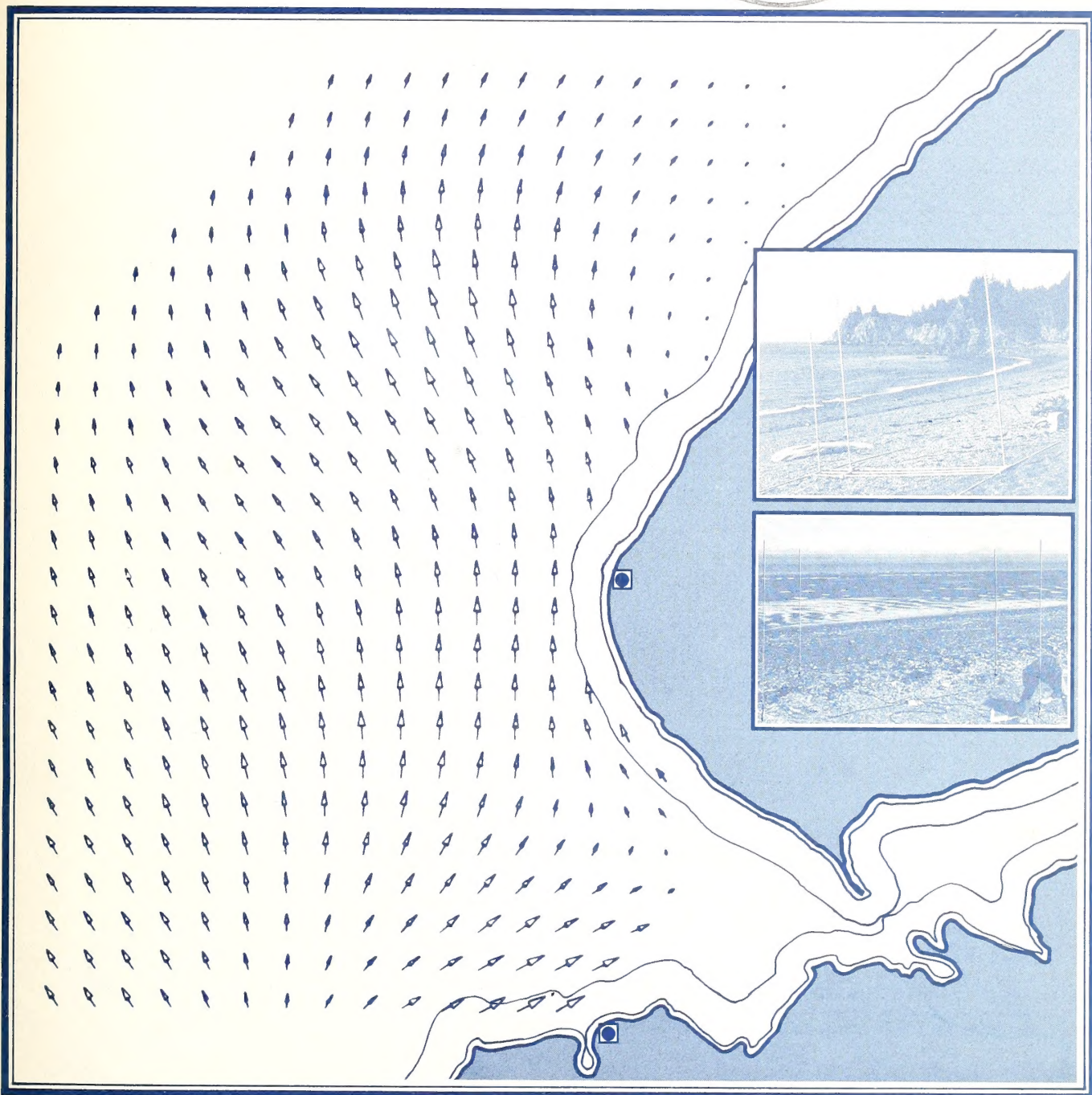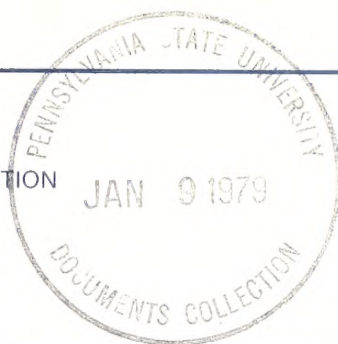# COLLECTED REPRINTS

1976·77

Wave Propagation Laboratory

NATIONAL OCEANIC AND ATMOSPHERIC ADMINISTRATION
Environmental Research Laboratories

September 1978

Cover figure--A novel high-frequency radar system developed at the Wave Propagation Laboratory produced this map of surface current vectors in Alaska's Lower Cook Inlet near Kachemak Bay. Each of two sites--located at the dots (38 km apart)--employs easily erectable, transmit antennas (upper inset) and receiving antennas (low inset). Each antenna pair operates in a backscatter radar mode. A current map, like that on the cover, is obtainable after fifteen minutes operation. Each such map consists of several hundred data points. The large volume of available data, continuous in space and time, suggests many unique applications of the radar system in oceanographic research and services.

COLLECTED REPRINTS

1976·77

Wave Propagation Laboratory

September 1978

Boulder, Colorado

FOREWORD

The Wave Propagation Laboratory acts as the focal point within NOAA for the development and research application of new methods for remote sensing of man's geophysical environment. Since its creation in May 1967, the Laboratory has pioneered in the development and application of a large number of new remote sensing methods, involving the use of optical, radio and acoustic waves. The new techniques have many significant advantages over standard, in situ methods; in particular, it is often possible to provide the researcher with one-, two- or three-dimensional data sets possessing excellent continuity and resolution in both time and space. In many cases, these data sets are much richer than those available by other techniques, and are providing important new insights into atmospheric and oceanographic processes.

This fifth volume of Collected Reprints comprises material published between 1 January 1976 and 31 December 1977. To avoid unnecessary duplication in the case of WPL/NOAA Technical and Memorandum Reports, only the abstracts are included.

As in the case of previous volumes of WPL Collected Reprints, we expect that this volume will be well received by colleagues in many fields, as a convenient and helpful compilation of WPL research. Remote sensing remains a somewhat specialized field and is still regarded by many atmospheric and oceanographic researchers as somewhat peripheral to their interests. This attitude is changing; we expect that this volume will help accelerate this change by bringing to the attention of our colleagues in these fields the unique advantages and capabilities of remote sensing.

C. Gordon Little

C. Gordon Little, Director
Wave Propagation Laboratory

Synopsis of Contents

CONTENTS

B.   Radio Wave Propagation

II. Measurements Utilizing Remote Sensing

A. Remote Sensing Using Optical Waves

B.   Remote Sensing Using Radio Waves

III.   Geophysical Studies

A.   Atmospheric Boundary Layer

D.   Refractive Index Structure Parameter

For measurement of the refractive index structure
parameter using remote sensing see also paper 39

E.   Other Studies

IV. Remote Sensing Systems

A. Descriptions of Remote Sensing Systems

MOLECULAR AND PARTICULATE EXTINCTION IN THE ATMOSPHERE

BETWEEN 8 AND 15 μm WAVELENGTH

R. F. Calfee and V. E. Derr

Although the spectral region near 10 μm is relatively free of atmospheric attentuation of electromagnetic radiation, it becomes necessary for long path measurements to take into account gaseous molecular absorption and particulate scatter and absorption. The design of remote sensing techniques must take into account these attentuation factors. This report provides the computed values of absorption coefficient for water vapor, the principal absorber, and the extinction coefficients for hydrometeors. The information is presented in graphic form for quick reference. Tabulated values are provided for use in detailed calculations.

Physical properties of the atmosphere in relation to laser probing

S. F. CLIFFORD
Wave Propagation Laboratory, Environmental Research Laboratories NOAA, Boulder, Colorado 80302 USA

This paper is concerned with the properties of the atmosphere that limit the effectiveness of laser probing. We analyse the fluctuations in amplitude and phase of a laser signal that are induced by propagation through the irregular refractive-index structure of the atmosphere.

1. Introduction

The refractive index of air at optical frequencies can be written

$$n = n_r + in_i, \qquad (1)$$

where n_r is the real part of the refractive index and n_i is the imaginary part. In general, n_r is a function of temperature, humidity and optical wavelength λ and n_i is a function of humidity and λ. (An extensive treatment of optical refractive index is found in [1].) If the atmosphere is transparent, and this is a good approximation for visible wavelengths, the real part of the refractive index is most important. In the infrared region of the spectrum, moderate to severe attenuation can occur and both n_r and n_i will have a significant effect on propagation.

Both n_r and n_i are random variables with $\langle n_r \rangle \simeq 1$ and $\exp(-k\langle n_i \rangle z) = T$, the average transmittance, where the angle brackets indicate an ensemble average and $k = 2\pi/\lambda$ is the wavenumber of the radiation. The fluctuating part of the real refractive index δn_r and the fluctuating part of the imaginary refractive index δn_i produce random variations in both the irradiance and phase of a propagating optical beam. Lee and Harp [2] show from the first order perturbation theory that irradiance/(phase) fluctuations produced by variations in real refractive index have the identical statistical properties, i.e., power spectral density as the phase/(irradiance) fluctuations produced by the variations in imaginary refractive index. It is then sufficient, within the limits of validity of the

first order theory, to analyse the statistics of the fluctuating wave parameters produced by variations in real refractive index alone.

2. Spatial and temporal variations of turbulent refractive index fluctuations

The real refractive index varies markedly in space and time. Fig. 1 shows the temperature contribution to δn_r measured at a height of 1.5 m on a clear sunny day for 0.3 s duration. (Lee and Harp [2] demonstrate that, although both humidity and temperature contribute to δn_r, only the temperature term will have significant scintillation-producing effects. The humidity term will be dominant in producing fluctuations in δn_i which will then cause irradiance fluctuations by means of random variations in attenuation.) There are large excursions of temperature, amounting to several °C, that occur in sharply bounded regions of warm air with quiescent intervening cool regions. The intermittent character of the temperature record of Fig. 1 is normally observed.
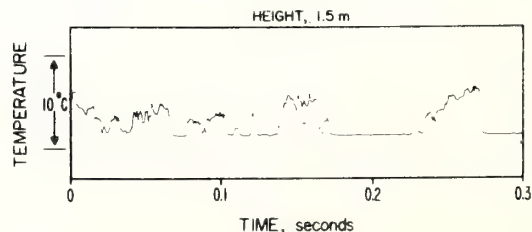
Figure 1 High speed temperature measurements made 1.5 m above the ground on a clear, sunny day.

95
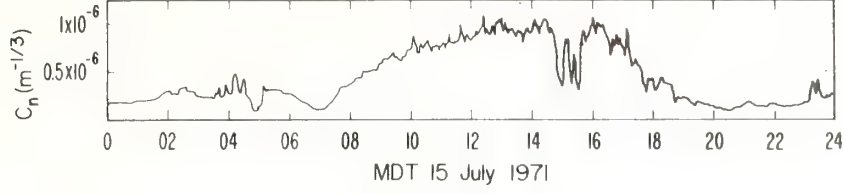
Figure 2 Behaviour of the square root of the refractive-index structure constant at 1.5 m above the ground (MDT is Mountain Daylight Time.) From [5].

Because δn_r is a random variable, we must settle for a statistical rather than deterministic description of its properties. The description most relevant to the optical propagation problem is the refractive-index structure function defined by

$$D_n(r) \equiv \langle [n(x) - n(x+r)]^2 \rangle \qquad (2)$$

Equation 2 states that the refractive-index structure function is determined by subtracting, squaring and averaging the fluctuations in refractive index measured at two points separated by a distance r. From a relationship derived by Kolmogorov for velocity turbulence [3, 4] we can derive a theoretical prediction of the behavior of this quantity as a function of spacing between some inner scale size of refractive index fluctuation l_0 and the largest or outer scale size fluctuation L_0, i.e.,

$$D_n(r) = C_n^2 r^{2/3}, \qquad (3)$$

for $l_0 \ll r \ll L_0$. (Typically, l_0 is of the order of mm to cm and L_0 is of the order of the height above the ground.) The statistical parameter that describes the atmosphere's turbulent interaction with optical waves is the structure constant of the refractive-index fluctuations C_n^2. It is C_n^2 that determines the intensity of optical scintillations observed on atmospheric paths.

The behavior of C_n^2 with altitude and time are shown in Figs 2-4. Fig. 2 shows the typical diurnal behavior of C_n^2; namely, low values during the early morning hours, rising to a maximum as solar heating of the ground produces convective instability in the afternoon and, finally, decreasing to minimum values at sunset and into the nighttime. These data were taken at a height of 1.5 m above a flat grassy mesa during a sunny day [5]. Fig. 3 shows the theoretically predicted [4] behavior of the temperature structure constant C_T^2 which is related to C_n^2 by the expression

$$C_n^2 = \left(\frac{79P}{T^2} \times 10^{-6} \right)^2 C_T^2, \qquad (4)$$
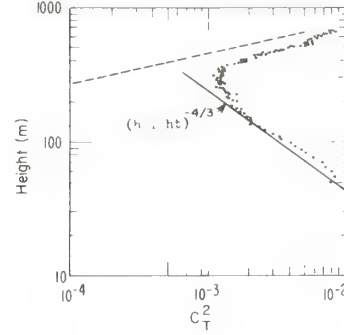
Figure 3 Acoustic-sounder determined values of the temperature structure constant (dots) compared with theoretical prediction (solid line. Data from [6].

where P and T are the mean background pressure in mb and temperature (°K), respectively. The dots are determinations of C_T^2 by an acoustic echo-sounder [6]. The theory and experiment agree quite closely in the first 100 m, or so, of the atmospheric boundary layer so that it is reasonable to assume that C_T^2 and hence C_n^2 will decrease in this height range roughly as height to the minus four thirds power and less optical scintillation will be observed if the average path height is raised. Finally, Fig. 4 illustrates the erratic behavior of C_n^2 with
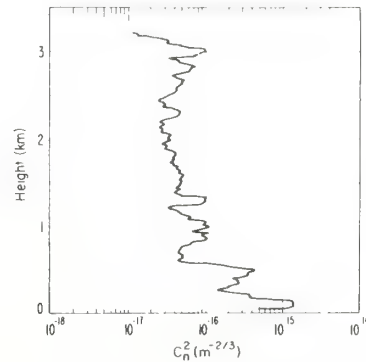
Figure 4 Behaviour of refractive-index structure constant with height.

96

3
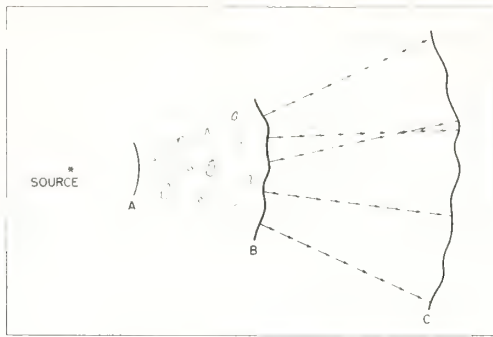
Figure 5 Schematic of the propagation of a spherical wave through refractive turbulence.

directions and eventually interfere, producing irradiance fluctuations (scintillations) at C.

At B, we would observe only phase fluctuations, the scintillations have not yet had enough path to fully develop. If we placed a phase-sensitive detector at B, we would observe the record of Fig. 6, where the relative phase is seen to wander randomly over many cycles in one minute. Fig. 6 illustrates the phase fluctuations measured by a Michelson-type interferometer (see [8]) on a 50 m path at a height of 1.6 m above the ground. Fig. 7 shows our statistical measure of these fluctuations, the phase structure function, defined in analogy to Equation 2, as

$$D_\phi(\rho) = \langle [\phi(x) - \phi(x + \rho)]^2 \rangle \qquad (5)$$

where $\phi(x)$ is the phase fluctuation observed at a position x in the plane transverse to the direction of propagation. The crosses represent actual data from [9] taken on the number of independent runs indicated by the adjacent circled number. The behavior of $D_\phi(\rho)$, increasing as $\rho^{5/3}$, indicates, in contrast to the case of scintillations, that the largest refractive-index irregularities are most effective in producing phase fluctuations. It is important to note this fact because, as we have mentioned above, the scintillations produced by δn_i have the same spectral characteristics as the phase fluctuations produced by δn_r.

As we have noted, because of interference, irradiance fluctuations will appear at position C.

height up to 3.2 km. These data have been smoothed over a height interval of 100 m. Actual unsmoothed data [7] exhibit even more drastic fluctuations sometimes amounting to more than an order of magnitude in a few meters height range.

3. Production of scintillations by refractive turbulence

To analyse the scintillation-producing process we consider a light wave (such as that shown in Fig. 5) propagating outwards from a point source. The wave is initially spherical until it encounters refractive-index irregularities between A and B. These irregularities selectively slow down or speed up adjacent segments of the wave such that, at B, the wave has a distorted wavefront. Various portions of the wave will now travel in different

Figure 6 Optical phase variations versus time determined by a Michelson-type interferometer. ($\lambda = 0.63\,\mu$m). From [8].

97

4
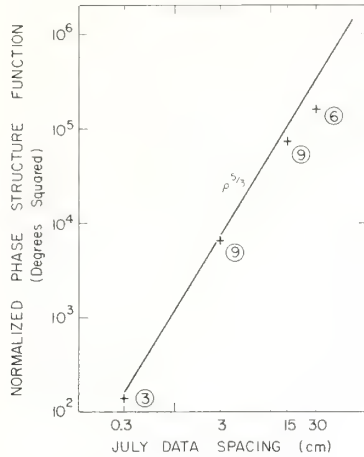
Figure 7 Measurements of the structure function of the optical phase fluctuations (crosses) compared with the theoretical prediction (solid line). Numbered circles represent the number of independent runs averaged to make one data point. Data from [9].

Figure 8 Geometry involved in determining the size of eddy that is most effective in producing scintillation in the weak turbulence case.
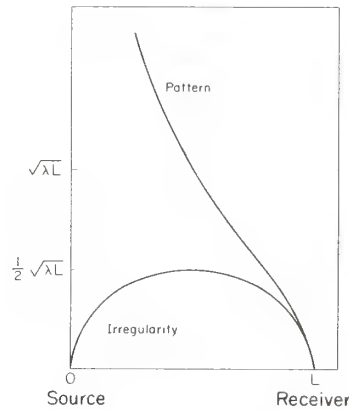
Figure 9 Size of most effective irregularity and resultant scintillation pattern size versus path position.

We now examine the criteria that determine which of the refractive-index irregularities at a given path position are most effective in producing these scintillations. In Fig. 8 we show, schematically, two irregularities on the line-of sight between the source and receiver. Consider the irregularity, labelled r, at mid-path. In order for this refractive-index fluctuation, or eddy, to be completely effective in producing an intensity fluctuation at the receiver, the extreme ray paths OBL and OZL must differ by at least one half wavelength. This minimum effective size turns out to be the optimum size. Working out the geometry we see that the size of the *most effective eddy* is

$$r = \sqrt{(\lambda L)}[(z/L)(1 - z/L)]^{\frac{1}{2}}, \qquad (6)$$

where z is the eddy path position and L is the total path length. Equation 6 indicates that the most effective eddies near the transmitter, such as shown at z_1 in Fig. 8, will be smaller than mid-path eddies and because of the symmetry of Equation 6, the same will be true for eddies near the receiver. Fig. 9 shows a plot of Equation 6 as a function of path position (the curve marked 'irregularity'). Note that it peaks at midpath at a size of one-half Fresnel zone $\sqrt{\lambda L}/2$ and tapers to zero size at the source and receiver. The other curve marked 'pattern' in Fig. 9 is the size of the disturbance at the receiving plane produced by the most effective eddy. Because we have assumed a

diverging spherical wave as the illumination incident upon the irregularity, there will be a projection effect such that the image of the eddy in the scintillation pattern will be magnified inversely as the distance from the source. Mathematically, we determine the size of this pattern r_p as

$$r_p = (L/z)r = \sqrt{(\lambda L)}(L/z - 1)^{\frac{1}{2}}. \qquad (7)$$

Equations 6 and 7 illustrate another important feature of scintillations; namely, small scale (spatial) irradiance fluctuations result from the effects of irregularities near the receiver and large scale irradiance fluctuations result from the effects of irregularities near the source.

We may push our model still further. To determine which portion of the path is most effective in producing scintillation, we need only determine the relative strength of the refractive-index fluctuations of each most effective eddy. This information is contained in the one-dimensional power spectrum of the refractive-index fluctuations $\Phi_n(K)$, which from [3, 4] is

$$\Phi_n(K) \propto C_n^2 K^{-5/3} \qquad (8)$$
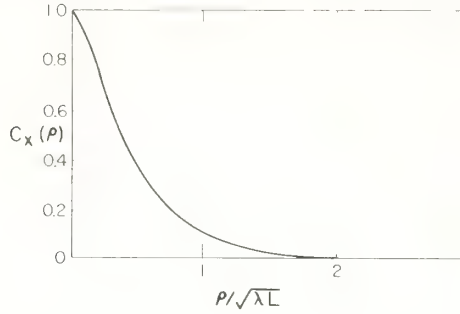
Figure 10 Normalized covariance of the log-amplitude fluctuations vs spacing in Fresnel zones.

where $K = 2\pi/r$ is the spatial frequency. This expression is an entirely equivalent relation in the spectral domain to the structure function of Equation 3. They are related by a transform pair [3, 4]. If we insert r from Equation 6 into Equation 8, we obtain the expression for the path weighting function of scintillation in the form

$$W(z/L) \propto [(z/L)(1 - z/L)]^{5/6}. \qquad (9)$$

This function is symmetric about a mid-path maximum and tapers to zero at the end points. This indicates that, according to the single-scatter theory, the turbulent refractive-index fluctuation located in the middle of the optical path will produce the most scintillation.

Finally, we may combine the weighting function (Equation 9) and the pattern size function

(Equation 7) to obtain the spatial spectrum of sizes observable in the received scintillation pattern. Fig. 10 illustrates the normalized log-amplitude covariance function defined by

$$C_\chi(\boldsymbol{\rho}) = \langle \chi(\mathbf{r})\chi(\mathbf{r} + \boldsymbol{\rho}) \rangle / \sigma_\chi^2 \qquad (10)$$

where $\mathbf{r}$ and $\boldsymbol{\rho}$ are displacement vectors in the plane of the receiver and σ_χ^2 is the variance of the log-amplitude. This function is a statistical measure of the spatial scale sizes of the irradiance fluctuations in the received scintillation pattern. This theoretically derived curve shows the predominance of the Fresnel zone size $\sqrt{(\lambda L)}$ irregularities as indicated by our geometric arguments.

The above analysis, based on the simple models discussed, although quite reliable in the realm of weak turbulence, must be dramatically modified to account for the observations of scintillation in strong turbulence.

4. Effects of multiple scattering on the production of scintillation

Our phenomenological model of scintillation discussed in the last section predicts that the variance of the log-amplitude, a typically measured indicator of the amount of scintillation, has the form [3, 4]

$$\sigma_\chi^2 = 0.124 k^{7/6} L^{11/6} C_n^2. \qquad (11)$$

Equation 11 implies that σ_χ is linear in C_n and nearly linear ($L^{11/12}$) versus path length. Fig. 11
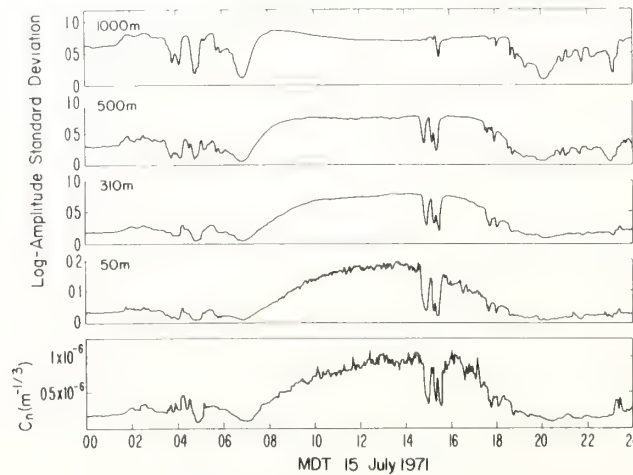
Figure 11 The variation of the square root of the log-amplitude variance at each of four path lengths compared to the square root of the refractive-index structure constant C_n^2 for a 24 hr period. $\lambda = 0.63\,\mu m$.

99

6
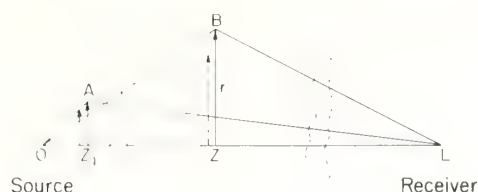
Figure 12 Geometry involved in determining the size of eddy that is most effective in producing scintillation in the presence of strong intervening turbulence.

Figure 13 Size of the most effective eddy and corresponding scintillation pattern size in the weak (solid) and strong (dashed) scintillation cases.

shows some scintillation data for $\lambda = 0.63\,\mu m$ taken at a 1.5 m height above a flat grassy mesa. The lowest curve is a 24 hour plot of C_n measured with high speed thermometers. The curves above are simultaneous measurements of σ_χ for paths of 50, 310, 500, and 1000 m. Note that the scintillation curves appear to be linear in C_n only for the 50 m path. On the longer paths increases in C_n do not produce corresponding increases in σ_χ and, in fact, on the 1000 m path σ_χ actually decreases with increasing C_n. This so-called saturation of scintillation was the first indication that the first order model we have discussed need modification.

The changes necessary in the mathematical model of propagation in strong turbulence were to account for multiple scattering effects, i.e., to include higher order perturbation terms in the series representation of the electric field. This problem proved to be extremely difficult and has only now begun to be handled satisfactorily. A phenomenological model [10], employing new physical assumptions to complement the mathematics, has provided quantitative predictions of scintillation phenomena that agree in detail with the experimental observations. Again, we may use our simple geometric approach to explain the important features.

Fig. 12 illustrates our new path geometry with refractive-index irregularities located at z and z_1 on a total optical path of length L. Because of the intervening turbulence, the eddy size determined by Equation 6 will no longer be most effective in producing scintillation. The turbulence will introduce a new random phase shift that will prevent the destructive interference that occurred before because of the $\lambda/2$ excess phase path OBL-OZL. The effects of intervening refractive turbulence are proportional to the path-average transverse separation of the two ray paths. If the extreme ray paths lie close together, there will be less effect
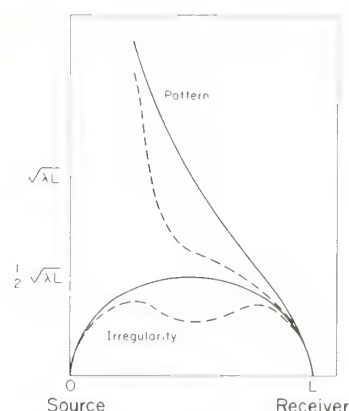
100

than if the extremes are far appart. This is true because more of the eddies that produce phase path changes will be large enough to affect both ray paths simultaneously and, because we need a phase-path difference between two extreme rays, these large eddies will have no scintillation-reducing effect. For larger transverse separation, more phase changing eddies will produce a relative phase shift of the two ray paths and hence a larger effect on scintillation; consequently, we expect that the refractive index irregularity at z, because of its larger size, will be reduced in scintillation-producing effectiveness much more severely than the irregularity at z_1. This is indicated in the figure by the dashed arrows representing the new, smaller, most effective irregularity sizes in the presence of multiple scattering. Note that, because the larger most effective eddy sizes are near mid path, these
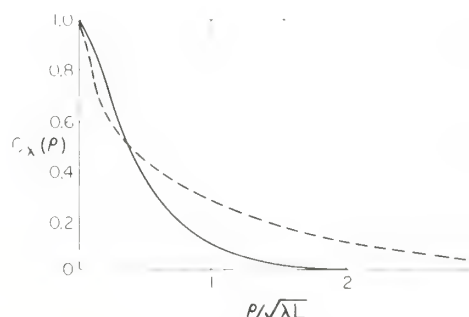
Fig. 14 Normalized log-amplitude covariance function in the cases of weak (solid) and strong scintillation (dashed) versus spacing in Fresnel zones.
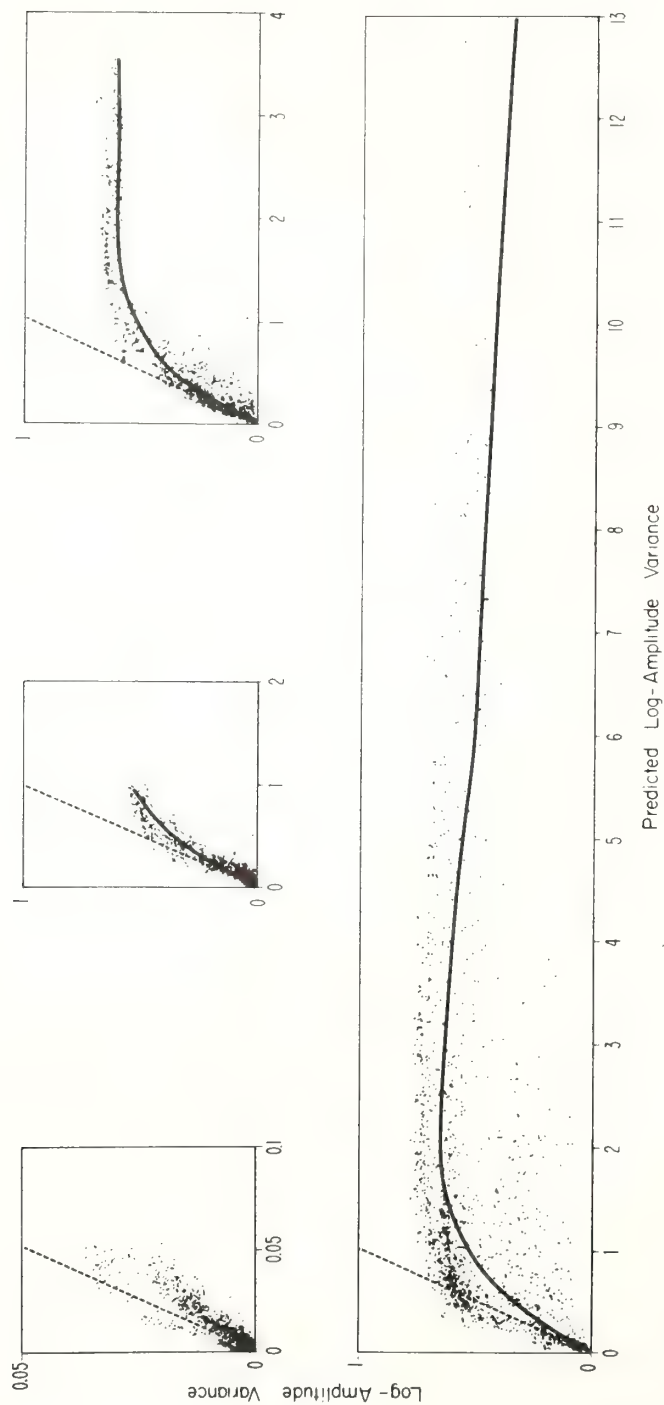
Figure 15 Measurements of log-amplitude variance σ_λ^2 versus the variance predicted from the weak turbulence theory. Solid lines are theoretical predictions. Dashed lines are the result expected if the weak scatter theory were valid. From [10].

will be most affected by intervening turbulence and we would expect maximum size changes in this region of the path.

Fig. 13 shows our modified curves (dashed lines) for the size of the most effective irregularity and resultant pattern size. Again, because of the power law nature of the turbulence spectrum, we expect the path weighting function for scintillation to have the same general shape as the dashed curve marked irregularity. This means that the ends of the path become more effective and the middle less effective. The combination of the weighting function and the pattern scale curves (the dashed line marked pattern) indicate that there will be less Fresnel zone size irregularities in the received scintillation pattern and relatively more smaller and larger spatial-scale scintillation observed. This is confirmed in Fig. 14 by the theoretical curve of $C_\chi(\rho)$. The dashed curve again is that for the multiple scattering case. Initially, the curve falls off faster than the same curve for single scattering, because of the presence of the now more influential small-scale structure and the curve has developed a much higher tail because of the presence of the now more influential large-scale structure in the scintillation pattern. In summary, we would expect to see a transition from the dominance of a single scale size $\sqrt{(\lambda L)}$ to a more uniformly structured pattern containing all sizes from extremely small up to sizes of many Fresnel zones.

Experimental results confirm our phenomenological model. Fig. 15 shows the same type of data as Fig. 11, that is, simultaneous observation of σ_χ^2 at each of 4 path positions, clockwise from the upper left, 50, 310, 500 and 1000 m plotted versus the theoretical prediction for σ_χ^2 from the first order theory $0.124 k^{7/6} L^{11/6} C_n^2$. If the data confirmed the single scattering theory all the dots would cluster about the dashed line shown. Note that this is a reasonable interpretation for the 50 m path but that once again we notice the saturation effect setting in on the longer paths. Scintillation does not endlessly increase with increasing turbulence or path length but proceeds to saturate and even decrease when $0.124 k^{7/6} L^{11/6} C_n^2$ increases beyond 0.3. The solid curves shown are the theoretical predictions from [10].

It is useful to define a new parameter

$$\sigma_t^2 = 0.124 k^{7/6} L^{11/6} C_n^2. \tag{12}$$
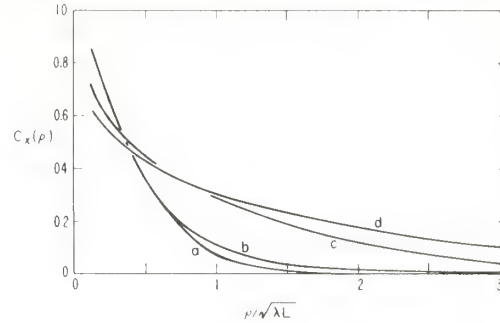
Figure 16 Measurements of the normalized log-amplitude covariance function in weak (a) and (b) to strong (c) and (d) refractive turbulence versus spacing in Fresnel zones.

This quantity describes the amount of integrated refractive turbulence and represents the key parameter for judging the onset of multiple scattering effects. Fig. 16 shows data on the effects of large values of integrated turbulence in the spatial structure of scintillation. Curve a is a experimental determination of C_χ under conditions of weak refractive turbulence and corresponds quite closely to the single scatter result (see Fig. 10). Curves b, c and d represent experimental data for progressively larger values of σ_t^2 and hence stronger integrated refractive turbulence. Note the quicker dropoff at small spacings and the longer tail as σ_t^2 increases, confirming our phenomenological model results (see Fig. 14). Finally, Fig. 17 shows the results of the full mathematical theory. The behavior of the curves quite closely follows that of the experimental data for all values of σ_t^2.

5. Aperture averaging and the reduction of scintillation

The classical method of reducing scintillation noise in a receiver is to increase the size of the receiving optics. The rationale is that larger receivers will tend to average the irradiance over the scintillation pattern and act as a low pass spatial filter on the received signal. Conventional wisdom indicates that the reduction in irradiance variance would go as $1/N$, when $N \to \infty$ where N is the number of independent scintillating patches in the receiving aperture. (This argument has its flaws; namely, no 'patches' in the receiving plane are really independent, the only statistically independent elements are the two-dimensional Fourier components of the scintillation pattern). From this reasoning, if we apply the results of the first
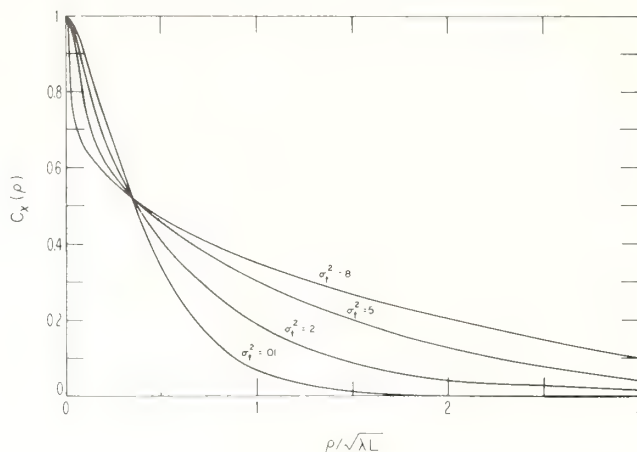
Figure 17 Theoretical curves of the log-amplitude covariance function in weak to strong refractive-turbulence conditions.
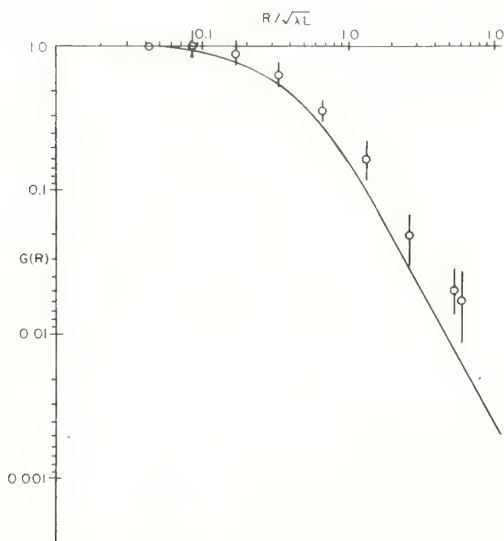
Figure 18 Aperture averaging factor $G(R)$ versus radius of receiving optics in Fresnel zones. Solid curve is predicted behavior for the weak turbulence theory. Circles are experimental data taken in weak refractive turbulence. $\lambda = 0.63 \, \mu m$. From [11].

Figure 19 Aperture averaging factor $G(R)$ versus radius of receiving optics in Fresnel zones. Solid curves are the predicted behaviour for weak turbulence theory. Circles are experimental data taken in strong refractive turbulence. $\lambda = 0.63 \, \mu m$. From [11].

order theory where an independent patch may be said to be Fresnel zone in diameter, we would expect scintillation to be reduced as $[R/\sqrt{(\lambda L)}]^{-2}$ with increasing aperture radius R. This convenient rule is incorrect as a detailed examination of Fig. 18 would show. Fig. 18, taken from [11], is a plot of the scintillation reduction factor $G(R)$ as a function of normalized aperture radius $R/\sqrt{(\lambda L)}$. The quantity $G(R)$ is the fraction of the variance measured with a point detector that one would observe with a receiver of radius R. The asymptotic slope of this function for $R/\sqrt{(\lambda L)} \gg 1$ is $[R/\sqrt{(\lambda L)}]^{-7/3}$. The rule of thumb $[R/\sqrt{(\lambda L)}]^{-2}$ certainly is a reasonable engineering approximation. The curve shown in Fig. 18 is the case where $\sigma_t^2 = 0.1$ and the data shown were taken in roughly the same amount of weak integrated turbulence.

Fig. 19, also from [11], shows what happens in strong refractive turbulence where multiple

103

scattering is important. (The theoretical curves, solid lines, are for the single scatter case.) The effectiveness of aperture averaging is greatly reduced. This is to be expected from our multiple scatter model where we showed the covariance function had a progressively longer tail, indicating the presence of larger scale scintillations in the receiving plane, as σ_t^2 increased. This implies that, in order to contain a larger number of independent scintillating patches when σ_t^2 is large, we must dramatically increase the size of the receiving optics. In summary, the amount of aperture averaging varies with the amount of refractive turbulence in such a way that receiving optics, which produce a large reduction in scintillation noise in weak turbulence, will no longer be as effective when the amount of integrated refractive turbulence is larger.

Another technique for reducing scintillation has been space diversity receivers. Again, this is quite easily evaluated in terms of our simple model, If the receivers are separated sufficiently far such that they each observe independent scintillating patches, they will reduce the variance of scintillation as $1/N$ where N is now the number of detectors. Unfortunately, the large scale sizes in the scintillation pattern present in strong turbulence, force progressively larger spacings as σ_t^2 increases. However, since σ_t^2 decreases as $\lambda^{-7/6}$, considerable improvement is obtained with longer wavelengths.)

Finally, to refer back to our discussion of the imaginary part of the refractive index fluctuations, the predominant scale size of these scintillations will be the outer scale of turbulence, approximately the height above ground of the optical path. Reducing these scintillations by either aperture averaging or space diversity requires either very large receiver optics or quite large spacings between detectors. Because the scintillation pattern sizes, in this case, are not functions of wavelength, changing wavelengths will not eliminate this requirement.

References

1. J. C. OWENS, *Appl. Optics* 6 (1967) 51-59.
2. R. W. LEE and J. C. HARP, *Proc. IEEE* 57 (1969) 375-406.
3. V. I. TATARSKI, *Wave Propagation in a Turbulent Medium*, McGraw-Hill, New York (1961).
4. V. I. TATARSKI, 'The Effects of the Turbulent Atmosphere on Wave Propagation', U.S. Dept. of Commerce, Nat. Tech. Info. Serv., Springfield, Va. (1971).
5. R. S. LAWRENCE, G. R. OCHS and S. F. CLIFFORD, *J. Opt. Soc. Am.* **60** (1970) 826-830.
6. W. D. NEFF, NOAA Tech. Rept. ERL 322-WPL 38 (1975).
7. J. L. BUFTON, P. O. MINOTT, M. W. FITZ-MAURICE and P. J. TITTERTON, *J. Opt. Soc. Am.* **62** (1972) 1068-1070.
8. G. M. B. BOURICIUS and S. F. CLIFFORD, *ibid* **60** (1970) 1484-1489.
9. S. F. CLIFFORD, G. M. B. BOURICIUS, G. R. OCHS and M. H. ACKLEY, *ibid* **61** (1971) 1279-1284.
10. S. F. CLIFFORD, G. R. OCHS and R. S. LAWRENCE, *ibid* **64** (1974) 148-154.
11. G. E. HOMSTAD, J. W. STROHBEHN, R. H. BERGER and J. M. HENEGHAN, *ibid* 162-165.

LIDAR TECHNIQUES FOR ANALYZING AND TRACING PARTICULATE POLLUTANTS FROM ENERGY PRODUCTION

Vernon E. Derr
Wave Propagation Laboratory
Environmental Research Laboratories
National Oceanic and Atmospheric Administration
U.S. Department of Commerce
Boulder, Colorado

INTRODUCTION

Particulate pollutants from energy-related sources disperse and mix with natural aerosols. Both remote sensing and in-situ identification, measurement and tracing techniques are required for impact assessment, prediction of climate variation and estimation of the character, concentration and dispersion of particulate pollutants arising from man's activities. In-situ sampling may provide specific identification, concentration estimates and size-distributions, but ground and aircraft vehicles cannot economically establish correct average measurements over large periods of time, are impractical for the study of drift, and unfeasible for the measurements of fluctuations. Lidar remote sensors, on the other hand, may be developed, with somewhat diminished accuracy, to identify, measure concentrations and size distributions, and are the economical instrument of choice to measure these quantities and their fluctuations over large volumes and extended time periods. Improvement of lidar techniques is required to increase accuracy of identification, and measurement of size-distribution, shape factors and concentration. Theoretical and experimental investigations of depolarization effects, multi-spectral back-scatter and absorption, and inelastic scatter are the most promising technique to achieve the required improvement for measurements from ground and aircraft. The first phase of depolarization field studies and the expansion of the lidar capabilities to two wavelengths have been completed. The depolarization technique has been used in the impact assessment program at Colstrip, Montana to distinguish stack emission from dust newly risen from strip coal mines.

TECHNICAL DISCUSSION

Unique identification of atmospheric aerosols may come from Raman spectra or (broad band) absorption and backscatter spectra, to be investigated later in the study. Severe technical limitations prevent immediate application of these techniques. Identification algorithms, under construction, will use impact data of many kinds to obtain the greatest precision. Identifiers including depolarization effects and multiple-frequency measurements are the first of the more complete series to be used finally.

Radiation backscattered from spherical particles is polarized in the same way as the incident radiation. Depolarization of the back-scattered beam can only occur when the scattering particles are non-spherical or when multiple scattering occurs. Thus depolarization is an indicator of departure from sphericity of particles.

The lidar system shown in Figure 1 has been carefully revised to provide accurate measurement of the depolarization of the backscattered radiance. The lidar transmitter, by means of addition polarizing elements inside the cavity, transmits a beam vertically polarized within a few percent. The dual polarization receiver has been constructed to provide the ratio of intensities, to within a few percent, in channels polarized parallel and perpendicular to the transmitted polarization.
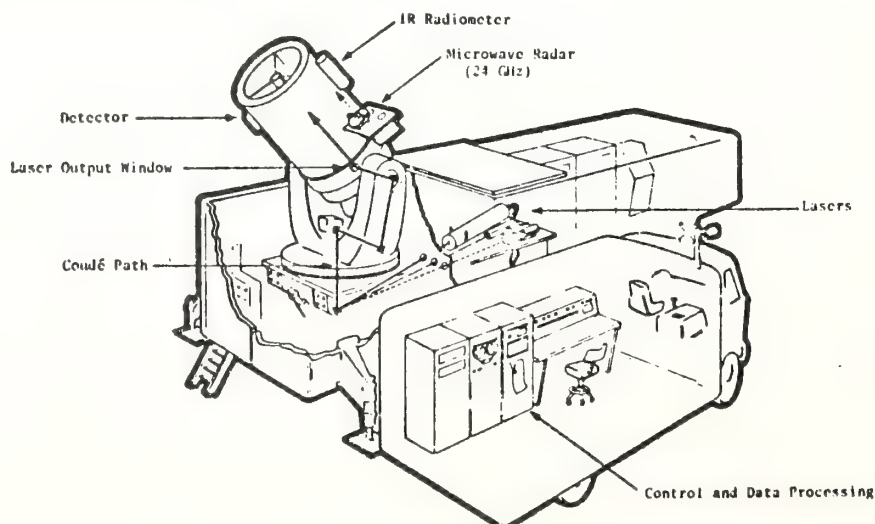
Figure 1. Cut-away view of remote sensing facility.

The revised polarization-sensitive lidar system has been employed in three major field experiments, examining the depolarization from many kinds of atmospheric particles. As a general rule, with a few exceptions, it has been found that particles from hot sources such as power plants, kilns, and automobiles, are generally spherical, producing very small depolarization. Invariably the non-sphericity of newly-risen dust is indicated by large (> 25%) depolarization. This technique has been employed to separate backscatter from the plume of stack emission in the impact assessment program at Colstrip, Montana, from the backscatter due to dust from the coal mines. This separation permits tracing of the plume without confusion with other sources. Figure 2 shows typical unprocessed data from a single lidar shot with mine dust at 6.8 km from the lidar, and stack emission from the Colstrip power plant at 11 km.

To proceed further in development of particle identifiers, a dual wavelength (.694 and .347 µm) lidar transmitter and detector have been constructed. Theorectical studies have shown that estimates of mean particle diameters may be deduced from multiple wavelength information. The two wavelength system will permit development of field and analytical techniques and the determination of optimum wavelengths and the number of channels required. Particle size estimates and depolarization ratios are powerful identifiers. The ultraviolet wavelength should extend the sensitivity of the system to particle diameters less than .05 µm

PROGRAM DISCUSSION

Two steps have been taken to improve remote detection and measuring methods for particulate pollutants. The first, depolarization techniques, has proven useful in studying plume dispersion in impact assessment programs and in distinguishing plumes from natural background aerosols. Preliminary results on two wavelength techniques have indicated potential for improved identification of particles. Theoretical studies have resulted in improved application of mathematical inversion algorithms to deduce the properties of particles from their electromagnetic signatures.

CONCLUSIONS

The effort to improve particle identification and determination of characteristics has successfully employed depolarization techniques in impact assessment studies at Colstrip, Montana. Initial tests of the dual wavelength system are encouraging for more accurate depolarization, and multiple wavelength studies are now complete. Theoretical studies have supported and directed the evolving techniques.

The immediate future will be occupied with field tests of the depolarization technique and the two wavelength technique. Plans are being formulated for the study of differential absorption and inelastic scatter techniques.

LIDAR BACKSCATTER
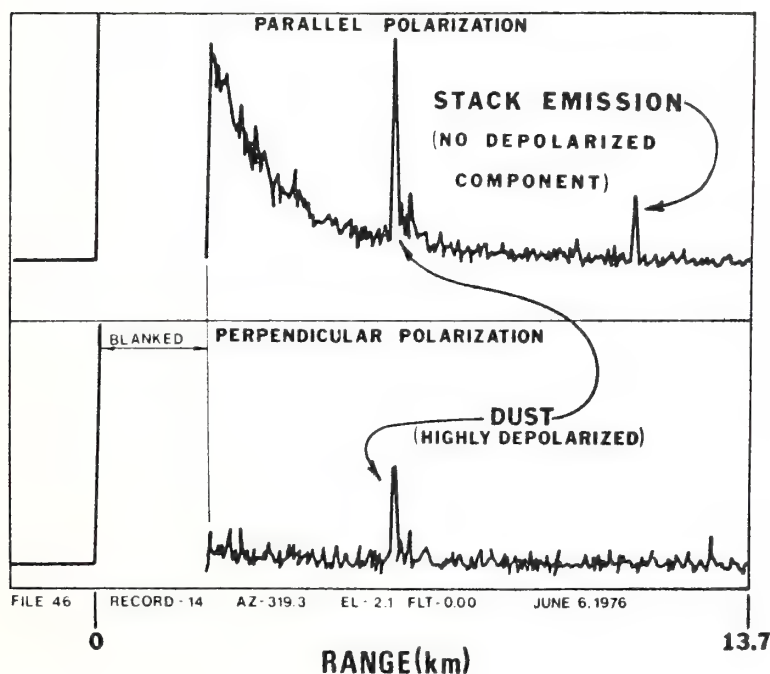
Figure 2. Depolarization of smoke-stack particulates and mine dust.

13

SPECTRAL TRANSMISSION OF WATER VAPOR FROM 1 to 12000 cm^{-1}
AT LOW CONCENTRATION AND LOW TEMPERATURE

V. E. Derr and R. F. Calfee

The transmittance of water vapor in the spectral range 0-12000 cm^{-1} is presented for T = 245 K, a pressure of 0.66 atmospheres, and for five values of total precipitable water content between 2.1 and 1070 μm.

THE BUMP IN THE VARIANCE OF LOG-INTENSITY

R. J. Hill and S. F. Clifford
NOAA/ERL/Wave Propagation Laboratory
Boulder, Colorado 80302

Accurate measurements of the spatial power spectrum of temperature fluc-
tuations in the atmospheric surface layer have been performed by Champagne et
al. [1977] and by Williams [1974]. These measurements reveal that at high
wave numbers the temperature spectrum becomes larger than the $K^{-11/3}$ law
predicted by Oboukhov [1949] and Corrsin [1951]; of course, at yet higher wave
numbers the temperature spectrum decreases rapidly due to the diffusion of
heat. Several theoretical models of the scalar transfer spectrum for quanti-
ties advected by turbulent flow have been developed by Hill [1977]. When
applied to temperature fluctuations in air one of these models is in excellent
agreement with the data of Champagne et al. [1977] and of Williams [1974].
Therefore there now exists an accurate model of the temperature spectrum for
use in calculating quantities relevant to optical propagation through turbu-
lence. Moreover, the scalar spectral model is capable of predicting the form
of such spectra as the humidity spectrum. The purpose of this paper is to
present results of a calculation of the variance of log-intensity for unsat-
urated conditions using the aforementioned realistic model of the temperature
spectrum. Only the case of point transmitters and receivers is considered.

In the inertial-convective range the temperature spectrum is given by

$$\Phi_T(K) = (4\pi)^{-1} \beta \chi \varepsilon^{-1/3} K^{-11/3} \tag{1}$$

where χ is the rate of dissipation of mean-squared temperature fluctuations
and ε is the rate of viscous dissipation of turbulent kinetic energy per unit
mass of fluid. The constant β is obtained by considering the measurements of
Champagne et al. [1977] and Williams [1974]; we take $\beta = .717$. Hitherto,
calculations of quantities relevant to optical propagation through turbulence
have used a temperature spectrum due to Tatarskii [1971], namely

$$\Phi_T(K) = (4\pi)^{-1} \beta \chi \varepsilon^{-1/3} K^{-11/3} \exp(-K^2/K_m^2) \tag{2}$$

where $K_m = 5.92/\ell_o$. The inner scale ℓ_o is defined as the value of the spacing
r at which the large-r and small-r asymptotic forms of the temperature struc-
ture function are equal. The Kolmogorov microscale η is given by $(\nu^3/\varepsilon)^{1/4}$,
where ν is the kinematic viscosity. Without reference to the actual form of
the temperature spectrum, other than equation (1), the following relationship
holds between ℓ_o and η:

$$\ell_o/\eta = \left[\frac{27}{5} \frac{\beta}{Pr} \frac{\Gamma(1/3)}{}\right]^{3/4}$$

where Pr is the Prandtl number and Γ is the Gamma function. For air we take Pr = .72 and obtain $\ell_o/\eta = 7.39$.
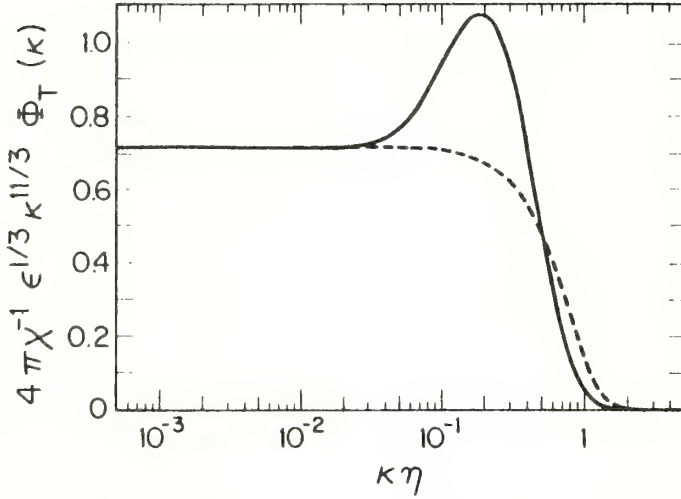
Figure 1. Spatial power spectrum of temperature fluctuations Φ_T. Solid curve: realistic model; dashed curve: from equation (2).

In Figure 1 we plot $4\pi\chi^{-1}\epsilon^{1/3}K^{11/3}\Phi_T(K)$ as a function of the scaled wave number (Kη). The solid curve is the realistic model given by Hill [1977] whereas the dashed curve is equation (2). The outstanding feature in figure 1 is the pronounced bump in the temperature spectrum which is not represented by equation (2). Equation (2) constitutes an assumption for $\Phi_T(K)$ which is not accurate for wave numbers higher than those at which equation (1) holds. Reference to equation (1) shows that the curves in figure 1 must tend to the constant β for wave numbers in the inertial-convective range. The curves in Figure 1 are universal in the sense that these curves do not change with changes in χ or ϵ (i.e., with changes in C_T^2).

The immediate implications of the bump in the temperature spectrum is that there is enhanced optical scintillation when the Fresnel zone size lies at a length scale corresponding to the bump. The variance of log-intensity is calculated for a spherical wave in a homogeneous medium using equation (T8) of Lawrence and Strohbehn [1970] for various values of $\sqrt{\lambda L}/\ell_o$. In the limit $\sqrt{\lambda L}/\ell_o \gg 1$ equation 1 implies that

$$\sigma_{\ell n I}^2 \rightarrow .5 \, C_n^2 \, k^{7/6} \, L^{11/6} \qquad , \qquad \sqrt{\lambda L}/\ell_o \gg 1. \tag{3}$$

16

The calculated $\sigma_{\ln I}^2$ scaled by the above limiting formula is presented in figure 2; the solid curve corresponds to the realistic temperature spectrum whereas the dashed curve is calculated using equation (2). For very large $\sqrt{\lambda L}/\ell_o$ both curves must tend to unity, whereas for small $\sqrt{\lambda L}/\ell_o$ the variance must tend to zero because of the rapid decrease of the temperature spectrum at high wave numbers. The bump in the temperature spectrum produces a corresponding bump in the variance of log-intensity.

A more conventional presentation of the variance of log-intensity is presented in Figure 3. For fixed $\sqrt{\lambda L}/\ell_o$ a value from Figure 2 is the slope of a straight line on Figure 3. The straight lines implied by the solid curve in Figure 2 and the corresponding values of $\sqrt{\lambda L}/\ell_o$ appear in Figure 3 along with
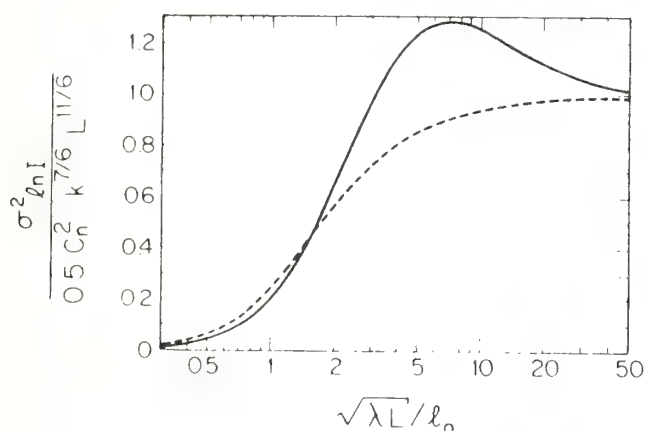
Figure 2. *The variance of log-intensity. Solid curve is from the realistic model of the temperature spectrum. Dashed curve is from equation (2).*
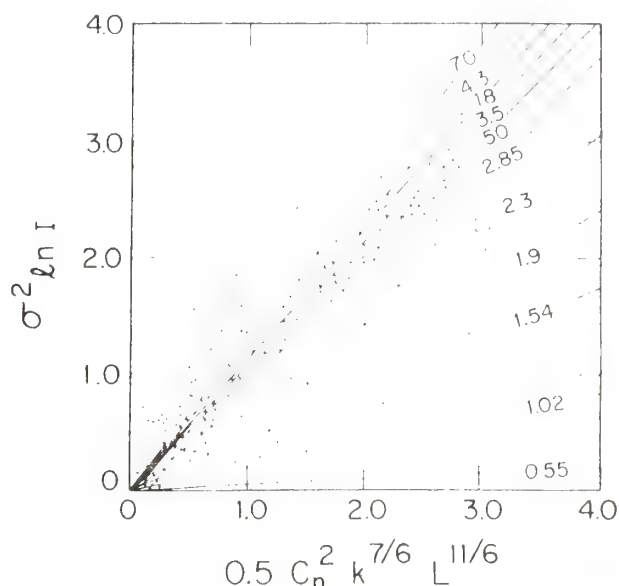
Figure 3. *Comparison of the variance of log-intensity with data.*

the data points obtained by Ochs [1969]. Much of the data is seen to lie to the left of the steepest straight line. This disagreement with theory remains even when the data is segregated according to estimates of ℓ_o. The discrepancy between data and theory is greater for the dashed curve in Figure 2 than for the solid curve.

17

Consider the case of red light propagating along a path a few meters above the ground. For a 50 m path $\sqrt{\lambda L}/\ell_o$ may be as small as .7. For a 500 m path, $\sqrt{\lambda L}/\ell_o$ may be as large as 6. Consequently, lasers used on short paths in the surface layer are typically operating on the steep portion of the solid curve in Figure 2. A $\sqrt{\lambda L}/\ell_o$ value of 30 would require a path length of roughly 150 km. Therefore the interpretation of the variance of log-intensity in terms of C_n^2 is never governed by the limiting formula in equation (3).

18

REFERENCES

Champagne, F. H., C. A. Friehe, J. C. LaRue and J. C. Wyngaard (1977), Flux measurements, flux estimation techniques, and fine-scale turbulence measurements in the unstable surface layer over land, *J. Atmos. Sci.*, 34, 515-530.

Corrsin, S. (1951), On the spectrum of isotropic temperature fluctuations in isotropic turbulence, *J. Appl. Phys.*, 22, 469-473.

Hill, R. J. (1977), Models of the scalar spectrum for turbulent advection, (in preparation).

Lawrence, R. S. and J. W. Strohbehn (1970), A survey of clear-air propagation effects relevant to optical communications, *Proc. IEEE*, 58, 1523-1545.

Oboukhov, A. M. (1949), Structure of the temperature field in turbulent flow, *Izv. Akad. Nauk. SSSR, Ser. Geogr. i Geofiz.*, 13, 58-69.

Ochs, G. R. (1969), Measurements of 0.63 μm laser-beam scintillation in strong atmospheric turbulence, *ESSA Tech. Rep. ERL 154-WPL 10*.

Tatarskii, V. I., *The Effects of the Turbulent Atmosphere on Wave Propagation*, Keter Press, Jerusalem, 1971.

Williams, R. M., Jr. (1974), High frequency temperature and velocity fluctuations in the atmospheric boundary layer, Ph.D. thesis, Oregon State Univ., 81 pp.

Analysis for Pulsed Coherent
Lidar System Performance

R. M. Huffaker and P. A. Mandics
Wave Propagation Laboratory
Environmental Research Laboratories
National Oceanic and Atmospheric Administration
Boulder, Colorado 80302

NOAA/WPL is developing pulsed coherent lidar systems for the long-range (~ 20 km) measurement of atmospheric wind velocity. Design studies have been completed for ground-based and airborne systems. In the design of a pulsed coherent lidar, a thorough analysis of the system parameters that affect the signal-to-noise ratio (SNR) is essential. A sensitivity analysis of parameters affecting the SNR of these systems was performed and these results will be presented.

Particular features of the SNR equation utilized in the analysis are:

a)   A shot-noise-limited system operation is assumed.

b)   The received signal is assumed to be within the bandwidth of a filter matched to the transmitted pulse.

c)   The effects of wind shear, wind variability, and signal amplitude fluctuations are not considered.

An expression for the signal-to-noise ratio has been derived by Sonnenschein and Horrigan (1971), excluding atmospheric effects. The effects of atmospheric turbulence and attenuation have been included in our analysis.

$$SNR = \frac{\eta J \beta c \tau \ D^2 \ e^{-2\mu R}}{32 h \nu \left[R^2 (1+a^2) + (\frac{\pi D^2}{4\lambda})^2 \ (1-\frac{R}{f})^2 \right]}$$

where η = total system and detector efficiency (10%),

J = transmitted energy in joules,

β = atmospheric backscatter coefficient in m^{-1},

c = velocity of light (3.0×10^8 m/s),

τ = pulse duration in seconds,

D = transmitter/receiver optics diameter in meters,

μ = atmospheric extinction coefficient in meters^{-1},

$h\nu$ = Planck's constant x frequency of the radiation (1.9×10^{-20} joules

R = range in meters,

λ = wavelength in meters (10.6×10^{-6} m),

f = focal length in meters,

$e^{-2\mu R}$ - represents the effect of atmospheric extinction for a two-way path,

$\frac{\pi D^2}{4\lambda}$ - accounts for near-field effects which cause non-planar wavefronts at close ranges,

$1-\frac{R}{f}$ - is a focusing term (it has an effect only in the near field),

$1+a^2$ - accounts for the effects of the atmospheric turbulence structure coefficient on system SNR performance,

$$a^2 = \frac{D^2}{(2r_e)^2}$$

$r_e = 0.1048 \, \lambda^{6/5} \, R^{-3/5} \, (C_n^2)^{-3/5}$ is a turbulence-limited effective optics radius, and

C_n = refractive index structure parameter ($m^{-1/3}$).

The study consisted of a careful evaluation of the following parameters:

Optics Size:

The primary factor affecting the optics size of a coherent lidar is the state of atmospheric turbulence characterized by C_n^2. The expected performance of a pulsed coherent lidar as a function of C_n^2, optics size, and range was determined. For a wavelength of 10.6 μm (CO_2 lidar) and a range of 20 km, an optics diameter of .5 m would allow C_n^2 values up to 10^{-14} m$^{-2/3}$ along the path without large signal-to-noise ratio losses.

Atmospheric Attenuation:

Models of clear-air atmospheric absorption were generated using data from McClatchey and Selby (1972) which included absorption by CO_2 and H_2O for five model atmospheres. Attenuation caused by rain, fog, and clouds is treated in a companion paper by Pratte and Westwater (1977).

Backscatter Coefficient (β) at 10.6 μm:

The backscatter coefficient as a function of altitude was determined from Mie calculations utilizing experimental particulate number densities and size distributions reported in the literature and assuming an average index of refraction.

The expressions for β (in m^{-1}) as a function of altitude are as follows:

$$\beta = 1.4 \times 10^{-7} e^{-.35H}, \quad 0 \text{ km} < H < 10 \text{ km}$$

$$\beta = 1.3 \times 10^{-7} e^{-.33H}, \quad 10 \text{ km} < H < 18 \text{ km}$$

$$\beta = 5.0 \times 10^{-9} e^{-.14H}, \quad 18 \text{ km} < H < 30 \text{ km}$$

where H is the height in meters.

Effects of Atmospheric Turbulence; the Refractive Index Structure Parameter:

The simple model for C_n^2 as a function of altitude used in the performance evaluation was (Ochs and Lawrence, 1972),

$$C_n^2 = C_{no}^2 \times H^{-4/3}$$

where $C_{no}^2 = 10^{-11} \text{ m}^{-2/3}$ is the near-surface (H = 1 m) value, and

H = height in meters.

Summary:

Parametric analysis for pulsed coherent lidar systems performance which shows effects of C_n^2, β, optics size, range, atmospheric attenuation, and precipitation for horizontal and slant paths has been completed. Figure 1 illustrates the expected SNR performance for the tropical model atmosphere and the listed system parameters. These results indicate the feasibility of developing a long-range (20 km) pulse coherent lidar for measuring atmospheric wind velocity.

References:

McClatchey, R. A. and J. E. A. Selby (1972), "Atmospheric Transmittance, 7-30 μm: Attenuation of CO_2 Laser Radiation," Air Force Cambridge Research Laboratories, Report AFCRL-72-0611 (Data in this report was updated for our study by McClatchey, Private Communication).

Ochs, G. R. and R. S. Lawrence (1972), "Temperature and C_n^2 Profiles Measured Over Land and Ocean to 3 km Above the Surface," NOAA Technical Report ERL 251-WPL 22.

Pratte, F. J. and E. R. Westwater (1977), "Characterization of High Extinction Weather for a Ground-Based Infrared Pulsed Doppler Lidar, Summary Volume, Optical Propagation Through Turbulence, Rain and Fog Meeting, August 9-11, 1977, University of Colorado, Boulder, Colorado.

Sonnenschein, C. M. and F. A. Horrigan (1971), "Signal-to-noise Relationships for Coaxial Systems that Heterodyne Backscatter from the Atmosphere," Applied Optics, 10 (7), 1600-1604.
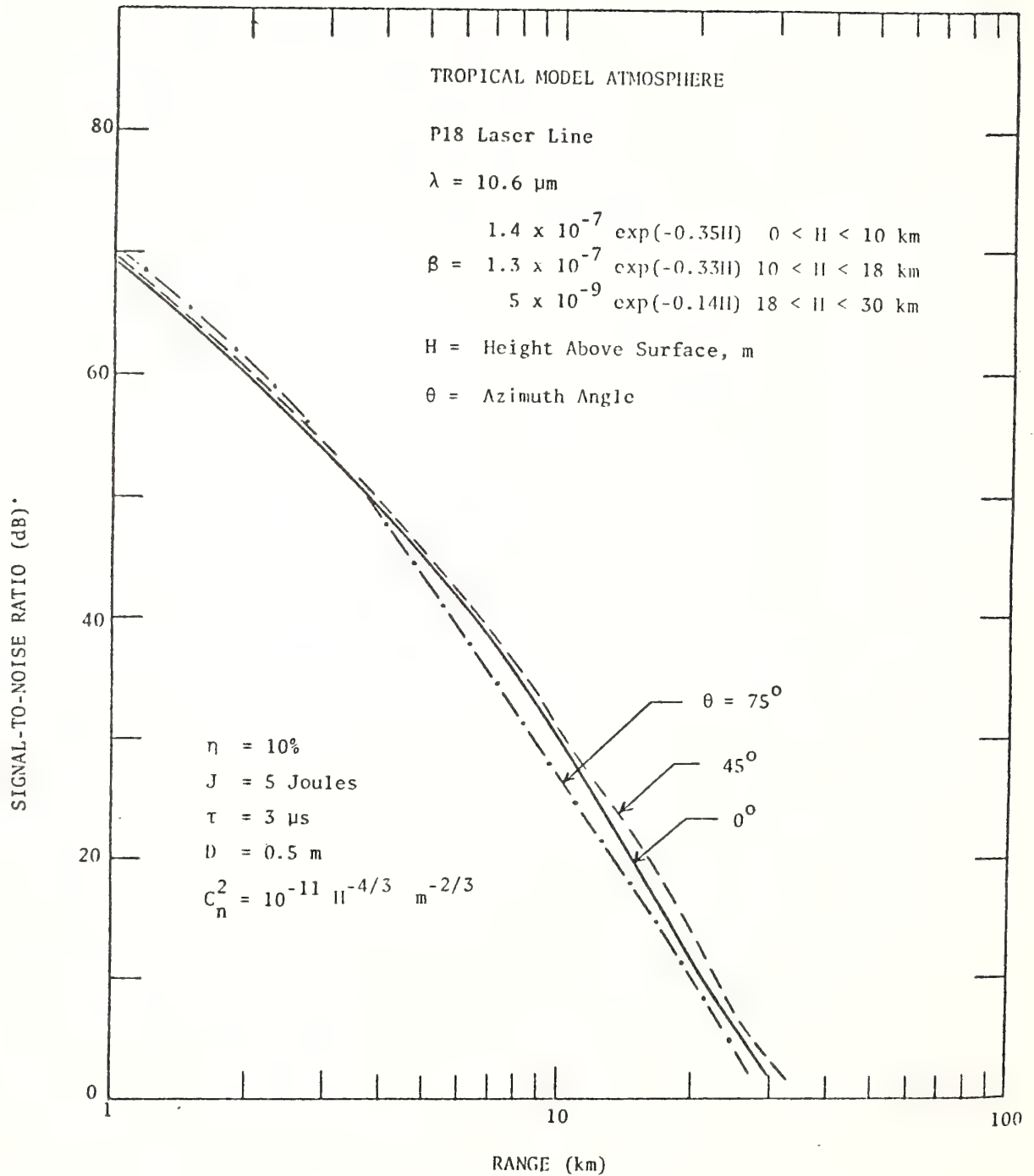
Figure 1. Performance of a ground-based pulsed coherent CO_2 lidar for various atmospheric propagation paths.

24

A REVIEW OF THE OPTICAL EFFECTS OF THE CLEAR TURBULENT ATMOSPHERE

Robert S. Lawrence
National Oceanic and Atmospheric Administration
Environmental Research Laboratories
Boulder, Colorado 80302

Abstract

The refractive irregularities that are responsible for the atmospheric degradation of optical images arise from variations in temperature of the atmosphere. We present a non-mathematical, physically based description of these irregularities and how they contribute to the degradation of an image. Irregularities near the image contribute only through the distortion of the wave front, thereby distorting or spreading the image of a point source. More distant irregularities produce, in addition, scintillations or fluctuations in the intensity of the light. The random apodization resulting from scintillations further degrades the image.

Introduction

Refractive-index variations in the clear atmosphere affect light waves passing through them and, in most cases, degrade the performance of optical systems. We shall describe the refractive-index variations with particular attention to the small-scale fluctuations associated with atmospheric turbulence. Then we shall consider the effects of the fluctuations on optical systems, emphasizing the motion, blur, and scintillation produced in the image of a point source. Although we shall usually describe the effects in the context of the image of a star seen with a ground-based telescope, that description applies with only minor and obvious modifications to other situations such as ground-to-ground paths.

We make no attempt to present mathematical details or a comprehensive bibliography. Readers desiring such information are referred to a review paper by Lawrence and Strohbehn[1] containing 95 references. More recent information will be found in a review by Fante[2] and in a forthcoming book being edited by Strohbehn.[3]

The Refractive Index of the Atmosphere

The refractivity of air at optical frequencies is, to a good approximation, simply

$$N = 79 \frac{P}{T} \tag{1}$$

Here, P is the atmospheric pressure in mb and T is the temperature in K. $N \equiv (n-1)10^6$ is the deviation of the refractive index from unity in parts per million. N is roughly 290 at sea level. This approximation neglects the variation of N with wavelength and the minor effect of the variation of air density caused by the presence of water vapor. The wavelength dependence of N is about 10 percent over the optical range; the humidity dependence is less than 1 percent but its small-scale structure may sometimes be significant. These matters have been reviewed in detail by Owens[4] and by Friehe et al.[5]

Large-scale Variations and Their Optical Effects

Large-scale variations in refractivity, referring to spatial sizes greater than about a meter and durations longer than about 10 seconds, are primarily caused by the exponential decrease of pressure with height and the tendency of a convectively stable air mass to support long-lived vertical temperature gradients of large horizontal extent.

An optical ray arriving at the surface of the earth from a star suffers downward bending as it passes through the atmosphere of steadily increasing refractive index. The bending τ of the ray is known as astronomical refraction. For a grazing ray at sea level, a typical value for τ is 10 mrad (34 minutes of arc; slightly more than the apparent angular diameter of the sun). Since the optical refractive index is approximated by the dry term of the radio refractive index, the discussion of average tropospheric radio refraction given by Bean and Dutton[6], including the use of the surface value N_s to estimate τ, is directly applicable to the optical case if the humidity is taken as zero. A more elaborate procedure, including a description of the appropriate computer program and applicable to all cases, including satellite-to-satellite paths, has been published by Garfinkel.[7]

The downward bending of an optical ray also occurs on ground-to-ground paths. The curvature of the ray is caused by the vertical gradient of refractive index. Following the procedure used by Bean and Dutton, [6] in their section 2.5.3, we may differentiate the equation for refractivity to obtain, for sea-level conditions at 0° C,

$$\frac{\Delta N}{\Delta h} = .28 \frac{\Delta P}{\Delta h} - 1.04 \frac{\Delta T}{\Delta h} \qquad \text{(Units mentioned below)} \qquad (2)$$

If we assume that the vertical pressure gradient $\frac{\Delta P}{\Delta h}$ maintains its standard sea-level value of -12.1 mb/100 m, we can calculate the temperature gradient needed to prevent bending ($\Delta N=0$) of the ray to be -3.3 °C/100 m. Although this temperature lapse rate is much greater than for a normal atmosphere (-0.6 °C/100 m) or an adiabatic atmosphere (-1.0 °C/100 m), even greater lapse rates can occur directly above a hot surface. Such conditions give rise to a "mirage". On the other hand, if the vertical temperature gradient becomes strongly positive, as may happen above a cold surface, downward curvature of the ray can be increased to approach the curvature of the earth's surface, causing "looming". The temperature gradient needed for this is 11.8 °C/100 m. An entertaining and easily readable discussion of mirages, looming, and many other optical effects has recently been prepared by Fraser and Mach.[8]

Natural variations in the vertical temperature gradient produce hour-to-hour changes in the apparent position of a distant object. A typical difference between day and night on a 15-km path is 100 μrad, corresponding to a temperature-gradient change of 0.7 °C/100m.

Refractive-Index Turbulence

Whenever we refer to "turbulence" we shall mean refractive-index (or temperature) turbulence rather than the mechanical or velocity turbulence commonly measured with hot-wire probes. The distinction is important because, when the atmosphere is in neutral thermal stability, i.e., when the temperature lapse rate is adiabatic, strong mechanical turbulence may exist with little or no optical effect.

The most widely accepted description of the structure of mechanical turbulence appeared when Kolmogorov[9] considered the structure function D between two components of velocity, call them α, β where $\alpha, \beta = x, y, z$,

$$D_{\alpha\beta}(r) = |v_\alpha(\xi) - v_\beta(\xi+r)|^2 \qquad (3)$$

for a span r along coordinate ξ. Purely from dimensional analysis he found $D_{\alpha\beta}$ to be proportional to the two-thirds power of the separation, i.e.,

$$D_{\alpha\beta}(r) = C_{\alpha\beta}|r|^{2/3} \qquad (4)$$

where $C_{\alpha\beta}$ is a parameter depending on the components and the energy involved.

An advance of direct interest to optical propagation came when Obukhov[10] and Corrsin[11] used a similar dimensional analysis to consider the temperature fluctuations in turbulence. The structure function of this scalar parameter turns out also to obey the two-thirds law, i.e.,

$$D_T(r) = C_T^2|r|^{2/3} \qquad (5)$$

where C_T^2, the "temperature structure parameter", depends on the energy involved in the turbulence.

The structure of mechanical turbulence has been treated in detail in a number of places, e.g. Lumley and Panofsky.[12]

Pressure fluctuations in turbulent air are smoothed out with the speed of sound, and are negligible compared to temperature fluctuations. Differentiating the equation for refractivity and eliminating δP, we see that the refractive-index fluctuations are related to the temperature fluctuations, by the formula

$$\delta N = -79 \frac{P}{T^2} \delta T \quad .$$ (6)

Accordingly, the refractive-index structure function,

$$D_N(r) = C_N^2 |r|^{2/3} = \left[\frac{79 \ P}{T^2}\right]^2 C_T^2 |r|^{2/3}$$ (7)

where $C_N^2 = C_n^2 \times 10^{12}$ and C_n^2 is the refractive-index structure parameter. The mean value of C_N^2 tends to decrease with height above the ground, excepting a slight peak that is commonly present near the tropopause where wind shear abounds. Local variations in C_N^2 exceeding a factor of fifty seem always to be present. A model for the height dependence of C_n^2 has been formulated by Hufnagel.[13] Measurements, taken with airplanes and balloons, have been published by Tsvang,[14] by Lawrence, Ochs and Clifford,[15] and by Bufton et al.[16]

Near the ground, C_N^2 varies significantly from day to night, being primarily controlled in the daytime by the unstable convection that results from solar heating of the ground. Fig. 1 shows a typical daily variation of C_n measured with fine-wire resistance thermometers 2 m above the ground. The minima near sunrise and sunset occur when the ground temperature equals that of the air because, as mentioned earlier, if air with uniform temperature (strictly speaking, with an adiabatic lapse rate) is mixed by mechanical turbulence no optical effects are produced. At night, the atmosphere tends to be stratified in layers of different temperature and wind-driven turbulent mixing produces measurable levels of C_N.
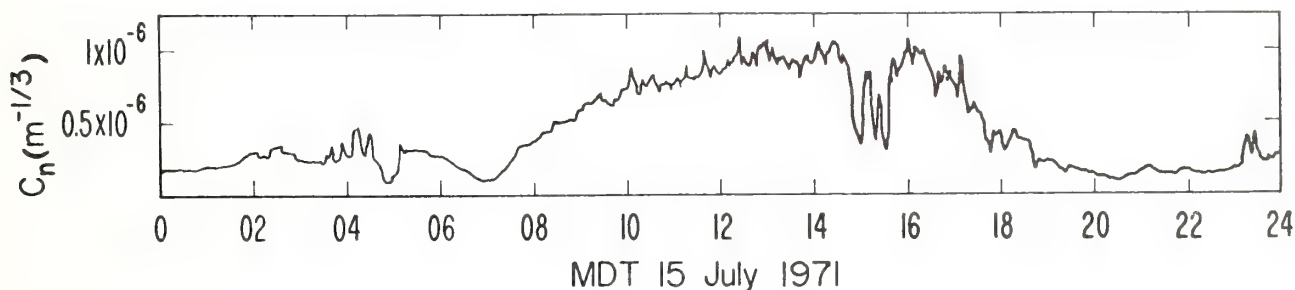
Fig. 1. Typical diurnal variation of the strength of refractive-index turbulence near the ground. The daytime peak results from heating of the ground; the dips at 15 hours are caused by clouds passing in front of the sun.

Optical Effects of Refractive-Index Turbulence

Phase and Amplitude Distortion of the Wave Front

Referring to Fig. 2, let us consider the behavior of a plane wave front A such as might arrive from a star, as it travels through the turbulent atmosphere. Immediately after passing through a region of irregular refractive index, the wave front B has been distorted. Since absorption and wide-angle scattering are negligible in the clear atmosphere, the energy density of the wave front B is still uniform and equal to its

free-space value. Thus an ordinary square-law detector placed at B would be unaffected by the wave-front distortions and incapable of measuring them. The distortions can, of course, be measured by a phase-sensitive detector such as an interferometer or a telescope.

As the wave progresses from B toward C, the various portions of the distorted wave front travel in slightly different directions and eventually begin to interfere. The interference is equivalent to a redistribution of energy in the wave and causes intensity fluctuations (scintillations) that can be detected by a square-law detector. On the way from B to C, the wave passes through additional refractive-index irregularities and so suffers additional phase perturbations. These new irregularities are, however, relatively ineffective in producing scintillations at C.

Let us examine the criteria that determine which of the turbulence irregularities along a line of sight are most effective in producing intensity fluctuations. In Fig. 3, consider an irregularity of diameter ℓ at an arbitrary point Z on the line of sight between the plane wave and the receiver at L. The irregularity can be fully effective in producing intensity variations only if the extreme ray paths AL and ZL differ in length by at least half a wavelength, i.e., the irregularity must be at least equal in size to the first zone of a Fresnel zone plate situated at Z. This minimum effective size is, in fact, the optimum size for the irregularity. Larger irregularities at the same point are ineffective because they do not diffract light through a large enough angle to reach the observer. While it is true that smaller irregularities produce intensity fluctuations at points closer than L and that these fluctuations persist in modified form until the wave reaches L, such smaller irregularities are relatively ineffective because of the steep increase in the Kolmogorov spectrum of atmospheric turbulence with irregularity size.
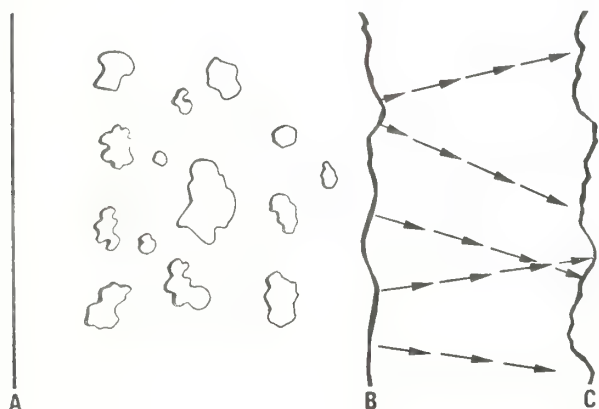
Fig. 2. The effect of atmospheric irregularities on a plane wave A. At B there are only phase distortions of the wave front; at C there are both amplitude and phase distortions.
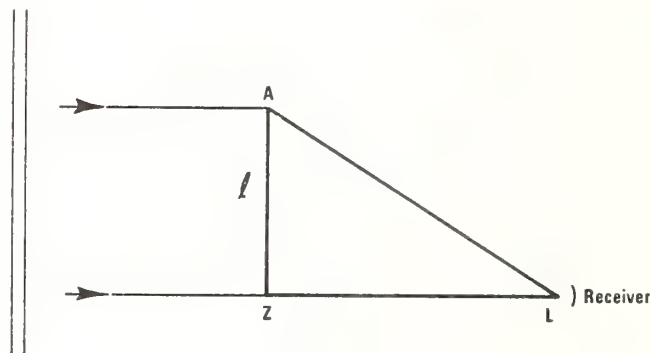
Fig. 3. The size ℓ of the irregularities most effective in producing scintillations is such that distance AL exceeds distance ZL by one-half wavelength.

From the geometry of Fig. 3, we see that the diameter of the most effective irregularity at height h is $\ell = \sqrt{\lambda h}$, where λ is the wavelength of the light. As a numerical example, for visible light of wavelength 0.5 μm and for a height of 10 km, ℓ = 7 cm.

If we assume, for the moment, that the turbulence is uniformly distributed along the path between the top of the atmosphere and the receiver, and that it has a Kolmogorov spectrum so that the large irregularities are more intense than the small, it is clear that the mean-square fluctuation of refractive index attributable to irregularities of optimum size varies systematically along the path. There is, therefore, a weighting function that expresses the relative effectiveness of turbulence in producing intensity fluctuations as a function of path position. It is clear that this weighting function must be a maximum at the top of the atmosphere (or at the middle of the path for a ground-to-ground path with a point source) and must decrease monotonically to zero at the receiver.

It is also clear that, for the plane-wave case of starlight, the intensity pattern at the receiver has the same scale size as the irregularities that produced it. Thus, in our numerical example, turbulence at a height of 10 km produces an intensity pattern on the ground that has a predominant size of 7 cm while turbulence at lower heights produces smaller scales.

The arguments given above assume simple superposition of the effects of irregularities at various points along the path. When the integrated turbulence on the entire path becomes too large, this assumption fails and the scintillations "saturate", i.e., the strength of the scintillations is no longer proportional to the strength of the turbulence that produced them. When saturation exists, the most effective portion of the path moves toward the receiver (or, for ground-to-ground paths with a point source, toward the ends of the path) and the scale sizes in the pattern are affected accordingly.

In summary, distortions in the phase of a plane wave from a star traveling through a clear, uniformly turbulent atmosphere are produced equally by turbulence at all locations. Because of the Kolmogorov spectrum, the large-scale eddies in the turbulence produce greater phase shifts than do the smaller scales. The amplitude, or intensity fluctuations in the wave front are produced predominantly by the turbulence high in the atmosphere, and the sizes of the pattern vary as the square root of the distance to the turbulence.

It is convenient to describe the magnitude of the phase fluctuations in terms of the phase structure function, $D_\phi(r)$, which is simply the mean square phase differences between two points a distance r apart on a plane parallel to the mean wave front. The Kolmogorov spectrum of turbulence produces wave front distortions that have a particular form of phase structure function, viz.,

$$D_\phi(r) \propto r^{5/3} . \tag{8}$$

Thus, for waves that have passed through natural turbulence in the atmosphere, the magnitude and nature of the phase fluctuations can be completely specified by a single number, r_o, known as the phase coherence length, which is the value of r for which $D_\phi(r)=1$.

For starlight at the ground

$$D_\phi(r) = \frac{28.8}{\lambda^2} r^{5/3} \int_0^\infty C_n^2 \, dh \tag{9}$$

in SI units, and r_o is of the order of 5 to 15 cm.

The strength of scintillations, on the other hand, is described in terms of the contrast between the light and dark areas. The most common measure of this contrast is the "log-amplitude variance"

$$\sigma_\chi^2 = \frac{1}{4} \left\langle \left[\log_e \frac{I}{I_o} \right]^2 \right\rangle \tag{10}$$

where I is the instantaneous intensity (or irradiance) of the wave and I_o is its long-term average. The pointed brackets denote averaging. Another frequently used measure of the strength of scintillations is the "scintillation index"

$$S_I = \frac{\left[\langle (I-I_o)^2 \rangle \right]^{1/2}}{I_o} . \tag{11}$$

For scintillations produced by the Kolmogorov turbulence in the atmosphere, the logarithm of the intensity has a normal or Gaussian probability distribution and the relation between log-amplitude variance and scintillation index is

$$\sigma_\chi^2 = \frac{1}{4} \log_e (1+S_I^2) \tag{12}$$

Notice that, unlike phase fluctuations, the scintillations are measured by quantities that give no indication of the scale size of the pattern. This is because the pattern size is usually determined by the distance to the turbulent layers and is independent of the strength of the turbulence. An exception occurs when the scintillations saturate, i.e., when $\sigma_\chi^2 \gtrsim 0.6$, and the Fresnel-zone sized irregularities begin to disappear relative to larger and smaller scales. For starlight, this happens only for stars near the horizon.

The log-amplitude variance is related to the strength of turbulence C_n^2 throughout the atmosphere by the formula

$$\sigma_\chi^2 = \frac{4.78}{\lambda^{7/6}} \int_0^\infty C_n^2 \, h^{5/6} \, dh \tag{13}$$

in SI units. The factor $h^{5/6}$ in this formula shows that the turbulence at great heights is more effective in producing scintillations than is the turbulence near the ground.

Effect of Wave-Front Distortions on a Stellar Image

The phase and intensity distortions of the wave front each affect the ability of a telescope to form a point image of a star, though in different ways. Considering first the phase distortions, we must discuss separately the effect of scale sizes larger than the telescope aperture diameter d and those smaller than d. If we call the mean-square variations of phase difference over the aperture due to the large scale sizes $\Delta\phi_\ell^2$ and the corresponding variations due to small sizes $\Delta\phi_s^2$, we can write

$$\Delta\phi_s^2 + \Delta\phi_\ell^2 = D_\phi(d) \tag{14}$$

The phase variations $\Delta\phi_\ell$ larger than d simply change the position of the stellar image in the focal plane of the telescope. Thus, for exposure times short compared with the time it takes for wind to blow across the diameter of the telescope, the quality of the image is unaffected by these large phase irregularities. On longer exposures, the image wanders through an angle λ/r_o, causing a long-exposure smearing of the image. This long-exposure smearing angle is independent of telescope diameter as long as $d > r_o$.

The phase variations $\Delta\phi_s$ smaller than the telescope aperture act as independent prisms of diameter r, each forming a separate image that is spread by a diffraction angle λ/r. These become important only as $D_\phi(r)$ approaches unity, and the integrated effect of all these small phase irregularities produces the "short-exposure" spreading which is of the order of λ/r_o^{ST}. The short-exposure phase coherence length r_o^{ST} is defined in the same manner as r_o, except that only phase irregularities smaller than the aperture diameter are involved. Yura[17] has shown that

$$r_o^{ST} \approx r_o[1+0.37(r_o/D)^{1/3}] \tag{15}$$

which is 10 to 40 percent greater than r_o for telescopes of modest diameter. We see that, as far as the formation of a small stellar image is concerned, there is no advantage to having a telescope diameter larger than r_o^{ST}.

The scintillations may also degrade the image if the scintillation index, as measured by a small-aperture receiver, is greater than about 0.2. Since the scintillations have a predominant size equal to a Fresnel zone $\sqrt{\lambda h}$ (where h is the height of the highest scintillation-producing layer in the atmosphere), the angle through which these random apodizers can spread the image is of the order of

$$\frac{\lambda}{\sqrt{\lambda}} = \sqrt{\lambda/h} \quad . \tag{16}$$

We see that scintillations cause significant image degradation relative to that caused by phase fluctuations only when $r_o > \sqrt{\lambda h}$. This, of course, depends on the relative strength of the turbulence in the upper atmosphere compared with that near the ground just above the observatory. The intensity of the blurred image caused by scintillation is always less than that caused by phase fluctuations, the ratio never exceeding about 0.2.

References

1. Lawrence, R. S. and Strohbehn, J. W., "A Survey of Clear-Air Propagation Effects Relevant to Optical Communications,", Proc. IEEE (Special Issue) 58:10, 1523-1545, 1970.

2. Fante, R. L., "Electromagnetic Beam Propagation in Turbulent Media," Proc. IEEE 63:12, 1669-1692, 1975.

3. Strohbehn, J. W. (ed), "Topics in Applied Physics; Laser Beam Propagation Through the Atmosphere," Springer-Verlag (to be published).

4. Owens, J. C., "Optical Refractive Index of Air: Dependence on Pressure, Temperature, and Composition," Appl. Opt. 6:1, 51-59, 1967.

5. Friehe, C. A., LaRue, J. C., Champagne, F. H., Gibson, C. H., and Dreyer, G. F., "Effects of Temperature and Humidity Fluctuations on the Optical Refractive Index in the Marine Boundary Layer,", J. Opt. Soc. Am. 65:12, 1502-1511, 1975.

6. Bean, B. R. and Dutton, E. J., Radio Meteorology, NBS Monograph 92, U. S. Government Printing Office, 1966. (also, Dover Publications, 1968.)

7. Garfinkel, B., "Astronomical Refraction in a Polytropic Atmosphere," Astron. J. 72:2, 235-254, 1967.

8. Fraser, A. B. and Mach, W. H., "Mirages," Sci. Amer. 234:1, 102-111, 1976.

9. Kolmogorov, A., Turbulence, Classic Papers on Statistical Theory, S. K. Friedlander and L. Topper, Eds., New York, 1941: Interscience p. 151, 1961.

10. Obukhov, A. M., "Structure of the Temperature Field in a Turbulent Flow", Izv. Akad. Nauk, SSSR. Ser. Geograf. Geofiz. 13:58, 1949.

11. Corrsin, S., "On the Spectrum of Isotropic Temperature Fluctuations in an Isotropic Turbulence", J. Appl. Phys. 22:, 469-473, 1951.

12. Lumley, J. L. and Panofsky, H. A., The Structure of Atmospheric Turbulence, John Wiley & Sons, 1964.

13. Hufnagel, R. E., "Variations of Atmospheric Turbulence," Optical Society of America Topical Meeting on Optical Propagation Through Turbulence, Boulder, Colorado July 1974.

14. Tsvang, L. R., "Some Characteristics of the Spectra of Temperature Pulsations in the Boundary Layer of the Atmosphere," Izv. Geophys. Ser., No. 10, 1594-1600, 1963.

15. Lawrence, R. S., Ochs, G. R. and Clifford, S. F., "Measurement of Atmospheric Turbulence Relevant to Optical Propagation," J. Opt. Soc. Am. 60:6, 826-830, 1970.

16. Bufton, J. L, Minott, P. O., Fitzmaurice, M. W., and Titterton, P. J., "Measurements of Turbulence Profiles in the Troposphere," J. Opt. Soc. Am. 62:9, 1068-1070, 1972.

17. Yura, H. T., "Short-Term Average Optical-Beam Spread in a Turbulent Medium," J. Opt. Soc. Am. 63:5, 567-572, 1973.

SATURATION OF SCINTILLATIONS AND ITS EFFECT ON REMOTE-SENSING
AND TELECOMMUNICATIONS SYSTEMS

R. S. Lawrence and S. F. Clifford
NOAA Research Laboratories
Boulder, Colorado 80302
(U. S. A.)

SUMMARY

As the strength of the turbulent fluctu-ations of refractivity distributed along an extended path increases, the resulting scin-tillations eventually saturate, i.e. their variance ceases to increase and, in fact, begins to decrease. When saturation appears, the spatial and temporal spectra of the scin-tillations are modified, as is the weighting function that describes the relative impor-tance of turbulent fluctuations at various points along the path. These modifications affect the interpretation of those remote-sensing systems that rely upon the presence of scintillations to deduce the turbulent structure or motions of the propagation medium, and they affect the performance of telecommunications systems, especially those using diversity or large-aperture techniques to reduce fading.

We present a physically based, heuristic theory for the onset of the saturation phenom-enon, and we show how it can be used to under-stand and predict the effects of saturation on remote-sensing and telecommunications systems.

1 - INTRODUCTION

The thin-screen diffraction theory of ionospheric scintillations first proposed by Booker, Ratcliffe, and Shinn (1950) and the diffraction theory for the twinkling of stars proposed by Little (1951) have been elaborated by many workers over the years (see especially Tatarski (1961, 1971)). These theories have been remarkably successful in predicting the effects on electromagnetic waves of random perturbations of the refrac-tive index, provided those perturbations are sufficiently weak or occur in a sufficiently restricted portion of the propagation path.

When, as in propagation near the ground through the turbulent atmosphere, the refrac-tivity fluctuations are strong and extend along a considerable portion of the path, the scintillations saturate, i.e. their variance no longer increases in proportion to an increase in the path-averaged fluctuation of refractivity. When saturation occurs, the scale sizes of the scintillation pattern change, and the scintillations are no longer described by the theories mentioned above.

An example of the saturation effect is shown in Figure 1, in which the normal diurnal variation in the square root of the refractive-
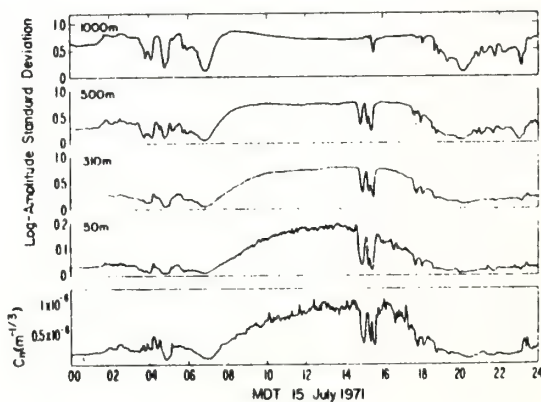
Fig. 1. The variation of the square root of the log-amplitude variance at each of four path lengths compared to the square root of the refractive-index structure constant C_n^2 for a 24 hr period. $\lambda = 0.63$ μm.

index structure parameter C_n^2 (lowest curve) is well reproduced by optical scintillations on a 50 m path but not on longer paths. Theories that permit quantitative prediction of the saturation effect have been presented by Clifford, Ochs, and Lawrence (1974), by Yura

(1974) and by Fante (1975). Clifford and Yura (1974) and Fante (1976) subsequently showed that all three theories are, in fact, equivalent. Here we review this theory briefly and indicate its application to some practical remote-sensing and telecommunications systems.

2 - THE THEORY OF SATURATION

The simple diagram in Figure 2 illustrates the geometry involved in the production of scintillations. Looking first only at the solid lines in the diagram, light from a
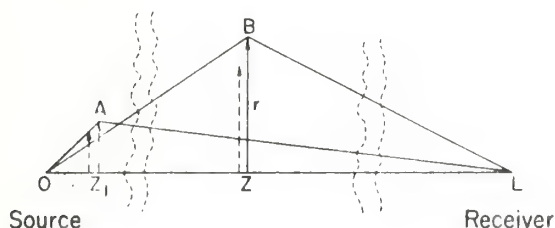
Fig. 2. The geometry involved in the discussion of the diffraction theory of scintillation. Weak scintillations are caused predominantly by irregularities such as Z_1A and ZB, represented by solid arrows. In saturation, the most effective irregularities are represented by dashed arrows.

source at the origin, point O, is received at point L. According to the diffraction theory of scintillations, a refractive irregularity of size r at point Z can be effective in producing scintillations at L only if it is large enough so that the difference between the paths OBL and OZL is at least one-half wavelength, $\lambda/2$, so that the two rays can interfere destructively. Working out the geometry, we see that this means

$$r \geq \sqrt{\frac{z}{L}(1-\frac{z}{L})} \quad \sqrt{\lambda L} \quad .$$

Now, an irregularity of size r will diffract light through an angle $\theta \leq \lambda/r$. The diffraction angle needed for the light to reach L is $\theta \geq r/(1-z)+r/z$. These two requirements are satisfied only when

$$r = \sqrt{\frac{z}{L}(1-\frac{z}{L})} \quad \sqrt{\lambda L}. \qquad (1)$$

and we see that this value of r is the most effective irregularity size at point Z. This size r is plotted as the lower solid curve of Figure 3. Notice that it reaches a maximum size, one-half a Fresnel zone radius for a plane wave at a distance L from the receiver, at the center of the path.
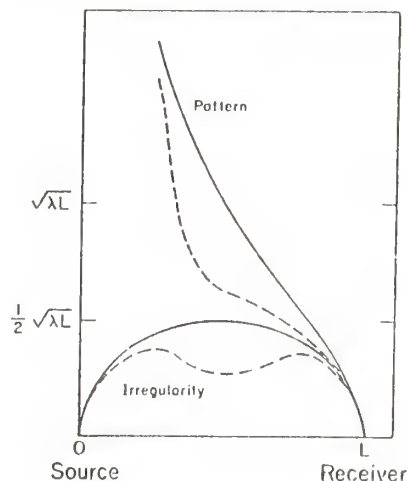
Fig. 3. Solid curves show the sizes of the most effective irregularities and of the resulting scintillation pattern for weak scintillations. Dashed curves illustrate the same quantities for partially saturated scintillations.

Because the light is emanating from a point source, the pattern produced at L by the irregularity at Z is magnified by the factor L/Z. Thus, the pattern size is

$$r_p = \sqrt{\frac{L}{z} - 1} \quad \sqrt{\lambda L} \quad ,$$

plotted as the upper solid curve in Figure 3. Notice that the small features in the scintillation pattern arise from refractive irregularities near the receiver, the large features arise from irregularities near the source, and the most prominent pattern size is the Fresnel-zone size $\sqrt{\lambda L}$.

This knowledge of the pattern size and the eddy size, along with information about the spectrum of turbulence, permits us to calculate the spatial autocorrelation function of the scintillation pattern. The solid curve of Figure 4 shows this function for the case of turbulence with a Kolmogorov spectrum distri-
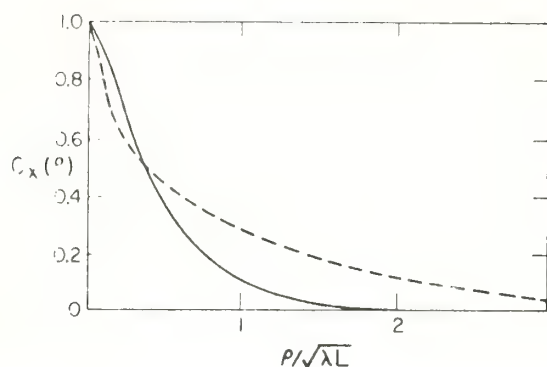
Fig. 4. The spatial autocorrelation function for eak scintillations (solid curve) and for partially saturated scintillations (dashed curve).

buted uniformly along the path. Here, again, we see that Fresnel-zone sized features are prominent in the pattern.

So far we have considered each refractive irregularity to act independently of the others. This is an adequate explanation of scintillations when the refractive irregularitie are sufficiently weak or when they are confined to a small portion (thin diffracting screen) of the path. Looking back at Figures 2, 3, and 4, but this time considering the dashed lines, we can understand the more complicated situation that results when the strong irregularities occur along the entire path. This is the situation that gives rise to saturation.

In Figure 2, when sufficient refractive perturbations (indicated by the wavy dashed lines) are present between O and Z, the irregularity of size r at Z can no longer be effective in producing a scintillation at L. This will be the case if the wavefront arriving at Z is already randomly distorted by more than about one radian relative to an unperturbed spherical surface. Then, some smaller size irregularity, indicated by the dashed arrow at Z, will be more effective.

To quantify the preceding argument, we introduce the concept of the "transverse coherence length" ρ_0 of the wave. This is roughly defined as the transverse distance over which the root-mean-square distortion of the wavefront exceeds one radian. As a wave propagates through a randomly varying medium

ρ_0 decreases continuously but, since refractive perturbations between Z and L are just as effective as those between O and Z in reducing scintillations at L, the value of ρ_0 for the entire path is the pertinent quantity for a discussion of saturation. A more precise definition of ρ_0 for the case of a spherical wave propagating through a uniform path distribution of C_n^2 is given by Yura (1974) as

$$\rho_0 = 0.16 \ \lambda^{6/5}(C_n^2)^{-3/5}L^{-3/5}. \qquad (2)$$

An equivalent formula valid for the case when the path distribution of C_n^2 is not uniform is

$$\rho_0 = 0.09 \ \lambda^{6/5} \left[\int_0^L C_n^2 \ (Z)(Z/L)^{5/3}dZ \right]^{-3/5}. (3)$$

When $\rho_0 = \sqrt{\lambda L}/2$ saturation begins and, as ρ_0 decreases, Fresnel-zone sized irregularities further and further from the center of the path lose their effectiveness. The dashed lines in Figure 3 illustrate what happens to the most effective irregularity sizes and to the corresponding pattern sizes as saturation begins. An equivalent indication of the onset of saturation is when scintillations become sufficiently strong that the log-amplitude variance of the received signal exceeds 0.3.

3 - EFFECTS OF SATURATION ON SYSTEMS

The dashed curve of Figure 4 illustrates schematically how the normalized spatial autocorrelation function of scintillations is distorted when saturation occurs. In terms of spatial sizes in the scintillation pattern, we see that there is a relative predominance of fine-scale structure producing the rapid initial drop in the autocorrelation function, and there is a relative predominance of large-scale structure producing the elevated tail in the autocorrelation function. In other words, the medium-scale features of the scintillation pattern have been selectively removed by the saturation phenomenon. The medium-scale features are those having a Fresnel-zone size $\sqrt{\lambda L}$ and they are the predominant features of a weak scintillation pattern.

Most optical and radio systems that are designed to coexist with scintillations are in some sense optimized with regard to Fresnel-zone sized variations in the received signal. For example, diversity systems work best when the antennas are separated by at least one Fresnel-zone distance. Large-aperture systems smooth out scintillations according to how many Fresnel-zone sized irregularities can be accommodated simultaneously in the area of the aperture. The simplest way to use scintillations to measure crosswinds depends on the fact that the predominant temporal frequency in the envelope of the scintillating signal is the frequency with which Fresnel-zone sized irregularities are carried across the path by the wind.

All such systems will be affected by saturation, as the Fresnel-zone sized components of the scintillation pattern are replaced by both smaller and larger components. For example, new fading frequencies appear in a communications system, less aperture averaging occurs, etc.

We can estimate the magnitude of these effects by remembering that, in saturation, the most effective irregularity size is ρ_0 and the most effective portions of the path are at Z_1 and Z_2, the two values of Z obtained when we solve for this condition by combining equation (1) with equation (2) or (3), i.e.

$$z_1 = \frac{L}{2}\left[1 - \sqrt{1 - \left(2\,\frac{\rho_0}{\sqrt{\lambda L}}\right)^2}\right], \qquad (4a)$$

$$z_2 = \frac{L}{2}\left[1 + \sqrt{1 - \left(2\,\frac{\rho_0}{\sqrt{\lambda L}}\right)^2}\right]. \qquad (4b)$$

The temporal frequency spectrum for weak scintillations peaks at a frequency $2V/\sqrt{\lambda L}$ where V is the wind speed component perpendicular to the propagation path. In saturation, this frequency increases to V/ρ_0.

The spatial size that predominates in the pattern of weak scintillations is $\sqrt{\lambda L}$. In saturation two sizes predominate; viz. $\rho_0 L/Z_1$ and $\rho_0 L/Z_2$. To be effective, a diversity system must be designed with a spacing greater than the larger of these sizes.

Aperture averaging of scintillations occurs when a receiving or transmitting aperture is large enough so that independently varying portions of the scintillation pattern are received simultaneously. For apertures greater than a few Fresnel zones, the variance of weak scintillations is reduced by the factor $(D/\sqrt{\lambda L})^{-7/3}$, while for saturated scintillations the factor is $[D/(\frac{L}{2}\rho_0)]^{-7/3}$, where Z_1 is calculated from formula (4a). As ρ_0 becomes much smaller than $\sqrt{\lambda L}$, the saturated scintillation factor finally reduces to $[D/(\frac{\lambda L}{\rho_0})]^{-7/3}$, exactly what is obtained by noting that the receiver is in the far field of the ρ_0-size irregularities.

4 - REFERENCES

Booker, H. G., J. A. Ratcliffe, and D. H. Shinn, "Diffraction from an irregular screen with applications to ionospheric problems" *Phil. Trans. Roy. Soc. A 242* No. 856 579-607 (1950).

Clifford, S. F., G. R. Ochs, and R. S. Lawrence, "Saturation of optical scintillation by strong turbulence" *J. Opt. Soc. Am. 64* No. 2 148-154 (1974).

Clifford, S. F., and H. T. Yura, "Physical Equivalence of two theories of strong optical scintillation" *J. Opt. Soc. Am. 64* No. 12 1641-1644 (1974).

Fante, R. L., "Electromagnetic beam propagation in turbulent media" *Proc. IEEE 63* No. 12 1669-1692 (1975).

Fante, R. L., "Comparison of theories for intensity fluctuations in strong turbulence" *Radio Sci. 11* No. 3 215-219 (1976).

Little, C. G., "A diffraction theory of the scintillation of stars on optical and radio wavelengths" *Mon. Not. Roy. Aetron. Soc. 111* No. 3 289-302 (1951).

Tatarski, V. I., *Wave Propagation in a Turbulent Medium*, translated by R. S. Silverman, McGraw-Hill Book Co., Inc. New York, N. Y. 286 pp. (1961).

Tatarski, V. I., *The Effects of the Turbulent Atmosphere on Wave Propagation*, translated by Israel Program for Scientific Translations, available from Nat'l Tech. Info. Service, Springfield, Va. (1971).

Yura, H. T., "Physical model for strong optical-amplitude fluctuations in a turbulent medium" *J. Opt. Soc. Am. 64* No. 1 69-67 (1974).

ON THE DISTRIBUTION OF TURBULENT FLUCTUATIONS
OF REFRACTIVE INDEX IN THE ATMOSPHERE

R. S. Lawrence, S. F. Clifford, and G. R. Ochs

NOAA Research Laboratories

Boulder, Colorado 80302

(U.S.A.)

SUMMARY

The turbulent fluctuations of temperature that are responsible for scintillation and image distortion of light waves and for most of the tropospheric forward scatter and scintillation of radio waves occur irregularly throughout the atmosphere. The refractive-index structure parameter C_n^2 is distributed irregularly in space so that a given volume often contains one hundred times the magnitude of an adjacent volume the same size. Measurements made with high-speed temperature probes reveal a number of interesting features of the distribution of C_n^2, and some of these will be discussed. However, an understanding of the climatology of refractive-index fluctuations will require continuous measurements from ground-based sensors. We describe a technique, already in use, for using scintillations of starlight to measure the smoothed vertical profile of C_n^2 throughout the atmosphere. We are presently developing methods for profiling C_n^2 along ground-to-ground line-of-sight paths.

1 - INTRODUCTION

Turbulent fluctuations of atmospheric refractive index with scale sizes less than 1 meter are responsible for scintillation and image distortion of light waves, for tropospheric forward scatter and clear-air radar returns of radio waves, and for backscattering of sound waves. For light waves and sound waves the refractive-index fluctuations are, for most practical purposes, proportional to temperature fluctuations (Tatarski, 1961) and can be characterized by the temperature structure parameter,

$$C_T^2 = \overline{[T(r) - T(r+\rho)]^2} \; \rho^{-2/3} \; ,$$

where ρ is the separation of the points at which the two temperature measurements are made. For radio waves the situation is complicated by the strong dependence of refractive index on water vapor. Near the ground where water vapor is often a significant constituent of the atmosphere, the refractive-index fluctuation may be either increased or decreased by the presence of the water vapor, depending on whether the water vapor is anti-correlated or correlated with the temperature (Gossard, 1960). Nevertheless, we shall limit the present discussion to the occurrence of C_T^2 in the atmosphere. At high altitudes this is closely related to the refractive-index structure parameter C_n^2. At middle and low altitudes, in the clear air, a description of C_T^2 gives at least a qualitative indication of the magnitude and spatial variability of C_n^2.

2 - NEAR THE SURFACE

Near the surface of the earth the nature of the temperature fluctuation depends largely on whether the atmosphere is stable or unstable, i.e. on whether the vertical temperature gradient is greater than or less than the adiabatic lapse rate. Generally speaking, in the daytime the air near the ground is heated, the atmosphere is unstable, and thermal plumes develop. These cause strong mixing of warm and cool air and result in large values of C_n^2. A typical value 1 meter above sunlit level ground is $10^{-12} m^{-2/3}$. Both theory and observation show (See Wyngaard, Izumi, and Collins, 1971; Frisch and Ochs, 1975) that, for the first few hundred meters or up to the first temperature inversion C_n^2 decreases with height h as $h^{-4/3}$. Because of the thermal plumes, the spatial distribution of C_n^2 is highly variable

as shown by acoustic echo sounders (See Frisch and Ochs, 1975). During stable conditions such as on a clear night the situation is more complicated and less amenable to theory. Gossard, Jensen, and Richter (1971) used a high-resolution FM/CW radar to show the thin, horizontal stratification that predominates in radio refractive index at such times.

3 - AT HIGH ALTITUDES

3.1 The distribution of temperature fluctuations at altitudes above the first inversion layer or above about 1 km is characterized by its complex structure and great variability. No quantitative theory exists and there are few observations from which to infer geographical or climatological variations.

3.2 Direct observations. The few observations that are available consist of measurements made with high-speed temperature sensors carried aloft by balloons or aircraft. Indirect measurements, deduced from the observed scintillation of starlight, offer less height resolution but permit a valuable continuity of observation. The samples of direct observations that follow are presented in terms of the dry-term refractive-index structure parameter

$$C_n^2 = \left[\frac{79 \cdot 10^{-6} P}{T^2}\right]^2 C_T^2.$$

Figure 1 shows a typical example of measurements made by Ochs and Lawrence (1972) with an airplane-borne temperature probe over the open ocean about 160 km southwest of San Diego, California. The relatively smooth curve on the right is the temperature profile; that on the left is the profile of C_n^2. Below the strong temperature inversion C_n^2 is relatively high and decreases as $h^{-4/3}$. At the inversion height there is a 100-fold increase in C_n^2, followed by an immediate decline to the high-altitude value of about $2 \times 10^{-17} m^{-2/3}$. Above the inversion layer, C_n^2 varies erratically by a factor of about 100, but its mean value shows little change with height, at least up to the 3 km limit of these observations.
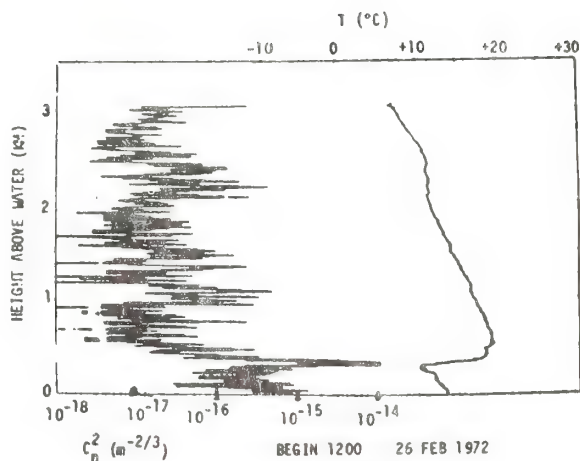
Fig. 1. Vertical profiles, over water, of the refractive-index structure parameter C_n^2 (left) and the temperature (right), obtained from a high-speed temperature sensor mounted on an airplane (From Ochs and Lawrence (1972)).

Figure 2 shows balloon-borne measurements made near Greenbelt, Maryland by Bufton (1973) to a height of 20 km. Here C_n^2, plotted on a linear scale, shows a mean value less than
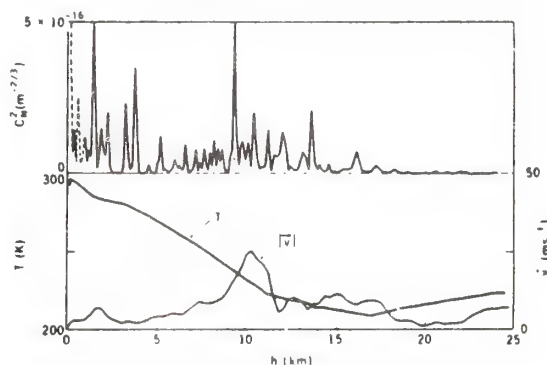
Fig. 2. Vertical profiles made in Maryland of refractive-index structure parameter C_n^2, temperature, and wind speed obtained from a balloon carrying fine-wire sensors. (From Bufton (1973)).

10^{-16} and little decrease with height up to at least 13 km. In fact, there is a noticeable increase in C_n^2 at about 9 km associated with wind shear at that altitude. Figure 3 shows similar measurements made by Barletti and his associates (1974) in the Canary Islands. In this case, the effect of the islands is evident up to a height of 3.5 km. Above that, C_n^2 displays its usual erratic nature and has a

mean value of about $10^{-17} m^{-2/3}$ that depends little on height.
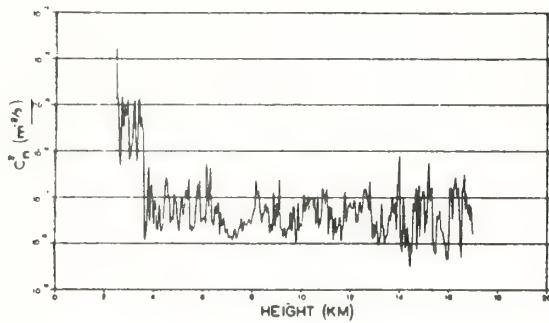
Fig. 3. Vertical profile, made in the Canary Islands, of refractive-index structure parameter C_n^2 deduced from balloon-borne temperature sensors. (From Barletti et. al. (1974)).

The ground effect, which shows clearly in Figure 3, is very pronounced and can extend large distances from irregular terrain. Figures 4 and 5 show contours of C_n^2 made from daytime airplane-borne measurements over the peak of 3-km Mt. Haleakala in Hawaii. There was a light wind, about 5 m/s, from the east. Effects of the terrain, even on the windward side of the mountain, increase C_n^2 by a factor of 100 and are evident more than a kilometer above the surface.
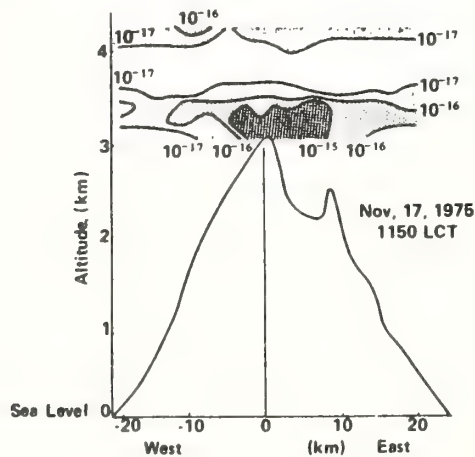
Fig. 4. Contours of the refractive-index structure parameter C_n^2 over Mt. Haleakala, Hawaii, deduced from airplane flights carrying high-speed temperature sensors.
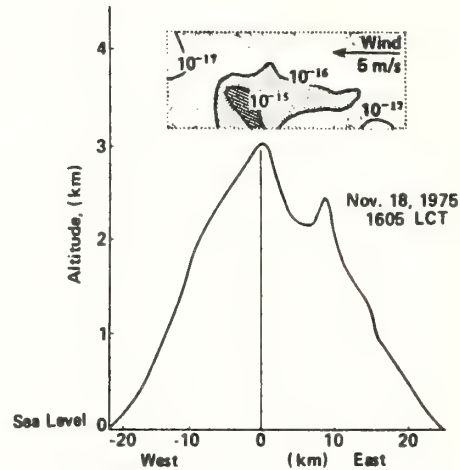
Fig. 5. Contours of the refractive-index structure parameter C_n^2 over Mt. Haleakala, Hawaii, deduced from airplane flights carrying high-speed temperature sensors.

3.3. Indirect observations. It has long been known that the twinkling of stars yields information about the turbulent refraction of the atmosphere. See, for example the qualitative discussions by Douglass (1897) and by Pickering (1925). More quantitative relationships were sought by Protheroe (1964), Townsend (1965), Vernin and Roddier (1973), and by Roddier and Roddier (1973). More recently, Rocca, Roddier, and Vernin (1974) and Vernin and Roddier (1975) devoted considerable attention to a method of deducing the height and spacing of turbulent layers from scintillation measurements.

Building on these ideas, Ochs, Wang, Lawrence, and Clifford (1976) constructed a spatial-filtering attachment to a 36 cm astronomical telescope and used it to measure smoothed profiles of C_n^2 above an altitude of 2.5 km. Figure 6 shows typical profiles taken with this instrument in Boulder, Colorado. They disclose a night-to-night variation of at least 50:1, and show a general decline with altitude. Measurements with the same instrument made in Hawaii show similar variations (Figure 7). The remarkable difference between the Colorado observations and the Hawaii observations is that the mean value of C_n^2 is only about one-tenth as large in Hawaii as it is in Colorado. We suggest that this difference is caused by the hundreds of kilometers of high
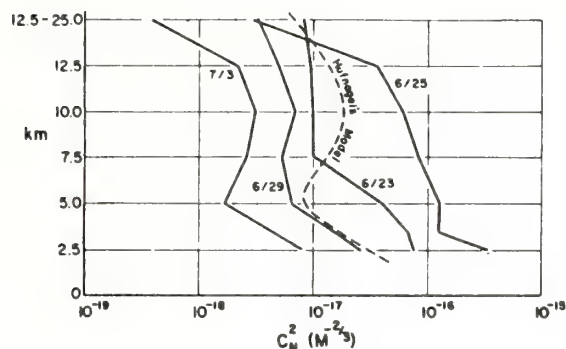
Fig. 6. Vertical profiles of C_n^2 in Boulder, Colorado, deduced from spatial filtering of stellar scintillations. The dashed curve is the model from Hugnagel (1974).

Fig. 8. Vertical profiles of C_n^2 in Hawaii, taken at 20-minute intervals, show large hour-to-hour variation in the structure of the atmosphere.

Fig. 7. Vertical profiles of C_n^2 in Hawaii, deduced from spatial filtering of stellar scintillations. The dashed curve is the model from Hufnagel (1974).

mountains that lie to the west (windward side) of Boulder, Colorado.

The typical profiles shown in Figure 8 were made at 20-minute intervals and disclose large variations from one hour to the next. Such variations suggest that the turbulent regions responsible for the refractive irregularities occur in isolated patches not unlike the occurrence of visible clouds.

3.4. Models. The first generally accepted, quantitative empirical model for the distribution of C_n^2 throughout the atmosphere was proposed by Hufnagel (1966). This early model was adjusted to have an integrated value of C_n^2 that agreed with observations of stellar scintillation, and to have an enhanced layer near the tropopause at about 12 km. As a result of the more recently published observations, Hufnagel (1974) has revised his empirical model and has added realistic variability to it. The new formula is

$$C_n^2 = 8.2 \times 10^{-56} u^2 h^{10} \exp(-h/1000) + 2.7 \times 10^{-16} \exp(-h/1500)$$

where h is the height in meters and u is the root-mean-square wind speed (m/s) in the height range 5 to 20 km. If u is unknown, Hufnagel suggests using 27 m/s. The correlation with wind velocity comes from a comparison, by Hufnagel, of extensive published measurements of stellar scintillation with available rawinsonde data.

The dotted curves in Figures 6 and 7 show the new Hufnagel model with a wind speed of 27 m/s. Figure 9 compares four Boulder, Colorado profiles with appropriate realizations of the Hufnagel model, using wind velocities measured by the National Weather Service six hours later.
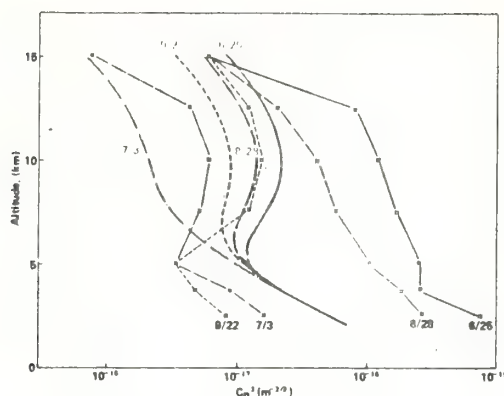
Fig. 9. A comparison between observed profiles of C_n^2 at Boulder, Colorado (solid lines) and Hufnagel (1974) models, using winds observed by nearby rawinsonde.

4 - CONCLUSIONS

While we now have models for the mean value of C_n^2, the enormous variability exhibited by this quantity, even high in the atmosphere, cannot be predicted. We know little or nothing about the geographical and climatic variations of C_n^2, though there is a suggestion that mountainous terrain may enhance refractive-index irregularities even at great heights. Further progress in our understanding of these matters requires extensive observations, observations that will be practicable only with ground-based sensors. The stellar-scintillation technique is useful, and the possibility exists of building similar profilers that will operate in the daytime by using the edge of the sun as a source of scintillations.

5 - REFERENCES

Barletti, R., G. Ceppatelli, E. Moroder, L. Paterno, and A. Righini, "A vertical profile of turbulence in the Atlantic air mass measured by balloon-borne radiosondes" *Journal of Geophysical Research 79* No. 30 4545-4549 (1974).

Bufton, J. L. "Comparison of vertical profile turbulence structure with stellar observations" *Applied Optics 12* No. 8 1785-1793 (1973).

Douglass, A. E., "Atmosphere, Telescope and Observer" *Popular Astronomy*, June, 1897 (Reprinted in *Amateur Telescope Making, Book Two*, 585-605, A. G. Ingalls, ed. Scientific American, Inc. (1957)).

Frisch, A. S., and G. R. Ochs, "A note on the behavior of the temperature structure parameter in a convective layer capped by a marine inversion" *Journal of Applied Meteorology 14* No. 3 415-419 (1975).

Gossard, Earl E., Power spectra of temperature, humidity and refractive index from aircraft and tethered balloon measurements" *IRE Transactions on Antennas and Propagation AP-8* No. 2 186-201 (1960).

Gossard, E. E., D. R. Jensen, and J. H. Richter, "An analytical study of tropospheric structure as seen by high-resolution radar" *Journal of the Atmospheric Sciences 28* 794-807 (1971).

Hufnagel, R. E., in *Restoration of Atmospherically Degraded Images*, Nat'l Academy of Sciences, Washington, D. C. Vol. 2, p. 14. (1966).

Hufnagel, R. E., "Variations in atmospheric turbulence" in *Digest of Technical Papers, Topical Meeting on Optical Propagation Through Turbulence*, July 9-11, 1974, Optical Society of America, Washington, D. C.

Ochs, G. R., and R. S. Lawrence, "Temperature and C_n^2 profiles measured over land and ocean to 3 km above the surface" NOAA Technical Report ERL251-WPL 22, Sup't of Documents, Washington, D. C. (1972).

Ochs, G. R., Ting-i Wang, R. S. Lawrence, and S. F. Clifford, "Refractive-turbulence profiles measured by one-dimensional spatial filtering of scintillations" *Applied Optics 15* No. 10 2504-2510 (1976).

Pickering, W. H., "The shadow bands" *Popular Astronomy 33* 1-2 (1925).

Protheroe, W. M., "The motion and structure of stellar shadow-band patterns" *Quarterly Journal Royal Meteorological Society 90* No. 388 27-42 (1964).

Rocca, A., F. Roddier, and J. Vernin, "Detection of atmospheric turbulent layers by spatiotemporal and spatioangular correlation measurements of stellar-light scintillation" *Journal of the Optical Society of America 64* No. 7 1000-1004 (1974).

Roddier, C., and F. Roddier, "Correlation measurements on the complex amplitude of stellar plane waves perturbed by atmospheric turbulence" *Journal of the Optical Society of America 63* No. 6 661-663 (1973).

Tatarski, V. I., *Wave Propagation in a Turbulent Medium*, translated by R. S. Silverman, McGraw-Hill Book Co., Inc. New York, N. Y. 285 pp. (1961).

Townsend, A. A., "The interpretation of stellar shadow-bands as a consequence of turbulent mixing" *Quarterly Journal Royal Meteorological Society 91* No. 387 1-9 (1965).

Vernin, J. and J. Roddier, "Experimental determination of two-dimensional spatio-temporal power spectra of stellar light scintillation. Evidence for a multilayer structure of the air turbulence in the upper troposphere" *Journal of the Optical Society of America 63* No. 3 270-274 (1973).

Vernin, J., and F. Roddier "Détection au Sol de la Turbulence Stratospherique par Intercorrélation Spatioangulaire de la Scintillation Stellaire" *Comptes Rendus Acad. Sci. Paris (French), Vol. 283(B)* 463-465 (1975).

Wyngaard, J. C., Y. Izumi, and Stuart A. Collins, Jr., "Behavior of the refractive-index-structure parameter near the ground" *Journal of the Optical Society of America 61* No. 12 1646-1650 (1971).

FEASIBILITY OF MONITORING AEROSOL CONCENTRATIONS

BY 10.6 µm BACKSCATTER LIDAR

Gordon Lerfald

The feasibility of remotely monitoring aerosol concentrations by means of backscatter lidar systems operating at the wavelength 10.6 µm was investigated by experimental tests and calculations. A prototype lidar system was built and was operated in conjunction with equipment that permitted direct measurement of particle size distribution of aerosols in essentially the same sampled volume. The backscattered signals measured by the test system agreed to within a factor of two with the backscatter computed from the measured particle size distributions. The experimental results are used to predict the performance of systems having transmitter powers and receiver collecting optics different from those used for the test system.

FINAL REPORT ON PHASE I
OF SOLAR RADIATION ATMOPSHERIC TRANSMISSION RESEARCH

G. M. Lerfald, V. E. Derr, R. F. Pueschel, and R. L. Hulstrom

The efficient use of solar energy requires a knowledge of the effects of clouds, atmospheric gasses and aerosols on insolation rates. Understanding must be of sufficient depth to project the effects on climate fluctuations and man-made changes in the absorbing and scattering constituents of the atmosphere. The feasibility of differentiating and quantizing the various atmospheric components which affect the transmission of solar radiation to ground level, has been tested by a program of experiment and analysis. The results show that available techniques can be effectively combined to obtain a rather complete knowledge of the roles of the individual components which scatter or absorb solar radiation. This data assists in development of improved models to predict solar irradiation at ground level. The atmospheric components of greatest importance to solar energy are:

(1) Rayleigh scattering by the standard atmosphere, (2) ozone absorption, (3) cirrus clouds, (4) other clouds, (5) suspended particulates (aerosols), (6) water vapor, and (7) other gaseous components. In addition, for some purposes ground albedo is of importance.

Remote sensing techniques (e.g., lidar, solar photometry, radiometry and acoustic sounding) and both ground based and airborne in situ measurements of aerosol characteristics are combined to simultaneously measure the parameters of interest. The optimum complement of equipment turned out to differ somewhat from that originally anticipated.

WIND AND C_n^2 PROFILING WITH CROSSED LASER BEAMS AND SPATIAL FILTER DETECTORS

G. R. Ochs, S. F. Clifford, and Ting-i Wang

We analyze the potential of crossed laser beams and array receivers to profile wind and C_n^2 along the optical path. The theory of profiling is developed for the cases of multi-detector arrays and two transmitting sources, which may or may not be resolvable. Numerical results based upon the theory are presented, and preliminary experimental results are shown. Finally, we discuss the design of a proposed profiling system, based upon the theory, that will path-resolve wind and C_n^2 into 6 parts over the middle two-thirds of an optical path 0.5 to 2 km long.

Laser wind sensing: the effects of saturation of scintillation

G. R. Ochs, S. F. Clifford, and Ting-i Wang

We have developed a physically based extension of the first-order perturbation theory of optical scintillation that accounts for the observed variance and covariance of the amplitude fluctuations in strong integrated turbulence. We use this model to analyze the experimentally observed changes in the operation of our laser wind sensor. The theory suggests a transmitter–receiver configuration that can nearly eliminate the performance-degrading effects of strong turbulence. Based on this analysis, we have developed a saturation-resistant optical wind sensor that maintains its calibration and wind-weighting function throughout the observed range of integrated-turbulence values.

I. Introduction

We have developed a laser-beam system that uses the naturally occurring scintillations produced by atmospheric refractivity variations to derive the path-averaged transverse wind.[1] By measuring a time-lagged covariance function with spaced detectors, the path-averaged wind speed can be found directly from the slope of this function at zero time lag. By changing the separation between detectors, we emphasize different regions of the path as shown in Fig. 1. Our path-average sensor uses $\beta = 0.3$ Fresnel zones normalized spacing to achieve the most uniform path average. Figure 2 shows the resulting system performance in weak turbulence as compared with the average of six conventional anemometers spaced along the optical path. The excellent performance of the system based on the first-order scattering theory is achieved only as long as the integrated amount of refractive turbulence σ_T^2 is small. The quantity σ_T^2 for a point source is given by

$$\sigma_T^2 = 0.124 k^{7/6} L^{11/6} C_n^2, \qquad (1)$$

where k is the wavenumber of the radiation, L is the pathlength, and C_n^2 is the refractive-index structure parameter.[2,3] As the strength of refractive-turbulence increases, the scintillations saturate,[4] and the system performance changes dramatically in a hitherto unpredictable manner.

There are two significant questions to be asked about the effects of strong turbulence on our original wind sensor. First, how does the relation between the slope of the time-lagged covariance at zero delay and wind speed change? Second, how does the path-weighting function change? These two questions are related because the area under the weighting function is the slope-wind proportionality constant.

Ultimately, an understanding of the mechanisms responsible for these changes should lead to the development of a new system that is relatively unaffected by strong turbulence. In this paper, we derive the formulas that describe the performance of the optical wind sensor in strong turbulence and, based on this theory, describe the design and testing of an optical wind sensor that maintains its wind-weighting function and calibration throughout the observed range of turbulence values.

II. Theory

In a recent paper,[4] we developed an equation for the log-amplitude covariance function $C_\chi(\rho) = \langle \chi(\rho_1 + \rho)\chi(\rho_1) \rangle$ in strong Kolmogorov turbulence[5,6] in the form

$$C_\chi(\rho) = 2.94 \int_0^1 du \sigma_T^2(u)[u(1 - u)]^{5/6} \int_0^\infty \frac{dy \sin^2 y}{y^{11/6}}$$

$$\times \exp\left\{ -\sigma_T^2(u)[u(1 - u)]^{5/6} F(y) \right\} J_0\left\{ \left[\frac{4\pi y u}{(1 - u)} \right]^{1/2} \rho \right\}. \qquad (2)$$

where $\sigma_T^2(u) = 0.124 k^{7/6} L^{11/6} C_n^2(u)$.

In Eq. (2), $u = z/L$ is the normalized path position, ρ is the separation between two detectors in Fresnel zones $(\lambda L)^{1/2}$, where λ is the wavelength of the radiation, and $F(y)$ is given by

$$F(y) = 7.02 y^{5/6} \int_{0.7y}^x d\xi \xi^{-8/3}[1 - J_0(\xi)]. \qquad (3)$$

45
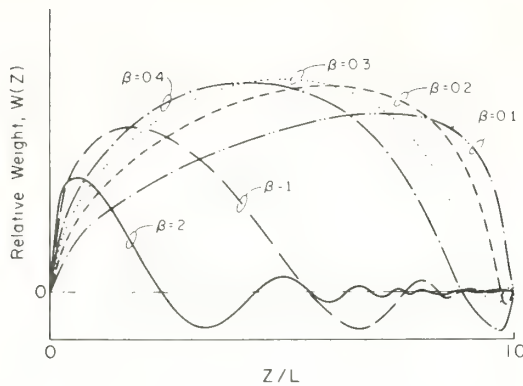
Fig. 1. The relative weight of the different portions of the path in determining the optically measured wind. The parameter $\beta = \rho(\lambda L)^{-1/2}$ is the separation of the sensors. These curves are calculated for point sensors; the finite area of a real sensor will tend to remove the negative weights near the receiver.

To incorporate the effects of wind into Eq. (2), we use Taylor's hypothesis and replace ρ by $|\rho - \mathbf{v}\tau(\lambda L)^{-1/2}u^{-1}|$. For simplicity, we define

$$g(u, y) = y^{-11/6} \sin^2 y \exp\{-\sigma_T^2[u(1 - u)]^{5/6}F(y)\}. \quad (4)$$

Information about the wind is then derived from the slope at zero time lag, i.e., $m = \partial C_\chi(\rho,\tau)/\partial\tau$ at $\tau = 0$. After differentiating, we obtain

$$m = 2.95 \int_0^1 du \sigma_T^2(u)[u(1-u)]^{1/3}(\hat{\rho} \cdot \mathbf{v}_n) \int_0^\infty dy g(u, y)(4\pi y)^{1/2}$$
$$\times J_1\left[\left(\frac{4\pi y u}{1 - u}\right)^{1/2} \rho\right], \quad (5)$$

where J_1 is the first-order Bessel function of the first kind, $v_n = v/(\lambda L)^{1/2}$, and $\hat{\rho} = \rho/\rho$. (Note that only winds parallel to $\hat{\rho}$ will contribute to the measured wind speed.) When we use the one-bit correlator technique[1] to obtain $C_\chi(\rho,\tau)$, this function is automatically normalized to the signal variance $C_\chi(0,0)$,

and we actually obtain a normalized slope m_N of the form

$$(\lambda L)^{1/2} m_N = \int_0^1 du v(u) W_1(u) / \left[\int_0^1 du W_2(u)\right], \quad (6)$$

where

$$W_1(u) = [u(1 - u)]^{1/3} \int_0^\infty dy g(u, y)(4\pi y)^{1/2} J_1\left[\left(\frac{4\pi y u}{1 - u}\right)^{1/2} \rho\right] \quad (7)$$

and

$$W_2(u) = [u(1 - u)]^{5/6} \int_0^\infty dy g(u, y). \quad (8)$$

[Note in using the particular form of Eq. (2), we have assumed a uniform distribution along the optical path, i.e., that C_n^2 is a statistically uniform function of u.] Under the above assumption, $W_1(u)$ is proportional to the path-weighting function for the transverse wind speed under all refractive-turbulence conditions.

For use in the next section of this paper, we need to generalize Eq. (6), (7), and (8) to the case of finite, circular, transmitting, and receiving apertures. Details of this procedure are contained in Ref. 7. The essential modification of the theory is to replace $g(u,y)$ with

$$g'(u, y) = g(u, y)\left\{\frac{2J_1\left[\left(\frac{\pi y u}{1 - u}\right)^{1/2} D\right]}{\left(\frac{\pi y u}{1 - u}\right)^{1/2} D}\right\}^2$$
$$\times \left(\frac{2J_1\left\{\left[\frac{\pi y(1 - u)}{u}\right]^{1/2} t\right\}}{\left[\frac{\pi y(1 - u)}{u}\right]^{1/2} t}\right)^2, \quad (9)$$

where D and t are, respectively, the diameters of the receiver and transmitter normalized to a Fresnel zone for the optical path.
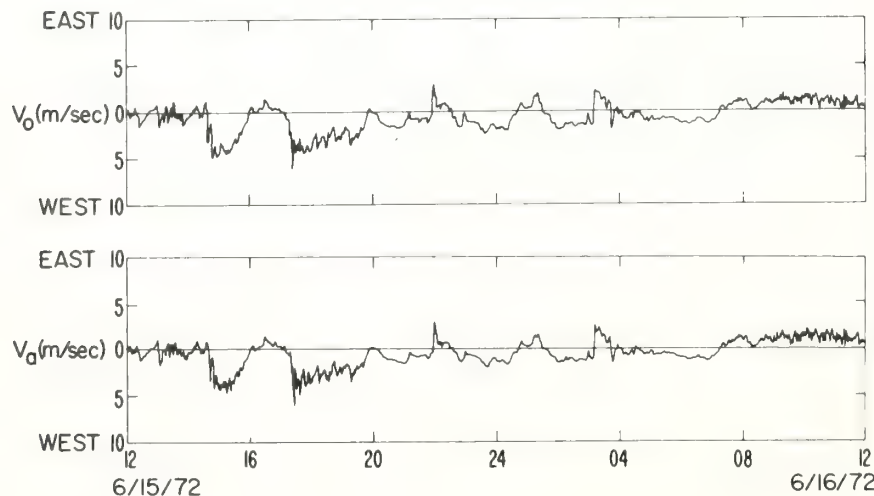
Fig. 2. A comparison of the average wind speed (V_o) measured optically with the average of the readings of six propellor anemometers (V_a) uniformly spaced along the optical path. Both the anemometers and the optical system measure the component of wind that is horizontal and at right angles to the path. The path is 300 m long, oriented north–south, and 3 m above the ground.
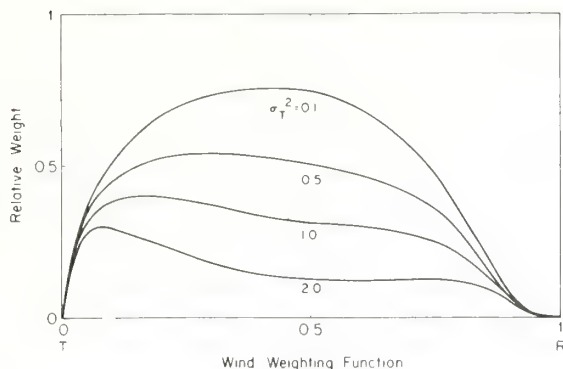
Fig. 3. Weighting functions for wind measurement with the original instrument, as calculated from saturation theory. These curves are calculated vs the integrated amount of turbulence σ_T^2, where $\sigma_T^2 = 0.124k^{7/6}L^{11/6}C_n^2$, k is the wavenumber of the radiation, L is the pathlength, and C_n^2 is the refractive-index variation. A point transmitter and tangent circular receivers, 0.35 Fresnel zone in diameter, are assumed. The slope-wind calibration of the instrument is proportional to the area under the curves. Note the decrease in area at high turbulence levels.

Figure 3 illustrates the wind-weighting functions for our original laser wind sensor as calculated from Eq. (7) after modifying this equation according to Eq. (9). These curves are calculated for a point transmitter and tangent circular receivers 0.35 $(\lambda L)^{1/2}$ in diameter (i.e., $\rho = D = 0.35$) for integrated-turbulence values ranging from $\sigma_T^2 = 0.1$ to $\sigma_T^2 = 2.0$. The slope-wind calibration of the instrument is proportional to the area under the curves. The change in shape of the weighting function and the decrease in area under the curve are pronounced at higher levels of σ_T^2. These effects are easily explained in the context of the earlier theory.[4] For low values of integrated turbulence, the scintillation arising from Fresnel-zone-sized turbulent eddies dominates the scintillation process. In saturation their effect is greatly reduced, and smaller eddies, the size of the wave-coherence length,[8] become more important. This is the reason for the dip in the center region of the weighting function in the saturation region. The Fresnel-zone-sized eddies near the center of the path are no longer most effective for producing scintillation. One way to avoid the difficulties experienced by the original instrument then is to devise an optical system that avoids observing the motion of Fresnel-zone-sized eddies for wind measurement. A system with transmitter and receiver optics more than a Fresnel zone in diameter would satisfy this requirement because it biases the refractive-turbulence weighting toward larger sizes. However, it must be a spatially incoherent system, i.e., the phase coherence over the apertures must be small compared to a Fresnel zone. With a coherently illuminated aperture, small eddies near the transmitter would produce scintillation, and the system would not be biased toward larger size eddies as we require to eliminate the effects of saturation.

In Fig. 4, we show the effects of enlarging the transmitter and receiver apertures. These curves are for a $3(\lambda L)^{1/2}$-diameter incoherent transmitter and tangent receiver apertures that are $\rho(\lambda L)^{1/2}$ in diameter. The solid curves are for $\sigma_T^2 = 0.1$, and the dotted curves are for $\sigma_T^2 = 5$. As suggested by our phenomenological model,[4] the change in shape and area of the curves over large variations in integrated turbulence is quite small, and this difference decreases with increasing aperture size ρ.

Because we have now shown, by the use of the saturation theory, that large aperture systems are nearly immune to the effects of high integrated refractive-index turbulence, we may proceed to calculate weighting functions for various sizes of incoherent transmitters and tangent receivers with the useful constraint that the maximum of the weighting function curves be at midpath. Curves are shown in Fig. 5 for $t = 0, 0.25, 0.5, 1, 2,$ and 4 Fresnel zones. The
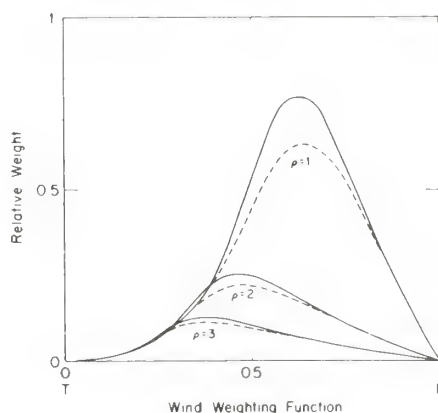
Fig. 4. Weighting functions for wind measurement using an incoherent transmitter, three Fresnel zones in diameter, and tangent receiver apertures, $\rho = 1, 2,$ and 3 Fresnel zones in diameter. The solid curves are for $\sigma_T^2 = 0.1$, and the dotted curves are for $\sigma_T^2 = 5$. The decrease in area under the curves is small even for high values of integrated turbulence.
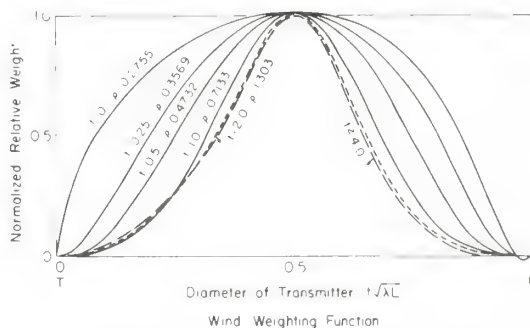
Fig. 5. Weighting functions calculated from first-order theory for various sizes of incoherent transmitters (diameter t Fresnel zones) and tangent receivers (diameter ρ Fresnel zones), with the constraint that the slope of the weighting-function curves be zero at midpath. The plots are normalized to 1 at midpath. Note that for $t > 2$ and $t/\rho = 1.53$, the shape of the weighting function is essentially constant.

47

Fig. 6. The receiving system. Wind speed is computed by the electronics package under the Fresnel lens receivers.

(rather than the logarithm of the irradiance) is used, however, because there is essentially no difference between the two at the low signal variances observed with the larger receiving and transmitting apertures.

The system as outlined cannot discriminate against unwanted stray light (such as lights fluctuating at 120 Hz) as effectively as can a laser system that has interference filters at the receivers. In practice, lights in the field of view of the receivers at about the same range as the light source are not troublesome because they are generally much dimmer. However, light sources near the receivers, but outside the field of view, do provide significant amounts of energy scattered from the Fresnel lenses to the photodiodes. To help eliminate this problem, a second photodiode is placed in the focal plane of the Fresnel lens to observe an area 2.4° from the first. Both photodiodes observe an angular area 0.6° in diameter. By subtracting the signal received by the second photodiode from the first, background light, including light scattered from the Fresnel lens surfaces, is effectively canceled. Obviously, this method does not cancel very bright single lights present only in one of the fields of view, and this situation must be avoided.

Some experimental results are shown in Fig. 7. The solid line is interpolated from the area under the curves of Fig. 3 and predicts the change in calibration that may be expected at high values of σ_T^2, using the original (nonsaturation-resistant) version of the optical wind-measurement system. The circles are values of 1–3-h averages of observations using the original instrument on our 500-m path, 1.5 m above the ground. The agreement with theory is gratifying. Each data point is an average over a σ_T^2 interval of 0.2. The performance of the saturation-resistant system is shown by the crosses and shows no observable decrease in the calibration factor with increasing values of σ_T^2. The square apertures of this system were set as follows: the transmitting aperture 3 Fresnel zones on a side and the adjacent receiving apertures 1.95 Fresnel zones on a side.

required value of ρ for a midpath maximum is also shown. One can see that, for values of $t > 2$, there is essentially no change in the shape of the weighting function. All these curves are normalized to unity at midpath.

III. Implementation

We have constructed an optical wind measurement system based upon these principles and tested it on a 500-m optical path instrumented with ten anemometers aligned to measure the horizontal crosswind component. The system uses a quartz–iodine lamp operating at 12-V dc as a light source. The lamp is at the focus of the Fresnel lens. A photograph of the receiver is shown in Fig. 6. The light is detected by two photodiode detectors at the foci of two adjacent square Fresnel lenses. The instrument analyzes the fluctuations of irradiance at the receiving apertures to obtain the mean crosswind in much the same manner as in Ref. 1. The slope, at zero time delay, of the normalized covariance of the irradiance fluctuations

Fig. 7 Comparison of standard (o) and saturation (+) optical wind-measurement calibration as a function of σ_T^2. The saturation-resistant system used square apertures, with the incoherent transmitters 3 Fresnel zones on a side and the adjacent receivers 1.95 Fresnel zones on a side.

48
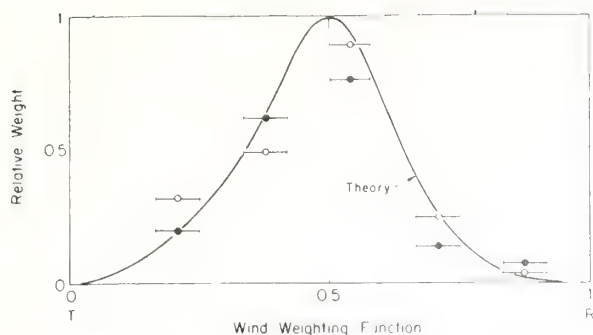
Fig. 8. Experimental wind-weighting function obtained by comparison of the optical measurement over a 500-m path with five pairs of anemometers arranged to measure the horizontal crosswind component. The data from one 25-h run are indicated by the solid data points; open circles are from the second 25-h run. The ends of the horizontal data bars indicate the location of the ten anemometers. The optical system used square apertures, with the incoherent transmitter 3 Fresnel zones on a side and the adjacent receivers 1.95 Fresnel zones on a side. The solid curve is the weighting function for a circular transmitter and receivers, 3, and 1.95 Fresnel zones in diameter, respectively.

The transmitter-to-receiver size ratio was chosen to peak the weighting function at the center of the path according to Fig. 5. The form of this weighting function has been checked experimentally by comparing measurements from the ten anemometers along the path, averaged in groups of two, with the optical reading. (Detailed description for computing the weighting function can be found in Ref. 7.) All sensors were provided with 10-sec time constants; and every 10 sec, a computer sampled the optical system and the output from each of the five anemometers pairs. After thirty-eight 10-sec intervals had elapsed, the computer solved, by least-squares, for the weight that must be applied to each anemometer pair so that the weighted sum of the readings from all anemometers best agreed with the time-varying measurements made by the optical system. The result of such a measurement is shown in Fig. 8. The solid curve is the theoretical weighting function from Eq. (7) for a circular transmitter and receivers, 3 and 1.95 Fresnel zones in diameter, respectively. The experimental results are indicated by the solid and open circles. [We may use the monochromatic theory of Eq. (7), if we interpret λ as the mean wavelength of the incoherent illumination.[7]] The results of two separate runs, each of 25-h duration, are shown by the solid and open circle data points. The ends of the horizontal bars indicate the location of the ten anemometers.

Finally in Fig. 9, we compare the wind measurement from the saturation-resistant optical system with the average of five anemometers, reading the horizontal crosswind component in the middle $\frac{1}{3}$ of the optical path. During this period, $\sigma_T^2 > 1$. The agreement is good, even though the anemometer readings were not weighted according to the expected

weighting function of the optical system, and the experimental unit had square, not round, apertures. The wind-slope calibration has been determined experimentally for the 500-m path. By introducing two square-wave calibrating signals of frequency f_c,[1] in phase quadrature, the system can be calibrated. As shown previously, if the receiver separation and transmitter size are sufficiently larger than a Fresnel zone, the calibration may be stated in terms of receiver separation and transmitter size. For the present system, we determined experimentally that the value of f_c corresponding to a wind speed of 10 m/sec is

$$f_c = (1.6)/d,$$

where $d = \rho(\lambda L)^{1/2}$ is the receiver separation in meters. This determination was made for $\sigma_T^2 \leq 1.2$, $1.3 \leq \rho \leq 2.6$, and for $t = 1.53\rho$.

From information such as that contained in Fig. 4, it can be shown that for $\rho = 1.95$ Fresnel zones, changes in the system calibration will be less than $\pm 3\%$ for $\sigma_T^2 < 5$. Where very high integrated turbulence values along the path are expected, it may be desirable to use larger transmitter size and receiver spacing to account for the increasing scale sizes in the scintillation pattern as σ_T^2 increases.

IV. Conclusions

We have extended the theory of optical wind sensing to the strong integrated refractive turbulence, or saturation, regime. We have shown that the performance-degrading effects of saturation of scintillation on our original laser wind-sensing system may be overcome by redesigning the instrument in a manner suggested by our phenomenological model of saturation. The model has indicated, and our experimental tests have confirmed, that increasing the aperture size of the receivers and illuminating them with light from an extended incoherent source make the system sensitive to such large eddy sizes so that the resultant instrument is nearly immune to changes in refractive-turbulence strength, even well into the saturation regime. The new prototype sensor, based on these design principles, has proven that it will maintain its calibration and wind-weighting function throughout the observed range of integrated-turbulence values.
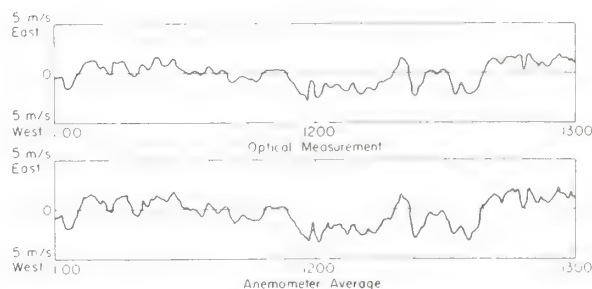
Fig. 9. Comparison of the saturation-resistant system measurement with the average of five anemometers, reading the horizontal crosswind component in the middle $\frac{1}{3}$ of the optical path.

References

1. R. S. Lawrence, G. R. Ochs, and S. F. Clifford, Appl. Opt. **11**, 239 (1972).
2. V. I. Tatarski, *Wave Propagation in a Turbulent Medium* (McGraw-Hill, New York, 1961).
3. V. I. Tatarski, *The Effects of the Turbulent Atmosphere on Wave Propagation*, IPST Catalog 5319 (National Technical Information Service, Springfield, Va., 1971).
4. S. F. Clifford, G. R. Ochs, and R. S. Lawrence, J. Opt. Soc. Am. **64**, 148 (1974).
5. A. N. Kolmogoroff, *Turbulence, Classic Papers on Statistical Theory*, S. K. Friedlander and L. Topper, Eds. (Interscience, New York, 1961), p. 151.
6. S. F. Clifford, *Remote Sensing of the Troposphere*, V. E. Derr, Ed. (U.S. Government Printing Office, Washington, D.C., 1972), Chap. 11.
7. S. F. Clifford, G. R. Ochs, and Ting-i Wang, NOAA Tech. Rept. *ERL 312-WPL 35* (U.S. Government Printing Office, Washington, D.C., 1974).
8. S. F. Clifford and H. T. Yura, J. Opt. Soc. Am. **64**, 1641 (1974).

Refractive-turbulence profiles measured by one-dimensional spatial filtering of scintillations

G. R. Ochs, Ting-i Wang, R. S. Lawrence, and S. F. Clifford

Stellar scintillations, when appropriately analyzed, yield information about the turbulence throughout the atmosphere. We describe an instrument involving a 36-cm telescope and an on-line minicomputer that provides, after 20 min of observation, the refractive-turbulence profile of the atmosphere. The height resolution is sufficient to divide the atmosphere into about four independent regions. The principal limitation to greater accuracy and resolution is the nonstationary behavior of the atmosphere during the 20-min observing period.

I. Introduction

Atmospheric turbulence-induced optical scintillations have long been a problem to astronomical observations. However, it has also been realized that observations of the twinkling of stars and the motion of stellar images yield information about the turbulence and the wind speed in the upper atmosphere.[1-9] As early as 1897, Douglass[1] reported that he was able to deduce the altitude of the atmospheric currents by observing the stellar scintillation in the vicinity of the focal plane of a telescope. He also mentioned that the direction and the speed of the atmospheric currents could be determined, although no quantitative results were given. In 1925, Pickering[2] described some features of shadow bands he had observed in 1878: "... that the irregular shadows produced by the hot air currents near at hand were much finer and more sharply marked than those produced by the currents acting at a greater distance." Again, no quantitative results were recorded. In recent years, renewed interest has been shown[3-17] in deducing the turbulence intensity and the wind speed high in the troposphere from ground-based measurement of stellar scintillation. Protheroe[4] presented some quantitative values of the height, speed, and direction of tropospheric winds from observing the motion and structure of stellar shadow-band patterns. His results seemed to agree as well as could be expected with raw-insonde measurements taken some distance away. Townsend[5] extended Protheroe's analysis to obtain the fluctuation of velocity and temperature in the troposphere. Roddier and his colleagues[6-8] used the spa-

tio–temporal and spatio–angular correlation of the scintillation of a single star to deduce the altitude, the turbulence intensity, and the wind speed of a turbulent layer. They are also able to separate the contributions from more than one turbulent layer; and, with the help of meteorological wind-sounding data, the altitudes of the different layers could be determined.

More recently, considerable attention has been devoted to deducing the vertical profile of refractive-index turbulence from ground-based measurements of stellar scintillations.[8-17] Though Peskoff[10,11] and Fried[12] pointed out that the exact profile can be obtained theoretically under certain assumptions, their proposed methods ignore the practical problems of sensitivity to experimental errors and nonstationarity of the atmosphere. More careful theoretical studies[13-15] have shown that these problems would severely limit the remote probing performance of their methods. Ochs et al.[16] have discussed the feasibility of using either a single star or a double-star pair as the light source to obtain the vertical profile of the atmospheric turbulence. Roddier and his colleagues[8,9] were able to monitor as many as three turbulent layers, obtaining $C_n{}^2$ and the altitude of each layer, between 2 km and 20 km by use of a double-star pair as the source. However, in their measurements of $C_n{}^2$, they had to assume the thickness of the turbulent layer. Wang et al.[17] have discussed a crossed-path technique to obtain the profile by using two stars as sources. Relatively good path resolution has been obtained with horizontal-path simulation experiments.

Although there are definite advantages to using a double star as a source,[16,17] there are a few useful double stars in the sky. Because of this limitation, it seemed worthwhile to build a single-star instrument, even though the altitude resolution cannot be so good as might be obtained from the crossed-path method using

The authors are with National Oceanic and Atmospheric Administration, Boulder, Colorado 80302.

51

a double-star pair. We discuss here a technique for measuring the vertical profile of refractive-index turbulence by using a single star as a source and a spatially filtered detector as a receiver.

The general philosophy of our approach is to view the spatial structure of the stellar scintillation pattern through filters that pass only a narrow band of spatial frequencies. By running many such signals through filters of different spatial wavelength and combining the outputs with appropriate weights, we obtain a set of reasonably sharp-peaked path-weighting functions centered at different heights; and this gives us a measurement of the vertical turbulence profile.

II. Theory

We assume that the star irradiance I, perturbed by the atmospheric turbulence and received on the ground, can be decomposed into a fluctuating part I' and a mean irradiance $\bar{I}$. Then the variance of the filtered intensity scintillation normalized to the mean irradiance is defined by

$$\sigma_{I_f}^2$$
$$= \left\langle \frac{\int_{-D/2}^{D/2} I'(x') \cos(2\pi x'/d)dx' \int_{-D/2}^{D/2} I'(x'') \cos(2\pi x''/d)dx''}{\int_{-D/2}^{D/2} \bar{I}dx' \int_{-D/2}^{D/2} \bar{I}dx''} \right\rangle,$$
$$(1)$$

when we use a one-dimensional sinusoidal spatial filter of length D and wavelength d. The brackets denote an ensemble average. The denominator of Eq. (1), assuming statistical homogeneity of I in the receiving plane, is simply $D^2\bar{I}^2$. Hence Eq. (1) can be simplified to

$$\sigma_{I_f}^2 = D^{-2} \int_{-D/2}^{D/2} dx' \int_{-D/2}^{D/2} dx'' \cos(2\pi x'/d)$$
$$\times \cos(2\pi x''/d)C_I(x'-x''). \quad (2)$$

In Eq. (2), C_I is the covariance of the unfiltered irradiance scintillation given in the weak scattering limit by[18]

$$C_I(x'-x'') = \langle I'(x')I'(x'')\rangle/\bar{I}^2$$
$$= 0.528\pi^2 k^2 \int_0^\infty dz C_n^2(z) \int_0^\infty dK K^{-8/3} \sin^2[K^2 z/(2k)]$$
$$\times J_0[K(x'-x'')], \quad (3)$$

where $k = 2\pi/\lambda$, λ is the wavelength of the incident starlight, and K is a two-dimensional spatial wavenumber. (Stellar scintillations observed near the zenith are sufficiently weak that we may use the first-order scattering theory of Tatarskii.[18]) The function J_0 is a Bessel function of the first kind of order zero. In Eq. (3) we have inserted the well-known turbulence spectrum suggested by Kolmogorov,[19]

$$\Phi_n(K) = 0.033 \, C_n^2 K^{-11/3}; \, L_0^{-1} \ll K \ll l_0^{-1}, \quad (4)$$

where C_n^2 is the structure constant of the atmospheric refractive-index fluctuations and l_0 and L_0 are, respectively, the microscale and outer scale of turbulence that define the inertial subrange.

To simplify Eq. (2), we make the change of variables from x',x'', to $\xi = x' - x''$ and $2\eta = x' + x''$. The integration over η can be performed easily and reduces Eq. (2) to

$$\sigma_{I_f}^2 = (1/D) \int_0^D d\xi C_I(\xi) \left\{ \frac{\sin[K_0(D-\xi)]}{K_0 D} \right.$$
$$\left. + (1 - \xi/D) \cos(K_0\xi) \right\}, \quad (5)$$

where $K_0 = 2\pi/d$. There is a useful identity[16] that, substituted into Eq. (3), permits the ξ integration to be performed easily, viz.,

$$J_0(K\xi) = \pi^{-1} \int_{-\infty}^\infty dK'(K^2 - K'^2)^{-1/2}$$
$$\times \exp(iK'\xi); 0 < |K'| < |K|. \quad (6)$$

After substituting Eq. (3) into Eq. (5) and integrating over ξ, we obtain

$$\sigma_{I_f}^2 = 0.264\pi k^2 \int_0^\infty dz C_n^2(z) \int_0^\infty dK'$$
$$\times \left\{ \frac{\sin[(K_0 - K')D/2]}{(K_0 - K')D/2} + \frac{\sin[(K_0 + K')D/2]}{(K_0 + K')D/2} \right\}^2$$
$$\times \int_{K'}^\infty dK K^{-8/3}(K^2 - K'^2)^{-1/2} \sin^2[K^2 z/(2k)]. \quad (7)$$

Making the change of variables $y = K'/K_0$, $u^2 = (K^2/K'^2) - 1$ and defining the parameters $\beta = D/d$ and $x = \pi z\lambda/d^2$, we may write Eq. (7) in the form of a weighting function, i.e.,

$$\sigma_{I_f}^2 = \int_0^\infty dz C_n^2(z) W(z), \quad (8)$$

where

$$W(z) = (0.528\pi^2 k^2/D)$$
$$\times \int_0^\infty dy \beta \left[\frac{\sin[\pi\beta(y-1)]}{\pi\beta(y-1)} + \frac{\sin[\pi\beta(y+1)]}{\pi\beta(y+1)} \right]^2$$
$$\times (K_0 y)^{-8/3} W_0(xy^2), \quad (9)$$
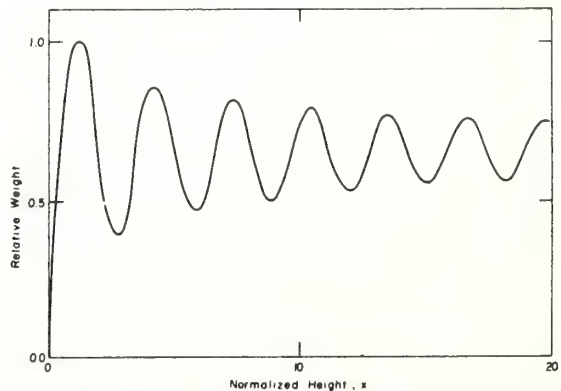
Fig. 1. Weighting function of an infinite linear array of detectors observing the scintillations of a monochromatic plane wave source. The relative weight is shown as a function of normalized height $x = \pi z \lambda^2/d$, where z is the height of the turbulence and d is the spatial wavelength of the array of detectors.

52
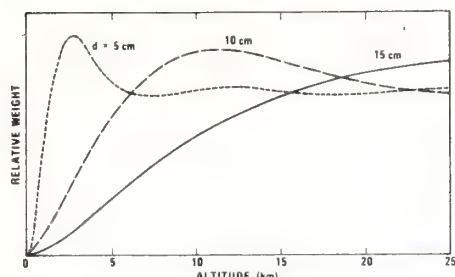
Fig. 2.   Weighting function of a finite linear array of detectors (array length = 35.6 cm) observing stellar scintillations for various spatial wavelengths d.   The finite bandwidth of the light source has been included.

and W_0 is the weighting function when $D \to \infty$, given by

$$W_0(x) = \int_0^\infty du(1 + u^2)^{-11/6} \sin^2[x(1 + u^2)]. \quad (10)$$

III.   Path-Weighting Function

For a monochromatic source and an infinitely long spatial filter at the receiver, the path-weighting function is given by Eq. (10).   The relative weight is shown in Fig. 1 as a function of normalized height $x = \pi z \lambda^2/d$.   Because a star is a broadband source, the path-weighting function must be averaged over the bandwidth of the detected signal, which is mainly limited by the response of the photomultiplier (PM) tube.   We assume that the response follows a Gaussian curve centered at λ_0 with standard deviation σ_λ.   Then the broadband path-weighting function is given by

$$W'(z) = (\pi/2)^{-1/2}\sigma_\lambda^{-1}\{1 + \Phi[\lambda_0/(\sqrt{2}\sigma_\lambda)]\}^{-1}$$

$$\times \int_0^\infty d\lambda W(z) \exp[-(\lambda - \lambda_0)^2/2\sigma_\lambda^2], \quad (11)$$

where Φ is the error function.

For our experimental setup the parameters of the PM tubes are $\lambda_0 = 0.4$ μm and $\sigma_\lambda = 0.1$ μm.   We use a 35.6-cm Schmidt-Cassegrain telescope, so the parameter β in Eq. (9) is equal to 35.6/d, where d is the spatial wavelength of the receiver in centimeters.   Inserting Eq. (9) into Eq. (11) we can obtain, for the above parameters, the path-weighting functions for different spatial wavelengths, as shown in Fig. 2.   The oscillation seen in Fig. 1 is smeared out because of the broadband effect.

It is clear that for smaller spatial wavelengths there is more contribution from the lower atmosphere.

The weighting functions shown in Fig. 2 are good enough to measure the average turbulence strength above a certain scale height.   However, the height resolution is too poor to measure directly the vertical profile of turbulence.   To improve the height resolution, we measure the variance of the signal at many different spatial wavelengths.   Combining them all with appropriate weights, we obtain a set of reasonably sharp-peaked path-weighting functions centered at different heights; and we are able to measure the vertical turbulence profile.

The composite path-weighting function is given by

$$W_c(z) = \sum_{i=1}^{N} R_i K_i^{8/3} W'(z,d_i), \quad (12)$$

where N is the number of different wavelengths used, R_i is the appropriate weight given to the ith spatial wavenumber $K_i = 2\pi/d_i$, and d_i is the ith spatial wavelength.   Restricting ourselves to $N \le 3$, we obtained, by trial and error, a family of seven weighting functions peaked at different heights from 2.25 km to 14.5 km and above (see Fig. 3).   The peak altitude, the three spatial wavelengths d_i needed for each linear combination, and the relative weights R_2 and R_3 ($R_1 \equiv$ 1) are shown in Table I.   It is clear, from Fig. 3, that the height resolution becomes poorer at higher altitude.   We could, in principle, obtain a sharper weighting function by combining more than three spatial wavelengths, but we would then need a higher accuracy for the measurements.   So we restrict the number of linear combinations to three or less.   From this information we obtain data from four independent layers (e.g., the odd-numbered Ws).   Some redundancy is provided by
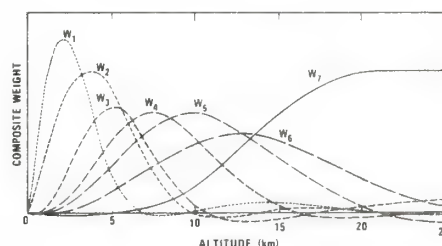
Fig. 3.   Composite path-weighting functions obtained by linearly combining weighting functions at three different spatial wavelengths (see text and Table I for details).

Table I.   The Peak Altitudes and Relative Inverse Areas [see Eq. (14)] of Each of the Seven Weighting Functions W_i shown in Fig. 3

	W_1	W_2	W_3	W_4	W_5	W_6	W_7
Peak altitude (km)	2.25	3.75	5.25	7.5	9.75	12.75	>14.5
$B \times 10^{14}$	2.39	1.91	2.57	1.84	1.38	1.46	0.87
d_1 (cm)[a]	5	6.5	7	8.5	10	11.5	14
d_2 (cm)	8	9	5	6	6.5	7.5	9
d_3 (cm)	15	15	11	13	15	15	7
R_2	−0.65	−0.6	−0.38	−0.35	−0.27	−0.24	−0.73
R_3	−0.33	−0.36	−0.53	−0.56	−0.66	−0.67	+0.23

[a] The d_i are the spatial wavelengths that must be combined to produce each W, the relative weights being R_2 and R_3 ($R_1 \equiv$ 1).

53
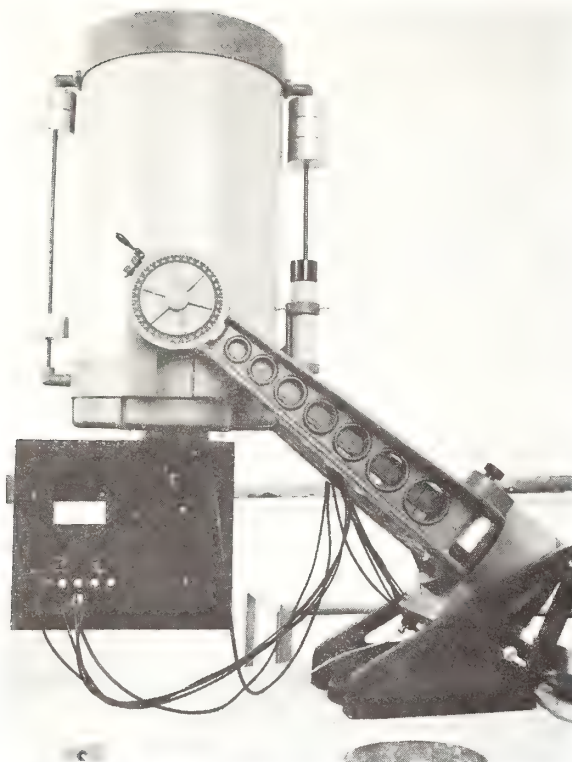
Fig. 4. The telescope and the attached instrument box.

calculating C_N^2 for seven heights, because these measurements are not independent.

The C_n^2 of each measurement can be expressed as

$$C_n^2 = B \sum_{i=1}^{N} R_i K_i^{8/3} \sigma_{I_f}^2(d_i),$$
(13)

where

$$B = 1.87 \times 10^{-13} \left[\int_0^\infty dz\, W_c(z) \right]^{-1}.$$
(14)

In Eqs. (13) and (14), C_n^2 is in m$^{-2/3}$, K_i is in cm^{-1}, z is in km, and $\sigma_{I_f}^2(d_i)$ is the normalized irradiance variance detected by a one-dimensional spatial filter with spatial wavelength d_i. By measuring the areas under the curves shown in Fig. 3 (for W_7, we cut it off at 25 km), we obtain the calibration factor B shown for each layer in Table I.

IV. Profiling Instrument

We have developed a system that uses a spatial filtering technique and makes an on-line computation of the refractive-index profile. An instrument package attached to a 35.6-cm Schmidt-Cassegrain telescope (Fig. 4) sequentially measures the normalized standard deviation of the irradiance scintillation at different spatial wavelengths and converts this information to electrical signals, which are fed to a minicomputer. After a series of measurements are completed at spatial wavelengths from 5 cm to 15 cm, the computer is programmed to compute values of C_n^2 at seven ranges from the instrument.

The instrument package contains the optical spatial filter and the electronics shown in Fig. 5. The optical spatial filter is formed by placing a reticle, consisting of aluminized stripes 0.5 mm wide on 1.0-mm centers, outside the focus of the telescope. The starlight passing between the stripes is collected by one PM tube, while that reflected from the stripes is directed to the other tube. The reticle is angled slightly with respect to the telescope optical axis so the reflected light may be directed to the second tube by an off-axis mirror. By subtracting the electrical output of one tube from that of the other, we form a spatial filter that is sensitive to only one narrow band of spatial wavelengths in the scintillation pattern incident upon the telescope aperture. The spatial harmonics generated by the sharp edges of the strips make a negligible contribution because the energy contributed from higher wavenumbers falls off according to the Kolmogorov spectrum [Eq. (4)].

The wavelength d sensed by the spatial filter is $d = d'F/f$, where d' is the spatial wavelength of the reticle, F is the focal length of the telescope, and f is the telescope focus-to-reticle distance. This wavelength is changed by varying f continuously with the motor-driven reticle mount. The electrical output of the filter is a fluctuating signal whose frequency content is determined by scintillation pattern movement relative to the orientation of the filter. We are interested only in the amplitude of the signal; however, the frequency spectrum of the signal will affect the observed amplitude if it extends outside the electrical passband of the system. For this reason we rotate the reticle continuously so the filter measures at all angles with respect to the direction of movement of the scintillation pattern.

We wish to measure σ_{I_f} (Eq. 1), which, in terms of measured quantities, is

$$\sigma_{I_f}^2 = \left[\overline{\left(\frac{I_1'}{\bar{I}_1} - \frac{I_2'}{\bar{I}_2} \right)^2} \right]^{1/2}.$$
(15)

Here $\bar{I}_1$ and I_1' are the mean and fluctuating part of the signal from PM tube 1 and $\bar{I}_2$ and I_2' are the same for PM tube 2. For $I_1'/\bar{I}_1 \ll 1$, $I_2'/\bar{I}_2 \ll 1$, and with high pass filtering of the difference signal, it can be shown that

$$\sigma_{I_f} \approx \{\overline{[\ln(\bar{I}_1 + I_1') - \ln(\bar{I}_2 + I_2')]^2}\}^{1/2}$$
(16)

with negligible error. We choose to measure σ_{I_f} by the
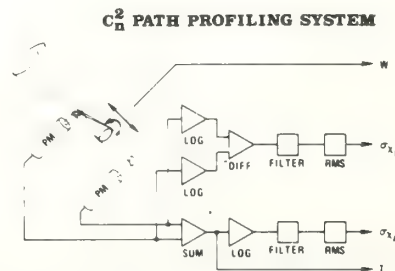
Fig. 5. Schematic of the optical spatial filter and the electronics.
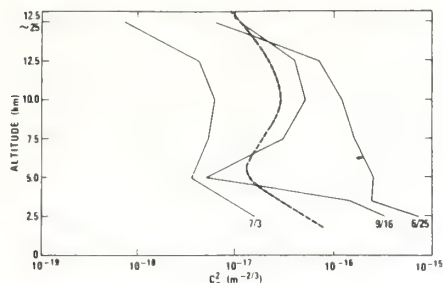
Fig. 6. Typical optically measured C_n^2 vertical profiles at Boulder, Colorado. Each curve is the average of the measurements of a single evening. The dashed line represents the statistical average profile of Hufnagel's latest model.

differencing method described in Eq. (16) because the differencing procedure improves dynamic range and stability. It is particularly important that the circuit be insensitive to gain differences of the optical and electronic circuits between PM tube 1 and PM tube 2, since a gain balance cannot be maintained in all positions as the reticle rotates and translates. We obtain a voltage proportional to σ_{I_f} by using analog circuitry (Fig. 5) to take the difference of the logarithms of signals 1 and 2. We bandpass-filter (6–900 Hz) that voltage and obtain the 1-sec rms average. The measured σ_{I_f} is then insensitive to both the gain of the system and the mean intensity of the starlight. The bandpass ratio is a compromise between wind speed range and SNR, and the range chosen covers atmospheric wind speeds from approximately 0.9 m/sec to 45 m/sec. The low frequency cutoff is also determined by the necessity of removing any signal fluctuations due to reticle movement.

We compute σ_I, the log-irradiance standard deviation of the whole aperture, by taking the logarithm of the sum of PM tube signals 1 and 2, bandpass filtering (6–900 Hz), and obtaining the 1-sec rms average.

The instrument package supplies four signal voltages to the minicomputer. They are proportional to the following:

σ_{I_f}, the fractional standard deviation of the spatially filtered signal as defined by Eq. (7),
d, the wavelength of the spatial filter,
σ_I, the log-irradiance standard deviation of the whole telescope aperture,
I, the irradiance of the whole telescope aperture.

From the first three inputs we calculate a C_n^2 profile according to the theory presented earlier. The fourth input (I) is used to set signal levels, monitor the guiding of the telescope, and provide a record if clouds obscure the star. The log-irradiance standard deviation of the whole aperture σ_I is a weighted measurement of the refractive-index turbulence, which approximately covers the region over which the instrument profiles C_n^2. Though, in principle, this measurement is not needed to compute C_n^2 profiles, we have found it allows us to compensate partially for the nonstationarity of the atmosphere during the 20-min measurement cycle. This compensation is accomplished by continuously

multiplying $\sigma_{I_f}^2$ by the factor $\overline{\sigma_I^2}/\sigma_I^2$, where $\overline{\sigma_I^2}$ is the mean of σ_I^2 over the 20-min measurement cycle.

Even with this correction, the largest error arises from atmospheric nonstationarity. We obtain a relative measure of nonstationarity, and hence profile quality, by calculating the fractional standard deviation of 24-sec averages of σ_I^2 over the measurement cycle.

One-second samples of σ_{I_f}, d, σ_I, and I are digitized. From this information, the computer forms 24-sec averages of $\sigma_{I_f}^2 d^{-8/3}$, d, σ_I^2, and I. The 24-sec average is necessary because that is the period of one revolution of the reticle. To suppress measurement noise, we use a triangular smoothing window (with halfwidth = 2 cm] centered at the required spatial wavelength (shown in Table I) to obtain $\sigma_{I_f}^2$ at that spatial wavelength and compute C_n^2 at seven ranges according to the theory presented in Sec. II.

V. Experimental Results

The instrument described in the previous section is designed for use with stars of second magnitude or brighter. To guarantee enough SNR, we first pointed the telescope to a zero magnitude star, Vega. The measurement was taken at Table Mountain, a mesa located 12 km north of Boulder, Colorado. Some measurements of the typical C_n^2 vertical profiles are shown in Figs. 6 and 7. Each curve represents an average of the measurements of a single evening. Variations from night to night are large, extending over a range of one hundred to one. The dashed line represents the statistical average profile of Hufnagel's latest
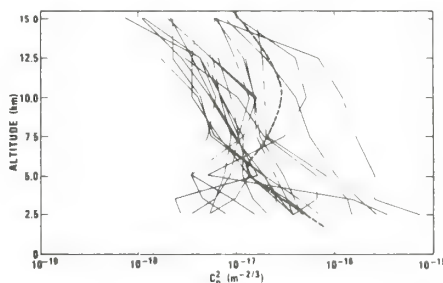
Fig. 7. More measurements of C_n^2 profiles at Boulder, Colorado. Each curve is the average of the measurements of a single evening. The dashed line represents the statistical average of Hufnagel's latest model.
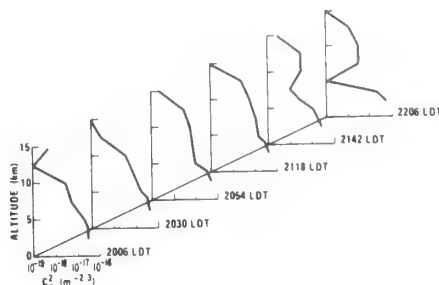
Fig. 8. Typical variation of the vertical C_n^2 profile in a single evening.

55
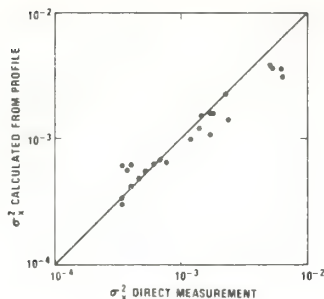
Fig. 9. A comparison between direct measurements of the whole aperture log-amplitude variance and calculations based on the measured C_n^2 profiles.
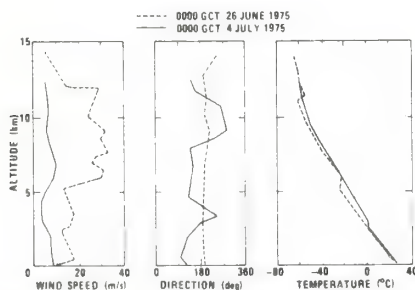
Fig. 10. Rawisonde measurements of wind speed, wind direction, and temperature taken at Denver.

model.[20] Our measurements show general agreement with this model. Since we are in the lee of the Rocky Mountains where mountain-wave effects are common, we expect to see large night to night variations of the vertical C_n^2 profile. The typical variation over a period of 2½ h in a single evening is shown in Fig. 8. We see that there are noticeable changes within a couple of hours.

It is difficult to compare quantitatively our measurements to other independent simultaneous measurements. However, a self-comparison is possible. When we were measuring the spatially filtered intensity scintillations, we also measured the variance of the whole-aperture scintillation of the telescope. We can calculate the expected log-amplitude variance of the whole aperture scintillation by inserting the measured C_n^2 profile into the following equation[16]:

$$\sigma_\chi^2 = 0.132\pi^2 k^2 \int_0^\infty dz C_n^2(z) \int_0^\infty dK K^{-8/3} \sin^2(K^2 z/2k)$$
$$\times \left[\frac{2J_1(KD/2)}{KD/2} \right]^2, \quad (17)$$

where D is the diameter of the telescope and $\sigma_I^2 = 4\sigma_\chi^2$. (It can be shown that the hole in the middle of a Schmidt-Cassegrain telescope has a negligible effect on the log-amplitude variance of the whole aperture scintillation.) The results of the calculated variances compared with the direct measurements are shown in Fig. 9. The agreement is encouraging evidence that the spatial filters and detectors worked as expected.

We picked the measurements of two nights, one with

a strong turbulence profile (25 June 1975) and the other with a weak turbulence profile (3 July 1975) (see Fig. 6), for comparison with rawinsonde data taken at Denver at 0000 GCT, 26 June 1975 and 0000 GCT, 4 July 1975, respectively (see Fig. 10). Unfortunately the National Weather Service measurements occurred several hours before our own and are taken more than 60 km away; hence a quantitative comparison is impossible. However, we note that during the night of 25–26 June both the wind-shear and the temperature gradient are larger than on the night of 3–4 July. We expect a strongly turbulent atmosphere on the evening of 25 June and a relatively weak turbulent atmosphere on the evening of 3 July, and this agrees with our measurements.

A different qualitative comparison between the optical measurements and the rawinsonde measurements has been suggested by Hufnagel.[21] By inserting the wind speed profiles measured by the rawinsonde into Hufnagel's latest model,[20] the vertical C_n^2 profiles can be obtained for each evening.

Four particular evenings with a variety of turbulence strengths have been chosen for such a comparison. The results are plotted in Fig. 11. The crosses represent the optical measurements, and the smooth curves denote the model C_n^2 profiles. Again, a quantitative comparison is impossible because the measurements differ in time and in location. However, the general qualitative agreement is remarkable, especially for heights above 5 km. For the evenings of 24 June, 28 August, 22 September, and 3 July, C_n^2 increases sequentially for both the optical as well as the model profiles. Although the optical profiles have higher values of C_n^2 than the Hufnagel prediction, this result could well be due to the measurement location in the lee of the Rocky Mountains. Nevertheless, the night-to-nght differences, predicted and measured, are similar.

VI. Conclusions

We have demonstrated that the vertical C_n^2 profile of the atmosphere can be measured by observing the turbulence-induced optical scintillation of a single star
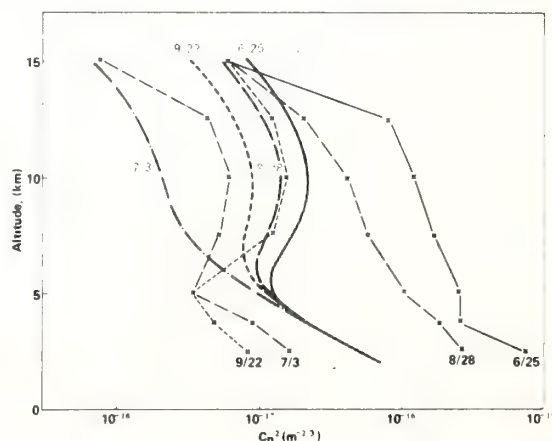
Fig. 11. Comparison of optical measurements (x) and the Hufnagel model (smooth curves) that results from using the wind speed profiles measured by the rawinsonde.

with a ground-based spatially filtered telescope. The whole atmosphere can be divided into four nearly independent layers. This is an accurate, practical, inexpensive, and potentially useful device to measure the vertical turbulence profile, provided that a high altitude resolution is not required.

References

1. A. E. Douglass, *Popular Astronomy* (1897). Reprinted in *Amateur Telescope Making* (*Book Two*) (Scientific American, Inc., New York, 1957), p. 585.
2. W. H. Pickering, Pop. Astron. **33,** 1 (1925).
3. F. Gifford and A. H. Mikesell, Weather **8,** 195 (1953).
4. W. M. Protheroe, Q. J. R. Meteorol. Soc. **90,** 27 (1964).
5. A. A. Townsend, Q. J. R. Meteorol. Soc. **91,** 1 (1965).
6. J. Vernin and F. Roddier, J. Opt. Soc. Am. **63,** 270 (1973).
7. C. Roddier and F. Roddier, J. Opt. Soc. Am. **63,** 661 (1973).
8. A. Rocca, F. Roddier, and J. Vernin, J. Opt. Soc. Am. **64,** 1000 (1974).
9. J. Vernin and F. Roddier, C. R. Acad. Sci. (Paris) **280** 463 (1975).
10. A. Peskoff, J. Opt. Soc. Am. **58,** 1032 (1968).
11. A. Peskoff, TRW Systems, Tech. Rept. 99900-6692-R0-00 (1968).
12. D. L. Fried, Proc. IEEE **57,** 415 (1969).
13. L. C. Shen, IEEE Trans. Antennas Propag. **AP-18,** 493 (1970).
14. J. W. Strohbehn, J. Opt. Soc. Am. **60,** 948 (1970).
15. J. W. Strohbehn, Boundary-Layer Meteorol. **3,** 476 (1972).
16. G. R. Ochs, S. F. Clifford, R. S. Lawrence, and Ting-i Wang, NOAA Tech. Rept. *ERL 397-WPL 30* (Government Printing Office, Washington, D.C., 1974).
17. Ting-i Wang, S. F. Clifford, and G. R. Ochs, Appl. Opt. **13,** 2602 (1974).
18. V. I. Tatarskii, *Wave Propagation in a Turbulent Medium* (McGraw-Hill, New York, 1961).
19. A. N. Kolmogorov, Dokl. Akad. Nauk SSSR **30,** 299 (1941).
20. R. E. Hufnagel, in *Digest of Topical Meeting on Optical Propagation Through Turbulence* (Optical Society of America, Washington, D.C., 1974).
21. R. E. Hufnagel, Perkin-Elmer Corp.; private communication (1976).

Limitations of cloud droplet size distribution by Backus-Gilbert inversion of optical scattering data

Madison J. Post

National Oceanic and Atmospheric Administration, Environmental Research Laboratories, Wave Propagation Laboratory, Boulder, Colorado 80302
(Received 22 September 1975)

The feasibility of using the Backus-Gilbert inversion technique to recover size distributions of water droplets in clouds from laser scattering data is investigated. The set of multiparameter lidar returns that yields the best inversion is a polarized set taken at multiple scattering angles. For the type of distributions found in natural clouds, experimental noise effects are minimal, but the small size portion of the spectrum is not well recovered because of low scattered intensity and large spread in the recovery function's resolution. However, recovery of precisely known, but less extensive distributions of cloud-sized water droplets is demonstrated for laboratory data.

Westwater and Cohen[1] first investigated the application of the Backus-Gilbert inversion technique[2] to the recovery of size distributions from optical scattering measurements. In theory they found that the technique was useful for multispectral data from narrow size distributions.

This work is a continuation of their studies. It investigates the feasibility of using the technique for a wider range of distributions—in particular for cloud-type water droplet distributions—and for multiangular as well as multispectral polarized data. In addition, laboratory data are taken from precisely known distributions, and they are accurately inverted.

I. SUMMARY OF THE BACKUS-GILBERT INVERSION TECHNIQUE

The Backus–Gilbert technique is applicable to linear inverse problems that take the form

$$g_i = \int_a^b w_i(r)f(r)\,dr + \epsilon_i, \quad i = 1, 2, \ldots, n, \tag{1}$$

where g_i is the ith of n physical measurements, ϵ_i is the noise included in the measurement, $w_i(r)$ is a known "weighting function," and $f(r)$ is the function to be recovered.

For the optical scattering case, the i's represent measurements taken at different angles, different frequencies, different polarizations, or any combination of these parameters. The weighting function $w_i(r)$ is the scattered intensity for a single particle of radius r. It is known from Mie theory for spherical shapes, as in water droplets; for irregular shapes, it may be known empirically. The size distribution $f(r)$ for $a \le r \le b$ is to be determined from a multiparameter set of measurements g_i.

It is known that

$$f(r_1) = \int_a^b \delta(r - r_1)f(r)\,dr \quad, \tag{2}$$

where $\delta(r - r_i)$ is the Dirac delta function. The Backus-Gilbert method finds a set of coefficients b_{i1} forming an averaging kernel K_1 which in some sense approximates a delta function at r_1:

$$K_1 = \sum_{i=1}^n b_{i1}w_i(r) \approx \delta(r - r_1). \tag{3}$$

Then, using that same set,

$$\sum_{i=1}^n b_{i1}g_i = \int_a^b \left(\sum_{i=1}^n b_{i1}w_i(r)\right) f(r)\,dr \simeq f(r_1) \tag{4}$$

by (2) above.

To investigate another radius r_2, a different set of coefficients b_{i2} is found such that

$$\sum_{i=1}^n b_{i2}w_i(r) \approx \delta(r - r_2) \quad. \tag{5}$$

With a sufficient number of coefficient sets one may then recover the entire distribution $f(r)$, $a \le r \le b$.

The recovery is complicated by the noise ϵ_i and the fact that the kernels do not perfectly simulate delta functions. In practice these difficulties are quantified by defining variance and spread. Variance is a measure of the range in the recovered value for f due to the statistical variation of measurement errors. Spread is a measure of the resolution inherent in a peaked function, defined so that the function's equivalent rectangle (that is, of equal peak height and area) is of width given by the spread.

It is found that the only way to decrease the variance is to increase the spread. Thus a compromise must be effected, and this is facilitated by choosing a point on a tradeoff curve which is parameterized by γ. A value for γ of 0° represents minimum spread in K_k and $\gamma = 90°$ represents minimum variance (see Fig. 1).

The mathematical technique for determining the inversion coefficients b_{ik}, and therefore the kernels K_k, may be found in the work by Westwater and Strand.[3] Note that this technique requires no *a priori* information about the form of $f(r)$, and that absolute, not relative, number densities are determined.

II. NATURE OF THE KERNELS

For this study, the weighting functions $w_i(r)$ were generated using Dave's[4] Mie scattering program. Thes were calculated for each 0.1 μm increment in radius in the range 0.1–30.4 μm, at each of 16 scattering angles, $135° \le \theta \le 150°$. The five values in each 0.5 μm increment were then averaged and normalized by $\lambda^2/4\pi$ to represent the value of $w_i(r)$ for that range. This process was repeated for two polarizations—one perpendicular to the scattering plane and one lying in
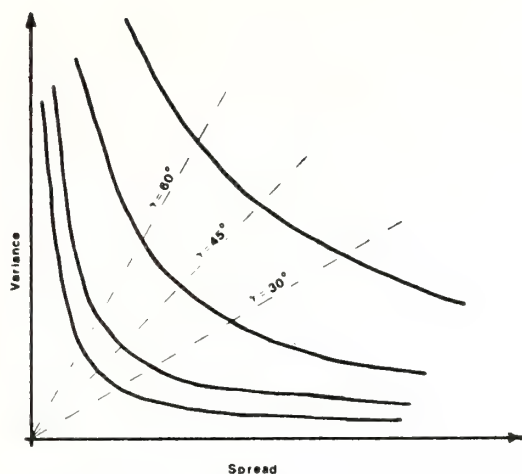
FIG. 1. Tradeoff curves for different sets of scattering parameters.
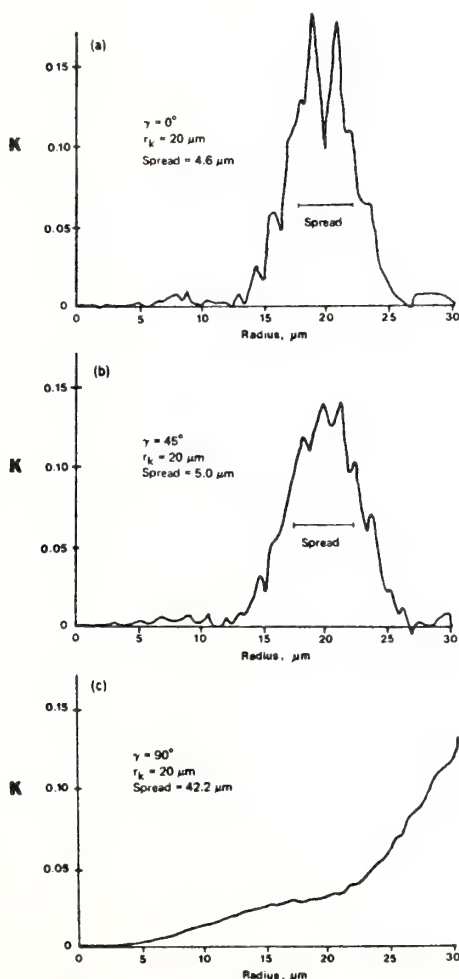
FIG. 2. Averaging kernels for different choices of tradeoff parameter γ, $r_k = 20\mu m$.
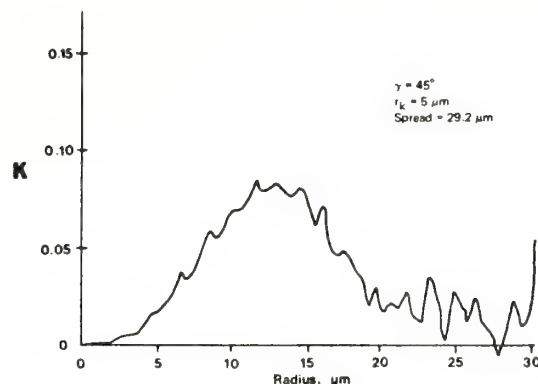
FIG. 3. Averaging kernel for $\gamma = 45°$, $r_k = 5$ μm.

it—for nine wavelengths across the visible spectrum. The range in the parameter θ was chosen to correspond to an observed peak in the scattering functions which also would allow for a realistic bistatic configuration in a field system.

These functional values were then used in Westwater and Strand's[3] Backus-Gilbert program to produce the inversion coefficients b_{ik} and kernels K_k at $r_k = 5$, 10, 15, 20, 25, and 30 μm for avrious choices of tradeoff parameter γ. The program also graphs the averaging kernels for various points on the tradeoff curve and outputs the spreads and variances for different choices of relative error on the signal.

With the Backus-Gilbert technique one can achieve physical insight by examining the details of the kernels K_k. Different sets of inversion coefficients, together with their corresponding kernels, are generated at a particular r_k for different points chosen on the tradeoff curve. One normally uses a point well removed from the end points of the tradeoff curve as the best compromise between sensitivity of the result to experimental errors (variance) and narrowness of the size interval over which f is determined (spread). In this work, however, it was found appropriate under some circumstances to use the $\lambda = 0°$ solution.

Averaging kernels for $r_k = 20$ μm and $\lambda = 0°$, 45°, and 90° are shown in Figs. 2(a)–2(c), along with integral properties of these approximations to delta functions. Note the combined smoothness and accuracy of the $\gamma = 45°$ kernel compared with the others. These functions are typical of those generated by this technique for the weighting functions encountered.

The quality of the averaging kernels for small radii (the one for $\gamma = 45°$, $r_k = 5$ μm is shown in Fig. 3) is poor. This is caused by the lack of the radial variations in the weighting functions, an example of which is shown in Fig. 4. There is very little structure in these functions, or between them, at lower radii. It is impossible to superimpose such similar functions linearly to approximate a delta function satisfactorily. In fact, the minimization procedures must try to negate the large contributions from the weighting functions of larger radii, leaving a kernel that does not
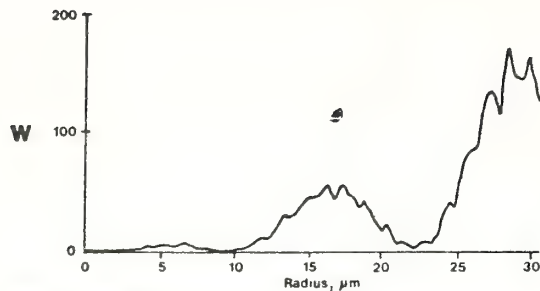
FIG. 4. Weighting function for $\theta_{scat} = 148$.

even peak at the correct radius. The opposite case is true for kernels that peak at larger radii, where weighting function oscillations are strong and varied. Here satisfactory kernels are created.

By analyzing the properties of the kernels that the technique creates (Table I), it was found that the optimum combination of scattering parameters for data taking includes polarization information and narrow beam scattering over multiple scattering angles. That is, these parameters result in the curve closest to the origin in Fig. 1. As may be deduced from the table, multiple frequency data improve results slightly, particularly if the frequencies are widely spaced, but in practice the amount of improvement probably does not warrant the effort.

III. THEORETICAL AND EXPERIMENTAL INVERSIONS

After the optimum combination of scattering parameters was established, the abilities of the Backus-Gilbert technique to recover number densities from distributions were investigated. To do this a stepped-size distribution was used to create theoretical signals from the known weighting functions. The response of inversion process to this "impulse" in size distribution could then be analyzed. The theoretical signals were processed with Backus-Gilbert inversion coefficients to recover a distribution. Results are depicted

in Fig. 5. It was found that if recovery over the radius range 0–30 μm is required, the recovery in the range 0–10 μm is poor. This has two causes. First, the minimization procedure used to create averaging kernels that peak at small radii must weight its efforts to cancel out high scattering values at larger radii. The result is a kernel of poor resolution that does not peak at proper radius. Second, even if the contributions from the larger radii do not overpower those from the smaller, the variation of the weighting functions with radius still is not intense enough at small radii to permit the construction of as good an averaging kernel as is possible at larger radii. These facts explain why Westwater and Cohen[1] were able to recover a narrow distribution when they limited their range of radii.

These and other limitations rule out detection of meaningful cloud-type size distribution parameters, such as mode radius and slope at large radii, at least for those distributions popularly used by modelers,[5,6] which in character include most measured distributions. For the mode radius, which typically occurs in the 0–10 μm range, recovered distributions are questionable because of the facts just presented. Even if the total range in radius were limited to 10 μm, as is the case with some cumuli, spreads would be too wide to yield useful results. To detect slope at large radii, the averaging kernels are well constructed with narrow spread, but pickup in their wings limits their usefulness to working with only two orders of magnitude range in number density. Because number densities at 30 μm are at least 10^5 below the mode radius density in most models, they are undetectable.

TABLE I. Spreads (μm) for various combinations of weighting functions.

Radius (μm)	$\gamma = 45°$					
	A	B	C	D	E	F
5	60.3	48.5	40.4	106.6	81.7	152.7
10	20.5	10.7	10.0	43.7	33.1	66.9
15	7.0	5.8	5.4	17.7	11.6	21.0
20	5.1	4.4	4.7	6.5	7.7	7.1
25	4.2	3.7	4.2	4.6	6.1	6.7
30	5.6	7.4	5.7	8.9	9.6	13.0

A: Finer quadrature, $0 \le r \le 30$ μm
B: One polarization, $\lambda = 6943$ and $\lambda = 3471$ Å
C: One polarization, $\lambda = 6328$ and $\lambda = 5890$ Å   } Multiangle
D: Angle scan limited to eight angles
E: Polarizations added
F: Two polarizations, nine wavelengths, one angle

FIG. 5. Actual and recovered size distributions—theoretical noisy data.

60
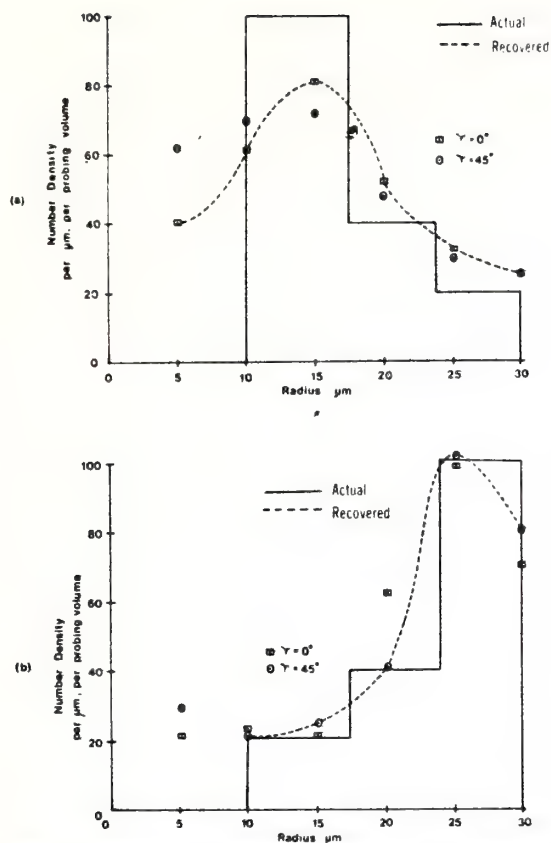
FIG. 6. Actual and recovered size distributions—experimental noisy data.

all discrepancies between recovered and actual distributions may be explained in terms of spread and noise, since there is no uncertainty about the actual distributions.

IV. CONCLUSIONS

It is concluded that recovery of size distributions from optical scatter of cloud-sized droplets is possible, but that the imperfect resolution inherent in the scattering process itself limits the types of distributions that are recoverable, and rules out meaningful inversions for cloud model distributions.

It must be emphasized, however, that useful applications of the Backus-Gilbert technique are possible for polydisperse systems with smaller ranges in number density and radius than are found in natural clouds; such distributions have been recovered in the laboratory. Also, there is hope that fog distributions (0–3 μm) may be recovered from multiangular or widely spaced multifrequency data because of their narrow range in radius. It may be possible to recover the total number density of narrowly distributed cumuli (0–10 μm) using this technique, if a distribution shape may be assumed. By using this same shape, one could also determine the total water content of the cloud.

Such possible applications of the Backus-Gilbert technique should be studied in more detail. Other inversion techniques should also be investigated, particularly those which may circumvent the imperfect resolution inherent in the optical scatter process associated with water cloud size distributions.

It was found theoretically that noise on the data up to a level of 10% does not affect recovery accuracy as much as the imperfect resolution of the kernels. Therefore it is wise to choose a point on the tradeoff curve nearer to $\gamma = 0°$ for this type of noisy scattering data.

After the properties and limitations of the Backus-Gilbert technique were investigated theoretically, the method was applied to noisy laboratory data with no unexpected results. The inversion values are depicted in Figs. 6(a) and 6(b). The data set itself is unusual in that the exact size distribution which created the data is known. This was accomplished by forming single water droplets in the 10–30 μm range and scattering from individual droplets. A cloud signal was then created by summing intensities from the various size droplets, weighted by the distribution function. For details of this process see Post.[7] For the experimental data,

[1] E. R. Westwater and A. Cohen, "Application of Backus-Gilbert inversion technique to determination of aerosol size distribution from optical scattering measurements," Appl. Opt. 12, 1340 (1973).
[2] G. Backus and E. Gilbert, "Uniqueness in the inversion of inaccurate gross earth data," Philos. Trans. R. Soc. London 266, 123 (1970).
[3] E. R. Westwater and O. N. Strand, "A generalized inversion program," NOAA Tech. Rpt. ERL-309-WPL34, GPO, Washington, D. C. (1974).
[4] J. V. Dave, "Subroutines for computing the parameters of the electromagnetic radiation scattered by a sphere," IBM Scientific Center Rpt. No. 320-3237, Palo Alto, Calif. (1968).
[5] D. Deirmendjian, Electromagnetic Scattering on Spherical Polydispersions (Elsevier, New York, 1969).
[6] T. Takahashi, "Study of warm rain, Part 2," submitted to J. Atm. Sci. (1975).
[7] M. J. Post, "Cloud droplet size distribution by Backus-Gilbert inversion of optical scattering data," Master's Thesis, Dept. of Astro-Geophysics, University of Colorado, Boulder, Colo. (1975).

Characterization of High Extinction Weather for a Ground-Based Infrared Lidar

F. Pratte and E. R. Westwater
Wave Propagation Laboratory
Environmental Research Laboratories
National Oceanic and Atmospheric Administration
Boulder, Colorado 80302

Extinction of infrared radiation by clouds and precipitation appears to
be the most significant limiting factor on a pulsed coherent lidar used to
remotely sense the atmosphere. Numerous articles have appeared in the litera-
ture describing Mie scattering calculations of extinction in atmospheric poly-
disperse suspensions, and there exists a limited amount of experimental data.
The sparseness of experimental data and the uncertainty of the calculations
makes quantifying the scattering properties of clouds to the degree required
by system simulation studies a difficult project. Here, we combine data and
calculations to estimate the range of variation of infrared transmission
through clouds and precipitation. Our data base resulted largely from an ex-
tensive literature survey. Infrared extinction and other scattering proper-
ties of the cloudy atmosphere have been deduced from passive measurements in
the atmospheric transmission window, from suitable measurements in the visible,
or from scattering calculations based on measured and hypothetical droplet-
size spectra. These results on cloud transmission properties were combined
with cloud occurrence statistics to form a simple model for system simulation
studies. Results summarizing the cloud transmission study are given in Table 1.

In general, cloud extinction at all wavelengths decreases as cloud base
altitude increases because of the relationships between liquid water content
and bulk scattering properties. From the evidence presented, most low alti-
tude clouds will prohibit probing from beyond the cloud, while many middle
and high clouds will be sufficiently transparent for usable returns to be
obtained from beyond the cloud. In rain, measured transmission losses are
much less than those estimated for low clouds.

Data also show that in most clouds the transmission improvement at 10.6 μm over
visible wavelengths is not large and appears to vary considerably. This im-
provement is generally a factor of three decrease in extinction coefficient,
but can range widely between one and ten under normal conditions.

Table 1: Model Characteristics of High-Extinction Phenomena

oud Type	$\overline{h}$(km)	$\overline{\Delta h}$(km)	$\overline{w}$(g m^{-3})	$\overline{r_m}$(μm)	$\overline{N}$(cm^{-3})	$\overline{b_{EXT}}$(km^{-1})	b_{BACK}(km^{-1})
ratus	.1-.7	.2-.8	.2-.4	5.5	100-400	30-100	.75-2.5
ratocumulus	.6-1.5	.2-.8	.02-.2	5.0	100-400	3-30	.075-.75
g	0	0-.15	.05-.2	2	25-800	.1-20	.002-.5
mbostratus	.1-1.0	2-3	.2-.9	6-7	100-400	30-100	.6-2
in	---	---	R=1-100	1000	.002 R$^{.21}$	.21R$^{.74}$	1.3x10^{-3}R
tostratus/ cumulus	2-6	.2-2	.1-.2 / .04 (ice)	4.8 / ---	100 / .3-2.0(ice)	10-30 / 1-3(ice)	.1-.75 / .002-.005(ice)
mulus	.5-1.0	.5-5	.005-.4	3.5	100-300	10-40	.25-1.0
mulonimbus	.5-1.0	2-12	.4-8.0	7.0	50-500	30-100	.2-2.5
rriform (ice)	6-10	1.0-2.5	.02-.1	50	.2-1	.3-1.4	.003-.001

NOTES: $\overline{h}$ = cloud base height (AGL); $\overline{\Delta h}$ = cloud thickness; $\overline{w}$ = water content; $\overline{r_m}$ = modal drop radius (or equivalent spherical drop radius for ice clouds); $\overline{N}$ = total concentration of droplets larger than r = 1 μm; b_{EXT} = bulk extinction coefficient (λ = 10.6 μm); b_{BACK} = bulk backscatter cross section coefficient (λ = 10.6 μm); R = rain rate (mm hr^{-1}); Overbars indicate typical or representative values. Natural variability of microscopic properties ($\overline{w}$, $\overline{r_m}$, $\overline{N}$, b_{EXT}, b_{BACK}) is exceedingly large. Some of the variability is a function of location, season, time of day and weather regime.

The exact Mie scattering theory has frequently been the basis for esti-
ting extinction and backscatter in clouds (Carrier, et al., 1967). The
gle particle scattering functions are integrated over measured or modelled
p-size distributions. These estimates appear to underestimate the extinc-
n and overestimate the backscatter as suggested by the experimental work re-
ted by Lawrence, et al., (1973), Zuev (1966), May (1961) and Cato et al., (1965).

Water content appears to be a reasonable and convenient indicator of ex-
ction for water clouds. The large natural and sampling variability of the
plet spectra, even within clouds of the same type, precludes more accurate
ermination. From the results of Platt (1976) and a general knowledge of
scattering behavior of cloud droplets it appears that for most liquid
se clouds

$$b_{EXT} \ (10.6 \ \mu m, \ km^{-1}) \cong 80 \ w^{.65} \ (g \ m^{-3})$$

where b_{EXT} is the bulk extinction coefficient and w, the water content.

Our survey indicates that extinction in low altitude liquid water clouds falls typically between 3 and 100 km^{-1} and backscatter cross section lies between .075 and 2.5 km^{-1}. In mid- and high-level ice phase clouds the extinction is substantially lower, typically between .3 and 2.2 km^{-1}. Lacking direct measurements, one cannot realistically claim that the current values represent better than order-of-magnitude estimates.

Cloud climatology provides information on the microscopic distribution of cloud types. For a ground-based lidar, the method of Lund and Shanklin (1973) was employed to estimate the frequency of occurrence of clouds by type along some elevated line of sight. This information was combined with the estimated cloud extinctions to yield the probability of two-way path attenuation. An example of this type of calculation is shown in Fig. 1. Thus on an annual basis for a vertically pointed lidar located at Columbia, Missouri, the probability for a 50 db or less two-way attenuation to 10 km is about 64%.

References:

Carrier, L. W. G. A. Cato and K. J. vonEssen (1967), "The backscattering and extinction of visible and infrared radiation by selected major cloud models," Applied Optics, 6 (7), 1209, July.

Cato, G. A., L. W. Carrier, K. J. vonEssen (1965), "Laser systems study, Part III: Effects of clouds," Final Report, Electro-Optical Systems, Inc., Pasadena, CA., December X66-17656 EOS Report 4440-Final III.

Lawrence, T. R., M. C. Krause, L. K. Morrison, C. E. Craven (1973), "A study on laser Doppler velocimeter atmospheric wind interrogation systems," Final Report, Lockheed Missiles and Space Co., Inc., Huntsville, Ala., LMSC-HREC TR D306888, October.

Lund, I. A., and M. D. Shanklin (1973), "Universal methods for estimating probabilities of cloud-free lines-of-sight through the atmosphere," JAM, (12), p. 29, February.

May, K. R. (1961), "Fog-droplet sampling using a modified impactor technique," Quart. J. Roy. Met. Soc. (87), p. 535.

Platt, C. M. R. (1976), "Infrared absorption and liquid water content in stratocummulus clouds," Quart. J. Royal Met. Soc. (102) 433, p. 553, July.

Zuev, V. E. (1966), Atmospheric Transparency in the Visible and the Infrared, Translation, U. S. Department of Commerce, 1970.
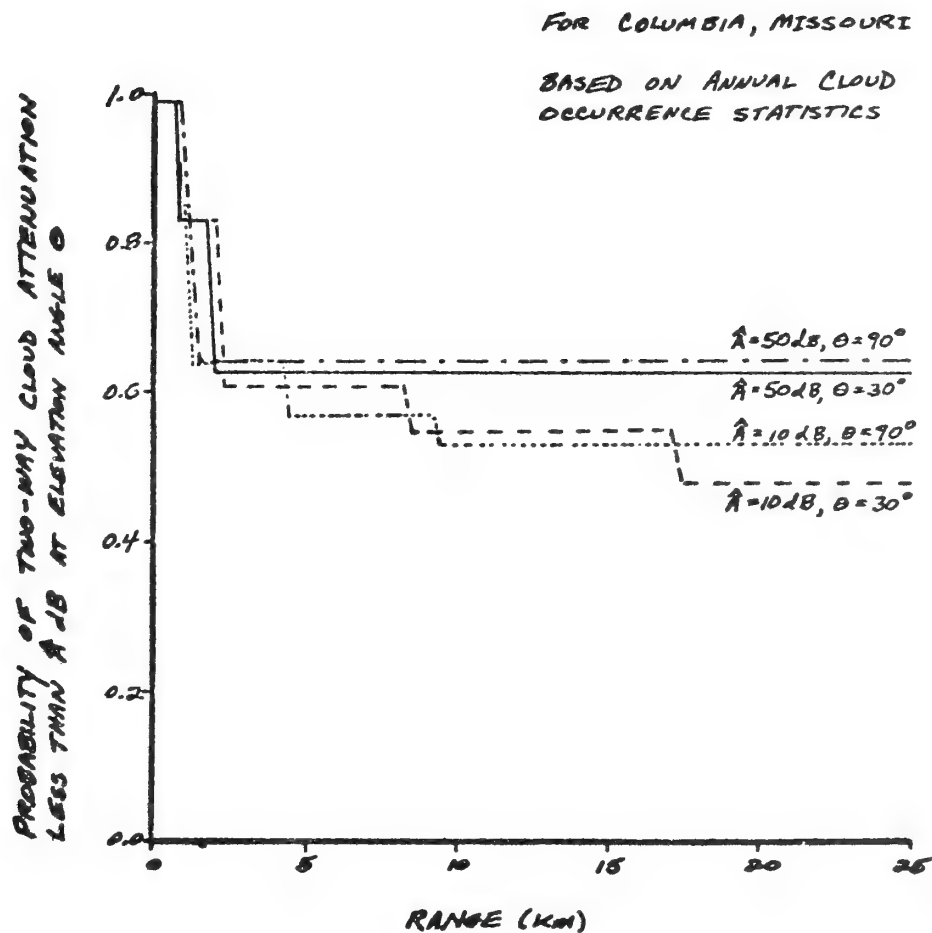
Figure 1. Expected two-way path attenuation due to clouds on an annual basis for a system located at Columbia, Missouri. Percentage of time for which the attenuation is less than 10 dB and 50 db for elevation angles of 30° and 90°.

Measurement of rain parameters by optical scintillation: computer simulation of the correlation method

Ting-i Wang and R. S. Lawrence

Earlier analysis of the use of laser-beam scintillations to measure path-averaged rainfall rate and drop-size distribution has been well verified for pathlengths up to 140 m even though, for such a path, overlapping of the scintillation patterns violates a simplifying assumption of the analyses. Analytic extension of the theory to the case where the scintillation patterns overlap appears intractable, so a computer simulation has been used to investigate that limitation of the theory. That simulation, presented here, verifies that the original scintillation–covariance technique for measuring rainfall parameters is, with only a slight modification, still applicable in the presence of overlapping scintillation patterns from many raindrops.

I. Introduction

Recently, Wang and Clifford[1] and Wang et al.[2] presented theoretical studies and preliminary experimental results of the use of rainfall-induced optical scintillations to measure path-averaged rain parameters. The general philosophy of the approach is to measure the raindrop-induced irradiance (or amplitude) scintillations with two vertically spaced detectors. The temporal covariance function of the signals detected by the two sensors yields the path-averaged terminal velocity distribution of the raindrops. Because there is a monotonic relationship between drop size and terminal velocity,[3] the measured velocity distribution can be converted to path-averaged drop-size distribution and hence to rain rate. However, one important assumption used in their derivation is that the time-lagged covariance function of the irradiance scintillation induced by many raindrops from different locations can be considered as the sum of the covariance functions of the scintillation patterns of the individual drops. This assumption is valid if the receiver detects only one diffraction pattern at a time. For a line detector, many patterns are detected simultaneously, and some of the irradiance scintillations will be canceled. Here, we discuss the result of a computer simulation to study the effect of the cancelation on measurements of path-averaged drop-size distribution and rain rate.

II. Theory

For a line detector with a length l much longer than a Fresnel-zone size for the path position x [i.e., $l \gg (\lambda x)^{1/2}$], the amplitude scintillation χ (equal to one-half of the irradiance scintillation) caused by a raindrop located at coordinates (x,y,z) is given by Eq. (2) of Ref. 2.

$$\chi(x,y,z) = \begin{cases} -(\eta/k)(2\pi x/k)^{1/2} \sin[kz^2/(2x) + \pi/4]J_1(\eta z/x)/(zl); & \text{if } |y| < l/2 \\ 0; & \text{if } |y| > l/2. \end{cases} \quad (1)$$

where $\eta = ka$ is the drop-size parameter; a is the drop radius and $k = 2\pi/\lambda$; λ is the wavelength of the source. The line detector is assumed to extend in the y direction. A typical pattern is shown in the upper diagram of Fig. 1 for $ka^2/x = 0.1$ which is the case for a drop with 1-mm radius at a path position 100 m from the line detector and the wavenumber $k = 10^7$ m^{-1} (He–Ne laser). The time-lagged autocovariance function of the irradiance scintillation of this pattern is shown in the lower diagram of Fig. 1. For any drop velocity, there is a corresponding covariance function that would be observed by a pair of vertically separated, horizontal line detectors. The circles in Fig. 2 show the superposition of 255 such covariance functions resulting from 255 drops of various sizes at various locations, assuming the line detectors had a vertical separation of 3 cm. Here we used a Marshall-Palmer drop size distribution[4] for a rain rate $h = 74$ mm/h. The theoretically obtained time-lagged covariance function is given by[2]

$$C_\chi^l(z_0, \tau) = 4.1 \times 10^{-16} z_0^2 l^{-1} \tau^{-3} \int_0^L dx h(x) p(a', x), \quad (2)$$

where

$$a' = 2.5 \times 10^{-5} z_0^2 \tau^{-2}. \quad (3)$$

The authors are with NOAA Wave Propagation Laboratory, Boulder, Colorado 80302.

66

In obtaining Eqs. (2) and (3), we assume that the relationship of the terminal velocity and the drop-size follows $v = 200\sqrt{a}$, where v is in m/sec and a is in m. This is equivalent to assuming that the function $g(v)$ in Eq. (9) of Ref. 2 is equal to unity. The solid line in Fig. 2 shows the corresponding theoretical curve. Because of the limited number of drops in the computer simulation, the largest drop in the group has a radius of 1.67 mm, corresponding to a time delay of 3.7 msec. This explains the discrepancy in the region $\tau = 2.4$–4 msec. However, the over-all agreement is excellent.

III.   Removal of the Baseline

Both the theoretical and simulated results shown in Fig. 2 are based on the assumption that the covariance function of many drops equals the ensemble average of the covariance functions of the individual drops. In
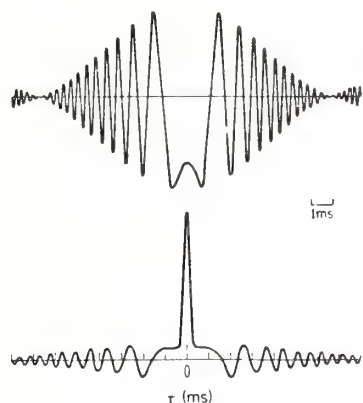
Fig. 1.   The raindrop-induced irradiance scintillation detected by a line detector for $ka^2/x = 0.1$ (upper diagram). The time-lagged autocovariance function of the irradiance scintillation is shown in the lower diagram.
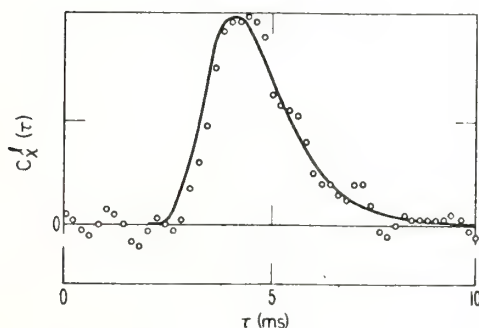
Fig. 2.   The time-lagged covariance function of the rain-induced irradiance scintillations detected by two line detectors with a 3-cm vertical separation. The covariance function is assumed equal to the sum of the covariance functions of 255 individual drops. Solid line—theoretical model; circles—simulation.

effect the signal detected by a line detector is the superposition of the electric fields induced by drops at different locations simultaneously. For an intensity detector, the signal detected is $I = |\Sigma_i E_i|^2$. If we decompose the electric field into $E_i = E_{s_i} + E_o$, where E_o is the unscattered field (assumed real) and E_{s_i} is the scattered field caused by the ith drop, we have $I = [E_o + \text{Re}(\Sigma_i E_{s_i})]^2 + [\text{Im}(\Sigma_i E_{s_i})]^2$, where Re and Im are the real- and imaginary-part operators, respectively. For the weak scattering case (i.e., $|\Sigma_i E_{s_i}| \ll E_o$), the detected signal is approximately equal to $I \simeq E_o^2 + 2E_o \text{Re}(\Sigma_i E_{s_i})$. The fluctuating part of I is defined as $I_1 = I - I_0$, where $I_0 = E_o^2$ is the unscattered intensity. Hence we obtain $I_1/I_0 \simeq 2 \text{Re}(\Sigma_i E_{s_i})/E_o$. The proportionality of the intensity fluctuation and the electric field fluctuation enables us to superpose the scintillation patterns instead of the electric fields. Some scintillation must be canceled by this superposition. Thus, we may question the assumption used in Fig. 2. In order to assess the magnitude of the error, we have performed a computer simulation. In the simulation, we assume that, at a given time, 255 different-sized drops are randomly located in that portion of a collinated 20-cm diam laser beam lying 25–175 m from the line detectors. The drops fall with their appropriate terminal velocities, and when each drop leaves the beam, another drop of the same size enters the top of the beam at a randomly chosen path position. We assume that the drops have a size distribution given by the Marshall-Palmer model for a rain rate of 10 mm/h. The line detectors observe the overlapping scintillation induced simultaneously by the 255 drops. The signal from the upper detector is delayed and correlated with that from the lower detector. The vertical separation of the detectors is taken to be 2 cm. After averaging 44 msec of data, we obtained the time-lagged covariance function shown in Fig. 3. The sizable background correlation is caused by the overlapping of the simultaneous scintillation patterns of the individual drops. However, if we remove this background by using the dashed line as a baseline, the original shape of the covariance function is preserved. A practical way to remove the background correlation is to take the difference between the covariance functions with positive and negative delays
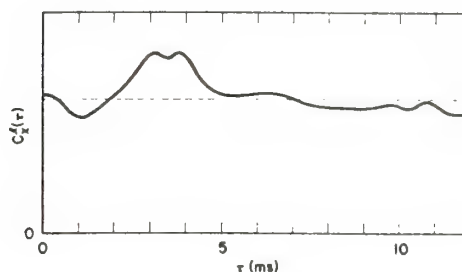
Fig. 3.   The time-lagged covariance functions of two line detectors on a 200-m path obtained by many drops from different locations (vertical separation = 2 cm).

$C_x{}^l(\tau) - C_x{}^l(-\tau)$. The result is shown by the solid line in Fig. 4, obtained after 200 msec of data averaging, which is equivalent to a total of 20,000 drops with 255 drops in the beam at any instant. The corresponding theoretical result is shown by the dashed line in Fig. 4. The path-averaged drop-size distribution can be retrieved by the relationship[2]

$$N_v(a') \sim z_0{}^{-9}\tau^{10}C_x{}^l(z_0, \tau),\qquad(4)$$

where a' is as defined in Eq. (3). The results are shown in Fig. 5.
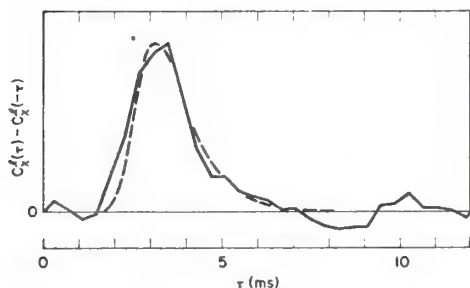
Fig. 4. Similar to Fig. 3 except that background correlation is removed by taking the difference between the covariance functions of positive and negative delays.
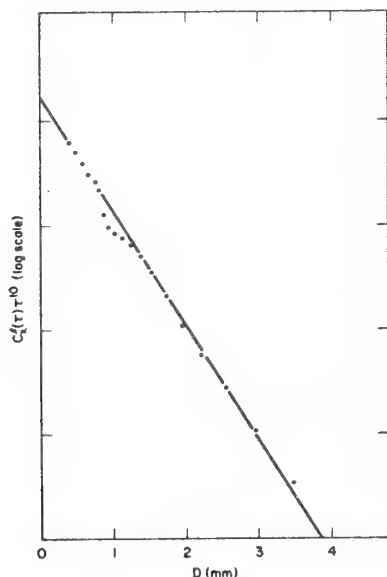
Fig. 5. The quantity $C_x{}^l(\tau)\tau^{10}$, from the correlation function obtained in Fig. 4, agrees well with the drop-size distribution (solid line) used in the simulation.

IV. Path Weighting Function and Drop-Size Distribution

From Eq. (2), the theoretical path-weighting function of the temporal–spatial covariance function is uniform along the path. In practice, because of the effect of overlapping patterns the actual path-weighting function may change. To obtain the weighting function by computer simulation, we used a model of a sheet of rainfall 50 m thick with the center of the sheet varying from 50 m to 2000 m from the detectors. We took eighty-five raindrops as being simultaneously inside the beam. The drop-size distribution is assumed to follow a Marshall-Palmer distribution of rain rate of 10 mm/h. The vertical separation of the detectors is fixed at 2 cm for all simulations. The ratio of the area A under the temporal–spatial covariance function (using the subtraction technique) to the rain rate R is shown in Fig. 6 as a function of distance L from the detectors. The path-weighting function is reasonably uniform, as predicted. The slight decline at large distances may be caused by the limited size of the laser beam (20 cm).

The retrieved drop-size distribution for different values of pathlength L is shown in Fig. 7 compared with the input model (solid line). For drops smaller than 0.4 mm, the retrieved distribution deviates from the model, especially at large distances. We presume this is because the small 2-cm vertical separation of the detectors provides insufficient velocity resolution for the large scintillation patterns that occur on a long path. A comparison between the retrieved drop-size distributions for vertical separations of 2 cm and 4 cm is shown in Fig. 8, where we see that better results are obtained for larger vertical separation. However, the magnitude of the temporal–spatial covariance function is smaller ($C_x{}^l \simeq z_0{}^{-1}$), and the signal is more sensitive to noise (mainly caused by turbulence) for the larger separation. For the purpose of measuring the path-averaged rain rate, we believe a 2-cm separation is optimum for pathlengths up to 2 km.
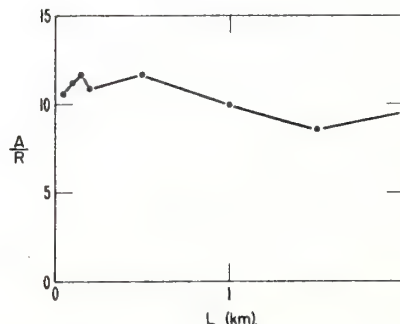
Fig. 6. Path-weighting function of the ratio of the area A under the temporal-spatial covariance function (using the subtraction techniques) to the rain rate R.

68
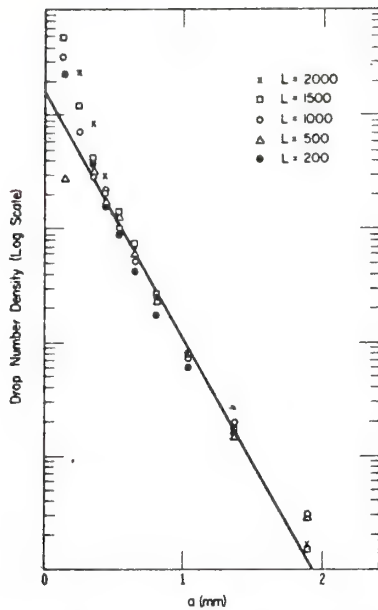
Fig. 7.   The retrieved drop-size distribution for different values of
L.   Solid line—theoretical model.
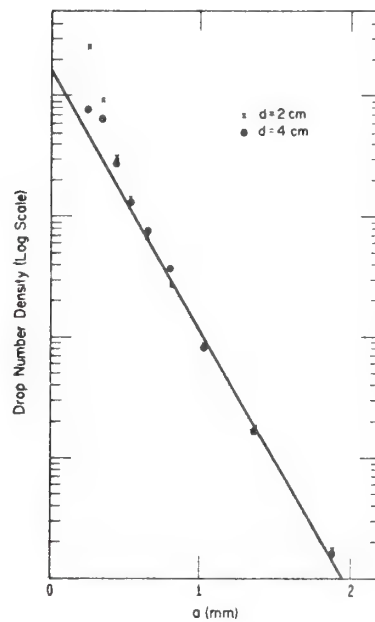
Fig. 8.   A comparison of the retrieved drop-size distributions for
vertical separations of 2 cm and 4 cm.   Solid line—theoretical
model.

V.   Conclusion

A computer simulation shows that, if the subtracting technique is used, the use of rainfall-induced optical scintillations to measure path-averaged rain parameters by computing the temporal–spatial covariance of two vertically separated line detectors is practical, even in the presence of the overlapping patterns from many drops.

References

1. T-i Wang and S. F. Clifford, J. Opt. Soc. Am. 65, 927 (1975).
2. T-i Wang, G. Lerfald, R. S. Lawrence, and S. F. Clifford, Appl. Opt. 16, 2236 (1977).
3. R. Gunn and G. D. Kinzer, J. Meteor. 6, 243 (1949).
4. T. S. Marshall and W. McK. Palmer, J. Meteorol. 4, 186 (1948).

69

Measurement of rain parameters by optical scintillation

Ting-i Wang, G. Lerfald, R. S. Lawrence, and S. F. Clifford

We describe a technique for measuring path-averaged rain parameters by analyzing the rainfall-induced scintillations of a laser beam. From the time-lagged covariance function of two vertically spaced line detectors, we determine the average rainfall rate and drop-size distribution along the optical path. This technique requires no prior assumption of the form of the drop-size distribution. Sample measurements on a 140-m path confirm that the path-averaged drop-size distribution of a steady rain follows a Marshall-Palmer distribution. The optically measured path-averaged rain rate also shows good agreement with conventional tipping-bucket rain-gauge data.

I. Introduction

Recently, Wang and Clifford presented a theoretical study of the use of rainfall-induced optical scintillations to measure path-averaged rain parameters.[1] The general philosophy of the approach is to measure the raindrop-induced irradiance (or amplitude) scintillations with two vertically spaced detectors. The temporal covariance function of the signals detected by the two sensor yields the path-averaged terminal velocity distribution of the raindrops. Because there is a monotonic relationship between drop size and terminal velocity,[2] the measured velocity distribution can be converted to path-averaged drop-size distribution and hence to rain rate. In that paper,[1] the use of vertically separated, point detectors was analyzed. In practice, because of the presence of horizontal wind, some form of distributed detectors, e.g., line detectors, must be used. In this paper, we generalize the previous results to include the line-detector case. We then describe the design of an experimental instrument, and, finally, we show sample measurements of path-averaged rain rate and drop-size distribution.

II. Theory

Figure 1 illustrates the geometry of an incident plane wave propagating along the x direction and scattered by randomly located raindrops. We assume that the raindrops are spherical and that the wavelength λ of the incident wave is much smaller than the radius a of the raindrop. In the far field, the normalized amplitude scintillation χ measured by a point detector is expressed by Eq. (4) of Wang and Clifford.[1] For a line detector, the amplitude scintillation χ caused by a raindrop located at coordinates (x,y,z) is

$$\chi(x,y,z) = -\eta/(kl) \int_{-l/2}^{l/2} dy' \sin\{k[(y-y')^2 + z^2]/(2x)\}$$
$$\times J_1\{\eta[(y-y')^2 + z^2]^{1/2}/x\}/[(y-y')^2 + z^2]^{1/2}, \quad (1)$$

where $\eta = ka$ is the drop-size parameter; a is the radius of the raindrop, and $k = 2\pi/\lambda$, the line detector is of length l, extending in the y direction. If we assume that the length l is much longer than a Fresnel-zone size for the pathlength L [i.e., $l \gg (\lambda L)^{1/2}$] and $a \ll (\lambda L)^{1/2}$, the integration of Eq. (1) can be accomplished by the method of stationary phase (see Appendix B of Ref. 1) with the result that

$$\chi(x,y,z) = \begin{cases} -(\eta/k)(2\pi x/k)^{1/2} \sin[kz^2/(2x) + \pi/4]J_1(\eta z/x)/(zl); \\ \quad \text{if } |y| < l/2, 0; \quad \text{if } |y| > l/2. \end{cases}$$
$$(2)$$

For $|y| < l/2$, the raindrop induced scintillation is plotted in Fig. 2. The result was confirmed by photographing the signal detected by a line detector at a distance of 18 m from laboratory-produced falling water drops illuminated by a collimated laser beam (Fig. 3).

We consider only the single scattering case, a reasonable simplification for laser-beam propagation through a moderate rainfall on paths up to 1 km (see Appendix of Ref. 1). Closely following the development of Secs. II and III of Ref. 1, we obtain the time-lagged cross-correlation function of the amplitude scintillation of two line detectors with a vertical separation z_0, i.e.,

$$C_\chi{}^l(z_0, \tau) = \frac{2\pi}{kl^2} \int_0^L x dx \int_0^\infty a^2 dN_V(a,x)$$
$$\times \int_{-l/2}^{l/2} dy \int_{-\infty}^\infty dz \sin[kz^2/(2x) + \pi/4]$$
$$\times \sin[k(z - z_0 + \upsilon\tau)^2/(2x) + \pi/4]$$
$$\times \frac{J_1(\eta z/x)}{z} \frac{J_1[\eta(z - z_0 + \upsilon\tau)/x]}{(z - z_0 + \upsilon\tau)}, \quad (3)$$

where a is the drop radius, υ is the terminal velocity of the drop, and L is the pathlength.

In Eq. (3), $dN_V(a,x)$ is the differential number den-
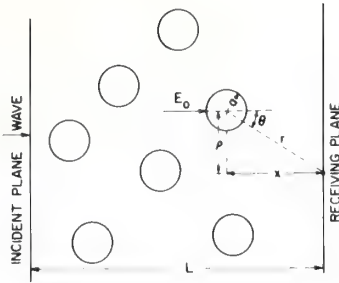
Fig. 1. Geometry of an incident plane wave scattered by randomly placed raindrops, $P = (y^2 + z^2)^{1/2}$.
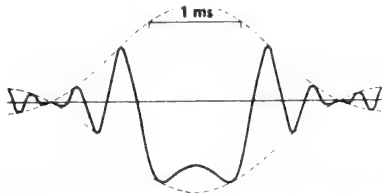
Fig. 2. The water-drop induced scintillation detected by a line detector as shown by Eq. (2) for $|y| < l/2$, $x = 18$ m, $\eta = ka = 9.5 \times 10^3$ and $k = 10^7$ m^{-1}.
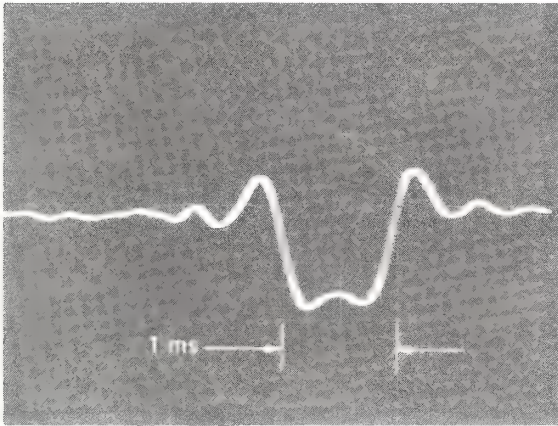
Fig. 3. The signal detected by a line detector at a distance 18 m from falling water drops (laboratory-produced) illuminated by a collimated He–Ne laser beam. The drop radius is about 1 mm.

sity of raindrops with radius a at path position x. The subscript V denotes the number density measured for a fixed volume. From Eq. (7) of Ref. 1, we have

$$dN_V(a,x) = \frac{dh(a,x)}{4.8\pi \times 10^6 a^3 v}, \qquad (4)$$

where $dh(a,x)$ is the differential rain rate contributed from raindrops with radius a at path position x. It can be shown (see Sec. IV, Ref. 1) that

$$dh(a,x) = h(x)p(a,x)da, \qquad (5)$$

where $h(x)$ is the total rain rate at position x in mm/h, and $p(a,x)$ is the probability-density function of raindrop size at that position given by

$$P(a,x) = \frac{N_t(a,x)\frac{4}{3}\pi a^3}{\int_0^\infty da N_t(a,x)\frac{4}{3}\pi a^3} \qquad (6)$$

[see Eq. (25), Ref. 1]. In Eq. (6), $N_t(a,x)$ is the number density of raindrops measured in a fixed time period. [The difference between the number densities $N_V(a,x)$ and $N_t(a,x)$ is discussed in detail in the Appendix.]

Inserting Eq. (4) into Eq. (3) and performing the integration over y, we obtain

$$C_x{}^l(z_0,\tau) = 1.33 \times 10^{-7} \frac{\pi}{kl} \int_0^L dx\, x h(x)(I_1 + I_2), \qquad (7)$$

where

$$I_1 = \int_{-\infty}^\infty dz \int_0^\infty \frac{dv}{v^2} P\left[\frac{v^2 g(v)}{4 \times 10^4}, x\right] \frac{J_1\left[\frac{kzv^2 g(v)}{4 \times 10^4 x}\right]}{z}$$
$$\times \frac{J_1\left[\frac{kv^2 g(v)}{4 \times 10^4 x}(z - z_0 + v\tau)\right]}{z - z_0 + v\tau} \sin[kz^2/x - kz(z_0 - v\tau)/x$$
$$+ k(z_0 - v\tau)^2/(2x)] \times \left[1 + \frac{vg'(v)}{2g(v)}\right]; \quad (8)$$

$$I_2 = \int_{-\infty}^\infty dz \int_0^\infty \frac{dv}{v^2} P\left[\frac{v^2 g(v)}{4 \times 10^4}, x\right] \frac{J_1\left[\frac{kzv^2 g(v)}{4 \times 10^4 x}\right]}{z}$$
$$\times \frac{J_1\left[\frac{kv^2 g(v)}{4 \times 10^4 x}(z - z_0 + v\tau)\right]}{z - z_0 + v\tau} \cos[kz(z_0 - v\tau)/x$$
$$- k(z_0 - v\tau)^2/(2x)] \times \left[1 + \frac{vg'(v)}{2g(v)}\right]. \quad (9)$$

In obtaining Eqs. (8) and (9), we used the relationship between the raindrop radius and its terminal velocity given by $g(v)v^2 = 4 \times 10^4 a$, where $g(v) = 2c$; c is the drag coefficient given by Gunn and Kinzer,[2] and $g'(v)$ denotes the derivative of $g(v)$ with respect to v. Here a is in meters, and v is in m/sec.

If we assume that $\tau \gg (2L/k)^{1/2}\sigma_v{}^{-1}$ and $\tau \gg 0.01(L/k)^{1/4}$, where σ_v is the standard deviation of the terminal velocity of the different size raindrops, the integration over v in Eqs. (8) and (9) can be performed by the method of stationary phase with respect to v at $v = (z_0 - z)/\tau$ (see Sec. V and Appendix B of Ref. 1 for details of the restrictions of the application of the method of stationary phase). Accordingly, we obtain

$$\left.\begin{matrix}I_1\\I_2\end{matrix}\right\} = 1.25 \times 10^{-5} \int_{-\infty}^{z_0} dz \left(\frac{2\pi k}{x\tau^2}\right)^{1/2}$$
$$\times P\left[\frac{(z_0 - z)^2 g(v_1)}{4 \times 10^4 \tau^2}, x\right] \frac{J_1\left[\frac{kz(z_0 - z)^2 g(v_1)}{4 \times 10^4 x\tau^2}\right]}{z}$$
$$\times \left\{\begin{matrix}\sin\\\cos\end{matrix}\right\} \{\pi/4 + kz^2/(2x)\} \cdot [g(v_1) + v_1 g'(v_1)/2], \quad (10)$$

where $v_1 = (z_0 - z)/\tau$. Using the method of stationary

phase once more with respect to z at $z = 0$, we have $I_2 = 0$ and

$$I_1 = 9.83 \times 10^{-10} \left(\frac{k z_0^2}{x \tau^3} \right) P(a',x)$$
$$\cdot \left[g(z_0/\tau) + \left(\frac{z_0}{\tau} \right) \frac{g'(z_0/\tau)}{2} \right], \quad (11)$$

where

$$a' = 2.5 \times 10^{-5} z_0^2 \tau^{-2} g(z_0/\tau). \quad (12)$$

Inserting Eq. (11) into Eq. (7) gives

$$C_\chi{}^l(z_0, \tau) = 4.1 \times 10^{-16} z_0^2 l^{-1} \tau^{-3} \left[g(z_0/\tau) \right.$$
$$+ \left(\frac{z_0}{\tau} \right) \frac{g'(z_0/\tau)}{2} \right] \int_0^L dx \, h(x) P(a',x)$$
$$\sim \overline{P(a')} \, \tau^{-3} \left[g(z_0/\tau) + \frac{z_0}{\tau} \frac{g'(z_0/\tau)}{2} \right], \quad (13)$$

where $\overline{P(a')}$ is the path-averaged probability-density function of raindrop size. The path-averaged rainfall rate is obtained by integration over all sizes. If we multiply Eq. (13) by τ^3 and integrate over a', we obtain

$$\bar{h} = \frac{1.22 \times 10^{11} l}{L} \int_0^\infty d\tau \, C_\chi{}^l(z_0, \tau). \quad (14)$$

Equation (14) shows that the path-averaged rainfall rate is proportional to the area under the time-lagged cross-covariance function of the rainfall-induced scintillation detected by two horizontally oriented line detectors with a vertical separation z_0.

In order to demonstrate how we can obtain the path-averaged rain rate, we assume that the raindrop size distribution follows the Marshall-Palmer distribution,[3] i.e.,

$$N_V(a,x) = N_0 \exp[-2\Lambda(x)a], \quad (15)$$

where N_0 is the value for $a = 0$, and $\Lambda(x)$ is a function of rainfall rate $h(x)$. It has been reported that[3]

$$N_0 = 8 \times 10^6 \text{ m}^{-4} \quad (16)$$

for any intensity of rainfall and that

$$\Lambda(x) = 4100 h(x)^{-0.21} \text{ m}^{-1}, \quad (17)$$

where $h(x)$ is in mm/h. (The assumption of a known drop-size distribution is only an example. The measured covariance will depend on the actual size distribution.) The number-density $N_t(a)$ can be obtained from Eq. (A4) in the Appendix, i.e., $N_t(a) = N_V(a)v(a)$. Since the measurements depend only on the path-averaged values, we need only give the path-averaged rainfall rate $\bar{h}$ instead of the path dependent rainfall rate $h(x)$. The quantity $\bar{h}$ is varied from 0.1 mm/h to 100 mm/h in the following plots. The normalized time-lagged covariance functions are shown in Fig. 4 (for a fixed separation $z_0 = 10$ cm). Since there are more large raindrops in the heavier rainfall rate, the peak of the covariance function occurs at a shorter time lag. The shape of the curves is dependent on the path-averaged raindrop size distribution. For different size distributions, we expect the covariance function will be
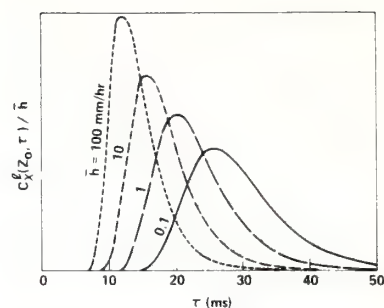
Fig. 4. Normalized time-lagged covariance functions for a fixed vertical separation $z_0 = 10$ cm and variable $\bar{h}$. The drop-size distribution is assumed to follow a Marshall-Palmer distribution.
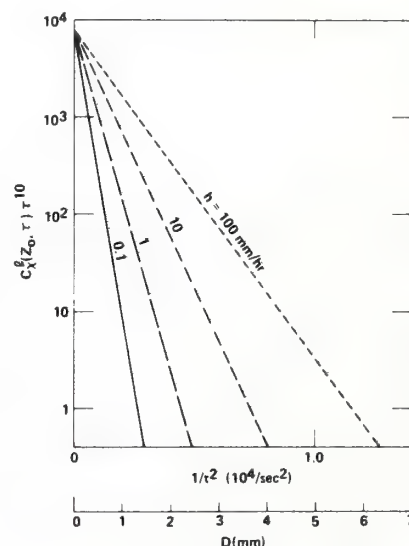
Fig. 5. The quantity $C_\chi{}^l(z_0, \tau) \tau^{10}$ (for fixed $z_0 = 10$ cm) vs $1/\tau^2$. The corresponding raindrop diameter is shown on the lower horizontal axis.
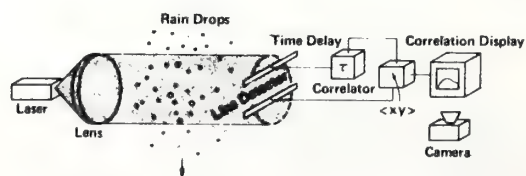
Fig. 6. Schematic diagram of a prototype optical rain gauge.

72

different. The areas under the curves, however, are a constant.

Inserting Eq. (6) into Eq. (13), we obtain the path-averaged number-density of raindrops in a fixed time period from the space–time covariance function, i.e.,

$$\overline{N_t(a')} \sim z_0^{-8}\tau^9 C_\chi{}^l(z_0,\tau)g^{-3}(z_0/\tau)$$
$$\times \left[g(z_0/\tau) + \frac{z_0}{\tau}\frac{g'(z_0/\tau)}{2} \right]^{-1}. \quad (18)$$

From Eq. (A4), we can also obtain the number-density for a fixed volume, i.e.,

$$\overline{N_V(a')} = \overline{N_t(a')}/v(a')$$
$$\sim z_0^{-9}\tau^{10} C_\chi{}^l(z_0,\tau)g^{-3}(z_0/\tau)\left[g(z_0/\tau) + \frac{z_0}{\tau}\frac{g'(z_0/\tau)}{2} \right]^{-1}. \quad (19)$$

Again, for a Marshall-Palmer distribution, the results of $C_\chi{}^l(z_0,\tau)\tau^{10}$ (for fixed $z_0 = 10$ cm) vs $1/\tau^2$ are plotted in Fig. 5. [In this figure, we assume that $g(v) = 1$. However in obtaining the experimental results, we use Eq. (19) to obtain the path-averaged raindrop number-density.] The corresponding raindrop diameter is also shown in the horizontal axis. The results agree with the assumed raindrop size distribution. In plotting Fig. 5, we assume that $N_0 = 8 \times 10^6$ m^{-4} since we have no information about N_0 when we use Eq. (19) as the raindrop size distribution. From Eq. (13), a uniform path-weighting function is obtained when we use Eqs. (14) and (18) to measure the path-averaged rain rate and drop-size distribution, respectively.

One important assumption used in the previous derivation is that the time-lagged covariance function of the irradiance scintillation produced by many raindrops from different locations can be considered as the sum of the covariance functions of the scintillation pattern of each individual drop. The assumption is valid if the receiver detects only one diffraction pattern at a time. With a line detector, many patterns may be detected simultaneously, and some of the irradiance scintillations will be smeared out. In order to see how much the smearing effect distorts the deduced rain rate and drop-size distribution, we have performed a computer simulation. The result shows that, in practical cases, the smearing effect will change only the baseline but not the shape of the covariance function. The path-averaged drop-size distribution and rain rate can still be obtained according to the previous analysis.

IV. Experimental System and Results

A prototype system, illustrated schematically in Fig. 6 and composed of the following components, was built and tested initially using falling water drops generated in the laboratory:

(a) Transmitter: A 5-mW He–Ne laser, followed by an optical system that expanded the collimated beam to produce a uniform beam 20 cm in diameter.

(b) Receiver: Two horizontal line detectors 25 cm long and 0.25 cm high on a mounting frame that allowed their vertical separation to be adjusted easily. Interference filters with a bandpass of 0.002 μm centered at 0.6328 μm were used to exclude extraneous light.

(c) Correlation/Integration: An analog delay device

and analog multiplier and integrator were used to obtain the time-lagged covariance function between the two detector outputs as a function of time lag.

(d) Display/Recorder: An oscilloscope and a 35-mm camera with continuously moving film (0.5 mm/sec) were used to display and record the integrator output. A scan of the time-lagged covariance was obtained every 7.5 sec.

Following laboratory tests, which indicated satisfactory operation, the system was used on an outdoor path with the transmitter near ground level and the receiver 140 m distant in a fourth floor window. A tipping-bucket rain gauge that sent a pulse to a chart recorder for each 0.25 mm of accumulated rainfall was located on the roof of the building at the receiving end of the path.

The instrument operated during short thundershowers on 22 May and during steady rains on 28 and 29 May 1975. The latter periods afforded an opportunity to test the technique against theoretical expectations.

The white lines in Fig. 7 show typical examples of the covariance curves. The hollow black line is the baseline as distorted by 120-Hz fluctuations of the laser source. The baseline is taken from the same film when there is no rain. The 7.5-sec scans of time-lagged covariance were then averaged for each time interval during which the tipping-bucket rain gauge was accumulating 0.25 mm of rain. From Eq. (14) the area under the convariance curve is proportional to the path-averaged rainfall rate. Figure 8 compares these areas with the rain rate determined by the tipping-bucket gauge, and Fig. 9 shows the linear regression of these two quantities. The
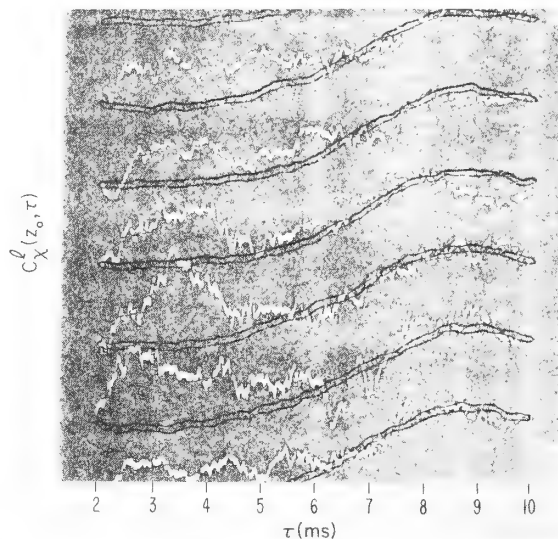
Fig. 7. Typical measured time-lagged covariance functions of the signals detected by two vertically separated line detectors with a separation $z_0 = 2$ cm. The pathlength $L = 140$ m, and the rain rate $h \simeq 3$ mm/h. The black line is the baseline due to 120-Hz fluctuations of the laser.

73
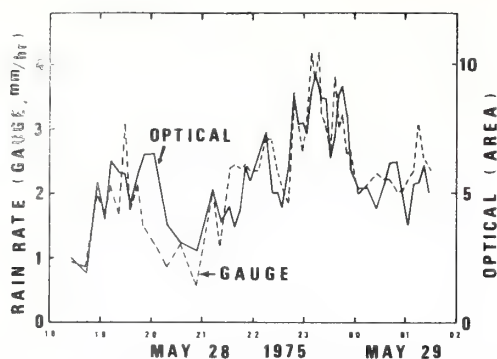
Fig. 8. The time variation of rain rates measured by a tipping-bucket rain gauge and by an optical rain gauge during an 8-h period.
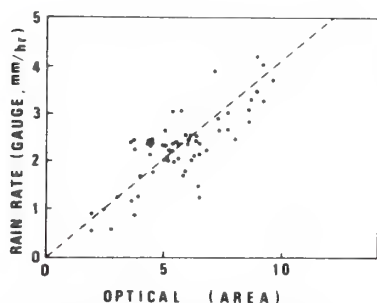
Fig. 9. Gauge rain rates vs optical measurements. Dashed line denotes the best linear regression fit.
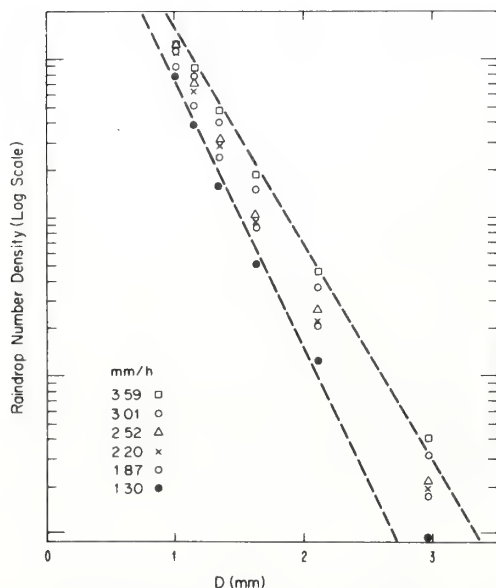
Fig. 10. The path-averaged raindrop size distribution vs the drop diameter for six groups of data divided according to the rainfall rate. The range of the number density of a Marshall-Palmer distribution is shown by the dash lines.

agreement between the rain gauge and the optical measurements is good, with a correlation coefficient greater than 0.95, and might have been improved by using several rain gauges deployed along the path.

From Eq. (19), the path-averaged raindrop number density vs the drop diameter is shown in Fig. 10 for rain rates varying from 1.3 mm/h to 3.59 mm/h. Because we do not know N_0 of Eq. (15) in our measurements, we display the curves on an arbitrary vertical logarithmic scale. The corresponding range of the number density of a Marshall-Palmer distribution is shown by the dashed lines. The agreement between the number density deduced from the scintillation measurements and the empirical Marshall-Palmer distribution is good.

V. Conclusions

We have demonstrated that the path-averaged rainfall rate and the drop-size distribution can be measured by using two vertically separated line detectors and observing the time-lagged covariance function of the irradiance fluctuations induced by falling raindrops. This technique has definite advantages. First, the measured quantities are not a function of the variations along the path of the rainfall rate or of the drop size. They depend only on the path-averaged values. Second, the measurement of the path-averaged rainfall rate is independent of any assumption as to the probability density function of raindrop size. Third, the actual path-averaged probability density function or the number density function of raindrop size can be measured. We believe this is a potentially useful device for measuring the path-averaged rain parameters.

We are presently investigating such limitations as the maximum usable range, the effects of multiple scattering in heavy rains, and the effects of atmospheric turbulence.

Appendix: Difference Between $N_V(a)$ and $N_t(a)$

In the text, we have defined two different number densities of raindrops, one $N_V(a)$ is measured in a fixed volume, the other $N_t(a)$ is measured by the drops falling through a horizontal plane in a fixed time interval. In this Appendix, we derive the relationship between them.

Number density is usually defined as the number of particles per unit volume. It is obtained by counting the number of different sized particles in a fixed volume and dividing by the total volume. The notation $N_V(a)$, where a is the radius of a raindrop, will be used to represent the number density for a fixed volume. Integrating the quantity $(4\pi a^3/3)N_V(a)$ over all sizes, we obtain the total water content M per unit volume, i.e.,

$$M = (4\pi/3) \int_0^\infty da N_V(a) a^3. \qquad (A1)$$

This quantity is not proportional to the rainfall rate. The relationship between the rainfall rate h and the number density for a fixed volume $N_V(a)$ can be found as follows. The total amount of water falling into a rain gauge with cross-section area A in a time period Δt is

74

$hA\Delta t$. The volume swept out by falling raindrops is $v(a)A\Delta t$ for drops with radius a and terminal velocity $v(a)$. The total amount of water in the swept volume is

$$(4\pi/3)\int_0^\infty da N_V(a)a^3 v(a)A\Delta t.$$

Hence,

$$h = (4\pi/3)\int_0^\infty da N_V(a)a^3 v(a). \qquad (A2)$$

Comparing Eqs. (A1) and (A2), we find that the quantities h and M differ by the factor $v(a)$ inside the integral. Defining a new number density $N_t(a)$ measured in a fixed time interval instead of fixed volume, we have

$$h \equiv (4\pi/3)\int_0^\infty da N_t(a)a^3. \qquad (A3)$$

From Eqs. (A3) and (A4), the relationship between $N_V(a)$ and $N_t(a)$ is

$$N_t(a) = N_V(a)v(a). \qquad (A4)$$

Both $N_V(a)$ and $N_t(a)$ are physically measurable. For example, drop counts from a photograph of falling rain yield $N_V(a)$. Measurements involving exposure of a horizontal surface for a short time yield $N_t(a)$.

When calculating the quantities related to raindrop-size distribution, we must be careful to distinguish between $N_V(a)$ or $N_t(a)$. To calculate the attenuation of a wave propagating through the rainfall, $N_V(a)$ must be used. To calculate the rainfall rate, $N_t(a)$ must be used. Taking a photo of rainfall and counting the raindrops to obtain the total amount of water in the volume is not a correct way to measure the rain rate. It is equally wrong if we use a moving vehicle passing through a rainfall with a speed faster than the raindrop-terminal velocities (e.g., an airplane) to carry a sensor to measure the drop-size distribution of the rainfall and try to obtain the rainfall rate by counting the number density collected without introducing a correction for the terminal velocity of the falling raindrops.

Some confusion has occurred in the literature between $N_V(a)$ from $N_t(a)$. Laws and Parsons[4] measured $N_t(a)$, whereas Marshall et al.[5] and Marshall and Palmer[3] present an empirical relationship between $N_V(a)$ and the rainfall rate. In Wang and Clifford's paper,[1] the number density in Eqs. (25), (26), and (41) should be $N_t(a)$. In all the other equations, the number density is $N_V(a)$. To give an example, they also used the Marshall-Palmer distribution as $N_t(a)$ instead of $N_V(a)$. Although this is a misuse of Marshall-Palmer distribution, their results were not affected.

References

1. T-i Wang and S. F. Clifford, J. Opt. Soc. Am. **65**, 927 (1975).
2. R. Gunn and G. D. Kinzer, J. Meteorol. **6**, 243 (1949).
3. T. S. Marshall and W. McK. Palmer, J. Meteorol. **4**, 186 (1948).
4. J. O. Laws and D. A. Parsons, Trans. Am. Geophys. Union **24**, Part 2, 452 (1943).
5. J. S. Marshall, R. C. Langville, and W. McK. Palmer, J. Meteorol. **4**, 186 (1947).

Extraction of wave parameters from measured HF radar sea-echo Doppler spectra

Donald E. Barrick

Wave Propagation Laboratory, Environmental Research Laboratories, National Oceanic and Atmospheric Administration, US Department of Commerce, Boulder, Colorado 80302

Computerized techniques for extracting rms wave height and dominant wave period from HF radar sea-echo Doppler spectra are derived. Earlier theoretical models for first- and second-order sea backscatter (derived elsewhere) are employed to obtain the simple, closed-form inversion equations giving these two radar-deduced quantities. The results are general in that no specific models for the radial or azimuthal form of the wave height directional spectrum need be assumed; the resulting formulas are only weakly dependent upon the radar/wind direction. Approximations made in the derivation are stated, and they are ultimately tested by comparing wave heights and periods extracted from the inversion model with the actual values input to the original equations for scatter. The derived relationships are then tested against some eighty hours of radar measurements taken at a variety of frequencies and buoy-measured sea conditions. Theoretically predicted and empirically determined correction factors for wave height and period are in agreement. Finally, the measurements show that when sea wave height is greater than one twentieth of the radar wavelength, wave height extraction (rms) errors are less than 23%, and wave period extraction errors less than 12%.

1. INTRODUCTION

Since the discovery over two decades ago that the simple Bragg-scatter mechanism is responsible for the characteristics of the sea-echo Doppler spectra [*Crombie*, 1955], considerable interest has ensued in the utilization of MF and HF radars, both in the short-range surface-wave mode and in the long-range skywave mode, for the remote sensing of sea state. Theoretical advances since that time have not only accounted for the dominant "first-order" Doppler peaks in the sea echo [*Barrick*, 1972*a,b*], but have explained the observed "second-order" continuum around the first-order peaks [*Barrick*, 1972*b*, 1971*b*]. *Hasselmann* [1971] advanced the notion that the second-order Doppler sidebands should be replicas of the wave height nondirectional temporal spectrum. Using only the hydrodynamics portion of the total second-order transfer coefficient, along with a given wave directional model, *Stewart* [1971] obtained an expression (following Hasselmann's suggestion) relating the mean-square wave height to the ratio of the second-order to the first-order echo energy. *Barrick* [1977] derived and evaluated a general expression for finding the wave height nondirectional temporal spectrum from the measured second-order Doppler

spectrum—after weighting by a theoretical function and normalization with respect to the first-order echo energy. Of course, the ultimate goal is to invert the general nonlinear integral equation for the complete wave height directional spectrum from the measured second-order echo spectrum. In the subsequent paper in this issue, *Lipa* [1977] presents one approach to this general inversion problem and successfully tests the technique theoretically.

Of all possible simple descriptors of sea state, the rms wave height is perhaps the most useful and important, followed by mean wave direction and dominant wave period (or velocity). By postulating possible models for ocean-wave directionality about the mean wind direction, various investigators [*Long and Trizna*, 1973; *Tyler et al.*, 1974; *Stewart and Barnum*, 1975] have employed measured data to test the accuracy of inferring wind/wave direction from use of the first-order sea-echo only. No one, however, has either derived or tested a general or complete model for extracting wave height and wave period from HF sea-echo records. The present paper presents such a model and tests its accuracy against some eighty hours of HF surface-wave radar observations.

In the next section we set forth and briefly discuss the equations for first- and second-order Doppler spectra in terms of the ocean wave height directional

spectrum. In the following two sections we then obtain simple models for wave height and period based upon these equations for sea echo; these are used to derive theoretical curves relating the radar-deduced wave height/wave period to the true values which were input to the model. A series of surface-wave observations taken with a multifrequency HF radar are then discussed. Using independent observations of the wave parameters, these same parameters are then deduced from the radar sea-echo by computerized algorithms. Comparisons are made to the theoretical predictions, and the variance (and hence rms error) is calculated for these measured parameters based upon the models. Finally, some guidance is given as to where the models can be expected to be acceptably accurate.

2. BACKGROUND SCATTER THEORY

Results for the HF sea-echo Doppler spectrum, to first and second order, have been published elsewhere [Barrick, 1972b, 1971b]. We repeat the results here only to facilitate the derivations and explanations of the inversion techniques that we will apply subsequently to measured data. To first order, the Doppler spectrum (for backscattered, near-grazing, or surface wave incidence conditions, and for the vertical polarization states) can be expressed in terms of the average radar cross section per unit (mean) sea surface area per rad/s bandwidth as

$$\sigma_{(1)}(\omega_d) = 2^7 \pi k_o^4 \sum_{u,l} S_\pm(\kappa_{rx}, \kappa_{ry}) \delta(\omega_d \mp \omega_{or}) \qquad (1)$$

where $\bar{\kappa}_r$ is the total radar wavenumber vector, defined as $\bar{\kappa}_r \equiv \bar{k}_s - \bar{k}_i$. The coordinate system selected here has the backscatter wavevector, $\bar{k}_s$, taken at an angle ϕ with respect to the x direction; hence $\bar{k}_i$ lies in the direction $\phi + \pi$, and is identically $\bar{k}_i = -\bar{k}_s$ for backscatter. Therefore, $\bar{\kappa}_r$ becomes $2k_o \cos\phi\hat{x} + 2k_o \sin\phi\hat{y}$, with k_o being the scalar radio wavenumber. The summation convention (u,l) refers to the upper and lower subscripts and signs in the equation. The quantity ω_d is the radian Doppler shift of the received signal, defined as $\omega_d \equiv \omega_s - \omega_i$, with ω_s and ω_i being the radian frequencies of the scattered and incident signals, respectively. The gravity-wave dispersion relation is employed for the definition

$$\omega_{or} \equiv \text{sgn}(\kappa_{rx})(g\kappa_r)^{1/2} = \text{sgn}(2k_o \cos\phi) \omega_B$$

where $\omega_B = (2gk_o)^{1/2}$ is referred to as the "Bragg" frequency for first-order scatter, with g being the acceleration of gravity. The expression $\text{sgn}(x)$ is a sign indicator that takes on the values ± 1 depending upon whether x is $\pm$. The average wave height directional spectrum is separated into two components, S_+ and S_-. Each component is symmetric since it represents pure real waves; i.e., $S_\pm(\kappa_x, \kappa_y) = S_\pm(-\kappa_x, -\kappa_y)$. Both components are employed to define a general wave field that propagates over $360°$ of azimuth; the only restriction used here for convenience is that the wave field peaks in azimuth along the $+x$ direction (when $\kappa_y = 0$). Inasmuch as this is often the wind direction for fully developed seas, ϕ can be thought of as the angle between the radar direction and the wind direction for such situations. The quantity $\delta(x)$ is the Dirac-delta function of argument x.

The corresponding result for second-order sea echo is

$$\sigma_{(2)}(\omega_d) = 2^8 \pi k_o^4 \sum_{u,l} \sum \iint_{-\infty}^{\infty} d^2\bar{\kappa}_l |\Gamma_T|^2$$
$$\cdot S_\pm(\kappa_{1x}, \kappa_{1y}) S_\pm(\kappa_{2x}, \kappa_{2y}) \delta(\omega_d \pm \omega_{o1} \pm \omega_{o2}) \qquad (2)$$

where

$$\bar{\kappa}_1 \equiv (1/2)\bar{\kappa}_r + \bar{\kappa}_l; \quad \bar{\kappa}_2 \equiv (1/2)\bar{\kappa}_r - \bar{\kappa}_l;$$
$$\omega_{o1} = \text{sgn}(\kappa_{1x})(g\kappa_1)^{1/2}; \quad \omega_{o2} = \text{sgn}(\kappa_{2x})(g\kappa_2)^{1/2};$$
$$\Gamma_T = \Gamma_H + \Gamma_{EM}$$

where

$$\Gamma_H = -(i/2)\{\kappa_1 + \kappa_2 + (\kappa_1\kappa_2 - \bar{\kappa}_1 \cdot \bar{\kappa}_2)[(\omega_B^2 + \omega_d^2)$$
$$\div (\omega_B^2 - \omega_d^2)]g/\omega_{o1}\omega_{o2}\}$$
$$\Gamma_{EM} = (1/2)(\kappa_{1x}\kappa_{2x} - 2\bar{\kappa}_1 \cdot \bar{\kappa}_2)/[(\bar{\kappa}_1 \cdot \bar{\kappa}_2)^{1/2} + k_o\Delta)]$$

and where the integration wavevector may be defined as $\bar{\kappa}_l = p\hat{x} + q\hat{y}$. Here, Δ is the normalized electrical impedance for the rough sea surface for vertical polarization at grazing incidence, as defined and derived by Barrick [1971a]. The coupling coefficients, Γ_H and Γ_{EM}, are obtained from hydrodynamic and electromagnetic theory, respectively; they are derived by expanding the nonlinear equations for the free water surface and the scattered fields into a perturbational series and retaining the second-order terms [Barrick, 1972b].

As seen from (1) above, the first-order sea-echo Doppler spectrum consists of two impulse functions symmetrically spaced about the carrier frequency, each originating from two sets of wave trains one half the radar wavelength, advancing toward and receding from the radar; this is identically the Bragg-scatter mechanism. In practice, these "spikes" will not be infinite in height. Their widths will be proportional normally to the receiver's spectral processing resolution, and hence their heights will adjust accordingly so that the area under them, as expressed by the factor multiplying the delta function, remains constant as given in (1). This area is proportional to the heights of the two sets of Bragg-scattering waves, as expressed by the two wave height directional spectra factors evaluated at the Bragg wavenumber. Figure 1 shows a measured sea-echo Doppler spectrum at 13.40 MHz, where the first-order peaks are much in evidence; their widths here are proportional to the receiver spectral resolution. (More will be said subsequently about the details of these measurements.)

The second-order Doppler spectrum represented by (2) is a continuous function of frequency, in contrast to the "spiky" nature of the first-order scatter. Equation (2) shows that this is due to a double-interaction process between two sets of ocean waves having wavevectors $\bar{\kappa}_1$ and $\bar{\kappa}_2$. The measured spectrum of Figure 1 shows where this structure appears. It is this second-order sea echo and its more prominent features, when normalized with respect to the first-order sea echo, that we shall employ subsequently to extract wave height and wave period.

3. WAVE HEIGHT APPROXIMATION

Hasselmann [1971] initially suggested that the second-order Doppler sidebands around each first-order peak ought to be proportional to the wave height nondirectional temporal spectrum, centered at the first-order Bragg frequency, $\pm\omega_B$. If this were strictly true, the area under these sidebands would be proportional to the mean-square sea wave height. *Stewart* [1971] followed this suggestion to derive a simple proportionality relationship between the mean-square wave height and the ratio between the second-order and first-order spectral energies. However, his model was quite restrictive, based upon (i) neglect of the electromagnetic coupling factor Γ_{EM}; (ii) the assumption of a cosine-square azimuthal model for the wave height directional spectral dependence; and (iii) radar propagation only in the "upwind" direction (i.e., $\phi = 0$ according to our geometry here).

On the basis of these suggestions, we initially attempted (using buoy measurements for wave height "sea truth") to empirically relate the total second-order spectral area, divided by the first-order area, to mean-square waveheight. Furthermore, using the theoretical models above, we derived curves for this relationship as a function of the input wave height and the radar-to-wind direction, ϕ. Although theoretical and experimental results were in reasonably good agreement, the results were rather disappointing for the following reasons: (i) we did not have a simple, closed-form relationship for this area-to-wave height ratio; (ii) both the theoretical curves and the data points appeared to follow a law that could not be described over the region of interest by a simple power-law relationship with a small number of parameters; and (iii) the ratio was highly dependent upon ϕ, the radar-to-dominant-wave direction.

Hence, we derived an approximation on a step-by-step basis, starting from (2), to show that under certain conditions, the concept of forming a ratio
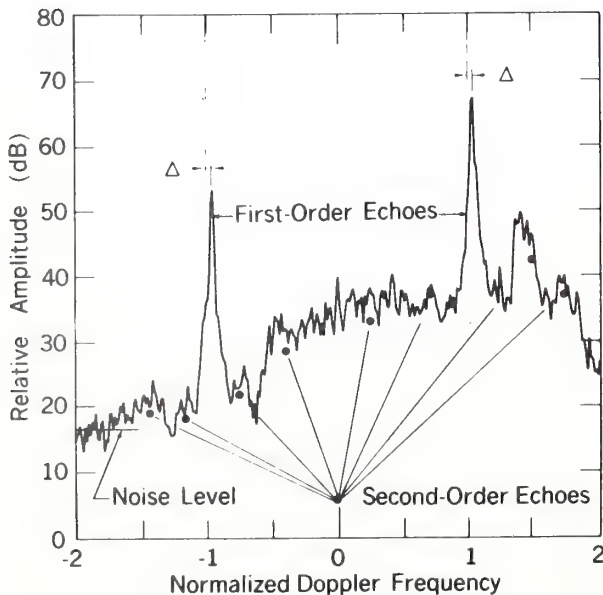
Fig. 1. Measured HF surface-wave sea-echo Doppler spectrum at 13.40 MHz from San Clemente Island.

of second-order to first-order energy could be used to obtain wave height. The differences in the approach taken here are: (i) the assumptions required in the approximations we employ are obvious, and the use of these approximations in turn permits us to derive a simple, closed-form result; and (ii) the use of a weighting function for the second-order energy, obtained from the theoretical model, allows the result to be relatively insensitive both to the form of the wave spectrum directionality and to the radar-to-wind direction, ϕ. Details of the steps of the derivation are found in *Barrick* [1977], where the wave height nondirectional temporal spectrum is related to the ratio of the weighted second-order Doppler sidebands to the first-order spectral energy. In this section, we take a different, simple approach to show how one can obtain mean-square wave height; that both analyses lead to the same result will be obvious shortly.

To illustrate the method, let us start from the following integral:

$$I_H = \sum_{u,l} \sum \iint_{-\infty}^{\infty} d^2\bar{\kappa}_1 S_{\pm}(\kappa_{1x},\kappa_{1y}) S_{\pm}(\kappa_{2x},\kappa_{2y}) \tag{3}$$

The integrand has two significant regions on the p-q plane: one near $\bar{\kappa}_2 = \bar{0}$ (i.e., at $\bar{\kappa}_I \cong (1/2)\bar{\kappa}_r$), and the other near $\bar{\kappa}_1 = \bar{0}$ (i.e., at $\bar{\kappa}_I \cong -(1/2)\bar{\kappa}_r$). In effect, one wave height spectrum is shifted out from the origin to a new origin at $\bar{\kappa}_2 \simeq \bar{0}$ ($\bar{\kappa}_I = (1/2)\bar{\kappa}_r$), but is weighted and shaped by the other spectrum factor with argument $\bar{\kappa}_1 \cong \bar{\kappa}_r$. Likewise, the other spectrum is located at $\bar{\kappa}_1 = \bar{0}$ ($\bar{\kappa}_I = -(1/2)\bar{\kappa}_r$), but weighted and shaped by the other spectrum with argument $\bar{\kappa}_2 \cong \bar{\kappa}_r$. This is illustrated in Figure 2 by employing a currently popular spectral model $S_{\pm}(\bar{\kappa}) = f(\kappa)g_{\pm}(\theta)$, where $f(\kappa)$ follows the Phillips model for wind-driven, fully developed seas [*Phillips*, 1966], and the directional factor $g_{\pm}(\theta)$ has a form deduced empirically by *Tyler et al.* [1974]. These factors are

$$f(\kappa) = .005/2\pi\kappa^4 \qquad \text{for } \kappa > \kappa_{co} \tag{4}$$

$$g_{\pm}(\theta) = (4/3)\cos^4[\pm|\theta|/2] \tag{5}$$

where $\kappa_{co} \equiv g/u^2$, with g being the acceleration of gravity and u being the wind speed. The original "one-sided" spectrum is shown in Figure 2(a), i.e., $(4/3)f(\kappa)\cos^4(\theta/2)$. Plotted in Figure 2(b) is the symmetricized spectrum $S(\bar{\kappa}) \equiv S_+(\bar{\kappa}) + S_-(\kappa)$ required for real wave fields. Shown then in (c)
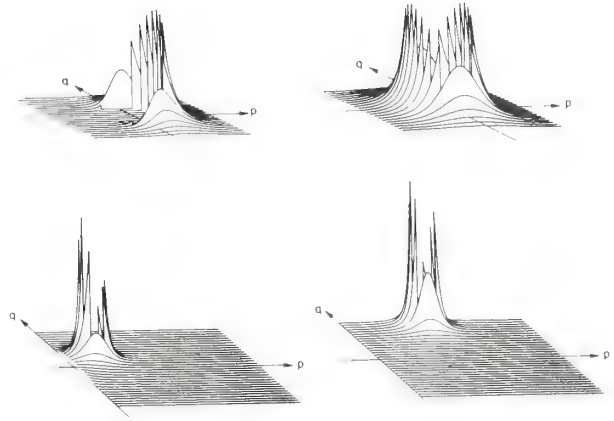
Fig. 2. Three-dimensional plots of single and product wave height directional spectra following (4). Upper left: One-sided spatial spectrum, $S_+(\bar{\kappa})$ for $0 < |\theta| < 90°$ and $S_-(\bar{\kappa})$ for $90° < |\theta| < 180°$. Upper right: two-sided spatial spectrum, $S(\bar{\kappa}) = S_+(\bar{\kappa}) + S(\bar{\kappa})$. Lower left: product functional, $S(\bar{\kappa}_1)S(\bar{\kappa}_2)$ for $\beta/2 = 4$ and $\phi = 45°$. Lower right: product functional, $S(\bar{\kappa}_1)S(\bar{\kappa}_2)$ for $\beta/2 = 10$ and $\phi = 45°$.

and (d) are the product functionals (for positive p only, since symmetry obtains for negative p), i.e., $S(\bar{\kappa}_1)S(\bar{\kappa}_2)$. From the definitions following (2) we write this as

$$S(\bar{\kappa}_1)S(\bar{\kappa}_2) = S(\kappa_{1x},\kappa_{1y})S(\kappa_{2x},\kappa_{2y})$$

$$= S(k_o\cos\phi + p, k_o\sin\phi + q)$$

$$\cdot S(k_o\cos\phi - p, k_o\sin\phi - q)$$

$$= S[(\kappa_{co}\beta/2)\cos\phi + p, (\kappa_{co}\beta/2)\sin\phi + q]$$

$$\cdot S[(\kappa_{co}\beta/2)\cos\phi - p, (\kappa_{co}\beta/2)\sin\phi - q]$$

where $\beta/2 = k_o/\kappa_{co}$ is a dimensionless parameter. As can be seen, this product functional has the effect of taking the single spectrum in (b)—located at $p = q = 0$ and creating two, one located at $p = (\kappa_{co}\beta/2)\cos\phi$, $q = (\kappa_{co}\beta/2)\sin\phi$, and the other at its mirror position $p = -(\kappa_{co}\beta/2)\cos\phi$, $q = -(\kappa_{co}\beta/2)\sin\phi$. Figure 2(c) illustrates this effect for $\beta/2 = 4$ and $\phi = 45°$, while Figure 2(d) has $\beta/2 = 10$ and $\phi = 45°$. At a typical HF radar frequency of 15 MHz, $\beta/2 = 10$ would correspond to an rms wave height of 1.592 m.

The figure demonstrates that as β becomes larger so that the centers of the product-functional spectra move farther apart (as in going from (c) to (d)), the spectrum $S(\bar{\kappa}_2)$ at and near $p = (\kappa_{co}\beta/2)\cos\phi$, $q = (\kappa_{co}\beta/2)\sin\phi$ is "weighted" by an $S(\bar{\kappa}_1)$ which

approaches a constant, i.e.,

$$S(\bar{\kappa}_1) \rightarrow S(\kappa_{co}\beta\cos\phi, \kappa_{co}\beta\sin\phi) = S(\bar{\kappa}_r)$$

Hence in this limit of large β, we could remove $S(\bar{\kappa}_1)$ from the integrand for positive p, q, giving

$$I_H \cong 2[S_+(\bar{\kappa}_r) + S_-(\bar{\kappa}_r)] \sum_{u,l} \iint_{-\infty}^{\infty} d^2\bar{\kappa}_1 S_\pm(\kappa_{2x},\kappa_{2y}) \tag{6}$$

The sum/integral factor, however, is identically the mean-square wave height, h_*^2, by definition of a wave height spectrum. Hence we have

$$I_H \cong 2h_*^2 [S_+(\bar{\kappa}_r) + S_-(\bar{\kappa}_r)] \tag{7}$$

There are two quantities in the integrand of (2) for $\sigma_{(2)}(\omega_d)$ that keep it from being equal to the I_H of (3): one is the coupling coefficient $|\Gamma_T|^2$, and the other is the δ-function. The former is a function of ω_d and also the integration parameters. We remove it in an approximation that retains its functional dependence on ω_d but averages it over the variable of integration; this defines our dimensionless "weighting function," $w(\nu)$, as [Barrick, 1977]:

$$\overline{|\Gamma_T|^2} = (k_o^2/8)w(\nu) \tag{8}$$

where $\nu \equiv \omega_d/\omega_B$ is Doppler frequency normalized to the Bragg frequency. Figure 3 shows a plot of $w(\nu)$ for $0 \le |\nu| \le 2.4$. The singularities at $2^{1/2}$ and $2^{3/4}$ result from regions of mathematical stationarity which are interpretable physically in terms of the radar/ocean wave interactions; such interpretation is found in Barrick [1977].

When (2) is divided by $w(\nu)$ we obtain

$$\frac{\sigma_{(2)}(\omega_d)}{w(\omega_d/\omega_B)} \cong 2^5\pi k_o^6 \sum_{u,l}\sum \iint_{-\infty}^{\infty} d^2\bar{\kappa}_1 S_\pm(\kappa_{1x},\kappa_{1y})$$
$$\cdot S_\pm(\kappa_{2x},\kappa_{2y})\delta(\omega_d \mp \omega_{o1} \mp \omega_{o2})$$

The δ-function can be eliminated by integrating the entire equation with respect to ω_d, at which point we arrive at (8):

$$\int_{-\infty}^{\infty} \frac{\sigma_{(2)}(\omega_d)}{w(\omega_d/\omega_B)} d\omega_d = 2^5\pi k_o^6 \sum_{u,l}\sum \iint_{-\infty}^{\infty}$$
$$\cdot d^2\bar{\kappa}_1 S_\pm(\kappa_{1x},\kappa_{1y})S_\pm(\kappa_{2x},\kappa_{2y}) = 2^5\pi k_o^6 I_H$$
$$\cong 2^6\pi k_o^6 h_*^2 [S_+(\bar{\kappa}_r) + S_-(\bar{\kappa}_r)] \tag{9}$$
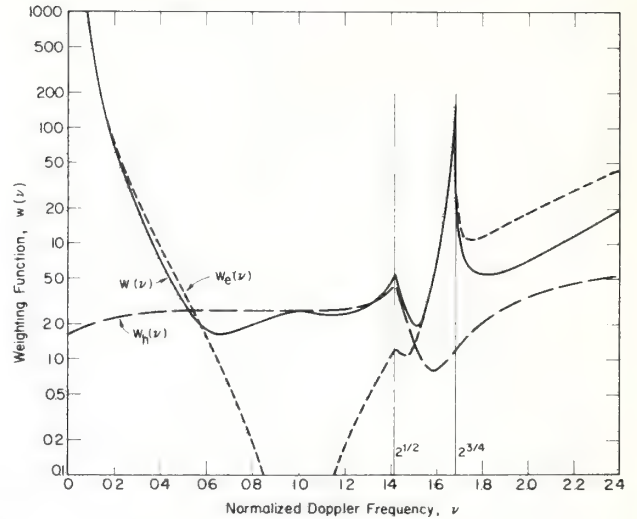
Fig. 3. Weighting function $w(\nu)$ as defined in (8). Also shown are the contributions to this function of the electromagnetic (e) and hydrodynamic terms (h) when each acts alone.

The unknown wave height directional spectrum evaluated at the Bragg radar wavenumber, $\bar{\kappa}_r$, is obtained from the first-order Doppler spectrum, (1), by integrating over ω_d:

$$\int_{-\infty}^{\infty} \sigma_{(1)}(\omega_d)d\omega_d = 2^7\pi k_o^4[S_+(\bar{\kappa}_r) + S_-(\bar{\kappa}_r)] \tag{10}$$

Dividing the two equations gives the desired result:

$$k_o^2 h_*^2 = \frac{2\int_{-\infty}^{\infty} [\sigma_{(2)}(\omega_d)/w(\omega_d/\omega_B)]d\omega_d}{\int_{-\infty}^{\infty}\sigma_{(1)}(\omega_d)d\omega_d} \tag{11}$$

Thus we have shown via two approximations how one can obtain an expression for the radar-deduced mean-square wave height, h_*^2, in terms of the weighted second-order spectral area divided by the first-order area; the validity of those approximations will be tested in a subsequent section. It is not necessary to integrate the spectral quantities in numerator and denominator over the entire Doppler region (i.e., $-\infty < \omega_d < \infty$). Many measured Doppler spectra will have one very strong side, while the other may be uncomfortably near the noise level; in this case, one can integrate both numerator and denominator only over the stronger side (i.e., $-\infty$

$< \omega_d < 0$ or $0 < \omega_d < \infty$). Also, while (11) is given in terms of $\sigma_{(2)}(\omega_d)$ and $\sigma_{(1)}(\omega_d)$, it is not necessary to know the absolute values of these quantities. Any unknown path loss or system gain factors multiplying one will also multiply the other, and the division process removes all such unknown factors. To apply (11) to measured data, it is necessary only that $\sigma_{(2)}$ and $\sigma_{(1)}$ both be identifiable and above the noise level.

4. WAVE PERIOD APPROXIMATION

Barrick [1977] derived an expression, as initially suggested by *Hasselmann* [1971], for the wave height nondirectional temporal spectrum in terms of one of the weighted Doppler second-order sidebands. Again, taking the side with the stronger power density, this expression is:

$$S_t[\omega_B|\nu - 1|] = [4\sigma_{(2)}(\omega_B\nu)/w(\nu)] \bigg/ k_o^2 \int_0^\infty \sigma_{(1)}(\omega_d)d\omega_d$$

(12)

where it is assumed that the spectral sidebands from 0 to ∞ are stronger, and that either one of the two sidebands near $\nu = 1$ is used (or better yet, their average).

We define the mean wave frequency in a "centroid" sense, i.e.,

$$\bar{\omega} = \int_0^\infty \omega S_t(\omega)d\omega \bigg/ \int_0^\infty S_t(\omega)d\omega$$

and its reciprocal as the mean wave period, i.e., $\tau \equiv 2\pi/\bar{\omega}$. Hence, our radar-deduced mean wave period would be

$$\frac{\omega_B\tau_*}{2\pi} = \frac{\displaystyle\int_{0,1}^{1,\infty} [\sigma_{(2)}(\omega_B\nu)/w(\nu)]d\nu}{\displaystyle\int_{0,1}^{1,\infty} |\nu - 1|[\sigma_{(2)}(\omega_B\nu)/w(\nu)]d\nu}$$

(13)

where again the integrations could run from either 0 to 1 or 1 to infinity.

The mean wave velocity may be defined in terms of this mean wave period obtained from the centroid by using the gravity-wave dispersion equation:

$$v_* = g\tau_*/2\pi$$

(14)

5. ACCURACY OF INVERSION MODELS: RECOVERED VS. ORIGINAL PARAMETERS

One method of testing the accuracy of the inversion techniques for wave height, h_*, and wave period, τ_*, and hence the validity of the approximations employed, is to see how well the technique recovers the desired parameter when one uses a known expression for the wave height directional spectrum in the original theoretical expressions, (1) and (2). Thus one knows precisely h and τ corresponding to the wave height directional spectrum used, then obtains $\sigma_{(1)}(\omega_d)$ and $\sigma_{(2)}(\omega_d)$ from (1) and (2), and finally recovers h_* and τ_* from (11) and (13).

To test the inversion models, we employed two different forms for the radial wavenumber dependence of the wave height spectrum, $f(\kappa)$ (as defined in connection with (7)). One was the Phillips model with the sharp cutoff for fully developed seas, as given in (7); the κ^{-4} spatial wavenumber dependence of this spectrum in the equilibrium region in turn transforms (via the first-order gravity-wave dispersion relation) to an ω^{-5} temporal frequency dependence. In addition, we employed a truncated version of the Phillips temporal spectrum, such that this model followed the ω^{-5} dependence for $\omega > 2^{1/2}\omega_{co}$, was flat for $\omega_{co} < \omega < 2^{1/2}\omega_{co}$, and zero for $\omega < \omega_{co}$ ($\omega_{co} \equiv (g\kappa_{co})^{1/2} = g/u$); the latter model would be more representative of seas that have not yet reached full development. In addition, we employed the $\cos^4\theta/2$ directional dependence given in (5) and three different radar/wind directions: $|\phi| = 0°$, $45°$, and $90°$ (by symmetry, identical results are obtained for $|\phi| = 180°$, $135°$, and $90°$).

Initially, we derived values of h_* and τ_* from the inversion models (11) and (13) as functions of $\beta(=2k_o/\kappa_{co})$ for the three values of ϕ. We found, however, from comparing results for the sharply cutoff spectrum with those for the truncated spectrum that a more universal parameter than β is (normalized) wave height, either k_oh (actual rms wave height) or k_oh_* (radar-deduced rms wave height). *In fact, the results to be presented here are independent of whether the spectrum is sharp or flat-topped if they are plotted as functions of k_oh_*.* This means in effect that the expressions for radar-deduced wave height and wave period do *not* depend upon the shape (or stage of development) of the spectrum, a fact that confirms the
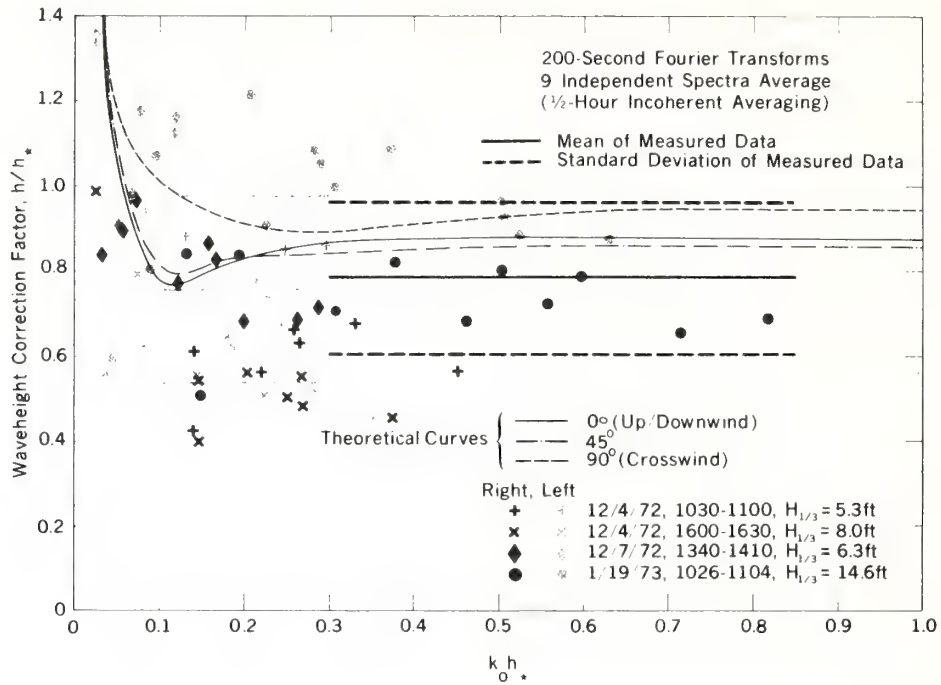
Fig. 4. Theoretical and experimental results of use of wave height inversion model; h_* is radar-deduced rms wave height, using (11), while h is actual (or buoy-measured) wave height.
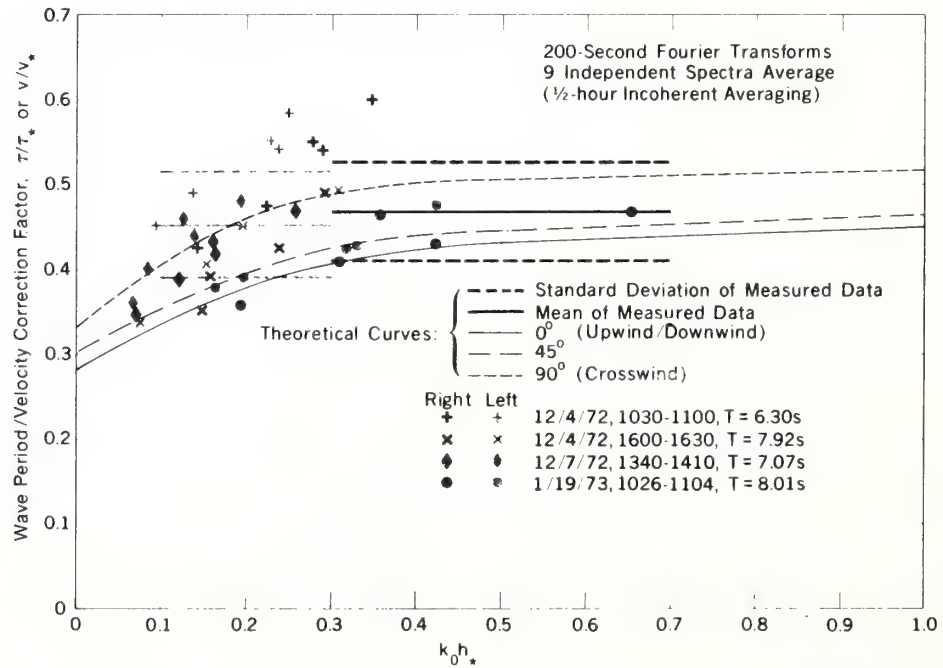
Fig. 5. Theoretical and experimental results of use of wave period inversion model; τ_* is radar-deduced mean wave period, using (13), while τ is actual (or buoy-measured) wave period.

82

general nature of the technique as derived in the mathematics.

In Figure 4, therefore, we plot h/h_* recovered from (11) as a function of $k_o h_*$ for the three values of radar look direction, ϕ. These curves represent correction factors by which one must multiply the radar-deduced wave height, h_*, in order to obtain the actual wave height (i.e., the input to the models here). Note that the rapidly diverging region for low values of $k_o h_*$ (i.e., $k_o h_* < .15$) implies that the approximations break down for low sea states and/or radar frequencies, as anticipated earlier. Secondly, note that while the curves do not converge exactly to unity for $k_o h_* \to \infty$, their asymptotes always lie closer to unity than 15%. Finally, we note that there is some small directional ϕ-dependence to the curves; this theoretical dependence is not nearly so pronounced, however, as it was when we did not weight the second-order Doppler spectra.

The curves for τ/τ_* do appear to approach unity asymptotically (Figure 5) for large $k_o h_*$. Again, the "sharp" and the "truncated" Phillips models gave the same correction curves for Figure 5, validating our use of the independent variable $k_o h_*$.

In theory then, one would employ the following steps to deduce precisely h and τ, the wave height and wave period: (i) Determine (if possible) the direction ϕ by using an alternate, independent technique (such as those described by *Long and Trizna* [1973], *Tyler et al.* [1974], or *Stewart and Barnum* [1975]). (ii) Determine h_* using (11). (iii) Enter the graph of Figure 4 with the values for ϕ and $k_o h_*$, obtaining the correction factor for converting h_* to h. (iv) Determine τ_* using (13). (v) Enter the graph of Figure 5 with the values for ϕ and $k_o h_*$, obtaining the factor for converting τ_* to τ.

If one does not know the radar look direction, ϕ, the figures give a range of uncertainty for the desired wave parameters, h and τ, which, as illustrated in the figures, is not all that great anyway. Hence for many applications, it may be just as convenient to ignore the dependence on ϕ in order to simplify the approach.

6. MEASURED DATA

HF surface-wave sea-echo measurements were made at a radar facility located on the west coast of San Clemente Island in late 1972 and early 1973.

The system was built by the Institute for Telecommunication Sciences of the US Department of Commerce and was operated under contract with the Wave Propagation Laboratory for this series of measurements.

Surface-wave radar data were obtained simultaneously at 10 frequencies extending from about 2.4 to 25 MHz. Receiver range gates were set to sample cells centered 22.5, 30.0, and 37.5 km from the radar. The receiving antenna consisted of an array of 13 monopoles phased and switched to alternately produce two beams each having a nominal beamwidth of 10° centered at azimuth angles of 240° and 270°. The combination of 10 frequencies, 3 ranges, and 2 antenna beams resulted in a total of 60 different data samples being recorded.

The transmitting antenna was a two-bay, vertically polarized, log-periodic antenna having a nominal half-power beamwidth of 60° over the HF band. Since this beamwidth illuminated both sectors covered by the receiving beams, no transmitter antenna steering was used. Power patterns of both receiving and transmitting antennas were measured from a small boat to verify gain and beamwidth performance. Radar characteristics are summarized in Table 1.

An on-line computer processed the received signals and computed the power spectrum for each of the 60 data channels. The power spectra that were processed on-line were calculated from signals that had been coherently sampled over a 200-sec window. Since a typical measurement period was 30 min, a total of 9 spectra would be computed during this time. These power spectra and the unprocessed IF data were recorded on magnetic tape to permit subsequent off-line analysis.

Wave heights and periods were measured

TABLE 1. Summary of San Clemente Island surface-wave radar characteristics.

Operating frequency range	2 to 25 MHz
Range gate distances	22.5, 30.0, 37.5 km
Available pulse lengths	20, 50, 100 μs
	(3.0, 7.5, 15.0 km)
Pulse repetition frequency	20 Hz per frequency
Transmitter peak power	40 kw
Antenna beamwidths	
Receiving (2 beams)	10° at 240° and 270° azimuth
Transmitting	60° at 255° azimuth
Antenna gain product	18 dB at center of HF band decreasing to 0 dB at band edges

independently by a Waverider Data Buoy moored 29.4 km from the radar site on an azimuth of 240°. These values of h and τ, taken here as the "sea truth," were confirmed (to ~10%) by comparisons with hindcasts from surface winds made over the same area and for the same time periods. Data from four different days were selected because of the fairly wide range of sea states and stages of development for these days. Because of the difficulty involved, no attempt was made to (directly) measure the dominant wave direction, ϕ, with respect to the radar look direction.

Computerized algorithms based on the use of (11) and (13) were developed to automatically extract wave height, h_*, and period, τ_*, from sample-averaged Doppler spectra such as those of Figure 1. First of all, the algorithm locates the first-order echo peaks. By searching for the nulls on either side of the dominant first-order peak, the algorithm identifies and separates the first-order echo from the second-order echo. To illustrate with an example, the remaining second-order echo after the first-order positive peak is removed from Figure 1 is shown as the solid curve of Figure 6. The computer then divides this second-order spectral energy by the weighting function, $w(\nu)$; the result

Fig. 6. Example from Figure 1 showing second-order portion of Doppler spectrum on positive side before weighting (solid) and after weighting (dotted).

is shown as the dotted curve of Figure 6. Finally, integrating both the weighted second-order energy and the first-order energy, as called for in (11) and (13), values for $k_o h_*$, h_*, and τ_* are obtained at the different frequencies, sea states, range gates, and beam positions. Knowing the buoy-measured values of h and τ, the resulting points were then plotted on Figures 4 and 5. Again, uncertainty regarding sea wave direction, ϕ, makes it impossible to identify the points with regard to this parameter. Over eighty hours of observations are represented by the data points on these plots.

The measured data points show a greater spread at the lower end, where the theoretical curves indicate that the approximations employed should be least valid. Consequently, we have calculated and shown the means and standard deviations over two regions of $k_o h_*$: for $0.1 < k_o h_* < 0.3$ and for $0.3 < k_o h_* < \infty$. For $k_o h_* > 0.3$, the empirically determined mean wave height correction factor is 0.785 and the mean wave period correction factor is 0.935. As can be seen, these are consistent with the theoretically deduced correction factors in each case. The percentage error for $k_o h_* > 0.3$, defined as the standard deviation of the measured data points divided by their mean, is 22.7% for wave height and 12.4% for wave period.

7. DISCUSSION AND CONCLUSIONS

This paper has concentrated upon developing and testing (against measured surface-wave sea echo) simple, closed-form models for estimating wave height and wave period with an HF radar. Unlike techniques described in the literature [*Long and Trizna*, 1973; *Tyler et al.*, 1974; *Stewart and Barnum*, 1975] for deducing mean wave direction, the methods described here are *not* based on the assumption of a given model for either the azimuthal directionality or the radial wavenumber dependence of the wave height directional spectrum. A goal here also was to obtain a simple inversion scheme that does not require *a priori* knowledge of the angle, ϕ, between the radar and mean wave direction.

Both theoretical predictions and measured data show that one can deduce both wave height and wave period reasonably accurately, so long as the parameter $k_o h_*$ is greater than 0.1. Measured data show that for $k_o h_* > 0.3$, wave height, h, can be deduced to an rms accuracy of ~23%, while wave period, τ, to an accuracy of ~12%. Theoretical
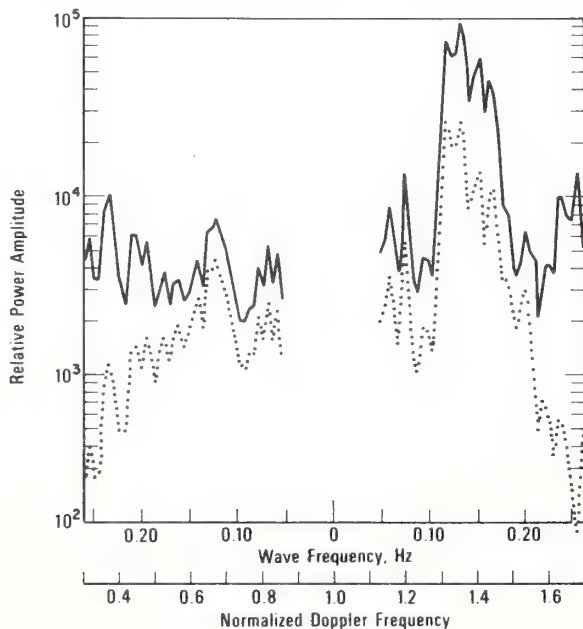
predictions show that part of this spread or error is due to the dependence of the results on the radar look angle, ϕ. Thus if one wishes to obtain better accuracy, he should employ alternate techniques to estimate ϕ, and then use this information, along with the curves of Figures 4 and 5, to find a closer estimate for the required correction factor. Hence the accuracies quoted above apply for the crudest and simplest inversion process, where one does not wish to bother with direction in order to estimate wave height and period. The models are straightforward, closed-form equations requiring measurement of the HF sea-echo Doppler spectrum and the use of a simple dimensionless weighting function presented here in Figure 3; the latter is a single curve over Doppler frequency, which is independent of radar frequency, look direction, wave height, or any other parameter. Obviously, further simplification is possible if one is willing to treat the weighting function as a constant over the region of greatest importance ($0.5 \leq |v| \leq 1.5$); how much further error such a simplification will produce has not been studied here.

Several things could degrade further the accuracy in estimating these parameters from measured data. Poor system Doppler resolution will produce some error; the above accuracies should apply if one can realize a Doppler resolution (at mid-HF) of ~0.02 Hz or better, requiring a 50-sec coherent processing period or longer. Inadequate incoherent averaging will also produce some error. With processing times exceeding 50 sec, one cannot afford to add hundreds of sequentially measured spectra to obtain an average. Thus a sample average of, say, ten Doppler spectra will still be somewhat random in appearance; curves for the confidence vs. number of samples for HF Doppler spectra were presented by *Barrick and Snider* [1977]. External (atmospheric) additive noise at HF will result in further error in the use of any inversion techniques such as this when the noise level is significant compared with the echo. This happens, for example, with surface-wave radars for operations at higher frequencies and at greater distances. For skywave radars (using ionospheric reflections), higher additive noise often contaminates the data at nighttime. Finally, skywave radar propagation often smears the dominant features of the Doppler spectra because of turbulence in the reflecting ionospheric layers. This has the effect of reducing the effective

Doppler resolution of the received spectra, and can be so bad at times that it is not possible to distinguish the first-order from the second-order portions of the signal spectrum. We and others are presently engaged in extending these methods and developing new techniques to handle such cases of severe ionospheric signal distortions.

REFERENCES

Barrick, D. E. (1971a), Theory of HF/VHF propagation across the rough sea, 1 and 2, *Radio Sci.*, 6, 517–533.

Barrick, D. E. (1971b), Dependence of second-order sidebands in HF sea echo upon sea state, paper presented at IEEE G-AP International Symposium, Los Angeles, California, September 1971.

Barrick, D. E. (1972a), First-order theory and analysis of MF/HF/VHF scatter from the sea, *IEEE Trans. Antennas Propagat.*, AP-20, 2–10.

Barrick, D. E. (1972b), Remote sensing of sea state by radar, in *Remote Sensing of the Troposphere*, edited by V. E. Derr, chap. 12, US Government Printing Office, Washington, DC.

Barrick, D. E. (1977), The ocean wave height nondirectional spectrum from inversion of the HF sea-echo Doppler spectrum, *Remote Sensing Environ.*, in press.

Barrick, D. E., and J. B. Snider (1977), The statistics of HF sea-echo Doppler spectra, *IEEE Trans. Antennas Propagat.*, AP-24, 19–28.

Crombie, D. D. (1955), Doppler spectrum of sea echo at 13.56 Mc/s, *Nature*, 175, 681–682.

Hasselmann, K. (1971), Determination of ocean wave spectra from Doppler radio return from the sea surface, *Nature Phys. Sci.*, 229, 16–17.

Lipa, B. (1977), Derivation of directional ocean-wave spectra by integral inversion of second-order radar echoes, *Radio Sci.*, 12, this issue.

Long, A. E., and D. B. Trizna (1973), Mapping of North Atlantic winds by HF radar sea backscatter interpretation, *IEEE Trans. Antennas Propagat.*, AP-21, 680–685.

Phillips, O. M. (1966), *Dynamics of the Upper Ocean*, pp. 109–139, Cambridge University Press, London.

Stewart, R. H. (1971), Higher-order scattering of radio waves from the sea, paper presented at IEEE G-AP International Symposium, Los Angeles, California, September 1971.

Stewart, R. H., and J. R. Barnum (1975), Radio measurements of oceanic winds at long range: An evaluation, *Radio Sci.*, 10, 853–857.

Tyler, G. L., C. C. Teague, R. H. Stewart, A. M. Peterson, W. H. Munk, and J. W. Joy (1974), Wave directional spectra from synthetic aperture observations of radio scatter, *Deep Sea Res.*, 21, 989–1016.

The Ocean Waveheight Nondirectional Spectrum from Inversion of the HF Sea-Echo Doppler Spectrum

DONALD E. BARRICK

NOAA/ERL/Wave Propagation Laboratory, Boulder, Colorado 80302

The measured HF sea-echo Doppler spectrum consists of prominent first-order peaks, around which exist second-order sidebands of a continuous nature. Theoretical models developed elsewhere are interpreted here and shown to satisfactorily account for these first and second-order measured spectral features. Employing these theoretical models, this paper derives a simple inversion technique for obtaining the waveheight nondirectional spectrum. The result is a closed-form expression, independent of the wave directionality factor, the radar look direction, or the stage of development of the waveheight spectrum. Approximations required in the derivation are stated along the way, and are shown to become increasingly valid in the limit of high seas and/or radar frequencies. The technique is tested by attempting to recover several input waveheight nondirectional spectra for various radar look directions. Comparisons show that the technique produces acceptable results for $k_o h > 0.2$, where k_o is the radar wavenumber and h is the rms waveheight. Application of the inversion technique to measured data is straightforward. One employs one of the stronger second-order Doppler sidebands (vs. Doppler frequency with respect to the first-order Doppler-peak frequency) and divides it by a parameterless, dimensionless weighting function derived in this paper. He then divides this result by the adjacent first-order spectral energy. The latter normalization (i) serves to remove any unknown radar path loss or system gain factors, and (ii) also eliminates the need for any *a priori* knowledge of the wave or radar directionality and/or the assumption of a model for these latter quantities.

1. Introduction

The use of HF radar to measure various parameters characterizing sea state was suggested by Crombie (1955) over two decades ago; he correctly deduced from measured echo spectra that the dominant (first-order) return was explained by the simple Bragg or diffraction-grating mechanism. More recently, analyses by Barrick (1972a, b) have developed theoretical models for the first-order sea echo which are compatible with Crombie's interpretations. Barrick (1971b, 1972b) extended these analyses to second-order, thereby accounting for the continuum in the observed Doppler spectrum between the first-order peaks; this theory reveals that a double (ocean) wave-wave interaction with the incident radar wave accounts for the scattered signal. Valenzuela (1974) obtained results that agree with those of Barrick, thereby lending credence to the conclusion that present models are correct to first and second order.

Hasselmann (1971) first suggested that the second-order Doppler sidebands ought to be proportional to the waveheight nondirectional temporal spectrum. He also suggested a convenient normalization of dividing these sidebands by the first-order echo, thereby canceling un-

known factors such as path loss and system gains. Stewart (1971) further explored conditions under which Hasselmann's hypothesis should be valid for a given sea-spectral model and radar-to-wind direction, deriving a result for mean-square waveheight. This paper derives precisely the relationships suggested by Hasselmann; no models for the waveheight directional spectrum are required, and the result is independent of the radar look direction. Approximations that are needed are stated along the way. These approximations—and their implicit requirements in terms of radar frequencies and sea roughness—are established by comparing nondirectional spectra recovered via our inversion technique with the original input to the model.

One can obtain many important descriptors of sea state from the waveheight nondirectional-spectrum, including rms waveheight, the dominant windwave period, swell periods, and the general stage of development of a wind-driven sea. This spectrum is readily obtained by oceanographers from time-series records of waveheight, as measured by wavestaffs or buoys with vertical accelerometers. (See Kinsman, 1965, for a general treatment of waves and their measurement.) The possibility of measuring this oceanographic quantity with skywave [over-the-horizon] or surface-wave HF radars (Barrick, 1973) represents an important step forward in replacing *in-situ* observing devices with remote-sensing techniques.

Results obtained in Barrick (1972a) show that the average, first-order sea-echo Doppler spectrum (for vertically polarized backscatter at grazing incidence), expressed as radar cross section per mean surface area per rad/s bandwidth, is:

$$\sigma_{(1)}(\omega_d) = 2^7 \pi k_o^4 \sum_{u,\ell} S_{\pm}(\kappa_{rx}, \kappa_{ry}) \delta (\omega_d \mp \omega_{or}),$$

(1)

where $\bar{\kappa}_r$ is the total radar wavenumber vector, defined as $\bar{\kappa}_r \equiv \bar{k}_s - \bar{k}_i$. The coordinate system selected here has the backscattering wavevector, $\bar{k}_s$, taken at an angle ϕ with respect to the x-direction; hence the incidence radar wavevector, $\bar{k}_i$, lies in the direction $\pi + \phi$. Therefore, $\bar{\kappa}_r$ becomes $2k_o \cos\phi \bar{x} + 2k_o \sin\phi \bar{y}$, with k_o being the scalar radio wavenumber. The summation convention refers to the upper (u) and the lower (ℓ) subscripts and signs in the equation. The quantity ω_d is the radian Doppler shift of the received signal, defined as $\omega_d \equiv \omega_s - \omega_i$, with ω_s and ω_i being the frequencies of the scattered and incident signals, respectively. The deep-water gravity-wave dispersion relation is employed to define ω_{or}: $\omega_{or} = \text{sgn}(\kappa_{rx}) \times \sqrt{g\kappa_r} = \text{sgn}(\cos\phi) \omega_B$, where $\kappa_r = |\bar{\kappa}_r|$, g is the acceleration of gravity (~ 9.81 ms^{-2}), and ω_B is referred to as the first-order Bragg frequency ($\omega_B \equiv \sqrt{2gk_o}$). The expression sgn ($x$) is a sign indicator, which takes on the values ± 1 depending on whether x is $\pm$. The average waveheight directional spectrum—represented as S_+ and S_-—is defined and discussed in App. A; suffice it to say here that S_+ is defined to peak azimuthally along the $+x$-axis. The quantity $\delta(x)$ is the Dirac-delta function of argument x.

From Barrick (1972b), the corresponding result for second-order sea echo is

$$\sigma_{(2)}(\omega_d) = 2^8\pi_o^4 \sum_{u,\ell}\sum \int\int_{-\infty}^{\infty} d^2\bar{\kappa}_I \, |\Gamma_T|^2$$

$$S_\pm(\kappa_{1x},\kappa_{1y}) \, S_\pm(\kappa_{2x},\kappa_{2y}) \, \delta \, (\omega_d \mp \omega_{o1} \mp \omega_{o2}),$$

$$(2)$$

where $\bar{\kappa}_1 \equiv 1/2\bar{\kappa}_r + \bar{\kappa}_I; \; \bar{\kappa}_2 \equiv 1/2\bar{\kappa}_r - \bar{\kappa}_I;$

$$\omega_{o1} \equiv \mathrm{sgn}\,(\kappa_{1x})\sqrt{g\kappa_1}; \; \omega_{o2} \equiv \mathrm{sgn}\,(\kappa_{2x})\sqrt{g\kappa_2};$$

$$\Gamma_T = \Gamma_H + \Gamma_{EM}, \text{ where}$$

$$\Gamma_H = -\frac{i}{2}\,\{\kappa_1 + \kappa_2 + (\kappa_1\kappa_2 - \bar{\kappa}_1 \cdot \bar{\kappa}_2)\times$$

$$\left(\frac{\omega_B^2 + \omega_d^2}{\omega_B^2 - \omega_d^2}\right)\frac{g}{\omega_{o1}\omega_{o2}} \, \},$$

$$(3a)$$

$$\Gamma_{EM} = \frac{1}{2}\,(\kappa_{1x}\kappa_{2x} - 2\bar{\kappa}_1 \cdot \bar{\kappa}_2) / (\sqrt{\bar{\kappa}_1 \cdot \bar{\kappa}_2}$$

$$+ k_o\Delta),$$

$$(3b)$$

and where we take the integration variables here to be p, q, such that $\bar{\kappa}_I = p\hat{x} + q\hat{y}$. The quantity $\triangle$ is the normalized electrical impedance for the rough sea surface at grazing incidence, as defined and derived in Barrick (1971a).

The coupling coefficients Γ_H and Γ_{EM} are obtained from the second-order terms in the perturbational expansions for the sea waveheight and electromagnetic scatter, respectively; the equations describing these processes are nonlinear.

In the next section, we demonstrate how one can employ the waveheight directional spectrum in (1) and (2) to predict the average sea-echo signal spectrum as seen at the output of a receiver; this is then compared to measurements to establish the validity of the theoretical models. The third section shows and explains the approximation whereby one of the two waveheight spectrum factors appearing in (2) is removed from the integrand as a constant, while the remaining integral is evaluated. Sec. 4 discusses the approximation in which the coupling coefficient, Γ_T, is removed and evaluated at each Doppler shift, ω_d. Finally, Sec. 5 shows examples of the use of the complete inversion technique to recover input waveheight spectra to the theoretical model; thus the accuracy of the method is established for a variety of sea-state/radar-frequency conditions.

2. The Doppler Spectrum: Interpretation and Direct Solution

The preceding theoretical expressions show that the Bragg—or diffraction grating—effect is responsible for the scatter. Equation (1) shows that the ocean wavevector responsible for first-order backscatter is $\bar{\kappa}_r = \bar{k}_s - \bar{k}_i$; likewise the temporal wavenumbers follow the same first-order Bragg condition, i.e., $\omega_d = \pm \, \omega_B = \omega_s - \omega_i$. To second order, (2) shows that the two ocean wavesets responsible for scatter, having wavevectors $\bar{\kappa}_1$ and $\bar{\kappa}_2$, obey the relation $\pm \bar{\kappa}_1 \pm \bar{\kappa}_2 = \bar{k}_s - \bar{k}_i$, and the wave

frequencies are related as $\pm \omega_{O1} \pm \omega_{O2} = \omega_s - \omega_i$; thus two sets of ocean waves are interacting simultaneously to produce the scatter. Of course, the lowest-order dispersion equation relates ω_{Or} to κ_r, and ω_{01}, ω_{02} to κ_1, κ_2.

By transforming (2) properly, the delta function in the integrand can be used to simplify the double integral, reducing it to a single integral. Of the various transformations possible, we have chosen one discussed in App. B. Its use results in the following expression for the second-order Doppler spectrum:

$$\omega_B \sigma_{(2)}(\omega_B \nu) = (2k_o)^8 \pi \nu^7 \, \underset{\nu,\alpha}{\Sigma\Sigma} \int_{\alpha_1}^{\alpha_2} \frac{d\alpha \mid \gamma_T(\nu,\alpha) \mid^2 S_{\pm}[\bar{\kappa}_1(\nu,\alpha)] S_{\mp}[\bar{\kappa}_2(\nu,\alpha)] \, \sin 2\alpha}{f^{16}(\alpha) \sqrt{2\nu^4 f^4(\alpha) - \nu^8 \cos^2 2\alpha - f^8(\alpha)}} \, , \tag{4}$$

where

$$\gamma_T(\nu,\alpha) = -\frac{i2f^4(\alpha)\nu^2}{\sqrt{\sin 2\alpha}} \left[\sqrt{2\sin 2\alpha} \, (\cos\alpha + \sin\alpha) + \mathrm{sgn}(\kappa_{1x}) \mathrm{sgn}(\kappa_{2x})(1 + \sin 2\alpha - \frac{f^4(\alpha)}{\nu^4}) \times \right.$$

$$\left. (\frac{1 + \nu^2}{1 - \nu^2}) \right] + \left[\frac{4\nu^4 f^4(\alpha) - 3f^8(\alpha) - \nu^8 \cos^2 2\alpha}{\sqrt{f^4(\alpha) - \nu^4 + \Delta f^2(\alpha)/\sqrt{2}}} \right] \, ,$$

with all of the remaining quantities being defined in App. B. The Doppler frequency is normalized here to the first-order Bragg frequency as follows: $\omega_d \equiv \nu \omega_B$.

One advantage of this transformation is that it explains a prominent feature of the Doppler spectrum: the peak at $\nu = 2^{3/4}$. This feature arises when the radical in the denominator of the second term of γ_T (i.e., the electromagnetic coupling factor) vanishes. Physically, the significance of this radical vanishing is that the intermediate radio wave interacting with the two sets of ocean waves having wavevectors $\bar{\kappa}_1$ and $\bar{\kappa}_2$ — which

has wavevector κ_I — is equal in magnitude to the free-space radio wavenumber, k_o, and is propagating along the surface. This means that the radio wave is at a transition point between being scattered and being evanescent; it therefore results in the greatest possible transport of (radio) energy between the two sets of ocean waves. The value of α, i.e., α_e, that causes the radical to vanish (vs ν) is that solution to the transcendental equation $f(\alpha_e) = \nu$; it is shown plotted in Fig. B-1. In this case, the peak at $\nu = 2^{3/4}$ is explained via our transformation by a simple "corner-reflector" effect. Two sets of ocean waves that produce intermediate scatter along the surface—as shown in Fig. 1—must propagate at angles α_e and $\pi/2$-α_e with respect to the backscatter direction. Furthermore, their wavelengths must be $L_1 = \pi/(k_o \cos\alpha_e)$ and $L_2 = \pi/(k_o \sin\alpha_e)$. From simple considerations, one can calculate the Doppler shift imparted by two such sets of ocean waves — both moving either toward or away from the radar — as $\nu = \pm[\cos^{1/2}\alpha_e + \sin^{1/2}\alpha_e]$. Now, as α_e varies, one sees that this ex-

pression has a maximum value — and in fact a point of mathematical stationarity — for $\alpha_e = 45°$, which occurs at $\nu = 2^{3/4}$. Thus two sets of waves at 45° with respect to the backscatter direction and 90° with respect to each other produce maximal intensity, as explained from elementary physics. This intensity manifests itself as a spectral peak at $\nu = 2^{3/4}$.

Before one launches into techniques for inverting the nonlinear integral equation, (4), to obtain the waveheight spectrum from the observed second-order Doppler spectrum, it is instructive to examine the numerical solution of the direct problem. Furthermore, the combination of the second-order echo with first-order, and their comparison with observations, should lend sufficient credibility to the entire theory that one could trust an inversion technique based upon these models. In order to perform such a numerical calculation, we employ a Phillips model for the spatial wavenumber spectrum, with a $\cos^4\theta/2$ directionality in azimuth. Thus we use

$$S_-(\kappa\cos\theta, \kappa\sin\theta) = \begin{cases} \dfrac{10^{-2}}{3\pi\kappa^4} \cos^4\theta/2 & \text{for } \kappa > \kappa_{co} = g/u^2 \\[2ex] 0 & \text{for } \kappa < \kappa_{co} = g/u^2, \end{cases} \tag{5}$$

where u is the wind speed in m/s. (This expression yields a rms waveheight $h = 0.05\ u^2/g$.) The above simplified model is only adequate for fully developed seas, that is, sea conditions where the wind duration is sufficient that the waves are in equilibrium with the wind. To obtain a result using (5) in (4), we assume as an example here that the radar looks in a direction $\phi = 45^\circ$ with respect to the dominant wave direction. Furthermore, we assume a radar operating frequency of 13.40 MHz ($k_o = 0.281\ \text{m}^{-1}$). In order to combine the first-order Doppler spectrum with the second-order portion, we assume that the two pass through a radar receiver whose effective windowing width is 40 s (giving an effective Doppler resolution of .025 Hz). Finally, a wind speed of 25 knots (12.86 m/s is assumed, giving an rms waveheight in this case of 2.765 ft (0.843 m). The result is shown as the solid curve in Fig. 2.

Many HF Doppler spectra were measured in the 1972-1973 period with a multi-frequency radar on San Clemente Island; details of the measurements and equipment are found in Barrick et al. (1974). One typical set of three spectra (measured on three frequencies, 13.40, 13.41, and 13.43 MHz) are shown in Fig. 2 for comparison. A sample average of 9 independent 200-second Doppler spectra on each frequency were produced in this case, and then passed through the same 40-second windowing function as the theoretical spectrum. The observed wind speed was 25 knots, the seas were fully developed, and the radar beam looked in a direction of 50° with respect to the wind. Since path losses in a system such as this are always somewhat

uncertain, the spectrum levels were adjusted until the first-order peaks were approximately aligned. The agreement of the second-order structures lends credibility to the models.

In general for this frequency range (5-30 MHz), the first-order peaks are constant in amplitude because they are sampling the sea spectrum in the saturated (equilibrium) region having κ^{-4} dependence. Hence, as waveheight and/or radar frequency increases, the second-order peaks of the spectrum increase both in their amplitudes and in their proximity to the first-order peaks. As the angle, ϕ, between dominant waves and radar varies between 90° and 0° or 180°, the shape of both portions of the Doppler spectrum varies between perfect symmetry about the carrier (at $\nu = 0$) to greatly skewed shapes in the $+\nu$ or $-\nu$ directions.

3. The Non-directional Spectrum Approximation

As a step in the inversion problem as postulated here, we show in this section that the integral

$$I_T = \underset{u,\ell}{\Sigma\Sigma} \int_{-\infty}^{\infty} dp \int_{-\infty}^{\infty} dq\ S_\pm(\kappa_{1x},\kappa_{1y})$$

(6)

$$S_\pm(\kappa_{2x},\kappa_{2y})\ \delta\ (\omega_d \mp \omega_{o1} \mp \omega_{o2}),$$
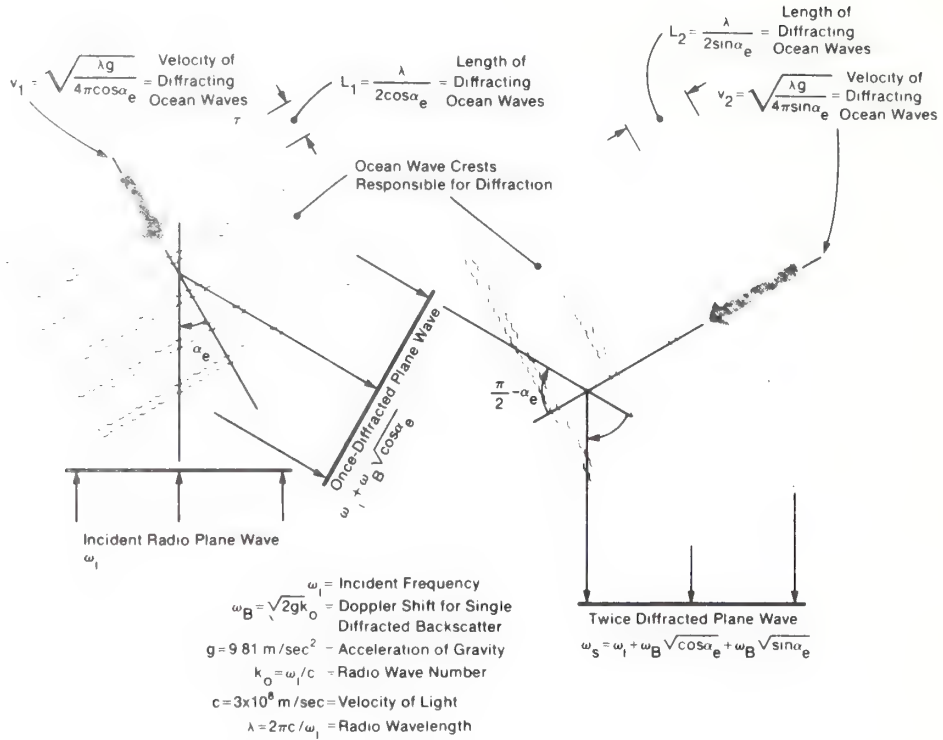
FIG. 1. Sketch showing second-order diffraction grating and Doppler effects when inter-mediate wave propagates along the surface.

can be approximated in terms of the waveheight non-directional spectrum when waveheight and/or radar frequency is large. Employing the same transformations outlined in App. B to derive (4) from (2), one can show that

$$\omega_B I_T = 8k_o^2 \nu^7 \sum_{\nu,\alpha}\sum \int_{\alpha_1}^{\alpha_2} \frac{d\alpha \, S_{\pm}\left[\bar{\kappa}_1(\nu,\alpha)\right] \, S_{\pm}\left[\bar{\kappa}_2(\nu,\alpha)\right]\sin 2\alpha}{f^4(\alpha)\sqrt{2\nu^4 f^4(\alpha) - \nu^8 \cos^2 2\alpha \quad f^8(\alpha)}} \cdot (7)$$
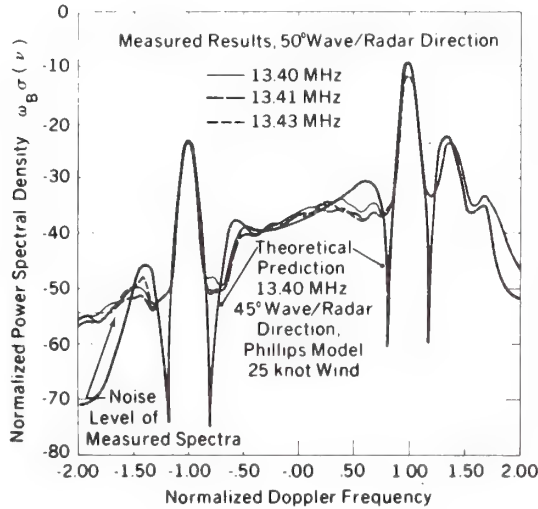
FIG. 2. Comparison of theoretical and experimental Doppler spectra (in decibels) at $\sim$13.4 MHz. Zero frequency corresponds to the carrier frequency position and ± 1 corresponds to 0.374 Hz. Gausian smoothing is used on all curves.

Referring to Fig. B-1, the more heavily shaded regions near $\nu = \pm 1$ produce a much greater contribution to the integral than those farther removed; in this region, α is close to 0 and $\pi/2$. We plan to concentrate here only on simplification of the above integral in the region where ν is slightly greater than unity and α is near zero; results for the other seven corners follow by analogy. For $1 < \nu < 1.3$, one can see from Fig. B-3 that two product functionals contribute to the integral: $S_+(\bar{\kappa}_1)\,S_-(\bar{\kappa}_2)$ and $S_+(\bar{\kappa}_1)\,S_+(\bar{\kappa}_2)$. We will expand normalized frequency, ν, as $\nu \equiv 1 + \mu$ in this region, where the assumption to be made is that μ is small. Then we change variables twice, and arrive at an integral over the azimuthal angle, θ_2, of the second spectrum. This essentially results

in the removal of the directional dependence of the waveheight spectrum, leaving the non-directioanl waveheight spectrum—evaluated at normalized temporal frequency μ—as being proportional to I_T for $\nu > 1$. In the process, all quantities will be expanded as series in μ, and all higher-order terms will be dropped. The error involved in this approximation for various radar frequencies and waveheight spectra will be examined in a subsequent section.

Higher sea states—characterized by large waveheights—result in smaller values of κ_{co} (the spatial wavenumber near which most of the energy exists). Hence, for increasing sea states and/or radar frequency, the parameter $\beta\ (= 2k_o/\kappa_{co})$ increases in size, and the dominant energy in the Doppler spectrum lies near $\mu = 0$, $\alpha = 0$. We will prove this here by deriving an approximation for μ_c in terms of β, where μ_c is the initial (normalized) frequency displacement from the Bragg line at which the Doppler energy begins to be significant. This is done by employing the Phillips cutoff relationship (the first of Eqs. (B-3)), eliminating α by employing (B-2), and expanding in a series of $\beta^{-n/2}$:

$$\mu_c = 1/\beta^{1/2} - 1/(2\beta) + 0(\beta^{-2}). \qquad (8)$$

Thus for example, for $\beta = 10$ (corresponding to an rms waveheight of 0.8 m and a radar frequency of 15 MHz for a fully developed sea), $\mu_c = 0.266$, which is reasonably small. At this point, the largest value of α is .09 rad or $5°$; hence, for $\beta > 10$ the claim becomes increas-

93

ingly valid that the region of ν,α space which is important occurs for μ and α small. (Complementary symmetry would show that the same is true for μ and $\pi/2$-α small.)

Next we derive approximations for α_2 and α_1 (the α-integration limits) in this region in terms of μ: these expressions come from expanding the Jacobian of (B-2) in terms of (small) α and μ:

$$\alpha_1 \cong \mu^2(1 - \mu)$$

and

$$\alpha_2 \cong \mu^2(1 + \mu). \qquad (9)$$

Thus α is indeed small even though μ may be only moderately small. Furthermore, the total excursion in α over this region of integration is even smaller, i.e., $2\mu^3$. We first use a transformation representing a linear shift in integration variables from α to δ, where $\delta \equiv \alpha - \alpha_1$: the integration limits on δ are now 0 and $2\mu^3$. Now expanding all quantities appearing explicitly in the integrand in terms of μ and δ, we retain only the lowest-order terms. As to orders of smallness, we note that $\delta \sim 0(\mu^3)$. Thus we find:

$$\kappa_{1x} \cong 2k_0\cos\phi \quad ; \quad \kappa_{1y} \cong 2k_0\sin\phi; \qquad (9a,b)$$

$$\kappa_{2x} \cong 2k_0[(\mu^2 - \delta/\mu)\cos\phi \pm \sqrt{2\mu\delta - \delta^2/\mu^2}\,\sin\phi]; \qquad (9c)$$

$$\kappa_{2y} \cong 2k_0[(\mu^2 - \delta/\mu)\sin\phi \mp \sqrt{2\mu\delta - \delta^2/\mu^2}\,\cos\phi]; \qquad \text{hence} \qquad (9d)$$

$$\kappa_1 \cong 2k_0; \kappa_2 \cong 2k_0\mu^2; \theta_1 \cong \phi; \qquad \text{and} \qquad (9e)$$

$$\theta_2 = \tan^{-1}\left[\frac{(\mu^2 - \delta/\mu)\sin\phi \mp \sqrt{2\mu\delta - \delta^2/\mu^2}\,\cos\phi}{(\mu^2 - \delta/\mu)\cos\phi \pm \sqrt{2\mu\delta - \delta^2/\mu^2}\,\sin\phi}\right]. \qquad (9f)$$

The other quantities in the integrand become

$$f^4(\alpha) \cong 1 \; ; \; \sin 2\alpha \cong 2\mu^2 \; ; \qquad (9g,h)$$

$$\sqrt{2\nu^4 f^4(\alpha) \, - \, \nu^8 \cos^2 2\alpha \, - \, f^{\,8}(\alpha)} \, \cong$$

$$2\sqrt{2\mu\delta \, - \, \delta^{\,2}/\mu^2}. \qquad (9\text{i})$$

Our previous statement that one of the waveheight spectrum factors, $S_+(\kappa_1)$ —which is common to both of the two terms in the integrand—can be removed from the integrand as a constant is now evident under these approximations. Thus the integral contribution to I_T from this region of $\nu > 1$, α near zero, can now be written as

$$\omega_B I^{\,\alpha\curvearrowright 0}_{\quad\nu\curvearrowright 1+} \, = \, 8k_O^4\mu^2 S_\pm(2k_O\cos\phi, 2k_O\sin\phi)\times$$

$$\sum_{u,\ell} \int_O^{2\mu^3} S_\pm[\bar{\kappa}_2(\mu,\delta)]\frac{d\delta}{\sqrt{2\mu\delta-\delta^2/\mu^2}}. \quad (10)$$

At this point, we make a final transformation to an integration over θ_2. Note that our initial representation in p-q space mapped doubly onto the allowed regions of ν-α (or μ-δ) space. Thus, going back to κ_2, θ_2, we see from (9f) that the selection of one set of signs covers only half the total possible variation of θ_2 (from 0 to 2π). For example, using the upper signs, we see that at $\delta=0$, $\theta_2=\phi$, at $\delta=\mu^3$, $\theta_2=\pi/2+\phi$, and at $\delta=2\mu^3$, $\theta_2=\pi+\phi$. The lower sign choice covers the remaining region $\phi-\pi<\theta_2<\phi$, as δ varies between its limits 0 to $2\mu^3$.

Using the upper sign choice and the Jacobian

$$d\theta_2 = \frac{d\delta}{\mu\sqrt{2\mu\delta-\delta^2/\mu^2}} \quad \text{gives} \qquad (11)$$

$$\omega_B I^{\,\alpha\curvearrowright 0}_{\quad\nu\curvearrowright 1+} = 8k_O^2\mu^3 S_+(2k_O\cos\phi, 2k_O\sin\phi)\times$$

$$\sum_{\mu,\ell} \int_\phi^{\phi+\pi} S_\pm(2k_O\mu^2\cos\theta_2, 2k_O\mu^2\sin\theta_2)d\theta_2. \quad (12)$$

This is the desired result, for it shows that the approximations permit one to integrate out the angular dependence in the waveheight directional spectrum. Noting from App. A that by definition S_+ and S_- are symmetric, we can relate the integral to the nondimensional temporal spectrum using (A-6), (A-7), and (A-8), obtaining

$$I^{\,\alpha\curvearrowright 0}_{\nu\curvearrowright 1+} = \frac{1}{2} S_+(2k_O\cos\phi, 2k_O\sin\phi)S_t(\omega_B\mu). \quad (13)$$

Up to now, we have considered only the contribution to I_T from the region near $\alpha=0$ (for $\nu>1$); an identical expression is obtained for the region near $\alpha=\pi/2$ ($\nu>1$). Hence we must double the above result to account for the total integral over α for $\nu>1$:

$$I_{\nu>1} = S_+(2k_O\cos\phi, 2k_O\sin\phi)S_t(\omega_B\mu). \qquad (14)$$

By analogy, one can derive an identical result for the region of ν slightly less than 1, defining in that case $\mu\equiv 1-\nu$. Finally, comparable results for the region of ν slightly greater and less than -1 give the same result as (14), but with S_+ replaced by S_-.

95

4. The Weighting-Function Approximation

Eq. (6) is similar—but not identical—to the second-order sea-echo Doppler spectrum as given in (2). Aside from multiplicative constants, it differs only in the presence of $|\Gamma_T|^2$ in the integrand of (2). The approximation to be made in this section involves the removal of $|\Gamma_T|^2$ from the integrand.

Let us refer to (4) and compare it with (7). Here, the non-common integrand factor is $2^5 k_0^6 \pi |\gamma_T(\nu,\alpha)|^2 / f^{12}(\alpha)$. For a given Doppler frequency, ν, this factor weights the remaining integrand over α. The simplest approximation would be to remove this factor and treat it as a constant, as though it varies neither with ν nor with α. Our approximation will be somewhat better. We will retain the ν-dependence of the factor, and then average it over α. Thus, the approximation goes as follows:

$$\omega_B \sigma_{(2)}(\omega_B\nu) = 2^5 k_O^6 \pi \left[|\gamma_T(\nu,\alpha)|^2 / f^{12}(\alpha) \right]_\alpha \times$$

$$8 k_O^2 \nu^7$$

$$\underset{\nu,\alpha}{\Sigma\Sigma} \int_{\alpha_1}^{\alpha_2} \frac{d\alpha S_\pm [\bar{\kappa}(\nu,\alpha)] S_\pm [\kappa_2(\nu,\alpha)]\sin 2\alpha}{f^4(\alpha)\sqrt{2\nu^4 f^4(\alpha) - \nu^8 \cos^2 2\alpha - f^8(\alpha)}}, \quad (15)$$

$$\text{or } \sigma_{(2)}(\omega_B\nu) = 2^5 k_O^6 \pi w(\nu) I_{\nu>1} =$$

$$2^5 k_O^6 \pi w(\nu) S_+ (2k_o\cos\phi, 2k_o\sin\phi) S_t(\omega_B\mu), \quad (16)$$

where we have used (7) and (14), and we define the "weighting function", $w(\nu)$, as follows

$$w(\nu) \equiv \overline{\left[|\gamma_T(\nu,\alpha)|^2 / f^{12}(\alpha) \right]_\alpha}$$

$$= \frac{1}{\alpha_2 - \alpha_1} \int_{\alpha_1}^{\alpha_2} \frac{d\alpha\, |\gamma_T(\nu,\alpha)|^2}{f^{12}(\alpha)}, \quad (17)$$

and where we again note that for $\nu > 1$, $\mu \equiv \nu - 1$.

Thus we have derived an approximation whereby the waveheight non-directional temporal spectrum is expressed in terms of the second-order Doppler spectrum divided by a weighting function; the latter quantity is readily determined by performing the integration (numerically) of the theoretical coupling coefficient, $|\gamma_T|^2 / f^{12}(\alpha)$.

Figure 3 shows a plot of the weighting function numerically evaluated for $0 < \nu < 2.4$. (It is symmetric for $\nu < 0$.) Also shown are the contributions to $w(\nu)$ from the square of each of the two terms of $\gamma_T(\nu,a)$ taken separately. This permits one to obtain a feeling for where over ν the hydrodynamic second-order effects dominate the electromagnetic second-order effects, as expressed separately by w_h and w_e. Notice that w_e—and hence w—have peaks at $2^{1/2}$, $2^{3/4}$, and increase toward infinity as $\nu \rightarrow 0, \infty$. These characteristics will tend to correct the Doppler sidebands bringing their behavior more in line with the actual waveheight temporal spectrum that produced the Doppler sidebands.
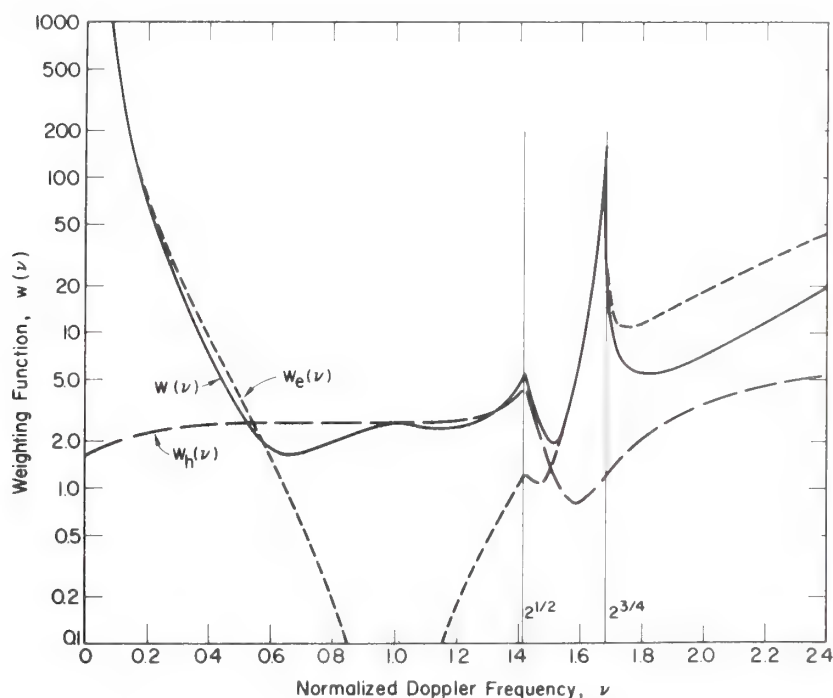
FIG. 3. Weighting function $w(\nu)$ as defined in (17). Also shown are the contributions to this function of the electromagnetic (e) and hydrodynamic terms (h) when each acts alone.

5. Application and Evaluation

Equation (16) contains the directional waveheight spatial spectrum, $S+$, evaluated at the Bragg wavenumbers $2k_0\cos\phi$, $2k_0\sin\phi$. It is a simple matter to remove this factor by noting that it appears in the expression for first-order scatter, Eq. (1). Integrating (1) over positive Doppler frequencies ($\nu>0$), and assuming $\phi<\pi/2$, we obtain

$$\int_0^\infty \sigma_{(1)}(\omega_d)d\omega_d$$

$$= 2^7\pi k_0^4 S_+(2k_0\cos\phi, 2k_0\sin\phi). \quad (18)$$

Hence for $\nu>0$, we have (using $\omega_d\equiv\omega_B\nu$):

$$S_t[\omega_B|\nu\ 1|] = \frac{4\sigma_{(2)}(\omega_B\nu)/w(\nu)}{k_0^2\int_0^\infty \sigma_{(1)}(\omega_B\nu)d(\omega_B\nu)} .(19)$$

When dealing with measured data, this result says the following. If one can isolate the dominant first-order Doppler peak, one simply integrates this portion of the power spectral density to obtain the total first-order energy. Either of the second-order sidebands near that first-order peak is then divided by this first-order quantity, af-

97

ter the second-order sideband has it-self been divided by the weighting function calculated here. This expression is self-normalizing, because any unknown path-loss or system constants multi-plying the entire Doppler spectrum will cancel in the division process.

The ultimate worth of any inversion technique such as this will be estab-lished by comparing radar measurements with exact "sea-truth" data for the wave-height temporal spectrum. Until such measurements can be made, we can ob-tain a feel for the validity of the approxi-mation behind this inversion by starting with a given form for the waveheight temporal spectrum, employing the theory here to calculate the average first and se-cond-order Doppler spectra, and then in-verting them via (19), attempting to recover the original waveheight spectrum. The magnitude of the departure of the recovered from the original waveheight spectra gives an indication of the quality and regions of validity of the approxi-mations.

To illustrate the accuracy of the tech-nique, we employ the classic ω^{-5} Phillips model for the waveheight temporal spec-trum and give it a $\cos^4\theta/2$ directional dependence; this is expressed in (5). In particular, we choose three radar direc-tions (with respect to the dominant wave directions): $\phi = 0$, $45°$, and $90°$. Finally, we employ a "sharp" lower-end cutoff, as well as a truncated or flat-top-ped lower end[1]. The parameter β is the

ratio $2k_o/\kappa_{co}$, where κ_{co} is the actual lower-end cutoff. In the case of the trun-cated spectrum, the flat top extends from cutoff, ω_{co} ($\omega_{co} = \sqrt{g\kappa_{co}}$) out to $\sqrt{2\omega_{co}}$. In employing (19) to re-cover S_t, both Doppler sidebands near the dominant first-order peak (at $\nu=+1$) were used; they were added and halved to obtain an average. Figures 4 and 5 show the comparisons between the re-covered and the original spectra.[2]

Qualitative comparison of the shapes of the recovered vs input spectra—when done on semi-logarithmic graphs as in Figs. 4 and 5—leaves some doubt as to the exact accuracy of the technique. A meaningful quantitative comparison is the relationship between the areas under the curves. This area is in fact the mean-square waveheight of the sea, perhaps the single most important descriptor of sea state. Let us denote by h_* the rms "radar-deduced" waveheight as recovered using the inversion technique based upon the area under the gray curves, and h, the rms waveheight from the input spec-tral model. Then Table 1 summarizes the ratio h/h_* for the models repre-sented in Figs. 4 and 5; unity represents a perfect recovery. Further detailed

_____

[2] To provide some feel for the parameter β, if we take 15 Mhz (a typical HF radar frequency), for $\beta/2=4$ and 10, we obtain rms waveheights of 0.636 m and 1.592 m for the sharp spectrum, with 0.469 m and 1.173 m for the truncated spectrum.

_____

[1] Although many other shapes have been proposed for the waveheight spectrum, we frequently observed nondirectional spectra with our Waverider buoy during the San Clemente Island experi-ments which closely resembled the models used here. The model with the "sharp" lower-end cutoff appeared more characteristic of fully-developed seas, while the truncated or "flat-topped" model was often seen in seas which were not yet fully developed by the wind.
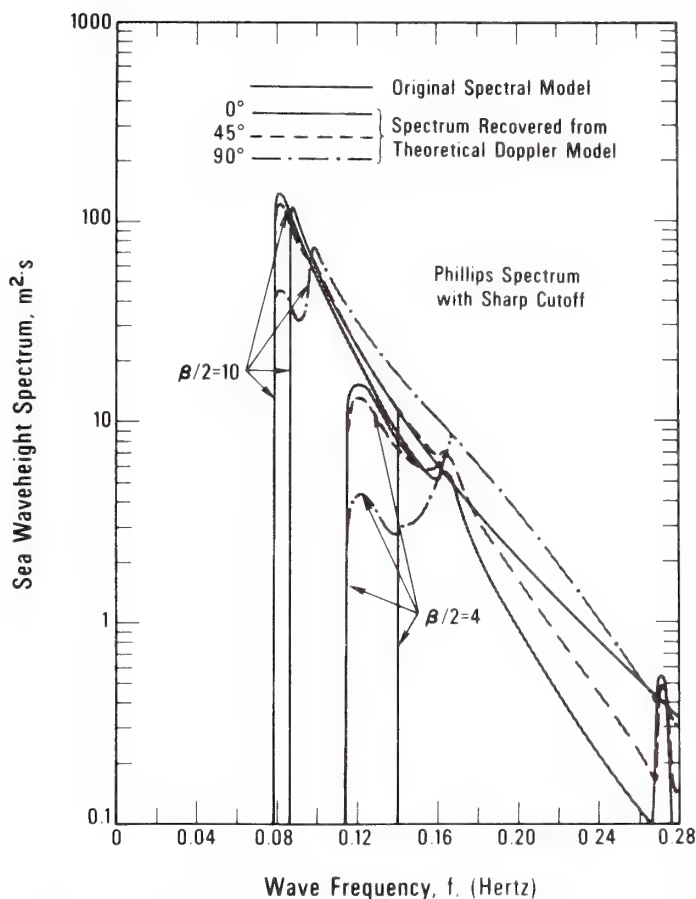
FIG. 4. Comparisons between input (original) and output (recovered) waveheight temporal spectra obtained from inversion result (19) for three different radar/wind directions. Phillips model with sharp cutoff is used as input.

studies of waveheight extraction and comparisons with measured data are found in Barrick [1977].

As one can see from Figs. 4 and 5 and Table 1, the quality of the approximation improves for increasing seas and/or frequency, as represented by increasing β. For remote-sensing applications, this is a satisfying trend, since accuracy is probably least important for low seas.

Likewise, observe that the ω^{-5} dependence of the input spectrum is best recovered at the lower end representing the longer, higher waves. Notice also that the singularities which occur in the Doppler spectrum at $2^{1/2}$ and $2^{3/4}$ are effectively removed by the use of the weighting function, helping thereby to recover the original shape of the waveheight spectrum.
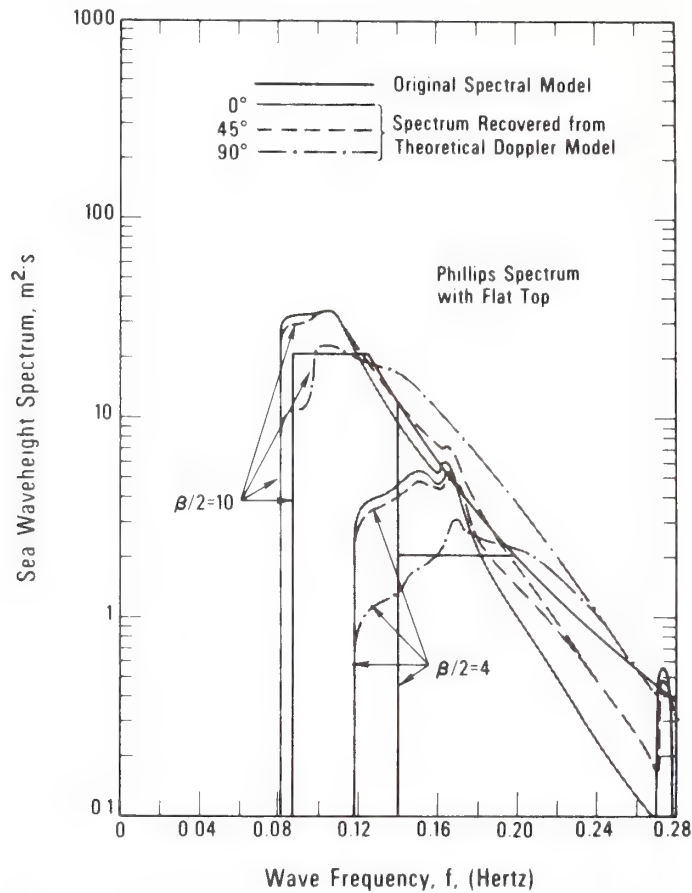
FIG. 5. Comparisons between input (original) and output (recovered) waveheight temporal spectra obtained from inversion result (19) for three different radar/wind directions. Phillips model with flat top is used as input

6. Conclusions

Ever since the solution relating the second-order HF Doppler sea echo to the integral of the product of two waveheight directional spectra appeared over five years ago, it has been evident that one should be able to sense many waveheight parameters with a single radar observation from a single direction. Published works to this time have mainly been concerned with the direct problem, i.e., given a waveheight spectral model, calculate the received Doppler spectrum. Such an approach – while it has permitted verification of the theoretical model – has limited application to remote sensing, for it requires a person to estimate wave characteristics by selecting from many the one precomputed Doppler

TABLE 1
h/h∗

	Radar/wind direction		
	$0°, 180°$	$45°, 135°$	$90°$
Sharp cutoff			
$\beta/2 = 4$	0.848	0.833	0.901
$\beta/2 = 10$	0.870	0.851	0.923
Flat top			
$\beta/2 = 4$	0.827	0.824	0.940
$\beta/2 = 10$	0.880	0.856	0.913

pattern that most nearly matches his observations.

The ultimate goal should be derivation of an exact inversion scheme for the nonlinear integral eq. (2). A step in this direction is Lips' recent work (1977). We have produced the derivation of a simple closed-form solution, which is based upon Hasselmann's suggestion (1971) that the second-order Doppler sidebands ought to replicate in some sense the nondirectional waveheight temporal spectrum. Our derivation involves the calculation and normalization of the second-order Doppler spectrum by a simple, dimensionless weighting function, calculated and presented here. Our technique has the advantage that no model—either for the directional or for the radial portions—need be assumed for the waveheight directional spectrum appearing (twice) in the integrand, as seen from the theory. Although we chose to illustrate the accuracy of the inverted results in this paper by employing specific models having (i) abrupt lower-end cutoffs, with both sharply peaked and flat radial wavenumber shapes, and (ii) a $\cos^4(\theta/2)$ angular dependence, we have tested the technique against a variety

of other models. These include spectra whose radial wavenumber dependence follows empirical models near the lower end suggested by Neumann and Pierson, Pierson and Moskowitz (Kinsman, 1965), and whose angular dependence has both the semi-isotropic nature suggested by Phillips (1966) (i.e., no waves opposing the wind) and for $\cos^s(\theta/2)$ models with s as high as 16. The inversion results there have identical trends and accuracies as those presented here; they are omitted for lack of space. These additional case studies do support the claim that the inversion technique is indeed general, and does not depend upon a given model behavior for the waveheight directional spectrum.

By employing our result to recover various waveheight nondirectional spectra used to calculate the Doppler spectrum, we have determined that the approximations leading to our result are valid under conditions of higher seas and/or radar frequencies. Both the magnitude, shape, and area of the recovered curves resemble those of the original waveheight spectrum under these conditions, with only slight differences depending upon the radar direction with respect to the dominant

wave direction. In particular, if one defines a parameter $k_0 h$, where k_0 is the radar wavenumber and h is the rms waveheight, our comparisons show that reasonable agreement can be expected when this parameter exceeds 0.2.

Having obtained the non-directional waveheight spectrum from measurements in this manner, one can establish many important descriptors of the sea state, such as rms waveheight, the dominant wave period, the presence and frequency of any swell components, and the stage of development of a wind-driven sea.

HF surface-wave radars can regularly produce Doppler spectra with sufficient resolution that the first-order and second-order components can be clearly recognized and used with this approach. However, skywave radar Doppler spectra will frequently be "smeared" by ionospheric multipath effects so that it will not always be possible to readily distinguish the first from the second-order energy. In such cases, direct application of the technique derived here will not be possible without further refinements and approximations.

Appendix A. The Waveheight Spatial-Temporal Spectrum

We define our coordinates such that the +x-direction coincides with the azimuth along which the traveling ocean waves have maximum strength; otherwise, the waveheight spatial spectrum can have a completely arbitrary angular distribution. We assume that in general waves moving in the back half-space (i.e., with a velocity component along the -x- direction) can exist. Furthermore, we employ the lowest-order dispersion relation for first-order ocean waves. Finally, with the requirement that the ocean waveheight be a real number, we employ the following definition for the waveheight, ζ, as a function of space and time (where a Fourier-series representation is used over space):

$$\dot{\zeta}(x,y,t) = \sum_{m,n=-\infty}^{\infty} P_+(m,n) \, e^{iamx+iany-i\omega_{mn}t}$$

$$+ \sum_{m,n=-\infty}^{\infty} P_-(m,n) \, e^{iamx+iany+i\omega_{mn}t},$$

$$(A-1)$$

where $P_+(-m,-n) = P_+^*(m,n)$ and $\omega_{mn} = $ sgn $(m) \sqrt{g[(am)^2 + (an)^2]^{1/2}}$, with "$a$" being a fundamental spatial frequency, assumed to be much less than the smallest wavenumbers actually present on the ocean. Here, $P_\pm$ describes the amplitudes of those waves having velocity components in the ±x-directions, respectively. We note that such a definition of real waves is required in all of the

perturbational scattering theories patterned after Rice (1951), where the real spatial waveheight series is extended to include time variation, as in Barrick (1972a).

The average spatial-temporal waveheight spectrum may now be defined in the following manner, where the Fourier coefficients are taken to be independent random variables:

$$S(\kappa_x, \kappa_y, \omega) = \frac{1}{(2\pi)^3} \iiint_{-\infty}^{\infty} <\zeta(x,y,t)\zeta(x+\tau_x, y+\tau_y, t+\tau_t)> \times$$

$$e^{-i\kappa_x\tau_x - i\kappa_y\tau_y + i\omega\tau_t} d\tau_x d\tau_y d\tau_t$$

$$\equiv S_+(\kappa_x, \kappa_y)\,\delta\,(\omega-\omega_o) + S_-(\kappa_x, \kappa_y)\,\delta\,(\omega+\omega_o), \qquad\qquad\text{(A-2)}$$

where $\omega_o = sgn\ (\kappa_x)\ \sqrt{g\kappa}$, with $\kappa = \sqrt{\kappa_{\bar{x}}^2 + \kappa_{\bar{y}}^2}$ and $\kappa_x = am$, $\kappa_y = an$. In terms of the coefficient averages, we have

$$<P_\pm(m,n)P_\pm^*(k,l)> = \begin{cases} a^2 S_\pm(\kappa_x, \kappa_y) \text{ for } k=m, l=n; \\ \\ 0 \qquad\qquad \text{for other } k,l. \end{cases} \qquad\text{(A-3)}$$

This definition requires the following normalization for mean-square waveheight:

$$h^2 = <\zeta^2(x,y,t)> = \iiint_{-\infty}^{\infty} S(\kappa_x, \kappa_y, \omega)d\kappa_x\,d\kappa_y\,d\omega = \sum_{u,l} \iint_{-\infty}^{\infty} S_\pm(\kappa_x, \kappa_y)\,d\kappa_x\,d\kappa_y. \quad\text{(A-4)}$$

103

Note also that because waveheight and its spatial correlation coefficient must be pure real, $S_+(-\kappa_x,-\kappa_y) = S_+(\kappa_x,\kappa_y)$, with an analogous symmetry requirement for S_-.

Oceanographers using tilt-buoys (Tyler et al., 1974) for measurements would define a waveheight directional spectrum in polar coordinates, $S_s(\kappa,\theta)$ (for a spatial spectrum) or $S_t(\omega,\theta)$ (for the temporal version) with the following interrelationships:

$$h^2 = \int_0^\infty d\kappa \int_{-\pi}^{\pi} d\theta S_s(\kappa,\theta) = \int_0^\infty d\omega \int_{-\pi}^{\pi} d\theta S_t(\omega,\theta); \tag{A-5}$$

$$\text{with} \quad S_t(\omega,\theta) = \frac{2\omega}{g} S_s(\frac{\omega^2}{g}, \theta) \tag{A-6}$$

from the dispersion relation, and the simple non-directional spectra defined as

$$S_s(\kappa) = \int_{\pi}^{\pi} S_s(\kappa,\theta)d\theta \qquad\qquad S_t(\omega) = \int_{-\pi}^{\pi} S_t(\omega,\theta)d\theta. \tag{A-7}$$

The quantity $S_s(\kappa,\theta)$ is related to our spectrum as

$$S_s(\kappa,\theta) = \begin{cases} 2\kappa S_+(\kappa\cos\theta, \kappa\sin\theta) & \text{for } -\frac{\pi}{2} < \theta < \frac{\pi}{2}, \\[2mm] 2\kappa S_-(\kappa\cos\theta, \kappa\sin\theta) & \text{for } -\frac{3\pi}{2} < \theta < -\frac{\pi}{2}. \end{cases} \tag{A-8}$$

Attention is directed to frequent confusion involving a factor of two in relating oceanographically observed (Teague et al., 1975) or modeled (Barrick, 1972a) waveheight spectra to scattered sea echo. Scattering theory requires waveheight descriptions similar to (A-1), and hence waveheight spectra of a form (A-2); thus we must employ (A-8) to relate these to the oceanographic observables.

Appendix B. The Integral Transformation

Equation (2) for the second-order scatter can be reduced from a double to a single integral by employing the sifting property of the Dirac-delta function. While the left side of the equation is an explicit function of one independent variable, ω_d, the integrand is a function of three: ω_d, p, and q. The delta function implies an interdependence among the three such that only two are strictly independent; one of the two is then eliminated in the final single integration. To employ the delta function to eliminate one of the two integrals, one must transform variable from p and q to two other variables with a (generally) multivalued mapping. The choice of transformation variables is optional, and various investigators have made different selections. There are problems encountered in each method. Ours has the advantages that a cubic (or higher) equation does not arise within the delta function argument, and that the final integration limits are finite; the disadvantage is that these integration limits must be found by solving a transcendental equation (numerically) for each value of ω_d and θ.

Our transformation process goes basically as follows:

(a) $p,q \rightarrow \kappa_1, \kappa_2$ $(-\infty<p,q<\infty;\ \kappa_1,\kappa_2 > 0)$, where κ_1 and κ_2 are as defined following (2).

(b) $\kappa_1, \kappa_2 \rightarrow r,\alpha$ $(r>0;\ 0 < \alpha < \frac{\pi}{2})$, where $\kappa_1 \equiv r\cos\alpha$ and $\kappa_2 \equiv r\sin\alpha$.

(c) $r \rightarrow \eta$ $(-\infty < \eta < \infty)$, where $\eta \equiv \pm\ \omega_{o1} \pm\ \omega_{o2} = grf(\alpha)$, where $f(\alpha) \equiv \pm\ \text{sgn}(\kappa_{1x})\cos^{1/2}\alpha \pm\ \text{sgn}(\kappa_{2x})\sin^{1/2}\alpha$, the upper/lower sign choices depending upon which of the four terms of the integrand in (2) is being used.

The Jacobian of the *total* transformation process is

$$J(\eta,\alpha) = \frac{2\eta^7 \sin 2\alpha}{g^2 f^4(\alpha)\sqrt{8g^2 k_0^2\, \eta^4 f^4(\alpha) - \eta^8 \cos^2 2\alpha - 16g^4 k_0^4 f^8(\alpha)}} \qquad \text{(B-1)}$$
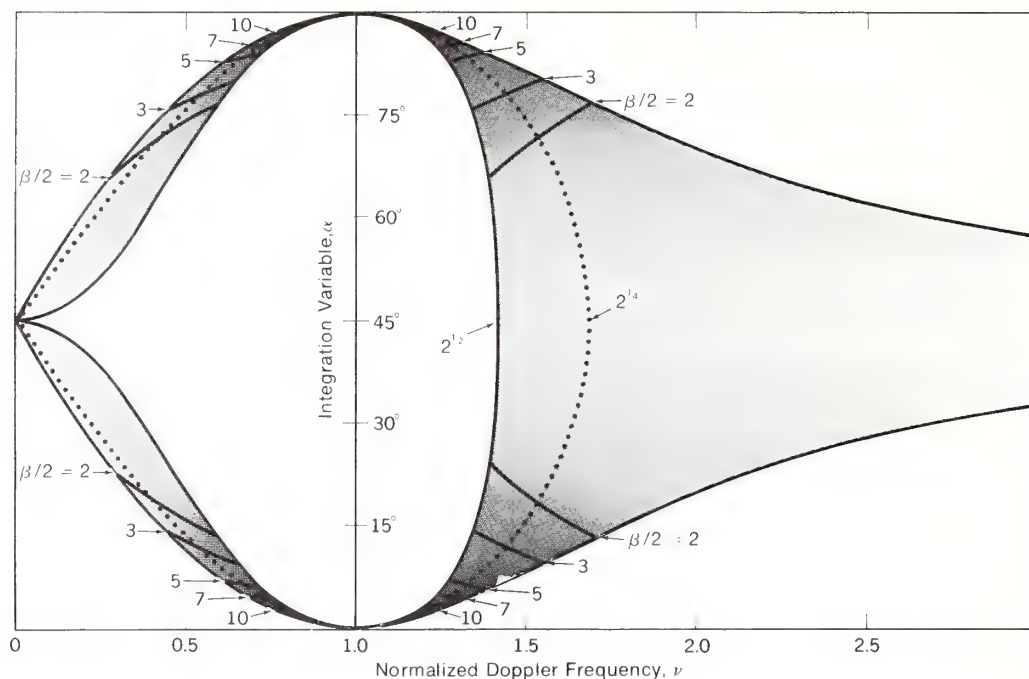
FIG. B-1. Plot showing regions over $\nu-\alpha$ space used for integration of (4). Solid lines delimiting regions of heavier shading are solutions to (B-3). Dotted lines indicate electromagnetic singularity, obtained as solution to equation $f(\alpha_e) = \nu$.

At this point the argument of the delta function becomes $\omega_d - \eta$; the integral over η is thus eliminated by dropping the delta function and replacing η everywhere by ω_d. With a further normalization of Doppler frequency ω_d as $\nu \equiv \omega_d/\omega_B$, one obtains (4).

Several details of this transformation must be outlined carefully. The first has to do with the integration limits on α. There are three types of limits:

(a) Jacobian-imposed limits. This limit is dictated by the fact that the argument of the radical in the denominator of J must be positive in order for the mapping to be real. In terms of ν, the inequality defining this limit, α_j, is

$$2\nu^4 f^4(\alpha_j)-\nu^8 \cos^2 2\alpha_j - f^8(\alpha_j) \geqslant 0. \quad \text{(B-2)}$$

(b) Spectral-model limits. Certain types of waveheight spectral models—such as the Phillips (1966) model—are nonzero by definition only when the wavenumber exceeds a lower cutoff value; for fully developed seas, this is often given in terms of wind speed, u, as $\kappa > \kappa_{co} = g/u^2$ (see Eq. (5) of the text.) Thus, for a model such as this, the integrand is nonzero only when κ_1 and κ_2 exceed this cutoff, giving rise to the inequalities

106

$$\nu^2 \cos\alpha_w / f^2(\alpha_w) \geqslant 1/\beta$$

and

$$\nu^2 \sin\alpha_w / f^2(\alpha_w) \geqslant 1/\beta, \qquad \text{(B-3)}$$

where β is a dimensionless parameter ($\beta \equiv 2k_0/\kappa_\omega$) that is basically a measure of the roughness height normalized to radio wavelength.

Figure B-1 shows the region (for $\nu > 0$) in ν-α space within which the mapping occurs, as defined by Eq.

(B-2). Shown also are lines obtained from Eqs. (B-3); these along with the heavy shading indicate which regions of ν–α space are most important for higher sea states and/or radar frequencies (i.e., higher values of β).

(c) Sign-change limits. The sign of the Doppler shift, ω_d, in (2) for each of the four terms of the integrand depends upon whether κ_{1x} and κ_{2x} are less or greater than zero. Thus, p–q space can be divided into three bands, as shown in Fig. B-2(a). The vertical, dashed lines delineating these regions are given by

$$-f^4(\alpha_{\underset{n}{p}})\cos\phi = \nu^4 \cos\phi\cos 2\alpha_{\underset{n}{p}} \pm \sin\phi\sqrt{2\nu^4 f^4(\alpha_{\underset{n}{p}}) - \nu^8 \cos^2 2\alpha_{\underset{n}{p}} - f^8(\alpha_{\underset{n}{p}})}, \text{ and}$$

$$\text{(B-4)}$$

$$\nu^4 \cos\phi\cos 2\alpha_{\underset{n}{p}} \pm \sin\phi\sqrt{2\nu^4 f^4(\alpha_{\underset{n}{p}}) - \nu^8 \cos^2 2\alpha_{\underset{n}{p}} - f^8(\alpha_{\underset{n}{p}})} = f^4(\alpha_{\underset{n}{p}})\cos\phi;$$

The two values, α_p and α_n (going with the upper and lower signs, respectively, in these equations) originate because p and q have two solutions in terms of κ_1 and κ_2 (which are transformed to α, ν as):

$$p/k_0 = (\nu^4 \cos\phi\cos^2 2\alpha \pm \sin\phi\sqrt{2\nu^4 f^4(\alpha) - \nu^8 \cos^2 2\alpha - f^8(\alpha)})/f^4(\alpha), \text{ and}$$

$$\text{(B-5)}$$

$$q/k_0 = (\nu^4 \sin\phi\cos^2 2\alpha \mp \cos\phi\sqrt{2\nu^4 f^4(\alpha) - \nu^8 \cos^2 2\alpha - f^8(\alpha)})/f^4(\alpha).$$
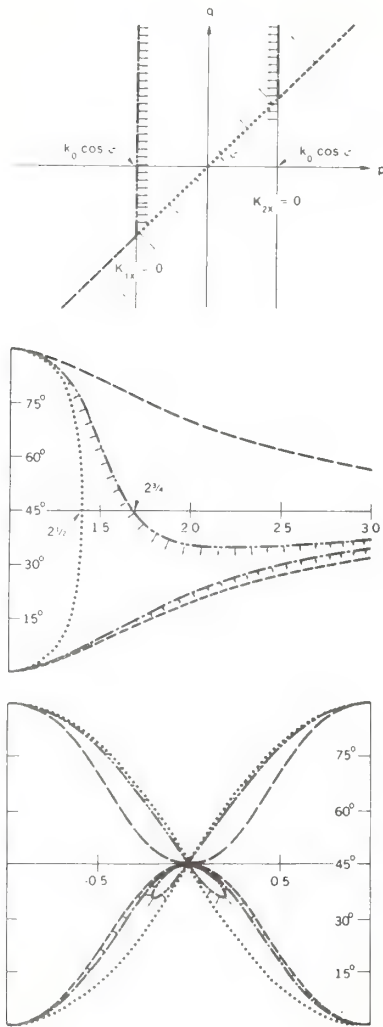
FIG. B-2. Plot showing how lines from $p-q$ space (upper) map onto $\nu-\alpha$ space for $1<|\nu|<3$ (middle) and $-1<\nu<+1$ (lower). A radar/wind direction of $\phi = 45°$ is used for this example, and arrows show movement of boundaries as ϕ goes from $45°$ toward $90°$ (crosswind case).

This further defines regions on the $p-q$ plane delineated by the dotted line with slope ϕ. This line is obtained by noting that the sign change is obtained at $\alpha = \alpha_j$, where one can solve the above two equations for the line to obtain $q/p = \tan \phi$.

For the sake of example, we show several of the relevant lines in Fig. B-2(b)

obtained from the above inequalities, mapped into $\nu - \alpha$ space; we employ $\phi = 45°$ for the curves of Fig. B-2. Furthermore, we indicate by arrows how these various lines collapse as $\phi \to 90°$, i.e., in the "crosswind" case.

Finally, we illustrate by chart form in Fig. B-3 how all of the four terms in the integrand of (2) map onto $\nu - \alpha$ space (again pictured for $\phi = 45°$). As can be seen, the entire four-term integrand over all $p - q$ space maps onto $\nu - \alpha$ space in a double-valued manner. This is important when one solves (4) numerically and attempts to take advantage of the various complementary

symmetries of the mapping to reduce the computations. The solution of the inversion problem as formulated in the text is also clarified by understanding the mappings described here for solving the direct integral.

In effect, the coordinate system and transformation employed here accounts for radar/wave direction, ϕ, by changing the boundaries of the mapping (in both $p - q$ and $\nu - \alpha$ space), while keeping the waveheight spectra in the integrand invariant with ϕ. Transformations used by others (Lipa, 1977) keep the mapping boundaries constant, but include direction, ϕ, within the arguments of the waveheight spectra.
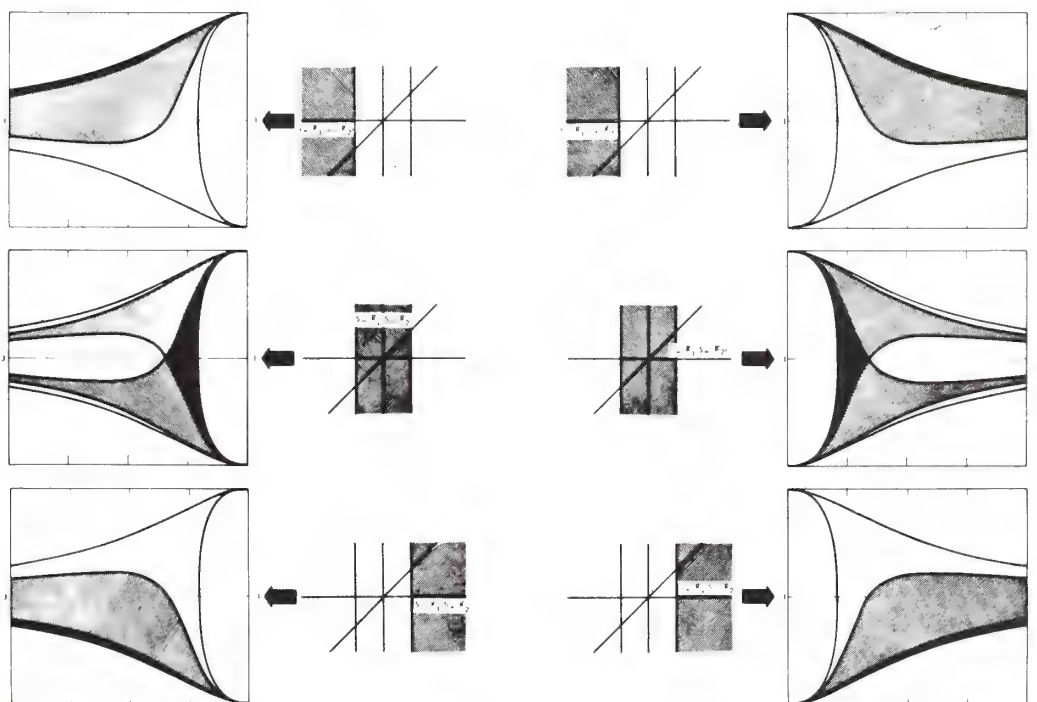
FIG. B-3(a). Plot showing how the various terms of the integrand of Eq. (2) map from $p - q$ space onto $\nu - \alpha$ space for $\phi = 45°$ and $1 < |\nu| < 3$.
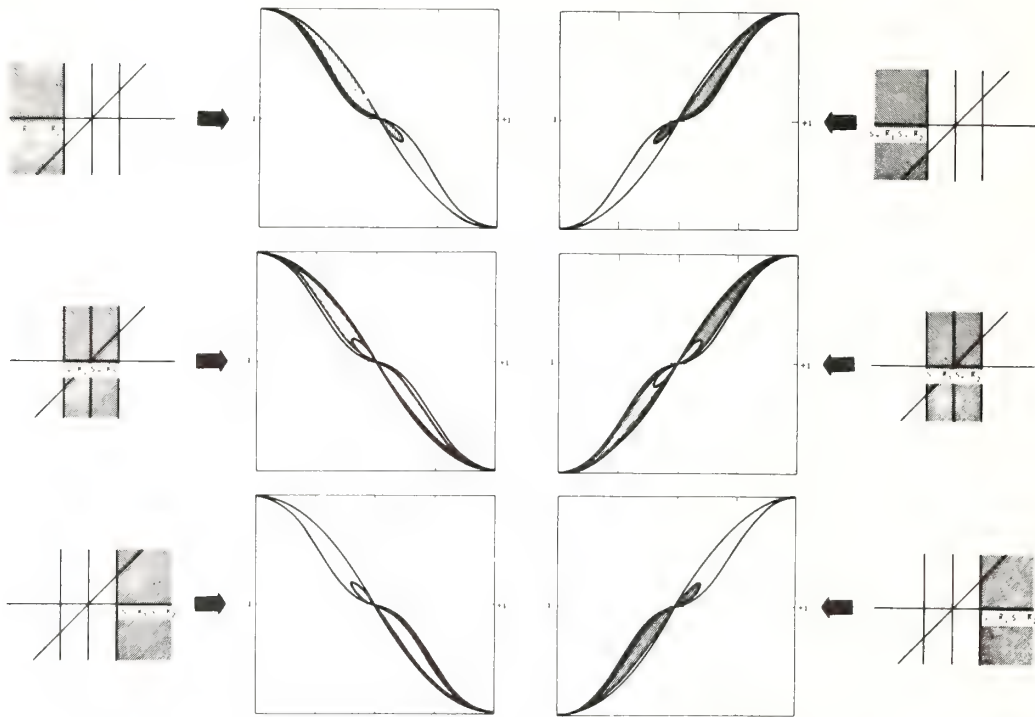
FIG. B-3(b). Plot showing how the various terms of the integrand of Eq. (2) map from $p-q$ space onto $\nu-\alpha$ space for $\phi = 45°$ and $-1 < \nu < +1$.

References

Barrick, Donald E. (1971a), Theory of HF/VHF propagation across the rough sea, Parts I and II, *Radio Science* **6**, 517-533.

Barrick, Donald E. (1971b), Dependence of second-order sidebands in HF sea echo upon sea state, *IEEE G-AP International Symposium Digest*, (Sept. 21-24, 1971, Los Angeles, Calif.), pp. 194-197.

Barrick, Donald E. (1972a), First-order theory and analysis of MF/HF/VHF scatter from the sea, *IEEE Transactions on Antennas and Propagation*, Vol. AP-20, pp. 2-10.

Barrick, Donald E. (1972b), Remote sensing of sea state by radar in *Remote Sensing of the Troposphere*, V. E. Derr, ed., Chap. 12, U. S. Government Printing Office, Washington, D.C.

Barrick, Donald E., Headrick, James M., Bogle, Robert W., and Crombie Douglass D., (1974), Sea backscatter at HF: Interpretation and utilization of the echo, *IEEE*, Vol. 62, pp. 673-680.

Barrick, Donald E. (1973), The use of skywave radar for remote sensing of sea states, *Marine Technol. Soc. J.* **7(1)**, 29-33.

Barrick, Donald E. (1977), Extraction of wave parameters from measured HF radar sea-echo Doppler spectra, *Radio Science* 12, No.3.

Crombie, Douglass D. (1955), Doppler spectrum of sea echo at 13.56 Mc/s, *Nature* **175**, 681-682.

Hasselmann, Klaus (1971), Determination of ocean wave spectra from Doppler radio return from the sea surface, *Nature Physical Science* **229**, 16-17.

110

$$S(\vec{K}_1)S_-(\vec{K}_2) + S_-(\vec{K}_1)S_-(\vec{K}_2) +$$
$$+ S_-(\vec{K}_1)S_-(\vec{K}_2) + S_-(\vec{K}_1)S_-(\vec{K}_2)$$
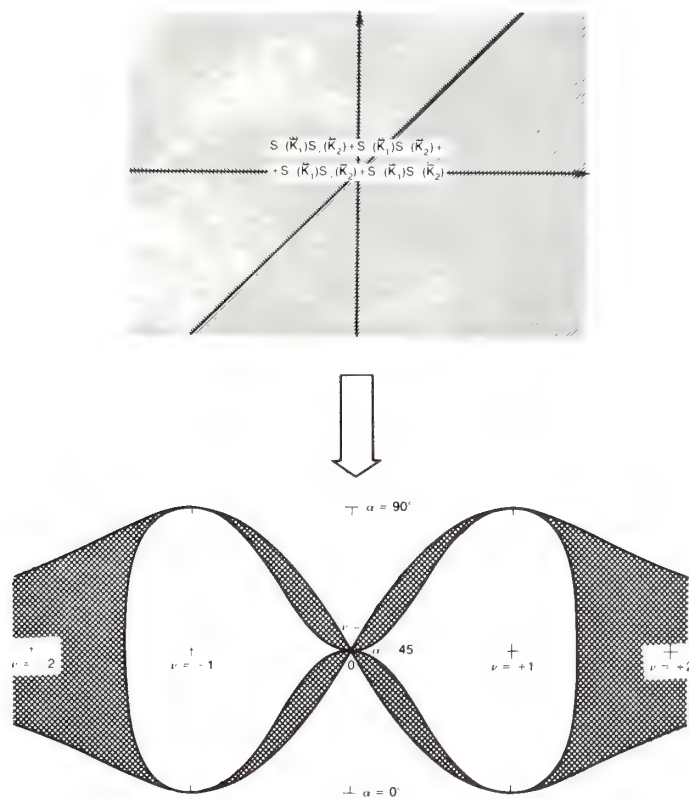
FIG. B-3(c). Total combination of mappings of previous two
figures.

Kinsman, Blair (1965) *Wind Waves*, Prentice-Hall, Inc., Englewood Cliffs, New Jersey.

Lipa, Belinda J. (1977), Derivation of Directional ocean wave spectra by integral inversion of second order radar echoes, *Radio Science* 12, No. 3.

Phillips, Owen M. (1966), *Dynamics of the Upper Ocean*, Cambridge University Press, London, England, pp. 109-139.

Rice, Stephen O. (1951), Reflection of electromagnetic waves from slightly rough surfaces, in *Theory of Electromagnetic Waves*, M. Kline ed., Interscience Publishers, New York, pp. 351-378.

Stewart, Robert H. (1971), *Higher order scattering of radio waves from the sea*, IEEE G-AP International Symposium Digest, (Sept. 21-24, 1971, Los Angeles, Calif.), pp. 190-193.

Teague, Calvin C., Tyler, G. Leonard, and Stewart, Robert H. (1975), The radar cross section of the sea at 1.95 MHz: Comparison of in-situ and radar determinations, *Radio Science* **10**, 847-852.

Tyler, G. Leonard, Teague, Calvin C., Stewart, Robert H., Peterson, Allen M., Munk, Walter H., and Joy Joseph W., (1974), Wave directional spectra from synthetic aperture observations of radio scatter, *Deep Sea Research* **21**, 989-1016 (Pergamon Press, printed in Great Britain).

Valenzuela, Gaspar R. (1974), The effect of capillarity and resonant interactions on the second-order Doppler spectrum of radar sea echo, *Geophys. Res.* **79**, 5031-5037.

The Statistics of HF Sea-Echo Doppler Spectra

DONALD E. BARRICK, MEMBER, IEEE, AND JACK B. SNIDER, MEMBER, IEEE

Abstract—Several important statistical properties of the HF sea echo and its Doppler power spectrum, which are useful in optimizing the design of radar oceanographic experiments, are established. First- and second-order theories show that the echo signal (e.g., the voltage) should be Gaussian; this is confirmed with experimental surface-wave data i) by comparison of the normalized standard deviation of the power spectrum at a given frequency with its predicted value of unity, and ii) by cumulative distribution plots of measured spectral amplitudes on Rayleigh probability charts. The normalized standard deviation of the dominant absolute peak amplitudes of the power spectrum (which wander slightly in frequency) are shown from experimental data to be ~ 0.7 for the first-order peaks and ~ 0.5 for the second-order peaks. The autocorrelation coefficient of the power spectra is derived from measured data and interpreted in terms of the spectral peak widths; from this information, the correlation time (or time between independent power spectrum samples) is shown to be ~ 25–50 s for radar frequencies above 7 MHz. All of these statistical quantities are observed to be independent of sea state, scatter- ing cell size, and relatively independent of radar operating frequency. These quantities are then used to establish the statistical error (and confidence interval) for radar remote sensing of sea state, and it is shown, for example, that 14 power spectral samples result in a sample average whose rms error about the true mean is 1.0 dB.

I. INTRODUCTION

TWO DECADES AGO, Crombie [1] experimentally deduced the physical mechanism responsible for first-order HF sea echo. The unique characteristics of his high-resolution Doppler records led to the conclusion that the dominant spectral peaks resulted from Bragg scatter; i.e., only those ocean wavetrains will backscatter near grazing whose spatial period is exactly one-half the radar wavelength and which move directly toward and/or away from the radar. In later deterministic analyses, Wait [2] confirmed this deduction and showed further that the strength of this first-order echo is proportional to the height of the resonant "Bragg-scattering" ocean waves. These con-

clusions suggested the exciting possibility of employing HF radars (both sky-wave and surface-wave) to measure the ocean waveheight directional spectrum—or "sea state." Recently a number of groups have been investigating the use of such HF radar techniques for remotely sensing ocean surface conditions via the sea-echo Doppler spectrum.

One of the very important properties of the HF sea echo, however, is its random nature. This point is often overlooked because resonant (or Bragg) scatter is such a precisely describable physical phenomenon that many have assumed that a single echo record describes the scattering surface satisfactorily. Since the heights of the Bragg-scattering waves within the radar resolution cell are random variables (in fact, the entire sea-surface height is a random variable best described via the Fourier–Stieltjes integral or the Fourier series with random coefficients), the sea echo must also be a random variable. This fact was employed in the analyses of Barrick and Peake [3] and Barrick [4], [5], who showed that to first and second order, the *average* sea-echo Doppler spectrum is related to the *average* sea waveheight directional spectrum evaluated at the required first and second-order Bragg wavenumbers.

All of the suggested methods for extracting sea-state parameters from the sea-echo Doppler spectrum involve the comparison (i.e., division) of one part of the echo spectrum by another part [6], [7]. Failure to note that the sea echo is a random variable will lead to a statistical fluctuation in the desired parameter. Hence, appropriate averaging of each sea-echo feature is necessary before the deduction of the desired mean sea-state descriptor. Since "averaging time" in a practical experiment is not unlimited,[1] the number of independent samples used to approximate the average may in fact be small. Therefore, in order to calculate the accuracy of predicting the desired sea parameter, one must know something about the statistics of the echo, such as the power spectrum variance, correlation time, etc. While it is often customary to assume Gaussian statistics for the scattered electric field, this assumption in many cases remains to be proven. In the microwave region, for example, where the physical mechanism behind near-grazing sea backscatter is considerably more complex than at HF, Trunk [8] has found that the echo voltage distribution in certain cases can be log-normal, while in others it follows the Gaussian (or normal) model.

First, we provide a heuristic theoretical rationale explaining why the complex components of the first- and second-order sea echo are Gaussian random variables. Then we examine the properties of Gaussian processes, in particular, deriving the probability density and the normalized standard deviation of the power for each Doppler frequency spectrum taken as the random variable. Next, we calculate both the normalized standard deviation and the

temporal correlation function of the Doppler spectrum from HF suface-wave sea-echo measurements. We compare these experimental results with the theoretical predictions for Gaussian processes (where the latter are available). Finally, we give an example of the use of the derived statistical properties of the sea echo in the analysis/design of an HF radar experiment.

II. SEA ECHO AND THE GAUSSIAN PROCESS

It is often customary to assume that in general random signals (e.g., voltages) are Gaussian because i) the Gaussian model has desirable mathematical properties, making manipulations with it easy, ii) if the signal is synthesized as the sum of several independent events, the Central Limit Theorem states that as the number of events becomes large, the sum signal approaches a Gaussian random variable, iii) wideband spectrally flat random signals after narrowband filtering (such as at the output of a finite Fourier transform) tend to Gaussian under most conditions [9], and conversely, iv) a wideband signal synthesized by the summation of Gaussian random narrowband signals will be Gaussian because linear operations on Gaussian variables produce Gaussian variables [10]. Since one can always find mathematical exceptions to these generalizations, and since the sea-echo spectrum is *not* flat, we will establish separate, independent proofs from the scattering theory to justify the Gaussian assumption.

The conventional method for analyzing HF sea echo employs the classical statistical boundary perturbation approach first set forth by Rice [11]. This technique requires that the surface waveheight be small in terms of the radar wavelength and that the surface slopes be small; both of these conditions are satisfied (in the mean) by the sea surface at HF. By ordering the terms in the scattered field solution according to the above "smallness" parameters, expressions have been derived for the first-order and second-order sea echo [4], [5]. These expressions show that Bragg scatter—the mechanism originally proposed by Crombie [1]—does, in fact, account for the echo.

In the formulation of this theory, the sea surface height is represented by an exponential spatial Fourier series with random complex coefficients $P(m,n) (= X(m,n) + iY(m,n))$, where m and n are running indices corresponding to the x and y directions (the latter taken as lying in the mean surface plane). The total sea surface height has been shown by oceanographers [12] to be representable as a Gaussian random variable *to first-order*. The requirement that the sea height be a real quantity means that $P^*(m,n) = P(-m,-n)$ (or $X(-m,-n) = X(m,n)$ and $Y(-m,-n) = -Y(m,n)$). The average sea waveheight directional spectrum $S(\kappa_x, \kappa_y)$, is then defined in terms of these coefficients as

$$\langle P(m,n)P^*(m',n') \rangle$$

$$= \begin{cases} a^2 S(am, an), & \text{for } m',n' = m,n \\ 0, & \text{for } m',n' \neq m,n \end{cases} \quad (1)$$

where $a \equiv 2\pi/L$, L being defined as the fundamental spatial period of the Fourier series. These first-order height co-

---

[1] The total observation time is proportional to the coherent integration time multiplied by the number of sequential beam scans times the desired number of samples per radar resolution cell. The coherent integration time is the reciprocal of the required Doppler resolution. The total observation time should not exceed the interval over which the sea is statistically stationary; the latter time may typically vary between 1 and 12 h.

efficients $P(m,n)$ may be taken to be uncorrelated random variables [13]; inasmuch as the waveheight can be considered a spectrally flat process over a nominally wide band of spatial wavenumbers, the random Fourier coefficients can also be taken to be Gaussian [9].

To first order, the backscattered electric field at the receiver is [4]

$$E^{(1)} = KP_{\pm}(m_*,n_*) \exp\{-i[\omega_0 \mp \sqrt{ag(m_*^2 + n_*^2)^{1/2}}]t\} \quad (2)$$

where K is a complex constant which depends upon the propagation loss to the scattering patch, incidence angle, and other fixed factors of the geometry. The quantity ω_0 is the transmitted radian carrier frequency; the Doppler shift of the scattered signal from the carrier,

$$\sqrt{ag(m_*^2 + n_*^2)^{1/2}} \quad (\equiv \omega_B),$$

originates as a result of the first-order dispersion relation between the spatial and temporal wavenumbers of a gravity wave, with g being the acceleration of gravity (~ 9.81 m/s^2). Hence, $\kappa_* = a(m_*^2 + n_*^2)^{1/2}$ is the spatial wavenumber of the particular Fourier-series components responsible for the scatter. The theory shows that only a very small number of Fourier-series components can contribute to scatter. These have wavenumbers along and perpendicular to the radar line of sight (for backscatter at grazing incidence) such that $\kappa_{x*} = am_* \approx 2k_0$, and $\kappa_{y*} = an_* \approx 0$, where k_0 is the radar spatial wavenumber ($k_0 = \omega_0/c = 2\pi/\lambda$); these are precisely the required conditions for first-order Bragg scatter, as originally deduced empirically by Crombie.

Equation (2) essentially shows that if $P(m,n)$ is a Gaussian random variable, as assumed in our description of the ocean, then the signal is itself a random variable which is directly proportional to the waveheight coefficient. Since any linear operation on a Gaussian random variable produces another Gaussian random variable, the received signal is therefore itself Gaussian. Hence one has a proof that the first-order sea echo is Gaussian *so long as one can assume that the height of the sea can be represented by a Gaussian random variable to first order.*

To second order, the signal scattered from the sea is [5]

$$E^{(2)} = iK \sum_m \sum_n \Gamma_T(m,n)P_{\pm}(m,n)P_{\pm}(m_* - m, n_* - n)$$

$$\times \exp\{-i[\omega_0 \mp \sqrt{ag[m^2 + n^2]^{1/2}}$$

$$\mp \sqrt{ag[(m_* - m)^2 + (n_* - n)^2]^{1/2}}]t\} \quad (3)$$

where K has the same value as in (1), and m_*,n_* are as defined after (2), i.e., a narrow band of numbers satisfying the first-order Bragg-scatter criterion. Equation (3) is actually an expression of second-order Bragg scatter, where one set of the double-interacting ocean waves has spatial wavenumber $\bar{\kappa}_1 = am\hat{x} + an\hat{y}$ and the other has spatial wavenumber $\bar{\kappa}_2 = a(m_* - m)\hat{x} + a(n_* - n)\hat{y}$. The summation over m,n indicates that there is an infinite number of double sets of ocean waves possible which can interact to second order (to first order, only one single set was possible

for each Doppler shift). Each double set in turn produces its own echo Doppler shift from the carrier, as seen from the argument of the exponential; in the limit the summations merge into a double integral, and the Doppler spectrum is seen to be a continuous function. The "transfer coefficient" Γ_T has been derived and presented elsewhere [5]; it is a deterministic constant which results from the second-order terms from both the nonlinear boundary condition at the water–air interface (the hydrodynamic contribution) and also the second-order terms in the nonlinear perturbation expansion of the scattered fields (the electromagnetic contribution).

Writing (3) in this manner expresses the hypothesis that if each of the two different P in each term of the summation is a Gaussian random variable, the second-order scattered field is also a random variable. However, each term of the summation, consisting of a product of two Gaussian random variables, is no longer Gaussian.[2] Nevertheless, many terms of the series of (3) can be seen to contribute to the signal at a given Doppler shift, hence, one can argue by the central limit theorem [13] that the result for each Doppler shift, being the sum of many independent non-Gaussian terms, nonetheless will tend toward Gaussian.

The point of this section was to show from the presently accepted theoretical derivations that the real and imaginary parts of the instantaneous complex signal at each Doppler shift are predicted to be Gaussian random variables. Since the temporal Fourier transform, as obtained from a digital processor at the output of an HF receiver, is nothing more than a weighted sum of the coefficients of the Doppler time series given by (2) and (3), this complex transform at each spectral point should also be Gaussian (i.e., the real and imaginary parts of the Fourier transform have Gaussian probability distributions). Thus, for example, if the Fourier transform is obtained with 0.02 Hz resolution (requiring 50 s of signal data), the complex parts of this transform should be Gaussian random variables. This will be true regardless of the integration time.

This latter fact is often erroneously overlooked by some, who feel that the longer the sample in time (or the larger the basic scatter area in space for a given scatter sample), the "smoother" the signal should be because of "temporal" or "spatial" averaging.[3] It will be shown from experimental data that the components of the complex received signal (in both the first-order and second-order spectral regions) appear in fact to be Gaussian, regardless of the coherent processing time or the size of the scatter area.

---

[2] The real and imaginary part of each *product* term can be shown to have an exponential probability density function given by $p(U) = \exp\{-U/\sigma_1\sigma_2\}/(2\sigma_1\sigma_2)$; $p(V) = \exp\{-|V|/\sigma_1\sigma_2\}/(2\sigma_1\sigma_2)$, where $U = X(m_1,n_1)X(m_2,n_2) - Y(m_1,n_1)Y(m_2,n_2)$ and $V = X(m_1,n_1) \cdot Y(m_2,n_2) + X(m_2,n_2)Y(m_1,n_1)$ are the real and imaginary parts of the product coefficients; $2\sigma_1^2 = a^2 S(am_1,an_1)$, and $2\sigma_2^2 = a^2 S(am_2,an_2)$. The probability density functions of the single coefficients, being Gaussian, are given by $p(X) = \exp\{-X^2/(2\sigma^2)\}/\sqrt{2\pi\sigma^2}$; $p(Y) = \exp\{-Y^2/(2\sigma^2)\}/\sqrt{2\pi\sigma^2}$.

[3] Temporal and/or spatial averaging can and are in fact often used to smooth the signal spectrum, but not within a single signal transform; several transforms (squared) must be added (incoherently) for different times and/or scatter areas to produce this type of averaging.
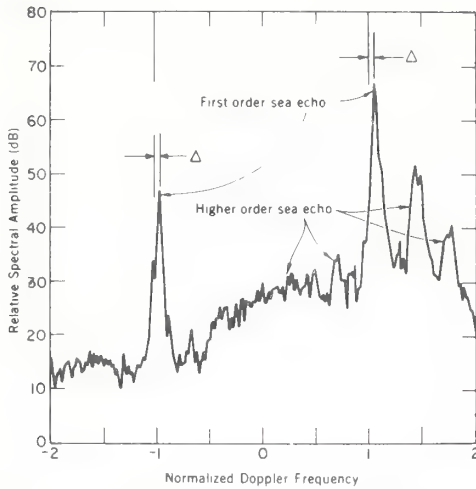
Fig. 1. Typical 9-sample average of 200-s surface-wave HF sea-echo power spectra at 9.4 MHz. Doppler frequency is normalized with respect to expected position of the first-order Bragg peaks (here 0.313 Hz). Δ is the normalized shift of the record due to underlying current.

III. STATISTICS OF THE SPECTRUM FOR A GAUSSIAN VOLTAGE SIGNAL

In the preceding section we gave a theoretical justification for the hypothesis that the first- and second-order sea-echo voltage signals (and their complex Fourier transforms) are Gaussian random variables. The quantity of interest for extraction of sea-state parameters, however, is the power spectrum of this received voltage signal; hence, our present radar processing equipment outputs this spectrum versus Doppler frequency automatically. Fig. 1 shows an example of a measured nine-sample-averaged surface-wave Doppler spectrum of the sea echo at 9.4 MHz.[4] The specific parameters of the system, and geometry behind this record will be discussed in the next section. The Doppler frequency units of the abscissa are normalized such that 0 corresponds to the carrier position, and ±1 refers to the predicted positions of the first-order Bragg echo peaks (i.e., $\omega_B/2\pi = \sqrt{2gk_0}/2\pi = \sqrt{g/\pi\lambda} \simeq 0.313$ Hz at a 9.4 MHz carrier). The ordinate is proportional to received power spectral density, and is obtained by taking the sum of the squares of the real and imaginary parts of the digital fast Fourier transform (FFT) output of the receiver. In this case, the FFT was taken on a 200-s coherent echo sample (giving 0.005 Hz Doppler resolution, or 0.016 in the normalized frequency units of Fig. 1). Nine consecutive spectra were averaged (i.e., added together) to produce Fig. 1, the entire figure therefore representing 0.5 h of sea-echo data.

A practical reason for wanting to know whether the received signal is Gaussian has to do with the assessment of error bounds (or confidence) in approximating the true average Doppler spectrum by the average of a finite number of samples. If the signal components are (nearly) Gaussian,

such confidences and errors can be readily established, since the required tables for Gaussian statistics are widely available. Hence, we shall establish the variance of the power spectrum for a Gaussian signal in terms of its mean. We shall use this test as an initial indicator of whether the original signal is sufficiently close to Gaussian that further testing is desirable. The further testing will then consist of plotting (on Rayleigh probability paper) the cumulative distribution of the FFT amplitude samples (i.e., the square root of the spectral power); if the original signal were Gaussian, these points should fall along a straight line with a 45° slope.

The sea-echo signal, as represented by (2) and (3) and exemplified in Fig. 1, is a narrow-band zero-mean signal which can be represented in the time domain in the following ways [13].

$$v(t) = A(t) \cos \left[\omega_0 t + \phi(t) \right]$$

$$= \sum_k A_k \cos \left[(\omega_0 + k\omega_f)t + \phi_k \right]$$

or

$$v(t) = \frac{2}{T} \sum_k \left[X_k \cos (\omega_0 + k\omega_f)t - Y_k \sin (\omega_0 + k\omega_f)t \right] \quad (4)$$

where ω_0 here represents the radian carrier frequency. The latter two forms of the above equation cast the signal in terms of a Fourier series with a fundamental frequency (in the absence of the carrier) of $\omega_f \equiv 2\pi/T$. Following the technique of Rice in Davenport and Root [13], one could allow the period T to become infinite, in which case the series with constant, uncorrelated coefficients could be used to represent a nonperiodic continuous process. Here, however, since in reality a digital FFT treats the process as a Fourier series whose fundamental period T is the window over which the signal is sampled, the last form of (4) is better suited to our purposes.

Following Davenport and Root, we assume that X_k and Y_k are uncorrelated coefficients with zero mean and variance σ_k^2. We shall now determine the variance of the Doppler power spectrum, assuming X_k and Y_k are Gaussian. The output of the FFT for the kth point will be $V(\omega_0 + k\omega_f) = X_k + jY_k$, and we define the power spectrum to be

$$P_k = \frac{|V(\omega_0 + k\omega_f)|^2}{T} = \frac{X_k^2 + Y_k^2}{T}. \quad (5)$$

Since X_k and Y_k are orthogonal by definition (and hence uncorrelated) we have $\langle X_k^2 \rangle = \langle Y_k^2 \rangle = \sigma_k^2$ and $\langle X_k Y_k \rangle = 0$; because they are Gaussian, all joint moments are the product of the individual moment factors (i.e., $\langle X_k^m Y_k^n \rangle = \langle X_k^m \rangle \langle Y_k^n \rangle$). Using the properties of the Gaussian probability density function, it can be shown that

$$\frac{\langle X_k^4 \rangle - \langle X_k^2 \rangle^2}{\langle X_k^2 \rangle^2} = \frac{\langle Y_k^4 \rangle - \langle Y_k^2 \rangle^2}{\langle Y_k^2 \rangle} = \frac{3\sigma_k^4 - \sigma_k^4}{\sigma_k^4} = 2$$

$$(6)$$

---

[4] Examples of the extraction of sea-state and surface-wind data from

and that P_k is chi-squared-distributed with two degrees of freedom such that

$$\frac{\langle P_k{}^2 \rangle - \langle P_k \rangle^2}{\langle P_k \rangle^2} = 1 \ (\equiv \sigma_p). \tag{7}$$

The latter equation is the desired result, for it gives the (normalized) variance of the individual Doppler power spectral density estimates (about their true mean value) for a Gaussian signal. Any Gaussian signal must have this property, and therefore it is a necessary condition for a Gaussian process (although possibly not sufficient). Since Doppler spectra are the natural output of our existing radar system, we intend to use (7) as a test to determine experimentally whether the signal is Gaussian.

Likewise, higher normalized moments[5] can be established from the general rule $\langle P_k{}^n \rangle = n! \langle P_k \rangle^n$. In this paper, we go no higher than the second—as defined in (7)—for our initial testing. The reason for this is the fact that our experimental sample bases are very small, containing only nine samples per ensemble. (The total number of such separate sample ensemble bases, on the other hand, is five hundred.) When dealing with such a small number of samples per ensemble, higher moments can be expected to become increasingly noisy and thus inaccurate for statistical testing. In general, one can predict that inasmuch as the sea-echo probability density must depart from Gaussian in its tails (since the signal can never approach infinity), these normalized higher empirical moments should fall increasingly short of their predicted values for a true Gaussian process.

The power spectral sample P_k (being the sum of the squares of two uncorrelated Gaussian variables) is predicted to be chi-squared with two degrees of freedom [15]; the probability density for P_k is therefore, the simple exponential function. Hence, the amplitude (i.e., $A_k \equiv \sqrt{P_k}$) of the FFT output is Rayleigh-distributed; this fact will be also employed subsequently for additional statistical testing.

IV. Description of Radar Facility

Sea-state measurements were made by an HF radar located on the west coast of San Clemente Island. The radar system was built by the Institute for Telecommunication Sciences of the Department of Commerce and was operated under contract for the Wave Propagation Laboratory for this series of measurements. Approximately 25 h of data were recorded between December 1972 and April 1973.

Surface-wave radar data were obtained simultaneously at 10 frequencies extending from about 2.4 to 25 MHz. Receiver range gates were set to sample cells centered 22.5, 30.0, and 37.5 km from the radar. The receiving antenna consisted of an array of 13 monopoles phased and switched to alternately produce two beams each having a nominal beamwidth of 10° centered at azimuth angles of 240° and 270°. The combination of 10 frequencies, 3 ranges, and 2

[5] The nth normalized moment is defined as

$$\langle (P_k - \langle P_k \rangle)^n \rangle / \langle P_k \rangle^n.$$

TABLE I
Summary of San Clemente Island Surface-Wave Radar Characteristics

Operating Frequency Range	2 to 25 MHz
Range Gate Distances	22.5, 30.0, 37.5 km
Available Pulse Lengths	20, 50, 100 μs
	(3.0, 7.5, 15.0 km)
Pulse Repetition Frequency	20 Hz per frequency
Transmitter Peak Power	40 kw
Antenna Beamwidths	
Receiving (2 beams)	10° at 240° and 270° az
Transmitting	60° at 255° az
Antenna Gain Product	18 dB at center of HF band
	decreasing to 5 dB at band
	edges

antenna beams resulted in a total of 60 different data samples being recorded.

The transmitting antenna was a two-bay, vertically polarized log-periodic antenna having a nominal half-power beamwidth of 60° over the HF band. Since this beamwidth illuminated both sectors covered by the receiving beams, no transmitter antenna steering was used. Power patterns of both receiving and transmitting antennas were measured from a small boat to verify gain and beamwidth performance. Radar characteristics are summarized in Table I.

An on-line computer processed the received signals and computed the power spectrum for each of the 60 data channels. The power spectra which were processed on-line were calculated from signals that had been coherently sampled over a 200-s window. Since a typical measurement period was 30 min, a total of 9 spectra would be computed during this time. These power spectra and the unprocessed IF data were recorded on magnetic tape to permit subsequent analysis of the raw data.

V. Measured Sea Echo Properties

A. Standard Deviation of Spectral Peaks

The normalized standard deviation σ_p of the power at the spectral peaks was computed for power spectra having coherent integration times of 200 s. Thus, the quantity σ_p for a 30-min sample represents the standard deviation of $N = 9$ spectral peaks divided by the average maximum of the 9 spectra in the sample. Normalized standard deviations were calculated for both the absolute maxima of the spectra in the vicinity of the first- and second-order Bragg frequencies and for the spectral power at constant Doppler frequencies near $\pm f_B$ and $\sqrt{2} f_B$. The Bragg frequency f_B is defined as $f_B = \omega_B / 2\sqrt{g/\pi \lambda}$.

The data studied consisted of approximately $7\frac{1}{2}$ h of measurements for a wide variety of sea states with significant waveheights ranging from 1 to 4 m (wave characteristics were measured by a Waverider Data Buoy moored 29.4 km from the radar site on an azimuth of 240°); 500 individual spectra have been considered in our analysis. Mean values of σ_p versus range are listed in Table II for the different spectral lines. We see there is no systematic tend of σ_p with

TABLE II
MEAN NORMALIZED STANDARD DEVIATIONS AT DIFFERENT RANGES FOR
ABSOLUTE MAXIMA AND SPECTRUM AT FIXED DOPPLER FREQUENCY

Doppler Line	Range			All Data Combined
	22.5 km	30.0 km	37.5 km	
	Fixed Doppler near Maxima			
1 +	0.912	0.917	0.918	0.916
1 -	0.921	0.930	0.974	0.942
2 +	0.948	0.954	0.954	0.952
	Absolute Maxima			
1 +	0.736	0.719	0.707	0.720
1 -	0.740	0.712	0.675	0.709
2 +	0.496	0.468	0.485	0.483

Note: 1 + and 1 - are first-order advancing and receding lines
near f_B; 2 + is the second order advancing line near $\sqrt{2}\, f_B$

TABLE III
NORMALIZED STANDARD DEVIATIONS FOR TWO PULSE LENGTHS
TRANSMITTED DURING ADJACENT 30-MIN PERIODS

Doppler Line	Range			All Data Combined
	22.5 km	30.0 km	37.5 km	
	Fixed Doppler - 20 µs Pulse			
1 +	0.816	0.876	1.024	0.905
1 -	0.927	0.990	0.947	0.955
2 +	0.929	0.940	0.886	0.918
	Fixed Doppler - 100 µs Pulse			
1 +	0.972	0.859	0.928	0.920
1 -	0.951	0.901	0.891	0.914
2 +	0.878	0.966	0.913	0.919
	Absolute Maxima - 20 µs Pulse			
1 +	0.659	0.796	0.733	0.729
1 -	0.719	0.861	0.646	0.742
2 +	0.502	0.442	0.515	0.486
	Absolute Maxima - 100 µs Pulse			
1 +	0.786	0.747	0.737	0.757
1 -	0.735	0.772	0.732	0.746
2 +	0.506	0.414	0.466	0.462

range, and hence none with cell size. Similarly, no dependence of σ_p with operating frequency was observed. The normalized standard deviation is slightly less than unity for the spectra at a fixed Doppler frequency indicating that the Gaussian model is approximately correct. The ratio is about 0.71 for the absolute power maxima of first order peaks; no model has yet been pursued which explains this result. The second-order average for the absolute maxima is about 0.5, indicating that perhaps still a different model applies to this spectral line.

As a further check of possible dependence of σ_p on range cell size, two pulse widths (20 and 100 µs) were transmitted for consecutive 30-min periods, during which significant waveheight and direction remained fairly constant. The normalized standard deviations obtained at each pulse length are shown in Table III. We see that the results

for different pulse lengths are not significantly different from the values obtained for all data combined. Therefore, we conclude that there is little, if any, dependence of σ_p upon cell size.

The correlation coefficient between normalized standard deviation and significant waveheight during the sample period was computed to determine whether the quantity σ_p can be used as a predictor of sea state. Since the observed correlation values were not statistically significant, we must conclude that σ_p is *not* a useful indicator of sea state.

B. Cumulative Distributions of Measured Data

The measured standard deviations σ_p for the spectral power at fixed Doppler frequency are sufficiently close to the predicted values for a Gaussian process (i.e., 0.916, 0.942, and 0.952 compared to unity) that further statistical testing is desirable. This is especially true since the theoretical analyses of Section II predict Gaussian processes. No further testing will be done, however, on the spectral data at the absolute spectral maxima, since the normalized standard deviations are quite different from Gaussian predictions (0.720, 0.709, and 0.483 compared to unity). Furthermore, no simple model (with a minimum of undetermined parameters) exists which can shed light on this spectral statistic; hence, it will not be examined further in this paper.

As an additional check to establish the Gaussian nature of HF sea echo, we examined the distribution of spectral power at a fixed Doppler frequency. From Section III, the FFT amplitude should be distributed according to the Rayleigh distribution if the echo signal is a Gaussian random variable. Therefore, our second test consisted in determining whether the spectral amplitude recorded over a period when the sea was statistically stationary was Rayleigh-distributed.

To obtain an adequate sample size, we calculated 72 spectra with 25-s integration time from continuous IF sea-echo data recorded over a 30-min period. First- and second-order ($\pm f_B$ and $\sim\sqrt{2}\, f_B$) data points were sorted into 0.5-dB intervals for computation of cumulative distributions of spectral amplitude. The distributions were expressed in decibels and plotted on special "Rayleigh-distribution" graph paper. This paper is constructed such that a Rayleigh-distributed variable will fall along a straight line having a slope of -1.

Fig. 2 shows the result for the first-order advancing and receding Bragg lines. The data points are the cumulative distributions obtained at three operating frequencies; the solid lines indicate the slope which a Rayleigh-distributed quantity would have. Except for some departures in the higher percentage tails, the data points appear to fall along straight lines having the slope criterion required for the Rayleigh distribution.

Data for the second-order approaching lines at the same three frequencies are plotted in Fig. 3. Again, the solid line shows the slope characteristic of a Rayleigh-distributed quantity. Although there appears to be a somewhat larger
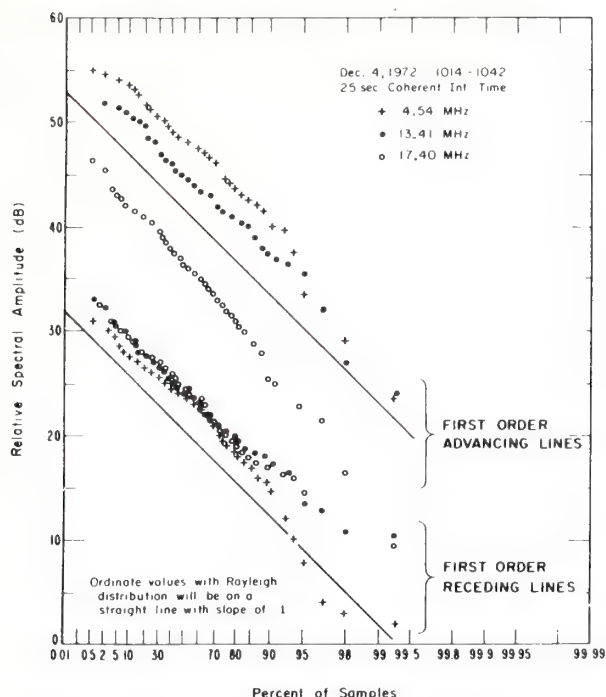
Fig. 2. Cumulative distribution of spectral amplitudes at fixed Doppler frequency ($\pm f_B$) for three sets of 72 spectra. Solid lines indicate slope $= -1$.
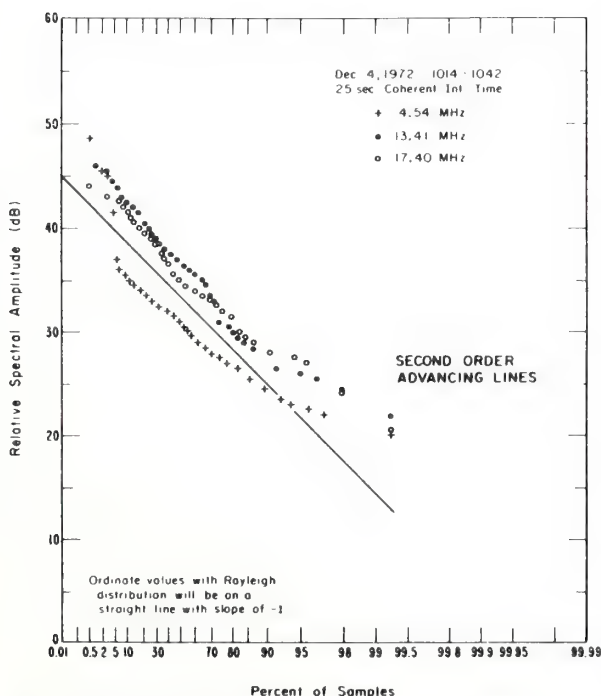
Fig. 3. Cumulative distribution of spectral amplitudes at fixed Doppler frequency ($\sqrt{2} f_B$) for three sets of 72 spectra. Solid line indicates slope $= -1$.
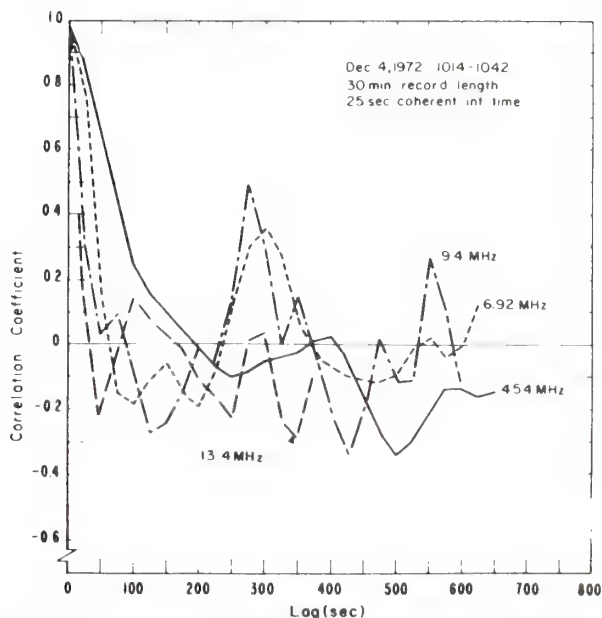
Fig. 4. Autocorrelation of first-order advancing maxima versus operating frequency.

departure from a straight line than was observed for the first-order lines, the data points have nearly the required slope.

We consider the apparent Rayleigh-distribution of spectral amplitudes at fixed Doppler frequency as additional confirmatory evidence that HF sea echo is described reasonably well by a Gaussian process.

C. Autocorrelation of Spectral Peaks

To determine the time between independent samples and the associated implications as to optimum measurement periods, we computed the autocorrelation $\rho(\tau)$ of first- and second-order portions of the power spectrum. This quantity is the correlation between spectral peaks separated by integral multiples of the coherent integration time; thus the autocorrelation is computed for lags τ equal to nT, $1 < n < N - n$, where T is the coherent integration time and N is the total number of spectra in the record length. We made calculations for coherent integration times of 25, 50, 100, and 200 s; the total record length was 30 min. As in the case of the normalized standard deviation, calculations were performed for both absolute peaks and power near these peaks but occurring at a constant Doppler frequency. Because of the fairly large amount of computer time required, only two sea states were considered. The first sample had a significant waveheight ($H_{1/3}$) of 1.5 m while the second had $H_{1/3} = 4$ m.

In Fig. 4 we present $\rho(\tau)$ observed on December 4, 1972 ($H_{1/3} = 1.5$ m) for the first-order advancing line. This result is very similar to that observed during the period with $H_{1/3} = 4$ m; thus, over the range of significant waveheights used in this analysis, waveheight does not appear to affect

TABLE IV

Time Required for Correlation Coefficients to Decrease to $1/e$ (0.368). Range = 22.5 km; Pulsewidth — 50 µs. Data Taken December 4, 1972, 1014–1042 PST

Frequency (MHz)	Time(s)					
	Absolute Maxima			Fixed Doppler Maxima		
	+ 1	- 1	+ 2	+ 1	- 1	+ 2
2.41	140	65	*	140	25	*
4.54	85	40	*	80	55	*
6.92	35	35	35	30	40	20
9.40	20	30	20	20	20	20
13.41	20	20	15	25	20	20

* There is no well defined second order component at this frequency

the correlation between spectral peaks for the predominant line. In addition, for the first-order advancing lines, the "correlation function" is very similar for both the absolute peaks and for the spectra at a fixed Doppler. However, the first-order receding and second-order advancing lines show a much more rapid decrease in correlation coefficient with lag time; in fact, the spectral peaks are uncorrelated after a single lag period of 25 s.

For the first-order advancing line, the correlation at the lower operating frequencies decreases more slowly than at higher frequencies. At frequencies greater than about 7 MHz, all these major spectral components are uncorrelated after a single lag interval. To show the behavior of the correlation coefficient of the spectral lines with frequency, in Table IV we tabulate the time required for the correlation coefficient to decrease to $1/e$. These values were obtained for a coherent integration time of 25 s. Since the correlation does not change significantly with range, data for only a single range are given.

When considering the correlation results for the longer coherent integration times, we find little difference in the general shape of the correlation function. Although some detail is smoothed out at the longer integration times, it is clear that there is no important difference in $\rho(\tau)$ for either a 25 or 50 s time interval. At 100 and 200 s integration times, sufficient detail is lost that comparison with the shorter times is difficult. However, to generalize the results at these longer times, we find that the peaks are uncorrelated after a single lag period at all frequencies.

The fact that spectral peaks at higher frequencies are largely uncorrelated after 25 s has important implications for over-the-horizon (OTH) sensing of sea state. Since higher frequencies are likely to be used in the OTH work, especially at the longer ranges, independent samples would be obtained with a 25 s coherent integration time. This is fortunate since the ionosphere is unlikely to remain stable for much longer periods. For sea-state sensing using an HF surface-wave radar, independant samples are always obtained using coherent integration times of 200 s.

A possible physical interpretation of the observed time between independent spectral samples can be deduced by noting that this time is approximately the reciprocal of the width of the respective spectral peak (measured in hertz) at

which the correlation time was measured. Meteorologists have established this relationship for radar spectra of rain echoes [16], [17]. The explanation for the spectral peak widths in that case relates to the differential raindrop fall velocities, and how long it takes for two typical raindrops with different velocities to produce a scattered signal phase change of 180°. The corresponding explanation for first-order scatter from the sea, for example, would suggest that the reciprocal of the first-order spectral peak width is essentially the time it takes for two typical periodic Bragg-scattering ocean wavetrains (within the resolution cell)— but having slightly different velocities—to slide one-half wavelength with respect to each other.

VI. Sample Extrapolation to System Design

The statistical analyses of the HF sea-echo signal undertaken in the previous sections have application to system design. The two results which are most immediately useful are the facts that i) the narrowband time signal is (approximately) Gaussian, and ii) the time between independent spectral samples is ~25–50 s over most of the HF region.

As an example, plans are underway to construct and operate a skywave research radar on San Clemente Island for sea-echo observations. Due to antenna scan time, a Doppler spectrum can be constructed for a given ocean patch only every T_s s (for the San Clemente Island skywave radar planned for the Gulf of Alaska observations, one mode of operation has $T_s \simeq 500$ s, with a coherent integration time per spectrum of 25 s). Since T exceeds 50 s, each spectrum is uncorrelated and independent of all others, according to the results of the preceding section. In order to extract average sea-state data from the echo, an "average" Doppler power spectrum must be constructed. This "average" is actually the sum of N independent spectral samples taken T_s s apart. An ensemble average—in which the spectrum fluctuations vanish as the spectrum approaches its true mean—is obtained as N approaches infinity. However, one cannot generally afford to wait this long; 1 or 2 h may be the practical upper limits of desirable system operation, due both to operating costs and also to the fact that sea state can change after several hours, making the statistics "nonstationary." During 1 h, for example, where $T_s \simeq 500$ s, only about $N = 7$ independent samples would be used to form the "average." This therefore is not a true "average" power spectrum, but is itself a random sample fluctuating about the true mean. The greater N, the less the fluctuation of the "sample average," and hence the less error involved in estimating the desired sea-state parameters. Thus one has the trade-off between reducing statistical errors in the desired output data versus requiring too much time to gather the data, with the resulting question—what is the optimum or "break-even" point in terms of the total number of independent samples, N (or the total data collection time NT_s)?

If one cannot assume Gaussian statistics, there is nothing one can do short of a massive program of gathering data and extracting empirical results. Since we can assume that the signal here is Gaussian, we can readily derive errors and
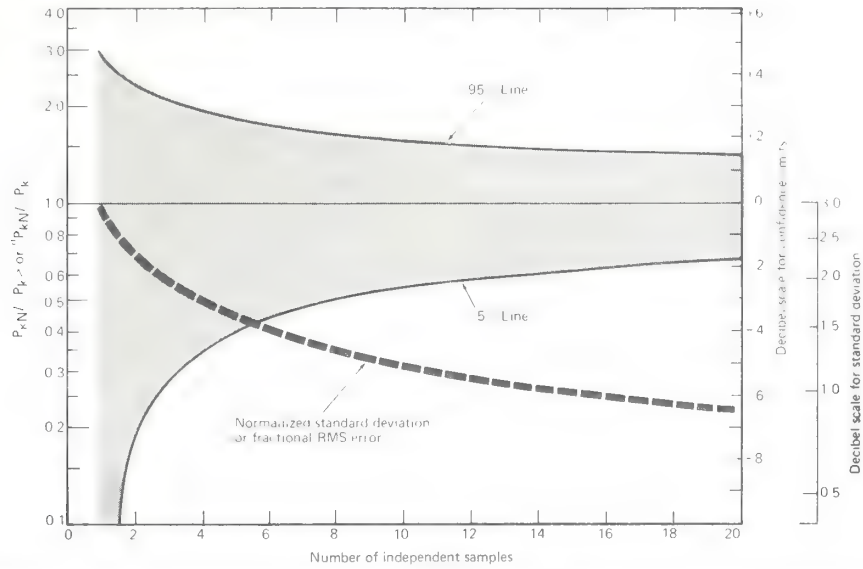
Fig. 5. Normalized standard deviation and 90 percent confidence interval for power spectra of Gaussian process versus number of independent samples.

confidence limits of the power spectrum versus the number of independent samples. Let us define P_{kN} as the sample average over N independent samples, with $\langle \cdot \rangle$, as before, signifying the true average over an infinite ensemble. We define the variance of the sample average as

$$\sigma_{P_{kN}}^2 = \langle P_{kN}^2 - \langle P_{kN} \rangle^2 \rangle$$

$$= \left\langle \left[\frac{1}{N} \sum_{n=1}^{N} \frac{X_{kn}^2 + Y_{kn}^2}{T} \right] \right\rangle^2 - P_k^2$$

$$= \frac{1}{T^2 N^2} \left[\sum_{n=1}^{2N} \langle X_{kn}^4 \rangle \right.$$

$$\left. + \sum_{m=1}^{2N} \sum_{n=1}^{2N} \langle X_{km}^2 \rangle \langle X_{kn}^2 \rangle - (2\sigma_k^2)^2 \right]. \quad (8)$$

Noting that X_{kn} and Y_{kn} have the same (Gaussian) distribution, and are uncorrelated, we arrive at the following answer for the (normalized) variance and standard deviation (or fractional rms error) in the spectral average of N samples:

$$\sigma_{P_{kN}}^2 / \langle P_k \rangle^2 = 1/N \quad \text{or} \quad \sigma_{P_{kN}} / \langle P_k \rangle = 1/\sqrt{N}. \quad (9)$$

The latter normalized standard deviation is shown plotted in Fig. 5, both on an absolute scale and in decibels. By multiplying the abscissa by T_s (the time between samples), one has a measure of the fractional rms spectral error versus operating time.

Another measure of the quality of an average of N independent samples is the confidence interval. This can be found by noting that since X_{kn} and Y_{kn} have the same statistics but bare uncorrelated, one can write

$$P_{kN} = \frac{1}{N} \sum_{n=1}^{N} \frac{(X_{kn}^2 + Y_{kn}^2)}{T} = \frac{1}{NT} \sum_{n=1}^{2N} X_{kn}^2. \quad (10)$$

Now, since X_{kN} is Gaussian, it is true that NP_{kN} is chi-squared with $2N$ degrees of freedom (see for example Hogg and Craig [15]). Thus one can use the standard tables for this distribution to estimate the confidence. A 90 percent confidence interval for $P_{kN}/\langle P_k \rangle$ is shown in Fig. 5 for the power spectral average consisting of N samples. The upper and lower limits are set symmetrically so that 5 percent of the points will fall above the upper line and 5 percent below the lower line. Therefore, the shaded zone represents the region (for given N) where 90 percent of the "average" spectral estimates P_{kN} will fall.

From both sets of curves, one can see for example that increasing the averaging time from 1 to 2 h (where $T_s = 500$ s) will decrease the rms error from 1.4 to 1.0 dB, and will decrease the total 90 percent confidence spread from 5.57 to 3.87 dB. This decrease in the statistical error may be considered marginal in terms of operating costs for the additional hour for certain applications.

VII. CONCLUSIONS

Our investigation into the statistics of HF sea scatter observed at San Clemente Island has revealed the following facts.

1) The first- and second-order portions of the received echo signal voltage are described reasonably well by a Gaussian process. This empirically implies that the sea wave-height is nearly Gaussian, a fact which has been ascertained and known to oceanographers for many years. Consequences of this result are the facts that i) the normalized standard deviation of the echo power at any given spectral frequency is unity and ii) the amplitude (square-root of power) at any given spectral frequency is Rayleigh-distributed.

2) The normalized standard deviation of the maximum of the first-order power spectral peak (which wanders slightly in frequency from record to record), on the other hand, is observed to be 0.7. The same quantity for the second-order peak is observed as ~0.5. While it is physically reasonable that these standard deviations should be less than unity, we presently have no satisfactory model which explains these results quantitatively.

3) The normalized standard deviations observed above appear from the data to be independent of range, radar resolution cell size, radar operating frequency, and sea state (i.e., significant waveheight).

4) The autocorrelation function (versus time) of the power spectra appears to be independent of sea state (i.e., waveheight) and cell size, but is slightly dependent upon radar operating frequency below 7 MHz. Above 7 MHz, the power spectra are essentially uncorrelated after 25 s. The heretofore accepted explanation that the correlation time should be roughly the time it takes the scattering wavetrains to pass through the cell (e.g., ~1550 s for a 7.5-km cell size at 10 MHz) is entirely inadequate to explain our observations. A more likely explanation relates this time to the reciprocal of the width of the respective spectral peak: this latter quantity in turn can be related to the differential velocities between the scattering ocean wavetrains, which resembles a "turbulence" phenomenon.

5) The implication of the previous result is that uncorrelated samples of sea-echo power spectra are obtained for intervals greater than 25 s in the upper HF band (where a skywave OTH radar would normally operate). This fact—combined with the Gaussian nature of the sea echo also established herein—makes it possible to predict the statistical errors inherent in spectral samples of finite number. For example, a power spectral average of 14 independent samples was shown to have an rms error (or fluctuation) about the mean of 1.0 dB.

REFERENCES

[1] D. D. Crombie, "Doppler spectrum of sea echo at 13.56 Mc/s," *Nature*, vol. 175, pp. 681–682, 1955.
[2] J. R. Wait, "Theory of HF ground wave backscatter from sea waves," *J. Geophys. Res.*, vol. 71, pp. 4832–4839, 1966.
[3] D. E. Barrick and W. H. Peake, "A review of scattering from surfaces with different roughness scales," *Radio Science*, vol. 3, pp. 865–868, 1968.
[4] D. E. Barrick, "First-order theory and analysis of MF/HF/VHF scatter from the sea," *IEEE Trans. Antennas Propagat.*, vol. AP-20, pp. 2–10, 1972.
[5] ——, "Remote sensing of sea state by radar," in *Remote Sensing of the Troposphere*, V. E. Derr (Ed.), U.S. Government Printing Office, Washington, DC: 1972, ch. 12.
[6] A. E. Long and D. B. Trizna, "Mapping of North Atlantic winds by HF radar sea backscatter interpretation," *IEEE Trans. Antennas Propagat.*, vol. AP-21, pp. 680–685, 1973.
[7] D. E. Barrick, J. M. Headrick, R. W. Bogle, and D. D. Crombie, "Sea backscatter at HF: Interpretation and utilization of the echo," *Proc. IEEE*, vol. 62, pp. 673–680, 1974.
[8] G. V. Trunk, "Radar properties on non-Rayleigh sea clutter," *IEEE Trans. Aerospace and Electronics Syst.*, vol. AES-8, pp. 196–204, 1972.
[9] A. Papoulis, "Narrowband systems and Gaussianity," *IEEE Trans. Inform. Theory*, vol. IT-18, pp. 20–27, 1972.
[10] ——, *Probability, Random Variables, and Stochastic Processes.* New York: McGraw-Hill, 1965, p. 583.
[11] S. O. Rice, "Reflection of electromagnetic waves from slightly rough surfaces," *Theory of Electromagnetic Waves*, M. Kline, Ed. New York: Interscience, 1961, pp. 351–378.
[12] B. Kinsman, *Wind Waves.* Englewood Cliffs, NJ: Prentice-Hall, 1965, p. 676.
[13] W. B. Davenport, Jr., and W. L. Root, *An Introduction to the Theory of Random Signals and Noise.* New York: McGraw-Hill, 1958, p. 393.
[14] J. L. Ahearn, S. R. Curley, J. M. Headrick, and D. B. Trizna, "Tests of remote skywave measurement of ocean surface conditions," *Proc. IEEE*, vol. 62, pp. 681–687, 1974.
[15] R. V. Hogg and A. T. Craig, *Introduction to Mathematical Statistics.* New York: Macmillan, 1959, p. 245.
[16] R. M. Lhermite, "Motions of scatterers and the variance of the mean intensity of weather radar signals," Sprery Rand Res. Center Program 38310, Rept. No. SRRC-RR-63-57, Atmospheric Physics Dept., Sudbury, MA, 1963.
[17] F. E. Nathanson, *Radar Design Principles.* New York: McGraw-Hill, 1969.

METEOROLOGICAL DOPPLER RADAR WITH DOUBLE PULSE TRANSMISSION

W. C. Campbell and R. G. Strauch
NOAA/ERL/Wave Propagation Laboratory
Boulder, Colorado 80302

1.   INTRODUCTION

Microwave pulse Doppler radars presently used in meteorological research transmit pulses that are uniformly spaced in time. The maximum unambiguous range (R_m) is directly proportional to the time separation of the pulses while the maximum unambiguous velocity (V_m) is inversely proportional to the pulse spacing. For this conventional pulse radar transmission the product ($R_m V_m$) is $\pm c\lambda/8$, where λ is the radar wavelength and c is the velocity of propagation. The maximum detection range of precipitation echoes may exceed 300 km and velocities can exceed $\pm$ 50 m/s. Hence the radar meteorologist, analyzing radar data taken with 3, 5, or 10 cm wavelength radars, must always be alert to the possibility that range or velocity aliasing may occur in the data. These aliasing problems can frequently be resolved with total confidence if other data are available. However, in severe weather with regions of high shear, the interpretation of velocity aliasing may be ambiguous. The usual operational procedure is to record data only if range aliasing is not a problem. Even 10 cm radars have difficulty in obtaining data in extensive severe weather regimes such as squall lines. The problems are particularly acute for 3 cm radars. These problems are not unique to radar meteorology; for example, the measurement of radar auroral motions presents an identical problem because 6 m wavelength radars are used to measure radar returns at ranges of 1000 km or more and velocities as high as 2000 m/s are encountered (Greenwald and Ecklund, 1975).

2.   DOUBLE PULSE TRANSMISSION

One method that can alleviate the problem of range and velocity aliasing is the transmission of a pair of pulses separated in time by T_1 with a repetition period of the pulse pair of T_2 where T_2 is much greater than T_1. T_2 is chosen so that the range $cT_2/2$ exceeds the maximum range of any radar return and T_2 exceeds $\lambda/(2\sigma_v\sqrt{2\pi})$, the correlation time of the weather echoes, where σ_v is the standard deviation of the velocity distribution of the scatterers (Nathanson, 1969). Fig. 1 illustrates the pulse sequence. Target velocity is obtained from the phase of the covariance function of the complex signal obtained with each pair of pulses. The maximum unambiguous range is therefore proportional to T_2, while the maximum unambiguous velocity is inversely proportional to T_1. This idea is not new (Rummler, 1968; Doviak and Sirmans, 1973); in fact double pulse transmission has been successfully adapted to an HF radar for radar auroral measurements (Greenwald and Ecklund, 1975). However, double pulse transmission has not been used in radar meteorology even though measurement of the phase of the covariance function has rapidly become the most widely-used method of estimating mean velocities for meteorological Doppler radars. We have implemented the double pulse technique on a computer-controlled research radar and it will be tested in an airport environment for 9 months
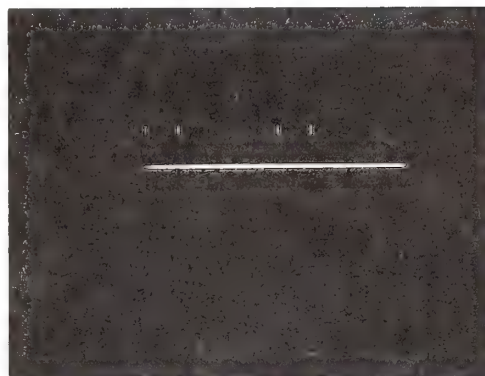
Figure 1. Radar pulses for double pulse transmission.
   T_1 = 256 microseconds
   T_2 = 1024 microseconds

starting in July 1976. After this period we plan to test it further on the new NOAA research aircraft (WP-3D).

3.   IMPLEMENTATION

A minicomputer controls the radar pulsing, range gate sampling, antenna positioning, etc. with all parameters entered on a keyboard. The spacing between pairs of triggers (T_2) can be selected from 512 to 8192 microseconds and the spacing of the pulses in the pair (T_1) can be selected from 200 microseconds to $T_2/2$. Estimates of the mean velocity are calculated (software) using bipolar video from 64 pairs of pulses or 128 radar samples. Mean velocity estimates can be averaged for as many as 1024 dwell times or 65,536 pulse pairs. A block of range sampling gates (up to 255 gates) are generated following each transmitted pulse. These gates can be positoned by selecting a time delay and a spacing between gates. Fig. 2 shows the transmitted pulses and the blocks of range gates when the total depth of coverage of the range gates is less than the spacing between pulses in the pair. In the top trace the maximum target range is less than $cT_1/2$, in the center trace the minimum target range is greater than $cT_1/2$, and in the bottom trace the second transmitted pulse occurs while the samples are being acquired for the first pulse. In this latter case data will be lost during receiver recovery. If the depth of echo exceeds $cT_1/2$, then the two blocks of range gates overlap as shown in Fig. 3. When this occurs, the pulse spacing is automatically adjusted so that in the overlap region a single sample serves as the data sample for both the first and second pulses. Therefore we can analyze data when the depth of the radar echo exceeds $cT_1/2$, even though one or both of the samples of a pulse pair contains echo power from both radar pulses. Radar return from ranges separated by $cT_1/2$ can occur in a given sample.

123
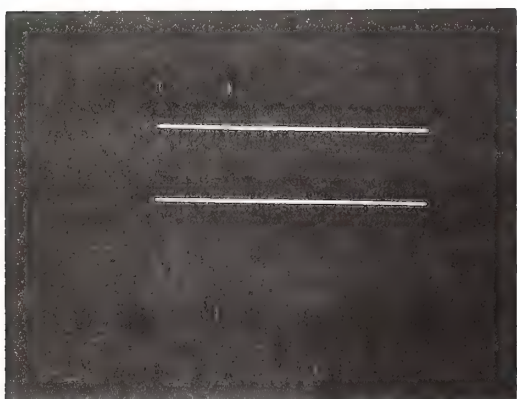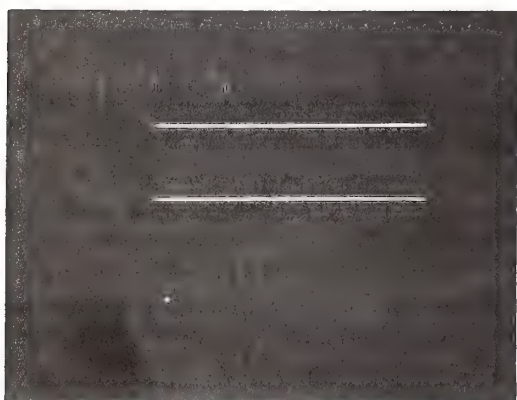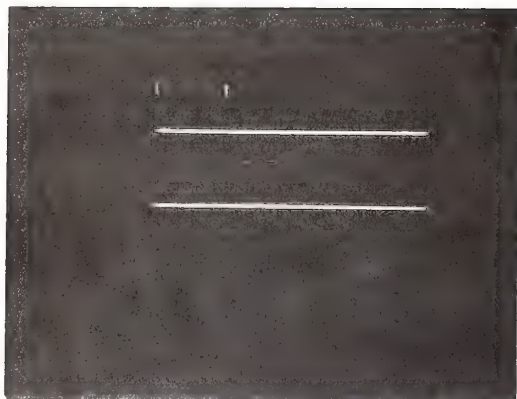
Figure 2. *Radar pulses (upper trace) and range gates (lower trace) for double pulse transmission.*

top: maximum range less than $cT_1/2$

center: minimum range greater than $cT_1/2$

lower: samples for first pulse are acquired when the second pulse occurs.

Figure 3. *Radar pulses (upper trace) and range gates (lower trace) when the depth of echo exceeds $cT_1/2$.*

4.   DISCUSSION

If the depth of echo does not exceed $cT_1/2$ then the estimation of radial velocities by measuring the phase of the covariance function is the same as that for radars with conventional pulsing. If the radar pulses are equally spaced the number of pulse-pairs may be considered to be N-1 (where N is the number of radar samples in the dwell time) by calculating the complex correlation of adjacent pulses. Alternatively, the number of pulse-pairs may be taken as N/2 by calculating the complex correlation of the pulses in groups of two. Since consecutive samples must be dependent, the number of independent pulse-pairs is the same for either computation. The latter method is identical to that used with double-pulse transmission. The standard deviations of the estimates of the mean velocity for double pulse transmission are predicted from results de-rived by Rummler (1968) when the depth of the echo does not exceed $cT_1/2$. Note that double pulse transmission increases the maximum unambiguous velocity V_m and also decreases the normalized width of the velocity spectra, and this decreases the standard deviation of the mean velocity esti-mate.

We have usually operated our conven-tional 3 cm pulse radars with a repetition period of about 500 microseconds (R_m=75 km, V_m=± 15 m/s). Frequently we observe isolated thunderstorms in the high plains with storm diameters of 30 to 40 km so that a spacing (T_1) of 250 microseconds can be used to double the maximum unambiguous velocity. In addition we can utilize double pulse transmission on larger storms when we scan at higher antenna elevation angles. We will use the double pulse mode for measuring radial velocities near an airport where the antenna elevation angle will be 10° to 20°, and we will use it for aircraft tests.

Doviak and Sirmans (1973) proposed to treat the case for which the depth of echo exceeded $cT_1/2$ by transmitting the two pulses of each

43

pair with orthogonal polarization. They proposed
to operate a dual channel system that would be
limited only by the depolarization of the hydro-
meteors. Before resorting to the complexity of
dual channel operation we propose to test the
double pulse transmission described above even
when the depth of echo exceeds $cT_1/2$, as illustrated
in Fig. 3. Since T_2 can be selected to be greater
than the correlation time, the spectrum of the echo
power that is received as an interfering signal
will appear as white noise. Hence we can treat
cases for which the echo depth exceeds $cT_1/2$ the
same as those without interfering signals but
which have degraded signal-to-noise ratio. Note
that either one or both samples of a given pair of
pulses may contain echo power from the undesired
pulse. However, if the interfering signal is
uncorrelated between pairs of pulses it should be
possible to obtain satisfactory mean velocity
estimates by increasing the number of pulse pairs
used to calculate the phase of the covariance
function. This method can be used if longer dwell
times are acceptable. Ecklund (private communi-
cation) reported that most of the radar auroral
measurements were made when the depth of the echo
exceeded $cT_1/2$. The HF radar normally uses a
large number of pulse pairs and the data is
treated as though there were no interfering
signals. One application of meteorological radar
that permits long dwell times is the measurement
of radial velocities along the glide slope (approxi-
mately 3 deg. elevation angle) of an airport
runway. We plan to test this operating mode when
the received signal power from the two pulses
overlap.

5.   CONCLUSION

        A low power 3 cm pulse Doppler radar
has been constructed with versatile pulsing
characteristics so that double pulse transmission
can be tested. It promises to alleviate some of
the range and velocity aliasing that occurs with
conventional pulse radars. Double pulse trans-
mission enables us to increase the maximum
unambiguous velocity of the 3 cm radar to $\pm$ 32 m/s
if the depth of radar echo is less than 38 km.
If the echo depth exceeds 38 km the mean radial
velocities can still be measured but longer dwell
times are required. Double pulse transmission
should help alleviate aliasing problems but it is
not a total solution.

6.   REFERENCES

Doviak, R. J. and D. Sirmans (1973), Doppler
        radar with polarization diversity, *J. Atmos.
        Sci.*, 30, 737-738.

Greenwald, R. A. and W. L. Ecklund (1975), A new
        look at radar auroral motions, *J. Geoph. Res.*,
        80, 3642-3648.

Nathanson, F. E. (1969), Radar Design Principles,
        McGraw-Hill, New York, p. 90.

Rummler, W. D. (1968), Two pulse spectral mea-
        surements, Tech. Memo. MM-68-4121-15, Bell
        Teleph. Lab., Whippany, N.J.

Microwave radar wind measurements in the clear air

R. B. Chadwick, K. P. Moran, R. G. Strauch, G. E. Morrison, and W. C. Campbell

NOAA-Environmental Research Laboratories, Wave Propagation Laboratory, Boulder, Colorado 80302

It is shown that an FM-CW radar can be used as a Doppler radar to measure winds. A description of the processing used to measure Doppler shifts is included. An analysis of scattering by refractive-index fluctuations shows that, under certain conditions, a Doppler FM-CW radar should be able to measure winds continuously in the boundary layer. Experimental results comparing horizontal winds measured by a tethered balloon and the FM-CW radar show very good agreement.

1. INTRODUCTION

A basic requirement of applied meteorology is the measurement of wind speed and direction as a function of height. Tethered or free balloons are most commonly used for in-situ wind measurements. Three usual disadvantages of wind measurement by balloon are (1) slow response time, (2) inability to monitor the winds continuously in time, and (3) inability to measure the winds simultaneously at all altitudes. All of these disadvantages may be circumvented by using Doppler radars that measure backscatter from either hydrometeors or from clear air refractive index fluctuations moving with the wind.

The techniques for measuring the motion of hydrometeors carried by the wind are well developed and in wide research use. The usual technique is to transmit a sequence of coherent pulses and then spectrally analyze the return sequence to obtain the velocity spectrum. Two problems that arise are: (1) lack of suitable hydrometeors and (2) nonzero fall velocity of the hydrometeors. Both of these problems vanish when a clear air radar is used.

During the past decade, radars have been developed that are sensitive enough to obtain returns from turbulent eddies which cause refractive index fluctuations in the clear atmosphere. One way to achieve the required sensitivity is simply to increase the power and antenna size of a conventional pulse radar. The result is a large and expensive radar system with a significant minimum range. Because antenna sidelobes inhibit its use at very short ranges, no advantage can be taken of the fact that for

beam-filling targets, the received signal is inversely proportional to range squared. An ability to take measurements close to the radar would greatly enhance the capability to sense refractive index fluctuations in the clear air.

Other radar techniques avoid this problem by transmitting a relatively low power continuous signal modulated in such a way that range information is easily recovered. A technique in which the frequency is linearly modulated was applied by *Richter* [1969] to the problem of sensing the clear atmosphere. The success of this effort resulted in at least three other frequency-modulated continuous-wave (FM-CW) radars being built: a second one by Richter, one by the Institute for Telecommunication Sciences [*Bean et al.*, 1971], and one by the Wave Propagation Laboratory (WPL). These radars measure atmospheric phenomena close to the radar with very good resolution; however, until recently there was no known method of measuring the velocity spectrum of distributed atmospheric targets with a microwave FM-CW radar.

Recently another clear air atmospheric radar was developed by *Green et al.* [1975]. This is a pulse-Doppler radar of 7-m wave length with an extremely large aperture (7200 m²). The large aperture gives excellent system sensitivity and detection of continuous return from altitudes of 4 to 16 km has been reported. The continuous return is Bragg scattering from refractive index fluctuations and is discernible from background noise only when the signal can be processed for Doppler information. The question naturally arises, "Can the microwave FM-CW radar detect background fluctuations of the refractive index to measure winds aloft?" Using comparison
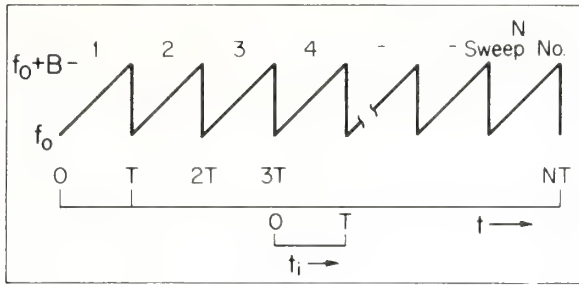
Fig. 1. FM-CW frequency sweep. The starting frequency is f_0, the bandwidth is B, and the sweep period is T.

techniques developed by *Chadwick and Little* [1973], we calculated that the present WPL FM-CW radar should be able to detect refractive index fluctuations to an altitude of 1 to 2 km, if the system described by *Green et al.* [1975] can detect fluctuations of similar magnitude to a height of 16 km. But, to measure winds, Doppler processing must be incorporated into the FM-CW radar.

Doppler processing has been used in over-the-horizon FM-CW radars at HF to measure sea state and two signal-processing methods have been described by *Barrick* [1973]. Using the signal-processing hardware and software from a pulse-Doppler system, *Strauch et al.* [1976] demonstrated the capability to measure vertical velocities in both rain and clear air with the WPL's microwave FM-CW radar. The present paper reports results of a field experiment using this same equipment with the addition of antenna-scanning capability. This added feature makes it possible to measure off-vertical radial velocities, components essential for inference of horizontal winds.

The next section is a brief discussion of the Doppler processing technique as applied to the FM-CW radar. A more complete description is given by *Barrick* [1973].

2. DOPPLER PROCESSING FOR FM-CW RADAR

The WPL FM-CW radar transmits a continuous waveform in which the frequency is linearly modulated over a sweep period T as shown in Figure 1. The conventional (range only) processing technique is easily explained by the fact that the round trip propagation delay causes the frequency sweep of the return signal to be shifted slightly to the right. The frequency difference between transmitted and received return signals is then proportional to

the time delay or range to the target. This frequency difference can be measured by mixing the transmitted signal with the received signal and measuring the power spectrum of the difference signal over a sweep period. The spectra from several successive frequency sweeps are then averaged and the resultant spectrum is proportional to the received power as a function of range.

There are two Doppler processing techniques that can be applied to the FM-CW radar and, since this paper presents data that could have been obtained with either of them, both will be described. Both yield nearly the same results and use the same number of computer arithmetic operations; however, the output formats differ. More complete discussion of the two techniques has been published by *Barrick* [1973].

2.1 *Two-dimensional spectral analysis.* The first technique requires a two-dimensional Fourier transform and is similar to the processing done in most pulse-Doppler radars. The RF portion of the Doppler FM-CW radar is essentially unchanged from that of a non-Doppler FM-CW radar; the difference lies in the signal processing. During any sweep, M samples of the mixed signal are acquired as shown in Figure 2. The guard time, τ, is necessary to avoid sampling large signals at the sweep turnaround. The value of τ is not at all critical and it can even be zero if the sampling A/D converter will not saturate. The sequence of M data points is then transformed by an FFT algorithm (off-line) and the resulting sequence of M complex numbers is stored in the first column of a data matrix. (Since the input sequence is real, the complex output
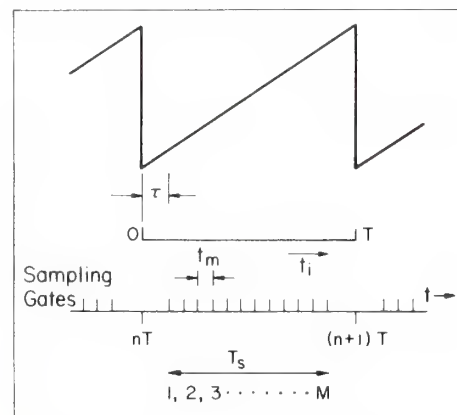
Fig. 2. Timing for signal sampling in the ith sweep.

127

sequence is symmetric so that only $M/2$ complex numbers are stored.) During the next sweep, M samples are acquired in a similar manner and processed with the FFT algorithm. The resulting $M/2$ nonredundant complex numbers are stored in the second column of the data matrix. This process continues until the end of the Nth sweep at which time the data matrix has N columns and $M/2$ rows and is filled with complex numbers. For the experiments described here, M and N are 64 and 32, respectively. The required storage of 1024 complex numbers, or 2048 real numbers, is easily achieved on a minicomputer.

The N one-dimensional Fourier transforms, referred to above, perform much the same function as that of the analog power spectrum analyzer in a non-Doppler FM-CW radar by transforming the mixed signal into a spectral estimate of return signal as a function of range (or frequency). The important difference is that the phase of the return signal from a given range is retained in the complex numbers, and it is this phase change from sweep to sweep that makes possible the measurement of the Doppler spectrum.

The rows of the data matrix contain complex numbers that characterize the magnitude and phase of the return signal from a given range for consecutive sweeps or as a discrete function of time. Thus the power spectral density of the data in a row of the matrix gives the Doppler or velocity spectrum at the range represented by that row, just as in a pulse-Doppler radar. The N point power spectrum is calculated for each of the $M/2$ rows of the data matrix. The result of this second sequence of Fourier operations is an output matrix with N columns and $M/2$ rows and each element of the matrix contains a positive real number representing power from a particular range and having a particular velocity. The output matrix is a map of the power returned from the distributed target as a function of range (by columns) and velocity (by rows). Such a map is shown in Figure 3.

2.2 *One-dimensional technique.* It is known that a two-dimensional Fourier transform is entirely equivalent to a single (long) one-dimensional Fourier transform, e.g., *Gossard and Hooke* [1975]. For our purposes the procedure is to form a long sequence of data by sampling the output signal of the mixer as illustrated in Figure 2. The long sequence of data is obtained over many (e.g., 100)
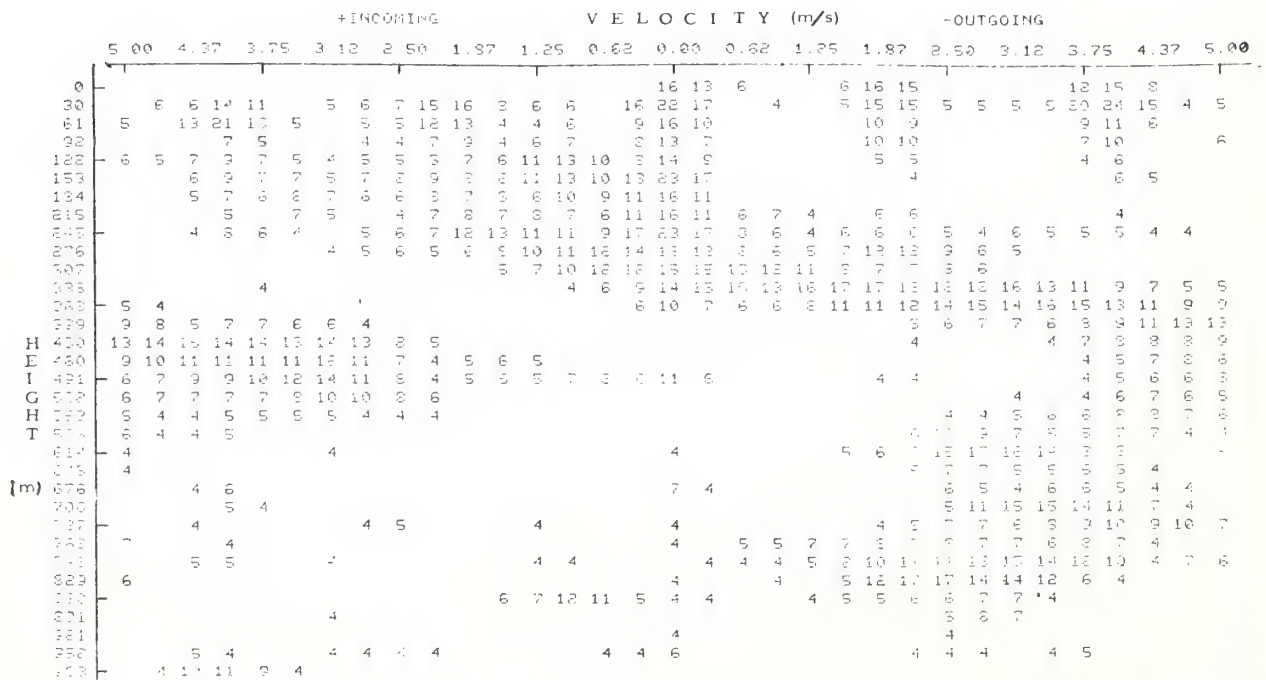
Fig. 3. Map of height-velocity characteristics of a clear air wind shear region (output for two-dimensional processing method). The numbers represent power in db. Velocity folding has occurred (see text).

sweeps, as though it were sampled uniformly from a continuous signal, and then transformed as a single long sequence. The squared magnitude of this single long transform is entirely equivalent to the output range-velocity map of the two-dimensional technique. *Barrick* [1973] showed not only that the two outputs are the same, but also that the required number of computer operations is the same for both techniques. We used the one-dimensional technique because existing software could easily be converted to this type of analysis.

Depending on the desired output format, the power spectrum can be presented as a range-velocity map as in Figure 3, or a one-dimensional A-scope display as in Figure 4. The A-scope display can be thought of as simply a rearrangement of the individual spectra in the range-velocity map so that they appear end to end rather than side by side. Each successive spectrum in the A-scope display is from the next range bin so the spectra are range-ordered. Furthermore, when velocity folding occurs, the folded return just appears in the next range bin. The height markers on the horizontal axis in Figure 4 represent the zero velocity point for the spectrum at that height. To further clarify the relationship between Figures 3 and 4, compare the spectrum at 276 m with that at 399 m in both figures. The close one is approximately centered about zero velocity, while the further one is "folded" and approximately centered about the maximum unambiguous velocity point which is midway between two zero velocity points.

In both the first and last range location the velocity spectra are folded so that velocity sense in these range cells is lost.
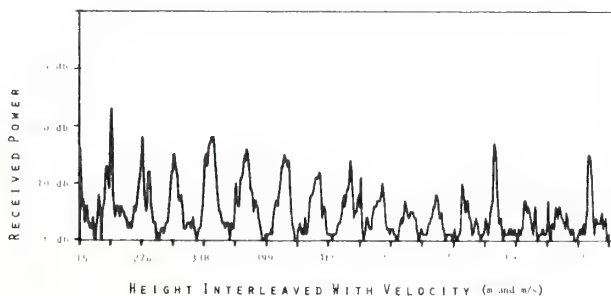
Fig. 4. A-scope display (output for one-dimensional processing method). Each mark on the horizontal axis represents the zero velocity point in that range bin. The folding velocity, halfway between two marks, is ±5 m/s.

3. EXPECTED SENSITIVITY TO SPATIALLY CONTINUOUS FLUCTUATIONS

The 10-cm FM-CW radar backscatter depends on fluctuations in the refractive index of 5-cm size. Although non-Doppler FM-CW radars readily detect regions of the atmosphere where the fluctuations are greatly enhanced, the intensity of fluctuations present elsewhere is generally below the level detectable by non-Doppler FM-CW radars at ranges of most interest. There are two reasons for this. The first, a sensitivity problem, is discussed next.

The power received from a beam-filling target is given by

$$P_r = 0.445 \, P_T A_e \, \Delta \, \eta / 16R^2 \qquad (1)$$

where P_T is the transmitted power, A_e is the effective aperture, Δ is the range resolution, η is the radar cross section per unit volume, and R is the distance to the range cell. The factor 0.445 is the Probert-Jones correction for beam-filling targets. The radar cross section per unit volume for fluctuations in the inertial subrange of turbulence is given by

$$\eta = 0.38 \, C_n^2 \lambda^{-1/3} \, (\text{m}^{-1}) \qquad (2)$$

where C_n^2 is the structure constant for the refractive index fluctuation and λ represents wavelength. The WPL FM-CW radar transmits a power of 200 W with a wavelength of 10 cm from an 8-ft antenna. The minimum detectable signal is about −155 dbm. Thus, the minimum detectable C_n^2 is given by

$$C_n^2 \min = 2.67 \times 10^{-20} \, R^2/\Delta \, (\text{m}^{-2/3}) \qquad (3)$$

For non-Doppler operation in typical FM-CW radar observations, $R \simeq 1$ km and $\Delta = 1.5$ m, so C_n^2 min $= 1.8 \times 10^{-14}$ (m$^{-2/3}$). *Ochs and Lawrence* [1972] measured average values (dry term only) of C_n^2 as ~3 × 10^{-17} (m$^{-2/3}$) at an altitude of 1 km over land or water. The structure constant, C_n^2, has a high variance and thus an average value for C_n^2 is not very useful. R. S. Lawrence (personal communication, 1975) stated that during any one sounding, the rapid fluctuations in C_n^2 can vary ±10 db about the mean and the mean can change ±10 db from day to day. Thus, one can realistically expect C_n^2 to be less than 3 × 10^{-15} (m$^{-2/3}$) at an altitude of 1 km. The C_n^2 measured by Ochs and Lawrence assumed a dry atmosphere as they measured temperature only. Below a height of 2 km, the water vapor component will typically in-

crease the $C_n{}^2$ value by an order of magnitude depending on air mass. Even with this 10 db increase, the peaks of the strongest fluctuations, on the strongest days, are only slightly above the minimum detectable $C_n{}^2$ for the FM-CW radar.

At altitudes where water vapor contributes significantly to the refractive index fluctuations, $C_n{}^2$ may sometimes be well above the minimum detectable $C_n{}^2$ of the non-Doppler FM-CW radar. If these fluctuations of $C_n{}^2$ are above the minimum detectable signal, the effect is a slight increase in the return signal at all ranges because the return signal is from all ranges. For the output of the radar this is simply a slight rise in the noise baseline and is masked by other effects.

We made two changes from the conventional operating mode of an FM-CW radar in order to improve detection of weak fluctuations in refractive index. First, we employed Doppler processing as described in the previous section and gained about 3 db from increased time of integration. Doppler processing caused the signal to appear in a localized area of the output rather than to appear as a slight increase in the baseline of the output. The second change was to decrease the range resolution (increase spatial integration). This is acceptable because there is usually no operational requirement for very fine range resolution when measuring the height profile of horizontal wind. Using a 120-m range cell for some of the data we added +19 db to our system sensitivity. The total sensitivity increase was +22 db and this reduced the minimum detectable $C_n{}^2$ to 1.1×10^{-16} $(m^{-2/3})$ at 1 km elevation. This was about 5 db above the average $C_n{}^2$ measured by *Ochs and Lawrence* [1972], but well below that to be expected when the effect of humidity is included.

In the seven years during which FM-CW radar sounders have been in use in the non-Doppler mode there have been no reports of detection of returns continuous in range. However, analysis of the sensitivity of the FM-CW radar used in our research indicates that in the Doppler mode we should be able to detect returns continuously for ranges up to 1 to 2 km. This conclusion agrees well with the experimental data we have collected so far. The next section presents some of these data.

4. WIND MEASURING EXPERIMENT

We operated our Doppler FM-CW radar for a two-week period in September 1975 in southeastern
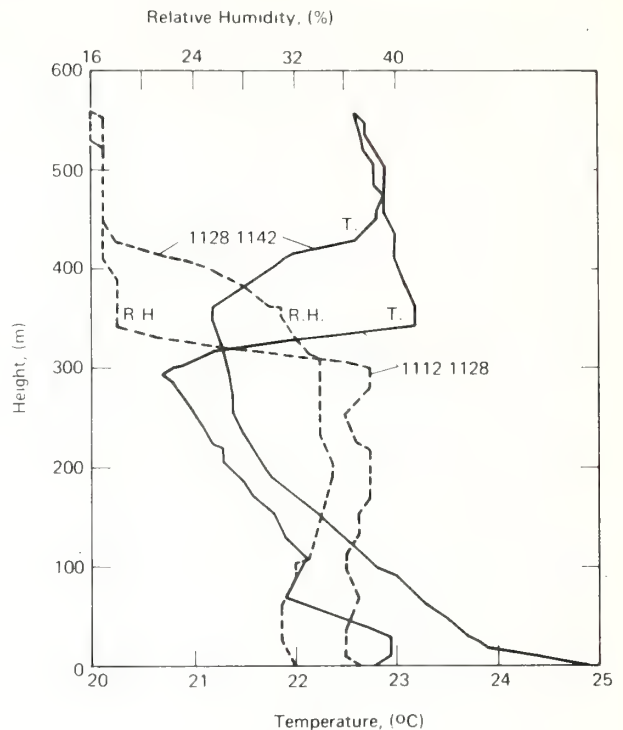
Fig. 5. Temperature and relative humidity profiles from tethered balloon.

Colorado near a 152-m tower and a tethered balloon system. The tethered balloon was instrumented to measure temperature, humidity, wind speed, and direction for elevations up to 600 or 700 m. This equipment was described by *Morris et al.* [1975]. The location near Haswell, Colorado, is a typical high plains meteorological regime with active convection developing during clear days. The data described here were collected on a day when ground fog was present at 0700 MDT. The fog "burned off" and was followed by a 2/10 cover of stratocumulus by 0900. At 1100 the sky was completely clear. To further characterize the meteorology, temperature and humidity soundings from the tethered balloon are shown in Figure 5. The ascent occurred from 1112 to 1128 and the descent occurred from 1128 to 1142.

At 1140, the radar was operating with an elevation angle (from horizontal) of 60°, a maximum range of 1171 m, and a maximum unambiguous horizontal velocity of ±5.0 m/s. Because of the existence of a strong capping inversion, we assume that the vertical velocity is negligible compared to the hori-
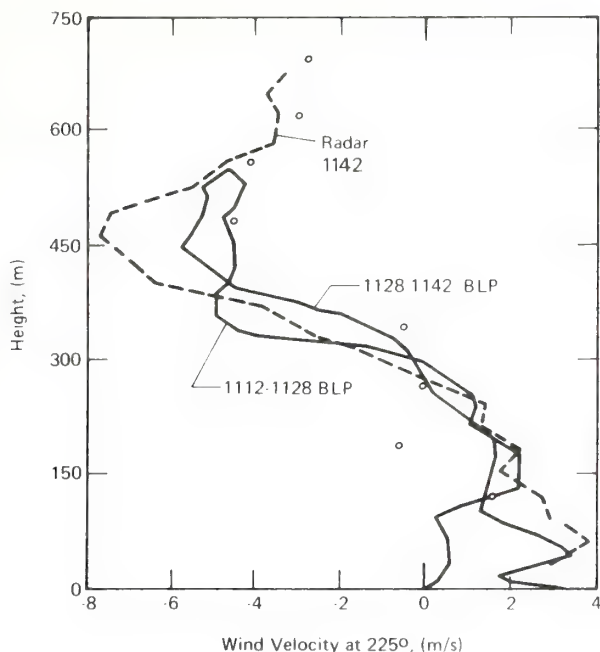
Fig. 6. Wind profiles on 225° bearing as measured by FM-CW radar and tethered balloon. The small circles are from a rawinsonde launched at 1100.

zontal velocity. We averaged 39 velocity spectra from each range interval to arrive at one output range velocity map representing 10 s of data. Such a map is shown in Figure 3, where the individual numbers represent the relative return power (in db) for that range velocity cell. The axes represent atmospheric height and horizontal wind. For ease in interpretation, output power weaker than the 3-db level has been suppressed. Near ±1.87 and ±3.75 m/s, in the lowest four or five range bins, there are equipment-generated harmonics caused by saturation of an audio amplifier. These harmonics are negligible above about 150 m. Because the radar points along only one azimuth at a time, the data in Figure 3 represent only the horizontal wind component along the 225° azimuth. This component of wind has a significant shear from ~215 to 522 m. Spectral folding has occurred from ~399 to ~614 m. That is, the return from 399 to 614 m, on the left-hand side of Figure 3, is really a continuation of the spectrum running off the right-hand margin. This folding can be easily resolved so that absolute components of the wind velocity can be obtained.

With a computer algorithm, we can estimate means of the spectra and thus derive profiles for the particular component of wind along the given direction. A profile of the wind component along 225° is shown in Figure 6 with profiles of this same wind component obtained over 30 min by the tethered balloon Boundary Layer Profiler (BLP) system. The agreement is remarkably good considering that the BLP was located ~300 m to the east of the radar and the radar data are averaged over only 10 s. An estimate of how the radar data change with time is provided by the data in Figure 7, which show the next four radar wind profiles (each a 10-s average). The radar wind profiles from Figures 6 and 7 show the radar wind data at 225° over a 50-s interval. Figure 8 shows the radar wind component along the 315° azimuth at approximately the same time as that measured by the BLP. It is clear that the strong, persistent shear layer is along the 225° azimuth only. Figure 9 shows the four 10-s averages of the wind component immediately prior to the profile in Figure 8. Note how rapidly the wind was changing in the lower levels compared with the 225° azimuth wind.

When wind velocities are estimated in this manner, there are two main causes for variations in the estimates. The first is nonstationarity of the convectively unstable atmosphere. Clear evidence for this is shown by the differences in profiles taken roughly 15 min apart during balloon ascent and
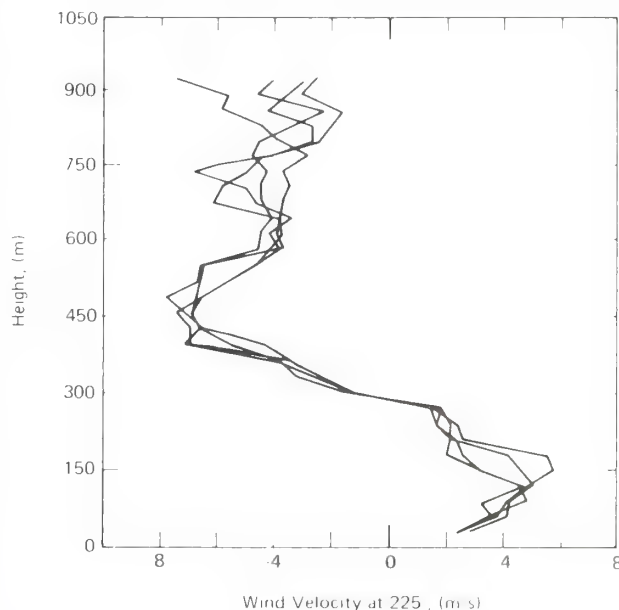
Fig. 7. Four wind profiles on 225° bearing as measured by FM-CW radar at 10-s intervals.

131

descent (Figures 6 and 8), and also in the much more rapid sequence radar wind profiles, taken 10 s apart (Figures 7 and 9). The second main cause degrading the velocity estimate is low signal-to-noise ratio. An examination of Figure 4 (which has had the R^{-2} range dependence removed and in which signal levels below 3 db are set to zero) shows that in the upper few range gates there is a signal-to-noise ratio problem. Therefore, the random error of the wind component estimate in Figures 6 and 8 increases in the upper few range gates. The variance of wind estimates in Figure 7 appears to be lower within the shear region than either above or below it. A possible cause for this is that the relatively strong mechanical turbulence associated with the shear layer produces a larger C_n^2, thus increasing the backscatter and signal-to-noise ratio. The amount of error in the measurement is difficult to estimate, especially in the upper levels where the signal-to-noise ratio is not large. However, we feel that for the data given here, the rms error for a 10-s integration time is less than 0.5 m/s for heights less than about 900 m.

It is important to note that there is significant return power for altitudes up to 900 m or more, well above the elevated temperature inversion. This
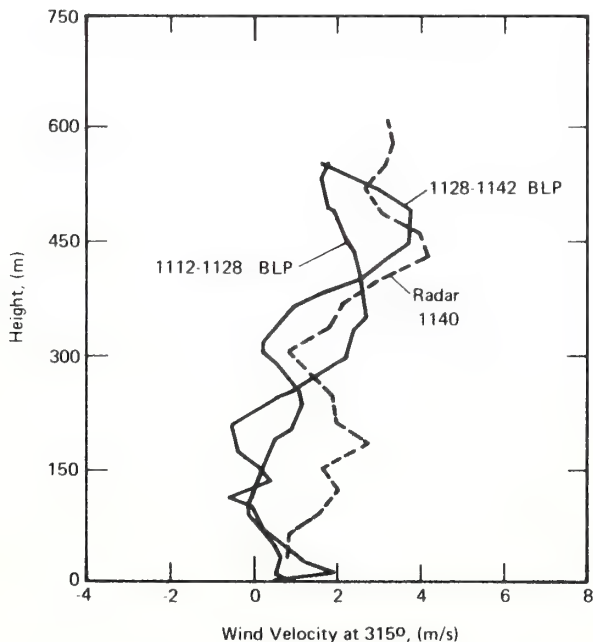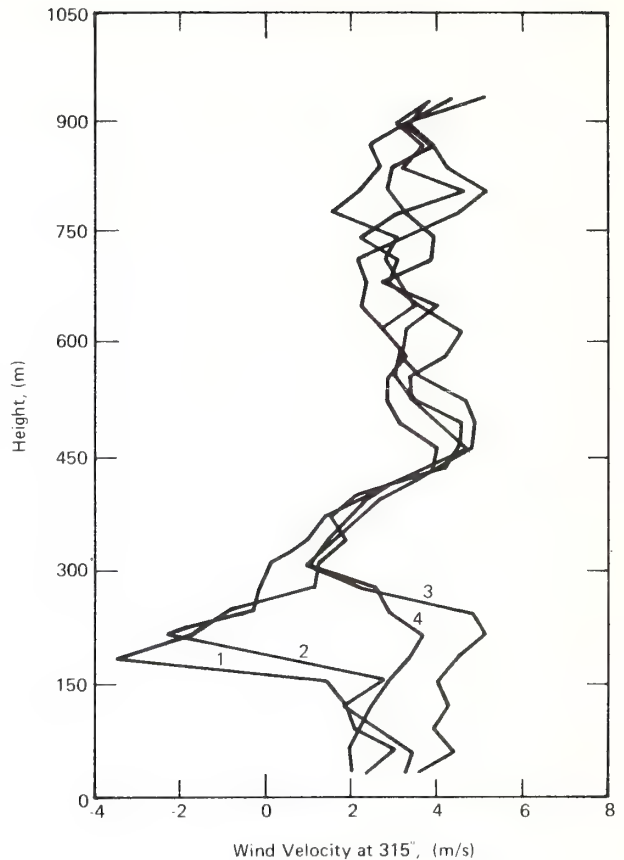
Fig. 9. Four wind profiles on 315° bearing as measured by FM-CW radar at 10-s intervals.

indicates that the radar is sensitive enough to detect refractive index fluctuations even in the region above the inversion. In this connection, it is perhaps significant that the radar wind profiles of Figures 7 and 9 indicate the existence of stronger variability of wind in the region above the inversion than within the inversion itself.

5. CONCLUSIONS

We conclude that measurement of winds in the clear lower atmosphere with a Doppler FM-CW radar is possible with appropriate signal processing. We have measured winds continuously to heights in excess of 2 km, but the maximum height depends on current meteorological conditions. Furthermore, we have measured winds continuously to ranges in excess of 3 km when looking at an elevation angle of 30°.

However, much remains to be done to develop

Fig. 8. Wind profiles on 315° bearing as measured by FM-CW radar and tethered balloon.

the FM-CW radar into a practical wind measuring system. Statistics of return signal strength based on climatology and air mass need to be obtained. Proper averaging times need to be determined. More efficient data processing techniques need to be developed. Techniques for clear air Velocity Azimuth Display also need to be developed.

For the meteorological conditions that existed during the experiment, we have demonstrated the capability to measure winds continuously (in height and time) up to, within, and significantly above the elevated inversion layer. Therefore we feel that an FM-CW radar with Doppler capability represents a significant advance in wind measurement in the lower atmosphere and points the way to an all-weather wind measurement capability. In addition, even from the small amount of data we have studied, it appears that a region of strong shear may return enhanced power. If this is true, it implies that regions of strong wind shear may be relatively easy to detect and measure.

REFERENCES

Barrick, D. E. (1973), FM-CW radar signals and digital processing, *NOAA Tech. Rep. ERL 283-WPL-26*, US Government Printing Office, Washington, DC 20402.

Bean, B. R., R. E. McGavin, R. B. Chadwick, and B. D. Warner (1971), Preliminary results of utilizing the high resolution FM radar, *Boundary Layer Meteorol.*, *1*, 466–473.

Chadwick, R. B., and C. G. Little (1973), The Comparison of Sensitivities of Atmospheric Echo-Sounders, *Remote Sensing Environ.*, *2*, 223–234.

Gossard, E. E., and W. H. Hooke (1975), *Waves in the Atmosphere*, 456 pp., Elsevier, Amsterdam.

Green, J. L., J. M. Warnock, R. H. Winkler, and T. E. Van Zandt (1975), A sensitive VHF radar for the study of winds, waves, and turbulence in the troposphere, stratosphere, and mesosphere, paper presented at the 16th Radar Meteorological Conference, Houston, Texas.

Morris, A. L., D. B. Call, and R. B. McBeth (1975), A small tethered balloon sounding system, *Bull. Amer. Meteorol. Soc.*, *56*, 964–969.

Ochs, G. R., and R. S. Lawrence (1972), Temperature and C_n^2 profiles measured over land and ocean to 3 km above the surface, *NOAA Tech. Rep. ERL 251-WPL-22*, US Government Printing Office, Washington, DC 20402.

Richter, J. H. (1969), High resolution tropospheric radar sounding, *Radio Sci.*, *4*, 1261–1268.

Strauch, R. G., W. C. Campbell, R. B. Chadwick, and K. P. Moran (1976), Microwave FM-CW Doppler radar for boundary layer probing, *Geophys. Res. Lett.*, *3*, 193–196.

133

Microwave Sensing of Atmospheric Temperature and Water

M. T. Decker, E. R.Westwater, and F. O. Guiraud
NOAA/ERL/Wave Propagation Laboratory

Introduction

Thermal radiation from the atmosphere at microwave frequencies originates
primarily from oxygen, water vapor, and liquid water, and depends on their
temperature and spatial distribution. For a gas such as oxygen whose density
as a function of height is well known given the surface pressure, the radiation
contains information primarily on the atmospheric temperature. It is thus
possible to infer temperature structure from surface-based radiation measure-
ments in the 60 GHz oxygen absorption complex. These measurements are
"contaminated" by radiation from water vapor and especially from cloud liquid
and so improved accuracy and operation during cloudy conditions are possible if
measurements are also made of radiation from these components at frequencies
outside the oxygen band. In addition to their use in temperature profiling
these observations can also be used to infer line integrals of water vapor
(and the resulting wet component of refractivity) and cloud liquid. In some
cases vapor profile information can also be obtained.

Theoretical Temperature Retrieval Accuracy

As an example of a possible application of these microwave radiometric
techniques a theoretical and experimental study is being made of ocean buoy-
mounted sensors for temperature profiling. The National Weather Service
desires that the temperature of layers, 100 mb in thickness, be determined
with accuracy ± 1 K. Although data up through 850 mb would be useful,
retrievals to 500 mb are wanted. Since the system must operate under a
variety of cloud conditions, a large portion of our theoretical effort was to
retrieve profiles from cloud-contaminated brightness observations. Although
an angular-scanned radiometric technique was initially considered, this
technique was quickly eliminated by the difficulty of correcting for buoy
motion. The results of this theoretical study (Westwater et al., 1976) show
that for ocean climatologies a three-frequency zenith measurement of oxygen
thermal emission (instrumental noise of 0.5 K) made during clear conditions
can be mathematically inverted to infer 100-mb layer averages of temperature
with rms accuracies that range from 0.5 K at the lowest altitudes to 1.7 K at
500 mb. To correct for cloud emission, brightness measurements are added
near 21 and 31 GHz and equivalent clear-air brightness is determined from
the cloud-contaminated measurements. With the five-channel system the rms
temperature retrieval error for cloudy conditions in the ocean climatology
is degraded (relative to clear air) by at most 0.3 K.

Experimental Temperature and Vapor Profiles

An experimental program to confirm the theoretical predictions is being conducted jointly by NOAA and the Jet Propulsion Laboratory. Five-channel observations were taken at Pt. Mugu, Calif. and kindly provided by B. Gary and N. Yamane of JPL. Their radiometer is similar to that used on the Nimbus 6 satellite (Staelin et al., 1975). During the three-week period of observations, thrice-a-day radiosondes obtained standard meteorological soundings of temperature, pressure, and humidity. Before the data were inverted, calculations of brightness temperature from radiosonde profiles, using Rosenkranz's (1975) O_2 line shape theory with Liebe's (1977) laboratory radiometric observations. Table 1 shows rms and average differences between calculations and clear-air observations. Considering the difficulties in making absolute radiometric measurements and in observing the same volume of air with radiosonde and radiometer, the agreement is quite good. After inserting bias corrections, determined from 11 visually clear profiles, a statistical inversion method

Table 1.

Average and rms differences (K) between measured and calculated brightness temperatures (N = 24 radiosonde observations)

Frequency (GHz)	22.235	31.65	52.85	53.85	55.45
Aver. diff.	2.47	1.67	.18	.14	-1.33
rms diff.	3.39	1.81	1.77	0.76	1.41

was used to retrieve 21 profiles of both water vapor and temperature. Measured values of surface temperature, pressure, and relative humidity were included with the five radiometer channels. Although some of the 21 profiles were obtained when there were visual observations of clouds, the radiometrically estimated liquid content was less than 0.02 mm; hence, the clear-air retrieval algorithms were used exclusively. Examples of retrieved temperature and water vapor profiles together with the radiosonde measurements are shown in Figures 1 and 2. As expected, these indicate that temperature structure near the surface may be retrieved, while elevated temperature structure and details of water vapor profiles will be smoothed. Figure 3 shows the theoretical accuracies expected for the Pt. Mugu climatology and an rms instrument error of 1 K together with the achieved accuracies for the 21 temperature and absolute humidity profiles. Included in these figures are the rms errors in profile prediction from surface meteorological observations alone and from a three-month mean profile. The achieved profile retrieval accuracies
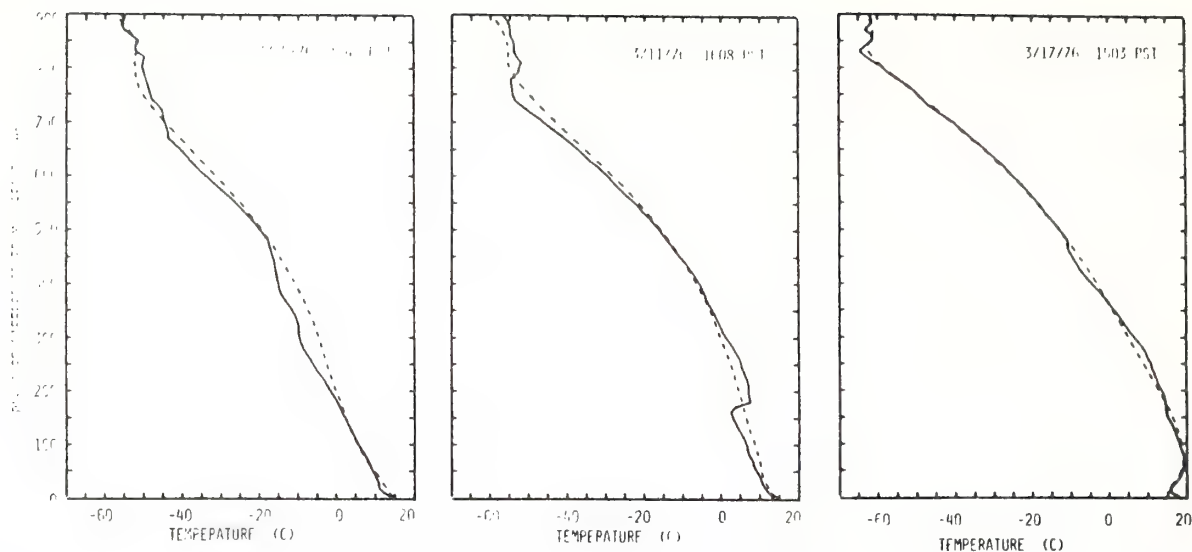
Figure 1. *Examples of temperature profiles retrieved from radiometric data (dashed lines) compared to concurrent radiosonde profiles (solid lines).*
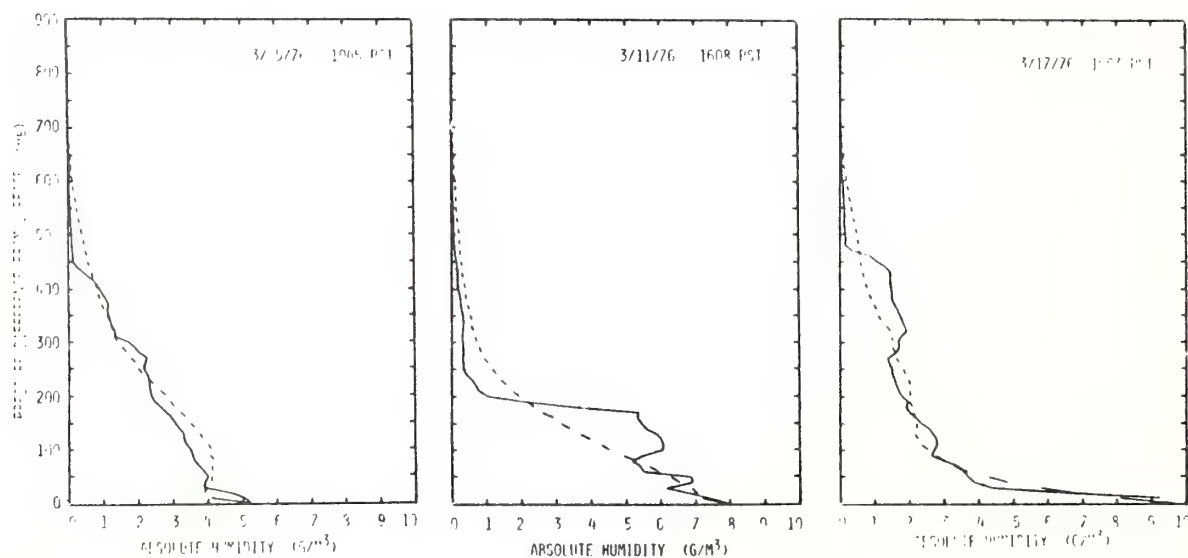
Figure 2. *Examples of water vapor profiles retrieved from radiometric data (dashed lines) compared to concurrent radiosonde profiles (solid lines).*

are quite close to theoretical predictions suggesting that an adequate modeling of the direct problem was achieved. Although the desired accuracy of ± 1 K was not reached it is felt that the rms difference of about 2 K up to the 350-mb level (650 mb pressure difference from the surface) is encouraging. Another set of observations at Pt. Mugu has been completed but is not yet analyzed. Finally, current plans include operating the radiometer at Weather Station P in the Gulf of Alaska.
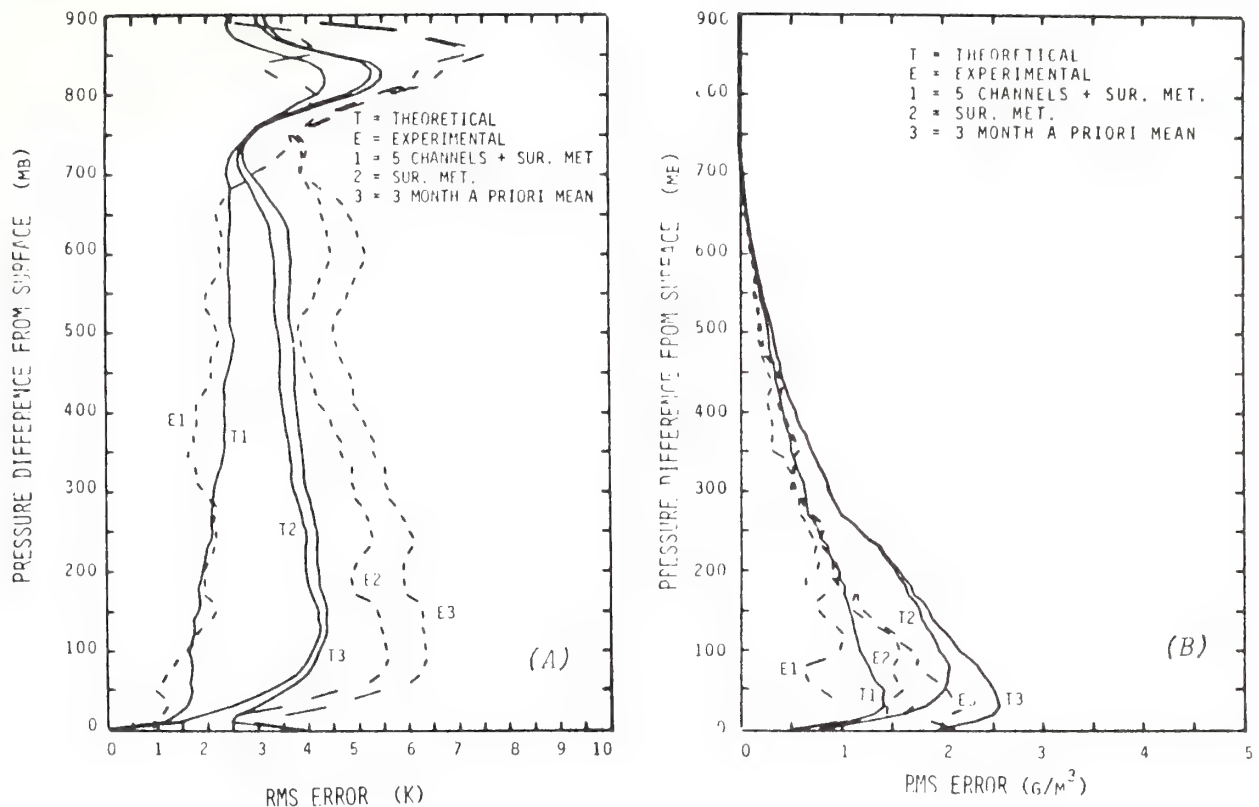
Figure 3. RMS accuracy in retrieval of temperature profiles (A) and absolute humidity profiles (B). Experimental data from 21 profiles.

Line integrals of vapor and liquid

The two-cloud correcting channels mentioned above can also yield measurements of the integrated amounts of liquid water and water vapor. Simulations indicate that if an instrumental noise level of 0.5 K can be achieved the rms measurement accuracies for zenith values should be about 0.04 mm for liquid and range from about 0.5 to 0.8 mm for vapor going from clear to cloudy conditions.

An example of the measurement of zenith line integrals of water vapor and cloud liquid using radiometers at 20.6 and 31.65 GHz is shown in Figure 4. This measurement over a period of ten hours was made at Boulder, Colo., and may be compared with radiosonde water vapor measurements at 0600 and 1800 local time from Denver, 40 km from the Boulder site. It illustrates the ability of a two-channel system to measure vapor in the presence of clouds - the single-channel data at 20.6 GHz would be in error by more than a factor of two during the last part of this period. No independent measure of cloud liquid is available to compare with the radiometric data. Precipitation began at the Boulder site at approximately 1800.
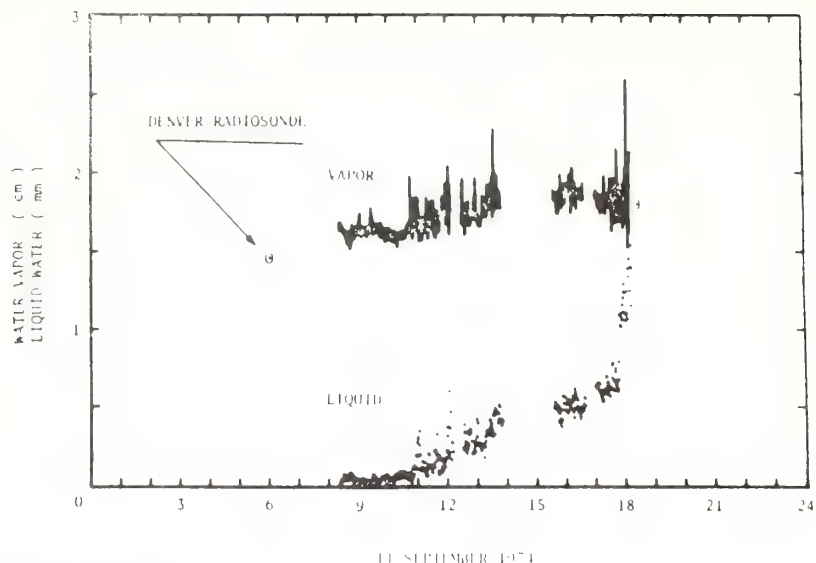
Figure 4. Vertical line integrals of water vapor and cloud liquid measured at 20.6 and 31.65 GHz.

Conclusions

The foregoing examples serve to illustrate the usefulness of microwave radiometry in the remote sensing of atmospheric parameters. They also show that it is possible to make a reasonable prediction of the accuracy to be expected from a specific application. Systems may, of course, be designed for other purposes; for example, to measure refractivity (Decker et al., 1973), to concentrate on the lowest part of the atmosphere, observe at angles other than the zenith, or make use of airborne platforms.

References

Decker, M. T., F. O. Guiraud, and E. R. Westwater, Correction of electrical path length by passive microwave radiometry, Proc. of Conference on Propagation of Radio Waves at Frequencies above 10 GHz, London, April 10-13, 1973.

Liebe, H. J., G. Gimmestad and J. Hopponen, Atmospheric oxygen microwave spectrum-experiment versus theory. To be published in IEEE Trans. Ant. Prop. AP25, March 1977.

Rosenkranz, P. W., Shape of the 5-mm oxygen band in the atmosphere, IEEE Trans. Ant. Prop. AP-23, 498-506, 1975.

Staelin, D. H. et al., The scanning microwave spectrometer (SCAMS) experiment. Nimbus-6 Users Guide, Goddard Space Flight Center, Greenbelt, Md., 1975.

Westwater, E. R., M. T. Decker, and F. O. Guiraud, Feasibility of atmospheric temperature sensing from ocean data buoys by microwave radiometry, NOAA Tech. Rept. ERL 375-WPL 48, 32 pp, 1976.

Error Estimation in Wind Fields Derived from Dual-Doppler Radar Measurement

RICHARD J. DOVIAK AND PETER S. RAY

National Severe Storms Laboratory, NOAA, Norman, Okla. 73069

RICHARD G. STRAUCH AND L. JAY MILLER

Wave Propagation Laboratory, NOAA, Boulder, Colo. 80305

(Manuscript received 24 July 1975)

ABSTRACT

Variance in horizontal and vertical winds are predicted when these components are computed from dual-Doppler velocity measurements combined with terminal velocity estimates and the continuity equation. Errors in horizontal wind magnitude and direction are shown to be functions of wind direction and speed as well as spatial location. Vertical wind could be estimated with errors less than a few meters per second up to altitudes near 14 km over a region $4d \times 4d$, where $2d$ is the radar separation. Vertical wind variance at high altitudes is related to accumulation of errors due to the integration of the continuity equation. The cause of wind variance is assumed to be uncertainty in mean Doppler velocity estimates produced by spectrum broadening mechanisms (e.g., shear, turbulence). Two interpolation methods, used to estimate Doppler velocity at common grid locations, are compared and their contribution to Doppler velocity variance reduction is calculated. Terminal velocity variance has been related to uncertainties in drop-size distributions and reflectivity estimate variance. The methods derived herein are applied to determine the errors in wind speeds calculated from dual-Doppler data.

1. Introduction

Wind fields can be inferred by combining Doppler velocities, measured by two spaced radars, with particle terminal velocity estimates and subsequently solving the continuity equation (Lhermitte, 1970; Miller and Strauch, 1974; Ray *et al.*, 1975). Wind field determination is greatly simplified if synthesis is performed in cylindrical coordinates with an axis colinear with the line connecting the two radars. Lhermitte and Miller (1970) suggested that Doppler data acquisition be confined to planes in this frame (COPLAN method) so that winds in each plane could be deduced directly with minimal data interpolation. Irrespective of the acquisition mode, wind synthesis is facilitated when executed in cylindrical coordinates and Cartesian wind components are derived from the synthesized cylindrical components. We shall determine wind estimate variance assuming this synthesis procedure. Although we can solve directly for Cartesian wind components, this necessitates a solution of a linear, inhomogeneous, hyperbolic partial differential equation to derive vertical wind (Armijo, 1969). Lhermitte and Miller (1970) estimated errors in dual-Doppler derived horizontal wind for regions where the particle's vertical motion can be neglected. In this paper, error in both horizontal and vertical wind related to interpolated mean Doppler velocity variance and error reduction associated with interpolation is evaluated. Further,

vertical velocity variance is related to height-dependent mass density and station separation.

To determine wind we must interpolate Doppler data to a grid common to both radars. We analyze two interpolation methods: 1) linear 4-point interpolation appropriate for COPLAN data acquisition and 2) distance-weighted spatial averaging applicable to data acquired using azimuthal sector scans stepped in elevation angle.

2. Wind estimate variance (cylindrical components)

Although we seek Cartesian component velocity variance for dual-Doppler derived wind, we first evaluate the variance of the wind components illustrated in the cylindrical coordinate system depicted in Fig. 1. Following Miller and Strauch (1974) the particle velocity at a grid point in a plane elevated by angle α is specified by

$$U_\rho(\rho,s) = \frac{r_1(s+d)V_1 - r_2(s-d)V_2}{2d\rho}, \quad (2.1a)$$

$$U_s(\rho,s) = \frac{r_2V_2 - r_1V_1}{2d}, \quad (2.1b)$$

where V_1, V_2 are the interpolated estimates of mean

(i.e., pulse-volume averaged)[1] Doppler velocities measured by radars 1, 2, and U_ρ and U_s are particle velocity components perpendicular and parallel to the baseline. The wind field is then

$$W_\rho = U_\rho - V_t \sin\alpha, \quad W_s = U_s, \qquad (2.2)$$

where V_t is the particle's interpolated mean terminal velocity estimate. Because V_1, V_2 are composed of independent measurements, W_ρ and W_s variances are directly determined from

$$\mathrm{var}[W_\rho] \equiv \sigma_\rho{}^2 = \frac{r_1{}^2(s+d)^2\sigma_1{}^2 + r_2{}^2(s-d)^2\sigma_2{}^2}{4d^2\rho^2}$$

$$+ \sigma_t{}^2 \sin^2\alpha, \quad (2.3\mathrm{a})$$

$$\mathrm{var}[W_s] \equiv \sigma_s{}^2 = \frac{r_2{}^2\sigma_2{}^2 + r_1{}^2\sigma_1{}^2}{4d^2}, \qquad (2.3\mathrm{b})$$

where $\sigma_1{}^2$, $\sigma_2{}^2$, $\sigma_t{}^2$ are variances of V_1, V_2, V_t. Wind perpendicular to the plane is determined by solving the continuity equation

$$\nabla \cdot \gamma \overline{\mathbf{W}} = 0, \qquad (2.4)$$

where $\gamma = \gamma_0 \exp(-\Gamma \rho \sin\alpha)$ is the mass density. Solving (2.4) we have

$$W_\alpha = -\frac{1}{\gamma} \int_0^\alpha \left[\frac{\partial}{\partial\rho}(\rho\gamma W_\rho) + \rho\frac{\partial}{\partial s}(\gamma W_s) \right] d\alpha, \quad (2.5)$$

in which $W_\alpha(\rho,0,s) = 0$ has been used as a boundary condition. Now the variance in W_α is

$$\mathrm{var}[W_\alpha] \equiv \sigma_\alpha{}^2 = \frac{1}{\gamma^2}\left\{ \mathrm{var}\left[\int_0^\alpha \frac{\partial}{\partial\rho}(\rho\gamma W_\rho)d\alpha \right] \right.$$

$$\left. + \mathrm{var}\left[\int_0^\alpha \rho\frac{\partial}{\partial s}(\gamma W_s)d\alpha \right] \right\}, \quad (2.6)$$

where the terms in (2.5) are assumed uncorrelated. This assumption is satisfied if contiguous interpolated grid values V_1 (or V_2) are uncorrelated and if the finite-difference approximation used to evaluate the partial derivatives does not use common grid values. Evaluating the first term in (2.6) using finite differences we obtain the approximate expression

$$\frac{1}{\gamma^2}\mathrm{var}\left[\int_0^\alpha \frac{\partial}{\partial\rho}(\rho\gamma W_\rho)d\alpha \right]$$

$$\approx \frac{1}{(2\gamma\Delta\rho)^2}\rho^2\,\mathrm{var}\left[\int_0^\alpha \gamma(W_{\rho2} - W_{\rho1})d\alpha \right], \quad (2.7)$$

where $2\Delta\rho \equiv \rho_2 - \rho_1$ is twice the grid spacing $\Delta\rho$, and $W_{\rho2}$, $W_{\rho1}$ are radial wind components evaluated at
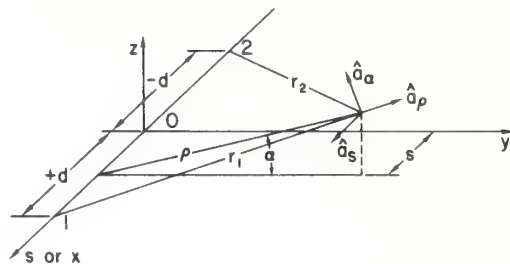
Fig. 1. Dual-Doppler COPLAN coordinate system.

ρ_2, ρ_1. We assumed $\rho \gg \Delta\rho$ and that $\gamma(\rho_2) \approx \gamma(\rho_1)$. Considering the integral to be a sum of terms having independent errors, (2.7) reduces to

$$\frac{2\rho^2\alpha\Delta\alpha}{(2\gamma\Delta\rho)^2}\frac{1}{\alpha}\int_0^\alpha \gamma^2\sigma_\rho{}^2 d\alpha, \qquad (2.8)$$

where $\Delta\alpha$, the step size used in the integration of ΔW_ρ, is the spacing between grid planes. Even though $\sigma_\rho{}^2$ is a function of ρ, α and s, we assumed $\sigma_{\rho2}{}^2$ equal to $\sigma_{\rho1}{}^2$, a reasonable approximation when variance changes across $\Delta\rho$ are small. Applying similar methods to evaluate the second term in (2.6) and substituting this and (2.8) into (2.6), we have $\sigma_\alpha{}^2$ given by

$$\sigma_\alpha{}^2 = \frac{2\Delta\alpha\rho^2}{(2\gamma\Delta\rho)^2}\left[\int_0^\alpha \gamma^2\sigma_\rho{}^2 d\alpha + \int_0^\alpha \gamma^2\sigma_s{}^2 d\alpha \right], \quad (2.9)$$

in which we equated $\Delta\rho$ and Δs. Substituting (2.3) into (2.9), we obtain the solution

$$\sigma_\alpha{}^2 = 2\alpha\Delta\alpha\left(\frac{\rho}{2\Delta\rho} \right)^2\left[\frac{r_1{}^2 r_2{}^2}{4(d\rho)^2}C_1 + C_2 \right] \qquad (2.10)$$

for variance in the α component of wind, where

$$C_1 = \frac{1}{\gamma^2\alpha}\int_0^\alpha \gamma^2(\sigma_1{}^2 + \sigma_2{}^2)d\alpha, \quad C_2 = \frac{1}{\gamma^2\alpha}\int_0^\alpha \gamma^2\sigma_t{}^2 \sin^2\alpha\, d\alpha.$$

The mass-density weighted variance factors C_1 and C_2 have values that depend upon height. Assuming α small and σ_1, σ_2 to be α-independent, C_1 is given by the approximate formula

$$C_1(\rho\alpha) \approx (\sigma_1{}^2 + \sigma_2{}^2)F_1(\rho\alpha)$$

$$= (\sigma_1{}^2 + \sigma_2{}^2)\left[\frac{\exp(2\Gamma\rho\alpha) - 1}{2\Gamma\rho\alpha} \right]. \quad (2.11)$$

Thus for a constant arc height $\rho\alpha$, F_1 is a constant. Eq. (2.11) shows that C_1 increases monotonically from $\sigma_1{}^2 + \sigma_2{}^2$ at $\rho\alpha = 0$ to nearly four times this value for an arc height of 10 km (for $\Gamma = 0.113$ km^{-1}). Therefore decreasing mass density contributes significantly to $\sigma_\alpha{}^2$. In like manner we can obtain an approximate expression for C_2. However, for fixed arc height, C_2

is proportional to α^2 and hence is much less than unity for α small. Eqs. (2.10) and (2.11) show that variance increases faster than linearly with α because C_1 and C_2 both increase with α.

We do not make any numerical assessment of cylindrical wind component variance but instead use the above formulas to infer Cartesian wind component variance (Section 4).

3. Interpolated Doppler velocity variance

The previously derived formulas provide estimates of synthesized wind variance, given σ_1^2, σ_2^2. Herein we shall relate σ_1^2 to mean Doppler estimate variance, $\sigma^2(\hat{V})$, grid point range, wind shear and antenna beam width. Mean Doppler estimate variance at a grid point is decreased through interpolation by an amount proportional to a variance reduction factor R^2. That is,

$$\sigma_1^2 = (1 - R^2)\sigma^2(\hat{V}), \qquad (3.1)^2$$

where $\sigma^2(\hat{V})$ is assumed constant over the interpolation domain. [In Appendix A, $(1-R^2)$ is derived for different interpolation schemes but is, approximately, inversely proportional to the number of mean Doppler estimates interpolated.] The $\sigma^2(\hat{V})$ is a function of Doppler spectrum width, signal-to-noise ratio (S/N), beam pointing precision, etc. Spectrum width ω_s depends on beamwidth, wind shear, turbulence, and many other factors (Nathanson, 1969 p. 206). Turbulence and wind shear are the dominant spectrum-width-producing mechanisms (Sirmans and Doviak, 1973), although at range more than 30 km shear is expected to predominate (Nathanson, 1969). However, Waldteufel (1976) shows that within a severe storm the shear contribution is small compared to other broadening factors. We now assess errors in V and gauge the magnitudes of $\sigma^2(\hat{V})$ and $\sigma^2(\hat{V}_t)$, the variance in mean terminal velocity estimates.

a. Systematic errors

Both systematic and random errors contribute to $\hat{V}$. Although systematic (bias) errors are introduced by certain Doppler processing techniques (Sirmans and Bumgarner 1975), we assume these errors can be ignored. However, causes for other bias errors include 1) non-uniform reflectivity Z within a radar sample volume, 2) use of incorrect V_t, Z relationship (Section 3c), 3) inaccuracies in beam position. For the latter cause, Doppler bias error δ_v, due to an antenna azimuthal (or elevation) position inaccuracy $\delta\phi$ (rad), for small elevation is

$$\delta_v = K_\phi r_1 \delta\phi, \qquad (3.2)$$

where K_ϕ is the azimuthal (or vertical) wind shear of the Doppler velocity. Assuming 5×10^{-3} s^{-1} for K_ϕ

[2] The caret is used to designate single data sample estimates of, for example, mean Doppler velocity.

(Donaldson et al., 1972) a 0.2° error causes a Doppler bias error of about 1 m s^{-1} for a ρ distance of 60 km. Using (2.1 a, b) we note that in this case bias error δ_v produces spatially dependent systematic errors in W_ρ, W_s, but may not contribute significantly to error in W_α because bias errors tend to cancel in the partial derivative of (2.5).

b. Random errors

Doppler spectrum width relates to random errors in mean Doppler estimates. For example, assuming radial velocity shear as the dominant width-producing mechanism. Sirmans and Doviak (1973) showed, for small elevation angles and Gaussian-shaped antenna pattern, that spectrum width is given by

$$\omega_s = 0.3 K_t r_1 \theta_w, \qquad (3.3)$$

where K_t is the transverse shear of radial velocity, r_1 the pulse volume range, and θ_w the one-way 3 dB beamwidth (rad). The interpolated mean Doppler velocity variance is defined as

$$\sigma_1^2 \equiv (1 - R^2)\frac{\omega_s^2}{N_t}, \qquad (3.4)$$

where N_t, the equivalent number of independent echo samples coherently processed, is given by

$$N_t = \frac{\omega_s^2}{\sigma^2(\hat{V})}. \qquad (3.5)$$

Because $\hat{V}$'s derived from the argument of signal covariance for time lag T (T is the pulse repetition time) have minimum variance for covariance estimated from a sequence of uncorrelated sample pairs (Miller and Rochwarger, 1972), we restrict our attention to velocities estimated by that technique. Berger and Groginsky (1973) demonstrate that, when covariance is an average of estimates from contiguous sample pairs comprising a uniform train of samples as is usually obtained from pulse Doppler radars, variance at large S/N ratio is simply

$$\sigma^2(\hat{V}) = \frac{\omega_s V_m}{2\sqrt{\pi}M} \quad \text{for } \omega_s \leqslant \frac{V_m}{\pi}, \qquad (3.6)$$

where V_m is the maximum unambiguous Doppler velocity (i.e., $V_m = \lambda/4T$) and a Gaussian-shaped spectrum is assumed. Thus the interpolated velocity variance is

$$\sigma_1^2 = \frac{0.3 K_t r_1 \theta_w \Delta V}{4\sqrt{\pi}} (1 - R^2), \qquad (3.7)$$

where $\Delta V = 2V_m/M$ is the Doppler velocity resolution. To estimate σ_1, we assume $K_t = 10^{-2}$ s^{-1}, $r_1 = 60$ km and $\theta_w = 1°$. We obtain from (3.3) a value $\omega_s = 3$ m s^{-1}

and if $\Delta V = 1$ m s^{-1}, then $\sigma(\hat{V}) = 0.63$ m s^{-1}. Now if $R^2 = 0.9$ (i.e., assuming that about 10 independent $\hat{V}$ estimates are averaged) then σ_1 is 0.2 m s^{-1}.

Random errors in the beam positioning angle $\delta\phi$ will generate additional random errors in Doppler velocity as is evident from (3.2). For example, an rms error of 0.1° will result in a 1 m s^{-1} rms error in $\hat{V}$ for the conditions assumed above. This value compares with the rms error in $\hat{V}$ due to w_s. Random errors in $\hat{V}$ can be reduced by increasing the number of echo samples coherently processed, but random errors due to other sources (e.g., $\delta\phi$) are not decreased by this processing and may require variance reduction by interpolation. Because a 10^{-2} s^{-1} wind shear can be maintained over large regions of severe storms, errors in beam pointing may place an upper limit on radar dwell time (i.e., the number of radar pulses processed coherently). For example, a 10 cm Doppler radar with $V_m = 32$ m s^{-1} needs to process no more than 64 samples to achieve a Doppler estimate variance less than that produced by a 0.1° rms beam pointing error.

c. Terminal velocity variance

To determine wind, a V_t estimate must be made. An estimate can be derived from application of a V_t, Z relationship, adjusted for air density variation with height. The relationship (Atlas *et al.*, 1973)

$$V_t = 2.65 Z^{0.114}\left(\frac{\gamma_0}{\gamma}\right)^{0.4} \left[\text{m s}^{-1}\right] \qquad (3.8)$$

well represents experimental data over a large range of Z (i.e., $1 \leqslant Z \leqslant 10^5$ mm^6 m^{-3}) for regions of liquid water. Terminal velocity variance $\sigma^2(\hat{V}_t)$ is caused by reflectivity estimate variance $\sigma^2(\hat{Z})$ and variance in the V_t, Z relation. We now compare errors from these two mechanisms.

Since Eq. (3.8) shows V_t is a slowly varying function of Z, we can relate $\sigma^2(\hat{V}_t)$ to $\sigma^2(\hat{Z})$ (Papoulis, 1965, p. 212) in the form

$$\sigma^2(\hat{V}_t) = \left[\frac{dV_t}{d\hat{Z}}\sigma(\hat{Z})\right]^2_{\hat{Z}=\bar{Z}}, \qquad (3.9)$$

where the derivative is evaluated at the mean $\bar{Z}$. Sirmans and Doviak (1973) have shown for logarithmic receivers that $\sigma^2(\hat{Z})$ may be written

$$\sigma^2(\hat{Z}) = \frac{1.28\bar{Z}}{K}, \qquad (3.10)$$

where K, the equivalent number of independent intensity estimates, is given approximately by

$$K = \frac{\sqrt{\pi}w_sM}{V_m}. \qquad (3.11)$$

Thus

$$\sigma^2(\hat{V}_t) = \frac{0.116(\hat{Z})^{-0.772}}{K}. \qquad (3.12)$$

Note that the number of independent velocity estimates N_i as computed from (3.5) is two times larger than K; the difference is related to the minimum variance properties of the velocity estimates. Using previously specified values for the parameters and assuming $\hat{Z} \geqslant 1$ we find that $\sigma(\hat{V}_t)$ is less than 0.13 m s^{-1}.

Eq. (3.11) gives $\sigma^2(\hat{V}_t)$ associated with reflectivity estimate uncertainty. However, the results of Joss and Waldvogel (1970) show variability in drop-size distributions within a storm produce standard deviations in terminal velocity nearer 1 m s^{-1} independent of Z. Therefore unless an accurate measure of drop-size distribution can be made we should assume $\sigma(\hat{V}_t)$ equal to 1 m s^{-1}. Moreover, if the drop-size distribution is invariant of data location within the interpolation domain (i.e., over 1-2 km), the errors in $\hat{V}_t$ will not benefit reduction from interpolation (Appendix A). Variance reduction results only if $\hat{V}_t$ estimates are uncorrelated, a condition not expected with errors due to uncertainties in the V_t, Z relation. Therefore we assume $\sigma_t = \sigma(\hat{V}_t) = 1$ m s^{-1}.

Larger errors, up to several meters per second, in V_t estimates can be caused by erroneously relating regions of hail with a V_t, Z relation appropriate for liquid water. Usually there is little or no information to uniquely identify these regions, and bias errors δV_t will result in an error in W_ρ although not in W_s [Eq. (2.2)]. If δV_t is ρ-independent, the bias error in W_α tends to cancel because of differentiation in (2.5). We will now show, for typical dual-Doppler geometry (i.e., $\alpha \leqslant 1$ rad), that the error in W_z is significantly smaller than δV_t.

Assume V_t has the spatial dependence of (3.8) and substitute $V_t + \delta V_t$ for V_t in (2.2) and the result into (2.5). It can be shown that the bias error δW_α for small α is

$$\delta W_\alpha = \delta V_t(0)\alpha^2\left[1 + \frac{1}{0.6\Gamma\rho\alpha} + \frac{1 - \exp(0.6\Gamma\rho\alpha)}{(0.6\Gamma\rho\alpha)^2}\right]$$

$$\equiv \frac{\alpha^2}{2}\delta V_t(0)F, \qquad (3.13)$$

where $\delta V_t(0)$ is the terminal velocity error at zero height. F monotonically decreases from unity to zero at about an arc distance $\rho\alpha = 3.3$ Γ, a direct result of a height-dependent mass density. Thus, although error increases with height because of α^2 in (3.13), this increase is offset by a decrease in F. For example, even when α is as large as 45° (0.79 rad) the error is W_α is less than 0.2 of the error in V_t at heights of 10–15 km. Because W_z is well approximated by W_α for α small, it is concluded that bias errors in W_z are significantly less than those in V_t and small, as will be seen in Section

4, compared to the random errors. Only for near vertical incidence does the error in W_z equal the error in V_t.

We now determine the standard deviation in Cartesian wind components and its dependence upon grid location.

4. Standard deviation of Cartesian wind components

The standard deviation (SD) of Cartesian wind components is obtained from the cylindrical component SD through use of geometric transformations and recognition that errors in W_ρ and W_α are uncorrelated. Therefore

$$\text{SD}[\hat{W}_x] \equiv \sigma_x = \sigma_s, \qquad (4.1a)$$

$$\text{SD}[\hat{W}_y] \equiv \sigma_y = (\sigma_\rho^2 \cos^2\alpha + \sigma_\alpha^2 \sin^2\alpha)^{\frac{1}{2}}, \qquad (4.1b)$$

$$\text{SD}[\hat{W}_z] \equiv \sigma_z = (\sigma_\rho^2 \sin^2\alpha + \sigma_\alpha^2 \cos^2\alpha)^{\frac{1}{2}}. \qquad (4.1c)$$

The independence of W_ρ and W_α errors derives from assuming that interpolated Doppler errors are uncorrelated and because the finite-difference approximation

FIG. 2. Isopleths of normalized vertical wind standard deviation σ_z/σ_1 on constant altitude surfaces.

employed to evaluate W_α uses four grid values different than the grid value at which W_ρ is evaluated.

a. Vertical wind standard deviation σ_z

To estimate vertical wind SD σ_z at various heights, for illustrative purpose we evaluated (2.3) and (2.10) for $d = 20$ km, $\Delta\rho = 0.5$ km, $\Delta\alpha = 0.5°$, and assumed a vertical mass density variation $\gamma/\gamma_0 = \exp(-0.113z)$. Furthermore, we choose $\sigma_1^2 = \sigma_2^2$ equal to a constant independent of grid-point location, a condition that results if a 4-point linear interpolation of range-averaged Doppler values is used (Appendix A) and for convenience $\sigma_t = \sigma_1$. Equal interpolated variance $\sigma_1^2 = \sigma_2^2$ also occurs when isotropic turbulence is the dominant variance-producing mechanism (instead of shear) and linear interpolation is applied to data that is not range-averaged. Combining (A4) with (3.7), we obtain

$$\sigma_1^2 = \sigma_2^2 = \frac{0.019 K_t \theta_w \Delta V}{n_r \Delta\theta}. \qquad (4.2)$$

Even though $\sigma^2(\hat{V})$ increases with range, range averaging maintains σ_1^2 independent of r_1. Fig. 2 shows the normalized SD σ_z/σ_1 as isopleths (for $\sigma_1 = 1$) on constant height surfaces. Although we cannot normalize σ_z to d, we have [for small α where the second term in (2.10) is assumed negligible] $\sigma_z \approx \sigma_\alpha$, and [for fixed arc height and grid spacing] σ_z becomes proportional to $(d/20)^{\frac{1}{2}}$. Therefore, Fig. 2 isopleths multiplied by $(d/20)^{\frac{1}{2}}$ will give σ_z for other station separations and is the reason why x and y are normalized to d in this and following figures. Similarly, when σ_1 differs from 1, σ_z can be obtained by multiplying isopleth value by σ_1. Finally, σ_z can be deduced for small α and grid or angle spacings different than that stipulated in Fig. 2 by multiplying it by $0.5/\Delta\rho$ or $(\Delta\alpha/0.5)^{\frac{1}{2}}$.

Assuming $\sigma_1 = \sigma_2 = 10^{-1}$ m s^{-1} as a reasonable standard deviation for interpolated grid values, it is seen (Fig. 2) that vertical velocity estimates have probably acceptable precision for altitudes up to 10 km. At $z = 14$, $y = 60$ km, the vertical velocity SD is 2.4 m s^{-1}.

The precision could be improved by increasing 1) the number of radar echos processed per $\hat{V}$ estimate (at the expense of longer scan time) and 2) the number of $\hat{V}$'s which are spatially averaged (at the expense of spatial resolution). The first procedure reduces σ_1 if errors are substantially due to finite spectrum width w_s. Wind estimate variance, related to beam pointing errors (Section 3), can only be decreased by spatial averaging. Interpolated Doppler variance depends on $\hat{V}$ sample density, mean Doppler variance $\sigma^2(\hat{V})$, and interpolation method (Appendix A).

b. Standard deviation of horizontal wind magnitude and direction

Since dual-Doppler derived horizontal wind most likely would be displayed on horizontal planes as wind
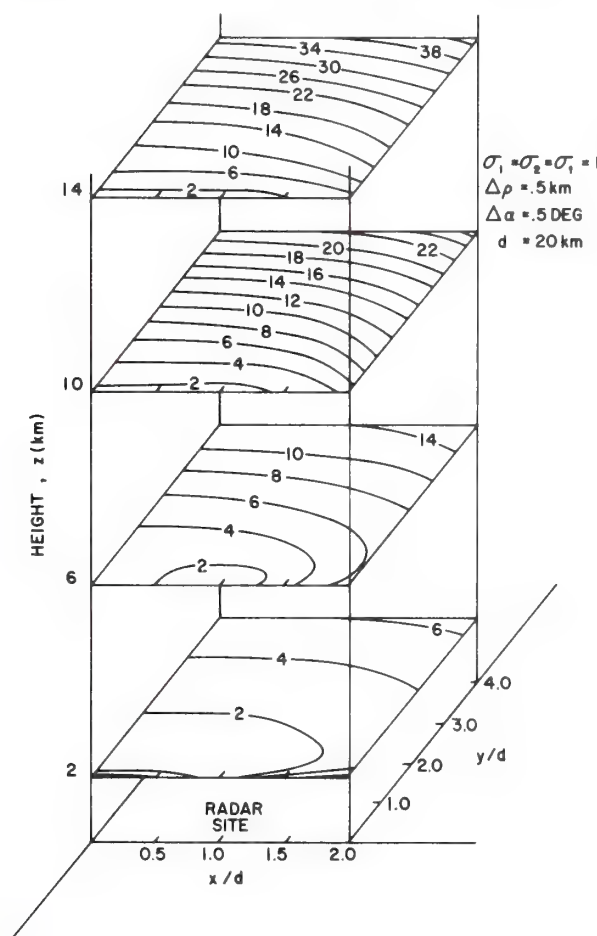
magnitude W_H and direction ψ, it is preferable to have SD's of these quantities. Using the definitions

$$W_H = (W_x{}^2 + W_y{}^2)^{\frac{1}{2}}, \quad \psi = \tan^{-1}\left(\frac{W_y}{W_x}\right), \quad (4.3)$$

and assuming errors concentrated about the expected values $\bar{W}_x$, $\bar{W}_y$, the magnitude variance $\sigma_H{}^2$ and direction variance $\sigma_\psi{}^2$ can be approximated by (Papoulis, 1965, p. 212),

$$\sigma_H{}^2 \approx \left(\frac{\partial W_H}{\partial W_x}\right)^2 \sigma_x{}^2 + \left(\frac{\partial W_H}{\partial W_y}\right)^2 \sigma_y{}^2 + 2\left(\frac{\partial W_H}{\partial W_x}\right)\left(\frac{\partial W_H}{\partial W_y}\right)\mu_{xy}, \quad (4.4)$$

with a similar formula for $\sigma_\psi{}^2$. The covariance μ_{xy} of W_x and W_y is defined as

$$\mu_{xy} \equiv E[(W_x - \bar{W}_x)(W_y - \bar{W}_y)] = \sigma_x \sigma_y r, \quad (4.5)$$

where r is the correlation coefficient of W_x, W_y. Expressing W_x, W_y in terms of the independent variables V_1, V_2, V_t, W_α and substituting into (4.5), we obtain

$$r = -\frac{r_2{}^2(s-d)\sigma_2{}^2 + r_1{}^2(s+d)\sigma_1{}^2}{(2d)^2 \rho \sigma_x \sigma_y} \cos\alpha, \quad (4.6)$$

where σ_x, σ_y are determined from (4.1). Solving (4.4) yields the magnitude and direction variance formulas

$$\sigma_H{}^2 = \sigma_x{}^2 \cos^2\bar{\psi} + \sigma_y{}^2 \sin^2\bar{\psi} + 2\sigma_x\sigma_y r \sin\bar{\psi} \cos\bar{\psi}, \quad (4.7a)$$

$$\bar{W}_H{}^2 \sigma_\psi{}^2 = \sigma_x{}^2 \sin^2\bar{\psi} + \sigma_y{}^2 \cos^2\bar{\psi} - 2\sigma_x\sigma_y r \sin\bar{\psi} \cos\bar{\psi}. \quad (4.7b)$$

Comparing (4.7a) and (4.7b) we notice that normalized wind direction variance $W_H{}^2\sigma_\psi{}^2$, at direction $\bar{\psi}$, is obtained from $\sigma_H{}^2$ for wind direction $\bar{\psi} + \pi/2$. Therefore we can obtain direction SD from magnitude SD.

Fig. 4. Normalized standard deviation for horizontal wind magnitude σ_y/σ_1. Wind perpendicular to baseline ($\bar{\psi} = \pi/2$). $d = 20$ km.

Fig. 3. Isopleths of normalized standard deviation for horizontal wind magnitude σ_x/σ_1 at $z = 0$. Wind parallel to baseline ($\bar{\psi} = 0$).

In Fig. 3 we show the isopleths of normalized magnitude SD, σ_H/σ_1, for $\bar{\psi} = 0$ (i.e., σ_x/σ_1) at $z = 0$ km. Since σ_x is identical to σ_s it can be shown from (2.3) that σ_x is relatively independent of height and that the normalized SD is less than 2 everywhere over the x, y domain indicated in the figure. Fig. 4 shows the normalized SD for wind perpendicular to the baseline. We see, as expected when both radar radials have directions close to that of the wind, that the smallest SD occurs in a region about the baseline bisector. Again, if the interpolated Doppler SD is less than 10^{-1} m s^{-1}, the SD in y-directed wind will be less than 1 m s^{-1} up to 14 km for most of the area displayed.

Although $\sigma_H(\bar{\psi} = 0)$ and $\sigma_H(\bar{\psi} = \pi/2)$ are symmetrical about the plane $x = 0$, σ_H is not symmetric in general because μ_{xy} has, for arbitrary $\bar{\psi}$, odd symmetry about plane. For example $\sigma_H(\bar{\psi} = 45°)$ for x negative has the same value as $\sigma_H(\bar{\psi} = 135°)$ for x positive. Thus, σ_H isopleths for $\bar{\psi} = 45°$, $x < 0$ are the mirror image of isopleths for $x > 0$, $\bar{\psi} = 135°$.
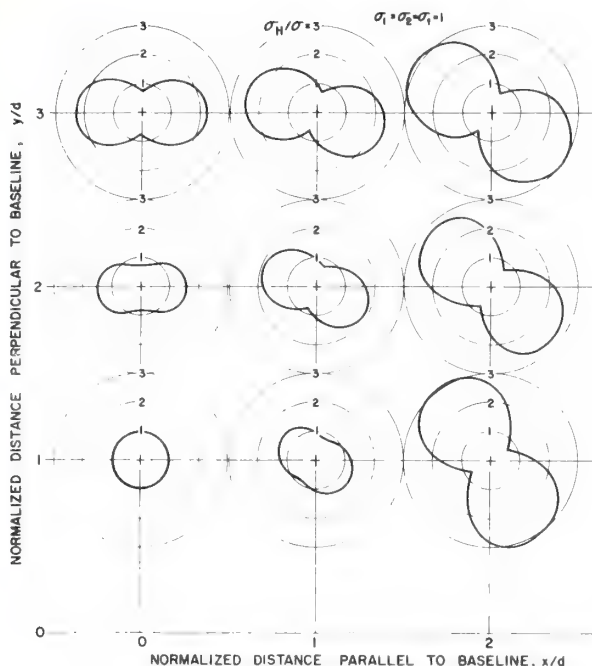
FIG. 5. Polar plots of horizontal wind speed standard deviation σ_H/σ_1 at $z=2$ km. $x=0, d, 2d$; $y=d, 2d, 3d$. Wind direction standard deviation is obtained by rotating each polar diagram by 90°.

Since the SD of wind magnitude and direction are functions of wind direction and speed, we have illustrated this dependence in Fig. 5 for nine selected points ($x=0, 20, 40$; $y=20, 40, 60$) at $z=2$ km. From the displays of σ_H vs $\bar{\psi}$, the normalized wind direction SD, $\bar{W}_H\sigma_\psi$, can be obtained by rotating the figures 90°. Thus where magnitude SD is smallest, the normalized wind direction SD is largest.

This is seen in Fig. 6 which shows the relation between standard deviations of wind (W) and interpolated Doppler velocities ($\hat{V}_1$, $\hat{V}_2$). In Fig. 6 the expected values $\hat{V}_1$, $\hat{V}_2$, $\bar{W}$ are identified as vectors and the Gaussian-shaped functions depict the scatter, proportional to σ_1, σ_2, about $\hat{V}_1$, $\hat{V}_2$. In case 1, where the

expected wind is along the bisector of angle β, the projection of the distributions $P(V_1)$, $P(V_2)$ along the direction W is, for small β, accomplished without large increase in width along $\bar{W}$. However in case 2, where W is directed orthogonal to the bisector, we note that the distributions projected along $\bar{W}$ have increased standard deviations. Although the magnitude SD of W in case 1 is small, the uncertainty in W direction is larger than in case 2 because there is a large angular region in case 1 over which the projected values of V_1, V_2 have intersections. It can be shown, neglecting V_t, that wind speed on constant α planes has minimum variance when the wind is directed along the bisector of the angle β. This fact is evident in the polar diagrams of Fig. 5. Finally, because of symmetry, it is deduced that the polar plots for negative x are those in Fig. 5 rotated about the axis $\bar{\psi}=90°$.

An estimate of the errors in wind speed and direction can best be illustrated by example. Suppose that for $x=20$ km, $y=40$ km, $z=2$ km we estimate a dual-Doppler mean wind $W_H=10$ m s^{-1} and mean direction $\hat{\psi}=45°$, and assume the interpolated SD. σ_1 is about 1 m s^{-1}. Then σ_z (Fig. 2) is 2.5 m s^{-1}, σ_H (Fig. 5) is about 1 m s^{-1}, and the wind direction SD σ_ψ, obtained by rotating the polar diagram by 90°, is

$$\sigma_\psi \approx \frac{1.8\sigma_1}{\hat{W}_H} = 0.18 \text{ rad,}$$

that is, the wind direction SD is about 10°. Of course the smaller the wind speed the larger the error in wind direction.

5. Wind variance dependency on radar separation

In this section we treat the relation between wind variance and radar separation for α small, whereby W_α approximates W_z, and σ_α at constant arc height $\rho\alpha$ estimates σ_z at constant height z. We also assume σ_1, σ_2 independent of grid location. The factor multiplying $\sigma_1^2+\sigma_2^2$ [in Eq. (2.10)] is larger than unity
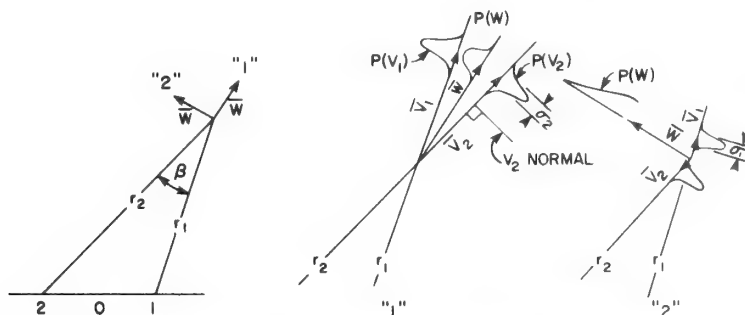
FIG. 6. Wind magnitude standard derivation depicted as projections of intersections between $\hat{V}_1$, $\hat{V}_2$ normals on true wind vector $\bar{W}$ line. Case "1" wind parallel to bisector of β and case "2" orthogonal to bisector. Vectors lie on a constant α plane. $\bar{V}_1$, $\bar{V}_2$ and $\bar{W}$ are vectors.

and if σ_t^2 is equal to or less than $\sigma_1^2 + \sigma_2^2$, we can neglect C_2.

Using d as a normalizing factor for the range distances r_1, r_2 and ρ, the variance of the quasi-vertical wind W_z at the unnormalized height $\rho\alpha$ is then

$$\sigma^2(W_z) = \frac{2d\Delta\alpha\rho\rho'(r_1'r_2')^2 F_1(\rho\alpha)}{(2\Delta\rho)^2(2\rho')^2}(\sigma_1^2 + \sigma_2^2), \quad (5.1)$$

where primes denote distances normalized to d. Eq. (5.1) shows that, for fixed arc height, grid spacing and normalized location, the quasi-vertical wind variance $\sigma^2(W_z)$ is linearly proportional to station separation.

However, grid spacings $\Delta\rho$, Δs and interpolation radius r_0 would probably be set proportional to the data spacing $r_2\Delta\theta$ (for $s \geqslant 0$) as discussed in Section 2b of the Appendix. Similarly the angle increment $\Delta\alpha$ would be proportional to $r_2\Delta\theta/\rho(s \geqslant 0)$. Therefore we assume

$$\rho\Delta\alpha = \Delta\rho = \Delta s = C_3 r_2\Delta\theta, \quad \text{for} \quad s \geqslant 0, \quad C_3 \geqslant 1,$$

where C_3 is a constant of proportionality that determines the number of data, spaced angularly at $\Delta\theta$, used in interpolation (Appendix A, Section 2b). Substituting these and (A14) for $1 - R^2$ into (3.7) to obtain σ_1^2, σ_2^2 and solving (5.1), we find

$$\sigma^2(W_z) \approx \frac{0.01 K_t\theta_w\rho\alpha\Delta V}{dn_r C_3^4(\Delta\theta)^2}\left(\frac{r_1'}{r_2'}\right)^2\left[\frac{(r_1')^3 + (r_2')^3}{(\rho')^2}\right]F_1(\rho\alpha),$$
$$s \geqslant 0. \quad (5.2)$$

We conclude that when shear is the dominant variance-producing mechanism and grid spacing is proportional to data spacing, $\sigma^2(W_z)$ is, at fixed arc height and normalized grid location, inversely proportional to station separation, proportional to the beamwidth, and inversely proportional to the range sample density n_r. The surprising result that $\sigma^2(W_z)$ decreases as d increases, along with the fact that σ_ρ^2, σ_s^2 are independent of d, implies that dual-Doppler coverage area can be increased to any desired size without increasing wind estimate variance. However, the resolution[3] $2\Delta\rho(=2C_3 r_2\theta_w)$ of vertical velocity will be linearly proportional to d for constant normalized grid location. As an example, a $1°$ beamwidth, range $r_2' = 2^{\frac{1}{2}}$ and $d = 20$ km results in a 1 km resolution. As shown below, $r_2' = 2^{\frac{1}{2}} = r_1'$ is a location where $\sigma^2(W_z)$ is a minimum. Furthermore when $\rho \gg d$ and $s \ll d$, $\sigma^2(W_z)$ becomes proportional to ρ at fixed arc height and to the square of ρ for fixed α.

To estimate $\sigma^2(W_z)$ assume that $r_1' = 2^{\frac{1}{2}} = r_2'$, $K_t = 10^{-2}$ s^{-1}, $n_r = (200 \text{ m})^{-1}$, $d = 20$ km, $\Delta\theta = \theta_w = (1/60)$ rad, $C_3 = 1$, $\Delta V = 1$. For an arc height $\rho\alpha = 10$ km, $F_1(\rho\alpha) \approx 4$; thus

$$\sigma(W_z) \approx 4 \text{ m s}^{-1}.$$

---

[3] The factor of 2 is present because the finite-difference approximation used is centered differences.

To assess an approximate spatial dependence of σ_α^2 on constant α planes, we ignore the $\rho\alpha$-dependence in C_1 and assume σ_1^2, σ_2^2 are constant. Thus σ_α^2 is proportional to

$$\sigma_\alpha^2 \propto \frac{r_1^2 r_2^2}{4d^2}.$$

Along lines of constant radius $R_0^2 = s^2 + \rho^2$ we find that

$$\sigma_\alpha^2 \propto \frac{d^2}{4}\left(\frac{R_0^2}{d^2} - 1\right)^2 + \rho^2.$$

Therefore σ_α^2 is minimum along a circular arc passing through the radar sites, a line near which we should have the most precise W_z estimates. The angle subtended by r_1, r_2 is equal to $\pi/2$ along this line.

6. Application to an experiment (20 April 1974)

The derived formula can be used to estimate error in dual-Doppler deduced wind where error is assumed related to spectrum width. We have selected the dual-Doppler data and analysis presented in a companion paper (Ray et al., 1975) to compute wind SD derived from that experiment. For sake of simplicity we calculate horizontal wind speed errors at a height of 1 km where we can ignore vertical velocity variance. Contours of speed SD superimposed on a field of wind vectors are shown in Fig. 7. The SD is obtained from (4.7a) in which wind direction estimates are used for $\bar{\psi}$ and σ_x, σ_y are approximated by σ_s, σ_ρ [Eq. 2.3)]. The interpolated Doppler velocity variances σ_1^2, σ_2^2 are computed using the distance-weighted interpolation technique described by Ray et al. This interpolation is similar to that described in the Appendix, the exception being that the influence radius on a horizontal plane is 1.5 km while along the vertical it is 1 km. Therefore σ_1^2, σ_2^2 are computed using (A7) and (3.6) to relate spectrum width w_s to interpolated Doppler estimate variance. Doppler width estimates, computed using
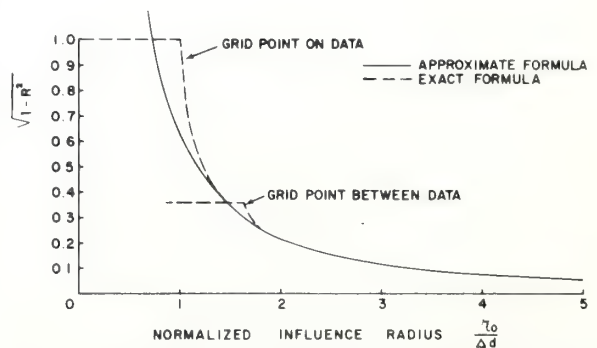
Fig. 7. Contours of wind speed standard deviation (m s^{-1}) for data collected at 1610 CST 20 April 1974. Wind vectors derived by Ray et al. (1975).

the pulse pair technique described by Berger and Groginsky (1973), were typically 5–6 m s⁻¹ showing a slight increase with range.

The wind speed SD is relatively uniform between 0.2 and 0.4 m s⁻¹ over a large region of the storm (Fig. 7). Higher SD (i.e., 0.6 m s⁻¹) in the northeast sector of the storm is a result of the wind being nearly perpendicular to the bisector of $\bar{r}_1$, $\bar{r}_2$. This location corresponds to $y/d=2$, $s/d=1$ (Fig. 5), where we see the ratio of speed SD for winds perpendicular and parallel to the bisector is about 2, a result supported by the error field of Fig. 7. Insofar as wind estimate errors are spectral-width-related, the error fields shown in Fig. 7 give the confidence one has in the dual-Doppler results published by Ray *et al.* (1975).

7. Summary and conclusions

The results of this work predict the variance of Cartesian wind components synthesized from dual-Doppler velocity estimates combined with the terminal velocity and the continuity equation. We give an example of the wind variance field and relate it to interpolated Doppler velocity variance for two interpolation schemes: a linear 4-point bivariate and a distance-weighted interpolation.

Vertical wind has variance larger than horizontal wind for most grid locations. Using an example it is concluded that vertical velocity can be estimated with a standard deviation less than a few meters per second up to heights near 14 km for extended regions of space (i.e., about $4d \times 4d$ where $2d$ is radar separation).

When the interpolation volume is matched to data spacing, it is shown that the dual-Doppler coverage area can be increased by increasing station separation without increasing wind estimate variance. However, increased coverage area is compromised by poorer resolution.

We show that horizontal speed estimate variance is a function of true wind direction, and that direction estimate variance is an inverse function of wind speed as well as a direct function of true direction. Best wind magnitude estimates are made when the true direction lies along the bisector of the angle between radius vectors drawn to the radars and the best direction estimate when the wind is perpendicular to this bisector. Results predict, for station separations of 40 km and altitudes below 6 km, minimum vertical velocity variance near the circular arc through the radar positions and, for higher altitude, near the radar's vertical.

Terminal velocity, determined from reflectivity estimates and an assumed dropsize distribution, has more variance due to uncertainties in the size distribution than in reflectivity estimates. For typical dual-Doppler geometry, bias errors in vertical wind velocity due to particle fallspeed are significantly smaller than those in terminal velocity estimates for any reasonable heights (e.g., 0–20 km). Thus the selection of a V_t, Z

relation should not be critical. Finally an air density decrease with height significantly increases the vertical velocity estimate variance.

APPENDIX

Variance Reduction for Interpolated Velocities

Doppler velocity data collected with equal spacings of radar range and beam position result in dual-Doppler radar fields having no data location coincidence. Therefore interpolation is required to locate data on a common grid. Although there are many different interpolation techniques, discussion is limited to two methods. A linear 4-point bivariate interpolation is applicable if data are acquired on constant α planes. A second method concerns data weighted in proportion to the space-time distance between data and grid location. If data are not acquired on planes of constant α, then interpolation must be four-dimensional (three space plus time). More than assigning Doppler values at grid locations, interpolation provides Doppler estimates V_1, V_2 that have variance smaller than that associated with $\hat{V}$. We now determine variance reduction for each interpolation scheme so that with $\sigma^2(\hat{V})$ as an input one may estimate the SD of dual-Doppler derived wind.

Although there are elegant techniques to determine weighting functions and a rigorous formula to estimate variance of interpolated values (Panchev, 1971), these solutions require spatial correlation functions of error and unknown wind fields. For simplicity, we assume a weighting function and present an estimate of variance reduction.

1. Linear interpolation on constant α planes

Each grid point will be in a block bounded by four data points (two at constant range and two at constant beam position); thus the interpolated value is given by

$$V_\theta = V(\theta_0 + \Delta\theta, r_1 + q\Delta R)$$
$$= (1-p)(1-q)V_{00} + p(1-q)V_{10}$$
$$+ q(1-p)V_{01} + pqV_{11}, \quad (A1)$$

where V_{00} is the data value at θ_0, r_1; r_1 and θ_0 define pulse volume position on an α plane. V_{01} is the data point at constant range, but displaced $\Delta\theta$, where $\Delta\theta$, ΔR are data-point spacings and p and q ranging from 0 to 1, define grid location within the data block.

Assuming $\sigma^2(\hat{V})$ equal around the block, the variance σ_1^2 at the grid point is

$$\sigma_1^2/\sigma^2(\hat{V}) = (1-p)^2(1-q)^2 + p^2(1-q^2)$$
$$+ q^2(1-p)^2 + p^2q^2 \equiv F(q,p). \quad (A2)$$

It has been shown (Miller and Strauch, 1974) that if p and q are independent and uniformly distributed over the block $(\Delta\theta)$ (ΔR), then the expected variance is

$$E[\sigma_1^2/\sigma^2(\hat{V})] = \int_0^1 F(q,\rho)dpdq = 4/9 \equiv 1-R^2. \quad (A3)$$

Thus the normalized variance reduction R^2 of interpolated velocity is 5/9 independent of grid location. If grid density is uniform and coarse, not all data may be used to reduce variance and resolution will be lost without benefiting variance reduction. On the other hand, if grid density is fine, interpolated values are correlated and the SD σ_z of the quasi-vertical wind derived earlier needs to be modified to account for this correlation. However no adjustment is required in this case for the variance in W_ρ, W_s. Because data spacing increases with r_1, it may be preferable to use a grid spacing Δ_ρ that increases in proportion to the larger data spacing $r_2\Delta\theta$ (for $s \geqslant 0$). Furthermore since radial sample density is usually more than azimuthal density, range averaging of samples over the interval $r_1\Delta\theta$ (and $r_2\Delta\theta$ for $\hat{V}_2$) would give a further variance reduction with a resolution consistent with beamwidth (i.e., assuming $\Delta\theta$ proportional to θ_w). In this case,

$$R^2 = 1 - \frac{4}{9n_r r_1 \Delta\theta}, \quad (A4)$$

where n_r is the range sampling density and we assume range-averaged data density equal to or larger than grid density.

2. Volume averages of Doppler estimates

a. Spherical volume

We now determine R^2 when data are averaged within a volume of constant radius. The interpolated velocity V_1 (or V_2) is assumed to be a linear combination

$$V_1 = \frac{\Sigma C_i \hat{V}_i}{\Sigma C_i} \quad (A5)$$

of data values V_i, where C_i is a weight determined by the assumed function

$$C_i = \begin{cases} \dfrac{r_0^2 - r_i^2}{r_0^2 + r_i^2}, & 0 \leqslant r_i \leqslant r_0 \\ 0, & \text{otherwise} \end{cases} \quad (A6)$$

where r_0 is the so-called influence radius, and r_i the grid

to data point distance. The interpolated velocity variance follows directly from (A5) and is

$$\sigma_1^2 = \frac{\Sigma C_i^2 \sigma^2(\hat{V}_i)}{(\Sigma C_i)^2}, \quad (A7)$$

where we assume equal data variance $\sigma^2(\hat{V}_i)$ within the averaging volume. When data samples are uniformly dense within the volume, the above discrete sum formula can be replaced by the integral

$$\frac{\sigma_1^2}{\sigma^2(V)} = \frac{1}{3N} \int_0^1 C^2(X)dX \Big/ \left[\int_0^1 C^2(X)X^2dX\right]^2$$
$$= 1-R^2, \quad (A8)$$

where $X \equiv r_i/r_0$ and N is the total number of data points within the volume. Substituting (A6) into (A5) and carrying out the lengthy although elementary integrations we obtain normalized variance reduction

$$R^2 = 1 - \frac{1.69}{N}. \quad (A9)$$

For uniform data spacing Δd, N is

$$N = \frac{4\pi r_0^3}{3(\Delta d)^3}, \quad (A10)$$

which, when substituted into (A9), gives

$$(1-R^2)^{\frac{1}{3}} = \frac{0.64}{(r_0/\Delta d)^{\frac{1}{3}}}. \quad (A11)$$

Eq. (A11) is plotted in Fig. A1. Because (A11) is only
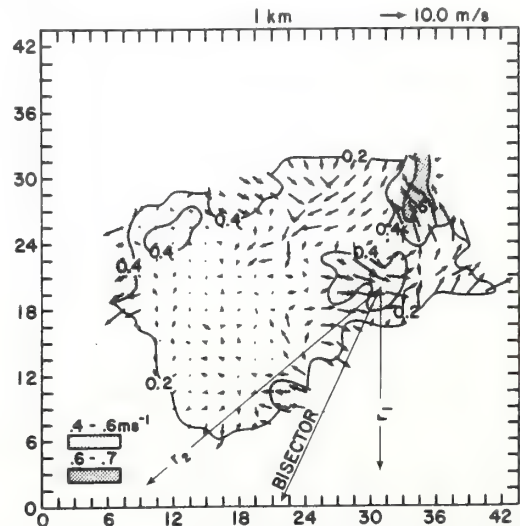
Fig. A1. Multiplying factor to obtain grid estimate standard derivation from data standard derivation for distance-weighted interpolation, using spherical averaging volume and uniform data spacing. Δd is data spacing.

applicable when N is large (i.e., $r_0 \gg \Delta d$) we need to determine R for small N. In order to assess the range of r_0 for which (A11) is a good approximation we evaluated R using the exact formula (A7) for grid points on and midway between data points. These solutions (dashed lines in Fig. A1) show the approximate formula (A11) is good when $r_0/\Delta d \geqslant 1.5$.

The variance reduction R^2 obtained from (A11) is applicable to uniform distribution of data within r_0, a condition not usual in radar data acquisition schemes. Therefore if data samples are range averaged over the interval $r_1 \Delta \theta$, then

$$R^2 = 1 - \frac{0.41 (r_1 \Delta \theta)^2}{r_0^3 n_r}. \tag{A12}$$

b. Cylindrical volume

An averaging volume which fits naturally into the cylindrical coordinate system is one bounded about a grid point ρ, s, α with respective limits $\pm \Delta \rho/2$, $\pm \Delta s/2$, $\pm \Delta \alpha/2$. This "pie" shaped averaging volume gives the advantage that interpolated grid value errors are uncorrelated and hence the error analysis presented in this paper is applicable without correction. Furthermore this averaging volume may prove useful in recognizing data anomalies because only one grid value is affected by an anomolous data value. In any case, because angular data spacing increases with range it is most reasonable to assume an interpolation volume that accordingly increases. However the evaluation of R appears difficult. To make an R estimate we assume that the volume is nearly cubic (i.e., $\rho \Delta \alpha = \Delta s = \Delta \rho$) and use (A9) as an approximation for R, where N is now the number of data contained in the averaging volume. If r_0 is set equal to the volume diagonal $\sqrt{3}\rho_0 \Delta \alpha/2$, and if data spacing Δd within the volume is uniform and equal to $r_1 \Delta \theta$, the variance reduction R is

$$R = 1 - \frac{1.1}{(r_0/\Delta d)^3}. \tag{A13}$$

In this case R^2 is smaller than in (A11) for spherical volume because for given r_0 we have smaller N in the quasi-cubic volume. Substituting for r_0 and again assuming range sample averaging plus a grid spacing $\Delta \rho = C_3 r_2 \Delta \theta$ (for $s \geqslant 0$), we obtain a variance reduction

factor for V_1

$$R_1^2 = 1 - \frac{1.7}{C_3^3 n_r r_1 \Delta \theta} \left(\frac{r_1}{r_2}\right)^3, \tag{A14a}$$

and for V_2

$$R_2^2 = 1 - \frac{1.7}{C_3^3 n_r r_2 \Delta \theta}, \tag{A14b}$$

where C_3 is a constant, equal to or larger than unity, which determines grid spacing. R^2 for $s \leqslant 0$ is obtained by exchanging r_2 with r_1.

REFERENCES

Armijo, L., 1969: A theory for the determination of wind and precipitation velocities with Doppler radars. *J. Atmos. Sci.*, **26**, 570–573.

Atlas, D., R. C. Srivastava and R. S. Sekhon, 1973: Doppler radar characteristics of precipitation at vertical incidence. *Rev. Geophys. Space Phys.*, **2**, 1–35.

Berger, T., and H. L. Groginsky, 1973: Estimation of the spectral moments of pulse trains. Presented at International Conference of Information Theory, Tel Aviv, Israel.

Donaldson, R. J., G. M. Armstrong, K. J. Banis and R. M. Dyer, 1972: Measurement of wind gradients in convective storms by Doppler radar. *Preprints 15th Radar Meteorology Conf.*, Champaign-Urbana, Amer. Meteor. Soc., 22–26.

Joss, J., and A. Waldvogel, 1970: Raindrop size distributions and Doppler velocities. *Preprints 14th Radar Meteorology Conf.*, Tucson, Amer. Meteor. Soc., 153–156.

Lhermitte, R. M., 1970: Dual-Doppler radar observation of convective storm circulation. *Preprints 14th Radar Meteorology Conf.*, Tucson, Amer. Meteor. Soc., 139–144.

——, and L. J. Miller, 1970: Doppler radar methodology for the observation of convective storms. *Preprints 14th Radar Meteorology Conf.*, Tucson, Amer. Meteor. Soc., 133–138.

Miller, K. S., and M. M. Rochwarger, 1972: A covariance approach to spectral moment estimation. *IEEE Trans. Information Theory*, **IT-18**, 588–596.

Miller, L. J., and R. G. Strauch, 1974: A dual Doppler radar method for the determination of wind velocities within precipitating weather systems. *Remote Sensing Environ.*, **3**, 219–235.

Nathanson, F. E., 1969: *Radar Design Principles*. McGraw-Hill, 596 pp.

Panchev, S., 1971: *Random Functions and Turbulence*. Pergamon Press, p. 381.

Papoulis, A., 1965: *Probability, Random Variables and Stochastic Processes*. McGraw-Hill, 576 pp.

Ray, P. S., R. J. Doviak, G. B. Walker, D. Sirmans, J. Carter and B. Bumgarner, 1975: Dual Doppler observations of a tornadic storm. *J. Appl. Meteor.*, **14**, 1521–1530.

Sirmans, D., and B. Bumgarner, 1975: Numerical comparison of five mean frequency estimators. *J. Appl. Meteor.*, **14**, 991–1003.

——, and R. J. Doviak, 1973: Meteorological radar signal intensity estimation. NOAA Tech. Memo. ERL-NSSL 64.

Waldteufel, P., 1976: An analysis of Doppler spectra width estimates for a tornadic storm. NSSL Tech. Memo. 76, 80 pp.

MEASUREMENT OF WINDS IN THE OPTICALLY CLEAR AIR
WITH MICROWAVE PULSE-DOPPLER RADAR

L. Hennington, R.J. Doviak, D. Sirmans, D. Zrnic'
National Severe Storms Laboratory
Norman, OK

and

R. G. Strauch
Wave Propagation Laboratory
Boulder, CO

About a year ago one of the authors
(Richard Strauch) raised the question as to
whether a pulse-Doppler radar with antenna of
moderate diameter (4-10 m) would have sufficient
sensitivity to observe diffuse scatter continu-
ously from the optically clear atmosphere. Doppler
processing can enhance the minimum detectable
signal by an order of magnitude (section 3) and
hence medium resolution weather radars might
have a detection capability matching that more
commonly associated with large aperture (18-27 m
diameter) antennas used with incoherent radars.
Furthermore, a coherent radar provides a way in
which ground clutter can be distinguished from
moving atmospheric targets and allows data acqui-
sition at closer ranges thereby taking advantage
of the R^{-2} dependence in echo power. An affirma-
tive answer has practical significance in that
pulse-Doppler ASR radars under development by the
FAA could then also measure wind shear hazards
near airports under all weather conditions.
Important economic advantage can be achieved if
these radars can serve a dual purpose.

Echoes from the clear air have been almost
observed from the inception of radar observations
and speculation abounded as to whether diffuse
angel echoes were refractive index fluctuations
or insects. It was not until 1966 that clear air echo
measurements with ultrasensitive, multiwavelength
radars at Wallops Island confirmed that radar
detects minute fluctuations in refractive index
(Hardy and Glover, 1966).

Although many impressive results were
obtained with the large diameter (18 m) aperture
antennas at Wallops Island (e.g., see Preprints,
14th Radar Meteor. Conf., 1970, Am. Meteor. Soc.,
Boston) and with the 27 m diameter antenna at
Defford, England (Starr and Browning, 1972) radar
observation of the clear air need not be entrusted
to large aperture antennas and high power radars.
Richter (1969) demonstrated that a moderate power
(150 w average), vertically pointing FM-CW radar
with 3 m diameter antennas, shrouded to suppress
ground clutter, can detect clear air refractive
fluctuations. The absence of appreciable ground
clutter permits radar measurement to ranges 20
to 100 times smaller than typically used with large
aperture, thus enhancing enormously (13 to 40 dB)
the weak echoes. Richter's experiments showed

radar echoes confined for the most part to thin
layers several meters in vertical extent and to
boundaries of convective cells (Arnold et al. 1975).

Simultaneous acoustic sounder and FM-CW mea-
surements show radar echoes to be confined to
convective cell boundaries whereas acoustic signals
appear to be continuously distributed in height
to convection tops (Richter and Jensen, 1975).
This has been attributed to the fact that radar
target cross section is mostly from moisture fluc-
tuations whereas the acoustic sounder principally
senses temperature fluctuations. However, we
submit that a radar of modest resolution, but
with Doppler processing, should detect these
temperature fluctuations.

Pulse-Doppler radar with single shrouded
antenna should have ground clutter immunization
equivalent to that of an FM-CW and hence permit
observation at near ranges. Gorelik, Knyazev and
Uglova (1973) and Dobson (1970) are among the
first to use Doppler processing to observe clear
air.

2.   HEIGHT DISTRIBUTION OF REFRACTIVE INDEX
     STRUCTURE CONSTANT

In 1971 Ochs and Lawrence (1972) made tempera-
ture fluctuation measurements using a sensor
mounted on an aircraft and sounded the atmosphere
in the lower 3 km. Results show that the tempera-
ture contribution to refractive index structure
constant was consistently above $10^{-17}m^{-2/3}$ over
land and ocean within the measured height interval.
A profile of averaged C_n^2 due to temperature
fluctuations over land in November 1971 is shown
in Fig. 1. These results suggest Doppler radars
with minimum detectable structure constant of
$10^{-17}m^{-2/3}$ might be able to continuously monitor
the wind within the lower troposphere. Doviak,
Goldhirsh and Miller (1972) used a bistatic radar
to detect the presence of diffuse scatter in the
upper troposphere (1972). Their measurements at
7 km infer a diffuse-scatter related C_n^2 value
that could be as large as $10^{-17}m^{-2/3}$ which
compares with those values at 3 km reported by
Ochs and Lawrence. Crane (1970), using the 25.6 m
diameter Millstone Hill Radar antenna, reports
results that suggest C_n^2 is less than $4x10^{-16}m^{-2/3}$

for heights above 7 km in contrast to values as large as $10^{-15} \mathrm{m}^{-2/3}$ observed with the 7.4 m radar at Sunset, Colorado (Green et al. 1975).

Also shown in the figure are two curves which depict the minimum detectable C_n^2 for NSSL's 10 cm radar using Doppler spectral averaging techniques (section 3). The radar has been configured to principally observe severe storms and it is not optimized for clear air detection. Nevertheless, the present system (4/19/76) should be able to confirm the presence of spatially continuous diffuse scatter. The radar can be reconfigured to improve its detection performance (solid curve labeled 'best') but the biggest limitation to date is the presence of masking ground clutter. Even with Doppler processing, close-in observation of echo power near receiver noise is masked by ground clutter power that exceeds the limited dynamic range of the 12 bit A/D converters. Because of ground clutter, observations were usually limited to ranges beyond 5 to 6 km. Shrouded antenna or location of the antenna in a ground depression LaGrone et al. 1964) should suppress significantly these pesky returns.
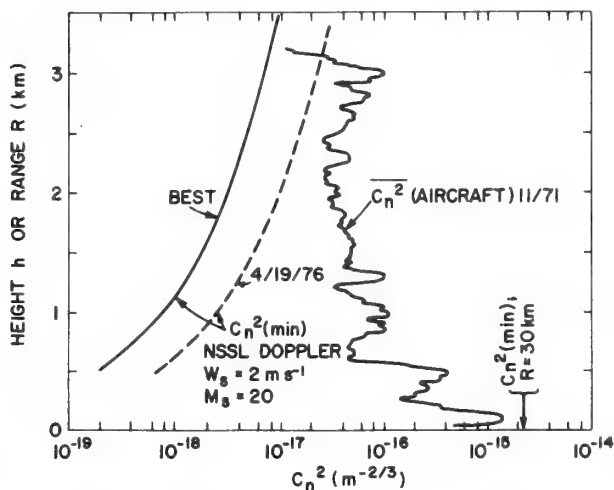
Figure 1. Profile of average structure constant $\overline{C_n^2}$ due to temperature fluctuations versus height h (Ochs and Lawrence,1972). Smooth lines are minimum radar detectable C_n^2 at range R using NSSL's Doppler system as configured on 4/19/76 (dashed line) and for system if reconfigured (solid line) to provide lower system noise temperature and higher transmitted power.

3. MINIMUM DETECTABLE REFLECTIVITY WITH DOPPLER RADAR

Consider the receiving system (Fig.2) with indicated gains, losses and noise figure. T_a is the antenna temperature estimated at $80^\circ K$ from an assumed sky temperature of $50^\circ K$ and an earth temperature of $290^\circ K$ viewed by antenna sidelobes. Measurements at the calibration port showed the receiver noise figure to be 3.7 dB and when referred to points immediately outside the radome 5.7 dB giving a noise power P_{no} at these points equal to:

$$P_{no} = kT_{so} B_N = -111.2 \text{ dBm} \qquad (1)$$

where k is the Boltzman constant, $T_{so}=867^\circ K$ and $B_N=6.37 \cdot 10^5$ Hz.

(a)
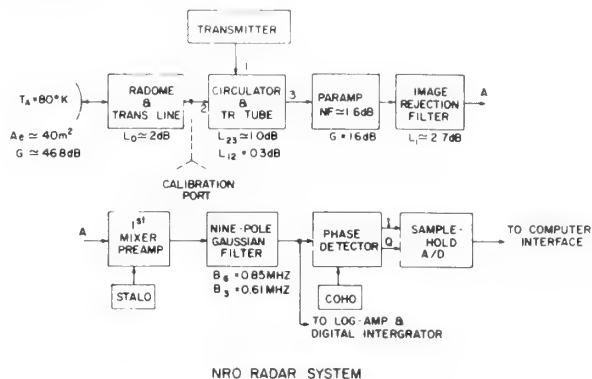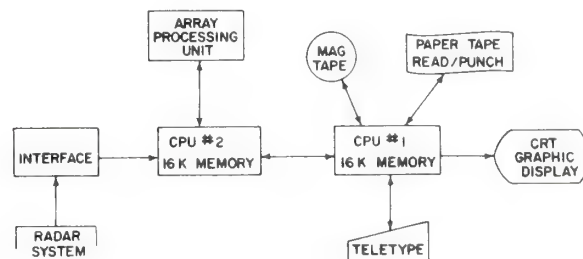
(b)

Figure 2(a) Norman radar system. Losses L and gains G are indicated, B_6 and B_3 are the 6 and 3 dB filter bandwidths. (b) The minicomputer and graphic display.

Considerable increase in scatter signal detection sensitivity can be achieved through spectral processing. The power density S(V) (V is the Doppler velocity) is a statistically varying quantity with an amplitude having a probability density given by

$$\text{Prob}[\hat{S} + \hat{N}] = \frac{e^{-(\hat{S}+\hat{N})/(\overline{S}+\overline{N})}}{\overline{S}+\overline{N}} \qquad (2)$$

where $\hat{S}+\hat{N}$ is an estimate of the mean signal and noise power density and $\overline{S}$, $\overline{N}$ are the mean values. (We have dropped the explicit notation of Doppler velocity V.) $\overline{S}$ is the quantity that is to be estimated whereas the mean spectral noise power density $\overline{N}$ is assumed known. Thus, for any V, the computed spectral coefficient will have a dc value plus random signal when viewed from one spectral estimate to the next. It can be shown (Sirmans and Doviak, 1973) that the spectral coefficient estimate variance is proportional to $(\overline{S}+\overline{N})^2$ and that averages of estimates will reduce variance by the number, M_s, of spectra averaged. That is

$$\text{VAR}[\hat{S}+\hat{N}] = (\overline{S}+\overline{N})^2/M_s \qquad (3)$$

151

Thus we consider the power density to have signal amplitude $\bar{S}$ (the dc value) with power $\bar{S}^2$ contaminated by a fluctuation noise power N_f

$$N_f = (\bar{S} + \bar{N})^2 / M_s \qquad . \qquad (4)$$

The minimum detectable signal is defined as one which produces an output signal power $\bar{S}^2_{min}$ equal to the fluctuation noise power for $\bar{N}$ alone. That is

$$\bar{S}^2_{min} = \bar{N}^2 / M_s$$

or

$$\bar{S}_{min} = \frac{\bar{N}}{\sqrt{M_s}} \qquad (5)$$

The mean spectral power density noise level is the system noise power P_{no} distributed uniformly over the Nyquist co-interval $\lambda/2T$. Thus

$$\bar{N} = \frac{P_{no} 2T}{\lambda} \qquad (6)$$

where T is the radar's pulse repetition time, and the minimum detectable signal power density is

$$\bar{S}(min) = \frac{P_{no} 2T}{\lambda \sqrt{M_s}} \qquad (7)$$

For Gaussian shaped spectra the peak signal spectral density is

$$\bar{S}_p = \frac{\bar{P}_s}{\sqrt{2\pi}\, W_s} \qquad (8)$$

where $\bar{P}_s$ is the mean signal power and W_s the signal power spectrum standard deviation or simply the spectrum width. Thus the minimum detectable signal power is

$$P_s(min) = \frac{2TW_s}{\lambda} \cdot \sqrt{\frac{2\pi}{M_s}} \; P_{no} \qquad (9)$$

Eq. 9 assumes that there is sufficient spectral resolution, or number of spectral lines (Discrete Fourier Transform coefficients), within the signal spectrum, to resolve the modal value. The above formula shows that the minimum signal power increases (detection ability weakens) in direct proportion to the ratio of spectrum width W_s to Nyquist co-interval $\lambda/2T$.

3.1 Minimum Detectable C_n^2

For Gaussian weighted pulse volumes which are uniformly filled with scatterers the signal power P_s (outside radome) is related to the reflectivity $\eta(m^{-1})$ of the scatter volume as

$$\eta = \frac{8\pi \; R^2 \; P_s \; L_d}{P_t \; \Delta R \; A_e} \qquad (10)$$

where the radar parameters for 5/19/76 are:

P_t is the peak transmitted power after all losses have been substracted (4.73×10^5 watts)
L_d is the "matched" filter loss (2.7 dB)
ΔR is the range resolution (150m)
A_e is the effective antenna area ($40m^2$)

The refractive index structure constant is

$$C_n^2 = \frac{\eta}{.39 \; \lambda^{-1/3}} \qquad (11)$$

Thus in terms of the system parameters the minimum detectable structure constant becomes

$$C_n^2(min) = \frac{8\pi R^2 \; L_d \; P_s(min)}{.39 \; \lambda^{-1/3} \; P_t \; \Delta R \; A_e} \qquad (12)$$

Substituting (9) into (12) we obtain

$$C_n^2(min) = \frac{16\pi\sqrt{2\pi} \; R^2 \; W_s \; T \; L_d \; P_{no}}{.39 \; \lambda^{2/3} \; P_t \; \Delta R \; A_e \sqrt{M_s}} \qquad (13)$$

Substituting NSSL radar parameter values we find

$$C_n^2(min) = \frac{5.5 \times 10^{-24} \; W_s R^2}{\sqrt{M_s}} \; m^{-2/3} \qquad (14)$$

Equation (13) and (14) were used to obtain the $C_n^2(min)$ versus range R curves plotted in Fig. 1. 'Best' values are obtained increasing P_t by 3 dB and relocating the parametric amplifier near the feed horn.

4. REAL TIME DOPPLER SPECTRUM PROCESSING AND DISPLAY

The real-time minicomputer system (Fig.2b) consists of two sixteen bit parallel processors (CPU) with one microsecond cycle times. Each CPU has 16 K of memory and one Direct Memory Access (DMA) channel with multiple ports. Time series data for 16 range bins is transferred from the Doppler radar to CPU No.2 and processed by the Array Processing Unit (APU). The APU is a versatile array processor and the Discrete Fourier Transform (DFT) is accomplished with multiple array manipulations using the Cooley-Tukey algorithm. The spectral coefficient power is calculated and 'M_s' summations are performed. The time to calculate each 64 complex point transform and compute power is approximately 1 m sec. Therefore, the time required for the display shown in Fig.3 is approximately $16M_s$ m sec. Other calculation times, such as summation and logarithms, are small compared to DFT calculation time.

The power spectra are then sent to CPU No.1 where they are made ready for output to the CRT graphic display. Sixteen gates of power spectra, in dB, are plotted vs. frequency or velocity and are scaled according to the operator's input via the teletype.

The output display (see Fig. 3) consists of the multispectra graphs as well as pertinent housekeeping parameters. Azimuth, elevation, time and spacing between gates in kilometers are shown. 'TH' is a threshold in dB usually set to a value corresponding to 10 Log P_n where P_n is noise power. DB/DIV is the number of dB's per unit as depicted by the graticule which are dashed lines of lower intensity. 'NS' is the number M_s of spectra averaged. 'BS' is the beginning step or block corresponding to sixteen gates. Any one of 8 blocks may be displayed which, depending on gate spacing, allows the operator to scan a fraction or the entire unambiguous range (115 km). 'RNG' is the horizontal distance from the radar to the sample volume. 'HGT' is the height above the radar's local horizontal plane. Only every other gate

152

or sample volume is labeled. The width of each graph covers the Nyquist co-interval.
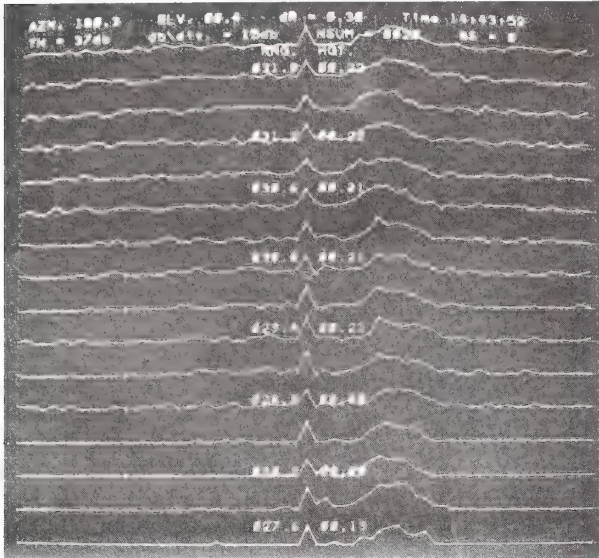
Figure 3. NSSL's display of real time averaged spectra for 16 range gates. Graticule vertical scale corresponds to 15 dB/div and is approximately 4 ms^{-1}/div along the horizontal. The narrow spike in the center is at zero velocity. Positive velocities are to the right of zero and negative to the left.

5. AUTOCOVARIANCE METHOD OF VELOCITY MEASUREMENT; IMPLICATION FOR CLEAR AIR STUDIES

Pulse pair processing is another attractive coherent processing technique to estimate Doppler velocity measurements in clear air (Berger and Groginsky, 1973). Although the autocorrelation at lags equal to pulse repetition periods can provide "good" power estimates with noise immunity similar to spectral processing when spectra are narrow (WT < .05), this technique's advantage is that it's a maximum likelihood velocity estimator. The Discrete Fourier Transform (DFT) technique to derive mean Doppler velocities has certain advantages over the pulse pair autocovariance method because spurious point targets and ground clutter effects can be removed. However, the pulse pair method does provide, in absence of spurious targets, a minimum variance estimate of mean Doppler velocity and spectrum width (Miller and Rochwarger, 1972). Furthermore, the pulse pair technique is computationally more efficient than the DFT one if only the principal Doppler spectra moments are required.

NSSL's dual-Doppler radars at Norman (NRO) and Cimarron are equipped with hard-wired calculators that can process up to 256 pairs of time samples in 762 contiguous range gates. Typical outputs displayed on the oscilloscope (Fig. 4) shows meaningful velocities (estimates with small variance out to ranges nearly 80 km for this day (6/29/76) when elevation angle is 1.4°. On the photograph are also pulse pair width estimates, logarithmic video and integrated log video signals. Systematic measurement with NRO Doppler shows that accurate (1-2 ms^{-1} rms error) velocities within the

boundary layer can be obtained typically to ranges of 60 km. We feel that densely spaced two Doppler data combined with a reasonable interpolation scheme can provide horizontal wind over vast regions prior to precipitation and thus amplify our ability to analyze the atmosphere.
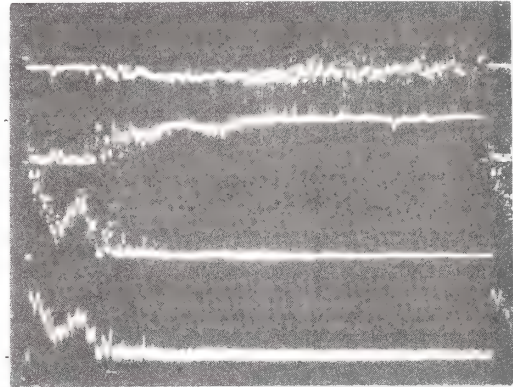
Figure 4. Oscilloscope display of Doppler spectrum moments from the covariance estimator. Traces from top are: Mean velocity (34 ms^{-1}/cm), spectrum width (16 ms^{-1}/cm), integrated logarithmic video and raw logarithmic video. Horizontal scale is 12 km/cm. AZ = 180°; EL = 1.3°. Ground clutter extends to about 18 km and causes zero velocities and widths. Between 18 and 60 km, velocities of -8ms^{-1} (ragged trace with small standard deviation) are due to clear air echoes and further out the velocities gradually become randomly distributed between ± 34 ms^{-1} (last 20 km) when signal is lost. Note the increase of spectrum width (no noise correction) with distance that also characterizes signal weakening. Number of pairs coherently processed is 256.

6. WIND PROFILE MEASUREMENTS

In order to ascertain usefulness of the radar for pre-precipitation convection studies, the experimental setup (Fig. 5) was utilized. Mean velocities obtained from averages of spectra were subjectively examined and biases due to ground clutter and point targets removed. Spectra were taken every 45° in azimuth and at 30 km range. Elevation angle was stepped in increments corresponding to height differences of about 300 m. Spectra in sixteen contiguous range gates (150 m deep and 600 m apart) were simultaneously recorded and radar measurements coincided in time with a nearby (300 m) rawinsonde sounding. Experiments conducted for several days during November 1975 and the Spring of 1976 provide data for our analysis. We focus our attention to May 19, 1976, a perfectly clear day with mild southerly winds. Estimates of the divergence and wind velocity are from a Discrete Fourier Transform fit on the 8 azimuthal data points at constant heights. Fitted curve (Fig. 6) shows a d-c offset indicating slight convergence and an extremely close match with experimental points suggesting uniform wind while at higher altitudes the deviation is larger because echo power is weaker (smaller SNR) making precise measurements more difficult. Nevertheless rawinsonde

153

record (wind speed and direction) throughout the boundary layer agrees very well with that measured by radar (Fig.7). Temperature and dew point soundings (Fig. 8) indicate presence of an inversion layer that is restraining convective activity to the lower 1.5 km, within which the radar consistently detected, what is interpreted to be, fluctuations of refractive index. The measured structure constant C_n^2 varied from a maximum of $1.7 \ 10^{-13}$ to $1.7 \ 10^{-15} m^{-2/3}$, the latter within 1dB of the theoretically established minimum detectable value for a width of $2 \ ms^{-1}$. Data of May 19 show C_n^2 relatively uniform in height with somewhat enhanced reflectivity at .5 km and 1.3 km above ground.

S = 600m
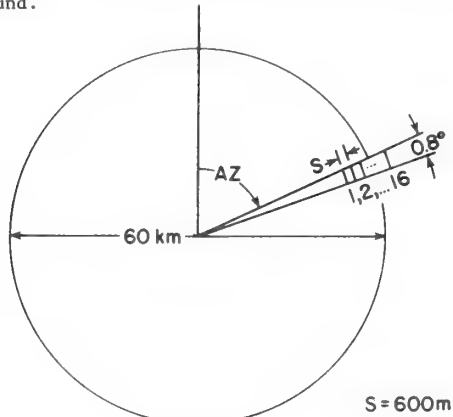
Figure 5. Arrangement of pulse-Doppler gates for clear air VAD measurements.
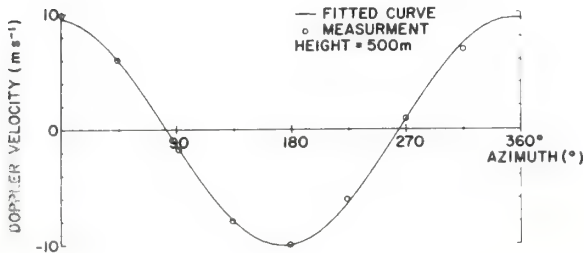
Figure 6. Velocity azimuth display for 5/19/76. Fitted curve contains the zeroth and first harmonic.
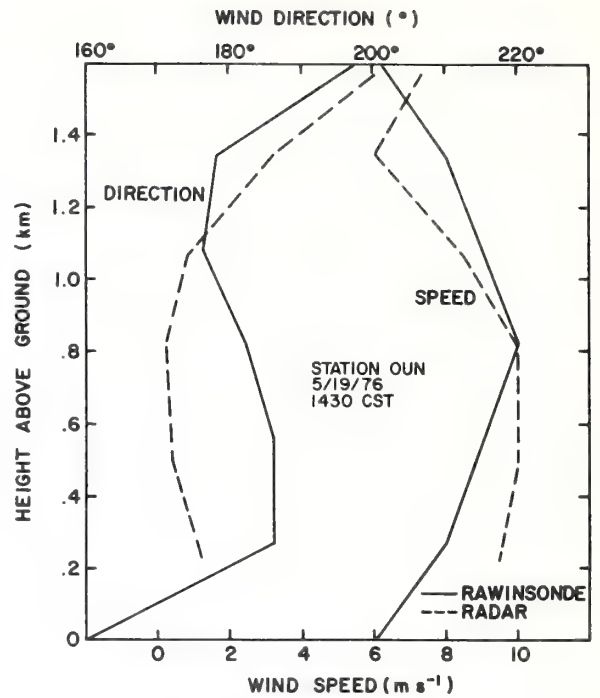
Figure 7. Comparison between rawinsonde and radar measurements of wind velocities.
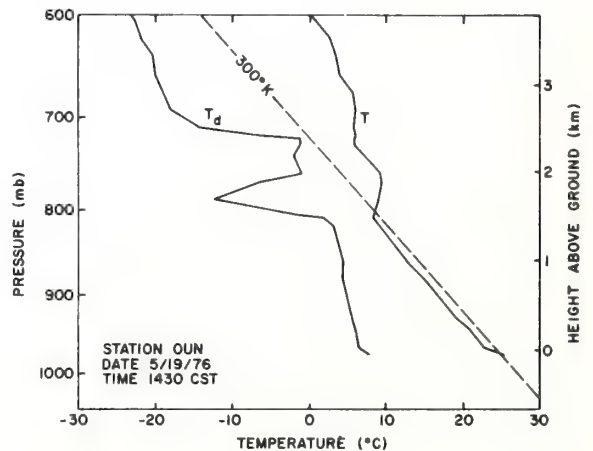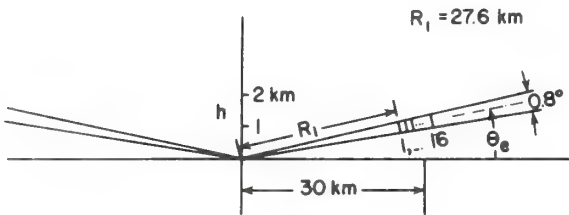
Figure 8. Temperature and dewpoint from the rawinsonde.

154

Table I contains the average vertical. velocities over the circular region 60 km in diameter at various heights, the divergence, and sample values of the structure constant. Root mean square error for the average vertical velocity is less than .3 cms^{-1}.

Table I

Height (km)	Divergence (s^{-1})	Average vertical velocity (cms^{-1})	Structure Constant $C_n^2 (m^{-2/3})$
.2	0	0	$4.5 \cdot 10^{-14}$
.5	$-6.3 \cdot 10^{-6}$	.4	$5.8 \cdot 10^{-14}$
.8	$-12.5 \cdot 10^{-6}$	1.4	$6.0 \cdot 10^{-14}$
1.0	$-29.2 \cdot 10^{-6}$	2.4	$4.5 \cdot 10^{-14}$
1.3	$-16.6 \cdot 10^{-6}$	3.0	$8.9 \cdot 10^{-14}$
1.5	$-6.3 \cdot 10^{-6}$	3.4	$3.9 \cdot 10^{-14}$

7. COMPARISON WITH FM-CW

The FM-CW radar is inherently coherent and Strauch et al.(1975) have exploited this property to measure Doppler shift of echoes from the optically clear atmosphere. Linear sawtooth modulation of the microwave frequency gives this radar characteristics that have analogy to the pulse-Doppler radar. The reciprocal of frequency deviation can be considered analogous to an effective pulse length for pulse radar, while the modulating frequency is equivalent to the PRF.

Because peak-to-average power ratio is unity, we immediately infer that resolution can be increased without changing the effective "per pulse" transmitted energy; not so with pulse radar where decrease in pulse width reduces transmitted pulse energy. Therefore per pulse S/N is decreased in proportion to the square of pulse-width whereas the equivalent signal to noise ratio of the FM-CW radar decreases linearly with effective pulse-width. We have assumed naturally that system bandwidth is matched to the pulse-width or frequency deviation. This unquestionable advantage of the FM-CW radar changes markedly when considering pulse-Doppler radar and coherent echoes.

If echoes are coherent, loss in detection sensitivity of the pulse-Doppler radar is not different than than lost by FM-CW even though the per pulse transmitted energy decreases. This is because echo signal adds coherently and when pulse width is decreased we assume PRF is proportionally increased to maintain constant average power as in FM-CW radar. Thus pulse-Doppler has capabilities that should rival the Doppler FM-CW radar.

As a matter of fact, aside from the power supply design advantage of the FM-CW system, the pulse-Doppler may prove more advantageous for the following reasons:

(1) Pulse-Doppler has a 3 dB noise figure advantage because the FM-CW radar employs homodyne mixing and suffers increased noise from image frequencies.

(2) A single shrouded antenna is required for pulse-Doppler radar thus giving economic advantage over the two antenna FM-CW system.

(3) Pulse-Doppler range resolution is independent of range, not so for FM-CW.

Saunders (1970) points out that the FM homodyne radar is seldom, if ever, limited by thermal noise in the first mixer and that a well-designed one may come within 20-30 dB of the performance of a pulse-Doppler radar, a surprisingly large departure. Saunders does not detail reasons for this degradation but some of it might be due to transmitter leakage and excessive noise produced in the homodyne mixer. However, low noise r-f preamplifiers may reduce the undesirable 1/f noise of this mixer.

We have as yet to determine if pulse-Doppler can indeed match or better FM-CW radars at short ranges. Pulse-Doppler radar limitations for near range (i.e., less than 1-2 km) observations are caused by receiver recovery time in conventional duplexer/TR tube systems but this can be alleviated through the use of high power circulators and magnetic switches. These switches have on-off time response less than 0.05 μ sec thus permitting radar observation to a minimum range limited by receiver response to transmitter pulse leakage which may set the minimum detectable echo power level for close-in targets. It appears that only a shrouded antenna need be mated to a pulse-Doppler radar to answer the question whether it can indeed provide comparable performance as the FM-CW.

8. CONCLUSIONS

Doppler processing provides an improvement in echo power detection in proportion to the Nyquist co-interval $\lambda/2T$ spectrum width W_s ratio. Aircraft measurement of temperature structure constant up to 3 km altitude and theoretical computation demonstrate that a moderate power (1 kw average) pulse-Doppler radar with a single shrouded antenna of modest diameter (4-10 m) should detect spatially and temporally continuous temperature fluctuations within the first one or two kilometers. As yet radar measurement has not completely confirmed this prediction. There is evidence that WPL's FM-CW radar does measure continuous scattering in the boundary layer (Chadwick et al.1976), and NSSL pulse-Doppler radars have consistently measured spatially continuous echoes at 17 km (3 dB beamwidth=.8°) up to heights of 1 to 2 km whenever observations were made (morning, noon or late afternoon).

Pulse-Doppler radar should have measurement capability approaching that already exhibited by FM-CW radar. Differences in FM-CW and pulse-Doppler detection sensitivities need to be experimentally investigated and effects of ground clutter on each system needs evaluation.

We have demonstrated that Doppler processing has substantially improved the detection capability of pulse radar. It appears that NSSL's two-Doppler radars have the potential to measure covergence, without chaff, within the boundary layer prior to formation of precipitation. Furthermore,

155

comparison of two-Doppler wind patterns with closely spaced ground station anemometers may answer the question: what surface station spacing is required to resolve meteorological parameters on scales significant for convection preceding thunderstorms?

9. ACKNOWLEDGMENTS

10. REFERENCES

Arnold, A., J.R. Rowland, T.G. Konrad, J.H.Richter, D.R. Jensen, and V.R. Noonkester, 1975: Simultaneous observations of clear air convection by a pulse radar, an FM-CW radar, an acoustic sounder, and an instrumented aircraft. Preprints 16th Radar Meteor. Conf., Am. Meteor. Soc.,Boston, 290-295.

Berger, T. and H.L. Groginsky, 1973: Estimates of spectral moments of pulse trains. Paper presented at the Inter. Conf. on Information Theory, Tel-Aviv, Israel.

Chadwick, R.B., W.C. Campbell, K.P. Moran, R.G. Strauch, 1976: Boundary layer wind measurement with an FM-CW Doppler radar. Preprints 17th Radar Meteor.Conf., Am. Meteor.Soc., Boston.

Crane, R.K., 1970: Measurement of clear air turbulence in the lower stratosphere using the Millstone Hill L-Band Radar. Preprints 14th Radar Meteor. Conf., Am.Meteor.Soc., Boston, 101-106.

Dobson, E.B., 1970: Doppler radar measurements of mean wind variations in the clear atmosphere. Preprints 14th Radar Meteor. Conf., Am.Meteor.Soc., Boston, 69-78.

Doviak, R.J., J. Goldhirsh and A.R. Miller,1972: Bistatic radar detection of high-altitude clear-air atmospheric targets. Radio Science, 7, 993-1003.

Gorelik, A.G., L.V. Knyazev and L.N. Uglova, 1973: Radar echoes from the "clear sky" in the decimeter radio band. Izv., Atmos. & Oceanic Physics, 9, 190-194.

Green, J.L., J.M. Warnock, R.H. Winkler and T.E. VanZandt, 1975: A sensitive VHF radar for the study of winds, waves and turbulence in the troposphere, stratosphere and mesophere. Preprints 16th Radar Meteor.Conf., Am.Meteor. Soc., Boston, 313-315.

Hardy, K.R. and K.M. Glover, 1966: Twenty-four hour history of radar angel activity at three wavelengths. Proc. 12th Conf. on Radar Meteor., Am.Meteor.Soc., Boston, 269-274.

LaGrone, A.H. A.P. Deam and G.B. Walker, 1964: Angels, Insects, and Weather. Radio Science, 68D, 895-901.

Miller, K.S. and M.M. Rochwarger, 1972: A covariance approach to spectral moment estimation. IEEE Trans. on Info. Theory, IT-18, 588-596.

Ochs, G.R. and R.S. Lawrence, 1972: Temperature and $C_n{}^2$ profiles measured over land and ocean to 3 km above the surface. NOAA Tech. Rpt. ERL 251-WPL 22, Boulder,CO, 39 pp.

Richter, J.H., 1969: High resolution tropospheric radar sounding. Radio Science, 4, 1261-1268.

Richter, J.H., D.R. Jensen, 1975: Simultaneous acoustic and FM-CW radar observations. Preprints 16th Radar Meteor.Conf., Am.Meteor. Soc., Boston, 282-289.

Saunders, K.W., 1970: CW and FM Radar in Radar Handbook edited by M.I. Skolnik, McGraw-Hill Bk. Co., New York, p 16-1.

Sirmans, D. and R.J. Doviak, 1973: Meteorological radar signal intensity estimation. NOAA Tech. Memo ERL NSSL-64. 80 pp.

Starr, J.R. and D.A. Browning, 1972: Doppler radar measurements of clear air turbulence. Preprints 15th Radar Meteor.Conf., Am.Meteor.Soc., Boston, 248-253.

Strauch, R.G., W.C. Campbell, R.B. Chadwick, K.P. Moran, 1975: FM-CW boundary layer radar with Doppler capability. NOAA Tech Rpt. ERL 329-WPL 39, Boulder, CO

ANALYSIS OF THE RELATIONSHIP BETWEEN LF REFLECTION COEFFICIENTS AND D-REGION PROFILES

R. Michael Jones

In calculating D region electron density profiles from LF reflection coefficient measurements, it is important to order those measurements according to depth of penetration into the ionosphere. A ray theory analysis, a set of full-wave reflection coefficient calculations, and reflection coefficient mesurements support the approximation that those waves with the larger equivalent frequency $f \cos^2 i_0$ (where f is the wave frequency and i_0 is the angle of incidence on the ionosphere) will penetrate further into the ionosphere. This approximation is more accurate for those waves that reflect below the height where the collision frequency equals the gyrofrequency (about 65 km at midlatitudes), where the earth's magnetic field has negligible effect.

Scintillation Correlation at Different Wavelengths

C. L. Rufenach[1]

NOAA/Space Environment Laboratory, Boulder, Colorado 80302

Scintillation cross-correlation coefficients at two radio wavelengths are investigated on the basis of a shallow-modulated phase screen for several different spectral descriptions of the scattering medium. For the relevant simplification, a sufficiently large outer-scale dimension, it is argued that the normalized correlation coefficient is primarily dependent on spectral shape and wavelength separation and is independent of anisotropy and outer-scale dimension. Ionospheric and interplanetary scintillation measurements are compared with this result.

INTRODUCTION

In the past the interpretation of the scintillation cross-correlation coefficients at two different radio wavelengths was based on irregularities in electron density described in terms of a Gaussian wave number spectrum with an outer scale approximately equal to the Fresnel radius (see, e.g., *Budden* [1965]). A Gaussian description is mathematically convenient and, in the absence of other information, was thought to be reasonable. More recently, measurements support a power law variation in spatial wave number, $P_N(\kappa) \propto \kappa^{-\alpha_3}$ with $\alpha_3 \simeq 4$ and a large outer-scale dimension. This description is relevant for both the F region ionosphere [*Rufenach*, 1974] and interplanetary [*Jokipii and Hollweg*, 1970] scintillation.

In the present work the need for a realistic expression for the scintillation correlation coefficient at two wavelengths is recognized. The correlation coefficient is given for several different spectral shapes (Gaussian and power law) of the irregular scattering layer. Those coefficients, based on the shallow-modulated phase screen, are given as closed form expressions.

The coefficient based on a Gaussian shape can be useful in assessing the importance of anisotropy on the scintillation correlation but does not give a realistic description of the wavelength variations. In contrast, this coefficient based on a power law shape can give useful information on the wavelength variation but does not contain information on anisotropy, since a closed form expression for a general power law shape could not be found. However, for the relevant special case, large outer-scale dimension, a closed form expression is available which simplifies the dependence on irregularity parameters. This simplification is used to model the correlation coefficient, which is compared with measurements.

PHASE SCREEN THEORY

Consider a horizontally stratified irregular layer located at a distance z above a flat earth with the plane $z = 0$ at the center of the layer. Let the irregularities be considered a stochastic process described by random electron density fluctuations with zero mean. Furthermore, consider two plane wave fronts at radio wavelength λ_1 and λ_2 incident on the irregular layer with $\lambda_1 > \lambda_2$. Following *Salpeter* [1967] and *Cronyn* [1970], the cross-correlation coefficient of intensity fluctuations between λ_1 and λ_2 at one observing point is

$$\langle I(\lambda_1)I_2(\lambda_2) \rangle \propto \lambda_1\lambda_2 \iint\limits_{-\infty}^{\infty} P_N(\kappa_x, \kappa_y)$$
$$\cdot \sin\left(\frac{\kappa^2\lambda_1 z}{4\pi}\right) \sin\left(\frac{\kappa^2\lambda_2 z}{4\pi}\right) d\kappa_x \, d\kappa_y \quad (1)$$

provided $\langle I^2(\lambda_1) \rangle$ and $\langle I^2(\lambda_2) \rangle$ are sufficiently small, where $P_N(\kappa_x, \kappa_y)$ is the power spectrum of electron density fluctuations, κ_x and κ_y are the spectral wave number components in the x and y directions, and $\kappa^2 = \kappa_x^2 + \kappa_y^2$. A typographic error in Salpeter's (60) is corrected to read κ^2 rather than κ. The normalized cross-correlation coefficient Γ_I is defined as

$$\Gamma_I = \langle I(\lambda_1)I(\lambda_2) \rangle / [\langle I^2(\lambda_1) \rangle \langle I^2(\lambda_2) \rangle]^{1/2} \quad (2)$$

IRREGULARITY DESCRIPTION

The irregularities are considered to be aligned along the magnetic field with a circular cross section. Furthermore, the anisotropy is defined in terms of an effective axial ratio β obtained by rotating the axes in wave number space into a plane normal to the radio path [*Rufenach*, 1975]. The Gaussian and power law spectral forms are then given by

$$P_N(\kappa_x, \kappa_y) \propto \exp\left[-(\kappa_x^2 + \beta^2\kappa_y^2)/\kappa_o^2\right] \quad (3)$$

$$P_N(\kappa_x, \kappa_y) \propto [1 + \kappa_o^{-4}(\kappa_x^2 + \beta^2\kappa_y^2)^2]^{-\alpha_3'/4} \quad (4)$$

where $\kappa_o = 2\pi/L_o$ is the outer-scale wave number, L_o being the outer-scale dimension; $\beta^2 = \cos^2\psi + \alpha^2\sin^2\psi$; ψ is the angle between radio path and magnetic field direction; and α is the axial ratio. The power law variation in (4) was selected in this special form including a spectral cutoff. Under certain conditions this form is amenable to the integration required by the closed form expression in (1).

The spectral features are a constant spectral density for $\kappa' < \kappa_o$, where $\kappa'^2 = \kappa_x^2 + \beta^2\kappa_y^2$, and a monotonically decreasing density for $\kappa' > \kappa_o$. The power law spectrum for $\kappa' < \kappa_o$ in (4), $P_N(\kappa') \propto \kappa'^{-\alpha_3}$, decreases more slowly than the Gaussian spectrum for realistic $\alpha_3 \simeq 4$; therefore the power law irregularities represent more abrupt spatial density changes than the Gaussian spectrum. The power law spectrum corresponds to a one-dimensional spectral index $\alpha_1 \simeq 2$ [*Tatarski*, 1971], in reasonable agreement with reported in situ measurements in the F region ionosphere and interplanetary medium.

MODEL CALCULATIONS

In this section the normalized cross-correlation coefficients Γ_I are developed on the basis of anisotropic spectral shapes

---

[1] Now at NOAA/Ocean Remote Sensing Laboratory, Miami, Florida 33149.

(Gaussian and power law) given by (3) and (4). The closed form results based on power law irregularities are limited to two special cases, $\beta = 1$ for a constant spectral index $\alpha_3 = 4$ and a sufficiently large outer-scale dimension, whereas a general result is available for the Gaussian irregularities. Furthermore, it is shown that $\langle I(\lambda_1)I(\lambda_2)\rangle$ is separable into two factors, one dependent on anisotropy and the other dependent on wavelength provided the outer-scale dimension is sufficiently large. Under this simplification it can be shown that Γ_I is independent of anisotropy.

The normalized cross-correlation coefficient Γ_I based on anisotropic Gaussian irregularities using (1)–(3) and *Gradshteyn and Ryzhik* [1965] is given by

$$\Gamma_I = \{\cos^{1/2}\theta_\Delta \cos^{1/2}\theta_{\Delta\beta} \cos\left[\tfrac{1}{2}(\theta_\Delta + \theta_{\Delta\beta})\right]$$
$$- \cos^{1/2}\theta_\sigma \cos^{1/2}\theta_{\sigma\beta} \cos\left[\tfrac{1}{2}(\theta_\sigma + \theta_{\sigma\beta})\right]\}/\{1$$
$$- \cos^{1/2}\theta_{\sigma+\Delta} \cos^{1/2}\theta_{\sigma\beta+\Delta\beta} \cos\left[\tfrac{1}{2}(\theta_{\sigma+\Delta} + \theta_{\sigma\beta+\Delta\beta})\right]\}^{1/2}$$
$$\cdot \{1 - \cos^{1/2}\theta_{\sigma-\Delta} \cos^{1/2}\theta_{\sigma\beta-\Delta\beta}$$
$$\cdot \cos\left[\tfrac{1}{2}(\theta_{\sigma-\Delta} + \theta_{\sigma\beta-\Delta\beta})\right]\}^{1/2} \qquad (5)$$

where

$$\Delta = \frac{\pi(\lambda_1 - \lambda_2)z}{L_o^2} \qquad \sigma = \frac{\pi(\lambda_1 + \lambda_2)z}{L_o^2}$$

$$\tan\theta_\Delta = \Delta \qquad\qquad \tan\theta_{\Delta\beta} = \Delta/\beta^2$$
$$\tan\theta_\sigma = \sigma \qquad\qquad \tan\theta_{\sigma\beta} = \sigma/\beta^2$$
$$\tan\theta_{\sigma+\Delta} = \sigma + \Delta \qquad \tan\theta_{\sigma\beta+\Delta\beta} = (\sigma+\Delta)/\beta^2$$
$$\tan\theta_{\sigma-\Delta} = \sigma - \Delta \qquad \tan\theta_{\sigma\beta-\Delta\beta} = (\sigma-\Delta)/\beta^2$$

The numerator in (5), which is proportional to $\langle I(\lambda_1)I(\lambda_2)\rangle$, reduces to the β dependence given by *Briggs and Parkin* [1963]:

$$\langle I^2(\lambda_1)\rangle \propto 1 - \cos^{1/2}\theta_\sigma$$
$$\cdot \cos^{1/2}\theta_{\sigma\beta} \cos\tfrac{1}{2}(\theta_\sigma + \theta_{\sigma\beta}) \qquad \lambda_1 = \lambda_2$$

The variation of Γ_I based on the anisotropic Gaussian irregularities from (5) is illustrated in Figure 1 for several wavelength separations and effective axial ratios. The abscissa is a measure of the distance below the irregular layer; the near field corresponds to $L_o^2 \gg \pi\lambda_o z$, whereas the far field corresponds to $L_o^2 \ll \pi\lambda_o z$, where λ_o is the geometric mean between λ_1 and λ_2, $\Delta\lambda/\bar{\lambda}_o$ is the normalized wavelength separation, and $\bar{\lambda}_o$ is the arithmetic mean. The variation of Γ_I in Figure 1 illustrates several interesting features:

1. The cross-correlation coefficient Γ_I is dependent on the radio wavelength separation, the angle of incidence, and the physical properties of the irregularities including the abruptness of the density fluctuations (spectral shape), axial ratio, and outer-scale dimension. The dependence on axial ratio and angle of incidence is included in the β dependence. Changes in Γ_I are most pronounced for $\Delta\lambda/\bar{\lambda}_o > 20\%$ and $L_o^2 \gtrsim \pi\lambda_o z$.

2. The cross-correlation coefficient Γ_I is essentially independent of β and approximately equal to 1 for all $\Delta\lambda/\bar{\lambda}_o$ provided $L_o^2 \gg \pi\lambda_o z$.

No closed form expression could be found for Γ_I based on the anisotropic power law form in (4). Two simplifications were considered in an attempt to obtain a closed form expression. First, the irregularities are considered isotropic, $\beta = 1$,
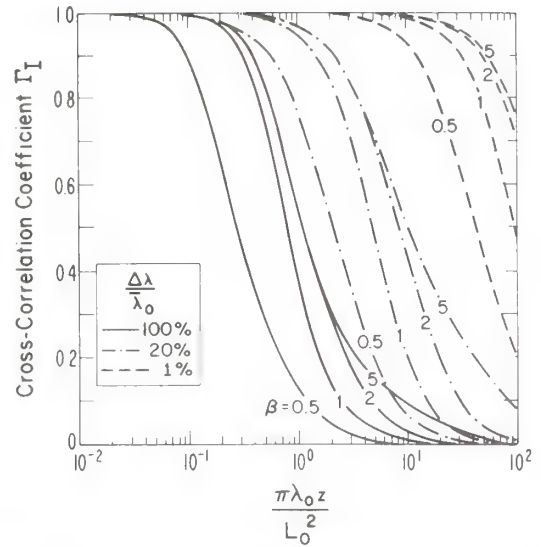
Fig. 1. Model calculations of cross-correlation coefficient based on anisotropic Gaussian irregularities. The abscissa is a measure of the distance below the irregular layer (near and far field). L_o is the outer-scale dimension, and $\Delta\lambda/\lambda_o$ is the normalized wavelength separation, where $\Delta\lambda = \lambda_1 - \lambda_2$, $\bar{\lambda}_o = (\lambda_1 + \lambda_2)/2$, and $\lambda_o = (\lambda_1\lambda_2)^{1/2}$.

with a constant spectral index $\alpha_3 = 4$, which by using (1), (2), and (4) and *Gradshteyn and Ryzhik* [1965] yields

$$\Gamma_I = \frac{\exp(-\Delta) - \exp(-\sigma)}{[1 - \exp(-\Delta - \sigma)]^{1/2}[1 - \exp(\Delta - \sigma)]^{1/2}} \qquad (6)$$

This expression allows the comparison of Γ_I based on isotropic Gaussian and power law irregularities as given in Figure 2. The differences in Γ_I for Gaussian and power law irregularities clearly show the dependence of Γ_I on spectral shape.

The large differences in Γ_I for the relevant approximation,
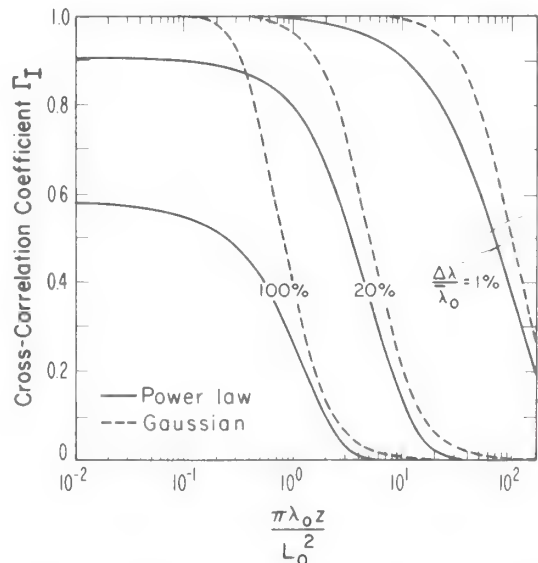
Fig. 2. Model comparison of cross-correlation coefficients based on isotropic power law and Gaussian irregularities. The special form for the power law spectrum includes a spectral cutoff and constant spectral index $\alpha_3 = 4$.

$L_o{}^2 \gg \pi\lambda_o z$, suggest that further investigation of this approximation is required. For a sufficiently large outer scale and substitution of either (3) or (4) into (1) it can be shown that

$$\langle I(\lambda_1)I(\lambda_2)\rangle \propto F(\sigma, \Delta)f(\beta) \qquad (7)$$

where $F(\sigma, \Delta)$ is dependent on λ_1 and λ_2 and $f(\beta)$ is dependent on anisotropy. Therefore for $\lambda_1 = \lambda_2$, $\langle I^2(\lambda_1)\rangle = \langle I^2(\lambda_2)\rangle \propto f(\beta)$, and it follows that Γ_I is independent of anisotropy. For example, substituting the power law irregularities in (4) into (1) with $\kappa_x = \kappa \cos\theta$ and $\kappa_y = \kappa \sin\theta$ and assuming $L_o{}^2 \gg \pi\lambda_i z/[1 + (\beta^2 - 1)\sin^2\theta]$, where $i = 1, 2$, we have [Gradshteyn and Ryzhik, 1965]

$$F(\sigma, \Delta) = \Delta^{(\alpha_3-2)/2} - \sigma^{(\alpha_3-2)/2} \qquad (8)$$

$$f(\beta) = \frac{1}{2\pi}\int_0^{2\pi}[1 + (\beta^2 - 1)\sin^2\theta]^{-\alpha_3/2}\,d\theta \qquad (9)$$

Following a similar procedure for the Gaussian irregularities, we have

$$F(\sigma, \Delta) = \sigma^2 - \Delta^2 \qquad (10)$$

$$f(\beta) = \frac{1}{8\beta^4}(3\beta^4 + 2\beta^2 + 3) \qquad (11)$$

Indeed, even though a closed form expression for the anisotropy based on the power law form could not be found, it is not needed, since the normalized cross-correlation coefficient is independent of anisotropy. Furthermore, the relevant expression for this coefficient can be given in a slightly different form:

$$\Gamma_I = \left(\frac{\lambda_o}{\bar{\lambda}_o}\right)^{(2-\alpha_3)/2}\left[1 - \left(\frac{\Delta\lambda}{2\bar{\lambda}_o}\right)^{(\alpha_3-2)/2}\right] \qquad (12)$$

A further simplification is available if we assume $\lambda_o \simeq \bar{\lambda}_o$, which is reasonable provided $\Delta\lambda/\bar{\lambda}_o \gtrsim 1.4$:

$$\Gamma_I \simeq \left[1 - \left(\frac{\Delta\lambda}{2\bar{\lambda}_o}\right)^{(\alpha_3-2)/2}\right] \qquad (13)$$

which gives the cross-correlation coefficient in terms of the wavelength separation and spectral index as illustrated in Figure 3. The principal result is that a flatter spectral shape, smaller α_3, is associated with smaller cross-correlation coefficients. For the purpose of the present work, (12) and (13) are considered the most useful representation of Γ_I and hence will be compared with measurements in the following section.

DISCUSSION

Measurements of the cross-correlation coefficients have been extensively reported by using ionospheric scintillation signals, while only limited measurements are available for interplanetary scintillation. The correlation coefficient for the ionospheric measurements varies over a wide range for results at similar wavelength separations (see discussion of Aarons et al. [1967]). The cause of these large variations is not well understood; however, one likely explanation is a possible strong dependence on scintillation level. Other possibilities are changes in spectral shape and the effects of an inner-scale dimension, which is important when it is approximately equal to the Fresnel radius. The theory in the present work is based on small scintillation levels and neglects the effects of the inner scale. In practice, comparison of measurements at wide wavelength separations with theory may be difficult, since wide
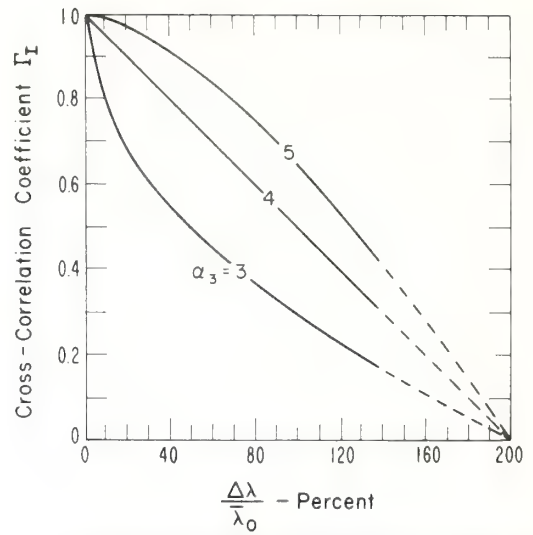
Fig. 3   Model calculations of cross-correlation coefficient based on a power law spectrum with an infinite outer-scale dimension and a variable spectral index α_3.

separations usually produce large scintillation levels at the longer wavelength, which is not covered by the theory in the present work.

The simplified model used here describes the correlation coefficients for ionospheric scintillation signals caused by F region irregularities generally considered to be aligned along the magnetic field lines and for interplanetary scintillation signals caused by irregularities usually considered isotropic or nearly isotropic. Two radio-stellar scintillation measurements, ionospheric [Aarons et al., 1966] and interplanetary [Little et al., 1966], were selected as the measurements most likely associated with small scintillation levels.

The measured cross-correlation coefficients Γ_I are compared with the model results of (13). These results, based on Γ_I independent of β, are given in Table 1, which illustrates that the model-deduced α_3 values are in reasonable agreement with direct in situ measurements. Small deviations of Γ_I may be caused by statistical fluctuations in measured values. Therefore the measurements of the cross-correlation coefficient should include some measure of the statistical error limits.

Although the measurements of the cross-correlation coefficient alone yield limited information about the irregularities, measurements of this coefficient in conjunction with a full autospectral and cross-spectral analysis could lead to a more comprehensive understanding of the wave propagation effects and hence a better description of the irregularities.

TABLE 1.   Comparison of Model Parameters With Measured Cross-Correlation Coefficients

Source	Measured Γ_I	λ_o, m	$\Delta\lambda$ $\bar{\lambda}_o$	α_3
Interplanetary scintillation at 81.5 and 178 MHz [Little et al., 1966]	(0.5) 0.65 (0.8)	2.49	0.74	(3.5) 4 (5)
Ionospheric scintillation at 113 and 228 MHz [Aarons et al., 1967]	(0.5) 0.7 (0.9)	1.87	0.68	(3.3) 4.2 (>5)

Parentheses indicate estimates of the upper and lower bounds for the coefficient.

CONCLUSIONS

Cross-correlation models of scintillation show a strong dependence on radio wavelength separation and the physical properties of the scattering medium. Furthermore, these expressions, based on a shallow-modulated phase screen, show that the outer-scale dimension and anisotropy are less important provided the outer-scale dimension is sufficiently large if the normalized cross-correlation coefficient is considered. The measurements of this coefficient could be especially useful in conjunction with other available methods such as autospectral and cross-spectral analysis in inferring information about the scattering medium.

REFERENCES

Aarons, J., R. S. Allen, and T. J. Elkins, Frequency dependence of radio star scintillation, *J. Geophys. Res.*, *72*, 2891, 1967.

Briggs, B. H., and I. A. Parkin, On the variation of radio star and satellite scintillations with zenith angle, *J. Atmos. Terr. Phys.*, *25*, 339, 1963.

Budden, K. G., The theory of the correlation of amplitude fluctuations of radio signals at two frequencies, simultaneously scattered by the ionosphere, *J. Atmos. Terr. Phys.*, *27*, 883, 1965.

Cronyn, W. M., The analysis of radio scattering and space probe observations of small-scale structure in the interplanetary medium, *Astrophys. J.*, *161*, 755, 1970.

Gradshteyn, I. S., and I. M. Ryzhik, *Tables of Integrals, Series and Products*, pp. 415, 421, 490, Academic, New York, 1965.

Jokipii, J. R., and J. V. Hollweg, Interplanetary scintillation and the structure of the solar wind fluctuations, *Astrophys. J.*, *160*, 745, 1970.

Little, L. T., A. Hewish, and P. A. Dennison, Correlation of interplanetary scintillation at different frequencies, *Planet. Space Sci.*, *14*, 1221, 1966.

Rufenach, C. L., Wavelength dependence of radio scintillation: Ionosphere and interplanetary irregularities, *J. Geophys. Res.*, *79*(10), 1562, 1974.

Rufenach, C. L., Ionospheric scintillation by a random phase screen: Spectral approach, *Radio Sci.*, *10*(2), 155–165, 1975.

Salpeter, E. E., Interplanetary scintillation, 1, Theory, *Astrophys. J.*, *147*, 433, 1967.

Tatarski, V. I., *The Effects of the Turbulent Atmosphere on Wave Propagation*, translated from Russian by Israel Program for Scientific Translations, pp. 25, Nat. Tech. Inform. Serv., U.S. Dep. of Commer., Springfield, Va., 1971

MICROWAVE FM-CW DOPPLER RADAR
FOR
BOUNDARY LAYER PROBING

R. G. Strauch, W. C. Campbell, R. B. Chadwick and K. P. Moran

NOAA/ERL/Wave Progagation Laboratory
Boulder, Colorado 80302

Abstract. A microwave FM-CW radar can obtain the complete spectrum of radial velocities of both precipitation particles and refractive-index fluctuations in the optically clear air. Heretofore the extraction of the Doppler spectrum from this type of radar was believed to be a formidable, if not impossible, task. We have implemented a Doppler processing technique that uses a data acquisition system developed for pulsed Doppler radar. We present Doppler spectra obtained with a zenith-pointing FM-CW radar that demonstrate this new capability. In addition to the strong refractive-index layers observed by the FM-CW radar in the optically clear air, there is evidence that scattering from a background continuum of C_n^2 can be detected when a Doppler operating mode is employed.

High resolution probing of the atmosphere with a microwave FM-CW radar was first demonstrated by Richter [1969]. The FM-CW radar, normally operated in a zenith-pointing mode, has been used as a boundary layer probe to detect clear air refractive-index fluctuations with a range (height) resolution of less than 2 m [Richter, 1969; Gossard et al., 1970a; Bean et al., 1971; Richter et al., 1973]. Clear air radar echoes in the boundary layer are usually found in layers, often with wavelike structure [Gossard and Richter, 1970b; Gossard et al., 1971, 1972]. Radar reflectivity for scattering from turbulent fluctuations in refractive-index is given by $\eta = 0.38$ $C_n^2 \, \lambda^{-1/3}$ [Ottersten, 1969] for homogeneous isotropic turbulence where C_n^2 is the radio refractive-index structure constant and λ is the radar wavelength. The original motivation for adding Doppler processing to the FM-CW radar was to obtain data that would reveal the role that wind shear may play in the production of turbulence associated with scattering layers.

Although the frequency of the detected signal depends on both range and velocity for an FM-CM radar, the complete Doppler velocity spectrum can be measured in each range resolution cell by measuring the change in phase of the signal from sweep-to-sweep. The Doppler velocity spectrum is measured from the radar signal obtained during many sweeps, whereas the power spectrum of the signal obtained during each sweep is measured for conventional FM-CW data processing. Doppler processing has been used with FM-CW radars that measure sea state [Barrick, 1973] but these radars, operating at HF, transmit signals whose phase repeats from sweep-to-sweep, thereby enabling the phase changes of the return signal to

be measured. The transmitted signal for microwave FM-CW radars, obtained from YIG-tuned transistor oscillators, is not phase coherent from sweep-to-sweep. However, the time delay (range) between transmitted and received signals is only a few tens of microseconds for boundary layer probing, so the signal phase at the output of the homodyne detection system is sufficiently coherent from sweep-to-sweep. Therefore, the same processing technique used for the HF radar data can be used for microwave FM-CW radars [Strauch, et al., 1975].

Doppler processing can be accomplished in a variety of ways that offer flexibility in range and velocity resolution. The particular way presented here provides 33 contiguous range-resolution elements, from 0 to a selectable maximum range. Thirty-one of the range cells have 33 velocity resolution increments, from 0 to plus or minus a selectable maximum velocity. The first and last range increments have 17 velocity resolution elements, and the sign of the velocity is not resolved in these range cells; i.e., the negative velocity portion of the spectrum is folded onto the positive portion. An arbitrary number of velocity spectra can be averaged, thereby reducing the variance of the estimate of each spectral density value.

Velocity spectra of falling raindrops and the height profile of fall speeds measured with a zenith-pointing FM-CW Doppler radar are shown in Figure 1. The data were acquired with a coherent integration time, T_c, of 0.034 sec (data window for a single spectrum consisting of 32 sweeps) and an averaging time, T_A, of 1.7 sec (averaging 50 spectra); the entire data sample was acquired in 10 sec (T_0). The velocity profile (Fig. 1a) is a profile of the mode of the averaged velocity spectrum. Figure 1a shows the fall speed profile with a height resolution of 32 m. The heights shown are above ground level (AGL), with the radar located at 1500 m MSL. The melting layer [Battan, 1973, p. 194] is indicated by the change in fall speed between 740 and 930 m AGL. Figure 1b is a plot of the 33 power spectral density values measured in the height interval 224 to 256 n. Ground clutter appears at the zero velocity spectral point (in the middle of the spectrum) and, because of the width of the spectral window, also appears at the two adjacent velocity points. For the sweep parameters used in this data sample, the interval of unambiguous velocity is ± 8 m sec^{-1} and the velocity distribution is not completely encompassed by this interval. The velocity spectrum is therefore partly folded, and for the data processing scheme used here, the folded portion of the spectrum appears in adja-

Rainfall
5-12-75
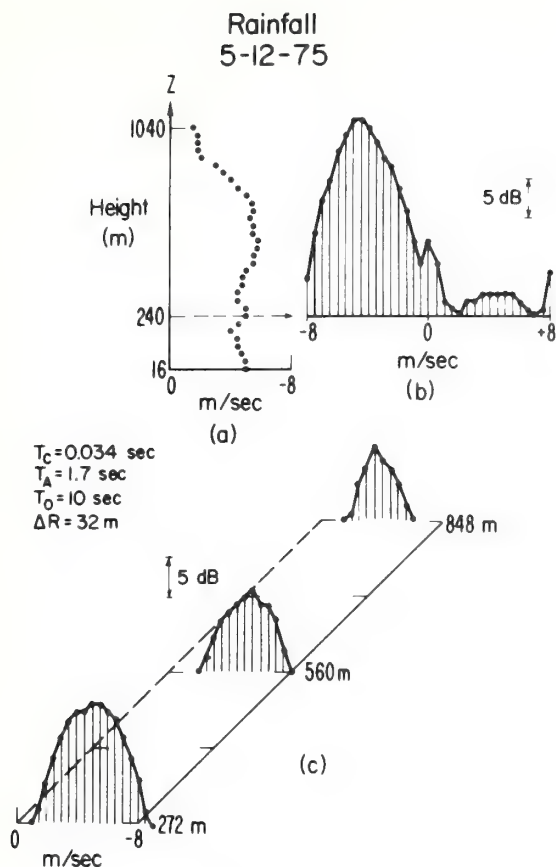
Figure 1. (a) Modal fall speeds of raindrops measured with FM-CW Doppler radar. (b) Averaged velocity spectrum in height interval 235-257 m. (c) Sample Doppler spectra after applying threshold.

cent range cells. One technique used to estimate the moments of the spectrum in the presence of noise is to discard all spectral values below a threshold level and compute the moments based on the remaining spectral points. Figure 1c shows the spectral density at three height intervals after a threshold level has been subtracted.

Figure 2 (a-c) illustrates results obtained with the FM Doppler radar when a strong atmospheric refractive-index scattering layer was observed in the optically clear air. The data were acquired prior to the onset of convective mixing to minimize the contamination of the atmospheric scattering layer by insects or particles such as seeds. The radar antennas were zenith-pointing so the mean radial (vertical) velocity was approximately zero. Figure 2a shows the radar reflectivity measured before and after the FM-CW Doppler velocity measurements on 29 June 1975. The background intensity setting of the display oscilloscope was reduced so that only the strongest returns were observed. Figure 2b shows the Doppler spectra measured in the scattering layer. The averaging time was 3.6 sec, and the total observation time was 15 sec. In Figure 2a the radar reflectivity of the atmo-

spheric scattering layer is much stronger than that of other targets (probably insects), indicating a large C_n^2. Large C_n^2 values may often be associated with relatively strong mechanical turbulence so spectral widths of several m sec^{-1}, as in Figure 2b, may be characteristic of scattering from the strong refractive-index fluctuations found in layers. Figure 2c shows spectra measured from scattering at altitudes below the strong layer but much higher than the minimum observable altitude. These spectra were measured at the same time as those shown in Fig. 2b. In Figure 2c ground clutter, detected through the antenna sidelobes, is the dominant feature. It appears at zero velocity and the two adjacent spectral points. The spectra measured at the height interval near 198 m and 254 m can be attributed solely to ground clutter, but the spectra at 367.5 and 424 m altitudes result from ground clutter and clear air returns with near-zero velocity. Since Figure 2a does not reveal anything about the spatial or temporal structure of reflectivity at these altitudes, it was necessary to examine multiple profiles of the spectra to insure that the signals were not caused by insects. Ground clutter, even in moderate winds, was always confined to the three spectral points at and adjacent to zero velocity.

6-29-75
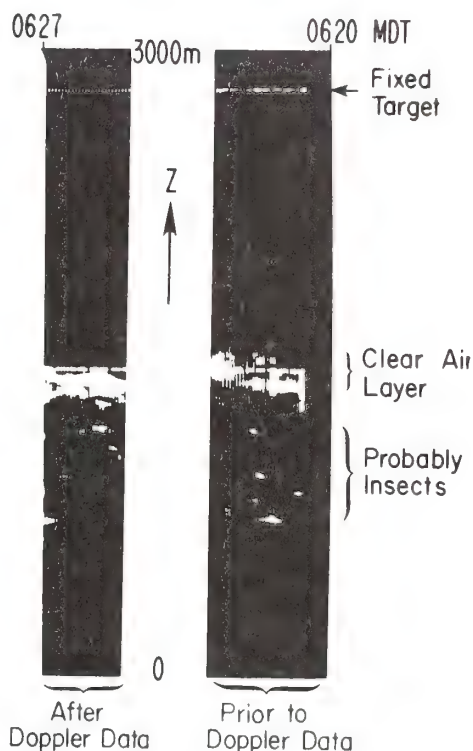
Figure 2a. Radar scattering intensity from refractive-index fluctuations in a strong scattering layer.

163
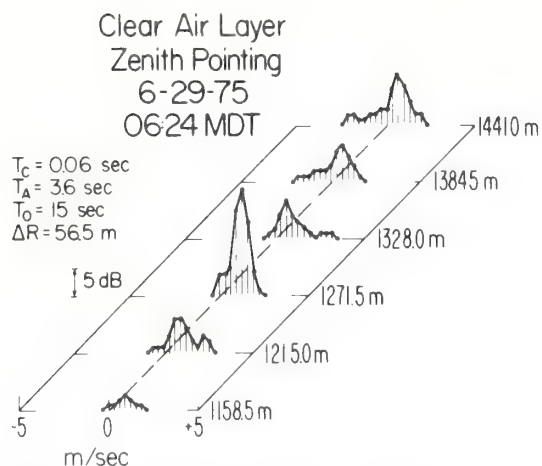
Figure 2b. Doppler spectra of clear air return from a scattering layer (vertical velocity).

Figure 3. Doppler spectra measured in a region where atmospheric signals were not observed by the FM-CW radar without Doppler processing.

Another early morning test was conducted on 30 June when a strong scattering layer, similar to that shown in Figure 2a, was observed near 1300 m altitude. The spectra measured at the scattering layer (not shown) are similar to those in Figure 2b. The spectra in Figure 3 show refractive-index scattering either from a second layer that was much weaker than the layer at 1300 m, or from nonlayered or background refractive-index fluctuations. The signal spectra from this second region are only partially masked by the strong ground clutter. The signal spectra were spatially continuous with a 56.5 m range resolution and were also temporally continuous for several minutes during Doppler data recording. If these returns were not associated with a layered structure whose height or radar reflectivity factor changes with time, it would be very difficult to detect them with a data processing system

that measures only the intensity of the radar signal. Backscatter that does not change in time or height would not be distinguishable from ground clutter. Doppler processing enables us to detect refractive-index scattering much weaker than the ground clutter.

The FM-CW radar, heretofore used primarily to observe qualitatively the structure of atmospheric layers with large C_n^2, should find additional meteorological applications because it can measure Doppler velocity spectra. It may prove very useful in wind measurements in the boundary layer, particularly if Doppler processing enables us to detect weak atmospheric signals that cannot be detected by radar systems that measure only the scattered intensity.

References

Barrick, D. E., FM-CW radar signals and digital processing, NOAA TR ERL 283-WPL 26, U.S. Dept. of Commerce, Boulder, Colo., 1973.

Battan, L. J., Radar observations of the atmosphere, Univ. of Chicago Press, Chicago, 1973.

Bean, B. R., R. W. McGavin, R. B. Chadwick, and B. D. Warner, Preliminary results of utilizing the high resolution FM radar as a boundary-layer probe, Boundary-Layer Meteor., 1, 466-473, 1971.

Gossard, E. E., J. H. Richter, and D. Atlas, Internal waves in the atmosphere from high-resolution radar measurements, J. Geophys. Res., 75, 3523-3536, 1970a.

Gossard, E. E., and J. H. Richter, The shape of internal waves of finite amplitude from high-resolution radar sounding of the lower atmosphere, J. Atmos. Sci., 27, 971-973, 1970b.

E. E. Gossard, D. R. Jensen, and J. H. Richter, An analytical study of tropospheric structure as seen by high-resolution radar, J. Atmos. Sci., 28, 794-807, 1971.

E. E. Gossard, J. H. Richter and D. R. Jensen, Effect of wind shear on atmospheric wave instabilities revealed by FM-CW radar observations, Boundary-Layer Meteor., 4, 113-131, 1972.

Figure 2c. Sample Doppler spectra measured below the scattering layer. Spectra at 198 and 254 m are caused solely by ground clutter.

Ottersten, H., Radar backscattering from the
     turbulent clear atmosphere, Radio Sci., 4,
     1251-1255, 1969.
Richter, J. H., High resolution tropospheric
     radar sounding, Radio Sci., 4, 1260-1268,
     1969.
Richter, J. H., D. R. Jensen, R. A. Pappert, and
     V. R. Noonkester, New developments in FM-CW
     radar sounding, Boundary-Layer Meteor., 4,
     179-200, 1973.

Strauch, R. G., W. C. Campbell, R. B. Chadwick,
     and K. P. Moran, FM-CW boundary layer radar
     with Doppler capability, NOAA TR ERL 329-WPL
     39, U.S. Dept. of Commerce, Boulder, Colo.,
     1975.

MEASUREMENT CAPABILITIES OF FM-CW DOPPLER RADARS

R. G. Strauch and R. B. Chadwick
NOAA/ERL/Wave Propagation Laboratory
Boulder, Colorado 80302

1.   INTRODUCTION

FM-CW radars have been used for high resolution measurements of the radar reflectivity of the optically clear air since Richter (1969) first demonstrated the technique. The primary utilization of FM-CW radar has been in qualitatively portraying the structure of radar reflectivity. Frequently the radar returns in optically clear air show wave motions and these waves have been studied extensively [Gossard et al. 1970a; Gossard and Richter, 1970b; Gossard et al. 1971, 1972]. It was widely believed that extracting the Doppler velocity spectrum of distributed targets with this type of radar was a formidable task because the signal frequency depends on both target range and target velocity. However, the phase of the signal obtained from repetitive sweeps of the transmitted frequency depends only on target velocity and the Doppler spectrum is readily obtained by power spectrum analysis. We have implemented Doppler processing on an FM-CW radar [Strauch et al. 1975] and have demonstrated the applicability of FM-CW Doppler radar for measurements of the Doppler spectrum of hydrometeor scattering as well as radar scattering from the optically clear air [Strauch et al. 1976]. In this paper the measurement properties of FM-CW Doppler radars are discussed and comparisons are made with the more familiar pulse Doppler radar.

2.   THE RADAR AMBIGUITY FUNCTION

The measurement properties of a radar waveform can be described by the ambiguity function [Deley, 1970]. The ambiguity function for the FM-CW radar waveform without Doppler processing is that of a single linear FM ("chirp") pulse (Fig. 1) and is given by [Deley, 1970]:

$$\chi_1(\delta,\phi) = \frac{e^{j\pi\delta\phi} \sin[\pi(B/T\delta+\phi)(T-|\delta|)]}{\pi(B/T\delta+\phi)} \, \text{rect}[\delta/2T]. \quad (1)$$

T is the sweep duration, B is the sweep bandwidth, δ is the time variable, ϕ is the frequency variable, and rect[x] is 1 if $|x| < 1/2$ and is 0 if $|x| > 1/2$. A 3-dimensional plot of the magnitude of this function shows the radar response to targets with time delays (ranges) and frequency shifts (velocities) that differ from those of the target of interest at $\delta = \phi = 0$.
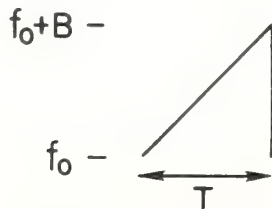
Figure 1. Transmitted signal of an FM-CW radar without Doppler processing. f_0 is the transmitted frequency at the start of the sweep and B is the sweep width.

Fig. 2 shows a top view of the magnitude of χ_1. The dark area represents the region where targets with different velocities and ranges cannot be resolved. The axis of this area is the line $B/T \delta + \phi = 0$ which can be written $V = -(\lambda B/cT)R$ where λ is the radar wavelength, c is the velocity of propagation, V is the target velocity and R is the target range, with R and V relative to the target of interest. Typical sweep parameters for the boundary layer FM-CW radar without Doppler are T = 0.05 s and B = 100 mHz so the axis of the ambiguity area is V = -2/3 R where R is in m and V is in m/s. Thus there is no simultaneous range and velocity discrimination for meteorological scatterers.
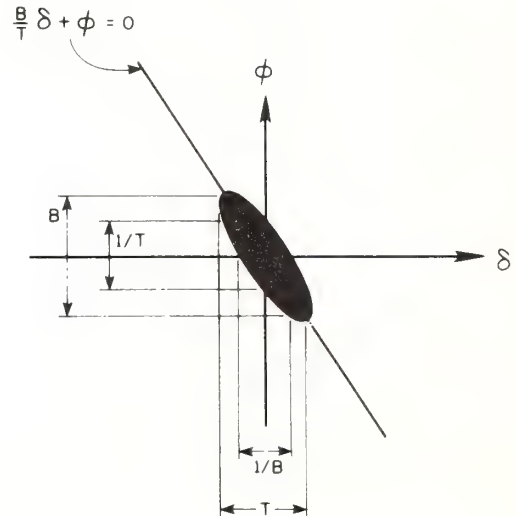
Figure 2. Central peak of the magnitude of the ambiguity function for FM-CW radar without Doppler processing.

The FM-CW Doppler radar utilizes a repetitive sweep as illustrated in Fig. 3. The ambiguity function for this transmitted waveform is given by [Deley, 1970]:

$$\chi(\delta,\phi) = e^{j n \pi \phi T'} \chi_1(\delta-nT',\phi) \frac{\sin[(N-|n|)(\pi\phi T')]}{N \sin(\pi\phi T')} \quad (2)$$

for $|\delta-nT'| \leq T$, n = -(N-1) ..., 0, ... (N-1), and zero elsewhere. T' is the repetition period and N is the number of sweeps used in the signal processing. The peaks of the magnitude of this ambiguity function are shown in Fig. 4. Equation (2) is valid for T' $\geq$ 2T but the peaks of the ambiguity function are the same as those shown in Fig. 4 when a sawtooth sweep (T'=T) is used.

The range ambiguities for the FM-CW radar with repetitive sweeps occur with a spacing of cT'/2 and the velocity ambiguities are spaced
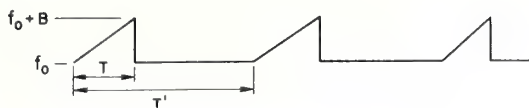
Figure 3. Transmitted signal of an FM-CW Doppler radar.
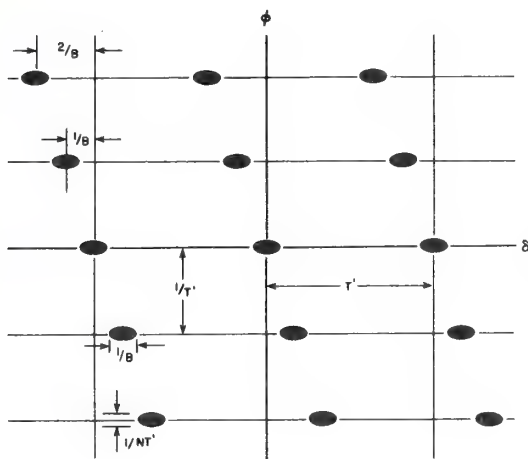
Figure 4. Peaks of the magnitude of the ambiguity function of an FM-CW Doppler radar.

by $\lambda/2T'$. The frequency resolution is $1/NT'$ or the velocity resolution is $\lambda/2NT'$. The time resolution is $1/B$ or the range resolution is $c/2B$. The range resolution is the same as that for a single sweep. Fig. 4 shows that the range and velocity measurement properties of the FM-CW Doppler radar are essentially the same as those of a pulse Doppler radar with one exception: targets whose velocity exceeds the maximum unambiguous velocity (V_m) appear in an adjacent range resolution cell with an FM-CW radar, whereas with a pulse radar the velocity spectrum folds at the same maximum velocity but the target remains in the same range resolution cell. With either type of radar we need additional information such as that provided by spatial or temporal continuity to resolve the folding. There are no practical differences in the problems encountered in resolving ambiguities with either type of radar. Thus, an FM-CW Doppler radar with sweep bandwidth B and sweep repetition time T' will have essentially the same measurement properties as that of a pulse Doppler radar with pulse width $\tau = 1/B$ and pulse repetition time T'.

A basic limitation with both pulse Doppler and FM-CW Doppler is that the product of the maximum unambiguous range and the maximum unambiguous velocity is $R_m V_m = \pm c\lambda/8$ or constant for a given radar. For this reason, neither radar technique can be applied to acoustic sounders or laser probes. A 2 kHz acoustic sounder has a value of $R_m V_m$ of only 5.6 m^2/s, and this product is 18.76 m^2/s for a visible laser. A CO_2 laser

has a $R_m V_m$ product of 375 m^2/s and thus would be useful only for extremely short ranges. The acoustic and laser systems must therefore measure the Doppler spectrum from the return of a single pulse. The velocity resolution and range resolution cannot be chosen independently when the velocity spectrum is measured with a single pulse. The range resolution is directly proportional to the pulse width while the frequency (velocity) resolution is inversely proportional to pulse width. This tradeoff leads to acceptable parameters for acoustic sounders, but pulse Doppler laser systems have thus far found limited atmospheric use. Although the FM-CW Doppler technique cannot be applied to acoustic or laser systems, non-Doppler FM-CW radar techniques may prove to be useful in both types of atmospheric probes.

3.   PROCESSING FM-CW DOPPLER RADAR SIGNAL

The technique used to measure the Doppler velocity spectrum of each range resolution cell of an FM-CW radar involves spectral analysis of the signal obtained from N consecutive sweeps rather than the signal from a single sweep as for conventional FM-CW radar. A complete description of the data processing is given by Strauch et al. (1975), but a simple explanation is available by considering the form of the output voltage of the receiver.

Fig. 5 shows the receiver output voltage for two stationary targets. In the top trace the target range is such that the period of signal frequency is an exact multiple of the sawtooth sweep repetition time (T). The signal is a continuous sinusoid except at the start of each sweep where the local oscillator has started a new sweep while the signal still corresponds to the previous sweep. (A short high frequency pulse occurs and a low pass filter at the mixer output causes a brief transient to occur at the start of each sweep.) In the lower trace the range is arbitrary so the period of the signal frequency is not a harmonic of $1/T$. In both cases however, the signal is repetitive with period T. Therefore, the power spectral density is zero except at harmonics of $1/T$. Note that the power spectrum of a single sweep (as used in conventional FM-CW data processing) is continuous with a $(\sin x)/x$ envelope but with repetitive sweeps the power spectrum of a single target is discrete. The power spectrum of the signal shown in the top trace of Fig. 5 consists of a single line at $f = 3/T$ (neglecting retrace effects) while the signal shown in the lower trace contains power at $f = 3/T$ as well as other harmonics. The important point to note is that all stationary targets (including ground clutter) will appear in the power spectrum at harmonics of $1/T$.

Fig. 6 shows the receiver output for a moving target. The phase of the signal changes from sweep to sweep because the range is changing. The rate of phase change is the radian Doppler frequency. The power spectrum of this signal is therefore that of a stationary target that has been frequency translated by the Doppler shift as shown in Fig. 7. Velocity away from the radar causes a translation to higher frequencies and velocity toward the radar translates the spectrum in the direction of decreasing range or lower

30

167
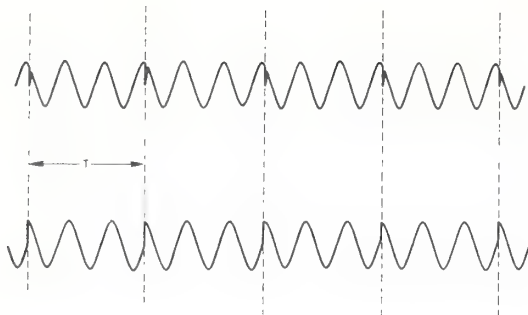
Figure 5. *Output voltage of an FM-CW Doppler radar receiver for stationary targets. Top trace shows a target at a range $R_3 = 3c/2B$. Bottom trace shows a target at an arbitrary range near R_3.*

Figure 6. *Output voltage of an FM-CW radar receiver for a moving target.*
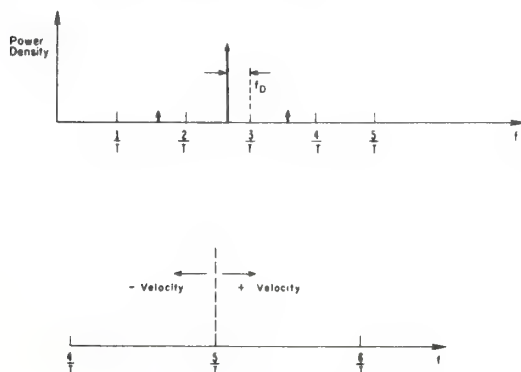
Figure 7. *Power spectrum of the output signal of an FM-CW Doppler radar.*

frequencies. The power spectral density plot is therefore a range and velocity map, with ground clutter appearing at harmonics of 1/T and moving targets at other frequencies. Each harmonic of 1/T corresponds to a range resolution cell. Moving targets in a particular range resolution cell appear in the power spectrum at frequencies near the corresponding harmonic of 1/T. It is readily seen that the maximum Doppler frequency shift that can be measured unambiguously is 1/2T because at that frequency it is not possible to determine which range resolution cell the signal corresponds to. The spectrum folds into adjacent range cells as predicted by the ambiguity function.

4. CONCLUSION

The FM-CW Doppler radar can measure the Doppler velocity spectrum of meteorological scatterers (hydrometeors and clear air) with the same resolution and ambiguities as a pulse Doppler radar whose transmitted signal bandwidth and repetition rate are the same as the FM-CW radar. The choice of which type of radar to use for a given problem must be made on considerations other than velocity measurement capability. Some advantages of FM-CW Doppler radar compared with pulse Doppler radar are the very short (< 30 m) minimum range, the exceptionally good range resolution (< 10 m), and the selectable range resolution. Typically, it is more versatile and less expensive than pulse Doppler radars capable of clear air wind measurements.

There are also disadvantages of FM-CW radars. Data processing of FM-CW Doppler data is analogous to spectral processing of pulse Doppler data. There is (as of this time) no method available for estimating the moments of the Doppler spectrum for FM-CW Doppler signals without spectral processing whereas pulse Doppler signals do not require spectral analysis to obtain moment estimates. A second disadvantage of FM-CW Doppler radar is the dual antenna system. For a given total aperture the angular resolution is better with a pulse Doppler radar. Therefore, while the FM-CW Doppler radar can be used for a variety of research problems, its primary applications are those requiring low cost, short range, and good range resolution. It should be viewed not as a replacement for pulse Doppler radar but rather as a complement to it.

5. REFERENCES

Deley, G. W., Waveform Design, *Radar Handbook* Chap. 3, M. Skolnik, Editor, McGraw Hill, New York, 1970.

Gossard, E. E., J. H. Richter, and D. Atlas, Internal waves in the atmosphere from high-resolution radar measurements, *J. Geophys. Res.*, 75, 3523-3536, 1970a.

Gossard, E. E., and J. H. Richter, The shape of internal waves of finite amplitude from high-resolution radar sounding of the lower atmosphere, *J. Atmos. Sci.*, 27, 971-973, 1970b.

Gossard, E. E., D. R. Jensen, and J. H. Richter, An analytical study of tropospheric structure as seen by high-resolution radar, *J. Atmos. Sci.*, 28, 794-807, 1971.

Gossard, E. E., J. H. Richter and D. R. Jensen, Effect of wind shear on atmospheric wave instabilities revealed by FM-CW radar observations, *Boundary-Layer Meteorol.*, 4, 113-131, 1972.

Richter, J. H., High resolution tropospheric radar sounding, *Radio Sci.*, 4, 1260-1268, 1969.

Strauch, R. G., W. C. Campbell, R. B. Chadwick, and K. P. Moran, FM-CW boundary layer radar with Doppler capability, NOAA TR ERL 329-WPL 39, U.S. Dept. of Commerce, Boulder, Colo., 1975.

31

Strauch, R. G., W. C. Campbell, R. B. Chadwick,
and K. P. Moran, Microwave FM-CW Doppler
radar for boundary layer probing, *Geophys.
Res. Let.*, <u>3</u>, 193-196, 1976.

32

APPLICATION OF STATISTICAL INVERSION TO

GROUND-BASED MICROWAVE REMOTE SENSING

OF TEMPERATURE AND WATER

VAPOR PROFILES

E. R. Westwater and M. T. Decker
NOAA/ERL/Wave Propagation Laboratory

*Surface-based observations of downwelling microwave ther-
mal emission are related to temperature and humidity profiles
via a standard integral equation of radiative transfer. Both
in clear and in cloudy atmospheres, statistical inversion
techniques can be used to retrieve profiles from a data vector
of brightness observations and surface meteorological con-
straints. For the clear case, we illustrate accuracy pre-
dictions and profile retrievals for (a) single-frequency
angular-scanned data, (b) multi-frequency angular scanned data,
and (c) multi-frequency zenith data. For case (c) we compare
predicted and achieved accuracies in a recently conducted
joint NOAA-JPL radiometric experiment. Finally, we present
retrievals of cloud-contaminated radiometric data.*

I. INTRODUCTION

The continuous measurement of temperature and humidity in the
Earth's boundary layer is an important requirement in some areas
of meteorological research. Ground-based microwave radiometric
measurements of temperature structure show promise of meeting this
need and the technique has been investigated by several groups
(Refs. 1, 2, 3, and 4). Limited information on the moisture pro-
file is also radiometrically available (Refs. 5 and 6).

In this review, we outline the application of statistical

inversion methods to a few of the increasingly complex measuring techniques that have evolved over the years. For each method, statistical inversion appears capable of extracting maximum information from the measurements.

The extent to which inversion theory applies to a problem depends strongly on the solution of the direct problem; i.e., given the profile, can we calculate the measurements to within the experimental accuracy? We therefore spend some time discussing the accuracies of microwave thermal emission calculations.

We then review temperature retrieval results from single- and multiple-frequency angular scanning radiometers. Finally, we conclude with recent results in multi-frequency sensing of temperature and moisture profiles.

II. MICROWAVE ATTENUATION AND EMISSION IN CLEAR AND CLOUDY ATMOSPHERES

Measurements of microwave radiant power are commonly expressed as an equivalent black body temperature, or brightness temperature, T_b. Except during rain, atmospheric scattering is small relative to absorption. For a nonscattering atmosphere in local thermodynamic equilibrium, the downward brightness temperature at frequency ν is given by

$$T_b(\nu) = T_b^{(ext)} \tau_\nu + \int_0^\infty T \alpha_\nu \exp\left(- \int_0^S \alpha_\nu(s')ds'\right)ds \qquad (1)$$

where T is absolute temperature (K), α_ν is absorption coefficient (km^{-1}), $T_b^{(ext)}$ is brightness temperature external to the Earth's atmosphere (K), τ_ν is transmission through the atmosphere, and s is path length from the receiver to emitting volume (km). In the troposphere, microwave absorption is due principally to molecular resonances of O_2 (60 GHz) and H_2O (22 GHz) and to clouds and rain. In general, the absorption is a strong function of composition and a weak function of temperature. Thus, around 22 GHz, the emission varies principally because of variations in water concentration,

whereas at 60 GHz, the emission from the well-mixed constituent O_2 depends mainly on temperature. For ground-based applications, the term $T_b^{(ext)}$ describes discrete external sources, such as the Sun or Moon, and the continuum "big bang" contribution of 2.9 K. Calculations of the microwave absorption coefficient are shown in Fig. 1.

A. Water Vapor Attenuation

Water vapor attenuation arises from the rotational transition at 22.235 GHz and the nonresonant contribution of submillimeter and infrared lines. At frequencies below 100 GHz, the spectrum is the sum of a resonant term and a contribution from the higher fre- quency lines that varies as ν^2. An excellent summary and dis- cussion of the theoretical experimental basis of water vapor atten- uation calculations are given by Waters (Ref. 7).
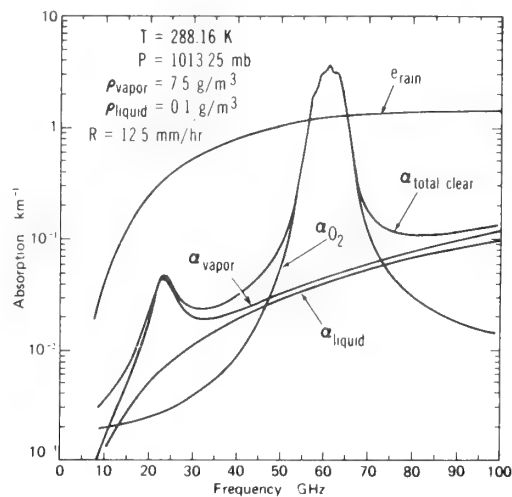
Fig. 1. Microwave atmospheric absorption in clear air, clouds, and rain. α = absorption coefficient, e = attenuation coefficient. (1 bar = 100 kPa)

172

For remote sensing of water and temperature, we must accurately calculate water vapor emission and attenuation from profiles of meteorological variables. Since several equations to calculate vapor attenuation exist in the literature (Ref. 7), we thought that a comparison of more recent models in brightness calculations would be at least suggestive of the accuracy to which the clear air direct problem is solved in the 20-35 GHz band. Thus, we present, in Table 1, comparisons of calculations of brightness temperature for five selected radiosonde profiles. The calculations labeled BA used constants derived by least squares from the absorption data of Becker and Autler (Ref. 8); L labels calculations using constants derived by Liebe (Ref. 9) using dispersion spectroscopy; finally W labels the results using parameters given by Waters (Ref. 7). BA and L assume the Van Vleck-Weisskopf line shape; W uses that of Gross-Zhevakin-Naumov. When compared with radiometric accuracies that approach 1 K, the agreement is not completely satisfactory, especially for the profiles with larger water content. If one accepts the more recent results (L and W), the agreement is within 5%.

B. Oxygen Attenuation

Beginning with the classic theoretical paper by Van Vleck (Ref. 10) on microwave absorption by molecular O_2, a large amount of theoretical, laboratory, and atmospheric research has been devoted to the understanding of attenuation from this constituent. As a consequence, the knowledge of O_2 absorption parameters and of related pressure broadening theory has steadily increased. Two recent advances are of note. The first is the development of the dispersion spectroscopy technique by Liebe and its application to the determination of the spectroscopic parameters of O_2 (Ref. 11). The second is Rosenkranz's (Ref. 12) theoretical attenuation model which accounts for overlapping lines in the oxygen complex.

As in the previous case of water vapor, we wanted to

TABLE 1

*Comparison of Calculated Zenith Brightness
Temperatures at 22 and 31 GHz Resulting
from Various Choices of Spectral
Line Parameters*

Pro-file	Liquid water content	22.235 GHz			31.65 GHz		
		BA	L	W	BA	L	W
1	0.8	23.4	22.3	21.4	14.7	15.0	14.5
2	1.1	28.6	27.2	26.1	16.5	16.9	16.3
3	1.3	31.1	31.5	30.1	18.1	18.5	17.7
4	2.8	68.2	64.5	61.5	29.0	30.1	28.3
5	3.6	74.9	70.8	67.5	31.2	32.4	30.4

determine the degree to which contemporary absorption models agreed
with each other. To this end, we performed calculations of zenith
brightness using three absorption models: the first (RMC) used
the Van Vleck-Weisskopf line shape with constants given by Reber,
Mitchell and Carter (Ref. 13); the second (R) used Rosenkranz's
(Ref. 12) line shape and the constants given in his paper; the
third (L) used Liebe's measurements (Ref. 11), the Rosenkranz line
shape, and Rosenkranz's value of the non-resonant line width. The
results are shown in Table 2.

There is close agreement between all three models at 53.8 and
55.5 GHz and R and L agree well also at 52.8 GHz. The difference
between RMC and the other two at the most transparent channel,
52.85 GHz, is almost constant ($\approx$ 4.2 K) and occurs primarily
because of the difference in absorption prediction in the pressure
range 100-500 mb.

C. Comparison of Clear Air Emission Measurement and Calculations

Five-channel microwave observations were taken at Pt. Mugu,
California and were kindly provided by B. Gary and N. Yamane of

174

TABLE 2

Comparison of Calculated Zenith Brightness
Temperatures (K) in the Oxygen Band
Resulting from Various
Absorption Models

Pro-file	52.85 GHz			53.85 GHz			55.45 GHz		
	RMC	R	L	RMC	R	L	RMC	R	L
1	194.8	190.6	191.3	251.2	250.8	251.2	281.5	281.6	281.7
2	191.5	187.2	187.7	250.7	250.3	250.6	280.8	281.0	281.0
3	193.8	189.6	190.0	257.0	256.8	256.9	289.7	289.8	289.9
4	190.6	186.3	187.0	248.3	248.0	248.4	278.7	278.9	278.9
5	189.9	185.5	186.0	252.4	252.1	252.4	287.4	287.6	287.6

Jet Propulsion Laboratory (JPL). Their radiometer was similar to
the SCAMS system used on the Nimbus 6 satellite (Ref. 14). During
the three-week period of observations, thrice-a-day radiosondes
obtained standard meteorological soundings of temperature, pres-
sure, and humidity. Calculations of brightness temperature were
made by using the constants of Becker-Autler for water vapor, and
those of Liebe for O_2. The comparison of measurements and cal-
culations are shown in Table 3. Considering the difficulties in
making absolute radiometric measurements and in observing the same
volume of air with radiosonde and radiometer, the agreement in the
O_2 band is quite good. Note, however, the relatively large vari-
ance at the 22 and 31 GHz channels. Because of the difficulty in
obtaining reliable direct measurements of humidity profiles by
radiosondes (Refs. 15 and 16), these differences may not be caused
by incorrect absorption coefficients.

D. Attenuation by Clouds and Rain

Attenuation from a distribution of spherical particles of known
dielectric properties can be calculated by classical electromag-
netic theory. Depending on the ratio of particle size to

TABLE 3

Average and Root-Mean-Square (rms) Differences
(K) between Measured and Calculated
Brightness Temperatures
(N = 24 Radiosonde
Observations)

Frequency (GHz)

Difference	22.234	31.65	52.85	53.85	55.45
Average	2.5	1.7	0.2	0.1	-1.3
Root-mean-square	3.4	1.8	1.8	0.8	1.4
Percent	12.6	11.2	0.9	0.3	0.5

wavelength, simplicity or complexity prevails. In the domain here this ratio is small, called the Rayleigh region, attenuation is independent of size distribution and is directly proportional to total mass of droplets. In addition, scattering is negligible relative to absorption. For large particles, Mie theory must be used, and attenuation depends on size distribution in both absorption and scattering. For our purposes, we will consider water clouds with modal radii less than 50 μm to be in the Rayleigh region for frequencies less than 100 GHz. Calculations of water absorption for a cloud liquid water content of $\rho_{liquid} = 0.1$ g/m^3 are shown in Fig. 1. Depending on the frequency, spherical ice particles absorb from one to two orders of magnitude less than an equivalent amount of water.

In contrast to nonprecipitating clouds, rain (and hail) both scatters and absorbs microwave energy. The attenuation coefficient e must be calculated from Mie theory for both absorption and scattering coefficients. Calculations of e for a moderate rain of 12.5 mm/hr are also shown in Fig. 1. We assumed a Laws and Parsons (Ref. 17) size distribution for this rain rate (liquid) water content = 0.6 g/m^3). It is clear that rain dominates all other sources of attenuation except in the vicinity of the oxygen complex.

The atmospheric thermal emission spectrum in the presence of a cloud can differ considerably from that obtained under clear conditions. In detail, the amount of contrast depends on the height profiles of temperature, humidity, and liquid content. However, the largest contribution to the difference is the liquid thickness with the emission being relatively insensitive to the height and geometric thickness of the cloud (Ref. 18). Table 4 shows estimated rms differences between clear and cloudy brightness temperatures for the July climatology of Pt. Mugu, California. These differences clearly show the need for cloud correction. Similar calculations for ocean climatologies indicated rms differences about twice as large as those of Table 4.

III. STATISTICAL INVERSION OF GROUND-BASED MICROWAVE RADIOMETER DATA TO RECOVER VERTICAL TEMPERATURE PROFILES

Minimum-variance statistical inversion is used to estimate a parameter vector $\underset{\sim}{p}$ from a data vector $\underset{\sim}{d}$ according to the well-known prescription

$$\hat{\underset{\sim}{p}} = <\underset{\sim}{p}> + <\underset{\sim}{p}'\ \underset{\sim}{d}'^{T}> <\underset{\sim}{d}'\ \underset{\sim}{d}'^{T}>^{-1}\underset{\sim}{d}' \tag{2}$$

In Eq. (2), $\hat{\underset{\sim}{p}}$ is the estimator of $\underset{\sim}{p}$, $<\cdot>$ refers to ensemble averages over joint distributions of $\underset{\sim}{p}$ and $\underset{\sim}{d}$, and primes denote

TABLE 4

Rms Differences between Clear and Cloudy
Zenith Brightness Temperatures

Frequency, GHz	Rms difference, K
22.235	3.6
31.65	7.6
52.85	6.4
53.85	2.0
55.45	0.1

departures from mean values. The assumptions and derivations leading to this equation are given by Rodgers (Ref. 19). The covariance matrix of this estimate, $S_{p-\hat{p}}$, is given by

$$S_{p-\hat{p}} \equiv \langle (p - \hat{p})(p - \hat{p})^T \rangle = \langle p' \ p'^T \rangle -$$

$$\langle p' \ d'^T \rangle \ \langle d' \ d'^T \rangle^{-1} \ \langle d' \ p'^T \rangle, \tag{3}$$

The ith diagonal element of $S_{p-\hat{p}}$ represents the residual variance of the estimate of the ith parameter and is a direct measure of solution quality. If p represents a discretized profile of some variable, then the matrix trace of $S_{p-\hat{p}}$ is a useful measure of overall solution quality. Here p usually represents vertical temperature or humidity profiles at a sufficiently dense set of height coordinates, and d is some function of observed brightness temperatures.

The application of these equations to ground-based (g.b.) sensing of meteorological profiles differs in several respects from the corresponding satellite retrieval problem:

(a) Satellite retrievals use *a priori* statistics appropriate to a latitudinal region; a ground-based application requires only single-station statistics. Consequently, the *a priori* variance of the g.b. ensemble is usually much less than that used for satellites.

(b) For the g.b. problem, direct observations of the desired profile at the surface can usually be obtained. This can be imposed as an exact constraint on the inferred profile, which, in addition, further reduces the *a priori* variance at all levels, since we are now averaging over an ensemble with fixed surface conditions.

(c) A practical consequence of (a) and (b) is that linear methods are frequently appropriate, because of the relatively small variation about the initial guess profile.

A.   Temperature Sensing by Inversion of Single-Channel Angular-
     Scanned Radiometric Data

     Initially, ground-based temperature sensing was attempted by
fixed-frequency angular scanning methods (Refs. 1,20, and 21). A
typical set of weighting functions is shown in Fig. 2. Although
these weighting functions attain their maxima at the surface,
linear combinations of them can be made to peak at various alti-
tudes yielding a spatial resolution that degrades with altitude
(Ref. 3).

     Weighting functions give the system response to a delta-
function input; another meaningful system characterization is the
total variance of the observations, and its partitioning into the
contributions from all relevant meteorological variables. An
example of this analysis is shown in Fig. 3, in which partial
variances in T_b from fluctuations in temperature, relative humidity,
and pressure are shown as a function of elevation angle. Although
this channel is in the O_2 band, the fluctuations due to humidity
exceed those from temperature for angles greater than 20°.
The reduction in "noise" due to surface constraints is shown in
Fig. 4, where, in particular, the variance in T_b due to pressure
fluctuations is reduced to almost zero. However, the contamination
of the temperature "signal" due to the humidity "noise" is still
extensive and really requires a water channel for its removal.

     As mentioned earlier, the diagonal elements of $S_{T-\hat{T}}$ are a
measure of solution quality. Plots of the square roots of these
diagonal elements as a function of altitude indicate the expected
standard deviation of the solution over an ensemble of profiles.
An example of this type of plot is Fig. 5, which shows theoretical
retrieval accuracy for several choices of operating frequency for
the August climatology of Salt Lake City, Utah. These calculations
predict an accuracy of somewhat better than 1 K up to 3 km in
altitude. Retrieval of profiles from radiometric data (clear
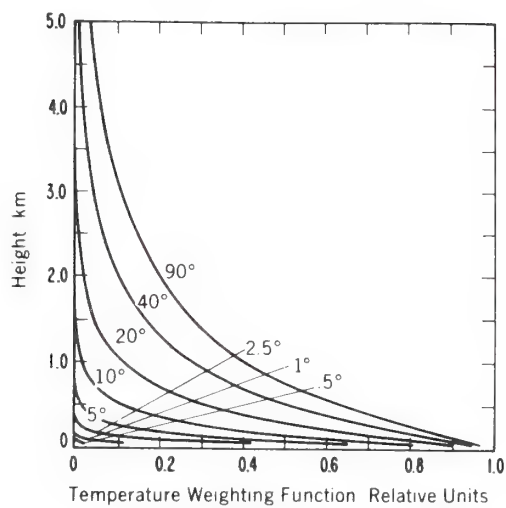
Fig. 2.   Temperature weighting functions for ground-based angular scanning at 54.5 GHz.
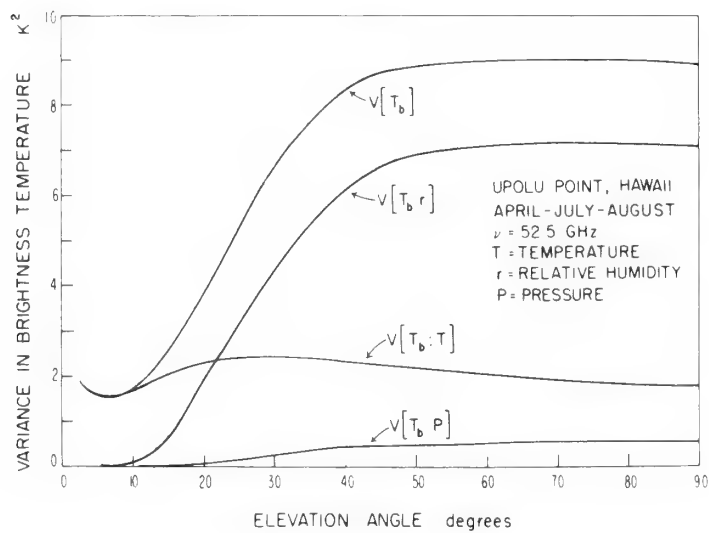
Fig. 3.   Contribution to fluctuations in brightness tempera-ture at 52.5 GHz from temperature, humidity, and pressure.
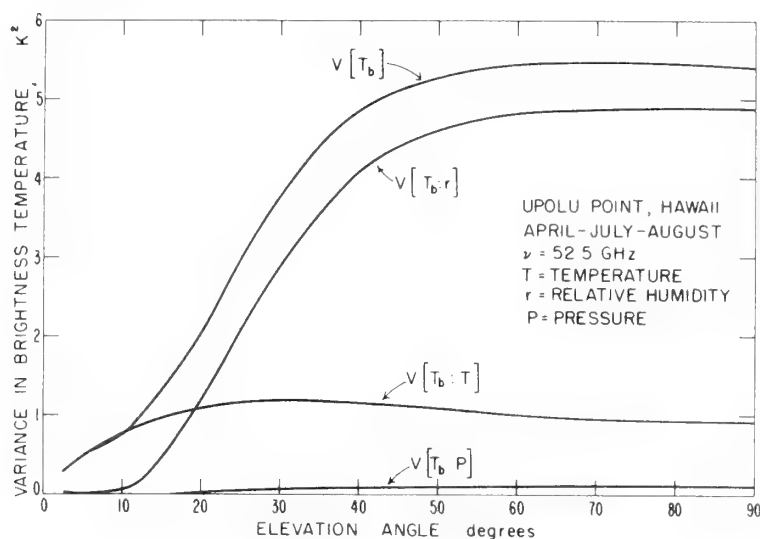
*Fig. 4. Contribution to fluctuations in brightness tempera-
ture at 52.5 GHz from temperature, humidity, and pressure.
Constrained surface conditions.*

skies only) gave accuracies very close to these predictions (Ref.
21). Examples of profile recoveries from single-channel angular
scan data are given in Figs. 6 and 7.

B. Temperature Sensing by Inversion of Multi-Spectral Angular-
    Scanned Radiometric Data

    Although the simplicity of a single-frequency angular-
scanning radiometer is attractive, scanning with a multi-channel
system can significantly improve retrieval accuracy (Ref. 22). An
example of the amount of improvement can be seen in Fig. 8 in which
theoretical retrieval accuracy for several systems is shown as a
function of altitude. Table 5 gives an explanation of the spec-
tral combinations of Fig. 8; combination 1A refers to experi-
mental noise level of 0.1 K and represents somewhat of a practical
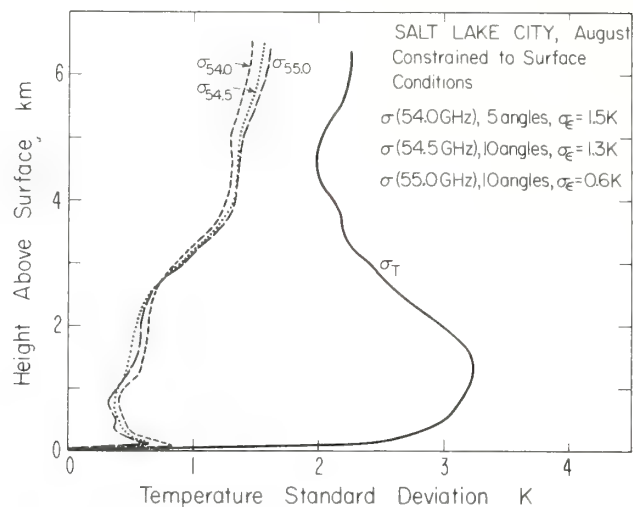
Fig. 5. Theoretical accuracy in retrieving vertical temperature profiles by inversion of single-frequency angular scanned radiometer data. σ_ε = *assumed instrument noise level.* σ_T = *a priori standard deviation for fixed surface conditions.*
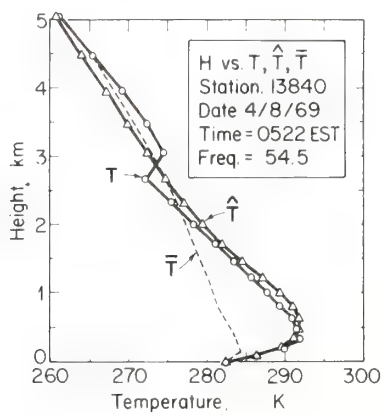
Fig. 6. Temperature profile derived from single-frequency angular scanned radiometer data at Cincinnati, Ohio. A priori statistics from Dayton, Ohio. T = *radiosonde profile.* $\bar{T}$ = *mean profile for constrained surface conditions.* $\hat{T}$ = *inferred profile.*
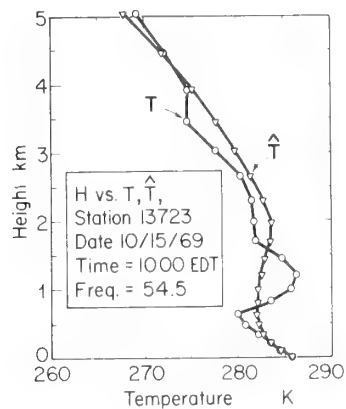
Fig. 7. *Temperature profile derived from single-frequency*
angular scanned radiometer data at Raleigh-Durham, North Carolina.
A priori statistics from Greensborough, North Carolina – radiosonde
profile. *T = inferred profile.*

TABLE 5

Explanation of Spectral Combinations
Employed to Estimate Temperature
Profiles

| | Input data | |
Combination	Elevation angle (deg)	Frequency (GHz)
1	5	54.5, 55.5
	10	54.5, 55.5
	15	54.5, 55.5
	30	53.5, 54.5, 55.5
	60	52.5, 53.5, 54.5
	90	52.5, 53.5, 54.5
2	90	52.5, 53.5, 54.5, 55.5

183
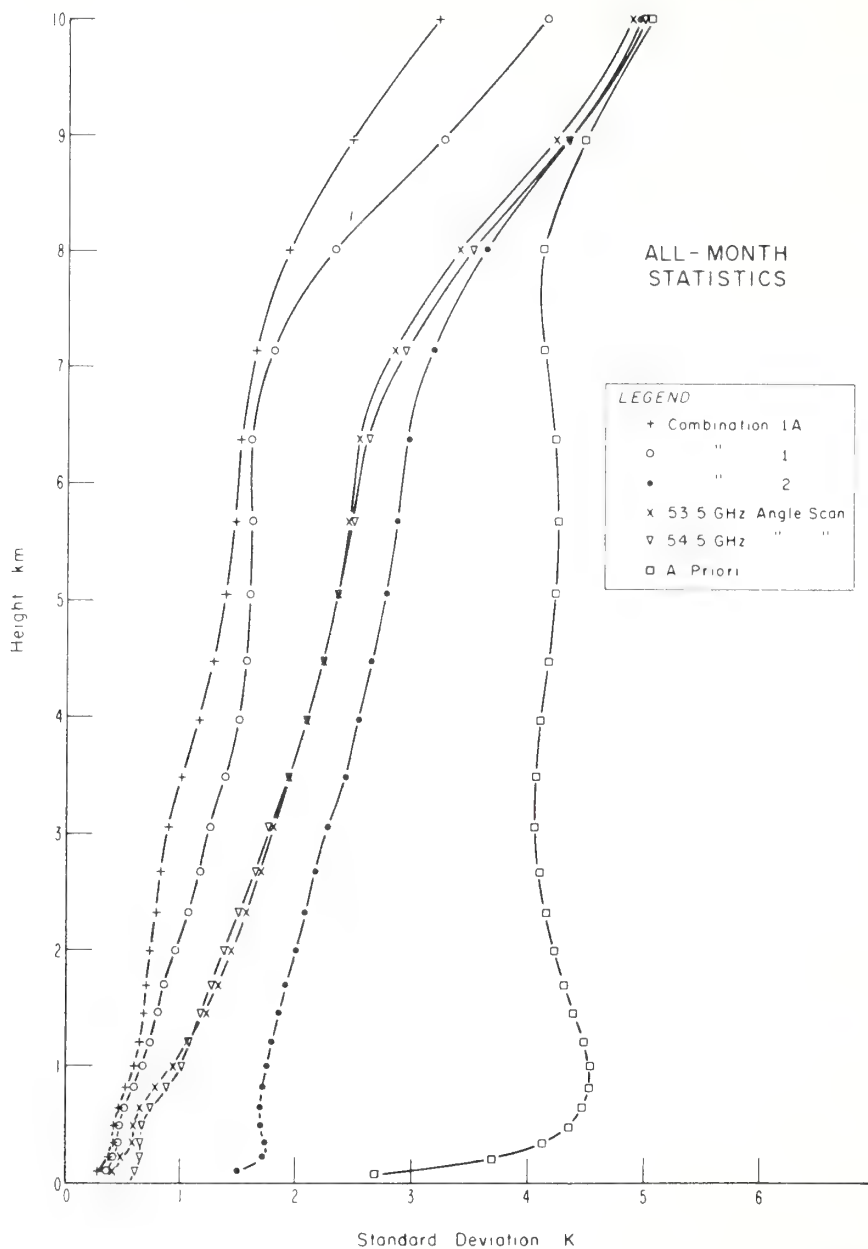
Fig. 8.   Theoretical accuracy in retrieving vertical temper-
ature profiles from various combinations of multi-spectral multi-
angle radiometer data,   Denver, Colorado (after Ref. 20).

limit in measurement accuracy; the noise levels in other combina-
tions were obtained from comparison of measurements and calcula-
tions of brightness temperature. The multi-spectral angular-scan
combination 1 improves the retrieval accuracy over the single-
frequency scans by a margin of about two to one.

Typical examples of the low-altitude temperature structure
that can be recovered is shown in Figs. 9, 10, and 11, which show
retrievals of a low altitude elevated inversion, a ground-based
inversion, and a low-level super-adiabatic profile. Note espe-
cially the improvement in the recovery of the elevated inversion
over the single-frequency result of Fig. 7.

IV.   RECENT RESULTS IN INVERSION OF GROUND-BASED MULTI-SPECTRAL
RADIOMETRIC DATA TO INFER TEMPERATURE
AND HUMIDITY PROFILES

We are currently investigating the feasibility of sensing of
temperature profiles from an ocean data buoy-mounted radiometer.
Because of buoy motion, the previously discussed angular scanning
techniques are not practical; in addition, the cloud problem dic-
tates the need for two moisture channels to sense and to correct
for clouds. Cloud correction algorithms appropriate for microwave
passing sensing have been published by Westwater, et al.,
Rosenkranz, et al., and Fowler, et al. (Refs. 18, 23, and 24).

The National Weather Service desires that the temperature of
layers, 100 mb in thickness, be determined with accuracy ± 1 K.
Although temperatures of the lowest two layers could be useful,
retrievals to 500 mb are wanted. Predictions for ocean clima-
tologies, using Eq. (3), showed that under clear conditions, a
three-frequency zenith looking radiometer could meet the lower
altitude requirements and could be reasonably close to those at
the higher altitudes (Ref. 18). Accuracy predictions are shown
in Fig. 12 for several systems under consideration; the tempera-
ture weighting functions for system C are shown in Fig. 13.
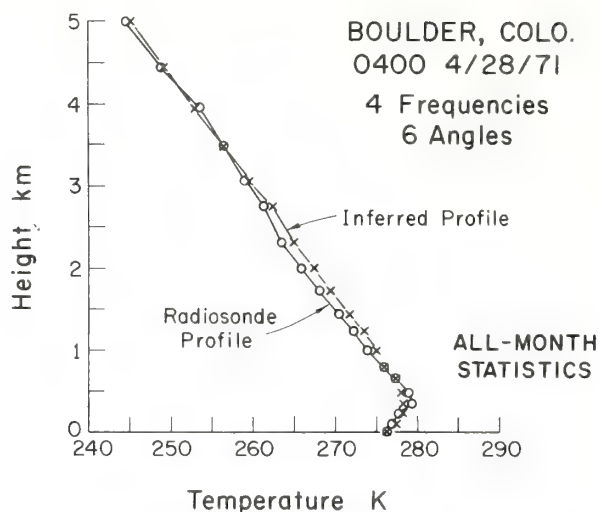
Fig. 9.   Inferred and radiosonde temperature profiles from
multi-spectral multi-angle radiometer data for 0400, April 28,
1971.   A priori statistics from Denver, Colorado.   (After Ref. 20.)
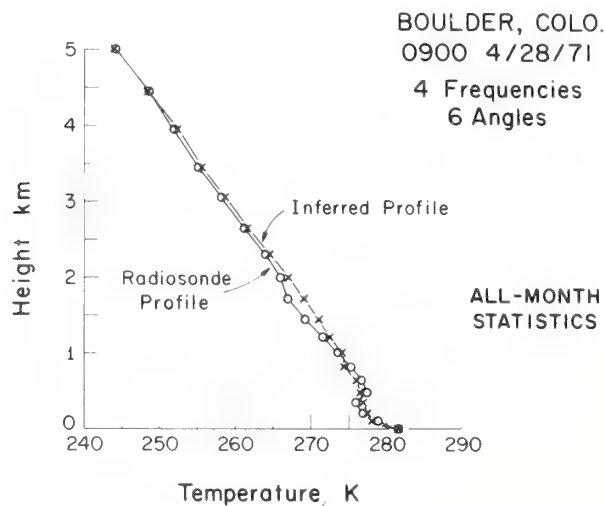
Fig. 10.   Inferred and radiosonde temperature profiles from
multi-spectral multi-angle radiometer data for 0900, April 28,
1971.

186
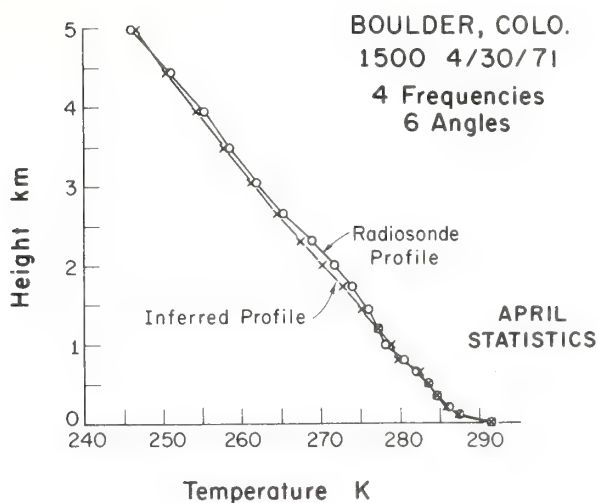
Fig. 11. *Inferred and radiosonde temperature profiles from multi-spectral multi-angle radiometer data for 1500, April 30, 1971.*
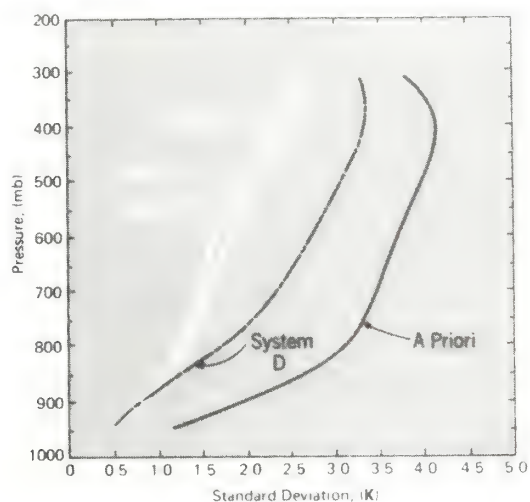
Fig. 12. *Comparison of several radiometric systems in retrieving temperature layers of 100-mb thickness during clear conditions at ocean climatologies. Five-station rms average. Instrumental error = 0.5K. Systems: A(52.8, 55.4, 58.8, 20.6, 31.65 GHz); B(54.0, 55.4, 58.8, 20.6, 31.65 GHz); C(52.8, 54.0, 55.4, 20.6, 31.65 GHz); D(55.4, 58.8 GHz).*
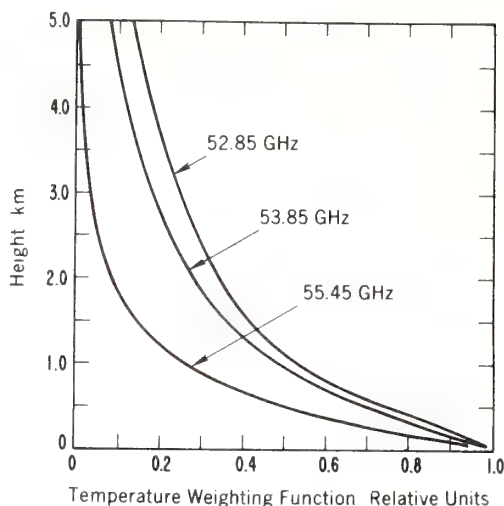
Fig. 13.   Temperature weighting functions for ground-based sensing by SCAMS radiometer.

As mentioned in Section II.D, both the 52.85 GHz and the 53.85 GHz channels require cloud correction. The results shown in Fig. 14 indicate that with the addition of the two water correcting channels, and with a careful choice of frequency in the O_2 band, retrieval accuracies approaching those in clear air can be obtained. On the basis of the calculations shown in Figs. 12 and 14, the radiometric system C (SCAMS) was chosen for experimental verification of the temperature sensing capability of the buoy-based system.

The experimental program to confirm the theoretical predictions is being conducted jointly by National Oceanic and Atmospheric Administration (NOAA) and the Jet Propulsion Laboratory. During a three-week measurement period in March 1976, at Point Mugu, California, 21 suitable radiometer-radiosonde observations were obtained. Although some of the data were taken when there were visual observations of clouds, the radiometrically estimated liquid content was less than 0.02 mm; hence, the clear air retrieval
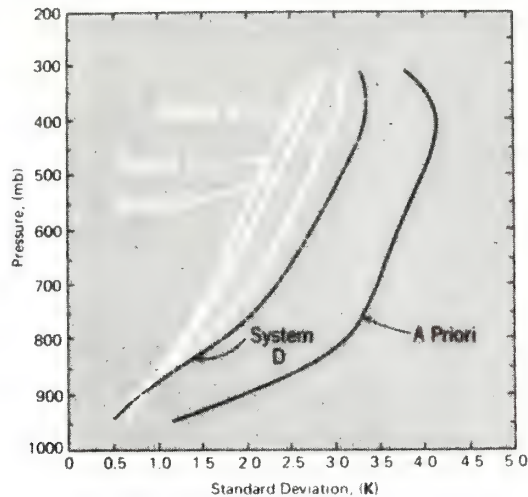
Fig. 14. Comparison of several radiometric systems in retrieving temperature layers of 100-mb thickness during cloudy conditions (liquid thickness < 4 mm H_2O). Five-station rms average. Instrumental error - 0.5 K. Systems: A(52.8, 55.4, 58.8, 20.6, 31.65 GHz); B(54.0, 55.4, 58.8, 20.6, 31.65 GHz); C(52.8, 54.0, 55.4, 20.6, 31.65 GHz); D(55.4, 58.8 GHz).

algorithms were used exclusively. The *a priori* data base was two years of twice daily soundings during February, March and April, taken in 1973-1974. The statistical summary of experiment results are compared with *a priori* predictions in Fig. 15. Although the observed variability of the 21 profiles about the three-month *a priori* is somewhat greater than the theoretical average, the achieved retrieval accuracies are in close agreement with predictions. It is somewhat unusual that theory predicts (a) no reduction in variance at about 750 mb above the surface, and (b) a modest reduction in variance above this level. The experiment results confirm this prediction.

Low resolution information on the water vapor distribution is also contained in the five-channel measurements. Typical water

189
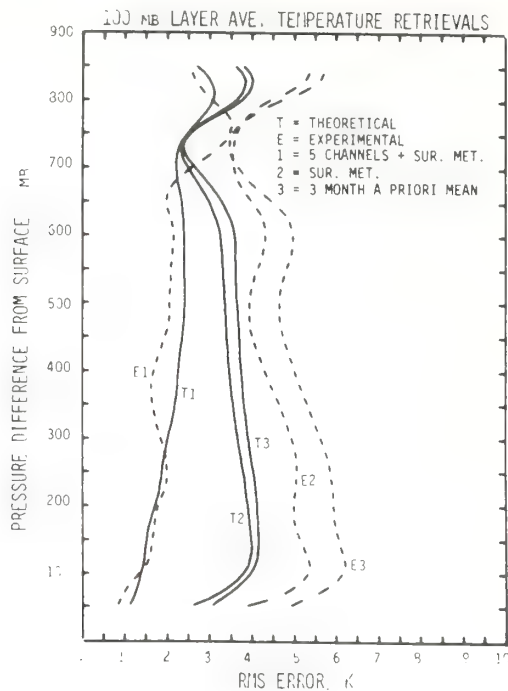
Fig. 15. RMS accuracy in retrieval of 100-mb layer averaged temperature, Pt. Mugu, California, March 1976, 21 profiles.

vapor weighting functions for the SCAMS system are shown in Fig. 16. Statistical retrieval algorithms were again applied to the 21 sets of radiometer observations to infer water vapor profiles. The summary of results is shown in Fig. 17, and typical temperature and humidity retrievals are given in Figs. 18 and 19.

Another set of observations was taken by JPL at Pt. Mugu in July 1976. In all, 22 concurrent radiometric and radiosonde observations were obtained. The statistical retrieval algorithm, in Eq. (2), was used to estimate the cloud liquid water content (LWC) of each of the profiles. As mentioned earlier, we classify a profile as cloudy if the estimated LWC is greater than 0.02 mm (a LWC of 0.02 mm will give a 1 K change in brightness temperature

190
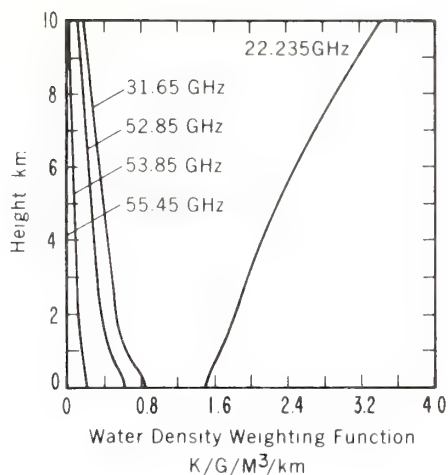
Fig. 16. *Water vapor density weighting functions for ground-based SCAMS radiometer.*
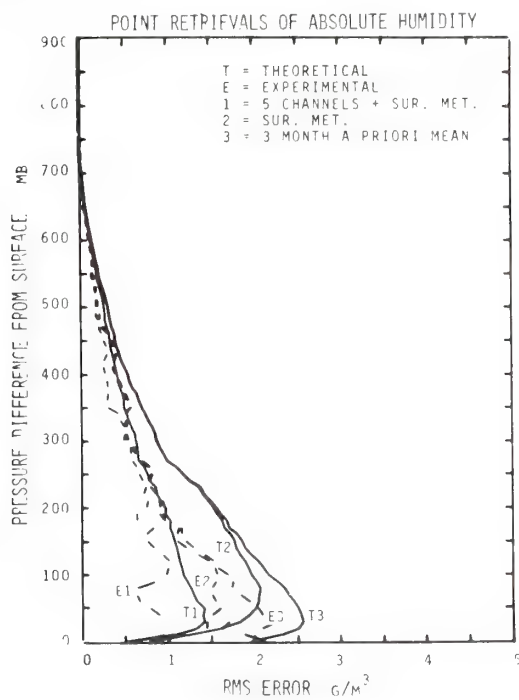
Fig. 17. *Rms accuracy in retrievals of absolute humidity, Pt. Mugu, California, March 1976, 21 profiles.*
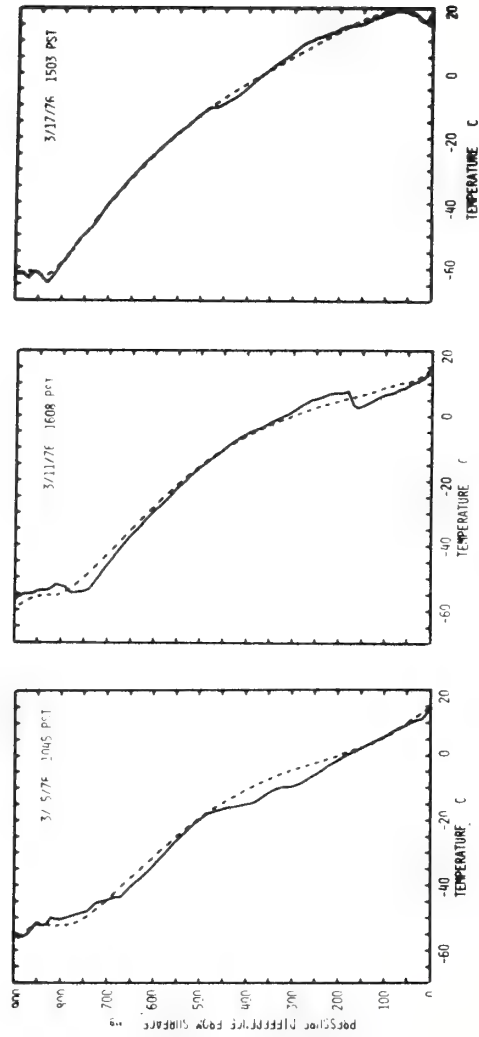
Fig. 18. Examples of temperature profiles retrieved from SCAMS radio-
metric data (dashed lines) compared with concurrent radiosondes (solid lines).

417
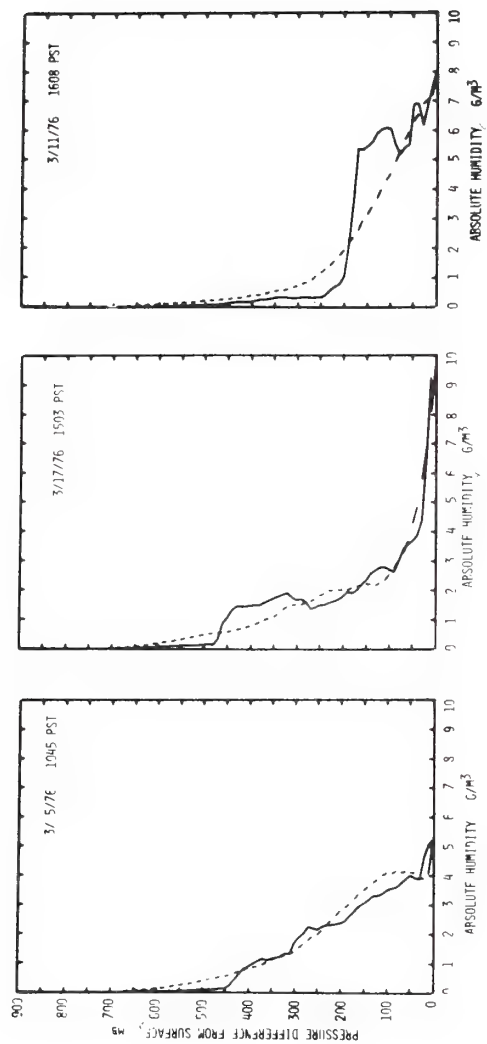
Fig. 19. Examples of water vapor profiles retrieved from SCAMS radio-
metric data (dashed lines) compared with concurrent radiosonde profiles (solid
lines).

418

193

in the window channel). With this classification, 17 of the 22
profiles were radiometrically cloudy. We are currently investi-
gating the application of various cloud correction algorithms to
these data. However, with a very simple correction method,
namely, no correction at all, the upper two channels can yield
useful retrieval. Examples of retrievals obtained during cloudy
conditions are shown in Figs. 20 and 21, and the statistical com-
parison of all 22 profiles is given in Fig. 22. Although there is
a substantial reduction in variance in the region from 50 to 150 mb
above the surface, it is likely that cloud correction can reduce
this variance still further.
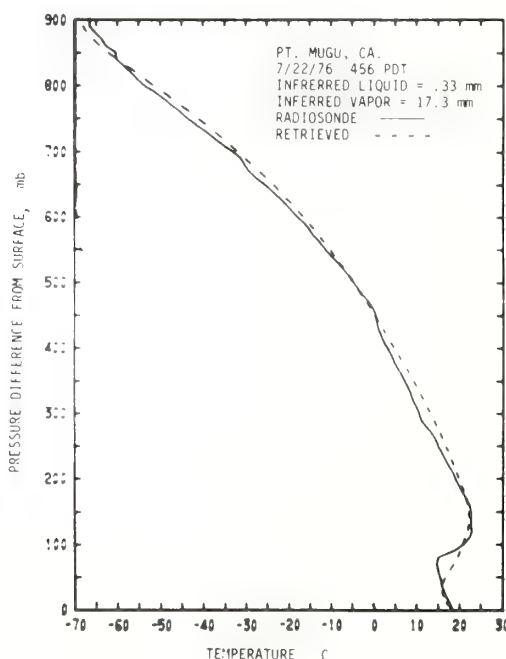
*Fig. 20. Example of temperature profile retrieved from two
oxygen channels during cloudy conditions.*
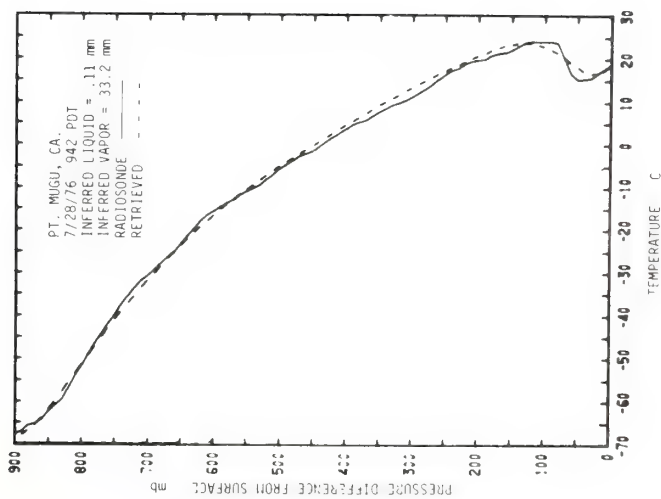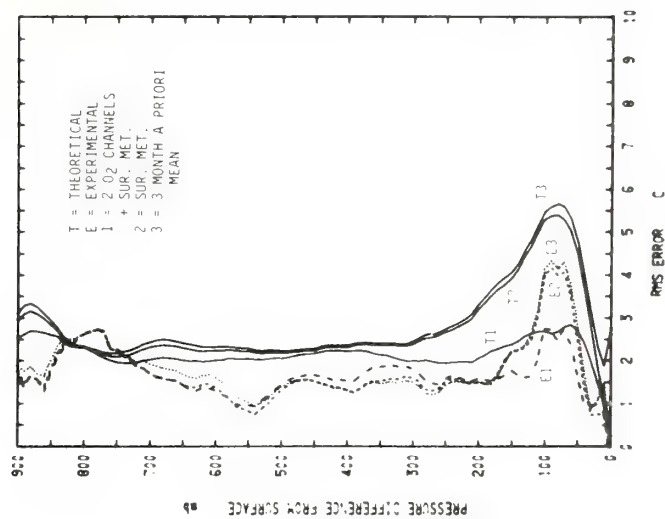
Fig. 22. Rms differences between radiometrically retrieved and radiosonde temperature profiles, 22 profiles: 5 clear + 17 cloudy.

Fig. 21. Example of temperature profile retrieved from two oxygen channels during cloudy conditions.

420

195

V. CONCLUSIONS

Statistical retrieval algorithms have proven to be quite useful in ground-based radiometric sensing, not only in profile recovery, but in making a reasonable *a priori* prediction of measurement achievability. Thus, we feel we can confidently answer questions relevant to system design, such as

   a. what is the climatological variation of retrieval accuracy?

   b. for a given number of channels, what is the optimum location of measurement ordinates?

   c. what noise levels are required to give specified retrieval accuracies?

We are currently investigating extensions of the statistical technique to the microwave cloud problem.

SYMBOLS

$\underset{\sim}{d}$	generalized data vector (Eqs. (2) and (3))
e_{rain}	extinction coefficient of rain, km^{-1} (Eq. (1))
$\underset{\sim}{p}$	generalized parameter vector (Eqs. (2) and (3))
$\hat{\underset{\sim}{p}}$	statistical estimator of p (Eqs. (2) and (3))
P	atmospheric pressure, mb (Figs. 1, 3 and 4)
r	relative humidity (Figs. 3 and 4)
R	rain rate, mm/hr (Fig. 1)
s,s'	path length, km from receiver to emitting volume (Eq. (2))
$S_{\underset{\sim}{q}}$	covariance matrix of random vector q (Eq. (3))
T	absolute temperature, K (Eq. (1), Figs. 1, 3 to 7)
$\bar{T}$	average absolute temperature (Fig. 6)
$T_b(\nu)$	brightness temperature, K (Eq. (1), Figs. 3 and 4)
$T_b^{(ext)}$	brightness temperature, K external to the Earth's atmosphere (Eq. (1))
$V[T_b]$	variance in brightness temperature, K^2 (Figs. 3 and 4)

$V[T_b;P]$ variance in brightness temperature, K^2 due to fluc-
              tuations in atmospheric profile parameter p (Figs. 3
              and 4)

α_ν absorption coefficient, km^{-1} (Eq. (1), Fig. 1)

ν frequency, GHz (Eq. (1))

ρ_{liquid} density of liquid water, g/m^3 (Fig. 1)

ρ_{vapor} absolute humidity, g/m^3 (Fig. 1)

σ standard deviation (Fig. 5)

σ_ϵ standard deviation of instrumental noise, K   (Fig. 5)

REFERENCES

1. C. R. Hosler and T. J. Lemmons, Radiometric measurements of
    temperature profiles in the planetary boundary layer, *J.
    Appl. Meteorol. 11*, 341 (1972).

2. G. F. Miner, D. D. Thornton, and W. J. Welch, The inference of
    atmospheric temperature profiles from ground-based measure-
    ments of microwave emission from atmospheric oxygen, *J.
    Geophys. Res. 77*, 975 (1972).

3. E. R. Westwater, J. B. Snider and A. V. Carlson, Experimental
    determination of temperature profiles by ground-based micro-
    wave radiometry, *J. Appl. Meteorol. 14*, 524 (1975).

4. A. T. Yershov, Y. V. Lebskiy, A. P. Naumov, and V. M. Plechkov,
    Determination of the vertical temperature profile from ground-
    based measurements of the atmospheric radiation at λ = 5 mm,
    Izv. Atmos. Oceanic Phys. 11, 1220 (1975).

5. J. W. Waters and D. H. Staelin, Statistical inversion of
    radiometric data, *Q. Prog. Rep. No. 89*, *Res. Lab. Elect.*,
    Massachusetts Institute of Technology, 1968.

6. A. T. Yershov, A. P. Naumov, and V. M. Plechkov, Determination
    of the vertical humidity profile from ground-based thermal-
    radar measurements of atmospheric absorption, *Izv. Vuz.
    Radiofizika, 15* (1972).

7. J. W. Waters, Absorption and emission by atmospheric gases,
    in "Methods of Experimental Physics" (M. L. Meeks, Ed.),
    Vol. 12, Part B, Ch. 2.3. Academic Press, New York, 1976.

8. G. E. Becker and S. H. Autler, Water vapor absorption of elec-
    tromagnetic radiation in the centimeter wavelength range,
    Phys. Rev. 70, 300 (1946).

9. H. J. Liebe, Calculated tropospheric dispersion and absorption
    due to the 22-GHz water vapor line, *IEEE Trans. Antennas
    Propag. AP-17,* 621 (1969).

10. J. W. Van Vleck, The absorption of microwaves by oxygen, *Phys.
    Rev. 71,* 413 (1947).

11. H. J. Liebe, et al., Atmospheric oxygen microwave spectrum-
    experiment versus theory, *IEEE Trans. Antennas Propag. AP-25
    3,* 327 (1977).

12. P. W. Rosenkranz, Shape of the 5-mm oxygen band in the atmos-
    phere, *IEEE Trans. Antennas Propag. AP-23,* 498 (1975).

13. E. E. Reber, R. L. Mitchell, and C. J. Carter, Attenuation of
    the 5-mm wavelength band in a variable atmosphere, *IEEE Trans.
    Antennas Propag. AP-18,* 472 (1970).

14. D. H. Staelin, A. H. Barrett, P. W. Rosenkranz, F. T. Barath,
    E. J. Johnson, J. W. Waters, A. Wouters, and W. B. Lenoir,
    The scanning microwave spectrometer (SCAMS) experiment,
    *The Nimbus 6 Users Guide, NASA, Goddard Space Flight Center,
    Greenbelt, Maryland,* 1975.

15.　F. Ostapoff, W. W. Shinners, and E. Augstein, Some tests on the radiosonde humidity error, *NOAA Tech. Rep. ERL 194-AOML 4, U.S. Dept. of Commerce*, 1970 [Superintendent of Documents: C55:13:ERL 194-AOML-4].

16.　J. F. Morrissey and F. J. Brousaides, Temperature-induced errors in the ML-476 humidity data, *J. Appl. Meteorol. 9,* 805 (1970).

17.　J. O. Laws and D. A. Parsons, The relation of raindrop size to intensity, *Trans. Am. Geophys. Union, 24,* 432 (1943).

18.　E. R. Westwater, M. T. Decker, and F. O. Guiraud, Feasibility of atmospheric temperature sensing from ocean data buoys by microwave radiometry, *NOAA Tech. Rep. ERL 375-WPL 48,* 1976.

19.　C. D. Rodgers, Retrieval of atmospheric temperature and composition from remote measurements of thermal radiation, *Rev. Geophys. Space Phys. 14,* 609 (1975).

20.　W. D. Mount, A. C. Anway, C. V. Wick, and C. M. Maloy, Capabilities of millimeter wave radiometers for remotely measuring temperature profiles pertinent to air pollution, *Final Report, Contract No. PH. 86-67-76, Sperry Rand Research Center, Sudbury, Massachusetts,* February 1968.

21.　E. R. Westwater, Ground-based determination of low altitude profiles by microwaves, *Mon. Weather Rev. 100,* 15 (1972).

22.　J. B. Snider, Ground-based sensing of temperature profiles from angular and multi-spectral microwave emission measurements, *J. Appl. Meteorol. 11,* 958 (1972).

23.　P. W. Rosenkranz, F. T. Barath, J. C. Blinn III, E. J. Johnston, W. B. Lenoir, D. H. Staelin, and J. W. Waters, Microwave radiometric measurements of atmospheric temperature and water from an aircraft, *J. Geophys. Res. 77,* 5833 (1972).

24. M. G. Fowler, N. D. Sze, and N. E. Gaut, The estimation of
    clear sky emission values from cloudy radiometric data,
    Air Force Cambridge Research Laboratories-TR-75-0440, 1975.

DISCUSSION

Susskind: When you do your analysis of the SCAMS data, do you subtract or do you find any bias in the brightness temperatures? I know Dave Staelin mentioned there was the possibility of a 2^O bias in the measurements. And when we do our analysis we have to subtract something from the brightness temperatures.

Westwater: On the first or the second slide that I showed, we did have a small bias in the upper channel--a 54.5 channel and this was a bias of about 1.3^O. The biases in the other two channels were essentially entirely below the noise levels. These were in the order of about 2/10 of a degree. Now with resepct to that question, we also did retrieval with subtracting a bias and retrievals with just the raw data. And for the temperature retrievals it made very little difference in the RMS errors. But there is somewhat of a bias in this in the data.

Susskind: I wonder if I could address this quickly to Dave Staelin. You mentioned that there was a bias of approximately 2^O with the SCAMS measurement. Is that still there? Namely, that due to instrument calibration.

Staelin: There are two origins for bias in the satellite instruments. One is the instrument calibration. We recalibrated in orbit using NMC data yielding corrections on the order of a degree or so. There is another correction in the case of our data from both the Nimbus 5 and 6 satellites, which I did not discuss, and that is the transmittances. Either they have systematic errors which are larger than anything that has been indicated in the laboratory spectroscope data, to date, or the radiosondes have systematic errors which are larger than their manufacturer would probably like to accept. This is still a residual effect on the order of one or two degrees. But we have yet to track down its origin. It can be removed empirically and is not a problem now.

Susskind: We do find roughly a systematic difference between the observations and our ability to calculate them of approximately 2^O. It's hard to tell if it is in the measurement or in our ability to calculate them.

Westwater: There is one other parameter in the Rosencrantz theory that is quite difficult to measure by Liebe's laboratory dispersion technique. This does not affect the calculated radiances at the strongly attenuating frequencies. However, at a frequency of around 50 GHz or 52 GHz, they are much more sensitive to this parameter that was not determined well from Liebe's measurements. In our calculations, we used the value of the nonresonant parameter that was given by Rosencrantz himself and it seemed to give a much better agreement with our measurements.

Fleming: Would you care to comment on just how you adjust for clouds when you sense them?

Westwater: The technique that we originally tried was to estimate the equivalent clear air brightness from the entire set of radiance observations and then use the equivalent clear brightness in retrieval. However, we ran into difficulties in applying this technique to the 52.8 GHz channel, so that the retrievals you saw were uncorrected brightness measurements at 53.8 and 55.45 GHz. We are still trying to unscramble the eggs again and what has happened to the cloud correction at the lower attenuating oxygen channel.

Fraser: Perhaps I misunderstood your last slide. I understood you to say that you were quite pleased with the water vapor retrieval. But, as I read the last slide, the theoretical and the experimental standard deviations, which I interpret as deviations in the radiosondes observations, except for 50 to 70 millibars above the ground, were essentially the same. If they are, then why are you so pleased with experimental data?

Westwater: The slide I showed at the end was the clear air data that was taken in March. And at least the total integrated water contents agreed quite well with that estimated by the radiosondes. However, in the period in July we did not obtain adequate agreement, primarily because of the cloud correction difficulties that I mentioned before. One of the reasons I am really pleased with the data is we really expected to get one parameter and one parameter alone. That would just be the total integrated water content. The amount of structure shown in the retrievals was an order of magnitude greater than anything I would have expected or that anyone would have expected from a weighting function which is essentially constant with altitude. There is very little structure in the weighting function itself.

202

WESTWATER, E. R., DECKER, M. T. and GUIRAUD, F. O.
NOAA/ERL/Wave Propagation Laboratory, Boulder, Colorado, USA

Atmospheric Temperature and Moisture Sensing from Ocean Data Buoys by Microwave Radiometry

Ocean-based data buoys are currently providing useful surface meteorological
observations of temperature, pressure, humidity, and wind. The utility of
buoy observations would be much enhanced if vertical profiles of these
meteorological parameters could be measured. We report here on theoretical
and experimental studies of remotely sensing vertical temperature structure
with a passive microwave radiometer.

The U.S. National Weather Service desires that the temperature of layers,
100 mb in thickness, be determined with accuracy ± 1 K. Although data up
through 850 mb would be useful, retrievals to 500 mb are wanted. Since the
system must operate under a variety of cloud conditions, a large portion of
our theoretical effort was to retrieve profiles from cloud-contaminated
brightness observations. A byproduct of our system is some information
on water vapor profiles and liquid water content.

Theoretical Retrieval Accuracy under Clear Conditions

Although an angular-scanned radiometric system was initially considered,
this technique was quickly eliminated by the difficulty of correcting for
buoy motion. A vertically-pointing two-channel radiometer, operating in
the 60 GHz O_2-band, showed promise of meeting accuracy requirements from
the surface to 850 mb. To infer profiles to 500 mb, a third channel is
required. Figure 1 shows the estimated rms retrieval accuracy, for five
ocean climatologies, for several multifrequency systems.

Theoretical Retrieval Accuracy under Cloudy Conditions

To correct oxygen-band observations for clouds, a channel sensitive to
water vapor, 20.6 GHz, and one sensitive to clouds, 31.65 GHz, were added.
Our cloud correction algorithm determined equivalent clear-air brightness
from the multi-frequency cloud-contaminated measurements. Figure 2 shows
estimated temperature retrieval accuracy under cloudy conditions. The
results in figures 1 and 2 indicated that system C yielded the smallest rms
temperature retrieval error; hence, channels operating near these frequen-
cies were selected for field evaluation.

Experimental Results

Five-channel microwave observations were taken at Pt. Mugu, Calif. and kindly
provided by B. Gary and N. Yamane of Jet Propulsion Laboratory (JPL). Their
radiometer was similar to that used on the Nimbus 6 satellite[1]. During the
three-week period of observations, thrice-a-day radiosondes obtained standard
meteorological soundings of temperature, pressure, and humidity. Before the
data were inverted, calculations of brightness temperature from radiosonde

profiles, using Rosenkranzs' O_2 line shape theory[2] with Liebes' laboratory measurements of O_2 spectroscopic parameters[3], were compared with JPL's radiometric observations. Table 1 shows rms and average differences between calculations and clear-air observations. Considering the difficulties in making absolute radiometric measurements and in observing the same volume of air with radiosonde and radiometer, the agreement is quite good. After inserting bias corrections, determined from 11 visually clear profiles, a
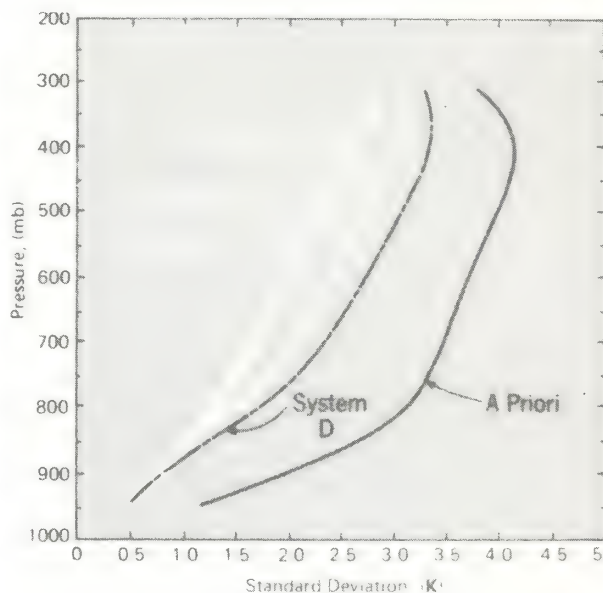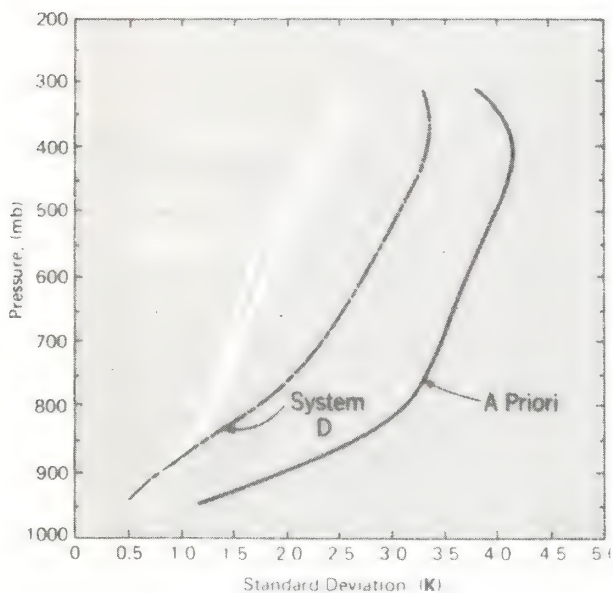
Figure 1. *Comparison of several radiometric systems in retrieving temperature layers of 100-mb thickness during clear conditions. Five-station rms average. Instrumental error = 0.5 K. Systems:*
A(52.8, 55.4, 58.8, 20.6, 31.65 GHz),
B(54.0, 55.4, 58.8, 20.6, 31.65 GHz),
C(52.8, 54.0, 55.4, 20.6, 31.65 GHz),
D(55.4, 58.8 GHz).

Figure 2. *Comparison of several radiometric systems in retrieving temperature layers of 100-mb thickness during cloudy conditions (liquid thickness < 4 mm H_2O). Five-station rms average. Instrumental error = 0.5 K. Systems: same nomenclature as Figure 1.*

Table 1.

Average and rms differences (K) between measured and calculated brightness temperatures (N = 24 radiosonde observation)

Frequency (GHz)	22.235	31.65	52.85	53.85	55.45
Aver. diff.	2.47	1.67	.18	.14	1.33
rms diff.	3.39	1.81	1.77	0.76	1.41

statistical inversion method was used to retrieve 21 profiles of both
water vapor and temperature. Although some of the 21 profiles were
obtained when there were visual observations of clouds, the radiometrically
estimated liquid content was less than 0.02 mm; hence, the clear-air
retrieval algorithms were used exclusively. Figures 3 and 4 show theoretical
and achieved retrieval accuracies for temperature and absolute humidity.
Included in these figures are the rms errors in profile prediction from
surface meteorological observations alone and from a 3-month mean profile.
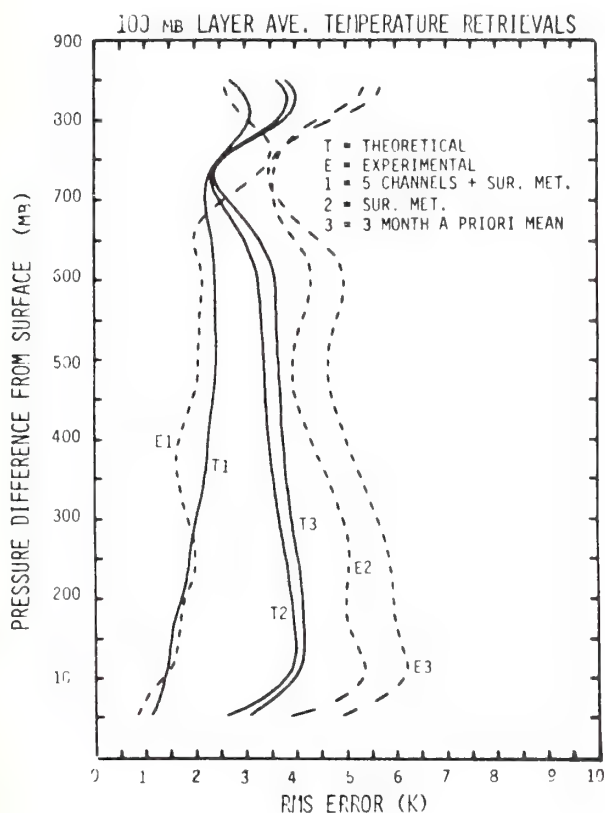
Figure 3. Rms accuracy in retrieval
of 100 mb layer averaged tempera-
ture. 21 profiles.
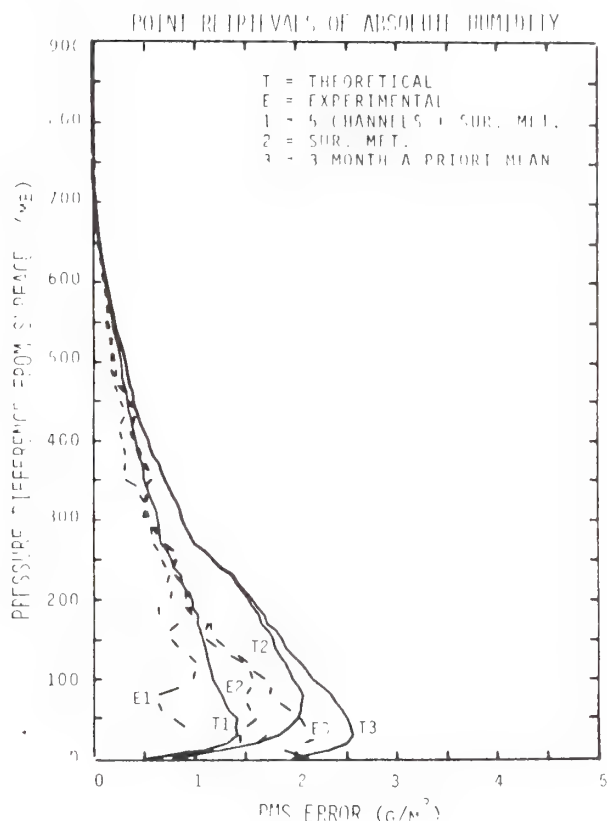
Figure 4. Absolute humidity retrievals.
Same nomenclature as figure 3.

Conclusions

The achieved profile retrieval accuracies are quite close to theoretical
predictions suggesting that an adequate modeling of the direct problem was
achieved. Although the desired accuracy of ± 1 K was not reached it is felt
that the rms difference of about 2 K up to the 350-mb level is encouraging.
Another set of observations at Pt. Mugu has been completed but is not yet
analyzed. Finally, current plans include operating the radiometer at Weather
Station P in the Gulf of Alaska.

References

1. Staelin, D. H. et al., The Scanning Microwave Spectrometer (SCAMS) Experiment. Nimbus-6 Users Guide, Goddard Space Flight Center, Greenbelt, MD., 1975.

2. Rosenkranz, P. W., Shape of the 5-mm Oxygen Band in the Atmosphere, IEEE Trans. Ant. Prop. AP-23, 498-506, 1976.

3. Liebe, H. J., G. Gimmestad and J. Hopponen, Atmospheric Oxygen Microwave Spectrum-Experiment Versus Theory. To be published in IEEE Trans. Ant. Prop. AP25, March, 1977.

FEASIBILITY OF ATMOSPHERIC TEMPERATURE SENSING
FROM OCEAN DATA BUOYS BY MICROWAVE RADIOMETRY

E. R. Westwater, M. T. Decker, and F. O. Guiraud

The feasibility of measuring atmospheric temperature structure by using
a microwave radiometer mounted on an ocean-based data buoy has been investigated
with simulated measurements. The accuracy of layer-averaged temperature re-
trievals was studied as a function of radiometer noise level, various choices
of frequency, number of channels, layer pressure thickness, clear vs. cloudy
skies, and five ocean climatologies. A three-frequency zenith measurement of
O_2 thermal emission (instrumental noise of 0.5 K) made during clear conditions
can be mathematically inverted to infer 100-mb layer averages of temperature
with rms accuracies that range from 0.5 K at the lowest altitudes to 1.7 K at
500 mb. To correct for cloud emission, additional brightness measurements are
required near 21 and 31 GHz. With the five-channel system the rms temperature
retrieval error for cloudy conditions is degraded (relative to clear air) by
at most 0.3 K. The two cloud-correcting channels also yield measurements of
integrated liquid water and water vapor content.

On the attenuation of sound by turbulence

E. H. Brown and S. F. Clifford

*Atmospheric Acoustics Program, National Oceanic and Atmospheric Administration, Environmental
Research Laboratories, Boulder, Colorado 80302*
(Received 2 February 1976; revised 2 July 1976)

We present a theory of attenuation of sound by turbulence. The mechanism underlying this theory is the
turbulence-induced broadening of finite beams of sound. It is thus conjectured that attenuation of sound by
turbulence is not an intrinsic property of the medium, nor even of its dynamic state, but depends on the
particular details of the experiment, such as beamwidth, beam orientation, etc. This point of view is at odds
with that of some other theories, in which attenuation by turbulence is regarded primarily as a scattering
process. Some conceptual flaws in these other theories are pointed out. It is shown that the present theory
yields results which are in qualitative agreement with observations.

Subject Classification: [43]28.40, [43]28.60; [43]20.35.

INTRODUCTION

Ever since the work of Tyndall[1] in 1874 researchers,
such as Duff,[2] have assumed that scattering of sound
out of a finite beam by turbulent temperature and ve-
locity fluctuations would contribute to a loss of acoustic
energy—so-called *excess attenuation*—beyond that due
to classical and molecular absorption. By molecular
absorption we imply both that due to oxygen and the so-
called "anomalous absorption" due to nitrogen. But,
whether the magnitude of such excess attenuation
reached levels high enough to affect applications of
acoustics remained an unanswered question for many
years and, in fact, remains a subject of controversy
today. In a study on the effects of meteorological con-
ditions on sound propagation made in 1953 Ingard[3] con-
cluded that "most of the time in the case of short-range
propagation (over distances less than a mile) the at-
tenuation due to irregularities in the wind structure,
gustiness, seems to be of major importance in com-
parison with..." classical and molecular attenuation,
attenuation caused by fog, rain, and snow, and apparent
attenuation due to the refractive effects of wind and
temperature gradients.

The experiment of Duff[2] in 1898 produced values of
total attenuation not in accord with predicted values of
the absorption coefficient. Duff determined the maxi-
mum distance of audibility for varying numbers of
whistles, and found attenuations roughly twice the
spherical spreading losses despite negligible values of
classical attenuation. Measurement across a quiet
river minimized "ground attenuation." Duff briefly con-
sidered excess attenuation (due to scattering), then dis-
missed the possibility in light of the low wind speeds dur-
ing the tests. He ascribed to "radiation" the additional at-
tenuation now known to depend on molecular relaxation.
In 1953 Delsasso and Leonard[4] obtained the first quanti-
tative support for significant levels of excess attenua-
tion. To minimize ground attenuation they measured
the losses over a path of somewhat over a mile across
a deep mountain canyon for a number of frequencies and
under various meteorological conditions. They con-
cluded that "the average value of the attenuation in the
field exceeds the measured value in the laboratory in
all cases from 22 to 81%," which implies that the im-
portance of excess attenuation may roughly equal that of
ordinary attenuation.

In 1946 Blokhintzev[5] obtained estimates of excess at-
tenuation using the primitive scattering theory available
at that time. His analysis divided the turbulent motion
of the fluid into two parts: "macroscopic" motions with
wave numbers less than some value K_0, and "micro-
scopic" motions with wave numbers greater than K_0. By
integrating the energy scattered by the microscopic
components of the turbulence in a localized scattering
volume on the path over that part of a sphere with scat-
tering angle greater than the angle ψ_f that a beam of
sound would have due to diffraction alone, Blokhintzev
derived a series in ψ_f for the excess attenuation which
varied as the $\frac{1}{3}$ power of the frequency and gave reason-
able magnitudes of the excess attenuation for typical
experimental values of turbulence parameters. Light-
hill[6] included a similar theoretical study of excess at-
tenuation due to scattering by velocity fluctuations
alone in his article on the interaction of turbulence with
sound waves. Lighthill integrated the energy flux due
to the farfield scattering cross section over all angles
on a spherical surface to obtain the total power re-
moved from a beam of sound. This approach leads
directly to a quadratic frequency dependence, whereas
measurements appear to behave more like a cube root.
A field experiment by Ingard and Wiener[7] also found an
amount of excess attenuation much smaller than pre-
dicted by Lighthill and a frequency dependence much
milder than quadratic.

Beran[8] and Beran *et al.*[9] attempted an intriguing ex-
periment by mounting a sound source on a glider, then
observing the sound intensity on the ground during suc-
cessive passes as the glider spiralled down. This pro-
cedure gave both total (accumulated) attenuation and at-
tenuation profiles. If the attenuation varied linearly
with path length the derivative of the profile would fur-
nish the attenuation coefficient. (We shall see later,
however, that the dependence is not linear.) The
studies found excess attenuation coefficients varying
from 0.01 to 10 times the ordinary (classical plus mo-
lecular) coefficients, and that large excess attenuation
coefficients correlated closely with thin wind-shear
layers; they found also a variation with frequency much
smaller than ordinary attenuation. Unfortunately,
Gething[10] has brought the quantitative value of the re-

sults of these studies into question by finding an error in the computer program used to calculate the ordinary attenuation from humidity measurements. Although the error implies much smaller observed values of total excess attenuation, the conclusions on frequency dependence and on correlation with wind shear appear to remain valid.

Ingard[11] studied two interesting anomalies in atmospheric sound propagation that cast some light on the problem of excess attenuation. He showed that in a low-frequency band (about 300 to 600 Hz) the multipath effect produced by interference between the ground-reflected wave and the direct wave can reduce the expected signal by as much as 50 dB. In contrast, at higher frequencies (say 6000 Hz) multipath effects can produce an apparent *negative* excess attenuation—that is, received signals *greater* by up to 50 dB than expected from average attenuation-coefficient calculations. Such a multipath effect arises because the transmissivity depends exponentially rather than linearly on the attenuation coefficient, so that a path with an attenuation slightly less than the average over the set of all paths acts as a partial "short circuit," contributing the main part to the received signal. Howe[12] has studied an attenuation process, an example of the reverse of Lighthill's[13] mechanism for the generation of aerodynamic sound. Again, however, the effect is small, amounting at most to 2 or 3 dB/km.

In view of the previous conflicting experimental results Aubry *et al.*[14] undertook a more careful experiment. They stationed a tethered balloon carrying two microphones and a package of sensors for wind, temperature, and humidity at various heights above a sound source fitted with an exponential horn on the ground. The experiment furnished profiles up to about 800 m of both total attenuation of sound at a number of frequencies and the meteorological conditions. The authors concluded that "(1) Within the range of meteorological conditions studied the excess attenuation was much smaller than the molecular attenuation. It was generally smaller than the uncertainty in the molecular attenuation. (2) Some excess attenuation was observed in relation with larger turbulent intensity on April 16. This excess attenuation seemed to increase with frequency and reached a value of about 10 dB/km at 4000 Hz . . . . If the first statement is confirmed by further experiments, it is most significant because it means that in average conditions the excess attenuation could be ignored for practical pruposes." Immediately, however, a question of the meaning of "average conditions" arises. Through most of the experiment the values of the temperature fluctuations structure parameter C_T^2 varied between about $2 \times 10^{-5} K^2 m^{-2/3}$ and $2 \times 10^{-6} K^2 m^{-2/3}$, down by factors of over one hundred to one thousand from the values found by Neff[15] on a typical, mild summer morning with moderate wind (5 m/sec). Under convective conditions C_T^2 may reach values as high as 0.1 $K^2 m^{-2/3}$, but usually ranges between $1 \times 10^{-3} K^2 m^{-2/3}$ and $5 \times 10^{-3} K^2 m^{-2/3}$. In the one case (statement (2) above) showing a significant excess attenuation (roughly comparable with the ordinary attenuation), the measured C_T^2 reached $2 \times 10^{-4} K^2 m^{-2/3}$—that is, a more

"typical" value. No estimates of the corresponding velocity fluctuations structure parameter C_V^2 were included in the article. The low values of C_T^2 are possibly due to the presence of cloud cover sufficient to reduce significantly the turbulent heat flux—but no information on such conditions was included.

DeLoach[16] made an extensive survey of most of the previous experimental and theoretical work on excess attenuation and also introduced a variation of the theory proposed by Blokhintzev.[5] His summary of experimental results concludes that "(1) excess attenuation has as much effect on the propagation of outdoor sound as ordinary attenuation. (2) The instantaneous value of the excess-attenuation coefficient undergoes rapid fluctuations over a wide range of magnitudes. The ratio of the excess-attenuation coefficient to the ordinary attenuation coefficient can change by an order of magnitude in the period of a few minutes. (3) The excess-attenuation coefficient is a function of altitude; it is larger near the surface than at higher altitudes. (4) The excess attenuation exhibits a weak frequency dependence. At least one observer has noted a cube-root frequency dependence. In any case, the frequency dependence of the excess attenuation is much milder than that of the ordinary attenuation. (5) There is a correlation between the excess attenuation and gradients in the wind speed. The more irregular the wind, the greater the excess attenuation; however, the excess attenuation is nonzero even when the wind shear is negligible. (6) The data from at least one investigation indicates a correlation between the average magnitude of the excess attenuation and the time of day, larger values being obtained in the early morning than in the late afternoon."

The theory proposed by DeLoach follows that of Blokhintzev[5] and Lighthill[6] in integrating the scattering cross section over solid angle. Unfortunately, these theories invoke a single scatter model that does not conserve energy. DeLoach assumes that any energy that is scattered is lost and in doing so he ignores the quite significant contribution to the average intensity of the energy that is scattered to the detector by off-axis irregularities in refractive index. The theory that we propose conserves energy and there is supporting theoretical and experimental evidence that it is valid in the strong turbulence or multiple scatter regime.[19]

I. ANALYSIS

We now present a theory for the existence and behavior of excess attenuation that agrees with the observations listed by DeLoach, explains the apparently contradictory results of the various experimenters, and is based on the well-developed theories of forward propagation through turbulence begun by Tatarskii[17,18] and extended by Lutomirski and Yura,[19] and Yura,[20] among others. We note that the forward-propagation theories mentioned deal with optical propagation through turbulence. These theories remain valid for acoustic propagation if most of the energy is scattered through narrow angles. A discussion of this assumption will appear below. The presence of refractivity fluctuations produces *beam broadening* of any finite beam in excess

209
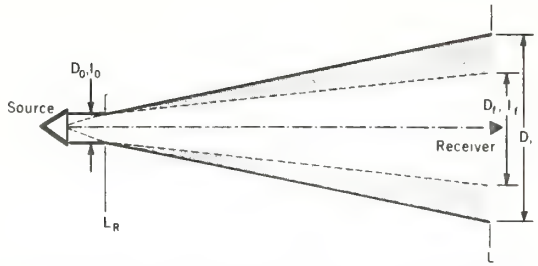
FIG. 1. Geometry of an acoustic beam propagating through turbulence.

of that due to diffraction alone ("R^2 spreading"). As the beam cross-sectional area increases, the energy-flux density decreases, and any receiver smaller than the local beam diameter will measure decreasing acoustic intensities. Forward propagation is determined[19] by the point source "modulation transfer function" or MTF defined as $\mathrm{MTF}(\vec{\rho}, L) = \langle P_s(\vec{\rho}_1 + \vec{\rho}, L) P_s^*$ $\times (\vec{\rho}_1, L)\rangle$, where the angle brackets indicate an ensemble average and the pressure fields P_s, produced by a spherical wave emitted from the observation point, are measured at the two points $\vec{\rho}_1$ and $\vec{\rho}_1 + \vec{\rho}$ in the transmitting plane. Tatarski[17,18] shows that $\mathrm{MTF}(\vec{\rho}, L)$ $= \exp[-\tfrac{1}{2}D_W(\vec{\rho}, L)]$ where $D_W(\vec{\rho}, L) = D_x(\vec{\rho}, L) + D_\phi(\vec{\rho}, L)$ is the wave structure function and D_x and D_ϕ are respectively, the structure function of the logarithm of the amplitude and phase. Since, for pathlengths greater than a few tens of meters, D_x is insignificant compared with D_ϕ, we conclude that beam broadening and, thus, excess attenuation, as defined by our model, are determined primarily by the phase fluctuations rather than the amplitude fluctuations.

The fact that excess attenuation depends on beam broadening caused by phase fluctuations has an immediately significant consequence. Phase fluctuations of a beam do not have a symmetric path weighting function, that is, interchange of transmitter and receiver affects the observations. The path weighting function includes[18] a factor $(L-s)^{5/3}$ (with s the distance from the transmitter and L the total pathlength), which causes the importance of the refractivity fluctuations to decrease along the path: *the most significant turbulence for excess attenuation lies directly in front of the transmitter.* For forward propagation the structure parameter for refractivity fluctuations C_n^2 depends on C_T^2 and C_V^2 according to the relation[17]

$$C_n^2(z) = C_T^2(z)/4T^2 + C_V^2(z)/c^2, \tag{1}$$

assuming horizontal homogeneity, where T is the mean temperature, c the mean speed of sound, and z the height above the ground. Because of the structure of the atmosphere the largest values of $C_n^2(z)$ appear near the ground. Then, interchange of transmitter and receiver on a vertical propagation path will produce widely disparate results since, in one case, the intense turbulence will lie in front of a transmitter situated on the ground and, in the other, only weak turbulence will appear in front of a transmitter elevated by a balloon

or tower. Thus, even discounting differences in C_n^2, we cannot expect an experiment such as that of Aubry et al.[14] to give the same magnitude of excess attenuation as that obtained from the experiment of Beran et al.[9] For the experiment of Delsasso and Leonard[4] the chaotic behavior of C_n^2 over rugged mountainous terrain makes any predictions difficult. As one example of the applications, the theory clearly implies one cannot obtain the proper excess attenuation for monostatic echosonde observations by merely doubling the excess attenuation measured on a one-way path.

In the following, for simplicity, we assume zero ordinary attenuation—that is, attenuation due to the classical and molecular absorption coefficients, which always can be introduced separately. Beam diameters are defined by the points where the power is down by the factor e^{-1} (4.3 dB). We also assume that the beam diameter is larger than the outer scale of turbulence so that only beam spreading occurs and the beam center of gravity does not wander about the propagation axis. If this is not the case, the theory can be modified as discussed in Fante[23] to include both short and long term beam spread. Figure 1 shows the various distances and beam diameters involved in the analysis. D_0 is the diameter of the source and D_f is the diameter the farfield beam would have at the distance L if only Fraunhofer diffraction were involved, so that $D_f^2 = D_0^2$ $+ 16 L^2/k^2 D_0^2$ (with k the wave number $2\pi/\lambda$). D is the actual diameter of the beam at the distance L due both to diffraction and turbulent beam spreading, or D^2 $= D_f^2 + D_t^2$. Since the total acoustic power is constant, the long-term average intensity $\langle I \rangle$ at L is simply related to the intensity I_f that would exist at L in the absence of turbulence by the relation

$$\langle I \rangle / I_f = D_f^2/D^2 \tag{2}$$

or, defining the total excess attenuation A_e measured in dB by $A_e = 10 \log(I_f/\langle I \rangle)$, then,

$$A_e = 10 \log(D^2/D_f^2) = 10 \log(1 + D_t^2/D_f^2). \tag{3}$$

Clearly, turbulent beam spreading will not be important for short paths or low turbulence intensities. Fortunately, for a broad range of parameters Yura[20] has already obtained the solution for the effective turbulent beam spreading in the form

$$D_t^2 = 25 k^{2/5} \left[\int_0^L ds (L-s)^{5/3} C_n^2(s) \right]^{6/5}, \tag{4}$$

where the integration over the beam path runs from the transmitter to the receiver. (Yura obtained this result by employing the form of the MTF suggested by Tatarski for a weak-turbulence model. Fante[23] showed that this form also applies in strong turbulence, where multiple scattering predominates, to a reasonable approximation; therefore, the results of this paper apply even when the pathlength and turbulence strengths exceed the weak turbulence constraints. As mentioned above, the application of the theories of Yura, Fante, and Tatarski to acoustic propagation is somewhat suspect because of the assumption of narrow-angle scattering. A sufficient condition for narrow-angle scattering is that $\lambda \ll l_0$ where λ is the wavelength of the

TABLE I. Comparisons of excess attenuations.

f(Hz)	$\alpha \times 10^3$ (dB/m)	$\overline{\alpha}_e \times 10^3$ (Theor.) (dB/m)	$\overline{\alpha}_e \times 10^3$ (exp) (dB/m)	$1.63(f/1000)^{1/3}$
125	0.072	0.85	0.65	0.82
250	0.285	1.08	1.75	1.02
500	1.148	1.31	2.38	1.29
1000	4.592	1.58	1.63	1.63

sound and l_0 is the smallest scale (microscale) irregularity in the refractive turbulence field. For typical values of the microscale $l_0 \sim 1$ cm, this assumption is not valid for acoustic wavelengths in the kilohertz range. However, Clifford and Brown[21] have shown that the assumption $\lambda \ll l_0$ is too restrictive and that the same form of D_ψ and hence the MTF, as suggested by Tatarski and applied by Yura, should apply for acoustic wavelengths of the order of up to a few meters. Then, assuming the receiving point in the farfield, or $4L/kD_0^2 \gg 1$, and substituting Eq. (4) in Eq. (3) immediately gives

$$A_e = 10 \log\left\{1 + 1.56\, k^{12/5} D_0^2 \left[\int_0^L ds \left(\frac{L-s}{L}\right)^{5/3} C_n^2(s)\right]^{6/5}\right\}, \quad (5)$$

or, for the case of constant C_n^2,

$$A_e = 10 \log(1 + 0.48\, k^{12/5} D_0^2 L^{6/5} C_n^{12/5}). \quad (6)$$

Either Eq. (5) or Eq. (6) provides profiles or average values of the "excess-attenuation coefficient" by using the definitions $\alpha_e = \partial A_e / \partial s$ or $\overline{\alpha}_e = A_e/L$. The above results remain valid up to ranges where the wave coherence length[20] decreases to values comparable with the inner scale of turbulence—at distances much farther than are likely to be of practical importance. (Note that the weighting factor $[(L-s)/L]^{5/3}$ appearing in Eq. (5) differs from the factor $(s/L)^{5/3}$ appearing in Table I of Yura[24] because our integration runs from transmitter to observer, while Yura's runs from a test point source placed at the observing point backwards towards the transmitter.)

Note that the factor $(L-s)^{5/3}$ in the integrand of Eq. (5) always weights the turbulence near the transmitter most heavily. For the case of constant C_n^2 (such as for horizontal paths) the asymmetry of the path weighting factor has no effect on the wave propagation. The situation is quite different for vertical paths; here, the combination of path weighting asymmetry and atmospheric structure produces large differences in the observations under reflection of the source-path-receiver combination. We cannot expect agreement between the results obtained with the transmitter on the ground and those with an elevated source. A further important insight on observations results from the theory if we rewrite Eq. (5) in the form

$$A_e = 10 \log\left\{1 + 61.6(D_0/\lambda)^2 k^{2/5}\left[\int_0^L ds\left(\frac{L-s}{L}\right)^{5/3} C_n^2(s)\right]^{6/5}\right\}. \quad (7)$$

Then—as is appropriate for a point source—letting $D_0/\lambda \to 0$ gives the not unexpected result that

$$A_e = 0 \quad (8)$$

for a point source. Clearly, the total angular beam-

width $\psi = 3.2\lambda/\pi D_0$ of the antenna has an important influence on the magnitude of the expected values of the excess attenuation. Thus, the value of ψ should be measured and included in any experimental report on excess attenuation. Note also that, since the factor $k^{12/5}$ appears under the logarithm in Eq. (5), the frequency dependence varies with the magnitude of A_e. For $A_e = 1$ dB the dependence is approximately quadratic; by the time A_e reaches 10 dB, however, the exponent has dropped to less than one.

The above analysis, that results in the excess attenuation given in Eq. (5), gives only a measure of the average reduction in received intensity due to turbulent refractive index fluctuation. Of course, the instantaneous intensity will fluctuate wildly about this value such that a sound pressure level meter will record dB readings that will vary significantly with averaging times. To calculate the perceived sound level, information about the statistics of these fluctuations is essential. Clifford and Yura[24] and Fante[23] have studied this problem theoretically and conclude that the standard deviation of the intensity fluctuations for most paths and C_n^2 values of interest in noise-propagation problems, i.e., 1 km $\lesssim L \le 10$ km and $C_n^2 \sim 10^{-7}$ m$^{-2/3}$ is approximately equal to the mean intensity or, more precisely, $\sigma_I \approx \langle I \rangle$. There is some doubt as to the form of the probability distribution in this range of path-lengths and C_n^2. The log-normal probability density is probably the most reasonable assumption but one must be cautious because experimental evidence suggests[23] that the log-normal density tends to overestimate the number of extreme values.

II. ATMOSPHERIC PROFILES

The above discussion emphasizes the need for atmospheric profiles in the prediction of excess attenuation. Although mean wind and temperature profiles produce chiefly refractive effects, the profiles of C_V^2 and C_T^2 affect the excess attenuation directly, through their contribution to C_n^2 [as given by Eq. (1)], and by the effect of the C_n^2 profile on A_e shown in Eq. (5). Since we hope to apply echosondes eventually to the remote measurement of the same turbulence parameters C_V^2 and C_T^2, and since the accuracy of such measurements depends on knowing the values of A_e, a possible difficulty exists. Fortunately, the smallness of the correction for A_e implies that use of reasonable mean profiles using parameters determined by ground measurements should give acceptable results.

Both the height and the structure of the boundary layer depend strongly on whether the atmosphere is stable or unstable—conditions obtaining mainly during the night or the midpart of the day, respectively. Here, for illustrative pruposes, we will consider only typical daytime, unstable boundary-layer profiles. Such a boundary layer possesses three regions, differing in structure: the *shear layer* (or surface layer) extending a few tens of meters above the ground, and strongly influenced by the surface friction; the *free-convection layer* reaching up to about one-tenth the total height z_i of the boundary layer, where the turbulent heat flux

211
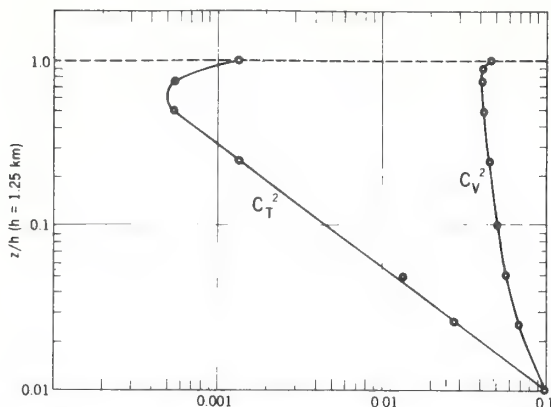
FIG. 2. Variation of turbulence intensities with altitude.

remains the only important dynamic parameter; and the *mixed layer* extending to z_i which, as the name implies, contains well-mixed velocity fluctuations of approximately constant intensity. As a result, in the mixed layer C_V^2 is roughly constant; then, descending to the free-convection layer, C_V^2 increases; finally, in the shear layer C_V^2 approaches a curve varying as $z^{-2/3}$. Thus, the mean profile of C_V^2 is roughly modeled by the empirical curve

$$C_V^2 = A + B(z/z_i)^{-2/3}. \tag{9}$$

Studies of boundary-layer structure relate the constants A and B to other atmospheric parameters, but these relations need not concern us here. In addition, the validity of such profiles terminates at some height related to the thickness of the laminar flow just above the ground. The behavior of C_T^2 is somewhat different. Experimental studies have found, instead, the mean profile

$$C_T^2 = C(z/z_i)^{-4/3} \tag{10}$$

throughout the boundary layer. Figure 2, derived from a study by Kaimal *et al.*,[22] shows average experimental C_V^2 and C_T^2 profiles for a typical midday, unstable boundary layer with a total height of $z_i = 1.25 \times 10^3$ m. (The change in behavior of both C_V^2 and C_T^2 just below $z = z_i$ is due to entrainment from the flow just above the boundary layer.) The experimental curves in Fig. 2 are expressed approximately by the equations

$$C_V^2 = 0.04 + 0.33\ z^{-2/3} \tag{11}$$

and

$$C_T^2 = 2.9\ z^{-4/3}.$$

At heights typical of echosonde measurements, C_T^2 is from one to two orders of magnitude smaller than C_V^2 but, below 12.5 m, just the region in which ground-situated transmitters and receivers would be located, C_T^2 becomes considerably larger than C_V^2. Of course, instantaneous curves of C_V^2 and C_T^2 may vary from the profiles given in Eq. (9) and Eq. (10), and the constants involved also may vary considerably from those in Eq. (11).

III. COMPARISON WITH EXPERIMENT

Since none of the past experimenters have known which parameters played the most important roles in

excess attenuation, experimental reports invariably lack key values. Thus, to compare the predictions of the present theory with previous observations will require some judicious guesses. As an example, we consider the work of Delsasso and Leonard who give $\overline{\alpha_e}$ for a horizontal path. In their experiment they calculated A_e by comparing the signal from a microphone at a reference distance $L_r = 104$ ft (32 m) with the signal from a microphone at the distance $L = 8652$ ft (2637 m), using the spherical spreading formula

$$A_e = 10 \log(I_r/I) - 10 \log(L/L_r)^2 = 10 \log(L_r D/LD_r)^2, \tag{12}$$

where D_r is the diameter of the beam at L_r. We note that Eq. (12) is correct only if L_r is in the farfield. In the farfield case, $D_r^2 = D_0^2 + 16\ L_r^2/k^2 D_0^2 \approx 16\ L_r^2/k^2 D_0^2$. Substituting this in Eq. (12) immediately gives the correct result Eq. (5). By using the farfield relation $D_f = LD_r/L_r$ in Eq. (3) we obtain Eq. (12) or, in another form,

$$A_e = 10 \log(1 + L_r^2 D_t^2/L^2 D_r^2), \tag{13}$$

with D_t^2 given by Eq. (4).

We now consider what will happen if we use Eq. (12) or Eq. (13) to reduce the experimental data even if the reference microphone position L_r lies in the *nearfield*. This procedure is equivalent to defining a new (unphysical) quantity $\hat{A}_e$ which, for appropriate ranges of parameters, represents an approximation to the physically defined excess attenuation A_e. Since $D_r^2 = D_0^2 + 16\ L_r^2/k^2 D_0^2$, substituting the farfield distance $kD_0^2/8$ for L_r shows that D_r varies approximately 10% from D_0 over the entire nearfield. Thus, the value of $\hat{A}_e$ is given approximately by

$$\hat{A}_e \approx 10 \log(1 + L_r^2 D_t^2/L^2 D_0^2). \tag{14}$$

Delsasso and Leonard used a cannon for a sound source. Since the equivalent aperture is probably represented by a region of nonlinear interaction rather than the mouth itself, we arbitrarily assume that L_r is in the nearfield and that $D_0 = 1$ m. Since the microphones were mounted on masts and the entire experiment took place at an altitude of 10 000 ft, we arbitrarily assume $C_n^2 = 10^{-7}$ m$^{-2/3}$ and $c = 335$ m/sec.

We cannot compare our theory with Delsasso and Leonard's summary table of field measurements of the total of ordinary plus excess attenuation since these are averages over a wide range of relative humidity. Instead, we choose the average of five representative values of the mean of their maximum and minimum measurements for which the relative humidity is 30% or more; then, we scale the measured value of the ordinary-attenuation coefficient α at 1000 Hz by the square of the frequency to obtain average values of experimental excess attenuation. Table I gives a comparison of α, the theoretical values of $\overline{\alpha_e}$ from Eq. (14), and the experimental values of $\overline{\alpha_e}$ derived from Delsasso and Leonard. The final column in Table I shows the expected behavior if $\overline{\alpha_e}$ varies as the $\frac{1}{3}$ power of the frequency. The close agreement with the theoretical behavior suggests that some of the departures of the experimental values are due to the small number of samples in the average. In fact, if data are expressed by using a fixed L_r, the frequency dependence of $\hat{A}_e$ ap-

pears as the $\frac{2}{5}$ power under the logarithm and, thus, the dependence will vary with the magnitude of $\hat{A}_e$.

We now consider two examples of the true excess attenuation A_e on vertical paths, one with an elevated transmitter as in the experiment of Beran *et al.*, the other with a ground-based transmitter as in the experiment of Aubry *et al.* For illustrative purposes we use the experimental profiles of C_V^2 and C_T^2 obtained by Kaimal, as expressed by Eq. (11). When $T = 283$ K the relation for C_n^2 becomes $C_n^2 = 8.8 \times 10^{-6} (C_V^2 + 0.35 \ C_T^2)$. Suppose in the first case that the receiver is at $z = 1$ m; and, in the second case, the transmitter is at $z = 1$ m; then, the integral appearing in Eq. (5) becomes equal to $L \ \overline{C_n^2}$ or $L \ \underline{C_n^2}$, where

$$\overline{C_n^2} = \frac{1}{L} \int_1^L dz \left(\frac{z}{L}\right)^{5/3} C_n^2(z) \qquad \text{(elevated transmitter)}$$

(15)

$$\underline{C_n^2} = \frac{1}{L} \int_1^L dz \left(\frac{L-z}{L}\right)^{5/3} C_n^2(z) \qquad \text{(ground-based trans-mitter).}$$

(16)

Substituting the expression

$$C_n^2 = 8.8 \times 10^{-6} (0.04 + 0.33 \ z^{-2/3} + 1.015 \ z^{-4/3}) \qquad (17)$$

in Eq. (12) and integrating gives

$$\overline{C_n^2} = 1.3 \times 10^{-7} (1 + 11 \ z^{-2/3} + 51 \ z^{-4/3}). \qquad (18)$$

For the ground-based transmitter, however, $\underline{C_n^2}$ depends only weakly on z. Since $[(L-z)/L]^{5/3}$ peaks sharply at $z = 0$, substituting $z = 0$ in Eq. (16) gives a reasonable approximation for the integral, that is,

$$\underline{C_n^2} \approx 4.6 \times 10^{-6}. \qquad (19)$$

We now apply the above values to a calculation from Eq. (5) of the mean excess attenuation coefficient over a 600-m path for a 4-kHz beam assuming $D_0 = 1$ m. The results are

$$\overline{\alpha_e} = 1.5 \text{ dB/km} \qquad \text{(elevated transmitter)}$$

and

(20)

$$\overline{\alpha_e} = 8.0 \text{ dB/km} \qquad \text{(ground-based transmitter).}$$

These results show almost an order of magnitude difference between the excess attenuation for an elevated transmitter and that for a ground-based transmitter for the same path. In the first case, the excess attenuation does not appear very important but, in the second, the magnitude has risen to a significant value.

IV. CONCLUSIONS

We have shown that forward-propagation formulas applied to the problem of excess attenuation lead to a theory that predicts the right orders of magnitude and the correct behavior (with regard to other parameters) obtained in previous experiments. The theory gives values of the excess-attenuation coefficient for typical path lengths and turbulent intensities that are significant when compared with ordinary attenuation coefficients, and that agree well with observations. When the data are displayed in terms of a fixed nearfield reference distance L_r, the frequency dependence ap-

pears in the form $\log(1 + af^{2/5})$ which, for typical magnitudes of the excess attenuation, appears close to the $f^{1/3}$ dependence observed. More properly, if the results are displayed in terms of the nonturbulent beamwidth, which is itself a function of frequency, the dependence changes to $\log(1 + af^{12/5})$. For downward transmission the results include (in the argument of the logarithm) an altitude dependence from the combined effect of a factor $z^{6/5}$ and the rapid decrease of the intensity of refractivity fluctuations C_n^2. For low altitudes the magnitude of C_n^2 depends, first, on the intensity of velocity fluctuations C_V^2 and—with a factor of about one-third—on the intensity of temperature fluctuations C_T^2. Thus, the magnitude of the excess attenuation should correlate strongly with the wind shear, yet not fall completely to zero when the shear—and thus C_V^2—vanishes. Finally, the experimental values of the excess attenuation depend highly on the geometry of the path; typical values may reach an order of magnitude higher when sound propagates upward than when it propagates downward. Equation (5) and the comments following Eq. (8) show that excess attenuation is not an intrinsic property of air, or even the dynamic state of the atmosphere. Excess attenuation depends strongly on the geometry (that is, acoustic-beam parameters) and orientation. Also, as indicated above, the comparison of theory with existing data suffers from inadequate reporting of both equipment parameters and relevant supporting meteorological information. Hopefully, the design of future experiments will include measurement of wind, temperature profiles, C_V^2, and C_T^2 as well as, transmitting aperture characteristics. Without this sort of information such experiments will have only limited value.

In conclusion, we believe that substitution of the appropriate parameters in the theory presented here will lead to reasonable estimates of the amount of excess attenuation in the propagation of sound or noise through the atmosphere if refractive effects and ordinary attenuation are handled separately.

[1]J. Tyndall, "On the atmosphere as a vehicle of sound," Philos. Trans. R. Soc. London, Sec. A:164, 183 (1874).
[2]W. Duff, "The attenuation of sound and the constant of radiation of air," Phys. Rev. 6, 129 (1898).
[3]U. Ingard, "A review of the influence of meteorological conditions on sound propagation," J. Acoust. Soc. Am. 25, 405 (1953).
[4]L. P. Delsasso and R. W. Leonard, "The attenuation of sound in the atmosphere," Summary Report, U. S. Air Force Contract W-28-099-AC-228 (University of California, Berkeley, 1953).
[5]D. Blokhintzev, "The propagation of sound in an inhomogeneous and moving medium II," J. Acoust. Soc. Am. 18, 329 (1946).
[6]M. J. Lighthill, "On the energy scattered from the interaction of turbulence with sound or shock waves," Proc. Cambridge Philos. Soc. 49, 531 (1953).
[7]U. Ingard and F. M. Wiener, "On the scattering of sound by atmospheric turbulence," J. Acoust. Soc. Am. 30, 670 (1958).
[8]D. W. Beran, "Turbulence detection," Ph. D. thesis (University of Melbourne, 1970) (to be published).
[9]D. W. Beran, R. M. Reynolds, and J. T. Gething, "Sound attenuation in the free atmosphere," Project Ear, Report V (University of Melbourne, Melbourne, 1970).

[10] J. T. Gething, (personal communication via D. W. Beran, 1975).

[11] U. Ingard, "On sound transmission anomalies in the atmosphere," J. Acoust. Soc. Am. **45**, 1038 (1969).

[12] M. S. Howe, "Multiple scattering of sound by turbulence and other inhomogeneities," J. Sound Vib. **27**, 455 (1973).

[13] M. J. Lighthill, "On sound generated aerodynamically," Proc. R. Soc. London, Sec. A: **211**, 564 (1952).

[14] M. Aubry, F. Baudin, A. Weill, and P. Rainteau, "Measurement of the total attenuation of acoustic waves in the turbulent atmosphere," J. Geophys. Res. **79**, 5598 (1974).

[15] W. D. Neff, "Quantitative evaluation of acoustic echoes from the planetary boundary layer," NOAA Technical Report ERL 322-WPL 38 (U. S. GPO, Washington, D.C., 1975).

[16] R. DeLoach, "On the excess attenuation of sound in the atmosphere," NASA TN D-7823 (National Technical Information Service, Springfield, VA 1975).

[17] V. I. Tatarskii, Wave Propagation in a Turbulent Medium (McGraw–Hill, New York, 1969).

[18] V. I. Tatarskii, The Effects of the Turbulent Atmosphere on Wave Propagation (National Technical Information Service, Springfield, VA 1971).

[19] R. F. Lutomirski and H. T. Yura, "Propagation of a finite optical beam in an inhomogeneous medium," Appl. Opt. **10**, 1652 (1971).

[20] H. T. Yura, "Atmospheric turbulence induced laser beam spread," Appl. Opt. **10**, 2771 (1971).

[21] S. F. Clifford and E. H. Brown, "Propagation of sound in a turbulent atmosphere," J. Acoust. Soc. Am. **48**, 1123 (1970).

[22] J. C. Kaimal, J. C. Wyngaard, D. A. Haugen, O. R. Coté, Y. Izumi, J. S. Caughey, and C. J. Readings, "Turbulent structure in the convective boundary layer," Q. J. R. Meteorol. Soc. (to be published).

[23] R. L. Fante, "Electromagnetic beam propagation in turbulent media," Proc. IEEE 63, 1669 (1975).

[24] S. F. Clifford and H. T. Yura, "Equivaline of two theories of strong optical scintillation," J. Opt. Soc. Am. **64**, 1641 (1974).

The Range Limitation on Radar-Acoustic Sounding Systems (RASS) due to Atmospheric Refractive Turbulence

STEVEN F. CLIFFORD AND TING-I WANG

Abstract—The effects of acoustic refractivity fluctuations on the operation of a radar-acoustic sounding system (RASS) have been calculated. Using the Born approximation, the electromagnetic field scattered from a spherical acoustic pulse whose sphericity is perturbed by transmission through the turbulent medium between the source and scattering volume was determined. The resultant system gain reduction factor changes the dependence on range R of the total received power from an R^{-2} dependence for a homogeneous atmosphere to $R^{-18/5}$ in strong turbulence. This new range dependence can occur at distances of the order of a few hundred meters for sufficiently strong turbulence.

INTRODUCTION

RECENTLY, considerable interest has been generated in the potential of a combined radar-acoustic sounder system (RASS) to measure temperature profiles in the lower atmosphere. Marshall *et al.* [1] discuss the history of the technique and its unique advantages for atmospheric probing.

The advantages of this system over conventional acoustic or radiowave sounding of the clear atmosphere arise from the fact that the RASS system scatters a radiowave from an effective spherical reflector produced by a collocated acoustic sounder. An acoustic pulse of wavelength λ_a is transmitted first, and then a radiowave of wavelength λ_e is scattered from the refractivity fluctuations produced by the wavefronts of the acoustic wave. The acoustic wave satisfies the Bragg scattering condition for backscatter of the EM wave so that $\lambda_a = \lambda_e/2$; hence, as long as it maintains its proper shape, the spherical acoustic wave perfectly focuses the incident EM energy on the receiver to produce a large gain in scattering efficiency over clear air scattering.

The purpose of this paper is to analyze the perturbing effects of the intervening turbulent medium that destroy the sphericity of the acoustic wavefronts and to compute the consequent gain reduction.

ANALYSIS

From Tatarski [3], we can calculate the electric field, scattered from a weak refractive index perturbation η_1 located at position r_1 to an observer at r (see Fig. 1) from the integral

$$E_s(r) = \frac{k_e^2}{2\pi} \int_V d^3r_1 \frac{e^{ik_e|r-r_1|}}{|r-r_1|} \eta_1(r_1)E_0(r_1) \tag{1}$$

where $k_e = 2\pi/\lambda_e$ with λ_e equal to the wavelength of the
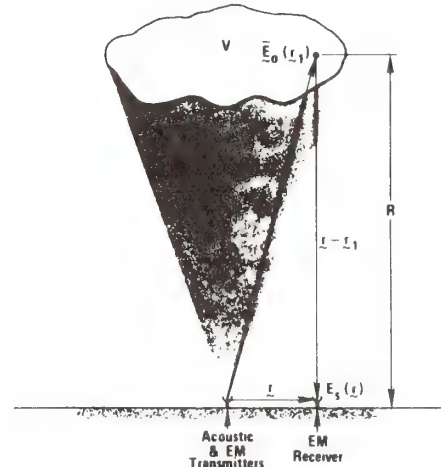
Fig. 1. Geometry of transmitters, receivers, and scattering volume for RASS.

electric field $E_0(r_1)$ incident upon the volume V. The origin of coordinates in (1) is at the transmitter. The refractive index fluctuations must satisfy the relation $\eta_1 \ll 1$ to be considered sufficiently weak for (1) to be valid.

For the RASS problem $\eta_1(r_1)$ is due to the transmitted acoustic pulse, that has the form

$$\eta_1(r_1) = \begin{cases} \xi_0 \, \text{Re}\left[\dfrac{e^{ik_a r_1 + \psi(r_1)}}{r_1}\right], \\[2mm] \qquad\qquad R - \dfrac{N\lambda_a}{2} < r_1 < R + \dfrac{N\lambda_a}{2} \\[2mm] 0, \qquad\qquad \text{otherwise} \end{cases} \tag{2}$$

where $k_a = 2\pi/\lambda_a$ with λ_a the acoustic wavelength, R is the range to the scattering volume, and N is the total number of cycles in the acoustic pulse. The quantity ξ_0/R is the refractive index perturbation at $r_1 = R$. We take the real part in (2) because we assume that η_1 is pure real. The factor e^ψ is included to account for the effects of the refractive turbulence that the incident acoustic wave encounters on its way to the scattering volume. It is this quantity that causes departures of η_1 from perfect sphericity and degrades system performance. The quantity in brackets is the total acoustic field incident upon the scattering volume. Both the unperturbed field (spherical pulse) and its first-order perturbation are included. If we call this total acoustic field u and its spherical pulse component u_0, then clearly (2) is equivalent to $u_1(r_1) =$

$u_0(r_1)e^{\psi}$. Now, by assumption $\eta_1(r_1)$ is also equal to $\eta(r_1)$; therefore, ψ must be defined by $\psi = \ln(u/u_0)$. Finally we let u and u_0 be represented as phasors, i.e., $u_0 = A_0 \exp(is_0)$ and $u = A \exp(is)$; then $\psi = \ln(A/A_0) + i(s - s_0)$ where A is the amplitude of the total acoustic wave and s is its total phase and A_0 and S_0 are the amplitude and phase of the unscattered wave.

In (1) $E_0(r_1)$ is the incident electromagnetic signal, a spherical wave emitted from a source collocated with the sounder, i.e.,

$$E_0(r_1) = A_0 \frac{e^{ik_e r_1}}{r_1}. \tag{3}$$

This field also suffers degradation due to the intervening turbulence, but for radiowaves this is significantly less than for acoustic waves. Inserting (2) and (3) into (1), we obtain

$$E_s(r) = \frac{k_e^2 \xi_0 A_0}{2\pi} \int_{V(R)} d^3 r_1 r_1^{-2} \frac{e^{ik_e |r-r_1|}}{|r - r_1|}$$

$$\cdot \exp[ik_e r_1 + \chi(r_1)] \cos[k_a r_1 + s_1(r_1)] \tag{4}$$

where $s_1 = s - s_0$ and $\chi = \ln A/A_0$.

The flux of scattered power in watts/(meter)^2 in the direction toward the receiver is proportional to $|E_s|^2$, and we are interested in its average value, i.e., $S = \langle E_s E_s^* \rangle$. Substituting (4) into the definition of S, we obtain

$$S = \frac{k_e^4 \xi_0^2 A_0^2}{(2\pi)^2} \int_{V(R)} d^3 r_1 \int_{V(R)} d^3 r_2$$

$$\cdot \frac{c^{ik_e(r_1 - r_2)}}{r_1^2 r_2^2} \frac{e^{ik_e|r-r_1|}}{|r - r_1|} \frac{e^{-ik_e|r-r_2|}}{|r - r_2|}$$

$$\langle e^{\chi(r_1) + \chi(r_2)} \cos[k_a r_1 + s_1(r_1)] \cos[k_a r_2 + s_1(r_2)] \rangle. \tag{5}$$

Equation (5) is a good approximation to the radial power density if $R \gg \lambda_e$. We assume that χ and s_1 are random variables and that they are normally distributed. In Appendix I the expected value of the quantity in the angle brackets is computed to be

$$\langle e^{\chi(r_1) + \chi(r_2)} \cos[k_a r_1 + s_1(r_1)] \cos[k_a r_2 + s_1(r_2)] \rangle$$

$$\cong \frac{1}{2} \cos[k_a(r_1 - r_2)] e^{-\frac{1}{2} D_w(r_1, r_2)} \tag{6}$$

where D_w is the wave structure function defined in Tatarski [3], [5]. The exponential quantity is a measure of the acoustic waves decreasing coherence as it propagates through the intervening turbulent medium. (Note, if there were no turbulence, $\exp[-\frac{1}{2}D_w] \to 1$.) Substituting this expression into (5), we

obtain

$$S = \frac{k_e^4 \xi_0^2 A_0^2}{8\pi^2} \int_{V(R)} d^3 r_1 \frac{e^{ik_e r_1}}{r_1^2} \frac{e^{ik_e|r-r_1|}}{|r - r_1|}$$

$$\cdot \int_{V(R)} d^3 r_2 \frac{e^{-ik_e r_2}}{r_2^2} \frac{e^{-ik_e|r-r_2|}}{|r - r_2|}$$

$$\cdot \cos[k_a(r_2 - r_1)] e^{-\frac{1}{2} D_w(r_1, r_2)} \tag{7}$$

There are several assumptions that can be made to simplify (7). First, the fluctuations in the wave parameters, e.g., amplitude and phase, have the properties that their statistics depend separately upon the difference in coordinates along the spherical shell perpendicular to the radius of the outgoing wave and, to a good approximation, upon the center of mass of the two radial dimensions. (This is more fully discussed in Tatarski [4].) Therefore we may write

$$D_w(r_1, r_2) = D_w\left(r_1 \sin\theta_1 - r_2 \sin\theta_2, \frac{r_1 + r_2}{2}\right) \tag{8}$$

where θ is the angle between the normal to the wavefront at an arbitrary position and the z axis. Finally, if the pulse-width is not too large. i.e., $N\lambda_a \ll R$, the dependence of D_w upon r_1 and r_2 in (7) and their variation in the denominator is sufficiently weak that we can replace r_1 and r_2 by R; consequently,

$$D_w(r_1, r_2) = D_w[R(\sin\theta_1 - \sin\theta_2), R]. \tag{9}$$

What we have ignored in going from (8) to (9) is the decrease of longitudinal coherence in the propagating wave. Tatarski [4] states that the coherence length in this direction is of the order of R and therefore this effect is negligible.

With (9) substituted into (7), after integrating out the ϕ variation and assuming that the receiver is also located at the origin of the coordinates, i.e., $r = 0$, since D_w has azimuthal symmetry, we obtain the expression

$$S = \frac{\gamma^4 k_e^4 \xi_0^2 A_0^2}{8R^2} I(R) \int_{R-\frac{N\lambda_a}{2}}^{R+\frac{N\lambda_a}{2}} dr_1 \int_{R-\frac{N\lambda_a}{2}}^{R+\frac{N\lambda_a}{2}} dr_2$$

$$\cdot e^{i2k_e(r_1 - r_2)} \cos[k_a(r_1 - r_2)] \tag{10}$$

where

$$I = \frac{4}{\gamma^4} \int_0^{\gamma} d\theta_1 \int_0^{\gamma} d\theta_2 \sin\theta_1 \sin\theta_2$$

$$\cdot \exp\{-\frac{1}{2} D_w[R(\sin\theta_1 - \sin\theta_2), R]\}. \tag{11}$$

In (11), γ is the smaller of the acoustic half-beamwidth γ_a or the electromagnetic half-beamwidth γ_e, and (11) is normalized so that $I(R) = 1$ in the absence of turbulence, i.e., when $D_w = 0$. The double integral in (10) is easily integrated by elementary means and, when evaluated, it takes the form

$$S = \frac{\gamma^4 k_e^4 \xi_0^2}{16 R^2} A_0^2 (N\lambda_a)^2 \left\{ \frac{\sin\left[(k_a - 2k_e)(N\lambda_a/2)\right]}{(k_a - 2k_e)(N\lambda_a/2)} \right\}^2 I(R). \tag{12}$$

The R^{-2} dependence comes from the spherically diverging acoustic wave. (We have also assumed that $r_1 \sim R$ and $r_2 \sim R$ in the denominator over the range of integration in (10).) If $I = 1$, (12) would agree with the expression in Marshall [2]. In general $I \leq 1$ and produces the gain reduction caused by the intervening turbulence. All that remains is to evaluate I from (11).

REFRACTIVE TURBULENCE ATTENUATION FACTOR

To evaluate I, we use the form of D_w for spherical waves from Lutomirski and Yura [6],

$$(1/2)D_w \left[R(\sin\theta_1 - \sin\theta_2), R\right]$$

$$= 0.132\pi^2 k_a^2 \int_0^R dz \, C_n^2(z) \int_0^\infty dK \, K^{-8/3}$$

$$\cdot \left\{1 - J_0\left[Kz(\sin\theta_1 - \sin\theta_2)\right]\right\} \tag{13}$$

where J_0 is the zero order Bessel function of the first kind and C_n^2 is the refractive turbulence structure parameter, an estimate of the "intensity" of refractive turbulence. (The validity of the assumption that we can use an optical wave result for an acoustic wave as we have done in choosing the particular form of (13) is demonstrated in a paper by Clifford and Brown [7].) Lutomirski and Yura assume that the Kolmogorov spectrum of turbulence is valid such that, in the so-called inertial subrange between some inner scale l_0 and some outer scale L_0, this universal wavenumber spectrum applies

$$\Phi_n(K) = 0.033 C_n^2 K^{-11/3}, \qquad L_0^{-1} \ll K \ll l_0^{-1}. \tag{14}$$

In writing (13), we have assumed $L_0 = \infty$. This assumption is valid provided $L_0 > \gamma R$.

Equation (13) can be simplified by integrating out the K variation. Using the integral table of Wheelon [8] and letting $u = z/R$, we obtain

$$(1/2)D_w = 1.46 k_a^2 R^{8/3} \, |\sin\theta_1 - \sin\theta_2|^{5/3}$$

$$\cdot \int_0^1 du \, C_n^2(u) u^{5/3}. \tag{15}$$

We can now identify a single parameter D where

$$D = 1.46 k_a^2 R^{8/3} \int_0^1 du \, C_n^2(u) u^{5/3} \tag{16}$$

and write (11) in the form

$$I = \frac{4}{\gamma^4} \int_0^\gamma d\theta_1 \, \sin\theta_1 \int_0^\gamma d\theta_2 \, \sin\theta_2 \, e^{-D|\sin\theta_1 - \sin\theta_2|^{5/3}} \tag{17}$$

The parameter D can be thought of as the total amount of integrated turbulence between the ground and the scattering volume. Note that the $u^{5/3}$ weighting inside the u integral emphasizes C_n^2 values at higher altitudes ($u = 0$ is at the ground).

We can reduce (17) to a single integral by assuming that γ is sufficiently small that the small angle approximation $\sin\theta \sim \theta$ applies in both integrals. We then transform variables to $\xi = \theta_1 - \theta_2$ and $2\eta = \theta_1 + \theta_2$. This produces the expression

$$I = \frac{8}{\gamma^4} \int_0^\gamma d\xi \, \exp\{-D\xi^{5/3}\} \int_{\frac{\xi}{2}}^{\gamma - \frac{\xi}{2}} d\eta \left(\eta^2 - \frac{\xi^2}{4}\right). \tag{18}$$

The inside integral can be performed by elementary means and (18) becomes

$$I = \frac{8}{3} \int_0^1 dy \, \exp\left[-Hy^{5/3}\right] \left(1 - \frac{3y}{2} + \frac{y^3}{2}\right) \tag{19}$$

where $y = \xi/\gamma$ and H is a new parameter defined by

$$H = D\gamma^{5/3} = 1.46 k_a^2 R^{8/3} \gamma^{5/3} \int_0^1 du \, C_n^2(u) u^{5/3}. \tag{20}$$

(A physical interpretation of H is that it is the mean-square phase difference at two points separated by a distance γR along the acoustic wavefront at a range R.) Fig. 2 shows the behavior of $I(H)$ versus H.

Since $I(H)$ is linear in the log-log plot of Fig. 2, when H becomes large, we should be able to generate a convenient asymptotic expression in this region. In (19) as H increases, the exponential truncates the integration closer and closer to $y = 0$; therefore, we should be able to ignore the y and y^3 terms compared to unity and also increase the upper limit to infinity with negligible error. If we change variables to $z = y^{5/3}$, the integral can be solved by elementary means and we obtain

$$I = \frac{8}{5} H^{-3/5} \Gamma(3/5) = 2.38 H^{-3/5} \tag{21}$$

This asymptote is the dashed line in Fig. 2.
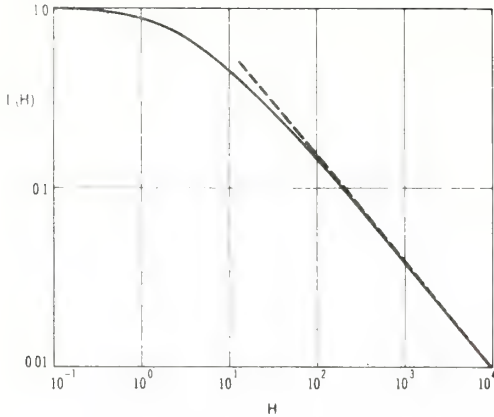
Fig. 2.   Plot of gain reduction factor for RASS system due to atmospheric turbulence effects versus H, parameter expressing amount of integrated turbulence between acoustic source and scattering volume

Fig. 3.   Plot of 3 dB and 10 dB range limitation curves as function of acoustic wavenumber k_a, beamwidth γ, and strength of refractive turbulence C_n^2.

In Appendix II, we derive the expression for the received power in terms of the various system parameters in the form

$$P_r = 4.6 \times 10^{-17} \frac{N^2 P_a P_t}{R^2} \left\{ \frac{\sin\left[(k_a - 2k_e)(N\lambda_a/2)\right]}{(k_a - 2k_e)(N\lambda_a/2)} \right\}^2 I(H)$$

$$\cdot \begin{cases} g_a, & \text{if } \gamma_e \leqslant \gamma_a \\ g_e^2/g_a, & \text{if } \gamma_e \geqslant \gamma_a \end{cases} \tag{22}$$

where

$$H = 1.46 k_a^2 R^{8/3} \gamma^{5/3} \int_0^1 du\, C_n^2(u) u^{5/3} \tag{23}$$

and γ is the smaller of the acoustic or electromagnetic half-beamwidths γ_a or γ_e, respectively, and $I(H)$ is plotted in Fig. 2. In (22), $k_a = 2\pi/\lambda_a$ where λ_a is the acoustic wavelength, $k_e = 2\pi/\lambda_e$ where λ_e is the electromagnetic wavelength, R is the range to the scattering volume, g_e and g_a are the electromagnetic and acoustic antenna gains, respectively. N is the number of cycles in the acoustic pulse, C_n^2 is the acoustic refractive-turbulence structure parameters [3, p. 119] and P_a and P_t are the radiated powers of the acoustic and radar antennas, respectively. Fig. 3 illustrates the range limitation as determined from $I(H)$ as a function of k_a, γ and C_n^2 for both 3 dB and 10 dB reductions in received signal power. If we use the asymptotic form of $I(H)$ from (21) we obtain

$$P_r = 9.6 \times 10^{-18} \frac{P_t P_a N^2 \lambda_a^{6/5}}{R^{18/5} \left[\displaystyle\int_0^1 du\, C_n^2(u) u^{5/3} \right]^{3/5}}$$

$$\cdot \left\{ \frac{\sin\left[(k_a - 2k_e)(N\lambda_a/2)\right]}{(k_a - 2k_e)(N\lambda_a)/2)} \right\}^2 \begin{cases} g_a/\gamma_e, & \gamma_e \leqslant \gamma_a \\ g_e^2/(\gamma_a g_a), & \gamma_e \geqslant \gamma_a \end{cases} \tag{24}$$

for $H \gg 1$, or strong integrated turbulence.

DISCUSSION

We have calculated the effects of acoustic refractivity fluctuations on the operation of a RASS system. Fig. 2 shows the reduction in gain one would observe, over that calculated by Marshall *et al.* [1] or Marshall [2], due to refractive turbulence located along the path to the scattering volume. This turbulence perturbs the sphericity of the acoustic wavefronts causing reduced effectiveness in focusing the incident electromagnetic energy. In effect the acoustic wavefronts became "bumpier" reflectors as the wave propagates further into the medium and this effect causes the subsequent gain reduction. Equation (24) is an asymptotic expression for the received power for large values of integrated refractive turbulence. This expression contains an additional $R^{-8/5}$ decrease in received power with range over that predicted when turbulence effects are ignored.

APPENDIX I

The quantity in the angle brackets in (5) is most easily computed by expanding the cosine terms into their exponential constituents, i.e.,

$$\langle\,\rangle = \tfrac{1}{4} \left\langle \exp\left[\chi(r_1) + \chi(r_2)\right] \left[e^{ik_a r_1 + is_1(r_1)} + e^{-ik_a r_1 - is_1(r_1)}\right] \right.$$

$$\left. \cdot \left[e^{ik_a r_2 + is_1(r_2)} + e^{-ik_a r_2 - is_1(r_2)}\right] \right\rangle. \tag{A1}$$

We intend to use the property of a mean-zero Gaussian random process, B, that

$$\langle \exp(B) \rangle = e^{1/2\langle B^2 \rangle}. \tag{A2}$$

From scattering theory we know that it is reasonable to assume that $\langle S_1 \rangle = 0$ but $\langle \chi \rangle$ cannot be zero, in fact, to conserve energy $\langle \chi \rangle$ must satisfy

$$\langle \chi \rangle = -\sigma_\chi^2 \tag{A3}$$

where σ_χ^2 is the variance of χ defined by

$$\sigma_\chi^2 = \langle [\chi - \langle \chi \rangle]^2 \rangle. \tag{A4}$$

The relation in (A3) follows directly from the fact that $\langle I \rangle$, the expected value of the irradiance, must equal its unperturbed value I_0; i.e.,

$$\frac{\langle I \rangle}{I_0} = \frac{\langle u u^* \rangle}{u_0^2} = \langle e^{\chi + i s_1} e^{\chi - i s_1} \rangle = 1 \tag{A5}$$

where u is the total acoustic field.

After subtracting off the mean value of χ in the exponents and using (A2), we obtain

$$\exp \{ 2\langle \chi \rangle + 2\sigma_\chi^2 \} = 1 \tag{A6}$$

and obviously (A3) follows from (A6).

In (A1) we add and subtract $\langle \chi(r_1) \rangle = \langle \chi(r_2) \rangle = \langle \chi \rangle$ to make the resulting variable mean zero and we obtain four resulting terms

$$\langle \, \rangle = \frac{1}{4} \left\{ e^{i k_a (r_1 - r_2) + 2\langle \chi \rangle} \langle e^{\chi'(r_1) + \chi'(r_2) + i s_1(r_1) - i s_1(r_2)} \rangle \right.$$
$$+ e^{-i k_a (r_1 - r_2) + 2\langle \chi \rangle} \langle e^{\chi'(r_1) + \chi'(r_2) - i s_1(r_1) + i s_1(r_2)} \rangle$$
$$+ e^{i k_a (r_1 + r_2) + 2\langle \chi \rangle} \langle e^{\chi'(r_1) + \chi'(r_2) + i s_1(r_1) + i s_1(r_2)} \rangle$$
$$\left. + e^{-i k_a (r_1 + r_2) + 2\langle \chi \rangle} \langle e^{\chi'(r_1) + \chi'(r_2) - i s_1(r_1) - i s_1(r_2)} \rangle \right\} \tag{A7}$$

where $\chi' = \chi - \langle \chi \rangle$. We now use (A3) and (A2). After dropping the covariance of the amplitude and phase in the exponential term because of its smallness compared with the terms retained, we obtain

$$\langle \, \rangle = \frac{1}{2} \cos [k_a(r_1 - r_2)]$$
$$\cdot e^{-2\sigma_\chi^2 + \frac{1}{2}\langle [\chi'(r_1) + \chi'(r_2)]^2 \rangle - \frac{1}{2}\langle [s_1(r_1) - s_1(r_2)]^2 \rangle}$$
$$+ \frac{1}{2} \cos [k_a(r_1 + r_2)]$$
$$\cdot e^{-2\sigma_\chi^2 + \frac{1}{2}\langle [\chi'(r_1) + \chi'(r_2)]^2 \rangle - \frac{1}{2}\langle [s_1(r_1) + s_1(r_2)]^2 \rangle} \tag{A8}$$

The first term in (A8) differs from the second primarily because of the phase difference in the exponent rather than the sum as in the second term.

Consider the function

$$\langle [s_1(r_1) \mp s_1(r_2)]^2 \rangle = 2\sigma_s^2 \mp 2C_s(r_1, r_2) \tag{A9}$$

where σ_s^2 is the phase variance and C_s is the phase covariance function defined by $C_s(r_1, r_2) = \langle s_1(r_1) s_1(r_2) \rangle$. When the minus sign applies (A9) becomes the definition of the structure function D_s, i.e.,

$$D_s(r_1, r_2) = 2\sigma_s^2 - 2C_s(r_1, r_2). \tag{A10}$$

This quantity varies from zero when $r_1 = r_2$ to $2\sigma_s^2$ when $|r_1| \gg |r_2|$. When the plus sign applies the resulting function has a minimum value of $2\sigma_s^2$ when $|r_1| \gg |r_2|$ and a maximum of $4\sigma_s^2$ when $r_1 = r_2$. Consequently, the maximum error we can make by dropping the second term is a factor of two. (Actually, it can be shown, because the most important region of integration in (5) occurs when $r_1 = r_2$, that the error caused by ignoring the second term is considerably less than a factor of two.)

We now direct our attention to the terms in (A8) that involve χ', first expand in the usual way

$$-2\sigma_\chi^2 + \frac{1}{2} \langle [\chi'(r_1) + \chi'(r_2)]^2 \rangle$$
$$= -2\sigma_\chi^2 + [\sigma_\chi^2 + C_\chi(r_1, r_2)]. \tag{A11}$$

Combining these two terms we note that the result is the structure function for χ

$$D_\chi(r_1, r_2) = 2\sigma_\chi^2 - 2C_\chi(r_1, r_2). \tag{A12}$$

Taking these simplifications into account, we may finally write (A8) as

$$\langle \, \rangle = \frac{1}{2} \cos [k_a(r_1 - r_2)] e^{-1/2 D_w(r_1, r_2)}. \tag{A13}$$

The quantity D_w is defined in Tatarski [5] as the wave structure function and in terms of the log-amplitude and phase structure function is given by

$$D_w = D_\chi + D_s. \tag{A14}$$

APPENDIX II

The problem considered here is to relate the expression in (12) to that of Marshall [2]. First, Marshall calculated the total power received in terms of the total power emitted by the acoustic source. In (12), $S = \langle E_s^2 \rangle$ and from antenna theory the total power received P_r is

$$P_r = \frac{S}{4\pi z_0} \lambda_e^2 g_e \tag{A15}$$

where g_e is the electromagnetic antenna gain and z_0 is the characteristic impedance of free space. Equation (A15) implies the validity of the local plane wave assumption, which is not obviously applicable in case of a focused spherical wave. However, in Appendix III we discuss this problem and find that the local plane wave assumption is valid where the beamwidth of the focused wave is less than 1 rad. Similarily we can relate the total transmitted power P_t to the quantity A_0^2/R^2 by the formula

$$\frac{A_0^2}{R^2 z_0} = \frac{P_t g_e}{4\pi R^2}. \tag{A16}$$

After inserting these two expressions into (12) we obtain the expression for the total backscattered power received

$$P_r = \frac{\pi^2}{16} \gamma^4 \left(\frac{\lambda_a}{\lambda_e}\right)^2 N^2 \frac{\xi_0{}^2 P_t g_e{}^2}{R^2}$$

$$\cdot \left\{ \frac{\sin\left[(k_a - 2k_e)\left(\frac{N\lambda_a}{2}\right)\right]}{(k_a - 2k_e)\left(\frac{N\lambda_a}{2}\right)} \right\}^2 I. \tag{A17}$$

Now, we assume that $\lambda_e/\lambda_a \sim 2$ in the coefficient from the Bragg condition and then (A17) becomes

$$P_r = \pi^2 \frac{\xi_0{}^2 \gamma^4 P_t N^2 g_e{}^2}{64R^2} \left\{ \frac{\sin\left[(k_a - 2k_e)\left(\frac{N\lambda_a}{2}\right)\right]}{(k_a - 2k_e)\left(\frac{N\lambda_a}{2}\right)} \right\}^2 I. \tag{A18}$$

Finally we must construct the relation between ξ_0 and the acoustic antenna parameters. From (2) $\xi_0/R \equiv \Delta n/n$, the refractive index perturbation produced by the acoustic transmitter at the scattering volume. The formula for atmospheric acoustic refractive index is given by [3]

$$n = 7.9 \frac{P}{T} \times 10^{-5} \tag{A19}$$

where P and T are the atmospheric pressure and temperature, respectively. To find Δn we linearly perturb (A19)

$$n + \Delta n = 7.9 \frac{(P_0 + \Delta p)}{(T_0 + \Delta T)} \times 10^{-5} \tag{A20}$$

where P_0 and T_0 are the background pressure and temperature and Δp and ΔT are the perturbations produced by the acoustic sounder. Retaining terms to first order only, we obtain

$$\frac{\Delta n}{n} \cong 7.9 \times 10^{-5} \frac{\Delta p}{T_0} - 7.9 \times 10^{-5} \frac{P_0 \Delta T}{T_0{}^2}. \tag{A21}$$

At STP $T_0 \cong 273$ K and $P_0 \cong 1013$ mbar, therefore (A21) becomes

$$\frac{\Delta n}{n} = 2.9 \times 10^{-7} \Delta p - 1.07 \times 10^{-6} \Delta T. \tag{A22}$$

For an adiabatic process

$$T = Bp^{\frac{\gamma-1}{\gamma}} = Bp^{0.286} \tag{A23}$$

where γ is the ratio of specific heats ($\gamma \sim 1.4$) and B is a constant. After linearly perturbing (A23)

$$\Delta T = 0.286 B (P_0)^{-0.714} \Delta P \tag{A24}$$

and noting that $B = T_0 P_0{}^{-0.286}$, we obtain

$$\Delta T = 0.077 \Delta p. \tag{A25}$$

Substituting (A25) into (A22), the expression for $\Delta n/n$ becomes

$$\frac{\Delta n}{n} = 2.1 \times 10^{-7} \Delta p. \tag{A26}$$

Since Δp is in millibars and all other quantities are in MKS units we should convert the coefficient 2.1×10^{-7} to that for Δp in MKS. One millibar is approximately 10^2 N/m^2 so the new equation is

$$\frac{\Delta n}{n} = 2.1 \times 10^{-9} \Delta p \tag{A27}$$

where Δp is in newtons/meter^2. The only remaining task to find $\xi_0{}^2$ is to relate Δp to the relevant antenna and atmospheric parameters. The acoustic pressure fluctuation produced by a point source with power flux S_a(W/m^2) is

$$\Delta p = [2\rho_0 C S_a]^{1/2} \tag{A28}$$

where ρ_0 is the mean density of air and C is the speed of sound in air, both quantities at STP. The power density at a distance R is related to the total acoustic power output P_a (watts) and the antenna gain g_a by the relation

$$S_a = \frac{P_a g_a}{4\pi R^2}. \tag{A29}$$

Substituting (A29) and (A28) into (A27), we obtain the expression for the refractive index perturbation

$$\frac{\Delta n}{n} = \frac{2.1 \times 10^{-9}}{R} \sqrt{\frac{\rho_0 C P_a g_a}{2\pi}}. \tag{A30}$$

Now, since $\xi_0{}^2 = R^2 \Delta n^2/n^2$ we obtain

$$\xi_0{}^2 = 7.0 \times 10^{-19} P_a g_a \rho_0 C \tag{A31}$$

(the constant factor has dimensions of meter^2/newton). Again at STP $\rho_0 = 1.29$kg/m^3 and $C = 331$ m/s, therefore,

$$\xi_0{}^2 = 3.0 \times 10^{-16} P_a g_a. \tag{A32}$$

Inserting (A32) into (A18) we obtain the final expression

$$P_r = 4.6 \times 10^{-17} \frac{\gamma^4 P_a g_a P_t g_e{}^2 N^2}{R^2}$$

$$\cdot \left\{ \frac{\sin\left[(k_a - 2k_e)\left(\frac{N\lambda_a}{2}\right)\right]}{(k_a - 2k_e)\left(\frac{N\lambda_a}{2}\right)} \right\}^2 I. \tag{A33}$$

Equation (A33) agrees with result of Marshall [2] to within about 30 precent. The difference is attributable to differing assumptions about the values of T_0, P_0, ρ_0 and C.

Finally we can obtain the results for the cases $\gamma_e < \gamma_a$ and $\gamma_e > \gamma_a$, where γ_e and γ_a are the electromagnetic and acoustic half beamwidths, respectively,

$$P_r = 4.6 \times 10^{-17} \frac{N^2 P_a P_t}{R^2} \left\{ \frac{\sin \left[(k_a - 2k_e) \left(\frac{N\lambda_a}{2} \right) \right]}{(k_a - 2k_e) \left(\frac{N\lambda_a}{2} \right)} \right\}^2 I(R)$$

$$\cdot \begin{cases} g_a, & \text{if } \gamma_e \leqslant \gamma_a \\ g_e^2/g_a, & \text{if } \gamma_e \geqslant \gamma_a \end{cases} \qquad (A34)$$

where we have used the appropriate relation $g_e \sim \gamma_e^{-2}$ or $g_a \sim \gamma_a^{-2}$.

APPEXDIX III

For (A15) to be used to evaluate the total received power, the local plane wave assumption must be valid in the vicinity of the receiving antenna. This condition is not satisfied for an antenna located at the focal plane of a focused spherical wave. The range of validity of this assumption will be discussed in this appendix.

Let us first assume that there is no turbulent medium between the receiver and the spherical acoustic wave fronts. Then (4) can be simplified as

$$E_s(R) = \frac{k_e^2 \xi_0 A_0}{2\pi} \int_{V(R)} d^3 r_1 \frac{e^{ik_e r_1}}{r_1^2} \cos (k_a r_1) \frac{e^{ik_e |r_1 - r|}}{|r_1 - r|}. \qquad (A35)$$

Here, the transmitter is at the origin of coordinates and the receiver is at r. If we assume that $|r_1| (\sim R) \gg |r|$, then $|r_1 - r|$ can be replaced by R in the denominator and by $r_1 + r [\sin \theta \sin \theta_1 \cos (\phi_1 - \phi) + \cos \theta \cos \theta_1]$ in the exponential, where the θ and the ϕ are the angles in spherical coordinates. Then (A35) becomes

$$E_s(R) = \frac{k_e^2 \xi_0 A_0}{2\pi R} \int_{R - \frac{N\lambda_a}{2}}^{R + \frac{N\lambda_a}{2}} dr_1 \exp (2ik_e r_1)$$

$$\cdot \cos (k_e r_1) \int_0^\gamma d\theta_1 \sin \theta_1 \int_0^{2\pi} d\phi_1$$

$$\cdot \exp \{ ik_e r [\sin \theta \sin \theta_1 \cos (\phi_1 - \phi) + \cos \theta \cos \theta_1] \} \qquad (A36)$$

where γ is the smaller of the acoustic beamwidth γ_a or the electromagnetic beamwidth γ_e. Performing the integral over r_1 and ϕ_1, we obtain

$$E_s(R) = \frac{k_e^2 \xi_0 A_0}{\pi^2 R} \frac{\sin [(k_a - 2k_e)N\lambda a/2]}{(k_a - 2k_e)N\lambda a/2} N\lambda_a$$

$$\cdot \exp [i(2k_e - k_a)R] I_1(\gamma) \qquad (A37)$$

where

$$I_1(\gamma) \equiv \int_0^\gamma d\theta_1 \sin \theta_1 \exp [ik_e r \cos \theta \cos \theta_1]$$

$$\cdot J_0 [k_e r \sin \theta \sin \theta_1].$$

At the receiving plane, $\theta = \pi/2$, hence

$$I_1(\gamma) = \int_0^\gamma d\theta_1 \sin \theta_1 J_0 [k_e r \sin \theta_1]. \qquad (A38)$$

It is difficult to evaluate $I(\gamma)$ for arbitrary γ without introducing further approximations. If we assume that $\gamma \ll 1$, then $\sin \theta \cong \theta$. In this case $I(\gamma)$ can be simplified as

$$I_1(\gamma) = \int_0^\gamma d\theta_1 \theta_1 J_0 [k_e r \theta_1] = \gamma^2 \frac{J_1(k_e r\gamma)}{k_e r\gamma}. \qquad (A39)$$

To generate a perfect section of spherical wave with beamwidth γ_e, the transmitter antenna pattern should be

$$F(r) = \frac{2J_1(k_e r\gamma_e)}{k_e r\gamma_e}. \qquad (A40)$$

Because we use the same antenna for both transmitting and receiving, the receiving antenna has the same pattern as the transmitting antenna. Hence the receiving power is

$$P_r = \int d^2 r \, E_s \cdot E_s^* F^2(r) = \frac{2k_e^4 \xi_0^2 A_0^2}{\pi^3 R^2}$$

$$\cdot \left\{ \frac{\sin [(k_a - 2k_e)N\lambda_a/2]}{(k_a - 2k_e)N\lambda_a/2} \right\}^2 (N\lambda_a)^2 \int_0^\infty dr \, rF^2(r) I^2(\gamma). \qquad (A41)$$

Inserting (A39) and (A40) into (A41), we have

$$P_r = \frac{2k_e^4 \xi_0^2 A_0^2}{\pi^3 R^2} \left\{ \frac{\sin [(k_a - 2k_e)N\lambda_a/2]}{(k_a - 2k_e)N\lambda_a/2} \right\}^2$$

$$\cdot (N\lambda_a)^2 \frac{4\gamma^4}{k_e^2 \gamma_e^2} \int_0^\infty dr \frac{J_1^2(k_e r\gamma)J_1^2(k_e r\gamma_e)}{k_e^2 r^3 \gamma^2}. \qquad (A42)$$

The integration over r in the above equation is not easy to evaluate. However, because γ is the smaller of γ_e and γ_a, we will discuss the case $\gamma_e < \gamma_a$ and $\gamma_e > \gamma_a$ seperately. If $\gamma_e < \gamma_a$, then $\gamma = \gamma_e$. The integral in this case is simply a constant.

If $\gamma_e > \gamma_a$, then $\gamma = \gamma_a < \gamma_e$. The most important contribution to the integral comes from the region in the vicinity of $\gamma = 1/(k_e r_e)$. In this case, the Bessel function $J_1(k_e r\gamma) \cong k_e r\gamma/2$. The integral can be simplified as $\int_0^\infty dr\, J_1^2(k_e r\gamma_e)/(4r)$. Again, this is a constant. Hence (A42) can be written as

$$P_r \sim \frac{\xi_0^2 A_0^2}{R^2} \frac{\gamma^4}{\gamma_e^2} \left(\frac{\lambda_a}{\lambda_e}\right)^2 N^2 \left\{\frac{\sin\,[(k_a - 2k_e)N\lambda_a/2]}{(k_a - 2k_e)N\lambda_a/2}\right\}^2.$$

(A43)

Inserting (A16) and (A32) into (A43), we have ($g_a = 1/\gamma_a^2$ and $g_e = 1/\gamma_e^2$)

$$P_r \sim \frac{P_t P_a}{R^2} \frac{\gamma^4}{\gamma_e^4 \gamma_a^2} \left(\frac{\lambda_a}{\lambda_e}\right)^2 N^2 \left\{\frac{\sin\,[(k_a - 2k_e)N\lambda_a/2]}{(k_a - 2k_e)N\lambda_a/2}\right\}^2.$$

(A44)

This result is consistant with the result of (A33) which is obtained by using (A15) to calculate the received power. Therefore, we have proven that if the beamwidth γ is not large ($\gamma \leqslant 1$ rad), the local plane wave assumption is valid even in the focal plane of the spherical beam.

The dependence of P_r on the P and the γ of (A44) can be expressed as

$$P_r \sim \begin{cases} P_t P_a g_a, & \text{if } \gamma = \gamma_e \leqslant \gamma_a; \\ P_t P_a g_e^2/g_a, & \text{if } \gamma = \gamma_a \leqslant \gamma_e. \end{cases}$$

(A45)

The physical interpretation of (45) is as follows. If $\gamma = \gamma_e < \gamma_a$, the transmitting acoustic and EM power are $P_a g_a$ and $P_t g_e$, respectively. The received power is proportional to the product of the acoustic and EM power and the square of the beam size γ_e^2, hence $P_r \sim P_t g_e P_a g_a \gamma_e^2 = P_t P_a g_a$, which agrees with (A45). However, the situation changes when $\gamma = \gamma_a < \gamma_e$. We use the same EM antenna as transmitting and receiving antenna. When the transmitting beam and receiving beam have the same width, all the power can be picked up by the antenna. In case the effective receiving beam (γ_a) is smaller than the transmitting beam (γ_e), the power picked up by the EM antenna is only γ_a^2/γ_e^2 of the total power. Hence the receiving power becomes $P_r \sim P_t g_e P_a g_a \gamma_a^2 (\gamma_a^2/\gamma_e^2) = P_t P_a g_e^2/g_a$. This is also consistent with the result of (A45)

REFERENCES

[1] J. M. Marshall, A. M. Petersen, and A. A. Barnes, Jr., *Appl. Opt.*, vol. 11, pp. 108–112, (1972).
[2] J. M. Marshall, Scientific report No. 39, National Aeronautics and Space Administration, Grant No. NGL05-020-014, Feb. 1972.
[3] V. I. Tatarski, *Wave Propagation in a Turbulent Medium.* New York: McGraw-Hill, 1961
[4] ——, *Sov. Phys. J.E.T.P.*, vol. 22, pp. 1083–1088, (1966).
[5] —— *The Effects of the Turbulent Atmosphere on Wave Propagation.* (Translated from the Russian by the Israel Program for Scientific Translations; originally published in 1967), U.S. Dept. of Commerce, Nat. Tech. Info. Ser., Springfield, VA 472 pp. (1971).
[6] R. F. Lutomirski and H. T. Yura, *J. Opt. Soc. Am.*, vol. 61, pp. 482–487, (1971).
[7] S. F. Clifford and E. H. Brown, *J.A.S.A.*, vol. 48, pp. 1123–1127, (1970).
[8] A. D. Wheelon, *Table of Summable Series and Integrals Involving Bessel Functions.* San Francisco: Holden-Day, 1960.

An Acoustic Doppler Sounder for Measuring Wind Profiles in the Lower Boundary Layer

J. C. Kaimal and D. A. Haugen

NOAA ERL Wave Propagation Laboratory, Boulder, Colo. 80302

(Manuscript received 22 April 1977, in revised form 24 September 1977)

ABSTRACT

A simplified acoustic Doppler wind sensor that can be built around an existing sounder is described. The instrument consists of two fan-beam transmitters and a pencil-beam receiver in an orthogonal configuration. Considerable improvement in signal-to-noise ratio over previous techniques is realized with this approach. Field tests show good agreement between the Doppler sounder measurements and wind measurements with *in situ* sensors on a 150 m tower. The system operated satisfactorily in an airport environment under fog conditions as well as in light rain. It failed only during periods of jet aircraft activity directly over the sounder and under conditions of moderate-to-heavy rainfall.

1. Introduction

In recent years descriptions of various acoustic Doppler techniques for measuring winds have appeared in the literature (e.g., Beran *et al.*, 1971; Beran and Clifford, 1972; Beran, 1975; Balser *et al.*, 1976; Kaimal and Haugen, 1975). The monostatic systems used in earlier Doppler experiments had a major drawback that limited their usefulness for continuous wind profiling. Monostatic echoes are produced entirely by temperature fluctuations in the sampling volume. Therefore the returns tend to be discontinuous with resulting gaps in the wind information. Often the neutral atmosphere yields no information at all.

Bistatic systems, in which the transmitting and receiving antennas are separated in space but aimed at a common volume, yield more continuous returns since both wind and temperature fluctuations contribute to the scattering. Wind profiles can be obtained by moving the common volume up and down, or by steering one of the beams either mechanically or electronically. Alternative systems using a combination of fan-beam receivers and a narrow-beam transmitter have been tested successfully (e.g., Beran *et al.*, 1974; Haugen, 1976). Such systems use pulse transmission (the spatial resolution of the wind measurement is a function of the pulse length chosen) and time-gating techniques to track the acoustic pulse as it propagates upward. However, with fan-beam receivers, the potential for poor signal-to-noise ratio exists, since the elevation coverage for unwanted noise is always much larger than that for the acoustic pulse.

In the approach described here we have attempted to improve the signal-to-noise ratio by reversing the positions and beam patterns of the transmitters and receivers. A single, vertically pointing receiver collects the scattered returns from acoustic pulses generated by two fan-beam transmitters placed in an orthogonal array.[1] Doppler shifts in the two transmitted signals (of differing frequencies) are detected and converted to velocity information. By time-gating the received signal, it is possible to get useful wind profile data to heights that are twice the antenna separation distance. In such a system, receiver performance can be optimized for maximum sidelobe rejection. Since the receiver points in the direction of minimum background noise, a further advantage is gained in the signal-to-noise ratio. The burden of performance, therefore, falls on the transmitters, which now have to radiate sufficient acoustic energy over a wide elevation angle. This problem can be handled by proper antenna and cuff design. An attractive aspect of this approach is the ease with which a conventional acoustic sounder can be converted for Doppler wind measurement by the addition of a few off-the-shelf commercial components. The system discussed here was developed for the Air Force Geophysical Laboratories (AFGL), for low-altitude, low-wind-speed applications in an airport environment.

2. Principle of operation

The theory of sound propagation and scattering has been covered in sufficient detail elsewhere (Little, 1969; Beran and Clifford, 1972) and will not be repeated here. The derivation of wind speed from the measured Doppler frequency shift for the bistatic configuration

---

[1] Two wind sensing systems based on the same concept have been developed recently, one by J. W. Wescott (private communication), the other by Davey (1976).
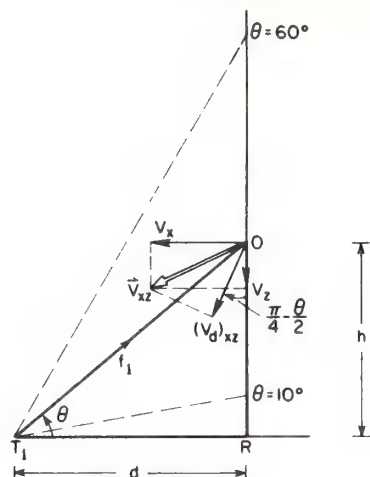
FIG. 1. Ray geometry for Doppler wind sensing in the x-z plane. T_1 is a transmitter, R the receiver and d is the horizontal distance between them.

described here is best explained by Fig. 1. V_z and V_x are the horizontal and vertical components of the instantaneous wind vector $\mathbf{V}_{xz}$ in the x-z plane, which contains the transmitter (T_1) and receiver (R) beams. The Doppler wind velocity $(V_d)_{zz}$ is the component along the direction bisecting the transmitter and receiver beams.

If Δf_1 is the frequency shift measured at elevation angle θ in the transmitted frequency f_1, and if C is the velocity of sound in air, the Doppler wind equation for the x-y plane would become

$$\Delta f_1 = \frac{2f_1}{C}\left[(V_d)_{zz} \sin\left(\frac{\pi}{4}+\frac{\theta}{2}\right)\right]. \quad (1)$$

The Doppler wind component can be expressed in terms of the horizontal and vertical wind components as

$$(V_d)_{zz} = \left[V_z \cos\left(\frac{\pi}{4}+\frac{\theta}{2}\right) - V_x \cos\left(\frac{\pi}{4}-\frac{\theta}{2}\right)\right]. \quad (2)$$

Equations for the Doppler frequency shifts Δf_1 and Δf_2 in the x-y and y-z planes, respectively, reduce to

$$\Delta f_1 = (f_1/C)[V_x \cos\theta - V_z(1+\sin\theta)], \quad (3)$$

$$\Delta f_2 = (f_2/C)[V_y \cos\theta - V_z(1+\sin\theta)]. \quad (4)$$

To measure V_x and V_y accurately, one needs either an independent measure of V_z or a method of averaging the readings over a period long enough to insure that $\bar{V}_z = 0$ (the overbar denotes time average). Eqs. (3)

and (4) then reduce to

$$\bar{V}_x = \left(\frac{C}{f_1 \cos\theta}\right)\overline{\Delta f_1}, \quad (5)$$

$$\bar{V}_y = \left(\frac{C}{f_2 \cos\theta}\right)\overline{\Delta f_2}. \quad (6)$$

The importance of time averaging cannot be over-emphasized since the V_z contribution could seriously contaminate horizontal wind measurements, particularly at the higher levels, if $\bar{V}_z$ is not made sufficiently small. As shown in Fig. 2, the sensitivity of the Doppler wind component to the vertical wind velocity exists for all scattering angles but rises very rapidly above $\theta = 60°$. The length of the averaging period required for $\bar{V}_z$ to approach zero, over reasonably flat terrain, is a function of height. In the unstable convective boundary layer, a 3–5 min averaging period may be adequate for the first few meters above the ground, but for heights on the order of 1 km, a minimum averaging period of 15–20 min is needed. In thermally stable air, the requirement for averaging length is less severe— a 5 min averaging time should be adequate at all heights within the stable boundary layer. A discussion of the relationship between length scales and height is given by Kaimal (1973) and Kaimal et al. (1976). In applications where such long averaging intervals are unacceptable, as in airport wind-shear monitoring or when sloping terrain produces a nonzero $\bar{V}_z$, simultaneous measurement of V_z is essential to remove its contributions in Eqs. (3) and (4).

The elevation angle range between 10° and 60° is best suited for Doppler wind measurement. Below 10° the strength of the scattered signal drops rapidly, approaching zero at 0°; above 60° the resolution of the horizontal wind measurement is degraded by the large inclination angle in V_d. In our data processing routine, the elevation range from 7° to 63.5° is covered, which corresponds to a height range of d/8 to 2d.
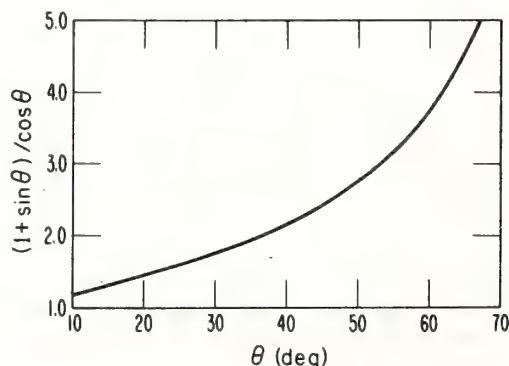
FIG. 2. Sensitivity of the Doppler wind component to V_z relative to V_x. V_z is defined positive upward.

Analog Inputs to Computer
1. Doppler Shift (Δf_1)
2. Doppler Shift (Δf_2)
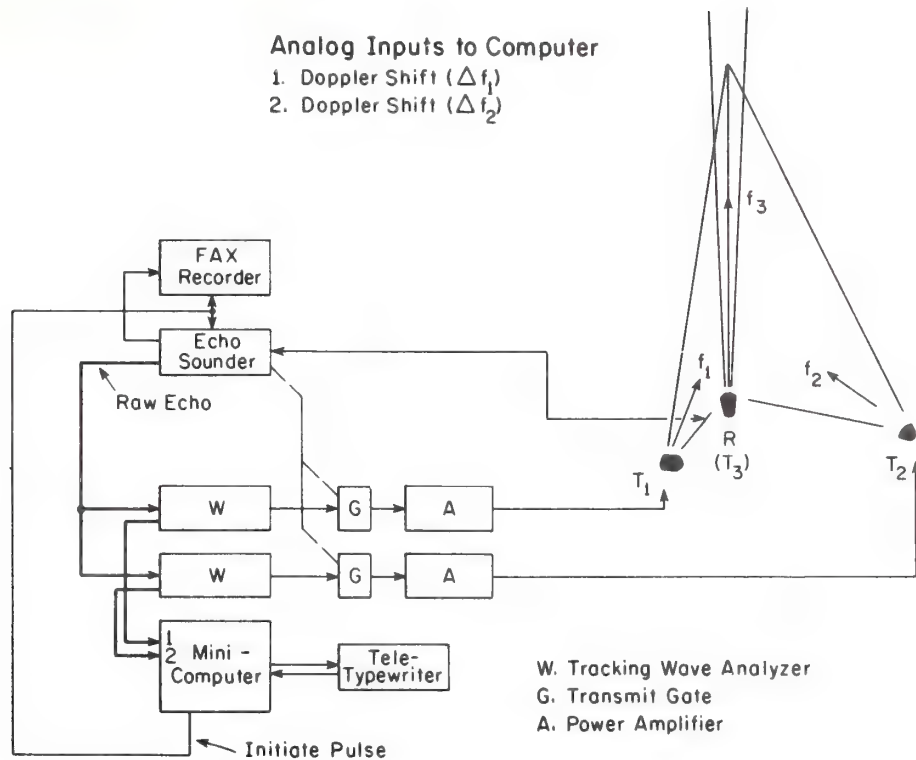
FIG. 3. Block diagram of the acoustic Doppler sounder.

3. System configuration

The Doppler sounder is designed to provide full control over all operating parameters so that performance characteristics such as velocity sensitivity, wind speed range and height resolution can be varied to suit the requirements of a particular experiment. All parameters (with the exception of the height range which depends on the length of the baseline) are adjustable either through dial settings on the instrument panels or by changes requested through the computer keyboard.

A simplified block diagram of the AFGL system is shown in Fig. 3. The system is built around a standard NOAA Mark VII acoustic sounder (Owens, 1975) and utilizes its antenna and receiver electronics to collect the bistatic returns from sound pulses emitted by the fan-beam transmitters T_1 and T_2. The carrier frequencies f_1 and f_2 for the two transmitters are generated by two tracking wave analyzers (Quan-Tech, Model 304 TDL). The frequency of each analyzer can be tuned manually over a range of 1 to 5000 Hz. The preferred settings for AFGL's low-level applications are $f_1 = 3.6$ kHz and $f_2 = 3.0$ kHz. These settings provide adequate sensitivity with low background noise and do not interfere with the Mark VII acoustic sounder frequency options ($f_3 = 2.0$, 2.5 and 3.3 kHz).

The oscillator outputs are applied to a pair of transmission gates (operated synchronously with the transmit gate in the echo sounder) to produce the tone bursts that drive T_1 and T_2. The duration of the tone burst is controlled by thumb-wheel settings on the acoustic sounder. The transmitters are driven by two power amplifiers (Crown, Model DC-300A modified for monaural operation) capable of delivering 300 W to each transmitter.

The three transmitters[2] (T_1, T_2, T_3) are pulsed simultaneously under software control. An "initiate" pulse generated by the computer not only opens the transmitter gates, but also sets the delay time needed to blank out any ringing in the receiver antenna, initiates the ramp voltage (which, multiplied by the received raw echo, corrects for attenuation due to spherical divergence of the scattered signals), and starts the facsimile recorder scan of the vertical backscatter intensity in f_3. The direct transmissions from T_1 and T_2 arrive at R after time $t = d/C$ (neglecting the wind component along the base line). Tracking of Doppler shifts in f_1 and f_2 begins soon after the trailing edge of the tone burst has passed the receiver. For extraction of the Doppler frequency shifts Δf_1 and Δf_2, the raw echo from the echo sounder is fed back to the inputs of the two tracking wave analyzers, as shown in Fig. 3. Bandpass filters in the wave analyzers reject all unwanted frequencies in the raw echo and measure

[2] The receiver antenna R switches to transmitter T_3 mode for the duration of the tone burst.

the departure of the first moment of the Doppler spectrum from the transmitted frequency. Since the passband always remains centered on the transmitted frequency, the measured frequency shift is insensitive to small drifts in the frequency setting. Available as outputs from the tracking wave analyzers are analog signals representing the frequency shift in each channel. These signals are presented to the multiplexer inputs of the minicomputer (Data General, Nova 820) where they are sampled, digitized and stored in temporary memory locations for processing.

A critical factor in the design of any acoustic Doppler system is the beam pattern of the transmitting and receiving antennas. The locus of all scatterers contributing to signal intensity at any instant is an ellipsoid that has its foci at the transmitting and receiving antennas. A large segment of the ellipsoid is illuminated by the fan-beam transmitters, so it is imperative that side-lobe rejection in the receiver be exceptionally good. It is desirable to limit the beamwidths of the transmitting antennas in the azimuth direction, partly to conserve power, but more importantly to minimize reflections from nearby objects. Beam patterns for the transmitting and receiving antennas at frequencies near the upper and lower ends of the operating range are shown in Fig. 4. (The axis of the transmitting antenna is tilted upward at a 45° angle from the horizontal to obtain the necessary elevation range.)

Fig. 5 shows the receiver antenna. The 1.2 m parabolic dish and driver-horn assembly are part of the standard NOAA Mark VII acoustic sounder, but the cuff design is new and accounts for the 50 dB side lobe attenuation at 90° in this receiver. The cuff is a 1.8 m high, six-sided structure made of external-grade plywood and lined internally with 5 cm foam absorber. Sandwiched in

the foam is a lead septum that effectively blocks acoustic transmission through the cuff walls. Our selection of the flare angle for the cuff (16°) is based on numerical studies of gain patterns reported by Strand (1971) and Adekola (1977). Their studies had anticipated optimum side-lobe rejection at this flare angle and our beam pattern measurements confirm their predictions.

The transmitting antenna consists of an array of three sectoral dispersion horns (Altec Model 311-90) mounted as shown in Fig. 6a. Each horn is driven by a 100 W high-frequency driver (Altec 290-4G) connected in series to present a 12 Ω load impedance to the power amplifier. The absorbing cuff (lined with the same absorbing material used in the receiver cuff) fits over the horn enclosure to reduce side-lobe energy in the horizontal plane. A view of the electronic hardware including the dual-channel storage scope, minicomputer and teletypewriter is shown in Fig. 6b.

4. Signal processing

A minor modification of the tracking wave analyzer (schematic available on request) is necessary to extract the frequency-shift information from its phase-comparator circuit. The voltage output is a nonlinear function of the frequency deviation and requires linearization before it can be used in the Doppler wind computation. This linearization is provided by the computer software. It is apparent from Fig. 7 that the sensitivity of the frequency discriminator is a function of filter bandwidth. The relationship between frequency shift Δf, bandwidth B and voltage output (E_0) can be approximated empirically by

$$E_0 = 2.3 \sin(\pi \Delta f / 2B), \qquad (7)$$

where E_0 is in volts.
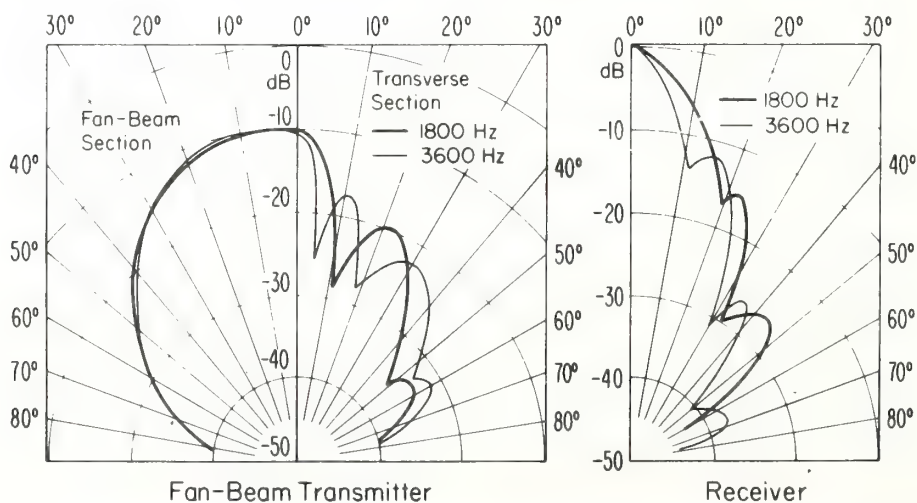
FIG. 4. Polar patterns of the acoustic beam in the fan-beam and transverse directions for transmitters T_1 and T_2 and of the acoustic beam for receiver R.

Thus,

$$t_i = C^{-1}[h_i^2 + d^2)^{\frac{1}{2}} + h_i] + \tfrac{1}{2}\tau, \qquad (8)$$

where τ is the duration of the tone burst.

Expressions for V_x and V_y in terms of the frequency discriminator outputs are obtained by rearranging Eq. (7) and substituting for Δf_1 and Δf_2 in Eqs. (5) and (6).
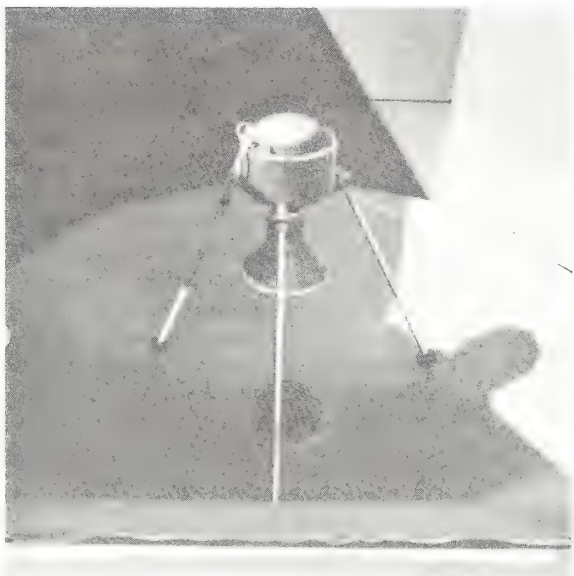
FIG. 5. External view (a) of the vertically pointing acoustic sounder, and internal view (b) showing 1.2 m parabolic dish and transducer.

The frequency-discriminator outputs E_{01} and E_{02} are sampled along with the detected intensities in f_1 and f_2 at time t_i following the "initiate" pulse (where $i = 1, 2, 3, \ldots, N$ and N is the total number of heights requested). The elapsed time t_i equals the total transit time for the center of the acoustic pulse to reach height h_i and for the scattered sound from that height to propagate vertically down to the receiver.

FIG. 6a. Fan-beam transmitter with absorbing cuff. The horn enclosure protects the three drivers attached at the rear. 6b. Electronic components including storage scope, minicomputer (left) and teletypewriter (center). The components in the instrument rack (from above) are the storage scope, sounder electronics, two tracking wave analyzers, frequency generator and three power amplifiers.
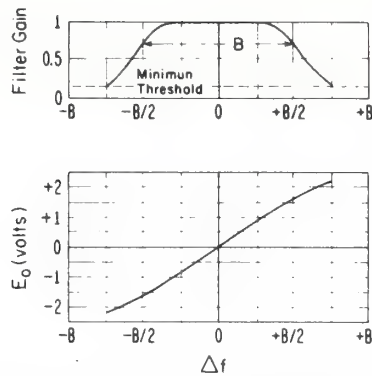
FIG. 7. Relationship between filter bandwidth and frequency discriminator output.

The averaged wind components at each level become

$$\bar{V}_x = \frac{2BC}{\pi f_1 \cos\theta} \overline{[\sin^{-1}(E_{01}/2.3)]}, \tag{9}$$

$$\bar{V}_y = \frac{2BC}{\pi f_2 \cos\theta} \overline{[\sin^{-1}(E_{02}/2.3)]}. \tag{10}$$

The frequency discriminator output from any single transmission sequence appears spikey as seen in Fig. 8. Since most of these spurious readings are associated with either a signal loss or a large external noise input, the detected echo intensity can be used as a criterion for eliminating them from the data sample. But even more effective in reducing scatter in the derived wind information is a moving average filter applied to the voltage outputs E_{01} and E_{02}. No significant bias is introduced since positive and negative spikes are equally probable in each scan. The width of the moving average is set equal to τ, the duration of the tone burst, to retain
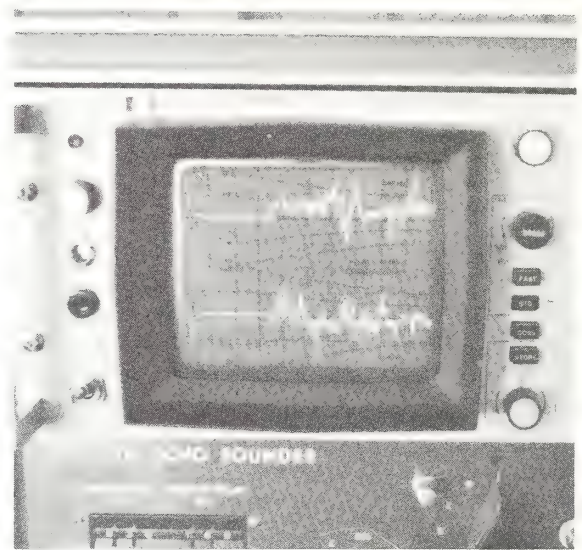
FIG. 8. Typical Doppler frequency shifts along the N–S (top trace) and E–W (bottom trace) directions from a single scan sequence displayed on a storage scope. The vertical axis denotes frequency shift and the horizontal axis time delay. The blanked regions correspond to the time interval between initiation of the transmit pulses at T_1 and T_2 and passage of the direct transmission across R.

the spatial resolution of the velocity measurement. To accomplish this, E_{01} and E_{02} are sampled and digitized once every millisecond and the readings stored in memory. Block averages over time interval $\pm \tau/2$ are then constructed around readings corresponding in time to the profile levels requested by the operator. (The software can accommodate up to 16 separate height levels.) The block-averaged data are retained in memory for developing the time averages that are printed out on the teletypewriter.
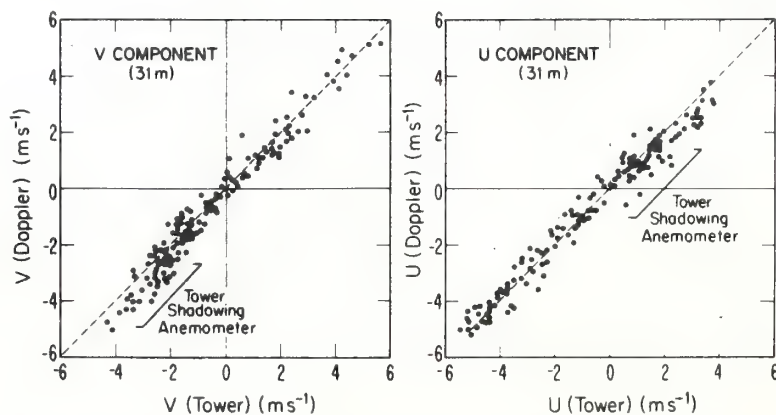
FIG. 9. Scatter diagram of wind components measured at 31 m by the tower sensors and the Doppler sounder. The V and U components correspond to the N–S and E–W components, respectively.
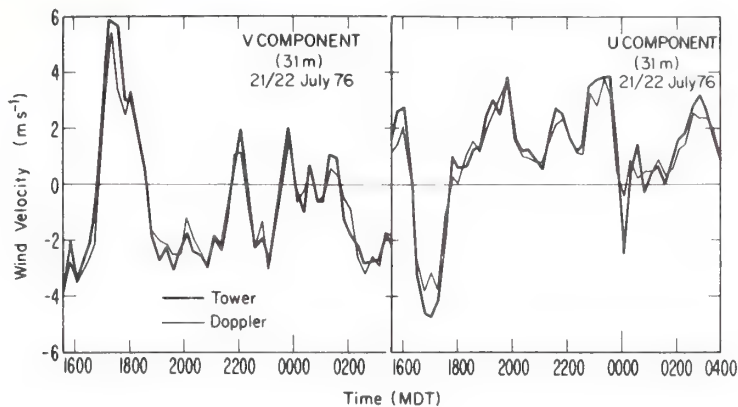
FIG. 10. Comparison of 15 min averaged winds measured by the tower sensors and the Doppler sounder during a 12 h observation period.

5. Test results

Extensive tests were conducted at the NOAA field site on Table Mountain to compare wind measurements from the Doppler sounder with measurements from *in situ* sensors (R. M. Young Co., propeller-vane anemometer Model 8002) on a 150 m tower. The test site is a flat, slightly elevated area about 2 mi² in extent. A 40 m baseline and a pulse repetition interval of 2 s were chosen to provide maximum accuracy and resolution in the 20–80 m height range critical to the fog modification program at AFGL.

During the initial tests, comparisons were made at heights of 31 and 67 m. Only 15 min averaged wind components were compared to minimize the effect of spatial separation (300 m) between the two systems. The agreement was good for most atmospheric conditions. The Doppler sounder did not operate satisfac-

torily in moderate-to-heavy rainfall but was unaffected by light showers or drizzle.

In Fig. 9 the scatter diagram of the north to south and east to west wind components (denoted by V and U, respectively) at 31 m indicates a spread of approximately ± 0.5 m s⁻¹. The largest departures correspond to periods when the anemometer was in the shadow of the tower.

Fig. 10 shows the time history of the mean wind field at 31 m during a 12 h period that included the neutral hour during the evening transition from an unstable to a stable lapse rate. The ability of the Doppler sounder to track the wind field during periods of greatly reduced temperature fluctuations was encouraging. Plots of the data taken at 67 m showed much the same behavior as in Fig. 10. In general, the agreement between the two systems was what would be expected for two identical sensors 300 m apart.

To determine how close an agreement one might expect in vertical profiles observed with the two techniques, we computed 10 min averaged wind velocities from the Doppler sounder at 5 m height intervals from 25 to 80 m. Tower profiles were also obtained for the same periods. The primary objective of this test was to establish system reliability under near calm, slightly stable atmospheric conditions. A sample 10 min profile obtained around 0400 MDT is shown in Fig. 11. Except for the 25 m U component, which seemed to read consistently low, agreement was good up to 80 m with winds <2 m s⁻¹.

The performance of the Doppler sounder in an airport environment was qualitatively assessed after the system was installed at AFGL's Otis Air Force Base test site in September 1976. The single major source of acoustic interference at the site was jet aircraft noise from an adjacent runway. The wave analyzers successfully tracked the Doppler frequency shift during these periods, including take-offs, and failed only when an aircraft appeared within the beam width of the receiver.
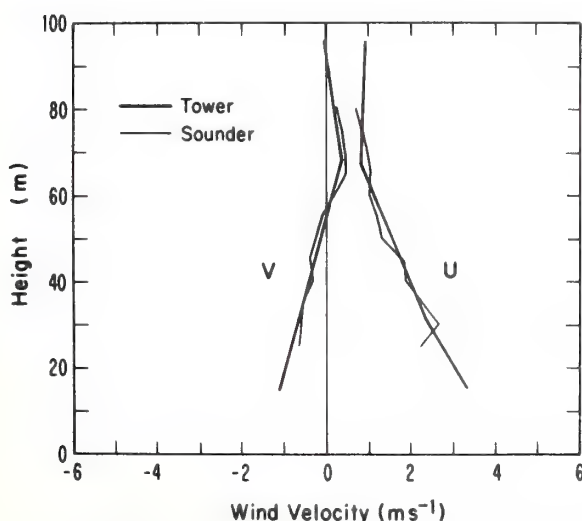
FIG. 11. Typical velocity profiles under stable lapse rate conditions around 0400 MDT.
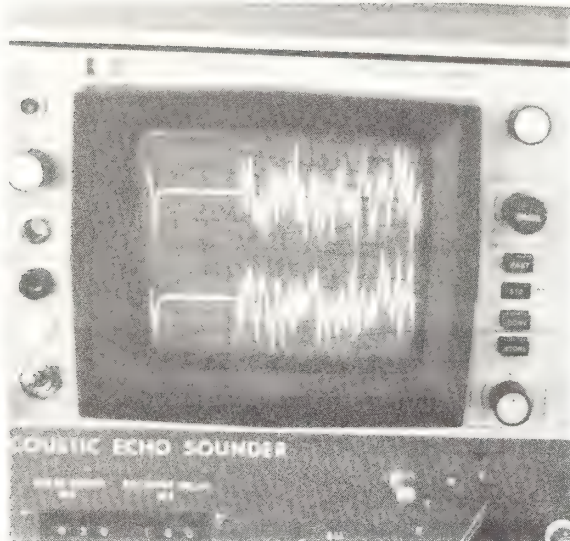
FIG. 12. Effect of jet aircraft noise on the Doppler signal. Compare with Fig. 8 for signal in the absence of such noise. The amplitude of the large positive and negative excursions in the trace is found to increase in proportion with the audible aircraft noise.

A typical scan of the frequency shift output during one take-off is shown in Fig. 12. The erratic appearance of the trace notwithstanding, the block-averaging technique was able to extract the velocity information. Only when the positive and negative excursions exceeded the bandwidth of the frequency discriminators, as when an aircraft was flying immediately overhead, did the measured wind velocities depart significantly from *in situ* measurements. Often, the net effect of any such noise episode on the 10 or 15 min averaged wind velocity was negligible, but several such episodes within a single averaging interval caused the velocity readings to be underestimated.

The operational limits of the system under strong wind conditions were not tested in these experiments. Experience with the vertically pointing antenna described here indicate that wind-generated noise becomes significant at wind speeds > 10 m s^{-1}. For high wind applications the useful range of the system can be extended by lowering the receiver antenna into the ground, bringing the cuff opening to a level flush with the surface of the ground.

REFERENCES

Adekola, S. A., 1977: The effects of phase front distribution on echosonde antenna radiation patterns. *Radio Sci.*, **12**, 11–22.

Balser, M., C. A. McNary, A. E. Nagy, R. Loveland and D. Dickson, 1976: Remote sensing by acoustic radar. *J. Appl. Meteor.*, **15**, 50–58.

Beran, D. W., 1975: Remote sensing wind and wind shear system. Interim Rep. FAA-RD-74-3.

——, and S. F. Clifford, 1972: Acoustic Doppler measurement of the total wind vector. *Preprints Second Symp. Meteorological Observations and Instrumentation*, San Diego, Amer. Meteor. Soc., 412–417.

Beran, D. W., C. G. Little and B. C. Willmarth, 1971: Acoustic Doppler measurements of vertical velocities in the atmosphere. *Nature*, **230**, 160–162.

——, B. C. Willmarth, F. C. Carsey and F. F. Hall, Jr., 1974: An acoustic Doppler wind measuring system. *J. Acoust. Soc. Amer.*, **55**, 334–338.

Davey, R. F., 1976: A coherent acoustic Doppler radar for real-time wind measurement. *Preprints 17th Conf. Radar Meteorology*, Seattle, Amer. Meteor. Soc., 270–275.

Haugen, D. A., 1976: Performance test results for a Xonics acoustic Doppler sounder. NOAA Tech. Memo ERL-WPL-16, 13 pp.

Kaimal, J. C., 1973: Turbulence spectra, length scales and structure parameters in the stable surface layer. *Bound. Layer Meteor.*, **4**, 289–309.

——, and D. A. Haugen, 1975: Evaluation of an acoustic Doppler radar for measuring winds in the lower atmosphere. *Preprints 16th Radar Meteorology Conf.*, Houston, Amer. Meteor. Soc., 312.

——, J. C. Wyngaard, D. A. Haugen, O. R. Coté, Y. Izumi, S. J. Caughey and C. J. Readings, 1976: Turbulence structure in the convective boundary layer. *J. Atmos. Sci.*, **33**, 2152–2169.

Little, C. G., 1969: Acoustic methods for the remote probing of the lower atmosphere. *Proc. IEEE*, **57**, 571–578.

Owens, E. J., 1975: NOAA VII Acoustic Echo Sounder. NOAA Tech. Memo. ERL WPL-12, 71 pp.

Strand, O. N., 1971: Numerical study of the gain pattern of a shielded acoustic antenna. *J. Acoust. Soc. Amer.*, **49**, 1698–1703.

Depolarization of Lidar Returns from Virga and Source Cloud

V. E. Derr, N. L. Abshire, R. E. Cupp and G. T. McNice

NOAA/ERL/Wave Propagation Laboratory, Boulder, Colo. 80302

(Manuscript received 13 February 1976, in revised form 4 October 1976)

ABSTRACT

The observed depolarization of polarized lidar signals scattered from virga and a source cloud may be interpreted to show that the source cloud is largely glaciated, and the virga is composed of ice crystals not randomly oriented. The orientation of the ice crystals in the virga, generally possible only in a nonturbulent atmosphere, is demonstrated by depolarization ratios greater than 1. The cloud processes suggested by this observation are in agreement with other independent observations.

1. Introduction

The study of cloud characteristics by remote sensing lidar techniques has been reported by Collis (1965), Cohen and Graber (1971), Poultney (1971), Plass and Kattawar (1971), Zuev and Balin (1972), and others. Efforts have been made to extend the method to include polarized radiation and polarization sensitive detectors by Harris (1969), Tyabotov (1969), Schotland *et al.* (1971), Pal and Carswell (1973), Balin *et al.* (1974), Carswell *et al.* (1974), Cohen and Graber (1974), Derr *et al.* (1974), Liou and Lahore (1974), and others. The remote sensing of cloud characteristics by lidar has potential in cloud physics for studying transformations, transformation rates, and the spatial distribution of ice and water in clouds and precipitation. Combined with infrared radiometry lidar is useful for determining the radiation characteristics of clouds. In weather modification it may aid in evaluation of cloud potential for effective seeding, and post-seeding assessment by detecting the degree of glaciation. The results obtained by many authors on depolarization of lidar signals by clouds are not completely consistent, primarily because of the insufficiency of *in situ* data necessary to evaluate the validity of remote sensing. We have at this time only an accumulation of partial data, with a few definitive observations, to explain the wide variety of effects observed (Pal and Carswell, 1973).

A recent observation of the depolarization of a ruby lidar beam by virga and its cumulus source exemplifies the significant information obtained by this technique and its interpretation demonstrates both the firmness of the foundation and the assumptions necessitated by remaining basic and eventually removable uncertainties. The new lidar observation of virga reported here illustrates that the method, under some meteorological circumstances, provides useful interpretation of cloud characteristics and ambient conditions. Caution in the use of the depolarization technique is required when cloud density is so high that multiple scattering may introduce interfering depolarization. Assumptions required in the interpretation of the data are discussed below.

2. Lidar scattering principles

Linearly polarized electromagnetic radiation backscattered from a homogeneous or spherically symmetric layered sphere remains linearly polarized (Kerker, 1969). Nonspherical shapes generally produce some depolarization in backscatter (Kerker, 1969; Liou and Lahore, 1974; Dugan *et al.*, 1971). Table 1 shows results obtained by several authors from theoretical, experimental, or field studies. This evidence, while not wholly consistent nor obtained under equally well-defined conditions, strongly supports the view that since liquid hydrometeors are approximately spherical and frozen hydrometeors (with a few notable exceptions) are usually nonspherical, we may use the depolarization of lidar backscattered radiance to determine whether clouds are in liquid or solid state.

Although large raindrops depart from sphericity, Schotland *et al.* (1971) have shown by laboratory and field studies (the latter with an elevation of the laser beam of 30°) when diameters lie in the range of 10–2000 μm the depolarization in backscatter is less than 0.03. Because the drop sizes in the source cumulus studied herein were probably considerably less than 2 mm (Auer, 1967), we accept that the depolarization was not due to distorted raindrops; however, we reserve the opinion that definitive laboratory experiments on larger drop sizes are desirable. So far as the authors can ascertain such experiments have not been performed.

There is a region of ambiguity in the interpretation of the depolarization ratio from Table 1, but low values (<10%, indicating water droplets only) and high

TABLE 1. Percent depolarization by hydrometeors according to several authors.

Authors	Water and possible multiscatter	Young ice (no orientation)	Ice unspecified	Oriented ice	Observed dependence on orientation	Water and ice clouds	Haze	Haze and drizzle	Rain	Snow	Type of data*
					Hydrometeor characteristics						
Liou and Lahore (1974)	2–4	35–40		45	Yes	10–20					T,E
			28								T
			29								T
Dugan et al. (1971)	0			>100	Yes						E,T
Balin et al. (1974)	5–35(A)		30–60		No		2–5(B)	12–25(C)	7–10(D)	20–45(E)	E
										50–85(F)	
Schotland et al. (1971)	3	38	81		No	35			3	94	E,F

$\sigma\,(\mathrm{km}^{-1})$

(A) 4 –40   (D) 0.6– 1
(B) 0.1– 0.2   (E) 0.5– 0.8 (crystals up to 0.5 mm diam.)
(C) 0.7– 1.5   (F) 1 – 3.5 (crystals up to 1–4 mm diam.)

* T, theoretical; E, experimental; F, field.

values (>30%, indicating substantial glaciation) can be interpreted consistently with all the authors quoted.

The depolarization ratio is defined as the ratio of the backscatter radiance in the receiver channel that accepts radiation polarized perpendicular to the emitted laser polarization to the backscatter radiance observed polarized parallel to the laser polarization, sometimes expressed as percentage. One hundred percent depolarization indicates that the emitted radiation is scattered in such a way that equal power is observed in each detector channel. Greater than 100% depolarization indicates that more power is observed in the detector channel sensitive to polarization perpendicular to that emitted by the lidar. We comment on the conditions under which this can occur after a short description of the lidar system.

The lidar system has an output of 1 J in a 10 ns pulse at a rate of 1 pulse per 2 s. The wavelength is 694.3 nm. The laser beam divergence is 0.5 mr. The Newtonian receiving telescope has a 71 cm diameter primary mirror, with an angular field of view of 2 mr. The received signal is split into two beams with perpendicular polarization by a Glan-Thompson prism, collimated, filtered and detected by photomultipliers. One receiver channel (herein called parallel) accepts components radiation polarized parallel to the emitted beam, whose polarization vector is horizontal. The second channel (perpendicular) accepts radiation components polarized perpendicular to the emitted beam.

The radiation from the lidar is coherent and polarized horizontally. However, the backscattered radiation from many randomly situated particles adds incoherently, that is, the power (rather than the radiation amplitude from each scatterer) is added to form the total signal. A nonspherical backscatterer generally introduces a component of polarization other than the incident polarization (Liou and Lahore, 1974). A large number of randomly ordered ice particles can produce no greater than 100% depolarization, by symmetry. Thus, observed cases of more than 100% depolarization must arise from oriented groups of scatterers. Dugan et al. (1971) have shown that hexagonal prisms of ice in a nephelometer rotate the polarization of the incident beam, when scattered at angles of 175°. In their case the incident beam was horizontally polarized. The theory of scattering from irregular particles is insufficient to precisely account for this experimental result, but is shown possible in principle by Liou and Lahore (1974).

Depolarization by multiple scatter may occur in dense water clouds. It is a function of optical depth, the phase function, and receiver beamwidth. It can approach depolarization values found in ice clouds without multiple scatter (Werner, 1974). It will be seen that it is not important in the observation presented here.

3. Observation

Lidar observations of virga were made at Boulder, Colo., on 20 August 1974 with the polarization sensitive lidar system. Fig. 1 shows typical signals received in the two detector channels from cumulonimbus with virga. The larger signals in both channels are from the cloud; the smaller signals at shorter range are due to scatter from the virga. The depolarization is the ratio of the signal in the perpendicular channel to that in the parallel channel. In this case the cloud shows strong depolarization and the virga below it shows depolarization greater than 100%. The cloud base height was
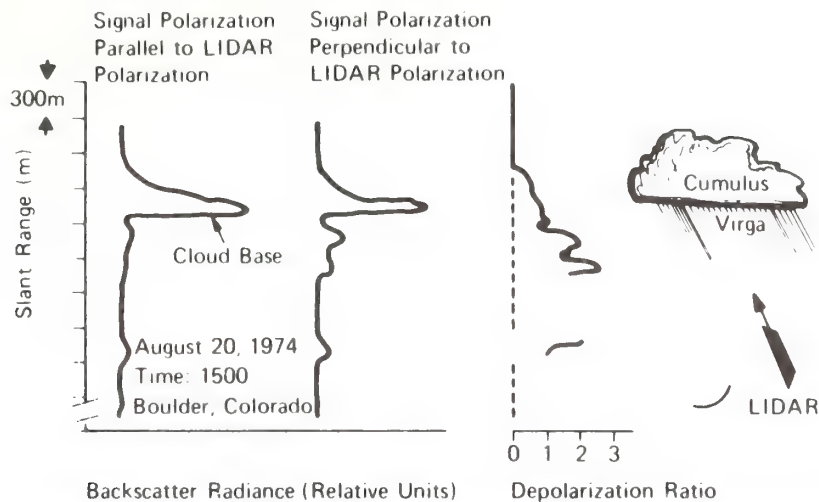
FIG. 1. Lidar signals received from cumulonimbus and depolarization ratio as a function of range. Cloud base height, 3819 m above ground; observation angle, 30° from zenith.

3819 m above the ground, which lay at 1800 m MSL. The virga extended, in patches, approximately 900 m below the cloud. The freezing level estimated from the 1800 MDL 20 August 1974 sounding at Denver was 2713 m above the ground, but the different time of the observation (1500 MDL) and the difference of location (approximately 48 km) render the exact freezing level uncertain.

4. Discussion

a. Interpretation of the measurement

We first examine the question of whether the depolarization effects may be attributed to multiple scatter, which produces depolarization in dense water clouds. An estimate of the magnitude of multiple scatter may be made if the absolute backscatter coefficient at the base of the cloud is known. At the time of this observation the lidar had not been calibrated against a standard target. Therefore many cumulus clouds, not yet precipitating, and typical of those later glaciating, were examined. These showed depolarization effects less than 4% indicating insufficient optical density to produce large multiple scatter effects. We may conclude that largely spherical particles are involved in the non-precipitating cumulus; they may be ice spheres or water spheres. The initial formation of ice in cumulus clouds is so unlikely to be spherical (Auer, 1967) that we accept the hypothesis that the cumulus showing no depolarization are water clouds of density below that required for multiple scatter.

Most of the cloud described in Fig. 1 shows depolarization near 80%, indicating (see Table 1) a highly glaciated condition. The depolarization in the virga region significantly exceeds 100%. By the arguments advanced above, the virga must consist of nonspherical ice particles falling in a nonturbulent atmosphere with an average orientation, perhaps as found in falling leaves. The argument for orientation does not depend

on the details of the scattering process. A complete lack of orientation would prevent depolarization greater than 100%.

It may be questioned whether ice has an optical rotatory power sufficient to enter into the process. Ice is a birefringent, uniaxial crystal, but its birefringence is so extremely low ($n_E - n_O = 0.0014$) that it is unlikely to be involved (Hobbs, 1974). Here n_E and n_O are the extraordinary and ordinary indices of refraction. However, the theory of backscatter from non-uniform, crystalline substances is not capable of giving immediate answers, so the question must remain open.

Insufficient information exists to correlate the observed large depolarization with specific meteorological conditions. However, more than a dozen observations of virga have shown only three cases of greater than 100% depolarization, although all but one case has shown large (>60%) depolarization. Qualitatively, depolarizations of more than 100% appeared only when cloud appearances showed little turbulence. At no time has virga been observed to give greater than 100% depolarization when cloud appearances showed signs of large turbulence. Thus, observations of greater than 100% depolarization strongly suggest a minimum of atmospheric turbulence.

b. Agreement with independent observations

A typical summer day in Boulder begins cloudless, with cumulus composed initially of liquid droplets forming over the continental divide and drifting eastward, with some showery precipitation forming toward the Kansas border by late afternoon. Eastward of the foothills of the Rockies, over the high plains, virga, almost invariably ice (Toutenhoofd, 1975), is frequently observed. Clouds in this continental area often are optically less dense than marine clouds (Auer, 1967), resulting in less multiple scatter effects. The cloud bases are often above the freezing level and the precipitation

forms by the Bergeron-Findeisen process. The clouds are thus glaciated, at least partially, and the precipitation often appears as virga. The observation presented above gives some support for these processes. In the early stages the cumulus is composed of liquid water droplets. As the cloud develops by updrafts well above the freezing level it glaciates and precipitation is observed below the cloud. The cloud observed closely followed this history.

c. Potential uses

In conclusion, we may state that this new lidar observation of virga and cumulus adds further evidence to the usefulness of lidar in differentiating between ice and water content of clouds. Although the observation presented here is not surprising to cloud physicists, it shows the potential of lidar remote sensing of cloud processes. Observations of the relative efficiency of ice formation, drop coalescence in precipitation, and the rates of cloud glaciation are important information for cloud physics and weather modification efforts (Knight et al., 1974; Cannon et al., 1974; Dye et al., 1974). The observations may be carried out night or day from ground or aircraft and offer operational information for cloud seeding and assessment. Range in clear air is not severely limited; clouds have been observed with useful signal-to-noise ratio at 45 km.

Lidar and radar supplement each other in cloud observations. Lidar is of shorter range than the larger radars. On the other hand, it can detect clouds with much less density and smaller hydrometeor size distribution than radar. The observation of cirrus, for example, can be done with a simple lidar, cheap relative to a standard weather radar. The formation and growth of clouds, before precipitation allows observation by radar, may be continually observed by lidar. Because the interaction of visible and near visible radiation with clouds is larger than that of microwaves, the penetration of lidar is less than that of radar. The combined use of lidar and radar will permit extended observational capability in cloud studies. A major disadvantage of present lidar systems is that they must generally be shut down in precipitation. Suitable windows over the transmitter and receiving telescope will undoubtedly be developed, and radiation at a wavelength of 10.6 μm may permit some penetration of severe weather.

Further developments underway include multiple-wavelength backscatter observations to obtain information on drop-size distribution (Post, 1975) and combined lidar and microwave radiometric observations to estimate water content.

REFERENCES

Auer, A. H. Jr., 1967: A cumulus cloud design for continental airmass regimes. *J. Rech. Atmos.* 3, 91–100.

Balin, Yu. S., G. O. Zadde, V. E. Zuev, G. G. Matvienko, I. V. Samokhualov and V. W. Shamanaev, 1974: Lidar investigations of polarization characteristics of meteorological formations. *Proc. Intern. Conf. Structure, Composition and General Circulation of the Upper and Lower Atmospheres and Possible Anthropogenic Perturbations*, Melbourne, 186–191.

Cannon, T. W., J. E. Dye and V. Toutenhoofd, 1974: The mechanism of precipitation formation in Northeastern Colorado cumulus. II Sailplane measurements. *J. Atmos. Sci.*, 31, 2148–2151.

Carswell, A. I., J. D. Houston and S. R. Pal, 1974: Lidar polarization studies of the lower atmosphere. *Preprints 1974 International Laser Radar Conference, Conference on Laser Atmospheric Studies*, Sendai, Japan, Amer. Meteor. Soc., 161–162.

Cohen, A., and M. Graber, 1971: Application of laser techniques to investigation of clouds and particles in the atmosphere. Final Report, Contract ESSA E-100-67 (E), Hebrew University, 309 pp.

——, and ——, 1974: Double-scattering calculations compared with laboratory dye-laser multiple scattering measurements. *Preprints 1974 International Laser Radar Conference, Conference on Laser Atmospheric Studies*, Sendia, Japan, Amer. Meteor. Soc., 126–128.

Collis, R. T. H., 1965: Lidar observations of cloud. *Science*, 149, 978–981.

Derr, V. E., R. E. Cupp, G. T. McNice, N. L. Abshire, M. J. Post and R. L. Schwiesow, 1974: The design and operation of á tropospheric remote sensing system. *Preprints 1974 International Laser Radar Conference, Conference on Laser Atmospheric Studies, 3–6 September 1974*. Sendai, Japan, Amer. Meteor. Soc., 8–9.

Dugan, V. P., B. M. Golubitskiy, S. O. Mirumyants, P. I. Paramonov and M. V. Tantashev, 1971: Optical properties of artificial ice clouds. *Atmos. Ocean. Phys.*, 7, 871–877.

Dye, J. E., C. A. Knight, V. Toutenhoofd and T. W. Cannon, 1974: The mechanism of precipitation formation in northeastern Colorado cumulus. III. Coordinated microphysical and radar observations and summary. *J. Atmos. Sci.*, 31, 2152–2159.

Harris, F. S., Jr., 1969: Changes in polarization and angular distribution of scattered radiations during cloud formation. *Appl. Opt.*, 8, 143–145.

Hobbs, P. V., 1974: *Ice Physics*. Clarendon Press, p. 202.

Kerker, M., 1969: *The Scattering of Light*. Academic Press, 666 pp.

Knight, C. A., N. C. Knight, J. E. Dye and V. Toutenhoofd, 1974: The mechanism of precipitation formation in Northeastern Colorado cumulus. I. Observations of the precipitation itself. *J. Atmos. Sci.*, 31, 2142–2147.

Liou, Kuo-Nan, and H. Lahore, 1974: Laser sensing of cloud composition: A backscattered depolarization technique. *J. Appl. Meteor.*, 13, 257–263.

Pal, S. R., and A. I. Carswell, 1973: Polarization properties of lidar backscattering from clouds. *Appl. Opt.*, 12, 1530–1535.

Plass, G. N., and G. W. Kattawar, 1971: Reflection of light pulses from clouds. *Appl. Opt.*, 10, 2304–2310.

Post, M. J., 1976: Limitations of cloud droplet size distribution by Backus-Gilbert inversion of optical scattering data. *J. Opt. Soc. Amer.*, 66, 483–486.

Poultney, S. K., 1971: Theoretical observational and analytical study of the optical properties of clouds. Final Rept., Dept. of Physics and Astronomy, Grant ESSA-E264-68, University of Maryland, 145 pp.

Schotland, R. M., K. Sassen and R. Stone, 1971: Observations by lidar of linear depolarization ratios for hydrometeors. *J. Appl. Meteor.*, 10, 1011–1017.

Tyabotov, A. E., V. I. Shlayakhov and A. B. Shupyatsky, 1969: *Izv. Atmos. Phys.*, 5, 192–195.

Werner, Ch., 1974: Determination of multiple scatter by means of laser radar techniques. *Preprints 1974 International Laser Radar Conference, Conference on Laser Atmospheric Studies*, Sendai, Japan, Amer. Meteor. Soc., 127–128.

Zuev, V. E., and Yu. S. Balin, 1972: Investigation of atmospheric boundary layers and clouds by the laser tracking method. *Fizika*, 15, No. 5, 125–128.

LIDAR OBSERVATIONS OF ATMOSPHERIC PARTICULATES NEAR
DENVER, COLORADO

V. E. Derr, G. T. McNice, N. L. Abshire, R. E. Cupp,
R. F. Calfee, and M. J. Ackley

        Lidar observations were made by WPL-(NOAA) of the cloud of pollution
often observed near the Platte River Valley north of Denver, Colorado, during
the EPA sponsored Denver Air Pollution Field Study of November 1973. The lidar
was located at the Adams County Fair Grounds, near Henderson, during the period
15-29 November. During this time four days of data were obtained on smog
conditions, namely 16, 21, 26, 29 November. This data is reported, analyzed
and compared with other observations taken simultaneously. From the lidar,
estimates may be made of total aerosol content up to the inversion level,
given a ground calibration.

STELLAR-SCINTILLATION MEASUREMENT OF THE VERTICAL PROFILE
OF REFRACTIVE-INDEX TURBULENCE IN THE ATMOSPHERE

G. R. Ochs, R. S. Lawrence and T. Wang
National Oceanic and Atmospheric Administration
Environmental Research Laboratories
Boulder, Colorado 80302

and

P. Zieske
AVCO Everett Research Laboratory
Puunene, Hawaii 96784

Abstract

We observe the turbulence-induced scintillation (twinkling) of a single star to measure, from the ground, the vertical profile of refractive-index turbulence in the atmosphere. A linear combination, with appropriate weights, of the strength of the scintillations observed with receivers of various spatial wavelengths allows us to synthesize a path weighting function centered at a specific height. The central height and height resolution of the measurement can be controlled by changing the relative coefficients and spatial wavelengths of the receiver outputs. Twenty-minute measurements, made with stars of second magnitude or brighter and with a 36-cm Schmidt-Cassegrain telescope, show that the atmospheric turbulence can be divided into four independent height regions with reasonable accuracy. The measurements of the different spatial wavelengths are made sequentially with the same telescope, and the statistical stationarity of the atmosphere during the 20-minute observation period is crucial to the accuracy of the deduced profile. Stationarity is roughly checked by continuously monitoring the whole-aperture scintillation of the star. The observed profiles agree with the strength and general shape of accepted models of the atmosphere and with profiles obtained from aircraft-mounted and previously used balloon-borne in-situ sensors.

Introduction

For centuries, it has been known that observations of astronomical sources, particularly the twinkling of stars and the motion of stellar images, yield information about the turbulence in the atmosphere.[1-12] Scintillation measurements have usually been used by astronomers for site-selection purposes but, in recent years, some attention has been given to the problem of deducing the vertical profile of refractive-index turbulence from ground-based measurements of stellar scintillation.[8-12] The application of these developments to the design of an optical instrument for measuring refractive-index turbulence will permit the gathering of synoptic data relevant to problems of ground-based imaging of astronomical and orbital objects.

We have previously discussed[10] the feasibility of using either a single-star or a double-star pair as the source for remote probing of the vertical atmospheric turbulence profile. The advantage of using a double star as a source is that a relatively good height resolution would be obtained by use of the crossed-path technique.[11] However, there are few useful double stars in the sky, so it seemed to us worthwhile to build a single-star instrument although the altitude-resolution may not be so good as could be obtained from the crossed-path method. In a previous paper,[12] we discussed a technique for measuring the atmospheric turbulence profile aloft by using a single star as a source and a spatially-filtered detector array as a receiver. Here, we present some quantitative results in the form of measured vertical profiles of refractive-index turbulence at Boulder, Colorado and at Mt. Haleakala, Hawaii. A comparison of the ground-based measurements and airplane in-situ measurements is also presented.

Theory and Implementation

The general philosophy of our approach is to view the spatial structure of the stellar scintillation pattern through filters that pass only a narrow band of spatial frequencies. By observing the signal intensity through filters of different spatial wavelengths and combining the outputs with appropriate weights, we obtain a set of reasonably sharp-peaked path-weighting functions centered at different heights, and so measure the vertical turbulence profile.

If we assume that the turbulence is described by a Kolmogorov spectrum, then, from Eq. (12) of reference 12, the composite path-weighting function resulting from a combination of N filters is given by

$$W_c(z) = \sum_{i=1}^{N} R_i \, K_i^{8/3} \, W_i'(z,d_i) \, , \tag{1}$$

where z is the height above the ground, N is the number of different wavelength filters used, R_i is the appropriate weight of the ith spatial wavenumber $K_i = 2\pi/d_i$, and d_i is the ith spatial wavelength. The W_i' in Eq. (1) are the weighting functions of the corresponding spatial wavelengths d_i given by Eqs. (9) to (11) of reference 12. In calculating the W_i', we have included the effect of a finite-sized array and the effect of a broad-band source (see ref. 12 for details). The number N of filters used is arbitrary. The larger N will give theoretically sharper weighting functions but the results will be more sensitive to experimental error and to non-stationarity of the atmosphere. In order to tolerate the non-stationarity and noise found in real observations, we restrict N to 3 or less. By trial and error combinations of the values of d_i and R_i, we obtained, with the help of a computer, a family of seven weighting functions peaked at different heights ranging from 2.25 km to 14.5 km and above (see Fig. 1). The peak altitude, the three spatial wavelengths needed for each linear combinations and the relative weights R_2 and R_3($R_1 \equiv 1$) are shown in Table 1. The seven profile values are not independent. They can roughly be divided into four nearly independent layers (e.g., the odd-numbered combinations).
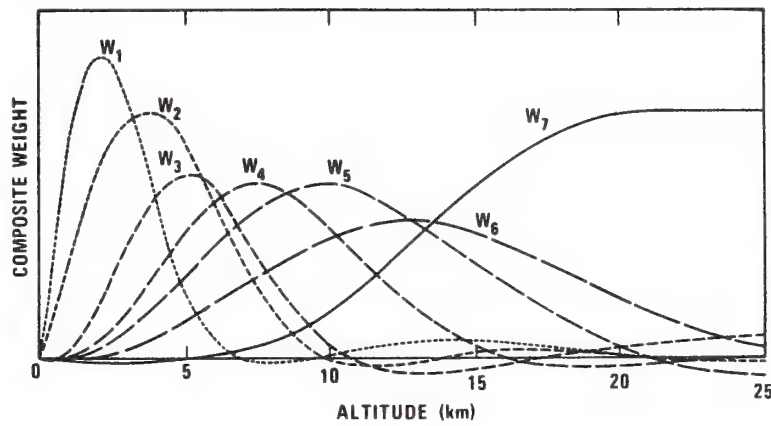
Fig. 1. Composite path-weighting functions obtained by linearly combining the weighting functions of three different spatial wavelengths (see text and Table 1 for details.)

Table 1. The peak altitudes and relative inverse areas (see Eq. (14)) of each of the seven weighting functions W_i shown in Fig. 1. The d_i are the spatial wavelengths that must be combined to produce each W, the relative weights being R_2 and R_3($R_1 \equiv 1$).

	W_1	W_2	W_3	W_4	W_5	W_6	W_7
Peak(km) altitude	2.25	3.75	5.25	7.5	9.75	12.75	>14.5
$B \times 10^{14}$	2.39	1.91	2.57	1.84	1.38	1.46	0.87
d_1(cm)	5	6.5	7	8.5	10	11.5	14
d_2(cm)	8	9	5	6	6.5	7.5	9
d_3(cm)	15	15	11	13	15	15	7
R_2	− .65	− .6	− .38	− .35	− .27	− .24	− .73
R_3	− .33	− .36	− .53	− .56	− .66	− .67	+ .23

237

The C_n^2 of each profile value is given by

$$C_n^2 = B \sum_{i=1}^{N} R_i K_i{}^{8/3} \; \sigma_I{}^2(d_i), \qquad (2)$$

where

$$B = 1.87 \times 10^{-13} [\int_0^{\infty} dz \; W_c \; (z)]^{-1} \qquad (3)$$

In Eq. (2), $\sigma_I{}^2(d_i)$ is the measured irradiance variance of spatial wavelength d_i, C_n^2 is the refractive-index structure constant in $m^{-2/3}$, K_i is the spatial wavenumber in cm^{-1} and z is in km. By measuring the areas under the curves shown in Fig. 1 (for W_7, we cut it off at 25 km), we obtain the calibration factor B shown for each layer in the second line of Table 1.

We have developed a system that uses the spatial filtering technique to make an on-line computation of the refactive-index profile. An instrument package attached to a 36 cm Schmidt-Cassegrain telescope (Fig. 2) sequentially measures the variance of the intensity scintillation at different spatial wavelengths. The instrument package supplies to the analog-to-digital minicomputer four signal voltages proportional to the following:

Fig. 2. The telescope and the attached instrument box.

$\sigma_I(d)$, the standard deviation of the spatially filtered signal for a specific spatial wavelength d,

d , the wavelength of the spatial filter,

σ_I , the log-irradiance standard deviation of the whole telescope aperture,

I , the irradiance of the whole telescope aperture.

From the first two inputs we calculate a C_n^2 profile according to Eq. (2). The fourth input (I) is used to set signal levels, monitor the guiding of the telescope, and provide a record if clouds obscure the star. The log-irradiance standard deviation of the whole aperture is a weighted measurement of the refractive-index turbulence which approximately covers the region over which the instrument profiles C_n^2. While in principle this measurement is not needed to compute C_n^2 profiles, we have found it useful to compensate partially for the non-stationarity of the atmosphere during the 20-min measurement cycle. (See section IV of Ref. 12 for details of the design of the instrument.)

Results

The instrument is designed for use with stars of second magnitude or brighter. In order to guarantee enough signal-to-noise ratio (SNR), we first pointed the telescope to a zero magnitude star, Vega. The measurement was taken at Table Mountain, a flat mesa located 12 km north of Boulder, Colorado. Some measurements of the typical C_n^2 vertical profiles are shown in Fig. 3. The "altitude" shown is actually slant range from the observatory 1.7 km above sea-level. Zenith-angle corrections, amounting to less than 2 percent, have been neglected. Variations from night to night are large, extending over a range of one hundred to one. Our measurements show general agreement with Hufnagel's model.[13] Since we are in the lee of the Rocky Mountains where mountain-wave effects are common, we expect to see large night-to-night variations of the vertical C_n^2 profile. A typical variation over a period of two and one-half hours in a single evening is shown in Fig. 4. We see that there are noticeable changes in a couple of hours.

238
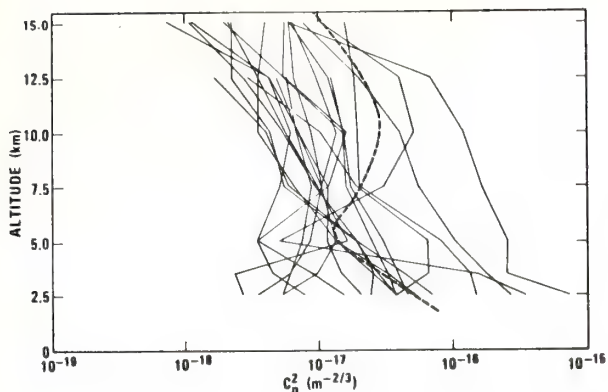
Fig. 3. Typical optically measured C_n^2 vertical profiles at Boulder, Colorado. Each curve is the average of the measurements of a single evening. The dashed line represents the statistical average profile of Hufnagel's latest model.[13]
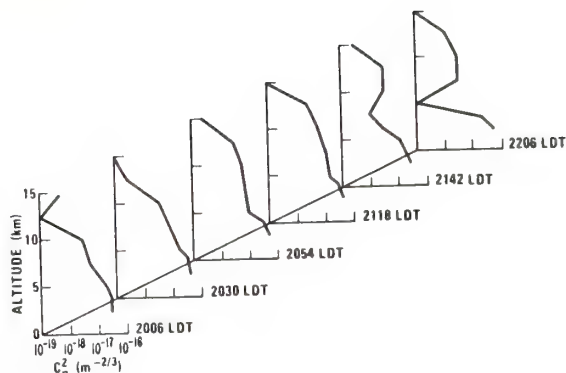
Fig. 4. Typical variation of the vertical C_n^2 profile in a single evening.

The instrument was then moved to Maui, Hawaii and installed at the ARPA Maui Optical Station (AMOS), an observatory located on the top of Mt. Haleakala, 3 km above sea level. The night-to-night variations are shown in Fig. 5. Again the "altitude" is range from the observatory. Zenith-angle corrections, always less than 10 percent, have been neglected. Hour-to-hour variations in a single evening are shown in Fig. 6. Both Figs. 5 and 6 show variations similar in magnitude to those in the data from Colorado. However, the mean value of C_n^2 is smaller than in the Colorado data. This result might be expected since the AMOS observatory is on an isolated peak 3 km above sea level whereas the Colorado measurements were taken at the level of the surroundings and in the lee of 2000 km of mountainous terrain, and since the winds aloft (and therefore, presumably, the wind shear) are weaker in the tropics.
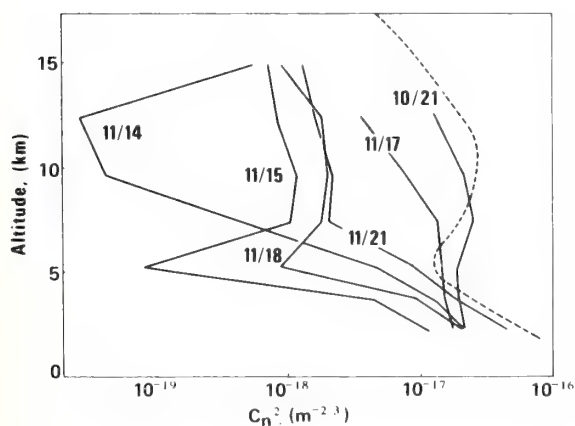
Fig. 5. Typical optically measured C_n^2 vertical profiles at Mt. Haleakala, Hawaii. Each curve is the average of the measurements of a single evening. The dashed line represents the statistical average profile of Hufnagel's latest model.[13]
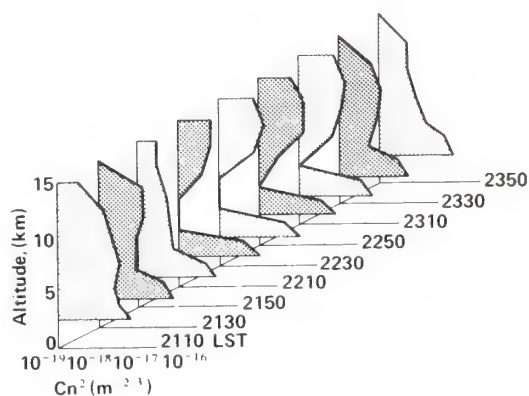
Fig. 6. Typical variation of the vertical C_n^2 profile in a single evening.

It is difficult to obtain an independent confirmation of our C_n^2 measurements. Rawinsonde data are available but such wind and temperature information does not have sufficient detail to make estimates of C_n^2. It is possible, however, to derive C_n^2 from direct small-scale measurements of the temperature field, and we made measurements of this type from a light aircraft over Haleakala. Only the lowest data point obtained with the optical instrument could be compared because of aircraft altitude limitations.

We derive C_n^2 by assuming that, over small scale sizes, air density and therefore C_n^2 are affected primarily by temperature irregularities, and very little by variable pressure and composition. At optical wavelengths,

$$C_n^2 = \left(\frac{79P}{T^2} 10^{-6} \right)^2 C_T^2 \quad , \tag{4}$$

where P is the pressure in millibars, T is the Kelvin temperature, and C_T^2 is the temperature structure parameter. Assuming that the spectrum of turbulence follows the Kolmogorov law, a single sensor mounted on an aircraft traveling at velocity v, and arranged to respond to angular frequencies from ω_L to ω_H, may be used to measure C_T^2. It can be shown that[14]

$$C_T^2 = \frac{2.68 [<T^2>_{AV} - \bar{N}^2]}{(v/\omega_L)^{2/3} - (v/\omega_H)^{2/3}} \quad , \tag{5}$$

where $<T^2>_{AV}$ is the mean-square temperature fluctuation, and $\bar{N}$ is the noise from all sources, principally the aircraft engine and propellor.

The sensor is mounted on the wing of the aircraft, and consists of a platinum wire 6μm in diameter, wound on an open square form 0.35 cm on a side and 2 cm long. The low-frequency cutoff is $\omega_L = 1.45 \text{ sec}^{-1}$ (0.23 Hz), and the high-frequency limit ω_H is 2070 sec^{-1} (330 Hz). A detailed description of the measurement of C_n^2 with this temperature probe can be found in reference 14.

Profile measurements were made during spiral descents over Haleakala, as there is less background noise at reduced engine power. In Fig. 7, we compare aircraft measurements and optical measurements made during the evening hours of November 17, 18, and 21, 1975 over Mt. Haleakala.
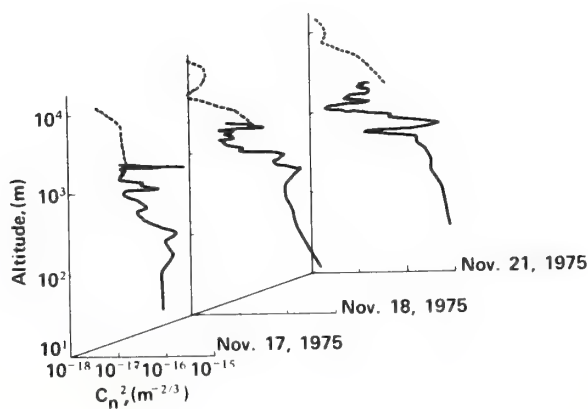
Fig. 7. Comparison of aircraft in-situ measurements (solid line) and optical measurements (dotted line).
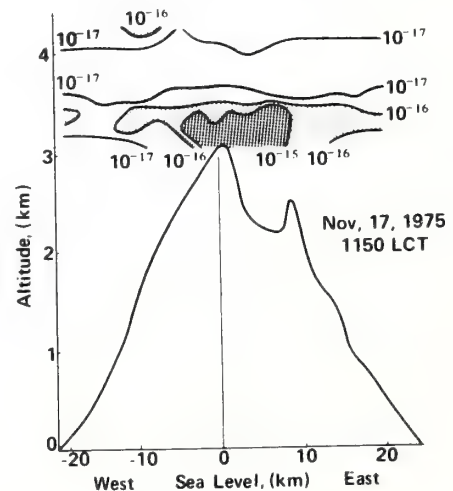
Fig. 8. Two-dimensional C_n^2 contours above Mt. Haleakala, Hawaii during daytime.

There are several difficulties with such a comparison. First, the spatial average of the lowest optical measurement covers about 3 km in height whereas the aircraft measurement is averaged over a height range of only 75 m. Also, the measurements do not exactly correspond in time or space. The horizontal variation of C_n^2 can be seen in
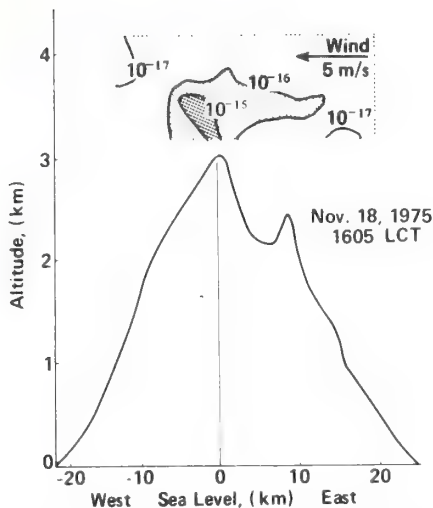
Fig. 9. Two-dimensional C_n^2 contours above Mt. Haleakala, Hawaii during daytime.
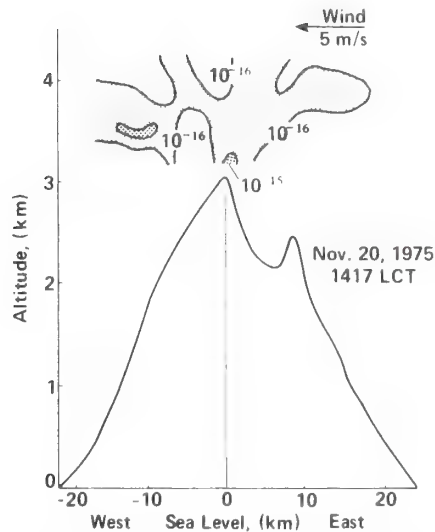
Fig. 10. Two-dimensional C_n^2 contours above Mt. Haleakala, Hawaii during daytime.

Figs. 8 - 10, obtained from horizontal aircraft flights along the direction of the prevailing wind. The horizontal separation of the aircraft and optical meaurements was perhaps a kilometer or more, and one can see that a considerable variation might be expected from such a separation. Allowing for these factors, we feel that the agreement is quite satisfactory.

Conclusions

We have demonstrated that the vertical C_n^2 profile can be measured by observing the turbulence-induced optical scintillation of a single star with a ground-based, spatially-filtered telescope. The whole atmosphere can be divided into four nearly independent layers. There is good agreement between the optical remote measurements and aircraft in-situ measurements. Night-to-night and hour-to-hour variations have been observed in the measured C_n^2 profiles taken at Boulder, Colorado, and on top of Mt. Haleakala in Hawaii. This is a potentially useful device to measure the vertical turbulence profile provided that a sharp altitude resolution is not required.

References

1. Douglass, A.E., "Atmosphere, Telescope and Observer" Popular Astronomy, June, 1897 (Reprinted in Amateur Telescope Making, Book Two, pp. 585-605, A. G. Ingalls, ed. Scientific American, Inc. (1957)).

2. Pickering, W. H., "The Shadow Bands," Popular Astronomy, 33:, 1-2, 1925.

3. Gifford, F., and Mikesell, A. H., "Atmospheric Turbulence and the Scintillation of Starlight,", Weather 8:7, 195-197, 1953.

4. Protheroe, W. M.,"The Motion and Structure of Stellar Shadow-band Patterns," Quart. J. Roy. Met. Soc. 90:388, 27-42, 1964.

5. Townsend, A. A.,"The Interpretation of Stellar Shadow-bands as a Consequence of Turbulent Mixing," Quart. J. Roy. Met. Soc 91:387, 1-9, 1965.

6.   Vernin, J. and Roddier, J.,"Experimental Determination of Two-Dimensional Spatio-Temporal Power Spectra of Stellar Light Scintillation. Evidence for a Multilayer Structure of the Air Turbulence in the Upper Troposphere," J. Opt. Soc. Am. 63:3, 270-274, 1973.

7.   Roddier, C. and Roddier, F.,"Correlation Measurements on the Complex Amplitude of Stellar Plane Waves Perturbed by Atmospheric Turbulence," J. Opt. Soc. Am. 63:6, 661-663, 1973.

8.   Rocca, A., Roddier, F., and Vernin, J.,"Detection of Atmospheric Turbulent Layers by Spatiotemporal and Spatioangular Correlation Measurements of Stellar-Light Scintillation," J. Opt. Soc. Am. 64:7, 1000-1004, 1974.

9.   Vernin, J. and Roddier, F, "Détection au Sol de la Turbulence Stratospherique par Intercorrélation Spatioangulaire de la Scintillation Stellaire," Comptes Rendus Acad. Sci. Paris (French), 280:B, 463-465, 1975.

10.   Ochs, G. R., S. F. Clifford, R. S. Lawrence, and Ting-i Wang, "Development of a Ground-Based Optical Method for Measuring Atmospheric Turbulence Aloft", NOAA Tech. Rept. ERL297-WPL30, Superintendent of Documents, U.S. Gov't Printing Office, Washington, D. C. 20402, 1974.

11.   Wang, Ting-i, S. F. Clifford, and G. R. Ochs,"Wind and Refractive-Turbulence Sensing Using Crossed Laser Beams," Appl. Opt 13:11, 2602-2608, 1974.

12.   Ochs, G. R., Ting-i Wang, R. S. Lawrence, and S. F. Clifford, "Refractive-Turbulence Profiles Measured by One-Dimensional Spatial Filtering of Scintillations, " (submitted to Applied Optics, 1976).

13.   Hufnagel, R. E.,Variations of Atmospheric Turbulence, Optical Society of America Topical Meeting on Optical Propagation Through Turbulence, Boulder, Colorado July 1974.

14.   Lawrence, R. S., G. R. Ochs, and S. F. Clifford,"Measurement of Atmospheric Turbulence Relevant to Optical Propagation," J. Opt. Soc. Am. 60:6, 826-830, 1970.

Lidar Observation of a Mixed-Phase Altostratus Cloud

C. M. R. Platt[1]

Division of Atmospheric Physics, CSIRO, Aspendale, Victoria, Australia, 3195

(Manuscript received 8 September 1976, in revised form 15 March 1977)

ABSTRACT

Measurements by monostatic lidar of linear depolarization ratios and backscatter coefficients in an altostratus cloud revealed a horizontally layered structure. Three different types of layers were observed. The bottom and central layers had depolarization ratios varying from 0.3 to 0.4, which identified them as layers containing mainly ice. The backscatter coefficients were similar to those found in cirrus ice clouds. A central, transient layer had depolarization ratios characteristic of a high-density water cloud, although the total integrated backscatter of 2.3±1.2 was high for this type of cloud. The top layer had a depolarization ratio of 0.2 at the cloud base, decreasing to 0.04 at the cloud center. Backscatter coefficients ranged up to 30 km⁻¹ and the total integrated backscatter was about 7.6±3.8. This value is considerably higher than the range of values predicted for water or cirrus ice clouds and one possible explanation is that specular reflection was occurring from horizontally aligned ice crystal plates.

The variation of backscatter coefficient within each layer was rather regular, with a maximum at the center of the layers. The cloud was situated in a stable air stream and its evolution appeared to be slow.

1. Introduction

The potential of lidar depolarization for discrimination between water, ice and mixed phases in clouds was recognized by Schotland *et al.* (1971) who observed appreciable depolarization of a linearly polarized lidar beam by ice crystals. Although depolarization ratios approaching unity have been observed in some ice clouds, they are typically about 0.4. Sassen (1974) has since shown that the depolarization ratio is dependent on the ratio of ice crystal to water droplet concentration. The theoretical value of the depolarization ratio for water spheres in the back direction is zero (Liou and Schotland, 1971), while the measured value near the bases of water cloud is about 0.03 (Sassen, 1974). However, for any appreciable cloud thickness, the depolarization ratio is found to increase almost linearly with increasing cloud penetration, reaching values of 0.4–0.5 within a depth of about 150 m (Pal and Carswell, 1973). This effect is due to multiple scattering of radiation in the lidar beam, although theoretical studies have as yet been unable to simulate the measured figures (e.g., Eloranta 1972; Liou and Schotland, 1971).

Depolarization measurements can be usefully supplemented by measurements of the backscatter coefficients of the clouds. Platt (1973) has shown that the integrated backscatter from a cloud tends, as the cloud becomes denser, to a value which is related by a constant factor to the backscatter to extinction ratio of the cloud particles. This quantity varies with cloud phase and type (Platt and Bartusek, 1974).

Recently a high-power ruby lidar system was installed at Aspendale with facilities for depolarization studies and fast digitization of data. Preliminary measurements of depolarization ratios in cirrus and water clouds have broadly verified the work of other authors. These results will be published elsewhere. Here we report some interesting observations of depolarization ratios and backscatter coefficients from one altostratus cloud system which showed a vertical structure of distinct layers with differing optical properties.

2. Instrumental and experimental technique

The Aspendale system is a monostatic lidar with facilities for rapid comparison between normal and depolarized returns. The ruby laser has an output energy of 1.5 J and a pulse width of 20 ns. The maximum pulse rate is 1 s⁻¹. The reflected light is imaged by a 14-inch Celestron telescope. The polarizer is placed near the telescope focus and can be rotated rapidly between pulses. The photomultiplier output voltage is digitized by a BIOMATION 8100 Recorder with a minimum sampling time of 10 ns. A 2100 Hewlett–Packard computer controls the laser firing time and the transfer of data to tape. The pulse energy is also measured and recorded and received amplitudes are normalized to unity pulse energy. Returns from cloud were calibrated by comparison with returns from

---

[1] Present affiliation: Cooperative Institute for Research in Environmental Sciences, University of Colorado/NOAA, Boulder, Colo. 80309 (until September 1977).
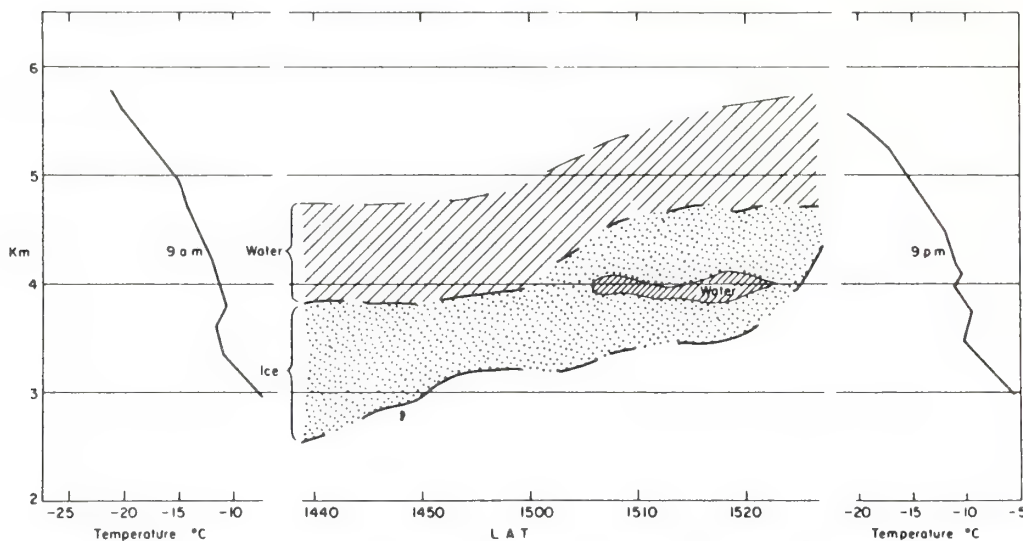
FIG. 1. Time-height representation of the altostratus cloud over the total time of observation. The dashed contours indicate the main separation of the different phases when data were available. The designation of phase is only tentative. Radiosonde temperature profiles are shown at 0900 and 2100 local apparent time.

dust-free air of known backscatter coefficient and corrected for attenuation between the cloud and ground (Platt, 1973). The estimated error in calibration was ±25%.

For the present experiment the lidar was fired in the vertical every 5s and between each pulse the polarizer was rotated through 90°. This was the minimum rate achievable at the time of the experiment. The optimum rate of rotation of the polarizer of 1 s^{-1} has since been achieved. The output voltage from the photomultiplier was sampled by the BIOMATION recorder at 20 ns intervals. The transmitted lidar pulse had a beamwidth of 1 mrad and the receiver system beamwidth was adjusted to 10 mrad. The wide receiver aperture enabled better penetration of the cloud via multiple scattering processes (Platt, 1973).

3. Analysis of data

The depolarization ratio $\delta(z)$ at altitude z is given by Schotland et al. (1971) as

$$\delta(z) = \frac{B(\pi,z)_\perp}{B(\pi,z)_\parallel}[\exp(\tau_\parallel - \tau_\perp)], \quad (1)$$

where $B(\pi,z)_\perp$ and $B(\pi,z)_\parallel$ are the backscatter coefficients at altitude z for the perpendicular and parallel polarized returns, respectively. The exponential term allows for a difference in cloud transmittance for the two components due to, say, preferentially aligned ice crystals, but here as in Schotland et al. (1971) it will be taken as unity. If the crystals are not oriented, then they would present the same mean extinction cross section to either polarization. The transmittance could possibly be affected by differences in the angular

scattering functions in the back hemisphere affecting the two multiple scattered returns, but again the random orientation of the crystals would be expected to partially smooth out such differences.

In this case, $\delta(z)$ is given simply by the ratio of the return intensities $P_\perp(z)$ and $P_\parallel(z)$ at the lidar receiver. It is noted that other terms in the lidar equation such as range, receiver gain, etc., do not appear in the expression for $\delta(z)$.

A first viewing of the values of $P_\perp(z)$ and $P_\parallel(z)$ revealed a situation where cloud properties were varying slowly in the interval between firings. To allow for a linear change of $P_\parallel(z)$ within the 10 s between observations of this quantity $\delta(z)$ was defined as the ratio of $P_\perp(z)$ at time t seconds to the mean of $P_\parallel(z)$ $(t-5)$ and $P_\parallel(z)$ $(t+5)$. The data, which were stored on tape, were processed by computer to give values of the quantities $\delta(z)(t)$ and $\frac{1}{2}[P_\parallel(z)(t-5)+P_\parallel(z)(t+5)]$ at time intervals of 10 s minimum.

4. Observations

Lidar returns were obtained from an altostratus cloud during the period from 1438 to 1525 hours[2] on 9 August 1975. The returns were obtained sufficiently often to build up time-height cross sections of the cloud as shown in Figs. 1 and 2. Periods when observations were not made are shown as breaks in the line defining the cloud base. The designations of the cloud phases in Figs. 1 and 2 are only very tentative, being based on previous depolarization results reported by other workers, as discussed in Section 1. The analysis of the integrated backscatter, which is discussed in

[2] Local apparent time.

Section 5b, casts doubt on the reality of some of the above designations.

The current synoptic map showed a large, complex, low-pressure system centered about 600 km east of Aspendale. A front had passed through Aspendale during the previous 24 h and the cloud was situated in a rather stable air mass behind the front. This stability is evident in the temperature profiles illustrated in Fig. 1 which were measured by radiosonde at Laverton, some 40 km west of Aspendale.

5. Discussion of results

The discussion of the cloud observations is divided for convenience into three sections. In Section 5a the depolarization patterns from some single lidar returns during the period 1518 to 1524 are discussed in detail, and the phases of the particles in the layers are interpreted in terms of these patterns. In Section 5b, the backscatter coefficients and the integrated backscatter are evaluated and discussed for different layers and for the same period as Section 5a. Section 5c is devoted to a discussion of the cloud structure and its evolution as it passed through the lidar's field of view.

a. Interpretation of depolarization patterns

Four displays are shown in Figs. 3a–3d which indicate the patterns in the backscatter and depolarization observed between 1518 and 1524.

The "noise" evident in the depolarization ratio is due not only to photon noise in the original returns but also to the limited resolution of the BIOMATION recorder. The output of this instrument was restricted to 0–128 counts. When the backscatter returns from

the most intense layers were matched to the upper end of this range, the returns from the weaker ice layers measured about 10 counts in the case of $B_{\parallel}$ and only about 4 in $B_{\perp}$. The "noise" in $\delta(z)$ caused by this effect was thus about 25%.

Fig. 3a shows the return from a layer of cloud with its base at an altitude of 3.35 km and with a depolarization ratio of about 0.4, which is typical for an ice cloud containing very little, or no, water (Sassen, 1974). Overlying this layer, at an altitude of 3.70 km, is a highly reflecting layer with a very low value of $\delta(z)$ of about 0.03. The layer is thus identified as a water cloud. A second layer immediately above it is also highly reflecting but has an increasing depolarization ratio with increasing altitude. These characteristics identify the layer from past work as a dense water cloud with a high extinction coefficient (Pal and Carswell, 1973). The depolarization behavior, coupled with an absence of returns from above this layer, points to complete extinction of the lidar pulse.

Fig. 3b shows the situation 1 min after that depicted in Fig. 3a. The lower water layer has disappeared and the layer at 3.90 km has both a smaller depth and backscatter coefficient. As a result, the laser pulse can now penetrate the water layers to reveal two further layers above. The first extends from about 3.9 to 4.5 km and appears to be an ice layer. The second extends from about 4.5 to 5.4 km and within this range, the depolarization ratio decreases to a low value.

After a further minute and three-quarters (Fig. 3) the lower water layer at 3.8 km has nearly disappeared and the topmost layer is seen to be nearly 1 km deep. The backscatter from the layers above 3.8 km has increased in intensity which can be attributed to the
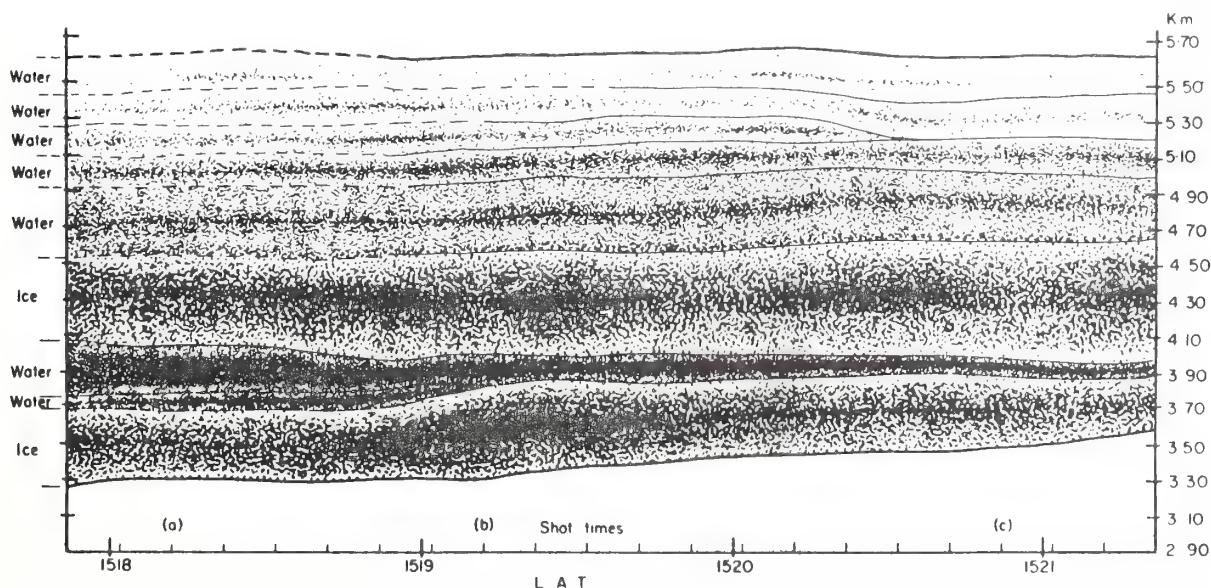
FIG. 2. Time-height representation of the cloud evolution from 1518 to 1522 hours 9 August 1975. Times of depolarized returns are shown on the horizontal axis. Parallel returns were received at intermediate times. The letters in brackets refer to depolarized returns used in Figs. 3a–3c. The representation of the layer intensities is only qualitative, and the phase designation is tentative.

245
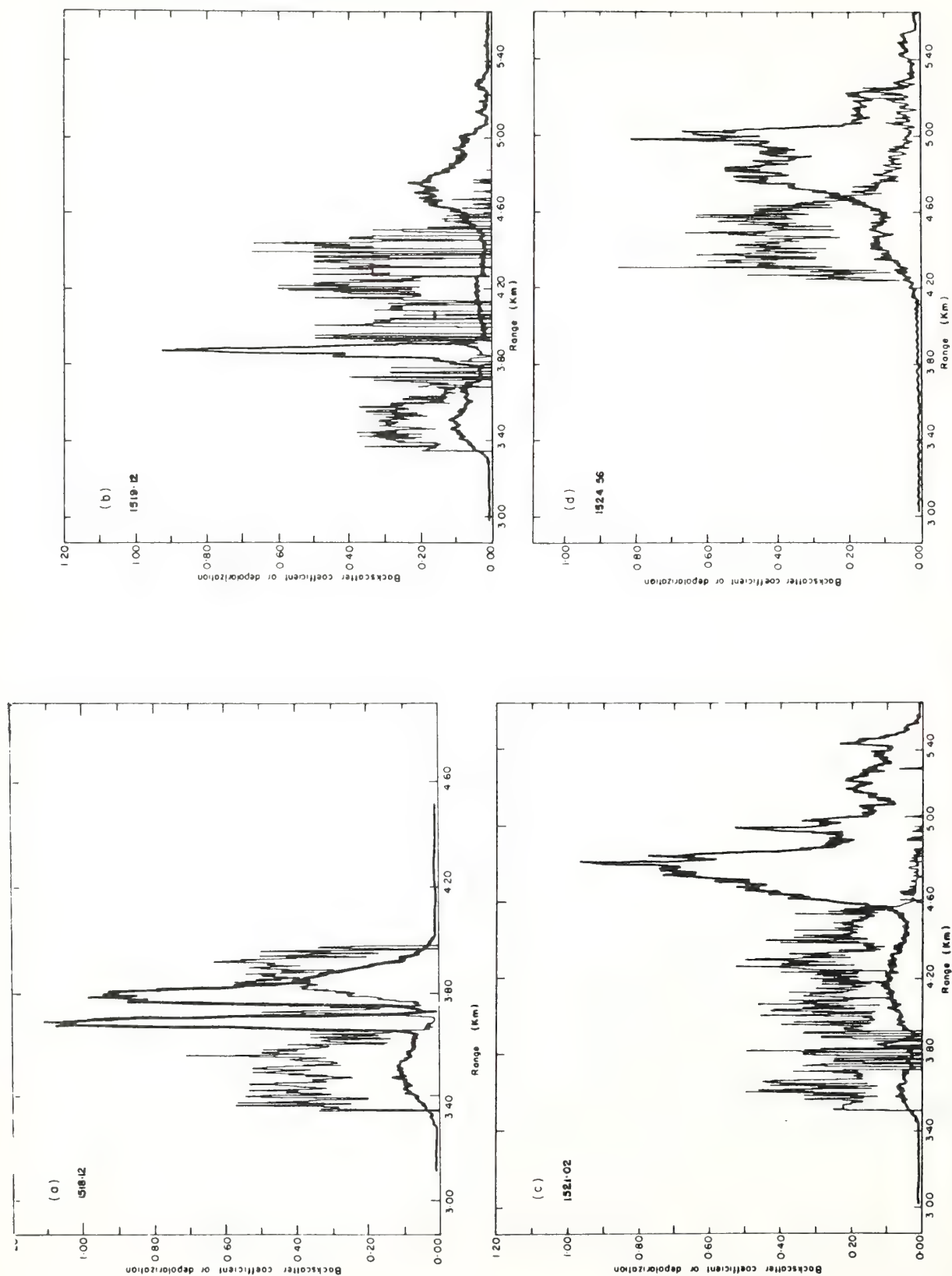
Fig. 3. Altitude dependence of backscatter coefficient and depolarization ratio at four local apparent times on 9 August 1975. Backscatter coefficient is shown as the fuller line and the units are km^{-1} when the vertical scale is multiplied by 10.

decreased extinction below these layers. Above 4.6 km the depolarization is apparently very small, which would indicate that this layer was also composed of small water drops. However, the zero value of $\delta(z)$ above 5 km is a result of the small depolarized returns from this region being unresolvable by the BIO-MATION recorder. These returns can be better resolved if a logarithmic amplifier is used at the output of the lidar receiver photomultiplier and such a return is shown in Fig. 3d. Here $\delta(z)$ is seen to fall to a value of about 0.04 at 5 km. It is interesting that between 4.8 and 5 km, $\delta(z)$ gradually decreases, signifying a slow change in the cloud composition from a predominantly ice layer to what is apparently a water layer (Sassen, 1974).

b. Interpretation of backscatter characteristics of layers

The above identification of cloud layers purely in terms of their depolarization ratios is based on previous work. Additional information on the nature of the cloud layers is available from measured backscatter coefficients and calculations of the integrated backscatter. The following analysis indicates that this information contradicts, in some aspects, designation of the "water" layers in Figs. 1 and 2.

The total backscatter coefficient $B(\pi)$ is equal to the sum of $B(\pi)_{\shortparallel}$ and $B(\pi)_{\perp}$. The *measured* backscatter $B'(\pi,z)$, at range (altitude) z is less, due to attenuation of the lidar pulse during its passage through the cloud. Thus

$$B'(\pi,z) = B(\pi,z) \exp\left[-\int_{z_0}^{z} 2\eta(z'')\sigma(z'')dz'' \right], \quad (2)$$

where z_0 is cloud-base altitude, $\eta(z'')$ a multiple scattering factor and $\sigma(z'')$ the cloud extinction coefficient. It is assumed that $\sigma(z'')$ and $\eta(z'')$ are both equal for the two polarization directions.

A quantity $\gamma'(\pi)$ is defined in Platt (1973) as

$$\gamma'(\pi) = \int_{z_0}^{h} B'(\pi,z)dz, \quad (3)$$

where h is cloud top altitude. If it is assumed that $\eta(z'') [=\eta]$ is constant, then substitution of (2) into (3) and integrating gives

$$\gamma'(\pi) = (k/2\eta)[1 - \exp(-2\eta\tau_\varepsilon)], \quad (4)$$

where

$$\tau_\bullet = \int_{z_0}^{h} \sigma(z'')dz'' \quad \text{and} \quad k = B(\pi,z)/\sigma(z).$$

The assumption that η is constant is not always valid (Kunkel and Weinman, 1976). However, Eq. (4) is convenient for the analysis of cloud data. When $\tau_\bullet$ becomes large, $\gamma'(\pi)$ tends to $k/2\eta$. Thus, a series of measurements of $\gamma'(\pi)$ for different values of $\tau_\bullet$ can

give an experimental value of $k/2\eta$ (Platt, 1973). If η is not constant then an effective value, $k/2\bar{\eta}$, is measured where

$$\bar{\eta} = \frac{1}{2} \int_{z_0}^{h} k\sigma(z)\left[\exp - \int_{z_0}^{z} 2\eta(z'')\sigma(z'')dz'' \right]dz. \quad (5)$$

Although relatively few determinations of $k/2\bar{\eta}$ have been made, its value was found to lie between 0.3 and 0.6 for several different cirrus and cirrostratus systems (Platt, 1973; and unpublished data), and that a similar range of values occurred in some middle-level clouds (Platt and Bartusek, 1974). Some of this variation was due to the use of different receiver beamwidths, which varied between 3 and 10 mrad. $\bar{\eta}$ would decrease with increasing beamwidth. Also, those authors calculated theoretical values of k for two water clouds as 0.64 and 0.67, respectively. The corresponding value of $\bar{\eta}$ for water clouds is estimated to lie between 0.6 and 0.9 (Kunkel and Weinmann, 1976), so that $k/2\bar{\eta}$ for water clouds is predicted to lie within the range of 0.36 to 0.54. However, with the wide receiver beamwidth of 10 mrad, the value of $\bar{\eta}$ is likely to be at the low end of the quoted range.

The relevance of the above discussion to the present article is that some of the values of $\gamma'(\pi)$ determined for different layers in the altostratus cloud were considerably higher than any of the above quoted values, even allowing for an estimated 50% error. Values of $\gamma'(\pi)$ are listed in Table 1. Some of the layers overlap because values were calculated from two separate lidar returns, as indicated. Except for layer 2, none of the layers were opaque to the lidar pulse so that values of $\gamma'(\pi)$ [Eq. (4)] for layers 1, 3 and 4 were actually *less* than the corresponding values of $k/2\bar{\eta}$. Values of $\gamma'(\pi)$ for each layer above the first were corrected for attenuation by the layers beneath, using the mean value of $k/2\bar{\eta}$ (the effective backscatter to extinction ratio) measured for cirrus.

Layers 1 and 3 had backscatter (and depolarization) values which were similar to those of cirrus clouds. However, layers 2 and 4 had backscatter values which were respectively about 2–4 times and 8–16 times the predicted theoretical values for water clouds. Despite assumptions made about the behavior of $\eta(z)$ or the transmittance of the layers, layers 2 and 4 apparently

TABLE 1. Integrated backscatter through different layers of the altostratus cloud.

Layer No.	Figure No.	Altitude (km)	$\gamma'(\pi)$	$\gamma'(\pi)$*
1	3a	3.3–3.65	0.17	0.17±0.04
2	3a	3.75–4.0	1.42	2.3 ±1.2
3	3c	3.85–4.6	0.36	0.6 ±0.3
4	3c	4.6–5.6	2.30	7.6 ±3.8

* Corrected for attenuation below the layer.

possess backscatter characteristics which are different from those of either cirrus or water clouds, while their depolarization characteristics are similar to those of water clouds. Thus the interpretation of the layers solely in terms of their depolarization characteristics must be called into question. It is still possible that layer 3 could have been a water cloud. It was very dense, and attenuated the lidar pulse within a few hundred meters. This interpretation could imply that $\gamma'(\pi)$ was in error by more than 100%, which is a possibility. However, the value of $\gamma'(\pi)$ for layer 4 was more than an order of magnitude greater than that predicted for a water cloud and even then the layer did not seem to attenuate the lidar pulse completely. A possible explanation for the high backscatter was that reflection was occurring from horizontally aligned hexagonal ice plates. The observed temperature range in layer 4 (-12 to $-20°C$) was just that range in which hexagonal ice plates form. The low depolarization ratio would also be consistent with this explanation (Liou and Lahore, 1974). Scattering by ice plates will be explored further in a subsequent paper. Suffice it to say here that a low depolarization ratio may *not necessarily* imply automatically a cloud of water droplets.

c. Cloud structure and evolution

In the time-height representations of Figs. 1 and 2, spatial and temporal variations in cloud structure could not be separated. However, there are reasons for thinking that most of the variations were spatial. Although the cloud was situated in a complex low-pressure system it was not in an active frontal zone, but in an area of stability to the rear of a front. Clouds in such a region are often in a mature phase of growth and layered in structure (Borovikov *et al.*, 1963; Mason, 1971). Ascending motions are rather weak (~ 1 cm s^{-1}) and cloud evolution is accordingly quite slow. This would be particularly true for mature ice layers, such as the bottom layer in Fig. 2, which are known to evolve more slowly than water clouds.

An interesting feature of the cloud structure is the local maximum in cloud backscatter coefficient which tends to occur at the center of each layer. This structure is shown best in Fig. 3c, particularly for the ice layers. Assuming that the cloud particle size distribution was constant with height in each layer, the variation in backscatter coefficient would imply similar variations in both the particle number density and the cloud water content. One possible explanation for this structure is that the cloud initially formed in thermally stratified air in which there was a variation in cloud condensation nuclei. Certainly, on the day of observation, the temperature profiles indicated considerable stratification (Fig. 1) at cloud height. Another factor which might be important is variations in shear-induced mechanical mixing.

In contrast to the generally stable nature of the cloud, the dense "water" layer observed between 1506 and 1521 at about 3.8 km must have represented a local active growth phase in the cloud. The top of this layer was probably defined by the temperature inversion near 4 km.

6. Summary

Layers with very different optical properties have been observed in an altostratus cloud using a calibrated lidar with depolarization facilities. The identification of the layers as given in Figs. 1 and 2 is necessarily very tentative due to a lack of any definitive set of lidar measurements coupled with simultaneous direct sampling of cloud particles. Furthermore, the measured integrated backscatter casts doubt on whether those layers which gave a small depolarization ratio were actually water drop clouds. Very high backscatter coefficients, coupled with a low depolarization ratio, were observed in the top cloud layers, which had air temperatures varying from -12 to $-20°C$. A possible explanation advanced to explain these properties is that reflection was occurring from horizontally aligned ice plates.

The measurement of the integrated backscatter $\gamma'(\pi)$ is obviously an important additional quantity in the interpretation of cloud lidar depolarization measurements; for instance, the above observations indicate that a low depolarization ratio may not unambiguously identify a water cloud.

One method of testing the hypothesis of specular reflection from ice crystals would be to take lidar measurements at various angles to the vertical. If specular reflection was occurring, then the measured lidar backscatter would decrease dramatically as the lidar was scanned away from the vertical.

Other interesting features observed in the cloud were the highly opaque, transient "water" layers in the center of the cloud and the regular variations of backscatter within each layer. In fact, each layer was bounded and defined by regions of low backscatter.

In order to make the integrated backscatter measurements more definitive, the dependence of $\bar{\eta}$ and depolarization ratio on receiver beamwidth and cloud type is at present under study, both theoretically and experimentally.

REFERENCES

Borovikov, A. M., A. Kh. Khrgian, and others, 1963: *Cloud Physics.* [Israel Program for Scientific Translations, 329 pp.]
Eloranta, E., 1972, Calculation of doubly scattered lidar returns. Ph.D. thesis, University of Wisconsin, 115 pp.

Kunkel, K. E., and J. A. Weinmann, 1976, Monte Carlo analysis of multiply scattered lidar returns. *J. Atmos. Sci.*, **33**, 1772 1781

Liou, Kuo-Nan, and R. M. Schotland, 1971: Multiple backscattering and depolarization from water clouds for a pulsed laser system. *J. Atmos. Sci.*, **28**, 772 784.

——, and H. Lahore, 1974 Laser sensing of cloud composition A backscattered depolarization technique *J. Appl. Meteor.*, **13**, 257 263.

Mason, B. J., 1971, *The Physics of Clouds*, 2nd ed. Oxford University Press, 671 pp.

Pal, S. R., and A. I. Carswell, 1973, Polarization properties of lidar backscattering from clouds *Appl. Opt.*, **12**, 1530 1535

Platt, C. M. R., 1973, Lidar and radiometric observations of cirrus clouds. *J. Atmos. Sci.*, **30**, 1191 1204.

——, and K. Bartusek, 1974 Structure and optical properties of some middle-level clouds *J. Atmos. Sci.*, **31**, 1079 1088

Sassen, K., 1974, Depolarization of laser light backscattered by artificial ice clouds *J. Appl. Meteor.*, **13**, 923 933.

Schotland, R. M, K. Sassen and R. Stone, 1971 Observations by lidar of linear depolarization ratios for hydrometeors. *J. Appl. Meteor.*, **10**, 1011–1017.

Experimental Measurements of Atmospheric Aerosol Inhomogeneities

Madison J. Post and Gordon M. Lerfald

Wave Propagation Laboratory
Environmental Research Laboratories/NOAA
Boulder, CO 80302

Observations

In "clear air" a lidar may depend on backscattering from aerosols for its signal. Short-term variations in the signal level arise from inhomogeneities in the aerosols, i.e., spatial variations in the number density, size distribution, chemical composition, shape, etc.

We have used two instruments to measure these spatial variations, a focused CO_2 lidar (CW) of 10.6 μm wavelength and a pulsed nitrogen lidar of 337 nm wavelength. The infrared system responds to particles of radius 0.5 - 5.0 μm radius, while the U-V system is sensitive to nearly all sizes of aerosols. Particle size distributions were determined during data taking.

The CO_2 lidar points into the wind and measures the Doppler shift of the energy backscattered by aerosols moving with the air. Its sensing volume is the shape of a garden hose - 20 m long and 3 cm in diameter - positioned 30 m above the ground. The total energy back-scattered, or 0th moment of the Doppler frequency spectrum, is a measure of the total aerosol loading. By assuming Taylor hypothesis, one can then construct a spatial history of the aerosol variations from the time history of the aerosol variations. The distribution and structure functions of these spatial fluctuations of aerosols are then computed, much the same way spatial temperature fluctuations are analyzed.

The basic arrangement for the U-V measurements involves a dual-beam bistatic lidar system and in-situ sensors of wind, temperature and humidity. The lidar system is located next to a tower on which the in-situ sensors are mounted. A beam-steering arrangement on the lidar system permits the volumes of intersection of the transmitted laser beams and receiver tele-scope beams to be positioned in the plane containing the tower and the

250

receiving telescopes. The aerosol backscatter volumes can therefore be positioned in height and any desired separation between the backscatter volumes can be chosen.

The humidity sensor, the thermistor probes and the wind instruments are mounted on booms attached to the tower. The lidar backscatter volumes are normally positioned near the in-situ sensors. Data are recorded on a 14-channel analog tape recorder operating at a tape speed of 1-7/8 inches/sec. The lidar pulse rate is 100 pulses per sec.

Infrared Results

Preliminary results from the Doppler lidar data indicate that the aerosol passive additive follows approximately the expected $x^{2/3}$ structure function relation, but does depart from it in several significant areas. During daylight conditions, the outer scale of the structure function "rolls off" at much larger separations, typically 200-300 m, than should be observable for isotropic eddies at the 30-m level. This suggests a stretching of the horizontal dimensions, or pancaked-shaped eddies, perhaps due to organized convection. At night, the outer scale drops to 40-60 m, so isotropic theory holds for this more stable condition.

Another observed departure from the expected $x^{2/3}$ relation appeared at small separations. Consistently, the slope of the structure function was greater in this region, typically nearer 4/5 than 2/3, a 20% increase. Maximum errors in data taking and reducing can only account for an 8% increase.

The day-night change in the level of the structure function (the nighttime data being lower) is approximately one order of magnitude, considerably less than the variance experienced for similar temperature fluctuations. Possibly this means that the aerosols are not strongly coupled to the temperature or turbulence fields, or that the source is different for the aerosols.

Distribution functions for the infrared data follow a consistent pattern of being bell-shaped but skewed toward lower levels. That is, excursions of the signal toward high levels (or high aerosol concentrations) occur less frequently than excursions to lower levels.

Over 30 data sets were taken, spanning all seasons but Fall. No significant departure from the general results reported above was observed. Possible variations with observation level will be investigated next.

Analysis of Ultra-Violet Data

The analog taped data were digitized and written onto digital magnetic tape for analysis. Individual data channels are computer-processed to obtain distribution functions and an intermittancy function. The latter measures the distribution of times for recurrence of specified signal values. Cross correlations and spatial structure functions are computed from pairs of data channels, (e.g., the two lidar backscatter signals).

One of the primary analysis goals is to obtain information on the decay rates of aerosol eddy structure from cross correlations for different spacings between the aerosol backscatter columns.

At the time of this writing final results and comparisons are not available, but they will be presented during the conference.

Remote Doppler velocity measurements of atmospheric dust devil vortices

R. L. Schwiesow and R. E. Cupp

ERL/NOAA Wave Propagation Laboratory, Boulder, Colorado 80302.
Received 17 October 1975.
Sponsored by F. S. Harris, Jr., Old Dominion University.

We report here what we believe to be first remote measurement of the velocity structure in a small-scale, natural atmospheric vortex. While the dust devil data are interesting in their own right, the practical demonstration of the applicability of the optical Doppler technique to field measurements on natural vortices, such as for waterspout and tornado research, is the point we wish to stress.

Basically, the cw ir (10.6-μm) Doppler system measures the line-of-sight velocity components of atmospheric aerosols within the diffraction-limited focal volume of the optical system. This sensing volume at the 3% irradiance level is approximately a cylinder $1.88 \times 10^{-3} r^2$ m long by $1.70 \times 10^{-4} r$ m diam, where r is the range in meters,[1] for our present system. At typical ranges the azimuth and elevation resolution is very good, but the range resolution element includes the entire depth of the vortex. Because the return signal is aerosol-concentration weighted, good range resolution is not required to distinguish the vortex from ambient flows. Principles of the homodyne extraction of Doppler velocity information from the return signal have been discussed elsewhere.[2-6]

The velocity spectra obtained are actually line integrals over the range resolution element, weighted by the aerosol backscatter coefficient at 10.6 μm. Although calculations on water aerosols have been done at 10.6 μm,[7] ir backscatter data for dusts are not available in a form suitable for direct use in our analysis. In general, one expects the most significant Doppler return from aerosols in the 1–10-μm diam range, whereas visual aspects are more strongly affected by smaller aerosols. Our qualitative observations have shown that some visually dense dust devils are only fair ir scatterers, though other dust devils invisible to the eye return a strong Doppler signal. Only estimates of the dimensions of the vortices were made since an investigation of dust devil morphology was not an objective of this study.

Data were collected on over forty dust devils during July

1975 at the Gila Indian Reservation south of Phoenix and at the Nevada test site of ERDA. Figure 1 reproduces velocity spectra from a small representative vortex. The vortex, at approximately 300-m range, was scanned 7 m above the surface. The visual diameter of the optically thin vortex at this height was approximately 2 m. Correlation with cinematography taken simultaneously with the velocity data reveals that the corresponding dust devil was of the broad, turbulent type (vase configuration), which often shows subvortices, rather than the narrow, intense, singular variety.[8] The mean wind of 3.5 msec^{-1} was perpendicular to the line-of-sight direction, so that ambient velocity effects are negligible in the spectra of Fig. 1.

Although the data will be analyzed in more detail later from the point of view of dust devil velocity structure, three preliminary observations can be reported.

(1) Peak horizontal velocity components in dust devils are small. We observed components up to 10 msec^{-1} near Phoenix and up to 22 msec^{-1} at the Nevada test site in these series of tests. Such values are larger than those observed with cup anemometers at other locations[9] but are not surprising in light of the very high spatial and temporal resolution of the ir Doppler system.

(2) The characteristic double-hump velocity spectrum associated with the complex vase configuration vortices, evident on two traces in Fig. 1, gives quantitative evidence for the embedded subvortices inferred by Sinclair from direction-vane data.[10] In general, subvortex tangential velocities (one-half the peak separation) were about 25% of the parent vortex rotational velocity, but one case of a subvortex velocity of 0.9 msec^{-1} in a 1.4-msec^{-1} mean rotational flow was observed.

(3) Data taken through the axis of the vortex, where only turbulent velocity components along the line of slight are expected, reveal a definite periodicity in both peak wind observed and the velocity at the spectral intensity peak. This suggests either the effect of large, slow subvortices or the existence of waves on the circumference of the main vortex itself. Such waves may be the precursor of the formation of embedded subvortices.

The characteristic behavior of the velocity spectra in dust devils as one scans across the diameter from the visual edge to the center is expressed in Fig. 1. A rather sharp tangential velocity peak at the edge of the vortex gives way to a broader spectrum as various velocity components con-
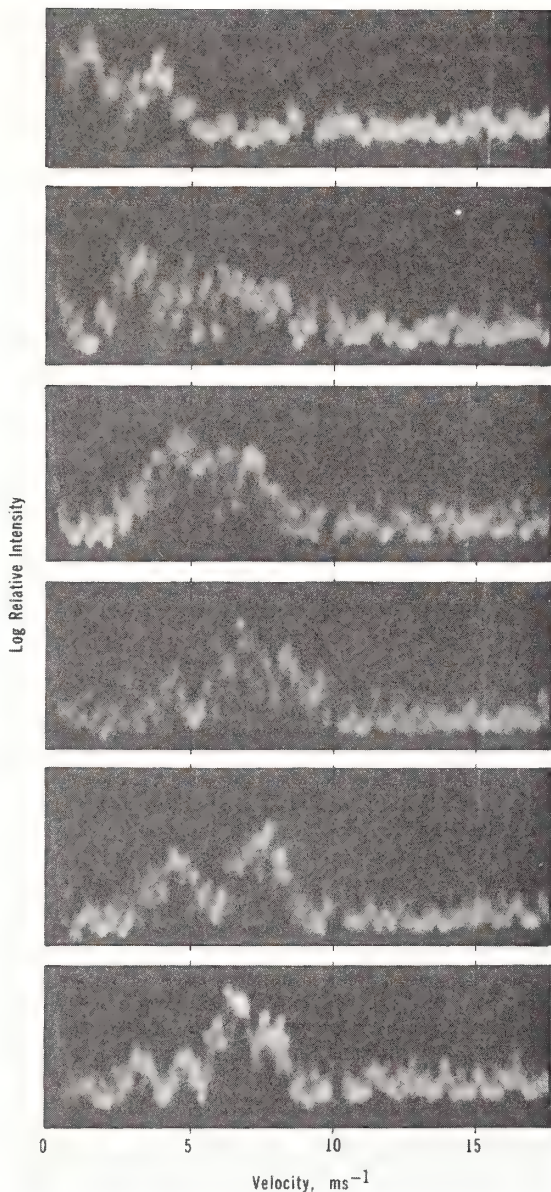
Fig. 1. Representative velocity spectra of a dust devil with spectra from the outer edge to the center of the vortex corresponding to the bottom and the top of the figure. respectively.

tribute within the sensing volume. For the vase-type vortices, the broad spectrum breaks into double peaks as subvortices are detected. As the measurement angle moves toward the vortex axis, the turbulent spectrum fills in toward zero velocity. When the mean wind is a significant fraction (20% or more) of the rotational velocity, the leading edge of the vortex (downwind side) has a more sharply defined spectrum than the upwind edge.

For practical optical applications, the remote Doppler velocity measurement system has proven utility. Experience has shown that, partly because of optical simplicity and the ir wavelengths, such a system can operate without realignments or adjustments after more than 1500-km transport on a heavy-duty, four-wheel drive vehicle. On-site setup time was demonstrated to be less than 10 min on initial starting and less than 2 min after detector cooldown. Power requirements for such a highly mobile system allow it to be self-contained with its own 5-kW generator. It has been found that effective operation is facilitated by a two-man crew.

This reported experiment demonstrates the feasibility of the remote, ir Doppler velocity measurement of natural atmospheric vortices. Application of the system to waterspouts and tornadoes are obvious extensions of the work.

References

1. See, for example, R. L. Schwiesow, J. Opt. Soc. Am. **59**, 1285 (1969).
2. R. M. Huffaker, Appl. Opt. **9**, 1026 (1970).
3. R. M. Huffaker, A. V Jelalian, W. H. Keene, C. M. Sonnenschein, and J. A. L. Thomson, in *Aircraft Wake Turbulence and Its Detection*, J. H. Olsen, A. Goldburg, and M. Rogers, Eds. (Plenum, New York, 1971), pp. 113–124.
4. A. J. Hughes, J. O'Shaughnessy, E. R. Pike, A. McPherson, C. Spavins, and T. H. Clifton, Opto-electronics **4**, 379 (1972).
5. T. R. Lawrence, D. J. Wilson, C. E. Craven, I. P. Jones, R. M. Huffaker, and J. A. L. Thomson, Rev. Sci. Instrum. **43**, 512 (1972).
6. C. M. Sonnenschein and F. A. Horrigan, Appl. Opt. **10**, 1600 (1971).
7. F. S. Harris, Jr., Appl. Opt. **8**, 143 (1969).
8. S. B. Idso, Am. Sci. **62**, 530 (1974).
9. J. A. Ryan and J. J. Carroll, J. Geophys. Res. **75**, 531 (1970).
10. P. C. Sinclair, J. Atmos. Sci. **30**, 1599 (1973).

VELOCITY STRUCTURES OF WATERSPOUTS AND DUST DEVILS
AS REVEALED BY DOPPLER LIDAR MEASUREMENTS

R. L. Schwiesow, R. E. Cupp and M. J. Post

Wave Propagation Laboratory, ERL/NOAA
Boulder, Colorado

R. F. Abbey, Jr.

Division of Reactor Safety Research, NRC
Washington, D.C.

P. C. Sinclair

Atmospheric Science Dept., Colorado State University
Ft. Collins, Colorado

1. INTRODUCTION

A knowledge of the velocity structure of atmospheric vortices can be useful in understanding the nature of some damaging winds associated with severe local storms. We have used a Doppler lidar technique to determine certain aspects of the flow in dust devils and waterspouts. Previous studies have used either photogrammetry, as for example Golden (1974), or *in situ* probes, as reported by Sinclair (1973) and Leverson, *et al.* (1977).

In order to understand the experimental results, one must understand the technique used. Because Doppler lidar is not yet a common tool in severe storms research, and because the applicability of this tool extends beyond the scope of this report, we explain Doppler lidar principles and implementation in some detail. Observations of both dust devils and waterspouts lead to similarities and differences in the interpretation of the results obtained from the two types of vortices. We conclude by indicating other applications of Doppler lidar to the detailed study of tornado and cloud dynamics aspects of severe local storms.

2. EXPERIMENTAL TECHNIQUE

2.1 Doppler Lidar Principles

Optical radiation scattered from a moving target will be Doppler-shifted in frequency (wavelength) because of target motion. This frequency shift is quite small. The fractional shift is the order of the particle velocity divided by the speed of light.

Practical Doppler lidars operate with a backscatter geometry. For a transmitter laser at 10.59 μm wavelength, a frequency shift of 189 kHz is observed for a 1 ms^{-1} target velocity component along the lidar line-of-sight. A single-axis lidar can only measure the line-of-sight or longitudinal component of the velocity.

The lidar transmitter can operate with pulsed or continuous wave (CW) output. In the latter case, range resolution is achieved only by the depth-of-focus of the lidar optics.

2.2 Implementation

For studies of the velocity structure of atmospheric vortices we have chosen to use an infrared, CW Doppler lidar with a CO_2 laser. A number of reasons suggested operation in the infrared rather than the visible. These reasons include relative eye safety, freedom from sky background interference, high frequency resolution, heterodyne or homodyne detection and conversion gain, and laser power efficiency.

The lidar unit uses a 30 cm transmit-receive telescope and radiates 3W. Data is recorded on 4 channel analog magnetic tape and on a time-code-correlated super 8 movie film using a 60 mm camera lens boresighted with the lidar axis. Signal detection involves homodyne operation (transmitter and local oscillator frequencies identical) so that only the magnitude, and not the sign, of the longitudinal velocity component is determined. A liquid-nitrogen-cooled, HgCdTe detector is the basic signal detector-mixer.

This Doppler system was mounted on the starboard side of a Cessna TC-207 aircraft. Some of the characteristics of the system are shown in Table 1.

Table 1
Lidar system operational characteristics

range	1 km, demonstrated
range resolution cell	10 m @ 100 m (-3 db)
angle resolution	<0.2 mr
velocity range	0-250 ms^{-1}
velocity resolution	1% full scale (variable)
velocity accuracy	±3 cm s^{-1}

data rate   10 ms/full spectrum
                             54 fps photographic

scan range   ±15° az and el

weight   175 kg

power in   750 W

2.3   Available Data

Although the CW infrared lidar exhibits very good resolution in azimuth and elevation, the length of the sensitive volume increases with the square of the range and includes essentially the entire vortex in the line-of-sight direction. Within the volume sensed by the lidar will be many scatterers having different longitudinal velocity components. It is not possible to characterize this velocity ensemble by a single value. A useful way of characterizing the sampled velocity information is by means of the complete velocity-component spectrum for the array of scatterers.

The velocity spectrum can be thought of as arising from an integral of the distributed velocity function throughout the resolution volume, weighted by the aerosol backscatter intensity function in the volume. In practice, this means that the data comes from the vortex since the ambient atmosphere scatters much more weakly than the dust or cloud droplets in the dust devil and waterspout respectively.

Basic velocity spectra can be correlated with azimuth or location with respect to the vortex axis. As the resolution volume is scanned across the vortex by aircraft translation, the sudden increase in velocity-integrated spectral intensity signals the edge of the visible funnel. Further detail on the visual aspects of the funnel is obtained from the boresighted cinematography.

3.   OBSERVATIONS

3.1   Dust Devils

Dust devil observations with a truck-mounted lidar have been reported by Schwiesow and Cupp (1976). The spectral data showed two characteristically different types of devils. One class of spectra exhibited spectral widths of approximately 20% of the maximum observed velocity, characteristic of a relatively laminar flow. Visually, these devils had a high aspect ratio of visual length to diameter and a cylindrical configuration. By contrast, highly turbulent devils were observed where the spectral width was often 80% of the maximum. The configuration of these devils was roughly inverted conical with an aspect ratio near 5.

Sequential spectra of the cylindrical devils showed a smooth transition between successive traces for the 20 or more spectra taken on a single scan of the vortex. Turbulent, conical devils on the other hand, gave spectra where spectral doublets would intermittently appear and disappear from the data. Examples are shown in Schwiesow and Cupp (1976). Residual turbulent velocities of typically 5 ms^{-1} were observed on the vortex axis, where a laminar flow would be expected to yield zero longitudinal component.

3.2   Waterspouts

Two characteristically different types of waterspouts were also observed. In contrast to dust devils, both spout types were cylindrical and of very high aspect ratio. The more common type exhibited a smoothly progressing series of spectra with fractional spectral widths of approximately 20%. A less common type of waterspout was the "double-walled" waterspout also mentioned by Golden (1974). A typical composite of raw spectral data is shown in figure 1.
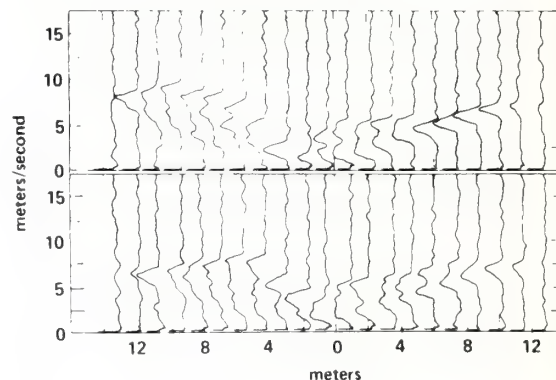
Figure 1. Raw spectral data for double-walled waterspout. The "third dimension" for each trace is relative spectral intensity on a log scale. Upper composite is taken on the same spout approximately 2 minutes after the lower composite.

Spectra to the far right of each composite in figure 1 exhibit the same character as spectra from the less complex, single-walled spouts. Typical spouts observed in this experiment did not extend completely from cloud base to sea surface. For example, cinematography and recorded visual observations indicate the funnel length of the spout of figure 1 was 100 ±30 m long, or approximately 15% of the cloud base to ground distance.

Note the smooth transition of spectral character from trace to trace in figure 1, except for the sudden onset of a persistent spectral doublet at 6 to 7 m from the vortex axis. Although all velocities are shown positive, it is obvious that the spectra must be reflected about the zero velocity axis for one half of the pass.

4.   CONCLUSIONS

4.1   Maximum Horizontal Velocity Component

A useful, although not particularly exciting, result is the maximum observed vortex tangential velocities in a horizontal plane. From the spectra it is objectively easy to determine the maximum velocity with intensity above the instrumental noise. For example, in figure 1 the maximum observed horizontal velocity is approximately 10 ms^{-1}, although the pure rotation part of this value is somewhat less because of slight relative motion between the vortex axis and the aircraft. The spectra were not affected by the forward motion of the aircraft because before each pass the lidar azimuth was adjusted

to bring the observed airspeed component with respect to the air approximately 500 m from the aircraft to 0 ±0.5 ms^{-1}.

In the Arizona dust devil field experiment the maximum observed velocity was 10 ms^{-1}. At a Nevada site where devils were less frequent, but larger, values to 22 ms^{-1} were measured. The relationship between maximum velocity and qualitative statistics is consistent with notions of the buildup and release of instability. These maximum velocity values do not represent upper limits to dust devils, but do represent the largest values observed from more than 40 devils measured.

A preliminary value from 20 waterspout passes is a maximum horizontal velocity component of 25 ms^{-1}, although this value may be revised after more complete analysis is done. These passes ranged between an altitude of 68 ±8 m (the judged lowest safe altitude) to cloudbase, and in every case were above the spray ring on the sea surface. Because of the cylindrical shape of the vortex, it is our opinion that maximum velocities in the spray ring region are not higher than those measured above the 68 m altitude, but we have no direct supporting data. Some waterspouts were probed at different altitudes when in an apparently slowly changing state, but these height-profile data are not yet analyzed except for maximum velocity, independent of height value.

Spectral progressions show that the maximum observed horizontal velocity is just inside the visible funnel wall.

4.2   Vortex Velocity Structure

The variations of the shape of the velocity spectrum as the sensing volume is scanned across the vortex can be correlated with data from visual imagery. The intermittent spectral doublets in the dust devil case are always associated with turbulent, conical vortices. These spectral signatures are taken as evidence for embedded subvortices, which are not coaxial with the parent vortex. Subvortex tangential velocities in the horizontal plane (one-half of the doublet separation) were usually about 25% of the parent vortex rotational velocity, but one case of a subvortex tangential rotation velocity of 0.9 ms^{-1} in a 1.4 ms^{-1} parent rotation was observed. Based on the persistence time of the doublets in the progression of spectra, we estimate that typical subvortex diameters were less than 10% of the parent vortex diameter. This size ratio means that quite high radial accelerations may be present in the subvortices even though their rotational velocities are comparatively small.

Spectral doublets in the waterspout case are taken as evidence for a concentric, two-vortex structure because of the persistence of the doublet feature. In contrast to the dust devil case, double-walled spouts do not exhibit higher turbulence than do the simpler variety. Figure 2 shows some features of a double-walled waterspout.
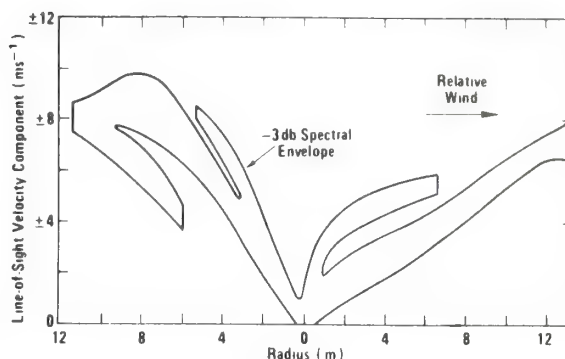
Figure 2. Reduced spectral data for a double-walled waterspout. The contour is for a 3 db-down point of spectral intensity.

A number of conclusions can be drawn from the reduced spectral data. First, note the difference in slope of the right and left branches of the plot. This feature is because of relative motion between the vortex axis and the aircraft in a longitudinal direction. The spout was viewed on the starboard side of the aircraft with the storm outflow approaching the aircraft from the front quarter. Forward in time is right to left on the plot. Therefore we can conclude the waterspout was cyclonic. If we extrapolate the linear portions of the plot, we conclude that the vortex axis was approaching the aircraft line-of-sight with a 3 ±0.5 ms^{-1} component perpendicular to the flight path.

The most striking feature is the sudden onset, at approximately 6.5 m from the vortex axis, of another distinct velocity value. This is from the rotation of a separate (in backscatter intensity and velocity) inner vortex, we believe. This observation is consistent with the visual data, but is not a necessary conclusion from the cinematography alone. This structure invites phenomenological modeling, which is underway.

Interaction with the storm outflow, which is the ambient environment of the spout, is quite strong. A slight increase in turbulence is evident on the downwind edge of the funnel (to the right) where some shear would be expected. Much larger turbulence (spectral width) is seen the upwind edge of the spout (to the left). If one extrapolated the linear upwind side of the plot to the edge of the funnel, as is the case on the downwind side, a longitudinal velocity component of approximately 14 ms^{-1} would be expected. However, a deficit of 4 ms^{-1} is evident because of interaction with the ambient flow moving past the vortex from left to right on the plot. We suggest that strong turbulent mixing distorts the vortex rotation on the upwind side of the funnel. Dust devils also show increased turbulence on the upwind side of the vortex as a result of interaction with the faster-moving ambient flow.

The third vortex shell is a low-velocity element existing for only a short arc on the upwind side of the spout. This feature was not evident in the visual data. We postulate that

this is sub-visible condensation in the moist
outflow from the storm, which has been given some
rotational component and backscatter enhancement
by interaction with the vortex in the turbulent
mixing fashion discussed above.

5.   OTHER DOPPLER LIDAR APPLICATIONS

5.1   Tornados

    An obvious extension of this work is to
the maximum horizontal component of the rotational
velocity in tornados and to the velocity struc-
ture in tornados, especially the question of
subvortices and velocity variation with height.
The problem of a safe, highly mobile platform is
a significant one, especially if a range of 1 km
from the tornado is attempted.

    It is possible that the present air-
borne infrared Doppler lidar system would give
usable return from a tornado at ranges up to 5
km. This would require that the infrared back-
scatter coefficient of a tornado be approximately
15 db larger than that of a waterspout. This is
possible, especially considering the difference
in the imaginary part of the refractive index of
dust and water, but is not known. System improve-
ments are possible, especially in data processing.
The presently-used scanning spectrum analyzer
operates at a 0.5% duty factor. Other means of
spectral analysis are under consideration.

5.2   Cloud Dynamics

    We have obtained velocity data from
young cumulus at a range of 1.8 km. At this
range the CW lidar has no range resolution, but
the signal is coming from the strongest backscat-
ter region in the beam, which is the air-to-cloud
interface. If the azimuth of the lidar is set to
show some small airspeed component, then two vel-
ocity peaks are observed — one from the cloud
and one from approximately 300 m from the air-
craft. The difference in observed velocity
represents the longitudinal component of the
entrainment into the cloud at the level scanned
by the lidar. That is, the difference in longi-
tudinal velocity component between a parcel in
the region of the aircraft and a parcel at the
condensation interface is observed.

    Direct applications of this technique
to entrainment and/or mixing beneath a growing
cumulus, especially the echo-free vault, at the
side of a cumulus at various altitudes, and at
the top of a stratus deck can be envisioned, for
example.

6.   ACKNOWLEDGMENTS

    We appreciate the continuing support
and interest in this work by V. E. Derr. The
enthusiasm of W. N. Hess was instrumental in
beginning the lidar application to vortices.

7.   REFERENCES

Golden, J. H., 1974: The life cycle of Florida
    Keys' waterspouts. I. J. Appl. Meteor., 13,
    678-692.

Leverson, V. H., P. C. Sinclair and J. H. Golden,
    1977: Waterspout wind, temperature, and
    pressure structure deduced from aircraft
    measurements. Mon. Wea. Rev., 105, (June
    issue).

Schwiesow, R. L., and R. E. Cupp, 1976: Remote
    Doppler velocity measurements of atmospheric
    dust devil vortices. Appl. Opt., 15, 1-2.

Sinclair, P. C., 1973: The lower structure of
    dust devils. J. Atmos. Sci., 30, 1599-1619.

Coherent differential Doppler measurements of transverse velocity at a remote point

R. L. Schwiesow, R. E. Cupp, M. J. Post, and R. F. Calfee

We consider the analysis and results of a laser remote velocity sensing experiment in which both the longitudinal and transverse velocity components at one location were simultaneously measured from a range of 33 m. Fully coherent homodyne detection was used with a test target that simulates many aspects of distributed atmospheric aerosol targets.

I. Significance of the Results

This paper describes the concept of and actual results from a new signal processing technique for Doppler velocity measurements at ranges of at least 30 m. The significance of the results is twofold: (1) we are able to measure all three velocity components of a target at a remote point using the same analysis apparatus for each component (although in a time-shared mode with present simple hardware) and (2) the differential Doppler analysis is carried out in a· fully coherent manner with the advantages of conversion gain, detector noise suppression, and narrow bandwidth detection, which are characteristic of optical heterodyne signal processing.

II. Technique

The technique consists of illuminating a region of the atmosphere with two coherent, focused beams converging at a small angle (approximately 6 mrad in our test case) and intersecting at a common focus. A scatterer in the focal volume simultaneously scatters radiation back along each transmitted beam direction and from each transmitted beam into the other. If the scatterer is in motion, the frequency of the scattered radiation will in general be different in each direction. At the single detector, the four scattered signals are combined with one another and with a relatively much more powerful optical local oscillator in a homodyne or heterodyne mode on a single detector. A schematic diagram of the optical arrangement is shown in Fig. 1. The output of the detector contains a triplet of rf signals. Modifications of this basic procedure, such as using a separate detector and local oscillator offset for each received signal to remove sign ambiguity, are possible.

The authors are with NOAA Environmental Research Laboratories, Wave Propagation Laboratory, Boulder, Colorado 80302.

The actual experiment described later used homodyne detection for simplicity. Target velocity was controlled to assure the optical homodyne beat was well removed from zero frequency so that no spectral folding occurred. For purposes of general analysis it is easiest to assume heterodyne operation so that, in even the general case where the longitudinal (line-of-sight) velocity component may go to zero, spectral folding about zero frequency is avoided.

For a scatterer of velocity V at an angle θ with the lidar axis (bisector of the transmitter beams) and an incident beam convergence angle of ϕ between beams as shown in Fig. 2, the three Doppler frequency shifts (from the fixed local oscillator-to-transmitter frequency difference) for an incident laser frequency ν are

$$\Delta\nu_0 = (-2\nu V/c)(\cos\theta \, \cos\phi/2),$$

$$\Delta\nu_1 = (-2\nu V/c)(\cos\theta \, \cos\phi/2 + \sin\theta \, \sin\phi/2), \quad (1)$$

and

$$\Delta\nu_2 = (-2\nu V/c)(\cos\theta \, \cos\phi/2 - \sin\theta \, \sin\phi/2).$$

The optical signals with these frequency shifts yield a rf triplet that results from coherent optical heterodyne detection in the photodiode detector. The interbeam frequency component at $\Delta\nu_0$ should be twice the intensity of either wing of the triplet. Approximating $\cos\phi/2 = 1$ and $\sin\phi/2 = \phi/2$ since ϕ is very small, we can write the average frequency shift of the triplet from the local oscillator offset as f_L, where

$$f_L = |(-2\nu V/c) \cos\theta|. \quad (2)$$

This situation is illustrated schematically in Fig. 3.

The rf triplet centered at f_L arises from a linear translation process, namely, the subtraction of the local oscillator frequency from the optical triplet frequencies. To conveniently measure the spacing between frequencies in the triplet, the resulting rf triplet is passed through a nonlinear device to give a beat frequency between the frequencies comprising the triplet.
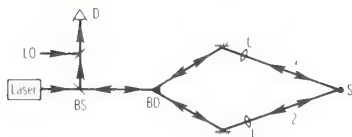
Fig. 1. Schematic indication of apparatus used for the coherent differential Doppler experiment. The laser beam is divided by beam divider BD and focused at the sample region S by optical elements L. Scattered radiation is collected and recollimated by the same optical system as used for the transmitter. At beam splitter BS the four signals (1 back to 1, 2 into 1, 1 into 2, and 2 back to 2) are directed to the detector D where they are combined with local oscillator LO.
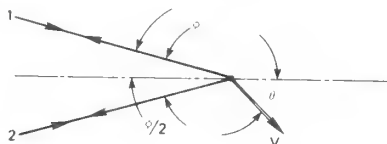
Fig. 2. Scattering geometry used for remote lidar sensing of transverse velocity at a point.

After such nonlinear detection the frequency difference between the center of the triplet and either sideband is f_T, where

$$f_T = |(-\nu V/c)\phi \sin\theta|. \qquad (3)$$

This triplet spacing frequency is a result of a rf nonlinear detection process. An additional beat between the two sidebands of the triplet will occur at a frequency $2f_T$ and will be down in intensity by a factor of 4 below the signal at f_T.

To a very good approximation, the average frequency of the triplet is proportional to the longitudinal (along lidar axis) component of the velocity V_L, and the beat (difference) between either sideband and the center frequency gives the transverse (perpendicular to lidar axis) component of the velocity V_T in the plane of the transmitted beams.

III. Practical Application

A key consideration for the practical application of the technique is the effect of atmospheric refractive index fluctuations on the transmitted and received signals. Heterodyning requires temporal coherence along each ray so that efficient mixing with the local oscillator can occur. Each separate path need not be phase coherent with the other, since the signal scattered back along the transmitted path and that scattered from one path to the other are mixed separately with the local oscillator. The question of atmospheric phase fluctuations is treated in a number of review articles including those by Hodara[1] and Lawrence and Strohbehn.[2]

Our analysis contrasts the temporal coherence requirements of the coherent system with the more familiar spatial coherence requirements associated with amplitude scintillation patterns. Experimentally, one could study temporal coherence with an unequal-arm interferometer and spatial coherence by two-aperture amplitude correlations in the far field. A clear understanding of the difference between temporal and spatial coherence, or between path-integrated frequency effects and differential phase changes across an aperture, helps one interpret the coherent differential Doppler technique.

A. Coherent System

For the geometry of Fig. 1, we consider a wavelength λ, pathlength L, transverse velocity V_T, atmospheric structure parameter $C_n{}^2$, effective optical aperture for each beam in the system D_e, and beam separation d at the transmitter. Note that the convergence angle ϕ is just d/L. Temporal phase fluctuations introduce an rms frequency modulation[1] given by

$$\langle \Delta f^2 \rangle^{1/2} = V_T D_e{}^{-1/6} (\lambda^{-2} L C_n{}^2)^{1/2}.$$

Strictly speaking, this expression applies only for collimated beams. We use this form for a useful approximation to our situation. To evaluate the range limit L_T allowed by temporal coherence requirements, it is reasonable to require $\langle \Delta f^2 \rangle^{1/2}$ to be some small fraction of f_T from Eq. (3), for example, 1%. Applying this restriction results in a limit

$$L_T = (10^{-2} d D_e{}^{1/6}/C_n)^{2/3}, \qquad (4)$$

which is independent of wavelength. For typical atmospheric boundary layer values of $d = 0.3$ m, $D_e = 0.1$ m, and $C_n = 3 \times 10^{-8}$ m$^{-1/3}$, the range is limited to $L_T = 1.67 \times 10^3$ m by temporal coherence considerations. Note that L_T increases with increasing beam separation so that longer coherent ranges are possible by going to a larger geometry. This increase in range limit with d is a result of the larger f_T associated with increasing convergence angle ϕ.

B. Incoherent System

For an incoherent system that relies on fringe formation, the important coherence consideration is spatial coherence between the two beams that form the fringes. The effective aperture of the system for beam-to-beam coherence is the extreme ray separation d. The aperture over which the rms phase difference (fluctuation) is less than 1 rad is given by[1]

$$d = [2.9(\lambda/2\pi)^{-2} L C_n{}^2]^{-3/5}.$$
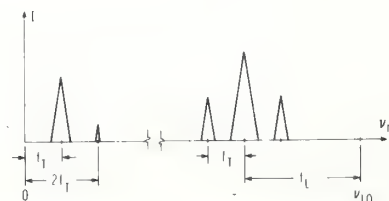
Fig. 3. Optical heterodyne frequency spectrum showing the triplet centered at f_L from the local oscillator (unresolved in practice) resulting from linear detection and the experimentally resolved intratriplet beat at f_T resulting from nonlinear detection. Frequency f_L is proportional to the longitudinal component of the velocity and f_T is proportional to the transverse component.

260

This expression, valid for collimated beams, is used for the system focused at 33 m as an approximation for helpful range estimates as was done in the temporal coherence case. The spatial coherence limit on range L_S is then

$$L_S = (\lambda/2\pi C_n)^2 d^{-5/3}/2.9. \qquad (5)$$

For the same conditions as for the temporal limit, with $\lambda = 10.6 \times 10^{-6}$ m, the range is limited to $L_S = 8.11 \times 10^3$ m by spatial coherence considerations. Note that the spatial coherence limit decreases with increasing beam separation, in contrast to the case for temporal coherence. To compare the ir with the visible, it is more meaningful when changing range to fix the convergence angle ϕ than the beam separation d. Recasting Eq. (5) with convergence angle gives the expression

$$L_S = [(\lambda/2\pi C_n)^2 \phi^{-5/3}/2.9]^{3/8},$$

which shows that the ϕ-fixed range satisfying the spatial coherence criterion goes as $\lambda^{3/4}$. Using this ratio gives a limiting range for the visible $L_S(\text{vis}) = 833$ m, which is less than the temporal limit in the ir for a similar geometry.

The ratio L_T/L_S indicates whether the coherent (heterodyne) or incoherent (fringe) technique is more severely range limited. This ratio is given by

$$L_T/L_S = 5.31\lambda^{-2}C_n{}^{4/3}D_e{}^{1/9}d^{7/3},$$

and for the ir conditions assumed has a value $L_T/L_S = 0.206$. In the ir (for the assumed conditions) the coherent system, which relies on temporal coherence, is slightly more range limited than the incoherent or fringe system, which is limited by spatial coherence. In the visible, however, the range limit for the coherent technique is predicted to be eighty times larger than that for the incoherent technique.

Note that this discussion of atmospheric coherence limitations touches on only one aspect of the four-way remote-sensing systems comparisons among coherent and incoherent techniques operating in the ir and the visible. The coherence considerations are intended to illuminate the coherent technique and to indicate that atmospheric refractive index fluctuations should not limit the reported experiment.

The values assumed for the examples above are based on a C_n average for data taken 30 m above the surface.[3] A smaller range limit would result for a C_n of approximately 3×10^{-7} m$^{-1/3}$ observed in another experiment done 1.6 m above the terrain.[4] In this case the temporal range limit given following Eq. (4) would be approximately 360 m. On the other hand, C_n approximately equal to 1×10^{-8} m$^{-1/3}$ is more reasonable for a slant range at distances beyond 500 m. Values for the atmospheric structure parameter $C_n{}^2$ from experiments in the visible are also used in the range limit estimates for ir wavelengths (10.6 μm). Near strong ir absorption lines the refractive index of air changes markedly,[5] but at 10.6 μm the atmospheric transmission exhibits only very weak absorption features. In the absence of absorption lines, the difference between the refractive index of air and of vacuum $(n - 1)$ changes by less than

5% over the 0.6–10.6-μm region.[6] It is therefore reasonable to use the same value of $C_n{}^2$ for the visible and 10.6-μm wavelengths.

We conclude from these considerations that the coherent differential Doppler technique in the configuration tested is not restricted by atmospheric coherence limitations to a range of at least 360 m. Observed fringes are not a reliable indicator of the possibility of efficient heterodyne detection of transverse velocities.

To be useful in the atmosphere as a remote probe, which implies a need to sample much larger volumes than are characteristic of laboratory Doppler velocimeters, as well as more stringent coherency requirements than for laboratory systems, a practical Doppler velocity measurement system must operate when a number of scattering targets with a distribution of velocities are present within the sampling region (focal volume). A distribution of velocity components with a characteristic spread δV will give rise to frequency distributions of magnitude

$$\delta f_L \sim 2\nu(\delta V)/c, \qquad (6)$$

and

$$\delta f_T \sim \nu(\delta V)\phi/c \sim (\phi/2)\delta f_L.$$

The expressions above, and the order of magnitude arguments following, are not to be thought of as equations applicable to all situations. Rather, the arguments discuss typical or generalized scale sizes. For example, the spread in longitudinal velocity components δV_L is approximately equal to that for the transverse component δV_T in typical boundary layer situations. For purposes of scaling argument it is sufficiently accurate to characterize the velocity spread by a representative value δV.

In our Doppler lidar experience the range of the spread is typically given by

$$0.1 \le \delta V/V \le 0.5. \qquad (7)$$

Incidentally, this empirical observation for Doppler lidar is in contrast to the usually smaller spreads noted for Doppler radar.[7] It is reasonable to expect lidar spreads to be larger than radar-derived values since the small tracers (typically 2–10-μm diam) characteristic of lidar measurements should follow the fluctuations in the wind field more faithfully than do larger hydrometeors or chaff. The larger volume average of the radar will also tend to smooth out some of the variability present in the smaller lidar sensing volume. In any case, for small $\phi/2$ it is clear that

$$\delta f_L \gg f_T, \qquad (8)$$

and there is no hope of observing the triplet splitting due to transverse velocity components in the frequency region near f_L when a number of targets with a distribution of velocities are present in the sensing volume. However the intratriplet beats are distributed only over a narrow frequency bandwidth $\delta f_T < f_T$ and are in fact observable in the frequency region near f_T. Frequency spectral analysis, over the region 0 to $\sim 2f_L$ on either

261

side of the heterodyne local oscillator offset, gives a measure of the longitudinal velocity component and its variation for a scattering target. Spectral analysis in the region 0 to $\sim 2f_T$, where typically the scale relationships $f_T \sim (\phi/2)f_L \tan\theta$ and $\phi \lesssim 0.01$ are representative, gives a measure of the transverse velocity component and its variation. For unambiguous analysis, the local oscillator offset should be chosen to be significantly larger than the greater of $2f_T$ and f_L.

In addition to the signal triplet from each scattering center that we have analyzed, additional noise frequencies must be considered to understand the results and applicability of our experiment. Frequencies from nonlinearly detected intertriplet beats, when multiple scattering centers are simultaneously contributing to the signal, will cause noise in the frequency region near f_T. If there are n simultaneous scatterers, an intratriplet beat signal proportional to n will occur over a bandwidth δf_T, while an intertriplet beat proportional to approximately n^2 (in the limit of large n) will be spread over a much larger bandwidth δf_L. For small n, the fact that $\delta f_T \ll \delta f_L$ will dominate the signal-to-noise situation so that the SNR will increase with increasing number of scatterers. In the limit of very large n the SNR near f_T goes to zero. More research is required on the effect on SNR from a distributed target with a range of signal intensities as well as a range of signal frequencies. Since the intensity from the scatterers varies, the effective n for a particular situation can be chosen to be less than the actual n by setting an intensity threshold on the received signal spikes before the nonlinear mixing occurs. The fact that some intermediate value of n, rather than the largest possible, is preferred indicates a possible preference for the ir over the visible for practical systems.

Comparison of this coherent differential Doppler technique with other transverse velocity measuring schemes helps to illuminate this method. Incoherent differential Doppler or incoherently detected real fringe systems detect the amplitude modulation of the nearly backscattered signal when inhomogeneities in the atmospheric aerosol distribution pass through the illuminated region.[8-10] Although the SNR analysis of such systems is difficult,[11] the coherence requirement on the two beams forming the fringes, which leads to Eq. (5), must be satisfied to maintain good fringe contrast. Temporal coherence requirements apply to the so-called "coherent fringe system" discussed by Hughes and Pike.[11] In this context, we mean by coherency that two scattered beams are collected by separate optical paths and combined at the detector, rather than considering the beam interference to occur at the scattering volume and then to be collected along a simple optical path as in the incoherent fringe system. This coherent fringe system does not involve the use of a local oscillator for heterodyne conversion. We are not aware that such a coherent fringe system has been tried in the atmosphere at significant ranges, say beyond 10 m, although the analysis by Drain[12] suggests that coherent processing is preferred over incoherent when the number of particles involved in the scattering becomes large. None

of these transverse techniques is effective in measuring the longitudinal component of velocity.

Operationally the coherent and incoherent techniques can be contrasted by considering velocity measurement where the target is a uniform, white diffuse scatterer such as a sheet of paper. No amplitude variations would be detected as the paper moved through the fringe system. However, the scattered light would be shifted in frequency, and the frequency shift detected by a coherent system. Another contrast is apparent if one notes that the incoherent (fringe) technique is sensitive only to the velocity component perpendicular to the beam angle bisector, whereas the coherent technique measures only the longitudinal (line-of-sight) velocity component along the beam. The coherent differential Doppler method studied here measures the small difference in two longitudinal components separated slightly in angle to determine the component transverse to the beam angle bisector.

The present full-coherent approach combines the differential Doppler geometry with the optical homodyne or heterodyne detection already successfully applied in the atmosphere for the longitudinal velocity component.[13,14] The use of a local oscillator requires that the coherence limits of Eq. (4) must be satisfied if efficient heterodyning is to occur.

IV. Instrumentation

To test some of these ideas, velocity components of the surface of a belt sander moving at approximately 45° to the lidar axis were measured at a range of 33 ± 0.2 m. The lidar path varied from 0.5 m to 3 m above an asphalt surface with strong solar heating. This condition provided a worst-case test for the immunity of the technique from decohering effects and from background interference, for a given pathlength. The two sensing beams were separated at the transmitter by 20 ± 0.5 cm, converging on the target at approximately 6.05 mrad $\pm$ 3%. The focal region on the target was approximately 5 mm × 2 mm. The optical system for each coaxial transmit–receive path used a collecting optics area of 50 cm^2 and radiated less than 120 mW at 10.6-μm wavelength. The aperture of each optical system subtended approximately 1.8 mrad in the plane of the two beams as seen from the target. For simplicity and economy the four received signals were combined with the local oscillator on a single nonlinear (power law) ir detector. The resulting rf optical-beat signal and the nonlinearly detected intratriplet beat signal were subsequently analyzed with a conventional scanning spectrum analyzer having a duty cycle of approximately 0.5% coupled to a signal averager with a 5-sec time constant.

V. Results

The belt sander target approximated a distributed atmospheric target sufficiently well that the velocity spread or spectrum width of the return analyzed with a 5-sec time constant satisfied the inequality (8). That is, there was no evidence of a triplet structure in the velocity spectrum. The spectral full width at half-maximum at the expected triplet center, near 500 kHz

for a 2.5-msec^{-1} longitudinal velocity component, was 20% ± 5%, or $\delta f_L / f_L = 0.2 \pm 0.05$.

The frequency spread is partly attributed to the velocity changing rapidly within times shorter than the analysis time as a result of observed vibration, for example, rather than solely to multiple velocities existing in the sensing volume at any instant. Thus this target, while simulating some aspects of a velocity-distributed multiple-target situation, does not represent an atmospheric aerosol target well enough to prove definitely the feasibility of the technique for such an atmospheric target. However, the experimental results, together with the analysis, do give a reasonable expectation that transverse velocity measurements are possible from aerosol targets at ranges beyond 30 m. Even with no averaging time, the scanning spectrum analyzer would not be expected to observe the rf triplet from the intensity-fluctuating variable-frequency signal, since the time to scan the triplet spread of $2f_T$ was equal to or greater than the duration of each signal burst.

In order to measure the instantaneous triplet spacing and thereby determine the frequency f_T and the transverse component of the target velocity, the rf signal bursts from the detector were amplified by 40 dB, fed through a series diode, and analyzed by the same time-averaged scanning spectrum analyzer used to study the spectrum near the longitudinal component frequency. The spectrum analyzer sweep range was changed by a factor of 5×10^{-3}, near the factor $\phi/2$ difference expected from Eqs. (2) and (3).

The intratriplet beat expected was observed at a frequency f_T near 3 kHz corresponding to a transverse velocity component of approximately 2.5 msec^{-1}. Two departures from the idealized situation were evident. First, the spectral full width at half-maximum of the transverse frequency was 50% ± 10%, or $\delta f_T / f_T = 0.5 \pm 0.1$, although one would expect the velocity distribution statistics to be the same for both longitudinal and transverse velocity components. The increased spectral width for the transverse component is attributed to geometric broadening. Each beam subtended an angle greater than 25% of the beam separation. In relation (6) a spectral width $\delta f_T / f_T$ can arise from both a velocity spread $\delta V/V$, common to both components, and from a distribution in convergence angle $\delta\phi/\phi$, which strongly affects only the transverse component. Secondly, a weak spectral peak was observed at a frequency $2f_T$ with an intensity less than 10% of the peak at f_T. The weakness of this intratriplet beat with respect to the expected 25% of the f_T intensity is attributed to the nonlinear character of the mixing process in the simple series diode.

Infrared Doppler lidar sensing of longitudinal (along the line-of-sight) velocity components, at ranges of at least 1 km using velocity-distributed targets, is a well-established technique. To help establish the validity of this newer technique, variations in the transverse velocity component experiment were tried. These tests produced the expected results and strengthened confidence in the technique analysis presented earlier in the paper.

First, an increase in the angle between the lidar axis and the constant-velocity target velocity from 30° to 60° shifted the peak of the f_T frequency distribution by the expected factor of 1.7 ± 10% for the change in transverse velocity component.

Second, rotation of the plane of the intersecting beams by 90° about the beam angle bisector, so that the beam plane was perpendicular to the plane containing the lidar axis and the target velocity, resulted in a transverse frequency $f_T < 0.1$ kHz, consistent with the expected value 0 (no triplet splitting). This accuracy limitation is not fundamental but arises from the zero-beat width of the spectrum analyzer at the setting used. The longitudinal frequency spectrum, in the region of $f_L \sim 500$ kHz, underwent no detectable change when the beam plane was rotated.

The third verification test consisted of simultaneously reducing the beam separation and increasing the individual beam aperture, leaving the outer limits of the optical system unchanged. For each stage of the two-step beam separation modification, the transverse frequency spectrum of f_T was observed to increase in integrated intensity, to shift in peak value to lower frequency, and to broaden. The spectral intensity increase was consistent with that resulting from increasing the original 50-cm^2 optics area to 85 cm^2 and then to 100 cm^2 for each beam. The reduction of f_T at the spectral peak is a result of, and qualitatively proportional to, the reduction in effective mean interbeam convergence angle ϕ. Geometric broadening due to both increasing $\delta\phi$ and decreasing ϕ is responsible for the increasing width of the spectrum. During the decreasing separation and increasing aperture system modification, no part of the frequency spectrum above the original spectral peak changed, which is expected if the maximum-convergence-angle portion of the optical system remained unchanged.

A fourth check of the experiment was to determine if the sensing paths really intersected at the target and were coherent. On a thermally sensitive screen the 10.6-μm wavelength field intensity at the target consisted of three interference fringe maxima within an overall envelope 5 mm × 2 mm. The long dimension of the pattern was in the plane of beam intersection, consistent with the diffraction-limited spot size of the single beam aperture dimensions, which were in a ratio of approximately 4:10 parallel and perpendicular to the intersection plane, respectively. The measured fringe spacing of 1.75 mm ± 5% agreed well with a calculated value of the fringe spacing, $d = \lambda/\phi = 1.75$ mm ± 3%. The pattern at the target also rotated 90°, as expected, when the plane of beam intersection was rotated by 90° about the convergence angle bisector.

VI. Conclusions

We conclude from this experiment that it is possible to measure remotely at one point in the flow field all three velocity components of a target, both transverse to and along the optical line of sight, simultaneously, by using a fully coherent optical homodyne (and by simple extension, heterodyne) technique. The measurement is made effectively from a single location. In addition, the analysis and experiment give reasonable expectation

that the technique will work on multiple targets, occurring intermittently throughout the sensing volume, with a significantly wide distribution of velocities. With readily available apparatus, interbeam convergence angles as small as 6 mrad pose no difficulty in practice.

The practical limits of the technique, with respect to the statistics of signal distribution in time and frequency and with respect to minimum convergence angle, remain to be determined.

References

1. H. Hodara, Proc. IEEE **56,** 2130 (1968).
2. R. S. Lawrence and J. W. Strohbehn, Proc. IEEE **58,** 1523 (1970).
3. I. Goldstein, P. A. Miles, and A. Chabot, Proc. IEEE **53,** 1172 (1965).
4. G. M. B. Bouricius and S. F. Clifford, J. Opt. Soc. Am. **60,** 1484 (1970).
5. R. F. Calfee, Appl. Opt. **7,** 1652 (1968).
6. L. D. Lorah and E. Rubin, in *Handbook of Military Infrared Technology,* W. L. Wolfe, Ed. (U.S. Government Printing Office, Washington, D.C., 1965), p. 839.
7. F. E. Nathanson, *Radar Design Principles* (McGraw-Hill, New York, 1969), pp. 208–209.
8. W. M. Farmer and J. O. Hornkohl, Appl. Opt. **12,** 2636 (1973).
9. C. M. Penney, IEEE J. Quantum Electron. **QE-5,** 318 (1969).
10. P. J. Bourke and C. G. Brown, Opt. Laser Technol. **3,** 23 (1971).
11. A. J. Hughes and E. R. Pike, Appl. Opt. **12,** 597 (1973).
12. L. E. Drain, J. Phys. D **5,** 481 (1972).
13. T. R. Lawrence, D. J. Wilson, C. E. Craven, I. P. Jones, R. M. Huffaker, and J. A. L. Thomson, Rev. Sci. Instrum. **43,** 512 (1972).
14. R. L. Schwiesow and R. E. Cupp, Appl. Opt. **15,** 1 (1976).

BOUNDARY LAYER WIND MEASUREMENTS WITH AN FM-CW RADAR

R. B. Chadwick, W. C. Campbell, K. P. Moran, and R. G. Strauch
NOAA/ERL/Wave Propagation Laboratory
Boulder, Colorado 80302

1.   INTRODUCTION

An FM-CW radar equipped with Doppler data processing is able to measure the velocity spectra of both hydrometeor scatterers and refractive-index fluctuations in the optically clear air [Strauch et al. 1976]. The FM-CW Doppler radar is therefore potentially able to measure wind profiles in all weather conditions. The FM-CW radar without Doppler capability has been used primarily as a high resolution probe of the reflectivity structure of the optically clear air. It has usually detected scattering from layered regions but could not detect spatially continuous radar scattering even at low altitudes. However, the addition of Doppler processing to the FM-CW radar means that it can be used in different and more versatile modes. For example, the FM-CW radar has heretofore operated almost exclusively as a zenith-pointing device; with Doppler processing it will usually be operated off the zenith to measure horizontal wind components. Without Doppler processing the FM-CW radar typically operates with a range resolution of a few meters; with Doppler it has applications as a wind sensor with coarse range resolution as well as applications requiring fine resolution. The FM-CW radar without Doppler processing uses integration times of a few seconds so that the spatial structure of reflectivity can be measured in detail as it passes overhead; an FM-CW Doppler radar may use integration times of more than one minute to measure wind profiles. The FM-CW radar without Doppler capability is relatively insensitive to reflectivity structure that does not change in height or with time; with Doppler processing the presence of scattering from non-layered regions of the atmosphere is readily detected, even if the signals are much weaker than the background ground clutter. Therefore, the FM-CW Doppler can measure wind profiles in regions where the non-Doppler FM-CW radar detects no scattering layers.

Green et. al. (1975) report the measurement of winds in the optically clear air by measuring spatially continuous scattering between 4 and 16 km altitude with a 7-m pulse Doppler radar. When we compare the sensitivity of an FM-CW radar to that of the 7-m pulse radar using the techniques of Chadwick and Little (1973), we find that we should detect the same refractive-index fluctuations at an altitude of 1 km with an FM-CW radar that the 7-m pulse radar detects at 10 km altitude. Because refractive-index fluctuations at 1 km altitude are much stronger than those at 10 km altitude the FM-CW Doppler radar can be expected to measure boundary layer wind profiles.

2.   RADAR SENSITIVITY

The minimum detectable radar reflectivity of an FM-CW Doppler radar is given by: (Strauch, 1976)

$$\eta_{min} = \frac{256 \ R^2 \ k \ T_{op} \ \sigma_v}{\sqrt{\pi} \ P_t \ A_e \ \Delta R \sqrt{\lambda_o} (\Delta V) T_o} \qquad (1)$$

where   k is the Boltzmann constant

T_{op} is the operating temperature of the receiver

R is the range

σ_v is the standard deviation of the Doppler velocity distribution

P_t is the transmitted power

A_e is the effective antenna aperture

ΔR is the range resolution

λ_o is the radar wavelength

ΔV is the velocity resolution of the radar

and T_o is the total observation time.

The radar reflectivity is related to the refractive-index fluctuations in the inertial subrange by: (Ottersten, 1969)

$$\eta = 0.38 \ C_n^2 \ \lambda^{-1/3} \qquad (2)$$

where C_n^2 is the refractive-index structure constant. We can predict the minimum C_n^2 needed for detection using the following parameters that apply to the Wave Propagation Laboratory FM-CW radar:

T_{op} = 527 K
P_t = 200 Watts
A_e = 2.33 m^2
ΔR = 32 m
λ_o = 0.1 m.

The width of the Doppler spectrum is assumed to be 1 m/s. A velocity resolution of 15/32 m/s and a total observation time of 64 s are assumed. The minimum value of C_n^2 that can be detected at 1 km range is 5×10^{-17} m$^{-2/3}$. (The minimum detectable reflectivity factor for hydrometeor scattering is -47 dBZ at 1 km range.) Measurements made by Kropfli et. al. (1968) and Ochs and Lawrence (1972) indicate that a radar with this sensitivity should be able to measure wind profiles in the lowest 1 to 2 km of the optically clear atmosphere in nearly all the cases measured by the in situ sensors. This conclusion is supported by the experimental data that we have obtained since Sept. 1975 with our FM-CW radar operating in the adverse conditions of relatively dry air masses in Colorado.

3.   WIND MEASUREMENTS

The Doppler processing scheme for FM-CW radars is described by Barrick (1973) and Strauch et. al. (1976). Strauch and Chadwick (1976) give a simplified description of how the spectral indicies of the power spectrum of the signal obtained from repetitive sweeps correspond to both target range and target velocity. Figs. 1-3 show examples of this range/velocity display with radar
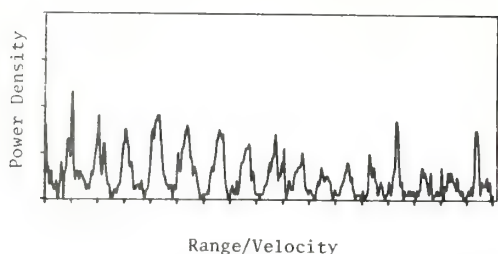
Figure 1. *Power spectrum of the FM-CW radar return from the optically clear air. Spectrum shown is the average of 39 spectra obtained in 20 s. Spectrum calculations were performed off-line by minicomputer.*
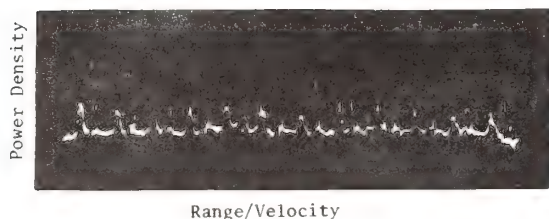
Figure 2. *Real-time display of the power spectrum of FM-CW radar signals. Sharp lines are ground clutter at consecutive range resolution cells while signal spectra occur at spectral points corresponding to non-zero velocity.*

Figure 3. *Time-height display of the range/velocity data obtained in real time from radar returns in the optically clear air.*

returns from the optically clear air. Fig. 1 shows the average of 39 power spectra that were calculated off-line with a minicomputer. The mixer output signal was digitized and tape recorded and each of the 39 spectra were obtained from 32 radar sweeps. Ground clutter appears as a sharp line at the spectral index values on the axis labeled as range/velocity (at zero velocity) while the spectra of moving targets are broader and are displaced

from the zero-velocity lines. The strong signal spectra in the range intervals near 399 m are actually folded in velocity; it is not possible to tell from this display whether the velocities are toward or away from the radar. (The ambiguity is easily resolved with clear air returns by simply increasing the elevation angle of the radar antenna to reduce the Doppler shift caused by horizontal winds.) Fig. 2 shows a similar display obtained from the output of the real-time spectrum analyzer. Again, the ground clutter appears as a sharp line so that the presence of strong ground clutter does not prevent the detection of weak atmospheric returns if the Doppler spectrum is shifted sufficiently by the horizontal wind. Fig. 3 shows the same type of output on a time/range display. In this display, the power density of the spectrum analyzer output modulates the intensity while the film advances slowly. The y axis is the range/velocity axis. The horizontal lines on the film are the ground clutter corresponding to consecutive range intervals while the signal spectra are displaced from the clutter by the mean wind which, in this case, has a periodic component. One component of the horizontal wind can be obtained from data of this type. In order to measure the vector wind we have mounted the dual antennas on a fully steerable mount. We have operated at full rf power at elevation angles as low as 30 deg.

We operated our Doppler FM-CW radar for a two-week period in September 1975 in southeastern Colorado near a 152-m tower and a tethered balloon system. The tethered balloon was instrumented to measure temperature, humidity, wind speed, and direction for elevations up to 600 or 700 m. This equipment was described by Morris et. al. (1975). The location near Haswell, Colorado, is a typical high plains meteorological regime in which active convection develops during clear days. The data described here were collected on a day when ground fog was present at 0700 MDT. The fog "burned off" and was followed by a 2/10 cover of strata cumulus by 0900. At 1100 the sky was completely clear. To further characterize the meteorology, temperature and humidity soundings from the tethered balloon are shown in Fig. 4. The ascent occurred from 1112 to 1128 and the descent occurred from 1128 to 1142.

At 1140, the radar was operating with an elevation angle (from horizontal) of 60°; the maximum observed range was 1171 meters, and the maximum unambiguous horizontal velocity of the radar was ± 5.0 m/s. Because of the existence of a strong capping inversion, we assume that the vertical velocity is negligible compared to the horizontal velocity. We averaged 39 velocity spectra from each range interval to arrive at a range/velocity map representing 10 s of data. With a computer algorithm, we estimated the mean radial velocity and derived profiles of a component of the horizontal wind along a given direction. A profile of the wind component along 225° azimuth is shown in Fig. 5 with profiles of the same component obtained over 30 min by the tethered balloon Boundary Layer Profiler (BLP) system. The agreement is remarkably good considering that the BLP was located ∿ 300 m to the east of the radar and the radar data are averaged over only 10 s. An estimate of how the radar data change with time is provided by the next four wind

327
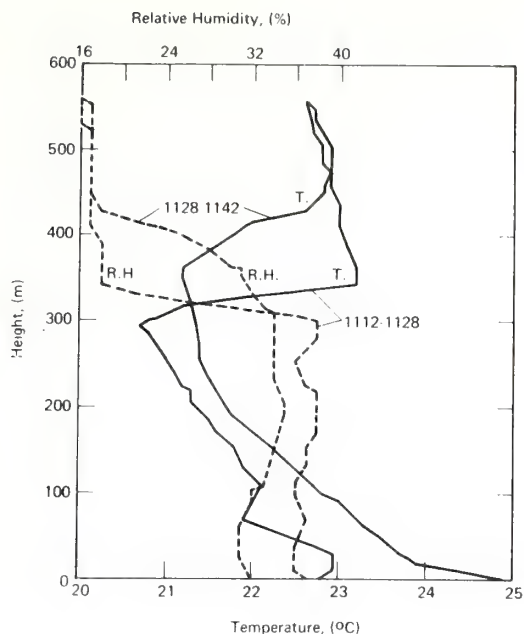
Figure 4. Temperature (T) and relative humidity (RH) profiles measured by tethered balloon.

Figure 6. Four wind profiles on 225° bearing as measured by FM-CW radar at 10-sec intervals.

profiles plotted in Fig. 6. The radar wind profiles from Figs. 5 and 6 show the radar wind data at 225° over a 50-s interval. Fig. 7 shows the radar wind component along the 315° azimuth at approximately the same time as that measured by the BLP. It is clear that the strong, persistent shear layer is along the 225° azimuth only. Fig. 8 shows the four 10-s averages of the radar-derived wind component immediately prior to the profile in Fig. 7. Note how rapidly the wind was changing in the lower levels compared with the 225° azimuth wind.

Figure 5. Wind profiles on 225° bearing as measured by FM-CW radar and tethered balloon. The small circles are from a rawinsonde launched at 1100.
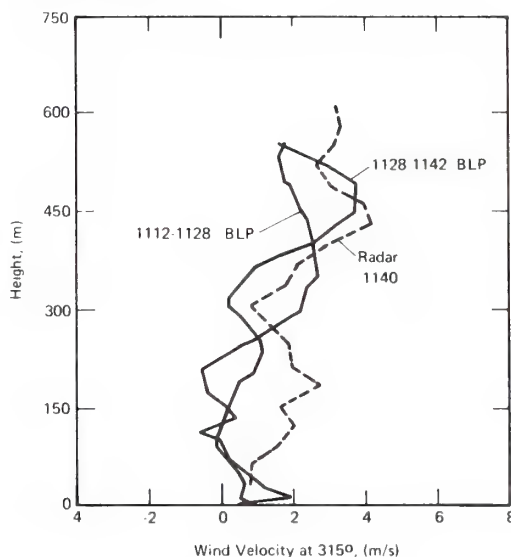
Figure 7. Wind profiles on 315° bearing as measured by FM-CW radar and tethered balloon.

328

267
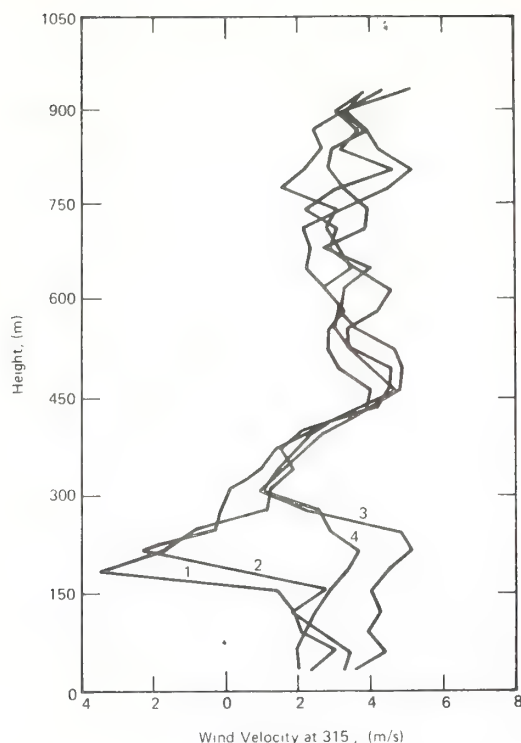
Figure 8. *Four wind profiles on 315° bearing as measured by FM-CW radar at 10-sec intervals.*

4. CONCLUSION

An FM-CW Doppler radar can measure wind profiles in the lower atmosphere in the optically clear air. Since the measurement of winds in the presence of hydrometeors is readily achieved with Doppler radar (Strauch et. al. 1976), the FM-CW Doppler radar has potential for important applications as a device for measuring winds in the lower atmosphere in all weather conditions. Such a device may be useful for measuring wind-shear hazards at airports, predicting dispersal of air pollutants in valleys, near cities, or near power plants, and predicting the formation and dispersal of fog. It will also enable us to determine the role that wind shear plays in the formation of layers of high radar reflectivity. In addition, the second moment of the Doppler spectrum can be used to estimate turbulent dissipation rates which are important in understanding boundary layer dynamics.

5. ACKNOWLEDGMENT

The authors wish to thank A. L. Morris of Ambient Analysis, Inc. of Boulder, Colorado, for providing excellent in situ data with his tethered balloon boundary layer profile system.

6. REFERENCES

Barrick, D. E. (1973): FM-CW radar signals and digital processing, *NOAA Technical Report ERL 283-WPL-26,* U.S. Govt. Printing Office, Washington, D.C. 20402.

Chadwick, R. B. and C. G. Little (1973): The comparison of sensitivities of atmospheric echo-sounders, *Remote Sensing of the Environment,* 2, 223-234.

Green, J. L., J. M. Warnock, R. H. Winkler and T. E. Van Zandt (1975): A sensitive VHF radar for the study of winds, waves and turbulence in the troposphere, stratosphere and mesosphere, 16th Radar Meteorological Conference, April 22-24, Houston, Texas.

Kropfli, R. A., I. Katz, T. G. Konrad and E. B. Dobson (1968): Simultaneous radar reflectivity measurements and refractive index spectra in the clear atmosphere, *Radio Sci.,* 3, 991-994.

Morris, A. L., David B. Call and Robert B. McBeth (1975): A small tethered balloon sounding system, *Bulletin of the AMS,* 56, no. 9, 964-969, Sept. 1975.

Ochs, G. R. and R. S. Lawrence (1972): Temperature and C_n^2 profiles measured over land and ocean to 3 km above the surface, *NOAA Technical Report No. ERL 251-WPL 22,* U.S. Govt. Printing Office, Washington, D.C. 20402.

Ottersten, H. (1969): Radar backscattering from the turbulent clear atmosphere, *Radio Sci.,* 4, 1251-1255.

Strauch, R. G. (1976): Theory and application of the FM-CW Doppler radar, Ph.D. Thesis.

Strauch, R. G. and R. B. Chadwick (1976): Measurement capabilities of FM-CW Doppler radars, Preprints, 17th Radar Meteorology Conference, Oct. 26-29, Seattle, WA.

Strauch, R. G., W. C. Campbell, R. B. Chadwick and K. P. Moran (1976): Microwave FM-CW Doppler radar for boundary layer probing, *Geophysical Research Letters,* 3, no. 3, 193-196.

CELL INTERACTION AND MERGER IN A SOUTH FLORIDA THUNDERSTORM

Harold W. Frank
NOAA/ERL/Wave Propagation Laboratory
Boulder, Colorado 80302

Roger M. Lhermitte
Division of Atmospheric Sciences
University of Miami
Coral Gables, Florida 33124

1.   INTRODUCTION

Mechanical forcing produced by cold outflow at downdraft bases is recognized by thunderstorm researchers as a powerful mechanism, often vital to storm sustenance and propagation. The conceptual models of Newton and Newton (1959), Browning (1962), and others describe this mechanism and emphasize that when there is substantial vertical wind shear in the storm environment, updrafts and downdrafts with opposing horizontal momentum can coexist adjacent to each other and interact to maintain a quasi-steady configuration often associated with severe or tornadic storms. More often steadiness is not achieved; instead, outflowing downdraft air stimulates the formation of new and separate convective cells, thus maintaining a multi-cell storm by discrete propagation. Convergence and lifting are especially intense where cold thunderstorm outflow collides with outflow from another storm or with a sea-breeze current. Indeed, the latter situation has been observed in association with several south Florida tornados and waterspouts (Holle and Maier, 1974; Boyd, 1965; Gerrish, 1969; Senn et al., 1969). In fact many south Florida tornados occur when synoptic scale shear is weak and local winds are dominated by thunderstorms and the sea breeze (Senn et al., 1969). The bulk of summer rainfall in this area is derived from numerous convective storms of moderate intensity, formed and maintained under the influence of sea breeze and intra-cell interactions (Pielke, 1973). Often the cells form lines or clusters, and rainfall production is greatly enhanced when individual cells merge to form larger and more intense storms (Simpson and Woodley, 1971; Woodley et al., 1971).

In this paper we present three dimensional air flow patterns obtained by the University of Miami dual Doppler radar system, which document the role of downdraft interaction in promoting one cell merger as described. We feel these observations are highly relevant to weather modification efforts, particularly in south Florida where researchers aim to effect mergers by cloud seeding (Simpson et al., 1972). The utility of multiple Doppler radar in thunderstorm research is discussed in light of the fact that quasi-real time processing of multi-Doppler data may soon be possible (Lhermitte, 1975).

2.   CONDITIONS IN THE STORM ENVIRONMENT

During the summer of 1973 the University of Miami dual Doppler system was operated in south Florida in conjunction with the Florida Area Cumulus Experiment (FACE), conducted by the National Oceanic and Atmospheric Administration - Experimental Meteorology Laboratory (NOAA-EML). Its purpose was to study convective rainstorms in the south Florida area and to test the results of dynamic seeding on Florida cumulus clouds (Staff,
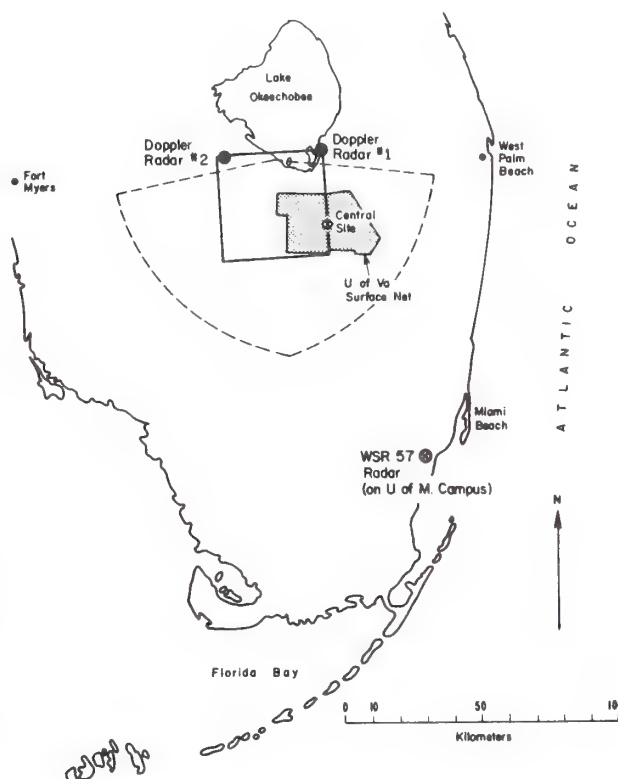
Figure 1. During FACE 1973 the University of Miami dual Doppler system was located just south of Lake Okeechobee. The dashed line indicates the total area of dual Doppler coverage, but this study is concerned with dual Doppler measurements in the heavily outlined square. The University of Virginia surface instrument network covers the stippled area.

EML, 1974). For this experiment the University of Miami radars were located near the south shore of Lake Okeechobee, as shown in figure 1. The radars were separated by about 35 km, and were able to provide dual Doppler observations within the area delineated in the figure by dashed lines. Measurements to be discussed in this paper are confined to the 37 km x 37 km square bounded in the figure by solid lines. These results pertain to a complex of thunderstorm cells that was observed on the afternoon of July 30, 1973. Dual Doppler data were collected from 13:48 to 17:17 EDT on that day, but this analysis is concerned with developments between 15:30 and 16:30.

Figure 2 depicts a series of WSR 57 PPI photographs that show the evolution over a 90 minute period of radar echos near the area of dual Doppler coverage. We will consider flow patterns
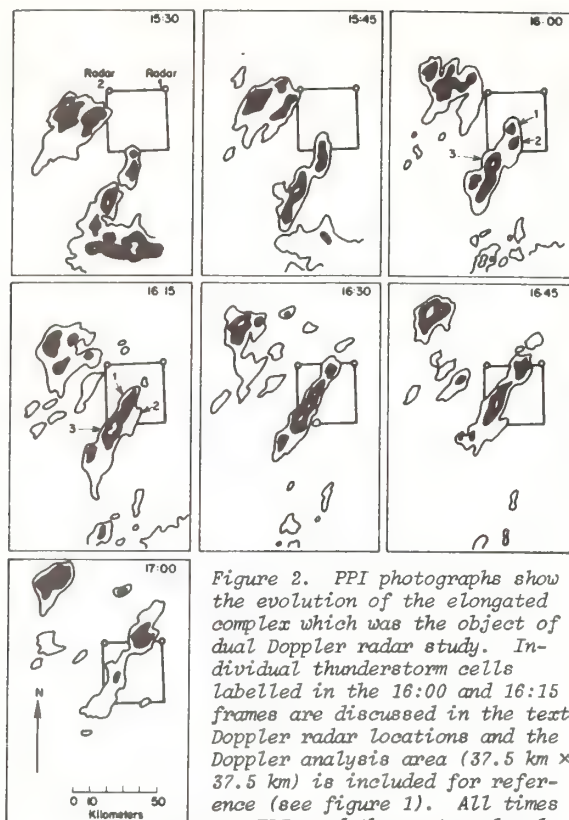
Figure 2. PPI photographs show the evolution of the elongated complex which was the object of dual Doppler radar study. Individual thunderstorm cells labelled in the 16:00 and 16:15 frames are discussed in the text. Doppler radar locations and the Doppler analysis area (37.5 km × 37.5 km) is included for reference (see figure 1). All times are EDT, and the contour levels are drawn for radar reflectivity factors of 16, 30 and 41 dBZ.

in the echo region containing cells 1 and 2, which are pointed out in the 16:00 photo of the figure. Cells 1 and 2 present a convenient situation for dual Doppler analysis for several reasons. They are in an optimum location around 16:00, and until about 16:10 the pair is distinguishable from

surrounding cells and thus can be treated to some extent as a separate cell complex. Furthermore, the eventual dissipation of cell 2 and the merging of cell 1 with cell 3 (see the 16:15 photo) is an interesting development which we will attempt to explain with the help of the Doppler measurements.

Synoptic conditions over south Florida on this day are described as "weakly disturbed" (Staff, ERL, 1974) due to the presence in the area of a stationary trough with minor perturbations. The Showalter stability index is +4 for the 8:00 EDT Miami sounding, and slightly less than +3 for the 14:30 EDT sounding at Central Site (shown in figure 1). The latter sounding is shown in figure 3a. Small circles on the temperature sounding indicate a suggested in-cloud profile referring to a parcel which entrains saturated air of environment temperature according to 1/M dM/dZ = 0.2, where M is parcel mass and Z is height in kilometers The entrainment calculation is discussed in Frank (1976).
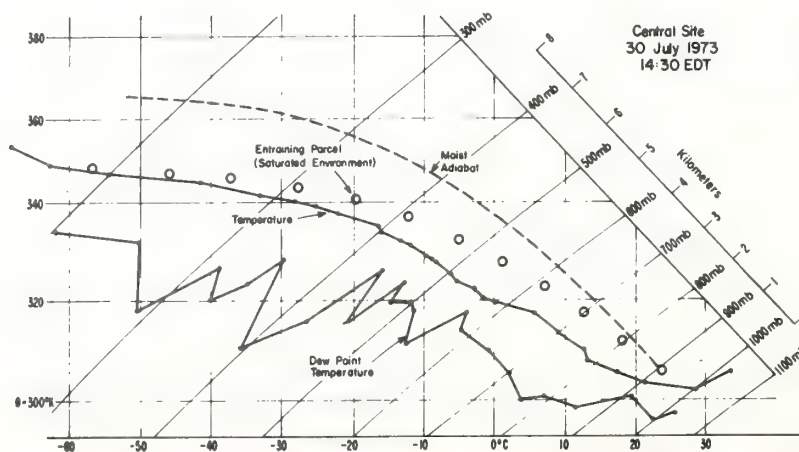
Figure 3a. Central site sounding for 14:30 EDT, about one hour earlier than the dual Doppler observations presented in this study. Circles refer to an updraft of 1 km radius which entrains saturated air at the environment temperature, assuming entrainment coefficient K = 0.2.

152

In figure 3b the wind profile from the 15:00 EDT MIA sounding is shown along with a profile of equivalent potential temperature, θ_E, derived from the central site sounding. Southerly winds of 5 to 8 ms^{-1} in the lowest 4 km give way to 8 to 10 ms^{-1} northeasterly winds above 7 km, with weak easterly flow between. Warm, moist air gives rise to large θ_E below 2 km, confirming that abundant moisture is available to drive convection. Between 2 km and 5 km, on the other hand, θ_E is relatively low, so evaporative cooling and downdraft formation are favored in this layer.

The radar echo pictures in figure 2 show that the cells we are to describe are part of an elongated complex which has new cells periodically developing on the northeast end. Individual cells move almost straight northward, from 190° at about 8 ms^{-1}, and the complex simultaneously propagates toward the northeast as new cells appear. Careful study of a more complete set of photos (not all included in figure 2) reveals that cells toward the southeast dissipate while those on the northwest grow and tend to merge. It appears that the complex is fed primarily by air that originates at low levels on the west side, and this supposition is reinforced by photographs taken from research aircraft, revealing a shelf-like structure just above cloud base on the west.

The propagation of this complex along a line from southwest toward northeast suggests the presence of a convergence line, perhaps associated with colliding outflows from thunderstorms dissipating at this time to the south and to the northwest. Winds measured in the University of Virginia surface network (shaded in figure 1) were southerly; it is likely that they had a westerly component in the area toward the west.

3. VERTICAL VELOCITY PATTERNS

The Doppler observations are derived from a succession of three dimensional scan sequences accomplished by the coplanar scanning technique of Lhermitte and Miller (1970). Each sequence covers about seven minutes, during which time ten planes tilted at 0°, 2°, ..., 18° are scanned. Horizontal slices are constructed for each sequence at 400 m intervals up to 5600 m, with data for each slice represented on a 1 km horizontal grid. Using quasi-horizontal two-dimensional velocities measured by the radars, we integrate the continuity equation to arrive at vertical velocities. Incompressible flow is assumed and contamination of measured quasi-horizontal velocity fields by vertical target motion is ignored. Details of the technique used and uncertainties in the results are discussed by Frank (1976). The field of horizontal motion is quite accurately determined, but some vertical velocities may be in error by as much as several meters per second. Nevertheless updraft and downdraft locations and other salient features of the vertical velocity field are well represented at scales larger than one kilometer.

The analysis is focused on four sequences, with starting times at 15:42, 15:56, 16:03 and 16:10 EDT. Vertical velocity fields for these sequences are shown in figure 4 for horizontal planes at 400 m, 2000 m, and 3600 m heights; sparse data prevented the computation of w fields

at higher levels. In the figures, numerals represent downward velocities in meters per second, while letters represent upward velocities, for example, A = 1 ms^{-1}, B = 2 ms^{-1}, etc. Contours are drawn for w = 0, with updrafts areas shaded. The locations of cells 1, 2, and 3 are indicated in figure 4b.

At the 400 m subcloud level (figure 4a) we see that vertical motion is weak and predominantly downward except at 16:10, when significant updraft occurs in the rapidly developing echo between cells 1 and 3. However, the patterns of vertical flow show strong features and rapid evolution at 2000 m and 3600 m. Updrafts dominate cell 1 and cell 2 at 15:42 (cell 3 is not covered at this time), increasing with height; the flow is typical of the late cumulus stage. No significant downdraft has developed, but a substantial amount of precipitation is present at this time, as evidenced by the 15:45 radar echo shown in figure 2. An additional cell is seen to the south of cell 2 at 15:42, but the evolution of this cell cannot be traced because the echo is of insufficient strength (perhaps a result of attenuation) to allow Doppler measurements at later times. The echo history of figure 2 shows that this area dissipates about 16:00.

Circulation indicative of the mature stage is evident in cells 1 and 2 at 15:56. Downdraft dominates in the observed portions of cell 2, although some updraft is apparent at 3600 m, probably extending to higher levels. In cell 1 the downdraft is less extensive and weaker, suggesting a slightly less advanced stage of development than cell 2. At 16:03 we see weaker downdraft at 2000 m and a substantial shrinking of the radar echo at 3600 m as cell 2 begins to dissipate. At the same time cell 1 exhibits an intensified downdraft at 2000 m, but at 3600 m both updraft and radar echo have increased. In addition, the filling in of the echo pattern between cells 1 and 3 points to stimulated convective activity in that area. Cell 3 is characterized at this time by updraft at 400 m and 2000 m, although there is not yet sufficient echo to yield Doppler data at 3600 m.

At 16:10 cell 2 is essentially dissipated, while vigorous convection in the cumulus stage is now apparent in the adjacent area to the northwest. Cell 3 displays a well organized updraft, with the appearance of downward flow at 2000 m suggesting the onset of the early mature stage.

The most interesting event revealed by these results takes place near cell 1 around 16:10. While downdraft began in this cell by 16:03 and is apparent on the north and east at 16:10, the cell does not dissipate in the manner of cell 2. Rather, the updraft that remains appears to merge with upward flow in the adjacent new growth to the southwest, and an intense updraft results on the southwest edge of what was previously labeled cell 1. The updraft velocity here reaches at least 15 ms^{-1} (denoted by 0 in figure 4c) at the 3600 meter height; this is the most intense updraft observed in this storm complex. Due to uncertainties discussed in Frank (1976) this is very likely an underestimate of the true peak updraft, and furthermore it is likely that the updraft is even stronger higher up in the cell.

153
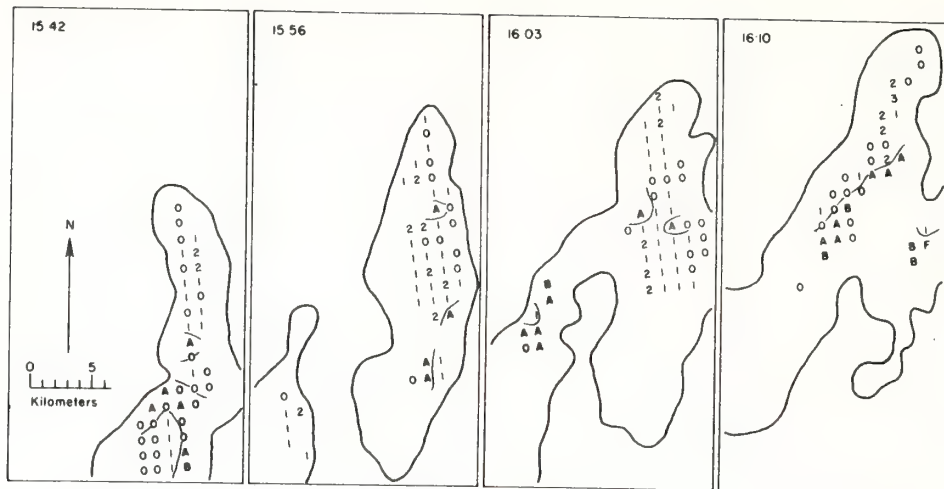
Figure 4a. Vertical velocity field in a horizontal plane at 400 meters height derived from dual-Doppler radar measurements. Speed is represented at one meter per second intervals by letters (upward) or numerals (downward); updrafts are shaded. Times (all EDT) refer to the beginnings of respective seven minute dual-Doppler scan sequences. Heavy curves outline the radar echo near the ground as seen by the U. of M. Doppler radars.
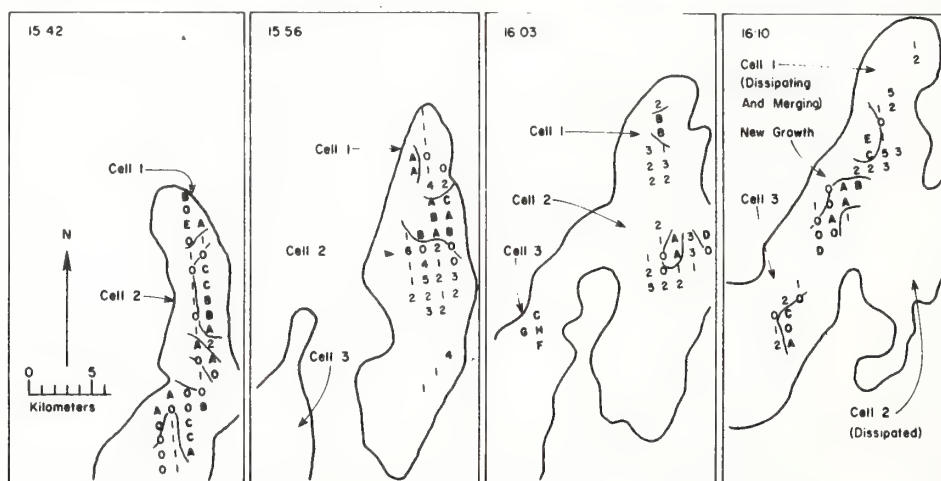
Figure 4b. Vertical velocity (m s^{-1}) as in figure 4a except height = 2000 meters.
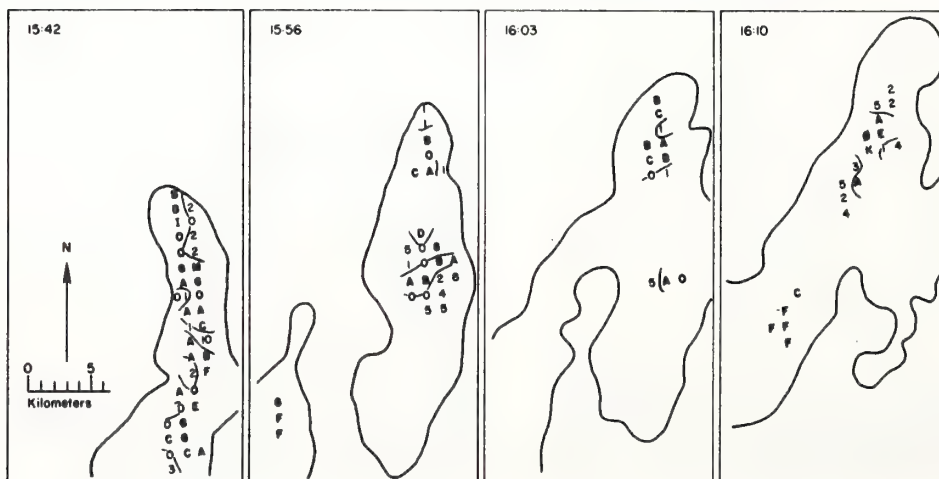
Figure 4c. Vertical velocity (m s^{-1}) as in figure 4a except height = 3600 meters.

Evolution of the flow pattern in this rapidly changing complex is further illustrated by several height profiles of lateral inflow (i.e., inflow through the side boundaries of the radar echo) shown in figure 5. These curves represent inflow ($m^3 \ s^{-1}$) per 400 m height interval, and were obtained at by integrating the component of horizontal velocity normal to the echo boundary along a closed rectilinear curve surrounding the contiguous echo area. More precisely, the contiguous area that is considered is the one for which Doppler velocities are available, and therefore is not identical to the one with the radar echo.
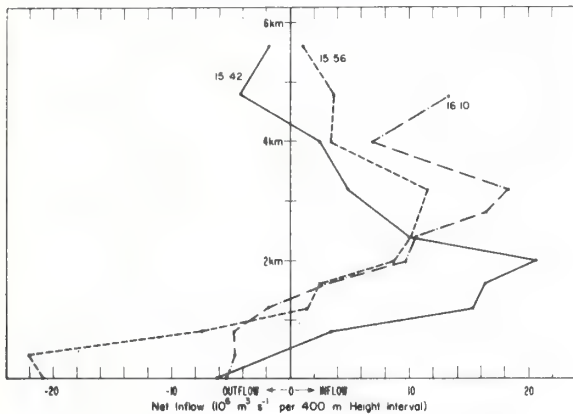
Figure 5. *Net inflow (m^3s^{-1} per 400 m height) to the region for which Doppler measurements are available; this region is called the "Doppler echo" and is not identical with the precipitating region. Inflow dominates between 1 km and 4 km at all times, and dramatic outflow at 15:56 is confined to the lowest 1 km.*

The 15:42 inflow profile shows weak outflow in the lowest 500 meters, topped by well-defined inflow extending above 4 km and totaling approximately $8 \times 10^7 \ m^3 \ s^{-1}$. The area for which this profile applies includes cells 1 and 2, and the predominance of inflow reflects the vigorous growth characterizing both these cells while they are in the cumulus stage. At the higher levels we see relatively weak outflow, a fact consistent with the divergence expected at the summit of a penetrating jet or vortex bubble. In the 15:42 sequence the Doppler radars covered essentially the entire height of the storm. This is not true of later sequences, hence the top-level outflow is not observed in them.

The curve in figure 5 for 15:56 also applies to cells 1 and 2, and a dramatic change is apparent as the cells enter the mature stage. The striking feature at this time is an outflow layer confined to the lowest 1000 meters, through which there is an outflow of $4 \times 10^7 \ m^3 \ s^{-1}$. Substantial inflow of air ($6.1 \times 10^7 \ m^3 \ s^{-1}$) continues, but is now concentrated at about 3 km height rather than around the 1.8 km level as was the case fourteen minutes earlier. The height interval in which inflow occurs at 15:56 is seen to correspond

roughly to the region of low θ_E noted in figure 3b. It is therefore likely that much of this inflow feeds downdrafts that create the low level outflow, with the remainder sustaining continuing updrafts at higher levels.

It is more difficult to interpret the third (16:10) inflow profile, which no longer involves cell 2 but includes cells 1 and 3 and the active intervening region. Cells 1 and 2 progressed almost simultaneously through the cumulus and mature stages (with cell 2 always slightly more advanced). In the 16:10 case matters are complicated by the fact that cell 1 has reached a mature stage and is producing some outflow while vigorous cumulus-stage activity proceeds nearby. In addition, the merger discussed earlier has stimulated a strong updraft near the top of the observed height interval. Thus at this time, we see moderate outflow of $1.4 \times 17^7 \ m^3 \ s^{-1}$ in the lowest 1.5 km probably associated mostly with the proximity of cell 1, but this is far outweighed by the inflow seen throughout the rest of the observed region. Observed inflow totals $7.8 \times 10^7 \ m^3 \ s^{-1}$, and actual inflow into this part of the storm is certainly larger as it is evident that the observed height interval does not include all significant inflow. Most inflow occurs well above 2 km, unlike that seen in the early stages represented at 15:42, and reflects the fact that updrafts are now higher than they were at the earlier time (see figure 4). In particular the updraft of cell 1 accounts for much of the inflow seen at the highest observed level.

5.   FACTORS INFLUENCING THE OBSERVED MERGER

In the introduction we mentioned that in Florida the merging of small isolated rainstorms has been found to have important impact on overall precipitation production from local convective storms. For example, Simpson and Woodley (1971) and Woodley et al. (1971) cite observed cases in which rain production by storms resulting from mergers of smaller cells exceeds by an order of magnitude the rain output that could be expected from the individual components had merging not occurred. This finding has in fact prompted researchers to adopt cloud seeding techniques designed specifically to promote such mergers (Simpson et al., 1972). Although results have been encouraging, it appears that improved understanding of the dynamics of mergers is essential to a successful modification program. Although the case presented here is not particularly spectacular in terms of precipitation amounts, it is hoped that these rather unique observations will shed some light on the subject of mergers.

Evidently in the present results *timing* is a crucial factor. The stage is set by the presence of cells (1 and 3) in an active stage of their temporal development at the precise time that strong new activity is taking place adjacent to them. Of course this is not surprising, as we expect a merger resulting in strengthened activity to involve juxtaposition of active cells, and merger is favored if component cells are in similar stages of development.

However, in this case it appears that merger is further promoted by the timely collapse

155

of cell 2. As mentioned earlier, the outflow from this cell as it matures and dissipates is instrumental in stimulating convection to the southwest of cell 1 at a time when cell 1 and 3 are still quite active. It may be conjectured that had the timing been different, the new convection might not have matched that in the existing cells enough to allow the merger.

6. CONCLUSIONS

In short, Doppler data support the conclusion, suggested by the radar echo evolution shown in figure 2, that the rapid development of convective activity within and between cells 1 and 3 results in merging of the cells around 16:15 and is intimately associated with the collapse of cell 2. Although we must keep in mind that only one specific case is described here, it is important to recognize the role of the collapsing cell in this event. In cloud clusters, where a potential for merger exists, cells in the late mature or dissipating stages will often be found in the vicinity of active cells that may be ripe for merger. These results demonstrate that cells approaching their demise may strongly influence the behavior of neighboring cells, and must be considered when assessing the potential for growth and merger in convectively active areas.

In south Florida, modification efforts have followed the "dynamic seeding" approach in which the aim is to enhance the intensity and duration of updrafts. The present results suggest that coordination of seeding activity with local downdraft/outflow events might vastly improve the chances of promoting mergers when the effect of seeding would otherwise be marginal or inadequate. While additional and more quantitative studies similar to the one presented here might tell us whether or not such coordination would be feasible and how to accomplish it, the actual implementation would require quasi-real-time availability of air flow measurements. Lhermitte (1974, 1975) has described a data processing method that provides real-time display of multi-Doppler measurements, and that method is employed, except for the necessary data telemetry, in the University of Miami system. We feel that this observing capability can help optimize the use of resources available for cloud seeding operations, and will in fact be an essential part of many future weather modification efforts.

7. ACKNOWLEDGMENTS

Thanks are due W. L. Woodley, R. L. Holle and other members of the NOAA National Hurricane and Experimental Meteorology Laboratory staff for providing FACE data. Much of this report is taken from a Master's Thesis prepared while the first author was at the University of Miami on a NOAA training assignment.

8. REFERENCES

Boyd, J. G., 1965: Observation of two intersecting radar fine lines. *Monthly Weather Review*, 93, 188.

Browning, K. A. and F. H. Ludlam, 1962: Airflow in convective storms. *Quarterly Journal Royal Meteorological Society*, 88, 117-135.

Byers, H. B. and R. R. Braham, 1949: *The Thunderstorm; Report of the Thunderstorm Project*. U.S. Government Printing Office, Washington, D.C.

Frank, H. W., 1976: Cell interaction, merger and cumulus tower growth in a south Florida thunderstorm observed by dual Doppler radar. Master's Thesis at the University of Miami, Coral Gables, FL.

Gerrish, H. P., 1969: Intersecting fine lines and a south Florida tornado. Preprints of 6th Conference on Severe Local Storms, AMS, Boston, 188-191.

Holle, R. L. and M. W. Maier, 1974: Development of a Florida tornado related to downdraft interaction. Preprints of Conference on Cloud Physics, AMS, Boston, 453-458.

Lhermitte, R. M., 1974: Real time monitoring of convective storm processes by dual Doppler radar. *Atmospheric Technology*, winter 1974-75, National Center for Atmospheric Research, Boulder, 26-32.

Lhermitte, R. M., 1975: Real time velocity observations by multi-Doppler radar. *Preprints of 18th Radar Meteorology Conference*, American Meteorological Society, Boston, 107-114.

Lhermitte, R. M. and L. J. Miller, 1970: Doppler radar methodology for the observation of convective storms. *Preprints of 14th Radar Meteorology Conference*, AMS, Boston, 133-138.

Newton, C. W. and H. R. Newton, 1959: Dynamical interactions between large convective clouds and environment with vertical shear. *Journal of Meteorology*, 16, 483-496.

Pielke, R., 1973: An observational study of cumulus convection patterns in relation to the sea breeze over south Florida. NOAA Technical Memorandum ERL OD-16, Office of the Director, Environmental Research Laboratories, Boulder, 81 pp.

Senn, H. V., C. L. Courtwright and H. W. Hiser, 1969: Preliminary characteristics of south Florida tornadoes in the summer of 1968. Preprints of 6th Conference on Severe Local Storms, AMS, Boston, 192-196.

Simpson, J. and W. L. Woodley, 1971: Seeding cumulus in Florida: new 1970 results, *Science*, 172, 117-126.

Simpson, J., W. L. Woodley and R. M. White, 1972: Joint federal-state cumulus seeding program for mitigation of 1971 south Florida drought, *Bulletin of the American Meteorological Society*, 53, 334-343.

Staff, Experimental Meteorology Laboratory, 1974: *1973 Florida Area Cumulus Experiment (FACE) Operational and Preliminary Summary*, NOAA Technical Memorandum ERL WMPO-12, Weather Modification Program Office, Boulder.

Woodley, W. L., J. Norwood and B. Sancho, 1971: Some aspects of Florida showers and thunderstorms, *Weatherwise*, 24, 106-113.

A NOTE ON DUAL DOPPLER RADAR OBSERVATIONS OF POST-FRONTAL
STORMS OVER THE OLYMPIC PENINSULA

A. S. Frisch, W. C. Campbell, R. G. Strauch and N. M. Kohn

NOAA/ERL/Wave Propagation Laboratory
Boulder, Colorado 80302

1.   INTRODUCTION

During the month of March 1976 in the state of Washington on the Olympic Peninsula, the WPL-NOAA dual Doppler radar system was operated in conjunction with a rain scavenging experiment conducted by Battelle, Northwest Laboratories. As the frontal storms arrived at the coast from the west, radars scanned areas within their 75 km range. From the data taken during these scans, we were able to reconstruct some of the motion fields within these storms.

2.   TECHNIQUE

The two radars were located on top of Bahokus peak at the tip of Cape Flattery and at the Quilliute Airfield near Forks, Washington (Figure 1). The radars scanned in a series of tilted planes (Lhermitte and Miller, 1970) in 1° increments. Because of blockage and trees at both sites, the lowest COPLAN scanned was not at 0° but varied from 1-1/2° to 3-1/2° depending upon the azimuth. The beamwidth of the radars was about 0.9° and there were between 32 and 64 range gates separated by 450 m for each radar beam. The data were smoothed in COPLAN space to obtain better statistical estimates. By this smoothing operation, the standard deviation of the error in the velocity was made less than 20 cm/s for the 128 samples used for each pulse volume (Miller and Strauch, 1974).
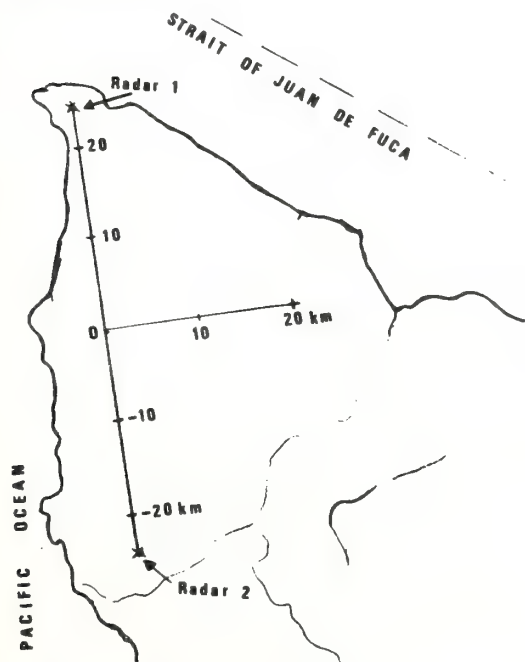
Figure 1. *Location of the two NOAA-WPL Doppler radars. Scale (in km) is also used for reference in later figures.*

Horizontal projections of the wind fields were calculated in a series of horizontal planes by ignoring the component of velocity normal to each tilted plane and using only the calculated component of velocity in each plane. The contribution of error in the horizontal wind fields using this technique was small since a calculation of the magnitude of the normal component of velocity showed it to be small (< 2 m/s). Since the plane angles were less than 12°, this further reduced the contribution of this component to errors in the horizontal wind fields. Mathematically the contribution to the horizontal component is $u_\alpha \sin \alpha$, where u_α is the component of velocity normal to the plane and α is the angle of the plane relative to the ground.

3.   RESULTS

Figure 2 shows an example of the horizontal motion field relative to the mean horizontal motion at 2 km height. Some of the motion at the upper righthand side of the figure shows a vortex-like structure about 5 km across. Other divergence and convergence patterns also appear in the figure with some regions extending for distances of 7 km or more. Figure 3 shows more data taken at a height of 2 km over a ridge of hills that are parallel to the Strait of Juan de Fuca and over the straits themselves. One can see definite cellular structure not only over the straits, but also over the land, with scales of 5 to 6 km. Figure 4 shows another set of observations in the same region 15 minutes later. In this figure there are fewer measurements over the staits because the precipitation there had diminished, offering fewer radar targets as air motion tracers. Over the land, there was more precipitation forming, and this is visible as new velocity structure to the south.

The next two figures, 5 and 6, represent more data taken 12 minutes apart. Data for figure 5 are the same as data appearing in figure 2, enlarged to show more detail. Some of the features in the structure appearing in figure 5 also appear in figure 6, but are displaced horizontally. For example, the divergence pattern centered at x = 29, y = -24 in figure 5 appears in figure 6 centered, at x = 31, y = -21, to be somewhat distorted compared with figure 5. The convergence pattern centered at x = 23, y = -20 with the vortex at the upper end in figure 5 appears in figure 6 centered at x = 26, y = -19 with the convergence line lengthened and lacking the vortex that appeared in figure 5. In addition, a whole new cell is showing at the top in figure 6, having formed since the data for figure 5 was taken.
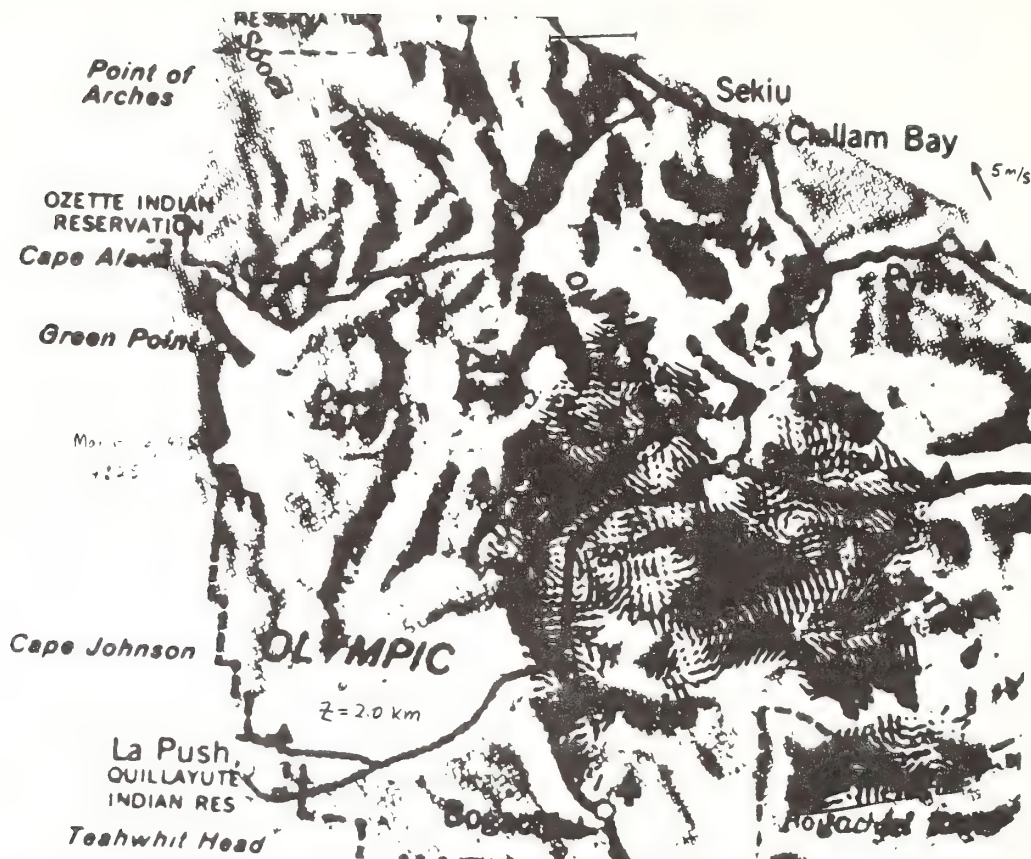
Figure 2. *Horizontal projection of the velocity field onto a plane 2 km above sea level. A mean wind vector of 11 m/s from the SWW has been removed in order to see the detailed structure of the velocity fluctuations. Taken March 16, 1975 @ 14:23.*

Figure 3. *Horizontal projection of the velocity field onto a plane 2 km above sea level. A mean wind vector of 13 m/s from the SWW has been removed in order to see the detailed structure of the velocity fluctuations. Note the cellular-like structure delineated by regions of convergence and divergence. Taken March 16, 1975 @ 12:00.*

229

276
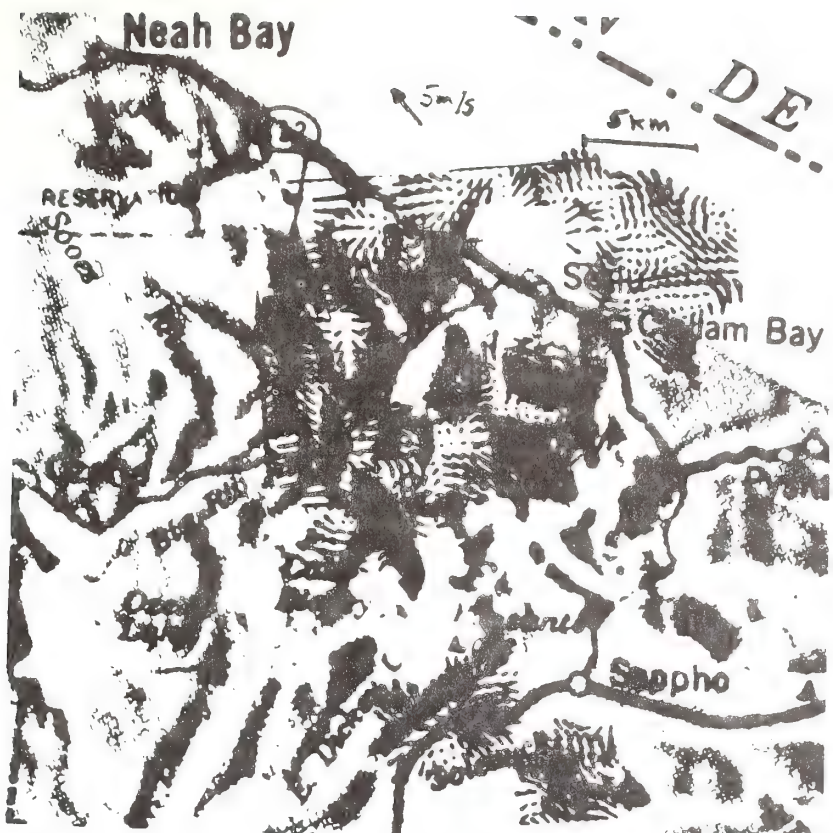
Figure 4. Horizontal projection of the velocity field onto a plane 2 km above sea level. A mean wind vector of 13 m/s from the SWW has been removed in order to see the detailed structure of the velocity fluctuations. Note the cellular-like structure delineated by regions of convergence and divergence. Taken March 16, 1975 @ 12:15.

Figure 5. Horizontal projection of the velocity field onto a plane 2 km above sea level. A mean wind vector of 11 m/s from the SWW has been removed in order to see the detailed structure of the velocity fluctuations. Co-ordinates are relative to the map in figure 1. Taken March 16, 1975 @ 14:23.
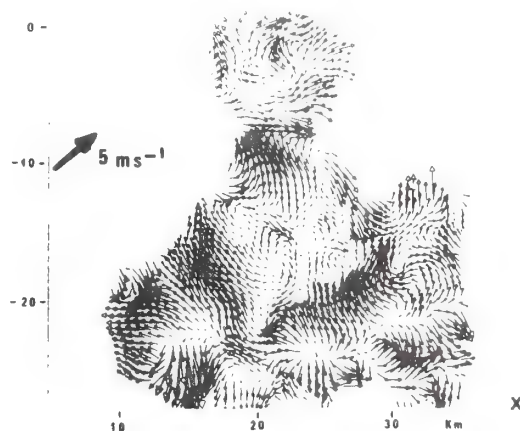
Figure 6. Horizontal projection of the velocity field onto a plane 2 km above sea level. A mean wind vector of 11 m/s from the SWW has been removed in order to see the detailed structure of the velocity fluctuations. Co-ordinates are relative to the map in figure 1. Taken March 16, 1975 @ 14:35.

230

277

4.   DISCUSSION AND CONCLUSIONS

        The velocity data presented show that
the coastal storms have scales of motion approxi-
mating 5 to 7 km, and in some cases show very
definite cellular structure with scales of approxi-
mately 5 km. Some of the features in the velocity
fields appear to hold their identity for at least
12 minutes and to move horizontally at a much
slower rate than the average wind speed. The
patterns that appear may be functions not only
of the dynamics of the atmosphere, but also of
the local topography, which is certainly not level
for the Olympic Peninsula. Much more analysis
will have to be done to separate these two effects.

5.   REFERENCES

Lhermitte, R. M. and L. J. Miller, 1970: Doppler
        radar methodology for the observation of
        convective storms. *Preprint Vol.* AMS 14th
        Radar Meteorol. Conf., 133-138.

Miller, L. J. and R. G. Strauch, 1974: A dual
        Doppler radar method for the determination
        of wind velocities within precipitating
        weather systems. *Remote Sensing of Environ.*
        3, 219-235.

231

OBSERVATIONS OF BOUNDARY-LAYER CONVECTION CELLS MEASURED BY DUAL-DOPPLER RADAR AND ECHOSONDE, AND BY MICROBAROGRAPH ARRAY

A. S. FRISCH, R. B. CHADWICK, W. R. MONINGER, and J. M. YOUNG

NOAA/ERL/Wave Propagation Laboratory, Boulder, Colo., U.S.A.

Abstract. Three-dimensional air motion, observed with radar in a convective planetary boundary layer under light wind conditions, is organized in cellular structures scaled from 2 to 5 km; simultaneous acoustic echosonde measurements indicate that near the ground there are smaller cells than those observable by the radar. At heights of 400 m, cell scales become as large as those observable by the radar. Pressure fluctuations at the ground measured with spatial pressure transducers, at the same time as the radar and echosonde observations, traveled at the same speed and direction as the radar volume-averaged wind. The length scale determined at the ground with pressure fluctuation data was between 1.2 and 2.4 km. smaller than the largest radar-measured motion scales.

1. Introduction

Measurements of the wind field in the planetary boundary layer can help us determine diffusion properties, length scales that contain maximum energy (and thus knowledge as to how energy is input), and the nature of atmospheric motions.

The way the energy is distributed in the boundary layer depends on the type of atmospheric motion which in turn depends on atmospheric properties such as wind speed and temperature gradient. For example, when Woodcock (1942) observed the soaring habits of gulls over the ocean, he found their patterns dependent upon the temperature difference between the air and ocean-surface temperature and the horizontal wind speed. At low wind speeds, the soaring was circular, changing to line soaring at high wind speeds. The circular soaring indicated presence of large convection cells at lower wind speeds.

Taylor (1958) observed that near the ground during day-time convection, there was evidence of organized thermal structures extending vertically for several metres superimposed on a background of random disturbances. Vulf'son (1961) considered these small thermals as jets and with a statistical model, he inferred the average diameter to be on the order of 50 to 100 m to heights of 3 km. Telford and Warner (1964) examined how the vertical temperature flux was carried by eddies much smaller than the thermals which were the obvious feature of the temperature records. However, the importance of these smaller eddies in the transport of temperature fluctuations decreased with height. In a later paper, Warner and Telford (1967) found temperature pulse widths to be about 300 m in diameter below a height of 3 km. While these diameters were at variance with Vulf'son's observed diameters, lapse rate data were not available to compare the effects of thermal stability between the two sets of observa-

tions. The lapse rate has a particularly important effect on the diameters at low levels as shown by Frisch and Businger (1973). High-power radar observations by Hardy and Ottersten (1969) and by Konrad (1970) showed convection cells originating several hundred metres above the surface with disorganized returns having scale sizes between 100 and 200 m in diameter near the surface, increasing to well-developed cell structures 1 to 3 km in diameter at heights of over a kilometer. With an instrumented aircraft, Lenschow (1970) found convection scales 800 m in diameter. With wind shear present, the types of motion can change dramatically. For example, LeMone (1973) found two-dimensional horizontal roll vortices 2 km wide in the convective boundary layer when the wind speed was in excess of 7 m s^{-1}.

Our calculations use data from a dual-Doppler radar system, an acoustic echosonde, and a microbarograph array to describe features of the convective boundary layer. The Doppler radar system determined the three-dimensional wind fields over a horizontal area of 5×5 km^2 to a height of 1 km. Chaff was used as an air motion tracer. The echosonde was used to infer the spatial scales of the fluctuations of temperature variance observed in the convective boundary layer, for comparison with the velocity spatial scales observed by the dual-Doppler radar system. The micro-barograph array gave the size, direction, and speed of pressure disturbances at the ground.

2. Measurement and Analysis Techniques

2.1. DUAL-DOPPLER RADAR.

This work used the COPLAN scanning method originated by Lhermitte and Miller (1970). The dual-Doppler techniques used for the total three-dimensional wind field measurements are summarized here; a comprehensive discussion of them can be found in Miller and Strauch (1974).

To obtain velocity estimates of the air motion, each radar needs targets that follow the air motion. These targets can be chaff (a reflective coated mylar filament cut to $\frac{1}{2}$ wavelength) or precipitation. Since the targets move randomly, the return signal fluctuates in both phase and amplitude. The signal is converted to a spectrum of the velocity component parallel to the beam axis of each radar. The spectrum is weighted by the backscattering cross-section of the particles moving at each particular velocity within the pulse volume. The weighted average of this velocity spectrum is the mean radial velocity of the particles. We obtain the true air motion by combining radar radial velocity measurements with the equation of mass continuity and an independent estimate of the mean terminal fall velocity of the radar targets. Such determinations of three-dimensional air motion by dual-Doppler radar have been presented by Frisch et al. (1974), Miller and Frank (1974), and Kropfli and Miller (1974).

We calculate the spatial spectra of the velocity fields with the maximum entropy spectral analysis technique because, for short data samples, it provides spectral estimates with higher resolution at a given confidence level than classical methods do (Burg, 1967; LaCoss, 1971; Markel, 1972; Ulrych, 1972; Chen and Stegen, 1974). In many problems, better frequency resolution can be achieved by increasing the

length of the data sample. However, in our case the length of the data sample is determined by the size of the area covered with chaff, which is not under the complete control of the experimenter.

When we first calculated spectra from the dual-Doppler radar data, using the conventional maximum entropy technique described by Burg (1967), the limited sample size introduced large errors into the estimates of the autocorrelation functions. Such errors can make the function mathematically inadmissible. Under certain conditions the inadmissible autocorrelation functions caused invalid peaks in the maximum entropy spectrum that could easily lead to a complete misinterpretation of the spectra. Therefore, a more general algorithm was developed that safeguards against these errors. This algorithm tapers the possible inadmissible estimate of the correlation function in an unconventional manner that causes it to be admissible. This allows use of more lags in the autocorrelation function for a given data sample size. This new processing procedure is described by Strand and Chadwick (1975). All spectra in this study were calculated with this 'tapered' version of the maximum entropy technique.

2.2. ECHOSONDE

The theory of acoustic sounding has been discussed by Little (1969) and its potential uses described by Beran and Hall (1973). An echosonde system similar to the one used in this experiment has been described by Owens (1974). The echosonde was operated in a direct vertical backscatter mode. The intensity of the backscattered acoustic waves may be calculated as a function of the magnitude of the fluctuations in the refractive index of the medium if it is assumed that the fluctuations result from isotropic turbulence. The theory of interactions of sound waves with the turbulent atmosphere has been investigated by many authors (e.g., Tatarski, 1961). In the direct backscatter mode, the scattering cross-section is a function only of C_t, which depends on the turbulent kinetic energy dissipation rate, ε, and on the rate of destruction of temperature fluctuations. Such actions between acoustic waves and the atmosphere have been used to investigate atmospheric phenomena such as gravity waves and plumes (Bean *et al.*, 1973; Emmanuel *et al.*, 1972; Hooke *et al.*, 1973; Wyckoff *et al.*, 1973; Frisch and Clifford, 1974; Kjelaas *et al.*, 1975). When the boundary layer is unstable, the echosonde shows large values of C_t intermittent in time and coherent from a height of about 50 m to a few hundred metres. These have been associated with plumes or families of plumes that are generated in the surface layer and carried aloft by some scale of motions larger than the plumes, as suggested by LeMone (1973) and Kjelaas and Ochs (1974).

2.3. MICROBAROGRAPH ARRAY

The microbarograph used in this study (Cook and Bedard, 1971) consisted of a variable-capacitance differential pressure sensor in conjunction with an acoustic high-pass filter. This instrument measures pressure fluctuations with periods from 1 to 1000 s and has a noise level of 10^{-3} μbar. The data from a triangular array of microbarographs spaced about 300 m apart were used to determine the correlation distance,

speed, and direction of arrival of pressure fluctuations at the ground. This was done by 'steering' the array beam; i.e., by systematically varying the phase relationships between different sensors (see Gossard and Hooke, 1975, pp. 337–341). For the analysis of our pressure data, we used Young's algorithm for digital array processing (Young and Hoyle, 1975). The technique has been described by Kjelaas *et al.* (1975) who used it to study a storm-generated system of gravity waves.

3. Experiment and Results

A site near Haswell, Colorado, was the location of the measurement program. We determined the average value of the Richardson number from measurements on a 152-m tower and from a laser triangle located 2 m above the ground (Kjelaas and Ochs, 1974). The tower and laser triangle were in the vicinity of the echosonde and microbarograph array. Radar targets, consisting of aluminium coated mylar rods $1\frac{1}{2}$ cm in length and 0.0025 cm in diameter, were dispersed from an airplane at about
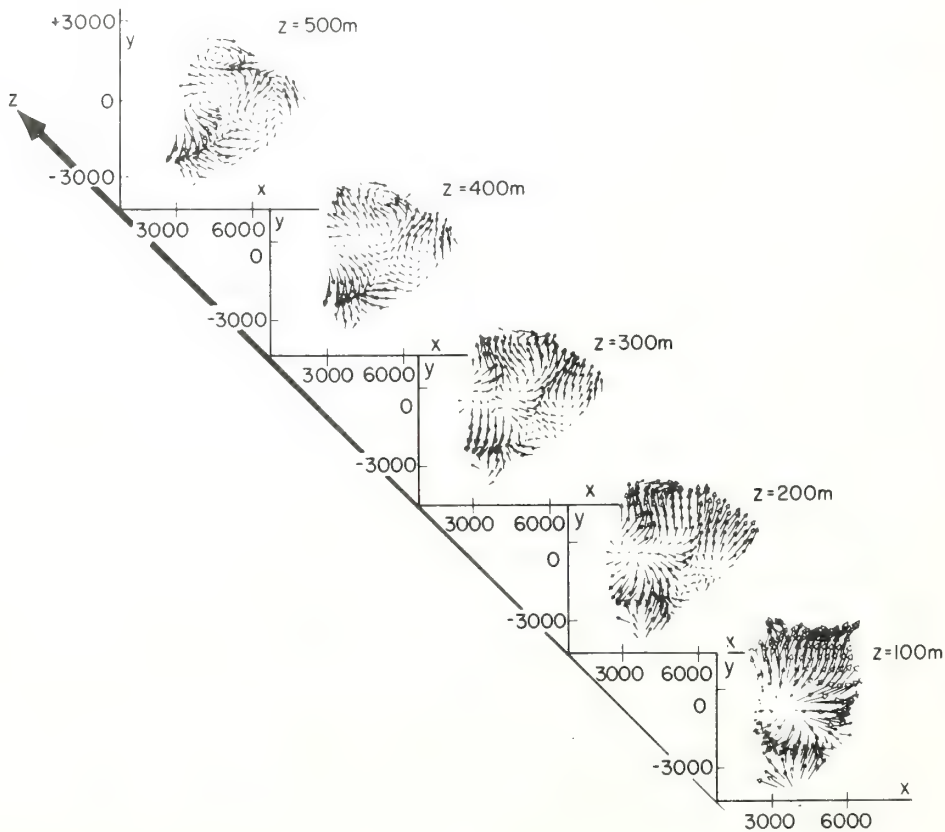
Fig. 1.   Projections of the velocity vectors in a series of horizontal planes. The volume-averaged wind (5 m s^{-1} in the negative x-direction) has been removed. Dimensions are in metres.
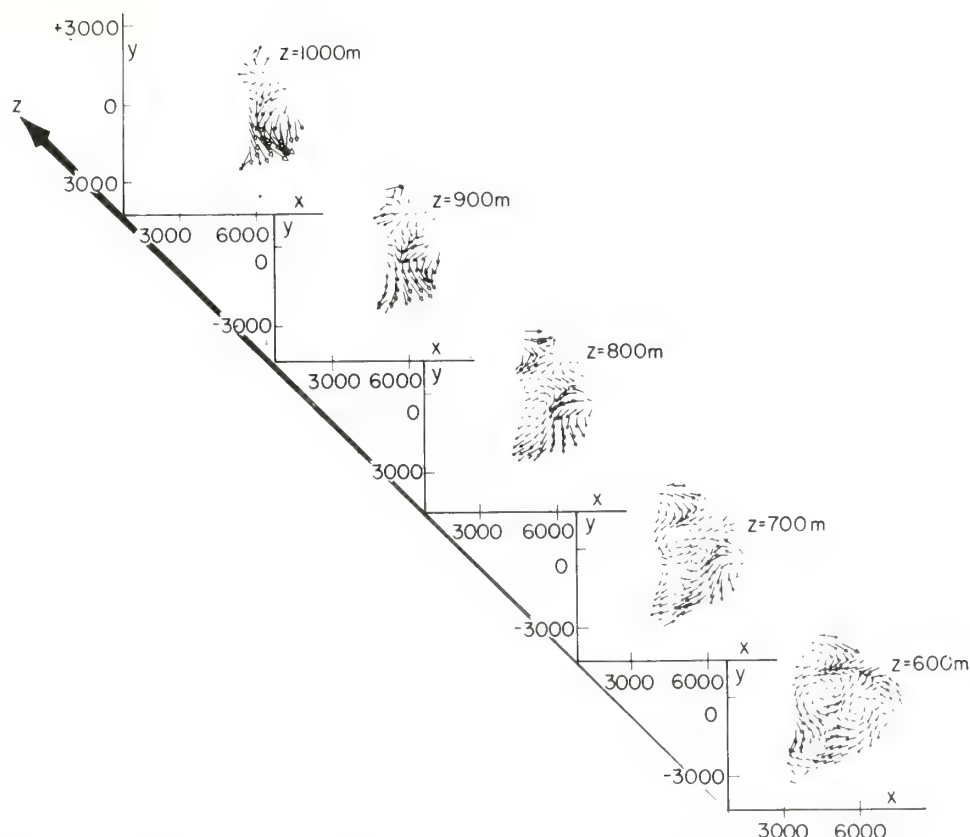
Fig. 2. Projections of the velocity vectors in a series of horizontal planes. The volume-averaged wind (5 m s⁻¹ in the negative *x*-direction) has been removed. Dimensions are in metres.

1230 MDT on 10 August 1972. As soon as the chaff had diffused enough to fill a significant volume (after a time of about 25 min), radar data were taken in conjunction with data from the acoustic echo sounder and microbarograph array. The wind speed was about 5 m s^{-1} from the SE, and the Richardson number, measured between 33 and 2 m, was -2.

3.1. Velocity fields

The mean wind velocity was obtained by averaging all of the radar velocity measurements in the scan volume (about $5 \text{ km} \times 5 \text{ km} \times 1 \text{ km}$). Velocity fields are displayed by projecting the vector field onto sets of orthogonal planes: one set parallel to the ground, and two vertical sets parallel and perpendicular to the volume-averaged wind direction. To display more detail in the velocity field, the volume-averaged velocity was removed from each velocity vector to obtain a fluctuation field. The errors in the estimate of these fluctuations are less than 4 cm s^{-1} in the horizontal and less than 15 cm s^{-1} in the vertical.

Figures 1 and 2 show the velocity vectors projected onto a series of horizontal planes. The data are plotted in a coordinate system whose origin is the center of the baseline joining the radars. The x-axis is horizontal and perpendicular to the baseline. The z-axis is vertical. At $z = 100$ m, the horizontal field diverges over most of the area measured. As z increases, an organized rotational pattern in the velocity fluctuation field emerges. This is especially apparent at $z = 600$ m, where two complete vortices and a third incomplete vortex may be seen within the chaff cloud. The largest has a diameter between 2.5 and 3.0 km and the smallest has a diameter of about 1.2 km.

Figures 3 and 4 are projections of the velocity vectors onto planes approximately parallel to the volume-averaged wind. In the plane $y = -900$ m (Figure 3), convective cellular structure is apparent, with two downdraft regions approximately 3.5 km apart having vertical velocities slightly less than 1 m s^{-1}. Adjacent to the left-hand region of downward moving air is upward moving air. The magnitude of this updraft is somewhat less than that of the downdraft. This feature is coherent through all planes between $y = -600$ and 600 m. In Figure 4 some closed vortices are to be seen in the
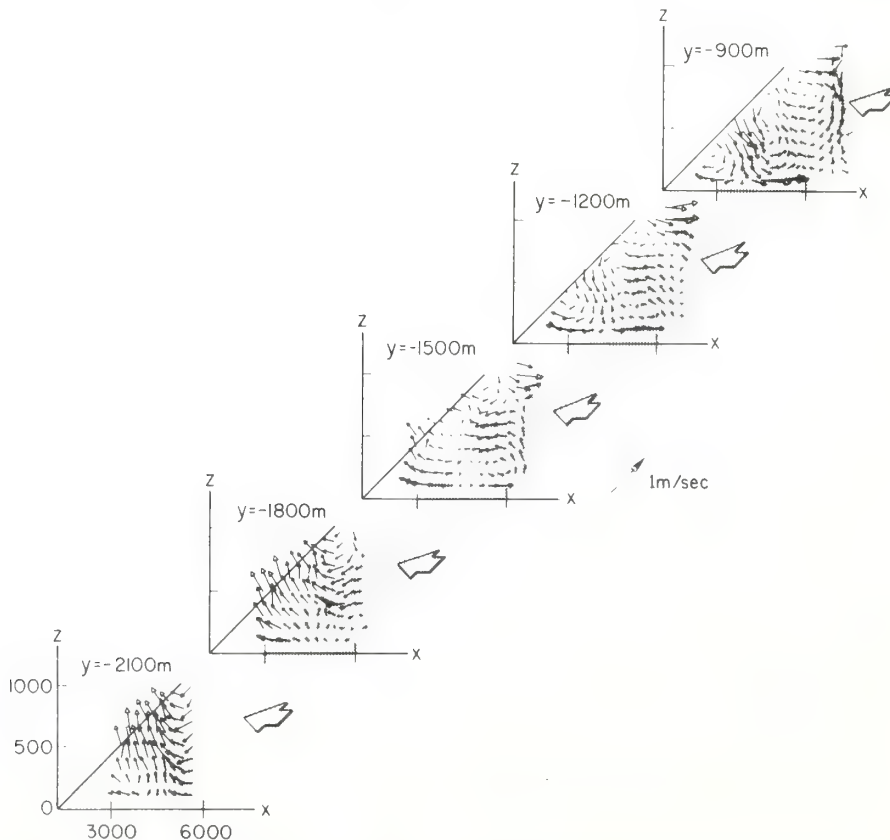
Fig. 3. Projections of the velocity vectors on vertical planes parallel to the volume-average wind. The volume-averaged wind has been removed from each vector. The y scale gives the relative location of each plane. Dimensions are in metres.
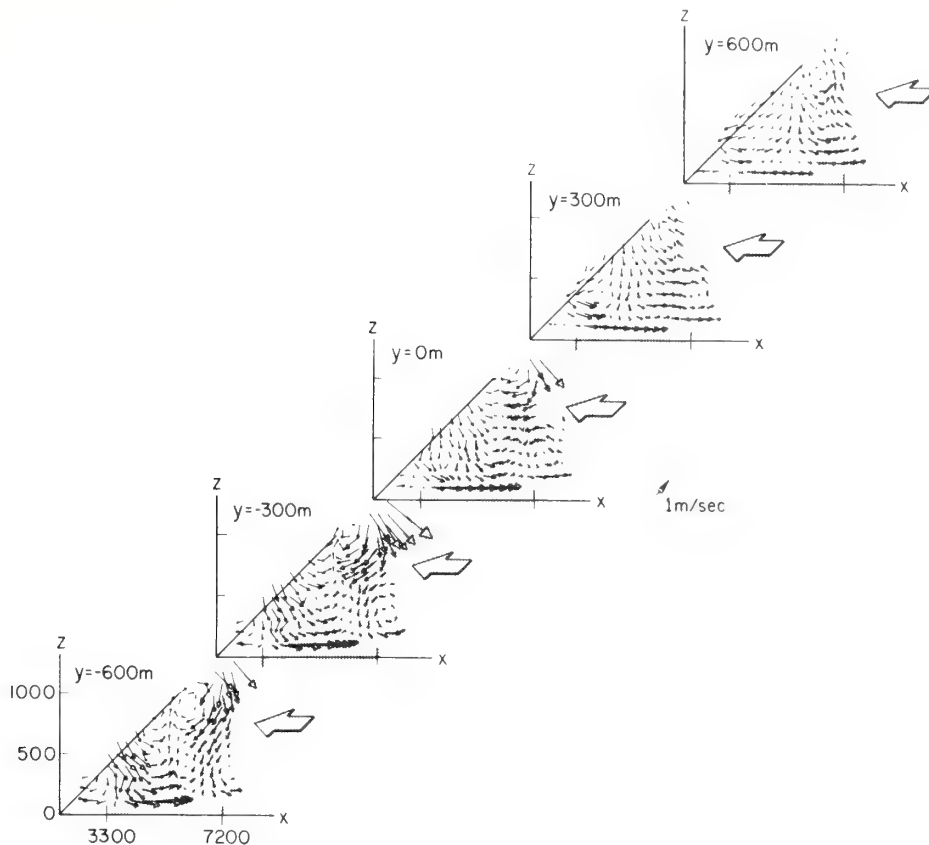
Fig. 4. Projections of the velocity vectors on vertical planes parallel to the volume-averaged wind. The volume-averaged wind has been removed from each vector. The y scale gives the relative location of each plane. Dimensions are in metres.

plane $y = -600$ m between $x = 5400$ m and $x = 7200$ m from $z = 800$ m to $z = 1200$ m. Part of another rotating feature can be seen in the $y = 0$ plane at $z = 0$ to $z = 700$ m for $x > 6300$ m. At $y = -300$ m this rotation is even more apparent and this type of motion can be traced to the $y = 900$ m plane.

Figures 5 and 6 show the projections of the velocity vectors in vertical planes perpendicular to the volume-averaged wind. Between the planes $x = 3300$ m (Figure 5) and $x = 5100$ m (Figure 6), one can again see a cellular structure with distinct updraft and downdraft regions. The cells extend from the lowest plane, $z = 100$ m, to a height of $z = 800$ m. Their scale in the y direction is approximately 2 km. A portion of this cell can be seen at $x = 4200$ m, where a rotary motion starts to appear from $y = 0$ to 2100 m and from $z = 300$ to 700 m. This motion is coherent through $x = 6000$ m before it disappears at $x = 6300$ m. In addition, at $x = 4800$ m, part of another cellular-like structure appears with the motion field counter-rotating relative to the other cell.

3.2. VELOCITY SPECTRA

Spatial power spectra of velocity give the distribution of kinetic energy density as a function of wavelength. Such spectra have been estimated from velocity measurements obtained from instrumented towers or aircraft (e.g., Lumley and Panofsky, 1964; Panofsky, 1973; Pasquill, 1972). Because the Doppler radar measurements yield a three-dimensional velocity field over a volume of the planetary boundary layer, it is possible to calculate estimates of the spatial velocity spectra within that volume. Comparing these spectra with spectral estimates found by other techniques under similar atmospheric conditions, we can judge the generality of our observations. We chose the horizontal plane 600 m above the ground for analysis and calculated the spectra of the orthogonal velocity components u, v (Figure 7). We calculated spectral estimates of only the u and v components, since they are much less sensitive to errors in the integration of the equation of continuity than the vertical component (Miller and Strauch, 1974). The results are shown as $k\phi_{uu},x(k)$, etc., vs $\log k$, where k is the wavenumber in the direction determined by the subscript after the comma in ϕ.
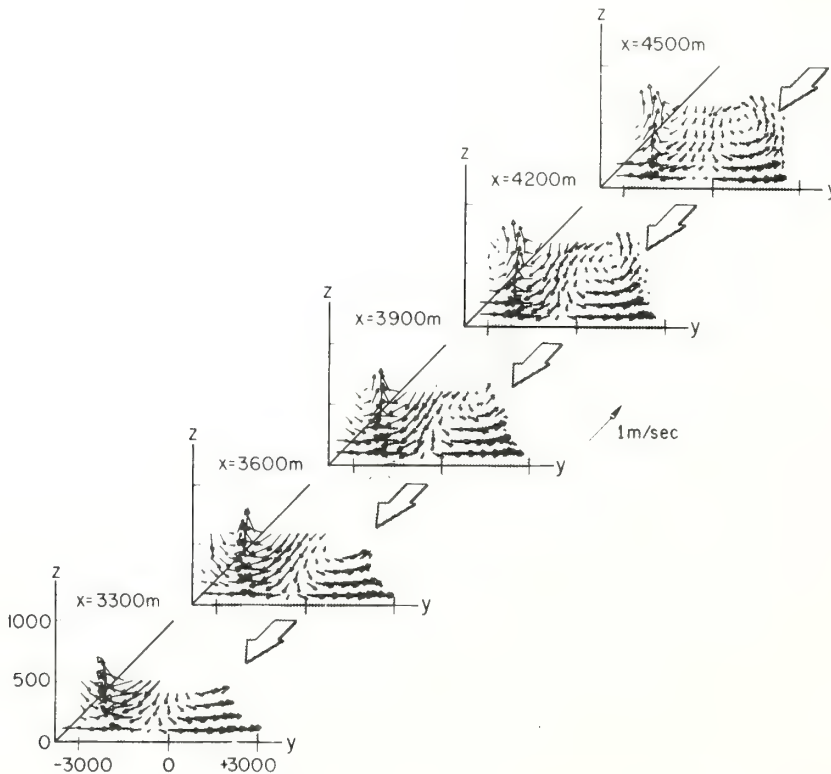
Fig. 5. Projections of the velocity vectors on vertical planes perpendicular to the direction of the volume-averaged wind. The volume-averaged wind has been removed from each vector. The x-scale gives the relative location of each plane. Dimensions are in metres.
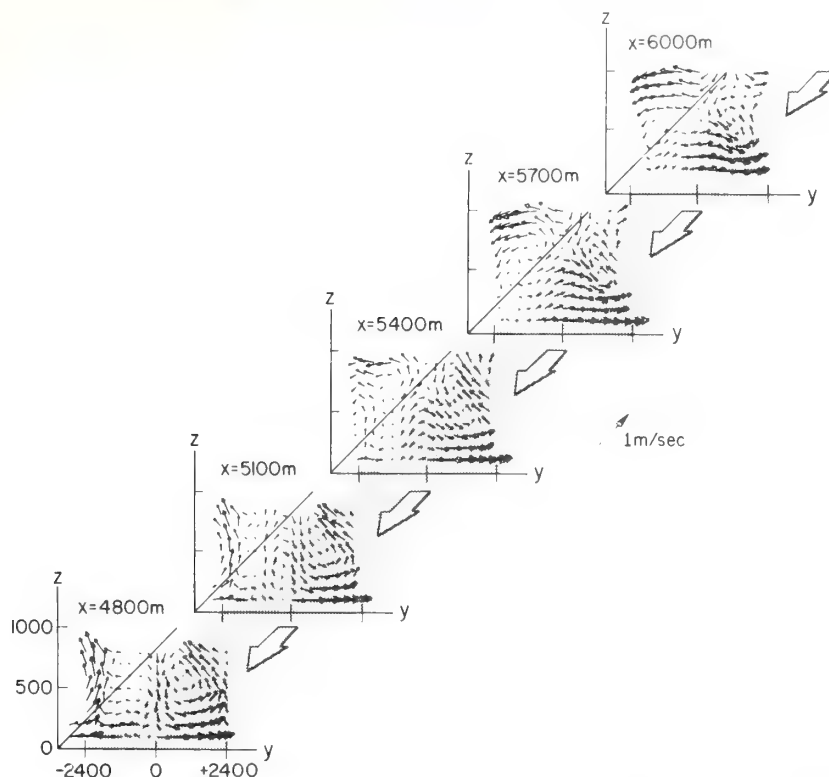
Fig. 6. Projections of the velocity vectors on vertical planes perpendicular to the direction of the volume-averaged wind. The volume-averaged wind has been removed from each vector. The x-scale gives the relative location of each plane. Dimensions are in metres.

The spectrum of the u component in the x direction shows two peaks, one at an approximate wavelength of 5 km, and the other at 2 km. Examining the $z = 600$-m plane in Figure 2, one can see parts of three counter-rotating features. In the smaller cell, located at $x = 6000$ m and $y = 0$, the u component reverses itself in a distance of 1 km, which corresponds to a wavelength of 2 km. Considering the features centered at $x = 4000$ m and $y = 0$, the u component reverses itself in a little over 2.5 km which would give a wavelength of 5 km, corresponding to the second peak in the $\phi_{uu,x}(k)$ spectrum. The v-component spectrum appears to behave in a similar manner in the x direction although the spectral peaks are shifted toward longer wavelengths compared to the u spectral peaks. The spectra of the u component in the y direction show a major peak at slightly greater than 3 km with a smaller one slightly under 2 km. Again looking at the velocity field projection in Figure 2 at 600 m, the u component in the larger cell reverses itself within about 1.5 km in the y direction and about 1 km in the smaller cell. These correspond to scale sizes of 3 and 2 km, respectively. Similarly, the v spectrum in the y direction has peaks at 5 and 2 km, associated with scales appearing in Figure 2.
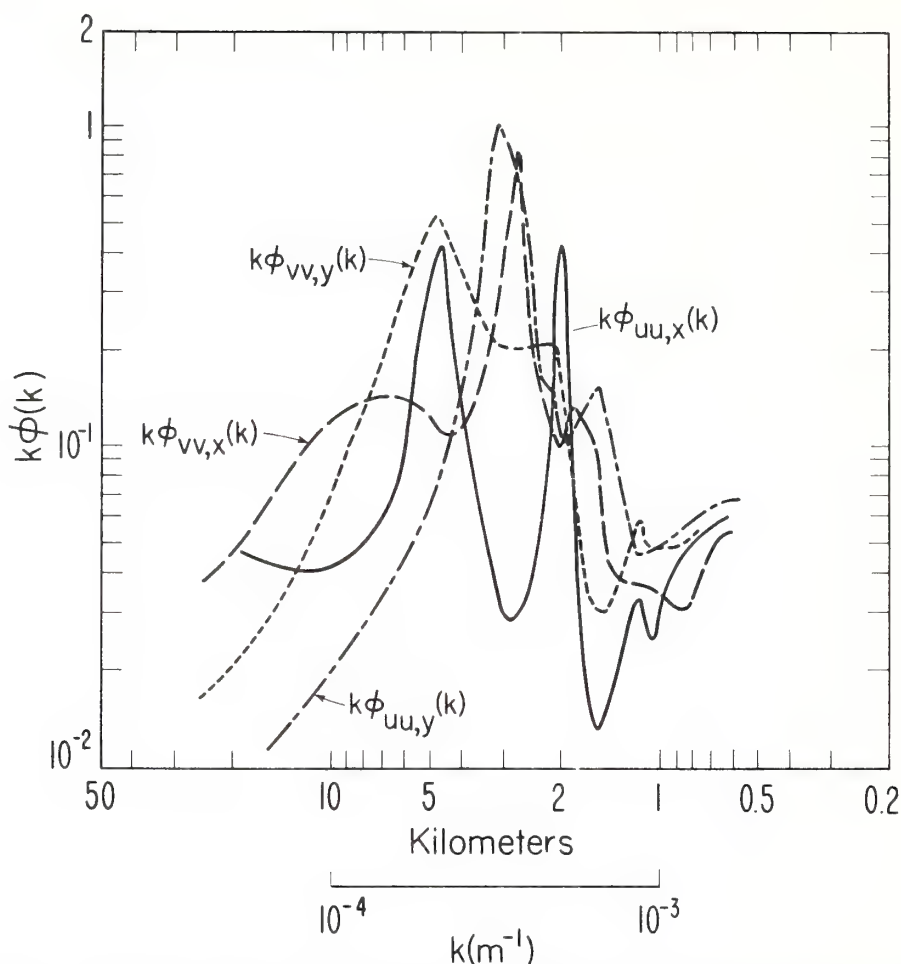
Fig. 7. Wavenumber spectra for the components perpendicular and parallel to the mean wind. (Here the mean wind (*v* component) is in the *Y* direction.)

3.3. ECHOSONDE DATA

The echosonde was located at approximately $x = 8000$ m and $y = 300$ m in the radar coordinate system in which the origin is at the center of the radar baseline. The *x*-axis is horizontal and perpendicular to the baseline. Figure 8 shows the echosonde facsimile record for a time interval that includes that of the dual-Doppler radar observations. The darker the record, the stronger the backscattered signal. Thus the plot displays echo strength as a function of time and height. It shows the acoustic intensity increasing and then decreasing over periods of a few minutes except near the ground (< 100 m) where the intensity is more continuous. Near the ground the periods are shorter. Furthermore, the larger values of C_T^2 seem to last longer than do weak values of C_T^2. Since there is an updraft in the convective boundary layer less than 50% of the time
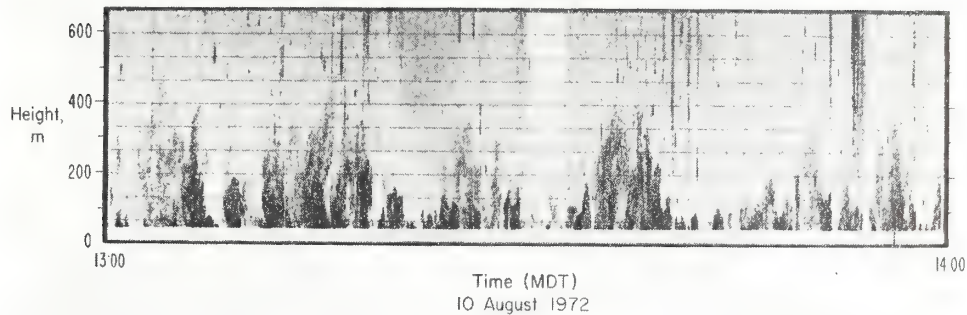
Fig. 8.   Acoustic backscattered intensity vs time and height.

(Frisch and Businger, 1973), either some of the temperature fluctuations causing the large acoustic echoes are in part of the downward moving air, or the angular resolution of the acoustic beam is insufficient to separate the structure in the lower part of the records.

Higher in the boundary layer, acoustic Doppler measurements have indicated that most of the larger values of C_T^2 are associated with upward moving air (Beran *et al.*, 1971). Unfortunately, the chaff did not fill the region above the echosonde (as can be seen in Figure 1, recalling the fact that the echosonde was at $x = 8000$ m and $y = -300$ m). Thus it is not possible to compare directly the echosonde data with the radar measurements. Adopting Taylor's hypothesis using 5 m s^{-1} as the mean wind speed, one can see that near the ground the fluctuations of C_T^2 are of much smaller scale than the distances between updrafts in the radar data. The radars can only resolve features larger than 300 m, and thus may be filtering out the smaller scales resolved by the echosonde.

At approximately 400 m, the echosonde record shows two very strong echoes at 1300 and 1318 MDT (roughly the time of the Doppler radar measurements). Again using Taylor's hypothesis, the separation distance is roughly 5 km – comparable to the distance between updrafts observed by Doppler radar. Although these are only two events, a similar scale was observed by Fitzjarrald (1975) using more echosonde data and longer time intervals. The similarity of the updraft separation distances to the separation distances between the large values of C_T^2 indicates that the large-scale updrafts may be important in transporting the temperature fluctuations upward above the surface layer, as suggested by LeMone (1973) and Kjelaas and Ochs (1974).

3.4. MICROBAROGRAPH ARRAY

Because of high noise in the pressure data and because the chaff volume was not over the array (located near the echosonde), it was not possible to compare the pressure fluctuations directly with patterns seen in the radar data. Using cross-spectrum analysis to process the micro-barograph array data, we found that most of the energy of

coherent pressure fluctuations was in a frequency band between 8.8×10^{-4} and 4.7×10^{-3} Hz. The propagation velocity of these coherent fluctuations was the same as the radar volume-averaged wind. The corresponding scales of the pressure disturbances were between 1.2 and 2.4 km, i.e., in the same range as one of the spectral peaks of $\phi_{uu,x}(k)$. However, at lower frequencies (longer wavelengths) the spectral estimates were unusable because of contamination by contributions due to power-line fluctuations.

4. Discussion and Conclusions

The observations we have described show the kinematic structure of convection cells in the boundary layer. The maximum kinetic energy in the residual velocity field in a horizontal plane 600 m above the ground was at scales between 2 and 5 km, with slightly more energy in the along-wind component than in the transverse component. Pennell and LeMone (1974) found that most of the momentum flux in the unstable trade-wind boundary layer over the ocean occurred at scales between 800 m and 10 km, with two peaks at 800 m and 6 km, comparable to the peaks in our spectral data (Figure 7). During BOMEX, Grossman (1973) observed similar scales in the u and v spectra with peaks occurring in the 2 to 3 km wavelength range. The echosonde data indicate that near the ground, scales smaller than the radar grid resolution are important, with a transition to the dominance of the larger scale motion as the height above the ground increases. This is in agreement with observations of Telford and Warner (1964) showing that near the ground, small scales are important in transferring temperature fluctuations vertically, with larger scales becoming more important with increasing height.

The surface pressure data indicate that there is at least one scale size in the range between 1.2 and 2.4 km that propagates at the same speed and direction as the wind velocity averaged over the first kilometre of the atmosphere. We cannot say with certainty from the present data whether or not the velocity features revealed by the Doppler radar are correlated with the pressure fluctuations at the ground.

Comparison of our spectral results with those of other investigators (Grossman, 1973; Pennell and LeMone, 1974) suggests that the velocity patterns or structures in the unstable boundary layer may be similar over the ocean and over land.

References

Bean, B. R., Frisch, A. S., McAllister, L. G., and Pollard, J. R.: 1973, 'Planetary Boundary-layer Turbulence Studies from Acoustic Echo Sounder and *in situ* Measurements', *Boundary-Layer Meteorol.* **4**, 449–474.
Beran, D. W. and Hall, F. F., Jr.: 1973, 'Remote Sensing Applications in Air Pollution Meteorology', *ISA Proc. 2nd Joint Conf. on Sensing of Environmental Pollutants*, 231–246.
Beran, D. W., Little, C. G., and Willmarth, B. C.: 1971, 'Acoustic Doppler Measurements of Vertical Velocities in the Atmosphere', *Nature* **230**, 160–162.
Burg, J. P.: 1967, 'Maximum Entropy Spectral Analysis', *37th Annual Intl. SEG Meeting*, Oklahoma City, Okla.
Chen, W. Y. and Stegen, G. R.: 1974, 'Experiments with Maximum Entropy Power Spectra of Sinusoids', *J. Geophys. Res.* **79**, 3019–3022.

Cook, R. K. and Bedard, A. J.: 1971, 'On the Measurement of Infrasound', *Geophys. J. R. Astr. Soc.* **26**, 5–11.

Emmanuel, C. B., Bean, B. R., McAllister, L. G., and Pollard, J. R.: 1972, 'Observations of Helmholtz Waves in the Lower Atmosphere with an Acoustic Sounder', *J. Atmos. Sci.* **29**, 886–892.

Fitzjarrald, D. E.: 1975, 'A Field Observation of Atmospheric Free Convection', submitted to *J. Appl. Meteorol.*

Frisch, A. S. and Businger, J. A.: 1973, 'A Study of Convective Elements in the Atmospheric Surface Layer', *Boundary-Layer Meteorol.* **3**, 301–328.

Frisch, A. S. and Clifford, S. F.: 1974, 'A Study of Convection Capped by a Stable Layer Using Doppler Radar and Acoustic Echo Sounders', *J. Atmos. Sci.* **31**, 1622–1628.

Frisch, A. S., Miller, L. J., and Strauch, R. G.: 1974, 'Three-Dimensional Air Motion Measured in Snow', *Geophys. Res. Letters* **1**, 86–89.

Gossard, E. E. and Hooke, W. H.: 1975, *Waves in the Atmosphere,* Elsevier, Amsterdam, 456 pp.

Grossman, R. L.: 1973, 'An Aircraft Investigation of Turbulence in the Lower Layers of the Marine Boundary Layer', Ph. D. Dissertation, Colorado State University, 182 pp.

Hardy, K. R. and Ottersten, H.: 1969, 'Radar Investigation of Convective Patterns in the Clear Atmosphere', *J. Atmos. Sci.* **26**, 666–672.

Hooke, R. H., Hall, F. F., Jr., and Gossard, E. E.: 1973, 'Observed Generation of an Atmospheric Gravity Wave by Shear Instability in the Mean Flow of the Planetary Boundary Layer', *Boundary-Layer Meteorol.* **5**, 29–41.

Kjelaas, A. G. and Ochs, G. R.: 1974, 'Study of Convergence in the Boundary Layer Using Optical Propagation Techniques', *J. Appl. Meteorol.* **13**, 242–248.

Kjelaas, A. G., Gossard, E. E., Young, J. M., and Moninger, W. R.: 1975, 'Dispersion and Spectra of Gravity Waves Probably Generated by a Convective Storm', *Tellus* **27**, 25–32.

Konrad, T. G.: 1970, 'The Dynamics of the Convective Process in Clear Air as Seen by Radar', *J. Atmos. Sci.* **27**, 1138–1147.

Kropfli, R. A. and Miller, L. J.: 1974, 'Dual-Doppler Radar Measurements Within a Hail Producing Storm in Northeast Colorado', *Preprints, AMS Conf. on Cloud Physics*, 227–282.

LaCoss, R. T.: 1971, Data Adaptive Spectral Analysis Methods', *Geophysics* **36**, 661–675.

LeMone, M. A.: 1973, 'The Structure and Dynamics of Horizontal Roll Vortices in the Planetary Boundary Layer', *J. Atmos. Sci.* **30**, 1077–1091.

Lenschow, D. H.: 1970, 'Airplane Measurements of Planetary Boundary Layer Structure', *J. Appl. Meteorol.* **9**, 874–884.

Lhermitte, R. M. and Miller, L. J.: 1970, 'Doppler Radar Methodology for Observation of Convective Storms', *Preprints, AMS Proc. 14th Radar Meteor. Conf.*, 133–138.

Little, C. G.: 1969, 'Acoustic Methods for the Remote Probings of the Lower Atmosphere', *Special Issue on Remote Environ. Sensing. Proc. IEEE-7*, 571–578.

Lumley, J. L. and Panofsky, H. A.: 1964, *The Structure of Atmospheric Turbulence*, Wiley, London, 239 pp.

Markel, J. D.: 1972, 'Digital Inverse Filtering – A New Tool for Format Trajectory Estimation', *IEEE Trans. Audio Electro-acoustics, AU-20*, 129–137.

Miller, L. J. and Frank, H. W.: 1974, 'Three-dimensional Air Motion Within a North-East Colorado Rainstorm', *Preprints, AMS Conf. on Cloud Physics*, 321–327.

Miller, L. J. and Strauch, R. G.: 1974, 'A Dual-Doppler Radar Method for the Determination of Wind Velocities Within Precipitating Weather Systems', *Remote Sensing of Environ.* **3**, 219–235.

Owens, E. J.: 1974, 'Development of a Portable Acoustic Echo Sounder, *NOAA Tech. Report, ERL 258-WPL 31*, U.S. Dept. of Commerce.

Panofsky, H. A.: 1973, 'Boundary Layer Above 30 m', *Boundary-Layer Meteorol.* **4**, 252–264.

Pasquill, F.: 1972, 'Some Aspects of Boundary-layer Description', *Quart. J. Roy. Meteorol. Soc.* **98**, 469–494.

Pennell, W. R. and LeMone, M. A.: 1974, 'An Experimental Study of Turbulence Structure in the Fair-Weather Trade Wind Boundary Layer', *J. Atmos. Sci.* **31**, 1308–1323.

Strand, O. N. and Chadwick, R. B.: 1975, 'A New Procedure for Computing and Analyzing Whitening Filters and Maximum Entropy Spectral Estimates', submitted to *Math. of Computation.*

Tatarski, V. I.: 1961, *Wave Propagation in a Turbulent Medium*, McGraw-Hill, New York, 285 pp.

Taylor, R. J.: 1958, 'Thermal Structures in the Lowest Layers of the Atmosphere', *Australian J. Physics* **11**, 168–176.

Telford, J. W. and Warner, J.: 1964, 'Fluxes of Heat and Vapor in the Lower Atmosphere Derived from Aircraft Observations', *J. Atmos. Sci.* **21**, 539–548.

Ulrych, T. J.: 1972, 'Maximum Entropy Power Spectrum of Truncated Sinusoids', *J. Geophys. Res.* **77**, 1396–1400.

Vulf'son, N. I.: 1961, 'Convective Motions in a Free Atmosphere', Israel Program for Scientific Translations, Jerusalem (Trans. 1964), Clearinghouse, U.S. Dept. of Commerce, π64–11017, 188 pp.

Warner, J. and Telford, J. W.: 1967, 'Convection Below Cloud Base', *J. Atmos. Sci.* **24**, 374–382.

Woodcock, A. H.: 1942, 'Soaring over the Open Sea', *The Scientific Monthly* **55**, 226–232.

Wyckoff, R. J., Beran, D. W., and Hall, Jr., F. F.: 1973, 'A Comparison of the Low-level Radiosonde and the Acoustic Echo Sounder for Monitoring Atmospheric Stability', *J. Appl. Meteorol.* **12**, 1196–1204.

Doppler Radar Measurements of Turbulent Kinetic Energy Dissipation Rates in a Northeastern Colorado Convective Storm

A. S. FRISCH AND R. G. STRAUCH

NOAA/ERL/Wave Propagation Laboratory, Boulder, Colo. 80302

(Manuscript received 19 November 1975, in revised form 19 July 1976)

ABSTRACT

In this paper we report the results of measurements of turbulent kinetic energy dissipation rates within a convective storm. The measurements were obtained with two Doppler radars, one scanning the storm from a distance at low elevation angles and the other pointing vertically with the storm passing overhead. With the scanning radar we measured the wind shear in the radial velocity field and the turbulent kinetic energy dissipation rates within the storm. These dissipation rates showed good agreement with those measured by the zenith-pointing radar data; dissipation rates ranged from 30 cm² s⁻³ to greater than 3500 cm² s⁻³ in the region between the updraft and downdraft.

1. Introduction

The spatial distribution of turbulence within severe storms is of interest in studies of hazards to aircraft, the diffusion of seed material within storms, the microphysics of drop-size growth and hail formation, and the basic physics of turbulence itself. In the past, turbulence measurements in convective storms have been made primarily with sensors on aircraft (Steiner and Rhyne, 1962; Sand *et al.* 1974). However, the volume of the storm that can be sampled by an aircraft is small compared with the total volume, and a long time is required to collect even such a limited sample. On the other hand, Doppler radars can sample almost the complete volume of a storm in a very short time, collecting enormous amounts of spectral information about the movements of scatterers within the storm. This information includes the radial component of the mean velocity of the scatterers in the pulse volume, obtained from the Doppler shift of the mean (first moment) frequency, and the variance of scatterer velocity within the pulse volume, obtained from the width (second central moment; hereinafter referred to as the second moment) of the Doppler spectrum.

The second moment of the spectrum contains information about turbulence that can be used to calculate the turbulent kinetic energy dissipation rate when other contributors to the second moment can be ignored or calculated (Frisch and Clifford, 1974; Gorelik and Mel'nichuk, 1963, 1968). We used this method to calculate the spatial distribution of turbulent kinetic energy dissipation rate in a severe storm in northeastern Colorado on 9 July 1973. With one Doppler radar we scanned the storm from a distance at low elevation angles. The storm passed almost

directly over a second radar, whose antenna was pointed vertically to obtain a time-height cross section of vertical velocity through the storm as it passed overhead. From the second moment of the spectra, obtained with the distant radar, we calculated turbulent dissipation rates; these were compared with dissipation rates calculated from the first moment data acquired at a height of 4.5 km by the vertically pointing radar. In one region common to the two radars the values from the second moment of the Doppler spectra varied between 280 and 800 cm² s⁻³, showing good agreement with the first moment value which was 700 cm² s⁻³.

2. Method

There are three potentially important contributors to the width or second moment of the Doppler spectrum for a narrow beam radar: turbulence, wind shear and the spread of particle fallspeeds. If we can determine the contributions of the last two, we can isolate the contribution of turbulence for use in our calculations. If we assume the turbulence to be homogeneous and isotropic we can then calculate the turbulent kinetic energy dissipation rate ϵ.

The contribution of fallspeed to the second moment is $\sigma_D{}^2 \sin^2\theta$, where θ is the elevation angle and $\sigma_D{}^2$ the variance of particle fall velocity in quiet air. The spread of particle fallspeeds is nearly independent of rainfall rate and is about 1 m² s⁻² (Lhermitte, 1963). Thus, for the low elevation angles ($<15°$) at which the distant radar scanned the storm, the fall velocity contribution is less than $\frac{1}{16}$ m² s⁻² and may be ignored.

The contribution of wind shear to the second moment is most easily discussed in terms of (i) shear in the radial velocity along the radial direction, i.e., *parallel*

to the beam axis, and (ii) shear in the radial velocity *transverse* to the beam axis.

The contribution of shear parallel to the beam axis is (Sirmans and Doviak, 1973)

$$\sigma_s{}^2 = (k_r h)^2/12, \qquad (1)$$

where k_r is the component of the shear parallel to the beam (s⁻¹), and h is the radar range resolution (m).

The contribution of shear transverse to the beam axis is given by (Sloss and Atlas, 1968)

$$\sigma_s{}^2 = (0.3 k R \phi)^2, \qquad (2)$$

where k is the shear of the radial velocity across the beam (s⁻¹), R range (m), and ϕ the one-way, half-power beamwidth. It is convenient to divide the transverse shear into two perpendicular components, $k^2 = k_v{}^2 + k_h{}^2$. Then the total contribution of shear to the second moment is given by

$$\sigma_s{}^2 = (k_h{}^2 + k_v{}^2)(0.3 R \phi)^2 + k_r{}^2 h^2/12. \qquad (3)$$

A scanning Doppler radar can measure the mean radial velocity throughout a storm, so k_r, k_h and k_v can be calculated. The beamwidth of our antenna was 0.9°, the range R was between 40 and 55 km, and the resolution h was 75 m. Therefore, it is clear from Eqs. (1) and (3) that the second moment contributions from k_v and k_h are about an order of magnitude greater than that from k_r. The second moment remaining after removal of the shear contribution is a result of small-scale velocity fluctuations within the radar pulse volume. For narrow beam radars the second moment produced by these fluctuations is related to the turbulent structure by

$$\sigma_{11}{}^2 = \int d\mathbf{k}^3 \phi_{11}(\mathbf{k})[1 - (2\pi)^6 |F_p(\mathbf{k})|^2], \qquad (4)$$

where $\phi_{11}(\mathbf{k})$ is the radial component of the spectral density tensor of the velocity field, $F_p(\mathbf{k})$ the filter function of the radar illumination pattern, and $\mathbf{k}$ the vector wavenumber. Thus the Doppler spectrum width depends not only on the velocity spectrum along the radar beam axis, but on the beam illumination function. The beam illumination function depends on the physical width of the beam (Frisch and Clifford, 1974) and thus varies with distance from the radar.

If we assume that the scales of motion within the pulse volume that cause the measured $\sigma_{11}{}^2$ lie within an inertial subrange, we can relate the turbulent kinetic energy dissipation rate ϵ to $\sigma_{11}{}^2$ (Frisch and Clifford, 1974):

$$\epsilon \approx \frac{1}{\alpha}\left(\frac{\sigma_{11}{}^2}{1.26 A}\right)^{\frac{3}{2}}, \qquad (5)$$

where $A = 0.53$ (Wyngaard and Pao, 1972) and α, the beamwidth parameter, is $R\theta/1.66$ for a Gaussian beam

or $0.0094R$ for our radar, where R is the pulse volume range from the radar (m) and θ the one-way half-power beamwidth. Eq. (5) applies when the antenna beamwidth is much larger than the range resolution. To confirm the validity of their method of estimating dissipation rates, Frisch and Clifford (1974) compared their radar-measured dissipation rates with those measured from an instrumented tower and found good agreement.

In applying this method to a thunderstorm, we assume that the outer scale of the inertial subrange is larger than the maximum dimension of the beam illumination function. This assumption seems reasonable since aircraft observations in thunderstorm inflow regions indicate that the velocity spectra behave in the manner characteristic of an inertial subrange (Foote and Fankhauser, 1973), with the inertial subrange existing at wavelengths as large as 4 km. Aircraft penetrations of thunderstorms by Steiner and Rhyne (1962) have also yielded one-dimensional spectra characterized by an inertial subrange having an outer scale of several kilometers.

3. Experiment and results

Data were collected for a storm on 9 July 1973 during the field program of the National Hail Research Experiment (NHRE). Two Doppler radars from the Wave Propagation Laboratory (WPL), situated 50 km apart along an approximately north-south line, observed the storm. Additional observations made with instrumented aircraft, a 10 cm radar and a surface meteorological network assisted in interpreting the Doppler radar data. The storm passed over the south radar which was zenith-pointing, and moved in a southerly direction at approximately 7 m s⁻¹ (Chalon *et al.*, 1976). This storm produced pea-sized hail, mixed with rain. A few larger hailstones, up to 1.5 cm in diameter, were collected on the ground. [The storm is described by Browning *et al.* (1976).]

The moments of the Doppler spectra were estimated from the power spectral densities calculated from 128 complex radar samples that were acquired in 65 ms. A Hamming weighting function was used. Prior to calculating the moments a velocity window was applied to the signal plus noise power spectrum so that the noise spectrum was eliminated except for those spectral points that also contained signal power. The velocity window extended from both sides of the mean velocity to the points where the spectral power exceeded the mean noise level by 3 dB.

Fig. 1 shows radar reflectivity, radial velocity and the width of the spectra measured by the north radar in a vertical plane through the two radar locations. (The reflectivity contours are not corrected for attenuation.) This plane is approximately parallel to the direction of echo motion. The direction of echo motion, to the right in Fig. 1, is away from the radar so that

Radar Reflectivity

radial velocity field shows air motion toward the region of high reflectivity. Behind and at the same level of the 44 dBZ contour, the radial velocity field shows the air motion to be toward the high-reflectivity region. At the top and behind the 44 dBZ contour the radial velocity field shows motion away from the high-reflectivity region. Data obtained by the zenith-pointing radar showed a strong updraft just ahead of this high-reflectivity region (>44 dBZ). The data in Fig. 1

Fig. 1. Contours of radar reflectivity, radial velocity and second moments of the Doppler spectrum in a vertical plane through the two Doppler radars. The echo motion (measured by the north radar) was approximately parallel to this plane and the storm was moving away from the north radar. Positive radial velocity is in the direction of echo motion. Shaded region is the trailing edge of the updraft. Data are measured with a 3 cm radar located about 55 km NNW of the storm. Zenith-pointing radar was located at $y=3.7$ km.

positive velocities are in the direction of echo motion. When we use the radar echo as the frame of reference, i.e., subtract 7 m s^{-1} toward the south from the total velocity, the reflectivity and radial velocity measurements show that within the highest reflectivity regions (>44 dBZ), the N-S component of relative air motion was approximately zero. Ahead of (i.e., in the direction of storm motion) and below the 44 dBZ contour the

Fig. 2. Radar reflectivity, radial velocity, and second moments of the Doppler spectrum at 5 km altitude. Data are measured with a 3 cm radar located about 55 km NNW of the storm. Positive radial velocity is in the direction of echo motion. Zenith-pointing radar was located at $x=8.3$, $y=3.7$ km.

suggest convergence of the air entering the storm at low- and mid-level, and divergence of the air at the top of the updraft.

The radial velocity fields shown in Fig. 1 can be used to calculate the shear components k_v and k_r in the vertical plane passing through the two radars. Calculating k_v, we find it to be largest in the rear of the storm with a maximum value of about $6 \times 10^{-3} \text{ s}^{-1}$.

The radial shear component k_r, also calculated from the radial velocity in Fig. 1, has a maximum value of 10^{-2} s^{-1} at a height of 4 km, between $y = 3$ km and $y = 4$ km, i.e., between the low- and mid-levels of the storm and slightly in front of the high-reflectivity region in the direction of echo motion. Part of an updraft (denoted by the shaded area in Fig. 1) was observed by the south radar with its antenna pointing vertically as the storm passed overhead (Strauch and Merrem, 1976). This region contained updraft velocities as high as 16 m s^{-1}. After the echo advected less than 3 km, the zenith-pointing radar observed downdrafts as large as 12 m s^{-1}. This horizontal shear of the vertical wind does not contribute appreciably to the width of the Doppler spectrum observed by the north radar because the elevation angle of the radar antenna in the region of high shear was less than 8°. Second-moment contours measured by the north radar show a distinct maximum at altitudes between 4 and 8 km, just ahead of the highest reflectivity region which is also the region between the updraft and downdraft.

Fig. 2 shows mid-level contours in a horizontal plane at a height of 5 km. Comparing contours of reflectivity and radial velocity we note strong convergence of air overtaking the storm from the north and air entering the storm from the south near the highest reflectivities. The velocity variance is large in a region about 5 km in diameter, just ahead of the high-reflectivity core (at $x = 7$ km, $y = 3$ km). The third component of shear, k_h, was calculated from the radial velocity fields in Fig. 2. These values are generally very small but show a maximum of $4 \times 10^{-3} \text{ s}^{-1}$ at the southwest edge of the coverage area. The total shear contribution to the spectrum width measured by the north (low-angle) radar was only a small portion of the total width in the region where the highest second moments were observed. Therefore, the high second moment values shown in Figs. 1 and 2 portray regions with high turbulent kinetic energy dissipation rates. The largest spectral widths were measured just ahead of the high-reflectivity region, where a transition between updraft and downdraft occurred (Browning et al., 1976).

From the second moments measured by the north radar scanning at low elevation angles (maximum of 15°), we calculated the turbulent kinetic energy dissipation rate ϵ using Eq. (5) after correcting for the shear contribution to the velocity second moment. If the total shear contribution to the width of the Doppler spectrum is less than 50%, it was removed from the
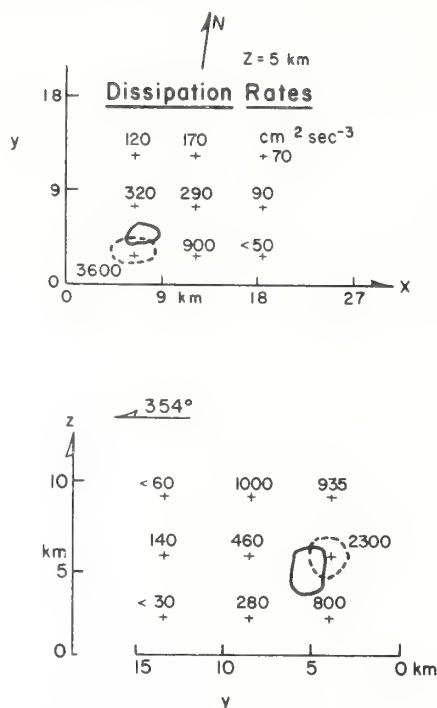
FIG. 3. Dissipation rates measured by the scanning radar at 5 km altitude (top) and in the same vertical plane shown in Fig. 1 (bottom). The solid line is the 44 dBZ reflectivity contour and the dashed line is the 14 m² s⁻² second moment contour. The dissipation rate is not estimated when the shear contribution to the width is more than half the total width.

total width and a corrected variance for turbulence only was calculated. If the shear contribution was greater than 50% of the total, the width measurement was not used for dissipation rate calculations. The measured first and second moments of the Doppler spectrum, obtained with a range spacing of 600 m and an elevation and azimuth spacing of about 900 m, were interpolated to a 900 m Cartesian grid using linear interpolation. The dissipation rates were calculated from the interpolated values of the first and second moments at various locations throughout the storm. The wind shear was calculated from finite differences of the interpolated mean radial velocity at adjacent grid points. The interpolation process filters the measured data field and thereby attenuates scale sizes on the order of the grid spacing. Hence velocity fluctuations at scale sizes large compared to the pulse volume are treated as shear and their contributions to the width of the spectrum are removed. Velocity fluctuations on scale sizes of the order of the pulse volume are not treated as shear because mean velocity fluctuations on these scale sizes are not distinguishable from statistical uncertainties in the estimate of the mean velocity. This means that we may not have removed the effects of all velocity fluctuations at scale size greater then the pulse volume. For this reason we did not attempt to calculate the dissipation rate when the shear contribution was greater than 50% of the total
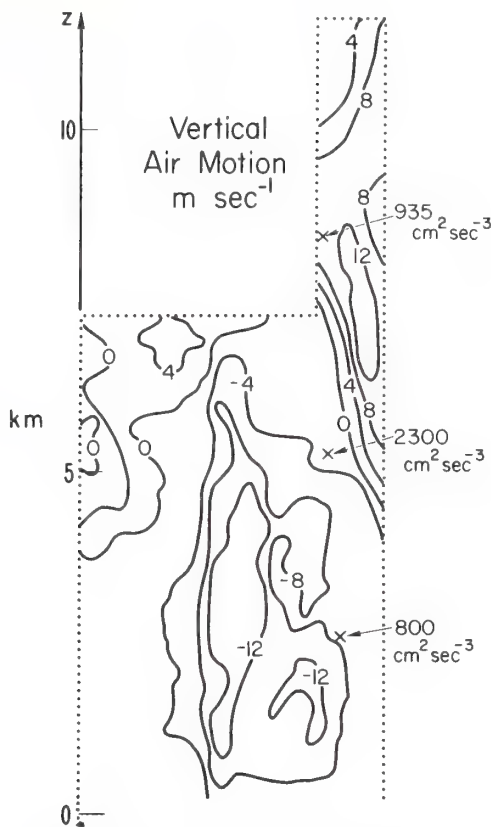
FIG. 4. Vertical air motion measured by the zenith-pointing radar. Vertical velocity measurements were corrected for the fall velocity of the particles in still air. Note that high dissipation rates were measured between updraft and downdraft. The spatial scale was obtained by assuming $x = \bar{u}t$, where $\bar{u}$ was approximately 7 m s^{-1}.

spectrum width. Fig. 3 shows the calculated dissipation rates in the same vertical plane (bottom) shown in Fig. 1 and the same horizontal plane (top) shown in Fig. 2. The calculated dissipation rates vary by two orders of magnitude in different areas of the storm. In the rear of the storm (relative to the radar echo motion) the dissipation rates are small (< 30 cm^2 s^{-3}). In the region with the highest second moment, the rates are > 2000 cm^2 s^{-3}; the highest dissipation rate found was 3600 cm^2 s^{-3} which considerably exceeds the rates usually associated with severe clear air turbulence (Trout and Panofsky, 1969). The position of the highest value of ϵ shown in Fig. 3 (~ 3600 cm^2 s^{-3}) coincides with the region between the updraft and downdraft shown in Fig. 1. The region can be seen more readily in Fig. 4 which shows it to be also a region of large horizontal shear of the vertical velocity (3×10^{-2} s^{-1}). The high dissipation rate found here is expected because of shear production of turbulent kinetic energy.

We compared values of ϵ calculated from the second moment measured by the scanning radar with those calculated from the first moment, i.e., from mean velocity measurements acquired by the vertically pointing radar. The transverse structure function of the mean

vertical velocity [$D_{ww}(r)$] at an altitude of 4.5 km was calculated from the vertical velocity measurements taken every $\frac{5}{8}$ s as the storm advected overhead. Assuming Taylor's hypothesis to be valid, the temporal record can be treated as a spatial record with $r = \bar{u}t$, where $\bar{u}$ is the average horizontal motion of the storm (7 m s^{-1}) and t time. The radar pulse volume was 75 m in depth by about 65 m in diameter at the height of 4.5 km. For values of r where $D_{ww}(r)$ varied as $r^{\frac{2}{3}}$, $D_{ww}(r)$ is related to the dissipation rate by

$$D_{ww}(r) = B\epsilon^{\frac{2}{3}} r^{\frac{2}{3}} = B\epsilon^{\frac{2}{3}} (\bar{u}t)^{\frac{2}{3}},$$

where

$$D_{ww}(r) = \overline{[w(x) - w(x+r)]^2} = \overline{[w(x) - w(x+\bar{u}t)]^2} \quad (6)$$

and B is a constant equal to 1.4 (Record and Cramer, 1966; Tatarski, 1961). The vertical velocity time record was 240 s long, and in computing $D_{ww}(r)$ we used delays up to 40 s. We assumed that the changes in the particle fall velocity in still air were unimportant. At a height of 4.5 km (above ground level) and with a mean horizontal wind speed of 7 m s^{-1}, Eq. (6) yielded an average value of $\epsilon = 700$ cm^2 s^{-3}. The temporal record of vertical velocity corresponds to the location (Fig. 3) where the scanning radar measured ϵ values ranging from 280 to almost 800 cm^2 s^{-3}. Thus there is reasonable agreement between the two entirely different radar measurement techniques.

Although we had no direct measurements with which to compare our calculated results for this storm, data taken by aircraft penetrating other storms verify that our indirectly derived values were consistent with direct measurements. For example, using storm data from Steiner and Rhyne (1962), we found maximum values of $\epsilon \approx 10^4$ cm^2 s^{-3}. Using Foote and Fankhauser's (1973) velocity spectra from another storm, we calculated values for ϵ of about 620 cm^2 s^{-3} in the outflow and 68 cm^2 s^{-3} in the inflow regions. Dissipation rates of 3000 cm^2 s^{-3} were measured by Sand et al. (1974) in another northeast Colorado thunderstorm. Thus, our values lie within the range of values found by other investigators.

Another check on the order of magnitude of the dissipation rate is given by $\epsilon \approx q^3/l$ (Tennekes and Lumley, 1972) where q is the average velocity variation within the storm and l a characteristic scale for the storm. Examination of Figs. 1 and 2 indicates that the variation in the mean radial velocity field is ~ 8–10 m s^{-1} and the scale of the storm is ~ 10 km. This yields $\epsilon \approx 500$ to 10^3 cm^2 s^{-3}, which is in the range of values we calculated from our storm measurements.

4. Discussion

Aircraft measurements of the turbulent kinetic energy dissipation rate with *in situ* sensors provide data along the flight path, but during the time required for the aircraft to make a single pass through the storm,

the radar can obtain estimates throughout the entire storm. For example, the radar data we used were acquired in 160 s. In addition, the probability is small that the aircraft will pass through the most turbulent region of a storm, and the safety of doing so is questionable. Kyle (1974) used an aircraft measurement to arrive at an average dissipation rate of 512 cm² s⁻³ throughout the height of a storm to compute the diffusion of seed material. An aircraft flying through the storm we studied might well have measured this average value depending on the track and record length used. However, the radar measurements show that the distribution of ϵ is not constant, and any model for diffusion within this storm must include a small but intense turbulent region at mid-level.

Dissipation rates measured by aircraft in clear air turbulence are summarized by Trout and Panofsky (1969). The highest rate they report is 1160 cm² s⁻³ with a geometric mean of 675 cm² s⁻³ for "severe turbulence." They believe the average estimates to be conservative and may easily be in error by 50%. The rates we calculated using the Doppler radar measurements range from their classification for "light turbulence" to greater than their numbers for "severe turbulence." The highest dissipation rates we measured were in the area between the updraft and the downdraft; an aircraft would certainly have experienced severe turbulence in that region.

5. Conclusion

The three-dimensional scalar field of the second moment of the Doppler spectrum, measured in a convective storm by a Doppler radar scanning at low elevation angles, shows regions of high shear and severe turbulence. Shear of the radial velocity can be estimated from the gradients of the radial velocity field, so the contribution of shear to the width of the spectra can be assessed. Turbulent kinetic energy dissipation rates can be derived from the portion of the second moment that is not related to the shear. Dissipation rates derived from the second moment of the Doppler spectra measured in a northeast Colorado thunderstorm ranged from rates associated with little or no turbulence to rates associated with severe turbulence. The highest dissipation rates were found in the mid-levels of the storm where there was large shear between the updraft and downdraft. Remote measurement of the dissipation rate throughout the storm provides essential data for calculating the diffusion of seed material injected along a line or at a point. It is also potentially important in identifying hazardous areas for aircraft.

REFERENCES

Browning, K. A., J. C. Fankhauser, J-P. Chalon, P. J. Eccles, R. G. Strauch, F. H. Merrem, D. J. Musil, E. L. May and W. R. Sand, 1976: Structure of an evolving hailstorm. Part V: Synthesis and implications for hail growth and hail suppression. *Mon. Wea. Rev.*, **104**, 603–610.

Chalon, J.-P., J. C. Fankhauser and P. J. Eccles, 1976: Structure of an evolving hailstorm, Part I: General characteristics and cellular structure. *Mon. Wea. Rev.*, **104**, 564–575.

Foote, G. B., and J. C. Fankhauser, 1973: Airflow and moisture budget beneath a northeast Colorado hailstorm. *J. Appl. Meteor.*, **12**, 1330–1353.

Frisch, A. S., and S. F. Clifford, 1974: A study of convection capped by a stable layer using Doppler radar and acoustic echo sounders. *J. Atmos. Sci.*, **31**, 1622–1628.

Gorelik, A. G., and Yu. V. Mel'nichuk, 1963: Radar study of dynamic processes in the atmosphere. *Tr. Vses. Nauchno Meteor.*, **5** [Amer. Meteor. Soc. Trans. T-R-667, 12 pp.]

——, and ——, 1968: A new method for measuring dissipation rate of turbulence in clouds and precipitation using conventional radar. *Proc. Third All-Union USSR Conf. on Radar Meteorology*, [Jerusalem, Israel Program for Scientific Translations, 150–156.]

Kyle, T. G., 1974: The dispersal of seeding material in the updraft of storms. *Preprints 4th Conf. Weather Modification*, Ft. Lauderdale, Amer. Meteor. Soc., 69–72.

Lhermitte, R. M., 1963: Motions of scatterers and the variance of the mean intensity of weather radar signals. SRRC-RR-63-57, Sperry-Rand Research Center, Sudbury, Mass., 43 pp.

Record, F. A., and H. E. Cramer, 1966: Turbulent energy dissipation rates and exchange processes above a non-homogeneous surface. *Quart. J. Roy. Meteor. Soc.*, **92**, 519–532.

Sand, W. R., D. J. Musil and T. G. Kyle, 1974: Observations of turbulence and icing inside thunderstorms. *Preprints 6th Conf. Aerospace and Aeronautical Meteorology*, El Paso, Amer. Meteor. Soc., 299–304.

Sirmans, D., and R. J. Doviak, 1973: Meteorological radar signal intensity estimation. NOAA TM ERL NSSL-64, U. S. Dept. of Commerce, Norman, Okla., 30 pp.

Sloss, P. W., and D. Atlas, 1968: Wind shear and reflectivity gradient effects on Doppler radar spectra. *J. Atmos. Sci.*, **25**, 1080–1089.

Steiner, R., and R. H. Rhyne, 1962: Some measured characteristics of severe storm turbulence. NSSL Rep. No. 10, U. S. Dept. of Commerce, Norman, Okla.

Strauch, R. G. and F. H. Merrem, 1976: Structure of an evolving hailstorm, Part III: Internal structure from Doppler radar. Mon. Wea. Rev., **104**, 588–595.

Tatarski, V. I., 1961: *Wave Propagation in a Turbulent Medium*. McGraw–Hill, 285 pp.

Tennekes, H., and J. L. Lumley, 1972: *A First Course in Turbulence*. The MIT Press, 187 pp.

Trout, D., and H. A. Panofsky, 1969: Energy dissipation near the tropopause. *Tellus*, **21**, 355–358.

Wyngaard, J. C., and Y. H. Pao, 1972: Some measurements of the finestructure of large Reynolds number turbulence. *Lecture Notes in Physics, Statistical Models and Turbulence*, J. Ehlers, K. Hepp and H. A. Weidenmuller, Eds., Springer-Verlag, 384–401.

OBSERVATION OF WINDS IN THE CLEAR AIR USING AN FM-CW DOPPLER RADAR

E. E. Gossard, R. B. Chadwick, K. P. Moran, R. G. Strauch,
G. E. Morrison, and W. C. Campbell

NOAA/ERL/Wave Propagation Laboratory
Boulder, Colorado 80302, USA

SUMMARY

The Wave Propagation Laboratory of NOAA has developed a frequency-modulated, continuous-wave, clear air radar with a Doppler capability for measuring both the mean wind and turbulent intensity. In this paper, observations of turbulence are shown and related to the background wind and temperature structure. The radar's capability for measuring the structure parameters of both velocity and refractive index is discussed.

1 - INTRODUCTION

It has been known for some time (Richter, 1969), that frequency-modulated, continuous-wave (FM-CW) radar has the capability of revealing many details of clear-air structures in the planetary boundary layer. Its value lies mainly in its ability to "see" structure close to the radar (near the ground), and in the fine resolution with which the atmosphere can be observed. It is fundamentally very flexible, and the range resolution, observed range, and integration time can be varied more-or-less at will.

The capabilities of the FM-CW radar for observing the atmosphere attracted considerable attention for some time after its invention, and much was learned about wave motions and convection in the lower atmosphere (Gossard et al., 1970; Atlas et al., 1970; Bean et al., 1972). However, acoustic sounders were under development at about the same time (Little, 1969; McAllister, 1968), and the acoustic sounders had the great advantage that Doppler velocity information was easy to extract from the backscattered signal. Although it was well known that Doppler velocity information about discrete targets could be obtained by the FM-CW radar, it was widely believed that the extraction of velocity information from backscatter that was continuous in range was impossible because this kind of radar uses the frequency difference between the outgoing and returning signal to get range information. How, then, could the backscattered signal also be used to provide Doppler velocity information?

Strauch et al. (1975) of NOAA's Wave Propagation Laboratory have recently described the theory of how Doppler information can be extracted through digital processing, and demonstrated the technique (Strauch et al., 1976) by observing the fall velocity of rain and snow. The essence of the technique is to observe phase changes in the return signal from sweep to sweep. They further pointed out the potential of the radar for clear-air studies and showed examples of clear air vertical velocity.

2 - MEAN WIND OBSERVATIONS

Still more recently, Chadwick et al. (1976) have made clear-air observations of the horizontal wind velocity and discovered the startling fact that the Doppler information is fundamentally available even without additional digital data processing if the FM-CW radar is suitably configured. This is because the output of this radar appears in the frequency domain. The equipment configuration is similar to that used by Richter (1969), the only changes being in parameters.

The FM sweep period used by Richter was 50 ms while Chadwick et al. (1976) used a few ms sweep period. Richter coherently processed over only one sweep while Chadwick et al. coherently processed over 50 or so sweeps. An example of velocity spectra displayed on an A Scope without digital processing is shown in Figure 1. Figure 2 (from Chadwick et al.) shows the corresponding wind profile acquired along an azimuth of 225° at an elevation angle of 45°. The profile is compared with winds measured by a captive balloon (solid lines) at the beginning times of ascent and descent indicated. The circles show a RAWINSONDE ascent made at the same time. The radar sounding represents a 10-second average, whereas many minutes were needed for the balloon soundings. In the system used by Chadwick et al., the radial wind and wind-shear data can easily be displayed on a PPI, revealing the clear-air wind structure over a volume in the vicinity of the radar.
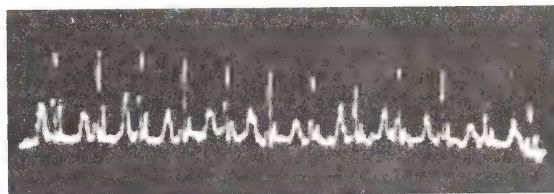
Fig. 1 A-SCOPE DISPLAY OF CLEAR AIR DOPPLER WIND SPECTRA. SPIKES ARE FROM GROUND CLUTTER AND REPRESENT ZERO VELOCITY POINT IN RANGE CELLS SPACED 122 METERS APART FROM 165 M RANGE OUT TO 1805 M. THE VELOCITY SCALE IS 20 M/S BETWEEN SPIKES; THE CLEAR-AIR SPECTRA ARE THE BROAD PEAKS SHIFTED FROM ZERO BY THE HORIZONTAL WIND.
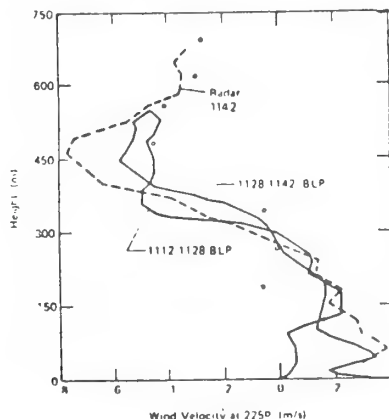
Fig. 2 FM-CW RADAR AND TETHERED BALLOON WIND PROFILES FOR 16 SEPTEMBER 1975. WIND COMPONENT IS AT 225° AZIMUTH. SMALL CIRCLES SHOW RESULTS OF RAWINSONDE RELEASE AT 1100 MDT. TETHERED BALLOON AND RAWINSONDE RELEASE ABOUT 300 M EAST OF RADAR SITE.

299

3 - TURBULENCE INTENSITY MEASURED BY FM-CW DOPPLER RADAR

The mean radial velocity is found from the displacement of the wind velocity spectrum from zero as shown in Figure 1. However, the finite width of the velocity spectrum is a result of either random turbulent air motions toward and away from the radar within the range cell or of shear of the radial wind transverse or parallel to the beam axis. However, shear transverse to the beam axis can usually be determined by scanning the beam; shear parallel to the beam can be found from the range cell-to-cell wind information, and shear effects then removed. When the radar is pointing vertically, the shear component is nearly always negligible because the mean radial wind component is then almost always small. Thus the width of spectra measured by Doppler radars can be interpreted in terms of mechanical turbulence intensity (Frisch and Clifford, 1974).

Figure 3 shows an example of an FM-CW radar record obtained on 29 April 1976 with the antennas pointing vertically. The left side shows intensity of the backscatter on a height vs time display. An A Scope display of log intensity vs height is shown by the left-hand solid curve. The backscattered intensity is a direct measure of the turbulent structure parameter C_N^2, as demonstrated by Ottersten (1969). The Doppler spectra in 87 m height increments are shown by the curves at the right. As in Figure 1, the range axis is also a velocity axis. In this case the vertical velocity is zero within the error of reading from the display so the peaks of the spectra are at zero velocity. The velocity range from peak-to-peak is 10 m/s and the corresponding height range is 87 m. The first and second moments of the spectra were calculated from the mean-value theorem using the trapezoidal rule.

On 29 April there was a nearly stationary front along the eastern slope of the Rocky Mountains so the boundary layer displayed by the radar was in a nearly steady-state condition. We therefore have compared the radar data with the RAWINSONDE data from Denver, Colorado, almost 60 km from Boulder where the radar
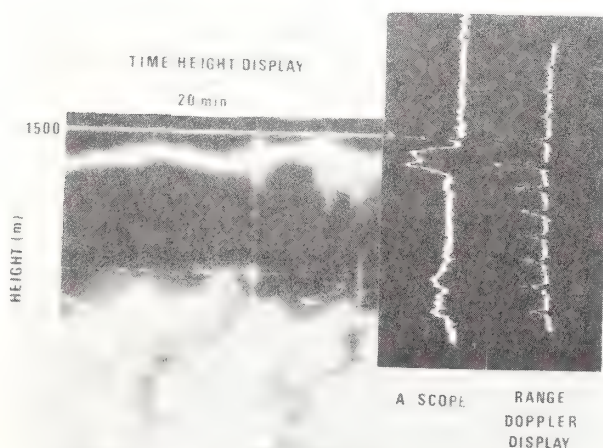
was located. The RAWINSONDE data taken at 0500 MST shows the frontal inversion to be 1400 meters above the ground in remarkable agreement with the thin, intense scattering layer on the radar record. The sounding data are shown in Figure 4 with the wind variance profile for comparison. The variance reaches a maximum below the inversion, falling off to less than a tenth of its maximum value above the inversion. The structure parameter C_N^2 (or equivalently, the backscattered intensity) has a strong maximum at the base of the inversion, in agreement with aircraft-borne-refractometer results reported by Gossard (1960) and with balloon-borne-refractometer results reported by Lane (1967).
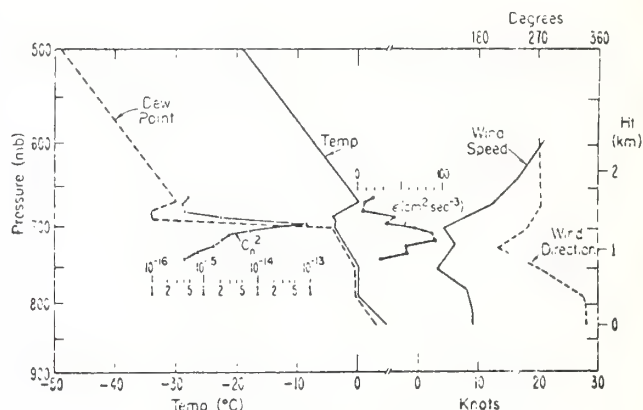
Fig. 4   METEOROLOGICAL SOUNDING DATA FROM THE DENVER RAWIN AND TURBULENT DISSIPATION RATE ϵ AND C_n^2 MEASURED BY THE RADAR.

4 - CONCLUSIONS

The FM Doppler radar is a powerful new research tool for studying wind structure and turbulence in the planetary boundary layer. If it can be established that it can operate to several km ranges a large percent of the time, it will have many practical applications as well as research applications. These include the monitoring of wind shear and severe turbulence in the neighborhood of airports.

5 - REFERENCES

Atlas, D., J. I. Metcalf, J. H. Richter, and E. E. Gossard, 1970: The birth of "CAT" and microscale turbulence, *J. Atmos. Sci.*, vol. 27, 903-913.

Bean, B. R., R. E. McGavin, R. B. Chadwick, and B. D. Warner, 1971: Preliminary results of utilizing the high resolution FM radar, *Boundary Layer Meteor.*, 1, 466-473.

Chadwick, R. B., K. P. Moran, R. G. Strauch, G. E. Morrison, and W. C. Campbell, 1976: A new radar for measuring winds, *Bull. Amer. Meteor. Soc.*, vol. 57, 1120-1125.

Frisch, A. S., and S. F. Clifford, 1974: A study of convection capped by a stable layer using Doppler radar and acoustic echo sounders, *J. Atmos. Sci.*, vol. 31, 1622-1628.

Gossard, E. E., 1960: Spectra of atmospheric scalars, *J. Geophys. Res.*, vol. 65, 3339-3351.

Fig. 3   BACKSCATTERED INTENSITY VS HEIGHT AND TIME WITH WIND SPECTRA SHOWN AT FAR RIGHT.   SPECTRA ARE CENTERED ON ZERO VELOCITY BECAUSE RADAR IS POINTING VERTICALLY.

Gossard, E. E., J. H. Richter, and D. Atlas, 1970: Internal waves in the atmosphere from high-resolution radar measurements, *J. Geophys. Res.*, vol. 75, 3523-3536.

Lane, J. A., 1967: Measurements with a spaced-cavity microwave refractometer, *Atmospheric Turbulence and Radio Wave Propagation*, ed. by A. M. Yaglom and V. I. Tatarsky, Publishing House Nauka, Moscow., 201-204.

Little, C. G., 1969: Acoustic methods for the remote probing of the lower atmosphere, *Proc. IEEE* vol. 57, 571-578.

McAllister, L. G., 1968: Acoustic sounding of the lower troposphere, *J. Atmos. Terr. Phys.*, vol. 30, 1439-1440.

Ottersten, H., 1969: Atmospheric structure and radar backscattering in clear air, *Radio Sci.*, vol. 4, 1179-1193.

Richter, J. R., 1969: High resolution tropospheric radar sounding, *Radio Sci.*, vol. 4, 1261-1268.

Strauch, R. G., W. C. Campbell, R. B. Chadwick, and K. P. Moran, 1975: FM-CW boundary layer radar with Doppler capability, *NOAA Technical Report ERL 329-WPL 39*, U.S. Government Printing Office, Washington, D.C. 20402 USA.

Strauch, R. G., W. C. Campbell, R. B. Chadwick, and K. P. Moran, 1976: Microwave FM-CW Doppler radar for boundary layer probing, *Geophys. Res. Lett.*, vol. 3, 193-196.

A DUAL DOPPLER RADAR STUDY OF THE URBAN BOUNDARY LAYER:
A SUMMARY OF METROMEX RESULTS

Robert A. Kropfli

The two WPL/NOAA Doppler radars participated in METROMEX from July 15, 1975 through August 15, 1975 in an effort to document the three-dimensional wind field in the urban planetary boundary layer. Convective motions within the PBL were utilized to distribute aircraft-dispensed chaff to heights of 2 km and over areas as large as 250 km^2. Coplane scanning and analysis revealed the presence of persistent horizontal rolls for three of the seven cases analyzed. Persistent localized updrafts were observed over the heavily industrialized locations within the Metropolitan St. Louis area. Numerous other features·were also revealed in the wind fields generated for the seven cases presented in this report.

DUAL-DOPPLER RADAR OBSERVATIONS OF THE CONVECTIVE
MIXING LAYER AT ST. LOUIS

R. A. Kropfli and N. M. Kohn
NOAA/ERL/Wave Propagation Laboratory
Boulder, Colorado 80302

1.   INTRODUCTION

         Since 1971 the urban planetary boundary
layer in the St. Louis metropolitan area has been
under intensive study as part of the Metropolitan
Meteorological Experiment (METROMEX). During the
summer of 1975 the Wave Propagation Laboratory
(WPL) of NOAA joined forces with the 5 other par-
ticipating agencies and the WPL dual-Doppler radar
system was used to study the urban wind field in
clear air and in precipitation. This paper pre-
sents a preliminary sampling of three-dimensional
wind fields within the urban planetary boundary
layer on six clear days. These data were selected
because they were all taken on clear days over
the same general area of the city during mid-
afternoon. Thus in this analysis the number of
important variables that might affect the flow
field is reduced to two: the static stability
and the mean environmental wind. Patterns that
are repeated on several days may thereby be more
easily related to their causative factors. Later
studies will include rural-urban comparisons and
hopefully will lead to knowledge of the relative
importance of surface roughness and heat island
effects.

2.   METHODOLOGY

         The coplan method of scanning and data
reduction described by Miller and Strauch (1974)
was used here. This method has been adequately
discussed in the literature and has been recently
used with minor variations to measure flow fields
in diverse meteorological situations such as a
sea breeze (Lhermitte and Gilet, 1975), a tornadic
storm (Ray et al., 1975), a non-tornadic convec-
tive storm (Kropfli and Miller, 1976), and snow
(Frisch et al., 1974). In this experiment
dry convection was observed in the urban boundary
layer by having chaff continuously distributed
from an aircraft flying repeated 15 km paths across
the wind at 500 m AGL. On most days convective
and diffusive processes carried the chaff over an
area of a few hundred square kilometers throughout
most of the mixing layer ($\sim$ 2 km). Typical chaff
densities were 10^3 to 10^4 per km^3.

         On one of the six days (7/27/75) the
aircraft was not available and chaff was released
from a car travelling through downtown St. Louis.
Convection carried the chaff to nearly 2 km and
these results are also shown below.

         The two x-band radars were located
relative to the city as shown in Figure 1. All
data shown are given in a right-handed coordinate
system with the origin at the midpoint between
the radars, y increasing from the origin along
the baseline to the C radar and the z axis positive
upward.
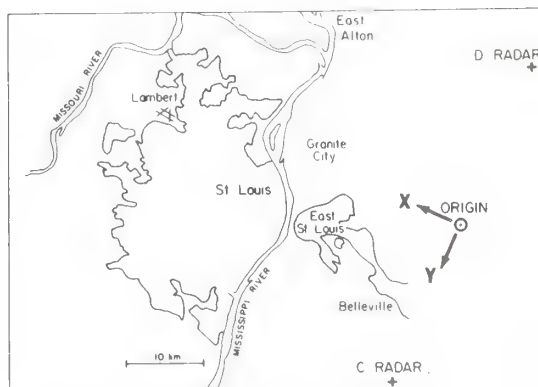
*Figure 1. Radar locations relative to St. Louis
metropolitan area.*

         The data was passed through a Gaussian
filter in coplan space. Some results shown here
were run with a 2 km wide spatial filter and
other higher resolution data were run at 1.2 km.
Figure captions will note the differences.

3.   RESULTS

         Observations on 7/27/75 were the only
ones made in which ground-released chaff was
used. The release was made in downtown St. Louis
between the Gateway Arch and Forest Park having
x,y coordinates (23,9) and (29,11) respectively
in Figure 2. A mean echo speed of 2.8 m/s was
removed from the velocity field in this figure.
The complete set of flow patterns, of which
Figure 2 is a part, shows that the size of the
observable flow field is three times larger
in area at 1200 m than it is at 250 m due to the
diffusion of the chaff as it rises. Near the
surface the echo remained relatively compact during
the 40 minute observation time and was observed
to drift with the same velocity as the mean
Doppler velocity in the lowest plane. The large
scale divergence pattern at 1500 m in Figure 2
persisted over this time interval whereas the
smaller scale structure at mid-levels (1000 m)
became unrecognizable after about 10 min.

         An area over 200 km^2 was filled with
echo after the aircraft chaff release on 7/28/75.
The horizontal eddy fields (mean removed) are
shown in Figures 3 and 4 at two times, 31 minutes
apart on this day. The 300 m planes show eddy
flow away from the baseline with a line of convergence
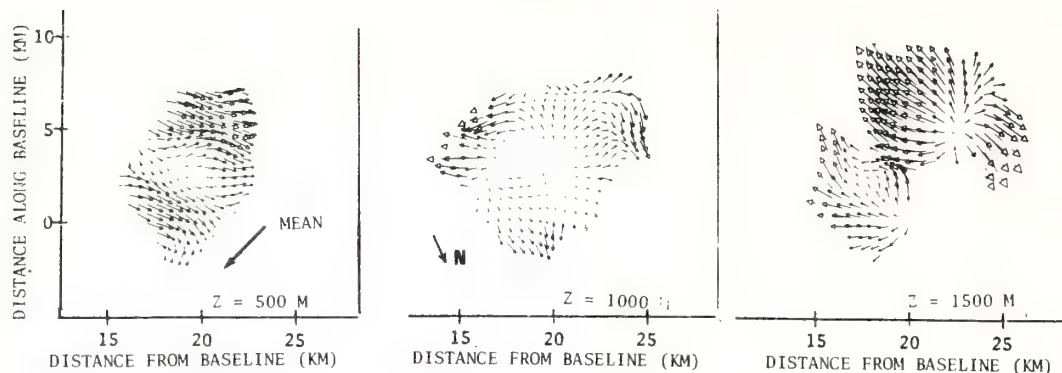
Figure 2. Horizontal eddy wind fields for 1509 CDT on 7/27/75. Mean wind of 2.8 m/s and north pointing vectors are indicated. Gaussian spatial filter width was 2.0 km.

parallel to the baseline and nearly along the mean flow. The means were taken over the entire chaff volume in all cases shown here. Other data show that this feature persisted for more than an hour. Just a few km to the right of the convergence line in the 300 m level of Figure 3 was an equally persistent line of divergence at x = 26 km. At mid-levels smaller scale features on the order of 4 km could not be identified for more than 10 min but they did appear to be moving with the mean Doppler wind, shown in the figure.

The 1300 m levels of Figures 3 and 4 show a line of divergence at x = 22.5 km which is directly above the line of convergence near the surface. This convergence-divergence pair is a manifestation of an updraft being reduced to zero as it reaches the top of the mixing layer. Results for other days also exhibit these large scale features in the convergence-divergence patterns.
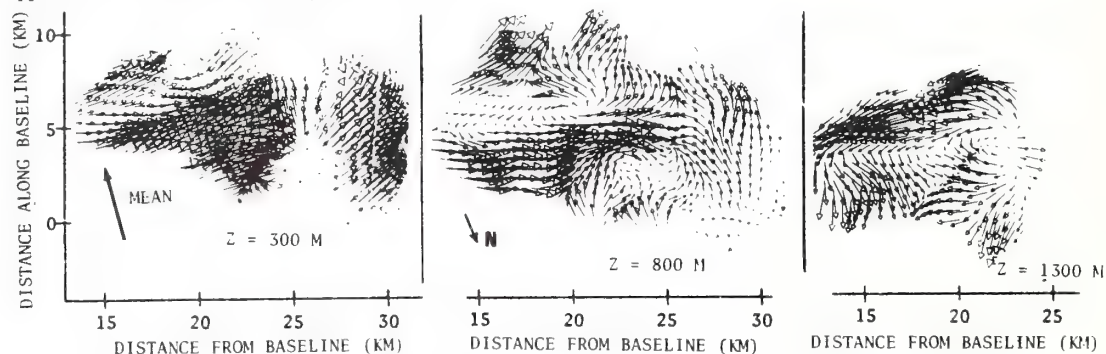
Figure 3. Horizontal eddy wind fields for 1506 CDT on 7/28/75. Mean wind of 3.8 m/s is indicated. Gaussian spatial filter width was 2.0 km.
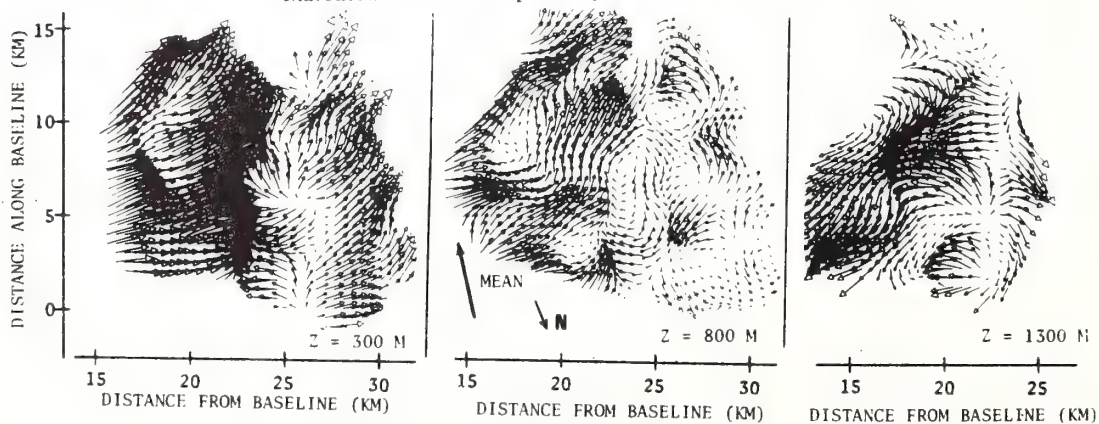
Figure 4. Horizontal eddy wind fields for 1537 CDT on 7/28/75. Arrow scaling and spatial filtering is the same as Figure 3.

322
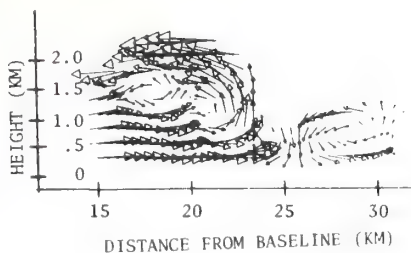
Figure 5. Vertical eddy wind field for 1506 CDT on 7/28/75 at y = 4 km looking downwind. Arrow scaling and spatial filtering is the same as Figure 3.

A vertical view of the eddy field is presented in Figure 5. The plane shown is nearly across the mean wind direction. Clearly shown is a large roll vortex about 8 km across and about 2.3 km deep. This roll structure appears similar to that observed in the planetary boundary layer by LeMone (1973), and has nearly the same width to depth ratio reported by her. Other examples of such structures are shown below.

Data not shown here indicates that the roll circulation in this eddy field extended throughout the echo for at least 8 km along the mean-wind direction. The updraft strength at the 800 m level on the right edge of this roll was about 1 m/s. This pattern persisted throughout the observations, about one hour. A smaller roll circulation of the same sense is shown on the right of Figure 5.

It is curious that the chaff density in the region between these rolls at x = 25 km was always very low even though the chaff dispensing aircraft repeatedly ran a course from (14,2) to (33,-4) and the release was continuous. Seemingly the flow pattern carried the chaff away from this line and concentrated it in other areas.

The case of 7/31/75 was one of much stronger environmental wind of 8 m/s roughly normal to the baseline in the +x direction. The eddy fields of Figure 6 show nearly parallel rows of convergence and divergence at 300 m and at 1050 m. It can be seen that convergence near the surface overlaps with divergence above so that an integration of the continuity equation results in near-zero vertical velocities near the top of the mixing layer.

Again a roll structure is exhibited in the vertical yz plane in Figure 7. This 4 km wide roll was seen to extend along the x-axis throughout the echo for more than 8 km.

The surface environmental winds on 8/4/75 were similar to those on 7/28/75 and the large scale features in the eddy field near the surface were also similar as shown in Figure 8. Although there are gaps in the data at 300 m it can be seen that a line of convergence near the line x = 25 km is paralleled by two lines of divergence. Similar to other cases we see in
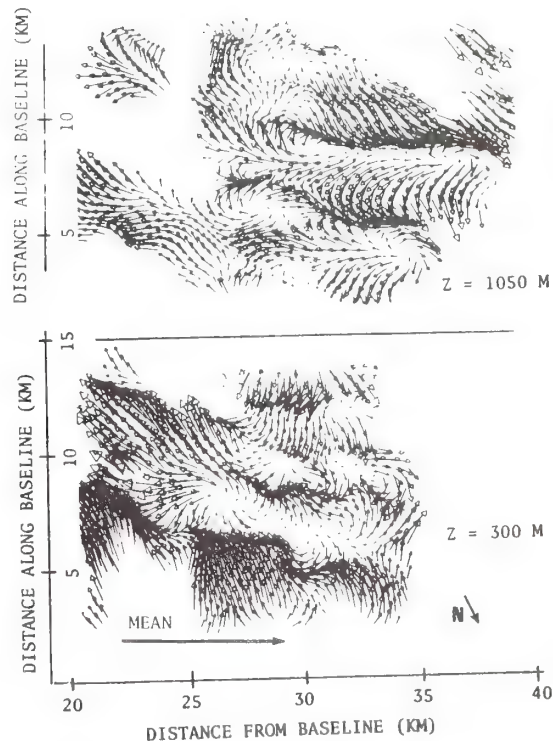
Figure 6. Horizontal eddy wind fields for 1436 CDT on 7/31/75. Mean wind of 7.9 m/s is indicated. Gaussian spatial filter width was 1.2 km.

the 300 m and 1300 m levels of Figure 8 that convergence superimposes with divergence. The alignment of the convergence lines corresponds closely to the direction of the mean Doppler-derived wind. Figure 9 displays a roll couplet that in the xz plane at y = 5 km that was aligned along the wind vector for at least 5 km. Note the nearly zero vertical velocities near the top of the field as would be expected near the top of the mixing layer. Unfortunately no temperature sounding data are available as of this writing to determine the exact depths of the mixing layer on these days.
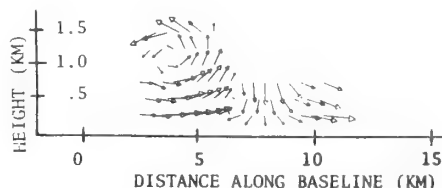
Figure 7. Vertical eddy wind field for 1436 CDT on 7/31/75 at x = 26 km looking downwind. Arrow scaling and spatial filtering is the same as Figure 5.

323

305
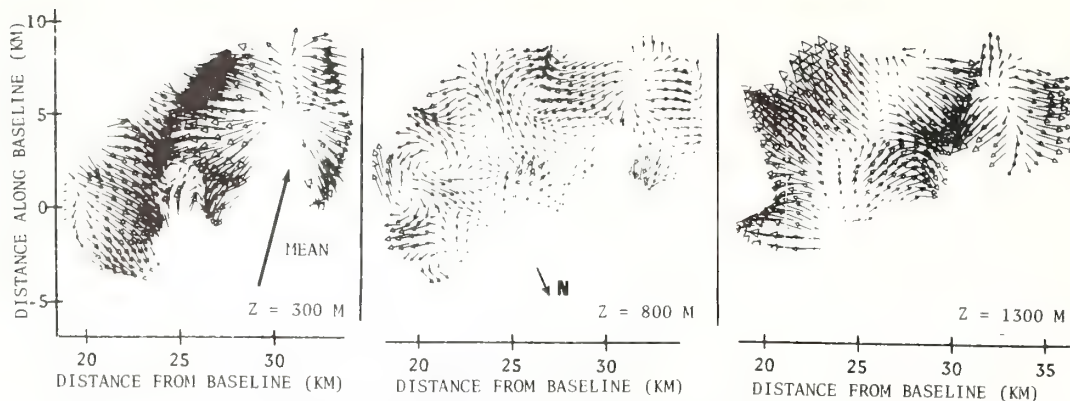
Figure 8. Horizontal eddy wind fields for 1447 CDT on 8/4/75. Mean wind field of 4.6 m/s is indicated. Spatial filter width was 2.0 km.
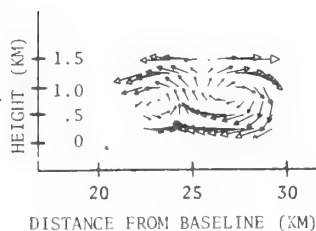
Figure 9. Vertical eddy wind fields for 1447 CDT on 8/4/75 approximately along the mean wind direction. Spatial filter width and arrow scaling is the same as in Figure 7.

The total horizontal wind field at 550 m in Figure 10 shows surprisingly large changes in total wind direction on 8/11/75. These data were taken over East Alton about 30 km downwind of downtown St. Louis and may indicate a downstream urban induced wind perturbation. A horizontal roll in the eddy field nearly identical to that observed on 7/28/75 (see Figure 5) is displayed in Figure 11.

The last example is shown in Figure 12 for 8/12/75. As on 8/11/75 these data were taken about 30 km downwind of downtown St. Louis near East Alton, Illinois. In this case a small scale vortex most clearly seen in the horizontal plane at 850 m was observed to move across the mean flow at about 5.5 m/s. This was the only small scale feature that was observed to move with a velocity much different from the mean wind.
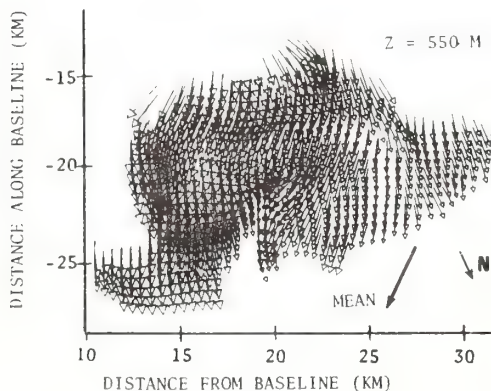
Figure 10. Horizontal total wind field for 8/11/75. Mean wind field of 2.4 m/s is indicated. Spatial filter width was 2.0 km.
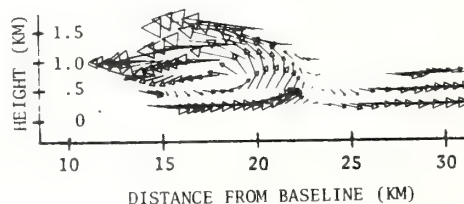
Figure 11. Vertical eddy wind field for 1612 CDT on 8/11/75 at y = -19 km looking upwind. Spatial filtering and arrow scaling is the same as in Figure 9.

324
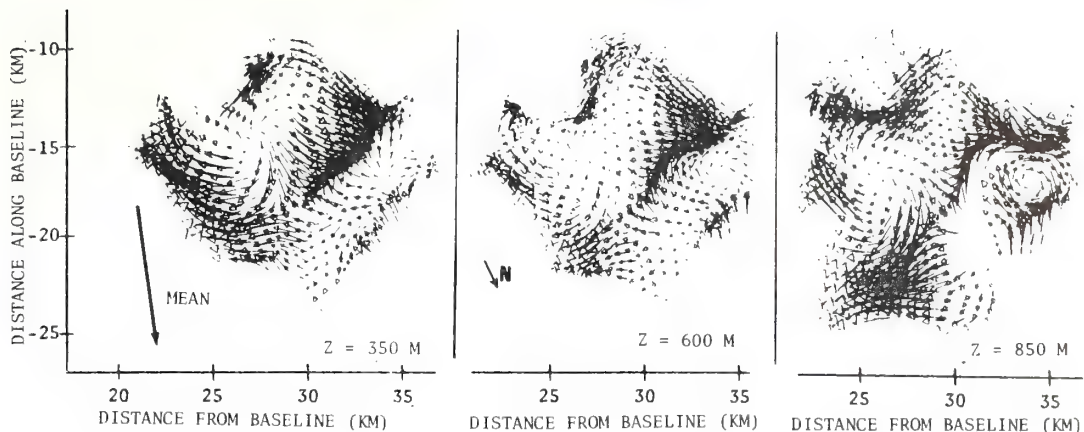
Figure 12. Horizontal eddy wind field for 1515 CDT on 8/12/75. Mean wind of 4.4 m/s is indicated. Spatial filter width was 2.0 km.

4.   SUMMARY

A preliminary sampling of wind fields in the urban boundary layer has been given for six days in which clear conditions prevailed. The most striking aspect of the eddy fields was the complexity of the patterns on scales from 2 to 15 km. One feature that did appear on several days was a long-lasting horizontal roll-vortex pattern oriented along the wind. Large scale divergence fields near the surface were often seen to be accompanied by divergence of the opposite sign at higher levels. Chaff was seen to disperse very quickly within the convective boundary layer, whether released from the ground or from aircraft.

5.   REFERENCES

Frisch, A. S., L. J. Miller and R. G. Strauch, 1974: Three dimensional air motion measured in snow. *Geophys. Res. Lett.*, 1, 86-89.

Kropfli, R. A. and L. J. Miller, 1976: Kinematic structure and flux quantities in a convective storm from dual-Doppler radar observations. *J. Atmos. Sci.*, 33, 520-529.

LeMone, Margaret Anne, 1973: The structure and dynamics of horizontal roll vortices in the planetary boundary layer. *J. Atmos. Sci.*, 30, 1077-1091.

Lhermitte, Roger M. and Marc Gilet, 1975: Dual-Doppler radar observation and study of sea breeze convective storm development. *J. Appl. Metoerol.*, 14, 1346-1361.

Miller, L. J. and R. G. Strauch, 1974: A dual-Doppler radar method for the determination of wind velocities within precipitating weather systems. *Remote Sensing Environ.*, 3, 217-233.

Ray, Peter S., R. J. Doviak, G. B. Walker, D. Sirmans, J. Carter and B. Bumgarner, 1975: Dual-Doppler observation of a tornadic storm. *J. Appl. Meteorol.*, 14, 1521-1530.

325

307

PERSISTENT HORIZONTAL ROLLS IN THE URBAN MIXING LAYER
AS REVEALED BY DUAL DOPPLER RADAR

R. A. Kropfli and N. M. Kohn

NOAA/ERL/Wave Propagation Laboratory
Boulder, Colorado 80302

1. INTRODUCTION

The general objective of the Wave Propagation Laboratory (WPL) in METROMEX (Metropolitan Meteorological Experiment) is to study the nature of the perturbation wind field within the urban convective mixing layer during clear conditions. The observational effort was concentrated during the mid-afternoon hours since it was found that convective motions were necessary for the echo-producing chaff to be dispersed throughout the mixing layer from the surface to several kilometers in height. Specific questions that may be resolved by these measurements are the following: 1) How is the perturbation wind field affected by profiles of mean wind and temperature? 2) How significant is the heat island and increased surface roughness on the urban wind field? 3) Are there frequently occurring, persistent wind patterns over a large metropolitan area? 4) Can such patterns explain the downwind precipitation anomaly that has been documented by other METROMEX participants (Semonin and Changnon, 1974)? Answers to such questions will impact on air quality in large metropolitan areas and may shed light on the extent to which large cities inadvertently modify the local climate.

2. METHOD OF DATA COLLECTION AND ANALYSIS

The two X-band Doppler radars used in these clear air observations have been used in a similar fashion to observe air motions in severe storms (Kropfli and Miller, 1976). Details of the coplan method of generating wind fields from radial velocities measured by two Doppler radars have been documented elsewhere (Miller and Strauch, 1974) so that only the essentials will be mentioned here. The two radars are set to scan synchronously through a common tilted plane passing through the echo and the radar baseline. After completion of a scan, the tilt angle is incremented and a similar scan is performed. The process is repeated until the entire echo volume is observed. The duration of such a volume scan in this experiment was about 1 min, which is small compared with time scales important in kilometer-deep convection. Aircraft dispensed chaff was used to trace air motions.

3. ANALYSIS OF 7/28/75 WIND FIELD

The St. Louis metropolitan area and the region extensively probed by the Doppler radars are shown in Figure 1. Superimposed on this map is the field of potential temperature at 300 m for 7/28/75. These temperature measurements were obtained by the University of Wyoming aircraft* and they will be related to the boundary layer wind field. Note that the solid block in this figure is the area displayed in Figures 2 and 4.

*This temperature map was taken from the Univ. of Wyo. M.S. Thesis by K.K. Wong entitled "Urban perturbations on the mixing layer airflow in St.Louis.
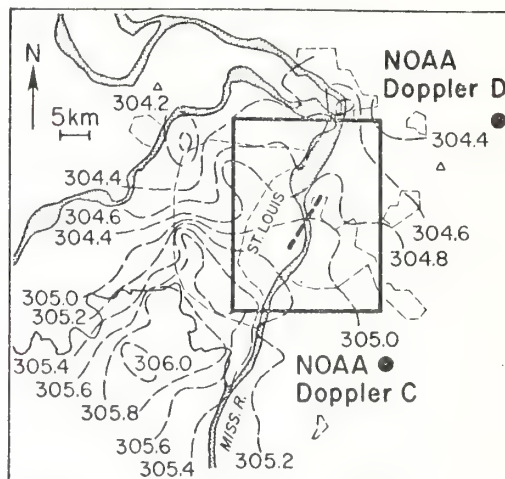
Figure 1. St. Louis metropolitan area with superimposed θ contours at 300 m AGL derived from University of Wyoming aircraft data at ∿ 1430 CDT on 7/28/75. Solid square indicates region within which chaff drops were made and is the region displayed in Figures 2 and 4.

The total wind field near the mid-point of the convectively mixed layer on 7/28/75 is shown in Figure 2a. This wind field represents an average of 17 volume scans taken during a 70-min period. All other wind fields presented for this date also represent such long term averages. It is apparent that the mean wind is from about 20° at about 4 m sec⁻¹. The chaff-dispensing aircraft had been flying a pattern across the northeastern edge of the wind field from a point on the northern tip of St. Louis to just NE of East St. Louis on this day. Note that an area of approximately 250 km² was filled with chaff to the extent that reliable wind measurements were possible.

The mean velocity of the entire chaff cloud was removed from the data and the resulting perturbation wind field at 0.3 km is shown in Figure 2b. Immediately apparent in Figure 2b is a 12 km line of convergence extending about 10° to the right of the mean wind direction at this level. Adjacent to this line of convergence is a line of divergence 3 or 4 km to the NW and a less obvious region of divergence to the SW. There is also a localized area of enhanced convergence which did not move with the mean wind on the NE end of the convergence line. This 1.5 km diameter region had a convergence of 1.4 x 10⁻³ sec⁻¹ in contrast to values of about half this amount farther downstream along the convergence line.

13
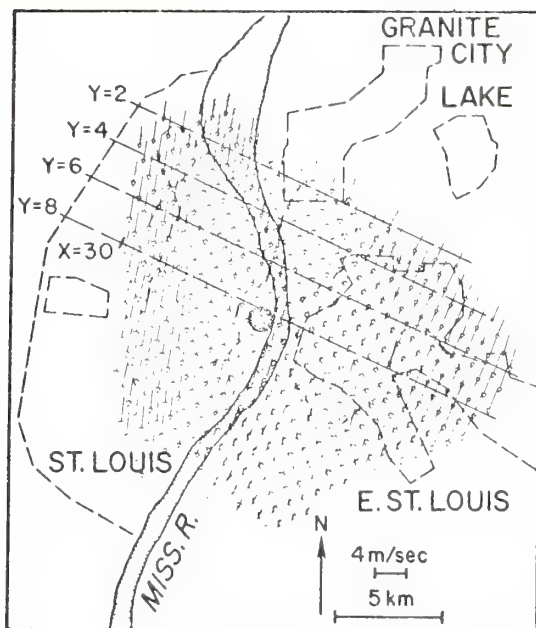
Figure 2a. *Total wind field at 0.8 km AGL on 7/28/75. Winds are obtained from an average of 17 volume scans taken during a 70 min. period ending at 1557 CDT. The Gateway Arch is indicated by the dot just to the west of the Mississippi River at the location X=22.6, Y=8.5.*

Figure 2b. *Eddy wind field at 0.3 km AGL. Winds are obtained from an average of 17 volume scans taken during a 70 min period ending at 1557 CDT. The mean wind over the entire chaff cloud has been subtracted from these data.*

It appears that this convergence pattern is the result of heat sources within the heavily industrialized area around Granite City and the central business district to the SW. There is reasonable consistency between the convergence line, shown as a heavy dashed line in Figure 1, and the thermal ridge also shown in the figure. The thermal pattern at 500 m indicates a 0.2° contrast between the region of convergence and neighboring regions of divergence to either side.

At the time of this writing, surface temperature maps had not been constructed, but it is believed that this line of convergence follows an elongated heat island from Granite City and across the St. Louis central business district just west of the Gateway Arch. The Mississippi River to the west of Granite City and the small lake to the east contributed to this temperature contrast.

Most illustrative of the character of the perturbation field is the series of vertical cross-sections shown in Figure 3. These cross-sections are taken at a spacing of 2 km along the lines indicated in Figure 2a. From the similarity of the velocity patterns on different vertical cross-sections it is apparent that the mode of convection favored on this day was the horizontal roll oriented nearly along the mean wind. Three such rolls can be seen on each cross section.

Figure 3. *Vertical cross-sections of eddy wind field through lines indicated in Figure 2a. This is from the same data set used in Figure 2.*

14
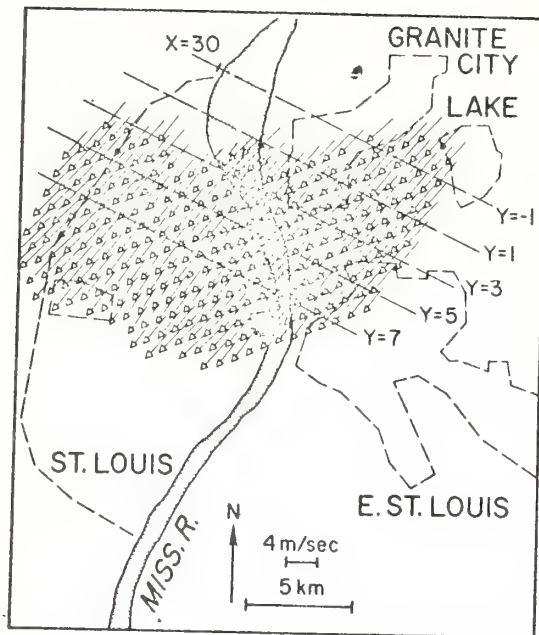
Figure 4a. Same as Figure 2a except this figure represents an average of 15 volume scans over a 20 min period ending at 1445 CDT on 8/4/75. Height is 0.8 km AGL.

Figure 4b. Same as Figure 2b except this figure represents an average of 15 volume scans over a 20 min period ending at 1445 CDT on 8/4/75. Height is 0.3 km AGL.

The largest roll, located over East St. Louis, has a counterclockwise circulation when observed from the NE and has the urban heat island as its source. An intermediate-sized roll of the same sense is located to the west. Less well defined and much smaller is a clockwise roll between the two larger rolls. The main updraft at X = 23 km had a magnitude of up to 1 m sec^{-1} for the 1 hr period; single volume scans indicated that the updraft may have been as high as 2 m sec^{-1} over a short time period. An explanation for the size differences in these rolls is be offered after the discussion of the 8/4/75 data.

4. ANALYSIS OF 8/4/75 WIND FIELD

Figure 4a shows that the total mid-level wind field on 8/4/75 was very similar to that on 7/28/75 (see Figure 2a). The mean wind in the lower half of the mixing layer differed by less than 1.5 m sec^{-1}. As will be discussed later, the notable difference between the total wind fields on these two days was the lack of shear on 8/4/75. All data shown for this day represent an average of 15 volume scans during a 20-min period.

As one would expect, the vertical component is small near the top of the boundary layer as shown in the vertical cross-sections of Figure 5. These cross-sections are taken through the lines indicated on Figure 4a. Figure 5 again shows that the convective structure was in the form of horizontal rolls, although of equal size on this occasion.

Figure 5. Vertical cross-sections of eddy wind field through line indicated in Figure 4a. This is from the same data set used in Figure 4.

15

310

It should be emphasized that the features described above were long-lasting on both days and were apparent in the data regardless of how the averages were taken. The roll structure was indicated even when single volume scans were considered. In such "instantaneous" samples, however, there were smaller less persistent features that were smoothed out in the longer-term averages.

5. CONCLUSIONS

The hodograph in Figure 6 indicates the mean radar-derived wind at each level for the two cases considered here. It is evident that, while the mean wind in the lower half of the boundary layer was not very much different, there was in fact a significant difference in the shear on the two days. The cross-roll component of shear on 7/28/75 was 1.5×10^{-3} sec^{-1} and nearly zero on 8/4/75. It is suggested that this difference may account for the difference in roll size on these two days. Rolls of opposite senses were the same size on 8/4/75 (the no-shear case) but were very different in size when the cross-roll shear existed on 7/28/75. It is suggested that the cross-roll linear wind shear enhanced the rolls having CCW sense in Figure 3 but acted to suppress the CW roll. The reason for the CCW roll on the left of this figure being larger than the CCW roll on the right is presumably that the heat island forced this roll, while there was no equivalent forcing for the CCW roll on the right. Since there was no shear in the boundary layer on 8/4/75 there was no such enhancing-suppressing mechanism, and the rolls are the same size in Figure 5. A stream function analysis of a hypothetical wind field derived from the superposition of counter-rotating horizontal rolls and linear cross-roll shear supports this interpretation.

These observations indicate that under certain conditions the horizontal roll mode of convection is dominant over an urban area. Shear does not seem to be a necessary condition for the existence of these rolls. Although horizontal rolls have been predicted by theory (Brown, 1972) for an inflection point instability in a stratified Ekman boundary layer, and their existence has been deduced from tower and aircraft measurements (LeMone, 1973), such rolls have not, to the authors' knowledge, been observed in connection with strong forcing from an urban heat island. The orientation and relative sizes of these persistent rolls can be understood in terms of urban thermal effects, mean wind direction, and wind shear. Other cases with different boundary layer wind profiles that have not been shown here also reveal persistent features in the wind patterns. In these cases however the horizontal roll structure is not observed. These cases are also being investigated and will be reported at a later time.

These experiments have shown that hundreds of square kilometers of the clear boundary layer wind field can be monitored over extended periods of time by dual-Doppler radar. The data reduction and analysis problem, while still a formidable task, is becoming manageable.
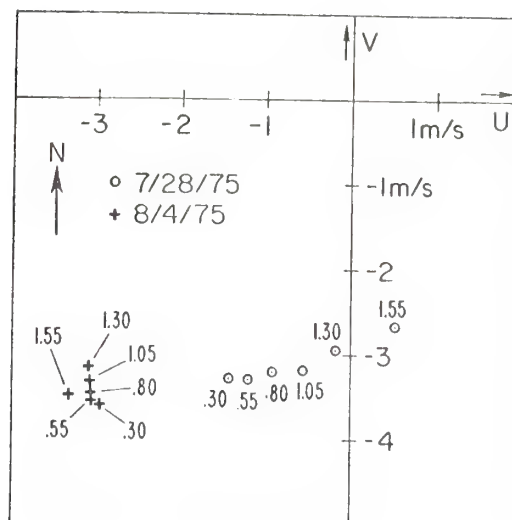
Figure 6. Radar derived hodograph for 7/28/75 and 8/4/75. Heights are in km.

REFERENCES

Brown, R. A., 1972: On the inflection point instability of a stratified Ekman boundary layer. *J. Atmos. Sci.* 29, 850-859.

Kropfli, R. A. and L. J. Miller, 1976: Kinematic structure and flux quantities in a convective storm from dual-Doppler radar observations. *J. Atmos. Sci.* 33, 520-529.

LeMone, M. A., 1973: The structure and dynamics of horizontal roll vortices in the planetary boundary layer. *J. Atmos. Sci.* 30, 1077-1091.

Miller, L. J. and R. G. Strauch, 1974: A dual Doppler radar method for the determination of wind velocities within precipitating weather systems. *Remote Sensing Environ.* 3, 217-233.

Rumler, W. O., 1968: Two-pulse spectral measurements. Tech. Memo. MM-68-4121-15, Bell Telephone Laboratories, Whippany, N. J.

Semonin, Richard G. and S. A. Changnon, Jr., 1974: METROMEX: Summary of 1971-1972 results. *Bull. Amer. Meteor. Soc.* 55, 95-100.

16

Kinematic Structure and Flux Quantities in a Convective Storm from Dual-Doppler Radar Observations

R. A. Kropfli and L. J. Miller

Wave Propagation Laboratory, NOAA, Boulder, Colo. 80302

(Manuscript received 14 April 1975, in revised form 13 November 1975)

ABSTRACT

The NOAA/WPL dual-Doppler radar system has been used to determine the three-dimensional kinematic structure of a convective storm during its decaying stage which grew in a weakly sheared environment. The internal flow appears similar in many respects to the Wokingham storm described by Browning and Ludlam even though the latter existed in a strongly sheared environment. Among the similar features are an upshear tilted updraft, a surface gust front, the intrusion of middle-level cool dry air, a precipitation-filled downdraft, and a vortex pattern suggestive of obstacle flow.

Quantitative flux results are presented. Profiles of mass, water vapor, energy, momentum and vorticity fluxes were computed using the Doppler data and other supporting data from the National Hail Research Experiment surface network and upper air soundings.

1. Introduction

It has been widely recognized that a comprehensive understanding of convective storms must have as a basis the interaction of microphysical and dynamical processes. As emphasized by Mason (1969), "Progress has been hindered by a poor appreciation of interrelations between the air motion and the microphysical events which, acting in concert, culminate in the release of precipitation." Laboratory investigations have added greatly to our understanding of the microphysical processes involved in the formation of raindrops, snowflakes and hailstones. However, these investigations usually have been performed in a controlled environment of uncertain relevancy to the real atmosphere. In addition, numerical calculations of microphysical processes have been performed and again the weakness has been a lack of knowledge of the environment in which these processes actually take place. In particular, incomplete information about kinematics, for example the updraft and downdraft structure and vorticity distribution, has been a shortcoming.

The three-dimensional wind field described here for a convective storm in northeast Colorado is the first step in an analysis plan that will eventually include the microphysics. At this time we have computed three-dimensional streamlines for a storm velocity field determined from measurements with the NOAA/Wave Propagation Laboratory 3 cm wavelength dual-Doppler radar system. These streamlines have been used to infer air parcel trajectories within the storm. Precipitation fallspeeds determined from modeled microphysical growth processes must be combined with these wind fields to deduce the needed precipitation and cloud particle trajectories. Such particle trajectories clearly have implications regarding optimal artificial seeding for hail suppression or precipitation enhancement. A study of storm kinematics and microphysics is currently being pursued in collaboration with the National Hail Research Experiment (NHRE).

In acquiring the initial radial velocity data we have used the coplane method of scanning first suggested by Lhermitte and Miller (1970). The results presented here are from three separate volume scans of a thunderstorm which occurred on 28 July 1973 in northeast Colorado. The observations were made around 1730 (all times Mountain Daylight Time) while the storm was over the NHRE surface mesonet in which temperature, pressure, humidity, wind speed and direction were measured and hail samples were collected. The Doppler results show the kinematical structure during a 5 min period near the end of the storm's mature state. A preliminary description of this storm is given by Kropfli and Miller (1975).

2. The coplane method

The coplane method for coordinated scanning with two Doppler radars is fully described by Miller and Strauch (1974) in which an error analysis is also included. Only a brief overview is presented here. The Doppler radars are synchronized to scan in a common plane tilted 15° or less from the horizon. After each 10 s scan, the tilt angle is changed by a radar beamwidth (~1°) and the next plane is scanned. The entire storm volume scan is completed in 160 s. Because of the way

the data are acquired, a cylindrical coordinate system with its axis along the baseline between the radars is used.

Radial velocity estimates are made from data acquired with each radar by means of a pulse-pair technique by Rumler (1968). From his results, the standard deviation of the pulse-pair estimate of radial velocity is about 0.1 to 0.5 m s^{-1} for signal-to-noise power ratios >5 dB. These radial velocities are vectorially combined to yield the two-dimensional velocity field within each tilted plane. A correction for particle fall velocity is then made with an empirical relationship from Joss and Waldvogel (1970). This relationship provides an estimate of the terminal velocity V_T as a function of the measured reflectivity factor Z. Because of the weak dependence of V_T on Z, i.e., $V_T \propto Z^{0.1}$, we have found that the estimate of the vertical air velocity w is insensitive to errors in Z. Setting the entire Z field to zero, for example, changed the computed w field by no more than 1 m s^{-1} for these data. To obtain the components normal to each plane, the mass continuity equation in the form $\nabla \cdot [\rho(z)\mathbf{V}]=0$ (ρ is air density, z the vertical coordinate, and $\mathbf{V}$ the vector air motion), is integrated in this cylindrical coordinate system. The boundary condition requires that the vertical velocity vanish at the surface of the earth. Finally, an interpolation procedure is used to transform wind fields to a Cartesian coordinate system.

3. Storm environment

Five rawinsondes were released from different locations within 50 km of the NHRE test area at 1800, just 30 min after the dual-Doppler measurements. These soundings showed that the convective condensation level, assumed to represent cloud base, was at 610 mb or 4.1 km (all heights above mean sea level except where indicated otherwise). Ground level is at 1.5 km in the test area.

These soundings and five others at about 1620 indicated that the mixing ratio in the lowest kilometer of the subcloud layer was 6.2 g kg^{-1} with little change observed in both time and space. A parcel lifted dry adiabatically from near the surface to cloud base and then pseudoadiabatically to 500 mb would have been 3°C warmer than the environment. Cloud top was observed near the tropopause at 13 km. This was 2.5 km above the airflow measurements discussed here.

A hodograph of relative winds determined from the average of the five soundings at 1800 is shown in Fig. 1. A 3 m s^{-1} echo advection, determined by inspection of the echo positions, has been removed from the plotted winds to display the environmental winds relative to the moving storm. The subcloud relative winds were less than 3 m s^{-1} from the southeast, and middle and upper-level relative winds were approximately 10 m s^{-1} from the west. Weak shear (9×10^{-4} s^{-1}) is indicated from cloud base to the tropopause.
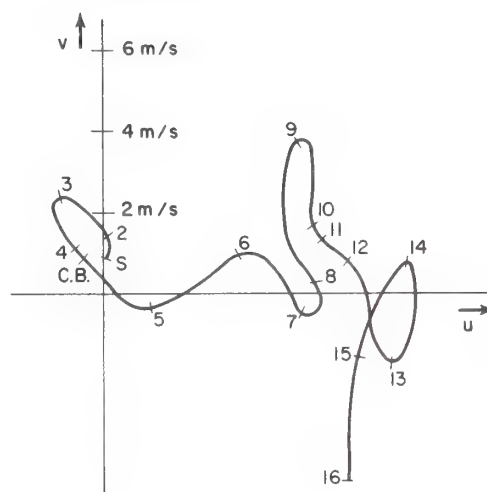
FIG. 1. Hodograph of relative winds synthesized from five rawinsondes. A 3 m s^{-1} storm motion toward the east has been removed. Heights are kilometers above mean sea level.

A time-height distribution of equivalent potential temperature (θ_e) is shown in Fig. 2. This plot reveals a layer of air centered at 5 km with $\theta_e = 325$ K compared with values of ~334 K near the surface at around 1600. This potentially cool dry layer aloft contributed to downdraft generation (Fawbush and Miller, 1954) by supplying unsaturated air which could be cooled by evaporation. The passage of this layer from the area around 1700 preceded the decay of the storm by 30 min.

4. Radar echo evolution

The NHRE 10 cm radar at Grover scanned the storm from about 1600 until it had dissipated at about 1814. Fig. 3 shows the radar reflectivity structure near cloud base at 15 min intervals centered on the time of the
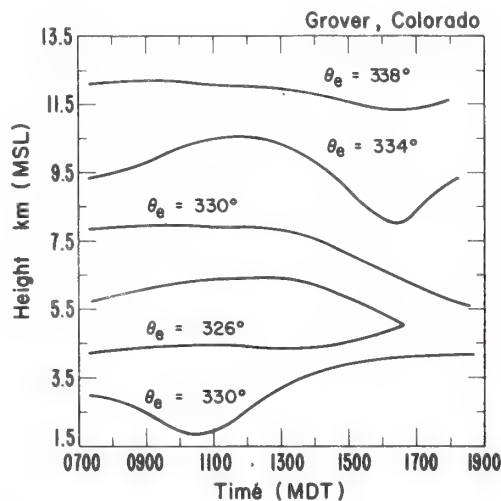
FIG. 2. Time-height distribution of equivalent potential temperature (θ_e) from five soundings released at Grover.
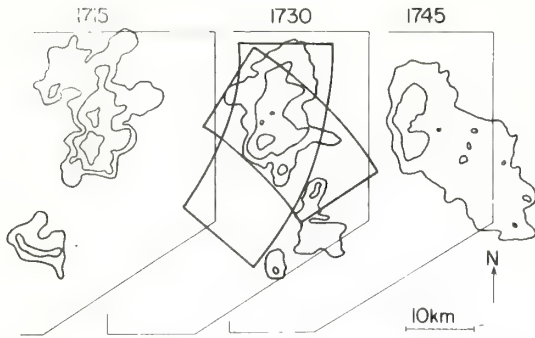
FIG. 3. Cloud base radar echo from 10 cm radar at Grover at the times shown. The outer contour is 30 dBZ, and the increment 10 dB. Solid lines superimposed on the 1730 frame show the areas covered by the two Doppler radars. The boundaries of the NHRE test area are shown by the thin solid line.

dual-Doppler measurements, i.e., 1730. At this time the echo top was near 12 km with the cloud top about 1 km higher. The high-reflectivity core was decreasing during the 15 min period prior to the Doppler measurements. This decrease suggests that the observations described here were during the decaying phase of the storm's mature stage. However, the peak reflectivity remained in excess of 50 dBZ during these observations. Following these observations the storm weakened at a more rapid rate.

5. Kinematical description

A series of horizontal projections of wind velocity *relative to the moving storm* are shown in Figs. 4 and 5. A 3 m s^{-1} eastward component of echo advection has been removed from the original vectors. The coordinate system used in all flow patterns has its origin at the midpoint of the baseline between the radars. Since the baseline that defines the y axis is only 5.9° away from true north, the x direction is nearly eastward and approximately in the direction of storm motion. These figures display the flow field at 1728:44 and 1734:09 which were the starting times for these two volume scans. Below the flow patterns are shown both the reflectivity (solid lines) and the updraft contours (dashed lines) obtained from the Doppler radars. The lower boundary is assumed rigid ($w=0$) so only reflectivity is shown in the $z=1.5$ km plane at the surface. In order to minimize the effects of attenuation at the 3 cm wavelength, the larger of the two reflectivity estimates available from the two Doppler systems were used in these drawings. It should be recognized that the entire cloud mass cannot be observed with these radars since only precipitation-sized particles are detected.

At 1728:44 the most apparent feature of the surface wind field ($z=1.5$ km in Fig. 4) is the highly divergent flow coincident with the high-reflectivity region. A peak divergence of 8×10^{-3} s^{-1} is found only 1 km east of the
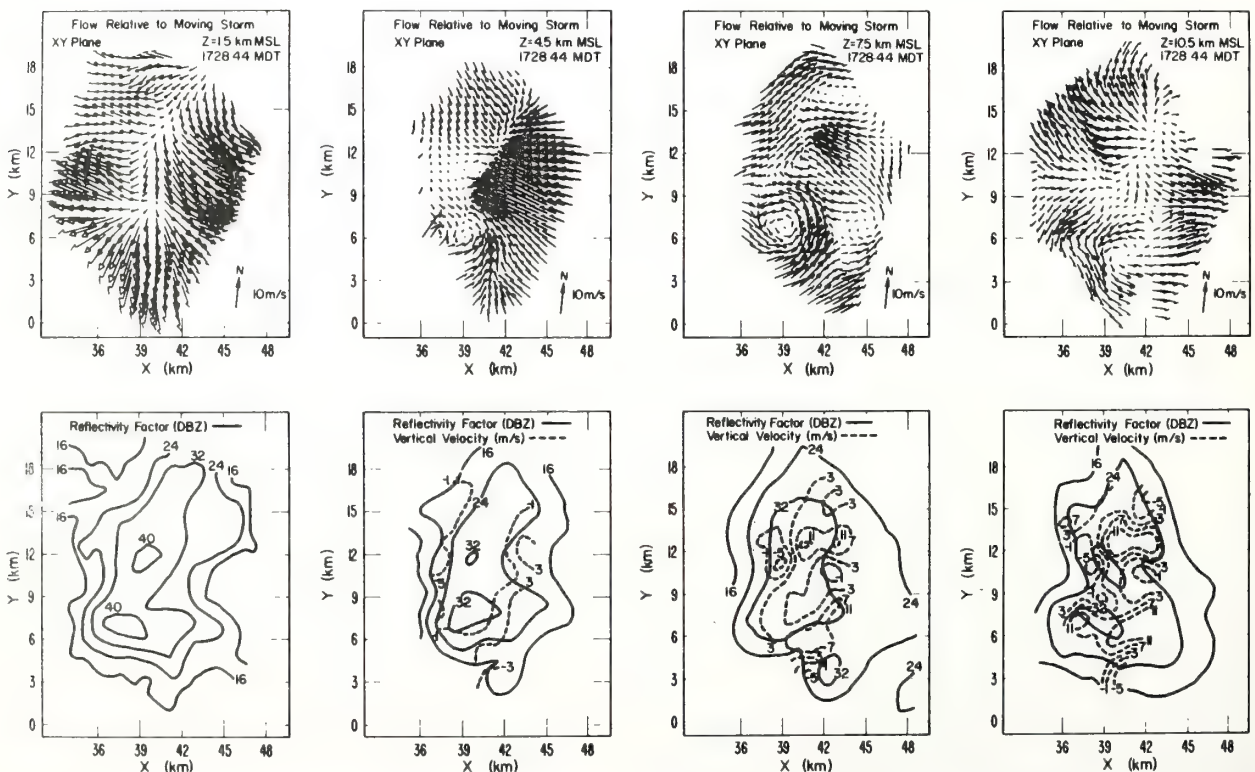
FIG. 4. Two-dimensional relative airflow in horizontal planes at heights 1.5 (surface), 4.5 (~cloud base), 7.5 and 10.5 km MSL. At the bottom are reflectivity contours at 16, 24, 32 and 40 dBZ. The vertical velocity contours (dashed lines) are −5, −1, +3, +7 and +11 m s^{-1}. The time of these results was 1728:44 MDT.
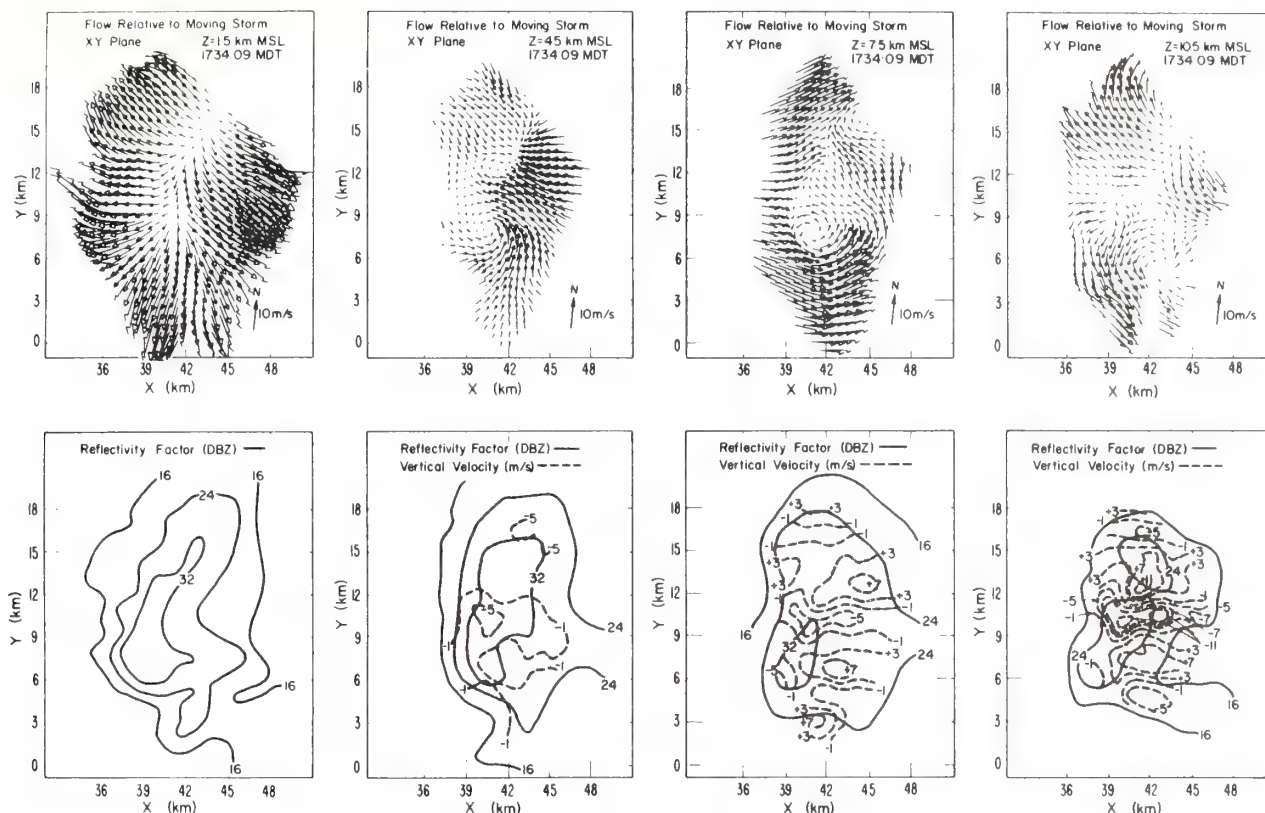
Fig. 5. As in Fig. 4 except at 1734:09 MDT.

southernmost 40 dBZ area. There exists a similar coincidence of divergent flow with high reflectivity for the 40 dBZ region to the north. A local maximum of 4×10^{-3} s^{-1} is found less than 1 km northeast of the northern 40 dBZ region. This correspondence of divergent flow with high reflectivity is consistent with the notion that gravitational loading by the precipitation is important in the initiation and maintenance of the downdraft.

The plane at $z = 4.5$ km clearly shows upward moving inflow air on the eastern half of the storm. This air, the lower edge of the updraft, enters the storm from the ESE with a vertical velocity of 3 m s^{-1}. It is detrained into the downdraft and is seen to descend at about 4 m s^{-1} in the center of the storm at this level. At 7.5 km the inflow air had penetrated the eastern two-thirds of the storm. A 3 m s^{-1} updraft contour runs from the x, y coordinate (42, 17) to the position (38, 6) with the entire region to the east of this line in a vigorous updraft. Regions of cyclonic curvature to the south and anticyclonic curvature to the north can clearly be seen in the horizontal flow pattern especially at 10.5 km. It is apparent that this feature is a result of the outer portions of the updraft beginning to take on upper level westerly environmental momentum.

Near the top of the observed flow ($z = 10.5$ km) the updraft had attained a peak value of 19 m s^{-1} compared

with an estimate of 25 m s^{-1} from parcel theory. The sparse data between 10.5 and 11.5 km (not shown) indicated divergence values between 5×10^{-3} and 8×10^{-3} s^{-1} in the updraft region. Divergence here reflects deceleration of the upward airflow and its subsequent conversion to upper level outflow into the anvil.

Cloud top (where $w = 0$) was observed to be at 13 km as determined from the NCAR Saberliner dropsonde flight at 1712.[1] Thus a divergence of 7.6×10^{-3} s^{-1} would be required to reduce the 19 m s^{-1} updraft to zero in the 2.5 km interval between the very highest level velocity measurement at 10.5 km and cloud top. Such a value is consistent with divergence measurements near this height.

Fig. 5 also shows the horizontal velocity components, reflectivity, and vertical velocity contours but at 1734:09, 5 min and 28 s after the volume scan shown in Fig. 4. Many of the features at the earlier time remain; however, both updraft speeds and reflectivity do show some signs of weakening. On the other hand, the downdraft at 10.5 km has intensified from near zero to 12 m s^{-1}.

Vertical (x, y) cross sections of the relative velocity components in the plane of the echo motion and through the northern updraft core at 1728:44 and 1734:09 are

---

[1] Personal communication with J. C. Fankhauser.

shown in Figs. 6a and 6b. Note the general collapsing of the precipitation region as evidenced by the descent of the reflectivity contours. The velocity field, particularly the vertical motion, exhibits a decrease in magnitude. The salient features in these figures are summarized schematically in Fig. 7. Included are the middle-level (6 km) intrusion of potentially cool ($\theta_e \approx 326$ K, see Fig. 2) dry air from the backside, a precipitation-filled downdraft with reflectivities in excess of 36 dBZ, and a gust front consisting of air originating near the 6 km level. Note that only the portion of the storm contained within the dashed lines of Fig. 7 was visible to the Doppler radars, and not the entire cloud mass. Certain details in the reflectivity structure appear to be consistent with the flow pattern. Note, for example, the indentation of the reflectivity contours on the backside near middle levels. This indentation is undoubtedly the result of erosion of the precipitation-filled volume by the intrusion of relatively dry air. The reflectivity contours on the front side show a migration of precipitation toward the back of the storm. This area is seen to be within the inflow region.

Fig. 8 displays a vertical (y,z) cross section transverse to the storm motion at 1728:44. The view is into the storm or toward the west. This figure demonstrates the complex three-dimensionality of the storm in contrast to the impression given by Fig. 6. Note that in Fig. 8 a
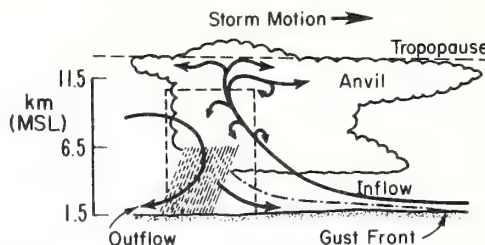
FIG. 7. Schematic representation of salient kinematic features. Dashed lines roughly indicate region of the measured flow field.

line of near-zero vertical air motion at about 6 km divides ascending from descending air. Below this level air in the downdraft is generally moving toward the viewer whereas higher level air in the updraft is moving away from the viewer.

Streamlines were calculated for initial points near the storm edge for the scan beginning at 1728:44. Fig. 9 displays a sampling of these three-dimensional streamlines that enter the storm at the 5.5 km level. Wide arrows indicate that several air parcels which followed approximately the same path were combined and that a larger volume of air was involved in the flow. In order to give a rough estimate of speed we have indicated times in the figure to specify how long an air parcel would take in traversing a particular streamline. It should be emphasized that these streamlines represent the flow at a particular instant and can be interpreted as parcel flow only in the steady state. Although the storm rapidly decayed after these observations, it is believed that the streamlines give a general representation of air parcel flow during the earlier mature stage when the echo structure was less variable.

Fig. 9 shows that the gust front on the storm's right forward flank at the surface has its source on the left rear flank at 5.5 km. Air descends anticyclonically from the left rear portion of the storm and exits under the
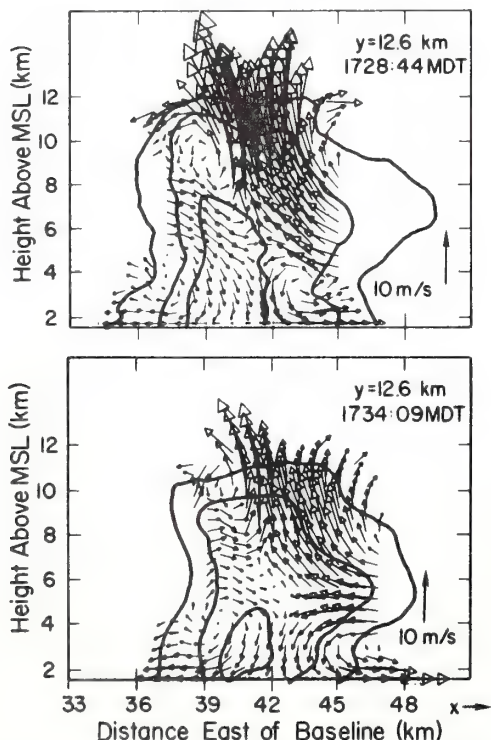
FIG. 6a. Vertical (x,z) cross section of relative velocities with superimposed 20, 28 and 36 dBZ reflectivity contours at 1728:44 MDT (a) and 1734:09 MDT (b). These planes are oriented parallel to the direction of echo motion. The arrow tail indicates the location of the measurement.
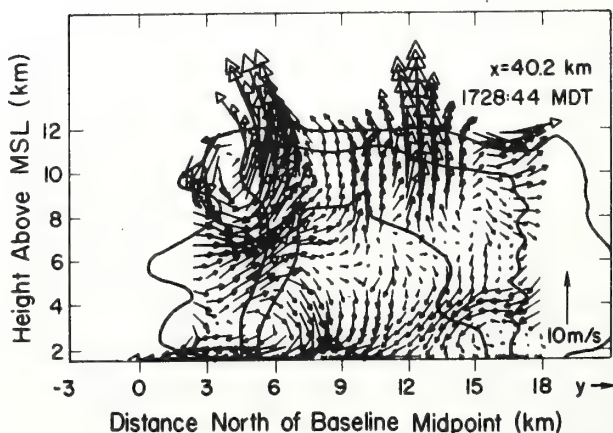
FIG. 8. Vertical (y,z) cross section of relative velocities at $x=40.2$ km with superimposed 20, 28 and 36 dBZ reflectivity contours at 1728:44 MDT. This plane is oriented normal to storm motion. The viewer is looking upstream into the storm.
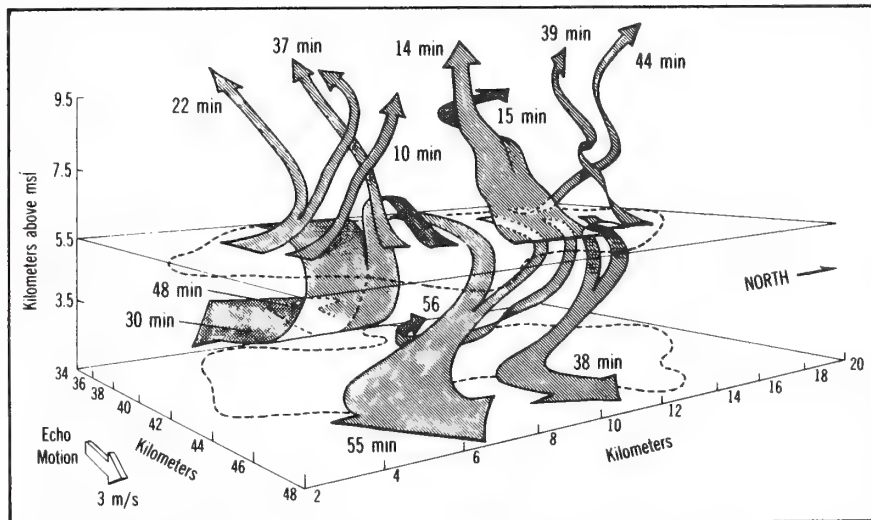
FIG. 9. Streamlines entering storm at 5.5 km level. Dashed lines
indicate 25 dBZ reflectivity contours.

updraft at the surface. The source air for the northern portion of the gust front is air entering from the left forward flank that becomes entrained into the anticyclonic downdraft. Air entering at this level on the right rear flank descends with little rotation and exits at the rear about 0.5 km from the surface. Some of the inflowing air that starts at the lower edge of the updraft is detrained into the downdraft and also exits near the surface on the backside. Air entering on the right flank and right forward flank moves upward with cyclonic curvature and exits near the 11 km level. Most of the broad sheet of upward moving air near the forward central edge of the storm at this level moves directly upshear with a 25° backward tilt. It ascends with little rotation and eventually exits near the top of the scanned volume. However, the northern portion of this sheet splits off, turns anticyclonically, and exits the left rear flank at the upper levels.

Surface winds derived from the NHRE mesonet are displayed relative to the moving storm at 1730 (Fig. 10). Superimposed in the figure are isochrones of sudden wind increase and temperature decrease to depict the movement of the gust front through the area. A broad area of surface divergence beneath the storm is apparent. The station at the southeast corner of the NHRE test area had shown light (<3 m s^{-1}) and variable winds just prior to this time. The sudden increase to 11 m s^{-1} is interpreted as the passage of the gust front indicated schematically in Fig. 7. At this time ($\sim$1730) the gust front is seen to precede the echo by 7–14 km. The gust front was also accompanied by a rapid decrease in θ_e from 335 K at 1715 to 326 K at 1745. As shown in Fig. 2, air with $\theta_e = 326$ K was found near the 5.5 km level. Using θ_e as a tracer we conclude that the air just behind the gust front must have originated near the 5.5 km level. This implies that the

streamlines in Fig. 9 are indeed reasonably representative of a quasi-steady state.

The gust front moved at more than twice the speed of the echo motion as indicated by the isochrones of the gust line in Fig. 10. Sixty minutes earlier the gust front had been located near the leading edge of the echo. A factor contributing to the rapid decay of the storm was undoubtedly the undercutting of the updraft by the gust front, tending to reduce the forced convergence in the surface layer ahead of the storm. In addition, there would have been an increase with time in the surface area between the gust front and the overriding updraft. This would have resulted in greater mixing
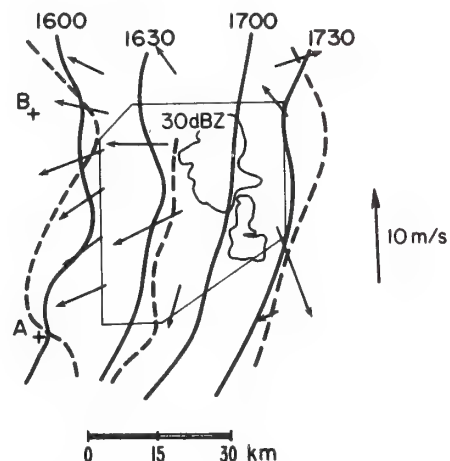
FIG. 10. Relative surface winds (vectors) from NHRE mesonet at 1730 MDT with superimposed 30 dBZ contour near cloud base. Also shown are isochrones of temperature break (dashed) and wind gust (solid) derived from the NHRE mesonet. The + symbols indicate the locations of the Doppler radars A and B.

between the potentially cold air in the gust front and the warmer updraft air.

There are some similarities between the kinematic structure observed in this storm (see Fig. 9) and the three-dimensional model of the Wokingham storm described by Browning and Ludlam (1962). Briefly, the following are apparent:

1) Both storms are persistently fed from opposite sides; the updraft slopes in the upshear direction from near the surface and the downdraft air enters the backside at middle levels.

2) The downdraft descended from middle levels with little curvature and much of it exited the backside at the surface.

3) Environmental air in middle and upper levels overtook the storm and flowed to either side as if around an obstacle.

4) The updraft source was on the right forward flank of the storm.

A significant difference, however, is apparent in the structure of the gust front. Browning and Ludlam (1962) show air within the gust front entering from the left forward flank near 3 km AGL and passing across the front of the storm transverse to the storm's motion. They show air within the gust front leaving the storm at the surface near the right rear flank. In contrast to this, the Doppler result shows that the gust front air entered the storm from near 4 km AGL on the left rear side and exited at the surface, moving away from the storm and slightly to the right of its direction of motion.

6. Quantitative results

In addition to a qualitative description of the kinematic structure within thunderstorms, other quantitative information can be derived from the derived air motions. Software has now been developed to compute the areal and volume averages of any of the computed field variables over the updraft or downdraft regions. If desired, these averages can also be computed over

any region in which any other field variable assumes a specified range of values.

This capability was used in computing the updraft mass flux $\overline{\rho w A}$, where ρ is the air density and A the updraft area. It appeared from updraft contours such as those in Figs. 4 and 5 that nearly all of the updraft had been detected by the radars from heights of 8.0 to 10.0 km MSL. Reliable estimates of updraft mass flux were made through these levels and the resulting mass flux profiles are shown in Fig. 11. The profile to the right represents the mass flux in the entire updraft ($w>0$) and the profile to the left shows the upward mass flux by air with $w>4$ m s^{-1}.

These profiles show that the total updraft was weakly detraining air at a rate of 0.026 km^{-1} in this region. [The entrainment rate is computed from $(1/F_m) \times (dF_m/dz)$ where F_m is mass flux.] It is also seen that no air was detrained from the portion of the updraft with $w>4$ m s^{-1} where the mass flux profile is constant. It was also found that the areas of the entire updraft ($w>0$) and the "strong" updraft ($w>4$ m s^{-1}) were nearly constant with height at 75 km^2 and 41 km^2, respectively, in this height interval. Thus 84% of the mass was being carried upward through only 55% of the updraft area.

Table 1 is a summary of quantities computed from the volume scan at 1728:44. Included in the table are results published by other observers for comparison. Updraft flux quantities were derived from values at 8.5 km where the entire updraft was observed. The eastern edge of the updraft was missing from planes below this level. Water vapor flux in the updraft was computed under the assumptions that the source of the updraft was near the surface where the mixing ratio is known (6.2 g kg^{-1}) and that there was a 3% per kilometer entrainment rate below the 8.5 km level. Mass flux through cloud base was calculated with a similar entrainment assumption. The resulting flux quantities were therefore estimates of the mass and water vapor feeding the storm from below cloud base.

The updraft energy flux through the 8.5 km level was computed from the standard relationship

FIG. 11. Updraft mass flux profiles for entire updraft on the right (triangles) and for "strong" updraft on the left (circles). A best fit by eye to each data set is shown by the straight lines.

$$F_e = F_m \left[\overline{C_p T'} + \overline{Lq'} + \frac{\overline{(u'^2 + v'^2 + w'^2)}}{2} + \overline{gz'} \right].$$

Primes indicate deviations within the storm from environmental values. The temperature excess and moisture excess, T' and q', were computed from parcel theory and the 1800 MDT soundings at Sterling and Sidney. These soundings were located east of the storm and therefore more accurately described the inflow air than did the other soundings. It was assumed that the updraft was saturated above cloud base. The kinetic energy term was computed from measured three-dimensional velocities and was found negligible compared with the temperature and humidity terms. Storm kinetic energy, however, was more than an order of

TABLE 1. Quantities computed from convective storm volume scan at 1728:44 MDT.

Quantity	Present result	Published value	Source[*]
Updraft mass flux at cloud base	230×10^9 g s^{-1}	335×10^9 g s^{-1}	1
Downdraft mass flux at 3 km	-220×10^9 g s^{-1}		
Updraft energy flux at 8.5 km	1.9×10^{11} cal s^{-1}		
Updraft vapor flux at cloud base	1.4×10^9 g s^{-1}	3.4×10^9 g s^{-1}	1
Updraft area	75 km^2	85 km^2	1
Downdraft area	87 km^2		
Precipitating volume (>20 dBZ)	2.4×10^3 km^3		
Vorticity flux ($\overline{\zeta w}$)	1.8×10^{-3} m s^{-2}		
Storm kinetic energy	6.2×10^{13} cal	6.2×10^{14} cal	2
Environment kinetic energy	2.6×10^{12} cal		
Mean updraft speed (storm average)	3.8 m s^{-1}	4.4 m s^{-1}	1
Mean downdraft speed (storm average)	-2.3 m s^{-1}		
Flux of eastward momentum ($\overline{\rho u w}$)	-6.2 N m^{-2}		
Flux of northward momentum ($\overline{\rho v w}$)	1.3 N m^{-2}		
Updraft detrainment rate $(1/F_m)(dF_m/dz)$	2.6% km^{-1}		

[*] 1. Auer and Marwitz (1968)—eight northeast Colorado storms. 2. Sellers (1972)—average summer storm.

magnitude larger than that in an equivalent volume of environmental air. The last term, expressing the potential energy due to a vertical displacement z' of the density surface, was also negligible for reasonable values of z'.

The downdraft mass flux was computed from the density-weighted average of the downdraft speed through the 3 km plane in which most of the downdraft was observed.

The vertical flux of the vertical component of vorticity per unit area, when averaged over the storm volume, $\overline{\zeta w}$, was large and positive at this time in the life cycle of the storm. As will be shown in more detail in Section 7, both the updraft and the downdraft contributed to a net upward flux of cyclonic vorticity.

Eastward and northward components of momentum flux were computed over the storm volume and the results are also shown in Table 1. In these calculations the u (eastward) and v (northward) components were taken relative to the environmental winds shown in Fig. 1. Knowing that storms are effective in the vertical exchange of air, we expect from the hodograph that air transported from the surface to the upper levels would have a strong relative component toward the west and a somewhat weaker component to the north. The relative magnitudes and signs of the momentum flux components in Table 1 are therefore consistent with the hodograph of Fig. 1.

Except for kinetic energy, the measurements appearing in Table 1 are similar to estimates previously published. These results indicate that dual-Doppler radar is a powerful tool to remotely determine important storm parameters.

7. Vorticity

The most striking feature of the horizontal velocity fields of Figs. 4 and 5 is the locally high value of the vertical component of vorticity. Two regions of high vorticity are seen to be separated along a line having an azimuth about 20° through the center of the storm at the 7.5 km level. Both vortex axes appear vertical in contrast to the updraft axis which is tilted 25° from the vertical. The southernmost vortex column most clearly seen at (39, 7) in the 7.5 km plane extends from below cloud base to the highest level of the Doppler data, around 11 km. The peak vorticity in the column is 1.0×10^{-2} s^{-1} at 5.5 km, while the generally weaker anticyclonic column to the north has a peak value of 0.7×10^{-2} s^{-1} near the 9 km level. This weaker column extended from the 5.5 km level to the top of the observed wind field. Vorticity profiles within the core of the southern vortex are given in Fig. 12 for the three volume scans.

One possible explanation for these cyclonic and anticyclonic vorticity columns is that the storm acted, to some extent, as an obstacle to the environmental wind. This resulted in the generation of cyclonic curvature on the right flank of the storm and anticyclonic curvature on the left flank as the environmental air moved past the storm from behind. Newton and Newton (1959) arrived at a similar conclusion. In-cloud winds were slower than the environmental winds at all levels which indicates that environmental air was indeed overtaking the storm. Therefore, this air must have been diverted to some extent around the storm.

As indicated in Table 1, a strong positive correlation between the updraft strength and vorticity yielded a large net upward flux of cyclonic vorticity. It should be stressed that although this correlation did exist, the updraft and vortex axes did not exactly coincide. The vortex axes were located near the interface between the updraft and downdraft. Fig. 13 shows a plot of areal averages of updraft strength versus vorticity. It is evident that the downdraft aided in the net upward transport of cyclonic vorticity. This upward flux of vorticity may be significant in light of the large-scale vorticity budget of Reed and Johnson (1974). They
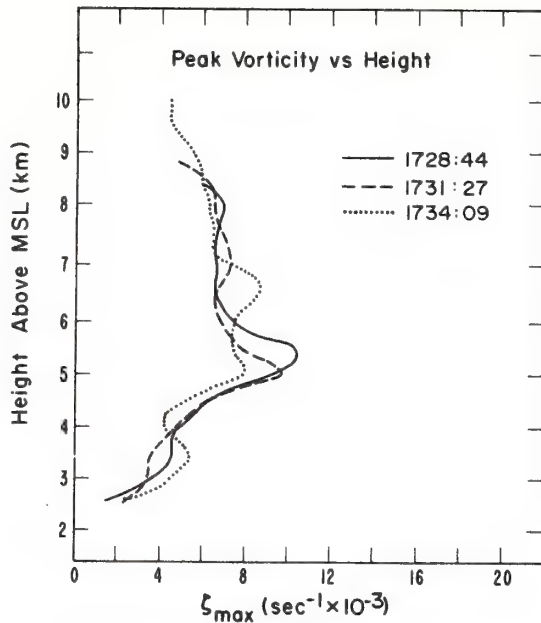
FIG. 12. Vertical profiles of the peak value of the vertical component of vorticity at the times shown. These values were taken along the axis of the southern vortex.

have shown that there is an apparent sink of vorticity near the surface and a source aloft in convectively active regions. It is possible that mesoscale convective elements not resolvable by large-scale measurements are a mechanism for the generation and upward transport of synoptic-scale vorticity. Other case histories are now under study to determine the generality of the ζ-w correlation and its possible relationship to this synoptic-scale vorticity source-sink.

Flux profiles of vorticity and momentum have been generated for this storm but are not presented here.
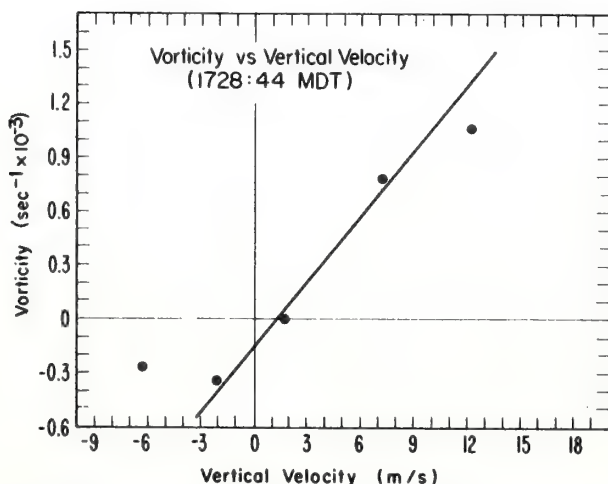
FIG. 13. Vorticity as a function of vertical velocity areally averaged at various levels within the precipitating volume. The straight line indicates a best fit by eye.

8. Summary

The NOAA/WPL dual-Doppler radar system has been used to determine the kinematic structure of the decaying stage of a convective storm which grew in a weakly sheared environment. The following features of the kinematic structure were observed:

1) Divergence was coincident with high reflectivity at the surface.
2) The updraft was fed by potentially warm (high θ_e) air from ahead of the storm. Potentially cold (low θ_e) air overtook the storm and participated in the downdraft circulation. Similar low values of θ_e were measured just behind the surface gust front located 14 km ahead of the forward edge of the radar echo. The conclusion that middle level air ($\sim$5.5 km) was the source for the gust front was consistent with the Doppler-derived three-dimensional streamline.
3) Regions of cyclonic and anticyclonic vorticity were found respectively on the right and left sides of the storm. This flow pattern indicates that the mass of air within the storm may have acted, to some extent, as an obstacle to the environmental flow.
4) The main updraft was in the form of a sheet of upward flowing air inclined 25° in the upshear direction. This sheet was composed of two jets of relatively high speed flow separated by a less intense updraft. Peak updraft speeds of 19 m s^{-1} were observed at 10.5 km (9 km AGL).
5) The kinematic structure of this storm was similar to the structure of the Wokingham storm described by Browning and Ludlam (1962) despite the fact that the latter storm developed in a strongly sheared environment.
6) Quantitative flux results computed from the Doppler data generally fell within the range of prior observations. A detrainment rate of 0.026 km^{-1} was measured in the updraft from 8.0 to 10.0 km MSL. Finally, vorticity and vertical velocity were found to be positively correlated.

There are significant kinematical differences between this storm and one observed in the same area only a few days later (31 July 1973) as reported by Miller *et al.* (1975). These differences must be related to the different environmental conditions within which each storm grew. For example, the environmental shear on 31 July was three times larger and more moisture was available than on 28 July. A comparison of several case histories such as these should lead to a more complete understanding of the necessary environmental conditions that ultimately produce a particular kinematic structure and precipitation distribution.

team effort extending over several years. In particular, the engineering effort of Richard Strauch and the computer programming of Nathan Kohn deserve recognition here. The authors are also grateful for the valuable discussion with Keith Browning. Supporting data used in Figs. 1, 2, 3 and 10 were made available by the NHRE.

REFERENCES

Auer, A. H., and J. D. Marwitz, 1968: Estimates of air and moisture flux into hailstorms on the high plains. *J. Appl. Meteor.*, **7**, 196–198.

Browning, K. A., and F. H. Ludlam, 1962: Airflow in convective storms. *Quart. J. Roy. Meteor. Soc.*, **88**, 117–135.

Fawbush, Ernst J., and R. C. Miller, 1954: A basis for forecasting peak wind gusts in non-frontal thunderstorms. *Bull. Amer. Meteor. Soc.*, **35**, 14–19.

Joss, J., and A. Waldvogel, 1970: Raindrop size distributions and Doppler velocities. *Preprints 14th Radar Meteor. Conf.*, Tucson, Ariz., Amer. Meteor. Soc., 133–138.

Kropfli, R. A., and L. J. Miller, 1975: Thunderstorm flow patterns in the dimensions. *Mon. Wea. Rev.*, **103**, 70–71.

Lhermitte, R. M., and L. J. Miller, 1970: Doppler radar methodology for the observation of convective storms. *Preprints 14th Radar Meteor. Conf.*, Tucson, Ariz., 133–138.

Mason, B. J., 1969: Some outstanding problems in cloud physics—the interaction of microphysical and dynamical processes. *Quart. J. Roy. Meteor. Soc.*, **95**, 449–485.

Miller, L. J., J. D. Marwitz and J. C. Fankhauser, 1975: Kinematic structure of a Colorado thunderstorm. *Preprints 16th Radar Meteor. Conf.*, Houston, Tex., Amer. Meteor. Soc., 128–133.

——, and R. G. Strauch, 1974: A dual-Doppler radar method for the determination of wind velocities within precipitating weather systems. *Remote Sensing Environ.*, **3**, 217–233.

Newton, C. W., and H. R. Newton, 1959: Dynamical interactions between large convective clouds and environment with vertical shear. *J. Meteor.*, **10**, 483–496.

Reed, R. J., and R. H. Johnson, 1974: The vorticity budget of synoptic-scale wave disturbances in the tropical western Pacific. *J. Atmos. Sci.*, **31**, 1784–1790.

Rumler, W. D., 1968: Two-pulse spectral measurements. Tech. Memo. MM-68-4121-15, Bell Telephone Laboratories, Whippany, N. J.

Sellers, W. D., 1972: *Physical Climatology.* The University of Chicago Press, p. 13.

UPDRAFT INTENSIFICATION AND HAIL PRODUCTION AFTER CELL MERGER

L. Jay Miller

NOAA/ERL Wave Propagation Laboratory
Boulder, Colorado 80302

1. INTRODUCTION

Using data from aircraft, radar (including Doppler), surface mesonetwork, and rawinsondes, Browning et al. (1976) were able to synthesize a schematic model of an evolving multicell hailstorm. They stated that such storms are characterized by a succession of individual cells, each having a life cycle similar to the one described by Byers and Braham (1949). Each cell begins as a cumulus cloud, usually on the right flank, which grows rapidly in the vertical as it moves into and toward the back of the main cloud mass. New cells typically exhibit a detectable radar echo in about 15 min near the $-12°C$ (~7km MSL) level. Radar-detectable cells continue moving through the main cloud mass, producing rain and hail at the ground and eventually dissipating. The total lifetime of each identifiable cell is about 45 min. This overall behavior is similar to that of hailstorms in western South Dakota as described by Dennis et al. (1970), who further report that merging of cells with the main radar echo is often followed by bursts of heavy rain or hail at the ground.

This paper describes the sequence of events as revealed by detailed internal airflow measurements with two Doppler radars, in a similarly evolving multicell hailstorm that developed on 23 July 1974 in northeastern Colorado. During the 1974 summer field program of the National Hail Research Experiment* (NHRE), two Wave Propagation Laboratory 3-cm mobile Doppler radars were operated in the Lhermitte and Miller (1970) coplane scan mode for data acquisition. These radial velocity and reflectivity data were combined using coplane analysis (Miller and Strauch, 1974; Doviak et al., 1976) to obtain the three-dimensional airflow. The time-evolving core draft and the internal airflow, including draft structure, following the merger of three radar cells are described.

2. STORM ENVIRONMENT

The sounding from a rawinsonde released at Grover, Colorado, at 1620 (all times MDT) was assumed to represent the environmental conditions. This sounding was taken 45 min before the appearance of the radar echo and was located 20 km northeast (downshear) of the main echo complex. From Fig. 1 it can be seen that a nearly dry adiabatic layer existed in the subcloud region. As shown, a parcel of air near the surface lifted dry adiabatically to the convective condensation level (assumed to be cumulus cloudbase), then lifted moist adiabatically above cloudbase, was $3°C$ warmer than the environment at 500 mb. Note that

significant negative buoyancy at cloudbase was probably not present. This is contrary to the typical situation accompanying the more severe storms that occur in this area. Marwitz (1973) reported that inflow air for these storms is almost always negatively buoyant just below cloudbase. This would tend to help stabilize the surface layer thereby enabling a deep moist layer to develop, which may later be overturned by mechanical lifting. A lack of significant negative buoyancy was also found in a non-steady moderate intensity thunderstorm described by Miller (1975).

The environmental winds (Fig. 2) were generally easterly in the surface layer and backed to west-southwesterly in the upper levels. Subcloud winds were light, and moderate shear $(1.9 \times 10^{-3} s^{-1})$ existed in the cloud layer. These are considered distinguishing environmental characteristics of multicell hailstorms (Marwitz, 1972). Conditions accompanying this hailstorm are summarized in Table 1.

Table 1.
Environmental Conditions on 23 July 1974 as Determined From the 1620 Grover Rawinsonde

Subcloud	
Water vapor mixing ratio	$8 gm kg^{-1}$
Mean winds	$050°: 3.5 m s^{-1}$
Cloudbase	
Height	4.3 km MSL
Temperature	$3°C$
Cloud layer (base to 14 km)	
Mean Winds	$305°: 7m s^{-1}$
Shear	$232°: 1.9 \times 10^{-3} s^{-1}$
Layer of minimum equivalent	
potential temperature	< 330 K
Height	5.8 km MSL
Thickness	1.5 km
Mean winds	$325°: 8.5 m s^{-1}$

3. RADAR ECHO EVOLUTION

A series of low-level constant elevation scans obtained with the Grover 10-cm radar is shown in Fig. 3. The tracks of the 45 and 55 dBZ* reflectivity factor contours are also shown. The storm is seen to consist of two main multicell radar echo complexes, an easternmost (E prefix) and a westernmost (W prefix) one. Overall echo motion determined from the reflectivity was from 325° at 6 m s^{-1}. This total motion, propagation plus translation, was along, and 2 m s^{-1} slower than

$$\overline{*dBZ \equiv \log Z/1 \ mm^6 m^{-3}}.$$
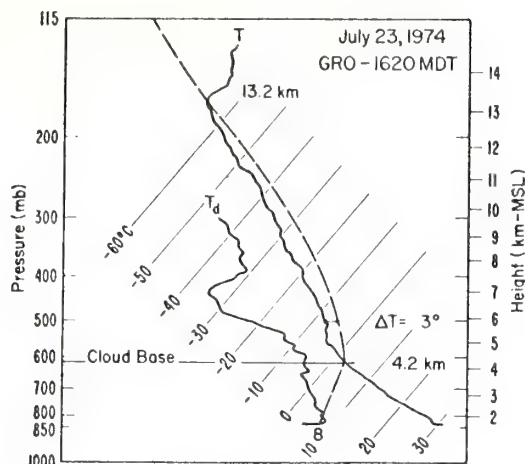
Fig. 1. *Temperature (T) and dewpoint temperature (T_d) profiles from Grover rawinsonde release. Isotherms are the thin solid lines that slope upward to the right and the subcloud water vapor mixing ratio (g/Kg) isopleth is the dashed line marked 8. The trajectory of parcel ascent along the dry and moist adiabats is shown as a dashed line.*
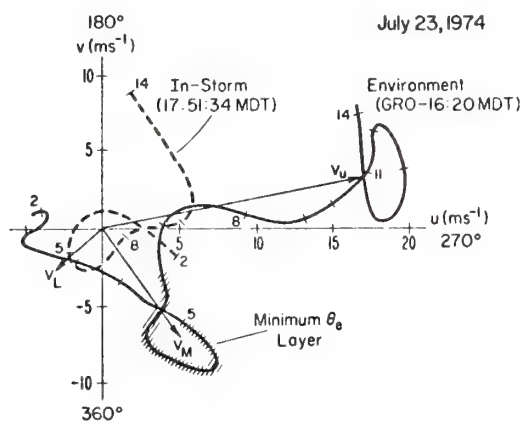
Fig. 2. *Hodographs of environmental and in-storm horizontal winds. Heights are in kilometers above mean sea level. The minimum equivalent potential temperature (θ_e) layer is shown as cross-hatching along the environmental wind hodograph. Average winds over the subcloud (V_L), minimum θ_e layer (V_M) and upper levels (V_u) are shown as vectors.*

the mean winds in the layer of minimum equivalent potential temperature (θ_e). New echoes tended to form on the flanks of the main echo complexes. Those cells on the left flank (northeast side) moved cyclonically into the main echo, whereas those on the right flank (southwest side) moved anti-cyclonically. From the analysis of airflow, described in Section 4, it was found that this was confluent motion into the main updraft.

The location of hailstones collected at the surface by NHRE mobile chase teams suggests that hail grew in the easternmost echo complex. Hailstone diameters ranged mostly between 1 and 2 cm with some as large as 2.5 cm. However, no major hailfall was found.

4. INTERNAL AIRFLOW

Shown in Fig. 4 are contours of vertical air motion and horizontal streamlines on several horizontal planes. These planes show the near-instantaneous (total radar scan time was about 3 min) picture of airflow in the volume of the storm covered by the two Doppler radars. These data were obtained shortly after cells marked E0, E4, and E5 in Fig. 3 were no longer distinguishable as individual radar cells. Some ambiguity must always exist regarding cell merger, depending on the criteria used to define a radar cell. Here the intent was to relate the order of events so that cells were considered indistinguishable when they were enclosed by a single 45 dBZ contour. Somewhat poor temporal and spatial resolution, particularly in the Doppler data, did not warrant following the small-scale, high reflectivity regions or "hot spots." Complete Doppler scans were only repeated every 10 min or so. Also, the requirement of spatial smoothing to obtain reliable velocity estimates degraded the resolved spatial scales to those larger than 5 km. This is consistent with the relative smoothness of vertical air motion contours.

At this time (17:51:34), the easternmost echo complex was found to consist of a large updraft on the right flank. The updraft extended outside the detectable echo at all levels as shown by contours opening to the south at the echo boundary. A cell (E6) to the northeast had appeared as a first echo some 14 min earlier at a height of 6.5 km.

From the horizontal streamlines* (Fig. 4b), it is inferred that updraft air entered the storm on the right flank (southwest) and exited on the left flank (east-northeast). The horizontal velocity, mostly direction, of the surface outflow downdraft air is consistent with this air having originated from the layer of minimum θ_e. However, no θ_e measurements were obtained at the surface to confirm this inference. There was a confluence line near the center of the echo complex particularly in the layer from 5 to 8 km. As this was the layer containing most first echoes, it appears that the motion of echoes growing to either side of this line was in response to a kinematic structure that was more steady than the precipitation structure.

---

* Streamlines are shown relative to the ground. Echo translation was slow (<2m s^{-1} as determined by averaging the horizontal winds over the storm volume scanned) so that echo motion was dominated by propagation.

111

323
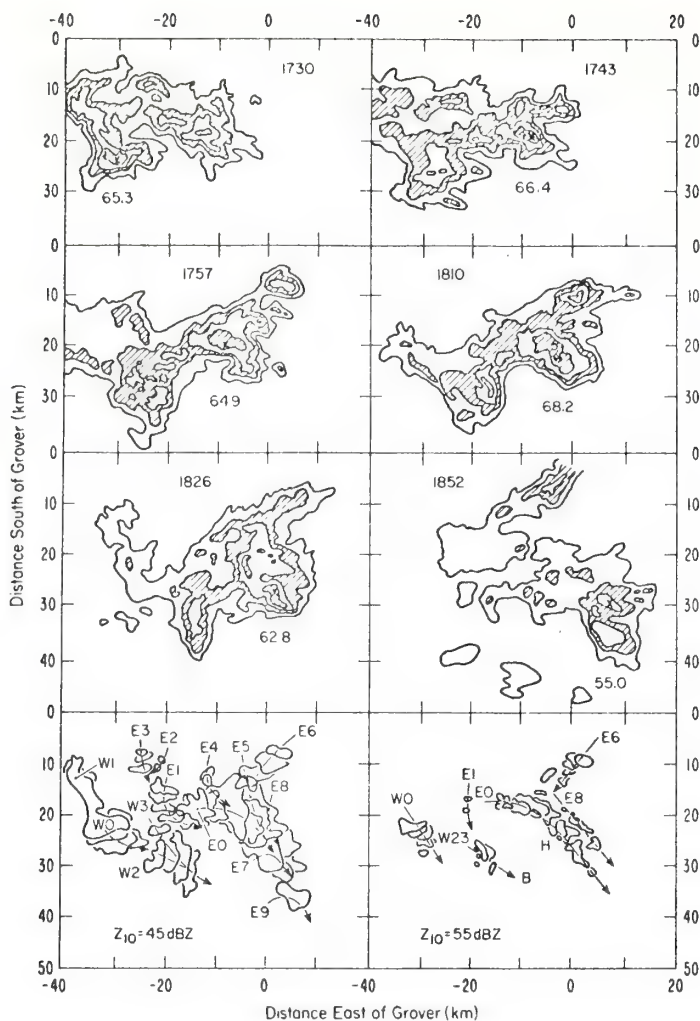
Fig. 3. A series of low-level 10-cm radar constant elevation angle scans. The radar is located at coordinates (0, 0). Times and values of maximum radar reflectivity factor are shown on each frame. Contours of reflectivity are at 10 dB increments above 25 dBZ, cross-hatched for 35-45 and 55-65 intervals. Lower frames show 45 and 55 dBZ (contour) tracks with individual cells marked with a prefix letter for westernmost (W) and easternmost (E). Numeral suffixes are roughly in chronological order. Hailstones (near H) were collected at the surface 10 km northeast of Briggsdale (B) marked on 55 dBZ track frame.

In fact, when one considers the total echo motion, the kinematic structure moved from 280° at <2 m s^{-1} implying a propagation of the precipitation structure from 342° at 4.5 m s^{-1}. This means that the precipitation field (radar echo) outran the kinematic perturbation (deviation from environmental flow) because of propagation. At a later time (18:02 not shown here), the major draft area was located farther back in the storm with precipitation echo in front of it suggesting that the inflow was being cut off. This storm persisted for about 2 hours, remaining intense for only 30-45 min. Previously, Miller (1975) found in a case study of another storm that precipitation fell into inflow air thereby cutting off the updraft and forcing the storm to decay.

Representative profiles of the time-evolving core draft were constructed (Fig. 5) by following the eastern cell complex. These profiles are associated more with a larger scale airflow cell than with individual radar or visible cells. As noted before, such interpretations are sometimes dictated by poor spatial and temporal resolution. During the growing stage, profile at 17:28:54, there was a secondary updraft maximum of 10 m s^{-1} about a kilometer above cloudbase. It is easy to see that updraft profiles determined from tracking chaff could be interpreted as having updraft maxima within 1-4 km of cloudbase (Marwitz, 1973). For example, any chaff released into this storm could not have been tracked above the secondary maximum since the echo from precipitation exceeded 30 dBZ (Marwitz, 1973). Whether or not this is the explanation, in general, it seems to be a likely candidate for many updraft maxima detected at relatively low levels. Here an updraft maximum was clearly found in the upper levels.

Since the cell E6 was distinguishable both as a radar echo and circulation cell for most of its lifetime, a core draft profile was also constructed for this cell and is shown in Fig. 6. The previous profiles (Fig. 5) are interpreted as more nearly representative of the large-scale updraft, whereas the profiles in Fig. 6 represent the evolution

112

324
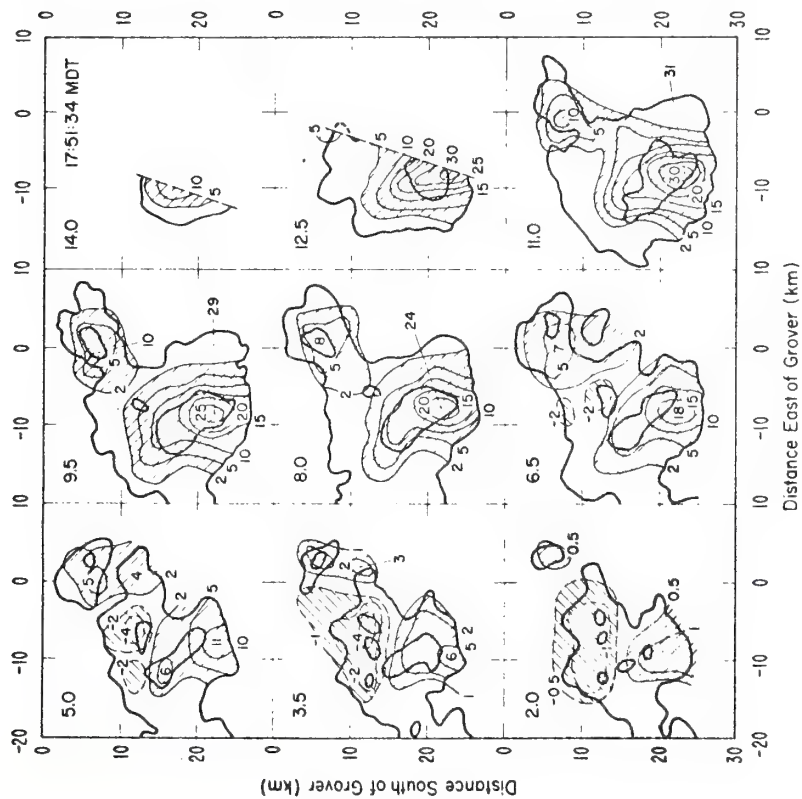
Fig. 4a. Contours of vertical air motion are shown at nine heights (km MSL). Downdrafts are dashed line contours with cross-hatching sloping upward to the right. Updrafts are solid thin lines with cross-hatching sloping upward to left. The thick solid lines are 3-cm 20 and 45 dBZ contours. Only the easternmost cell complex was scanned by the Doppler radars.
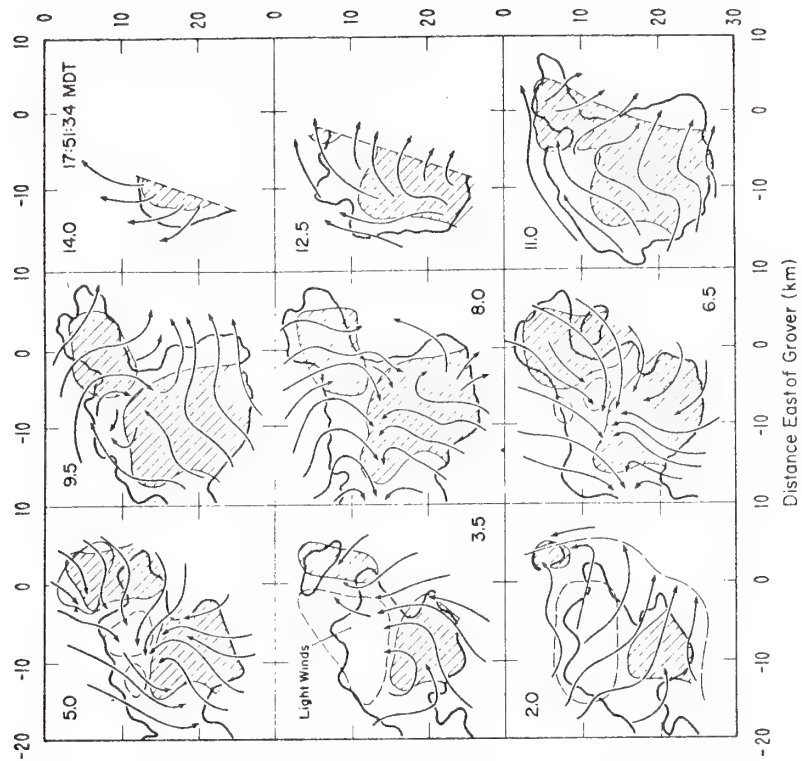
Fig. 4b. Streamlines of horizontal flow relative to the ground at. same heights as in Fig. 4a. The updraft regions are cross-hatched and the downdraft is delineated with a thin dashed contour. The thin dashed line (2.0 km frame) mostly outside radar echo is a wind shift line as determined by one Doppler radar about 30 km east of the echo. Dual radar data were not obtained outside this line because of lack of return signal for one of the radars.

113

325
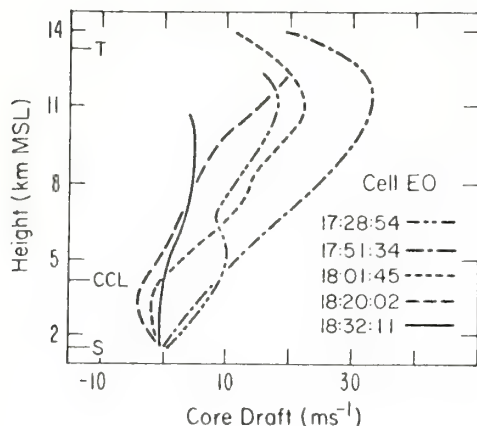
Fig. 5. Vertical profiles of vertical air motion in core of easternmost draft region. These profiles were constructed from Doppler radar scans centered at times shown. The most intense phase (17:51:34) corresponds to Fig. 4.
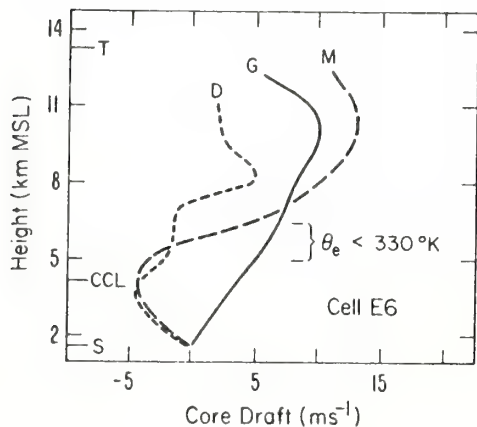
within any single cell. Cell E6 appeared as a first radar echo at 17:37 near 6.5 km (-12°C). Within 14 min the first profile (G in Fig. 6) was obtained when the echo extended to the ground. Maximum upward motion of 13 m s^{-1} was found aloft 24 min after first echo. Downdrafts were found below the minimum θ_e layer. After 42 min, the cell was dissipating with only weak updrafts aloft. This sequence is qualitatively similar to the one described by Byers and Braham (1949). Cell E6 reached a maximum diameter (of 20 dBZ reflectivity contour) of 7.5 km and was dissipating before it was indistinguishable from the rest of the easternmost complex.

5. SUMMARY

Data obtained with two 3-cm Doppler radars have been analyzed to reveal the temporal and spatial behavior of the airflow in an evolving multi-cell hailstorm. The airflow and individual cell evolution were found to resemble those in a schematic model described by Browning et al. (1976). It was found that vertical air motions in the main draft were most intense shortly after three radar cells had merged. Also, maximum radar reflectivity increased to 65 dBZ shortly after merger. Though no significant hailfall was found, hailstones as large as 2.5 cm diameter were collected. Their location suggested that the hail grew in the merged cell complex. Insufficient data on specific times of hail fall preclude determining the most probable location of hail growth. However, there seems to be qualitative agreement with the notion of hail embryos grown in so-called "feeder" clouds naturally seeding a main storm complex to continue their growth to hailstone sizes (e.g., Musil, 1970; Dennis and Musil, 1973).

Fig. 6. Core draft profiles during growth (G), mature (M), and decay (D) phases of cell E6. The heights of the surface (S), convective condensation level (CCL) and tropopause (T) are marked on the left vertical axis.

114

6. REFERENCES

Browning, K.A., J.C. Fankhauser, J.P. Chalon, P.J. Eccles, R.G. Strauch, F.H. Merrem, D.J. Musil, E.L. May, and W.R. Sand, 1976: Structure of an evolving hailstorm, Part V: Synthesis and implications for hail growth and hail suppression, *Mon. Wea. Rev.* 104, 603-610.

Byers, H.R., and R.R. Brahan, Jr., 1949: The Thunderstorm, U.S. Government Printing Office, Washington, D.C., 287 pp.

Dennis, A.S., C.A. Schock, and A. Koscielski, 1970: Characteristics of hailstorms of Western South Dakota, *J. Appl. Meteorol.*, 9, 127-135.

Dennis, A.S., and D.J. Musil, 1973: Calculations of hailstone growth and trajectories in a simple cloud model, *J. Appl. Meteorol.*, 30, 278-288.

Doviak, R.J., P.S. Ray, R.G. Strauch, and L.J. Miller, 1976: Error estimation in windfields derived from dual-Doppler radar measurement, *J. Appl. Meteorol.*, 15, 868-878.

Lhermitte, R.M., and L.J. Miller, 1970: Doppler radar methodology for the observation of convective storms, Preprints, AMS 14th Radar Meteorol. Conf., 121-127.

Marwitz, J.D., 1972: The structure and motion of severe hailstorms, Part II: Multi-cell Storms, *J. Appl. Meteorol.*, 11, 180-188.

Marwitz, J.D., 1973: Trajectories within the weak echo regions of hailstorms, *J. Appl. Meteorol.*, 12, 1174-1182.

Miller, L.J., 1975: Internal airflow of a convective storm from dual-Doppler radar measurements, *Pure and Appl. Geophys.*, 113, 765-785.

Miller, L.J., and R.J. Strauch, 1974: A dual-Doppler radar method for the determination of wind velocities within precipitating weather systems, *Remote Sens. of Environ.*, 3, 219-235.

Musil, D.J., 1970: Computer modeling of hailstone growth in feeder clouds, *J. Atmos. Sci.*, 27, 474-482.

115

Structure of an Evolving Hailstorm, Part III:
Internal Structure from Doppler Radar

R. G. Strauch and F. H. Merrem

NOAA/ERL/Wave Propagation Laboratory,[1] Boulder, Colo. 80303

ABSTRACT

Two X-band Doppler radars observed a hailstorm that passed directly over one of the radars during the 1973 National Hail Research Experiment (NHRE). While one of the radars scanned the storm at low elevation angles the other radar, which operated simultaneously in a zenith-pointing mode, measured part of an updraft. Observations by other NHRE participants assisted in interpreting the radial velocity fields so that inflow and outflow could be identified from the scanning radar measurements. The peak updrafts occurred just ahead of the highest reflectivity while the strongest downdrafts were found only 6 km behind the updraft. Strong turbulence was generated in the transition region between updraft and downdraft as evidenced by large velocity variances. A substantial part of the downdraft appeared to have been fed by air that had ascended in the updraft. Low-level velocity fields were in general agreement with surface measurements and showed the outflow toward the front of the storm in the gust front as well as outflow opposite the echo motion behind the storm. There was strong outflow opposite the direction of echo motion at the top of the storm which agreed with photographs of the anvil overhang.

1. Introduction

The observations discussed in this paper were made with two X-band Doppler radars on a storm that passed directly over one of the radars near Raymer during the 1973 field program of the National Hail Research Experiment (NHRE) in northeast Colorado. The two radars normally were operated as a dual-Doppler system to acquire data for analysis of three-dimensional wind fields. However, when a storm passed directly over one radar, it was operated in a zenith-pointing mode while the second radar scanned an azimuth sector encompassing the zenith-pointing radar with a raster scan stepped in elevation. Browning *et al.* (1968) conducted a similar experiment to observe the horizontal and vertical air motion in a shower, except their second radar scanned in elevation at a single fixed azimuth. The operational mode we selected enabled us to determine the two-dimensional velocity in a vertical plane through the radars, and it also allowed us to observe the reflectivity and one component of air motion throughout the storm volume. Several storms were observed in this operating mode, but the Raymer storm of 9 July 1973 discussed here combines two fortuitous factors in addition to the extensive measurements obtained with other instruments:

1) The storm track was within 5° of the line joining the radars. Thus, inflow and outflow parallel to the

direction of storm motion were observed as radial velocity. These regions were clearly seen by the scanning radar and assisted in interpreting the measured radial velocity field in terms of the storm structure.

2) An updraft region passed directly over the zenith-pointing radar. The vertical velocity data could therefore be used to locate the updraft precisely in relation to the storm echo.

2. Doppler radar observations

The location of Doppler radars A and B relative to the NHRE operational area is shown in Fig. 1. The radars were separated by 52.2 km with a baseline angle of 354° from north. The 9 July 1973 hailstorm passed directly over the southern radar (Radar A). Fig. 1 also shows the reflectivity contours, just below cloud base, measured by the NHRE 10 cm radar located at Grover, Colo., at the time the storm was over Radar A. Radar A acquired data in a zenith-pointed mode from 1725:55 to 1736:15 MDT. During this same time, Radar B was scanning an azimuth sector at elevation angles of 0° to 15° in 1° steps. The 16 elevation steps were scanned in 160 s. The area covered by Radar B during its initial scan sequence is outlined by the dashed lines. A representative echo motion was 7 m s⁻¹ along the radar baseline during the time interval of interest for the Doppler data. Seven meters per second is an intermediate value between the motion of the storm as a whole and the motion of individual cells (Part I). The dotted line in Fig. 1 shows the coverage of the zenith-pointing radar as the storm advected overhead. The Doppler radar observations pertain to cell W4.

The characteristics of the X-band Doppler radars have been described by Frisch *et al.* (1974), but will be briefly summarized here. The complex video signals were digitally recorded for postanalysis. The zenith-pointing radar acquired data at 24 fixed heights with a dwell time of 0.065 s corresponding to 128 radar samples in each height increment. From these data the complete Doppler velocity spectrum was obtainable 96 times per minute at each height. The radar beamwidth of 0.9° provided a horizontal resolution better than 250 m at the maximum altitude. The height resolution was 75 m and the minimum height that could be observed was 1.8 km (MSL). (The radar altitudes were 1.5 km MSL.) The height spacing between data locations was 600 m, with the lowest location centered at 1.9 km and the highest at 15.7 km during the period 1725:55 to 1728:05. From 1728:05 to 1736:15 the height spacing was 300 m with the lowest location centered at 1.9 km and the highest at 8.8 km.

The scanning radar used the same dwell time (0.065 s for 128 radar samples) and acquired data for 384 (16 azimuth × 24 range) radar resolution elements in 10 sec for each fixed elevation step. Four complete elevation scan sequences were made during the 12 min observation period. The 0.9° beamwidth resulted in a spatial resolution of 600 to 800 m at the location of the storm. The data locations were separated by 600 m in range and about 1.5° (1300 m) in azimuth. The entire Doppler velocity spectrum was calculable for each measurement point of the scanning radar so the radial velocity, velocity variance, and radar reflectivity were estimated at each data point.

3. Data analysis procedure

The radar reflectivity and the first and second moments of the velocity spectra were estimated from the 128 radar samples recorded at each range location. A fast Fourier transform algorithm was used with a general purpose computer to calculate the Doppler velocity spectra. Each radar acquired data for approximately 28,000 velocity spectra during the 12 min observation period, so that estimates of the spectral moments of the signal had to be made by a high speed computer from the Doppler signal plus noise data. The spectra were estimated from the 128 radar samples and the moments were computed after a velocity window was applied to the spectra. The velocity window ranged on both sides of the peak of the spectrum to points where the power density fell to within 3 dB of the receiver noise level. The windowed spectra were manually checked to ensure that the automated method selected the correct signal spectra and properly accounted for velocity folding. The first and second moments of the velocity spectra were also estimated with a "pulse-pair" algorithm (Berger and Groginsky, 1973). The radar reflectivity factor Z was also calculated from the signal power estimates. The radar reflectivity values were not
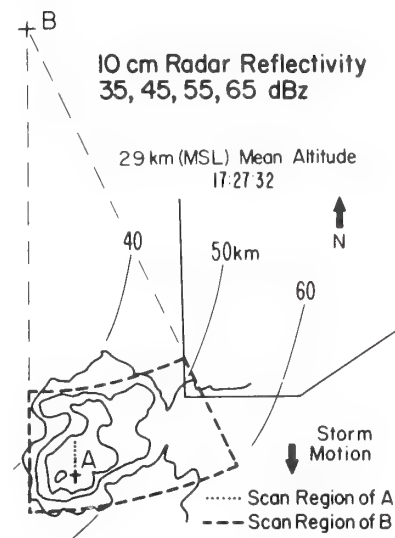
FIG. 1. PPI presentation of NHRE 10 cm radar reflectivity contours near cloud base at 1727 MDT and scan regions for the Doppler radars.

corrected for attenuation and are, therefore, only approximate. The vertical air motion, W, was estimated by subtracting the terminal fall speed of the particles, V_T, from the measured, reflectivity-weighted particle velocity, V_z. The terminal fall speed of the particles was estimated using the empirical relation $V_T = 2.6\, Z^{0.107}$ of Joss and Waldvogel (1970) as suggested by Atlas *et al.* (1973), with a correction for air density variations proposed by Foote and du Toit (1969). Since the V_T vs Z relationship is relatively insensitive to Z, the estimate of V_T should be accurate to within ± 1 m s^{-1} in rain. The Joss-Waldvogel empirical equation underestimates the fall speed if hail is present in the pulse volume; consequently the updraft would be underestimated.

The reflectivity factor, mean radial velocity, and velocity variance measured by the scanning radar were interpolated into a Cartesian coordinate system with the y axis along the radar baseline. The various quantities were then contoured and displayed in horizontal and vertical planes. Interpolation smoothed out large gradients because adjacent measurement points were used to calculate values on a Cartesian grid. Consequently, examination of the original measurements indicated that maximum gradients of the various quantities were reduced by a factor of about 2 after interpolation. The radial velocity sign convention is such that motion away from the radar is registered as positive. The vertical motion of the particles, V_z, contributes a radial velocity component of magnitude $V_z \sin \theta$ to the velocity measured by the scanning radar, where θ is the elevation angle of the radar antenna. This contribution was always less than 1.5 m s^{-1} in this experiment and was not removed from the radial velocity fields except in the vertical plane containing both
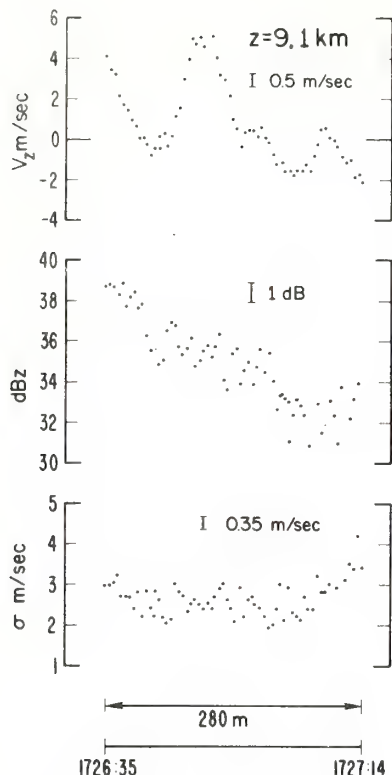
FIG. 2. Forty-second sample of data measured by the zenith-pointing radar. Vertical velocity of the scattering particles of +5 m s^{-1} indicate updraft in excess of 13 m s^{-1}. Bars denote predicted standard deviation of the estimates.

radars because it was known only above the zenith-pointing radar.

In the region where both radars acquired data, two-dimensional air motion was calculated by combining the observations of vertical air motion by the zenith-pointing radar with the horizontal air motion along the radar baseline observed by the scanning radar. The horizontal component of motion, V_h, in the vertical plane through the two radars was derived from the measured radial velocity, V_R, using the relationship $V_R = V_z \sin\theta + V_h \cos\theta$. The two-dimensional air motion field was corrected for echo motion by removing a 7 m s^{-1} component from the horizontal velocity.

4. Nature of the data

An example of the data acquired by the zenith-pointing radar is shown in Fig. 2 to illustrate the temporal variability of the vertical structure. Sixty-four data points from a sample obtained in the updraft region over a period of 40 s are shown. The terminal fall speed computed from the Joss-Waldvogel equation varied from 8.2 to 9.4 m s^{-1} for the reflectivity values shown in Fig. 2 (center), so the maximum updraft must have exceeded 13 m s^{-1}. The particle velocity V_z changed 6 m s^{-1} in 8 s with little change in reflectivity, demonstrating that rapid changes can occur in the up-

draft. The beamwidth was about 120 m at 9.1 km altitude, and the pulse length was about 75 m. The 6 m s^{-1} velocity change, therefore, occurred while the echo was advected about $\frac{1}{2}$ beamwidth. If the velocity change had been caused by horizontal shear within the updraft, a shear of 10^{-1} s^{-1} would have been required. A vertical velocity gradient of 7×10^{-2} s^{-1} in an updraft of 10 m s^{-1} would also account for the velocity change.

Fig. 2 can also be used to estimate the accuracy of the measured data. The standard deviation of the mean particle velocity, V_z, (top trace) is given by Miller and Rochwarger (1970) as

$$\left[\frac{\lambda\sigma}{4T_D} \right]^{\frac{1}{2}},$$

where T_D is the dwell time, λ the radar wavelength (0.0322 m) and σ the width of the velocity spectrum. The dwell time is the pulse repetition period (512 μs) multiplied by the number of pulses making up the sample from each volume increment (128), so $T_D = 0.065$ s. The average width of the spectra (bottom trace) is about 2.5 m s^{-1} so the standard deviation of the mean velocity estimate is about 0.5 m s^{-1}. The reflectivity estimates (center trace) are calculated from 128 radar samples, but the number of independent samples is given by Nathanson (1969, p. 89) as

$$N_I = \frac{4\sqrt{\pi}\sigma T_D}{\lambda}.$$

In this experiment there are about 30 independent samples. The standard deviation of the reflectivity estimates is therefore about 1 dB. The standard deviation of the estimates of spectral width, σ, is given by (Miller and Rochwarger, 1970)

$$\left[\frac{3\lambda\sigma}{32T_D} \right]$$

and is about 0.35 m s^{-1} for the data in the lower trace of Fig. 2.

Fig. 3 shows examples of vertical profiles of vertical particle velocity measured in the 0.065 s dwell time. The spatial samplings are for range gate spacings of 600 m (at 1726:01 MDT) and 300 m (1735:01 and 1730:31). The profile measured at 1726:01 illustrates the vertical variability of the velocity structure, particularly in the updraft region about 6.5 km. At 1730:31 the maximum altitude of the measurements had been reduced from 15.7 to 8.8 km. The profile in the center trace of Fig. 3 indicates a downdraft existed over the radar at that time. The profile measured at 1735:01 in the back portion of the storm shows weak downdrafts. Particle velocities as high as +12 m s^{-1} were measured in the updraft at 1726:01, but 4.5 min later, after the

storm had advected less than 2 km, velocities of -20 m s^{-1} were measured.

5. Results

a. Air motion in the vertical plane through the radar sites

Fig. 4a shows the time vs height plot of the 10 cm radar reflectivity above the zenith-pointing radar. The dotted line outlines the time and height of the data acquired by the zenith-pointing radar. As can be seen in Fig. 4a the operator of the zenith-pointing radar reduced the maximum observed altitude shortly after the upper-level high reflectivity region had passed overhead. Radar B scanned all of the echo structure shown in Fig. 4a except for the very earliest and latest portions.

Fig. 4b shows contours of vertical air motion derived from the Doppler velocities and reflectivity measured by the zenith-pointing radar using the Joss-Waldvogel equation to remove the V_T component. Five-second averages (8 values) of Z and V_z were used to derive an estimate of W every 5 s, or 35 m for an echo motion of 7 m s^{-1}. The time-height values of W represent the region inside the dotted outline of Fig. 4a. No updrafts were observed below 6.5 km, but the trend of the data suggests that the low-level portion of the updraft had advected past Radar A before 1725. The boundary of the surface outflow passed the radar at 1715 while the leading edge of the low-level echo arrived at 1725. Maximum updraft values occurred between 8.0 and 10.3 km altitude. The slope of the updraft contours indicates that the updraft was tilted toward the north— opposite to the direction of echo motion. This tilt was about 20° from the vertical at 9 km altitude. Highest downdrafts were measured between 3 and 5.5 km altitude and occurred just behind the updraft. The back portion of the storm contained weak downdrafts in the lower levels, but near the highest altitude observed there were weak updrafts, even after the portion of the storm with highest reflectivity had advected past.

The two-dimensional air motion in a vertical plane through the storm observed by both radars is shown in Fig. 4c. The vector representation shows the air motion relative to the storm in the region outlined by the dotted lines in Fig. 4a. The transition between strongest updraft and strongest downdraft probably took place over a distance of about 3 km, and as we shall show, strong turbulence was generated in this region. The most intense part of the downdraft appears to have been fed by air which had ascended in the updraft, as postulated by Newton (1963). The peak downdraft occurred in the region of highest reflectivity and water loading probably contributed to the downdraft.

Reflectivity contours measured by Radar B in the vertical plane through the radars are shown in Fig. 5a. The highest reflectivity factors measured by the 3 cm radar were about 50 dBZ and occurred at an altitude of 5.5 km and 2 km west of the baseline joining the
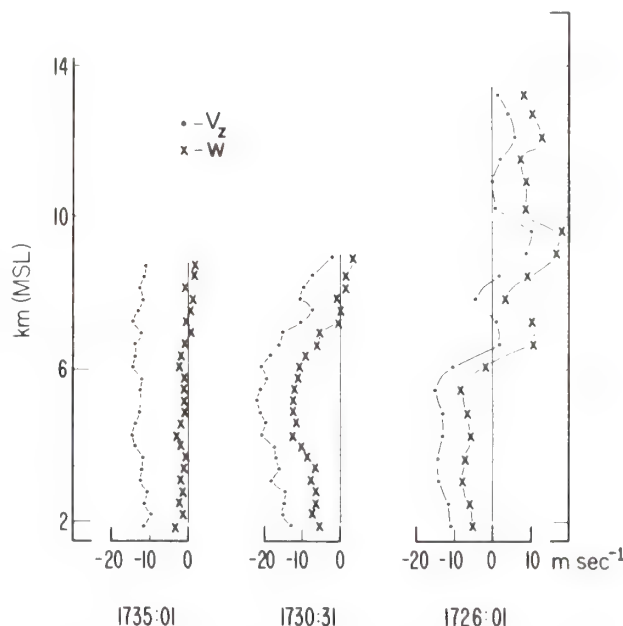
Fig. 3. Vertical particle velocity (V_z) profiles measured by the zenith-pointing radar and vertical wind (W) estimates derived from the Joss-Waldvogel $V_T - Z$ relation.

radars. The 3 cm radar reflectivity contours shown in Fig. 5a are plotted from data acquired between 1727 and 1729:40 while the radar scanned through 16 elevation angles. The time-height plot of 10 cm radar reflectivity factor shown in Fig. 4a is a 30 min history of the reflectivity over Radar A. Reflectivity plotted in Figs. 4a and 5a should have been the same if 1) attenuation of the 3-cm radar was negligible, 2) the storm track was from 354° during the time period 1720 to 1750, 3) the storm was in steady-state during this time, and 4) both radars were properly calibrated. None of these conditions was precisely satisfied. Reflectivity gradients at the leading and trailing edges of the storm appear similar in the two plots, although the measured reflectivity values were greatly different. Attenuation of the 3 cm radar signals would be most noticeable at mid-level of the leading edge of the storm, but the 3 cm radar reflectivity contours portray a structure similar to that depicted by the 10 cm radar.

The radial velocity field (measured by Radar B) shown in Fig. 5b corresponds to the time and location of the reflectivity data shown in Fig. 5a. The velocity contours are absolute velocities; there is no correction for the echo motion and no correction for the terminal fall velocity contribution. Negative velocities are directed toward Radar B and positive velocities are directed away from it. Strong updrafts were measured above Radar A during the time these data were collected by Radar B. The velocity field in Fig. 5b suggests the location of the updraft even without verification from Radar A. Air feeding the updraft entered the storm from the right side of Fig. 5b (Part I). Fig. 5b indicates that the air was moving into the storm at mid-levels

(a)
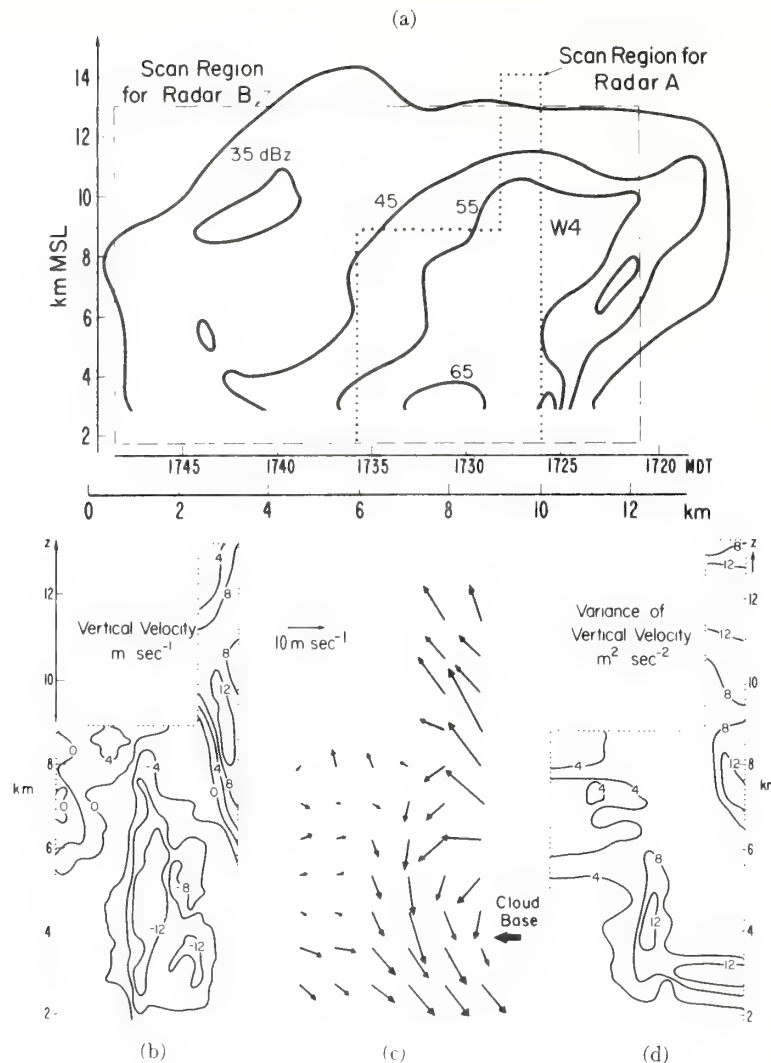
FIG. 4. (a) Time-height presentation of 10 cm reflectivity contours measured over the zenith-pointing Doppler radar and the scan regions for the Doppler radars. (b) Averaged vertical wind contours measured by the zenith-pointing radar from 1726 to 1736 MDT. (c) Two-dimensional air motion relative to the storm echo motion in the vertical plane through the two Doppler radars. (d) Averaged velocity variance measured by the zenith-pointing radar.

with a horizontal velocity component as high as 10 m s⁻¹ relative to the storm. The region of high radial velocity gradient above Radar A clearly defines the interface that existed between the updraft and downdraft. The measured component of air flow at the rear of the storm above 7.5 km was generally similar to that in the near environment as measured by the nearest representative radiosonde. Mid-level air was overtaking the storm from the backside at 6.5 to 8.5 km altitude. The outflow at the top of the storm had a strong northward component of more than 15 m sec⁻¹ relative to the storm. The trend of the radial velocity in the y direction suggests that weak outflow at the top of the storm could have occurred in the direction of echo motion. It

seems unlikely that this implied weak outflow would have been strong enough to have led to particle recirculation to account for the few larger hailstones found in this storm. The velocity field shown in Fig. 5b is in agreement with photographs which show a small anvil overhang in the direction of echo motion (Part II) and a large anvil overhang toward the northeast. The surface anemometer readings of 13 to 17 m s⁻¹ are higher than the velocities seen by the radar in the gust front, and they therefore indicate that the strongest low-level outflow in the direction of echo motion occurred in the lowest few hundred meters; this was not observed by the radar.

b. Air motion in horizontal planes

Fig. 6(a)–(c) shows the radial velocity fields measured by Radar B at 3 altitudes. These data were acquired during the time period 1727 to 1729:40. The lowest altitude is labeled 1.8 km, but the antenna pattern at elevation angles corresponding to this altitude was distorted by ground blocking so the data shown for this altitude are actually more representative of the wind field at about 2.1 km. The radial velocity fields in Fig. 6 are not corrected for echo motion. The velocity field at low altitude reveals outflow in the direction opposite the echo motion and also outflow in the gust front. The radial velocity field at 6.5 km (Fig. 6b) shows the strong convergence of the updraft air at the south or leading edge of the storm and the downdraft air from the backside that was overtaking the storm over a wide area. Two regions of air moving into the storm (contours labeled -2 m s^{-1}) probably correspond to the two distinct inflow branches toward W4 and W5 as identified in Part I. The main updraft of W4 had just advected past Radar A at this altitude when these data were acquired. The maximum radial velocity shear indicated by these contours is about 5×10^{-3} s^{-1} whereas the data prior to interpolation indicate peak shear values greater than 10^{-2} s^{-1}. The updraft and downdraft regions of the storm were readily distinguished on the basis of the radial velocity fields measured by Radar B because inflow and outflow parallel to the direction of storm motion was observed as radial velocity. The low and mid-level radar data in Fig. 6 show that the cell that passed over Radar A was contiguous with a line of cells that formed about 30 km to the east.

The radial velocity contours at 11.5 km (Fig. 6c) show the strong divergence near the top of the updraft. Particle velocities at this level appeared as though the particles were ejected from a fountain. The motion relative to the storm was strongly toward the north over a wide area at the back of the storm. The environmental winds at this altitude were from the west-southwest at about 12 m s^{-1}, corresponding to a radial component of only about 3 m s^{-1}. Particle velocity with a southerly component of 4 to 7 m s^{-1}, nearly equal to the echo motion, occurred in front of the updraft at 11.5 km altitude so that some outflow in the direction of echo motion was likely.

c. Distribution of turbulence inferred from the variance of the velocity

There are three major factors that can contribute to the variance or second moment of the Doppler spectrum measured by a radar with a narrow beamwidth: wind shear, turbulence, and the spread of particle fall speed in still air (Atlas, 1964). The contribution to the variance caused by fall speeds is given by $\sigma_D^2 \sin^2\theta$ where σ_D^2 is the variance that would be observed in still air
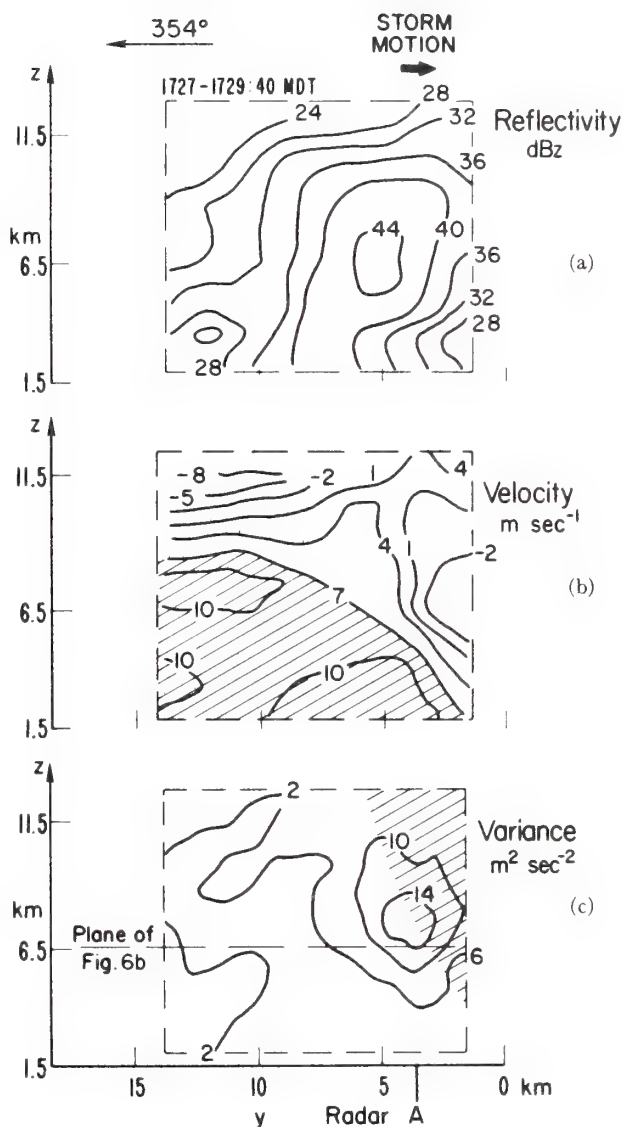
FIG. 5. (a) Three-centimeter radar reflectivity, (b) radial particle velocity, and (c) velocity variance measured by Radar B in the vertical plane through the two Doppler radars. The region inside the dashed lines corresponds to the scan region for Radar B shown in Fig. 4a. The shaded region in b indicates radial velocities that exceed the echo motion of 7 m s^{-1}. The shaded region in (c) indicates where the zenith-pointing radar measured the main updraft. Radar B was located at $y = 52.2$ km.

at vertical incidence. σ_D^2 is about 1 m^2 s^{-2} for rainfall and is nearly independent of rainfall rate (Lhermitte, 1963). For hail with a maximum diameter of 1.5 cm, as occurred in this storm, σ_D^2 is 4 to 6 m^2 s^{-2} (Battan, 1974). The variance caused by wind gradients parallel to the radar beam is given by (Sirmans and Doviak, 1973)

$$\frac{(k_R h)^2}{12}$$
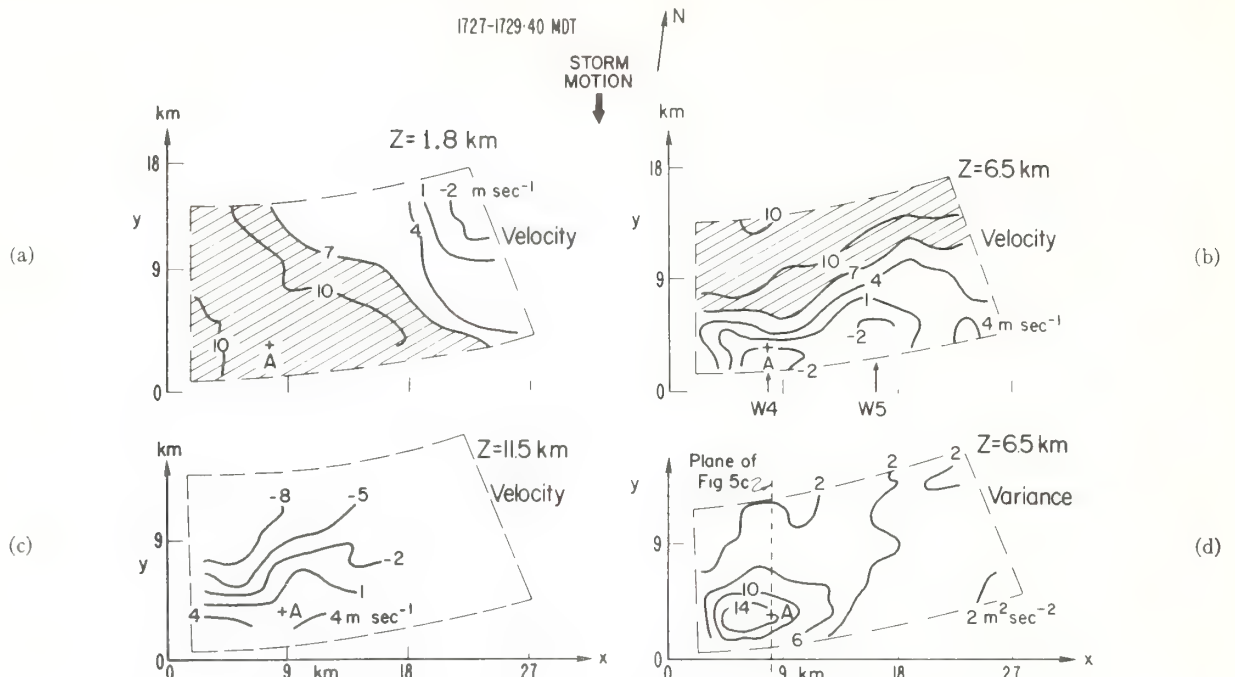
Fig. 6. Radial particle velocity (absolute) at (a) 1.8 km altitude, (b) 6.5 km altitude, and (c) 11.5 km altitude measured by Radar B located 50 km north of the storm. The shaded regions indicate radial velocities that exceed the storm motion of 7 m s⁻¹. (d) Velocity variance at 6.5 km altitude. The scan regions are the same as those shown in Fig. 1.

where k_R is the radial shear (s⁻¹) along the beam and h is the pulse length. For shear across the beam, the variance contribution is given by $(0.3\ k_T\ R\Phi)^2$, where k_T is the radial shear transverse to the beam (Nathanson, 1969, p. 207), R is the range, and Φ is the one-way half-power beamwidth.

All factors that contribute to the variance must be considered for the zenith-pointing radar but the fall speed spread can be neglected for the quasi-horizontally scanning radar because the contribution caused by fall speed was at most 0.08 m² s⁻² in rain and 0.5 m² s⁻² in hail. The measured variances in this storm were much greater than 0.5 m² s⁻² in regions where hail was probably present and much greater than 0.08 throughout the storm. Since the fall speed spread was negligible for the scanning radar and since the radial velocity field was measured throughout the storm, thus making the radial shear known, the turbulence throughout the storm could be calculated from the variance field measured by the scanning radar (Strauch et al., 1975).

The velocity variance measured by Radar A is shown in Fig. 4d and the variance measured by Radar B is shown in Figs. 5c and 6d. Variance data from the zenith-pointing radar were contoured after smoothing by taking an 8-point (5 s) average. High variances were observed by Radar A in two regions of the storm: at mid-levels where Radar B also measured high variances and just below cloud base where Radar B did not measure high variance. The low-level band of high vari-

ance must therefore be attributed to spread in particle fall speeds. In fact, shear or turbulence would have caused Radar B to measure larger variances than Radar A because the pulse volume of Radar B was much larger. The large variance at mid-levels seen by Radar A were caused, in part, by shear and turbulence. Fig. 2 shows that its beamwidth was too large to resolve strong local horizontal gradients in the updraft, so this kind of local shear would be interpreted as turbulence in its contribution to the variance. Variances measured by Radar B (Figs. 5c and 6d) at the back of the storm were less than 2 m² s⁻² and can be attributed to vertical gradients of the radial velocity since the vertical shear of 5×10^{-3} s⁻¹, seen in Fig. 5b, is sufficient to cause a variance exceeding 2 m² s⁻². On the other hand, the core of large variance between 5.5 and 9.5 km in Figs. 5c and 6d cannot be attributed to shear because the large shear in this region was parallel to the beam, and its contribution to the variance was small since the pulse length was only 75 m. This region contains large gradients in the vertical velocity (Fig. 4c) but these gradients do not contribute significantly to the variance observed by Radar B. We conclude that the high variance core measured by Radar B was caused mainly by turbulence generated by the large horizontal shear of the vertical wind at the interface between updraft and downdraft. The dissipation rate, ϵ, derived from the velocity variance field measured by Radar B varied from less than 30 cm² s⁻³ at the back of the storm to

more than 3000 cm² s⁻³ in the region between the up-draft and downdraft (Strauch *et al.*, 1975). These values span the entire range of values measured by aircraft in clear air turbulence.

We assumed that the outer scale in the inertial sub-range was larger than the largest dimensions of the radar pulse volume (800 m). Energy spectra with a −5/3 power law to scales greater than 1.5 km have been measured with penetration aircraft in thunder-storms (Steiner and Rhyne, 1962). The radial velocity fields shown in Figs. 5b and 6a seem to indicate that the outer scale is no larger than the radar resolution since they do not contain fluctuations at scales of 1 to 2 km. However, the interpolations used to transform the measured data to Cartesian grid points filtered the energy spectrum at scale sizes between the radar beam-width and the outer scale so the radial velocity fields show only organized motions. Spectra measured with penetration aircraft in severe Oklahoma storms (Steiner and Rhyne, 1962) showed dissipation rates that ex-ceeded those measured by our radar.

6. Conclusions

The Doppler radar measurements described consti-tute a unique data set because, for the first time, a zenith-pointing radar observed part of the storm as it advected overhead while, at the same time, a scanning Doppler radar obtained the three-dimensional field of reflectivity, radial velocity, and the velocity variance of the radial velocity in a volume that included the updraft of a convective storm. The Doppler radar data do not provide the total picture, but they display more of the kinematic structure than can be obtained by other instruments.

The data obtained by the scanning Doppler radar illustrate both the utility and the limitations of single Doppler radar measurements. The radial velocity field from a single radar cannot yield the unambiguous three-dimensional wind fields that can be derived from dual-Doppler measurements; however, many features of the overall air motion in convective storms can be inferred from the radial velocity fields. This is especially true if, as in this case, the primary motion of the air entering and leaving the storm is in a vertical plane radial to the radar.

The second moment of the Doppler spectrum, ob-tained by a Doppler radar scanning the entire storm at low elevation angles, portrays regions of high shear and turbulence. The turbulence contribution can be isolated because shear can be inferred from the radial velocity fields. Measurement of the second moment fields and their evolution requires only a single radar. These data have not previously been fully utilized by radar mete-orologists, but they can, in principle, provide a warning of dangerous turbulence or wind shear conditions and can aid in understanding how seed material or tracers will diffuse in a storm.

REFERENCES

Atlas, D., 1964: Advances in radar meteorology. *Advances in Geophysics*, Vol. 10, Academic Press, 318–478.

——, R. C. Srivastava and R. S. Sekhon, 1973: Doppler radar characteristics of precipitation at vertical incidence. *Rev. Geophys. Space Phys.*, **11**, 1–35.

Battan, L. J., 1974: Doppler radar observations of a hailstorm. *J. Appl. Meteor.*, **14**, 98–108.

Berger, T. and H. L. Groginsky, 1973: Estimation of the spectral moments of pulse trains. International Conf. Information Theory. Tel Aviv, Israel.

Browning, K. A., T. W. Harrold, A. J. Wyman and J. G. C. Beimers, 1968: Horizontal and vertical air motion and pre-cipitation growth within a shower. *Quart. J. Roy. Meteor. Soc.*, **94**, 498–509.

Foote, G. B., and P. S. du Toit, 1969: Terminal velocity of rain-drops aloft. *J. Appl. Meteor.*, **8**, 249–253.

Frisch, A. S., L. J. Miller and R. G. Strauch, 1974: Three-dimen-sional air motion measured in snow. *Geophys. Res. Lett.*, **1**, 86–89.

Joss, J., and A. Waldvogel, 1970: Raindrop size distribution and Doppler velocities. *Preprints 14th Radar Meteor. Conf.*, Tucson, Ariz., Amer. Meteor., Soc., 153–156.

Lhermitte, R. M., 1963: Motions of scatterers and the variance of the mean intensity of weather radar signals. Sperry Rand Res. Center, 5RRC-RR-63-57, 25–28, Sudbury, Mass.

Miller, K. S., and M. M. Rochwarger, 1970: On estimating spectral moments in the presence of colored noise. *IEEE Trans. Inform. Theory*, **IT-16**, 303–309.

Nathanson, F. E., 1969: *Radar Design Principles; Signal Proces-sing and the Environment*. McGraw-Hill, 626 pp.

Newton, C. W., 1963: Dynamics of severe convective storms. *Meteor. Monographs*, **5**, No. 27, 33–58.

Sirmans, D., and R. J. Doviak, 1973: Meteorological radar signal estimates. NOAA Tech. Memo. *ERL-NSSL-64*, U. S. Dept. of Commerce, Norman, Okla., 80 pp. [NTIS No. COM-73-11923/2AS].

Steiner, R., and R. H. Rhyne, 1962: Some measured character-istics of severe storm turbulence. National Severe Storms Project, Report No. 10, U. S. Dept. of Commerce [NTIS No. N62-16401].

Strauch, R. G., A. S. Frisch, and W. B. Sweezy, 1975: Doppler radar measurements of turbulence, shear, and dissipation rates in a convective storm. *Preprints 16th Radar Meteor. Conf.*, Houston, Tex., Amer. Meteor. Soc., 83–88.

A Field Observation of Atmospheric Free Convection

D. E. FITZJARRALD

NOAA Environmental Research Laboratories, Boulder, Colo. 80302

(Manuscript received 17 March 1975, in revised form 1 December 1975)

ABSTRACT

Measurements during periods of atmospheric free convection have been made using acoustic echo sounders and conventional wind sensors on a meteorological tower. Comparison of data from the two instrument systems shows good agreement. Fourier analysis of the data indicates that the predominant horizontal scales of motion are approximately six times the depth of the convecting layer, in good agreement with laboratory convection experiments.

1. Introduction

The purposes of this paper are twofold. The first is to analyze and interpret time variations in the velocity and temperature structure measured during a period of atmospheric free convection. The second purpose is to compare an *in situ* measurement of wind with an acoustic sounder during convective activity.

The atmospheric data presented below are taken from sensors which are fixed in position. To get approximation of spatial variations using Taylor's hypothesis the flow irregularities must be passively advected past the measuring point. Spatial disturbances that propagate at some velocity in addition to the wind will cause the observer to misinterpret their size. Thus, convection rolls that are lined up along the wind and propagate slowly in a lateral direction appear the same as large convection cells. Since both these possibilities are observed in atmospheric convection, single-point measurements of time variations will not yield unambiguous pictures of the spatial changes. In the interpretation of the data given here, the ambiguities in interpretation of time variations will be noted.

A particularly important characteristic of turbulent convection which is the object of the present investigation is the predominant horizontal scale of motion observed in the flow. Laboratory experiments in closed convection boxes using air as the working fluid (Deardorff and Willis, 1967; Fitzjarrald, 1976) have established that there exists a predominant horizontal scale, which depends upon the amount of thermal instability present. At high thermal instability the dominant horizontal scale measured midway through the layer is found to be several times larger than the depth of the convecting layer. Other laboratory experiments, using silicon oils or water as the working fluid, allow better visualization (Busse and Whitehead, 1974) and have clarified the process by which the convection proceeds from the readily understood convection rolls through a series of flow instabilities to a complex superposition of time-varying motion. A flow instability which leads to motions of a horizontal scale similar to those observed in turbulent experiments in air has been termed the "collective instability" (Busse and Whitehead, 1974). While no theoretical analysis has yet been possible, the occurrence of similar horizontal scales in different experiments suggests that such motions are ubiquitous in turbulent convective flows.

Of course, atmospheric convection differs in several respects from closed-box, Rayleigh convection experiments. The latter are symmetric about the mid-plane with a cold upper boundary and hot lower boundary, while the atmospheric convection has no fixed upper boundary and is not symmetric. Atmospheric convection generally occurs together with a larger scale wind field, so that there is shear present in the lowest layers. No shear is present in laboratory convection experiments.

In spite of these differences Rayleigh convection experiments remain the best candidates with which to compare measurements of the horizontal scale in atmospheric free convection. In these cases the shear is confined to a thin layer, with the Monin-Obuhkov length L being quite small. The velocity and temperature variances in Rayleigh experiments and atmospheric convection above the shear layer scale with the convective velocity w_* and temperature T_* (Deardorff, 1970; Willis and Deardorff, 1974; Fitzjarrald, 1976). Until reliable measurements of the dominant horizontal scales are possible in experiments that more closely resemble the atmosphere, such as the apparatus of Willis and Deardorff (1974), the Rayleigh convection experiments are the closest link between easily observed and controlled laboratory flows and atmospheric observations. We will therefore attempt to
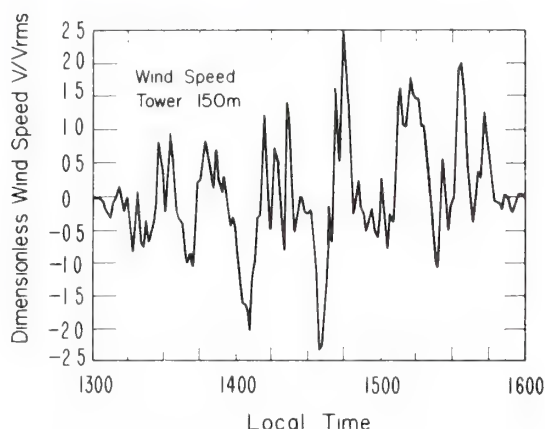
FIG. 1a. Time variation of tower wind speed at 150 m. Mean wind speed of 4.6 m s^{-1} has been removed, and values scaled by rms wind speed of 1.4 m s^{-1}. First and last 10% are tapered to zero using cosine. Data are filtered and decimated using $d = 15$.
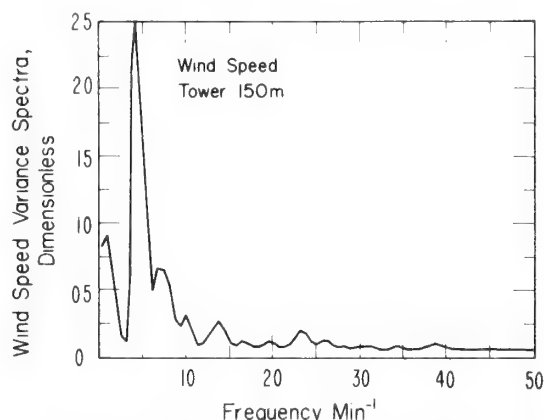
FIG. 1b. Variance spectra of wind speed. Highest frequency unattenuated by low-pass filter is 0.37 min^{-1}.

compare the predominant horizontal scales as measured in laboratory and atmospheric convection, taking care to stay well away from the boundaries in both cases.

2. Instrumentation and data acquisition

The data to be discussed below were acquired on 10 August 1972 at Haswell, Colo. We shall be concerned with horizontal and vertical velocities measured by a bivane at a height of 150 m on a meteorological tower and with acoustic echo sounder data from a vertically pointing sounder. Kjelaas and Ochs (1974) have described the tower arrangement and compared surface convergence, as measured by a laser array, with the acoustic sounder output. The measurement array and acoustic sounder setup have been described in detail by Gaynor et al. (1974), together with comparisons of vertical vorticity and convergence from

the laser array. Both of the aforementioned studies were concerned with the time period from 1400 to 1500 local time on 10 August 1972, while in the present study we shall analyze the entire period from 1300 to 1600 local time.

The acoustic sounder operated at 2750 Hz with 40 ms pulse length and had a beam width of approximately 4°. The repetition period was 4 s, and the intensity of echo return for each sounding was digitized into 248 records, resulting in a height resolution of 2.7 m. Nine digitized values centered at a height of 300 m were averaged together, corresponding approximately to a 25 m thick layer centered at 300 m.

The tower data were transferred from the original records to digital tape with one record each second. Four of these records were averaged together so that the time series for all measured quantities were identical with one data point every 4 s.

To minimize computations and to concentrate on frequencies of interest in the present case, the data have been low-pass filtered (Ormsby, 1961) and decimated; that is, the digital filters were centered every d data points, where d is the decimation ratio. The new Nyquist frequency is therefore reduced by d and becomes $S/2d$, where S is the sampling frequency (0.25 Hz). The low-pass filter was chosen to have unity gain at frequencies below 0.75 $S/2d$, with a linear decrease to zero gain at the reduced Nyquist frequency $S/2d$. The value of d used below is 15, so that there is one data point per minute. The highest frequency which is unattenuated is therefore 0.00625 Hz. The half-widths of the digital filters were at least $10d$ in all cases to be discussed below. The mean was removed from the raw data before filtering, and the values were scaled by the rms deviation.

3. Filtered data and variance spectra

The results of the above process are shown in Fig. 1a for the wind speed measured at 150 m on the tower. To avoid difficulties with the spectral analysis to follow, the first and last 10% of the filtered data series have been tapered down to zero using a cosine taper. The mean wind speed for the entire time sequence was 4.6 m s^{-1} and the rms deviation from the mean by which the values in Fig. 1a are scaled was 1.4 m s^{-1}. There are 160 points in the filtered, decimated time series from 1300 to 1600. Using conventional techniques the variance spectra were calculated for the data of Fig. 1a, and the spectral results are shown in Fig. 1b. The spectra have been smoothed so that the variance at frequency f has been replaced by

$$V'(f) = \tfrac{1}{4} V(f - \Delta f) + \tfrac{1}{2} V(f) + \tfrac{1}{4} V(f + \Delta f).$$

A strong spectral peak is seen to occur at a period of 23 min, a periodicity which can readily be identified in the filtered data in Fig. 1a.

Using identical procedures the data for acoustic intensity at 300 m were calculated and are presented in Fig. 2a. Monostatic acoustic sounders are sensitive to temperature fluctuations of the order of one-half the acoustic wavelength. This half-wavelength is ~7 cm in the present case. In convective conditions the echo returns are strongest in the center of convective elements which originate at the surface and weak in the descending air between. Facsimile records of the echo intensity from 1400 to 1500 local time have been presented by Gaynor *et al.* (1974) and by Kjelaas and Ochs (1974), together with an overlay of the surface convergence. A detailed study of acoustic echo intensity within convective plumes has been presented by Hall *et al.* (1975).

It is clear that areas of strong echo intensity are characterized by surface convergence and rising motion. Thus, analyzing the echo intensity gives a clear picture of time variance of convective elements being advected across the measuring volume. The variance spectra of echo intensity at 300 m are shown in Fig. 2b.
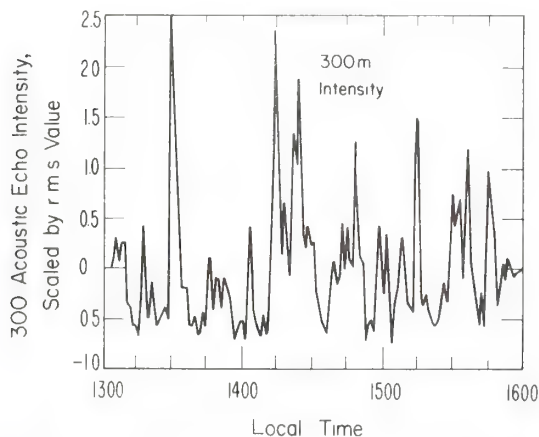
Fig. 2a. As in Fig. 1a except for acoustic-sounder echo intensity at 300 m.
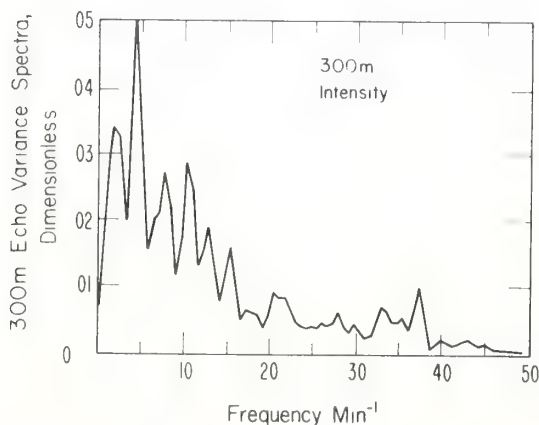
Fig. 2b. As in Fig. 1b except for variance spectra of echo intensity at 300 m.
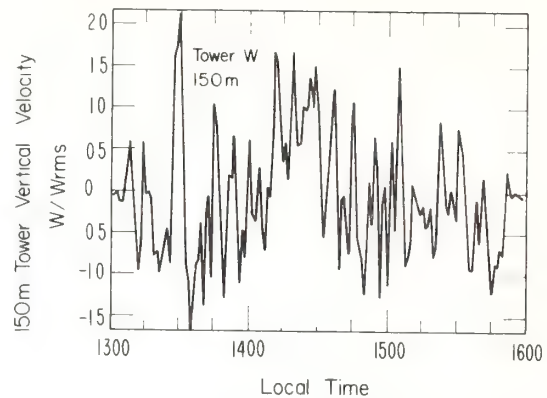
Fig. 3a. As in Fig. 1a except for tower vertical velocity at 150 m and a mean vertical velocity of 0.46 m s⁻¹, rms vertical velocity of 1.15 m s⁻¹.
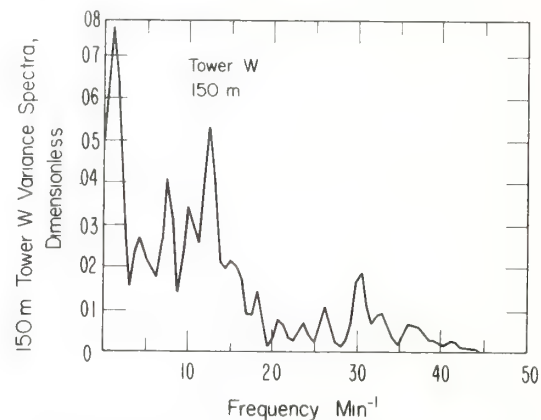
Fig. 3b. As in Fig. 1b except for variance spectra of tower vertical velocity.

The dominant peak at 23 min can again be clearly seen. Since there are over seven waves of 23 min periods in the total time series, it is believed that this is a significant peak. Examination of the filtered data shows it to be evident, especially in the data of Fig. 1a.

In Fig. 3a, the vertical velocity measured at 150 m on the tower is presented. We see that there is more high-frequency variance, and this is confirmed by the variance spectra in Fig. 3b. A strong peak is evident at a period of 8 min. In addition, a strong low-frequency peak is seen at a period of 80 min. This low-frequency change can be seen in the data of Fig. 3a and is caused by the period of very strong convection from 1400 to 1500. No significance is attached to this very low frequency peak, since there are only two waves in the entire time series.

4. Discussion of results

A strong peak at 23 min is evident in both the spectra of the 150 m wind speed and 300 m acoustic

intensity. Inspection of the data of Figs. 1a and 2a shows that these two time series are indeed highly correlated, with the only notable exception in the entire 3 h period being the intensity peak at 1405 that corresponds to a minimum of the wind speed. Obtaining the same frequency with two such dissimilar instruments indicates that this frequency does represent a significant temporal variation in the flow.

However, the same frequency is not apparent in the vertical velocity spectra of Fig. 3b. Evidently, the horizontal wind field adjusts well to the large-scale oscillation at 23 min and damps out the higher frequencies present in the vertical velocity. The oscillations which show up in Figs. 1 and 2 represent convective elements large enough to have significant small-scale temperature fluctuations at 300 m and a significant effect on the wind field. The depth of the layer of significant motion, as measured by a Doppler radar sensing chaff (Frisch and Chadwick, 1975), is ~1 km. Therefore, these thermal elements are well into the convecting layer. These deep convective elements of low frequency that are evident in Figs. 1 and 2 are most suitable for comparison with laboratory experiments and will be emphasized here.

Keeping in mind the limitations of inferring spacial scales from single-point temporal measurements, the oscillation of 23 min corresponds to a scale of 6350 m using the mean wind. The study of Kjelaas and Ochs (1974) has shown that there is very little shear above the 90 m level, so that convective elements are nearly vertical as they are advected past the sensors. The scale found above is in good agreement with that found by a true spatial measurement taken with the Doppler radar at 1300 local time (Frisch and Chadwick, 1975).

The horizontal wavelength is therefore about six times the depth of the convective layer, which is in close agreement with the dominant scale obtained in Rayleigh convection experiments (Fitzjarrald, 1976). This is an important result and should be useful in further investigations of both the atmospheric flows and the nature of convective turbulence.

As was noted in the Introduction, there are other possible interpretations of the time spectra presented here. We have assumed that the convective cells are of indeterminant but rather uniform horizontal extent and are simply advected past the sensor by the mean wind. An equally plausible explanation would be long, steady convection rolls which propagate slowly across the sensors. However, in the absence of any further indications, such as aircraft data or cloud lines, we must regard the uniform horizontal advected cells as at least equally probable. Certainly, both convection rolls and cells are both often observed in atmospheric flows.

5. Conclusions and suggestions for further work

We have seen an indication that horizontal scales of motion exist in atmospheric free convection and scale to those measured in laboratory experiments. Further work along this line should include examination of longer time series to increase the confidence in spectral peaks which were found here and aircraft data to determine the horizontal extent of convective elements. Data taken during different stability conditions and with differing convection layer depths are necessary to establish their effects on the horizontal scales of motion.

An investigation of the vertical dependence of horizontal scales in both atmospheric and laboratory convective flows will also be a useful contribution. The upper bounding analyses (Busse, 1969) provide a guide to the vertical variation in convection, but these theories may be of limited use in analyzing the results of real flow (Fitzjarrald, 1976).

The present study has presented further comparison between data obtained with the indirect measurements of acoustic sounders and with *in situ* measurements on a meteorological tower. Each time that these instruments are used their usefulness and limitations become more apparent. Further studies will also contribute to this knowledge.

Preliminary work has begun on analysis of the acoustic sounder records obtained during the GATE experiment of 1974. A number of very long, mostly steady convective conditions were recorded that should provide the opportunity to investigate the above-mentioned topics.

REFERENCES

Busse, F. H., 1969: On Howard's upper bound for heat transport by turbulent convection. *J. Fluid Mech.*, **37**, 457–477.
——, and J. A. Whitehead, 1974: Oscillatory and collective instabilities in large Prandtl number convection. *J. Fluid Mech.*, **64**, 67–79.
Deardorff, J. W., 1970: Convective velocity and temperature scales for the unstable planetary boundary layer and for Rayleigh convection. *J. Atmos. Sci.*, **28**, 1211–1213.
——, and G. E. Willis, 1967: Investigation of turbulent thermal convection between horizontal plates. *J. Fluid Mech.*, **28**, 675–704.
Fitzjarrald, D. E., 1976: An experimental study of turbulent convection in air *J. Fluid Mech.* (in press).
Frisch, A. S., and R. B Chadwick, 1975: Observations of velocity fields and velocity spectra in the convective boundary layer

using a dual-Doppler radar system *Preprints 16th Radar Meteorology. Conf.*, Houston, Tex., Amer. Meteor. Soc., 237–242

Gaynor, J. E., F. F. Hall, Jr., J. G. Edinger and G. R. Ochs, 1974: Measurement of vorticity in the surface layer using an acoustic sounder array. Submitted to *Remote Sens. Environ.*

Hall, F. F., Jr., J. G. Edinger and W. D. Neff, 1975: Convective plumes in the planetary boundary layer, investigated with an acoustic echo sounder. *J. Appl. Meteor.*, **14**, 513–523.

Kjelaas, A. G., and G. R. Ochs, 1974: Study of divergence in the boundary layer using optical propagation techniques. *J. Appl. Meteor.*, **13**, 242–248.

Ormsby, J. F. A., 1961: Design of numerical filters with applications to missile data processing. *J. Assoc. Comput. Mach.*, **8**, 440–466.

Willis, G. E., and J. W. Deardorff, 1974: A laboratory model of the unstable planetary boundary layer. *J. Atmos. Sci.*, **31**, 1297–1307.

Acoustic Doppler Measurement of Atmospheric Boundary Layer Velocity Structure Functions and Energy Dissipation Rates

J. E. Gaynor

Wave Propagation Laboratory, NOAA Environmental Research Laboratory, Boulder, Colo. 80302

(Manuscript received 2 April 1976, in revised form 24 January 1977)

ABSTRACT

Acoustic echo sounder (echosonde) and meteorological tower measurements of the turbulent velocity structure parameters $D(\mathbf{r})$ and C_v^2 and the rate of dissipation of turbulent energy ϵ are compared. The two acoustic Doppler methods attempted, utilizing pulse differencing and Taylor hypothesis approaches, show good agreement. The small discrepancy in these parameters between the tower and echosonde is explained by the wind noise and ambient noise characteristics of the echosonde and by the effects of pulse volume averaging. Time-averaged, acoustically derived C_v^2 values are compared with acoustic facsimile records in both stable and unstable atmospheric conditions. The temporal and (implicitly) the spatial variations of C_v^2 were observed to be large, and correlated well with echosonde-detected waves, turbulent layers and thermal plumes. The hour-average vertical ϵ profiles for the two stability cases show reasonable comparison with those calculated by other investigators.

1. Introduction

The ability to measure the intensity of velocity turbulence in the atmosphere either *in situ* or remotely has been of great concern to meteorologists over the years. A knowledge of the turbulence structure can allow a derivation of the dissipation of turbulent energy, which, at times, is a very important parameter in the energy balance of the atmosphere.

The next section offers a brief discussion of the relations between measures of velocity turbulence, acoustic scattering and rate of dissipation of turbulent kinetic energy ϵ. Methods of measuring ϵ are identified; a new method, based on an acoustic Doppler echosounding technique, is described in this paper.

2. Velocity turbulence and acoustic scattering

A common measure of the velocity turbulence, the longitudinal velocity structure function, is defined by Tatarskii (1971) as

$$D_{rr}(\mathbf{r}) = \langle [V_r(\mathbf{r}_1) - V_r(\mathbf{r}_1 + \mathbf{r})]^2 \rangle, \quad (1)$$

where, following his notation, $V_r(\mathbf{r}_1)$ is the velocity along $\mathbf{r}$ at a position $\mathbf{r}_1$ and $V_r(\mathbf{r}_1 + \mathbf{r})$ is the velocity along $\mathbf{r}$ at position $\mathbf{r}_1 + \mathbf{r}$. The angle braces denote a mean value. The direction of $\mathbf{r}$ relative to a particular wind component will depend on the data analysis method and will be described later. We can use a similar equation for $V_t(\mathbf{r}_1)$ and $V_t(\mathbf{r}_1 + \mathbf{r})$, velocity components perpendicular to $\mathbf{r}$, to obtain the transverse structure function $D_{tt}(\mathbf{r})$.

For locally isotropic turbulence, Tatarskii (1971) derived the spectral form of the structure function

$$D_{11}(\mathbf{r}) = 2D_{tt}(\mathbf{r}) + D_{rr}(\mathbf{r}) = 2 \int\int_{-\infty}^{+\infty}\!\!\!\int (1 - \cos\mathbf{k}\cdot\mathbf{r})$$
$$\times \Phi_{11}(\mathbf{k})d^3\mathbf{k}, \quad (2)$$

where $\mathbf{k}$ is the vector wavenumber and $\phi_{11}(\mathbf{k})$ the three-dimensional spectral density function of the wind velocity.

The structure parameter of turbulent velocity C_v is related to the velocity structure function $D_{11}(\mathbf{r})$ by

$$C_v^2(\mathbf{r}) = \frac{D_{11}(\mathbf{r})}{r^{\frac{2}{3}}}. \quad (3)$$

The term C_v^2, related to the acoustic refractive-index variations of the atmosphere caused by turbulent velocity fluctuations, is one of the important parameters included in the scattering equation of acoustic waves (Little, 1969):

$$\sigma(\theta) = 0.03k^{\frac{1}{3}}\cos^2\theta\left[\frac{C_v^2}{c^2}\cos^2(\theta/2) + 0.13\frac{C_T^2}{T^2}\right]$$
$$\times (\sin\theta/2)^{-11/3}, \quad (4)$$

where $\sigma(\theta)$ is the acoustic power of wavelength λ scattered, per unit volume, per unit incident power. The quantity θ is the scattering angle measured from the incident direction, $k = 2\pi/\lambda$, c is the speed of sound,

T the absolute air temperature and $C_T{}^2$ the temperature structure parameter. In the derivation of (4) the Kolmogorov spectrum of turbulence is assumed. The value of $C_v{}^2$ in (4) is derived from the longitudinal structure function $D_{rr}(\mathbf{r})$.

The relation between the velocity structure parameter and the important (but difficult to measure) rate of dissipation of turbulent kinetic energy ϵ is (Tatarskii, 1971)

$$\epsilon^{\frac{1}{3}} = \frac{C_v{}^2}{\beta}, \tag{5}$$

where $\beta \approx 2$. Eq. (5) assumes locally isotropic turbulence and that the data are measured at scales less than the outer scale of turbulence, i.e., in the inertial subrange. The assumption in (5) is that in this subrange

$$E(k) \propto \epsilon^{\frac{2}{3}} k^{-5/3}, \tag{6}$$

where $E(k)$ is the scalar spectral energy density function and $k = |\mathbf{k}|$. Eqs. (2) and (3) show that $C_v{}^2$ can be related to the energy density for any component and therefore to ϵ. The proportionality factor β in (5) can be determined experimentally by measuring $E(k)$ and $C_v{}^2$ in the inertial subrange (Kaimal, 1973).

Some investigators (e.g., Taylor, 1955; Ball, 1961; Record and Cramer, 1966; Volkovitskaya and Ivanov, 1970) have used the definition of $D_{rr}(\mathbf{r})$ in (1) to estimate ϵ using meteorological tower data. Eq. (1) was usually altered to account for the rather slow response of the instruments. More recently, much work has been done (e.g., Ivanov, 1962; Lenschow, 1970; Taylor, 1972; Lenschow, 1974) in applying the spectral definition of $D_{11}(\mathbf{r})$ in (2) using tower and aircraft data.

In the past few years electromagnetic Doppler radar has presented a new data source for turbulent energy dissipation measurements. Gorelik and Mel'nichuk (1968) and Knyazev (1971) have used these data to obtain ϵ employing the spectral technique. Mel'nichuk (1968) used Doppler radar data to derive ϵ using (1). Velocity turbulence can also broaden the width of the Doppler spectrum in an electromagnetic radar return (Kapitanov et al., 1972) and an acoustic return (Brown, 1974). This effect allows for another method of calculating ϵ using the second moment of a Doppler return. For radar, this was done very approximately by Gorelik and Patsaeva (1968) and in much more detail by Frisch and Clifford (1974).

The very brief discussion presented above on velocity turbulence and its relation to scattering of acoustic energy in (4) suggests three possible methods of obtaining $C_v{}^2$ or $D_{11}(\mathbf{r})$ and hence ϵ using echosondes. These methods were also alluded to by Derr and Little (1970). One obvious but experimentally difficult technique would be to use (4). Knowing $\sigma(\theta)$ from the scattered return and measuring $C_T{}^2$ from monostatic backscatter ($\theta = 180°$) (Neff, 1975), we could solve for $C_v{}^2$ at inertial subrange scales. This method presents

some problems as discussed by Neff: the requirement of extremely accurate instrument calibrations and the failure of the beam-filling assumption in the presence of thin, stable lamina in the boundary layer. A second method would be to follow the work of Frisch and Clifford (1974) who used radar data and measure the second moment of the acoustic Doppler return. This would allow calculations of ϵ in the lower few hundred meters where radar data are difficult to obtain because of ground clutter; the acoustic Doppler return would not depend on the presence of rain, snow, chaff or other scatterers as with most microwave Doppler radars. The second-moment technique is now being developed using echosonde data. The method requires considerable care because spectral widening does not result from velocity turbulence alone, but to noise, finite beamwidth and pulse modulation, all of which could be of the same order (Spizzichino, 1974). The second moment integrates the effect of the turbulence on scales up to the dimension of the pulse volume ($\sim$30 m), while the angle dependence method [Eq. (4)] measures $C_v{}^2$, the strength of turbulence at spatial scales $(\lambda/2)\sin(\theta/2)$ [$\sim$0.1 m], where λ is the acoustic wavelength and θ is the scattering angle. The third technique of deriving ϵ using echosonde data would be to obtain Doppler derived winds and use (1) to calculate $D_{rr}(\mathbf{r})$ or $D_{tt}(\mathbf{r})$. Two versions of this method, one measuring $D_{rr}(\mathbf{r})$ and the other $D_{tt}(\mathbf{r})$, were used in this study.

The Doppler method (as it will be termed) is simple and measures the effect of the turbulence on scales up to the separation of the pulse volumes ($>$30 m). In the future, it is hoped to combine all three techniques to derive ϵ from measurements at various scales. The objective of the current work is to prove the reliability of the Doppler-differencing method only.

3. The experimental method

The data were taken from an August 1972 field experiment conducted near Haswell, Colo. (Little and Gossard, 1975). The site consisted of a 150 m meteorological tower equipped with bivanes at five equally spaced levels, the lowest being at 30 m above the surface of the ground. Three echosondes in a triangular array were located about 300 m northwest of the tower. A schematic map of the site including the sounder array is shown in Fig. 1. One echosonde was pointed vertically, and the other two were tilted so that their antenna beams intersected at about 150 m above the surface.

The Doppler frequencies were identified using a tracking filter. When this filter tracks during a period of time when the signal-to-noise ratio is occasionally low, the resulting averaged winds would be slightly underestimated compared to the tower values. Using the method described by Beran and Clifford (1972), the component of the wind along the beam was calculated using digitized monostatic acoustic backscattered Doppler and intensity returns. Because of problems in
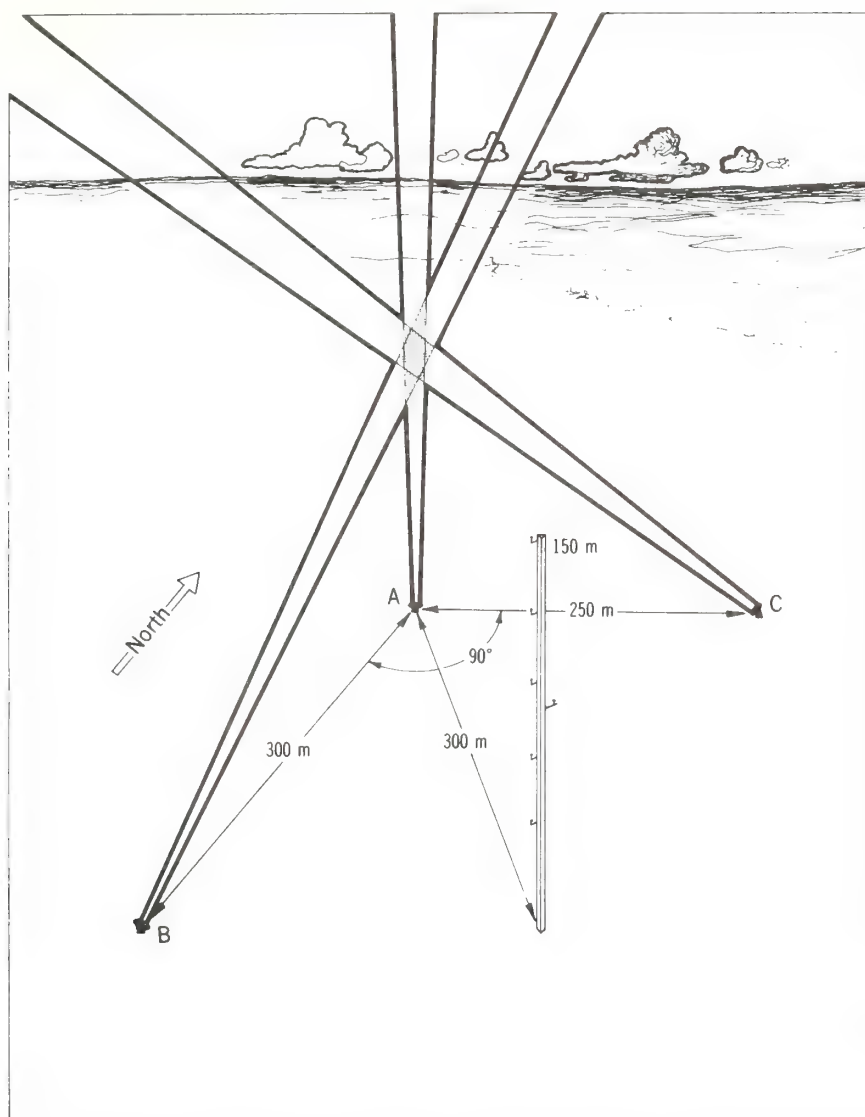
Fig. 1. Schematic of the experimental configuration at Haswell, Colo., in 1972, including the three echosondes (A vertical, B and C tilted to meet A at a common sounding volume) and the 150 m meteorological tower located 300 m southeast of echosonde A.

the electronics of one of the echosondes, the fluctuating part of the Doppler wind along the slanted beam in the north-south direction (or what we call the y direction) was not available. Except for the common volume, the three wind components were not measured in precisely the same region. However, averaging the derived structure functions for no less than 5 min and up to 1 h and being interested in data taken only in the inertial subrange seems to provide adequate average winds.

Two time periods were chosen for analysis to represent convectively unstable and statically stable boundary layers. The three echosondes synchronously pulsed every 8 s during the stable period (0600–0700 MST 5 August) and every 4 s during the unstable period (1400–1500 MST 10 August).

Because C_v^2 is a scalar function of the vector $\mathbf{r}$, we can calculate this function for various orientations of $\mathbf{r}$ relative to the wind components. Using (1) and (3) we calculated C_{vz}^2 (for $\mathbf{r}$ horizontal and the wind vertical) and C_{vx}^2 (for $\mathbf{r}$ horizontal and the east-west wind component along the beam) from the acoustic Doppler data. The bivanes on the five levels of the tower allowed us to calculate C_v^2 for the three orientations of wind velocity relative to the horizontal at those levels using (1) and Taylor's hypothesis. The velocity orientations were orthogonal, being vertical, east-west and north-south. The C_{vz}^2 values from tower and sounder could be compared exactly at similar heights above the surface while the C_{vx}^2 values, with the velocity vector tilted from the horizontal for the sounder and horizontal for the tower, could be compared only approxi-

mately. The true horizontal wind component for C_v^2 could have been calculated from the three-echosonde combination, but use of the fluctuating vertical wind component must be made for this calculation. This means the horizontal and vertical values of C_v^2 would not be independent, making the usefulness of these measurements somewhat doubtful. In any case, a tilted wind component for C_v^2 allows for a measure of the degree of anisotropy of velocity turbulence. The normal boundary-layer convention is to use orthogonal components relative to the mean horizontal wind. We are forced to use coordinates relative to north because data from echosonde B (Fig. 1) were noisy. The boundary layer convention requires velocity variance data from echosonde B.

The velocity structure function in (1) can be calculated in two ways. The first is to calculate two-point vertical velocity differences between the fixed levels of the tower and, in a similar way, between gates on an acoustic pulse return (pulse differencing). This is a longitudinal measure of the structure function $D_{rr}(\mathbf{r})$. The second method uses Taylor's relation $\bar{V}\tau = r$, where τ is time, $\bar{V}$ the average horizontal wind and $r = |\mathbf{r}|$, to transform (1) into a time domain. Then we calculate a transverse structure function $D_{tt}(\mathbf{r})$ at a particular level. For the echosondes, $\bar{V}$ was calculated using the three Doppler components from the three sounders averaged for 1 h. Table 1 shows the comparison of the two methods for $r \approx 35$ m and centered at a height of 150 m after using (3) to compute C_{vz}^2. We use the C_{vz}^2 notation for both longitudinal and transverse measures for simplicity. Also included are the tower data. The comparison is fairly good when we consider the three orders of magnitude difference between the stable and unstable cases. Through the remainder of this work the results of the Taylor method are reported because the results are closer to the tower values. Also, this method allows us to calculate C_v^2 at fixed levels for a wide range of effective separations r.

4. Results

An example of the calculated results of the vertical structure function, denoted by D_z (a notation for D_{tt} computed using the vertical winds), is presented in Fig. 2 for the unstable case comparing the tower and echosonde values. The height chosen was 150 m. An

TABLE 1. Results of two methods of calculating C_{vz}^2 ($m^2 s^{-2} m^{-\frac{1}{3}}$) for $r \approx 35$ m at a height of 150 m above the ground, averaged for an hour in each case using echosonde data. Also included are the tower data for the two cases.

Stability case	Pulse differencing	Taylor hypothesis	Tower
0600–0700 5 August	1.30×10^{-3}	0.78×10^{-3}	0.58×10^{-3}
1400–1500 10 August	0.122	0.109	0.084
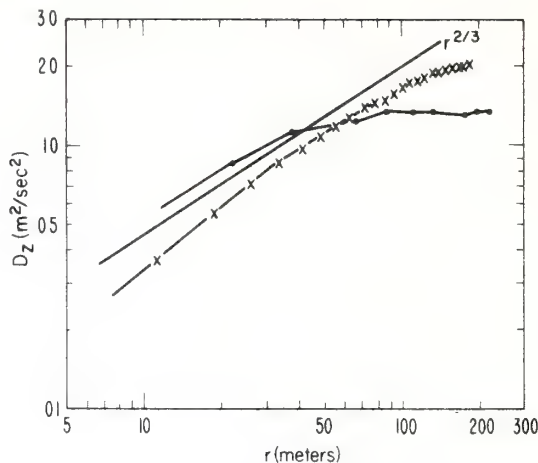
Fig. 2. The vertical velocity structure function D_z for the tower (crosses) and echosonde A (dots) for the unstable period. The $r^{\frac{1}{3}}$ line is shown for reference. The decrease of the slope of the echosonde data at larger scales can be explained by pulse volume filtering of the one-dimensional velocity spectrum.

$r^{\frac{1}{3}}$ line is shown for reference. Where the slopes of the curves are near $\frac{2}{3}$ is generally considered the vicinity of the inertial subrange.

Some of the flatness associated with the curve of the echosonde data may be the result of some wind or instrument (or other) noise. These noise spikes have been carefully identified and replaced by a weighted average of the four data points on each side of the spike. However, some random noise does leak through. This will be shown to be a small effect for the average C_v^2 values.

MacCready (1953), Taylor (1955), Ball (1961), Mel'nichuk (1968) and others have shown the falloff of the structure function from the $\frac{2}{3}$ slope when the separation distance r is of the order of the height of measurement (in this case 150 m). This similar behavior is shown in Fig. 2 for the tower data. The major discrepancy between echosonde-derived and tower-derived D_z, shown in Fig. 2, is the echosonde data's falloff from an approximate $\frac{2}{3}$ slope at smaller r than for the tower data. The explanation of this discrepancy, concerning electromagnetic radar pulse volume filtering, is given by Srivastava and Atlas (1974). They showed that energy at scales large compared to the beam dimensions can be reduced for a one-dimensional spectrum because small scales in orthogonal directions, contributing to the energy, are attenuated due to the pulse volume filtering compared to a one-dimensional point-sensor spectrum. Fig. 6 of their work gives a good qualitative picture of their argument. Srivastava and Atlas used a Gaussian illumination function which is also a good approximation for the echosonde (Hall and Wescott, 1974).

It is necessary here to tie their results briefly into our discussion in Section 2. To do this, we will follow the spectral definition of the velocity structure function.
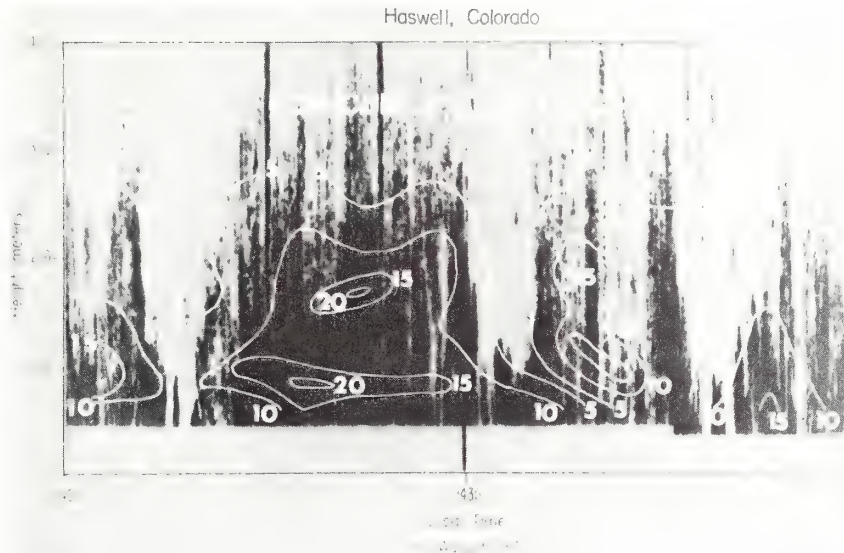
FIG. 3. Acoustic facsimile record with overlayed acoustic Doppler derived values of C_{vz}^2 ($\times 10^{-2}$ m^2 s^{-2} m$^{-\frac{1}{3}}$) with $r \approx 35$ m from the vertically pointing echosonde block averaged for 5 min for the unstable regime.

Using spherical coordinates, we may integrate (2) over the angles to get

$$D_{11}(r) = 8\pi \int_0^\infty \left(1 - \frac{\sin k_1 r}{k_1 r}\right) \Phi_{11}(k) k_1^2 dk_1, \quad (7)$$

where we take k_1 as the wavenumber along the beam and r is measured along the direction of k_1. The velocity spectral density tensor $\phi_v(k)$ is given by

$$\phi_v(k) = \left(1 - \frac{k_1^2}{k^2}\right) \frac{E(k)}{4\pi k^2} \quad (8)$$

for isotropic and incompressible turbulence. Srivastava and Atlas obtained the equation for the beam-filtered spectral density in one dimension, i.e.,

$$\Phi_{11}(k) = \phi_v(k) \left[\frac{\sin(k_1 l/2)}{k_1 l/2}\right]^2 \exp(-\sigma_2 k_2^2 - \sigma_3 k_3^2) \quad (9)$$

after assuming a Gaussian illumination function. In (9), k_1, k_2 and k_3 are the orthogonal wavenumbers, $l = h/2$ (where h is the pulse length) and

$$\sigma_i = 0.3003 B_i, \quad i = 2, 3, \quad (10)$$

with B_2 and B_3 the linear dimensions of the beam perpendicular to the beam axis; $B_2 \approx B_3$ for the echosonde case. Using (9) in (7) yields

$$D_{11}(r) = 8\pi \int_0^\infty \left(1 - \frac{\sin k_1 r}{k_1 r}\right) \phi_v(k) \left[\frac{\sin(k_1 l/2)}{k_1 l/2}\right]^2 k_1^2 dk$$

$$\times \exp[-\sigma^2(k_2^2 + k_3^2)]. \quad (11)$$

Eq. (11) gives the effect of the beam filtering on the velocity structure function for the echosonde. Assuming a half-power beam width between 4° and 5° (Hall and Wescott, 1974), B_i is approximately 12 m for the 150 m level and for the vertical echosonde. The pulse length h is about 13.5 m for the unstable case.

According to the interpretation of the beam filtering in (11) given by Srivastava and Atlas, the smaller effective scale of filtering causes a lessening of the energy falloff at and beyond what we may call the outer scale of the inertial subrange $r = L_0$ (refer to Fig. 2 of Srivastava and Atlas, 1974). This corresponds to the value of r where the slope becomes less than $\frac{2}{3}$ on the graph of D_z for the tower data shown in Fig. 2. The particular value of r, for which this falloff from the $\frac{2}{3}$ slope begins for the echosonde data, depends on the variable relation between the outer scale of turbulence and the effective beam size.

Robinson and Konrad (1974), in a careful spectral comparison of electromagnetic radar Doppler wind fluctuations and winds measured by an aircraft, showed a decrease in spectral density of the Doppler winds beyond scales of about 100 m. Although they attribute this discrepancy to the possible low-frequency drift of the aircraft, it could be that the difference results from the pulse volume filtering discussed above. Mandics (1971) showed a similar decrease of spectral density of acoustic phase difference at much smaller sizes (5–11 m), which he explains as near the outer scale of turbulence. His measurements were taken quite close to the ground, which accounts for the small outer scales.

From (1) and (3), we calculated C_{vz}^2 and C_{vz}^2 for the unstable and stable cases, respectively, with $r \approx 35$

m. Fig. 3 shows C_{vz}^2 5 min block averaged, contoured and overlayed on the echosonde facsimile record. A detailed explanation of echosonde facsimiles is given by McAllister *et al.* (1969). Fig. 4 shows the overlay for C_{vz}^2 averaged for 5 min for the stable period. Both cases indicate large temporal variability but correlate well with the facsimile records. C_v^2 is obviously important in the acoustic scattering equation (4), but can also be related to two-point velocity differences through (1). The larger the C_v^2 values, the larger the velocity variability. We expect this variability to be relatively large within the thermal plumes of Fig. 3 and the layers of breaking waves in Fig. 4, as well as near the surface in both cases. Although it is doubtful relation (5) is valid for such short averaging periods of C_v^2, the large variability of C_v^2 in Figs. 3 and 4 do tend to indicate a large intermittency of ϵ.

C_v^2 was not calculated above 300 m in Fig. 3 nor above 400 m in Fig. 4 because the signal-to-noise ratios became too low for reliable Doppler data above those levels. A note of caution must be introduced when interpreting the contoured C_v^2 values. Signal-to-noise characteristics are at their best for the darker areas of the facsimiles (except when these darker areas represent wind noise on the transducer). The Doppler wind measurements and therefore the dissipation rates may be biased toward these darker areas. Poor signal-to-noise ratios would increase the variance of the Doppler estimates. At the same time, the tracking filter is biased toward zero Doppler shifts when a low signal-to-noise ratio is encountered. This zero bias would decrease the

average value of r in (3) derived from Taylor's hypothesis and therefore increase C_v^2 and ϵ [Eqs. (3) and (5)]. This bias of echosonde-derived C_v^2 and ϵ toward slightly larger values compared with C_v^2 from tower-derived measurements is especially noticeable in Table 1, in Fig. 5 and in the lower levels of Fig. 6. A bistatic system recently tested at the Wave Propagation Laboratory shows promise in overcoming some of the above-stated limitations of direct backscatter data. Scattering at angles other than 90° and 180° is directly sensitive to C_v^2 [Eq. (4)] which is not only a stronger scatterer of acoustic waves on the average, but usually is more widespread in the boundary layer.

An example of 1 h averaged vertical profiles of ϵ derived from C_{vz}^2 ($r \approx 35$ m) using (3) for the unstable case is shown in Fig. 5 for the tower and echosonde data. The agreement between tower and echosonde is good and constancy of ϵ with height above the surface layer is well documented (e.g., Lenschow, 1974).

Assuming stationarity and horizontal homogeneity the turbulence kinetic energy budget in the boundary layer is given by

$$\frac{g}{T}\overline{w'T_v'} - \frac{\partial}{\partial z}\overline{w'(e'+p'/\rho)} + \frac{\tau}{\rho}\cdot\frac{\partial \bar{V}}{\partial z} - \epsilon = 0, \quad (12)$$

where the primes denote a departure from a mean value. T_v' is the virtual temperature, e' the turbulent kinetic energy [$\frac{1}{2}(u'^2+v'^2+w'^2)$], τ the stress and $\partial V/\partial z$ is the mean vertical shear. The nearly constant ϵ with height in Fig. 5 can be explained by the sum of the

Haswell, Colorado
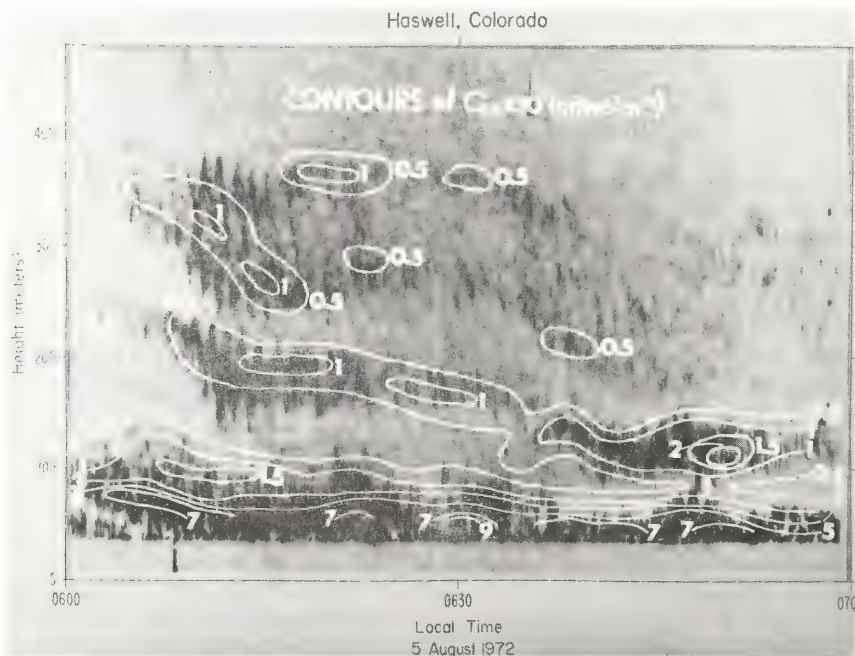
FIG. 4. As in Fig. 3 except for the stable case, $C_{vz}^2 \times 10^{-4}$ m² s⁻² m⁻¹, and a 4 min average.
Note that the contour values at the lower levels are not linearly separated.

approximately linearly decreasing buoyancy generation term with height, represented by the first term in (12), and the linearly increasing vertical transport term, represented by the second term in (12), above the surface layer. The third term in (12), the shear generation, is quite small above the surface layer (Lenschow, 1974). As a further check on the data's validity, the unstable surface layer equation given by Wyngaard and Coté (1971), i.e.,

$$\epsilon = \frac{u_*^3}{\kappa Z}(1+0.5|Z/L|^{\frac{2}{3}})^{\frac{3}{2}},\qquad(13)$$

was used, where κ is von Kármán's constant, u_* the friction velocity, and L the Obukhov length. Using August afternoon data from the 1968 Kansas boundary layer experiment (Izumi, 1971), with $Z=22.63$ m, $u_*=0.33$ m s^{-1} and $Z/L=-1.19$, gives us the circle in Fig. 5. The agreement is excellent. Also, the hourly averaged Richardson number for the Colorado data was calculated to be -1.15 (Gaynor et al., 1977) between 2 and 30 m, which, for an unstable boundary layer, should be (and is) close to Z/L.

The ϵ profile for the stable case derived from C_{vx}^2 ($r \approx 35$ m) is shown in Fig. 6. A similar decrease with height above 30 m is also shown in the results of Readings and Rayment (1969), but the results presented here are about an order of magnitude smaller than their calculations. Using values of u_* and Z/L for stable cases during the 1968 Kansas experiment and using an equation similar to (13) for the stable surface layer from Wyngaard and Coté (1971), we calculate ϵ values approximately twice as large as those in Fig. 6. A likely reason for our smaller ϵ values is that, at the lower levels, ϵ may be based on structure functions calculated for r larger than the outer turbulence scale. A plot similar to that in Fig. 2 for both tower and
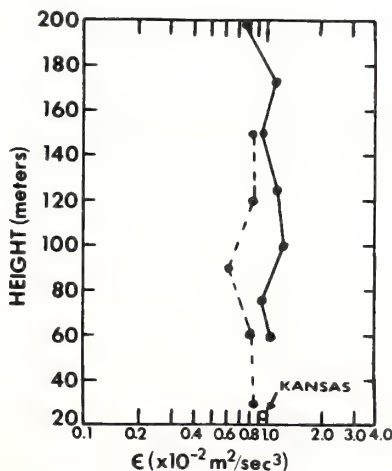
Fig. 5. One-hour averaged vertical profiles of the rate of energy dissipation ϵ for the tower (dashes) and echosonde A (solid line) during the unstable period derived from the structure function of vertical velocity.
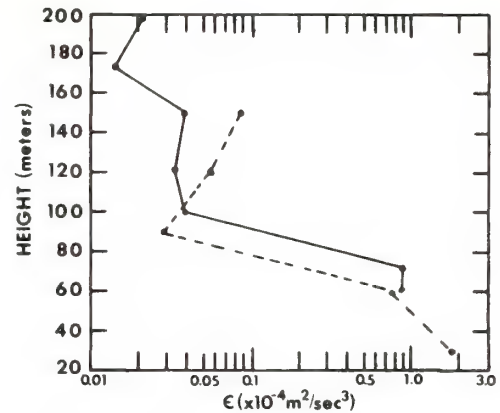
Fig. 6. One-hour averaged vertical profiles of ϵ derived from the structure function of the east-west velocity component from the tower (dashes) and the east-west tilted velocity component from echosonde C (solid line) for the stable case.

echosonde data at the 30 m level does indicate a falloff from a $\frac{2}{3}$ slope at ground $r=15$ m. Because we are using structure functions with $r=35$, ϵ is calculated from D outside the inertial subrange.

In the stable layer, shear generation is important and buoyancy generation is likely small as is vertical transport. Eq. (12) does not contain horizontal transport terms, which may be important in these layers of Kelvin–Helmholtz waves shown in the facsimile records (Fig. 4). The tendency for ϵ values to increase above 90 m may be the effect of energy dissipation in the vicinity of these Kelvin–Helmholtz layer. Such an increase was also noted by Readings and Rayment (1969) at inversion base.

5. Conclusions

The ability of the echosonde to measure the turbulent velocity structure functions $D(r)$ and C_v^2 using Doppler techniques has been demonstrated. Assuming an inertial subrange, the rate of turbulent dissipation ϵ can be calculated for time-averaged data. Compared with the pulse Doppler radar, the echosonde can provide values of ϵ below the lowest height a radar can reliably detect because of ground return. A profile of ϵ can then be obtained down to heights of the order of 40 m with the larger echosondes and, perhaps, down to the order of a few meters with the new microsounders now being tested at the Wave Propagation Laboratory.

As discussed earlier, the Doppler method of obtaining the rate of turbulent energy dissipation is only one of three possible acoustic methods. It is hoped that we can explore the other two methods in the future.

Doppler expertise and to Drs. C. Gordon Little, Freeman Hall, Jr., John Wyngaard and Chandran Kaimal for their helpful suggestions during manuscript preparation.

REFERENCES

Ball, F. K., 1961: Viscous dissipation in the atmosphere. *J. Meteor.*, **18**, 553–557.

Beran, D. W., and S. F. Clifford, 1972: Acoustic Doppler measurements of the total wind vector. *Preprints Second Symp. Meteorological Observations and Instrumentation*, San Diego, Calif., Amer. Meteor. Soc., 100–109.

Brown, E. H., 1974: Turbulent spectral broadening of backscatter acoustic pulse. *J. Acoust. Soc. Amer.*, **56**, 1398–1406.

Derr, V. E., and C. G. Little, 1970: A comparison of remote sensing of the clear atmosphere by optical, radio, and acoustic radar techniques. *Appl. Opt.*, **9**, 1976–1992.

Frisch, A. S., and S. F. Clifford, 1974: A study of convection capped by a stable layer using Doppler radar and acoustic echo sounders. *J. Atmos. Sci.*, **31**, 1622–1628.

Gaynor, J. E., F. F. Hall, Jr., J. G. Edinger and G. R. Ochs, 1977: Measurement of vorticity in the surface layer using an acoustic sounder array. *Remote Sensing Environ.* (in press).

Gorelik, A. G., and V. A. Parsaeva, 1968: Radar study of turbulent-flow structure in earth-adjacent layer for sub-frontal clouds and precipitation. *Proc. Third All-Union Conf. Radar Meteorology*, Moscow [Jerusalem, Israel Program for Scientific Translations, 142–150].

——, and Yu V. Mel'nichuk, 1968: A new method for measuring dissipation rate of turbulence in clouds and precipitation using conventional radar. *Proc. Third All-Union Conf. Radar Meteorology*, Moscow [Jerusalem, Israel Program for Scientific Translations, 150–156].

Hall, F. F., Jr., and J. W. Wescott, 1974: Acoustic antennas for atmospheric echo sounding. *J. Acoust. Soc. Amer.*, **56**, 1376–1382.

Izumi, Y., 1971: Kansas 1968 field program data report. Environ. Res. Pap., No. 379, Air Force Cambridge Research Laboratories, Bedford, Mass.

Ivanov, V. N., 1962: Turbulent energy dissipation in the atmosphere. *Izv. Akad. Nauk SSSR Bull. Geophys. Ser.*, **9**, 788–791.

Kaimal, J. C., 1973: Turbulent spectra, length scales and structure parameters in the stable surface layer. *Bound-Layer Meteor.*, **4**, 289–309.

Kapitanov, V. A., Yu. V. Mel'nichuk and A. A. Chernikov, 1972: The shape of the spectrum of radar echoes from precipitation. *Izv. Atmos. Oceanic Phys.*, **8**, 963–972.

Knyazev, L. V., 1971: Determination of the rate of dissipation of turbulent energy from radar data. *Izv. Atmos. Oceanic Phys.*, **7**, 1201–1205.

Lenschow, D. H., 1970: Airplane measurements of planetary boundary layer structure. *J. Appl. Meteor.*, **9**, 874–884.

——, 1974: Model of the height variation of the turbulence kinetic energy budget in the unstable planetary boundary layer. *J. Atmos. Sci.*, **31**, 465–474.

Little, C. G., 1969: Acoustic methods for the remote probing of the lower atmosphere. *Proc. IEEE*, **57**, 571–578.

——, and E. E. Gossard, 1975: The 1972 Haswell, Colorado, atmospheric boundary layer experiment. *Preprints Third Symp. Meteorological Observations and Instrumentation*, Washington, D. C., Amer. Meteor. Soc., 187–192.

MacCready, P. B., Jr., 1953: Structure of turbulence. *J. Meteor.*, **10**, 434–449.

Mandics, P. A., 1971: Line-of-sight acoustical probing of atmospheric turbulence. Tech. Rep. 4502-1, Stanford Electronics Labs., Stanford, Calif., 92 p.

McAllister, L. G., J. R. Pollard, A. R. Mahoney and P. J. R. Shaw, 1969: Acoustic sounding-A new approach to the study of atmospheric structure. *Proc. IEEE*, **57**, 579–587.

Mel'nichuk, Yu. V., 1968: Structure of horizontal wind fluctuations in precipitation according to radar data. *Proc. Third All-Union Conf. Radar Meteorology*, Moscow [Jerusalem, Israel Program for Scientific Translations, 132–142].

Neff, W. D., 1975: Quantitative evaluation of acoustic echoes from the planetary boundary layer. NOAA Tech. Rep., ERL 322-WPL 38, U. S. Govt. Printing Office, Washington, D. C., 34 pp.

Readings, C. J., and D. R. Rayment, 1969: The high frequency fluctuation of the wind in the first kilometer of the atmosphere. *Radio Sci.*, **4**, 1127–1131.

Record, F. A., and H. E. Cramer, 1966: Turbulent energy dissipation rates and exchange processes above a non-homogeneous surface. *Quart. J. Roy. Meteor. Soc.*, **92**, 519–532.

Robinson, F. L., and T. G. Konrad, 1974: A comparison of the turbulent fluctuations in clear air convection measured simultaneously by aircraft and Doppler radar. *J. Appl. Meteor.*, **13**, 481–487.

Spizzichino, A., 1974: Discussion of the operating conditions of a Doppler sodar. *J. Geophys. Res.*, **79**, 5585–5591.

Srivastava, R. C., and D. Atlas, 1974: Effect of finite radar pulse volume on turbulence measurements. *J. Appl. Meteor.*, **13**, 472–480.

Tatarskii, V. I., 1971: *The Effects of the Turbulent Atmosphere on Wave Propagation.* [Jerusalem, Israel Program for Scientific Translations, 472 pp].

Taylor, R. J., 1955: Some observations of wind velocity auto-correlations in the lowest layers of the atmosphere. *Aust. J. Phys.*, **8**, 535–544.

——, 1972: Aircraft measurements of dissipation of turbulent kinetic energy. *Quart. J. Roy. Meteor. Soc.*, **98**, 658–661.

Volkovitskaya, Z. I., and V. N. Ivanov, 1970: Turbulent energy dissipation in the atmospheric boundary layer. *Izv. Atmos. Oceanic Phys.*, **6**, 435–444.

Wyngaard, J. C., and O. R. Coté, 1971: The budgets of turbulent kinetic energy and temperature variance in the atmospheric surface layer. *J. Atmos. Sci.*, **28**, 190–201.

Measurement of Vorticity in the Surface Layer Using an Acoustic Echo Sounder Array

J. E. GAYNOR, F. F. HALL, JR., J. G. EDINGER*, and G. R. OCHS

NOAA/ERL/Wave Propagation Laboratory, Boulder, Colorado 80302

The earth's atmospheric surface layer is usually defined as that region of the lower atmosphere (generally below about 10 m above the earth's surface) where surface friction causes vertical fluxes of heat, moisture and momentum to be constant with height. Within the surface layer, either in response to surface friction or to the atmosphere above, horizontal circular eddies often develop. These circular motions may provide the source of rotation for dust devils so often seen on hot and dry days particularly in desert regions. Also, at larger scales ($\sim$ 1 km in diameter) regions of warm and therefore buoyant upward moving air, called thermal plumes, may acquire rotation. These plumes may extend from the earth's surface to more than a kilometer in height on a warm afternoon. Fluid dynamicists quantify this horizontal rotation with a parameter known as the vertical component of vorticity. Vorticity is very difficult to measure in the earth's atmosphere at scales of close to a kilometer because the calculation involves wind-speed differences over horizontal distances of about 500 m. The winds must be measured quite accurately because the differences can be quite small and, therefore, the errors in these measurements are often quite large. This work describes a method of measuring vertical vorticity at scales down to 500 m using an array of three acoustic sounders about 2 m above the earth's surface which overcomes some of the accuracy problems mentioned above. We relate these vorticity measurements to other atmospheric parameters and compute temporal spectra of these quantities to help explain the relationship between vorticity, thermal plume activity, and the smaller-scale dust devils.

Introduction

In the earth's atmosphere, the vertical component of vorticity is defined as

$$\zeta = \frac{\partial v}{\partial x} - \frac{\partial u}{\partial y}, \qquad (1)$$

where v is the north-south component of the wind, u is the east-west component, x is a distance-measurement in the east-west direction horizontal to the earth's surface (which is assumed flat in (1) for the relatively short distances considered here), and y is a distance-measurement in the north-south direction. Because ζ is

twice the local average angular velocity, it is a very useful measurement which can be used in momentum equations which include rotating motion.

Improved methods of measuring vorticity in the lower atmospheric layers of the earth are important for a better understanding of atmospheric dynamics. In particular, good vorticity measurements may help to explain how vorticity organizes into dust devils in the unstable boundary layer (usually the layer below 1 km above the earth's surface) and how organized cells with vorticity help in the vertical heat transport from the warm earth's surface.

This paper describes an acoustic method for measuring relatively small-scale (0.5

*Also with Atmospheric Science Dept., UCLA

km $< x$ or $y < 8$ km) vorticity in the surface boundary layers. Supporting data were obtained from acoustic Doppler-derived and meteorological-tower vertical-wind speeds (w) and laser detection of convergence/divergence of the surface wind. Divergence of air-flow from a two-dimensional horizontal area is mathematically defined as

$$D = \frac{\partial u}{\partial x} + \frac{\partial v}{\partial y}, \qquad (2)$$

where the variables are as those defined in (1). If the air is flowing into the region, then we have convergence (or $-D$). Time series of vorticity, vertical wind speed and convergence/divergence data as well as their temporal spectra (plots of the variance of a quantity versus frequency) indicate that these parameters are all closely related signatures of convective thermal plume activity. Thermal plumes are regions of relatively warm, buoyant air rising from the earth's surface particularly on warm days.

Instrumentation and Data Acquisition

The data were acquired at Haswell, Colorado during a summer field experiment in 1972, using echosondes (acoustic echo sounders, Beran et al., 1971) optical lasers (Kjelaas and Ochs, 1974) and a 150-m meteorological tower equipped with temperature sensors and bivanes, which measure the three wind components, at five levels (Little and Gossard, 1975). The site is situated near the center of a shallow "bowl-like" depression, approximately 20 km across and 70 m in depth at an elevation of 1307 m MSL.

The terrain is flat near the tower, with clumps of sparse buffalo grass 15-cm high for a minimum of 3-km radius from the tower. Figure 1 is a map of the echosonde configuration in relation to the optical laser array and to the tower. The sensors in both arrays were located approximately 2-m above the prairie surface.

The method of calculating the vertical component of atmospheric vorticity using the echosondes, each operating at a different audio frequency, and pulsing simultaneously, took advantage of the echosondes' imperfect side-lobe rejection. Each of the three echosondes contained a transducer which translates an electronic pulse into an acoustic pulse which propagated nearly vertically into the atmosphere. However, some of the acoustic energy also "leaks out" horizontally with the earth's surface. When the echosondes are in the receiving mode, this side-lobe acoustic energy from the other nearby echosondes propagates directly to the receiving echosonde. Since each sounder is operating at a different frequency, the source of the received side-lobe can be determined. Because the velocity of sound propagation between the echosondes is

$$V_T = C_d + V, \qquad (3)$$

where C_d is the velocity of sound in dry air ($C_d = 20.05 \sqrt{T}$, where T is the air temperature in K) and V is the velocity caused by the wind vector in the line between two adjacent antennas, all that is necessary is an accurate measurement of the travel times of the sound pulses propagating in each direction between antenna pairs.

HASWELL,COLORADO,FIELD SITE
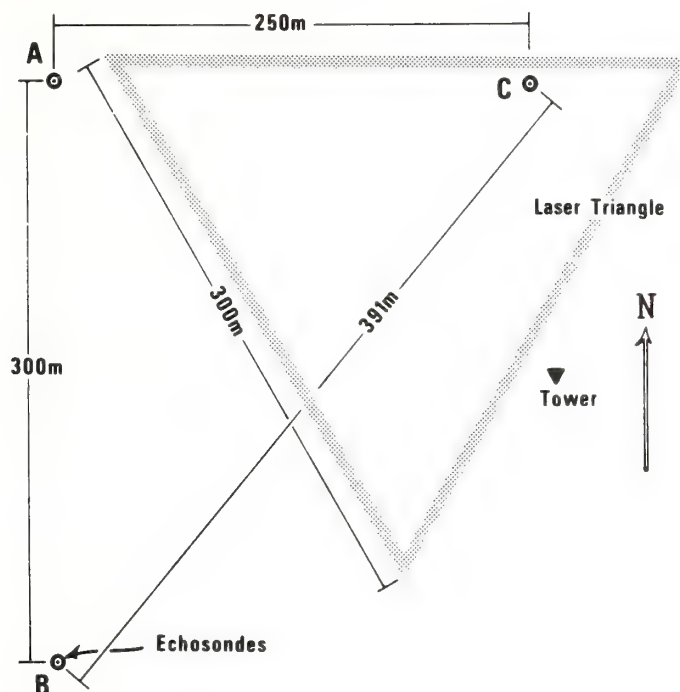
FIG. 1. Location map of the echosonde and laser arrays and the tower.

Using the travel-times of these direct pulses, we do not need to know the temperature of the air to obtain C_d. The average of the two travel-times between antenna pairs would be the expected travel-time between the two antennas if there were no wind parallel to the antennas. This method is similar to that used in acoustic anemometers (Miyake et al., 1971) which give wind speed magnitudes in the direction of acoustic propagation over very short paths. Once C_d and V_T (from the time of travel between one echosonde pair) is known, we can compute V. Obtaining V in the same way for all three echosonde pairs, we calculate the circulation, C, horizontal to the earth's surface using

$$C = V_a X_a + V_b X_b + V_c X_c ,$$

where the V's represent the wind velocities along sides a, b, and c of the echosonde triangle and the X's are the distances along each side. We then divide C by the area enclosed by the array to obtain a measure of vorticity (essentially Stokes' theorem).

Accurately measuring the time required for the direct pulse to travel between

antenna pairs is critical for the vorticity calculations. The received sound intensity data from each antenna were sampled every 2 msec and converted to digital form for computer analysis. The pulse repetition period of the antennas was 4 sec, with all three echosondes synchronized.

The method used to obtain travel times for the vorticity calculations was a "centered-pulse" technique. The first data point on the digital tapes which was three times noise was found; then the next point which was back down to three times noise was located. If these two points were found to be within a certain specified temporal region, the average of the times associated with the two points was taken as the center of the pulse. This was assumed to be the travel time of the direct pulse. The "noise" periods on the tapes were defined as those time periods between the opening of the receivers and the earliest times that the direct pulses could be expected. During those intervals we assumed the antennas were only receiving some background noise and the digitized received intensities averaged for those periods were assumed to represent this noise. At times, perhaps due to refraction of the sound path from strong gusts of vertical wind or cross wind, or because the pulses were buried in ambient noise (mainly caused by wind blowing against the transducers), these direct pulses could not be found and vorticity calculations were not made for those times. This occurred for at least one sounder pair about one-half the time for the 50-min run considered here. The missing points were replaced with a value obtained by linear interpolation between neighboring points.

The largest error in the vorticity results comes from the uncertainty in the exact time of the arrival of the center of the pulse. To illustrate what a timing error can do to the results, suppose an average 10-msec timing error around the array for one pulse event was calculated. (Because of the temporal narrowness of the pulses, this is an extreme error.) This will result in an error of 0.042 sec^{-1} for an instantaneous vorticity measurement, or of 6.5×10^{-3} sec^{-1} for a 2.8-min average. Figure 2 shows that this error is relatively small when compared to the calculated values of the vorticity.

The results of the vorticity measurements are shown in Fig. 2. These are low-pass filtered using the Ormsby digital filter (1961) such that variations with periods of less than 2.8 min are eliminated. The filtering was necessitated by the size of the array. Using an advection speed of vorticity fluctuations of 4 msec^{-1} taken from the horizontal wind speed profiles in Fig. 4 and a resolvable scale of twice the average length of the sides of the echosonde triangle (Fig. 1), we find that variations of periods less than 2.8 min cannot be resolved with an array this large.

Measured convergence/divergence from a laser triangle as described in detail by Kjelaas and Ochs (1974) for the same time period and filtered in the same way as the vorticity data is also presented in Fig. 2. The laser technique uses the drifting scintillation pattern caused by wind-transported refractive-index irregularities in the atmosphere. Using a laser transmitter and two horizontally-spaced

Haswell, Colorado
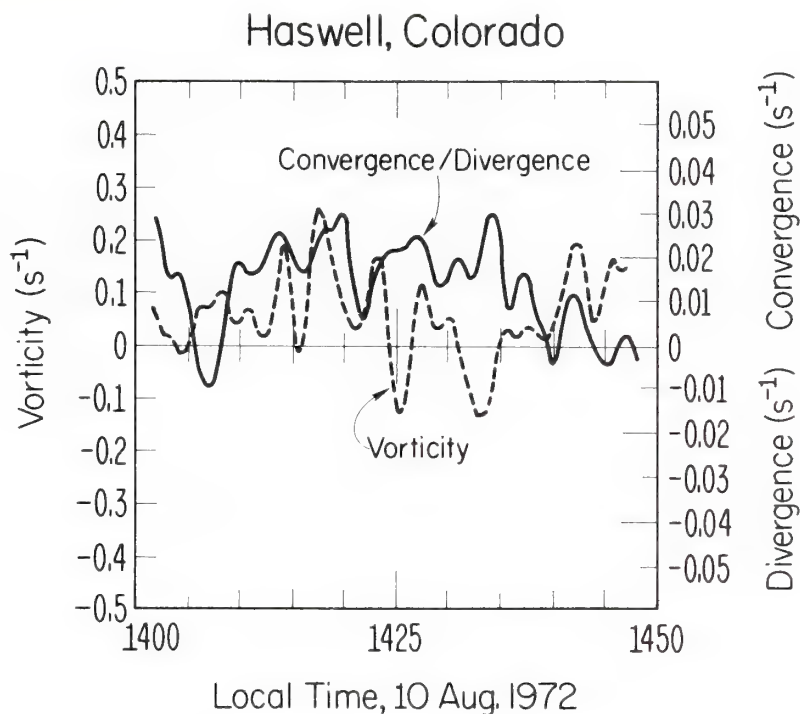
FIG. 2. 2.8-min low-pass filtered vorticity, using a centered pulse technique, and convergence/divergence between 1400-1450 (MDT) on 10 August 1972. Note the different vertical scale for each data set.

detectors a small distance apart and located about 300 m from the transmitter, the horizontal average of the wind perpendicular to the path of light can be calculated. This method requires the assumption of a uniform refractive-index structure constant $(C_n{}^2)$ along the path, and a relation between the slope of the normalized covariance of the logarithms of the signals received at the two detectors at zero delay and the average horizontal wind across the path (Lawrence et al., 1972). With a triangular array of transmitters and receivers as in Fig. 1, a relation essentially the same as that in Eq. (2) can be used to measure the hori-

zontal divergence within the array. Supporting data came from the acoustically-derived, Doppler, vertical velocities (Beran, et al., 1971). This method gives a vertical velocity, w, with an accuracy of 0.1 msec^{-1}. Figure 3 shows a facsimile record of acoustic-echo intensity taken from the vertical echosonde, A, (the other two echosondes were tilted) for the unstable period 1400-1450 hrs. The overlaid contours of Doppler vertical velocities indicate downward motion by the horizontal hatching. The acoustic facsimile in Fig. 3 is a time-height cross-section of backscattered acoustic intensity. The vertically oriented dark streaks which are widest at

HASWELL, COLORADO
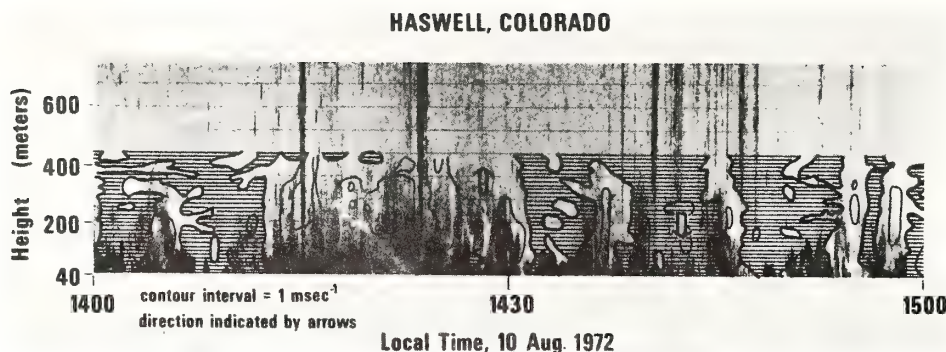
FIG. 3. Facsimile record from vertically pointing sounder during the unstable plume time period on 10 August 1972, with overlayed contours of acoustic Doppler-derived vertical velocities in intervals of 1 msec^{-1} Hashed areas indicate sinking motion.

the top of the record are caused by wind noise blowing on the transducer and echosonde cuff. The less sharp regions darkest at the base of the record and generally disappearing at 400 m are backscattered acoustic signals from the warm and buoyant plumes naturally occurring on an afternoon with an unstable temperature (or density) lapse rate within the surface layer. At the edges and within the plumes we expect considerable turbulent mixing of the warmer air in the plumes with the cooler air outside them. This mixing produces small-scale (~ 0.1 m) temperature differences which can be related to acoustic refractive index variations (Tatarskii, 1971) that cause a portion of the sound to be scattered back (180°). The upward motion agrees well in time with the occurrence of plumes.

Analysis of the Data

Profiles of the average, horizontal wind-speed, wind direction, and temperature from in-situ measurements on the 150-m tower between 1400 and 1500 hrs are shown in Fig. 4. The 2-m level wind has been derived from the laser array. The Richardson number between the 2-m level and the 30-m level averaged for the hour was computed to be -1.15. The Richardson number is defined by the relation

$$ R = \frac{g}{T_0} \frac{\partial \theta}{\partial z} / (\frac{\partial v}{\partial z})^2, \tag{4} $$

where $g = 9.8$ msec^{-2}, the acceleration of gravity, T_0 is the average temperature in some vertical distance $\triangle z$, $\frac{\partial \theta}{\partial z}$ is the potential temperature change in that layer, and $\frac{\partial v}{\partial z}$ is the vertical change of horizontal

TOWER PROFILES

Haswell, Colorado, 1400 - 1500 Local Time, 10 Aug. 1972
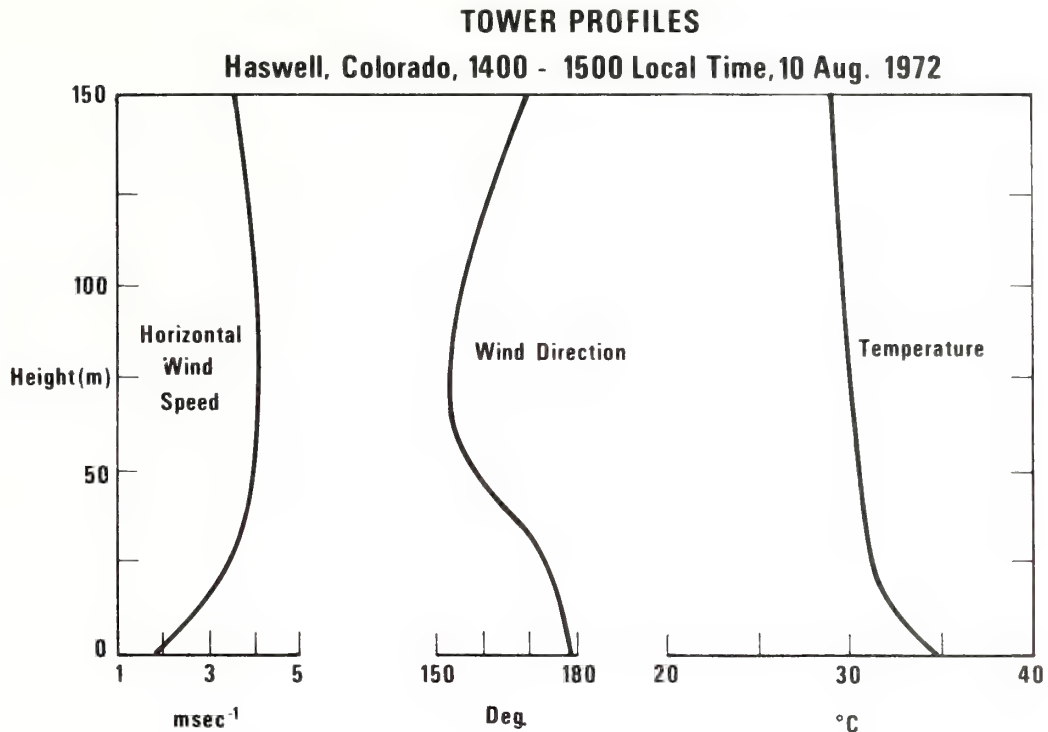
FIG. 4. Average horizontal wind speed, wind direction, and temperature profiles, using the tower data between 1400-1450 (MDT) on 10 August 1972. The surface wind speed and wind direction are taken from the laser array data.

wind (vertical wind shear) within the layer. The potential temperature (θ) is defined as that temperature corresponding to an adiabatic increase from the level of measurement to that level corresponding to an atmospheric pressure of 1000 mb. Therefore, if $\frac{\partial \theta}{\partial z} < 0$, we have an unstable lapse rate within the layer. R is the measure of the relative magnitude of vertical mixing due to buoyancy (the numerator in Eq. (4)) to vertical mixing due to vertical shear (the denominator). Lumley and Panofsky (1964) have pointed out that "free" convection

occurs for $R < -0.03$. During the period considered in this paper, the lower boundary-layer appears well within the free-convection regime.

The filtered-vorticity time-series of Fig. 2 shows a maximum positive value of 0.27 sec^{-1}. This is much smaller than the measurements of Carroll and Ryan (1970) using a paddle-type vorticity meter, but is close to those obtained by Fitzjarrald (1973). Fitzjarrald averaged his vorticity results for about 20 sec.

A large dust devil of nearly 20-m diameter moved through the area enclosed by

the arrays at around 1422-1423 hrs. Vorticity and convergence peaks (negative of divergence is a positive number) in Fig. 2 approximately agree in time with the arrival of the dust devil, and its observed cyclonic-rotation agrees with the positive sign of vorticity. Two, small dust devils appeared near the arrays at 1417-1418 hrs, and a large vorticity-peak occurs at this time with an indication of a broad convergence-peak. The apparent ability to measure the effects of rotation of a dust devil over such a large area compared with the relatively small, dust-devil core size is in disagreement with a hypothesis of Fitzjarrald that the effect of dust-devil rotation does not extend very far from the dust devil itself. Carroll and Ryan, however, indicated a high correlation between the direction of dust-devil rotation and their environmental vorticity measurements. In addition, many of the positive vorticity peaks of Fig. 2 agree well in time with the more intense (darker) plumes seen in Fig. 3.

Temporal spectra were computed for: Doppler-derived and tower w; vorticity; and convergence/divergence; all for the time period from 1400 to 1450 hrs. All the data were highpass filtered to remove variance of periods greater than 17 min and low-pass filtered to remove variance of periods less than 1.6 min. The filter used was that of Ormsby (1961) which improves upon the running ("box") average because of the tapered edges of its response function. A fast-Fourier-transform was used to obtain the spectra and the estimates were smoothed in frequency space using a simple 3-point running average to increase the confi-

dence in the spectral peaks.

Figure 5 shows a temporal spectrum (variance versus frequency) for Doppler-derived w from echosonde A. The 50-min time series was calculated at a level centered at 71.5 m above the surface of the ground. The echosonde actually illuminates a nearly cylindrically-shaped volume approximately 30 m in diameter by 30 m high. The vertical wind speeds are representative of this volume as opposed to the tower vertical wind speeds which are essentially point measurements. The echosonde-w measurements were taken every 4 secs corresponding to the pulse repetition rate. The tower-w measurements were taken every second and at a height of 61 m above the surface. Figure 5 also shows the spectrum of tower w. The tower was located about 300 m upwind from echosonde A. The bimodality of both spectra is quite evident. The higher frequency peak is associated with the individual plumes as seen on the acoustic facsimile in Fig. 3. If we assume the plumes are advected at near the speed of the wind in the boundary layer (Hall et al., 1975), the wind profile in Fig. 4 will give us scales of around 500 m. This is comparable with approximate plume sizes seen by Warner and Telford (1967) and Grant (1965) near the surface. The peak at the lower frequency may correspond to roll vortices (LeMone, 1973) or cellular patterns (Krueger and Fritz, 1961). It is doubtful these larger structures advect at the speed of the mean wind, so scales would be difficult to identify with measurements in one location.

The spectra for the vorticity and convergence/divergence in Fig. 6 do not show

Spectra of Echosonde and Tower w
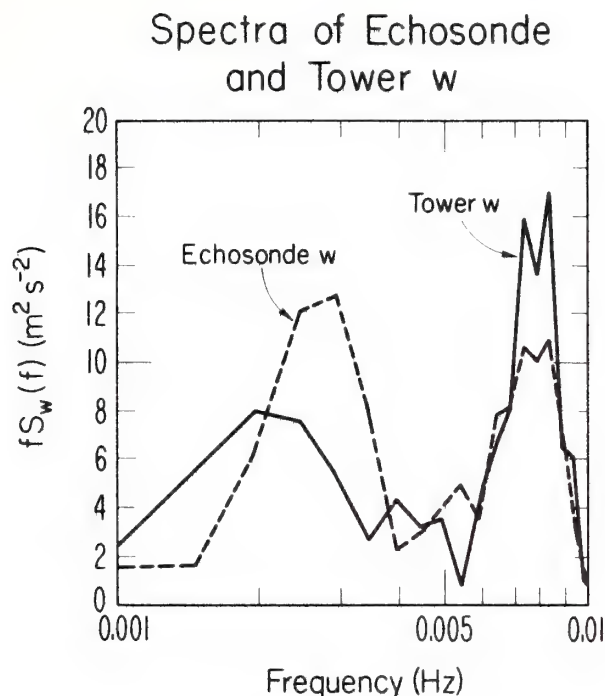
FIG. 5. Spectra of acoustic Doppler-derived and tower w.

a clear bimodality. The vorticity does not have significant variance at the smaller scales (higher frequencies), which is in agreement with the results of Kaimal and Businger (1970) that small individual plumes do not rotate, but the larger scale plume organizations do show rotation. The convergence/divergence spectrum indicates that the small and large plumes also have significant convergence into their bases. The broad regions of rather large variance in vorticity and convergence/divergence at lower frequencies, although not located at precisely the same frequency as the secondary peak of w (Fig. 5), suggest that vorticity, and, to a lesser extent, convergence/divergence are important at the frequencies associated with the larger-scale roll or cellular structures.

Conclusions

The ability of an echosonde array to measure vorticity in the surface layer has been demonstrated for an unstable boundary layer. A few dust devils in and around the echosonde array indicate rotation in the same sense as the larger-scale vorticity-field and correspond to vorticity peaks and regions of convergence. Spectra of vertical velocity from

Spectra Of Vorticity
And Convergence/Divergence
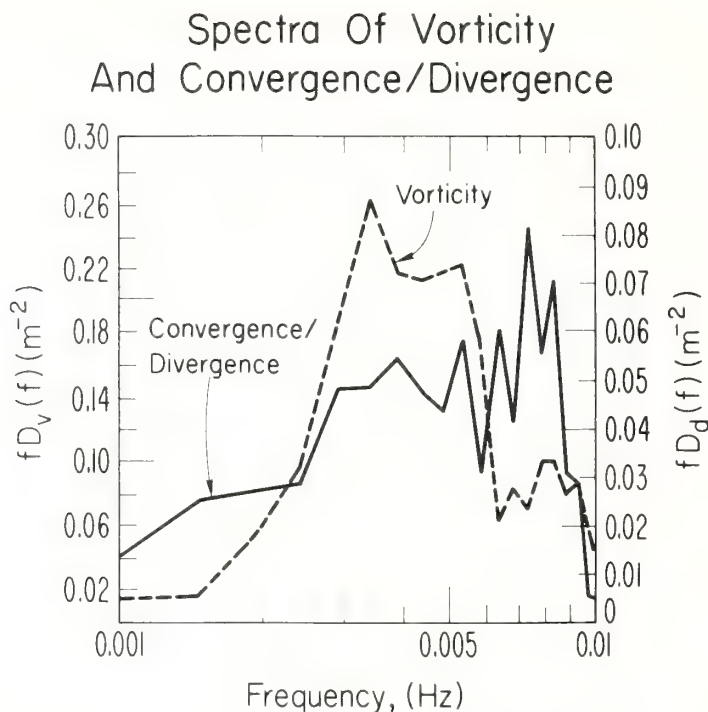
FIG. 6. Spectra of vorticity and convergence/divergence. Note the different vertical scale for each data set. $Dv(f)$ is the spectral density of vorticity and $D_d(f)$ is the spectral density of convergence/divergence.

acoustic Doppler methods and from a nearby meteorological tower show a bimodality, with one mode associated with the individual plume-scales and the other peak perhaps due to larger-scale roll or cellular organization. Although the convergence/divergence spectrum indicates significant variance at the plume scales, the vorticity spectrum shows little variance at the smaller scales and, in particular, significant variance at frequencies approaching the larger-scale organization.

The authors are greatly indebted to J. C. Kaimal and C. G. Little for their very helpful suggestions while preparing this manuscript.

References

Beran, D. W., Little, C. G., and Wilmarth, B. C. (1971) Acoustic Doppler measurements of vertical velocities in the atmosphere, *Nature* **230**, 160-162.

Brooks, F. B. (1960), Rotation of dust devils, *J. Meteor.* **17**, 84-86

Carroll, J. J., and Ryan, J. A. (1970), Atmospheric vorticity and dust devil rotation, *J. Geophys. Res.* **75**, 5179-5184.

Fitzjarrald, D. E., (1973), A field investigation of dust devils, *J. Appl. Meteor.* **12**, 808-813.

Grant, D. R., (1965), Some aspects of convection as measured from aircraft, *Quart. J. Roy. Meteor. Soc.* **91**, 268-281.

Hall, F. F., Jr., Edinger, J. G., and Neff, W. D. (1975), Convective plumes in the planetary boundary layer, investigated with an acoustic echo sounder, *J. Appl. Meteorol.* **14**, 513-523.

Kaimal, J. C., and Businger, J. A. (1970), Case studies of a convective plume and a dust devil, *J. Appl. Meteor.* **9**, 612-620.

Kjelaas, A. G., and Ochs, G. R., (1974), Study of divergence in the boundary layer using optical propagation techniques, *J. Appl. Meteor.* **13**, 242-248.

Krueger, A. F., and Fritz, S. (1961), Cellular cloud patterns revealed by Tyros I, *Tellus,* **13**, 1-7.

Lawrence, R. L., Ochs, G. R., and Clifford, S. F. (1972), The use of scintillations to measure average wind across a light beam, *Appl. Opt.* **11**, 239-243.

LeMone, M. A., (1973), The structure and dynamics of the horizontal roll vortices in the planetary boundary layer, *J. Atmos. Sci.* **30**, 1077-1091.

Little, C. G., and Gossard, E. E. (1975), The 1972 Haswell, Colorado, atmospheric boundary layer experiment, *Preprints, Third Symp. on Meteor. Obs. and Instr.,* Washington, D.C., 10-13 Feb., Amer. Meteor. Soc., 187-192.

Miyake, M., Stewart, R. W., Burling, R. W., Tsvang, L. R., Koprov, B. M., and Kuznetzov, O. A. (1971), Comparison of acoustic instruments in an atmospheric turbulent flow over water, *Boundary-Layer Meteor.* **2**, 228-245.

Ormsby, J. F. A.(1961), Design of numerical filters with application to missile data processing, *J. ACM* **8**, 440-466.

Tatarskii, V. I. (1971), *The Effects of the Turbulent Atmosphere on Wave Propagation,* Israel Program for Scientific Translations, N72-18163, available from NTS, Springfield, Virginia, 472 pp.

Warner, J., and Telford, J. W., (1967), Convection below cloud base, *J. Atmos. Sci.* **24**, 374-382.

STUDIES OF THE TROPICAL MARINE BOUNDARY
LAYER USING ACOUSTIC BACKSCATTERING DURING GATE

J. E. Gaynor, P. A. Mandics, A. B. Wahr, and F. F. Hall, Jr.
Wave Propagation Laboratory
NOAA Environmental Research Laboratories
Boulder, Colorado 80302

1.   INTRODUCTION

        The NOAA Ship OCEANOGRAPHER was out-
fitted with one vertically pointing and two tilted
acoustic antennas, all gyro-mounted, for the GARP
Atlantic Tropical Experiment (GATE). Although the
tilted antenna data quality was degraded by sea
scatter and the noisy ship environment, the ver-
tical antenna provided good quality quantitative
backscattered data. The acoustic facsimile re-
cords showed long periods of weak thermal plume
activity (compared with those observed over land)
produced by ocean surface temperatures that were
consistently 0.5 - 1.0°C warmer than the air 10 m
above. The plume activity was occasionally broken
by periods of increased atmospheric stability re-
sulting from outflows of slightly cooler, drier
and therefore denser air. These outflows were
generated by isolated cumulonimbus cells and per-
sisted for up to 5 hours. During these events,
the tropical marine mixed layer collapsed from
500-600 m thickness to 200 m or less. Organized
squall-line activity similarly stabilized the
mixed layer for up to 17 hours. Results showing a
profile of the rate of dissipation of turbulent
kinetic energy immediately following an outflow
event are presented.

        Under suppressed (fair) weather condi-
tions, "hummock"-shaped echoes appeared at times
with bases near the top of the mixed layer and
above the plume echoes. Evidence is presented
that these hummock echoes are associated with low-
level tropical cumuli. Doppler-derived vertical
velocities show relatively strong upward motions
within these hummocks compared with the plumes
below. Preliminary results indicate that much, if
not most, of the scattering in the plumes and
hummocks is associated with humidity fluctuations.

2.   CONVECTIVE OUTFLOWS

        Fig. 1 illustrates the spectacular
alteration of the mixed layer associated with a
cold air outflow (less than 2°C cooler than the
ambient air) generated by a nearby isolated
tropical convective cell. The figure shows a
time-height facsimile record of the intensity of
the backscattered acoustic returns from refractive
index fluctuations at the λ/2 scale size to
which the acoustic sounder is sensitive when
operating in the backscatter mode. The darker
areas correspond to more intense scattering while
the lighter areas indicate lack of scatter. The
occasional vertical dark lines are caused by am-
bient ship noise. The dark horizontal echo
centered at about 350 m just before the outflow's
arrival at 1620 represents specular acoustic
reflection from the Boundary Layer Instrumentation
System (BLIS) balloon. The event shown in Fig. 1
appears to be quite similar to gravity currents
often occurring over land (Hall et al., 1976).
The cooler air is generated within the cumulo-
nimbus cloud by raindrop evaporation and forced
down by a combination of the air parcel's own

negative buoyancy and the drag on the air by the
falling raindrops. The arrival of the cooler and
drier air strongly increases heat and moisture
fluxes from the sea surface, but the stability
between about 200 and 600 m causes strong con-
vergence of these fluxes in the region between
these levels. The undulating dark echoes between
these two levels are indicative of the turbulent
moisture and temperature mixing between the warmer
and moister air above and the cooler, drier, and
denser air below.

OSS OCEANOGRAPHER
GATE POSITION NO. 4
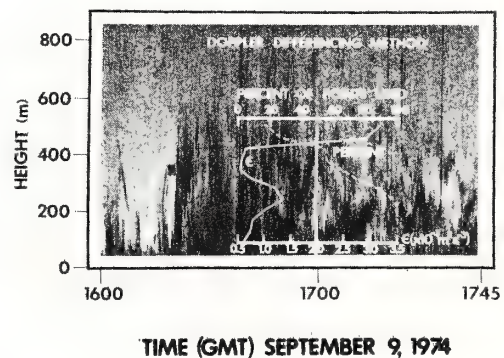
Figure 1. Facsimile record of an outflow generated
by a nearby convective cell. Overlaid is a profile
of the acoustically-derived rate of turbulent energy
dissipation, ε, averaged between 1630 and 1730.

        Also plotted in Fig. 1 is the rate of
turbulent energy dissipation, ε, which was de-
rived using the structure function of vertical
velocity in a manner similar to Gaynor (1976). An
attempt to use the turbulence widening of the
Doppler spectrum failed due to the deleterious
effects of strong ambient noise and the inability
to obtain adequate spectral resolution even at
very high digitizing rates. The vertical velocity
structure function is

$$D(\Delta z) = \overline{[w(z_1) - w(z_1 + \Delta z)]^2},$$

where $w(z_1)$ is the vertical velocity at some
level z_1 and $w(z_1 + \Delta z)$ is the vertical velocity
at a higher level $z_1 + \Delta z$. The overbar indicates
a time average. In our case the levels are about
35 m apart. The squared differences are averaged
from 1630 to 1730 in Fig. 1 and only velocities
obtained under good signal-to-noise ratio con-
ditions are included in the average. A profile of
the percentage of points accepted is also in-
cluded in the figure. In the inertial subrange,
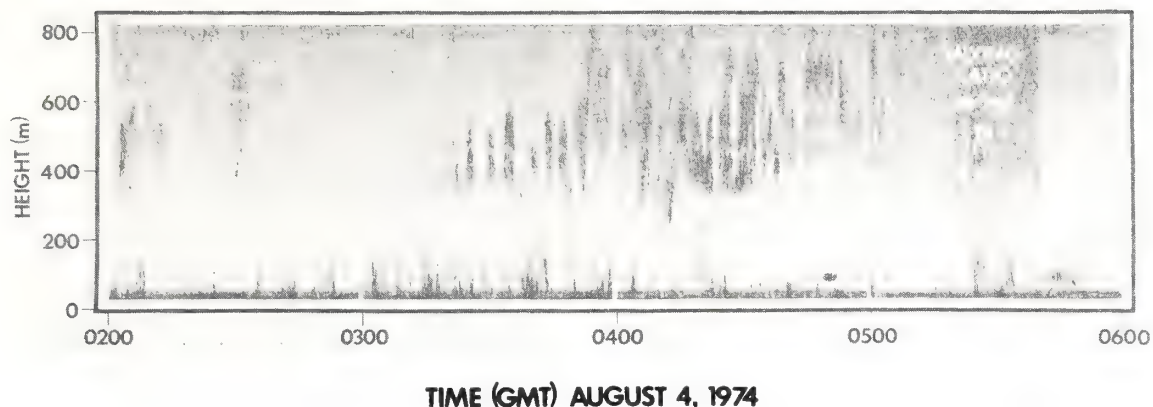
Figure 2. *Hummocky echoes with mixing ratio time series evaluated from BLIS data at 450 m.*

the energy dissipation is related to the structure function by (Tatarskii, 1971)

$$\varepsilon^{2/3} = \frac{3D(\Delta z)}{8(\Delta z)^{2/3}}$$

The marked increase in ε around 250 m could be related to dissipation occurring in the layer of strong convergence of heat flux mentioned above, or it may be caused by dissipation of energy in the gravity waves at the density interface centered on the temperature inversion. It should be noted that in order to calculate ε from the structure function $\Delta z/z \ll 1$ must hold. At the lowest level of our calculations (90 m), the inequality is not quite satisfied and the ε values may be slightly smaller than if a smaller Δz were used. However, the ε values of Fig. 1 compare

quite favorably to those calculated by Gaynor (1976) over land using a similar method. His ε values varied from 5×10^{-6} m^2 s^{-3} for a very stable boundary layer to 1×10^{-2} m^2 s^{-3} for a free convective boundary layer and compared well with nearby tower measurements.

3.   HUMMOCKS

Fig. 2 shows acoustic returns during a hummocky period with the mixing ratio calculated from BLIS data at 450 m overlaid on the facsimile record. The hummocks are quite moist with mixing ratios at times peaking over 17 g/kg. The strongest indication that these hummocks represent clouds is presented in Figs. 3 and 4. Availability of all-sky camera photos on the OCEANOGRAPHER provided an opportunity to correlate the appearance of hummocks on the acoustic facsimile with
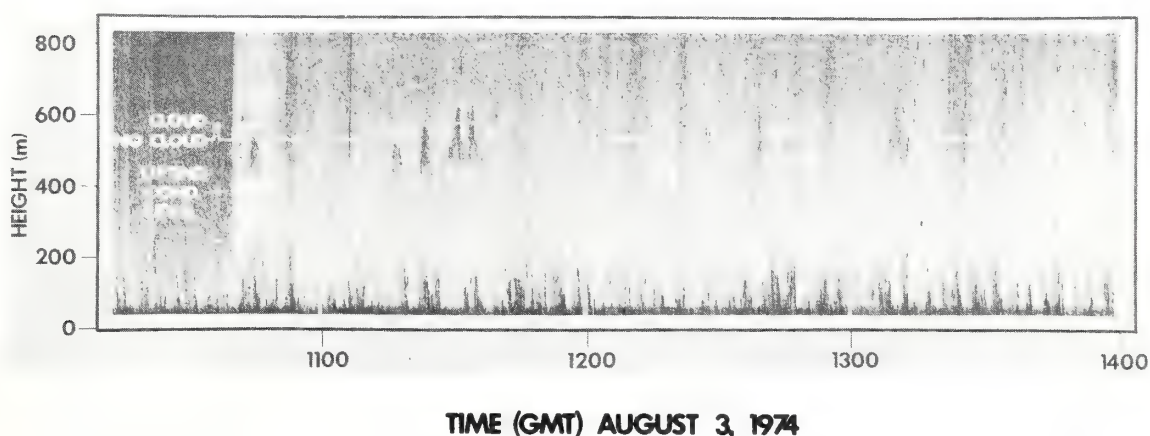
Figure 3. *Hummocky echoes correlated with the appearance of clouds overhead as seen by an all-sky camera, and condensation level calculated from surface data.*

304

low-level cumuli overhead. Fig. 3 indicates that the correlation is good. Quite often, however, low-level cumuli existed overhead with no hummocks recorded by the sounder. Because acoustic scattering is caused by small-scale temperature and humidity fluctuations which in this case are enhanced by mixing of clouds with the environment, the appearance of hummocks or lack thereof when clouds are overhead suggests important differences in the small-scale cloud dynamics. The computed lifting condensation levels agree well with hummock bases in Fig. 3. However, for a larger sample, Fig. 4 shows that hummock bases are slightly higher on average than the computed condensation level.
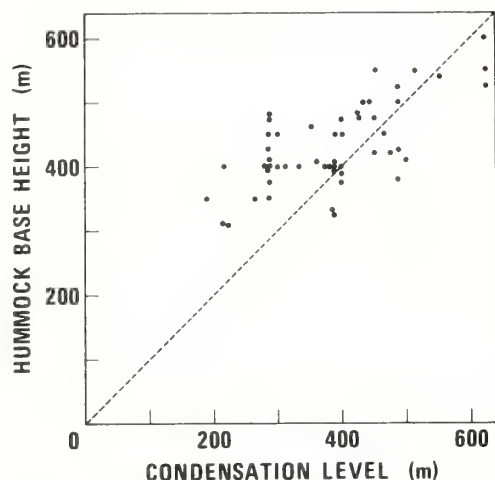
Figure 4. Scatter diagram of the computed condensation levels versus observed hummock base heights for all GATE hummock occurrences.

An adaptive linear prediction filter technique (Griffiths, 1975) was used to extract vertical acoustic Doppler and velocity information. This method is much faster and more straightforward than the standard Fast Fourier Transform approach. Contours of Doppler-derived vertical velocity are shown in Fig. 5 for a hummocky case. In the figure the zero velocity line is located between the clear and hatched areas. The adaptive filter technique offers a non-dimensional spectral estimator, the magnitude of which is inversely proportional to the width of the spectrum. Its peak value is therefore an indirect measure of the signal-to-noise ratio — the larger the estimator, the more reliable the data. Very noisy data gave peak values below 50. High signal-to-noise ratio regions increased the peaks well above 1000. A minimum cutoff of 200 was chosen as optimum when the estimator was compared to regions of good signal on the acoustic facsimiles. Vertical velocity data are omitted from Fig. 5 when this measure drops below the threshold. Maximum velocities in the plumes are of the order of 1 m s^{-1}; in the hummocks velocities range up to 2 m s^{-1} because of vertical accelerations caused by the release of latent heat. The upward motion in the plumes is not well coupled with the motion in the hummocks for this time period. When the sounder is in a region of synoptic-scale low-level convergence, a much better coupling between the plumes and hummocks appears on the acoustic facsimile and vertical velocity data.

For the moist tropical marine boundary layer, we must consider the contributions of both temperature and humidity fluctuations to acoustic scattering. Over most land areas, humidity is relatively low and its fluctuations contribute very little. However, because the tropical marine mixed layer contains at least an order of magnitude more water vapor than the continental boundary layer, contributions due to moisture fluctuations

OSS OCEANOGRAPHER, GATE POSITION NO. 1

TIME (GMT) AUGUST 4, 1974
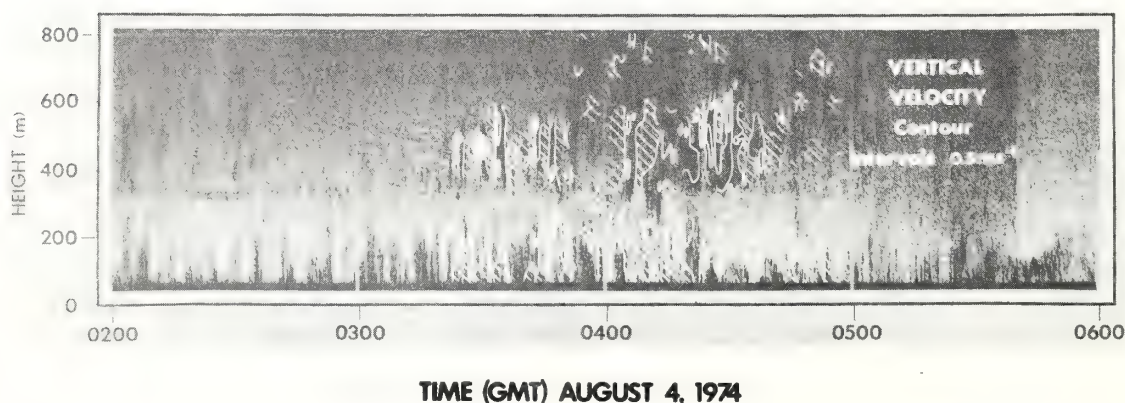
Figure 5. Contours of Doppler-derived vertical velocities overlaid on facsimile record showing hummocky echoes. Hatched areas indicate downward motion and contour intervals are 0.5 m s^{-1}

305

must be considered. If we assume that temperature and humidity fluctuations at acoustic scattering scales (~ 0.1 m) are uncorrelated, then the refractive index fluctuations caused by temperature and humidity, respectively, are given by (Wesely, 1976)

$$(C_n)^2_T = \frac{C^2_T}{4\overline{T}^2} \quad \text{and}$$

$$(C_n)^2_\rho = 0.094 \, \frac{C^2_\rho}{4\overline{p}^2} \quad , \tag{1}$$

where C^2_T and C^2_ρ are the structure parameters of temperature and water vapor pressure, respectively, $\overline{T}$ is the average temperature, and $\overline{p}$ is the average total pressure. Spectra of temperature and water vapor pressure were calculated from a 16-min aircraft run at 153 m altitude during GATE (Fitzjarrald, 1976) to exemplify the relative importance of T and ρ fluctuations to acoustic scattering in a very moist environment. On the assumption that the Kolmogorov model is valid, the spectra have been extended down along a -5/3 slope to describe their relative magnitudes at scales to which the acoustic sounder is sensitive. Using the relation $\phi_n(k_1) = 0.25 \, C^2_n k_1^{-5/3}$ (Friehe et al., 1975), where $\phi_n(k_1)$ is the one-dimensional power spectrum of n, and k_1 is the wave-number component in the stream-wise direction, and using Eq. (1), we find that humidity fluctuations account for at least 28% of the total acoustic backscatter. Quite possibly at cloud level this percentage is even higher. Theory (Wesely, 1976) and measurements (Friehe et al., 1975) indicate that the degree of correlation of ρ and T is an important factor in evaluating the contributions of temperature and humidity to acoustic backscatter in a moist environment. More aircraft data are needed to describe the relative importance of humidity and temperature fluctuations and their correlation as a function of height and atmospheric condition.

4. CONCLUDING REMARKS

GATE offered an unusual atmospheric environment for acoustic sounder application. The strength of scattering from the dynamically weak thermal plumes was surprising as was the spectacular appearance of the relatively weak convective outflows. The importance of humidity fluctuations to acoustic scattering in the tropical marine boundary layer offers some insight into the turbulent dynamics of T and ρ, both correlated and individually, as a function of height and atmospheric conditions. The agreement between hummocky acoustic echoes and clouds overhead and the absence of hummocks for some clouds may be related to the small-scale dynamics of developing and dissipating low-level tropical cumuli. Dissipation of turbulent kinetic energy and vertical velocities measured acoustically are expected to clarify some aspects of mixed-layer energetics with applications to parameterization of the dynamics of the lower tropical marine boundary layer for large-scale numerical models.

5. REFERENCES

Fitzjarrald, D. E., 1976: Horizontal scales of motion in atmospheric free convection observed during the GATE experiment. Submitted to *J. Appl. Meteorol.*

Friehe, C. A., J. C. La Rue, F. H. Champagne, C. H. Gibson, and G. F. Dreyer, 1975: Effects of temperature and humidity fluctuations on the optical refractive index in the marine boundary layer. *J. Opt. Soc. of Amer.*, 65, 1502-1511.

Gaynor, J. E., 1976: Acoustic Doppler measurement of atmospheric boundary layer velocity structure functions and energy dissipation rates. Submitted to *J. Appl. Meteorol.*

Hall, F. F., Jr., W. D. Neff, and T. V. Frazier, 1976: Wind shear observations in thunderstorm density currents. Submitted to *Nature*.

Griffiths, L. J., 1975: Rapid measurement of digital instantaneous frequency. *IEEE Transactions on Acoustics, Speech, and Signal Processing*, 23, 207-222.

Tatarskii, V. I., 1971: *The Effects of the Turbulent Atmosphere on Wave Propagation*, Israel Program for Scientific Translations, N72-18163, available from NTIS, Springfield, Virginia, 472 pp.

Wesely, M. L., 1976: The combined effect of temperature and humidity fluctuations on refractive index. *J. Appl. Meteorol.*, 15, 43-49.

306

Wind shear observations in thunderstorm density currents

F. F. Hall, Jr & W. D. Neff

Wave Propagation Laboratory, National Oceanic & Atmospheric Administration, Environmental Research Laboratories, Boulder, Colorado 80302

T. V. Frazier

Department of Physics, University of Nevada, Reno, Nevada 89507

Acoustic sounder observations of thunderstorm density currents reveal a complicated but ordered internal structure. Fast-response anemometers on a 150-m tower reveal a succession of internal shear layers which occur following the leading portion or nose of the current. The measured wind shear revealed by the anemometers is found to be a function of the temperature differential between the ambient air and the interior of the gust, measured near the surface. An heuristic model is developed to explain this observation.

DENSITY currents flowing out from thunderstorms, sometimes referred to as gust fronts or microfronts, can constitute a hazard to the landing and takeoff of aircraft. The associated wind shear results in the aircraft experiencing rapid changes in air speed; vertical shears > 0.1 s^{-1} in the lowest 100 m have been shown to be hazardous to large, swept-wing, jet-powered aircraft in a study by Snyder[1]. An improved knowledge of density current dynamics and structure is also important in understanding the interaction of the thunderstorm with its environment. Since the cold air outflows from storms are statically stable, but highly turbulent, such currents exhibit large acoustic index of refraction fluctuations, leading to strong acoustic echoes when the flows are probed with sound waves. Using an acoustic sounder as a guide in the interpretation of meteorological tower data we present new observations of the internal structure and shear in gust fronts, and find a strong correlation between the strength of the current and its temperature contrast with the ambient air.

Wind shear measurements

During field experiments in 1972 and 1974, five different thunderstorm density currents were observed at the National Oceanic and Atmospheric Administration (NOAA), Haswell, Colorado site. The meteorological tower at Haswell, 150 m tall and located 300 m from an acoustic sounder, was instrumented at 30-m intervals with fast response wind and temperature sensors; data were recorded at 1.0-s intervals. In addition, heavy-duty wind sensors were located at 15 m and 150 m, and were able to withstand the high winds which in two cases destroyed the fast response instruments.

In the two more severe storms observed, wind-generated noise at the acoustic antenna masked the reception of echoes, but for the other cases, the internal shear structure was observed in detail with the sounder. The structure for the August 11, 1972 current is shown in Fig. 1. This outflow originated near a line of small thunderstorms which had levelled off at a peak altitude of 8.5 km above sea level, and were observed to dissipate 20 km NE of Haswell at 2300 by the National Weather Service weather radar in Limon, Colorado. When last observed the storms were moving 6 m s^{-1} from an azimuth of 330°. The maximum wind speeds within the current were 5 m s^{-1} from between 280° and 340°. This density current flow was opposed to an ambient flow of 10 m s^{-1} from 135° before the event, producing a vector change in wind speed, Δu of 15 m s^{-1}. A temperature drop of 2 °C at 30 m occurred with the passage of the microfront or head of the current. Maximum shears at the lower edge and in the interior of the current reached values of $\partial u/\partial z = 0.13$ s^{-1} as measured by the tower bivanes; the strongest shear events correlated with temperature shifts measured
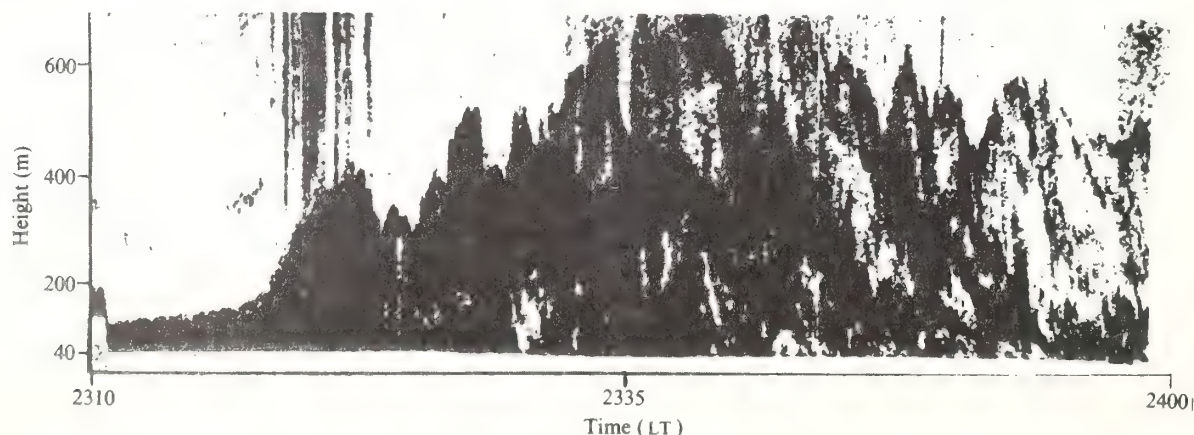
Fig. 1 Acoustic sounder facsimile record obtained on August 11, 1972 at Haswell, Colorado, of a density current originating from a line of weak storms more than 20 km away. Wind noise associated with the passage of the current nose led to the vertical noise-lines in the upper part of the record at 2320. The postulated shears and temperature gradients at the edge of the current, and in descending layers within the current, are revealed as darker regions on the facsimile record because of increased acoustic scattering cross sections.
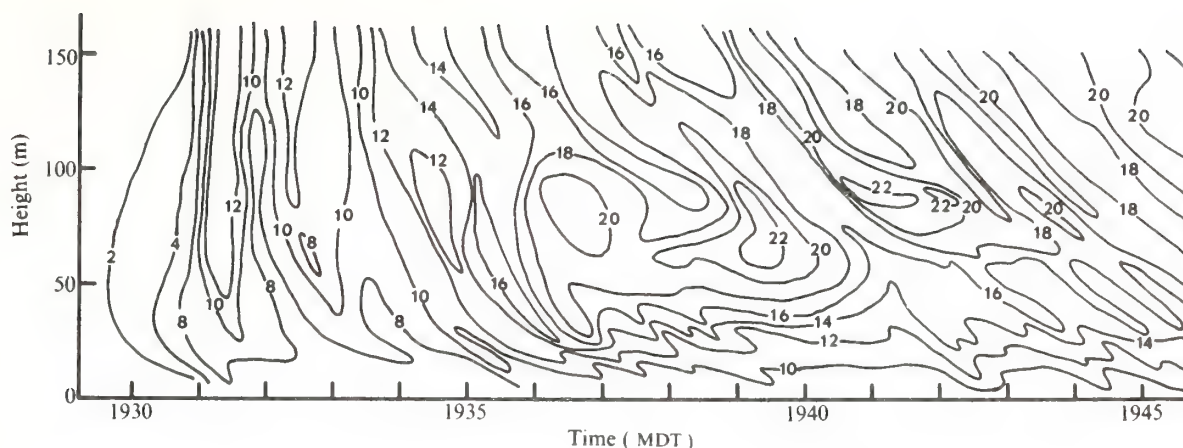
Fig. 2 Isotachs in m s^{-1} drawn against height and time as derived from wind measurements at six levels on the Haswell tower, 10-s averaged data for the density current of August 5, 1972. The resulting pattern of shear is consistent with the layered structure shown by acoustic sounder observations of much weaker currents as in Fig. 1.

on the tower and with the observation of scattering regions on the acoustic sounder facsimile record. This correlation is to be expected since theory predicts that the acoustic scattering is produced by small scale temperature fluctuations associated with turbulence in regions of temperature and wind gradients.

This prediction has been verified quantitatively by Neff[2] for a number of cases including elevated scattering layers. The thin, tilted echo layers, internal to the current but above the height of the tower, are thus presumably of such an origin. Although not verifiable from the present data, the local enhancement of the shear and consequent production of turbulence may arise from internal waves generated at the interface or large-scale overturning within the current.

Two more vigorous density currents from closer and larger thunderstorms passed the tower on August 2 and 5, 1972. In these cases, the wind noise was so great that acoustic records could not be obtained. By using the August 11 facsimile record as a guide in interpreting the wind data from the tower, however, a consistent set of isotachs could be plotted for the August 5 event following the form suggested by Fig. 1, with tilted shear layers gradually sloping or descending with time. These are shown in Fig. 2, plotted from data averaged over 10 s. One minute of data averaging proved to be too long to delineate the thin shear regions within the currents; therefore, internal shear layers were not revealed in the recent comprehensive thunderstorm outflow study by Goff[4], who used 2-min wind averages.

From Fig. 2, it is immediately obvious that the vertical shear $\partial u/\partial z$ in the lower 50 m is consistently large and above the aircraft safety criterion set by Snyder[1]. It must be realised that the spatial slope of the higher shear zones is greatly accentuated in Figs 1 and 2; if one assumes the zones are advected with the mean wind, the actual slopes for the shear regions at 100 m are found to be < 2°. The fluctuating nature of the shear at higher levels yields an undulatory pattern of shears > 0.1 s^{-1}. Regions where this critical shear value is exceeded are shown in Fig. 3, indicating that even 16 km from this quite averagely-sized prairie thunderstorm (with radar echoes extending to an altitude of 14.6 km), the clear air wind shear exceeded the safety limits consistently in the lower 100 m for > 10 min. Shortly after 1946 on August 5, a gust of more than 25 m s^{-1} destroyed two of the light weight propellers on the fast response sensors, or bivanes, eliminating further data.

The even more energetic density current of August 2, 1972 arose from a storm just 5 km away with radar tops observed to be above 17 km. Maximum velocities in this current exceeded 42 m s^{-1}, which quickly destroyed all bivanes on the tower. A recorded wind shear of 0.26 s^{-1} was observed over the 135-m separation of the two more rugged but slower response wind sensors. Thus the actual shear internal to the current (which otherwise might have been measured with 30-m height resolution provided by the bivanes) was probably greater than that recorded over the greater height increment separating the rugged sensors.
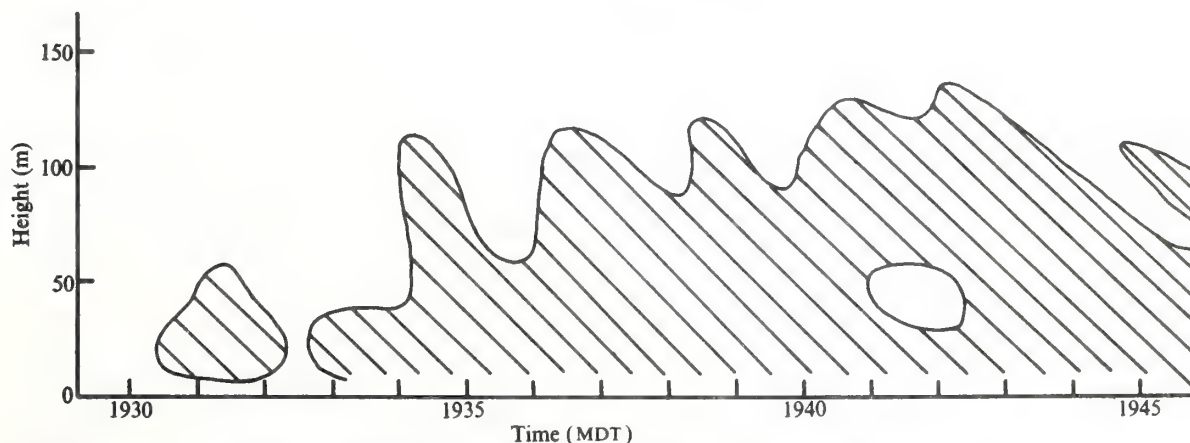
Fig. 3 Height against time plot of those regions where the wind shear exceeded 0.1 s^{-1} for the August 5, 1972 density current at Haswell, Colorado.

A model of density current wind shear

A feature common to the density current events observed was the drop in temperature with the arrival of the first gust. Empirically, it was found that the larger the temperature drop, the greater the observed shear, consistent with the primitive equation model of gust fronts by Mitchell[5]. This suggested that temperature measurements relatively near the surface might serve as a quantitative predictor of the severity of density current shears. We now outline a simple model relating temperature drop to wind shear.

An obviously relevant parameter in density current modelling is the speed of the current, u_g. This is given by Turner[6] as

$$u_g = \alpha[gH(T_a - T_g)/T_a]^{1/2} \tag{1}$$

where g is the acceleration of gravity, H is the depth of the current following the head, T_a the ambient air temperature, and T_g the temperature of the gust. Equation (1) comes from hydraulic theory. When dissipative processes are neglected the constant, α, is $\sqrt{2}$. Laboratory investigations yield an empirical value for α of 1.1 (ref. 3).

We consider first the shear along the upper boundary of the current near its nose. In this region of warm air overlying the colder current, we hypothesise that the turbulence generated there self-adjusts to gradient Richardson numbers, $Ri \sim 0.2$, as observed in thin inversion surfaces in the real atmosphere (Turner[6], Hall et al.[7]). From the definition of Ri we write

$$\frac{\partial u}{\partial z} = \frac{1}{Ri} \frac{g}{\theta} \frac{\partial \theta}{\partial z} \bigg/ \frac{\partial u}{\partial z} \tag{2}$$

This can be approximated as

$$\frac{\partial u}{\partial z} \simeq \frac{1}{Ri} \frac{g}{T} \frac{\Delta T}{\Delta u} \tag{3}$$

where the vertical gradients are assumed to occur over the same depths, the temperature lapse rates within and outside of the current are nearly equal, and $\Delta T = T_a - T_g$, measured near the surface. Assuming the ambient flow velocity is zero, $\Delta u = u_g$. Then equation (3) becomes

$$\frac{\partial u}{\partial z} = \frac{1}{\alpha Ri} \left(\frac{g\Delta T}{HT}\right)^{1/2} \tag{4}$$

Taking $H = 500$ m, which the sounder reveals to be a characteristic value for a number of such currents observed, $Ri = 0.2$, $\alpha = 1.1$ and $T = 300$ K, we have

$$\frac{\partial u}{\partial z} = 0.037(\Delta T)^{1/2} \tag{5}$$

For $\Delta T > 7$ °C at the upper boundary of the current, equation (5) predicts wind shears > 0.1, the safety limit derived by Snyder[1].

At the lower boundary of the current, where the shear is actually measurable on the tower, the speed must go to zero through some boundary layer thickness δ. We can then use equation (1) to estimate

$$\frac{\partial u}{\partial z} = \frac{u_g}{\delta} = \alpha \left(\frac{gH\Delta T}{\delta^2 T}\right)^{1/2} \tag{6}$$

Taking again $H \simeq 500$ m and 50 m $< \delta < 100$ m (typically observed values) we have

$$0.044 (\Delta T)^{1/2} < \frac{\partial u}{\partial z} < 0.089 (\Delta T)^{1/2} \tag{7}$$

expressions surprisingly similar to equation (5), but predicting shears near the surface somewhat larger than at the upper boundary of the current.

A summary of the maximum observed wind shear for five density currents as recorded at Haswell is shown in Fig. 4, where the dated data points show the values recorded by bivanes on the 150-m tower, except for the August 2, 1972 event. Other points shown were recorded by Charba[8] and by Marks[9] at the WKY tower near Oklahoma City. The Goldman and Sloss[10] data were obtained at the 150-m Kennedy Space Center, Florida tower. A least-squares linear fit to the data, relating wind shear to temperature drop observed in the density current, is shown as a solid line. The equation for this line is

$$\frac{\partial u}{\partial z} = 0.024 \,\Delta T + 0.03 \tag{8}$$

The area bounded by the limits of equation (7) is plotted as the stippled overlay which agrees well with the data. Equation (5) would plot near the lower bound of the stippled zone. The non-zero intercept in Fig. 4 probably reflects our neglect of the background shear.

The fact that the observed shear varies nearly linearly with ΔT may reflect an indirect dependence of H on ΔT as suggested in the two-dimensional primitive equation model of Mitchell[5]. Our simple heuristic model also avoids the variability in the static stability of the ambient air. Equation (7) is thus useful mainly to set approximate bounds on the shear using values of H typical of the few cases observed by the sounder.

If the simple relationships shown in Fig. 4 prove to be typical for an even larger data set, it would be a relatively simple matter to measure ΔT on a grid surrounding airports to warn of the wind shear produced by density currents moving across the area.

Conclusions

We conclude that even at distances > 16 km from thunderstorms, the wind shear in density currents from such storms can be a hazard to aircraft landing and taking off. Unless such density currents are delineated by blown dust, as in desert regions, they will be undetectable to the unaided observer. The temperature drop associated with these currents, however, gives
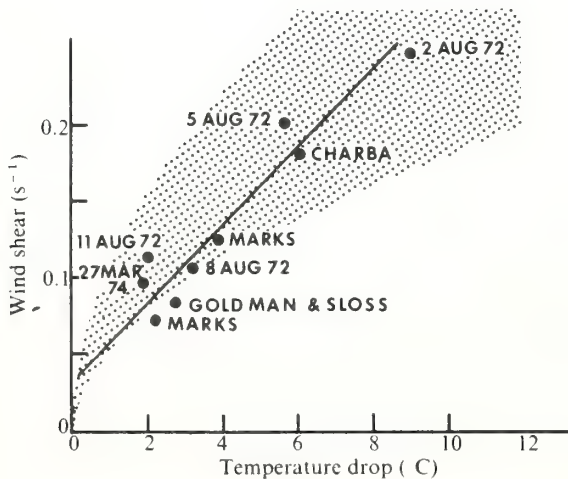
Fig. 4 Measured wind shear plotted against temperature drop from the ambient atmosphere to the density current. The experimental data points, as described in the text, nearly fit a straight line, while the overlay stippled area represents approximate bounds on the shear predicted by equation (7).

366

a good measure of the wind shear to be expected. In addition, the ability of the acoustic sounder to detect such turbulent shear layers may provide new insight into the internal dynamics and structure of such currents in the atmosphere.

We thank D. W. Beran, W. H. Hooke, C. G. Little and P. A. Mandics for discussions. G. Gertig assisted with the data reduction and the plotting. Support for this study was provided by the Federal Aviation Administration.

[1] Snyder, C. T., *Analogue study of longitudinal response to wind shear and sustained gusts during landing approach* (NASA TN D-4447, Ames Research Center, Moffett Field, California, 1968).

[2] Neff, W. D., *Quantitative evaluation of acoustic echoes from the planetary boundary layer* (NOAA Tech. Rep. ERL 322-WPL 38, Environmental Research Laboratories, Boulder, Colorado 1975).

[3] Benjamin, T. B., *J. Fluid Mech.*, 31, 209–248 (1968).

[4] Goff, R. C., *Thunderstorm-outflow kinematics and dynamics* (NOAA Tech. Memo. ERL NSSL-75, National Severe Storms Laboratory, Norman, Oklahoma, 1975).

[5] Mitchell, K. E., *A numerical investigation of severe thunderstorm gust fronts* (NASA Report CR-2635, Pennsylvania State Universities, Contr. NAS8-27334, 1975).

[6] Turner, J. S., *Buoyancy Effects in Fluids* (Cambridge, University Press, 1973).

[7] Hall, F. F., Jr, Edinger, J. G., and Neff, W. D., *J. appl. Meteorol.*, 14, 513–523 (1975).

[8] Charba, J., *Gravity current model applied to analysis of squall-line gust front* (NOAA Tech. Memo. ERL NSSL-61, National Severe Storms Laboratory, Norman, Oklahoma, 1972).

[9] Marks, J. R., *Acoustic radar investigations of boundary layer phenomena* (Sci. Rep. on NAS8-28659, Department of Meteorology, University of Oklahoma, Norman, Oklahoma, 1973).

[10] Goldman, J. L., and Sloss, P. W., *Structure of the leading edge of thunderstorm cold-air outflow*, 75–79 (Sixth Conference on Severe Local Storms, American Meteorological Society, Boston, 1969).

Comments on "A Mesoscale Phenomenon Revealed by an Acoustic Sounder"

F. F. Hall, Jr., and W. D. Neff

NOAA/ERL/Wave Propagation Laboratory, Boulder, Colo. 80302

27 August 1976

We cannot agree with the interpretation of the acoustic sounder facsimile record published by Petersen and Jensen (1976). The narrow band acoustic echo which the authors interpret as a specular reflection from a mesoscale front separating moist land breeze air from colder air is not supported by the appearance of the facsimile record nor by the wind and temperature data presented in their Fig. 2. The initial rising trace of their Fig. 1 lasts for 2.5 h and passes through regions of marked turbulence on the facsimile record as at 0545, 0615 and 0650. How can the hypothesized sharp gradient (<5 m in thickness) maintain its integrity through such turbulent regions?

Then there are the sudden discontinuities in layer height as at 0635 and 0710. In the latter case the layer drops over 70 m instantaneously. Such transients do not occur geophysically, certainly not in nonturbulent environments where the layer appears to be at these times.

But let us assume for the moment that a smooth gradient of acoustic refractive index is the explanation of the layer. The velocity of sound c is given by

$$c = 20.05 \sqrt{T}(1 + 0.14e/p),$$

so that we must consider both changes in absolute temperature T and in water vapor pressure e (p is the atmospheric pressure) in calculating the change in refractive index from one air mass to the next. We see from Petersen and Jensen's facsimile record that the layer passed the instrumented 117 m level on the Risø tower at about 0635. Referring to the temperature trace at that time, we find that there are no inflections measured. On the contrary, there is a smooth linear increase in temperature from 0600 to 0700. Thus we must attribute the change in index to changes in water vapor pressure. Let us assume that the humid air, conditioned by passage over the nearby fjord is *saturated* and at a temperature of 3°C. We will assume that the land air is *completely dry*. Then the maximum possible difference in the index of refraction is $\Delta n = 1.05 \times 10^{-3}$. As described by Ottersten (1970) the calculation of the layer reflectivity is sensitive to the precise profile of refractivity. A linear gradient through a depth h gives a power reflectivity of $R = (\lambda \Delta n / 4\pi h)^2$. Assuming that $h = 1$ m and $\lambda = 0.2$ m yields the value $R = 2.8 \times 10^{-10}$. We now inquire what value of the temperature structure parameter C_T^2 would provide the same returned power as the gradient reflectivity and find this value to be

$C_T{}^2 = 2 \times 10^{-3}$ K^2 m$^{-\frac{2}{3}}$. This value is somewhat less than hourly averages and much less than peak values of the temperature structure parameter observed in ground-based and elevated inversions (Neff, 1975).

In the specularly reflecting layer model used above, the discontinuous derivatives of the index of refraction at the boundaries of the layer lead to a *maximum* estimate of reflectivity. More realistic profiles with smoothly rounded edges lead to reflectivities *many orders of magnitude less* than the sharp edged model (Ottersten, 1970), but such weakly reflecting layers would be inconsistent with the observed layer echo which appears to equal in intensity the return from the turbulent ground-based layer in Petersen and Jensen's Fig. 1.

The shortest pulse usually available with the Aerovironment Type 300 Acoustic Radar used by the authors is $t = 50$ ms, providing a spatial resolution $ct = 16.7$ m. Their "specular" layer measures less than 10 m thick on the facsimile record, however. The more ragged layer, which rises to about 200 m shortly before 0800 and descends again before 0900, measures to be somewhat thicker than the minimum resolvable distance, or about 30 m, as one might expect for a turbulent region. We believe *this* layer is the land breeze interface: it reaches 117 m at 0745, just when the wind and temperature at that level change, and descends past 117 m at 0850 when the *in situ* instruments also show inflections.

The NOAA Atmospheric Acoustics Group has made several efforts in the past to identify unambiguously layers in the stable planetary boundary layer producing specular returns. The highly stable, low wind conditions at Fairbanks, Alaska, seemed to offer an optimum environment for such tests. However, no changes in facsimile intensity could be found for two acoustic sounders, one transmitting vertically and one tilted at an angle of 35° from the vertical (Beran *et al.*, 1973). Indeed, if the Petersen and Jensen layer were a specular reflector and the layer advected with the low-level

winds of about 1 m s^{-1}, the rise of the layer from 200 to 500 m in 26 min would lead to a slope of the layer of greater than 10°; thus the specular return would not be seen by the sensitive main beam of the sounder but instead would return near the first null in the beam pattern.

We have observed fascimile records, similar to the authors', that have proved to be non-atmospheric, caused by acoustic noise background or equipment problems. At our Haswell, Colo., tower site, a narrow band of wind velocities causes the carriage cable on the tower to oscillate and clank against the tower structure. This background noise can be nearly synchronous with the sounder returns, producing sloping and curved *apparent layers* in the records. Occasionally, when we have had problems with triggering the transmit pulse in sounders, secondary pulses nearly synchronized with the pulse repetition rate have leaked through our diode protective bridge causing similar striped patterns. We suggest that such background noise sources or equipment problems are the more likely explanation for the thin layer echoes reported by Petersen and Jensen, and that specularly reflecting layers for acoustic energy at normal incidence have yet to be observed.

REFERENCES

D. W. Beran, W. H. Hooke and S. F. Clifford, 1973: Acoustic echo-sounding techniques and their application to gravity-wave turbulence, and stability studies. *Bound. Layer Meteor.*, 4, 133–153.

Neff, W. D., 1975: Quantitative evaluation of acoustic echoes from the planetary boundary layer. NOAA Tech. Rep. ERL 322-WPL 38, Boulder, Colo., 34 pp.

Ottersten, H., 1970: Radar angels and their relationship to meteorological factors. FOA Reports, Vol. 4, Res. Inst. Nat. Defense, Stockholm, 1–33.

Petersen, E. L., and N. O. Jensen, 1976: A mesoscale phenomenon revealed by an acoustic sounder. *J. Appl. Meteor.*, 15, 662–664.

369

Some Properties of Convective Plume and Small Fair-Weather Cumulus Fields as Measured by Acoustic and Lidar Sounders

Raúl Erlando López

NOAA/ERL/Wave Propagation Laboratory, Boulder, Colo. 80302

31 January 1977 and 28 May 1977

ABSTRACT

Results of a preliminary experiment are described in which a lidar-acoustic sounder system was used to measure plume and cloud width and depth. These parameters are shown to be lognormally distributed. By applying the theory of the genesis of the lognormal to the formation process of convective cells it is suggested that clear air plumes and small cumulus clouds grow by the merger or agglomeration of smaller elements.

1. Introduction

In spite of considerable progress in the formulation of models of cloud growth and development, the initiation of cumulus clouds is not clearly understood at this time. the existence of convective plumes and bubbles in the planetary boundary layer has been confirmed by various sensing devices. Among these the following examples can be mentioned: instrumented towers (Kaimal and Businger, 1970; Taylor, 1958), instrumented aircraft (Vul'fson, 1961; Warner and Telford, 1963), acoustic sounders (Hall, 1972), and ultrasensitive radars (Hardy and Katz, 1969). It is generally supposed that water clouds are formed when these plumes and bubbles somehow break through the stable layer that usually caps the well-mixed layer in convective situations. However, the exact mechanism by which this occurs is imperfectly understood.

In a recent paper Coulman and Warner (1976) concluded from aircraft observations that successions of parcels of air from the convective layer produce the larger parcels of cooler, moister air present in the stable layer beneath cloud base. These larger parcels were often found to be associated with fair weather clouds. The implication is that convective elements agglomerate in the formation of larger parcels, which can eventually form water clouds. On the other hand, López (1976) analyzed cumulus cloud populations for many different geographic and climatic situations around the world and found that cloud and radar echo diameter, height and duration are distributed lognormally. By extending the stochastic process that determines the genesis of this probability law to the formation process of clouds, he concluded that cumulus clouds of all scales are probably formed by the progressive union of smaller elements. Thus, these two sets of observations would indicate that cumulus clouds ranging in size from the small·fair-weather·cumuli through cumulus congestus and cumulonimbi are formed and grow by a process of agglomeration of smaller convective elements. An example of this agglomeration in

the case of cumulus congestus is the merging of clouds very often observed in undisturbed and disturbed shower production (e.g., Woodley *et al.*, 1971; López, 1976).

The present paper presents some preliminary results of an experiment designed to improve the understanding of cloud initiation. A high-power (5 J) ruby lidar firing at one pulse per second and using a 71 cm telescope was utilized. In addition, an acoustic sounder and a movie camera were employed.

2. The experimental setup

The data was obtained at a site in Boulder, Colo., during a day in August 1976. The lidar, the acoustic sounder and the movie camera employed were pointed at the zenith. Thus, clouds and convective plumes were monitored as they drifted over the site with the ambient wind. The lidar was fired once every second and the acoustic sounder once every 12 s. The lidar provided precise measurements of the heights of cloud base and cloud top above ground and of the time during which the clouds were over the instrument (± 1 s). Similarly, the acoustic sounder provided measurements of the time during which the convective thermals were overhead (± 12 s). An estimate of the wind speed at cloud base of 7 m s^{-1} was obtained from cloud motion vectors calculated from the movie photographs and the range obtained from the lidar. From this wind estimate the time intervals during which the clouds were overhead were translated into cloud transect lengths. The winds in the well-mixed layer, where the convective plumes were observed, were estimated at 3 m s^{-1} by extrapolating the winds at cloud base with an exponential wind profile (Smith, 1973). Thus, convective plume transect lengths were also estimated.

It is possible that on many occasions the clouds and plumes did not go directly overhead of the acoustic sounder and lidar. By assuming a geometrical model for the plumes and clouds and by using a statistical model, it is possible, as Vul'fson (1961) has done, to

370

obtain a better estimate of the plume and cloud diameter. For the purposes of this preliminary note it can be assumed that the plume and cloud fields are populations of vertical cylinders which are transected along a straight line oriented with the mean wind direction by the acoustic sounder and lidar. Using the statistical scheme and tables developed by Vul'fson (1961) the plume and cloud transect lengths distributions have been converted into plume and cloud diameter distributions.

3. Results

A frequency distribution of plume widths was obtained from the acoustic sounder observations. The data were derived from fascimile records which provide a time history of the strength of the returned signal with height. The estimate of the time interval during which a plume was overhead was obtained by counting the number of contiguous fascimile traces making up an identifiable element and multiplying this number by the time interval between traces (12 s). Using the wind speed calculated for the well-mixed layer (3 m s^{-1}) an estimate of the plume transect length can be finally obtained assuming Taylor's hypothesis. The system results in an uncertainty of ± 36 m in all the measurements. In addition, some of the plumes with widths less that 36 m might not be detected. This is not felt to cause a severe bias in the distribution of plume sizes since the average diameter of plumes as recorded in the literature (see above) ranges from 50 to 300 m.

Fig. 1 shows the frequency distribution of plume transect lengths (large dots). The data have been plotted on logarithmic probability paper—the ordinates on a
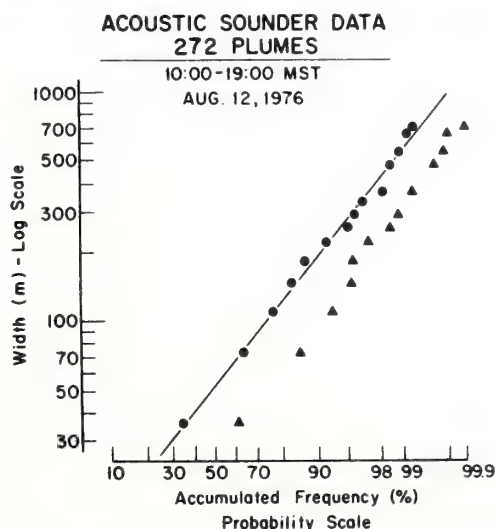
logarithmic scale and the abscissas on a normal probability scale. A lognormal distribution would thus describe a straight line on this coordinate system. As can be seen from the graph the data points closely approximate a straight line. The straight line in the figure corresponds to the lognormal distribution that minimizes the value of chi-square for the present sample. This minimum value is 1.15. The value of chi-square at a 5% level of significance corresponding to this data is 9.49, so that the hypothesis of lognormality would not be rejected at the 5% level. In fact the probabiltity of obtaining a value of chi-square as high or higher than the value obtained for the observations is 88%.

It is interesting to note that the lognormal distribution obtained shows no indication of truncation or biasing. If a distribution is obtained from a lognormal population by truncating it at the low end (not including elements below a certain size), the resulting log-probability graph would curve away from a straight line at the lower end indicating lower frequencies of the smaller elements than called for by the pure lognormal distribution. No such truncation or biasing is apparent in the present distribution.

The triangles in the graph correspond to the distribution of plume diameters obtained from the transect length data using Vul'fson (1961) techniques. Again the hypothesis of lognormality cannot be rejected at a level of 5% or better. In fact the best lognormal fit yields a value of chi-square of 0.31 compared to 1.15 for the uncorrected distribution. The geometrical mean of the original distribution (54.5 m) (intersection of the 50% ordinate axis) is seen to be higher than the mean of the diameter distribution (28.0 m). This seemingly contradictory result (also noted by Vul'fson in his data) is due to the fact that the statistical model includes the very small convective elements that are unlikely to be intercepted by the acoustic sounder, and which contribute in a negligible amount to the frequency distribution of transect lengths. In the derived distribution of diameters they will appear significantly, thus lowering the mean diameter for the entire population. If only those plumes which were intersected were considered, however, their average diameter would be larger than the average length of the intercepted chords.

Cloud transect lengths were obtained from the lidar observations. The data were derived from a height vs time display of the strength of the returned signal. A procedure similar to that employed with the acoustic sounder was used to obtain cloud transect lengths. The uncertainty in the measurements was ± 7 m. In some cases of considerable vertical wind shear, cumulus clouds tend to tilt with height. Under those conditions the method employed in this study to measure cloud transect lengths would result in an overestimate of the real values. An inspection of the height vs time lidar display of the data as well as of the movie photographs

FIG. 1. Logarithmic probability graph of the accumulated frequency distribution of the convective plume transect lengths measured with an acoustic sounder. The straight line corresponds to the lognormal distribution that best fits the data. The triangles represent the distribution of plume diameters obtained from the transect length data.
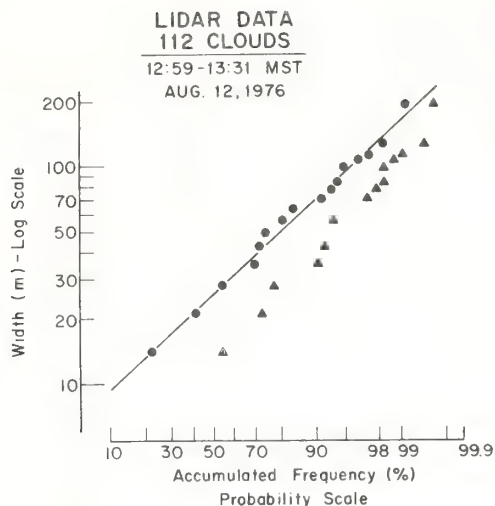
FIG. 2. As in Fig. 1 except for cloud transect lengths measured with a lidar plotted on logarithmic probability paper. The triangles represent the distribution of cloud diameters obtained from the transect length data.

taken at the same time did not indicate any apparent tilting of the clouds. Actually because of the small depths of these clouds (80% had depths under 100 m) a strong vertical wind shear would be necessary to show appreciable tilting.

The frequency distribution of cloud transect lengths is displayed in Fig. 2. It can be seen that the widths of the clouds detected by the lidar are also lognormally distributed. Applying a chi-square test again shows that the hypothesis of lognormality for the distribution would not be rejected at the 5% level of significance. Again, the distribution of cloud diameters obtained from the cloud transect length data is shown by triangles. This corrected distribution is also lognormal at better than the 5% level of significance and yields a smaller chi-square value for the best fit than the original distribution. The diameters in the mean are also smaller than the transect lengths due to the inclusion of smaller clouds which were less likely to be intercepted by the lidar.

The depths of the clouds were obtained by noting the greatest depth observed for each particular cloud from the lidar records. In general, the attenuation of visible lidar beams is considerably high. For a ruby lidar, for example, the penetration in a dense cloud would only be a few hundred meters. However, in many cases a lidar beam can penetrate several layers of cloud which together obscure the sun. Derr (1977) has computed from Mie scattering theory the penetration of different types of clouds by a ruby lidar beam. For a newly formed low-density cloud he obtained penetration depths of 357 m for a signal-to-noise ratio of 10 and 715 m for a signal-to-noise ratio of 100. The clouds observed in this study were very small, incipient thin clouds. On the basis of Derr's computations we would expect penetrations of around 400 m. Actually, a few hours

after the small clouds were measured, a larger, denser cumulus congestus cloud drifted over the site from the mountains. The returned signals from this cloud were in general 2–3 times as intense as in the case of the early clouds and came from depths of up to 400–700 m inside the cloud. The small clouds used in this study were under 300 m in depth and about 80% of them were under 100 m. According to the above considerations we feel confident that the cloud depths measured were real and were not penetration depths.

The frequency distribution of depths is portrayed in Fig. 3. It also describes very closely a lognormal distribution, and the hypothesis of lognormality would not be discarded at a level of significance of 5% or better.

The lognormal distribution can be considered (Aitchison and Brown, 1957) the frequency distribution of a variate that is subject to the law of proportionate effects, i.e., a variate whose change in value at any step of a process is a random proportion of the previous value of the variate. Thus, something that forms, grows or changes according to the law of proportionate effects will yield a lognormal size distribution. López (1976, 1977) has hypothesized that large cumulus clouds grow and develop by a process which follows the law of proportionate effects, thus producing the observed lognormal distributions of cloud characteristics. Such a process can be postulated as follows: In a given region many small convective elements are randomly generated throughout the subcloud layer. These agglomerate randomly into larger elements. The larger elements, covering a greater area, intercept a larger number of other elements and thus grow more rapidly than the smaller ones, i.e., growth proceeds according to the law of proportional effects. In this way a cloud population develops where the eventual size
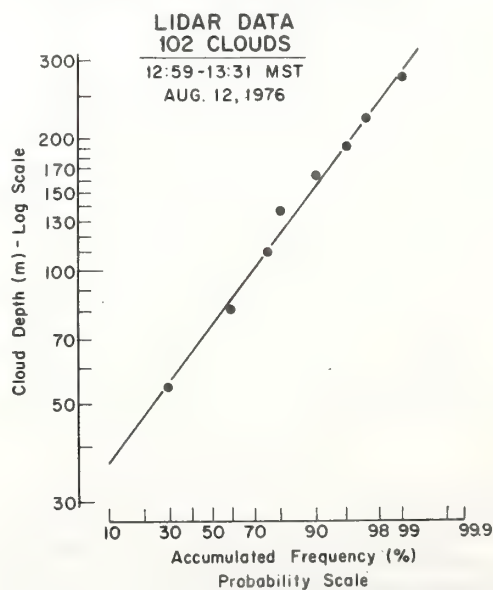
FIG. 3. As in Fig. 1 except for the depths of clouds measured with a lidar.
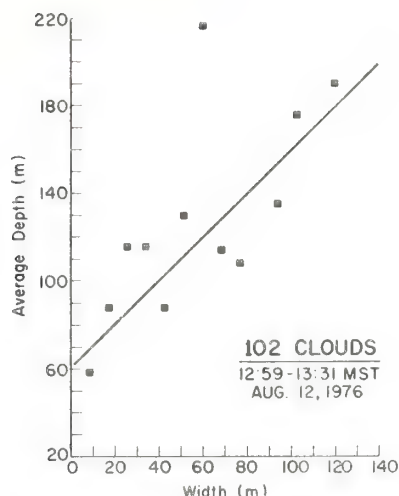
FIG. 4. The average depth of all the clouds within each cloud transect width interval as measured with a lidar.

distribution is lognormal. On the basis of that interpretation, the lognormality of plumes in the boundary layer and small fair weather cumuli as revealed by the present measurements suggests that the convective plumes and small clouds also grow by the merging or agglomeration of smaller elements.

It is interesting to notice from these distributions that on the average the small clouds are 2–3 times deeper than they are wide. This is more evident in Fig. 4 where the average depth of all the clouds within each cloud transect width interval is portrayed. Notice that

those clouds with smaller widths tend to have large aspect ratios of depth to width, while the wider clouds tend to be as deep as they are wide. In other words, the small clouds (supposedly formed by a few convective elements) tend to look like plumes, whereas the larger ones (supposedly formed by the merger of many convective cells) tend to look like bubbles.

Fig. 5 shows as a function of time the height of the base of the clouds above ground measured with the lidar. A fluctuation with a duration of about 30 min can be seen. This time interval can be equated to a horizontal distance of about 12 km by using the wind estimate at cloud base and by assuming that the pattern of cloud-base height remained constant as the clouds were advected over the site by the wind. This mesoscale variation could have been due to wavelike perturbations in the subcloud layer on the scale of about 12 km, or due to time changes in the thermal structure of the boundary layer on the scale of 30 min.

4. Summary and discussion

It has been shown here that both clear air convective plumes and small cumulus clouds yield lognormal size distributions. Similar distributions for larger cumulus clouds have been interpreted by López (1976, 1977) as an indication of growth by the agglomeration of smaller cloud elements. Applying the same interpretation to the present data it is suggested that both convective plumes and small fair-weather cumuli are formed by the agglomeration of smaller elements.

The relationship between the plumes and the clouds cannot be ascertained from the present data. However, the concept of growth by agglomeration in both clear air plumes and very small cumulus clouds is suggestive of a continued process of grwoth from the clear air convection to the cloud stage. In any case, the preliminary data presented in this note are an indication of the capability of a lidar-acoustic sounder system to study the problem of cumulus cloud initiation by convective plumes in the boundary layer. A more extensive and complete experiment is planned where this system will be supplemented with instrumented tower and aircraft observations.

FIG. 5. The height of the average cloud base above ground as a function of time. The vertical bars represent ±1 standard deviation of cloud base height around the corresponding average. Time has been equated to horizontal distance by using the wind at cloud base and by assuming that the cloud-base height patterns remained constant as the clouds were advected by the wind over the site.

REFERENCES

Aitchison, J., and J. A. C. Brown, 1957: *The Lognormal Distribution.* Cambridge University Press, 176 pp.

Coulman, C. E., and J. Warner, 1976: Aircraft observations in the subcloud layer over land. *Preprints Int. Conf. Cloud Physics,* Boulder, Amer. Meteor. Soc., 270–274.

Derr, V. E., 1977: Some directions in laser meteorology. Paper presented at the Eighth Int. Laser Radar Conf., Drexel University.

Hall, F. F., 1972: Temperature and wind structure studies by acoustic echo-sounding. *Remote Sensing of the Troposphere,* V. E. Derr, Ed., Chap. 18. [Govt. Printing Office, Cat. No. 0323-0011].

Hardy, K. R., and I. Katz, 1969: Probing the clear atmosphere with high power, high resolution radar. *Proc. IEEE,* **57,** 468–480.

Kaimal, J. C., and J. A. Businger, 1970: Case studies of a convective plume and a dust devil. *J. Appl. Meteor.,* **9,** 612–620.

López, R. E., 1976: Radar characteristics of the cloud populations of tropical disturbances in the northwest Atlantic. *Mon. Wea. Rev.,* **104,** 269–283.

——, 1977: The lognormal distribution and cumulus cloud populations. *Mon. Wea. Rev.,* **105,** 865–872.

Smith, M. E., Ed., 1973: *Recommended Guide for the Prediction of the Dispersion of Airborne Effluents.* Amer. Soc. Mech. Eng., 85 pp.

Taylor, R. J., 1958: Thermal structures in the lowest layers of the atmosphere. *Aust. J. Phys.,* **11,** 168–176.

Vul'fson, N. I., 1961: *Convective Motions in a Free Atmosphere* [Israel Program for Scientific Translations, Jerusalem, 188 pp.].

Warner, J., and J. W. Telford, 1963: Some patterns of convection in the lower atmosphere. *J. Atmos. Sci.,* **20,** 313–318.

Woodley, W. L., B. Sancho and J. Norwood, 1971: Some precipitation aspects of Florida showers and thunderstorms. *Weatherwise,* **24,** 106–119.

Preliminary Results from the GATE Acoustic Echo Sounder

P. A. Mandics and F. F. Hall, Jr.

Wave Propagation Laboratory, ERL/NOAA, Boulder, Colo. 80302

Abstract

An acoustic echo sounder mounted on the NOAA ship *Oceanographer* during GATE proved to be a valuable tool for investigating the structure and dynamics of the tropical marine boundary layer up to 800 m in height. Under suppressed weather conditions the facsimile-recorded echo intensity returns depicted a mixed layer characterized by convective plumes rising from the surface of the water to 400 m. Disturbed weather events resulted in a substantial modification of the boundary layer; layered structures formed that at times limited the depth of the mixed layer to 100 m. The Doppler frequency shift of the acoustic returns made it possible to determine the vertical velocity field.

1. Introduction

During the past few years, acoustic echo sounders have become valuable remote-sensing tools for investigating the lower atmospheric layers of continents. For example, facsimile-recorded backscattered echo intensities have been used to study atmospheric stability and convective plumes in the planetary boundary layer (Hall *et al.*, 1975; Wyckoff *et al.*, 1973; Cronenwett *et al.*, 1972). Recently, Neff (1975) has shown that the intensity of acoustic returns can be related to the strength of temperature fluctuations in a quantitative manner. Beran *et al.* (1974) have succeeded in determining wind velocity from the Doppler frequency shift of acoustic returns.

Only a very limited amount of data has been gathered in the ocean environment using acoustic echo sounders (Ottersten *et al.*, 1974; Mandics and Owens, 1975). GATE presented a unique opportunity to deploy and operate an echo sounder over the ocean in conjunction with a number of other boundary-layer probes. A three-

axis acoustic echo sounder was mounted on the NOAA ship *Oceanographer* to obtain data on the structure of the marine boundary layer and to measure wind velocity in the subcloud layer. The echo sounder was in operation during a large percentage of the time in GATE, especially during Phases 2 and 3. In the present paper, we describe some of the main features of the echo sounder and the results of the preliminary data analysis.

2. The echo sounder system

The operation of the acoustic echo sounder is dependent on backscattering produced by small-scale (about one-half acoustic wavelength in size) temperature and, to a lesser extent, humidity fluctuations. Short bursts of acoustic energy were transmitted every 5 s by the echo sounder antennas. The acoustic frequency was selected to minimize interference by the ship's ambient noise; frequencies between 2 and 3 kHz were used during GATE. After the transmission of the pulse, the same antennas served to collect the backscattered acoustic energy in a monostatic fashion. Sensitive circuitry incorporating low-noise, high-gain amplifiers and narrow-band filters was used to condition the received signals (Simmons *et al.*, 1971). The data were recorded on 14-channel analog magnetic tape for later digitization and analysis. In addition, the intensity of the vertically backscattered signal provided valuable information on the atmospheric structure as displayed on a facsimile recorder in real time.

To resolve the vector wind velocity, three acoustic antennas were located on the forward weather deck of

TIME (GMT) SEPTEMBER 15-16, 1974
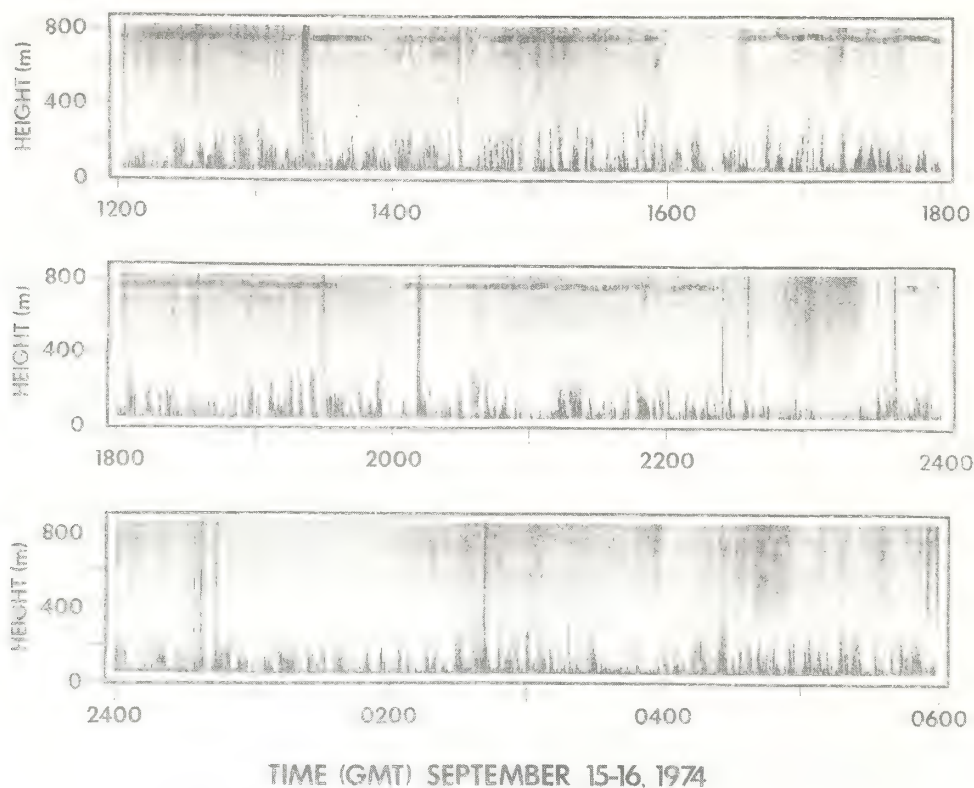
FIG. 1. Facsimile record of backscattered acoustic intensity during undisturbed weather conditions, from the *Oceanographer* at GATE position 4.

the *Oceanographer* about 8.5 m above the water line. One was pointed vertically and two others were elevated at 45° and separated by 90° in azimuth. Each antenna consisted of a 1.2 m parabolic dish fed by a commercial, high-power acoustic transducer. The antennas were surrounded by 1.8 m tall anechoic shielding cuffs to reduce interference from airborne ambient noise and to minimize the annoyance of ship's personnel by the transmitted tone bursts. Depending on the frequency used, half-power antenna beamwidths varied from 5° to 8°. To compensate for the ship's pitch and roll motions the antennas were mounted on a gyro-controlled stable platform. Rubber vibration isolation pads reduced the ship's structure-borne noise to a tolerable level.

The ambient noise generated by the ship's engines proved to be the main limitation to the sounder's performance. Calculations based on the estimated strength of scattering, measured ambient noise level, and known sounder parameters indicated that the maximum range of the sounder should be about 300 m (Mandics and Owens, 1975). Data gathered during GATE generally agreed with these range estimates; however, there were occasions when returns were obtained from as high as 800 m. On occasion, heavy rains and strong surface winds (12 m s^{-1} and higher) produced sufficient acoustic noise to mask any returns, and thus rendered the sounder inoperative.

The automatic frequency-tracking circuit of the acoustic receiver was able to resolve the Doppler frequency shift of the returns as long as the received signal-to-noise ratio remained above 3 dB within the passband of the receiver (30 Hz for the vertically pointed antenna and 100 Hz for the tilted antennas). Digital spectral analysis of the tape-recorded data is being performed in the laboratory to determine Doppler shifts (and the corresponding velocities) for lower signal-to-noise ratios.

3. Typical suppressed condition results

Fair weather (undisturbed) conditions existed during a large percentage of the time at the positions occupied by the *Oceanographer*. Figure 1 illustrates typical time-height facsimile recordings of the backscattered acoustic intensity obtained from the vertical antenna under these conditions. Records of this type were observed 94, 74, and 69% of the time when the sounder was in operation during Phases 1, 2, and 3, respectively. Because the acoustic sounder antennas were covered and the equipment was not in operation whenever it rained, the data collected were biased toward undisturbed conditions for Phase 1 and to a lesser extent for Phases 2 and 3. The
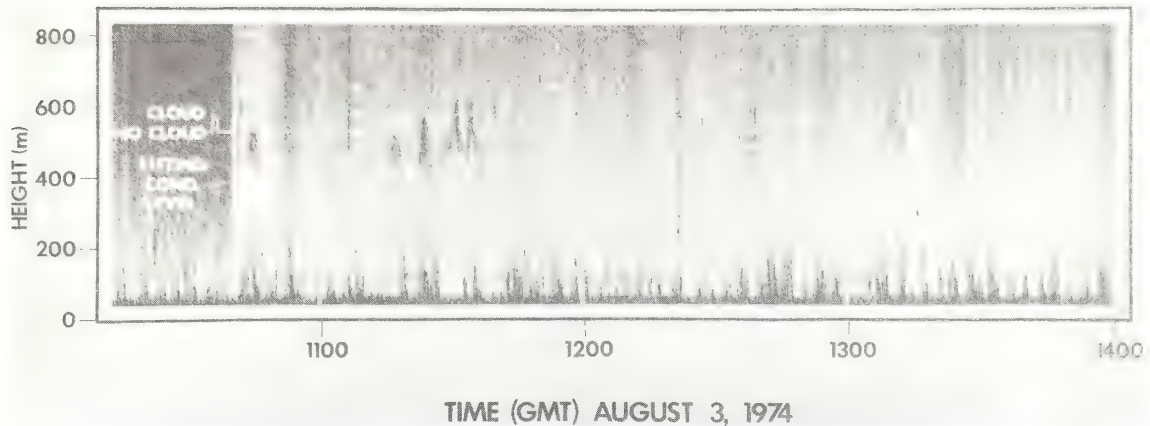
FIG. 2. Facsimile record of backscattered acoustic intensity with the presence or absence of clouds (solid white line) and calculated lifting condensation level (dashed white line), from the *Oceanographer* at GATE position 1.

sounder was in operation for 33, 64, and 83% of the time during Phases 1, 2, and 3, respectively.

In Fig. 1, darker regions correspond to more intense scattering while white areas indicate the lack of scatter. The gradual darkening of the record with height is caused by the amplification of ambient noise by the automatic range-compensation network in the receiver. The transmitter was turned off for 1 min at the end of each hour to provide a time mark on the record. The resultant lightly shaded bars also serve as a convenient qualitative measure of the signal-to-noise ratio. Reflections from the Boundary Layer Instrumentation System (BLIS) balloon produced strong acoustic returns that resulted in the heavy dark line at 750 m. Shifts in wind direction and ship heading changed the relative position of the balloon and acoustic beam and caused the BLIS echoes to fade out at times. Noise from ship maintenance and interference by radio transmissions produced the continuous vertical dark lines such as those seen at 1320 GMT.

The "spiky" dark traces extending from the surface to about 300–400 m in height were produced by convective plumes rising from the warm surface of the water. The fact that no returns were obtained from above 400 m does not necessarily mean that the mixed layer extends no higher. Because temperature variations that produce acoustic scattering decrease with height, a point is reached above which returns are masked by the ambient noise. Generally, as long as the water temperature exceeded that of the overlying air, convective plumes were observed both day and night. This was in sharp contrast with the diurnal pattern (thermal plumes during the day and more stable, layered stuctures at night) usually seen over land. During GATE, acoustically observed plume heights ranged from 100 to 400 m. Assuming that plumes were advected with the mean wind, we were able to estimate their spatial extent. On the average, the along-the-wind plume dimension was 750 m at 60 m above the water's surface; however, plumes as

wide as 3000 m and as narrow as 200 m were also observed on occasions.

About 20% of the time, convective plumes were accompanied by patchy, "hummocky" returns from between 400 and 600 m as shown in Fig. 2. Shaw (1971) observed similar acoustic returns in the semitropical environment of Darwin, Australia, and was able to correlate the patchy echoes with the presence of individual, low-level cumulus clouds overhead. To resolve the question of whether the hummocks seen in Fig. 2 were produced by clouds, we examined all-sky photographs for the presence or absence of clouds directly over the *Oceanographer*. The solid white line in Fig. 2 shows excellent correlation between hummocks and clouds. Not all clouds seen on the photographs registered as hummocks on the acoustic records, however. For example, the cloud indicated at 1156 GMT in Fig. 2 has no hummock accompanying it. We have also evaluated the lifting condensation level from 12 min averages of surface meteorological data and plotted it with dashed lines in Fig. 2. The calculated condensation levels agree well with the hummock base heights.

Because cloud droplets in general are much less effective scatterers of acoustic energy than temperature variations, we do not believe that the hummocks were produced by such scattering (Little, 1972). Temperature fluctuations enhanced by the release of latent heat of condensation are a much more likely source of the returns. Entrainment and detrainment near cloud boundaries could also be responsible for more intense temperature variations. The "witch's hat" appearance of many of these returns (for example, the hummock at 1045 GMT in Fig. 2) tends to support the latter mechanism.

There is convincing evidence indicating that hummocky acoustic returns are produced by low-level cumulus clouds. A further interesting feature of these returns is that quite often individual hummocks were associated with plumes directly below them. A more detailed investigation of these structures could shed val-

TIME (GMT)   SEPTEMBER 9, 1974
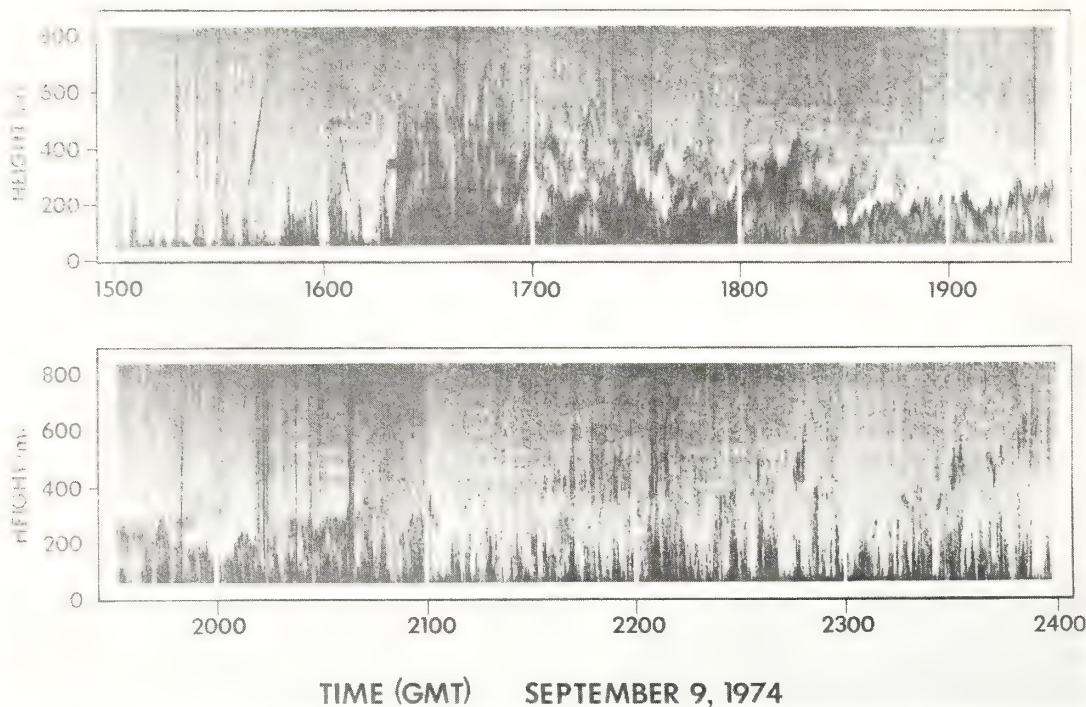
Fᵢɢ. 3. Facsimile record of backscattered acoustic intensity during a cumulonimbus-generated downdraft, from the *Oceanographer* at GATE position 4.

uable light on subcloud processes and possibly on the origins of cloud formation itself. Are hummocks (clouds) produced by convection from individual plumes, or do they (once formed) set up a circulation including the generation of convective plumes underneath to sustain themselves?

4. Disturbed events

Disturbed weather conditions resulted in pronounced changes in the structure of the boundary layer, and these changes were also reflected in the observed acoustic records. Figure 3 illustrates the effects of a cumulonimbus-generated downdraft. At the beginning of the record, plumes characteristic of suppressed conditions were seen. Suddenly at 1620 GMT the intensity and height of the acoustic echoes increased considerably as a result of the cold air outflow. A low-level, multilayered, undulating inversion formed, which persisted for almost 5 h. By 2100 GMT the inversion had dissipated and the undisturbed-condition boundary layer with convective plumes and occasional hummocks above reestablished itself.

Several intense squall lines with winds gusting over 15 m s⁻¹ passed over the ship during Phase 3. Figure 4 illustrates one that occurred on 12 September. The passage of the squall line at 1255 GMT was followed by 3 h of heavy rain, which resulted in the almost total blackening of the record due to acoustic noise generated by raindrops falling on the antenna. The formation of a strong, low-level inversion layer started during the rain

and became clearly visible after 1600 GMT. Wavelike undulations on the multilayered inversion at times exceeded 200 m in amplitude (for example, shortly after 1900 GMT), and features resembling Kelvin-Helmholtz breaking waves from 0020 to 0230 GMT suggested the presence of strong wind shear between 450 and 650 m. The depth of the mixed layer was considerably reduced during the disturbance; at 1725 GMT it became less than 100 m. It took the boundary layer about 16 h to return to its typical fair weather state.

The acoustic records have clearly shown that disturbances resulted in a stable stratification of the lower boundary layer in agreement with the conclusions of Garstang and Betts (1974). The significance of the resultant strong inversions was that they provided a lid over the mixed layer that prevented the vertical transfer of latent and sensible heat to higher elevations. As a result, no new disturbances could have developed until after the inversion dissipated. The sounder records have also provided valuable information on the temporal extent of disturbances. Modifications of the boundary layer caused by cumulus downdrafts typically lasted for 5–6 h, whereas those due to squall lines persisted for 12–16 h. During disturbed conditions, the facsimile records also delineated the depth of the mixed layer.

5. Quantitative results

Up to this point we have examined only facsimile records of backscattered acoustic intensity, which pro-
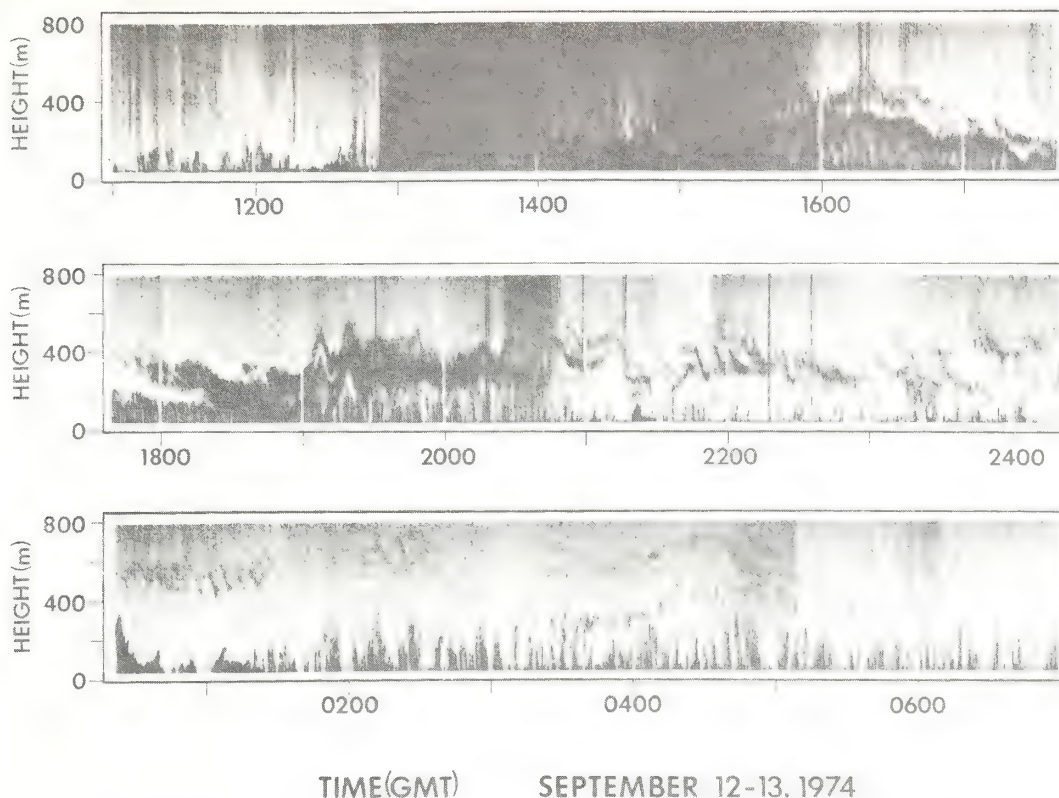
Fɪɢ. 4. Facsimile record of backscattered acoustic intensity during the passage of an intense squall line, from the *Oceanographer* at GATE position 4.

vided qualitative and semiquantitative information about the structure of the boundary layer. The tape-recorded acoustic data are also amenable for analyses to yield quantitative information about boundary-layer processes. For example, the Doppler frequency shift of the returns can be used to resolve the motion of scatterers, and hence wind velocity. Figure 5 shows a comparison of acoustic Doppler-derived and BLIS anemometer-measured vertical velocities at the 138 m level following the gust-front event depicted in Fig. 3. Although the sounder sampled a volume of about 6×10^3 m³ (with a vertical resolution of 34 m) at this height level while the BLIS provided a point measurement, the agreement between the two is good. The two records show the best agreement for the larger velocity variations caused by the waves shown in Fig. 3; however, there is considerable disagreement in the finer details.

Our attempts to evaluate horizontal wind components from the two tilted antennas have not been successful yet. For reasons not fully explained, the signal-to-noise ratio for these antennas has been markedly inferior to that obtained for the vertically pointed antenna. The wider receiver bandwidths used with the tilted antennas and the fact that they faced into the wind may have contributed to the increased noise level.

Assuming that acoustic scattering is caused mainly by

small-scale temperature variations, we can relate the intensity of scattering to the magnitude of temperature fluctuations (more precisely to C_T, the temperature structure parameter) in a quantitative manner at the various height levels. Following the method of Neff (1975), we will use C_T to estimate the surface sensible heat flux under free convection conditions. Work is already well underway on this aspect of the data analysis, and preliminary results indicate fair agreement between acoustically derived sensible heat fluxes and those obtained from surface meteorological data using bulk methods.

6. Discussion

Our GATE experience has proven the value of probing the marine atmosphere with an acoustic echo sounder. Facsimile-recorded acoustic backscatter data provided a unique and hitherto unavailable description of processes taking place in the tropical marine boundary layer. From these records, one can determine directly parameters such as the temporal extent of disturbances and the depth of the mixed layer during these disturbances, which should be of interest to researchers attempting to parameterize the subcloud and cloud layers.

We have been able to, show only a limited sample of the acoustic facsimile records here. Microfilm copies of facsimile-recorded vertically backscattered acoustic inten-
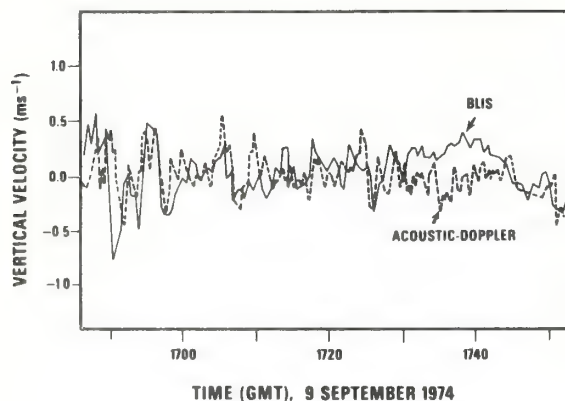
FIG. 5. Comparison of acoustic Doppler-derived and BLIS anemometer-measured vertical velocities at 138 m, from the *Oceanographer* during Phase 3 of GATE.

sities for all three phases of GATE have been archived at World Data Centers A and B and are available for distribution.

Our present efforts are aimed at evaluating some of the quantitative aspects of the acoustic data. Because of the computer costs involved, we can calculate vertical velocities (and possibly horizontal wind components as well) for selected time periods only. Because we believe that the maximum usefulness of the acoustic data will be realized only if they are combined with data from other sources, we would welcome suggestions from other investigators as to what time periods should be given priority in our analysis.

Acknowledgments. We are indebted to Drs. D. H. Sargeant and J. L. Rasmussen of the U.S. GATE Project Office for their encouragement and support. We would like to thank Capt. W. D. Barbee, Chief Bosun W. J. Halama, the crew, and officers of the *Oceanographer* for their cooperation and help during GATE. We are grateful to D. Wylie and W. D. Neff for the BLIS- and

acoustic-determined vertical velocities, respectively, which are presented in Fig. 5.

References

Beran, D. W., F. F. Hall, B. C. Willmarth, R. J. Keeler, and D. Hunter, 1974: Operational test results of acoustic Doppler wind shear detector. *Preprints of Papers, Sixth Conference on Aerospace and Aeronautical Meteorology*, (El Paso, Tex.), Boston, Mass., Amer. Meteor. Soc., 412–417.

Cronenwett, W. T., G. B. Walker, and R. L. Inman, 1972: Acoustic sounding of meteorological phenomena in the planetary boundary layer. *J. Appl. Meteor.*, **11**, 1351–1358.

Garstang, M., and A. K. Betts, 1974: A review of the tropical boundary layer and cumulus convection: Structure, parameterization, and modeling. *Bull. Amer. Meteor. Soc.*, **55**, 1195–1205.

Hall, F. F., Jr., J. G. Edinger, and W. D. Neff, 1975: Convective plumes in the planetary boundary layer, investigated with an acoustic echo sounder. *J. Appl. Meteor.*, **14**, 513–523.

Little, C. G., 1972: On the detectability of fog, cloud, rain and snow by acoustic echo-sounding methods. *J. Atmos. Sci.*, **29**, 748–755.

Mandics, P. A., and E. J. Owens, 1975: Observations of the marine atmosphere using a ship-mounted acoustic echo sounder. *J. Appl. Meteor.*, **14**, 1110–1117.

Neff, W. D., 1975: Quantitative evaluation of acoustic echoes from the planetary boundary layer. NOAA Tech. Rept. ERL 322-WPL 38, U.S. Government Printing Office, Washington, D.C., 34 pp.

Ottersten, H., M. Hurtig, G. Stilke, B. Brümmer, and G. Peters, 1974: Shipborne sodar measurements during JONSWAP 2. *J. Geophys. Res.*, **79**, 5573–5584.

Shaw, N. A., 1971: Acoustic sounding of the atmosphere. Ph.D. thesis, Dept. of Phys., Univ. of Melbourne, Melbourne, Australia, 266 pp.

Simmons, W. R., J. W. Wescott, and F. F. Hall, Jr., 1971: Acoustic echo sounding as related to air pollution in urban environments. NOAA Tech. Rept. ERL 216-WPL 17, U.S. Government Printing Office, Washington, D.C., 77 pp.

Wyckoff, R. J., D. W. Beran, and F. F. Hall, Jr., 1973: A comparison of the low-level radiosonde and the acoustic echo sounder for monitoring atmospheric stability. *J. Appl. Meteor.*, **12**, 1196–1204.

ACOUSTIC SOUNDER MEASUREMENTS OF THE SOUTH POLE
BOUNDARY LAYER

W. D. Neff and F. F. Hall, Jr.
Wave Propagation Laboratory
NOAA Environmental Research Laboratories
Boulder, Colorado 80302

1.   INTRODUCTION

A monostatic acoustic sounder was operated
at the South Pole for the twelve months of 1975.
The facsimile records, showing the intensity of the
backscattered acoustic energy, provide a detailed
picture of the planetary boundary layer structure
over the Antarctic ice plateau. Interpretation of
the records has been aided by rawinsonde data
obtained at the pole, synoptic scale charts pre-
pared for Antarctica, and surface layer turbulence
measurements made by University of California,
Davis scientists at the pole. In this paper we
report on the experiment and progress we have made
in the interpretation of the facsimile records.

2.   EQUIPMENT DESCRIPTION

The sounder antenna used was a 1.2 m
diameter parabolic dish surrounded by a plywood
and foam absorbing cuff 1.2 m high. The antenna
was located 120 m east of the Skylab tower, part
of the New Pole Station complex. A door was pro-
vided in the cuff for snow removal and the winter-
ing-over NOAA technician, Ken Martinsson, brushed
the snow accumulation from the dish several times
during the winter night. The antenna was located
atop aluminum legs .4 m tall so the snow drifting
near the surface would not accumulate and bury
it. This design proved to be very practical since
at sunrise in September 1975, a drift extended
100 m downstream with no accumulation at the
antenna itself.

The electronic equipment was located
in the Skylab and was connected to the preamplifier
at the antenna by a multiconductor shielded cable.
Six inches of polystyrene foam around the remote
preamp at the antenna plus a ten-watt heater
within the preamp chassis assured that the
temperature of the components did not drop lower
than -40°C. No significant electronic problems
or voice coil failures were experienced in spite
of temperatures which reached -75°C. An operating
frequency of 2 kHz with a 100 ms pulse repeated

every 4 s gave the sounder a nominal range of
600 m, and echoes were frequently received from
this maximum height.

3.   THE GROUND-BASED LAYER (GBL) ECHO

The most persistent acoustic-echo fea-
ture observed on the facsimile recordings at the
pole we designate the Ground-Based Layer (GBL).
It appears to be closely related to the Ekman
Layer depth. This feature is also very similar to
the "herringbone" pattern described by McAllister
et al. (1969). It shows rather closely spaced,
descending or tilted turbulent layers as illus-
trated in Figure 1. From the Davis data the
Richardson number near the ground was near
zero but increased somewhat in magnitude above
the surface. From rawinsonde-derived tempera-
ture and wind gradients in the upper parts of
such layers, it appears that the gradient
Richardson number (Ri) is larger than 0.25 al-
though the slow response of the rawinsonde does
not allow resolution of the local Ri in such thin
regions. The turbulence in this layer seems to be
maintained at Richardson numbers approaching 1.0.

This is in contrast with some of our measure-
ments over the plains of Colorado, using higher-
resolution tower data, which has shown that the
Richardson number within the echoing region seldom
exceeds 0.25. The reasons for the turbulence at
these higher values of Ri at the pole still needs
to be explored and higher resolution data obtained.

The terrain around the pole is smooth
and homogeneous with a slope of 10^{-3}. The only
terrain features are several hundred kilometers
away, towards the Transantarctic Mountains and the
Ross Ice Shelf. The depth of the GBL which over-
lay this nearly uniform surface varied from 50 m
to 300 m. The average depth for the year was 158 m
with a standard deviation of 42 m. Under "undis-
turbed" inversion conditions, when wind direction
and speed as well as temperatures showed little
change from day to day, the GBL depth was generally
less than 100 m. This band of acoustic returns
corresponded to the region of largest rawinsonde
measured temperature gradient.

When the wind speed above the inversion
increased, particularly when warmer air was ad-
vected over the pole from the quadrant west of the
Greenwich meridian, the depth of the layer some-
times increased to as much as 300 m. Such in-
creases of the depth of the GBL corresponded with
the rapid warmings which occurred at the surface
on twelve occasions between March and August 1975,
showing durations of several days. Following the
passage of such "warm front" events, the GBL
relaxed in 8 to 12 hours to its normal depth near
100 m. On several occasions, this recovery process
occurred in conjunction with cold front passages.
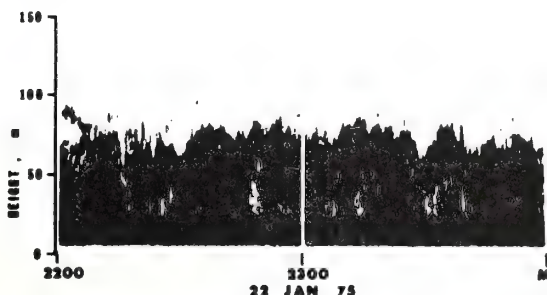
Figure 1. *Acoustic facsimile recording obtained
on 22 January 1975 at the South Pole showing the
detailed layering or "herringbone" pattern charac-
teristic of the surface-based echo structure.*

The acoustic sounder, when operating in a backscatter mode, provides a vertical profile of the intensity of small-scale (10 cm) temperature fluctuations. Such fluctuations are generally associated with turbulence within regions of non-zero potential temperature gradient. Temperature inversions are thus well delineated by the sounder. In the detailed comparison of sounder records with rawinsonde temperature profiles, we found that the top of the GBL corresponded gen-erally with the top of the principal ground-based inversion. The exceptions arose when thin elevated echo layers were present, at which time the first layer above the GBL corresponded with the top of the principal inversion. These two cases are illustrated in Figures 2 and 3. In Figure 2, the absence of echo at low levels (other than the transmitter-pulse leak-through that extends to about 40 m) is related to the nearly adiabatic lapse rate where vertical mixing will not produce temperature inhomogeneities.
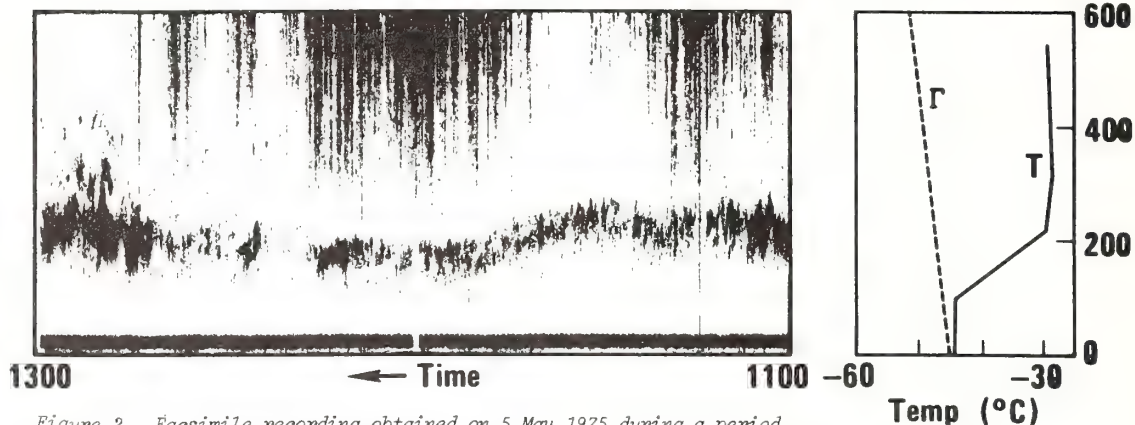
Figure 2. *Facsimile recording obtained on 5 May 1975 during a period when the surface-based inversion was destroyed. The absence of echo at lower levels is due to the nearly adiabatic lapse rate. The rawinsonde was launched at 1115 (SPT).*
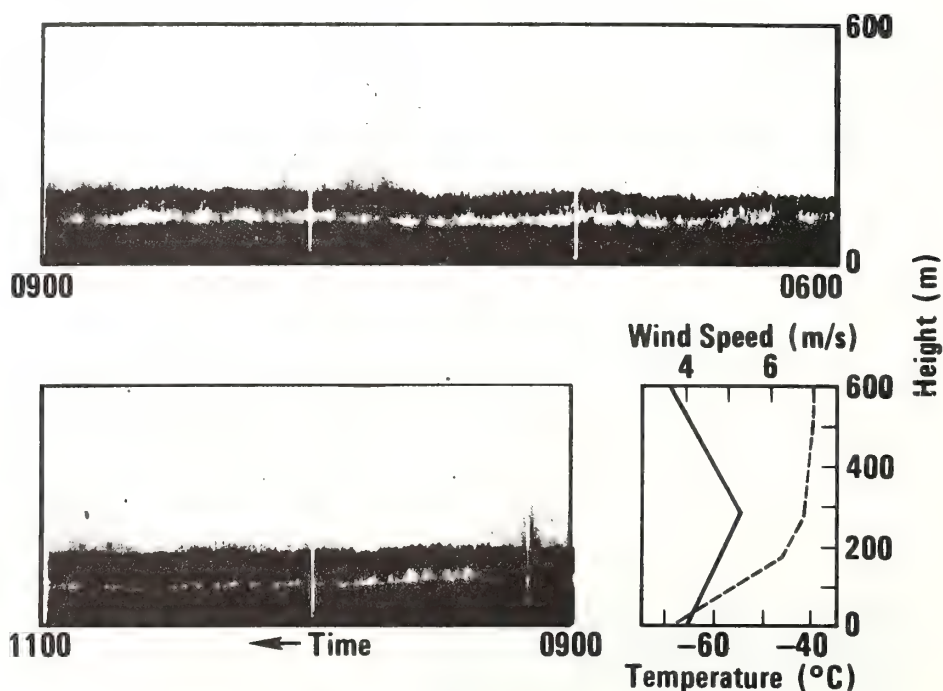
Figure 3. *Facsimile recording obtained on 4 June 1975 showing the ground-based layer (GBL) with an elevated layer with short-period "waves" near the top of the inversion. The rawinsonde launched at 1115 SPT, with a one-minute averaging for the wind, suggests the presence of a low-level inversion jet.*

298

The slight separation in the otherwise continuous GBL echo in Figure 3 probably results from the presence of a low level inversion jet; the upper layer then occurs as a result of dynamic instability above the jet. This explanation requires weak geostrophic winds above the inversion which was the case on 4 June, as shown in Figure 3.

A comparison between the GBL depth derived from the sounder and the top of the principal inversion from the daily rawinsonde records is shown in Figure 4. The scatter is similar to that observed by Wyckoff et al. (1973). South Pole rawinsonde data may also be complicated by the location of the balloon launch site downwind of the station, where wave perturbations in the inversion may have been sampled by the rising balloon. The sounder was upwind of the station and would have been unaffected by these hypothesized waves.

Figure 5. *Comparison of hourly averages of the GBL depth for a six-day period with daily measurement of the inversion depth from rawinsonde.*

equation estimates the maximum depth of the Ekman layer (Zilitinkevich, 1972),

$$h_E^- = \sqrt{\frac{K}{f}} = \sqrt{\frac{-Ru_*^4}{\beta Qf}}$$

where R is a universal constant empirically determined to be approximately 10, K is the eddy diffusivity, f is the Coriolis parameter, u_* the surface friction velocity, $\beta = g/T_o$, and Q is the surface temperature flux (heat flux normalized by ρc_p). Using values of $10^{-1} < K < 10^{+1}$ m^2/s, which seems to be the nominal range for the South Pole (Dalrymple et al., 1966; Miller, 1974) we find 27 m < h_E < 267 m, which is the range observed with the sounder.

Figure 4. *Comparison of the ground-based-echo layer depth from the sounder facsimile with the top of the ground-based inversion obtained from the daily rawinsonde. The dashed line represents perfect agreement. A least-squares fit gave a slope of 0.94 with an x intercept of 10 m. The standard deviation from the best-fit line was 20 m.*

Significant variations do occur from hour to hour in the depth of the GBL in response to changes in the surface stress. Figure 5 shows a six-day comparison of sounder GBL depth with the rawinsonde inversion tops comparing the daily balloon measurements with hourly sounder GBL depths. Although the point-by-point comparison has considerable scatter the trend in layer thickness is clearly traced out.

It appears plausible to interpret the sounder GBL depth as the Ekman layer depth. The sharp cut-off on the upper boundary of the layer is explained by the decrease in turbulence at that height as suggested by the higher order closure calculations of Wyngaard (1975). This is also observed in NOAA bistatic acoustic sounding data that have not yet been published. The following

Figure 6. *Depth of the ground-based layer echo compared with vertical temperature gradient obtained from the daily rawinsonde, suggesting the inverse dependence of the Ekman-layer depth on the static stability.*

299

It might be expected that the Ekman layer depth is an inverse function of static stability. A plot of this parameter shown in Figure 6 tends to confirm this. Because of the slow response of the rawinsonde temperature sensor, the inversion strength and depth were used to calculate $\partial T/\partial z$. The dashed-line plot of $(\partial T/\partial z)^{-1}$ is intended for comparison purposes. The scatter in the points may be caused by short term variations in stress and horizontal inhomogeneity. When short-term surface stress measurements become available from the Davis data we expect these comparisons to be further refined.

4. ELEVATED LAYERS AND FRONTS

The elevated scattering layers which occasionally occur to heights of 600 m, the maximum range of the sounder, have not been documented in previous Antarctic studies. In an otherwise stable atmosphere, such layers may be the result of a local reduction of the Richardson number with the consequent production of turbulence, because of perturbation of the velocity field by internal waves. Alternatively, they may indicate turbulence generated at the boundary of two air masses, as in a frontal passage.

At times during the period from March to September, the existence of a "geotriptic thermal jet," a geostrophically balanced current driven by the horizontal temperature gradient in an inversion overlying a sloped surface, was also

suggested by the sounder and radiosonde data. The top of this jet generally occurred at heights of 200 m and was marked by short period waves or dynamical instabilities. These jets and other multiple elevated layers generally correlate with weak and barotropic winds aloft, between the passages of synoptic scale disturbances. We conjecture that the condition of weak winds with small shears aloft allows for critical level encounters of low frequency internal waves propagating out of the boundary layer. We plan to test this hypothesis during a continuation of the experiment scheduled for 1977, using a microbarograph array around the sounder to analyze internal-wave motion within the boundary layer.

Occasional, but dramatic, variations in boundary layer structure were observed in association with tropospheric jet streams. One such case occurred during the period 20-25 May 1975. Early in this period, a 25 m/s jet directed from 90°W was centered at a height of 2 km. The 700 mb maps prepared at McMurdo at the beginning of this period showed high pressure over the entire continent, followed by the formation of a large depression off the Ross Sea area by 24 May with some influx of altostratus over the pole. Until this time the skies had been clear. The thermal wind relation applied to the 20 May rawinsonde profile suggested strong baroclinicity (3.25°C/100 km). The wind speed then dropped to 2 to 3 m/s and shifted to 150°E. At 0600 22 May, a wedge of cold air arrived at the pole dropping the surface temperature by 8°C over the next 24 hours. The facsimile record for this event is shown in Figure 7. Initially, the principal
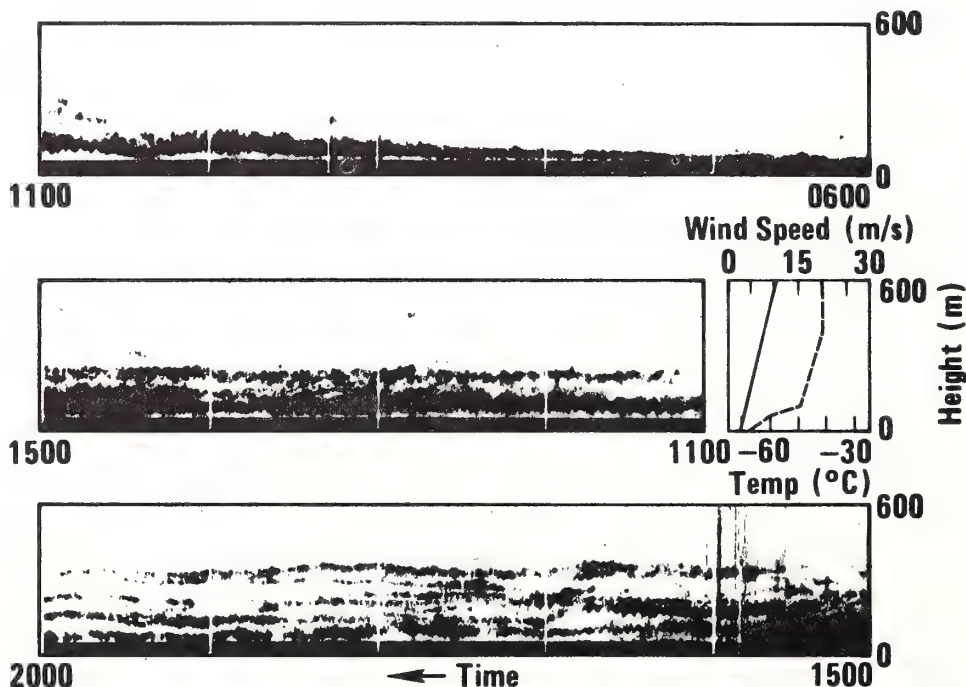
Figure 7. *Facsimile recording obtained on 22 May 1975 showing a cold "front" arrival at South Pole station. The surface pressure minimum occurred at 0700 SPT. It is postulated that the elevated layers that follow the front are associated with subsidence aloft.*

300

384

thermal wind was confined to the lower kilometer. On succeeding days the flow remained baroclinic but the region of large shear deepened to 4 km. From the thermal wind relation the horizontal temperature gradient at the time of the front was 2°C/100 km. Figures 8 and 9 give a synopsis of the surface and radiosonde observations for the event. The rawinsonde, unfortunately, reveals very little detail about the wind and temperature structure of this enhanced downslope flow of cold air. Also of interest is the occurrence of the surface pressure minimum in conjunction with the front. The absence of layered structure prior to the event may be associated with the divergence aloft ahead of the front and the presence of layers after the event with the subsequent convergence aloft and sinking motion.
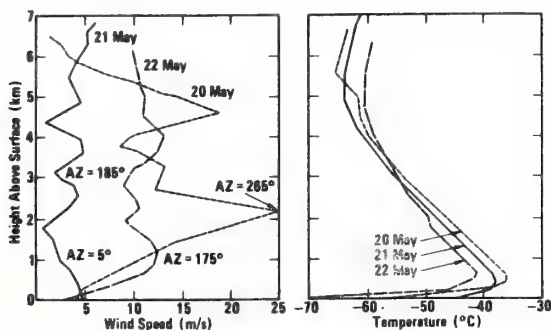
At times the multilayered acoustic echo structure exhibited significant sinusoidal oscillations at an extremely uniform frequency. For example, on 9 February, during the intrusion of cold air, such oscillations were observed in multiple layers between 200 and 600 m above the surface. Between 0900-1400 there were 10 to 17 wave periods per hour with 30 to 70 m peak to peak amplitude. From 1700 to 2200, there was a uniform 13 waves per hour with the nearly sinusoidal patterns exhibiting 60 m peak to peak amplitude. The rawinsonde ascent at 11:15 showed a stable layer between 254 and 736 m with the convectively unstable superadiabatic lapse below and a nearly unstable layer just above 736 m. Computing the Brunt-Väisälä wave frequency N for the stable layer from the expression $N^2 = (g/\theta)d\theta/dz$, the period for the waves is 17 waves per hour. This is in such good agreement with the observed period that it seems clear the wave events were indeed gravity waves. Data to be obtained during 1977 using a microbarograph array to define the wave phase velocity relative to the ground should give further insight into such events.

5. CONVECTIVE PLUMES

During 58 hours of the more than 6,000 hours during which the sounder operated, convective plumes originating at the ice surface were detected by the sounder. Five separate such events occurred, each during a rapid decrease in surface temperatures. A series of well-defined plumes occurred between 10:30 and 13:30 on 9 February 1975, SPT (Z+12) as shown in Figure 10. The temperature had dropped from -27.7°C at 0700 to -37.4°C by 2300. It is hypothesized that since the ice surface had become heated by the relatively warmer air during the early hours of the day, the rapid intrusion of colder air found the ice relatively warmer than the atmospheric surface layer, thus setting off the convection. A radiosonde ascent at 11:15 showed a superadiabatic lapse rate in the lowest 138 m of the atmosphere. Probably because of convective overshoot, some of the plumes detected by the sounder extended to more than 200 m. The other events showing convective plumes occurred on 5 February between 2000 and 2100, on 6 February between 1000 and 1500; two additional cases occurred late in the year. On 8 December convection lasted for 23 hours while on 17 December plumes extended to 400 m for 18 hours. The latter case also showed a gradually-rising, capping inversion which eventually exceeded the 600 m range of the sounder.

Other events showing abrupt cooling were not accompanied by convective plumes that could be detected on the facsimile record. On several such occasions in March and April, the sounder depicted subsident layers above the ground-based layer, which probably resulted in high static stability in the lower few hundred meters. If there was any convection because of cold air intrusion, the plume heights must have been kept below the 40 m minimum range of the sounder by such subsidence.

Figure 8. Time series plot of hourly surface observations of wind speed and direction, and temperature before and after the event shown in Figure 7.

Figure 9. Rawinsonde observations taken at 1115 on 20, 21, and 22 May 1975 which show the events precursing and during the event shown in Figure 7. Selected wind azimuths are shown that reveal the wind shift relative to the continental slope prior to the occurrence of the front.

301

6. FUTURE PLANS

During 1977, we plan to operate a bistatic acoustic sounder to provide continuous vertical profiles of C_T^2 and C_V^2. Together these quantities give a measure of the local dissipation of turbulent kinetic energy and the effects of the turbulent mixing process on the local thermal structure. In 1978 we hope to update the sounder system to a full three-axis Doppler wind profiling system. This should alleviate the difficulty with rawinsonde data, which was the inability to resolve detailed gradients in the wind, especially when multiple layers are present.

7. CONCLUSIONS

An acoustic sounder operating for a year at South Pole Station has provided a detailed climatology of the statically stable boundary layer which overlies the Antarctic ice dome. During the six-month austral winter, when this boundary layer is unperturbed by the direct effects of solar heating, the sounder provided a continuous record of the response of the boundary layer to synoptic-scale influences. This included the passage of warm and cold fronts, which are usually only schematically indicated in the once-daily rawinsonde flights. The ground-based layer echo was found to be closely related to the Ekman layer depth and reflected changes in surface stress and heat flux. On several occasions rapid changes in air masses and the effect of transient heat storage in the ice led to vertical convection of heat from the ice surface. Finally, elevated layers and internal waves were frequently observed and appeared to relate to changes in the synoptic flow.

9. REFERENCES

Dalrymple, P., H. Lettau, and S. Wollaston, 1966: South pole micrometeorological program: data analysis. *Antarctic Research Series* 9, 13-58.

McAllister, L. G., J. R. Pollard, A. R. Mahoney, and P. J. R. Shaw, 1969: Acoustic sounding - a new approach to the study of atmospheric structure. Proc. IEEE 57, 579-587.

Miller, S. T., 1974: An analysis of heat and moisture budgets of the inversion layer over the antarctic plateau, for steady state conditions, Ph.D. thesis, Dept. Meteor., University of Wisconsin, Madison, 68 pp.

Wyckoff, R. J., D. W. Beran, and F. F. Hall, Jr., 1973: A comparison of the low-level radiosonde and the acoustic echo sounder for monitoring atmospheric stability. *J. Appl. Meteor. 12*, 1196-1204.

Wyngaard, J. C., 1975: Modeling the planetary boundary layer - extension to the stable case. *Boundary-Layer Meteor. 9*, 441-460.

Zilitinkevich, S. S., 1972: On the determination of the height of the Ekman boundary layer. *Boundary-Layer Meteor. 3*, 141-145.
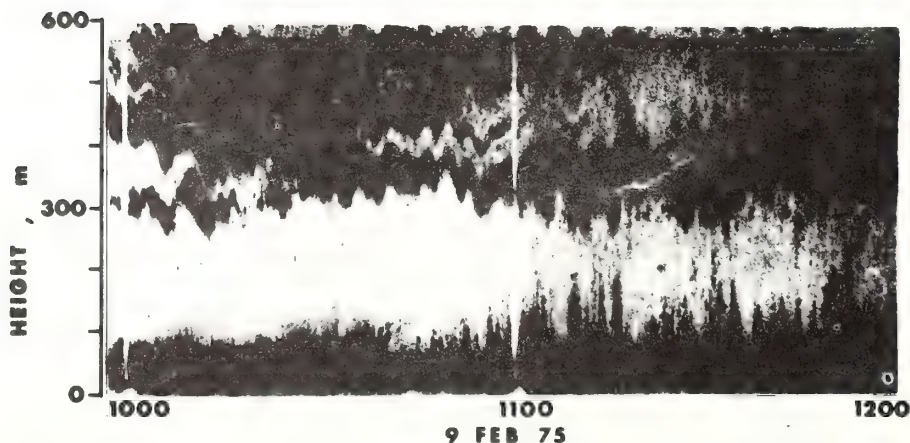
Figure 10. Facsimile recording obtained on 9 February 1975 showing convective plumes beneath multiple elevated scattering layers.

302

Acoustic echo sounding of the atmosphere boundary layer at the South Pole

W. D. NEFF *and* F. F. HALL, JR.
Wave Propagation Laboratory
Environmental Research Laboratories
National Oceanic and Atmospheric Administration
Boulder, Colorado 80302

An atmospheric acoustic echo sounder, with a vertical range of 600 meters, was operated successfully at Amundsen-Scott South Pole Station throughout 1975. The sounder operates on a backscatter principle similar to that of radar. It utilizes as scatterers small-scale (10-centimeter) temperature inhomogeneities produced by turbulence in regions of larger scale temperature gradients. Such gradients occur typically in temperature inversions and in superadiabatic regions associated with convection from a warm surface. The facsimile recordings obtained from the sounder thus allow one to trace the evolution of inversion layers such as those that generally occur at the South Pole.

The records obtained during 1975 provide a de-
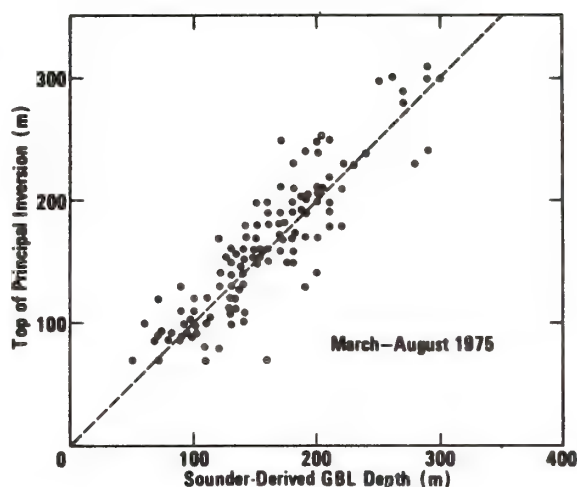
Figure 2. Comparison of the depth of the ground-base layer (GBL) from the sounder facsimile with the depth of the principal ground-based inversion obtained from the daily rawinsonde. The dashed line represents perfect agreement. A least-squares fit gave a slope of 0.94 with an x intercept of 10 meters. The standard deviation from the best-fit line was 20 meters.

tailed climatology of the atmospheric boundary layer at the Pole. They show the response of the boundary layer to synoptic scale disturbances. Events such as cold fronts are revealed well (figure

South Pole Acoustic Sounder
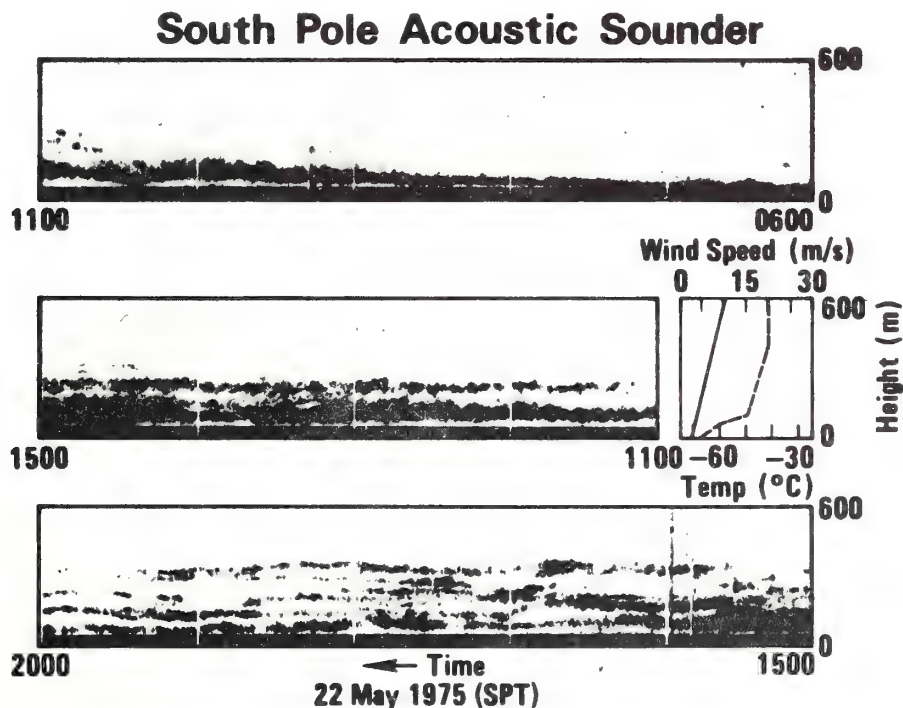
Figure 1. Facsimile recording obtained on 22 May 1975 showing cold "front" arrival at South Pole Station. The surface pressure minimum occurred at 0700 local time (1900 Greenwich Mean Time, 21 May 1975).

1) because of the increased scattering at the boundary of the cold air mass. Such events, because of the filtering effect of the surface inversion and the sparsity of rawinsonde observations, have in the past been ill-defined over the ice dome.

The "undisturbed" inversion layer usually was associated with an almost continuous echo that extended beyond the 40-meter minimum range of the sounder to heights as great as 300 meters. The deepest layers generally occurred during the strong winds that typify warm, moist advection from the quadrant west of the Greenwich meridian. The top of the echo region corresponded to the top of the principal ground-based inversion measured by the daily rawinsonde. Figure 2 is a scatter diagram based on the period March to August 1975. The depth of the echo layer was found to vary inversely with the static stability. This behavior, described in more detail by Neff and Hall (in press), suggests a turbulent Ekman layer. We are testing this hypothesis in cooperation with the University of California at Davis using the University's micrometeorological data from the Pole.

During 58 hours of the more than 6,000 hours the sounder operated, the sounder detected convective plumes originating at the ice surface. Five such events occurred, each during a rapid decrease in surface temperature. We hypothesize that rapid intrusion of colder air over the relatively warmer ice sets off the convection. On 17 December plumes extended to 400 meters for 18 hours. This event showed a gradually rising, capping inversion that eventually exceeded the sounder's 600-meter range.

We plan further studies using a bistatic acoustic sounder during 1977 to obtain quantitative information on the turbulence structure above the layer that can be studied using surface instruments. A microbarograph array is to be installed in January 1977 to aid in the interpretation of the acoustic sounder data.

Reference

Neff, W. D., and F. F. Hall, Jr. In press. Acoustic sounder measurements of the South Pole boundary layer. American Meteorological Society *Proceedings of the 17th Radar Meteorology Conference*.

144

Acoustic sounder operations at South Pole Station

W.D. Neff, H.E. Ramm, *and* F.F. Hall, Jr.

*Wave Propagation Laboratory
Environmental Research Laboratories
National Oceanic and Atmospheric Administration
Boulder, Colorado 80302*

An acoustic sounder was in operation at South Pole Station throughout 1975 (Neff and Hall, 1976 a, b). In the backscatter mode, sound waves are scattered by small-scale thermal fluctuations, thus defining the location of turbulent inversion layers. At other scattering angles turbulent velocity fluctuations also contribute, giving a measure of the intensity of the small-scale turbulence and its spatial distribution. The mean motion of the air volume advecting the small-scale eddies also induces a Doppler shift that can be detected using either analog or digital computer techniques.

During January and February 1977, we set up a sounding system, utilizing bistatic geometry and Doppler principles, at Amundsen-Scott South Pole station to study the turbulence structure and evolution of the statically stable boundary layer over the ice plateau. Because waves and dynamical instabilities are an ever present feature of such layers, we installed a sensitive pressure sensor array to track the movement of such events across the site. We also mounted a sensor on the 8-meter micrometeorological mast to measure the root mean square (RMS) temperature difference between two platinum wire probes spaced 20 centimeters apart in the horizontal. The so-called structure parameter, C_T, derived from this measurement is a function of the surface heat flux and allows us to correlate surface events with waves and instabilities aloft as seen by the sounder. All these sensors are shown schematically in figure 1.

The sounders operated in the bistatic mode for a few days prior to the departure of summer personnel. From these data we have determined that the elevated scattering layers documented during 1975 are the result of turbulence oc-curring within an essentially laminar flow. Since the uppermost of these multiple layers marks the top of the inversion (or the bottom of the isothermal layer), this implies that the inversion depth is not always determined by the effects of surface friction and "eddy diffusive" effects, but depends at times on larger scale dynamics. However, the acoustic sounder does allow one to identify the surface layer within the deeper inversion and will provide a means of testing theories that relate the depth of this layer to surface parameters.

During a short portion of the recording we obtained Doppler information from the tilted (15° from the vertical) monostatic sounder. In this mode the velocity component along the beam is given by

$$v_{Beam} = v_{Hor} \sin 15° + w \cos 15°$$

Since the vertical velocity, w, averages to zero, this allows one to determine the mean wind component along the beam. The fluctuations in horizontal velocity are also weighted by sin 15° or a factor of 0.26. We calculated the mean wind for the turbulent breaking wave case shown in figure 2, and found a value near 4.5 meters per second.
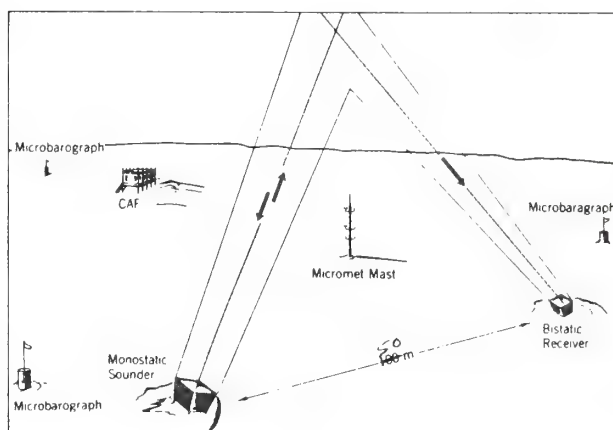
Figure 1. Site plan showing the locations of the acoustic sounders, microbarographs, and micrometeorological mast relative to the new Clean Air Facility (CAF) at South Pole Station. The main station is 200 meters to the left (to the west) of the sounders.
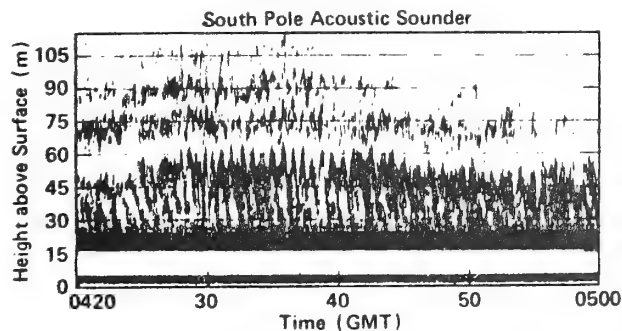
Figure 2. Acoustic sounder facsimile recording obtained on 10 February 1977 at South Pole Station.

389

Assuming a fluctuation in horizontal wind one-quarter the mean wind, this leads to a maximum error of 0.3 meter per second in the vertical velocities. The traces in figure 3 show, however, that the vertical velocities approach 1 meter per second aloft in the breaking waves. Note also the strong correlation between the pressure variation at the surface and the vertical velocities. The acoustic system, as installed, was not intended to produce the horizontal wind component; the values observed were nonetheless in reasonable agreement with the 4.2 meters per second wind from 112° at 8 meters on the University of California at Davis micrometeorology mast. The C_T sensor mounted at 8 meters also showed, on occasion, the effect of vertical mixing and increased heat flux associated with these breaking wave motions.

The system is being maintained through the austral winter by Gary Rosenberger and Brad Halter of the NOAA-Global Monitoring for Climatic Change project. During 1978 we will set up a complete Doppler wind system which will provide continuous wind profiles from about 30 meters to as high as 400 meters. This will allow us to monitor the relation between the wind at the top of the surface inversion and the surface wind and turbulent fluxes. Surface fluxes will be provided by a three-axis sonic anemometer,

adapted to cold temperatures, and a collocated fast response platinum wire thermometer. This sytem is to be operated during the winter of 1978 by Hans Ramm following the setup in January.

References

Neff, W.D., and F.F. Hall. 1976a. Acoustic sounder measurements of the south pole boundary layer. *Preprint Volume — 17th Radar Meteorological Conference.* American Meteorological Society, Boston. 297-302.

Neff, W.D., and F.F. Hall. 1976b. Acoustic echo sounding of the atmospheric boundary layer at the south pole. *Antarctic Journal of the U.S.*, XI(3): 143-144.
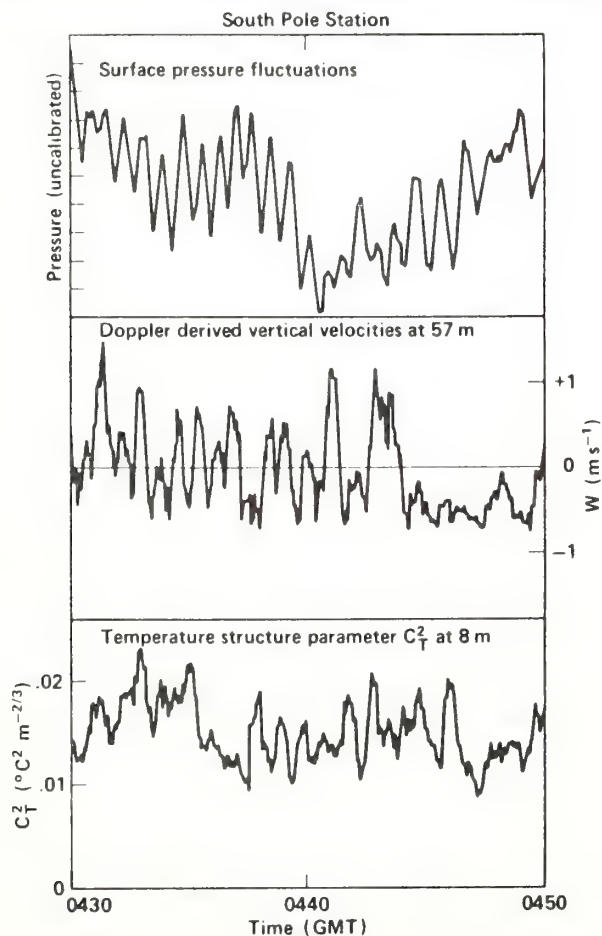
Figure 3. Time series of the temperature structure parameter (which is related to the surface heat flux), the pressure fluctuations from one element of the microbarograph array, and the acoustically-derived vertical velocity. These are for the case shown in figure 2.

Vertical heat flux in the convective boundary layer

By S. J. CAUGHEY   and   J. C. KAIMAL

Meteorological Research Unit,   *NOAA/ERL Wave Propagation Laboratory*
RAF Cardington   *Boulder, Colorado 80302*
Bedford, England

SUMMARY

The variation of heat flux with height in inversion-capped convective boundary layers is discussed. Cospectral shapes at levels above approximately one-tenth the height of the lowest inversion base (z_i) are shown to depart significantly from surface layer forms. The characteristic wavelength for heat flux increases rapidly in the first 150 m of the boundary layer but shows little variation between 150 and 300 metres. Around sunset, the transition to negative heat flux occurs first in the upper regions of the boundary layer and propagates downwards to the surface.

1. INTRODUCTION

In a recent paper, Kaimal *et al.* (1976) described a joint experiment conducted by the Meteorological Research Unit (MRU), RAF Cardington, England, and the Air Force Cambridge Research Laboratories, Bedford, Mass., USA, in the autumn of 1973. The objectives were to make measurements of the vertical fluxes of momentum and heat, and of the profiles of wind velocity and temperature, within the planetary boundary layer. The experiment was conducted over a very flat, sparsely populated area in northwestern Minnesota. By using tower-mounted sensors in conjunction with turbulence probes, attached to the tethering cable of a large, 1300 m³, kite balloon, it was possible to obtain wind and temperature statistics at seven levels between 4 m and the height of the lowest inversion base (denoted in this paper by the symbol z_i). The paper by Kaimal *et al.* examined data obtained in convective conditions within the framework of mixed-layer similarity.

In this paper we consider some aspects of heat flux and its variation in the first few hundred metres above the ground, using data from eight runs, each of seventy-five minutes duration, representing cloud-free convective conditions. Additionally, data obtained during the evening transition to stable conditions are used to illustrate the breakdown of the convective boundary layer. For details of the experiment and information on z_i and other scaling parameters for each run the reader is referred to earlier papers by Readings *et al.* (1974) and Kaimal *et al.* (1976). Information on the instrumentation and data reduction techniques are in the report by Izumi and Caughey (1976).

2. VARIATION OF THE HEAT FLUX WITH HEIGHT

The heat flux in the convective boundary layer is expected to decrease monotonically with height, becoming negative in the upper half of the boundary layer. The dimensionless profiles available from this experiment (Fig. 1) show the cross-over to negative (downward) flux occurring around $0.6z_i$, with a spread from 0.4 to $0.8z_i$. These profiles resemble those obtained from aircraft measurements (Lenschow 1974; Pennell and LeMone 1974), laboratory experiments (Willis and Deardorff 1974), and numerical model calculations (Deardorff 1972; Wyngaard and Coté 1974), except for a tendency for the profiles of Fig. 1 to cross zero at slightly lower heights.

The negative heat flux in the upper boundary layer has been traced to downward transport of warmer air entrained into the boundary layer through the inversion base by the return flow associated with large convection cells in the boundary layer (Kaimal *et al.* 1976). The effects of such entrainment have been observed in the temperature and heat flux statistics down to heights of the order of $0.5z_i$. The observed variation in the level of zero heat flux is probably a reflection of the variation in entrainment intensity from run to run.

3. HEAT FLUX COSPECTRA

The negative heat flux in the upper boundary layer appears in cospectral plots as large negative

391
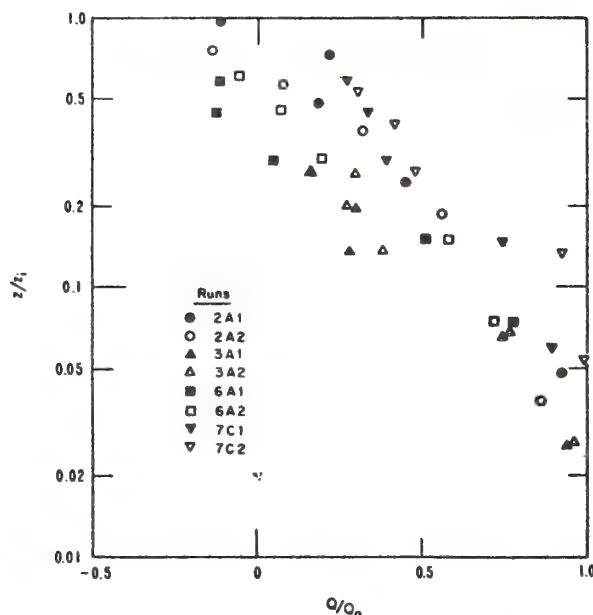
Figure 1.   Variation of dimensionless heat flux (Q/Q_0) with logarithmic dimensionless height (z/z_i).
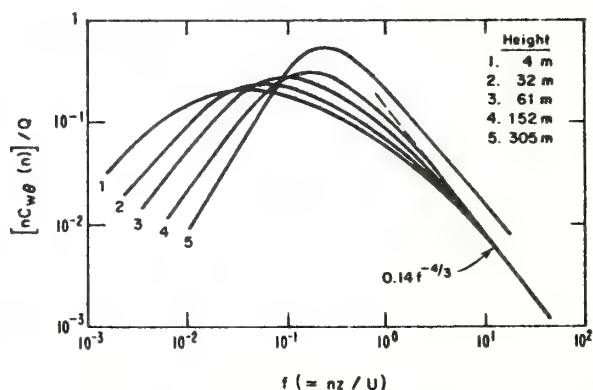
Figure 2.   Composite curves for heat flux cospectra at five heights.

contributions in the frequency range 10^{-2} to 10^{-4}Hz. Cospectral behaviour at those heights is not consistent enough to justify the development of composite plots, but in the height range of $z < 0.2z_i$ (below about 300 m for the Minnesota data) the flux is almost entirely upwards and one can expect some order to emerge. Composite curves for the logarithmic cospectra, normalized by the local kinematic heat flux Q ($= \overline{w\theta}$)m, show a small but systematic variation with height in the first 150 m (Fig. 2) when plotted as a function of dimensionless frequency f ($= nz/U \approx z/\lambda$); n is cyclic frequency, z height above ground, U mean wind speed, and λ wavelength ($= U/n$). In the inertial subrange they all converge to a single curve as in the Kansas results (Kaimal *et al.* 1972) and follow the same empirical relationship,

$$nC_{w\theta}(n)/Q = 0.14f^{-4/3} \qquad . \qquad . \qquad . \qquad . \qquad (1)$$

Here w and θ are the fluctuating vertical wind component and temperature, respectively, and $C_{w\theta}(n)$ is their cospectral density at frequency n.

At lower frequencies the 4 and 32 m curves of Fig. 2 fall within the narrow cospectral band defined by the scatter in the unstable Kansas cospectra. Within this band, the Minnesota data show a systematic shift to higher f values with height. But as the low frequency end continues to shift with height above 32 m, the cospectral curves move farther and farther away from the Kansas results.
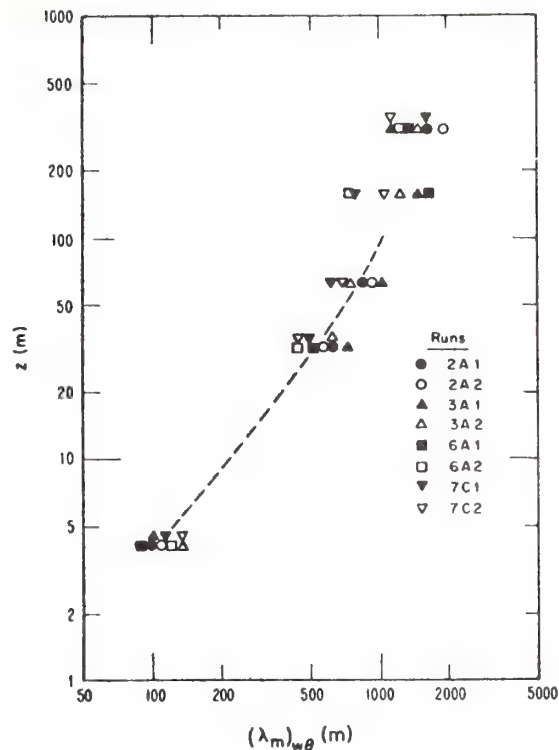
Figure 3. Plot of the wavelength of the maximum heat flux versus height.

Above 150 m a more abrupt change occurs as the inertial subrange cospectrum breaks away from the surface layer form represented by Eq. (1).

The plot of λ_m (wavelength corresponding to the cospectral peak) versus height in Fig. 3 shows λ_m increasing with height between 4 and 152 m and levelling off to a constant value between 152 and 305 m. This constant value (different for each run) is of the order of $1 \cdot 5z_i$, which is also the limiting value for λ_m in the Minnesota temperature and velocity spectra (Kaimal *et al.* 1976). The Minnesota data show z_i emerging as the important length scale at $z > 0 \cdot 1z_i$ and the limiting wavelength of $1 \cdot 5z_i$ as the approximate spacing between large thermals in the boundary layer.

4. BREAKDOWN OF THE CONVECTIVE BOUNDARY LAYER

The Minnesota experiment provided an excellent opportunity to observe in detail the progression of heat flux at different heights as the convective boundary layer disintegrated shortly before sunset. Much recent work has been devoted to the study of the evolution of the convective boundary layer between sunrise and noon (see, e.g., Richter *et al.* 1974; Neff 1975; Zilitinkevich 1975; Tennekes 1975; Chorley *et al.* 1975; Mahrt and Lenschow 1976), yet not much is known about the details of its dissolution near sunset. The time/height plot of heat flux (15-minute averages) in Fig. 4 shows that this breakdown is rapid, occurring in a matter of minutes. During this period the level of zero heat flux, located normally around $0 \cdot 6z_i$, makes a sudden descent to the surface. This occurs almost an hour before local sunset and is typical of other evening transitions observed during this experiment. It is surprising that the transition to negative heat flux propagates downwards to the surface, and not upwards as one might expect. Following this event a surface-based inversion begins to develop in line with the conventional view of nocturnal layer build-up, and we see a gradual intensification of the downward heat flux near the surface. This surface inversion may break down and form again during the course of the evening.

5. CONCLUDING COMMENTS

These results serve to emphasize the importance of entrained heat flux in the inversion-capped
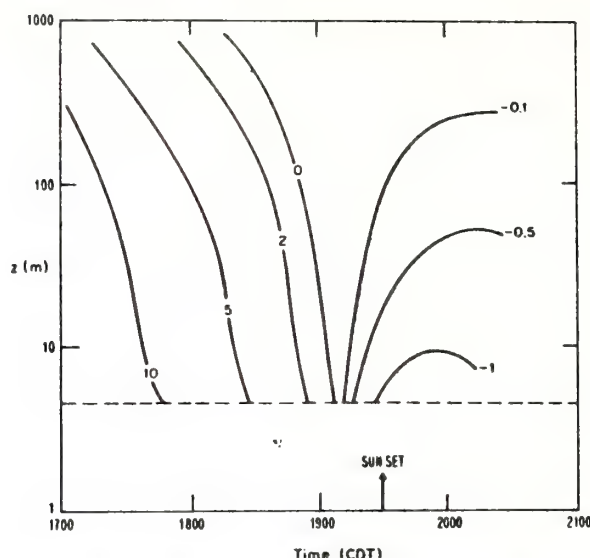
Figure 4. Isopleths of the 15-minute heat fluxes for run 7 covering the transition period around sunset.
Units are cm s^{-1}K.

convective boundary layers which were present during the Minoesota experiment. The low height
values obtained for cross-over to negative heat flux is an indication of the intensity of entrainment
in the upper boundary layer on these occasions. Cospectral shapes differ significantly from the
surface layer forms above $0.1z_i$ and at these heights the characteristic wavelength for heat flux
approaches 1·5 times the inversion height, the length scale of the large convection systems in the
boundary layer. The observed lag between the cross-over to negative heat flux aloft and at the
surface around sunset needs closer study because of its implications in the modelling of stable
boundary layers.

REFERENCES

Chorley, L. G., Caughey, S. J. and Readings, C. J.	1975	The development of the atmospheric boundary layer: three case studies, *Met. Mag.*, **104**, 349–360.
Deardorff, J. W.	1972	Numerical investigation of neutral and unstable planetary boundary layers, *J. Atmos. Sci.*, **29**, 91–115.
Izumi, Y. and Caughey, S. J.	1976	Minnesota 1973 Atmospheric Boundary Layer Experiment Data Report, Environmental Research Paper No. 547 (Air Force Geophysic Laboratory, Bedford, Mass. 01731).
Kaimal, J. C., Wyngaard, J. C., Haugen, D. A., Coté, O. R., Izumi, Y., Caughey, S. J. and Readings, C. J.	1976	Turbulence structure in the convective boundary layer, *J. Atmos. Sci.*, **33**, 2152–2169.
Kaimal, J. C., Wyngaard, J. C., Izumi, Y. and Coté, O. R.	1972	Spectral characteristics of surface layer turbulence, *Quart. J. R. Met. Soc.*, **98**, 563–589.
Lenschow, D. H.	1974	Model of the height variation of the turbulence kinetic energy budget in the unstable planetary boundary layer, *J. Atmos. Sci.*, **31**, 465–474.
Mahrt, L. and Lenschow, D. H.	1976	Growth dynamics of the convectively mixed layer, *Ibid.*, **33**, 41–51.
Neff, W. D.	1975	Quantitative evaluation of acoustic echoes from the planetary boundary layer, *NOAA Tech. Report*, *ERL 322–WPL 38* (Environmental Research Laboratories NOAA, Boulder, Colo. 80302).
Pennell, W. T. and LeMone, M. A.	1974	An experimental study of turbulence structure in the fair-weather trade-wind boundary layer, *J. Atmos. Sci.*, **31**, 1308–1323.
Readings, C. J., Haugen, D. A. and Kaimal, J. C.	1974	The 1973 Minnesota boundary layer experiment, *Weather*, **29**, 309–312.

Richter, J. H., Jensen, D. R.,   1974   Clear air convection: a close look at its evolution and
    Noonkester, V. R.,   structure, *Geophys. Res. Letters*, **1**, 173–176.
    Konrad, T. G., Arnold, A.
    and Rowland, J. R.
Tennekes, H.   1975   Reply to comments on 'A model for the dynamics of the
                                                   inversions above a convective boundary layer', *J.
                                                   Atmos. Sci.*, **32**, 340–350.
Willis, G. E. and   1974   A laboratory model of the planetary boundary layer, *Ibid.*,
    Deardorff, J. W.   **31**, 1297–1307.
Wyngaard, J. C. and Coté, O. R.   1974   The evolution of a convective planetary boundary layer –
                                                   a higher-order closure model study, *Boundary Layer
                                                   Met.*, **7**, 289–308.
Zilitinkevich, S. S.   1975   Comments on 'A model for the dynamics of the inversion
                                                   above a convective boundary layer', *J. Atmos. Sci.*,
                                                   32, 991–992.

Flux Measurements, Flux Estimation Techniques, and Fine-Scale Turbulence Measurements in the Unstable Surface Layer Over Land

F. H. Champagne, C. A. Friehe[1] and J. C. LaRue

Department of Applied Mechanics and Engineering Sciences,
University of California-San Diego, La Jolla 92093

J. C. Wyngaard

Cooperative Institute for Research in Environmental Sciences, University of Colorado/NOAA,
Boulder 80307 and Wave Propagation Laboratory, NOAA, Boulder 80302

(Manuscript received 21 May 1976, in revised form 12 November 1976)

ABSTRACT

An AFCRL-UCSD joint experiment in Minnesota in 1973 has provided a comparison of direct and indirect measurements of the surface-layer fluxes of momentum, heat and moisture under unstable conditions. The direct momentum and heat flux measurements of the two groups agreed well, and also agreed well with values inferred by the direct dissipation technique. The moisture flux estimates from the inertial-dissipation technique also agreed well with the directly measured values.

Several of the important terms in the budgets of turbulent kinetic energy and turbulent scalar variances were evaluated directly. The imbalance (or pressure transport) term in the energy budget was estimated, and the ratio of the imbalance term to the dissipation term determined from the present experiment agrees well with the Kansas results. The dissipation rate of temperature variance exceeded its production rate, in contrast with the Kansas results, implying an imbalanced temperature variance budget. Several possible contributors to this imbalance are discussed.

The one-dimensional spectra of the temperature and streamwise velocity fluctuations are presented in Kolmogorov normalized form. Spectral moments to fourth order are shown to agree with earlier results. Values of the universal velocity and temperature spectral constants of $\alpha_1 = 0.50 \pm 0.02$ and $\beta_\theta = 0.45 \pm 0.02$ were obtained.

1. Introduction

The turbulent fluxes of momentum, heat and moisture in the atmospheric surface layer are important to many aspects of meteorology and oceanography. Consequently, the surface layer has been studied in some detail, with emphasis on understanding turbulent transport processes under a wide range of stability conditions and on developing instrumentation and techniques to determine the turbulent fluxes. For a review of experimental methods used in atmospheric boundary layer studies, see *Atmospheric Technology*, No. 7, 1975.

There are several methods for determining surface layer fluxes, including the direct covariance method which requires the measurement of the covariance of the turbulent variables, and the profile, inertial-dissipation and direct dissipation rate techniques where the fluxes are obtained indirectly, using measurements of related statistical quantities. The direct covariance method, while straightforward, generally requires the use of expensive equipment to obtain accurate measure-

ments. In ship or aircraft applications, instrument platform motion can severely contaminate the velocity signals, thereby degrading the flux measurements. Correction for this contamination is extremely difficult since it requires precise, simultaneous measurement of the instrument platform motion (see Kaimal and Haugen, 1969).

The dissipation rate techniques are much less sensitive to instrument platform motion. The measurement of the dissipation rates of the turbulent velocity, temperature and humidity fields can be made at frequencies much higher than those of the platform motion so that contamination is minimized. The dissipation rate measurements are obtained either from spectral density or structure function data in the inertial subrange of frequency or spatial separation (the inertial-dissipation technique), or by direct measurement of the derivative statistics which define the dissipation rates (the direct dissipation technique). The turbulent fluxes are then estimated through the use of the budget equations for the turbulent kinetic energy, temperature variance and humidity variance, as discussed in detail later.

Here we present results for momentum, heat and

---

[1] Also Scripps Institution of Oceanography.

moisture fluxes obtained by direct and indirect techniques, as well as turbulent fine-structure revealed in the process of direct dissipation measurements.

2. Flux determination techniques

a. The direct covariance method

The vertical fluxes of momentum, sensible heat and moisture are defined by

$$
\left.\begin{array}{l}
\tau = -\rho \overline{uw} = \rho u_*^2 \\
H = \rho c_p \overline{w\theta} = -\rho c_p u_* T_* \\
E = \overline{wq} = -u_* q_*
\end{array}\right\}, \quad (1)
$$

where u and w are the streamwise horizontal and the vertical velocity fluctuations, θ is the temperature fluctuation, q the humidity[2] fluctuation, ρ air density, c_p specific heat at constant pressure u_* the friction velocity, T_* and q_* the temperature and humidity scales, respectively, and the overbar denotes a time average.

In the direct covariance method one forms the instantaneous product of the vertical velocity with the variable of interest and averages the result. The covariances $\overline{uw}$, $\overline{w\theta}$ and $\overline{wq}$ are also integrals of their respective cospectra over frequency. The bandwidth required to measure the entire $\overline{uw}$ cospectrum, for example, is typically on the order of $10^{-3} \leqslant fz/U \leqslant 10$, where f is frequency (Hz), z the height above the surface, and U the mean wind speed (see McBean, 1972).

b. Inertial-dissipation technique

This method, apparently first proposed by Deacon (1959) and demonstrated by Taylor (1961), has been applied by many investigators to the surface layer over the ocean. These include Smith (1967), Weiler and Burling (1967), Miyake et al. (1970), Smith (1970), Pond et al. (1971), Hicks and Dyer (1972), Stegen et al. (1973), Dyer (1975), and Leavitt and Paulson (1975). In the earlier works, neutral, locally isotropic, horizontally homogeneous, stationary surface-layer turbulence was usually assumed, with a kinetic energy balance

$$
-\overline{uw}\frac{\partial U}{\partial z} = \epsilon, \quad (2)
$$

where the first term represents shear production and ϵ is the rate of dissipation of turbulent kinetic energy. Under the assumed conditions, we have

$$
\frac{\partial U}{\partial z} = \frac{u_*}{\kappa z}, \quad (3)
$$

where κ is von Kármán's constant. Combining Eqs. (2) and (3) yields

$$
u_*^2 = -\overline{uw} = (\kappa \epsilon z)^{\frac{2}{3}}. \quad (4)
$$

The value of ϵ can be determined from a measurement of the one-dimensional velocity spectrum in the inertial subrange, i.e.,

$$
\varphi_{uu}(k_1) = \alpha_1 \epsilon^{\frac{2}{3}} k_1^{-5/3}, \quad \overline{u^2} = \int_0^\infty \varphi_{uu}(k_1) dk_1, \quad (5)
$$

where α_1 is the one-dimensional Kolmogorov constant, assumed known, and k_1 is the wavenumber obtained from the cyclic frequency f using Taylor's approximation (see Taylor, 1938, and Lumley, 1965), $k_1 = 2\pi f U^{-1}$. Equivalently, Taylor (1961) determined ϵ from the second-order structure function in the inertial subrange, i.e.,

$$
D_{uu}(r) = \overline{[u(x+r) - u(x)]^2} = 4.02\alpha_1 \epsilon^{\frac{2}{3}} r^{\frac{2}{3}}, \quad (6)
$$

where r is the magnitude of the separation vector.

Thus, from Eq. (4), the momentum flux under neutral conditions can be estimated using ϵ obtained from Eqs. (5) or (6). Away from neutral, however, the effects of stability on the mean profiles and on the turbulent energy budget should be considered.

The budget of the turbulent kinetic energy, $\frac{1}{2}\overline{e^2} = \frac{1}{2}(\overline{u^2} + \overline{v^2} + \overline{w^2})$, simplifies under the assumptions of horizontal homogeneity and stationarity to

$$
-\overline{uw}\frac{\partial U}{\partial z} + \frac{g}{T_v}(\overline{w\theta} + 0.61 T\overline{wm}) - \frac{1}{2}\frac{\partial}{\partial z}\overline{we^2}
$$
$$
-\frac{1}{\rho}\frac{\partial}{\partial z}\overline{pw} - \epsilon = 0, \quad (7)
$$

where $T_v = T(1 + 0.61M)$ is the virtual temperature, T is the mean absolute temperature, m the fluctuating specific humidity,[3] M the mean specific humidity and p the pressure fluctuation. The terms in Eq. (7) represent, respectively, the shear production, buoyant production (including the effect of humidity fluctuations), divergence of the turbulent flux of kinetic energy, divergence of the pressure-velocity covariance or pressure transport, and dissipation. Under unstable conditions, many investigators (see Busch and Panofsky, 1968; Pond et al., 1971; McBean et al., 1971; Hicks and Dyer, 1972) have approximated (7) by

$$
-\overline{uw}\frac{\partial U}{\partial z} + \frac{g}{T_v}(\overline{w\theta} + 0.61 T\overline{wm}) - \epsilon = 0, \quad (8)
$$

which states that total production balances dissipation.

---

[2] Precisely, q is water vapor density or absolute humidity ($g\ m^{-3}$).

---

[3] The specific humidity m is related to q by $m = 7.735 \times 10^{-4}$ $Tq/273$, where the units of m are grams of water vapor per gram of moist air, those of q are grams of water vapor per cubic meter of moist air, and T is in kelvins.

An extensive and systematic investigation of the energy budget was carried out during the 1968 AFCRL Kansas experiment (Haugen *et al.*, 1971; Wyngaard and Coté, 1971). All terms except pressure transport were measured, and the dissipation rate ϵ was obtained from hot-wire anemometer measurements extending over the dissipative range. Wyngaard and Coté (1971) concluded from their analysis of the Kansas data that the buoyant production and the flux divergence terms are approximately in balance for the stability range $-1 \leqslant z/L \leqslant 0$ so a better budget approximation than Eq. (8), at least for the over-land case, is

$$\overline{uw} \frac{\partial U}{\partial z} + \epsilon + I = 0, \qquad (9)$$

where I is the measured imbalance, a substantial gain term under unstable conditions. They suggested that this imbalance could be attributed to the only unmeasured term, pressure transport. A recent attempt to measure pressure transport directly by McBean and Elliott (1975; see also Elliott, 1975) gave general agreement with Wyngaard and Coté's conclusion. The empirical expression for the imbalance term given by Wyngaard and Coté (1971) is

$$\frac{\kappa z}{u_*^3} I = (1 - 15z/L)^{-\frac{1}{4}} - (1 + 0.5|z/L|^{\frac{2}{3}})^{\frac{3}{2}}, \qquad (10)$$

where L is the Monin-Obukhov length scale defined as

$$L = [-u_*^3 T_v / \kappa g (\overline{w\theta} + 0.61 T \overline{wm})]. \qquad (11)$$

Mean profiles are also strongly affected by stability. Dyer (1967) and Businger *et al.* (1971) found that under unstable conditions Eq. (3) is invalid, and instead

$$\varphi_M \left(\frac{z}{L} \right) = \frac{\kappa z}{u_*} \frac{\partial U}{\partial z} = (1 - 15z/L)^{-\frac{1}{4}}. \qquad (12)$$

The history of indirect flux measurement techniques presents a rather confused picture. Various expressions for the mean profiles and for the turbulent energy budget have been used. Further, stability effects have not always been consistently included, and various values have been used for the Kolmogorov and von Kármán constants. Possibly because of compensating errors, however, some of these earlier attempts have been fairly successful. For estimating the momentum fluxes from the slightly unstable BOMEX data, Pond *et al.* (1971) used Eq. (8), $\alpha_1 = 0.55$, and the logarithmic-profile form Eq. (3). Their results exhibit considerable scatter but appear to compare favorably with the directly computed flux values. They neglected the effects of stability on the velocity profile, although not on the scalar profile, as they obtained better results in doing so. Hicks and Dyer (1972) used Eqs. (5), (8)

and (12) to estimate the momentum flux over land and suggest the same for the surface layer over water. They concluded that their estimates of the momentum flux were adequate using a value of α_1 of 0.54, but pointed out the need for further investigation.

Until further results concerning the energy budget become available, it would seem preferable to use Eq. (9) along with Eqs. (10) and (12) to estimate momentum flux under unstable conditions by the inertial dissipation technique. Combining these equations gives

$$u_* = \left[\frac{\kappa z \epsilon}{(1 + 0.5|z/L|^{\frac{2}{3}})^{\frac{3}{2}}} \right]^{\frac{1}{3}}. \qquad (13)$$

Note that the presence of the stability-dependent term introduces further complications in that the sensible heat and moisture fluxes must be known to estimate the momentum flux. This means the state of stability of the surface layer must be established to determine the fluxes.

The budget equations for the scalar variances under stationary, horizontally homogeneous conditions are

$$-2\overline{w\theta} \frac{\partial T}{\partial z} - \frac{\partial}{\partial z} \overline{w\theta^2} = \chi_\theta, \qquad (14)$$

$$-2\overline{wq} \frac{\partial Q}{\partial z} - \frac{\partial}{\partial z} \overline{wq^2} = \chi_q, \qquad (15)$$

where Q is the mean humidity (g m^{-3}), and χ_θ and χ_q are the temperature variance and humidity variance dissipation rates, respectively. Note that the scalar variance equations (14) and (15) are written for the budgets of $\overline{\theta^2}$ and $\overline{q^2}$ rather than $\frac{1}{2}\overline{\theta^2}$ and $\frac{1}{2}\overline{q^2}$. The first term in each equation is the rate of production by interaction of the vertical turbulent flux with the mean scalar gradient. The second and third terms in each equation represent the divergence of the vertical flux of scalar variance and the rate of destruction by molecular diffusivity, respectively.

There have been fewer experimental studies of the scalar variance budget equations than of the kinetic energy budget equation. Wyngaard and Coté did not measure χ_θ, but found that the flux divergence term for temperature variance averaged about -5% of the production term in the unstable range $-1 \leqslant z/L \leqslant 0$. Thus

$$\chi_\theta = -2\overline{w\theta} \frac{\partial T}{\partial z}. \qquad (16)$$

This gave values of the Kolmogorov inertial subrange constant β_θ, where

$$\varphi_{\theta\theta}(k_1) = \beta_\theta \chi_\theta \epsilon^{-\frac{1}{3}} k_1^{-5/3}, \quad \overline{\theta^2} = \int_0^\infty \varphi_{\theta\theta}(k_1) dk_1, \qquad (17)$$

which agreed with most of the data available then.

Monji (1973) also found Eq. (16) to be valid over land [χ_θ was inferred from inertial subrange spectral measurements using Eq. (17)], and observed that the flux divergence term changed sign for $z/L < -1$, as did Wyngaard and Coté. Garratt (1972), from data taken over the surface of a lake, also found that production essentially balanced estimated dissipation. In all the referenced studies of the $\overline{\theta^2}$ budget the value of χ_θ was not directly measured but was inferred from Eq. (17) using a β_θ value of 0.4. Recent measurement of β_θ obtained over land by Williams (1974) and those reported herein are not significantly different and do not alter any of the conclusions reached in the referenced studies. Therefore, Eq. (16) will be considered a valid approximation for the temperature variance budget.

The Kansas result for the mean temperature gradient is (Businger *et al.*, 1971)

$$\varphi_T\left(\frac{z}{L}\right) = \frac{\kappa z}{T_*} \frac{dT}{dz} = \frac{1}{\alpha_T}\left(1 - 9\frac{z}{L}\right)^{-\frac{1}{4}} \qquad (18)$$

for unstable conditions, where α_T is the ratio of eddy transfer coefficients for heat and momentum. They found that for neutral conditions $\alpha_T = 1.35$ and also $\kappa = 0.35$, rather than the traditional value of 0.40. Combining (16) and (18) gives an expression for T_*,

$$T_* = -\left(\frac{\kappa z \chi_\theta}{2u_* \varphi_T}\right)^{\frac{1}{3}}, \qquad (19)$$

where the negative root is taken for the unstable conditions considered here. Since the right side depends on the stability of the surface layer, to obtain the desired estimate of the sensible heat flux we need to determine L and χ_θ. The latter can be obtained from spectral measurements in the inertial subrange and Eq. (17), while the former requires knowledge of the momentum and moisture fluxes.

The humidity variance budget is not as well-documented as those for the kinetic energy and temperature variance, primarily because moisture statistics are more difficult to measure (see Kaimal, 1975), and it is not presently possible to measure directly the dissipation rate χ_q. Some studies have been made over the open ocean (Pond *et al.*, 1971; Leavitt and Paulson, 1975), and based on those results we will assume that the humidity budget is similar to that for the temperature variance, so that

$$\chi_q = -2\overline{wq}\frac{\partial Q}{\partial z}. \qquad (20)$$

Values of χ_q are determined from inertial range spectral measurements using

$$\varphi_{qq}(k_1) = \beta_q \chi_q \epsilon^{-\frac{1}{3}} k_1^{-5/3}, \quad \overline{q^2} = \int_0^\infty \varphi_{qq}(k_1) dk_1, \quad (21)$$

where β_q is assumed to be known. Since there are no

direct measurements of β_q, it is usually assumed equal to β_θ. Paquin and Pond (1971) estimated β_θ and β_q from second- and third-order structure functions and found $\beta_\theta = \beta_q \approx 0.4$.

The mean humidity gradient is assumed to be given by

$$\varphi_q\left(\frac{z}{L}\right) = \frac{\kappa z}{q_*} \frac{\partial Q}{\partial z} = \frac{1}{\alpha_q}\left(1 - 9\frac{z}{L}\right)^{-\frac{1}{4}}, \qquad (22)$$

similar to Eq. (18) for temperature, and further α_q is assumed equal to α_T. Eqs. (20) and (22) can be combined to give

$$q_* = -\left(\frac{\kappa z \chi_q}{2u_* \varphi_q}\right)^{\frac{1}{3}}, \qquad (23)$$

so that both χ_q and L are required to estimate the moisture flux. Again, the negative root is taken for conditions with positive (upward) moisture fluxes.

Pond *et al.* (1971) used the inertial dissipation technique to estimate the scalar fluxes for BOMEX and San Diego data. In general, the estimates of the sensible heat flux from this technique were considerably higher (at times by a factor of 2 or more) than direct measurements, while the moisture flux estimates showed good agreement with their directly measured values. Hicks and Dyer (1972), from a similar study over land, concluded that the inertial dissipation technique provided adequate estimates for the sensible heat flux using a value of $2\beta_\theta$ of 0.71. Moisture effects were neglected.

In the inertial-dissipation technique, the dissipation rates ϵ, χ_θ and χ_q are obtained from spectral measurements of the appropriate variable in the inertial range of wavenumbers. An alternative is to measure these dissipation rates directly, as discussed in the next section.

c. The direct dissipation technique

Pond *et al.* (1963) and Gibson and Williams (1969) demonstrated that ϵ may be measured directly in the atmospheric boundary layer. Gibson *et al.* (1970) measured ϵ directly during project BOMEX and extended the technique to measure χ_θ. Invoking the assumption of local isotropy and using Taylor's hypothesis, the expressions for ϵ and χ_θ can be written

$$\epsilon = 15\nu\overline{\left(\frac{\partial u}{\partial x}\right)^2} = \frac{15\nu}{U^2}\overline{\left(\frac{\partial u}{\partial t}\right)^2}, \qquad (24)$$

$$\chi_\theta = 6\mathfrak{D}\overline{\left(\frac{\partial \theta}{\partial \dot{x}}\right)^2} = \frac{6\mathfrak{D}}{U^2}\overline{\left(\frac{\partial \theta}{\partial t}\right)^2}, \qquad (25)$$

where $\mathfrak{D}$ is the molecular diffusivity for temperature. Measurements of the variances of the time derivatives of u and θ require spatial resolution of the sensing

probes to nearly the Kolmogorov scale $\eta = (\nu^3/\epsilon)^{\frac{1}{4}}$ (typically about 1 mm in atmospheric flows), correspondingly high-frequency response of the associated circuitry and sensors, and good signal-to-noise ratios.

Heskestad (1965) and Lumley (1965) have shown that this use of Taylor's hypothesis overestimates ϵ in high-intensity turbulence. Lumley's fluctuating convection velocity model gives

$$\overline{\left(\frac{\partial u}{\partial t}\right)^2} = U^2 \overline{\left(\frac{\partial u}{\partial x}\right)^2}\left(1+\frac{\overline{u^2}}{U^2}+2\frac{\overline{v^2}+\overline{w^2}}{U^2}\right), \quad (26)$$

which is equivalent to Eq. (24) only in low-intensity flows. Heskestad also obtained Eq. (26), but in a completely different way. He squared and averaged the Navier-Stokes equation for u, assuming local isotropy and that velocity and velocity derivative fluctuations are uncorrelated.

We extended the Heskestad model to a scalar and obtained [in agreement with the extension of Lumley's model by Wyngaard and Clifford (1976)]

$$\overline{\left(\frac{\partial \theta}{\partial t}\right)^2} = U^2 \overline{\left(\frac{\partial \theta}{\partial x}\right)^2}\left(1+\frac{\overline{u^2}+\overline{v^2}+\overline{w^2}}{U^2}\right). \quad (27)$$

Thus we can rewrite (24) and (25) as

$$\epsilon = 15\nu\overline{\left(\frac{\partial u}{\partial x}\right)^2} = \frac{15\nu}{U^2}\overline{\left(\frac{\partial u}{\partial t}\right)^2}\left(1+\frac{\overline{u^2}}{U^2}+2\frac{\overline{v^2}+\overline{w^2}}{U^2}\right)^{-1}, \quad (28)$$

$$\chi_\theta = 6\mathcal{D}\overline{\left(\frac{\partial \theta}{\partial x}\right)^2} = \frac{6\mathcal{D}}{U^2}\overline{\left(\frac{\partial \theta}{\partial t}\right)^2}\left(1+\frac{\overline{u^2}+\overline{v^2}+\overline{w^2}}{U^2}\right)^{-1}. \quad (29)$$

Eqs. (28) and (29) were used to calculate ϵ and χ_θ. The values averaged 16% and 10% less than those indicated by Eqs. (24) and (25).

Stegen et al. (1973) compared momentum and sensible heat flux measurements from the direct dissipation technique with results from the direct covariance and inertial dissipation techniques obtained by other investigators during BOMEX. In general the comparisons were encouraging with the exception of the high estimates of the sensible heat flux inferred from the inertial dissipation technique using $\beta_\theta = 0.4$.

d. Computation of fluxes

We now have relations for u_*, q_* and T_* in terms of the measured dissipation rates and stability-dependent terms. The latter pose complications by coupling the equations and no simple, direct solution is possible. A solution procedure, however, was developed by combining the relevant equations for u_*, T_*, q_* and L such that an expression relating the measured quantities as a function of z/L was obtained. Hicks and Dyer
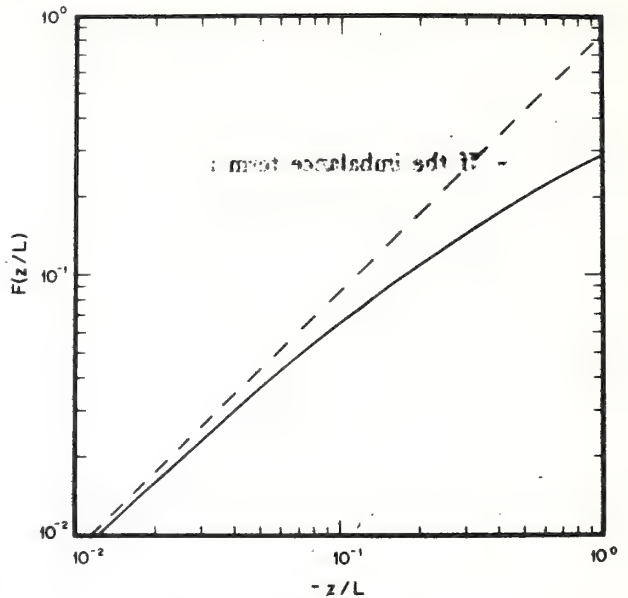
FIG. 1. The function $F(z/L)$ from Eq. (31) (solid) Eq. (32) (dashed).

(1972) used a similar procedure but they neglected humidity effects in their equations, often a good approximation over land but not in the marine boundary layer. The desired expression, including humidity effects, can be obtained as follows.

Eq. (11) may be written in the form

$$L = \frac{-u_*^3\left[1+0.472\times10^{-3}\left(\frac{T}{273}\right)Q\right]}{\kappa g\left[\frac{\overline{w\theta}}{T}+0.472\times10^{-3}\left(\frac{T}{273}\right)\overline{wq}\right]}. \quad (30)$$

Substituting the equations for u_*, T_* and q_* into Eq. (30) gives, after some manipulation,

$$\frac{(\kappa z\chi_\theta)^{\frac{1}{2}}\kappa z g\left[\frac{1}{T}+0.472\times10^{-3}\frac{T}{273}\left(\frac{\chi_q}{\chi_\theta}\right)^{\frac{1}{2}}\right]}{\sqrt{2}\,(\kappa z\epsilon)^{5/6}[1+0.472\times10^{-3}(T/273)Q]}$$

$$-\frac{z}{L}\left[\frac{1}{\alpha_T}\left(1-9\frac{z}{L}\right)^{-\frac{1}{2}}\right]^{\frac{1}{2}}$$

$$= \frac{}{[1+0.5|z/L|^{\frac{4}{3}}]^{5/4}} = F(z/L). \quad (31)$$

Values of $F(z/L)$ have been computed using $\alpha_T = \alpha_q = 1.35$ with the result shown in Fig. 1. Estimates of the fluxes can be obtained by first determining the value of $F(z/L)$ from the measured quantities ϵ, χ_θ, χ_q, T, Q and z, then determining z/L from Eq. (31) or Fig. 1, and finally computing u_*, T_* and q_* from Eqs. (13), (19) and (23), respectively, as the stability terms are now determined. The effect of the mean humidity can

normally be neglected as it changes the value of $F(z/L)$ by less than 1% for typical boundary layer conditions.

The z/L terms appearing in the brackets on the right side of Eq. (31) arise from the stability dependence of the imbalance term I and the generalized gradients ϕ_M and ϕ_T. If the imbalance term is set to zero and stability effects are not considered, as was originally done in the development of the dissipation technique, $F(z/L)$ becomes

$$F(z/L) = -\frac{1}{\sqrt{\alpha_T}}\frac{z}{L}. \qquad (32)$$

Eq. (32) is also plotted on Fig. 1 to show that stability effects and inclusion of the imbalance term are significant for even near-neutral conditions. At $F(z/L) = 0.1$, $z/L = -0.15$ from Eq. (32), whereas Eq. (31) gives -0.18; under more unstable conditions the discrepancy becomes much larger.

3. Experimental details

a. Site

Greater upper Minnesota was the location of the boundary layer experiment described here. A large section of farmland in the Red River Valley of the North ($48°34'$N, $96°52'$W) was specially prepared for the experiment, with a plowed soil surface with furrows approximately 20 cm deep and 40 cm apart, running east to west. The desired wind direction was from the north, and the fetch was uniform in this direction for several kilometers upwind of the instrument towers; the soil was plowed only about 25 m to the south of the towers. The surface was very flat, with a few shallow large-scale undulations, estimated at approximately 50 cm in height over horizontal distances of ~ 0.3 km. The soil was a dense black mixture of silt and clay, known locally as "gumbo."

Boundary layer observations reported herein were made simultaneously by the AFCRL and UCSD groups during the afternoon of 28 September 1973. The wind was from the north, and the sky was clear with a few scattered low clouds. Several days of intermittent heavy showers preceded that day and the soil was well-saturated, with only a few areas of standing water evident.

The AFCRL and UCSD instrument towers were located at the southern edge of the field, approximately 100 m apart in the east-west direction. The 32 m AFCRL tower had turbulence instrumentation at 4 and 32 m. The UCSD instrumentation was placed on mounting brackets on top of two 4 m, 5 cm diameter guyed poles. Turbulence instrumentation was on one pole, and monitoring instrumentation (cup anemometer, cooled-mirror aspirated dew-point unit) was on the other pole, 7 m away to avoid interference.

b. Instrumentation

1) LOW FREQUENCY

The AFCRL instrumentation is described in detail in papers covering other aspects of this field program (Readings et al., 1974; Kaimal et al., 1976). Here we mention only the relevant 4 m instrumentation, an EG&G Model 198-3 sonic anemometer and a Cambridge Systems platinum resistance thermometer.

UCSD low-frequency turbulence instrumentation consisted of an EG&G Model 198 sonic anemometer, a platinum resistance thermometer and a Lyman-alpha humidiometer. The UCSD sonic anemometer was directly calibrated in the UCSD low-speed wind tunnel prior to the field experiment. The calibration revealed that there was a slight distortion of the array due to misalignment of the vertical path, but this was accounted for in the subsequent data analysis. The fluctuating water vapor density was measured with an ERC Model B Lyman-alpha humidiometer. The device was calibrated in a Cambridge Systems hygrometric facility at the Naval Undersea Center, San Diego, prior to the field experiment. Calibration was also obtained *in situ* from the EG&G Model 110S(M) dewpoint unit. The bandwidth of the Lyman-alpha device appears to be dc to ~ 10 Hz. The exponential response of the instrument to humidity was accounted for in the digital analysis of the data. The temperature signal required for direct computation of the sensible heat flux was obtained by low-pass filtering the high-frequency temperature signal, which is discussed in the following section.

2) HIGH FREQUENCY

High-frequency measurements of the turbulent streamwise velocity component were obtained using a DISA 55M01 (constant temperature anemometer) and 55D10 (linearizer) system. A DISA 55F11 tungsten hotwire probe was used (5 μm diameter by 1.0 mm length), operated at an overheat ratio of 1.8 (210 K). Frequency response, with a 50 m probe cable, was measured to be ~ 18 kHz at a calibration velocity of 7 m s^{-1} using the square wave response technique. The temperature sensitivity was estimated and found to have a negligible contribution to the reported statistics. The anemometer system was calibrated at the field site prior to and after the experimental run. The hotwire sensor was in the horizontal plane, perpendicular to the mean flow direction.

Temperature fluctuations were measured with a resistance platinum thermometer (0.62 μm diameter by 0.65 mm length) which was formed from an etched section of Wollaston wire which was mounted on a Thermo-Systems 1210 probe. The sensor was operated in an ac Wheatstone bridge circuit designed by T. K. Deaton. Current through the 210 Ω wire was 255 μA rms. Bandwidth of a sensor of the above dimensions

and operated at the conditions of the experiment is estimated to be dc to approximately 2 kHz (LaRue *et al.*, 1975). Calibration of the fluctuating temperature signal was obtained by modulating the current through the sensor such that the output voltage change corresponded to 1.00 K (assuming a value of 0.0034 K^{-1} for the temperature-resistance coefficient for platinum). The velocity sensitivity of the sensor is estimated to be 1.4×10^{-2} K m^{-1} s and is neglected (Wyngaard, 1972; LaRue *et al.*, 1975).

c. Data analysis

1) SIGNAL PROCESSING

Signals were recorded digitally by AFCRL, and in analog form by UCSD. The AFCRL data acquisition system is described by Kaimal (1975). The analog signals from the UCSD instrumentation were preconditioned before being recorded on an FM tape recorder (Honeywell 7610, operated at 15 inches per second, bandwidth dc to 5 kHz), in order to use its dynamic range optimally. Amplitude levels were recovered on playback to within $\pm 1\%$ over the range dc to 5 kHz.

For some portions of the data analysis, the time derivatives of u and θ were required. These were obtained with an analog differentiator and low-pass filter combination having unity gain at 15.9 Hz and bandwidth dc to 10 kHz.

2) DATA SELECTION

From the several hours of data recorded, approximately 1 h was selected for detailed analysis. The period analyzed corresponded in time to 1544 to 1644 CST on 28 September 1973. During that period the wind was from the north and constant in speed and direction. There was, however, a small decrease with time of the sensible heat flux in the period. For this reason, and also to correspond with the standard AFCRL 15 min analysis period, the 1 h period was separated into four sections of about 15 min each which are designated as Runs 1, 2, 3 and 4.

3) DATA REDUCTION

The recorded signals were digitized in the laboratory at UCSD using a 12-bit resolution analog-to-digital converter with sample-and-hold circuits and a multiplexer for multi-channel analysis. The low-frequency signals of u, w, θ and q were sampled at 16.28 per second, while $\partial u/\partial t$ and $\partial \theta/\partial t$ were sampled at two rates (4170 and 521 s^{-1}) in order to give good spectral resolution from dc to $\sim$2 kHz. Data reduction was performed on the UCSD CDC 3600 computer using statistical and spectral programs developed at UCSD. The fluxes were computed directly from the simultaneously-sampled (16.28 s^{-1}) time series of u, w, θ and
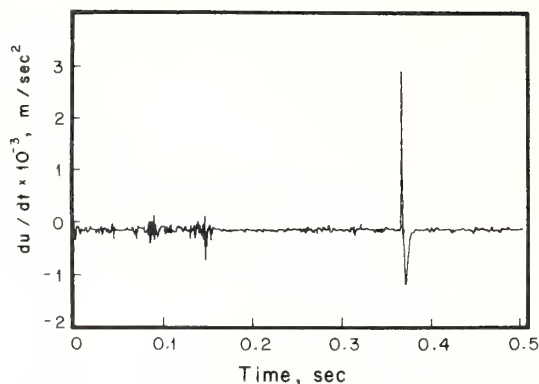
FIG. 2. Digital time series of a record of the velocity derivative $\partial u/\partial t$ showing the characteristic large spike at approximately 0.375 s. It is believed that the spike is caused by a particle striking the hot-wire anemometer probe.

q. To reduce the effects of nonstationarity and ultra-low-frequency fluctuations, the fluxes were computed from the ensemble averages of the covariances computed from fluctuations about 63 s means.

The dissipation rates of velocity and temperature were obtained from the variances of the 4170 s^{-1} digitized time series. The skewness and kurtosis values were also routinely calculated, and it was observed that the velocity derivative data in a few records (typically 10 out of the 1800 per run) contributed enormously to these higher moments. These records gave velocity derivative kurtosis values greater than 100, with maximum values of about 2000. For the velocity derivative signal, time series plots of these records revealed a characteristic asymmetric large amplitude spike, as shown in Fig. 2. It is believed that this spike signal is the result of the anemometer circuit responding to a small particle striking the active section of the hot-wire probe. The records with extremely large ($>$100) kurtosis values were deleted for the final calculation of the velocity statistics. No such characteristic spikes were found in the temperature derivative signal. However, since the temperature and velocity derivative signals were sampled simultaneously, the same temperature derivative records were dropped; these deletions caused less than 2% changes in the variances of $\partial u/\partial t$ and $\partial \theta/\partial t$.

The power spectra of the velocity and temperature derivative signals were obtained using a fast Fourier transform routine on the 4170 and 521 Hz sampled data. The resulting spectra were combined and smoothed with a 9-point running average, to cover the range 0.25 to 2086 Hz.

4. Results and discussion

a. Spectra

Since the flux estimation techniques require values for the dissipation rates as input, some of the measured
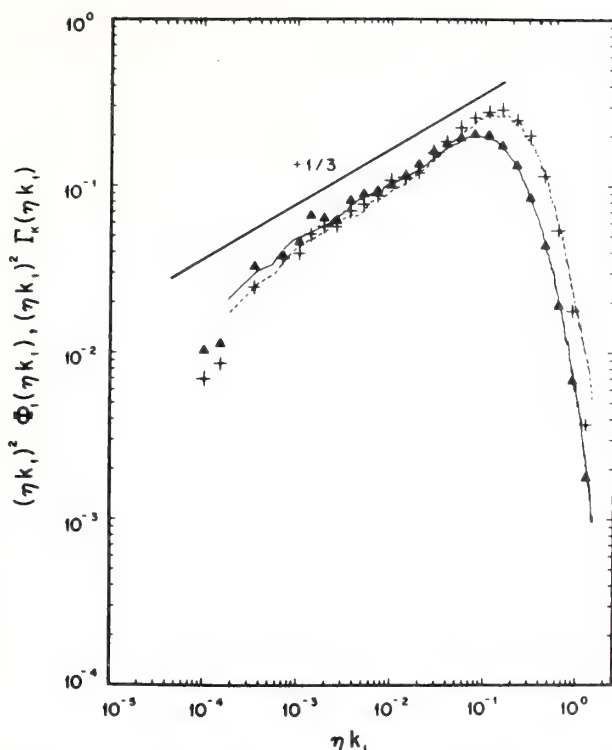
FIG. 3. Normalized velocity derivative and temperature derivative spectra. Run 1: $\dot{u}$ (solid), $\dot{\theta}$ (dashed); Williams: $\dot{u}$ (▲ ▲), $\dot{\theta}$ (+ +).

spectra will be presented to demonstrate the capability and limitations of the instrumentation used. The one-dimensional spectra of the derivatives $\partial u / \partial x$ and $\partial \theta / \partial x$ from Run 1 are presented in Fig. 3 in Kolmogorov-normalized form defined by

$$(\eta k_1)^2 \Phi_{11}(\eta k_1) = \frac{\nu^{\frac{1}{4}}}{\epsilon^{\frac{1}{4}}} k_1^2 \varphi_{uu}(k_1), \qquad (33)$$

$$(\eta k_1)^2 \Gamma_K(\eta k_1) = \frac{(\nu \epsilon)^{\frac{1}{4}}}{\chi_\theta} k_1^2 \varphi_{\theta\theta}(k_1), \qquad (34)$$

where $\Phi_{11}(\eta k_1)$ and $\Gamma_K(\eta k_1)$ are the Kolmogorov-normalized spectrum functions. An inertial subrange appears to exist for more than one decade in wavenumber as apparent from the agreement with a $+\frac{1}{3}$ slope, indicated by the solid straight line. Also shown for comparison are the surface-layer data of Williams (1974) for both temperature and velocity, which show good agreement with the present data. The dissipation rates ϵ and χ_θ in (33) and (34) were determined from the second moments of the spectra through the isotropic relations

$$\epsilon = 15\nu \int_0^\infty k_1^2 \varphi_{uu}(k_1) dk_1, \qquad (35)$$

$$\chi_\theta = 6\mathfrak{D} \int_0^\infty k_1^2 \varphi_{\theta\theta}(k_1) dk_1. \qquad (36)$$

Note that ϵ and χ_θ from (35) and (36) differ from the corrected values given by (28) and (29). It was necessary to use the uncorrected values here to permit comparison of the spectra with earlier results.

Fig. 4 shows the normalized derivative spectra on a linear-linear plot. The Kolmogorov frequency, i.e., the frequency corresponding to $\eta k_1 = 1$, was 1370 Hz for our data. Since the frequency response of the hot-wire anemometer was 17 kHz and that of the cold wire 2 kHz, the bandwidth of the instrumentation was adequate for determination of ϵ and χ_θ.

The length of the hot wire was $l_w = 1$ mm, corresponding to $\eta / l_w = 0.68$. Its spatial resolution was adequate since, according to Wyngaard's (1968) analysis, the spectral attenuation is less than 10% at $\eta k_1 = 1$ and causes no significant underestimate in ϵ (see Wyngaard, 1969). Similar results apply for the cold wire which was 0.65 mm in length (Wyngaard, 1971).

The tail of the normalized temperature spectrum does not approach the abscissa in Fig. 4 asymptotically because of noise in the ac bridge and associated circuitry. The effects of noise are probably insignificant until $\eta k_1 > 0.6$, as can be inferred from Fig. 5 which shows the fourth moments of the normalized spectra. The approximate normalized wavenumber for which the signal-to-noise ratio is unity is 1.0 for temperature and 1.3 for velocity. The low-pass filters used in data playback and digitizing were set at 2000 Hz or at $\eta k_1 = 1.46$. Thus the contribution of noise to the value of χ_θ is less than a few percent, while that to ϵ is negligible.

The magnitude and position of the peak values of the second- and fourth-moment curves for the normalized velocity spectrum agree well with those of Williams (1974) and of Wyngaard and Pao (1971). These results demonstrate that high quality spectral data were obtained for both velocity and temperature.

Values of the "universal constants" α_1 and β_θ were obtained as shown in Fig. 6. This linear-log plot allows closer examination of the data for inertial subrange behavior, since a straight line fit to the data in the inertial subrange region should have zero slope. For the wavenumber range $1 \times 10^{-3} < \eta k_1 < 2 \times 10^{-2}$ apparent inertial subranges exist for both u and θ with the measured values $\alpha_1 = 0.46 \pm 0.02$ and $\beta_\theta = 0.40 \pm 0.02$. Williams' data are also presented in Fig. 6 and agree quite favorably with our own. Both sets of normalized temperature spectral data exhibit an unexpected bump or relative peak near $\eta k_1 = 0.1$. No plausible theoretical explanation for the bump has yet been obtained.

Taylor's (1938) "frozen-flow" approximation was used to convert frequency to wavenumber in the spectral analysis. This breaks down in high-intensity turbulence, leading to underestimates of α_1 (Lumley, 1965) and β_θ (Wyngaard and Clifford, 1976). Our corrected values are $\alpha_1 = 0.50 \pm 0.02$ and $\beta_\theta = 0.41 \pm 0.02$. The failure of Taylor's approximation also distorts
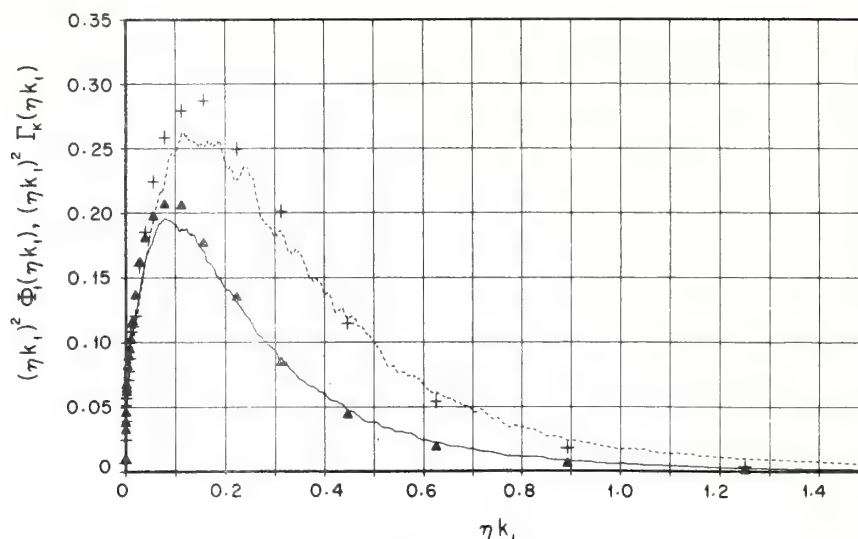
FIG. 4. Normalized velocity derivative and temperature derivative spectra.
Symbols as in Fig. 3.

high-wavenumber spectra, as will be shown in a forth-coming paper by Champagne *et al.*, but we have done no more than correct α_1 and β_θ here.

Another interesting feature of the Kolmogorov-normalized velocity and temperature spectra plots is the significantly greater spectral content in the normalized temperature spectrum for $\eta k_1 > 0.06$ than in the normalized velocity spectrum. This is at least partly due to the different relations between three-dimensional and one-dimensional spectra for velocity and temperature, i.e.,

$$\varphi_{uu}(k_1) = \int_{k_1}^{\infty} \left(1 - \frac{k_1^2}{k^2}\right)\frac{E(k)}{k}dk, \qquad (37)$$

$$\varphi_{\theta\theta}(k_1) = \int_{k_1}^{\infty} \frac{F(k)}{k}dk, \qquad (38)$$

respectively. Here E and F are the three-dimensional velocity and temperature spectra (Hinze, 1959). If the same forms are used for E and F, the one-dimensional spectra will differ because of the differences in the integrals in (37) and (38). We used the Corrsin (1964) and Pao (1965) three-dimensional spectral expression and numerically integrated to obtain Kolmogorov-normalized one-dimensional spectra. Their relative shapes were similar to the data (but there was no bump), with more content in the scalar spectrum at high wavenumbers.
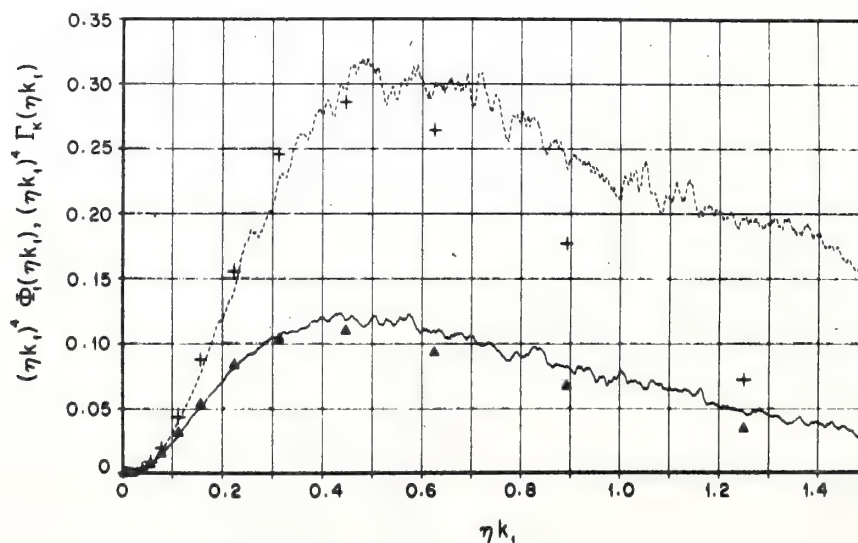
FIG. 5. Fourth moments of normalized velocity and temperature spectra.
Symbols as in Fig. 3.
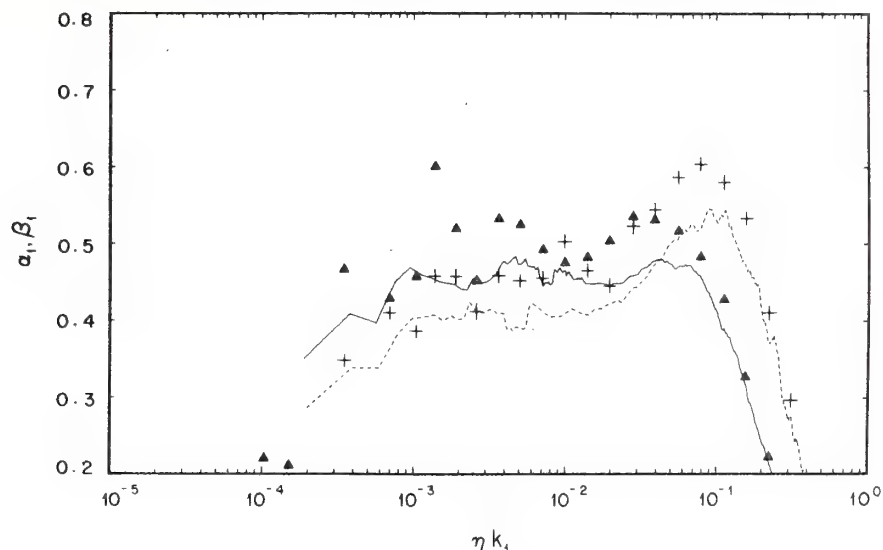
FIG. 6. Universal constants α_1 and β_θ. Run 1: α_1 (solid), β_θ (dashed); Williams: α_1(▲▲), β_θ(++). This is a plot of $(\eta k_1)^{5/3}$ times the power spectra and represents α_1 and β_θ only in the inertial subrange.

The measurement of the humidity fluctuations was limited by instrumentation response and resolution problems. The spatial separation of the Lyman-alpha detector and source tube was about 1.0 cm, which corresponds roughly to a frequency of 90 Hz for winds of 5.5 m s⁻¹. Evidently flow blockage or other effects limit the effective upper frequency to roughly 10 Hz.

The humidity spectrum for Run 1 is shown in Fig. 7. The spike at 60 Hz is caused by line noise. From the velocity and temperature spectral data, an inertial subrange in the humidity spectrum would be expected between frequencies of 1 to about 28 Hz. Fig. 7 indicates the start of an apparent inertial subrange around 1 Hz, and it appears to terminate near 8 Hz; but this roll-off is probably due to the response of the humidiometer. From the spectral level at 1 Hz, the value of χ_q was estimated using Eq. (21) with $\beta_q = 0.05$.

b. The fluxes

The mean conditions, turbulence levels and dissipation rates for Runs 1–4 are presented in Table 1. Fig. 8
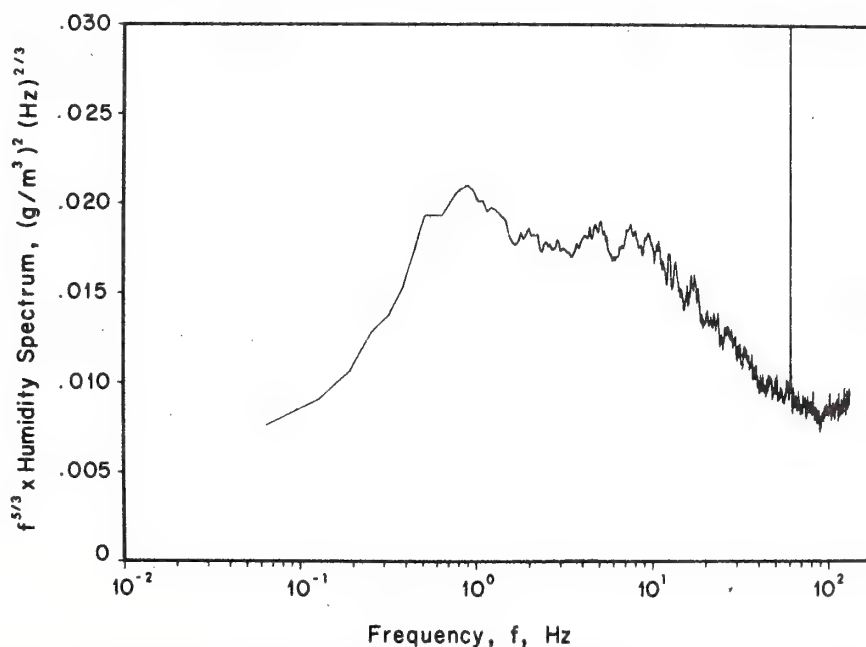
FIG. 7. Semi-logarithmic plot of the 5/3 moment of the humidity spectrum. The spike at 60 Hz is due to line noise pickup.

405

TABLE 1. Experiment conditions and dissipation rate values.[a]

Run	U (m s^{-1})	T (°C)	Q (g m^{-3})	$\overline{u^2}^{\frac{1}{2}}$ (m s^{-1})	$\overline{w^2}^{\frac{1}{2}}$ (m s^{-1})	$\overline{v^2}^{\frac{1}{2}}$ (m s^{-1})	$\overline{\theta^2}^{\frac{1}{2}}$ (K)	$\overline{q^2}^{\frac{1}{2}}$ (g m^{-3})	ϵ (10^2 m^2 s^{-3})	χ_θ (10^3 K^2 s^{-1})	χ_q (10^2 g^2 m^{-6} s^{-1})
1	5.48	23.0	9.4	0.94	0.38	1.59	0.32	0.47	1.94	6.41	1.18
2	5.28	23.1	9.4	0.97	0.39	1.28	0.27	0.48	1.65	3.82	1.10
3	6.21	23.2	9.3	1.20	0.43	1.35	0.19	0.45	1.99	2.18	1.10
4	5.67	23.2	9.3	1.05	0.44	1.49	0.18	0.39	2.32	2.33	0.91

[a] Values of ν and $\mathfrak{D}$ used were $\nu = 0.159$ cm^2 s^{-1}, $\mathfrak{D} = 0.219$ cm^2 s^{-1}, Pr$=0.725$. Mean pressure was 28.84 inches Hg.

presents the directly measured turbulent shear stress values and the values estimated by the direct dissipation technique. The length of the horizontal bars represents the time period over which the average was obtained. The UCSD directly computed results are generally higher by 10–15% than those of AFCRL, and this appears to be a general trend rather than scatter.

The directly computed $\overline{w\theta}$ and the estimated values are presented in Fig. 9. The UCSD and AFCRL directly computed values agree quite well, but the values estimated from the direct dissipation technique are consistently high. Also shown in Fig. 9 are the UCSD directly computed $\overline{wq}$ values and the indirect values, which show good agreement, on average. Table 2 presents the UCSD directly computed covariances and the values estimated by the dissipation technique.

c. The variance budgets

The directly measured values of $\overline{uw}$, $\overline{w\theta}$, $\overline{wq}$, ϵ and χ_θ and the estimated χ_q provide sufficient information to

evaluate several of the important terms in the three variance budgets. The mean gradient terms necessary for the various production terms were determined from the Businger et al. (1971) relationships using the measured values of z/L_m, where L_m denotes the value of L obtained from the directly measured covariances.

1) THE TURBULENT KINETIC ENERGY BUDGET

The turbulent kinetic energy equation (7) can be made dimensionless through multiplication by $-\kappa z/u_*^3$ to obtain

$$\varphi_M - \frac{z}{L} - \frac{1}{2}\frac{\kappa z}{u_*^3}\frac{\partial}{\partial z}\overline{we^2} - \frac{\kappa z}{u_*^3}I - \frac{\kappa z\epsilon}{u_*^3} = 0, \qquad (39)$$

where I, the imbalance term, is assumed to be pressure transport. Table 3 presents the various terms computed from the direct measurements: I_m/ϵ is the measured imbalance, as defined by Eq. (9), normalized by the measured dissipation rate; and $(I/\epsilon)_w$ is the same
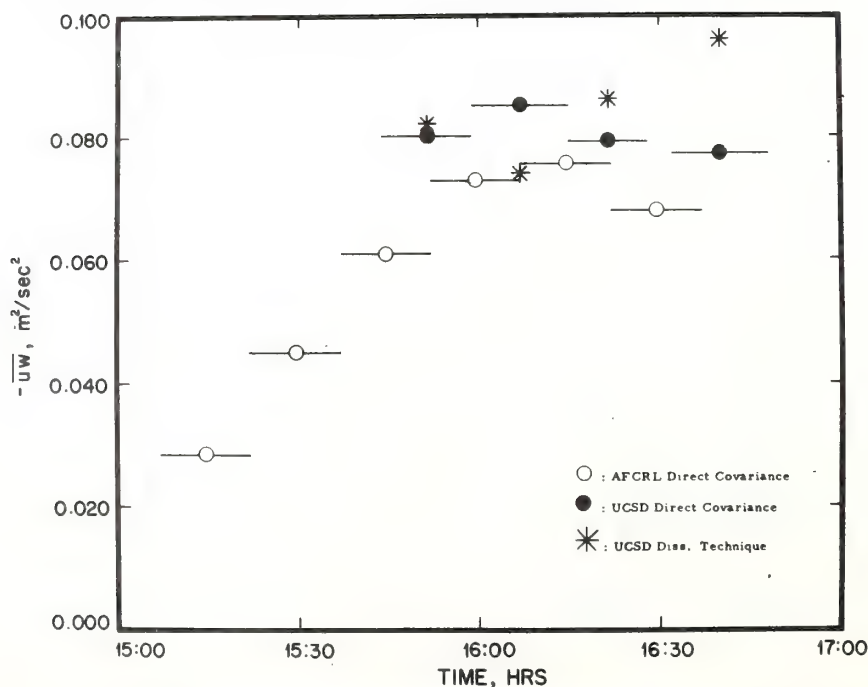
FIG. 8. Values of the turbulent shear stress during the experiment.
The length of the horizontal bar is the averaging time.
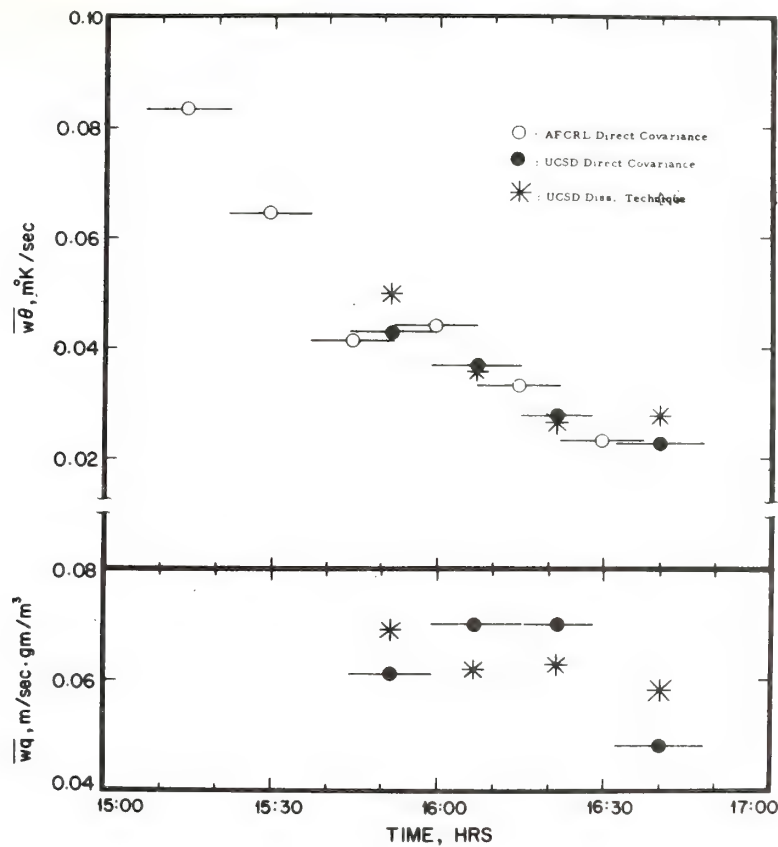
Fig. 9. Values of the turbulent fluxes of temperature and moisture during the experiment. Symbols as in Fig. 8.

variable computed from Wyngaard and Coté's (1971) results, which can be expressed as

$$\left(\frac{I}{\epsilon}\right)_W = \frac{[1-15(z/L)]^{-\frac{1}{4}}}{[1+0.5|z/L|^{\frac{2}{3}}]^{\frac{3}{2}}} - 1.0, \quad (40)$$

where the measured L values were used for computation. The values presented in Table 3 are shown in Fig. 10 together with the results of Wyngaard and Coté (1971). The agreement is good over the limited range of z/L

for the present data. The scatter in the directly measured values of ϵ perhaps can be attributed to the difficulty of measuring the variance of the signal $\partial u/\partial t$ which has a large kurtosis (Tennekes and Wyngaard, 1972).

2) THE SCALAR VARIANCE BUDGETS

The production, dissipation and flux divergence terms for the scalar variance budgets are presented in Tables 4 and 5. The flux divergence terms were esti-

TABLE 2. Summary of results.

Run	$-\overline{uw}$ (m² s⁻²)			$\overline{w\theta}$ (m° K s⁻¹)			$\overline{wq}$ (g m⁻² s⁻¹)			L_θ (m)	L_q (m)	$L_m{}^d$ (m)
	Direct	Dissipa- tion[a]	Error[b] (%)	Direct	Dissipa- tion[a]	Error[b] (%)	Direct	Dissipa- tion[c]	Error[b] (%)			
1	0.080	0.082	+3	0.043	0.051	+18	0.061	0.069	+13	−45.2	−210	−37.2
2	0.085	0.074	−13	0.037	0.038	+3	0.070	0.064	−9	−57.6	−204	−44.9
3	0.079	0.086	+9	0.028	0.028	+0	0.070	0.063	−10	−69.4	−180	−50.1
4	0.077	0.096	+25	0.023	0.029	+26	0.048	0.058	+21	−79.8	−257	−60.9
Average	0.080	0.084	+6	0.033	0.036	+12	0.062	0.063	+2	—		

[a] Direct dissipation technique.
[b] Error $= 10^2$ (dissipation−direct)/direct.
[c] Inertial dissipation technique.
[d] $L_m = (L_\theta^{-1}+L_q^{-1})^{-1}$, where L_θ is the Monin-Obukhov length due to sensible heat flux and L_q the Monin-Obukhov length due to moisture flux, from directly measured fluxes.

TABLE 3. Dimensionless kinetic energy budget terms, including measured and estimated imbalance term.

Run	φ_M	$-z/L_m$	$\frac{\kappa z}{u_*^3} I_m$ [a]	$\frac{\kappa z \epsilon}{u_*^3}$	$\frac{I_m}{\epsilon}$	$\left(\frac{I}{\epsilon}\right)_W$ [b]
1	0.783	0.110	−0.442	1.226	−0.36	−0.33
2	0.805	0.091	−0.144	0.949	−0.15	−0.30
3	0.819	0.082	−0.465	1.284	−0.36	−0.29
4	0.842	0.067	−0.721	1.563	−0.46	−0.25
Average	0.812	0.088	−0.443	1.255	−0.33	−0.30

[a] Eq. (9).
[b] Eq. (40).

mated from Wyngaard and Coté's (1971) results using a value of

$$\frac{\kappa z}{u_* T_*^2} \frac{\partial}{\partial z}\overline{-w\theta^2} = \frac{\kappa z}{u_* q_*^2} \frac{\partial}{\partial z}\overline{-wq^2}$$

of 0.2 for $z/L = -0.1$.

For the humidity variance budget, our results indicate that production is equal to dissipation, with the dissipation determined from the humidity spectrum using $\beta_q = 0.50$. Had we used $\beta_q = \beta_\theta = 0.41$, the ratio of production to dissipation for humidity variance would have been 0.79, close to that found for temperature variance.

The results for the temperature variance budget are presented in Table 5. Averaged over the four runs, the ratio of production to dissipation is 0.84. If we include the estimated flux divergence term, also a loss, the production rate is 28% less than the sum of dissipation and flux divergence.

There are many factors that could have contributed to this relatively small imbalance. We can rule out instrumental problems, because of the low noise levels, the

FIG. 10. The dimensionless turbulent kinetic energy budget components versus $-z/L$. The solid lines are from Wyngaard and Coté (1971). Run 1, circles; run 2, squares; run 3, diamonds; run 4, triangles.

TABLE 4. Humidity variance budget equation terms.

Run	$-2\overline{wq}\frac{\partial Q}{\partial z}$ [a] (10^2 g^2 m^{-6} s^{-1})	χ_q (10^2 g^2 m^{-6} s^{-1})	$\frac{\partial \overline{wq^2}}{\partial z}$ [b] (10^2 g^2 m^{-6} s^{-1})	$\frac{-2\overline{wq}\frac{\partial Q}{\partial z}}{\chi_q}$	$-2\overline{wq}\frac{\partial Q}{\partial z}$ [c] (10^2 g^2 m^{-6} s^{-1})
1	0.97	1.18	0.18	0.82	1.37
2	1.29	1.10	0.24	1.17	1.74
3	1.37	1.10	0.24	1.25	1.80
4	0.68	0.91	0.12	0.75	0.86
Average	1.08	1.07	0.20	1.01	1.44

[a] Eq. (22).
[b] Wyngaard and Coté (1971).
[c] Neglecting stability effects.

consistency of the high-frequency data with earlier results, and the good agreement between AFCRL and UCSD fluctuating temperature levels (see Fig. 11). However it is possible, for example, that the small-scale temperature field is slightly anisotropic, so that $\chi_\theta < 6\mathfrak{D}\overline{(\partial\theta/\partial x)^2}$. Evidence of anisotropy, in the form of skewed temperature derivatives, has been widely reported (Mestayer et al., 1976). We also found the skewness of $\partial\theta/\partial t$ to be non-zero, with typical values of -0.7.

The mean temperature gradient contribution to the temperature variance production term was not measured directly, but was estimated from Eq. (18), with $\kappa = 0.35$ and $\alpha_T = 1.35$. We also tried the Hicks and Dyer (1972) formulation

$$\varphi_T = \frac{1}{\alpha_T}(1 - 15z/L)^{-\frac{1}{4}} \tag{41}$$

with $\alpha_T = 1.0$ and $\kappa = 0.41$. This gave virtually identical production rates.

The flux divergence term was also not measured directly, but was taken from Wyngaard and Coté's (1971) results. Their data were quite scattered, however, rendering our estimates here somewhat uncertain.

TABLE 5. Temperature variance budget equation terms.

Run	$-2\overline{w\theta}\frac{\partial T}{\partial z}$ [a] (10^3 K^2 s^{-1})	χ_θ (10^3 K^2 s^{-1})	$\frac{\partial \overline{w\theta^2}}{\partial z}$ [b] (10^3 K^2 s^{-1})	$\frac{-2\overline{w\theta}\frac{\partial T}{\partial z}}{\chi_\theta}$	$-2\overline{w\theta}\frac{\partial T}{\partial z}$ [c] (10^3 K^2 s^{-1})
1	4.80	6.41	0.91	0.75	6.77
2	3.61	3.82	0.66	0.94	4.87
3	2.21	2.18	0.39	1.01	2.91
4	1.56	2.33	0.27	0.67	1.98
Average	3.04	3.68	0.56	0.84	4.13

[a] Eq. (18).
[b] Wyngaard and Coté (1971).
[c] Neglecting stability effects.

Fig. 11. Values of the rms temperature fluctuations during the experiment.
AFCRL (open circles), UCSD (solid circles).

Finally, we should mention that we used a horizontally homogeneous, stationary model of the temperature variance budget, and neglected radiation effects. From the work of Townsend (1958), Brutsaert (1972) and Coantic (1975), the radiation effects can be expected to be an order of magnitude smaller than our imbalance and of the opposite sign. Similarly, the observations of $\partial\overline{\theta^2}/\partial t$ (see Fig. 11) show it is of the same sign as the imbalance but an order of magnitude smaller. Inhomogeneity effects are more difficult to assess, but following the arguments of Wyngaard and Coté (1971) one can show that very large horizontal gradients in $\overline{\theta^2}$ (100% change in less than 1 km) or mean temperature (5 K km^{-1}) would be required to account for the imbalance. While (described in Section 3a) the soil was drying out during the runs, with some areas of standing water, it seems unlikely that this would have caused such strong inhomogeneity.

Thus while the causes for the temperature variance budget imbalance cannot be precisely identified, it seems likely that there could be a number of contributors.

d. Flux estimates neglecting stability effects

To determine the effect of neglecting stability, the fluxes were estimated using the expressions strictly valid only under neutral conditions. Thus Eq. (4) was used to estimate stress, and T_* and q_* were found from

$$T_* = -\left(\frac{\kappa z \chi_\theta \alpha_T}{2u_*}\right)^{\frac{1}{2}}, \qquad (42)$$

$$q_* = -\left(\frac{\kappa z \chi_q \alpha_q}{2u_*}\right)^{\frac{1}{2}}. \qquad (43)$$

These flux estimates also agreed well with the direct measurements, in spite of the neglect of stability effects. The stress estimate was 16% high, compared with the 6% overestimate (Table 2) with stability effects included. Heat flux was 3% low, compared with 12% high; and moisture flux was 10% low, compared with 2% high.

To investigate this apparent anomaly further, we calculated the magnitudes of the discarded stability contributions to the u_*^2 estimate. Combining Eqs. (9) and (12) yields

$$u_*^2 = (\kappa z \epsilon)^{\frac{2}{3}}\left(1+\frac{I}{\epsilon}\right)^{\frac{2}{3}}\left(1-15\frac{z}{L}\right)^{1/6}. \qquad (44)$$

From Table 3, values of I_m/ϵ and $-z/L_m$ were used to compute the last two factors in (44). It was found that their product was nearly unity even though the individual terms themselves were substantially different from unity. Thus although the simplified Eq. (4) gave good estimates of the momentum flux, one must be cautious in drawing the conclusion that stability effects are negligible. For example, the above could lead to the conclusion that shear production and dissipation are in balance, which is clearly not the case in unstable conditions.

5. Conclusions

The estimates of the momentum, heat and moisture fluxes from the dissipation techniques agree well with those measured directly.

The turbulent kinetic energy budget was found to agree with that presented by Wyngaard and Coté (1971) for unstable conditions. Viscous dissipation, the largest term, is balanced by shear production and an imbalance (presumably pressure transport) term. The production and dissipation terms in the humidity variance budget were found essentially in balance, which agrees with Wyngaard and Coté's temperature variance budget results if $\beta_q = 0.50$.

The present experiment is apparently the first in which the dissipation rate of temperature variance was directly measured simultaneously with $\overline{w\theta}$ and other variables which permitted estimation of its production rate. The average ratio of production to dissipation was 0.84. Together with the behavior of the flux divergence term, estimated from Wyngaard and Coté (1971), these results imply a slightly imbalanced temperature variance budget. Possible reasons for the imbalance are considered but none can be definitely identified as a significant contributor.

The one-dimensional spectra of the streamwise velocity fluctuations and temperature fluctuations, presented in Kolmogorov-normalized form, compare favorably with the results of Williams (1974). Values of the universal constants of $\alpha_1 = 0.50 \pm 0.02$ and $\beta_\theta = 0.41 \pm 0.02$ were obtained. The deviations from Taylor's hypothesis caused by high turbulence levels were found to have significant effects on the values of α_1 and β_θ and the dissipation rates ϵ and χ_θ.

REFERENCES

Busch, N. E., and H. A. Panofsky, 1968: Recent spectra of atmospheric turbulence. *Quart. J. Roy. Meteor. Soc.*, **94**, 132–140.

Brutsaert, W., 1972: Radiation, evaporation and the maintenance of turbulence under stable conditions in the lower atmosphere. *Bound.-Layer Meteor.*, **2**, 309–325.

Businger, J. A., J. C. Wyngaard, Y. Izumi and E. F. Bradley, 1971: Flux-profile relationships in the atmospheric surface layer. *J. Atmos. Sci.*, **28**, 181–189.

Coantic, M., 1975: An *Introduction to Turbulence in Geophysics and Air-Sea Interactions*. Course notes, University of California, San Diego, 283 pp.

Corrsin, S., 1964: Further generalization of Onsager's cascade model for turbulence spectra. *Phys. Fluids*, **7**, 1156–1159.

Deacon, E. L., 1959: The measurement of turbulent transfer in the lower atmosphere. *Advances in Geophysics*, Vol. 6, Academic Press, 211–228.

Dyer, A. J., 1975: Measurement of turbulent fluxes by fluxatron and NIFTI technique. *Atmos. Tech.*, **7**, 24–29.

——, 1967: The turbulent transport of heat and water vapor in an unstable atmosphere. *Quart. J. Roy. Meteor. Soc.*, **93**, 501–508.

Elliott, J. A., 1975: The measurement of pressure fluctuations in the atmospheric boundary layer. *Atmos. Tech.*, **7**, 30–32.

Garratt, J. R., 1972: Studies of turbulence in the surface layer over water (Lough Neagh). Part II. Production and dissipation of velocity and temperature fluctuations. *Quart. J. Roy. Meteor. Soc.*, **98**, 642–657.

Gibson, C. H., and R. B. Williams, 1969: Turbulence structure in the atmospheric boundary layer over the open ocean. *Proc. AGARD Conf. Aerodynamics of Atmospheric Shear Flows*, Vol. 48, 5–1 to 5–9.

——, G. R. Stegen and R. B. Williams, 1970: Statistics on the finestructure of turbulent velocity and temperature fields measured at high Reynolds number. *J. Fluid Mech.*, **41**, 153–167.

Haugen, D. A., J. C. Kaimal and E. F. Bradley, 1971: An experimental study of Reynolds stress and heat flux in the atmospheric surface layer. *Quart. J. Roy. Meteor. Soc.*, **97**, 168–180.

Heskestad, G., 1965: A generalized Taylor hypothesis with application for high Reynolds number turbulent shear flows. *J. Appl. Mech.*, **87**, 735–740.

Hicks, B. B., and A. J. Dyer, 1972: The spectral density technique for the determination of eddy fluxes. *Quart. J. Roy. Meteor. Soc.*, **98**, 838–844.

Hinze, J. O., 1959: *Turbulence*. McGraw-Hill, 586 pp.

Kaimal, J. C., 1975: Sensors and techniques for direct measurement of turbulent fluxes and profiles in the atmospheric surface layer. *Atmos. Tech.*, **7**, 7–14.

——, and D. A. Haugen, 1969: Some errors in the measurement of Reynolds stress. *J. Appl. Meteor.*, **8**, 460–462.

——, J. C. Wyngaard, D. A. Haugen, O. R. Coté, Y. Izumi, S. J. Caughey and C. J. Readings, 1976: Turbulence structure in the convective boundary layer. *J. Atmos. Sci.* (in press).

LaRue, J. C., T. Deaton and C. H. Gibson, 1975: Measurement of high-frequency turbulent temperature. *Rev. Sci. Instrum.*, **46**, 757–764.

Leavitt, E., and C. A. Paulson, 1975: Statistics of surface layer turbulence over the tropical ocean. *J. Phys. Oceanogr.*, **5**, 143–156.

Lumley, J. L., 1965: Interpretation of time spectra measured in high-intensity shear flows. *Phys. Fluids*, **8**, 1056–1062.

McBean, G. A., 1972: Instrument requirements for eddy correlation measurements. *J. Appl. Meteor.*, **11**, 1978–1084.

——, R. W. Stewart and M. Miyake, 1971: The turbulent energy budget near the surface. *J. Geophys. Res.*, **76**, 6540–6549.

——, and J. A. Elliott, 1975: The vertical transports of kinetic energy by turbulence and pressure in the boundary layer. *J. Atmos. Sci.*, **32**, 753–766.

Mestayer, P. G., C. H. Gibson, M. F. Coantic and A. S. Patel, 1976: Local anisotropy in heated and cooled turbulent boundary layers. *Phys. Fluids*, **19**, 1279–1287.

Miyake, M., M. Donelan, G. McBean, C. Paulson, F. Badgley and E. Leavitt, 1970: Comparison of turbulent fluxes over water determined by profile and eddy correlation techniques. *Quart. J. Roy. Meteor. Soc.*, **96**, 132–137.

Monji, N., 1973: Budgets of turbulent energy and temperature variance in the transition zone from forced to free convection. *J. Meteor. Soc. Japan*, **51**, 133–145.

Pao, Y. H., 1965: Structure of turbulent velocity and scalar fields at large wavenumbers. *Phys. Fluids*, **8**, 1063–1075.

Paquin, J. E., and S. Pond, 1971: The determination of the Kolmogoroff constants for velocity, temperature and humidity fluctuations from second- and third-order structure functions. *J. Fluid Mech.*, **50**, 257–269.

Pond, S., R. W. Stewart and R. W. Burling, 1963: Turbulence spectra in the wind over waves. *J. Atmos. Sci.*, **20**, 319–324.

——, G. T. Phelps, J. E. Paquin, G. McBean and R. W. Stewart 1971: Measurements of the turbulent fluxes of momentum, moisture and sensible heat over the ocean. *J. Atmos. Sci.*, **28**, 901–917.

Readings, C. J., D. A. Haugen and J. C. Kaimal, 1974: The 1973 Minnesota atmospheric boundary layer experiment. *Weather*, **29**, 309–312.

Smith, S. D., 1967: Thrust-anemometer measurements of wind-velocity spectra and of Reynolds stress over a coastal inlet. *J. Mar. Res.*, **25**, 239–262.

——, 1970: Thrust-anemometer measurements of wind turbulence, Reynolds stress and drag coefficient over the sea. *J. Geophys. Res.*, **75**, 6758–6770.

Stegen, G. R., C. H. Gibson and C. A. Friehe, 1973: Measure-ments of momentum and sensible heat fluxes over the open ocean. *J. Phys. Oceanogr.*, **3**, 86–92.

Taylor, G. I., 1938: The spectrum of turbulence. *Proc. Roy. Soc. London*, **A164**, 476–490.

Taylor, R. J., 1961: A new approach to the measurement of turbulent fluxes in the lower atmosphere. *J. Fluid Mech.*, **10**, 449–458.

Tennekes, H., and J. C. Wyngaard, 1972: The intermittent small-scale structure of turbulence: data-processing hazards. *J. Fluid Mech.*, **55**, 93–103.

Townsend, A. A., 1958: The effects of radiative transfer on turbulent flow in a stratified fluid. *J. Fluid Mech.*, **4**, 361–375.

Weiler, H. S., and R. W. Burling, 1967: Direct measurements of stress and spectra of turbulence in the boundary layer over the sea. *J. Atmos. Sci.*, **24**, 653–664.

Williams, R. M., Jr., 1974: High frequency temperature and velocity fluctuations in the atmospheric boundary layer. Ph.D. thesis, Oregon State University, 81 pp.

Wyngaard, J. C., 1968: Measurement of small-scale turbulence structure with hot wires. *J. Sci. Instrum.*, **1**, 1105–1108.

——, 1969: Spatial resolution of the vorticity meter and other hot-wire arrays. *J. Sci. Instrum.*, **2**, 983–987.

——, 1971: Spatial resolution of a resistance wire temperature sensor. *Phys. Fluids*, **14**, 2052–2054.

——, 1972: The effect of velocity sensitivity on temperature derivative statistics in isotropic turbulence. *J. Fluid Mech.*, **48**, 763–769.

——, and O. R. Coté, 1971: The budgets of turbulent kinetic energy and temperature variance in the atmospheric surface layer. *J. Atmos. Sci.*, **28**, 190–201.

——, and Y. H. Pao, 1971: Some measurements of the fine structure of large Reynolds number turbulence. *Statistical Models and Turbulence*, M. Rosenblatt and C. Van Atta, Eds., Springer-Verlag, 384–401.

——, and S. F. Clifford, 1976: Taylor's hypothesis and high-frequency turbulence spectra. Submitted to *J. Atmos. Sci.*

KINEMATIC MODELS OF A DRY CONVECTIVE
BOUNDARY LAYER COMPARED WITH DUAL-DOPPLER
RADAR OBSERVATIONS OF WIND FIELDS

EARL E. GOSSARD and A. S. FRISCH

NOAA/ERL/Wave Propagation Laboratory,
Boulder, Colorado, USA

Abstract. The kinematic structure of the convective boundary layer, observed by a dual-Doppler radar system, is compared with the structure predicted by simple shear models. We first consider the models to be inviscid, then add viscous effects. Model 1 assumes a linear ambient wind profile from the surface through the boundary layer, and a constant wind above. The shear layer is assumed to be statically neutral, but static stability is permitted in the region above the shear. Model 2 has a hyperbolic tangent ambient wind profile.

After considering the inviscid models, some of the effects of viscosity are incorporated into the models in a crude way, and the results are compared.

We conclude that although the presence of shear is important, the kinematic structure is relatively independent of the details of the wind and temperature profiles. Viscosity has important effects, especially near the critical level where the disturbance velocity is equal to the wind speed. The patterns predicted by both models agree very well with the dual-Doppler radar observations when viscosity is included.

1. Introduction

Dual-Doppler radar observations reveal the kinematic structure of the lower atmosphere in detail that has never before been attainable. In this paper we compare the kinematic structure revealed by the radars with some simple dry models. The models are steady, three-dimensional and permit speed shear in the ambient wind.

The dynamics of a fairly general inviscid model, including a surface-based superadiabatic layer and an inversion capping a shear layer, were examined by Gossard and Moniger (1975). The primary effect of the capping inversion was to confine the range of dynamic instability to a relatively narrow band of wave numbers. Because the general form of their model contained a statically unstable layer and a wind profile with an inflection point, both dynamic and convective instability were possible when $-1 < (N/\beta)^2 (m/k)^2 < 0$, where N is the Väisälä-Brunt frequency in the superadiabatic layer, β is the shear (assumed constant) in the shear layer, m is wave number of the disturbance, and k is the wave number component in the direction of shear. Thus m/k represents orientation of the disturbance and is just $(\sin \theta)^{-1}$ where θ is the angle between the direction of disturbance alignment and the shear direction. Below $(N/\beta)^2 (m/k)^2 = -1$, only convective instability is found; above zero, only dynamically unstable disturbances exist. Disturbances aligned transverse to the shear direction were found to be

most dynamically unstable, while those aligned parallel to the shear direction were most convectively unstable. Thus the analysis of the dynamics of the model recognizes two classes of disturbance in terms of their origin, one wave-like and the other convective.

In this paper we are interested in the kinematic structure rather than the dynamics. Because the flow patterns are determined by kinematic constraints, the velocity field is insensitive to whether the disturbance is from wave action or convection; the solutions may appear wave-like in one region and cell-like in another. If one were interested in making such a distinction, it would have to be on the basis of alignment of the disturbances, their scale relative to layer depth and the presence of an inflection point in the wind profile or a superadiabatic vs. a stable lower atmosphere. Because the radar measurements were made on an afternoon with active solar heating, we assume that the observed features were generated by convective instability, but the kinematic structure is "unaware" of this.

It is, of course, possible to calculate the vector wind perturbation fields in the full multi-layer model of Gossard and Moniger (1975). However, the number of parameters that must be specified in a model of such complexity is very large, and almost any pattern could be produced by a suitable choice of parameters. In the absence of a comprehensive, independent set of observations to define the environment in detail, it is reasonable to compare the simplest model with observation, and increase its complexity only as necessary to account for observations. We find that a simple three-dimensional, two-layer model consisting of an adiabatic lower layer, under various degrees of shear, capped by a stable upper atmosphere is capable of explaining nearly all features found in the dual-Doppler observations. If we included a shearless, superadiabatic surface layer beneath the shear layer, as in the model of Gossard and Moninger (1975), it would be a very important factor in the dynamics because it introduces both inflection point and thermal instability into the model, but such a layer has virtually no effect on the kinematics if it is fairly thin ($\simeq 0.1\ \Delta H$). The rigid lower-boundary constraint on vertical velocity must still be obeyed, and the interfacial displacement must match at the top of the superadiabatic layer. On the other hand, the kinematics in the two-layer model can be discussed independently of the dynamics, while the addition of another layer requires solution of the complete dynamical problem to satisfy the interfacial kinematic conditions because the quantity "A" in Gossard and Moninger (1975) must then be evaluated.

Shear has a very important influence on the observed flow patterns. In the vertical plane containing the shear vector, strong shear can produce adjacent vortices rotating in the same sense. However, if the shear is absent or weak, they rotate in opposite directions. Shear, if very weak, can also produce counter-rotating adjacent vortices in horizontal planes within the shear layer. As the shear becomes stronger, these patterns more nearly resemble flow about an obstacle.

An important conclusion of the present study is that most of the observed

413

kinematics of a convective boundary layer can be modeled without resorting to numerical methods in large computers which typically require large amounts of expensive computer time. This makes experimentation with the model much easier and facilitates isolation of the effects of various model changes. This kind of modeling can therefore serve as a valuable guide in the design of numerical models that may contain more complexity and also aid in the interpretation of results from those models. The kinematic model can aid in the design of measurement programs, since by making changes in input parameters, one can see the range of expected effects and determine type and placement of optimum instrumentation.

The techniques used by the Wave Propagation Laboratory in the collection and processing of the dual-Doppler radar data have been described in detail by Miller and Strauch (1974). The wavelength of each radar is 3.2 cm. The two radars are separated by a baseline and they scan a common volume of space in which there are air-motion tracers. These tracers may be snow (Frisch *et al.*, 1974), water drops (Miller, 1975; Kropfli and Miller, 1976), or chaff as in the observations to be described in this paper. The radars scan the volume by synchronously scanning, sequentially, a series of tilted planes, each common to both radars (Lhermitte and Miller, 1970). In the collection of data used in this paper, 24 range gates were used, and each co-plane was scanned in 16 azimuthal "beams." The radars were separated by 16 km. The chaff was injected from an aircraft flying a grid pattern at a height of 1 km on a convective afternoon with active solar heating. The chaff was injected high in the convective structure so it flowed mainly into the downdraft.

The chaff filled a depth of about 1 km, which we will therefore assume to be the depth of the convectively mixed layer. It took about 30 s to scan each plane and about 5 min to scan the volume. The radial velocities were accurate to ± 6 cm^{-1}. A description of the Doppler data, along with spatial spectra and analyses of the relation of the turbulent structure to the convective patterns, has already been published (Frisch *et al.*, 1976). In the present paper we have interchanged the x and y axes from the convention in Frisch *et al.*

In order to reveal the cell structure as clearly as possible, the mean air motion in the volume scanned was subtracted from the total velocity field. Therefore, in the models we have calculated flow relative to the cell motion.

2. Derivation of the Model Equations

For a mean flow $u_0(z)$ with vertical shear $\partial u_0/\partial z$ in the x direction, the equations of motion, continuity, and energy conservation for small, adiabatic perturbations are (see Gossard and Hooke, 1975, p. 122):

$$\frac{Du}{Dt} + \frac{1}{\rho_0}\frac{\partial p}{\partial x} + \frac{\partial u_0}{\partial z} w = 0 \qquad (1)$$

$$\frac{Dv}{Dt} + \frac{1}{\rho_0}\frac{\partial p}{\partial y} = 0 \tag{2}$$

$$\frac{Dw}{Dt} + \frac{1}{\rho_0}\frac{\partial p}{\partial z} + g\frac{\rho}{\rho_0} = 0 \tag{3}$$

$$\frac{D\rho}{Dt} + w\frac{\partial \rho_0}{\partial z} + \rho_0 \nabla \cdot \mathbf{v} = 0 \tag{4}$$

$$\frac{D\rho}{Dt} + w\frac{\partial \rho_0}{\partial z} = \frac{1}{c^2}\left(\frac{Dp}{Dt} + w\frac{\partial p_0}{\partial z}\right) \tag{5}$$

where u, v, w are small perturbations of the x, y, z components of velocity, and ρ, p are perturbations of density and pressure. Unperturbed quantities are designated by zero subscripts, and c is sound velocity. We have chosen x to be the direction of the unperturbed flow, so that $v_0 = w_0 = 0$; the operator $D/Dt \equiv \partial/\partial t + u_0(z)\partial/\partial x$.

We eliminate ρ between Eqs. (4) and (5) and adopt the transformation

$$U, V, W, P^{-1} = [\rho_0(z)/\rho_s]^{1/2}(u, v, w, p^{-1}) \tag{6}$$

where ρ_s is the density at some reference level such as the surface. The four partial differential equations are linear and homogeneous, and solutions representing a simple form of three-dimensional disturbance are

$$U, V, W, P = \tfrac{1}{2}[U(z), V(z), W(z), P(z)][\exp i(kx + ly - \sigma t)$$
$$\pm \exp i(kx - ly - \sigma t)] \tag{7}$$

where k and l are the horizontal wave numbers of the perturbation and σ is frequency. The partial differential equations are satisfied by the following phasing of the variables:

$$P = P(z)\cos ly \sin (kx - \sigma t) \tag{8}$$

$$U = U(z)\cos ly \sin (kx - \sigma t) \tag{9}$$

$$V = V(z)\sin ly \cos (kx - \sigma t) \tag{10}$$

$$W = W(z)\cos ly \cos (kx - \sigma t). \tag{11}$$

Eliminating $P(z)$, $U(z)$, and $V(z)$, we obtain the classical ordinary differential equation in $W(z)$,

$$\frac{d^2 W(z)}{dz^2} - \left[m^2 - \frac{u_0'' k}{\omega} - \frac{N^2 m^2}{\omega^2}\right]W(z) = 0, \tag{12}$$

where $m^2 \equiv k^2 + l^2$, $u_0'' \equiv d^2 u_0/dz^2$ and $\omega \equiv iD/Dt = k[C - u_0(z)]$ is the intrinsic frequency. In deriving (12), we have defined $N^2 \equiv -g(\rho_0^{-1}d\rho_0/dz + g/c^2) = (g/\theta_0)(d\theta_0/dz)$, where N is the Väisälä-Brunt frequency and θ is potential temperature. We have neglected the quantity $(2\rho_0)^{-1}d\rho_0/dz + g/c^2$, compared with $\partial/\partial z$

applied to the field variables, and we have assumed that the phase velocity $C = \sigma/k \ll c$. This is a form of the Boussinesq approximation. It implies that we have assumed the scale depth of the atmosphere to be large compared with the scale depth of the disturbance and that the disturbance propagates slowly compared with the speed of sound. It is important to note that Equation (12) is identical to the wave equation for a two-dimensional disturbance except that m^2 has replaced k^2 as the first term in brackets and $N^2 m^2/k^2[C - u_0(z)]^2$ has replaced $N^2/[C - u_0(z)]^2$ as the last term in brackets. Therefore, solutions for the two-dimensional case can be applied to the three-dimensional case by simply substituting $N' = Nm/k$ for N.

The solution of (12) is generally difficult because of singularities in the coefficient where the intrinsic frequency becomes zero, i.e., at the height where the disturbance velocity and the background wind velocity are equal. Solutions for some special cases are well known, e.g., in the case of no shear when ω is constant and u_0'' is zero. If N is also constant with height, the coefficient in (12) is constant, and its solutions are simply combinations of exponentials with the exponent being either real or imaginary depending on whether N/ω is less than or greater than unity.

The solutions are also simple when the shear is constant and $N = 0$ (homogeneous medium). Then $u_0'' = 0$, and important solutions are $\exp(\pm mz)$, $\cosh mz$, $\sinh mz$, and combinations thereof, as needed to satisfy prescribed boundary conditions. If the vertical velocity varies as the cosh or the exponential, the streamline pattern is essentially the cat's eye of Kelvin (1880) near $z = 0$. However, if the solution in the neighbourhood of $z = 0$ goes as $\sinh mz$, the streamline pattern is the cockeyed cat's eye of G. I. Taylor (1931) shown in Fig. 2 (upper frame) along with the cat's eye pattern (lower frame). In order to satisfy the boundary condition that $W = 0$ at $z = \pm\infty$, the layer in which W varies as $\sinh mz$ must be bounded by layers in which W is evanescent. The bounding layers must therefore vary as $\exp(\pm\gamma z)$, where $\gamma = m[1 - (N/\omega)^2]^{1/2}$, if they are shearless and statically stable, or as $\exp(\pm mz)$ if they are neutral. This model is shown in the top frame of Figure 1.

Models in which the mean wind profile varies as $u_0(z) = \Delta u_\infty \tanh(z/\Delta H)$ have been analyzed by Drazin (1958), Holmboe (1960), and Garcia (1961). In the Holmboe model, the mean density distribution is represented by $\rho_0(z) = \rho_s \exp S\Delta H[\tanh(z/\Delta H)]$ where ρ_s is the density at the height $z = 0$ and S is the value of $\rho_0^{-1} d\rho_0/dz$ at $z = 0$. This model is shown in the bottom frame of Figure 1. If we wish to apply our model to the atmosphere, we use the profile of potential temperature instead of density. Then $S = -\theta_0^{-1} d\theta_0/dz$. The eigenfunction, W, for this model expressed in terms of $W_{\Delta H}$, is given (for $C = 0$) by

$$W(z) = (1.312)(0.851)^{-\alpha} W_{\Delta H}[\text{sech}(z/\Delta H)]^\alpha[\tanh z/\Delta H]^{1-\alpha} \qquad (13)$$

where $\alpha = m\Delta H$. The streamline patterns in the neighbourhood of $z = 0$ have
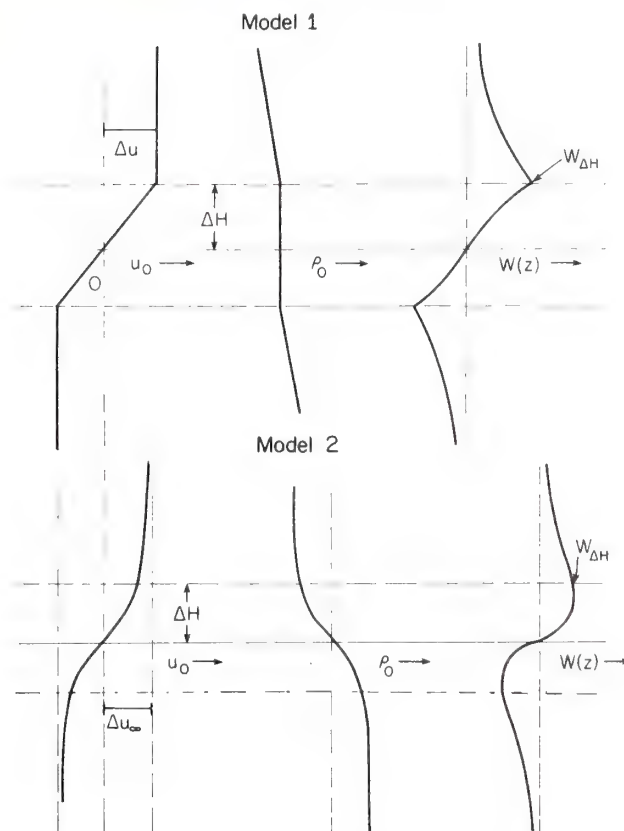
Model 1

Model 2

Fig. 1.   Model with statically neutral shear layer imbedded in stable medium (upper); model with hyperbolic tangent wind profile and some static stability (lower). Left and middle frames are ambient wind and density profiles, respectively. Right frame shows the resulting vertical velocity perturbation. When a rigid boundary (the earth's surface) is inserted at the center of the shear layer, the upper model becomes our Model 1 and the lower our Model 2.
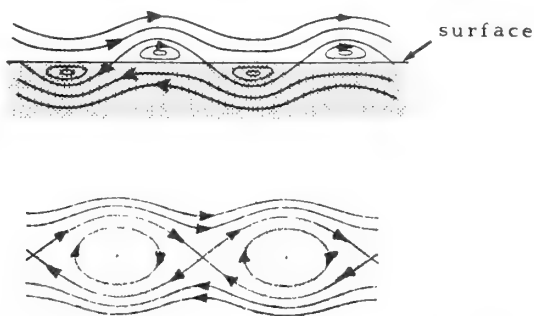
Fig. 2.   Streamlines in vertical planes containing a symmetrical shear layer in a homogeneous medium. The lower frame shows the Kelvin cat's eye pattern. The upper frame shows the cockeyed cat's eye of G. I. Taylor. When a rigid boundary is placed at the level streamline in the cockeyed cat's eye, the pattern is that of the streamlines in the two-dimensional case of Model 1 near the earth's surface. All vortices rotate in the same direction.

417

been plotted by Howard and Maslowe (1973) and are reproduced in Figure 3 for various α. When $\alpha = 1$ (frame a) the pattern is essentially that of the cat's eye and when $\alpha = 0$ (frame e) it resembles the cockeyed cat's eye.

Eliminating p between Equations (1) and (2) and then using the continuity Equation (4) in its incompressible form, i.e., $ikU + ilV + \partial W/\partial z = 0$ since $c^2 \gg C^2$, the relationship between $U(z)$ and $W(z)$ is found to be

$$U(z) = -\frac{k}{m^2}\left(\frac{\partial}{\partial z} - \beta \frac{k}{\omega}\frac{l^2}{k^2}\right)W(z). \tag{14}$$

Similarly,

$$V(z) = -\frac{l}{m^2}\left(\frac{\partial}{\partial z} + \beta \frac{k}{\omega}\right)W(z) \tag{15}$$

and

$$P(z) = -\rho_s \frac{\omega}{m^2}\left(\frac{\partial}{\partial z} + \beta \frac{k}{\omega}\right)W(z), \tag{16}$$

where β is the shear du_0/dz.

3. Boundary Conditions

The model with a homogeneous shear layer is shown in the top frame of Figure 1. We will call it Model 1 and call that shown in the bottom frame Model 2.
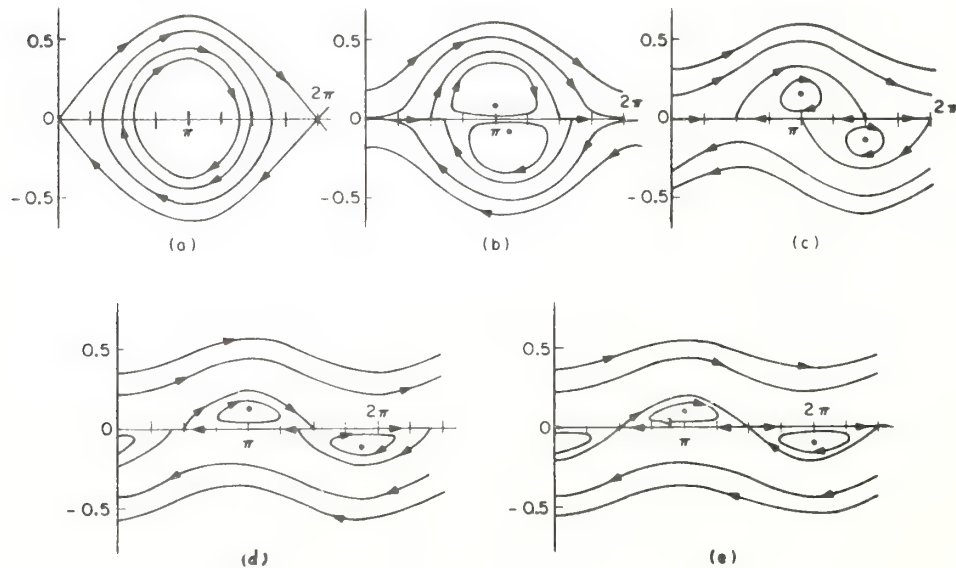
Fig. 3. Streamline patterns in vertical planes of Model 2. Frame (a) shows the case of $\alpha = 1$ (essentially the cat's eye) and frame (e) shows the case of $\alpha = 0$ (much like the cockeyed cat's eye). For purposes of calculation we choose $\alpha = 0.5$ in our Model 2. (Figure taken from Howard and Maslowe, 1973).

Satisfying the dynamic and kinematic boundary conditions at the interfaces between layers in Model 1 yields the eigenvalue relationship between C, α, N, and β. However, it is not our purpose here to examine the dynamics or stability of models but rather to describe their kinematics for comparison with flow patterns observed with a dual-Doppler radar system.

The kinematic conditions require that W must vanish at a level, rigid lower boundary and at infinity. In Figure 2 we notice that one of the two zero streamlines enclosing the vortices is horizontal at $z = 0$ in the cockeyed cat's eye pattern. Therefore, in contrast with the cat's eye, the vertical velocity is zero at $z = 0$ and we may put a rigid boundary there. Satisfactory solutions for Model 1, where a rigid lower boundary exists at $z = 0$, are

$$W(z) = W_{\Delta H} \frac{\sinh\left(\alpha \frac{z}{\Delta H}\right)}{\sinh \alpha}, \quad \frac{z}{\Delta H} \leqslant 1 \tag{17a}$$

$$W(z) = W_{\Delta H} \exp\left[-\alpha_0\left(\frac{z}{\Delta H} - 1\right)\right], \quad \frac{z}{\Delta H} > 1. \tag{17b}$$

(The eigenvalue equation for this model is $(\operatorname{ctnh} 2\alpha + \alpha_0/\alpha)\xi^2 - \xi - (\alpha^2 - \alpha + \alpha\alpha_0) = 0$ where $\xi = C/\Delta u$ and $\alpha_0 = \alpha(1 - N^2/\omega^2)^{1/2}$. Since the shear layer is surface-based (at $z = 0$), there is no inflection point in the wind profile and therefore no domain of dynamic instability.) We will assume that Model 1, with its adiabatic lower layer, approximately represents a dry, sheared convective boundary layer.

The streamlines for Model 2 have been plotted for several values of α by Howard and Maslowe (1973) using Equation (13) and they are shown in Figure 3. When $\alpha = 1$ (frame a), we see that the pattern is essentially that of the cat's eye, and when $\alpha = 0$, it is that of the cockeyed cat's eye. When $\alpha = 1$, $W(z) \propto [\cosh (z/\Delta H)]^{-1}$ so the kinematic conditions are satisfied at $z = \infty$ but not at $z = 0$. When $\alpha = 0$, $W(z) \propto \tanh (z/\Delta H)$ so the kinematic conditions are satisfied at $z = 0$ but not at $z = \infty$. For other values of α, both conditions are satisfied and in what follows we will choose $\alpha = 0.5$, which means that the horizontal scale is 17.8 ΔH. The features observed by the radars had horizontal scales of about 5 ΔH, but we chose a smaller ratio of vertical to horizontal scale in the model so that the linearizing assumptions in the theory would be more valid. Then from Equation (13),

$$W(z) = 1.422\, W_{\Delta H}[\cosh (\alpha z/\Delta H)]^{-1}[\sinh \alpha z/\Delta H]^{1/2}. \tag{18}$$

Equation (18) is not exactly a solution of (12) unless $C = 0$. However, it is a convenient approximation to use for W, and comparison with Model 1 will allow us to judge how sensitive the flow patterns are to the precise form of the assumed profiles.

Insertion of Equations (17) or (18) into Equations (14) or (15) essentially completes our problem of relating the velocity components within these inviscid shear models.

For Model 1, $\omega/\beta = (\alpha k/m)(\xi - z/\Delta H)$ where $\xi \equiv C/\Delta u$. For Model 2, $\omega/\beta_0 = (\alpha k/m)[\tanh \xi - \tanh (z/\Delta H)]$ where $\beta_0 = \Delta u_\infty/\Delta H$. At the critical level, $z/\Delta H = \xi$, so ω passes theorugh zero there and changes sign. Therefore $U(z)$, $V(z)$ and the vertical component of vorticity become infinite (Gossard and Moninger, 1975). This is a result of our neglect of viscosity. Figure 4 shows the velocity fields in four horizontal planes, the middle two of which are on opposite sides of the critical level at $z_c/\Delta H = 0.5$. The left column of frames shows the inviscid model. Note the opposite direction of rotation of the vortices below and above the critical level. The conditions assumed are given in the caption.

3. The Flow Fields with Viscosity

The reason the horizontal velocity components become infinite at the critical level is, of course, because we have neglected viscosity. In general, it is difficult to take viscosity and thermal conductivity into account. If both viscosity and thermal conductivity are included, Equation (12) becomes of 6th order and simple solutions exist for only a few special cases. For example when shear is included the coefficients cannot be treated as constant. It is therefore necessary to resort to computers to obtain solutions for realistic models with viscosity included.

However, some of the effects of viscosity and thermal conductivity can be represented qualitatively by assuming that the two quantities are constant and equal, and simply redefining the operator D/Dt in Equations (1) through (5) to include the $\nu\nabla^2$ operator through which viscosity enters the basic equations. Then

$$D/Dt = -i\omega = \frac{\partial}{\partial t} + u_0(z)\frac{\partial}{\partial x} - \nu\nabla^2.$$

For some eigenfunctions, viscosity is rigorously represented by this artifice, but in general it should be considered to provide only qualitative information about the effect of viscosity. It does incorporate some of the important viscous effects into the model and allows us to deal with a differential equation of only 2nd order. There is historical precedent for this kind of approximation, sometimes called the Darcy approximation (e.g., Kuo, 1963), but its main justification in this paper is that viscosity will be important only in a height region in the vicinity of the critical level, since we neglect the surface friction layer. Our goal is only to derive the kinematic structure of the disturbances; in this paper we ignore the dynamics and the flux properties of models.

For Model 1, letting $L' = \nu\nabla^2/\beta$,

$$\frac{\omega}{\beta} = \frac{k}{m}\alpha\left(\xi - \frac{z}{\Delta H}\right) - iL';$$
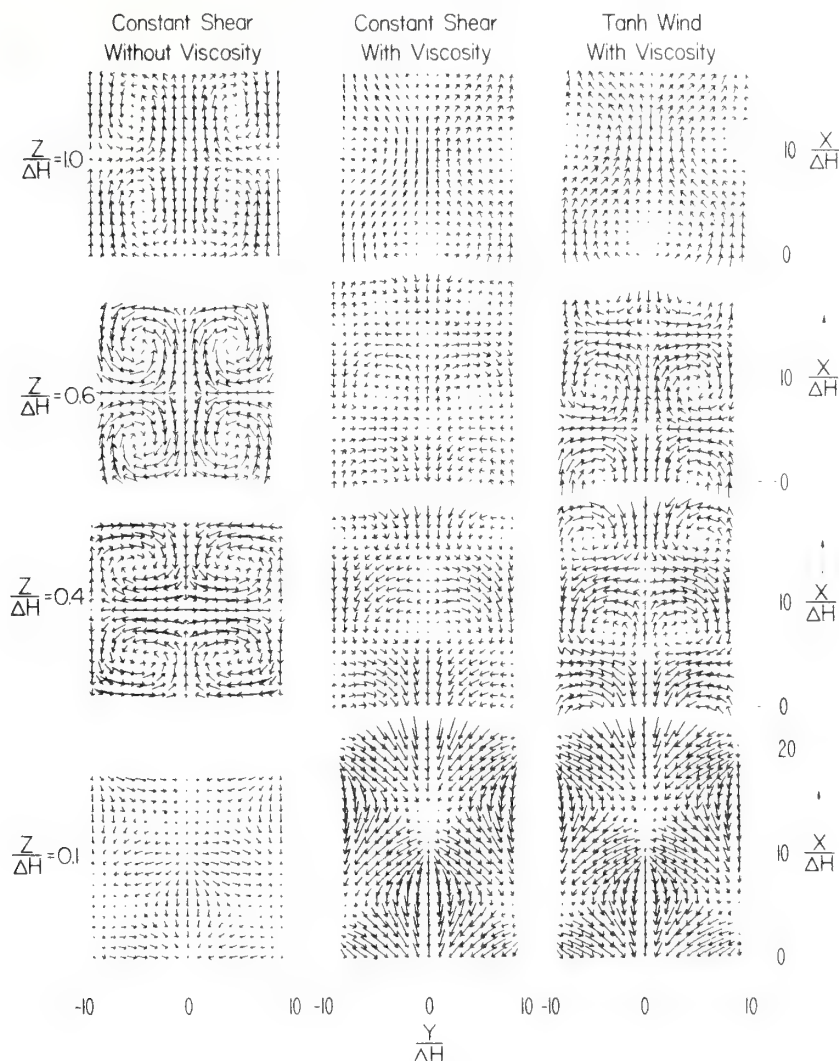
Fig. 4. Flow patterns in four horizontal planes through the shear layer. Set of patterns at the left shows Model 1 without viscosity. Middle set shows Model 1 with viscosity. Set of patterns at the right shows Model 2 with viscosity. The patterns look very similar in the two models but differ significantly from the inviscid case. Note especially the reversal in sign of the vorticity as it passes through $\pm\infty$ at the critical level. In the calculations it was assumed that $k = l$, $\alpha = 0.5$, $z_c/\Delta H = 0.5$, $L = L' = -0.14$, $\Delta u_\infty = 0.5 \text{ m s}^{-1}$, $W_{\Delta H} = 0.25 \text{ m s}^{-1}$ (Model 1) and $W_{\Delta H} = 0.176 \text{ m s}^{-1}$ (Model 2). Length of arrow indicates relative speed, and orientation indicates direction. The scale size of the arrows in the pattern at $0.6 \, \Delta H$ in the left set of patterns is one-half that used at the other levels. The position of the wind calculated from the model is at the head of the arrow.

and for Model 2, letting $L = \nu\nabla^2/\beta_0$,

$$\frac{\omega}{\beta_0} = \frac{k}{m}\,\alpha\left(\xi_0 - \tanh\frac{z}{\Delta H}\right) - iL$$

where $\xi = C/\Delta u$ and $\xi_0 = C/\Delta u_\infty$. Introducing an undisturbed environmental wind $u_0(z)$ to which the perturbations given by Equations (14) and (15) are added, we define the total perturbation of the x component u_T as

$$u_T = u_0(z) - \frac{k}{2m}\left[\frac{1}{m}\frac{\partial W(z)}{\partial z} - \frac{l^2}{k^2}(A + iB)\right]$$
$$\times (-i)[\exp i(kx + ly - \sigma t) + \exp i(kx - ly - \sigma t)].$$

The y component of the velocity perturbation and the vorticity are given by

$$V = -\frac{l}{2m}\left[\frac{1}{m}\frac{\partial W(z)}{\partial z} + (A + iB)\right]$$
$$\times (-i)[\exp i(kx + ly - \sigma t) - \exp i(kx - ly - \sigma t)]$$

$$(\text{vor})_H \equiv \frac{\partial V}{\partial x} - \frac{\partial u_T}{\partial y} = \frac{l}{2k\Delta H}(A + iB)$$
$$\times (-i)[\exp i(kx + ly - \sigma t) - \exp i(kx - ly - \sigma t)]$$

where it is understood that the real part is to be taken.

For Model 1,

$$\frac{\partial W}{\partial z} = \left(\frac{\alpha}{\Delta H}\right)\frac{W_{\Delta H}}{\sinh \alpha}\cosh\left(\alpha\frac{z}{\Delta H}\right), \quad z < \Delta H$$

$$\frac{\partial W}{\partial z} = -\left(\frac{\alpha_0}{\Delta H}\right)W_{\Delta H}\exp\left[-\alpha_0\left(\frac{z}{\Delta H} - 1\right)\right], \quad z > \Delta H$$

$$A = \frac{1}{\alpha}\frac{\left(\xi - \dfrac{z}{\Delta H}\right)W(z)}{\left(\xi - \dfrac{z}{\Delta H}\right)^2 + \left(\dfrac{m}{k}\dfrac{L'}{\alpha}\right)^2},$$

$$B = \frac{1}{\alpha}\frac{\dfrac{m}{k}\dfrac{L'}{\alpha}W(z)}{\left(\xi - \dfrac{z}{\Delta H}\right)^2 + \left(\dfrac{m}{k}\dfrac{L'}{\alpha}\right)^2},$$

$$u_0(z) = \beta z = \Delta u\left(\frac{z}{\Delta H}\right).$$

The W, herein assumed to be given by Equation (17) or (18), will really be complex in general. Writing $A + iB$ in exponential form, we recognize that the introduction of viscosity has introduced a phase change in the x direction. From Equations (14) and (15), we see that A and B are zero when β is zero and that the terms in A and B are also zero for two-dimensional perturbations ($l \equiv 0$).

For Model 2,

$$\frac{\partial W}{\partial z} = (1.312)(0.851)^{\alpha} \frac{W_{\Delta H}}{\Delta H} \left\{ (1-\alpha) \left[\operatorname{sech} \left(\frac{z}{\Delta H} \right) \right]^{2+\alpha} \left[\tanh \left(\frac{z}{\Delta H} \right) \right]^{-\alpha} \right.$$
$$\left. - \alpha \left[\operatorname{sech} \left(\frac{z}{\Delta H} \right) \right]^{\alpha} \left[\tanh \left(\frac{z}{\Delta H} \right) \right]^{2-\alpha} \right\}$$

$$A = \left(\frac{1}{\alpha} \right) \frac{\left[\xi - \tanh \left(\frac{z}{\Delta H} \right) \right] \left[\operatorname{sech} \left(\frac{z}{\Delta H} \right) \right]^2 W(z)}{\left[\xi - \tanh \left(\frac{z}{\Delta H} \right) \right]^2 + \left(\frac{m}{k} \frac{L}{\alpha} \right)^2}$$

$$B = \left(\frac{1}{\alpha} \right) \frac{\frac{m}{k} \frac{L}{\alpha} \left[\operatorname{sech} \left(\frac{z}{\Delta H} \right) \right]^2 W(z)}{\left[\xi - \tanh \left(\frac{z}{\Delta H} \right) \right]^2 + \left(\frac{m}{k} \frac{L}{\alpha} \right)^2}$$

$$u_0(z) = \Delta u_\infty \tanh \left(\frac{z}{\Delta H} \right).$$

Wind field patterns calculated from the models are shown in Figures 4–6. Arrowheads have been put on the arrows manually. The length of the line segment represents speed and its orientation indicates direction. The line segments are arrows flying with the wind.

In Figure 4 the wind fields for the two models are shown projected onto horizontal planes at four heights through the shear layer. For these plots, we arbitrarily chose $L' = L = -0.14$. This was approximately the minimum value giving smooth behavior of the wind patterns across the critical level. Choosing $\alpha = 0.5$, $\Delta u = 0.5$ m s^{-1}, $\Delta H = 1000$ m, and assuming $\nabla^2 \simeq m^2$ gives a value of $\nu \cong 300$ m^2 s^{-1} in contrast to the molecular value of $\sim 1.5 \times 10^{-5}$ m^2 s^{-1}. The wind fields of the models with viscosity are shown along with the corresponding wind fields from the inviscid case of the homogeneous shear-layer model (left column). We see that neither the horizontal velocity components nor the vorticity change sign or become infinite passing through the critical level when viscosity is included. There is a smooth transition from patterns dominated by divergence at the surface through patterns dominated by vorticity in the region of the critical level to patterns primarily again divergent aloft. The vorticity appears in the horizontal planes because the environmental vorticity vector in the y direction is "tilted" up and down periodically by the three-dimensionality of the model. In Figure 4, it was assumed that the critical level was at $0.5\Delta H$ for all models, and that the change in wind across ΔH was 0.5 m s^{-1}. $W_{\Delta H}$ was 0.25 m s^{-1} in Model 1 and 0.176 in Model 2 (i.e., $1.422 W_{\Delta H} = 0.25$ in Model 2).

Figure 5 shows the wind fields from Model 1 in vertical planes parallel to the mean wind at $y/\Delta H = 0$ for three shear conditions. When $\Delta u = 0$, the flow is a
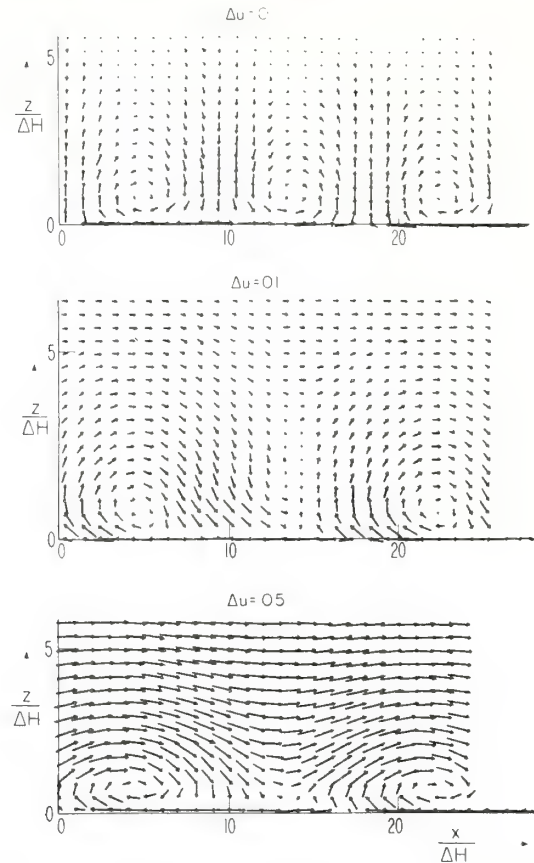
Fig. 5.   Velocity vectors projected onto planes parallel to the shear for three values of Δu in Model 1. For $\Delta u = 0.05 \text{ m s}^{-1}$, the counter-clockwise vortex is barely closed. It is assumed that $k = l$, $\alpha = 0.5$, $z_c/\Delta H = 0.5$, $L = -0.2$, $W_{\Delta H} = 0.25 \text{ m s}^{-1}$ and $y/\Delta H = 0$.

pattern of adjacent counter-rotating vortices with vertical up- and downdrafts. However, when $\Delta u = 0.1 \text{ m s}^{-1}$, the vortex rolling against the shear has disappeared, leaving a non-symmetrical pattern of tilted up- and downdrafts, and vortices rotating in the downwind direction. When the shear is further increased to $\Delta u = 0.5 \text{ m s}^{-1}$, the pattern is almost symmetrical and is essentially that of the cockeyed cat's eye with the lower half removed.

Figure 6 shows the wind fields projected onto vertical planes perpendicular to the direction of the mean wind. The top frame shows the fields at $x/\Delta H = 0$ and the bottom at $x/\Delta H = 3$. As expected, there is a simple symmetry in the planes perpendicular to the shear; the perturbation amplitude simply decreases co-sinusoidally on either side of $x/\Delta H = 0$.

5. The Effect of Wind Shear

The mean wind shear has an important effect on the kind of flow patterns found in the model.
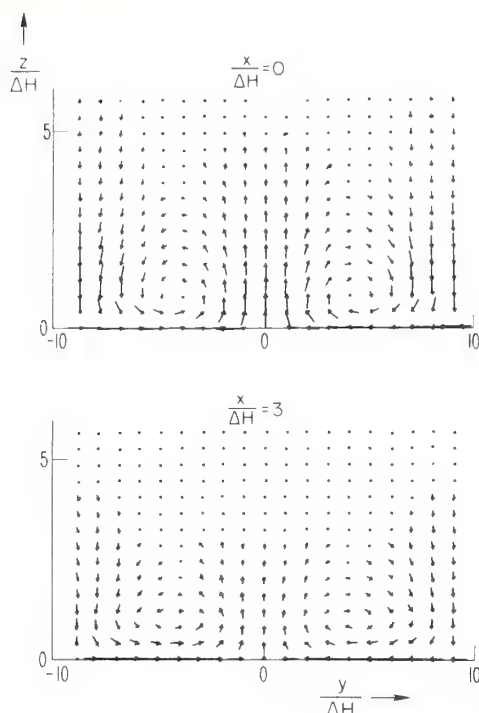
Fig. 6.   Flow patterns in planes perpendicular to the direction of shear at $x/\Delta H = 0$ (upper) and $x/\Delta H = 3$ (lower). Assumptions otherwise the same as in the caption of Fig. 5. Pattern of counter-rotating adjacent vortices is independent of shear.

Figure 7 shows velocity patterns in a horizontal plane, as shear is increased from zero to a value of $0.005 \, s^{-1}$. To facilitate comparison with real observations to follow, this figure has been plotted in terms of actual shear, β, rather than Δu. In doing this, we have made use of the observed fact that the chaff dispersed through a depth of about a kilometer and have therefore chosen 1 km as the depth of the adiabatic layer. Patterns are plotted for a height of 600 m; we have assumed the critical level to be at 250 m and have set $l = k$.

With no shear, the patterns represent simple convergence/divergence as expected. With some small shear, the patterns are more or less evenly spaced, counter-rotating vortices. As the shear is increased further, adjacent vortices crowd closer together, pairs become more widely separated and the pattern becomes much like the flow about an obstacle with each vortex pair the obstacle.

6. Comparison with Observation

In this section we present dual-Doppler radar observations of flow patterns in the boundary layer on a convective afternoon using chaff as the air-motion tracer. The data were collected at about 1230 MDT on 10 August 1972 near Haswell in

southeast Colorado. Unfortunately, there was no RAWINSONDE until about five hours later, so the mean wind data from the balloon sounding are of little value in determining shear conditions. The spatially-averaged Doppler radar wind observations suggest a wind profile with very small shear (0.0005 s^{-1}), which is in accord with the kind of flow patterns observed. We have compared the radar observations with a model in which $\Delta u = 0.05 \text{ m s}^{-1}$, so that $\beta = 0.00005 \text{ s}^{-1}$. A larger value completely suppresses the counter-clockwise roll in the vertical plane
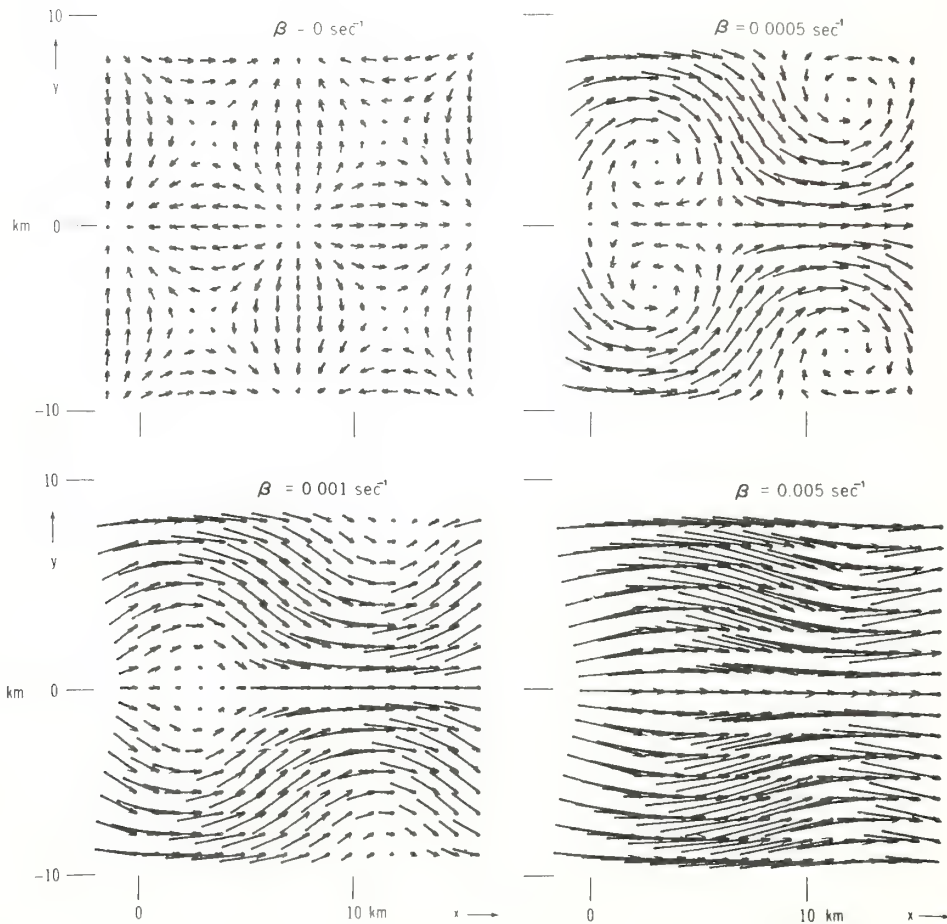
Fig. 7. The effect of environmental shear on the flow pattern in a horizontal plane near the middle of a shear layer (Model 1). When there is no shear, the pattern is simple convergence and divergence. With some very small shear, adjacent counter-rotating vortices appear. With stronger shear at a given level, the flow more nearly resembles streaming about an obstacle.

in the direction of shear, and there is some evidence for such rolls as seen in Figure 9, middle frames. The observed mean shear was small compared with the height fluctuations in wind velocity resulting from the disturbance field, so it can be considered only a crude approximation of the environmental wind. In accordance with the observations, we assumed, for the plots from the model, that the cells were horizontally symmetrical; thus $k/m = l/m = 0.707$. We assumed $\alpha = 0.5$ so that the horizontal scale of the disturbance is $17.8 \Delta H$. The chaff spread through a depth of about a kilometer, so it is reasonable to choose a value of $\Delta H = 1$ km, which gives a horizontal scale of about 18 km. The observed scale is about 5 km as seen in Figure 8, but we chose to keep the ratio of the perturbation magnitude to horizontal scale size small in accord with the small perturbation
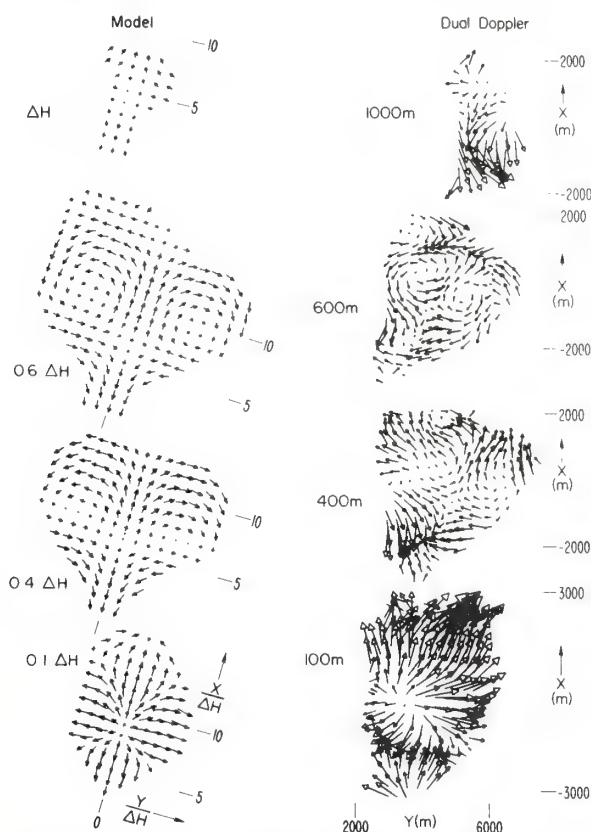
Fig. 8. Calculated velocity vectors projected onto four horizontal planes (left), compared with velocity vectors measured by dual-Doppler radars in clear-air convection (right) using chaff. In the model calculations, we chose the same assumptions as in the caption of Fig. 4 except that a very weak shear ($\beta = 0.00005$ s^{-1}) was assumed. The x axis of the model has been rotated clockwise to achieve a best fit with the observations. Only that portion of the calculated pattern is shown which corresponds to the portion of the cells seen by the radars, i.e., the chaff cloud. The position of the observed wind is at the tail of the arrow, as plotted in the display from the CDC 3800 computer, in contrast with the wind vectors calculated from the model, whose position is indicated by the arrowhead. The length of the arrows on the right-hand x scale corresponds to a measured wind speed of 1 m s^{-1}.

approximation used in linearizing the basic Equations (1) to (5). We assumed $W_{\Delta H} = 0.176$ m s^{-1} and $L = -0.14$ as explained in the description of Figure 4.

The plots of the dual-Doppler data were made from the CRT display of a large computer and the tail of the arrow indicates position. Plots for the model were made from a desk computer and xy plotter, and the head of the arrow indicates position. In all cases the volume-averaged wind has been subtracted from the total wind, so the residual winds are shown in the plots.

Figure 8 compares flow patterns in a series of horizontal planes in Model 2 with patterns observed by dual-Doppler radar on a convective afternoon when chaff was injected into the atmosphere by an aircraft flying a grid pattern at a height of 1 km. The data are processed in a coordinate system in which the x and y directions are chosen parallel and perpendicular, respectively, to the baseline between the radars. In Figure 8 we have tilted the patterns of the model slightly clockwise to achieve a better fit with the patterns seen by the radar in its coordinate system. The similarities between the patterns in the model and those observed by radar are unmistakable. Since the model assumes temporal stationarity and horizontal homogeneity of the environment, the patterns from the model repeat themselves indefinitely in the horizontal plane. Those parts of the model patterns are displayed that most closely coincide with the parts of the pattern revealed by the chaff. The chaff was injected in the upper region of the boundary layer, so that the chaff flowed toward and into the downdraft. Therefore it is the downdraft portion of the convection cell that is mainly revealed to the radars as shown by the radar winds in the vertical planes in Figure 9.

Figure 9 shows observed flow patterns in vertical planes parallel to the radar baseline for the same case as Figure 8 and compares them with flow patterns in the model for various conditions of wind shear and critical level height. It demonstrates that most patterns observed by the radars can be reproduced from the model with only minor changes in environmental parameters. In the model, the wind speed increases with height and the shear is directed toward the right in the figure. In the top two frames, the critical level is chosen to be at $0.5\,\Delta H$. When $\Delta u = 0.1$ m s^{-1}, the counterclockwise vortex of the shearless case, seen in the top frame of Fig. 5, has disappeared, and only clockwise rotating vortices remain. An example from the radar observations is shown to the right of the model winds for comparison. When $\Delta u = 0.05$ m s^{-1}, the counterclockwise vortex is barely closed. A similar case from the radar wind measurements is also shown. Finally, the bottom frame shows the case of larger shear ($\Delta u = 0.5$ m s^{-1}) and higher critical level ($z_c = 0.8\,\Delta H$). A col is now seen between the rotating vortices and this feature can also be sometimes found in the radar wind fields as shown at the bottom right of Figure 9.

Figure 10 shows the model flow pattern in a plane perpendicular to the mean shear, and also the observed winds in a plane perpendicular to the radar baseline. The observed patterns are less clear in this set of planes and the vortex motions are not so evident. The maximum height of the observations slopes upward away
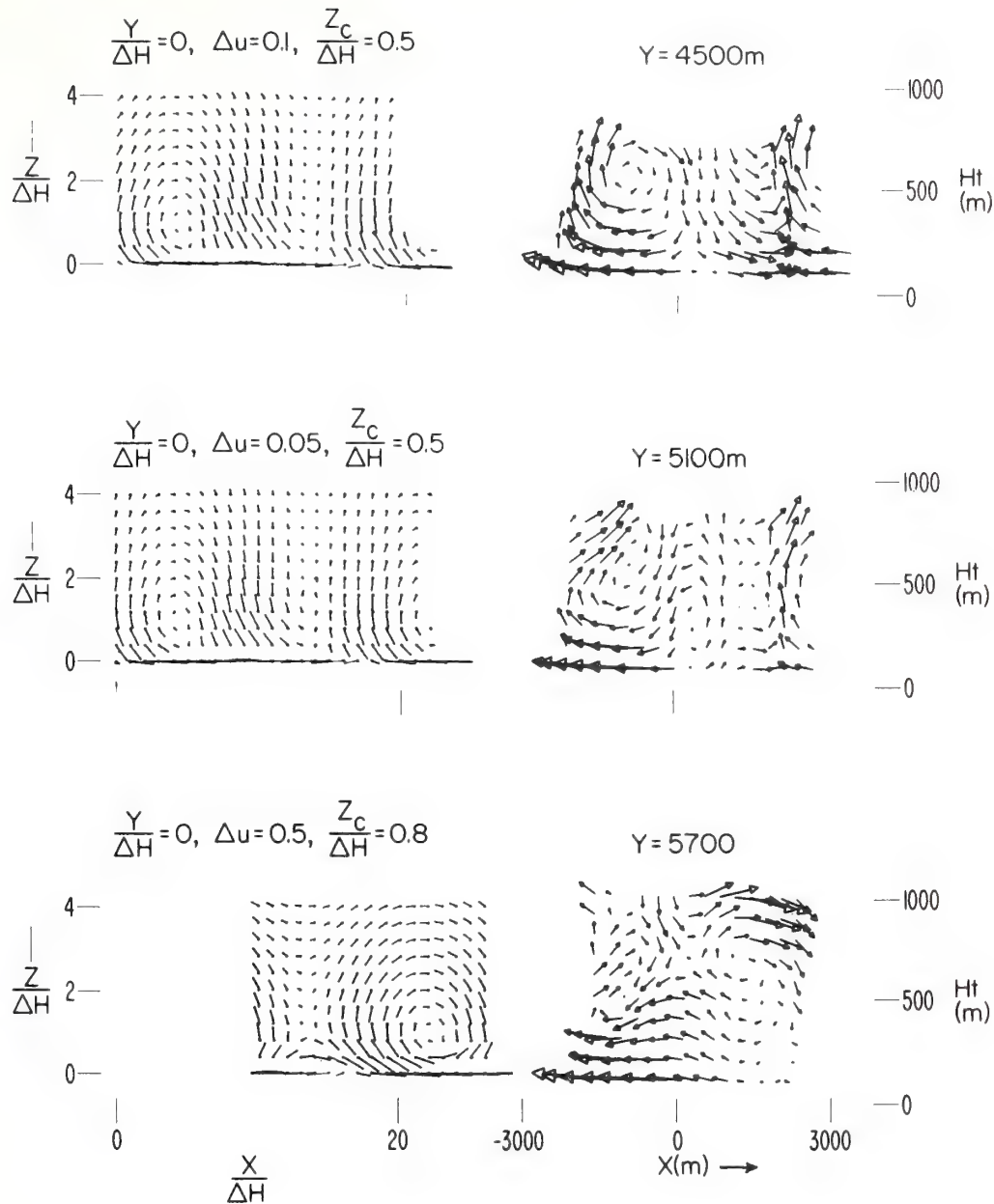
Fig. 9. Calculated velocity vectors (left) projected onto vertical planes parallel to the shear. Several values of Δu and $z_c/\Delta H$ are chosen to compare with various features in the dual-Doppler observations (right) of winds in planes parallel to the baseline. In the top and middle frames, we assumed $z_c/\Delta H = 0.5$, but in the bottom frame, we chose $z_c/\Delta H = 0.8$ to emphasize the col between the vortices. Otherwise, assumptions are as given in the caption of Fig. 5. Only that portion of the model winds is shown which corresponds to the portion of the cells seen by the radars, i.e., the chaff cloud. The length of the arrow on the x scale corresponds to a measured wind speed of 1 m s^{-1}.
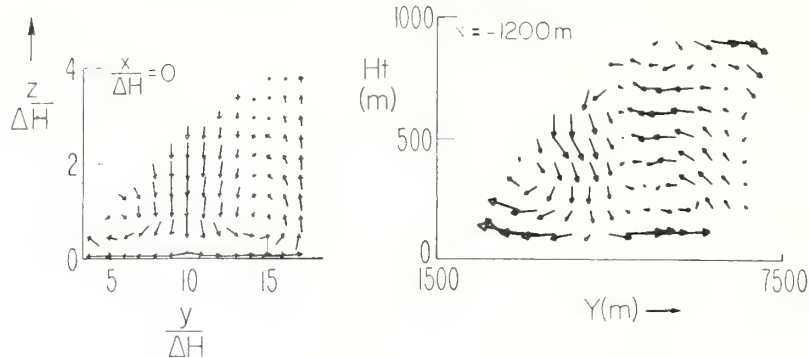
Fig. 10.   Calculated velocity vectors projected onto a plane perpendicular to the direction of shear. The winds observed by dual-Doppler radars in a plane perpendicular to the baseline are shown for comparison (right). The upper limit of the observed winds slopes upward toward the right at the tilt angle of the highest co-plane scanned by the radars. Assumptions as given in captions of Figs. 5 and 6. The length of the arrow on the y scale corresponds to a measured wind of 1 m s^{-1}.

from the radar baseline at an angle corresponding to the tilt of the highest angle co-plane scanned by the radars.

7. Results and Conclusions

We have compared two simple shear models of convection in the boundary layer with observations made with a dual-Doppler radar system. We first considered the models to be inviscid; then we added viscosity in a crude way.

The viscous models simulate some of the observed patterns very satisfactorily, especially the transition from a pattern dominated by simple horizontal divergence near the surface to one dominated by vorticity in horizontal planes near the middle levels. The models predict counter-rotating vortices in horizontal planes and in vertical planes perpendicular to the shear vector. They also predict counter-rotating adjacent vortices in vertical planes parallel to the shear vector when the wind shear is absent or very weak, but they predict adjacent vortices rotating in the same direction when the vertical shear is significant.

We conclude that some (very small) shear in the environmental wind is necessary to explain the observed flow patterns, but that the patterns are relatively insensitive to the exact shape of the mean shear profile. The effects of viscosity on the kinematics are important, expecially near the critical level.

8. Acknowledgment

We wish to thank Drs. F. Caracena and M. LeMone for their careful reading and criticism of the manuscript.

References

Drazin, P. G.: 1958, The stability of a shear layer in an unbounded heterogeneous inviscid fluid. *J. Fluid Mech.* **4,** 214–224.

Frisch, A. S., Miller, L. J. and Strauch, R. G.: 1974, Three-dimensional air motion measured in snow. *Geophys. Res. Letters* **1,** 86–89.

Frisch, A. S., Chadwick, R. B., Moninger, W. R., and Young, J. M.: 1976, Observations of boundary-layer convection cells measured by dual-Doppler radar and echosonde, and by microbarograph array. *Boundary-Layer Meteorol.* **10,** 55–68.

Garcia, R. V., 1961. Unpublished lecture, Univ. California, Los Angeles.

Gossard, E. E. and Hooke, W. H.: 1975, *Waves in the Atmosphere*, Elsevier, Amsterdam, 456 pp.

Gossard, E. E. and Moninger, W. R.: 1975, The influence of a capping inversion on the dynamic instability of a convective boundary layer model with shear. *J. Atmos. Sci.* **32,** 2111–2124.

Holmboe, J.: 1960, Unpublished lecture notes. (See Miles, 1963).

Howard, L. N. and Maslowe, S. A.: 1973, Stability of stratified shear flows, *Boundary-Layer Meteorol,* **4,** 511–523.

Kelvin, Lord,: 1880, On disturbing infinity in Lord Rayleigh's solution for waves in a plane vortex stratum. *Nature* **XXIII,** 45–46.

Kropfli, R. A. and Miller, L. J.: 1975, Kinematic structure and flux quantities in a convective storm from dual-Doppler radar observations. Submitted to *J. Atmos. Sci.*

Kuo, H. L.: 1963, Perturbations of plane Couette flow in stratified fluid and origin of cloud streets. *Phys. Fluids* **6,** 195–211.

Lhermitte, R. M. and Miller, L. J.: 1970, Doppler radar methodology for the observation of convective storms. *AMS 14th Radar Meteorol. Conf.,* 133–138.

Miller, L. J.: 1975, Internal airflow of a convective storm from dual-Doppler measurements. *Pure & Appl. Geophys.* **113,** 765–785.

Miller, L. J. and Strauch, R. G.: 1974, A dual Doppler radar method for the determination of wind velocities within precipitating weather systems, *Remote Sensing of Environ.* **3,** 219–235.

Taylor, G. I.: 1931, Effect of variation in density on the stability of superposed streams of fluid. *Proc. Roy. Soc. Lond.* **A132,** 499–523.

Turbulence Structure in the Convective Boundary Layer

J. C. Kaimal,[1] J. C. Wyngaard,[2] D. A. Haugen,[1] O. R. Coté and Y. Izumi

Air Force Geophysics Laboratory, Hanscom AFB, Mass. 01731

S. J. Caughey and C. J. Readings[3]

Meteorological Research Unit, RAF Cardington, Bedford, England

(Manuscript received 23 March 1976, in revised form 16 July 1976)

ABSTRACT

Results from a boundary layer experiment conducted over a flat site in northwestern Minnesota are discussed. Wind and temperature fluctuations near the ground were measured with AFCRL's fast-response instrumentation on a 32 m tower. Measurements between 32 m and the inversion base z_i were made with MRU probes attached at five different heights to the tethering cable of a 1300 m³ kite balloon. The daytime convective boundary layer appears to be well-mixed with evidence of significant heat and momentum entrainment through the capping inversion.

The spectra of velocity components are generalized within the framework of mixed-layer similarity. The characteristic wavelength for w increases linearly with height up to $z = 0.1z_i$ following free convection prediction, but approaches a limiting value of $1.5z_i$ in the upper half of the boundary layer. The characteristic wavelengths for u and v are maintained at approximately $1.5z_i$ down to heights very close to the ground. This limiting wavelength corresponds to the length scale of large convective elements which extend to the top of the boundary layer.

The behavior of the temperature specra above $0.1z_i$ cannot be generalized in the same manner. Below that height the θ spectra follow behavior observed in the surface layer; $z = 0.1z_i$ is also the upper limit for the free convection predictions of the w and θ variances.

The high-order moments and the structure parameters reveal the strong influence of entrainment at heights above $0.5z_i$.

1. Introduction

An experiment to investigate the structure of turbulence in the atmospheric boundary layer was conducted in 1973 by members of the Air Force Cambridge Research Laboratories (AFCRL), Bedford, Mass., the Meteorological Research Unit (MRU), Cardington, Bedford, England, and the Air Weather Service, Tinker Air Force Base, Okla. The experiment was carried out over a flat, sparsely populated section of northwestern Minnesota, 80 km south of the Canadian border.

This joint experiment was the culmination of nearly four years of preparation following the 1968 Kansas surface layer experiment (Haugen *et al.*, 1971). The Kansas experiment provided a comprehensive picture of turbulence structure in the surface layer, but it also

indicated a clear need for similar data from greater heights. Turbulence in the surface layer appeared to be strongly influenced by scales of motion large enough to encompass the whole boundary layer. By the late 1960's scientists at MRU had developed turbulence probes which could be attached to the tethering cable of large, captive balloons (Readings and Butler, 1972) and had gained considerable experience gathering data to heights of the order of 1 km. It appeared that such a technique could easily be integrated with the instrumentation and data handling capability developed at AFCRL for tower-based measurements.

Before any full-scale experiment could be mounted it was necessary to establish that the two techniques were compatible. Experiments were conducted to determine whether differences in sensor design, frequency response, data reduction techniques and the movement of the MRU probe as it swayed with the balloon cable produced significant differences in the observations. The first comparison test, performed at Bedford, Mass., in 1969, showed excellent agreement in the means, variances and covariances of velocity components and temperature when the two sensors were mounted 2 m apart on a 16 m tower (Readings

---

[1] Present affiliation: Wave Propagation Laboratory, NOAA, Boulder, Colo. 80302.

[2] Present affiliation: Wave Propagation Laboratory, NOAA, Boulder, Colo. 80302 and Cooperative Institute for Research in Envrionmental Sciences, University of Colorado/NOAA, Boulder, Colo. 80309

[3] Present affiliation: Ministry of Defense, Whitehall, London, England.

and Butler, 1972). The second test, designed to isolate possible effects of cable movement on the measured statistics, was conducted in 1971 on a 370 m tower (Haugen *et al.*, 1975) at Eglin AFB, Fla. The AFCRL sonic anemometers were mounted on booms at 150 and 305 m, while the MRU probes were flown at the same heights on the tethering cable of a 1300 m³ kite balloon. The results showed that the mean and variance of the horizontal wind speed were overestimated (about 10% and 20%, respectively) by the balloon-borne probe, but the variances of the vertical wind component and temperature and the fluxes of momentum and heat compared well. Spectrum analysis of these data provided essential information on the distribution of probe movement error needed to correct velocity spectra obtained subsequently at the Minnesota site.

2. Experimental details

The tower and balloon-launch facilities for the Minnesota experiment were located on the southern edge of a flat uniform 1 mi² plot of land. At the time of this experiment most crops in the area had been harvested, so the fetch in the northerly direction was uniform in its roughness for about 10 km. Only differences in color that normally exist between freshly harvested, plowed and fallow areas remained as inhomogeneities in terrain cover. A description of the site with plot plan and aerial photographs of installations at the site can be found in a paper by Readings *et al.* (1974).

AFCRL's profile and turbulence sensors were mounted on a 32 m tower. The tethered balloon launch and mooring point was 90 m east-southeast of the tower. Two-axis sonic anemometers were used for measuring mean horizontal winds at 1, 2, 4, 8, 16 and 32 m. Quartz-crystal thermometers measured mean temperatures at 0.5 m in addition to the heights listed above. Wind component and temperature fluctuations were measured with three-axis sonic anemometers and fine platinum-wire thermometers at 4 and 32 m on the tower. Five MRU probes were used for the balloon-borne measurements. These were the same probes used in the comparison experiments except for a modification to measure azimuth wind direction. The heights at which they were flown varied from one observational period to another, depending on operating conditions. The maximum height range was 61 to 1219 m.

During periods of data gathering, the actual heights of the probes were measured periodically with a double theodolite system. Their motions were also monitored by tracking a rawinsonde attached to the balloon cable just above the top probe. Slow-rise rawinsonde ascents made every 2 h during observational periods by the Mobile Weather Squadron, Air Weather Serivce, provided information on wind and temperature fields above the instrumented heights. From these data we were able to determine the height of the lowest inversion base, the upper limit of the convective boundary layer and its variation as a function of time.

Data collection was restricted to periods when the wind was northerly. The sky was clear during the periods chosen for this study, with occasional patches of cirrus clouds visible around the horizon. As it happened, each period began during convective conditions, usually late morning or early afternoon. An observational period was terminated when either wind speed or direction became unfavorable or when turbulence at all levels vanished as often happened around midnight. The northerly winds occurred with high pressure systems moving over the site rapidly. Thus the period of consistent northerly winds seldom lasted more than 12 h. As a result, the data obtained are effectively restricted to the convective boundary layer.

All data recording was accomplished by the AFCRL computer-controlled data acquisition system (Kaimal *et al.*, 1966). The turbulence probes on the tower and the balloon cable were sampled 10 times per second; the wind and temperature profile sensors on the tower, once a second. Details of the experimental techniques and the data reduction procedures are reported by Izumi and Caughey (1976). Eleven 75 min periods of observations of the convective boundary layer provide the data base for the analyses described in this paper.

3. Description of data

The observational periods included in this study are listed in Table 1. They all fall within the time interval 1200–1800 CDT, when the height of the inversion base was roughly constant and the surface heat flux was directed upward. Listed in Table 1 are time periods for each run, the average values of the height of the lowest inversion base, the surface heat flux and other relevant boundary layer parameters. The reference heights for the five MRU probes are given in Table 2. The common averaging period for all data is 75 min. The fluctuation data are filtered with a high-pass, recursive digital filter to minimize long-term trends. The filter effectively attenuates frequencies below 0.001 Hz (12 dB per octave roll-off with −3 dB point at 0.001 Hz). A detailed discussion of data-reduction procedures is given by Izumi and Caughey (1976).

Computation of spectra and cospectra followed procedures used earlier in the analysis of the Kansas data (Kaimal *et al.*, 1972). The available bandwidth was covered in overlapping stages: the higher range (0.0025–5.0 Hz) by dividing each 75 min segment into shorter segments and averaging the spectral estimates over frequency bands, the lower range (0.0002–0.04 Hz) by block-averaging the original time series to reduce the number of points. The low-frequency ends of the spectra were later corrected for the attenuation caused by the high-pass filter.

TABLE 1. List of runs with significant boundary-layer parameters expressed in MKS units.

Run	Date	Period (CDT)	Q_0	u_*	$-L$	z_i	w_*	θ_*
2A1	10 Sept 73	1217–1332	0.196	0.45	41.7	1250	2.00	0.098
2A2	10 Sept 73	1332–1447	0.209	0.45	38.0	1615	2.23	0.094
3A1	11 Sept 73	1510–1625	0.186	0.37	24.0	2310	2.41	0.077
3A2	11 Sept 73	1625–1714	0.116	0.32	24.3	2300	2.06	0.056
5A1	15 Sept 73	1622–1737	0.069	0.18	7.1	1085	1.35	0.051
6A1	17 Sept 73	1401–1516	0.210	0.24	5.7	2095	2.43	0.086
6A2	17 Sept 73	1516–1631	0.162	0.23	6.4	2035	2.21	0.073
6B1	17 Sept 73	1652–1807	0.072	0.26	22.7	2360	1.77	0.041
7C1	19 Sept 73	1415–1530	0.221	0.28	8.8	1020	1.95	0.114
7C2	19 Sept 73	1530–1645	0.181	0.30	13.1	1140	1.89	0.096
7D1	19 Sept 73	1650–1805	0.099	0.25	13.5	1225	1.58	0.063

4. General characteristics of the boundary layer

The convective boundary layer is defined as that part of the atmosphere most directly affected by solar heating on the earth's surface. In mid-latitudes over land, this layer typically reaches a height of 1–2 km by midafternoon. Its upper limit is often delineated by a capping inversion. This layer exhibits a near-constant distribution of wind speed and potential temperature, obviously a consequence of the strong vertical mixing produced by convection. The name "mixed layer" is therefore used synonymously with the convective boundary layer in much of the literature on the subject.

The wind speed and temperature profiles of Fig. 1 are fairly typical of daytime convective conditions. Almost all the wind shear and all the potential temperature gradient in the boundary layer are confined to a very shallow region close to the ground. The sharp increase in wind speed across the capping inversion appears consistently in many daytime runs and has possible implications for momentum and heat transport in the upper regions of the boundary layer. It should be pointed out that the dashed portion of the curves is obtained from rawinsonde measurements and tends to be less precise than those from the balloon-borne measurements. Also, the rawinsonde data are obtained from discrete observations made every 2 hr, while the solid curves represent a 75 min average. However, the

strong winds observed above the inversion in successive rawinsonde ascents suggest a fairly persistent pattern of wind shear across the inversion in the early afternoon runs analyzed here.

The boundary layer over land may be idealized as a three-layer structure in terms of the parameters considered relevant to the turbulence in each.[4] Proceeding upward from the surface, we have:

1) *The surface layer* where wind shear plays a dominant role. Here Monin-Obukhov similarity applies and the controlling parameters are z, τ_0, Q_0 and g/T. The scaling velocity and temperature for this layer are, respectively,

$$u_* = (\tau_0/\rho)^{\frac{1}{2}}, \tag{1a}$$

$$T_* = -Q_0/u_*. \tag{1b}$$

Dimensionless groups formed with u_* and T_* become universal functions of z/L. The Kansas results with the exception of u and v statistics support this (Businger *et al.*, 1971; Wyngaard and Coté, 1971; Kaimal *et al.*,

TABLE 2. Reference heights (m) for the balloon-borne probes.

Run	Probe 1	Probe 2	Probe 3	Probe 4	Probe 5
2A1	61	305	610	914	1219
2A2	61	305	610	914	1219
3A1	61	152	305	457	610
3A2	61	152	305	457	610
5A1	61	152	305	457	610
6A1	152	305	610	914	1219
6A2	152	305	610	914	1219
6B1	152	305	610	914	1219
7C1	61	152	305	457	610
7C2	61	152	305	457	610
7D1	61	152	305	457	610
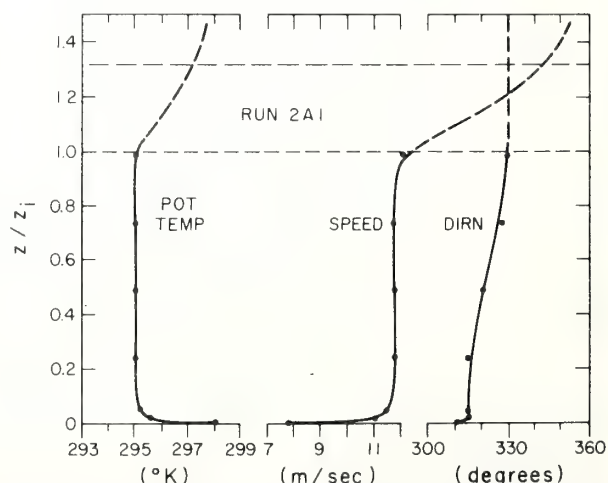
FIG. 1. Profiles of wind speed, wind direction and potential temperature for Run 2A1. The near-adiabatic lapse rate and the negligible mean wind shear in the mixed layer are typical for observational periods in this experiment.

[4] A list of symbols is given in an appendix.

1972; Busch, 1973). The shear layer is confined to a height range, $z < |L|$.

2) *The free convection layer* where τ_0 is no longer important but height z continues to be the significant length scale. The governing parameters reduce to three: z, Q_0 and g/T, which yield a scaling velocity u_f and a scaling temperature T_f given by

$$u_f = [Q_0 z(g/T)]^{\frac{1}{3}}, \qquad (2a)$$

$$T_f = Q_0/u_f. \qquad (2b)$$

Dimensionless groups formed with u_f and T_f should be constants according to the "local free-convection" predictions of Wyngaard *et al.* (1971a). The very unstable $(-z/L > 1)$ data from Kansas support these predictions for the most part. A definition of the upper limit for free convection scaling is one of the objectives of this analysis. Our data suggest an upper limit of approximately $0.1 z_i$ for this layer.

3) *The mixed layer* where the structure of turbulence is insensitive to z as well as τ_0. The thickness of the boundary layer, defined as the height of the lowest inversion base z_i, emerges as the controlling length scale, so that the scaling velocity and temperature for this layer become

$$w_* = [Q_0 z_i(g/T)]^{\frac{1}{3}}, \qquad (3a)$$

$$\theta_* = Q_0/w_*. \qquad (3b)$$

Within this region dimensionless groups formed with w_* and θ_* should be functions only of z/z_i. This expectation is based on model studies (Deardorff, 1972; Wyngaard *et al.*, 1974) which show wind and temperature data scaling with w_* and θ_*. In the analyses to follow, the Minnesota data will be examined within the framework of such scaling.

Controversy exists regarding the choice of z_i for the thickness of the convective boundary layer. Some investigators (Tennekes, 1970; Zilitinkevich, 1972; Clarke and Hess, 1973) have suggested that this thickness is a function of u_*/f, the Ekman layer depth, but

the modeling studies of Deardorff (1974a) show that z_i, the height of the lowest inversion base, determines the boundary layer depth. He found the heights of the boundary layer for both heat and momentum to be nearly the same and approximated by z_i.

Estimating z_i presented no difficulty in our observations as the base of the capping inversion was sharply defined in all the rawinsonde plots. The height of the inversion base varied from day to day and from one observational period to another, but its diurnal trend, at least in the limited sample obtained at Minnesota, followed a pattern which is typified by the curve in Fig. 2. Similar patterns have been observed with FM-CW radars (e.g., Richter *et al.*, 1974) and acoustic sounders (e.g., Neff, 1975) at other sites. Also shown on the same plot is the diurnal trend of Q_0 observed during the experiments.

The following observations can be made from Fig. 2. Between sunrise and local noon (1300 CDT) z_i grew rapidly in response to the steadily increasing surface heat flux. The growth of z_i slowed down between 1300 and 1600 CDT as Q_0 reached its maximum value. The growth rate of z_i for this period agrees with the numerical model prediction of Mahrt and Lenschow (1976) which assumes a constant Q_0 for the 3 h following local noon. But as Q_0 decreased through the late afternoon, z_i began to level off to a nearly constant value which it maintained even after Q_0 turned negative.

Examining data obtained during the evening transition, we find the dissolution of the convective boundary layer to be rather abrupt, especially when compared to its evolution in the morning. The heat flux over the entire layer turned negative within minutes, but surprisingly this trend propagated downward from the top with Q_0 the last to cross zero. The transition took place almost an hour before sunset. With surface temperatures dropping rapidly after sunset, an inversion layer often developed near the ground and continued to deepen through the evening. Remnants of the capping inversion were found to persist through the development of the nocturnal boundary layer and some-
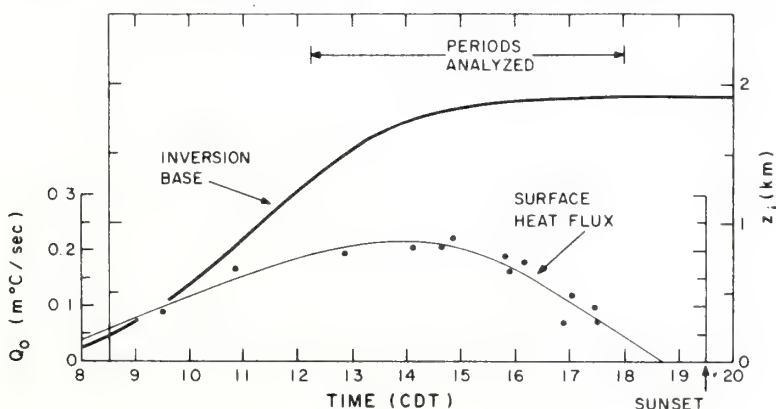
FIG. 2. Diurnal trend in the surface heat flux and corresponding inversion rise for a typical day.
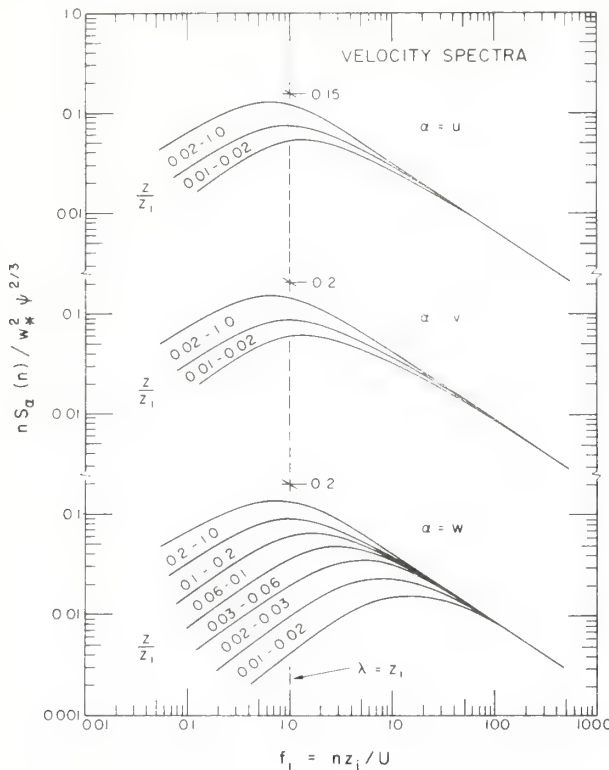
FIG. 3. Universal curves for velocity spectra expressed in mixed-layer similarity coordinates. The function ψ in the spectral normalization is the dimensionless energy dissipation rate $\epsilon/(g/T)Q_0$.

times well into the next morning, when they either merged with the newly rising surface inversion or existed as a separate layer aloft.

Even though the convective boundary layer evolves in response to the roughly sinusoidal variation in surface heating as described above, there is justification for treating its midday structure as if it were in steady state. The time scale characteristic of convectively driven turbulence is z_i/w_*. Under typical conditions ($z_i = 1.25$ km, $Q_0 = 0.2$ m °C s^{-1}) this turns out to be 10 min, much smaller than the time scale of changes in Q_0 and z_i, or changes in the pressure field that drives the flow. Thus, we expect that near midday the mixed layer quickly adjusts its structure in response to the slowly changing boundary conditions and keeps itself in a condition of moving equilibrium or quasi-steady state. This quasi-steady state assumption is implicit in the analyses described in the sections to follow.

5. Spectra of velocity components

Data obtained in the 1968 Kansas experiment had shown that atmospheric spectra and cospectra from the first 22 m, when expressed in appropriate similarity coordinates, reduce to a set of universal curves that converge into a single curve in the inertial subrange, but spread out as a function of z/L at lower frequencies (Kaimal et al., 1972). In this section we will attempt to

see if the spectral properties of the convective boundary layer above 22 m can similarly be generalized through proper normalization of spectral intensities and frequency scales.

Two facts emerge as we examine velocity spectra obtained from the mixed layer. The energy in the inertial subrange remains essentially constant with height, in contrast with the sharp decrease with z observed near the ground, and the spectral peaks tend to be invariant both in their intensities and their positions on the frequency scale. These observations imply a near-uniform spectral behavior over much of the boundary layer, so the use of mixed-layer scaling appears logical. Extending the similarity argument to the mixed layer, we can expect the mixed-layer velocity spectrum, normalized by w_*^2, to be a function of only two variables, z/z_i and λ/z_i (where λ is the wavelength approximated by U/n). Thus, the one-dimensional logarithmic u spectrum in the inertial subrange can be expressed as

$$\frac{nS_u(n)}{w_*^2} = \frac{\alpha_1}{(2\pi)^{\frac{2}{3}}}\psi^{\frac{2}{3}}f_i^{-\frac{2}{3}}, \qquad (4)$$

where α_1 is the spectral constant for u, ψ is the dimensionless dissipation rate $(\epsilon T/gQ_0)$ appropriate to the mixed layer and f_i is the dimensionless frequency (nz_i/U) for that layer; ψ and f_i are analogous to ϕ_ϵ and f in the surface layer formulation [Eq. (5), Kaimal et al., 1972]. By our similarity argument, ψ, the ratio of kinetic energy dissipation rate to buoyancy production rate at the surface, should be a function only of z/z_i.

Taking α_1 to be 0.5 and rearranging terms, Eq. (4) becomes

$$\frac{nS_u(n)}{w_*^2\psi^{\frac{2}{3}}} = 0.15f_i^{-\frac{2}{3}}. \qquad (5)$$

Spectral forms for the one-dimensional v and w spectra differ from Eq. (5) by a factor of $\frac{4}{3}$ as a consequence of isotropy, so that

$$\frac{nS_v(n)}{w_*^2\psi^{\frac{2}{3}}} = \frac{nS_w(n)}{w_*^2\psi^{\frac{2}{3}}} = 0.20f_i^{-\frac{2}{3}}. \qquad (6)$$

Logarithmic spectra normalized in this manner show systematic behavior when plotted as a function of f_i (see Fig. 3). Inclusion of $\psi^{\frac{2}{3}}$ in the normalization forces all spectra to collapse into a single curve in the inertial subrange. At lower frequencies we find the curves separating as a function of z/z_i. The separation is not nearly so systematic as in the Kansas spectra, but the demarcations between the different z/z_i categories in the composite plots are, nevertheless, clear enough to justify the curves in Fig. 3. Over 90% of the spectra in each z/z_i category fall within the areas indicated. The spectra used for constructing the composite plots
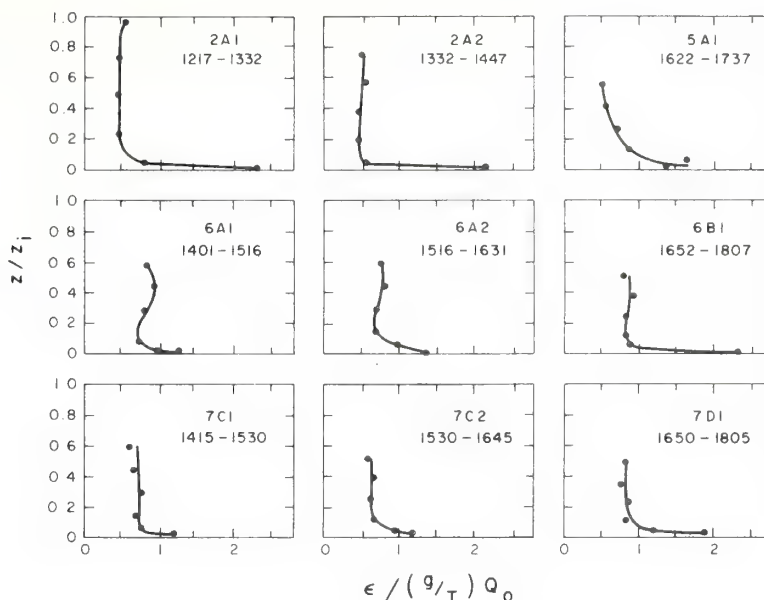
Fig. 4. Dimensionless energy dissipation rate ψ plotted as a function of z/z_i.

were subjected to minor smoothing by eye to average out the larger peaks and valleys near the low-frequency end. The only alterations made to the spectral shapes were the corrections for attenuation caused by the high-pass digital filter and the distortions introduced by balloon movement at the high-frequency end.

Of the three velocity components w shows the largest spread with height. Our normalization tends to exaggerate the spread in the ordinate, but the separation in the abscissa comes as no surprise because the length scales of w are known to be strongly height dependent in the lower layers of the atmsophere. As z/z_i increases from 0.01 to 1.0, the position of the spectral peak shifts to increasingly lower values of f_i rather rapidly at first up to $z/z_i = 0.1$, then more gradually above that.[5] For u and v only two categories exist: 0.01 to 0.02 and 0.02 to 1.0, and the shift in spectral peak is virtually insignificant.

The dimensionless dissipation rate ψ, which appears in the normalization of the spectral intensities, assumes a nearly constant value in the mixed layer (see Fig. 4). In the fully convective runs this value falls between 0.5 and 0.7. Slightly larger values are observed in the near-transition runs close to sunset. In general these curves resemble the dissipation rate profiles obtained by Lenschow (1974), Frisch and Clifford (1974), Rayment (1973), Volkovitskaya and Ivanov (1970) and Kaimal and Haugen (1967). In the convective atmospheric boundary layer with negligible wind shear across the capping inversion, one would expect negligible shear-

production rates of turbulent energy in the mixed layer. The height-averaged energy budget should then represent a balance between buoyant production and dissipation. With a linear heat-flux profile, one would then expect a mid-layer dissipation rate of 0.4–0.5 times the buoyant production rate. Our values are somewhat larger, perhaps because the large stress values observed at the Minnesota site caused appreciable shear production rates in some runs.

The limiting wavelength for the inertial subrange appears to be a function of z_i in the mixed layer. Based on Fig. 3 we can define the limit as $\lambda \leqslant 0.1z_i$. In the surface layer this limiting wavelength is approximately the height above ground (Kaimal et al., 1972), so we have to assume the transition from the z to the z_i dependence occurs within the height range 0.01 to $0.1z_i$.

The peak wavelength λ_m in the w component also undergoes a similar transition with height. This wavelength is important for studies of turbulent transport in the boundary layer and therefore merits close examination. In Fig. 5 we have λ_m normalized with z_i, plotted as a function of z/z_i. At $z \leqslant 0.1z_i$ the relationship is a linear one approximated by

$$\lambda_m/z_i = 5.9(z/z_i), \qquad (7)$$

which is precisely the free-convection limit $z/\lambda_m = 0.17$ observed in the Kansas data (Kaimal et al., 1972). Above $0.1z_i$, λ_m increases more gradually with height and finally approaches a constant value ($\approx 1.5z_i$) in the range $0.5z_i < z < z_i$. An exponential relationship for its behavior above $0.1z_i$ has been suggested by D. H. Lenschow (personal communication) whose aircraft w spectra show similar behavior. Combining the results

[5] An alternate presentation of the spectra in free-convection layer scaling (i.e., normalizing with $u_f\psi^{\frac{1}{3}}$ and plotting against f) will cause all w spectra in the height range 0.01 to $0.1z_i$ to collapse into a single curve over the entire frequency range.
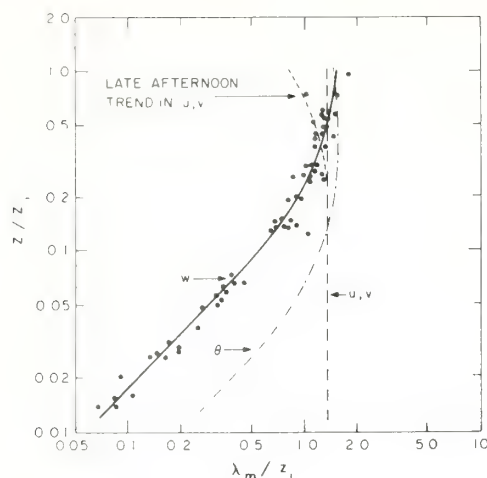
FIG. 5. Dimensionless peak wavelength for the velocity components and temperature plotted as a function of z/z_i. Scatter in the u, v and θ data points (not shown) is about twice as large as for w.

from Kansas[6] and Minnesota we can approximate λ_m for w in different regions of the convective boundary layer as follows:

$$(\lambda_m)_w \approx \begin{cases} z/(0.55 - 0.38|z/L|), & 0 \leqslant z \leqslant |L| \\ 5.9z, & |L| \leqslant z \leqslant 0.1z_i \quad (8) \\ 1.5z_i[1 - \exp(-5z/z_i)], & 0.1z_i \leqslant z \leqslant z_i \end{cases}$$

For the u and v components λ_m/z_i shows little, if any, variation with z/z_i. The scatter in the data (not shown in this plot) is larger than for w, by at least a factor of 2. But their average value (1.3), shown by the dashed line, comes close to the asymptotic limit of 1.5 for w. Thus, in the mixed layer we see a strong tendency for the wavelength in all components to be the same and roughly equal to 1.5 times the boundary layer thickness.

A curious behavior observed toward the end of the day is noted in Fig. 5. In the runs immediately before sunset we see a contraction in the λ_m for u and v at the upper levels. No corresponding decrease is observed in w at the same heights.

These observations are in general agreement with those reported by other investigators. Deardorff's (1974b) numerical experiments showed λ_m/z_i for the w spectra to be approximately 1.0 for z/z_i between 0.38 and 0.69. The aircraft measurements of Kukharets (1974) showed λ_m for w increasing with height between 50 and 500 m and approaching a constant value above 500 m. He found λ_m sensitive to changes in terrain type (steppe, desert and ocean), which might possibly be the response to changes in z_i. The u spectra from the 300 m tower at Obninsk, reported by Ivanov et al. (1973), show behavior very similar to the Minnesota spectra. The single characteristic time scale observed at all levels on their tower is attributed to organized

mesoscale convective circulations in the boundary layer.[7] In the surface layer we had found (Kaimal et al., 1972; Busch, 1973) that λ_m for u and v do not obey Monin-Obukhov similarity under unstable conditions. The absence of any systematic behavior with z/L indicated that some length scale other than z and L controls the behavior of λ_m. It appears from our Minnesota data that this controlling length scale is z_i.

The low-frequency roll-off observed in our velocity spectra at $f_i < 1.5$ (Fig. 3) appears to be real. It represents the limit of three-dimensional turbulence in the boundary layer. With the flow at synoptic scales being quasi-horizontal, the roll-off in w should continue to very low frequencies. The u and v spectra, on the other hand, should curve upward following the -3 power law (-2 slope in the logarithmic spectral representation) predicted for two-dimensional flows. The Wangara u spectra (Hess and Clarke, 1973) show a slope somewhat smaller, but nevertheless provide a fairly realistic representation of spectral behavior at very low frequencies. The existence of a spectral gap between the three-dimensional boundary layer turbulence and the quasi-horizontal large-scale motions, found in many recent observational studies (Hess and Clarke, 1973; Smedman-Högström and Högström, 1975) and strongly indicated by the low-frequency roll-off in our u and v spectra, appears to be a function of the spectral behavior in the mesoscale region. Energy contribution from large disturbances, like thunderstorms and frontal passages, would easily fill the gap, but the boundary layer as defined in this study would not exist during such periods. If the predominant scales of motion in the convective boundary layer are indeed controlled by the inversion height as implied in the Minnesota data, these scales will appear prominently in any spectral representation of the undisturbed boundary layer, and the gap separating this region from the synoptic scales of motion becomes an essential feature of boundary layer spectra.

This is a good point at which to speculate on the significance of the spectral peak at $\lambda_m \approx 1.5z_i$ observed in all three velocity spectra. Longitudinal roll vortices found in convective boundary layers with mean mixed-layer wind speeds in excess of 7 m s^{-1} (LeMone, 1973) come to mind, since they provide an effective mechanism for transporting heat and momentum between the earth's surface and the inversion base. The mean mixed-layer wind speeds for all runs used in this study (except Run 5A) exceed 7 m s^{-1}. LeMone (1973) has shown that these rolls have wavelengths roughly three times the boundary layer thickness. However, it is very unlikely that the rolls will appear in the logarithmic spectra at $\lambda_m \approx 1.5z_i$ because of their slow translation velocities across a fixed observation

---

[6] The 4 m Minnesota spectra are in exact agreement with the Kansas spectra and follow the relationship in Eq. (8) for $z < -L$.

[7] The small shift in the u and v spectral peaks at $0.01z_i < z < 0.02z_i$ in Fig. 3 is more a reflection of the decreased U near the ground than an increase in n_m.

point. The rolls tend to line up at a small angle to the mean wind and move laterally at a fraction of the mean wind speed. The time interval between the passage of successive convergent zones shows up in the time traces of uw as periods of intense activity (Haugen *et al.*, 1971, and Section 7 of this paper) but it is seldom apparent in the velocity traces *per se*.

Interestingly enough, the observed λ_m matches the horizontal length scale of large convective plumes or thermals which extend through the depth of the boundary layer. The existence of organized convection on this scale has been observed by other investigators: Hardy and Ottersten (1969) and Konrad (1970) with the help of high-powered radars, Rowland and Arnold (1975) with FM-CW radar, and Frisch *et al.* (1975) with a combination of dual-Doppler radar, acoustic sounder and microbarograph array. In the Minnesota data evidence of such structures can be found in the temperature records from heights above $0.1z_i$ (see Section 7 for details). The temperature traces show positive bursts spaced 4–5 min apart, the time scale represented by λ_m in the mixed layer. The records show a high degree of correlation between these fluctuations and the long-period fluctuations in the velocity field responsible for the peaks in Fig. 3 which suggests that the length scales of three-dimensional turbulence in the boundary layer are determined primarily by the prevailing convection pattern. In the u and v components, where the length scales are not limited by the height above ground as in w, those long-period fluctuations can be observed down to very small heights above the ground.

The prevailing convective field during these runs probably resembles the "thermal streets" in Konrad's (1970) radar observations, where individual thermals line up in the direction of the mixed-layer mean wind vector (spaced roughly $1.5z_i$ apart and transported at the mean wind speed) with a row separation approximating $3z_i$, the roll wavelength observed by LeMone (1973). Under more unstable conditions (mean mixed-layer wind speeds <7 m s^{-1}), the pattern could conceivably be different, with individual thermals arranging themselves into open rings or hexagons with diameters 5–6 times z_i as observed by Hardy and Ottersten (1969). Such a pattern could yield the longer wavelengths ($6z_i$) observed by Fitzjarrald (1976) under low wind conditions. More observations and analysis of convection patterns are needed to confirm these speculations.

6. Spectrum of temperature

The spectrum of temperature, unlike velocity spectra, cannot be conveniently generalized within the framework of mixed-layer similarity. The difficulty stems mainly from run-to-run variations in the low-frequency variance introduced by entrainment effects in the upper half of the boundary layer. However, some broad generalizations can be made about spectral shapes and
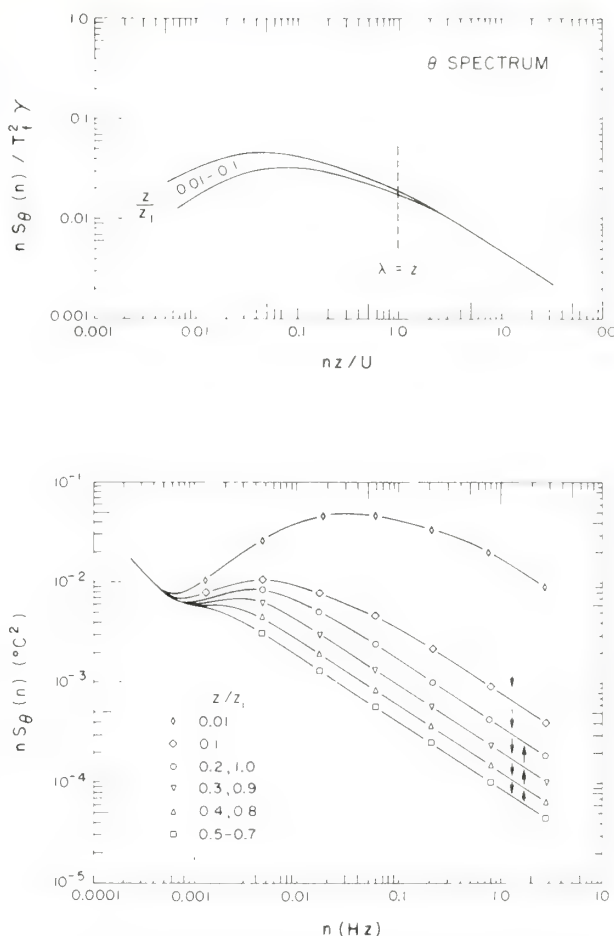
FIG. 6. Universal curve for the θ spectrum (upper figure) in the range $0.01z_i \leqslant z \leqslant 0.1z_i$. T_f is the free-convection scaling temperature and γ represents a dimensionless grouping which is constant ((≈ 0.83) in this height range. Idealized temperature spectra in dimensional coordinates (lower figure) show variation in spectral behavior as a function of z/z_i.

inertial subrange intensities in the convective boundary layer. These generalizations are embodied in the set of idealized spectral curves shown in the lower plot of Fig. 6. At the low-frequency end they all converge to a single curve which extends upward in response to the diurnal trend in temperature. At inertial subrange frequencies the spectral intensity drops steadily with height up to $0.5z_i$, stays at a low value between 0.5 and $0.7z_i$ and starts to rise again above $0.7z_i$. The arrows near the right edge of the figure illustrate this trend. The leveling off and subsequent increase in the spectral level in the upper regions of the boundary layer clearly reflect the mixing produced by the entrainment of warm air through the capping inversion. Further evidence of this entrainment will be presented in Section 7.

The only region where spectral generalization is possible is in the height range $z \leqslant 0.1z_i$, where the θ spectra behave much like those obtained in the Kansas experiment (Kaimal *et al.*, 1972). Since the controlling
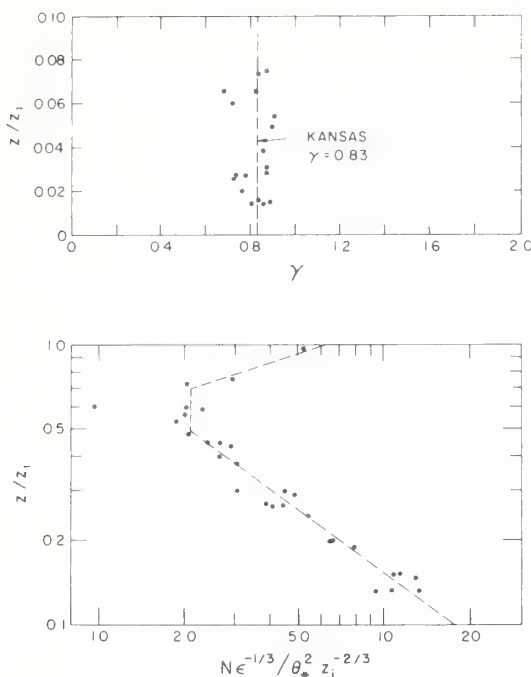
FIG. 7. The upper figure shows γ plotted as a function of z/z_i. The dashed line corresponds to the value 0.83 obtained in the Kansas experiments. In the lower figure the behavior of $N\epsilon^{-\frac{1}{3}}$ with height is presented in mixed-layer coordinates.

length scale in this region is z, not z_i we use f for the dimensionless frequency scale.

The logarithmic one-dimensional θ spectrum for the inertial subrange can be expressed in the form (Kaimal et al., 1972)

$$ nS_\theta(n) = \frac{\beta_1}{(2\pi)^{\frac{2}{3}}} N\epsilon^{-\frac{1}{3}} z^{\frac{2}{3}} f^{-\frac{2}{3}}, \tag{9} $$

where β_1 is the spectral constant for θ assumed to be 0.8 from the Kansas results, and N is the dissipation rate of $\theta^2/2$. Substituting the value for β_1, normalizing the spectral intensity with T_f^2, where T_f is the free-convection scaling temperature and rearranging terms, we have

$$ \frac{nS_\theta(n)}{T_f^2\gamma} = 0.235 f^{-\frac{2}{3}}, \tag{10} $$

where

$$ \gamma = N\epsilon^{-\frac{1}{3}} Q_0^{-1} (g/T)^{\frac{2}{3}} z^{\frac{1}{3}}. \tag{11} $$

This normalization brings all θ spectra into coincidence in the inertial subrange as seen in Fig. 6. At mid and low frequencies they collapse into a relatively narrow band with no apparent tendency to separate according to z/z_i. λ_m for this composite spectrum approximates $20z$, the free-convection limit in the Kansas spectra (Kaimal et al., 1972). As z approaches $0.1z_i$ we see λ_m approaching the characteristic wavelength $1.5z_i$ found in the velocity components (see Fig. 5). Above $0.1z_i$, λ_m shows a tendency to increase slightly with height up to

$0.5z_i$ and to decrease again above $0.7z_i$ consistent with the idealized spectral behavior in Fig. 6.

The function γ is essentially a dimensionless form of the structure parameter C_T^2. We can write

$$ C_T^2 = 4\beta_1 N\epsilon^{-\frac{1}{3}} \approx 3.2 N\epsilon^{-\frac{1}{3}}. \tag{12} $$

The Kansas data provide the relationship between C_T^2 and surface layer parameters for local free convection (Wyngaard et al., 1971b):

$$ C_T^2 \approx 2.67 Q_0^{\frac{4}{3}} (g/T)^{-\frac{2}{3}} z^{-\frac{4}{3}}. \tag{13} $$

From Eqs. (11), (12) and (13), we have $\gamma \approx 0.83$ for the free-convection layer. The plot in Fig. 7 shows this approximation is valid for the Minnesota data as well. The value of γ stays surprisingly constant up to $0.5z_i$, indicating that the $z^{-\frac{4}{3}}$ decrease in the inertial subrange intensity continues well above $0.1z_i$. The behavior of $N\epsilon^{-\frac{1}{3}}$ above $0.1z_i$, nondimensionalized with mixed layer parameters θ_* and z_i, is shown in Fig. 7 and can be approximated as

$$ \frac{N\epsilon^{-\frac{1}{3}}}{\theta_*^2 z_i^{-\frac{2}{3}}} = \begin{cases} 0.83(z/z_i)^{-\frac{4}{3}}, & z \leqslant 0.5z_i \\ 2.1, & 0.5z_i \leqslant z \leqslant 0.7z_i \\ 6.1(z/z_i)^3, & 0.7z_i \leqslant z \leqslant z_i \end{cases} \tag{14} $$

This behavior of the temperature spectrum agrees qualitatively with the ϵ and N profiles presented by Caughey and Rayment (1974).

The above empirical relationship can be used to collapse all inertial-subrange temperature spectra into a single curve in a plot similar to Fig. 3. Here the dimensionless ratio of Eq. (14) plays the same role as $\psi^{\frac{2}{3}}$ in Eq. (5). Bringing the inertial-subrange θ spectra together in this manner causes the low-frequency end to spread out, but no systematic trend emerges in the composite plots because of run-to-run variations in the details of their low-frequency behavior.

7. Heat flux and stress

The cospectra of heat flux and stress measured near the ground ($z < 0.1z_i$) follow the same universal forms observed in the Kansas data (Kaimal et al., 1972). But cospectral shapes depart significantly from those forms as z exceeds $0.1z_i$ and as large excursions in both positive and negative directions become a characteristic feature of heat flux and stress cospectra in the mixed layer. The patterns that emerge are not consistent enough to justify development of universal forms, although individually they provide interesting perspective into the nature of turbulent transport in the boundary layer.

In Fig. 8, for example, we see how the range of frequencies contributing to the upward transport of heat near the ground narrows down to a relatively small band centered around 0.003 Hz (the frequency corresponding to λ_m) at a height of 610 m. At 1219 m,
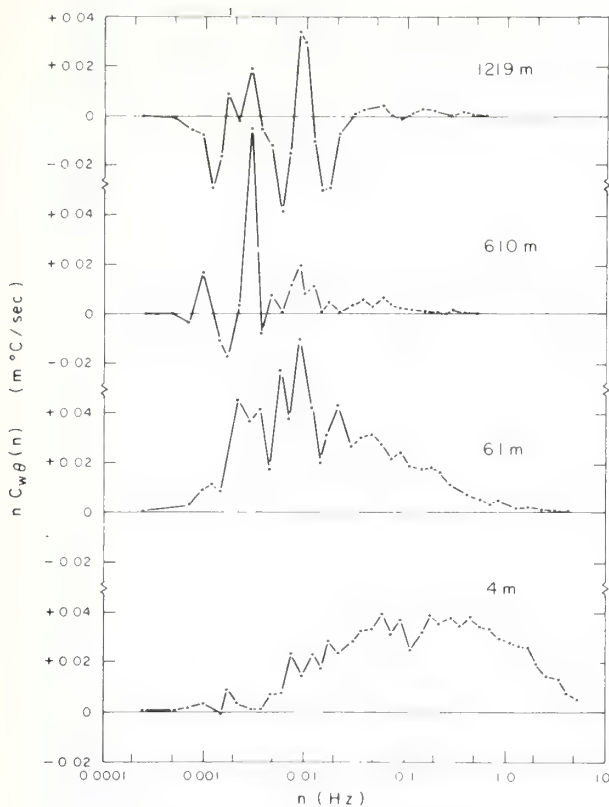
FIG. 8. Cospectra of heat flux at four heights during
Run 2A1.

close to the inversion base, there is still some upward flux at 0.003 Hz, but the net flux is distinctly downward. Adiabatic transport of air downward through the capping inversion would produce this negative flux which, in turn, suggests substantial entrainment of air into the boundary layer from above (Ball, 1960). The temperature and heat flux traces in Fig. 9 provide clear evidence of such entrainment. Only portions of the $w\theta$ traces where significant heat flux exists are shown and these regions are shaded to distinguish them from the temperature traces. The regions of upward heat flux are obviously thermals which originate near the surface shear layer. The regions of downward heat flux appear between the tops of the thermals, but these are also characterized by positive bursts in the temperature trace. The structure of the bursts strongly suggest that the entraining warm air descends in the form of discrete plumes. They display a characteristic saw-tooth appearance with the largest discontinuity and the highest temperatures at the leading edge, not at the trailing edge as in buoyant plumes near the earth's surface (Kaimal and Businger, 1970). Such a structure is not surprising because the warmer air from higher up in the inversion layer has proportionally higher wind speeds (assuming positive wind shear across the inversion) and will therefore tend to concentrate on the downwind side of the plume.

The shape of the updraft region in the thermals, as delineated by the curves in Fig. 9, resembles the three-
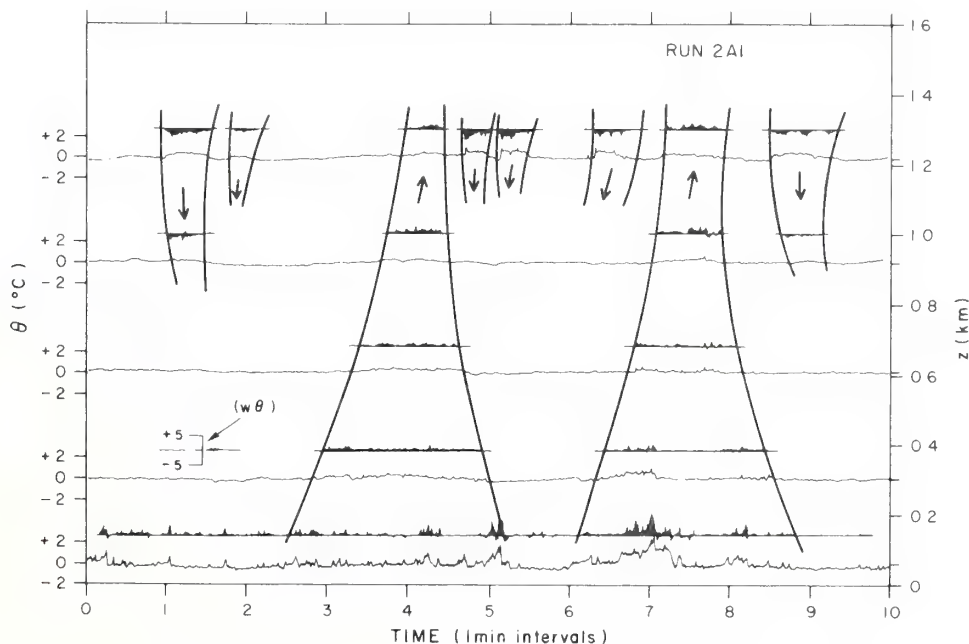
FIG. 9. Temperature fluctuations observed during the 10 min period from 1321 and 1331 CDT toward the end of Run 2A1. The top of the figure represents the inversion base for this period. The instantaneous vertical heat flux at each level is indicated by the shaded fluctuations traced above it. Only regions of significant flux are shown. Scale for $w\theta$ is in m °C s^{-1}.

441

dimensional convection patterns observed by Frisch et al. (1975) with their dual-Doppler radar. According to our observations these thermals develop from the merging of smaller ground-based plumes (Kaimal and Haugen, 1967; Kaimal and Businger, 1970) in the vicinity of $0.1z_i$ and extend to the top of the boundary layer. The observations of Arnold et al. (1975) and Rowland and Arnold (1975) suggest that this rising air spreads out laterally as it reaches the inversion base, producing a dome-like depression at the interface, and returns as a downdraft along the "sidewall" of the thermal. Arnold et al. find the dome-like structures, observed by their FM-CW radar, to be co-located with the thermals detected simultaneously in the lower boundary layer by their acoustic sounder. The juxtaposition of the cool moist air in the interior of the thermal with the warmer drier air above it makes the top dome visible to radars. But the strong returns from the sidewalls indicate the presence of entrained air from the inversion in the downdraft. The inverted U structures in the vertical sections and doughnut-shaped patterns in the plan views observed by Hardy and Ottersten (1969) and by Konrad (1970) thus represent the sidewalls where refractive index gradients are large enough to produce radar returns.

Arnold et al. conclude from their data that most of the entrainment takes place along the top of the dome. Here, either the Kelvin-Helmholtz instability described by Rayment and Readings (1974) or the wave-like overturning of the dome structure envisaged by Carson and Smith (1974) could provide the mechanism for entrainment. But the mechanism responsible for draw-ing this entrained air deep into the mixed layer, where its effects can be observed to heights of the order of $0.5z_i$, must be the downdraft in the gap between the thermals. The Doppler wind measurements of Hall et al. (1975), Rowland and Arnold (1975) and the Minnesota results described here seem to support this view. Laboratory convection experiments, now being conducted by G. E. Willis (personal communication) at the National Center for Atmospheric Research, simulating an inversion layer overlying the mixed layer, show tongues of fluid from the inversion being drawn into the mixed layer by the return flow between thermals. The separation distance for these thermals range from 1.3 to $1.4z_i$.

In our results, the consequences of entrainment are most apparent in the profiles of vertical heat flux (see Fig. 10). The negative heat flux below the inversion is quite apparent. Profiles observed around midday are generally similar to those from aircraft measurements (Lenschow, 1974; Pennell and LeMone, 1974), laboratory experiments (Willis and Deardorff, 1974) and model calculations (Deardorff, 1972; Wyngaard and Coté, 1974). They are approximately linear and cross zero somewhere in the upper half of the mixed layer. Zilitinkevich (1975) and Tennekes (1975) have recently discussed how the rate of growth of the convective layer can affect heat flux near z_i. Unfortunately, the uppermost instrument levels for most runs were well below z_i, so nothing very specific can be said about the magnitude of the negative heat flux in relationship to Q_0. But Fig. 10 demonstrates how variable the heat flux profile can be from one run to another and how the transition to negative flux is initiated near the top of
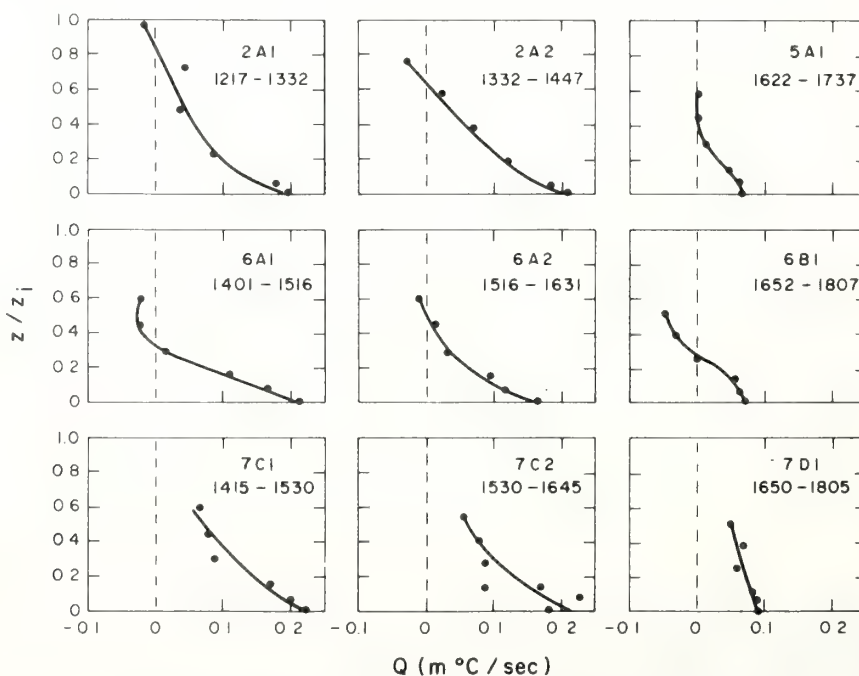
FIG. 10. Vertical profiles of heat flux for nine of the runs observed.
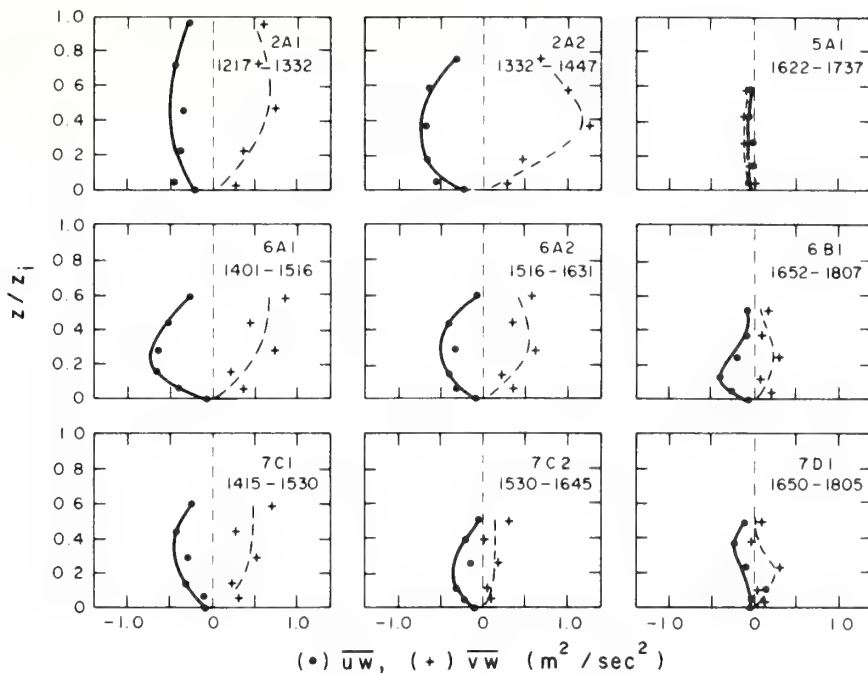
FIG. 11. Vertical profiles of stress for nine of the runs observed. The coordinate axes for
u and v are referred to the mean wind field at the 4 m level.

the mixed layer even before the surface heat flux drops to zero at the end of the day.

The behavior of the stress profiles provides the largest surprise of all. Fig. 11 shows $\overline{uw}$ and $\overline{vw}$ increasing in magnitude with height, reaching a maximum value near $0.5z_i$ and decreasing above that height. In this figure the coordinate system for the stress components is referred to the vector-mean direction at 4 m. In the barotropic, nonentraining, convective boundary layer one would expect $\overline{uw}$ to decrease monotonically with height, approaching zero at $z = z_i$, and $\overline{vw}$ to vanish over the entire depth. The profiles in Fig. 11 look quite different: they are strongly curved, with $\overline{uw}$ and $\overline{vw}$ of approximately the same magnitude. Large stress values of this magnitude can arise from several causes. One possible cause may be baroclinicity (Arya and Wyngaard, 1975). The baroclinicity needed to explain these observations require positive horizontal temperature gradients of the order of 1°C per 15 km to the northwest, a condition not present on the synoptic scale during the experiments. Gradients of this magnitude are likely to be on the 1–2 km scale because of albedo variations introduced by differences between harvested and plowed areas. Whether such gradients existed on scales large enough (20–30 km) to affect the stresses is not known.

Deardorff (1973) has shown that a wind profile such as the one observed in Fig. 1 can generate large stresses through entrainment of momentum in the upper portions of the mixed layer. We tested this idea through a numerical simulation of Run 2A1 using the updated

higher-order-closure model described by Wyngaard (1975). The observed values of surface geostropic wind, surface roughness and Q_0 for Run 2A1 were used. A barotropic model with no subsidence at z_i was assumed. Initial wind and temperature profiles at the morning transition were assumed and the model then calculated the evolution of the convective boundary layer. The calculated wind and stress profiles for the time corresponding to Run 2A1 are shown in Fig. 12. The results compare well with observations, except for the fact that the stress maxima occur in the vicinity of the inversion and not well within the boundary layer.
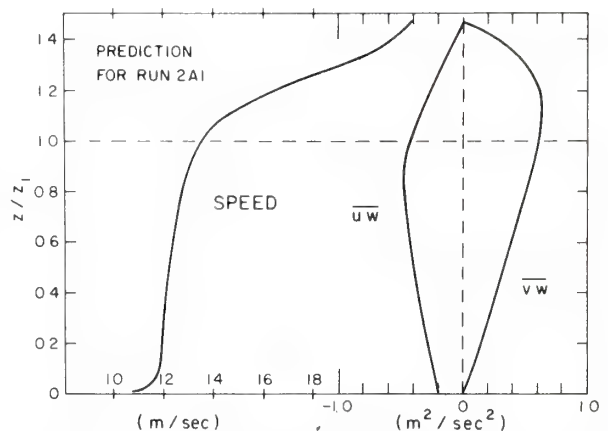
FIG. 12. Numerical predictions for wind speed and stress profiles for Run 2A1. Actual observations are given in Figs. 1 and 11.

Another possible explanation for the large stresses is that our averaging period is too short to include the entire range of cospectral contributions to the stress. Given a sufficiently long averaging period (or measurements over sufficiently long distances with an instrumented aircraft), the stress profile might possibly show a steady decrease with height. Implicit in the argument is the assumption that cospectral contributions from frequencies outside the present spectral bandwidth will be sufficient to offset the large contribution now measured in the range $0.001 < n < 5$ Hz. In the case of uw this would mean a large upward transport of momentum at very low frequencies ($n < 0.001$ Hz). This argument cannot be discounted without definite proof to the contrary. A few runs (6A1 and 6A2) show evidence of positive uw and negative vw correlations at the low end of the cospectrum, but how far that trend continues beyond our spectral bandwidth cannot be ascertained. It is conceivable that the large stresses we observe result from a combination of factors, not any one by itself, so that even a small loss of cospectral energy at the low-frequency end could be significant. More data over longer averaging periods are needed to determine the relative importance of the various factors discussed here.

However, data obtained in this experiment provide some interesting details of the momentum transport process. The largest contributions to the stress cospectra come from frequencies in the range $0.002 < n < 0.1$ Hz, the energy-containing region for the velocity spectra. This range is at least a decade too low for balloon-movement effects (Haugen et al., 1975) and other mechanically induced correlations. Fig. 13 shows uw traces for the 2.5 h period covering Runs 6A1 and 6A2

with the isopleths of 15 min averaged wind inclination angles observed by the MRU probes superimposed on them. The isopleths indicate well-defined longitudinal roll vortices with the updraft regions spaced roughly 1 h apart. Most of the vertical momentum transport in the boundary layer occurs within this updraft region. (Evidence of such roll circulation can be found in all the early afternoon runs selected for this study.) Within this updraft region the amplitude of the uw burst increases with height. This increase continues to a height of approximately $0.5z_i$. The downdraft region, on the other hand, is more diffused and occupies a longer time interval compared to the updraft region. Here the amplitude of uw fluctuations decreases rapidly with height and remains small throughout most of the boundary layer depth. The opposing stress gradients in the updraft and downdraft regions tend to cancel out in the surface layer, resulting in a near-constant distribution of stress with height; but above the surface layer in the time scale of our observations, the averaged stress profiles reflect the gradient in the updraft region.

Examining the structure of the uw bursts in the updraft region, we find that it consists of smaller discrete bursts with vertical continuity through the depth of the boundary layer. These small bursts in fact correspond to the thermals discussed earlier in this section. It appears that the bulk of the downward momentum transport in the boundary layer is carried out by the thermals located in the updraft regions between the longitudinal roll vortices. The convective elements in the downdraft region do not seem to play an active role in transporting momentum.
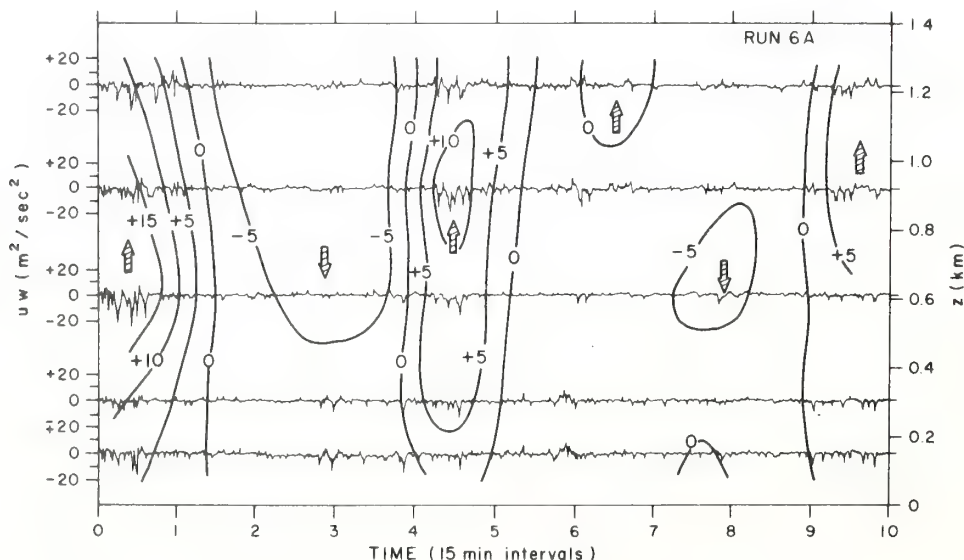
Fig. 13. Instantaneous uw at five levels observed during the 150 min period covering Runs 6A1 and 6A2. Isopleths of wind inclination angle (15 min averaged) at 5° intervals are shown superimposed on the uw fluctuations. Each division on the scale represents 15 min.

8. Moments and structure parameters

In this section we will examine the vertical profiles of some higher order moments and structure parameters to determine to what heights the Kansas free-convection predictions apply and how the profiles are modified by entrainment in the upper regions of the mixed layer. We had observed earlier that the free-convection predictions for the peak wavelengths in the w and θ spectra are valid to a height of $0.1 z_i$. Above that they tend to stay approximately constant with height. Only the moments involving w and θ will be examined here because they are least affected by balloon-movement effects.

The asymptotic predictions for $\overline{w^2}$ and $\overline{\theta^2}$ expressed in terms of surface layer parameters (Wyngaard *et al.*, 1971a) are

$$\overline{w^2}/u_*^2 \approx 3.6(-z/L)^{\frac{2}{3}}, \tag{15}$$

$$\overline{\theta^2}/T_*^2 \approx 0.9(-z/L)^{-\frac{2}{3}}. \tag{16}$$

These expressions convert directly to mixed layer parameters with only a change in the value of the constant. Thus, replacing Eqs. (15) and (16) we have

$$\overline{w^2}/w_*^2 \approx 1.8(z/z_i)^{\frac{2}{3}}, \tag{17}$$

$$\overline{\theta^2}/\theta_*^2 \approx 1.8(z/z_i)^{-\frac{2}{3}}. \tag{18}$$

These predictions are shown as dashed lines in Fig. 14. We find the above predictions followed to a height of
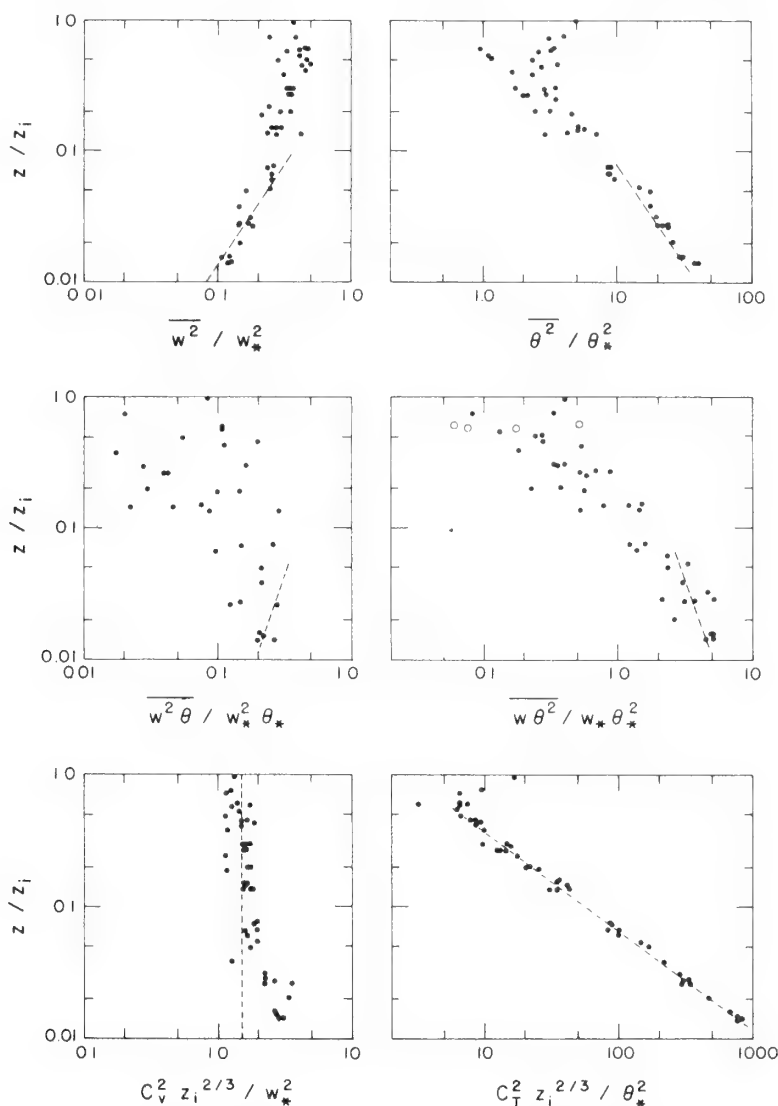
FIG. 14. Vertical profiles of high-order moments and structure functions for the fully convective runs in Table 1 (Runs 5A1, 6A1 and 7D1 are excluded). The dashed lines are free-convection predictions based on the Kansas data. The open circles represent negative values.

$0.1z_i$. (Only the fully convective runs are used in constructing these and other plots in Fig. 14.) Above $0.1z_i$ we see data points deviating from the predictions, exhibiting much more scatter than is apparent at the lower levels.

Comparing our w variance data above $0.1z_i$ with aircraft, water tank and numerical model results [as surveyed by Deardorff and Willis (1974)] we find the aircraft results fall within the scatter of our data points. The magnitudes observed in the tank and numerical experiments tend to be slightly larger than the atmospheric measurements. As for the height of maximum variance, the tank data show a peak around $0.5z_i$—as in the aircraft data and barely suggested in the Minnesota data—while the numerical model has its peak somewhat lower. The most significant departure from the tank and numerical results is the absence of any significant drop in w variance near the inversion base. This is consistent with the spectral behavior observed in Fig. 3 showing no appreciable change in spectral intensity or shape above $0.1z_i$ and probably reflects the different upper boundary conditions that exist in the atmosphere compared to the experiments.

The θ variance above $0.1z_i$ shows a steeper decrease with height than predicted by local free-convection similarity. The decrease continues to $0.5z_i$ where it reaches a minimum value. Above $0.5z_i$ the variance increases with height, clearly the result of mixing produced by entrainment of warm air into the boundary layer through the inversion.

The third-order moments $\overline{w^2\theta}$ and $\overline{w\theta^2}$, which represent the vertical transports of heat flux and temperature variance, respectively, deviate from their free-convection predictions at heights considerably below $0.1z_i$. The asymptotic values for these moments (Wyngaard et al., 1971a) expressed in mixed-layer similarity parameters become

$$\overline{w^2\theta}/w_*^2\theta_* \approx 0.9(z/z_i)^{\frac{1}{3}}, \qquad (19)$$

$$\overline{w\theta^2}/w_*\theta_*^2 \approx 1.1(z/z_i)^{-\frac{1}{3}}. \qquad (20)$$

The vertical gradients of these triple moments represent the local gain or loss of the quantity ($\overline{w\theta}$ and $\overline{\theta^2}$, respectively) that results from turbulent transport. Eqs. (19) and (20) imply a local loss of $\overline{w\theta}$ and a local gain of $\overline{\theta^2}$ resulting from turbulent transport in their budget equations. Our observations show free-convection predictions approached at fairly low heights (0.02 and $0.05z_i$, respectively) for $\overline{w^2\theta}$ and $\overline{w\theta^2}$. In the case of $\overline{w^2\theta}$ even the sign of the gradient is different above $0.02z_i$ indicating a gain rather than a loss from turbulent transport in the $\overline{w\theta}$ budget. The transport term in the $\overline{\theta^2}$ budget remains a gain throughout. Note the negative values of $\overline{w\theta^2}$ (open circles) above $0.5z_i$ showing downward flux of temperature variance,

another manifestation of the entrainment process discussed earlier.

The lack of agreement between the observations and predictions might very likely be a consequence of inadequate averaging time. With longer observational periods it is conceivable that the scatter in the results will be greatly reduced and the free-convection predictions will be followed to a height of $0.1z_i$ as in the second moments. On the other hand, it is possible that the turbulent transports of $\overline{w\theta}$ and $\overline{\theta^2}$ are in fact confined to a shallow layer around $0.1z_i$ and the data reflect the true state of affairs in the atmospheric boundary layer. Further measurements are needed to establish the reasons for the observed departures from prediction. Spatial measurements over long distances offer the best hope for statistically stable third moments, being free of contamination from the diurnal trends that inevitably affect single-point measurements.

The structure parameters C_V^2 and C_T^2 reflect the inertial subrange behavior in the velocity and temperature spectra, respectively. Their chief application is to studies of acoustic and optical propagation in the atmosphere. The expression for C_V^2, analogous to the one for C_T^2 in Eq. (12), is (Kaimal, 1973)

$$C_V^2 = 4\alpha_1\epsilon^{\frac{2}{3}} \approx 2\epsilon^{\frac{2}{3}}. \qquad (21)$$

The asymptotic surface-layer prediction for C_V^2, derived from the surface layer relationship for ϕ_ϵ (Wyngaard and Coté, 1971), shows that

$$\frac{C_V^2 z_i^{\frac{2}{3}}}{w_*^2} = \text{constant}, \qquad (22)$$

which is unity for the Kansas data but is higher (~ 1.5) for the Minnesota data. It is interesting that this constant value is reached only at heights above $0.1z_i$. A useful approximation for the dimensionless C_V^2 in the range $0.01z_i \leqslant z \leqslant 0.1z_i$ from Fig. 14 would be

$$\frac{C_V z_i^{\frac{2}{3}}}{w_*^2} = 1.3 + 0.1(z/z_i)^{-\frac{2}{3}}. \qquad (23)$$

The C_T^2 measurements provide by far the best fit to the Kansas free-convection predictions in the lower half of the boundary layer with considerably less scatter than any other parameter examined. From Eqs. (12) and (14) we have

$$\frac{C_T^2 z_i^{\frac{2}{3}}}{\theta_*^2} = 2.67(z/z_i)^{-\frac{2}{3}}, \qquad (24)$$

which is indicated by the dashed line in Fig. 14. These results are in agreement with Tsvang's (1969) observations that showed the $-\frac{4}{3}$ power law extending to heights of the order of 500 m in the atmosphere. The trend stops at about $0.5z_i$, and C_T^2 begins to increase with height above $0.7z_i$, once more reflecting the mixing

produced by warm air entraining into the boundary layer. This modification of the $-\frac{4}{3}$ law above $0.5z_i$ has also been observed by Neff (1975) from acoustic sounder returns over land and by Frisch and Ochs (1975) in aircraft measurements within the marine boundary layer.

9. Conclusions

The conclusions to emerge from this study can be summarized as follows:

1) The convective boundary layer observed at the Minnesota site was well-mixed down to approximately $0.1z_i$, with a near-uniform wind speed and potential temperature distribution over that depth. A well-defined capping inversion was observed in all daytime runs.

2) The spectra of velocity components in the boundary layer can be generalized within the framework of mixed layer similarity. With appropriate normalization the w spectrum can be reduced to a family of curves which spreads out as a function of z/z_i at low frequencies, but converge to a single universal curve in the inertial subrange. The u and v spectra generalized in the same manner show universal behavior, but without the z/z_i dependence apparent in w. The onset of the inertial subrange in the mixed layer occurs at wavelength $\lambda \approx 0.1z_i$.

3) The temperature spectra above $0.1z_i$ cannot be generalized in the same manner as the velocity spectra because of variability in the low-frequency behavior. However, the inertial subrange level is more predictable, decreasing as $(z/z_i)^{-\frac{4}{3}}$ up to $0.5z_i$ and increasing as $(z/z_i)^3$ above $0.7z_i$. Below $0.1z_i$ they behave much like the surface layer spectra.

4) The characteristic wavelength λ_m for w and θ increases linearly with z in the height range $-L$ to $0.1z_i$, following free-convection prediction, but levels off to a nearly constant value ($\lambda_m \approx 1.5z_i$) above that height. λ_m for u and v stays approximately the same (at $\lambda_m \approx 1.5z_i$) throughout the depth of the boundary layer.

5) The wavelength $\lambda_m \approx 1.5z_i$ observed in the velocity and temperature spectra corresponds to the length scale of large thermals that appear to dominate the circulation in the boundary layer.

6) Free-convection predictions for the variances of w and θ also appear valid to a height of $0.1z_i$. The triple moments indicate a much shallower free-convection layer but this may be the result of inadequate averaging time. C_V^2 reaches its asymptotic limit only above $0.1z_i$, while C_T^2 fits the prediction to a height of $0.5z_i$.

7) There is evidence of substantial heat and momentum entrainment into the boundary layer through the capping inversion. The entrained warm air descends in the form of inverted plumes strongly affect-

ing the temperature and heat flux statistics in the upper half of the boundary layer. The unexpectedly large stress values observed in the boundary layer can be explained, at least partly, in terms of momentum entrainment across the velocity jump within the inversion. Any theoretical or numerical model for the mixed layer must take into account the effects of entrainment through its upper boundary.

APPENDIX

List of Symbols

U	mean wind speed
u, v, w	fluctuating wind components in the longitudinal, lateral and vertical directions
T	mean temperature
θ	fluctuating temperature
ρ	density of air
τ_0	surface shear stress $[= -\rho\overline{uw}$ at 4 m$]$
Q	vertical kinematic heat flux $[= \overline{w\theta}]$
Q_0	surface kinematic heat flux $[= \overline{w\theta}$ at 4 m$]$
(g/T)	buoyancy parameter
ϵ	dissipation rate of turbulent kinetic energy
k	von Karman's constant
ϕ_ϵ	dimensionless dissipation rate $[= kz\epsilon/u_*^3]$
ψ	dimensionless dissipation rate $[= \epsilon T/gQ_0]$
N	dissipation rate for one-half of the temperature variance
γ	a dimensionless structure parameter
α_1	spectral constant for one-dimensional u spectrum
β_1	spectral constant for the one-dimensional θ spectrum
z	height above ground
z_i	height of lowest inversion base (from rawinsonde ascents)
L	Obukhov length $[= -u_*^3/k(g/T)Q_0]$
n	cyclic frequency

n_m frequency of logarithmic spectral peak

λ_m wavelength corresponding to $n_m [= U/n_m]$

f dimensionless frequency $[= nz/U]$

f_i dimensionless frequency $[= nz_i/U]$

$S(n)$ one-dimensional spectral density

$C_T{}^2$ structure parameter for temperature

$C_V{}^2$ structure parameter for velocity

u_*, T_* scaling velocity and temperature for the surface shear layer

u_f, T_f scaling velocity and temperature for the free-convection layer

w_*, θ_* scaling velocity and temperature for the mixed layer.

REFERENCES

Arnold, A., J. R. Rowland, T. G. Konrad, J. H. Richter, D. R. Jensen and V. R. Noonkester, 1975: Simultaneous observations of clear air convection by a pulse radar, an FM-CW radar, an acoustic sounder and an instrumented aircraft. *Preprints 16th Radar Meteorology Conf.*, 22–23 April, Houston, Tex., Amer. Meteor. Soc., 290–295.

Arya, S. P. S., and J. C. Wyngaard, 1975: Effect of baroclinicity on wind profiles and the geostrophic drag law for the convective planetary boundary layer. *J. Atmos. Sci.*, 32, 767–778.

Ball, F. K., 1960: Control of inversion height by surface heating. *Quart. J. Roy. Meteor. Soc.*, 86, 483–494.

Busch, N. E , 1973: The surface boundary layer. *Bound.-Layer Meteor.*, 4, 213–240.

Businger, J. A., J. C. Wyngaard, Y. Izumi and E. F. Bradley, 1971: Flux-profile relationships in the atmospheric surface layer. *J. Atmos. Sci.*, 28, 181–189.

Carson, D. J., and F. B. Smith, 1974: Thermodynamic model for the development of a convectively unstable boundary layer. *Advances in Geophysics*, Vol. 18A, Academic Press, 111–124.

Caughey, S. J., and R. Rayment, 1974: High-frequency temperature fluctuations in the atmospheric boundary layer. *Bound.-Layer Meteor.*, 5, 489–503.

Clarke, R. H., and G. D. Hess, 1973: On the appropriate scaling for velocity and temperature in the planetary boundary layer. *J. Atmos. Sci.*, 30, 1346–1353.

Deardorff, J. W., 1972: Numerical investigation of neutral and unstable planetary boundary layers. *J. Atmos. Sci.*, 29, 91–115.

——, 1973: An explanation of anomalously large Reynolds stresses within the convective planetary boundary layer. *J. Atmos. Sci.*, 30, 1070–1076.

——, 1974a: Three-dimensional numerical study of the height and mean structure of a heated planetary boundary layer. *Bound.-Layer Meteor.*, 7, 81–106.

——, 1974b: Three-dimensional numerical study of turbulence in an entraining mixed layer. *Bound.-Layer Meteor.*, 7, 199–226.

——, and G. E. Willis, 1974: Computer and laboratory modeling of the verical diffusion of nonbuoyant particles in the mixed layer. *Advances in Geophysics*, Vol. 18B, Academic Press, 187–200.

Fitzjarrald, D. E., 1976: A field observation of atmospheric free-convection. *J. Appl. Meteor.*, 15, 259–263.

Frisch, A. S., and S. F. Clifford, 1974: A study of convection capped by a stable layer using Doppler radar and acoustic echo sounders. *J. Appl. Meteor.*, 31, 1622–1628.

——, and G. R. Ochs, 1975: A note on the behavior of the temperature structure parameter in a convective layer capped by a marine inversion. *J. Appl. Meteor.*, 14, 415–419.

——, R. B. Chadwick, W. R. Moninger and J. M. Young, 1975: Observation of boundary layer convection cells measured by dual-Doppler radar and echosounder and by microbarograph array. *Bound.-Layer Meteor.*, 3, 199–226.

Hall, F. F., Jr., J. G. Edinger and W. D. Neff, 1975: Convective plumes in the planetary boundary layer. *J. Appl. Meteor.*, 14, 513–523.

Hardy, K. R., and H. Ottersten, 1969: Radar investigation of convective patterns in the clear atmosphere, *J. Atmos. Sci.*, 26, 666–672.

Haugen, D. A., J. C. Kaimal and E. F. Bradley, 1971: An experimental study of Reynolds stress and heat flux in the atmospheric surface layer. *Quart. J. Roy. Meteor. Soc.*, 97, 168–180.

——, ——, C. J. Readings and R. Rayment, 1975: A comparison of balloon-borne and tower-mounted instrumentation for probing the atmospheric boundary layer. *J. Appl Meteor.*, 14, 540–545.

Hess, G. D., and R. H. Clarke, 1973: Time spectra and cross-spectra of kinetic energy in the planetary boundary layer. *Quart. J. Roy. Meteor. Soc.*, 99, 130–153.

Ivanov, V. N., A. Ye. Ordanovich and L. I. Petrova, 1973: Certain properties of wind-velocity and air-temperature spectra in the low-frequency range in the presence of convection. *Izv. Atmos. Ocean. Phys.*, 9, 445–452.

Izumi, Y., and S. J. Caughey, 1976: Minnesota 1973 atmospheric boundary layer experiment data report. AFCRL Res. Rep. (in preparation). [Will be available on request from Y. Izumi, AFGL, Hanscom AFB, Bedford, Mass. 01731 or NTIS, Springfield, Va. 22151.]

Kaimal, J. C., 1973: Turbulence spectra, length scales and structure parameters in the stable surface layer. *Bound.-Layer Meteor.*, 4, 289–309.

——, and D. A. Haugen, 1967: Characteristics of vertical velocity fluctuations observed on a 430 m tower. *Quart. J. Roy. Meteor. Soc.*, 93, 305–317.

——, and J. A. Businger, 1970: Case studies of a convective plume and a dust devil. *J. Appl. Meteor.*, 9, 612–620.

——, D. A. Haugen and J. T. Newman, 1966: A computer-controlled mobile micrometeorological observation system. *J. Appl. Meteor.*, 5, 411–421.

——, J. C. Wyngaard, Y. Izumi and O. R. Coté, 1972: Spectral characteristics of surface layer turbulence. *Quart. J. Roy. Meteor. Soc.*, 98, 563–589.

Konrad, T. G., 1970: The dynamics of the convective process in clear air as seen by radar. *J. Atmos. Sci.*, 27, 1138–1147.

Kukharets, V. P., 1974: Spectra of the vertical wind velocity component in the atmospheric boundary layer. *Izv. Atmos. Ocean. Phys.* 10, 375–378.

LeMone, M. A., 1973: The structure and dynamics of horizontal roll vortices in the planetary boundary layer. *J. Atmos. Sci.*, 30, 1077–1091.

Lenschow, D. H., 1974: Model of the height variation of the turbulence kinetic energy budget in the unstable planetary boundary layer. *J. Atmos. Sci.*, 31, 465–474.

Mahrt, L., and D. H. Lenschow, 1976: Growth dynamics of the convectively mixed layer. *J. Atmos. Sci.*, 33, 41–51.

Neff, W. D., 1975: Quantitative evaluation of acoustic echoes from the planetary boundary layer. NOAA Tech. Rep., ERL 322-WPL 38, 34 pp. [Available from the author, NOAA Laboratories/WPL, Boulder, Colo. 80302 or Govt. Printing Office, Washington, D. C. 20402.]

Pennell, W. T., and M. A. LeMone, 1974: An experimental study of turbulence structure in the fair-weather, trade wind boundary layer. *J. Atmos. Sci.*, 31, 1308–1323.

Rayment, R., 1973: An observational study of the vertical profile of the high frequency fluctuations of the wind in the atmospheric boundary layer. *Bound.-Layer Meteor.*, 3, 284–300.

——, and C. J. Readings, 1974: A case study of the structure and energetics of an inversion. *Quart. J. Roy. Meteor. Soc.*, 100, 221–233.

Readings, C. J., and H. E. Butler, 1972: The measurement of atmospheric turbulence from a captive balloon. *Meteor. Mag.*, **101**, 286–298.

——, D. A. Haugen and J. C. Kaimal, 1974: The 1973 Minnesota atmospheric boundary layer experiment. *Weather*, **29**, 309–312.

Richter, J. H., D. R. Jensen, V. R. Noonkester, T. G. Konrad, A. Arnold and J. R. Rowland, 1974: Clear air convection: A close look at its evolution and structure. *Geophys. Res. Lett.*, **1**, 173–176.

Rowland, J. R. and A. Arnold, 1975: Vertical velocity structure and geometry of clear air convection elements. *Preprints 16th Radar Meteorology Conf.*, 22–23 April, Houston, Tex., Amer. Meteor. Soc., 296–303.

Tennekes, H., 1970: Free convection in the turbulent Ekman layer of the atmosphere. *J. Atmos. Sci.*, **27**, 1027–1034.

——, 1975: Reply to comments on "A model for the dynamics of the inversions above a convective boundary layer." *J. Atmos. Sci.*, **32**, 992–995.

Smedman-Högström, A. S., and U. Högström, 1975: Spectral gap in surface layer measurements. *J. Atmos. Sci.*, **32**, 340–350.

Tsvang, L. R., 1969: Microstructure of temperature fields in the free atmosphere. *Radio Sci.*, **4**, 1175–1177.

Volkovitskaya, Z. I., and V. N. Ivanov, 1970: Turbulent energy dissipation in the atmospheric boundary layer. *Izv. Atmos. Ocean. Phys.*, **5**, 249–253.

Willis, G. E., and J. W. Deardorff, 1974: A laboratory model of the unstable planetary boundary layer. *J. Atmos. Sci.*, **31**, 1297–1307.

Wyngaard, J. C., 1975: Modeling the planetary boundary layer—extension to the stable case. *Bound.-Layer Meteor.*, **9**, 441–460.

——, and O. R. Coté, 1971: The budgets of turbulent kinetic energy and temperature variance in the atmospheric surface layer. *J. Atmos. Sci.*, **28**, 190–201.

——, and ——, 1974: The evolution of a convective planetary boundary layer—a higher-order-closure model study. *Bound.-Layer Meteor.*, **7**, 289–308.

——, ——, and Y. Izumi, 1971a: Local free convection, similarity, and the budgets of shear stress and heat flux. *J. Atmos. Sci.*, **28**, 1171–1182.

——, Y. Izumi and S. A. Collins, Jr., 1971b: Behavior of the refractive-index structure parameter near the ground. *J. Opt. Soc. Amer.*, **61**, 1646–1650.

——, O. R. Coté and K. S. Rao, 1974: Modeling the atmospheric boundary layer. *Advances in Geophysics*, Vol. 18A, Academic Press, 193–211.

Zilitinkevich, S. S., 1972: On the determination of the height of the Ekman boundary layer. *Bound.-Layer Meteor.*, **3**, 141–145.

——, 1975: Comments on "A model for the dynamics of the inversion above a convective boundary layer". *J. Atmos. Sci.*, **32**, 991–992.

THE CHARACTERISTICS OF TURBULENT VELOCITY COMPONENTS IN THE SURFACE LAYER UNDER CONVECTIVE CONDITIONS

H. A. PANOFSKY and H. TENNEKES

The Pennsylvania State University, University Park, Pa., U.S.A.

D. H. LENSCHOW

National Center for Atmospheric Research*, Boulder, Colo., U.S.A.

and

J. C. WYNGAARD

Cooperative Institute for Research in Environmental Sciences, University of Colorado/NOAA, Boulder, Colo., U.S.A.

and

Wave Propagation Laboratory, NOAA, Boulder, Colo. 80302, U.S.A.

Abstract. It is proposed that the ratios of the standard deviations of the horizontal velocity components to the friction velocity in the surface layer under convective conditions depend only on z_i/L where z_i is the height of the lowest inversion and L is the Monin-Obukhov length. This hypothesis is tested by using observations from several data sets over uniform surfaces and appears to fit the data well. Empirical curves are fitted to the observations which have the property that at large $z_i/-L$, the standard deviations become proportional to w_*, the convective scaling velocity.

Fluctuations of vertical velocity obtained from the same experiments scale with z/L, where z is the height above the surface, in good agreement with Monin-Obukhov theory.

1. Introduction

According to the now classical Monin-Obukhov similarity theory, the characteristics of the standard deviations of horizontal turbulent velocity components σ in the surface layer are described by:

$$\frac{\sigma_\alpha}{u_*} = \phi_\alpha\left(\frac{z}{L}\right), \quad \alpha = u, v, w \tag{1}$$

where u_* is the surface friction velocity, z the height and L the Monin-Obukhov length. ϕ is presumed to represent a set of universal functions, different for each horizontal velocity component.

Lumley and Panofsky (1964) have already noted that Equation (1) applies well to vertical but not to horizontal velocity components. In particular, under convective conditions, a change in height has negligible effect on horizontal standard deviations, whereas a change in L has a pronounced effect.

---

* The National Center for Atmospheric Research is sponsored by the National Science Foundation.

We can get some insight into the relevant similarity variables for the horizontal velocity components by considering the limiting case of free convection. Even in the surface layer, it seems plausible that they should scale with the convective velocity scale for the boundary layer,

$$w_* \equiv \left(\frac{gHz_i}{c_p \rho T}\right)^{1/3} = u_* k^{-1/3}(z_i/-L)^{1/3}, \tag{2}$$

where g is gravity, H the vertical surface virtual heat flux, c_p the specific heat at constant pressure, ρ density, T temperature and k von Kármán's constant, since the horizontal components of the convective eddies would be expected to extend down to near the surface. Thus in the limit

$$\frac{\sigma_\alpha}{u_*} \sim (z_i/-L)^{1/3}, \qquad \alpha = u, v. \tag{3}$$

Therefore we suggest that the proper surface-layer scaling for σ is not as in Equation (1), but rather

$$\frac{\sigma_\alpha}{u_*} = f(z_i/L), \qquad \alpha = u, v. \tag{4}$$

Wyngaard and Coté (1974) have previously postulated equations of this form.

Recently, good observations have become available on the basis of which the reliability of Equation (4) will be tested. For completeness, the data obtained during the same periods will be used to test once again the agreement of the vertical velocity fluctuations with predictions from Monin-Obukhov theory.

2. Properties of Horizontal Wind Components

The analysis is based on several independent field experiments. In one of these, two research groups, representing, respectively, the Air Force Cambridge Research Laboratories of Bedford, Massachusetts and the Meteorological Research Unit, Cardington, Bedford, England, cooperated in a rather ambitious project over an extremely flat section of northwestern Minnesota. The experiment is described in detail by Readings *et al.* (1974) and Izumi and Caughey (1976). Observations up to 32 m were obtained by sonic equipment from a mast. Data above that level were taken from instrumentation carried aloft by a tethered balloon.

In the other experiments, measurements were obtained from either the de Havilland Buffalo or Lockheed Electra aircraft operated by the National Center for Atmospheric Research. With the exception of one observation over eastern Colorado (described by Lenschow, 1970), the measurements were obtained over water. These include measurements over one of the Great Lakes (Lenschow, 1973), near Puerto Rico (Pennell and Le Mone, 1974) and over the East China Sea near Okinawa, Japan, as part of the Air Mass Transformation Experiment (AMTEX) (Lenschow and Agee, 1976). Each observation was obtained from straight and level flight legs at heights less than $0.2\ z_i$ over a time period of about 10 min, which corresponds to a distance of 40 to 60 km. A linear trend was

removed from the data before calculating the turbulence statistics. The Monin-Obukhov lengths were obtained from flux measurements at flight level and z_i was obtained from rawinsonde and aircraft vertical soundings.

All particulars of the observations used in this section are shown in Table I. The standard deviations at Minnesota represent averages of observations at 4 and 32 m heights. No significant difference of horizontal fluctuations at these heights was detected. In contrast, fluctuations of vertical velocity rapidly increased upward. Further, there were no important differences between lateral and longitudinal components, and only averages were analyzed. The standard deviations computed from the airplane data represent such averages, and are simply called σ in Table I.

Table I shows the influence of z_i on σ/u_*. For example, the Minnesota data of September 15 and 17 have about the same L but quite different z_i, and σ/u_* is observed to increase as z_i increases.

Figure 1 shows the relation between σ/u_* and z_i/L. All observations fall quite well on the same line even though some of the airplane data were obtained at levels rather too high for the surface layer.

Two empirical curves were fitted to the points in Figure 1, both satisfying the condition that f varies as $(z_i/-L)^{1/3}$ at large $z_i/-L$, so that the standard deviations σ become proportional to w_*, independent of u_*.

The equation

$$\sigma/u_* = [4 + 0.6(z_i/-L)^{2/3}]^{1/2} \tag{5}$$

was selected because it was similar in form to that postulated by Wyngaard and Coté (1974); the other,

$$\sigma/u_* = (12 + 0.5 \, z_i/-L)^{1/3} \tag{6}$$

was chosen because it is somewhat simpler and because it is in better agreement with observations made at other sites and in wind tunnels under near-neutral stability conditions (see, e.g. Lumley and Panofsky, 1964). Both equations fit well. Also, both agree well with laboratory studies by Willis and Deardorff (1974) in the limit of large $z_i/-L$.

It is clear that the hypothesis expressed by Equations (4) and (6) is in general agreement with observations. However, all data analyzed here were obtained over flat surfaces. It is quite possible that mesoscale terrain features can influence the scale of horizontal velocity components. This hypothesis needs to be tested. Another question not yet answered is whether substitution of z_i for z in Monin-Obukhov scaling also accounts satisfactorily for the properties of spectra and other more complex statistics of the horizontal velocity components. Kaimal et al. (1976) have shown that their spectra in the mixed layer scale with z_i, not z, and have suggested that such scaling should apply to the energy-containing region of the surface-layer spectra as well.

TABLE I

List of observations used (SI units) of horizontal fluctuations

Northwest Minnesota (tower)

Date (1973)	Run No.	σ_u	σ_y	z_i	$-L$	u_*
10/9	2A1	1.36	1.41	1250	42	0.45
10/9	2A2	1.26	1.37	1615	38	0.45
11/9	3A1	1.48	1.50	2310	24	0.37
11/9	3A2	1.16	1.22	2300	24	0.32
15/9	5A1	0.72	0.75	1085	7	0.18
17/9	6A1	1.42	1.37	2095	6	0.24
17/9	6A2	1.26	1.34	2035	6	0.23
17/9	6B1	1.01	1.08	2360	23	0.26
19/9	7C1	1.34	1.22	1020	9	0.28
19/9	7C2	1.18	1.22	1140	13	0.30
19/9	7D1	1.03	1.15	1225	14	0.25

Date	σ	z_i	$-L$	u_*	z
Eastern Colorado (Airplane)					
4/25/68	1.39	1045	33	0.46	87
Lake Huron (Airplane)					
11/13/73	0.85	912	24	0.27	31
Carribbean (Airplane)					
11/15/72	0.93	610	357	0.45	30

East China Sea (Airplane)

Date (1975)	σ	z_i	$-L$	u_*	z
2/15	1.04	1296	70	0.38	110
2/15	1.10	1296	67	0.39	110
2/15	1.22	1296	36	0.39	110
2/15	1.19	1296	54	0.44	110
2/15	1.11	1296	20	0.30	110
2/15	1.03	1296	25	0.32	110
2/15	0.88	1296	32	0.24	226
2/15	1.07	1296	65	0.45	135
2/15	1.22	1296	54	0.45	135
2/15	1.23	1296	107	0.53	135
2/15	1.07	1296	66	0.47	135
2/15	1.24	1296	43	0.41	135
2/16	0.96	1435	61	0.36	99
2/16	1.06	1435	35	0.32	99
2/16	1.31	1435	24	0.30	99
2/16	1.09	1435	33	0.35	99
2/16	1.15	1435	56	0.46	99
2/16	1.16	1435	25	0.34	99
2/16	0.88	1435	35	0.35	132
2/16	0.93	1435	44	0.35	66
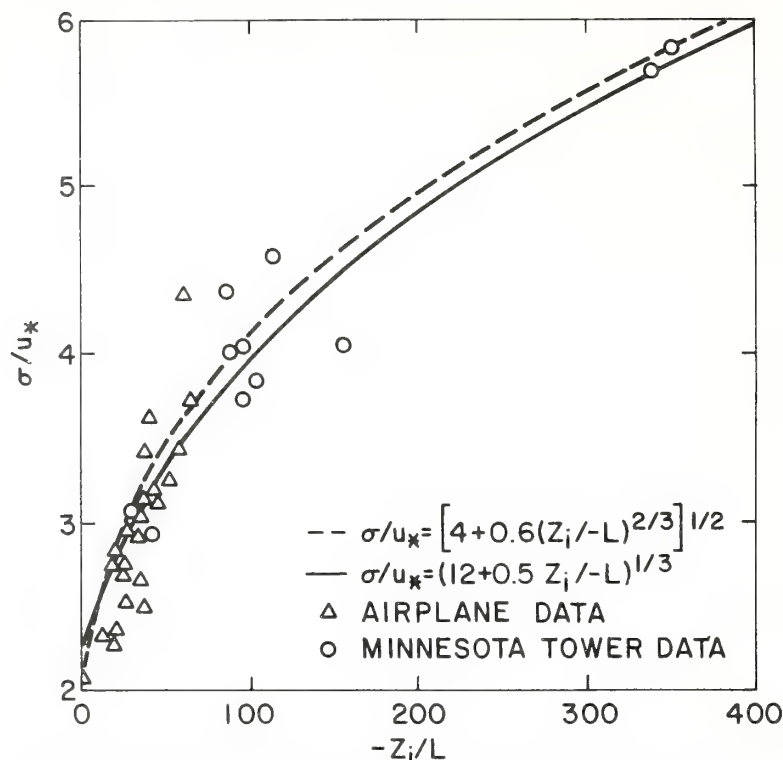
Fig. 1. Standard deviations of horizontal velocity components, normalized by u_*, as functions of $-z_i/-L$.

3. Properties of the Vertical Velocity Components

Figure 2 shows the variation of the ratio of σ_w, the standard deviation of the vertical velocity, to the friction velocity, plotted as a function of $z/-L$. The points are based on the same field experiments as those in Figure 1. The lack of random scatter of the Minnesota observations attests to their unusual excellence of these observations.

Again, two empirical relations have been fitted to the data, both subject to the conditions that σ_w/u_* should vary as $(z/-L)^{1/3}$ for large $z/-L$, and that it should approach approximately 1.3 as $z/-L \to 0$. The equation

$$\sigma_w/u_* = [1.6 + 2.9(z/-L)^{2/3}]^{1/2} \tag{7}$$

was selected because it is of the form postulated by Businger (1959) and by Wyngaard and Coté (1974). The equation

$$\sigma_w/u_* = 1.3[1 + 3z/-L]^{1/3} \tag{8}$$

is a little simpler and fits the observations better at large $z/-L$. It also provides a good fit to surface-layer observations collected by Merry and Panofsky (1976) from observations at the other sites, and is therefore believed to be slightly preferable to Equation (7).
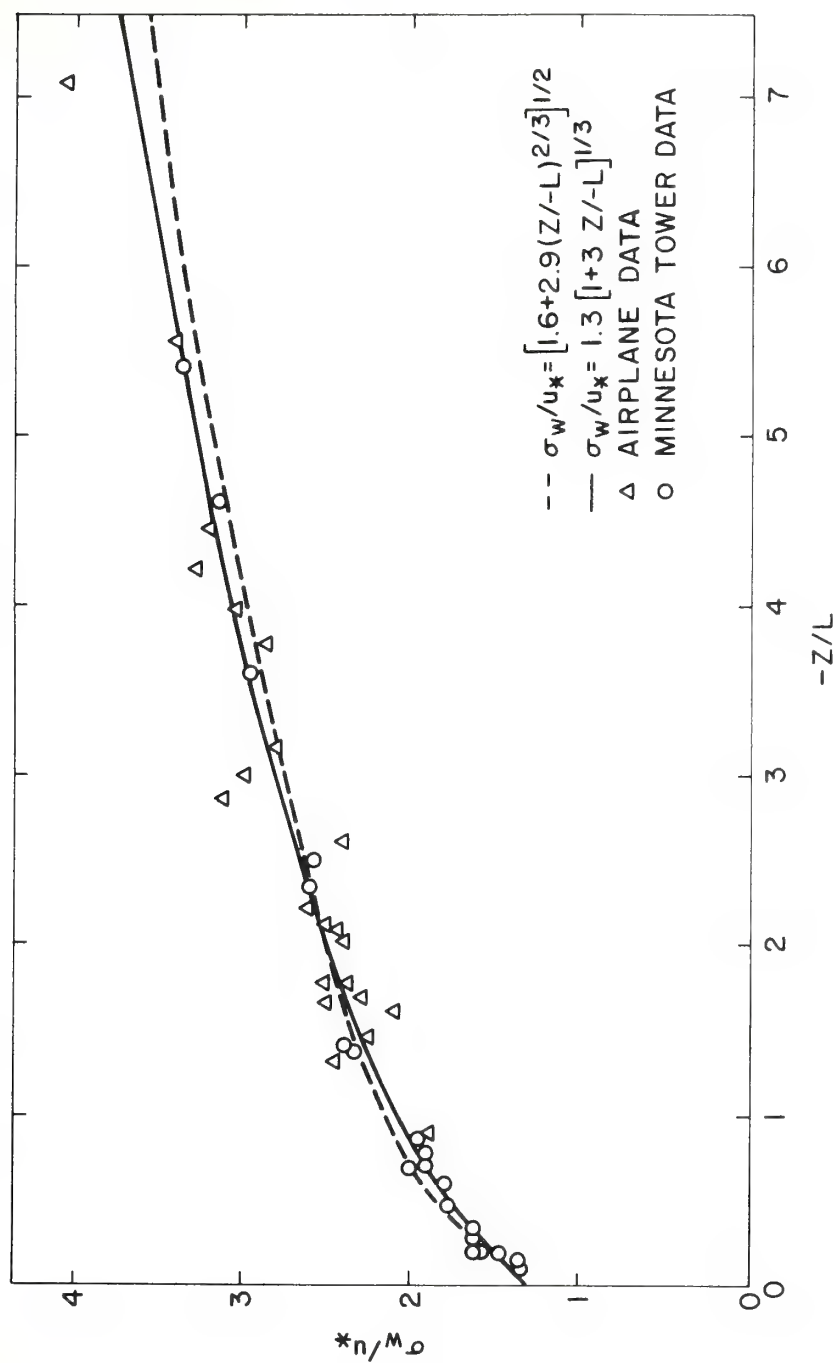
Fig. 2. Standard deviation of vertical velocity, normalized by u_*, as a function of $-z/L$.

References

Businger, J. A.: 1959, 'A Generalization of the Mixing-Length Concept', *J. Meteorol.* **16,** 516–523.

Izumi, Y. and Caughey, J. S.: 1976, 'Minnesota 1973 Atmospheric Boundary Layer Experiment Data Report', AFCRL-TR-76-0038, 29 pp.

Kaimal, J. C., Wyngaard, J. C., Haugen, D. A., Coté, O. R., Izumi, Y., Caughey, S. J., and Readings, C. J.: 1976, 'Turbulence Structure in the Convective Boundary Layer', *J. Atmos. Sci.* **33,** 2152–2169.

Lenschow, D. H.: 1970, 'Airplane Measurements of Planetary Boundary Layer Structure', *J. Appl. Meteorol.* **9,** 874–884.

Lenschow, D. H.: 1973, 'Two Examples of Planetary Boundary Layer Modification over the Great Lakes', *J. Atmos. Sci.* **30,** 568–581.

Lenschow, D. H. and Agee, E. M.: 1976, 'Preliminary Results from the Air Mass Transformation Experiment', *Bull. Am. Meteorol. Soc.* **57,** 1346–1355.

Lumley, J. L. and Panofsky, H. A.: 1964, *Structure of Atmospheric Turbulence*, Wiley-Interscience, New York.

Merry, M. and Panofsky, H. A.: 1976, 'Statistics of Vertical Motion over Land and Water', *Quart. J. Roy. Meteorol. Soc.* **102,** 255–260.

Pennell, W. T. and LeMone, M. A.: 1974, 'An Experimental Study of Turbulence Structure in the Fair-Weather Trade Wind Boundary Layer', *J. Atmos. Sci.* **31,** 1308–1323.

Readings, C. J., Haugen, D. A., and Kaimal, J. C.: 1974, 'The 1973 Minnesota Atmospheric Boundary Layer Experiment', *Weather* **29,** 309–312.

Willis, G. E. and Deardorff, J. W.: 1974, 'A Laboratory Model of the Unstable Planetary Boundary Layer', *J. Atmos. Sci.* **31,** 1297–1307.

Wyngaard, J. C. and Coté, O. R.: 1974, 'The Evolution of a Convective Planetary Boundary Layer – a Higher-Order-Closure Model Study', *Boundary-Layer Meteorol.* **7,** 289-308.

THE ATMOSPHERIC BOUNDARY LAYER OVER A SIMPLE INHOMOGENEOUS SURFACE

J. C. Wyngaard

Cooperative Institute for Research in Environmental Sciences
University of Colorado/NOAA
Boulder, Colorado 80309
and
National Oceanic and Atmospheric Administration
Wave Propagation Laboratory
Boulder, Colorado 80302

R. M. Jones

National Oceanic and Atmospheric Administration
Wave Propagation Laboratory
Boulder, Colorado 80302

1. INTRODUCTION

In many applications one needs to calculate the flow in the atmospheric boundary layer (ABL) under realistic conditions--such as over inhomogeneous terrain. Even with the recent advances in flow modeling, in numerical techniques, and in computers, this remains a formidable problem for several reasons. First, it can require a four-dimensional grid (three space plus time), and thus be very time consuming. Second, it is always necessary to account for the effects of turbulence ABL calculations, and while today's turbulence models are superior to those of a generation ago, they require a fine mesh, with grid spacing on the order of a turbulent integral scale or less. Thus computer capacity can limit the total grid volume to far less than that desired.

On the other hand, often one does not want the wealth of local detail such a calculation would give. In many problems, flow properties averaged over horizontal planes would suffice. In this paper we discuss a modeling approach in which contemporary turbulence modeling techniques are used in an attempt to satisfy these simpler needs.

2. THE MODEL

We will illustrate our approach by considering a simple case which has the essential elements of the full problem. The flow is taken as neutrally stratified, steady, with the lower boundary a horizontal surface whose roughness varies with x_1, the downstream coordinate. Near the surface the flow will change continuously with x_1 in response to the variable roughness, which we take to be *statistically* homogeneous. Thus the streamwise velocity derivative $\partial U_1/\partial x_1$ will in general be non-zero, generating

a non-zero vertical velocity U_3. The flow throughout the ABL will be modified by this forcing at the lower boundary, with flow variables depending on the vertical coordinate x_3 and on x_1. We assume that the conditions at the top of the ABL are fixed.

The mean momentum and continuity equations for this flow are (Busch, 1973)

$$U_{i,j}U_j + (\overline{u_i u_j})_{,j} = -P_{,i} - 2\,\varepsilon_{ijk}\,\Omega_j\,U_k$$

$$U_{i,i} = 0 \tag{1}$$

where U_i and u_i represent the (ensemble) mean and turbulent velocity, respectively, P is the mean kinematic pressure, Ω_j is the earth's rotation rate, a comma denotes differentiation, and repeated indices are summed. The turbulent stress $\overline{u_i u_j}$ has an important role in this equation and cannot be neglected, so we need additional information in order to close the system (1).

Much development work has been done in recent years on model equations for these turbulent stresses. These "higher order closure" models have largely replaced the eddy diffusivity approach in smaller-scale ABL research applications. While this field is still in an early stage of development, it is clear that such models can give very accurate predictions of turbulent flow structure. At the same time, it is also clear that much development work remains before a model suitable for use in a wide range of flow situations is produced. Bradshaw (1972) has reviewed this activity.

We will use a simple turbulence model of this type:

$$\frac{\partial}{\partial t}\overline{u_i u_k} = -U_{i,j}\overline{u_j u_k} - U_{k,j}\overline{u_i u_j} - (U_j\overline{u_i u_k})_{,j}$$

$$- A_1(\overline{q^2})^{1/2}(\overline{u_i u_k} - \frac{\overline{q^2}}{3}\delta_{ik})/\ell$$

$$+ A_2\overline{q^2}(U_{i,k} + U_{k,i}) - 2(\overline{q^2})^{3/2}\delta_{ik}/3\ell$$

$$- 2\epsilon_{ijm}\Omega_j\overline{u_m u_k}$$

$$- 2\epsilon_{kjm}\Omega_j\overline{u_m u_i} = 0 \qquad (2)$$

This is a parameterization of the exact $\overline{u_i u_k}$ equation under neutral conditions. The first three terms on the right represent (exactly) production and advection; the fourth and fifth are parameterizations of pressure covariances, and the sixth term is a parameterization of viscous dissipation. The final terms represent (exactly) the rotation effects. A_1 and A_2 are constants, and ℓ is a length scale of the turbulence. We use the notation $\overline{q^2} = \overline{u_i u_i}$.

This is a simplified version of the model used by Wyngaard (1975) in a study of the horizontally homogeneous ABL. We include it here only to demonstrate how a turbulence model can be used to calculate inhomogeneous flow structure, and not to advocate this particular form.

The turbulence equation (2), together with the mean field equation (1), represent a closed system. Our approach to the solution is to decompose the flow variables into a basic, undisturbed state (denoted by a superscript zero) plus contributions due to the forcing at the lower boundary. Thus for any flow variable f

$$f = f^{(0)}(x_3) + f^{(1)}(x_1, x_3) + f^{(2)}(x_1, x_3) \qquad (3)$$

We assume the deviations from the basic state are not large so that $f^{(1)}$ and $f^{(2)}$ are first and second order quantities, respectively, in some small parameter. We will take $f^{(1)}$ and $f^{(2)}$ to represent the linear and nonlinear responses. Since the mean and turbulent fields are intimately coupled through Eq (1) and (2), both will be disturbed by the forcing.

3.   CALCULATION OF THE LINEARIZED RESPONSE

Substitution of the decomposition (3) into the momentum equation (1) and neglecting terms of order higher than the first gives

$$U_{i,j}^{(0)}U_j^{(1)} + U_{i,j}^{(0)}U_j^{(0)} + U_{i,j}^{(1)}U_j^{(0)}$$

$$+ (\overline{u_i u_j}^{(0)} + \overline{u_i u_j}^{(1)})_{,j} = -P_{,i}^{(0)} - P_{,i}^{(1)}$$

$$- 2\epsilon_{ijk}\Omega_j(U_k^{(0)} + U_k^{(1)}) \qquad (4)$$

The basic flow satisfies

$$U_{i,j}^{(0)}U_j^{(0)} + (\overline{u_i u_j}^{(0)})_{,j} = -P_{,i}^{(0)}$$

$$- 2\epsilon_{ijk}\Omega_j U_k^{(0)} \qquad (5)$$

Subtracting Eq (5) from Eq (4) gives the first order mean momentum equation:

$$U_{i,j}^{(0)}U_j^{(1)} + U_{i,j}^{(1)}U_j^{(0)} + (\overline{u_i u_j}^{(1)})_{,j} = -P_{,i}^{(1)}$$

$$- 2\epsilon_{ijk}\Omega_j U_k^{(1)} \qquad (6)$$

In a similar way we can derive a first order turbulent stress equation from Eq (2):

$$U_{i,j}^{(1)}\overline{u_j u_k}^{(0)} + U_{i,j}^{(0)}\overline{u_j u_k}^{(1)} + U_{k,j}^{(1)}\overline{u_i u_j}^{(0)} + U_{k,j}^{(0)}\overline{u_j u_i}^{(1)}$$

$$+ (U_j^{(0)}\overline{u_i u_k}^{(1)} + U_j^{(1)}\overline{u_i u_k}^{(0)})_{,j}$$

$$= -A_1(\overline{q^2}^{(0)})^{1/2}(\overline{u_i u_k}^{(1)} - \overline{q^2}^{(1)}\delta_{ik}/3)/\ell$$

$$- A_1(\overline{q^2}^{(1)})^{1/2}(\overline{u_i u_k}^{(0)} - \overline{q^2}^{(0)}\delta_{ik}/3)/\ell$$

$$+ A_2\overline{q^2}^{(0)}(U_{i,k}^{(1)} + U_{k,i}^{(1)}) + A_2\overline{q^2}^{(1)}(U_{i,k}^{(0)} + U_{k,i}^{(0)})$$

$$- 2(\overline{q^2}^{(1)})^{3/2}\delta_{ik}/3\ell - 2\epsilon_{ijm}\Omega_j\overline{u_m u_k}^{(1)}$$

$$- 2\epsilon_{kjm}\Omega_j\overline{u_m u_i}^{(1)} \qquad (7)$$

The continuity equation becomes

$$U_{1,1}^{(1)} + U_{3,3}^{(1)} = 0 \qquad (8)$$

Eqs (6-8) are a closed set of linear differential equations for the first order quantities. Although they contain derivatives in both x_1 and x_3, the former can be eliminated by a Fourier transform over that coordinate, leaving a set of ordinary differential equations. They are to be solved as a boundary-value problem, with the conditions specified near the surface and at the top of the ABL. Lower boundary conditions can be generated from the equations themselves, and the no-slip condition, by observing their behavior as $x_3 \to 0$. Since there $\ell \sim x_3$, many of the terms in the linearized turbulence equations (7) can be dropped, and the set yields, near the surface,

$$\overline{u_1 u_3}^{(1)} = -2K^{(0)}U_{1,3}^{(1)} \qquad (9)$$

where $K^{(0)} = ku_* ^{(0)}x_3$ is the background eddy diffusivity. Noting that $\overline{u_1 u_3}^{(1)} = -2u_* ^{(0)}u_* ^{(1)}$ gives

$$U_{1,3}^{(1)} = \frac{u_* ^{(1)}}{k x_3}$$

$$U_1^{(1)} = \frac{u_* ^{(1)}}{k}\,\mathrm{Ln}\,x_3 + \text{constant} \qquad (10)$$

The constant can be evaluated by requiring the sum of $U_1^{(0)}$ and $U_1^{(1)}$ to vanish at the local roughness height $z_0(x_1)$. If we denote the constant background roughness length by z_{00}, this gives

61

$$U_1^{(0)} = \frac{u_*^{(0)}}{k} \operatorname{Ln} \frac{x_3}{z_{00}}$$

$$U_1^{(0)} + U_1^{(1)} = \frac{u_*^{(0)}}{k} \operatorname{Ln} \frac{x_3}{z_{00}} + \frac{u_*^{(1)}}{k} \operatorname{Ln} \frac{x_3}{z_0}$$

$$- \frac{u_*^{(0)}}{k} \operatorname{Ln} \frac{z_0}{z_{00}} \tag{11}$$

The resulting linearized expression for $U_1^{(1)}$ is

$$U_1^{(1)} = \frac{u_*^{(1)}}{k} \operatorname{Ln} \frac{x_3}{z_{00}} - \frac{u_*^{(0)}}{k} \operatorname{Ln} \frac{z_0}{z_{00}} \tag{12}$$

Differentiation of Eq (12) with respect to x_1, using the continuity equation (8), and integration over x_3 gives the lower boundary condition for $U_3^{(1)}$. In linearized form it is

$$U_3^{(1)} = -\frac{1}{k} \frac{du_*^{(1)}}{dx_1} \left[x_3 \operatorname{Ln} \frac{x_3}{z_{00}} - (x_3 - z_0) \right]$$

$$+ \frac{u_*^{(0)}}{k} \left\{ \frac{d}{dx_1} (\operatorname{Ln} z_0) \right\} (x_3 - z_0) \tag{13}$$

The advantage of these boundary bonditions over the no-slip condition alone is that (12) and (13) can be applied at some height which is well above z_0, but still small, thus saving computation time. At the top of the ABL, which can either scale with $u_*^{(0)}/f$ or be fixed by an upper-level inversion, the first order quantities are forced to vanish.

4.   RELATION TO THE ORR-SOMMERFELD EQUATION

This perturbation approach is also used in the linearized theory of the stability of viscous flow, where it gives the Orr-Sommerfeld equation (Schlichting, 1960) for the first order disturbance stream function. Often an ad-hoc extension to turbulent flow is made by replacing the molecular viscosity by an eddy viscosity K. Thus, in a steady neutral shear flow without rotation effects, the linearized disturbance equations would be represented as

$$U_{i,j}^{(0)} U_j^{(1)} + U_{i,j}^{(1)} U_j^{(0)} = -P_{,i}^{(1)} + K U_{i,jj}^{(1)}$$

$$U_{i,i}^{(1)} = 0 \tag{14}$$

It is usual to introduce a stream function χ,

$$U_1^{(1)} = -\chi_{,3}$$

$$U_3^{(1)} = \chi_{,1} \tag{15}$$

and to Fourier transform in the homogeneous (streamwise) direction

$$\chi(x_1, x_3) = \int_{-\infty}^{\infty} e^{i\kappa x_1} D(\kappa, x_3) \, dx_1 \tag{16}$$

The result of combining Eqs (14)-(16) is the Orr-Sommerfeld equation for this flow:

$$K D'''' + D'' (-\kappa^2 K - i\kappa U_1^{(0)}) + D(i\kappa U_1''^{(0)} + i\kappa^3 U^{(0)}) = 0 \tag{17}$$

Our set of equations (6)-(8) can also be combined to give a single linear differential equation for the disturbance stream function. If further assumptions about the relationships among components of $\overline{u_i u_k}^{(1)}$ are made, it can be reduced to a fourth order equation of the form

$$a_4 D'''' + a_3 D''' + a_2 D'' + a_1 D' + a_0 D^0 = 0 \tag{18}$$

where the a_i are functions of the background flow (both mean and turbulent) and wavenumber. Thus our approach gives a more general equation than the ad-hoc extension of the viscous Orr-Sommerfeld equation to turbulent flow.

The differences between our equation (18) and the Orr-Sommerfeld form (17) can be simply explained. In a laminar flow the viscosity is a property of the *fluid*. In turbulent flow the eddy viscosity is a property of the *flow*; in fact it can be independent of the fluid. If a turbulent flow is changed by adding a disturbance, the eddy viscosity is changed as well. Thus when one decomposes a turbulent flow into background plus disturbance components, he should also decompose the eddy viscosity. The stress conservation equation (2) amounts to an equation for a generalized eddy viscosity, and in perturbing it we have, in effect, allowed the eddy viscosity to be changed by the disturbance. The additional terms in our Eq (18) represent the effects of this disturbed eddy viscosity. Thus attempts to improve linear disturbance calculations in *turbulent* flow by using height-dependent eddy viscosity, while still ignoring its perturbations, neglect a substantial part of the physics.

5.   CALCULATIONS OF NONLINEAR EFFECTS

The perturbation equations through second order can be derived by following the same procedure. We average these equations over horizontal planes, denoting this by brackets. Recall that the flow is taken to be *statistically* homogeneous in the horizontal, so that horizontal derivatives of these averaged quantities vanish. Note also that first order quantities average to zero, since they have zero mean. It then follows from the averaged continuity equation that $[U_3^{(2)}] = 0$. Thus we need only consider the horizontal components of the second order mean momentum equation; the pressure gradient terms vanish upon averaging, and we have

$$U_{i,j}^{(0)} [U_j^{(2)}] + [U_{i,j}^{(2)}] U_j^{(0)} + [U_{i,j}^{(1)} U_j^{(1)}]$$

$$+ [\overline{u_i u_j}^{(2)}]_{,j} = -2 \, \varepsilon_{ijk} \Omega_j [U_k^{(2)}]$$

$$i = 1, 2 \tag{19}$$

The corresponding turbulence equation is

$$U_{i,j}^{(0)}[\overline{u_j u_k}^{(2)}] + [U_{i,j}^{(2)}]\overline{u_j u_k}^{(0)} + [U_{i,j}^{(1)}\overline{u_j u_k}^{(1)}]$$

$$+ U_{k,j}^{(0)}[\overline{u_j u_i}^{(2)}] + [U_{k,j}^{(2)}]\overline{u_j u_i}^{(0)} + [U_{k,j}^{(1)}\overline{u_j u_i}^{(1)}]$$

$$+ \left\{ [U_j^{(2)}]\overline{u_i u_k}^{(0)} + U_j^{(0)}[\overline{u_i u_k}^{(2)}] + [U_j^{(1)}\overline{u_i u_k}^{(1)}] \right\}_{,j}$$

$$= -A_1(\overline{q^2}^{(0)})^{1/2}([\overline{u_i u_k}^{(2)}] - [\overline{q^2}^{(2)}]\delta ik/3)/\ell$$

$$- A_1[(\overline{q^2}^{(2)})^{1/2}(\overline{u_i u_k}^{(0)} - \overline{q^2}^{(0)}\delta ik/3)/\ell$$

$$- A_1[(\overline{q^2}^{(1)})^{1/2}(\overline{u_i u_k}^{(1)} - \overline{q^2}^{(1)}\delta ik/3)]/\ell$$

$$+ A_2\overline{q^2}^{(0)}([U_{i,k}^{(2)}] + [U_{k,i}^{(2)}])$$

$$+ A_2[\overline{q^2}^{(2)}](U_{i,k}^{(0)} + U_{k,i}^{(0)})$$

$$+ A_2[\overline{q^2}^{(1)}(U_{i,k}^{(1)} + U_{k,i}^{(1)})]$$

$$- 2\,\delta ik[(\overline{q^2}^{(2)})^{3/2}]/3\ell$$

$$- 2\,\epsilon_{ijm}\,\Omega_j\,[\overline{u_m u_k}^{(2)}]$$

$$- 2\,\epsilon_{kjm}\,\Omega_j\,[\overline{u_m u_i}^{(2)}] \qquad (20)$$

The set (19) and (20) are linear, ordinary differential equations, with x_3 as independent variable, and with forcing functions generated from correlations of the first order solutions. Phase shifts in these first order variables will be generated by the turbulence, so in general these forcing functions are non-zero. Appropriate boundary conditions are vanishing second-order averages at the top of the ABL. Thus (within the restrictions of the small-amplitude expansion) this allows us to calculate the mean levels introduced into the disturbance field along with the streamwise periodic first order variations.

To pick a simple illustrative example, the averaged flow near the surface will be $U = U_1^{(0)} + [U_1^{(2)}]$, while the friction velocity averages to $u_* = u_*^{(0)} + [u_*^{(2)}]$. The velocity profile remains essentially logarithmic, giving

$$U = \frac{u_*}{k} \, \mathrm{Ln} \, \frac{x_3}{z_0 \text{ eff}} \qquad (21)$$

where $z_0 \text{ eff}$ is an "effective" roughness length, which in general is not simply $[z_0(x_1)]$.

One can calculate horizontally-averaged values for both mean field and turbulence quantities from Eqs (19) and (20). These should be useful for example in determining the effect of surface roughness inhomogeneities on the similarity and scaling laws which have been developed for the idealized, horizontally homogeneous ABL. In fact, they should be useful in interpreting the results of *any* ABL turbulence measurements.

The extension to stratified flows requires the inclusion of temperature terms in the momentum and turbulence equations and the addition of equations for these new terms, which involve both the mean temperature and turbulent temperature covariances. Several turbulence models which include these effects currently exist, and they can be incorporated into the scheme described here without additional difficulty beyond increasing the number of equations. Other types of boundary conditions can also be treated.

References

Bradshaw, D., 1972: The understanding and prediction of turbulent flow. *Aeronaut. J.*, *76*, 403-418.
Busch, N. E., 1973: On the mechanics of atmospheric turbulence. *Workshop On Micrometeorology*, D. A. Haugen, Ed., Amer. Meteor. Soc., 1-61.
Schlichting, H., 1960: *Boundary Layer Theory*. McGraw-Hill, New York.
Wyngaard, J. C., 1975: Modeling the planetary boundary layer--extension to the stable case. *Boundary-Layer Meteorology*, *9*, 441-460.

On the Nonlinear Theory for Gravity Waves on the Ocean's Surface.
Part II : Interpretation and Applications

D. E. Barrick and B. L. Weber

ABSTRACT

In a previous paper (Weber and Barrick, 1977), a generalization of Stokes' perturbational technique permitted us to obtain solutions to higher orders for gravity-wave parameters for an arbitrary, two-dimensional periodic surface. In particular, the second-order wave-height correction and the third-order dispersion relation correction were derived there. In this paper, we interpret and apply those solutions in a variety of ways. First of all, we interpret the dispersion relation (and its higher order corrections) physically, as they relate to the phase velocity of individual ocean wave trains. Second, the validity of the two results derived previously is established by comparisons in the appropriate limiting cases with classical results available from the literature. It is shown how the solutions—derived for periodic surface profiles—can be generalized to include random wave fields whose average properties are to be specified. Then a number of examples of averaged higher order wave parameters are given, and in certain cases a Phillips' one-dimensional wave-height spectral model is employed to yield a quantitative feel for the magnitudes of these higher order effects. Both the derivations and the examples have direct application to the sea echo observed with high-frequency radars, and relationships with the radar observables are established and discussed.

1. Introduction

In a previous paper (Weber and Barrick, 1977) a generalization of Stokes' (1847) perturbation technique was presented which permitted the derivation of higher order corrections to the linear solution of the (nonlinear) hydrodynamic equations describing waves near the air-water interface. The generalization consisted in assuming a Fourier series expansion for the wave height for deep-water gravity waves. The method ignores the dynamics of energy transfer between waves, between the atmosphere and ocean and viscous damping effects. Hence the solution is expected to be valid over space and time scales less in extent than those over which energy transfer variations are important.

While the overall method was general, that paper concentrated upon the derivation of two results: 1) the second-order correction to the wave height (and velocity potential), and 2) the first nonzero correction to the lowest order dispersion relation obtained by carrying the perturbation analysis to third order. Bits and pieces of these derived quantities have appeared from time to time in the literature (e.g., height corrections for two waves at a time, dispersion-relation correction for colinear waves), but this is the first time to our knowledge that Stokes' techniques have been generalized to an infinite field of two-dimensional waves in such a way that both wave height and dispersion-relation corrections can be derived in the same analysis in a self-consistent manner.

It is the purpose of this paper to interpret and apply the solutions derived in the previous paper. In particular: 1) the dispersion relation will be interpreted physically; 2) the validity of the results for second-order wave height and the third-order dispersion-relation correction will be established by comparisons with classical solutions in the appropriate limits; 3) it will be shown how the results for periodic waves can be generalized to include random wave fields whose average properties are desired; and 4) specific sample applications for the average wave-height directional spectrum and dispersion relation mean and variances will be given. The rationale for wanting to know these latter two quantities derives from the interpretation of high-frequency radar echoes from the sea surface, and this application will be discussed briefly.

2. Interpretation of the dispersion relationship

a. Series simplification

The basic Fourier series expansion of the wave-height as given in Eq. (4) of W-B[1] shows the summation indices over $\mathbf{k}$ and ω (two-dimensional space and time) as seemingly independent. They are *not*, however. Having chosen $\mathbf{k}$ and $\eta_1(\mathbf{k},\omega)$ as the independent variables of the problem, all other quantities are dependent upon these variables. Thus to the lowest order $\omega \approx \omega_0$, where ω_0 was derived in Eq. (15) of W-B, and is seen to be a function of $k(\equiv |\mathbf{k}|)$ only. If one wishes to include the first nonzero correction to ω (i.e.,

---

[1] Hereafter, W-B refers to Weber and Barrick (1977), Part I.

ω_2 since $\omega_1=0$), this was shown in Eq. (29) of W-B to be a function of both $\mathbf{k}$ and $|\eta_1(\mathbf{k},\omega)|^2$. Hence having specified $\mathbf{k}$ and η_1, one is no longer free to choose ω independently. Therefore, η_1 is actually only a function of $\mathbf{k}$. Furthermore, the Fourier representation of wave height is no longer a triple series over $\mathbf{k}$ ($=k_x\hat{x}+k_y\hat{y}$) and ω, but is reduced to an explicit double series over $\mathbf{k}$, where $\hat{x}$ and $\hat{y}$ are unit vectors.

This dependence of ω on $\mathbf{k}$ can be used to simplify the series by the use of Kronecker-delta indicators. For example, suppose that the dispersion relation to the lowest order is adequate for a given purpose. Then the series Eq. (4) of W-B can be rewritten to first order as

$$\eta_1(\mathbf{r},t)=\sum_{\mathbf{k},\omega_0}\eta_1(\mathbf{k},\omega_0)\delta_{\omega_0}^{\pm\sqrt{gk}}\exp[i(\mathbf{k}\cdot\mathbf{r}-\omega_0 t)]$$

$$=\sum_{\mathbf{k}}\{\eta_1(\mathbf{k})\exp[i(\mathbf{k}\cdot\mathbf{r}-\sqrt{gk}t)]+\eta_1^*(\mathbf{k})$$

$$\times\exp[-i(\mathbf{k}\cdot\mathbf{r}-\sqrt{gk}t)]\},\quad(1)$$

where we have defined and used the fact[2] that $\eta_1(\mathbf{k})\equiv\eta_1(\mathbf{k},\sqrt{gk})$ and $\eta_1^*(\mathbf{k})\equiv\eta_1^*(\mathbf{k},\sqrt{gk})=\eta_1(-\mathbf{k},-\sqrt{gk})$. A similar application of Kronecker deltas can be used to extend ω to its next nonvanishing order (i.e., $\omega=\omega_0+\omega_2$), except that now ω_2 is a function of wave heights $\eta_1(\mathbf{k})$, and hence a series in the exponential argument must be evaluated before the main series is summed. In a like manner, Kronecker-delta relationships between ω_0' (or ω') and k', as well as ω'' and $\mathbf{k}''$, can be used to simplify the series for the second-order wave height [Eq. (22) of W-B]. Hence one of the three summations can be dropped, with a single Kronecker-delta remaining in the double series. Finally, note that a single Kronecker-delta appears in the series for the second-order frequency correction, ω_2 [Eq. (29) of W-B]; this reduces the triple summation over $\mathbf{k}'$, ω' to a double summation over $\mathbf{k}'$, with the wave-height coefficients $\eta_1(\mathbf{k}',\omega')$, as before now only functions of $\mathbf{k}'$, i.e., $\eta_1(\mathbf{k}')$.

b. Interpretation

The gravity-wave dispersion relations have a simple interpretation in terms of the phase velocity of a wave train of wave vector $\mathbf{k}$. This quantity is the speed with which the crests of waves of length $2\pi/|\mathbf{k}|$ pass a given point, i.e., $v_{ph}=\omega(\mathbf{k})/k$ (where $k\equiv|\mathbf{k}|$). Since successive terms in the perturbation expansion for ω are small, we can write (to second order)

$$\omega(\mathbf{k})=\omega_0+\omega_2=\omega_0\left(1+\frac{\omega_2}{\omega_0}\right)=\sqrt{gk}\left(1+\frac{\omega_2}{\omega_0}\right),\quad(2)$$

and hence

$$v_{ph}(\mathbf{k})=\sqrt{\frac{g}{k}}\left(1+\frac{\omega_2}{\omega_0}\right)=\sqrt{\frac{g}{k}}[1+\Delta v_{ph}(\mathbf{k})].\quad(3)$$

Therefore, the correction term ω_2/ω_0 to the dispersion equation derived as (29) of W-B represents the correction to the phase velocity of an ocean wave of length $2\pi/k$. The general form of Eq. (29) indicates that this change in phase velocity comes about not only as a result of the existence of that wave alone, but as a result of the presence of all the other waves. Stokes (1847) showed that the phase velocity of a *solitary* wave train tended to increase slightly as its height increased. Longuet-Higgins and Phillips (1962) showed that a wave of length $2\pi/k$ whose own amplitude is infinitesimally small is affected by a second wave moving parallel to it. Our solution contains both of these two results as limiting cases, but also applies to an arbitrary number of waves moving in arbitrary directions.

In order to understand this effect physically, let us specialize (29) to the following two cases. We shall study the normalized phase velocity correction of a sinusoidal wave of length $2\pi/k$ due to both itself and a second wave of wavelength $2\pi/k'$ moving 1) parallel to the first wave and 2) perpendicular to the first wave. Thus (29) becomes[3]

Parallel waves

$$\Delta v_{ph}(\mathbf{k})=\omega_2/\omega_0=2k^2|\eta_1(\mathbf{k})|^2\pm 4\frac{\omega_0'k}{\omega_0}|\eta_1(\mathbf{k}')|^2$$

$$\times\begin{cases}k & \text{for}\quad k'>k\\k' & \text{for}\quad k'<k\end{cases}\quad(4)$$

Perpendicular waves

$$\Delta v_{ph}(\mathbf{k})=\omega_2/\omega_0=2k^2|\eta_1(\mathbf{k})|^2+\frac{k^2\omega_0'^2}{\omega_0^2\omega_\perp^2}F_\perp|\eta_1(\mathbf{k}')|^2.\quad(5)$$

In the first equation, the upper/lower sign is used if the second wave (with period $2\pi/k'$) is traveling in the same/opposite direction as the first wave (with period $2\pi/k$), respectively. In the second equation,

$$F_\perp\equiv\omega_0^2+\omega_0'^2-2\omega_\perp^2$$

$$+\frac{2(\omega_0^2+\omega_0'^2-\omega_\perp^2)(\omega_0^2\omega_0'^2-2\omega_0^4-2\omega_0'^4)}{[\omega_\perp^2-(\omega_0-\omega_0')^2][\omega_\perp^2-(\omega_0+\omega_0')^2]},\quad(6a)$$

where   (6b)

$$\omega_\perp^2\equiv\sqrt{\omega_0^4+\omega_0'^4}.$$

---

[2] While we required that $\eta_1^*(\mathbf{k},\omega)=\eta_1(-\mathbf{k},-\omega)$ we make no similar requirement on $\eta_1(\mathbf{k})$. Therefore, $\mathbf{k}$ is taken to lie in the direction of travel, and $|\eta_1(\mathbf{k})|\neq|\eta_1(-\mathbf{k})|$, since in general we want to allow waves traveling ·in opposite directions to have different amplitudes. Note, however, that the *total* spatial coefficient (dropping time), i.e., $\eta_1(\mathbf{k})+\eta_1^*(-\mathbf{k})$ *does* satisfy the complex conjugate relationship required for real wave fields.

[3] Note that because of the complex Fourier series representation used here for wave height, the actual amplitude of the sinusoid is $a(\mathbf{k})=2|\eta_1(\mathbf{k})|$.

Examining (4) and (5), we can represent the phase speed change as two separate effects: the self effect (first term) and the mutual effect (second term). Thus the nonzero height of the original wave tends to increase its speed slightly (just as predicted by Stokes, 1847). The second wave acting on the first may increase or decrease its speed, depending upon its direction with respect to the first wave. To obtain some feel for this "mutual" interaction effect, let us consider two lengths and three directions for the second wave (with wavenumber k'). First we rewrite the second wave in terms of its slope [i.e., $s' = 2k'|\eta_1(\mathbf{k}')|$], since in a fully developed sea it is the slope which is more nearly maintained at a constant value than the wave height. In Table 1 we present the change in the phase velocity of the first wave with wave vector $\mathbf{k}$ due to the second wave with wave vector $\mathbf{k}'$ when the second wave is i) twice as long ($k' = \frac{1}{2}k$), and ii) half as long ($k' = 2k$), and traveling in i) the same direction, ii) the perpendicular direction, and iii) the opposite direction with respect to the first wave.

As a simple summary of these interaction effects (expressed in terms of constant wave slope), the longer, higher second wave produces a greater phase velocity change on the first wave (by a factor of 4) than the shorter, lower second wave; when the wave trains are parallel, the velocity change is the same in magnitude, but its sign depends on whether the waves are moving in the same or opposite directions, entirely as one would expect. (Had the result been expressed in terms of the height of the second wave $2|\eta_1(\mathbf{k}')|$, the magnitude of the phase velocity change would *not* have depended upon the wavelength of the second wave train for any of the directions considered.).

It is interesting to note that there *is* a mutual interaction even when the second wavetrain is moving orthogonally to the first wave train, and this interaction is such as to *increase* the speed of the first wave train. However, this interaction velocity change is small compared with cases when they are aligned or colinear (i.e., it is only 2.78% of the value for colinear alignment), and hence for many purposes the perpendicular interaction might be considered negligible.

3. Comparison with Stokes (1847) and Longuet-Higgins and Phillips (1962)

As discussed previously, Stokes (1847) employed a technique—valid only for a solitary periodic wavetrain—which permitted him to obtain the second-order Fourier correction to the wave-height profile and the higher order correction to the dispersion equation. He showed that the second spatial harmonic (traveling at the same phase speed as the fundamental cosine wave) is also a cosine wave with amplitude $a_2 = \frac{1}{2}ka_1^2$, where a_1 is the amplitude of the fundamental cosine wave. If we reduce the exponential series (1) to two terms representing a cosine wave [where $\eta_1^*(\mathbf{k}) = \eta_1(\mathbf{k})$],

TABLE 1. Phase velocity change in wave with wave vector $\mathbf{k}$ due to wave with wave vector $\mathbf{k}'$.

	$k' = 2k$ (Second wavelength $= \frac{1}{2} \times$ first wavelength)	$k' = \frac{1}{2}k$ (Second wavelength $= 2 \times$ first wavelength)
Same directions	$+\dfrac{\sqrt{2}}{4}s'^2$	$+\sqrt{2}s'^2$
Perpendicular directions	$+\dfrac{(\sqrt{5}-2)}{24}s'^2$	$+\dfrac{(\sqrt{5}-2)}{6}s'^2$
Opposite directions	$-\dfrac{\sqrt{2}}{4}s'^2$	$-\sqrt{2}s'^2$

we obtain from Eq. (22) of W-B $\eta_2(2\mathbf{k}, 2\omega) = k\eta_1^2(\mathbf{k})$. Since $a_1 = 2\eta_1$ and $a_2 = 2\eta_2$, we see that the two results are identical. Furthermore, our second-order wave is seen to move with a phase velocity $\Omega/K = 2\omega/2k = \omega/k$, which is exactly the phase velocity of the fundamental or first-order wave; hence the total wave-train profile "stays together." However, the frequency $\Omega = 2\omega$ and wavenumber $K = 2k$ of the second-order wave do not satisfy the first-order dispersion relation (15) of W-B. That is, $\Omega_0^2 = 4\omega_0^2 = 4gk = 2gK$, rather than $\Omega_0^2 = gK$; hence the second-order component is *not* freely propagating, but is tied to or trapped by the fundamental, which is all consistent with Stokes' analyses.

The first term of (4) represents the normalized correction to the dispersion relation when only one wave is present. This should agree with the normalized phase-velocity increase derived by Stokes (1847) for a single periodic wave train. His normalized phase velocity correction is given as $\frac{1}{2}k^2a_1^2$, which is seen to be identical to the first term when one notes that $a_1 = 2|\eta_1(\mathbf{k})|$.

The second term of (4) is the normalized phase velocity (or dispersion-relation) correction to the first wave of wavenumber $\mathbf{k}$ due to a second periodic wave which is colinear with the first and having wavenumber $\mathbf{k}'$. Longuet-Higgins and Phillips (1962) specifically analyzed this case, and found the actual phase velocity correction to be $\omega_0'k'a_1'^2$ for $k' < k$ and $\omega_0'ka_1'^2$ for $k' > k$; they also note that the phase velocity correction has a negative sign if the waves are traveling opposite to each other. By using the identity $a_1' = 2|\eta_1(\mathbf{k}')|$ in the second term of (4) and multiplying by $\sqrt{g/k}$ to convert from a normalized to an actual phase velocity correction, we see that the two results are identical.

A curious but important fact should be noted about the two terms in (4): if one attempts to make the second wave (with wavenumber k') merge into and replace the first [i.e., let $\eta_1(\mathbf{k}) \to 0$, but allow $\mathbf{k}' \to \mathbf{k}$] so that only the second term remains, it is *twice* as large as the first. In other words, mutual and self effects on the phase velocity are different, and one cannot predict one effect starting from the other. Thus Stokes analysis gave only the self-effect term, while

Longuet-Higgins and Phillips' (1962) analysis gave only the mutual interaction term. Our generalized analysis, however, gives both terms, and each agrees properly with its respective classical predecessor. One point in common between all three analyses is the initial formulation of the problem in terms of periodic waves (i.e., Fourier series). We note in passing that Huang and Tung (1976), using instead a Fourier-Stieltjes approach, obtained a general expression for the phase velocity correction due to mutual interaction effects for colinear waves [the second term of their Eq. (22)] that does not agree with either our result [Eq. (4)] or Longuet-Higgins and Phillips' (1962) solution. Both of the latter results show that one must switch factors from k to k' depending upon whether $k \lessgtr k'$.

4. Generalization to random surfaces

This section will show how the Fourier series representation can be converted to describe a random surface in which averages rather than deterministic descriptions are desired; in the process summations become integrals (in the Riemann sense).

In any practical experiment, one is interested in a description of the sea surface only over some finite area of space, $L_x \times L_y$ and a finite interval of time, T. We assume here that the sea surface is statistically stationary over these intervals. If we are permitted the further assumption that these intervals are much larger than the dominant gravity-wave spatial and temporal periods of interest in the analysis, then Rice has shown (Davenport and Root, 1958) that the real and imaginary parts of the Fourier series coefficients, $\eta(\mathbf{k}, \omega)$, describing the sea can be taken to be random variables which become mutually uncorrelated when the spatial/temporal intervals greatly exceed the spatial/temporal wavelengths of the dominant waves. Since we are interested in describing the surface only within these limits, we can take L_x, L_y, T to be the fundamental periods of the Fourier series and allow the surface to be periodic (i.e., repeat itself) for other areas and times. Finally, it has been shown in many places (Kinsman, 1965) that the *first-order* sea-surface height coefficients can be allowed to be zero mean *Gaussian* random variables for most practical purposes.

With these assumptions, we can define the surface wave-height spectrum in terms of the height coefficients (for each order) as

$$\langle \eta_n(\mathbf{k}, w) \eta_n^*(\mathbf{k}', w') \rangle$$
$$= \begin{cases} \dfrac{(2\pi)^3}{L_x L_y T} S_n(\mathbf{k}, w) & \text{for} \quad \mathbf{k}' = \mathbf{k} \quad \text{and} \quad w' = w \\ 0 \text{ for other } \mathbf{k}', w', \end{cases} \quad (7)$$

where $\langle f \rangle$ denotes an ensemble average of f, and $S_n(\mathbf{k}, w)$ is the nth order directional wave-height spatial/

temporal spectrum for arbitrary spatial wave vector $\mathbf{k}$ and arbitrary temporal wavenumber w. By the zero mean assumption of the preceding paragraph, we have $\langle \eta_1(\mathbf{k}, w) \rangle \equiv 0$ for all $\mathbf{k}, w$.

If one is interested in the first-order wave-height spatial/temporal spectrum evaluated using the dispersion equation to lowest order, the following relation can be used:

$$\langle \eta_1(\mathbf{k}) \eta_1^*(\mathbf{k}') \rangle = \begin{cases} \dfrac{(2\pi)^2}{2 L_x L_y} S_1(\mathbf{k}) & \text{for} \quad \mathbf{k}' = \mathbf{k} \\ 0 \text{ for other } \mathbf{k}', \end{cases} \quad (8)$$

along with the last form of (1) to establish the following identity:

$$S_1(\mathbf{k}, \omega_0) = \tfrac{1}{2} S_1(\mathbf{k}) \delta(\omega_0 - \sqrt{gk}) + \tfrac{1}{2} S_1(-\mathbf{k}) \delta(\omega_0 + \sqrt{gk}), \quad (9)$$

where $\delta(x)$ is the Dirac-delta function.

Finally, if one is concerned with only one-dimensional (colinear) ocean waves so that (1) is a function of only x and t, then we have

$$\langle \eta_n(k, w) \eta_n^*(k', w') \rangle$$
$$= \begin{cases} \dfrac{(2\pi)^2}{L_x T} S_n(k, w) & \text{for} \quad k' = k, \ w' = w \\ 0 \text{ for other } k', w' \end{cases} \quad (10)$$

and

$$\langle \eta_n(k) \eta_n^*(k') \rangle = \begin{cases} \dfrac{2\pi}{2 L_x} S_n(k) & \text{for} \quad k' = k \\ 0 \text{ for other } k' \end{cases} \quad (11)$$

with identity (9) holding here also.

These wave-height spectra are defined with the following normalization[4] with respect to root-mean-square (rms) wave height h:

$$h^2 = \langle \eta^2(\mathbf{r}, t) \rangle = \int_{-\infty}^{\infty} \int_{-\infty}^{\infty} d^2\mathbf{k} \int_{-\infty}^{\infty} dw S(\mathbf{k}, w)$$

$$= \int_{-\infty}^{\infty} \int_{-\infty}^{\infty} d^2\mathbf{k} S(\mathbf{k}). \quad (12)$$

One can also define a temporal (only), nondirectional wave-height spectrum, a quantity which is readily measured with buoys and/or wave staffs as

$$S(w) \equiv \int_{-\infty}^{\infty} \int_{-\infty}^{\infty} d^2\mathbf{k} S(\mathbf{k}, w),$$

where

$$h^2 = \int_{-\infty}^{\infty} dw S(w). \quad (13)$$

---

[4] Attention is again called to the fact that, as per our definitions after (1) and (8), $S(\mathbf{k})$ is nonsymmetric so that it can represent wave fields traveling over 360° of space with arbitrary amplitudes.

One further identity will be used in subsequent higher order averaging processes; this identity, valid for Gaussian random variables such as η_1, is established in elementary statistics texts (e.g., Davenport and Root, 1958)

$$\langle \eta_1(\mathbf{k}_1)\eta_1{}^*(\mathbf{k}_2)\eta_1(\mathbf{k}_3)\eta_1{}^*(\mathbf{k}_4)\rangle$$
$$= \langle \eta_1(\mathbf{k}_1)\eta_1{}^*(\mathbf{k}_2)\rangle\langle\eta_1(\mathbf{k}_3)\eta_1{}^*(\mathbf{k}_4)\rangle + \langle\eta_1(\mathbf{k}_1)\eta_1(\mathbf{k}_3)\rangle$$
$$\times\langle\eta_1{}^*(\mathbf{k}_2)\eta_1{}^*(\mathbf{k}_4)\rangle + \langle\eta_1(\mathbf{k}_1)\eta_1{}^*(\mathbf{k}_4)\rangle\langle\eta_1{}^*(\mathbf{k}_2)\eta_1(\mathbf{k}_3)\rangle. \quad (14)$$

By employing (8), one can see that the first term on the right side can be nonzero only when $\mathbf{k}_2 = \mathbf{k}_1$ and $\mathbf{k}_4 = \mathbf{k}_3$. The second term can *never* be nonzero. The third term is nonzero only when $\mathbf{k}_4 = \mathbf{k}_1$ and $\mathbf{k}_2 = \mathbf{k}_3$. Under these conditions the right side of (14) becomes $[8\times(2\pi)^4/(L_xL_y)^2]S_1(\mathbf{k}_1)S_1(\mathbf{k}_3)$.

We will now apply these definitions and identities to show how the results derived in W-B for periodic, nonrandom, Fourier series descriptions of waves can be converted to integrals representing average spectra, etc. In this process, we form products, take ensemble averages [in the sense of (7) or (8)], interchange averaging and summation processes and finally convert remaining Fourier sums to integrals. This latter process is done in a Riemann sense, where, for example, $(2\pi)^2/L_xL_y \equiv d\mathbf{k}$ and $2\pi/T \equiv dw$, L_x, L_y and T being the observation periods. Let us illustrate this process on (22) of W-B, where our purpose is to derive an expression for the second-order wave-height spatial/temporal spectrum $S_2(\mathbf{K},\Omega)$ in terms of first-order wave-height spectra. First, we express the second-order wave height as follows [using (4) and (22) of W-B and the lowest-order dispersion relation]:

$$\eta_2(\mathbf{r},t) = \sum_{\mathbf{K}}\eta_2(\mathbf{K})\exp\{i[\mathbf{K}\cdot\mathbf{r}-(\omega_0+\omega_0')t]\}, \quad (15a)$$

where

$$\eta_2(\mathbf{K}) = \sum_{\mathbf{k},\omega_0}\sum_{\mathbf{k}',\omega'_0} A(\mathbf{k},\omega_0,\mathbf{k}',\omega_0')\eta_1(\mathbf{k},\omega_0)\eta_1(\mathbf{k}',\omega_0')$$
$$\times \delta_{\mathbf{K}}^{\mathbf{k}+\mathbf{k}'}\delta_{\omega_0}^{\pm\sqrt{gk}}\delta_{\omega_0'}^{\pm\sqrt{gk'}}. \quad (15b)$$

Therefore, we perform averaging on the spatial second-order coefficient, convert these sums to integrals, and then take the temporal Fourier integral of the result:

$$S_2(\mathbf{K},\Omega) = \frac{1}{2\pi}\int_{-\infty}^{\infty}\langle\eta_2(\mathbf{K})\eta_2{}^*(\mathbf{K})\rangle\cdot\left(\frac{L_xL_y}{(2\pi)^2}\right)$$
$$\times\exp[-i(\omega_0+\omega_0')t+i(\omega_0''+\omega_0''')(t+\tau)-i\Omega\tau]d\tau. \quad (16)$$

By employing (14) along with the Kronecker-delta functions, we can show that all of the summations contained in (16) reduce to a single vector wavenumber sum, which is then converted to an integral in the Riemann sense. Finally, the integral in (16) over τ becomes a Dirac-delta function, leaving as the final result (written in symmetrical form)

$$S_2(\mathbf{K},\Omega) = \frac{1}{2}\int_{-\infty}^{\infty}\int_{-\infty}^{\infty}d^2\kappa\sum_{u,l}\sum_{u,l}A^2(\mathbf{k},\pm\sqrt{gk},\mathbf{k}',\pm\sqrt{gk'})$$
$$\times S_1(\pm\mathbf{k})S_1(\pm\mathbf{k}')\delta(\Omega\mp\sqrt{gk}\mp\sqrt{gk'}), \quad (17)$$

where $\mathbf{k}\equiv\frac{1}{2}\mathbf{K}+\kappa$, $\mathbf{k}'\equiv\frac{1}{2}\mathbf{K}-\kappa$, and the summation indices refer to the upper and lower signs in the equation. The quantity $A(\mathbf{k},\omega_0,\mathbf{k}',\omega_0')$ is as derived and given in (23) of W-B. The Dirac-delta function permits one of the two integrations to be performed, leaving one which must (in general) be done numerically for a given form of the wave-height spatial spectrum.

An identical expression holds for one-dimensional spatial spectra due to colinear wave trains, where the double integral is replaced by a single integral (i.e., $d\kappa$ instead of $d^2\kappa$), and where the spatial wavenumber in all spectra is a scalar rather than a vector quantity; this case will be treated separately later.

Next we apply these statistical techniques to calculations of the mean and variance of the correction to the dispersion relation (or phase velocity), ω_2/ω_0, as given by Eq. (29) of W-B. So that the algebraic expressions will not be so cumbersome as to detract from the main points to be illustrated by the example, we restrict our attention here to colinear waves. Then the $C(\mathbf{k},\omega,\mathbf{k}',\omega')$ of (29) of W-B reduces to the factor multiplying the second term of (4), i.e., we have

$$\frac{\omega_2(k)}{\omega_0(k)} = \pm\frac{4k}{\omega_0}\sum_{k'>0}\omega_0'|\eta_1(k')|^2\cdot\begin{cases}k' & \text{for}\quad k'<k \\ k & \text{for}\quad k'>k\end{cases} \quad (18)$$

where, as before, $\omega_0 = \sqrt{g|k|}$ and $\omega_0' = \sqrt{g|k'|}$. The upper sign is used *except* when the wave whose desired phase velocity correction (with wavenumber k) is moving opposite to the direction of the waves with wavenumbers k'. Note that this expression is valid for all waves *except* the one at wavenumber k; at this wavenumber the corresponding term in (18) must be divided by two, as discussed after (4). Where many waves are present, however, this "self-induced" phase velocity correction is negligible compared to the mutual interaction effects; hence it will be ignored here as we proceed to a spectrum of many waves.

The average value of (18) is readily taken using the techniques discussed above:

$$\left\langle\frac{\omega_2(k)}{\omega_0(k)}\right\rangle = \pm\frac{k}{\omega_0}\sum_{k'=-\infty}^{\infty}\omega_0'S_1(k')\cdot\frac{2\pi}{L_x}\begin{cases}k' & \text{for}\quad k'<k \\ k & \text{for}\quad k'>k\end{cases}$$

or

$$\left\langle\frac{\omega_2(k)}{\omega_0(k)}\right\rangle = \pm\frac{2k}{\omega_0}\int_0^k\omega_0'k'S_1(k')dk'$$
$$\pm\frac{2k^2}{\omega_0}\int_k^{\infty}\omega_0'S_1(k')dk'. \quad (19)$$

This agrees with the expression given by Longuet-Higgins and Phillips (1962) in their Eq. (4.1).

Finally, we take the variance of ω_2/ω_0, inasmuch as this is a measure of the expected spread in the frequencies or phase velocities of first-order waves with wavenumber k. Of the three terms resulting from the use of (14), one cancels with the square of the mean. Here we initially allow the sums to run over negative wavenumbers and divide by 2:

$$\text{Var}\left[\frac{\omega_2}{\omega_0}(k)\right]=\left\langle\left(\frac{\omega_2(k)}{\omega_0(k)}\right)^2\right\rangle-\left\langle\frac{\omega_2(k)}{\omega_0(k)}\right\rangle^2$$

$$=\frac{4k^2}{\omega_0^2}\sum_{k'=-\infty}^{\infty}\sum_{k''=-\infty}^{\infty}\omega_0'\omega_0''\begin{Bmatrix}k'\\k\end{Bmatrix}\begin{Bmatrix}k''\\k\end{Bmatrix}$$

$$\times\langle\eta_1(k')\eta_1^*(k')\eta_1(k'')\eta_1^*(k'')\rangle$$

$$-\frac{4k^2}{\omega_0^2}\sum_{k'=-\infty}^{\infty}\sum_{k''=-\infty}^{\infty}\omega_0'\omega_0''\begin{Bmatrix}k'\\k\end{Bmatrix}\begin{Bmatrix}k''\\k\end{Bmatrix}\langle\eta_1(k')\eta_1^*(k')\rangle$$

$$\times\langle\eta_1(k'')\eta_1^*(k'')\rangle=\frac{2k^2}{\omega_0^2}\sum_{k'=-\infty}^{\infty}\left[\omega_0'\begin{Bmatrix}k'\\k\end{Bmatrix}S_1(k')\right]^2\cdot\left(\frac{2\pi}{L_x}\right)^2$$

or

$$\text{Var}\left[\frac{\omega_2}{\omega_0}(k)\right]=\frac{8\pi k^2}{\omega_0^2 L_x}\left[\int_0^k\omega_0'^2 k'^2 S_1^2(k')dk'\right.$$

$$\left.+k^2\int_k^{\infty}\omega_0'^2 S_1^2(k')dk'\right].\quad(20)$$

It is curious that in (20) one of the $2\pi/L_x$ factors is *not* used up as an integration increment dk', as in all other cases considered. Recall that initially we described L_x as the spatial increment over which the Fourier series with random coefficients was valid. Outside of this increment of space the surface profile repeats itself. Hence L_x physically corresponds to the region of space over which observations relating to this particular statistic of the sea are either made or desired. As one can see, the larger this observation window, the smaller the variance.

5. Examples of the second-order wave height and its spectrum

a. Two-wave interactions and diffraction grating analogies

Eq. (22) of W-B shows that the spatial wavenumber of the second-order wave, $\mathbf{K}$, is the vector sum of the wavenumbers of the first-order waves present. The same holds true for the temporal wavenumbers. In other words

$$\mathbf{K}=\mathbf{k}+\mathbf{k}'\quad\text{and}\quad\Omega_0=\omega_0+\omega_0'\quad(21)$$

(to lowest order, where $\omega_0=\sqrt{gk'}$ and $\omega_0'=\sqrt{gk'}$). These relationships have been referred to as representing second-order Bragg "scatter" or a second-order Feynman interaction (Hasselmann, 1966; Barrick, 1972).

To obtain a clearer physical picture of this interaction, let us consider the case of two first-order sinusoidal wave trains, where $\mathbf{k},\mathbf{k}'=\pm\mathbf{k}_a,\pm\mathbf{k}_b$. Eq. (22) of W-B shows that there will be several sinusoidal second-order wave trains whose Fourier coefficients $\eta_2(\mathbf{K},\Omega_0)$ are determined by the products of terms in the sum. Neglecting the second-order coefficients at zero wavenumber (which only redefine the mean sea level), we have four sets of second-order waves:

1)   The self-generating second-harmonic waves:

Wavenumbers $\mathbf{K}_{aa}=2\mathbf{k}_a$; $\mathbf{K}_{bb}=2\mathbf{k}_b$ (22a)

Frequencies $\Omega_{0aa}=2\omega_{0a}$; $\Omega_{0bb}=2\omega_{0b}$ (22b)

Phase Speeds $V_{aa}=\Omega_{0aa}/K_a=\omega_{0a}/k_a=v_a$;

$v_{bb}=\Omega_{0bb}/K_b=\omega_{0b}/k_b=v_b$.   (22c)

2)   The mutual cross-coupling waves:

Wavenumbers $\mathbf{K}_{s,d}=\mathbf{k}_a\pm\mathbf{k}_b$ (23a)

Frequencies $\Omega_{0s,d}=\omega_{0a}\pm\omega_{0b}$ (23b)

Phase Speeds $v_{s,d}=\Omega_{0s,d}/K_{s,d}=(\sqrt{gk_a}\pm\sqrt{gk_b})/K_{s,d}$.

(23c)

The first set (second harmonics) originates from the analysis of Stokes (1847) where one periodic wave train alone is considered. The second set originates because of the nonlinear (square-law) interaction between two separate sets of first-order waves, and cannot arise from Stokes analysis by mere superposition of his results.

An interesting interpretation of these second-order waves is obtained by analogy with Moirè patterns in diffraction gratings. Let us represent the peaks $(+)$ and troughs $(-)$ of two sets of first-order, arbitrarily oriented sinusoidal waves $(\mathbf{k}_a,\mathbf{k}_b)$ as shown at the top of Fig. 1. Where the peaks of one set reinforce with the peaks of the other set, we have a linear superposition (or "piling up") of water as shown by the circles with the plus signs (with a similar situation for negative reinforcement). These line "intersections" would appear as a separate dense pattern, known as the Moirè effect, if two diffraction gratings were overlain. Now, if each first-order wave train moves with its own characteristic phase velocity, these dense spots (circles) will also move as a solid pattern, but in a different direction than either of the two first-order gratings.

The second-harmonic waves are easy to describe: they lie parallel to the first-order wavesets, have half the spatial period of the fundamental, but move at the same phase velocity as the fundamental; they are shown at the lower left of Fig. 1. The "cross-coupling" waves, however (shown at the lower right), have their crests aligned along lines joining the dense spots at the corner of a triangle, the two sides of which lie along the first-order crestlines, one full period on each side. These second-order crestlines appear to stay attached to the dense spots or circles as they move, carried along
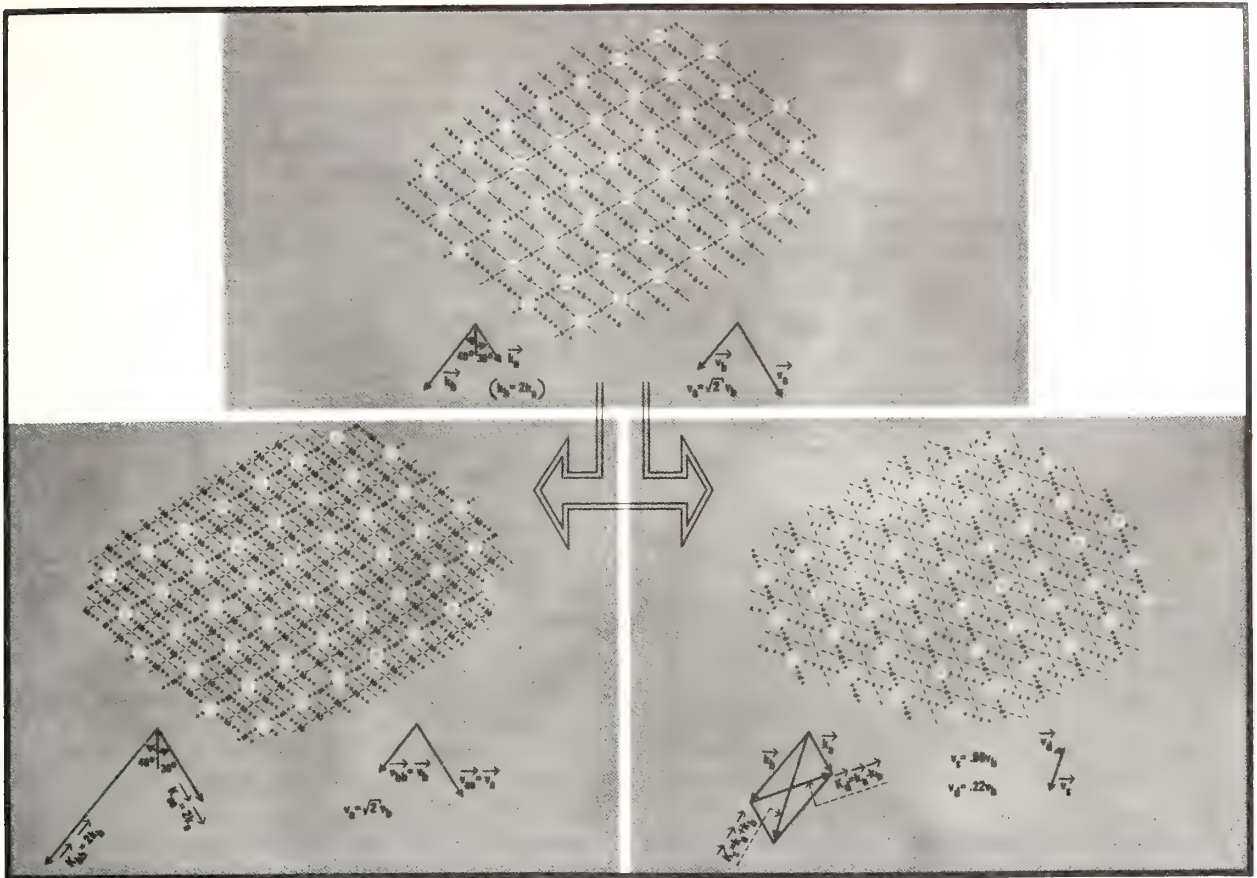
Fig. 1. Sketch showing crest (+)/trough (−) patterns for two sets of first-order sinusoidal wave trains (upper figure) and the second-order wave trains they produce. Lower left shows the "second-harmonic" wave trains, while the lower right shows the "cross-coupling" wave trains. Relative scales on wave vector wave trains reinforce positively ⊕ and negatively ⊖.

by the first-order waves. Their wavelengths and directions of propagation are of course predicted by the vector triads, coming from (21). Their phase speeds can be predicted trigonometrically by following the Moirè pattern temporally, and this identically corresponds to those derived rigorously and given in (23c). If Fig. 1 were indeed a double diffraction grating in which each grating moved in the direction and at the speed indicated, one would in fact notice these second-order "mutual" waves (when viewed from a distance), due to second-order optical nonlinearities (i.e., the abrupt change from transparent to opaque).

For the wavepatterns shown (and also in general), the heights of the "second-harmonic" second-order waves are of the same order as the heights of the "mutual" second-harmonic waves. For the example shown [letting $k_a = 1$ and $k_b = 2$, we have $\eta_2(K_{aa}, \Omega_{0aa})$ $= \eta_1^2(k_a)$, $\eta_2(K_{bb}, \Omega_{0bb}) = 2\eta_1^2(k_b)$, but $\eta_2(K_s, \Omega_{0s}) = 0.324$ $\eta_1(k_a)\eta_1(k_b)$ and $\eta_2(K_d, \Omega_{0d}) = 2.637$ $\eta_1(k_a)\eta_1(k_b)$]. The actual heights of these second-order waves are small compared to the first-order waveheights. Since the half-heights of the first-order waves *at maximum* (i.e., when breaking occurs) must be such that $|\eta_1(k)|$ $\leq \pi/(14k)$, we have (upon using the equality and allowing η_1 to be pure real) $\eta_1(k_a) = 0.2244$, $\eta_1(k_b)$ $= 0.1122$, $\eta_2(K_{aa}, \Omega_{0aa}) = 0.0504$, $\eta_2(K_{bb}, \Omega_{0bb}) = 0.0252$, $\eta_2(K_s, \Omega_{0s}) = 0.00816$, and $\eta_2(K_d, \Omega_{0d}) = 0.0664$. Therefore, even with the maximum possible first-order wave heights, the second-order wave heights are small in terms of them, and the perturbation analysis of W-B used to derive these results is justified.

As one generalizes from the case of two first-order waves to a spectrum of very many waves (say N), it is obvious that the number of second-order "cross-coupling" waves far exceeds the number of "second-harmonic" waves; the latter goes as N whereas the former goes as $N(N-1) \approx N^2$. Hence, the total second-order sea waveheight for many first-order waves for all practical purposes consists only of the "cross-coupling" waves; this becomes especially true in the limit of an infinite spectrum of first-order waves, as seen from (17).

b. Average second-order spectrum for colinear waves

Following (17), it was mentioned that in the case of colinear waves, that equation has vector wavenumbers replaced by scalar wavenumbers, and the double

integral becomes a single integral. This permits us to evaluate the integral exactly because of the Dirac-delta function. One must transform variables in order to employ the delta function, however. Let us assume that all of the waves are propagating along the $+x$ direction. Then we can break k space into two regions: $-\frac{1}{2}K < \kappa < \frac{1}{2}K$, and $\kappa < -\frac{1}{2}K$, $\kappa > \frac{1}{2}K$. Note first that $A^2(k,\omega_0,k',\omega_0') = K^2/4$. Now, considering the region $0 < \kappa < \frac{1}{2}K$, transform variables first to $u \equiv \sqrt{g(\frac{1}{2}K+\kappa)}$, and to $w \equiv u + \sqrt{gK - u^2}$. The upper signs in the delta-function argument must be used within the first region. Using the limits of the integral to define required inequalities for Ω, we arrive at the following expression (for $K > 0$ and for the total region $-\frac{1}{2}K < \kappa < \frac{1}{2}K$):

$$S_2(K,\Omega) = \begin{cases} \dfrac{K^2}{4g}\dfrac{(\Omega^2 - gK)}{\sqrt{2gK-\Omega^2}} S_1\left[\dfrac{1}{2}\left(K + \dfrac{\Omega}{g}\sqrt{2gK-\Omega^2}\right)\right] \\ \quad \times S_1\left[\dfrac{1}{2}\left(K - \dfrac{\Omega}{2g}\sqrt{2gK-\Omega^2}\right)\right] \quad (24) \\ \qquad \text{for} \quad \sqrt{gK} < \Omega < \sqrt{2gK} \\ 0 \quad \text{for} \quad \Omega > \sqrt{2gK}. \end{cases}$$

Likewise, the transformations required for $\kappa > \frac{1}{2}K$ are $u \equiv \sqrt{g(\frac{1}{2}K+\kappa)}$ and $\omega \equiv u - \sqrt{u^2 - gK}$. Opposite signs in the delta-function argument must be used in this region. Adding in the contribution from the region $\kappa < -\frac{1}{2}K$, we obtain (for $K > 0$)

$$S_2(K,\Omega) = \begin{cases} \dfrac{K^2[(gK)^2 - \Omega^4]}{8g\Omega^3} S_1\left[\dfrac{1}{4g\Omega^2}(gK-\Omega^2)^2\right] \\ \quad \times S_1\left[\dfrac{1}{4g\Omega^2}(gK-\Omega^2)^2\right] \text{ for } 0 < \Omega < \sqrt{gK} \\ 0 \text{ for } \Omega < 0. \qquad\qquad\qquad (25) \end{cases}$$

Hence (24) and (25) define the second-order one-dimensional spatial-temporal spectrum in terms of the one-sided first-order spatial spectrum. It is seen that, for positive K, the region over Ω in which the spectrum exists is bounded between 0 and $\sqrt{2gK}$; a square-root-type singularity occurs at $\Omega \to \sqrt{2gK}$, but the area is finite under this singularity. Since the waves are required to be real quantities, half the energy in the first and second-order spectra lies in the region $K < 0$. Hence (24) and (25) also apply, when $K < 0$, and in this case Ω lies in the region $-\sqrt{2g|K|} < \Omega < 0$.

Tick (1959) used a Fourier integral approach and statistical methods on colinear wave trains to obtain expressions involving second-order wave heights. While he never specifically derived an expression for the second-order wave-height spatial-temporal spectrum, one can obtain this quantity by Fourier transforming his Eq. (36) over the spatial distance variable ξ; this involves Dirac-delta functions and nonlinear transformations such as those used in obtaining (24) and (25). Furthermore, he works with first-order wave-height temporal spectra instead of our spatial spectra, which necessitates another transformation. Nonetheless, if one performs the required algebraic steps and transformations on his result, one obtains identically our (24) and (25) for $S_2(K,\Omega)$. Hence the agreement of the two results lends credence to our claims that 1) the techniques we demonstrated for going from periodic wave trains, representable by Fourier series to random wave fields whose average properties are sought, are generally valid; 2) our higher order expressions involving two-dimensional wave fields are also valid because they agree with Tick's (1959) and Longuet-Higgins and Phillips (1962) results in the limit of one-dimensional (colinear) wave fields.

c. Example of spatial spectra for colinear Phillips model

To show an example of how (22), (24) and (25) can be applied to indicate the shape, magnitude and distribution of second-order wave-height spectral energy, we employ the commonly used Phillips (1969) spectral model for fully developed seas, converted to a one-dimensional spatial form

$$S_1(k) = \begin{cases} \dfrac{B}{2k^3} & \text{for} \quad k_{c0} < k < k_\gamma \\ 0 & \text{for} \quad -\infty < k < k_{c0} \end{cases} \qquad (26)$$

where $k_{c0} = g/v^2$ (v = wind speed in m s^{-1}, g = gravitational constant = 9.81 m s^{-2}), and where $k_\gamma = \sqrt{\rho g/\gamma}$ is the upper cutoff at the capillary wave region, with ρ = water density (= 10^3 kg/m^3) and γ = surface tension (= 0.073 N m^{-1}). B is a dimensionless constant whose equilibrium value has been determined experimentally to be ~ 0.005. This spectrum is normalized such that the rms slope of the colinear waves is the same as that for a two-dimensional semi-isotropic spectrum (Phillips, 1969). This yields a first-order two-sided spatial-temporal spectrum whose temporal frequency ω_0 (to lowest order) is uniquely related to the spatial wavenumber as follows:

$$S_1(k,\omega_0) = \begin{cases} \dfrac{B}{4|k|^3}\delta(\omega_0 + \sqrt{g|k|}) & \text{for } -k_\gamma < k < -k_{c0}, \\ 0 & \text{for } -k_{c0} < k < k_{c0}, \quad (27) \\ \dfrac{B}{4k^3}\delta(\omega_0 - \sqrt{gk}) & \text{for } k_{c0} < k < k_\gamma. \end{cases}$$
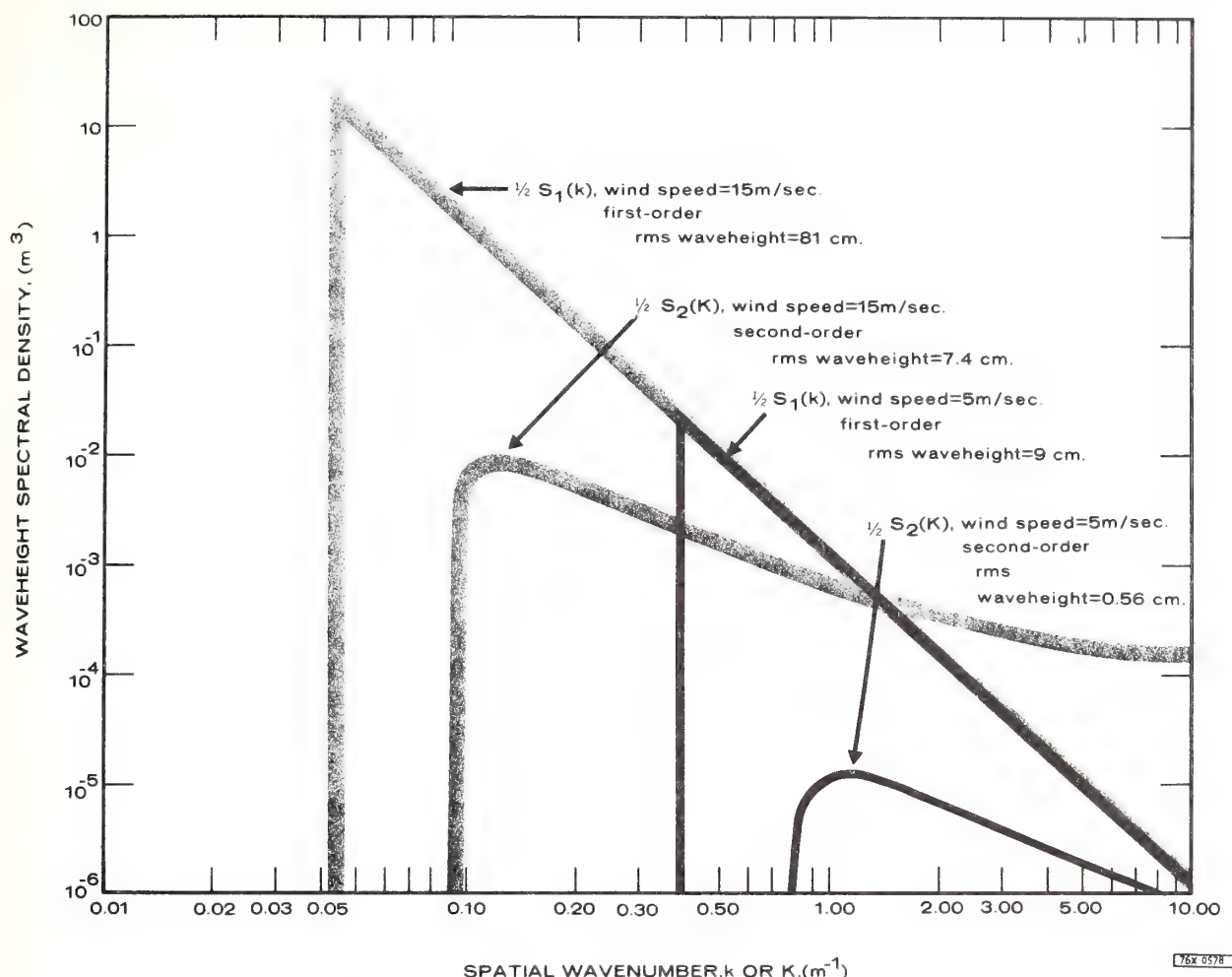
FIG. 2. Spatial wave-height spectra using Phillips' one-dimensional (colinear) first-order model.

This form defines waves traveling in the $+x$ direction (where k is positive).

Upon substituting (26) into (24) and (25), simplifying and converting the inequalities in (26) into appropriate temporal form, we arrive at the following result for the second-order spatial-temporal wave-height spectrum for $K > 0$:

$$\Omega_F S_2(K,\Omega)$$

$$= \begin{cases} \dfrac{2^7 B^2 \mu^9}{K^3(1-\mu^4)^5} & \text{for} \quad 0 < \mu^2 < 1 - 2\mu_{c0}\sqrt{1-\mu_{c0}^2} \\[2em] \dfrac{2^2 B^2}{K^3\sqrt{2-\mu^2}(\mu^2-1)^5} & \text{for} \quad 1 + 2\mu_{c0}\sqrt{1-\mu_{c0}^2} < \mu^2 < 2 \\[2em] 0 & \text{for other } \mu \end{cases}$$

$$\text{and} \quad 2\mu_{c0}^2 > 1 \quad (28)$$

where μ is a normalized temporal frequency $\mu \equiv \Omega/\Omega_F$, $\Omega_F \equiv \sqrt{gK}$; $\mu_{c0} \equiv \Omega_{c0}/\Omega_F$ and $\Omega_{c0} = g/v$; the spectrum is identical for negative K and Ω.

Whereas the first-order spatial-temporal spectrum appears at a discrete temporal frequency ($\omega_0 = \sqrt{gk}$), the second-order spectrum is distributed over a continuum of frequencies around $\sqrt{gK}$ between $\Omega = 0$ and $\Omega = \sqrt{2} \times \sqrt{gK}$; an integrable singularity occurs at the latter limit.

The one-sided second-order spatial spectrum $S_2(K)$ can be found by integrating (28) over positive Ω, the temporal wavenumber and dividing by two. This can be done from the tables, and the result expressed in closed form; it is not given here for lack of space. Rather, we give curves showing $S_1(k)$ and $S_2(K)$ over the gravity wave region for the above Phillips model and two different values of wind speed ($v = 5$ and 15 m s^{-1}) in Fig. 2. Also, the first-order and second-order rms wave heights h_1 and h_2 corresponding to these spectra are given

$$\left[\text{i.e.,} \; h_{1,2}^2 \equiv \int_0^\infty S_{1,2}(\kappa)d\kappa \right].$$

Note that even though the mean-square second-order

wave height (i.e., the area under the curve) is always less than the mean-square first-order wave height (as required in the perturbation theory), the second-order spectral power can exceed the first-order power at certain higher wavenumbers. This may at first appear strange, for the Phillips model measured by oceanographers (following a κ^{-4} or ω^{-5} law) should more realistically be thought of as the *total* spectrum, including all perturbation orders. Thus it may have been more meaningful in calculating the curves of Fig. 2 if we had "iterated" until the *sum* of the first and second-order curves satisfied the model given in (26). Our purpose here was only to provide an illustrative example of a second-order spectrum, given a first-order spectrum. In addition, Fig. 2 illustrates that the second-order portion does not begin to dominate until one has gone over four orders of magnitude down from the first-order spectral peak. Nearly all wave-height spectral measurements reported in the literature cover a dynamic range of only two orders of magnitude. An exception to this are very precise measurements by Mitsuyasu and Honda (as reported by Pierson, 1976), which in fact do show a departure from ω^{-5} law some three orders of magnitude down from the spectral peak; this departure is an *increase* from the inverse fifth-power law, commonly assumed to hold everywhere in the gravity-wave region.

6. Examples of first-order phase velocity mean and variances

Because Section 2 showed that the greatest correction to the dispersion equations occurs for parallel (colinear) rather than perpendicular wave trains, we will employ as an example the Phillips colinear spectral model (26) in (19) and (20). Using this model, we obtain for the mean

$$\left\langle \frac{\omega_2(k)}{\omega_0(k)} \right\rangle = 2B(\sqrt{k/k_{c0}} - \tfrac{2}{3})(\text{assuming } k > k_{c0}), \quad (29)$$

where $k_{c0} = g/v^2$.

The phase-velocity standard deviation (assuming an average over an infinite ensemble) using (20) is

$$\sqrt{\mathrm{Var}\left[\frac{\omega_2}{\omega_0}(k) \right]} = B\sqrt{\pi/(kL_x)} \cdot \sqrt{k^2/k_{c0}^2 - \tfrac{1}{2}}. \quad (30)$$

Note again that this result depends upon L_x, the length of the area under observation; as this quantity becomes very large compared to the water wavelength $2\pi/k$, the above standard deviation for an infinite ensemble average approaches zero.

A more sensible quantity than the infinite ensemble variance of phase velocity is the variance for a finite sample size. If, for example, one formed a sample average of ω_2^2 (consisting of the sum of N independent samples of ω_2^2 divided by N) and called it $N:\overline{\omega_2^2}$, one

can show that the sample phase velocity standard deviation correction is given by

$$\sqrt{\mathrm{Var}_N\left[\frac{\omega_2}{\omega_0}(k) \right]} = \frac{1}{\omega_0}[\langle (N:\overline{\omega_2^2})^2 \rangle - \langle N:\overline{\omega_2^2} \rangle^2]^{\tfrac{1}{4}}$$

$$= \left(\frac{2}{N}\right)^{\tfrac{1}{4}} \left\langle \frac{\omega_2(k)}{\omega_0(k)} \right\rangle = \left(\frac{2}{N}\right)^{\tfrac{1}{4}} 2B(\sqrt{k/k_{c0}} - \tfrac{2}{3}). \quad (31)$$

To illustrate the magnitudes of these various quantities, let us consider an HF radar application and assume the following parameters: wind speed $v = 15$ m s^{-1}; $2\pi/k = 5$ m (e.g., 5 m long ocean waves would be observed with an HF backscatter radar at 30 MHz having a wavelength of 10 m); the number of independent samples $N = 12$; the length of observed ocean patch $L_x = 3$ km; $B = 0.005$. For 5 m ocean waves, the phase velocity (to lowest order) is 2.794 m s^{-1}. The normalized phase velocity correction mean, standard deviation and 12-sample standard deviation for this example are then 0.04702, 0.00045345 and 0.03004, respectively. The actual phase velocity correction mean, standard deviation and 12-sample standard deviation corresponding to these numbers for the 5 m long ocean wave component are then 13.14, 0.13 and 8.9 cm s^{-1}, respectively.

7. Discussion and conclusions

In this series of two papers, we have presented a general perturbational formulation in which all desired higher order corrections to deep-water gravity wave parameters can be obtained at the same time; the approach is valid over temporal and spatial scales sufficiently small that energy exchange processes can be neglected. In particular, the technique was used to obtain the second-order wave height, velocity potential, and the first nonzero correction to the dispersion relationship (a third-order quantity). These results were interpreted physically and shown to agree with special limiting cases treated in the classical literature. It was shown how the solutions—based upon periodic two-dimensional wave trains—are readily converted to a form suited to random descriptions of the sea wave height. Finally, several examples were presented, primarily based upon colinear (one-dimensional) random wave fields and a Phillips spectral model for fully developed seas; these two simplifications led to closed-form solutions which are not possible in the general two-dimensional case, permitting one to obtain an insight into these higher order quantities.

The basic techniques leading to the derivation of these quantities were outlined in the literature over a decade ago (Tick, 1959; Phillips, 1960; Hasselmann, 1962, 1963a, b). In certain cases these authors indicated solutions in a formalistic manner, but did not complete the details of the algebra. Possibly this failure to complete and expand upon these solutions at that time

was due to the fact that experimental techniques were neither available nor of sufficient accuracy to permit confirmation of these higher order wave parameters. Two prospects in recent years have altered this picture, however: 1) the interest in energy transfer between different regions of the wave-height spectrum via nonlinear wave-wave interactions (Hasselmann *et al.*, 1973); and 2) the application of high-frequency radars (as a remote sensing tool) to the measurement of ocean-wave statistics and near-surface currents (along with the concomitant verification of theoretical models explaining this interaction; Barrick *et al.*, 1974; Stewart and Joy, 1974). It is the latter application which has led us to formulate and complete the steady-state derivations presented here.

In particular, the second-order wave-height spectrum and the higher order phase velocity correction for first-order waves are directly observable with HF radar systems. Theory (Barrick, 1972) and experiment (Barrick *et al.*, 1974) have shown that the average signal power spectral density (expressed as an average radar backscattering cross section per unit area per radian per second bandwidth for vertical polarization at grazing incidence) can be written

$$\sigma_{1,2}{}^0(\omega) = 2^7 \pi k_0{}^4 S_{1,2}(\kappa_r, \omega - \omega_0), \qquad (32)$$

where ω_0 is the radar carrier frequency (rad s^{-1}), k_0 is the magnitude of the incident and scattered radio wavenumbers (i.e., $k_0 = \omega_0/c$, c being the radiowave free-space velocity); $\kappa_r = \mathbf{k}_i - \mathbf{k}_s$ or $\kappa_r = 2\mathbf{k}_i = 2k_0\hat{k}_i$ for backscatter, since $\mathbf{k}_s = -\mathbf{k}_i$. Thus $\omega - \omega_0$, the radian frequency at which the ocean wave-height spectrum is being observed, appears in the radar receiver as the Doppler shift of the sea-scattered signal from the carrier. The spatial vector wavenumber κ_r indicates that the Bragg (or diffraction-grating) effect is giving rise to the scatter.[5]

We saw that $S_1(\mathbf{k},\omega)$ is an impulse function from the lowest order dispersion equation (centered at $\omega \approx \omega_0 \pm \sqrt{gk}$). Any finite width to this normal infinitesimally narrow impulse function in the (Doppler) frequency domain is therefore a measure of the variance of the dispersion equation for first-order waves (neglecting any frequency broadening due to system limitations, nonscatter-related mechanisms, current shears within the scattering patch). Hence the variance of ω_2, as discussed earlier, manifests itself here as the width of the first-order sea echo Doppler peak.

The second-order portion of the sea echo Doppler spectrum is related in its magnitude and shape to the wave-height spatial spectrum in a nonlinear manner via the integral (17). The fact that this second-order echo

energy is more sensitive to the longer, higher ocean waves than is the first-order echo energy at useful HF radar frequencies is generating considerable interest in utilizing this portion of the echo to remotely sense sea state. While the simple colinear wave models examined in detail here can provide some feeling for the general distribution of sea-echo energy, the complete solution to the two-dimensional model (17) must be pursued in order to study the effect of wave directionality on the echo spectral shape. Because of the complexity of solving (17) numerically for two-dimensional wave-height spectra, this topic must be undertaken separately.

REFERENCES

Barrick, D. E., 1972: Remote sensing of sea state by radar. *Remote Sensing of the Troposphere*, V. E. Derr, Editor, U. S. Govt. Printing Office, Washington, D. C., Chap. 12.

Barrick, D. E., J. M. Headrick, K. W. Bogle and D. D. Crombie, 1974: Sea backscatter at HF: Interpretation and utilization of the echo. *Proc. IEEE*, **62**, 673–680.

Davenport, W. B., Jr., and W. L. Root, 1958: *Random Signals and Noise.* McGraw-Hill, 393 pp.

Hasselmann, K., 1962: On the nonlinear energy transfer in a gravity-wave spectrum; Part 1. General theory. *J. Fluid Mech.*, **12**, 481–500.

——, 1963a: On the nonlinear energy transfer in a gravity-wave spectrum; Part 2. Conservation theorems, wave-particle correspondence, irreversibility. *J. Fluid Mech.*, **15**, 273–281.

——, 1963b: On the nonlinear energy transfer in a gravity-wave spectrum; Part 3. Evaluation of the energy flux and swell-sea interaction for a Neumann spectrum. *J. Fluid Mech.*, **15**, 385–398.

——, 1966: Feynman diagrams and interaction rules of wave-wave scattering processes. *Rev. Geophys.*, **4**, 1–32.

——, T. P. Barrett, E. Bouws, H. Carlson, D. E. Cartwright, K. Enke, J. A. Ewing, H. Gienapp, E. D. Hasselmann, P. Kruseman, A. Meerburg, P. Muller, D. J. Olbers, K. Richter, W. Sell and H. Walden, 1973: Measurements of wind-wave growth and swell decay during the Joint North Sea Wave Project (JONSWAP). *Erganzungsh. Deut. Hydrograph. Z. Reihe*, **A8**, No. 12, 95 pp.

Huang, N. E., and C. Tung, 1976: The dispersion relation for a nonlinear random gravity wave field. *J. Fluid Mech.*, **75**, 337–345.

Kinsman, B., 1965: *Wind Waves.* Prentice-Hall, 676 pp.

Longuet-Higgins, M. S., and O. M. Phillips, 1962: Phase velocity effects in tertiary wave interactions. *J. Fluid Mech.*, **12**, 333–336.

Phillips, O. M., 1960: On the dynamics of unsteady gravity waves of finite amplitude; Part 1. The elementary interactions. *J. Fluid Mech.*, **9**, 193–217.

——, 1969: *The Dynamics of the Upper Ocean.* Cambridge University Press, 261 pp.

Pierson, W. J., 1976: The theory and applications of ocean wave measuring systems at and below the sea surface, on the land, from aircraft, and from spacecraft. NASA Contract Rep. CR-2646, NASA Goddard Space Flight Center, Washington, D. C., 388 pp.

Stewart, R. H., and J. W. Joy, 1974: HF radio measurements of surface currents. *Deep-Sea Res.*, **21**, 1039–1049.

Stokes, G. G., 1847: On the theory of oscillatory waves. *Trans. Cambridge Phil. Soc.*, **8**, 441–455.

Tick, L. J., 1959: A nonlinear random model of gravity waves, I. *J. Math. Mech.*, **8**, 643–651.

Weber, B. L., and D. E. Barrick, 1977: On the nonlinear theory for gravity waves on the ocean's surface. Part 1. Derivations. *J. Phys. Oceanogr.*, **7**, 3–10.

---

[5] To second order, there is another term proportional to the second-order waveheight spectrum which originates from double radio-wave scatter (from two sets of ocean waves). This term—neglected here—is generally smaller than the "hydrodynamic" contribution considered here; it is derived elsewhere (Barrick, 1972) and given there.

Infrasound From Convective Storms: An Experimental
Test of Electrical Source Mechanisms

WILLIAM H. BEASLEY

Department of Electrical Engineering, University of Florida, Gainesville, Florida 32611

T. M. GEORGES AND MICHAEL W. EVANS

Wave Propagation Laboratory, NOAA Environmental Research Laboratories, Boulder, Colorado 80302

We performed an experiment to test the suggestion that the infrasound radiated by certain severe storms is caused by lightning. During the 1972 storm season we recorded at Boulder, Colorado, the rate and arrival direction of both VLF atmospherics and infrasound from severe thunderstorms in the midwestern United States. If infrasound were caused by lightning, we should have observed a good agreement in direction and time between the radio and acoustic emissions of lightning, within observational uncertainty. Fewer than half of the infrasound events showed such agreement with electromagnetic emissions. Those agreements can be attributed to noncausal coincidence. We argue that the correlation should be much higher if the infrasound emissions were caused by lightning. Some detailed case studies illustrate the differing phenomenologies of the emissions; for example, they show that the infrasound is probably emitted during an earlier stage of storm growth than that usually associated with lightning.

INTRODUCTION

Georges [1973] has reviewed the evidence linking observations of ultralow frequency sound waves (or infrasound) with certain severe convective storms that were hundreds and occasionally thousands of kilometers away. In a critique of several suggested models of the emitting mechanism, T. M. Georges (unpublished manuscript, 1976) defined theoretical predictions of each model that could be tested against observations. One of the hypothetical models examined was the possibility that the infrasound is just the low-frequency portion of the spectrum of thunder. Audible thunder is almost totally attenuated by atmospheric absorption in a few tens of kilometers, but any infrasonic component could travel hundreds or thousands of kilometers relatively undiminished because the acoustic absorption coefficient is proportional to the square of the frequency.

Thunder is the acoustic remnant of the cylindrical shock generated by lightning strokes. *Colgate and McKee* [1969], *Dessler* [1973], *Beasley* [1974], and T. M. Georges (unpublished manuscript, 1976) have examined the possibility that significant infrasonic energy is radiated not only by the lightning channel expansion but also by electrostatic relaxation in clouds following the discharge. Comparisons by Georges and Beasley of the energy required to account for the infrasound observations with the energy available from lightning strokes showed that only the most energetic strokes, occurring at least at the maximum observed rates, could possibly account for the observed infrasound intensities. But we could not conclusively rule out an electrical model on theoretical grounds alone because of uncertainties in the measured energy and spectral content of the acoustic radiation from lightning. An experimental test of the electrical models thus seemed appropriate.

It is well known that lightning also emits electromagnetic energy over a broad spectrum. Therefore one of the observational tests suggested was a simultaneous measurement of the infrasonic and electromagnetic (specifically, VLF radio) emissions from severe storms and a comparison of azimuths of peak sferics rates with azimuths of infrasound arrivals. This

paper reports the results of such a test. We find that the spatial and temporal correlation between the two kinds of emissions is much lower than we would expect if the two were causally related; therefore the source of severe storm infrasound is probably not electrical.

More details about the experimental procedure, the data collected, and the analysis and assumptions leading to our final conclusion can be found in the dissertation by *Beasley* [1974].

EXPERIMENT

Pressure measurements. To record the infrasonic waves from severe storms, we used the National Oceanic and Atmospheric Administration Wave Propagation Laboratory (NOAA/WPL) operational array of four microbarographs located near Boulder, Colorado. The microbarographs are of the National Bureau of Standards type described elsewhere [*Matheson*, 1964; *Georges and Young*, 1972] and have a sensitivity of about 0.01 μbar (10^{-8} atm). Sensor spacing averages about 8 km, and the array geometry is irregular. Spatial filters are attached to each microbarograph to reduce the noise of wind-advected turbulence. They are constructed of 1000 feet of iron pipe with capillary leaks to the atmosphere every 5 feet. The spectral passband of the sensing and processing system we used has 20-dB response points at about 2- and 100-s wave periods.

During the interval studied, May 22 to August 30, 1972, pressure variations from all sensors were recorded on magnetic tape in analog form at a central recording station. When we identified wave events of possible interest, we processed the tapes (to yield azimuths of wave arrival and coherence) on the NOAA analog-correlating device that has been described elsewhere [*Brown*, 1963; *Georges and Young*, 1972]. We identified severe storm waves using criteria similar to those described by *Georges and Greene* [1975]. Briefly, whenever an acoustic wave arrived during the time of and from the direction of severe thunderstorm activity, as indicated on the NOAA hourly radar summary charts, and the wave could not be identified with other known infrasound sources, we attributed the wave event to the storm. Extensive experimentation has proven the relia-

bility of this procedure [*Georges and Greene*, 1975]. Typical storm-associated waves have amplitudes of 0.5–1.0 μbar and periods of 20–40 s.

Sferics measurements. We wanted to record the direction of arrival of VLF atmospherics at Boulder as a function of time in a way that also preserved a rough indication of the relative intensity of sferics activity in each direction. The direction-measuring scheme we used is essentially that described by *Watson-Watt and Herd* [1926] and *Terman* [1943]. It employs a pair of crossed loop antennas whose relative responses to an incoming plane wave indicate the direction of arrival of the wave. The way in which we processed and recorded this information is illustrated in Figure 1. The azimuth-intensity information displayed on the oscilloscope face was quantized into 10° sectors, and a measure of the amount of sferics activity in each sector was obtained by counting the number of sferics impulses exceeding a preset amplitude threshold in each 10-min time interval. The data were stored on paper tape and then processed logarithmically to yield azimuth-time plots as shown in Figure 2. Each number indicates the amount of sferics activity in its azimuth-time cell. The other sferics plots in this paper were derived from such number arrays by manual contouring.

The threshold level we used was 0.5 V m⁻¹, which corresponds to the median field strength (measured, for example, by *Taylor* [1963]) of sferics from cloud-to-ground strokes about 700 km away, about the median distance from which severe storm infrasound is observed. The receiving system had 6-dB response points at 5 and 50 kHz.

Uman [1969] and *Kimpara* [1965] have established that almost all VLF sferics radiation comes from cloud-to-ground return strokes and that relatively little comes from intracloud strokes. Therefore, we interpret the VLF sferics rate measurements as indicating the rate of occurrence and intensity of cloud-to-ground lightning strokes.

Measurement uncertainties. Azimuth resolution and accuracy of the microbarograph array and processing system depend upon the signal-to-noise ratio, the array size and geometry, the suitability of the plane-wave assumption, and the workings of the analog-processing mechanism. Experiments have shown that we can reasonably assign an average uncertainty of ±3° to all infrasound bearing determinations.

Additional uncertainty in locating the apparent source of infrasound arises from acoustic refraction caused by atmospheric winds. *Beasley* [1974] has estimated the expected mag-

nitudes of these errors under various atmospheric wind conditions, using three-dimensional acoustic ray tracing. The difference between the true and apparent source bearings would not exceed about 11° more than 5% of the time. Therefore the total uncertainty between measured and true bearings to an infrasound source should exceed 14° no more than 5% of the time.

The sferics measurements have a maximum azimuth uncertainty of ±5°. The combined uncertainty in sferics and infrasound measurements is ±19°. It would be very improbable for the two kinds of emissions to have a common source and also arrive at Boulder with bearings differing by more than 19° more than 5% of the time.

RESULTS

Correlation Statistics

During the observing period we identified 144 distinct infrasonic events at Boulder. Of these, 59 were judged to be unrelated to severe weather (being associated with other known natural sources of infrasound). Because of equipment malfunctions we had VLF atmospherics data during only 64 of the 85 severe storm infrasound events. Of the 64 events, 28 (44%) showed an apparent coincidence in direction, within 19°, whereas in 36 cases (56%) the infrasound bearing differed from the bearing of most intense sferics activity by more than 19°. In 19 cases (30%) the difference was greater than 40°, and in 4 cases (6%) there were no sferics above threshold from any direction.

Fig. 2. Example of the way our processor displays sferics rates in the azimuth-time plane. Each digit indicates the relative number of sferics impulses in its azimuth-time cell of 10° by 10 min.

Fig. 1. System for recording direction and time of arrival of VLF atmospherics (sferics).

Fig. 3. Azimuth of peak sferics rate versus azimuth of infrasound arrival. Approximately 44% of both near and far cases show apparent coincidence within ±19°, the indication being that the degree of coincidence is independent of distance. The histograms on each axis show the number of infrasound or sferics arrivals in each 5° azimuth sector. (The tendency for sferics to peak from 80–90°, while infrasound shows a broader peak around 140°, may arise because of many squall line cases such as those of Figure 7.)

Figure 3 summarizes these results by showing how the infrasound bearings and the sferics bearings are related for each of the 64 cases when both were observed simultaneously (allowing for differences between the acoustic and electromagnetic travel times). The distance was measured from Boulder to the center of the radar-indicated storm area. The squares and circles mark, for each event, the measured infrasound arrival azimuth versus the azimuth of the most intense sferics activity (according to our counting scheme). The squares indicate events whose apparent source storm is less than 500 km from Boulder. The circles are for sources greater than 500 km away. We separated the data by distance to see if there were any difference in the correlation for distant and nearby storms. No such difference is visually apparent in the figure. The percentage of events (44%) whose azimuths coincide within 19° is independent of distance to the source storm. This agrees with our intuition because we expect both the infrasound and the VLF sferics to experience roughly cylindrical spreading. If so, the dependence of amplitude on distance should be about the same for both, and the correlation (if any) between the two emissions should not depend strongly on the distance to the emitting storm.

If the infrasound were generated where lightning activity was the most intense, we would expect almost all of the marks to fall within the ±19° uncertainty limits (dashed lines) on either side of the infrasound bearings (actually, only about 44% did). Greater differences could arise in a few cases where indicated maxima in sferics intensity are caused by the superposition of the effects of several separate storm systems in roughly the same direction but at different distances.

Case Illustrations

We chose five examples of simultaneous sferics and infrasound arrivals that clearly illustrate the different kinds of correlation we observed between the two emissions and with radar-indicated storm activity. We show all five cases here because they represent the important features of practically all of the events studied. We chose these particular examples because the data were relatively unambiguous and the radar charts were relatively uncluttered with other, possibly confusing events.

Each case is illustrated with a reproduction of a radar summary chart with its standard notations and a portion of the azimuth-time sferics record with superimposed information about the infrasound arrival. We have no way to check the accuracy of the radar-indicated echo heights, but the exact height is not critically important. The infrasound times have been corrected for acoustic travel time from the apparent source storm at an average transit speed of 300 m s^{-1}, so that they can be thought of as emission times. The symbols used in the illustrations are explained in Figure 4. Our interpretations follow the descriptions.

Case 1 (Figure 5). During this event, infrasound was recorded at Pullman, Washington, in addition to Boulder, and so it was possible to locate the apparent source by triangulation. The intersecting bearings are shown on the map. Two tornadoes were reported during this storm, and their locations are shown both on the map and in the azimuth-time plot. Radar charts for the adjacent hours show that the system was moving toward the southeast. Maximum radar echo heights were 65,000 ft. (19,800 m).

Fig. 4. Symbols used in case illustrations.

RADAR SUMMARY 0240 Z

5-50 kHz ATMOSPHERICS
BOULDER, COLO.

Fig. 5. Case illustration 1, July 31, 1972. Infrasound originates in tornado-bearing storm about 1 hour before any above-threshold sferics.

Infrasound began at 0200 UT, but sferics were not recorded until 0245 UT and did not reach their maximum rates until about 0500 UT. Furthermore, the infrasound arrived at Boulder from 38° azimuth, whereas sferics activity began from between 60° and 70°. Local wind noise obscured the infrasound at Boulder after about 0245 UT, but it seems clear that the infrasound emissions began rather early in the lifetime of this system (and prior to the sightings of the two tornadoes) while it was in southeastern South Dakota. The strongest sferics emissions appeared about 2 hours later, when the system moved into Nebraska and Iowa.

This case is a clear example of infrasound without any accompanying sferics at the time of infrasound emission. It is also a clear example of infrasound generation apparently preceding a tornado (by 30–40 min) and of infrasound from the tornado location. Several other such cases were recorded during this experiment.

Case 2 (Figure 6). In this example the infrasound came from the direction of maximum sferics rates and began and ended during strong sferics activity. The storm system was an area of many radar echoes with tops at 40,000 ft (12,200 m) or greater extending from northeastern New Mexico to north central Nebraska. Both emissions appeared to come from near the middle of this area. A funnel cloud aloft was reported at the location shown, several degrees clockwise from the infrasound bearing. This case is included as an example of the 44% of the cases which showed apparent coincidence.

Case 3 (Figure 7). Here, infrasound was received for 8

hours from the southern extremity of a squall line that extended from the Texas panhandle into northern Kansas. Maximum radar-indicated storm tops were at 54,000 ft (16,500 m), with the larger storms tending to be near the southern end of the squall line. Atmospherics consistently showed a peak in intensity at about 20° counterclockwise (northward) of the infrasound bearing. Several similar cases occurred during the observation period, the result being the peak in the sferics histograms (Figure 3) around 80°–90°, whereas infrasound peak was around 140°.

Case 4 (Figure 8). In this example the sferics and infrasound appeared to be completely unrelated. Infrasound arrived from 10° azimuth, which corresponds to the direction of heavy rainfall and flash flooding in the Rapid City, South Dakota, area. Sferics came from the east, however, with maximum rates from about 110°, the azimuth of a nearer storm system (with 42,000-ft (12,800 m) tops) in eastern Colorado; no counts above threshold were recorded from less than 70° azimuth. Whereas sferics activity at a low-count level did come from the Rapid City direction some 4 hours earlier, none remained by the time of the infrasound generation.

Case 5 (Figure 9). This case provides a clear example of infrasound coming from a relatively isolated nearby storm system, with the most intense sferics activity coming from another, more distant system. The infrasound azimuth (144°) agrees well with the direction and time of a 50,000-ft (15,200 m) storm that produced hail up to 2¾ in. (70 mm) in diameter in the Texas panhandle. Yet no sferics above threshold came from

the direction of this storm. The azimuth of the peak sferics count was about 105°, which corresponded to another relatively isolated system in southeastern Kansas (38,000-ft (11,600 m) tops), about twice as far as the infrasound-emitting storm. The isolated nature of these storm systems provides good evidence for the independence of the two wave generation mechanisms. If the infrasound emission were electrical, we would expect the nearer infrasound-emitting storm to dominate the sferics azimuth-time plot.

INTERPRETATION

Case illustrations 2 and 3 show that infrasound generation may arise from a relatively narrow sector for long periods of time, whereas sferics signals during the same interval vary greatly in rate and azimuth of arrival. This agrees with the interpretation that the conditions for infrasound generation are more restrictive than those for sferics generation.

If the mechanism that generates severe storm infrasound were any of the electrical mechanisms discussed by T. M. Georges (unpublished manuscript, 1976) and Beasley [1974], we would expect to see a close spatial and temporal correlation between the apparent sources of infrasound and the apparent sources of VLF atmospherics, i.e., cloud-to-ground lightning strokes. We would expect the two apparent source locations to coincide often by accident just because the most severe storms tend to be the most frequent emitters of both kinds of radiation. But a large number of cases where the emissions appear to be completely unrelated spatially or temporally would appear to rule out a causal connection. Our observations support this conclusion, both statistically and on the basis of individual

case studies of phenomenology; but before we can safely infer that lightning is not directly related to the infrasound source, we must answer some questions that could be raised about such an inference.

Some questions. Our sferics recording system responded mainly to radiation from cloud-to-ground strokes. What about infrasound generators related to intracloud strokes and electromechanical relaxation as discussed by T. M. Georges (unpublished manuscript, 1976) and *Beasley* [1974]? Observations by *Brook and Kitagawa* [1960], for example, have established that intracloud strokes are almost always accompanied by nearly equal numbers of cloud-to-ground strokes. Therefore virtually any kind of electrical discharge activity inside storms would usually be accompanied by VLF emissions. This would include the hypothetical electromechanical relaxation process, which requires a discharge to set it off.

Our correlation statistics were between infrasound azimuths and the directions of maximum sferics counts. But would electrical infrasound generation necessarily coincide with the generation of highest VLF emission rates? And what about the effects of distance to the source? Couldn't a nearby weak sferics emitter dominate our sferics receiving system while a more distant, stronger sferics (and infrasound) emitter goes undetected? In such a case the generation mechanism could be electrical, but the azimuth of peak sferics might not coincide with the infrasound azimuth. We argue against this possibility as follows.

1. As was mentioned previously, comparison of the energy of observed infrasound with the energy available as acoustic radiation from lightning shows that only the most energetic

RADAR SUMMARY 0240 Z

5–50 kHz ATMOSPHERICS
BOULDER, COLO.
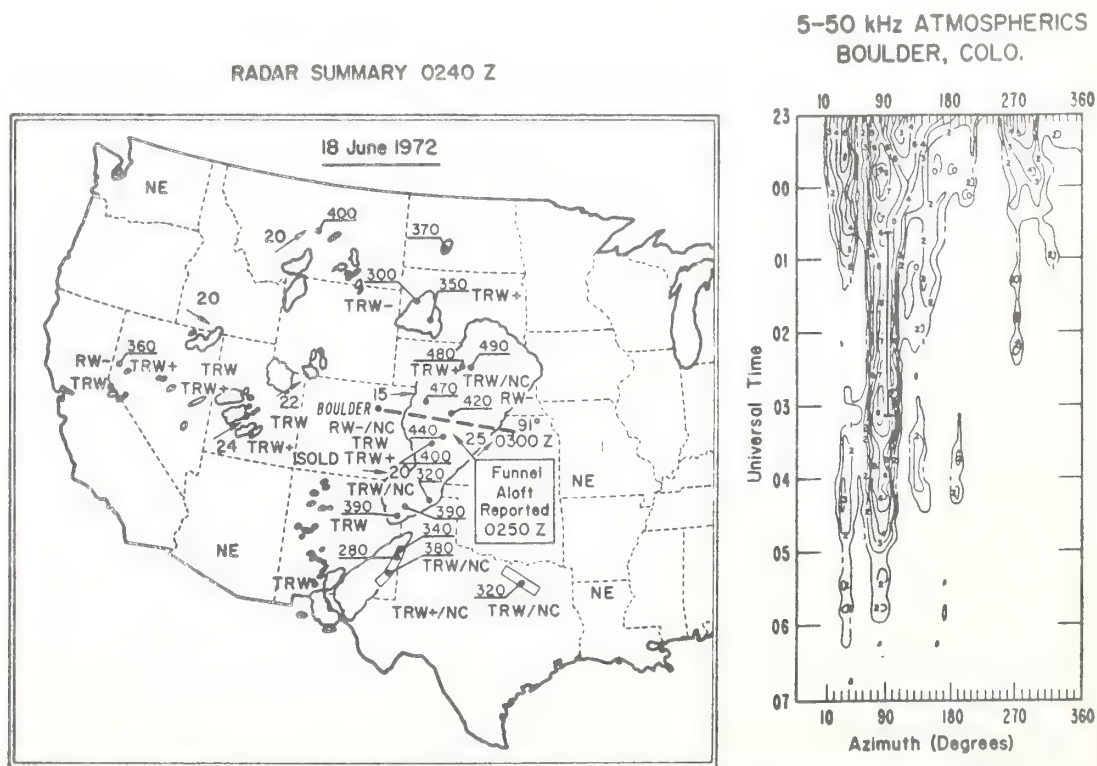
Fig. 6. Case illustration 2, June 18, 1972. The azimuths of infrasound and of maximum sferics rates coincide.
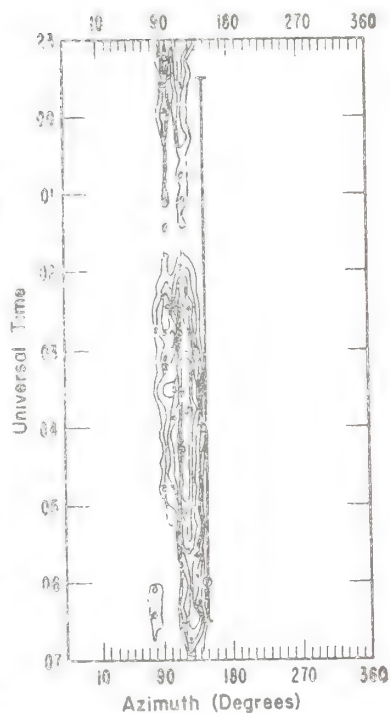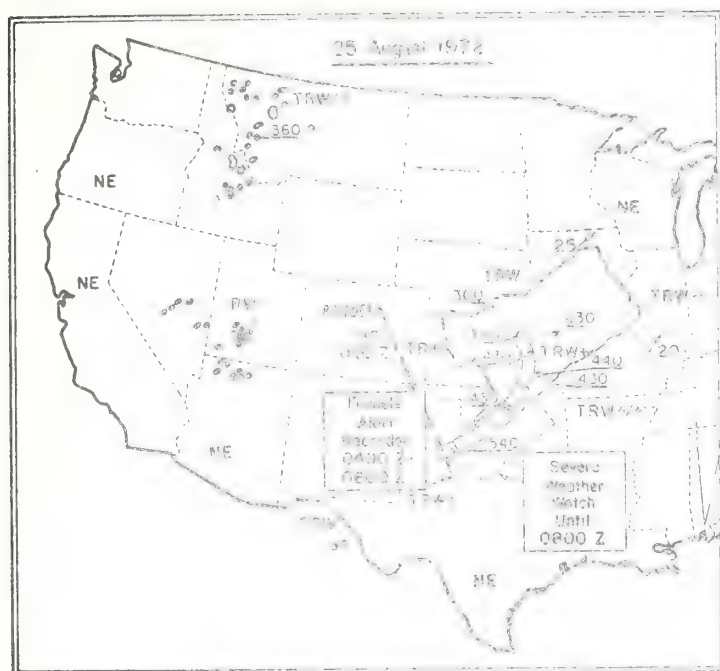
Fig. 7. Case illustration 3, August 25, 1972. Infrasound originates at the southern end of the squall line, while maximum sferics rates are received from the midpoint of the line, about 20° counterclockwise.
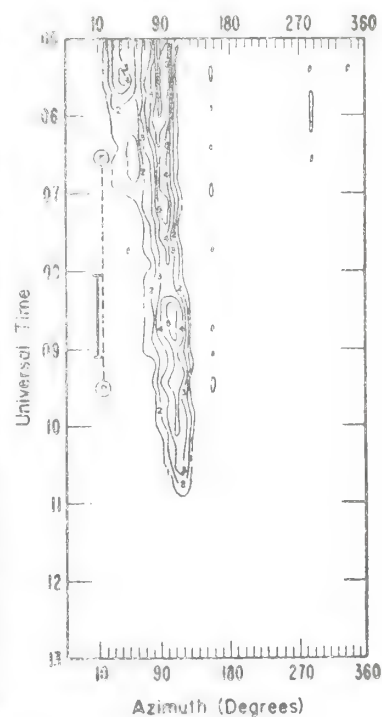
Fig. 8. Case illustration 4, June 10, 1972. Infrasound and sferics emissions appear to be completely unrelated and independent.
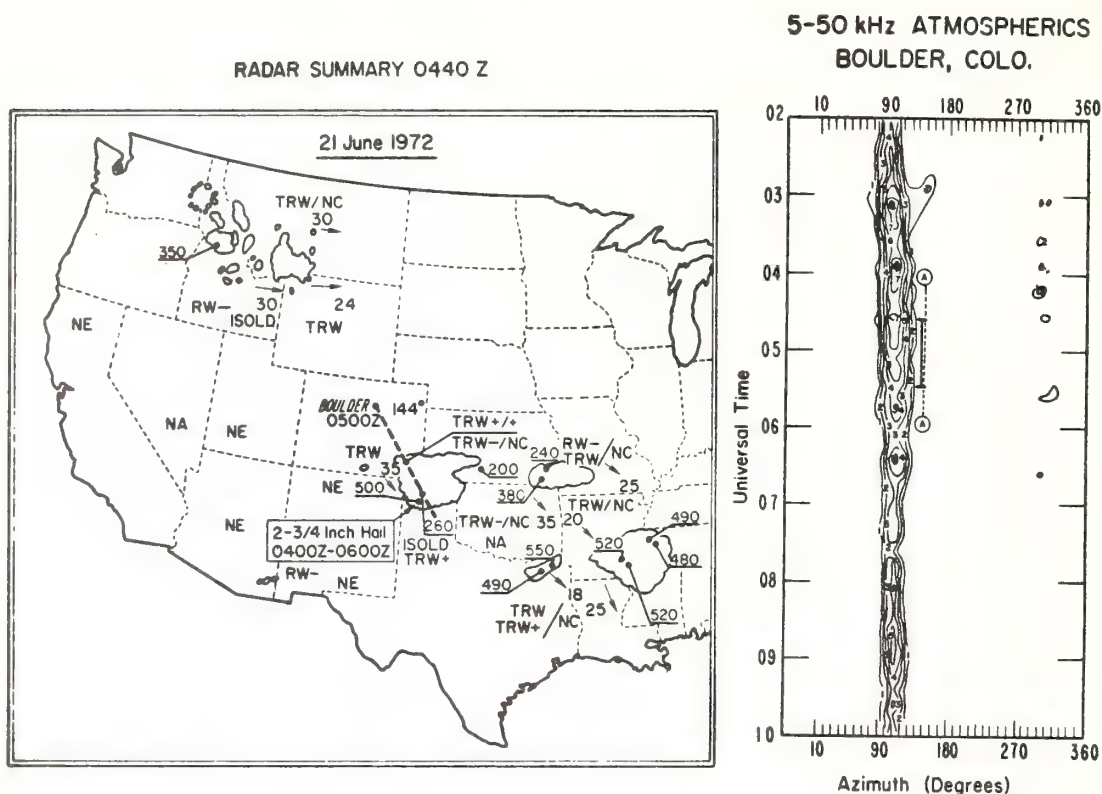
Fig. 9. Case illustration 5, June 21, 1972. Infrasound originates in a nearby storm, while sferics come from a group of storms about twice as far away, independence of emission mechanisms being suggested.

strokes occurring at the highest observed rates could possibly account for observed infrasound intensities.

2. We expect that an increase in the total energy input to lightning strokes results in proportionate increases in the energy coupled into both acoustic and electromagnetic radiation.

3. Because the long-distance propagation mechanisms for VLF sferics and infrasound are similar (cylindrical spreading), we expect roughly the same average rate of amplitude attenuation with distance.

Therefore if one kind of emission were stronger because the source storm was closer, then the other kind should also be stronger by about the same factor. This argument is strengthened by the observed lack of a distance dependence in the correlation statistics of Figure 3. There could, of course, be some qualitative difference between the electrical activity inside different storms such that one kind emits infrasound and another does not. However, we are unaware of any evidence for such a distinction.

Evidence that infrasound precedes sferics. Our case studies and other examples we studied in detail reveal a tendency for infrasound emission during an early stage of storm development, whereas the greatest electrical activity is usually associated with the 'mature' (precipitating) stage of cumulus development [e.g., *Byers,* 1974]. Case 1, for example, shows that infrasound emissions (and the two tornadoes) occurred when the storm system was in central South Dakota but that electrical activity peaked some hours later, after the system had moved toward the southeast. Case 3 shows infrasound emissions from the southern extremity of the squall line, where the

most severe storms (and funnels aloft) were observed; yet the most intense sferics activity came from storms farther northward along the squall line. This observation agrees with current models of squall line thunderstorm development which have proposed that new storm generation occurs at the southern end of the line, while the older storms are displaced northward along the line [*Browning and Ludlam,* 1962; *Newton and Fankhauser,* 1964].

These results suggest that the infrasound-generating mechanism is frequently associated with the early stages of cumulus formation, when the most vigorous convection occurs. Its frequent association with tornadoes and funnels aloft also provides a valuable clue to the actual generation mechanism [*Georges and Greene,* 1975].

REFERENCES

Beasley, W. H., An evaluation of lightning as a source of severe-storm infrasound, Ph.D. dissertation, Univ. of Tex. at Dallas, Richardson, 1974.
Brook, M., and N. Kitagawa, Some aspects of lightning activity and related meteorological conditions, *J. Geophys. Res., 65,* 1203–1210, 1960.
Brown, R. F., Jr., An automatic multichannel correlator, *J. Res. Nat. Bur. Stand., Sect. C, 67,* 33–38, 1963.

Browning, K. A., and F. H. Ludlam, Airflow in convective storms, *Quart. J. Roy. Meteorol. Soc., 88,* 117–135, 1962.

Byers, H. R., *General Meteorology,* 4th ed., pp. 374–378, McGraw-Hill, New York, 1974.

Colgate, S. A., and C. McKee, Electrostatic sound in clouds and lightning, *J. Geophys. Res., 74,* 5379–5389, 1969.

Dessler, A. J., Infrasonic thunder, *J. Geophys. Res., 78,* 1889–1896, 1973.

Georges, T. M., Infrasound from convective storms: Examining the evidence, *Rev. Geophys. Space Phys., 11,* 511–594, 1973.

Georges, T. M., and G. E. Greene, Infrasound from convective storms, 4: Is it useful for storm warning?, *J. Appl. Meteorol., 14,* 1303–1316, 1975.

Georges, T. M., and J. M. Young, Passive sensing of natural acoustic-gravity waves at the earth's surface, in *Remote Sensing of the Troposphere,* edited by V. E. Derr, chap. 21, U.S. Government Printing Office, Washington, D. C., 1972.

Kimpara, A., Electromagnetic energy radiated from lightning, in *Problems of Atmosphere and Space Electricity,* edited by S. C. Coroniti, Elsevier, New York, 1965.

Matheson, H., Instructions for the operation of NBS infrasonic equipment, *Nat. Bur. Stand. Rep. 8519,* U.S. Dep. of Commer., Washington, D. C., 1964.

Newton, C. W., and J. C. Fankhauser, On the movements of convective storms, with emphasis on size discrimination in relation to water-budget requirements, *J. Appl. Meteorol., 3,* 651–668, 1964.

Taylor, W. L., Radiation field characteristics of lightning discharges in the band 1 kc/s to 100 kc/s, *J. Res. Nat. Bur. Stand., Sect. C, 67*(5), 539–550, 1963.

Terman, F. E., *Radio Engineers' Handbook,* McGraw-Hill, New York, 1943.

Uman, M. A., *Lightning,* McGraw-Hill, New York, 1969.

Watson-Watt, R. A., and J. F. Herd, An instantaneous direct-reading radiogoniometer, *J. Inst. Elec. Eng., 64,* 611–622, 1926.

479

The asymmetry in infra-sound generation by travelling aurora

George Chimonas

Cooperative Institute for Research in Environmental Sciences, University of Colorado/NOAA,
Boulder, Colorado 80309

and

Wave Propagation Laboratory, National Oceanic and Atmospheric Administration,
Boulder, Colorado 80302, U.S.A.

Abstract—Ground level pressure signals are sometimes found to accompany equatorwards travelling auroral arcs, but have never been detected for polewards travelling ones, even though there are no obvious visual differences in the displays. It is shown that the visual similarities of the arcs in no way guarantee a similarity of their electrojets. The field characteristics of the recorded arcs indicate that those with detectable infrasound signatures belong to a special class in which the electrojet current is of an unusually concentrated nature. This concentration occurs when, in the frame of reference of the arc, the ionisation velocity field contains a convergence mode towards which all the arc ionisation is driven after production.

INTRODUCTION

Over the last decade, Wilson (1974, and references therein) has made an exhaustive study of the ground level sound pulses that accompany supersonically translating auroral arcs. There is little doubt that the sound is a result of the coupling of the arc currents to the neutral atmosphere through either Joule heating or the Lorentz force. The interaction was examined by Chimonas and Peltier (1970), who found excellent agreement between the observed pressure bow waves and a theory in which the current was concentrated into an electrojet of width about 10 km. Recently Wilson (1975) has established that in many thousands of arcs studied, not one whose direction of motion was towards the pole ever produced a detectable infrasound signature. Apart from this sense of motion, there appeared to be only minor differences in visual width and total current between the sound producing and non-producing varieties. Unfortunately this has led to some debate as to whether the linear interaction between electrojet and atmosphere could be responsible for the observed pressure signatures, since if two electrojets differ only in their senses of translation, their pressure signatures are equally strong. In this paper we show that the problem is easily resolved, in that a reversal of the sense of arc translation does not leave the electrojet unaffected. In particular, it will appear that only for a particular alignment of arc electric field and velocity can we obtain the strong narrow electrojets that produce the detectable bow waves. Reversing the arc motion, but keeping the electric fields and ionisation production patterns the same, leads to a very different electrojet and sub-noise level signatures. It is important to realise that we are not investigating the dynamics that drive arcs and interrelate their basic properties. Thus when we consider an arc and its reversed form (as above), we are comparing two distinct data sets. There is no suggestion that (say) any one real arc could ever reverse its sense of motion without major constitutional changes. Nor do we suggest any reason for the various types of arc structure. In this paper we only need to accept their observed existence.

The difference in the electrojet structures is a result of a simple ionisation collection process. If the electric fields that accompany the moving arc have the right form, they will sweep the ionisation produced in the visible arc region into a thin core. If on the other hand they are too weak or have the wrong form, the ionisation will be left behind as the arc translates, and a much wider and less intense electrojet will result. Piddington (1963) has suggested that the DS fields throughout the higher latitudes produce some convergence of ambinent ionisation. The work presented here could be regarded as an extension of this idea to the much smaller scales of an active arc. The dynamics of the process are also highly analogous to the corkscrew mechanism by which descending sporadic-E layers are formed and held at moving wind nodes (Chimonas and Axford, 1968).

FORMULATION

Auroral arcs are of course extremely complicated systems with strong variations in both space and

time. However, the observed asymmetry in pressure signatures must result from some very basic arc property that can be incorporated into a relatively simple and unsophisticated model of the arc. In fact, although Wilson has studied many thousands of auroral events, only the crudest features of the arcs were needed to compile the statistics and establish the symmetry. We may regard as 'available' data on (a) arc speed and direction at zenith crossing, (b) total equivalent line current at zenith, (c) pressure signature at ground level (if above noise level) and (d) a crude estimate of the visual width of the arc. This set does not supply quite enough detail to define the model parameters that prove relevant. We also really need information about the electric field in and about the arc. However many other features of real arcs, such as finite lengths and non-uniform time behaviour, are not fundamental to the asymmetry feature and can be ignored. Basically we can state the problem as follows: Particles of magnetospheric origin stream into a section of the E-region and generate a certain amount of ionisation. This bombardment is not stationary (at least in a frame of reference fixed to an earth point), but sweeps across the ionosphere with a supersonic velocity. The immediate location of the ionisation production is, of course, just the visible auroral arc. Strong electric fields through and about this location, act on the ionisation to form the electrojet. Given the space time form of the ion production and the electric fields, what is the shape of the electrojet?

We adopt a right-handed set of cartesian co-ords (x, y, z) with z set in the vertical direction. The incoming stream, and the ionisation it produces, is taken to be completely constant in one horizontal direction, say y. The uniform translation of the arc proceeds in the x direction, and we choose to work in the frame of reference that is fixed to the arc so that all functions in the problem become time independent. If the electric field $\mathbf{E}(x, z)$, the geomagnetic field $\mathbf{B}_0$, the ion-production rate $p(x, z)$ and the density of the neutral atmosphere are given, we can calculate the electron/ion density $n(x, z)$ and hence the electrojet current. But the form of $\mathbf{E}$ is unknown and can only be guessed in crude general terms, so we might just as well save a considerable amount of labour and guess instead the related function $\mathbf{V}_p (x, z)$, the projection of the electron velocity onto the (x, z), plane. Without any great loss to the physics, we may make the usual approximations that

(1) $\mathbf{B}_o$ is a vector in the z direction.

(2) The electrical conductivity in the z direction is infinite, so $\mathbf{E} \cdot \hat{z}$ is zero.

(3) The ion and electron partial pressure gradients are negligible compared with the other terms in the equations of motion of the charged species.

(4) Any neutral winds are space and time independent on the scales of interest.

Then $\mathbf{V}_p(x, z)$ becomes the (x, z) plane velocity of both ions and electrons and lies totally in the x direction, $\mathbf{V}_p(x, z) = \hat{x} V_p(x, z)$. The ion/electron distribution is governed by the continuity equation

$$p(x, z) - \alpha n^2(x, z) - \frac{\partial}{\partial x}[V_p(x, z) n(x, z)] = 0 \quad (1)$$

which is very easily solved on the computer for any given well behaved functions p and V. Of particular interest to us are the solutions when p and V are of the types shown in Figs. 1 and 2. Let us designate the system, shown in Fig. 1 a type 1 system. In it, all ionisation that is produced finds itself swept towards a convergence node, and a narrow highly peaked distribution of ionisation results. On the other hand, Fig. 2 displays a type 2 system in which the ionisation is swept at high speed out of the production region and hence through a very long tail stretching way behind the visible arc.

The frame of reference fixed with respect to the Earth's surface is the one in which $V(x) \rightarrow 0$ at $x \rightarrow \pm \infty$. But in this frame we see that the type 1 and type 2 shown have identical $\mathbf{E}$ (i.e., $\mathbf{V}_P$) fields, identical visible structures, identical speeds of translation, similar total electrojet currests but opposite directions of motion across the sky. From the calculations of Chimonas and Peltier (relating ground level pressure signal to the arc currents), we know that if the type 1 system produced a pressure bow wave strong enough to give a 10:1 signal to noise ratio at the ground, reversal of the arc motion to give the type 2 system would cause the signal to fall into the noise level. Since the very strongest bow waves so far observed have signal to noise ratios of about 3, we find a very simple explanation for the observational asymmetry. It is known from Wilson's observations that all arcs whose pressure signatures have been detected, contained electrojets in which ion and arc have the same sign for their component of velocity along the horizontal normal to the arc (observed in the ground based frame). On the other hand, all the pole-wards travelling arcs have opposite signs for these velocity components (which make them type 2) and produced no observable pressure waves. The inference is that even the strongest electrojets must be in the
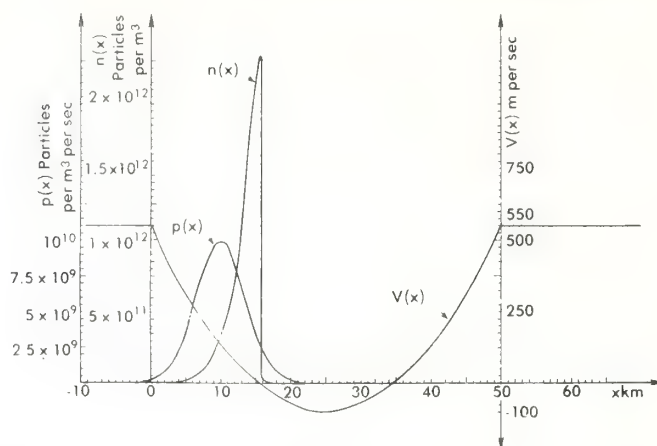
Fig. 1. The number density $n(x)$ that is the solution of equation (1) with z fixed and the functions p and V chosen to have the forms

$$p(x) = 10^{10} \exp\left[-(0.2x-2)^2\right] \text{ptcle/m}^3/\text{s}$$

$$v(x) = \begin{cases} 550 \text{ m/s} & x < 0 \quad \text{or} \quad x > 50 \text{ km} \\ -100 + 1.04 \cdot (x-25)^2 \text{ m/s} & 0 < x < 50 \text{ km}. \end{cases}$$

As the ions are produced, they are all swept towards the convergence node at $x = 15.2$ km. $n(x)$ is recombination limited in this region. α has been set at the typical E-region value of 10^{-14} m^3/ptcle/s. We define a type 1 arc as one having this convergence node. If the electric fields are zero for large $|x|$, then to a ground based observer the arc appears to sweep across the sky at 550 m/s, and the electric fields within the arc move ionisation in the direction of arc travel.
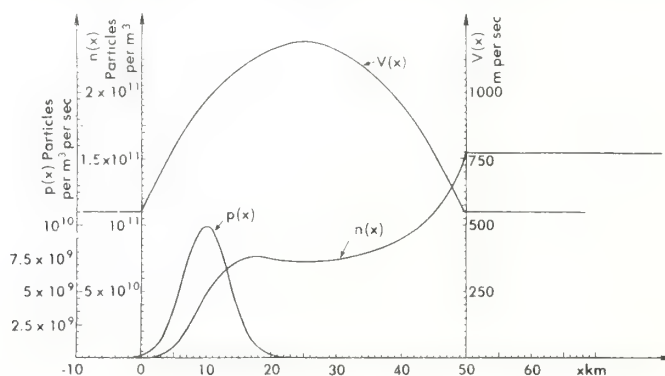
Fig. 2. The number density $n(x)$ that is the solution of equation (1) with z fixed and the shown functions p and V. p (and α) are the same as used in Fig. 1, but V now has the form

$$V(x) = \begin{cases} 550 \text{ m/s} & x < 0 \quad \text{or} \quad x > 50 \text{ km} \\ 1200 - 1.04 \cdot (x-25)^2 \text{ m/s} & 0 < x < 50 \text{ km} \end{cases}$$

Ionisation is swept away from the production region into a long tail. Note the order of magnitude change in the scale of $n(x)$. This system in which ionisation is continuously forced away from the production region is denoted type 2. Note that if the production function p and the arc electric fields of the system in Fig. 1 are kept constant but the velocity of the arc across the sky is reversed, we obtain this present system.

favoured type 1 configuration to produce a signature of detectable amplitude.

In principle the current distribution within travelling arcs could be accurately monitored. Then these currents could be fed into the theory for bow wave production and compared with the observed (or noise level) signals on the microbarographs. Of course, the magnetometer arrays usually used in

this work do not come within an order of magnitude of providing the needed resolution of the electrojet. There is probably more hope in using the auroral radar techniques recently developed by the team of GREENWALD et al. (1975).

However, it is doubtful that any great profit lies in these investigations, beyond, of course, the satisfaction of scientific curiosity.

In summary, the linear generation theory has no difficulty in providing a consistent picture of all that is known about arc induced infrasound. However, it has become necessary to suggest (and show feasible) a strong difference between the electrojet structures of sets of arcs that appear quite similar to a ground based observer.

It is not suggested that the matter *per se* merits the expense that would be required for a definitive experimental investigation, but it would be a worthwhile secondary task for any future project that happens to take sensors through the appropriate regions.

BASIS OF THE TYPE 1 ARC

The calculations given above illustrate the properties required of an arc in order that it should have a narrow and intense electrojet. Clearly the only fundamental requirement is that the electric field in or about the precipitation region must be able to collect the ionisation into a preferred region.

There is no *a priori* reason to use a stationary precipitation/electric field system (apart from ease of calculation). One could quite easily construct models for which the collection region had a speed of translation quite different from that of the precipitation region. Since real arcs are highly time dependent, it would in fact be rather surprising if these two speeds were identical. It is interesting to note here that Wilson's observations (WILSON, 1972) seem to indicate that the visible arc translates rather faster than its associated bow wave, suggesting perhaps that the trapping region falls progressively further behind the moving precipitation region.

However, this is all speculative; the arc morphology is not sufficiently well known. As mentioned above, Wilsons's observations do show that the sense of the electric fields is correct for type 1 in equatorwards and type 2 in polewards travelling arcs, but intensity and structure of the fields has not been observed.

COMPARISON WITH THE PRESSURE-WALL THEORY

When he first observed the asymmetry in bow-wave production by travelling aurora, WILSON (1972) was led to reject the linear arc/atmosphere interaction theory of sound production, and postulated instead that a nonlinear shock mechanism was required. In that approach collisions in the arc between ions and the neutral atmosphere were supposed to accelerate the neutral medium to supersonic velocities. An ion collection process relying on a similar electric field structure to the one used in this paper but producing very much greater ion densities was suggested to operate. It is not clear that such a super-mechanism is entirely impossible under the physical restraints known to exist in aurora, but it does seem unlikely. The work in this paper suggests that it is unnecessary, and that the asymmetry results simply from the localised geometry of type 1 electrojets.

However, there still remains the problem of the sign of the pressure signature (discussed by WILSON, 1972). It may be remarked here that SWIFT (1973) has performed a valuable service in showing that the instruments used by Wilson may not have a sufficient bandwidth to record the auroral signatures correctly, and this, combined perhaps with the complex geometrical forms of real arcs may account for any remaining discrepancy between theory and observation.

REFERENCES

CHIMONAS G. and AXFORD W. I.	1968	*J. geophys. Res.* **73,** 111.
CHIMONAS G. and PELTIER W. R.	1970	*Planet. Space Sci.* **18,** 599.
GREENWALD R. A., ECKLUND W. L. and BALSLEY B. B.	1975	*J. geophys. Res.* **80,** 3635.
PIDDINGTON J. H.	1963	*Geophys. J. R. Astron. Soc.* **7,** 415
SWIFT D. W.	1973	*J. geophys. Res.* **78,** 8205.
WILSON C. R.	1972	*J. geophys. Res.* **77,** 1820.
WILSON C. R.	1974	*Planet. Space Sci.* **22,** 151.
WILSON C. R.	1975	*J. atmos. terr. Phys.* **37,** 973.

A Possible Source Mechanism for Mountain-Associated Infrasound

GEORGE CHIMONAS

*Cooperative Institute for Research in Environmental Sciences, University of Colorado/NOAA,
Wave Propagation Laboratory, NOAA, Boulder 80302*

(Manuscript received 10 October 1975, in revised form 2 February 1977)

ABSTRACT

Mountain-associated sound is a well known natural acoustic signal that can be traced back to windy mountainous areas. Direct monitoring in such regions reveals much low-phase-velocity wind noise: in this paper we suggest that scattering of these wind oscillations from terrain irregularities produces at least part of the infrasound signal. An idealized (two-dimensional) calculation shows that the scattering mechanism is rather efficient. However, the more intricate question of how much infrasound could be expected in this manner from a real mountain range is not investigated.

1. Introduction

Every operator of infrasonic range microbarographs is familiar with the phenomenon of mountain-associated sound—MAS. It is an infra-sound signal with period between 10 and 100 s that emanates from mountainous locations in the seasons of strong local tropospheric wind. The geo-acoustic group of NOAA has made an extensive statistical study of MAS, and the interested reader is referred to papers by Greene and Howard (1975), Bedard (1975) and Larson *et al.* (1971).

Strong disturbances in the same period range are commonly observed at windy mountainous sites; however, these are not acoustic disturbances as they have horizontal propagation speeds of up to only a few tens of meters per second. The origin of these low-phase-velocity waves is unknown, although many suggestions have been offered, including rotor breakdown, eddy shedding at sharp irregularities in the terrain, and Kelvin-Helmholtz generation by strong low-level wind shears. Whatever, they are a well-verified set of low-frequency oscillations that may have amplitudes as large as a few millibars. In this paper we examine the possibility that they interact with undulations in the terrain to produce the sound waves recognized great distances away as MAS. Of course, we do not suggest that this is the sole, or even major source of MAS. At this stage it is merely one that lends itself to reasonably clear mathematical analysis and, hopefully, to experimental investigation at some future date. The semi-qualitative predictions of this paper indicate that the mechanism is at least viable.

2. Scattering across domains

In studying atmospheric disturbances with horizontal phase velocities of a few tens of meters per second or less, one more often than not employs the equations of motion for an incompressible fluid. On the other hand, if the disturbance of interest is in the sound domain, so that its horizontal phase velocity is at least equal to the sound speed, the equations used display the adiabatic compressions, but very often ignore gravitational stratification and mean atmospheric motions (winds). Both approaches give sufficiently correct treatment within their respective domains, but it is necessary here to point out that the two types of system do not obey different equations of motion, as is sometimes mistakenly imagined. In fact, both the Kelvin-Helmholtz instability (say) and acoustic noise (say) obey identical equations. It is only when different approximations are made in the two cases to more easily obtain representations of the solutions that differences in the equations are fabricated. If this is borne in mind, then no confusion should arise when we find low phase velocity waves (whose forms are conveniently derived from the incompressible equations of motion) being scattered into the acoustic wave domain.

Scattering from the very low phase velocity to the very high phase velocity domains is not particularly uncommon in geophysics. Perhaps the best formulated example is found in Longuet-Higgins' (1950) explanation of the storm generation of microseisms.

The essential mechanics can be displayed as follows. Suppose a wave system A, characterized by frequency ω_A and horizontal wavenumber K_A, interacts with a second system with the parameters ω_B and K_B. The products of the interaction will have frequencies $\omega_A \pm \omega_B$ and wavenumbers $K_A \pm K_B$. Although both $|\omega_A/K_A|$ and $|\omega_B/K_B|$ may be very small compared with C, the speed of sound, one of the scattered system's phase speeds, $|\omega_A \pm \omega_B/K_A \pm K_B|$, can be greater than C if the wavenumbers K_A and K_B have almost
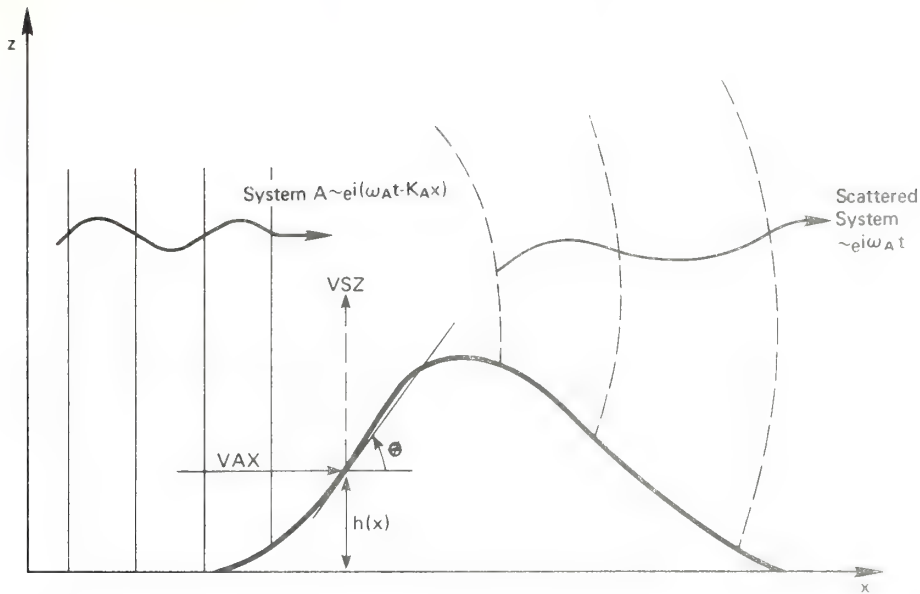
FIG. 1. Schematic showing an incident wave system A of the form $\exp[i(w_A t - K_A x)]$ scattering against a ridge $h(x)$ to produce waves with the same frequency $e^{i\omega_A t}$ but quite different phase speeds.

the same magnitude. In the particular situation to be studied in this paper, system A is a component of the wind noise in the mountainous area, while system B is a Fourier component of some terrain irregularity (say a hill or ridge) at the air-ground interface. In this case, ω_B is zero (in the familiar frame of reference) so the scattered waves have phase speeds $|\omega_A/K_A \pm K_B|$. We are now assured of supersonic components as $|K_A| \rightarrow |K_B|$, since no inconvenient cancellation can occur in the numerator.

3. The scattering amplitude

We will now calculate the strength of such a scattering interaction using an approximation that is entirely analogous to that of linear lee-wave theory. A more precise formulation is possible, but unnecessarily complex at this time, when a factor of 2 or less is inconsequential.

Fig. 1 is a schematic of the interaction. The wave system A, propagating in the (x,z) plane, satisfies the ideal boundary condition of zero normal velocity at the mean air-ground interface $z=0$. The wave field has velocity components $U_x(x,z)$ in the horizontal and $U_z(x,z)$ in the vertical. A uniform two-dimensional ridge aligned with the y axis provides a displacement $h(x)$ of the ground surface above its mean plane.

The system A incident upon this upthrust produces a contribution

$$U_x(x,h)\sin\theta - U_z(x,h)\cos\theta$$

to a flow normal to this solid surface, which must be balanced by an equal and opposite contribution from a scattered wave system with velocity components

(V_x, V_z), i.e.,

$$V_z(x,h) - V_x(x,h)\tan\theta = U_x(x,h)\tan\theta - U_z(x,h), \quad (1)$$

where $\tan\theta = dh/dx$. Assume now that $|dh/dx|_{max} \ll 1$ and that $|h|$ is much less than the vertical wavelengths of both incident and scattered fields. The fields at $z=h$ can be expressed as expansions about $z=0$, and to a satisfactory approximation only the first contributing term in each series need be retained, i.e.,

$$V_z(x,0) - V_x(x,0)\frac{dh}{dx} \approx U_x(x,0)\frac{dh}{dx} - 0 - \frac{\partial U_z(x,z)}{\partial z}\bigg|_{z=0} h. \quad (2)$$

It is seen that the amplitude of the scattered field is of order $|dh/dx|$ times the amplitude of the incident field, and thus to first order in $|dh/dx|$ the term $V_x(x,0)dh/dx$ may be dropped, giving

$$V_z(x,0) = U_x(x,0)\frac{dh}{dx} - \frac{\partial U_z(x,z)}{\partial z}\bigg|_{z=0} h. \quad (3)$$

Eq. (3) plus the upper boundary condition that the scattered field must either approach zero as $z \rightarrow \infty$ or correspond to an upward propagation of energy there provide two field constraints. These, applied to solutions of the linearized equations of motion for the atmosphere, completely determine the scattered fields.

The incident fields are low phase velocity waves. Hence they closely obey the incompressibility condition

$$\frac{\partial U_x(x,z)}{\partial x} + \frac{\partial U_z(x,z)}{\partial z} = 0,$$

which allows (3) to be recast as

$$V_z(x,0) = \frac{\partial h U_x(x,0)}{\partial x}. \tag{4}$$

Eq. (4) is a formulation in terms of velocity components; but since observations are usually made with pressure measuring devices, we must recast the equation accordingly.

Let $\rho(z)$ be the density and $W(z)$ the x component of wind, in the mean state of the atmosphere. The x component of the linearized Euler equation relates the pressure and velocity fields in the incident wave system through

$$\rho(z)\left(\frac{\partial}{\partial t}+W(z)\frac{\partial}{\partial x}\right)U_x(x,z)$$
$$+\rho(z)U_z(x,z)\frac{\partial}{\partial z}W(z) = -\frac{\partial}{\partial x}P_I(x,z).$$

At $z=0$, U_z is zero; hence

$$\rho(0)\left[\frac{\partial}{\partial t}+W(z)\frac{\partial}{\partial x}\right]U_x(x,0) = -\frac{\partial}{\partial x}P_I(x,0).$$

But the incident wave system is harmonic in t and x, i.e.,

$$(U_x,P_I)\sim \exp[i(\omega_A t-K_A x)],$$

so

$$P_I(x,0)=\rho(0)[\omega_A/K_A-W(0)]U_x(x,0).$$

Using this relation in (4) we obtain

$$V_z(x,0)=\frac{1}{\rho(0)[\omega_A/K_A-W(0)]}\frac{\partial}{\partial x}P_I(x,0)h. \tag{5}$$

At this stage it is not useful to attempt a general replacement of V_z by the scattered pressure amplitude P_S. The replacement will be made later for each specific case studied.

4. The Fourier representation of the scattered wave

Eq. (5) defines the scattered wave over the surface $z=0$. If we decompose it into its Fourier spectrum on x, and use the linearized equations of motion for each component, we can obtain the full (x,z) space solution. We will now do this, bearing in mind that when we use the exponential representation [as in (6)], it is implied that the real part of all equations corresponds to the real physical system.

We will use the notation

$$P_I(x,0)=p_I \exp[i(\omega_A t-K_A x)], \tag{6}$$

$$V_z(x,z)=\frac{e^{i\omega_A t}}{2\pi}\int_{-\infty}^{\infty}dk\,\hat{V}_z(z,k)e^{-ikx}. \tag{7}$$

From (5), (6) and (7) it follows that the Fourier amplitude of the scattered wave is given by

$$\hat{V}_z(0,k)$$

$$=\frac{p_I}{\rho(0)[\omega_A/K_A-W(0)]}\int_{-\infty}^{\infty}dx e^{ikx}\frac{d}{dx}h(x)e^{-iK_Ax} \tag{8}$$

$$=\frac{p_I}{\rho(0)[\omega_A/K_A-W(0)]}H(k-K_A)\quad\text{(say)}, \tag{9}$$

where (9) is an identity defining a shorthand symbol for the integral transform written explicitly in (8).

The system (8) [or (9)] specifies each (ω_A,k) component of the scattered wave's vertical velocity at the ground. Its form at all other z is defined by the causal boundary condition at $z\to\infty$ and the second-order differential equation in z derived from linearization of, and elimination between, the equations of motion for a perfect compressible fluid. A particularly succinct form of this equation is given by Warren (1968). We do not make explicit use of this general governing operator, although the approximations we use below could, of course, be derived from it. It also follows from this representation that the velocity transform can be written in terms of the pressure transform.

Thus suppose we formulate the wave equation for the pressure perturbation, and solve it under the correct upper boundary condition to obtain the function p_T [explicitly, $p_T(z,k,\omega_A)$]. This function uniquely defines an associated vertical velocity field w_T, and in particular the ground level value $w_T(0,k)$. But (9) defines the required ground level value, so

$$\hat{P}_I(z,k)=\hat{p}_T(z,k)\frac{\hat{V}_z(0,k)}{w_T(0,k)} \tag{10}$$

$$=\frac{p_I}{\rho(0)}\frac{\hat{p}_T(z,k)}{w_T(0,k)}\frac{H(k-K_A)}{[\omega_A/K_A-W(0)]}. \tag{11}$$

Inverting the transform on k then gives the spatial representation of the scattered pressure field

$$P_S(x,z)=\frac{e^{i\omega_A t}}{2\pi}\int_{-\infty}^{\infty}dk\frac{p_T(z,k)}{w_T(0,k)}$$

$$\times\frac{p_I}{\rho(0)}\frac{H(k-K_A)}{[\omega_A/K_A-W(0)]}e^{-ikx}. \tag{12}$$

5. Scattering into the atmospheric modes

At certain values (ω_A,k_i) the solution of the homogeneous wave equation on which we have imposed the (causal) upper boundary condition $\text{Lim}z\to\infty\hat{w}_T(z,k_i)=0$ also yields the condition $\hat{w}_T(0,k_i)=0$. Two factors contribute to the existence of these modal solutions. The first is an interplay of buoyancy and

compressibility that allows an exponentially decaying field at large z to evolve into a flow that is entirely parallel to the ground at $z=0$. Modes of this character are known as Lamb waves. Second, the vertical structure of the system may provide "sound channels" or height intervals resembling waveguide ducts. Modes originating in this way are known as the acoustic modes. In the real atmosphere the two effects can interact strongly, making the nomenclature somewhat arbitrary in certain regions of (ω,k) space.

Such natural modes of the atmosphere are particularly important for two reasons. First they can be observed at great distances from the source region where dispersion and high altitude dissipation have eliminated almost all the non-modal parts of the signal; and second, the atmospheric response is greatly enhanced where a mode exists so that even at intermediate distances from the source their presence makes detection of a signal much easier. [However, in and near the source region the signal cannot display its modal characteristics. See for example Pierce (1963).]

Modes are most strongly excited by sources located near the altitude of their maximum energy density. This is also the height at which they are, in principle, most easily observed.

Thus in MAS work modes must have a significant proportion of their energy in the lower troposphere to be of any interest. In a windless isothermal atmosphere the Lamb wave is the sole mode. It is also of just the correct form to be important to this work. However in the real, temperature-structured atmosphere there are numerous further modes. In particular the first gravity mode and the series of acoustic modes become important at periods <5 min because they also have considerable strength in the lowest 10 km of the atmosphere. In fact these modes become strongly coupled with the "isothermal" Lamb wave, and in part assume its properties over certain frequency intervals. Francis (1973) describes these modes in detail, and even defines a "pseudo Lamb wave" throughout most of the frequency spectrum.

We will evaluate the modal contributions to (12) for two situations: first the isothermal atmosphere (Lamb wave) model and then for the acoustic modes about minute periods. The Lamb wave calculation, interpreted in terms of Francis's pseudo mode, should be valid at the longer period end of the MAS observations, the acoustic mode calculations in the middle and high frequency range.

At a value k_i of k corresponding to a mode, the integrand in (12) is singular. The excitation strength of the mode is taken to be the integral over a very small k region about the singularity. This is the (theoretical) amplitude that a very narrow band width instrument tuned to k_i would record at a large distance from the source region. Then extracting all such residues from

(12) we obtain the modal response

$$P_S(x,z)\big|_{\text{modes}} = ie^{i\omega_A t}\sum_{i\text{ all modes}}\frac{p_I}{\rho(0)}\frac{H(k_i-K_A)}{[\omega_A/K_A-W(0)]}$$

$$\times\frac{p_T(z,k_i)}{\left(\dfrac{\partial w_T(0,k)}{\partial k}\right)_{k_i}}e^{-ik_i x},$$

where we must now evaluate the dominant terms in the sum.

6. The Lamb wave excitation

In an isothermal atmosphere the sum in (13) reduces to a single member, the Lamb wave. From the paper by Hines (1960), we obtain

$$\hat{p}_T(0,k)/\hat{w}_T(0,k) = i\gamma\omega_A(M+N)\frac{A}{(\omega_A{}^2-k^2C^2)},\quad (14)$$

where γ is the ratio of specific heats, A the atmospheric pressure at ground level, $N=(1-\gamma/2)g/C^2$, $M^2=g^2[\gamma^2/4-(\gamma-1)k^2C^2/\omega_A{}^2]/C^4-(\omega_A{}^2/C^2-k^2)$, and if $M^2>0$, M is chosen positive to satisfy the upper boundary condition.

The right-hand side of (14) has poles at $\pm k_L=\pm\omega_A/C$, the Lamb wavenumbers. The residue about the forward propagating mode is then obtained from

$$\hat{p}_T(0,k)\Big/\frac{\partial\hat{w}_T(0,k)}{\partial k}\bigg|_{k_L} = -i\gamma NA/C,\quad (15)$$

which, with (13), gives

$$P_S(x,0)_{\text{Lamb wave}} = (1-\gamma/2)\frac{g}{c}\frac{H(k_L-K_A)}{[\omega_A/K_A-W(0)]}p_I$$

$$\times\exp[i(\omega_A t-\omega_A x/c)].\quad (16)$$

Eq. (16) is of the general form we set out to obtain. It relates the ground level pressure perturbation in the scattered acoustic wave to the pressure perturbations p_I in the low-phase-velocity wind oscillations. It will be valid when ω_A allows the Lamb wave approximation.

Before considering its implications in more detail, we will obtain the acoustic mode counterpart that holds at the higher frequencies.

7. The acoustic mode excitation

For wave periods <2 min it is not realistic to use the isothermal model to obtain the modes of the low atmosphere. There is really no great difficulty in evaluating (13) for any given model of the atmospheric temperature and wind structure; modern fast computers make calculations of the modes and all other required informa-
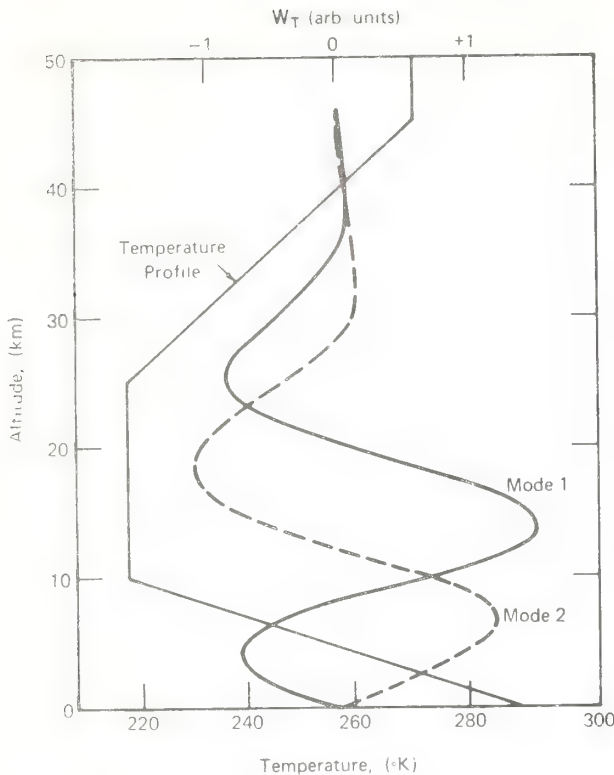
FIG. 2. The temperature profile and two of its modes used in the calculation of the response function. The profile is derived from the 1962 U. S. Standard Atmosphere up to 45 km, above which it is continued as an isothermal space. The modes are for $\omega = 0.2$ s^{-1} and $k_1 = 6.24 \times 10^{-4}$ m^{-1}, $k_2 = 6.49 \times 10^{-4}$ m^{-1}. The abscissa gives the vertical component of velocity of the mode.

tion a relatively quick and painless operation. We have made such an evaluation using a somewhat oversimplified model, which nevertheless will give as much accuracy as is needed here. At periods $\leqslant 60$ s the modes that are important in MAS are the A_3 and A_2 or A_1 acoustic modes (using the notation of Francis referenced above). Since we are only interested in modes that are confined to the lower sound channel, we use the atmospheric temperature structure shown in Fig. 2. It is based on the 1962 U. S. Standard Atmosphere (Valley, 1965) with the arbitrary continuation of the stratopause temperature throughout the space above 45 km altitude. We have not included either wind or viscosity in the calculations. The modal structures found at angular frequency 0.2 s^{-1} are shown in Fig. 2 superimposed over the temperature profile of the sound channel. In Table 1 we list the values found for the response factors

$$R_i = i \hat{p}_T(0, k_i, \omega) \Big/ \frac{\partial \hat{w}_T(0, k, \omega)}{\partial k} \Big|_{k_i}$$

for a number of mode sets (ω, k_i). These are to be used in the modal response formula (13). Comparing the values in Table 1 with the response factor $(1 - \gamma/2)g/C$ found

TABLE 1. A list of four response factors

$$R_1 = i \hat{p}_T(0, k_1) \Big/ \frac{d\hat{w}(0, k)}{dk} \Big|_1$$

calculated for modes of the temperature profile shown in Fig. 2.

$\omega = 0.2$ s^{-1}	$k_1 = 6.24 \times 10^{-4}$ m^{-1}	$R_1 = 3.5 \times 10^{-3}$ [mks]
$\omega = 0.2$ s^{-1}	$k_2 = 6.49 \times 10^{-4}$ m^{-1}	$R_2 = 1.1 \times 10^{-3}$ [mks]
$\omega = 0.1$ s^{-1}	$k_1 = 1.236 \times 10^{-4}$ m^{-1}	$R_1 = 7.3 \times 10^{-3}$
$\omega = 0.1$ s^{-1}	$k_2 = 1.256 \times 10^{-4}$ m^{-1}	$R_2 = 2.8 \times 10^{-3}$

$$R_{\text{Lamb}} = (1 - \gamma/2)g/C \approx 9 \times 10^{-3} \text{ [mks]}$$

for the Lamb wave [Eq. (16)], we see that there is no great difference in this instance between the isothermal model and the "real" atmosphere.

8. The terrain factor H

To obtain a quantitative measure of the scattering process we need to assign a value to the terrain factor H that appears in (15) as

$$H(k - K_A) = \int_{-\infty}^{\infty} dk e^{i(k - K_A)x} \left(\frac{dh}{dx} - iK_A h \right). \quad (17)$$

As an example, suppose the ridge is Bell-shaped with a maximum height h_m and a half-height width b, i.e.,

$$h(x) = h_m / [1 + (x/b)^2]. \quad (18)$$

Then we find

$$H(k - K_A) = i\pi k h_m b \exp[-|k - k_A| b]. \quad (19)$$

This expression maximizes against the parameter b for $|k - K_A| b = 1$, or since $k \ll K_A$, $K_A b = 1$. Thus, as was to be expected, this type of scattering is most effective when the ridge width is of the same order as the wave length of the incident wave. At such an "optimum" ridge we have

$$H(k - K_A)_{\text{opt}} = i\pi h \frac{k}{K_A} \frac{m}{e}. \quad (20)$$

Finally we evaluate the strength of the mode ($\omega = 0.1$ s^{-1}, $k = k_1$) excited by a wind oscillation with an associated pressure fluctuation of 1 mb incident on a ridge of height of 100 m and optimum width. Eqs. (13) and (20) with Table 1 then give

$$P_S(z = 0, \omega_A = 0.1 \text{ s}^{-1}, k_1 = 1.24 \times 10^{-4})_{\text{mode}}$$
$$\approx 3 \exp[i(\omega_A t - k_1 x)], \quad (21)$$

in microbars.

This pressure amplitude of 3 μb may be compared with the observed "typical" value of a 1 μb.

9. Discussion

The idealized calculation performed above bears only an indirect and tentative relation to the true generation

problem posed by wind oscillations in a mountainous terrain. The numerical result indicates that the mechanism could be responsible for the observed signals, but in no wise guarantees it. A full treatment of the problem requires four steps:

1) Calculation of the modal excitation by scattering of a wind oscillation against a three-dimensional obstacle.

2) Definition of the space-time statistics of the wind oscillations across the mountainous area.

3) Definition of the statistics of "suitable" scattering obstacles across the area.

4) Calculation of the signal strength that should be expected at large distances from the area when the many incoherent contributions to a particular mode are summed.

Clearly much research remains to be done in this area.

REFERENCES

Bedard, A. J., 1977: Infrasound originating near mountainous regions in Colorado. Submitted to *J. Appl. Meteor.*
Francis, S. H., 1973: The acoustic-gravity modes and large-scale traveling ionospheric disturbances of a realistic, dissipative atmosphere. *J. Geophys. Res.,* 78, 2278–2301.
Greene, G. E., and J. Howard, 1975: Natural infrasound: A one-year global study. NOAA Tech. Rep. ERL317, WPL 37 [NTIS COM75-10639].
Hines, C. O., 1960: Internal atmospheric gravity waves at ionospheric heights. *Can. J. Phys.,* 38, 1441–1481.
Larson, R. J., L. B. Craine, J. E. Thomas and C. R. Wilson, 1971: Correlation of winds and geographic features with production of certain infrasonic signals in the atmosphere. *Geophys. J. Roy. Astronom. Soc.,* 26, 201–214.
Longuet-Higgins, M. S., 1950: A theory of the origin of microseisms. *Phil. Trans. Roy. Soc., London,* A243, 1–35.
Pierce, A. D., 1963: Propagation of acoustic-gravity waves from a small source above the ground in an isothermal atmosphere. *J. Acoust. Soc. Amer.,* A35, 1798–1807.
Warren, F. W. G., 1968: A note on Howard's proof of Miles' theorem. *Quart. J. Mech. Appl. Math.,* 21, 433–437.
Valley, L. S., Ed., 1965: *Handbook of Geophysics and Space Environments.* U.S.A.F. publication, Section 2.7.

Infrasonic Waves From Auroral Arcs

G. Chimonas

Cooperative Institute for Research in Environmental Sciences, University of Colorado/NOAA
Boulder, Colorado 80309
Wave Propagation Laboratory, National Oceanic and Atmospheric Administration
Boulder, Colorado 80302

The infrasonic bow wave from a traveling auroral arc of finite length is calculated, and the results of the infinite length approximation are essentially recovered. The finite length results in a distinct, separate, second trailing pulse that is weaker than, and of the opposite sign from, the main pressure wave. It is shown that the sign-reversed signatures sometimes observed may be due to arc currents that have strongly defined trailing ends and relatively diffuse frontal structures.

Introduction

Auroral arcs that move across the sky at supersonic speeds may produce a detectable infrasonic pressure wave at ground level. These signals have been studied in some detail [*Wilson*, 1969a, b, c, 1972] with arrays of microbarographs to record the pressure signature, with all-sky cameras to record the arc motion, and with magnetometers to monitor the electrojet current.

The two most obvious mechanisms by which the arc can generate the acoustic signal in the neutral atmosphere are Joule heating and Lorentz coupling in the electrojet region. Calculations show that both of these sources are able to produce ground level perturbations of the observed magnitude if certain assumptions are made about the spatial form of the electrojet currents. If then it is assumed that the basic mechanisms have been correctly identified, it becomes possible to invert the problem to some extent and to use the pressure records to obtain information about the structure of the arc currents.

Thus *Chimonas and Peltier* [1970], using a model arc of infinite length, found that if wave dispersion is neglected, the pressure pulse is a direct map of the height-integrated current in the arc. When Wilson observed that only equatorward propagating arcs produced detectable signals, it seemed reasonably clear that only these arcs had sufficiently sharply defined electrojets to produce signals in the observing window. Their poleward translating counterparts, although visually similar and of a comparable total current flow, would then have to contain a more diffuse current distribution that resulted in bow waves outside the detection limits of the apparatus. This was shown to be a reasonable consequence of the observed electric field structure within the arcs, which could lead to a much greater localization of the currents in the equatorward moving system [*Chimonas*, 1977].

However, *Swift* [1973] made calculations for arcs of finite length indicating that end effects are responsible for much of the observed signal. The pressure fields that he obtained are strikingly different from those of the infinitely long arc system and suggest detectable signals from much broader current distributions than are possible in the infinite case. To some extent this negates the explanation given above for the observed asymmetry in bow wave production. Swift was, however, able to explain the signature of the pressure observations. This is sometimes the negative of that expected from the simpler theory, and Swift found that the convolution of his

calculated pressure field with apparatus response would yield this result. He also obtained an explanation of the second pressure pulse that is sometimes found to follow the bow wave that comes in at the predicted time. Wilson has suggested that this second arrival is the reflection from higher altitudes of the upgoing arm of the primary bow wave, while Swift obtains it as the direct consequence of the finite length of the arc.

In this paper the pressure fields expected from an arc of finite length are reexamined. An analytical argument shows that the complexly structured fields obtained by Swift should not be expected, and this is confirmed by numerical computation. It is shown that the broad current distributions used in his calculations will not result in detectable ground level pressure signals and end effects are considerably less dramatic.

However, Swift's two major points can be recovered in one sense or another. Although the electrojet scales must be made much smaller to obtain a detectable signal (recovering the explanation of the north-south propagation asymmetry mechanism), end effects do produce a (weaker and well separated) trailing pulse. Moreover, the signal filtering introduced by the apparatus can reverse the apparent sign of the pressure signature.

Thus although the fields found in this paper are radically different from those obtained by Swift, his basic postulates hold good, and these two effects considerably augment our understanding of the bow wave phenomenon.

Formulation

We will follow very closely the formulation set up by *Swift* [1973]. The only modifications made are to use mks rather than cgs units, to drop the Joule heating term, and to displace the defining coordinates of the source function. Since the Joule heating and Lorentz terms are related by a simple constant, dropping one of them affects the amplitude but not the form of the calculated fields. The displacement of the source function is a convenience that slightly simplifies the bookkeeping in the numerical work but otherwise has no significance.

The geometry of the arc, similar to that in Swift's work, is shown in Figure 1. The current is along the arc axis, is uniform on $-L < x < L$, and is zero outside this range. Translation takes place at constant speed V ($V > C$, the sound speed) in the y direction. Across the arc the current is assumed to be narrowly confined to a height range about z_A and to have a height-integrated density of trapezoidal form in the y direction. The pressure field will be calculated at the field point $(x, y, z, t) = (0, 0, 0, t)$, and the time origin is selected so that the leading edge of the arc reaches $y = 0$ at $t = 0$.
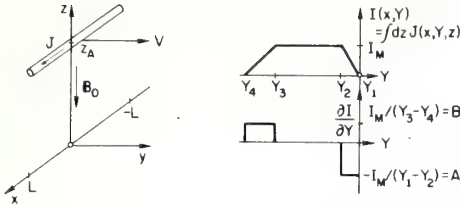
Fig. 1. Geometry of the arc current showing its alignment, motion, and finite length. Drawing at right shows the y distribution of the current integrated over the vertical coordinate and the y derivative of this function.

Then from *Swift* [1973, equation (11)], the pressure at the selected field point is

$$p(0, t) = -\left(\frac{n_0(0)}{n_0(z_A)}\right)^{1/2} \frac{B_0}{4\pi} \int dx' \, dz' \, dy' \, dt'$$

$$\cdot \left[\delta\left(t' - t + \frac{|x'^2 + y'^2 + z'^2|^{1/2}}{c^2}\right)\right]$$

$$\cdot \left(|x'^2 + y'^2 + z'^2|^{-1/2}\right) \frac{\partial}{\partial y'} J(x', y' - Vt', z') \quad (1)$$

The integration over z' can be performed by replacing J by I on the assumption that the vertical extent of the current arc is very much less than the mean arc height z_A. Hence

$$p(0, t) = -\left(\frac{n_0(0)}{n_0(z_A)}\right)^{1/2} \frac{B_0}{4\pi} \int dx' \, dy' + \frac{1}{(x'^2 + y'^2 + z_A^2)^{1/2}}$$

$$\cdot \left\{\frac{\partial}{\partial Y} I(x', Y)\right\}_{Y = y' - Vt + (V/C)(x'^2 + y'^2 + z_A^2)^{1/2}} \quad (2)$$

FIRST ARRIVAL TIMES

Equation (2) relates the pressure at the observation point (0, 0, 0, t) to the spatial source density at its retarded times. By construction, $I(x', Y)$ is zero for all values of $Y > 0$.

Thus no signal from source point x', y' can be received at the observation point until $[y' - Vt + (V/C)|x'^2 + y'^2 + z_A^2|^{1/2}]$ becomes zero.

Solving

$$y' - Vt + (V/C)|x'^2 + y'^2 + z_A^2|^{1/2} = 0$$

as an equation in y' gives

$$y' = \left\{-Vt \pm \frac{V}{C}\left[V^2 t^2 - \left(\frac{V^2}{C^2} - 1\right)\left(x'^2 + z_A^2\right)\right]^{1/2}\right\}$$

$$\cdot \left(\frac{V^2}{C^2} - 1\right)^{-1} \quad (3)$$

which requires that

$$t \geq t_{x'} = \frac{1}{V}\left|\left(\frac{V^2}{C^2} - 1\right)\left(x'^2 + z_A^2\right)\right|^{1/2} \quad (4)$$

Clearly, $t_{x'}$ is the earliest time that any source point with coordinate x' can affect the pressure signal at our selected field point.

The very first such signal comes in from $x' = 0$ at time

$$t_0 = \frac{1}{V}\left[\left(\frac{V^2}{C^2} - 1\right)z_A^2\right]^{1/2}$$

while the first signal to come in from the end of the arc at $x' = \pm L$ arrives at time

$$t_L = \frac{1}{V}\left[\left(\frac{V^2}{C^2} - 1\right)\left(L^2 + z_A^2\right)\right]^{1/2}$$

Thus between times $t = t_0$ and $t = t_L$ the received pressure signal must be identical with that from an arc of infinite length.

However, consider Figure 2. The upper trace is the pressure signal calculated by Swift for the finite arc of the specified parameters, while the lower trace is that expected from its infinitely long counterpart [see *Chimonas and Peltier*, 1970; *Swift*, 1973, appendix]. Between the marked times t_0 and t_L the traces should be identical. Since they are not, something is seriously amiss.

CALCULATION OF THE PRESSURE FIELD

Figure 1 shows the function $\partial/\partial Y \, I(x', Y)$ for the trapezoidal current distribution. There are four critical values of Y (Y_1, Y_2, Y_3, Y_4) that define its behavior. In formula (2), Y is replaced by the function $y' - Vt + (V/C)(x'^2 + y'^2 + z_A^2)^{1/2}$. It is therefore necessary to locate these critical values in (x', y', t) space, and this is done through the equation

$$y' - Vt + (V/C)(x'^2 + z_A^2 + y'^2)^{1/2} = Y_i \quad (5)$$

for $i = 1$ through 4.

Solving (5) for y' gives

$$y' = \left\{-(Vt + Y_i) \pm \frac{V}{C}\left[(Vt + Y_i)^2 - \left(\frac{V^2}{C^2} - 1\right)\right.\right.$$

$$\left.\left. \cdot (x'^2 + z_A^2)\right]^{1/2}\right\}\left(\frac{V^2}{C^2} - 1\right)^{-1} \quad (6)$$

This is a real solution for y' only if

$$t \geq t_{x',i} = -\frac{Y_i}{V} + \frac{1}{V}\left[\left(\frac{V^2}{C^2} - 1\right)(x'^2 + z_A^2)\right]^{1/2} \quad (7)$$

(Note that the sign of the radical must be positive, since this
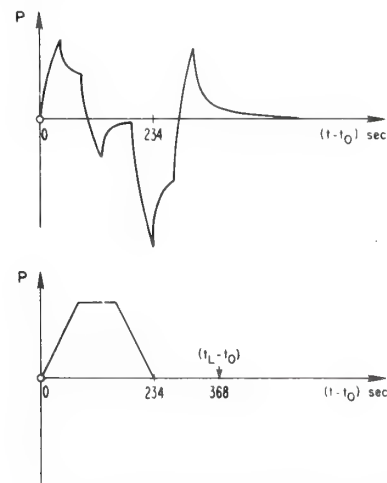
Fig. 2. Bow wave pressure profiles. Upper trace [after *Swift*, 1973] is for an arc of length $L = 220$ km, speed $v = 0.64$ km/s, and cross-section parameters $Y_1 - Y_2 = Y_2 - Y_3 = Y_3 - Y_4 = 50$ km centered at height $z_A = 110$ km. The ambient sound speed is 0.32 km/s. Lower trace is that obtained from the arc with infinite length but all other parameters unchanged. The time t_L marks the instant at which the first signal from $x = L$ can reach the observation point.

corresponds to the retarded solution. The other sign corresponds to the advanced, or time-reversed, 'world.')

The time $t_{x',i}$ is the earliest time at which the field point receives signals from a source point on x' in the functional state $\{\partial/\partial Y\, I(x', Y)\}_{Y_i}$. Thus if $i = 1$, it is the very first time that signals come in from distance x'; if $i = 2$, it means that some point with coordinate x' has sent in its final signal from the current growth stage; and so forth.

Figure 3 shows the evolution of the retarded source function on a constant x' coordinate. At fixed (x', t) the integration on y' in (2) reduces to one, two, three, or four integrations of the form $\int_{y_A}^{y_B} dy'\ [\mathrm{const}/(x'^2 + y'^2 + z_A^2)^{1/2}]$. Standard tables give the result

$$\int ds\ \frac{1}{(x'^2 + z_A^2 + s^2)^{1/2}} = \ln\left|s + (x'^2 + z_A^2 + s^2)^{1/2}\right| \qquad (8)$$

However, this expression must be interpreted with considerable care. To avoid its misuse, it is best to break the region of integration into domains $y' > 0$ and $y' < 0$ and then transform domains on $y' < 0$ to the variable $y'' = -y'$. Formula (8) can then be used in domains with $s \geq 0$, where its meaning is unambiguous.

With this precaution the integration over y' in (2) is obtained in a simple if somewhat laborious form. The remaining integration on x' is then performed numerically.

Figure 4 shows the result of these computations for the same parameters used by Swift in obtaining the upper trace in Figure 2. There is a lack of similarity. It is seen that our computations do indeed reproduce the pressure trace of the infinite arc systems for the period $t_0 < t < t_L$ and that only at

Fig. 4. Bow wave pressure profile recalculated for the finite length arc given in Figure 2.

later times is there any difference between the infinite and finite cases.

RESPONSE OF MICROBAROGRAPHS TO PRESSURE PULSE

The leading part of the trace shown in Figure 4 is an exact reproduction of the current distribution fed into the model. If we had used a smooth current profile, as would be expected for a real arc, instead of the trapezoidal form, we would again have reproduced its form. The only time scale that can realistically be associated with this leading pulse is its duration of 234 s. If the filters in microbarographs are optimally matched to the signal period, atmospheric pressure oscillations with amplitudes as small as 0.1 mks (= 1 dyn/cm²) can be detected. But the apparatus used by Wilson has a very reduced sensitivity at 234 s and so can only detect correspondingly stronger signals. However, for a total arc current of 10^5 A and a density amplification factor $n_0(0)^{1/2} n_0(z_A)^{-1/2}$ of 3.5×10^3 the peak pressure of this pulse is only 0.1 mks. This includes an additional factor of 2 to allow for the wave reflection at the ground. It is safe to assume that the entire pulse would remain undetected by Wilson's instruments.

DETECTABLE PRESSURE PULSES

To allow the microbarographs to detect these bow waves, it is necessary to introduce an arc time scale that fits more closely the apparatus passband of 10–100 s. Figure 5 shows the ground level pressure pulse from an arc whose width is one tenth of that used above. As was previously shown by *Chimonas and Peltier* [1970], such an arc is detectable for quite moderate currents. However, note that the finite length of the arc produces a trailing pulse some 350 s behind the leading bow wave.

SIGNATURE REVERSAL

Swift [1973] applied the apparatus passband filter to his calculated pressure form and found that the detected signal could differ radically from the true pressure signal. In this manner he found that the apparatus could 'detect' a pressure signature of the opposite sign from that of the true signal. This is important, since the form of the bow wave may be compared

Fig. 3. Illumination of the source region. The source function $\partial/\partial Y\, I(x', Y)$ must be evaluated at the retarded position $Y = y' - Vt + (V/C)(x'^2 + z_A^2)^{1/2}$. The figure shows the contributing regions of y' space at a fixed source coordinate x'. The determining parameters are $t_{x',i} = -Y_i/V + [(V^2/C^2 - 1)(x'^2 + z_A^2)]^{1/2}/V$ and $(YP_i, YN_i) = \{-Vt + Y_i \pm V/C[(Vt + Y_i)^2 - (V^2/C^2 - 1)(x'^2 + z_A^2)]^{1/2}\}/(V^2/C^2 - 1)$.
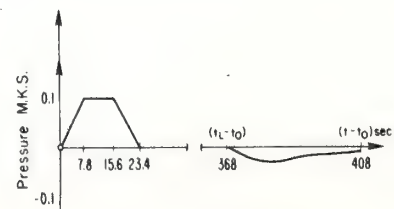
Fig. 5. Bow wave pressure profile like that in Figure 4 but with $Y_1 - Y_2 = Y_2 - Y_3 = Y_3 - Y_4 = 5$ km. Normalization is to a total arc current of 10^4 A.
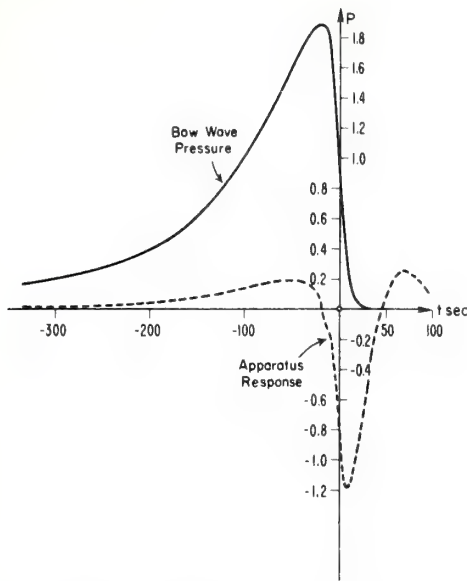
Fig. 6. Hypothetical pressure bow wave and response to it of the microbarographs. The wave form is $p(t) = [1 - \tanh{(t/10)}]/[1 + (t/100)^2]$, and the response is $R(t) = \int_{-\infty}^{t} p(\tau)Y(t - \tau)$ with $Y(s) = \delta(s) - (4/\pi)\{[\sin{(0.11\pi s)}\sin{(0.09\pi s)}]/0.09s^2\}$ [Swift, 1973, equation (30)].

with the theoretical predictions; if the theory cannot even give the correct sign for the perturbation pressure, it is of little use. However, if it is the apparatus rather than the theory that is misleading, the remedy must be sought in a more adequate analysis of the raw data.

Although the pressure forms to which Swift applied the filtering appear to be erroneous, the procedure is valid, and its consequences can be exactly as he suggested.

Consider the pressure bow wave shown in Figure 6. It would be obtained from a current distribution of the same shape. There are two very different time scales in this pulse: a long one for the pressure rise and a much shorter one for the pressure relaxation. If only the latter time scale is within the response range of the detector, its output signal will indicate a negative pressure perturbation.

This is shown quantitatively in Figure 6, where the signal is convoluted with the apparatus response function given by *Swift* [1973, equation (30)]. If the noise obscures the relatively small positive excursions, the signal will be seen with the 'wrong' sign. It is not known if the arc currents can contain such structure. It could perhaps be even more complex. Ideally, the ground level pressure detection systems would answer these questions.

REFERENCES

Chimonas, G., The asymmetry in infra-sound generation by travelling aurora, *J. Atmos. Terr. Phys.*, in press, 1977.
Chimonas, G., and W. R. Peltier, The bow wave generated by an auroral arc in supersonic motion, *Planet. Space Sci.*, *18*, 599, 1970.
Swift, D. W., The generation of infrasonic waves by auroral electrojets, *J. Geophys. Res.*, *78*, 8205, 1973.
Wilson, C. R., Auroral infrasonic waves, *J. Geophys. Res.*, *74*, 1812, 1969a.
Wilson, C. R., Infrasonic waves from moving auroral electrojets, *Planet. Space Sci.*, *17*, 1107, 1969b.
Wilson, C. R., Two station infrasonic wave observations, *Planet. Space Sci.*, *17*, 1817, 1969c.
Wilson, C. R., Auroral infrasonic wave-generation mechanism, *J. Geophys. Res.*, *77*, 1820, 1972.

F. Einaudi

Cooperative Institute for Research
in Environmental Sciences,
University of Colorado/NOAA,
and Aeronomy Laboratory,
National Oceanic and Atmospheric Administration,
Boulder, Colo.

D. P. Lalas

Department of Mechanical Engineering Sciences,
Wayne State University,
Detroit, Mich.

The Effect of Boundaries on the Stability of Inviscid Stratified Shear Flows

The influence of the presence and position of solid boundaries on the stability of an inviscid, stratified shear flow, is examined numerically for the case of a hyperbolic tangent velocity profile and an exponentially decreasing density. The presence of solid boundaries is shown to stabilize short wavelengths and destabilize large wavelengths. Furthermore, extra unstable modes, not present in an infinite domain, are found for large wavelengths, both for symmetric and asymmetric boundaries. Finally, the validity of the principle of exchange of stability is examined, and it is shown to be unreliable even for the case of symmetric boundaries.

Introduction

The stability of inviscid, nonconducting, stably stratified shear layers, in the presence of a gravitational field, has been investigated extensively by many authors, and stability criteria have been established. For the case of the background flow U_0, varying with height z only, these criteria are mainly functions of the background velocity, density, and their derivatives. The boundary conditions usually imposed are either radiation conditions for infinite domains or zero normal velocity conditions on impermeable boundaries. Reviews of such work can be found in, among others, Drazin and Howard [1][1] and Thorpe [2].

Recently, Hazel [3] has obtained stability curves and selected growth rates for a variety of flow configurations, by numerical methods. In particular, one of the cases he investigated was the flow with velocity profile given by $U_0(z) = \tanh(z)$ and density profile $\rho_0(z) = \rho_g \exp[-\sigma \tanh(z)]$, where σ is a typical density measure and ρ_g the density at $z = 0$. Hazel adopted the Boussinesq approximation and neglected the inertial terms of the density stratification, so that the Taylor-Goldstein equation became the governing equation. He found that as the boundaries are moved in from infinity, the longer wavelengths are destabilized, while the shorter wavelengths are stabilized at a different rate. The second effect dominates as the distance between the boundaries reaches a certain minimum value, so that eventually the flow becomes stable for all values of the Richardson number and for all wavelengths, as was already shown, theoretically, by Howard [4]. Hazel's numerical program for the neutral curves could only operate for waves with phase velocity equal to the background velocity at the inflection point, and therefore it could only be used when the principle of exchange of stabilities is applicable (see Miles [5]).

Drazin [6], on the other hand, investigated analytically the stability of the same velocity profile, but with an exponentially decaying background density and without solid boundaries. He obtained an expression for the neutral curve separating stable from unstable roots in the Richardson number-wave number plane, based on the preliminary assumption that the principle of "exchange of stabilities" holds for stationary, singular neutral modes. This is again equivalent to restricting one's attention to waves with phase velocity equal to the background velocity at the inflection point. As recognized by Drazin [6] and discussed by Howard [7], the adoption of the principle of exchange of stabilities in shear stratified flows can lead to neutral curves which may not be stability boundaries or may result in overlooking some possible modes.

In this paper, we have numerically analyzed, in detail, the stability characteristics and the eigenvalue structure of a hyperbolic tangent shear layer with an exponential density profile, i.e., Drazin's profiles, in the presence of solid boundaries. We have focused on three main points: the effect of the relative position, with respect to the inflection point of the velocity, of the two solid boundaries; the effect of the usually neglected inertial terms; and, finally, the validity of the principle of the exchange of stabilities for the Taylor-Goldstein equation (inertial terms neglected) even when the boundaries are symmetric.

In the second section the governing equations are derived, and a
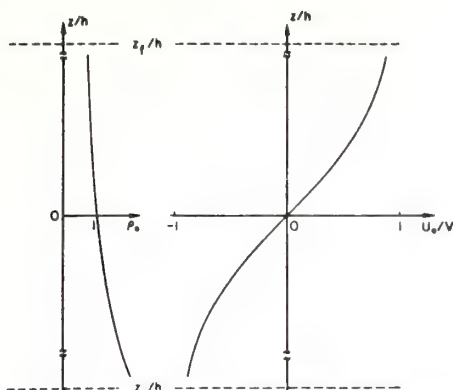
Fig. 1 The density and velocity profiles and geometry of the basic flow (not in scale)

discussion of the stability analysis is given, together with a brief description of the numerical programs used, while in the third section the numerical results are presented and analyzed.

The Stability Equations

Let us first define our background system. We assume a background velocity $U_0(z)$ and a background density $\rho_0(z)$ of the form

$$\mathbf{U}_0(z) = V \tanh\left(\frac{z}{h}\right) \hat{\imath}_x, \qquad \rho_0(z) = \rho_0(0) \exp\left[-\frac{z}{H}\right], \quad (1)$$

where $\hat{\imath}_x$ is the unit vector in the x-direction. In terms of these quantities, one can define the square of the Brunt-Väisälä frequency n^2 and the Richardson number R_i as follows:

$$n^2 = -g\left[\frac{1}{\rho_0}\frac{d\rho_0}{dz} + \frac{g}{c_0^2}\right], \qquad R_i = \frac{n^2}{(dU_0/dz)^2}, \quad (2)$$

where c_0 is the speed of sound, and g is the acceleration of gravity acting in the negative z-direction. If the fluid is incompressible, the second term in n^2 goes to zero. In the atmosphere, if the background temperature is assumed constant, as often done, c_0 is constant and related to H by $c_0^2 = \gamma g H$, where γ is the ratio of specific heats. In any case, since we demand that the fluid is stably stratified, n^2 will be taken as a positive constant in the following treatment.

To examine the stability of the system to infinitesimal disturbances, we write each dependent variable as the sum of a background quantity and a perturbation, denoted by a suffix zero and one, respectively. The basic flow quantities are constant or functions of z only. The background vertical component of velocity is set equal to zero. Assuming that the perturbations are small with respect to the background quantities, we can write the linearized equations of motion in the Boussinesq approximation as follows:

$$\rho_0\frac{d}{dt}u_1 + \rho_0\frac{dU_0}{dz}w_1 + \frac{\partial p_1}{\partial x} = 0 \quad (3)$$

$$\rho_0\frac{d}{dt}w_1 + \frac{\partial p_1}{\partial z} + g\rho_1 = 0 \quad (4)$$

$$\frac{d}{dt}\rho_1 - \frac{n^2}{g}\rho_0 w_1 = 0 \quad (5)$$

$$\frac{\partial}{\partial x}u_1 + \frac{\partial}{\partial z}w_1 = 0 \quad (6)$$

where u_1, w_1, p_1, and ρ_1 are the perturbations of the horizontal velocity, vertical velocity, pressure and density, respectively, and

$$d/dt \equiv \partial/\partial t + U_0\partial/\partial x. \quad (7)$$

Equations (3) and (4) are the equations of conservation of horizontal and vertical momentum, respectively; equation (5) expresses

the condition of incompressibility, and equation (6) is the equation of continuity.

The system of equations (3)–(6) is linear in the four unknowns u_1, p_1, ρ_1, and w_1. Assuming a plane-wave type of solution in x and t, and eliminating u_1, p_1, and ρ_1 in favor of w_1, we obtain the following equations:

$$\frac{d^2 Z_s}{dy^2} - F_1 Z_s - F_2 Z_c = 0,$$

$$\frac{d^2 Z_c}{dy^2} - F_1 Z_c + F_2 Z_s = 0, \quad (8)$$

where, for convenience in the numerical analysis, we choose to work in the real domain, so that

$$w_1(x,z,t) = \rho_0^{-1/2}\, e^{\omega_i t}[Z_c(y)\cos(k_x x - \omega_r t) + Z_s(y)\sin(k_x x - \omega_r t)]. \quad (9)$$

The horizontal wave number $k_x = 2\pi/\lambda_x$ is assumed real, and ω_r and ω_i are the real and imaginary parts, respectively, of the frequency of oscillation. In (8), F_1 and F_2 are given by

$$F_1 = \alpha^2 + \sigma^2/4 - J\frac{c_{re}^2 - c_i^2}{|\Omega|^4} - \left[\frac{d^2 u_0}{dy^2} - \sigma\frac{du_0}{dy}\right]\frac{c_{re}}{|\Omega|^2}, \quad (10)$$

$$F_2 = -\frac{c_i}{|\Omega|^2}\left[2J\frac{c_{re}}{|\Omega|^2} + \frac{d^2 u_0}{dy^2} - \sigma\frac{du_0}{dy}\right]. \quad (11)$$

and

$y = z/h$ = normalized height coordinate
$\alpha = hk_x$ = normalized horizontal wave number
$c_r = \omega_r/k_x V$, $c_i = \omega_i/k_x V$ = real and imaginary part of the normalized frequency of oscillation
$c_{re} = c_r - u_0$ = real part of the normalized Doppler frequency
$\Omega = c_{re} + ic_i$ = normalized Doppler frequency
$\sigma = h/H$ = ratio of the length scale of velocity to that of density
$u_0(y) = U_0(y)/V$ = normalized background velocity
$J = n^2 h^2/V^2$ = value of the Richardson number at $y = 0$, which is also the minimum Richardson number in the flow domain.

Except for Z_c and Z_s which are the two parts of the vertical velocity scaled with respect to the square root of the background density, all the other variables in (8) are nondimensional. Since we choose h as the characteristic scale for length and V for velocity, the normalized background velocity and the local Richardson number become

$$u_0(y) = \tanh(y), \qquad R_i = J/(du_0/dy)^2. \quad (12)$$

Now $R_i = J$ at $y = 0$ and $R_i > J$ everywhere else, so that J is the most useful parameter in the stability analysis: unstable solutions will exist only in the range $0 \leq J \leq \frac{1}{4}$, as required by the Miles-Howard theorem [8, 9], and its extension to compressible fluids (Chimonas [10]). If $J > \frac{1}{4}$, the flow is stable. The parameter σ is a measure of the height dependence of the density in the inertial term of the momentum equation. It gives rise to various contributions in (8), which we shall henceforth call inertial terms. They are often neglected on the ground that density variations across the whole shear layer are usually small. We retain the terms multiplying σ because they appear to have some effect on the position of the critical level in the flow, and hence on the phase velocity of the waves. The critical level is defined as that level where the horizontal phase velocity of the disturbance is equal to the background wind at that level.

The stability analysis inquires into the set of eigenvalues ω_r and ω_i, for given k_x, for which equations (8) admit nontrivial solutions satisfying the usual boundary conditions on the solid boundaries, located at $z = z_i$ and $z = z_f$, i.e.,

$$Z_c = Z_s = 0 \text{ at } z = z_i \text{ and } z = z_f, \quad (13)$$

with the origin of the z-axis at the inflexion point of the velocity profile.

The two coupled second-order differential equations (8) in the

two unknowns, Z_c and Z_s, are of course equivalent to the single second-order differential equation in the unknown complex amplitude of the vertical velocity used by Drazin: the boundary conditions differ since $w_1 = 0$ at finite distances rather than at infinity as in Drazin's case. We wish to solve (8) numerically and obtain growth rates and phase velocities for the range of parameters α and J, where the system is unstable, as well as the family of neutral modes for which $c_i = 0$, since the neutral stability boundary would be composed of such modes. A brief description of the numerical programs utilized follows:

(i) Program for Unstable Waves. In order to determine growth rates, a point in the (α, J) plane is specified. For some assumed values of c_r and c_i, equations (8) are integrated from the lower to the top boundaries, located at $y_i = z_i/h$ and $y_f = z_f/h$, respectively. If the boundary conditions at the top are satisfied, the assumed values of c are accepted as eigenvalues; otherwise, the whole process is repeated with new guesses for c_r and c_i. The new guesses are provided by a root-finding subroutine. The integration routine used is the one of Bulirsch and Stoer [11] which yields consistently reliable results in our study. For a brief comparison of this technique to other integration routines, see Acton [12] and Hull, et al. [13]. We consider growth rates c_i that are less than 10^{-5} to be zero. No convergence problems have been encountered for the entire (α, J) plane.

(ii) Program for Neutral Curves. When $c_i = 0$, equations (8) reduce to just one second-order differential equation in Z, say, satisfying the boundary conditions (13). The equation is singular at the critical level y_c where $\Omega = 0$. For assumed values of y_c and J, starting from both boundaries, we integrate numerically to within a small but finite distance y_m, $0 < y_m \ll 1$, from y_c. If y_c and J are indeed eigenvalues, the two solutions above and below y_c can be matched to the Frobenius expansion about y_c (see Ince [14]). Otherwise, new values of y_c and J are assumed, and the process is repeated. This program differs from Hazel's program for neutral waves in that it does not *a priori* assume the phase velocities of these waves to be zero, but rather searches for the correct value of c_r appropriate to the eigenvalue problem.

Although no insurmountable difficulties were encountered in the program for the neutral curves, we would like to point out that:

1 When R_c was very close to 0.25, very small steps in α were needed to derive the neutral curve.

2 Some convergence problems did arise as $J \to 0$ and $\alpha \to \alpha_{max}$, i.e., toward the right-hand corners of the first modes.

3 The results are somewhat sensitive to the choice of y_m, especially the values of y_c and hence c_r. For this reason, the calculations were carried out retaining the first three terms of the Frobenius expansion. This also resulted in smaller computing times since values of y_m as large as 0.01 could be used.

4 Some minor difficulties of convergence were encountered along the nearly vertical portions of the neutral curves for the higher modes.

5 For $y_f = 30$ and $y_i = -30$, some convergence problems occurred for α sufficiently large.

All calculations were carried out with at least four decimal points accuracy. The agreement between the results obtained with the two programs is excellent; indeed the unstable modes end on the neutral curves as can be seen from the figures.

Discussion of the Results

To investigate the effect of the boundaries, two cases have been considered. One is that in which the distance between the boundaries has been varied, keeping their position symmetric with respect to $y = 0$, which corresponds to the point of inflection of the velocity profile. The second case is that in which the distance of the boundaries is varied asymmetrically.

In presenting the results of the neutral curves, we have plotted J and R_c as a function of the normalized horizontal wave number α. Although from the knowledge of y_c and J, one can derive R_c, and
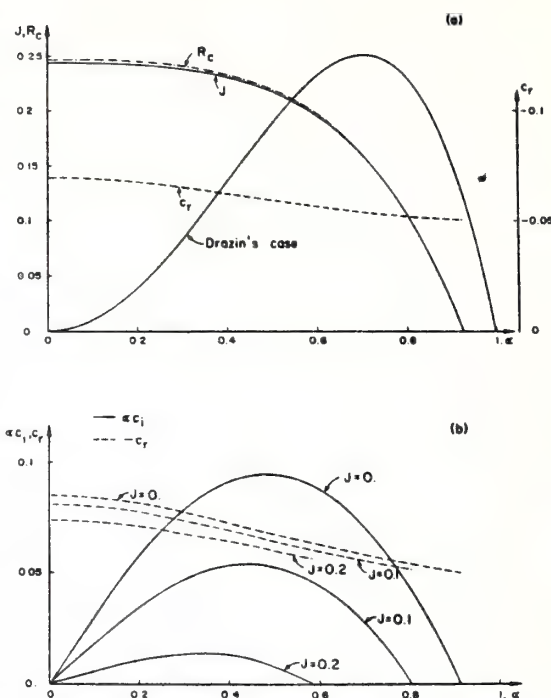
Fig. 2 Mode I stability characteristics for $y_i = -2$, $y_f = 2$, $\sigma = 0.1$; (*a*) J (solid lines), R_c (dashed-dotted lines) and corresponding c_r (dashed lines) as a function of α for the neutral curve. The solid line labeled "Drazin's case" corresponds to $\sigma = 0$, $y_i \to -\infty$ and $y_f \to \infty$. (*b*) αc_i (solid lines) and c_r (dashed lines) versus α for three different values of the parameter J, for unstable modes.

vice versa, we have plotted both quantities, since R_c is the quantity which is physically more important, while J is the one that is known *a priori* from the assigned values of the background quantities n^2, h, and V. On the same graph of the neutral curves, we have plotted the normalized Doppler frequency c_r, from which y_c can be obtained in a straightforward fashion.

For the unstable modes, we plot c_r and $\alpha c_i = h\omega_i/V$; the normalized growth rate, versus α, for given J.

In carrying out the analysis, we have taken the view that h, the normalizing length, is constant and the same for all figures. If the inertial terms are neglected, variations of $J \equiv n^2 h^2/V^2$ imply changes in the ratio n/V; that is, in the ratio of the static stability parameter to the total jump in velocity. If, on the other hand, the terms multiplying $\sigma = h/H$ are retained, one has two main choices: if σ is taken to be constant, H and therefore n must be regarded as constant, and variations in J must be attributed to variations in V; if V is taken to be a constant, then σ is proportional to J so that a change in J would imply a change in σ. We have carried out the calculations for $\sigma = 0.1$, constant, although the other choice is equally valid and presents no complications. In analyzing the results, one can take an alternate view: consider z_i and z_f given, and vary h from case to case as y_i and y_f change, but keep h constant in each case. If the inertial terms are neglected, no other adjustment is necessary; otherwise, n^2 must be changed from case to case so as to keep $\sigma = 0.1$.

Common features of the symmetric and nonsymmetric boundaries appear to be the following: (*a*) For the distance between boundaries larger than some minimum value, there exists a mode, which we shall call mode I, that in the limit of each boundary going to infinity tends to the mode found by Drazin; (*b*) For intermediate distances of the boundaries, other modes appear in the upper

496
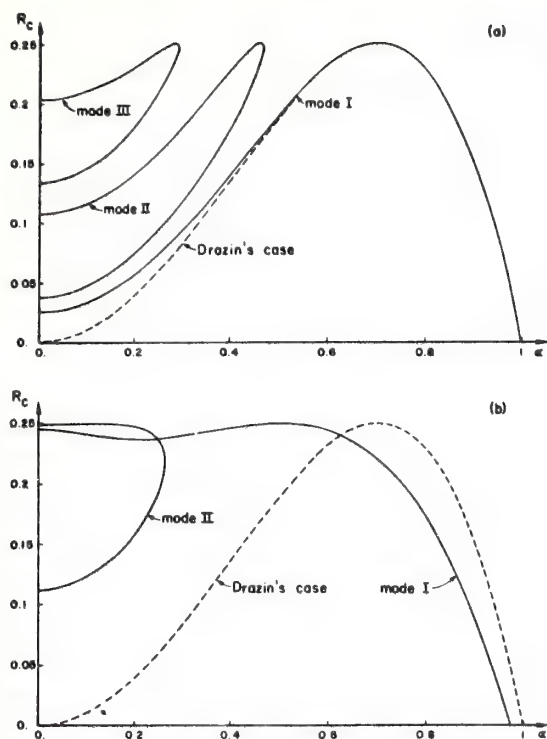
Fig. 3 (a) Stability boundaries for different modes, for $y_i = -10$, $y_f = 10$, $\sigma = 0.1$. Solid lines are plots of the Richardson number R_c at the critical level versus α. The dashed line, which merges into mode I, corresponds to Drazin's case. (b) The same as in (a), but for $y_i = -2$, $y_f = 10$, $\sigma = 0.1$.

Fig. 4 Neutral curves and growth rates as in Fig 2, i.e., mode I, but with $y_i = -10$ and $y_f = 10$

left corner of the (α, J) plane; (c) The critical levels are not at the origin, even for the case of symmetric boundaries.

Let us now comment on the various effects separately.

(i) Effect of Boundaries on the Smaller Wavelengths. Only mode I contains short wavelengths. These, as in the case considered by Hazel, for given J, are more stable than they would be if the domain were infinite. The right-hand branch of the neutral curves moves to the left of the infinite case considered by Drazin. The effect is entirely due to the boundaries, since the role of the inertial terms on the neutral curves is negligible at these wavelengths. This effect can be seen very well in Fig. 2(a). It disappears for $y_i = -10$ and $y_f = 10$ (Fig. 3(a)), but is still present, although somewhat reduced, for the asymmetric case $y_i = -2$, $y_f = 10$ (Fig. 3(b)).

(ii) Effect of Boundaries on the Longer Wavelengths: Mode I. The longer wavelengths are destabilized since the left-hand branch of the neutral curves rises above the infinite case. Here again the main cause is the boundaries and not the inertial effects. In Fig. 2(a) one can see that the intersection of the neutral curve with the $\alpha = 0$ axis has moved up to almost $J = 0.25$ from $J = 0$ for the infinite case. This effect is still present, although reduced, for $y_i = -10$ and $y_f = 10$ (Fig. 3(a)), while it is very large for $y_i = -2$, $y_f = 10$ (Fig. 3(b)).

(iii) Effect of Boundaries on the Longer Wavelengths: Additional Modes. Perhaps the most interesting result of these calculations is the appearance of other modes in the upper left part of the (α, J) plane (Fig. 3). In view of these new modes, it appears that there are situations for which waves with long wavelengths can be excited for values of J that are not available to mode I. For given J, the maximum growth rates of the additional modes are smaller
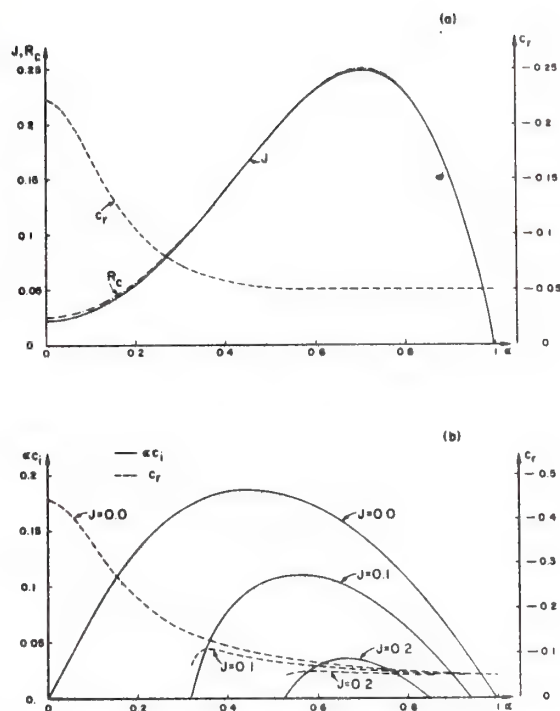
than those of mode I: the corresponding horizontal wavelengths, though, are very different and, depending on the generation mechanism and other factors, they may be excited together with, or instead of, mode I. Such a case has been reported by Reed and Hardy [15], who observed waves of 15–20 and 1.6 kilometers, created by a shear layer in the atmosphere.

(iv) Effect of Asymmetry in the Boundaries. As clearly illustrated by Fig. 3, the effect of asymmetry is substantial on the neutral curves giving R_c versus α. Comparing Fig. 4(a) with 6(a), however, one can see a much smaller effect on the curves giving J versus α, for mode I. This is due to the substantial changes in the position of the critical levels, and hence of the phase velocities of the disturbances, brought about by the asymmetry of the boundaries. Stronger changes are introduced as far as the second and third modes are concerned. For example, the third mode, which is present for $y_i = -10$, $y_f = 10$, disappears for $y_i = -2$, $y_f = 10$. We will return to this point later.

(v) Effect of the Inertial Terms and the Principle of Exchange of Stabilities. The main effect of the presence of the inertial terms is on the location of the critical level y_c and hence on the value of c_r for neutral waves. For the case of symmetric boundaries at $y_i = -10$ and $y_f = 10$ as an example, the critical level for modes I and III would go to zero if $\sigma \to 0$. The phase velocity c_r of the neutral waves of mode II, though, remains nonzero as $\sigma \to 0$. Thus this mode would have been overlooked if the principle of exchange of stabilities had been invoked, even in this case of symmetrically located boundaries. For the unstable waves, the exclusion of the inertial terms affects mostly the additional modes by increasing their growth rates slightly. The neutral curves in the (α, J) planes are affected somewhat for small values of α only. No uniform pattern in the change of the stability regions brought about by $\sigma \to 0$ can be established: this is not surprising in view of the fact that changes in both directions have been previously reported (Menkes [16], Maslowe and Kelly [17]).

497
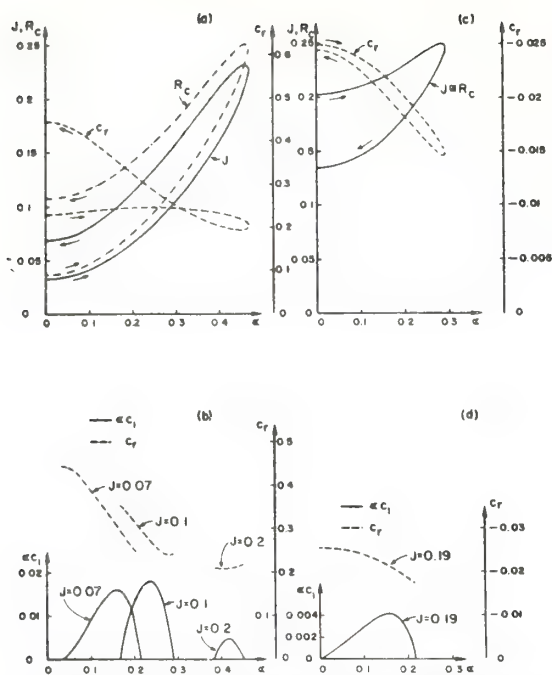
Fig. 5 Neutral curves and growth rates as in Fig. 4, but for mode II (a,b) and mode III (c,d); the arrows along the curves indicate the correspondence between the various branches
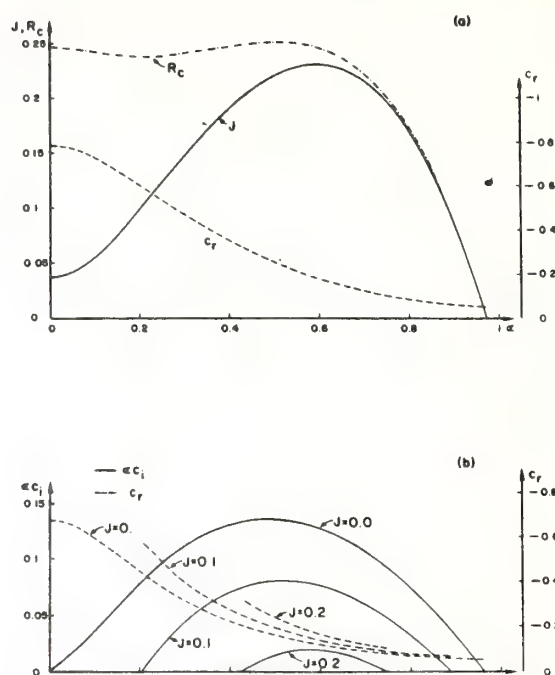
Fig. 6 Neutral curves and growth rates as in Fig. 2, i.e., mode I, but with $y_f = 10$

Fig. 7 Neutral curves and growth rates as in Fig. 6, but for mode II; the arrows along the curves indicate the correspondence between the various branches

Similar considerations hold for the case of asymmetrically located boundaries. Here, though, no neutral curves have critical levels at $y = 0$, even when $\sigma \to 0$.

We conclude this section with a brief discussion of what happens to each mode when, for given α, we change y_i and/or y_f by small steps. For $y_i = -2$ and $y_f = 2$, mode I is the only one present. As the distance between the boundaries is reduced, the unstable region in the (α, J) plane shrinks and disappears entirely near $-y_i = y_f = 1.1997$, which is the value derived theoretically by Howard [4]. If, on the other hand, the distance between the boundaries is increased from $y_i = -2$ and $y_f = 2$, symmetrically or not, the neutral curves and growth rates for mode I shown in Figs. 4 and 6 are reached in a continuous fashion.

Similar behavior is observed for modes II and III, as well as for any others. For symmetric boundaries, modes II and III disappear for $-y_i = y_f$ about 5.38 and 8.33, respectively. When the boundaries are asymmetric, the behavior is the same, so that, for example, with $y_i = -2$ mode II would disappear for y_f less than about 8.13.

For even larger values of $|y_i|$ and y_f, other modes appeared with yet smaller growth rates. The possibility of one extra mode in the limit of an unbounded system was discussed by Drazin and Howard [1] and indeed found very recently by Blumen, et al. [18], for a fully compressible but homogeneous shear layer.

Finally, it should be recognized that, although we have carried out a systematic search for the neutral and the unstable modes, additional modes, with even smaller growth rates, most likely exist. An infinite number of unstable modes was indeed found, in the long wavelength limit, by Lalas, et al. [19], for a Kelvin-Helmholtz profile bounded below by the ground.

Conclusions

We have presented a detailed analysis of the stability characteristics of a background flow with a hyperbolic tangent velocity profile, an exponentially decaying density, and solid boundaries located symmetrically and asymmetrically with respect to the inflection point. It is found that the presence of solid boundaries at finite distances stabilizes somewhat the shorter wavelengths and destabilizes substantially the long wavelengths. A modal structure appears which is present even in the limit of $\alpha \to 0$. The asymmetry of the boundaries substantially changes the position of the critical level and so do the inertial terms. The extra modes, which correspond to large horizontal wavelengths, are likely to be excited at relatively large values of the Richardson number, a situation of particular interest to atmospheric flows, where there is mounting evidence of gravity waves in the troposphere with horizontal wavelengths of the order of a few hundred kilometers that propagate over distances of several wavelengths (Uccellini [20]). For such waves to be unstable, at least initially, so as to enhance their abili-
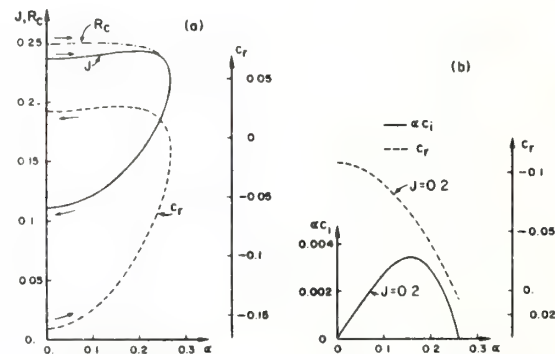
498

ty to overcome dissipative effects and often destructive interactions, if they were corresponding to mode I, they would require very small Richardson numbers, which are unlikely to be found in the atmosphere. To the extent that a flow between solid boundaries is a good representation of an atmospheric flow, as is often assumed (see, for example, the recent work by Tanaka [21]), the extra modes described in this paper could give a possible explanation for such phenomena.

Acknowledgments

References

1 Drazin, P. G., and Howard, L. N., "Hydrodynamic Stability of Parallel Flow of Inviscid Fluids," *Advances in Applied Mechanics*, Vol. 9, 1966, pp. 1–89.

2 Thorpe, S. A., "Turbulence in Stably Stratified Fluids: A Review of Laboratory Experiments," *Boundary-Layer Meteorology*, Vol. 5, 1973, pp. 95–119.

3 Hazel, P., "Numerical Studies of the Stability of Inviscid Stratified Shear Flows," *Journal of Fluid Mechanics*, Vol. 51, 1972, pp. 39–61.

4 Howard, L. N., "The Number of Unstable Modes in Hydrodynamic Stability Problems," *Journal de Mècanique*, Vol. 3, 1964, pp. 433–443.

5 Miles, J. W., "On the Stability of Heterogeneous Shear Flows, Part 2," *Journal of Fluid Mechanics*, Vol. 16, 1963, pp. 209–227.

6 Drazin, P. G., "The Stability of a Shear Layer in an Unbounded Heterogeneous Inviscid Fluid," *Journal of Fluid Mechanics*, Vol. 4, 1958, pp. 214–224.

7 Howard, L. N., "Neutral Curves and Stability Boundaries in Stratified Flow," *Journal of Fluid Mechanics*, Vol. 16, 1963, pp. 333–342.

8 Miles, J. W., "On the Stability of Heterogeneous Shear Flows," *Journal of Fluid Mechanics*, Vol. 10, 1961, pp. 496–508.

9 Howard, L. N., "Note on a Paper of John W. Miles," *Journal of Fluid Mechanics*, Vol. 10, 1961, pp. 509–512.

10 Chimonas, G., "The Extension of the Miles-Howard Theorem to Compressible Fluids," *Journal of Fluid Mechanics*, Vol. 43, 1970, pp. 833–836.

11 Bulirsch, R., and Stoer, J., "Numerical Treatment of Ordinary Differential Equations by Extrapolation Methods," *Num. Math.*, Vol. 8, 1966, pp. 1–13.

12 Acton, F. S., *Numerical Methods That Work*, Harper and Row, Publishers, New York, 1970.

13 Hull, T. E., et al., "Comparing Numerical Methods for Ordinary Differential Equations," *SIAM Journal Numer. Anal.*, Vol. 9, 1972, pp. 603–637.

14 Ince, E. L., *Ordinary Differential Equations*, Dover Publications, Inc., New York, 1956.

15 Reed, R. J., and Hardy, K. R., "A Case Study of Persistent Intense Clear Air Turbulence in an Upper Level Frontal Zone," *Journal of Applied Meteorology*, Vol. 11, 1972, pp. 541–549.

16 Menkes, J., "On the Stability of a Shear Layer," *Journal of Fluid Mechanics*, Vol. 6, 1959, pp. 518–522.

17 Maslowe, S. A., and Kelly, R. E., "Inviscid Instability of an Unbounded Heterogeneous Shear Layer," *Journal of Fluid Mechanics*, Vol. 48, 1971, pp. 405–415.

18 Blumen, W., Drazin, P. G., and Billings, D. F., "Shear Layer Instability of an Inviscid Compressible Fluid—Part 2," *Journal of Fluid Mechanics*, Vol. 71, 1975, pp. 305–316.

19 Lalas, D. P., Einaudi, F., and Fuá, D., "The Destabilizing Effect of the Ground on Kelvin-Helmholtz Waves in the Atmosphere," *Journal Atmos. Sci.*, Vol. 33, Jan. 1976.

20 Uccellini, L. W., "A Case Study of Apparent Gravity Wave Initiation of Severe Convective Storms," *Month. Weath. Rev.*, Vol. 103, 1975, pp. 497–513.

21 Tanaka, H., "Quasi-Linear and Nonlinear Interactions of Finite Amplitude Perturbations in a Stably Stratified Fluid With Hyperbolic Tangent Shear," *Journal of the Meteorology Society of Japan*, Vol. 53, 1975, pp. 1–32.

INFRASOUND FROM CONVECTIVE STORMS, PART II:
A CRITIQUE OF SOURCE CANDIDATES

T. M. Georges

I critically examine several acoustic radiation mechanisms that have
been suggested to explain the ultra-low-frequency emissions from certain severe
thunderstorms that are observed on the ground and in the ionosphere. The
candidates are: (a) simple acoustic sources (monopole, dipole) related to
the expansion of heated storm air and to the storm-scale circulation pattern;
(b) the random acoustic noise from "turbulent" motions inside storms; (c)
low-frequency thunder, i.e., the radiation from lightning discharges or
electrostatic relaxation inside storms; (d) vortex sound, the radiation
from several kinds of unsteady vorticity or the interaction of multiple-vortex
systems; and (e) thermo-mechanical oscillations driven by the interaction
between latent-heat release and the storm's updraft. Each mechanism is
evaluated for realism in terms of actual storm processes, and the predicted
acoustic power and its spectral content are compared with those required by
acoustic measurements. The mechanism most consistent with the observations
appears to be a form of vortex radiation, in which instabilities and,
ultimately, multiple vortices form about the periphery of a larger, mesoscale
vortex, and radiate narrow-band sound as they spin about a common axis.

Refraction of infrasound by upper-atmospheric winds

T. M. Georges

Wave Propagation Laboratory, NOAA Environmental Research Laboratories, Boulder, Colorado 80302

William H. Beasley

Department of Electrical Engineering, University of Florida, Gainesville, Florida 32611
(Received 17 May 1976; revised 24 September 1976)

We used realistic models of upper-atmospheric winds in a three-dimensional acoustic ray-tracing program to calculate how much wind refraction alters acoustic transit speed and azimuth of arrival for long-distance paths. Transit speed varied by 20% or more, and bearing deviations of up to ten degrees were found, depending on the season and on the direction the waves travel. On the average, the predicted seasonal trends corresponded to osbervations, but the calculated standard deviations exceed the mean seasonal values, making simple corrections useless in individual cases. Furthermore, it is doubtful that variations of horizontally uniform winds alone can account for the large observed variability in refractive effects, specifically the large differences in bearing error at adjacent observatories. We show that realistic horizontal gradients of either temperature or wind could cause as much azimuthal refraction as our height-dependent wind models.

INTRODUCTION

Audible sound is so strongly absorbed by atmospheric viscosity that propagation to distances greater than a few tens of kilometers is seldom observed, and then only in cases of very large explosive sources. (The explosion of Krakatoa in 1883 was reportedly heard 16 000 km away in Texas as the sound of a distant cannon.)[1] But, because the classical coefficient of absorption is proportional to the square of the wave frequency,[2] infrasound, especially waves whose frequencies are less than about 1 Hz, can travel global distances relatively unattenuated. (Krakatoa's pressure waves were recorded on barographs after several circuits around the earth.[3])

Acoustic waves that travel so far are subject to significant refraction by the atmosphere's wind and temperature structure. The principal refractive effects are caused by the atmosphere's vertical temperature structure; waves launched at elevation angles (from horizontal) less than about 60° are bent back to earth by positive temperature gradients near 30- and 100-km altitudes (Fig. 1). This well-known effect allows acoustic waves to bounce back and forth between the ground and the upper atmosphere and thus to travel great distances along the earth's surface.

Upper-atmospheric winds also refract the acoustic ray paths: The wind component along the path changes the waves' effective phase velocity and thus alters the ray-path geometry. The wind component transverse to the path changes the azimuthal direction the waves travel. High-altitude winds have a greater effect on acoustic propagation than those at lower altitudes for two reasons: High-altitude winds tend to be stronger, and the acoustic waves spend more time at the greater heights than near the ground (Fig. 1).

In the study of infrasound from natural and artificial sources, we often try to locate the source and estimate the time of the emissions by looking back in the direction the waves appear to come from; if bearings can be measured at two or more observatories, triangulation on the source is possible.

A potential application of improved refractive corrections would be in the location of the sources of severe-storm infrasound emissions, which might be useful for storm warning, tracking, and diagnosis.[6] If bearings cannot be corrected for wind refraction, then it appears that storms cannot be located better than within about 100 km.

I. SUMMARY OF PREVIOUS WORK

Measurements of infrasonic waves from natural and manmade explosions have shown that bearing errors of up to 6° are common and that much larger deviations are occasionally observed.[7,8] Based on such observa-
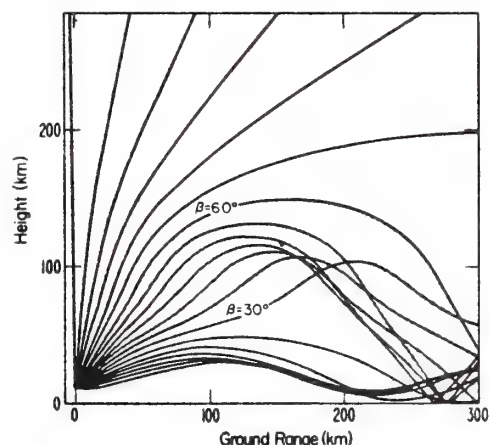
FIG. 1. A set of acoustic ray paths launched at a height of 10 km in a still atmosphere with a Standard-Atmosphere temperature profile. Three groups of rays are evident: those which enter the thermosphere and never return to earth, those which reflect in the thermosphere, and those which reflect in the mesosphere.
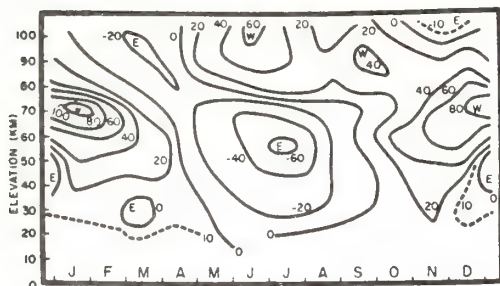
FIG. 2. A time-height cross section of the zonal wind between 30° and 40° latitudes. Speed contours are labeled in m sec, with positive values indicating an eastward flow (from Batten, [10]). Our models correspond to midsummer and midwinter, but this figure illustrates the seasonal transition between the two extremes.

tions, simple empirical bearing corrections have been devised, which taken into account the season of the year (because upper-atmospheric winds exhibit seasonal variations) and the direction the sound travels. Even though these corrections have apparently never been published, various forms seem to be widely known and used in the infrasonic research community.

For example, one simple model says, that, at mid-latitudes, the mesospheric winds (which exert the dominant effect) blow eastward during the winter and westward during the summer, so that a correction for the angle of arrival takes the form

$$\theta = \theta_0 - \delta\theta \cos\theta_0, \qquad (1)$$

where θ_0 is the true bearing (in degrees east of north) of the source from the observer, θ is the bearing from which the sound appears to come (π plus the wave-normal direction), and $\delta\theta$ is a constant whose magnitude is typically about 3° or 4°. The sign of $\delta\theta$ is positive during the summer and negative during the winter, to account for the seasonal zonal-wind reversal (Fig. 2). For example, a wave from a source at 45° bearing would arrive from about 42.5° in the summer and from about 47.5° in the winter.

Wind-induced fluctuations in wave transit speed are also commonly observed. But we are not concerned here with the part of those fluctuations that is caused by the intrinsic dispersive properties of low-frequency acoustic-gravity waves. Such effects are best modeled by normal-mode analysis. [4] We are concerned instead with the part that operates on nondispersive acoustic waves and is caused by alteration of the effective sound speed and the ray-path geometry by atmospheric winds. In practice, simple empirical (but unpublished) formulas, based on measurements from known explosive sources, are used. Such a formula might be

$$V = V_0 + \delta V \sin\theta_0, \qquad (2)$$

where, typically, $V_0 = 300$ m sec^{-1} and $\delta V = 15$ m sec^{-1} (Ref. 5); δV has a positive sign in summer and a negative sign in winter. The waves in the example given earlier would thus have average transit speeds of 311 and 289 m sec^{-1}.

In practice, using formulas like Eqs. (1) and (2) tends to reduce the mean error of a large number of measurements, but the observed error variance seems too large to make the corrections useful in individual cases. Therefore, we wanted to see if we could improve upon (or at least lend physical support to) the empirical corrections by calculating what the refractive effects should be for the best existing models of the atmospheric wind and temperature fields. We also wanted to find out whether realistic variations of a horizontally uniform wind model could account for the variability of the refractive effects and for the occasional extreme bearing deviations. If not, then the effects of horizontal wind and temperature structure would have to be examined.

In searching the literature for previous theoretical work on wind-induced bearing and transit-speed variations, we found very little of direct relevance.

The effects of wind on acoustic propagation were recognized by Lord Rayleigh, [9] who demonstrated that a uniform wind translates spherical wavefronts undistorted at the wind speed. The geometry of such a model yields, to first order in u/c, an effective wave transit speed of $c + u \cos\phi$ and an angle between the true and apparent source directions of $\sin^{-1}[(u/c)\sin\phi]$, where c is the sound speed in still air, u is the wind speed, and ϕ is the angle between the wind and the wave normal.

Practically no refinements of Rayleigh's model have been attempted for estimating bearing deviations caused by nonuniform transverse winds. Diamond, [10] for example, used the approximation $\tan\phi \simeq u/c$ to estimate the effects of cross winds on the angle of arrival of sound waves from explosions at about 32-km altitude. To account for the observed height variability of the winds, he used a model in which winds were constant within layers 5000 ft thick, and added the suitably weighted contributions of each layer to get the total bearing deviation.

The effects of the global wind structure on the directions of arrival of acoustic-gravity waves from nuclear explosions have been carefully studied, but to the best of our knowledge, only empirical models have been constructed. The details of these models are not yet available in the unclassified literature.

Numerical methods for calculating the effects of realistic winds on acoustic energy distribution in the atmosphere have included ray tracing (geometrical acoustics) and normal-mode analysis, which is better suited to modeling some aspects of long-distance propagation of very-low-frequency acoustic and acoustic-gravity waves.

Several authors have incorporated transverse and/or longitudinal winds into waveguide-mode analyses to predict the wind-induced changes in acoustic intensity, the frequency dispersion, and the spectral content of waves that travel global distances. [5,11-14] The wind models are generally crude and limited in height, however, and, although mode transit time is predicted, azimuth deviations are not.

Rothwell[15] incorporated winds into an early ray-tracing procedure, in which atmospheric wind and temperature profiles were represented by layers in which wind and sound speed varied linearly with height. He neglected cross winds and applied it only to the atmosphere up to 3500 m. A number of authors have since reported numerical computations of acoustic ray paths and signal amplitudes in temperature- and wind-stratified atmospheres,[16–21] but the effects of cross winds (lateral deviation) were always neglected. Pierce[41] introduced a computational method for including cross-wind effects into the ray-tracing equations, but no results using realistic atmospheric wind models have been published. Georges[22] developed a flexible, three-dimensional acoustic-gravity-wave ray-tracing program using a Hamiltonian formulation in spherical (earth-centered) coordinates. It computes and displays three-dimensional acoustic-gravity ray paths, and allows three-dimensional wind and temperature fields. This is the program we used to calculate the results of this paper.

II. WIND AND TEMPERATURE MODELS

We used a single height profile of atmospheric temperature and five different wind models; two represent seasonal midlatitude averages and the other three are estimates of extreme variations, based on observed standard deviations (Fig. 3). The standard deviations are applied to the summer-wind model only, but they are applied in three ways that are intended to represent extreme wind conditions. The notations "2σ Shift East" and "2σ Shift West" mean that the mean wind profile is shifted eastward (or westward) by an amount equal to twice the standard deviation of the wind speed at each height. The notation "2σ Magnitude" means that the mean profile is increased in magnitude by an amount equal to twice the standard deviation of the wind speed at each height. This creates a profile with extreme shear. After examining a large number of winter-wind profiles, we concluded that the winds are much more variable in winter than in summer. Therefore, we did not attempt to construct 2σ winter profiles. The wind models used in the ray tracing are Fourier series fits to measurements made by Essenwanger and Dudel,[23] Groves,[24] Kantor and Cole,[25] Kohl and King,[26] Gringorten et al.,[27] Mitchell,[28] Amayenc,[29] Elford,[30] Kantor,[31] and several measurements cited by Murgatroyd et al.[32] The temperature model is an analytic fit to the 1962 U. S. Standard Atmosphere.[33]

III. THE CALCULATED REFRACTIVE EFFECTS

We calculated acoustic ray paths for various elevation angles from a source on the ground, using each of the wind models, and we recorded the bearing deviations and transit-speed variations in each case.

The effects of the two seasonal-mean wind models on ray geometry are shown in Fig. 4. To represent rays that converge on a receiver from different ranges, source heights and elevation angles, we calculated these ray paths through a wind model in which wind direction is reversed compared with reality. Changing

the wind direction has the effect of reversing time and allows us to compute the ray paths terminating at a single receiver. Notice that when the infrasound travels with the wind (eastward in winter, westward in summer), most of the wave energy is concentrated in the troposphere and stratosphere (i. e., below about 30-km altitude), as indicated by the ray-density plots. The height where the rays are bent back towards the ground also changes with ray orientation. This could influence the amount of absorption upwind compared with downwind; for example, Donn and Rind[21,34] have invoked this absorption difference to infer upper-atmospheric winds using microbaroms. Ray density and absorption both contribute to the field strength on the ground.

Another confirmation of upwind versus downwind propagation effects comes from observations of severe-storm infrasound from the Midwestern U. S. at Boulder, Colorado, and Washington, D. C.[35] Even though severe storms apparently radiate throughout the spring and summer, infrasound is seldom observed in Boulder before mid-May or in Washington, D. C., after mid-May, when the mesospheric winds usually reverse direction (Fig. 2).

The calculated bearing deviations and transit-speed variations are shown for the summer-mean and winter-mean models in Figs. 5(a)–5(d). (Similar plots are available for the other three wind models, but are not shown here in the interest of brevity.) They are plotted in the plane azimuth of arrival versus elevation angle of arrival (from horizontal). This format is useful if elevation and azimuth are both measured, but unfortunately, they frequently are not. A format giving the deviations explicitly as a function of ground range would be more useful, but, as the ray plots of Fig. 4 show, ground range is a complicated and multivalued function of elevation angle. For very long-distance propagation at infrasonic frequencies, attenuation is lowest for the low-elevation-angle rays (because their total path length is shorter and because the kinematic viscosity of the atmosphere is lower at the lower heights), so that only the deviation results for less than about 10° or 20° elevation angle concern us. For distances shorter than a few hundred kilometers, approximate relations between range and elevation angle can be derived from ray plots.

Bearing deviations for all five wind models are shown versus azimuth, for 0° elevation angle, in Fig. 6. The corresponding plot for transit speed is shown in Fig. 7. The winter-mean results tend to validate the sinusoidal form of the empirical formulas [Eqs. (1) and (2)], but the magnitude of $\delta\theta$ should be about 8°; δV should be about 50 m sec^{-1}, and V_0 should be 275 m sec^{-1}. The summer-mean and 2σ-magnitude models predict very small bearing deviations (usually less than 1°), but the 2σ-shifted summer-wind models predict maximum deviations of opposite sign, with $\delta\theta \simeq \pm 6°$. If the 2σ bearing deviations really are $\pm 6°$, then it would appear useless to consider models to correct individual bearings. Because wintertime winds seem to be much more variable than those in summer, even larger 2σ bearing

J. Acoust. Soc. Am., Vol. 61, No. 1, January 1977

503
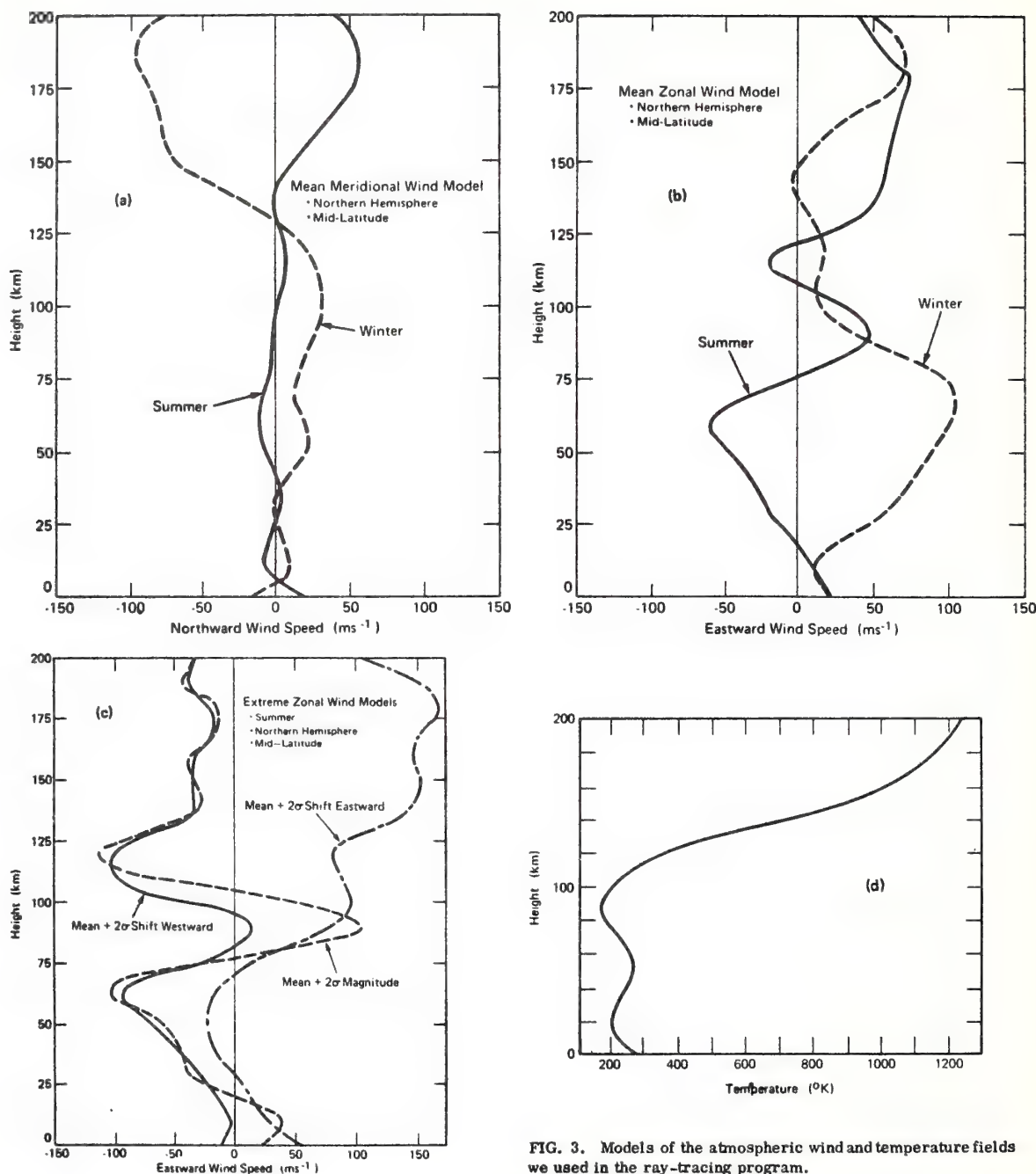
FIG. 3. Models of the atmospheric wind and temperature fields we used in the ray-tracing program.

deviations might be expected during winter. Refraction always appears to be small for eastward and westward propagation, however, making those bearing measurements more reliable, regardless of season.

Unfortunately, very few accurate measurements of bearing deviation or transit speed exist for known sources at midlatitudes. Therefore, we can't decide whether the empirical formulas or the ray-tracing re-

sults are more accurate. Another difficulty is that the calculations shown in Figs. 6 and 7 are for 0° elevation angle. We sometimes observe azimuth deviations from a given source that vary by several degrees over a time of a few minutes.[7] This could be explained from a ray viewpoint as the successive arrival of energy from different elevation angles over ray paths that traverse different parts of the atmosphere, specifically rays that reach different altitudes. (See Fig. 4, for example.)

J. Acoust. Soc. Am., Vol. 61, No. 1, January 1977

504
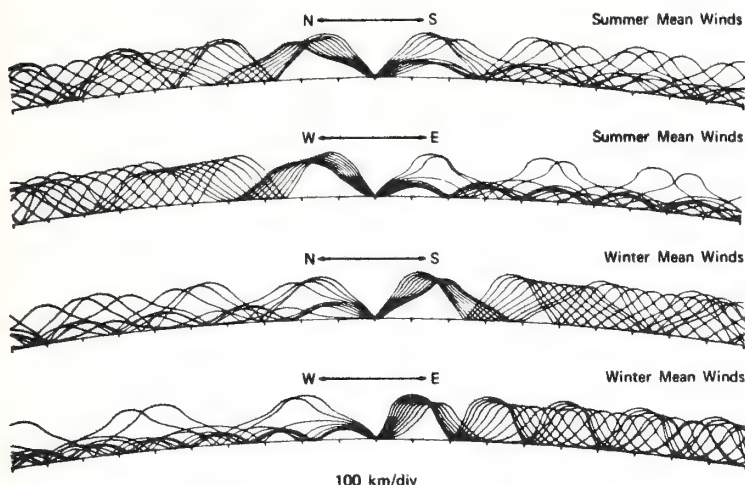
FIG. 4. Acoustic ray paths projected onto vertical north–south and east–west planes, for the winter- and summer-mean wind models. These ray paths differ from the usual representation, in that the receiver is located at the center of each plot, where the rays converge, and the rays travel toward the center as though they were radiated from sources distributed along the ground. The effect is to show where in the atmosphere an acoustic sensor is "looking" under various wind conditions. The paths were calculated with a wind field $u'(z) = -u(z)$, where $u(z)$ is the model of the actual winds. The rays arrive at the receiver from elevation angles spaced every 5° between 0° and 45°.

IV. ARE HORIZONTAL GRADIENTS IMPORTANT?

Our wind and temperature models depend only on height, even though we know that both wind and temperature actually do exhibit horizontal structure. But our knowledge of the horizontal variability of the atmosphere is still inadequate to permit us to construct representative models, even though our ray-tracing program could handle them.

It is possible that horizontal gradients cause most of the observed refraction. To appreciate this possi-
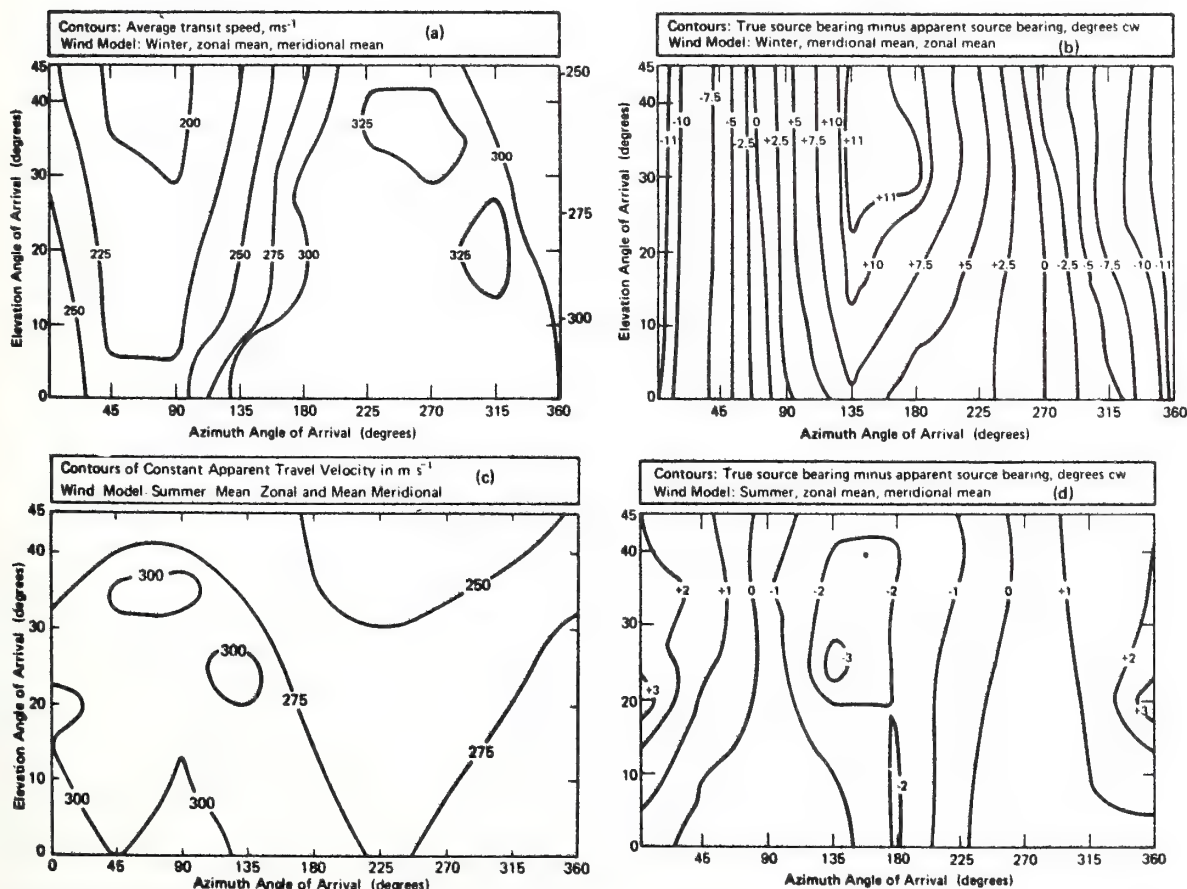
FIG. 5. Bearing-deviation and transit-speed contours in the elevation-azimuth plane for the summer- and winter-mean wind models.

J. Acoust. Soc. Am., Vol. 61, No. 1, January 1977

505

bility, consider the acoustic ray bending caused by simple linear gradients of wind U and sound speed C (which is proportional to the square-root of the temperature T). In each case, the acoustic ray paths are circular arcs (to first order in U/C and $\Delta C/C$) whose radii of curvature κ are proportional to the respective gradients

$$\kappa = C^{-1}dC/dx = (2T)^{-1}dT/dx \qquad (3)$$

for temperature gradient dT/dx, and

$$\kappa = C^{-1}dU_y/dx \qquad (4)$$

for a wind shear dU_y/dx. A circular ray traveling a distance D bends through an angle $\theta = \kappa D$. Let us ask what wind or temperature gradients would cause a 1° bend over a distance D of 1000 km. The required temperature gradient is

$$dT/dx = 2T\theta/D \qquad (5)$$

or 10.5 °K in 1000 km. The required wind shear is

$$dU_y/dx = C\theta/D$$

or 5.9 m sec⁻¹ in 1000 km. Even our limited knowledge of the real atmosphere[36] suggests that horizontal gradients of at least these magnitudes would be common, and that gradients five times as large would not be exceptional.

It is not uncommon to observe widely differing bearing deviations at two nearby observatories on the same signal from a distant source. For example, two Colorado observatories only about 50 km apart recorded infrasound from a Chinese nuclear test, whose arrival directions differed by 6°. This could be explained only by horizontal refractive-index gradients. Calculations by Georges[37] show, for example, that atmospheric vortices of even moderate intensity can cause substantial angular ray deviations, and that the deviations change rapidly depending on whether rays pass through the

FIG. 7. Average transit speed, versus azimuth, for all five wind models.

vortex center or its periphery. Furthermore, observations of such waves' spatial coherence[38] tend to confirm Gossard's prediction[39] that horizontal inhomogeneities in refractive index produce a loss of wave coherence, both along the wavefronts (caused by waves at a given frequency arriving from a small range of directions) and in the direction the waves travel (caused by refractive fluctuations in phase velocity).

V. CONCLUSIONS

Simple formulas for bearing corrections and transit-speed variations are probably useless because standard deviations far exceeding the mean occur. Furthermore, horizontal refractive-index gradients could easily cause as much bearing deviation as the variations predicted by our horizontally stratified models. Discrepancies in bearing errors and loss of wave coherence measured at adjacent infrasound observatories suggest the importance of horizontal structure.

FIG. 6. Bearing deviation versus azimuth for all five wind models.

[1]D. Wallechinsky and I. Wallace, *The People's Almanac* (Doubleday, Garden City, NY, 1975), p. 544.

[2]J. W. Reed, "Attenuation of blast waves by the atmosphere," J. Geophys. Res. 77, 1616–1622 (1972).

[3]R. K. Cook, "Strange sounds in the atmosphere, Part 1," Sound 1, 12–16 (1962).

[4]N. K. Balachandran and W. L. Donn, "Dispersion of acoustic-gravity waves in the atmosphere," in *Acoustic Gravity Waves*

in the Atmosphere (U.S. GPO, Washington, D. C., 1968), pp. 179–193.

[5]A. D. Pierce, "Propagation of acoustic-gravity waves in a temperature-and-wind-stratified atmosphere," J. Acoust. Soc. Am. 37, 218–227 (1965).

[6]T. M. Georges and G. E. Greene, "Infrasound from convective storms: Pt. IV. Is it useful for storm warning?" J. Appl. Meteorol. 14, 1303–1316 (1975).

[7]V. H. Goerke, J. M. Young, and R. K. Cook, "Infrasonic observations of the May 16, 1963, volcanic explosion on the island of Bali," J. Geophys. Res. 70, 6017–6022 (1965).

[8]H. Mack and E. A. Flinn, "Analysis of the spatial coherence of short-period acoustic-gravity waves in the atmosphere," Geophys. J. Roy. Astron. Soc. 26, 255–269 (1971).

[9]Lord Rayleigh, Theory of Sound (Dover, New York, 1945), Vol. 2.

[10]M. Diamond, "Cross-wind effect on sound propagation," J. Appl. Meteorol. 3, 208–210 (1964).

[11]D. Pridmore–Brown, "Sound propagation in a temperature and wind-stratified atmosphere," J. Acoust. Soc. Am. 34, 438–443 (1962).

[12]R. MacKinon, "The effects of winds on acoustic-gravity waves from explosions in the atmosphere," Q. J. R. Meteorol. Soc. 93, 436–454 (1967).

[13]J. E. Thomas, "An investigation of acoustic-gravity wave propagation in a realistic atmosphere," Research Rept. No. 3, Engineering Experiment Station, University of Idaho, Moscow, ID (1970) (unpublished).

[14]J. E. Thomas and L. B. Craine, "Acoustic-gravity wave propagation in a measured atmosphere," Geophys. J. Roy. Astron. Soc. 26, 311–321 (1971).

[15]P. Rothwell, "Calculation of sound rays in the atmosphere," J. Acoust. Soc. Am. 19, 205–221 (1947).

[16]G. Barry, L Griffiths and J. Taenzer, "HF radio measurements of high-altitude acoustic waves from a ground-level explosion," J. Geophys. Res. 73, 448–451 (1966).

[17]O. Essenwanger, "Wind influence upon acoustic focusing," 2nd National Conference of Atmospheric Propagation, U. S. Army Electronics Research and Development Activity, 151–171, White Sands Missile Range, NM (1963) (unpublished).

[18]R. Thompson, "Computing sound ray paths in the presence of winds," Sandia Rept. SC-RR-67-860, Sandia Corp., Albuquerque, NM (1967) (unpublished).

[19]W. L. Donn and E. Posmentier, "Infrasonic waves from natural and artificial sources," in Acoustic-Gravity Waves in the Atmosphere (U.S. GPO, Washington, D. C., 1968).

[20]N. K. Balachandran and W. L. Donn, "Characteristic of infrasonic signals from rockets," Geophys. J. R. Astron. Soc. 26, 135–148 (1971).

[21]W. L. Donn and D. Rind, "Natural infrasound as an atmospheric probe," Geophys. J. R. Astron. Soc. 26, 111–133 (1971).

[22]T. M. Georges, "A program for calculating three-dimensional acoustic-gravity ray paths in the atmosphere," NOAA Tech. Report ERL 212-WPL 16 (U.S. GPO, Washington, DC., 1971).

[23]O. M. Essenwanger and H. P. Dudel, "Seasonal models of air density, temperature and wind between surface and 25 km

for four geographic zones," Report No. RR–TR–65–8, U. S. Army Missile Command, Redstone Arsenal, AL (1965) (unpublished).

[24]G. V. Groves, "Atmospheric structure and its variations in the region from 25 to 120 km," Environmental Research Papers No. 368, (AFCRL, Bedford, MA, 1971).

[25]A. J. Kantor and A. E. Cole, "Zonal and meridional winds to 120 km," J. Geophys. Res. 69, 5131–5140 (1964).

[26]H. Kohl and J. W. King, "Atmospheric winds between 100 and 700 km and their effects on the ionosphere," J. Atmos. Terrest. Phys. 29, 1045 (1967).

[27]I. I. Gringorten, R. W. Lenhard, Jr., H. A. Salmela, and N. Sissenwine, "Winds," in Handbook of Geophysics and Space Environments, edited by S. L. Valley (AFCRL, Bedford, MA, 1965), Chap. 4.

[28]L. V. Mitchell, "Variability of the monthly mean zonal wind, 30–60 km," Tech. Rept. 195, USAF Air Weather Service (MAC) (1970) (unpublished).

[29]P. Amayenc, "Tidal oscillations of the meridional neutral wind at midlatitudes," Radio Sci. 9, 281–293 (1974).

[30]W. G. Elford, "A study of winds between 80 and 100 km in medium latitudes," Planet. Space Sci. 1, 94–101 (1959).

[31]A. J. Kantor, "Strong wind and vertical wind shear above 30 km," Environmental Research Papers No. 303, AFCRL-69-0346 (1969) (unpublished).

[32]R. J. Murgatroyd, F. K. Hare, B. W. Boville, S. Teweles, and A. Kochanski. "The circulation in the stratosphere mesosphere and lower thermosphere," WMO Tech. Note No. 70, Geneva, Switzerland (1975) (unpublished).

[33]Handbook of Geophysics and Space Environments, edited by S. L. Valley (McGraw–Hill, New York, 1965).

[54]W. L. Donn and D. Rind, "Further use of natural infrasound as a continuous monitor of the upper atmosphere," J. Atmos. Sci. 32, 1694–1704 (1975).

[35]T. M. Georges, "Infrasound from convective storms: Examining the evidence," Rev. Geophys. Space Phys. 11, 571–594 (1973).

[36]H. S. Bowman and A. J. Bedard, "Observations of infrasound and subsonic pressure disturbances related to severe weather," Geophys. J. R. Astron. Soc. 26, 215–242 (1971).

[36]R. A. Craig, The upper atmosphere, meteorology and physics (Academic, New York, 1965).

[37]T. M. Georges, "Acoustic ray paths through a model vortex with a viscous core," J. Acoust. Soc. Am. 51, 206–209 (1972).

[38]T. M. Georges and J. M. Young, "Passive sensing of natural acoustic gravity waves at the earth's surface," Remote Sensing of the Troposphere, edited by V. E. Derr (U.S. GPO, Washington, DC, 1972), Chap. 21.

[39]E. E. Gossard, "The effect of bandwidth on the interpretation of the cross-spectra of wave recordings from spatially separated sites," J. Geophys. Res. 74, 325–335 (1969).

[40]E. S. Batten, "Wind systems in the mesosphere and lower ionosphere," J. Meteorol. 18, 283–291 (1961).

[41]A. D. Pierce, "Geometrical acoustics' theory of waves from a point source in a temperature- and wind-stratified atmosphere," AVCO Report AVSSD-0135-66-CR, Scientific Report No. 2, AVCO Corp., Wilmington, MA (1966) (unpublished).

507

Rossby-Planetary Waves, Tides, and Gravity Waves in the Upper Atmosphere

8

WILLIAM H. HOOKE
Wave Propagation Laboratory
National Oceanic and Atmospheric Administration

8.1 PROLOGUE

The outstanding structural feature of all planetary atmospheres is their effectively exponential density decrease with height under the action of gravity. In the earth's atmosphere, the density decreases by 12 orders of magnitude between the surface and the base of the exosphere. As we have seen in previous chapters, this enormous variation of density with height and the changes in composition associated with it combine to produce an atmospheric photochemistry correspondingly rich in variety. The qualitative nature of the photochemistry presents a different aspect with every change in altitude of a scale height or so, and the chemistry as a whole changes from an essentially neutral regime in the lower atmosphere to a plasma regime in the magnetosphere. Thus the upper atmosphere presents us with a sophisticated photochemistry and plasma-physics laboratory, available to us to the extent that we are able to probe and monitor it using *in situ* sensors on rocket or satellite platforms or ground- and satellite-based remote-sensing devices such as ionosondes, radars, lidars, radiometers, and spec-

trometers. In recent years, our utilization of this laboratory has become increasingly active. We are now able to modify a number of upper atmospheric processes—stimulating artificial airglow and aurora and heating the ionospheric plasma in controlled ways.

But the upper atmosphere is more than a laboratory. It serves as a shield, protecting us from the harsh particle and radiative environment of the interplanetary medium. In recent years, we have come to learn that this shield is possibly more fragile, more vulnerable to man's depredations than we had previously supposed. Because our understanding of the processes sustaining this shield and our impact upon it is so fragmentary, the photochemistry and plasma physics of the upper atmosphere are now urgent problems that we must face.

As the earlier chapters of this volume serve to indicate, the complexity of these problems would severely tax our modeling capabilities for some time to come even if the atmosphere were stationary. In fact, however, the air is in a pronounced state of motion, ranging in scale from circulations that are truly global to turbulent eddies that may be only centimeters in dimension. The result is that the

continuity equations describing the photochemistry and plasma physics of both major and minor atmospheric constituents must contain divergence or transport terms associated with these motions. For example, any model of the ozone balance of the upper atmosphere, to be complete, must incorporate or parameterize stratospheric dynamics, as indicated in Chapters 9 and 10. Similarly, if we are to understand the effects on high-frequency radiowave propagation of phenomena such as traveling ionospheric disturbances and ionospheric storms, we must include dynamical processes in the models.

Thus the subject of atmospheric dynamics forms a large part of this study, being considered explicitly or implicitly in every chapter. Other chapters treat the electrically neutral atmospheric dynamics in its largest and smallest aspects—from the global circulations engendered by nonuniform heating (Chapter 3) to the turbulent motions producing local transport and diffusion, as well as an energy cascade into molecular dissipation (Chapters 7 and 9)—and the plasma dynamics involved in the interaction between the charged particles of the upper atmosphere and the earth's magnetic field (Chapters 1, 2, and 5). But we observe that the large-scale circulations account for only part of the transport in the upper atmosphere. We find similarly that small-scale, turbulent motions do not account for the rest. The remainder—an important fraction—occurs as a result of neutral atmospheric motions on six orders of magnitude of intermediate scale—motions between a few meters and a few thousand kilometers in spatial dimension and having temporal scales between a few seconds and several days.

It happens that most of the atmospheric motions on these scales can be interpreted as wavelike in nature. The time series they display on various records are often nearly sinusoidal. They exhibit a high degree of spatial correlation. They propagate with well-defined phase and group speeds that appear to exhibit appropriate dispersion. The study of these wave motions is thus attractive from two points of view. On the one hand, the waves appear to be an important part of the dynamics of the upper atmosphere, contributing significantly to the transport processes that occur there. On the other, a wide variety of mathematical tools are available for analyzing atmospheric wave motions; the wave approach to the study of atmospheric dynamics has consistently proven to be a powerful one. In this chapter we present in broad outline a summary of the progress of this subject and its prospects for the future.

In general, wave motions involve an interchange of energy of various forms—kinetic, internal, electromagnetic, and gravitational potential, for example. Because the earth's upper atmosphere provides a wide variety of forms of energy storage, it sustains a rich spectrum of wave motions of different types, including at various ends of the spectrum hydromagnetic waves, inertial oscillations, acoustic waves, and the like. However, the observationally important wave motions of the electrically neutral upper atmosphere fall for the most part into one of the three dominant classes—the Rossby-planetary waves, the tides, and the gravity waves. In this chapter we shall describe briefly the physical characteristics basic to each of these three wave types, the various complicating factors affecting their propagation in the real atmosphere, and the processes governing their generation and dissipation. In addition to the wave kinematics, we consider wave dynamics, which plays a greater role in atmospheric physics than most people realize. One of the striking features of geophysical fluid dynamics is that wave motions are so often nearly monochromatic. All of us have often seen displayed, either on the ocean surface or in clouds, patterns revealing wavefront after wavefront, evenly spaced so that the wave nature of the phenomenon leaps out at us in a way that would not be nearly so apparent if the wave spectrum were fairly broad and all we saw was the chaotic superposition of many waves. An example is shown in Figure 8.1, which shows wave motions on two scales modulating noctilucent clouds at 85-km altitude—the height of the mesopause. With examples such as this before us, and with the mathematics of linear monochromatic plane waves being relatively simple and straightforward, it is no wonder that theorists have found the interpretation of such events so tempting. But it turns out that atmospheric wave motions are much more than a mere curiosity of the atmospheric motion field; because waves so effectively transport momentum and energy without requiring a concomitant mass transport, they are dynamically quite important, even when they are of relatively small amplitude. In the troposphere, planetary waves provide significant meridional transports of momentum and energy, while gravity waves produce corresponding vertical transports of these quantities. The effect of these transports is to produce a global climate that is much more temperate than it would otherwise be. In the upper atmosphere, analogous processes are at work but with greater intensity. Because the waves propagate

FIGURE 8.1 Noctilucent clouds at the mesopause revealing wave motions (after Witt, 1962).

their energy upward into regions of lesser density, con-
servation of energy requires that the wave amplitude
increase to compensate. The effect is so extreme that
while lower atmospheric wave energy fluxes are small
compared with solar radiative energy fluxes, in the upper
atmosphere the dynamical and radiative fluxes can be of
comparable magnitude; more is said about this effect in
Section 8.5.

The decrease in atmospheric density with height af-
fects the wave dynamics, and indeed the fundamental
structure of the upper atmosphere, in yet another way,
through the associated increase in atmospheric kinematic
viscosity (inversely proportional to the density) with
height. Just above the tropopause this viscosity is small in
the sense that the observed atmospheric motions can be
considered inviscid to good approximation; not only are
the motions inviscid, but they tend to engender turbu-
lence and concomitant mixing. Turbulent, or eddy, vis-
cosity is orders of magnitude larger than its molecular
analog; the latter plays a negligible role in the observable
dynamics. However, molecular kinematic viscosity in-
creases steadily with height; at 100 km, it is some six
orders of magnitude greater than its surface value. Not far
above this altitude, turbulence can no longer be main-
tained; turbulent mixing ceases, and the different atmo-
spheric constituents diffusively separate according to
their molecular weights (Chapters 3 and 7). At the same
time, the atmospheric motions become increasingly sub-
ject to viscous dissipation. For the same reason, the time
constants for radiative transitions eventually become
shorter than the collision times for the particles involved,
so that the atmosphere can no longer be considered in

local thermodynamic equilibrium. Similarly, the increas-
ing relative plasma density introduces a new dimension
to the fluid motion. Thus the same density decrease that
causes the upper atmosphere to present us with a richly
varied photochemistry and plasma-physics laboratory
provides a diversity of fluid-dynamics regimes, ranging
from inviscid and turbulent to laminar and from electri-
cally neutral to plasma, for our scrutiny.

8.2 ROSSBY-PLANETARY WAVES, TIDES, AND GRAVITY WAVES

The upper atmosphere supports a wide variety of oscilla-
tions and wave modes, ranging on the large-scale end
from the quasi-biennial oscillation of the tropical upper
atmosphere and the atmospheric semiannual oscillation
through Rossby-planetary waves and the tides to inertial
oscillations, gravity waves, and acoustic waves with
periods of a few seconds at the smallest scale. The most
important of these from a fluid-dynamical standpoint are
the Rossby-planetary waves, the tides, and the gravity
waves. These motions are, of course, implicit in, and
represent solutions to specialized forms of, the equations
of motion for the upper atmospheric fluid. One form of
these equations is given in Table 8.1 (for a complete and
thorough development of the equations the interested
reader is referred to Batchelor, 1967); they are simple in
appearance but complex in implication. Three of these
equations (one vector equation and two scalar equations)
express conservation of momentum, energy, and matter,
respectively; these are *prognostic*, in the sense that they

TABLE 8.1   Equations of Motion

$$\rho\,\frac{\partial \mathbf{u}}{\partial t} + \rho(\mathbf{u}\cdot\nabla)\mathbf{u} + 2\rho\Omega_\varepsilon \times \mathbf{u} = -\nabla p + \rho\mathbf{g} + \mu\left[\nabla^2\mathbf{u} + \nabla(\nabla\cdot\mathbf{u})/3\right] + \rho\mathbf{F}$$

$$\frac{\partial e}{\partial t} + (\mathbf{u}\cdot\nabla)e = -p\,\frac{\partial\rho^{-1}}{\partial t} - p(\mathbf{u}\cdot\nabla)\rho^{-1} + \phi + \frac{1}{\rho}\nabla\cdot(K_T\nabla T) + J$$

$$\frac{\partial\rho}{\partial t} + \nabla\cdot(\rho\mathbf{u}) = 0$$

$$p = \rho R T$$

ρ = density
$\mathbf{u}$ = velocity
Ω_ε = earth's angular rotation vector
p = pressure
$\mathbf{g}$ = acceleration of gravity
μ = coefficient of viscosity
$\mathbf{F}$ = body force/unit mass (e.g., Lorentz force, solar, lunar gravitational forces)
e = internal energy/unit mass
ϕ = rate of mechanical energy dissipation/unit mass due to viscosity
K_T = thermal conductivity
J = heat input/unit mass (e.g., radiation transfer, chemical reactions, water-phase transformations)
R = atmospheric specific gas constant
T = temperature

predict evolutions of the system resulting from its present state. The fourth—an equation of state—is *diagnostic*, in that it only states a necessary constraint relating instantaneous values of the system pressure, density, and temperature; for most purposes the ideal gas law suffices. Together with the appropriate boundary conditions, these equations are capable of describing the whole of atmospheric dynamics (exceptions arise in those cases for which the dynamics of each of the atmospheric constituents is substantially different, as is the case with ions and neutrals; then separate sets of equations must be written for each constituent). This comprehensiveness may be welcome in some respects, but it is most unwelcome in others, in that solution of the equations in their fullest generality requires more initial information than we are able to provide and would yield more information than we could assimilate. Thus the science of atmospheric dynamics involves a search for simplifications and idealizations to these equations and their boundary and initial conditions that drastically reduce the amount of input required and output retained while reproducing the essential features of the particular phenomena of interest.

A major source of such simplification derives from the fact that the different terms in the equations depend in different ways on spatial and temporal derivatives of the pressure, density, temperature, and velocity fields. The result is that the different terms of the equation may or may not be important to a given phenomenon, depending on its spatial and temporal scales. It is for this reason that the Rossby-planetary waves, tides, and gravity waves each have such a distinct character, as indicated by Tables 8.2 and 8.3.

Rossby-planetary waves are oscillations of the atmosphere having wavelengths of the order of several days or more. These motions are global in scale and have periods exceeding the period of the earth's rotation; they arise as a result of the earth's sphericity and rotation, which combine to produce a Coriolis force that increases with latitude. The inertial term in the equation of motion is small compared with the Coriolis term; hence the wave-associated motions are the result of an approximate balance between Coriolis and pressure-gradient forces, i.e., they are nearly geostrophic. Similarly, vertical accelerations are small in the sense that there is a nearly complete balance between the vertical pressure gradient and the buoyancy term; i.e., the motions are hydrostatic. Their horizontal wave phase speeds are the order of 10 m sec^{-1}; these are comparable with the mean zonal wind speed at temperate latitudes, and the sensitivity of planetary waves to and their interaction with the zonal flow is strong. Inspection of the wave dispersion equation in Table 8.3 indicates this; the wave-phase speed is always smaller than the mean zonal flow u_0 and decreases with increasing wavelength, vanishing when $k^2 = 2\Omega_e \sin \theta / u_0$; R_0; for $\theta = 45°$ and $u_0 = 10$ m sec^{-1}; this occurs for $\lambda = 2\pi/k \approx 5000$ km. Because Rossby-planetary waves produce at alternate phases of their cycles, the familiar "highs" and "lows" of weather maps, their discovery and the understanding of their motion constituted a major advance in our understanding of the weather. In the troposphere, Rossby-planetary waves contain orders of magnitude more energy than their tidal or gravity-wave counterparts; however, their theoretical study is much more recent, dating from pioneering work by Rossby in the late 1930's.

The tides, although producing only weak oscillations in the atmospheric surface pressure (fluctuations ~ 1 mbar as opposed to changes ~ 30–100 mbar that are associated with the Rossby-planetary waves), are strongly evident in the oceans. As a result, they attracted early theoretical interest; late in the seventeenth century Newton explained the so-called "equilibrium" tide that would develop on a nonrotating earth under the gravitational influ-

TABLE 8.2 Summary of Wave Properties

Wave	Horizontal Wave-length, λ	Period, τ	Horizontal Wave Phase Speed, λ/τ	Motion	Source Mechanisms
Rossby-planetary waves	$\sim R_E$	$\sim 5\tau_E$	$\ll R_E/\tau_E$	Geostrophic Hydrostatic	Instability Topographical forcing Differential heating
Tides	$\sim \dfrac{2\pi R_E}{n}$, $n = 1,2,\ldots$	$\sim \dfrac{\tau_E}{n}$, $n = 1,2,\ldots$	$\sim 2\pi R_E/\tau_E$	Nongeostrophic Hydrostatic	Solar, lunar gravitational fields Solar heating
Gravity waves	$\ll R_E$	$\ll \tau_E$	$< C_0$	Nongeostrophic Nonhydrostatic (except for largest τ)	Instability Topographical forcing Differential heating Wave–wave interaction

$R_E \cong$ radius of the earth
$\tau_E \cong$ solar day
$2\pi R_E/\tau_E \cong 460$ m sec^{-1}
$C_0 \cong$ speed of sound (~ 300 m sec^{-1} at altitudes <100 km, increasing to 10^3 m sec^{-1} above)

TABLE 8.3   Wave Dispersion Equations

Rossby-planetary waves: $\psi = \psi_0 \exp i (\omega t - kx)$

$$k^2 = \frac{2\Omega_E \sin \theta / R_E}{u_0 - \omega/k}$$

Tides: $\psi^{\omega,s} = \sum_n \Theta_n^{\omega,s}(\theta) \exp i (\omega t - s\phi - nz) \exp (z/2H)$

$$\left[\frac{1}{\sin \theta} \frac{\partial}{\partial \theta} \left(\frac{\sin \theta}{\omega^2/4\Omega_E^2 - \cos^2\theta} \frac{\partial}{\partial \theta} \right) - \frac{1}{\omega^2/4\Omega_E^2 - \cos^2\theta} \left(\frac{s}{\omega/2\Omega_E} \cdot \frac{\omega^2/4\Omega_E^2 + \cos^2\theta}{\omega^2/4\Omega_E^2 - \cos^2\theta} + \frac{s^2}{\sin^2\theta} \right) \right] \Theta_n^{\omega,s} = - \frac{4R_E^2\Omega_E^2}{gh_n^{\omega,s}} \Theta_n^{\omega,s}$$

$$n = \left(\frac{\gamma - 1}{\gamma H h_n^{\omega,s}} - \frac{1}{4H^2} \right)^{1/2}$$

Gravity waves: $\psi = \psi_0 \exp (z/2H) \exp i (\omega t - ky - nz)$

$$\omega^4 - \omega^2 C_0^2(k^2 + n^2) + (\gamma - 1)g^2k^2 - \gamma^2 g^2\omega^2/4C_0^2 = 0$$

$x \equiv$ zonal (east–west) coordinate	$u_0 \equiv$ mean zonal wind
$y \equiv$ arbitrary horizontal coordinate	$\phi \equiv$ longitude
$z \equiv$ vertical coordinate	$g \equiv$ acceleration of gravity
$t \equiv$ time	$h_n^{\omega,s} \equiv$ "equivalent depth"
$\Omega_E \equiv$ earth's angular rotation velocity	$\gamma \equiv$ ratio of atmospheric specific heats
$R_E \equiv$ earth's radius	$H \equiv$ atmospheric scale height
$\theta \equiv$ colatitude	$C_0 \equiv$ speed of sound

ence of the sun and the moon; his work was extended in the 1800's by Laplace, who treated the dynamic case of tides on a rotating planet. Except in the tropics, the weak tidal pressure fluctuations are masked by planetary-wave fluctuations in the daily records; thus the determination of their amplitudes has required extensive, careful statistical analysis. As this was done, it was discovered that the dominant tidal component in the surface observations was the solar semidiurnal mode. This was quite a puzzle; if the tidal forcing were predominantly gravitational, then it would appear that the lunar semidiurnal tide should be dominant, while if the forcing were primarily thermal, then it would appear that the solar diurnal mode should be larger in amplitude. In the 1880's, Thomson (later to become Lord Kelvin) postulated an explanation in terms of a resonant response of the atmosphere to the solar gravitational forcing. This theory was vulnerable to the criticism that the resonance had to be quite sharp to enhance the solar semidiurnal tide relative to the corresponding lunar mode, which should be stronger by a factor of 2 in the absence of resonance. The result was that

the popularity of the theory waxed and waned for nearly 80 years, its fortunes changing with each new discovery concerning new details of the temperature structure of the upper atmosphere, to which the theory was quite sensitive; during this period some of the best minds in atmospheric science applied themselves to this problem.

As the resonance theory was finally seen to be untenable, the problem was approached from the opposite point of view, namely, that the predominant forcing was thermal and that the amplitude of the solar diurnal mode at the surface was somehow suppressed. Upper atmospheric research was an important factor in resolving the problem. In the 1950's and 1960's, researchers showed that stratospheric ozone absorption of solar radiation could account for most of the observed surface amplitude of the solar semidiurnal tide. High-altitude rocket data provided another clue when their analysis revealed that in the stratosphere and mesosphere the dominant tidal component was indeed a solar diurnal mode. The final resolution to the mystery of the tides was provided by Lindzen in the mid-1960's. Lindzen considered the set of eigen-

values of the tidal problem known as the "equivalent depths" (Table 8.3); he showed that this set was complete only if it included negative values for the square of the vertical wavenumber, corresponding to wave energy trapping in the vertical. He then showed that most of the solar energy input goes into such a vertically trapped mode. At one stroke, this explained both the dominance of the solar semidiurnal mode at the earth's surface and the dominance of the diurnal mode in the upper atmosphere (for a complete development of tidal theory as well as an interesting historical account, the reader is referred to the book by Lindzen and Chapman, 1970). The tides, like the planetary waves, are global in dimension; however, for tidal motions the inertial terms are comparable to the Coriolis terms and the motions are therefore nongeostrophic. The vertical accelerations remain small, so that the motions are hydrostatic. Wave-phase speeds are much larger than zonal wind speeds; hence the vertical propagation of the important tidal modes is only weakly affected by the mean zonal winds.

The gravity waves, the third major wave type, occur on spatial scales much smaller than the earth's radius and with periods much less than a day; as a result, the earth's sphericity and rotation play a negligible role in their description. These, together with their closely related oceanic counterparts, the wind waves, have been studied for more than a century. However, the interpretation of upper atmospheric motions in terms of gravity-wave theory effectively begins only with Hines (1960; Hines has recently published a collected works including his 1960 paper and subsequent research together with interesting annotation, 1974). Gravity waves exist because of a subtlety of the atmospheric density decrease with height; for the most part, that density decrease occurs in such a way that the atmospheric stratification is *statically stable*. Consider the motion of a parcel of air in such a region after it has been displaced upward from its equilibrium position. Finding itself denser than its surroundings, it decelerates, and sinks back to its equilibrium level, and overshoots, whereupon it finds itself warmer and lighter than its surroundings, so that it decelerates, and so on. In this way it finds itself in oscillation about its equilibrium position. It does this with a characteristic oscillation frequency N called the Brunt-Väisälä frequency after its discoverers. In the Boussinesq (incompressible) approximation, N is given in terms of the density stratification and the acceleration of gravity g by

$$N^2 = -\frac{g}{\rho}\frac{d\rho}{dz},$$

where z is the height; more properly, since the atmosphere is compressible, N^2 is expressible in terms of potential temperature θ as

$$N^2 = -\frac{g}{\theta}\frac{d\theta}{dz},$$

The Brunt period has a value of the order of 10 min in the

atmosphere between the surface and 100 km; above that height it decreases to a value of 5 min.

The Brunt-Väisälä frequency has a critical importance for gravity waves. Examination of the wave dispersion equation of Table 8.3 shows that in an isothermal atmosphere, gravity waves with frequency $\omega < N$ are internal; the vertical wavenumber n is real, and there is vertical phase and energy propagation. Gravity waves having frequencies $\omega < N$ are evanescent; for these the vertical wavenumber n is imaginary and there is no phase or energy propagation in the vertical. (It should be noted that the dispersion equation given in Table 8.3 is a general dispersion relation encompassing both acoustic and gravity waves, as suggested by the fact that it is fourth order in ω; care must be taken to avoid confusion between the two sequences.) Gravity-wave motions are in no way geostrophic, since in their description the curvature and rotation of the earth are ignored. Waves having frequencies $\omega \ll N$ are nearly hydrostatic, but for those waves for which $\omega \to N$ the vertical accelerations are important enough to invalidate the hydrostatic assumption. For some gravity-wave components, the horizontal wave-phase speeds may approach the speed of sound; however, for the most part the wave-phase speeds are a few tens of meters per second or less. In an inviscid atmosphere, the wave-phase speeds, and indeed the wavelength, can in principle be arbitrarily small. It is appropriate to note at this point another property of gravity waves satisfying the Boussinesq approximation (phase speeds $V_{ph} \ll C_0$, vertical wavelengths $\lambda_z \leqslant H$, where H is the scale height); to good accuracy these obey the dispersion relation $n^2 \doteq k^2[(N/\omega)^2 - 1]$, where n is the vertical wavenumber and k the horizontal wavenumber. This is an approximate form of the general result in Table 8.3 and shows that in this limit the vertical tilt of the wave-phase fronts (related to the ratio n/k) is dependent only on ω/N. This result applies for the tides and the Rossby-planetary waves as well; it shows that for all waves having periods much greater than the Brunt period, the wavefronts are nearly horizontal. For a review of the theory of gravity waves in the atmosphere, the reader is referred to the book by Gossard and Hooke (1975).

8.3 FACTORS COMPLICATING WAVE PROPAGATION IN THE UPPER ATMOSPHERE

In the preceding section we reduced the physics of each of the three wave types to its barest essentials; however, to apply the wave theory successfully to interpretation of the upper atmospheric observations we must incorporate a number of complicating factors in our models. These complications are many and varied, but for the most part they may be thought of as producing (a) wave refraction, (b) wave coupling, or (c) wave dissipation. Since most of these complications have proved sufficiently severe to defy comprehensive analysis, and since

observational data user requirements are becoming increasingly demanding, investigations of the effect of these processes on wave propagation constitute an active area of current research.

Most familiar of the refractive influences is the temperature structure of the upper atmosphere, specifically that associated with the mean height structure: the stratospheric temperature increase, the mesospheric temperature decrease, and the thermospheric temperature increase with height. These produce both wave refraction and partial or total wave energy trapping. The equations governing the wave motion in an isothermal atmosphere have constant coefficients; introduction of the vertical atmospheric temperature structure introduces height-variable coefficients. The mathematical difficulties thus encountered are usually surmounted by (a) WKB or ray-tracing methods, which assume that the temperature varies slowly over a wavelength, so that the dispersion equations of Table 8.3 hold locally; (b) use of multilayer models in which the temperature is constant within each layer and matching of boundary-conditions determines the wave solutions at layer interfaces; (c) analytical solutions for special profiles; and (d) a variety of numerical techniques. All illustrate the wave refraction, trapping, and partial ducting; they serve to identify the trapped modes and in many cases lead to good comparison with observation.

Wind structure of the upper atmosphere introduces analogous complications, producing wave refraction and trapping, and its effects can be handled in exactly the same way as the effects of the temperature structure, with one important exception. That exception occurs in the immediate vicinity of so-called critical levels, which mark heights at which the component of the background wind speed in the direction of wave propagation matches the horizontal wave-phase speed. Dispersion equations incorporating the effects of atmospheric winds all reveal singularities at such heights—singularities associated with the fact that at such heights the wave frequency measured by an observer moving with the mean wind vanishes. Careful analyses show this to have a number of interesting implications. Inspection of the group velocity of wave packets in the WKB approximation reveals that the packets approach such critical levels asymptotically. Full-wave calculations, providing matching across the critical level, tend to confirm the WKB picture, showing that for slowly varying shear flows the wave energy penetration through such critical levels is very slight. Furthermore, the WKB approach indicates that in the vicinity of a critical level, the vertical wavelength becomes vanishingly small while amplitudes of wave-associated fluctuations in horizontal velocity and shear tend to infinity; this implies that the usual linearized, inviscid models of the wave motions must break down there. Critical-level encounters are consequently quite difficult to treat in the models. It is apparent from our earlier discussion of wave phase speeds that both Rossby-planetary waves and gravity waves, with their low phase speeds, are quite suscep-

tible to critical-level encounters as they propagate through the upper atmosphere; by contrast most tidal components are relatively immune.

Two other refractive effects deserve passing mention. Above about 100 km, the atmosphere ceases to be well mixed; instead it approaches a state of diffusive separation in which lighter elements and molecules tend to overlie heavier ones; as a result the atmosphere scale height increases with height quite independently of the thermospheric temperature increase. (In addition to the refractive effects, diffusive separation produces dissipative effects, which are discussed separately below.) Similarly, the $1/r^2$ decrease of gravity with radial distance r from the center of the earth also influences the scale height and the Brunt-Väisälä frequency. The result is some contribution to wave refraction; however, this effect is slight compared with those listed above.

A second set of complications arises from the fact that the decrease in atmospheric density with height generally causes the various wave modes to grow in amplitude with height. For plane waves, constancy of vertical energy flux implies constancy of the quantity $\rho u'^2$, where ρ is the atmospheric density and u' is the wave-associated perturbation velocity. Since ρ varies as $\exp(-z/H)$, u' must vary as $\exp(z/2H)$. Thus, in the absence of wave reflection and energy dissipation, wave amplitude increases exponentially in the upper atmosphere, by orders of magnitude between the tropopause and the base of the thermosphere. Thus even the smallest-amplitude wave motions in the troposphere tend to violate the linearization assumption at some point in the upper atmosphere; at this point the effect of the nonlinearities must be taken into account explicitly. This is done only with difficulty.

The simplest result of the nonlinearity is a self-interaction of the wave; this turns out to be weak, because the wave motions considered here happen to be nearly incompressible, but it does result in steepening of the waves into shocks. In addition to the self-interaction produced by nonlinearity, there arises coupling between different wave modes. In its simplest form, this manifests itself because small-scale, short-period waves find themselves propagating in an atmosphere in which the dominant temperature and wind structure is not that associated with the mean but rather that associated with larger-scale, longer-period waves of large amplitude. In its more complex form, coupling arises between different wave modes that happen to form resonant triads, satisfying the conditions

$$\mathbf{k}_3 = \mathbf{k}_1 \pm \mathbf{k}_2$$

and

$$\omega_3 = \omega_1 \pm \omega_2.$$

where the $\mathbf{k}$'s represent the wave vectors of three waves, while the ω's represent the corresponding wave frequencies, and the ω's and $\mathbf{k}$'s individually satisfy the dispersion

equation. Higher-order resonances are also possible, as are forced couplings of wave energy into modes that do not satisfy the dispersion equation. There is a continuous interchange of wave energy among modes in this way. This energy exchange is more rapid, the larger the amplitudes of the wave involved. Considerable study has been devoted to the generation of gravity waves by the atmospheric tides through this means. At altitudes the order of 100 km, tidal-associated density perturbations become a significant fraction of the ambient, while tidal velocity fluctuations become a substantial fraction of the speed of sound. Above this height, tidal-wave amplitudes cease their growth, while gravity-wave amplitudes increase; there is considerable interest in the question of whether wave–wave interaction (as opposed, for example, to simple tidal dissipation by viscosity) is responsible for this.

Associated with the increase of wave amplitude with height is the increase potential for wave-induced instability. On the small scale, the relevant stability is that in the vertical; this is characterized by the so-called Richardson number R_i, defined as

$$R_i = \frac{N^2}{(du/dz)^2} ;$$

here du/dz is the vertical shear of the horizontal wind u. Stability theory shows that shear flows are dynamically stable to infinitesimal perturbations as long as $R_i > \frac{1}{4}$. However, wave-associated velocity and temperature perturbations may become so large in the upper atmosphere as to cause R_i to fall below $\frac{1}{4}$ locally, inducing dynamic instability, or even cause R_i to become negative, inducing convective instability (in this extreme case the atmospheric density structure is not even statically stable). This results in the generation of small-scale motions at a rate much faster than that allowed by conventional wave–wave interaction. The result may be a cascade of wave energy into smaller and smaller scales and eventually into molecular dissipation; at the same time, the unstable modes produce enhanced diffusion and transport of energy in such a way as to limit the growth of the originally unstable mode. The problem has only been treated successfully numerically, and very little is currently known about wave dynamics once wave amplitudes reach unstable levels. It has been suggested, however, that nonlinear, unstable wave fields may account for much of atmospheric diffusion and transport.

In addition to nonlinearities, wave–wave coupling, and instability, which may be thought of in one sense as processes tending to limit wave amplitudes, there are a number of other dissipative processes operative in the upper atmosphere. Radiative damping is a major source of wave energy dissipation; this complication is sufficiently taxing that it is usually entered into the analysis not in a general way but through a parameterization. The most common approach is to add a term linear in the wave-associated temperature perturbation, and of the opposite sign; this is the so-called Newtonian cooling. Analyses of

the effect of this cooling show that it is of major importance in damping Rossby-planetary waves in the stratosphere and mesosphere.

Molecular relaxation also produces wave energy damping. This process arises as a result of the failure of a molecular gas to equipartition energy among translational, vibrational, and rotational states of the molecules in a time short compared with a wave period. At the earth's surface, the relevant time constant is the order of 10^{-5} sec; but because the time constant is inversely proportional to the pressure, this process becomes relevant to gravity waves at altitudes the order of 100 km or so. Only preliminary analyses have been carried out on its precise effects, but it appears that molecular relaxation could be a major source of wave damping in the lower thermosphere (above that height the dominant constituents are atomic and the process no longer so important).

Atmospheric viscosity and thermal conductivity have a major influence on the upper atmospheric wave physics; their influence on wave propagation increases with height, and, when it becomes significant, it introduces radical changes in the wave behavior. This may be seen from the equations of motion of Table 8.1, which show that introduction of the viscous and thermal-conduction terms produces equations with nonconstant coefficients, in addition to raising the order of the differential equation. The result is that exact analytic solutions no longer obtain. Several methods exist for sidestepping this difficulty. The first involves parameterization of the viscous effects by the substitution of a term that is simply linearly proportional to the wave-associated velocity perturbations and oppositely directed. This is the so-called Rayleigh friction; it is useful in the sense that it removes a number of mathematical difficulties, but it is deficient in the respect that it suppresses the scale-dependence of the viscous effects, which are greatest for the smallest-scale waves. A second method of solution involves arbitrarily requiring that the viscosity μ and the thermal conductivity K_T vary with height in the way necessary to reduce the equations to equations with constant coefficients. This approach is most useful in analyzing the propagation of waves having vertical wavelengths small compared with a scale height, the scale of variation of the viscosity, and the thermal conductivity. Analysis of the wave propagation in this case shows that the lowest-order effect of viscosity and thermal conduction is wave damping, but that higher-order effects involve refraction as well. In addition, the effect of raising the order of the differential equations is to introduce new modes of oscillation: viscous (or shear) waves and thermal conduction waves. A third approach is numerical. Analyses of this type show that the atmosphere can be thought of as consisting of four regions as far as wave motions are concerned. The lowermost region is a boundary layer in contact with the earth's surface; viscous and thermal conduction modes coexist with the other wave modes here in order to satisfy boundary conditions at the surface. Above this relatively thin layer there exists a region in which viscosity and

thermal conductivity are relatively unimportant; in this region the wave motion is dominated by the Rossby-planetary waves, tides, and gravity waves. With increasing height, the viscous and thermal conduction terms increase in importance, until finally a height region is reached in which there is significant coupling between the nondissipative modes and the former; above this height region is a fourth, in which only the viscous and thermal conduction modes are important. This is a highly idealized picture, but it does appear to reflect processes at work in the thermosphere, where theoretical analyses indicate the mode conversion to be substantial. Such analyses permit an examination of the competing effects of dissipation and wave amplitude growth with height to determine whether the waves in question will ever become nonlinear before they are damped by viscosity.

From the tropopause to the mesopause, the molecular kinematic viscosity and thermal conductivity are relatively small; in particular their effects are small relative to the effects of small-scale waves and turbulence in dissipating energy of the larger-scale modes through either wave–wave interaction or instability. The effects of these interactions on the waves are parameterized by effective "eddy" viscosities and thermal conductivities that are orders of magnitude larger than the molecular values. It is these that produce the mixing and vertical transports in this region of the atmosphere; their distribution with height is uncertain, and indeed any attempt to make these distributions precise would necessarily be artificial, but they can be taken to be roughly constant with altitude. To the extent that the parameterization is valid, then, the approximation of constant coefficients should also be valid. However, at altitudes not far above 100 km, molecular viscosity and thermal conductivity become so large that they suppress turbulence and the related mixing. In this region, the Reynolds number of the flow is small but sufficiently large for the development of turbulence; nevertheless, molecular viscosity and thermal conductivity hold full sway and grow exponentially with height.

The photochemistry of the upper atmosphere may play some role in wave dynamics. This occurs by wave generation through absorption of solar radiation and the heat release associated with it. Wave-associated density and temperature changes modify the photochemistry and produce certain phase-related heat release and absorption; if this heat release is of the correct phase, then instability results and there may be wave growth. Heat release of the opposite phase may work to suppress wave amplitudes. This is known to happen in the lower atmosphere as the result of water-vapor condensation; the effects of analogous photochemical reactions in the upper atmosphere have been only cursorily treated. Much more work needs to be done in this research area, which requires a synthesis of dynamics and photochemistry. Diffusive separation of molecular constituents above 100 km also produces wave energy loss, because the different constituents respond to the impressed wave motion in

different ways. Thus the different species tend to move with different velocities, and wave energy loss results from collisions between molecules of the different species.

A final factor complicating the propagation of Rossby-planetary waves, tides, and gravity waves in the upper atmosphere is the increasing concentration of ionized particles relative to neutral particles with increasing height. The relevant quantity here is the neutral–ion collision frequency—the frequency with which neutrals experience collisions with ions. In the E region, this collision frequency is of the order of 1 day^{-1}, so that for motions of Rossby-planetary wave or tidal period, the effects of ion drag are comparable with inertial effects here. In the F region, near the ionization density maximum, the collision frequency rises to about one collision each 30 min. Thus here, even waves of gravity-wave period experience significant ion drag. In addition, the introduction of charged particles and the earth's magnetic field into the equations of motion introduces new modes of oscillation—mixed hydromagnetic modes that couple with the incident wave energy.

8.4 WAVE SOURCES

In the previous sections, we took for granted the existence of the waves of interest here and discussed the basic aspects of their physics and propagation and modification of this propagation by various complicating factors. However, for waves to exist, they must be generated, and in this section we treat the manner of their generation.

Rossby-planetary waves are primarily generated by three mechanisms: instability of the mean zonal flow, topographical forcing, and differential heating. The relevant instabilities are of two types: the barotropic instability, which is analogous to the shear-flow instability of a homogeneous fluid, and baroclinic instability, which results in a statically stably stratified shear flow in the presence of a north–south temperature gradient. For a further description of these instabilities, the reader is referred to the introductory text by Holton (1972). Planetary waves generated by such instabilities have relatively short wavelengths of several thousand kilometers. The topographical forcing results from the vertical velocity component imposed on the zonal airflow over the continents. Similarly, the differential heating arises from the difference in the heat input to the atmosphere encountered over the continents and over the oceans. Both the topographical forcing and the differential heating result in wavelengths of the order of half a global circumference at 45° latitude, i.e., about 2×10^4 km.

The tides, as their name implies, are generated by lunar and solar gravitational forcing and by solar heating. The dispersion equation shown in Table 8.3 represents free tidal oscillations; in analyses of the tidal forcing, inhomogeneous terms appear in the vertical structure equation, and the response of the atmosphere to these is

determined. As mentioned in the previous section, it is found that the predominant forcing is thermal; the major diurnal thermal mode is trapped, while that of the semidiurnal mode is propagating.

Sources of gravity-wave excitation are many and varied. Gravity waves, like the Rossby-planetary wave, may be generated by the shearing instability of larger-scale flows for which the Richardson number drops below the critical value of ¼. This is probably the single most important source mechanism for such wave motions, since wave generation by shear instability is the process effective in limiting the intensification of large-scale circulations. The waves may also be generated in similar ways by the airflow over irregular and unevenly heated topography. They may also be generated by photochemical destabilization. In addition, gravity waves are generated in the auroral zone by the heat and momentum input associated with variations in energetic particle precipitation. We mentioned in the previous section that many waves owe their existence to wave–wave interactions, involving either other gravity-wave modes or the interaction of tidal modes. The distinction between gravity waves and turbulence may be artificial (the latter representing a highly nonlinear, interactive, and broad spectrum of the former), but to the extent that the distinction has some value, gravity waves may also be considered to be generated by turbulent fields. The process is analogous to that of the generation of acoustic waves by turbulent fields. However, there is a considerable difference in the efficiency of the two processes. Calculations made of acoustic-wave generation by low-Mach-number turbulence that assume that the turbulence is unaffected by the wave generation confirm that the generation is relatively weak and inefficient, while similar calculations of gravity-wave generation by turbulent fields show that the power output per unit volume is infinite. This shows that the original assumption that the turbulence is unaffected by the wave generation is invalid but follows physically from the fact that acoustic waves, unlike the turbulent eddies, are longitudinal motions propagating with the speed of sound, while the gravity waves are qualitatively similar to the turbulence in that they are rotational and may have arbitrarily small phase speeds. Finally, gravity waves may be launched by penetrative convection of air parcels from convectively unstable regions of the atmosphere (those for which $N^2 < 0$) into stable regions.

It should be recognized in reviewing this catalog of sources that from the standpoint of those of us interested in the upper atmosphere, they can be cataloged in another way, i.e., as arising locally or in the lower atmosphere. Much has been made of this fact, but it cannot be stressed too often. All else being equal, atmospheric wave sources below the height of observation will tend to dominate because of the decrease of atmospheric density with height and the concomitant increase in wave amplitude. For the three wave types considered here, phase propagation and energy propagation have oppositely directed vertical components, so that waves that are observed to have a downward phase propagation are associated with upward energy propagation. Such waves do indeed dominate the observations of every level in the upper atmosphere.

8.5 WAVE DYNAMICS

The study of atmospheric wave physics has progressed substantially beyond the point of a mere analysis of wave propagation characteristics to the study of wave dynamics and its role in determining the atmospheric motion field (and indeed atmospheric structure). At issue is the hand-over of energy and momentum from the mean atmospheric flow to the waves during wave generation, the transport of this energy and momentum by the waves as they propagate, and the return of that energy and momentum to the mean flow accompanying the wave damping. Wave-dynamical processes are important even in the troposphere, but they assume additional importance in the upper atmosphere because of the decrease in atmospheric density with height and the concomitant increase in wave amplitudes required by energy conservation. If we consider the upward propagation of energy from a Rossby-planetary wave whose amplitude at the tropopause is ~10 m sec⁻¹, at the 100-km level the corresponding wave amplitude would be ~10⁴ m sec⁻¹ if the wave propagates its energy vertically. This is a factor of 10 greater than the molecular thermal velocity at these heights and would result in thermospheric temperature of the order of 10⁵ K, some two orders of magnitude greater than that observed. The earth's gravitational field would be too weak to prevent a rapid boiloff of such a hot atmosphere. Explaining why this process does not occur is therefore a matter of considerable interest. Research on this subject reveals that Rossby-planetary wave energy is prevented from reaching the thermosphere either by the effects of atmospheric zonal winds, which, depending on the season (there is a seasonal wind reversal), trap the wave energy by causing the waves to encounter a critical level or levels below 50 km (Charney and Drazin, 1961) or by the effects of radiative damping (Dickinson, 1969). Even at these lower altitudes the effect of the waves on atmospheric temperatures and mean flows is substantial. Stratospheric warmings may have their origin in dynamic processes of this sort.

In contrast to the Rossby-planetary waves, the tides are only slightly affected by atmospheric temperature and wind structure and are thus efficient in propagating their energy vertically upward. These have amplitudes negligible compared with the planetary waves at the earth's surface, but at thermospheric heights the tidal energy flux is nevertheless substantial. Lindzen and Blake (1970) estimate that tidal heating of the upper atmosphere is sufficient by itself to maintain the temperature of the thermosphere at some 400 K; this is about one third of the observed value and suggests that this dynamical heat flux is the same order of magnitude as the solar EUV heat flux

responsible for the strong day–night thermospheric temperature variation.

Similarly, gravity waves provide substantial heat input into the upper atmosphere. Hines (the relevant papers are contained in his 1974 volume) estimated that gravity waves should provide heat inputs comparable to the tidal flux, but the exact contribution is difficult to assess because of uncertainties about the variability of this flux with latitude, season, time of day, and other parameters. Hines went so far as to suggest that gravity-wave heating might account for the observed warm temperature of the polar wintertime mesopause, an explanation that remains intriguing to this day.

Associated with the large wave-energy fluxes just described there are substantial momentum fluxes as well. Hines has estimated that the tidal fluxes to the upper atmosphere should be so large as to provide accelerations of the mean zonal wind of the order of 20 m sec^{-1} day^{-1}. The gravity waves, if all propagating in the azimuthal direction (an admittedly unlikely assumption), should lead to even larger local thermospheric accelerations of ~70 m sec^{-1} h^{-1}. Fluxes of this magnitude could account for the observed upper-thermosphere superrotation and certain other anomalies following magnetic substorms.

The quasi-biennial oscillation, a unique feature of the tropical stratosphere, is now believed to be the result of the interaction between gravity waves and the semi-annual oscillation. The former encounter critical levels created by the latter and deposit their momentum and energy there, changing the wind profile in such a way as to lower the height of the critical level at subsequent times. It might be noted that within a few degrees of the equator, gravity waves may have periods of the order of days before Coriolis effects become important. Waves of such long period are internal within a narrow equatorial region; outside that latitude belt they are trapped (by the increased value of the Coriolis parameter). It is these long waves, termed Kelvin and Yanai waves depending on their symmetry properties, that are relevant to the quasi-biennial oscillation. Wallace (1973) reviews this subject and gives pertinent references.

The major wave types discussed here also produce important dynamical effects in the ionized upper atmosphere. These range from tidal driving of the so-called Sq current system producing magnetic fluctuations observed at ground level to gravity-wave production of traveling ionospheric disturbances and ionospheric storms. These topics are considered in other chapters.

8.6 THE UPPER ATMOSPHERE AS A FLUID-DYNAMICS LABORATORY

The upper atmosphere is an interesting astrogeophysical fluid-dynamics laboratory, for several reasons. First and foremost, it exhibits the full range of wave phenomena we wish to study for astrogeophysical application, including the Rossby-planetary waves, tides, and gravity waves, which we have considered in detail, as well as a number of wave types that for reasons of space we could not discuss—inertial oscillations and acoustic waves being among them. The earth's upper atmosphere mirrors all the observed tropospheric wave motions but usually with greater amplitudes so that they are easier to see. Wave–wave interactions and wave-associated instabilities mirror analogous processes in the oceans. The earth's thermosphere is truly a "geocorona" in the sense that the dynamical heating provided by the tides and gravity waves provides a close analog to the heating of the solar corona by wave processes. The density stratification of the upper atmosphere allows us to study these phenomena under a wide range of conditions from small-amplitude to highly nonlinear, from inviscid and turbulent to laminar, and from electrically neutral to ionized. And it permits us to study these phenomena on a geophysical scale free from the severe compromises in scaling imposed by laboratory models.

In addition, the upper atmosphere facilitates the study of fluid dynamics by providing tracers of the neutral dynamics. These range from constituents with unique optical properties such as ozone, to airflow chemistry for revealing gravity-wave motions, to ionization for revealing the motions of the neutral atmosphere on all scales.

REFERENCES

Batchelor, G. K. (1967). *An Introduction to Fluid Dynamics*, Cambridge U. Press, New York.

Charney, J. G., and P. G. Drazin (1961). Propagation of planetary-scale disturbances from the lower and the upper atmosphere, *J. Geophys. Res. 66*, 83.

Dickinson, R. E. (1969). Vertical propagation of planetary Rossby waves through an atmospheric with Newtonian cooling, *J. Geophys. Res. 74*, 929.

Gossard, E. E., and W. H. Hooke (1975). *Waves in the Atmosphere*, Elsevier, New York.

Hines, C. O. (1960). Internal atmospheric gravity waves at ionospheric heights, *Can. J. Phys. 38*, 1441.

Hines, C. O., *et al.* (1974). *The Upper Atmosphere in Motion*, American Geophysical Union, Washington, D.C.

Holton, J. R. (1972). *An Introduction to Dynamic Meteorology*, Academic Press, New York.

Lindzen, R. S., and D. Blake (1970). Mean heating of the thermosphere by tides, *J. Geophys. Res. 75*, 6868.

Lindzen, R. S., and S. Chapman (1970). *Atmospheric Tides*, D. Reidel, Dordrecht, Holland.

Wallace, J. M. (1973). General circulation of the tropical lower stratosphere, *Rev. Geophys. Space Phys. 11*, 191.

Witt, G. (1962). Height structure, and displacements of noctilucent clouds, *Tellus 14*, 1.

Infrasound from convective storms. III. Propagation to the ionosphere

R. Michael Jones and T. M. Georges

Wave Propagation Laboratory, NOAA Environmental Research Laboratories, Boulder, Colorado 80302
(Received 23 July 1975; revised 1 December 1975)

We model mathematically the spectral features of infrasound observed in the ionosphere and believed to be radiated by severe thunderstorms. We explain the dominant 2–5-min wave period as an effect of atmospheric filtering; shorter periods are excessively attenuated by absorption in transit to the ionosphere, and longer periods are attenuated in portions of the atmosphere where the waves are evanescent because their frequencies are below the acoustic cutoff. An observed spectral "fine structure" within the 2–5-min band is explained in terms of resonant interactions between the waves and the atmospheric temperature structure. Accurate quantitative modeling of all these details of the storm-to-ionosphere transmission coefficient requires numerical integration of the acoustic-gravity wave equation, including the effects of ground reflection, absorption, and partial reflections in the atmosphere.

Subject Classification: [43]28.30.

INTRODUCTION

This is one of a series of papers about the ultra-low-frequency acoustic energy that some convective storms radiate. Necessary background information is given in Pt. I,[1] which summarized what was then known about two different manifestations of the waves: one in the radio soundings of the ionospheric F region; the other in recordings of microbarometric pressure fluctuations at the earth's surface. This paper attacks some problems that the ionospheric effects pose.

I. THE PROBLEM

The two different wave effects display remarkably similar phenomenologies, and indeed have been observed concurrently during some storms, so it is tempting to suggest that a single generating mechanism is responsible for both effects. Yet the waves observed at the surface and those observed in the ionosphere differ markedly in one respect, their spectral content. The pressure waves observed on the ground have periods that usually fall between about 10 and 40 sec and may be either broad- or narrow band (the distinction depending somewhat on the length of the observation interval), whereas the ionospheric waves always have periods between about 2 and 5 min, and analog records of the oscillations present a nearly monochromatic appearance. Why do the ionospheric waves exhibit this peculiar narrow-band characteristic?

Another aspect of the ionospheric waves was uncovered by Davies and Jones,[2] who found that their frequency spectra consistently reveal a fine structure, whose principal features are response peaks at 3.5- and 4.5-min wave periods (Fig. 1). What is the physical explanation of these peaks?

At least two competing explanations for these observations have been advanced: Georges[3] has argued that a narrow-band acoustic "window" to the ionosphere exists between wave periods of about 2 and 5 min, bounded by increased absorption at higher frequencies and acoustic-cutoff effects at lower frequencies. Later, Chimonas and Peltier[4] recognized that the observed

peaks in the fine structure occur at the frequencies of modal resonances revealed by theoretical analyses of acoustic waveguide propagation in the atmosphere's temperature structure (e.g., Francis, Ref. 5). This would permit a single broadband generating mechanism to explain both the ionospheric and surface observations; the spectral differences could be caused entirely by atmospheric filtering and some other observational biases.

Moo and Pierce[6] have argued, on the other hand, that the frequency of the ionospheric response is characteristic of buoyancy oscillations and nonlinear frequency doubling at the source. This would seem to require a separate mechanism to explain the surface infrasound observations.

The difference is important to those studying severe-storm dynamics; if storms tend to radiate only in a certain narrow frequency band, very special (and un-
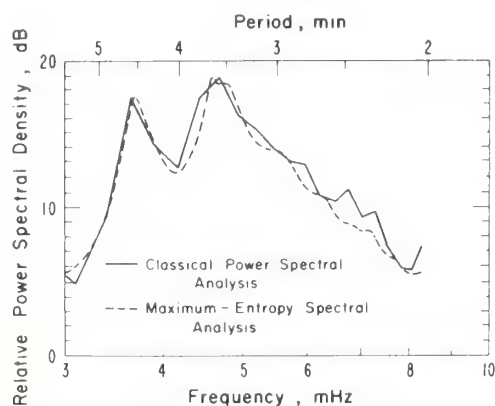
FIG. 1. Composite power-spectral analysis (average of 18 individual spectra) of a total of 54 h of observations of severe-storm ionospheric waves over six different sounding paths. We reanalyzed all the data scaled by Davies and Jones[2] using both classical power spectral analysis[28] and the maximum-entropy spectral-analysis technique.[29,30] Individual spectra obtained with the two techniques sometimes differed substantially in the sharpness of the major features, but the average spectra are quite similar.

known) dynamical processes must be occurring. To decide between these two explanations, we need to compare in further detail the predictions of each model with the observed ionospheric response. In this paper, we formulate a quantitative model of the atmospheric-filtering process and compare its predictions with the spectra of the ionospheric response measured by Davies and Jones.[2] If atmospheric filtering is to be a viable model for the observed ionospheric spectra, we must show that the rapid low-frequency falloff of the ionospheric response is quantitatively explained by decreased tunneling of lower-frequency acoustic waves through atmospheric layers where propagation is evanescent; we also need to match the observed high-frequency falloff of the response with the calculated increase in absorption with frequency. Further, to explain the observed fine-structure peaks in terms of modal resonances, we have to verify that the modes are sufficiently leaky to permit some energy to reach the ionosphere, while not being leaky enough to extinguish the resonances. We believe that our results do so and thus strengthen the case for the atmospheric-filtering explanation.

II. APPROACH

Our approach to modeling the ionospheric window is to try first the simplest method likely to reproduce the gross features of the window, and then to successively add whatever refinements we need to explain as many of the waves' observed spectral features as possible. We first tried a simple WKB method, which means just integrating the acoustic-gravity-wave attenuation coefficient, as a function of frequency, between the source (which we assume to be at 10 km height) and observation heights in the ionosphere. The WKB method does partially explain the gross shape and spectral location of the window, but it does not reproduce the observed fine structure. To do so, we needed to account for partial reflections and resonant interactions caused by the atmosphere's temperature structure, and to do that, we had to resort to direct numerical integration of a form of the acoustic-gravity-wave equation that includes dissipation.

This "full-wave" approach raises several difficult questions, specifically: (a) What are the appropriate upper and lower boundary conditions? (b) How can we handle the infinite coupling of upgoing and downgoing waves at reflection levels? (c) How can we unambiguously separate the total waves into upgoing and downgoing components in an inhomogeneous medium? A substantial part of this paper explains how we answered these questions.

To model the changes in window shape from day to night, we needed a model atmosphere whose acoustic absorbing and amplifying properties varied correctly as we changed from one model to another. Therefore, we constructed a model for continuous height profiles (not isothermal layers) of all the relevant atmospheric state variables, which can be derived from a single height profile (pressure scale height), assuming horizontal stratification and hydrostatic equilibrium (Appendix A).

We also formulated a version of the acoustic-gravity-wave dispersion relation that includes both viscous and thermal dissipation as well as the effects of temperature gradients on the definition of the Brunt–Väisälä frequency. Although our formulas and method apply to both vertical and oblique propagation between the troposphere and the ionosphere, all the results presented here are for vertical ray paths ($k_x = 0$). We found that the major effect of introducing oblique ray paths is to change the geometrical focusing. We examine this effect in Sec. III C.

A. WKB approach

For our purposes, it is convenient to model the atmosphere as a medium whose acoustic properties vary only in the vertical (z) direction. (It seems unlikely that horizontal gradients cause any of the effects we seek to explain.) The details of this model are given in Appendix A. The propagation of waves in such a medium can be described by a wave equation of the form

$$\frac{\partial^2 \theta}{\partial z^2} + q^2 \theta = 0 , \tag{1}$$

where θ is some wave-amplitude variable. The quantity q represents the z component of the (generally complex) vector wave number; the relation between q, the other wave variables and the atmosphere's properties is called a dispersion relation.

The WKB method provides approximate solutions of the form

$$\theta \sim q^{-1/2} \exp \pm i \int q \, dz , \tag{2}$$

which are valid (roughly speaking) to the extent that changes in $q(z)$ are small (compared with $|q|$) in one wavelength. (See, for example, Einaudi and Hines[7] for more explicit validity conditions.) The two signs are associated with upgoing and downgoing waves. This means that we can estimate the ground-to-ionosphere transmission coefficient merely by performing the integration in Eq. (2), after appropriately defining θ and $q(z)$ for the acoustic-gravity waves having frequencies near our hypothetical ionospheric window.

Einaudi and Hines[7] have already examined in detail the applicability of the WKB method to acoustic-gravity-wave propagation in a nonisothermal atmosphere. They found that the value of q to be used in a WKB approximation, such as Eq. (2), depends on which of the several possible wave variables is identified with θ. (In an isothermal atmosphere, all the q's reduce to the same value, called q_0.) But they also concluded that the differences among the various nonisothermal q's are insignificant; that is, the different q's yield solutions that differ by less than the errors attributable to the WKB approximation itself. However, the differences between the nonisothermal q's and q_0 can sometimes be significant; Einaudi and Hines therefore recommend the use of a particular form of q called q_M given by

$$q_M^2 = q_0^2 + \frac{g k_x^2}{H \omega^2} \frac{dH}{dz} \tag{3}$$

in the absence of dissipation and winds. The isothermal q_0 is the same as that given by Hines[8]:

$$q_0^2 = (\omega^2 - \omega_a^2)/C^2 + k_x^2(\omega_g^2/\omega^2 - 1) . \tag{4}$$

The remaining symbols are defined as follows: ω is the angular wave frequency, k_x is the horizontal wave number, C^2 is the square of the classical sound speed in air and equals $\gamma g H$, where γ is the usual specific-heat ratio, g is the acceleration of gravity, and H is the pressure scale height of the atmosphere; ω_a is the acoustic-cutoff frequency and equals $\gamma g/2C$, and ω_g is the so-called "isothermal" Brunt–Väisälä frequency and equals $(\gamma - 1)^{1/2}g/C$. It follows that q_M differs from q_0 only in that ω_g in Eq. (4) is replaced by a quantity ω_B defined by

$$\omega_B^2 = \omega_g^2 \left(1 + \frac{\gamma}{\gamma - 1} \frac{dH}{dz}\right) , \tag{5}$$

where the term in parentheses is sometimes called the "gradient correction" to the Brunt–Väisälä frequency. Others have contemplated a similar correction for the acoustic-cutoff frequency ω_a, but Einaudi and Hines assert that such a correction is not meaningful.

For our computations we used the dependent variable ϕ defined by

$$\phi = (\mathrm{div}\,\vec{U}) \exp - \int_0^z \frac{dz}{2H} , \tag{6}$$

where $\vec{U}$ is the wave-associated air velocity, and we changed the independent (height) variable to ζ, such that

$$d\zeta = \frac{dz}{H} . \tag{7}$$

Einaudi and Hines[7] showed that the wave equation for ϕ is then

$$\frac{\partial^2 \phi}{\partial \zeta^2} + (q_M^2 H^2)\phi = 0 . \tag{8}$$

We used the wave variable ϕ in our calculations because its q (which is q_M) is much easier to work with than the q's associated with other wave variables; also, the change of independent variable required to get the wave equation in the form of Eq. (1) is less involved.[7]

The price we pay for using the variable ϕ is that, after calculating it, we have to convert it to U_g, the wave variable associated with the observed Doppler effects.[1] We do this with the "polarization relation"

$$U_g = \frac{\gamma g}{\omega^2} \frac{(g k_x^2 H/\omega^2 - \frac{1}{2})\phi + d\phi/d\zeta}{g^2 k_x^2/\omega^4 - 1} e^{\zeta/2} , \tag{9}$$

which has been derived from Eqs. (20) and (21) of Pitteway and Hines.[9]

Because we think that an essential feature of the ionospheric window is caused by acoustic absorption at the higher frequencies, we cannot use the dissipationless form [Eq. (3)] of the dispersion relation, but have to use a form that accounts for losses. Both Francis[5] and Midgley and Liemohn[10] have derived such a relation. We used the form given in the Appendix of Francis's paper, but we left out the terms related to iondrag forces, because they are unimportant at acoustic frequencies. We call the wave number obtained from Francis's dispersion relation, including losses, q_L. However, when the dissipative terms are removed from q_L, it reduces, not to q_M, but to q_0, the isothermal form. (This is because Francis approximates the real atmosphere with isothermal layers; he accounts for the effects of gradients in the boundary conditions at layer interfaces.) But we want a form of q that includes both the gradient correction and dissipative effects.

Instead of rigorously deriving a dispersion relation that includes both effects (which would lead to a sixth-order polynomial equation in q), we defined a new wavenumber,

$$Q^2 = (q_L^2 + q_M^2 - q_0^2)H^2 , \tag{10}$$

which, in effect, simply adds the gradient correction to q_L. (We multiply by H^2 to nondimensionalize for later convenience.) Therefore, the final form of the wave equation we use is

$$\frac{\partial^2 \phi}{\partial \zeta^2} + Q^2 \phi = 0 , \tag{11}$$

where Q^2 is as defined in Eq. (10). The WKB solution of (11) is

$$\frac{\phi(\zeta_2)}{\phi(\zeta_1)} = \left(\frac{Q(\zeta_1)}{Q(\zeta_2)}\right)^{1/2} \exp \int_{\zeta_1}^{\zeta_2} \pm iQ \, d\zeta . \tag{12}$$

Although we did not rigorously justify this ad hoc approach, we found that, in application to acoustic waves in the atmosphere, both the temperature-gradient and the dissipative effects are never simultaneously important. In the thermosphere (above 150 km) where dissipation is important but the gradient correction is not, our dispersion equation reduces to Francis's form; below the thermosphere, where the gradient correction is needed but dissipation is negligible, it reduces to the nondissipative form given by Einaudi and Hines. In the case of vertical propagation, however, the gradient correction in Eq. (3) disappears, and Francis's dissipative dispersion relation is correct at all heights.

Note that Eq. (9) is the nondissipative polarization relation between ϕ and U_g. It does include the gradient correction, however. Derivation of a polarization relation that includes both effects is very involved, so we used Eq. (9) throughout the atmosphere. We checked its accuracy at ionospheric heights by comparing it with a form that includes dissipation but not gradients. The differences were negligible everywhere except at the greatest heights and for the highest frequencies, where we found errors of about 1 dB.

Yanowitch[11] has pointed out that the gradient of kinematic viscosity at thermospheric heights can cause significant partial reflection for some long waves, and that for these waves, a term in the gradient of kinematic viscosity should be included in the dispersion relation. However, we did not include such a term, because Yanowitch's estimate of the reflection coefficient, $\exp(-qH)$, predicts significant reflections only for waves much longer than the ones of interest here.

In addition to damping the acoustic-gravity waves, the dissipative terms in the equations of motion give rise to two more kinds of waves called heat conduction and viscosity waves. These dissipative waves appear as the additional solutions to the cubic equation in q^2 when dissipation is included. In practice, we found that we could identify the smallest root with the acoustic solution.

We investigated the possibility of coupling between the acoustic and dissipative waves by searching for equal roots in the complex height plane. We never found a situation in which an acoustic root was nearly equal to one of the other two roots. Thus, as others have found, coupling is evidently not important for the cases we considered, and we didn't pursue it further.

In Sec. III B we investigate the properties of the ionospheric window that the WKB method predicts. We know in advance that, for the waves we are studying, the WKB validity condition is sometimes met, and sometimes it is not, depending on wave frequency. Specifically, we expect WKB solutions to be accurate for wave periods of about 4 min and less, and to break down for longer periods, for which there are levels in the atmosphere where q approaches zero. But to find out exactly how accurate the WKB solutions are, and for what frequencies, we need to compare them with exact solutions of Eq. (1). We make this comparison in Sec. III D 2.

B. Outline of full-wave approach

The WKB method predicts some of the observed properties of the ionospheric wave spectra, but, because the method neglects coupling between upgoing and downgoing waves, it cannot be used to look for resonances caused by multiple partial reflections within the atmospheric temperature structure. To include these effects, we have to solve the wave equation numerically for the total wave field in the real atmosphere. The easiest way to do this is to write Eq. (11) as two coupled first-order equations instead of one second-order equation.

There are many ways to separate Eq. (11) into two first-order equations; Eqs. (20) and (21) of Pitteway and Hines[9] are examples that use wave-associated air velocity and divergence as dependent variables. But we want to compare the full-wave solution with the WKB calculations (to check the regions of validity of the latter), and we also need to match solutions with upgoing and downgoing radiation at the source; therefore, we want solutions that correctly distinguish between upgoing and downgoing waves. Although it is not possible, in general, to identify unambiguously purely upgoing and downgoing components in an inhomogeneous medium, Budden (Ref. 12, p. 137) shows that useful approximations are given by

$$\phi_1' = (-iQ - Q'/2Q)\phi_1 + (Q'/2Q)\phi_2 \qquad (13)$$

and

$$\phi_2' = (iQ - Q'/2Q)\phi_2 + (Q'/2Q)\phi_1 , \qquad (14)$$

where primes indicate derivatives with respect to ζ, and the total field $\phi = \phi_1 + \phi_2$, the sum of the upgoing and downgoing waves. The last terms in Eqs. (13) and (14) represent coupling between ϕ_1 and ϕ_2; in the absence of gradients of Q, ϕ_1 and ϕ_2 reduce to the upgoing and downgoing WKB solutions, thus retaining the insight that the WKB method provides.

Unfortunately, this method of separating the total wave into upgoing and downgoing components fails near "turning points," that is, where $Q^2 = 0$. There the coupling becomes infinite. This presented two problems. The first was simply the computational awkwardness of dividing by zero. We fixed this by merely adding to Q^2 a constant imaginary part that is small enough to be physically insignificant but large enough to allow the integration to proceed [see Fig. 2(b)].
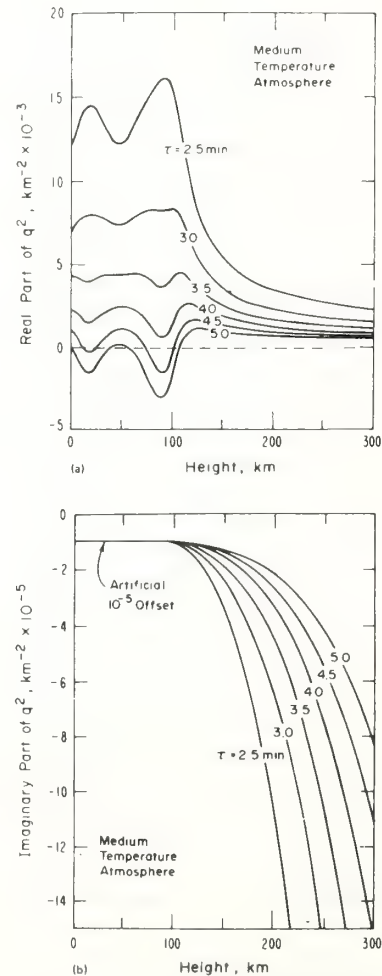
FIG. 2. (a) Plots of the real part of $q^2(z)$ for six wave frequencies, and $k_x = 0$, showing "inverted refraction" at the lowest frequencies. Where $q^2 < 0$, the wave is evanescent. (b) Plots of the imaginary part of $q^2(z)$ for six wave frequencies, and $k_x = 0$, showing attenuation caused by viscous damping and thermal conduction at thermospheric heights. A constant (-10^{-5}) was added to facilitate numerical integration, but is physically insignificant.

The second difficulty arose because turning points occur both near the ground and near the source height (10 km) within the range of frequencies we are interested in. In these cases, ϕ_1 and ϕ_2 do not accurately represent the purely upgoing and downgoing waves that have to be matched with upward and downward source radiation, and are used to relate incident to ground-reflected waves. The solution we chose was to identify the upgoing and downgoing waves with new wave variables, ψ_1 and ψ_2, which are linear combinations of ϕ_1 and ϕ_2 that are forced to behave like Airy functions in the vicinity of turning points. Airy functions are exact solutions of the wave equation [Eq. (11)] in regions where Q^2 varies linearly with ζ, and furthermore, they are the only uncoupled solutions (cf. Budden, Ref. 12). Far from turning points, where the WKB solutions accurately represent upgoing and downgoing waves, the ψ's reduce to the ϕ's, but near turning points, the Airy-function representation is a higher-order approximation to the partition into upgoing and downgoing components. We calculate the ψ's after we numerically integrate Eqs. (13) and (14) for the ϕ's. (See Appendix B for further details.)

1. Solving the wave equation

The general solution of the wave equation, Eq. (11), is any linear combination of two independent particular solutions. The two arbitrary constants in our case are determined by the upper and lower boundary conditions We obtained two particular solutions by numerically integrating the equivalent first-order equations, Eqs. (14a) and (14b), first by specifying an upper boundary condition and integrating downward, then by specifying a lower boundary condition and integrating upward. The two solutions were then combined so that the total field meets both correct boundary conditions, and so that an appropriate discontinuity exists at the source height to represent an energy input.

The boundary conditions for our two particular solutions are arbitrary and need not be the correct boundary conditions for the total wave. In particular, we chose a lower boundary condition one would use if the ground were absent; the effects of the ground were introduced after the numerical integration on combining the two particular solutions. This was a convenient way to isolate the effects of ground reflection.

The integrations calculate ϕ_1 and ϕ_2 from Eqs. (13) and (14) as functions of height, whose sum is repartitioned to form ψ_1 and ψ_2, the Airy-function representations of upgoing and downgoing components at each height. This repartitioning was necessary because we were not able to find a way to carry out the integrations directly in ψ. We call the ψ's that were computed starting with the upper boundary condition ψ_{1U} and ψ_{2U}; those computed starting with the lower boundary condition are called ψ_{1L} and ψ_{2L}. Subscripts 1 and 2 indicate upgoing and downgoing waves, respectively. The upper and lower boundary conditions we used are described in the following two subsections.

2. Boundary condition at the top of the atmosphere

Because we cannot extend our integration indefinitely in height, we have to specify a boundary condition for our wave variable at some height in the atmosphere. The boundary condition we chose was that, at a height of 300 km, only an upgoing wave exists. This is true to the extent that there are no wave reflections above 300 km, that is, to the extent that the atmosphere is isothermal above that height. The problem is that the atmosphere is not isothermal, and we cannot uniquely define upgoing and downgoing waves in a nonisothermal atmosphere. We have several choices. If we associate ϕ_1 and ϕ_2 with the upgoing and downgoing waves, the boundary condition is just

$$\phi_2(300) = 0 . \tag{15}$$

A slight improvement results from making the total wave, $\phi_1 + \phi_2$, look like an upgoing WKB solution in the vicinity of the upper boundary. The method we finally used was again to identify the upgoing and downgoing waves with the uncoupled Airy-function solutions, ψ_1 and ψ_2 (see Appendix B), and set

$$\psi_{2U}(300) = 0 . \tag{16}$$

This is equivalent to assuming that $Q^2(\zeta)$ above 300 km is just a linear extrapolation with a gradient equal to its value at 300 km.

Because all of these conditions are identical for the case of an isothermal atmosphere in the vicinity of the upper boundary, and because our thermospheric models are nearly isothermal, all three methods give nearly the same results for ψ_{1U} and ψ_{2U}. We also tried using 600 km as the upper boundary and found negligible differences in the results.

3. Boundary condition at the ground

To calculate ψ_{1L} and ψ_{2L}, we chose a lower boundary condition identical to the upper one; that is, at the ground level only a downgoing wave exists. We therefore used the same Airy-function representation of the field that we did at the upper boundary, and set

$$\psi_{1L}(0) = 0 . \tag{17}$$

This is not the correct boundary condition for the *total* field at the ground; it is the boundary condition we would use if the ground did not exist and the atmosphere extended (with the same gradient of Q^2) below ground level. We did this to isolate the effects of the ground-reflection process. To account correctly for the presence of the ground, we defined a ground reflection coefficient for ϕ, which we use in combining the ψ_U and ψ_L solutions to get the total field. We derived this ground-reflection coefficient as follows:

The boundary condition for U_z is well known as

$$U_z(0) = 0 . \tag{18}$$

From Eq. (9), therefore, the boundary condition for ϕ is

$$(gk_x^2H/\omega^2 - \tfrac{1}{2})(\phi_1 + \phi_2) + \phi_1' + \phi_2' = 0 , \tag{19}$$

where primes again indicate derivatives with respect to

ζ. The ground-reflection coefficient for ϕ is then

$$R \equiv \frac{\phi_1(0)}{\phi_2(0)} = - \frac{\frac{1}{2} - gk_x^2 H/\omega^2 - \phi_2'(0)/\phi_2(0)}{\frac{1}{2} - gk_x^2 H/\omega^2 - \phi_1'(0)/\phi_1(0)} . \qquad (20)$$

The functions ϕ_1'/ϕ_1 and ϕ_2'/ϕ_2 can be calculated in several ways, depending on the degree of approximation employed. For example, if the medium above the ground can be assumed homogeneous, these terms become simply $\pm iQ$. But because gradients (and, for some frequencies, turning points) exist near the ground, we again used the Airy-function representations, ψ_1 and ψ_2, from which we calculated ψ_1'/ψ_1 and ψ_2'/ψ_2 for use in Eq. (20). [See Eqs. (B5) and (B6) in Appendix B.]

4. Calculating the total source-to-ionosphere transfer function

To compute the atmospheric-filtering effects on waves reaching the ionosphere from an elevated source, we have to combine our two particular solutions in a way that accounts not only for the direct upward source-to-ionosphere path, but also accounts for the path with an intermediate ground reflection. In addition, since we know that the atmosphere's inhomogeneity gives rise to continuous partial reflections (that is, coupling between up- and downgoing waves) at practically all heights, we have to allow also for all the possible combinations and orders of internal reflections within the atmosphere, including the ground. Indeed, this is how we expect to determine whether modal resonances could explain the observed fine structure in the ionospheric wave spectra. Our final formula for the field strength in the ionosphere not only accounts for all of these effects, but makes it possible to examine separately the relative importance of each. Following is a summary of its development.

From our integration that begins with the upper boundary condition [that is, $\psi_{2U}(300) = 0$], we obtain the following transfer functions:

$$T_1 = \psi_{1U}(z)/\psi_{1U}(10) , \qquad (21)$$

$$T_2 = \psi_{2U}(10)/\psi_{1U}(10) , \qquad (22)$$

$$T_3 = \psi_{1U}(z)/\psi_{1U}(0) , \qquad (23)$$

$$T_4 = \psi_{2U}(10)/\psi_{1U}(0) , \qquad (24)$$

where the arguments indicate the height in kilometers, and z is the ionospheric height for which we want the total transfer function.

From our integration that begins with the lower boundary condition [that is, $\psi_{1L}(0) = 0$ in the absence of the ground], we obtain the following transfer functions:

$$T_5 = \psi_{1L}(10)/\psi_{2L}(10) , \qquad (25)$$

$$T_6 = \psi_{2L}(0)/\psi_{2L}(10) . \qquad (26)$$

If we denote the total upgoing wave at the ionosphere by ψ_U^I, and call the upward and downward radiation from the source ψ_U^s and ψ_D^s, we can solve for ψ_U^I. Drawing a picture of these transfer functions helps in visualization.

The result is

$$\psi_U^I(z) = \frac{\psi_U^s T_1 + \psi_D^s (RT_6 T_3 + T_1 T_5)}{1 - (RT_6 T_4 + T_2 T_5)} . \qquad (27)$$

The first term in the numerator represents the contribution of the direct wave between the source and the ionosphere. The second term in the numerator represents the energy reaching the ionosphere by way of ground reflection (first term in parentheses) and by way of partial reflections in the lower atmosphere between the source and the ground (second term in parentheses).

The denominator reveals the possibility of resonance effects and we call its inverse the "resonance factor." It fully accounts for all phase reinforcement caused by multiple reflections involving the ground (first term in parentheses) and multiple partial reflections within the atmospheric temperature structure (second term in parentheses). These resonances are equivalent to the waveguide modes found by others. We will show that this resonance factor is essentially responsible for the fine structure of the ionospheric response spectrum.

By adjusting the relative phase and amplitude of ψ_U^s compared with ψ_D^s, we can examine the roles of the direct and ground-reflected waves as well as the sensitivity to various hypothetical radiation mechanisms (monopole, dipole, etc.). We show these results in Sec. III D 3.

III. RESULTS: CALCULATIONS OF WINDOW SHAPE

Our many calculations of the window shape showed the changes caused by varying each of many different atmospheric and wave parameters. Although each effect is interesting, there are so many variables that we confine our attention to just a few effects that are related to the changing conditions under which the ionospheric waves are observed; we show only how the window changes with respect to (a) observing height in the ionosphere, (b) thermospheric temperature changes resembling the transition from day to night, and (c) the relative phase of upward and downward source radiation.

To display the effects of varying the observer height and the model atmosphere, we found it satisfactory to use the results of the WKB calculations. The main effects of these two variables are related to absorption and the rate of exponential amplitude growth with height, both of which are given accurately by the WKB method. To show how the acoustic energy disperses spatially, we also calculated some acoustic ray paths from a point source, for a few frequencies within the window.

To examine the fine structure of the window, and to see what effect varying source phase has, we show the results of the full-wave calculations. We examine specifically the contribution to the window shape by the "resonance factor" in Eq. (27), and we compare the full-wave results with the WKB solutions. Finally, we compare our calculated spectra with the observed one and assess how well they agree.

A. Behavior of $q(z,\omega)$ and inverted refraction

We obtained some useful insights into the physical mechanisms that form the ionospheric filter by looking at the way q depends on wave frequency and height in the atmosphere. In what follows, calculations of q^2 are made for $k_x = 0$ with the formulas of Francis mentioned earlier.

Figure 2(a) shows the real part of $q^2(z)$ for various wave frequencies in the vicinity of the hypothetical window, using the medium-temperature atmospheric model (Appendix A). Plotting q^2 instead of q allows us to show in a single plot where the waves are vertically propagating ($q^2 > 0$) and where they are evanescent ($q^2 < 0$).

Because of dissipation, q^2 is not purely real; it also has an imaginary part that is significant only at thermospheric heights. Figure 2(b) shows the imaginary part of q^2 as a function of height for several wave frequencies. As expected, essentially all of the absorption occurs above about 200 km and at the higher wave frequencies.

These curves illustrate a phenomenon that we have called *inverted refraction*. Normally (that is, for ordinary acoustic waves) $\mathrm{Re}(q^2)$ depends inversely on the atmospheric temperature T, so that (for a given ω and k_x) maxima in $q^2(z)$ correspond to minima in $T(z)$, and vice versa. Such behavior is evident in the top (highest frequency) curve of Fig. 2(a), which essentially reproduces the inverse of the atmospheric temperature profile. But the remaining (lower frequency) curves show successive stages in transition to the reverse behavior, until, at a wave period of 4 min, for example, maxima in $q^2(z)$ occur at heights of the temperature maxima. At frequencies where an increase in sound speed (temperature) causes an increase in q^2 (a decrease in vertical wavelength), we say that refraction is inverted, being opposite to the high-frequency acoustic case. Mathematically, inverted refraction occurs when

$$\frac{dq^2}{dC^2} > 0 . \qquad (28)$$

For the case of dissipationless acoustic-gravity waves in a locally isothermal atmosphere (the case treated by Hines[8]), Eq. (28) is true if the acoustic wavelength λ exceeds $2\pi C/\omega_a$ or, assuming $\gamma = 1.4$, if

$$\lambda > 8.98\, C^2/g . \qquad (29)$$

According to Fig. 2(a), refraction appears to be normal for wave periods shorter than about 2.5 min, and inverted for periods longer than about 4 min; for periods in between, refraction seems to be normal at some heights and inverted at others. Inverted refraction at the lower frequencies means that, as frequency is lowered, the portion of the atmosphere to become evanescent ($q^2 < 0$) first will be the temperature minimum at about 85 km; next the minimum at about 15 km will become evanescent. It also means that ducting (and modal resonances) can occur in the vicinity of temperature maxima, in contrast to the high-frequency case where ducting occurs in temperature minima.

The frequency for which q^2 first drops below zero at any height represents the low-frequency end of the ionospheric window; at lower frequencies, the wave must tunnel through the lowest temperature layers where $q^2 < 0$, in which wave amplitude decreases exponentially with distance into the layer. Because the thickness of these evanescent layers increases as frequency is lowered, total attenuation through them also increases rapidly.

B. Window shape in WKB approximation

Using the medium-temperature atmospheric model (Appendix A), we calculated the transmission factor from Eqs. (9) and (12) for plane waves traveling vertically ($k_x = 0$) from a source height of 10 km to various heights in the ionosphere, neglecting ground reflection. This factor gives the amplitude of the wave-associated vertical air velocity U_z relative to that at 10 km height; U_z is proportional to the observed radio Doppler shift.

1. Dependence on observer height

Figure 3 shows transmission factor $[U_z(z)/U_z(10)]$ as a function of frequency, near the hypothetical window, for several ionospheric heights. The large amplitude growth with height is caused by the exponential factor in Eq. (9), which is a consequence of wave-energy conservation in an atmosphere with exponentially decreasing density with height. Consequently, a 3-min period wave with a 10 m/sec velocity amplitude at 300 km height would, in the plane wave approximation, have only a 10^{-4} m/sec amplitude at 10 km height.

The low-frequency shape of the window is relatively independent of height in the ionosphere, whereas the high-frequency falloff, caused by absorption in the thermosphere, increases at the greater heights. Within this frequency range, there is for each frequency, a
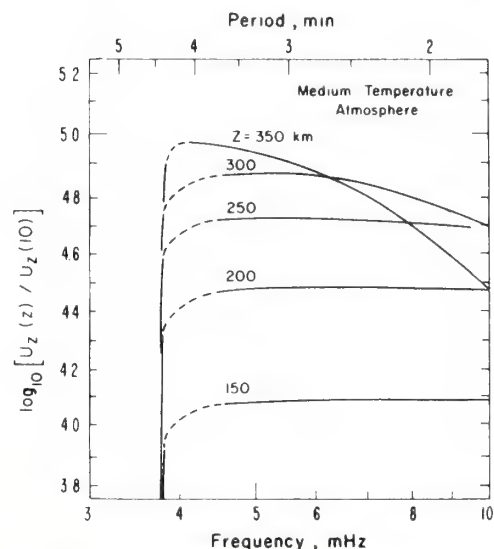
FIG. 3. Window shapes calculated with the WKB approximation and $k_x = 0$ for five different observer heights in the medium-temperature atmosphere. The window narrows and wave amplitude increases as height increases. The dashed portions indicate regions where the WKB solutions are inaccurate.

height where the dissipation rate just equals the amplitude growth rate with height; that height is where the wave amplitude attains its maximum value. This height of maximum amplitude decreases with increasing frequency and can be visualized, as a function of frequency, as the upper "envelope" of these amplitude-vs-frequency curves. The largest amplitude occurs at about 4 mHz and at about 350 km height.

Davies and Jones[2] report observing the ionospheric waves from heights below 150 km to over 300 km, but no systematic dependence of spectrum shape on height is evident from their observations. Thus we cannot yet verify this aspect of our window calculations.

2. Dependence on model atmosphere

We calculated window shape using three model atmospheres that differ only in their thermospheric temperature above 120 km (Fig. 11). We call them "high," "medium," and "low." The high and low models represent the temperature extremes available from the CIRA models; the high model is for near midday, the low model is for near midnight, and the medium model lies in between, probably best representing average conditions, especially in morning and evening hours. Although the difference between the high and low models is extreme and doesn't represent the actual range of diurnal change, we used them to reveal the range of possible window shapes.

We found that the main differences in the models' effects on the window are in different absorption rates at the higher frequencies and in different exponential growth rates. The latter effect is independent of frequency and simply shifts the entire window up or down in amplitude. To illustrate, Fig. 4 shows the window shape in the WKB approximation at an observer height of 300 km, for the three model atmospheres. The difference in the high-frequency falloff rate from model to model is substantial, making the window much narrower for the low model. But the exponential-growth rate is greater for the low model, so that it produces the high-
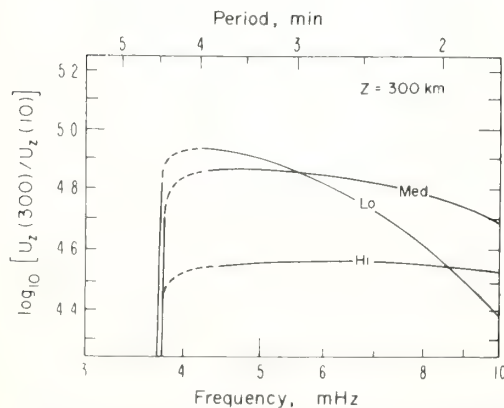
FIG. 5. Two sets of acoustic ray paths calculated with an acoustic-gravity ray-tracing program on a digital computer. The model atmosphere used resembles the medium-temperature model. The top plot is for wave periods of 1 min or shorter (where propagation is nondispersive); the lower plot is for a wave period of 4.5 min. For slightly longer periods, all rays reflect at about 85 km height, where $q^2 < 0$ [see Fig. 2(a)]. The ray density is about twice as great at ionospheric heights for the 4.0-min rays, compared with the high-frequency case.

est overall amplitudes in the ionosphere. Less geometrical defocusing of upgoing rays, not accounted for in our plane-wave representation, also contributes to relatively larger ionospheric wave amplitudes with the low model, as discussed next.

C. Acoustic ray paths: A spatial window

Within the accuracy of the WKB method, we can also calculate acoustic ray paths that show how the acoustic energy disperses spatially from a point source. Figure 5 shows two sets of acoustic ray paths computed with a ray-tracing computer program for acoustic-gravity waves,[13] using a model closely resembling the medium-temperature model. The wave source is at an elevation of 10 km, and the lower set of rays is for a wave period of 4 min, long enough for the waves to be influenced by gravity but not so long that the WKB approximation is invalid. For wave periods shorter than about 1 min, the ray paths are essentially the same as those shown in the upper set. Dispersion begins to be strong, and the validity of the ray viewpoint becomes questionable for periods longer than 4 min. The rays pictured were launched from the source every 5° in elevation angle (from horizontal) between 0° and 90°.

FIG. 4. Window shapes at 300 km height calculated with the WKB approximation with $k_x = 0$ and the three model atmospheres. The low-temperature atmosphere produces the narrowest window. A lower exponential growth rate causes the lower amplitudes with the high-temperature (midday) model.

The feature most interesting to us is that only rays within about a 90° cone centered about the vertical reach ionospheric heights. (No horizontal winds were used in our atmospheric model, but if they were the cone would essentially be tilted slightly in the direction of the wind.) We calculated the horizontal distance at which the U_z amplitude falls to one half the value directly overhead at a height of 300 km, based on ray density. In the high-frequency limit, that distance is about 170 km; for the 4-min wave period, it is about 150 km. This is probably why the ionospheric effects are seldom seen more than about 300 km from severe storms. This is also why we confine our attention to nearly vertically propagating sound waves.

Note also that the ray density is substantially greater above the source for the 4-min rays compared with the high-frequency rays. This is caused by inverted refraction, and tends to enhance the energy density at the low-frequency end of the window. For example, the intensity 300 km overhead is about 6 dB higher at 4-min period than at 1 min, because of increased focusing alone. This effect has not been included in our window-shape calculations, which are based on plane-wave propagation for $k_x = 0$, but an estimated focusing correction has been included in Fig. 10.

D. Full-wave calculations of window shape

1. Resonance factor

Separate calculations of the resonance factor in Eq. (27) (Fig. 6) show that modal resonances occur at frequencies of about 3.7, 4.6, 5.3, and 6.6 mHz (corresponding to wave periods of about 4.5, 3.6, 3.1, and 2.5 min). We concluded from the vertical distribution of total field strength for these four frequencies that the three higher frequencies are the result of second-, third-, and fourth-order acoustic resonances between the ground and the base of the thermosphere. (The fre-
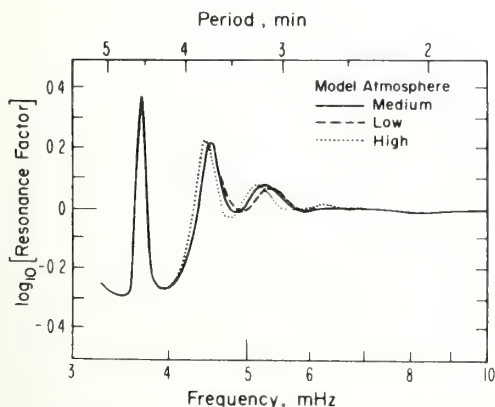
FIG. 6. Plot of the "resonance factor" alone, the inverse of the denominator of Eq. (27), for the three model atmospheres. The higher-order resonances that depend somewhat on the model are apparently between the ground and the base of the thermosphere; the lowest-frequency resonance seems to be in the temperature maximum near 50 km, which is the same for all three models.
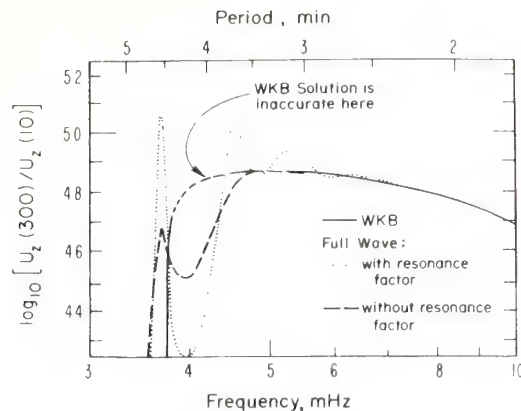
FIG. 7. Comparison of the window shapes calculated by the WKB method and by the full-wave method [Eq. (27) with $\psi_U^S = 1$, $\psi_D^S = 0$], for $z = 300$ km, $k_x = 0$ and the medium-temperature atmosphere. The curve labeled "without resonance factor" shows the effect of leaving out all reflections below the source height in calculating internal resonances in the atmosphere.

quencies of these resonances depend slightly on the model atmosphere, as shown in Fig. 6.) A first-order mode between the ground and the base of the thermosphere apparently does not exist, because, as frequency decreases toward where a first-order resonance might occur, refraction becomes inverted (Sec. III A), and a duct centered at 50 km interposes [see Fig. 2(a)]. The lowest-frequency resonance at 3.7 mHz appears therefore to be due to trapping in the temperature *maximum* at 50 km. This resonance is independent of the model atmospheres we used, which were identical below 120 km. Small changes in the lowest-frequency resonance were obtained when we changed the mesospheric temperature profile (not shown).

2. Comparison with WKB results

We calculated the window-shape using Eq. (27), and found reasonable agreement with the WKB results, except for the effect of the resonance factor. Figure 7 shows the window shape as calculated by the two methods. A third curve shows the full-wave results, but without the resonance factor; comparing this curve with the WKB curve best reveals where the WKB method is inaccurate.

Although the dashed curve was calculated without the resonance factor, some resonance effects are still evident at 4.5-min period, but the higher-order resonances disappear. Omitting the resonance factor effectively removes the ground, which is necessary for the higher-order resonances, but only partly contributes to the 4.5-min resonance.

3. Effect of source phase

We wrote our final expression for the ionospheric field [Eq. (27)] in a way that allows us to specify independently the amplitude and phase of the upward and downward radiation from the source. We found that, for a source height of 10 km, interference effects between the direct and ground-reflected waves play an im-
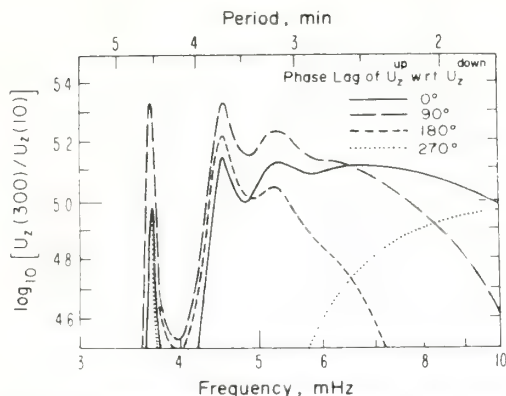
FIG. 8. Window shape calculated with Eq. (27) with $|\psi_D^S|$ $= |\psi_U^S| = 1$, for four different phases of the upward source radiation U_z^{up} with respect to U_z^{down}. Medium-temperature atmosphere, $z = 300$ km, $k_x = 0$. Phase greatly affects the high-frequency falloff of the window shape.

portant role in shaping the higher frequency part of the window; therefore, the shape of this part of the window depends strongly on the relative phases of these two components. To illustrate, Fig. 8 shows the window shape with several values of relative phase. By source phase we mean the relationship between the upward and downward radiated components of U_z; because there is a frequency-dependent phase between U_z and ϕ, the corresponding phases between upward and downward radiated ϕ differ from those for U_z. The peak levels are higher in Fig. 8 than in Fig. 7, because we have added downward radiation from the source equal in intensity to the upward radiation previously considered alone.

E. Comparing the window shape with observed spectra

If the shape of the spectrum of the ionospheric waves depended only upon the atmospheric filter (that is, if the source spectrum were white), then we could hope for close agreement between the observed spectra and the calculated window shapes. To see if this is so, we have compared in Fig. 9 the composite experimental spectrum (the same as the dashed curve in Fig. 1) with some of the calculated spectra.

The match at the low-frequency edge of the window and in the peaks of the fine structure is within the tolerances introduced by the uncertainties in the atmospheric models, but at the high-frequency end, the observed spectrum seems to fall off more rapidly than the calculated ones. The window produced with the low-temperature atmospheric model better matches the observed high-frequency falloff rate; but this model is not appropriate for the level of solar activity during which most of the observations were made. Furthermore, the match with observations applies only at the greatest heights; if the shape of the actual spectra depended on such a window, we would expect to see more high-frequency waves at the lower heights. No such tendency is evident in the experimental spectra. Thus, filtering alone appears inadequate to explain the high-frequency falloff of the observed spectra.

1. Possible reasons for disagreement

(a) We haven't accounted for all the possible wave-absorption mechanisms.

If so, the high frequencies may be actually attenuated more than our calculations based only on viscous and thermal damping predict. However, at this time we cannot find any additional absorbing mechanism strong enough to produce alone the observed high-frequency falloff (see Appendix C).

(b) We haven't correctly accounted for source phase in calculating the phase interference between direct and ground-reflected waves.

For certain phases, the interference greatly diminishes the net field strength in the ionosphere (Fig. 8). Although such interference effects could explain the more rapid observed falloff, it seems unlikely that the relationship between source phase and source height could remain as consistent as the observed falloff rate. This is difficult to check because we don't yet know the source mechanism or what phase to expect.

(c) Refraction causes decreased focusing at ionospheric heights as frequency increases.

We made some calculations that show decreased focusing at high frequencies (Fig. 10), but the amount is not great enough to account for the disagreement.

(d) Our assumption of a white source spectrum is incorrect.

Actually, we should represent the observed ionospheric spectrum, $I(\omega)$, as the product of some source spectrum $S(\omega)$ and the atmospheric-window function $W(\omega)$. [We assume here the $S(\omega)$ is independent of $W(\omega)$, which may not be true.] The fact that $I(\omega)$ and the calculated $W(\omega)$ agree fairly well except in their high-frequency falloff rates suggests that some simple form for $S(\omega)$, say a power-law spectrum, could bring $I(\omega)$ into agreement with the calculated $S(\omega)W(\omega)$. [The falloff at the low-frequency end of the window is so steep that it is difficult to compare the observed with
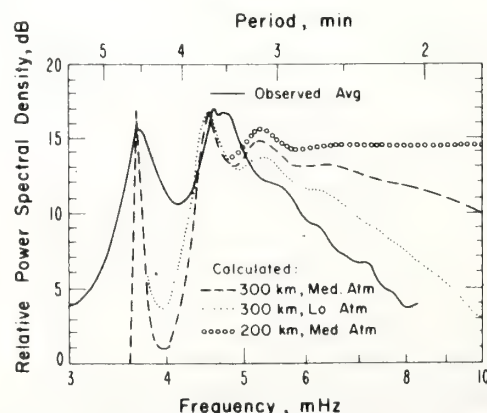
FIG. 9. Comparison of the average of the observed spectra (maximum-entropy method) with three calculated windows, in which the observation height and model atmosphere are varied.
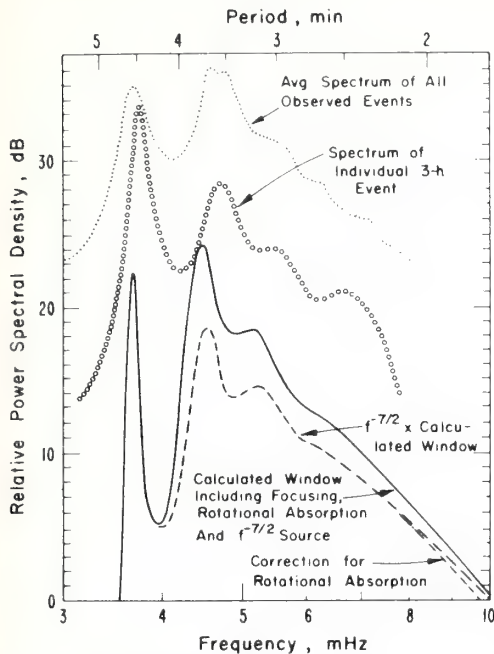
FIG. 10. Comparison of observed spectra with calculated window, including the effects of rotational absorption and focusing. The calculated windows are multiplied by an $f^{-7/2}$ source function. The spectrum of an individual event (09-12 UT, 5/12/70, Long Branch, IL to Boulder, CO) is included to show how the 4.5-min resonance is broadened in the averaging process. The vertical separation of the curves is for clarity and has no other significance.

the predicted rate; multiplying $W(\omega)$ by some power-law form for $S(\omega)$ would not make a material difference there.] Our thesis, that the window explains the principal features of the observations, would then be only slightly modified. We will now see how well this works.

2. Possible source spectrum

In proposing a simple, realistic source spectrum for severe-storm waves, we look both to measurements of pressure spectra in the atmosphere and to the local and radiated pressure fluctuations predicted theoretically for "turbulent" air flows.

Experiments in the atmosphere consistently reveal a nearly f^{-2} dependence of the intensity (square) of pressure fluctuations in the frequency range of interest to us (cf. Kimball and Lemon,[14] Meecham,[15] and the references they cite), but it is seldom clear what portion of these fluctuations represents *in situ* sampling of random pressure fluctuations, and what portion is acoustic radiation from remote air motions.

One proposed theoretical model of severe-storm radiation is based on a stochastic description of the air motions inside storms.[16] A turbulent description of the radiation mechanism is based mainly on dimensional arguments and is not very satisfactory from the point of view of insight into storm processes, but it may suffice for predicting an average radiation spectrum.

Suppose, for example, that we adopt a turbulent description of severe-storm air motions, such that energy is supplied to the fluid motions (by convective instability) on an "outer scale" L equal to the scale of the convection cell itself. According to the Kolmogorov hypothesis,[17] motions on smaller scales merely partake of an energy-cascade process that transfers energy to smaller and smaller scale motions, until an "inner scale" is reached, where the energy can be efficiently dissipated by molecular viscosity. In the inbetween or so-called inertial range of scales, where energy is neither supplied to nor removed from the fluid motions but is merely transferred by means of nonlinear interactions between scale sizes, the statistical and spectral properties of the turbulence do not depend on the geometry of the driving mechanism. From dimensional arguments, it is possible to establish that the frequency spectrum of (squared) pressure fluctuations in such a fluid obeys an $f^{-7/3}$ law,[17] but that the power spectral density of its acoustic radiation falls off with frequency as $f^{-7/2}$ (Ref. 18, Sec. 11.4; Ref. 19). This supports the idea that the measured f^{-2} spectra for pressure fluctuations are mainly spectra of the local pressure fluctuations and not of acoustic radiation.

At wave frequencies of about $u/2\pi L$, where u is a representative velocity fluctuation on the scale of L, we expect the radiated spectrum to peak and to fall off again at lower frequencies, because L is the largest scale of fluctuations in the fluid. For a large thunderstorm, we can take $u \simeq 30$ m/sec and $L \simeq 10$ km, which gives a wave period of about 30 min. So, it seems reasonable to hypothesize a wave spectrum for thunderstorm radiation that peaks in the vicinity of 30 min (actually, these would be gravity waves) and falls off at lower and higher frequencies, with the high-frequency falloff approaching an $f^{-7/2}$ rate.

Let us therefore make the tentative (but certainly questionable) assumption that motions of about a 3-min time scale are fully in the inertial range, and that $S(\omega)$ in that range has an $f^{-7/2}$ slope. Figure 10, then, compares the $S_t(\omega)W(\omega)$ product [t subscript for "turbulent"] with $I(\omega)$ for 300 km calculated with the medium-temperature model. The height and model atmosphere used best represent the observational conditions. The agreement is certainly much better. Adding the approximately 6-dB enhancement between about 3- and 4-min period (to account for focusing) even further improves the agreement.

IV. CONCLUSIONS

From our comparison of the calculated ionospheric window with the observed ionospheric spectra, we conclude that the major features of the spectra are explained by our model of the source-to-ionosphere transfer function, and that there is no need to invoke a narrow-band source mechanism. However, the failure of the model to match accurately the observed high-frequency spectral-falloff rate led us to propose a source spectrum whose average power spectral density is proportional to $f^{-7/2}$, the same variation expected of a turbulent sound source.

The need to invoke an $f^{-7/2}$ source spectrum to explain the observed high-frequency falloff of the ionospheric spectra raises a question about the relative level of the higher-frequency infrasound observed at ground level (nominally at 30-sec wave period). If the $f^{-7/2}$ source spectrum extends through the higher frequencies of the ground-level observations, then 30-sec waves would be emitted with about 1.3×10^{-3} times the power of 200-sec waves; their pressure amplitude should then be about 28 times lower. To check this with the observations, we took Davies and Jones's measurements[2] of three ionospheric events where the height in the ionosphere was determined with ionosondes, and we calculated the equivalent ground-level pressure fluctuations using model atmospheres appropriate to the measurement time. The average equivalent pressure fluctuation amplitude was 0.3 μbar, which is quite close to the average amplitude of storm-associated infrasound measured at the ground. The much lower amplitudes we would expect would not be detected in the presence of local pressure fluctuations at the sensors.

Many effects could be invoked to circumvent this difficulty; for example, overestimates of the ionospheric reflection height (this is critical), enhanced geometrical focusing for ground-observed waves, and a source radiation pattern with horizontal directivity. In the absence of such effects, however, the discrepancy appears to argue against a single $f^{-7/2}$ average spectrum extending through the frequency ranges of both observations. Another difficulty is that, to be consistent with both an $f^{-7/2}$ source spectrum and the observed level of higher-frequency infrasound, the ionospheric waves would have to grow to nonlinear amplitudes, an effect that we have not considered at all.

APPENDIX A: MODEL ATMOSPHERES

We wanted to compare the source-to-ionosphere transfer functions for three different atmospheres. The transfer function depends at least indirectly on the height profiles of pressure, density, temperature and molecular weight. We could have used three different models in which all these profiles were specified independently, but we couldn't be sure that the proper relationships among all the variables would be preserved as one, say temperature, varied. If one parameter were

TABLE AI.

ATMOSPHERIC MODEL
(PARAMETERS DEPEND ONLY ON HEIGHT)

PARAMETER	METHOD OF CALCULATION	FORMULA
SCALE HEIGHT	ANALYTIC FIT TO CIRA PROFILES	$H = H(z)$
PRESSURE	FROM SCALE HEIGHT	$P = P_{u_0} EXP\left(-\int_{z_0}^{z} dz/H\right)$
DENSITY	HYDROSTATIC EQUILIBRIUM	$\rho = P/gH$
MOLECULAR WEIGHT	ANALYTIC FIT TO CIRA FUNCTION OF PRESSURE	$M = M_0 - 2.6 \, LOG\left(1 + (P_0/P)^{2/3}\right)$ $M_0 = 28.996, \; P_0 = 3 \times 10^{-3} \, N/M^2$
TEMPERATURE	EQUATION OF STATE	$T = PM/\rho R$
VISCOSITY	AROC FUNCTION OF TEMPERATURE	$\mu = 145.8 \times 10^{-8} \, T^{5/2}/(T + 110.4)$
THERMAL CONDUCTIVITY	PRANDTL NUMBER FOR N_2	$K = 1.91 \mu R/(\gamma - 1)M$
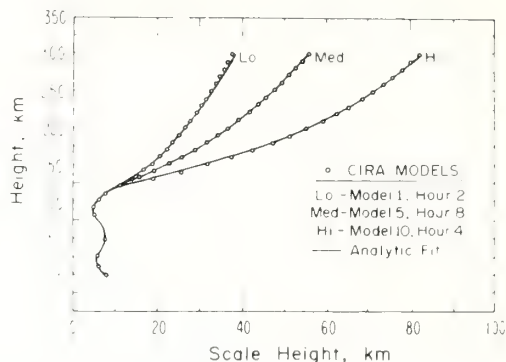
FIG. 11. Analytic height profiles of pressure scale height for the three model atmospheres we used, compared with three CIRA models (circles).[31] All the other required atmospheric parameters were derived from these profiles.

varied without proper attention being paid to how the others depended upon it, spurious results could emerge, e.g., for the dependence of absorption on temperature.

To avoid the possibility of such confusion, we adopted a method of calculating a self-consistent model atmosphere, in which all relevant parameters are derived from a single specified profile, which we decided should be the pressure scale height. Table AI summarizes how we obtained all the other required parameters from the $H(z)$ profile, assuming horizontal invariance and hydrostatic equilibrium. The integration required to compute the pressure profile is carried out at the same time as the numerical integration of the wave equation. The gas constant R and γ are assumed independent of height, and g follows an inverse-square height dependence.

Figure 11 gives the three $H(z)$ profiles we have identified with "high," "medium," and "low" temperature thermospheres. All three are analytical fits to CIRA tabular models.

APPENDIX B: BOUNDARY CONDITIONS AND GROUND-REFLECTION COEFFICIENT

Here are some more details about the upper and lower boundary conditions and the ground-reflection coefficient in terms of our Airy-function representation of the upgoing and downgoing waves. First, we need to define the particular Airy-function solutions we use.

When Q^2 is a linear function of ζ, we can write Eq. (11) in the form

$$\phi'' = -Q^2\phi = -(Q^2)'(\zeta - \zeta_0)\phi \,, \tag{B1}$$

where $(Q^2)'$ is now a constant equal to its local value. All primes without explicit arguments indicate derivatives with respect to ζ, and ζ_0 is the location of a turning point. The uncoupled solutions of Eq. (B1) are the Airy functions Ai and Bi defined, for example, in Abramowitz and Stegun (Ref. 20, p. 446). We want particular combinations of Airy functions that reduce to the upgoing and downgoing WKB solutions far from turning

points. Such combinations are[21]

$$w_1(t) = \sqrt{\pi} \left[\text{Bi}(t) - i\, \text{Ai}(t) \right] \qquad (B2)$$

and

$$w_2(t) = \sqrt{\pi} \left[\text{Bi}(t) + \text{Ai}(t) \right] , \qquad (B3)$$

where

$$t = \left[-(Q^2)' \right]^{1/3} (\zeta - \zeta_0) . \qquad (B4)$$

The cube root in Eq. (B4) is chosen closest to the real axis, so that t is nearly positive real in an evanescent region and nearly negative real in a propagating region. (In other words, t and Q^2 have opposite signs.)

After numerically solving Eqs. (13) and (14), for ϕ_1 and ϕ_2, we define new variables ψ_1 and ψ_2 that are linear combinations of ϕ_1 and ϕ_2 and that behave like Airy functions in the vicinity of turning points. [It is important to note here that the total field, $\phi_1 + \phi_2$, which we calculate by integrating Eqs. (13) and (14) is exact; we are concerned here about repartitioning $(\phi_1 + \phi_2)$ into components $(\psi_1 + \psi_2)$ that we can reasonably call "upgoing" and "downgoing" waves near turning points.] The kind of Airy functions we use depends on whether $(Q^2)'$ is positive or negative locally. For $(Q^2)' > 0$, we want

$$\psi_1'/\psi_1 = t'(\zeta) w_1'(t)/w_1(t) \qquad (B5)$$

and

$$\psi_2'/\psi_2 = t'(\zeta) w_2'(t)/w_2(t) , \qquad (B6)$$

where, from Eq. (B4),

$$t' = \left[-(Q^2)' \right]^{1/3} . \qquad (B7)$$

[For the case where $(Q^2)' < 0$ locally, we interchange w_1 and w_2 here and in all the following results.]

To calculate ψ_1 and ψ_2 we set

$$\psi_1 = b_{11}\phi_1 + b_{12}\phi_2 \qquad (B8)$$

and

$$\psi_2 = b_{21}\phi_1 + b_{22}\phi_2 . \qquad (B9)$$

The b coefficients are taken to be locally constant and are determined from Eqs. (B5) and (B6), together with the additional requirement that

$$\psi_1 + \psi_2 = \phi_1 + \phi_2 . \qquad (B10)$$

It follows that

$$b_{11} + b_{21} = 1 \qquad (B11)$$

and

$$b_{12} + b_{22} = 1 . \qquad (B12)$$

The solutions for the b's are then

$$b_{11} = (1 + \beta)/(\beta - \alpha) , \qquad (B13)$$

$$b_{12} = -\alpha(1 + \beta)/(\beta - \alpha) , \qquad (B14)$$

$$b_{21} = (1 + \alpha)/(\alpha - \beta) , \qquad (B15)$$

and

$$b_{22} = -\beta(1 + \alpha)/(\alpha - \beta) , \qquad (B16)$$

where

$$\alpha = \frac{-iQ\phi_1 - (Q'/2Q)(\phi_1 - \phi_2) - t'[w_1'(t)/w_1(t)]\phi_1}{iQ\phi_2 - (Q'/2Q)(\phi_2 - \phi_1) - t'[w_1'(t)/w_1(t)]\phi_2} , \qquad (B17)$$

and β is equal to the same expression with the w_1's replaced by w_2's.

Our upper boundary condition for beginning the downward integration of ϕ was that $\psi_2(300) = 0$. The corresponding condition for ϕ is, from Eq. (B9), that b_{21} and $b_{22} = 0$. From Eqs. (B15) and (B16), this requires that $\alpha = -1$. Therefore, the upper boundary condition on ϕ is, from Eq. (B17),

$$\frac{\phi_2}{\phi_1} = \frac{iQ + t'[w_1'(t)/w_1(t)]}{iQ - t'[w_1'(t)/w_1(t)]} . \qquad (B18)$$

Similarly, the lower boundary condition that $\psi_1(0) = 0$ implies that $\beta = -1$ and that the lower boundary condition for beginning the upward ϕ integration is

$$\frac{\phi_1}{\phi_2} = \frac{iQ - t'[w_2'(t)/w_2(t)]}{iQ + t'[w_2'(t)/w_2(t)]} . \qquad (B19)$$

The values of ψ_1'/ψ_1 and ψ_2'/ψ_2 to be used in place of the ϕ's in the ground-reflection coefficient [Eq. (20)] are given in Eqs. (B5) and (B6), when $Q^{2\prime} > 0$ at the ground. If $Q^{2\prime} < 0$ at the ground, w_1 and w_2 are interchanged.

APPENDIX C: OTHER ABSORPTION MECHANISMS

Our calculations of q^2 from Francis's dispersion relation[5] included dissipation caused only by classical (viscous and thermal conduction) absorption mechanisms. To be sure that nonclassical absorption mechanisms do not contribute significantly to the shape of the ionospheric-transmission window, we roughly estimate the absorption coefficients associated with the excitation of rotational and vibrational energy states in molecular oxygen and nitrogen.

1. Rotational relaxation

The largest nonclassical contribution probably comes from absorption by rotational transitions in molecular oxygen and nitrogen. Greenspan[22] calculated the absorption by rotational relaxation and measured it in N_2, O_2, and air; his results show an increase in absorption coefficient by a factor of about $\frac{4}{3}$, when $p/(\omega\mu)$ is greater than about 4, where p is the pressure, ω is the angular wave frequency, and μ is the coefficient of viscosity. For $p/(\omega\mu)$ less than about 1, the effects of rotational relaxation appear to be negligible. The factor of $\frac{4}{3}$ is very close to the discrepancy between absorption coefficients calculated from classical formulas and those measured in air (cf. Reed, Ref. 23, and the references he cites). This reinforces the idea that rotational relaxation is the most important nonclassical process.

We now estimate the correction factor for values of the parameters of interest to us.

At infrasonic frequencies (10 mHz is the highest frequency we consider), essentially all the classical absorption takes place above 200 km [see Fig. 2(b)]; therefore, any multiplicative correction would be important only above that height. In the upper atmosphere, however, we encounter a further complication: a con-

TABLE C1. The fraction of the atmosphere that is diatomic (for heights between 200 and 400 km), $p/(\omega\mu)$ for a frequency of 10 mHz and the medium-temperature atmosphere, the factor F_R to multiply the classical absorption coefficient by (at that height) to include rotational relaxation, and an estimate of the factor that applies to integrated absorption up to that height.

z, km	Fraction diatomic	$p/(\omega\mu)$	$F_R(z)$	Correction factor for propagation up to z
200	0.75	40	1.25	$1.25 \rightarrow 1.33$
250	0.63	10	1.21	$1.21 \rightarrow 1.25$
300	0.50	4	1.167	$1.167 \rightarrow 1.21$
350	0.42	2	1.14	$1.14 \rightarrow 1.167$
400	0.33	0.8	1.0	$1.00 \rightarrow 1.14$

siderable fraction of the atmosphere is atomic oxygen, which plays no role in rotational absorption. The rotational correction should be multiplied by the fraction of the atmosphere that is diatomic. (See Table C1.)

In estimating the integrated factor, we reason that, for example, the total absorption up to 300 km would be underestimated if we used 1.167, because we would be using too small a value for lower heights; on the other hand, most of the classical absorption occurs above 250 km, so we would overestimate the total if we used 1.21. Therefore, the two factors roughly form upper and lower bounds for the correction on waves traveling up to 300 km.

These factors have been applied to the window calculation shown in Fig. 10. The contribution by rotational relaxation appears to be insignificant.

The reason that rotational relaxation absorption can be so easily combined with classical absorption (i.e., a simple multiplying factor), is that the characteristic temperatures for transitions between rotational states in O_2 and N_2 are only a few degrees Kelvin. Therefore, at normal atmospheric temperatures, the discrete rotational energy levels are so close together that they behave like a continuum. This is not the case for vibrational relaxation, considered next.

2. Vibrational relaxation

Vibrational transitions in molecular oxygen and nitrogen also absorb sound energy. The vibrational frequencies (conventionally divided by c, the free-space speed of light) for O_2 and N_2 are 1580.361 and 2358.07 cm^{-1}, respectively (Gray, Ref. 24, pp. 7–178 and 179). These are converted to temperature θ_{vib} by multiplying by hc/k, where h is Planck's constant and k is Boltzmann's constant. Values of θ_{vib} for O_2 and N_2 are thus 2274 and 3393 °K, respectively. Therefore, the vibrational states are very widely spaced, compared with atmospheric temperatures, and we must consider the quantum effects of the discrete vibrational energy levels.

Hines et al. (Ref. 25, p. 380) give a correction to be added to the absorption coefficient to account for relaxation processes. For our application, it reduced to

$$\alpha_{vib} = \frac{\gamma-1}{\gamma} \frac{\omega}{2C} \frac{n}{f} \frac{1}{\omega_m/\omega + \omega/\omega_m} ,\qquad (C1)$$

where ω_m is the frequency where the relaxation absorption is maximum, C is the sound speed, and f is the number of degrees of freedom associated with molecular translation and rotation, 5 for diatomic molecules. (This formula applies strictly only when $\omega \gg \omega_a$.)

The number n is the effective number of classical degrees of freedom associated with molecular vibration. If the atmosphere's temperatures were much greater than θ_{vib}, n would equal 2; for lower temperatures, we can calculate n from formulas given by Sears (Ref. 26, p. 303) so that

$$n = 2R^2 e^R/(e^R - 1)^2 ,\qquad (C2)$$

where $R = \theta_{vib}/T$. In the atmosphere, then, n is usually substantially less than 2.

In applying these formulas to the atmosphere, we find that the absorption coefficient depends on height mainly through the relaxation frequency ω_m and in particular on the height where $\omega = \omega_m$. It is easy to show that, because ω_m depends mainly on pressure, the integrated absorption is roughly equal to its maximum value times three times the scale height. To estimate the total absorption A we used the formula

$$A_{vib}(dB) = \frac{20}{\ln 10} \frac{\gamma-1}{\gamma} \frac{\omega}{2} (\gamma g H)^{-1/2} \frac{2}{5} \frac{R^2 e^R}{(e^R-1)^2} \tfrac{1}{2} 3H[O_2, N_2] ,\qquad (C3)$$

where $[O_2, N_2]$ means the fraction of O_2 or N_2 present, and where all parameters are evaluated at the height where $\omega = \omega_m$.

We calculated the relaxation frequency ω_m from formulas given by Sutherland et al.[27] for N_2 and O_2 and found that the greatest possible height where ω might equal ω_m within our window could not exceed 120 km, and is probably much lower. Because of the exponential factors in Eq. (C3), the total absorption increases with the height assumed; therefore, assuming 120 km should give an upper bound to the total absorption. Using conditions at a height of 120 km, we get a total absorption for O_2 of 0.085 dB and for N_2 of 0.034 dB, clearly negligible compared with classical absorption.

Finally, we estimated the absorption caused by eddy viscosity below 100 km and found it negligible.

[1] T. M. Georges, "Infrasound from convective storms: Examining the evidence," Rev. Geophys. Space Phys. 11, 571–594 (1973).

[2] K. Davies and J. F. Jones, "Ionospheric disturbances produced by severe thunderstorms," NOAA Professional Paper No. 6 (U. S. GPO, Washington, DC, 1972).

[3] T. M. Georges, "HF Doppler studies of traveling ionospheric irregularities," J. Atmos. Terr. Phys. 30, 735–746 (1968).

[4] G. Chimonas and W. R. Peltier, "On severe storm acoustic signals observed at ionospheric heights," J. Atmos. Terr. Phys. 36, 821–828 (1974).

[5] S. H. Francis, "Acoustic-gravity modes and large-scale traveling ionospheric disturbances of a realistic, dissipative atmosphere," J. Geophys. Res. 78, 2278–2301 (1973).

[6] C. A. Moo and A. D. Pierce, "Generation of anomalous iono-

spheric oscillation by thunderstorms," *Effects of Atmospheric Acoustic-Gravity Waves on Electromagnetic Wave Propagation* AGARD Conf. Proc. No. 115 (1972).

F. Einaudi and C. O. Hines, "WKB approximation in application to acoustic-gravity waves," Can. J. Phys. 48, 1458–1471 (1970).

C. O. Hines, "Internal atmospheric gravity waves at ionospheric heights," Can. J. Phys. 38, 1441–1481 (1960).

[3]M. L. V. Pitteway and C. O. Hines, "The reflection and ducting of atmospheric acoustic-gravity waves," Can. J. Phys. 43, 2222–2243 (1965).

[1]J. E. Midgley and H. B. Liemohn, "Gravity waves in a realistic atmosphere," J. Geophys. Res. 71, 3729–3748 (1966).

[11]M. Yanowitch, "Effect of viscosity on gravity waves and the upper boundary condition," J. Fluid Mech. 29, 209–231 (1967).

[12]K. G. Budden, *Radio Waves in the Ionosphere* (Cambridge University, Cambridge, UK, 1961).

[13]T. M. Georges, A program for calculating three-dimensional acoustic-gravity ray paths in the atmosphere, NOAA Tech. Report No. ERL 212-WPL 16 (U. S. GPO, Washington, DC, 1971).

[14]B. A. Kimball and E. R. Lemon, "Spectra of air pressure fluctuations at the soil surface," J. Geophys. Res. 75, 6771–6777 (1970).

[15]W. C. Meecham, "On aerodynamic infrasound," J. Atmos. Terr. Phys. 33, 149–155 (1971).

[16]T. M. Georges, "Infrasound from convective storms. part 2. A critique of source candidates" (unpublished).

[17]J. L. Lumley and H. A. Panofsky, *The Structure of Atmospheric Turbulence* (Wiley, New York, 1964).

[18]P. Morse and K. Ingard, *Theoretical Acoustics* (McGraw-Hill, New York), 1968.

[19]W. C. Meecham and G. W. Ford, "Acoustic radiation from isotropic turbulence," J. Acoustic Soc. Am. 30, 318–322 (1958).

[20]*Handbook of Mathematical Functions with Formulas, Graphs, and Mathematical Tables*, Natl. Bur. Stand. Appl. Math. Ser. No. 55, edited by M. Abramowitz and I. A. Stegun (U. S. GPO, Washington, DC, 1964).

[21]J. R. Wait, "A diffraction theory for LF sky-wave propagation," J. Geophys. Res. 66, 1713–1723 (1961).

[22]M. Greenspan, "Rotational relaxation in nitrogen, oxygen, and air," J. Acoust. Soc. Am. 31, 155–160 (1959).

[23]J. W. Reed, "Attenuation of blast waves by the atmosphere," J. Geophys. Res. 77, 1616–1622 (1972).

[24]D. E. Gray, *American Institute of Physics Handbook*, 3rd ed. (McGraw-Hill, New York, 1972).

[25]C. O. Hines, *et al. The Upper Atmosphere in Motion*, Geophysical Monograph No. 18 (American Geophys. Union, Washington, DC, 1974).

[26]F. W. Sears, *An Introduction to Thermodynamics, the Kinetic Theory of Gases and Statistical Mechanics*, 2nd ed. (Addison-Wesley, Reading, MA, 1956).

[27]L. C. Sutherland, J. E. Piercy, H. E. Bass, and L. B. Evans, "A method for calculating the absorption of sound in the atmosphere," J. Acoust. Soc. Am. 56, S-1(A) (1974).

[28]P. D. Welch, "The use of the fast Fourier transform for the estimation of power spectra: a method based on time averaging over short, modified periodograms," IEEE Trans. Audio Electroacoust. AU-15, 70–73 (1967).

[29]J. Makhoul, "Linear prediction: A tutorial review," Proc. IEEE 63, 561–580 (1975).

[30]T. J. Ulrych and T. N. Bishop, "Maximum entropy spectral analysis and autoregressive decomposition," Rev. Geophys. Space Phys. 13, 183–200 (1975).

[31]*COSPAR International Reference Atmosphere* (North-Holland, Amsterdam, 1965).

On the Characteristics of Gravity Waves Generated by Atmospheric Shear Layers

D. P. Lalas

Department of Mechanical Engineering Sciences, Wayne State University, Detroit, Mich. 48202

F. Einaudi

Cooperative Institute for Research in Environmental Sciences, University of Colorado/NOAA, Boulder 80309 and Aeronomy Laboratory, NOAA, Boulder, Colo. 80302

ABSTRACT

The stability analysis of a hyperbolic tangent velocity profile in an isothermal atmosphere in the presence of the ground is presented. It is shown that such a system has a number of modes in addition to the one studied by Drazin and that unstable waves can be excited, for finite values of some minimum Richardson number of the flow, even in the limit of horizontal wavelengths going to infinity. Some of the unstable waves belonging to these new modes are able to propagate energy and momentum away from the shear zone and may therefore play an important role in microscale flow dynamics and in coupling of small-scale phenomena to mesoscale flow motions.

1. Introduction

The excitation of gravity waves by shear flow instability has been extensively investigated in order to explain a variety of phenomena in the ocean and the atmosphere. We will focus here on only some of the pertinent results. The interested reader is referred to the review articles of Drazin and Howard (1966), Thorpe (1973) and Howard and Maslowe (1973) for more complete and detailed discussion of previous work. Of the wind profiles utilized to model a shear layer, the simplest is the Helmholtz profile, which has a background horizontal velocity $U_0(z)$ constant in each of two semi-infinite media and a sharp discontinuity at the separating interface. Recently, some new properties of this profile have been reported by Lindzen (1974), and also by Einaudi and Lalas (1974) who, in addition, take into account temperature discontinuities and condensation effects. Other models utilized are, in order of increasing correspondence to reality and difficulty, a constant shear layer between constant velocity layers (Taylor, 1931; Goldstein, 1931; Miles and Howard, 1964; Jones, 1968; Gossard, 1974), and a $U_0(z)$ given by a hyperbolic tangent (Drazin, 1958; Maslowe and Kelly, 1971; Thorpe, 1973). The stability investigations of the above profiles are complemented by the general stability results of Miles (1961), Howard (1961) and Chimonas (1970) that provide bounds on the range of the phase velocities and growth rates of the unstable waves through the so-called semicircle theorem, as well as a sufficient condition for stability.

The primary aim of these investigations is to specify, for given velocity and density or temperature profiles, the characteristics of the most unstable wave to be excited, i.e., its wavelength, period, phase velocity and growth rate, as well as the range of horizontal wavelengths λ_x that are unstable for a given value of some characteristic Richardson number of the flow. Thus, Drazin (1958), investigating a hyperbolic tangent velocity profile with an exponentially decreasing density in an infinite medium, finds that the neutral stability boundary is given by $J = \alpha^2(1 - \alpha^2)$, where J is the minimum Richardson number in the flow and α the product of the horizontal wavenumber $k_x = 2\pi/\lambda_x$ of the disturbance and half the depth of the shear layer. The most unstable wave corresponds to $J = 0$ and $\alpha \approx 0.44$ (Maslowe and Kelly, 1971). For the Miles and Howard (1964) model, of a constant shear layer with linearly decreasing density between two semi-infinite layers of uniform velocity and density, the most unstable wave is associated with $J = 0$ and $\alpha \approx 0.41$. Both results have been used extensively in analyzing experimental observations in the atmosphere (Atlas *et al.*, 1970; Emmanuel, 1973; Hooke *et al.*, 1973) and the ocean (Woods, 1968).

A common property of Drazin's and Miles and Howard's models is the existence of one mode only, for which the instability domain in the (α, J) plane is bounded by its singular neutral mode; furthermore, unstable waves with $\alpha \to 0$ require correspondingly small values of the Richardson number, which are un-

common in the atmosphere. Because of such properties, the above two models may not be able to explain satisfactorily some recent observations obtained by improved remote sensing techniques such as FM-CW radars, acoustic sounders, Doppler radars, etc., together with microbarograph arrays and instrumented high meteorological towers. In particular, the appearance on a number of occasions (Reed and Hardy, 1972; Hooke and Hardy, 1975) of more than one wave with different horizontal wavelengths and the detection of gravity waves with horizontal wavelengths of the order of 100–500 km (Uccellini, 1975; Lilly, private communication) may require, in our opinion, the existence of a modal structure associated with a given velocity and temperature profile, with at least one mode associated with very large wavelengths.[1]

Jones (1968) indeed finds a modal structure in one of the three profiles he considers. He examines numerically three models of a constant shear layer capped by a semi-infinite layer of constant velocity, with a background density which decreases exponentially with height; adjacent to the bottom of the shear layer in the first case is the ground, in the second case another finite layer of constant velocity and then the ground, and in the third a semi-infinite layer of constant velocity with no ground at all. Jones finds that the first model is always stable, the second unstable for all wavenumbers, and the third unstable for wavenumbers larger than some wavenumber k_0. In the second model, he finds one mode only whose singular neutral curve has two branches, one of which corresponds to propagating waves in the top layer. In the third model, he finds two singular neutral modes, bounding two areas of instability that overlap for a finite range of wavenumbers, $k_1 \geqslant k_x \geqslant k_0$ within which one mode is evanescent in the upper semi-infinite layer and the other in the lower. For $k_x > k_1$ only one mode exists and is evanescent in both top and bottom layers. More recently, Dickinson and Clare (1973) and Dickinson (1973) have analyzed numerically an unbounded hyperbolic-tangent barotropic shear flow, and the corresponding baroclinic shear problem, respectively. In both studies, two modes exist for sufficiently small values of the longitudinal wavenumbers, one of which is propagating. Finally, very recently, Blumen et al. (1975) have found a second unstable mode, which exists only when the Mach number is greater than 1, in a hyperbolic-tangent shear layer profile in the absence of gravity and stratification. This new mode decays away from the shear zone much more slowly than the subsonic one.

The fact that unstable modes are present in the limit $k_x \rightarrow 0$, in Jones' second model, while no unstable mode exists for $k_x < k_0$ when the ground is removed, suggests

that the presence of the ground may destabilize the longer horizontal wavelengths. This is confirmed by the results of Hazel (1972), who investigates numerically a class of shear flows with different velocity and density profiles, bounded on top and bottom by solid surfaces. His results clearly indicate that the presence of solid boundaries destabilizes the long wavelengths and stabilize the short wavelengths at a smaller rate. When, on the other hand, the boundaries are brought too close to each other, the system becomes completely stable in accordance with Howard's (1964) calculations. Similar results are obtained by Einaudi and Lalas (1976) who considered the stability of Drazin's profile in the presence of two solid boundaries. In addition to the mode that would correspond to Drazin's if the boundaries were removed, they find a number of new modes, all of which are unstable, for finite values of J, as $\alpha \rightarrow 0$. The presence of a solid top boundary is unrealistic for atmospheric applications, at least as far as the propagating modes are concerned, because it does not allow leakage of energy away from the shear layer. To rectify this shortcoming, Lalas et al. (1976) have investigated the characteristics of a Helmholtz profile with a solid lower boundary at a finite distance below the velocity discontinuity. Contrary to the results without the ground (Einaudi and Lalas, 1974), they find that an infinite number of unstable modes exists even for horizontal wavelengths of the order of tens of kilometers with the most unstable new modes in reasonable agreement with experimental observations.

In an attempt to determine all possible modes of an atmospheric shear flow configuration that is more realistic than a Helmholtz profile, or a constant shear profile, we examine in this paper the inviscid stability of a semi-infinite hyperbolic-tangent horizontal background flow along the x direction, i.e.,

$$U_0(z) = V \tanh(z/h), \qquad (1)$$

with the origin of the coordinate system (x,z) at the height of the inflexion point and the ground some finite distance $|z_i|$ below. The effective width of the shear layer obeying (1) is given by $2h$. We also assume the atmosphere to have a background density ρ_0 given by

$$\rho_0(z) = \rho_g \exp(-z/H), \qquad (2)$$

where H is the scale height of the atmosphere and ρ_g the density at the inflexion height. A density of the form given by Eq. (2) implies a constant Brunt–Väisälä frequency n and a constant background temperature $T_0 = g/RH$, where g is the gravitational acceleration acting in the negative z direction and R is the gas constant for air. The velocity U_0 and density ρ_0 are shown, not in scale, in Fig. 1.

The mode previously discussed by Drazin is recovered, but with some significant differences in the values of the frequency at large wavelengths. Furthermore, additional modes are shown to exist with most

---

[1] For convenience, we will, in this paper, refer to unstable waves that end on different neutral curves in the normalized (α, J) plane as belonging to different modes, even though in a different projection of the stability boundary, one mode may simply be the continuation of another.

unstable wavelengths, for the same J, that are two or three times longer than the most unstable one of the main mode. Unstable waves can be excited at finite J, even in the limit of $\alpha \to 0$. Some of these additional modes are predominantly propagating, rather than evanescent, at large heights where there is no shear. Growth rates and stability boundaries for these modes are calculated, and the effect of the distance of the shear layer to the ground is discussed. Finally, the effect of a sudden increase in stability at large distances from the ground, as is often the case at the tropopause, is explored briefly.

2. The governing equations

As previously mentioned, we assume a stratified shear flow in the atmosphere with a hyperbolic-tangent wind profile and constant Brunt–Väisälä frequency, bounded below by a solid surface, the ground, and above by an infinite layer with constant wind and temperature, as shown in Fig. 1. We are interested in investigating the characteristics of unstable and neutral gravity waves that can be supported in such an atmosphere. If this background flow is perturbed by disturbances that are small enough so that they are adequately described by the linearized version of the inviscid hydrodynamic equations, and if use is made of the Boussinesq approximation, the equations of conservation of mass, horizontal momentum and vertical momentum, and the condition of incompressibility take the form

$$\frac{\partial u_1}{\partial x} + \frac{\partial w_1}{\partial z} = 0 \qquad (3)$$

$$\rho_0 \left(\frac{\partial}{\partial t} + U_0 \frac{\partial}{\partial x} \right) u_1 + \rho_0 \frac{dU_0}{dz} w_1 + \frac{\partial p_1}{\partial x} = 0 \qquad (4)$$

$$\rho_0 \left(\frac{\partial}{\partial t} + U_0 \frac{\partial}{\partial x} \right) w_1 + \frac{\partial p_1}{\partial z} + g\rho_1 = 0 \qquad (5)$$

$$\left(\frac{\partial}{\partial t} + U_0 \frac{\partial}{\partial x} \right) \rho_1 - \frac{n^2}{g} \rho_0 w_1 = 0. \qquad (6)$$

In Eqs. (3)–(6), u_1, w_1, p_1 and ρ_1 denote the horizontal velocity, vertical velocity, pressure and density, respectively, of the disturbance; U_0 and ρ_0 are defined by (1) and (2), respectively; and n^2 is given by

$$n^2 = -g \left(\frac{1}{\rho_0} \frac{d\rho_0}{dz} + \frac{g}{c_0^2} \right) = g \frac{d\theta_0}{dz} \Big/ \theta_0, \qquad (7)$$

where c_0 is the speed of sound and θ_0 the potential temperature. To be consistent with the Boussinesq approximation utilized in (3)–(6) the term g/c_0^2 in (7) should be omitted. This point and the validity of the Boussinesq approximation will be discussed later. In this investigation, since we are not interested in con-
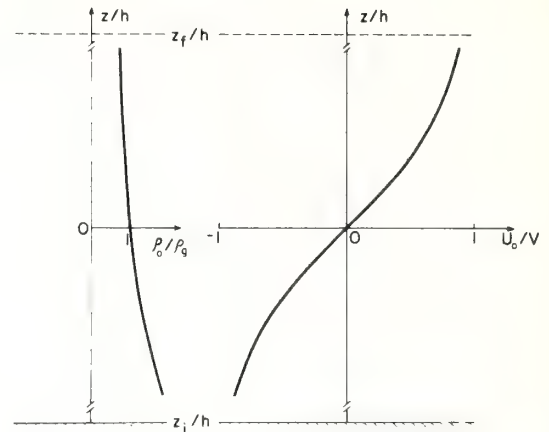
FIG. 1. The normalized density and velocity profiles and the geometry of the basic flow (not in scale).

vectively unstable flows n^2 is taken to be real and positive.

For a disturbance of wavelength λ_x, wavenumber $k_x = (2\pi/\lambda_x)$ and complex frequency $\omega = \omega_r + i\omega_i (\omega_i > 0)$, we assume a perturbation vertical velocity w_1 of the form

$$w_1 = \rho_0^{-\frac{1}{2}} \operatorname{Re}\{\psi(z) \exp[i(k_x x - \omega t)]\}. \qquad (8)$$

Eliminating u_1, p_1 and ρ_1, also assumed to possess similar forms, in favor of w_1 in (3)–(6), we obtain the following equation for ψ:

$$\frac{d^2\psi}{dy^2} - \Lambda(y)\psi = 0, \qquad (9)$$

with

$$\Lambda = \left[\alpha^2 + \frac{\sigma^2}{4} - \frac{J}{\Omega^2} - \left(\frac{d^2u_0}{dy^2} - \sigma \frac{du_0}{dy} \right) \Omega^{-1} \right]. \qquad (10)$$

The normalized quantities that appear in Eq. (10) are defined as follows:

$y = z/h$	normalized height coordinate
$\alpha = hk_x$	normalized horizontal wave-number
$c_r = \omega_r/k_x V$	normalized horizontal phase velocity of the wave
$c_{re} = c_r - u_0$	normalized Doppler-shifted phase velocity
$c_i = \omega_i/k_x V$	normalized imaginary part of the frequency of oscillation
$\Omega = c_{re} + ic_i$	normalized Doppler frequency
$\sigma = h/H$	ratio of the scale length of velocity to that of density
$u_0(y) = U_0/V = \tanh y$	normalized background velocity
$J = n^2 h^2 / V^2$	value of the Richardson number at $y=0$; also the minimum Richardson number of the flow domain.

In the present notation, the local Richardson number

Ri becomes

$$\mathrm{Ri} = J\left(\frac{du_0}{dy}\right)^{-2}, \qquad (11)$$

so that $\mathrm{Ri} > J$ everywhere in the flow domain except at $y=0$, the inflexion point, where $\mathrm{Ri} = J$.

Even though the Boussinesq approximation has been utilized, it should be pointed out that the effect of the background density variation in the inertial term of the momentum equation is included in (9) and gives rise to the terms, proportional to σ, which we shall henceforth call inertial terms of the density gradient.

The boundary or radiation conditions to be imposed on ψ are as follows:

(i) At $y=y_i=z_i/h$, where z_i is the distance of the ground from the inflexion point,

$$\psi(y_i) = 0. \qquad (12)$$

(ii) Above some height $y_f=z_f/h$, u_0 is virtually constant and so is $\Lambda(y)$. In this region, the solution takes the form $\psi \sim \exp(iKy)$ [see Hines, 1974], where K is the normalized vertical wavenumber given by

$$K = \pm[-\Lambda(y=y_f)]^{\frac{1}{2}} = K_r + iK_i. \qquad (13)$$

The perturbation amplitude has to go to zero at $y=\infty$ or, if the wave is neutral and propagating, it has to obey the usual radiation condition. This is assured if the sign in (13) is chosen so that either $K_i > 0$ or, when $K_i=0$, $dc_r/dK_r > 0$. For a wave of the form $\psi \propto \exp(iKy)$, the following relation has to hold between ψ and $d\psi/dy$:

$$\frac{d\psi}{dy} = iK\psi \quad \text{at} \quad y=y_f. \qquad (14)$$

It may be noted that for all values of $y>5$, du_0/dy is essentially zero and (14) holds for all $y_f \geqslant 5$.

All unstable waves of given horizontal wavelength that can be supported by a stratified shear, described by Eqs. (1) and (2) and characterized by a given J and α, will have frequency c_r and growth rate αc_i given by the eigenvalue problem for c_r and c_i comprising Eq. (9) and boundary conditions (12) and (14). Similarly, singular neutral waves that exist in a flow characterized by some J will have frequency c_r and wavenumber α given by the same eigenvalue problem with $c_i=0$ in (9), (12) and (14). The fact that now $c_i=0$ introduces possible singularities in (9) and the numerical difficulties that result and their resolutions will be discussed in the next section.

3. Numerical procedure

A stability analysis of a fluid flow should be able to provide the main characteristics of unstable modes such as frequency, phase velocity and growth rate in terms of the parameters of the basic flow, i.e., in terms of z_i, n^2, V and h. In addition, it should provide stability boundaries in the (α, J) plane that can specify the range of unstable wavelengths λ_x for a given physical situation. The domain of unstable modes will be bounded by contiguous neutral modes. Since according to the semi-circle theorem (Miles, 1961; Howard, 1961) the horizontal phase velocity of unstable modes has to be equal to the background velocity at some height y_c, known as the critical level, contiguous neutral modes will possess a critical level as well, where now (9) becomes singular. The altered nature of (9) when $c_i=0$ necessitates the use of one program for unstable waves and another for singular neutral modes. For both, the integrating subroutine utilized is the one developed by Bulirsch and Stoer (1966). A comparison of its performance versus other standard techniques, like the Runge–Kutta, can be found in Hull et al. (1972). The details of the two programs follow.

a. Program for the unstable modes

To determine the appropriate c_r and c_i for given α and J, some trial values of c_r and c_i are assumed and Eq. (9) is then integrated from $y=y_i$ to $y=y_f$. If the resulting values of ψ and its derivative at $y=y_f$ satisfy (14), the trial values of c_r and c_i are accepted as the true ones. Otherwise new values for c_r and c_i are assumed and the procedure is repeated until (14) is satisfied. No difficulty is encountered in obtaining the correct c_r and c_i, after a few iterations, for the entire range of α and J. All eigenvalues are correct to at least four significant figures.

b. Program for the singular neutral modes

In this case, for given α, values for c_r and J are assumed and Eq. (9) is integrated starting simultaneously at both $y=y_i$ and $y=y_f$ to within a small distance y_m away from the critical level y_c, i.e., up to $y=y_c-y_m$ and down to $y=y_c+y_m$, respectively, where $0 < y_m \ll 1$.

The analytical Frobenius expansion of ψ (Ince, 1956), valid in $y_c - y_m \leqslant y \leqslant y_c + y_m$, is used to match the numerically calculated ψ at both sides of the critical level, if the assumed c_r and J are indeed eigenvalues. If the matching is not possible, new values of c_r and J are assumed, as before, and the entire procedure is repeated until the matching is obtained.

The difference between this program and Hazel's (1972) second program discussed in his Appendix A, apart from the integrating routine, is the ability of our program to investigate neutral modes of arbitrary phase velocity and unknown position of the critical level.

The values of c_r and hence y_c are found to be sensitive to the value of y_m. If y_m is too large, a large number of terms in the Frobenius expansion is necessary, and in some cases up to three terms are utilized. If y_m is too small, numerical difficulties arise because of the large values of the derivatives near y_c. Usually, a value of
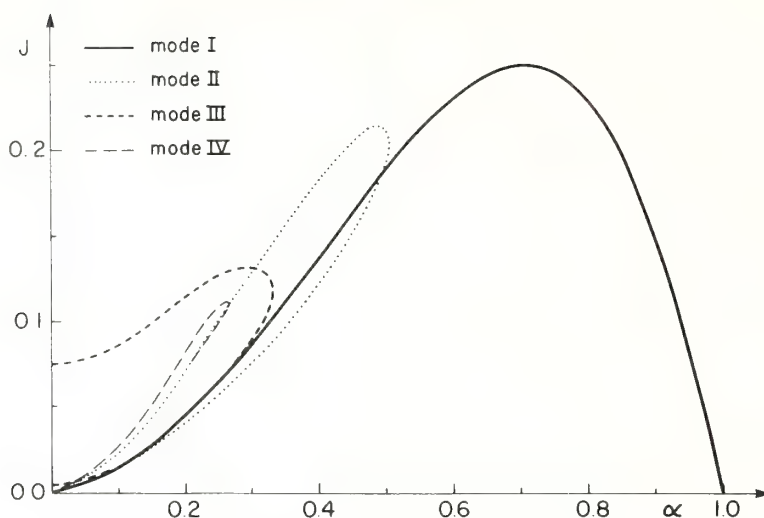
FIG. 2. Stability boundaries, in the normalized wavenumber, minimum Richardson number (α, J) plane for modes I, II, III and IV for $y_i = -10$, $y_f = 10$, $\sigma = 0.1$. Note that the lower branches of modes II and III overlap in part with mode I and the lower branch of mode IV with the upper branch of mode II.
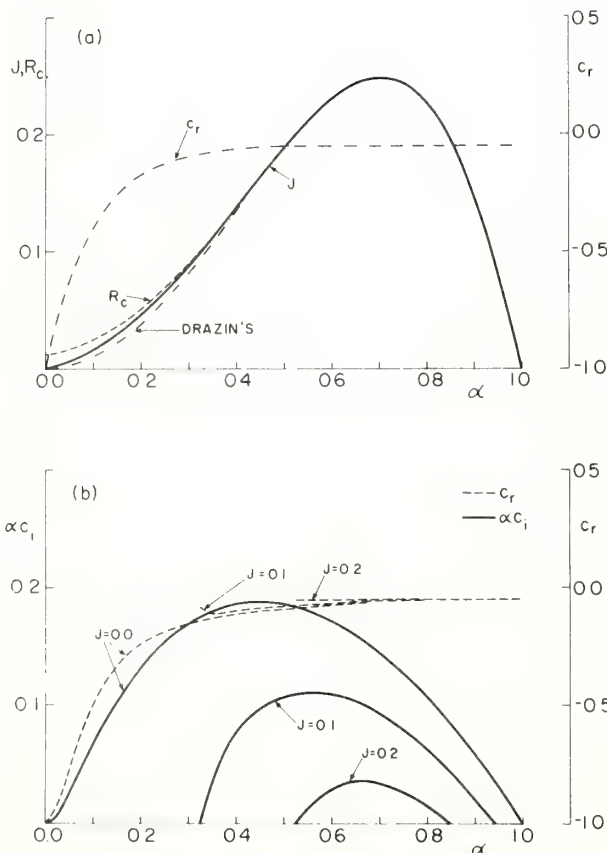
FIG. 3. Mode I stability characteristics for $y_i = z_i/h = -10.0$, $y_f = z_f/h = 10.0$ and $\sigma = 0.1$. (a) J (solid line), R_c (dashed line) and corresponding c_r (dot-dashed line) as a function of $\alpha = k_x h$ for the neutral waves. The dash-double dotted line labeled "Drazin's" corresponds to $\sigma = 0.0$ and $y_i \rightarrow -\infty$, $y_f \rightarrow \infty$; (b) normalized growth rates αc_i (solid lines) and phase velocities c_r (dashed lines) as a function of α for different values of J for the unstable waves.

$y_m = 10^{-4}$ and a one-term series expansion are found to be adequate.

The agreement between the two programs is excellent and, as can be seen from the figures, unstable modes end exactly on neutral modes in the (α, J) plane, except for those modes which intersect the $\alpha = 0$ axis and thus do not end on a neutral curve.

4. Results

The number of the parameters specifying the background flow, i.e., n^2, h, V, J, z_i, etc., is so large that one is forced to limit the investigation to specific parametric studies, three of which are presented below.

a. Results for constant shear thickness 2h

The neutral curves and the properties of the unstable waves are calculated for three different locations of the shear layer inflexion point with respect to the ground. Specifically, the normalized distance between the ground and the inflexion point $y_i = z_i/h$ is taken to be -10.0, -5.0 and -2.0. The normalized height, $y_f = z_f/h$, above which we consider the velocity to be uniform and at which we take (14) to hold, is taken to be 10.0, although any value larger than 5.0 is adequate and no appreciable effect on the eigenvalues and the eigenfunctions is noted. The ratio σ of half the shear layer thickness h to the density scale height H is taken to be $\sigma = h/H = 0.1$; calculations with $\sigma = 0$ are also carried out to ascertain the effect of inertial terms of the density gradient.

Following Thorpe (1969), we choose J as the main stability parameter. For given J, once the phase velocity of a particular mode is known, the value of R_c, the

Richardson number at the critical level for that wave, where $u_0 = c_r$, can be calculated from the relation

$$R_c = \mathrm{Ri}(y_c) = J/(1 - c_r^2)^2. \qquad (15)$$

For each particular geometry we calculate the characteristics of both unstable and neutral modes that may be excited. For the unstable modes, normalized growth rates $\alpha c_i = \omega_i h/V$ and phase velocities c_r are plotted versus $\alpha = k_x h$, for selected values of J. For the neutral modes, c_r, J and R_c are plotted versus α.

For $z_i/h = -10.0$, at least four modes, which we shall call modes I, II, III and IV in order of decreasing growth rates, are found. The neutral curves that comprise the stability boundary for each mode are shown in Fig. 2. The properties of the first three modes are shown in more detail in Figs. 3 and 4. The additional modes IV, V, etc., have growth rates too small to plot and in addition the range of α over which they exist is very narrow. We shall therefore ignore them in the following discussion. For relatively large values of α, only mode I is allowed, with c_r of the order of -0.05. If $\sigma = 0$, the growth rates and the neutral curve for mode I remain the same to less than 1% but c_r is now zero for large α. As $z_i \to -\infty$, mode I coincides with the one found by Drazin (1958) and shown for comparison in Fig. 3a. Modes I and II correspond to waves that are mostly evanescent at large y, i.e., $K_i \gg |K_r|$ with K defined in (13), while mode III corresponds to mostly propagating waves, i.e., $|K_r| \gg K_i$. Near the ground, on the other hand, mode II is mostly propagating, mode I is mostly evanescent, while mode III can be either, depending on the particular values of α and J.
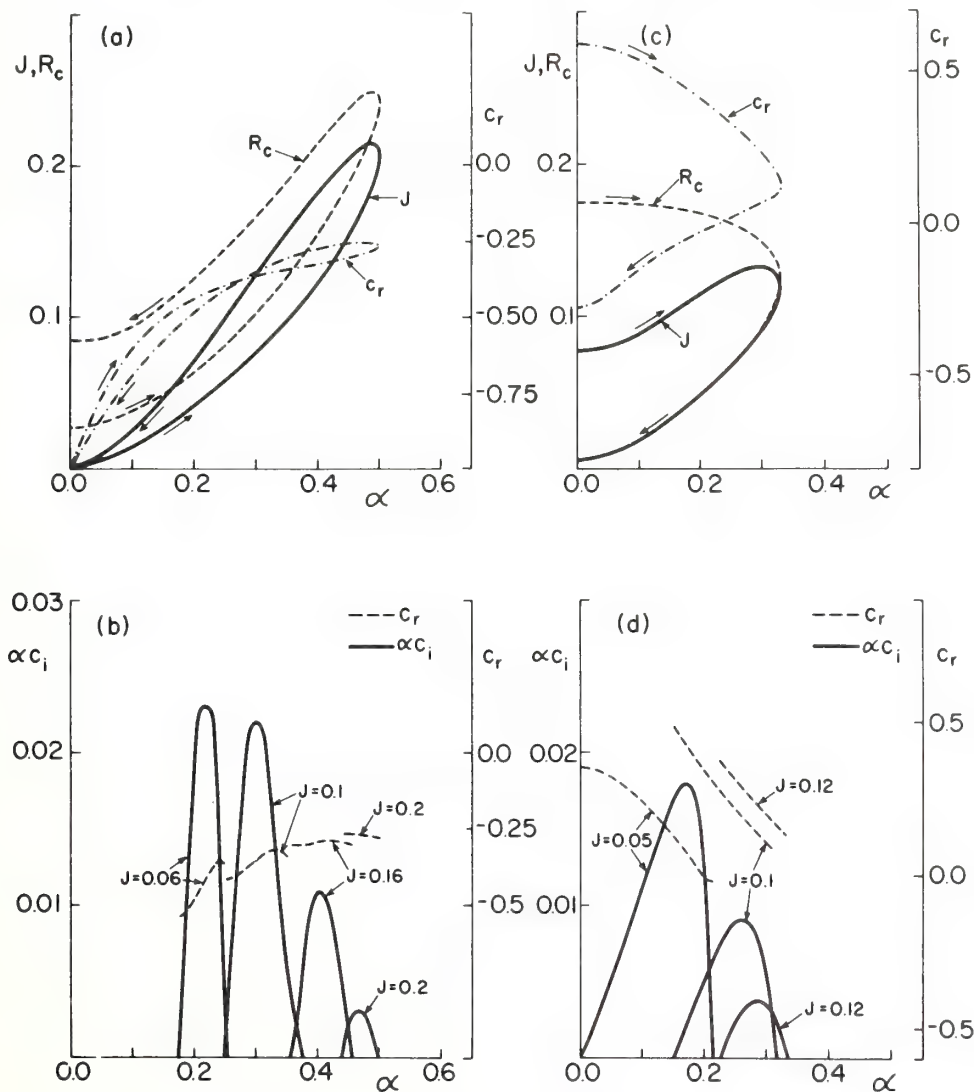
FIG. 4. Mode II and III characteristics for $y_i = -10.0$ and $y_f = 10.0$ and $\sigma = 0.1$ as in Fig. 3: (a) J (solid), R_c (dashed) and c_r (dot-dashed) vs α for mode II neutral waves; (b) αc_i (solid) and c_r (dashed) vs α for different J of mode II unstable waves; (c) as in (a) but for mode III; (d) as in (b) but for mode III.
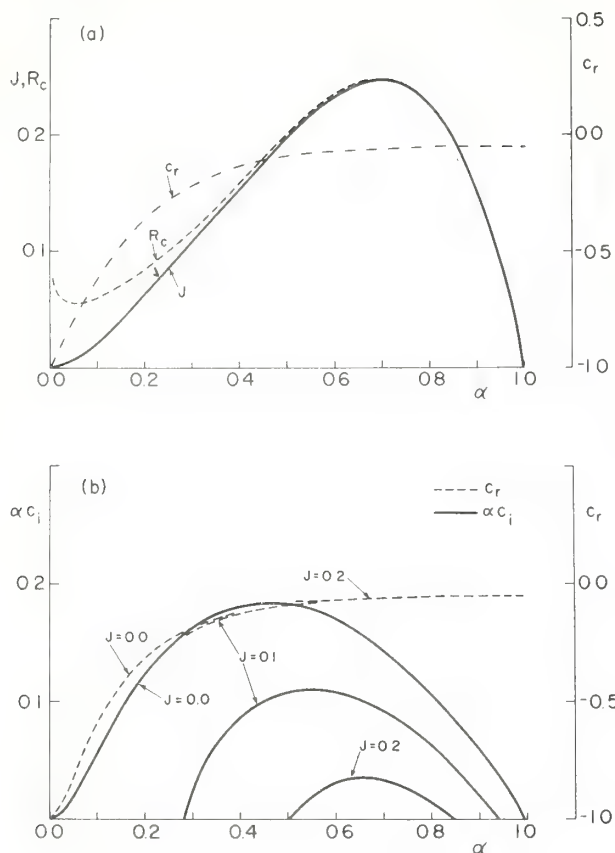
FIG. 5. As in Fig. 3 except for $y_i = z_i/h = -5.0$, mode I.

Figs. 5 and 6 show the wave characteristics for the case of $z_i/h = -5.0$. In this case, mode II has disappeared. The growth rates of mode III are larger than the ones for $z_i/h = -10.0$. Finally, for $z_i/h = -2.0$, the results are plotted in Fig. 7. Mode III has now disappeared as well. The maximum value of α for unstable modes to exist has decreased to $\alpha \approx 0.96$; if $|z_i/h|$ is decreased even further, this maximum value of α will

decrease more and eventually even mode I will disappear in agreement with the results of Jones (1968, first model).

The effect of the distance from the inflexion point to the ground for the propagating mode can be seen more clearly in Fig. 8 where c_i of mode III for $\alpha = 0.01$ is plotted versus z_i/h, for different values of J.

For mode I, at $J = 0.0$, the most unstable wavelength corresponds approximately to $\alpha_{max} \approx 0.46$. The value of α_{max} changes somewhat as J varies between 0 and 0.25; the growth rate αc_i undergoes much larger relative changes as J varies and reaches its maximum at $J = 0.0$, as can be seen from Figs. 3b, 5b and 7b. For modes II and III the most unstable wavelength for given J is a much stronger function of J than for mode I as can be seen from Figs. 4b, 4d and 6b; for example, in Fig. 4d for mode III, at $J = 0.1$, $\alpha_{max} \approx 0.25$ while at $J = 0.05$, $\alpha_{max} \approx 0.15$. The loci of the most unstable wavelengths for each J of modes II and III are lines running almost parallel to the neutral curves that comprise the lower neutral boundary (i.e., bottom solid lines in Figs. 4a, 4c and 6a). Again the actual growth rate αc_i changes as J changes. The approximate values of α and J at which the growth rate αc_i is maximum over the entire (α, J) plane, are given in Table 1, for each mode and for each of the three values of z_i/h considered.

The phase velocity of all modes that are mostly evanescent on top (i.e., I, II, IV, etc.) is seen to go to -1 for long wavelengths, with corresponding critical levels going toward the lower edge of the shear layer, where the local Richardson number is large; thus the growth rates will be small.

The eigenfunctions $Z_c = \mathrm{Re}(\psi)$ and $Z_s = -\mathrm{Im}(\psi)$ that correspond to the most unstable wavelengths of each mode for $z_i/h = -10.0$ and $J = 0.1$ are plotted in Fig. 9. The normalization is with respect to the value of their
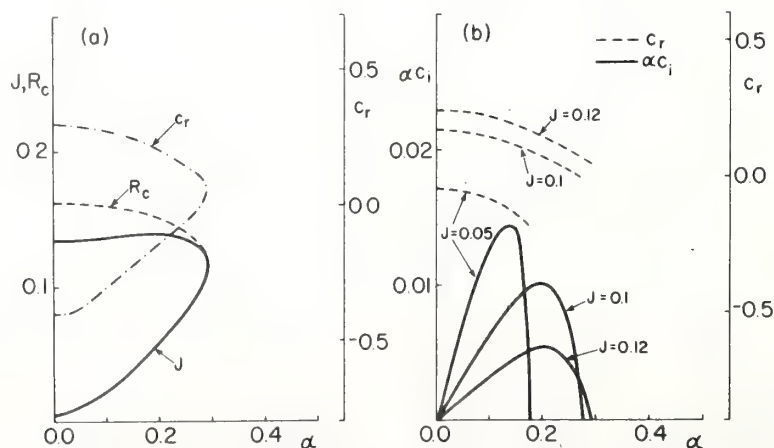
FIG. 6. As in Figs. 4c and 4d except for $y_i = -5.0$, mode III.

derivatives on the ground so that

$$\left(\frac{dZ_c}{dy}\right)_{y_i} = \left(\frac{dZ_s}{dy}\right)_{y_i} = 1.0. \qquad (16)$$

This normalization scheme is chosen with the idea that microbarograph data on the ground can be used to provide the amplitude for specific cases. In Fig. 10, the eigenfunctions of mode I for $J=0.0$ and $\alpha=0.01$ are plotted for $z_i/h = -10.0$ and $z_i/h = -2.0$ to demonstrate the effects of the distance of the ground from the inflexion point.

Additional information concerning the modes described in Fig. 9 is given in Table 2, where the normalized vertical wavelength $\lambda_z = 2\pi/K_r$ and the normalized vertical e-folding length $\delta_z = 1/K_i$ are expressed in terms of the distance $\Delta y = |(y_i - y_c)|$ between the critical level and the ground. The values of λ_z and δ_z are calculated at $y = y_f$ and $y = y_i$, i.e., well in the regions of almost constant velocity. As can also be seen from Fig. 9, mode I is mostly evanescent above and below while mode II is mostly evanescent above but propagating below. Mode III is mostly propagating above; in the lower region it is propagating but K_i and K_r are of the same order. Furthermore, in the bottom
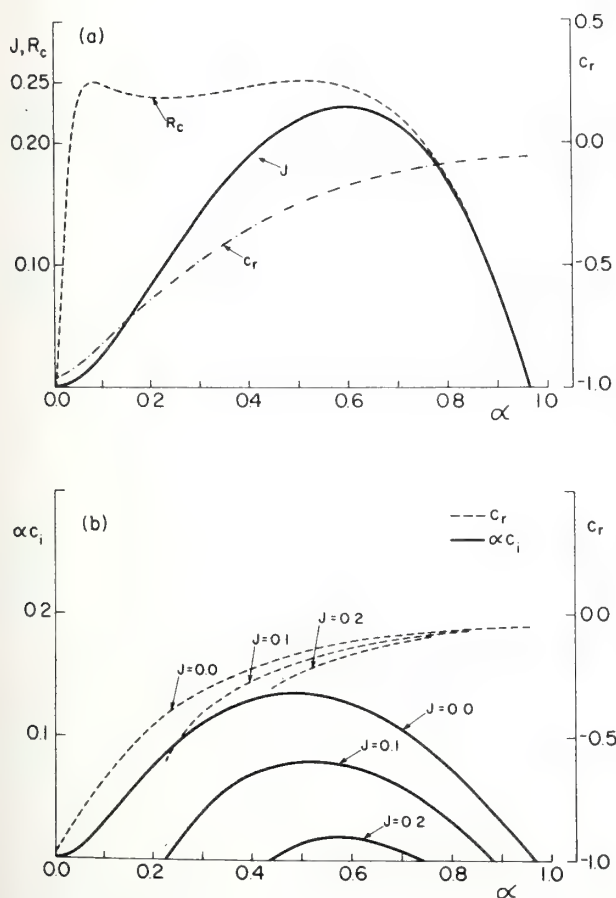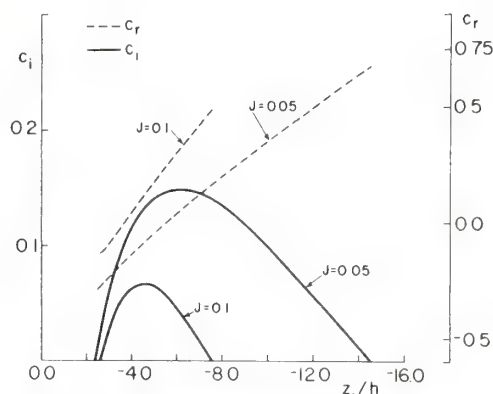
FIG. 8. Normalized imaginary c_i (solid line) and real c_r (dashed line) parts of the horizontal phase velocity of mode III unstable waves, for two different values of J, as a function of the normalized distance y_i between the inflexion point and the ground. Here $y_f = 10.0$, $\alpha = 0.01$ and $\sigma = 0.1$.

layer and for $J=0.1$, mode II has a λ_z which is approximately twice Δy and mode IV (which is not shown in Fig. 9 but which has similar characteristics to those of mode II) has a horizontal phase velocity which is about twice that of mode II and a $\lambda_z/\Delta y$ of about 1. It appears therefore that the modes which are mostly propagating in the bottom layer may be due to resonance between the critical level and the solid surface below, as suggested by Lilly (private communication) and in qualitative agreement with the "quantization of the real part of the vertical wavenumber" observed by Lindzen and Rosenthal (1976).

To check the range of applicability of the above results, the validity of the Boussinesq approximation and the influence of the inertia terms, we have carried out extensive calculations with the fully compressible equations, as well as with $\sigma = 0.0$ in Eq. (10). The results were substantially the same with the most noticeable difference in the values for c_r. This change in c_r does not affect the neutral boundary of mode I at all and results in a small shift upward, for mode II, of no more than 5%, and a shift downward, for mode III, of approximately 25% in the most extreme cases and of much less elsewhere. In future calculations, it is recommended that the fully compressible equations, as given for example by Chimonas (1970), be used since they do not introduce any new numerical problems. Thus approximations which are adequate for the present profiles need not be invoked.

FIG. 7. As in Fig. 3 except for $y_i = z_i/h = -2.0$, mode I.

TABLE 1. The approximate values of α and J at which αc_i is maximum of the entire αJ plane.

	$z_i/h = -10.0$		$z_i/h = -5.0$		$z_i/h = -2.0$	
	α	J	α	J	α	J
Mode I	0.46	0.0	0.46	0.0	0.48	0.0
Mode II	0.25	0.07	—		—	
Mode III	0.17	0.05	0.135	0.05	—	
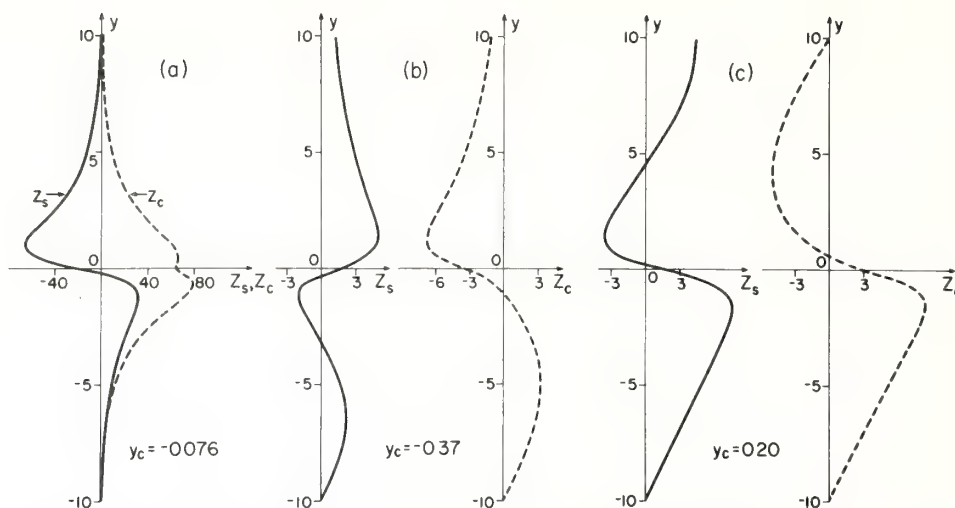
FIG. 9. Plots of $Z_c = \mathrm{Re}(\psi)$ and $Z_s = -\mathrm{Im}(\psi)$, the vertical velocities weighted by $\rho_0^{-\frac{1}{2}}$, for $J = 0.1$ and $\sigma = 0.1$: (a) mode I with $\alpha = 0.56$, $c_r = -0.07581$ and $c_i = 0.1974$; (b) mode II with $\alpha = 0.3$, $c_r = -0.3539$ and $c_i = 0.07298$; (c) mode III with $\alpha = 0.26$, $c_r = 0.1953$ and $c_i = 0.03475$. The wavelengths for each mode correspond to the most unstable wave for $J = 0.1$ as can be seen from Figs. 3 and 4.

For the results presented up to now, h is considered constant and therefore variations in $J = n^2 h^2 / V^2$ are due to variations in n^2/V^2. In Figs. 2–7 we choose $\sigma = h/H = 0.1$ which implies that H and n^2 are also constant, and thus variations in J are due entirely to variations in V. Yet since the presence of σ is found to have a small effect on the results as discussed above, within reasonable accuracy, variations in J can also be attributed to variations in n^2. In this approximation, the results can be applied to boundary layer situations

as well. In either case, one cannot compare these results with the limiting case of the discontinuous Helmholtz profile studied by Lalas et al. (1976) for which $h \to 0$, but z_i and k_x remain finite.

b. Results for z_i constant and varying h

To study the effect of varying h, the equations are renormalized with respect to a length L, which we take to be proportional to z_i, a constant. The minimum
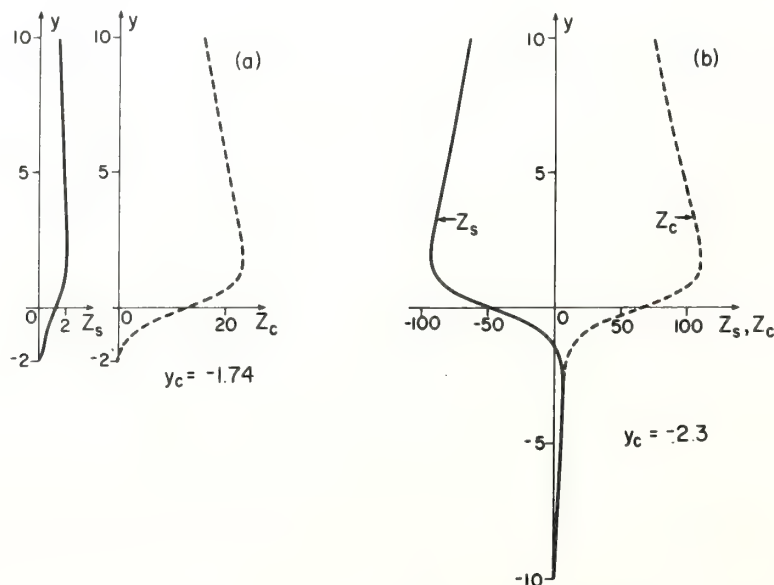
FIG. 10. Plots of Z_c and Z_s, the vertical velocities weighted by $\rho_0^{-\frac{1}{2}}$, for an unstable wave of mode I with $J = 0.0$, $\alpha = 0.01$ and $\sigma = 0.1$ to illustrate the effect of a change in y_i. (a) $y_i = z_i/h = -2.0$ for which $c_r = -0.9399$ and $c_i = 0.01969$; (b) $y_i = z_i/h = -10.0$ for which $c_r = -0.9802$ and $c_i = 0.08801$.

Richardson number J now becomes

$$J = \left(\frac{n^2 L^2}{V^2}\right)\left(\frac{h^2}{L^2}\right) = \tilde{J}\left(\frac{h}{L}\right)^2, \qquad (17)$$

and its variation is now due to changes of the ratio h/L, if we keep $\tilde{J}$ constant. For the following calculations, we choose $L = |z_i|/10$ and $\tilde{J} = 0.0748$. These values of L and $\tilde{J}$ make the eigenvalues equal to the ones of the constant h case with $y_i = -10.0$, at $\alpha = 0.01$ and $h/L = 1.0$, which implies $J = 0.0748$. The singular neutral mode plots in the $(\tilde{\alpha}, J)$ plane, with $\tilde{\alpha} = k_x L = \alpha(L/h)$, are shown in Fig. 11. The limit $\tilde{\alpha} \to 0$ corresponds to $k_x \to 0$, and the limit $J \to 0$ corresponds to the Kelvin–Helmholtz discontinuous profile. The values of $\tilde{\alpha}$ for which the neutral curves cut the $J = 0$ axis are $\tilde{\alpha}_{Ia} = \tilde{\alpha}_{Ib} \approx 0.25$, $\tilde{\alpha}_{II} \approx 0.185$ with $c_{rIa} \approx -0.081$, $c_{rIb} \approx 0.0$ and $c_{rII} \approx -0.46$; the renormalized vertical wavenumber K at large y is now approximately zero for all three modes although the zero is approached through imaginary values for modes Ia and II and real values for mode Ib. These values are in complete agreement with the results of Lalas *et al.* (1976) and can be calculated from their Eq. (31), with the appropriate translation of variables and normalizing quantities. In future numerical work, Eq. (31) of Lalas *et al.* (1976) can be used to provide initial starting points for all modes at $J = 0.0$.

It should be pointed out that for $J = 0.0$, we now have at least two modes, as opposed to the case with h constant, in which $J = 0.0$ corresponds to zero stratification, and then only one, the Rayleigh (1880), mode is present.

Mode Ia,b is equivalent to the neutral mode calculated by Jones in his second model and shown in his Figs. 5 and 6. Mode II and the additional smaller modes not plotted here were not found by Jones.

The phase velocity of mode Ia varies between -0.08

TABLE 2. Values of λ_z and δ_z as a function of Δy.

	Modes		
	I ($\Delta y = 9.92$)	II ($\Delta y = 9.65$)	III ($\Delta y = 10.19$)
$\delta_z/\Delta y$ above	0.206	0.527	4.28
$\lambda_z/\Delta y$ above	20.8	43.8	2.13
$\delta_z/\Delta y$ below	0.217	1.48	2.10
$\lambda_z/\Delta y$ below	12.8	1.72	14.17

at $\tilde{\alpha} = 0.253$ to a minimum of -0.104 at $\tilde{\alpha} = 0.37$ and goes toward -0.05 for large $\tilde{\alpha}$. Mode Ia is evanescent near the ground and at large heights. Mode II is also evanescent at large heights but propagating near the ground with $-1.0 < c_r < -0.46$, while mode Ib is propagating on top and evanescent near the ground with c_r varying between 0.6 down to -0.03 as $\tilde{\alpha}$ increases. The neutral curves for modes Ia and II appear to asymptotically approach zero as $\tilde{\alpha}$ increases. The numerical calculation is stopped at the points shown in Fig. 11 only for the purpose of reducing computing time.

c. The effect of an abrupt increase of the static stability at large heights

The static stability of the atmosphere is often observed to increase substantially at tropopause heights—a fourfold increase in n^2 is not unusual. Such an abrupt change in n^2 has been found in other studies, as, for example, in lee wave dynamics (Klemp and Lilly, 1975), to give rise to constructive interaction between upgoing and downgoing waves. To examine this effect, we modify the background Brunt–Väisälä frequency so that n^2 above $y = y_f$ is four times the value below. The neutral mode curve in the (α, J) plane is shown for h fixed, $y_i = -10.0$, $y_f = 10.0$ and $\sigma = 0.0$ in Fig. 12. The main feature is that the distinct structure of each
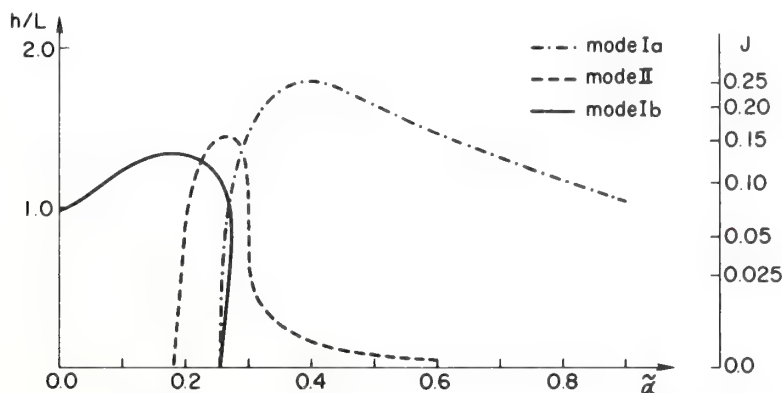
FIG. 11. Neutral wave plots in the $(\tilde{\alpha}, J)$ or $(\tilde{\alpha}, h/L)$ plane $[J = 0.0748(h/L)^2]$ for the case of a variable thickness shear layer with the distance between the inflexion point and the ground equal to $10L$. The variation of density in the inertial term of the momentum equation is included. Note that $\tilde{\alpha} = k_x L = \alpha L/h$. Mode I comprises two branches, Ia evanescent and Ib propagating in the top layer.
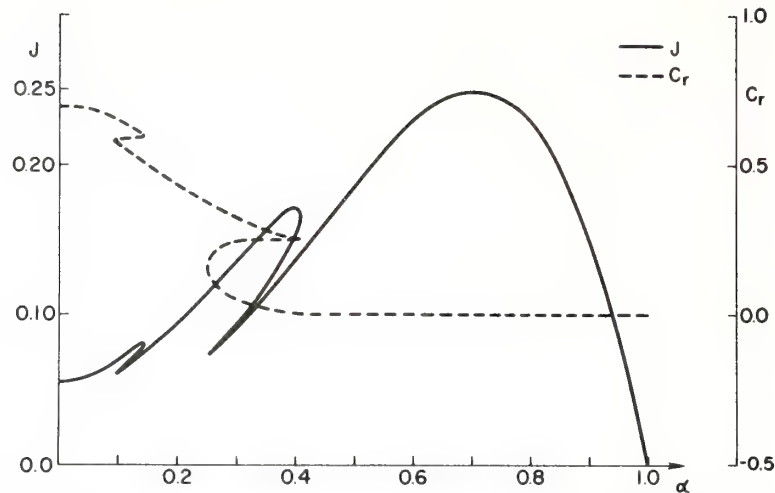
Fig. 12. Neutral wave plots in the (α, J) plane for $y_i = -10.0$, $y_f = 10.0$ and $\sigma = 0.0$ with n^2, the square of the Brunt–Väisälä frequency, above $y_f = 10.0$ equal to four times n^2 below $y_f = 10.0$.

mode has now disappeared. Vestiges of the modal structure remain, but now there are no separate neutral boundaries for each mode in the (α, J) plane projection. The neutral waves are propagating in the top layer $y > y_f$ and so are the unstable ones except for large values of α where they become mostly evanescent. The transition, though, in this case is continuous, with K_r/K_i going through 1 smoothly as α increases. No specific resonance was noticed in this particular example; the growth rates do not differ substantially for the case without a jump in static stability and the changes in the total unstable region in the (α, J) plane are small.

5. Conclusions

We have shown in this paper that an atmospheric shear layer, modeled by a hyperbolic-tangent velocity profile and a constant background temperature, in the presence of the ground, can support a number of unstable modes, in addition to the classical one discussed in the literature and labeled I in our figures. The properties of these modes and the consequences of their existence can be summarized as follows:

1) For given J and for each mode there exists a most unstable wave with wavelength λ_m. The values of λ_m for the additional modes are much larger than λ_m for mode I.

2) Unstable waves exist, for non-zero J, in the limit of $k_x \to 0$ and are always propagating in the top region. In the region near the ground they are either mostly propagating or mostly evanescent dependent on the actual value of J.

3) For a shear layer of given thickness, small wavelengths correspond to evanescent waves both above and below the shear layer. For large wavelengths there

exist modes that are mainly propagating both above and below, or only above, or only below the layer. Such waves always belong to the additional modes, while mode I is always evanescent above and below the shear layer. The consequences of the ability of these waves to propagate and thus transport energy away from the shear layer are bound to be important in determining the vertical structure of the atmosphere and the coupling of mesoscale motions to microscale phenomena.

4) The growth rates of the additional modes are usually smaller than the corresponding ones for mode I and for the same J. As pointed out by Jones (1968), this is probably due to the fact that the propagation of energy away from the shear zone by the waves reduces the amount of energy available to them for temporal growth.

5) The system has the capability of exciting more than a single wavelength with maximum growth rate. This capability seems to be due to the presence of the ground which allows the kinematic conditions at the interface to be satisfied by more than one frequency and phase velocity by introducing an up-going wave in the layer between the shear zone and the ground. The ultimate wavelengths which will be observed in such a shear flow in the atmosphere will depend on a number of factors such as topography, horizontal inhomogeneities, initial growth rates as predicted by linear theory, as well as nonlinear effects. The latter have been studied recently by Tanaka (1975) who indicates that, for the only mode he has, long wavelength waves which have linear growth rates much smaller for given J than the short wavelength ones, may attain larger asymptotic amplitudes and may eventually become dominant.

Finally it should be mentioned that the possibility of

additional modes existing especially in the region of small values of α and large values of J cannot be excluded.

Characteristics of wave generation in actual atmospheric flows, once the velocity and temperature profiles are known, can be readily obtained by the present numerical technique, although care should be taken to insure that all modes of interest have been identified.

REFERENCES

Atlas, D., J. I. Metcalf, J. H. Richter and E. E. Gossard, 1970: The birth of "CAT" and microscale turbulence. *J. Atmos. Sci.*, **27**, 903–913.

Blumen, W., P. G. Drazin and D. F. Billings, 1975: Shear layer instability of an inviscid compressible fluid. Part 2. *J. Fluid Mech.*, **71**, 305–316.

Bulrisch, R., and J. Stoer, 1966: Numerical treatment of ordinary differential equations by extrapolation methods. *Num. Math.*, **8**, 1–13.

Chimonas, G., 1970: The extension of the Miles–Howard theorem to compressible flows. *J. Fluid Mech.*, **43**, 833–836.

Dickinson, R. E., 1973: Baroclinic instability of an unbounded zonal shear flow in a compressible atmosphere. *J. Atmos. Sci.*, **30**, 1520–1527.

——, and F. J. Clare, 1973: Numerical study of the unstable modes of a hyperbolic-tangent barotropic shear flow. *J. Atmos. Sci.*, **30**, 1035–1049.

Drazin, P. G., 1958: The stability of a shear layer in an unbounded heterogeneous inviscid fluid. *J. Fluid Mech.*, **4**, 214–224.

——, and L. N. Howard, 1966: Hydrodynamic stability of parallel flow of inviscid fluids. *Advances in Applied Mechanics*, Vol. 9, Academic Press, 1–89.

Einaudi, F., and D. P. Lalas, 1974: Some new properties of Kelvin–Helmholtz waves in an atmosphere with and without condensation effects. *J. Atmos. Sci.*, **31**, 1995–2007.

——, and ——, 1976: The effect of boundaries on the stability of inviscid stratified shear flows. *J. Appl. Mech.* (in press).

Emmanuel, C. B., 1973: Richardson number profiles through shear instability wave regions observed in the lower planetary boundary layer. *Boundary-Layer Meteor.*, **5**, 19–27.

Goldstein, S., 1931: On the stability of superposed streams of fluids of different densities. *Proc. Roy. Soc. London*, **A132**, 524–547.

Gossard, E. E., 1974: Dynamic stability of an isentropic shear layer in a statically stable medium. *J. Atmos. Sci.*, **31**, 483–492.

Hazel, P., 1972: Numerical studies of the stability of inviscid stratified shear flows. *J. Fluid Mech.*, **51**, 39–62.

Hines, C. O., 1974: *The Upper Atmosphere in Motion. Geophys. Monogr.*, No. 18, Amer. Geophys. Union, 248–328.

Hooke, W. H., F. F. Hall and E. E. Gossard, 1973: Observed generation of an atmospheric gravity wave by shear instability in the mean flow of the planetary boundary layer. *Boundary Layer Meteor.*, **5**, 29–41.

——, and K. R. Hardy, 1975: Further study of the atmospheric gravity waves over the eastern seaboard on 18 March 1969. *J. Appl. Meteor.*, **14**, 31–38.

Howard, L. N., 1961: Note on a paper by John W. Miles. *J. Fluid Mech.*, **10**, 509–512.

——, 1964: The number of unstable modes in hydrodynamic stability problems. *J. Mec.*, **3**, 433–443.

——, and S. A. Maslowe, 1973: Stability of stratified shear flows. *Boundary Layer Meteor.*, **4**, 511–523.

Hull, T. E., W. H. Enright, B. M. Fellen and A. E. Sedgwick, 1972: Comparing numerical methods for ordinary differential equations. *SIAM J. Num. Anal.*, **9**, 603–637.

Ince, E. L., 1956: *Ordinary Differential Equations.* Dover, 405 pp.

Jones, W. L., 1968: Reflexion and stability of waves in stably stratified fluids with shear flow: A numerical study. *J. Fluid Mech.*, **34**, 609–624.

Klemp, J., and D. K. Lilly, 1975: The dynamics of wave-induced downslope winds. *J. Atmos. Sci.*, **32**, 320–339.

Lalas, D. P., F. Einaudi and D. Fua, 1976: The destabilizing effect of the ground on Kelvin–Helmholtz waves in the atmosphere. *J. Atmos. Sci.*, **33**, 59–69.

Lindzen, R. S., 1974: Stability of a Helmholtz velocity profile in a continuously stratified, infinite Boussinesq fluid. Applications to clear air turbulence. *J. Atmos. Sci.*, **31**, 1507–1514.

——, and A. J. Rosenthal, 1976: On the instability of Helmholtz velocity profiles in stably stratified fluids when a lower boundary is present. Submitted to J. Geophys. Res.

Maslowe, S. A., and R. E. Kelly, 1971: Inviscid instability of an unbounded heterogeneous shear layer. *J. Fluid Mech.*, **48**, 405–415.

Miles, J. W., 1961: On the stability of heterogeneous shear flow. *J. Fluid Mech.*, **10**, 496–508.

——, and L. N. Howard, 1964: Note on a heterogeneous shear flow. *J. Fluid Mech.*, **20**, 331–336.

Rayleigh, Lord, 1880: On the stability, or instability, of certain fluid motions. *Proc. London Math. Soc.*, **11**, 57–70.

Reed, R. J., and K. R. Hardy, 1972: A case study of persistent, intense, clear air turbulence in an upper level frontal zone. *J. Appl. Meteor.*, **11**, 541–549.

Tanaka, H., 1975: Quasi-linear and non-linear interactions of finite amplitude perturbations in a stably stratified fluid with hyperbolic tangent-shear. *J. Meteor. Soc., Japan*, **53**, 1–31.

Taylor, G. I., 1931: Effect of variation in density on the stability of superposed streams of fluid. *Proc. Roy. Soc. London*, **A132**, 499–523.

Thorpe, S. A., 1969: Experiments on the stability of stratified shear flows. *Radio Sci.*, **4**, 1327–1331.

——, 1973: Turbulence in stratified fluids: A review of laboratory experiments. *Boundary Layer Meteor.*, **5**, 95–119.

Uccellini, L. W., 1975: A case study of apparent gravity wave initiation of severe convective storms. *Mon. Wea. Rev.*, **103**, 497–513.

Woods, J. D., 1968: Wave induced shear instability in the summer thermocline. *J. Fluid Mech.*, **32**, 791–800.

The Destabilizing Effect of the Ground on Kelvin-Helmholtz Waves in the Atmosphere

D. P. LALAS

Department of Mechanical Engineering Sciences, Wayne State University, Detroit, Mich. 48202

F. EINAUDI

Cooperative Institute for Research in Environmental Sciences, University of Colorado/NOAA and Aeronomy Laboratory, NOAA, Boulder, Colo. 80302

D. FUA[1]

Cooperative Institute for Research in Environmental Sciences, University of Colorado/NOAA, Boulder, Colo. 80302

ABSTRACT

The simple Kelvin-Helmholtz model for shear zones in the atmosphere is modified, by introducing a solid boundary below to account for the effect of the ground. The new characteristics of neutral and unstable waves that can exist in such configuration are analyzed for various values of wind velocity, depth of the bottom layer, and Brunt-Väisälä frequency. It is shown that the presence of the ground considerably destabilizes waves with long horizontal wavelengths. In particular, long wavelengths are always unstable, so that no neutral stability boundary exists. Furthermore, the solid lower boundary introduces an infinite number of neutral modes, all of which correspond to evanescent waves in the top layer. Finally, the model with the ground is used to calculate the characteristics of the most unstable waves that would be generated for some well-documented observed cases and the calculated values are found to be in reasonable agreement with observations.

1. Introduction

Vertical shear of the horizontal background wind velocity is known to be the cause of a variety of dynamic phenomena in the atmosphere, such as clear air turbulence, generation of gravity waves, billow clouds, etc. If the shear is concentrated over a height interval small compared with vertical wavelengths of interest, the situation can be modeled by two semi-infinite layers with constant but different velocities. In each layer, the temperature and, hence, the Brunt-Väisälä frequency are also assumed constant. The characteristics of this model are well known, and additional features have been analyzed lately by Lindzen (1974) and Einaudi and Lalas (1974).

Recently, the number of waves detected in the atmosphere that may be attributed to shear zones has been increasing. The observed wavelengths are, at times, considerably longer than the longest possible unstable wavelengths predicted by the Kelvin-Helmholtz model. This may be due to a number of reasons, the most apparent of which are the discontinuity of the background profiles and the absence of a solid lower boundary.

Continuous velocity and temperature profiles in an infinite medium have been analyzed by various authors (Drazin, 1958; Miles and Howard, 1964), and we refer to the paper by Drazin and Howard (1966) for a complete review of the subject. A continuous velocity profile indeed allows longer wavelengths to be excited, but only at very small Richardson numbers, which are seldom observed in the atmosphere. In particular, horizontal wavelengths of the order of 50–100 km have been reported (Lilly, private communication) by ground-based pressure measurements without evidence of particularly small Richardson numbers aloft, thus suggesting that the continuous profile alone does not eliminate the discrepancy between theory and observations.

We propose in this paper to analyze the second effect, i.e., the presence of the ground which requires that the vertical velocity vanish there. Such a boundary condition is known to influence the wavelength spectrum considerably (Yih, 1969) and to cause the appearance of a variety of new modes which, as we

---

[1] On a fellowship from the National Research Council of Italy.
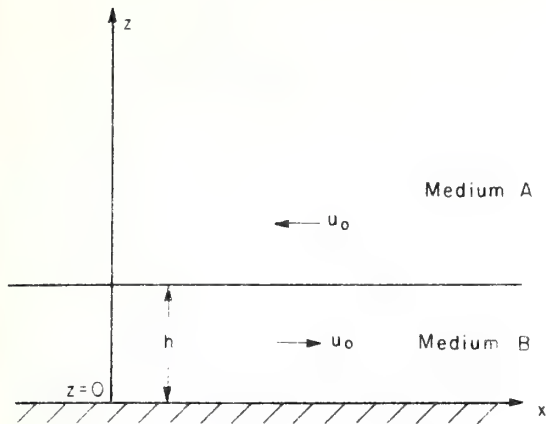
FIG. 1. The geometry of the system.

shall demonstrate, bring theory in much closer agreement with observations.

A three-layer model in the presence of the ground has been considered recently by Gossard (1974); his model, however, includes a neutrally stable isentropic middle layer, so that the effect of the ground itself cannot be separated and analyzed. Jones (1968) analyzes numerically three models in which the background density is an exponentially decreasing function of height. Model I has a constant shear layer bounded from below by a solid surface and from above by a fluid of infinite depth whose velocity is constant. Model II is a similar model, but with an intermediate layer of uniform velocity between the ground and the bottom of the shear layer; the velocity in the layer adjacent to the ground is equal to that at the bottom of the shear zone. Model III is like model II, with the ground removed. Jones finds that the first model is always stable, that the second model is unstable for all wavenumbers, while the third model is unstable only for large wavenumbers. By comparing models II and III, one can conclude that the ground destabilizes the system. However, comparing models I and II, one concludes that the position of the ground may have a stabilizing effect on all wavelengths, since no instability exists for model I.

Our calculations are carried out, in the Boussinesq approximation, for a Kelvin-Helmholtz profile bounded from below by a solid surface, and with the temperature of the two layers, in general, different. When the temperature in both layers is the same, our model can be viewed as a limiting case of Jones' model II. It reveals, however, a modal structure which appears to be absent in Jones' example.

In Section 2, the equations are stated in linearized form, and the governing dispersion equation is derived. An examination of this dispersion equation is carried out in Section 3, and the existence of a whole new family of modes directly attributable to the bottom is identified. In Section 4, unstable modes are investigated, and their growth rates are calculated and

displayed as functions of the horizontal wavelength. It is demonstrated that the effect of the ground is destabilizing. Finally, in Section 5, a comparison of some of these unstable modes with observations of shear waves in the atmosphere is presented, and a recent conjecture by Lindzen (1974) of the role of neutral waves in smoothing out shear layers is re-examined in the light of our calculations of growth rates in the presence of the ground.

2. The governing equations and the resulting dispersion relation

The linearized equations governing the propagation of small perturbations in a stratified atmosphere with a background wind are given by:

$$\frac{d}{dt}\rho' + \rho_0\left(\frac{\partial u'}{\partial x} + \frac{\partial w'}{\partial z}\right) + w'\frac{d\rho_0}{dz} = 0 \tag{1}$$

$$\rho_0\frac{du'}{dt} + \frac{\partial p'}{\partial x} + \rho_0 w'\frac{du_0}{dz} = 0 \tag{2}$$

$$\rho_0\frac{dw'}{dt} + \frac{\partial p'}{\partial z} + \rho' g = 0 \tag{3}$$

$$\rho_0 c_v \frac{dT'}{dt} + p_0\left(\frac{\partial u'}{\partial x} + \frac{\partial w'}{\partial z}\right) = 0 \tag{4}$$

$$p' = R(\rho' T_0 + \rho_0 T'). \tag{5}$$

In the above, p, ρ, u, w, T are the pressure, density, horizontal velocity, vertical velocity and temperature, respectively, with primes indicating perturbation quantities and subscripts 0 referring to background quantities of the unperturbed state, which are assumed to be a function of z only; R is the gas constant; c_v is the specific heat at constant volume; and g is the gravitational acceleration acting in the negative z direction. The total derivative operator d/dt is defined by

$$\frac{d}{dt} = \frac{\partial}{\partial t} + u_0 \frac{\partial}{\partial x}. \tag{6}$$

We wish to consider here a model of the atmosphere that consists of two layers, the properties of which are denoted by subscripts A and B, as shown in Fig. 1. We assume that the temperature is constant in each layer, and we consider a background velocity given by

$$\begin{aligned}\mathbf{u}_{0A} &= -u_0\hat{\mathbf{e}}_x \\ \mathbf{u}_{0B} &= u_0\hat{\mathbf{e}}_x\end{aligned}\Biggr\}, \tag{7}$$

where u_0 is a constant and $\hat{\mathbf{e}}_x$ the unit vector in the x direction. The layer A is semi-infinite, and the depth of layer B, adjacent to the ground, is given by h.

Let us assume that the perturbations are of the form

$$p'(x,z,t) = P \exp(i\theta - z/2H)$$
$$\rho'(x,z,t) = D \exp(i\theta - z/2H)$$
$$u'(x,z,t) = U \exp(i\theta + z/2H)$$
$$w'(x,z,t) = W \exp(i\theta + z/2H)$$
$$\theta = \omega t - k_x x + kz$$
$$\omega = \omega_r + i\omega_i$$

(8)

with ω being the frequency of oscillation, $\lambda_x = 2\pi/k_x$ and $\lambda_z = 2\pi/k$ the horizontal and vertical wavelengths, respectively, $H = RT_0/g$ the scale height for an isothermal atmosphere, and P, D, U, W constant amplitudes. The dispersion relation for propagation in either layer that results from the above assumptions is (Hines, 1960)

$$\Omega^4 - \Omega^2 c^2 (k_x^2 + k^2) + c^2 n^2 k_x^2 - \Omega^2 c^2/(4H^2) = 0, \quad (9)$$

with the Doppler frequency Ω, the sound speed c, and the Brunt-Väisälä frequency n given by

$$\Omega = \omega - k_x u_0, \quad (10)$$

$$c^2 = RT_0 \left(1 + \frac{R}{c_v}\right), \quad (11)$$

$$n^2 = -g \left(\frac{1}{\rho_0} \frac{d\rho_0}{dz} + \frac{g}{c^2}\right). \quad (12)$$

Solving (9) for k, we obtain

$$k_A = \pm \frac{k_x u_0}{c_A} \left\{ (\phi+1)^2 \right.$$
$$\left. - \frac{c_A^2}{u_0^2} \left[1 + \frac{1}{4H_A^2 k_x^2} - \frac{n_A^2}{k_x^2 u_0^2} \frac{1}{(\phi+1)^2} \right] \right\}^{\frac{1}{2}}, \quad (13)$$

for layer A, and

$$k_B = \pm \frac{k_x u_0}{c_B} \left\{ (\phi-1)^2 \right.$$
$$\left. - \frac{c_B^2}{u_0^2} \left[1 + \frac{1}{4H_B^2 k_x^2} - \frac{n_B^2}{k_x^2 u_0^2} \frac{1}{(\phi-1)^2} \right] \right\}^{\frac{1}{2}}, \quad (14)$$

for layer B. In both cases

$$\phi = \omega/(k_x u_0) = \phi_r + i\phi_i \quad (15)$$

is the normalized complex phase velocity.

For waves propagating in the system shown in Fig. 1, one has to impose the appropriate boundary conditions at the ground, at the displaced interface between the two layers, and at infinity. Specifically, at the ground, the boundary condition to be imposed is that the vertical velocity is zero. This necessitates, for a non-trivial solution, the existence of an up-going as well as a down-going wave, denoted, respectively, by the superscripts u and d. The boundary condition at the ground then is

$$W_B^{(u)} + W_B^{(d)} = 0. \quad (16)$$

At the top, we require that the wave decay to zero at infinity or, if it is a neutral propagating wave, that the direction of its energy transport be away from the interface and toward infinity. This implies only one wave and specifies the sign of k_A so that either

$$\text{Im}(k_A) > 0, \quad (17)$$

or, for real k_A,

$$\frac{d\omega}{dk_A} > 0. \quad (18)$$

Finally, at the displaced interface between the two layers we demand that the vertical displacements, calculated on each side, match, i.e.,

$$\frac{W_A}{\Omega_A} \exp(ik_A h + h/2H_A) = \frac{1}{\Omega_B} [W_B^{(u)} \exp(ik_B h)$$
$$+ W_B^{(d)} \exp(-ik_B h)] \exp(h/2H_B), \quad (19)$$

and that the total pressure is continuous, i.e.,

$$-g\rho_{0A}(z=h) \frac{W_A}{i\Omega_A} \exp(ik_A h + h/2H_A)$$
$$+ P_A \exp(ik_A h - h/2H_A)$$
$$= -g\rho_{0B}(z=h) \frac{W_A}{i\Omega_A} \exp(ik_A h + h/2H_A)$$
$$+ P_B^{(u)} \exp(ik_B h - h/2H_B)$$
$$+ P_B^{(d)} \exp(-ik_B h - h/2H_B). \quad (20)$$

Using polarization coefficients derived from Eqs. (1)–(5), we can express P_A in terms of W_A, and $P_B^{(u)}$ and $P_B^{(d)}$ in terms of $W_B^{(u)}$ and $W_B^{(d)}$, so that Eqs. (16), (19) and (20) become three homogeneous equations for the unknowns W_A, $W_B^{(u)}$, $W_B^{(d)}$. Setting the determinant of their coefficients equal to zero, we obtain

$$\rho_{0A}(z=h) \left\{ -g + \frac{c_A^2}{g} \frac{(\Omega_A^2 - n_A^2)}{\left[1 - \frac{c_A^2}{g}\left(\frac{1}{2H_A} - ik_A\right)\right]} \right\}$$
$$= \rho_{0B}(z=h) \left\{ -g + \frac{c_B^2}{g}(\Omega_B^2 - n_B^2)\Phi_0 \right\}, \quad (21)$$

where

$$\Phi_0 = \frac{1}{[\exp(ik_B h) - \exp(-ik_B h)]} \left\{ \frac{\exp(ik_B h)}{\left[1 - \frac{c_B^2}{g}\left(\frac{1}{2H_B} - ik_B\right)\right]} \right.$$
$$\left. - \frac{\exp(-ik_B h)}{\left[1 - \frac{c_B^2}{g}\left(\frac{1}{2H_B} + ik_B\right)\right]} \right\}. \quad (22)$$

If we make use of the Boussinesq approximation, namely, if in (21) as well as in the individual dispersion relations (13) and (14) we consistently neglect terms of order $1/H_A$ compared with k_A, $1/H_B$ compared with k_B, and $(\omega/k_z)^2$ compared with either c_A^2 or c_B^2, we obtain the following simplified form for Eq. (21):

$$g(1-r)+r\frac{\Omega_A{}^2-n_A{}^2}{ik_A}$$

$$=\frac{\Omega_B{}^2-n_B{}^2}{ik_B}\left[\frac{\exp(ik_Bh)+\exp(-ik_Bh)}{\exp(ik_Bh)-\exp(-ik_Bh)}\right], \quad (23)$$

with

$$r=(\rho_{0A}/\rho_{0B})_{z=h}, \quad (24)$$

$$k_A=\pm\frac{k_z}{(\phi+1)}\left[\frac{n_A{}^2}{k_z{}^2u_0{}^2}-(\phi+1)^2\right]^{\frac{1}{2}}, \quad (25)$$

$$k_B=\frac{k_z}{(\phi-1)}\left[\frac{n_B{}^2}{k_z{}^2u_0{}^2}-(\phi-1)^2\right]^{\frac{1}{2}}. \quad (26)$$

The sign in (26) is arbitrarily taken to be positive since its choice does not affect (23). Our main results will stem from the solutions of (23) with the help of (25) and (26) and inequalities (17) or (18).

When the depth h of the bottom layer becomes infinite, Eq. (23) reduces to the one previously studied by Einaudi and Lalas (1974). The effect of the finite depth of the layer results in the presence of the term

$$[\exp(ik_Bh)+\exp(-ik_Bh)]/[\exp(ik_Bh)-\exp(-ik_Bh)]$$

which multiplies the right-hand side of the equation. We will show in the next section that this is sufficient for excitation of other very interesting modes.

3. The neutral modes

Stability boundaries, if any, of a flow separate stable from unstable regimes in parameter space and so by definition belong to the family of solutions of (23) for real eigenvalues ϕ. To examine the existence and location of such stability boundaries, we will investigate all neutral modes that satisfy (23) for different values of the parameters. To facilitate matters, we introduce new non-dimensional variables:

$$\alpha=k_zh \quad (27)$$

$$J_A=\left(\frac{n_Ah}{u_0}\right)^2 \quad (28)$$

$$J_B=\left(\frac{n_Bh}{u_0}\right)^2=J_A/r \quad (29)$$

$$G=\frac{c_p}{R}\frac{H_B}{h}. \quad (30)$$

Here c_p is the specific heat at constant pressure. In terms of these new non-dimensional variables, we rewrite (23) in the form

$$G(1-r)J_B+r\frac{[\alpha^2(1+\phi)^2-J_A]}{i(k_Ah)}$$

$$=\frac{[\alpha^2(1-\phi)^2-J_B]}{i(k_Bh)}\left[\frac{\exp(ik_Bh)+\exp(-ik_Bh)}{\exp(ik_Bh)-\exp(-ik_Bh)}\right]. \quad (31)$$

We notice here again that (31) is independent of the sign of k_B but not of k_A which is to be chosen to satisfy the radiation conditions (17) or (18). Furthermore, one should also notice that for neutral modes, i.e., ϕ real, k_B can be either real or purely imaginary, but in either case the right hand side (R.H.S.) of (31) is always real. This automatically dictates one of two choices: either k_A is imaginary, or the second term in the left hand side (L.H.S.) of (31) is zero. The second term in the L.H.S. of (31) would be zero if either

$$\phi_r=-1, \quad (32)$$

or

$$J_A=\alpha^2(\phi+1)^2. \quad (33)$$

On the other hand, if

$$J_A<\alpha^2(\phi+1)^2, \quad (34)$$

k_A is imaginary. We can then distinguish three classes of neutral curves.

CLASS 1. $\phi_r=-1$, i.e., (32) is satisfied.
The real part of (31) then becomes

$$G(1-r)J_B=i4k_Bh\left[\frac{\exp(ik_Bh)+\exp(-ik_Bh)}{\exp(ik_Bh)-\exp(-ik_Bh)}\right], \quad (35)$$

with

$$hk_B=-\tfrac{1}{2}[J_B-4\alpha^2]^{\frac{1}{2}}. \quad (36)$$

If J_B is larger than $4\alpha^2$, k_B is real and (35) has a countably infinite number of solutions. None of the solutions of (35) goes through the origin of the (α,J_B) plane. The solution corresponding to $k_B=0$ is represented in the (α,J_B) plane by the point

$$J_{B0}=4\frac{R}{c_p}\frac{h}{H_B}\frac{1}{1-r}, \quad \alpha_0=J_B{}^{\frac{1}{2}}/2, \quad r\neq1,$$

while for $J_B<4\alpha^2$, the solution of (35) is given by a single curve in the (α,J_B) plane starting at (α_0,J_{B0}) and proceeding toward larger values of α and J_B. When $r=1$, only the neutral curves corresponding to k_B real are present.
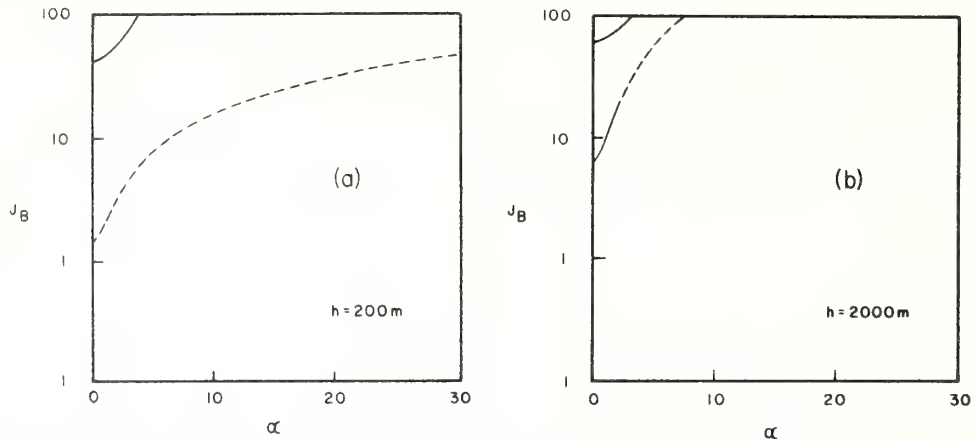
FIG. 2. Neutral curves of class 1 (see text). Solid lines are the neutral curves for waves with k_B real, dashed lines for waves with k_B imaginary; $r = 280/285$: (a) $h = 200$ m, (b) $h = 2000$ m.

CLASS 2. $J_A = \alpha^2(\phi+1)^2$, i.e., (33) is satisfied.

In view of the fact that $J_A = rJ_B$ and $(\phi-1)^2 = [(J_A{}^{\frac{1}{2}}/\alpha) - 2]^2$, Eq. (31) takes the form

$$G(1-r)J_B = i[(rJ_B)^{\frac{1}{2}} - 2\alpha]^2$$

$$\times \frac{k_B h}{\alpha^2} \left[\frac{\exp(ik_B h) + \exp(-ik_B h)}{\exp(ik_B h) - \exp(-ik_B h)} \right], \quad (37)$$

with

$$k_B h = \frac{\{J_B - [(rJ_B)^{\frac{1}{2}} - 2\alpha]^2\}^{\frac{1}{2}}}{\left[\dfrac{(rJ_B)^{\frac{1}{2}}}{\alpha} - 2 \right]}. \quad (38)$$

Since $rJ_B = \alpha^2(\phi+1)^2$, it follows that $(rJ_B)^{\frac{1}{2}} < 2\alpha$ and, from (38), that k_B will be real, zero, or purely imaginary depending on whether J_B is larger, equal to, or smaller than $[2\alpha/(1+r^{\frac{1}{2}})]^2$, respectively. For $r \neq 1$, the same considerations as in class 1 can be repeated here except that ϕ varies now between -1 and 1, and all the neutral curves corresponding to k_B real tend toward the origin of the (α, J_B) plane as $\phi \rightarrow 1$. When $r = 1$, only the curves corresponding to $\phi > 0$, i.e., k_B real, exist.

CLASS 3. Inequality (34) is satisfied, which implies an evanescent wave in the top layer.

In this case, (31) is completely real so that we have only one rather than two relations between α, J_B and ϕ, for fixed r.

It is interesting to compare these results with the ones for two semi-infinite layers for which, following the same non-dimensionalization scheme, with h now being some reference height, the governing equation is

$$G(1-r)J_B + r \frac{[\alpha^2(1+\phi)^2 - J_A]}{ik_A h} = \frac{\alpha^2(1-\phi)^2 - J_B}{ik_B h}. \quad (39)$$

The sign of k_B is now specified by the appropriate radiation conditions at $z = -\infty$. The only difference

between (39) and (31) is the absence of the term

$$[\exp(ik_B h) + \exp(-ik_B h)]/[\exp(ik_B h) - \exp(-ik_B h)].$$

This means that the R.H.S. of (39) can now be real or imaginary. Furthermore, all the countably infinite modes of classes 1 and 2 with k_B real are prohibited for the case of the two semi-infinite layers, and all the remaining modes go through the origin of the (α, J_B) plane.

The existence and nature of the extra modes for the finite bottom eliminate the possibility of a stability boundary. For the neutral curves of (39), the curve $\phi = -1$ constitutes an envelope, so that for given α and r, no neutral curves exist for values of J_B higher than the one satisfying (39) with $\phi = -1$ (see Einaudi and Lalas, 1974). Unstable modes exist only for the points (α, J_B) below this curve. Such an envelope does not exist for the neutral curves of (31), because the modes of class 1 do not go through the origin. Instead, they start at non-zero values of J_B for $\alpha = 0$ and, for given α and r, no matter how large J_B is, there is always a neutral curve above that point in the (α, J_B) plane. If unstable modes exist below each neutral curve of (31), as will be shown to be the case, then the effect of the presence of the ground is to completely destabilize the flow through the introduction of whole new categories of stable and unstable modes that drastically alter the classical Kelvin-Helmholtz (K-H) instability results.

To clarify the above point, we consider in more detail the case $r = 1$, with and without the ground. When the ground is absent, the neutral curves are given by

$$J = 2(1+\phi^2)\alpha^2, \quad (40)$$

which derives from (39). These curves have envelopes given by $J = 4\alpha^2$ for $\phi = \pm 1$ and $J = 2\alpha^2$ for $\phi = 0$. This implies that k_A and k_B are both real.
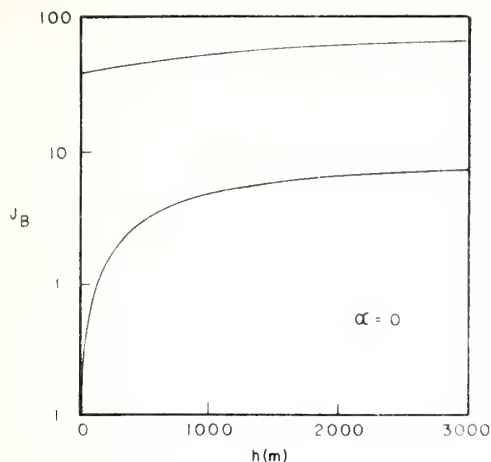
FIG. 3. Neutral curves of class 1 (see text) as a function of the depth of layer B, for very large wavelengths ($\alpha=0$). Solid lines are for $r=280/285$, dotted for $r=1$.

By contrast, in the presence of the ground, the curves of class 1 are now given by

$$J = 4\alpha^2 + \pi^2(2m+1)^2, \quad m=0, 1, 2, \cdots, \quad (41)$$

and are always higher than those given by (40).

The modes of classes 2 and 3 are not relevant for this point since they all tend toward the origin, and

are bounded from above by the modes of class 1 and therefore do not play a major role in trying to find a possible stability boundary for the system.

In Figs. 2a and 2b the lowest two neutral curves are plotted against α for different values of h and for $r=280/285$. In Fig. 3, the lowest two neutral curves of class 1 are plotted against h, for $\alpha=0$: the solid lines refer to the previous value of r and the dotted horizontal ones to $r=1$. The value of $\alpha=0$ has been chosen because the effect of the ground is more pronounced for long wavelengths.

A word of caution may be in order here since class 1 curves demand that $\phi=-1$ which implies that the vertical wavelength in the top (but not in the bottom) layer is zero. This brings the validity of the K-H configuration into question, but does not necessarily invalidate it since k_B is still finite and can still be much smaller than the thickness of the real shear zone.

4. The nature of the unstable modes

If we return now to (31) and allow ϕ_i to be non-zero, we can investigate the possible unstable modes of the system. This was done by solving (31) numerically for given r, J_B, α and G. The results are shown for some typical values of the above parameters in Figs. 4, 5 and 6. Since the equation contains only G, r, J_B
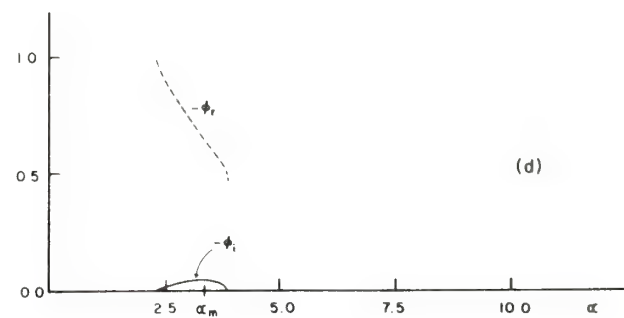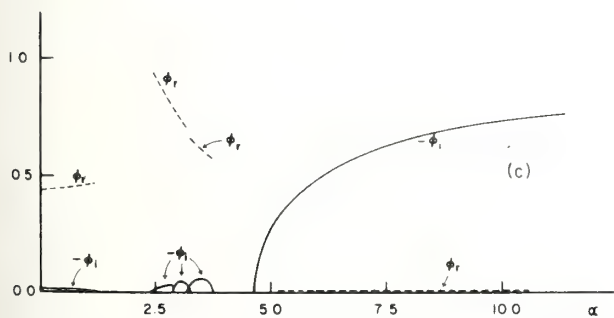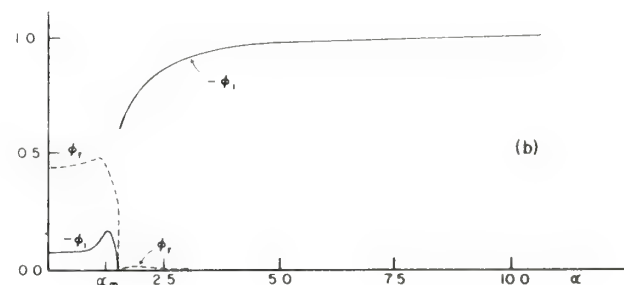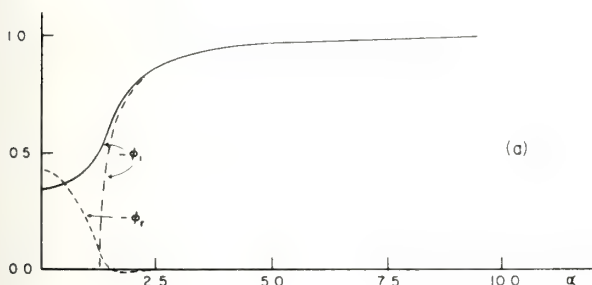
FIG. 4a. Normalized growth rates $-\phi_i = -\omega_i/k_x u_0$ (solid line) and normalized phase velocity $\phi_r = \omega_r/k_x u_0$ (dashed line) as a function of α, for $u_0 = 2$ m s^{-1}, $h=200$ m, $r=1$ and $J_B=3.43$ (corresponding to B-V frequency $n_B = 1.85 \times 10^{-2}$ s^{-1}). The dot-dash line is the normalized growth rate for the same u_0 and n_B but for an infinite bottom layer for which $\phi_r=0$.

FIG. 4b. As in Fig. 4a, mode II.

FIG. 4c. As in Fig. 4a, but with $r=280/285$, corresponding to $\Delta T = 5$ K between the two layers.

FIG. 4d. As in Fig. 4c, additional mode.

and α, one does not have to specify explicitly u_0, T_0 and h, although these are connected through the definitions of J_B and G.

Some features of the normalized phase velocity and growth rate should be pointed out.

1) ϕ_i is not zero for $\alpha=0$, i.e., there is no value of α, no matter how small, for which unstable modes do not exist.

2) The number of modes varies with the value of parameters, even at $\alpha=0$. To make this point clearer,
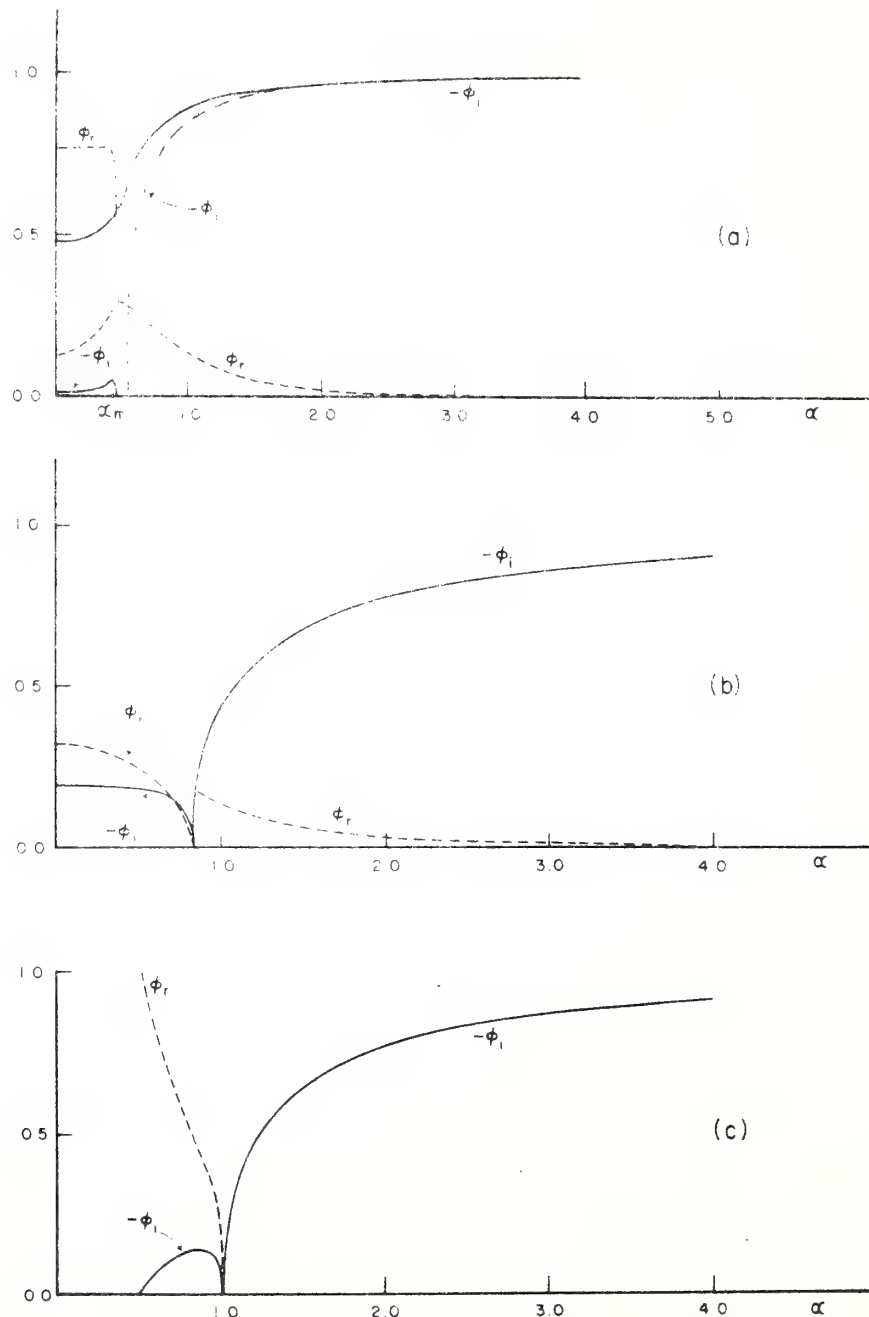
FIG. 5a. As in Fig. 4a but with $u_0=5$ m s^{-1}. Here $h=200$ m, $r=1$ and
$n_B=1.85\times10^{-2}$ s^{-1}, but $J_B=0.549$.

FIG. 5b. As in Fig. 5a but with $r=280/285$, i.e., $\Delta T=5$ K between layers.

FIG. 5c. As in Fig. 5b but with an infinite bottom layer,
for comparison purposes.
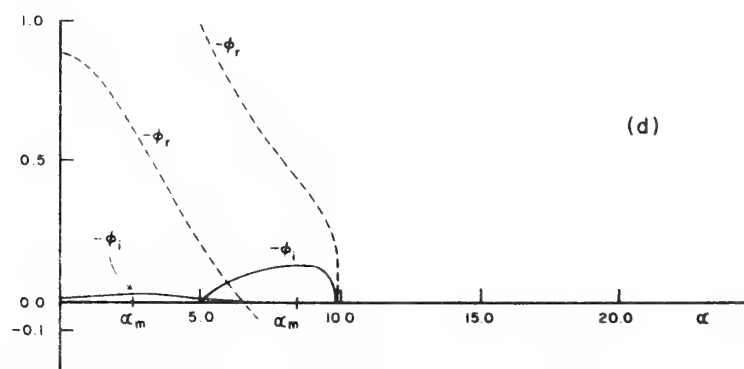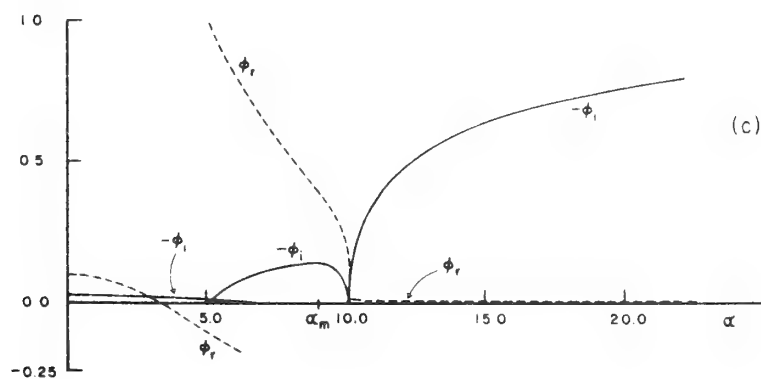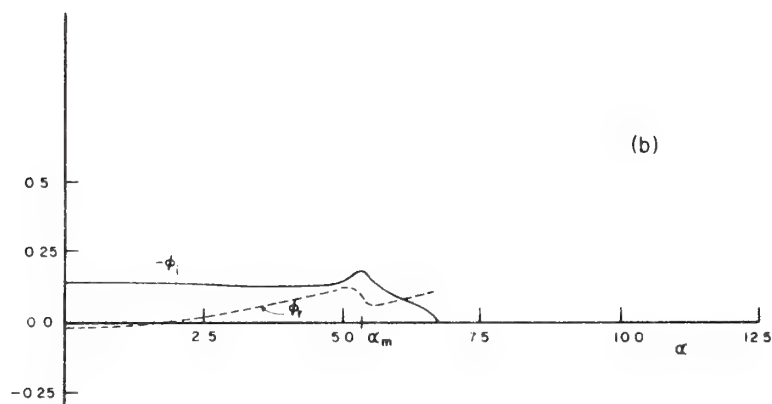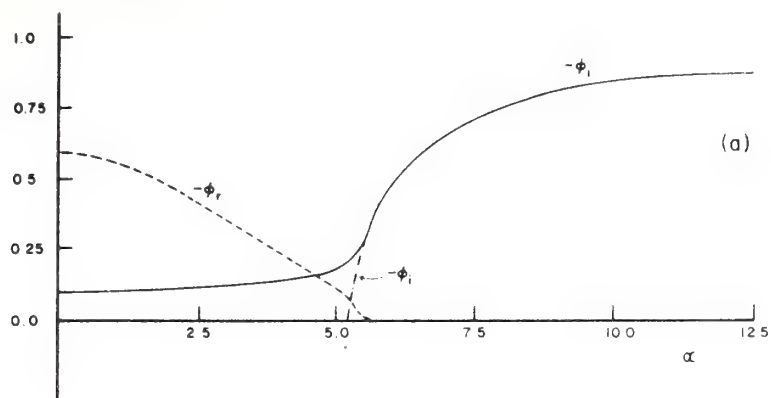
FIG. 6a. As in Fig. 4a but with $u_0 = 5$ m s^{-1} and $h = 2000$ m. Here $n_B = 1.85 \times 10^{-2}$ s^{-1} and $r = 1$ but $J_B = 54.88$.

FIG. 6b. As in Fig. 6a, mode II.

FIG. 6c. As in Fig. 6a but with $r = 280/285$, i.e., $\Delta T = 5$ K between layers.

FIG. 6d. As in 6c, additional modes.

we plot in Fig. 7 ϕ_r and ϕ_i at $\alpha=0$ as a function of h for $r=1$ and $u_0=5$ m s^{-1}. We only show the three largest modes, although there are an infinite number, each starting at the origin and ending on one of the neutral curves of class 1 which are given by (41) and shown as dotted lines in Fig. 3.

3) All cases possess a mode which we shall call mode I with $\phi_r\approx0$ and $\phi_i\approx-1$ for large α. This mode may or may not continue all the way to $\alpha=0$ depending mostly on the value of r. When $r=1$, it always reaches $\alpha=0$ with $\phi_i\neq0$. This mode exists even when $h\to\infty$, i.e., for the case of two semi-infinite layers; it becomes neutral, though, at a finite but non-zero value of α.

4) For all cases, a large number of unstable modes is possible. The growth rates, though, of some of these modes are so small ($|\phi_i|$ of the order of 10^{-3} or less) that it would be impossible to show them in Figs. 4–6. By comparison, for infinite bottom layer, the dispersion relation (39) allows at most four unstable modes as is demonstrated by Einaudi and Lalas (1974).

5) All the modes that terminate at some finite value of α (which we shall call mode II, III, etc.) possess a maximum in their growth rate for some finite value of α, which we can call α_m. For example, when $h=200$ m, $r=1$ and $u_0=2$ m s^{-1}, $\alpha_{mII}=1.35$ ($\lambda_x \approx931$ m); while for $r=280/285$, $\alpha_{mII}=3.1$ ($\lambda_x\approx406$ m), $\alpha_{mIII}=3.4$ ($\lambda_x\approx370$ m), $\alpha_{mIV}=3.55$ ($\lambda_x\approx354$ m). For most of these modes, particularly when $r=1$, the maximum is very pronounced. It should be pointed out that when h goes to infinity, these extra modes either disappear when $r=1$, or terminate at some non-zero value of α when $r\neq1$. They still possess a maximum as can be seen from Figs. 7, 9 and 11 of Einaudi and Lalas (1974) but at smaller wavelengths. For the previous example, i.e., $u_0=2$ m s^{-1}, $r=280/285$, the maximum would be at $\lambda_x\approx300$ m.

6) All unstable modes, regardless of whether $r=1$ (except for mode I at large α), have a non-zero ϕ_r. In addition, all the outgoing waves in the top layer are not purely evanescent.

7) As can be seen analytically from the dispersion equation, if ϕ is a complex root, so is its complex conjugate. This property was also true for the case of two semi-infinite media.

From the growth rate calculations, it becomes obvious that the major effect of the presence of a solid boundary at a finite distance from the velocity discontinuity of the K-H configuration, is the destabilization of the longer wavelengths (α small) and the introduction of extra modes both unstable and neutral. To be able to pinpoint this ground effect, we turn our attention to some simple cases below.

In the K-H instability configuration of Fig. 1, there are at least four competing effects. One is the shear at the interface which, in the absence of gravity, is always unstable with waves of phase speed equal to
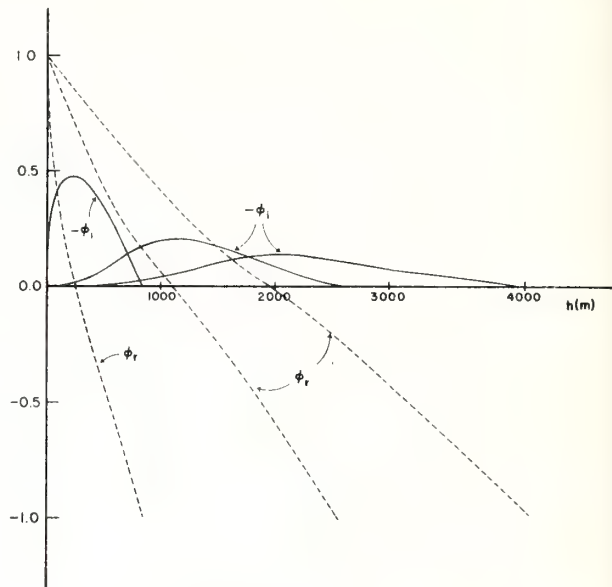
FIG. 7. Normalized growth rates ϕ_i (solid lines) and normalized phase speeds ϕ_r (dashed lines) as a function of the depth of the bottom layer for $\alpha=0$ and $u_0=5$ m s^{-1}, with $r=1$ and $n_B=1.85 \times10^{-2}$ s^{-1}, obtained from Eq. (45). Only the first three modes are shown.

the average between the two layers and growth rate $\phi_i=\pm1$. The next one is the density jump with lighter fluid on top, which, because of gravity, stabilizes some of the large wavelength disturbances of the shear instability. It gives rise mainly to the term $G(1-r)$ in (31). A third effect is the continuous density stratification which is expressed by J_A and J_B. This stratification usually stabilizes the flow but its stabilizing influence is not clearcut as is well known, and situations have been found in which its influence is destabilizing (Chimonas, 1974). This may be due to the introduction of extra modes that can propagate upward. Finally we have the effect of the ground. Let us try to isolate its influence on the other three contributors.

If we go back to (31) and eliminate stratification by putting J_A and J_B equal to zero, but retaining gravity so that r, defined by (24), is in general different from unity, we obtain

$$\phi=\left(\frac{D-r}{D+r}\right)\pm i\left[1-\left(\frac{D-r}{D+r}\right)^2-\frac{\tilde{G}(1-r)}{\alpha(r+D)}\right]^{\frac{1}{2}}, \quad (42)$$

with

$$D\equiv\coth(k_xh)\geqslant1, \quad \tilde{G}=gh/u_0^2.$$

When $r=1$, we have just a shear flow with no stabilization (since we have already neglected viscosity) and from (42) we see that the effect of the ground is to reduce the growth rate from 1 to

$$\left[1-\left(\frac{D-r}{D+r}\right)^2\right]^{\frac{1}{2}}$$

but not to reduce the range of unstable wavelengths. To see the effect of the density jump, i.e., $r \neq 1$, we rewrite (42) as

$$\phi = \left(\frac{D-r}{D+r}\right) \pm i\left(\frac{1+r}{D+r}\right)D^{\frac{1}{2}}\left[\frac{4r}{(1+r)^2} - \frac{\tilde{G}(1-r)}{\alpha(1+r)}\Lambda\right]^{\frac{1}{2}}, \quad (43)$$

where

$$\Lambda = (r+D)/D(1+r) \leqslant 1.$$

The stability boundary is obtained by setting the square bracket equal to zero, which gives

$$\lambda_x = \frac{8\pi r u_0^2}{g(1-r)(1+r)\Lambda}. \quad (44)$$

When the ground is not present, $h = \infty$ and $\Lambda = 1$. Since, for finite h, $\Lambda < 1$, the largest horizontal wavelength that may be unstable in the presence of the ground is bigger than without the ground. Thus, the effect of the ground, when $r \neq 1$, is to increase the range of the unstable wavelengths of the system. Notice that up to now, with J_A and J_B zero, k_A and k_B have to be imaginary, and the introduction of the ground has not introduced any additional modes.

To see the effect of stratification, we go back to (31) and allow J_A and J_B to be non-zero, and we take $r = 1$ so that the density jump disappears. If we look for the largest horizontal wavelength for which a wave can still be unstable, we see that there is none since there are unstable roots of (31) for $r = 1$ and $\alpha = 0$, i.e., $\lambda_x = \infty$ given by the equation

$$\phi = \exp[-2iJ_B^{\frac{1}{2}}/(\phi - 1)], \quad (45)$$

which can be shown to have an infinite number of solutions. Thus the effect of the ground in the presence of continuous stratification is to again destabilize the larger wavelengths through the introduction of an infinite number of additional modes. The numerical analysis shows that the growth rates of the unstable modes in the presence of the ground are always larger than the ones for two semi-infinite media.

The presence of the ground does not affect waves with small horizontal wavelengths, since they usually correspond to largely evanescent waves, which will have negligible amplitude on the ground. Thus the reflected wave necessary to satisfy the zero vertical velocity boundary condition would be even smaller at the shear zone so that no substantial re-enforcement takes place.

5. Comparison with some observations

Lindzen (1974) considered the case of two semi-infinite layers with velocity u_0 and $-u_0$ and with the same temperature. For this configuration, (40) is the governing equation that admits either an unstable

mode (and its conjugate) or two neutral modes which may be either propagating or evanescent. He then proposed that the neutral propagating modes may be as efficient in carrying momentum and energy away from the shear zone as the unstable ones. In this fashion they can modify the basic flow. He also indicated that the presence of the ground may enhance this process through reflection.

However, (31) does not admit neutral upward propagating waves in the top layer, in the presence of the ground. For such waves to exist, we have shown that equalities (32) or (33) must hold. They, in turn, imply that $|k_A| \to \infty$ and $|k_A| \to 0$, respectively. In either case, the group velocity of such waves is zero, as can immediately be verified from the expression of the vertical component of the group velocity in an isothermal atmosphere, with constant background wind. Hence, the transport of momentum and energy away from the shear zone and its readjustment have to be attributed to unstable waves, which have a non-zero vertical wavelength and propagate upward. Indeed, the examples mentioned by Lindzen in his Table 1 can be approximately explained by unstable waves if reference is made to the growth rate curves of Figs. 4–6. In every case, all modes except mode I have a maximum growth rate, as previously pointed out, at some finite value of α. This maximum becomes very pronounced when $r = 1$.

Assuming that the unstable waves with α equal to α_m are excited, let us see how they compare with observations. In Table 1, we reproduce the four cases mentioned by Lindzen along with his calculated most efficient neutral wavelength (for his two semi-infinite layers with $r = 1$) and the wavelength and period of our most unstable modes. These growth rates and unstable wavelengths were calculated by assuming two layers of constant velocity with the velocity jump taken from Lindzen's (1974) Table 1. The Brunt-Väisälä frequencies of the two layers are equal ($r = 1$), and their values again are the same as the ones used by Lindzen. Given the uncertainties in the experimental data and the departures of the actual velocity and density profiles from the simple configuration utilized, the agreement (within 25% or less) is good enough to suggest that instabilities are still the dominant smoothing mechanism of shear zones. Furthermore, if one took into account the fact that unstable modes themselves are capable of propagating energy away from the shear zone, their role becomes even stronger.

Finally, if the model were chosen so that the Brunt-Väisälä frequency of the top layer is larger than the bottom one, as the data of Hooke *et al.* (1973) or Hooke and Hardy (1975) seem to indicate, then one finds that the most unstable wavelength is even larger, which would improve the agreement with observations.

Table 1. Characteristics of the four cases referred to by Lindzen (1974).

	Case 1 Wallops Is., Va. 7 Feb 1968 (Ottersten et al., 1968)	Case 2 Haswell, Colo. 12 Nov 1971 (Hooke et al., 1973)	Case 3 Wallops Is., Va. 19 Feb 1970 (Hardy et al., 1973)	Case 4 Wallops Is., Va. 18 Mar 1969 (Hooke and Hardy, 1975)
Bottom layer height h (km)	11	0.12	2.5	9
Velocity jump $u_0 = \Delta u_0/2$ (m s^{-1})	10	1	7	28
Brunt-Väisälä frequency n (s^{-1})	2×10^{-2}	2.7×10^{-2}	2×10^{-2}	1.3×10^{-2}
Observed wavelength λ_x (km)	6	0.350	2.7	15–20, 1.6
Lindzen's optimal λ_x (km)	4.44	0.329	3.1	19.1
Mode II, most unstable λ_x (km)	4.46	0.320	3.05	20.0
Mode III, most unstable λ_x (km)	4.44	0.362	—	—
Mode II, growth rate $|\omega_i|$ (s^{-1})	1.208×10^{-3}	5.167×10^{-3}	8.96×10^{-4}	9.95×10^{-4}
Mode III, growth rate $|\omega_i|$ (s^{-1})	1.241×10^{-3}	1.45×10^{-3}	--	—
Phase velocity[a], observed (m s^{-1})	not given	2.9–3.8	20	47
Phase velocity[b], Mode II (m s^{-1})	23.6	3.67	23.5	53.2
Phase velocity[b], Mode III (m s^{-1})	25.9	3.98	—	—
Period, observed[c] (s)	not given	100	152	300
Period, Mode II (s)	189	85	172	377
Period, Mode III (s)	172	91	—	—

[a] This phase speed is relative to an observer stationary on the ground.

[b] To calculate the phase speed of the wave, the mean wind velocity at the interface at $z = h$ had to be used. From the data, the values extracted were 25, 3.5, 17 and 43 m s^{-1} for cases 1 to 4, respectively. There is considerable uncertainty as to the exact location of the interface and thus the previously mentioned mean wind values are only approximate.

[c] The previously mentioned mean wind, with its uncertainty, had to be utilized here as well.

6. Conclusions

From the previously outlined results, it becomes clear that:

(i) The presence of the ground cannot be neglected in calculations of shear-associated waves in the atmosphere.

(ii) The inclusion of the solid lower boundary has a destabilizing effect on the Kelvin-Helmholtz waves with long horizontal wavelengths.

(iii) Additional families of modes, unstable and neutral, are made possible by the presence of the ground.

(iv) The modifications to the classic Kelvin-Helmholtz waves bring the calculated results in reasonable agreement with observations.

It should be noted that, although the presence of the ground gives a more realistic model, it increases the computational complexity of the problem by only a minor amount. A similar effect, i.e., destabilization of long wavelengths, is to be expected if the jump discontinuity of the velocity profile is replaced by a smooth transition and further studies with such a continuous model are now in progress by the present authors.

REFERENCES

Chimonas, G., 1974: Considerations of the stability of certain heterogeneous shear flows including some inflection free profiles. *J. Fluid Mech.*, **65**, 65–69.

Drazin, P. G., 1958: Stability of a shear layer in an unbounded heterogeneous inviscid fluid. *J. Fluid Mech.*, **4**, 214–224.

——, and L. Howard, 1966: Hydrodynamic stability of parallel flow of inviscid fluids. *Advances in Applied Mechanics*, Vol. 9, Academic Press, 1–89.

Einaudi, F., and D. P. Lalas, 1974: Some new properties of Kelvin-Helmholtz waves in the atmosphere with and without condensation effects. *J. Atmos. Sci.*, **31**, 1995–2007.

Gossard, E. E., 1974: Dynamic stability of an isentropic shear layer in a statically stable medium. *J. Atmos. Sci.*, **31**, 483–492.

Hardy, K. R., R. J. Reed and G. K. Mather, 1973: Observation of Kelvin-Helmholtz billows and their mesoscale environment by radar, instrumented aircraft, and a dense radiosonde network. *Quart. J. Roy. Meteor. Soc.*, **99**, 279–293.

Hines, C. O., 1960: Internal gravity waves at ionospheric heights. *Can. J. Phys.*, **38**, 1441–1481.

Hooke, W. H., and K. R. Hardy, 1975: Further study of the atmospheric gravity waves over the eastern seaboard on 18 March 1969. *J. Appl. Meteor.*, **14**, 31–38.

——, F. F. Hall and E. E. Gossard, 1973: Observed generation of an atmospheric gravity wave by shear instability in the mean flow of the planetary boundary layer. *Bound.-Layer Meteor.*, **5**, 29–42.

Jones, W. L., 1968: Reflection and stability of waves in stably stratified fluids with shear flow: A numerical study. *J. Fluid Mech.*, **34**, 609–624.

Lindzen, R. S., 1974: Stability of a Helmholtz velocity profile in a continuously stratified, infinite Boussinesq fluid. Applications to clear air turbulence. *J. Atmos. Sci.*, **31**, 1507–1514.

Miles, J. W., and L. Howard, 1964: Note on a heterogeneous shear flow. *J. Fluid Mech.*, **20**, 331–336.

Ottersten, H., K. R. Hardy and C. G. Little, 1973: Radar and sodar probing of waves and turbulence in statically stable clear-air layers. *Bound.-Layer Meteor.*, **4**, 47–90.

Yih, S-C, 1969: *Fluid Mechanics*. McGraw-Hill, Chap. 4.

Generation of Gravity Waves by Jet Streams in the Atmosphere

G. Mastrantonio[1], F. Einaudi[2] and D. Fua[1]

Cooperative Institute for Research in Environmental Sciences, University of Colorado/NOAA, Boulder 80309

D. P. Lalas[3]

Department of Mechanical Engineering Sciences, Wayne State University, Detroit, Mich. 48202

(Manuscript received 25 February 1976, in revised form 4 May 1976)

ABSTRACT

The characteristics of internal gravity waves generated by tropospheric jet streams are analyzed and discussed. By solving numerically the equations of motion in the linear, inviscid and Boussinesq limit, it is shown that a modal structure exists. Some of these modes have the ability to propagate vertically away from the jet and are likely to be responsible for some of the observed wave activities in the ionosphere as well as at the ground. For selected values of the minimum Richardson number of the flow, growth rates and horizontal phase velocities are given as functions of the horizontal wavenumber, for jet streams of varying width. Finally, a brief study of the stability of the so-called low-level jet, whose spectrum of generated waves undoubtedly will contribute to the dynamics of the nocturnal boundary layer, is undertaken.

1. Introduction

Atmospheric gravity waves are thought to play an important role in the observed dynamical processes in the ionosphere, as well as in the upper and lower atmosphere. Hines (1960) originally suggested that some of the ionospheric disturbances can be interpreted in terms of internal gravity waves generated at tropospheric heights. Gossard (1962) confirmed Hines' suggestion and found that a window can exist, for an atmosphere without background wind, at periods of about 10 min to 2 h, through which substantial amounts of energy can leak out of the troposphere. The tides, of course, can substantially reduce such a leakage, and even eliminate it. Among the possible sources of gravity waves in the troposphere (such as topographic features, tropospheric storms and synoptic-scale events) likely ones are wind shears in general, and jet streams in particular, because they possess a considerable amount of kinetic energy with velocities comparable to some of the horizontal phase velocities associated with the upper atmospheric effects.

Similarly, in the lower atmosphere pressure fluctuations at the ground, with periods of a few minutes to several hours and horizontal wavelengths of tens of meters to a few hundreds of kilometers, have been successfully correlated to gravity waves generated by the previously mentioned sources. In particular, Madden and Claerbout (1968), Claerbout and Madden (1968), Cook (1968), Tolstoy (1968), Herron and Tolstoy (1969), Tolstoy and Herron (1969), Herron *et al.* (1969), Keliher (1975) and others have presented evidence that pressure fluctuations monitored with an array of microbarographs at the ground can be related to the overhead tropospheric jet stream. The correlation consists mainly in showing that the horizontal disturbance phase velocities of the order of 10–100 m s^{-1}, say, are well within the range of velocities of the jet stream aloft and that the direction of the pressure disturbances coincides, within limits, with that of the jet stream. The latter is particularly important since the streaming direction remains fairly constant throughout the jet profile. Herron and Tolstoy (1969) show that a good correlation can persist for weeks between the direction of the jet stream winds and the pressure fluctuations recorded by the microbarograph array. The order of magnitude and power spectra for microbarographic fluctuations (in the 5–60 min period range) that would be expected on the ground due to disturbances of known spectra in the jet stream aloft (Kao and Woods, 1964) have been calculated by Tolstoy and Herron (1969) via a simple linear model and were found to be in reasonable agreement with observations.

New observational support to the idea that jet-stream-associated gravity waves are responsible for some of the pressure fluctuations revealed by microbarograph arrays has been recently given by Reed and Hardy (1972) and Hooke and Hardy (1975). They

---

[1] On a Fellowship from the National Research Council of Italy. Present affiliation: CNR-LPS, cp 27, 00044 Frascati, Italy.

[2] Also affiliated with the Wave Propagation Laboratory, National Oceanic and Atmospheric Administration, Boulder, Colo. 80302.

[3] Present affiliation: Department of Meteorology, University of Athens, Greece.

have directly related gravity-wave-associated pressure fluctuations recorded by a microbarograph array in the Washington, D. C., area to wave structure in the upper troposphere recorded during the same time interval by the Wallops Island 10 cm wavelength radar.

In an attempt to obtain information concerning the nature and the characteristics of gravity waves generated by a tropospheric jet stream in the atmosphere, we carry out in this paper a detailed numerical stability analysis of an idealized model of such a jet stream. In particular, we calculate the range of horizontal wavelengths which, with the plane wave assumption, corresponds to unstable waves, i.e., waves which grow exponentially in time. The range of such unstable waves is bounded in the (α, J) plane (α, normalized horizontal wavenumber; J, minimum Richardson number in the basic state flow) by singular neutral modes (no exponential temporal growth). If in such a plane we refer to unstable waves that end on different neutral curves as belonging to different modes, we will then show that the tropospheric jet stream can support a number of modes, some of which are essentially evanescent and others essentially propagating away from the shear zone. Both types of waves can contribute to the turbulence measured *in situ* (Kao and Woods, 1964; Reed, 1969; Kennedy and Shapiro, 1975), while the propagating ones are most likely responsible for some of the wave motions observed at ionospheric heights and at the ground. The analysis follows the lines of standard stability theory as applied to jets (Curle, 1957; Tatsumi and Kakutani, 1958; Howard, 1958; Sato, 1960; Batchelor and Gill, 1962; Drazin and Howard, 1966; Hazel, 1972). It differs from these previous studies in the form of the background temperature and wind profiles and in the boundaries which, to better model the actual atmosphere, are here chosen to be the ground below and a semi-infinite isothermal layer with constant background wind at the top.

As an illustration of the scope and utility of our analysis, we compare the theoretically predicted characteristics of the specific event of 18 March 1969 over the Eastern Seaboard to the actual ones reported by Hooke and Hardy (1975) and find that the agreement is good.

Finally, we briefly investigate the so-called low-level jet, which denotes a sharp maximum in the wind profile, usually within a height of 1.5 km above the ground. The jet is best developed at night and its maximum often coincides with the top of the nocturnal inversion. We refer to the paper by Bonner (1968) for a review of its properties and its role. We believe that waves generated by the low-level jet may contribute to the spectrum of fluctuations observed in the nighttime boundary layer by microbarograph arrays and various remote sensing techniques.
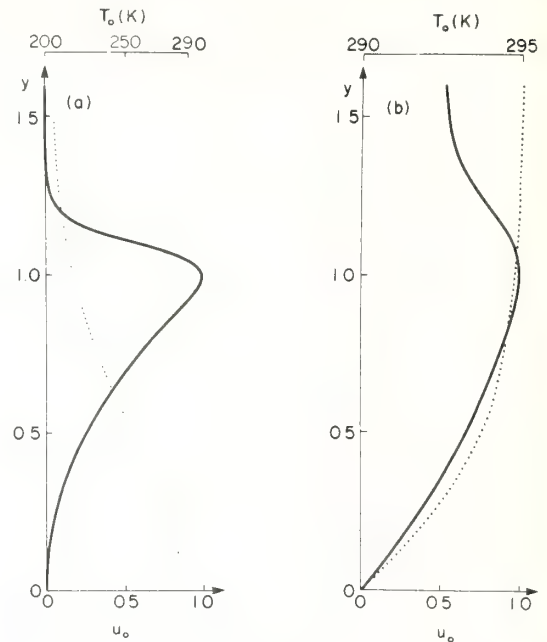
FIG. 1. Background temperature T_0 (dotted lines) and normalized background velocity u_0 (solid lines) versus normalized height y: (a) tropospheric jet stream corresponding to $m_1 = 30$, $m_2 = 2$, $T_\infty = 203$ K, $\theta = 100$ K, $k_T = 1.8$ and $y_0 = 0.5$; (b) low-level jet stream corresponding to $m_1 = 14$, $\theta = 5$ K and $T_g = 290$ K.

2. The model and the governing equations

Atmospheric flows which possess wind maxima can be classified as low-level or tropospheric jets depending on whether the maximum occurs within approximately 1.5 km of the ground or near the tropopause, respectively. The background vertical wind component for both jet types is usually negligible, and the background horizontal wind in the x direction and temperature are considered to vary with the height coordinate z only, since we restrict our attention to horizontal wavelengths of up to a few hundred kilometers for the high-level jet and a few kilometers for the low-level one.

The background temperature associated with a tropospheric jet is typically linearly decreasing with height to a minimum at the tropopause and constant, or slightly increasing, for the next 10–20 km. To model the tropospheric jet we choose (among others) the following analytical expressions:

$$u_0(y) = \frac{m_1/m_2}{[(m_1 - m_2)/m_2] + y^{m_1}} y^{m_2}, \tag{1}$$

$$T_0(y) = T_\infty + \theta \frac{\exp[-k_T(y - y_0)]}{\exp[k_T(y - y_0)] + \exp[-k_T(y - y_0)]}. \tag{2}$$

In the above $u_0(y)$ is the background velocity U_0 normalized with respect to its maximum value V, which we take to occur at $z = h$ the height of the tropopause, and y is the normalized height given by $y = z/h$.

The constants m_1 and m_2 in (1) control the shape of the velocity profile in general and its width Δ in particular, Δ being the normalized distance between the two heights where $u_0 = 0.5$. Similarly, θ, k_T, T_∞ and y_0 in (2) control the temperature, with θ a measure of the total temperature difference between the ground and the tropopause. Typical profiles generated by (1) and (2) are shown in Fig. 1a.

The low-level jet differs from the tropospheric jet in that its velocity does not decrease as much as the latter above the maximum. In addition, the temperature has a profile typical of the nighttime boundary layer with an inversion approximately at the height of velocity maximum. To account for these differences the analytical expressions for the normalized velocity u_0 and the temperature T_0 of the low-level jet are taken to be

$$u_0(y) = \frac{1}{1+\tanh(2)}\left[\frac{m_1}{m_1-1+y^{m_1}}y+\tanh(2y)\right], \quad (3)$$

$$T_0(y) = \theta \tanh(2y) + T_g. \quad (4)$$

The maximum value of u_0 takes place at $y \approx 1$; m_1 controls the thickness Δ of the jet and θ is proportional to the temperature increase across the inversion. Characteristic profiles described by (3) and (4) are shown in Fig. 1b.

With the temperature profiles specified by (2) and (4) the Brunt-Väisälä frequency n, defined in terms of the potential temperature θ_0 and the acceleration of gravity g acting in the negative z direction, given as

$$n^2 = \frac{g}{\theta_0}\frac{d\theta_0}{dz} = \frac{g}{T_0}\left[\frac{\partial T_0}{\partial z}+\frac{g}{c_p}\right], \quad (5)$$

can be evaluated to be

$$n^2(y) = \frac{g}{T_0}\left\{\frac{g}{c_p}\right.$$
$$\left. -2k_T\frac{\theta/h}{\{\exp[k_T(y-y_0)]+\exp[-k_T(y-y_0)]\}^2}\right\} \quad (6)$$

for the tropospheric jet and

$$n^2(y) = \frac{g}{T_0}\left\{\frac{g}{c_p}+2\frac{\theta}{h}\text{sech}^2(2y)\right\} \quad (7)$$

for the low-level jet, c_p being the specific heat at constant pressure for the atmosphere. The background quantities of both jets [specified by Eqs. (1)–(4)] become constant for y larger than some height y_f since du_0/dy and $dT_0/dy \to 0$ as $y \to \infty$, so that the system can be considered capped by an isothermal, semi-infinite layer with constant background wind.

To analyze the stability of the above configurations, we follow closely the approach and notation of Lalas and Einaudi (1976), hereafter referred to as I, who con-

sider the stability of atmospheric flows with $u_0 = \tanh(y)$ and $T_0 = $ constant, and assume a perturbation vertical velocity w_1 of infinitesimal amplitude and of the form

$$w_1(x,z,t) = \rho_0^{-\frac{1}{2}}\text{Re}\{\psi(z)\exp[i(k_x x-\omega t)]\}, \quad (8)$$

where ρ_0 is the background density, and $k_x = 2\pi/\lambda_x$, λ_x and $\omega = \omega_r + i\omega_i$ are the horizontal wavenumber, wavelength and complex frequency of the disturbance, respectively. If we further assume that the perturbations of horizontal velocity, pressure and density are also infinitesimal and of the same form (8), then the linearized equations of motion can be reduced (in the inviscid and Boussinesq limit and with rotational effect neglected) to the following second-order differential equation (see I):

$$\frac{d^2\psi}{dy^2} - \Lambda(y)\psi = 0, \quad (9)$$

with

$$\Lambda = \alpha^2 - \frac{1}{4}\frac{1}{\rho_0^2}\left(\frac{d\rho_0}{dy}\right)^2 + \frac{1}{2}\frac{1}{\rho_0}\frac{d^2\rho_0}{dy^2} - \frac{n^2h^2}{V^2}\frac{1}{\Omega^2}$$
$$-\frac{1}{\Omega}\left[\frac{1}{\rho_0}\frac{d\rho_0}{dy}\frac{du_0}{dy}+\frac{d^2u_0}{dy^2}\right]. \quad (10)$$

The normalized quantities in (10) are defined as follows:

$\alpha = hk_x$ normalized horizontal wavenumber

$c_r = \dfrac{\omega_r}{k_x V}$ normalized horizontal phase velocity of the wave

$c_i = \dfrac{\omega_i}{k_x V}$ normalized imaginary part of the frequency of oscillation

$\Omega = c_r - u_0 + ic_i$ normalized Doppler frequency.

It should be noted that, although the Boussinesq approximation has been utilized, the so-called inertial terms, for example those which depend on the density variation in the inertial term of the momentum equation, are retained.

The solution ψ of (9) must satisfy the usual boundary condition at the ground

$$\psi(0) = 0. \quad (11)$$

At large heights the velocity and temperature are nearly constant so that for $y \gtrsim y_f$, $\Lambda(y)$ is essentially constant and equal to $\Lambda(y_f)$. In such a region, the solution of (9) takes the form (Hines, 1960, 1974)

$$\psi \propto \exp[iKy], \quad K = \pm[-\Lambda(y=y_f)]^{\frac{1}{2}} = K_r + iK_i, \quad (12)$$

and the boundary condition to be imposed becomes

$$\frac{d\psi}{dy} = iK\psi \quad \text{at} \quad y = y_f, \quad (13)$$

with the sign of K, given by (12), chosen so that either $K_i > 0$ or, if $K_i = 0$, $dc_r/dK_r > 0$: this choice assures that the perturbation amplitude decays to zero as $y \to \infty$ or, if the wave is neutral and propagating, that the energy is transported away from the shear zone toward infinity, i.e., the vertical group velocity is positive.

Following Thorpe (1969), we choose J, the minimum value of the Richardson number Ri in the flow, as the main stability parameter, so that

$$J = [\text{Ri}]_{\min} = \frac{h^2}{V^2}[n^2/(du_0/dy)^2]_{\min}. \quad (14)$$

We then attempt to specify, for the given background quantities, the range of horizontal wavelengths λ_x that correspond to unstable waves for each value of J, and to calculate the periods, phase velocities and growth rates of such waves. This is accomplished by solving (9) numerically for given α and J, and by determining c_i and c_r so that the conditions (11) and (13) are satisfied. The numerical algorithms used are the same as in I and we shall not repeat their description here. Note that if $J > \frac{1}{4}$ throughout the flow, the system is stable so that all possible unstable modes correspond to the range $0 \leqslant J < \frac{1}{4}$. (We are only concerned here with statically stable situations, so that $n^2 > 0$.) The only procedural difference from I is the use of the program for unstable waves with $c_i = 5 \times 10^{-4}$, which we consider to be zero, to evaluate most but not all of the singular neutral modes. This is done because the program for neutral modes with c_i identically zero utilizes a Frobenius expansion near the singularities of (9) which, in this case, occur at two critical levels (where $u_0 = c_r$) rather than at only one as in I. This results in some convergence difficulties and in excessive use of computing time. The second program is used only to check the accuracy of the results obtained by the program for unstable modes with $c_i = 5 \times 10^{-4}$. The accuracy is found to be satisfactory.

3. Analysis of the results

The number of parameters characterizing the problem is so large that we are forced to limit our investigation to a few representative cases. Other specific profiles, including splines from experimentally obtained points, can be analyzed with the present technique. We choose to keep the reference height h constant in each case we examine, since Eq. (14) requires that variations in the stability parameter J, once the normalized velocity and temperature are fixed, be attributed to variations in V. However, the numerical analysis also shows that the inertial terms in (10), i.e., the terms $(d^2\rho_0/dy^2)/\rho_0$, $[(d\rho_0/dy)/\rho_0]^2$ and $[(d\rho_0/dy)/\rho_0](du_0/dy)$, have a small effect (less than 10% in the most serious cases when α is very small). Now, if these terms are neglected, the ex-
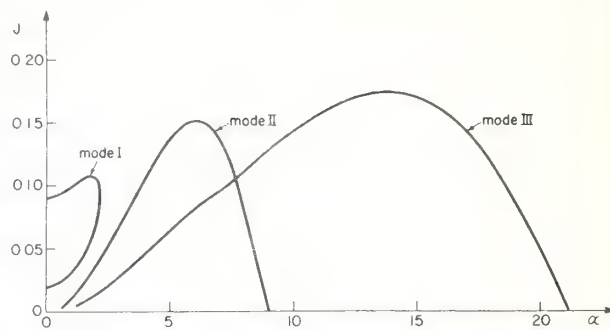
FIG. 2. Neutral curves giving the minimum Richardson number J in the flow versus the normalized horizontal wavenumber α for the case $\Delta \approx 2.28$ km specified by Eq. (16a).

pression for Λ in (10), with the help of (14), becomes

$$\Lambda(y) = \alpha^2 - (Jn^2/\Omega^2)/[n^2/(du_0/dy)^2]_{\min} \\ - (d^2u_0/dy^2)/\Omega. \quad (15)$$

If n^2 [given by (6) or (7)] is independent of h, then h does not explicitly appear anywhere in the governing equation (u_0 does not explicitly depend on h) and the results are applicable to a much broader range of flows with different h. If the ratio θ/h, the only term in which h appears in (6) and (7), is kept constant, then n^2 is indeed independent of h and in this sense variations of J can also be attributed to variations of h for fixed V. The numerical calculations presented here have been carried out using (10). We now describe the results for the tropospheric and low-level jets, separately.

a. Tropospheric jet stream

Limitations in computing time have forced us to consider only the effect of varying the thickness Δ of the jet. The values for m_1 and m_2 used in (1) and the corresponding Δ are

$$m_1 = 30, \qquad m_2 = 10, \qquad \Delta \approx 2.28 \text{ km}, \qquad (16a)$$

$$m_1 = 30, \qquad m_2 = 2, \qquad \Delta \approx 5.10 \text{ km}, \qquad (16b)$$

$$m_1 = 10, \qquad m_2 = 2, \qquad \Delta \approx 7.83 \text{ km}. \qquad (16c)$$

The background temperature profile remains the same for all cases, with $h = 12$ km, $k_T = 1.8$, $y_0 = 0.5$, $T_\infty = 203$ K and $\theta = 100$ K.

The case of thickness $\Delta = 2.28$ km is shown in Figs. 2, 3 and 4. In Fig. 2 the parameter J [defined by (14)] is plotted as a function of the normalized horizontal wavenumber α for the neutral curves which, as already mentioned, actually correspond to $c_i = 5 \times 10^{-4}$. Three modes are present, each of which defines a range of values of α for given J, within which the solutions of (9) satisfying the boundary conditions (11) and (13) are unstable ($c_i > 0$). Mode I corresponds to neutral curves which are propagating in the top semi-infinite layer ($y > y_f$). Mode II corresponds to evanescent waves, while mode III supports neutral waves which
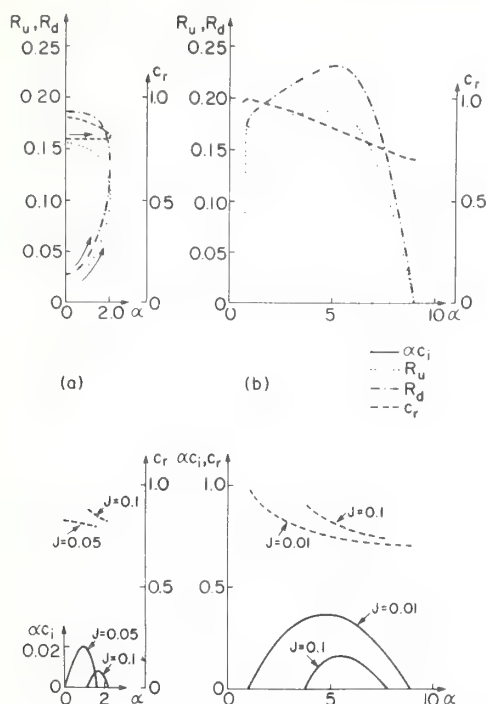
FIG. 3a. Top part: values of the Richardson numbers R_d and R_u at the two critical levels y_d and y_u, respectively, and the normalized horizontal phase velocity c_r as a function of the normalized horizontal wavenumber α for the neutral curve of mode I described in Fig. 2. Bottom part: normalized growth rates αc_i and normalized horizontal phase velocities c_r as a function of α for mode I and for given values of J.

FIG. 3b. As in Fig. 3a but for mode II.

It is of interest to note that over some ranges of α, the calculated waves display very little dispersion. For example, c_r for the neutral waves of mode I varies between 0.8 and 0.9 over the entire range of α. Such absence of dispersion has also been observed in nature and reported by Madden and Claerbout (1968).

The second case, corresponding to the values of the parameters given by (16b), is obtained from the first by decreasing m_2 and thus increasing Δ. The instability area corresponding to mode I progressively shrinks as m_2 decreases and disappears altogether at $m_2 \approx 6$. The remaining two modes appear to coalesce into one as shown in Fig. 5 where J, c_r and R_u (R_d essentially greater than $\frac{1}{4}$ throughout) are plotted vs α in (a), while in (b) the growth rates αc_i and phase velocities c_r are given in terms of α. The neutral curves are evanescent in the top layer for all the values of α.

By keeping $m_2 = 2$ and decreasing m_1 to 10, we obtain an even broader jet with $\Delta = 7.83$ km. The characteristics of the neutral curves are described in Fig. 6. Although the neutral curve gives the appearance of being made of two separate branches, the waves are evanescent in the top region over the entire range of values of α. This latter example has little more than an illustrative meaning if indeed h and θ are kept at the values of 12 km and 100 K, because the values of V required to bring the values of J to less than $\frac{1}{4}$ are too large. For this case to be physically meaningful, one has to reduce h and θ so that θ/h remains equal to $1/120$ K m^{-1}, as discussed earlier.

are propagating or evanescent in the top layer depending on whether or not α is smaller or larger than about 7.16. For each wave there are two critical levels y_d and y_u, with $y_u > y_d$, where the horizontal phase velocity c_r is equal to the background velocity u_0, i.e., $c_r = u_0(y_u) = u_0(y_d)$. Associated with each critical level there is a corresponding value of the Richardson number, $R_d = \mathrm{Ri}(y_d)$ and $R_u = \mathrm{Ri}(y_u)$. For the neutral modes described in Fig. 2, the values of c_r, R_d and R_u are given (in terms of α) in the upper parts of Figs. 3a, 3b and 4, for modes I, II and III, respectively. For modes II and III, the curves are not completed near the origin due to some convergence difficulties in the program as $\alpha \to 0$ and $J \to 0$. In general, when both R_d and R_u are less than $\frac{1}{4}$, the question of whether the wave is generated at one or another or at both critical levels cannot be answered conclusively. As in mode III, with $9.6 < \alpha < 14.95$, if one of the two Richardson numbers, in this case R_d, is greater than $\frac{1}{4}$, then it is established that the wave is generated at $y = y_u$. To give an idea of the behavior of the unstable roots, the normalized growth rates $\alpha c_i = \omega_i h/V$ and the normalized horizontal phase velocities c_r are plotted as a function of α in the bottom parts of Figs. 3a, 3b and 4, for modes I, II and III, respectively. Each curve corresponds to a selected value of J, which is kept constant along it.

FIG. 4. As in Fig. 3a but for mode III.

FIG. 5a. Minimum Richardson number J in the flow, values of the Richardson number R_u at the upper critical level and normalized horizontal phase velocities c_r as a function of α for the case $\Delta \approx 5.10$ km specified by Eq. (16b). $R_d > \frac{1}{4}$.

FIG. 5b. Corresponding normalized growth rates αc_i and normalized horizontal phase velocities c_r as a function of α for given values of J.

We now turn our attention to the waveforms and fluxes associated with the solution just presented. In Fig. 7 the eigensolutions $Z_c = \mathrm{Re}(\psi)$ and $Z_s = -\mathrm{Im}(\psi)$ corresponding to the maximum growth rates for the specified values J of modes I, II and III are shown for the case with $\Delta \approx 2.28$ km. The arbitrary amplitude of the disturbance is chosen so that

$$\frac{dZ_c}{dy} = \frac{dZ_s}{dy} = 1 \quad \text{at} \quad y = 0. \quad (17)$$

In order to compare pressures, displacements, etc., with data from an observed case, one would choose the amplitude by matching some measured parameter at a given height, as will be done in the next section. As can be seen by the behavior of Z_s and Z_c, mode I shown in Fig. 7a is essentially propagating above and below the jet, while mode II (Fig. 7b) and mode III (Fig. 7c) are evanescent above and below. In addition, the energy flux $\overline{p_1 w_1}$, i.e., the product of the perturbation pressure and vertical velocity averaged over a horizontal wavelength, is plotted. Energy is shown to be radiated away from the region between the two critical levels in both directions, out to considerable distances for the propagating mode I. The energy flux had to be zero at the ground, so that if these waves were not unstable, the flux would have been zero below the bottom critical level. For all modes shown, the Richardson number is below 0.25 at both critical levels. For different α (not shown) Ri is below 0.25 at only one critical level, in which case, as expected, there is strong absorption at the other critical level.

b. Low-level jet

For this configuration we have only analyzed one case with $h = 300$ m, $\theta = 5$ K, so that $\theta/h = 1/60$ K m^{-1},

with the temperature at the ground $T_g = 290$ K and $m_1 = 14$. The results are shown in Fig. 8. The neutral waves of Fig. 8a are all evanescent in the top layer. Unstable waves of large wavelengths are now possible, in contrast to the flow with a boundary-layer type velocity profile and the same temperature difference between the ground and the inversion height studied by Fua *et al.* (1976). Even though we have not yet analyzed a wide variety of profiles for the low-level jet, we feel that these partial results indicate the need for consideration of such wave modes in boundary layer dynamics.

4. An illustrative application of the results

We carry out in this section a comparison between the theoretical results of our model and those observed
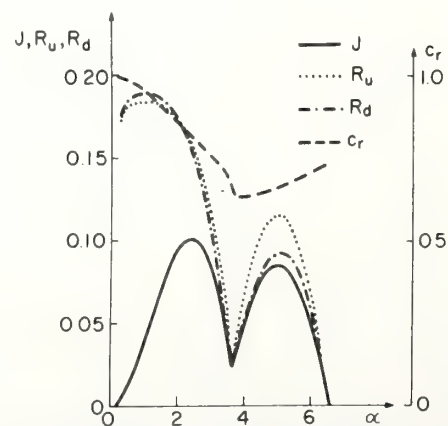
FIG. 6. As in Fig. 5a, but for the case $\Delta \approx 7.83$ km, specified by Eq. (16c).
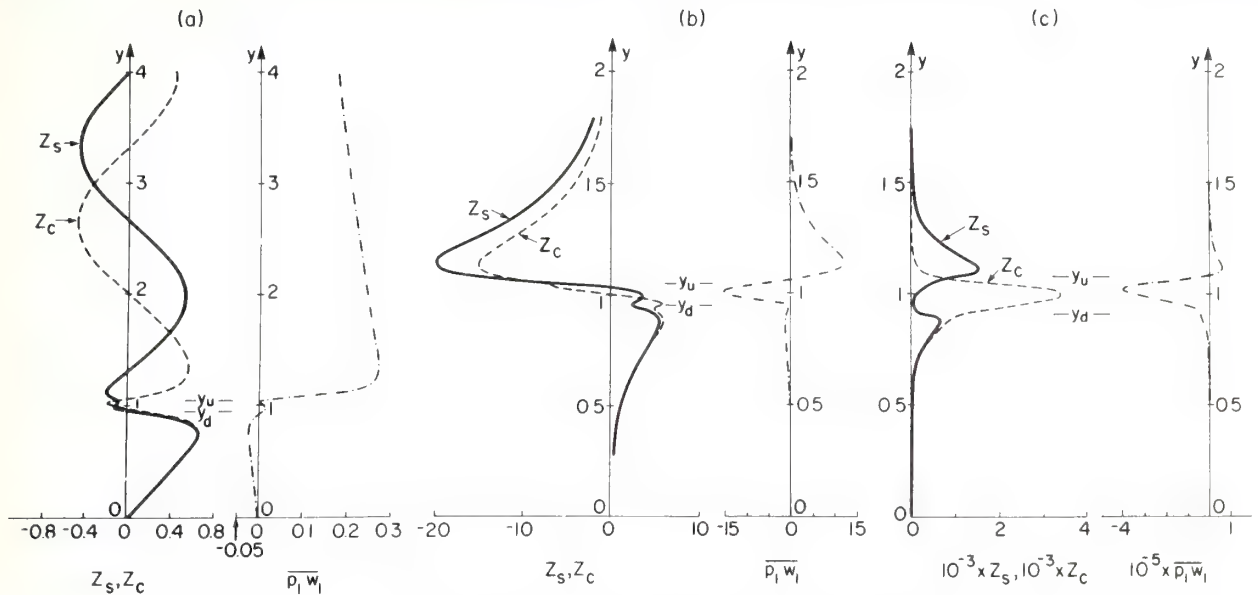
FIG. 7. Plots of $Z_c = \mathrm{Re}(\psi)$ and $Z_s = -\mathrm{Im}(\psi)$, the vertical velocities weighted by $\rho_0^{-\frac{1}{2}}$ and the wave energy flux $\overline{p_1 w_1}$, all normalized so as to satisfy (17), as a function of the normalized height y for $\Delta \approx 2.28$ km and for the following three values of α, each approximately corresponding to the maximum growth rate, for given J: (a) mode I: $J = 0.05$, $\alpha = 1.0$, $c_i = 0.0206$, $c_r = 0.8087$, $y_d = 0.95$ and $y_u = 1.045$; (b) mode II: $J = 0.1$, $\alpha = 5.4$, $c_i = 0.0302$, $c_r = 0.7986$, $y_d = 0.948$ and $y_u = 1.047$; (c) mode III: $J = 0.1$, $\alpha = 12$, $c_i = 0.0479$, $c_r = 0.5517$, $y_d = 0.907$ and $y_u = 1.078$.

in the case study (Reed and Hardy, 1972; Hooke and Hardy, 1975) mentioned in the Introduction. For this event the background velocity reaches a maximum slightly in excess of 80 m s^{-1} at about 12 km, with an essentially linear decrease in the background temperature from 289 to 217 K. Of the cases described in the previous section, the one corresponding to $m_1 = 30$ and $m_2 = 2$ and shown in Fig. 5 is closest to the actual profiles. The correspondence is only approximate, however, and no special attempt has been made to improve it because some doubts exist about the accuracy of the original profiles, especially above 12 km, where no

direct data are available and a sounding taken about 250 km away had to be utilized to complete them.

Since no accurate determination of J can be obtained from the data, we take $J = 0.1$, so that the maximum velocity $V \approx 89$ m s^{-1}. Hooke and Hardy indicate that the observed wavelength is between 14 and 15 km. We take the wavelength to be 14.7 km so that $\alpha = 5.1$, and from Fig. 5b we then determine c_r and αc_i, and therefore the two critical levels $z_d = h y_d$ and $z_u = h y_u$. In addition, from the measured peak-to-peak pressure variation on the ground of 200 dyn cm^{-2}, we calculate through the usual gravity wave polariza-
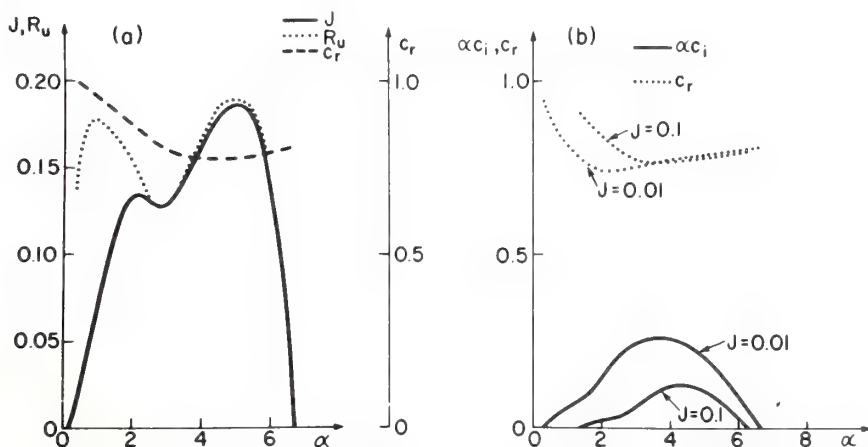
FIG. 8. Stability characteristics for the low-level jet shown in Fig. 1b. (a) Plots of J, R_u and c_r for the neutral curve as a function of α for $R_d > \frac{1}{4}$. (b) Corresponding normalized growth rates αc_i and horizontal phase velocities c_r as a function of α for $J = 0.1$ and $J = 0.01$.

tion relations the corresponding displacement at 8.3 km, where the actual displacement has been measured directly by the radar. In Table 1, we present the observed and the calculated quantities for this case.

Since $R_u = 0.125$ and $R_d = 1.36$, the disturbance is generated in the upper part of the jet. The waveforms, however, which we do not display here, have rather large gradients near both critical levels, much in the manner of the waveforms described in Fig. 7. Thus a wave may indeed be detected by radar at the lower critical level even though the wave is generated above. In view of the observational uncertainties, the agreement is satisfactory. If the background velocity profile were better known, so that more accurate modeling of it would be meaningful, and the value of J could be calculated *a priori*, even better agreement could be expected.

5. Conclusions

We have presented in this paper the results of the linear stability analysis of a tropospheric, as well as of a low-level, jet stream. By solving numerically the governing equations of motion in the inviscid and Boussinesq limit, we have shown that a tropospheric jet stream can in general support a number of modes whose characteristics (namely growth rates and horizontal phase velocities) have been calculated in terms of the corresponding horizontal wavelengths. Some of these modes correspond to waves which can propagate energy and momentum away from the main region of shear and which can therefore play an important role in mesoscale dynamics. Of particular significance in this respect is the fact that, for one of the cases examined, a propagating mode exists (mode I of Fig. 2) for non-zero values of the minimum Richardson number in the flow, even for very small values of α. Wavelengths of the order of ten as well as a few hundred kilometers have been recently detected and appear to be responsible for triggering various kinds of atmospheric events along their path (Uccellini, 1975; Goff, 1976). The calculations presented here confirm the idea that tropospheric jet streams can be a source, among many, for such waves. More cases should be analyzed to have a more complete knowledge of the spectra of waves that can be excited. In particular, one might wish to include the effect of a rather sharp increase of the Brunt-Väisälä frequency near the tropopause as it is often observed (Klemp and Lilly, 1975). The numerical program utilized in this paper can make use of spline functions determined from experimentally obtained points.

Similarly, the results presented here for the low-level jet streams should be extended to include a larger number of cases with different temperature and velocity profiles.

Finally, we should mention that although an extensive search for possible extra modes has been carried out, the

TABLE 1. Comparison of observed and calculated characteristics for the case study analyzed by Reed and Hardy (1972) and Hooke and Hardy (1975).

	Observed	Calculated
Phase velocity (m s^{-1})	~47	62
Period (s)	~300	236
Growth rate ω_i (s^{-1})	—	$8.32 \cdot 10^{-4}$
Critical levels (km)	—	9.732
		12.996
Displacement at $z = 8.3$ km (peak-to-peak, in meters)	680	635

possibility exists that we might have missed some. This is particularly probable in the region of small values of α and large values of J, where there are indications both for the calculations we have carried out here and in I, that modes might exist which define a rather narrow area in the (α, J) plane and which therefore have very small growth rates. These modes are difficult to determine. An analysis of this region, with all compressibility terms included, is presently under way.

REFERENCES

Batchelor, G. K., and A. E. Gill, 1962: Analysis of the stability of axisymmetric jets. *J. Fluid Mech.*, **14**, 529–551.

Bonner, W. D., 1968: Climatology of the low level jet. *Mon. Wea. Rev.*, **96**, 833–850.

Claerbout, J. F., and T. R. Madden, 1968: Electromagnetic effects of atmospheric gravity waves. *Proc. Acoustic-Gravity Waves Symp.*, T. M. Georges, Ed., U. S. Printing Office (C52.2:Ac7), 135–155.

Cook, R. H., 1968: Subsonic atmospheric oscillations. *Proc. Acoustic-Gravity Waves Symp.*, T. M. Georges, Ed., U. S. Printing Office (C52.2:Ac7), 209–213.

Curle, N., 1957: On hydrodynamic stability in unlimited fields of viscous flows. *Proc. Roy. Soc. London*, **A238**, 489–501.

Drazin, P. G., and L. N. Howard, 1966: Hydrodynamic stability of parallel flow in inviscid fluid. *Advances in Applied Mechanics*, Vol. 9 Academic Press, 1–89.

Fua, D., F. Einaudi and D. P. Lalas, 1976: The stability analysis of an inflexion-free velocity profile and its application to the nighttime boundary layer in the atmosphere. *Bound.-Layer Meteor.*, **10**, 35–54.

Goff, R. Craig, 1976: Character of thunderstorm-generated long-period solitary waves. (Submitted to *J. Appl. Meteor.*)

Gossard, E. E., 1962: Vertical flux of energy into the lower ionosphere from internal gravity waves generated in the troposphere. *J. Geophys. Res.*, **67**, 745–757.

Hazel, P., 1972: Numerical analysis of the stability of inviscid stratified shear flows. *J. Fluid Mech.*, **51**, 39–61.

Herron, T. J., and I. Tolstoy, 1969: Tracking jet stream winds from ground level pressure signals. *J. Atmos. Sci.*, **26**, 266–269.

——, —— and D. W. Kraft, 1969: Atmospheric pressure background fluctuations in the mesoscale range. *J. Geophys. Res.*, **74**, 1321–1329.

Hines, C. O., 1960: Internal atmospheric gravity waves at ionospheric heights. *Can. J. Phys.*, **38**, 1441–1481.

——, 1974: *The Upper Atmosphere in Motion. Geophys. Monog.*, No. 18, Amer. Geophys. Union, Washington, D. C., 248–328.

Hooke, W. H., and K. R. Hardy, 1975: Further study of the atmospheric gravity waves over the Eastern Seaboard on 18 March 1969. *J. Appl. Meteor.*, **14**, 31–38.

Howard, L. N., 1958: Hydrodynamic stability of a jet. *J. Math. Phys.*, **37**, 283–298.

Kao, S.-K., and H. D. Woods, 1964: Energy spectra of mesoscale turbulence along and across the jet stream. *J. Atmos. Sci.*, **21**, 513–519.

Keliher, T. E., 1975: The occurrence of microbarograph-detected gravity waves compared with the existence of dynamically unstable wind shear layers. *J. Geophys. Res.*, **80**, 2967–2976.

Kennedy, P. J., and M. A. Shapiro, 1975: The energy budget in a clear air turbulence zone as observed by aircraft. *Mon. Wea. Rev.*, **103**, 650–654.

Klemp, J., and D. K. Lilly, 1975: The dynamics of wave induced downslope winds. *J. Atmos. Sci.*, **32**, 320–339.

Lalas, D. P., and F. Einaudi, 1976: On the characteristics of gravity waves generated by atmospheric shear layers. *J. Atmos. Sci.*, **33**, 1248–1259.

Madden, T. R., and J. F. Claerbout, 1968: Jet-stream-associated gravity waves and implications concerning jet stream stability. *Proc. Acoustic-Gravity Waves Symp.*, T. M. Georges, Ed., U. S. Govt. Printing Office (C52.2:Ac7), 121–134.

Reed, R. J., 1969: A study of the relation of clear air turbulence to the mesoscale structure of the jet stream region. *Proc. Clear Air Turbulence and Detection Symp.*, Y.-H. Pao and A. Goldburg, Eds., Plenum Press, 288–307.

——, and K. R. Hardy, 1972: A case study of persistent, intense, clear air turbulence in an upper level frontal zone. *J. Appl. Meteor.*, **11**, 541–549.

Sato, H., 1960: The stability and transition of a two-dimensional jet. *J. Fluid Mech.*, **7**, 53–80.

Tatsumi, T., and T. Kakutani, 1958: The stability of a two-dimensional laminar jet. *J. Fluid Mech.*, **4**, 261–275.

Thorpe, S. A., 1969: Experiments on the stability of stratified shear flows. *Radio Sci.*, **4**, 1327–1331.

Tolstoy, I., 1968: Mesoscale pressure fluctuations in the atmosphere. *Proc. Acoustic-Gravity Waves Symp.*, T. M. Georges, Ed., U. S. Govt. Printing Office (C52.2:Ac7), 107–120.

——, and T. J. Herron, 1969: A model for atmospheric pressure fluctuations in the mesoscale range. *J. Atmos. Sci.*, **26**, 270–273.

Uccellini, L. W., 1975: A case study of apparent gravity wave initiation of severe convective storms. *Mon. Wea. Rev.*, **103**, 497–513.

Note on a New Solution of the Taylor-Goldstein Equation and Applications to the Atmosphere

WILLIAM R. MONINGER[1]

Coe College, Cedar Rapids, Iowa 52402

EARL E. GOSSARD

NOAA/ERL/Wave Propagation Laboratory, Boulder, Colo. 80302

8 September 1975 and 8 December 1975

ABSTRACT

A model having smooth wind and density profiles, for which a new solution of the Taylor-Goldstein equation can be found, is described. This model is particularly suitable for comparison with the analogous piecewise linear model so that the influence of "corners" in profiles can be judged. Such corners are found in models studied by Rayleigh, Goldstein, Taylor, Howard, Holmboe, and Gossard.

1. Introduction

Small perturbations in the atmosphere obey the equation (Gossard and Hooke, 1975)

$$\frac{d^2W(z)}{dz^2} + \left[\frac{N^2}{(u-c)^2} - \frac{u''}{u-c} - k^2 - \frac{2\Gamma u'}{u-c} - \Gamma^2 \right] W(z) = 0. \quad (1)$$

In this equation $W(z) = [\rho(z)/\rho_0]^{\frac{1}{2}} w$, where w is the vertical component of the velocity perturbation, ρ the unperturbed density of the fluid, and ρ_0 the density at some reference level. The Väisälä-Brunt frequency squared is represented by $N^2 = g\,d(\ln\theta)/dz$, where θ is the potential temperature. The ambient wind and its second derivative with respect to height z are u and u'', respectively. The phase velocity of the disturbance is c, and

$$\Gamma = (g/2c_s^2)(1 - N^2 c_s^2/g^2),$$

where c_s is the speed of sound.

When c_s is large, the terms containing Γ are negligible compared with the first term in the coefficient for reasonable values of u'. Eq. (1) then reduces to

$$\frac{d^2W(z)}{dz^2} + \left[\frac{N^2}{(u-c)^2} - \frac{u''}{u-c} - k^2 \right] W(z) = 0, \quad (1a)$$

which has been studied by Taylor (1931), Goldstein (1931), and many other authors. This approximation is equivalent to the Boussinesq approximation.

An important feature of Eq. (1a) is that the first and second terms in the brackets may become infinite where $u = c$. This problem may be circumvented by

[1] This work was carried out while under a temporary appointment at the NOAA/ERL Wave Propagation Laboratory.

requiring that $N^2(z)$ and $u''(z)$ go to zero at the height z_c where $u = c$ (the critical level) rapidly enough to overcome the zeroes in their respective denominators. Alternatively, one may require that $W(z)$ tend to zero more rapidly than $u - c$ does as z_c is approached. In this study we have chosen the former course.

Because we wish our model to represent the earth's atmosphere as nearly as possible, we choose to describe the stratification in terms of potential temperature $\theta(z)$ instead of density $\rho(z)$. For static stability $\theta(z)$ must increase with height. In an atmosphere whose lapse rate is exactly adiabatic $d(\ln\theta)/dz = 0$.

2. The model

The profiles we chose for the potential temperature and the ambient wind are

$$\theta = \theta_0 \exp\left[N_\infty^2 \frac{\Delta H}{g} \left(\frac{z}{\Delta H} - \tanh\frac{z}{\Delta H} \right) \right], \quad (2)$$

$$u = u_\infty \tanh\frac{z}{\Delta H}, \quad (3)$$

where N_∞^2 and u_∞ are the Väisälä-Brunt frequency and ambient wind, respectively, at $z \to \infty$. This model is shown in Fig. 1. Models having a hyperbolic tangent wind profile have been studied by Drazin (1958), Holmboe (1960), and others. This wind profile has simple analytic properties and is a reasonable representation of real shear layers.

We chose Eq. (2) because it is a smooth profile model that can be compared directly with the corresponding piecewise linear model and so can be used to assess the effect of corners on the profile. However, such profiles

566

may sometimes represent actual atmospheric conditions during the onset of intense mixing associated with a wind discontinuity. The mixing of momentum would tend to erase the shear as well as the gradient of potential temperature in the eventual steady state, but if the shear is maintained by some process external to the model, the profiles might look much like those of our model during the transient thickening of the mixed layer.

The almost linear appearance of θ away from the shear layer is due to the very small (typical atmospheric) value of $N_\infty{}^2$ in the exponent. In this model

$$N^2 = N_\infty{}^2 \tanh^2 \frac{z}{\Delta H}, \qquad (4)$$

$$u'' = -2\frac{u_\infty}{\Delta H^2} \operatorname{sech}^2 \frac{z}{\Delta H} \tanh \frac{z}{\Delta H}, \qquad (5)$$

both of which vanish at $z=0$.

Eq. (1) applies to a two-dimensional disturbance propagating in the x direction. Thus $c=\sigma/k$, where σ is the frequency and k the wavenumber in the x direction. Solutions for which the frequency (and hence the phase speed) is complex will represent unstable perturbations. However, we only seek solutions where c is real because such solutions define the stability boundary [see Miles, (1963) and the discussion below]. In addition, because of the symmetry of the profiles, we assume that $c=0$. In this case, using Eqs. (4) and (5), Eq. (1) becomes

$$\frac{d^2 W(z)}{dz^2} + \frac{1}{(\Delta H)^2}\left[\left(\frac{N_\infty}{\beta_0}\right)^2 - \alpha^2 + 2\operatorname{sech}^2\frac{z}{\Delta H}\right]W(z) = 0, \quad (6)$$

where $\beta_0 = u_\infty/\Delta H$ and $\alpha = k\Delta H$.

A solution to Eq. (6) which satisfies the boundary conditions $W(\pm\infty)=0$ is

$$W(z) = A \operatorname{sech} \frac{z}{\Delta H} \qquad (7)$$

and

$$\left(\frac{N_\infty}{\beta_0}\right)^2 = \alpha^2 - 1. \qquad (8)$$

FIG. 2. Neutral curves: solid for this model; dashed for Gossard's three-layer model.

Another solution to Eq. (6) is $W(z) = A \cosh^2(z/\Delta H)$. However, this does not satisfy the boundary conditions and we disregard it. Eq. (8) defines a curve shown as the solid line in Fig. 2. According to an important result of Miles (1963), such a locus of stable solutions in the α, $(N_\infty/\beta_0)^2$ plane implies the existence of a contiguous region of unstable solutions. Eq. (8) thus defines the stability boundary. The unstable region lies above the curve.

3. Comparison with other models

Perhaps the principal practical value of this solution is that it permits us to compare the stability boundary of this model, which has smooth profiles with continuous derivatives, with the stability boundary of the corresponding three-layer, piecewise linear model. This comparison will permit an assessment of the effects of "corners" on the profiles of models such as those of Goldstein (1931), Taylor (1931), Howard (1963), Holmboe (1962) and Gossard (1974). This is important because piecewise linear models can be synthesized that

FIG. 1. Wind and potential temperature profiles for this model.
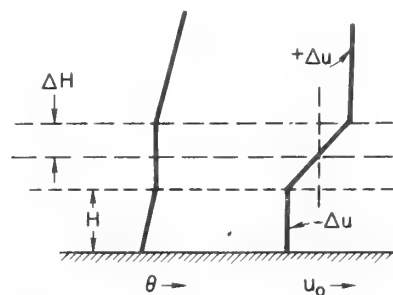
FIG. 3. Wind and potential temperature profiles for Gossard's three-layer model.
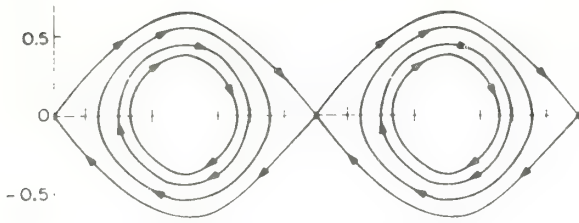
FIG. 4. Streamline pattern for this model.

represent very general conditions including a rigid lower boundary at an arbitrary distance below the shear layer and discontinuities at the edges of the shear layer.

The general eigensolution for a three-layer model, piecewise linear (almost) but continuous in wind and potential temperature and containing a rigid lower boundary, has been given by Gossard (1974). The model is shown in Fig. 3 and the required relation between σ, α in terms of H, ΔH, N_1, N_3 and β is

$$\left[\left(1+\frac{\alpha_1\alpha_3}{\alpha^2}\right)\tanh 2\alpha+\frac{\alpha_1+\alpha_3}{\alpha}\right]\left(\frac{\sigma}{\beta}\right)^2$$

$$+\left[\left(\frac{\alpha_1-\alpha_3}{\alpha}\right)\tanh 2\alpha\right]\frac{\sigma}{\beta}+(2\alpha-\alpha\alpha_1-\alpha\alpha_3)$$

$$-(1+\alpha^2-\alpha_1-\alpha_3+\alpha_1\alpha_3)\tanh 2\alpha=0, \quad (9)$$

where

$$\alpha_1=\gamma_1\Delta H\,\mathrm{ctnh}\gamma_1 H$$

$$\alpha_3=\gamma_3\Delta H$$

$$\gamma_1=k\left[1-\left(\frac{N_1/\beta}{\sigma/\beta+\alpha}\right)^2\right]^{\frac{1}{2}}$$

$$\gamma_3=k\left[1-\left(\frac{N_3/\beta}{\sigma/\beta-\alpha}\right)^2\right]^{\frac{1}{2}}$$

The subscripts 1, 3 apply to the lower and upper layers, respectively. N_1 and N_3 are assumed to be constant in the lower and upper layers so the profile of θ is exponential and thus not quite linear above and below the shear layer. However, applied to the real atmosphere, it is very nearly linear in those regions when N is constant. Within the shear layer $N_2=0$.

When $N_1=N_3$, $H=\infty$ and $\sigma/\beta=c=0$, this becomes the three-layer analog of the smooth model we study in this paper. Under these conditions Eq. (9) simplifies to

$$[(\alpha_\infty-1)^2+\alpha^2]\tanh 2\alpha+2\alpha(\alpha_\infty-1)=0, \quad (10)$$

where $\alpha_\infty^2=\alpha^2-(N_\infty/\beta)^2$ and the subscript ∞ designates the value in both layers 1 and 3. The stability boundary plotted from Eq. (10) is shown plotted as the dashed curve in Fig. 2. The general shape is the same as that of the solid curve plotted from Eq. (8). Both curves pass through $(N_\infty/\beta_0)^2=-1$ at $\alpha=0$.

When the model shown in Fig. 3 has a homogeneous density distribution (or $d\theta/dz=0$) it becomes a special case studied by Rayleigh (1945). Then $N_\infty=0$ so $\alpha_\infty=\alpha$ and (10) reduces to the Rayleigh condition for stability:

$$\frac{\tanh 2\alpha}{1+\tanh 2\alpha}-\alpha(1-\alpha)>0, \quad (11)$$

which yields $\alpha>0.64$. Therefore, the stability boundary for the three-layer model passes through 0.64 at $N_\infty/\beta=0$ as seen in Fig. 2.

Two smooth models in which the Richardson number does not vanish at the critical level were analyzed by Drazin (1958) and Holmboe (1960). For density (or, similarly, potential temperature) Drazin uses a simple exponential; Holmboe uses a hyperbolic tangent exponent. For example, the Holmboe function is, in our notation

$$\theta=\theta_0\exp\left[N_0^2\frac{\Delta H}{g}\tanh\left(\frac{z}{\Delta H}\right)\right], \quad (12)$$

where N_0 represents the Väisälä-Brunt frequency at $z=0$. Both Drazin and Holmboe use a hyperbolic tangent wind profile.

The eigensolutions and stability boundaries for both models are similar in form:

$$W(z)=A\left[\mathrm{sech}\left(\frac{z}{\Delta H}\right)\right]^\epsilon\left[\tanh\left(\frac{z}{\Delta H}\right)\right]^{1-\epsilon}, \quad (13)$$

$$\left(\frac{N_0}{\beta}\right)^2=\epsilon(1-\epsilon). \quad (14)$$

For the Drazin model, $\epsilon=\alpha^2$; for the Holmboe model, $\epsilon=\alpha$.

Eq. (14) has a maximum at $(N_0/\beta)^2=\frac{1}{4}$ in either model. This is in agreement with a theorem of Miles (1961) and Howard (1961) which states that a sufficient condition for stable fluid flow is that the local Richardson number $[(N/\beta)^2]$ be greater than $\frac{1}{4}$ everywhere in the fluid. The stability boundary curves shown in Fig. 2 exhibit no such limit. This is because $(N/\beta)^2=0$ at $z=0$ and thus the Miles-Howard theorem cannot be satisfied. Instead, the curves increase monotonically as α increases and there is always instability at some α.

Both of the eigenfunctions represented by Eq. (13) become that of our model [Eq. (1)] in the special case of $\alpha=1$. However, our solution and the stability boundary we find are valid for all α's.

At $N_0=N_\infty=0$, corresponding to a homogeneous fluid, or an adiabatic atmosphere, all three smooth models give $\alpha=1$ as the stability boundary. The piecewise linear model, however, yields $\alpha=0.64$, as mentioned earlier. This difference between the smooth and the piecewise linear models is obviously due to the different wind profiles (compare Figs. 1 and 3).

The streamlines for our model resemble the cat's eye pattern that is often seen in radar and acoustic sounder records (see Fig. 4). The Drazin and Holmboe models only yield the cat's eye when $\alpha = 1$, which implies an entirely homogeneous atmosphere, i.e., $(N/\beta)^2 = 0$ (see Howard and Maslowe, 1973).

The cat's eye pattern only occurs when $W(z_c) \neq 0$. This can occur only if all the terms of the Taylor-Goldstein equation [Eq. (1a)] remain finite at $z = z_c$. Thus, the existence of the cat's eye depends critically on the property of our model that $N^2(z_c) = 0$, that is, on our assumption of an adiabatic atmosphere at the critical level. Mathematically, this is a very special case, but observationally the cat's eye pattern is a common pattern found in records from many kinds of remote sensors.

A model due to Garcia (1961), $u = u_\infty \tanh(z/\Delta H)$, $\theta = \theta_0 \exp[(\text{const}) \tanh^3(z/\Delta H)]$, also yields the cat's eye and instability for all α. However, in the Garcia model the atmosphere becomes homogeneous at $z = \pm\infty$, i.e., the environment away from the shear layer is nearly homogeneous. Our model may provide some insight as to why the cat's eye pattern is often seen even when the shear layer is imbedded in a non-homogeneous environment.

Fig. 2 also suggests a generalization of a result reported by Gossard and Moninger (1975). They analyzed a fairly complicated model with profiles composed of wind and temperature segments. The model was three-dimensional and included a surface superadiabatic layer, a shear layer, and an inversion capping the shear layer. Because the model contained a superadiabatic layer and a shear layer, two kinds of instability were found—one convective and the other dynamic. Dynamically unstable disturbances were most unstable when aligned transverse to the wind shear, while those disturbances aligned along the shear were most convectively unstable. Both kinds of instability are found in the range $-1 < (N_1/\beta)^2 (m/k)^2 < 0$, where N_1 is the Väisälä-Brunt frequency of the superadiabatic layer, β the shear of the shear layer, m wavenumber, and k the component of wavenumber in the direction of shear. Thus this single dimensionless number includes magnitude of stability, shear, and orientation. Only convective instability exists below $(N_1/\beta)^2 (m/k)^2 = -1$ and only dynamic instability above 0. The cutoff in dynamic instability at -1 was found to be very general and is not affected by the stability of the upper atmosphere or the presence of the capping inversion. The present note demonstrates that this cutoff also does not depend on the "corners" in the profiles of the model. (In the two-dimensional models dealt with here, $m/k = 1.0$.)

REFERENCES

Drazin, P. G., 1958: The stability of a shear layer in an unbounded heterogeneous inviscid fluid. *J. Fluid Mech.*, **4**, 214–224.

Garcia, R. V., 1961: Unpublished lecture (see Miles, 1963).

Goldstein, S., 1931: On the stability of superposed streams of fluids of different densities. *Proc. Roy. Soc. London*, **A132**, 524–548.

Gossard, E. E., 1974: Dynamic stability of an isentropic shear layer in a statically stable medium. *J. Atmos. Sci.*, **31**, 483–492.

——, and W. H. Hooke, 1975: *Waves in the Atmosphere*. Elsevier, 456 pp.

——, and W. R. Moninger, 1975: The influence of a capping inversion on the dynamic and convective instability of a boundary layer model with shear. *J. Atmos. Sci.*, **32**, 2111–2124.

Holmboe, J., 1960: Unpublished lecture notes (see Miles, 1963).

——, 1962: On the behavior of symmetric waves in stratified shear layers. *Geophys. Publ.*, **24**, No. 2, 67–113.

Howard, L. N., 1961: Note on a paper of John W. Miles. *J. Fluid Mech.*, **10**, 509–512.

——, 1963: Neutral curves and stability boundaries in stratified flow. *J. Fluid Mech.*, **16**, 333–342.

——, and S. A. Maslowe, 1973: Stability of stratified shear flows. *Bound.-Layer Meteor.*, **4**, 511–523.

Miles, J. W., 1961: On the stability of heterogeneous shear flows. *J. Fluid Mech.*, **10**, 496–508.

——, 1963: On the stability of heterogeneous shear flows, Part 2. *J. Fluid Mech.*, **16**, 209–227.

Rayleigh, J. W. S., 1945: *The Theory of Sound*, Vol. 2 (reprint of 2nd ed. of 1896). Dover, Chap. 21.

Taylor, G. I., 1931: Effect of variation in density on the stability of superposed streams of fluid. *Proc. Roy. Soc. London*, **A132**, 499–523.

On the Nonlinear Theory for Gravity Waves on the Ocean's Surface.
Part I: Derivations

B. L. WEBER AND D. E. BARRICK

*National Oceanic and Atmospheric Administration, Wave Propagation Laboratory,
Sea State Studies Program, Boulder, Colo. 80302*

ABSTRACT

A general hydrodynamic solution is derived for arbitrary gravity-wave fields on the ocean surface by extending Stokes' (1847) original perturbational analysis. The solution to the nonlinear equations of motion is made possible by assuming that the surface height is periodic in both space and time and thus can be described by a Fourier series. The assumption of periodicity does not limit the generality of the result because the series can be made to approach an integral representation by taking arbitrarily large fundamental periods with respect to periods of the dominant ocean waves actually present on the surface. The observation areas and times over which this analysis applies are assumed small, however, compared to the periods required for energy exchange processes; hence an "energy balance" (or steady-state) condition is assumed to exist within the observed space-time intervals. This in turn implies the condition of statistical stationarity of the Fourier height coefficients when one generalizes to a random surface. Part I confines itself to the formulation of a perturbation solution (valid to all orders) for the higher order terms resulting from a two-dimensional arbitrary periodic description of the surface height. The method is demonstrated by deriving (to second order) the height correction to the sea and (to third order) the first nonzero correction to the lowest order gravity-wave dispersion relation.

1. Introduction

In recent years, it has become evident that radio waves can be used to measure an appreciable portion of the directional ocean wave-height spectrum. Barrick (1972) has presented a theory that relates this spectrum to the radar Doppler spectrum, which is observed when radio waves are scattered from the sea surface.

The purpose of this paper is 1) to derive the hydrodynamic part[1] of Barrick's theoretical results and 2) to derive the general correction term for the deepwater gravity-wave dispersion relation.

The approach taken here to solve the nonlinear hydrodynamic equations for ocean waves is similar to the approach that was used by Stokes (1847). That is, the general form of the solution is first postulated and then the details of this solution are performed starting with the equations of motion. In his classic work, Stokes sought a solution for a single gravity wave that propagates with a rigid, periodic profile and a constant velocity. He found that the wave height contained higher spatial frequency components in addition to the fundamental sinusoid predicted by the linear solu-

tion and that the higher order correction to the wave velocity depended upon the wave height.

The present problem is to find a general periodic wave train (consisting of an arbitrary number of individually distinct gravity waves) whose profile need not be rigid and whose spectral components need not all have the same phase velocity. The condition that the wave train is periodic allows the wave height to be expanded in a spatial and temporal Fourier series, which greatly simplifies the solution. The assumption of periodicity is a mathematical device that does not limit the generality of the solution because the fundamental spatial and temporal periods of the series can be made large compared with the physical area and time interval over which observations are made. In fact when these periods become very large—approaching infinity—we intend to use the fact that the series converge to integrals in the Riemann sense. It is assumed that such a periodic wave train can be used to give an approximate description of real ocean waves. The apparent stochastic character of these waves can then be included, if desired, by allowing the wave heights to be random variables.

It is more common to use a spatial and temporal Fourier-Stieltjes representation for analyzing ocean

---

[1] The electromagnetic scattering part of the theory will be derived in another paper.

waves. For example, Tick (1959) and Huang (1971) obtained straightforward nonlinear solutions by using this approach, but they also neglected the wave-height dependence in the dispersion relation. Tick's first and second-order perturbation derivations are essentially the same as those presented here, although Tick confined himself to one-dimensional ocean waves. Huang obtained a Fourier-Stieltjes integral equation relating wave height to velocity potential (to all orders); this expression could have been expanded in a perturbation series to solve for wave height correctly to second order, but that result was not pursued in Huang's treatment. Huang and Tung (1976) derived a general dispersion relation which was a function of wave height but which was also a function of space and time. However, their derivation appears inconsistent because they did not treat the wave frequency as a function of space and time throughout the entire derivation.

Phillips (1957, 1960) and Hasselmann (1962, 1963a,b) used a Fourier-Stieltjes integral for the spatial coordinates alone, leaving the wave height a general function of time. In this way, the original equations of motion, which contain both space and time derivatives, are replaced by differential equations with time derivatives only. Longuet-Higgins and Phillips (1962) and Benney (1962) used this general formulation to study the wave height dependence of wave velocity for the simpler case of one-dimensional wave trains. They used formal expressions for wave height that are essentially Fourier series, where the Fourier coefficients are slowly varying functions of time. This approach leads to a number (equal to the number of terms in the Fourier series) of coupled differential equations. Therefore, it is understandable why these studies were restricted to cases with small numbers of waves. The approach used in the present paper allows for an arbitrary number of waves (of different spatial periods and directions) by requiring that the sea surface be periodic.

Although we have neglected the energy transfer due to wind-wave interactions, wave-wave interactions, viscous damping, etc., the present problem is well-defined and soluble. The perturbation approach used by Stokes is valid mathematically (see, Lamb, 1932, p. 420); thus, we believe that the present generalization of Stokes' solution is also valid. In addition, since the energy transfer rates are relatively low compared with the periods of gravity waves, we expect the present description of these waves to give an accurate physical picture of the sea surface just as Stokes' waves closely resemble simple wave trains such as swells. The various energy transfer mechanisms are discussed in detail elsewhere by Phillips (1966), Hasselmann (1966), Miles (1967), Willebrand (1975) and Whitham (1967), just to name a few. Our main concern here is the correct description of the sea surface over times and areas such that energy transfer is not a dominant feature in the propagation of the gravity waves on the surface.

This paper confines itself to the derivational details and their justification. Fourier-series forms are used in this paper. A companion paper shows that this generalized two-dimentional solution checks, in the appropriate limiting cases, with the simpler but well-established results of Stokes (1847) for wave velocity and height corrections for a single wave; with Longuet-Higgins and Phillips' (1962) phase velocity correction for one wave due to the presence of another colinear wave; and with Tick's (1959) result for the second-order wave height of a one-dimensional wave-train profile. It is shown how the Fourier series approach can be converted to integral form suitable for statistical averaging processes. Finally, that paper gives several applications of these derivations to physical situations, which provide some appreciation for the utility of the results. Thus we believe that this work represents the first truly complete generalization of Stokes' technique which stands up to comparisons with all of the previously accepted specialized cases.

2. The generalization of Stokes' problem

The problem to be solved here is a generalization of the problem that was solved earlier by Stokes (1847). In that problem, Stokes sought a periodic wave train which propagates with a rigid profile and a constant velocity. The present problem is to find a general periodic wave train whose profile need not be rigid and whose spectral components need not all have the same phase velocity. The method of solution is based upon the perturbation technique used by Stokes. Also, the equations of motion are essentially the same simplified hydrodynamic equations that Stokes employed.

To begin with, the ocean is assumed to be infinitely deep and unbounded along its surface. Also, atmospheric effects are taken to be absent so that the interface is a free surface. Next, the water is treated as a homogeneous fluid that is incompressible, inviscid and without surface tension. All of these restrictions are generally accepted as being approximately valid for the description of the free propagation of gravity waves. Phillips (1966), Lamb (1932) and Batchelor (1970) are just a few who discussed these simplifying restrictions in detail. These assumptions can now be used to simplify the general hydrodynamic equations.

The first equation derives from the conservation of mass equation, which reduces to $\nabla \cdot \mathbf{v} = 0$, where $\mathbf{v}$ equals the local velocity of the water. For an inviscid fluid, initially irrotational motion will remain irrotational (i.e., $\nabla \times \mathbf{v} = 0$). In this case, a velocity potential ϕ can be defined such that $\mathbf{v} = \nabla \phi$, and the conservation of mass is then expressed by

$$\nabla^2 \phi = 0. \tag{1}$$

For these same conditions the Navier-Stokes equation (or conservation of linear momentum equation) at the

surface can be used to obtain

$$\left[\frac{\partial\phi}{\partial t}+\frac{1}{2}\nabla\phi\cdot\nabla\phi\right]_{z=\eta}=-g\eta, \tag{2}$$

where η is the vertical displacement of the surface due to waves. The coordinate system for this equation was chosen so that the positive (vertical) z axis is up and the x and y axes are in the plane (flat-earth approximation) of the undisturbed surface at $z=0$.

The third and final equation comes from the requirement that the surface remain intact. Then the vertical velocity $v_z=\partial\phi/\partial z$ of the water at the surface must equal the vertical velocity $d\eta/dt$ of the surface. That is,

$$\left[\frac{\partial\phi}{\partial z}\right]_{z=\eta}=\frac{\partial\eta}{\partial t}+\nabla\eta\cdot\left[\nabla\phi\right]_{z=\eta}. \tag{3}$$

Now a periodic waveform for η is sought. Therefore, η is expanded in spatial and temporal Fourier series as follows:

$$\eta(\mathbf{r},t)=\sum_{\mathbf{k},\omega}\eta(\mathbf{k},\omega)\exp[i(\mathbf{k}\cdot\mathbf{r}-\omega t)], \tag{4}$$

where $\mathbf{r}=\hat{x}x+\hat{y}y$ gives the position in the x, y plane. All of the spatial and temporal frequencies are harmonics of the fundamental frequencies, which may be taken to be infinitesimal.

It is obvious from (4) that η is a function of only the x and y spatial coordinates and time t. However, the velocity potential ϕ depends upon the z coordinate also. The form of the z dependence in ϕ is determined by (1) and the condition that $\phi\to 0$ as $z\to-\infty$. Therefore,

$$\phi(\mathbf{r},z,t)=\sum_{\mathbf{k},\omega}\phi(\mathbf{k},\omega)\exp[kz+i(\mathbf{k}\cdot\mathbf{r}-\omega t)]. \tag{5}$$

These expressions (4) and (5) give a general form for a periodic wavetrain. The fact that $\eta(\mathbf{r},t)$ and $\phi(\mathbf{r},z,t)$ are real physical quantities requires that the conditions $\eta^*(\mathbf{k},\omega)=\eta(-\mathbf{k},-\omega)$ and $\phi^*(\mathbf{k},\omega)=\phi(-\mathbf{k},-\omega)$ be satisfied by the series (4) and (5), respectively.

The fact that (2) and (3) are nonlinear suggests a perturbation approach. Stoker (1957), Tick (1959) and others preferred to make the perturbation expansions on $\eta(\mathbf{r},t)$ and $\phi(\mathbf{r},z,t)$. However, Whitham (1974) and Cole (1968) pointed out that such an approach may omit the amplitude dependence in the dispersion relation. On the other hand, Stokes' perturbation method does produce an amplitude dependence for the dispersion relation, and thus it is believed to be more general.

Therefore, the Fourier coefficients for wave height $\eta(\mathbf{k},\omega)$, velocity potential $\phi(\mathbf{k},\omega)$ and the frequency ω are expanded in perturbation series as follows:

$$\eta(\mathbf{k},\omega)=\eta_1(\mathbf{k},\omega)+\eta_2(\mathbf{k},\omega)+\cdots, \tag{6}$$

$$\phi(\mathbf{k},\omega)=\phi_1(\mathbf{k},\omega)+\phi_2(\mathbf{k},\omega)+\cdots, \tag{7}$$

$$\omega=\omega_0+\omega_1+\omega_2+\cdots, \tag{8}$$

where the subscripts give the perturbation order. For example, $\eta_2\sim\eta_1\eta_1$, $\phi_1\sim\eta_1$, $\phi_2\sim\eta_1\eta_1$, etc. Similarly, $\omega_1\sim\eta_1,\omega_2\sim\eta_1\eta_1$, but ω_0 is independent of wave height. Thus η_1 is considered an independent parameter and $\mathbf{k}$ is the independent variable of the present problem. The perturbation approach is valid if the wave heights are sufficiently small such that

$$\sum_{\mathbf{k},\omega}|\eta(\mathbf{k},\omega)|\times k<1. \tag{9}$$

This condition limits the slope of the surface to small values so that the perturbation expansion will converge.

Later, it will become evident that the wave heights of various orders in (6) do not all exist in the same domains of wave vector frequency space. In other words, the dispersion relation is in general different for each order of the ocean wave. For example, the first- and second-order wave-height spectra do not overlap in wave vector frequency space. Therefore, it will become convenient to use different notation for the wavevectors and frequencies of different orders of ocean waves.

3. The first-order solution

The perturbation expansions (6), (7) and (8) can be used along with the Fourier series (4) and (5) in order to solve the equations of motion for a periodic wave train. In this solution, the first-order wave heights $\eta_1(\mathbf{k},\omega)$ are arbitrary and all of the other variables are expressed in terms of them. The solution begins by substituting the Fourier series (4) and (5) into the equations of motion (2) and (3).

When the Fourier series are substituted into the equations of motion, the exponential $\exp(kz)$ in (5) becomes $\exp[k\eta(\mathbf{r},t)]$ because these equations are evaluated at the surface $z=\eta(\mathbf{r},t)$. Then the exponential is represented by its power series, and the wave height in each term is replaced by its Fourier series (4). Finally, the resulting equations are integrated over the spatial and temporal periods of the wave train. Because of the orthogonality of the Fourier components, (2) becomes

$$-i\omega\phi(\mathbf{k},\omega)+\sum_{\mathbf{k}',\omega'}\left[-i\omega'k'\phi(\mathbf{k}',\omega')\eta(\mathbf{k}-\mathbf{k}',\omega-\omega')\right.$$

$$+\tfrac{1}{2}[k'|\mathbf{k}-\mathbf{k}'|-\mathbf{k}'\cdot(\mathbf{k}-\mathbf{k}')]\phi(\mathbf{k}',\omega')\phi(\mathbf{k}-\mathbf{k}',\omega-\omega')\Big]$$

$$+\sum_{\mathbf{k}',\omega'}\sum_{\mathbf{k}'',\omega''}\left[-i\omega'\frac{k'^2}{2}\phi(\mathbf{k}',\omega')\eta(\mathbf{k}'',\omega'')\right.$$

$$\times\eta(\mathbf{k}-\mathbf{k}'-\mathbf{k}'',\omega-\omega'-\omega'')+\tfrac{1}{2}(k'k''-\mathbf{k}'\cdot\mathbf{k}'')(k'+k'')$$

$$\times\phi(\mathbf{k}',\omega')\phi(\mathbf{k}'',\omega'')\eta(\mathbf{k}-\mathbf{k}'-\mathbf{k}'',\omega-\omega'-\omega'')\Big]$$

$$+O(4)=-g\eta(\mathbf{k},\omega). \tag{10}$$
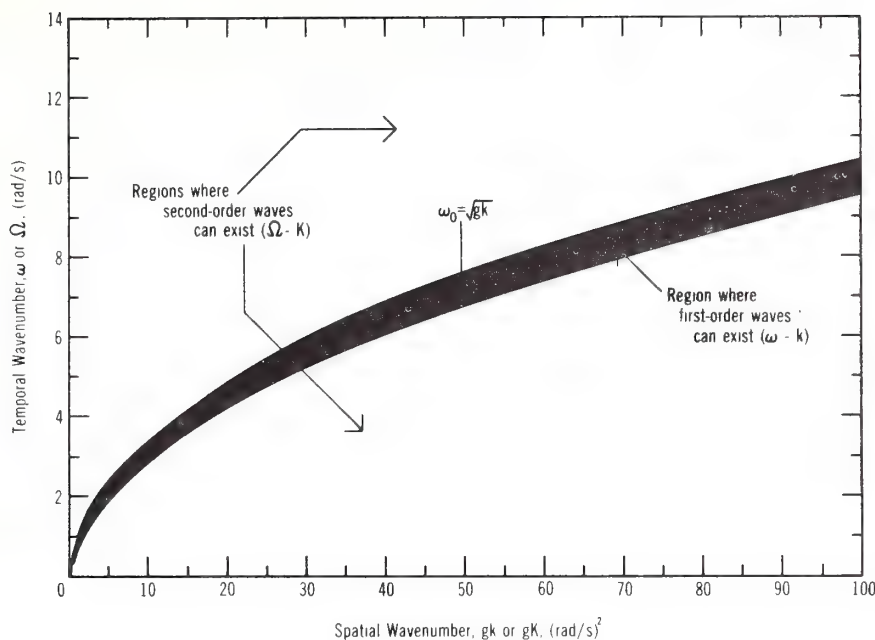
FIG. 1. Gravity-wave dispersion relationship diagram. First-order waves exist in heavily shaded region centered on $\omega_0 = \sqrt{gk}$. Second-order waves exist in remainder of diagram.

Similarly, the other equation of motion [(3)] becomes

$$k\phi(\mathbf{k},\omega) + \sum_{\mathbf{k}',\omega'} k'^2\phi(\mathbf{k}',\omega')\eta(\mathbf{k}-\mathbf{k}',\,\omega-\omega')$$

$$+\sum_{\mathbf{k}',\omega'}\sum_{\mathbf{k}'',\omega''}\frac{k'^3}{2}\phi(\mathbf{k}',\omega')\eta(\mathbf{k}'',\omega'')$$

$$\times\eta(\mathbf{k}-\mathbf{k}'-\mathbf{k}'',\,\omega-\omega'-\omega'')+O(4)=-i\omega\eta(\mathbf{k},\omega)$$

$$+\sum_{\mathbf{k}',\omega'}-\mathbf{k}'\cdot(\mathbf{k}-\mathbf{k}')\phi(\mathbf{k}',\omega')\eta(\mathbf{k}-\mathbf{k}',\,\omega-\omega')$$

$$+\sum_{\mathbf{k}',\omega'}\sum_{\mathbf{k}'',\omega''}-\mathbf{k}'\cdot\mathbf{k}''k'\phi(\mathbf{k}',\omega')\eta(\mathbf{k}'',\omega'')$$

$$\times\eta(\mathbf{k}-\mathbf{k}'-\mathbf{k}'',\,\omega-\omega'-\omega'')+O(4). \quad (11)$$

Next, the perturbation expansions will be used in (10) and (11) in order to separate the various orders of perturbation solution. The first-order terms in (10) are equated to give

$$-i\omega_0\phi_1(\mathbf{k},\omega)=-g\eta_1(\mathbf{k},\omega), \quad (12)$$

while the corresponding terms in (11) are

$$k\phi_1(\mathbf{k},\omega)=-i\omega_0\eta_1(\mathbf{k},\omega). \quad (13)$$

Hence

$$(\omega_0^2-gk)\eta_1(\mathbf{k},\omega)=0. \quad (14)$$

This equation can be satisfied if either the wave height $\eta_1(\mathbf{k},\omega)$ vanishes or

$$\omega_0^2=gk. \quad (15)$$

Therefore, for finite wave heights (15) becomes a dispersion relation which must be satisfied. It is important to note, however, that this condition (15) puts a restriction only upon the value of the first term ω_0 of

the perturbation expansion of the frequency ω. The higher order terms in (8) are determined by the higher order terms in (10) and (11). Also, it is the total frequency ω, and not just ω_0, which must be a harmonic frequency of the fundamental frequency. In Stokes' case of a rigid profile, the frequency of the first-order wave is the fundamental frequency. In the general case with many first-order waves present, the fundamental frequency need not be equal to the frequency of any of these waves.

4. The second-order solution

The second-order solution to (10) is

$$-i\omega_0\phi_2(\mathbf{k},\omega)-i\omega_1\phi_1(\mathbf{k},\omega)+\sum_{\mathbf{k}',\omega'}\{-i\omega_0'k'\phi_1(\mathbf{k}',\omega')$$

$$\times\eta_1(\mathbf{k}-\mathbf{k}',\,\omega-\omega')+\tfrac{1}{2}[k'|\mathbf{k}-\mathbf{k}'|-\mathbf{k}'\cdot(\mathbf{k}-\mathbf{k}')]$$

$$\times\phi_1(\mathbf{k}',\omega')\phi_1(\mathbf{k}-\mathbf{k}',\,\omega-\omega')\}=-g\eta_2(\mathbf{k},\omega). \quad (16)$$

Likewise, the second-order solution to (11) can be written

$$k\phi_2(\mathbf{k},\omega)+\sum_{\mathbf{k}',\omega'}\mathbf{k}'\cdot\mathbf{k}\phi_1(\mathbf{k}',\omega')\eta_1(\mathbf{k}-\mathbf{k}',\,\omega-\omega')$$

$$=-i\omega_0\eta_2(\mathbf{k},\omega)-i\omega_1\eta_1(\mathbf{k},\omega), \quad (17)$$

where terms on both sides of (11) have been combined.

There are two ways of attempting to satisfy (16) and (17) and solving for the desired second-order wave height η_2 and/or velocity potential ϕ_2. These can best be explained by dividing the frequency wavenumber $(\omega-k)$ domain into two distinct regions as illustrated in Fig. 1. The heavily shaded ridge is the region, for a given k, where the lowest order solution (zero-order)

for ω must satisfy the dispersion equation (15) given in the preceding section, viz., $\omega_0 = \pm\sqrt{gk}$. Since we have expanded ω in a perturbation series about ω_0, then ω_1, ω_2, ... should be increasingly small corrections to ω_0 by the very nature of the perturbation expansions. The center of the deep-shaded ridge is therefore defined by $\omega_0 = \sqrt{gk}$, and the width of the ridge (within which ω_1, ω_2, ... must lie), defining the complete ω, is kept small. We call the region within this ridge the region of first-order waves; we continue to denote the temporal frequencies in this region by ω, ω_0, ω_1, etc., i.e., lower case. Over the remainder of the diagram, no such restriction is required on the lowest order temporal frequency; to avoid confusion, we henceforth redefine the frequencies and wavenumbers corresponding to this region as $\mathbf{k} \equiv \mathbf{K}$ and $\omega \equiv \Omega$, with $\mathbf{K}$ as before being the independent variable. Just as with ω, we expand Ω in a perturbation series, $\Omega = \Omega_0 + \Omega_1 + \Omega_2 + \cdots$; but here we do *not* require that $\Omega_0 = \sqrt{gK}$. It will be shown that second-order ocean waves lie in this lightly shaded region exclusive of the ridge around $\omega_0 = \sqrt{gk}$ and that the two regions are in fact nonoverlapping. In other words, second-order waves cannot even approximately satisfy the first-order dispersion relationship normally identified with freely propagating ocean waves.

In order to eliminate the first possible way of solving (16) and (17), let us attempt to solve for η_2 and ϕ_2 at frequencies ω which could lie in the first-order zone. Since ω, ω' and ω'' all appear as arguments of first-order wave heights and velocity potentials, to lowest order we saw that we must require that $\omega_0 = \sqrt{gk}$, $\omega_0' = \sqrt{gk'}$ and $\omega_0''(=\omega_0 - \omega_0') = \sqrt{g|\mathbf{k}-\mathbf{k}'|}$. If these three equations cannot be satisfied, then in general *no* solution can exist within the ridge for ω, since if the lowest perturbation order ω_0 fails to meet the requirement, then the overall frequency ω also fails (i.e., each perturbation order must be satisfied separately).

To show this zero-order failure, the three separate dispersion equations $\omega_0^2 = gk$, $\omega_0'^2 = gk'$ and $\omega_0''^2 = gk''$ can be combined to give

$$\omega_0^2 + \frac{(3 - \hat{k}\cdot\hat{k}'')}{2}\omega_0\omega_0'' + \omega_0'^2 = 0,$$

which has real roots only if $\hat{k}\cdot\hat{k}'' = -1$. The solution in this event is $\omega_0 = -\omega_0''$ (requiring also $k = k''$), which leads to $\omega_0' = 0$ and $\mathbf{k}' = 0$. Thus of all the terms in the series of (16) and (17), only one is permissible: that with $\mathbf{k}'$ and $\omega_0' = 0$. There cannot be any waves with $k' = 0$, however, because this would produce a change in the mean level of the ocean, requiring the creation or destruction of water. We already defined the $x-y$ plane to lie in the mean plane of the ocean, implying that $\eta_1(0,\omega) = 0$. Hence, the summations in (16) and (17) must vanish, leaving

$$-i\omega_0\phi_2(\mathbf{k},\omega) - i\omega_1\phi_1(\mathbf{k},\omega) + g\eta_2(\mathbf{k},\omega) = 0, \quad (18)$$

$$k\phi_2(\mathbf{k},\omega) + i\omega_0\eta_2(\mathbf{k},\omega) + i\omega_1\eta_1(\mathbf{k},\omega) = 0. \quad (19)$$

Now if we multiply the first equation by k, multiply the second by $i\omega_0$, and add the two, then using the fact that $\omega_0^2 = gk$ we obtain $i\omega_1 k\phi_1(\mathbf{k},\omega) + \omega_0\omega_1\eta_1(\mathbf{k},\omega) = 0$. Upon substitution of (13) into this, we have $2\omega_0\omega_1\eta_1(\mathbf{k},\omega) = 0$. Since in general $\eta_1(\mathbf{k},\omega)$ is not equal to zero (i.e., η_1, $\mathbf{k}$, and hence ω_0, are the independent variables of the problem), then $\omega_1 \equiv 0$. This leaves (18) and (19) for the second-order wave height and velocity potential idential identical to (12) and (13) for the equivalent first-order quantities. Hence, there is no unique second-order solution for η_2 and ϕ_2 (within the "ridge" of Fig. 1 where first-order waves can exist) which is dependent upon and expressible in terms of η_1 and/or ϕ_1. Since there is no difference between the ϕ_2 and η_2 remaining in (18) and (19) and ϕ_1 and η_1 in (12) and (13), we can define all quantities which lie in the ridge and satisfy these required first-order equations as first order.

Therefore we have established the following facts thus far in this section:

1) First-order waves—by definition—exist within the narrow region in ω centered about ω_0, with ω_1, ω_2, ... being higher order (perturbation) corrections which are small compared to ω_0; η_1, ϕ_1, and ω_0 satisfy the first-order relation given by (12), (13) and (15).

2) The first-order correction to ω_0 (viz., ω_1) is identically zero. Therefore, the first possible correction to the lowest-order dispersion relation is second-order; this fact might have been suspected from Stokes' original derivations as well as later works (e.g., Lamb, 1932).

3) Second-order waves η_2 (and velocity potentials ϕ_2) which are dependent upon and expressible in terms of double products of η_1 and/or ϕ_1 cannot exist within the narrow region in ω near ω_0 which contain the first-order waves (such that the lowest-order dispersion equation $\omega_0^2 = gk$ is satisfied). They can exist and will be derived subsequently over the remainder of the temporal frequency region.

We now go back to (16) and (17) and solve for η_2 and ϕ_2 in the region where they can in fact exist: that region of Fig. 1 considerably away from the first-order ridge. As mentioned before, we change wavenumber notation to upper case (i.e., $\mathbf{K},\Omega$) to indicate that in this region the first-order dispersion relation does not apply, i.e., $\Omega_0^2 \neq gK$. Thus whenever $\mathbf{k}$ and ω appear, we change to $\mathbf{K}$ and Ω. However, $\mathbf{k}'$ and ω' remain, and all arguments of η_1 and ϕ_1 are still required to satisfy the first-order dispersion equation; i.e., $\omega_0'^2 = gk'$ and $(\Omega_0 - \omega_0')^2 = g|\mathbf{K} - \mathbf{k}'|$. Also, the second term on the left side of (16) and the last term on the right side of (17) are zero, because, as shown above, ϕ_1 and η_1 cannot exist in the second-order region (where $\mathbf{k} = \mathbf{K}$ and $\omega = \Omega$). Thus (16) can be rewritten as follows:

$$-i\Omega_0\phi_2(\mathbf{K},\Omega) + \sum_{\mathbf{k},\omega}\left[-\omega_0^2 - \tfrac{1}{2}\omega_0(\Omega_0 - \omega_0)\left(1 - \frac{\hat{k}\cdot(\mathbf{K}-\mathbf{k})}{|\mathbf{K}-\mathbf{k}|}\right)\right]$$
$$\times\eta_1(\mathbf{k},\omega)\eta_1(\mathbf{K}-\mathbf{k},\Omega-\omega) = -g\eta_2(\mathbf{K},\Omega), \quad (20)$$

where (13) was used to replace the first-order potentials inside the summation in (16). Similarly, (17) becomes

$$K\phi_2(\mathbf{K},\Omega) + \sum_{\mathbf{k},\omega} -i\omega_0\hat{k}\cdot\mathbf{K}\eta_1(\mathbf{k},\omega)\eta_1(\mathbf{K}-\mathbf{k},\ \Omega-\omega)$$
$$= -i\Omega_0\eta_2(\mathbf{K},\Omega). \quad (21)$$

These last two equations can be combined to obtain an expression for $\eta_2(\mathbf{K},\Omega)$ and one for $\phi_2(\mathbf{K},\Omega)$.

The second-order wave height becomes

$$\eta_2(\mathbf{K},\Omega) = \sum_{\mathbf{k},\omega} \sum_{\mathbf{k}',\omega'} A(\mathbf{k},\omega,\mathbf{k}',\omega')\eta_1(\mathbf{k},\omega)\eta_1(\mathbf{k}',\omega')$$
$$\times \delta_{\mathbf{K}}^{\mathbf{k}+\mathbf{k}'}\delta_{\Omega}^{\omega+\omega'}, \quad (22)$$

where this expression has been written in a symmetrical form with the help of the Kronecker delta functions, and where

$$A(\mathbf{k},\omega,\mathbf{k}',\omega') = \begin{cases} \dfrac{1}{2}\left[k+k'+\dfrac{\omega_0\omega_0'}{g}(1-\hat{k}\cdot\hat{k}')\left(\dfrac{gK+\Omega_0^2}{gK-\Omega_0^2}\right)\right] \\ 0 \quad \text{if} \quad \mathbf{k}'=-\mathbf{k} \quad \text{and} \quad \omega'=-\omega. \end{cases} \quad (23)$$

This last expression was simplified by taking advantage of the lowest order dispersion relation.

Since it has been proven earlier that $\Omega_0^2 \neq gK$, the denominator in (23) cannot vanish for any real values of $\mathbf{k}$, $\mathbf{k}'$, ω, ω' satisfying the Kronecker deltas. It can be shown that the two terms on the left side of (21) vanish for $K=0$. Because the velocity $\mathbf{v}=\boldsymbol{\nabla}\phi$, it is obvious that $\mathbf{v}(\mathbf{k},\omega)=i\mathbf{k}\phi(\mathbf{k},\omega)$ for all perturbation orders. Now, it is always possible to choose our coordinate system so that the undisturbed ocean is stationary (i.e., there is no current). Hence, $\mathbf{v}(\mathbf{k},\omega)=0$ for $k=0$ to all perturbation orders and the first term on the left side of (21) vanishes. Similarly, the second term vanishes because K is a multiplying factor. As a result, $A(\mathbf{k},\omega,\mathbf{k}',\omega')$ in (23) is defined to be identically zero when $\mathbf{k}+\mathbf{k}'=0$.

Since second-order waves cannot satisfy the first-order dispersion equation, these waves are not "free" in that they do not remove energy from the first-order waves, and hence cannot propagate freely without the two first-order waves with wavenumbers $\mathbf{k}$, ω and $\mathbf{k}'$, ω'; they are said to be "trapped" or "evanescent" ocean waves. By the same token, whenever the first-order waves are present, the second-order waves will always accompany them.

The second-order wave height (22) was used by Barrick (1972) in order to calculate the theoretical radar Doppler spectrum that is continuously distributed about the first-order solution. The coefficient $A(\mathbf{k},\omega,\mathbf{k}',\omega')$, which appears in this wave-height expression and is given by (23), is equal to $i\Gamma_H$ in Barrick's integral expression for the Doppler spectrum. There is also another quantity in this integral which accounts for second-order electromagnetic contributions.

In a similar manner, (20) and (21) can be combined to obtain an expression for the second-order velocity

potential. Hence,

$$\phi_2(\mathbf{K},\Omega) = \sum_{\mathbf{k},\omega} \sum_{\mathbf{k}',\omega'} B(\mathbf{k},\omega,\mathbf{k}',\omega')\eta_1(\mathbf{k},\omega)\eta_1(\mathbf{k}',\omega')$$
$$\times \delta_{\mathbf{K}}^{\mathbf{k}+\mathbf{k}'}\delta_{\Omega}^{\omega+\omega'}, \quad (24)$$

where

$$B(\mathbf{k},\omega,\mathbf{k}',\omega') = \frac{-i\Omega_0\omega_0\omega_0'(1-\hat{k}\cdot\hat{k}')}{(gK-\Omega_0^2)}. \quad (25)$$

By using the same line of reasoning that followed (23), it is clear that $KB(\mathbf{k},\omega,\mathbf{k}',\omega') \to 0$ for $K \to 0$ because the current velocity vanishes by definition.[2]

5. The third-order solution

The higher order equations from (10) and (11) can in principle be solved to all perturbation orders. However, the complexity of these equations becomes prohibitive for large orders. In general, the nth order equations will have solutions for all orders of waves from first order up to and including nth order. That is, there are n different solutions for the nth order equations. Each of these solutions uses all of the previous solutions to all of the lower order equations.

The discussion here will be limited to the third-order solution for first-order waves. In other words, just as we did for second-order waves, we initially assume that these third-order waves can exist over all $\mathbf{k}-\omega$ space, both in the "ridge" region of Fig. 1 near which $\omega_0^2=gk$ and over the remaining region where $\Omega_0^2 \neq gK$. We proved in the preceding section that second-order waves *cannot* exist in the first-order region near the ridge. A similar argument can be presented for third- and higher order waves. We will concern ourselves here with only those solutions which exist within the first-order wave region.

By following the pattern of the second-order solution and by using the first- and second-order results, it is possible to obtain the following simplified equations. The third-order expression for (10) becomes

$$-i\omega_0\phi_3(\mathbf{k},\omega) - i\omega_2\phi_1(\mathbf{k},\omega) + \sum_1 = -g\eta_3(\mathbf{k},\omega). \quad (26)$$

Likewise, (11) leads to

$$k\phi_3(\mathbf{k},\omega) + \sum_2 = -i\omega_0\eta_3(\mathbf{k},\omega) - i\omega_2\eta_1(\mathbf{k},\omega), \quad (27)$$

where the terms $\sum_1$ and $\sum_2$ are abbreviations which represent expressions that have the form of

$$\sum_{\mathbf{k}',\omega'} \sum_{\mathbf{k}'',\omega''} (\ldots)\eta_1(\mathbf{k}',\omega')\eta_1(\mathbf{k}'',\omega'')$$
$$\times \eta_1(\mathbf{k}-\mathbf{k}'-\mathbf{k}'',\ \omega-\omega'-\omega'').$$

---

[2] Expressions obtained by Hasselmann (1962) for the second-order wave height and velocity potential coefficients can be shown to reduce exactly to our (23) and (25). Because that approach ignores corrections to the dispersion relation, however, wave height and velocity potential solutions of order higher than third will differ from those obtained with our formulation.

Now, both $\eta_3(\mathbf{k},\omega)$ and $\phi_3(\mathbf{k},\omega)$ can be simultaneously eliminated from (26) and (27) by using the first-order dispersion relation (15); thus, they are indeterminant and can be taken to be identically zero because they are physically indistinguishable from first-order waves.[2] One then obtains an expression for the second-order frequency term ω_2:

$$\omega_2\eta_1(\mathbf{k},\omega)=\sum_{\mathbf{k}',\omega'}\sum_{\mathbf{k}'',\omega''}(\dots)\eta_1(\mathbf{k}',\omega')\eta_1(\mathbf{k}'',\omega'')$$
$$\times\eta_1(\mathbf{k}-\mathbf{k}'-\mathbf{k}'',\omega-\omega'-\omega''). \quad (28)$$

At first, this equation seems to contain an inconsistency because ω_2 is real, while the first-order wave heights $\eta_1(\mathbf{k},\omega)$ are arbitrary complex parameters. However, this equation also implies that there must be four waves such that $\omega'''=\omega-\omega'-\omega''$ and $\mathbf{k}'''=\mathbf{k}-\mathbf{k}'-\mathbf{k}''$. As was discussed in detail earlier with respect to the second-order solution, this equality between the temporal frequencies must and does hold for all perturbation orders.

All of these equations of different perturbation order (i.e., $\omega_n'''=\omega_n-\omega_n'-\omega_n''$) cannot be simultaneously satisfied unless pairs of the frequencies are identically equal. That is, $\omega=\omega'$ and $\omega''=-\omega'''$, or $\omega=\omega''$ and $\omega'=-\omega'''$, or $\omega=\omega'''$ and $\omega'=-\omega''$. At the same time, there must be the analogous equalities among the spectral wavenumber vectors. In the case that $\omega=\omega'$ and $\omega''=-\omega'''$, for example, it is also true that $\mathbf{k}=\mathbf{k}'$ and $\mathbf{k}''=-\mathbf{k}'''$. Consequently, $\eta_1(\mathbf{k},\omega)$ is a factor in every term on both sides of (28). Thus, (28) reduces to

$$\omega_2=\omega_0\sum_{\mathbf{k}',\omega'}C(\mathbf{k},\omega,\mathbf{k}',\omega')\,|\,\eta_1(\mathbf{k}',\omega')\,|^2, \quad (29)$$

where

$$C(\mathbf{k},\omega,\mathbf{k}',\omega')=-\frac{1}{2}\left[k'^2+\frac{\omega_0'}{\omega_0}\mathbf{k}\cdot\mathbf{k}'\left(2+\frac{k}{k'}\right)\right]$$

$$\times\left[1-\tfrac{1}{2}\delta_{\omega'}^\omega\delta_{\mathbf{k}'}^{\mathbf{k}}-\tfrac{1}{2}\delta_{\omega'}^{-\omega}\delta_{\mathbf{k}'}^{-\mathbf{k}}\right]+A\left(\mathbf{k},\omega,\mathbf{k}',\omega'\right)$$

$$\times\left[-k'+\frac{\omega_0'}{\omega_0}\frac{\mathbf{k}\cdot\mathbf{k}'}{k'}\right]-\frac{B(\mathbf{k},\omega,\mathbf{k}',\omega')}{i\omega_0}\left[\mathbf{k}\cdot(\mathbf{k}+\mathbf{k}')\right.$$

$$\left.-k|\mathbf{k}+\mathbf{k}'|+\frac{\omega_0'}{\omega_0}\frac{k}{k'}\mathbf{k}'\cdot(\mathbf{k}+\mathbf{k}')\right]. \quad (30)$$

The expressions for $A(\mathbf{k},\omega,\mathbf{k}',\omega')$ and $B(\mathbf{k},\omega,\mathbf{k}',\omega')$ are given by (23) and (25), respectively. Since $B(\mathbf{k},\omega,\mathbf{k}',\omega')$ contains a factor of i, the i in (30) is cancelled so that $C(\mathbf{k},\omega,\mathbf{k}',\omega')$ is clearly real. Here we see one advantage

in retaining series formulations rather than integral notation, at least to this point. The step from (28) to (29) would be more difficult mathematically had we been using integrals.

Higher order correction terms to the frequency ω in (8) can be computed in principle, but they are small compared to ω_2. Thus, the dispersion relation for first-order ocean waves is given (to second order) by $\omega=\omega_0+\omega_2$, where ω_0 is defined by (15) and ω_2 is defined by (29). It is recalled that the first-order correction term ω_1 was shown to be zero for these waves. Once the dispersion relation is known for first-order waves it is also known for second-order waves because the Kronecker-delta functions in (22) imply that $\Omega=\omega+\omega'$, where Ω is the frequency of a second-order wave and ω and ω' are the frequencies of first-order waves. Hence to second-order $\Omega=\omega_0+\omega_0'+\omega_2+\omega_2'$. Some interesting numerical examples will be presented in a companion paper.

6. Discussion and conclusions

The nonlinear solution presented here for a two-dimensional deep-water surface of arbitrary profile—periodic in space and time—can be evaluated to any perturbation order following the technique presented here. To second order, we determined expressions for the wave height and velocity potential and showed that those do not represent free waves, i.e., waves which follow (approximately) the first-order dispersion equation $\omega_0^2=gk$. We then carried the solution to third order to solve for the first nonzero correction to the first-order dispersion equation.

This solution gives a complete mathematical description (but only an approximate physical description) of the sea surface; it must be restricted in area and time. The sizes of the observed area and time intervals over which the solutions are valid are such that they are large compared to the spatial periods $2\pi/|\mathbf{k}|$ and temporal periods $2\pi/|\omega|$ of the dominant waves present, but small in terms of the areas and times over which energy transfer takes place (i.e., both nonlinear wave-wave energy transfer, energy transfer between the atmosphere and ocean and viscous effects). The waveheights $\eta_1(\mathbf{k},\omega)$ are in general complex random variables whose statistics change over areas and times larger than those required for energy transfer.

So long as the above area/time restrictions are understood, the Fourier series solution can be generalized to allow one to perform statistical averaging, and sums are readily converted to integrals, with average waveheight spectra evolving from the height coefficients. This process will be illustrated in a companion paper. In certain (but not all) averaging processes, one must define a length or time period associated with the series-integral conversion, and this quantity remains in the final result. For the radar problem, this length (or area) period must logically be taken as the actual areal resolu-

---

[2] These waves are interesting in another context because, as was shown in the works of Hasselmann (1963a,b) and Phillips (1966), since these waves do satisfy the first-order dispersion equation—and hence are indistinguishable physically from first-order waves—they can and do carry energy (in contrast with the evanescent or trapped second-order waves $\eta_2(\mathbf{K},\Omega)$). Therefore, nonlinear wave-wave energy redistribution of the original spectrum can and does occur via third-order waves.

tion cell observed by the radar. Likewise, the temporal period (if needed explicitly in the final result) would be the coherent observation time associated with the buoy or radar experiment. An example will be given in the companion paper.

REFERENCES

Barrick, D. E., 1972: Remote sensing of sea state by radar. *Remote Sensing of the Troposphere*, V. E. Derr, Ed., U. S. Govt. Printing Office, Washington, D. C., Chap. 12.

Batchelor, G. K., 1970: *An Introduction to Fluid Dynamics*. Cambridge University Press, 615 pp.

Benney, D. J., 1962: Nonlinear gravity wave interactions. *J. Fluid Mech.*, **14**, 577–584.

Cole, J. D., 1968: *Perturbation Methods in Applied Mathematics*. Blaisdell Publishing Co., p. 84.

Hasselmann, K., 1962: On the nonlinear energy transfer in a gravity-wave spectrum; Part 1. General theory. *J. Fluid Mech.*, **12**, 481–500.

——, 1963a: On the non-linear energy transfer in a gravity-wave spectrum; Part 2. Conservation theorems, wave-particle correspondence; Irreversibility, *J. Fluid Mech.*, **15**, 273–281.

——, 1963b: On the non-linear energy transfer in a gravity-wave spectrum, Part 3. Evaluation of the energy flux and swell-sea interaction for a Neumann spectrum. *J. Fluid Mech.*, **15**, 385–398.

——, 1966: Feynman diagrams and interaction rules of wave-wave scattering processes. *Rev. Geophys.*, **4**, 1–32.

Huang, N. E., 1971: Derivation of stokes drift for a deep water random gravity wave field. *Deep-Sea Res.*, **18**, 255–259.

——, and C. Tung, 1976: The dispersion relation for a nonlinear random gravity wave field. *J. Fluid Mech.*, **75**, 337–345.

Lamb, H., 1932 *Hydrodynamics*, 6th ed. Dover Publications, 738 pp.

Longuet-Higgins, M. S., and O. M. Phillips, 1962: Phase velocity effects in tertiary wave interactions. *J. Fluid Mech.*, **12**, 333–336.

Miles, J. W., 1967: On the generation of surface waves by shear flows, Part 5. *J. Fluid Mech.*, **30**, 163–175.

Phillips, O. M., 1957: On the generation of waves by turbulent wind. *J. Fluid Mech.*, **2**, 417–445.

——, 1960: On the dynamics of unsteady gravity waves of finite amplitude; Part 1. The elementary interactions. *J. Fluid Mech.*, **9**, 193–217.

——, 1969: *The Dynamics of the Upper Ocean*. Cambridge University Press, 261 pp.

Stokes, G. G., 1847: On the theory of oscillatory waves. *Trans. Cambridge Phil. Soc.*, **8**, 441–445.

Stoker, J. J., 1957: *Water Waves*. Interscience, 567 pp.

Tick, L. J., 1959: A nonlinear random model of gravity waves, I. *J. Math. Mech.*, **8**, 643–657.

Willebrand, J., 1975: Energy transport in a nonlinear and inhomogeneous random gravity wave field. *J. Fluid Mech.*, **70**, 113–126.

Whitham, G. B., 1967: Variational methods and applications to water waves, *Proc. Roy. Soc. London*, A299, 6–25.

——, 1974: Dispersive waves and variational principles. *Nonlinear Waves*, S. Leibovich and A. R. Seebass, Eds., Cornell University Press, Chap. V.

DETECTION OF GUST FRONTS USING SURFACE SENSORS

A. J. Bedard, Jr. and D. W. Beran

Properties of thunderstorm gust fronts and the surface effects they produce are reviewed with emphasis on density currents and their associated wind shear as a hazard to aircraft. Methods of detection are reviewed in terms of their utility in warning systems for airports. A first-generation warning system developed at NOAA/ERL's Wave Propagation Laboratory is described. It consists of an acoustic Doppler system, a Doppler radar, and a dense array of pressure-jump detectors. It overcomes deficiencies of systems developed previously, which lack sufficient spatial resolution and areal extent for measurements of evolving gust fronts. The research program continuing at WPL to evaluate and optimize the system is documented.

ATMOSPHERIC PRESSURE JUMPS MEASURED WITH ARRAYS
OF SENSITIVE PRESSURE SENSORS IN THE VICINITY
OF CHICAGO'S O'HARE INTERNATIONAL AIRPORT

A. J. Bedard, Jr. and M. M. Cairns

We describe an experiment designed to evaluate the use of arrays of sensitive pressure sensors for gust-front detection. First results of the experiment (which is still underway at Chicago's O'Hare airport in conjunction with the Transportation Systems Center of the Department of Transportation) have demonstrated the feasibility of predicting the motion of such density currents by using an array of such sensors. Using data sets obtained in June through August of 1976 we discuss their implications for the design of arrays to provide warnings of gust front systems in airport environments. Although we tracked over 80% of the pressure jumps over the O'Hare system, several events went undetected at two or more of the outer array locations. We there-fore conclude that the optimum array density will involve a compromise between practicality and a need for high reliability in detection. The current outer array configuration of absolute pressure sensors seems to represent the mini-mum array dimensions and density needed for detection and tracking. Although a 1 km spacing permits resolution of small-scale features, to obtain accurate velocity computations (permitting prediction) increased spacings (to about 2 km) and/or more pressure jump detectors seem necessary.

MEASURING THUNDERSTORM GUST FRONTS USING SURFACE SENSORS

A. J. Bedard and M. M. Cairns

NOAA/ERL/Wave Propagation Laboratory
Boulder, Colorado

1.   INTRODUCTION

A concept has evolved for using the sudden pressure rise associated with the leading edge of cold air outflows from thunderstorms as a means of detecting such systems and the hazardous wind shears associated with them (Bedard and Beran, 1977). We describe here our efforts (funded by the Federal Aviation Administration) to evaluate the use of pressure sensors to detect thunderstorm outflows. Although we have several other measurement efforts using pressure sensors currently in progress (e.g., at Dulles airport (Bedard, Hooke and Beran, 1977) and with the National Severe Storms Laboratory), space and time considerations caused us to restrict our presentation here to studies involving the Chicago O'Hare airport area.

Pressure disturbances accompany a wide range of meteorological phenomena. Figure 1 depicts some mechanisms that cause pressure changes on scales of tens of kilometers. Large pressure changes occur with hydraulic jumps (Tepper, 1954), gravity-shear waves (Flauraud, et al., 1954) and frontal passages (Clarke, 1961) in addition to thunderstorm gust fronts (Goff, 1976). Moreover, vertical accelerations of air parcels are another source of "minor" changes in pressure (Perry, 1976). Thus a need exists for statistical studies to determine the frequency with which various source mechanisms cause significant pressure perturbations.

We have developed for the Chicago O'Hare airport area statistics on the relative frequency of the various sources of pressure disturbances (to find methods of distinguishing between them and to provide quantitative bases for the design of sensitive pressure jump detectors). Data are also available from an array of pressure sensors operated at O'Hare International Airport since the spring of 1976 in a field program to evaluate the ability of such arrays to detect and track the motions
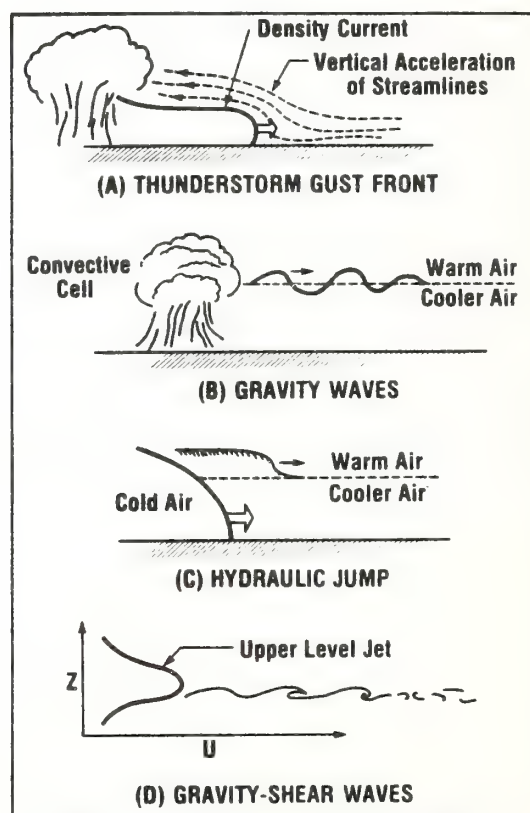
Figure 1. Causes of atmospheric pressure disturbances.

of pressure discontinuities. (This is part of a cooperative study with the Transportation Systems Center (TSC) of the Department of Transportation). We present here results from our statistical study and from the O'Hare array of pressure sensors. These results indicate that it is possible to detect and track thunderstorm-gust-front motions and estimate their severity using arrays of pressure sensors.

154

2. PRESSURE DISTURBANCE STATISTICS FOR CHICAGO'S O'HARE AIRPORT

Details of the statistics presented in this section appear in a Federal Aviation Administration Final Report (Greene et al., 1977a) reviewing the wind shear problem. Papers by Greene et al. (1977b) and Frank and Moninger (1977) in these proceedings are also based upon that final report.

We analyzed the occurrences of pressure jumps in the Chicago O'Hare Airport area for the period 1968 through 1972, using standard National Weather Service 24-hour barogram traces in the analysis. Daily surface weather maps and station weather for 0700, EST, Storm Data and Severe Weather Phenomena (which included location, date, time, and character of the storm), and radar summaries for the United States were used to determine the type of local weather phenomena occurring at the time of the event. We applied several criteria in defining a significant pressure disturbance. Here we present data for one of them -- a pressure rise exceeding one millibar in ten minutes (600 sec), which is the threshold for one type of sensitive pressure jump detector designed for possible use as part of a future shear warning system.

Figures 2 through 4 show the occurrence of pressure jumps meeting this criterion as a function of time-of-year for events related to thunderstorms, gravity-shear waves, and frontal activity respectively. It is evident that thunderstorm-related pressure disturbances occurred mainly during the months of April through September, the peak months being May and June. Figure 3 shows that gravity shear wave activity peaks in March, April, and November with few events in the summer. December and January have no events in contrast to the winter maximum observed by Flauraud et al., (1954). This may reflect the movement of the upper level jet to lower latitudes. We categorized oscillatory pressure disturbances of long duration (> 1 hour) as related to gravity-shear waves (especially when they occurred in the presence of an intense jet stream aloft). Figure 4 presents time-of-year occurrence of disturbances related to frontal passages. It shows no clear peak in the yearly statistics for these events.

Figures 5 and 6 show the sources of pressure disturbances by percentage of occurrence. Figure 5 shows the data for the entire year, and figure 6 shows only the months of May through September. Thus, a variety of source mechanisms are responsible for pressure disturbances at this location
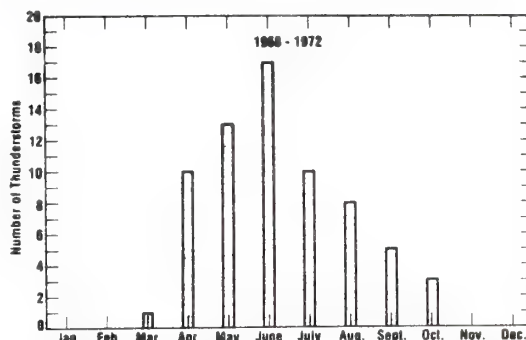
Figure 2. Time-of-year variation of pressure disturbances due to thunderstorms.
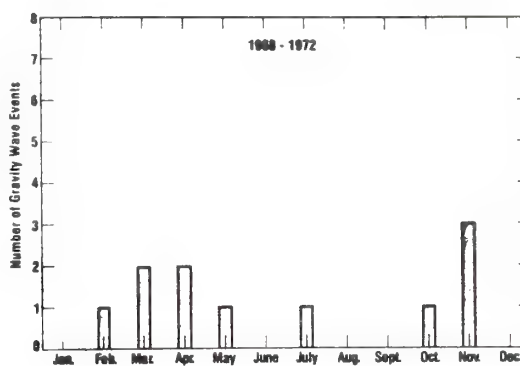
Figure 3. Time-of-year variation of pressure disturbances due to gravity-shear waves.
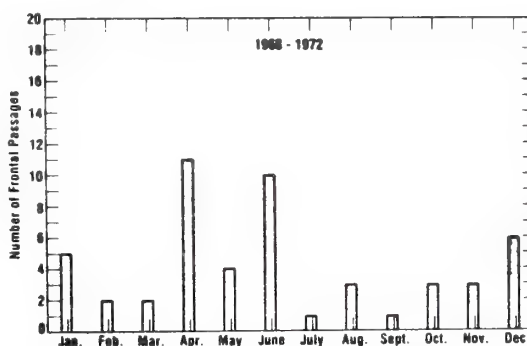
Figure 4. Time-of-year variation of pressure disturbances due to frontal activity.

regardless of season. Most of them (over 82%) probably correlate with shear events at lower altitudes.

155
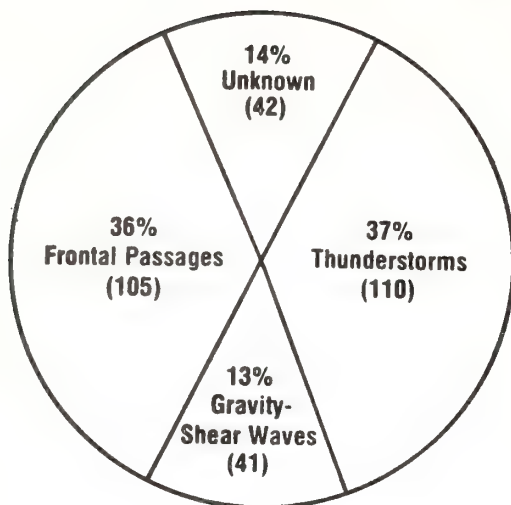
Figure 5. *Sources of pressure disturbances at Chicago's O'Hare International Airport by percentage of occurrence (1968-1972).*
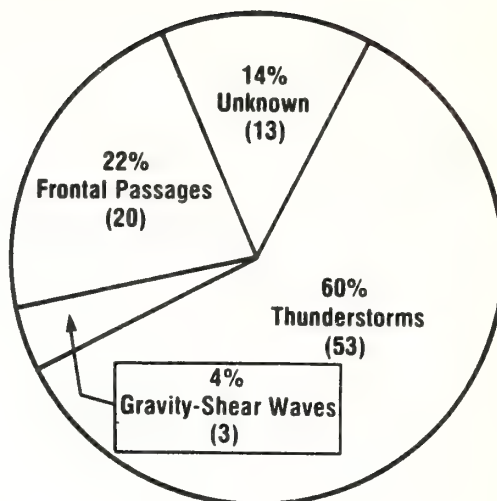
Figure 6. *Sources of pressure disturbances at Chicago's O'Hare International Airport by percentage of occurrence (May-September;1968-1972).*

Figure 7 is a plot of ΔP, the maximum pressure change in millibars as a function of τ, the rise time of the jump in minutes. This plot is shown only for the thunderstorm-related cases. These data in conjunction with the time-of-year source frequency statistics can be used to make estimates concerning detection rates for pressure detectors.

We analyzed anemometer recordings for O'Hare Airport for the 5-year period during the months of May through September and noted the maximum

change in speed (ΔU) for all cases in which a sudden wind surge appears (an increase greater than 4.5 m sec^{-1} -- 10 mph), usually occurring within 5 minutes). The ΔU values constitute minimum changes of horizontal wind speed, not taking into account changes in wind direction often associated with the passage of gust fronts. We measured the maximum pressure change and rise time, τ, for each of the events and present these data in two ways. Figure 8 is a plot of ΔP as a function of ΔU and appears as a scatter plot with no evidence of the $(\Delta P)^{1/2}$ law frequently assumed for density currents. On the other hand if we plot $\Delta P/\tau$ as a function of ΔU, a better correlation is evident (Figure 9).

We interpret these results as evidence that atmospheric gust-fronts frequently move due to driving forces in the central outflow region, as opposed to pressure gradients across the density discontinuity at the nose of the current. A simple model of a source-driven density current appears in the report by Greene et al. (1977a). Our data imply that statistically some value of gust-front severity can be chosen as a warning threshold for operational systems. For example, some threshold level of $\Delta P/\tau$ could be related to the speed of motion of the discontinuity and magnitude of the shear. However, we need more statistics about these relationships.

Figure 7. *Pressure amplitude versus rise time statistics for thunderstorm-related cases.*
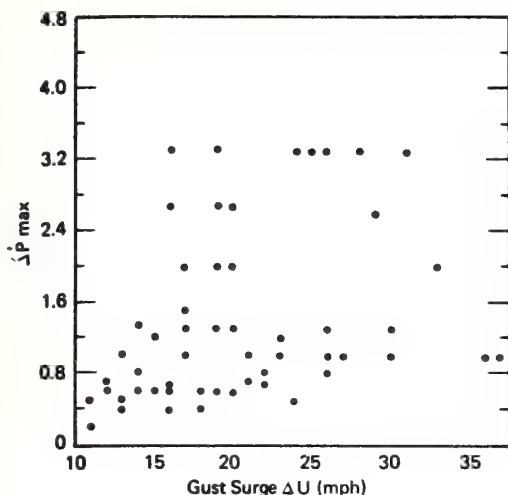
Figure 8. *Plot of maximum pressure change versus gust surge maximum (1968-1972).*
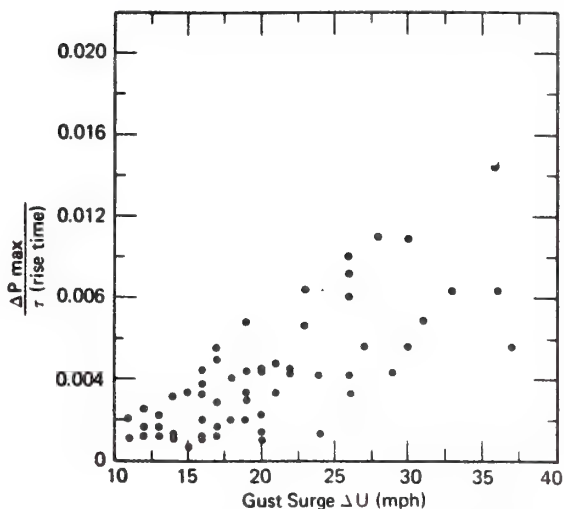
Figure 9. *Plot of the ratio $\Delta P/\tau$ versus gust surge.*

3.   DETECTION OF THUNDERSTORM GUST FRONTS USING AN ARRAY OF PRESSURE SENSORS NEAR CHICAGO'S O'HARE AIRPORT

Figure 10 shows the passage of a pressure discontinuity across the array of pressure sensors at O'Hare International Airport. Using the arrival times of the pressure maximum at the P_0 (absolute pressure sensor) locations in the outer arrays we computed the azimuth of arrival and horizontal trace speed. We assumed a plane wave front for the disturbance and show its measured arrival times by the dashed lines. The disturbance arrived from an azimuth of 226.7° at a speed of 12.6 ms^{-1}, apparently originating from thunderstorm cells southwest of the airport.

In addition we used these data to compute the arrival time of the pressure maximum at the location of the airport anemometer. Figure 11 presents the anemometer trace corresponding to this event with the dashed lines indicating the predicted arrival times of the start and maximum of the pressure jump. Note the good agreement between time of the gust surge and the computed arrival time of the pressure maximum. South and west departures were stopped because of heavy cells shortly after the arrival of the wind surge.

We are preparing a detailed report describing the operation of the O'Hare airport pressure sensor array during the spring and summer of 1976. Between June and August we detected ten events similar to the one described. A key conclusion is that the speed of motion of thunderstorm gust-fronts often does not change significantly over distances of about 10 km, thus permitting prediction of discontinuity position as a function of time. In the future we hope to compare pressure sensor data from such events with data from an array of rain gauges operated by the Illinois State Water Survey (Changnon and Huff, 1976). We also hope to obtain data from additional anemometers, pressure sensors, and temperature sensors now operating near the ends of runways at O'Hare airport as part of a cooperative effort with TSC.

One weakness of these experiments is that we have no quantitative measurement of the wind shear to compare with the surface array data. On-going experiments with surface pressure sensor arrays at Dulles airport and at the National Severe Storms Laboratory should help fill this gap. At Dulles an acoustic/microwave radar system measures wind and wind-shear continuously from the surface to 500 m (Hardesty et al., 1977). Bedard, Hooke and Beran (1977) describe the dense array of surface sensors installed at Dulles airport. A meteorological tower near Oklahoma City, Oklahoma, provides the reference for the NSSL experiment.
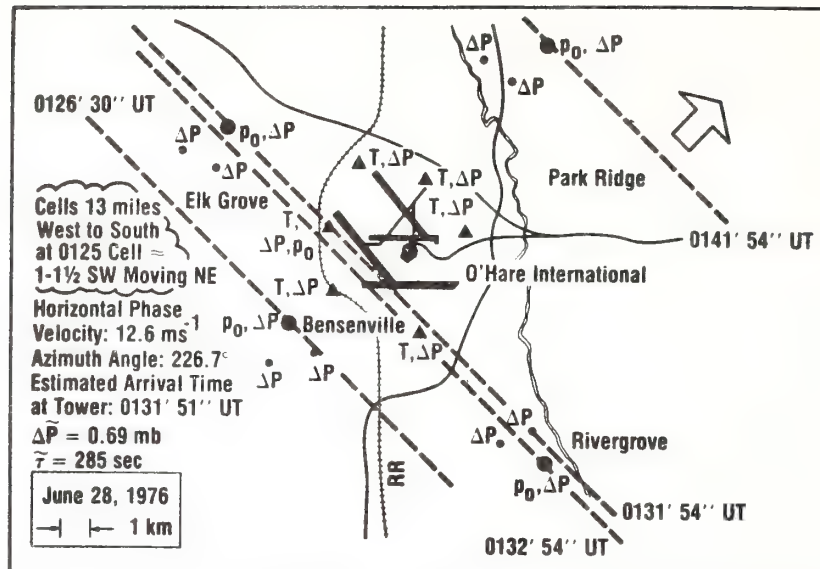
Figure 10. *Motion of a pressure jump across Chicago's O'Hare International Airport on 28 June 1976.*
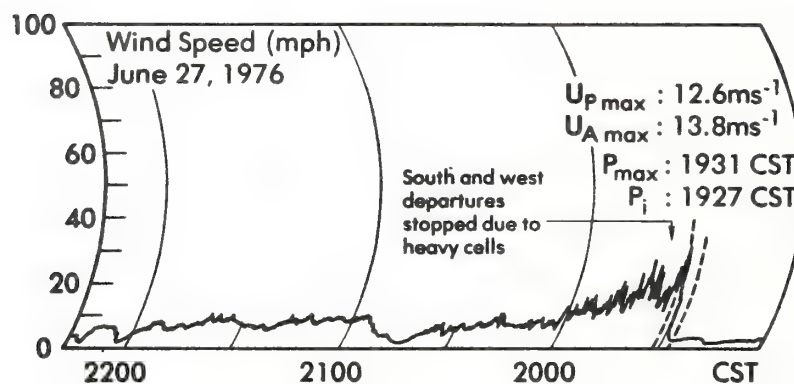
Figure 11. *Comparison showing the arrival of a gust surge relative to the predicted arrival time of the pressure jump.*

4.   IMPLICATIONS FOR DETECTION
            AND ANALYSIS OF THUNDER-
            STORM GUST-FRONT EVENTS

        Observations showing that gust fronts often move with little change in speed over distances of about 10 km indicate the usefulness of surface sensors to predict system motion and provide warnings. The events accompanied by pilot reports of weather-related problems in the vicinity of the airport were all detected by at least three of the outer arrays and we could compute azimuths and speeds of motion. However, other data sets from O'Hare show pressure disturbances that were spatially complex. For these, the plane wave assumption is not valid, and detection requires a dense array of surface sensors to resolve their form and motion. Such a dense array is currently being tested in the vicinity of Dulles airport.

158

The statistical studies indicate the frequency with which various mechanisms produce significant pressure disturbances. Although thunderstorms and frontal activity accounted for most of the events, gravity-shear waves also produced large pressure perturbations. We are currently working on methods for distinguishing between various source mechanisms. The observation of a correlation between the peak surface wind surge and the ratio $\Delta P/\tau$ suggests that estimates of the speed of motion of the system are possible by the use of pressure data alone. We hope to extend these statistical studies to other regions of the country.

5. ACKNOWLEDGMENTS

6. REFERENCES

Bedard, J. A., Jr. and D. W. Beran (1977). "Detection of gust fronts using surface sensors." NOAA Tech. Memo. ERL WPL-20, 15p.

Bedard, A. J., Jr., W. H. Hooke and D. W. Beran (1977). "The Dulles airport pressure-sensor array for gust-front detection." Submitted to Bull. Amer. Meteor. Soc.

Changnon, S. A., Jr. and F. A. Huff (1976). "Chicago hydrometeorological area project: A comprehensive new study of urban hydrometeorology." First interim report. Program of Advanced Environmental Research and Technology Research Applied to National Needs, Atmospheric Sciences Section, Illinois State Water Survey, 69p.

Clarke, R. H. (1961). "Mesostructure of dry cold fronts over featureless terrain." J. Meteor., *18*, 715-735.

Flauraud, E. A., A. H. Mears, F. A. Crowley, Jr. and A. P. Carey (1954). "Investigations of microbarometric oscillations in eastern Massachusetts." Tech. Rept. 54-11 Geophys. Res. Paper 27, Air Force Cambridge Res. Lab., Mass., 61p.

Frank, H. W. and W. R. Moninger (1977). "Observations of atmospheric density currents with severe wind shear." Proc. 10th Conference on Severe Local Storms, Oct. 18-21, Omaha, Nebr., Amer. Meteor. Soc., Boston, Mass.

Goff, R. C. (1976). "Vertical Structure of Thunderstorm Outflows." Mon. Wea. Rev., *104*, No. 11, 1429-1440.

Greene, G. E., J. A. Korrell and P. A. Mandics (1977a). "An analysis of the gust-front hazard." Proc. 10th Conference on Severe Local Storms, Oct. 18-21, Omaha, Nebr., Amer. Meteor. Soc., Boston, Mass.

Greene, G. E., H. W. Frank, A. J. Bedard Jr., J. A. Korrell, M. M. Cairns and P. A. Mandics (1977b). "Wind shear characterization." Final report to the Federal Aviation Administration, prepared by the Wave Propagation Laboratory, NOAA.

Hardesty, R. M., P. A. Mandics, D. W. Beran and R. G. Strauch (1977). "The Dulles airport acoustic/microwave radar wind and wind-shear measuring system." Submitted to Bull. Amer. Meteor. Soc.

Perry, J. D. (1976). "An analysis of pressure jumps at Luqa, Malta, in the years 1968-1972." Meteor. Magazine, *105*, 166-184.

Tepper, M. (1954). "Pressure Jump Lines in Midwestern United States, January-August 1951." U. S. Dept. of Commerce, Weather Bureau Research Paper No. 37.

Structure of an Evolving Hailstorm, Part V: Synthesis and Implications for Hail Growth and Hail Suppression

K. A. Browning[1], J. C. Fankhauser, J.-P. Chalon[2] and P. J. Eccles

National Center for Atmospheric Research,[3] Boulder, Colo. 80303

R. G. Strauch and F. H. Merrem

NOAA/ERL/Wave Propagation Laboratory, Boulder, Colo. 80303

D. J. Musil, E. L. May and W. R. Sand

Institute of Atmospheric Sciences, South Dakota School of Mines and Technology, Rapid City, S. Dak. 57701

(Manuscript received 17 September 1975, in revised form 6 January 1976)

ABSTRACT

A model of an evolving hailstorm is synthesized from data presented in four related papers in this issue. The storm model, which is applicable to a class of ordinary multicell hailstorms and similar to earlier models derived by workers in South Dakota and Alberta, is discussed in terms of the growth of hail and its implications for hail suppression. Hail is grown in time-evolving updrafts that begin as discrete new clouds on the flank of the storm. Low concentrations of embryos develop rapidly within each of these clouds. The embryos subsequently grow into small hailstones while suspended near or above the −20°C level as each new cloud grows and becomes the main updraft. Recycling is not a feature of this model as it is in supercell models. To improve the chance of silver iodide seeding being effective in suppressing the growth of hail in multicell storms, it is proposed that the seeding should be carried out not in the main updraft as is often the practice, but, rather, in the regions of weaker updraft associated with the early stages of developing clouds on the flank of the storm.

1. Introduction: the ordinary multicell storm as a distinct hailstorm type

Several categories of hailstorms have recently been proposed (Marwitz, 1972 a, b, c; Chisholm and Renick, 1972). According to Browning (1975), one of the most important distinctions is between ordinary multicell storms and supercell storms. The essential difference between these two types is that, whereas a supercell storm is dominated by a single cell which attains a quasi-steady structure with updrafts and downdrafts coexisting symbiotically for long periods, an ordinary multicell storm consists of a sequence of evolving cells each of which may go through a life-cycle resembling that first described in the Thunderstorm Project (Byers and Braham, 1949). Both kinds of storms can produce damaging hail and, although the biggest and most damaging hailstorms tend to be supercells, the majority of hailstorms in the North American continent appear to be of the ordinary multicell variety.

Each new updraft cell in an ordinary multicell storm is seen first as a discrete new growing cumulus cloud. During Project Hailswath (Goyer *et al.*, 1966) these became known as feeder clouds. This term can be misleading when applied to ordinary multicell storms in the sense that the clouds do not *feed* the mature hail cloud but, rather, grow and *become* the mature hail cloud. Therefore, we refer to them instead as daughter clouds. Such clouds have been discussed by Dennis *et al.* (1970) and Musil (1970). They consider them to be one of the most striking visual phenomena associated with Great Plains thunderstorms. They find that the daughter clouds begin forming at distances up to 30 km away from the hailstorm core. Each cloud grows rapidly as it approaches and merges with the main cumulonimbus cloud mass. For an eastward-moving storm the merger usually takes place on the southwestern side of the main cloud mass and occurs 15–40 min after the initial formation of the daughter cloud. As shown in Fig. 1, a first radar echo usually appears in a daughter cloud just before it merges fully with the main cloud mass. A burst of heavy rain or hail usually reaches the ground soon after the merger. The evolution of the individual areas of heavier precipitation associated with
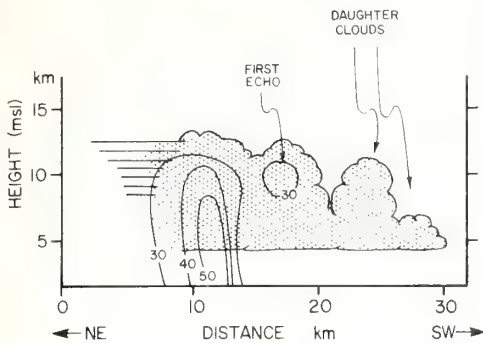
FIG. 1. Schematic diagram showing an NE-SW cross section through a typical hailstorm of western South Dakota. Stippled shading denotes cloud; solid contours represent radar reflectivity in dBz (adapted from Dennis et al., 1970).

successive cells has been studied by Renick (1971). He shows that the individual cells may produce hail for periods of up to 30 min. At the surface this gives rise to families of what Changnon (1970) refers to as hail-streaks. Since the new cells usually form on the right flank, the storm as a whole propagates discretely to the right of the cell motion (Browning, 1962; Renick, 1971; Marwitz, 1972b).

The purpose of this paper is to present a model of the storm that gave hail in the vicinity of Raymer, Colorado, on 9 July 1973, synthesized from data in Parts I through IV. As we shall show, the model conforms in many ways to the above description of ordinary multicell storms. Of course, this is not to say that all such storms can be expected to fit this model. The maximum temperature excess in the updraft, assuming unmixed parcel ascent, was 5°C; the mean wind shear in the layer from cloud base to cloud top (650–150 mb) was about 2×10^{-3} s^{-1}; and the mean wind in the subcloud layer was 8 m s^{-1}. According to Marwitz (1972b) these values are characteristic of the environment of multi-cell hailstorms. In terms of the updraft intensity, the frequency of development of new cells and the resulting hail size, the Raymer hailstorm can be categorized as being of moderate intensity.

2. Model of the Raymer hailstorm

Figures 2 and 3 are simplified representations of the Raymer storm, each depicting a vertical section along the storm's direction of travel (approximately north to south). The former figure is highly schematic; the latter is rather more realistic.

Figure 2 shows the configuration of the updraft circulation derived from the observations, and also the way it depends on the environmental winds. The wind pattern was rather complex but the main feature distilled here is that the storm traveled roughly with the winds in the middle troposphere, the winds in the lower and upper troposphere having a component from south to north relative to the storm. As in the case of

some low-latitude storms (e.g., Ludlam, 1963; Zipser, 1969), this caused air to feed the updraft from the front of the storm and to leave it as an anvil trailing to the rear. Owing to strong veer of the environmental winds with height relative to the storm, the inflow actually approached the updraft with a small component also from beneath the page in Fig. 2 and the anvil outflow left with a strong component back into the page. However, because of the general rearward tilt of the updraft most of the small hailstones which grew within the updraft probably descended directly into the underlying downdraft rather than re-entering the updraft. Thus, although turbulent motions may have transferred some particles from an older updraft cell to a younger one, the majority of particles would probably have been denied the chance of a second ascent in which to continue their growth into larger stones. A similar (although steadier) updraft configuration to that in Fig. 2 has been inferred for a supercell storm by Browning and Foote (1976) but in that case strong winds blowing around the storm in the middle tropo-sphere were able to carry particles around the periphery of the updraft so that they could indeed re-enter the foot of the updraft.

Figure 3 (top) embellishes the model with more de-tailed information from Parts I–IV. Plotted at the bottom of the figure are curves showing the variation of updraft velocity and water content along the line NS at a height of 7.2 km (all heights are above MSL). Different parts of Fig. 3 were derived from different sources of data obtained over a period of about an hour during which a sequence of five cells was observed. Times and sources of the data are plotted in Table 1.

The model in Fig. 3 can be interpreted in two ways. It can either be regarded as an instantaneous view of a typical structure with four different cells at different stages of evolution or it can be regarded as showing four stages in the evolution of an individual cell. Thus Cell n, which had developed a "first echo" shortly before the time portrayed in Fig. 3, began growing out of the shelf cloud as a distinct daughter cloud $(n+1)$
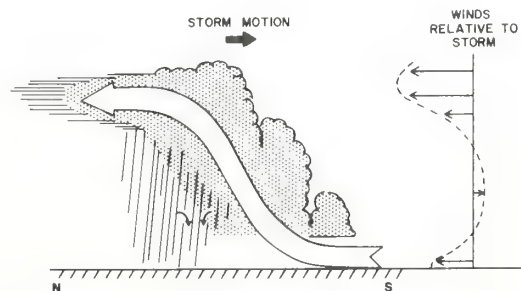
FIG. 2. Schematic diagram showing the configuration of the updraft in the Raymer hailstorm in relation to the environmental flow. (Strictly the updraft was in the form of a chain of con-tiguous updraft elements with centers lying along the arrow shown in the figure.)

about 15 min earlier. Cell $n-1$, which has almost reached its maximum reflectivity, is in its mature stage; it has a vigorous updraft but part of it has been converted into a vigorous downdraft. The decaying Cell $n-2$ is characterized by weak downdrafts at most levels, with a residual weak updraft in places aloft. The
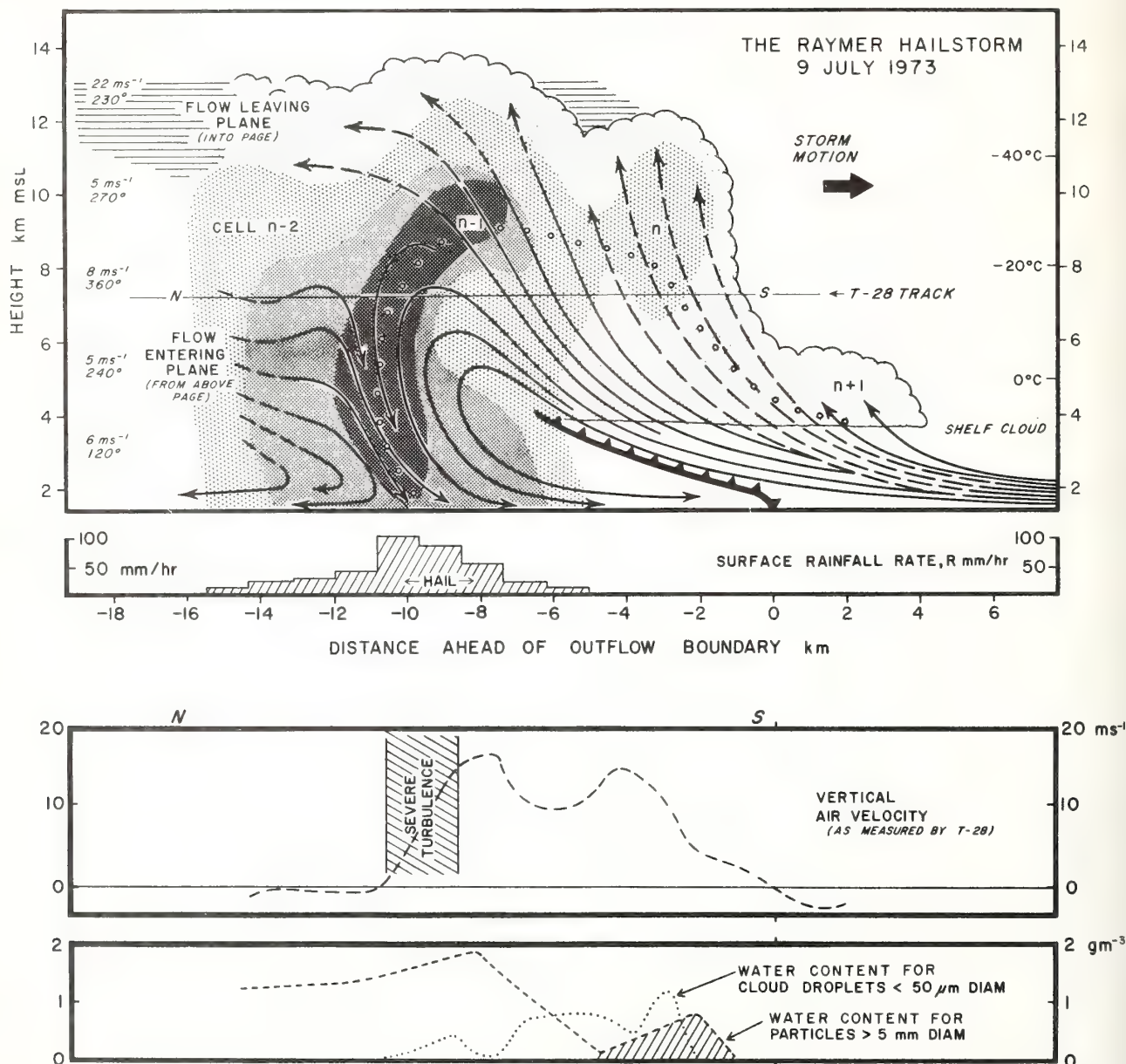
FIG. 3. Schematic model (top) of the Raymer hailstorm showing a vertical section along the storm's direction of travel through a sequence of evolving cells. Solid lines are streamlines of flow relative to the moving system; they are shown broken on the left side of the figure to represent flow into and out of the plane and on the right side of the figure to represent flow remaining within a plane a few kilometers closer to the reader. The open circles represent the trajectory of a hailstone during its growth from a small droplet at cloud base (see text). (Actually the airflow in each cell has been drawn relative to the individual cell and, since the developing Cells $n+1$ and n traveled more slowly (5 m s^{-1}) than either the mature cells (7 m s^{-1}) or the storm as a whole (10 m s^{-1}), the streamlines in the young cells would have had a stronger component from the south relative to the storm as a whole. This explains why in the model the trajectory of the growing hailstone crosses over the streamlines during its early growth as shown in the figure.) Lightly stippled shading represents the extent of cloud and the three darker grades of stippled shading represent radar reflectivities of 35, 45, and 50 dBz. The temperature scale on the right side represents the temperature of a parcel lifted from the surface. Winds (m s^{-1}, deg) on the left side are environmental winds relative to the storm based on soundings behind the storm. Surface rainfall rate averaged over 2 min intervals during the passage of the storm is plotted below the section. The horizontal line NS through the section at 7.2 km shows the track of the T-28 penetration aircraft, smoothed data from which are plotted at the foot of the figure. Although the T-28 data were not quite synchronous with the data in the vertical section, a comparison of the T-28 updraft velocity measurements with the flow pattern in the vertical section shows that the agreement is reasonably good.

TABLE 1. Times and sources of data in Fig. 3.

Data	Source	Time (MDT)
Radar echo	Grover 10 cm radar (See Part I)	1716–1717
Visual cloud	Airborne photographs (Part II)	1719
Inflow to updraft and gust front	4 aircraft at sub-cloud levels (Part II)	1642–1727
	Surface mesometeorological network (Part II)	1655–1727
Airflow within interior of storm	2 Doppler radars (Part III)	1727–1736
Microphysical measurements in relation to vertical air motion	T-28 penetration aircraft (Part IV)	1717–1720

time interval between development of successive cells was 15 ± 2 min; it took 15 min for n to evolve to the stage of development of $n-1$, and similarly for $n-1$ to evolve to $n-2$. The total lifetime of each cell was about 45 min. The lifetime for individual radar echoes was rather longer than the average figure for singlecell echoes reported by Battan (1953).

The entire inflow toward the updraft originated close to the ground ahead of the storm; at a distance of 20 km upwind of the updraft the inflow was about 500 m deep. The inflow rose unmixed to cloud base, consistent with the laminar flow generally observed below cloud base in earlier studies (e.g., Auer et al., 1970). The lateral dimensions of individual updraft cells, about 8 km at cloud base level, are similar to the average value for High Plains hailstorms found by Auer and Marwitz (1968). Cell dimensions decreased in the present case to roughly 5 km in the middle troposphere. Successive updraft cells may have been separated by an area of weak subsidence at cloud base level but they were contiguous at higher levels, giving rise to a fairly broad region of general updraft aloft. The *maximum* updraft velocity in a mature cell reached 6 to 8 m s^{-1} at cloud base and 20 m s^{-1} at 7 km MSL just above the level of maximum parcel buoyancy. The *average* value of the updraft at cloud base was 4 m s^{-1}, again similar to that measured by Auer and Marwitz (1968) in typical High Plains hailstorms. Horizontal momentum was conserved in parts of the updraft, the relative southerly component being 10 to 12 m s^{-1} in the inflow below cloud base and also in the updraft core at 7 km, but decreasing by a few meters per second in the core at 10 km. The outflow from the updraft formed an anvil which was directed mainly toward the left rear flank of the storm (to the left and into the page). The entire updraft was tilted toward the rear of the storm and, as noted above, there seemed to be little opportunity for precipitation particles grown within one cell to be recycled into a younger cell.

As for the downdraft, part of it originated in the midtroposphere at the level of lowest equivalent potential temperature (6 km) and descended unmixed to the

surface; this air entered the storm on its right rear flank (from the left of and above the page). Some of the downdraft was also probably generated within former updraft air. This is suggested by the form of the streamlines in Fig. 3 but the possibility of motion out of the plane weakens the inference somewhat. The maximum observed downdraft velocity of 15 m s^{-1} was located in the region of highest radar reflectivity, close to cloud base level. Downdraft velocities greater than 10 m s^{-1} occurred in a region 2 km wide extending from a height of 2 to 6 km. A pronounced maximum of turbulence intensity existed at the updraft-downdraft interface of the mature cell; it reached a peak near the level of maximum parcel buoyancy (7 km). The depth of the surface outflow exceeded 1 km ahead of the storm, but behind the storm the depth of downdraft air that was directed rearward relative to the storm was less than 500 m. Surface divergence beneath the strongest downdraft was 4×10^{-3} s^{-1}. Maximum surface convergence at the inflow-outflow interface was 1 to 2×10^{-3} s^{-1}. On average the gust front extended 5 km ahead of the leading edge of the surface precipitation, a feature which according to Auer et al. (1969) is typical of intense and persistent hailstorms.

Measurements with the penetration aircraft indicated that supercooled water was most abundant in the young updraft regions in the vicinity of the "first echo." Small supercooled droplets (diameter <50 μm) were present at the 7 km level in amounts of about 1 g m^{-3}. This is about a third of the adiabatic content. The "first echo" in each cell occurred typically at $-12°C$ (7 km MSL), rather lower than usual for High Plains hailstorms (Browning, 1975). Shortly after the appearance of the first echo it contained particles 5 mm in diameter in a number concentration of 1 m^{-3}; most of these larger particles were frozen but a few (up to 25%) appeared to be entirely water. The mature cell ($n-1$) contained particles with diameter 8 to 10 mm in concentrations of about 0.5 m^{-3} at a height of 7 km. These particles, which accounted for most of the maximum radar reflectivity, were almost entirely of ice and were most abundant on the rear edge of the updraft and in the downdraft. Large concentrations of water corresponding to possible "accumulation zones" (Sulakvelidze et al., 1967) were not found. Heavy rain (~100 mm h^{-1}) and hail (maximum diameter 15 mm) reached the surface, giving a total of 12 mm in 20 min of which 5% was due to hail. Although no hail was collected for the particular storm of interest, in a nearby storm 25% of the hailstone embryos were frozen drops and 75% were graupel.

3. Growth of hail in the Raymer storm

In the previous section we summarized the bare facts about the storm structure as derived in Parts I to IV. We now attempt to piece some of these facts

together in a more speculative way to infer the likely growth conditions for the hail and also the possible influence of silver iodide seeding.

Large hailstones have fallspeeds V_t of 20 m s^{-1} or more and in any theory their production requires that the updraft in which they are grown shall have comparable speeds. However, in the early stages of its growth (when $V_t < 10$ m s^{-1}) the fallspeed of a hailstone embryo increases rather slowly and a steady strong updraft would carry it through the supercooled zone of a cloud before it could attain a large size (Ludlam, 1958). A favorable growth regime can occur in at least two ways. One way is for an embryo to grow during an ascent on the edge of a quasi-steady updraft where the vertical velocity is relatively weak and then, after its terminal fallspeed has reached about 10 m s^{-1}, for it to get carried around to the inflow side of the main updraft to enter the core of the updraft at a low level. Such a behavior probably applies to supercell storms (Browning and Foote, 1976) but is not applicable to the Raymer storm because individual updraft cells were short-lived and in any case there were no significant components of flow aloft capable of causing the embryos to recycle in this way; neither does it seem likely that turbulence can have transferred many such particles from the mature cells into the daughter clouds against the mean flow. A second way for the embryos to grow, exemplified in this case study, is for them to grow in a time-developing updraft. The young daughter clouds which characterize an ordinary multicell storm are thus favored regions for the growth of embryos because they do not develop into strong updrafts until some time after the initial cloud formation (Musil, 1970).

In the Raymer storm the early growth of embryos typically 5 mm in diameter from small cloud particles seems likely to have occurred within newly rising daughter clouds going from the $n+1$ position in Fig. 3 to the n position (see trajectory in Fig. 3). The subsequent motion of the embryos was determined by tracking local volumes of relatively high reflectivity through the storm echo (see Part I). This showed that the further growth of the embryos into hailstones which reached the ground 10 to 15 mm in diameter occurred while the particles (mean terminal fallspeed $\sim$20 m s^{-1}) were essentially balanced within the updraft as Cell n moved into the $n-1$ position in Fig. 3. Recall, now, that the flow pattern in Fig. 3 is drawn relative to each individual cell and that the developing cells were moving relatively at 5 m s^{-1} into the main storm system. During their growth most of the small hailstones probably will have remained within the same updraft cell as the cell moved through the storm system. In this case, the apparent crossing of the hail trajectory from one cell to another in Fig. 3 can be construed as a stone staying within a single cell as the cell goes through successive phases of development. On the other hand,

hailstone embryos growing on the northern edge of Cell n may have descended into part of the older updraft associated with Cell $n-1$, just as the stones in the unsteady hailstorm observed by Battan (1975) sometimes appeared to be falling from one small updraft core into another. In either event the hailstones at this stage were evidently encountering updraft velocities sufficient to keep them aloft without major fluctuations in altitude.

The final stage in the hailstone growth history was for the particle content to increase to about 2 g m^{-3} near the region in Fig. 3 where the reflectivity exceeds 50 dBz. It appears that precipitation loading and, more importantly, mixing with low-θ_e air, began to have an effect here, for the lower portions of the updraft were quickly converted into a downdraft, and the hailstones cascaded rapidly to the ground with negligible further growth in a region almost depleted of supercooled water. Taking a mean terminal fallspeed of 23 m s^{-1} for hailstones 15 mm in diameter and a mean downdraft velocity of 10 m s^{-1}, such particles will have descended from 8 km to the ground at 1.5 km MSL in as little as 200 s. For a period of about 120 s the stones will have been descending below the 0°C level. As a result of melting such stones will have reached the ground about 13 mm in diameter (Ludlam, 1958).

Growth of the hailstones from embryos nominally 5 mm in diameter to stones 15 mm across is believed to have occurred as they were carried more or less horizontally relative to the storm system through a distance of 6 km at an ambient temperature between -20 and -30°C (Fig. 3). Taking a relative horizontal velocity of 8 m s^{-1}, consistent with the Doppler radar measurements in Part III, gives a period of 750 s. According to Ludlam (1958), this period is sufficient to account for growth from 5 to 15 mm diameter in the presence of a cloud water content of 1 g m^{-3}. This is broadly consistent with the values measured by the T-28.

The most difficult stage of growth to reconstruct is the development of the 5 mm embryos during the approximately 15 min period of initial growth of the daughter cloud. It has been suggested that the ice-crystal/graupel mechanism is the dominant process in High Plains storms (e.g., Dye *et al.*, 1974), and the fact that 75% of the embryos in a nearby storm on this occasion were graupel tends to support this view. However, there remains the problem of accounting for the remaining 25% of frozen-drop embryos in the nearby storm and the similar proportion of large all-water drops in the region of the first echo in the Raymer storm. We have already shown that the flow pattern in this storm was not conducive to such particles having been recycled from other, more mature, parts of the storm. Possibly these large drops did begin as graupel and experienced a brief turbulent excursion below the 0°C level during the growth of an individual daughter

cloud. Alternatively the few large water drops encountered in the region of the first echo may have been due to growth by coalescence. As shown by Danielsen *et al.* (1972), for coalescence to account for the observed growth rate, it is necessary to assume the existence of rare large cloud droplets at cloud base. Perhaps these arose due to the presence of a few large aerosol particles; such particles have been detected within hailstones and are probably due to wind-raised dust (Rosinski, 1966; Rosinski and Kerrigan, 1969).

The above discussion indicates that the nature of the early growth is still open to question although the balance of evidence suggests that the ice crystal/graupel mechanism is likely to predominate. It is clearly important that more aircraft penetrations of daughter clouds (i.e., first echo regions) should be made, especially using instruments which are specially designed to identify the phase of the hydrometeors (e.g., Cannon, 1974). However, the uncertainties that exist should not detract from the general conclusions that (1) the embryos originate in the young daughter clouds, (2) they grow into hailstones while suspended at high levels after the updraft has become strong, and (3) they follow a trajectory broadly resembling that depicted in Fig. 3. These conclusions are similar to those reached by Musil (1970) and Renick (1971).

It is instructive to compare the vertical section in Fig. 3 with that through supercell storms—see e.g., Fig. 11 of Browning and Foote (1976). In both cases the updraft enters the storm within a weak echo region (WER). In the supercell the WER is in the form of a vault bounded by an overhanging curtain of echo containing embryos which have formed elsewhere and have circulated around the edge of the updraft so as to re-enter it on its forward side. In the ordinary multicell storm the WER is not bounded: there are probably no recirculating embryos either. Instead the embryos form in situ during relatively weak ascent on the leading edge of the WER. In a supercell the re-entering embryos grow into hailstones while crossing over the vault from front to back; the newly-grown embryos in an ordinary multicell storm, on the other hand, grow into hailstones while they (and their associated first echo) are first suspended above and then descend into the WER. In a supercell the growth of the hailstones on the edge of the vault is favored since they are the first large particles to encounter undepleted cloud water in the updraft: to use the terminology of Browning and Foote (1976), they "compete unfairly" for the cloud water in the updraft. To some extent this may still be true of particles above the WER in an ordinary multicell storm as they descend into the WER. However, there is evidence that, whereas the updraft in a supercell is sufficiently strong and continuous both to prevent any cloud droplets attaining precipitation size within the vault and to prevent precipitation from entering it from its periphery, the same does not necessarily apply

in the WER of an ordinary multicell storm. Perhaps because of rapid growth on very large aerosol particles or because of turbulence bringing in particles from the side, additional precipitation particles appear beneath the particles descending from the original first echo. They can be seen, for example, as the extensive region of relatively weak echo on the inflow side of the high reflectivity hailshaft in Fig. 3; in supercells this region is usually absent and there is instead an abrupt transition from no detectable echo in the vault to the high-reflectivity hailshaft bounding the vault. The presence of such particles, provided they are frozen, would have the effect of depleting the cloud water from which the original large embryos are able to grow and might account for the low cloud water content measured aloft by the T-28. These additional precipitation particles, being situated close to where the updraft is converted into a downdraft, are not themselves likely to grow into hail since they fall out of the updraft prematurely. Any effect of this kind would of course tend to suppress hail growth naturally by diminishing the ability of the first-born embryos to compete unfairly for the available water.

4. Some implications for hail suppression

One way of attempting to suppress hail is to try to emulate nature by generating further competing embryos in the parts of the updraft containing abundant supercooled water just beneath the main region of growing hailstones. According to Browning and Foote (1976), this approach may be be possible in the case of supercells because it requires the generation of competing particles within the vault where the updraft is persistently too strong to give enough time for competing particles to develop. The situation appears to be better in an ordinary multicell storm provided one is able to take advantage of the time-evolving character of the individual updrafts and attempts to seed each cell prior to the development of the first. In this way one cannot only try to insure that the newly-introduced embryos are able to start depleting the cloud water before the development of the precipitation particles responsible for the first echo, but also, if the seeding is begun early enough, one can exploit the relatively slow updraft velocity during the earliest stage of growth of the daughter cloud so as to give more time for the competing embryos to become effective.

Much of the growth of the initial embryos in the Raymer storm was accomplished during ascent from cloud base to the first echo at the $-12°C$ level. The level of formation of the first echo on this occasion was rather lower than usual for hailstorms; it can be as high as the $-40°C$ level although perhaps a more typical value would be $-20°$ to $-30°C$ (Browning, 1975). If seeding is to be effective in slowing down the growth of such embryos and in producing many more of comparable size, it is probably necessary for it to

cause the liquid water content to be substantially depleted by the $-20°C$ level. In some recent calculations Young (1975) has derived the seeding rate required to deplete (through glaciation) different proportions of the cloud water at different altitudes. He finds that the required seeding rate depends very sensitively on the updraft velocity. For a very weak updraft of 2 m s^{-1} at about 3 km MSL increasing upward linearly at 0.75 m s^{-1} km^{-1}, the seeding rate required to achieve 90% glaciation by the $-20°C$ level is of order 1 g min^{-1} km^{-2} of silver iodide; for an updraft of 4 m s^{-1} at 3 km increasing upward at 1.5 m s^{-1} km^{-1} the corresponding seeding rate is of the order of 30 g min^{-1} km^{-2}. For comparison, a typical seeding rate as used by NHRE is only 1 g min^{-1} km^{-2}, although this seeding rate could reasonably be increased by at least an order of magnitude. Of course, Young's calculations are highly simplified. No allowance is made for the decrease in concentration of silver iodide in the cloud due to turbulent diffusion. The assumed mode of nucleation may also be in error. Consequently these results must not be relied on in a highly quantitative way. However, they do suggest that a significant proportion of the supercooled water can be glaciated by the $-20°C$ level only if the seeding is applied at an early stage in the growth of each successive daughter cloud while the vertical velocities are still very weak. Updrafts often intensify quite rapidly in daughter clouds, however, and so it appears to be desirable to act quickly as soon as a growing daughter cloud is identified. As shown in Fig. 3, the developing daughter clouds are located many kilometers ahead (or to the right) of the mature updraft region: according to the above arguments this is where the seeding should be concentrated.

It is not clear for how long one should continue seeding a daughter cloud as it develops into the main updraft. One hopes that the early seeding will produce more and smaller embryos in the initial stages of growth so that they will compete among themselves for the available water when they later find themselves in the intensifying updraft. In some ways one would have liked to have been able to glaciate the mature updraft in order to be more certain of preventing significant further hailstone growth but, as Young has shown, there comes a stage in the intensification of the updraft beyond which reasonable seeding rates will no longer have any worthwhile effect. In any case there is good reason to avoid seeding the strong updraft very heavily since, according to Young, this might cause a reduction in surface rainfall. Seeding at moderate rates in a weak updraft on the other hand is more likely to have the opposite effect.

Seeding the regions of initial embryo development is the approach adopted by Schock (1971), Summers *et al.* (1972), and Abshaev and Kartsivadze (1973). Abshaev and Kartsivadze recommend seeding near the leading edge of the radar echo, up to 3 to 5 km ahead of it, as
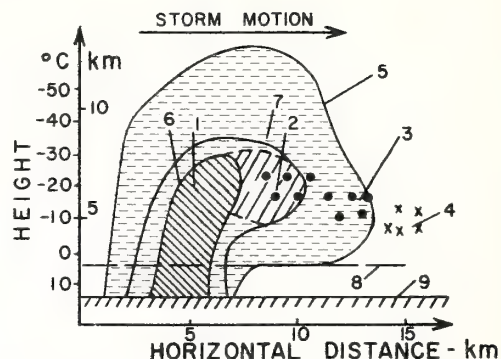
FIG. 4. Schematic diagram showing the preferred seeding location in an ordinary multicell hailstorm (after Abshaev and Kartsivadze, 1973). Features are identified by numbers as follows: (1) main hailshaft, (2) hail growth zone, (3) hail embryo formation zone, (4) seeding zone, (5) radar echo boundary, (6) zone of highest reflectivity, (7) boundary of region of fairly high reflectivity, (8) cloud base level, (9) surface level. The dots and crosses are discussed in the text.

shown by the crosses in Fig. 4. The region denoted by the dots in Fig. 4, within the radar overhang, was the primary target of the seeding carried out by Sulakvelidze, Bibilashvili, and Lapcheva (1967), based upon the "accumulation zone" concept. The latter corresponds to the common practice of seeding in the mature updraft, which we now suggest is not the best procedure. Abshaev and Kartsivadze (1973) used radar to determine where to seed; however, since the initial embryo development is within daughter clouds before the "first echo" stage, it may sometimes be easier to identify the seeding locations visually (Summers *et al.*, 1972). Visibility from the ground is often obscured and so such observations are most reliably obtained from an aircraft.

It is important to keep in mind the limitations of the above discussion regarding the possibilities for hail suppression. What we have suggested on the basis of indirect inference is that the prospects for at least partial success in hail suppression seem rather more promising in ordinary multicell storms than in the archetypal supercell storms discussed by Browning and Foote (1976). We have also suggested a way of improving the chance of seeding having a beneficial effect. However, this suggestion is tentative; the observational evidence is scanty. Much more research is needed in the areas of the cloud dynamics, the hail trajectories, and the processes of natural hail growth (especially during the early stages of growth) before we can predict the outcome of different seeding procedures with any confidence. The possibility that a given seeding technique may have a different (sometimes adverse) effect on the precipitation in different kinds of storms makes it imperative that we avoid indiscriminate seeding and put more effort into developing a sounder, more quantitative, physical understanding.

Acknowledgments (Parts I through V). The authors are grateful to D. Atlas, G. B. Foote, C. A. Knight, W. C. Macklin, and J. D. Marwitz for helpful discussions and comments on the manuscripts and to all those within NHRE and collaborating agencies who contributed to the data collection and analysis.

REFERENCES

Abshaev, M. T. and A. I. Kartsivadze, 1973: Radar methods and equipment for hail suppression. *Proc. WMO/IAMAP Sci. Conf. Weather Modification*, WMO. No. 399, 343–350.

Auer, A. H., Jr. and J. D. Marwitz, 1968: Estimates of air and moisture flux into hailstorms on the High Plain. *J. Appl. Meteor.*, **7**, 196–198.

——, D. L. Veal and J. D. Marwitz, 1969: Updraft deterioration below cloud base. *Preprints, Sixth Conf. Severe Local Storms*, Chicago, Amer. Meteor. Soc., 16–19.

——, D. L. Veal and J. D. Marwitz, 1970: The identification of organized cloud base updrafts. *J. Rech. Atmos.*, **6**, 1–6.

Battan, L. J., 1953: Duration of convective radar cloud units. *Bull. Amer. Meteor. Soc.*, **34**, 227–228.

——, 1975: Doppler radar observations of a hailstorm. *J. Appl. Meteor.*, **14**, 98–108.

Browning, K. A., 1962: Cellular structure of convective storms. *Meteor. Mag.*, **91**, 341–350.

——, 1975: The structure and mechanism of hailstorms. A review paper presented at the NHRE Symposium, Sept. 1975. To be published.

——, and G. B. Foote, 1976: Airflow and hail growth in supercell storms and some implications for hail suppression. *Quart. J. Roy. Meteor. Soc.*, **102**. To be published in the July issue.

Byers, H. R. and R. R. Braham, Jr., 1949: *The Thunderstorm.* U. S. Gov't. Printing Office, Washington, D. C., 287 pp.

Cannon, T. W., 1974: A camera for photography of atmospheric particles from aircraft. *Rev. Sci. Instrum.*, **45**, 1448–1455.

Changnon, S. A., Jr., 1970: Hailstreaks. *J. Atmos. Sci.*, **27**, 109–125.

Chisholm, A. J. and J. H. Renick, 1972: The kinematics of multicell and supercell Alberta hailstorms. Alberta Hail Studies 1972, Research Council of Alberta Hail Studies Report No. 72-2, 24–31.

Danielsen, E. F., R. Bleck and D. A. Morris, 1972: Hail growth by stochastic collection in a cumulus model. *J. Atmos. Sci.*, **29**, 135–155.

Dennis, A. S., C. A. Schock and A. Koscielski, 1970: Character-

istics of hailstorms of Western South Dakota. *J. Appl. Meteor.*, **9**, 127–135.

Dye, J. E., C. A. Knight, V. Toutenhoofd and T. W. Cannon, 1974: The mechanism of precipitation formation in northeastern Colorado cumulus, III. Coordinated microphysical and radar observations and summary. *J. Atmos. Sci.*, **8**, 2152–2159.

Goyer, G. G., W. E. Howell, V. J. Schaefer, R. A. Schleusener and P. Squires, 1966: Project Hailswath. *Bull. Amer. Meteor. Soc.*, **47**, 805–809.

Ludlam, F. H., 1958: The hail problem. *Nubila*, **1**, 12–96.

——, 1963: Severe local storms: A review. *Meteor. Monog.*, **5**, No. 27, 1–30.

Marwitz, J. D., 1972a: The structure and motion of severe hailstorms, Part I. Supercell storms. *J. Appl. Meteor.*, **11**, 166–179.

——, 1972b: The structure and motion of severe hailstorms, Part II. Multicell storms. *J. Appl. Meteor.*, **11**, 180–188.

——, 1972c: The structure and motion of severe hailstorms, Part III. Severely sheared storms. *J. Appl. Meteor.*, **11**, 189–201.

Musil, D. J., 1970: Computer modeling of hailstone growth in feeder clouds. *J. Atmos. Sci.*, **27**, 474–482.

Renick, J. H., 1971: Radar reflectivity profiles of individual cells in a persistent multicellular Alberta hailstorm. *Preprints Seventh Conf. on Severe Local Storms*, Kansas City, Mo., Amer. Meteor. Soc., pp. 63–70.

Rosinski, J., 1966: Solid water-insoluble particles in hailstones and their geophysical significance. *J. Appl. Meteor.*, **5**, 481–492.

—— and T. C. Kerrigan, 1969: The role of aerosol particles in the formation of raindrops and hailstones in severe thunderstorms. *J. Atmos. Sci.*, **26**, 695–715; corrigendum, **27**, 178–179.

Schock, M. R., 1971: The North Dakota Pilot Project: 1971 work plans. Inst. of Atmos. Sci., South Dakota School of Mines & Technology, Rapid City, Report No. 71-8, 23 pp.

Sulakvelidze, G. K., N. Sh. Bibilashvili and V. F. Lapcheva, 1967: Formation of precipitation and modification of hail processes. Israel Program for Scientific Translations, Jerusalem, 208 pp.

Summers, P. W., G. K. Mather and D. S. Treddenick, 1972: The development and testing of an airborne droppable pyrotechnic flare system for seeding Alberta hailstorms. *J. Appl. Meteor.*, **11**, 695–703.

Young, K. C., 1975: Growth of the ice phase in strong cumulonimbus updrafts. *Pure and Applied Geophysics*, **113**, 1005–1017.

Zipser, E. J., 1969: The role of organized unsaturated convective downdrafts in the structure and rapid decay of an equatorial disturbance. *J. Appl. Meteor.*, **8**, 799–814.

OBSERVATIONS OF ATMOSPHERIC DENSITY

CURRENTS WITH SEVERE WIND SHEAR

Harold W. Frank and Wm. R. Moninger

NOAA/ERL/Wave Propagation Laboratory
Boulder, Colorado 80302

1.   INTRODUCTION

A number of phenomena that produce strong winds and wind shear in the lower atmosphere can be described as density currents; among these are synoptic and sea-breeze fronts, and thunderstorm outflow currents or gust fronts. Recently atmospheric density currents have received considerable attention, largely due to the serious threat that severe low-level wind shear presents to large jet aircraft.

Laboratory studies performed by Keulegan (1957, 1958), Simpson (1969, 1972) and Middleton (1966) have revealed a great deal about the nature of density currents in water, and have established a conceptual model and non-dimensional descriptive parameters that apply to currents of widely different dimensions and intensity. Unfortunately the rules governing laboratory density flows cannot be transferred directly to atmospheric counterparts with substantially different Reynolds numbers, ambient stabilities and generating mechanisms. Limited observations of density currents in the atmosphere show encouraging similarities, but the great difficulty of obtaining needed measurements has precluded a thorough description of atmospheric density currents. Simpson (1972) pointed out similarities between density current models and atmospheric density flows associated with both sea breeze and thunderstorm conditions. Using data from the National Severe Storms Laboratory's (NSSL) surface observation network and an instrumented 481 m tower, Charba (1972) analyzed one gust front and compared it to the density current model. Goff (1975) analyzed 20 gust fronts of varying intensities observed at NSSL. A two-dimensional numerical model of the thunderstorm gust front, developed by Mitchell (1975), investigates regions of wind shear and the effects of the temperature drop and ambient stability upon the gust-front structure. Other gust-front studies have been conducted by Colmer (1971), Goldman and Sloss (1969), Idso et al. (1972) and Hall et al. (1976).

In this report we discuss four density currents observed at the Wave Propagation Laboratory (WPL) instrumented tower near Haswell, Colorado. The four cases vary widely in size and severity, but each is found to contain potentially dangerous wind shear, and in each the overall structure is grossly similar to that displayed by laboratory currents. However, we find that certain scaling

parameters are substantially different, and that mixing is apparently more intense in the atmosphere than in the laboratory studies. In the following we will outline a conceptual model of density current structure that relies primarily on laboratory observations, and then discuss our results in terms of that model.

2.   DENSITY CURRENT STRUCTURE

The atmospheric density current is a mass of relatively dense air propagating along the ground within a thin layer, typically less than 2 km deep. Figure 1 shows the characteristic shape and features of a density current. At the leading edge of the dense mass a sharp density gradient defines the current front, or gust front; the passage of the front is marked at the surface by a sharp pressure rise. An elevated head of dense air is maintained behind the front, followed by a turbulent wake that expands in depth with increasing distance behind the front. Photographs of laboratory and atmospheric density flows, and acoustic sounder observations presented in this report, suggest that the wake may extend well above the head height.

Friction retards the current at the ground so the leading edge, or nose, of the current may be found some distance above the surface. Dense fluid moves forward with respect to the front in the lower portion of the current (under the wake), diverging upward in the forward part of the head close behind the front. A large roll may be formed in the top of the head as shown in Figure 1, with downward flow behind the head and upward motion in
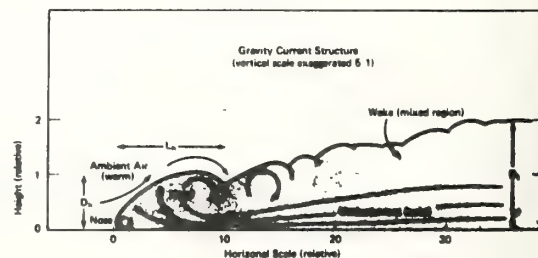
Figure 1. Depiction of atmospheric density current structure based on descriptions of laboratory flows.

the front part of the head. Updrafts are also found ahead of the front where ambient fluid is lifted over the head. The roll feature was observed in laboratory flows by Simpson (1972) and is predicted by Mitchell's (1975) atmospheric model. The maximum speed of the forward flow, or undercurrent, occurs beneath the downflow at the rear of the head, where the forward current is compressed and pushed toward the ground. This location of the high-speed wind "core" is verified by Middleton's (1966) experiments and by Mitchell, who also finds that peak surface wind is found below the core. Because of surface friction, the maximum wind is always some distance above the ground (up to several hundred meters), reaching its lowest height in the core region where the wind speed is about 1.5 times the front speed. Mean velocity within the steady dense current following the front is generally somewhat greater than the front speed, providing an excess of dense fluid that must be entrained into the wake.

In the initial stage of outflow from a dense fluid source (for example, when a thunderstorm downdraft first reaches the ground) the gravity current model clearly does not apply, as the head and horizontal flow pattern have not reached an equilibrium state. The laboratory experiments indicate, however, that the gravity current configuration is attained soon after the flow begins and persists until the current dissipates after the source of dense fluid is depleted. As the supply of dense fluid diminishes, the depth and velocity of the current decrease, but the current maintains a similar structure in that its shape is preserved and key parameters of the flow do not change appreciably. "Similarity" for gravity currents can be expressed in terms of the non-dimensional Froude number, F, of the head region:

$$ F = \frac{C_p}{(g \, D_h \, \Delta\rho/\rho_0)^{\frac{1}{2}}} $$

where C_p is the front propagation speed, D_h the head depth, $\Delta\rho/\rho_0$ the relative density in the head of the current, and g the gravitational acceleration. The theoretical value of F for the head region of an idealized flow is near unity (see Benjamin, 1968). However, observations in the laboratory (e.g., Keulegan, 1958; Middleton, 1966) indicate smaller values for F, in the neighborhood of 0.76. Limited observations in the atmosphere (Simpson, 1969; Charba, 1972) suggest F values ranging from 0.4 to 1.1.

3.   OBSERVATIONS

The four events to be discussed in this paper occurred on August 2, 5 and 11, 1972 and March 27, 1974, henceforth referred to as cases 1, 2, 3, and 4, respectively. Data are displayed in time-height coordinates in Figures 2-5.

The 152 m Haswell tower was instrumented with bivanes and temperature sensors at 30 m intervals beginning at 30 m, except that temperature was measured at the surface and not

at 120 m for cases 3 and 4. Calibration of these instruments was performed daily, but offsets in the vertical velocity were not recorded and these data were adjusted by assuming zero mean vertical motion in the ambient air outside gravity flows. Occasional uncertainties in the offset of temperature instruments were resolved by hygrothermograph recordings at 0, 30, 100, and 152 m. Wind and temperature data were recorded at one-second intervals on magnetic tape, and one minute block averages were later computed to construct time-height plots. Twelve-second averages were used for a portion of case 4 as discussed below. Gust-front propagation speeds and directions were determined from pressure disturbances at three surface microbarographs near the tower. The local frontal motions determined this way may not represent the average motions because of possible irregularities and unsteadiness at the fronts such as those described by Simpson (1969, 1972). Horizontal wind components normal to the fronts (along the propagation direction) and parallel to the fronts were computed using these estimates of propagation direction. Contours were drawn by hand from the averaged data, smoothing out scales smaller than one or two grid intervals. Vertical velocity at the 152 m level is included for the first three cases, and is similarly hand smoothed from averaged data.

The four cases will be discussed together following brief descriptions of the individual events.

Case 1. After an initial rapid temperature drop of about 5°C at 1827 hr (all times MDT), the temperature continued to decrease throughout the observed time. Although the coldest area was apparently above the tower top, a well-defined wind maximum was located near 60 m height and ahead of the temperature minumum. Contoured fields show evidence of retardation (elevated nose) in the temperature field, and clearly indicate that the wind profile nose is about 150 m high. Large eddies (i.e., large with respect to the data intervals) are indicated by flow reversal below the wind nose. Data collection was stopped around 1910 hr as a number of the instruments were destroyed by high winds. Acoustic signals were masked by wind noise; therefore, the depth was estimated at 450 m on the basis of temperature drop, ΔT, and propagation speed, C_p, assuming that the Froude number was 0.76.

Case 2. With the arrival of the gust front at 1931 hr, temperatures dropped very rapidly at all tower levels by about 10°C. All temperature recorders were off scale for approximately 7 min, preventing us from plotting temperatures in the front vicinity. Since the initial drop occurred almost simultaneously at all levels, the front must have had a nearly vertical slope in the tower layer. The wind maximum was apparently just above the tower at about 200 m, but the earliest evidence of wind increase in the lowest 150 m occurred near the ground, 10 min ahead of the temperature transition. A well-defined cold-air mass and wind core persisted for about 30 min after the frontal passage, followed by relatively constant temperatures and winds.

161
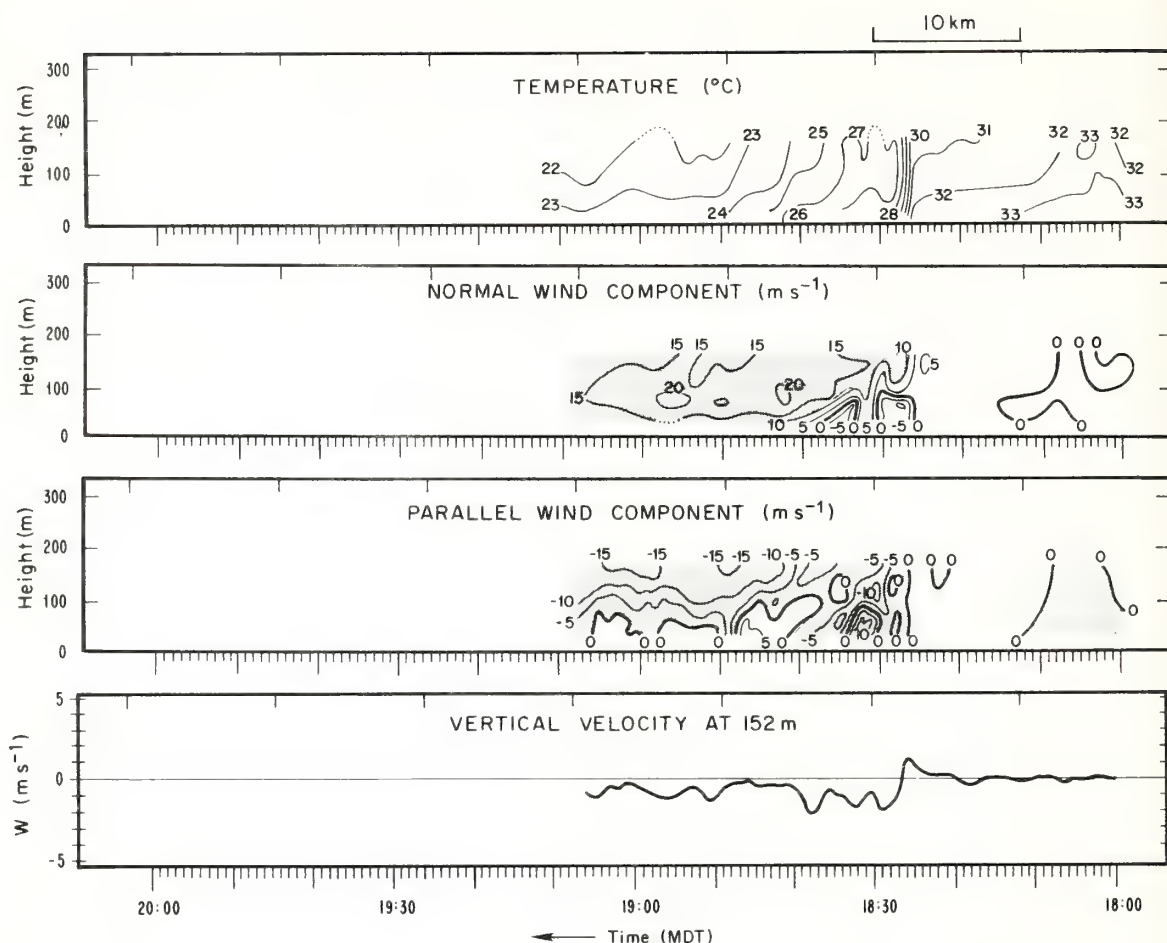
Figure 2. Case 1, August 2, 1972. Time-height displays of temperature and wind structure. Stippled areas indicate where the normal wind is forward with respect to the front, and where the parallel wind is directed to the right of the propagation direction.

As in the preceding case, intense eddies appeared near the leading edge of the maximum wind core, and again there was no usable acoustic sounder record. Outflow depth was estimated at about 1400 m by the same method as mentioned above. A brief period after 2000 hr when no data were recorded is indicated in the plots by a dashed section of the time axis.

Case 3. This and case 4 were relatively mild density currents that nevertheless provided exceptionally good descriptions of atmospheric gravity flow structure because they were fairly shallow with respect to the tower height. A number of features described in Section 2 are illustrated in Figure 4; the current head, 375 m deep, is clearly outlined on the acoustic sounder display between 2317 and 2323 hr. Minimum temperature and a well-defined wind core appear in the head region. Vertical velocity at 152 m is upward ahead of the front and downward in the rear portion of head, suggestive of the expected roll within the head.

The maximum normal wind in this case, 4.3 m sec^{-1}, is less than the 6.7 m sec^{-1} propagation speed of the front, a surprising observation that may result from the irregular local motion of the front (which might cause a poor estimate of propagation speed). Middleton (1966) observed similar cases in dissipating currents and suggests that the front may temporarily move faster than the following flow if the head depth is decreasing. It appears possible, therefore, that at the time of these observations the current was approaching dissipation, and the head was beginning to collapse.

A surface-based temperature inversion observed before this event was disrupted only temporarily near the ground, and was reestablished soon after passage of the head. The stability of the ambient atmosphere may have had a suppressing effect, contributing to the shallowness of the flow.

162
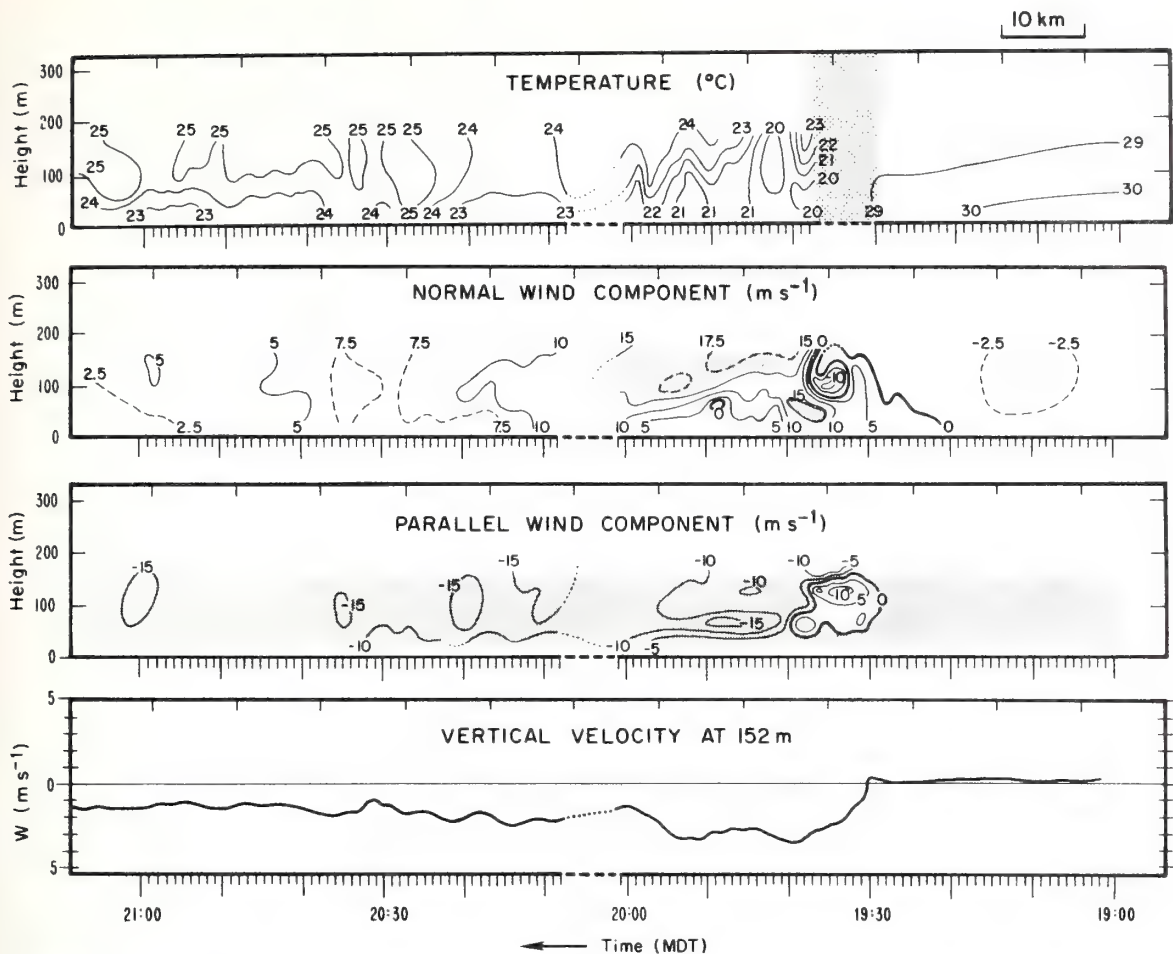
Figure 3. Case 2, August 5, 1972. Same as Figure 2.

Case 4. Being only 100 m deep, this current was contained in the tower height interval, but the 30 m spacing of instruments proved inadequate to resolve the detailed structure. The wind maximum was close to the ground, below the lowest tower instrument level at 30 m, and near the center of the head. From 0005 to 0025 hr, tower data were plotted at 12 sec rather than 1 min intervals to emphasize the turbulent wake and the detailed correspondence of the acoustic sounder record.

Table 1 lists the parameters which were chosen to represent vital features observed in the various case studies. For the most part these descriptors are derived from the time-height plots, and therefore represent time scales generally greater than one minute. Instantaneous peak values of some parameters are likely to exceed the listed values.

For most of the Haswell density currents, the forward flow with respect to frontal motion persists for fairly short periods. There are two likely explanations for this: (1) the currents may be separated from

their source when they reach the tower site and are thus not sustained by a steady flow of new dense air, and (2) the currents might dissipate significantly during the observation period. In the first three cases, for which vertical velocity is recorded, there is a clear indication of downflow behind the fronts. Significant updrafts ahead of the fronts are apparent only in the shallower cases 1 and 3; presumably, similar updrafts would have been recorded for case 2 had the measurement been taken at a higher level, i.e., above the wind core. Maximum vertical velocity is on the order of 2 m sec^{-1} in each case. We find clear evidence of the head feature and of forward flow beneath the head with respect to the front. Middleton (1966) observed in laboratory flows that the ratio of front propagation speed, to the core wind speed increased with distance traveled, and a similar observation was made by Simpson (1964) for sea-breeze currents. The ratios observed ranged from about 0.5 to 1.0. Charba (1972) found the ratio to be 0.63 for one thunderstorm outflow current, and Goff (1975) observed an average ratio of 0.67 for thunderstorm gust fronts. Our data do not allow us to

163
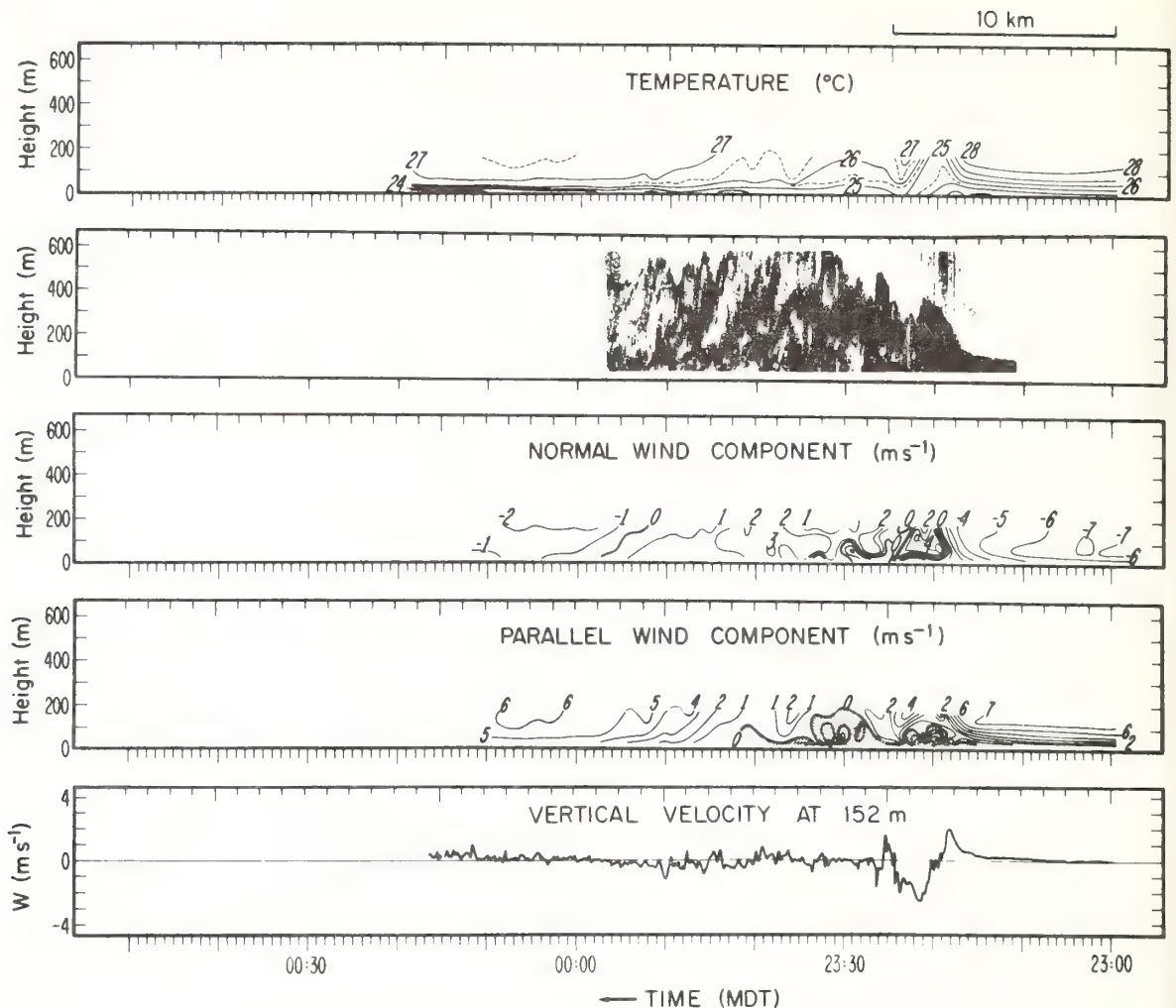
Figure 4. Case 3, August 11, 1972. Same as Figure 2 except acoustic sounder record is included.

evaluate the effect of distance traveled, but they are fairly consistent with other observations. (The anomalous behavior of case 3 was discussed earlier.) Also we observe a strong relationship between the heights of wind maxima, $H(U_n)$, and depths of the heads (see Table 1) with an average observed ratio $H(U_n)/D_h$ around 0.15. The shapes of the Haswell currents are consistently longer and shallower than their laboratory counterparts. For example Keulegan (1958) and Middleton (1966) found that current heads had depth-to-length ratios, D_h/L_h, of about 0.4, but in all the Haswell currents this ratio is much smaller, averaging 0.11.

Figure 6 shows pressure traces for cases 2 and 3. These data were recovered from microbarographs having high-pass filters, hence the pressure magnitude is uncertain. We are confident of the shape of the pressure surge before the gust fronts; the high winds obscure the pressure trend after the gust fronts have

passed by the sensors. Case 2 shows a dip in the pressure surge at 1927 hr slightly ahead of the front. This dip correlates with the gust in the normal wind component seen in Figure 3. A similar pressure dip just ahead of the front was seen by Charba (1972). Case 3 shows evidence of a gravity wave-like structure ahead of the front. Analysis of the velocity of this structure suggests that it is not associated with the front. In both these cases the initial pressure rises precede the density fronts and are roughly coincident with the earliest wind disturbances, consistent with the observations of Charba (1972) and Goff (1975). Sharp pressure peaks occur near the density fronts.

Evidence of mixing and turbulent wakes behind the heads is seen in cases 2, 3, and 4, as average temperature increases and temperature gradients weaken with time. Well behind the fronts the mixed layer extends down to the ground or to the tops of thin surface

164
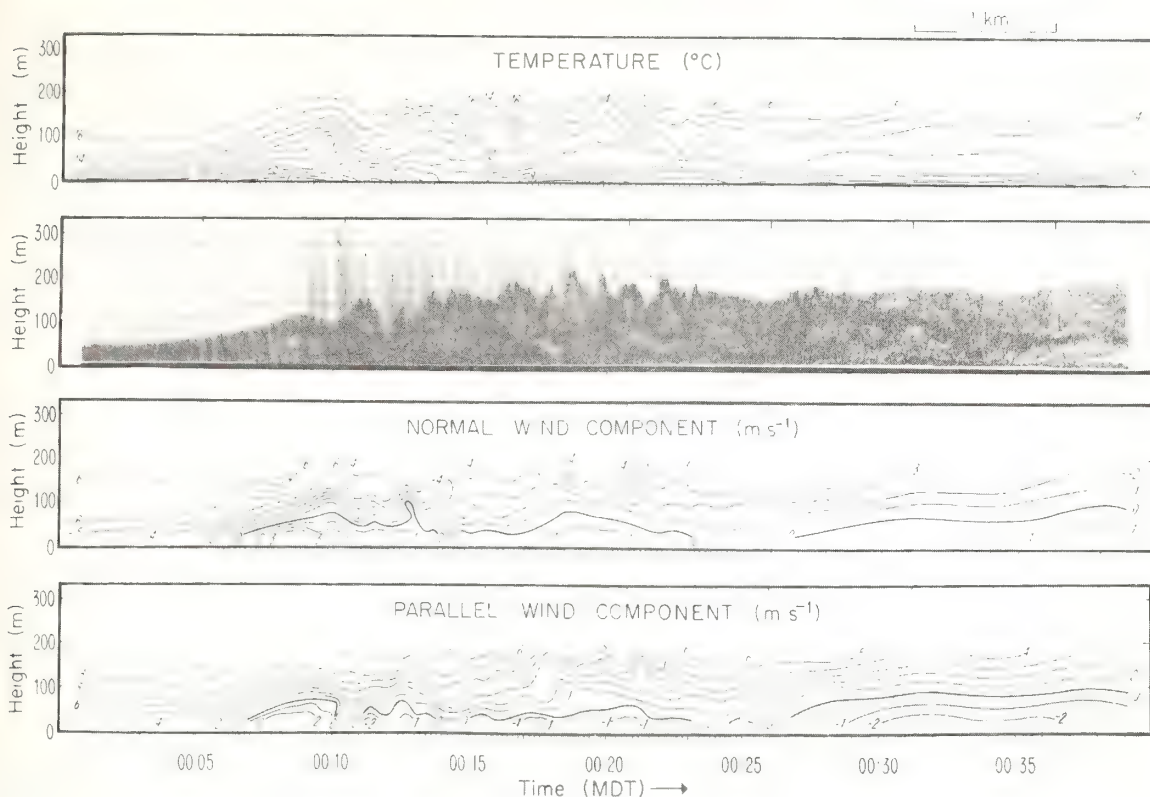
Figure 5. Case 4, March 27, 1974. Same as Figure 4 except vertical velocity is not included.

inversion layers. Acoustic sounder data show the mixing also extends upward above the heads, and turbulence in the wake region is evidenced by fine-scale fluctuations in all the measured quantities. Wave-like patterns behind the heads suggest gravity waves or large turbulent eddies. Since the patterns break down into smaller and smaller scales with time, the latter seems more likely. The measured vertical velocity patterns are consistent with the presence of large rolls in the heads that would produce deep downward intrusions of warm air, thereby initiating the mixing process on a fairly large scale immediately behind the heads.

Our observations indicate that mixing in atmospheric gravity currents is considerably greater than in laboratory experiments, and this might significantly affect the behavior of thunderstorm gust fronts. If an outflow current is disrupted by mixing close behind the initial front, a new front must form provided that the outflow supplying the cold air persists. In the absence of a steady supporting current, the initial front must eventually dissipate. This mechanism might explain some cases in which multiple surges have been observed in storm outflows (for example, Goff, 1975), and have been attributed to merging of outflows from pulsating or separate downdrafts.

4.   SUMMARY AND CONCLUSIONS

Using data from an instrumented tower, acoustic sounder and surface microbarographs, we have described the wind and temperature structure within four atmospheric density currents. The observed cases compare quite well with laboratory and model counterparts, but several essential differences are noted. The atmospheric currents are relatively longer and shallower, and in the two milder cases frontal slopes are observed to be less than the minimum slope achieved in the laboratory by eliminating surface friction. On the other hand, the more intense cases 1 and 2 have nearly vertical slopes near the ground (i.e., in the tower interval), but they were too deep to determine frontal slopes from the tower data. The high speed wind core is observed at a height about 0.15 times the depth of the current head, and wind and pressure disturbances precede the density fronts in agreement with other investigators. Mixing is found to be greater in the atmosphere than in laboratory flows, suggesting that multiple surges often observed in gust fronts may result from disruption (by mixing) and subsequent reforming of the front and current head. Multiple surges have previously been attributed to multiple or pulsating downdrafts.

Table 1. Haswell Density Current Parameters

Parameter	Case Number			
	1	2	3	4
Temp drop, ΔT (^{o}C)	≥ 9.7	≥ 9.8	4.0	5.5
Head depth, D_h (m)	450	1394	375	100
Head length, L_h (km)	7.0	25	3.2	1.0
Max shear, S (s^{-1})	0.7	1.1	0.23	0.16
Max normal wind, U_n (ms^{-1})	20.0	>19.5	4.2	4.0
Height of U_n, $H(U_n)$ (m)	60	200	60	15
Front speed, C_p (ms^{-1})	9	16	6.7	3
Reynold number, Re($x10^{-8}$)	2.6	15	1.7	0.21
Froude number, F	--	--	0.96	0.69
C_p / U_n	0.44	<0.82	1.6	0.75
$H(U_n)$ / D_h	0.13	0.14	0.16	<0.3
D_h / L_h	0.07	0.16	0.12	0.10

Figures 2-5 indicate areas where aircraft safety might be threatened. Most notably, severe wind shear occurs in the head region both above and below the wind core, strong turbulence is seen near the front ahead of the wind core, and there is a significant updraft-downdraft couplet associated with the roll within the head. The severity of these conditions is clearly related to overall intensity of the respective cases, and the data suggest that temperature contrast, maximum wind speed, propagation speed, and possibly other parameters might serve as indicators. (See Greene, et al. (1977) for a discussion of the possible warning parameters.) While the data set used in this report is not adequate for evaluating these indicators, one important point is illustrated in the plots of Figures 2-5: surface measurements of wind or temperature often will not represent the true severity of the disturbance at higher levels. This suggests that propagation speed may be the most reliable of the easily measured parameters as an indicator of density current wind and wind shear hazards.
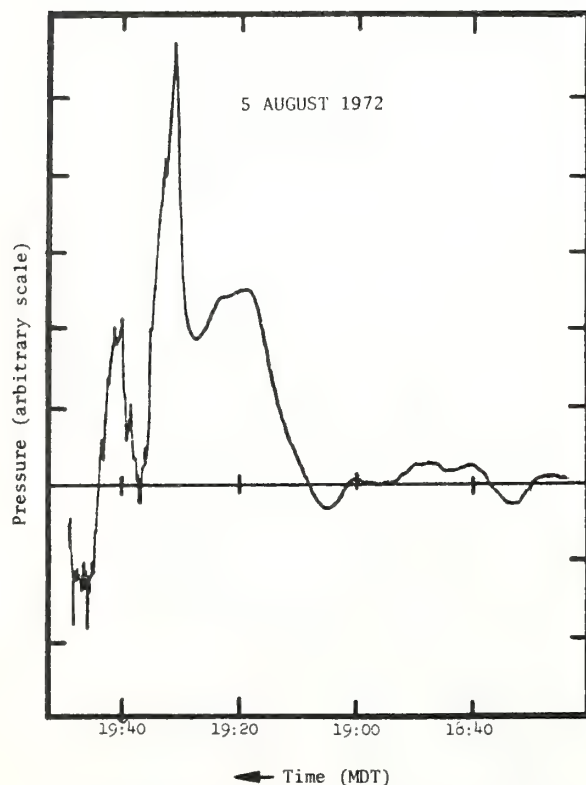
Figure 6(a). Pressure record for case 2 (arbitrary pressure scale). See text for discussion.
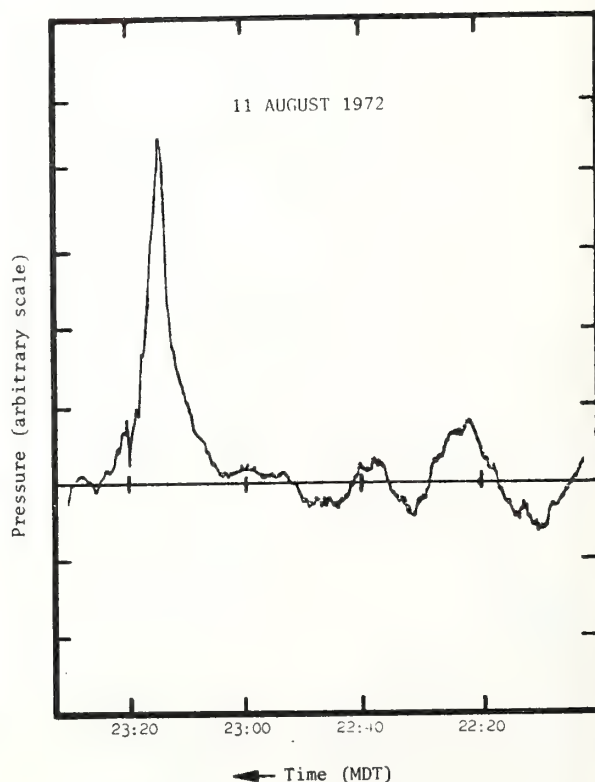
Figure 6(b). Pressure record for case 3, as in Figure 6(a).

166

6.   REFERENCES

Benjamin, T. B. (1968). "Gravity currents and
      related phenomena." J. Fluid Mech., *31*,
      Part 2, 209-248.

Charba, J. (1972). "Gravity current model
      applied to analysis of squall-line gust
      front." Mon. Wea. Rev., *102*, 140-156.

Colmer, M. J. (1971). "On the character of
      thunderstorm gust fronts." Royal Aircraft
      Ext., Tech. Memo. Aero 1316, Bedford, Eng.

Goff, R. C. (1975). "Thunderstorm-outflow
      kinematics and dynamics." NOAA Tech.
      Memo. ERL NSSL-75.

Goldman, J. L. and P. W. Sloss (1969).
      "Structure of the leading edge of thunder-
      storm cold-air outflow." Proc. Sixth
      Conf. on Severe Local Storms, Amer.
      Meteor. Soc., Boston, Mass., 71-79.

Greene, Gary E., Harold W. Frank, Alfred
      J. Bedard, Jr., J. Ann Korell, Mary Cairns,
      and Peter A. Mandics (1977). "Wind shear
      characterization." Final Report to the
      Federal Aviation Administration, prepared
      by Wave Propagation Laboratory, NOAA
      under Interagency Agreement No. DOT
      FA76WAI-622.

Hall, F. F., W. D. Neff, and T. V. Frazier
      (1976). "Wind shear observations in
      thunderstorm density currents." Nature,
      264, 408-411.

Idso, S. B., R. S. Ingram, and J. M. Pritchard
      (1972). "An American haboob." Bull.
      Amer. Meteor. Soc., *53*, 930-935.

Keulegan, G. H. (1957). "An experimental study
      of the motion of saline water from locks
      into fresh water channels." Natl. Bur.
      Standards, Rept. No. 5168.

Keulegan, G. H. (1958). "Twelfth progress
      report on model laws for density currents;
      the motion of saline fronts in still
      water." Natl. Bur. Standards,
      Rept. No. 5831.

Middleton, G. V. (1966). "Experiments on the
      density and turbidity currents. I.
      Motion of the head." Can. Journ. Earth
      Sci., *3*, 523-546.

Mitchell, K. E. (1975). "A numerical investi-
      gation of severe thunderstorm gust
      fronts." NASA CR-2635.

Simpson, J. E. (1964). "Sea-breeze fronts
      in Hampshire." Weather, *19*, No. 7,
      208-219.

Simpson, J. E. (1969). "A comparison between
      laboratory and atmospheric density cur-
      rents." Quart. J. Roy. Meteor. Soc.,
      95, 758-765.

Simpson, J. E. (1972). "Effects of the
      lower boundary on the head of a gravity
      current." J. Fluid Mech., *53*, Part 4,
      759-768.

WIND SHEAR CHARACTERIZATION

Gary E. Greene, Harold W. Frank, Alfred J. Bedard, Jr.,
J. Ann Korrell, Mary M. Cairns, and Peter A. Mandics

A brief review of the major causes of severe low-level wind shear indicates that the thunderstorm gust front is the most dangerous source of potential aircraft accidents. The study constains the analysis of several gust-front events in detail using meteorological tower, acoustic echo sounder, and pressure sensor data. The results have been compared with theoretical models and laboratory studies. Our analyses show that gust front can probably be detected reliably with a suitable array of different ground-based sensors. However, the determination of wind-shear severity is a more difficult problem. The results thus far show a promising relationship between the gust-front speed of motion and maximum shear.

AN ANALYSIS OF THE GUST-FRONT HAZARD

G. E. Greene, J. A. Korrell, and P. A. Mandics

NOAA/ERL/Wave Propagation Laboratory
Boulder, Colorado 80302

1.   INTRODUCTION

Low-level wind shear is a major hazard to the safe performance of aircraft, particularly during take-offs and landings. A sudden change in the speed and/or direction of the wind can affect the lift on an aircraft abruptly enough that the pilot may be unable to take corrective action in time, especially if the plane is close to the ground. Therefore, it is important to develop methods for predicting both the occurrence and severity of low-level wind shear.

The three major sources of significant low-level wind shear are the low-level jet (Blackadar, 1957), the synoptic-scale frontal zone, (Sowa, 1974), and the thunderstorm gust front (Simpson, 1972; Goff, 1975; Hall et al., 1976). However, sub-synoptic discontinuities and meso-scale fronts as well as orographic features such as strong airflow over mountains can also produce significant shear. Of all of these sources, one of the more frequent causes of severe low-level wind shear is the gust front associated with thunderstorms. Consequently we have focused our investigation on gust-front dynamics with a view toward potential detection and forecasting of the resultant wind shear.

The magnitude of shear that can produce potentially hazardous conditions is difficult to determine because it depends on several parameters such as the flight characteristics of the aircraft and its proximity to the ground. A frequently used value has been defined by Sowa (1974) as significant when a change in airspeed greater than 8.4 m sec^{-1} occurs within 100 m, a shear of 0.08 sec^{-1}. This value is in close agreement with the one derived by Snyder (1968) from a theoretical analysis of swept-wing aircraft dynamic response.

2.   THE GUST FRONT

Thunderstorm gust fronts result from downdrafts of relatively cold, dense air produced in the storms by evaporative cooling. As the dense air collides with the ground it spreads outward, away from the source, displacing the warmer air surrounding the thunderstorm. This outflow is often referred to as a "density current" or "gravity current" since the primary motive force is provided by gravity and the density gradient. The cold-air outflow propagates as a micro-cold front and can create strong wind gusts up to 20 km away from the parent thunderstorm in a clear-air environment that makes it difficult to detect.

Our study consisted of thorough analyses of several gust-front events for which considerable meteorological data were available and of statistical analyses of other available

data such as barograph and anemometer records. Detailed studies of individual gust front events are presented by Frank and Moninger (1977) in a companion paper. Some of the statistical results and the potential use of surface-based sensors are discussed by Bedard and Cairns (1977) in a second companion paper. More details of this work are presented in a Federal Aviation Administration Report (Greene et al., 1977) along with a review of the overall wind-shear problem.

3.   RESULTS

Results from our detailed case studies show that several features of observed atmospheric gust fronts compare quite well with laboratory and theoretical models; however, important differences are also evident. Some of these features are discussed in detail by Frank and Moninger (1977). For example, they point out that the temperature drop measured near the ground is frequently unrelated to the magnitude of shear at higher elevations.

This effect has been observed when stable inversion layers were present. In his numerical model of gust fronts, Mitchell (1975) considered the effect of ambient stability on several gust-front parameters and found that high stability results in a far smaller frontal temperature decrease than does a neutral atmosphere. Figure 1 shows his predicted effect in terms of
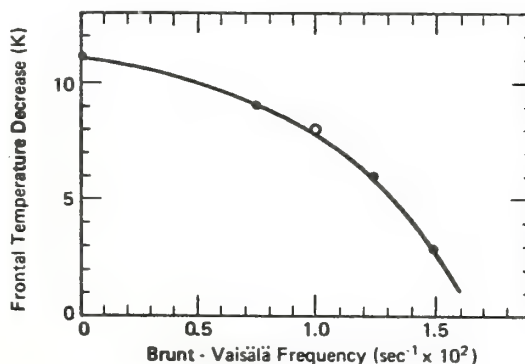
Figure 1. Gust-frontal temperature decrease as a function of ambient stability.

the Brunt-Vaisälä frequency,

$$\omega = (g/\theta(Z) \cdot d\theta(Z)/dZ)^{1/2},$$

where θ is the potential temperature, g is the acceleration due to gravity, and Z is the height

above the surface. Using 10-min 150-m time-height profile data from several case studies presented by Goff (1975), we estimated both the drop in potential temperature near the surface (Z<50m) and the maximum change in horizontal wind speed normal to the gust front, U_n. We also estimated ω for these events by evaluating the temperature difference between the surface and 450 m height from Goff's isotherms. Although these estimates are quite coarse, Figure 2 shows a significant
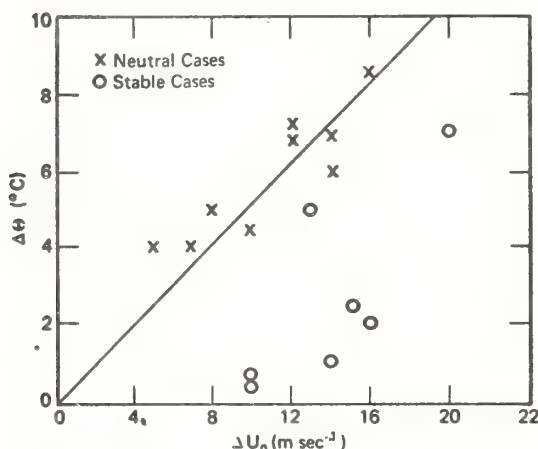
Figure 2. *Horizontal wind change vs. surface temperature decrease for neutral and stable cases.*

difference between the neutral or near-neutral ($\omega \times 10^{-2} \mathrm{sec}^{-1}$) and stable cases. Neutral conditions indicate a linear relationship between temperature drop and wind change (or gust surge) whereas increased stability results in a much smaller temperature drop with accompanying large wind changes. The same limitation appears to hold for measurements of wind near the surface. These, too, frequently fail to reflect the greater intensity of wind fluctuations at higher levels. As a consequence, the effectiveness of surface-based anemometers and thermometers can be greatly influenced by the state of atmospheric stability during the passage of a gust front. A promising ground-based gust-front detection technique that is not affected by atmospheric stability uses the measurement of atmospheric pressure jumps; this is discussed by Bedard and Cairns (1977). This has great potential because the surface pressure change results from the integrated mass change aloft and hence reflects conditions aloft.

A vivid example of the gust-front hazard has been presented by Caracena (1976) who performed a detailed streamline analysis of the wind field at the time that Continental Flight 426 crashed at Stapleton International Airport in Denver, Colorado, while attempting to take-off on August 7, 1975. Figure 3 shows the streamline pattern over the runway resulting from a nearby downdraft. The aircraft began its take-off with a slight tail wind, entered a head wind about a third of the way along the runway, thereby obtaining additional lift, but then abruptly encountered
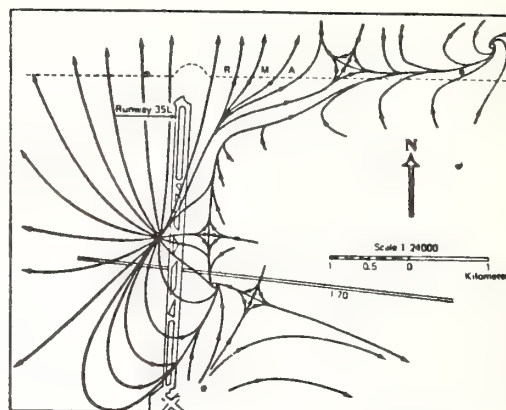
Figure 3. *Surface airflow pattern in the vicinity of Runway 35L at 1610 MDT on August 7, 1975.*

a strong tail wind, lost its lift and was unable to compensate for it with sufficient power before impact with the ground. Fortunately there were no fatalities in this case; however, other accidents, thought to be caused by the gust-front phenomenon, have been more serious (Fujita and Caracena, 1977). The need to develop reliable methods for detecting dangerous conditions produced by severe gust fronts is an important one that requires considerable additional study.

4.   SUMMARY AND CONCLUSIONS

As mentioned above, a detailed summary of all this work, together with an extensive reference list, is available in a Federal Aviation Administration Report by Greene et al. (1977). As a result of this study the investigators of the Wave Propagation Laboratory have reached a number of conclusions, some of which are summarized below.

1) The state of atmospheric stability at the time of a gust-front arrival has a significant effect on surface-based measurements. Because low-level surface inversions inhibit mixing, none or only part of the dynamics within the density current may reach the ground. We have found a linear relation between vertical wind shear and the maximum temperature decrease across the front; however, the maximum temperature change occurred well above the surface, especially when an inversion was present.

2) A linear relationship has been found between the speed of motion of the density outflow and the maximum vertical shear. Consequently, a warning system should have the capability to measure the gust-front motion directly (companion paper by Frank and Moninger).

3) Statistics comparing pressure and anemometer records have shown that the time rate of change of the pressure disturbance caused by a cold-air density-current passage is related to the gust surge, or change in horizontal wind speed produced by the event. Thus pressure measurements may provide some indication of wind-shear severity (companion paper by Bedard and Cairns).

4) Atmospheric density currents were found to be considerably longer and shallower than those measured in laboratory flows. Also, much greater mixing occurs in the atmosphere than indicated by laboratory experiments, suggesting that observed multiple surges may be produced by the formation of a new current head in place of the previous one disrupted by intense mixing. Previously these surges have usually been attributed to the merging of outflows from pulsating or separate downdrafts.

5. REFERENCES

Bedard, A. J., Jr. and M. M. Cairns (1977). "Measuring thunderstorm gust fronts using surface sensors." Proceedings 10th Conference of Severe Local Storms, Oct. 18-21, Omaha, Nebraska, Amer. Meteor. Soc., Boston, Mass.

Blackadar, A. K. (1957). "Boundary layer wind maxima and their significance for growth of nocturnal inversions." Bull. Amer. Meteor. Soc., *38*, 283-290.

Caracena, F. (1976). Weather Analysis. NTSB Exhibit No. 5E-1 of Stapleton accident.

Frank, H. W. and W. R. Moninger (1977). "Observations of atmospheric density currents with severe wind shear." Proceedings 10th Conference of Severe Local Storms, Oct. 18-21, Omaha, Nebraska, Amer. Meteor. Soc., Boston, Mass.

Fujita, T. T. and F. Caracena (1977). "An analysis of three weather related aircraft accidents." (To be published in Bull. Amer. Meteor. Soc.).

Goff, R. C. (1975). "Thunderstorm-outflow kinematics and dynamics." NOAA Tech. Memo. ERL NSSL-75.

Greene, G. E., H. W. Frank, A. J. Bedard, Jr., J. A. Korrell, M. M. Cairns, and P. A. Mandics (1977). "Wind shear characterization." Final report to the Federal Aviation Administration, prepared by the Wave Propagation Laboratory, NOAA.

Hall, F. F., W. D. Neff, and T. V. Frazier (1976). "Wind shear observations in thunderstorm density currents." Nature, *264*, 408-411.

Mitchell, K. E. (1975). "A numerical investigation of severe thunderstorm gust fronts." NASA CR-2635.

Simpson, J. E. (1972). "Effects of the lower boundary on the head of a gravity current." J. Fluid Mech., *53*, Part 4, 759-768.

Snyder, C. T. (1968). "Analogue study of longitudinal response to wind shear and sustained gusts during landing approach." NASA TD D-4477, Ames Res. Center, Moffett Field, California.

Sowa, D. (1974). "Low-level wind shear effects on approach and climbout." D. C. Flight Approach, No. 20, McDonald Douglas Corp., 10-17.

A Transmission Line Model With General Velocities for Lightning

J. A. Leise and W. L. Taylor

Environmental Research Laboratories, Wave Propagation Laboratory, NOAA, Boulder, Colorado 80302

A transmission line model which incorporates general discharge velocities is presented, and formulas for the current and charge densities are derived. The resultant formulas for the electromagnetic fields are given in a form applicable to intercloud and intracloud discharges. A spectral study of a vertical discharge results in a velocity equation. This equation relates the velocity of ionization of the discharge to the current at the base of the discharge and the radiation field of the sferic. Analysis of a dimensionless parameter for a Bruce-Golde type discharge and an example suggest that vertical discharges may become horizontal after entering the cloud.

Introduction

This paper consists of two rather interwoven parts. The first part is directed at the theoretical problem of constructing models of lightning discharges. The general model pursued is patterned after the transmission line models of *Uman and McLain* [1969] and *Uman et al.* [1975b]. In particular, our formulation incorporates general velocities along the discharge path. Such models do not seem to be completely developed in previous literature. Also, formulas for the electromagnetic fields are presented in a form applicable not only to vertical discharges but also to intercloud and intracloud discharges. Realistic models of intercloud and intracloud discharges are needed for analyzing and interpreting sferic data. It is hoped that this work will be a constructive step in this direction.

In the development of the general model it is shown that for a lossless transmission line all points on the discharge path see the same time-retarded current. In other words, a point farther down the channel will see the same current at a later time. We also show how current losses can be included in this formulation.

Models of this kind can be expected to yield good first-order approximations of cloud-to-ground discharges because the current is usually very sharply peaked. Conceptually, if most of the charge is considered as being carried or as occurring in a region near this peak, then the charge velocity can be modeled as the propagation velocity of the peak current. To say this another way, if the current were a delta function, then the formulation given below (with losses) would be exact.

The second part of the paper is more specific and perhaps of more immediate interest. Here a somewhat specialized cloud-to-ground discharge model is used, and the Fourier transform is applied to obtain the velocity equation (33), which can be used to compute discharge velocities when sferic data and the current at the base of the discharge are given. This specialized model is further analyzed and compared with data. Specifically, if t_x is the crossover time of a sferic and f_m is the frequency of peak spectral amplitude, it is shown that the parameter $t_x f_m$ is bounded by a constant for Bruce-Golde type discharge models. This bound, in turn, is inconsistent with *Taylor*'s [1963] group 1 sferic data for normal sferics. It is interesting to note that rescaling the time axis of any sferic will leave $t_x f_m$ unchanged and consequently, $t_x f_m$ can be considered as a measure of the shape.

Finally, one possible way of resolving this discrepancy is presented by way of an example and indicates that perhaps the path of the discharge becomes horizontal after the discharge

enters the cloud. Some evidence to this effect is given by *Uman et al.* [1975a], *Brantley et al.* [1975], *Few* [1974], and *Teer and Few* [1974]. We should, nonetheless, emphasize that inferences which can be drawn from *Taylor*'s [1963] data and the example are bound to be somewhat controversial. Perhaps the most important thing to come out of this analysis is the need to develop models which can account for spectral as well as temporal properties of sferics. The difficulty is that both must be done at the same time.

General Aspects of Lightning Models

One of the main problems confronting lightning research is to determine the currents and charges associated with a return stroke of a lightning discharge. For us this amounts to finding methods for computing the charge and current densities, given electromagnetic field data at some distance from the source. This is what is sometimes called the inverse source problem. The realistic problem is made more difficult in that all relevant propagation effects should be included, and consequently, the solution of the inverse source problem requires a propagation model. Unfortunately, even with a free space propagation model no exact solution of the general inverse source problem is known. For this reason there seems to be no alternative but to simplify the general problem by making restrictive assumptions about the source in the form of a discharge model.

Bruce and Golde [1941] seem to have formulated the first successful model of the discharge process. This model was, however, unrealistic in that it assumed that charge could be transferred instantaneously along the discharge path. Two notable modifications which corrected this difficulty were made by *Dennis and Pierce* [1964] and *Uman and McLain* [1969]. The model developed here is patterned after these models insofar as it is a transmission line model. However, the way in which velocity is incorporated in our formulation is more precise.

Ideally, the propagation model should include the propagation effects attributed to a finitely conducting curved earth and ionosphere. Again, however, no solution of the inverse source problem is known for any realistic discharge model. Fortunately, this last difficulty can be circumvented for the analysis of the ground wave of a sferic because the ionosphere plays no role in ground wave propagation and a suitable transformation can be used to convert the remaining curved earth problem to a flat earth problem. A good approximation of this transformation is given by *Wait and Howe* [1956], which we describe as follows. Let ϵ_F denote the vertical electric field for an infinitely conducting flat earth at a linear distance R from the source. Also let ϵ_C denote the vertical electric field for a

spherical earth of conductivity σ at a circular distance R from the source. If both fields are produced by identical sources, then their Fourier transforms will satisfy $\mathcal{F}(\epsilon_C) = \mathcal{F}(\epsilon_F)W(R, \sigma)$, where the transfer function $W(R, \sigma)$ is a certain complex-valued function which has been computed and tabulated for selected values of the parameters R and σ by them. Thus when data ϵ_C are given, the flat earth equivalent is the inverse Fourier transform of $\mathcal{F}(\epsilon_C)/W(R, \sigma)$. *Taylor*'s [1963] spectral data used later are, as has been published, converted in this manner. For these data, however, computing the inverse Fourier transform was unnecessary.

We remark that the height of the ionosphere limits the range for which the ground wave can be separated from the total sferic. Consequently, the practical relevance of this method is limited to distances from the source which are usually less than about 500 km.

In summary, the restricted inverse source problem pursued in this paper will amount to modeling the discharge process up to a number of appropriate unknown functions of parameters. These functions or parameters can, hopefully, then be computed from converted ground wave data in the context of an infinitely conducting flat earth propagation model. A partial solution of this problem can be found in the velocity equation, derived later.

TRANSMISSION LINE MODEL

We begin by supposing that the path of the lightning discharge (henceforth referred to as the antenna) is a continuous nonintersecting curve of finite length d with distinct endpoints P_0 and P_1. Then the main assumptions are that charge always moves from P_0 toward P_1 and that the propagation characteristics of the antenna do not change with time or with the amount of charge being propagated. In other words, suppose that before time $t = 0$ a quantity of charge Q_0 is stored at the point P_0. If $Q(t)$ denotes the charge remaining at the point P_0 at time t, then the charge leaving P_0 is a current $I(t) = -\dot{Q}(t)$. We then assume that the quantum of charge $I(t)\,dt$ leaving P_0 between times t and $t + dt$ is propagated as a wave packet (or via the billiard ball effect) in such a manner that its velocity $v(s)$ depends only on its distance s from P_0 and that this velocity is always positive.

Thus for any time t, $I(t)\,dt$ arrives at a distance s from P_0 at some time $t + \tau(s)$. That is, $\tau(s)$ is the 'antenna time' required for $I(t)\,dt$ to travel this distance. Now s can also be considered as a function of antenna time t. In fact, s is a solution of the first-order autonomous differential equation

$$\dot{s}(\tau) = v[s(\tau)] \qquad (1)$$

because $u(\tau) = \dot{s}(\tau)$ is velocity as a function of time. Moreover, $\tau'(s) = 1/\dot{s}(\tau)$, and consequently, $\tau(s)$ can be calculated as

$$\tau(s) = \int_0^s \frac{dx}{v(x)} \qquad (2)$$

For example, suppose that v decays linearly with distance:

$$v(s) = v_0(1 - s/d) \qquad v_0 > 0 \qquad (3)$$

Then from (1) and (2) we deduce

$$u(\tau) = v_0 e^{-\gamma\tau} \qquad \tau(s) = -\gamma^{-1} \log(1 - s/d) \qquad (4)$$

where $\gamma = v_0/d$.

From our assumptions on the antenna, charge density $\rho(s, t)$ satisfies

$$\int_0^s \rho(x, t)\,dx = Q[t - \tau(s)] - Q(t) \qquad (5)$$

and consequently,

$$\rho(s, t) = (d/ds)Q[t - \tau(s)] = I[t - \tau(s)]/v(s) \qquad (6)$$

Moreover, the current density $\mathbf{J}(s, t)$ is computed from (6) by a standard application of the equation of continuity and the divergence theorem:

$$\mathbf{J}(s, t) = I[t - \tau(s)]\mathbf{e}_A(s) \qquad (7)$$

where $\mathbf{e}_A(s)$ is the unit vector tangent to the antenna at s, pointing in the direction in which charge is being propagated. Thus if the antenna is linear, $\mathbf{e}_A = (P_1 - P_0)/d$. Equations (6) and (7) are then the main ingredients of a lossless transmission line model. In particular, it should be noted that for a lossless transmission line every point on the antenna eventually sees the same current.

Transmission line losses can be included as follows. First, modify (7) to include a current loss:

$$\mathbf{J}(s, t) = G[\tau(s)]I[t - \tau(s)]\mathbf{e}_A(s) \qquad (8)$$

where G is an attenuation factor.

The charge density can then be recomputed from the equation of continuity and the divergence theorem:

$$\rho(s, t) = \{G[\tau(s)]I[t - \tau(s)] - \dot{G}[\tau(s)]S(t, s)\}/v(s) \qquad (9)$$

where

$$S(t, s) = \int_0^t I[\theta - \tau(s)]\,d\theta \qquad (10)$$

We remark that this model differs from the classical model of *Bruce and Golde* [1941] in that for their model, v is assumed to decay linearly with height (see (3)) and is interpreted as the velocity of the wave front or as the velocity at which the discharge channel is being energized (i.e., ionized). Moreover, behind this wave front the channel is assumed to be infinitely conducting with uniform current $I(t)$.

One of the first steps in refining the model of Bruce and Golde was taken by *Dennis and Pierce* [1964], who observed that the assumption of uniform current is unrealistic.

In a later model, *Uman and McLain* [1969] dealt with this difficulty by using a current density of the form

$$\mathbf{J}(s, t) = I[t - s/\langle u(s)\rangle]\mathbf{e}_A \qquad (11)$$

where $\langle u(s)\rangle$ is the average of u from ground to height s. If u is a constant, then (7) and (11) agree. Otherwise, (7) and (11) are different.

FREE SPACE SOLUTION

We now obtain the electromagnetic fields for the charge and current densities derived above for a lossless transmission line. The field expressions for a lossy transmission line would be completely analogous but more complicated. It should be emphasized that the solutions obtained below do not account for the presence of the earth. Although it is not difficult to include the boundary data of an infinitely conducting flat earth by using mirror images and ray tracing techniques, it would be cumbersome to do so here, and consequently, this is left to the reader. Moreover, formulas for vertical discharges which include the presence of the earth are given by *Uman et al.* [1975b].

A solution of the inhomogeneous wave equation with free space propagation constant and no boundary data is given by *Panofsky and Phillips* [1962, p. 248]. We write this solution as follows:

$$\mathbf{E}_{\text{STAT}} = \frac{1}{4\pi\epsilon_0} \int_V \frac{\rho_{ret}\mathbf{e}_r}{r^2} \, dv \tag{12}$$

$$\mathbf{E}_{\text{IND}} = \frac{1}{4\pi\epsilon_0 c} \int_V \frac{2\mathbf{e}_r(\mathbf{e}_r \cdot \mathbf{J}_{ret}) - \mathbf{J}_{ret}}{r^2} \, dv \tag{13}$$

$$\mathbf{E}_{\text{RAD}} = \frac{1}{4\pi\epsilon_0 c^2} \int_V \frac{(\dot{\mathbf{J}}_{ret}' \times \mathbf{e}_r) \times \mathbf{e}_r}{r} \, dv \tag{14}$$

where $\mathbf{E}_{\text{STAT}}$, $\mathbf{E}_{\text{IND}}$, and $\mathbf{E}_{\text{RAD}}$ are the static, induction, and radiation components of the electric field and the subscript *ret* refers to the retarded field. Note in particular that the static field obeys an inverse-square law only when no boundary conditions are imposed. The integration is performed over a volume V containing the charge and current densities, while r and $\mathbf{e}_r$ denote the distance and unit direction from a source point in V to the point of observation (the origin). Thus when (6) and (7) are substituted into (12)–(14), we have the free space solution of our lossless transmission line model. For example, when (7) is substituted into (12), we obtain

$$\mathbf{E}_{\text{STAT}} = \frac{1}{4\pi\epsilon_0} \int_0^d \frac{I[t - \tau(s) - r(s)/c]}{r^2(s)v(s)} \mathbf{e}_s \, ds + \mathbf{D} \tag{15}$$

where $\mathbf{e}_s = \mathbf{e}_{r(s)}$ and as was true above, d is the total length of the antenna. The term $\mathbf{D}$ accounts for the charge remaining at P_0 and any charge which collects at P_1. However, we observed in (1) that s can be considered as a function of antenna time τ. Consequently, by a simple change of variable we obtain the following fundamental representations of these fields:

$$\mathbf{E}_{\text{STAT}} = \frac{1}{4\pi\epsilon_0} \int_0^\infty \frac{I[t - \tau - r(\tau)/c]}{r^2(\tau)} \mathbf{e}_r \, d\tau + \mathbf{D} \tag{16}$$

$$\mathbf{E}_{\text{IND}} = \frac{1}{4\pi\epsilon_0 c} \int_0^\infty \frac{I[t - \tau - r(\tau)/c]u(\tau)}{r^2(\tau)} [2\mathbf{e}_r(\mathbf{e}_r \cdot \mathbf{e}_A)] \, d\tau \tag{17}$$

$$\mathbf{E}_{\text{RAD}} = \frac{1}{4\pi\epsilon_0 c^2} \int_0^\infty \frac{I[t - \tau - r(\tau)/c]u(\tau)}{r(\tau)} (\mathbf{e}_A \times \mathbf{e}_r) \times \mathbf{e}_r \, d\tau \tag{18}$$

where $r(\tau) = r[s(\tau)]$, $\mathbf{e}_r = \mathbf{e}_{s(\tau)}$, and $u(\tau)$ is the velocity (see (1)) as a function of time. Also, the upper limit of infinity on these integrals makes use of the assumption that $I(x) = 0$ when $x < 0$.

In a similar fashion the magnetic fields can be shown to be

$$\mathbf{B}_{\text{IND}} = \frac{\mu_0}{4\pi} \int_0^\infty \frac{I[t - \tau - r(\tau)/c]u(\tau)}{r^2(\tau)} \mathbf{e}_A \times \mathbf{e}_r \, d\tau \tag{19}$$

$$\mathbf{B}_{\text{RAD}} = \frac{\mu_0}{4\pi c} \int_0^\infty \frac{I[t - \tau - r(\tau)/c]u(\tau)}{r(\tau)} \mathbf{e}_A \times \mathbf{e}_r \, d\tau \tag{20}$$

We remark that (16)–(20) can be improved for computer computation. For example, with $T = t + r(t)/c$, (18) can be written as

$$\mathbf{E}_{\text{RAD}}(T) = \frac{1}{4\pi\epsilon_0 c^2} \int_0^t \frac{I[T - \tau - r(\tau)/c]u(\tau)}{r(\tau)} (\mathbf{e}_A \times \mathbf{e}_r) \times \mathbf{e}_r \, d\tau \tag{21}$$

The principal advantage of (21) over (18) is that the upper limit of integration is precisely known. Vector integrals of this kind have been coded for the computer with no serious difficulties. The presence of the earth is also easy to incorporate on the computer. In short, for computer solutions no further simplification is needed.

We remark that (16)–(20) can be used to obtain equations similar to those given by *Uman et al.* [1975b] with one important change. Conventions standard to lightning research require a change of sign in both electric and magnetic fields. Thus (16)–(20) should all be multiplied on the right by -1. Perhaps a more useful exercise for understanding these equations is to recover the electric dipole approximation from them. All that is needed is some careful vector arithmetic.

VELOCITY EQUATION

We here analyze the transmission line model for a vertical discharge at a distance large enough to make the charge moment equation applicable. By solving this equation for the radiation field we obtain the general equation (33), which relates the observed radiation field to the current of the base of the channel and the velocity along the channel. By assuming the form of the current at the base of the channel we can then solve for velocity when the transmission line is lossless.

Again suppose that the antenna is vertically oriented on an infinitely conducting flat earth and that the point of observation is likewise on the earth. A typical length of the antenna is 5 km. *McLain and Uman* [1971] analyzed (12)–(14) in this situation and concluded that if the distance R from the point of observation to the antenna is greater than 50 km, then the variable distance r in (12)–(14) can be replaced by the constant distance R. The only additional restriction on this approximation is that the significant spectral frequencies lie below about 1 MHz. Since the spectral amplitude of most atmospherics peaks in the very low frequency (VLF) range (3–30 kHz) with a typical value of 5 kHz [*Taylor*, 1963], this approximation can be used. In any case, when the above boundary conditions hold and when this approximation is valid, the charge moment equation also holds. This equation is a second-order linear differential equation:

$$\ddot{m}(t) + A\dot{m}(t) + A^2 m(t) = \epsilon_F \tag{22}$$

where $A = c/R$ and

$$m(t) = (2\pi\epsilon_0 c^2 R)^{-1} \int_0^\infty \rho(s, t)s \, ds \tag{23}$$

is the charge moment. Moreover, the terms $A^2 m$, $A\dot{m}$, and $\ddot{m}$ in (22) are known to represent the static, induction, and radiation fields, respectively. This equation is sometimes credited to *Lejay* [1925]. It was used by *Bruce and Golde* [1941], and it was analyzed by *McLain and Uman* [1971].

The traditional use of (22) has been to calculate ϵ_F when a charge density ρ was given. We shall, however, take the opposite point of view. That is, given data ϵ_F, we can recover the vertical radiation field ϵ_z as the second derivative of the particular solution of the differential equation (22). The results of this computation are

608

$$m(t) = a^{-1} \int_0^t \epsilon_F(\tau) e^{-b(t-\tau)} \sin\left[a(t-\tau)\right] d\tau \qquad (24)$$

and

$$\epsilon_z(t) = \epsilon_F(t) - A^2 a^{-1} \int_0^t \epsilon_F(\tau) e^{-b(t-\tau)} \sin\left[a(t-\tau) + \pi/3\right] d\tau \tag{25}$$

where $a = (3)^{1/2} A/2$ and $b = A/2$.

We remark that for distances R greater than about 200 km the transformation (25) is usually unnecessary, since the 'difference' between total and radiation fields is less than about 5%. We next compare this computed radiation field with the radiation field predicted from the general transmission line model.

For the above boundary conditions the vertical component of the electric field is the only nonzero component and is twice as large as (12)–(14) because of the ground-reflected image. Consequently, if E_z denotes the (negative) vertical component of the radiation field and $\epsilon_z(t) = E_z(t + R/c)$, then (18) becomes

$$\epsilon_z(t) = K \int_0^t I(t-\tau) u(\tau) d\tau \tag{26}$$

where $K = 1/2\pi\epsilon_0 c^2 R$. A change of sign in (26) has been introduced for consistency with field conventions standard to lightning research.

Now the Fourier transform $\mathcal{F}(g)$ of a function g which is zero for times less than zero is

$$[\mathcal{F}(g)](\omega) = \int_0^\infty g(t) e^{-i\omega t} dt \tag{27}$$

and transforms convolutions into products. But (26) is a convolution, and consequently,

$$\mathcal{F}(\epsilon_z) = K\mathcal{F}(I)\mathcal{F}(u) = i\omega K\mathcal{F}(I)\mathcal{F}(u) \tag{28}$$

When transmission line losses (8) are included in this calculation, we get

$$\mathcal{F}(\epsilon_z) = i\omega K\mathcal{F}(I)\mathcal{F}(Gu) \tag{29}$$

In order to exploit the full potential of (28) we make use of the following estimate for current at the base of the discharge:

$$I(t) = I_0(e^{-\alpha t} - e^{-\beta t}) \qquad t \geq 0$$
$$\tag{30}$$
$$I(t) = 0 \qquad\qquad\qquad t < 0$$

where $\beta > \alpha > 0$. Such currents have often been used in discharge models. But then

$$\mathcal{F}(I) = I_0(\beta - \alpha)/[(\alpha + i\omega)(\beta + i\omega)] \tag{31}$$

which gives, when $\mathcal{F}(u)$ in (28) is solved for,

$$\mathcal{F}(u) = \frac{\alpha\beta/i\omega + (\alpha + \beta) + i\omega}{KI_0(\beta - \alpha)} \mathcal{F}(\epsilon_z) \tag{32}$$

The inverse transform of (32) gives us the velocity equation:

$$u(t) = \frac{2\pi\epsilon_0 c^2 R}{I_0(\beta - \alpha)} \left[\alpha\beta \int_0^t \epsilon_z(x) dx + (\alpha + \beta)\epsilon_z(t) + \frac{d}{dt}\epsilon_z(t) \right] \tag{33}$$

The importance of the velocity equation is almost self-evident, since it provides a straightforward way of computing velocities

from data. It should also be pointed out that the above analysis could be reversed. We could have assumed a known velocity and solved for the current.

Finally, if the losses (8) are included, then $u(t)$ in (33) is replaced by $G(t)u(t)$. It is interesting to note that the product $G(t)u(t)$ may be interpreted as a 'pseudo' velocity insofar as (33) is concerned.

ANALYSIS OF $t_x f_m$

We here analyze the radiation field of a vertically oriented discharge in the case when the velocity is given by (4) and the current is given by (30). This case is of particular interest because such currents and velocities have been widely used in the literature. When the distance R is large enough to use the approximation (26), it will be shown that the resultant wave forms have the property that the product $t_x f_m$ is bounded by about $1/2\pi$, where t_x is the crossover time and f_m is the spectral frequency at which the amplitude attains a maximum. In other words, the product $t_x f_m$ is quite insensitive to the parameters in a Bruce-Golde type model. Now according to *Taylor* [1963] a typical value of f_m is 5 kHz, and this quantity has already been converted to a flat earth propagation model. However, the corresponding value of 53 μs for t_x has not been so adjusted. Nevertheless, an estimate of 48 μs for the adjusted value can be obtained by using the calculations of *Wait and Howe* [1956]. But then the flat earth value of $t_x f_m$ is approximately 0.25 and, consequently, is much too large to be realized by using traditional currents and velocities. We remark that the average distance from the source for these data was about 300 km, and consequently, we equate the total electric field with the radiation field.

To begin, a straightforward computation using (26) for the currents and velocities under consideration gives

$$\epsilon_z(t) = \frac{k}{\alpha - \gamma}[\alpha e^{-\alpha t} - \gamma e^{-\gamma t}] + \frac{k}{\beta - \gamma}[\gamma e^{-\gamma t} - \beta e^{-\beta t}] \quad (34)$$

where $k = v_0 I_0 K$ and α, β, and γ are assumed to be positive distinct parameters, β being the largest. For this calculation it is useful to replace the upper limit of infinity in (26) by the variable t. Now $\epsilon_z(t)$ starts at zero, increases to a positive maximum, decays back to zero (the crossover time t_x), and then stays negative. In particular, the crossover time is less than the value of t which makes the first three terms in (34) vanish. We therefore arrive at the following bound for t_x:

$$t_x \leq \frac{1}{\gamma - \alpha} \log(\gamma/\alpha) + \frac{1}{\gamma - \alpha} \log\frac{\beta - \alpha}{\beta - \gamma} \tag{35}$$

But for $y > -1$, $\log(1 + y) \leq y$, and so if we write $(\beta - \alpha)/(\beta - \gamma) = 1 + (\gamma - \alpha)/(\beta - \gamma)$, we can replace (35) by

$$t_x \leq \frac{1}{\gamma - \alpha} \log(\gamma/\alpha) + \frac{1}{\beta - \gamma} \tag{36}$$

Next, by (28) the Fourier transform $\mathcal{F}(\epsilon_z)$ of (34) satisfies

$$|\mathcal{F}(\epsilon_z)|^2 = K^2\omega^2|\mathcal{F}(I)|^2|\mathcal{F}(u)|^2$$
$$= k^2\omega^2(\beta - \alpha)^2/[(\alpha^2 + \omega^2)(\beta^2 + \omega^2)(\gamma^2 + \omega^2)] \tag{37}$$

By setting the logarithmic derivative of (37) to zero it is easily verified that the spectral frequency f_m at which the amplitude attains a maximum satisfies $U(2\pi f_m) = 0$, where

$$U(\omega) = 1 - \left[\frac{1}{(\alpha/\omega)^2 + 1} + \frac{1}{(\beta/\omega)^2 + 1} + \frac{1}{(\gamma/\omega)^2 + 1} \right] \tag{38}$$

However, U is monotonically decreasing, and $U[(\alpha\gamma)^{1/2}] < 0$; thus $f_m \le (\alpha\gamma)^{1/2}/2\pi$. The following inequality then combines this with (36):

$$2\pi t_x f_m \le \frac{(\alpha\gamma)^{1/2}}{\gamma - \alpha} \log(\gamma/\alpha) + \frac{(\alpha\gamma)^{1/2}}{\beta - \gamma} \qquad (39)$$

From (39) we finally obtain the basic inequality

$$2\pi t_x f_m \le \beta/(\beta - \gamma) \qquad \gamma > \alpha$$
$$\qquad\qquad\qquad\qquad\qquad\qquad\qquad (40)$$
$$2\pi t_x f_m \le \beta/(\beta - \alpha) \qquad \alpha > \gamma$$

Because the verification of (40) in both cases is similar, only the case $\gamma > \alpha$ will be treated.

First, the inequality

$$\log(y^2) \le y - y^{-1} \qquad y \le 1 \qquad (41)$$

may be verified by using elementary calculus. With $y = (\gamma/\alpha)^{1/2}$ it then follows that the first term on the right in (39) is bounded by 1. Also, $(\alpha\gamma)^{1/2} < \gamma$, and consequently, (39) becomes

$$2\pi t_x f_m \le 1 + [\gamma/(\beta - \gamma)] = \beta/(\beta - \gamma) \qquad (42)$$

which establishes (40).

We remark that either inequality of (40) is valid when $\alpha = \gamma$. This case is, however, relatively easy to verify by first applying a limit to (34) and is therefore left to the reader.

Now a crude upper bound for γ can be obtained from (4), $\gamma = v_0/d$, by setting $v_0 = c$ and $d = 3$ km to obtain

$$\gamma \le 1 \times 10^5 \qquad (43)$$

Typical values of γ are usually less than $\frac{2}{3}$ of this value. For an example, see *Srivastava* [1966].

According to *Cianos and Pierce* [1972, p. 60], typical rise times (the time to the maximum) for currents lie between 1.5 and 2 μs, while typical times to half of the peak value (this time occurs after the rise time) lie between 40 and 50 μs. For these ranges it can be shown that

$$\alpha \le 3 \times 10^4 \qquad \beta \ge 1 \times 10^5 \qquad (44)$$

It then follows from (40) for such ranges of parameters that the largest value of $t_x f_m$ must be less than about 0.18, which is inconsistent with *Taylor*'s [1963] value of 0.25.

There are at least four possible errors which could cause this inconsistency.

First, using a lossless transmission line could introduce significant error. We choose to neglect these losses in order to keep the analysis as simple as possible. The intelligent use of current losses would require answers to the following questions. What percent of the current is lost to branches? What percent is lost in neutralizing the main channel? How are current losses correlated with velocities? Is there any practical advantage in including such losses? For example, the practical way to handle losses might be to reinterpret the product $G(t)u(t)$ as a pseudo velocity (see the statement following (33)).

Furthermore, it is possible that all transmission line models are incorrect. In this respect, however, other models seem equally unsatisfactory in that they do not yield values of $t_x f_m$ much above 0.18. In particular, this is true for the model of *Bruce and Golde* [1941] and the model of *Dennis and Pierce* [1964].

Second, *Taylor*'s [1963] group 1 data might not be typical. However, the value of 0.25 for $t_x f_m$ is based on a frequency f_m of 5 kHz, which according to *Cianos and Pierce* [1972, p. 103]

is typical. It therefore seems unlikely that the crossover time t_x of 48 μs would be abnormal. It is also interesting that the data from *Taylor and Jean* [1959] give an average value of 0.282 for $t_x f_m$. These data were not, however, adjusted for propagation effects.

Third, the currents (30) could be in error. However, the current at the base of the discharge is one of the better documented quantities in the discharge process and, consequently, a less likely source of the inconsistency.

Last, the velocities (4) could be inappropriate. Because velocities are difficult to measure, especially when the discharge enters the cloud, this would seem to be another explanation for the above discrepancy. The following example suggests a suitable modification of the velocities (4) to obtain consistent results.

EXAMPLE

We here illustrate the use of the velocity equation when $R = 100$ km to show one way of resolving the difficulty of the preceding section. For this we consider the wave form shown in Figure 1, which was constructed by the authors to meet certain conditions. In particular, this wave form has a rise time of about 4 μs, a crossover time of about 50 μs, and no dc component. Moreover, the amplitude of the Fourier spectrum peaks at a frequency of 5 kHz. This wave form should be interpreted as the ground wave of the vertical radiation field generated by the first return stroke of a vertical cloud-to-ground lightning discharge in the presence of an infinitely conducting flat earth. It should be noted that the derivative changes abruptly at about 60 μs, which we will refer to as the break time. We do not claim that this is a typical wave form, although something like this might be. Neither do we claim that such an abrupt break is realistic. In fact, the only reason for depicting such a sharp break is to help clarify the exposition. However, the authors do not know of a viable way to construct a wave form with these properties for which the time to the minimum differs very much from 70 μs.

The result of computing the velocities for two different currents is then shown in Figure 2. The currents, as usual, are given by (30) and have rise times of 2 μs along with peak values of 12.5 kA. The solid line v_2 corresponds to a current with a time to half peak of 20 μs, while the dashed line v_1 corresponds to a current with a time to half peak of 40 μs. The current parameters (α, β) are 3.96204×10^4 and 2.00053×10^5 for v_2 and 1.84385×10^4 and 2.46649×10^5 for v_1. The current for v_1 is a typical one, while the current for v_2 is not. In remarkable agreement with this observation are the computed antenna
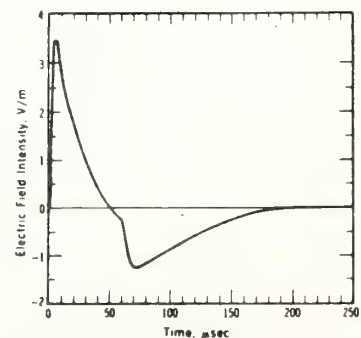
Fig. 1. Constructed sferic wave form.
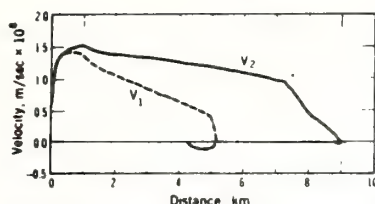
Fig. 2. Velocities computed from the constructed wave form by using two different currents.

lengths of about 5.2 km for v_1 and about 9 km for v_2, as can be seen in Figure 2. The length of 5.2 km is a typical one, while the length of 9 km is not.

We next observe that there is an abrupt break in the velocities v_1 and v_2 at about 5 km and 7.4 km and that these breaks correspond to the break time. Note that smoothing out the break in the original wave form will simply smooth out the breaks in the velocities v_1 and v_2; the overall characteristics will be the same.

We further note that both velocities are approximately linear over the major part of the discharge path. The linear part of v_1 has a slope of about 2.2×10^6. The velocity as a function of time can therefore be approximated as follows:

$$u(t) = v_0 e^{-\gamma t} \qquad 0 \le t \le T$$
$$u(t) = 0 \qquad\qquad t \ge T \tag{45}$$

where v_0 is about 1.5×10^8 m/s, $\gamma = 2.2 \times 10^6$ units/s, and $T = 60\,\mu s$ is the break time. If the time T is omitted from (45), we again have (4), in which case the values of v_0 and γ are in good agreement with the literature. In fact, $\gamma = 3 \times 10^6$ was used by *Bruce and Golde* [1941]. It therefore appears that the truncated linear velocities of (35) provide the minimal modification of the velocities of (4) necessary to remove the inconsistency of the preceding section. Computer solutions using velocities similar to (45) have been obtained to check this conclusion.

Another observation of some relevance in favor of a break is that the crossover time for a sferic is usually quite well defined. In other words, the slope of a sferic at crossover is consistently much steeper than is predicted by traditional model wave forms. This, in turn, suggests that the break usually occurs before crossover rather than after crossover, as is seen in this example.

We consider how this might be interpreted. First, the break time is roughly the time length of the vertical discharge path. After this time, something rather dramatic probably happens to the movement of charge. There seem to be two possibilities.

Either the charge stops abruptly by combining with the ions in the clouds, or the discharge path changes from a vertical path to a predominantly horizontal one. Experimental results seem to support the latter conclusion, although much remains to be done.

We finally point out that *Uman et al.* [1975a] have used models in which the discharge channel is also abruptly terminated and qualitatively, our analysis is in good agreement with their model sferics.

References

Brantley, R. D., J. A. Tiller, and M. A. Uman, Lightning properties in Florida thunderstorms from video tape records, *J. Geophys. Res., 80,* 3402–3406, 1975.

Bruce, C. E. R., and R. H. Golde, The lightning discharge, *J. Inst. Elec. Eng., Part 2, 88,* 487–520, 1941.

Cianos, N., and E. T. Pierce, A ground-lightning environment for engineering usage, SRI Project 1834, *Rep. L.S.-2817-A3,* 147 pp., McDonnell Douglas Astronautics Co., Huntington Beach, Calif., and Bell Teleph. Lab., Whippany, N. J., Aug. 1972.

Dennis, A. S., and E. T. Pierce, The return stroke of the lightning flash to earth as a source of VLF atmospherics, *Radio Sci., 68D,* 777–794, 1964.

Few, A. A., Thunder signatures, *Eos Trans. AGU, 55,* 508–514, 1974.

Lejay, P., Les perturbations orageuses du champ électrique et leur propagation à grand distance, *C. R. Acad. Sci., 181,* 678–679, 1925.

McLain, D. K., and M. A. Uman, Exact expression and moment approximation for the electric field intensity of the lightning return stroke, *J. Geophys. Res., 76,* 2101–2105, 1971.

Panofsky, K. W., and M. Phillips, *Classical Electricity and Magnetism,* 2nd ed., 400 pp., Addison-Wesley, Reading, Mass., 1962.

Srivastava, K. M. L., Return stroke velocity of a lightning discharge, *J. Geophys. Res., 71,* 1283–1286, 1966.

Taylor, W. L., Radiation field characteristics of lightning discharges in the band 1 kc/s to 100 kc/s, *Radio Sci., 67D,* 539–550, 1963.

Taylor, W. L., and A. G. Jean, Very-low-frequency radiation spectra of lightning discharges, *Radio Sci., 63D(2),* 199–204, 1959.

Teer, T. L., and A. A. Few, Horizontal lightning, *J. Geophys. Res., 79,* 3436–3441, 1974.

Uman, M. A., and D. K. McLain, Magnetic field of lightning return stroke, *J. Geophys. Res., 74,* 6899–6910, 1969.

Uman, M. A., R. D. Brantley, Y. T. Lin, J. A. Tiller, E. P. Krider, and D. K. McLain, Correlated electric and magnetic fields from lightning return strokes, *J. Geophys. Res., 80,* 373–376, 1975a.

Uman, M. A., D. K. McLain, and E. P. Krider, The electromagnetic radiation from a finite antenna, *Amer. J. Phys., 43,* 33–38, 1975b.

Wait, J. R., and H. H. Howe, Amplitude and phase curves for ground-wave propagation in the band 200 cycles per second to 500 kilocycles, *Nat. Bur. Stand. U.S. Circ., 574,* 1956.

WSMR ATMOSPHERIC STRUCTURE CONSTANT (C_n^2) SURVEY

R. B. Fritz and R. S. Lawrence

Between March 25 and April 5, 1977, a multi-sensor cooperative atmospheric survey was carried out at White Sands Missile Range, New Mexico. The Atmospheric Sciences Laboratory of WSMR conducted ground-based and rawinsonde measurements of the refractive index structure constant C_n^2 (at heights of 8 and 32 meters on two meteorological towers), wind, temperature, humidity, and pressure. The Optical Propagation Group of the NOAA/ERL Wave Propagation Laboratory (Boulder, Colorado) carried out measurements of C_n^2 using an aircraft-mounted temperature probe, including vertical profiles to 3000 meters above ground and constant altitude circuit surveys. The aircraft measurements and concurrent rawinsonde launches took place at approximately local midnight, dawn, noon, and sunset. This report describes and summarizes the aircraft measurements only.

Index of Refraction Structure Parameter in the Real Atmosphere - an Overview

Freeman F. Hall, Jr.

Wave Propagation Laboratory

NOAA Environmental Research Laboratories

Boulder, Colorado 80302

The index of refraction structure parameter, C_n^2, is simply the difference
in optical index, squared and averaged as measured at two points divided by
the 2/3 power of the distance, r, separating the measurements or

$$C_n^2 = \overline{(n_1 - n_2)^2}/r^{2/3}.$$

For a given meteorological condition the principal meteorological parameter
determining C_n^2 is the temperature structure parameter, C_T^2, although the
humidity structure parameter, C_e^2, may also be important where turbulent fluxes
of water vapor are large. (Density or pressure fluctuations, C_p^2, can be
neglected in the real atmosphere as only important when C_T^2 and C_e^2 are very
small, or when C_n^2 is less than $10^{-20} m^{-2/3}$.) Wesely (1976) has shown that
a convenient form for the index of refraction structure parameter is

$$C_n^2 = 6.2 \times 10^{-9} \; C_T^2 (\overline{p}/\overline{T}^2)^2 \left[1 + (0.03\beta^{-1})^2\right],$$

where β is the Bowen ratio, the ratio of sensible turbulent heat flux to mois-
ture flux. This expression assumes that there is no correlation between the
temperature and humidity fluctuations. This assumption may be quite safe in
the upper regions of the planetary boundary layer, but in the surface layers,
over evaporating lakes or over the tropical ocean the correlation in temperature
and moisture fluctuations may be very high and the Bowen ratio may be as low as
0.1. For such a case,

$$C_n^2 = 6.2 \times 10^{-9} \; C_T^2 (\overline{p}/\overline{T}^2)^2 \; (1 + 0.03\beta^{-1})^2$$

where it is assumed that the correlation is $r_{et} = \pm 1$. (The correlation may be
negative as when warm dry air entrains downward through a temperature inversion

into a cool, moist region. More measurements need to be made in cloud-free marine inversions to confirm such anti-correlation, however.) Curves summarizing the correction factor α for no correlation or ± 1 correlation of C_T and C_e are shown in Figure 1, after Wesely.

In discussing C_n^2 in the atmosphere, there are clearly three regions where the conditions determining the structure parameter are quite different. These three regions are the planetary boundary layer, the free troposphere, and the stratosphere. Characteristics of C_n^2 in the three regions will now be discussed.

Figure 1. Correction factor, α, to be used in computing C_n^2 from C_T^2 for various values of the humidity-temperature correlation, r_{et}, as a function of Bowen ratio, β. After M. L. Wesely (1976).

Over dry land at midday, the planetary boundary layer is characterized by convective plumes of turbulent, rising, warm air separated by regions of somewhat cooler well-mixed air with temperature fluctuations one or two orders of magnitude less than in the rising plumes. The convective plumes are characterized by scale sizes of several hundred meters and they advect with the mean wind which shows little shear above the lowest few tens of meters to the top of the convectively mixed layer.

At a height of one meter in the convective plumes over grass covered terrain, typical midday, summertime values of C_n^2 may average $6 \times 10^{-13} m^{-2/3}$. In such well mixed convective regimes, C_n^2 decreases with height, z, as $z^{-4/3}$ so that

at 40 m, on the average, $C_n{}^2 = 4 \times 10^{-15} m^{-2/3}$. Measured values of $C_T{}^2$, obtained using fast response, spaced temperature sensors show rapid fluctuations; the distribution of the measured values follows approximately a log-normal distribution spread over two decades between 1% and 99% probability. Since $C_n{}^2$ is a simple function of the sensible turbulent heat flux at ground level (Wyngaard et al., 1971), measured $C_n{}^2$ values will be larger over dry desert surfaces and especially over blacktop areas.

The warm, moist convective plumes found over tropical oceans will average $C_n{}^2$ about one-half the values mentioned above with at least 40% of the contribution occurring because of $C_e{}^2$, as determined from acoustic scattering measurements made during the GATE experiment. (The acoustic index of refraction structure parameter is determined by almost the same relative contributions from $C_T{}^2$ and $C_e{}^2$ as for the optical case. Therefore it is possible to determine the optical parameter from acoustic scattering measurements (Neff, 1975).)

Temperature inversions in the planetary boundary layer, where the temperature (more exactly, the potential temperature) increases with height are almost always dynamically unstable and turbulent, at least intermittently, although statically stable. The downward turbulent transport of heat through such inversions leads to values of $C_n{}^2$ on the order $1 \times 10^{-15} m^{-2/3}$ and typically these values will decrease with height more slowly than for the convective case. The assumption of the Kolmogorov spectrum of turbulence is not so well justified in the stably stratified nocturnal inversion case, and in some instances, $C_n{}^2$ may actually increase with height, although in general it does fall off as a $z^{-2/3}$. The distribution of values in the stably stratified atmosphere also seems to follow a log-normal distribution although the spread in values will be less than for the convective case; typically between the 1% and 99% scales only one order of magnitude difference will be found in the stably stratified atmosphere. In developing tropical cumulus clouds, $C_n{}^2$ may reach $6 \times 10^{-15} m^{-2/3}$ because of turbulent entrainment at the edges of the clouds and the release of sensible heat from condensation. Optical rays which graze developing clouds will thus experience considerable scintillation.

In the free atmosphere, the model of $C_n{}^2$ given by Hufnagel (1974) is proving to be quite reasonable. This model takes into account the wind shear found

615

between 5 km and 20 km altitude. A number of optical measurements of C_n^2 by Ochs et al. (1976) show rather good agreement with this model. It must be emphasized that even in the free atmosphere, which is generally statically stable, that a given profile of C_n^2 will change rapidly as shear zones develop and dissipate. Thus balloon-borne measurements of C_n^2, which resolve the fine scale altitude differences, quite impossible to detect with the path averaging optical methods, typically show extreme excursions in thin layers with the number of these layers increasing in zones of more intense wind shear. Van Zandt et al. (1977) present a model explaining such intermittent C_n^2 layers.

Wind shear values frequently increase near the top of the troposphere, especially in the vicinity of jet streams. This will in general produce an increase in C_n^2 (the high altitude hump in the Hufnagel model). Once above the tropopause, wind shear and turbulence generally decrease in the stratosphere and a decrease of C_n^2 with height is usually found. Since we know so little about stratospheric turbulence there are no really good models to explain the observations although balloon-borne microthermal probes and optical phase measurements are beginning to shed more light on the upper atmosphere. Figure 2 summarizes our knowledge of C_n^2 throughout the three atmospheric regions with the solid line representing a typical daytime profile from the surface to 15 km and with the dashed lines representing 3σ from the mean.
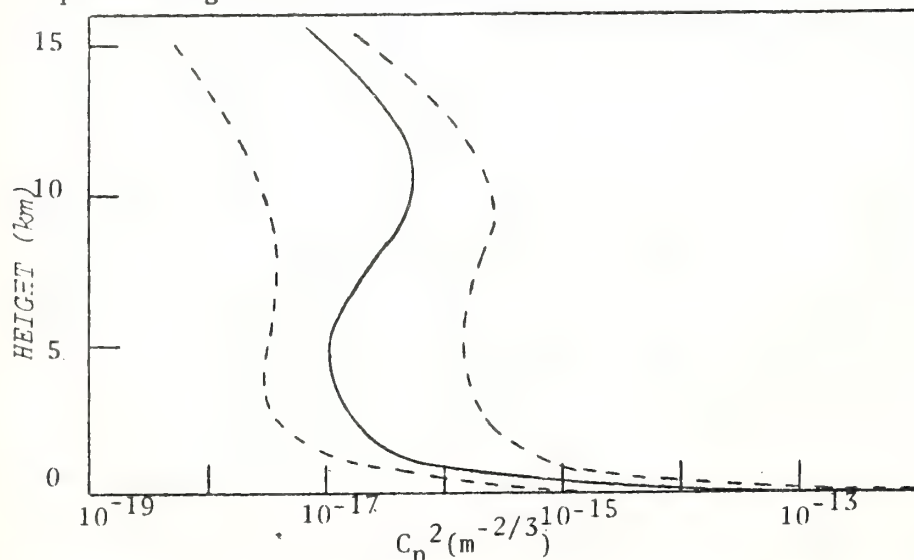
Figure 2. C_n^2 profiles in the temperate region, daytime atmosphere

Hufnagel, R. E., Opt. Prop. through Turbulence, OSA, paper Wa 1 (1974)
Neff, W. D., NOAA TR ERL 322-WPL 38 (1975)
Ochs, G. R., et al., Appl. Optics 15, 2504 (1976)
Van Zandt, T. E., et al., URSI Comm F. Proc., La Baule, FR, 519 (1977)
Wesely, M. L., J. Appl. Meteor. 15, 43 (1976)
Wyngaard, J. D., et al., J. Opt. Soc. Amer. 61, 1646 (1971)

THE DISTRIBUTION OF RADIO REFRACTIVE INDEX STRUCTURE PARAMETER IN BOUNDARY LAYERS UNDERGOING SPATIAL OR TEMPORAL TRANSITION

E. E. Gossard

NOAA/ERL/Wave Propagation Laboratory

Boulder, Colorado 80302, USA

SUMMARY

The height distributions of C_ϕ (the structure parameter of potential refractive index) in a steady, horizontally uniform boundary layer are calculated assuming power-laws for meteorological quantities. The results are then compared with those of more rigorous models examined by Wyngaard et al. (1971). It is shown that the results are in very satisfactory agreement when m is properly chosen. Finally, power-law profiles are used to calculate horizontal and temporal variations in vertical profiles of C_ϕ and to calculate radio-duct thickness for several boundary transitional conditions.

1 - INTRODUCTION

With the widespread realization of the capabilities of new clear-air Doppler radars, there is renewed interest in the spatial distribution of radio refractive index and its statistics. Of particular interest is the refractive index structure parameter C_ϕ^2, which is the turbulence-related quantity of primary concern for the prediction of clear-air backscatter. The Wave Propagation Laboratory of NOAA has developed a frequency-modulated, continuous-wave (FM-CW) radar with Doppler capability whose principal value is that it can monitor wind and wind shear in the planetary boundary layer. Therefore, it is urgent to determine how changes and modifications in the boundary layer affect C_ϕ^2 and the performance of the radar. This paper presents methods for calculating the height distribution of C_ϕ^2 in boundary layers undergoing spatial or temporal transition.

2 - FORMULATION OF THE PROBLEM

The refractive index parameter to be used is the potential refractive index ϕ, which is defined as the refractive index of a parcel of air brought adiabatically and without change in absolute humidity to a pressure level of 1000 mbars. In terms of meteorological quantities

$$\phi = \frac{77.6}{\theta} \left(P - \frac{4810 \, e_p}{\theta} P \right), \qquad (1)$$

where θ is potential temperature and e_p is the potential vapor pressure (see, e.g., Bean and Dutton, 1966). So defined, the quantity ϕ can be considered to diffuse much as θ, e_p, or any passive additive undergoing turbulent mixing. The approach that will be followed in this paper is to solve the diffusion equation for $\phi(z,x,t)$ and $C_\phi(z,x,t)$, where x,y,z and t are the three space coordinates and time, respectively, with z being the vertical direction. The quantity of primary interest is C_ϕ, where (Corrsin, 1951; Ottersten, 1969)

$$C_\phi^2 \approx 3.2 \, \epsilon^{-1/3} \epsilon_\phi. \qquad (2)$$

ϵ is the turbulent-dissipation rate and ϵ_ϕ is the rate of destruction of the variance of ϕ. For a steady-state regime of turbulence, the kinetic energy balance equation under conditions of forced convection can be represented, according to Lumley and Panofsky (1964), by

$$\epsilon \approx - \overline{u'w'} \frac{\partial u}{\partial z} (1 - R_f), \qquad (3)$$

where R_f is related to the more common Richardson Number, $Ri = (g/\theta)(d\theta/dz)/(du/dz)^2$, by the ratio of the eddy coefficients of heat to momentum. Under neutral or stable conditions that ratio is near unity. Symbols with a prime refer to turbulent perturbations. Furthermore, assuming that the destruction of variance of ϕ is balanced by shear production,

$$\epsilon_\phi \approx - \overline{\phi'w'} \frac{\partial \phi}{\partial z} . \qquad (4)$$

Both Eqs. (3) and (4) neglect potentially important terms such as radiative flux divergence and divergence of energy and pressure forces. This has been customary in studies of this type, because of difficulties in evaluating the neglected terms experimentally. Nevertheless this approximation must ultimately be justified by experiment.

Defining the eddy coefficient K for ϕ by $\overline{\phi'w'} = K(\partial\phi/\partial z)$ and defining the friction velocity u_* such that $u_*^2 = - \overline{u'w'}$, Eqs. (3) and (4) can be substituted into Eq. (2) yielding

$$\frac{C_\phi^2}{z^{4/3}(\frac{d\bar{\phi}}{dz})^2} = 3.2\ k_o^{4/3}(1-\alpha Ri)^{4/3}(1-Ri)^{-1/3}, \qquad (5)$$

where a log-linear velocity profile has been assumed so that $K/u_* = k_o z(1-\alpha Ri)$. The universal constant α is estimated by Businger et al. (1971) to be 4.7.

$$C_T^2\ /\ z^{4/3}(\partial\Theta/\partial z)^2$$
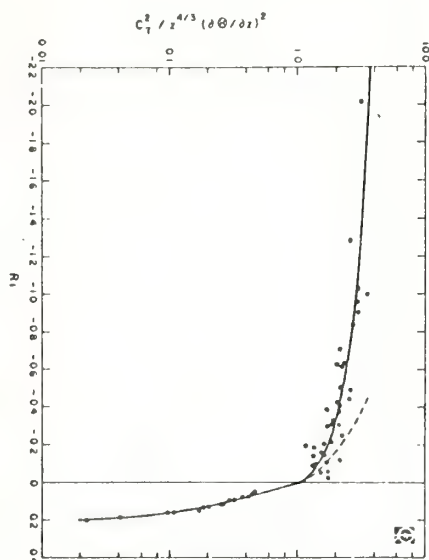
FIGURE 1.

The result of Eq. (5) may be compared with measured data reported by Wyngaard et al. (1971) and is shown in Fig. 1. The right side of Eq. (5) is plotted as a dashed curve. Throughout the stable range it nearly coincides with the solid curve that fits the data but fails seriously in the range of negative Ri. From this we can conclude that the assumptions and the balance equations we have used are an adequate representation of conditions in the steady-state, uniform surface layer of the atmosphere under neutral or stable conditions.

Under unstable conditions, Wyngaard et al. suggest that

$$C_\phi^2 = k_o \phi_*^2\ z^{-2/3} g(z/L) \qquad (6)$$

is a good fit to their data, where

$$g(z/L) = 4.9\ [1-7(z/L)]^{-2/3}.$$

L is the Monin-Obukov length representing static stability, and

$$\frac{z}{L} = Ri/(1-\alpha Ri). \qquad (7)$$

Plots of C_ϕ vs. height from Eqs. (5) and (6) are shown in the lower frame of Fig. 2 for several stabilities represented by L. These curves represent the probable best estimate of the height distribution of C_ϕ in the idealized boundary layer. However, the model used cannot be applied to the diffusion equation to obtain useful solutions except by numerical methods and high-speed computers. On the other hand, if power-law profiles had been used instead of log-linear profiles, then

$$u = bz^m, \qquad \theta - \theta_s = b_1 c^m, \qquad \phi - \phi_s = b_2 z^m,$$

where ϕ_s and θ_s are surface values and b, b_1, and b_2 are constants. Then

$$C_\phi^2 = 3.2(\frac{u_*}{bm})^{4/3} z^{4(1-m)/3}(1-Ri)^{-1/3}(\frac{\partial\phi}{\partial z})^2. \qquad (8)$$

The term that includes Ri stays very near unity for reasonable values of Ri because of the small negative power to which the expression is raised. The effect of stability is almost completely a function of m. The resulting distribution of C_ϕ vs. height is shown in the top frame of Fig. 2 for several values of m.
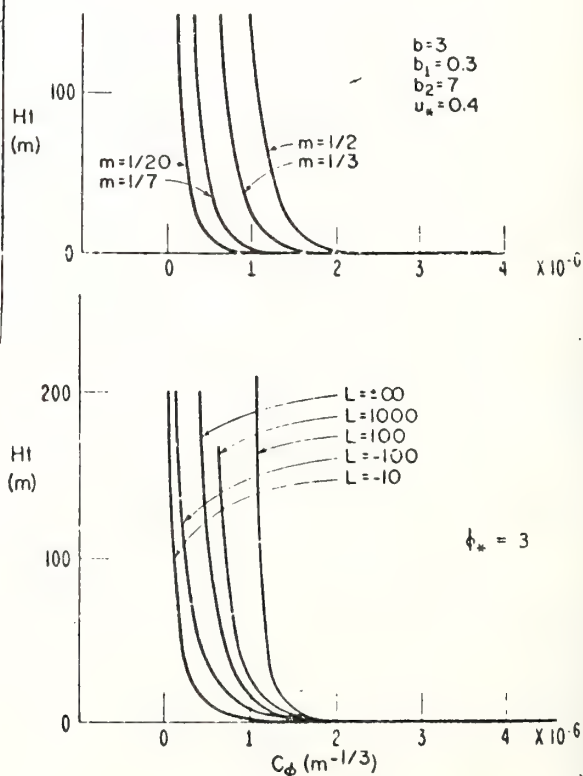
FIGURE 2.

To further test the adequacy of the power law, it is revealing to compare the predictions of surface duct thickness for the two models. The thickness of the duct in meters is the height at which $d\psi/dz = 0.131$ (m^{-1}). The results for the two models are shown in Fig. 3.

$$\phi_r - \phi_s = -40$$

$$d = -\left[\frac{0.131 \left(\ln \frac{z_r}{z_o} + a \frac{z_r}{L} \right)}{M_r - M_s - 0.131 z_r} + \frac{a}{L} \right]^{-1}$$

$$\phi_r - \phi_s = -40$$

$$d = \left[-\frac{0.131 z_r^m m^{-1}}{M_r - M_s - 0.131 z_r} \right]^{\frac{1}{M-1}}$$
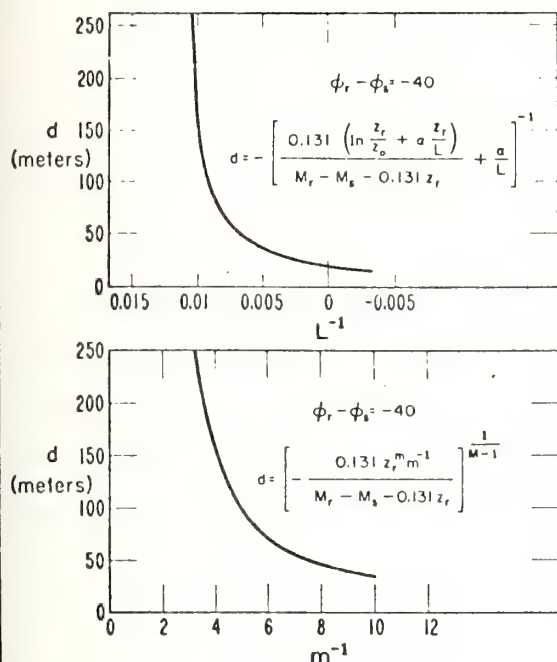
FIGURE 3.

It is evident that the power-law profiles with properly chosen values of m can give a very adequate representation of the more rigorous model. They have the important advantage that classical solutions to the diffusion equations can then be applied.

3 - BOUNDARY LAYERS UNDERGOING MODIFICATION

Written in general form, the diffusion equation for ϕ is

$$\underbrace{\frac{\partial \phi}{\partial t}}_{\substack{\text{temporal} \\ \text{term}}} + \underbrace{u \frac{\partial \phi}{\partial x} + v \frac{\partial \phi}{\partial y} + w \frac{\partial \phi}{\partial z}}_{\text{advective terms}}$$

$$= \frac{\partial}{\partial x} \left(K_x \frac{\partial \phi}{\partial x} \right) + \frac{\partial}{\partial y} \left(K_y \frac{\partial \phi}{\partial y} \right) + \frac{\partial}{\partial z} \left(K_z \frac{\partial \phi}{\partial z} \right) , \qquad (9)$$

where the quantities K_x, K_y, K_z are the eddy diffusion coefficients of ϕ in the x, y, and z directions, and u, v and w are the corresponding velocity components.

Thus formulated, the eddy coefficients can be considered functions of position. This use of the eddy coefficients in diffusion problems is classical. However, it lacks any fundamental physical basis and depends on a tenuous analogy with molecular diffusion for its justification. With the use of modern computers one can numerically solve a more rigorous formulation. However, it is the intent in this paper to go as far as possible without relying on large computers, and also to provide useful functional relationships for predicting system performance. In the past analytic solutions of Eq. (9) have provided numerical results in close agreement with observations, except under conditions of relatively extreme stability.

When the boundary layer is temporally stationary ($\partial\phi/\partial t = 0$) and horizontally uniform with w = 0 (i.e., the advective terms are zero) the left side of (9) is zero, and $k_z \partial\phi/\partial z$ is constant. This is the constant flux approximation that is usually valid near the ground. For a transition taking place in the x direction $\partial\phi/\partial x$ is no longer zero, although the x divergence of flux in the x direction $(\partial/\partial x)(K_x \partial\phi/\partial x)$ can still be considered negligible. Then

$$u \frac{\partial \phi}{\partial x} = \frac{\partial}{\partial z} \left[K(z) \frac{\partial \phi}{\partial z} \right] . \qquad (10)$$

Using power-law distributions we find $k = (u_*^2/bm)z^{1-m}$. Frost (1946) dealt with the corresponding problem in moisture flux (evaporation) and found that the variable transformation to $\zeta = z^{2m+1}/ax(2m+1)^2$ permitted straight-forward solution of (10). The corresponding solution for $\partial\psi/\partial z$ may then be used in Eq. (5) to obtain C_ϕ. The results are shown in Fig. 4 for three offshore distances, and Fig. 5 shows the corresponding duct thickness.

For a horizontally uniform boundary layer that is not in steady state Eq. (9) reduces to

$$\frac{\partial \phi}{\partial t} = \frac{\partial}{\partial z} \left[K(z) \frac{\partial \phi}{\partial z} \right] . \qquad (11)$$

There are simple solutions to this equation if K is assumed constant. Although this assumption is unrealistic, the resulting solution may be expected to reveal some of the qualitative features to be observed during diurnal cycles or other quasi-sinusoidal variations in temperature or humidity at Earth's surface. Data recorded at O'Neill, Nebraska, and Manor, Texas, USA, were used to fit a trochoidal function to the

$$c_\phi = 17 \frac{(\phi_s - \phi_0)\left(\frac{u_*}{bm}\right)^{2/3}(2m+1)^{1/(2m+1)} - m/(2m+1)(m-1)/3}{\Gamma\left(\frac{m}{2m+1}\right)}(ax) \, \ell \, \exp\left[-\frac{\ell^{2m+1}}{ax(2m+1)^2}\right]$$

FIGURE 4.

$$d = \left[\frac{0.131 \, \Gamma\left(\frac{m}{2m+1}\right)(2m+1)^{-1/(2m+1)}}{(\phi_s - \phi_0)}(ax)^{m/(2m+1)}\right]^{\frac{1}{m-1}}$$
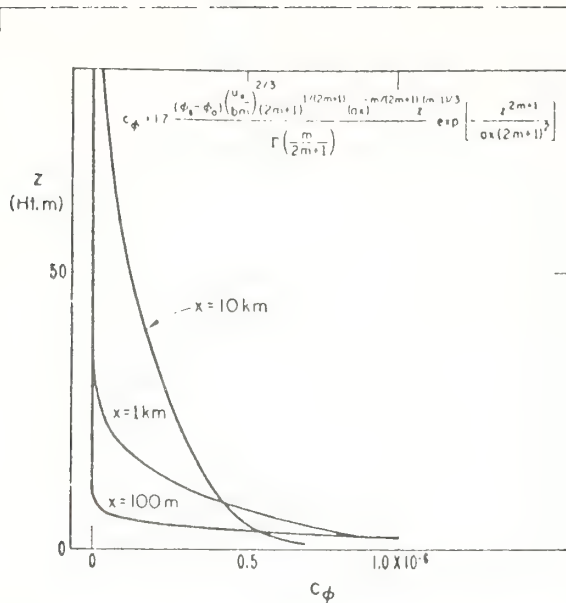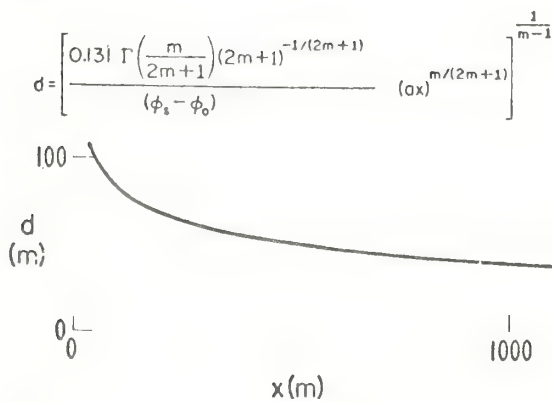
FIGURE 5.

temperature at $z = 0$ and at a few meters above the
ground. A best average value of K was determined from
the amplitude difference and phase lag at the two
heights. The resulting distributions of ϕ, C_ϕ, and
$M = \phi + 0.131z$ are shown in Fig. 6. Although the
model is crude, it shows features (such as the small
C_ϕ values before sunrise) that are observed with
acoustic and radar sounders.

$$C_\phi = 1.95 \, (K/u_*)^{2/3} \, \Delta\theta \, \sqrt{\sigma/2K} \, z \, e^{\sqrt{\sigma/2K} \, z} \, (\sin y - \cos y) + f_\phi \sqrt{\sigma/K} \, e^{\sqrt{\sigma/2K} \, z}(\sin y' - \cos y')$$

where $y = \sigma t - \sqrt{\sigma/2K} \, z$ and $y' = 2\sigma t - \sqrt{\sigma/K} \, z$
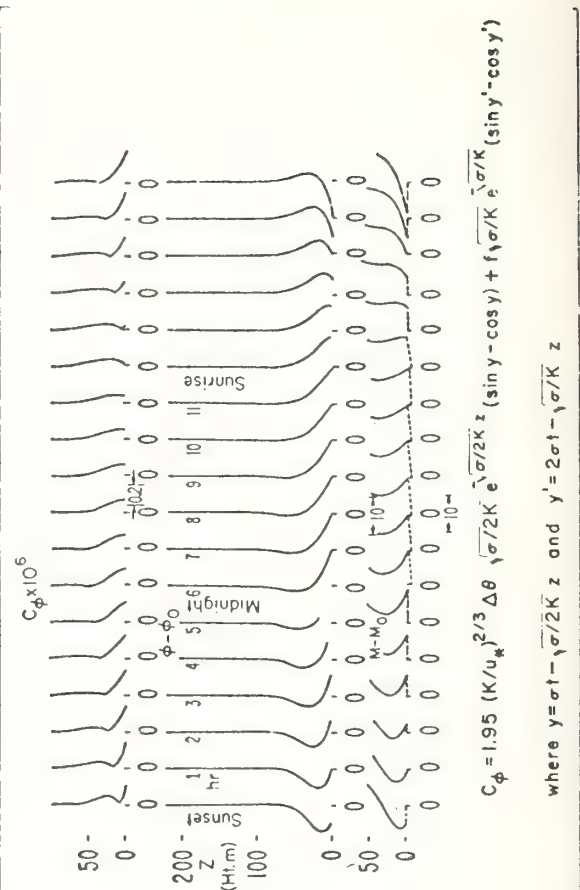
FIGURE 6.

REFERENCES

Bean, B. R., and E. J. Dutton (1966), *Radio Meteorology*,
National Bureau of Standards Monograph 92
(U.S. Government Printing Office, Washington,
D.C. 20402), Sec. 6.3.3

Businger, J. A., J. C. Wyngaard, Y. Izumi, and E. F.
Bradley (1971), Flux-profile relationships in the
atmospheric surface layer, *J. Atmos. Sci.*, **28**,
181-189.

Corrsin, S. (1951), On the spectrum of isotropic
temperature fluctuations in an isotropic turbu-
lence, *J. Appl. Phys.*, **22**, 417-423.

Frost, R. (1946), Turbulence and diffusion in the
lower atmosphere, *Proc. Roy. Soc. London, Ser. A.*,
186, 20-35.

Lumley, J. A., and H. A. Panofsky (1964), *The Struc-
ture of Atmospheric Turbulence*, Wiley and Sons,
New York, 239 pp.

N PAGES

620

Ottersten, H. (1969), Atmospheric structure and radar
backscattering in clear air, *Radio Sci.*, 4,
1179-1193.

Wyngaard, J. C., Y. Izumi, and S. A. Collins, Jr
(1971), Behavior of the refractive-index-
structure parameter near the ground, *J. Optical
Soc. of Amer.*, 61, No. 12, 1646-1650.

Refractive index variance and its height distribution in different air masses

Earl E. Gossard

Wave Propagation Laboratory, Environmental Research Laboratories, National Oceanic and Atmospheric Administration, US Department of Commerce, Boulder, Colorado 80302

With the advent of radars capable of detecting backscatter from turbulent inhomogeneities in the clear air, there is renewed interest in the refractive character of the atmosphere. The radio refractive index structure constant and its spatial and temporal distribution are of particular importance. The general refractive properties of air masses are discussed in this paper. Based on certain assumptions, the distribution of optical and radio refractive index structure constants are then calculated and the results are compared with the limited observational data available.

INTRODUCTION

The coverage of microwave radar and communications systems depends critically on the refractive structure of the atmosphere, and its refractive properties have been investigated for many years [see *Kerr*, 1951; *Bean and Dutton*, 1966]. It has also been long recognized that turbulent fluctuations in atmospheric refractive index can produce a kind of Bragg scattering of energy beyond the geometrical horizon that can greatly extend the coverage of microwave communications systems [*Booker and Gordon*, 1950]. However, such scattering strongly favors the forward direction and seemed to be of little interest for monostatic radar systems, although a long lasting controversy developed about the subject of "angels" producing radar returns from the clear air. One school of thought argued that the returns were indeed from refractive index fluctuations in the clear air, while another argued that they were from birds or insects. With the advent of powerful, narrow-beam radar systems with sophisticated processing capabilities, such as the NASA radar at Wallops Island and the Lincoln Laboratory radar at Millstone Hill in the USA, and the Royal Aircraft Establishment's radar at Defford, England, it became evident that returns from the clear air could, in fact, occasionally be detected [*Browning*, 1972; *Hardy*, 1972; *Ottersten*, 1969].

A further breakthrough occurred with the development of a frequency modulated, continuous wave radar (FM-CW) sounder capable of sensing targets

very close to the radar, thus taking advantage of the inverse-range-squared strength of the received signal to study the lower atmosphere [*Richter*, 1969]. This sounder also had a capability of viewing the atmosphere with very fine resolution, and it was immediately evident that there were commonly returns both from diffuse clear air structures [*Gossard et al.*, 1970] and from point targets such as insects and birds [*Atlas et al.*, 1970]. More recently a Doppler capability of measuring the velocity of distributed, clear air targets has been demonstrated in a microwave FM-CW radar at NOAA's Wave Propagation Laboratory [*Strauch et al.*, 1976], and actual wind profiles have been measured in the clear air to a height of about 2 km [*Chadwick et al.*, 1976]. Finally, a near vertically pointing Doppler radar at VHF has been shown to be able to measure winds in the clear air to heights of many kilometers [*Green et al.*, 1972].

One approach to developing a refractive index climatology is through the classification of air masses and the mechanisms of their modifications. In developing any climatology it must be recognized that the deviation of any chosen parameter (such as temperature) from its average, within any given air mass, is likely to be much greater than the variation of the average from air mass to air mass. Thus the results of this paper should only be regarded as typical for a given air mass and large variations are to be expected depending on the modification the air mass has undergone and the geographical location of the air mass. In Figures 10–12 and 14–16 the distribution of structure parameter in the same air mass at more than one location

is shown to illustrate its variability. For any given synoptic situation, the air mass refractive index structure must therefore be judiciously interpreted in terms of the modification it has undergone and the geographical location of interest. However, in a climatological sense, the frequency of occurrence of the various air masses in a certain locality and season should provide a statistical base on which to judge the performance of a particular radar or optical system.

This paper includes a description of an air mass classification system, and a discussion of air mass modification. The radio refractive index is then analyzed and its dependence on the meteorological variables summarized. Special emphasis is placed on the relationship of refractive index variance to the variance of meteorological properties. Height profiles of the ratio of the radio refractive index structure constant to the temperature structure constant are calculated. This ratio is believed to be important because many more measurements of optical refractive index structure constant (which depends only on temperature) have been made than of radio refractive index. In fact, a tentative model of the height variation of optical refractive index structure has been proposed by *Hufnagel* [1974].

This report attempts to "calibrate" the radio refractive index structure constant using the Hufnagel optical model and thus to deduce absolute quantities from what would otherwise be only a relative comparison between air mass types. Finally, the deduced height distributions of refractive index structure constant are compared with the very limited amount of observational data that exist— data collected by the powerful Millstone Hill *L*-band radar of Lincoln Laboratory described by *Crane* [1970].

AIR MASS CLASSIFICATION

An air mass is an extensive portion of the earth's atmosphere with meteorological properties which approximate horizontal homogeneity. Thus the refractive index within an air mass is also approximately horizontally homogeneous.

One classification of air masses divides them into two basic types according to latitude in the northern hemisphere. Those originating in sources north of approximately 40° lat are designated "arctic" (A) or "polar" (P), depending on their temperature, and those originating south of 40° lat are called "tropical" (T). Source regions are classified as "primary" or "secondary." A primary source region is an extensive area favorable to air stagnation for appreciable periods of time. A secondary source region is one in which stagnation does not occur, but in which the air trajectories are so long that the air mass takes on characteristics associated with the underlying surface.

The air mass types, arctic, polar, and tropical, are further subdivided according to the nature of the surface in the source region. Air masses originating over snow, ice, or land surfaces are called continental, while those originating over the sea are called maritime. Continental air masses are designated by a lower case letter c preceding the capital A, P, or T designations and a lower case letter m indicates maritime. The average location of the various air masses is shown for January and July in Figure 1 [from *Chromov*, 1937].

In addition to the air masses described above, a third classification called "Superior" is often used. This describes a mass of air formed at high levels in the atmosphere. However, this air mass may, on occasion, descend to the surface of the earth. In midwestern United States this most commonly occurs during sustained subsidence in a southward moving cP air mass. Superior air usually has a large lapse rate; in addition, it is low in humidity, so such air masses tend to be comparatively subrefractive except at night when clear skies may lead to a surface-based inversion due to strong radiational cooling at the ground. In this paper the temperature and humidity profiles published by *Showalter* [1939] were used.

Further subclassifications are often used. Probably the most common indicates the temperature of the air mass relative to the surface over which it is passing. If the air mass is warmer than the surface, a lower case letter w follows the capital P or M, and if it is colder it is so designated with a lower case letter k. Air masses with the k designation are thermally unstable, gusty, and turbulent with cumuliform clouds and showers. Those with the w designation are stable with steady winds, stratiform clouds, and drizzle. The k and w designations are an effort to extend air mass classification to include modification processes and will not be used in this paper. We prefer to treat the "typical" air mass separate from its modification, because modification of the boundary layer can often be dealt with using analytical and numerical methods,
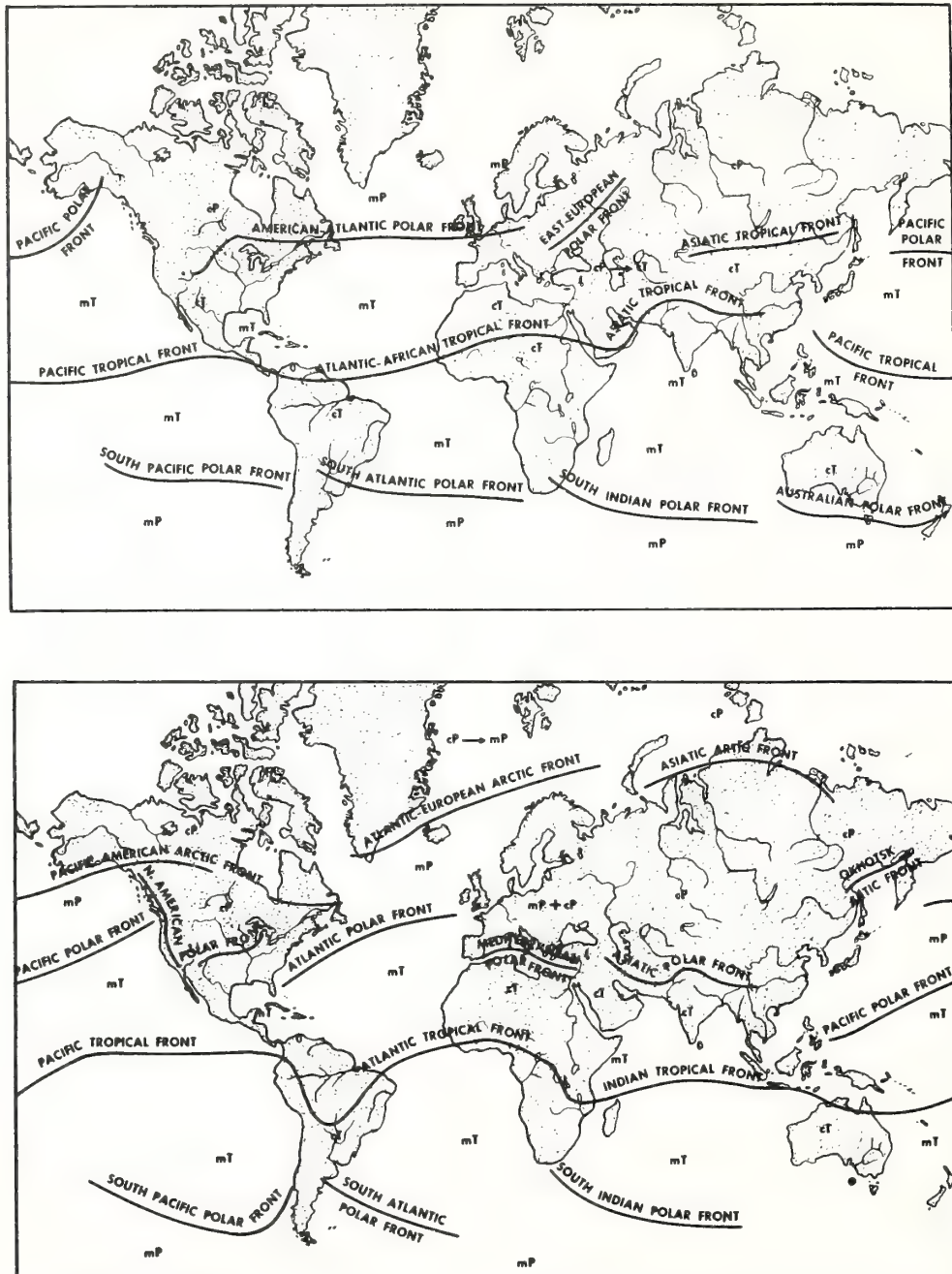
Fig. 1. Mean global air mass distribution for summer (top) and for winter (bottom) [from *Chromov*, 1937].

and because assumptions about independence of properties can legitimately be made in the deep air mass which may not apply to its boundary layer undergoing modification. Thus air mass types other than Superior may at one time or another be either warmer or colder than their underlying surface with corresponding stability or instability within their boundary layer causing either stratified or convective conditions to prevail. In this paper we consider the "typical" air mass in more or less neutral equilibrium with the underlying surface. The secondary source regions are really regions in which

624

the modification process has proceeded essentially to completion forming a new air mass that can again be treated as "typical."

AIR MASS MODIFICATION

Air mass modification occurs primarily due to two classes of processes: (a) transfer processes that take place at the air-earth boundary, (b) dynamical processes that cause convergence and divergence within the air mass.

The first class of processes includes transfer of heat, moisture, or momentum between the atmosphere and the earth's surface. Transfer processes are especially active when a dry continental or arctic air mass moves out over a relatively warm sea surface. However, significant modification of the surface layers also occurs when air moves over a relatively cooler surface. An example of the modification of the refractive structure in the lower layers as air moves southward from its source region in central Canada is shown in Figure 2. Refractive index can also be modified by transfer processes that result from radiational heating or cooling. Temporal changes in structure then occur that are somewhat analogous to spatial changes that result from transport over a different surface. Diurnal radiational cooling of the earth-air interface is an important example of this kind of modification. In the calculation of mean refractive index structure and refractive variance for air masses, it must be remembered that an important diurnal variation in the lower layers should in fact be superimposed on the means. Temporal changes can also occur over a much longer time span due to radiational cooling when a winter air mass stagnates for a considerable length of time in an arctic source region. An example is shown in Figure 3 which illustrates the progressive cooling of the surface layers of an air mass at Fairbanks, Alaska.

The second class of processes results in stretching or subsidence within the air mass. If stretching due to convergence takes place, the air mass will tend toward thermal instability and turbulent mixing, its temperature lapse will approach the adiabatic, and the potential refractive index gradient will tend toward zero. The refractive index variance will be small compared with that of stratified air masses for a given intensity of mechanical mixing. Such convergence is typically associated with a northward-moving cyclonic trajectory.

Subsidence within an air mass can be the result of descent of the air mass due to topography or it can result from divergence in the lower levels. One classical example of topographic subsidence occurs when air from the high desert interior of
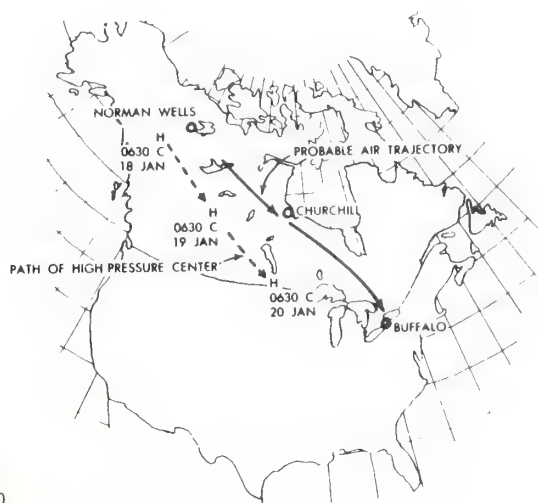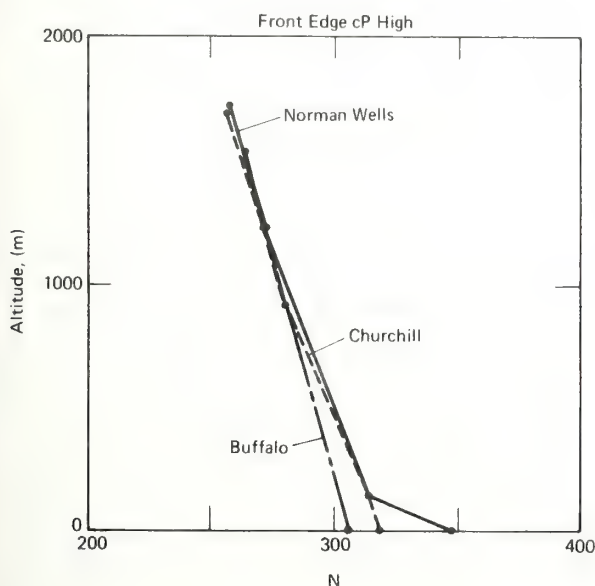
Fig. 2. Modification of the surface layers of an air mass as it moves southward along a trajectory shown by the solid arrows on the map at the right [adapted from *Plank*, 1952].

625
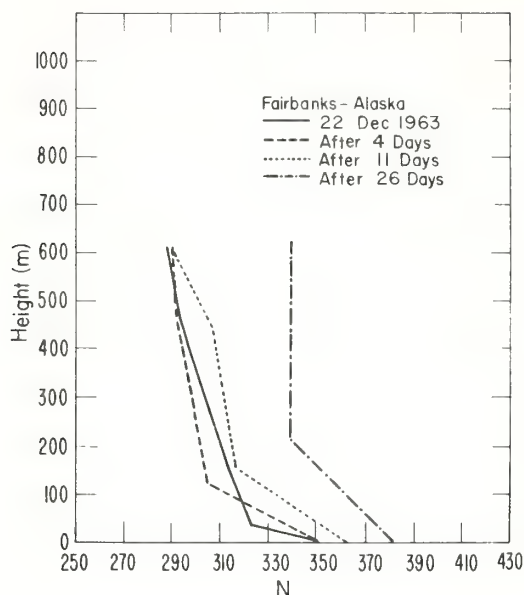
Fig. 3. Modification of the surface layers of an air mass in its source region as radiational cooling of the underlying surface proceeds.

the western United States flows down toward the coast of southern California and out over the sea. A strong low-level inversion forms, often surface based, in the air over the coastal water. A very strong refractive gradient results from the temperature inversion and also from the evaporation of moisture into the dry continental air.

A somewhat different kind of topographic subsidence is common on the eastern slope of the Rocky Mountains and the adjacent plains. This subsidence occurs when a deep, wide-spread westerly circulation dominates the area. When enhanced by a surface-based radiation inversion, it can produce severe air pollution in the Denver area as well as strong radio refraction. An example of the refractive index distribution during this subsidence condition (without the surface radiation duct) is shown by the Denver sounding in Figure 4. In spite of subsidence, solar heating often creates a nearly adiabatic layer near the ground.

Another type of subsidence occurs within an air mass due to divergence. This commonly occurs in a southward moving air mass having an anticyclonic circulation pattern [see, for example, *Byers, 1944*]. The following generalizations can be stated:

1) Decreasing vorticity (increasing anticyclonic

circulation) at a given latitude leads to subsidence within the air mass and vice versa.

2) In the absence of lateral convergence or divergence, increasing vorticity results from a northerly (equatorward) flow in the northern hemisphere or a southerly flow in the southern hemisphere.

3) If vorticity in the air mass is conserved, subsidence (i.e., divergence) occurs in a northerly (equatorward) flow in the northern hemisphere or a southerly flow in the southern hemisphere.

An example of the modification of radio refractive index due to air mass subsidence resulting primarily from (1), but also with some contribution from (3), is shown in Figure 5. That is, it results from a southward flow pattern in which the anticyclonic circulation is increasing. An example of a radio refractive index profile resulting primarily from (3) is illustrated by the San Diego sounding in Figure 4. This sounding is typical of an mP air mass originating in the north Pacific and moving southward around the periphery of the large subtropical high pressure system which dominates the eastern Pacific during the period June through October. During this period, radio refraction can be so strong that television coverage can be greatly enhanced for these transmitters located at elevations just
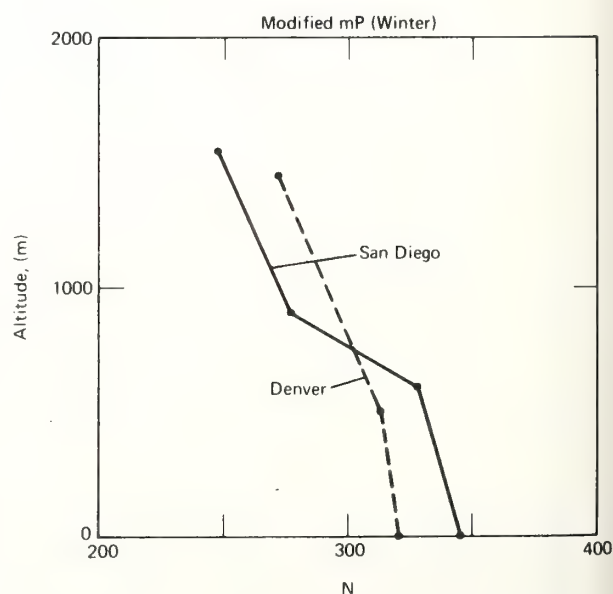
Fig. 4. Refractive index distribution resulting from two kinds of subsidence in different climatic regimes.
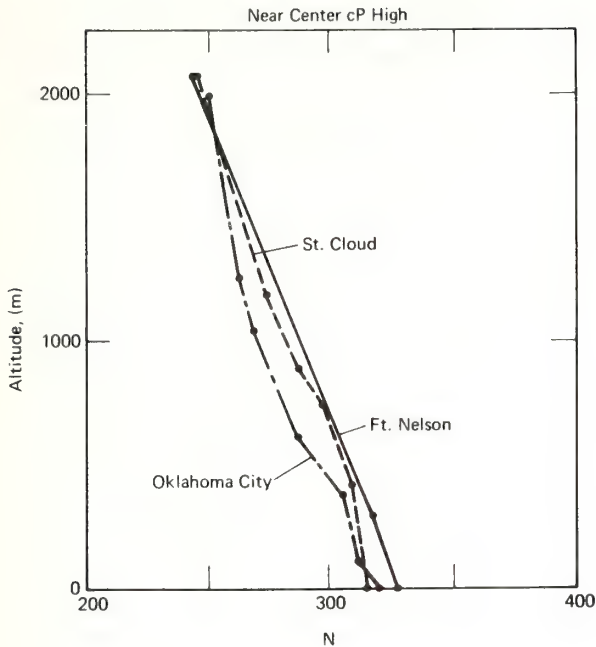
Fig. 5. Height distribution of radio refractive index N in an air mass which is subsiding as it moves southward anticyclonically along the trajectory shown by the solid arrows on the map to the right [adapted from *Plank*, 1952].

beneath the inversion. However, such coverage tends to be quite sporadic and is characterized by fading.

The topography of the western United States can modify mP air from the Pacific by "wringing it out," and creating what amounts to a new air mass aloft in the central US. The moist, cool air from the Pacific is lifted topographically, causing condensation and precipitation on the western slope of the Sierra Nevada and Cascade mountain ranges. It may then pass inland across the Great Basin where it may stagnate or be carried to the Rocky Mountains where it is again topographically lifted removing still more moisture in the form of precipitation on the western slope. It then is warmed adiabatically as it descends the eastern slope forming a dry, relatively warm mass of one kind of superior air often found overlying cP or cA air in the midwest. The equivalent potential temperature distribution in the original mP air can be used to estimate the refractive index distribution in the air mass that results after the topographic modification.

RADIO REFRACTIVE INDEX AT MICROWAVE FREQUENCIES

The refraction of radio waves in the non-ionized atmosphere depends on both nonpolar and polar gaseous constituents. However, for comparable concentrations, the effect of the polar constituent, i.e., water vapor, is much greater than that of the nonpolar. The expression relating the refractive index m to the various meteorological measurables is:

$$(n - 1) \times 10^6 = K_1 \frac{p_d}{T} + K_2 \frac{e}{T} + K_3 \frac{e}{T^2} + K_4 \frac{p_c}{T}$$

(1)

where K_1, K_2, K_3, and K_4 are constants, T is absolute temperature, p_d is partial pressure of the dry air constituents, e is partial pressure of water vapor and p_c is partial pressure of carbon dioxide. The first and fourth terms· represent the effects of nonpolar constituents and the second and third represent the effects of polar constituents. A summary of the values of K found by various workers

627

has been given by *Bean and Dutton* [1966]. Here, we simply adopt the values of Smith and Weintraub. If we define $N = (n - 1) \times 10^6$, this gives

$$N = 77.6 \frac{p_d}{T} + 72 \frac{e}{T} + 3.75 \times 10^5 \frac{e}{T^2} \qquad (2)$$

where p_d and e are in millibars. Because total pressure p is the easy quantity to measure, substitute $p_d = p - e$ and (2) becomes

$$N = 77.6 \frac{p}{T} - 5.6 \frac{e}{T} + 3.75 \times 10^5 \frac{e}{T^2}$$

Therefore, for $T \simeq 300$,

$$N = 77.6\, p/T + (e/T^2)(3.75 \times 10^5 - 5.6T) \simeq 77.6\, p/T$$
$$+ 3.73 \times 10^5\, e/T^2 \qquad (3)$$

which is commonly written in the form

$$N = (77.6/T)\,[p + (4810\, e/T)] \qquad (4)$$

REFRACTIVE INDEX VARIANCE

In problems dealing with scatter and backscatter of radio waves from the clear air it is important to know how perturbations of the meteorological quantities e, p, and T affect perturbations of N. At a fixed height in the atmosphere, perturbations of T, e, and p are essentially independent, so

$$dN = (\partial N/\partial T)dT + (\partial N/\partial e)de + (\partial N/\partial p)dp \qquad (5)$$

Rigorously, potential temperature, potential vapor pressure, and potential refractive index should be used here, but the relationship is to be applied at a constant pressure level (i.e., constant height) so no distinction need be made. Then from (4),

$$\partial N/\partial T = -77.6\, p/T^2 - 7.46 \times 10^5\, e/T^3 = -a$$

$$\partial N/\partial e = (3.73 \times 10^5)/T^2 = b$$

$$\partial N/\partial p = 77.6/T = c$$

which define the quantities a, b, and c. Thus,

$$N' = -aT' + be' + cp'$$

where primed quantities denote deviations from the mean. The variance of refractive index is related to the variance of the meteorological quantities by

$$\overline{N'^2} = a^2\, \overline{T'^2} + b^2\, \overline{e'^2} + c^2\, \overline{p'^2} - 2ab\, \overline{T'e'}$$
$$- 2ac\, \overline{T'p'} + 2bc\, \overline{p'e'} \qquad (6)$$

where the overbar denotes average (usually temporal). The possible importance of the term in $\overline{T'e'}$, when temperature and humidity fluctuations are correlated, was pointed out and evaluated by *Gossard* [1960].

REFRACTIVE INDEX STRUCTURE FUNCTION

Suppose the refractive index fluctuations are spatially statistically uniform and define $N = \bar{N} + N'$. The structure function $D_N(l)$ is then defined as

$$D_N(l) = \overline{[N'(r) - N'(r + l)]^2}$$
$$= 2\, \overline{N'^2(r)}\,[1 - \overline{N'(r)\, N'(r + l)}/\overline{N'^2(r)}\,] \qquad (7)$$

where we recognize the last term inside the brackets as just the spatial autocorrelation function, say $\rho_N(l)$. Then similarly,

$$D_T(l) = \overline{[T'(r) - T'(r + l)]^2} = 2\, \overline{T'^2(r)}\,[1 - \rho_T(l)]$$
$$D_e(l) = \overline{[e'(r) - e'(r + l)]^2} = 2\, \overline{e'^2(r)}\,[1 - \rho_e(l)]$$
$$D_p(l) = \overline{[p'(r) - p'(r + l)]^2} = 2\, \overline{p'^2(r)}\,[1 - \rho_p(l)]$$

For convenience we redesignate $N'(r) = N_1$, $N'(r + l) = N_2$, etc. Then from (7),

$$D_N(l) = \overline{N_1^2} + \overline{N_2^2} - 2\, \overline{N_1 N_2} \qquad (8)$$

From our assumptions of statistical uniformity and (6),

$$\overline{N_1^2} = \overline{N_2^2} = a^2\, \overline{T'^2} + b^2\, \overline{e'^2} + c^2\, \overline{p'^2} - 2ab\, \overline{T'e'}$$
$$- 2ac\, \overline{T'p'} + 2bc\, \overline{p'e'}$$

Also, assuming $\overline{T_1 T_2} = \overline{T_2 T_1}$, etc.,

$$\overline{N_1 N_2} = a^2\, \overline{T_1 T_2} + b^2\, \overline{e_1 e_2} + c^2\, \overline{p_1 p_2} - 2ab\, \overline{T_1 e_2}$$
$$- 2ac\, \overline{T_1 p_2} + 2cb\, \overline{e_1 p_2}$$

Recalling that $D_T(l)$, $D_e(l)$, $D_p(l)$ are of the same form as (8), e.g.,

$$D_T(l) = \overline{T_1^2} + \overline{T_2^2} - 2\, \overline{T_1 T_2}$$

we see that

$$D_N(l) = a^2\, D_T(l) + b^2\, D_e(l) + c^2\, D_p(l)$$
$$- 2ab\,[\,\overline{T(r)\, e(r)} - \overline{T(r)\, e(r + l)}\,] - 2ac\,[\,\overline{T(r)\, p(r)}$$
$$- \overline{T(r)\, p(r + l)}\,] + 2bc\,[\,\overline{e(r)\, p(r)} - \overline{e(r)\, p(r + l)}\,]$$

Therefore:

TABLE 1.   Continental polar-winter.

Ht(m)	a	b	c	a^2	b^2	c^2	$2ab$	$2ac$	$2bc$
				Oklahoma City					
0	1.09	5.19	0.29	1.19	26.9	0.08	11.3	0.63	3.00
500	1.02	5.17	0.29	1.05	26.7	0.08	10.6	0.59	2.98
1000	0.96	5.15	0.29	0.92	26.5	0.08	9.88	0.55	2.97
1500	0.90	5.19	0.29	0.81	26.9	0.08	9.37	0.52	3.00
2000	0.84	5.15	0.29	0.71	26.5	0.08	8.70	0.49	2.97

$$D_N(l) = a^2 D_T(l) + b^2 D_e(l) + c^2 D_p(l) - 2ab D_{Te}(l)$$
$$- 2ac D_{Tp}(l) + 2cb D_{ep}(l) \qquad (9)$$

where

$$D_N(l) = 2\,\overline{N'^2}\,[1 - \rho_N(l)]$$

$$D_T(l) = 2\,\overline{T'^2}\,[1 - \rho_T(l)]$$

$$D_e(l) = 2\,\overline{e'^2}\,[1 - \rho_e(l)]$$

$$D_p(l) = 2\,\overline{p'^2}\,[1 - \rho_p(l)]$$

$$D_{Te}(l) = 2\,\overline{T'e'}\,[1 - \rho_{Te}(l)]$$

$$D_{Tp}(l) = 2\,\overline{T'p'}\,[1 - \rho_{Tp}(l)]$$

$$D_{ep}(l) = 2\,\overline{e'p'}\,[1 - \rho_{ep}(l)]$$

and the ρ's are the spatial auto- and cross-correlation functions. They are, of course, normalized, so the variance and covariance appear as factors outside the brackets.

Within the inertial subrange we can express the structure function $D(l)$ in terms of the structure constant C^2, e.g.,

$$D_N(l) = C_N^2\, l^{2/3}$$

So, for any given l,

$$C_N^2 = a^2 C_T^2 + b^2 C_e^2 + c^2 C_p^2 - 2ab C_{Te}^2 - 2ac C_{Tp}^2$$
$$+ 2bc C_{ep}^2 \qquad (10)$$

It is reasonable to suppose that the quantity in brackets, in the expressions for D, is very nearly the same for all D, so all D (or C^2) can be expressed in terms of one (say C_T^2) by simply multiplying by the ratio of their variances or covariances, and the ratios of the factors a^2, b^2, c^2, ab, ac, cb multiplying the appropriate terms. The values of the coefficients in (9) and (10), for a variety of air masses and locations, are shown in Tables 1 through 8.

The pressure fluctuations are typically more than an order of magnitude smaller than the water vapor or temperature fluctuations, and c^2 and products of c with a and b are typically orders of magnitude less than a^2, b^2, or ab. Consequently, the important terms are

$$C_N^2 \simeq a^2 C_T^2 + b^2 C_e^2 - 2ab C_{Te}^2 \qquad (11)$$

where

$$C_e^2 = (\overline{e'^2} / \overline{T'^2})\, C_T^2$$

$$C_{Te}^2 = (\overline{T'e'} / \overline{T'^2})\, C_T^2$$

If we presume it is possible to acquire information about the height distribution of C_T^2 in a variety of air masses, a convenient form of (11) is

$$C_N^2 / C_T^2 \simeq a^2 + b^2 C_e^2 / C_T^2 - 2ab C_{Te}^2 / C_T^2$$

or

TABLE 2.   Maritime polar-winter.

Ht(m)	a	b	c	a^2	b^2	c^2	$2ab$	$2ac$	$2bc$
				Seattle					
0	1.27	4.76	0.28	1.62	22.6	0.08	12.1	0.71	2.63
500	1.22	4.84	0.28	1.49	23.5	0.08	11.8	0.68	2.71
1000	1.13	4.93	0.28	1.28	24.3	0.08	11.2	0.64	2.78
1500	1.06	5.05	0.28	1.13	25.5	0.08	10.7	0.61	2.88
2000	1.00	5.15	0.29	1.00	26.6	0.08	10.3	0.58	2.97
2500	0.29	2.01	−0.18	0.08	4.03	0.03	1.16	−0.10	0.72
3000	0.86	5.42	0.30	0.75	29.4	0.09	9.43	0.51	3.21
4000	0.77	5.73	0.30	0.60	32.8	0.09	8.87	0.47	3.48
5000	0.70	6.13	0.31	0.49	37.6	0.10	8.61	0.44	3.86

TABLE 3.   Maritime tropical-winter.

Ht(m)	a	b	c	a^2	b^2	c^2	$2ab$	$2ac$	$2bc$
Canal Zone									
0	1.64	4.21	0.26	2.69	17.7	0.07	13.8	0.85	2.19
500	1.56	4.28	0.26	2.44	18.4	0.07	13.4	0.82	2.25
1000	1.41	4.37	0.27	1.98	19.1	0.07	12.3	0.75	2.32
1500	1.26	4.46	0.27	1.60	19.9	0.07	11.3	0.68	2.39
2000	1.12	4.52	0.27	1.25	20.4	0.07	10.1	0.60	2.44
2500	0.99	4.59	0.27	0.99	21.0	0.07	9.11	0.54	2.49
3000	0.89	4.66	0.27	0.79	21.7	0.07	8.30	0.48	2.56
4000	0.76	4.81	0.28	0.58	23.1	0.08	7.33	0.42	2.67
5000	0.61	4.99	0.28	0.37	24.9	0.08	6.12	0.35	2.82
Pensacola									
0	1.54	4.36	0.26	2.37	19.0	0.07	13.4	0.82	2.31
500	1.42	4.40	0.29	2.02	19.4	0.07	12.5	0.76	2.35
1000	1.32	4.50	0.27	1.74	20.2	0.07	11.9	0.71	2.43
1500	1.16	4.60	0.27	1.35	21.2	0.07	10.7	0.63	2.51
2000	1.09	4.69	0.27	1.19	22.0	0.08	10.2	0.60	2.58
2500	1.01	4.81	0.28	1.01	23.1	0.08	9.69	0.56	2.68
3000	0.92	4.91	0.28	0.85	24.1	0.08	9.04	0.52	2.77
4000	0.76	4.91	0.28	0.58	24.1	0.08	7.46	0.43	2.77
5000	0.68	5.37	0.29	0.47	28.9	0.09	7.36	0.40	3.16

$$C_N^2 / C_T^2 \simeq a^2 + b^2 \, \overline{e'^2} / \overline{T'^2} - 2ab \, \overline{e' T'} / \overline{T'^2} \qquad (12)$$

To proceed further with the analysis of C_N^2, having only mean profile data from many air masses, requires additional assumptions. One method of deriving the relationship between the perturbation quantities and the mean profile is to adopt the mixing length concept. A more rigorous approach would be through the relationship of the vertical flux of temperature, moisture, and momentum to the eddy diffusion coefficients and profile gradients. However, both derivations lead to the same result and

TABLE 4.   Superior air-winter.

Ht(m)	a	b	c	a^2	b^2	c^2	$2ab$	$2ac$	$2bc$
Oklahoma City									
0	1.06	4.76	0.28	1.12	22.7	0.08	10.1	0.59	2.64
500	0.99	4.66	0.27	0.97	21.7	0.07	9.20	0.54	2.56
1000	0.92	4.59	0.27	0.85	21.1	0.07	8.45	0.50	2.50
1500	0.86	4.61	0.27	0.73	21.3	0.07	7.91	0.47	2.52
2000	0.80	4.73	0.28	0.64	22.4	0.08	7.56	0.44	2.61
2500	0.75	4.86	0.28	0.57	23.6	0.08	7.31	0.42	2.72
3000	0.69	4.89	0.28	0.48	24.0	0.08	6.77	0.39	2.75
4000	0.63	5.25	0.29	0.39	27.6	0.08	6.59	0.36	3.06
5000	0.56	5.54	0.30	0.32	30.7	0.09	6.26	0.34	3.32
Pensacola									
0	—	—	—	—	—	—	—	—	—
500	1.15	4.51	0.27	1.33	20.3	0.07	10.4	0.62	2.43
1000	1.06	4.71	0.27	1.12	21.7	0.07	9.8	0.58	2.55
1500	0.95	4.74	0.28	0.91	22.5	0.08	9.06	0.53	2.63
2000	0.89	4.79	0.28	0.79	23.0	0.08	8.53	0.49	2.67
2500	0.83	4.86	0.28	0.70	23.6	0.08	8.16	0.47	2.72
3000	0.79	4.96	0.28	0.63	24.6	0.08	7.85	0.45	2.81
4000	0.71	5.15	0.29	0.50	26.6	0.08	7.29	0.41	2.97
5000	0.63	5.40	0.29	0.40	29.2	0.08	6.83	0.37	3.19

TABLE 5.   Continental polar-summer.

Ht(m)	a	b	c	a^2	b^2	c^2	2ab	2ac	2bc
					Omaha				
0	1.22	4.42	0.27	1.48	19.5	0.07	10.8	0.65	2.36
500	1.25	4.35	0.27	1.57	18.9	0.07	10.9	0.66	2.31
1000	1.14	4.42	0.27	1.29	19.5	0.07	10.0	0.61	2.36
1500	1.06	4.51	0.27	1.11	20.3	0.07	9.53	0.57	2.43
2000	0.98	4.59	0.27	0.96	21.1	0.07	9.04	0.54	2.50
2500	0.91	4.67	0.27	0.83	21.8	0.07	8.52	0.50	2.57
3000	0.89	4.70	0.28	0.79	22.1	0.08	8.34	0.49	2.59
4000	—	—	—	—	—	—	—	—	—
5000	—	—	—	—	—	—	—	—	—

the mixing length approach contains more intuitive insight and requires less background in turbulence theory. It assumes that

$$e'_p, \theta' = L \, d(\overline{e_p}, \bar{\theta})/dz$$

where L is a mechanical mixing length, analogous to the molecular mean free path in Brownian diffusion, and e_p and θ are the potential vapor pressure and potential temperature, respectively. They are the values of e and T that a parcel of air would have if it were taken adiabatically to some reference pressure without change of state. The reference pressure is usually 1000 mb, so $\theta = T(1000/p)^{0.286}$ and $e_p \simeq e(1000/p)$. To illustrate, suppose the line segment in Figure 6 represents a portion of the

height profile of potential temperature. If an air parcel, A, with potential temperature $\bar{\theta}_2$ is mixed downward a distance L, it will cause a perturbation of θ at that level equal to $L \, d\bar{\theta}/dz$. In like manner, if an air parcel, B, with potential temperature $\bar{\theta}_1$ is mixed upward it will cause a similar perturbation in θ at its new level. The same arguments apply to e_p; so, if the same mechanical mixing length applies to θ and e_p,

$$\left(\frac{1000}{\bar{p}}\right)^{1.43} \frac{\overline{e'^2}}{\overline{T'^2}} = \frac{\overline{e'^2_p}}{\overline{\theta'^2}} = \frac{(d\bar{e}_p/dz)^2}{(d\bar{\theta}/dz)^2} \simeq \frac{\Delta \bar{e}^2_p}{\Delta \bar{\theta}^2} \quad (13)$$

and

TABLE 6.   Maritime polar-summer.

Ht(m)	a	b	c	a^2	b^2	c^2	2ab	2ac	2bc
					Spokane				
0	1.18	4.48	0.27	1.40	20.0	0.07	10.6	0.63	2.41
500	—	—	—	—	—	—	—	—	—
1000	1.05	4.35	0.27	1.09	18.9	0.07	9.11	0.55	2.31
1500	0.94	4.35	0.27	0.89	18.9	0.07	8.22	0.50	2.31
2000	0.88	4.54	0.27	0.78	20.7	0.07	8.03	0.48	2.46
2500	0.83	4.68	0.28	0.69	21.9	0.08	7.80	0.46	2.57
3000	0.78	4.79	0.28	0.60	22.9	0.08	7.44	0.43	2.67
4000	0.68	5.15	0.29	0.46	26.5	0.08	7.04	0.39	2.97
5000	0.58	5.29	0.29	0.34	28.0	0.08	6.14	0.34	3.09
					Omaha				
0	1.32	4.26	0.26	1.74	18.0	0.07	11.2	0.69	2.22
500	1.19	4.23	0.26	1.41	17.9	0.07	10.1	0.62	2.21
1000	0.98	4.26	0.26	0.96	18.1	0.07	8.38	0.52	2.23
1500	0.87	4.41	0.27	0.76	19.5	0.07	7.72	0.46	2.36
2000	0.80	4.52	0.27	0.64	20.4	0.07	7.25	0.43	2.44
2500	0.83	4.72	0.28	0.68	22.3	0.08	7.81	0.46	2.61
3000	0.77	4.84	0.28	0.58	23.4	0.08	7.41	0.43	2.70
4000	0.67	5.05	0.29	0.44	25.5	0.08	6.74	0.38	2.88
5000	0.58	5.29	0.29	0.33	28.0	0.08	6.12	0.34	3.09

TABLE 7.   Maritime tropical-summer.

Ht(m)	a	b	c	a^2	b^2	c^2	$2ab$	$2ac$	$2bc$
					Pensacola				
0	1.65	4.23	0.26	2.70	17.9	0.07	13.9	0.86	2.21
500	1.50	4.22	0.26	2.24	17.8	0.07	12.6	0.78	2.20
1000	1.35	4.30	0.26	1.82	18.5	0.07	11.6	0.71	2.27
1500	1.24	4.40	0.27	1.54	19.4	0.07	10.9	0.66	2.35
2000	1.13	4.49	0.27	1.28	20.2	0.07	10.2	0.61	2.42
2500	1.04	4.58	0.27	1.08	20.9	0.07	9.52	0.56	2.49
3000	0.94	4.67	0.27	0.88	21.8	0.07	8.79	0.52	2.56
4000	0.82	4.88	0.28	0.66	23.8	0.08	7.97	0.46	2.74
5000	0.69	5.09	0.29	0.48	25.9	0.08	7.07	0.40	2.92
					Omaha				
0	1.31	4.21	0.26	1.71	17.7	0.07	11.0	0.68	2.20
500	1.22	4.15	0.26	1.48	17.3	0.07	10.1	0.63	2.15
1000	1.10	4.13	0.26	1.20	17.1	0.07	9.06	0.56	2.13
1500	1.00	4.21	0.26	1.01	17.7	0.07	8.46	0.52	2.19
2000	0.93	4.33	0.26	0.87	18.7	0.07	8.07	0.49	2.28
2500	0.87	4.45	0.26	0.76	19.8	0.07	7.78	0.47	2.39
3000	0.81	4.56	0.27	0.66	20.8	0.07	7.41	0.44	2.47
4000	0.69	4.80	0.28	0.48	23.0	0.08	6.66	0.38	2.67
5000	0.61	5.09	0.29	0.37	25.9	0.08	6.18	0.35	2.92

$$\left(\frac{1000}{\bar{p}}\right)^{0.714}\frac{\overline{e'\,T'}}{\overline{T'^2}} = \frac{\overline{e_p'\,\theta'}}{\overline{\theta'^2}} \approx \rho\,\frac{\Delta \bar{e}_p}{\Delta \bar{\theta}} \qquad (14)$$

where ρ is the correlation coefficient of e_p and θ. In the examples shown in Figures 7 through 10, it was assumed that $\rho = 0.5$. From mean profile data in various air masses, the terms on the right-hand side of (12) can be estimated and thus an estimate of C_N^2/C_T^2 can be obtained.

If the quantities θ and e_p are used in (4) instead of T and e, the potential refractive index ϕ is obtained. The quantity C_N^2/C_T^2 could then have been found directly from the ratio $(d\bar{\phi}/dz)^2/(d\bar{\theta}/dz).^2$ However, the above derivation reveals
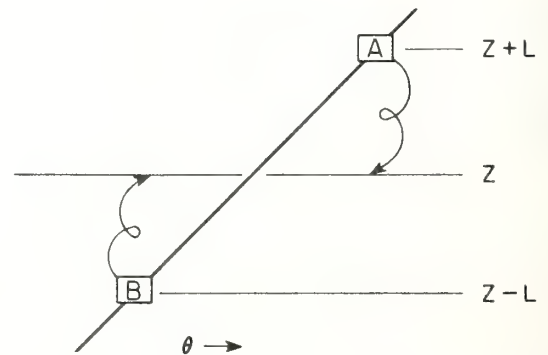
Fig. 6. Schematic illustration of turbulent mixing of air parcels.

TABLE 8.   Superior air-summer.

Ht(m)	a	b	c	a^2	b^2	c^2	$2ab$	$2ac$	$2bc$
					Omaha				
0	1.17	4.12	0.26	1.39	16.9	0.07	9.67	0.61	2.12
500	1.12	4.02	0.26	1.25	16.2	0.07	9.01	0.57	2.05
1000	1.00	4.06	0.26	1.00	16.3	0.07	8.13	0.51	2.08
1500	0.92	4.18	0.26	0.85	17.5	0.07	7.73	0.48	2.17
2000	0.82	4.29	0.26	0.67	18.5	0.07	7.04	0.43	2.26
2500	0.76	4.40	0.27	0.58	19.4	0.07	6.72	0.41	2.34
3000	0.72	4.54	0.27	0.52	20.7	0.07	6.53	0.39	2.46
4000	—	4.80	0.28	—	23.0	0.08	—	—	2.67
5000	0.54	5.08	0.29	0.30	25.8	0.08	—	—	2.90
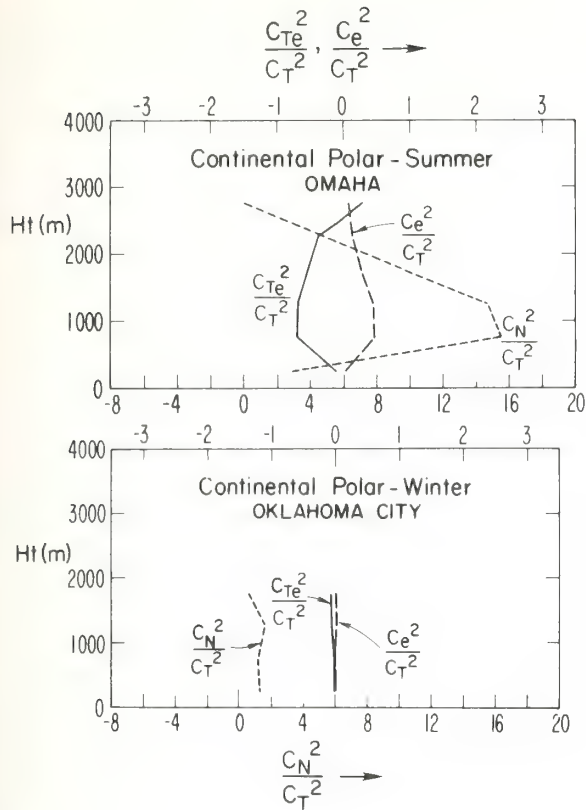
Fig. 7. Ratios of the structure constant of refractive index and humidity to the structure constant of temperature for various North American air masses at the season and location indicated.

the way it depends on the meteorological makeup of the air mass and therefore contains more information useful in judging how air mass modification is likely to change the refractive index structure.

With additional assumptions C_N^2 can be estimated, rather than just its relation to C_T^2. For convenience the following discussion will use C_ϕ^2 instead of C_N^2. Potential refractive index can be considered to diffuse like a passive property, so

$$C_\phi^2 = a \, \epsilon^{-1/3} \, \epsilon_\phi \qquad (15)$$

within the inertial subrange of turbulence [*Corrsin*, 1951]. Here ϵ is the turbulent kinetic energy dissipation rate and ϵ_ϕ is the rate of destruction of variance of the fluctuations in ϕ (actually $1/2$ variance).

For a fairly wide range of atmospheric conditions, the rate of dissipation of variance is approximately balanced by the rate of variance generation by

mixing in the mean gradient of the quantity (in this case ϕ). Then

$$\epsilon_\phi \simeq - \overline{\phi' \, w'} \, \partial \bar{\phi}/\partial z \qquad (16)$$

where w' is the perturbation of vertical velocity. This statement ignores some terms representing vertical divergence of flux, but such divergence is usually associated with modification processes such as those due to spatial transitions at the lower boundary or diurnal fluctuations. However, in this paper it is suggested that the various types of modification that air masses undergo be treated as deviations from the "typical" structure above the planetary boundary layer.
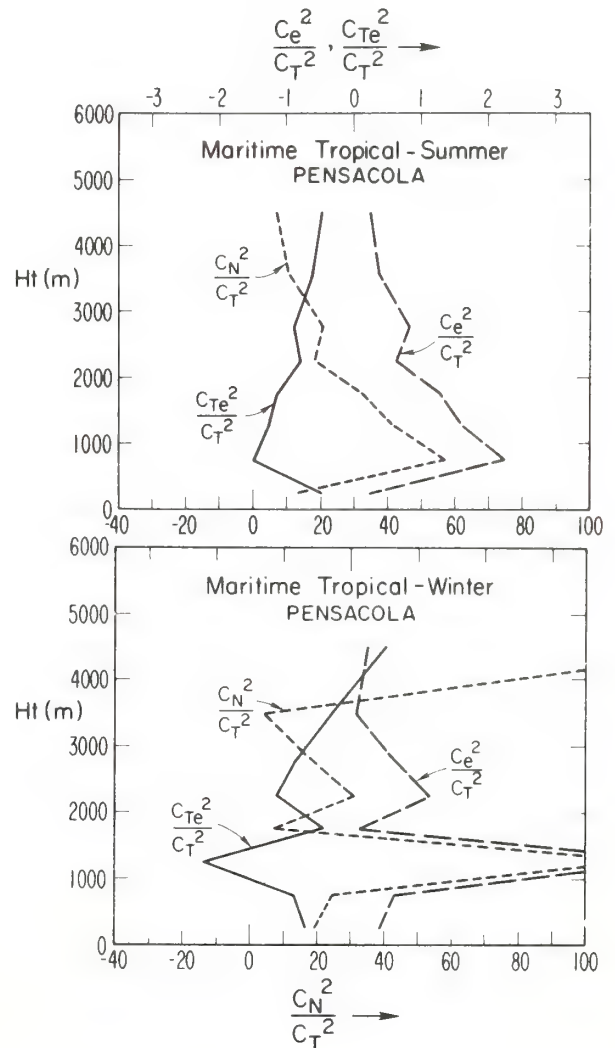
Fig. 8. See caption for Figure 7.

Noting that $\overline{\phi'w'}$ is the vertical flux of ϕ, the eddy diffusion coefficient is defined by

$$-\overline{\phi'w'} = K_\phi\, \partial\bar\phi/\partial z \qquad (17)$$

Inserting (16) and (17) into (15),

$$C_\phi^2 = a\,\epsilon^{-1/3} K_\phi (\partial\bar\phi/\partial z)^2 \qquad (18)$$

Most experiments find the diffusion coefficients of passive quantities such as ϕ to be similar to that for momentum so that $K_\phi \simeq K$, where K is the mechanical eddy viscosity. Therefore the factor $\epsilon^{-1/3} K$, which multiplies $(\partial\bar\phi/\partial z)^2$, represents the effect of mechanical turbulence. Note that ϵ appears to a very small power while $\partial\bar\phi/\partial z$ is squared.
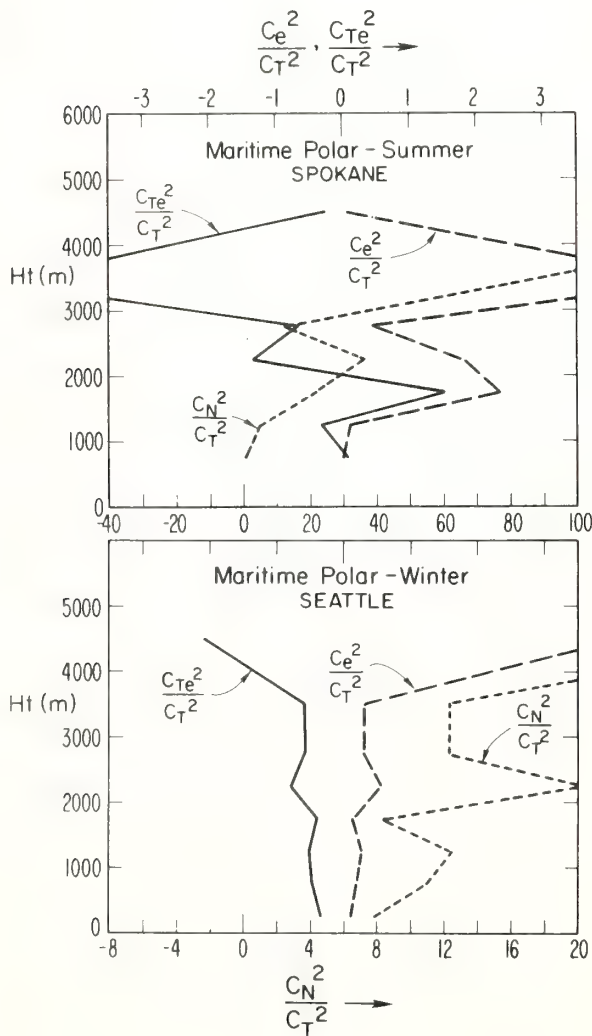
Fig. 9. See caption for Figure 7.
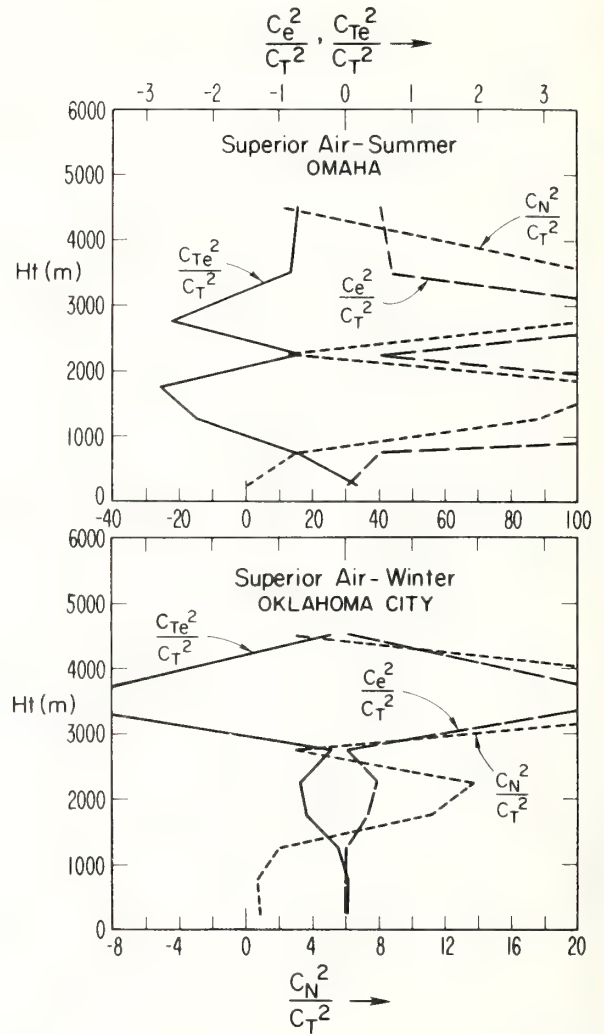
Fig. 10. See caption for Figure 7.

Furthermore, there seems to be little reason to expect $\epsilon^{-1/3} K$ to be *systematically* related to height, to height gradient of ϕ, or to air mass, except in frontal zones between air masses and in the planetary boundary layer where air mass modification processes are at work; there the $\epsilon^{-1/3} K$ factor may be closely related to $\partial\phi/\partial z$ as when an air mass moves over a warmer or colder surface producing intense or weak mechanical mixing in the lower layers. However, we have chosen to treat such modification as anomalies producing deviations about the "typical" air mass. Such modification of atmospheric boundary layers can be treated more or less independently using available analytical and numerical techniques.

If $\epsilon^{-1/3} K$ varies little, or if it is not systematically related to height, height gradient of ϕ, or to air mass, the distribution of C_ϕ^2 (or C_N^2) in the various air masses can be determined except for a common, unknown factor. A model proposed by Hufnagel for optical C_n^2 is then used to estimate the unknown factor.

DISCUSSION

Figures 7 through 10 show the height distribution of the ratios C_e^2/C_T^2, $C_{T_e}^2/C_T^2$ and C_N^2/C_T^2 for a variety of air masses and locations. These quantities are calculated from (12), (13), and (14). The assumption on which these plots are based is relatively defensible, requiring only that the quantities e_p, θ, and ϕ be mixed by turbulence in the same way; it is generally assumed that the eddy coefficients of the various conserved quantities are approximately the same. Because we deal with ratios, we need assume nothing about the intensity of mechanical turbulence.

One incentive for these plots is the belief that more measurements exist for C_T^2 (or the C_n^2 for optical refractive index) than exist for the C_N^2 of radio refractive index. Therefore, these plots permit one to make use of measurements made for optical systems to infer the scattering and scintillation characteristics of the atmosphere for radio waves. They also reveal the relative roles played by tem-

Fig. 12. Distribution of optical refractive index structure constant in maritime air masses at the locations shown. The winter and summer seasons are indicated by the small s and w following the air mass type. C_n^2 is in m$^{-2/3}$. Hufnagel model included for comparison.

perature, moisture, and their correlation within the various air masses.

Figures 11, 12, and 13 show the distribution of C_n^2 with height in various air masses, where C_n^2 is the structure constant for optical wavelengths. To make these calculations from mean temperature profile information, it was necessary to assume that the temperature variance caused by vertical mixing was proportional to the square of the height gradient of potential temperature. The validity of this as-

Fig. 11. Distribution of optical refractive index structure constant in continental air masses at the locations shown. The winter and summer seasons are indicated by the small s and w following the air mass type. C_n^2 is in m$^{-2/3}$.
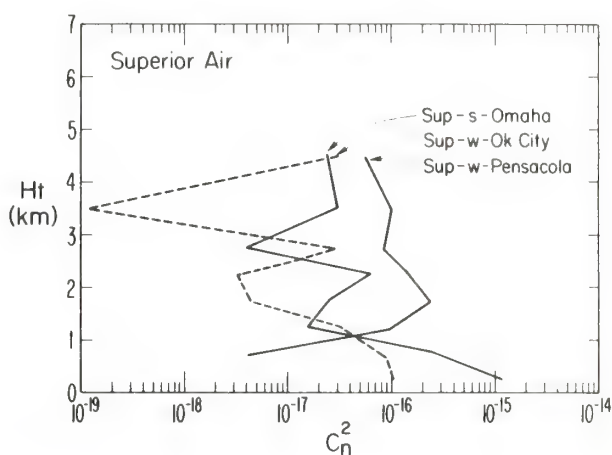
Fig. 13. Distribution of optical refractive index structure constant in superior air masses at the locations shown. The winter and summer seasons are indicated by the small s and w following the air mass type. C_n^2 is in m$^{-2/3}$.

sumption requires that $\epsilon^{-1/3}$ K bear no systematic relationship to air mass type or height within the air mass. After calculating profiles of $(\Delta\theta/\Delta z)^2$ for the various air masses, the plots were "calibrated" in terms of C_n^2 by assuming the Hufnagel model to represent a median profile for the various air masses. Hufnagel's model is shown superimposed on Figure 12. It is evident that the scatter of the air mass profiles about the Hufnagel profile is very large. However, measured profiles deduced from optical scintillation of stars show great scatter also, as seen in Figure 13, from *Ochs et al.* [1976]. In the calculated profiles C_n^2 occasionally drops to very low values. This occurs in height regions where the temperature gradient is very nearly the adiabatic lapse rate. There is some evidence of such deep troughs in the data of Ochs *et al.* even though the measurement technique had poor height resolution and must have smoothed the true profiles appreciably. These data were acquired in just one location (Boulder, Colorado) on only a few days.

Profiles of the radio refractive index structure constant, C_N, can be calculated from the relation $C_N^2 = [(\partial\bar{\phi}/\partial z)/(\partial\bar{\theta}/\partial z)]^2 \, C_n^2$ with no additional assumptions. These profiles are shown in Figures 14, 15, 16, and 17 and are labeled C_N^2 to distinguish them from the optical refractive index structure constant labeled C_n^2; however, C_N^2 has not had the factor 10^{-6} removed from the refractive index as has N in (2) and so differs from the structure constant of N by the factor 10^{-12}. There are several points worth noting:

(a) The value of radio C_N^2 is not always larger

Fig. 15. The height distribution of radio refractive index structure constant in some continental air masses at the locations indicated. The winter and summer seasons are indicated by w or s following the air mass type. The N subscript designates radio refractive index as opposed to optical refractive index. However, the factor $(10^{-6})^2$ is included in this structure constant in contrast to the definition of N given above (2). C_N^2 is in $m^{-2/3}$.

than the optical C_n^2. Note, for example, the topmost value in winter cP air at Oklahoma City (see Figures 11 and 15). This occurs when temperature and moisture fluctuations are positively correlated.
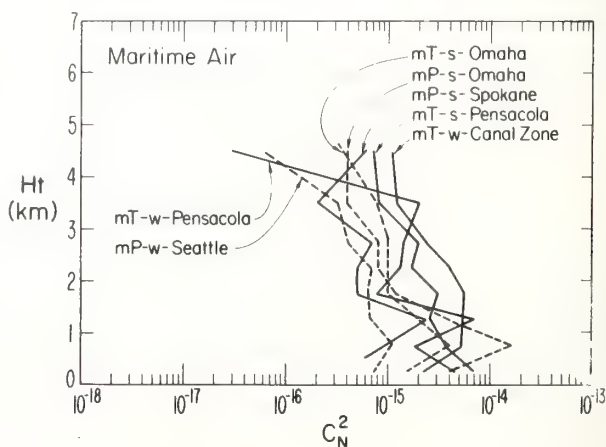
Fig. 16. The height distribution of radio refractive index structure constant in some maritime air masses at the locations indicated. The winter and summer seasons are indicated by w or s following the air mass type. The N subscript designates radio refractive index as opposed to optical refractive index. However, the factor $(10^{-6})^2$ is included in this structure constant in contrast to the definition of N given above (2). C_N^2 is in $m^{-2/3}$.

Fig. 14. Measured distribution of optical refractive index structure constant compared with Hufnagel model indicated by dashed curve [from *Ochs et al.*, 1976].
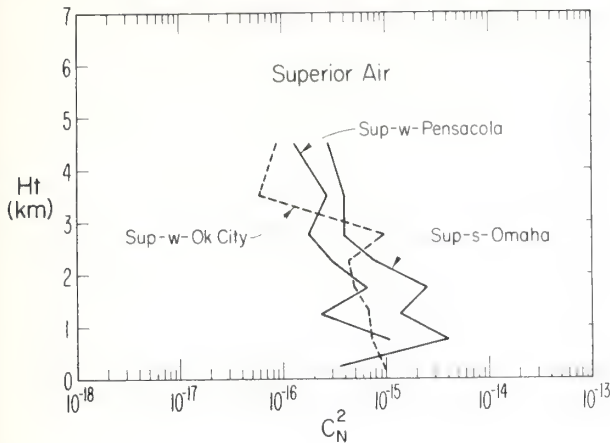
Fig. 17. The height distribution of radio refractive index structure constant in some superior air masses at the locations indicated. The winter and summer seasons are indicated by w and s following the air mass type. The N subscript designates radio refractive index as opposed to optical refractive index. However, the factor 10^{-12} is included in this structure constant in contrast to the definition of N given above (2). C_N^2 is in $m^{-2/3}$.

Then the last term in (12) can potentially subtract more from C_N^2 than is contributed by the moisture (middle term). This occurs when moisture increases with height, because potential temperature must always increase with height (except in rare super-adiabatic layers) in order that the atmosphere be statically stable.
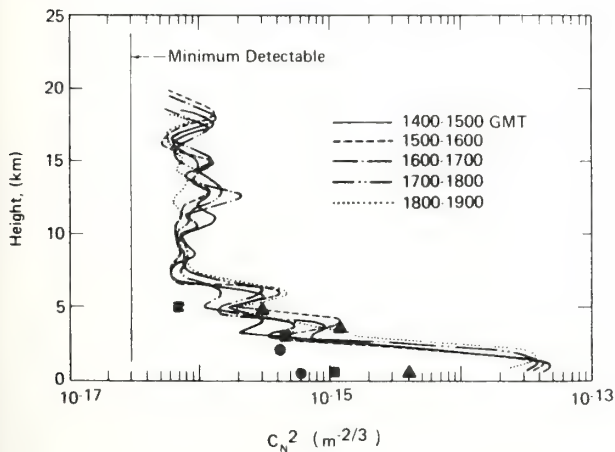
Fig. 18. Measured height distribution of radio refractive index structure constant recorded with the Millstone Hill radar described by Crane [1970] at the times indicated in December. The circles, squares, and triangles are calculated values for winter cP, winter mP, and winter mT air masses.
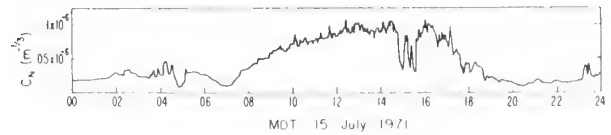
Fig. 19. Diurnal distribution of C_n measured at a height of 2 m above the ground [from Clifford et al., 1974].

(b) The scatter of C_N^2 is less than that of C_n^2. This is because the temperature lapse rate approaches the adiabatic more often than the gradient of potential refractive index approaches zero since nearly zero gradients of both humidity and potential temperature are usually required in the latter case. Thus C_n^2 reaches very low values more often than C_N^2.

(c) There is a dramatic decrease in C_N^2 above 2 km altitude in continental air masses, but in maritime air masses C_N^2 does not decrease with height any more rapidly than C_n^2 up to a height of 5 km.

The calculated values of C_N^2 agree fairly well with the limited observational data available. For example, Figure 18 shows profiles of C_N^2 reported by R. K. Crane (personal communication, 1975). These data were collected by the large, powerful Millstone Hill L-band radar in December 1967. A, that time of year one of three air masses might well have been in the area. Consequently, points representative of winter cP (circles), winter mP (squares), and winter mT (triangles) air masses were superimposed on Crane's data. The agreement is generally satisfactory except for the surface values. This discrepancy probably represents a diurnal effect, as Crane's observations were made near midday when surface heating and turbulent convection were probably occurring. Figure 19 taken from Clifford et al. [1974], shows the diurnal variation of C_n measured at a height of 2 m. Apparently more than an order-of-magnitude enhancement in C_n^2 is to be expected around midday. Such an enhancement would bring our calculated values into good agreement with Crane's observations.

REFERENCES

Atlas, D., J. I. Metcalf, J. H. Richter, and E. E. Gossard (1970), The birth of "CAT" and microscale turbulence, J. Atmos. Sci., 27, 903–913.

Bean, B. R., and E. J. Dutton (1966), Radio Meteorology, Nat.

Bur. Stand. Monogr. 92, 423 pp., US Government Printing Office, Washington, DC

Booker, H. G., and W. E. Gordon (1950), A theory of radio scattering in the troposphere, *Proc. IRE, 38*, 401–412.

Browning, K. A. (1972), Atmospheric research using the Defford radar facility, *Weather, 27*, 2–8.

Byers, H. R. (1944), *General Meteorology*, 645 pp., McGraw-Hill, New York.

Chadwick, R. B., K. P. Moran, R. G. Strauch, G. E. Morrison, and W. C. Campbell (1976), Microwave radar wind measurements in the clear air, *Radio Sci., 11*, 795–802.

Chromov, S. P. (1937), *An Introduction to Synoptic Analysis*, 2nd Ed., Hydrometeorological Office, Moscow, USSR.

Clifford, S. F., G. R. Ochs, and R. S. Lawrence (1974), Saturation of optical scintillation by strong turbulence, *J. Opt. Soc. Amer., 64*, 148–154.

Corrsin, S. (1951), On the spectrum of isotropic temperature fluctuations in isotropic turbulence, *J. Appl. Phys., 22*, 417–423.

Crane, R. K. (1970), Measurement of clear air turbulence in the lower stratosphere using the Millstone Hill *L*-band radar, paper presented at the 14th Weather Radar Conference, American Meteorological Society, Boston, Mass.

Gossard, E. E. (1960), Power spectra of temperature, humidity, and refractive index from aircraft and tethered balloon measurements, *IRE Trans. Antennas Propagat., AP-8*, 186–201.

Gossard, E. E., J. H. Richter, and D. Atlas (1970), Internal waves in the atmosphere from high-resolution radar measurements, *J. Geophys. Res., 75*, 3523–3536.

Green, J. L., J. M. Warnock, R. H. Winkler, and T. E. VanZandt (1975), Studies of winds in the upper troposphere with a sensitive VHF radar, *Geophys. Res. Lett., 2*, 19–21.

Hardy, K. A. (1972), Studies of the clear atmosphere using high power radar, ch. 14, *Remote Sensing of the Troposphere*, edited by V. E. Derr, US Government Printing Office, Washington, DC.

Hufnagel, R. E. (1974), *Variations of Atmospheric Turbulence*, paper presented at Optical Society of America Topical Meeting on Optical Propagation through Turbulence.

Kerr, D. E. (Ed.) (1951), *Propagation of Short Radio Waves*, 706 pp., Dover, New York.

Ochs, G. R., T. Wang, R. S. Lawrence, and S. F. Clifford (1976), Refractive turbulence profiles measured by spatial filtering of scintillations, *J. Appl. Opt.*, in press.

Ottersten, H. (1969), Atmospheric structure and radar backscattering in clear air, *Radio Sci., 4*, 1179–1193.

Plank, V. G. (1952), Refractive properties of air masses, *Rep. No. 243*, 28 pp., US Naval Electronics Laboratory, San Diego, Calif.

Richter, J. H. (1969), High resolution tropospheric radar sounder, *Radio Sci., 4*, 1261–1268.

Showalter, A. K. (1939), Further studies of American air mass properties, *Mon. Weather Rev., 67*, 204–218.

Strauch, R. G., W. C. Campbell, R. B. Chadwick, and K. P. Moran (1976), Microwave FM-CW Doppler radar for boundary layer probing, *Geophys. Res. Lett., 3*, 193–196.

REFRACTIVE INDEX SPECTRAL STRUCTURE
IN THE ATMOSPHERIC BOUNDARY LAYER

J. C. Wyngaard
NOAA/CIRES, Boulder, Colo. 80302

1. Introduction

One frequently needs only the spatial spectrum of refractive index fluctuations in order to calculate the effects of turbulence on optical propagation. We will briefly discuss here the behavior of this spectrum at inertial range and smaller scales. We use one-dimensional spectra, since they are the type usually measured. The relation between the full refractive index spectrum Φ_n and the 1-D form F_n is

$$\int\int_{-\infty}^{\infty} \Phi_n(\underline{\kappa}) \, d\kappa_2 \, d\kappa_3 = F_n(\kappa_1) \tag{1}$$

2. Inertial Range

Inertial range structure is usually assumed to be isotropic, so the structure function of refractive index fluctuations n depends on $r = |\underline{r}|$:

$$\overline{[n(\underline{x}) - n(\underline{x} + \underline{r})]^2} = c_n^2 \, r^{2/3} \tag{2}$$

with c_n^2 the refractive index structure parameter. The 1-D spectrum is

$$F_n = 0.25 \, c_n^2 \, \kappa_1^{-5/3} \tag{3}$$

under the convention

$$\overline{n^2} = \int_0^{\infty} F_n(\kappa_1) \, d\kappa_1 \tag{4}$$

For optical wavelengths in the atmospheric boundary layer (ABL) the principal contributors to n are temperature and humidity fluctuations. We have

$$n = C(\theta + aq) \tag{5}$$

where θ and q are fluctuations in temperature and absolute humidity; a is a factor depending on, among other things, the wavelength of the radiation; and the conversion constant C we will ignore hereafter. From (5) the spectra are related by

$$F_n = F_T + 2a \, Co_{Tq} + a^2 \, F_q \tag{6}$$

where Co_{Tq} is the temperature-humidity cospectrum [Friehe et al., 1975]:

$$\overline{\theta q} = \int_0^{\infty} Co_{Tq}(\kappa_1) \, d\kappa_1 \tag{7}$$

It is well-known that F_T and F_q have $\kappa_1^{-5/3}$ inertial ranges; Wyngaard *et al.* [1977] have shown that Co_{Tq} does as well, so

$$Co_{Tq} = 0.25 \ C_{Tq} \ \kappa_1^{-5/3}$$

$$F_T = 0.25 \ C_T^2 \ \kappa_1^{-5/3} \tag{8}$$

$$F_q = 0.25 \ C_q^2 \ \kappa_1^{-5/3}$$

The joint temperature-humidity structure parameter C_{Tq} is not written as a squared quantity because it can be either positive or negative.

A starting point for describing the behavior of the structure parameters, and hence the inertial range refractive index spectrum, is the set of relations between structure parameters and other turbulence properties:

$$C_T^2 = 4\beta_1 \ \varepsilon^{-1/3} \ \varepsilon_\theta$$

$$\tag{9}$$

$$C_q^2 = 4\beta_1 \ \varepsilon^{-1/3} \ \varepsilon_q$$

Here β_1 is the one-dimensional inertial range scalar spectral constant, which currently is believed to be in the range 0.4-0.5 [Champagne *et al.*, 1977]; ε is the dissipation rate of turbulent kinetic energy, and ε_θ and ε_q are the dissipation rates of $\overline{\theta^2}$ and $\overline{q^2}$. Wyngaard *et al.* [1977] show that

$$C_{Tq} = 4\gamma_1 \ \varepsilon^{-1/3} \ \varepsilon_{\theta q} \tag{10}$$

and find $\gamma_1 \simeq \beta_1$; here $\varepsilon_{\theta q}$ is the destruction rate of $\overline{\theta q}$. They discuss the behavior of $\varepsilon_{\theta q}$ in the convective ABL.

Thus the budgets of $\overline{\theta^2}$, $\overline{q^2}$, $\overline{\theta q}$, and turbulent kinetic energy contain the information necessary for describing the behavior of C_T^2, C_q^2, and C_{Tq}. Recent data on C_T^2 are presented by Kaimal *et al.* [1976]. Data on C_q^2 remain relatively scarce.

3. Spectral Bumps

Recent fine-resolution temperature spectral data show a distinct "bump" at the small-scale end of the inertial range. The bump seems real, and has been reproduced by different workers with different equipment [*e.g.*, Williams, 1974; Champagne *et al.*, 1977].

Hill [1977] has developed a model of the scalar transfer spectrum in a turbulent fluid of arbitrary Prandtl number Pr (the ratio of molecular diffusivities for momentum and temperature). He finds that for air (Pr = 0.72) a bump appears in the spectrum, in agreement with data. This bump can be broad (typically one decade in the 1-D spectrum in the ABL) and rises about 30% above an extension of the $\kappa_1^{-5/3}$ line. Since the molecular diffusivities for water vapor and temperature are nearly the same, we expect a similar bump in the humidity spectrum, the temperature-humidity cospectrum and the refractive index spectrum. Some of the first calculations of the effect of this bump on optical propagation are presented by Hill and Clifford [1977].

4. Local Isotropy and Spectral Tails

The hypothesis of "local isotropy"--that the fine structure in a turbulent flow is statistically isotropic--is one of the cornerstones of turbulence theory. Recent measurements of scalar derivative statistics [see Mestayer *et al.*, 1976, for a summary] show *anisotropic* scalar fine structure and no indication of an approach to isotropy with increasing Reynolds number. Recent data from LaRue [personal communication] show that this anisotropy exists at the highest measureable wavenumbers. This area of research is severely hampered by experimental difficulties, and critical measurements are often not possible with present techniques. One obviously important but unanswered question is the extent to which level surfaces of the 3-D temperature spectrum at large κ depart from the sphericity implied by local isotropy.

A less important but easier-to-answer question involves the shape of the "tail" on the scalar spectrum at very large κ . Propagation calculations often use the Gaussian tail, with the spherically-averaged spectrum E falling as

$$E \sim \kappa^{-5/3} \exp(-\kappa^2/\kappa_m^2) \tag{11}$$

Turbulence workers, on the other hand, often use the Corrsin-Pao form [Pao, 1965]

$$E \sim \kappa^{-5/3} \exp(-\kappa^{4/3}/\kappa_p^{4/3}) \tag{12}$$

These models are now being tested against recent 1-D spectral measurements. The conversion between the measured frequency spectrum and the streamwise

wavenumber spectrum at these large wavenumbers has been found to be not as simple as $\kappa_1 = 2\pi f/U$ [Taylor's hypothesis]; it is necessary to correct for the spectral content aliased by the convection velocity fluctuations [Wyngaard and Clifford, 1977].

Optical techniques for determining the extent to which scalar fine structure is locally isotropic, or for measuring the shape of the spectral tail, would be very valuable.

References

Champagne, F. H., C. A. Friehe, J. C. LaRue and J. C. Wyngaard, 1977: Flux measurements, flux estimation techniques, and fine-scale turbulence measurements in the unstable surface layer over land. *J. Atmos. Sci.*, *34*, 515-530.

Friehe, C. A., J. C. LaRue, F. H. Champagne, C. H. Gibson, and C. F. Dreyer, 1975: Effects of temperature and humidity fluctuations on the optical refractive index in the marine boundary layer. *J. Opt. Soc. Am.*, *65*, 1502-1511.

Hill, R. J., 1977: Models of the scalar spectrum for turbulent advection (in preparation).

Hill, R. J., and S. F. Clifford, 1977: The bump in the variance of log-intensity (this volume).

Kaimal, J. C., J. C. Wyngaard, D. A. Haugen, O. R. Coté, Y. Izumi, S. J. Caughey, and C. J. Readings, 1976: Turbulence structure in the convective boundary layer. *J. Atmos. Sci.*, *33*, 2152-2169.

Mestayer, P. G., C. H. Gibson, M. F. Coantic, and A. S. Patel, 1976: Local anisotropy in heated and cooled turbulent boundary layers. *Phys. Fluids*, *19*, 1279-1287.

Pao, Y. H., 1965: Structure of turbulent velocity and scalar fields at large wavenumbers. *Phys. Fluids*, *8*, 1063-1075.

Williams, R. M. Jr., 1974: High frequency temperature and velocity fluctuations in the atmospheric boundary layer. Ph.D. thesis, Oregon State Univ., 81 pp.

Wyngaard, J. C., and S. F. Clifford, 1977: Taylor's hypothesis and high-frequency turbulence spectra. To appear, *J. Atmos. Sci.*

Wyngaard, J. C., W. T. Pennell, D. H. Lenschow, and M. A. LeMone, 1977: The temperature-humidity covariance budget in the convective boundary layer. Submitted to *J. Atmos. Sci.*

Log-normality of the vorticity at a fluid particle

R. J. Hill

Wave Propagation Laboratory, Environmental Research Laboratories, National Oceanic and Atmospheric Administration, Boulder, Colorado 80302
(Received 5 April 1977; final manuscript received 9 August 1977)

It is shown that the magnitude of the vorticity, at a given fluid particle in inviscid turbulent flow, is a log-normal random function of time.

Obukhov[1] introduced the assumption that the energy dissipation rate, when averaged over a volume of dimension much smaller than an outer scale but much larger than the microscale, is a log-normal random variable. Chen[2] has shown that the log-normal distribution cannot follow if the averaging is over a volume of dimension comparable to the dissipative scales. The analysis presented here is distinct from that of Obukhov in that (1) no averaging over spatial domains is introduced in the present analysis, and (2) the log-normality of the magnitude of the vorticity at a fluid particle is shown to follow from the vorticity equation.

The method of proof used here is similar to that used by Hill and Bowhill[3] who show that the magnitude of the gradient at a fluid particle, of a turbulently advected scalar is a log-normal random function of time. The present analysis does not apply to the magnitude of the vorticity at a fixed point in space nor to the case of non-zero viscosity because of the presence of spatial derivatives of the vorticity in the vorticity equation for those cases.

We now turn to the proof of the log-normality of the magnitude of the vorticity at a fluid particle within inviscid turbulent flow. We denote time by t and the position vector by $\mathbf{x}$; the jth component of $\mathbf{x}$ is denoted by x_j. For inviscid flow the equation for the vorticity, in an inertial reference frame, is

$$(\partial \omega_i / \partial t)_{\mathbf{x}} + V_j (\partial \omega_i / \partial x_j)_t = \omega_j S_{ij},$$

where ω_i is a component of the vorticity vector, S_{ij} is the rate-of-strain tensor, V_j is a component of the velocity field, and the subscripts t and $\mathbf{x}$ on the derivatives denote the variables held fixed. The position of the fluid particle that was at $\mathbf{x}_0$ at $t = 0$ is denoted by $\mathbf{X}(\mathbf{x}_0, t)$. Then, the position of a point relative to the fluid particle is denoted by $\boldsymbol{\xi}$, where

$$\boldsymbol{\xi} = \mathbf{x} - \mathbf{X}(\mathbf{x}_0, t).$$

We transform to a moving coordinate system which has its origin at the fluid particle and which has its axes always parallel to the axes of the inertial Eulerian coordinate system. Then, the velocity of the fluid relative to this moving coordinate system is

$$U_i(\boldsymbol{\xi}, t) = V_i(\mathbf{x}, t) - V_i(\mathbf{X}, t).$$

The vorticity vector and rate-of-strain tensor are unchanged by this coordinate transformation since

$$(\partial U_i / \partial \xi_j)_t = (\partial V_i / \partial x_j)_t$$

where both sides of the equation are evaluated at the same point. In this coordinate system the vorticity equation becomes

$$(\partial \omega_i / \partial t)_{\boldsymbol{\xi}} + U_j (\partial \omega_i / \partial \xi_j)_t = \omega_j S_{ij}.$$

We now define a rotating coordinate system, called the primed coordinate system, which has its origin at the fluid particle; thus,

$$\xi'_i = A_{ij}(t)\xi_j,$$

where the $A_{ij}(t)$ are the time-dependent direction cosines. The velocity field as observed from the rotating coordinate system is given by

$$U'_i(\boldsymbol{\xi}', t) = U_j(\boldsymbol{\xi}, t) A_{ij}(t) + \dot{A}_{ij}(t)\xi_j,$$

where the dot denotes differentiation with respect to time. The rate-of-rotation tensor of the primed coordinate system with respect to the unprimed, with its components resolved on the primed axes, is given by

$$\Omega_{ij} = A_{ik}\dot{A}_{jk}.$$

The vorticity equation may now be written

$$\left(\frac{\partial \omega'_i}{\partial t}\right)_{\boldsymbol{\xi}} + \omega'_j \Omega_{ij} + U'_j \left(\frac{\partial \omega'_i}{\partial \xi'_j}\right)_t = \omega'_j S'_{ij},$$

where ω'_i and S'_{ij} are the vorticity vector and rate-of-strain tensor at the fluid particle as observed from an inertial reference frame but with the components resolved on the rotating and translating primed axes. Note that ω'_i is not the vorticity observed from the rotating reference frame.

Hitherto, the rotation of the primed axes with respect to the unprimed axes was arbitrary. We now restrict this rotation to be such that the vorticity vector at the fluid particle lies along the one axis of the primed coordinate system for all time; that is, we let

$$\omega_i'(0, t) = W(t)\delta_{i1},$$

where δ_{i1} is the unit vector along the one axis, and $W(t)$ is the magnitude of the vorticity vector that an Eulerian observer would measure at the position of the fluid particle at time t. The vorticity equation is now evaluated at the position of the fluid particle and becomes

$$dW(t)/dt\,\delta_{i1} + W(t)\,\Omega_{i1} = W(t)\,S_{i1}'(0, t).$$

These three equations may be expressed as follows:

$$W(t)/W(0) = \exp[J(t)], \quad \text{for } i = 1, \tag{1}$$

with

$$J(t) \equiv \int_0^t S_{11}'(0, t)\,dt; \tag{}$$
$$A_{2i}\dot{A}_{1i} = S_{21}'(0, t), \quad \text{for } i = 2; \tag{2}$$
$$A_{3i}\dot{A}_{1i} = S_{31}(0, t), \quad \text{for } i = 3. \tag{3}$$

Equations (2) and (3) partially determine the $A_{ij}(t)$ in terms of the rate-of-strain tensor at the position of the fluid particle. There are three independent direction cosines; thus, there exists another condition on the $A_{ij}(t)$. This other condition corresponds to the arbitrariness of the rotation of the primed system about the 1th primed axis. Equation (1) is the solution for the time dependence of the magnitude of the vorticity at the fluid particle.

These results apply to laminar as well as turbulent flow. Equation (1) implies that a stretching along the 1-primed axis results in an increase in the vorticity W, whereas a compression along the 1-primed axis leads to a decrease in W. Moreover, the exponential function weights the positive excursions of $J(t)$ more than its negative excursions. The positive excursions of $J(t)$ tend to increase W. Thus, in turbulent flow we expect that $W(t)$ should increase, on the average, provided that $J(t)$ is not an excessively negatively skewed random function of time.

The statistics of integrals is described by Tennekes and Lumley.[4] In turbulent flow $S_{11}'(0, t)$ has some finite correlation time τ. For times t very long compared with τ, the integral $J(t)$ can be divided into segments each of which is an integral over a time long compared with τ. Then, for these long times, $J(t)$ is expected to be a normal random function by an extension of the central limit theorem. In this case $W(t)$ is seen to be a log-normal random function of time by virtue of Eq. (1). The existence of times $t \gg \tau$ requires that the turbulent flow exhibits a sufficient degree of statistical stationarity and homogeneity.

In the presence of viscosity it is expected that the magnitude of the vorticity will be more limited than as given by Eq. (1). Thus, it is expected that the probability density of the magnitude of the vorticity at a fluid particle within turbulent flow will converge to zero more rapidly for large values of W than does the log-normal probability density.

[1]A. M. Obukhov, J. Fluid Mech. 13, 77 (1962).
[2]W. Y. Chen, Phys. Fluids 14, 1639 (1971).
[3]R. J. Hill and S. A. Bowhill (to be published).
[4]H. Tennekes and J. Lumley, *A First Course in Turbulence* (MIT Press, Cambridge, Mass., 1972), p. 218.

Estimation of Viable Airborne Microbes Downwind from a Point Source

BRUCE LIGHTHART* AND A. S. FRISCH

Ecological Effects Research Division, Corvallis Environmental Research Laboratory, U. S. Environmental Protection Agency, Corvallis, Oregon 97330, and Wave Propagation Laboratory, National Oceanographic and Atmospheric Administration, Boulder, Colorado 80301*

Modification of the Pasquill atmospheric diffusion equations for estimating viable microbial airborne cell concentrations downwind from a continuous point source is presented. A graphical method is given to estimate the ground level cell concentration given (i) microbial death rate, (ii) mean wind speed, (iii) atmospheric stability class, (iv) downwind sample distance from the source, and (v) source height.

Microorganisms may be introduced into the atmosphere from various sources, transmitted downwind via the airstream, and finally deposited on some surface (B. Lighthart, A. B. Akers, and J. C. Spendlove, in press). The airborne microorganisms may originate from human sources and activities, such as dust generated by urban and rural vehicles (J. W. Roberts, M. S. thesis, Univ. of Washington, Seattle, 1973), manufacturing processes, and construction. Microbial aerosols may be produced also from solid waste and sewage treatment plants (26; C. R. Albright, M. S. thesis, Univ. of Florida, Gainesville, 1958; B. Lighthart, Ph.D. thesis, Univ. of Washington, Seattle, 1967), talking, coughing, sneezing (3), and skin shedding.

Nonhuman sources of airborne microbes may be aquatic, such as bubble bursting of microbial-laden surface films of rivers, lakes, and oceans or from spray generated by breaking waves (20, 28) and rainwater splashes (2, 27), or terrestrial sources, such as dislodgement from vegetation or soil as a result of wind action or thermal convection (10–12). A new and potentially significant source of airborne microbes could be those originating from huge air draft cooling towers associated with nuclear and fossil-fueled power plants. The source of microorganisms is the water being used as the liquid coolant in the towers.

While airborne, microbial death is a function of many factors, including cellular physiological differences (1), relative humidity (9, 15), temperature (8), oxygen concentration (4, 16), light (22), and air pollutants (7, 17, 19, 23). Depending upon the quality and quantity of these factors, the death rate (see reference 6 for definition) may increase or decrease (e.g., 17).

Deposition of airborne bacteria may be by gravitational fallout, wind impaction of particles onto surfaces, and other mechanisms (13, 14).

It is the purpose of this communication to present a relatively simple graphical method to estimate the potential concentration of viable microorganisms at ground level downwind from a continuous point source given: (i) microbial death rate, (ii) wind speed, (iii) atmospheric stability class, (iv) source height, and (v) microbial source concentration.

METHODS

Microbial diffusion model. The downwind concentration of viable microbes may be estimated by using a modified Pasquill inert particle dispersion model (21, 24). The inert particle dispersion model is an empirical model, based on many observations of the dispersion of tracers in the atmosphere. For this reason we used it as the basis of our calculations of the numbers of microbes downwind from a source. We can use this model if we know: (i) the initial concentration of cells at the injection site, (ii) the death rate of the microorganisms in the ambient atmospheric after injection, and (iii) the meteorological conditions (i.e., wind velocity and diffusion factors) about the injection site.

The microbial death rate (λ) in the "real world" atmosphere is a dynamic function of many biological and environmental variables and, to our knowledge, has not been measured. Laboratory measurements of the death rate of airborne microbes as a time function of several variables (see B. Lighthart, C. Mason, G. Vali, and R. Edmonds, *in* R. L. Edmonds (ed.), *Ecological Systems Approaches to Aerobiology,* in press, for a description of these variables) have been made under steady-state and, to a limited extent, dynamic environmental conditions (15). Because of the lack of data describing death rates in the natural environment, it is assumed for the purposes of this communication that laboratory-

measured values will at least roughly approximate mean death rates in the dynamically changing atmosphere. Laboratory measurements vary from very rapid death rates for sensitive cells in hostile environmental conditions, e.g., $\lambda = 10^{-4}$/s, to moderate death rates, e.g., $\lambda = 10^{-1}$/s, to negligible rates for certain endospores (see Table 1). In any event, they are the only measurements we have and must suffice for the moment.

Atmospheric dispersion of inert materials $[\chi(x,y,z:H)]$ from a point source, given the source height (H) and meteorological conditions (see Table 2 for categories of weather conditions [24]), may be predicted by Pasquill's models:

$$\chi(x,y,z:H) = Q/(2\Pi(\sigma_y \sigma_z)\bar{U})$$

$$\times \; \text{EXP}[-0.5(Y/\sigma_y)^2] \times \{\text{EXP}[-0.5((Z \quad (1)$$

$$- H)/\sigma_y)^2] + [-0.5((Z + H)/\sigma_z)^2]\}$$

where χ is number of particles per cubic meter, Q is number of particles emitted from the source per second, $\bar{U}$ is mean air speed in meters per second, and σ_y, σ_z are the diffusion factors in the y and z plans and are functions of meteorological conditions and downwind distance from the source. The source height (H) and x, y, and z are coordinates, all in meters.

BD modification of dispersion model. The maximum number of viable particles remaining in the atmosphere after some time (t) depends upon atmospheric and cellular conditions. Knowing the biological death (BD) constant (λ) under various specific conditions, we may modify equation 1 to account for these factors by letting

$$\chi(x,y,z:H)_{BD} = \chi(x,y,z:H)\text{EXP}(-\lambda t) \quad (2)$$

where $\chi(x,y,z:H)_{BD}$ is the concentration with a death rate, t is the average time in seconds for transit of the bacteria, and λ is the microbial death constant

TABLE 1. *Some reported death rate constants[a] of certain airborne bacteria at the indicated relative humidities and temperatures*

Organism	% Relative humidity	Death rate constant		Source
		Temp (C)	λ (s^{-1})	
Serratia	1.2–3.4	15	7.5×10^{-2}	Ref. 17
marce-	23.4–26.5	15	8.1×10^{-2}	Ref. 17
sens	45.0–51.5	15	2.4×10^{-1}	Ref. 17
8UK	73.0–75.5	15	1.3×10^{-1}	Ref. 17
	88.0–96.0	15	1.1×10^{-1}	Ref. 17
Sarcina lu-	1.2–3.4	15	4.6×10^{-2}	Ref. 17
tea	23.4–25.5	15	1.1×10^{-2}	Ref. 17
	45.0–51.5	15	5.5×10^{-3}	Ref. 17
	73.0–75.5	15	5.5×10^{-3}	Ref. 17
	88.0–96.0	15	5.8×10^{-4}	Ref. 17
Pasturella	90	26.8	2.4×10^{-3}	Ref. 5
tularen-	80	26.8	5.5×10^{-3}	Ref. 5
sis LVS	0	26.8	7.1×10^{-2}	Ref. 5

[a] Data include aerosols up to 1 h old.

TABLE 2. *Relation of turbulence types to meteorological conditions (from reference 24)[a]*

Surface wind speed (m/s)	Daytime insolation			Nighttime conditions	
	Strong	Moder-ate	Slight	Thin over-cast or $\geq$[4,8] cloudi-ness[b]	$\leq$[3,8] cloudi-ness
<2	A	A-B	B		
2	A-B	B	C	E	F
4	B	B-C	C	D	E
6	C	C-D	D	D	D
>6	C	D	D	D	D

[a] A, Extremely unstable conditions; B, moderately unstable conditions; C, slightly unstable conditions; D, neutral conditions applicable to heavy overcast, day or night; E, slightly stable conditions; F, moderately stable conditions.

[b] The degree of cloudiness is defined as that fraction of the sky above the local apparent horizon that is covered by clouds.

(per second) experimentally determined for the particular atmospheric conditions. We may approximate t by $x/\bar{U}$. Thus equation 2 becomes

$$\chi(x,y,z:H)_{BD} = \chi(x,y,z:H)\text{EXP}(-\lambda x/\bar{U}) \quad (3)$$

where $\chi(x,y,z:H)_{BD}$ is the concentration of microorganisms per cubic meter with the microbial death constant included. Figure 1 shows examples of computed viable cell concentrations downwind from a continuous point source for the given conditions.

Knowing the microbial death constants, atmospheric conditions, σ_y, and σ_z, we may apply this model to give the concentration of microorganisms as a function of the distance (x) from the source with some effective height (H). If the death rates change with time, equation 2 can be modified to account for this change. For example, let λ_1 be the first death rate until time t_1, and let λ_2 be for times greater than t_1. Then

$$\chi(x,y,z:H)_{BD} = \chi(x,y,z:H)\text{EXP}(-\lambda_1 t) \text{ for } t \leq t_1 \quad (4)$$

Since the mean distance traveled in time t is

$$x = \bar{U}t \quad (5)$$

then

$$\chi(x,y,z:H)_{BD} = \chi(x,y,z:H)\text{EXP}(-\lambda_1 x/\bar{U}) \quad (6)$$

for $x < x_1$ (where $x_1 = \bar{U}t_1$), and

$$\chi(x,y,z:H)_{BD} = \chi(x,y,z:H)\text{EXP}(-\lambda_1 x_1/\bar{U}) \cdot \text{EXP}[-\lambda_1 (x-x_1)/\bar{U}] \quad (7)$$

for $x < x_1$ (see reference 18 for further details).

Using equation 1, and letting $y = 0$ and $z = 0$, equation 3 may be rewritten

$$\frac{\chi}{Q} \cdot \frac{\bar{U}}{\text{EXP}(-\lambda x/\bar{U})} = \frac{1}{2\Pi \sigma_y \sigma_z}$$

$$\cdot \text{EXP}\left[-\left(\frac{H^2}{2\sigma^2 z}\right)\right] \cdot g \quad (8)$$
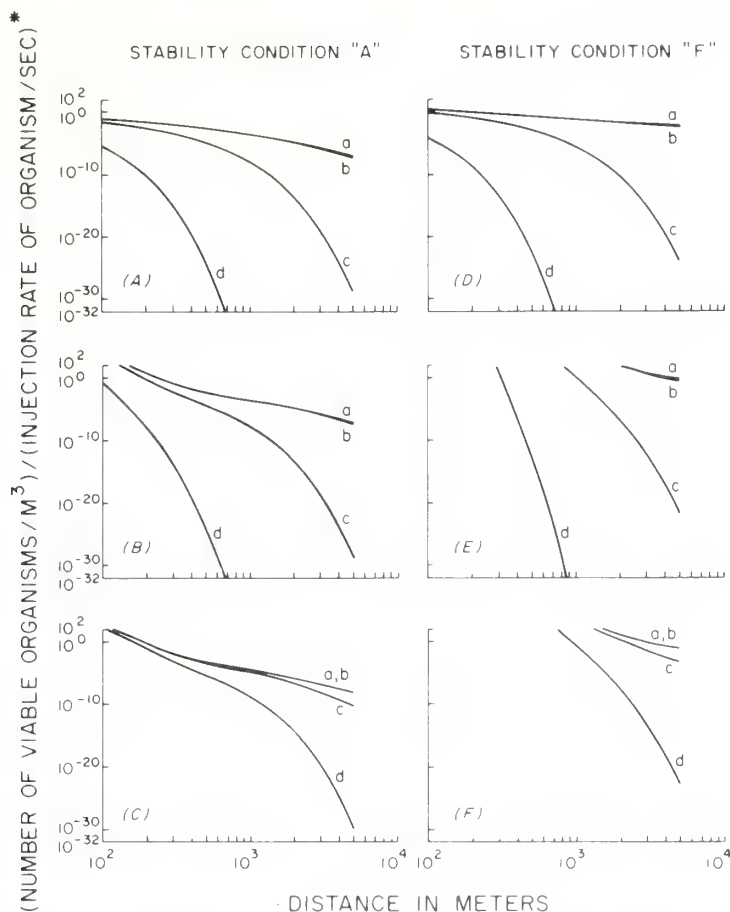
FIG. 1. *Examples of the relative number of viable cells per cubic meter divided by the number per second injected into the atmosphere downwind from a continuous point source (using equation 2) at a sample height of 2 m and a microbial death rate of 0 (a), 10^{-1} (b), 10^{-2} (c), and 10^{-3} (d) per s for stability classes "A" and "F." (A) and (D) Source height, 0 m; mean air speed, 1 m/s. (B) and (E) Source height, 200 m; mean air speed, 1 m/s. (C) and (F) Source height, 200 m; mean air speed, 10 m/s. *Percentage of viable organisms.*

Once this function is evaluated for a certain source height, stability class, wind speed, and distance, one can use any death rate to evaluate the ratio of the concentration, χ, to source strength Q. For convenience, g versus x for several source heights are shown in Fig. 2 for the stability classes defined in reference 24. With these figures, the user can estimate the viable microbial concentration downwind at a distance from a source of height H and strength Q and for a given stability class and death rate λ.

EXAMPLE AND DISCUSSION

The question asked was how many viable microorganisms at ground level (i.e., sample height = 0) are there per cubic meter downwind some distance (x in meters) from a continous point source, given an emission source strength of Q bacteria per second? One must first know or estimate (i) the microbial death constant (λ

in seconds) under the prevailing atmospheric conditions, (ii) the mean wind speed ($\bar{U}$ in meters per second), (iii) the meters downwind from the source, (iv) the atmospheric stability class (Table 2), and (v) the source height (H in meters). With this data one can use equation 8 with the appropriate values of σ_y and σ_z, or, alternatively, one can use Fig. 2, which is based on equation 8, to evaluate g.

For example, a hypothetical 200-m-high point source (H) might have an emission rate, Q, of 10^{10} bacteria/s in particles assumed to be distributed about a 10-μm diameter (Lighthart et al., in press). Assuming that these viable particles were dispersed from the source into a class "A" stability atmosphere with winds of 10 m/s, using our calculations, one might expect that viable bacteria having a mean death rate (λ) of 10^{-1}/s (e.g., see Table 1) would be found at
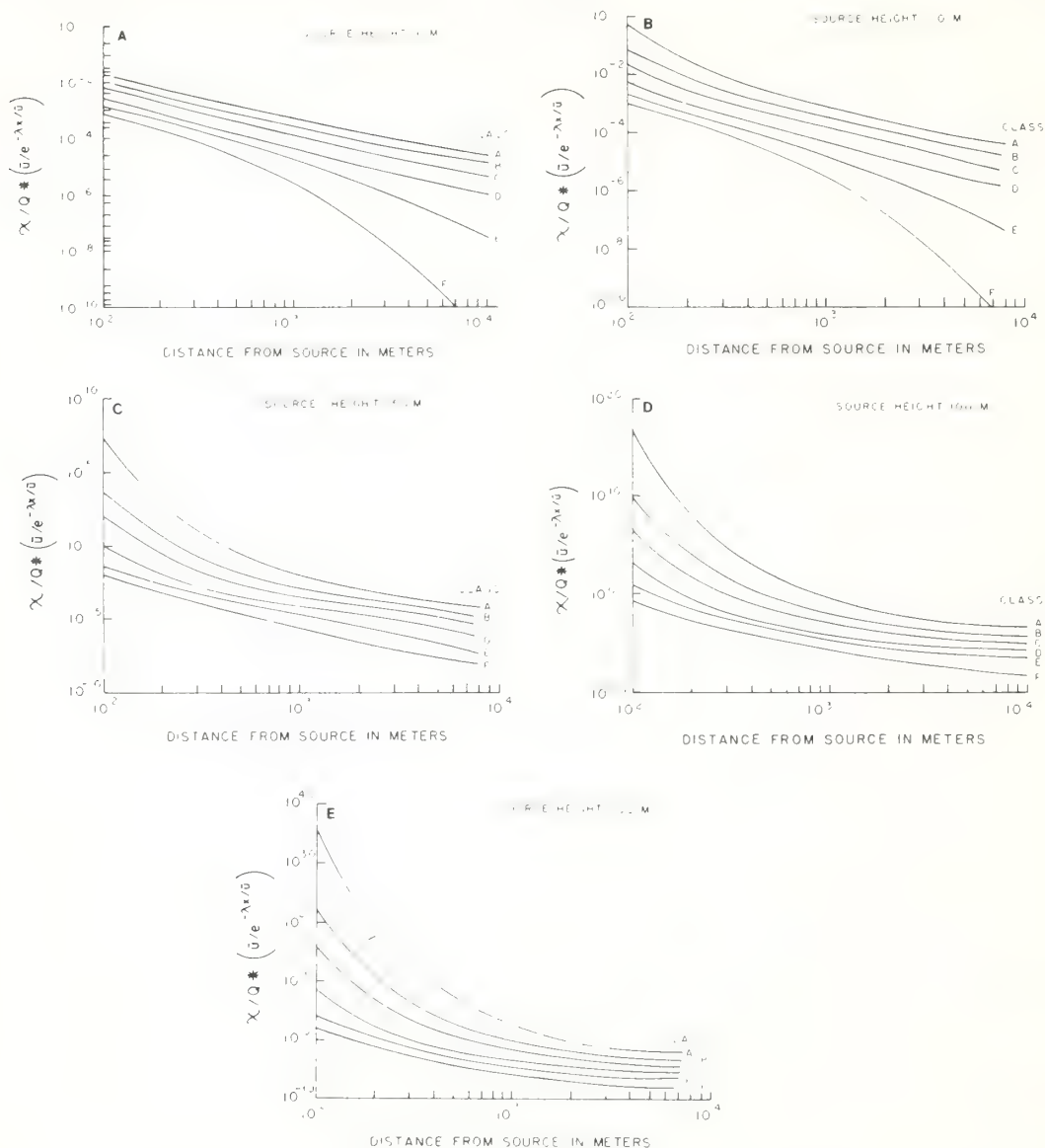
FIG. 2. Function $\chi/Q \times (\bar{U}/e^{-\lambda x/\bar{U}})$ versus distance from the source in meters for the indicated stability classes and several source heights. χ is the downwind concentration of viable bacteria per cubic meter, Q is the injection rate of live bacteria (number per second), and $\bar{U}$ is the mean wind velocity in meters per second, x the downwind distance (meters), and λ the microbial death rate (number per second).

a concentration of 1.4×10^4 viable bacteria/liter in the ground level atmosphere 1,000 m downwind from the source. That is, from Fig. 2, g is found to be 316/m²; solving for $\chi = (Q/\bar{U}) \times g$ [$\text{EXP}(-\lambda x/\bar{U})$] = $(10^{10}$ bacteria/s)/10 m per s $\times$ 316/m² $\times$ [$\text{EXP}(-10^{-1}$/s $\times 10^3$ m/10 m per s)] = 1.4×10^7 bacteria/m³. It is also estimated that a person with a 0.5-liter lung tidal-volume breathing rate of 12 cycles/min would inhale 8.4

$\times 10^4$ bacteria/min at this same location (25). This estimate is significant even if the diffusion model is in error by a factor of 10. In this example, the pathogenic and allergenic potential of the phenomena remains problematical.

Albeit the flavor of this technique of estimating viable airborne cells is quantitative, it is anticipated that present and future research in the areas of atmospheric turbulence and model

development, microbial death mechanisms, atmospheric injection phenomena, and particle sizing of airborne microorganisms will result in more precise estimates of airborne microbial loads downwind from sources.

ACKNOWLEDGMENTS

LITERATURE CITED

1. Anderson, J. D., and C. S. Cox. 1967. Microbial survival. *In* Airborne microbes. Proceedings of the 17th symposium. Society for General Microbiology, Cambridge.

2. Blanchard, D. C., and L. Syzdek. 1970. Mechanism for the water-to-air transfer and concentration of bacteria. Science 170:626–628.

3. Buchbinder, L., M. Solowey, and M. Solotorovsky. 1945. Comparative quantitative studies of bacteria in air of enclosed places. Air Pollution Survey of New York, Part I. Heat. Piping Air Cond., p. 389–397.

4. Cox, C. S. 1967. The toxic effect of oxygen upon the aerosol survival of *Escherichia coli* B. J. Gen. Microbiol. 49:115–117.

5. Cox, C. S., and L. J. Goldberg. 1972. Aerosol survival of *Pasteurella tularensis* and the influence of relative humidity. Appl. Microbiol. 23:1–3.

6. Dimmick, R. L., and A. B. Akers (ed.). 1969. An introduction of experimental aerobiology. Wiley-Interscience, John Wiley & Sons, New York.

7. Druett, H., and K. May. 1969. The open air factor. New Sci., p. 579–581.

8. Ehrlich, R., and S. Miller. 1973. Survival of airborne *Pasturella tularensis* at different atmospheric temperatures. Appl. Microbiol. 25:369–372.

9. Ehrlich, R., S. Miller, and R. L. Walker. 1970. Effects of atmospheric humidity and temperature on the survival of airborne *Flavobacterium*. Appl. Microbiol. 20:884–887.

10. Fulton, J. D. 1966. Microorganisms of the upper atmosphere. III. Relationship between altitude and micropopulation. Appl. Microbiol. 14:237–240.

11. Fulton, J. D. 1966. Microorganisms of the upper atmosphere. V. Relationship between frontal activity and the micropopulation at altitude. Appl. Microbiol. 14:245–250.

12. Fulton, J. D., and R. B. Mitchell. 1966. Microorganisms of the upper atmosphere. II. Microorganisms in two types of air masses at 690 meters over a city. Appl. Microbiol. 14:232–236.

13. Gregory, P. H. 1973. The microbiology of the atmosphere. John Wiley & Sons, New York.

14. Gregory, P. H., and J. L. Monteith. 1967. Airborne microbes. Proceedings of the 17th symposium. Society for General Microbiology, Cambridge.

15. Hatch, M. T., and R. L. Dimmick. 1966. Physiological responses of airborne bacteria to shift in relative humidity. Bacteriol. Rev. 30:597–602.

16. Hess, G. E. 1965. Effects of oxygen on aerosolized *Serratia marcescens*. Appl. Microbiol. 13:781–787.

17. Lighthart, B. 1973. Survival of airborne bacteria in a high urban concentration of carbon monoxide. Appl. Microbiol. 25:86–91.

18. Lighthart, B., and A. S. Frisch. 1973. A model to evaluate the airborne bacterial concentration from a continuous source, 139–149. *In* R. L. Edmonds and W. S. Benninghoff (ed.), Proc. of workshop/conference ecological systems approaches to aerobiology. II. Development and demonstration, and evaluation of models. US/IBP Aerobiology Program Handbook no. 3. University of Michigan, Ann Arbor.

19. Lighthart, B., V. E. Hiatt, and A. T. Rossano, Jr. 1971. The survival of airborne *Serratia marcescens* in urban concentrations of sulfur dioxide. J. Air Pollut. Control Assoc. 21:639–642.

20. Parker, B., and G. Barsom. 1970. Biological and chemical significance of surface microlayers in aquatic ecosystems. Bioscience 20:87–93.

21. Pasquill, F. 1962. Atmospheric diffusion. D. van Nostrand Co., Ltd, London.

22. Riley, R. L., and J. E. Kaufman. 1972. Effect of relative humidity on the inactivation of airborne *Serratia marcescens* by ultraviolet radiation. Appl. Microbiol. 23:1113–1120.

23. Serat, W. F. 1969. Approaches to the bioassay of airborne pollution, p. 123–125. *In* R. L. Dimmick and A. B. Akers (ed.), An introduction to experimental aerobiology. Wiley-Interscience, John Wiley & Sons, New York.

24. Slade, D. H. (ed.). 1968. Meteorology and atomic energy, 1968. U.S. Atomic Energy Commission, Publication no. TID-24190, Washington, D. C.

25. Sodeman, W. A. 1961. Pathogenic physiology. W. B. Saunders Co., Philadelphia.

26. Spendlove, J. C. 1974. Industrial, agricultural and municipal microbial aerosol problems. Dev. Ind. Microbiol. 15:20–27.

27. Woodcock, A. H. 1955. Bursting bubbles and air pollution. J. Hyg. 42:339–353.

28. Zobell, C. E. 1946. Marine microbiology. Chronica Botanica Co., Waltham, Mass.

The Lognormal Distribution and Cumulus Cloud Populations

RAÚL ERLANDO LÓPEZ[1]

Institute of Tropical Meteorology, University of Puerto Rico, Rio Piedras

(Manuscript received 14 December 1976, in final form 24 March 1977)

ABSTRACT

It is shown that the lognormal distribution describes the frequency distributions of height, horizontal size, and duration of cloud and radar echo populations in many different regions and convective situations. Two hypotheses are suggested to explain this phenomenon. The first postulates a *growth* process of cloud parcels, in which growth by entrainment of environmental air occurs by a random process that obeys the law of proportionate effects. The second postulates a *formation* process for clouds, in which the clouds are formed by the merger of random boundary-layer convective elements.

The information presented in this paper should be useful for the parameterization of cumulus convection in larger scale models, and for the understanding and modeling of cloud formation and development.

1. Introduction

In a recent paper, López (1976) found that the frequency distributions of the height and maximum horizontal area attained by radar echoes of tropical disturbances in the northwest Atlantic, follow lognormal[2] distributions. At the same time, Biondini (1976) found that the duration and rainfall volume of Florida radar echoes are also lognormally distributed. A question immediately arises: Is this a characteristic particular to cumulus cloud populations of tropical maritime systems, or is this a general property of cumulus cloud populations everywhere? If lognormality is indeed a general characteristic of cumulus convection, the efforts to parameterize the effects of clouds in large-scale numerical models would be greatly benefited. In addition, by extending the theory of the genesis of lognormal distributions to cumulus convection, our knowledge of cloud-formation processes would be enhanced.

Accordingly, the objective of this paper is to determine if lognormality is a general characteristic of cumulus convection. For this purpose, many cloud and radar echo populations (for different regions and varying large-scale conditions) are examined to see if their frequency distributions of height, horizontal size and duration are lognormal. As will be seen, the vast majority of cases do indeed indicate lognormality. The few cases that depart from this tendency are shown to respond to physical bounds to growth which produce *truncated* lognormal distributions.

---

[1] Present affiliation: Wave Propagation Laboratory, NOAA, Boulder, Colo. 80302.

[2] A variable is said to be lognormally distributed when its logarithm follows the normal probability law.

2. Characteristics of cumulus cloud populations

a. Height

Figs. 1 and 2 present the cloud and echo height distributions of six different cumulus cloud populations. For convenience they are separated into tropical and extratropical situations. The frequency distributions are plotted on logprobability paper: the ordinate is plotted in a logarithmic scale, while the abscissa is plotted in a normal probability scale. A lognormal distribution would thus describe a straight line in this coordinate system (Aitchison and Brown, 1957, pp. 31–35). The straight lines drawn through the different sets of points correspond to the lognormal distributions that best fit the data and give a smaller x^2 value for each population. Table 1 shows the best-fit parameters of the different distributions.

A chi-square test for goodness-of-fit has been applied to these data sets. This test has been amply described in the literature (see, e.g., Meyer, 1975). For the purposes of this paper it suffices to say that if a population is distributed lognormally (with geometric mean and standard deviation μ' and σ', and with interval frequencies f_i') and if random samples are drawn from that population (with N interval frequencies f_i each), then the sample chi-squared statistic

$$\chi^2 = \sum_{i=1}^{N} \frac{(f_i - f_i')^2}{f_i'}$$

would be distributed according to the χ^2 function with $N-3$ degrees of freedom. Moreover, this function has the property that large values for χ^2 have a small probability of occurring under random sampling. Thus, if a random sample from a supposedly lognormal popu-
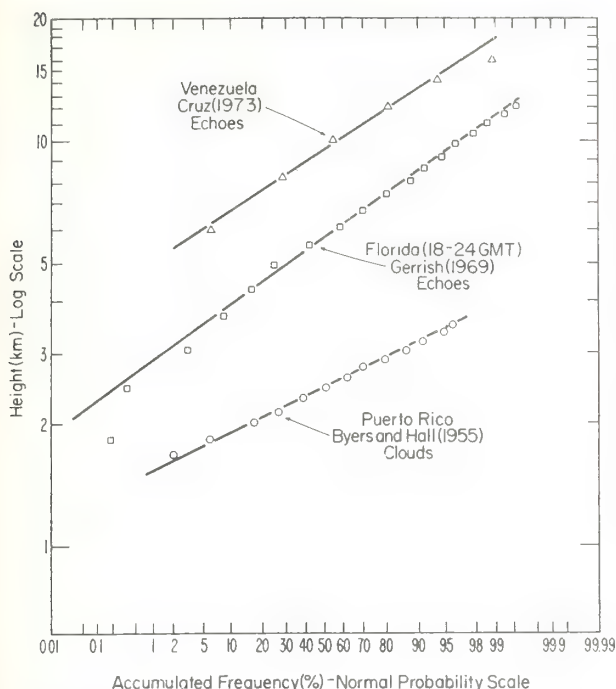
FIG. 1. Accumulated frequency distributions of cloud and radar echo height for tropical data sets. The straight lines correspond to the lognormal distributions that best fit the different data sets.
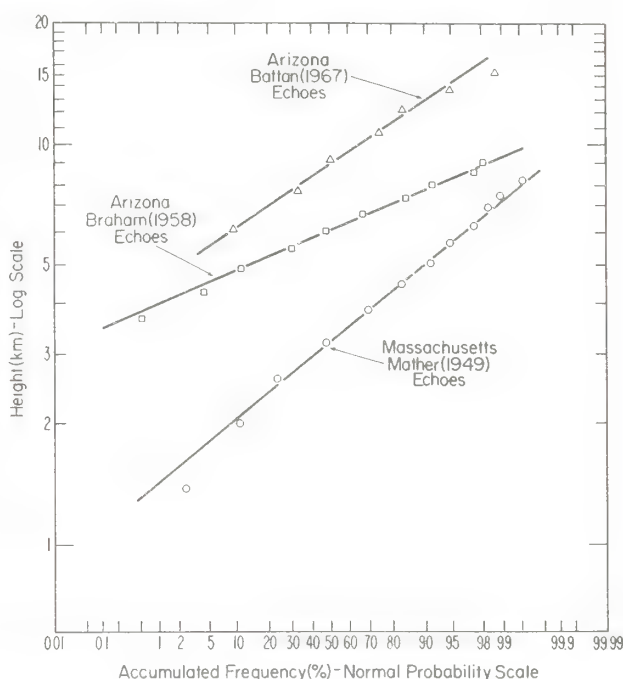
FIG. 2. As in Fig. 1 except for extratropical data sets.

lation (null hypothesis) produces a large χ^2 value which has a small probability of occurrence according to the corresponding χ^2 distribution, then the null hypothesis is rejected. The "small" probability level has been selected at 5% for the present application, which is a value commonly used. The next to the last column of Table 1 gives the corresponding χ^2 value for this probability for each of the distributions.

As can be seen from the table the χ^2 values obtained from the samples are in all cases smaller than the value at a level of significance of 5%. Thus the lognormal hypothesis is consistent with the data at this level of significance. In fact the probability of obtaining a value of χ^2 as large as or larger than the value measured is generally high (last column of Table 1). The case giving the worst fit is Battan (1967). It is shown below

that data by Battan (1953) also produce the worst lognormal fit in respect to echo horizontal dimension. In both cases, however, the lognormal hypothesis cannot be rejected at a level of significance of 5%.

Notice how the lognormal probability law describes the height distribution of echoes and clouds in a wide variety of situations: from the trade winds to maritime and continental tropical conditions, and from moist to dry mid-latitude environments. Although the shape of the distributions is the same for all cases, the means and standard deviations vary considerably from case to case. In general, it can be observed from Figs. 1 and 2 that the echoes tend to increase (the geometric mean corresponds to the 50% intercept of the lines) as one moves from oceanic to continental conditions in the tropics, and from moist to dry conditions in the middle latitudes.

TABLE 1. Cloud and radar echo height distribution.

| | | | Best-fit parameters (lognormal) | | | | | |
Author	Location	Feature	Geometric mean	Geometric sigma	Degrees of freedom	χ^2	Value of χ^2 at a level of significance of 5%	Probability of χ^2 value as large as measured or larger
Gerrish (1969)	Miami over water	Echo height (km)	5.71	1.97	8	3.74	15.50	88%
Braham (1958)	Arizona	First echo height (km)	6.08	1.23	5	3.02	11.07	70%
Battan (1967)	Arizona	Echo height (km)	8.87	2.98	4	7.79	9.49	10%
Cruz (1973)	Venezuela	Max echo height (km)	9.38	2.99	4	2.93	9.49	55%
Byers and Hall (1955)	Puerto Rico	Cloud height (km)	2.44	0.54	8	2.79	15.50	95%
López (1976)	NW Atlantic	Echo height (km)	4.47	2.58	12	3.61	21.03	99%
Mather (1949)	Massachusetts	Echo height (km)	3.17	1.31	5	3.79	11.07	58%
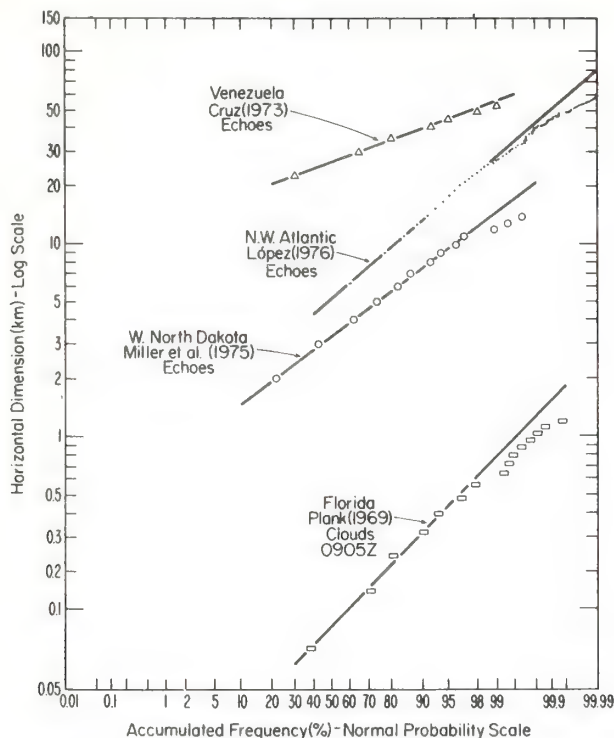
Fig. 3. Accumulated frequency distributions of cloud and echo horizontal dimension. The straight lines correspond to the lognormal distributions that best fit the different data sets.

Fig. 4. Continuation of Fig. 3.

b. Horizontal dimension

Figs. 3 and 4 show the distribution of horizontal size of eight cumulus cloud populations. Originally the data were expressed variously as diameter, radius, length and area distributions. For purposes of comparison, all the data points have been reduced to an equivalent diameter or characteristic horizontal dimension. Again, the distributions have been plotted on logprobability paper. Similarly, straight best-fit lines

have been drawn through the data points. Table 2 presents the corresponding parameters.

As in the case of height, the hypothesis that the frequency distributions of echo and cloud horizontal dimension are lognormal cannot be rejected at a level of significance of 5% or better. The fits are very good for the smaller 98% of the elements of the populations. The distribution of the larger 2% deviate somewhat from a lognormal law. This deviation, however, is not significant enough to warrant the rejection of the lognormal hypothesis. It will be shown that these small deviations correspond to a physical limit to growth. The resultant distribution can be better described by a truncated lognormal law. As in the case of the height distributions, the worst fit corresponds to the data obtained by Battan (1953). However, the data scatter is not large enough to justify rejecting the lognormality of this distribution at 5% level of significance. In general it can be said that the lognormal probability law

TABLE 2. Cloud and radar echo horizontal size distribution.

| | | | | | Best-fit parameters (lognormal) | | | |
| | | | | | | | | |
Author	Location	Feature	Geometric mean	Geometric sigma	Degrees of freedom	χ^2	Value of χ^2 at a level of significance of 5%	Probability of χ^2 value as large as measured or larger
Hudlow (1971)	Barbados	Echo length (km)	2.30	8.16	1	0.10	3.84	75%
Cruz (1973)	Venezuela	Echo max. area (100 km²)	5.64	4.90	3	1.96	7.81	59%
Mather (1949)	Massachusetts	Mean echo diameter (km)	6.22	4.03	5	0.82	11.07	98%
Battan (1953)	SW Ohio	Max. horiz. echo dimension (km)	3.59	1.84	2	4.68	5.99	10%
Plank (1969)	Florida, 0905 GMT	Equivalent cloud diameter (km)	0.11	0.15	3	2.68	7.81	44%
Miller et al. (1975)	NW Dakota	Echo diameter (km)	3.31	2.99	5	0.56	11.07	99%
Dennis and Fernald (1963)	Florida to California	Cloud length (km)	1.85	1.32	2	0.32	5.99	85%
Dennis and Fernald (1963)	Eniwetok	Shower radius (km)	1.75	1.71	3	2.19	7.81	53%
López (1976)	NW Atlantic	Max. echo area (km²)	20.96	71.20	3	0.03	7.81	99%
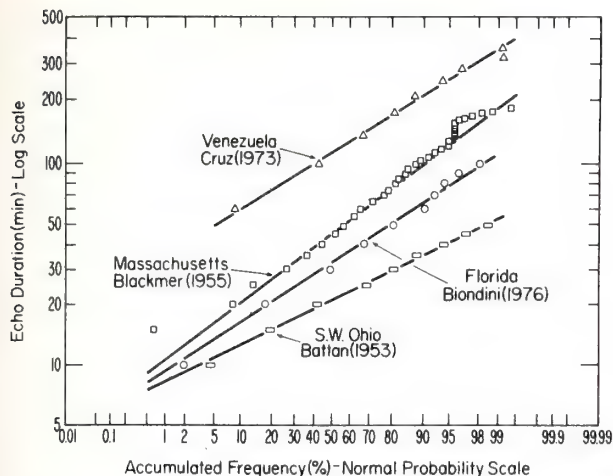
FIG. 5. Accumulated frequency distributions of radar echo duration. The straight lines correspond to the lognormal distributions that best fit the different data sets.

can be fitted very well to echo and cloud horizontal dimension distributions.

As in the case of height, it is worthwhile noting the wide range of climatic situations in which the lognormal has been found applicable: maritime and continental tropical regions; dry and moist, coastal and continental mid-latitudes. In general, continental tropical echoes tend to be larger than echoes in Atlantic tropical cloud clusters, and they are larger than the clouds induced by the Florida sea breeze.

c. Duration

Fig. 5 presents the lognormal plots of the frequency distributions of radar echo duration for four cumulus cloud populations. Again, best-fit straight lines have been drawn. Table 3 shows the pertinent statistical parameters. Once more, the hypothesis that the frequency distributions of echo duration are lognormal cannot be rejected at a level of significance of 5% or better. The lognormal law can be fitted very well to all of the echo duration distributions. Again, tropical and extratropical, maritime and continental populations all are lognormally distributed.

3. The lognormal distribution and cumulus cloud growth processes

a. The genesis of lognormal distributions

From the evidence presented in the last section it can be said that echo and cloud height, horizontal size and duration are distributed lognormally in a wide variety of convective situations. The question immediately arises: What is it in the formation and growth process of cumulus clouds that produces cloud populations which are lognormally distributed? It is reasonable to assume that the formation and growth processes in cumulus clouds follow the same stochastic processes that determine the genesis of the lognormal probability law. The lognormal distribution can be considered (Kapteyn, 1903; Aitchison and Brown, 1957, pp. 20–27) the frequency distribution of a variate that is subject to the law of proportionate effects, i.e., a variate whose change in value at any step of a process is a random proportion of the previous value of the variate. Thus, consider a variate whose value is x_0 at the start of the process and x_i at the ith step, reaching a value x_n at the end of n steps. At the ith step the change in value can be expressed as

$$x_i - x_{i-1} = \epsilon_i x_{i-1}, \tag{1}$$

where ϵ_i is a random variable, independent of x. Considering n steps,

$$\sum_{i=1}^{n} \frac{x_i - x_{i-1}}{x_{i-1}} = \sum_{i=1}^{n} \epsilon_i. \tag{2}$$

If the change at each step is small,

$$\sum_{i=1}^{n} \frac{x_i - x_{i-1}}{x_{i-1}} \sim \int_0^{x_n} \frac{dx}{x} = \ln x_n - \ln x_0, \tag{3}$$

so that

$$\ln x_n = \ln x_0 + \epsilon_1 + \epsilon_2 + \cdots + \epsilon_n. \tag{4}$$

By the additive form of the central-limit theorem, $\ln x_n$ is in the limit normally distributed and therefore x_n is lognormally distributed. So, something that is formed, grows or changes according to the law of proportional effects will yield a lognormal size distribution.

TABLE 3. Radar echo duration distribution.

| Author | Location | Feature | Best-fit parameters (lognormal) | | | | Value of χ^2 at a level of significance of 5% | Probability of χ^2 value as large as measured of larger |
			Geometric mean	Geometric sigma	Degrees of freedom	χ^2		
Cruz (1973)	Venezulea	Echo duration (min)	113.98	75.93	5	3.30	11.07	65%
Blackmer (1955)	Massachusetts	Echo duration (min)	44.72	38.58	11	5.57	19.68	90%
López (1976)	NW Atlantic	Echo duration (min)	2.29	9.89	5	2.27	11.07	81%
Battan (1953)	SW Ohio	Echo duration (min)	21.01	10.41	4	2.53	9.49	64%
Biondini (1976)	Florida	Echo duration (min)	32.38	22.84	4	3.87	9.49	42%

Both Biondini (1976) and López (1976), working simultaneously and independently, have hypothesized that cumulus clouds could grow and develop by a process which follows the law of proportionate effects, thus producing the observed lognormal distributions of echo characteristics. Although Biondini speculates about a "multiplicative diffusion process" to explain cloud formation, neither he nor López discussed the particular physical mechanism that could be responsible for the characteristic growth patterns. In the next two sections two hypotheses are advanced to explain how clouds could develop according to the law of proportionate effects. The first has to do with growth by turbulent diffusion and the second with growth by the merger of smaller cloud elements.

b. Stochastic growth process

Applying the stochastic process described above to the *growth* of clouds, a process like this can be hypothesized:

1) The large-scale features of the flow (convergence field, thermal stability, etc.) produce an initial population of small convective elements, the average size of this initial population probably being related to the depth of the local boundary layer.

2) These elements then develop by a process whereby growth is a random proportion of the size of the element, i.e., by the process of proportionate effects.

3) In this way a cloud population develops whose eventual size distribution is lognormal.

In terms of the mass m of a cloud parcel, step 2 above can be represented as

$$\frac{dm}{dt} = m\epsilon, \tag{5}$$

where ϵ is a random number. This can be rewritten as

$$\frac{1}{m}\frac{dm}{dt} = \epsilon. \tag{6}$$

It can now be seen that ϵ is just the fractional entrainment rate for the cloud parcel. This quantity figures prominently in parametric models of cumulus clouds. It has been variously parameterized in terms of the mean vertical velocity of the cloud parcel and its radius (e.g., Simpson and Wiggert, 1969) and in terms of the parcel turbulence intensity and its radius (López, 1973).

In order to understand physically how the entrainment rate could be a random quantity, consider the growth of the parcel by entrainment as a flux of mass through the surface of the parcel. Thus

$$\frac{dm}{dt} = \rho_e \bar{v}_e A, \tag{7}$$

where ρ_e is the density of the entrained air and $\bar{v}_e$ the mean velocity of the entrained mass averaged over the surface area A of the parcel. Let m be the mass of the parcel, where

$$m = \rho_p V, \tag{8}$$

V being the volume and ρ_p the density of the parcel. Dividing Eq. (7) by (8) and setting $\rho_p \approx \rho_e$, one obtains

$$\frac{1}{m}\frac{dm}{dt} = \frac{A}{V}\bar{v}_e. \tag{9}$$

Let the ratio of the surface to the volume of the parcel be

$$\frac{A}{V} = \frac{K}{R}, \tag{10}$$

where R is the parcel's radius and K a geometric constant depending on the configuration of the parcel. Eq. (9) now becomes

$$\frac{1}{m}\frac{dm}{dt} = K\frac{\bar{v}_e}{R}. \tag{11}$$

By comparing Eqs. (6) and (11) it can be seen that the entrainment rate would be random (and the cloud parcel would grow according to the law of proportionate effects) if the velocity of entrainment averaged over the surface of the parcel were a random variable.

Now, the entrainment of outside air into the cloud parcel is controlled by the turbulence near the surface of the cloud. The convolutions and invaginations of the cloud surface trap the exterior air and draw it inside (Turner, 1962, 1963). Thus, the mean velocity of entrainment at a given moment during the growth of a parcel depends on the particular turbulent configuration of the parcel's surface. This is, of course, a random variable. Thus, the mean velocity of entrainment would be a random variable, also. As a consequence, the fractional entrainment rate would be random. The law of proportionate effects would apply, and the resulting distribution of cloud size would be lognormal.

From strictly dimensional arguments it can be reasoned (Telford, 1966; Morton, 1968) that the velocity of entrainment fluctuates randomly around a value that is determined by the root-mean-square of the velocity fluctuations inside the parcel (turbulence intensity). Thus, although the value of the velocity of entrainment for the particular times during the growth of a parcel is going to vary randomly, its time average is going to be dependent upon the average turbulent intensity of the cloud parcel. Upon integration of Eq. (11), one obtains

$$\ln m = \ln m_0 + K \int_0^t \frac{\bar{v}_e dt}{R}, \tag{12}$$

where m is the final mass at time t, and m_0 the initial mass of the cloud parcel. Notice that, in addition to the initial mass, the final size depends on the mean ratio between the velocity of entrainment (fluctuating randomly around a value determined by the degree of turbulence) and the radius of the parcel. Thus, although this hypothesis would explain the observed lognormal size distribution of fields of clouds, it also retains the R^{-1} and turbulence intensity dependency in the entrainment formulation that have been well established in the cumulus dynamics literature.

It should be noted that in all of the entity type cloud models (e.g., Simpson and Wiggert, 1969; Weinstein and Davies, 1968; López, 1973) a different initial radius has to be specified to generate each cloud of different size under the same thermodynamic situation. In addition, nothing can be said about the different proportions of cloud types to be expected in a given case. The present hypothesis, however, by assuming a stochastic process and a characteristic initial convective element size, would explain the size distribution of the entire convective field under a given thermodynamic situation. The author is working on the theory of a stochastic cloud model based upon the present hypothesis to test the possibility of producing populations of clouds that are lognormally distributed in size and duration.

c. Stochastic formation process

In the previous section it was indicated that the lognormality of cloud and radar echo distributions can be explained by assuming that the clouds *grow* to their final size from an initially small volume by the process of random entrainment of environmental air. Lognormality can also be explained by postulating a process by which clouds of a particular size are *formed* by the merger of smaller elements. Thus, the following second hypothesis can also be made to explain the occurrence of lognormal cloud size distributions:

1) In a given region many small convective elements are randomly formed throughout the subcloud layer.

2) As they rise and expand they aglomerate into larger elements.
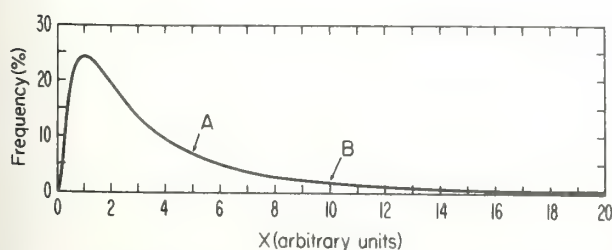
Fig. 6. A theoretical lognormal frequency distribution with geometric mean and standard deviation equal to 1 in arbitrary units of x. Points A and B are identified in Fig. 7.
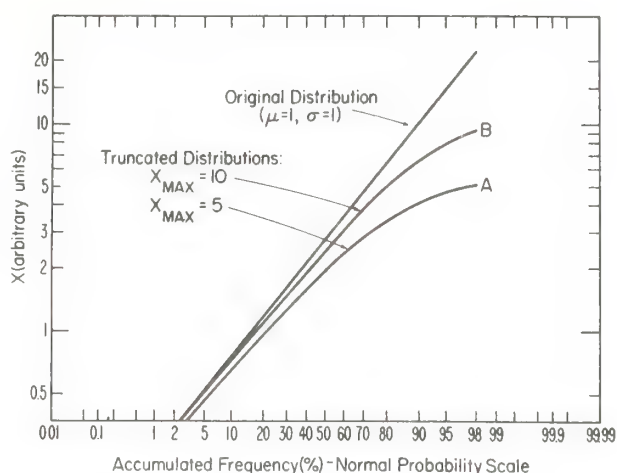
Fig. 7. The accumulated frequency distributions of a theoretical lognormal distribution (straight line) and the same for two truncated lognormals (curves A and B).

3) The larger elements, covering a greater area, intercept a larger number of other elements and thus grow more rapidly than the smaller ones, i.e., growth proceeds according to the law of proportional effects.

4) In this way a cloud population develops whose eventual size distribution is lognormal.

The author is also working on the development of a stochastic cloud formation model of this type.

This merging process probably continues during the latter stages of cloud life. Evidence for this mechanism can be seen in the studies of cloud mergers by Simpson and Woodley (1971) and López (1976). It is not the purpose of this paper to formulate the theoretical models that can be derived from the abovementioned hypotheses, but merely to advance these two hypotheses of growth and formation as possible explanations of the observed lognormal distributions of echo and cloud size and duration.

d. Truncated lognormals and limits to cloud growth

It was noted in Section 2 that some of the logprobability plots of size distributions departed to the right of a straight line (lognormal distribution) for the largest 2% of the echo and cloud sizes (see Fig. 3). This departure indicates that there are more echoes or clouds observed in that size range than are called for by the lognormal law, and at the same time that the lognormal predicts some elements with larger sizes that were not observed. This is exactly the situation to be expected if there is a physical limit to the growth of clouds.

In order to illustrate this limiting effect on a lognormal distribution some theoretical examples can be considered. Fig. 6 shows a theoretical lognormal frequency distribution with mean and standard deviation equal to 1 in arbitrary units of the variable x. The logprobability plot of this distribution is shown as the straight line of Fig. 7. The theoretical lognormal has
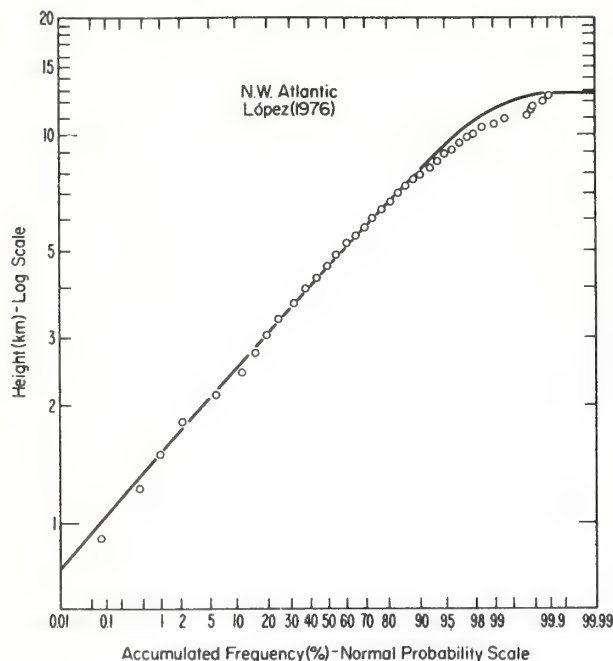
Fig. 8. Accumulated frequency distribution of radar echo height. The solid curve corresponds to the truncated lognormal distribution that best fits the data.

Fig. 9. Accumulated frequency distribution of radar echo horizontal dimension.

been arbitrarily truncated at $x = 5$ (point A) and $x = 10$ (point B) (Fig. 6). The logprobability plots of the resulting (renormalized) distributions are shown as curves A and B in Fig. 7. Notice that the curves depart to the right of the parent full lognormal in the same way as the size distributions of Fig. 5.

Accordingly, truncated lognormals were fitted to the three distributions that departed most from a full lognormal in the highest values. These three distributions were not pictured in Figs. 1–5, but their regular lognormal-fit parameters are shown in Tables 1–3. Figs. 8–10 portray the original distributions and the corresponding truncated lognormal fits. These were truncated at the maximum observed dimension. In general, the truncated lognormals fit the observed distributions much better than the corresponding regular lognormals do, especially in the range of largest sizes and durations. Still, however, some departure from the theoretical distributions toward higher frequencies is noticed in all three examples. It must be recalled that the theoretical distributions were arbitrarily truncated at the observed maximum dimension. This procedure tacitly assumes that only clouds that would grow to be smaller than the maximum size were initially generated. In reality, however, clouds might be generated that potentially could be larger than the maximum permitted by the environment. Those clouds would then be stunted in their development and would appear to be of the same size as clouds that just reach unhindered the maximum size. Thus the frequencies of the upper size range would appear inflated as observed.

4. Summary and conclusions

This paper has shown that the lognormal distribution describes well the frequency distributions of height, horizontal size and duration observed in cloud and radar echo populations in many different regions and convective situations.

Two hypotheses have been suggested to explain this phenomenon. One has to do with the growth process of cloud parcels by mixing with environmental air. Here *growth* by entrainment occurs by a random process that obeys the law of proportionate effects. The second hypothesis postulates a *formation* process of clouds by mergers of smaller elements. Here the size of the cloud being formed by the conglomeration of random boundary layer convective elements depends on how many elements have joined already.

The importance of the ideas presented in this paper should again be emphasized. First, here is the possibility of an analytical expression for cloud populations.
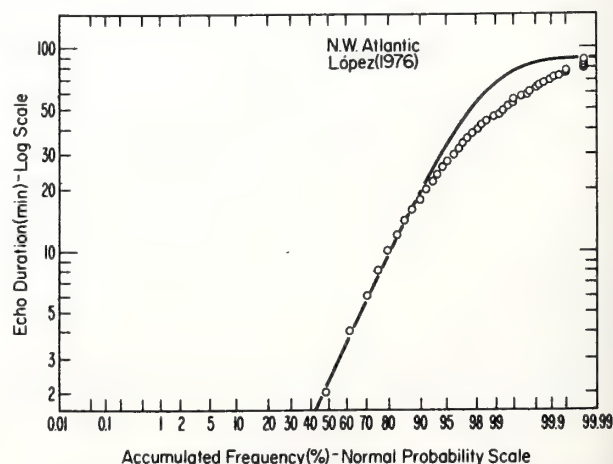
Fig. 10. Accumulated frequency distribution of radar echo durations.

This is of crucial importance for the parameterization effort. Second, the evidence presented here indicates that cloud formation and/or growth may not be an entirely deterministic process, but may instead involve a significant stochastic mechanism that follows the law of proportionate effects.

REFERENCES

Aitchison, J., and J. A. C. Brown, 1957: *The Lognormal Distribution.* Cambridge University Press, 176 pp.

Battan, L. J., 1953: Duration of convective radar cloud units. *Bull. Amer. Meteor. Soc.,* **34,** 227–228.

——, 1967: Silver iodide seeding and radar echoes from convective clouds. Sci. Rep. No. 23, Institute of Atmospheric Physics, University of Arizona, 11 pp.

Biondini, R., 1976: Cloud motion and rainfall statistics. *J. Appl. Meteor.,* **15,** 205–224.

Blackmer, R. H. Jr., 1955: The lifetime of small precipitation echoes. *Preprints Fifth Conf. Radar Meteorology,* Ft. Monmouth, N. J., Amer. Meteor. Soc., 103–108.

Braham, R. R., Jr., 1958: Cumulus cloud precipitation as revealed by radar—Arizona, 1955. *J. Meteor.,* **15,** 78–83.

Byers, H. R., and R. K. Hall, 1955: A census of cumulus-cloud height versus precipitation in the vicinity of Puerto Rico during the winter and spring of 1953–1954. *J. Meteor.,* **12,** 176–178.

Cruz, L. A., 1973: Venezuelan rainstorms as seen by radar. *J. Appl. Meteor.,* **12,** 119–126.

Dennis, A. S., and F. G. Fernald, 1963: Frequency distribution of shower sizes. *J. Appl. Meteor.,* **2,** 767–769.

Gerrish, H. P., 1969: Mesoscale studies of instability patterns and winds in the tropics. Radar Meteorological Laboratory, Institute of Marine and Atmospheric Sciences, University of Miami, 77 pp.

Hudlow, M. D., 1971: Three dimensional model of precipitation echoes for x-band radar data collected during BOMEX. Bomex Bulletin No. 10, BOMAP Office, NOAA, 51–63.

Kapteyn, J. C., 1903: *Skew Frequency Curves in Biology and Statistics.* Astronomical Laboratory, Groningen: Noordhoff (Quoted by Aitchison and Brown, 1957.)

López, R. E., 1973: A parametric model of cumulus convection. *J. Atmos. Sci.,* **30,** 1354–1373.

——, 1976: Radar characteristics of the cloud populations of tropical disturbances in the northwest Atlantic. *Mon. Wea. Rev.,* **104,** 269–283.

Mather, J. R., 1949: An investigation of the dimensions of precipitation echoes by radar. *Bull. Amer. Meteor. Soc.,* **30,** 271–277.

Meyer, S. L., 1975: *Data Analysis for Scientists and Engineers.* Wiley, 355–358.

Miller, J. R., A. S. Dennis, J. H. Hirsch and D. E. Cain, 1975: Statistics of shower echoes in western North Dakota. *Preprints 16th Conf. Radar Meteorology,* Houston, Tex., Amer. Meteor. Soc., 391–396.

Morton, B. R., 1968: Non-similar turbulent plumes. Dept. of Mathematics, GFDL Pap. No. 7, Geophysical Fluid Dynamic Lab., Monash University, Victoria, Australia, 50 pp.

Plank, V. E., 1969: The size distribution of cumulus clouds in representative Florida populations. *J. Appl. Meteor.,* **8,** 46–67.

Simpson, J., and V. Wiggert, 1969: Models of precipitating cumulus towers. *Mon. Wea. Rev.,* **97,** 471–489.

——, and W. L. Woodley, 1971: Seedling cumulus in Florida: New 1970 results. *Science,* **172,** 117–126.

Telford, J. W., 1966: The convective mechanism in clear air. *J. Atmos. Sci.,* **23,** 652–666.

Turner, J. G., 1962: The motion of buoyant elements in turbulent surroundings. *J. Fluid Mech.,* **16,** 1–16.

——, 1963: The flow into an expanding spherical vortex. *J. Fluid Mech.,* **18,** 195–208.

Weinstein, A. I., and L. G. Davies, 1968: A parameterized numerical model of cumulus convection. Dept. of Meteorology, Pennsylvania State University, NSF Rep. No. 11, GS-777, 44 pp.

Dye-laser scanning spectroscopy and fluorescence-quenching cross sections for the $B\,{}^3\Pi^+_{o,u}$ state of iodine

Michael H. Ornstein* and Vernon E. Derr

Wave Propagation Laboratory, NOAA, Environmental Research Laboratories, Boulder, Colorado 80302
(Received 14 June 1975)

A tuneable dye laser was used to study the energy-level structure near the dissociation limit of the $B\,{}^3\Pi^*_{o,u}$ state of I_2. The laser was continuously scanned from 498.0 to 520.0 nm while irradiating iodine vapor. Use of a wide-band filter, selected to pass only the third Stokes line of the fluorescence over the range of the laser scan, resulted in a continuous plot of the energy-level structure from about 35 vibrational levels below the dissociation limit to beyond the dissociation limit. From the spectrum, a value for the dissociation energy of the $B\,{}^3\Pi^*_{o,u}$ state was determined, corresponding to $\lambda = 498.8 \pm 0.3$ nm, in agreement with recent absorption-spectroscopy experiments. The laser was then set at each of two wavelengths: 517.1 nm, well below the dissociation limit, and 501.2 nm, close to the dissociation limit; the absolute self-quenching and foreign-gas (N_2) quenching cross sections for I_2 were measured by use of a digital detection system. The results were Stern-Volmer plots that yielded values of $\sigma^2\tau$, where $\pi\sigma^2$ is the quenching cross section and τ is the lifetime. Cross sections are reported on the basis of $\tau = 1.15 \times 10^{-6}$ s. A surprisingly large background fluorescence, due to collisional excitation transfer, was superimposed on the line spectrum in the foreign-gas quenching data, but not for self-quenching; appropriate corrections therefore were required for the former. Values obtained for $\lambda = 517.1$ and 501.2 nm were, respectively, $\sigma^2_{self} = 40 \pm 8$ and 75 ± 15 A², $\sigma^2_{N_2} = 3.7 \pm 1.0$ and 15 ± 3 Å².

Since the studies of Bernstein and co-workers[1] on laser Raman scattering of the $B\,{}^3\Pi^*_{o,u}$ state of I_2 above the dissociation limit indicated the possibility of using the resonance Raman effect to enhance Raman-scattering signals, there has been much interest in investigating the frequency dependence of the Raman-cross section approaching an absorption resonance of a molecule. The feasibility of using Raman lidar to measure meteorological parameters such as water-vapor and temperature profiles in the atmosphere has been demonstrated.[2,3] However, such measurements are extremely difficult, owing to the very small cross sections for Raman scattering. Fouche and Chang[4] reported resonance Raman scattering below the dissociation limit of the $B\,{}^3\Pi^*_{o,u}$ state of I_2, with an enhancement of 10^6 by use of an incident wavelength from an argon-ion laser about 2 GHz from the resonance center. However, St. Peters *et al.*[5] have disputed this finding, showing that in a very similar experiment the signal in the Raman channel was quenched and hence was not resonance Raman scattering but resonance fluorescence excited in the wing of the pressure-broadened profile.

In the present experiment, a tuneable dye laser was used to scan the region above and below the dissociation limit of the $B\,{}^3\Pi^*_{o,u}$ state of I_2, to measure the quenching cross section at various wavelengths within the transition region from resonance Raman scattering above the dissociation limit to resonance fluorescence below the dissociation limit. However, at the I_2 vapor pressures sufficiently low to ensure the absence of radiation trapping (which would invalidate the results unless complicated radiative-transfer corrections were made) it was not possible to observe resonance Raman scattering above the dissociation limit with the relatively low-power laser used in this experiment. (There is strong absorption in I_2 vapor even for λ above the dissociation limit.[6]) Instead, the experiment was confined to a study of the region of resonance fluorescence immediately below the dissociation limit of the $B\,{}^3\Pi^*_{o,u}$ state. As a prelude to the quenching studies, we decided to use the continuous tuneability of the dye laser to scan the energy levels of the molecule while moni-

toring the intensity of a single line in the fluorescence spectrum. A direct plot of the level structure of the $B\,{}^3\Pi^*_{o,u}$ state near the dissociation limit was thus obtained. Because this laser scan, when applied to the upper electronic state of the transition, gives essentially the counterpart of the usual monochromatically excited fluorescence spectrum obtained with a scanning spectrometer, which instead scans the lower electronic state, we refer to the method as "laser-scanning spectroscopy." Having investigated the level structure near the dissociation limit, we then selected two wavelengths at which to measure the absolute fluorescence-quenching cross sections for I_2, both for self-quenching and for foreign-gas quenching (due to collisions with N_2) using conventional Stern-Volmer plots of the scattered intensities. In addition to yielding new information about the I_2 molecule near the dissociation limit, these results should serve as a useful prelude for comparison to quenching cross sections of resonance Raman scattering above the dissociation limit if they are measured when more-powerful dye lasers become available.

I. THEORY

An excited I_2 molecule, after absorbing a photon of energy, $h\nu$, can either reradiate this energy as fluorescence or it can redistribute the energy in a collision with an unexcited I_2 molecule or with a foreign-gas molecule such as N_2. The various processes are indicated symbolically by

$$I_2^* \rightarrow I_2 + h\nu \quad \text{(fluorescence)}, \tag{1}$$

$$I_2^* + I_2 \rightarrow 2I \text{ (or } I_2) + I_2 \quad \text{(self-quenching)}, \tag{2}$$

$$I_2^* + N_2 \rightarrow 2I \text{ (or } I_2) + N_2 \quad \text{(foreign-gas quenching)}. \tag{3}$$

Quenching processes (2) and (3) may cause the excited molecule to be nonradiatively de-excited to the ground state or may cause the molecule to dissociate into two unbound iodine atoms. It has been shown[7,8] that the dominant quenching products are probably free iodine atoms, due to collision-induced predissociation to nearby repulsive electronic states whose potential

curves cross that of the state $B\,^3\Pi^*_{o,u}$. Both processes (2) and (3) are proportional to the concentration of excited iodine molecules, denoted $[I_2^*]$, and to the concentration of ground-state I_2 or the concentration of nitrogen buffer gas, respectively. In a steady state of absorption and decay (including atomic recombination via wall collisions), the number of excitation transitions per second can be equated to the number of decay transitions per second,

$$\pi\sigma^2_{ABS}I_0[I_2] = \tau^{-1}[I_2^*] + \pi\sigma^2_{SELF}\,\bar{v}_1[I_2][I_2^*]$$
$$+ \pi\sigma^2_{N_2}[N_2][I_2^*] \;, \tag{4}$$

where $\pi\sigma^2_{ABS}$ is the absorption cross section for photons of frequency ν (cm^2), I_0 is the irradiance by incident photons (cm^{-2} s^{-1}), τ is the effective lifetime of excited state (s), $\pi\sigma^2_{SELF}$ is the self-quenching cross section for I_2 (cm^2), $\pi\sigma_{N_2}$ is the I_2 quenching cross section due to collisions with N_2 (cm^2), and $\bar{v}_1, \bar{v}_2$ are the mean relative collision speeds (cm/s).

τ may contain a nonradiative component, in addition to the radiative lifetime, because of spontaneous predissociation. The fluorescence intensity for a particular transition from the excited state is given by

$$I_f = A[I_2^*] \;, \tag{5}$$

where A is the transition probability (per unit time). Combining Eqs. (4) and (5) gives a linear relation useful for determining the quenching cross sections (Stern-Volmer law[9]):

$$I_f^{-1} = \pi\sigma^2_{SELF}\quad \bar{v}_1(\pi\sigma^2_{ABS}AI_0)^{-1} + (\pi\sigma^2_{ABS}AI_0\tau)^{-1}[I_2]^{-1}$$
$$+ \pi\sigma^2_{N_2}\bar{v}_2(\pi\sigma^2_{ABS}AI_0[I_2])^{-1}[N_2] \;. \tag{6}$$

For experimental purposes, it is more convenient to

FIG. 1. Experimental arrangement. Q: quartz sample cell. P: photomultiplier. S: laser source. L: lens, adjustable in three axes. The I_2 reservoir is maintained at a fixed temperature.

convert concentrations to partial pressures (Torr). When this is done we see from Eq. (6) that if the partial pressure of N_2 buffer gas is zero, a plot of the reciprocal of I_2 fluorescence intensity versus the reciprocal of I_2 vapor pressure should yield a straight line with

$$\text{intercept/slope} = (\pi\sigma^2_{SELF}\,\bar{v}_1\tau)(7.501\times10^{-4}kT)^{-1} \;, \tag{7}$$

where

$$\bar{v}_1 = (8kT\pi^{-1}\mu^{-1})^{1/2}$$

and k is the Boltzmann constant (1.3805×10^{-16} erg/K), T is the absolute temperature (K), and μ is the reduced mass of I_2^*, I_2 collision partners (g). Similarly, if the partial pressure of I_2 is held constant, a plot of the reciprocal of I_2 fluorescence signal versus N_2 gas pressure yields

$$\text{slope/intercept} = \pi\sigma^2_{N_2}\,\bar{v}_2\,\tau(7.501\times10^{-4}kT)^{-1}$$
$$\times(1 + \pi\sigma^2_{SELF}\,\bar{v}_1\tau[I_2])^{-1} \;, \tag{8}$$

where

$$[I_2] = p_{I_2}(\text{Torr})/(7.501\times10^{-4}kT) \tag{9}$$

and $\bar{v}_2$ is the mean collision speed for I_2^*, N_2 collisions (cm/s). The use of these expressions to determine the cross sections is discussed in Sec. III.

II. EXPERIMENTAL CONFIGURATION

The optical system is shown schematically in Fig. 1. The light source was a flashlamp-pumped dye laser of 20 kW peak-power output per pulse (0.5 μs pulse width, 30 pps repetition frequency). The laser was continuously tuneable over most of the visible spectrum by rotating a reflection grating that, used in first order, formed the mirror for one end of the cavity. For the wavelength region of interest in this experiment, the dyes 1,2-dihydro-4-methoxybenzo/c/xanthylium fluoroborate and Coumarin 102 (Eastman Kodak trade name) were found most useful. The former dye tuned from 560.0 to 505.0 nm. Coumarin 102 tuned from 510.0 nm to well beyond the dissociation limit of the $B\,^3\Pi^*_{o,u}$ state of I_2 at $\approx$ 499.0 nm. Both dyes were dissolved in water to minimize thermal-dissipation problems and thus narrow the linewidth of the laser (Coumarin 102 was initially dissolved in a tiny amount of ethanol and 5% Ammonyx Lo was added to H_2O to keep the dye in solution). The linewidth of the laser source (full width at 10% maximum intensity) measured by a Spex 1401 Spectrometer (dispersive resolution = 0.005 nm) was approximately 0.05 nm.

The fluorescence cell consisted of a cylindrical quartz tube 30 mm long and 12 mm in diameter with flat windows sealed onto both ends. The curved side of the tube served as the exit window. A lens ($f = 40$ cm) with micrometer adjustments along three axes focused the laser into the cell and allowed for precise positioning of the beam. The fluorescent light was focused by the two-lens collecting optics, also with micrometer adjustments as indicated in Fig. 1, onto the slit of a Jarrell-Ash 0.5 m spectrometer oriented with the slit parallel to the laser beam to accept the central
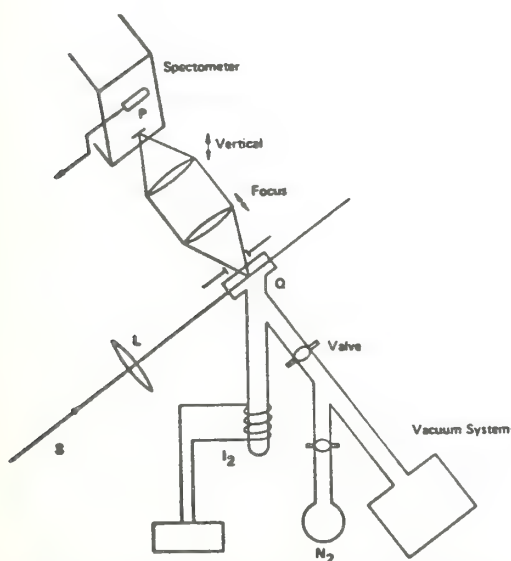
1.5 cm length of excitation region in the sample cell. The output of the spectrometer was detected by an RCA 1P28-A photomultiplier. The fluorescence cell contained a vertical tube extending below the cell that contained solid iodine. The temperature of this reservoir determined the vapor pressure of I_2 in the cell, which was found by using the vapor-pressure data of Gillespie and Fraser.[10] The I_2 reservoir was immersed in a Dewar containing ethanol; the temperature was accurately controlled by cooling coils that circulated coolant from a regulated cooling system. During the self-quenching studies, the reservoir temperature was maintained within ±0.05 °C for each data point, over the range −5 to +20 °C. (For computing cross sections, only data for $T < 14$ °C were used, to prevent radiation trapping.) During the foreign-gas quenching studies, the temperature of the reservoir was maintained at 285.0 ± 0.3 K. Temperatures were read to 0.01 °C from a Hg thermometer immersed in the reservoir. The upper part of the cell was maintained at room temperature (296 ± 1 K) throughout all runs. The cell was initially baked and pumped for over 24 h until a residual pressure of $\approx 5 \times 10^{-5}$ Torr was maintained. Baker reagent-grade iodine was then distilled into the cell under vacuum and the cell was sealed off at a pressure of $\approx 1 \times 10^{-4}$ Torr. The cell contained a side tube with a ground-glass valve through which N_2 could be introduced into the cell for the foreign-gas quenching experiments. Special halogen-resistant Halocarbon grease was used to coat the valve to prevent contamination by the I_2. In situ, the cell was permanently connected through this side tube to the vacuum system, which allowed easy evacuation of the cell and continual monitoring of the pressure in the cell to detect any leakage of the valve. No leakage was found. The N_2 pressure

in the cell was determined within ±0.01 Torr, over the range 0 to 8.5 Torr, by a manometer permanently affixed to the vacuum system. For more accurate reading, the manometer was filled with Kel-F No. 3 oil (halogen resistent), obtained from 3M Co., Minneapolis, Minn.

In the recording electronics, the signal from the photomultiplier went directly into a FET source-follower preamplifier and then into an integrate-and-hold circuit, which integrated the signal from several laser pulses and sent the integrated value through a multiplexer to an analog-to-digital converter to be printed in digital form on paper tape. To correct for fluctuations of laser intensity from one pulse to the next, a beam splitter separated a reference sample of the incident laser flux, which was simultaneously integrated, digitized, and recorded on paper tape. The recorded data were analyzed in a NOVA computer. The entire system was checked in situ for linearity by interposing interference filters, whose transmittances had been measured on a Cary spectrophotometer, in front of the spectrometer. The system was found to be linear within 10% over the range involved in the experiment.

III. RESULTS

A. Fluorescence spectra

Figure 2 shows an X-Y recorder plot of the fluorescence spectrum from I_2 with the excitation wavelength from the laser set at 517.1 nm, about 18 nm (701.5 cm^{-1}) below the dissociation limit (at about 499.0 nm) of the $B\ ^3\Pi_{o,u}^+$ state. This spectrum was obtained with the experimental arrangement described above, except that the digital recording system was replaced by an analog system in which the signals from the preamps were sent through separate channels of a boxcar integrator. The fluorescence signal was divided by the reference signal, in an analog divider, and the ratio was plotted on an X-Y recorder. The spectrometer slits were 400 μm wide for these spectra, corresponding to a dispersive resolution of 0.64 nm. In these low-resolution spectra, each vibrational transition, which in actuality consists of several rotational transitions, corresponding to the several rotational levels excited by the laser and also arising from $\Delta J = \pm 1$ transitions in emission, corresponds to a single line. In the lower plot of Fig. 2, four prominent Stokes lines can be seen. Also, one prominent and two weak anti-Stokes lines were present. The spacing between these lines (≈ 208 cm^{-1} or 6 nm) corresponds to the spacing of the vibrational levels of the ground state $X\ ^1\Sigma_g^+$, to which the excited molecule makes transitions.[11] These transitions arise primarily from molecules that were initially excited from $v'' = 0$ and 1, and to a lesser extent from $v'' = 2$ and 3. The upper plot in Fig. 2 shows the effect of introducing 1.0 Torr or N_2 buffer gas into the cell. A surprisingly large amount of excitation transfer to nearby vibration-rotation levels in the excited state is apparent from this plot. This transfer fluorescence complicated the determination of the foreign-gas quenching cross sections. The procedure for subtracting this effect is described in Sec. III.C
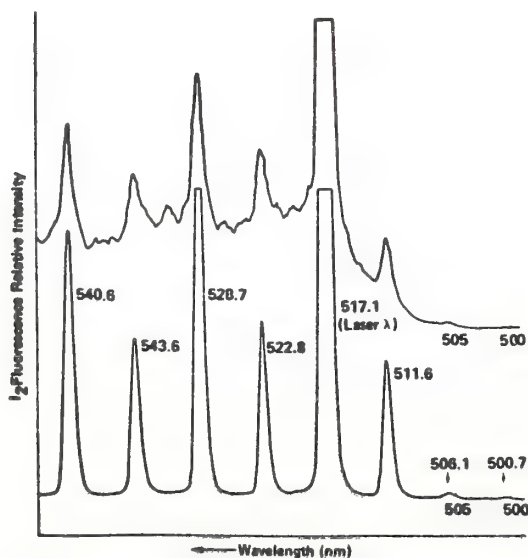
FIG. 2. Fluorescence spectrum of I_2, dye-laser excitation ($\lambda = 517.1$ nm). Bottom graph: I_2 vapor pressure = 0.12 Torr, $N_2 = 0$ Torr. Top graph shows effect of general background fluorescence due to N_2 added at 1.0 Torr vapor pressure.
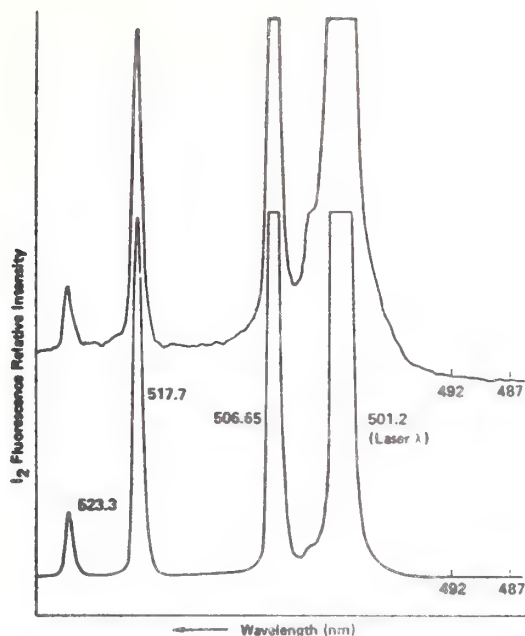
FIG. 3. Fluorescence spectrum of I_2, dye-laser excitation ($\lambda = 501.2$ nm). Bottom graph: I_2 vapor pressure $= 0.12$ Torr, $N_2 = 0$ Torr. Top graph shows effect of general background fluorescence due to N_2 added at 1.0 Torr vapor pressure.

A negligible amount of transfer fluorescence was observed in the self-quenching experiments. Figure 3 shows a similar set of plots with the laser wavelength shifted to 501.2 nm, only about 2.2 nm below the dissociation limit. In Fig. 3, the first, third, and fourth Stokes lines are again prominent. These transitions all arise from molecules that were initially excited from $v'' = 0$, because the laser wavelength is too close to the dissociation limit to excite fluorescence for $v'' > 0$. This accounts for the absence of any anti-Stokes lines. As described in Sec. III. B, we estimate $v' = 62$ for the excited state. The second line is missing, presumably due to a vanishing Franck-Condon factor for that transition. The small additional feature near the laser wavelength is not readily explained. It may be due to an intersection of the $B\,^3\Pi_{o,u}^+$ state with a nearby repulsive electronic state, which may also influence the vanishing of the second Stokes line. Higher-resolution spectroscopic studies of this region would be interesting and useful. This was not possible with the present system because of spatial instability of the laser beam, which caused the image on the entrance slit of the spectrometer to wander over a region of ± 200 μm, which limited narrowing of the slit to not less than 400 μm.

B. Laser-scanning spectroscopy

To obtain a direct display of the level structure near the dissociation limit of the $B\,^3\Pi_{o,u}^+$ state as a prelude to the quenching studies, we decided to use the continuous tuneability of the dye laser as a scanning probe. The data of Fig. 4 were obtained by use of the same recording system as in Figs. 2 and 3, but instead of

scanning the spectrometer with a fixed laser wavelength, we continuously scanned the laser wavelength, from 498.0 to 520.0 nm, by rotating the grating in the laser cavity with a motor. The spectrometer was used essentially as a variable-setting wide-band filter, by using a relatively narrow entrance slit (100 μm) and a wide exit slit (3 mm) with the spectrometer grating at a fixed setting, positioned so that only the third Stokes line passed through the exit slit. With the spectrometer grating now fixed, the laser wavelength was scanned. As the third Stokes line moved across the exit slit of the spectrometer it exhibited various peaks of intensity, corresponding to the vibrational energy levels of the $B\,^3\Pi_{o,u}^+$ state (see the schematic energy-level diagram in Fig. 4). (Use of the 100 μm entrance slit created additional fluctuations of the signal, owing to spatial instability of the laser beam, but this entered essentially as a random-noise factor and was compensated by additional filtering in the electronics.) The different scans in Fig. 4 correspond to different orientations of the spectrometer grating, and hence to different centers of the spectrometer pass band (used as a filter). Increased photomultiplier gain was used from one plot to the next as the dissociation limit was approached. For these scans, no N_2 buffer gas was present in the cell and the I_2 vapor pressure was 0.15 Torr. Spatial instability of the laser beam caused limited resolution, but the vibrational structure is clearly evident. Our best estimates for the positions of band heads are indicated as vertical lines on the graphs, out to the dissociation limit. The wavelength scale in Fig. 4 was determined by calibrating a micrometer scale on the laser-grating mount against laser wavelength determined by manually scanning the Jarrell-Ash spectrometer (with 100 μm slits) and detecting peak signals on an oscilloscope. The spectrometer, in turn, was calibrated by using the known emission lines of an argon-ion laser at 487.99, 496.51, 501.76, and 514.54 nm. The wavelength marks in Fig. 4 correspond to direct data from the calibration; they are not necessarily evenly spaced. Resolution was not deemed sufficient to warrant a detailed analysis to ob-
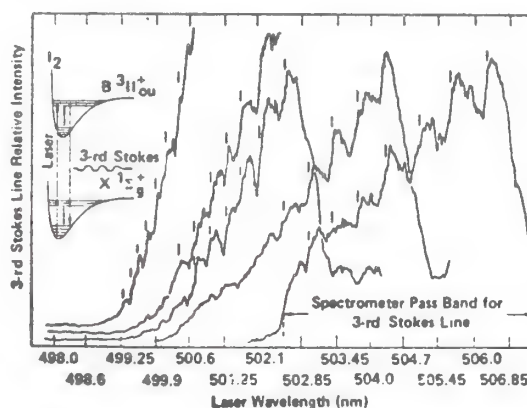
FIG. 4. Spectra of the vibrational structure of the $B\,^3\Pi_{o,u}^+$ state near the dissociation limit. Obtained by scanning the dye laser.

661

tain spectroscopic constants from the data. However, the spectra are useful for determining the vibrational levels excited in the quenching studies, and for visualizing the level structure in this region. The dissociation limit of the $B\ ^3\Pi^+_{o,u}$ state can also be estimated from the graph; it is estimated to be 498.8 ± 0.3 nm, in very good agreement with the value obtained by absorption spectroscopy.[12,13]

Excitation wavelengths 501.2 and 517.1 nm were used in the quenching experiments. The v' level excited by 517.1 nm can be determined from the precise spectroscopic constant of Wei and Tellinghuisen[14] for the $B\ ^3\Pi^+_{o,u}$ state, and of Rank and Rao[11] for the ground state, giving $v' = 40$. By determining the position of this wavelength on the extension of Fig. 4 to longer wavelengths, we assigned this v' value to a particular band. The v' level excited by 501.2 nm was then assigned by merely counting the vibrational bands in Fig. 4, which gave $v' = 62$. This value agrees with that determined by direct calculation for 501.2 nm by use of the spectroscopic constants of Ref. 14, which serves as a check on the assignment. This assignment assumed excitation from $v'' = 0$ of the ground state, the only level possible for the 501.2 nm excitation because of its proximity to the dissociation energy. For 517.1 nm, excitation from $v'' = 1$, 2, and possibly 3, are also permitted. By counting from the assigned bands to the dissociation limit, we resolved discrete levels up to $v' = 70$. In their high-resolution absorption-band study, Barrow and Yee[13] observed discrete levels to $v' = 77$. By extrapolation they estimated that the final bound vibrational level is $v' = 87$. The laser-scanning-spectroscopy technique that we employed has quite general applicability to excited-state molecular spectroscopy.

C. Quenching cross sections

The experimental system that we used for the absolute-quenching cross section measurements was as described in Sec. II. The dye-laser emission was predominantly polarized in the vertical plane; a Polaroid filter was inserted to obtain complete linear vertical polarization of the exciting light. The fluorescence signal collected at right angles (horizontally) to the laser beam was dispersed by the spectrometer (with 400 μm slits); to reduce leakage from unwanted scattered light, only the third Stokes line in the fluorescence was sent to the recording electronics. The detection electronics was designed to record only during the 0.5 μs duration of each laser pulse, which essentially eliminated photomultiplier noise from the signal. Figure 5 shows a plot of the I_2 fluorescence intensity for the third Stokes line as a function of I_2 vapor pressure. These data were obtained from a computer analysis of the recorded raw data. A computer subtracted the zero levels for each data set, divided the fluorescence signal by the reference intensity for each recorded set of values, averaged the results for 3 sets of values (320 laser pulses), and printed the results plotted on Fig. 5. Quenching cross sections were found by use of the reciprocal plots discussed in Sec. I. In order to eliminate error due to radiation trapping, only data for I_2 vapor pressure < 0.12 Torr were used for determining cross sections. Figure 6 shows Stern-Volmer plots obtained in this experiment for two laser excitation wavelengths, one (517.1 nm) well below the dissociation limit and the other (501.2 nm) close to the dissociation limit. There, wavelengths were chosen to coincide with the peaks of their respective fluorescence vibrational bands determined from Fig. 4 and the extension for Fig. 4 to longer wavelengths. The v' excited levels have been discussed in Sec. III.B The self-quenching cross sections (recorded in Table I) were determined by a least-squares linear fit to the data in Fig. 6 and by use of Eq. (7), assuming a lifetime for both excited states of $\tau = 1.15 \times 10^{-6}$ s. This lifetime was obtained by averaging all vibrational-state lifetimes for the $B\ ^3\Pi^+_{o,u}$ state obtained by Sakurai,

FIG. 6. Stern–Volmer graphs of the reciprocal of the I_2 fluorescence intensity as a function of the reciprocal of the I_2 vapor pressure. Laser $\lambda = 501.2$ nm for top graph; laser $\lambda = 517.1$ nm for bottom graph. No N_2 in cell. Small circles are experimental points.

FIG. 5. I_2 fluorescence intensity of the third Stokes line as a function of I_2 vapor pressure. Laser $\lambda = 517.1$ nm. N_2 pressure = 0 Torr.

662

FIG. 7. Stern–Volmer graphs of the reciprocal of the I_2 fluorescence intensity as a function of the buffer gas (N_2) pressure. I_2 vapor pressure = 0.0982 Torr. Top graph: λ = 501.2 nm. Bottom graph: λ = 517.1 nm. Background fluorescence was subtracted from data. Small circles are experimental points.

Capelle, and Broida.[15] No more-accurate value was found. However, the values of $\sigma^2\tau$, recorded in Table I, are the fundamental results of this study. More-accurate cross sections can be determined when future measurements yield more-accur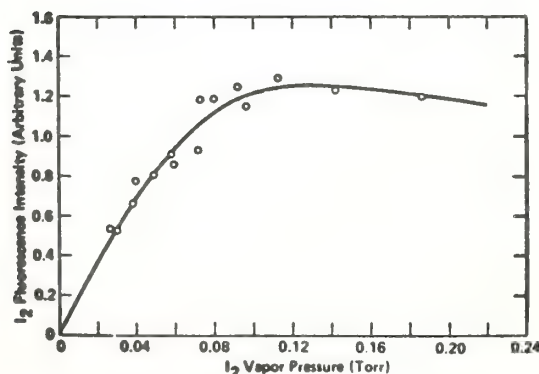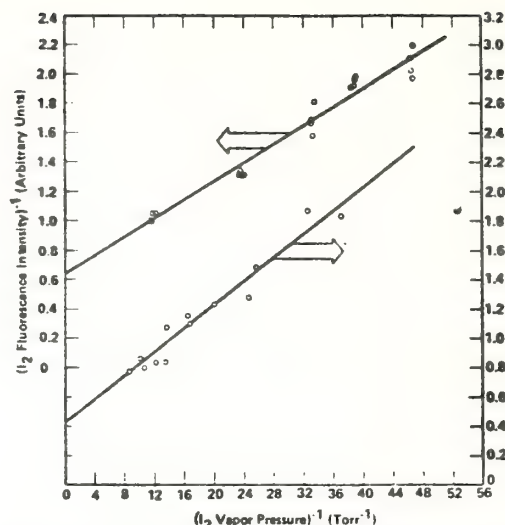ate values of τ for these states. (Although customarily called a cross section, σ^2 is the square of an effective collision diameter. The actual cross section is $\pi\sigma^2$.)

Figure 7 shows plots of the reciprocal of I_2 fluorescence signal versus N_2 gas pressure in the cell for fixed I_2 vapor pressure. As mentioned previously, the determination of the foreign-gas quenching cross sections was complicated by large background fluorescence caused by collisional excitation transfer to nearby levels in the excited state (see Figs. 2 and 3). In the quenching studies, the spectrometer slit width was 400 μm, which corresponded to a dispersive resolution (slit function) of 0.64 nm centered on the third Stokes line of the fluorescence. Because of the very close spacing of the rotational levels of the I_2 molecule[14] (≈ 0.002 nm at $v' = 40$, $J' = 1$ and ≈ 0.06 nm at $v' = 40$, $J' = 50$), the spectrometer slit function passes not only third Stokes fluorescence from the directly excited levels but also from several nearby rotational levels that are excited by excitation transfer. This transfer fluorescence must be subtracted from the data to obtain the true quenching cross section for the directly excited levels. This was done by taking two sets of data for each data point in Fig. 7. The first data were taken

with the spectrometer set to the peak of the third Stokes line. Then the spectrometer grating was rotated slightly to record the minimum intensity between the third Stokes line and the next adjacent line (see Figs. 2 and 3). The two signals were subtracted in the computer analysis, to yield the values plotted in Fig. 7; this assumes the transfer fluorescence to be a uniformly distributed background in the region of the third Stokes lines. This procedure was quite accurate for 501.2 nm exciting radiation. It was somewhat less accurate for 517.1 nm, where vibrational structure, in addition to rotational structure, appeared. Foreign-gas quenching cross sections for collisions with N_2 were determined from least-squares linear fits to the data in Fig. 7 by use of Eq. (8) with the previously determined values of $\sigma^2_{SELF}\tau$, and on the assumption of $\tau = 1.5 \times 10^{-8}$ s. The values are listed in Table I. For comparison, the values obtained by Brown and Klemperer[16] with Na D-line excitation are also given. These authors used a lifetime of 7.2×10^{-7} s to compute their cross sections. For comparison with our results, we computed new cross sections from their $\sigma^2\tau$ values, using $\tau = 1.15 \times 10^{-6}$ s. The error estimates in Table I represent an attempt to include the effects of systematic error, which is likely to be larger than the random errors in the data.

The two types of quenching involve different interactions. The self-quenching must arise from interactions of I_2 molecule in electronic states, whereas the foreign-gas (N_2) quenching surely involves transfer of energy among vibration/rotation substates of the excited electronic states. Thus they are very different processes. Their significance is that in certain kinds of measurements (e.g., I_2 in air) they can occur simultaneously; the separate measurements may be combined, if the pressure is not too high, to estimate a total quenching cross section. These results are important for any use of I_2 Raman or fluorescent spectra for identification. The cross sections are an average over many J values.

IV. DISCUSSION

A. Pressure broadening

A potential source of error in determining the quenching cross sections arises from collisional broadening of the I_2 absorption profile as the pressure of foreign gas is increased. Before foreign gas is introduced, the absorption profile, for the I_2 pressures employed,

TABLE I. Absolute quenching cross sections[a] for the $B\ ^3\Pi_{0_u^+}$ state of I_2.

	Excitation wavelength (nm)	Excited levels (v')	$\sigma^2_{SELF}\tau$ (10^{-21} cm^2 s)	σ^2_{SELF} (Å^2)	$\sigma^2_{N_2}\tau$ (10^{-22} cm^2 s)	$\sigma^2_{N_2}$ (Å^2)
This work	501.2	62	8.7 ± 1.7	75 ± 15	17 ± 3	15 ± 3
	517.1	40	4.6 ± 0.9	40 ± 8	4.3 ± 0.9	3.7 ± 1.0
Ref. 16	589.0	14, 15, 16	9.4	81.5	3.5	3.0

[a]The actual cross section is $\pi\sigma^2$ (σ^2 is the square of effective collision diameter). τ was assumed equal to 1.15×10^{-6} s (Sakurai *et al.*[15]).

M. H. Ornstein and V. E. Derr   238

663

is primarily Doppler broadened, with the width ~0.002 nm. (The laser-line width is ~0.05 nm.) If the absorption profile is appreciably pressure broadened, the amount of laser light absorbed will be different at different pressures, invalidating the analysis in Sec. I. For the foreign-gas pressures employed in the present experiment, the line width due to pressure broadening can be estimated to be about two orders of magnitude smaller than the laser-line width.[17,18] Hence, this source of error should be negligible, and the analysis is valid.

B. Radiation trapping

If the fluorescence is significantly reabsorbed by the I_2 vapor before it leaves the exit window of the cell, the fluorescence intensity recorded by the detection system at different I_2 pressures will not obey the working equations of Sec. I, because radiation-trapping effects were ignored in that analysis. Because the laser-line width was broader than the absorption line of the I_2 vapor, meaningful absorption data could not be obtained with which to estimate radiation trapping. We employed an approximate, satisfactory method to estimate the effect of this source of error. The laser beam was moved from the center of the cell to a position just next to the exit window by a slight horizontal movement of the lens that focuses the laser beam into the cell. (This of course required slight refocusing of the collecting optics.) The fluorescence intensity recorded for this beam position was compared to that recorded with the beam in the center of the cell. For I_2 reservoir temperature equal to 21 °C, corresponding to $P_{I_2} = 0.22$ Torr, the difference of intensity was found to be significant, about 20%. Figure 5 shows that, in this region, the curve of growth has reached its asymptotic value and is starting to decrease because of radiation trapping. To minimize this source of error, we determined cross sections by use of data only for P_{I_2} < 0.12 Torr. In this range, the error of the cross section due to radiation trapping is estimated to be ~10%. A potentially more accurate method, not employed, would be to insert an absorption cell in the fluorescence path.

C. Density measurement

To determine the absolute quenching cross sections, the absolute densities of I_2 and N_2 in the cell must be determined. This is likely to be the major source of error in this type of experiment. The pressure of N_2 was measured, with an oil manometer, with an estimated accuracy of ±5%. The I_2 vapor-pressure determination was likely to be considerably less accurate. We took many precautions to control accurately the I_2 reservoir temperature and allowed about 20 min. after each temperature change for re-establishment of equilibrium of the pressures in the reservoir and at the top of the cell. Initially we took data from high to low temperatures, as well as in the reverse sequence; the data were consistent to about ±10%. However, experience showed that equilibrium was established more rapidly from low to high temperature; hence, the runs for determining cross sections were taken in this di-

rection. The uncertainty of the I_2 density determination is estimated as ±15%.

D. Error estimate

In addition to the systematic errors mentioned, there is an additional error in the foreign-gas quenching cross sections associated with the transfer-fluorescence correction. This is accounted for, at least in part, by the random scatter of the data. The random scatter was more serious for $\lambda = 517.1$ nm than for $\lambda = 501.2$ nm. The systematic error was combined with the random error, determined by the least-squares fit to the data, by taking the square root of the sum of squares to give the error estimates listed in Table I.

A possible source of error arises from diffusion of molecules from the observation region before they decay. A simple estimate may be made of the fraction $(\Delta N/N)$ of molecules that decay before leaving the observation region. The mean speed of the molecules is $\bar{v} = (8kT/\pi M)^{1/2}$. For an I_2 molecule the molecular weight $M = 254$ amu. Thus $\bar{v} = 1.56 \times 10^4$ cm s^{-1} at $T = 293$ K. Then $\Delta N/N = [1 - \exp(-t/\tau)]$, where $\tau = 1.15 \times 10^{-6}$ s (Sakurai et al.[15]), the average lifetime, and t is the average time to traverse a 0.04 cm diam sample volume, that is $t = 2.56 \times 10^{-6}$ s. Thus $\Delta N/N = 0.89$. Hence, approximately 89% of the excited molecules decay before they leave the sample volume. Of the remaining 11% approximately one third travel along the direction of the laser beam parallel to the spectrometer slit, which increases the number observed to 93%. The effect of collision in the sample volume is to slow the diffusion of molecules; obviously, collisions occur, because quenching is observed. Therefore, the maximum error due to this effect is 7%. This error contributes little to the error estimate. The Stern-Volmer plots are not affected over the range of pressure used. This type of error is obviously smaller for the N_2 quenching studies.

The gating technique did not exclude any meaningful emission. The emission was continuously monitored with a range of ten times the gate width, and the gate was adjusted to a length at least double any observed emission. The error estimated from this source is much less than 1%.

*Present address: 2415 Gales Way, Forest Grove, Ore. 97116.
[1] W. Holzer, W. F. Murphy, and H. J. Bernstein, J. Chem. Phys. 52, 399 (1970).
[2] R. G. Strauch, V. E. Derr, and R. E. Cupp, Remote Sensing Environ. 2, 101 (1972).
[3] R. G. Strauch, V. E. Derr, and R. E. Cupp, Appl. Opt. 10, 2665 (1971).

[4]D. G. Fouche and R. K. Chang, Phys. Rev. Lett. 29, 536 (1972).

[5]R. L. St. Peters, S. D. Silverstein, M. Lapp, and C. M. Penney, General Electric Co. Tech. Inf. Ser., Schenectady, N.Y., Report No. CRD 297, Nov. (1972).

[6]Herzberg, *Spectra of Diatomic Molecules*, 2nd. ed. (Van Nostrand, Princeton, 1950), p. 38.

[7]E. Wasserman, W. E. Falconer, and W. A. Yager, J. Chem. Phys. 49, 1971 (1968).

[8]J. I. Steinfeld, J. Chem. Phys. 44, 2740 (1966).

[9]O. Stern and M. Volmer, Z. Phys. 20, 183 (1919).

[9]L. Gillespie and L. Fraser, J. Am. Chem. Soc. 58, 2260 (1936).

[11]D. H. Rank and B. S. Rao, J. Mol. Spectrosc. 13, 34 (1964).

[12]R. J. LeRoy and R. B. Bernstein, J. Mol. Spectrosc. 37, 109 (1971).

[13]R. F. Barrow and K. K. Yee, J. Chem. Soc. Faraday Trans. 2 69, 684 (1973).

[14]J. Wei and J. Tellinghuisen, J. Mol. Spectrosc. 50, 317 (1974).

[15]K. Sakurai, G. Capelle, and H. P. Broida, J. Chem. Phys. 54, 1220 (1971).

[16]K. Brown and W. Klemperer, J. Chem. Phys. 41, 3072 (1964).

[17]S. Y. Ch'en and M. Takeo, Rev. Mod. Phys. 29, 20 (1957).

[18]R. B. Kurzel and J. I. Steinfeld, J. Chem. Phys. 53, 3293 (1970).

Ocean Surface Currents
Mapped by Radar

Mobile coastal units can map variable surface currents
in real time to 70 kilometers, using ocean wave scatter.

D. E. Barrick, M. W. Evans, B. L. Weber

Currents within 1 meter of the ocean surface are highly variable, being driven by geostrophic forces and tides, but are strongly influenced by the local surface wind and wave fields. These currents transport floating matter and thus are of great importance in coastal areas, where considerable damage can be done by surface-borne pollutants and oil. In the case of the large oil spill by the tanker *Argo Merchant* off New England in December 1976, for example, catastrophic environmental damage was averted because strong offshore winds counteracted the normal surface-current drift toward shore. In a positive vein, the upper portion of the sea carries the zooplankton and phytoplankton, which are the dominant components at the bottom of the food chain and are responsible for production of most of the world's oxygen. Many types of fish eggs are borne by surface currents, which are therefore of concern to the fisheries industry. The transport of water with anomalous tem-

The authors are scientists with the Sea State Studies Area of the Wave Propagation Laboratories, Environmental Research Laboratories, National Oceanic and Atmospheric Administration, Boulder, Colorado 80302.

perature differences is now believed to be responsible for unusual weather patterns affecting entire continents.

Near-surface current patterns, and how they respond locally to the relevant prevailing forces, are a subject that is largely unknown. Yet the subject is a crucial ingredient for the effective management of operations in coastal waters, and an increasingly important input for global resource monitoring and weather predictions.

Current Measurements

In conventional methods of measuring currents moored meters are used; the most recent types are referred to as vector-averaging current meters and the Aanderaa meter (*1*). These devices must be moored at depths exceeding 10 m, and thus provide little indication of the current at the surface, which is often different. Furthermore, data must be either recorded aboard the buoy (to be picked up later for analysis) or telemetered to shore; the instrumentation for the latter often restricts the operating range from

the receiver to tens of kilometers. Surface currents have been measured by tracking floating objects. Qualitative estimates can be obtained by photographing the dispersal of dye packages from an aircraft, or by analyzing satellite infrared and optical imagery of suspended sediment (to a coarser area scale) (*2*). Quantitative measurements are made by photographically recording the positions of time-released floats dropped from the air, as described by Richardson *et al.* (*3*), or by tracking a drifting drogue buoy from a ship (*1*). In the latter case, a high-precision navigation system is required on the ship to accurately establish the drift of the buoy. Operations with aircraft or ships are both expensive and time-consuming for the meager amount of current data obtained (one vector over a period of about 1/2 hour). The velocity accuracy of these float-locating techniques appears to be of the order of 10 to 15 centimeters per second in magnitude and 5° in angle (*2*). The location of such drogues by triangulation, using high-frequency (HF) surface-wave emissions from the buoy, is described in (*3*); although such drogues are inexpensive ($175), the positional accuracy deteriorates with distance from shore, making this an unacceptable alternative near the edge of the continental shelf.

We discuss here a coastally located HF radar system that can measure and map near-surface currents to ranges about 70 kilometers from shore. This instrument deduces current velocity from the echoes scattered continuously from the ocean waves; buoys and drifters are not required. The radar units were built to be transportable and quickly deployable on a beach. A minicomputer controls the radar and processes the signals, permitting a current-vector map to be plotted in the field after 1/2 hour of operation. Two spatially separated radar units are presently employed, simultaneously

but independently, in order to yield the total current vector at each map grid point.

The principles underlying the system have been studied theoretically and experimentally over the past several years. The motion of the waves is seen by the radar as a translation of the frequency of the received echo signal from that of the transmitted signal; this frequency translation is called the echo Doppler shift. The radar can thus resolve and measure the component of scatter velocity along the line between the scatterer and the radar, referred to as the radial velocity. Crombie (4) first showed experimentally—and it was later confirmed theoretically (5)—that to first order the scatterers at high frequency are ocean wave trains moving toward and away from the radar, having spatial periods precisely one-half the radar wavelength. Thus the scattering mechanism is the diffraction grating or Bragg effect used in holography or in x-ray analysis of crystalline structures. The spectrum of the continuous-wave transmitted signal is a narrow peak at the carrier frequency location, as shown in Fig. 1. In the absence of current, the received first-order sea echo appears as two symmetrically spaced peaks about the carrier, whose Doppler shifts are given by the lowest-order dispersion relation of the scattering gravity waves; that is

$$\pm f_d = 2v_{ph}/\lambda =$$
$$2(gL/2\pi)^{1/2}/\lambda = (g/\pi\lambda)^{1/2} \quad (1)$$

where λ is the radar wavelength, $L = \lambda/2$ is the length of the ocean waves responsible for the first-order Bragg scattering, v_{ph} is the phase velocity of these waves, and g is the gravitational constant.

A current beneath the surface waves represents a transport of the water mass, and can be thought of as a translation of the entire coordinate frame for the waves with respect to the observer at the stationary radar on shore. Hence the two spectral peaks scattered from the waves will be shifted (with respect to the position of the carrier frequency) by a small amount proportional to the radial component of current velocity, as shown at the bottom of Fig. 1. This amount is $\Delta f = 2v_{cr}/\lambda$, where v_{cr} is the mean effective current velocity radial to the radar. In (6), radar-deduced radial current observations were compared with drifter measurements of currents at San Clemente Island; the narrow radar beam and short pulse kept the ocean patch size under observation to about 7 by 7 km. The agreement was about ± 10 cm/sec. In

these investigations (6, 7) the effect of a nonuniform current on the transport of the radar-observed surface waves was also analyzed as a function of depth.

Experiments such as those at San Clemente Island (6, 7), resolving the sea echo from narrow azimuthal sectors at high frequency, require long permanent phased-array antenna systems (> 300 m) on the beach to form a narrow beam. When one considers typical current patterns and the various echo-signal Doppler shifts they would produce at different azimuths from the radar, one can conceive of much smaller, simpler antenna systems for determining the direction of arrival of the echo. For example, by comparing the phase between two noninteracting antennas separated by less than one-half wavelength, one can uniquely determine the direction of arrival over 180° of space of a single signal at a given Doppler shift. Crombie (8) showed that this simple two-antenna system was adequate to azimuthally resolve sea-echo signals from Florida, looking eastward across the south-to-north Gulf Stream current flow.

Concepts Behind the Present System

Because seawater is nearly a perfect conductor at high frequency (3 to 30 megahertz), the "ground-wave" propagation mode is employed (9). In this mode, vertically polarized electric fields are transmitted and received. The propagating fields at these frequencies follow the curvature of the earth and continue well into the shadow region beyond the

horizon, even in the absence of atmospheric and ionospheric refractive index anomalies. Mathematical solutions for the ground wave—corrected to include the effects of sea-surface roughness (9)—are available. They show that (i) near the radiating source, the field decays with the expected inverse range dependence of free space, and (ii) far into the shadow region, the fields near the surface decay exponentially with range. This exponential range dependence ultimately dictates the maximum distance at which currents can be observed for a particular transmitted power. For the hardware described in the next section, the maximum range for the system—allowing for a 10-decibel signal-to-noise ratio (S/N) at the receiver (10)—is about 70 km; this has been verified in our recent experiments, which are discussed below.

Although the system does not employ ionospheric or atmospheric refraction to propagate beyond the horizon, it is incorrect to call it a "line-of-sight" radar (as is a microwave radar). In fact, trying to increase the useful range of the radar by elevating the antennas (in order to increase the distance to the horizon) is counterproductive, because there is a discontinuity in the propagation path in free space between the antennas and the highly conducting seawater. We have established this fact theoretically and also experimentally, by trying to put the antennas on roofs of buildings (but back several hundred meters from the water) to increase the range. We have found that the optimal locations for the antennas are at sea level on the beach, as close to the water as possible; in fact, it
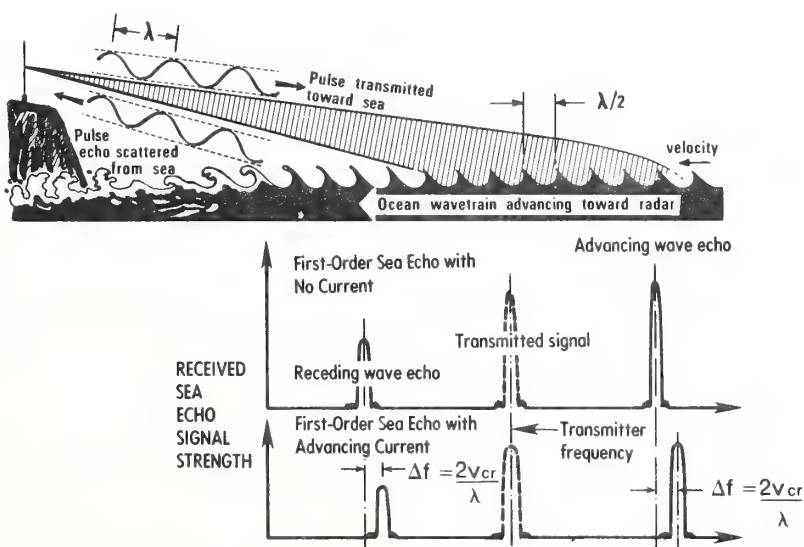

Fig. 1. Sketch showing the principles of first-order HF Bragg scatter from the sea, and resulting signal echo spectra without and with an underlying current.

is best if the grounding system beneath the antennas makes electrical contact with the seawater.

A separate antenna is used for transmitting. It produces a slightly directional pattern, peaked out toward the sea, with a half-power beam width of $\pm 90°$; its radiation in the backward direction is ~ 10 db lower than that in the forward direction, which minimizes unwanted illumination over land. As with nearly all radars, time gating of the received signal echo referenced to the transmitted pulse time determines the range to the sea echo. Our system transmits a 20-microsecond unmodulated pulse and digitizes the received echo signal every 20 microseconds after transmission. The signal sample from each range (time) gate thus represents the echo from an annulus of the sea surface 3 km in width, concentric with the radar location. A total of 25 consecutive range-gated signals are thus retained for every transmitted pulse, providing a total distance of about 75 km from the radar. The transmitted pulse repetition interval is 1 millisecond.

Since echo-signal Doppler shifts are to be related to current velocities, the time series for each range gate is spectrally processed. This is done digitally at the radar site with a fast Fourier transform (FFT) algorithm. Appropriate digital filtering of the signals is performed before the FFT to prevent spectral aliasing and to maximize S/N. Since the sea surface is a random variable, the sea echo is also a random variable. In fact, each spectral power point output from the FFT is an independent random variable, following a chi-square distribution with two degrees of freedom (11).

In the first series of experiments, three colinear independent receiving antennas were employed. The received signal was sampled on each antenna separately and sequentially for each transmission every millisecond, with the other two antennas switched open to minimize mutual interactions. Therefore the FFT outputs from the three antennas (for a given range gate) can be thought of as being measured simultaneously; the only theoretical difference between the signals at the antennas is due to the phase path differences undergone by an echo, at a particular Doppler frequency from a particular direction, arriving at the different positions of the three elements. Three antenna elements, each separated for our first experiments by one-quarter wavelength (3 m at 25 Mhz), aligned parallel to a straight coastline, can unambiguously resolve two sea-echo signals at a particular Doppler frequency from 180° of space. For two signals with complex amplitudes $\dot{A}_1$ and $\dot{A}_2$ from angles α_1 and α_2 (with respect to the perpendicular to the coastline), the three complex received voltages $\dot{V}_A$, $\dot{V}_B$, and $\dot{V}_C$ can be solved in closed form for the desired angles and amplitudes, with the following results (asterisks denote complex conjugates)

$$\alpha_{1,2} = \sin^{-1}\left[\frac{- \tan^{-1}\left(\frac{\text{Im}(x_{1,2})}{\text{Re}(x_{1,2})} \right)}{\pi/2} \right] \quad (2)$$

and

$$\dot{A}_{1,2} = \frac{\dot{V}_A x_{2,1} - \dot{V}_B}{(x_{2,1} - x_{1,2})} \quad (3)$$

where

$$x_{1,2} = \frac{(|\dot{V}_C|^2 - |\dot{V}_A|^2) \pm i(4|\dot{V}_C \dot{V}_B^* - \dot{V}_B \dot{V}_A^*|^2 - (|\dot{V}_C|^2 - |\dot{V}_A|^2)^2)^{1/2}}{2(\dot{V}_C^* \dot{V}_B - \dot{V}_B^* \dot{V}_A)}$$

In reality, since the sea-echo signal amplitudes $\dot{A}_1$ and $\dot{A}_2$ are random variables to which random noise is added, the angles of arrival determined from Eqs. 2 to 4 contain a random error that decreases with increasing S/N. Extensive simulations and special experiments have shown that for 10-db S/N, such angular errors are less than 1° for $|\alpha| < 70°$. We have recently changed to a four-antenna configuration (arranged in a square) to resolve two signals from 360°; this permits us to operate the radar on a peninsula or an island with ocean water subtending more than 180° around the site.

Two sites are required to obtain two radial current-vector components along lines pointing in different directions in order to construct a total current vector at a particular point on the sea. For a straight coastline, the question arises as to how far apart the sites should be. Since a total current vector can be constructed only within the common overlapping areas seen by both sites, it is desirable to maximize this area (by moving the sites closer together). On the other hand, as the sites become close (superposed in the limit), they see most points on the sea in the common area along nearly the same radial direction, which makes construction of the total vector inaccurate. Consequently, we defined the optimization criterion for site separation as the product of the common coverage area times the average of the sine of the angle between the lines to the two sites. This product has a broad maximum, indicating that for a coverage distance from a single site of about 70 km, a site spacing anywhere between 25 and 55 km is adequate.

Various trade-offs were considered in selecting the frequency range 25 to 26 Mhz for our first series of tests (the radar wavelength of 12 m is, to first order, scattered from ocean waves with a 6-m wavelength). At these frequencies atmospheric and external man-made electrical noise are often low, being equal to internal electrical receiver noise, whereas at lower frequencies atmospheric noise seen by the radar increases sharply. In addition, antenna sizes also increase with decreasing frequency, requiring larger structures and more ground area. On the other hand, ground-wave propagation loss decreases with decreasing frequency, offsetting the noise dependence. There are additional reasons for operating at higher frequencies, however. For one thing, above 25 Mhz ionospherically propagated echoes are rarely encountered, whereas at lower frequencies such distant echoes can be folded in with the desired short-range sea return. Two other important reasons for higher frequencies are oceanographic in nature. First, the Bragg-scattering 6-m ocean waves are relatively short and are likely to be present more of the time than longer waves, which require stronger winds to develop them. A wind with a velocity greater than 3 m/sec, blowing longer than 1 hour, will develop 6-m waves to their (equilibrium) root-mean-square height of ~ 10 cm. Inasmuch as the waves are used only as a "tracer" for the underlying currents, it is desirable that they be present as often as possible. Second, the shorter the ocean waves under observation, the more they are influenced by currents very near the surface. A rule of thumb (6, 7) is that the depth of the layer whose current will affect a surface wave of length L is $L/2\pi$ (about 1 m for $L = 6$ m). Hence, if one wants to observe currents in the uppermost ocean layers by measuring their effect on the phase speeds of gravity waves, he should use as high a radar frequency as possible. These factors led us to select 25 to 30 Mhz for our initial operations.

Hardware Description

The present two-unit radar system was designed as a prototype of an operational version, with considerably more flexibility than will ultimately be needed, in order to facilitate changes as experience is gained in the field. Yet this system was built to be transported by vehicle (see Fig. 2), easily erected on a beach, and capable of being operated from a portable power supply (a 2.2-kilowatt gaso-
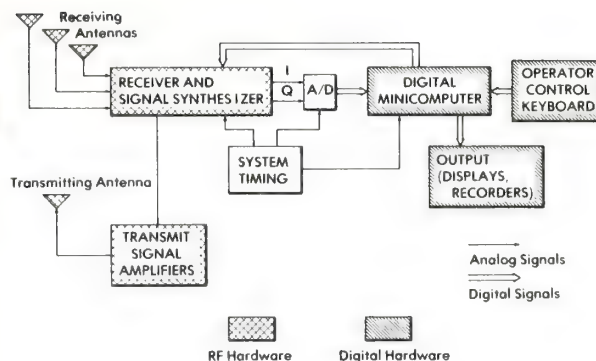
Fig. 2 (left). Sketch of the system as operated on the beach. Transmitting antennas are on the left and receiving antenna on the right. Fig. 3 (right). Block diagram of radar system.

line generator). The entire radar is controlled by a minicomputer, which also does the signal and data processing in the field. The end result is a map—drawn on a pen plotter—of the surface-current vector field.

The system radiates ~ 2.5-kw–peak pulse power, as a stream of 20-μsec pulses every millisecond; thus the average radiated power is only 50 watts. The radar is presently capable of transmitting any operator-selected frequency between 25 and 35 Mhz (in 200-khz increments), but so far we have operated primarily between 25 and 26 Mhz. The transmitting antenna is a log-periodic vertical monopole array of three (or four) elements designed especially for this application at Lawrence Livermore Laboratories (12). Both versions were designed to have an input impedance of ~ 50 ohms (real) from 25 to 27 Mhz; the three-element version has a half-power beam width of $\pm 90°$, while the four-element version has $\pm 43°$.

The individual receiving elements are readily available fiberglass–encased citizens-band whips cut to a height of 1.575 m and each fed against a quarter-wavelength, four-element, radial ground screen. The three (and currently four) receiving elements are aligned on the beach with a tape measure and compass. These elements are each connected through one-half wavelength of coaxial cable to a switching network and preamplifier box, which cycles sequentially through each of the antennas at a rate of 1 msec per antenna. From this switch, the signals then pass through a single preamplifier and coaxial line several tens

of meters in length to the receiver hardware in the van. From the antenna switch onward, the signals from each antenna pass through the same hardware, eliminating mismatch problems through separate channels. The entire antenna system can be unfurled by two men in about 1/2 hour.

The heart of the radio-frequency system is the receiver (Fig. 3), designed by Barry Research, Inc., especially for this radar. In addition to its obvious function, the receiver also synthesizes the desired

carrier frequency and the pulse stream to be transmitted. This stream is amplified in hardware designed and built in-house. Every 20 μsec, the receiver gain is changed under computer control, called a sensitivity time control (STC), in order to compensate for the decrease of echo strength with range. The echo is coherently mixed down to zero-intermediate-frequency in-phase and quadrature (I and Q) signals. These I and Q signals are then digitized with a ten-bit analog-to-digital (A/D) converter every 20 μsec,
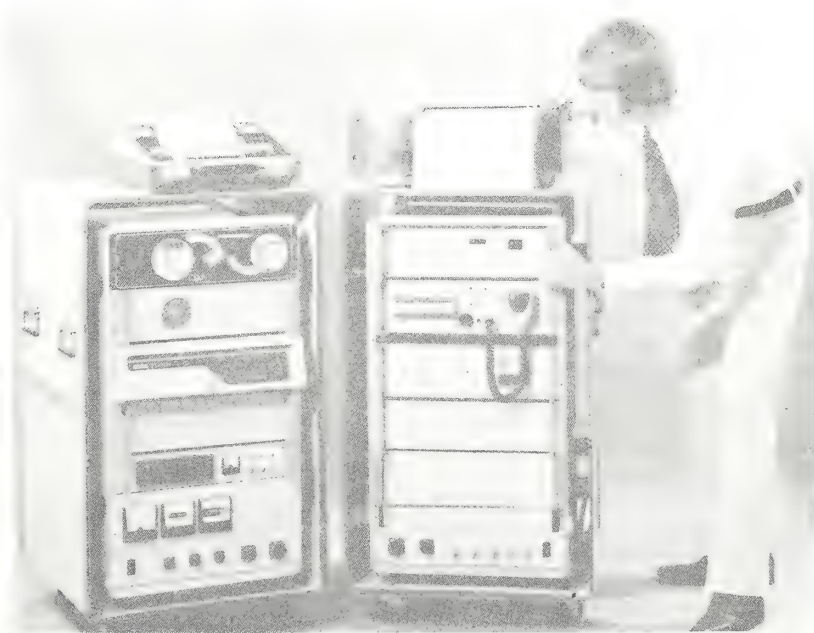
Fig. 4. Photograph of complete radar radio-frequency and digital hardware.

and all subsequent signal processing is done digitally. This includes filtering (called preaveraging, over 1/2 or 1/4 second) to reduce the signal bandwidth to 2 or 4 hertz. The filtered signals for each range gate and each receiving antenna are then collected for 128 or 256 seconds as the input to a 512-point complex FFT; thus, for the 128-second option, for example, the displayed spectrum has a Doppler resolution of 1/128 hertz over a window from − 2 to + 2 hertz. (These parameters can be selected by the operator.) The 1/128-hertz Doppler resolution translates into a radial current velocity resolution of ~ 5 cm/sec.

The heart of the digital system for radar control and data processing is a Digital Equipment Corporation PDP 11/34 minicomputer. The operator communicates with the system through a portable keyboard terminal. Moving-head magnetic disk and nine-track magnetic tape units are available for loading system software into the computer and also for recording and archiving processed radar data. Graphic displays and pen plotters are available to display raw spectra and current-vector plots. Further description of the system hardware is found in (10); a photograph of the complete digital and radio-frequency hardware (excluding antennas) for one site is shown in Fig. 4.

Experimental Results and Digital

Data Analysis

Initial field operations began with the new radar system in southern Florida during late 1976; there was an additional final week of operations in Florida from 20 to 26 March 1977, during which fairly extensive independent measurements of surface currents were made for comparisons. The Florida area was selected for initial operations and system calibrations because of the fairly regular but strong south-to-north Gulf Stream flow east of Miami. The two sites were located at South Miami Beach (20° 46′00″N,80°07′58″W) and Fort Lauderdale (26°05′01″N,80°06′38″W), approximately 36 km apart. The latitudes and longitudes of the two sites are entered into the computer, along with the azimuthal bearings of the two receiving antenna arrays. The software then calculates the x, y positions of a rectangular grid (3 by 3 km) of points to the east of the baseline joining the two sites—at which current vectors will be plotted from the radar data—after conversion from the radar-oriented polar coordinates (range and azimuthal bearing from each site). Most of the measurements

were made on 25.4 or 25.6 Mhz, with a 128-second coherent integration time (providing a Doppler resolution of 1/128 hertz).

The output of a single FFT is a complex random variable, having Rayleigh amplitude and uniform phase probability densities. The desired first-order portion of the sea echo is random because of the statistical nature of the scattering sea surface. The remaining portion of the FFT output can be thought of as additive random noise with respect to its effect on the desired first-order signal. In reality, there are at least four types of noise, originating from different sources: (i) external atmospheric or man-made noise, (ii) internal receiver noise, (iii) second-order radar sea echo (13), and (iv) processor noise due to limited system dynamic range, system nonlinearities, and quantization noise. Finally, the actual current field beneath the waves, instead of being uniform, is more likely to be somewhat turbulent within the spatial resolution scales seen by the radar. Hence, the total signal plus noise is ran-

dom, and from this we intend to extract (i) an estimate of the azimuth angle of arrival of the signal at each Doppler frequency output from the FFT, (ii) an estimate of the radial current velocity at this range and azimuth, and (iii) the sea-echo signal amplitude.

Since extraction of the angle of arrival, using the equations given above, requires the use of coherent simultaneous signals from each of three (or four) receiving antennas for a given range cell, we cannot average the individual outputs of the FFT's in order to reduce the effects of random signal fluctuation and noise. Instead, we go through the following process. Figure 5 is an example of the right half of the amplitude-squared output of the FFT processor for the 37.5-km range gate for sea echo measured at Fort Lauderdale. A threshold level is established for the usable portion of the signal (for example, 20 db down from the mean peak level), and the remainder of the FFT output is discarded. The solid curve shows the expected position of the echo in the absence of any current over the semicircular range cell; it occurs at a Doppler shift f_d (Eq. 1). All echo points at Doppler shifts different from f_d are therefore due to currents, and a radial current velocity scale centered on f_d can be given in terms of these Doppler shifts, as shown in Fig. 5. The angle of arrival of the signal at each of these Doppler shifts (or radial current velocities) is then obtained from the complex signals $\dot{V}_A$, $\dot{V}_B$, and V_C at each of the three antennas, using Eqs. 2 to 4.

At this point, for a given 128-second run and for each range gate, we have an array of azimuth angles and signal echo amplitudes as a function of radial current velocity. We then interchange the roles of the dependent and independent variables, considering radial velocity as a function of azimuth angle. After accumulating and storing radial velocity data over several consecutive 128-second runs (typically ten), we then average the radial velocities that fall within preset angular "bins."

This averaging is actually done in a manner that gives preference to higher-quality points. First of all, each sample radial velocity point in a particular angular bin is weighted by the ratio of the signal (amplitude squared) to the average noise power level for that same point; higher signal amplitude values give more accurate angle estimates. Second, other quality factors are used to weight the radial velocity samples. For example, in the absence of noise, the amplitudes of $x_{1,2}$ given in Eq. 4 will always be unity. Hence samples whose values of $|x_{1,2}|$ de-
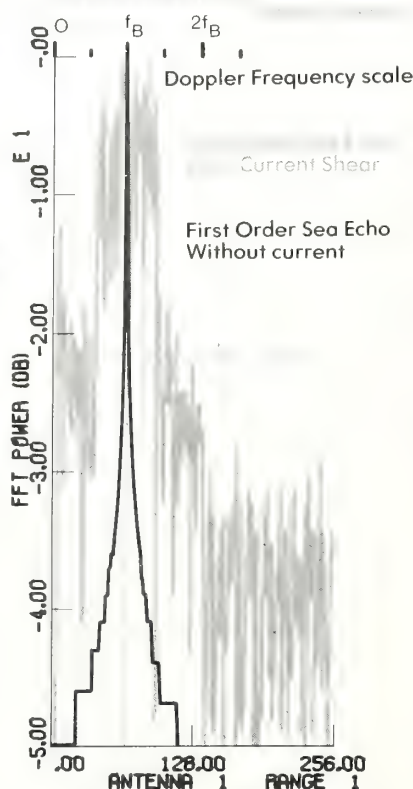

Fig. 5. Plot of FFT spectral power output. The black spectrum is the idealized test sea-echo spectrum in the absence of a current. The gray spectrum is the measured sea echo at 37.5 km from Fort Lauderdale, as modified by Gulf Stream current shear.
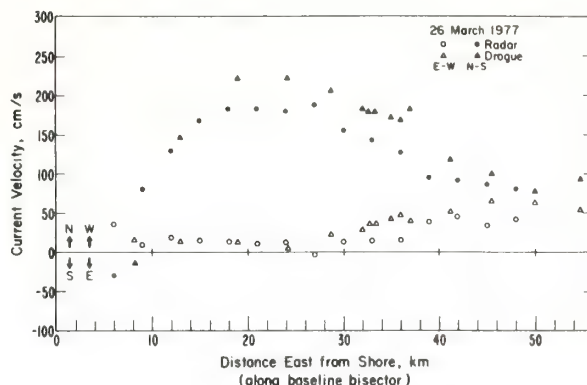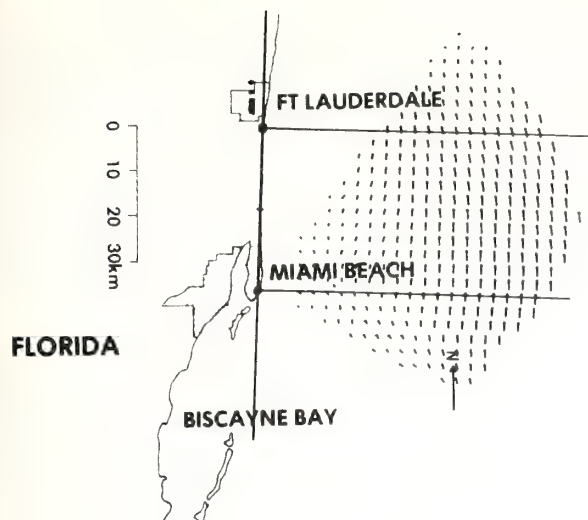
Fig. 6 (left). Computer-generated map of the Gulf Stream current on 20 October 1976 as deduced by radar. Fig. 7 (right). Comparison of radar-deduced surface currents and drifter measurements, resolved into north-south (solid symbols) and east-west (open symbols) components.

part significantly from unity are weighted lower. Finally, the signal-to-noise ratios for all of the samples in a particular angular bin are averaged; this is used in a final thresholding process to decide whether the (weighted) averaged radial velocity for that bin will ultimately be used. If it is not used (because the signals are too low) or if there were no values falling in the bin, then a value for the radial velocity at that angle is calculated by interpolation from the adjacent range-azimuth cells.

In the process of producing a map, the data from both sites are combined (in our case, either by data telemetry between the two sites or by physically transporting the data tapes from one site to the other). Then the arrays of radial current velocities from each radar site together with range and azimuth (in polar coordinates) are entered for each rectangular grid point; also, direction cosines at the grid point are calculated for the radial lines to the sites. This allows the total current vector to be plotted at that grid point. The angular sectors very near the shore are sometimes excluded because the nearly parallel radial velocities seen from each site at these grid points give rise to large vector errors; integration techniques to improve the quality of the maps near shore are being investigated. Figure 6 is an example of a map made in Florida by using these data processing steps. The well-known horizontal shear of the Gulf Stream (outward from the shore) is clearly visible in these maps.

The point to be emphasized is that all of the averaging, weighting, and thresholding procedures described above are done digitally (not arbitrarily or subjectively), according to rules that are being

optimized. The mathematical steps involved, beginning with the angle extraction, are nonlinear in nature. Hence it is not possible to obtain mathematical error estimates in closed form. The optimization of the processing algorithms must therefore be based on two methods of quality assessment. First, simulations are employed in which one begins with known current patterns, randomizes the first-order sea-echo spectrum, adds random noise, converts to a time series, and then processes this simulated echo signal to see how well the original current patterns are recovered. We have been using such simulations for nearly 3 years to arrive at our present algorithms. Second, independent measurements of surface currents are obtained during radar operations, using drifters and timed-released floats. Comparisons of these measurements with radar data are the subject of the next section.

Comparison with Drifters

As an ultimate calibration standard, one would like to employ independent measurements of near-surface currents as "ground truth." However, since differences of tens of centimeters per second have been documented in drifter current measurements, there is considerable doubt as to whether disagreements of this order between drifter- and radar-deduced currents are due to radar errors or drifter errors. Furthermore, the two techniques are so dissimilar in nature that there are many reasons why they should respond differently to conditions near the surface. Nonetheless, since drifters are the only established quantitative method of esti-

mating surface currents, we made a series of radar measurements on 23 to 26 March 1977 in Florida in conjunction with ship tracks of drifters in order to establish some initial credibility for this new remote-sensing technique. The Nova University vessel *Youngster III*—supported by a Hi-Fix Navigation system—tracked a drifter at several positions in the radar coverage area over 8- to 12-hour periods on 23 and 25 March. This drifter was drogued with rigid vertical aluminum baffle plates extending 46 cm below the surface float. Each track consisted of a 5- to 8-minute drift whose start and end points were marked navigationally; from this a mean (Lagrangian) drift velocity was calculated. In addition, the National Oceanic and Atmospheric Administration vessel *Virginia Key*—supported by a miniranger navigation system—tracked a cork float on 23 and 24 March at other locations in the coverage area. Again, each track lasted about 5 minutes.

The velocities deduced from both radar and drifter measurements, and the differences between them, were relatively similar in all cases. Significantly, the drifter velocities show considerable differences from day to day. For comparison, we show here our longest set of drifter measurements, made eastward from shore (at the midpoint between the two radar sites) to a range of 50 km; these drifter measurements, made with the *Youngster III* and the drogued buoy, required 12 hours to complete. These measurements are shown in Fig. 7 along with radar-deduced current velocities. The north-south and east-west components of the total velocity vectors are plotted in each case.

The agreement is very reasonable,

within the range of the expected drifter variances. Of possibly greater significance than the actual differences are the facts that (i) both the radar and the drifter observed the "countercurrent" flowing toward the south close to shore (this current element is seen only occasionally, and was not observed with the radar or drifters on the other 2 days); and (ii) both instruments recorded the considerable current shear with distance from shore. This shear was also seen to be variable in its magnitude and position from day to day. The maximum difference between the currents determined by the two techniques is about 50 cm/sec. The root-mean-square difference from this plot is 27 cm/sec, defined as

$$\left[\frac{1}{L} \int_0^L d^2(x)\ dx \right]^{1/2}$$

where d is the difference between straight-line segments joining radar and buoy points and L is the total length of the common path over which the two sets of measurements were made.

There are many possible explanations for the differences between the two techniques. First the radar was observing a wave phase-velocity change due to currents in a (mean) layer 1 m thick, while the drogue felt currents only within the top 0.46-m layer. Since currents nearest the surface are known to differ most from deeper currents, this may explain some of the difference. Second, some of the buoy motion was directly due to the wind; during the ship measurements over the easternmost 20 km, a strong wind (~12 m/sec) blew from the east-southeast. Third, breaking waves, which were prevalent with the high wind and wave conditions on these days, entrain floating surface objects, pushing them along (over short distances) at a much greater wave phase velocity. Fourth, the drifter and radar measurements at some locations were of necessity made several hours apart. And fifth, the drifter measurement is Lagrangian in nature, aver-

aged only over a short line (400 to 1000 m); the radar measurement is Eulerian, averaged over an area of about 3 by 3 km.

Applications and Future Directions

The HF radar remote-sensing system appears to provide considerably expanded observational capability for coastal physical oceanographic research. Since it is transportable and offers output current maps on site in near real time, the system has a great potential for operational coastal current monitoring and for quick response to offshore accidents. Inasmuch as surface currents are highly variable, elusive, and expensive to measure by existing in situ techniques, this instrument offers an attractive alternative. To duplicate the large areal volume of data vectors obtained with only a 1/2-hour radar operation would require many ships or aircraft tracking drifters simultaneously—an experiment that would cost hundreds of thousands of dollars. Our discussion with commercial manufacturers lead us to believe that streamlined operational versions of our prototype radar could be available for about $50,000 per complete radar pair.

The need to understand and better define the structure of currentlike water movement near the surface becomes more evident as we attempt to further interpret and refine the accuracy of this system. Both theoretical analyses and carefully planned experiments should be undertaken to quantify the effects of current turbulence within the radar cell, wave-wave interactions, and current shear with depth on the radar measurements. Furthermore, the actual linear horizontal drift of particles at the surface (for example, oil) and its relation to mean near-surface current velocity must be determined, especially under conditions of high winds and breaking waves. The similarities and differences between Eule-

rian areal and Lagrangian linear measurements need to be better understood. The prospect of having continuous surface-current data should provide the impetus to correlate currents with their short-term driving forces (such as winds, waves, and tides). Such a correlation is potentially a means of using the surface-current data to measure, indirectly, those driving forces.

Summary

A high-frequency radar remote-sensing system for measuring and mapping near-surface ocean currents in coastal waters has been analyzed and described. A transportable prototype version of the system was designed, constructed, and tested. With two units operating tens of kilometers apart, the currents were mapped in near real time at a grid of points 3 by 3 km covering areas exceeding 2000 km², out to a distance of about 70 km from the shore. Preliminary estimates of the precision of current velocity measurements show it to be better than 30 cm/sec.

References

1. P. M. Saunders, *Deep-Sea Res.* **23**, 249 (1976).
2. V. Klemas, G. Davis, J. Lackie, W. Whelan, G. Tornatore, *IEEE Trans. Geosci. Electron* **GE-15**, 97 (1977).
3. W. S. Richardson, H. J. White, Jr., L. Nemeth, *J. Mar. Res.* **30**, 259 (1972).
4. D. D. Crombie, *Nature (London)* **175**, 681 (1955).
5. D. E. Barrick, *IEEE Trans. Antennas Propag.* **AP-20**, 2 (1972).
6. R. H. Stewart and J. W. Joy, *Deep-Sea Res.* **21**, 1039 (1974).
7. D. E. Barrick, J. M. Headrick, R. W. Bogle, D. D. Crombie, *Proc. IEEE* **62**, 673 (1974).
8. D. D. Crombie, in *Proceedings of the IEEE Ocean '72 Conference* (IEEE Publ. 72 CHO 660-1 OCC, Institute of Electrical and Electronics Engineers, New York, 1972), pp. 173–179.
9. D. E. Barrick, *Radio Sci.* **6**, 517 (1971).
10. ———— and M. W. Evans, *NOAA (Natl. Oceanic Atmos. Adm.) Tech. Rep. ERL 373-WPL 47* (1976).
11. D. E. Barrick and J. B. Snider, *IEEE Trans. Antennas Propag.* **AP-25**, 19 (1977).
12. J. L. Willows and R. J. Lytle, *Lawrence Livermore Lab. Rep. UCID-17024* (1976).
13. D. E. Barrick, in *Remote Sensing of the Troposphere*, V. E. Derr, Ed. (Government Printing Office, Washington, D.C., 1972), chap. 12.

The Dulles Airport Pressure Jump Detector Array for Gust Front Detection

A. J. Bedard, Jr., W. H. Hooke, and D. W. Beran

Wave Propagation Laboratory
Environmental Research Laboratories, NOAA
Boulder, Colo. 80302

Abstract

Wind shear has long been recognized as one of the major aviation hazards in the airport environment. A principal source of dangerous wind shear is the thunderstorm gust front, a cold air outflow from the thunderstorm downdraft. The gust front is particularly hazardous not only because of the large surface wind shears associated with it, but also because of its highly localized character. Often the downdraft or downburst region producing such fronts is of the order of a few kilometers or less in dimension.

As a result, vertically profiling wind shear detection techniques such as the hybrid acoustic–microwave radar system described in the companion paper by Hardesty et al. (1977) do not provide adequate total protection. In this paper we describe an array of pressure sensors installed at Dulles International Airport in Washington, D.C., to detect and monitor gust fronts that could endanger aircraft operations. The pressure sensors (designed to respond only to sudden pressure increase) are so inexpensive that they can be used in dense networks of large spatial extent to monitor in detail the gust front progress as it approaches the airport. Some 125 sensors have been installed at Dulles. Indeed, a major cost of the installation is the cost of the phone lines required to return the information to a central data-processing location.

The system has been operating unattended for extended periods of time, registering the frontal passages that have also been detected by the acoustic–microwave radar system as they pass overhead. Results are presented showing the complementary nature of the two monitoring methods.

1. Introduction

In recent years the Federal Aviation Administration (FAA) has become increasingly concerned about the dangers posed by low-level wind shear to aircraft take-offs and landings. Some degree of wind shear is usually present at low levels; however, it has become apparent that in a number of instances low-level wind shear can reach magnitudes that exceed the design capabilities of the aircraft and the ability of the crew to implement corrective procedures. The problem is exacerbated by the highly localized nature of the hazardous condition, lack of unambiguous information on its presence, and an enormous economic price tag associated with sudden and unscheduled changes in airport operations (change of runways, airport closings, etc.) during peak traffic periods.

This paper and its companion (Hardesty et al., 1977) describe systems developed by NOAA's Wave Propagation Laboratory (WPL) for the detection and monitoring of low-level wind shear. Hardesty et al. describe a vertically profiling hybrid acoustic–microwave radar system for monitoring the wind shear associated with widespread inversions and frontal surfaces. In this paper we describe the use of an array of pressure sensors to detect highly localized thunderstorm gust fronts.

Cold air outflow from the base of a thunderstorm produces the gust front, which manifests itself as a sudden surge of wind speed along the discontinuity between the cold, dense air and the less dense ambient environment near the surface (Fig. 1). The convergence initially responsible for the familiar convective cloud becomes balanced by a divergence from the lower regions of the thunderstorm. This divergence, driven by the fall of rain and by cooling of the air by evaporation, can spread cool air many kilometers from the base of the cloud. The surface friction, the stability of the air being overrun, the speed of movement of the system as a whole, the amount of downdraft air and its momentum, and the proximity of nearby cells all combine to make gust front systems complex entities. Typically, the outflow air is ∼1 km high. Its flow pattern over the earth's surface is quite intricate and hard to predict, exhibiting effects of terrain, surface drag, low-level atmospheric stability, and prevailing wind direction. There is evidence of instability and lobing structure in the gust front flow (Figs. 1 and 2). Gust fronts have been known to move with speeds of the order of 10–20 m s⁻¹ for distances of ∼30 km, thus persisting for as long as 1 h after their development. Bedard and Beran (1977) give pertinent references.

Associated with the downdraft region and the gust front may be enormous wind shears and horizontal divergence (Byers and Braham, 1949; Lewellen et al., 1976; Fujita and Byers, 1977; Fujita and Caracena, 1977). It is these variations that pose a direct threat to aircraft takeoffs and landings. The lift on the aircraft is proportional to the square of the airspeed. If a plane were traveling at 70 m s⁻¹ and suddenly encountered a tail wind of 20 m s⁻¹, it would experience a 50% reduction in lift. Luers and Reeves (1973) performed numerical simulations to evaluate the influence of wind shear on a variety of aircraft and concluded that sudden decreases in relative velocity can result in potentially hazardous conditions. A review of the important factors in the Eastern 727 accident at Kennedy Airport in June 1975 indicates that downdrafts contributed to that accident (Fujita and Byers, 1977), as did variations of horizontal winds in the vertical (Lewellen et al., 1976). The study by Fujita and Caracena (1977) shows that there were downbursts (highly concentrated and severe downdrafts) in the vicinity at the time of three recent aircraft accidents. However,
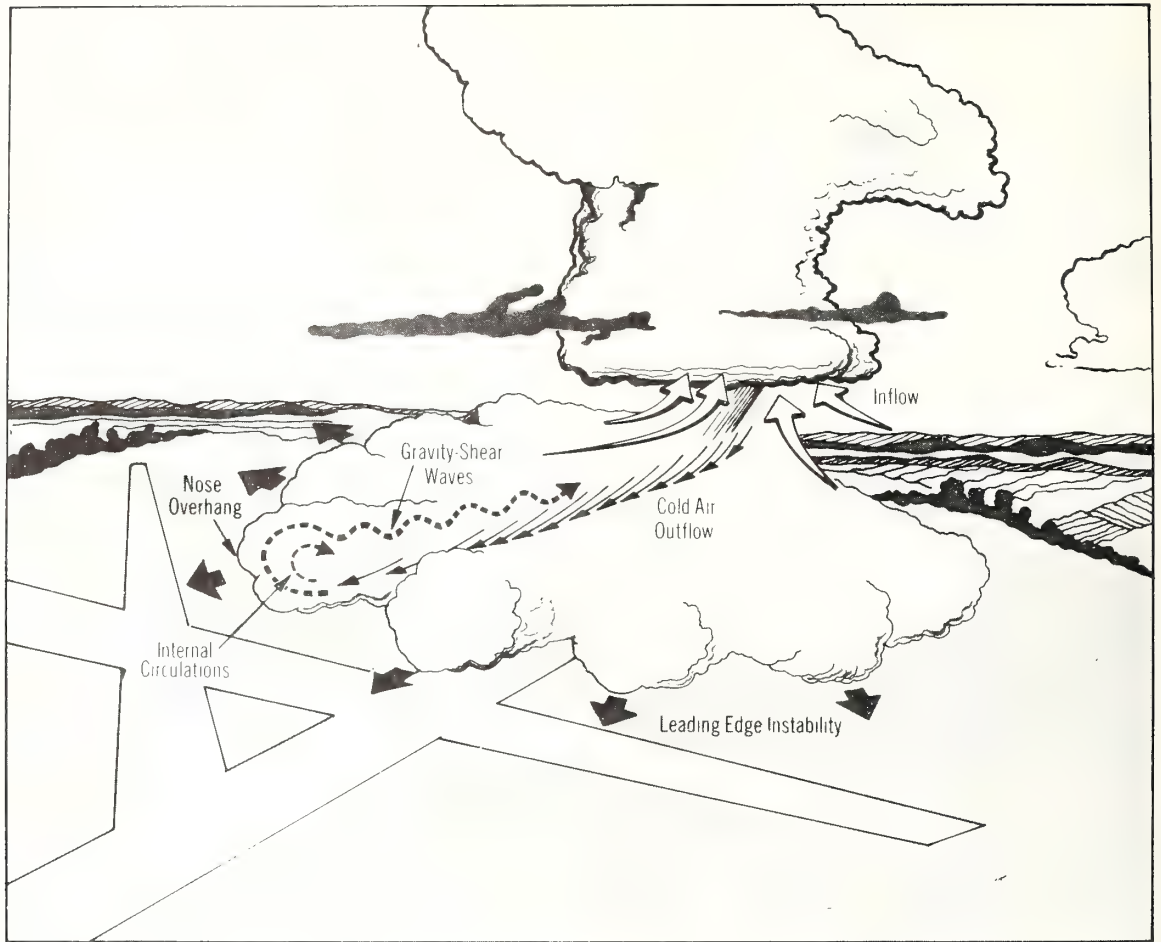
FIG. 1. Cross-sectional view illustrating the complex flow fields surrounding a thunderstorm.

FIG. 2. Leading edge of a gust front rendered visible by entrained dust (courtesy of
Dr. Sherwood B. Idso of the U.S. Department of Agriculture).

concern about this phenomenon dates back at least as far as the U.S. Weather Bureau Thunderstorm Project (1948).

Ultimately, the entire three-dimensional wind field within the gust fronts may be monitored by scanning radar and/or lidar systems, making all other approaches obsolete. In the interim, however, it seems attractive to explore the possibility of monitoring gust fronts through their associated surface effects. These include changes in surface wind speed and direction, reflecting the air-flow itself, temperature changes associated with the cooler air, and pressure changes associated with the weight of the gust front air mass. Of these, the most attractive from the standpoint of the surface monitoring of the gust front passage is the surface pressure change, for a variety of reasons given below.

1) Gust front pressure changes amount to the order of 1 mb in 600 s and are among the most rapid in nature. Devices triggering at such levels rarely will issue false alarms. The corresponding gust front changes in temperature, wind speed, and direction are not so unique.

2) The surface pressure change reflects the integrated change in air mass in the air column above the sensor; thus it is unique among the surface mani-festations in that it reflects changes occurring at aircraft altitudes. This can result in an improve-ment in timeliness, since gust fronts occasionally exhibit an overhang, manifested by a nose that ex-tends as much as 1 km ahead of the surface gust. It also results in improved false alarm rate, since

the system is less vulnerable to the effects of small dust devils and turbulent eddies of lesser practical consequence that can trigger other sensors. Since the detector only indicates positive pressure changes, large negative changes such as those associated with vortices do not cause the detectors to trigger.

3) A simple, inexpensive instrument suffices to mea-sure the gust front–associated pressure changes. The instrument does not have to be exposed to the ravages of weather during operation. It is easy to design the instrument so that it uses power only during gust front passage. Operation tends to be relatively maintenance free. Because the instrument is inexpensive it can be deployed economically in dense arrays, as required for effective detection (e.g., Sinclair et al., 1973; Fujita and Byers, 1977; Bedard and Beran, 1977).

4) The pressure sensor can be operated indoors, a not inconsiderable advantage (as indicated by the discussion of vandalism in Section 3) not enjoyed by anemometers and temperature sensors.

2. Pressure jump detector

Figures 3 and 4 shows the pressure jump detector and its block diagram, respectively. The basic sensor is a simple pressure switch, utilizing a diaphragm that flexes in response to imposed pressure changes across it. In fact, these switches are available commercially and are used in household dryers to prevent damage resulting from failure to clean the dryer lint trap. In operation the pressure jump detector uses a high-pass filter con-
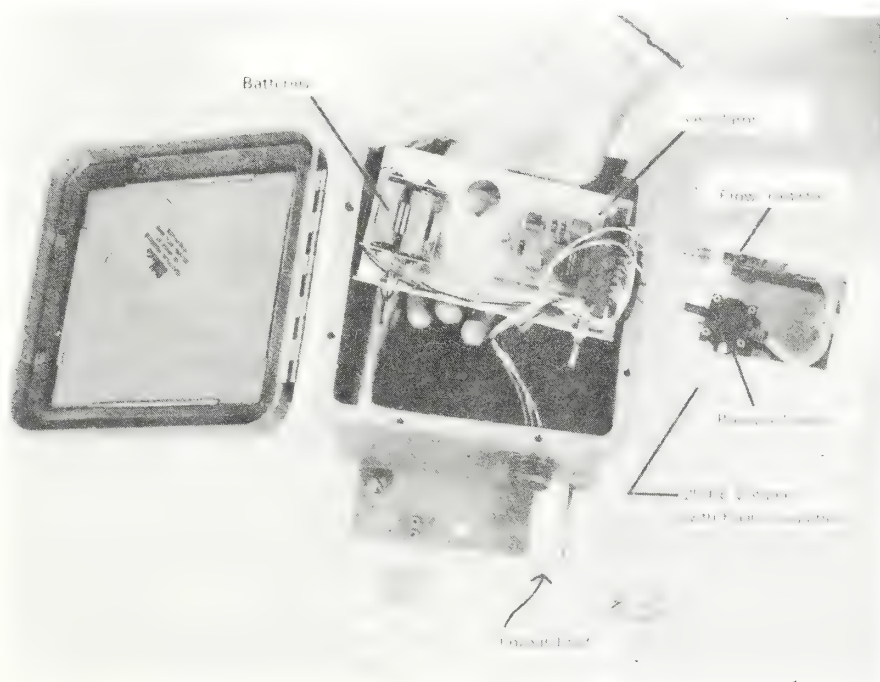
FIG. 3. View of pressure jump detector with major components identified.

675
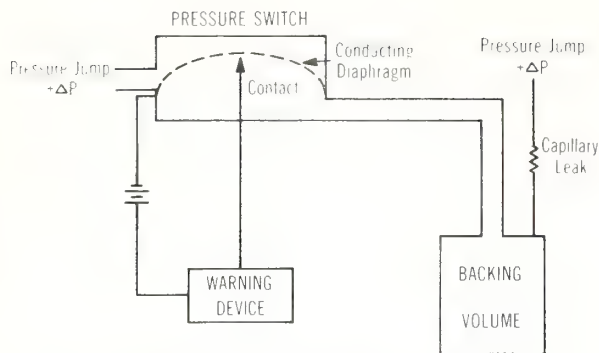
Fig. 4. Schematic view indicating pressure jump detector operation.

sisting of a thermally insulated backing volume and a capillary leak, in order to suppress long-period pressure changes associated with synoptic-scale weather. (In a prototype sensor these consisted of a hypodermic needle and a Coke bottle.) Thus the sensor responds to positive pressure changes dp/dt that exceed a certain threshold. After considering statistics on atmospheric pressure jumps available from Williams (1953) and Bleeker and Andre (1950) as well as some individual case studies (Byers and Braham, 1949; Tepper, 1950), we have used a trigger level that can be thought of in a loose sense as corresponding to a 1 mb pressure increase in 600 s. This detector presently uses a high-pass filter with a 3 min time constant. The pressure switch triggers for positive pressure differences in excess of $\frac{1}{2}$ mb. (For a precise description of the instrument response, the reader is referred to Bedard and Meade (1977).) Thus the instrument has a single moving part—the diaphragm. In the mode of operation shown here, the warning device is on and consuming power only during gust front passage. Thus, in effect, it places one level of processing (is an event occurring?) at the sensor itself, permitting more flexibility in multiplexing the sensor data over telephone lines and simplifying the entire data-processing task considerably. The capillary leak equalizes the pressure across the switch within a short time (typically several minutes), thus shutting itself off. Although the basic sensor is simple and inexpensive, it is a major task to build in the degree of reliability, ruggedness, and thermal stability required for outdoor use. This raises the cost of the pressure jump detector substantially. Figure 5 shows the sensor in its weatherproof case mounted on a telephone pole.

Laboratory tests indicate that the thermal time constant of the detector is >2 h. This means that the large temperature decreases caused by thunderstorm gust fronts (which can exceed 10°C over time scales of 10 min) will not produce rapid temperature changes (and hence pressure changes) in the reference volume. Longer-period, diurnal variations in temperature can vary the threshold of all the sensors of an array (typically 0.2 mb). All indications are that such changes do not degrade array performance.
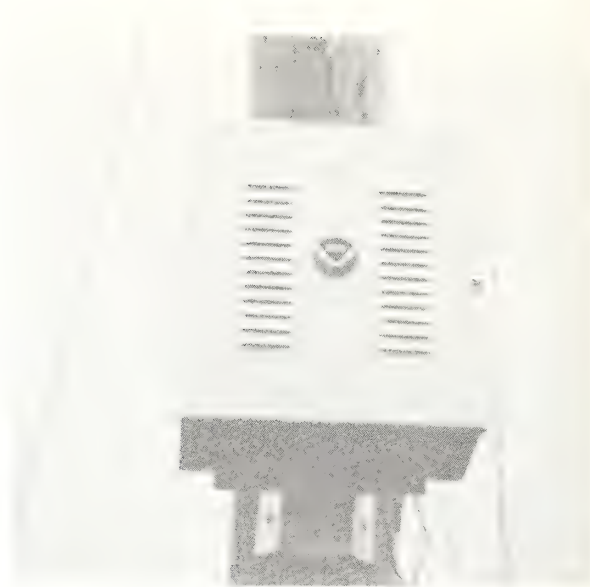
Fig. 5. View of pressure jump detector mounted on a telephone pole.

3. Dulles surface sensor array

With FAA funding and sponsorship, we have fabricated some 125 pressure jump detectors and deployed these in the vicinity of Dulles International Airport. Our goals included:

1) examination of the performance of the pressure jump detector system;
2) comparison of its performance with a sparser network of anemometers;
3) comparison of the surface array data with the acoustic–microwave radar profiles.

Figure 6 shows the locations of the pressure jump detectors, absolute pressure detectors (for examining which pressure waveforms actually triggered the detectors), anemometers, and temperature sensors in the vicinity of Dulles. Data from the pressure jump detectors and sensors were returned to a central recording site (the National Weather Service's Sterling Test and Evaluation Facility near Dulles) using leased phone lines. By using different tones for each detector, we multiplex up to eight pressure jump detectors on each leased line. Since the Dulles airport area is primarily rural, with few buildings or spare phone lines, we installed our sensors on existing telephone poles and had to arrange for the installation of a significant number of phone cables to complete the system. Because most of the pressure jump detectors are physically exposed, they are vulnerable to the ravages of both weather and vandalism (at this writing, 28 have been hit by firearms—our NOAA sticker is apparently too evocative of a bullseye). The installation of choice in more heavily populated areas (e.g., around Chicago's O'Hare Airport, where we

676
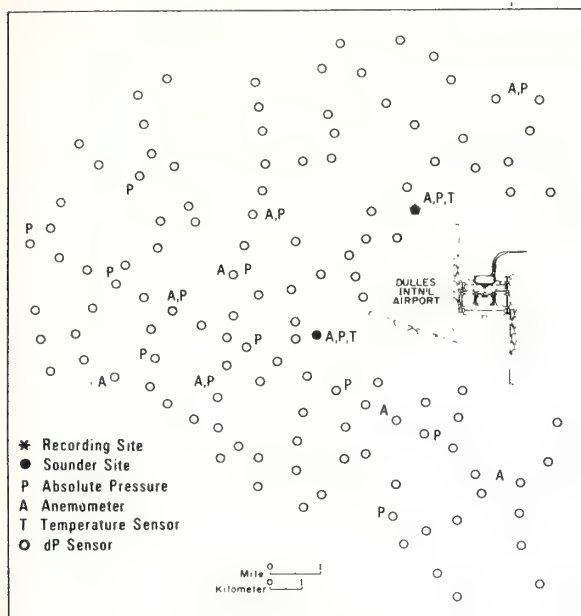
FIG. 6. Locations of surface sensors for the Dulles Airport system. The open circles indicate the positions of the pressure jump (dP) detectors.

FIG. 8. Motion of a pressure jump across the Dulles Airport array on 7 December 1976.

have a smaller installation) is inside buildings and would use existing phone lines. Operation of the pressure jump detector is virtually unaffected by being indoors.

A word about other sensors used in the Dulles installation is in order.

Absolute pressure sensors built by Ball Engineering (Model EX340B) are mounted on telephone poles collocated with certain of the pressure jump detectors. Each absolute pressure sensor uses a local 115 V, 60 Hz power drop and has a sensitivity of 0.1 V mb⁻¹ and a range of ±50 mb. A voltage-controlled oscillator sends an FM tone back to the recording site. The data from each absolute pressure sensor are multiplexed with three pressure jump detectors and sent over the same leased line.

FIG. 7. Block diagram of the system for recording and displaying the surface sensor array.

Ten Climatronics Wind Mark III systems, mounted on 20 ft aluminum towers, record the wind speed (0–100 mph) to ±5 mph and wind direction (0–540°) to ±1.5° on a strip chart collocated with each anemometer. The anemometers use local 115 V, 60 Hz power but have a battery backup that will last several days in the event of a power failure. The strip charts are changed once per month.

To look at the surface temperature changes associated with gust front passage, we use thermivolt temperature probe Type 705 and signal conditioning circuitry (manufactured by Yellow Springs Instrument Co.) with a Gill naturally ventilated radiation shield (R. M. Young Co., Type 43103) for temperature measurement at two sites within the array. The probes provide an accuracy of ±0.50°C from −30° to +100°C (sensors with specifications similar to the above should suffice in each case).

The system block diagram in Fig. 7 indicates the data flow for the recording system. Although a primary goal is the evaluation of the pressure jump detector array as a means of providing operational warnings to airports, the system is designed to record data for after-the-fact analyses. The absolute pressure and temperature data are collected and recorded once every 10 s. The entire array of pressure jump detectors is scanned about once per second and recorded if one or more of the sensors is in an alarm status.

Displays consisting of a map of the Dulles area with lights indicating the status of each sensor are provided at the Sterling and acoustic–microwave radar sites. These displays are updated once per second. The indicators latch at the initial alarm for each sensor, so that the display vividly depicts the encroaching discontinuity.

677
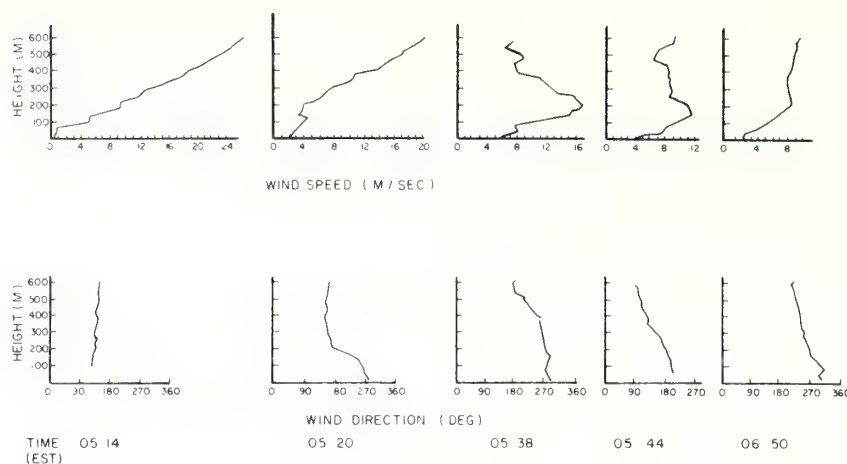
Fig. 9. Vertical profiles of wind speed and wind direction before and after the 7 December 1976 event at Dulles Airport.

4. The event of 7 December 1976

The operation of the complete Dulles system (see Hardesty *et al.* (1977) for a description of the vertically profiling portion) is illustrated by its performance during a wind shear event on 7 December 1976. On this date, at about 0530 EST, the array of pressure jump detectors tracked a disturbance approaching from the northwest at a speed of -20 m s^{-1}. The shaded areas in Fig. 8 depict the motion of the discontinuity by showing groups of triggered sensors together with the average of the initial trigger times for the earliest and latest sensors in each shaded area. The full complement of sensors operating on this date (47 in all) triggered during this event. Additional sensors to the west, south, and north of the airport were not installed at the time of this observation and thus the north-south limits of the shaded areas represent lack of data and not the limits of the discontinuity.

The discontinuity arrived at the sounder site at about 0532 EST. A time sequence of wind speed and direction profiles measured by the acoustic-radar portion of the system (Fig. 9) shows that a strong shear layer and shift in mean wind direction occurred near the arrival time of the pressure jump. The history of this event demonstrates the total wind shear system concept with a warning provided by the dense array of pressure jump detectors followed by a measurement of the shear magnitude and location by the vertically profiling portion of the system. In this case the pressure jump detectors provided about a 5 min warning of the arrival of the discontinuity at the airport. With the full array operating we estimate a warning time of 7 min for a discontinuity traveling at 20 m s^{-1}.

5. Concluding remarks

Current plans call for cross-comparisons between the surface array and the acoustic–microwave radar data sets for each event detected by the total system.

Parallel programs using our pressure jump detector arrays are being carried out at O'Hare Airport (in conjunction with the Transportation Systems Center of the Department of Transportation) and near Oklahoma City, Okla. (in conjunction with the National Severe Storms Laboratory gust front experiment). These are also providing data sets comparing pressure, wind, and temperature measurements.

References

Bedard, A. J., Jr., and D. W. Beran, 1977: Detection of gust fronts using surface sensors. NOAA Tech. Memo. ERL WPL-20, 15 pp.

——, and H. B. Meade, 1977: The design and use of sensitive pressure jump sensors to detect thunderstorm gust fronts, Part 1, Pressure jump detector design. *J. Appl. Meteor.* **16**(10), in press.

Bleeker, W., and J. M. Andre, 1950: Convective phenomena in the atmosphere. *J. Meteor.,* **7,** 195–209.

Byers, H. R., and R. R. Braham, Jr., 1949: *The Thunderstorm.* U.S. Dept. of Commerce, Weather Bureau, Washington, D.C., 287 pp.

Fujita, T. T., and H. R. Byers, 1977: Spearhead echo and downburst in the crash of an airliner. *Mon. Wea. Rev.,* **105,** 129–146.

——, and F. Caracena, 1977: An analysis of three weather-related aircraft accidents. *Bull. Amer. Meteor. Soc.,* **58**(11), in press.

Hardesty, R. M., P. A. Mandics, D. W. Beran, and R. G. Strauch, 1977: The Dulles airport acoustic–microwave radar wind and wind shear measuring system. *Bull. Amer. Meteor. Soc.,* **58,** this issue.

Lewellen, W. S., G. G. Williamson, and M. E. Teske, 1976: Estimates of the low-level wind shear and turbulence in the vicinity of Kennedy International Airport on June 24, 1975. NASA Rep. CR-2751, Space Sciences Labs., Marshall Space Flight Center, Huntsville, Ala., 40 pp.

Luers, J. K., and J. B. Reeves, 1973: Effect of shear on aircraft landing. NASA Rep. CR-2287, Space Sciences Labs., Marshall Space Flight Center, Huntsville, Ala., 53 pp.

Sinclair, R. W., R. A. Anthes, and H. A. Panofsky, 1973: Variation of the low-level winds during the passage of a thunderstorm gust front. NASA Rep. CR-2289, Space Sciences Labs., Marshall Space Flight Center, Huntsville, Ala., 65 pp.

Tepper, M., 1950: A proposed mechanism of squall lines: The pressure jump line. *J. Meteor.,* **7,** 21–29.

U.S. Weather Bureau Thunderstorm Project, 1948: A report on thunderstorm conditions affecting flight operations. U.S. Weather Bureau Tech. Pap. No. 7, Washington, D.C., 32 pp.

Williams, D. T., 1953: Pressure wave observations in the central Midwest, 1952. *Mon. Wea. Rev.,* **81,** 278–289. ●

WIND SHEAR TEST SITE UPGRADING

D. W. Beran and Duane Haugen

During late 1975 and early 1976 the FAA was faced with the problem of selecting one or two remote sensing techniques from many which might be used to solve the airport wind shear problem. To do this a suitable test site, along with test personnel were required. The Table Mountain field site near Boulder, Colorado, was chosen because it met most of the requirements.

This report describes the field site modifications that were made for the tests. In addition, the results from tests of a commercial acoustic Doppler system, a CW lidar system and a WPL owned FM-CW radar and prototype acoustic Doppler system are summarized. The commercial devices were tested for only a short period of time due to other contracted arrangements and limited resources for maintaining the systems on site. As a result the tests were useful but inconclusive. This limited availability for testing was also a problem with the FM-CW radar. However, it was possible to make the first comparisons of this device with an acoustic Doppler system. Winds measured by the two systems over approximately 5 minute averaging times compared well.

The WPL prototype acoustic Doppler system was operated for a much longer period and we now have a better understanding of its potential. This particular system is limited by surface winds above 10 meters per second and its performance is degraded by other background noises such as thunder. The limiting influence of rain is not as severe as had previously been expected, but it is a serious problem for intense rainfall.

Airport Weather Service: Some Future Trends

D. W. Beran,[1] W. H. Hooke,[1]
C. G. Little,[1] and F. Coons[2]

Abstract

The current state of aviation weather forecasting and its effect on weather-related aircraft accidents are reviewed. The authors predict that new approaches will be necessary if the technological gap is to be narrowed between weather forecasting and aircraft design and utilization. The importance of mesoscale modeling and new remote sensing devices is discussed. (Increased emphasis in these areas is to some extent a response to aviation needs and also to the need for improved synoptic-scale modeling.) Statistical and deterministic models that can assist in the prediction of the evolution of area weather are currently under development, but major obstacles, such as the difficulty in parameterizing the planetary boundary layer, suggest that useful models are at least 10 years away. Furthermore, it is predicted that, although weather modification and aircraft design will undoubtedly play important roles, the most immediate improvements will come from departures from traditional approaches to forecasting.

1. Introduction

The aviator's need for weather information parallels the history of manned flight. The fact that an aircraft depends on the atmosphere to function makes the motions and characteristics of that medium vitally important. It is clear from the large number of weather-related aircraft accidents that the vehicle and the medium that supports it are sometimes not in harmony. Accidents continue to occur despite our modern weather services. Even when tragedy is not the final result of foul weather, there may be a heavy cost in terms of delays and missed schedules. It is appropriate to ask if a stage has been reached where these delays and accidents are the price that must be paid for a highly efficient form of transportation. Given the present rapid rate of technological development, there is a basis for believing that the answer to this question is no.

By examining state-of-the-art technology and plans for future developments we can speculate about some of the advances that may occur in the next few years in aviation weather forecasting. Beyond that time, foreseeing the future becomes extremely difficult, because it is not possible to predict technological advances that may have a major impact on aircraft operation and on the way we forecast or control the weather. Highlighting critical problem areas may provide some guidance to those responsible for improving the safety of air travel.

Despite many efforts to improve observing and forecasting techniques (i.e., Crisci, 1975; Chisholm, 1976) the weather prediction component of aviation still lags behind the technology that has produced the sophisti-

cated aircraft of today. Compare, for example, modern airliners with radiosondes and other standard weather-observing devices. Although aircraft design has progressed from the Ford Tri-motor to supersonic jets, the mainstays of meteorological data-gathering equipment continue to be the radiosonde and a few ground-based *in situ* instruments that provide only a glimpse of mesoscale conditions. Despite this, meteorologists are expected to accurately forecast the occurrence of events ranging from a few minutes to >48 h in the future. Planned new developments like AFOS (Automation of Field Operations and Service) and AV-AWOS (Aviation-Automatic Weather Observing System) (SDO, 1976) are steps in the direction of improved communication and automation, a vitally important area, but they do not address the question of how to use radically new or different data sets. Radar is an important tool; however, its operational use has been confined to identification of regions of precipitation. The demonstrated potential of radar for measuring wind fields in the clear air remains untapped, and indeed there are no plans as yet to use it operationally.

The National Transportation Safety Board (1974) reported that 47% of aircraft accidents during the previous 4 years were weather related. This statistic bears out the assertion that there is a technological lag in aviation weather observations and forecasts relative to the activities they serve. To find reasons for this lag, several basic questions must be answered: Are the dynamics and driving forces of mesoscale weather events so poorly understood that we cannot use our present knowledge to make better predictions? Is the complexity of the problem so great that even a better understanding of the physics would offer little hope of predicting on all scales important to aircraft operations? Is the present data base sufficient for numerical models and prediction techniques? No simple answers can be found, but weaknesses in our present approach can be identified. By correcting these weaknesses it may be possible to significantly improve aviation weather services.

What conditions need to be forecast? Current critical aviation weather forecasting problems can be categorized into problems affecting airplanes in the terminal area and en route. The former category includes fog, winds (crosswinds, shear, and turbulence), thunderstorms, temperature, and precipitation; the latter category includes winds, turbulence, thunderstorms, and temperature. Meteorological conditions affecting the airport terminal are of two distinct time scales. The first, derived from the response time of the pilot and his aircraft, ranges in scale from the shortest time during which it is possible to maneuver the aircraft to the time required for the

[1] Wave Propagation Laboratory, ERL/NOAA, Boulder, Colo. 80302.

[2] Federal Aviation Administration, Department of Transportation, Washington, D.C. 20591.

final approach (on the order of a few minutes). These correspond to spatial scales up to 20 km. The second can be thought of as the response time of the aggregate of all aircraft under the terminal's control at any given time. At major airports, operations are tightly scheduled, and response to changes in the weather (diversions, runway closures, etc.) can take an hour or more and affect aircraft hundreds of kilometers away. Thus, the so-called terminal weather problem in fact extends to spatial scales up to synoptic.

Therefore, the associated weather forecasting problem is one of providing a mesoscale time forecast over a subsynoptic area, and it poses two fundamental, challenging questions: 1) What is the current status of the relevant volume of air? 2) How will this volume of air evolve over the next few hours?

Progress in understanding the laws of nature, the use of statistical methods, and the ability to use the computer has been substantial, but many experts feel that we are approaching a forecasting plateau that is far from perfect. This "leveling off" in forecasting skill is occurring despite the use of ever more powerful computers and complex numerical models; it is appropriate to ask why. The neglected areas of mesoscale modeling and observations may hold the key to further overall improvements, and these areas could be candidates for more intensive research and development.

Support for this assumption derives from the point of view that further improvement in synoptic-scale forecasting will occur if and when we gain a better understanding of mesoscale and synoptic-scale interactions. Forecasts for specific events and regions are now very dependent on synoptic-scale numerical prognosis in combination with the ability to properly interpret and use this information. Even new forecasting techniques such as MOS (Model Output Statistics) (Klein and Glahn, 1974), which are helping to improve present forecasts, must rely on synoptic-scale input. These same methods should be even more effective if they are used with a truly mesoscale data base. In other words, we work down from what is predicted or observed on the larger scales to local- or regional-scale forecasts. This is operationally proper, since for longer-term forecasts the synoptic pattern and its changes are a major control. However, this method falls short of perfection because of a poor understanding of mesoscale phenomena and of the interplay between the two scales. Large-scale patterns may help position a given event, but the importance of the smaller scale to the genesis of new conditions cannot be overlooked. From this we conclude that a major improvement is needed in understanding mesoscale and shorter-term atmospheric events.

Why has this important area of meteorology apparently been neglected? Rather than being neglected, it has been a case of taking the path of least resistance. The present data network is geared to the synoptic scale, making mesoscale research and forecasting difficult. With this limitation it has been far easier to show significant improvement by concentrating on forecasting the larger

scales and to take advantage of the technological advances in computers and statistical methods to reach present higher forecasting plateaus on all scales.

2. Improving forecasting—Mesoscale approach

We believe that major forecasting improvements will be made if more effort is directed toward the mesoscale. To be most efficient, how should this be accomplished? One approach would be to work down to smaller and smaller scales until we have reached our goal. An opposite approach would be to concentrate on acquiring a better understanding of the smaller scales and then to expand the sphere of interest until it merges with larger scales. Neither approach is totally satisfying. In the first, a point is soon reached where regional differences and the lack of high-resolution data are limiting factors. The second overlooks the important control functions exerted by the larger scale; we might soon discover that we knew a lot about a particular "tree," but very little about the "forest."

Both approaches will be needed. Our understanding of the mesoscale must be improved by concentrating more research in this area. Larger-scale influence cannot be neglected, and we must do more to introduce unique regional effects. This is not an easy task, since each mesoscale region will require special attention. It will be important to concentrate efforts in the areas of highest need, i.e., where the largest number of people are affected. Therefore, the environment of major airports will unquestionably have a high priority.

Most past efforts to improve mesoscale or short-term prediction have involved the use of richer data sets, persistence, local knowledge, and synoptic-scale prognosis. True mesoscale models for a given region have not been well developed, nor have the so-called "richer data sets" been adequate. Improved data sets have been provided by a "more-of-the-same" approach: the installation of a denser network of standard ground-based sensors and perhaps an increased launch rate of radiosondes. The need for high-resolution, real-time mesoscale data for short-term small-scale forecasts is apparent. It is equally important to know how many and what kinds of data are required for a given region and for a given phenomenon. Improved boundary layer models must play a key role, since they increase the understanding of meteorology and provide direction to the sensor developers. Furthermore, such work cannot proceed without a thorough understanding of present and potential observation techniques. Therefore, what is required is an iterative program emphasizing both a better understanding of mesoscale meteorology and the development of techniques for monitoring conditions on a real-time basis.

It is our assertion that the mesoscale will be the next important meteorological frontier. Furthermore, we believe that better observations on this scale combined with the development of new mesoscale models are key factors that will lead to improved forecasts. Insight can be gained by examining these two areas, now largely separated,

and by attempting to predict what might happen when they are properly merged.

The mesoscale monitoring challenge is awesome; what we require is the specification of atmospheric parameter fields within a volume ranging from 20–100 km wide to ~20 km deep. Specification of this volume must be most complete and must have its highest resolution in the kilometer closest to earth, where wind and turbulence profiles along glide paths are critical. Surface temperatures, visibilities, and precipitation conditions must also be accurately known. *In situ* meteorological instrumentation is incapable of accurately measuring these parameters. However, as the result of much research and development over the last decade, remote sensing instruments (both ground- and satellite-based) will soon be available for the monitoring requirements of the airport terminal. Although the majority of these new techniques have not been put into operational use, demonstrated capabilities of remote sensing techniques give an indication of future trends.

Both path averages and profiles of wind have been measured by optical, acoustic, and radar techniques (Beran, 1971; Lawrence *et al.*, 1972; Chadwick *et al.*, 1976). Complete three-dimensional clear-air wind fields have been measured with new radar techniques. Temperature sensing has been less tractable; however, radiometry and some optical techniques hold promise. We should also not overlook capabilities to measure second-order effects of the temperature field, such as mixing depth and structure constant (C_T), an indication of the intensity of turbulent fluctuations. Although these are not direct measures of the temperature field, they may prove to be significant parameters in forecasting techniques that are yet to be developed. They can be readily sensed by optical, acoustic, and radar techniques.

Moisture parameters in the form of path-averaged humidity and integrated water vapor content have been measured by differential absorption and by radiometers (Decker *et al.*, 1973). Measurements of path-averaged rainfall rates and drop sized distribution are both amenable to optical scintillation techniques, and integrated liquid water content and melting layer height can be measured by microwave radar methods. In addition, water-ice differentiation can be accomplished with polarized lidar, and visibility and ceiling-restricting cloud and fog can be monitored by both lidar and radar techniques.

The usefulness of these measurements will largely depend on how they are integrated into a total monitoring and forecasting plan. The particular platform, whether ground based, airborne, or satellite mounted, and the meteorological scale of interest will also have a bearing on how a particular device should be employed. (These comments are meant to give only a broad impression of the capabilities of remote sensor techniques. More details and references can be found in the works by Derr and Little (1970), Derr (1972), Little (1972, 1973), and Beran and Hall (1974).)

Mesoscale forecasting, even when the mesoscale data set is available, remains formidable, since there is little research or operational experience in this area. A great deal is known about the diurnal evolution of the convective boundary layer (e.g., Carson, 1973; Zeman and Lumley, 1976), but beyond this the best forecasting technique currently available is persistence. The forecaster examines the current atmospheric state, including the positions and speeds of such entities as storm cells and gust fronts, and then predicts that conditions will remain as they are, except that those observed features whose motions are currently known will continue to move at the same velocity. The next step is a big one, involving the prediction of the evolution of area weather—e.g., the development of a storm cell where currently none exists or a change in the motion or intensity of a gust front.

Two techniques appear to be available: statistical and deterministic. Statistical approaches analogous to those used in synoptic-scale prediction involve the study of linear regression analyses to determine optimal predictors of short-term changes in the weather. Algorithms based on this approach were mentioned earlier and are currently being developed by NOAA's Techniques Development Laboratory and by the U.S. Air Force's Air Weather Service, among others. Deterministic approaches involve the numerical modeling of mesoscale weather. This method is currently under extensive development at several institutions. The research involves several problems. The first is the same initialization problem facing those concerned with global circulation models (GCM). However, many of the difficulties are more serious in the case of mesoscale weather. For example, spurious gravity wave modes that arise from faulty initialization must be differentiated from actual storm-producing gravity wave modes (Uccellini, 1975). Thus it is critical that significant measurements not be rejected in the process. Another unique feature of most current mesoscale models is the need to "nest" or imbed them in the appropriate larger-scale flow. Although a number of procedures have evolved, the proper specification of such boundary conditions remains a problem. Parameterization of subgrid-scale processes is critical in the mesoscale models. First-order parameterizations incorporate fixed forcing terms to describe the subgrid-scale processes. Second-order parameterizations allow for forcing terms linear in the larger-scale variables, with the coefficients determined by various regression procedures. We are still far from being able to optimize such parameterizations. Foremost among the processes that need to be parameterized are those that occur within the planetary boundary layer (PBL). A broad range of PBL models are available; however, the best are prohibitively complex, and the simplest are often inadequate. Because of the many obstacles remaining, useful forecast models for the mesoscale are unlikely to be available for operational use within the next 10 years.

We believe that with improved understanding of the mesoscale and with better sensing techniques there could be radical departures from traditional forecasting methods. For example, remote sensors can detect anomalies

(i.e., sharp gradients, strong turbulence, or heavy precipitation) more readily than they can measure the standard, slowly varying distributions of wind, temperature, moisture, and pressure. This happens because regions such as strong baroclinic zones are associated with a more intense energy release. This, in turn, produces the necessary refractive index change or particulate concentration change that the remote sensor in large part depends on for a tracer. Such anomalies are also of vital importance to the forecaster since most significant weather events are embodied in these deviations from normal. Present synoptic models generally deal only with entire parameter fields that contain but do not always delineate the anomalies. Given the capability of remote sensors to detect anomalies more readily, we can foresee a shift from the emphasis now placed on parameters associated with the standard pressure surface to a stronger reliance on the significant weather event. This parallels Ramage's (1976) thinking that improved methods of observing turbulence bursts in their earliest stage may be one of the few ways of improving forecasts on the mesoscale.

Although many segments of society would benefit from improvement of short-range mesoscale prediction, it is most probable that the needs of aviation will provide the impetus for major changes. As emphasized earlier it is in the airport environment that inaccurate forecasts can have a major influence. We are already seeing the first indications of the interaction between need and the development of new techniques in such areas as wind shear and wake turbulence. Both of these conditions have become serious aviation hazards primarily because of our inability to observe and predict mesoscale conditions. This has led to new initiatives in the development of improved sensors and forecasting techniques. Although these efforts are narrowly confined to the subject problems, the instruments and techniques will undoubtedly have broader applications leading to general improvement in our ability to deal with aviation weather hazards.

3. The future of airport weather forecasting

It is convenient to divide our forecast of future developments into two parts: near term (<10 years) and long term (>10 years). For the near term we assume technological persistence; that is, those developments in airport weather forecasting that have already been made in the past 10 years will now be put into operational use. Prototypes of some of the observing systems and forecasting techniques are being tested; others will be tested shortly. This trend is expected to continue, so that during the next 10 years these systems will be optimized, adapted to operational use, and either installed at major airports or used by NWS to provide better service. Although recent developments in meteorological sensors have been outstanding, they have widened the gap between our ability to observe and our ability to forecast on the airport scale. New monitoring systems should permit improved nowcasts and persistence forecasts. Over

the long term, our "persistence" prediction of aviation weather breaks down. The development of operational regional and mesoscale models, hybrids of both the statistical and deterministic approaches, will make reliable airport terminal evolutionary forecasts a reality.

In attempting to foresee the long-term future of aviation weather forecasting we cannot take the narrow view that solutions will be restricted to meteorological approaches. Aircraft and flight system designers are equally aware of weather-related problems and are striving to design equipment that will compensate for, or will not be affected by, adverse weather conditions. A notable example is the development of Category III landing systems, which would virtually eliminate low visibility as a problem at least for commercial aviation.

Another area that cannot be overlooked in any long-term view concerns efforts to control the weather. At the present, forecasting represents the highest meteorological skill, but in the future this ultimate capability could be replaced by the ability to control or modify the weather. Evidence of this type of activity can be seen in present fog dispersal efforts. Future developments could, perhaps, lead to the suppression of thunderstorms near airports, the control of precipitation, and other modification efforts to improve the environment for aircraft operations. The feasibility and desirability of such weather control will certainly be the subject of future debates.

Given a continuing need for weather information and forecasting, it is likely that our capability will be significantly improved during the last quarter of this century. The most immediate improvements will come not from more-of-the-same but from marked deviations in traditional thinking. This change will result from a more intense effort to understand the mesoscale, especially the anomalies, coupled with use of radically new observation techniques.

References

Beran, D. W., 1971: A new approach for monitoring the environment near airports. *J. Aircraft,* **11,** 934–936.
——, and F. F. Hall, 1974: Remote sensing for air pollution meteorology. *Bull. Amer. Meteor. Soc.,* **55,** 1097–1105.
Carson, D. J., 1973: The development of a dry inversion-capped convectively unstable boundary layer. *Quart. J. Roy. Meteor. Soc.,* **99,** 450–467.
Chadwick, R. B., K. P. Moran, R. G. Strauch, G. E. Morrison, and W. C. Campbell, 1976: A new radar for measuring winds. *Bull. Amer. Meteor. Soc.,* **57,** 1120–1125.
Chisholm, D. A., 1976: Objective prediction of mesoscale variations of sensor equivalent visibility during advective situations. Air Force Geophysics Lab. (LYU) Rept. AFGL-TR-76-0132, Hanscom AFB, Mass.
Crisci, R. L., 1975: A development plan to improve short-range aviation weather forecasts. Paper presented at the Sixth Conference on Aerospace and Aeronautical Meteorology, El Paso, Tex., AMS.
Decker, M. T., F. O. Guiraud, and E. R. Westwater, 1973: Correction of electrical path length by passive microwave radiometry. *Proceedings of the Conference on Propagation of Radio Waves at Frequencies above 10 GHz,* IEE, London.

Derr, V. E. (Ed.), 1972: *Remote Sensing of the Troposphere.* U.S. Government Printing Office, Washington, D.C., 809 pp.

——, and C. G. Little, 1970: A comparison of remote sensing of the clear atmosphere by optical, radio, and acoustic radar techniques. *Appl. Opt.,* **9,** 1976–1992.

Klein, W. H., and H. R. Glahn, 1974: Forecasting local weather by means of model output statistics. *Bull. Amer. Meteor. Soc.,* **55,** 1217–1227.

Lawrence, R. S., G. R. Ochs, and S. F. Clifford, 1972: Use of scintillations to measure average wind across a light beam. *Appl. Opt.,* **11**(2), 239–243.

Little, C. G., 1972: Status of remote sensing of the troposphere. *Bull. Amer. Meteor. Soc.,* **53,** 936–939.

——, 1973: Remote sensing of the atmosphere. Atmospheric Technology, Rept. 2, NCAR, Boulder, Colo., pp. 51–56.

National Transportation Safety Board, 1974: Annual review of aircraft accident data. Rept. NTSB-ARC-76-1, Washington, D.C.

Ramage, C. S., 1976: Prognosis for weather forecasting. *Bull. Amer. Meteor. Soc.,* **57,** 4–10.

SDO, 1977: Programs and accomplishments—Systems Development Office, Fiscal Year 1976. NOAA S/T 77-2533, NWS, Silver Spring, Md., 38 pp.

Uccellini, L. W., 1975: A case study of apparent gravity wave initiation of severe convective storms. *Mon. Wea. Rev.,* **103,** 497–513.

Zeman, O., and J. L. Lumley, 1976: Modeling buoyancy driven mixed layers. *J. Atmos. Sci.,* **33,** 1974–1988.   ●

A WIND SHEAR AND GUST FRONT WARNING SYSTEM

D. W. Beran, P. A. Mandics
A. J. Bedard and R. G. Strauch

NOAA/ERL/Wave Propagation Laboratory
Boulder, Colorado 80302

1.   INTRODUCTION

An experiment to test the operational capability of an acoustic Doppler wind-shear detection system was described by Beran et al. (1974), and Beran (1974). This test was the forerunner of an extensive development program to produce a prototype acoustic system and an operational test unit for installation at Dulles International Airport. Highlights of this FAA-sponsored development program and modifications that have been made to produce a complete wind-shear and gust-front detection system are described. This is followed by a description of potential second-generation wind-shear detectors which have resulted from recent technological advances.

2.   WIND SHEAR TYPES

In 1972, at the inception of the FAA-sponsored program to develop a wind-shear detection system, the critical aircraft safety problem was perceived to be low level changes in horizontal wind speed or direction with height. These conditions occur at the interface between separate air masses, such as along a synoptic-scale frontal surface or across an intense radiation inversion. Cold air outflow from thunderstorms also produces wind shear, but this condition was then thought to be less of a detection problem since the generating thunderstorm is a highly visible phenomenon which should, at least, alert pilots to be cautious.

The record of several recent aircraft crashes suggests that the danger from gust fronts was underrated. There is also evidence indicating that the change in horizontal wind with height may not have been the only contributing factor, but that downdrafts or changes in the wind with horizontal distance were equally to blame.

The acoustic Doppler system was not designed to detect all aspects of these thunderstorm-related conditions. Its ability to measure a single vertical profile of the wind above a point is effective only for changes in the horizontal wind with height, conditions expected with synoptic-scale features having large horizontal extent.

The tendency to lump both types of wind conditions under the common title of "wind shear" is unfortunate and is a contributing factor to some of the confusion that now exists. It is recommended that wind changes associated with synoptic-scale fronts or strong radiation temperature inversions be referred to as "wind shear", and that those conditions associated with thunderstorms be called "gust-front wind shears." From the operations viewpoint, both situations can pose a hazard and should be detected.

3.   ACOUSTIC DOPPLER PROTOTYPE DEVELOPMENT

Following the Stapleton Airport tests (Beran et al., 1974) a program to upgrade that

acoustic Doppler system for a prototype installation was started. Improvements were made to the main transmitter, the receiver antennas and bunkers, and the data processing portions of the system. New transmitter designs, including an array antenna with Bessel function amplitude shading and an off-axis parabolic antenna with multiple driver feed were explored. The potential complexity and maintenance problems associated with arrays made them unattractive for operational use. For this reason, the off-axis parabolic horn antenna with a 12 driver manifold was selected for the prototype unit. This antenna has significant advantages over the simple on-axis feed parabolic dish used at Stapleton. It has much reduced side lobe radiation levels and is capable of generating nearly three times the acoustic power produced by the Stapleton unit.

A second conclusion from the early experiments was that a major signal-to-noise ratio improvement could be obtained by replacing the fan-beam receiver antennas with units employing narrow steerable beams to track the upward traveling transmitted pulse. An antenna was designed with three columns of seven receiver transducers, all but one of which were displaced from the parabolic antenna's prime focal point. Through electronic switching, three columns of seven receiver beams were produced in vertical planes along a major axis, and at plus and minus 10 degrees away from the central major axis.

This new design and the effect of the protective bunker structure on the beam patterns was thoroughly tested with a scale model in an anechoic chamber (Nagarkar and Finch, 1975). These tests demonstrated that the proper beams could be generated and that the effect of the bunker could be essentially eliminated if the structure acted like an acoustic absorber. This was accomplished by lining the internal bunker walls with highly absorbing material.

The system used at Stapleton employed analog Doppler extraction techniques; the NOVA 820 computer, which was part of the system, acted mainly as a data manipulation unit. The new, more advanced system design employed the computer for digitally extracting the Doppler frequency shift of the received signal and as the main control unit for the entire system. It controlled the pulse repetition rate, beam steering and data manipulation thus eliminating many of the analog functions of the previous system.

A prototype unit incorporating the design changes resulting from the Stapleton experiment was constructed at Table Mountain, a field site near Boulder, Colorado. This unit consisted of only one leg of a complete system; i.e., it had a main transmitter, but only one receiver bunker. Thus, only one wind component could be measured. The primary function of this installation was to test a full-scale mock-up of future operational test installations like that planned for Dulles

686

International Airport. Because of the urgency of the wind-shear problem, this testing was accomplished in parallel with the final design phases for the Dulles operational test unit.

The prototype receiver antenna bunker at Table Mountain incorporated an absorbing liner on critical surfaces and a receiver antenna with a beam which could be steered to seven positions along a vertical axis. Figure 1 shows a cutaway view of the prototype receiver bunker with the parabolic reflector in place. The acoustic signal enters through the acoustically transparent
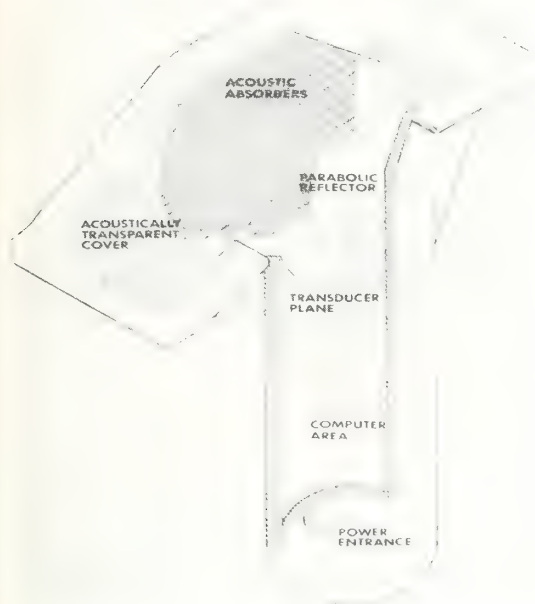
Figure 1. Isometric cut-away diagram of the Table Mountain prototype receiver bunker.

cover, is reflected by the parabolic surface, and is collected by the transducers mounted on the transducer plane shown in the figure. The final bunker installation, complete with earth backfill and transparent cover is shown in Figure 2. Beam pattern measurements of the receiver antenna mounted in the bunker were made (Willmarth et al., 1975) and have been compared with theoretical patterns for the seven separate beam positions. The comparison is shown in Figure 3, where the seven theoretical antenna patterns are shown above the measured ones.

The prototype main transmitter is shown in Figure 4. It is of the off-axis parabolic horn type discussed above and is driven by the array of manifolded transducers shown in Figure 5. Beam pattern measurements for this antenna indicated that absorptive liner and a cuff extension were needed to produce the necessary side lobe reduction.

Figure 2. Final prototype receiver bunker installation showing smooth transition between the surrounding terrain and the acoustically transparent cover.
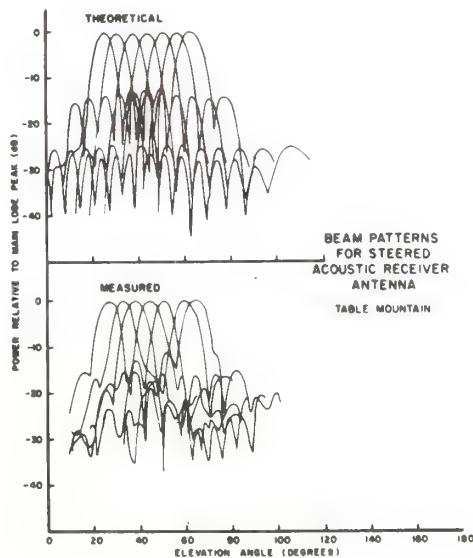
Figure 3. Theoretical (top) and measured (bottom) receiver antenna beam patterns. The elevation angles are measured from a line between the transmitter and receiver. The main lobes for each of the patterns shown indicate the positions through which the receiver can be steered.

168

Figure 4. Prototype main transmitter mounted on movable platform. The transducers (see Fig. 5) are located in the box at the left. The diameter of the exit portion of the horn is approximately 2 m.
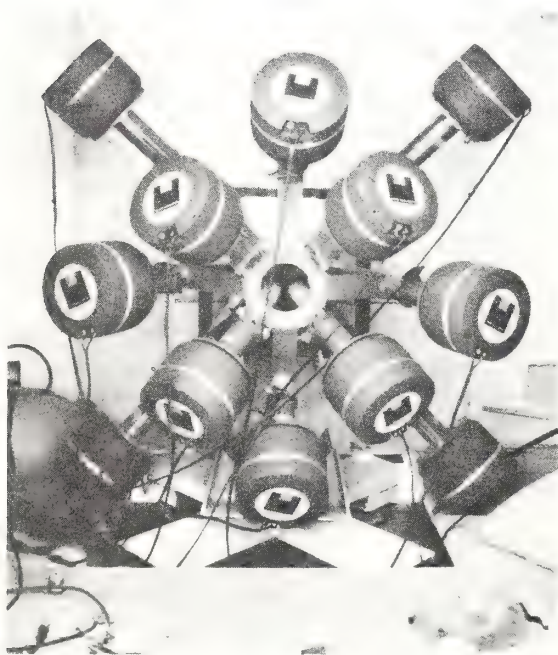
Figure 5. Main transmitter (see Fig. 4) transducers. Each unit is connected into a manifold which is attached to the entry cone of the horn reflector antenna.

In addition to serving as a first test of the major new design elements, the Table Mountain installation is also used as a test bed for hardware and software modifications that may later be incorporated into operational units. The Table Mountain system will also be used to determine the meteorologically-imposed operating limits for this acoustic Doppler system. The determination of these limits is a time consuming iterative process which is dictated by the necessity to wait for meteorologically-limiting conditions and then to make modifications that will improve the overall system performance. Such testing is further complicated by the necessity to use the facility for developing and testing other hardware and software modifications which account for a high proportion of the system down time.

These difficulties are exemplified by the work that has been required to identify an optimum bunker cover material. The primary function of the cover is to reduce receiver noise generated by strong surface winds. Several types of open cell foams are effective for this purpose, but the best material can be found only by subjecting the prime candidates to actual winds that are experienced at the bunker. This means that a cover material must be installed and left in place until sufficiently strong surface winds occur to determine its effectiveness. This procedure is further complicated by the fact that the direction of the wind also has a bearing on the noise-reducing qualities of the cover. The entire procedure must be repeated for each cover material before a final selection can be made.

169

The cover material is only one of the many elements and system parameters that have been changed during the prototype test period which started in October 1975. These necessary changes have made it impossible to collect a statistical data set on a fixed system for predicting down time and ultimate operating limitations. These modifications, of course, become fewer as the final system configuration and software are fixed, and a data set is now being collected. When the Dulles installation becomes active, giving us a second data set, operating limits will be easier to determine.

Despite the difficulties described above, we have obtained some preliminary estimates of system limits. For example, the best cover material tested to date has made it possible to measure a wind profile with surface winds of up to about 20 m/s. The maximum tolerable rain rate has not yet been established. Comparison of the acoustic Doppler winds and those measured by a balloon-borne anemometer have shown excellent agreement (see Figure 6), but the measurements are limited to wind speeds below 10 m/s, the operating limit of the balloon. The design goal of measuring winds within an accuracy of ± 1 m/s and ± 10° azimuth appears to be met for wind speeds below 10 m/s. Data for higher wind speeds, especially at the greater heights will not be available until acceptable standard sensors can be provided. Winds measured by a 150-m tower about 1 mile from the prototype installation provide some comparison information. However, the measurements are of limited use because of the distance between the two facilities and because there are no data for heights above 150 m. The FM-CW radar that is now under development at WPL and has been tested at Table Mountain may provide the needed calibration data. Unfortunately, this system is in the very early development stages and extensive work is still required before processed wind information is readily available. A preliminary comparison between winds
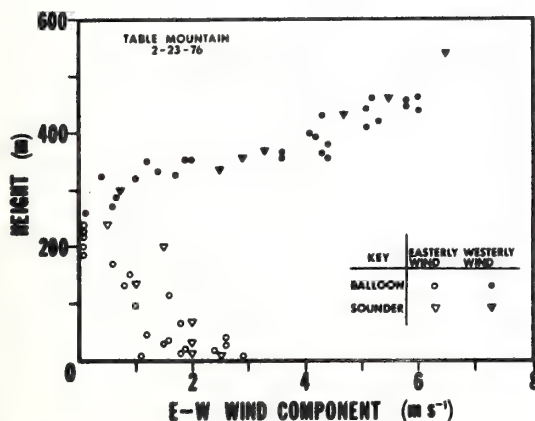
Figure 6. *Comparison of wind profiles measured by WPL acoustic echo sounder and balloon-borne anemometer.*

measured by the acoustic Doppler and by FM-CW radar is shown in Figure 7. The deviations seen between the two are the result of the different pulse volumes and Doppler resolution angles. These winds were measured at a height of about 200 meters on a hot day characterized by strong convective motions in the boundary layer. The geometry of the two sensors was such that the acoustic Doppler system sensed a larger component of the vertical velocity associated with the thermal plumes. Hence, larger oscillations appeared in the acoustic Doppler wind trace shown in Figure 7.
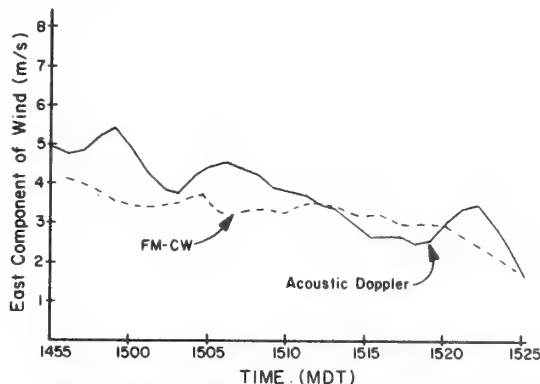
Figure 7. *Comparison of winds measured by FM-CW radar and acoustic Doppler at Table Mountain field site on 6/24/76. The curves shown have been filtered with a 10 min running average to remove differences due to different measurement volumes and separation.*

4.   THE DULLES INSTALLATION

The first operational test installation, made at Dulles during the summer of 1976, was designed to provide the maximum detectability for all types of wind shear. To do this, two new concepts were introduced into the overall system. Rain noise has long been recognized as a potential limitation for acoustic devices. To counter this problem, a dual-sensor approach using an acoustic Doppler for clear air conditions and a low-power, pulsed electromagnetic (EM) Doppler radar during precipitation has been employed. Wind measurement during precipitation with meteorological EM Doppler radars is a proven technique (Battan, 1973). The dual-sensor concept for continuous monitoring is, however, untried and will be tested for several months at Dulles during 1976 and 1977. If the concept proves successful the EM radar will be incorporated as part of the total system.

Because the acoustic Doppler has been designed for measuring a wind profile in the vertical and the EM radar requires hydrometeors, neither of these sensors will be effective for gust front monitoring. Gust fronts produce at least three distinct and detectable changes at the surface of the earth. These are: temperature drop, wind speed and direction change and sharp increase in pressure. While there is some debate as to the exact relationship between these changes and the severity of the wind shear produced by a given gust front, they are all recognized as

*Figure 8. Site of acoustic Doppler and EM radar installation at Dulles.
The location is labeled "site 2" in the photo.*

potential indicators. Based on extensive work with microbarographs (Bedard, 1966; Bedard and Meade, 1976; Bedard, 1976) it was concluded that an inexpensive, surface-based pressure jump detector could be designed to indicate the passage of a gust front over a point. Thus, providing a warning of the gust fronts presence, if not the magnitude of the shear aloft.

A comprehensive first-generation wind-shear detection system has evolved that uses the dual sensors and pressure detectors. Following an extensive site survey which placed prime emphasis on the climatology of wind shear, prevailing storm motion, and noise sources, the location of the acoustic Doppler system at Dulles International Airport was selected and is shown in Figure 8. The EM radar test unit is located at this same position.

To give an effective advanced warning of an approaching gust front, the pressure jump detectors must be placed at some distance from the active airport approach paths, and several units must be used to give broad coverage and indicate the speed and direction of the approaching disturbance. An optimum array would completely surround the airport, but for the sake of economy at this test installation the climatology of storm tracks was considered in selecting only a portion of the region around Dulles for the installation of a pressure jump detector array. The location of these detectors is shown in Figure 9.
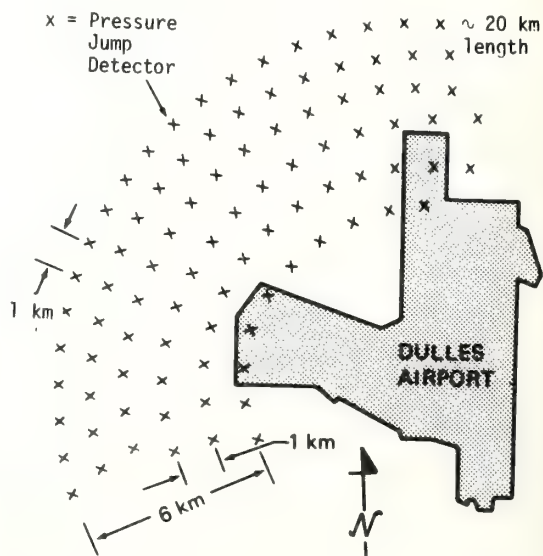
Figure 9. Location of pressure jump detectors around Dulles.

171

690

An artist's concept of the dual-sensor (acoustic/radar) installation is shown in Figure 10. The major elements of this part of the system are the main transmitter which projects a 1750 Hz acoustic tone burst vertically into the atmosphere, and three receivers, placed in bunkers, each spaced 290 m from the main transmitter on radii 120° apart. A smaller satellite transmitter is positioned 50 m in front of each receiver to provide wind measurements from 30 m up to 150 m in height. The main transmitter covers the region from 150 m up to 500 m. Information from any two of the three receiver legs is sufficient for measuring the wind profile.

When the rain rate reaches a point that significantly impairs the acoustic system, the EM radar is automatically turned on. Its exact mode of operation during this time has not yet been fixed. However, the first tests will employ a Velocity Azimuth Display (VAD) scan method for measuring the wind profile. Other operating modes, such as scanning along approach paths may also be explored. The central computer will accept data from both the acoustic and radar systems.

The central computer will also process the wind information to determine the magnitude of the wind shear and then relay these data to the airport control tower for display. As yet, the pressure jump detectors have not been tied directly to this central computer. A block diagram of the pressure jump detector portion of the system is shown in Figure 11. Because of the simplicity of the pressure sensors output, there may be no need for further processing before displaying the warning information. The test unit at Dulles will have a large map of the area, similar to that shown in Figure 9, with lights connected to each jump detector. When a segment of the array is triggered, corresponding lights will come on displaying the exact position and shape of the gust front. By providing the controller with this type of output, he will be able to tell at a glance when a dangerous condition is approaching the airport.

Figure 10. *Artist's concept of acoustic Doppler installation at Dulles International Airport.*

172

10 Absolute Pressure Sensors
10 Temperature Sensors

125
Pressure Jump Detectors
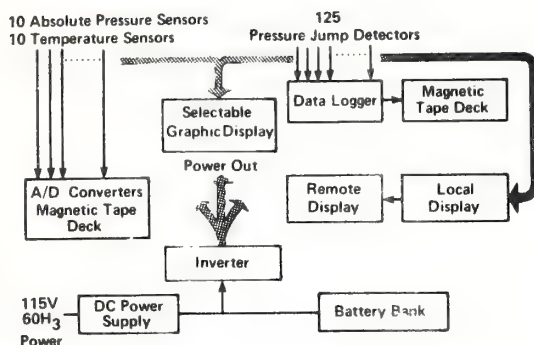
Figure 11. Block diagram of pressure jump detector system.

The total systems concept comes into play because the jump detectors can give only the location and speed of an approaching gust front. This would be sufficient information to issue a warning, but would not provide the equally important all clear indication. After the gust front has passed the airport, it is likely that dangerous shears will still occur at the interface between the cold air behind the front and the ambient air aloft, possibly for 30 minutes or longer. The vertically profiling part of the system can then be used to determine when such shear conditions have abated over the airport.

5.   SECOND-GENERATION DETECTORS

The system described above has the potential of detecting dangerous wind shears at an airport. However, as a total system its cost effectiveness must be questioned, especially in light of recent developments in related remote sensor technology. An analysis of all potential wind-shear detection techniques (Beran, 1974) concluded that laser systems, while having potential, were not sufficiently developed for early installation and that radar was limited because of its need for artificial tracers. Since that time, laser technology has advanced and systems such as the CO_2 pulsed lidar appear to have significant promise. In addition, a major breakthrough in radar processing has been achieved and winds in the clear air can now be measured by radar without the need for artificial tracers. Both of these systems have good range potential and can be engineered to scan over a wide region.

We define a second-generation wind-shear detection system as one capable of scanning the entire airport region out to something of the order of 20 km radius, with emphasis along approach and departure paths, under all weather conditions. Both the CO_2 pulsed lidar and radar now appear to have the potential of meeting these requirements. As an ultimate goal we would like to measure all three wind components at any point within the range of the system. This could be achieved with two Doppler sensors, as is done with dual Doppler radar, (Lhermitte and Miller, 1970) or potentially with only one sensor using new spatial filtering techniques that are now being explored. Basic development and testing of these second-generation sensors are still required.

Experiments with CO_2 lidars indicate that aerosol density, their tracer, is almost certainly large enough to allow full-time operation (DeLuisi et al., 1971; Huffaker et al., 1976). The question about cloud, fog and precipitation penetration still remains to be resolved, but there is some evidence that this problem may not be limiting. The desirability of developing an experimental wind-shear detection system based on the CO_2 pulsed lidar sensor is clear. Such a system should incorporate the latest laser and data processing improvements to provide a large increase in the signal-to-noise ratio over previous systems.

Sensitive EM radars using very large antennas can detect scattering from optically clear air (Hardy and Katz, 1972). Since wind measurements when hydrometeors are present are easily achieved, radar has high all weather potential. Both pulsed Doppler and FM-CW radar appear to have this potential. Recent experiments (Chadwick et al., 1976) have demonstrated that the FM-CW radar can measure the wind in the lowest kilometer of the clear air (see Figure 7). The FM-CW radar has advantages for shorter ranges, but it is probably equivalent to the pulsed system at longer ranges. This means that existing airport pulsed radars might be modified for use as wind shear detection systems.

The radar methods are very promising; however, a word of caution is necessary. Sufficient data have not yet been taken to clearly establish the climatological limits of the techniques. Until this is accomplished, we cannot say with certainty that all clear-air winds can be measured. It is encouraging to note, however, that the early FM-CW radar experiments have been conducted in the very dry climate of eastern Colorado, under conditions that are considered to be least favorable for clear-air radar operation. In addition, it is likely, but not yet firmly established, that the wind shear itself may enhance the scattering properties of the atmosphere and that the absence of echoes in clear air containing no shear will not pose an operational problem.

173

6. SUMMARY AND CONCLUSIONS

A first-generation wind-shear detection system has been installed at Dulles International Airport and is undergoing acceptance testing. The system consists of a dual remote wind sensor employing an acoustic Doppler to detect winds under all conditions except those when hydrometeors are present, at which time a low power pulsed EM Doppler radar takes over the measurement task. The acoustic/EM radar portion of the system is designed to measure a vertical profile of the horizontal wind to heights up to 500 m and to warn of shear layers produced by synoptic-scale fronts or low-level temperature inversions. In addition, an array of pressure jump detectors is installed around a portion of the airport to provide a warning of the approach of more localized and transient gust fronts. Because of the necessity to use three separate sensors to achieve total all-weather protection, this installation is considered to be a first-generation system.

Second-generation systems using lidars or radars that are capable of scanning the entire airport region from a single point, are under development and should eventually provide a more cost-effective solution to the airport wind-shear problem. These systems are, however, at least two years away from prototype installation at airports. Because the need for protection is immediate, we are faced with the dilemma of either rapidly installing complicated and expensive first-generation systems or waiting for the development of a second generation system, all the while realizing the possibility of the wind-shear risk.

The history of recent wind-shear related aircraft crashes suggests that an effective interim solution is possible and should be seriously considered. The majority of recent crashes have been associated with thunderstorms and most probably with the gust front. If some measure of protection from the gust front were provided quickly, we could reduce a major portion of future risks while awaiting the development of second-generation systems. It is recommended that some form of the inexpensive pressure jump detector array be installed soon at major airports that have a high incidence of thunderstorms. Although the protection provided would not be complete, the low cost and relative simplicity of such arrays would make them an effective, partial, interim solution.

7. ACKNOWLEDGMENTS

8. REFERENCES

Battan, L. J. (1973), *Radar Observation of the Atmosphere*, University of Chicago Press, Chicago, IL.

Bedard, A. J. (1966), Some observations of traveling atmospheric pressure disturbances, NBS Rept. No. 9364, 63 p.

Bedard, A. J. and H. B. Meade, (1976), The design of sensitive pressure jump detectors, (In preparation) NOAA/WPL, Boulder, CO.

Bedard, A. J. (1976), Detection of gust fronts using surface sensors (In preparation) NOAA/WPL, Boulder, CO.

Beran, D. W. (1974), Remote sensing wind and wind shear system, Report No. FAA-RD-74-3, Dept. of Transport. FAA, SRDS, Washington, D.C., 115 p.

Beran, D. W., F. F. Hall, B. C. Willmarth, R. J. Keeler and D. Hunter (1974), Operational test results of acoustic Doppler wind shear detector, 6th Conf. on Aerospace and Aeronautical Meteorology, El Paso, TX, Nov. 12-15, 1974. Publ. by Amer. Meteor. Soc., Boston, MA.

Chadwick, R. B., K. P. Moran, R. G. Strauch, G. E. Morrison and W. C. Campbell (1976), A new radar for measuring winds, *Bulletin AMS* (accepted).

De Luisi, J. J., I. H. Blifford Jr. and J. A. Takamine (1972), Models of tropospheric aerosol size distribution derived from measurements at three locations, *J. Geophys. Res.*, 77, No. 24, 4529-4538.

Hardy, K. R. and I. Katz, (1972), Probing the clear atmosphere with high power, high resolution radars, *Proc. IEEE*, 57, 468-480.

Huffaker, R. M., D. W. Beran and C. G. Little, (1976), Pulsed coherent lidar systems for airborne and satellite based wind field measurement, Proceedings 7th Conf. on Aerospace and Aeronautical Meteor., Nov. 16-19, 1976, Amer. Meteor. Soc., Boston, MA.

Lhermitte, R. M. and L. Jay Miller (1970), Doppler radar methodology for the observation of convective storms, 14th Radar Meteor. Conf., Amer. Meteor. Soc., Boston, MA., 133-138.

Nagarkar, B. N. and R. D. Finch (1975), Acoustic model study of a Doppler wind monitor receiver bunker, Final Report on NOAA order 01-5-022-2382 and 01-6-022-12172 for NOAA/WPL, Boulder, CO. Prepared at Applied Acoustics Corp., 7315 Ashcroft, Suite 112, Houston, TX, 77036, 61 p.

Willmarth, B. C., E. H. Brown, J. T. Priestley, and D. W. Beran, (1975), Beam pattern measurements for large acoustic antennas. 16th Radar Meteor. Conf. April 22-24, Houston, TX. Publ. by Amer. Meteor. Soc., Boston, MA.

a new radar for measuring winds

R. B. Chadwick, K. P. Moran,
R. G. Strauch, G. E. Morrison,
and W. C. Campbell

Wave Propagation Laboratory

NOAA/Environmental Research Laboratories

Boulder, Colo. 80302

Abstract

A new radar technique for measuring winds in the lower atmosphere is discussed. It is an extension of the well-known FM-CW technique and has the same advantages of relatively low cost and high flexibility for a clear-air radar. Two different types of wind data from clear-air returns are presented. The first is horizontal wind data by the FM-CW radar; these are compared with winds obtained from a tethered balloon. The second is radial velocities associated with convection cells drifting past the radar. Also, two types of data processing are illustrated. The first is off-line processing of recorded digital data, and the second is real-time processing using a commercial spectrum analyzer.

1. Introduction

Measuring winds in the atmosphere is a fundamental requirement in both research and operational meteorology. Anemometers continuously record wind near the ground, but they provide no information about winds aloft. On the other hand, rawinsonde balloons give wind profiles into the stratosphere, but they provide only "snapshots," typically every 12 h, at widely scattered locations. Furthermore, because a single sounding typically takes 80 min, it fails to provide simultaneous measurements at all altitudes.

To measure wind profiles more rapidly and to improve spatial and temporal resolution, new devices are being developed that use electromagnetic and acoustic waves to measure wind remotely. For example, the optical-scintillation technique (Lawrence et al., 1972) continuously records the average wind component blowing across an optical path, and refinements are being incorporated to yield the wind profile along the path. At present, however, vertical wind profiles (using stellar sources) can be obtained only at night and in clear weather. The acoustic-Doppler technique (Beran et al., 1971; Beran, 1974) measures the motion of wind-carried eddies from the Doppler shift of backscattered acoustic pulses. It can measure wind profiles up to 0.5 km but is ineffective in precipitation and in high winds. Acoustic absorption imposes height limits. Doppler lidars (Huffaker, 1974; Abshire et al., 1974) measure the velocity of wind-advected aerosols and so depend on the presence of such aerosols. Furthermore, they are vulnerable to attenuation by precipitation. Another problem is that CW Doppler lidars have a range resolution that degrades as the range is increased.

Here we describe a way to measure winds with a microwave radar, a technique that, in principle, is immune to most of the difficulties that limit the usefulness of the optical and acoustic techniques. The microwave technique offers an all-weather measurement capability.

2. Sensitivity consideration

Building a radar that can measure wind in the optically clear air is basically a matter of achieving the required radar sensitivity. A few years ago, pulse-Doppler radars were sensitive enough to measure wind fields only if artificial reflectors (chaff) were provided or if precipitation was present. Very-high-power pulse radars (Hardy and Katz, 1969) and FM-CW radars (Richter, 1969) can now detect layers of turbulence and temperature discontinuities in the clear air, but, so far, none has been adapted to wind measurement, which requires nearly continuous echoes in range. The pulse-Doppler radar recently developed by Green et al. (1975) has detected spatially continuous clear-air echoes between 4 and 16 km range at Sunset, Colo., by using 10 kW average power, a 7 m wavelength, and a 7200 m^2 aperture antenna. (Recent work with this radar indicates that the return may be due to layers that are not resolved owing to the coarse resolution used.) The continuous radar return is the result of Bragg scattering from refractive index (mainly temperature) fluctuations and is discernible from background noise only when the Doppler information is extracted from the signal. However, pulse radars cannot be used at short ranges (specifically, in the atmospheric boundary layer) because of receiver recovery and ground clutter, whereas FM-CW radars can see echoes as close as 15 m from the radar with good resolution. We calculated (Chadwick and Little, 1973) that if the Sunset radar could detect spatially continuous refractive-index fluctuations to 16 km range, then the Wave Propagation Laboratory FM-CW radar should be able to detect fluctuations of similar magnitude to 1 or 2 km range. To make this possible, however, we had to incorporate Doppler processing into the FM-CW system.

Until recently, there was no known way to extract the velocity spectrum of a distributed atmospheric target from an FM-CW echo. The supposed difficulty of measuring velocity spectra with an FM-CW radar lies in the fact that both range and Doppler information show up
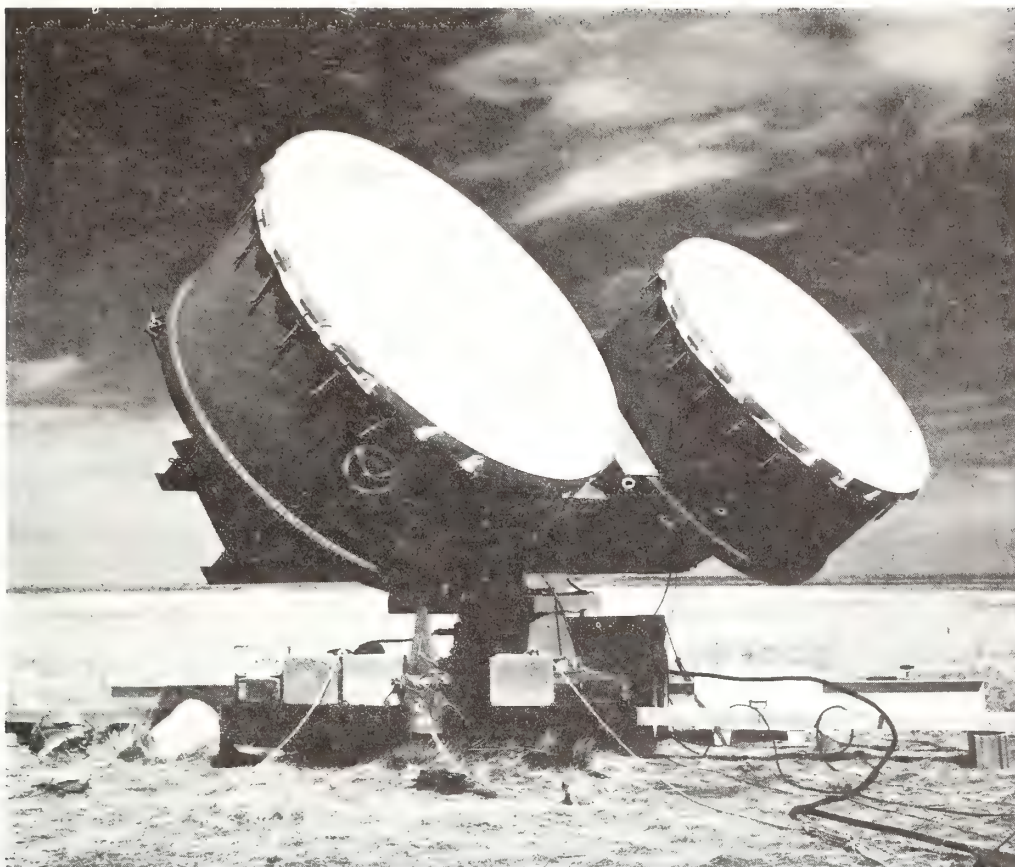
Fig. 1. FM-CW Doppler radar 8 ft parobolic antennas, one for transmitting and an identical one for receiving.

as frequency shifts of the radar echo. In conventional (range only) FM-CW processing, because the radar employs a linear-sweep frequency-modulated waveform, range is proportional to the frequency difference between the transmitted and received signal; any Doppler frequency shift introduces a small range error, but this is ignored. A power-spectral analysis of the echo yields echo intensity as a function of range (which is equivalent to frequency).

Recently, Barrick (1973), referencing work performed at Stanford, described signal-processing methods to measure sea state by extracting Doppler information from over-the-horizon FM-CW radars of a few meters wavelength. In an FM-CW Doppler system, the velocity spectrum is recovered by calculating the spectral estimate using a digital Fourier transform that preserves the phase as well as the amplitude of the spectral density of the radar signal obtained during each sweep. It is the change in this phase, from sweep to sweep, that contains the Doppler information.

Strauch *et al.* (1975) applied these techniques to the Wave Propagation Laboratory's FM-CW radar and measured the fall velocity of snow, demonstrating for the first time the applicability of this Doppler technique to centimeter wavelength radars. Later, Strauch *et al.* (1976)

demonstrated the ability of the same radar to sense movement of the clear air, with the radar looking vertically. It remained only to add antenna scanning to permit the measurement of horizontal wind.

Our FM-CW radar transmits at a wavelength of 10 cm with 200 W of power from an 8 ft parabolic-reflector antenna (Fig. 1). The adjacent receiving antenna is identical to the transmitting one, and the minimum detectable signal is about 155 dB below 1 mW. We further increased the radar sensitivity by sacrificing range resolution (increasing spatial integration). We used a 35 m range cell, which gives 30 m height resolution, for measuring height profiles of horizontal wind with an elevation angle of 60°. With the increased sensitivity provided by the Doppler capability and by increasing our spatial integration, we calculated that we should see continuous echoes and thus be able to measure wind to 1 or 2 km height. Our measurements demonstrated such a capability.

3. The results: Wind measurements

We operated our Doppler FM-CW radar for two weeks in September 1975, in southeastern Colorado, near a 152 m tower and a tethered-balloon system. The balloon system, described by Morris *et al.* (1975), measured tem-

695

870
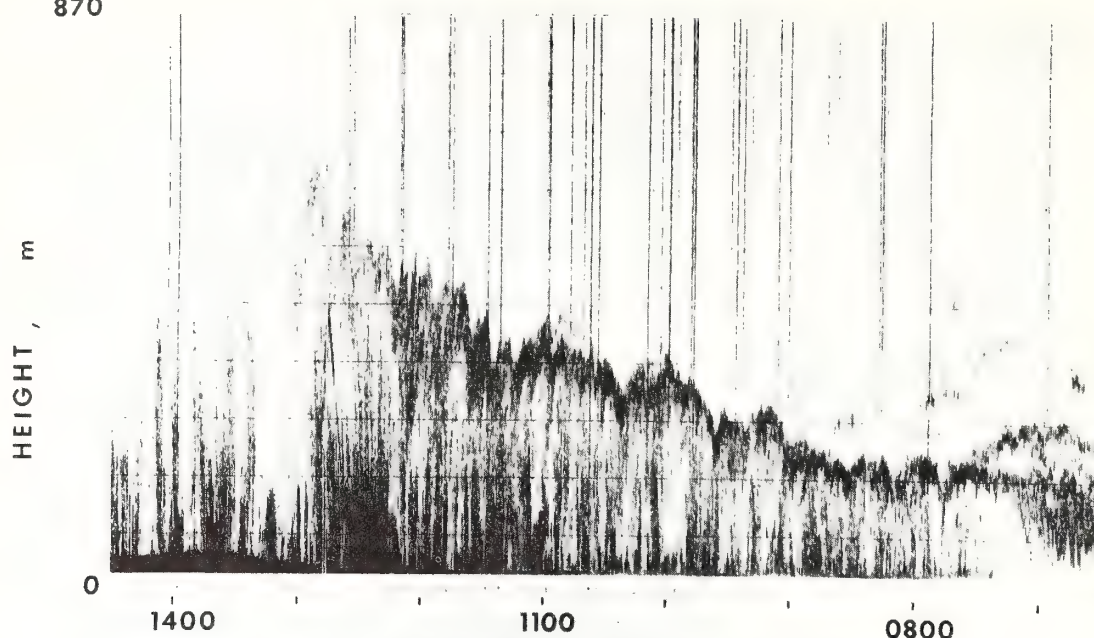
FIG. 2. Acoustic sounder record for 16 September 1975 at Haswell, Colo., showing a temperature inversion at about 150 m at 0700 MDT, rising to about 500 m before dissipating about 1300 MDT.
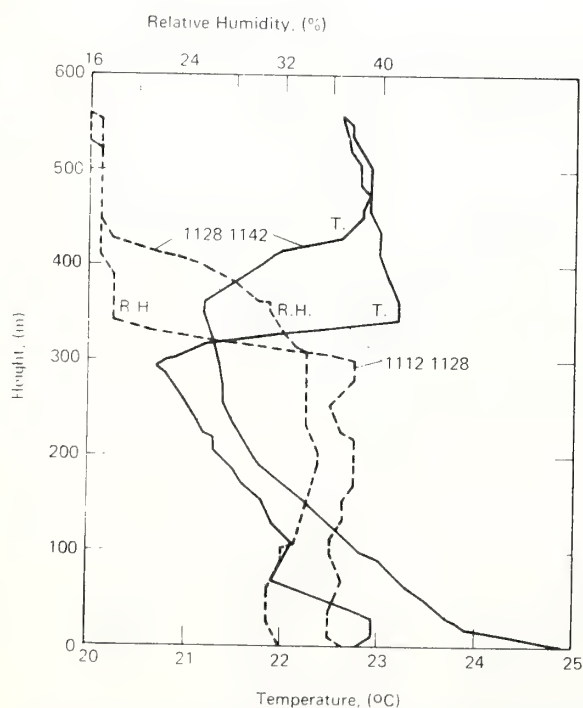
FIG. 3. Temperature and relative humidity profiles for 16 September 1975, as obtained with a tethered balloon, showing inversion between 300 and 400 m.

perature, humidity, and wind speed up to 600 or 700 m height, for comparison with the radar wind measurements.

On 16 September, the radar operated at an elevation angle (from horizontal) of 60° and at two orthogonal azimuth angles, 225° and 315°, to measure both horizontal wind components. The meteorology on this day is summarized as follows. Ground fog was present at 0700 MDT. By 0900 MDT the fog had "burned off" and there was 2/10 stratified cumulus cover. At 1100 MDT, the sky was completely clear. The record from an acoustic echo sounder operating nearby (Fig. 2) shows a temperature inversion starting at about 150 m and rising, owing to solar heating, to about 500 m before dissipating at about 1300 MDT. Temperature and humidity soundings made from the tethered balloon between 1112 and 1142 MDT are shown in Fig. 3, confirming the existence and location of the inversion between 300 and 400 m.

On days like this, when convection is inhibited by a low-level temperature inversion, vertical winds averaged over a short time period are probably negligible, whereas on days with vigorous convection the upward velocity may be comparable with the horizontal wind speed.

As an intermediate output, the radar produces a map of echo intensity in the height-velocity plane, as shown in Fig. 4. Here, 39 velocity spectra are averaged from each height interval, representing 10 s of data at azimuth 225°. The maximum unambiguous horizontal velocity is ± 5 m/s, so that spectral folding occurs whenever greater velocities are encountered. In Fig. 4, such folding

696
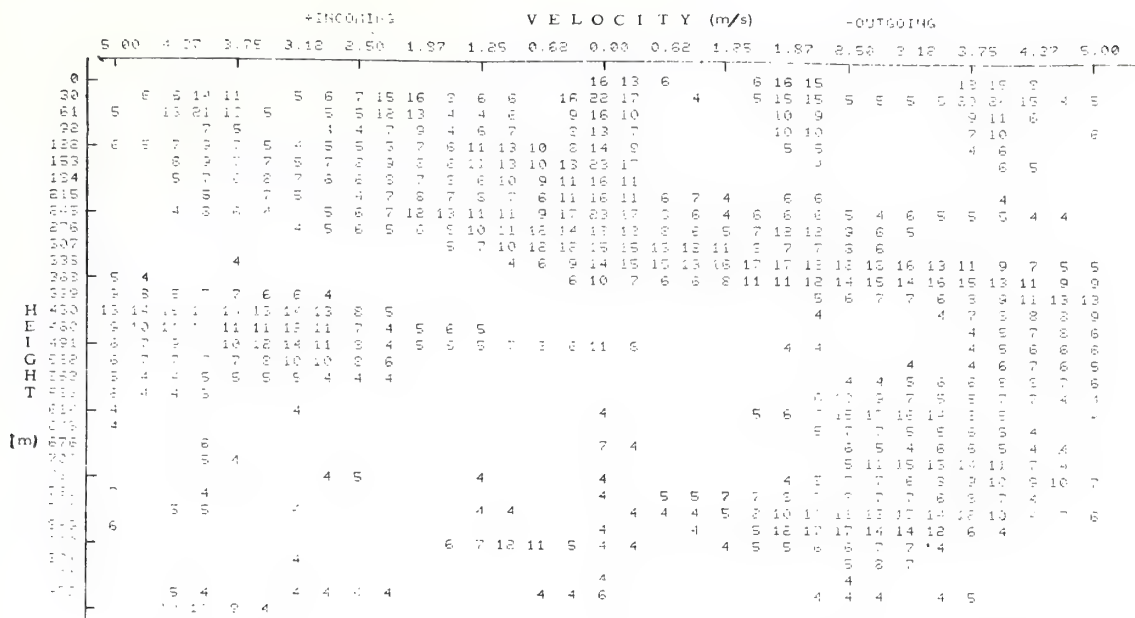
Fig. 4. FM-CW radar output as a function of height and horizontal velocity. The numbers are in decibles relative to the smallest value from that range. These are the data from which the radar wind profile in Fig. 5 was obtained.

is evident between about 399 m and 614 m height, so that in this height interval, the left portion of the spectrum is really a continuation of the spectrum that runs off the right margin. The height profile of the 225° wind component is obtained from the range-velocity map by estimating the spectral mean at each height. For example, at a height of 307 m in Fig. 4, the spectrum is centered about a small outgoing velocity. The two values of 15 dB near 0.00 m/s are partly due to ground clutter. Our algorithm selected a mean value of 0.93 m/s. The resulting profile is shown by the dashed line in Fig. 5, along with ascent and descent profiles measured by the balloon. The corresponding comparison for 315° azimuth is shown in Fig. 6. Considering the time differences (labeling on the curves), the 10 s averaging time of the radar, and the spatial separation (the radar was located 300 m west of the balloon system), the agreement seems remarkably good. Note from Fig. 4 that the radar is sensitive enough to give significant returns from above 900 m, well above the morning inversion. Evidently, the region of wind shear is about 3 times thicker than the depth of the inversion.

4. Effects of convection

As an example of the effects of convection on wind measurements, and to show another way to display the output of the radar, we show some data collected on another day, 23 September 1975. In Fig. 7 we display the time history of the Doppler spectra in each height cell by using the real-time output of the radar to intensity modulate a CRT display, which is photographed on slowly moving film. The straight horizontal lines repre-

sent the zero-velocity axis at that slant range, and the velocity spectra appear as the broader trace that changes position, width, and intensity with time. The position represents mean radial velocity; the width shows the spread of radial velocities in the range cell, and the in-
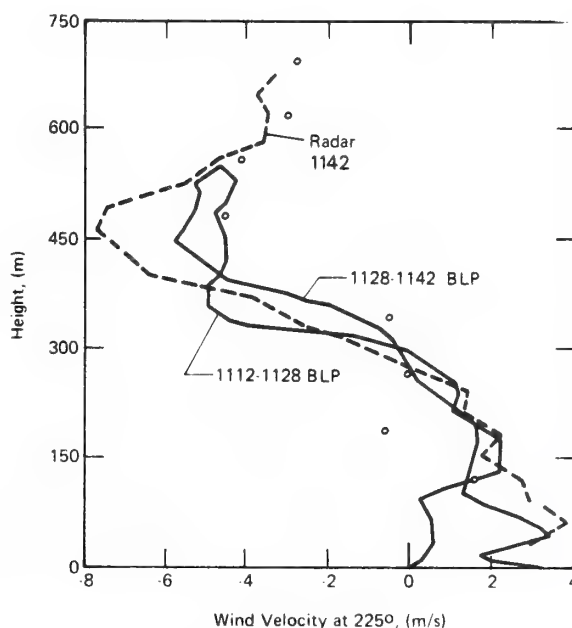
Fig. 5. FM-CW radar and tethered balloon (BLP) wind profiles for 16 September 1975. Wind component is at 225°. Small circles show results of rawinsonde release at 1100 MDT.
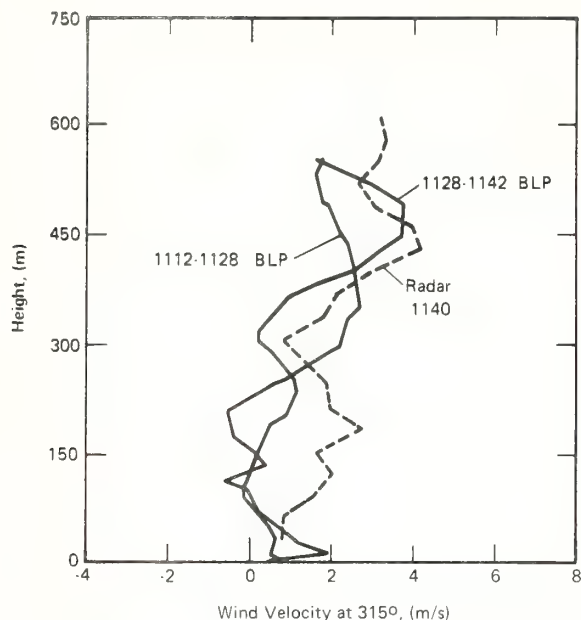
FIG. 6. FM-CW radar and tethered balloon (BLP) wind profiles for 16 September 1975. Wind component is at 315°.

tensity is proportional to radar reflectivity. When the spectrum lies below the zero-velocity marker, the radial wind component is toward the radar. The distance between the zero markers represents 10 m/s radial velocity, and their range separation is 122 m. The radial velocity resolution is 0.65 m/s, and the rms velocity error (which depends on signal-to-noise ratio) is about half this value.

In Fig. 7, we notice that the radial velocity at all heights regularly decreases to nearly zero at intervals of about 8 min. The antenna was pointed upwind. There are several possible explanations for these velocity perturbations. We interpret this pattern as the signature of a series of more-or-less evenly spaced convection cells being carried past the radar by the horizontal wind. The intensity enhancements that occur when the velocity suddenly decreases probably mark the turbulent-updraft portion of each cell, which produces enhanced radar echoes. The updraft is an outgoing radial velocity and thus, in this case, subtracts from the incoming radial-velocity contribution by the horizontal wind. (Our convection-cell structure seems to differ from those obtained by Hardy and Katz (1969), who find donut-shaped echoes on a plan position indicator (PPI) display, suggesting that the echoes come from a turbulent interface *between* up- and downdraft. We may not be looking through the centers of the cells, however.)

Assuming that the subsidence velocity associated with the convection cells is small, we attributed the non-enhanced portions of the velocity spectra to the horizontal wind component; we could then estimate the updraft speed from a simple geometrical construction. The value deduced in this case was about 4 m/s, not inconsistent with other measurements in similar cells. The same geometry gives a horizontal component of wind at this azimuth of about 10 m/s. Since this azimuth is in the direction of the prevailing wind, the total horizontal wind is perhaps only slightly larger than 10 m/s.

When vertical winds contribute significantly to the radial velocity measured by the radar, it may be necessary to make radar soundings at azimuths 180° apart to separate the vertical and horizontal components unambiguously. Suitable time averaging would be required to account for the slightly different volumes sampled.
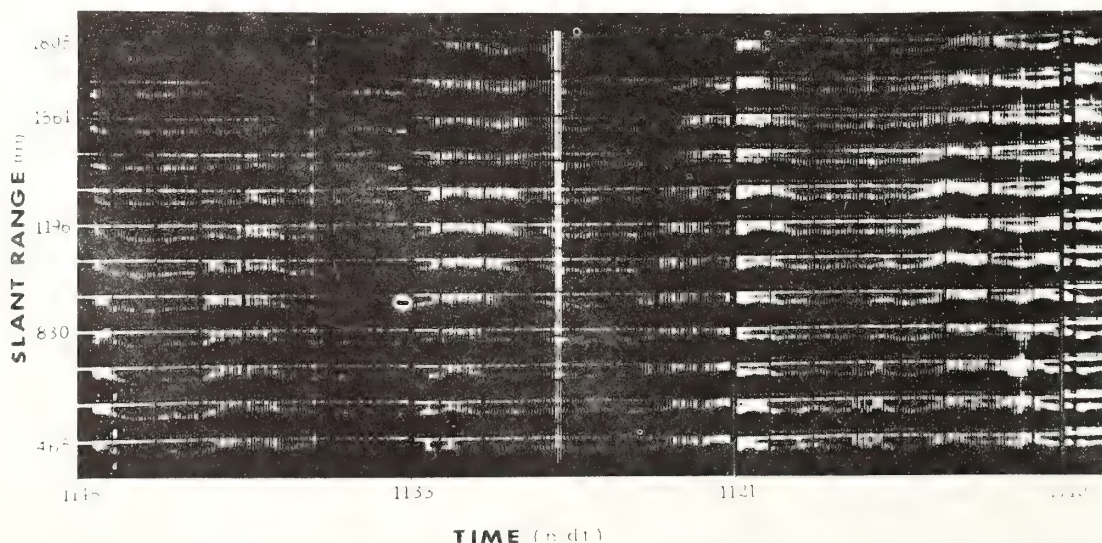
FIG. 7. FM-CW radar time-range-velocity display for 23 September 1975. The elevation angle is 45°, range cell size is 122 m, and velocity width from one zero velocity mark to the next is 20 m/s.

698

5. Summary

We have demonstrated an ability to measure winds in the clear air to heights in excess of 1 km using a microwave FM-CW radar with Doppler processing. Aside from system parameters, the maximum radar range depends on the availability of turbulent scatterers; with our system we have measured winds at ranges greater than 3 km when looking at 30° elevation. Furthermore, the time-range-velocity display (as in Fig. 7) is obtained in real time using a standard spectrum analyzer.

Radar wind measurement offers significant improvements in spatial and temporal coverage over *in situ* techniques. Using higher power and larger antennas, we should be able to probe greater heights.

References

Abshire, N. L., R. L. Schwiesow, V. E. Derr, 1974: Doppler lidar observations of hydrometeors. *J. Appl. Meteor.,* **13,** 951–953.

Barrick, D. E., 1973: FM-CW radar signals and digital processing. NOAA Tech. Rep. ERL 283-WPL-26.

Beran, D. W., 1974: Remote sensing wind and wind shear system. FAA Rep. FAA-RD-74-3. (Available from National Technical Information Service, Springfield, Va. 22151.)

——, C. G. Little, and B. C. Willmarth, 1971: Acoustic Doppler measurements of vertical velocities in the atmosphere. *Nature,* **230,** 160–162.

Chadwick, R. B., and C. G. Little, 1973: The comparison of sensitivities of atmospheric echo-sounders. *Remote Sensing Environ.,* **2,** 223–234.

Green, J. L., J. M. Warnock, R. H. Winkler, and T. E. VanZandt, 1975: A sensitive VHF radar for the study of winds, waves and turbulence in the troposphere, stratosphere and mesosphere. *Preprints of Papers, 16th Radar Meteorology Conference (Houston),* Boston, Mass., Amer. Meteor. Soc., 313–315.

Hardy, K. R., and I. Katz, 1969: Probing the clear atmosphere with high power, high resolution radars. *Proc. IEEE,* **57,** 468–480.

Huffaker, R. M., 1974: CO_2 laser Doppler systems for the measurement of atmospheric winds and turbulence. *Atmos. Technol.,* **6,** 71–76.

Lawrence, R. S., G. R. Ochs, and S. F. Clifford, 1972: Use of scintillations to measure average wind across a light beam. *Appl. Opt.,* **11,** 239–243.

Morris, A. L., D. B. Call, and R. B. McBeth, 1975: A small tethered balloon sounding system. *Bull. Amer. Meteor. Soc.,* **56,** 964–969.

Richter, J. H., 1969: High resolution tropospheric radar sounding. *Radio Sci.,* **4,** 1261–1268.

Strauch, R. G., W. C. Campbell, R. B. Chadwick, and K. P. Moran, 1975: FM-CW boundary layer radar with Doppler capability. NOAA Tech. Rep. ERL 329-WPL 39.

——, ——, ——, and ——, 1976: Microwave FM-CW Doppler radar for boundary layer probing. *Geophys. Res. Lett.,* **3,** 193–196.

The Boulder Atmospheric Observatory and Its Meteorological Research Tower

FREEMAN F. HALL, JR.

The author is with the Wave Propagation Laboratory, Environmental Research Laboratories, National Oceanographic and Atmospheric Administration, Boulder, Colorado 80302.

700

Remote sensing of the atmosphere by optical, acoustical, or radar means is becoming increasingly important in the meteorological community. Yet those of us in remote-sensing development are frequently asked the question, "How do you know your interpretation of the probing wave interactions with the atmosphere is correct?" Indeed, providing the independent verification of remote sensor performance has always been a challenge.

For the past ten years, the NOAA Wave Propagation Laboratory at Boulder, whose mission is remote-sensor development, has operated an instumented 150-m tall tower at

Figure 1. Artist's concept of the Boulder Atmospheric Observatory tower, located 25 km from the Rocky Mountain foothills.

Haswell, Colorado, in the southeast corner of the state. Many short-term but definitive atmospheric remote-sensing experiments have been conducted at this site. By 1969 we were aware of the limitations of the Haswell site because of the travel expense in operating so far from the home laboratory, because its intermittent use did not justify significant improvements in the instrumentation there, and because of the limited tower height. During the past four years we have been working hard to define the requirements for an improved tower and site and to obtain the monetary support to build such a facility. Now in 1977 we are constructing the tower. The purpose of this paper is to familiarize the optical community with the tower, its instrumentation, and its potential impact on atmospheric remote sensing. Possibly you, the reader, have in mind some atmospheric tests or experiments you would like to conduct at the site or use the tower instrumentation to support. The procedure for accomplishing such tests will be described.

THE TOWER STRUCTURE

The Boulder tower will be a guyed, open-lattice design 300 m tall. The structure will be galvanized steel with the three legs spaced 3 m apart. Flashing strobe lights will operate night and day to warn low-flying aircraft of the tower presence. A two-man elevator, internal to the tower, will allow access to the eight instrumentation levels while a movable carriage on one face of the tower provides for profiling or an intermediate platform between the fixed levels for sensing instruments. An artist's concept of the tower, showing these features and the general appearance of the facility, is illustrated in Fig. 1. The site is some 25 km from the nearest foothills of the Rocky Mountains so that the planetary boundary layer will be largely unaffected by the Rockies, except when strong downslope winds sweep over the prairie to the east of the mountains. The 300-m height of

the tower will ensure that the instruments extend above the nocturnal planetary boundary layer most of the time during all seasons. As the boundary layer depth is increased by convective mixing during the daytime, the capping inversion typically found at the top of the boundary layer will lift past the tower top by mid-morning. By afternoon the boundary layer may be one or two kilometers deep, so that it is not feasible to build any tower tall enough to sample this turbulent region continually. The planned 300-m tower is designed to allow extension to 500-m should the necessity for doing this be strongly apparent and the funding identified.

The location of the tower close to the mountains requires that special care be given to its design to withstand the winds and occasional icing conditions that can occur. The specification used was devised by the Electronic Industries Association and calls for the tower to withstand a

Figure 2. Drilling for the tower foundation piers, November, 1976.

wind loading of 3123 Nm^{-2} with 1.3 cm of radial ice on all members. At the altitude of Boulder, this is equivalent to a wind speed of 77 ms^{-1}. Safety factors of 2.5 were used in designing the tower structural members and guys.

The tower foundations must support not only the dead weight of the tower but also the pull-down tension of the guys. This required three concrete piers under the foundation cap, each pier 1.5 m in diameter and 17 m deep. Figure 2 shows the drilling rig on the site in November, 1976 preparing the holes for the foundation.

One of the operational goals was to place the tower close enough to the atmospheric sciences community in Boulder to keep the travel time from town less than 30 minutes. This was achieved when we identified an undeveloped section of land in Weld County, two miles east of the town of Erie, which was available for lease from the Colorado State Land Commission. The terrain is gently rolling prairie overlaying the Boulder–Weld Counties coal field. Many of the surrounding sections of land have been undermined during the past 80 years, and an operating mine is still worked on the adjoining section of land. Fortunately, we were able to locate a block upthrust or horst area which had not been undermined, wide enough to accommodate the tower guys. Coal deposits are generally thinner in such horst regions, explaining the lack of mining. Because the surrounding land is subject to subsidence over the old mines, there is little danger in future years of housing or commercial developments that might interfere with the low-level airflow past the tower. Most of the surrounding land is now used in alternate-strip, dry-land wheat farming.

Besides the NOAA investment in the tower and much of the instrumentation to be placed on and around it, the National Center for Atmospheric Reseasrch (NCAR), also located in Boulder, plans to move its Field Observing Facility to the site sometime in the future. The combined operation will be known as the Boulder Atmospheric Observatory. Through NCAR, we hope that many of the university groups in the atmospheric sciences will participate in experiments at the site.

INSTRUMENTATION ON THE TOWER

Prevailing winds at the tower site are from the southeast during the summer months and from the northwest during winter. For this reason, the tower instrumentation will be located on booms which can be extended 5 m from the tower to measure winds optimally from either the summer or winter prevailing direction. Instruments will probably need to be

Figure 3.   Details of an instrument level, showing the elevator landing platform, instrument boom, and external carriage.

moved twice a year to ensure proper exposure. Figure 3 is a blow-up of the earlier illustration to show one of the instrumentation levels. The elevator will stop at the steel grating platforms to allow access to the instruments. The booms can be cranked inward for instrument calibration and servicing, then repositioned away from the tower so as to reduce the effects of the structure on measurement accuracy. The booms will be located at 10, 20, 50, 100, 150, 200, 250, and 300 m heights. At each level we will have three-axis sonic anemometers, which can measure the three components of the wind independently twenty times per second. Conventional cup or propeller anemometers may be located at several levels for independent, average wind-speed measurement. Fast-response, platinum resistance thermometers will be colocated with the sonics to provide 10-Hz bandwidth temperature measurements. Slower response quartz crystal thermometers will provide averaged temperatures accurate to within 0.01 K.

A dewpoint hygrometer will be the standard humidity measuring instrument at each level with averaging times of several seconds for each reading. Lyman-α humidiometers will be added later to take advantage of the much faster response of these optical instruments. Pyroheliometers will be located at the base and the top of the tower to measure boundary-layer turbidity influence on solar flux.

The instrument carriage will be capable of handling loads of 1200 kilograms so that even the largest aerosol impactors or spectrometers can be profiled through the boundary layer. To avoid the necessity of trailing wires, we plan to telemeter the data from the carriage, probably utilizing an optical link for this purpose. At times, we may locate several three-axis sonic anemometers on the carriage together with high-frequency temperature and humidity instruments, thus requiring a communication bandwidth

of a megahertz or more. We are now working out details of the carriage instrumentation and telemetry.

Several remote sensors will also operate routinely at the tower. Surrounding the tower base will be a triangle of laser beams to measure the transverse wind across each leg of the triangle.[1] With the three independent transverse measurements we will be able to determine the wind convergence at the tower base. A typical instrument for such measurements is shown in Fig. 4. Three acoustic sounders, one at each corner of the laser triangle, will document the heights of the boundary layer and the presence of convective plumes or the occurrence of stably stratified layers. Sensitive microbarographs will also aid in the interpretation of gravity waves in the atmosphere propagating across the site.[2]

DATA ACQUISITION AND PROCESSING

The tower instrumentation, the laser triangle, and the microbarographs will be under the control of a digital computer housed at the base of the tower. The carriage telemetry receiver and the other instruments will be hard-wired to the computer through analog-to-digital converters with data being recorded on seven-track digital tapes. An XDS 920 computer, which has demonstrated its versatility through many years of field experiments, will be used initially. It will perform such chores as recording the raw or appropriately time-averaged data from each sensor, multiplying together the wind, temperature, and humidity fluctuations to provide averaged turbulent fluxes of momentum, heat, and moisture as well as performing other statistical manipulations of the data, printing out longer-period wind averages and variances, and correlating vertical velocities with the laser-triangle convergence measurements. We are working now on the formatting of the digital tapes and studying the optimum data-recording frequency and averaging times to provide a completely defined microclimatology of the boundary layer, and hope to limit
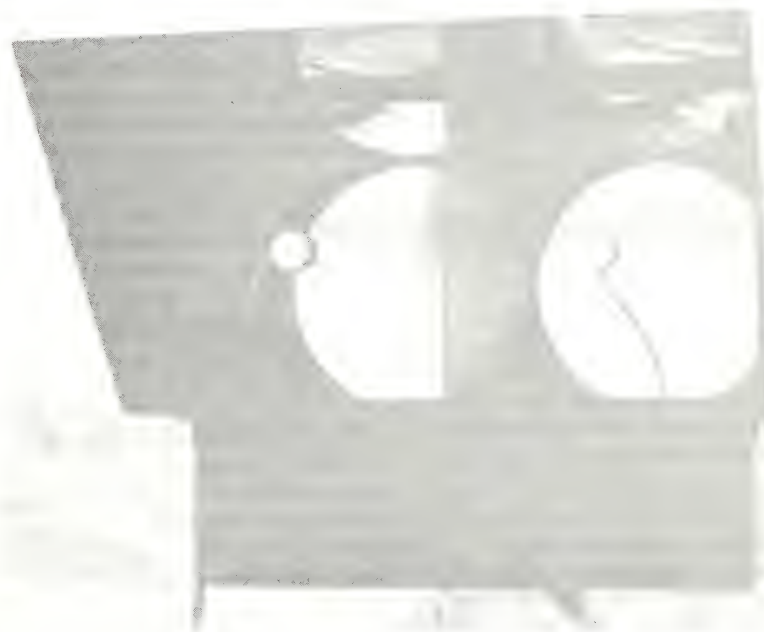
Figure 4.   Optical cross-beam wind sensor, as deployed in the field.

tape utilization to one or less per day. In addition, we will incorporate a more modern computer, at first for specialized, perhaps high-data-rate but short-time-period experiments, with the eventual goal of tying together the new tower computer with the Boulder Laboratories computer. This will allow experiments to be controlled in the future by scientists in Boulder without their even visiting the tower site. Eventually we may be able to link computer control to other users hundreds of miles away from the facility.

SOME SPECIFIC GOALS OF THE TOWER MEASUREMENT PROGRAM

The primary purpose of the tower, as previously stated, is to provide the *in situ* verification of atmospheric measurements made with remote sensors. The reliable comparison between remote sensors, which average over finite scattering volumes in the atmosphere, with the *in situ* instruments, which are essentially point sensors, requires the accumulation of significant statistics, something that the tower will be able to do since we plan to keep it in continual operation for a number of years. As the interaction of optical, acoustical, and radar waves with the atmosphere becomes better understood, we will be able to "virtually" extend the height of the tower past its 300-m limit through use of the remote probes. Indeed, one of the eventual goals is to replace many of the *in situ* instruments with remote sensors, eliminating the need for conventional instruments and possibly even for balloon-borne instruments.

With the information available at the tower from remote and *in situ* sensors, a unique data set on atmospheric dynamics will become available. By operating the tower continuously for an extended period, say five years or more, we will finally obtain a detailed microscale climatology of the planetary boundary

layer. We will have a reliable grasp on the statistics of turbulent heat, momentum, and moisture fluxes. We will be able to verify the importance of wave dynamics in boundary-layer processes and be able to understand the scattering mechanisms by which remote sensors record these events. For opticists, understanding the turbulent heat flux will permit better modeling and predicting of the effects of the turbulent atmosphere on optical wave propagation. We already have a good understanding of turbulent heat flux and optical index-of-refraction fluctuations under dry daytime convective conditions.[3] Better models are needed to help us to understand the stably stratified, nocturnal boundary layer, and we need to know the correlation between moisture and temperature fluctuations at different heights in the boundary layer so that the contribution of the latent heat fluxes on the optical index can be properly understood. Of course, this will require instrumenting the tower with fast-response humidity sensors, which we plan to do within the first year or two. Although the dry, high plains in Colorado are usually characterized by low moisture fluxes, on those occasions following rain storms we will be able to study the convariance of moisture and temperature fluctuations and should be able to extend this understanding to tropical or marine atmospheres by proper scaling. The improved understanding of moisture flux is also of great importance in understanding how the upward transport of water vapor through the boundary layer occurs. After all, this moisture is the source of clouds and large-scale weather in the atmosphere.

When the NCAR Field Observing Facility moves to the site, the measurement capability will be extended by the occasional deployment of its Portable Automated Mesonet (PAM) system, forty instrumented surface layer towers that can send telemetered data to a central location. In addition, NCAR and NOAA aircraft

will use the tower for calibration and be able to extend the range of tower measurements over wider horizontal and vertical scales.

The investment of tax dollars in the NOAA tower is significant. The data collected there will be of value not only to the Wave Propagation Laboratory in our mission of developing remote sensors, but to the entire atmospheric sciences community. It will be NOAA policy to treat the tower as a *national facility*, where others in the government, in universities, or in the private sector will be welcome to come and perform cooperative experiments with the NOAA personnel. The digital data tapes on which the routine tower data will be recorded will be available for anyone to duplicate, study, and evaluate for the cost of making the tape copy.

Eventually we hope that by obtaining better measurements and modeling of the boundary layer in its mesoscale (10–100 km) extent, we will be able to deduce better forecasting schemes for local weather. This goal, one of the most important in NOAA's list of priorities, will be continually kept in mind as this new national facility comes on line and as we gain experience in its first several years of operation.

Do you have an experiment you would like to conduct at the Boulder tower? After construction is completed in June, 1977, it will take several months to install the instruments and shake down the data acquisition system. We will then be ready for experiments on the tower. Get in touch with Dr. William H. Hooke at NOAA in Boulder, (303) 499-1000, X6378, and inform him of your experiment requirements.

REFERENCES

1. R.S. Lawrence, G.R. Ochs, and S.F. Clifford, Appl. Opt. **11**, 239 (1972).
2. W.H. Hooke, F.F. Hall, Jr., and E.E. Gossary, Boundary-Layer Meteorol. **5**, 29 (1973).
3. J.C. Wyngaard, Y. Izumi, and S.A. Collins, Jr., J. Opt. Soc. Am. **61**, 1646 (1971).

The Dulles Airport Acoustic-Microwave Radar Wind and Wind Shear Measuring System

R. M. Hardesty, P. A. Mandics,
D. W. Beran, and R. G. Strauch

Wave Propagation Laboratory
Environmental Research Laboratories, NOAA
Boulder, Colo. 80302

Abstract

Wind shear has been recognized as a major aviation hazard in the airport environment. A dual, acoustic Doppler–microwave Doppler radar system has been installed at Dulles International Airport near Washington, D.C., to measure the vertical profile of wind from the surface to 510 m in 30 m height increments. The acoustic system gathers data under clear-air conditions, and the microwave radar takes over automatically when precipitation is present. System performance is being assessed by comparing its output with National Weather Service radiosondes and with balloon-borne anemometers and by intercomparing the acoustic- and microwave-measured winds under light precipitation conditions. The dual-sensor system has been operating for several months, registering the passage of fronts, some with potentially hazardous wind shears.

1. Introduction

Analysis of several major aircraft accidents during the past few years has established beyond doubt that low-level wind shear can reach magnitudes that exceed the design capabilities of the aircraft and the ability of the crew to take corrective action (Laynor and Roberts, 1975; Fujita, 1976; National Transportation Safety Board, 1976; Fujita and Caracena, 1977; Caracena and Fujita, 1977). Wind shear of some magnitude is an expected feature of the atmosphere and can be found at nearly all temperature and density interfaces. On rare occasions it can reach magnitudes that are hazardous to aircraft. The critical attitude and slow response time of landing or departing jet-powered aircraft, combined with a lack of warning when strong low-level wind shear is present, can produce a very dangerous situation.

The Systems Research and Development Service of the Federal Aviation Administration (FAA) was aware of these dangers as early as 1972, when they initiated an interagency agreement with the Wave Propagation Laboratory (WPL) of NOAA to study and characterize the problem and to develop techniques that would provide adequate warning of low-level wind shear along the intended flight path of an aircraft. From the point of view of detection it is important to recognize two types of wind shear. One is associated with large-scale frontal or inversion surfaces and usually occurs above the ground with little or no surface manifestation other than a front that is in the general synoptic-scale region. The second one is related to the gust front that results from cold down currents generated by, or associated with, intense convective activity. In contrast to the synoptic-scale frontal shear, the gust front produces marked changes in surface wind, temperature, and pressure and is usually far more transient, lasting only minutes as compared to the possibly hour or more duration of the frontal type shear. The primary danger of the frontal shear is a change in wind speed or direction with height, whereas the hazard created by the gust front is more likely to be a change in wind speed or direction with horizontal distance. This paper describes a wind shear detection system that was designed to monitor large-scale, less transient types of wind shear produced by low-level inversions or frontal surfaces.

Preliminary results of the wind shear detector development effort have been described by Beran et al. (1976), Beran (1974), Beran et al. (1974a), and Beran et al. (1974b). The WPL development work consisted of the design and installation of a wind shear detection system at Dulles International Airport, Washington, D.C., during the summer of 1976. Because precipitation degrades the performance of acoustic sensors whereas it enhances the operation of microwave radar devices, the system includes both a microwave Doppler radar (Campbell and Strauch, 1976) and an acoustic sensor. This dual-sensor system measures the wind profile in a vertical column directly above the sensor. The shear typically produced by frontal surfaces is then derived from the vertical profile of the horizontal wind. It is assumed that shears associated with both fronts and inversions are nearly horizontally homogeneous over the entire area of low-level aircraft operations at the airport.

It should be recognized that the problem of wind shear in aviation is very complex and that until effective wind shear warning systems can be provided at all major airports, the use of other, more limited techniques still can improve safety. For instance, some success has been reported in forecasting frontal shears (Sowa, 1974). Use of existing onboard radar can be valuable for identifying dangerous regions associated with storm centers. In addition, by using the aircraft's inertial navigation system and surface-measured winds, information on the shear between an approaching aircraft and the touchdown point can be obtained.

2. Description of the dual-sensor system

Because of the prevailing westerly direction of storm motion at Dulles and the necessity to detect shears associated with storms before they reach the airport, the

Fig. 1. Artist's concept of the Dulles wind shear detection system.

shear detection system was located due west of the airport ⌣1.8 km from the west end of runway 12-30. Additional factors that affected the site selection included the desire to minimize acoustic background noise, availability of land, and planned airport expansion.

Figure 1 is an artist's concept of the installation. A centrally located transmitter projects short bursts of 1250 Hz acoustic energy vertically at 20 s intervals. Three receivers separated by 120° in azimuth surround the transmitter on a 580 m diameter circle. Electronically steered receiver beams track the upward propagating pulse from 150 to 510 m and collect signals scattered by the atmosphere. Smaller satellite transmitters positioned 50 m in front of each receiver cover the 30–150 m height interval. After amplification, the signals are digitized and spectrally analyzed. The spectra obtained from each height on each leg are exponentially averaged in time to improve the signal-to-noise ratio. The wind-induced Doppler shifts are then determined from the first moments of these spectra. By assuming that the vertical wind component averages to zero and using the known system geometry, the wind speed and direction profile is determined between 30 and 510 m in 30 m height increments. Table 1 lists the more important acoustic system parameters. Information from any two legs is sufficient to determine the horizontal wind. Therefore, the use of three legs provides a degree of system redundancy.

During precipitation, which may degrade the acoustic

system performance, the microwave radar is automatically activated. This system trade-off is made when the acoustic signal-to-noise ratio decreases below that of the microwave radar. The microwave radar measures the radial wind velocity along four orthogonal azimuths (north, east, south, and west) using an antenna mounted on top of the centrally located data-processing building. After emitting a short pulse along a given azimuth, the radar return is sampled every microsecond to cover a height range of 120–510 m with 30 m resolution. The microwave radar transmits 640 pulses along each azimuth, and the resultant four radial velocity profiles are combined to produce a total wind profile every minute by assuming that the vertical wind, raindrop fall speed, and horizontal wind are horizontally homogeneous. The maximum horizontal spacing of the measurements varies from 1.2 km at 120 m altitude to 5 km at 510 m altitude. Table 1 also lists the pertinent microwave radar system parameters.

Pulse pair processing (Miller and Rochwarger, 1972) is used to estimate mean radial velocities from the microwave radar. The error introduced into the horizontal wind estimates by differing particle fall speeds and vertical winds at azimuths separated by 180° is one-tenth of the difference between these vertical motions. If the magnitude of the horizontal component of the wind along the direction of the radar beam is different at the two colinear azimuths, the radar-measured wind component will be the mean value. By assuming

706

TABLE 1. Dulles dual-sensor system parameters.

	Acoustic Sensor			Microwave Radar
	Main (M)	Satellite (S)	M & S	
Transmitter				
Frequency	1250 Hz	1250 Hz		9310 MHz
Pulse duration	250 ms	100 ms		0.5 μs
Pulse interval	15–20 s	15–20 s		256 μs*
Peak power (electrical)	720 W	100 W		5 kW
Receiver				
Bandwidth			300 Hz	2 MHz
Sampling rate			10^3 samples s^{-1}	10^6 samples s^{-1}
Averaging time			2–6 min	2–6 min
Antenna beamwidth (and pointing)				
Transmitter	9° (vertical)	13° (elevated at 80°)		2.3° (elevated at 11.5°)
Receiver			8° × 12° (steerable)	same as transmitter
Measurement height interval			30–510 m	120–510 m
Height resolution			30 m	30 m
Measurement accuracy			±1 m s^{-1} (speed) ±10° (direction)	

* A pair of pulses (separated by 256 μs) is transmitted every 1024 μs. The signal return from each transmitted pulse is sampled with a 1 μs spacing between 120 and 510 m altitudes.

that the wind and particle fall velocities are horizontally uniform, the standard deviation of the measured wind components is expected to be <5 cm s^{-1}.

3. Initial test results

Following system checkout, a test program to establish the system measurement accuracy, operational limitations, and applicability as a wind and wind shear detector in the airport environment was initiated. Results presented in this section were obtained during the September 1976 through February 1977 period. Testing of the system is continuing under the direction of the FAA to assess its long-term capabilities and limitations. As with all remote sensors, it is inherently difficult to verify the sensor accuracy directly. At Dulles, two sources of independent wind measurements were used for the initial comparison: a balloon-borne anemometer and the radiosondes launched by the National Weather Service (NWS). In addition, under light precipitation conditions, both the acoustic and the microwave radar portion of the system can collect data simultaneously.

a. Comparisons with balloon-borne anemometer data

The Boundary Layer Profiler (BLP) consisting of a balloon-borne anemometer (Morris et al., 1975) produced data that were digitized and exponentially averaged with a 6 min time constant for comparison with the similarly averaged output of the acoustic system. Balloon instabilities at wind speeds approaching 10 m s^{-1} and limited battery lifetime severely restricted the use of the BLP. Even under favorable conditions, the balloon's vertical and lateral position fluctuated as much as 50 m, which increased the BLP measurement bias (Haugen et al., 1975) and resulted in inevitable measurement differences between the BLP and the acoustic system.

Despite these difficulties, ⁓12 h of BLP data were collected and compared with data from the acoustic portion of the system. Scatter diagrams of BLP versus acoustic wind speeds and directions for three height intervals (Fig. 2) show that >70% of the speed estimates differed by <1 m s^{-1}. Directional differences between the sensors were generally less than ±20°.

TABLE 2. Statistics of Boundary Layer Profiler (BLP) and acoustic sensor (A) wind comparisons.

Run	Date	Duration, min	Height, m	Mean Speed, m s^{-1} A	Mean Speed, m s^{-1} BLP	Mean Direction, deg A	Mean Direction, deg BLP	s.d. of Speed, m s^{-1} A	s.d. of Speed, m s^{-1} BLP	s.d. of Direction, deg A	s.d. of Direction, deg BLP	Speed rms Difference, m s^{-1}
1	10/15/76	105	60	6.5	6.3	200	205	1.16	1.27	6.3	4.8	0.81
2	10/29/76	120	300	4.5	4.7	253	254	2.42	3.08	36.3	37.5	1.3
3	11/4/76	30	410	2.1	2.4	145.4	169.5	0.29	0.59	18.9	25.0	0.79
4	11/24/76	120	300	4.8	4.5	214.5	224.4	1.58	1.64*	14.3	15.0	0.91
5	12/1/76	42	300	4.9	5.0	193.7	206.6	0.29	0.34	3.9	2.2	0.5
6	12/1/76	88	210	7.5	8.5	182.8	197.1	1.44	0.94	6.0	4.5	1.23
7	12/9/76	63	360	3.7	3.9	302.6	285.7	0.49	0.63	7.7	6.8	0.75
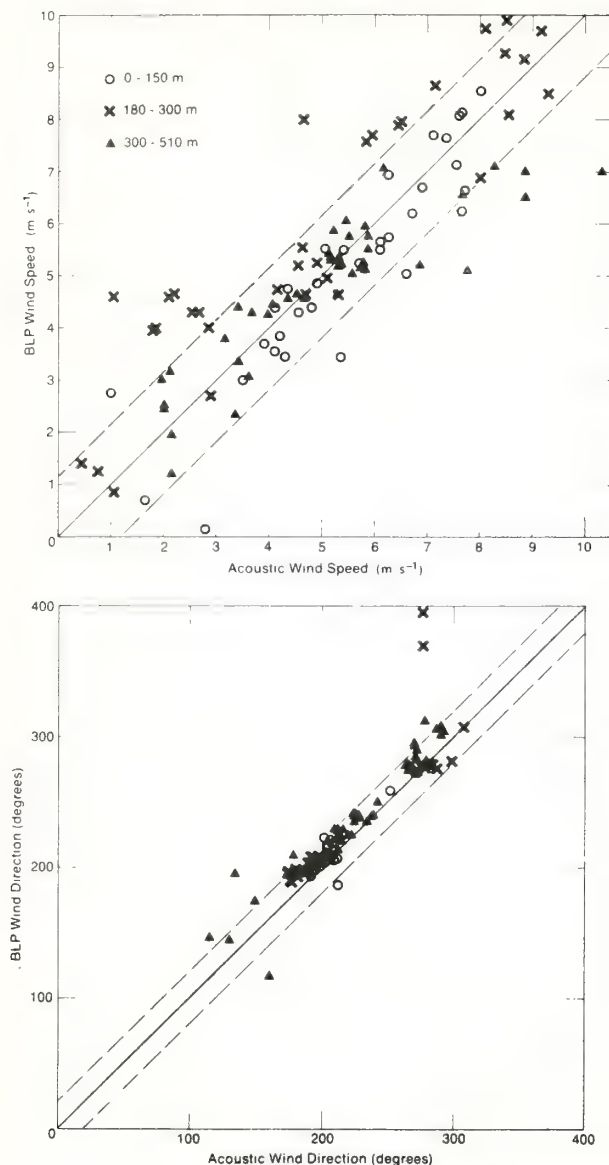
FIG. 2. Comparison of acoustic and BLP wind measurements for three height intervals. The dashed lines indicate rms measurement difference of 1.2 m s⁻¹ in speed and 20° in direction.

FIG. 3. Time series comparison of acoustic- and BLP-measured wind speeds at 300 m height level.

Table 2 contains a comparison of winds measured by the BLP and acoustic sensor for seven data runs. Mean wind speeds and directions were obtained by averaging data collected at the rate of 10 data points per hour for each run, which ranged from 30 min to 2 h in duration. The longer averaging time reduced differences caused by sensor separation, unequal sampling volumes, and random BLP displacements. Mean estimates for the runs agreed within ±1 m s⁻¹ (speed) and ±24° (direction).

Short-term (6 min) wind measurement accuracy is important in wind shear detection. A measure of comparability is given by the rms difference between sensor outputs. Table 2 shows that the rms difference exceeded 1 m s⁻¹ for only two of the seven runs and increased as

the standard deviation of wind speed increased, implying wider discrepancy between sensors under turbulent conditions. A comparison of the standard deviations of the wind speeds indicates that the acoustic estimates generally fluctuated more than those obtained by the BLP. The acoustic and BLP time series plotted in Fig. 3 bear this out. The standard deviation and rms difference can be decreased by increasing the exponential averaging time constant. However, this will also result in reduced system response time to wind changes.

b. Comparison with NWS radiosonde data

Radiosondes launched twice a day by the NWS at Sterling, Va., 6 km distant, provided comparison data for ~50 days under a greater variety of weather conditions. The degrading effects of differences in measurement volumes, techniques, and times and of the large spatial separation between the remote-sensing system and the radiosonde launch site are indicated in Fig. 4 by the greater scatter of the data. Despite the larger variability, the mean wind speeds measured by the acoustic–microwave radar system and the radiosondes are within 0.4 m s⁻¹. The corresponding mean directions are within 6°. The good agreement indicates that no significant measurement bias exists at 300 m, the only level for which data could be compared.

c. Acoustic–microwave radar internal consistency

Additional information on system performance was obtained through the analysis of simultaneous microwave radar and acoustic measurements. During periods of precipitation, the strong returns and high signal-to-noise ratios dictate the use of the microwave radar as the primary system sensor. Experience has shown, however, that if the precipitation is light or is in the form of snow, the acoustic signal-to-noise ratio is also sufficiently high to produce reliable wind estimates. An example of measurements taken during a light drizzle is shown in Fig. 5, which indicates excellent agreement between acoustic and microwave radar wind profiles. On many occasions, such conditions persisted for several hours. The time series of acoustic and microwave radar wind

708

FIG. 5. Wind profiles measured simultaneously by the acoustic (solid line) and microwave radar (dashed line) systems under light precipitation conditions.

FIG. 4. Comparison of acoustic–microwave radar system (acoustic/radar) and NWS radiosonde wind measurements over a 2-month time period at 300 m height level. The dashed lines indicate rms measurement difference of 3.3 m s⁻¹ in speed and 26.5° in direction.

estimates for such periods provided information on long-term agreement, sensor response time, and relative measurement variance. Two long-term comparisons of acoustic and microwave radar wind estimates at a height of 300 m (Figs. 6 and 7) show very good correlation for both periods. The microwave radar winds were block averaged for 1 min, and the acoustic measurements were exponentially averaged with a 6 min time constant. The smoothing effect of the longer averaging of acoustic estimates is apparent; they exhibit less high-frequency fluctuation. The large spike in the microwave radar wind direction estimate shown in Fig. 6 was apparently caused by localized turbulence that occurred immedi-

ately prior to the large-scale directional shift. Longer averaging of the acoustic data filtered out this directional anomaly. The trade-off obtained with averaging (better smoothing versus decrease in response) also shows up in the data. The acoustic measurement is seen to lag slightly behind the microwave radar estimate over much of the time.

The acoustic and microwave radar wind measurements are totally independent. Therefore, their excellent agreement strongly supports the validity of these two separate measurements. The probability of two independent sensors providing the same incorrect-wind measurement is quite small.

d. Observed wind shear events

During the first 4 months of system testing, a number of wind shear events were noted in the recorded data, and on at least two occasions, pilots confirmed the presence of shear. The utility of the dual-sensor system for wind shear detection was most dramatically demonstrated on the evening of 20 October 1976. During the day, a surface disturbance developed in the south Atlantic states and propagated northeastward, rapidly intensifying as it moved through the mid-Atlantic coastal region. The low-pressure center, accompanied by widespread precipitation, passed east of the Washington area about 0000 GMT, 21 October.

The synoptic frontal conditions indicated the potential for hazardous wind shear (Sowa, 1974) for the period beginning 2000 GMT, 20 October. The shear detected by the Dulles system (see Fig. 8) slowly developed after this time, reaching a value of 0.03 s⁻¹ over a 400 m depth around 0000 GMT. During this event, the wind direction at higher levels veered from east to west, while the lower level (below 200 m) wind direction backed from northeast to west. This behavior was consistent with the expected synoptic flow pattern of the developing system.

Figure 9 depicts the surface streamlines and frontal pattern at 0000 GMT, 21 October. As frequently occurs,
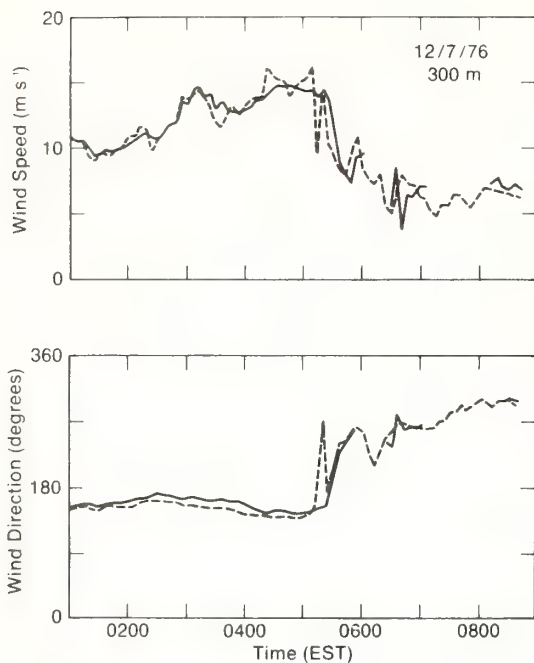
FIG. 6. Time series comparison of acoustic (solid line) and microwave radar (dashed line) measured winds at 300 m height level.

FIG. 7. Time series comparison of acoustic (solid line) and microwave radar (dashed line) measured winds at 300 m height level.

a shallow mass of modified cool air, characterized by weak northeasterly flow, was lying on the east side of the Appalachians this day. The 850 mb (1500 m) analysis at 0000 GMT indicated that a circulation center was located over southwest Pennsylvania and that a trough extended south-southeast through central Virginia. Prolonged low-level wind shear occurred across the interface between the cool, low-level flow and the stronger southeasterly flow on the east side of the upper (850 mb) trough. The cool, low-level northeasterly flow, overlain by warmer, moist air from the Atlantic, was gradually replaced after 0000 GMT by drier westerly flow at all levels in the boundary layer. The passage of the trough at the upper levels resulted in a uniform west-northwest wind direction below 510 m, eliminating the low-level shear. The associated meteorological conditions were typical for a developing coastal storm and, although the shear during this period was never very intense, the influence of the Appalachian highlands to the west of Dulles was noticeable both from the standpoint of trapping cool air in the lee and of funneling the westerly low-level flow after trough passage.

Only light drizzle occurred during the shear event. Returns from the microwave radar, which had operated in heavier rain through the day, became more intermittent because of the decreasing number of scatterers. As the rain rate decreased, the acoustic system gradually replaced the radar as the system sensor. During the transition period, continuous data were produced every 6 min regardless of which sensor was used to obtain the measurement. The excellent continuity of measurements from the different sensors indicated both the accuracy of
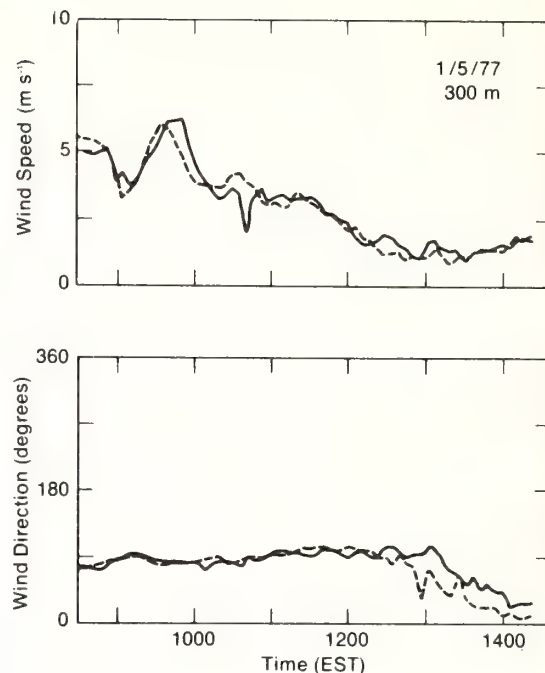
the measurements themselves and, because the sensed volumes were some 2 km apart, also the horizontal homogeneity of the wind field during the transition period. Thus the feasibility of using the dual-sensor system for wind measurements during front-generated wind-shear events was demonstrated.

e. System reliability and present operational status

Another objective of the system tests was the determination of long-term measurement reliability. The dual-sensor system has been in a test mode since the summer of 1976. There have been a few occasions during this time period when the received signal-to-noise ratio was so degraded that accurate determination of the wind became impossible. Ambient acoustic noise, a frequent source of problems for acoustic sensors, was the cause of most system failures at Dulles. Noise generated by aircraft, birds, and high surface winds at times altered or overwhelmed the scattered signal and resulted in decreased data reliability. The detrimental effects of noise increased as a function of its duration. For example, noise that was present for <5 min, such as that generated by arriving and departing aircraft, did not seriously affect system performance unless it recurred within a very short time. The most deleterious effects were produced by high surface winds, which often persisted for periods of several hours. Trees in the immediate vicinity of the receiver sites increased the wind noise significantly. Long-term analysis of data reliability indicated a substantial decrease in the percentage of acceptable wind estimates during periods when surface winds exceeded
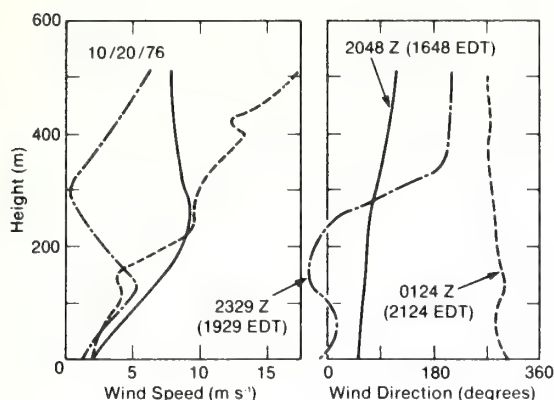
FIG. 8. Wind profiles for a front-generated wind shear event. (The 2048, 2329, and 0124 Z profiles correspond to the onset, peak, and dissipation of low-level shear, respectively.)

8 m s^{-1}. In contrast, during precipitation periods, when the microwave radar was operating, data reliability was generally very high.

The computer software detected and recorded those time periods during which data quality exceeded a preset acceptability threshold. Percentages of time when wind estimates were judged to be reliable are plotted in Fig. 10 as a function of height. The system produced acceptable measurements 90–95% of the time up to 300 m. Above 300 m the reliability decreased, and at 510 m, acceptable data were collected 70–80% of the time. The decrease in reliability at the higher altitudes is due primarily to increasing attenuation of the acoustic signal over the longer paths traveled. As a result, the received signal is weaker and is more susceptible to ambient noise.

In early tests at Dulles the acoustic system often produced unrealistically low or even zero wind values at the lower heights during periods of moderate winds. Analysis of received signal spectra indicated the presence of a large zero-Doppler-shifted signal. Side lobe radiation from the main transmitter, which was reflected by stationary objects on the ground and picked up by the receivers simultaneously with atmospherically scattered signals, was found to be the cause of these anomalies. The problem was eliminated by upgrading the background noise cancellation capability of the system.

Generally, wind profiles obtained by the system showed excellent continuity. However, on occasion a sharp discontinuity was observed. This occurred at heights where the acoustic system started using data from two receiver legs instead of three, because of inadequate signal reliability on one of the legs. Although occurring infrequently, the problem is potentially serious because of the possibility of interpreting the discontinuity as a wind shear. Computer simulations of the acoustic propagation paths indicate that wind acting on the transmitter and receiver beams causes slight measurement biases for each of the three wind components. The bias is proportional to the magnitude of the wind

along a given leg. When three legs are used to calculate the total wind, the biases tend to cancel because of the symmetry of the three receivers. However, when only two legs are used, the symmetry disappears and, depending on the wind direction, the biases may become cumulative resulting in the observed profile discontinuity. Work is currently under way to develop correction factors that would eliminate the biases along each leg.

4. Summary and conclusions

The acoustic–microwave radar concept tested at Dulles was selected because the associated technologies had been developed to the point where implementation as an operational test system was feasible within a relatively short time frame. The inherent limitations of an acoustic system coupled with the high cost of installation cast doubt on the ultimate usefulness of acoustic Doppler systems at airports. Although the cost might be reduced for production models, limitations such as those caused by high surface winds still must be assessed to determine the frequency of occurrence of limiting conditions when wind shear is present. For operational applications, the need for a microwave radar in conjunction with the acoustic system will remain essential unless unforeseen developments in signal processing or antenna design take place. Second-generation systems using clear-air lidar (Huffaker et al., 1976) or FM-CW microwave radar (Chadwick et al., 1976) have the potential to monitor winds directly along the takeoff and approach paths. Even though these techniques are promising, their operational implementation is still several years away.

Meanwhile, preliminary results of tests at Dulles demonstrate the feasibility of using the dual-sensor system for large-scale wind shear detection. Comparing
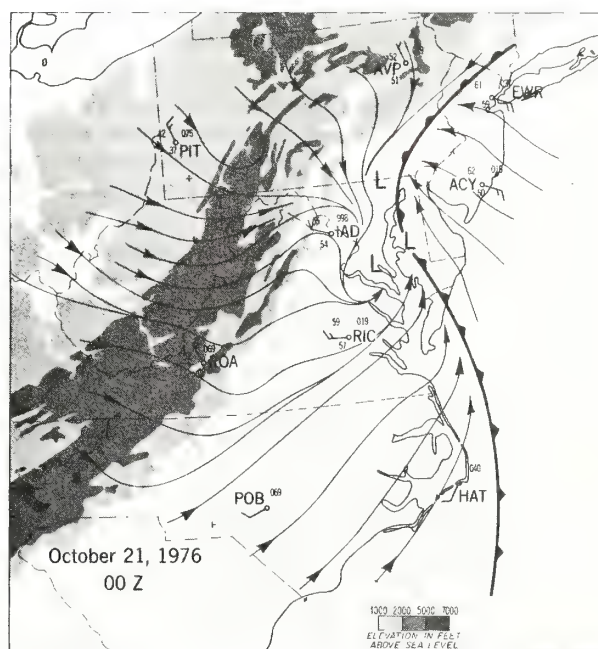
FIG. 9. Surface streamlines for wind shear event.
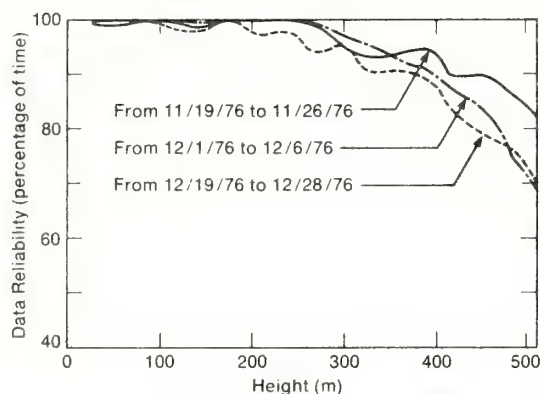
FIG. 10. Percentage of time during which acoustic–microwave radar system provided reliable wind estimates at the various measurement heights.

BLP with acoustic wind measurements and acoustic with microwave radar wind measurements, we find agreement within $\pm 1 \text{ m s}^{-1}$ (speed) and $\pm 20°$ (direction). The system has detected and monitored shear during typical shear-producing events. Analysis of archived data shows excellent correlation between system-monitored wind shears and frontal passages and/or pilot-reported shears.

Results of the initial test effort have supported our belief in the utility of the vertical profiling concept. Excellent agreement between the microwave radar and acoustic systems, which sensed volumes that were separated by several kilometers, indicates that under shear conditions the assumption of horizontal homogeneity of the wind field over the airport region is reasonable. Transitions between wind profiles taken by the acoustic and microwave radar systems at the beginning and cessation of precipitation have been smooth and continuous.

The optimum form of presentation of the system wind information remains to be determined. Examination of profiles derived from archived data has shown that a meteorologist observing winds measured by the system during a frontal passage could make a reasonable judgment in real time regarding the elevation and magnitude of shear. However, use of a meteorologist as the "alarm" would place an exorbitant responsibility on individual judgment, in addition to being generally inefficient because of the necessity of having personnel constantly available for profile monitoring. Because large-scale wind shear occurs only a very small percentage of the time (Grossman and Beran, 1975), a dedicated monitor would be inefficient.

Shear alerts could also be automated. However, before this can be accomplished, it is essential to develop a comprehensive definition of hazardous wind profiles. The criteria should be defined such that any conceivable shear profile is detected, while the probability of false alarm approaches zero. As an indication of the required degree of false alarm rejection, consider a system capable of measuring an average wind profile every 6 min. The corresponding probability of false alarm of 1% produces an erroneous warning once every 10 h, which is ob-

viously unacceptable. Work on hazardous shear definition is currently under way (Fichtl, 1972) and may result in a better understanding of the relative dangers associated with various wind profiles. Research relating extreme wind shear to the capabilities of various types of aircraft must be completed before detection and warning systems can be fully automated.

The additional tests now being conducted by the FAA should resolve a number of unanswered questions. The extent of limitations resulting from susceptibility to surface-wind-generated noise under potential shear conditions is critical in determining the eventual usefulness of this system. A study of the climatology associated with large-scale shear to determine the expected frequency of occurrence of conditions that degrade system performance should be performed. Continued testing will be needed to evaluate this and other aspects of system performance under a wide variety of meteorological conditions.

Complete protection against the hazard of low-level wind shear also must include a method of monitoring gust front motion and severity. The Dulles system includes this feature in the form of an array of pressure sensors that can detect gust front passage. The companion paper by Bedard *et al.* (1977) describes this portion of the system and shows data from an event that was first detected by the pressure sensors and then by the acoustic–microwave radar system.

References

Bedard, A. J., Jr., W. H. Hooke, and D. W. Beran, 1977: The Dulles Airport pressure jump detector array for gust front detection. *Bull. Amer. Meteor. Soc.,* **58,** this issue.

Beran, D. W., 1974: Remote sensing wind and wind shear system. Rep. FAA-RD74-3. (Prepared for U.S. Dept. of Transportation; available through National Technical Information Service.)

——, F. F. Hall, B. C. Willmarth, and R. J. Keeler, 1974a: Operational test results of acoustic Doppler wind shear detector. *Preprints, Sixth Conference on Aerospace and Aeronautical Meteorology (El Paso, Tex.),* AMS, Boston, pp. 412–417.

——, B. C. Willmarth, F. C. Carsey, and F. F. Hall, 1974b: An acoustic Doppler wind measuring system. *J. Acoust. Soc. Amer.,* **55**(2), 334–338.

——, P. A. Mandics, A. J. Bedard, and R. G. Strauch, 1976: A wind shear and gust front warning system. *Preprints, Seventh Conference on Aerospace and Aeronautical Meteorology and Symposium on Remote Sensing from Satellites (Melbourne, Fla.),* AMS, Boston, pp. 167–174.

Campbell, W. C., and R. G. Strauch, 1976: Meteorological Doppler radar with double pulse transmission. *Preprints, 17th Conference on Radar Meteorology (Seattle)*, AMS, Boston, pp. 42–44.

Caracena, F., and T. T. Fujita, 1977: Meteorological study of aircraft accident at Philadelphia Airport on June 23, 1976. To be published.

Chadwick, R. B., K. P. Moran, R. G. Strauch, G. E. Morrison, and W. C. Campbell, 1976: A new radar for measuring winds. *Bull. Amer. Meteor. Soc.*, **57**, 1120–1125.

Fichtl, G. H., 1972: Wind shear near the ground and aircraft operations. *J. Aircraft*, **9**, 765–770.

Fujita, T. T., 1976: Spearhead echo and downburst near the approach end of a John F. Kennedy Airport runway, New York City. Satell. and Mesometeor. Res. Proj. Pap. 137, Univ. of Chicago, Chicago, Ill., 51 pp.

——, and F. Caracena, 1977: An analysis of three weather-related aircraft accidents. *Bull. Amer. Meteor. Soc.*, **58**(11).

Grossman, R. L., and D. W. Beran, 1975: An investigation of extreme low-level wind shear at selected stations in the conterminous United States. *J. Appl. Meteor.*, **14**, 506–512.

Haugen, D. C., J. C. Kaimal, C. J. Readings, and R. Rayment, 1975: A comparison of balloon-borne and tower-mounted instrumentation for probing the atmospheric boundary layer. *J. Appl. Meteor.*, **14**, 540–545.

Huffaker, R. M., D. W. Beran, and C. G. Little, 1976: Pulsed coherent lidar systems for airborne and satellite based wind field measurement. *Preprints, Seventh Conference on Aerospace and Aeronautical Meteorology and Symposium on Remote Sensing from Satellites (Melbourne, Fla.)*, AMS, Boston, pp. 318–324.

Laynor, W. G., and C. A. Roberts, 1975: A wind shear accident as evidenced by information from the digital flight data recorder. Paper presented at the Society of Air Safety Investigators, International Seminar, Ottawa, Ont., Canada.

Miller, K. S., and M. W. Rochwarger, 1972: A covariance approach to spectral moment estimation. *IEEE Trans. Inform. Theory*, **IT-18**, 588–596.

Morris, A. L., D. B. McCall, and R. B. McBeth, 1975: A small tethered balloon sounding system. *Bull. Amer. Meteor. Soc.*, **56**, 964–969.

National Transportation Safety Board, 1976: Aircraft accident report—Eastern Air Lines, Inc., Boeing 727-225, N8B45E, John F. Kennedy International Airport, Jamaica, New York, June 25, 1975. Rep. NTSB-AAR-76-8, Washington, D.C., 47 pp.

Sowa, D. F., 1974: Low level wind shear. *DC Flight Approach*, No. 20, 10–15.

PULSED COHERENT LIDAR SYSTEMS FOR AIRBORNE AND
SATELLITE BASED WIND FIELD MEASUREMENT

R. M. Huffaker, D. W. Beran and C. G. Little
NOAA/ERL/Wave Propagation Laboratory
Boulder, Colorado 80302

1.   INTRODUCTION

A recent analysis by a National Academy of Sciences Panel has shown that the accuracy and temporal range of current numerical weather predictions are limited by the relatively wide separation of upper air data points in space and time. This limitation is, of course, particularly severe over the oceans and other data-sparse regions, but it is also limiting over the United States, where radiosonde measurements are made once every twelve hours at points an average of approximately 350 km apart. Preliminary analyses presented here indicate that satellite-borne Doppler lidar systems should be able to measure wind profiles around the globe with greatly improved spatial and temporal resolution. By obtaining global information on the horizontal velocity field as a function of height in the atmosphere, one is adding a fundamental and extraordinarily important new dimension to satellite meteorology, since the velocity field is the most important single unknown not currently available from the satellites. The addition of such data, therefore, holds great promise for improved meteorological research and services.

Our space exploits over the past several years, especially in the area of meteorological satellites, have helped to produce a better understanding of the general atmospheric circulation. In particular, we can now visualize entire synoptic-scale motions as observed by satellite cameras and traced by clouds. Quantitative measurements from space of important atmospheric parameters such as winds, temperature, and moisture have been far more difficult to achieve, and represent one of the major unconquered frontiers in satellite meteorology (Grantham et al., 1975; Hasler et al., 1975). Radiometric methods hold considerable promise for temperature and possibly moisture soundings from space, but truly quantitative wind measurement has eluded most past efforts. In some cases one can infer the wind fields from cloud motions (Johnson, 1973) and sea states observed from space. These methods are significant, but clearly limited, because they cannot provide measurements of the total global wind field throughout the depth of the troposphere.

New remote sensing techniques using lasers, coupled with technological advances in laser hardware, hold real promise for achieving global tropospheric wind measurements from a space platform. Resulting from a development effort for such a system we would also expect to see ground-based systems for mesoscale observation and research, and aircraft-mounted systems for aerial reconnaissance and support of large meteorological experiments such as the First Global GARP Experiment (FGGE). The development of coherent laser Doppler systems has made such a remarkable measurement capability appear feasible. The good spatial and velocity resolutions inherent with coherent Doppler systems lend themselves to the detailed study of the earth's wind field. This paper explores the feasibility of such measurements and attempts to identify the major problem areas that need to be attacked before a successful satellite-borne system is a reality.

2.   HISTORY

Coherent CO_2 lidar (optical radar) systems were developed in 1968 for the measurement of atmospheric wind velocity (Huffaker, 1970). Only limited use of these systems has been made for actual wind measurement. Both continuous wave (CW) and pulsed CO_2 coherent lidar systems have achieved accurate remote wind measurements (Huffaker, 1974-75). The CW system obtains range information by using an optical depth of focus effect which limits its useful range to < 1 km for most optical configurations. Range resolution for the CO_2 pulsed system is determined by the pulse length. The CW CO_2 coherent lidar systems have compared well with other types of wind sensing systems and have been used experimentally for tracking and measuring the properties of aircraft trailing vortices at airports (Huffaker, 1975).

The theoretical performance of coherent CO_2 lidar systems has been analyzed by Sonnenschein and Horrigan (1971), by Siegman (1966) and by Biernson and Lucy (1963). The experimental verification of coherent CO_2 systems performance has been reported by Teich et al. (1966), Brandewie and Davis (1972) and Huffaker et al. (1975). The coherent CO_2 lidar systems were calibrated against standard scattering targets and the overall systems efficiency determined (Huffaker et al., 1975).

A pulsed CO_2 coherent lidar system was developed in 1968-1970 by NASA. Later tests, including flights on the NASA Convair 990 during August 1972 and January 1973, (see figure 1 showing aircraft mounting) confirmed the feasibility of using a pulsed CO_2 lidar system for atmospheric wind velocity measurement. The extensive testing of the CW coherent lidar system specifically for wind velocity measurement and wake vortex tracking, and the feasibility demonstration of the pulsed CO_2 lidar system, lend strong support to the concept of using a pulsed CO_2 coherent lidar system for operational airborne and satellite based wind field measurements.

3.   SYSTEM DESCRIPTION

The basic CO_2 coherent lidar system consists of a very stable single frequency CO_2 laser, a Mach-Zehnder interferometer, transmit-receive optics, an infrared detector, a velocity-frequency analyzer, and a data processor and display. The pulsed system utilizes a modulator to achieve the desired pulse length and range resolution, and a laser amplifier to achieve the required laser energy. The laser beam is directed
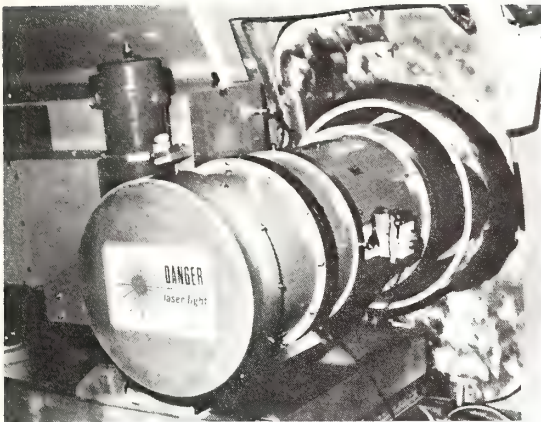
Figure 1. *Pulsed CO_2 coherent lidar aboard NASA CV-990.*

Figure 3. *Exterior view of aircraft pod for CO_2 pulsed lidar.*

optically to the point of interest in the atmosphere. The aerosol particulates, present in the lower atmosphere, scatter some of the transmitted radiation in all directions and, since the particles move with the atmosphere, the frequency of the scattered light is Doppler shifted from the frequency of the transmitted beam. Receiving optics collect the backscattered radiation and direct it onto an infrared detector where it is mixed with a small portion of the original beam. The total radiation seen by the detector fluctuates at a beat frequency that is proportional to the radial component of the wind velocity at the point of interest.

The pulsed CO_2 coherent lidar system shown in figure 1 uses a small, very stable, CW, master oscillator laser. This low-power, stable laser energy is gated into variable pulse lengths by a Gallium Arsenide Modulator. The pulses then enter a power amplifier chain and are amplified from approximately 10 W per pulse to 5 kW per pulse (figure 2).

Figure 2. *Schematic diagram for pulsed CO_2 coherent lidar system.*

The main transmitter characteristics are: a wavelength of 10.6 μm, a pulse length of 1-10 μs, a pulse rate of 140-160 pulses per second, a peak power of 5 kW, an average power of 3 W, and an optics diameter of 30.5 cm (12 in). Figure 3 shows an exterior view of the Ames

CV-990 with the CO_2 pulsed system on-board. The laser beam exits through the pod seen above the engine nacelle. The pod incorporates a germanium window 35.6 cm (15 in) in diameter. The telescope (see Fig. 1) is in the foreground and protrudes through the airplane into the external pod. The system was shock-mounted and the critical components insulated against noise and vibration. In figure 4, the photographs of typical display outputs taken during the flights show the intensity velocity display at a time of negligible turbulence and a range-velocity display when a wind shear was present ahead of the aircraft. For
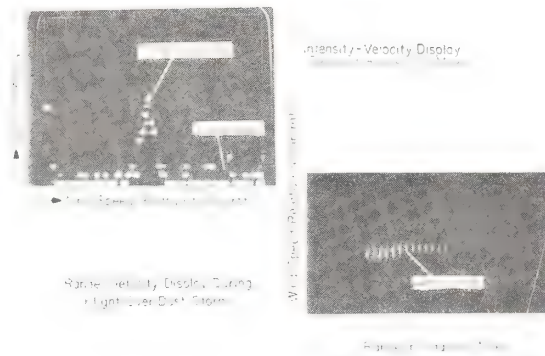
Figure 4. *Samples of output displays for CO_2 pulsed lidar.*

a selected range, the intensity velocity display shows the momentary velocity distributions from the filter bank. The signal intensity distribution forms a sharp peak and is a measurement of the wind speed relative to the aircraft. When the system is directed straight ahead, this speed corresponds to the true airspeed of the aircraft at close range.

319

The results of the existing pulsed system as reported by Huffaker (1974-75) have demonstrated the feasibility and potential of pulsed CO_2 lidar systems for long range wind measurements.

4. FEASIBILITY CONSIDERATIONS FOR SATELLITE GLOBAL WIND MONITORING

Several critical parameters affect the performance of a pulsed coherent infrared lidar global wind monitoring system. Some of these are the system signal-to-noise, aerosol size and number density, and scanning techniques. The following is a brief analysis of these crucial parameters as well as eye safety to give an indication of overall-feasibility.

4.1 Signal-to-noise: The power signal-to-noise ratio for a pulsed coherent lidar system focused at a range R, is

$$S/N = \frac{\eta_o \eta J \overline{n\sigma} \ c\tau}{32 \ h\nu} \ \frac{D^2}{R^2} \ e^{-2\mu R}$$

where

η_o = systems efficiency = 0.10;

η = detector efficiency = 0.30;

J = transmitted energy = 1-10 Joules;

$\beta = \overline{n\sigma}$ = backscatter cross section at 10.6 µ in units of m^{-1};

D = optics diameter = 1 meter;

$e^{-2\mu R}$ = round trip atmospheric transmission loss (assumed to be 5 dB);

$h\nu$ = Planck's constant x frequency of the radiation = 1.9×10^{-20} Joules;

R = range = 200 and 400 km;

c = velocity of light, m/s;

τ = pulse length, sec.

For a pulse length of 8 µs, an optics diameter of 1 m, a transmitted energy of 10 Joules, a β value of $10^{-8}m^{-1}$ and a range of 400 km, the expected power signal-to-noise ratio per pulse is 14 dB.

For a range of 200 km, which is typical of a low-orbit Spacelab mission, the expected system signal-to-noise ratio per pulse for the parameters listed above is equal to 20 dB. For a range of 200 km and a value of the backscatter coefficient β of $1.0 \times 10^{-9}m^{-1}$ the resulting signal-to-noise ratio is 10 dB. Figure 5 shows how the expected signal-to-noise ratio of the system depends on the backscatter cross-section β for two values of transmitted energy. These calculations indicate that, with state-of-the-art system parameters, the pulsed CO_2 coherent lidar mounted in a satellite would have a sufficient signal-to-noise ratio for backscatter cross-section values as low as $1.0 \times 10^{-9}m^{-1}$. With the optimization of system parameters, even smaller β values
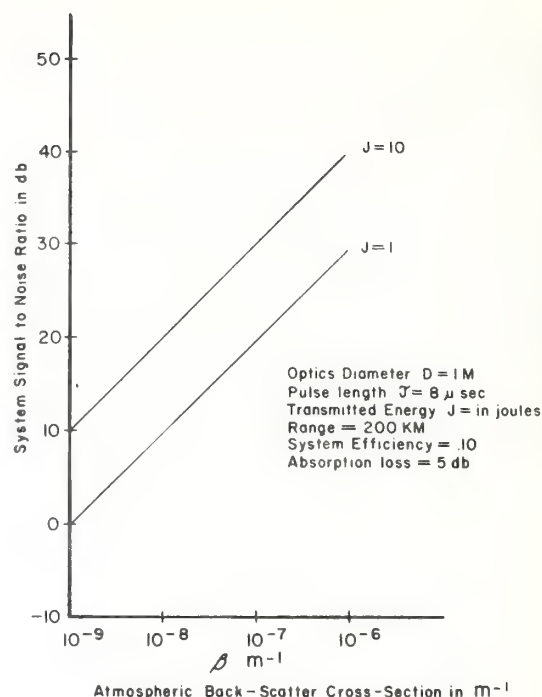
Figure 5. Signal-to-noise ratio for pulsed CO_2 coherent lidar satellite system.

could be detected. A backscatter coefficient of $\beta = 1.0 \times 10^{-9}m^{-1}$ corresponds to a density of approximately 3 particles per liter, with index of refraction that of spherical water droplets, having an average diameter of 2.0 µm. The index of refraction of spherical water droplets, for 10.6 µm radiation, is well established. The β value corresponding to silica particles, which are the expected ones to occur, is a factor of 10 greater than that for water droplets. Using the β values for silica-type particles increases the signal-to-noise ratio in the above cases by 10 dB.

4.2 Aerosol density

Uncertainties exist concerning the performance of a satellite-based pulsed CO_2 Doppler lidar under conditions of very clear atmosphere and also conditions of very dense clouds. The signal-to-noise ratio analysis showed the feasibility of measuring atmospheric winds from a range of 200 km for $\beta > 1.0 \times 10^{-9}m^{-1}$. The amount of data available on number density and size distribution of stratospheric aerosols is very limited. The available data on stratospheric aerosols must be analyzed and related to the pulsed CO_2 Doppler lidar performance. Several investigators have studied tropospheric aerosols. Their data from several sources indicate that 3 particles per liter is a very conservative value. If the particles were of a silica or Tektite-like composition the number of particles necessary to give sufficient signal-to-noise ratio would be only 0.3 per liter. These density values must be carefully related to the available data on global aerosol distributions to allow the proper system parametric trade-off analysis to be performed.

320

The performance of pulsed CO_2 Doppler lidar systems in clouds is relatively untested. Only limited experimental data exists; however, several investigators have developed theoretical models of CO_2 transmission in clouds and rain (Carrier et al., 1967; Rensch and Long, 1970). Past measurements, with an existing system, indicated that 22 km of cirrus and 5 km of cumulus clouds were penetrated. Figure 6 shows the backscatter signal intensity as a function of time and displays the return from the second cumulus cloud transmitting through the first one. The performance of a more sophisticated system as envisioned here, through clouds, must be determined by thorough analyses, and by ground and flight verification tests.
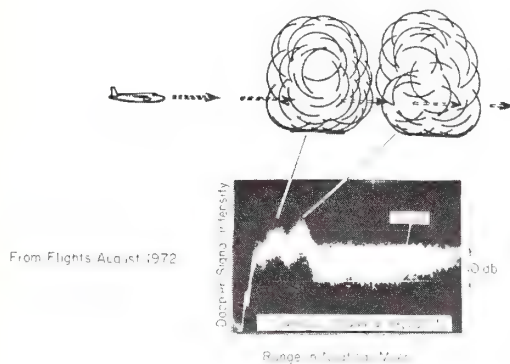
Figure 6. Doppler signal strength looking through a cumulus cloud.

Particle sampling equipment was operated by I. H. Blifford, Jr. of NCAR on the Ames CV 990 for 2 months during the pulsed-laser system flight tests. These tests were conducted over the ocean, desert areas, and the central United States and covered altitudes up to 12 1/2 km. The particulate number density and size distribution were measured and the backscatter cross-sections were calculated for a worst-case, in which the particles were assumed to be water droplets. The β values varied from 3.0×10^{-7} to $5.0 \times 10^{-9} m^{-1}$. The $5.0 \times 10^{-9} m^{-1}$ value corresponded to 15 particles/liter with an average size of 2μ. This low value occurred in only 1 sample time during the 2-month period. On previous flights, Blifford (1970) and De Luisi (1972) reported minimum particle densities in over 288 different measurements collected over Scottsbluff, Nebraska, the Pacific Ocean, and Death Valley. The lowest value of β, calculated for these particle number densities and size distributions, when the worst-case index of refraction of water was assumed, was $3.8 \times 10^{-9} m^{-1}$. Even with the very conservative estimates of β, the signal-to-noise ratio of the pulsed coherent lidar appears sufficient for satellite-borne global wind measurements.

4.3   Eye safety

Because of the long wavelength and large telescope diameter, the power density from the pulsed coherent lidar system is several orders of magnitude below safety limits. The eye-safety standard published by ANSI and the Dept. of the Army Tech. Bulletin TB-MED-279 gives the following information: For wavelengths between 1.4 and 1000 μ, and for exposure times between 10^{-7} and 10^{-1} sec, the maximum permissible exposure (MPE) is given by the following expression:

$$(MPE) = 0.56 \ \tau^{1/4} \ Joules/cm^2$$

where τ = pulse length = 10 μs.

For the CO_2 pulsed coherent lidar, the maximum permissible exposure (MPE) is 0.03 Joules/cm^2. The system must be designed such that the power density is less than 0.03 Joules/cm^2.

The actual power density that would be incident on the earth's surface from the pulsed CO_2 system in a 200 km orbit, is determined as follows: The pulse energy proposed in the pulsed coherent lidar system is a maximum of 10 Joules. The diameter of the beam at the earth, a range of 200 km, for a 1-m optical telescope is 2 meters. The cross sectional area is 31,400 cm^2. The energy density =

$$\frac{10 \ Joule}{31,400 \ cm^2} = 0.32 \times 10^{-3} \ \frac{Joules}{cm^2}$$

This value is a factor of 100 lower than the maximum permissible exposure of 0.03 Joules/cm^2.

4.4   Pointing accuracy required

Because of the very high orbital velocities and the requirement to measure winds very accurately ($\sim$ 1 m/s), there would be stringent requirements on the satellite pointing accuracy. Consider the following possible conditions;

- Orbital velocity $\sim$ 9000 m/s.
- Beam look angle is 45° from the vertical.
- The Doppler shift is approx. 1.3 GHz.
- The wind is blowing 1 m/s near the ground and the resulting frequency shift from the the air is $\sim$ 141 kHz.

If the air is stationary, the change in the pointing angle that produces a change in the 1.3 GHz Doppler shift of 141 kHz is $\sim$ 0.005°.

As an example, the NASA Spacelab Payload Accommodation Handbook gives the accuracy of the pointing information available to be 20 arc-seconds or 0.0055°. The positive control pointing accuracy requirements for the wind measuring task are much less. The actual positive control value available on the NASA Spacelab is ± 0.1°/axis, which should be sufficient to ensure the proper investigative area.

The pointing accuracy described would be required only when the pulsed coherent lidar system was not observing a ground return. The ground return, which is expected to be present most of the time, when compared with the known orbital velocity, would provide the correct angle

321

very accurately. The system is expected to see the ground at times when heavy cloud cover is not present. The extent to which the system is expected to see through clouds needs to be analyzed in more detail.

5.   POTENTIAL PROBLEMS

5.1   Scanning modes for airborne and satellite application

Air velocity is a vector quantity, but current Doppler radar techniques measure only one component of that velocity, specifically, the radial component, along the beam. Therefore, to define the full velocity, measurements are required of the radial velocity components of a given volume from three different directions. If, as is often the case, the vertical velocity can be ignored, then two measurements of each volume, preferably from widely different directions, will be required. The problem of how best to acquire such data from a single moving platform, by interrogating each volume from different points along the path, is a major one and warrants considerable study. The scanning concepts for the airborne and satellite system should be similar for looking in the downward direction. Scanning techniques already in use with ground-based microwave dual Doppler radar can be adapted for use by a system on a moving platform. Here two remotely located Doppler radars measure simultaneously two of the three velocity components as a function of position in the measurement volume. Since wind velocities are small compared with the speed of sound we can assume an incompressible atmosphere and then generate the third velocity component by integration of the continuity equation. This method assumes the boundary condition that the vertical velocity is 0 at the surface. The motion of the aircraft or satellite allows several look-angles thus providing the two-dimensional planes of velocity information from which the wind field can be constructed (Figures 7 and 8). Another scan technique that is well established in both microwave and laser Doppler radar systems is the Velocity-Azimuth Display (VAD). Here, the horizontal gradients in the wind vector are assumed to be small. The system scans in azimuth, at a constant elevation and from the Doppler velocity information obtains a measure of the horizontal wind vector.
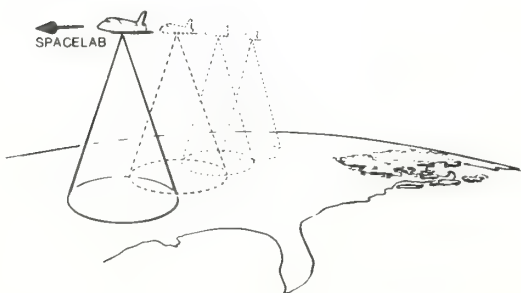
Figure 7. Concept for satellite-mounted pulsed CO_2 lidar for global wind measurements.
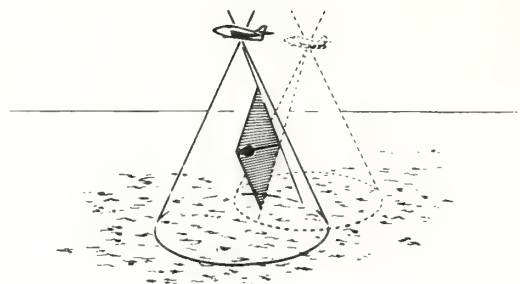
Figure 8. Concept for aircraft-mounted pulsed CO_2 lidar for tropospheric wind profiles.

6.   CONCLUSIONS & POTENTIAL APPLICATIONS

The preliminary calculations presented in this paper and limited tests indicate that atmospheric wind measurements with CO_2 lidars are possible. Although an extensive aerosol climatology throughout the depth of the troposphere and stratosphere is not yet available, the results from limited samplings are encouraging and suggest that a laser system could at least achieve a high percentage of the desired complete wind measuring capability. Cloud penetration capability, another potential limiting factor, is also not clearly established, but if the worst case of wind measurements in the clear air only, could be achieved, it would be a major contribution to our present sensing capability.

Studies are in progress at NOAA-WPL to determine the overall systems design of ground-based and airborne pulsed CO_2 lidar wind measuring systems. The result of these studies are expected to answer some of the questions raised in this paper.

The successful development of a CO_2 pulsed lidar wind measuring system would have major impact on the study and observation of all scales of atmospheric motion. An urgent need exists for a remote wind sensor that can scan over a large area and detect wind shear conditions at airports. First generation wind shear detection systems (Beran et al., 1976) lack the ability to scan and must rely on supporting ground measurements to achieve complete airport wind-shear surveillance. The ability to scan in a preprogrammed mode is easy to achieve through the use of rather simple and compact optics. This coupled with the expected range capability of approximately 20 km in the earth's atmospheric boundary layer make the pulsed CO_2 lidar a prime candidate for use as a second generation airport wind shear monitoring system. A single scanning pulsed CO_2 lidar centrally located at an airport is envisioned in Figure 9. This system could detect a component of wind shear both along approach and departure paths and the dangerous conditions associated with thunderstorm gust fronts.

While airport wind shear is an immediate and urgent problem that may be solved by a system such as that described above one should not overlook the great potential of this measurement

322

capability for less dangerous, but still important mesoscale meteorological applications. Short range weather forecasts, ranging from now-casts up to a few hours in duration are an important element in airport operations. A major limiting factor in making better short-range mesoscale forecasts is the lack of observations on this scale. Contrasting the present single ground-based anemometer and a twice daily wind profile with a system which can continuously define the wind field out to 20 km through a depth of 2 km gives one a picture of the vast potential of this observational system. Now-casts and short term forecasts cannot help being improved if the meteorologist has this ability to define his immediate wind environment. Such observational ability should also help to solve the wake vortex avoidance problems. It is known that wake vortices are strongly influenced by low level winds and the present solution to the problem is to construct conventional meteorological towers near the airport approach paths. The pulsed CO_2 lidar not only has the potential for measuring these winds, eliminating the need for costly and perhaps hazardous towers, but it would also be able to observe the position of the vortices, thus verifying the predicted vortex motion based on ambient winds.

The need for wind observations is, of course, not limited to the immediate airport environment. Wind profiles throughout the depth of the troposphere in regions where rawinsonde coverage is inadequate, are needed for certain operational applications, such as enhancing the data base for input into numerical models. In addition, vertical profiles of the wind form a vital part of the data base for research activities such as FGGE.

By placing the system on an aircraft, the potential of the concept is greatly enhanced and wind profiles above and below the vehicle as depicted in Figure 8 become feasible. This application would revolutionize present weather reconnaissance activities and support for such major experiments as FGGE.

Similarly, airborne systems with different scanning techniques (Figure 10) could also benefit severe storm research and monitoring. This type of installation coupled with an aircraft mounted pulsed Doppler radar would be capable of defining the "in cloud" and "clear air" wind fields in and around thunderstorms, tornadoes and hurricanes.
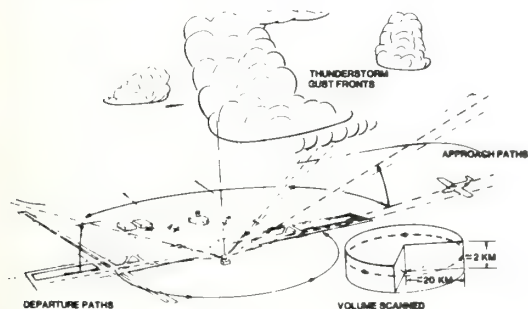
Figure 9. *Concept of an airport wind shear surveillance system using pulsed CO_2 lidar.*
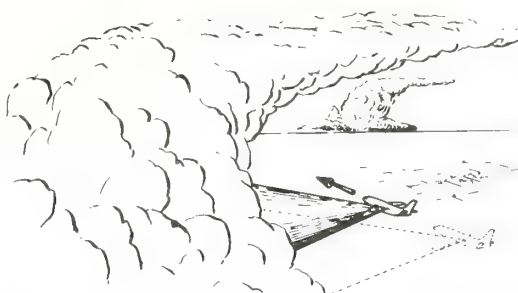
Figure 10. *Concept of an aircraft-mounted pulsed CO_2 lidar for severe storm wind measurements.*

The ultimate application remains the satellite-mounted pulsed CO_2 lidar having the capability of making truly global wind measurements throughout the depth of the troposphere. This concept, depicted in Figure 7, would provide coverage of the global circulation that has not previously been possible, for use in numerical prediction, airline operations, and atmospheric research.

The total potential capability of this single instrument, when used on the ground or on various platforms, is clearly exceptional. Its successful development would have major impact on many of our present meteorological activities, only a few of which have been mentioned here. Much work remains to be accomplished before a final proven system can be developed, but few modern devices have held such great promise not only in their ultimate planned application but at each stage of their development. Even if only part of the predicted capabilities are achieved a powerful remote sensing tool would become available.

REFERENCES

Beran, D. W., P. A. Mandics, A. J. Bedard and R. G. Strauch (1976), A wind shear and gust front warning system, *Proc. 7th Conf. on Aerospace and Aeronautical Meteor., Nov. 16-19, Amer. Meteor. Soc.,* Boston, MA.

Biernson, G. and R. F. Lucy, (1963), Requirements of a coherent laser pulse-Doppler radar, *Proc. of the IEEE,* 51, p. 202.

Blifford, Jr., I. H., (1970), Tropospheric aerosols, *J. Geophys. Res.,* 75, no. 15, p. 3099.

Brandewie, R. A. and W. C. Davis, (1972), Parametric study of a 10.6-μ laser radar, *Appl. Opt.,* 11, no. 7, p. 1526.

Carrier, L. W., G. A. Cato and K. J. Von Essen, (1967), The backscattering and extinction of visible and infrared radiation by selected major cloud models, *Appl. Opt.,* 6, no. 7, p. 1209.

De Luisi, J. J., I. H. Blifford, Jr. and J. A. Takamine, (1972), Models of tropospheric aerosol size distribution derived from measurements at three locations, *J. Geophys. Res.,* 77, no. 24, p. 4529.

323

Grantham, W. L., E. M. Bracalente, W. L. Jones,
J. H. Schrader, L. C. Schroeder, (1975),
An operational satellite scatterometer
for wind vector measurements over the ocean,
NASA-TMX-72672.

Hasler, A. F., W. Shenk, W. Skillman, (1975),
Wind estimates from cloud motions, NASA-TMS-
70826, 1974 and NASA-TMX-71061.

Huffaker, R. M., (1970), Laser Doppler detection
systems for gas velocity measurement,
Appl. Opt., $\underline{9}$, no. 5, p. 1026.

Huffaker, R. M., (Winter Issue, 1974-75), CO_2
laser Doppler systems for the measurement of
atmospheric winds and turbulence, *Atmo-
spheric Technology, NCAR*, p. 71.

Huffaker, R. M., H. B. Jeffreys, E. A. Weaver,
J. B. Bilbro (1975), Development of a laser
Doppler system for the detection, tracking
and measurement of aircraft wake vortices,
FAA Report FAA-RD-74-213.

Johnson, D. S., (1973), The impact of outer-space
technology on developments in meteorology,
Tenth Anniversary of the World Weather
Watch, WMO, Geneva pp 1i-32.

Rensch, D. B. and R. K. Long, (1970), Comparative
studies of extinction and backscattering by
aerosols, fog and rain at 10.6 µ and 0.63 µ,
Appl. Opt., $\underline{9}$, no. 7, p. 1563.

Siegman, A. E., (1966), The antenna properties of
optical heterodyne receivers, *Proc. of the
IEEE*, $\underline{54}$, no. 10, p. 1350.

Sonnenschein, C. M. and F. A. Horrigan, (1971),
Signal-to-noise relationships for coaxial
systems that heterodyne backscatter from the
atmosphere, *Appl. Opt.*, $\underline{10}$, no. 7, p. 1600.

Teich, M. C., R. J. Keyes and R. H. Kingston,
(1966), Optimum heterodyne detection at
10.6 µm in photoconductive Ge:Cu, *Appl. Phys.
Lett.*, $\underline{9}$, no. 10, p. 357.

324

THE BOULDER ATMOSPHERIC OBSERVATORY — A FACILITY
FOR ATMOSPHERIC RESEARCH AND INSTRUMENT COMPARISON

J. C. Kaimal

1. INTRODUCTION

A new facility designed to serve as a national resource for atmospheric research and instrument testing is now being constructed by the Wave Propagation Laboratory (WPL) at a site 20 km east of Boulder Colorado. Located on gently rolling terrain, the facility will consist of an instrumented 300-m tower, remote sensors of various types measuring atmospheric parameters, and a highly interactive computer system controlling the processing and display of the acquired data. The Boulder Atmospheric Observatory (BAO), as the facility will be called, is to be operated in collaboration with the National Center for Atmospheric Research (NCAR), located at Boulder. In the near future the Field Observation Facility of NCAR will be moved to the BAO site. The measurement capability of the BAO will then be augmented through the deployment of NCAR's Portable Automated Mesonet System and its instrumented aircraft, extending the range of the tower measurements over wider horizontal and vertical scales. This paper describes the BAO tower, the instrumentation on it, and its potential for atmospheric studies and for testing and calibrating meteorological sensors.

2. THE TOWER AND ITS SENSORS

The tower will be a guyed, open-lattice structure of galvanized steel with three legs spaced 3 m apart. A two-man elevator internal to the tower will provide access to the eight instrumented levels. A movable carriage on one side of the tower serves as a sensor platform for vertical profiling and for measurements at any desired height between the instrumented levels.

The meteorological sensors at each level will be mounted at the end of booms that extend 5 m from the tower. The tower levels chosen for instrumentation are the eight heights shown in Fig. 1. Atmospheric parameters measured at each height are indicated in the sketch. Both mean and fluctuating components will be measured. For example, the three wind components will be sensed by sonic anemometers which measure the absolute wind component over a 10-Hz bandwidth. Aspirated quartz crystal thermometers and dew point hygrometers will measure mean temperatures and dewpoints at each level, while platinum wire and Lyman α sensors will measure the fluctuating component of temperature and humidity. The pressure fluctuation sensors, designed primarily for detecting gust fronts and gravity waves, have response times of the order of 1 sec. The incoming solar radiation will be measured with a standard Eppley pyrheliometer. In addition to those indicated in Fig. 1, sensors for measuring net radiation, soil temperatures and soil heat fluxes will be installed in a separate location close to the tower.

From time to time the instrument carriage will carry such special sensors as aerosol impactors and spectrometers or a duplication of sensors at the standard heights, depending on the requirements of the specific experiment
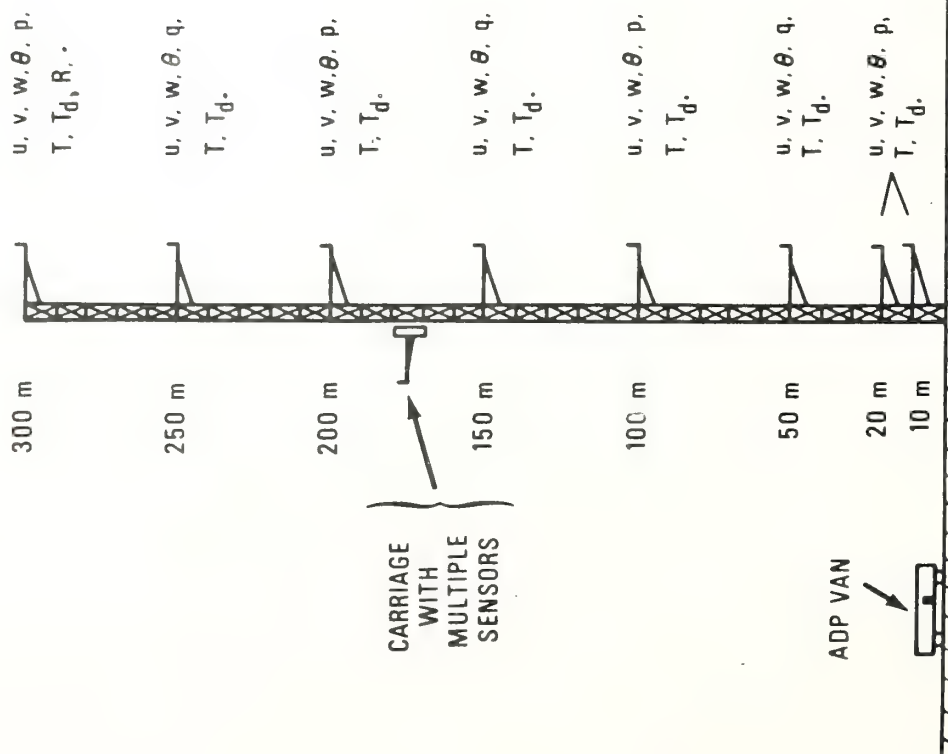
721

Figure 1. Tower instrumentation at the Boulder Atmospheric Observatory.

being conducted. The carriage will be capable of carrying loads up to 1200 kg. Details of the telemetry link for data transfer from the carriage to the ground station are now being worked out.

3. REMOTE SENSORS

Several remote sensors will operate continuously near the base of the tower. A triangle of laser beams centered around the tower will measure the surface wind convergence at the site. Three acoustic sounders will be used to detect the presence of stratified layers at night and convective plumes and capping inversions during the day. Acoustic Doppler techniques will also be utilized to measure wind components up to heights of 500 m. In addition we will have a variety of new remote sensors, such as those listed in Table 1, operating at different times at the BAO site.

TABLE 1: TYPES OF REMOTE SENSORS AVAILABLE AT WPL

	Technique used	Measured parameter	Comments
1.	Acoustic sounder (Monostatic)	C_T^2	Effects of excess attenuation not fully understood.
2.	Acoustic sounder (Bistatic)	C_v^2, C_T^2	Not fully tested.
3.	Acoustic sounder (Doppler, bistatic)	Wind components	50-500 m. Performance depends on atmospheric conditions.
4.	Pulse Dual-Doppler Radar	Wind velocities, variances, covariances, ε	Needs chaff or precipitation for long ranges. Processing requires large computer time.
5.	FM-CW Doppler Radar	Wind velocities, ε, C_n^2	Operates in clear air. Assumptions for converting VAD outputs to wind components need testing.
6.	Microwave Radiometry (Passive)	Integrated water-vapor content	Occasional large departures from radiosonde observations need to be resolved.
7.	CW Infrared Laser	Radial wind component	Resolution degrades with distance.
8.	Optical Scintillation	Cross wind component, C_n^2	Double-ended, requires transmitter (or receiver) at the other end.
9.	CW Laser	Rainfall rate	---
10.	Pulse Laser	Aerosol concentration	---
11.	Starlight scintillation	C_n^2	Range 2.5 km to tropopause.
12.	Infrared Radiometry (Passive)	Cloud surface temperatures	---

4. DATA ACQUISITION AND PROCESSING

All sensor outputs with the exception of the carriage sensors will be hardwired to the data acquisition computer at the BAO site through analog-to-digital converters or digital interface buffers, depending on their output characteristics. Data acquisition will be under software control with the fast-response sensors sampled 10 times a second and the slow-response sensors once every 10 sec. Some amount of real-time data processing will be performed at the site to provide essential information on instrument performance and some basic atmospheric parameters such as surface heat flux, Richardson number, and z/L, but all information will be transmitted through phone lines to a larger computer system at our laboratories in Boulder. Here the information will be sorted out for more detailed processing and analysis (e.g., correlations, FFT spectral and cospectral computations, higher order moments, energy budgets) in real time, for semipermanent disc storage allowing quick retrieval of the past week's observations, or for recording on magnetic tape for archiving. To conserve tape utilization we plan to record the fast-response data less frequently than the 10-Hz sampling rate, filling in the lost high-frequency information with 15-min averaged spectral and cospectral information. Studies to determine the optimum time interval between stored data samples and the bandwidths needed in the spectral computation are now in progress.

5. OBJECTIVES

The original and principal purpose of the tower is to provide in situ verification of atmospheric measurements made with remote sensors. We hope that as the performance of the remote sensors becomes better understood, we will be able to extend the useful range of our measurements beyond the 300 m limit imposed by the tower through the use of remote sensors in conjunction with the tower sensors. The BAO could serve as a calibration and test facility where instruments of different manufacture can be compared by the atmospheric science community both in the United States and abroad.

In addition to its uses for remote sensor development and instrument calibration, we hope to carry out a number of observational studies of turbulence structure and dynamics of atmospheric processes in the micro and mesoscales, atmospheric refractive index structure, and the propagation of acoustic and E-M waves in turbulent media. We are eager to see the resources of the BAO fully utilized and will welcome the opportunity to conduct cooperative experiments with interested groups.

REMOTE SENSING -- THE OTHER SIDE OF THE COIN

C. Gordon Little
Wave Propagation Laboratory
Environmental Research Laboratories
National Oceanic and Atmospheric Administration
Boulder, Colorado 80302

Introduction

Propagation measurements in the lower atmosphere tend to be con-
ducted by two largely separate groups of workers -- those tele-
communicators who need quantitative information on the propaga-
tion limitations and capabilities of the medium for telecommuni-
cation purposes, and those atmospheric scientists who use obser-
vations of atmospheric propagation to derive information on the
medium itself. These two activities can be thought of as being
at the two sides of a single coin -- the coin being the inter-
action of electromagnetic waves with the atmosphere. It is un-
fortunate that the two groups are so separate, for often results
obtained for one purpose can have direct relevance to "the other
side of the coin." In recent years, there has been considerable
progress on the remote sensing side of the coin; it is the pur-
pose of this paper to summarize this progress and discuss its
implications to local weather services.

Ground-Based Remote Sensing of the Lower Atmosphere

Before discussing the current status of ground-based remote sens-
ing of the atmosphere, it may be appropriate to list the poten-
tial advantages of remote sensors. These include the fact that
the data are conceptually available:

 in 1, 2, or 3 spatial dimensions,

 without the use of towers, balloons, or aircraft,

 with excellent continuity in space and time,

 with excellent resolution in space and time,

 over a wide range of parameters,

 as spatial averages,

 using systems which may be readily automated.

Any one of these advantages might justify the development of a
particular sensor; the combination of advantages in certain cases
provides an overwhelming justification for the development and
use of new remote sensors.

The present status of ground-based remote sensing of the primary
meteorological variables of wind, temperature, and humidity is
summarized in Table I. Because of the three-dimensional nature
of the atmosphere, it is appropriate to differentiate between
three levels of capability (a) measuring only the surface value
of some parameter, (b) the ability to measure the mean vertical

725

profile, and (c) the ability to measure the parameter as a function of position in three-dimensional space. Since each parameter typically exhibits small random fluctuations in time and space, we need to be concerned with the ability to measure not only the mean value, but also its small-scale variability. This variability is usually expressed in terms of its structure constant, which may be thought of as the root-mean-square difference between simultaneous values of the parameter at two points unit distance apart. Again, the structure constant may be measured only at the surface, or as vertical profiles, or as full three-dimensional fields.

The vertical fluxes of momentum, heat, and water vapor are of great importance to meteorology. These result primarily from the covariance of the turbulent components of vertical velocity with horizontal velocity, temperature, and humidity respectively. Once again, these vertical fluxes can be measured just at the surface, or as vertical profiles, or as full three-dimensional fields.

In Table I, a number is used to denote which research concepts have exhibited the ability to make that particular measurement. In general, however, operational hardware suitable for routine use is not yet available. The oral version of this paper will include slides illustrating the capabilities of active or passive radio systems to measure profiles of wind, temperature, and humidity.

We see from Table I that, in the research mode, it is possible to measure vertical profiles of wind, temperature, and humidity. Progress has been especially complete in the case of wind measurements, where three-dimensional measurements of mean wind and turbulence have been reported, and three-dimensional measurements of momentum flux for spatial scales larger than the pulse volumes are implicit in the Doppler data. At the moment, these capabilities do not exist in all weather conditions, though the recent demonstration of clear air microwave and infra-red Doppler radar capabilities makes wind measurement feasible in essentially all weather conditions. The passive microwave radiometric measurement of temperature and water vapor profiles has recently been demonstrated to be valid under cloudy as well as clear sky conditions, but is not likely to be applicable in rain.

In Table II, the status of remote sensing of precipitation, and of cloud and aerosol particles is indicated. Here the most important parameters to be measured are the three-dimensional distribution of the particles, and their size distributions; in the case of clouds and precipitation, the water-or-ice phase identification is important; for precipitation, the precipitation rate is also meteorologically important.

726

Remote Sensing -- A Complementary Approach to Short-Term Local
Weather Forecasting

The above status report indicates that continuous information on
the precipitation field, the cloud field, and the velocity field,
around an observing site could be provided by using a combination
of sensitive microwave and infrared Doppler radar systems. Opera-
tional ranges could range from a few tens of kilometers in clear
air, to greater than 100 kilometers in precipitation. In addition
(but not during rain), temperature and humidity profiles could be
monitored using a multi-wavelength microwave radiometer system;
the same system could also monitor integrated liquid water con-
tent.

Since virtually all changes in weather can be well described in
terms of the observed changes in the wind, cloud, and precipita-
tion fields, this immediately suggests that remote sensors could
be used to continuously and automatically observe the state of
the atmosphere over an urban area out to ranges of perhaps 100 kms.
Recent progress in data processing and display further suggest
that it would be possible to prepare, and disseminate in essen-
tially real time, (using a dedicated TV channel) "nowcasts" or
maps of the present state of the atmosphere over the area. Simple
extrapolation techniques, incorporating the effects of the ad-
vection and trends observed in the remote sensing data, could
then be used to prepare and issue short-term extrapolations or
forecasts of local weather conditions for the next two or three
hours.

Longer term (3-12 hour) forecasts would require meteorological data
from outside the 200 km diameter circle. Fortunately, these are
available from two sources -- geostationary satellites, and the
numerical forecasts of the National Weather Service's National
Meteorological Center. These data, plus the continuously avail-
able remote sensing data, could be used in local mesoscale numeri-
cal models to prepare detailed local weather forecasts for the
3-12 hour time frame. These local weather forecasts could be
much more accurate and detailed than the present NWS forecasts,
primarily because the local numerical models could take into
account local topography and other surface features which are
on too small a scale to be incorporated in the continental-scale
NWS models.

A program to establish a prototype regional observing and fore-
casting service (PROFS) based in large part on the above consi-
derations is now being discussed within the Department of
Commerce. If successfully implemented, it could have major
impact within the U.S. on short-term, local weather services
through widespread use of atmospheric remote sensing.

TABLE I. STATUS OF REMOTE SENSING OF PRIMARY
METEOROLOGICAL VARIABLES

Type of Measurement	Wind	Temperature	Humidity
Surface Values			
Mean	1	5	9
Structure constant	-	1	-
Vertical flux	-	1	-
Vertical Profiles			
Mean	2,3,4	6,7	6,9
Structure constant	2,4	8	-
Vertical flux	2	-	-
3-D Field			
Mean	2	-	-
Structure constant	2	-	-
Vertical flux	-	-	-

Measurement System Code

1	Optical scintillation	6	Multi-channel microwave radiometry
2	Doppler radar		
3	Doppler lidar (infra-red)	7	Hybrid radar-acoustic system
4	Acoustic Doppler	8	Monostatic acoustic sounder
5	Optical time-of-flight	9	Differential absorption lidar

TABLE II. STATUS OF REMOTE MEASUREMENT OF
HYDROMETEORS AND AEROSOL

Type of Measurement	Cloud Particles	Precipitation	Aerosol
Vertical line integral	1	1	2
3-D distribution	3	4	5
Particle size distribution	-	-	-
Phase identification	6	6	-
Precipitation rate	-	3,7	-

Measurement System Code

1	Multi-channel radiometer can measure integrated liquid water	4	Radar
		5	Lidar
2	Lidar	6	Polarized lidar
3	Short wavelength radar	7	Optical scintillation

STATUS REPORT ON GROUND-BASED REMOTE SENSING OF THE ATMOSPHERE

C. Gordon Little

NOAA/ERL/Wave Propagation Laboratory

Boulder, Colorado 80302

ABSTRACT

In recent years there has been major progress in the development of new methods for remotely sensing meteorological parameters from the surface of the earth. This talk attempts to summarize this progress in terms of acoustical, optical, infrared, and radio techniques for the remote measurement of wind, temperature, water vapor, cloud particles, precipitation, and aerosol.

1. INTRODUCTION - THE POTENTIAL ADVANTAGES OF REMOTE SENSING

· I understand that the last conference of this type was held roughly six years ago. In that six years, there has been considerable progress in the field of ground-based remote sensing of the atmosphere. Much of this work has been done by physicists and engineers from outside the field of meteorology, and it is therefore perhaps appropriate that I attempt to summarize the status of the field for you.

Conceptually, ground-based remote sensing has a number of important potential advantages. These advantages start with the fact that the observations are obtained remotely, in one, two, or three spatial dimensions, without the use of balloons, aircraft, or meteorological towers to carry in situ instruments to the desired observational location. Typically, the measurements have excellent resolution and continuity in both time and space, and do not require the expensive installation and telemetry capabilities implicit in arrays of in situ sensors. Potentially, a very wide array of meteorological parameters can be measured remotely, including such sophisticated parameters as spectra of turbulence and heat flux. Also, since the measurements automatically provide some degree of spatial averaging, they are often more representative of the region being measured than the data from a single in situ sensor, which is much more subject to transient or local perturbations. Although initial costs may be quite high, operating costs are often reduced, since in many cases the equipment operates in an unmanned mode, as contrasted with balloon or airborne measurements.

In many cases, any one of these advantages could justify the development of the instrument. The combination of advantages can make an overwhelming case for the development and exploitation of these new measurement capabilities in both research and services.

2. STATUS OF GROUND-BASED REMOTE SENSING

In order to summarize the status of remote sensing of meteorologically significant parameters, I have prepared a series of tables, one for each parameter. These list the various types of observations of each parameter for which remote sensing capability has been demonstrated, and the corresponding measurement technique. Superscript numbers and footnotes are used to indicate where an important limitation exists, typically because the system does not have all-weather capability. Thus, most optical and infrared measurement systems have greatly reduced measurement capabilities in fog, cloud, or precipitation; on the other hand some radar systems require the presence of precipitation (or chaff) to provide echoing targets. Acoustic systems are usually adversely affected by the impact noise produced by rain or hail, but, (unlike optical systems), they are not adversely affected by cloud or fog. Additional limitations are indicated in the text, as appropriate.

2.1 Remote Sensing of Wind and Turbulence

Table I summarizes the current ability to remotely sense wind and turbulence. Surface winds and surface convergence have been measured over paths of approximately 10 km in length, using the scintillations of optical beams (Kjelaas and Ochs, 1974). The superscript number and footnote denotes that the system does not operate under conditions of fog or significant precipitation.

Boundary layer profiles of wind and turbulence have been measured remotely using Doppler techniques at microwave and infrared wavelengths, and also using acoustic waves.

The newly developed FM/CW Doppler radar technique (Chadwick et al., 1976) has excellent capability in the boundary layer, and offers some promise of eventually providing winds and turbulence profiles to tropopause heights. Doppler acoustic systems (such as that installed at Dulles airport - Beran et al., 1976) are able to measure wind and turbulence profiles to roughly 500 meters height under most weather conditions, but require supplementing with a simple, low power Doppler microwave pulse radar if coverage during rain or hail conditions is required. Continuous wave infra-red Doppler systems are also capable of measuring wind and turbulence profiles in the boundary layer, with reasonably good all weather capability (Schwiesow and Cupp, 1976). Height resolution of these focused devices however deteriorates rapidly at the greater ranges; the height capability in fog or cloud conditions is not yet known.

The most dramatic demonstration of the ability to measure the three-dimensional velocity field has been the use of multi-station microwave Doppler radar systems (Miller and Strauch, 1974). These systems usually require precipitation or chaff to provide echoes, but recent work at NSSL

TABLE 1. STATUS OF REMOTE SENSING OF WIND AND TURBULENCE

Measurement	Technique
Path-averaged surface wind (including surface convergence)	Optical scintillations[1]
Boundary layer wind profile (including turbulence profile)	1. FM/CW radar 2. Acoustic sounder[2] 3. Pulsed μw radar[3] 4. Infrared lidar[4]
3-dimensional wind field (including turbulence field)	Multi-station Doppler radar[3]

ANTICIPATED DEVELOPMENTS

Improved clear air wind measuring capabilities, using pulsed IR Doppler lidar.

Measurement of both transverse and longitudinal components of wind from a single location.

(1) Performance adversely affected by haze, fog, or precipitation.

(2) Performance adversely affected by precipitation noise and wind noise.

(3) Requires high power system in clear air.

(4) Present CW systems have poor range resolution above approximately 300 m.

(Kessler 1976) has shown that at least in the atmospheric boundary layer, clear air echoes can be sufficiently strong to permit mapping by high power radars of the velocity fields over hundreds of square kilometers. It is not yet known to what extent these clear air measurement capabilities can be extended into the troposphere. The techniques could be applied to cloudy regions of the troposphere, if shorter wavelength radars were used.

The field of remote sensing of winds is not a static one. Current work at WPL includes efforts to improve clear air measurement capability by acquiring a pulsed IR Doppler lidar, with improved range resolution, and maximum range, over the existing continuous wave infrared Doppler lidar systems. A second promising area is the study of techniques permitting measurement of transverse velocities, as well as the longitudinal velocities normally measured by Doppler systems (Schwiesow et al., 1976).

2.2 Remote Sensing of the Temperature Field

Table 2 summarizes the status of ground-based remote sensing of the temperature field.

The path averaged surface temperature may be measured by an optical time-of-flight method, which in effect measures the average density of the air along the path. Recent unpublished measurements by Wyngaard have shown that the path-averaged vertical heat flux can be monitored by observing the intensity of optical scintillations along the path. The mixing depth of the atmospheric boundary layer can be monitored by microwave, infra-red, optical, and acoustic echo-sounding systems. Temperature profiles in the boundary layer can (under favorable wind conditions) be monitored using a hybrid radio/acoustic system in which the radar measures the velocity of a powerful sound wave as a function of height. Radio waves may also be used passively to derive atmospheric temperature profiles; in this case, multi-frequency microwave radiometers are used in the 5-6 mm wavelength oxygen absorption band. Here, recent unpublished work by Decker indicates that the addition of a water vapor channel and a window channel permits derivation of the temperature profile even in the presence of clouds.

2.3 Remote Sensing of the Water Vapor Field

Table 3 summarizes the status of remote measurement of water vapor. Path-averaged water vapor density can be measured by an optical differential absorption technique; there are good prospects that differential absorption lidar techniques will eventually make it possible to measure vertical profiles of water vapor from the earth's surface (Murray et al., 1976). The integrated water vapor content of the clear atmosphere can be measured on vertical or oblique paths using a microwave radiometer tuned to the 22 GHz water vapor line (Decker, Guiraud and Westwater, 1973); the addition of a "window" channel permits correction for the effect of clouds (Decker, 1976). Multi-channel microwave radiometers have also been used to derive approximate profiles of the water vapor distribution (Decker 1976).

TABLE 2. STATUS OF REMOTE SENSING OF THE TEMPERATURE FIELD

Measurement	Technique
Path-averaged surface temperature	Optical time-of-flight[1]
Path-averaged surface heat flux	Optical scintillations[1]
Mixing depth	FM/CW radar
	Acoustic sounder[2]
	Lidar[3]
Temperature profile	5-6 mm O_2 radiometer[4]
	Radar-acoustic[5]
C_T profile	Acoustic sounder[2]

ANTICIPATED DEVELOPMENT

FM/CW radar-acoustic system, providing boundary layer profiles of temperature, wind, turbulence, and C_T.

(1) Performance adversely affected by haze, fog or precipitation.
(2) Performance adversely affected by precipitation noise or wind noise.
(3) Performance adversely affected by fog or cloud.
(4) Performance adversely affected by rain.
(5) Performance adversely affected by strong winds.

TABLE 3. REMOTE SENSING OF THE WATER VAPOR FIELD

Measurement	Technique
Path-averaged water vapor density	Differential absorption[1]
Integrated water vapor content	2-λ μw radiometer[2]
Water vapor profiles	Multi-wavelength μw radiometers[2]

ANTICIPATED DEVELOPMENT

Water vapor profile by differential absorption lidar[3]

(1) Performance adversely affected by haze, fog or precipitation.
(2) Performance adversely affected by rain.
(3) Performance adversely affected by fog or heavy precipitation.

731

2.4 Status of Remote Measurement of the Precipitation Field

The status of remote sensing of the precipitation field is summarized in Table 4. Recent work by Wang and Clifford (1975) has shown that the scintillation of optical beams can be used to derive path-averaged drop size distribution and path-averaged rainfall rate. Passive microwave radiometry in the 3-30 GHz band can be used to derive the liquid water content of the atmosphere along a microwave beam, with the lower frequencies being used to measure the larger liquid water contents (Decker and Dutton, 1969). The three-dimensional distribution of liquid water and frozen precipitation, including the melting layer height, can be determined using microwave radar. The water-ice differentiation can be extended to cloud-size particles by means of polarized lidar (Sassen, 1976).

2.5 Status of Remote Sensing of Fog and Cloud Fields

Table 5 is a summary of the status of the remote sensing of fog and cloud particles. As indicated above, the integrated liquid water content can be measured using a two-channel microwave radiometer, and water-ice differentiation is achievable using polarized lidar. The three dimensional distribution of clouds is best obtained using a short wavelength radar, although infrared and optical lidars may be useful if the clouds are not too dense.

2.6 Status of Remote Sensing of Aerosol Particles

The status of remote sensing of aerosol particles is summarized in Table 6. Aerosol particles are too small to be registered on microwave radars or on acoustic sounders; the propagation effects

TABLE 4. STATUS OF REMOTE MEASUREMENT OF THE PRECIPITATION FIELD

Measurement	Technique
Path-averaged surface rainfall rate	Optical scintillations[1]
Path-averaged drop size distribution	Optical scintillations[1]
Integrated liquid water content	2λ μw radiometer
3-D liquid water distribution	μw radar
Melting layer height	μw radar
Water-ice differentiation	Polarized lidar

(1) Operational range dependent upon rainfall rate; performance adversely affected by fog.

TABLE 5. STATUS OF REMOTE SENSING OF FOG AND CLOUD FIELDS

Measurement	Technique
Integrated liquid water	2λ μw radiometer
3-D distribution	1. Short λ μw radar 2. Infrared lidar[1] 3. Optical lidar[1]
Water/ice differentiation	Polarized lidar[1]

ANTICIPATED DEVELOPMENTS

Pulsed IR lidar should give improved sensitivity and range resolution[1]

(1) Performance adversely affected by intervening fog, cloud, and precipitation.

732

TABLE 6.   STATUS OF REMOTE SENSING OF AEROSOL

Measurement	Technique
Vertical profile	Optical lidar[1]
3-D coverage	Optical lidar[1]
Shape differentiation	Polarized lidar[1]
Size differentiation	Multi-λ lidar[1]

(1) Not practicable in fog, cloud, or precipitation.

are limited to infrared and shorter wavelengths. Vertical profiles of total aerosol scattering cross-section may be obtained by lidar systems, which may also be used to monitor the distribution of the particles in three-dimensional space. Polarization measurements can be used to differentiate between spherical and non-spherical particles; some information on the size of the scatterers can be obtained from multi-wavelength observations.

3.   SUMMARY OF THE STATUS OF GROUND-BASED REMOTE MEASUREMENT OF THE THREE PRIMARY METEOROLOGICAL VARIABLES — WIND, TEMPERATURE, AND WATER VAPOR

Table 7 is an attempt to summarize the present status of ground-based remote measurement of the three primary meteorological variables of wind, temperature, and water vapor. Here, an "X" is used to denote that the measurement capability of this particular type has been demonstrated (at least in the research mode) and has withstood the test of publication. Unpublished capabilities, which have not yet received evaluation through open literature publication, are enclosed in parentheses.

Examination of Table 7 shows that a very full remote sensing capability exists for the velocity field, primarily because of the availability of a wide range of Doppler techniques. All-weather wind profiling capability is attainable in the boundary layer, with prospects good for all-weather wind profiling capability to tropopause heights, using some combination of microwave and infrared Doppler systems.

The ability to remotely sense the temperature and humidity fields is unfortunately much weaker, though progress in these areas is showing signs of acceleration. It seems likely to this author that it will be practicable to measure temperature and humidity profiles, perhaps to tropopause heights, under many meteorological circumstances within the next six years. However, it does not at this time seem likely that the three-dimensional temperature and humidity fields will be available from ground-based remote sensors on this time scale.

TABLE 7.   STATUS OF GROUND-BASED REMOTE SENSING OF WIND, TEMPERATURE, AND WATER VAPOR

Type of Measurement	Wind	Temperature	Water Vapor
Surface Values			
Mean	X	X	X
Vertical Flux	-	(X)	-
Vertical Profiles			
Mean	X	X	(X)
Structure Constant	X	X	-
Spectra	X	-	-
Flux	X	-	-
3-Dimensional Field			
Mean	X	-	-
Structure Constant	X	-	-
Spectra	X	-	-
Flux	X	-	-

733

3.1 References

Beran, D. W., P. A. Mandics, A. J. Bedard and R. G. Strauch, 1976: A wind shear and gust front warning system. *Proc. 7th Conf. Aerospace and Aeronautical Meteorology and Symposium on Remote Sensing from Satellites*, Melbourne, Florida, November 16-19, 1976.

Chadwick, R. B., K. P. Moran, R. G. Strauch, G. E. Morrison and W. C. Campbell, 1976: A new radar for measuring winds. *Bull. Amer. Met. Soc.*, 57, 1120-1125.

Decker, M. T. and E. J. Dutton, 1969: Radiometric observations of liquid water in thunderstorm cells. *Proc. 6th Conf. on Severe Local Storms*, Chicago, 163-164 April 8-10, 1969.

Decker, M. T., F. O. Guiraud and E. R. Westwater, 1973: Correction of electrical pathlength by passive microwave radiometry. *Proc. Conf. on Propagation of Radio Waves at Frequencies above 10 GHz*, London, April 10-13, 1973.

Decker, M. T., 1976: Private communication.

Kessler, E., 1976: Private communication.

Kjelaas, A. G. and G. R. Ochs, 1974: Study of divergence in the boundary layer using optical propagation techniques. *J. Appl. Meteor.*, 13, 242-248.

Miller, L. J. and R. G. Strauch, 1974: A dual Doppler radar method for the determination of wind velocities within precipitating weather systems. *Remote Sens. Environ.*, 3, 219-235.

Murray, E. R., R. D. Hake, J. E. van der Loan, and J. G. Hawley, 1976: Atmospheric water vapor measurements with an infrared (10 µm) differential-absorption lidar system. *Appl. Phys. Letters*, 28, 542-3.

Sassen, K., 1976: An evaluation of polarization diversity lidar for cloud physics research. Ph.D. thesis, Dept. of Atmospheric Science, University of Wyoming.

Schweisow, R. L. and R. E. Cupp, 1976: Remote Doppler velocity measurements of atmospheric dust devil vortices. *Appl. Optics*, 15, 1-2.

Schwiesow, R. L., R. E. Cupp, M. J. Post and R. F. Calfee, 1977: Coherent differential Doppler measurements of the transverse velocity component of a remote point. *Appl. Optics*, (accepted for publication).

Wyngaard, J. C., 1976: Private communication.

734

REMOTE SENSING WIND AND WIND SHEAR SYSTEM

Peter A. Mandics

The prototype development of an acoustic Doppler remote-sensing system to detect low-level wind shear generated by synoptic-scale features such as frontal surfaces is described. The detector system measured the vertical profile of wind by determining the Doppler frequency shift of vertically transmitted acoustic signals that are scattered by small-scale atmospheric inhomogeneities. Following earlier acoustic Doppler tests at Stapleton International Airport in Denver, Colorado, significant improvements have been accomplished on the acoustic transmitter and receiver antennas, and signal processing. A conical horn reflector antenna with a 2-m diameter aperture fed by 12 high-power acoustic drivers through a manifold increased the transmitted power by more than 100%. Substantial improvements have been achieved in received signal-to-noise ratio by developing a narrow-beam, off-focus steered receiver antenna that is capable of tracking the upward propagating acoustic pulse. Development of new system software made all-digital signal processing and computerized system control possible. Tests of one leg of the prototpyte at Table Mountain near Boulder, Colorado revealed that the system measured winds reliably up to a height of 600 m when surface wind did not exceed 10 m s ^{1}. The deleterious effects of precipitation on system performance have not been fully evaluated yet. A brief review of wind-shear types and their detection is followed by a discussion of second-generation wind-shear detection systems employing lidar and microwave radar devices.

PASSIVE REMOTE CROSSWIND SYSTEM

Thomas H. Pries, Ruben Rodriguez, Donald L. Walters,
Gerard R. Ochs, Robert S. Lawrence

INTRODUCTION

It is well known (Lawrence, Ochs, and Clifford, 1972) that atmospheric scintillation of light beams can be used to measure the average wind blowing across the beam. Optical crosswind monitors using this principle are in commercial production and are in use for a variety of applications. The optical-scintillation method produces excellent results, giving a true spatial average over the entire beam and, unlike mechanical anemometers, it has no low-speed threshold below which it fails to operate. Several modifications of the basic optical crosswind instrument are being investigated. Among these are profiling instruments which, through the use of multiple apertures, are able to localize wind measurement to a specific portion of the optical path.

A major improvement, which we shall describe in some detail, involves elimination of the artifical light source, replacing it by ambient light from a natural scene. The resulting passive crosswind system has obvious advantages in convenience of use, but the price that must be paid for this convenience is a non-uniform sensitivity along the line of sight, and occasional periods when the strength of scintillations becomes so small that the system cannot operate.

SYSTEM COMPONENTS

One of the major advantages of the Passive Remote Crosswind System (PRCS) is the fact that it does not have a transmitter; elimination of a transmitter reduces the size and power requirements considerably. The entire PRCS consists of an optical receiver, a photodiode array, and an electronic signal processor. The optical receiver has, in effect, four 2.5 cm apertures that are used in pairs to form wide band filters. These lens pairs focus the irregular patterns of the scintillating light reflected from the observed scene, onto the photodiode array. Electronic signals generated by the photodiodes are then combined to produce a covariance function of the scintillation pattern. A predetermined model covariance function is stored in the electronic receiver. Then using a 14 point analysis, the best-fit between the scintillation pattern covariance function and the model covariance function is obtained. Finally, the time scale of the best-fit is used to determine the time delay employed in the calculation of the wind speed. Use of this procedure yields the best compromise among the effects of variation in the scene spectrum, the spatial spectrum and distribution of refractive turbulence, and wind fluctuations.

Of significant importance to the operation of the PRCS is the weighting function, shown in Figure 1, which determines the relative importance of the crosswinds along the path, in the computation of the wind average. The present weighting function will accentuate more heavily the values out to 200 meters. The weighting function can be modified, by appropriate scaling of the apertures. The effective signal-to-noise ratio of the wind measurement is, in part, proportional to the product of the scene illumination and contrast, and the square root of the refractive-index structure constant. As a result, there may be times on dark or overcast days when operation is not possible with natural illumination. The PRCS, nevertheless, will operate during day or night if it is pointed at distant artificial lights. If a single light is used, the PRCS must be carefully aimed because its field of view is only 6 mrad.
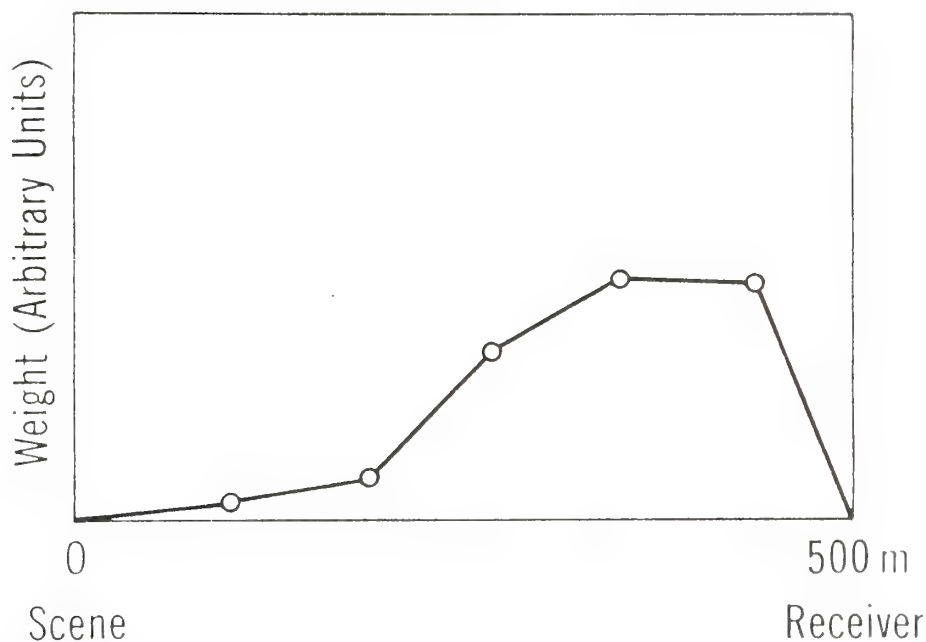
Figure 1. PRCS Weighting Function.

There is also a time constant associated with the wind measurements. The PRCS automatically adjusts this time constant according to the signal-to-noise ratio, from a minimum of 3 seconds to a maximum of approximately 10 seconds.

SYSTEM DESCRIPTION

The entire PRCS, shown in Figure 2, only weights 1.4 kgm, measures 12 cm by 26 cm by 31 cm, and is battery powered. Furthermore, the PRCS

can also be powered on 117 A.C. volts. Under internal battery operations, the PRCS can continuously run for 24 hours, after which period the batteries will have to be recharged for approximately 10 hours.
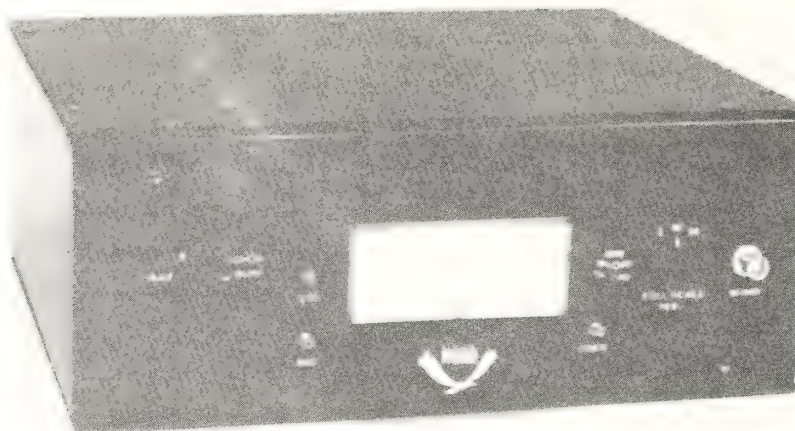
Figure 2. Passive Remote Crosswind System.

The PRCS is extremely simple to operate. The front panel of the PRCS consists only of three switches and a meter. One of the switches turns the system on and off, and places batteries in the recharge mode. The range switch sets the meter full scale deflection to three different wind speed ranges (5, 10, 20$\frac{m}{sec}$). Finally, the function switch determines whether:

1) The meter is used to calibrate the system (-, 0, + locations)

2) The system is to be in the run mode

3) The system is to be in the lock mode (to find out if there is enough signal to operate the system).

SYSTEM CAPABILITIES

As mentioned before, the optical crosswind receiver is designed to measure the wind vector across its line of sight out to a range of approximately 200 meters, when it is directed at backgrounds in this range or preferably farther away. The instrument calibration is especially insensitive to the spatial spectra of the scene when it is more than 500 meters away. Nevertheless, the PRCS is also capable of operating on

rather short paths (about 10 meters), because of its small angular field of view (6 mrad), if the illumination and refractive turbulence are large enough. In this mode of operation, the instrument measures the wind speed by observing the motion of angular fluctuations. For both modes of operation, the wind measurement is more heavily weighted near to the receiver as has been shown in Figure 1.

The PRCS has been tested under different weather conditions in order to evaluate its accuracy and precision. Considerable amounts of data have been gathered during recent evaluation and calibration tests; Figure 3 shows representative data taken during these tests.
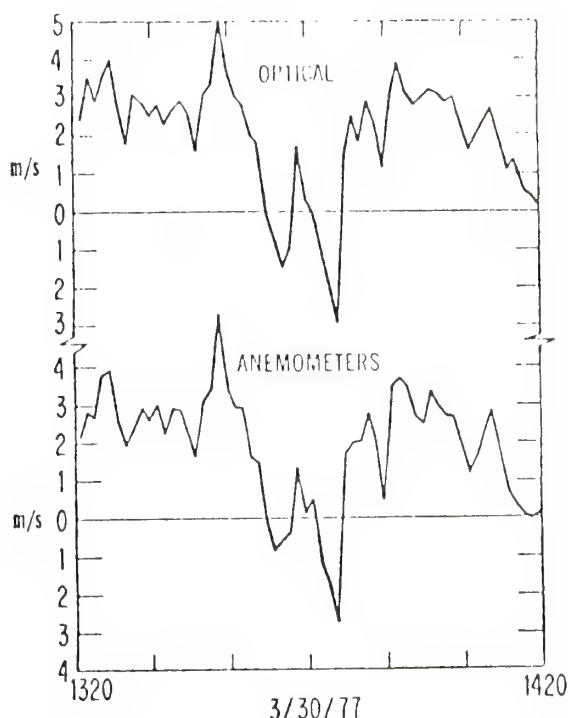
Figure 3. PRCS Evaluation Data.

POSSIBLE APPLICATIONS

There is a myriad of possible applications for the PRCS due to its small size, light weight, and battery-powered features as well as for its remote quasi-real-time measurement capabilities; a few of the most outstanding applications will be mentioned in the following paragraphs.

By strategically placing the PRCS at the top of a valley or any other advantageous location, the air pollutant flow can be evaluated. A modification of this application would locate the PRCS close to an industrial area to determine approximate pollutant flow rate as well as its general direction of movement, by monitoring average speed and direction of winds.

Many locations where it is desired to measure wind speed are inaccessible due to terrain features (rivers, ravines, etc.), or dangerous

environmental conditions (large concentrations of harmful gases). The PRCS can be advantagously employed at such locations because of the remote capability: it need only be placed within 200 meters of the measurement location.

An airplane, during landing, is very vulnerable to winds perpendicular to the runway; therefore, knowledge of the velocity of such winds is of extreme importance to pilots. Conventional anemometers are placed to the sides of the runway and provide wind speed at points other than over the runway itself. However, a PRCS, even though located on the side of the runway, is capable of measuring the wind speed directly over the runway.

CONCLUSIONS

There are times when it is desired to make wind measurements without having to set up permanent type or extensive instrumentation. At other times, it is necessary to obtain wind velocity at inaccessible locations. For these particular applications and also for general use, employing a PRCS is convenient and economical. Other advantages of the PRCS over other present systems include its light weight, small size, and battery-powered feature.

Although the PRCS measures wind velocity only along one axis, a biaxial system can be implemented by using two PRCS mutually perpendicular. Furthermore, once these two normal components are known, wind speed along any other direction can be calculated, by use of vector analysis.

REFERENCES

1. Lawrence, R. S., G. R. Ochs, and S. F. Clifford, "Use of Scintillations to Measure Average Wind Across a Light Beam," Applied Optics 11, p. 239-243 (1972).

2. Ochs, G. R., S. F. Clifford, and Ting-i Wang, "Wind and C_N^2 Profiling with Crossed Laser Beams and Spatial Filter Detectors," NOAA Tech Report ERL 367-WPL 45, Supt of Documents, U.S. Government Printing Office, Washington, D.C. (March 1976). Available also as ECOM Report 76-1.

DOPPLER LIDAR FOR MEASUREMENT OF POLLUTANT TRANSPORT

Ronald L. Schwiesow and Madison J. Post
Wave Propagation Laboratory
Environmental Research Laboratories
National Oceanic and Atmospheric Administration
U.S. Department of Commerce
Boulder, Colorado

INTRODUCTION

There are a number of environmental air quality problems for which Doppler lidar velocity sensing is a useful tool. As introductory material, we will first review operational characteristics of Doppler lidars, typified by the WPL mobile units used in this joint energy research. A brief summary of four problem areas that are being attacked using Doppler lidar measurements will serve to focus the more detailed discussions of progress and applications to follow.

This remote-sensing velocity measurement capability is being applied to four classes of problems in the research program discussed here. In the area of atmospheric diffusion, the lidar is being used to study the profile of mean wind and turbulent intensity at scales smaller than the resolution volume for various meteorological conditions and terrain configurations. For this application, the Doppler system acts as a mobile, high instrumentation tower for wind measurement. Wind characterization is an important part of diffusion experiments if the experimental results are to be applied to other topographic and atmospheric situations.

For measurements of the urban ventilation factor, the wind profile and the height of the mixed layer over the center of the urban area must be frequently measured. Here again the wind tower function of the Doppler lidar to heights of at least 300 m is important. The depth of the mixed layer as revealed by the height at which the concentration of large (>2μm diameter) particles falls off is under study for CO_2 lidar measurement.

In addition to pollutant concentrations, the stack effluent velocity from a stationary source is used to determine the total mass loading of the source. Doppler lidar appears promising for this application, and preliminary checks have been made.

Critical energy installations are subject to a structural wind loading from localized vortex phenomena, such as dust devils, waterspouts, and tornadoes, as well as from the more commonly considered straight-line winds. This project is also involved in a study of dust devils to determine if they provide a wind-loading threat to structures.

The Doppler lidar state-of-the-art in applications before this project is represented by

one-time trials of basically laboratory gear. Lawrence et al. (1972) reported on single-point wind measurements at a range of 30 m. Abshire et al. (1974) made similar measurements from hydrometeor targets. Other application tests have not been reported in the open literature, although work tracking aircraft wake vortices has been done on an in-house basis by NASA, and EPA has observed some stack returns using a CO_2 Doppler laser lidar. Work emphasizing lidar development, rather than applications, has been reported in the literature, but it is not relevant to our purpose in this paper.

RESEARCH PROGRESS

Technique Development

Guided by project applications, the infrared Doppler lidar technique is being refined for this research. The technique development is integrated with NOAA's own efforts in the Wave Propagation Laboratory. At this point we are using a compact, mobile Doppler lidar system mounted in a small camper shell on a pickup truck. With a towed, small generator, the unit is completely self-contained and can obtain data while underway. A similar unit has been installed aboard a single-engine Cessna. Its successful operation emphasizes the ruggedness and utility of the basic approach.

The laser, processing optics, and a 30 cm Newtonian transmit-receive telescope are fixed with respect to each other. Appropriate flat mirrors steer the beam anywhere within a full hemisphere in azimuth and elevation, although most work is done between -5° and +18° elevation or at 90° elevation. The range resolution element is determined by the focus of the telescope and is a roughly cylindrical volume less than 0.2 mrad in azimuth and elevation but with a length along the line-of-sight of 10 m at 100 m range. This length increases with the square of the range out to a range where essentially no ranging information is available.

Actual velocity information comes from the line-of-sight component of the motion of aerosol scatterers in the sensing volume. This tracer motion results in a Doppler shift of the backscattered radiation, which is directly interpretable as a velocity using the frequency to velocity conversion of 189 kHz per ms^{-1} velocity component. Since the scatterers are not in general in uniform motion, a frequency (velocity) spectrum is recorded as often as every 16 ms on magnetic tape. From the recorded spectrum, the relative total backscattered energy (0th moment), mean velocity (1st moment), and velocity spread (2nd moment) may be analyzed from each spectrum.

Part of the project is to determine the operating limitations of the system. Work on aerosol statistics (Post and Schwiesow, 1976) has revealed that approximately 5000 scatterers m^{-3} of diameter 2μm and larger are required for a range of 200 m. This corresponds to a typical rural environment with 50 km visibility. The operating range of the lidar in typical urban environments is 1 km because of the enhanced backscatter over rural areas. The clearest environments, such as atop 4250 m Mt.

infrared lidar is more sensitive to larger parti-
cles (greater than 2 μ diameter) than are the
visual aspects of the plume.

APPLICATIONS OF RESULTS

Atmospheric Diffusion

As a result of this study, we have demon-
strated that wind and turbulence profiles are meas-
urable using a rapidly-deployed remote sensing sys-
tem. Knowledge of the boundary-layer wind field
allows testing of diffusion models and transfer of
results under one set of conditions to another.

With respect to pibal wind measurement, the
Doppler lidar should allow increased cost-
effectiveness for obtaining micromet wind data
for input to diffusion models. This is especially
true for problems that require detailed coverage
in time and/or area. The lidar provides essen-
tially continuous time coverage of a fixed, rather
than drifting, point. With respect to wind-sensing
tower instrumentation, the lidar provides greater
profile height capability, portability, and cost-
effectiveness. As part of this project we have
made detailed comparisons between tower and lidar
wind measurements, which show correlations greater
than .998 for 1 minute averages of the data.

An immediate application of lidar wind data
could be to help provide a data base for extension
of Pasquill-Gifford type curves for elevated
sources and certain types of uneven terrain. Ob-
served wind shear and upper boundary layer accel-
eration in change-of-terrain seabreeze situations,
for example, should allow pollutant transport pre-
dictions to be made.

Urban Ventilation

FM-CW (frequency-modulated, continuous-wave)
ranging from a hard target with resolution to 10 m
has been demonstrated by using a simple modifica-
tion of NOAA's Doppler lidar system. This approach
is potentially applicable to determinations of the
aerosol pollution mixing depth.

The infrared lidar is expected to have in-
creased accuracy and cost-effectiveness over air-
borne in-situ aerosol mixed layer sensing methods
because of the general economic advantage of
ground-based systems over airborne platforms. Be-
cause a lidar measures aerosol profiles directly,
it gives the pollution mixing depth rather than the
thermal mixed layer inferred from acoustic sounder
data. With respect to pulsed visible lidars, the
infrared approach offers increased eye safety,
freedom from background light, and economy because
the same basic unit is also applicable to wind
sensing. The infrared depends on the less-numerous
larger particles (typically 1-5 μm diameter) for
backscatter.

We have demonstrated the ability to measure
one-component wind profiles along the mean wind in
an urban environment to 1 km range and 200 m
height. By increasing the elevation angle from
12° to 18°, the demonstration would be valid for
300 m height if a sufficient aerosol density
existed to that height.

In the urban environment, where principal
interest is in the lowest part of the atmosphere,
the lidar should provide increased height resolu-
tion and cost-effectiveness over labor-intensive
radiosonde measurements of boundary layer winds.
Furthermore, the lidar makes possible increased
time frequency coverage of wind profiles with
little increase in cost over measurements made a
few times daily. Possible effects of severe
weather on lidar penetration are not significant
for this problem, since under severe weather con-
ditions urban ventilation is not a concern.

Stack Effluent Velocity

We have analyzed the expected Doppler lidar
spectrum from a small mean velocity component in
the presence of large turbulence for a homodyne
(local oscillator frequency equal to the transmitter
frequency) system. Because homodyne detection does
not reveal the sign of the velocity component,
isotropic turbulence folds into a spectrum that
obscures a small mean velocity spectral shift.
This effect must be considered in interpretation
of homodyne lidar results from stacks.

It is obvious that for low elevation angles
(small line-of-sight stack velocity component) and
large turbulence values, an offset local oscilla-
tor or heterodyne lidar is essential to properly
interpret the return signal. For cases where the
ambient wind is not zero, the sign information from
heterodyne processing is extremely helpful in
separating ambient and stack velocity effects.

Field experimental stack returns using the
present mobile homodyne system have demonstrated
the feasibility of stack velocity monitoring with
a CO_2 Doppler lidar. This suggests that further
study would be profitable.

Vortex Structural Loads

The largest observed dust devil velocities in
the experiments discussed in the measurements sec-
tion of this summary were 22 ms^{-1}. It is fairly
obvious without detailed engineering analysis that
such winds pose negligible threat to energy-related
structures designed for higher straight-line winds.

Although the dust devil measurements represent
the conclusion of vortex studies for this joint
agency project, studies on waterspouts are continu-
ing under other sponsorship. Should experiments
reveal potentially damaging winds in these vortices,
the results could be important to the design of
energy-related structures. The subvortex struc-
tural details inferred from the dust devil data may
provide helpful information for tornado models,
since photographic evidence of subvortex structure
in tornadoes has been suggested by other observers.

STATUS

This research task is two years into a five-
year program. Milestones are on schedule. We

Evans, lead to a 50% signal dropout rate at 200 m range.

We have established concepts for system improvements to be made during the remaining 3 years of the program. These improvements include offset local oscillator, pulse ranging, and further differential Doppler work. Details of these efforts are given under future plans.

Measurement to Date

Profiles. One- and two-dimensional, single-component wind profiles have been measured for various locations. For these measurements the lidar is either scanned in range for a fixed elevation angle or is scanned in elevation (e.g. 0° to 18°) for a fixed range. Negligible vertical velocity is assumed to allow conversion from line-of-sight to horizontal wind component. This assumption on vertical velocity is weaker at higher elevation angles, so we have operationally limited the elevation to 18°.

We have measured a seabreeze situation with profiles 200 m over the water and 200 m inland using a variable elevation scan. Analysis of the terrain-induced wind modification is underway. A desert wind profile was determined using a fixed elevation scan, which shows an interesting mid-layer shear, as does a fixed elevation scan taken in Denver. Other profiles, using both fixed elevation and fixed range have been taken in a prairie environment under convective conditions, and in various locations near Boulder.

Conclusions from the profile measurements to date include the fact that operational wind profiles are available using a proven field lidar system (although not yet with real-time processing for resulting velocity). Feasibility is demonstrated. This field Doppler lidar unit in its present configuration measures velocity spectra to a range of 1 km and a usable height of 300 m using naturally-occurring aerosols. In contrast to towers, the setup time for a measurement is less than 1 minute. The measurement time for 10-point height resolution is approximately 5 minutes.

Vortices. We have measured the velocity spectra for dust devils, a measurement listed in the project plan, and for waterspouts, which represents additional benefit to this project from other related work. Both phenomena are representative of localized wind phenomena.

Although apparently vigorous because of the unusually large (for the atmosphere) radial accelerations involved, the largest dust devil velocity observed in a two-state field program was 22 ms^{-1} in the horizontal plane (Schwiesow and Cupp, 1976). Waterspout maximum velocities are still under analysis, but the observed spectra are generally similar to dust devil observations.

FM-CW Ranging. Frequency modulation of the continuous-wave CO_2 laser (FM-CW) allows one to determine range to a target by measuring the homodyne frequency difference between the instantaneous transmitted and received signal. We have performed such an experiment, ranging from a hard target (hillside).

A range of 6.8 km gave an easily observed signal with the FM-CW lidar in a breadboard stage. Although this experiment satisfied a project goal, the form of the observed signal spectrum was far from ideal. Rather than occurring at a single frequency, the return from fixed targets is spread significantly in frequency space. This means that it would be difficult, at best, to determine the profile of a distributed (e.g., aerosol) target.

The conclusion of this study is that it is more desirable for operational aerosol profiling purposes to explore some other type of modification to the Doppler lidar. Also, it has proven analytically difficult to separate range and velocity information from an infrared FM-CW return from a moving target. We are therefore pursuing a coherent pulsed lidar technique at 10.6 μm for this continuing project effort.

Three-Component Measurements. We have demonstrated a technique for measuring three components of atmospheric velocity at a single, remote point (Schwiesow et al., 1977). The experiment used two pairs of closely-spaced beams in a time-shared mode and a hard target at 30 m range.

This project on pollutant transport includes the goal of measuring profiles of all three components of the wind. The significance of the differential Doppler technique mentioned above is that a new, more effective way of determining all three components of the atmospheric velocity vector is potentially available. The comparative, conventional approach is based on some variation of an azimuth-scanning technique. Azimuth scanning involves an inherent assumption of horizontal homogeneity of the wind field and therefore represents an area average with departures from homogeneity as noise. The differential Doppler approach avoids the need for a homogeneity assumption. It can produce an area average by range and azimuth scanning or by averaging a time history. In the latter case, no mechanical scanning is required to measure all three components.

The present status of the study is that the theoretical analysis of the technique is complete. System design parameters for increased range have been established. Tests on aerosol targets at longer ranges are planned.

Stack and Cooling Tower Plumes. To establish the basic feasibility of stack and cooling tower plume measurements, Doppler lidar tests using the mobile system were performed on actual plumes. The question of signal return is important because liquid water is strongly absorbing at 10.6 μm.

The results of measurements on power plant plumes showed signal-to-noise ratios of 15 db and greater at a range of 500 ±100 m. Signal intensity from the stack varied by more than 10 db over time periods of a few minutes, presumably because of varying burner loads or tube cleaning. These results may not apply to all stacks since the

743

have made goal revisions, based on research results to date, in two areas. First, new concepts in optical signal processing (differential Doppler) allow transverse wind component measuring research to be an effective replacement for azimuth scanning geometries for the purpose of 3-component wind profiling. Differential Doppler is also applicable to low-elevation-angle stack velocity measurements. Second, FM-CW ranging has been found difficult to apply to aerosol targets in practice. Progress in digital data handling of high-frequency signals, done elsewhere, suggests that CO_2 laser pulse techniques with coherent detection are a viable method for obtaining aerosol profiles.

By using two existing Doppler lidar systems, we will be able to explore the extension of 3-component velocity sensing by differential Doppler to aerosol targets and longer ranges. Attempts will be made to determine the limiting angular beam separation required for operation and to relate observed signal-to-noise values obtained in the differential case to those seen in the normal pure backscatter geometry. Applications in diffusion, urban ventilation factor determination, and stack effluent velocity sensing should all benefit from progress in this area.

Work on heterodyne Doppler signal processing is designed to give the sign of the line-of-sight velocity component measured by the lidar. This capability is related to diffusion studies, especially vertical velocity measurements, and stack effluent velocity applications.

Various types of digital data processing, beginning with a high-speed clipped correlator, will be studied in an attempt to increase the signal-to-noise and therefore effective range of the system in low-signal conditions. Chances of success in this exploratory research are uncertain.

Coherently detected pulse ranging, without extracting Doppler information, will be attempted for aerosol profile measurements. This work is related to the urban ventilation factor application.

Studies of coherently detected, pulsed Doppler lidar, if successful, would lead to increased range resolution at ranges beyond approximately 500 m. A low duty cycle, pulsed return also opens the possibility of other types of signal processing than we now use. However, within the resource constraints and operational orientation of the project, successful pulsed Doppler experiments are not presented as a working objective.

Field experiments using the Doppler lidar are the basic part of the project. We will continue appropriate feasibility studies to apply our improved understanding and techniques to the measurement of wind profiles for atmospheric diffusion, urban ventilation factor profiles of wind and aerosol loading, and stack effluent velocity profiles.

REFERENCES

Abshire, N. L., R. L. Schwiesow and V. E. Derr, 1974: Doppler lidar observations of hydrometeors. J. Appl. Meteor., 13, 951-953.

Lawrence, T. R., D. J. Wilson, E. E. Craven, I. P. Jones, R. M. Huffaker and J. A. L. Thomson, 1972: A laser velocimeter for remote sensing. Rev. Sci. Instr., 43, 512-518.

Post, M. J. and R. L. Schwiesow, 1976: Temporal- and spatial-frequency spectra for atmospheric aerosols. In Atmospheric Aerosols, NASA Report NASA CP-2004, Dec. 13-15, 1976, TuC9-1 – TuC9-4.

Schwiesow, R. L. and R. E. Cupp, 1976: Remote Doppler velocity measurements of dust devil vortices. Appl. Opt., 15, 1-2.

Schwiesow, R. L., R. E. Cupp, M. J. Post, and R. F. Calfee, 1977: Coherent differential Doppler measurements of transverse velocity at a remote point. Appl. Opt., 16, lxxx-lxxx.

AN OPTICAL VELOCIMETER FOR PRECIPITATION

Ting-i Wang and K. B. Earnshaw
NOAA Environmental Research Laboratories
Boulder, Colorado 80302

I.   INTRODUCTION

We have developed a laser-beam system that uses raindrop-induced
scintillations to measure path-averaged rain parameters.[1] The general
philosophy of the approach is to measure the raindrop-induced irradiance (or
amplitude) scintillations with two vertically spaced horizontal detectors.
The time-lagged covariance function is obtained by delaying the signal from
the upper detector and then correlating with the signal from the lower
detector. This temporal covariance function yields the path-averaged terminal
velocity distribution of the raindrops. With a known relationship[2] between
drop-size and terminal velocity, the measured velocity distribution can be
converted to path-averaged drop-size distribution and hence to rain rate.
Sample measurements show that the path-averaged drop-size distribution of a
steady rain follows a Marshall-Palmer distribution.[1] The optically measured
path-averaged rain rate also shows good agreement with conventional tipping-
bucket rain-gauge data.[1]

This technique can also be used to measure the terminal velocity distribu-
tion of other precipitation, e.g., snow and hail. Because the relationship
between particle size and terminal velocity of these particles is not as well
determined as for raindrops, quantitative measurements of the amount of
precipitation is not as easy to achieve. However, this information is
useful for qualitative identification purposes.

II.   IMPLEMENTATION

The prototype velocimeter consists of a low-power laser, two line detectors
and an analog correlator to provide the computation of the temporal covariance
functions. The transmitter is a 4 mW He-Ne laser, followed by an optical system
that expands the collimated beam to produce a uniform beam 20 cm in diameter.

Two horizontal line detectors 25 cm long and 0.15 cm high are used as receivers. The detectors are mounted on a frame that allows their vertical separation to be adjusted easily. Interference filters with a passband of 0.002 μm centered at 0.6328 μm are used. Also, multiple field stops are used to exclude background light. The signals detected by the two detectors are then processed by a correlator that consists of analog delay devices, analog multipliers and integrators to obtain the time-lagged covariance functions.

The system was used during the summer and fall of 1976 on a 200-m flat path at Table Mountain, a mesa located 12 km north of Boulder, Colorado. Time-lagged covariance functions induced by rain, hail and snow were detected. Typical results are shown in Fig. 1, where z_o is the vertical separation of the two line detectors. The path-averaged velocity distributions converted from Fig. 1 are shown in Fig. 2. The typical falling speeds of snow, rain and hail are 2 m/s, 6 m/s and 10 m/s respectively. However, these values could vary for different storms. A bimodal distribution was detected on June 23, 1976, during a mixture of rain and hail. The time-lagged covariance functions (displayed for 5 min interval) of the signals detected by two vertically separated line detectors with z_o=4 cm are shown in Fig. 3. The shorter delay peak ($\tau \approx 4$ ms) contributed by hail-induced scintillations corresponds to a terminal velocity equal to 10 m/s. The long delay peak ($\tau \approx 9$ ms) is caused by raindrops with terminal velocity equal to 4.5 m/s. At the end of the storm, the hail peak disappeared; however, small raindrops
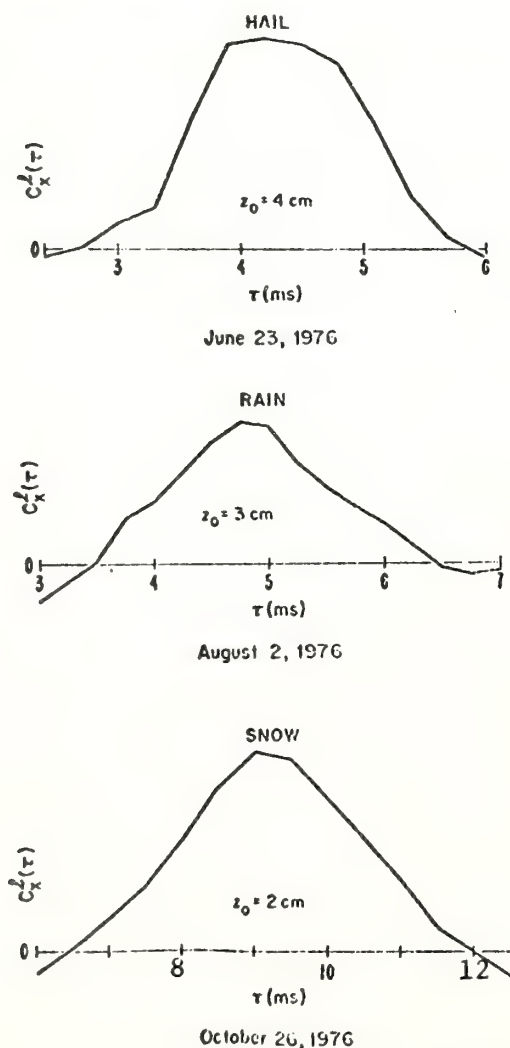
Fig. 1

746
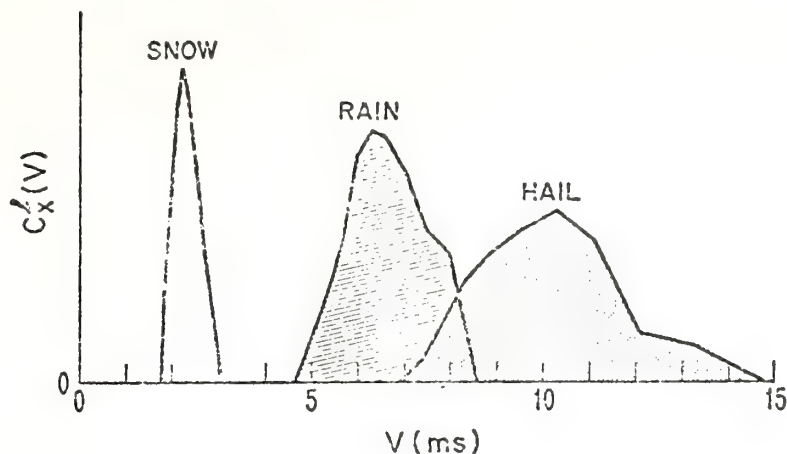
Fig. 2

were still falling. If we assume that the relationship between drop-size and the terminal velocity follows that given by Gunn and Kinzer,[2] we obtain the drop-size distribution as shown in Fig. 4. Because hail may not follow the relationship assumed, the results are only qualitatively correct for hail sizes. The dashed lines represent the corresponding Marshall-Palmer distribution[3] for the rain rate at that moment. With the presence of hail particles, the drop-size distributions have more large drops than a Marshall-Palmer distribution. At the end of the hail storm, the rainfall drop-size distribution agrees with the Marshall-Palmer distribution.

Fig. 3

Fig. 4

747
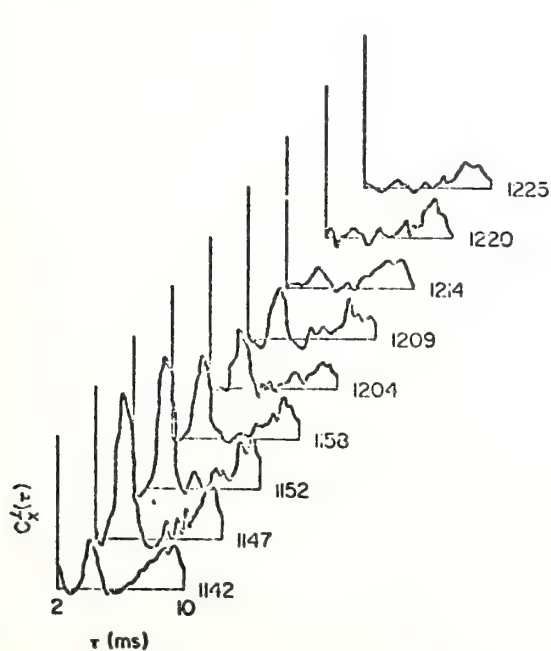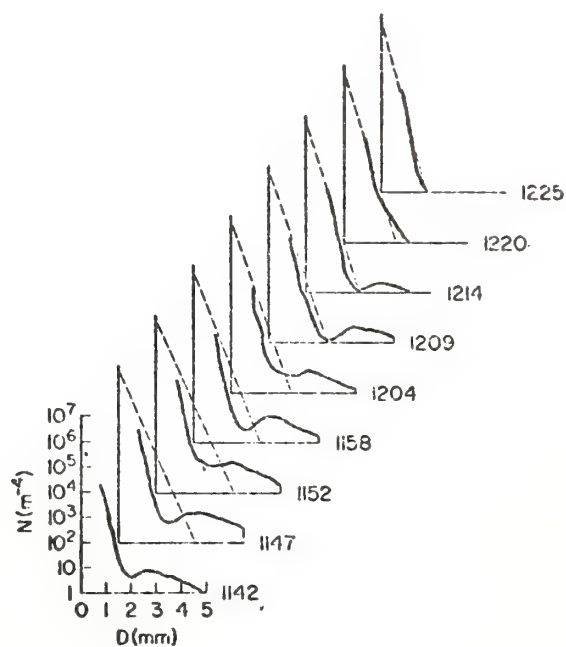
III. CONCLUSIONS

We have demonstrated that the path-averaged velocity distribution of precipitant particles can be measured by observing the time-lagged covariance function of the irradiance fluctuations of a laser beam induced by falling particles. We believe this is a potentially useful device for identification of various kinds of precipitation.

IV. REFERENCES

[1] Wang, T-i, G. Lerfald, R. S. Lawrence, and S. F. Clifford (*Applied Optics*, August 1977).

[2] Gunn, R., and G. D. Kinzer, *J. Meteorol. 6*, 243 (1949).

[3] Marshall, T. S., and W. McK. Palmer, *J. Meteorol. 4*, 186 (1948).

Concerning the influence of echo carrier frequencies and antenna dimensions on the performance of echosonde (acoustic-radar) antennas[a)]

S. Adeniyi Adekola[b)]

Wave Propagation Laboratory, Environmental Research Laboratories, National Oceanic and Atomspheric Administration, U. S. Department of Commerce, Boulder, Colorado 80302
(Received 3 April 1977)

A study of the influence of echo carrier frequencies and antenna dimensions on the performance of acoustic-radar antennas is reported with features of practical interest. For a steady-state plane-wave propagation, appropriate expressions are given for the acoustic impedance, the homogeneous boundary conditions analogous to the electromagnetic type of problems, and the time-averaged acoustic energy. Diffraction pattern integral equations for echosonde antennas are evaluated in closed forms using the Zernike polynomials and the generalized-hypergeometric functions, and physical interpretations are given where appropriate. Accurate computer simulations can contribute toward: (1) Better understanding of acoustic remote sensing of atomspheric structure/properties and (2) time-saving/avoidance of hidden problems in field work. Antenna-pattern simulations are examined using modifications of antenna design which improve antenna-system performance. By proper choices of echo carrier frequencies and antenna dimensions, quasiuniform phase distributions pertinent to modest phase shifts of experimental measurements (in striking contrasts with rapidly changing phases of previous results), are obtained. Severe side lobes are major detriments in acoustic remote sensing. Results presented include computer simulations of an antenna employed in probing the marine atmosphere remotely from a moving ship during a cruise in the Pacific Ocean/Caribbean Sea, and simulations of an antenna employed over dry-land; ground-level side lobes versus echo carrier frequencies; and 3-dB beamwidth variations with echo carrier frequencies and with antenna dimensions. For 1–5-kHz carrier-frequency range, acceptable antenna dimensions are 1.22, 1.8, and 1.8 m for the illuminating- transmitting-aperture diameters, and height of the absorbing cuffs, respectively. Half-power beamwidths within 7°–13.5° are obtained in the 1–2-kHz frequency range; and selection of antenna flare angles between 15° and 18° tends to give optimum side-lobe attenuations. Comparisons between theory and measurements show overall good agreements. Maximum relative side-lobe rejections of about −56.5 dB (in good accordance with measurements) in the 20° region near the ground, are obtained at 2-kHz carrier frequency.

INTRODUCTION

Efficient and highly directional antennas, with adequately suppressed sidelobes are needed for accurate-quantitative measurements of the characteristics of atmospheric scatterers using acoustic echo-sounding (echosonde) techniques.[1–5] This new and powerful technique has proved to be an efficient and valuable tool for investigating the structures and dynamics of the lower atmosphere.[6–8] Proper choices of antenna dimensions and operating carrier frequencies can produce sharp antenna beams with reduced sidelobes, thereby improving the efficiency of the entire system. Consequently, measurements of the characteristics of smaller atmospheric-scatterers than those measured at present would be possible. The antenna mainbeam is primarily responsible for the sounding operation. Severe detriments are interferences/ground echoes from the Earth's surface received through the sidelobes.[9] On transmission, the sidelobes may also constitute a noise-pollution problem to life near the antenna. Thus, sidelobes in the 20° region near the ground should be controlled.

Effects of variations of carrier frequencies on antenna gains are also of fundamental significance in view of the transmitting and receiving efficiencies which remarkably differ for different ranges of operating carrier frequencies. For example, for 1 W rms electrical input power, efficiencies of 50%, 10%, and 3%, have been reported for frequency ranges between 1–2, 2–3.5, and 3.5–6 kHz, respectively.[4]

Echosonde techniques provide excellent means of monitoring the lower boundary layer of the atmosphere because acoustic waves interact strongly with atmospheric structures. As one example, an echosonde system provides a convenient and accurate tool for sensing in real time the wind field around an airport for aircraft safety.[10] The system is highly sensitive to small-scale turbulent eddies of the order of one half the acoustic radar wavelength. For example, for a 2-kHz frequency (radar wavelength $\lambda = 0.17$ m), the strongest scatter is produced by turbulence components whose dimensions are of the order of half the radar wavelength (i.e., $\frac{1}{2}\lambda = 0.085$ m). This scattering phenomenon is known as Bragg scatter and has been observed in sea scatter with radars which are used for remote sensing of ocean waves.[11] Smaller-scale eddies at the lower boundary layer are of significance in that: Larger-scale motions can be deduced from them; they are related to eddy intensities at other scales of turbulence in the inertial subrange; and they are influenced by larger turbulent motions.[10]

In this paper, we first outline the theory of diffraction integrals for the echosonde antenna, and present some integral equations needed in the analysis of the antenna characteristics. The result lends itself readily to predicting the antenna behaviors by computer simulations. An account is also given for the fluid velocity normal to the radiating surface. Relations are developed for: the homogeneous boundary conditions analogous to the elec-

tromagnetic case, the time-averaged acoustic energy, and the acoustic impedance, using a steady-state plane-wave propagation assumption. Some of the developed integral equations are evaluated in closed forms using the Zernike polynomials, and the generalized-hyper-geometric functions.

Next, we examine pattern simulations for two antennas employed in remote sensing applications. In view of the system efficiencies stated above, the frequency ranges considered for the antennas are 1–5 and 1–3 kHz, for favorable practical applications. Considerations also include ground-level sidelobes versus carrier frequencies, and half-power beamwidth variations with carrier frequencies and with antenna dimensions. This paper also addresses the important problem of antenna simulations which seem to be at odds with measurements, particularly regarding the phase distributions across the radiating antenna aperture. By adequate choices of carrier frequencies, and modifications of antenna dimensions, modest phase shifts pertinent to experimental predictions are presented.

Finally, some of the computer-predicted beam patterns are compared with two sets of experimentally measured patterns, namely, the previously available experimental measurements,[1] and recent pattern measurements made with the radar now located at White Sands Missile Base in New Mexico—furnished by the Acoustic-Radar Group of the Wave Propagation Laboratory. For proper visualization of the antenna-radiation patterns, isometric plots are given for two cases of the pattern simulations.

I. ON THE DIFFRACTION INTEGRALS

The Kirchhoff–Fresnel diffraction integral has been modified for the echosonde antenna as[2–3]

$$P(\overline{R}) = \int_{S} \left[P(\overline{R}') \frac{\partial}{\partial n'} G(\overline{R}', \overline{R}) - G(\overline{R}', \overline{R}) \frac{\partial}{\partial n'} P(\overline{R}') \right] dS',$$
(1)

where $P(\overline{R})$ is the required pressure field of the antenna, $P(\overline{R}')$ is the source distribution, $\overline{R}$ and $\overline{R}'$ are the position vectors to the field and source points, respectively, $G(\overline{R}', \overline{R})$ is the Green's function, and $\hat{n}'$ is a unit vector pointing into the volume for which S is a surface. The radar-antenna configuration is depicted in Fig. 1. The lower illuminating antenna aperture (radius $\rho_{(max)}$) is smaller in size than the radiating aperture (radius $\rho_{s(max)}$) at the upper base such that the antenna is tapered as indicated in the figure. The antenna height H is made of shielding absorbing shrouds supported by a six-sided plywood structure on the outside. One side of the six sides has been removed from Fig. 1 so as to show the physical configuration more clearly. In order to be perfectly absorbing, the inside of the antenna is lined with absorbent materials like urethane foam or convoluted polyurethane. Some lead sheet or lead septum is then sandwiched between the absorbing urethane foam (on the inside) and the plywood structure (on the outside). The lead sheet is to further block the transmission of acoustic energy through the antenna walls. Any energy that is not absorbed by the convoluted polyure-
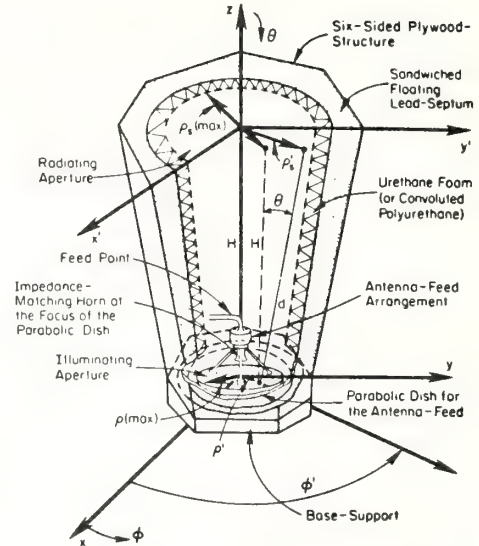
FIG. 1. Radar-antenna physical configuration for narrow-beam transmitter–receiver modes.

thane is reflected by the floating lead septum. The symbol d (as shown in the figure) represents the distance between two arbitrary points on the lower and upper apertures of the antenna, respectively.

In order to employ Eq. (1) in studying the characteristics of the radar antenna of Fig. 1 using the cylindrical coordinate system, one modifies Eq. (1) to give

$$P(\overline{R}) = \frac{jk}{4\pi} \int_{0}^{2\pi}$$

$$\times \int_{0}^{\rho(max)} F(\rho') \frac{\exp(-jkr')}{r'} (1 + \cos\theta)\rho' d\rho' d\phi',$$
(2)

where $F(\rho')$ is the excitation at the antenna-aperture in amplitude and phase, $\cos\theta = (z - z')/|\overline{R} - \overline{R}'|$, $r' = |\overline{R} - \overline{R}'|$, and the integration is performed along the antenna aperture in question. Throughout this paper, an $\exp(j\omega t)$ time variation is assumed and suppressed. Notice that Eq. (2) can be used to integrate along the illuminating aperture to obtain the near field of this aperture in amplitude and phase at a height H above the aperture. If this nearfield is truncated at $\rho_{s(max)}$ (radius of the radiating aperture), then it becomes the equivalent excitation at the radiating aperture. With this equivalent excitation, Eq. (2) can be used again to integrate along the radiating aperture to obtain the far-field of the antenna, with the entire antenna then acting like a point source. This point would be deferred until later, first we shall consider some pressure fields and boundary conditions.

A. Some pressure field considerations

On the radiating surface S, a requirement or boundary condition can be imposed such that the Green's function

J. Acoust. Soc. Am., Vol. 62, No. 3, September 1977

750

appearing in the integrand of Eq. (1) can be specified as

$$\frac{\partial G(\overline{R}', \overline{R})}{\partial n'} = 0 \quad \text{(on the radiating surface),} \tag{3}$$

where $\partial n'$ signifies the differentiation along a direction normal to the radiating surface. Thus, taking the requirement of Eq. (3) into consideration, the pressure field of Eq. (1) can be represented by

$$P(\overline{R}) = - \int_S G(\overline{R}, \overline{R}') \frac{\partial P(\overline{R}')}{\partial n'} dS', \tag{4}$$

where $G(\overline{R}, \overline{R}')$ satisfies the radiation condition for $\exp(j\omega t)$ time dependence. The arguments of the Green's function have been interchanged in view of the symmetry property of the Green's function. The quantity $\partial P(\overline{R}')/\partial n'$ appearing in the integrand of Eq. (4) can be expressed in terms of the fluid velocity $V_n(\overline{R}')$ normal to the radiating surface S at $\overline{R}'$ as

$$V_n(\overline{R}') = \frac{-1}{j\omega\rho_0} \frac{\partial P(\overline{R}')}{\partial n'}, \tag{5}$$

where ρ_0 is the mean fluid density, and ω is the angular frequency in radians. The fluid velocity describes the motion of the acoustic wave and it is assumed to have small amplitudes. Employing Eq. (5) in Eq. (4), the pressure field then becomes

$$P(\overline{R}) = j\omega\rho_0 \int_S G(\overline{R}, \overline{R}') V_n(\overline{R}') dS', \tag{6}$$

where $\overline{R}'$ is the position vector to an arbitrary point on the radiating surface. The entire radiating surface S in Eq. (6) may comprise any significant supporting structures, baffles, and piston faces.

For an idealized point source on the radiating surface S and located in a rigid baffle where $V_n(\overline{R}') = 0$, except at the source itself, and if $\overline{R}_0$ is the position vector of the location of the point source, then we have

$$V_n(\overline{R}') = Q(\overline{R}') \delta(\overline{R}_0 - \overline{R}'), \tag{7}$$

where Q is the strength of the point source, and $\delta(\overline{R}_0 - \overline{R}')$ is an impulse function. Substituting Eq. (7) in Eq. (6), and by virtue of the impulse function properties, one obtains

$$P(\overline{R}) = j\rho_0 ck G(\overline{R}, \overline{R}_0) Q(\overline{R}_0), \tag{8}$$

where the identity $\omega = kc$ has been used, c is the velocity of sound, and $\overline{R}_0$, $\overline{R}$, and $\overline{R}' \in S$. The strength Q of the point source can be defined as

$$Q = \lim_{\Delta S \to 0} V_n \Delta S. \tag{9}$$

For a source to be considered small, with d_s the maximum extent of the source, then $d_s/\lambda \ll 1$. Thus, for a small source in which there is no appreciable spatial phase delay between individual radiating elements we have

$$Q = \int_{S_0} V_n dS, \tag{10}$$

where S_0 is the radiating surface of the source.[26]

1. The acoustic impedance

By employing the fluid velocity $V_n(\overline{R}')$ along a normal direction to the radiating surface, and using the relationship between the fluid velocity and the derivative of the pressure field as given by Eq. (5), the surface acoustic impedance can be expressed in terms of the pressure field and its derivative. Thus, if ρ_0 is the mean fluid density, then the surface acoustic impedance denoted by the symbol Z_s is given by

$$Z_s = \frac{P}{V_n} = \frac{P}{-(1/j\omega\rho_0)(\partial P/\partial n)}. \tag{11}$$

In many instances, the field behavior is that of a plane wave or approximately so, and the plane-wave assumption simplifies the results significantly. Thus, if a steady-state plane wave is assumed to be propagating in the positive z direction, then

$$P = P_0 \exp(-jkz), \tag{12}$$

where P_0 is the amplitude of the wave which may be a complex quantity, and k is the wavenumber. Consequently, the characteristic impedance Z_c for plane-wave propagation can be obtained from Eq. (11) by replacing Z_s by Z_c as

$$Z_c = \frac{P_0}{(k/\omega\rho_0)P_0} = \frac{\omega\rho_0}{k} = \rho_0 c, \tag{13}$$

where the medium is a gas with characteristic impedance Z_c.

2. Homogeneous boundary conditions

The pressure-field homogeneous boundary condition, which is analogous to a corresponding electromagnetic problem, is discussed in this section. The following relationship between the pressure field P and the surface impedance Z_s follows directly from Eq. (11):

$$\frac{-Z_s}{j\omega\rho_0} = \frac{P}{\partial P/\partial n}. \tag{14}$$

The boundary condition then becomes

$$P + \frac{Z_s}{j\omega\rho_0} \cdot \frac{\partial P}{\partial n} = 0. \tag{14a}$$

This reduces to

$$\frac{\partial P}{\partial n} + jk\left(\frac{\rho_0 c}{Z_s}\right) P = 0. \tag{14b}$$

By virtue of Eq. (13), the above homogeneous boundary condition for the acoustic field can be expressed in the following form:

$$\frac{\partial P}{\partial n} + jk y_s P = 0, \tag{15}$$

where $y_s = Z_c/Z_s$ is the normalized surface acoustic admittance, Z_s is the acoustic impedance for the surface, and the pressure field P satisfies the radiation condition for $\exp(j\omega t)$ time dependence.[2,26] Equation (15) is the acoustic counterpart of the general homogeneous (impedance-type) boundary condition on the radiating surface usually encountered in electromagnetic problems.

751

3. Acoustic intensity $\overline{S}$, and the time-averaged energy $\langle \overline{S} \rangle$ in an acoustic plane wave

If the symbol $\overline{S}$ represents the instantaneous energy flux density, then the time-averaged energy flux density $\langle \overline{S} \rangle$ is given by

$$\langle \overline{S} \rangle = \tfrac{1}{2} \, \mathrm{Re}[P\overline{V}^*] \,, \tag{16}$$

where the angular brackets $\langle \cdot \rangle$ denote a time-averaged quantity in the complex notation, $\mathrm{Re}[\,\cdot\,]$ is the real part of the argument, the star sign ($*$) is a complex conjugate quantity, and $\overline{V}$ is the velocity given by

$$\overline{V} = (-1/j\omega\rho_0) \, \nabla P \,, \tag{16a}$$

where ∇P is the gradient of the pressure field. Substituting Eq. (16a) in Eq. (16), then the time-averaged energy flux becomes

$$\langle \overline{S} \rangle = \tfrac{1}{2} \, \mathrm{Re}[P(\nabla P)^*/j\omega\rho_0] \,. \tag{16b}$$

Employing the plane wave Eq. (12), then the velocity $\overline{V}$ of Eq. (16a) reduces to

$$\overline{V} = \hat{z} P/Z_c \,, \tag{16c}$$

where $\hat{z}$ is a unit vector in the positive z-propagation direction, and P and Z_c are defined in Eqs. (12) and (13), respectively. Consequently, the time-averaged energy flux $\langle \overline{S} \rangle$ reduces to

$$\langle \overline{S} \rangle = \hat{z}\,|P_0|^2/2Z_c \,, \tag{17}$$

where $|P_0|$ is the absolute value of the complex magnitude of the plane wave defined in Eq. (12). Equation (17) holds for a pure real characteristic impedance Z_c. However, for a complex Z_c in which Z_r and Z_i are, respectively, the real and imaginary components (i.e., if $Z_c = Z_r + jZ_i$), then the time-averaged energy flux $\langle \overline{S} \rangle$ is given by

$$\langle \overline{S} \rangle = \hat{z}\,|P_0|^2 Z_r/2(Z_r^2 + Z_i^2). \tag{17a}$$

The identity $PP^* = |P_0|^2$, which follows directly from Eq. (12), has been used. In subsequent sections, the diffraction patterns will be discussed.

B. Diffraction patterns

When the modified diffraction integral Eq. (2) is used to integrate along the radiating aperture of the antenna configuration of Fig. 1, the following diffraction pattern expression is obtained for the farfield[2-3]:

$$P(\theta) = \frac{jk(1+\cos\theta)}{2D} \exp(-jkD)$$

$$\times \int_0^{\rho_{s(\max)}} A(\rho_s')\exp[j\Phi(\rho_s')]J_0(k\rho_s'\sin\theta)\rho_s'\,d\rho_s', \tag{18}$$

where θ is the angle off the antenna axis in degrees, D is the distance from the center of the radiating aperture to the farfield point, $\rho_{s(\max)}$ is the radius of the radiating aperture, and J_0 is the zero-order Bessel function of the first kind. The excitation quantity $A(\rho_s')\exp[j\Phi(\rho_s')]$ in the integrand of Eq. (18) is obtained by using Eq. (2) to integrate along the illuminating antenna-aperture to obtain the two-dimensional Eq. (18a) from which $A(\rho_s')\exp[j\Phi(\rho_s')]$ can be computed. Thus,

$$A(\rho_s')\exp[j\Phi(\rho_s')] = \frac{j}{\lambda}\int_0^{2\pi}\int_0^{\rho(\max)} A(\rho')$$

$$\times \exp[j\Phi(\rho')]\exp\left[-j\,\frac{2\pi}{\lambda}\,(d-H)\right]\zeta(d)\,\rho'\,d\rho'd\phi', \tag{18a}$$

where d is given by

$$d(\rho', \phi') = [\,\rho'^2\sin^2\phi' + (\rho_s' - \rho'\cos\phi')^2 + H^2\,]^{1/2}$$

and $\zeta(d)$ is the decay of the signal with distance d given by

$$\zeta(d) = \frac{1 + H/d}{2d} \,.$$

The computed diffraction pattern is obtained by converting Eq. (18) to decibels thus

$$P_N(\theta) = 20\log_{10}\big|P(\theta)/P(0)\big|\,dB\,, \tag{18b}$$

where $P(0)$ is a normalizing factor obtained from Eq. (18), by setting θ equal to zero. From the practical standpoint, it is desirable to explore forms of the radial phase- and amplitude-distributions $A(\rho_s')\exp[j\Phi(\rho_s')]$, at the radiating aperture in which the resulting diffraction integral equations are expressed in closed forms. The integral equations arising from some phase distributions at the antenna aperture and their physical interpretations will be discussed in Sec. I C.

C. Radiation integrals arising from some aperture radial-phase distributions and their interpretations

New variables can be introduced in Eq. (18) as follows: If we let

$$r = \rho_s'/\rho_{s(\max)}$$

and

$$v = k\rho_{s(\max)}\sin\theta, \tag{19}$$

then, the quantity $A(\rho_s')\exp[j\Phi(\rho_s')]$ in the integrand of Eq. (18) goes over into the new quantity $A_0(r)\exp[j\Phi_0(r)]$, and the diffracted field $P(\theta)$ goes into a new function to be denoted for the present considerations as $P(v)$, then Eq. (18) reduces to

$$P(v) = \frac{jk(1+\cos\theta)}{2D}\exp(-jkD)\,\rho_{s(\max)}^2$$

$$\times \int_0^1 A_0(r)\exp[j\Phi_0(r)]J_0(vr)\,r\,dr. \tag{20}$$

If we let the complex amplitude and phase function $A_0(r)\exp[j\Phi_0(r)]$ be represented by

$$A_0(r)\exp[j\Phi_0(r)] = A_0(r)\exp[-j\alpha(r)]\,, \tag{20a}$$

where $A_0(r)$ and $\alpha(r)$ are real functions of r, and $\alpha(r)$ is a radial phase variation, then substituting Eq. (20a) in Eq. (20), we have

$$P(v) = \kappa(\theta)\int_0^1 A_0(r)\exp[-j\alpha(r)]J_0(vr)\,r\,dr\,, \tag{21}$$

where $\kappa(\theta)$ is given by

$$\kappa(\theta) = \frac{jk(1+\cos\theta)}{2D}\exp(-jkD)\,\rho_{s(\max)}^2\,. \tag{21a}$$

We shall next examine Eq. (21) for cases of practical interest and then interpret the results. The phase distribution $\alpha(r)$ of practical interest can be represented as

$$\alpha(r) = \tfrac{1}{2} u r^2 \ , \tag{21b}$$

where u is a dimensionless constant. Substituting Eq. (21b) into Eq. (21), we have

$$P(v) = \kappa(\theta) \int_0^1 A_0(r) \exp(-\tfrac{1}{2} j u r^2) J_0(vr)\, r\, dr \ . \tag{22}$$

The following physical interpretations are applicable to Eq. (22) above.

1. Physical interpretations

There are three interpretations that can be given to the expression of Eq. (22) thus:

(a) In the farfield region, the diffraction pattern $P(v)$ represents the pattern arising from an aperture excitation with amplitude $A_0(r)$ and with a quadratic phase modulation produced by defocusing the radiating system. Further discussions about the effects of phase modulation errors on the beam patterns have been considered in Ref. 3. When a radar antenna is defocused, beam widening, which may be useful in monopulse tracking applications, can be obtained. An aperture–antenna system can be defocused by ordinarily displacing the antenna-feed position without changing the aperture size of the antenna (in contrast with other methods of defocusing[12]). Such defocused systems would preserve the necessary phase and amplitude information in the beam pattern required for tracking applications.

(b) In the near-field region, if R_t represents the distance of the near-field region from the radiating antenna aperture, the expression of Eq. (22) is the field distribution arising from an in-phase radiating aperture excitation with circular symmetry and with u given by

$$u = k \rho_{s(max)}^2 / R_t \ . \tag{22a}$$

Equation (22) then becomes

$$P(v) = \kappa(\theta) \int_0^1 A_0(r) \exp\left(\frac{-jkr^2 \rho_{s(max)}^2}{2R_t}\right) J_0(vr)\, r\, dr \ . \tag{22b}$$

(c) The last interpretation applicable to the acoustic pressure field integral Eq. (22) is made if the quantities u and v are interpreted as follows:

$$u = k(\rho_{s(max)}/f) z \tag{22c}$$

and,

$$v = [k\rho_{s(max)}/f](x^2 + y^2)^{1/2} = k\rho_{s(max)} \sin\theta \ , \tag{22d}$$

where f is the focal length of the antenna aperture, and (x, y, z) are the rectangular coordinates at the focus, with z the axis of symmetry (i.e., the antenna axis). Using these definitions, then Eq. (22) is the three dimensional field distribution at the focus of the antenna system. The above interpretations are also applicable to nonuniform circular apertures.[13,14]

2. Integral evaluations

Some of the integral equations will be evaluated or expressed in closed forms by employing functions like the Zernike polynomials used in the theory of diffraction images. Since $A_0(r) \exp(-\tfrac{1}{2} j u r^2)$ is complex with circular symmetry then after a few steps (see Appendix A), Eq. (22) yields

$$P(v) = \kappa(\theta) \sum_{s=0,2,4,6,8\ldots} b_s (-1)^{s/2} \frac{J_{s+1}(v)}{v} \ , \tag{23}$$

where $J_{s+1}(v)$ is the $(s+1)^{\text{th}}$ order Bessel function of the first kind, and the coefficients b_s are given by

$$b_s = 2(s+1) \int_0^1 A_0(r) \exp(-\tfrac{1}{2} j u r^2) R_s^0(r)\, r\, dr, \tag{23a}$$

where $R_s^0(r)$ is one form of a set of Zernike polynomials[15] of the general form $R_s^m(r)$ (see Appendix A). The procedure of obtaining the diffraction pattern of Eq. (23), consists essentially of computing the coefficients b_s, which are of interest in diffraction theory. A few of the Zernike polynomial quantities are given in Appendix A. Equation (23a) has also been further simplified in Appendix A.

3. Uniform amplitude distribution: $A_0(r) = 1$

For the case of uniform amplitude distribution we set $A_0(r) = 1$ in the integrand of Eq. (22) giving

$$P(u, v) = \kappa(\theta) \int_0^1 \exp(-\tfrac{1}{2} j u r^2) J_0(vr)\, r\, dr \ . \tag{24}$$

By separating the above equation into real and imaginary components, the resulting expressions can be integrated by parts separately to yield the following expression for the diffraction pattern:

$$\begin{aligned}
P(u, v) = \tfrac{1}{2} \kappa(\theta) &\left\{ \frac{2}{u} \sin\left(\frac{v^2}{2u}\right) + \frac{\sin(\tfrac{1}{2} u)}{\tfrac{1}{2} u} V_0(u, v) \right. \\
&- \frac{\cos(\tfrac{1}{2} u)}{\tfrac{1}{2} u} V_1(u, v) - j\left[\frac{2}{u} \cos\left(\frac{v^2}{2u}\right) \right. \\
&\left. \left. - \frac{\cos(\tfrac{1}{2} u)}{\tfrac{1}{2} u} V_0(u, v) - \frac{\sin(\tfrac{1}{2} u)}{\tfrac{1}{2} u} V_1(u, v) \right] \right\} \ , \tag{24a}
\end{aligned}$$

where the V_n functions used in Eq. (24a) are the Lommel series functions which have been explicitly discussed elsewhere.[2,14] The slightly modified V_n functions of $V_0(u,v)$ and $V_1(u,v)$ used in Eq. (24a) above are given in Appendix B.

D. Some aperture amplitude distributions with uniform phase-fronts of the form $a(r) = 0$

For a uniform phase-front distribution of the type $\alpha(r) = 0$, Eq. (21) reduces to

$$P(v) = \kappa(\theta) \int_0^1 A_0(r) J_0(vr)\, r\, dr \ . \tag{25}$$

Amplitude functions $A_0(r)$ which are capable of representations by polynomials or series expansions can be used

J. Acoust. Soc. Am., Vol. 62, No. 3, September 1977

753

in Eq. (25). Thus, Eq. (25) can be transformed into diffraction patterns that can be represented by the generalized hypergeometric series. Two such cases will be discussed.

1. Amplitude distribution with a Taylor series expansion: $A_0(r) = \sum_{n=0}^{\infty} (r^n/n!) A_0(0)$

Amplitude distributions which are capable of a good polynomial approximation or a series expansion can be transformed or expressed in closed forms when they appear in diffraction pattern integral equations. The result from a Taylor series expansion of the amplitude distribution, for example, leads to a representation of the diffraction pattern integral by the generalized hypergeometric series. Thus, if the amplitude function $A_0(r)$ can be represented by a Taylor series expansion such that

$$A_0(r) = \sum_{n=0}^{\infty} \frac{r^n}{n!} A_0^{(n)}(0) , \qquad (26)$$

then, substituting Eq. (26) in Eq. (25), one obtains

$$P(v) = \kappa(\theta) \sum_{n=0}^{\infty} \frac{A_0^{(n)}(0)}{n!} \int_0^1 r^{n+1} J_0(vr)\,dr . \qquad (26a)$$

And by the property of the integrals of Bessel functions we have[16]

$$\int_0^1 r^{n+1} J_0(vr)\,dr = \frac{vJ_1(v)}{(n+2)^2} \,_1F_2(1;\, \tfrac{1}{2}n+2,\, \tfrac{1}{2}n+2;\, -\tfrac{1}{4}v^2), \qquad (26b)$$

where the symbol $_1F_2(\cdot)$ denotes the generalized hypergeometric series. Thus, Eq. (26a) reduces to

$$P(v) = \kappa(\theta)\, vJ_1(v) \sum_{n=0}^{\infty} \frac{A_0^{(n)}(0)}{n!\,(n+2)^2} \,_1F_2(1;\, \tfrac{1}{2}n+2,\, \tfrac{1}{2}n+2;$$
$$-\tfrac{1}{4}v^2). \qquad (27)$$

The diffraction pattern of Eq. (27) can be alternatively expressed by a series of Bessel functions since hypergeometric functions are expressible in terms of series of Bessel functions.[16]

2. Amplitude distributions of the form $A_0(r) = \cos(\tfrac{1}{2}\pi r)$

Since amplitude functions represented by cosine functions are capable of series expansions, the diffraction patterns arising from such amplitude distributions can also be expressed in closed forms using the hypergeometric series. A cosine-amplitude function can be represented by a power series containing factorials of the form[17]

$$A_0(r) = \cos(\tfrac{1}{2}\pi r) = \sum_{n=0}^{\infty} (-1)^n \frac{(\tfrac{1}{2}\pi r)^{2n}}{(2n)!} . \qquad (28)$$

Substituting Eq. (28) in Eq. (25), one obtains

$$P(v) = \kappa(\theta) \sum_{n=0}^{\infty} (-1)^n \frac{(\tfrac{1}{2}\pi)^{2n}}{(2n)!} \int_0^1 r^{2n+1} J_0(vr)\,dr, \qquad (28a)$$

and since[16]

$$\int_0^1 r^{2n+1} J_0(vr)\,dr = \frac{J_1(v)}{v} \,_3F_0\left(-n,\, -n,\, 1;\, \frac{-4}{v^2}\right) , \qquad (28b)$$

therefore, the diffraction pattern of Eq. (28a) reduces to

$$P(v) = \kappa(\theta) \frac{J_1(v)}{v} \sum_{n=0}^{\infty} (-1)^n \frac{(\tfrac{1}{2}\pi)^{2n}}{(2n)!} \,_3F_0\left(-n,\, -n,\, 1;\, \frac{-4}{v^2}\right) ,$$
$$(29)$$

where the symbol $_3F_0(\cdot)$ stands for the generalized hypergeometric function, and J_1 is the first-order Bessel function of the first kind.

II. COMPUTER SIMULATIONS OF THE DIFFRACTION PATTERNS OF AN ANTENNA EMPLOYED IN PROBING THE MARINE ATMOSPHERE FROM A MOVING SHIP

Pattern simulations of an antenna whose dimensions are similar to those of the antenna installed on a moving ship platform are presented in this section. The feasibility of echosonde system operation at sea from ships or buoys (with proper attention given to the antenna installation) appears to have first been demonstrated during JONSWAP (Joint North Sea Wave Project)2 experiment.[18] The echosonde antenna recently employed in shipborne remote sensing applications during GATE (Global Atmospheric Research Program Atlantic Tropical Experiments[19,20]), has an illuminating diameter of 1.2 m at the lower base which tapers to a larger diameter at the upper base with noise-suppressing shrouds of height 1.8 m. Figure 2 illustrates the pattern simulations of antennas with similar dimensions which approximately satisfy the relation

$$H = D_{R_s} = 1.5\, D_R , \qquad (30)$$

where H is the height of the noise-suppressing shrouds, and D_R and D_{R_s} are the illuminating-/radiating-aperture diameters, respectively (see Fig. 1). All dimensions are in meters. The symbols R and R_s are the radial variations across the illuminating- and radiating-apertures, respectively. These symbols are, respectively, used to represent ρ' and ρ'_s in the computer simulations for ease of programming purposes. The pattern behaviors with frequency variations in the range of 1–5 kHz are indicated in Fig. 2. The radiating-aperture excitations producing the beam patterns of Fig. 2, and some beam-pattern characteristics are discussed below. The beam-patterns are computed from the normalized version of Eq. (18), while the phase- and amplitude-field distributions at the radiating aperture are computed from Eq. (18a).

A. Quasiuniform phase excitations at the radiating antenna aperture

The diffraction patterns of Fig. 2 are produced by the near-uniform phase variations at the radiating aperture depicted in Fig. 3 for the respective frequencies. The phase distributions are shown for the radiating aperture diameters of 1.8 and 1.7 m, respectively. The phase distributions are fairly uniform across the aperture except at the edges. The distributions are symmetrical about the aperture axis, and only the variations from
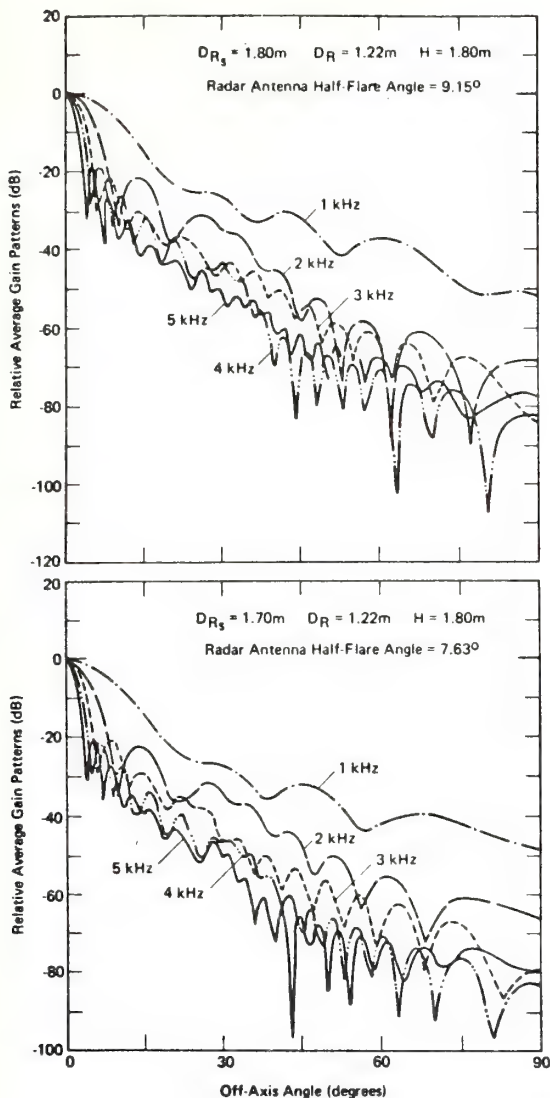
FIG. 2. Normalized echosonde-antenna gain patterns with the maximum directed along the zenith ($\theta = 0$ direction) for 1–5 kHz frequency variations.

the aperture center to the edge are indicated in the figure. The phase shifts are expressed in cycles across the aperture and are shown for carrier frequencies of 1–5 kHz. The phase variations show negligible departures from uniform phase fronts in accordance with predictions.[4]

Equivalent amplitude distributions

The variations of the symmetrical amplitude distributions (of the aperture field) with frequency are depicted in Fig. 4 for the radiating aperture diameters of 1.8 and 1.7 m. In most cases, the distributions are modified such that their intensities are peaked at the aperture center, and are tapered to small values at the aper-

ture edge. Such gradual amplitude tapers give reasonably low sidelobe patterns.[21] If the respective phase excitations depicted in Fig. 3 are represented by the symbol Φ, then the corresponding amplitude distributions of Fig. 4 are multiplied by an exponential function of the form $\exp(j\Phi)$ to obtain the aperture-field distribution in amplitude and phase.

B. Half-power (3-dB) beamwidth

The half-power beamwidth (HPBW) of an antenna pattern is the angular distance between the half-power points, i.e., the positions on the beam where the power has decreased to half its maximum value. The half-power points represent 70.7% of the total energy (or -3 dB relative to the maximum power of 0 dB). The 3-dB beamwidths can be estimated by using the usual relation[9]

$$\text{HPBW} = 1.13\lambda/D_a , \qquad (31)$$

where D_a is the diameter of the aperture and λ is the wavelength. The radiating aperture diameters expressed in wavelengths as given in Table I are 10.59λ and 16.36λ at 2- and 3-kHz carrier frequencies, respectively. Using these values in Eq. (31), estimated 3-dB beamwidths of $6.1°$ and $4°$ are obtained, respectively. These estimated 3-dB beamwidths are approximately of the same orders of magnitudes as the computed 3-dB
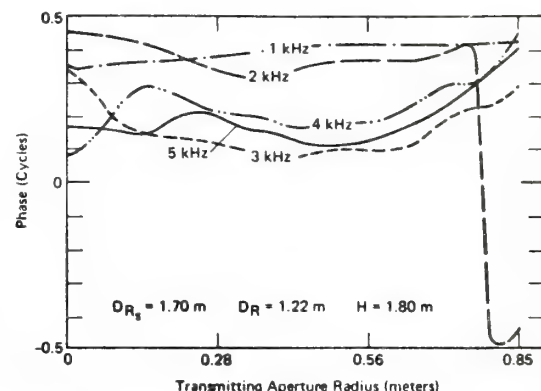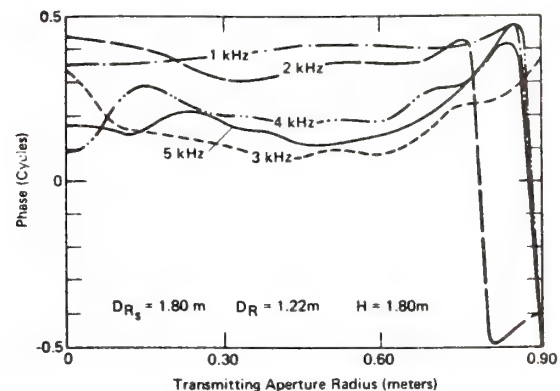

FIG. 3. Quasiuniform phase distributions of the signal at the radiating antenna aperture.

J. Acoust. Soc. Am., Vol. 62, No. 3, September 1977

755

TABLE I. Half-power beamwidths, dimensions of turbulent eddies producing strongest scatter, ground-level sidelobes for 1–5 kHz carrier frequencies, and antenna dimensions within $3.7\lambda - 25.7\lambda$ (D_{R_s}, D_R; and H are the radiating-, illuminating-aperture diameters; and antenna height, respectively).

Fre-quency (kHz)	Wave-length λ (m)	Dimensions of turbulent eddies producing the strongest scatter ($\lambda/2$) (m)	Half-power beamwidth (deg)	Relative ground level sidelobes (dB)	Relative maximum sidelobe levels in the 20° region adjacent to the ground (dB)	D_{R_s} (Wave-lengths)	D_R (Wave-lengths)	H (Wave-lengths)	
1	0.33	0.165	13.540	−49.378	−41.922 (at 70°)	5.45λ	3.70λ	5.45λ	
2	0.17	0.085	7.204	.−60.994	−56.506 (at 70°)	10.59λ	7.18λ	10.59λ	
									$D_{R_s} = 1.80$ m
3	0.11	0.055	4.836	−74.951	−58.580 (at 76°)	16.36λ	11.09λ	16.36λ	
									$D_R = 1.22$ m
4	0.08	0.040	3.738	−73.023	−68.027 (at 74°)	22.50λ	15.25λ	22.50λ	
									$H = 1.80$ m
5	0.07	0.035	3.156	−65.935	−63.096 (at 70°)	25.71λ	17.43λ	25.71λ	
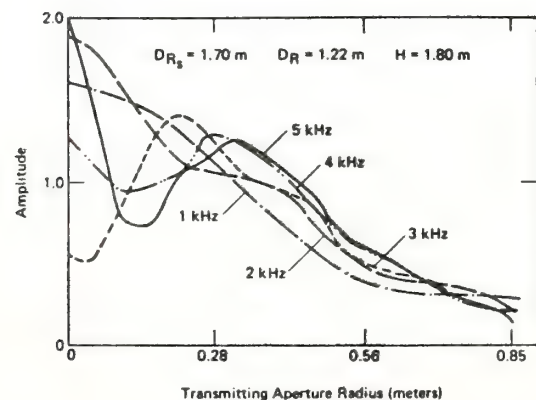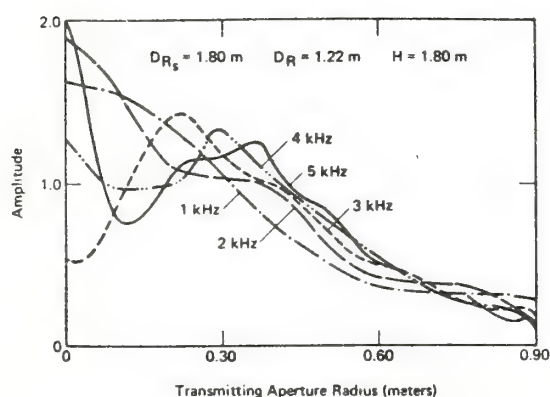
FIG. 4. Gradually tapered amplitude distributions at the radiating aperture.

beamwidths of 7.2° and 4.8° (at 2- and 3-kHz carrier frequencies, respectively) from the beam patterns of Fig. 2, and shown in Table I. Another beamwidth which can be used to describe a pattern behavior is the beamwidth between first nulls (BWFN).[22] Figure 5 illustrates most of the important features of an antenna beam in both the rectangular and polar formats.

1. Variations of 3-dB beamwidth with echo-carrier frequency and radiating antenna-aperture sizes

Figure 6 depicts the behaviors of the half-power beamwidth with echo-carrier frequency and with transmitting aperture diameters (D_{R_s}) of sizes 1.5, 1.6, 1.7, and 1.8 m, respectively. The beamwidth variations are shown for the antenna with and without the shielding ab-
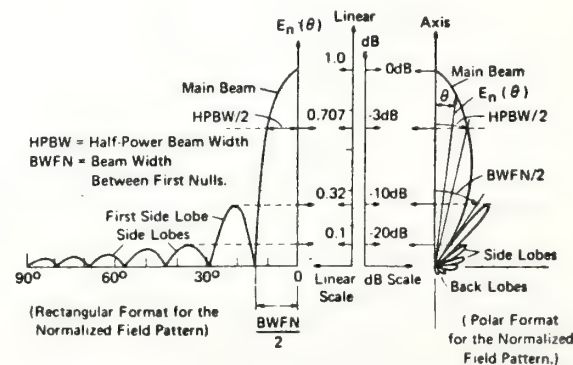
FIG. 5. The rectangular and polar formats of representing the normalized radiation pattern.

J. Acoust. Soc. Am., Vol. 62, No. 3, September 1977

756
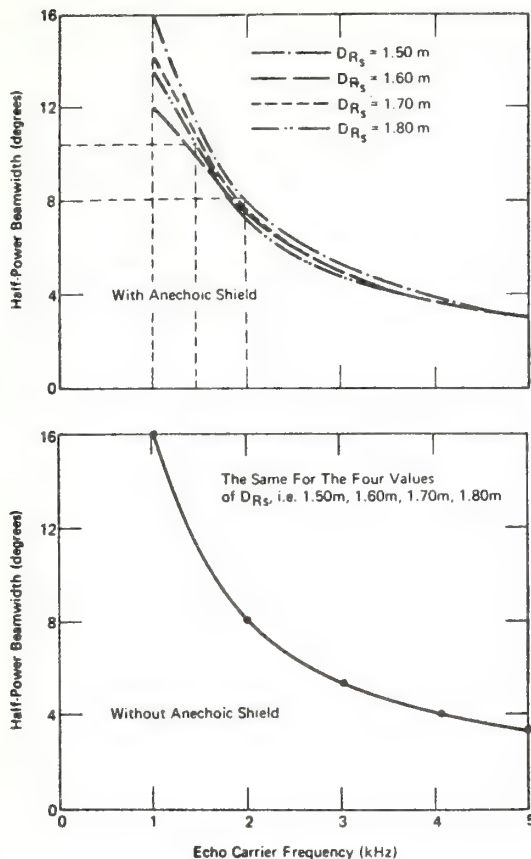
FIG. 6. Dependence of the 3-dB beamwidth on carrier frequency for different antenna dimensions.

2. Behaviors of sidelobe intensities with carrier frequency and radiating-aperture diameters

Major drawbacks in acoustic echosounding are the strong sidelobes particularly those adjacent to the ground. Low sidelobe patterns would reduce interference from extraneous noise sources and the signal-to-noise ratio of the system would be improved. The sidelobes could be raised or lowered depending on the type (and magnitude) of the aperture-field distributions. However, reduced sidelobes would tend to broaden the beamwidth (i.e., reduction in gain).

sorbing cuffs. Within the frequency interval between 1–2 kHz, half-power beamwidths in the range of 16°–8° are obtained as illustrated in Fig. 6. For the variations with transmitting aperture sizes shown in Fig. 7, larger beamwidths in the neighborhood of 1 kHz carrier frequency than the beamwidths within 2–5 kHz frequency range are noticed. Temperature refractions and wind gradients in the atmosphere can cause backscattered wavefronts to return at off-axis angles of several degrees.[3,4] Thus, 3-dB beamwidths greater than 5° may be necessary for satisfactory reception of the backscattered energy in acoustic remote sensing. As shown in Figs. 6 and 7, 3-dB beamwidths greater than about 5° are obtained for frequencies between 1–3 kHz. The variations of the half-power beamwidths with frequency (for the patterns of Fig. 2) are summarized in Table I. The beamwidth varies from 13.45° at 1 kHz through 3.16° at 5 kHz. The dimensions of turbulence components producing the strongest scatter at the lower boundary layer of the atmosphere, range from 0.165 m at 1 kHz to 0.035 m at 5 kHz. The antenna dimensions are of the order of several wavelengths ranging from a maximum of 25.7λ at 5 kHz to a minimum of 3.7λ at 1 kHz.

FIG. 7. Relations between the 3-dB beamwidth and radiating aperture diameter.

Figure 8 illustrates the behaviors of the maximum sidelobe intensities (within $70°-90°$ from the antenna axis) with carrier frequencies and with radiating-aperture diameters. The sidelobes adjacent to the ground are progressively reduced for increasing frequency as shown in the figure. The sidelobes also reduce with increasing aperture diameters. Although increasing the carrier frequency would somewhat suppress the sidelobes, the high propagation losses and the atmospheric acoustic signal absorption at high frequencies discourage system operations at high frequencies. As shown in Table I, the maximum relative sidelobe level near the ship's platform (ground level) for the 2 kHz carrier frequency is -56.51 dB with respect to the mainbeam (in good accordance with the prediction of -55 dB[19]). Relative sidelobes as low as -60.99 dB can be obtained as indicated in Table I.
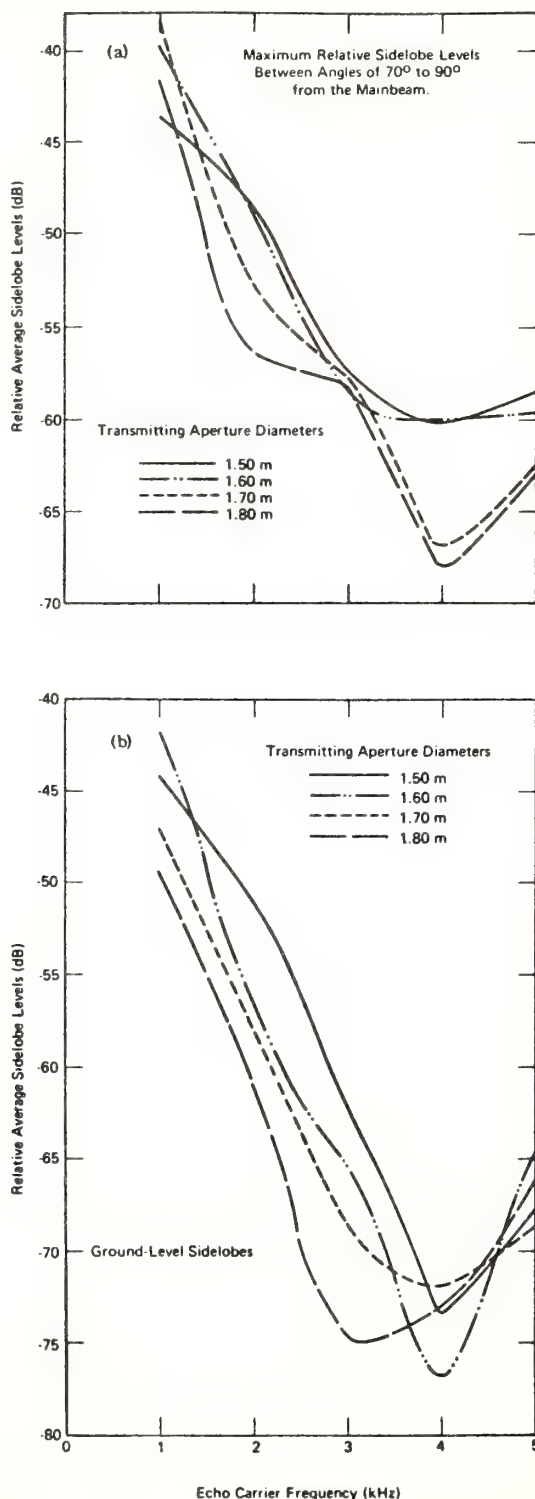

FIG. 8. The variations with echo carrier frequencies of (a) maximum sidelobe amplitudes in the 20° region adjacent to the ground and (b) ground-level sidelobes.
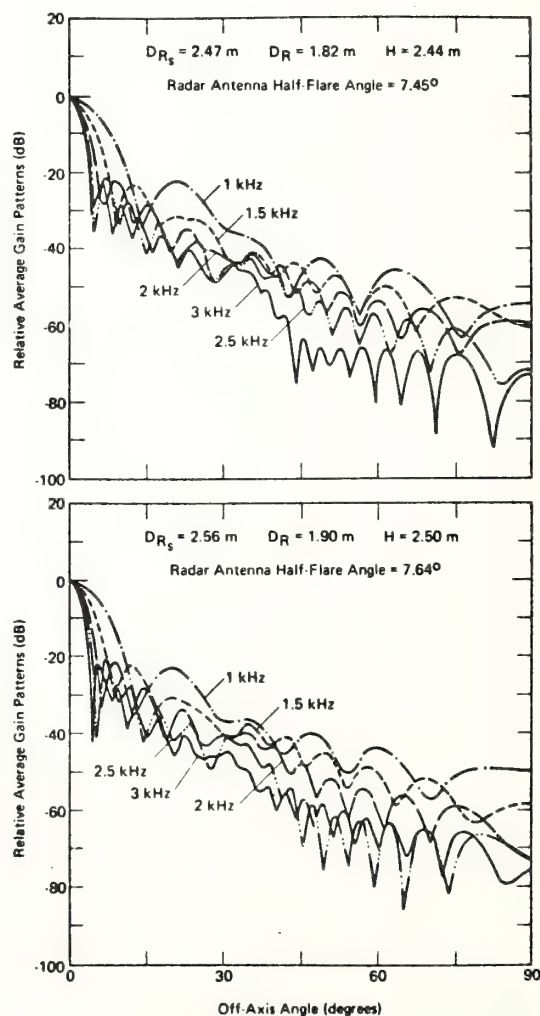
FIG. 9. Normalized echosonde-antenna gain patterns with the maximum directed along the zenith ($\theta = 0$ direction) for 1–3 kHz frequency variations.

J. Acoust. Soc. Am., Vol. 62, No. 3, September 1977

758

TABLE II. 3-dB beamwidths, dimensions of turbulent eddies producing strongest scatter, ground-level sidelobes for 1–3 kHz carrier frequencies, and antenna dimensions within $5.5\lambda - 22.5\lambda$ (D_{R_s}, D_R; and H are the radiating-, illuminating-aperture diameters; and antenna height, respectively).

| Frequency (kHz) | Wavelength λ (m) | Dimensions of turbulent eddies producing the strongest scatter ($\lambda/2$) (m) | 3-dB beamwidth (deg) | Relative ground level sidelobes (dB) | Relative maximum sidelobe levels in the 20° region adjacent to the ground (dB) | Dimensions of the radar antenna | | |
						D_{R_s} (Wavelengths)	D_R (Wavelengths)	H (Wavelengths)
1	0.33	0.165	9.80	−53.713	−50.471 (at 70°)	7.48λ	5.52λ	7.39λ
1.5	0.22	0.110	6.56	−60.217	−51.554 (at 74°)	11.23λ	8.27λ	11.09λ
2	0.17	0.085	4.99	−58.274	−54.788 (at 70°)	14.53λ	10.71λ	14.35λ
2.5	0.13	0.065	4.02	−70.894	−60.373 (at 75°)	19.00λ	14.00λ	18.77λ
3	0.11	0.055	3.34	−72.847	−67.206 (at 75°)	22.45λ	16.55λ	22.18λ

$D_{R_s} = 2.47$ m

$D_R = 1.82$ m

$H = 2.44$ m

III. SIMULATIONS OF THE RADIATION PATTERNS OF AN ANTENNA EMPLOYED IN REMOTE SENSING OVER DRY LAND

The antenna dimensions used for the pattern simulations of Fig. 9 approximately satisfy the relation

$$D_{R_s} = 1.34 \, D_R = H. \tag{32}$$

In the acoustic radar work at the Wave Propagation Laboratory, an antenna with similar dimensions (now located at White Sands Missile base in New Mexico) has been used over dry land for investigating the structures and dynamics of the lower boundary layer.[23] The pattern simulations of Fig. 9 are shown for frequency variations within 1–3 kHz. Table II summarizes some of the pattern characteristics. The antenna dimensions expressed in wavelengths vary between 5.5λ and 22.5λ. The highest 3-dB beamwidth (shown in Table II) is 9.8°, and the ground-region sidelobe level as low as -72.85 dB relative to the mainbeam maximum of 0 dB is obtained. Within 1–1.5 kHz carrier-frequency range, a maximum operating range of 1524 m (1.524 km) can be obtained. For a bistatic system, the baseline separation between the transmitter and the receiver can be taken as one-half of the maximum operating range (i.e.,

762 m if the transmitter is operated within 1–1.5 kHz frequency range). Summaries of the maximum (practical) operating echo ranges and possible baseline separations for the corresponding bistatic systems are given in Table III.[23] Other characteristics of the patterns of Fig. 9 are discussed below.

Figure 10 shows the phase distributions of the field at the radiating aperture for the patterns of Fig. 9 at the corresponding frequencies. The distributions appear reasonably uniform except for some phase shifts at 1- and 2-kHz frequencies in the lower illustration of Fig. 10. Some discontinuities in the distributions are noticed near the rim of the cuff. The corresponding amplitude distributions are shown in Fig. 11, and they are of similar characteristics with those described in Sec. II. The half-power beamwidths (computed from the patterns of Fig. 9) are depicted in Fig. 12 with and without the shielding absorbing shrouds. The beamwidth at a particular frequency is less for an antenna with the shielding shrouds than an antenna without the shrouds. Figure 12 also indicates that the beamwidth reduces with increasing frequency, for example, the beamwidth at 3 kHz is narrower than at 1.5 kHz by a factor of about 2 as expected. Figure 13 illustrates that there are significant reductions of

TABLE III. Specifications to be incorporated in the design of the antenna structure for favorable practical applications (J. W. Wescott, personal communications, 1976).

Height of shielding absorbing cuffs (m)	Illuminating aperture radius ρ (max) (m)	Radiating aperture radius ρ_s (max) (m)	Echo carrier frequency (kHz)	Radar wavelength (λ) (m)	Dimensions of turbulent eddies producing the strongest scatter ($\lambda/2$) (m)	Maximum practical echo ranges (m)	Baseline separation for a corresponding bistatic system (maximum echo range/2) (m)
1.83	0.61	0.92	2 to 3	0.17 to 0.11	0.085 to 0.055	762.20	381.10
2.44	0.91	1.22	1 to 1.5	0.33 to 0.22	0.165 to 0.110	1524.39	762.20

J. Acoust. Soc. Am., Vol. 62, No. 3, September 1977

759
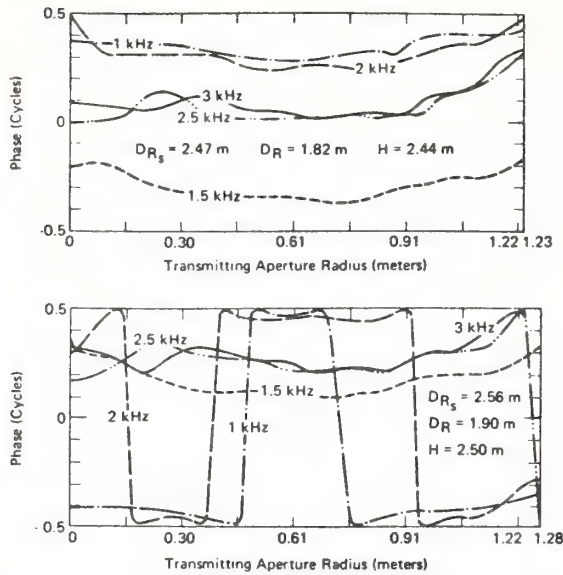
FIG. 10. Modest phase shifts of the signal at the radiating antenna aperture.

the ground-level sidelobes as the carrier frequency increases.

IV. MULTIPLE PHASE OSCILLATIONS AT THE RADIATING APERTURE FOR VERY LARGE ANTENNAS

Multiple phase oscillations at the radiating aperture (noticed from the pattern simulations of very large acoustic antennas) are undesirable in echosounding ap-
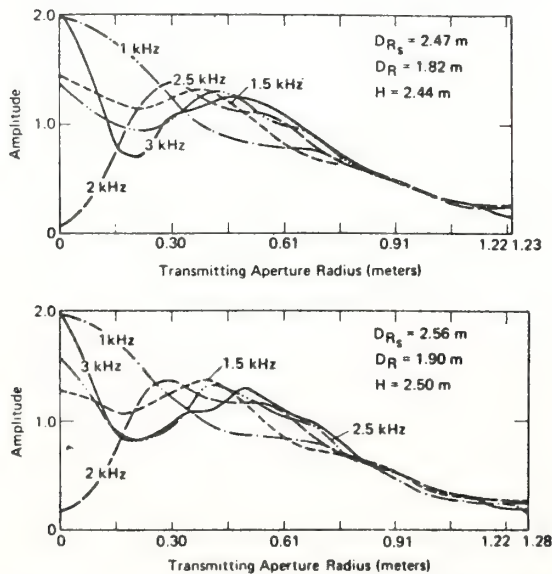
FIG. 11. Gradually tapered amplitude distributions at the radiating antenna aperture.

plications. The patterns depicted in the uppermost illustration of Fig. 14 are computed from an antenna whose dimensions satisfy the relation

$$D_{R_s} = H = 3 \ D_R . \qquad (33)$$
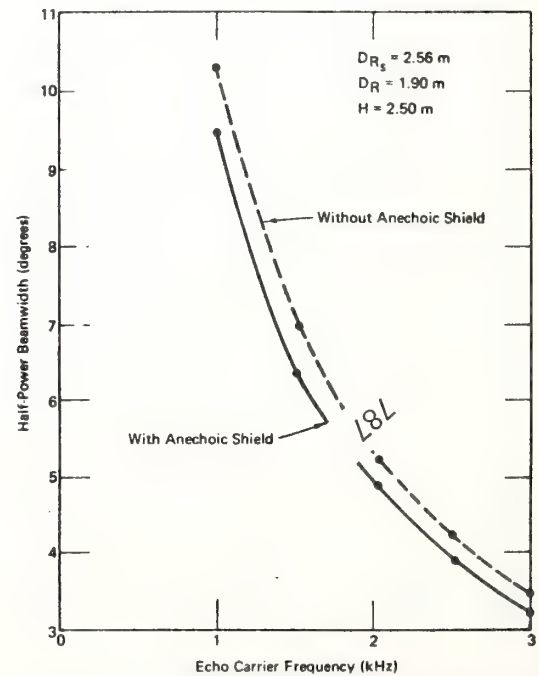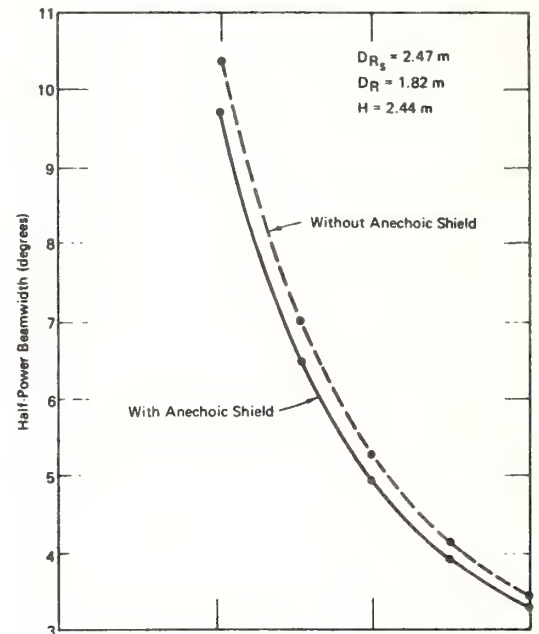
FIG. 12. Dependence of the 3-dB beamwidth on echo carrier frequency with and without shielding absorbing cuffs for the antenna.
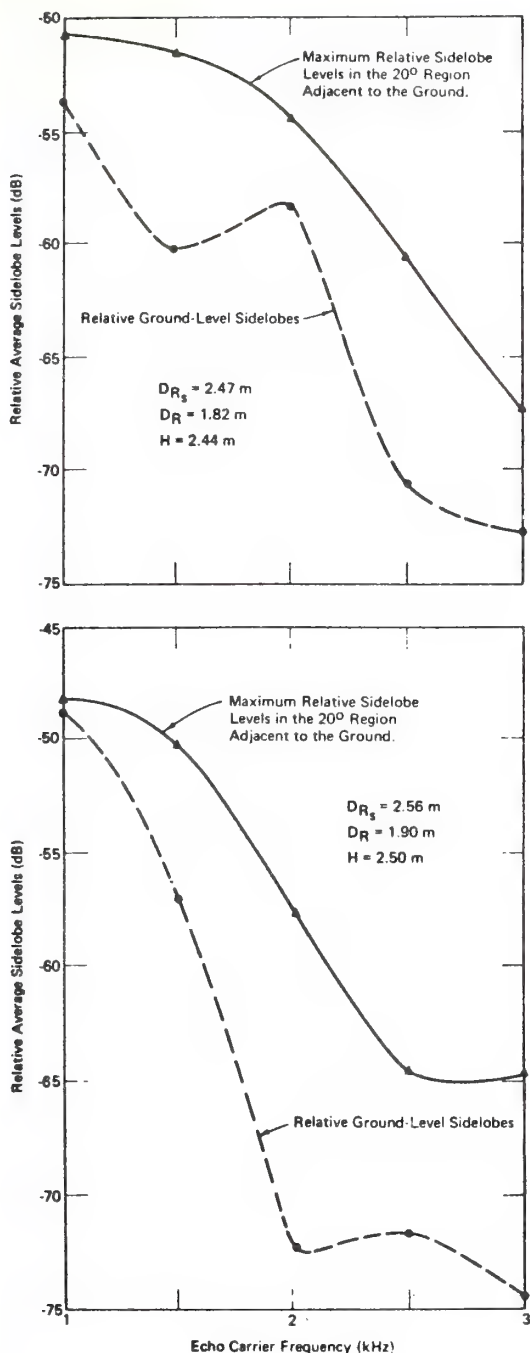
FIG. 13. Dependence of relative sidelobe amplitudes on echo carrier frequency. Notice that maximum sidelobe rejections of about −55 dB in the 20° region near the ground are obtained at 2 kHz.

The antenna half-flare angle (slope of shield wall from the vertical) is 18.44° and the half-power beamwidths of 18.52° and 7.56° are obtained at 1- and 2-kHz carrier frequencies, respectively. The corresponding

phase oscillations of the equivalent radiating-aperture field are shown in the uppermost illustration of Fig. 15. The relationship between the heights (H) and the illuminating aperture diameters (D_R), is the same for the antennas producing the three curves of the lower illustration of Fig. 14. The relationship is given by

$$H = 1.5\,D_R. \tag{34}$$

Employing Eq. (34), the effects of increasing the values of the radiating-aperture diameter (D_{R_s}) on the aperture field are considered, particularly regarding the phase distributions across the aperture. The antenna dimensions used for the three beam patterns denoted by the symbols A, B, and C in Fig. 14 are considered below.

The dimensions used to produce the pattern denoted by A satisfy the relation

$$D_{R_s} = 2H = 3\,D_R\,, \tag{34a}$$
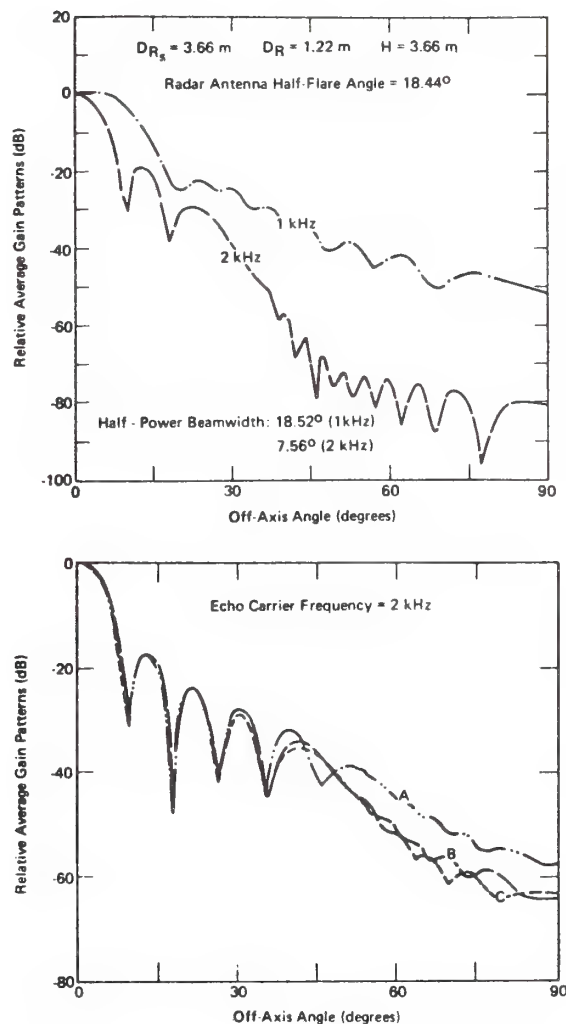
FIG. 14. Relative average gain patterns of very large antennas for 1–2-kHz carrier frequencies.
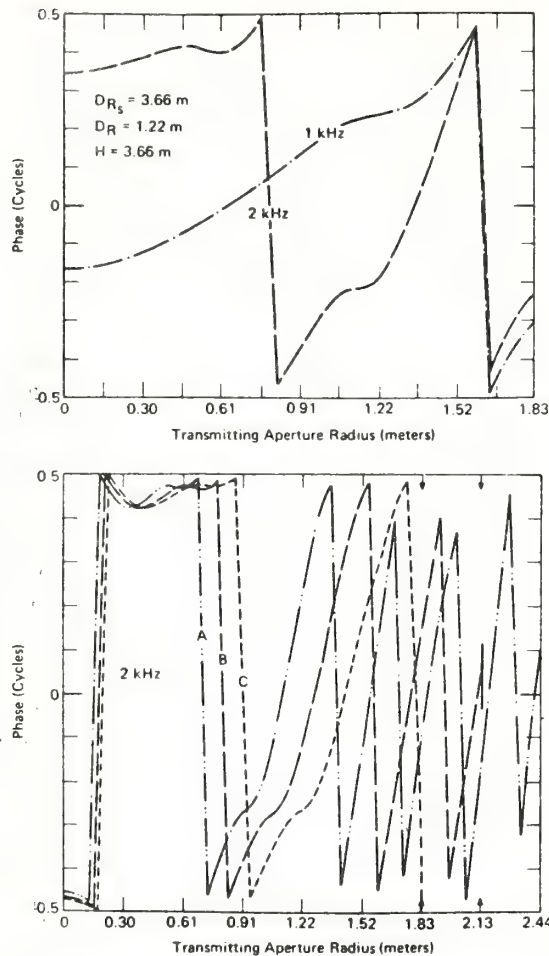
FIG. 15. Multiple phase oscillations at the radiating antenna apertures for very large antennas.

where D_{R_s}, D_R, and H are taken as 3.66, 1.22, and 1.83 m, respectively. The half-power beamwidth obtained is 8.1° and the antenna half-flare angle is 33.69°. For the pattern denoted by the symbol B, the antenna dimensions satisfy the relation

$$D_{R_s} = 2.33 \ H = 3.5 \ D_R, \tag{34b}$$

where the values of D_{R_s}, D_R, and H used are 4.27, 1.22, and 1.83 m, respectively. The half-power beamwidth is 8° and the half-flare angle of the antenna is 39.81°. The relationship between the antenna dimensions giving the curve C satisfies

$$D_{R_s} = 2.67 \ H = 4 \ D_R, \tag{34c}$$

where D_{R_s}, D_R, and H are taken as 4.88, 1.22, and 1.83 m, respectively. The half-power beamwidth is 8.1° and the antenna half-flare angle is 45°. An echo carrier frequency of 2 kHz is used for all the beam patterns A, B, and C. The phase curves for the equivalent excitation across the radiating aperture for the three

different conditions are given in the lower illustration of Fig. 15. One may notice the substantial phase oscillations for all the three aperture dimensions. The rapidly changing phase distributions shown in the figure are in sharp contrasts with the fairly uniform distributions of Figs. 3 and 10. Thus, undesirable multiple phase oscillations seem to be associated with very large antenna heights and radiating apertures. The amplitude distributions of the aperture field corresponding to the phase oscillations of Fig. 14 are of the same general forms as those of Fig. 11. The antennas whose dimensions satisfy the conditions of Eq. (33), (34)–(34c) may be too bulky for practical applications. The half-flare angles of the large antennas are between 18° and 45°. The phase distributions of the aperture field shown in Figs. 3, 10, and 15 illustrate that the equivalent aperture-field distributions are determined to some extent by the antenna dimensions.

The excess attenuation losses and the molecular absorption for acoustic energy propagating in the atmosphere at high frequencies, impose limitations on the carrier-frequency range and the associated antenna-aperture dimensions that may be used. The time and effort needed in fieldwork for assembly and disassembly of acoustic-antenna shrouds, the costs of acoustic shroud and absorbing materials (including the shipping and construction costs) also impose limitations on the height of the absorbing shroud that may be used. Thus, for favorable practical applications (as dictated by the above factors) the specifications given in Table III may be incorporated in the antenna design.

V. COMPARISONS BETWEEN THEORY AND EXPERIMENTAL MEASUREMENTS OF THE RADAR-ANTENNA BEAM PATTERNS

The experimental measurement reported for 1 kHz carrier frequency in Ref. 4, is compared with theoretical gain pattern at the same frequency in Fig. 16. For the theoretical pattern, the height of the shielding cuff, and the illuminating aperture diameter are each taken as 1.2 m. The antenna half-flare angle is 10°, and the excitation for the pattern is of the form $\exp(-0.35R^2)$ $\times \exp(-j\pi R^3)$. The experimental pattern is obtained from an antenna whose illuminating aperture diameter and absorbing cuff height are each 1.2 m. Several measurements were averaged to obtain the smooth experimen-
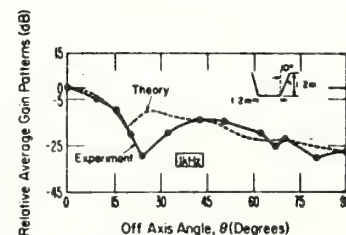

FIG. 16. Comparisons between theory and experimental measurements of Hall and Wescott (1974, Fig. 6) for 1-kHz frequency.

J. Acoust. Soc. Am., Vol. 62, No. 3, September 1977

762

tal pattern shown, and the details of the method of measurements have been reported elsewhere with other results.[4]

Figure 17 shows comparisons between the computer simulations and recent measurements made with the acoustic radar now located at White Sands Missile Base in New Mexico.[23] The transmitting frequency is 3 kHz. The experimental data are furnished by the Acoustic-Radar Group of the Wave Propagation Laboratory. The input electrical power of the transmitter for the experimental measurements is 1 W. The antenna-dimensions employed are 2.12, 2.12, and 1.23 m for the height of the shielding cuffs and the radiating- and illuminating-aperture diameters, respectively. The experimental data are acquired by a balloon carrying a microphone probe at the farfield of the antenna. The balloon technique of pattern measurements (developed in Ref. 24) is by aiming the antenna vertically and using a microphone probe (whose movements are controlled by a tethered weather balloon), moving in a fixed arc at the antenna farfield, to measure the field patterns. After bandpass filtering, the output of the probe preamplifier is rectified by a wave analyzer. The experimental patterns of Fig. 17(a) are the resulting log output registered on strip chart recorders. The slightly wavy nature of the patterns may be due to lateral drifts (as a result of wind breezes) experienced by the weather balloon which supports the probe. Two experimental curves are shown in Fig. 17(a) because the microphone probe traces the beam patterns on strip-chart recorders when the probe is moving one way, and also traces the pattern when moving back (along the same path) to its original position. The curves do not coincide because of the wind blowing the balloon up and down. The illumination at the lower aperture for the theoretical pattern is taken as $\exp(-cR^2)\exp(-j0.75\pi R^3)$, where c is a dimensionless constant. Four theoretical gain patterns are depicted in Fig. 17(a) for the constant c assuming values of 0.25, 0.4, 0.5, and 0.6, respectively. The average of the experimental patterns of Fig. 17(a) is depicted in Fig. 17(b) using standard error bars. The theoretical gain patterns with values of $c = 0.25$, and 0.6 are compared with the averaged experimental gain pattern as shown in the figure. Thus, as illustrated in Figs. 16 and 17, the agreement overall between theory and actual experimental measurements is good.

At 2 kHz transmitter frequency, the length of the baseline separation for the White Sands bistatic system is set at 300 m, thus giving the height range of 600 m, i.e., twice the baseline length (see Table III). More recently, some practical antennas have been built (for bistatic applications), with adequate antenna and cuff design along the lines outlined in this paper, to obtain continuous wind profiling and temperature fluctuations from the lower boundary layer of the atmosphere. The details of this new system, developed for the Air Force Geophysical Laboratories, are reported in Ref. 25. Adequate wind profile data are obtained with this system up to heights twice the baseline separation between the antennas. Maximum sidelobe reductions are reported, and the frequency tuning is between 1–5 kHz. The height of the shielding absorbing cuffs used is 1.8 m, and the illuminating aperture diameter is 1.2 m with

ground-level sidelobe rejections of about −50 dB relative to the mainbeam maximum of 0 dB. Also, antenna flare angle of 16° is used. Thus, the experimental study and the beam-pattern measurements reported in Ref. 25, are also in good agreement with the anticipated computer predictions of this paper.

Isometric plots for pattern visualizations

The computer simulations giving the isometric plots of Figs. 18 and 19 are viewed at colatitude and azimuth angles of (45°, 45°), respectively. The computer-program subroutine which computes the normalized version of Eq. (18) is used as the input to the contour-plot program (developed for the acoustic-radar antenna) to obtain the isometric plots. The plots are useful for beam-pattern visualizations of the antenna characteristics par-

FIG. 17. Comparisons between theory and recent measurements made with the acoustic radar now located at White Sands Missile Base in New Mexico (J. W. Wescott, personal communications, 1976), for 3-kHz frequency with $H = 2.12$ m, $D_{R_s} = 2.12$ m, and $D_R = 1.23$ m: (a) theory and recorded measurements on strip charts; (b) theory and averaged measurements indicated with standard error bars.

J. Acoust. Soc. Am., Vol. 62, No. 3, September 1977

763
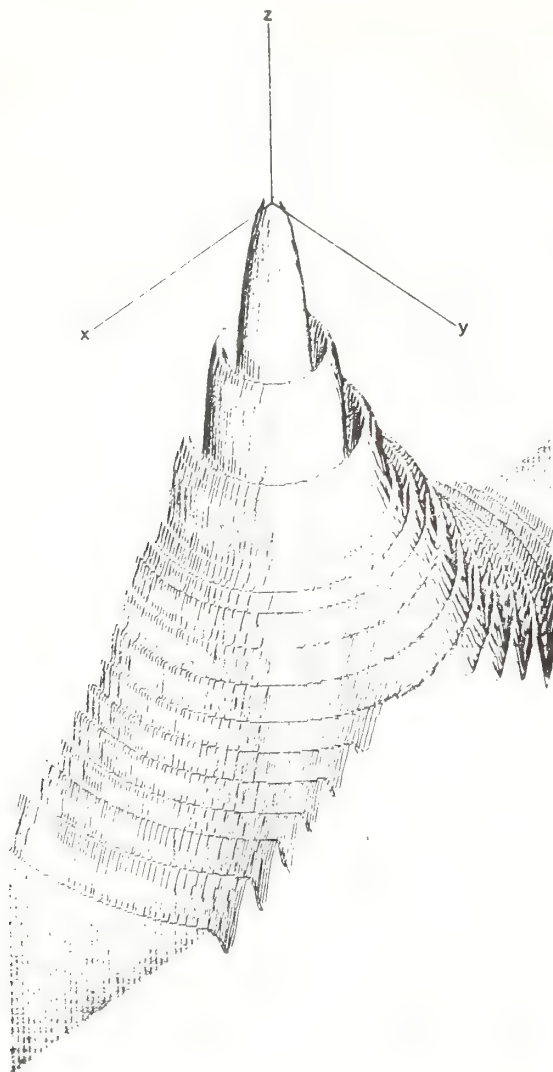
FIG. 18. A section of the isometric plot of the radiation pattern arising from a cosine-squared amplitude-tapered distribution at 2 kHz carrier frequency. Two major sidelobes; scale factor = 0.1.

ticularly regarding the relative positions of the sidelobes with respect to the mainbeam. The sectional plot of Fig. 18 arises from a cosine-squared tapered amplitude distribution at the illuminating aperture of the antenna. A carrier frequency of 2 kHz is used, the scale factor used for the plot is 0.1, and two major sidelobes are produced. The isometric plot of Fig. 19 arises from a cosine squared on a pedestal amplitude-tapered illumination at a carrier frequency of 5 kHz. The scale factor used for this plot is also 0.1. Several mini sidelobes are produced in this case, but four major sidelobes are noticed. The plots are self-explanatory.

VI. CONCLUDING REMARKS

In the present paper, some diffraction integral equations for echosonde antennas have been developed in closed forms using either the Zernike polynomials, the generalized hypergeometric functions, or the Lommel V_n functions each of which is also applicable in the theory of diffraction images. Appropriate expressions are given for the acoustic impedance, the homogeneous boundary condition, and the time-averaged acoustic energy using a steady-state plane-wave propagation assumption.

The influence of echo carrier frequencies and antenna dimensions on the performance of echosonde antennas has been examined. Computer simulations of the beam patterns have been presented for two practical antennas—an antenna employed in shipborne remote sensing applications, and an antenna used for remote sensing over dry land. Modifications of antenna design which improve antenna system performance have been considered. It has been shown that the antenna height (H) should be of the same order of magnitude as the radiating aperture diameter (D_{R_s}). Based on the results of

FIG. 19. Isometric plot for pattern visualization arising from a cosine squared on a pedestal amplitude-tapered distribution at 5 kHz carrier frequency. Four major sidelobes with several smaller sidelobes; scale factor = 0.1.

many computations, sizes of H and D_R, of about $1.5\,D_R$ are shown to be adequate, while sizes as large as $3\,D_R$ give undesirable multiple phase oscillations of the radiating aperture field. The problems of portability and costs also discourage the use of very large antenna apertures in addition to the difficulties of steering such large antennas.
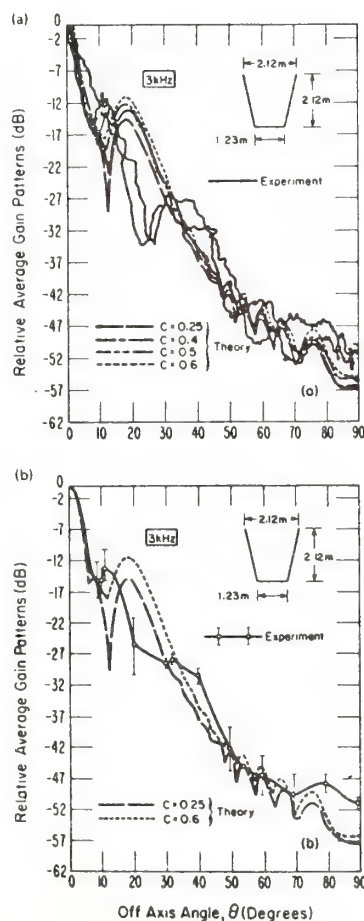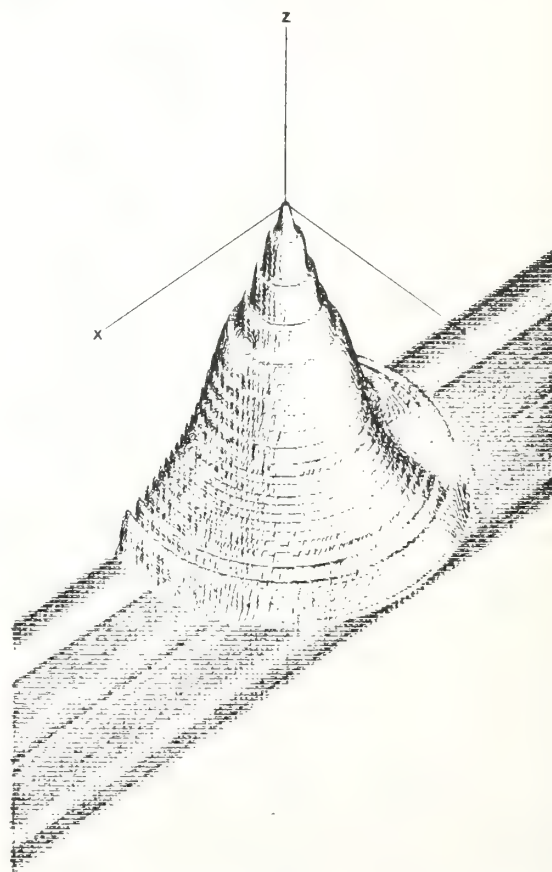
Supporting comparisons between theory and recent pattern measurements made with the acoustic radar now located at White Sands Missile Base in New Mexico are made. The overall agreements between theory and measurements are good. The isometric plot presented, shows the complete radiation pattern of the antenna. The advantages of using reasonably high operating carrier frequencies have been discussed. Narrow beamwidths are obtained for frequencies above 1 kHz. Recognizing that excess attenuation losses and strong molecular absorption occur for acoustic signal propagating in air at high frequencies, keeping the sidelobe levels relatively low is important for two reasons: First, the sidelobe reductions at high frequencies give improved signal-to-noise ratio (S/N) at the receiving mode of operation, and secondly, the noise pollution of the radiated field in the sidelobes is reduced in the transmitting mode. More Doppler shift sensitivity can be obtained at high frequencies since windspeed is proportional to frequency. However, the range of operation of the radar will dictate the optimum frequency that can be used. For example, an operating range of 150 m can be obtained at 5 kHz carrier frequency, whereas, a reduction to a lower frequency of 1 kHz will be necessary if the range is increased to 1.5 km. Larger antenna dimensions may be needed for the greater range of operation (at the lower frequency), since the larger antenna will tend to compensate for the higher noise level at the lower frequency by improving the directivity. For limited ranges, stronger echoes are normally expected as the transmitting frequency is increased because the turbulence spectrum tends to be stronger for the smaller scale structures. Little has shown that the Kolmogorov turbulence spectrum follows the $1/\lambda^{1/3}$ power law.[6]

Background considerations in the antenna design for favorable practical applications include: a compromise between portability and mechanical ruggedness; shipping and construction costs, easy assembly and disassembly of the antenna components; and compromise between aperture-size and echo carrier-frequency range that could be employed in applications. Echosonde antennas with moderate heights and weights as considered in this paper would survive rough handling and conditions of weather and wind, and would also give reliable operations. Such antennas could be disassembled into components which are of light weight and medium dimensions thereby facilitating the movements of the entire radar set to new sites if required. The susceptibilities of the antenna components to replacements and repairs under operating field conditions would also be enhanced.

ACKNOWLEDGMENTS

APPENDIX A: DETERMINATION OF THE COEFFICIENTS b_s ARISING FROM THE ZERNIKE POLYNOMIALS

The Zernike polynomials used in Eqs. (23) and (23a) to evaluate the integral Eq. (22) are discussed in this Appendix. For simplicity, we first let

$$f(r) = A_0(r)\exp\left(-\tfrac{1}{2}jur^2\right),\tag{A1}$$

such that Eq. (22) becomes

$$P(v) = \kappa(\theta)\int_0^1 f(r)J_0(vr)r\,dr,\tag{A2}$$

where $\kappa(\theta)$ is as defined in Eq. (21a). A convenient approach to solve Eq. (A2) is to use a set of orthogonal polynomials in which Eq. (A2) is a form of the integral transform of the orthogonal polynomials in question. The integral transforms can then be readily obtained in tabulated or analytical forms. Such polynomials, applicable in the present case, are the sets of Zernike polynomials represented by $R_n^m(r)$. These polynomials can also be applied in the theory of diffraction images.[13,15] The Zernike polynomials $R_n^m(r)$ have been shown to exhibit the following properties[15]:

$$\int_0^1 R_n^m(r)R_k^m(r)\,r\,dr = \begin{cases} 0 & n \neq k \\ \\ 1/2(n+1), & n = k \end{cases},\tag{A3}$$

and also

$$\int_0^1 R_n^m(r)J_m(ur)\,r\,dr = (-1)^{(1/2)(n-m)}\frac{J_{n+1}(u)}{u}.\tag{A4}$$

Thus, in the present case of interest in which the variable m identically equals zero, one obtains

$$\int_0^1 R_n^0(r)J_0(ur)\,r\,dr = \begin{cases} (-1)^{(1/2)n}\dfrac{J_{n+1}(u)}{u} & \text{if } n \text{ is even} \\ \\ 0 & \text{if } n \text{ is odd} \end{cases},\tag{A5}$$

J. Acoust. Soc. Am., Vol. 62, No. 3, September 1977

765

TABLE A1. Evaluated quantities for the $R_n^0(r)$, and $R_n^1(r)$ Zernike polynomials.

(i): $R_n^0(r)$: with n even, and $0 \leq n \leq 10$	(ii): $R_n^1(r)$: with n odd, and $1 \leq n \leq 11$
$R_0^0(r) = 1$	$R_1^1(r) = r$
$R_2^0(r) = 2r^2 - 1$	$R_3^1(r) = 3r^3 - 2r$
$R_4^0(r) = 6r^4 - 6r^2 + 1$	$R_5^1(r) = 10r^5 - 12r^3 + 3r$
$R_6^0(r) = 20r^6 - 30r^4 + 12r^2 - 1$	$R_7^1(r) = 35r^7 - 60r^5 + 30r^3 - 4r$
$R_8^0(r) = 70r^8 - 140r^6 + 90r^4 - 20r^2 + 1$	$R_9^1(r) = 126r^9 - 280r^7 + 210r^5 - 60r^3 + 5r$
$R_{10}^0(r) = 252r^{10} - 630r^8 + 560r^6 - 210r^4 + 30r^2 - 1$	$R_{11}^1(r) = 462r^{11} - 1260r^9 + 1260r^7 - 560r^5 + 105r^3 - 6r$

where $R_n^0(r)$ is defined in terms of the Legendre Polynomial as

$$R_n^0(r) = \begin{cases} P_{(1/2)n}(2r^2 - 1) & n \text{ even} \\ \\ 0 & n \text{ odd} \end{cases}, \quad (A6)$$

with the symbol P_n representing the Legendre Polynomial. In view of the above properties, Eq. (A1) can be written as

$$f(r) = \sum_{i=0,2,4,6,8,\ldots} b_i R_i^0(r). \quad (A7)$$

Consequently, by virtue of the property of Eq. (A3), we have

$$\int_0^1 f(r) R_s^0(r) r dr = \sum_{i=0}^\infty \int_0^1 b_i R_i^0(r) R_s^0(r) r dr = \frac{b_s}{2(s+1)}. \quad (A8)$$

Thus, the coefficients b_s are obtained from Eq. (A8) as

$$b_s = 2(s+1) \int_0^1 f(r) R_s^0(r) r dr. \quad (A9)$$

By using Eq. (A7), Eq. (A2) can be written in the following form:

$$P(v) = \kappa(\theta) \int_0^1 f(r) J_0(vr) r dr = \kappa(\theta)$$

$$\times \sum_{s=0}^\infty \int_0^1 b_s R_s^0(r) J_0(vr) r dr, \quad (A10)$$

which reduces to Eq. (23) of the text [after using the property of Eq. (A5)] as

$$P(v) = \kappa(\theta) \sum_{s=0,2,4,6,8,\ldots} b_s (-1)^{(1/2)s} \frac{J_{s+1}(v)}{v}. \quad (A11)$$

Using Eq. (A9), and substituting the expression of Eq. (A1) for $f(r)$, we obtain Eq. (23a) of the text given by

$$b_s = 2(s+1) \int_0^1 A_0(r) \exp(-\tfrac{1}{2} jur^2) R_s^0(r) r dr, \quad (A12)$$

where the subscript s assumes even integer values (i.e., $s = 0, 2, 4, 6, 8, \ldots$). A series representation of the Zernike polynomials $R_n^m(r)$, and some of the relevant Zernike polynomial quantities applicable for further simplifications of Eq. (A12) are discussed below.

Some relevant Zernike polynomial quantities

In the theory of diffraction images, the orthogonal polynomials $R_n^m(r)$ appear to have been first employed by Zernike in phase contrast and knife-edge techniques.[15] The polynomials are represented by

$$R_n^m(r) = \sum_{i=0}^{(1/2)(n-m)} (-1)^i$$

$$\times \frac{(n-i)! \; r^{n-2i}}{i! [(n+m)/2 - i]! [(n-m)/2 - i]!} \quad \begin{array}{l} n \geq m \geq 0 \\ (n-m): \text{ even.} \end{array}$$

$$(A13)$$

The properties are such that $n \geq m \geq 0$ and $(n - m)$ is even. The polynomials can also be expressed in terms of the generalized hypergeometric function denoted by the symbol $F(\cdot)$ as

$$R_n^m(r) = (-1)^{(1/2)(n-m)} \binom{\tfrac{1}{2}(n+m)}{m} r^m$$

$$\times F(\tfrac{1}{2}(n+m)+1, \; -\tfrac{1}{2}(n+m), \; -\tfrac{1}{2}(n-m), \; m+1, \; r^2). \quad (A14)$$

By using the representation of Eq. (A13) for the polynomials, the Zernike polynomial quantities $R_n^0(r)$ and $R_n^1(r)$ are computed and given in Table A1 below.[15]

By virtue of Table A1, further simplifications of the coefficients b_s of Eq. (A12) corresponding to Eq. (23a) of the text, can be made. Using the appropriate even values of the subscript "s" in b_s corresponding to $R_n^0(r)$ from Table A1 (with n assuming even values), the simplified b_s coefficients, given in Table A2, are obtained.

TABLE A2. Simplified versions of the coefficients b_s of the text, using the evaluated $R_n^0(r)$ Zernike quantities from Table A1.

$b_0 = 2 \int_0^1 A_0(r) \exp(-\tfrac{1}{2} jur^2) r dr$

$b_2 = 6 \int_0^1 A_0(r) \exp(-\tfrac{1}{2} jur^2) [2r^2 - 1] r dr$

$b_4 = 10 \int_0^1 A_0(r) \exp(-\tfrac{1}{2} jur^2) [6r^4 - 6r^2 + 1] r dr$

$b_6 = 14 \int_0^1 A_0(r) \exp(-\tfrac{1}{2} jur^2) [20r^6 - 30r^4 + 12r^2 - 1] r dr$

$b_8 = 18 \int_0^1 A_0(r) \exp(-\tfrac{1}{2} jur^2) [70r^8 - 140r^6 + 90r^4 - 20r^2 + 1] r dr$

$b_{10} = 22 \int_0^1 A_0(r) \exp(-\tfrac{1}{2} jur^2) [252r^{10} - 630r^8 + 560r^6 - 210r^4 + 30r^2 - 1] r dr$

APPENDIX B: THE LOMMEL V_n FUNCTIONS

The Lommel V_n functions discussed explicitly in Ref. 2, have been used in Eq. (24a) of the text in a somewhat similar but slightly modified fashion. The V_n functions $V_0(u, v)$ and $V_1(u, v)$ as used in Eq. (24a) of the text are given by

$$V_0(u, v) = J_0(v) - (v/u)^2 J_2(v) + (v/u)^4 J_4(v) - \dots , \quad \text{(B1)}$$

and

$$V_1(u, v) = (u/v) J_1(v) - (v/u)^3 J_3(v) + (v/u)^5 J_5(v) - \dots , \quad \text{(B2)}$$

where the $J_n(v)$'s are the appropriate nth-order Bessel functions of the first kind.

[1] S. Adeniyi Adekola, "Influence of echo carrier-frequencies and antenna-dimensions on the performance of echosonde antennas," J. Acoust. Soc. Am. 60, S69(A) (1976).

[2] S. A. Adekola, "Toward a more general integral formulation of the pressure field of an echosonde aperture antenna," J. Acoust. Soc. Am. 60, 230–239 (1976).

[3] S. Adeniyi Adekola and Dean T. Davis, "The effects of phase-front distributions on echosonde antenna radiation patterns," J. Radio Sci. 12, 11–22 (1977).

[4] F. F. Hall, Jr. and J. W. Wescott, "Acoustic antennas for atmospheric echo sounding," J. Acoust. Soc. Am. 56, 1376–1382 (1974) (also private communications).

[5] O. N. Strand, "Numerical study of the gain pattern of a shielded acoustic antenna," J. Acoust. Soc. Am. 49, 1698–1703 (1971).

[6] C. Gordon Little, "Acoustic sounding of the lower atmosphere," Proc. IEEE 57, 571–578 (1969).

[7] L. G. McAllister, J. R. Pollard, A. R. Maloney, and P. J. R. Shaw, "Acoustic sounding—A new approach to the study of atmospheric structure," Proc. IEEE 57, 579–587 (1969).

[8] D. W. Beran, "Acoustic echo sounding systems: their potential in forest fire control and research," J. For. 73, 633–639 (1975).

[9] A. Spizzichino, "Discussion of the operating conditions of a Doppler sodar," J. Geophys. Res. 79, 5585–5591 (1974).

[10] D. W. Beran, "Acoustics: A new approach for monitoring the environment near airports," (Am. Inst. Aeronautics and Astronautics), J. Aircr. 8, 934–936 (1971).

[11] D. E. Barrick and M. W. Evans, "Implementation of coastal current-mapping HF radar system progress report no. 1," NOAA Tech. Report ERL 373-WPL-47 (Boulder, CO, July 1976), 64 pp.

[12] H. W. Redlien, Jr., "Monopulse Operation with Continuously Variable Beamwidth by Antenna Defocusing," IEEE Trans. Antennas Propag. AP-16(4), 415–423 (1968).

[13] S. Cornbleet, "The diffraction fields of a non-uniform circular aperture," in Electromagnetic Theory and Antennas, edited by E. C. Jordan in International Series of Monographs on Electromagnetic Waves (Pergamon, New York, 1963), pp. 157–175.

[14] M. Born and E. Wolf, "Principles of optics," in Electromagnetic Theory of Propagation, Interference and Diffraction of Light (Pergamon, New York, 1959), pp. 434–438.

[15] E. H. Linfoot, Recent advances in optics (Oxford-Clarendon, Gt. Britain, 1955), pp. 51–54.

[16] Y. L. Luke, Integrals of Bessel functions (McGraw–Hill, New York, 1962), pp. 4–5, 18–26, 89–90.

[17] V. Mangulis, Handbook of Series for Scientists and Engineers (Academic, New York, 1965), pp. 17, 63.

[18] H. Ottersten, M. Hurtig, G. Stilke, B. Brümmer, and G. Peters, "Shipborne sodar measurements during Jonswap 2," J. Geophys. Res. 79, 5573–5584 (1974).

[19] P. A. Mandics and E. J. Owens, "Observations of the marine atmosphere using a ship-mounted acoustic echo sounder," J. Appl. Meteorol. 14, 1110–1117 (1975).

[20] P. A. Mandics, F. F. Hall, Jr., E. J. Owens, and D. Wylie, "Observations of the tropical marine atmosphere using an acoustic echo sounder during GATE," 16th Radar Meteor. Conf., April 22–24, Houston, Texas (published by Am. Meteor. Soc., Boston, MA), 257–259 (1975).

[21] S. Silver, "Microwave antenna theory and design," (Dover, New York, 1965), pp. 126, 190–196.

[22] J. D. Kraus and K. R. Carver, Electromagnetics (McGraw–Hill, New York, 1973), 2nd ed., pp. 601–604, 620–623.

[23] J. W. Wescott, Personal communications (1976).

[24] B. C. Willmarth, E. H. Brown, J. T. Priestley, and D. W. Beran, "Beam pattern measurements for large acoustic antennas," 16th Radar Meteor. Conf., April 22–24, Houston, Texas (published by Am. Meteor. Soc., Boston, MA), 278–281 (1975).

[25] J. C. Kaimal and J. W. Wescott, "An acoustic Doppler sounder for measuring wind profiles in the lower boundary layer," 17th Radar Meteor. Conf., Oct. 26–29, Seattle, Wash.; (published by Am. Meteor. Soc., Boston, MA), 290–296 (1976).

[26] R. G. Kouyoumjian, Personal communications (1975).

The effects of phase-front distributions on echosonde antenna radiation patterns

S. Adeniyi Adekola

Wave Propagation Laboratory, Environmental Research Laboratories, National Oceanic and Atmospheric Administration, Boulder, Colorado 80302

Dean T. Davis

Department of Electrical Engineering, The Ohio State University, Columbus, Ohio 43210

The effects of phase-front distributions on the radiation patterns of an echosonde (acoustic echo-sounding) antenna are studied. A radiation integral is used to compute an equivalent excitation at the transmitting antenna aperture at a height H above the illuminating aperture of smaller radius. A two-dimensional Fourier transform utilizing the Kirchhoff-Fresnel diffraction formula is used to obtain the far-field expressions. The results reported for linear, square-law, cubic, and periodic phase-front distributions, indicate that (while details of the antenna pattern depend upon the specific phase distribution used) all distributions tended to raise the sidelobes and broaden the mainlobe for stronger phase modulations. In some cases, the stronger phase modulations actually reduced the central portion of the mainlobe, producing a hollow conical beam. Some computed beam patterns at a carrier frequency of 2 kHz and with different phase modulation coefficients were compared with two recent sets of experimentally measured patterns. The agreement overall is good with any variations probably being due to the fact that the actual phase distributions on the antennas were not exactly known and also due to the lateral drifts that might be experienced by the tethered weather balloon supporting the microphone probe (used for some of the pattern measurements) as a result of wind breezes.

1. INTRODUCTION

For a better understanding of the atmospheric structure, there is a need to develop an efficient system for atmospheric turbulence detection and measurement. Acoustic waves are generally used for detection in turbulence since they tend to be more susceptible to variations in the atmosphere than electromagnetic waves such as microwaves or optical waves. *Little* [1969] points out that the refractive index for acoustic waves is 1000 times larger than that of electromagnetic waves. In addition, the bandwidth required by an echosonde system is 1,000,000 times less than the bandwidth of an electromagnetic system designed to probe the same volume of the atmosphere.

Some aspects of a radiating system applicable to non-ionized atmospheric sounding are considered in the present discussion. The emphasis is on acoustic waves as treated by other authors [*Derr et al.*, 1970; *Marshall et al.*, 1972; *McAllister*, 1968;

McAllister et al., 1969; *Little*, 1969; *Simmons et al.*, 1971]. However, the concepts are general and could be extended to the description of the radiation of electromagnetic waves (e.g., optical and microwaves). Doppler techniques (using three intersecting antenna beams sampling the same volume of the atmosphere) could permit the study of wind velocity distributions [*Beran et al.*, 1973, 1972; *Georges et al.*, 1972]. A formulation that would take distortions occurring in the radiation patterns into consideration, has been suggested by these authors. Some effects of distortions on the radiation patterns are treated in the present investigation. The antenna is a component part of the transmitter and receiver. The distortions produced in the antenna beams by the antenna configuration are of interest and these distortion effects are represented as phase error distributions over the illuminating aperture of the antenna. The effects of phase errors across the aperture on the mainlobe and sidelobes are considered. The phase-front distributions of interest are (a) linear, (b) square-law, (c) cubic, (d) periodic. A field-expedient antenna (set up in

the field and relatively easy to carry) is considered. The overall system could be a pulse-type atmospheric sounder.

The most desirable aperture field distributions are usually those in which the field is in phase across the aperture. For certain types of field distributions, there may be considerable departure from a uniform phase-front [*Jasik*, 1961]. In such cases, the need to investigate the effects of the phase distribution on the antenna radiation patterns becomes apparent. Antenna systems producing intersecting beams, such as those used in acoustic echo-sounding, belong to this group. Some of the above types of phase errors, e.g., linear, square-law, cubic, and periodic, may be inherent in the design of the antenna, and are usually dependent on antenna geometry. Phase-front errors may cause increases in sidelobe levels. For an array of radiating elements, the position and excitation errors of the elements in the array may also bring about phase errors. The phase errors may also be due to inability to illuminate the antenna aperture uniformly. From the ray optics point of view, phase errors may be incurred by the differences between direct rays and singly or doubly diffracted rays from objects in the environment of the echosonde antenna. These rays may add vectorially to create a phase interference pattern. A complete treatment of singly and doubly diffracted rays belongs to the realm of geometrical theory of acoustical diffraction (GTD) and will therefore not be considered in this article.

A treatment of typical phase distributions for the echosonde antenna, which is the major concern of this investigation, as stated above, does not appear to have been considered previously. Considerations in echosonde antenna studies have been primarily for zero phase, constant amplitude illuminations [*Strand*, 1971]. The phase-front distributions of interest are applied to a quasi-tapered, cylindrical anechoic structure with absorbing cuffs and operated at low acoustic carrier frequencies, although a horn reflector antenna shielded with fiberglass as the absorbent material could also be used.

2. THEORY

An approach similar to the method used by *Strand* [1971] for a three-dimensional model of the antenna is employed to obtain a radiation integral equation for the far field. The computational results are reported for a carrier frequency of 2 kHz and a frequency of 4 kHz for the contour plots. Other numerical results for the more commonly used carrier frequencies in acoustic radar work, namely 1, 3, 4, and 5 kHz, have been extensively considered by *Adekola* [1975]. Further integral formulations for the Fresnel zone fields which are expressed in closed forms using Lommel's series have also been considered [*Adekola*, 1976]. The Fresnel region representations are also suitable for computational techniques.

2.1. *Radiation integral for the echosonde antenna.* The Kirchhoff-Fresnel diffraction physical optics formula can be modified to produce the following radiation integral representation for an echosonde antenna:

$$P(\bar{R}) = \int_{S'} \{ P(\bar{R}')(\partial/\partial n') \, G_0(\bar{R}',\bar{R})$$

$$- \, G_0(\bar{R}',\bar{R})(\partial/\partial n') \, P(\bar{R}')] \, dS' \qquad (1)$$

where G_0 is the free-space Green's function, $P(\bar{R})$ is the component of the acoustic pressure field involved, $\bar{R} = (\rho,\phi,z)$ is the position vector to the field point, and $\bar{R}' = (\rho',\phi',z')$ is the position vector to the source point. The applicability of the formulation to scattering in a compressible fluid like the atmosphere and in an incompressible fluid like the ocean, justifies the use of the term "fluid-filled region" to describe both types of fluids. The present discussion deals with the former where the fluid is the atmosphere. Assuming a circularly symmetric source where z' is the axis of symmetry (e.g., see Figure 1), the source term $P(\bar{R}')$ is expressible in amplitude and phase as:

$$P(\bar{R}') = P(\rho',\phi',0) = A(\rho') \exp[j\Phi(\rho')] \qquad (2)$$

where $A(\rho')$ and $\Phi(\rho')$ are the amplitude and phase distributions respectively, and $\bar{R}' = (\rho',\phi',0)$ in the cylindrical coordinate system. Notice that (2) is independent of ϕ'. The source distribution could be either a pressure source or a velocity source in as much as it can be represented in amplitude and phase as indicated in (2) above. Using approximations similar to those employed by *Silver* [1965], the surface integral of (1) simplifies to:

$$P(\bar{R}) = \frac{jk}{4\pi} \int_0^{2\pi} \int_0^{\rho(\max)} A(\rho') \exp[j\Phi(\rho')]$$

$$\cdot \, \{[\exp(-jkr')]/r'\}(1 + \cos\psi)\rho' \, d\rho' \, d\phi' \qquad (3)$$

where $\rho(\max)$ is the radius of the aperture of the antenna, $r' = |\bar{R} - \bar{R}'|$ is the distance from the source point to the field point, $\cos\psi = (z - z')/|\bar{R} - \bar{R}'|$, and the variable of integration ϕ' is measured counter clockwise from the y axis for convenience. Equation (3) has also been used to obtain nearfield expressions for the echosonde antenna [Adekola, 1975, 1976].

2.2. *Far-field formula.* The physical configuration of the antenna is shown in Figure 1. The antenna geometry is that of a frustrum of a right circular cone which tapers from a smaller aperture of radius $R(\max)$ at the lower base to a larger aperture of radius $R_s(\max)$ at the upper base. The shielding absorbing cuff of the antenna is of height H feet. Upon transmission, the antenna is illuminated at the lower aperture and the signal radiation is at the larger aperture. For the purposes of analysis, the antenna is assumed to have perfectly absorbing walls on the inside and perfectly reflecting ones on the outside. Plywood could be used for the construction of the outside wall to provide a rigid structure and also for the attenuation of external noise interference. This could be followed by a layer of leadsheet for further attenuation of external noise interference. The inside of the antenna could be lined with urethane foam to achieve

Fig. 1. The tapered antenna structure.

good sound absorption to minimize internal reflections. Further discussions on the use of these materials for shielding echosonde antennas have been given by *Tombach et al.* [1973].

For notational simplicity, ρ, $P(\rho)$, and ψ are identically defined as R, $E(R)$, and θ respectively. Also, the primes on the coordinate variables are dropped for ease of programming purposes. Then, the integral equation (3) can be applied to the antenna configuration of Figure 1 to obtain the equivalent excitation $E_h(R_s)$ in amplitude and phase at the transmitting antenna aperture as:

$$E_h(R_s) = A(R_s)\exp[j\Phi(R_s)] = \frac{j}{\lambda}\int_0^{2\pi}\int_0^{R(\max)} A(R)$$

$$\cdot \exp[j\Phi(R)]\exp[-j(2\pi/\lambda)(d-H)]\Gamma(d)R\,dR\,d\phi$$

(4)

where R_s is the variation along the transmitting aperture of radius $R_s(\max)$, $R(\max)$ is the radius of the illuminating aperture, $A(R_s)\exp[j\Phi(R_s)]$ or $E_h(R_s)$ is the equivalent excitation at the transmitting aperture in amplitude and phase (see Figure 1), and $\Gamma(d)$ is the decay of the acoustic signal with distance d given by:

$$\Gamma(d) = (1 + \cos\theta)/2d = (1 + H/d)/2d \qquad (5)$$

where $\cos\theta = H/d$. The distance d inside the antenna structure, as shown in Figure 1, is a function of R and ϕ expressed as:

$$d(R,\phi) = [R^2\sin^2\phi + (R_s - R\cos\phi)^2 + H^2]^{1/2} \qquad (6)$$

The quantity $\exp(jkH)$ in (4) has been introduced in order to start from zero phase at the center of the upper aperture. The equivalent excitation at the transmitting aperture is a result of the illumination at the lower aperture represented in amplitude and phase by $A(R)\exp[j\Phi(R)]$. Equation (4) is used to study the effects of various phase variations $\Phi(R)$ at the lower aperture on the far-field radiation patterns.

Equation (3) can also be used to integrate along the transmitting aperture to obtain the far-field expression. Using the usual far-field approximations which can be found elsewhere [*Silver*, 1965; *Adekola*, 1975, 1976], and taking D as the distance from the center of the transmitting aperture to the far-field point, then the far-field expression is given by:
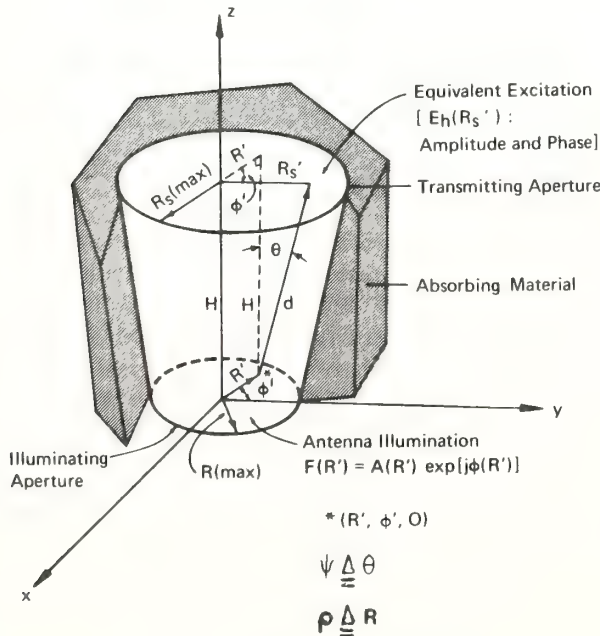
$$E(\theta) = [jk(1 + \cos\theta)/2D]\exp(-jkD)$$

$$\cdot \int_0^{R_s(\max)} A(R_s)\exp[j\Phi(R_s)]J_0(kR_s\sin\theta)R_s\,dR_s \quad (7)$$

where the two-dimensional expression (4) which computes the equivalent upper aperture excitation $E_h(R_s)$ serves as the excitation to the far-field expression, and it is represented in amplitude and phase by $A(R_s)\exp[j\Phi(R_s)]$ in the integrand of (7). J_0 is the zero-order Bessel function of the first kind, θ is the angle off the vertical axis of the antenna in degrees, $(1 + \cos\theta)/2$ is the obliquity factor, and an $\exp(j\omega t)$ time variation has been assumed and suppressed. Expression (7) is then used to compute the relative far-field signal strength by computing its normalized quantity as:

$$\text{Relative Power Pattern (dB)} = 20\log_{10}\left|\frac{E(\theta)}{E(0)}\right| \quad (8)$$

where $E(0)$ is the on-axis value of the field. Thus, (8) is the dB reduction of the acoustic far-field signal strength from the on-axis value.

3. PHASE-FRONT DISTRIBUTIONS

In the two-dimensional integral formula (4), the expression $A(R)\exp[j\Phi(R)]$, which is the illumination function in amplitude and phase at the lower illuminating aperture, will be used to study the effects of different phase-front distributions on the radiation patterns. The parameter β is designated as the phase coefficient. It is used in studying the effects of the phase-front modulations on the radiation patterns. The parameter is assigned various values and the effects of the variations of the parameter are studied with respect to the response of the echosonde antenna patterns to high and low values of the parameter. Sensitivity studies of the phase-front distributions could be considered by using small values of β. The simplest cases of the phase-front distributions are those in which the amplitude excitations have constant values. For simplicity, these distributions are only functions of the radial variation R. The linear phase distribution is represented as

$$A(R)\exp[j\Phi(R)] = \exp(-j\beta R) \quad (9)$$

the square-law distribution is

$$A(R)\exp[j\Phi(R)] = \exp(-j\beta R^2) \quad (10)$$

the cubic phase distribution is

$$A(R)\exp[j\Phi(R)] = \exp(-j\beta R^3) \quad (11)$$

and the periodic phase distribution is

$$A(R)\exp[j\Phi(R)] = \exp[j\cos(\beta R)] \quad (12)$$

In all the above cases, the amplitude distribution assumes a constant value of unity. The computation becomes more complicated when the amplitude illumination $A(R)$ is other than uniform. Thus, if $A(R)$ is gaussian for example, the contributions of the illuminations become for the

linear case:
$$A(R)\exp[j\Phi(R)] = \exp(-0.25R^2)\exp(-j\beta R) \quad (13)$$
square-law case:
$$A(R)\exp[j\Phi(R)] = \exp(-0.25R^2)\exp(-j\beta R^2) \quad (14)$$
cubic case:
$$A(R)\exp[j\Phi(R)] = \exp(-0.25R^2)\exp(-j\beta R^3) \quad (15)$$
periodic case:
$$A(R)\exp[j\Phi(R)] = \exp(-0.25R^2)\exp[j\cos(\beta R)] \quad (16)$$

The periodic phase contribution (16) is used in the present analysis to consider sensitivity effects of the phase contributions. The effects of the phase-front distributions are studied using values of the phase coefficients given by $\beta = 0$, $\pi/4$, $\pi/2$, $3\pi/4$, and π. The effects of shielding the echosonde antenna on the radiation patterns have some degree of similarity to the effects of the variations of the phase coefficients β on the radiation patterns. The latter criterion has also been previously discussed [*Adekola and Davis*, 1975; *Adekola et al.*, 1975].

4. RADIATION PATTERN CALCULATIONS

The expressions of the previous sections for the echosonde antenna are employed to calculate the radiation patterns of the antenna. The computational results were obtained on the OSU IBM 370/165 computer using Fortran IV. The universal curves produced are redrafted for comparison. Equation (7) gives the one-dimensional integral used for the far-field pattern calculations, where (8) gives the radiation power pattern in decibels. Proper attention is given to the oscillations of the integrand for accuracy in the computations. The truncation errors that may be incurred by not integrating all the way to the aperture edge are taken into consideration by properly truncating and floating the number of oscillations of the integrand accordingly. Equally

spaced points are used for the integral summation intervals and these are 0.10 and 0.15 for the lower and upper apertures, respectively. The more common trapezoidal method of integration could also be used. The output of the subroutine which computes (4) is used as the input to the second subroutine which computes (7). The first subroutine provides the equivalent excitation field distribution in amplitude and phase at a height H feet above the lower aperture. The equivalent upper aperture distribution serves as the source function used in (7) for the far-field pattern computations.

In Figures 2–7, the same antenna size is used with height $H = 12$ ft, the illuminating aperture radius $R(\text{max}) = 2$ ft, and the transmitting aperture radius $R_s(\text{max}) = 6$ ft. Also, the carrier frequency of 2 kHz (wavelength $\lambda = 0.55$ ft) is the same

Fig. 3. The equivalent upper aperture excitation in amplitude and phase for the curves of Figure 5; linear phase-front distribution, $\beta = \pi/4$, $\pi/2$, $3\pi/4$, and π; with gaussian tapered illumination.

for these figures. Figures 2, 3, and 4 depict the equivalent excitations at the upper transmitting aperture computed from (4) and used as the source functions in (7) to produce the relative gain patterns of Figure 5. The gaussian tapered distribution with zero phase at the illuminating aperture producing the plots of Figure 2 is of the form

$$A(R) = \exp(-R^2/4) \qquad (17)$$

the linear phase-front distribution with gaussian amplitude taper at the illuminating aperture giving the equivalent transmitting aperture excitations of Figure 3 is given by

$$A(R)\exp[j\Phi(R)] = \exp(-R^2/4)\exp(-j\beta R) \qquad (18)$$

while the distribution at the illuminating aperture producing the equivalent transmitting aperture ex-

Fig. 2. The equivalent upper aperture excitation in amplitude and phase for the curves $\beta = 0$ of Figure 5; with gaussian tapered illumination-zero phase.
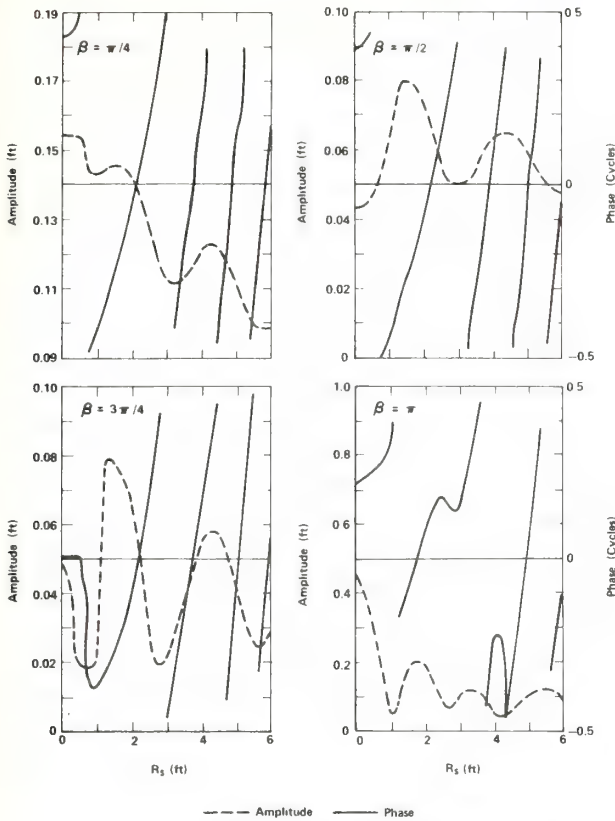
Fig. 4. The equivalent upper aperture illumination in amplitude and phase for the four curves of Figure 5; quadratic phase $\beta = \pi/4$, $\pi/2$, $3\pi/4$, and π; with gaussian tapered illumination.

citations of Figure 4 is of the form

$$A(R)\exp[j\Phi(R)] = \exp(-R^2/4)\exp(-j\beta R^2) \qquad (19)$$

with the phase coefficient β taking the values of $\beta = \pi/4$, $\pi/2$, $3\pi/4$, and π respectively. Figure 6 shows the equivalent distributions at the transmitting aperture used for the patterns of Figure 7, for the value of $H = 12$ ft. The cubic phase-front distribution at the illuminating antenna aperture giving the equivalent excitations of Figure 6 is of the form

$$A(R)\exp[j\Phi(R)] = \exp(-R^2/4)\exp(-j\beta R^3) \qquad (20)$$

The relative gain patterns for the value of $H = 8$ ft are also depicted in Figure 7. Adequate care is taken in computing the two-dimensional integration of (4) since any errors in the computation of this excitation quantity would be reflected in (7),

which in turn may give inaccurate or false far-field patterns.

In the relative far-field patterns of Figures 5 and 7, it is realized that the phase coefficient β can be used to regulate the 90° sidelobe levels. The 90° region corresponds to the ground level and the sidelobe level in the region is reduced to about 47 dB below the center value, which is the on-axis value. The figures are largely self-explanatory and are reported for a wavelength of $\lambda(2\text{ kHz}) = 0.55$ ft. A total of 70 dB reduction of the sidelobe level in the important 20° region between 70° and 90° may be obtained by protecting the antenna with shielding cuffs and by proper choice of phase distribution. The phase coefficient β is another
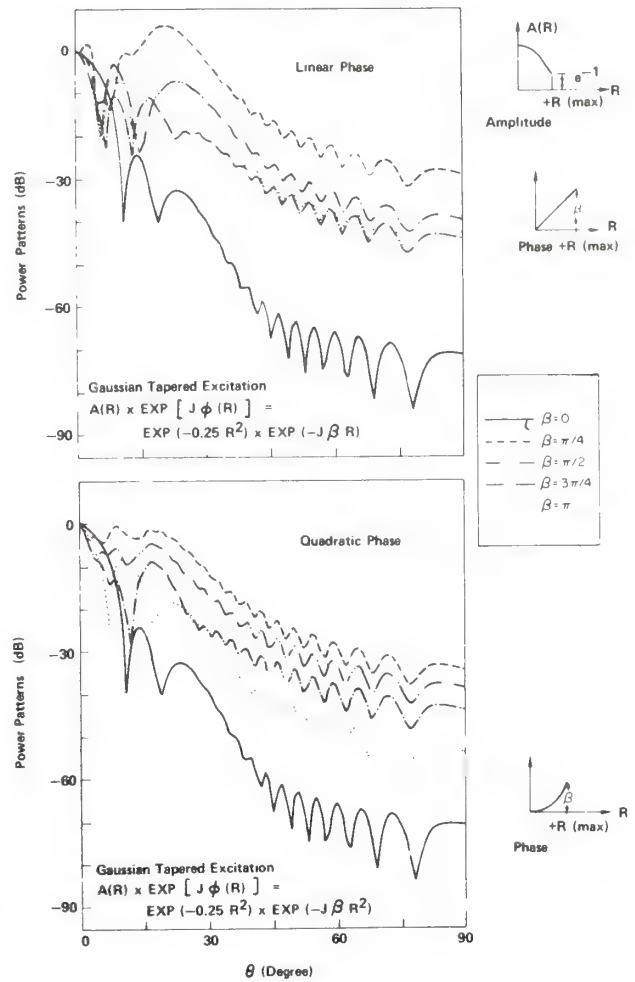
Fig. 5. Relative gain patterns for $H = 12$ ft. Notice that the main beam is nullified for the linear phase, $\beta = \pi/4$. The resulting pattern is conical in shape; $R \leq R(\text{max})$.

parameter for regulating the intensity of the sidelobe radiation in the same manner as the shielding. Notice that the 90° sidelobe levels are highly dependent on or sensitive to the combination of the amplitude and phase at the edge of the upper aperture (see the entries of Table 1 for the quadratic phase distribution). The effects of the shielding absorbing cuffs on sidelobe suppressions are substantiated in Figure 8. The high sidelobes exhibited without the cuffs are well suppressed when the antenna is shielded with absorbing cuffs particularly in the important 20° region adjacent to the ground. The same antenna size used in Figures 2–7 is employed for the curves of Figure 8. The antenna half-flare angle (slope of shield wall from vertical) is 18.43°. A frequency of 2 kHz is used.

Fig. 7. Relative gain patterns for $H = 12$ ft, and $H = 8$ ft, cubic phase-front distributions and gaussian tapered amplitude illumination. Notice the nonmonotone behaviors of the 90° sidelobe levels; $R \leq R(\max)$.
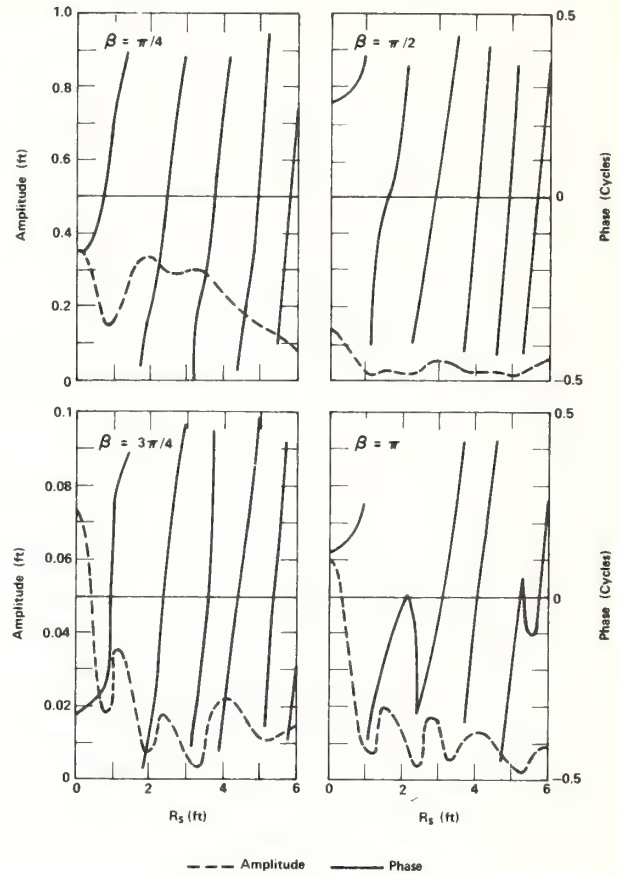

Fig. 6. The equivalent upper aperture excitations in amplitude and phase for the curves of Figure 7; cubic phase-front distribution, $\beta = \pi/4$, $\pi/2$, $3\pi/4$, and π; with gaussian tapered illumination.

TABLE 1. Truncation values of the equivalent excitation at the edge of the upper transmitting aperture for a gaussian tapered amplitude illumination with quadratic phase distribution at the lower illuminating aperture, i.e., $A(R)\exp[j\Phi(R)] = \exp(-R^2/4)\exp(-j\beta R^2)$.

Phase coefficients (β) (rad/ft²)	Amplitude (ft)	Phase (cycles)
0	0.020	−0.24
$\pi/4$	0.095	0.15
$\pi/2$	0.048	−0.03
$3\pi/4$	0.030	0.06
π	0.100	−0.06
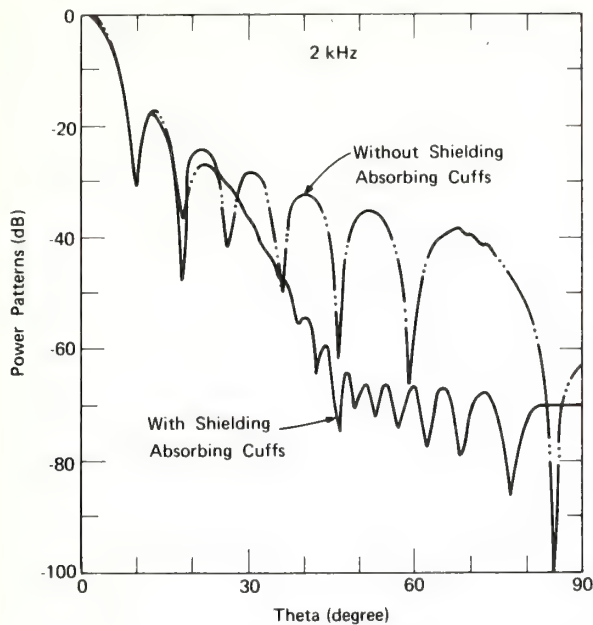
Fig. 8. The effects of the shielding absorbing cuffs on sidelobe suppressions.

4.1 Comparisons between theory and experiment for the directional characteristics of the echosonde antenna.

The computer-predicted radiation patterns for the echosonde antenna are compared with some experimental measurements in this section. The comparisons between theory and experiment are depicted in Figure 9. The experimental measurements of Figure 9a were obtained from the experimental data reported by *Hall and Wescott* [1974, Fig. 6]. The antenna was aimed in a horizontal direction while measuring the experimental far-field gain pattern of Figure 9a [*Hall and Wescott*, 1974]. The measurements were made with a 3.94 ft diameter antenna with a shielding material of height 3.94 ft. Several experimental measurements were averaged to produce the smooth experimental curve shown in Figure 9a, using a carrier frequency of 2 kHz. The theoretical curve is obtained from an antenna structure of height 3.94 ft, with a transmitting aperture of 3.94 ft diameter and an illuminating aperture of diameter 2.64 ft. A gaussian tapered illumination with a cubic phase-front distribution of the form

$$A(R)\exp[j\Phi(R)] = \exp(-0.25R^2)\exp(-j\pi R^3) \qquad (21)$$

is used for evaluating the antenna gains. The antenna

half-flare angle is 9.51°, and the computed 3 dB (half-power) beamwidth is 12.91°. This value of the half-power beamwidth is desirable in acoustic remote sensing. As already pointed out by *Hall and Wescott* [1974], a 3 dB beamwidth less than 4° or 5° is not worthwhile because atmospheric wind gradients and temperature refractions occasionally influence the backscattered wavefronts in such ways as to come back at off-axis angles of several degrees from the vertical axis of the antenna.
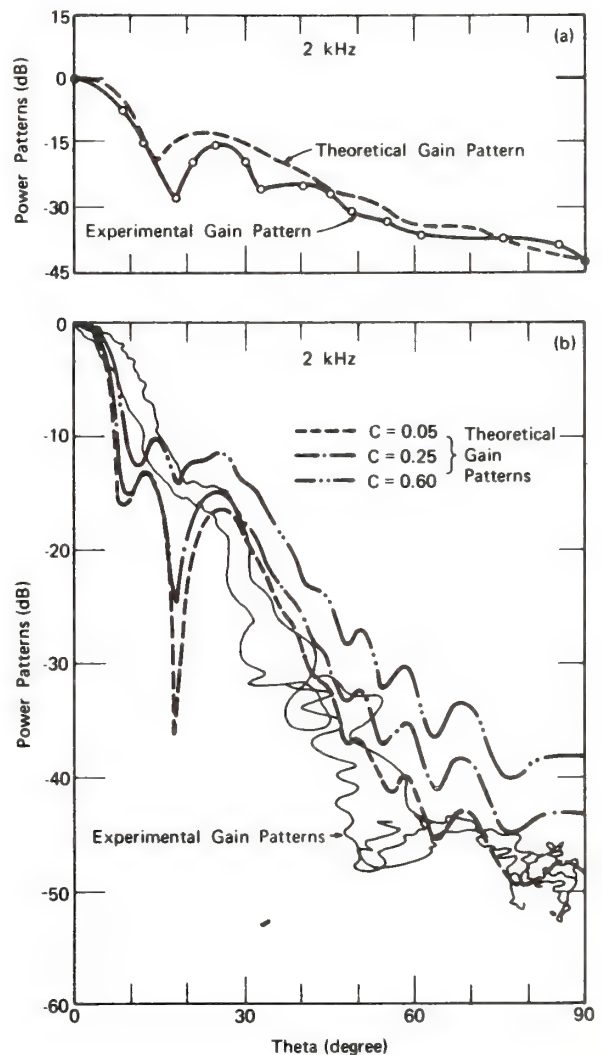
Fig. 9. Comparisons between theory and experiment: (a) computer-predicted radiation pattern and measurements of *Hall and Wescott* [1974, Figure 6] with $H = 3.94$ ft. (b) Computer-predicted radiation patterns and recent measurements registered on strip-chart recorders (J. W. Wescott, personal communication, 1976) with $H = 6.94$ ft.

Two recent experimental measurements (J. W. Wescott, personal communication, 1976) are compared with theory in Figure 9b. The experimental measurements were made with the echo-sonde system now located at White Sands Missile Range in New Mexico, at an operating carrier frequency of 2 kHz and 1 w electrical input power for the transmitter. Briefly, the method of measurements was by the movements of a microphone probe in a fixed arc at the antenna far-field, with the antenna aimed in a vertical direction. The microphone probe was supported and controlled by: a weather balloon (1200 gm), two fixed-length tethers, and a variable-length tether. Further details of this method of far-field pattern measurements have been discussed by *Willmarth et al.* [1975]. After the probe preamplifier output was bandpass filtered and rectified by a wave analyzer, the resulting log output was then registered on strip-chart recorders giving the experimental patterns of Figure 9b. The unsteady nature of the experimental patterns was due to mean wind breezes which might have caused the balloon to experience lateral drifts during measurements, thereby affecting the output as shown in the figure. If measurements were made under (rare) calm weather conditions, such problems would be alleviated. The antenna size used for the measurements is of height 6 ft, with transmitting and illuminating aperture diameters of sizes 6.94 and 4.04 ft respectively. The computer-predicted theoretical gain patterns for the same antenna dimensions are also shown in Figure 9b. The excitation at the illuminating aperture of the antenna used for the theoretical curves is a gaussian tapered illumination with cubic phase-front distribution of the form

$$A(R)\exp[j\Phi(R)] = \exp(-cR^2)\exp(-j \cdot 75\pi R^3) \quad (22)$$

where c is a dimensionless constant whose three different values used are as shown in the legend of the figure and are 0.05, 0.25, and 0.60 respectively. The antenna half-flare angle is 13.59°. The 3 dB beamwidths for the two experimental measurements are 10° and 16° respectively (i.e., giving 13° beamwidth when averaged), while the computed theoretical 3 dB beamwidths are 8°, 10°, and 12.8° for $c = 0.05$, 0.25, and 0.60 respectively.

4.2. *Contour plots.* In the contour plots of Figures 10 and 11, the angles with which the plots are viewed have been predetermined. These are taken as
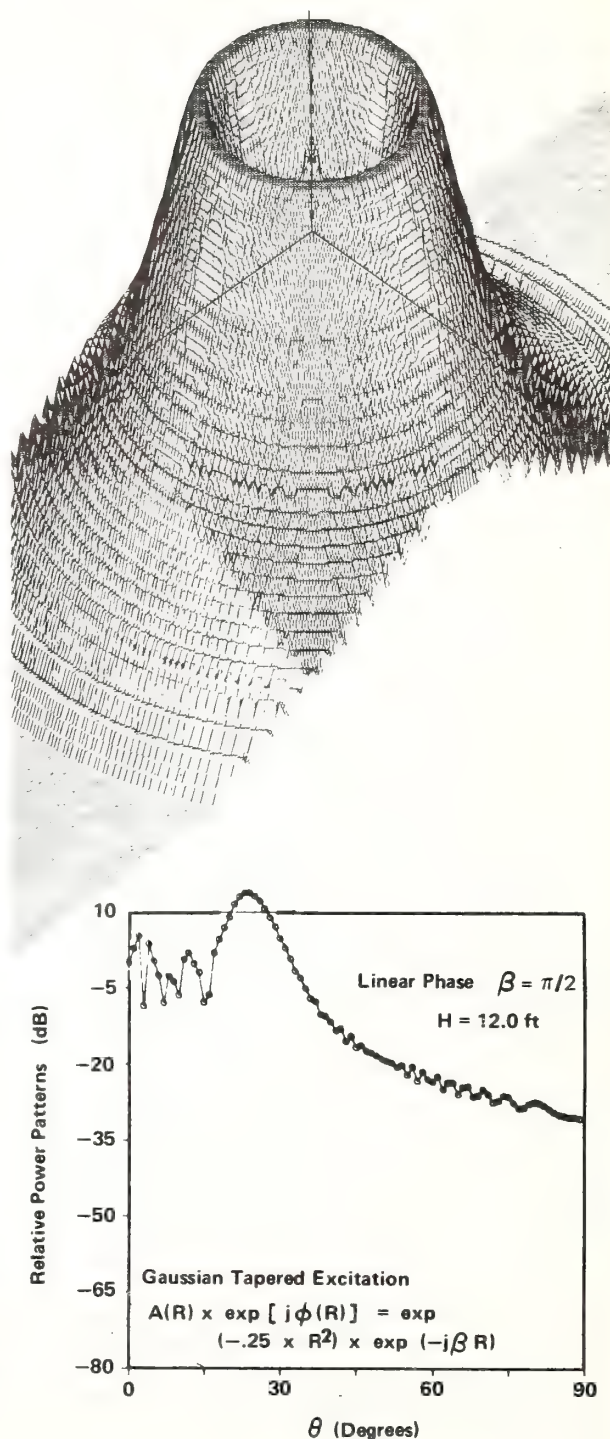
Fig. 10. Contour plot for the conical beam pattern resulting from the effects of linear phase-front distribution. The main-lobe is nullified by the phase distribution.
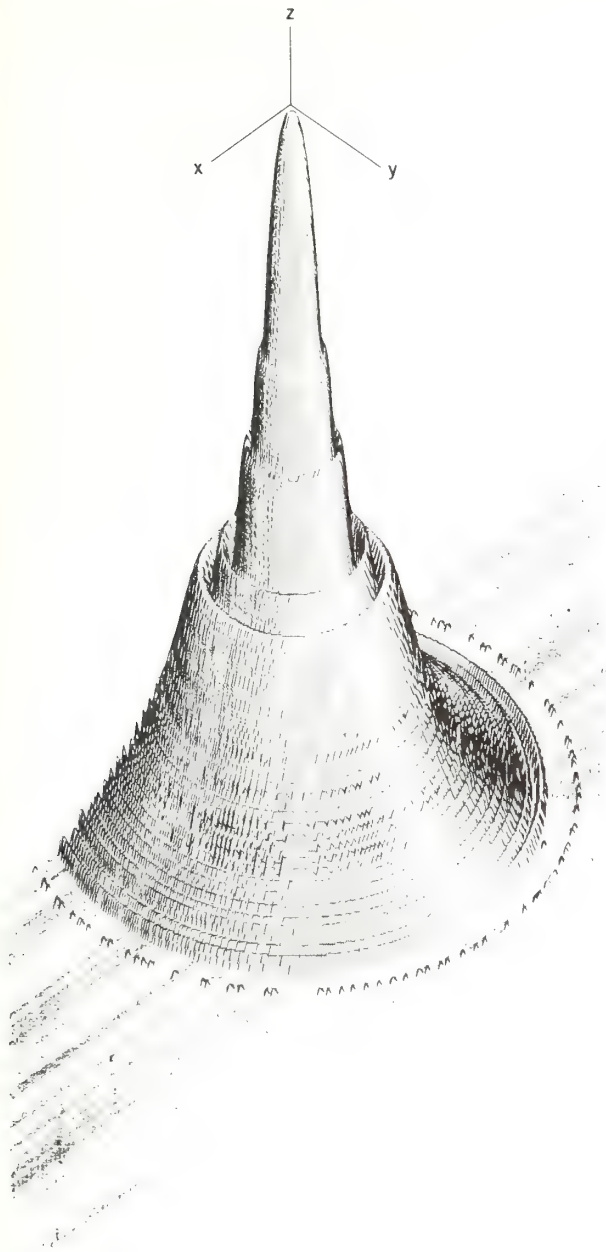
Fig. 11. The contour plot for the highly tapered pattern (with significant reduction in the 90° sidelobe level) arising from the periodic phase distribution.

$$(\theta_0, \phi_0) = (45°, 45°) \qquad (23)$$

where (θ_0, ϕ_0) are the angles of the spherical coordinate system. However, the computer program for the contour plots is a general one and any desired viewing angles may be used. The full details of

the contour plot program can be found elsewhere [*Adekola*, 1975]. The relative positions of the sidelobes are clearly shown in the contour plots. The effects of tapered aperture field distributions on the radiation patterns become apparent in the contour plots which serve as the pattern visualization of the acoustic echo-sounding antenna. In some cases, the stronger phase modulations produce conical beam distortion effects, the mainlobe being nullified by the phase modulations, while other minor sidelobes still remain. The gaussian tapered illumination with linear phase-front distribution producing the hollow conical beam distortion shown in Figure 10 is of the form:

$$A(R)\exp[j\Phi(R)] = \exp(-0.25R^2)\exp(-j\pi R/2) \qquad (24)$$

with an operating carrier frequency of 4 kHz (wavelength $\lambda = 0.27$ ft). The shielding is of height 12 ft, with the antenna radii of 6 and 2 ft for the transmitting and illuminating antenna apertures respectively. The 90° sidelobe level has a relative power level of -30.69 dB. The two-dimensional relative power pattern is shown in the legend of the figure.

The highly tapered pattern of Figure 11 arises from the periodic phase distribution with a $\cos^2$ on a pedestal tapered amplitude illumination of the form

$$A(R)\exp[j\Phi(R)] = [0.02 + \cos^2(\pi R/4)]$$
$$\cdot \exp[j\cos(\pi R/16)] \qquad (25)$$

Four major sidelobes with several smaller sidelobes are produced. The antenna dimensions are the same as those employed with Figure 10, and the operating carrier frequency is also at 4 kHz.

5.   CONCLUDING REMARKS

It has been shown that the tapered acoustic antenna structure considered here is a good model for studying the characteristics of the echosonde antenna. The computational results are in good accordance with available experimental data [*Hall and Wescott*, 1974; J. W. Wescott, personal communication, 1976].

The parameter H, which is the height of the echosonde antenna in feet, could be used to control the sidelobe levels in the 20° region within 70° through 90°, where 90° corresponds to the ground level. Most of the noise that may be irritating to

the nearby populace and the most significant radiation from the sidelobes come within this range. The present results are quite encouraging and further work would produce more information on the characteristics of this radiator particularly concerning beam scanning useful in acoustic radar work, and the near-field characteristics. The present consideration could be extended to include acoustic antenna arrays (with the necessary spacing considerations to prevent overlap), and the use of Dolph-Tchebyscheff polynomials for reduced and equal sidelobe levels.

The details of the pattern behaviors depend upon the specific phase distributions used, all phase distributions tended to raise the sidelobes and broaden the mainlobe for stronger phase modulations. The nonmonotone behaviors of the 90° sidelobes are depicted in the figures. Hollow conical beam distortions of the radiation patterns are produced by the stronger phase modulations in some cases, and the contour plot is shown for the linear phase modulation case. As depicted in the contour plot of Figure 10, the mainlobe disappears and it is replaced by the hollow region of the conical beam. For some phase modulations, the bifurcation appearing produces two peaks with a dip in the form of a valley in between (analogous to the bifurcation in circuit theory for overcoupled circuits). For the cubic phase distortion effect, the gain is reduced in addition to some broadening of the main beam. Operational techniques could also be used to compute the integrals involving the effects of the phase errors. The cubic phase-front errors could arise if the feed is moved off the axis of the antenna. The square-law phase modulations smooth the nulls and raise the sidelobe levels while the mainlobe fattens out. As the sidelobes blend with the mainlobe, they show as shoulders instead of appearing as distinct sidelobes. There is also a reduction in directivity for the quadratic phase errors. The effect of sinusoidal phase distribution is depicted in the contour plot of Figure 11. The 90° sidelobe levels are sensitive to small values of the phase coefficient β. The sidelobes coalesce with the mainlobe in some cases. The most significant effects of the periodic phase-front errors are on the sidelobes as shown in Figure 12. For weaker phase modulation coefficients, sharp nulls of the lower sidelobes are produced. Conical distortion effects are also present for β equals π/4 in this case. The antenna dimensions used for the plots
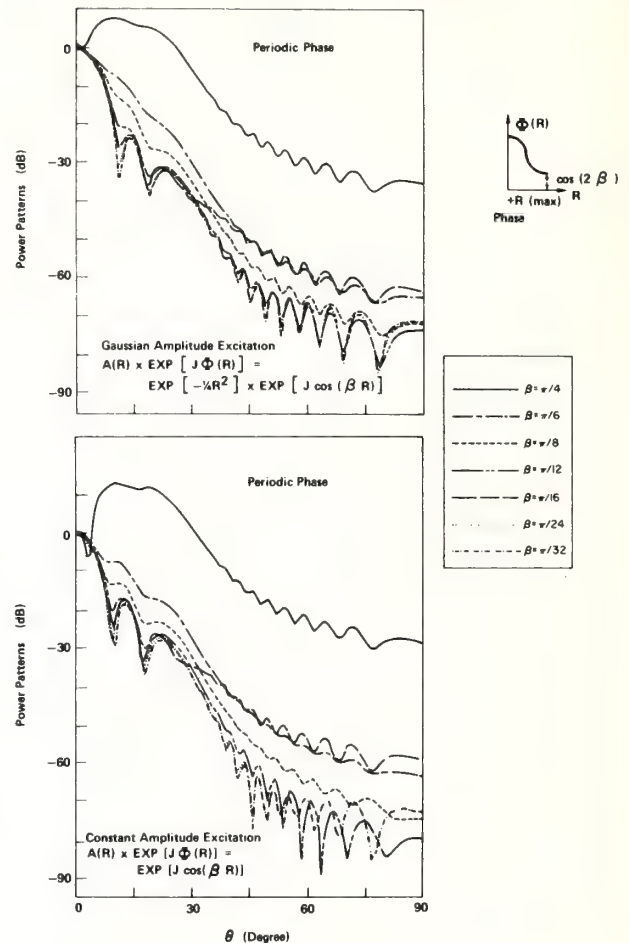
Fig. 12. The effects of periodic phase-front errors on the relative gain patterns of the shielded acoustic aperture antenna. The effects are shown for both the gaussian and constant amplitude excitations.

of Figure 12 are the same as those of Figure 11, but a carrier frequency of 2 kHz is employed instead of 4 kHz.

REFERENCES

Adekola, S. A. (1975), A Study of the radiation patterns of a shielded quasi-tapered aperture antenna for acoustic echo-sounding, Ph.D. Thesis, 301 pp., Department of Electrical Engineering, The Ohio State University, Columbus, Ohio.

Adekola, S. A., and D. T. Davis (1975), Effects of phase-front distributions and shielding on acoustic antenna patterns using a tapered cylindrical structure as a model, Proc. National USNC/URSI Meeting, University of Colorado, Boulder, pp. 238–239, October 1975.

Adekola, S. A., D. T. Davis, and T. A. Seliga (1975), Characteristics of a quasi-tapered acoustic radiator, Proc. Third International Conf. Atmospheric Acoustics, session III, p. 7, York University, Ontario, June 1975.

Adekola, S. A. (1976), Toward a More General Integral Formulation of the Pressure Field of an Echosonde Aperture Antenna, *J. Acoust. Soc. Amer.*, *60*(1), 230–239.

Beran, D. W., and S. F. Clifford (1972), Acoustic Doppler measurements of the total wind vector, Proc. AMS Second Symp. Meteorol. Obs. and Inst., pp. 100–109, San Diego, California.

Beran, D. W., W. H. Hooke, and S. F. Clifford (1973), Acoustic Echo Sounding Techniques and Their Application to Gravity-Wave, Turbulence, and Stability Studies, *Boundary-Layer Meteorol.*, *4*, 133–153.

Derr, V. E., and C. G. Little (1970), A Comparison of remote sensing of the clear atmosphere by optical, radio and acoustic radar techniques, *Appl. Opt.*, *9*(9), 1976–1992.

Georges, T. M., and S. F. Clifford (1972), Acoustic sounding in a refracting atmosphere, *J. Acoust. Soc. Amer.*, *52*(5), Part 2, 1397–1405.

Hall, F. F., Jr., and J. W. Wescott (1974), Acoustic antennas for atmospheric echo sounding, *J. Acoust. Soc. Amer.*, *56*, 1376–1382.

Jasik, H. (1961), *Antenna Engineering Handbook, First Ed.*, pp. 2-36 to 2-41, McGraw-Hill, New York.

Little, C. G. (1969), Acoustic methods for the remote probing of the lower atmosphere, *Proc. IEEE*, *57*(4), 571–578.

Marshall, J. M., A. M. Peterson, and A. A. Barnes, Jr. (1972), Combined radar-acoustic sounding system, *Appl. Opt.*, *11*(1), 108–112.

McAllister, L. G. (1968), Acoustic sounding of the lower atmosphere, *J. Atmos. Terr. Phys.*, *30*, 1439–1440.

McAllister, L. G., J. R. Pollard, A. R. Mahoney, and P. J. R. Shaw (1969), Acoustic sounding—A new approach to the study of atmospheric structure, *Proc. IEEE*, *57*(4), 579–587.

Silver, S. (1965), *Microwave Antenna Theory and Design*, pp. 165–167, Dover, New York.

Simmons, W. R., J. W. Wescott, and F. F. Hall, Jr. (1971), Acoustic echo sounding as related to air pollution in urban environments, *NOAA Tech. Rep. ERL 216-WPL 17*, 77 pp., National Oceanic and Atmospheric Administration, Environmental Research Laboratories, Boulder, Colorado.

Strand, O. N. (1971), Numerical study of the gain pattern of a shielded acoustic antenna, *J. Acoust. Soc. Amer.*, *49*(6), Part 1, 1698–1703.

Tombach, I., P. B. MacCready, and L. Baboolal, (1973), Use of a Monostatic Acoustic Sounder in Air Pollution Diffusion Estimates, Proc. 2nd Joint Conference on Sensing of Environmental Pollutants, Washington, DC, p. 140, December 1973. (Available from Instrument Soc. Am.; Instrumentation-Systems-Automation, 400 Stanwix Street, Pittsburgh, Pa. 15222.)

Willmarth, B. C., E. H. Brown, J. T. Priestley and D. W. Beran (1975), Beam pattern measurements for large acoustic antennas, Proc. 16th Radar Meteorology Conf., Houston, Texas, pp. 278–281, April 1975. (Published by the American Meteorological Society, Boston, Massachusetts.)

Toward a more general integral formulation of the pressure field of an echosonde aperture antenna*

S. A. Adekola[†]

Wave Propagation Laboratory, NOAA Environmental Research Laboratories, Boulder, Colorado 80302
(Received 15 February 1976)

The basis for improvements in acoustic echo-sounding (echosonde) antenna characteristics is analyzed. The results are based on a more general radiation integral formulated from the time-independent wave equation for an acoustic wave, using a cylindrical antenna as a model. Employing common forms of aperture field distributions across the upper transmitting aperture of the antenna, a Fresnel-region field quantity, which is expressed in a closed form using Lommel's series, is obtained. An echosonde antenna design meeting the requirements of previous specifications is made from the numerical results of the farfield patterns in order to show the validity of the results. The design permits the operation of the antenna in urban environments since irritating noise levels are kept low. The height of the antenna shielding cuffs reduces the 90° side-lobe level (ground level) by 3.85 dB at the height of 1 ft through 40 dB at 13 ft. A 90° side-lobe reduction of 38.6 dB, which agrees with predictions, is obtained for the more appropriate height of 12 ft; diameters of 4 and 12 ft for the lower illuminating—and upper transmitting—apertures, respectively. The results, reported for acoustic carrier frequencies of 2 and 5 kHz, indicate that small values of the antenna height are untenable in echo-sounding operation.

Subject Classification: [43]85.40.

INTRODUCTION

When considering the acoustic pressure field of an echosonde antenna, the starting point is the reduced time-independent, homogeneous wave equation for an acoustic wave:

$$\nabla^2 P(R) + k^2 P(R) = 0, \tag{1}$$

where ∇^2 is the Laplacian; P is the pressure field of the wave; $k = 2\pi/\lambda$; λ is the acoustic wavelength; and R is the distance to the field point. The method used in calculating the field produced by the acoustic antenna is the application of the free-space Green's function and the adaptation of the Kirchhoff–Fresnel diffraction formula to the antenna configuration. The configuration considered is a tapered cylinder with an open top. The radiation integrals developed from such a model are suitable for studying the characteristics of the echosonde antenna. The echosonde system is useful in studying the properties of the atmospheric structure.[1-4]

The Kirchhoff–Fresnel diffraction theory is applicable in both acoustic and electromagnetic-type problems. It is particularly useful in calculating the fields scattered by arbitrarily shaped objects at high frequencies in which the smallest dimension a of the scatterer satisfies[5,6] $a > 0.8\lambda$ (i.e., $ka > 5$), where λ is the corresponding wavelength. Advanced techniques have been developed for electromagnetic waves and such techniques are also applicable to acoustic waves (e.g., a microwave network approach can be adapted to acoustic waves and acoustic models have been made of radio antennas[7]). However, acoustic wave problems are more difficult than the corresponding electromagnetic field problems since two bulk-wave types occur in the acoustic wave problem as against one in the electromagnetic field problem, also acoustic wave boundary conditions are much more complicated, particularly in solids.

Horn reflector and cylindrical antenna structures have been used for boundary layer studies in acoustic

radar work.[8] The radiation integral developed in this paper is based on the antenna structure shown in Fig. 1. The developed integral computes the excitation at a horizontal level of height H ft above the lower illuminating aperture. The parameter H can be used to study the effects of shielding the antenna with absorbing cuffs which can be absorbent materials such as fiberglass or haybales. After truncating the excitation at $R_s(\max)$ which is the upper transmitting aperture radius at the height H ft, the farfield is obtained by a two-dimensional Fourier transform of the excitation function. The absolute value of the farfield signal is expressed in decibels relative to the on-axis value. The relative farfield signal strength gives the required power patterns.

The lower aperture excitation function represented as $F(\rho')\exp[j\Phi(\rho')]$ is the controllable illumination in amplitude and phase. The upper aperture illumination given as $F(\rho_s)\exp[j\Phi(\rho_s)]$ is computed through a two-
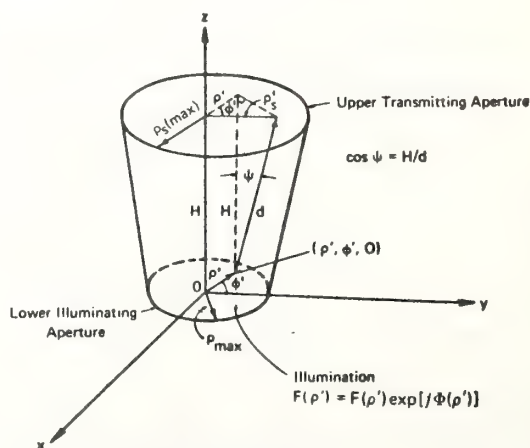
FIG. 1. Model for the shielded antenna.

dimensional Gaussian integration. In some cases of the present consideration, the field expressions in the Fresnel zone of the echosonde antenna are obtained when specific values are assumed for the quantities $F(\rho_s)$ and $\Phi(\rho_s)$. The resulting radiation integrals are expressed in closed forms using Lommel's series. For simplicity, circular symmetry is assumed. For optimum performance the height of the antenna and the diameter of the upper aperture are approximately three times the lower aperture diameter. In order to control sidelobes effectively, the height of the antenna and the phase coefficients can be adjusted.

I. KIRCHHOFF–FRESNEL DIFFRACTION FORMULA APPLIED TO THE PRESSURE FIELD OF THE ANECHOIC SHIELDED ECHOSONDE ANTENNA

The formulation applies to both liquid and gas. The term fluid-filled region is used to cover both cases of scattering in a compressible fluid like the atmosphere and an incompressible fluid like the ocean. The first type of problem is of interest here since we are considering applications in atmospheric boundary-layer studies. The Green's function that corresponds to the reduced wave Eq. (1) satisfies the equation

$$\nabla^2 G(\vec{R}, \vec{R}') + k^2 G(\vec{R}, \vec{R}') = -\delta(|\vec{R} - \vec{R}'|) , \qquad (1a)$$

where $G(\vec{R}, \vec{R}')$ is the Green's function, k the acoustic wave number and $\delta(|\vec{R} - \vec{R}'|)$ is an impulse function. The pressure field is given by

$$P(\vec{R}) = \int_S \{G(\vec{R}', \vec{R}) \nabla' P(\vec{R}') - P(\vec{R}') \nabla' G(\vec{R}', \vec{R})\} \cdot \hat{n}\, ds' , \qquad (2)$$

where $\hat{n}$ is a unit vector pointing out of a volume V bounded by surface S and spherical surface Σ. The surface Σ has no contribution to the integral for the exterior problem considered here. The Kirchhoff–Fresnel diffraction formula can then be written as

$$P(\vec{R}) = \int_S \{[\partial G(\vec{R}', \vec{R})/\partial n'] P(\vec{R}') - G(\vec{R}', \vec{R})$$
$$\times [\partial P(\vec{R}')/\partial n']\} ds' , \qquad (3)$$

where $\hat{n}'$ is a unit normal vector pointing into the volume V. The integral equation for a scalar diffracted field given in Eq. (3) can alternatively be written as

$$P(\vec{R}) = \int_S \{[\partial G_0(\vec{R}', \vec{R})/\partial n'] P(\vec{R}')$$
$$- G_0(\vec{R}', \vec{R})[\partial P(\vec{R}')/\partial n']\} ds' . \qquad (4)$$

$G_0(\vec{R}', \vec{R})$ is the free-space Green's function defined as

$$G_0(\vec{R}', \vec{R}) = \exp(-jkr')/4\pi r' , \qquad (5)$$

where r' is the distance from the source point to the field point (i.e., $|\vec{R} - \vec{R}'|$); $P(\vec{R})$ and $P(\vec{R}')$ are the field distributions at the field point and across the aperture respectively. It is shown that the term $\partial G_0/\partial n'$ is given by

$$\partial G_0(r')/\partial n' = (jk + 1/r') [\exp(-jkr')/r'] \hat{n}' \cdot \hat{r}' . \qquad (6)$$

In Eq. (4), we consider S as a large sphere having radius R'; consequently, if $\hat{R}'$ is denoted as the unit vector along the radius vector, then

$$\frac{\partial}{\partial n'} \sim \frac{\partial}{\partial R'} \quad \text{and} \quad |\vec{R} - \vec{R}'| \sim R' - \vec{R} \cdot \hat{R}' . \qquad (6a)$$

Therefore, the wavelength is small as compared with the radius of the large sphere. The requirements for the uniqueness condition for the field at infinity arise from the large sphere consideration. An outgoing wave is assumed. Sommerfeld[9] defines this vague requirement in a mathematical precision by stating the two conditions on the pressure scalar field P as

$$\text{(i)} \quad |RP| < K , \qquad (6b)$$
$$\text{(ii)} \quad R(\partial P/\partial R + jkP) \to 0 ,$$

where K is an arbitrary constant and the vertical bars denote an absolute quantity. However, the first of Eqs. (6b) may not be a necessary condition for the radiation problem.[9] By using the above Sommerfeld's condition Eq. (4) reduces to:

$$P(\rho) = \frac{jk}{4\pi} \int_0^{2\pi} \int_0^{\rho(\max)} F(\rho') \exp[j\Phi(\rho')] \frac{\exp(-jkr')}{r'}$$
$$\times (1 + \cos\psi) \rho' d\rho' d\phi' , \qquad (7)$$

where the formulation has been specialized to the cylindrical coordinate system of Fig. 2 and the other quantities used in the integrand of Eq. (7) are depicted in the shielded echosonde antenna model shown in Fig. 1.

II. FRESNEL-REGION APPROXIMATIONS

In order to obtain the Fresnel-zone field equation for the antenna model of Fig. 1, we let ρ_s' play the role of ρ' in Eq. (7) to give:

$$P(\psi) = \frac{jk}{4\pi} \int_0^{2\pi} \int_0^{\rho_s(\max)} F(\rho_s') \exp[j\Phi(\rho_s')] \frac{\exp(-jkr')}{r'}$$
$$\times (1 + \cos\psi) \rho_s' d\rho_s' d\phi' , \qquad (8)$$

where $\rho_s(\max)$ is the upper aperture radius and ρ_s' is

FIG. 2. Cylindrical coordinates.

J. Acoust. Soc. Am., Vol. 60, No. 1, July 1976

781
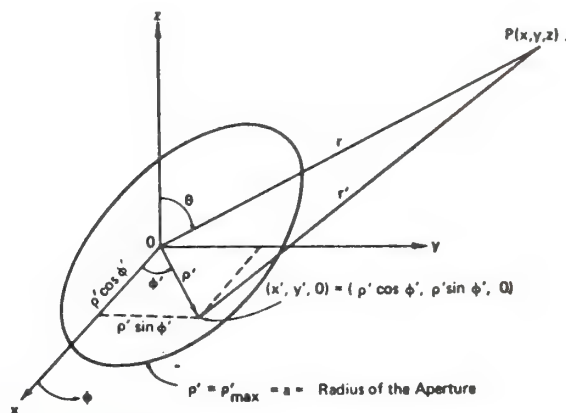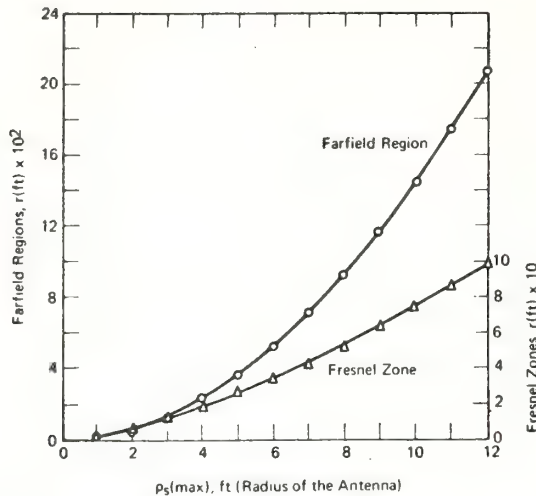
FIG. 3. Variations of the farfield/Fresnel regions for various values of the upper aperture radius of the antenna.

the variation across the upper aperture. It has been shown that the Fresnel zone is defined when the range r satisfies the condition[10]:

$$r \geq 0.6204\,(8\rho_s^3(\max)/\lambda)^{1/2} \quad [\text{or } 0.6204\,(D_u^3/\lambda)^{1/2}], \quad (9)$$

where $D_u = 2\rho_s(\max)$ is the diameter of the upper transmitting aperture and it is regarded as the maximum extent of the radiating source. The variations of the locations of the farfield/Fresnel zones are depicted in Figs. 3 and 4 for various values of the upper transmitting aperture radius and for various acoustic wavelengths, respectively. The usual farfield criterion of Eq. (9a) is used for computing the farfield locations:

$$r \geq 8\rho_s^2(\max)/\lambda \quad (\text{or } 2D_u^2/\lambda). \quad (9a)$$

Considering the field in a plane parallel to the xy plane one obtains:

$$\frac{\exp(-jkr')}{r'}$$

$$\simeq \frac{\exp\{-jk[z + \rho^2/2z - \rho\rho_s'\cos(\phi - \phi')/z + \rho_s'^2/2z]\}}{z}, \quad (10)$$

where $\rho < z$; $z > \rho_s(\max)$, and terms with $1/z^2$, $1/z^3$, ..., have been ignored. Using Eq. (10) in Eq. (8) one obtains:

$$P(\psi) = (jk/4\pi z)(1 + \cos\psi)\exp[-jk(z + \rho^2/2z)]U(\rho), \quad (11)$$

where $U(\rho)$ is a two-dimensional integral given by

$$U(\rho) = \int_0^{2\pi}\int_0^{\rho_s(\max)} F(\rho_s')\exp[j\Phi(\rho_s')]$$

$$\times \exp\{jk[\rho\rho_s'\cos(\phi - \phi')/z - \rho_s'^2/2z]\}\rho_s'\,d\rho_s'\,d\phi'. \quad (12)$$

For sufficiently small wavelengths and large k, the saddle point method can be used to evaluate Eq. (12). The equivalent upper aperture excitation function $F(\rho_s')$ $\times \exp(j\Phi(\rho_s'))$ contributes to the complexity of the above equations. The excitation function has been evaluated

by a two-dimensional Gaussian integration.[10] However, by assuming certain quantities for the equivalent upper aperture illumination, expressions will be obtained for the field values in the Fresnel zone of the antenna. Simplifications of the Fresnel zone field can be obtained for the special case of uniform illumination by using Lommel's series as originally used by Lord Rayleigh.[11] Expressions for illuminations other than uniform are more involved. Other considerations are discussed below.

A. Upper-aperture uniform amplitude and uniform phase distribution

When the equivalent illumination at the upper transmitting aperture is uniform both in amplitude and phase, then:

$$F(\rho_s')\exp(j\Phi(\rho_s')) = 1. \quad (13)$$

Using Eq. (13) and interchanging the order of integration Eq. (12) simplifies to

$$U(\rho) = 2\pi\int_0^{\rho_s(\max)} J_0(k\rho\rho_s'/z)\cos(k\rho_s'^2/2z)\rho_s'\,d\rho_s'$$

$$- j2\pi\int_0^{\rho_s(\max)} J_0(k\rho\rho_s'/z)\sin(k\rho_s'^2/2z)\rho_s'\,d\rho_s'$$

$$= C(\rho) - jS(\rho), \quad (14)$$

where the quantities $C(\rho)$ and $S(\rho)$ represent the Fresnel integrals. The Fresnel integrals are further reduced into simpler expressions using Lommel's series for two different values of the parameter ρ in Appendix A. The pressure field can then be represented as

$$P(\psi) = (jk/4\pi z)\exp[-jk(z + \rho^2/2z)](1 + \cos\psi)$$

$$\times [C(\rho) - jS(\rho)], \quad (15)$$
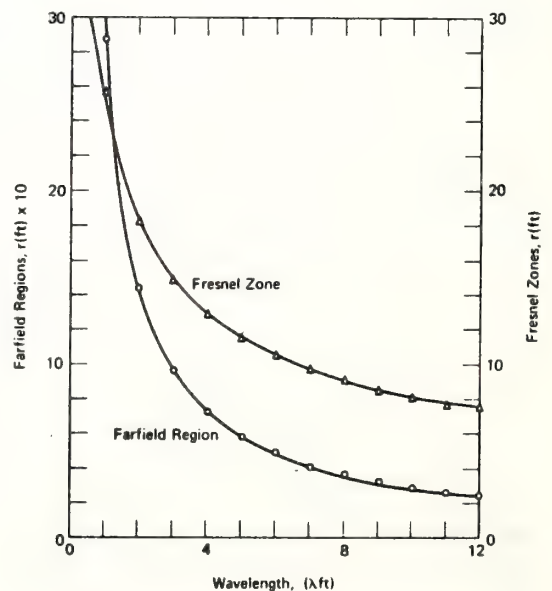
FIG. 4. Variations of the farfield/Fresnel regions for various acoustic wavelengths.

J. Acoust. Soc. Am., Vol. 60, No. 1, July 1976

782

where $C(\rho)$ and $S(\rho)$ are as defined in Appendix A. For the equivalent upper aperture illuminations that are different from uniform, the pressure field expressions for the Fresnel region are much more involved than the field expression given in Eq. (15).

B. Upper-aperture uniform amplitude and nonuniform phase distribution

When the upper aperture excitation has a nonuniform phase distribution, say in the form of the cubic phase-front error, the upper aperture illumination becomes

$$F(\rho_s') \exp[j\Phi(\rho_s')] = \exp(-j\beta\rho_s'^3) . \tag{16}$$

The pressure field in the Fresnel zone for this equivalent distribution then simplifies to

$$P(\psi) = (jk/2\pi z)\exp[-jk(z+\rho^2/2z)](1+\cos\psi)$$

$$\times \left(\int_0^{\rho_s(\text{max})} J_0(k\rho\rho_s'/z)\cos(k\rho_s'^2/2z + \beta\rho_s'^3)\rho_s'\,d\rho_s' \right.$$

$$\left. -j\int_0^{\rho_s(\text{max})} J_0(k\rho\rho_s'/z)\sin(k\rho_s'^2/2z + \beta\rho_s'^3)\rho_s'\,d\rho_s' \right). \tag{17}$$

For the linear and square-law distributions with uniform amplitude, the second entry of the cosine and sine functions of Eq. (17) is modified accordingly. Important aspects of the approximations are the farfield approximations and these will be considered in Sec. III. Both the Fresnel-field and the farfield expressions may be adapted to numerical computational techniques although the latter class of problems which are more commonly considered will be treated in this paper.

III. THE FARFIELD APPROXIMATIONS

Considerations of the farfield integral representations require further simplications of Eq. (8). The simplifications are particularly important in the quantity $\exp(-jkr')/r'$ [12] appearing in Eq. (8). If one considers the antenna model shielded with absorbing cuffs as depicted in Fig. 1, then r' can be expressed as

$$r' = [D^2 + \rho_s'^2 - 2D\rho_s'\sin\psi\sin\phi']^{1/2} . \tag{18}$$

Consequently, the usual approximations in the calculations of phase and amplitude terms are, respectively, given by

$$r' \simeq D - \rho_s'\sin\psi\sin\phi' \tag{18a}$$

and

$$r' \simeq D , \tag{18b}$$

where D is the distance from the center of the upper aperture to the farfield point. When these approximations are made in Eq. (8) and after reversing the order of integration and integrating with respect to the variable ϕ', then one readily obtains the following expression for the farfield:

$$P(\psi) = \frac{jk(1+\cos\psi)\exp(-jkD)}{2D}$$

$$\times \int_0^{\rho_s(\text{max})} F(\rho_s')\exp[j\Phi(\rho_s')]J_0(k\rho_s'\sin\psi)\rho_s'\,d\rho_s', \tag{19}$$

where J_0 is the zero-order Bessel function of the first kind. The equivalent upper aperture excitation function represented in amplitude and phase by $F(\rho_s')$ $\times\exp[j\Phi(\rho_s')]$ has been computed numerically to supply the input to Eq. (19) above. [10,13,14] Following the same approach used in the Fresnel-region fields considered earlier, expressions for the farfield Eq. (19) will be discussed when known forms are assumed for the excitation function by starting with the simple case of uniform excitation.

A. Upper-aperture uniform amplitude and uniform phase distribution

If the upper aperture excitation is uniformly distributed as given by Eq. (13), then the farfield Eq. (19) gives the $J_1(u)/u$ form of the field as

$$P(\psi) = \kappa\left(\frac{J_1[k\rho_s(\text{max})\sin\psi]}{k\rho_s(\text{max})\sin\psi} \right) , \tag{20}$$

where J_1 is the first-order Bessel function of the first kind; ψ is the angle off-axis in degrees; and κ is given by

$$\kappa = \left(\frac{jk(1+\cos\psi)\exp(-jkD)}{2D} \right)\left(\frac{\rho_s^2(\text{max})}{2} \right) . \tag{20a}$$

B. Upper-aperture uniform amplitude and nonuniform phase distribution

The farfield expression for the cubic phase distribution at the upper aperture as defined in Eq. (16) can be written as

$$P(\psi) = \frac{jk(1+\cos\psi)\exp(-jkD)}{2D}$$

$$\times \left(\int_0^{\rho_s(\text{max})} J_0(k\rho_s'\sin\psi)\cos(\beta\rho_s'^3)\rho_s'\,d\rho_s' \right.$$

$$\left. -j\int_0^{\rho_s(\text{max})} J_0(k\rho_s'\sin\psi)\sin(\beta\rho_s'^3)\rho_s'\,d\rho_s' \right). \tag{21}$$

The above expression is also true for the linear and quadratic phase distributions at the upper aperture with the cubic distribution replaced by the linear and quadratic phase-front distributions as the case may be. For computational simplicity, the primes in the integrand may be removed. The farfield expression is normalized with respect to the center value in order to obtain suitable patterns. The normalized value gives the relative power patterns in decibels. If R_s and θ are used to replace ρ_s and ψ, respectively, in the equations and the primes of the variable of integration are dropped, then the normalized field value giving the relative power patterns can be expressed as [10]:

$$E_N(\theta) = 20\log_{10}\left| \frac{1+\cos\theta}{2} \right.$$

$$\left. \times\left[\left(\int_0^{R_s(\text{max})} A(R_s)\exp[j\Phi(R_s)]J_0(kR_s\sin\theta)R_s\,dR_s \right) \right/ \int_0^{R_s(\text{max})} A(R_s)\exp[j\Phi(R_s)]R_s\,dR_s \right] \right|, \tag{22}$$

J. Acoust. Soc. Am., Vol. 60, No. 1, July 1976

783

FIG. 5. The effects of the size of the shielding cuffs of the antenna on the relative field strengths for different Gaussian coefficients (a) of the aperture illumination (constant phase coefficient). R_s(max) = 6 ft; R(max) = 2 ft; λ(5 kHz) = 0.22 ft.

where $E_N(\theta)$ is the normalized power pattern; θ is the angle off the vertical axis of the echosonde antenna; R_s(max) is the upper aperture radius of the antenna; $A(R_s)\exp[j\Phi(R_s)]$ is the equivalent excitation at the transmitting aperture of the antenna; R_s is the variable of integration at the upper aperture; and the vertical bars denote an absolute value. Since all digital machines are subject to limits of finite word lengths, adequate care is taken in computing Eq. (22) to avoid round-off errors.

IV. ANTENNA DESIGN FROM THE NUMERICAL RESULTS

The reduction in the side-lobe levels is depicted in Table I, which gives the numerical values from Fig. 5. The table shows that the height of the shielding cuffs reduces the side lobes within the range of 3.85 dB at 1 ft through 40 dB at 13 ft. It suffices to design an antenna from the results to meet the requirements of a specified side-lobe level and a specified beamwidth or gain. The appropriate illumination function which meets the requirements is chosen. Such considerations would show the usefulness of the numerical results obtained. For example, let us consider an echosonde antenna designed to meet the specifications given in Table II with a gain relative to the center value of − 7.13 and 40 dB side-lobe reduction at the ground level (i.e., 90° side-lobe level of 40 dB).

TABLE I. The effects of varying the parameter H (the shielding cuffs) obtained from the results of Fig. 5.

Antenna with anechoic shield	Gaussian coefficient											
	a = 0.125				a = 0.5		a = 0.75		a = 1.0		a = 2.5	
Height of the shield (ft)	H=0	H=1	H=12	H=13	H=10	H=11	H=4	H=5	H=6	H=7	H=8	H=9
90° side lobe level (SL) dB.	+1.3338	−3.8527	−37.2625	−38.7689	−27.0597	−30.4397	−17.2630	−29.0700	−28.6043	−28.0620	−30.8957	−34.6764
Reduction (dB) of the 90° SL from the value at $H=0$ ft	0	5.1865	38.5963	40.1027	28.3935	31.7735	18.5968	30.4038	29.9381	29.3958	32.2295	36.0102
Antenna without anechoic shield [a]												
20° power level (dB)	−13.5260	−13.5260	−13.5260	−13.5260	−13.5260	−13.5260	−13.5260	−13.5260	−13.5260	−13.5260	−13.5260	−13.5260
90° power level (dB)	−111.4415	−111.4415	−111.4415	−111.4415	−111.4415	−111.4415	−111.4415	−111.4415	−111.4415	−111.4415	−111.4415	−111.4415

[a]Note that for the case of the antenna without anechoic shield, the mainlobe and the sidelobes broaden out considerably. This is rather a surprising result particularly since the antenna dimensions are $> \lambda$. This may be due to the severe quadratic phase error distribution and the Gaussian function model assumed, otherwise this would not happen physically.

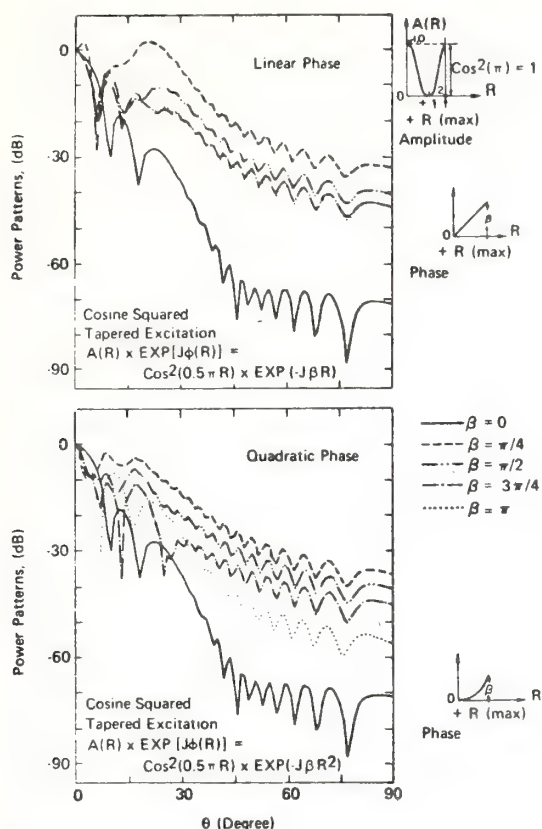J. Acoust. Soc. Am., Vol. 60, No. 1, July 1976

784

FIG. 6. The relative gain patterns depicting the nonmonotone behaviors of the 90° side-lobe levels. $H = 12$ ft; R_s(max) = 6 ft; R(max) = 2 ft; λ(2 kHz) = 0.55 ft; $\cos^2(\pi R/2)$ taper.

In order to meet the above antenna specifications, an examination of Table I shows that a side-lobe reduction of 38.6 dB is obtained if H equals 12 ft when a Gaussian excitation is used. With this serving as a guideline, a cosine-squared aperture distribution is chosen. The distribution is given by $A(R)\exp[j\Phi(R)] = \cos^2(\pi R/2) \times \exp(-j\beta R)$ using a wavelength λ of 0.55 ft; a height of 12 ft: the lower- and upper-aperture radii of the echosonde antenna model of 2 and 6 ft, respectively. The relative gain patterns are depicted in Fig. 6 (linear phase). The antenna design meeting the required specifications is illustrated in Table III where the numerical results of Fig. 6 have been used with and without shielding. It is thus demonstrated that the design of an antenna from the numerical results can meet the necessary specifications required. Although a cosine-squared distribution has been used, other commonly employed distributions can also be used depending on the requirements. The cosine aperture field distribution can also meet the requirements stated above. Further details are available elsewhere. [10]

V. DISCUSSION AND CONCLUSIONS

This paper outlines the theoretical basis for analysis of the echosonde antenna characteristics. The usefulness of the numerical results is shown in the previous section by designing an antenna from the results to meet the requirements of a specified beamwidth or gain and a specified side-lobe level. The excitation function satisfying the specifications with and without the absorbing cuffs is obtained from the results. Integrals for the Fresnel region representations of the radiated field have been obtained for certain upper transmitting aperture field distributions using Lommel's series. The integral equations developed are suitable for eval-

TABLE II. Antenna performance requirements.

	With shielding	Without shielding
Relative gain	-7.13 dB, with $BW = 4°$ (Gain relative to the center value or 18.47 dB absolute)	-7.2 dB, with BW = 6° (Gain relative to the center value or 18.4 dB absolute)
1st side-lobe level	5.6 dB below maximum at $\theta = 9°$	-21.3 dB at $\theta = 11°$
90° side-lobe level	90° SL = 40 dB below maximum	-63.9 dB
Extended requirements	Extension for future routine operation in urban environments subject to the additional conditions: (i) Further 90° SL reduction = 30 dB (ii) Maintain gain at -7.1 dB, but may tolerate additional 2° BW increase	(i) No further 90° SL reduction, i.e., further 90° SL reduction = 0 dB (remains as before) (ii) Maintain relative gain at -7.2 dB with BW = 6°
Beam maximum extending over a larger area	Maximum of beam extending to $\theta = 22°$ (i.e., operation on larger atmospheric volume with the disappearance of the main lobe): Peak power = + 2.40 dB	Power level = -24.2 dB

J. Acoust. Soc. Am., Vol. 60, No. 1, July 1976

785

TABLE III. Antenna design from Fig. 6 (linear phase) of the results to meet the required specifications of Table II.

	With Shielding	Without Shielding
Relative gain	From Fig. 6 (linear phase) $\beta = \pi/2$: Relative Gain= -7.1258 dB $\cong -7.13$ dB (relative to the center value); BW= $3.9999° \cong 4°$	Relative gain= -7.2001 dB $\cong$ -7.2 dB with BW= $5.9999° \cong$ $6°$
1st side-lobe level	$\beta = \pi/2$: -5.5708 dB $\cong 5.56$ dB below maximum at $\theta = 8.9999°$ $\cong 9°$	-21.2462 dB $\cong -21.3$ dB below maximum with $\theta = 10.9999°$ $\cong 11°$
90° SL	$\beta = \pi/2$: -40.0040 dB $\cong$ 40 dB below maximum	-63.8648 dB $\cong -63.9$ dB
Appropriate extended performance	$\beta = 0$: (i) 90° SL= -70.7834 dB $\cong$ -70.78 dB $\cong$ a further 30.8 dB reduction (ii) Gain= -7.3356 dB, BW= $5.9999° \cong 6°$ i.e., additional 2° BW increase	(i) 90° SL= -63.8648 dB $\cong$ -63.9 dB. Further 90° SL reduction= 0 dB (i.e., no reduction) (ii) Gain= -7.2001 dB $\cong$ -7.2 dB with BW= $5.9999° \cong 6°$
Appropriate extension of beam maximum over a larger area	$\beta = \pi/4$: Beam max. at $\theta = 21.9999°$ $\cong 22°$. (Mainlobe disappears). Peak power= $+2.3606$ dB $\cong$ $+2.40$ dB (relative)	Power Level= -24.2193 dB $\cong -24.2$ dB

uation by computer techniques and numerical results are obtained for the farfield representations.

The relative gain patterns of Figs. 5–9 are computed from Eq. (22). It is depicted in the figures that, for the relative gain patterns: the phase coefficient β; the Gaussian coefficient "a" in $\exp(-aR^2)$ of the excitation function; and the height of the echosonde antenna can all be used to advantage in controlling the side-lobe levels. Figure 5 shows that for small values of H— the absorbing cuffs of the antenna, the patterns are erratic in behavior thus indicating that small values of H are untenable. It is indicated in Fig. 8 that when H = 0 ft the undulatory nature of the signal departs markedly from the required directive main lobe with suppressed side lobes. The effects of varying the height of the antenna are also indicated in Table I using Fig. 5. The field pattern for H equals 0 ft is given within a multiplying constant by

$$E(\theta) = J_1(u)/u, \tag{23}$$

where $u = (2\pi R_{(max)} \sin\theta)/\lambda$; and for a carrier frequency of 2 kHz, an acoustic wavelength of 0.55 ft, and a lower aperture radius of 2 ft (Fig. 8), one obtains:

$$\sin\theta = 0.0437 u. \tag{24}$$

Table IV shows the locations of the zeros of the first-order Bessel function obtained from standard tables.[15] The zeros of the gain for uniform illumination for H = 0 ft are indicated in Table V. The values of Table V are obtained by numerical integration[10] using Eq. (22).

The effects of the parameter p of the field distribution of the form $[1 - (R/R_0)]^p$ on the relative gain are depicted in Fig. 9 and Table VI. The shapes of this
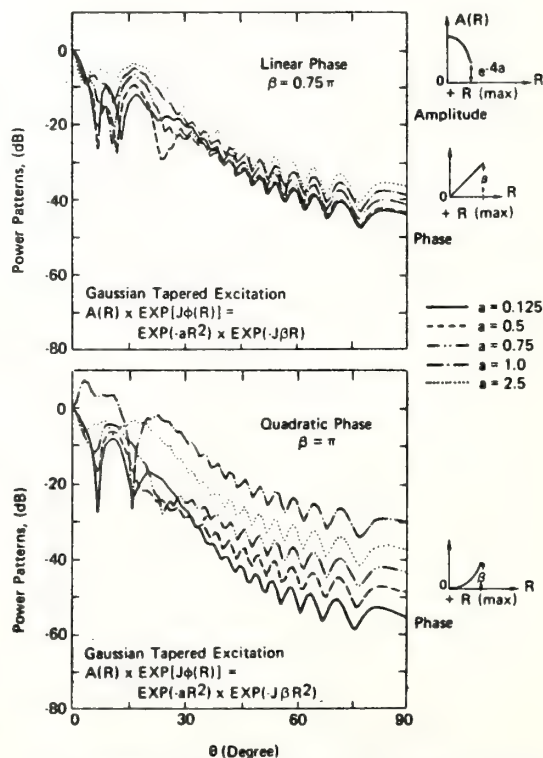

FIG. 7. Relative gain patterns showing the effects of Gaussian coefficients of the amplitude illumination on the gain. $H = 12$ ft; $R_s(max) = 6$ ft; $R(max) = 2$ ft; frequency= 2 kHz. Amplitude tapered to $\exp(-\frac{1}{2})$, $\exp(-2)$, $\exp(-3)$, $\exp(-4)$, and $\exp(-10)$ at the aperture edge for the respective values of a indicated.

TABLE IV. The successive locations of the Sth zero of the first-order Bessel function of the first kind (i.e., $J_1(u)$); $H = 0$ ft; $\lambda(2 \text{ kHz}) = 0.55$ ft; $R(\text{max}) = 2$ ft; (values obtained from standard tables[15]).

S	u: Sth zero of $J_1(u)$	$\sin\theta$	θ(deg)	Values of θ from numerical integration (deg)	Difference in the values of θ(deg)	% age difference
1	0.0000	0.0000	0.0000	0.0000	0.0000	0.0000
2	3.8317	0.1674	9.6000	10.5000	0.9000	8.6000
3	7.0156	0.3065	17.9000	18.5000	0.6000	3.2000
4	10.1735	0.4445	26.4000	28.5000	2.1000	7.3600
5	13.3237	0.5822	35.6000	35.5000	0.1000	0.3000

aperture distribution for the first three integer values of p are shown in the legends of the figure. The amplitude is tapered to zero at the aperture edge for all cases since $0 \le |R/R_0| \le 1$. The first side-lobe level decreases as p increases from 0–5 and increases for p greater than 5. However in the 20° region of interest near the ground, the maximum side-lobe level sharply decreases as p changes from 0 to 1 and increases with increasing values of p greater than 1.

The Gaussian excitation gives results that are compatible with practical realizability of the integral formulation. The main lobe is directive and the side lobes

are reasonably suppressed. A directive mainbeam with suppressed side lobes can be obtained by using a constant excitation across the illuminating aperture. A uniform amplitude and phase excitation gives maximum directivity, [16] although uniform distribution may not be easy to realize in practice. However, Hall and Wescott[1] have recently measured an extremely uniform pressure level across the aperture of an echosonde
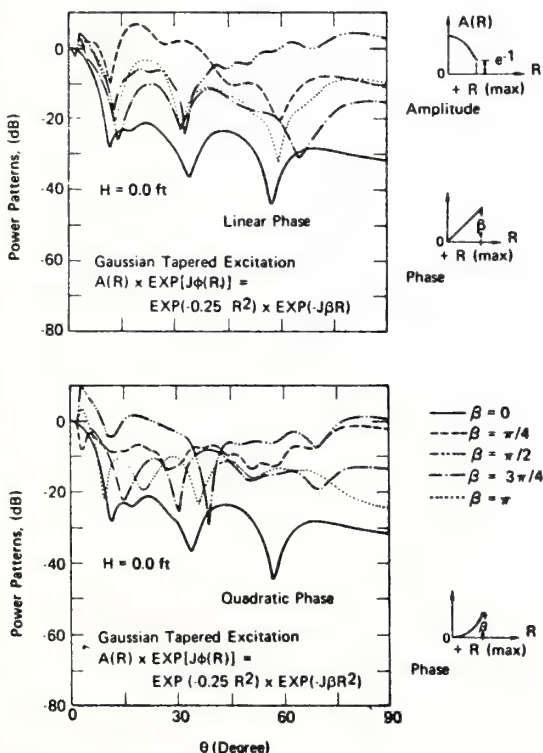
FIG. 8. Relative gains for the degenerate case of $H = 0$ ft. Notice the undulatory behaviors of the gains. $R(\text{max}) = 2$ ft; frequency = 2 kHz.
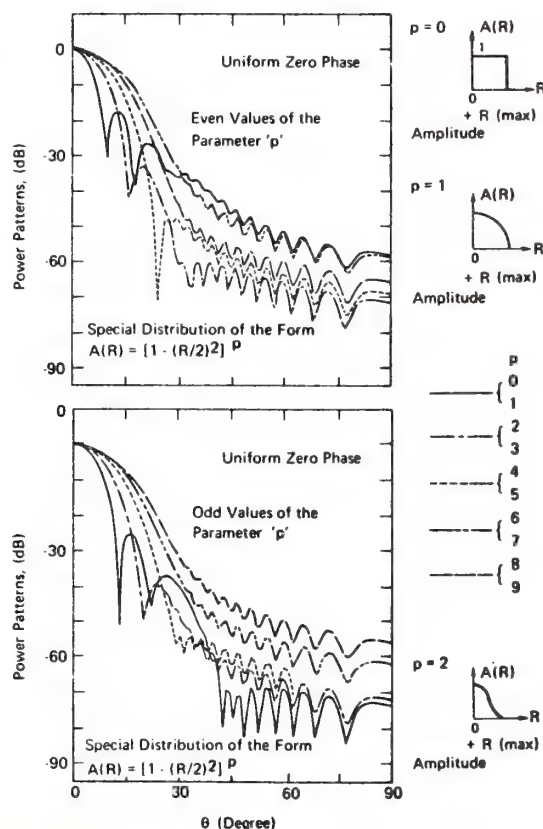
FIG. 9. The effects of a tapered aperture distribution of the form $[1 - (R/R_0)^2]^p$ on the relative gain with respect to the parameter p. Notice the behaviors of the side-lobe levels with respect to the variations of p [$H = 12$ ft; $R_a(\text{max}) = 6$ ft, $R(\text{max}) = R_0 = 2$ ft, $0 \le |R/R_0| \le 1$, frequency = 2 kHz].

J. Acoust. Soc. Am., Vol. 60, No. 1, July 1976

787

TABLE V. Apparent successive locations of the zeros of the gain for uniform illumination with zero phase distribution, i.e., $A(R) = 1.0$, $H = 0$ ft, $\lambda(2 \text{ kHz}) = 0.55$ ft; $R(\text{max}) = 2$ ft, (values obtained by interpolation of numerical integration results).

Theta (deg)	10.5000	18.5000	28.5000	35.5000	58.5000	71.5000
Relative gain (dB)	−22.4366	−24.5987	−27.0266	−38.2150	−40.3183	−28.0870

antenna, the measurement of the pressure levels being obtained by a sound-level meter. Such uniform distributions are desirable in acoustic radar work because of the associated directivity. The contour plot of the field strength shown in Fig. 10 gives an extremely directive mainbeam and significantly reduced side-lobe levels arising from a uniform aperture field distribution thus agreeing with experimental results. The contour plot is obtained from Eq. 22 for the carrier frequency of 2 kHz corresponding to a wavelength of 0.55 ft.

ACKNOWLEDGMENTS

APPENDIX

The Fresnel coefficients $C(\rho)$ and $S(\rho)$ used in Eq. (14) in expressing the Fresnel-zone fields are discussed in this section. For notational simplicity, let $\rho_s(\text{max})$ be represented as a, which is the radius of the upper transmitting aperture of the echosonde antenna. The Fresnel expressions have different representations

for two values of ρ depending on whether ρ is greater or less than the parameter a. $C(\rho)$ and $S(\rho)$ as used in Eq. (14) are then defined as:

$$C(\rho) = 2\pi \int_0^a J_0(k\rho\rho_s'/z) \cos(k\rho_s'^2/2z)\rho_s' d\rho_s'$$

and

$$S(\rho) = 2\pi \int_0^a J_0(k\rho\rho_s'/z) \sin(k\rho_s'^2/2z)\rho_s' d\rho_s'.$$

(A1)

Further simplification of Eqs. (A1) is possible by using integration by parts. The process results in Lommel's series representations of Eqs. (A1) for two different conditions on the parameter ρ thus[11,17]:

(1) *For* $\rho > a$; *Eqs.* (A1) *become*:

$$C(\rho) = (2\pi z/k)[\cos(ka^2/2z)U_1(\rho) + \sin(ka^2/2z)U_2(\rho)]$$

(A2)

and

$$S(\rho) = (2\pi z/k)[\sin(ka^2/2z)U_1(\rho) - \cos(ka^2/2z)U_2(\rho)],$$

where the quantities $U_1(\rho)$ and $U_2(\rho)$ are defined by

$$U_1(\rho) = (a/\rho)J_1(ka\rho/z) - (a/\rho)^3 J_3(ka\rho/z) + (a/\rho)^5 J_5(ka\rho/z) - \cdots$$

and

(A3)

$$U_2(\rho) = (a/\rho)^2 J_2(ka\rho/z) - (a/\rho)^4 J_4(ka\rho/z) + (a/\rho)^6 J_6(ka\rho/z) - \cdots,$$

where J_1, J_2, J_3, J_4, etc. are the Bessel functions of the first kind of orders one, two, three, four, etc.

TABLE VI. Relative magnitude of the first side-lobe level, and the maximum side-lobe level in the 20° region between 70° through 90° for the special distribution of the form $A(r) = (1 - r^2)^p$ ($0 \leqslant |r| \leqslant 1$; $r = R/2$; $H = 12$ ft; $R_s(\text{max}) = 6$ft; $R(\text{max}) = 2$ ft, $\lambda(2 \text{ kHz}) = 0.55$ ft).

| p		0	1	2	3	4	5	6	7
Relative magnitude of the first side-lobe level (SL) below the maximum of the main-beam.	dB relative to center value.	−17.5267	−25.0663	−32.9437	−39.2374	−48.3850	−54.2307	−48.0724	−45.0829
	θ (deg)	13.0000	16.0000	20.0000	22.9999	26.9999	29.9999	32.9999	35.9999
Maximum side-lobe level (SL) between the 20° region of 70°–90°	dB relative to center value	−61.7859	−84.0075	−78.7567	−77.9515	−75.0389	−74.8827	−71.5338	−66.7955
	θ (deg)	76.9997	76.9997	76.9997	76.9997	76.9997	76.9997	76.9997	76.9997

J. Acoust. Soc. Am., Vol. 60, No. 1, July 1976

788
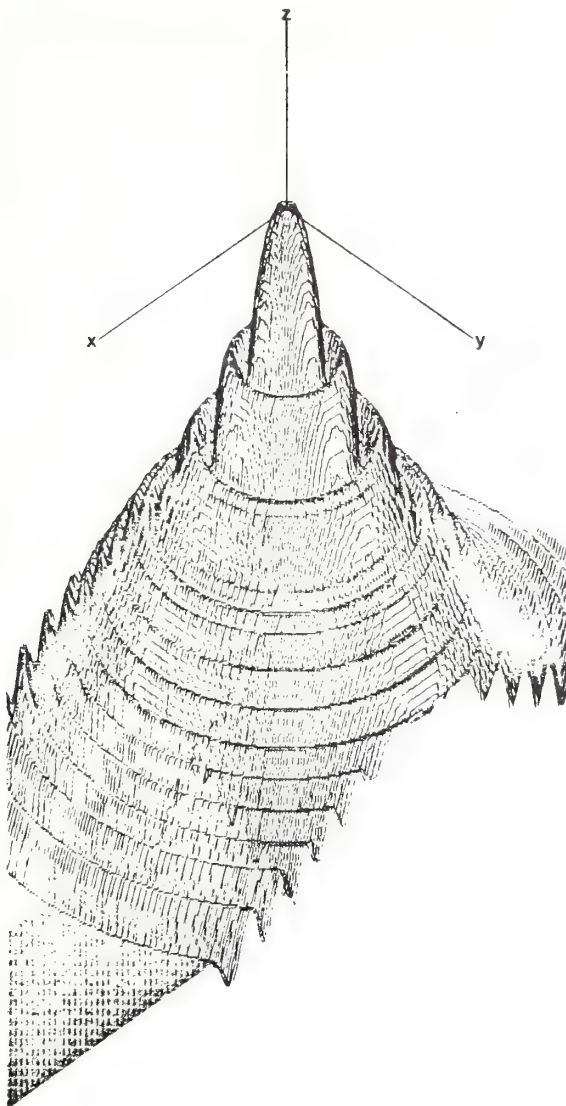
FIG. 10. Contour plot arising from a uniform excitation at the illuminating aperture of the antenna, i.e., $A(R)\exp[j\Phi(R)]$ $=1.0$; $H=10$ ft; $R_s(\max)=6$ ft; $R(\max)=2$ ft; $\lambda(2\text{ kHz})=0.55$ ft. Scale factor $=0.2$. Thirteen side lobes in all.

(2) For $\rho < a$; then Eqs. (A1) reduce to the form:

$$C(\rho) = (2\pi z/k)\left[\sin(k\rho^2/2z) + \sin(ka^2/2z)V_0(\rho)\right.$$
$$\left. - \cos(ka^2/2z)V_1(\rho)\right]$$

and   (A4)

$$S(\rho) = (2\pi z/k)\left[\cos(k\rho^2/2z) - \cos(ka^2/2z)V_0(\rho)\right.$$
$$\left. - \sin(ka^2/2z)V_1(\rho)\right],$$

where the quantities $V_0(\rho)$ and $V_1(\rho)$ are respectively defined as

$$V_0(\rho) = J_0(ka\rho/z) - (\rho/a)^2 J_2(ka\rho/z) + (\rho/a)^4 J_4(ka\rho/z) - \cdots$$

and

$$V_1(\rho) = (\rho/a)J_1(ka\rho/z) - (\rho/a)^3 J_3(ka\rho/z)$$
$$+ (\rho/a)^5 J_5(ka\rho/z) - \cdots, \tag{A5}$$

where J_0 is the zero-order Bessel function of the first kind and all other quantities are as defined above. Further considerations of Eqs. (A1)–(A5) can be obtained from reference[11] in which Lord Rayleigh gave the complete account of Lommel's memoir in an article on wave theory of light.

[1]F. F. Hall, Jr., and J. W. Wescott, "Acoustic Antennas for Atmospheric Echo Sounding," J. Acoust. Soc. Am. 56, 1376–1382 (1974) (also private communications).

[2]O. N. Strand, "Numerical Study of the Gain Pattern of a Shielded Acoustic Antenna," J. Acoust. Soc. Am. 49, 1698–1703 (1971) (also private communications).

[3]C. G. Little, "Acoustic Methods for the Remote Probing of the Lower Atmosphere," Proc. IEEE 57, 579–587 (1969).

[4]L. G. McAllister, J. R. Pollard, A. R. Maloney, and P. J. R. Shaw, "Acoustic Sounding—A New Approach to the Study of Atmospheric Structure," Proc. IEEE 57, 579–587 (1969).

[5]J. A. Stratton, Electromagnetic Theory (McGraw–Hill, New York, 1941), pp. 446–468.

[6]F. Kottler, "Electromagnetic Theory of Bending Around Dark Screens," Ann. Physik, 71, 457 (1923).

[7]E. C. Jordan, "Acoustic Models of Radio Antennas," Ph. D. dissertation (Ohio State University, 1940), pp. 7, 40.

[8]W. R. Simmons, J. W. Wescott, and F. F. Hall, Jr., "Acoustic Echo Sounding as Related to Air Pollution in Urban Environments," NOAA Tech. Report ERL 216-WPL-17 (Boulder, CO, May 1971), 77 pp.

[9]D. S. Jones, "The Theory of Electromagnetism," in International Series of Monographs in Pure and Applied Mathematics (Pergamon, Oxford, 1964), pp. 56–57, pp. 562–566.

[10]S. A. Adekola, "A Study of the Radiation Patterns of a Shielded Quasi-Tapered Aperture Antenna for Acoustic Echo-Sounding," Ph. D. dissertation (Ohio State University, 1975), pp. 66–69 (unpublished).

[11]Lord Rayleigh, "Wave Theory of Light," in Scientific Papers (Cambridge University, London, 1902), Vol. III, pp. 134–137.

[12]S. Silver, Microwave Antenna Theory and Design (Dover, New York, 1965), pp. 165–167.

[13]S. Adeniyi Adekola, Dean T. Davis, and Thomas A. Seliga, "Characteristics of a Quasi-Tapered Acoustic Radiator," 3rd International Conference on Atmospheric Acoustics, Toronto, Ontario, Canada, 24–27 June 1975 (unpublished).

[14]S. A. Adekola and Dean T. Davis, "Effects of Phase-front Distributions and Shielding on Acoustic Antenna Patterns Using a Tapered Cylindrical Structure as a Model," National USNC/URSI Conference, Boulder, CO, 20–23 Oct. 1975, pp. 238–239 (unpublished).

[15]Handbook of Mathematical Functions, edited by M. Abramowitz and I. A. Stegun (Natl. Bur. Stand., U. S. GPO, Washington, DC, 1964), p. 414.

[16]Henry Jasik, Antenna Engineering Handbook (McGraw–Hill, 1961), 1st ed. pp. 2-36–2-41.

[17]C. H. Walter, Travelling Wave Antennas (Dover, New York, 1970), pp. 58–63.

J. Acoust. Soc. Am., Vol. 60, No. 1, July 1976

789

SOME NEW APPROACHES IN DESIGN OF MILLIMETER-WAVE ANTENNAS

DAVID C. HOGG

NOAA/ERL/Wave Propagation Laboratory
Boulder, Colorado 80302

Abstract

Four designs of microwave antennas employing off-
set reflectors are discussed. In all cases the
reflectors are fed with dual or hybrid-mode horns.
The unblocked apertures, fed by a well-defined
illumination, result in measured radiation patterns
which compare well with theoretical predictions.

Introduction

It is necessary to pursue improvements in antenna
design regardless of wavelength; this is parti-
cularly so at millimeter wavelengths where special
problems arise. In addition to a good match (high
return loss), a clean radiation pattern devoid of
high immediate and far side lobes (proper aperture
illumination along with no blockage), wide band-
width, low cross-polarization, and low loss, it is
necessary to attain good mechanical precision and
to design so that environmental factors (rain,
snow, and temperature changes, in particular) do
not degrade performance.

Offset Reflectors

The elimination of blockage and attainment of a
good match[1] can be achieved by employing offset
reflectors*. An example of an offset paraboloid[2]
with a prime-focal feed is shown in Fig. 1a.
Because this arrangement is not symmetrical about
the axis of the generating paraboloid, an inherent
cross-polarization exists[3][4][5][6] with peaks
slightly removed from the axis of the main beam of
the antenna as shown by the radiation patterns at
19 GHz in Fig. 1b. This cross polarization is
important in communications where co-channel dual-
polarized transmission is contemplated. However,
the magnitude of the cross-polarization peaks
is a function of the offset angle, i.e., the angle

between the axis of the illumination pattern of
the feed and the axis of the generating paraboloid.
Figure 1c shows this dependence for the configura-
tion in Fig. 1a; theory and experiment agree
remarkably. The magnitude of the cross-polariza-
tion peaks can be limited to acceptably small
values (less than -30 dB, say) by choosing a
relatively small offset angle for the reflector*;
this can also be readily achieved in an offset
Cassegrainian antenna.

The return loss of offset prime-focus and
Cassegrainian antennas is essentially that caused
by reflection from the feeds per se since none of
the energy incident upon the reflectors is specu-
larly directed back to the feed. Likewise most of
the resistive loss in the antenna is inherent in
the feed, but the loss can be limited to very low
values even at millimeter wavelengths if properly
constructed hybrid-mode (corrugated) horns are
employed. These feed horns also produce a beam
that is essentially Gaussian and symmetrical about
the axis of the horn.

A Beam-Wave Antenna

Several modifications of offset paraboloids
appear attractive in the practical sense; one
example, called a beam-wave antenna, is shown in
Fig. 2. It is designed under the constraints that
the electronics be mounted below the antenna and
that the axis of the main beam of the radiation
pattern be horizontal. In this case the offset
angle between the axis of the hybrid-mode feed
(the vertical) and the axis of the generating
paraboloid is 30°; thus the cross-polarization
peaks are about 30 dB down. The radiation from
the offset paraboloid is reflected from a flat
into the horizontal direction; the flat can of
course be made adjustable for slight beam steering.
The aperture illumination is essentially axially-
symmetrical Gaussian because of the characteristic
of the hybrid-mode feed which also accommodates a
band of almost two to one.

---

* Although designs employing lenses can be con-
sidered, the lens always introduces some loss, and
some reflection, and, to some extent, limits the
bandwidth. Offset reflectors have been promoted
in the past by Carlyle Sletten and others.

---

* Unlike the horn-reflector antenna[7] (cornu-
copia) which has an offset angle of 90° and high
cross-polarization peaks.

The embodiment of Fig. 2 encompasses features that indicate the precautions taken against degradation by the environment. The weather cover, of thin low-loss material, is mounted at an angle with respect to the uniform phase front emerging from the flat reflector, thereby preventing reflection back to the feed. The function of the weather cover is, of course, to prevent rain, snow, dust, insects, and birds from entering the enclosure. The small amount of radiation specularly reflected from the cover is partially absorbed, as indicated in Fig. 2, to minimize multiple paths in the enclosure. Above the aperture is mounted a canopy to help prevent rain from falling on the weather cover. Wet weather covers can produce strong attenuations at centimeter wavelengths[8], and the degradation becomes even more severe at millimeter wavelengths.

Beam-Wave Transmission

At millimeter wavelengths, losses in waveguide and losses in transitions between various types of waveguides used as transmission lines to the antennas are factors of major concern. For this reason, beam-wave transmission in free space[9] has become an attractive option at millimeter wavelengths. It is possible to combine the low-loss properties of beam-wave transmission and offset reflectors as exemplified by the amusing design discussed in the following paragraphs.

The lower portion of Fig. 3 diagrams an installation operating at 8 mm that of necessity must be situated in a building on the ground, but whose antenna, in order to obtain path clearance, must be 100 feet above ground. Within the building, an offset reflector similar to that in Fig. 1 launches a quasi-Gaussian beam with a 20 dB diameter of about 20 inches. In combination with an elliptical reflector R_1, a collimated beam with a uniform phase front and diameter of 12 inches is produced 100 feet above ground. The two offset paraboloids, R_2 and R_3, tower-mounted at that height, are confocal (the focal point is indicated by F in Fig. 3 and the vertices of the paraboloids by V_2 and V_3). The diameter of the uniform phase front from below is simply magnified by the two-reflector combination and in the process of magnification, the beam negotiates a change in direction of 90° thereby producing a wave for horizontal transmission. The overall transmission from the building to the output aperture undergoes no attenuation other than that in the reflection process (which is kept low with proper precision of the surfaces) and in some spillover (which is minimized by oversized reflectors). Spurious radiation, if a problem, can be prevented by enclosing the beam in a shielding tower which also shelters the reflectors. However, because of the well-confined beam in the vertical, it is believed that this antenna will not contaminate the radio environment as the periscope antenna does. The cross polarization produced by such combinations of reflectors can be estimated analytically[5].

A Dual-Cylinder Offset Antenna

Another offset-reflector combination of interest is the Dragonian antenna[10], sketched in Fig. 4a, in which two offset parabolic cylinders are fed by a hybrid-mode horn. This arrangement produces a beam of elliptical cross-section over a wide band of frequencies. Although designed to cover the contiguous U.S. from a synchronous-orbit satellite (for bands at 20 and 30 GHz), the antenna can have application in terrestrial radio systems in the sense that a given tower stability may mandate a broader beam in the vertical plane than is necessary in the horizontal plane. An example of the excellent polarization properties is shown in Fig. 4b.

Conclusion

Configurations employing offset reflectors, or combinations of offset reflectors are shown to constitute useful microwave antennas.

References

(1) C. Dragone and D. C. Hogg, "The radiation pattern and impedance of offset and symmetrical near-field Cassegrainian and Gregorian antennas" IEEE Trans. Vol. AP-22, pp. 472-475, May/74.

(2) M. J. Gans and R. A. Semplak, "Some far-field studies of an offset launcher", Bell Syst. Tech. J., Vol. 54, No. 7, pp. 1319-1340, Sept./75.

(3) T. S. Chu and R. H. Turrin, "Depolarization properties of offset reflector mirrors", IEEE Trans. Vol. MTT-23, No. 4, pp. 377-379, April/75.

(4) A. W. Rudge, "Multiple-beam antennas: Offset reflectors with offset feeds", IEEE Trans. AP-23, pp. 317-322, May/75.

(5) M. J. Gans, "Cross polarization in reflector-type beam waveguides and antennas", Bell Syst. Tech. J., Vol. 55, No. 33, pp. 289-316, March/76.

(6) J. F. Kauffman, W. F. Croswell and L. J. Towers, "Analysis of the radiation patterns of reflector antennas", IEEE Vol. AP-24, No. 1, pp. 53-65, Jan./76.

(7) A. B. Crawford, D. C. Hogg and L. E. Hunt, "A horn-reflector antenna for space communication", BSTJ, Vol. 40, pp. 1095-1116, July/61.

(8) I. Anderson, "Measurements of 20 GHz transmission through a wet radome", IEEE Trans. Vol. AP-23, Sept./75.

(9) J. A. Arnaud, "Beam and fiber optics", Academic Press, 1976.

(10) C. Dragone, "An improved antenna for microwave radio systems consisting of two cylindrical reflectors and a corrugated horn", BSTJ Vol. 53, pp. 1351-1379, Sept./74.
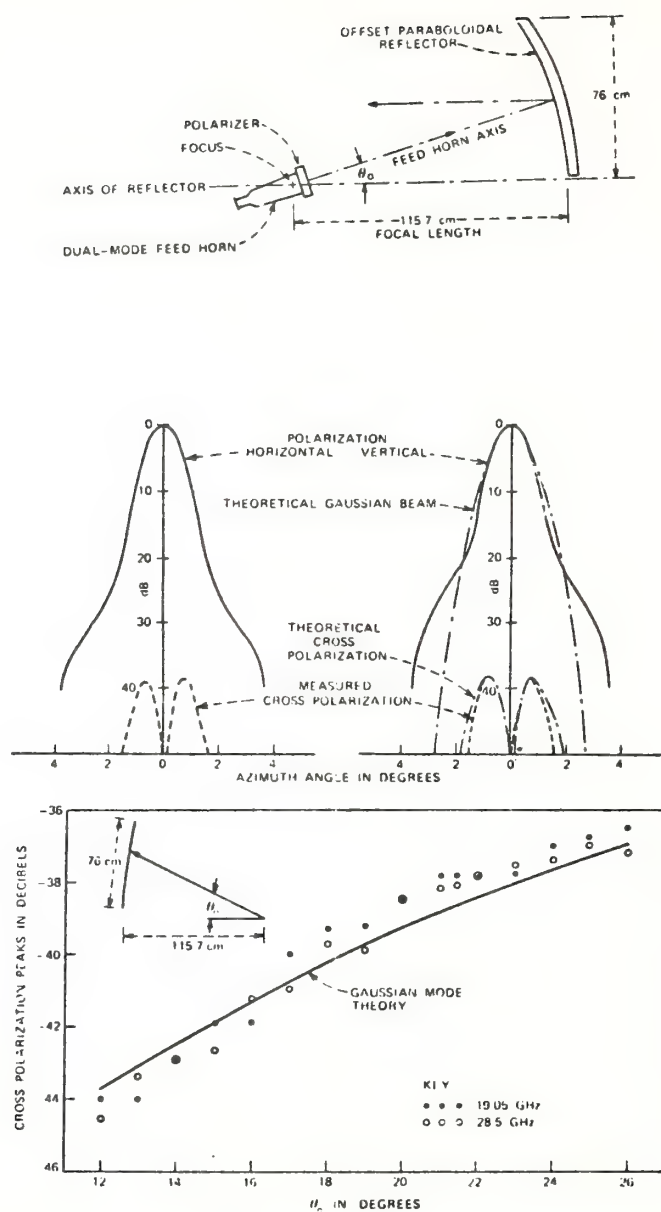
- Plot of cross-polarization peaks at 19.05 and 28.5 GHz introduced by the reflector itself as a function of offset angle, θ_o. Data are obtained by scanning the launcher in azimuth. Gaussian-mode theory is shown by the solid line. Incident polarization is horizontal.

Fig. 1.

Rain Shield

F
×

Generating
Axis of
Paraboloid

Paraboloid

Reflection from
Weather Cover

Absorber

Output Beam

Weather
Cover

Elliptical Flat
(at angle α)

α = 30°

θ_C = 15°

Phase
Center

Hybrid-Mode
Feed Horn
(Gaussian Illumination)

Electronics

CROSS-SECTION OF BEAM-WAVE ANTENNA WITH WEATHER COVER
SIDE VIEW

V_3 F
×
R_2 V_2

R_3

100 ft.

Building with
millimeter-wave
equipment.

R_1

2 ft.

BEAM-WAVE FEEDING OF A TWO-PARABOLOID MAGNIFIER

FIG. 3

793

(a)

Radiation patterns of vertically polarized double-cylinder antenna measured at 18.5 GHz in the $\phi = -45°$ plane for the main component (—·—) and the cross-polarized component (··—·) of the far field.

(b)

FIG. 4

IMPLEMENTATION OF COASTAL CURRENT-MAPPING HF RADAR SYSTEM
PROGRESS REPORT NO. 1

D. E. Barrick and M. W. Evans

A concept for radar remote-sensing of near-surface ocean currents in coastal regions is described, and progress is reviewed on the design and construction of the first operational units. The system employs pairs of low-power (50 W), transportable, HF (30 MHz) radars whose signals from the shore are scattered from ocean waves that serve as tracers, i.e., underlying currents impart a slight change in velocity to the ocean waves, which is detected by the radar receiver. Signals from each of the two geographically separated radar units of the pair, scattered from the same point on the sea, are used to construct a complete current vector for that point. In an operational system a radar pair will take simultaneous measurements over an ocean area with a grid having a 3-km spacing. Vectors will be constructed for each 3-km-square section, and a map of the near-surface current field will be output in real-time by a mini-computer on-site. All radar and digital gear is contained in two shock-mounted fiberglass cases, only 44 inches high and weighing under 200 pounds. The radar antennas are easily erectable frames holding three vertical aluminum pipes; the entire system can be set up in less than an hour. All of the individual components of the system have been designed and constructed. The system software has been essentially completed and checked out in the laboratory. Only a small amount of final assembly remains to be done before checkout and use in the field. System performance and simulation studies show that a radar pair can provide current data to a range from the coast of about 70 km. The optimum spacing between paired radars is nominally 40 km. Error analyses show that probable azimuthal position errors are less than 3° for signal-to-noise ratios exceeding 10 dB. Simulations using random sea-echo and noise signals indicates that probable rms current-velocity errors are not more than 5 cm/s.

THE D-C PRESSURE SUMMATOR: THEORETICAL OPERATION, EXPERIMENTAL TESTS AND POSSIBLE PRACTICAL USES

A. J. Bedard, Jr., National Oceanic and Atmospheric Administration

In studying low-amplitude acoustic-gravity waves in the presence of large-amplitude pressure fluctuations produced by atmospheric turbulence, some method is required for averaging out the incoherent turbulent noise by measuring pressure changes at distances greater than the turbulent wavelengths but smaller than the wavelengths of infrasonic waves. In practice this involves a requirement for measuring pressure changes at more than 100 locations on the earth's surface over a line 1000 feet long. The use of a microbarograph at each of these points is too expensive an approach, so a noise-reducing line microphone, a device for pneumatically adding pressures from a number of inputs, is used. This device is applicable to measurement problems where outputs from a number of pressure sensors are added together. Although applied by workers in geoacoustics for a number of years, the technique has seen few applications to other uses. My purpose is to describe the principle of operation for the device and suggest new applications for it such as in aircraft-wake vortex-detection and measurement of the pressure distribution within dust devils. Also, the sections that follow present results of tests and calibrations for a particular summator design. Such large-scale devices are difficult to test experimentally. The experimental data and techniques

presented here are to my knowledge the first for such a device. A simple analytical approach involving a d-c approximation for predicting the operation is described and compared with the experimental data. Finally, some practical applications are suggested.

DESCRIPTION OF NOISE-REDUCING LINE MICROPHONE

If microbarographs sample the atmosphere at only one point, local turbulence masks most infrasonic signals, which are typically 1 microbar P-P [Reference 5]. Such signals travel at acoustic velocities and in the frequency range 1 to 0.01 Hz are frequently measured with pressure amplitudes less than 1 microbar P-P, thus the signal wavelengths are in the range of 0.3 to over 30 kilometers. In practice, the effects on each microphone by local wind eddies are decreased by noise-reducing lines of pipe. In applications of the Geoacoustics Research Program Area of the National Oceanic and Atmospheric Administration (NOAA), these typically consist of 1000 feet of pipe of various diameters, tapering from 1.5-inch (inside diameter) pipe at the center in steps to 0.375-inch (inside diameter) at the ends (Figure 1). Usually, capillary ports to the atmosphere are set at 5-foot intervals. The input to the microphone is connected to the center of this spatial filter. For sound waves of periods longer than 10 seconds the line microphone is non-directional and the signal appears at each input of the adder; however, wind turbulence-induced noise is reduced considerably if there is little coherence between the various ports (inputs). Borsheverov et al. [Reference 3] present experimental data showing the reduction in local turbulent fluctuations of such a summator relative to a single point pickup. They used a line microphone patterned after the one described in this paper, but did not present experimental data concerning operational characteristics of the summator itself. It is also important to know information such as frequency response, internal attenuation and relative effectiveness of ports. Daniels [Reference 6] and Burridge [Reference 4] describe the theory of operation of line microphones, including acoustic inductive and capacitative effects. However, a simplified view of this line microphone as a purely resistive device predicts the operation quite well at low frequencies and offers clear insights into the principles of operation.

Design Criteria

Before considering the details of design, it is well to consider the design goals. Sampling ports need to be placed no farther apart than necessary for the background atmospheric turbulence to be incoherent. With closer spacing, the attenuation of background noise does not vary ideally (directly with the square root of the number of inlets). Placing the ports closer together than necessary will not necessarily degrade performance but this arrangement is probably more expensive. On the other hand, inefficient use of available space is the price paid for using inlet spacings larger than the distance necessary to produce incoherence. After deciding upon the length of array and the port separation, additional measures can be taken to insure that the internal reflections of sound waves do not occur within the line microphone, that all inlets are approximately equally effective and that the desired signals are not significantly attenuated.

   The port spacing distance might be chosen best by making experimental determinations of the correlation coefficient between the pressures measured with various single

797

Figure 1. Pipe Configuration and Equivalent Circuits
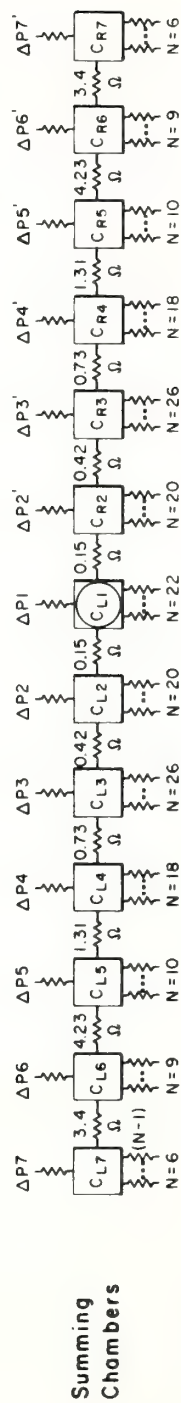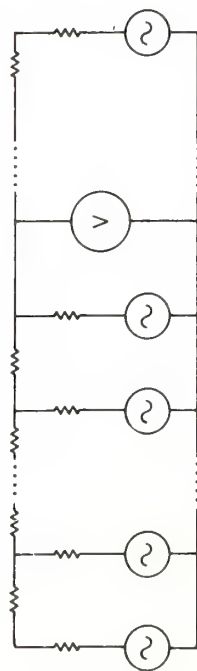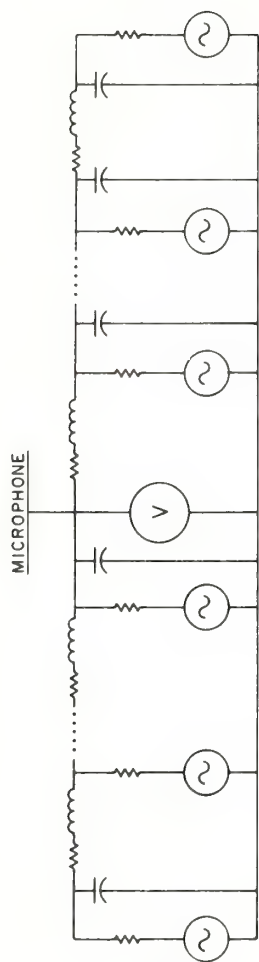
N equals total number of ports per chamber. All ports are equal in resistance.

inlet microphones as a function of spacing in the frequency range of interest as measured by Priestley[Reference 10], McDonald et al. [Reference 9], and Flores and Otero [Reference 7]. Finally, having determined the desired array length and port spacing from the above considerations, a method of determining that combination of acoustical resistances of the ports and sizes of pipe or tubing that constitutes a proper termination to reduce the internal reflections should be applied. The actual physical dimensions of noise-reducing arrays currently in use usually result from a compromise between theoretical design considerations, availability of tubing or pipe, and the type and amount of available terrain.

Termination of Sections of a Noise-Reducing Line Microphone for Minimum Internal Reflection

This section outlines the approach devised by Daniels [Reference 6] for noise-reducing line microphone design. For those with applications involving essentially static pressure measurements the criteria outlined in this section are not of paramount concern.

Internal reflections occur when sound waves propagate through a series of pipes of varying cross-sectional areas or through a pipe of constant cross section with side leaks. After determining the total array length and number of ports required, the next step involves computing the combinations of port resistances and pipe sizes that minimize internal reflections. By using a single value of port resistance throughout, one avoids the supply and installation problems presented by designs that require flow resistors of differing values.

Daniels [Reference 6] made the following assumptions in his design:

1. The impedance of the sampling ports is purely resistive.

2. Since the pipe sections are small compared with the wavelengths of interest, the port resistances for the pipe sections and combinations of pipe sections are considered as lumped parameters at a point.

3. There is no attenuation of sound within the pipe other than that caused by failure to maintain particle velocity across a junction of pipe diameters. In later sections, the assumption is shown to be invalid. It is, however, sufficient for design purposes when the goal is minimizing internal reflections.

4. The velocity of sound in the pipe is a constant and approximately equal to the velocity of sound in the local atmosphere.

Using these assumptions an equivalent pipe is devised by considering a sound wave incident on the junction of two pipes of differing cross-sectional areas and on a junction of two pipes of identical cross section at which there is an opening. By combining these two effects, the ideal, non-reflecting, noise-reducing array is approximated. It is possible to match combinations of lumped port resistances and changes of cross-sectional area so that there is no change in impedance along the line microphone. Although this process is an important, necessary step in the design of an infrasonic microphone, no additional detail is presented here. Many applications involve frequencies so low that inductive and capacitive effects are negligible, and a purely resistive transmission line represents a useful model.

Definition of a Particular Configuration

Daniels has developed his theory for a properly-terminated pipe using the assumption that the resistive attenuation effects within the pipe are so small as to be negligible. However, in the space filter, as it has been implemented in practice, this is not the case, and the resistive attenuation within the pipe array must be considered. In the sections that follow, experimental measurements of pipe arrays will be presented and a theoretical consideration of the array as a resistive summator will be outlined. We will view the space filter as a static summator and see what insights this will give into space filter operation.

Figure 1 shows the outline of the pipe array considered here. The pipe configuration is presented, and several equivalent circuits are defined. Details concerning the summing chamber equivalent circuit will be presented in a later section. It is usually instructive and helpful in understanding complex systems to consider them at their extremes. In so doing, important variables may be identified and guiding concepts chosen. The line microphone is now considered in the limit as a d-c pressure summator.

THE ACOUSTIC RESISTOR

Acoustic resistors are used as ports to the pipe. The pressure changes are fed through these ports into the pipe tubing. These ports typically take the form of controlled capillary leaks whose value is determined initially as indicated in the earlier section "Termination of Sections of a Noise-Reducing Line Microphone for Minimum Internal Reflection," if reduction of internal reflections is important. The value of the acoustic resistance of a capillary tubing of circular cross section in acoustic ohms may be computed using the Hagen-Poiseuille law

$$R = (8\mu L/ \pi a^4)$$

where a is the inner radius in centimeters, μ is the air viscosity in poises, L is the length of tubing in centimeters, and R is the flow resistance in acoustic ohms.

In practice, these ports have taken the form of drilled brass or plastic plugs, and hypodermic needles. The acoustic resistors may be measured using an acoustic ohm-meter [Reference 1]. This consists of a precision volume velocity source and a calibrated pressure transducer. The pressure change resulting from a known rate of flow through the resistor being tested is measured and the resistance may be computed from

$$\Delta P = QR$$

where ΔP is the pressure difference in μbar, and Q is the volume velocity in cc per sec.

Note that the resistance is one acoustic ohm when a flow of 1 cc/sec through the element produces a pressure change of 1 μbar. Because of the inverse fourth power dependence of the resistance on the inner capillary tube radius, it is important to insure that the capillaries are kept free of dirt.

For the details of an inlet found to be effective, see Figure 2. This inlet consists of a pipe tee, bushing plug drilled and tapped with a 6-32 thread, a hypodermic needle with a 6-32 thread on it, and a bent piece of tygon tubing. This tygon tubing connection acts as a rain shield and will place the effective sampling port at ground level. Keeping the effective sampling port as close to the ground as possible will reduce noise caused by a direct wind blast or Bernoulli effect at the inlet.

800
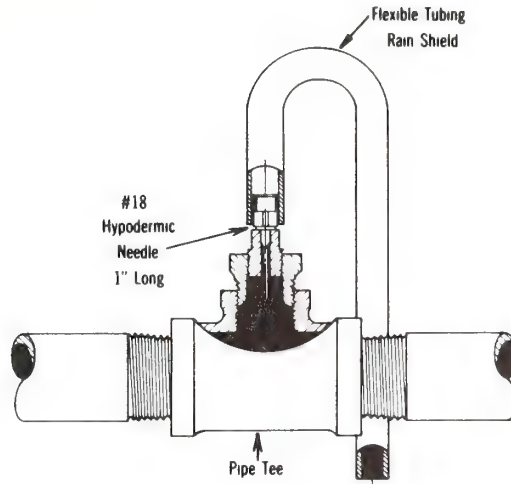
Figure 2. Typical Array Port Configuration

THE STATIC SUMMATOR

Consider a chamber with N acoustic resistors connecting the inside of the chamber to the atmosphere. The value of each of these parallel resistors is R. The pressure change applied to a single port is given relative to P_o, the ambient pressure and is designated ΔP_1. No pressure change is applied to the remaining $N - 1$ ports. The pressure in the chamber is designated ΔP_{C1}. Note that all pressure changes in this section shall be reference ambient. Zalmanzon [Reference 11] is a good reference for the dynamics of pneumatic chambers.

Now connect this chamber (chamber one) to an identical chamber (chamber two) through an additional resistive leak R_p, see Figure 3. For this case

$$\Delta P_{C1} = [\,(\Delta P_1 / R) + (\Delta P_{C2} / R_p)\,] / [\,(1/R_p) + (N/R)\,]$$

$$\Delta P_{C2} = [\,(\Delta P_2 / R) + (\Delta P_{C1} / R_p)\,] / [\,(1/R_p) + (N/R)\,]$$

Eliminating ΔP_{C2} from the above two equations, we obtain

$$\Delta P_{C1} \left\{ 1 - [\,(1/R_p) + (N/R)\,]^{-2} / (R_p^2) \right\} =$$
$$(\Delta P_1 / R) / [\,(1/R_p) + (N/R)\,] + (\Delta P_2 / RR_p) / [\,(1/R_p) + (N/R)\,]^2$$

For $\Delta P_2 = 0$, we have

$$\Delta P_{C1} = (\Delta P_1 / R) [\,(1/R_p) + (N/R)\,]^{-1} / \left\{ 1 - [\,(1/R_p) + (N/R)\,]^{-2} / (R_p^2) \right\}$$

801
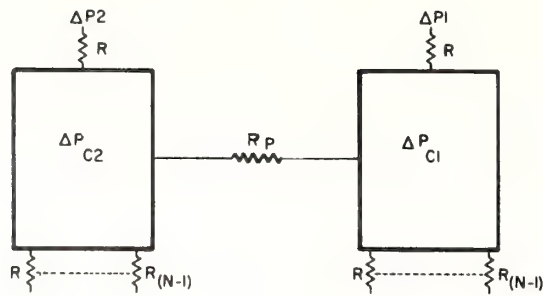
$$\frac{\Delta P'_{CI}}{\Delta P_{CI}} = \frac{1}{\left(1 + \dfrac{NR_P}{R}\right)}$$

N = NUMBER OF PORTS PER CHAMBER
R = PORT RESISTANCE
R_P = PIPE RESISTANCE

Figure 3. Pressure Summator

for $\Delta P_1 = 0$

$$\Delta P'_{C1} = (\Delta P_2 / RR_p)\left\{1/[(1/R_p) + (N/R)]\right\}^2 / \left\{1 - [(1/R_p) + (N/R)]^{-2}/(R_p^2)\right\}$$

Setting $\Delta P_1 = \Delta P_2$ we obtain that

$$(\Delta P'_{C1}/\Delta P_{C1}) = 1/[1 + (NR_p/R)]$$

The significance of this result is explained in the next section.

Line Microphone as a Static Summator

This system may be considered as a much simplified space filter and examined to see how the number of ports, port resistance, and resistance of the pipe will influence operation. The ratio $\Delta P'_{C1} / \Delta P_{C1}$ indicates the relative effectiveness of a pressure change applied to a port R of chamber 2 compared with the result for the same pressure change applied to a port R of chamber 1. This simple relation shows that to make the pressure measured in chamber 1 from ΔP_2 as similar as possible to that from ΔP_1, the ratio NR_p / R should be made small. This could be done by reducing the number N of the ports or by reducing the resistance R_p between the chambers. For the ideal case no resistive attenuation would be present within the space filter and the response of all ports would be equal. By increasing the value of R one would approach this ideal.

Implications of This View

Figure 1 shows a pipe array and its equivalent circuits made up of a set of summing chambers. The set of chambers shown in the figure may be represented by the group of equations shown below.

$$\Delta P_{CL1} = [\,(\Delta P_1/R) + (\Delta P_{CL2}/R_{1L}) + (\Delta P_{CR2}/R_{1R})\,]/[\,(N_1/R)$$
$$+ (1/R_{1L}) + (1/R_{1R})\,]$$

$$\Delta P_{CL2} = [\,(\Delta P_2/R) + (\Delta P_{CL3}/R_{2L}) + (\Delta P_{CL1}/R_{1L})\,]/[\,(N_{L2}/R)$$
$$+ (1/R_{2L}) + (1/R_{1L})\,]$$

$$\Delta P_{CL3} = [\,(\Delta P_3/R) + (\Delta P_{CL4}/R_{3L}) + (\Delta P_{CL2}/R_{2L})\,]/[\,(N_{L3}/R)$$
$$+ (1/R_{3L}) + (1/R_{2L})\,]$$

$$\vdots$$

$$\Delta P_{CL7} = [\,(\Delta P_7/R) + (\Delta P_{CL6}/R_{6L})\,]/[\,(N_{L7}/R) + (1/R_{6L})\,]$$

For Left Side of Summator

These equations can be combined so that the pressure measured in any chamber may be expressed in terms of the pipe resistances between chambers (R_{1L} --- R_{6L} --- and R_{1R} --- R_{6R}), the port resistance R, the number of ports in each chamber (N_{L1} --- N_{L7} and N_{R1} --- and N_{R7}) and the pressure ΔP applied to any given port. Thus, calculations may be made of the relative response of the various ports of a pipe array. Again, an underlying assumption has been either that the acoustic transmission line is properly terminated in its characteristic impedance so that internal reflections do not occur or that the frequency of use is so low that inductive effects are not important. At frequencies below about 0.05 Hz for the particular space filter used, resistive attenuation dominates, and the pipe array may be considered a d-c summator.

EXPERIMENTAL TECHNIQUES
Low Impedance Pressure Generators

The field pipe we used has an internal volume of about 50 gallons and hence can represent a large acoustic load to a device used to generate pressures at a port. For example, the calibrator used to assign pressure amplitude values to the NOAA microphone in the field has a volume smaller than the pipe array volume (by a factor of ten). It seemed desirable to apply a form of calibrator that would not be affected by the presence of an acoustic load of the form of the pipe array. Two types of low-output-impedance pressure generators have been devised and these will be described below. The calibrated infrasonic microphone normally used in making measurements monitors the pressures at the center of the pipe array being tested. But it is also necessary to monitor the input pressure to an array port. Several techniques were used to determine the value of acoustic pressure generated.
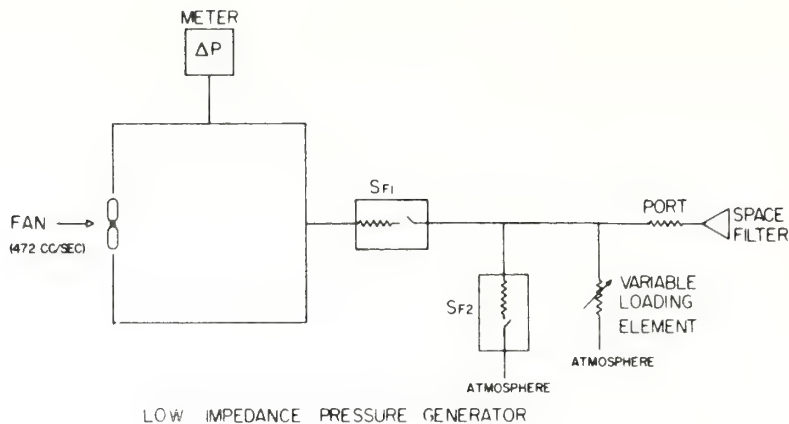
Figure 4. Schematic Diagram of Fan-Type Low Impedance
Pressure Generator

Fan Type Generator

Small, low-power, high-capacity fans are now available and these may be used as
pressure generating elements. A typical fan flow rate is 472 cc/sec with a pressure
differential developed across the fan of about 2500 μbar. This would mean that the
output impedance is about 5.3 ohms, considerably lower than the array port resistances
typically used (325 ohms). Figure 4 is a block diagram showing a fan configured into
an assembly suitable for calibration purposes. The pressure developed in the chamber
is measured with reference to ambient using a pressure gauge. The switches designated
"SF1" and "SF2" are used to control the pressure and to produce step functions. A
variable loading element was added so that sinusoidal pressure changes could also be
generated using this device. The switches themselves have some flow constriction so
that the output impedance will be higher than that due to the fan alone. A photograph of
the device is shown in Figure 5.

Centrifugal Type Generator

A second type of pressure generator used was a form of centrifugal calibrator. This
was applied as a pressure generator only; although a device based upon the principle
described by Kemp [Reference 8] was used as a standard in itself.

The centrifugal calibrator used here consists of a hollow arm open at both ends. This
is rotated about the center. The resulting pressure at the center, generated by centrif-
ugal forces, is monitored through the hollow shaft used to rotate the hollow arm. The
system is outlined in Figure 6. The pressure change for the device shown on this figure
is given by

$$\Delta P = (1/2) K\rho\omega^2 L^2$$

where ω is the angular frequency, ρ is the density of the medium, L is one-half of the
tube length, and K is a constant.

The end effects caused by the induced Bernoulli pressure about the ends of the tube
are probably the chief source of error.

804
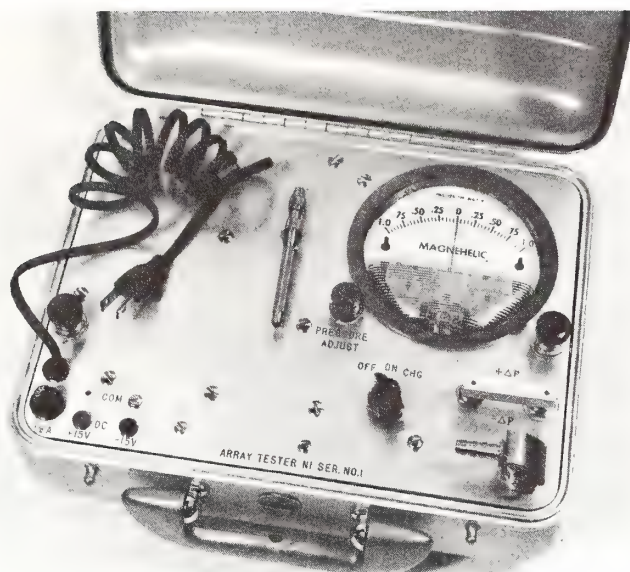
Figure 5. Photograph of Fan-Type Low Impedance Pressure Generator

   The centrifugal calibrator used as a generator of dynamic pressure also has a low output impedance. This was determined by loading the device with a controlled acoustic load and measuring the pressure changes generated with a water manometer. The measured impedance was found to be 3 ohms.

   A magnahelic pressure manometer was used to define the pressure change produced. By driving the system at a fixed rpm rate, a fixed differential pressure is generated. By superimposing a small sinusoidal variation in rpm rate upon a larger fixed rate of rotation, approximately sinusoidal variations of pressure will be generated super-imposed upon a larger fixed pressure change. The system was monitored with a milli-barograph to define the amplitude and the frequency response characteristics. All data presented are corrected for the frequency response of the detection system.

Variable Loading

A variable resistive load was designed by mounting an insert in a capillary tube. The insert was driven by a d-c motor and was eccentric so that the length of the insert in the capillary tubing could be varied, thus varying the acoustic resistance. The variable load produced a variable pressure output that was used to drive array ports. The frequency could be adjusted over a limited range by adjustment of the voltage to the d-c motor.

Figure 6. Centrifugal-Type Low Impedance Pressure Generator

Alternate Methods of Calibration

The ideal system of calibration would be an infrasonic source in the atmosphere capable of producing signals suitable for running the complete system response tests. Unfortunately, I know of no such infrasonic source that could be appl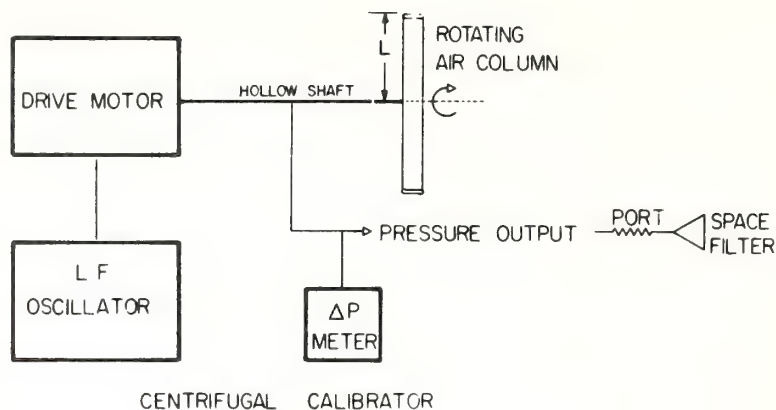ied to the problem of array testing below 1 Hz. Comparing a microphone output with an array to that obtained for the same far field signal without a pipe array would be another possible method. However, the increase in the wind-induced pressure noise for the microphone without the pipe would tend to mask the array effects.

At one time alternate plans were under way to (1) mount a complete microphone system including the 1000-foot pipe on a large shake table and calibrate the system using the pressures induced by controlled motions, and (2) build a pipe array coiled inside a test chamber, driving the chamber with a pressure generator. Because of other work, these efforts never got beyond the preliminary stages of preparation.

Another method of experimentally investigating the response of a large line microphone would be to connect thermophones to each of the ports. Phase differences between the various input signals could be included in such a test.

Because of the large size and weight of a pipe array, the most practical approach for testing was to apply portable pressure generators to an existing array already deployed at our field site. For the site chosen, the suffix N (North) or S (South) is added to the port numbers to distinguish between the two ends of the pipe.

Acoustic Resistors, Measurements and Types
General

Some of the characteristics of the required acoustic resistors have been mentioned previously in the earlier section "The Acoustic Resistor." Because a field pipe array was used in making these tests, the device tested must be considered dynamic (an insect can and frequently does crawl into a port, changing its properties from the ideal). In addition to the fact that the pipe array is susceptible to changes with time, the large number of ports involved (200) explains why it is desirable to have a simple and rapid method of accurately varying the port resistance values for the entire pipe array.

806

Changing toward Higher Resistance

One method used to vary the port resistance was to insert thin wires into a capillary. Ideally, the wire is perfectly centered, and the flow involved is through an annular section; however, an eccentric location of the wire would produce a different value of flow resistance [Reference 1] and this could also vary dynamically with wind or vibration. For a short, straight length of capillary tubing a solution is to insert a bent piece of wire. The flexing of the wire holds it at a fixed position in the bore and only slight changes caused by wire motion will be observed.

Experimental Techniques

The flow resistance of a brass port was measured, and then a set of wires of gradually increasing diameter was inserted and the flow resistance measured for each wire. In this way a plot of flow resistance versus wire insert size was generated. The necessary wire size to obtain a given flow resistance was determined from this plot and a set of wires was fabricated. Each wire was fitted with a loop at the top to prevent it from falling through the field port.

For example, for wires inserted in a brass field port of 310 ohms resistance, the following results were obtained:

Wire Diameter	Resistance in Ohms
0.0039 inches	405
0.007 inches	550
0.0126 inches	1000
0.0235 inches	5000

By walking the length of the array and inserting a set of wires in the ports, the port resistance for the entire pipe array may be increased in value above the 310 ohm port resistance value used for the field test pipe array.

Changing toward Lower Resistance

It is also of interest to test the field pipe array over a range of flow resistances lower than the 310 ohm port resistance. A different type of flow resistance was used to do this. Porcelain tubing frequently used to route thermocouple wires can be obtained at low cost in a multiple bore form showing uniform bore characteristics. A two-bore type was used with a nominal hole I.D. of 1 mm. The tubing length was chosen so that a resistance of 50 ohms was obtained for the parallel combination of the two bores. Then by inserting a wire in one of the bores with an O.D. which just permitted insertion, the resistance of one bore was made much higher than the other one. The net resistance obtained was changed to 100 ohms. By placing two of these elements in series, resistances of 150 and 200 ohms can be obtained. One element was mounted in an adaptor using silicone rubber sealant. The series connection of the second element was made using tygon tubing.
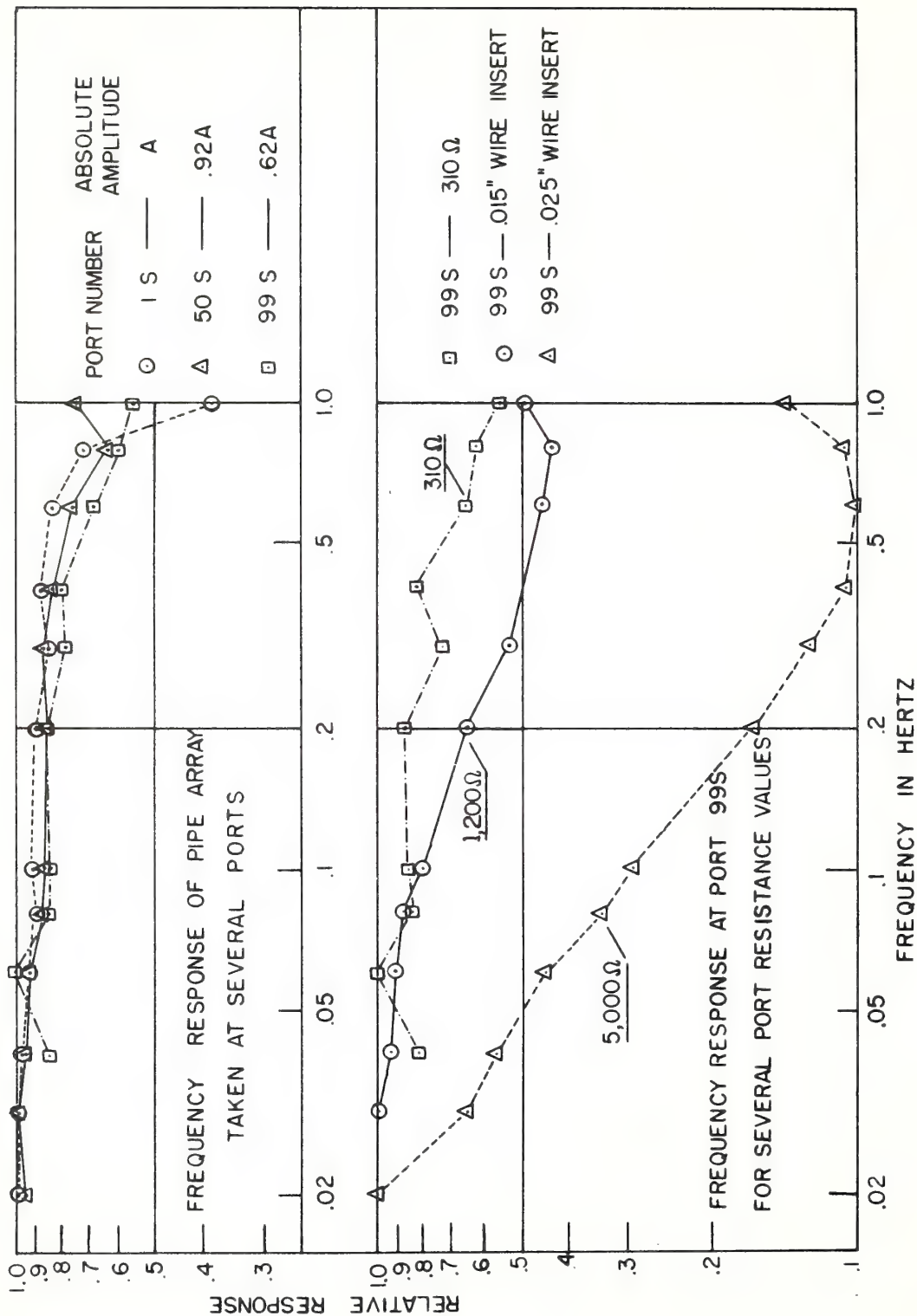
Figure 7. Frequency Response of Pipe Array as a Function of Port Resistance and Position

SOURCES OF EXPERIMENTAL ERROR

The chief sources of experimental error were wind-induced noise and possible changes in the calibrated array ports caused by dust, condensation or insects. The decision to perform this testing in the field was accompanied by the limitations of an uncontrolled environment. The solution to the problem of wind-induced noise was to wait for a period of low winds. The solution to the problem of dirt, dust, and insects in a field environment was to perform the tests as rapidly as possible to reduce the chances for change. But the uncertainty in amplitude measurements caused by background local pressure noise as well as far field signals and the possibility of port blockages remained the chief sources of error. Because of high local noise levels at times the amplitude uncertainty was above 20 per cent.

RESULTS OF EXPERIMENTAL TESTS AND THEORETICAL ANALYSIS

Frequency Response Characteristics of Pipe Array as a Function of Port Position and for Several Values of Array Port Resistance

The upper portion of Figure 7 shows frequency response data normalized using data at 0.25 Hz. This was done for ports 1S, 50S and 99S. These data are for a type of pipe array normally used with 310 ohm array ports.

The results indicate that there is little variation in the relative frequency response characteristics for this pipe array configuration regardless of the position of the port being tested. There was a variation in the absolute amplitude with port position. This information obtained at 0.25 Hz normalized reference port 1S data is indicated at the upper right hand side of the figure. The absolute amplitude data shows that signals near the ends of the pipe array are attenuated when compared to those near the center. Since this attenuation is frequency independent, resistive attenuation within the pipe array is indicated.

The lower portion of Figure 7 shows frequency response data taken at port 99S for several different values of array port resistance. The resistance of the entire set of array ports was changed by using wire inserts. An earlier section explains how the ports were calibrated under these conditions. Resistance values of 310 ohms, 1200 ohms and 5000 ohms were used. For each value of port resistance tested, the set of data obtained was normalized with reference to an amplitude measured at low frequency, and showing a good signal-to-noise ratio. This figure illustrates the pipe array operation as a function of port resistance and shows that it acts as a low pass filter; the shorter periods are reduced in amplitude as the value of port resistance is increased.

Static Summator Calculations of Pipe Array Attenuation

Considering the pipe array as a static summator, the attenuation of the pipe array has been computed as a function of port position for several values of port resistance. Figure 8 shows the results of these calculations performed for the pipe configuration defined as "normal."

In this figure the theoretical response normalized relative to the center port inputs has been plotted as a function of port location. Note that as the port resistance is
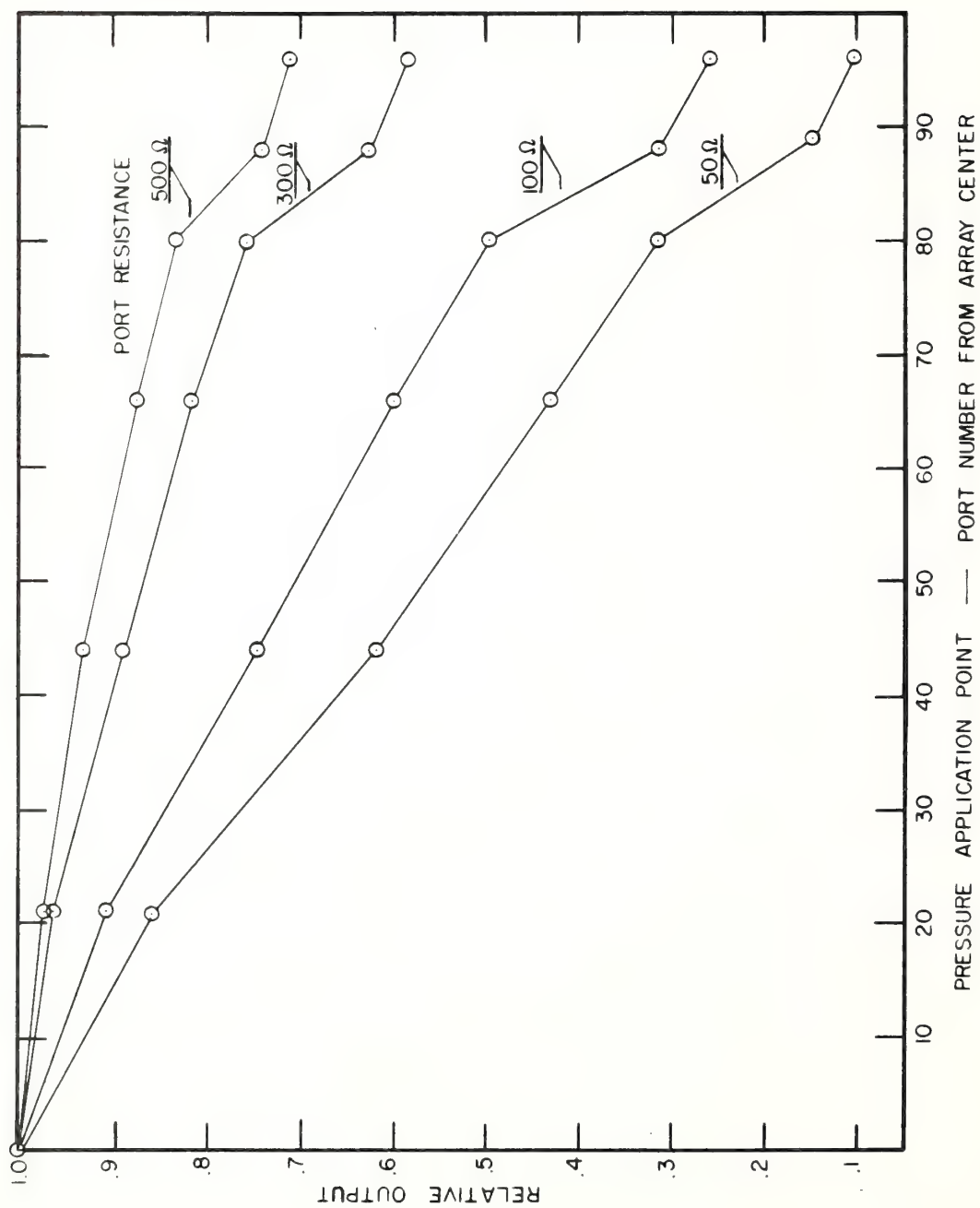
809

Figure 8. D-C Summator Computed Attenuation

reduced, the predicted attenuation increases greatly. For an array port resistance of 50 ohms the response at the ends of the pipe is about one-tenth of that at the center. For the array port resistance normally used ($\sim 300 \, \Omega$), just under 0.6 of the central port response is predicated for the end ports.

Step Functions of Pressure Applied
at Individual Ports

Figure 9 shows the plot of the relative response as a function of port location in feet from the center of the pipe array. These data were obtained by applying step functions of pressure to array ports located at various distances from the array center. Each resulting impulse measured at the center of the array was processed by measuring the amplitude from the zero position of an analog record to the first peak. The finite bandwidth correction for the electronics used was measured in the laboratory prior to performing the test so that the absolute pressure amplitudes were determined; however, the data were plotted on a relative amplitude basis together with the theoretical prediction for 300 ohm ports. Figure 7 demonstrated that there is little change in frequency response with port position with this configuration. Therefore, this attenuation is not produced by a change in passband varying the finite bandwidth correction for the step function, but rather reflects the broadband attenuation characteristics of the pipe array. Note that these results are in good agreement with the predicted ones assuming that the pipe array is a d-c summator.

Sine Wave Attenuation as a Function of Port Position

Figure 10 is a plot of relative response referred to the center port as a function of the port number from the array center. There are five-foot spacings between the array ports. These data were obtained using the fan-type pressure generator in conjunction with a variable resistive acoustic load which permitted approximate sine waves to be generated in a more convenient manner than did the centrifugal calibrator. Thus, the more portable fan-type generator was carried from port to port and operated for three different signal periods (10 sec, 8 sec and 3 sec). The resulting plot showed that for the three frequencies tested, the attenuation with distance toward the ends of the array is independent of frequency and is similar to the step function results shown in Figure 9.

Attenuation along Pipe Array with Alternate Ports Sealed

Figure 11 shows the data taken with 2-second period sine waves plotted as a function of port position for the pipe array. The predicted response has also been included for reference.

Alternate ports of the field array were capped off, and the experiment measuring the response as a function of port position was repeated. These normalized data show that there is less attenuation for the pipe array with alternate ports capped than for the normal array. This is expected from the decrease in N in accordance with the analysis of the earlier section "The Implications of this View."
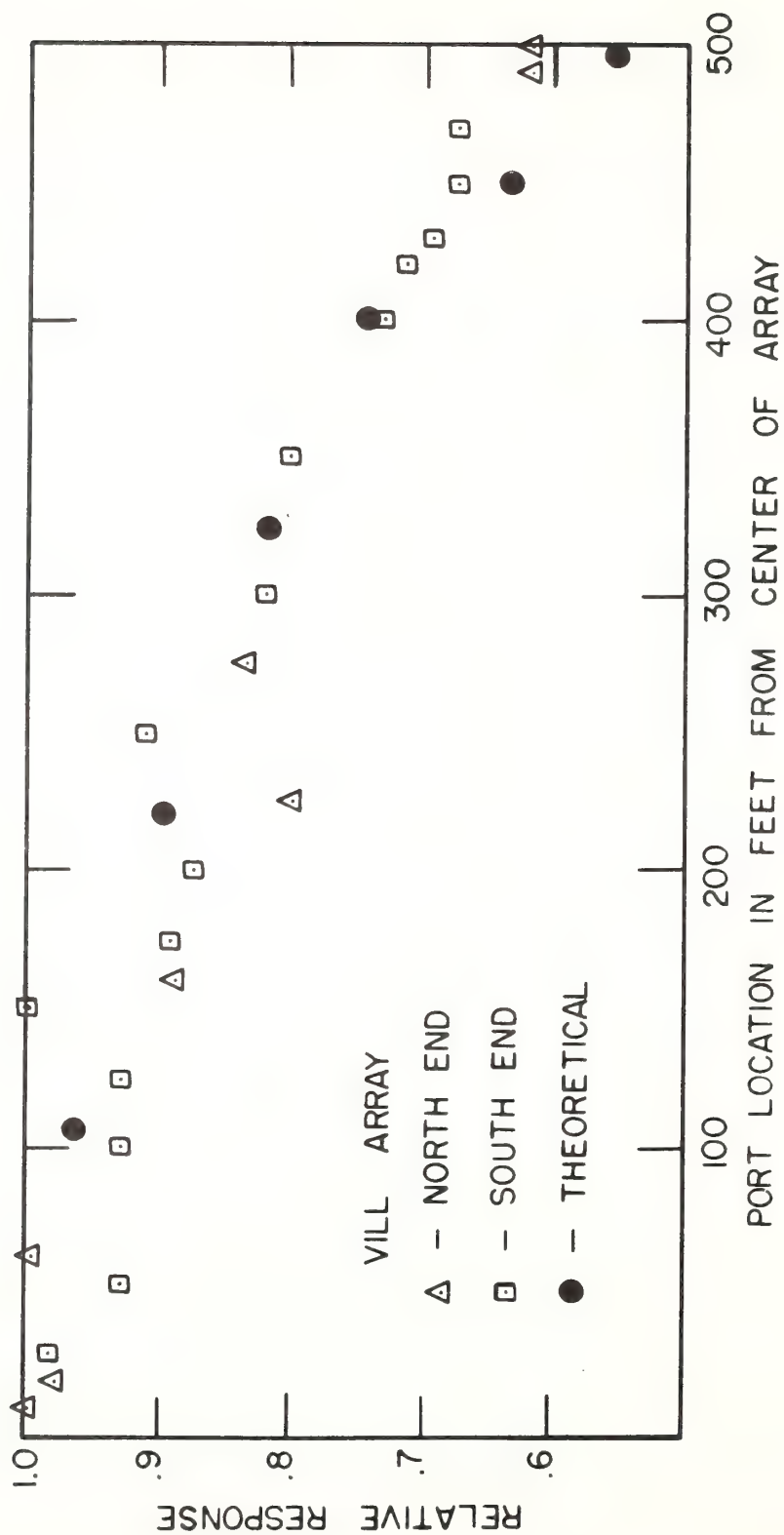
Figure 9. Step Function Response as a Function of Port Position,
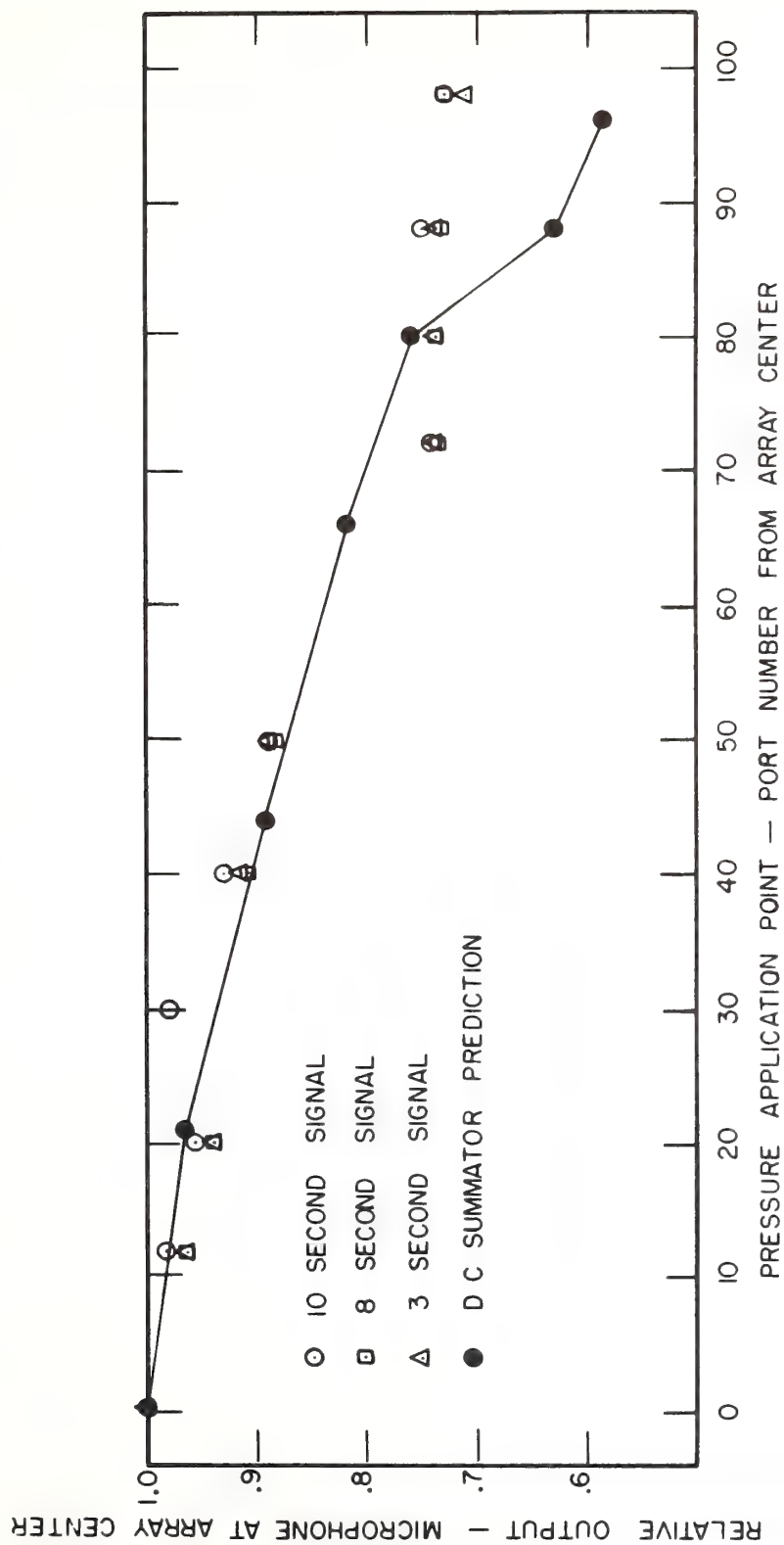Experimental and Theoretical

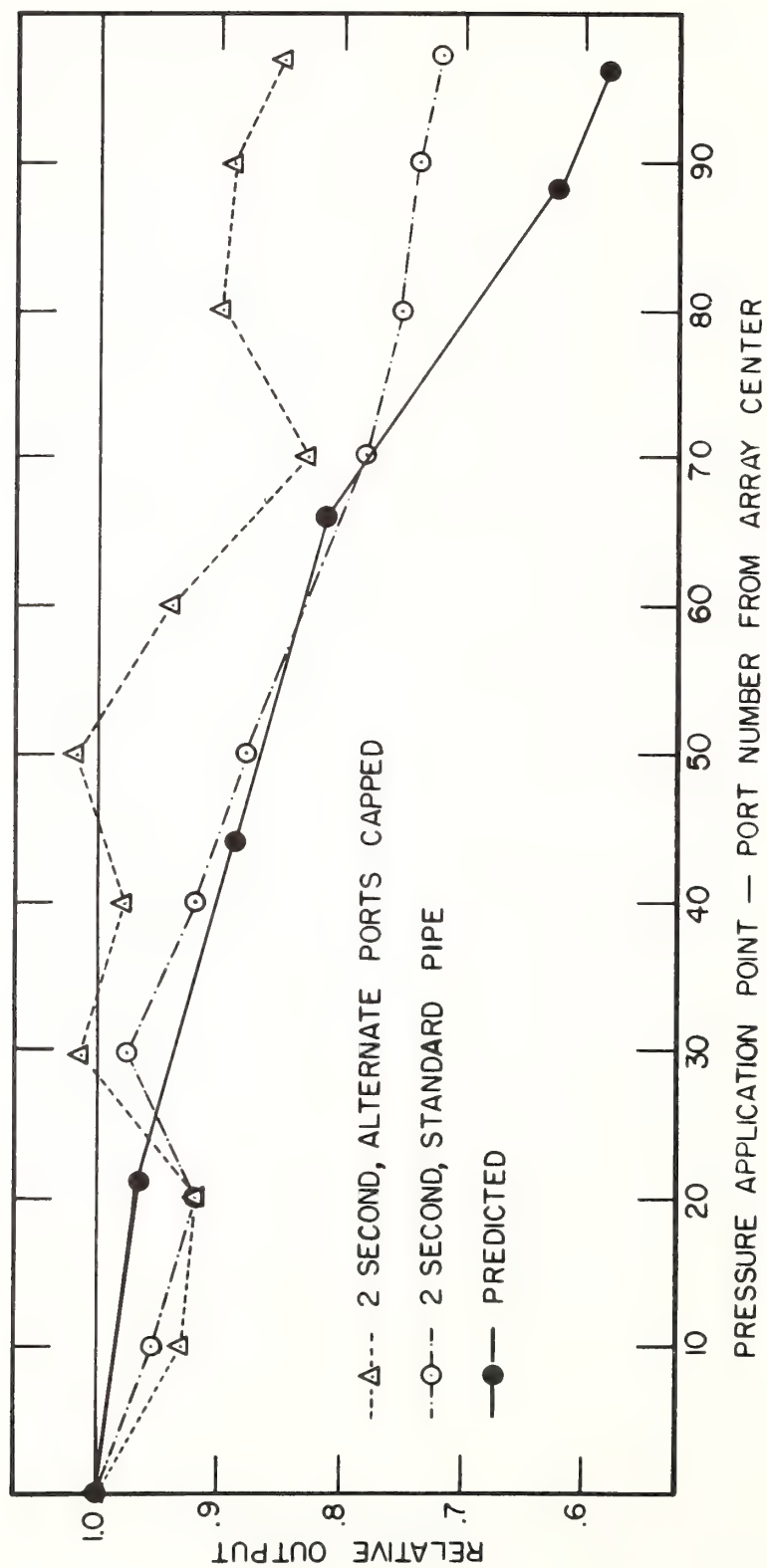Figure 10. Sine Wave Response as a Function of Port Position

813

Figure 11. Influence of Alternate Port Capping

Attenuation along Line Microphone for Low Values of Port Resistance

The port resistors described in the earlier section "Changing toward Lower Resistance" were installed so that the attenuation along the pipe array could be examined under these conditions. Measurements were made for a field pipe array and these are presented in Figures 12 and 13 for array port resistances of 50 ohms and 200 ohms. Note that the measured values for 50 ohms presented in Figure 12 are lower than those predicted using the d-c summator concept. Those values measured for 200 ohm inlets are more in agreement with the predicted values. Step functions were used in obtaining this data. The disagreement indicated in Figure 13 could be caused by a variation in the short period characteristics of the array response with port position.

Pressure Functions Applied to Pipe Array under Various Conditions of Leakage

It is important to investigate the operation of systems under abnormal conditions. Just as the functioning of a healthy person may frequently be best deduced in medicine by study of the sick; system operation under abnormal conditions can yield insights to an investigation.

Bushings were removed from the pipe at several port positions. This is equivalent to shorting a transmission line to ground because the acoustic resistance of a pipe inlet without a bushing is very low. Complete frequency response measurements were made at port 1 with the bushing removed at port 51S, and the test was repeated with only bushing 99S removed. The results of these tests appear in Figure 14. Note that at short periods the relative response is not changed much when compared with the greatly reduced response at long periods (upper curves, 51S removed). This indicates that inductive effects within the modified pipe are important at frequencies below 0.1 Hz. The data could not be extended to very low frequencies because of the increased local noise associated with a bushing removal.

POSSIBLE PRACTICAL APPLICATIONS

In cases where it is desirable to sense pressures at many points over a large area but where the cost of transducers would be prohibitive, pneumatic tubing with capillary leaks at the points of interest may provide a solution. Examples of such a situation are dust devil or tornado studies. It is conceivable that a researcher would wish to monitor an area and yet have insufficient mobility to be able to insert sensors in the flow field of a dust devil. Arrays of pneumatic summing devices offer economical means for sensing over large areas showing a high incidence of dust devil activity. The passage of a dust devil, which is tracked optically over an element of such an array, causes pressure signals which in turn give valuable information concerning the flow field.

It is possible to measure the speed of a vehicle using a summator along a roadbed. The time between the arrival of a vehicle wake system at various ports of a summator placed alongside a roadbed is a measure of vehicle speed. Information concerning the size of the vehicle is contained in the duration and pressure amplitude of the signal detected. Measurement of the pressure field caused by the transfer of aircraft weight to the surface of the earth [Reference 2] required the use of such a pipe array to detect the small pressure signatures in the presence of noise. Also sensitive barographs
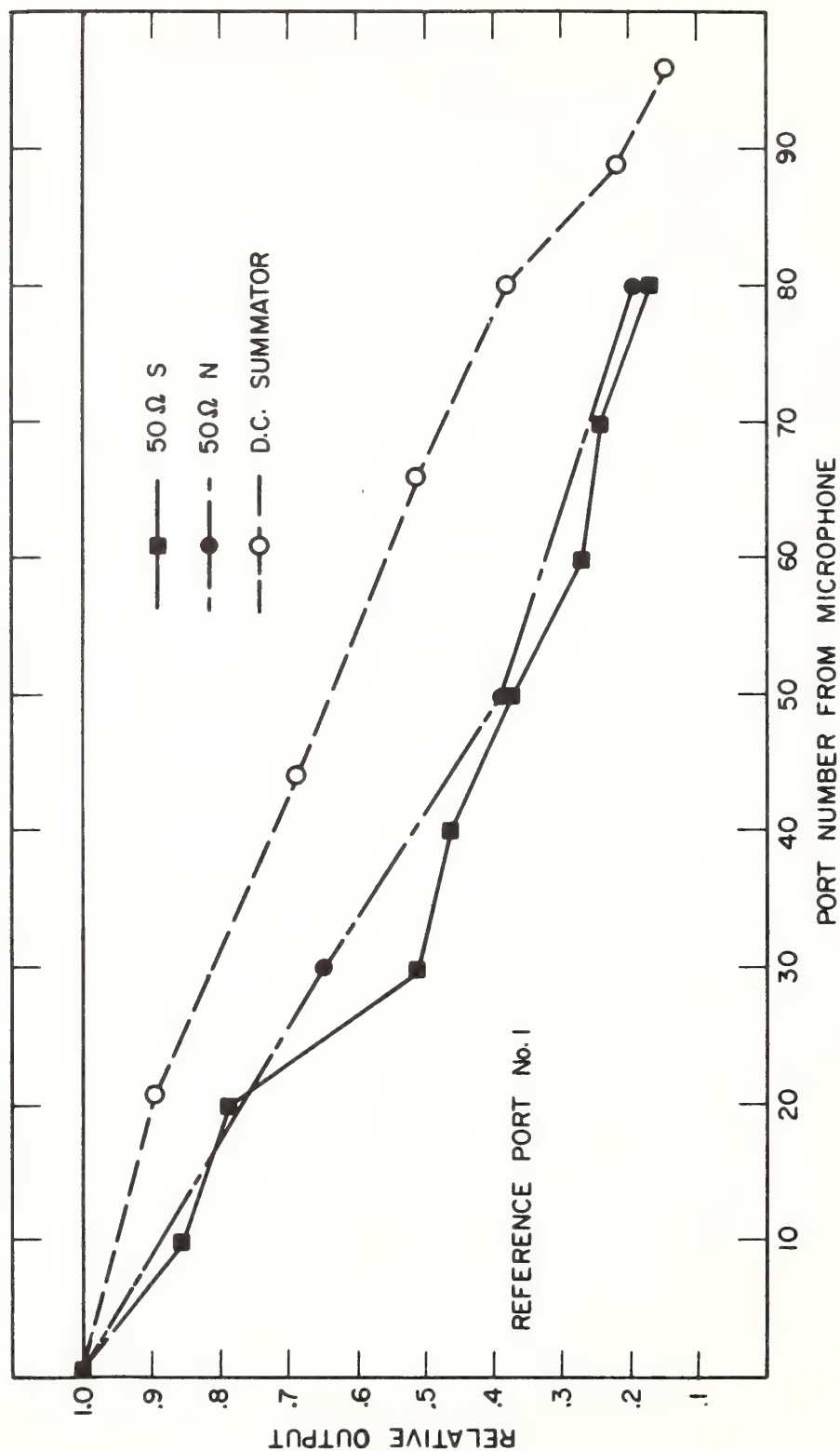
Figure 12. Attenuation along Pipe Array for 50 Ohm Port
Resistances, Experimental Step Function Response
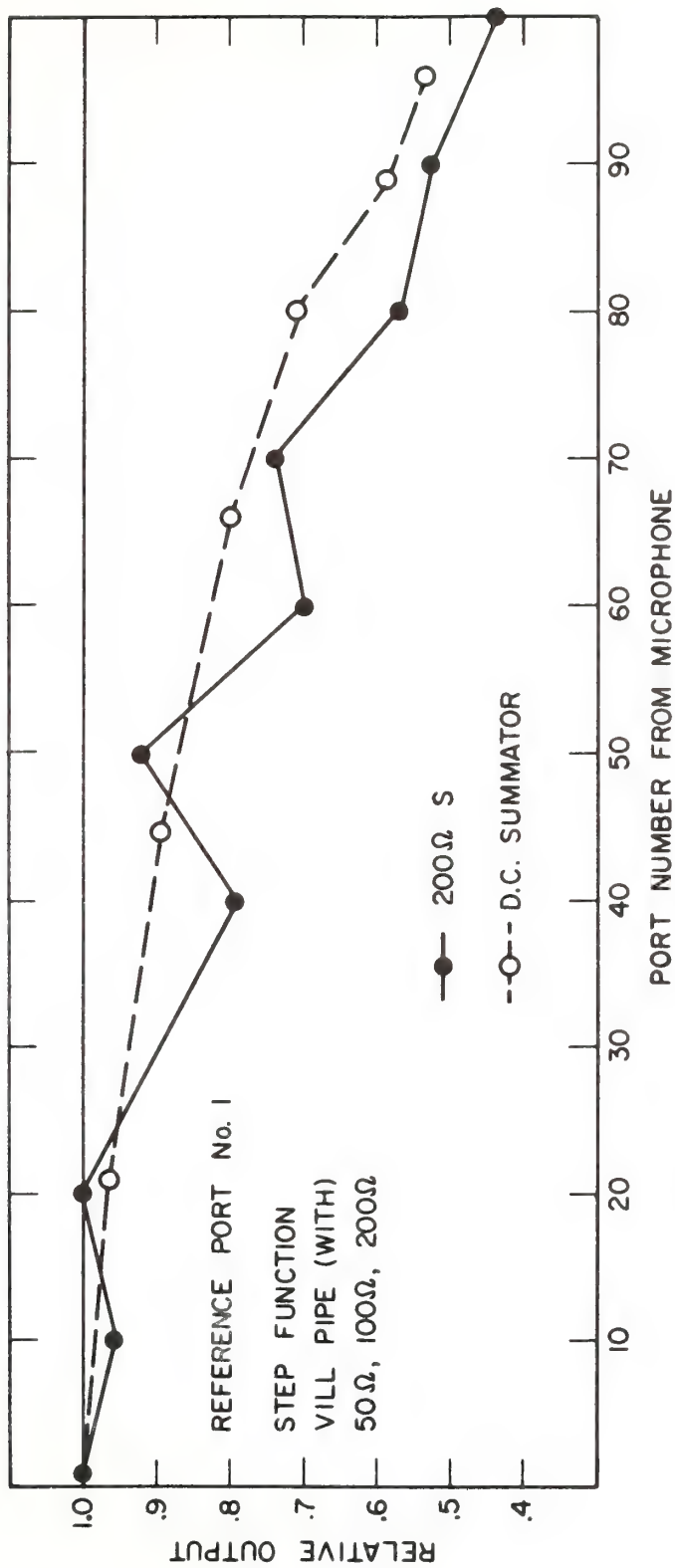compared to D-C Summator Prediction

Figure 13. Attenuation along Pipe Array for 200 Ohm Port
Resistances, Experimental Step Function Response
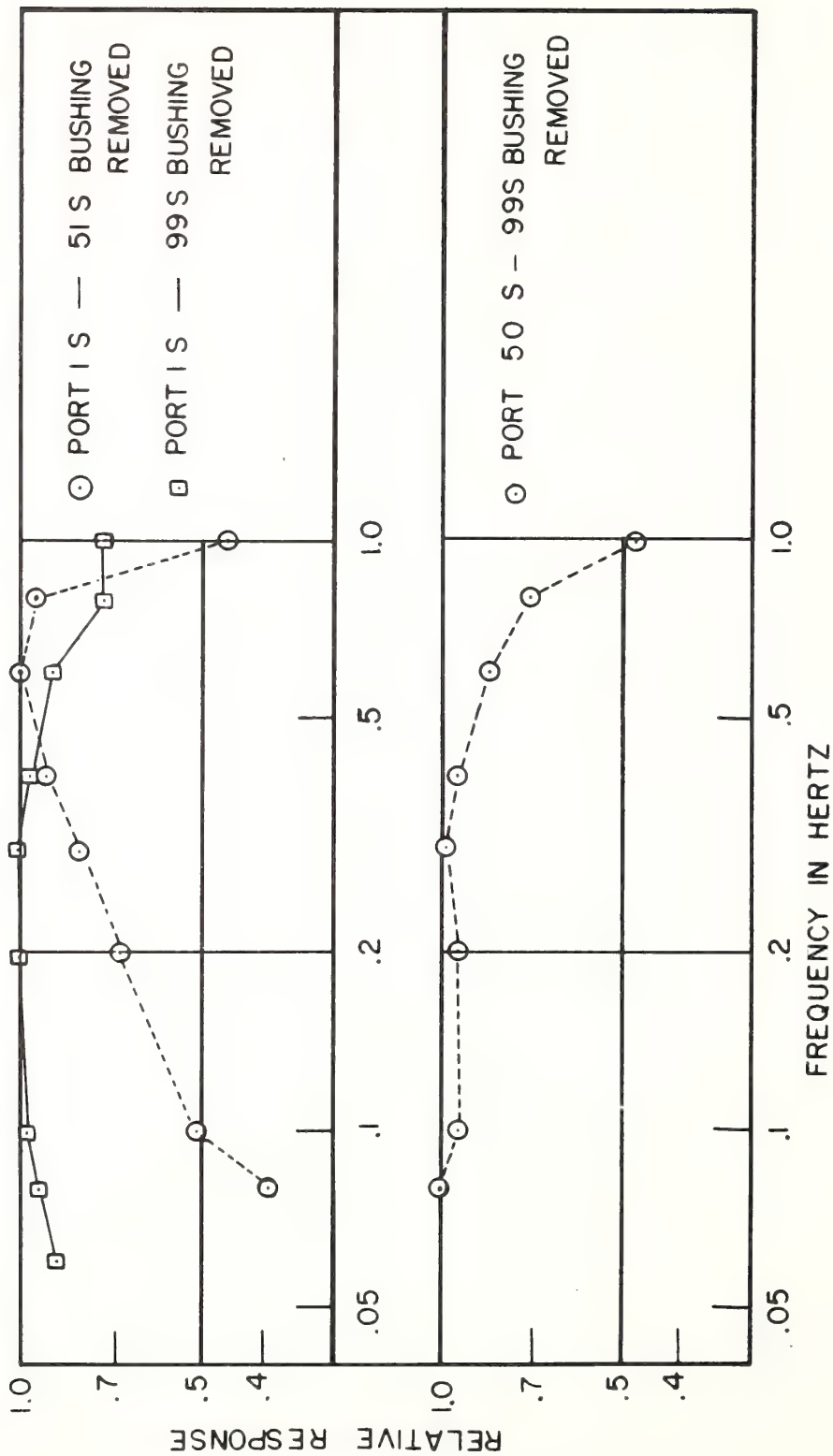compared to D-C Summator Prediction

817

Figure 14. Relative Frequency Response with Leaks in Pipe

vented to the atmosphere through forms of these summators provide better representation of the ambient pressure field in which the influence of the building housing the device is removed.

There are also a wide range of uses analogous to electronic adding circuits. Various combinations of input pressure signals can be monitored and functions activated if the summed signal becomes larger than some desired threshold at the pressure transducer. If one side of a differential pressure transducer is connected to a set of monitor points through a d-c summator, application of a pressure signal to the other side is equivalent to subtraction; therefore, a wide range of functions is possible using only one basic sensor, with the sensing points being distributed pneumatically.

A d-c summator placed along an aircraft runway offers an intriguing concept for use in the problem of aircraft-wake-vortex detection. When the long axis of a wing-tip vortex is oriented parallel to and above a line of ports, these sense the pressure field essentially coherently, and one detects a signal consisting of the summed pressures appearing at the ports. At the same time the distributed line reduces the incoherent pressure fluctuation noise caused by turbulence. Sensing pressure fields with a dimension that is small compared to the array length is possible while at the same time removing the more spatially coherent noise caused by atmospheric motions. Pressure changes caused by atmospheric gravity waves are an example of this class of noise. Subtraction by connecting two arrays differentially across a pressure transducer is an approach which removes such gravity wave noise when the spacing between the two arrays is small compared to a wavelength (typically 10 km) for atmospheric gravity waves. Finally, the test instruments and techniques described could be applied to the detection of leaks or stoppages in pneumatic lines.

Summary and Conclusions

A noise-reducing line microphone applied by geoacousticians was constructed of a 1000-foot length of galvanized iron pipe tapered from the center in steps to small diameters at the ends. Capillary leaks to the atmosphere at 5-foot intervals constitute the sensing inlets. The weight and size of this device necessitated tests at a field site in spite of the concerns about dust and insects changing its characteristics. We used portable low impedance pressure standards in the form of a centrifugal and a fan-type generator in these tests.

A theoretical model of the pipe as a d-c summator demonstrated the importance of resistive attenuation. The results of this analysis showed that significant attenuation occurs for the end ports relative to the center ports and that this attenuation is directly proportional to the number of ports and the resistance of a pipe section. Also the predicted attenuation varies inversely with the port resistance.

The experimental results were in good general agreement with the predicted attenuation. The frequency response of the pipe array was measured as a function of port resistance and position. Using step functions of pressure and sinusoidal pressure variations, we made detailed measurements for various array port positions.

The line microphone was operated under abnormal conditions (large leaks to the atmosphere), and frequency response data run under these conditions are presented. These data indicate that the cause of d-c summator malfunction can be deduced from frequency response data run at individual array ports.

Finally, the applications outlined included the possible uses of d-c summators for studies of tornadoes and dust devils. Their use for the detection of wingtip vortex systems near runways is also suggested and techniques for reducing "noise" due to

atmospheric gravity waves in such measurements are described. Application of pneumatic summing techniques is possible in a variety of geophysical problems.

Acknowledgments

References

1. A.J. Bedard, Jr. "The Design of a Temperature Independent D-C Flow Resistor," Fluidics Quarterly, Vol. 5, Issue 2 (April 1973), pp. 31-50.
2. A.J. Bedard, Jr. and R.K. Cook. "Transfer of Aircraft Weight to the Surface of the Earth," Abstract, J. Acoust. Soc., Am 44 (1968), p. 376.
3. V.M. Borsheverov, N.F. Gorshkov, S.O. Lomadze and M.I. Mordukhovich. "Spectral Characteristics of the Attenuation of Turbulent Pressure Fluctuations by Spatial Filtering," Izv. Atmospheric and Oceanic Physics, Vol. 9, No. 6 (1973), pp. 360-361.
4. R. Burridge. "The Acoustics of Pipe Arrays," Geophysical Journal, Royal Astronomical Society, Vol. 26 (1971), pp. 53-69.
5. R.K. Cook and A.J. Bedard. "On the Measurement of Infrasound," Geophysical Journal, Royal Astronomical Society, Vol. 26 (1971), pp. 5-11.
6. F.B. Daniels. "Noise Reducing Line Microphone for Frequencies Below 1 cps," J. Acoust. Soc., Am 31 (1959), pp. 529-531.
7. J.S. Flores and A.H. Otero. "Short-Period Infrasonic-Noise Spatial Coherence," J. Acoust. Soc., Am 56 (1974), pp. 204-205.
8. J.F. Kemp. "Centrifugal Manometer," Transactions of the ASME, Journal of Basic Engineering, 1959, pp. 341-348.
9. J.A. McDonald, E.J. Douze and E. Herrin. "The Structure of Atmospheric Turbulence and its Application to the Design of Pipe Arrays," Geophysical Journal, Royal Astronomical Society, Vol. 26 (1971), pp. 99-110.
10. J.T. Priestley. "Correlation Studies of Pressure Fluctuations on the Ground Beneath a Turbulent Boundary Layer," National Bureau of Standards (USA), Report 8942, 1965. This report is not available in the open literature.
11. L.A. Zalmanzon. "Components for Pneumatic Control Instruments," Pergamon Press, 1965. Translated from Russian.

Nomenclature

a Inner radius of tube

K Constant

L Length of tubing

N Number of flow resistors

P_o Ambient pressure

ΔP	Pressure difference with respect to P_o
ΔP_N	Pressure difference applied to flow resistor of Nth chamber
ΔP_{CN}	Pressure difference occurring within Nth chamber
$\Delta P'_{C1}$	Pressure difference in first chamber due to the application of pressure to flow resistor of 2nd chamber
Q	Volume velocity
R	Flow resistance of single capillary
R_P	Flow resistance of connecting pipe
S_f	Fluidic switch
μ	Viscosity of medium
ρ	Density of medium
ω	Angular frequency

The Design and Use of Sensitive Pressure-Jump Sensors to Detect Thunderstorm Gust Fronts. Part I: Pressure-Jump Detector Design

A. J. Bedard, Jr., and H. B. Meade[1]

Wave Propagation Laboratory, NOAA Environmental Research Laboratories, Boulder, Colo. 80302

(Manuscript received 4 March 1977, in revised form 28 July 1977)

ABSTRACT

We outline the known properties of atmospheric pressure jumps, including rise-time and pressure-amplitude statistics, and we indicate how these statistics guide the choice of pressure-jump detector components. We review design considerations and test procedures and discuss the practical constraints of inside and outside installations of such detectors. Our tentative conclusion is that a pressure switch with a threshold of 0.5 mb, used with a high-pass filter with about a 3 min time constant, can detect sudden pressure increases reliably. The final choice of components and the evaluation of the sensor for thunderstorm gust-front detection will depend upon the accumulation of operating experience under well-defined meteorological conditions.

1. Introduction

The official U. S. Weather Service definition of a pressure jump is a rise in pressure exceeding 0.005 inch of mercury (0.169 mb) per minute, totaling 0.02 inch of mercury (0.667 mb) or more. Such sudden increases in atmospheric pressure have a variety of meteorological sources including thunderstorm outflows and hydraulic jumps and can provide storm warning information. Tepper (1950) suggested that the detection of the pressure-jump line preceding squall lines can indicate the presence and the motion of a squall line. Subsequent measurements such as those of Williams (1953), Donn *et al.* (1954), Bedard (1966) and Bowman and Bedard (1971) demonstrated that the pressure jump can in fact be used to track the system motion. Bedard and Beran (1977) review the techniques available for detecting thunderstorm gust fronts using surface sensors.

One problem in making pressure-jump studies is that conventional Weather Service barographs do not have sufficient time or amplitude resolution for pressure-jump studies (since they are not designed for this purpose). Hence it is logical to design sensors to respond specifically to the pressure jump, while not responding to the large variety of pressure changes due to other sources, such as local turbulence, low- and high-pressure systems and atmospheric gravity shear waves aloft.

Responding to the analyses of Tepper, the U. S. Weather Bureau developed a pressure-jump detector and operated networks in the Fort Worth, Tex., and Washington, D. C., areas during 1955. Unfortunately, investigators did not publish either the details of the techniques used or the results obtained. Mr. William

Hass (private communication) of NOAA's Air Resources Laboratory, who worked with the project, indicates that the detectors operated quite satisfactorily. Using after-the-fact analysis the project scientists tracked pressure-jump lines across the network. (Although the project relied upon local observers to respond to local detector alarms and place phone calls to a central processing location, the designers of this pressure-jump detector network noted the desirability and feasibility of using automatic data transfer and processing.)

The purpose of this paper is to present the design considerations for such sensitive pressure-jump detectors including a description of the calibration techniques applied. These considerations must include a review of the statistics of pressure jumps important to the choice of detector components. Finally, we present an example illustrating the design and operation of this class of sensor.

2. Pressure-jump statistics

Although standard microbarographs are not well suited for such studies, several investigators, either using modified microbarographs or carefully studying standard traces, worked to compile statistics describing the causes and characteristics of atmospheric pressure jumps. The following review of some of these studies emphasizes pressure-amplitude and rise-time statistics. In addition, we consider how pressure amplitude is related to storm motion and intensity. This information is critical in choosing optimum time constants, trigger points and array element spacings. The reference by Bedard and Beran (1977) provides additional background. Unfortunately, the literature contains few references useful in defining the statistics of pressure

---

[1] Present affiliation: Federal Aviation Administration, St. Paul Sector, Grand Rapids, Minn. 55744.
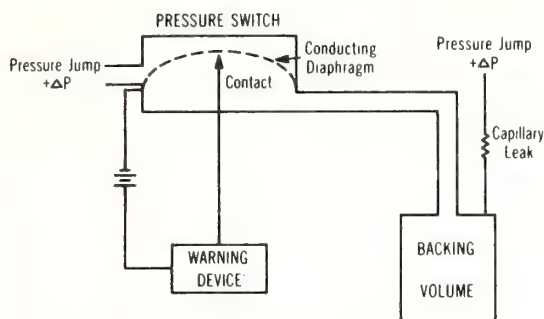
FIG. 1. Schematic view of pressure-jump detector.

jumps related to gust fronts. There is a need for more measurements with quality instruments under well-defined meteorological conditions.

a. Pressure-jump amplitude and rise time

Published case studies showing pressure-jump time series include those of Tepper (1950), Fujita (1959) and Charba (1974). These show positive changes in pressure that occur over a time scale of several minutes with typical amplitudes of several millibars. Bleeker and Andre (1950) summarized pressure-time data from 101 cases, 50 of which occurred in Ohio and 51 in Florida. They found that the most rapid portion of the pressure rise appears over a period of ~10 min. In studies using standard microbarographs the peak pressure is probably underestimated because of the influence of pen-paper friction. The application of a vibrator to the microbarograph reduces the friction considerably. Working with the properties of a squall-line event and averaging data from over 55 stations, Tepper (1950) found that the pressure rises sharply 2.3 mb in 5 min and then falls off gradually.

In a study of several squall-line thunderstorm events, Williams (1948) observed a pressure rise of from 2 to 6 mb sometimes occurring within 5 min. Williams (1953) summarized the pressure-amplitude characteristics for what he called "elevation type waves," which included both squall-line and cold-front related pressure increases as well as those due to "isolated discontinuities" (probably isolated thunderstorms). Goff (1975) found an average peak pressure rise of 2.5 mb for 20 case studies of thunderstorm gust fronts that ranged from 0.8 to 6.6 mb. For some cases he measured shorter rise times (~100 s) than past measurements indicate, which was perhaps due to the better quality instrumentation used.

b. The speed of motion of pressure-jump systems

Williams (1953) also summarized the statistics of propagation speeds for "elevation type waves." These data are pertinent to the choice of detector spacings as well as the estimation of warning lead time offered by a detector located some distance from a point of interest. Most of the disturbances traveled faster than 30 mph (13.4 m s⁻¹).

Tepper (1950), working with a pressure-jump case study, found a propagation speed for the pressure jump of 45.6 mph (20.4 m s⁻¹). Goff (1975) found the average speed of 17 thunderstorm gust fronts was 10 m s⁻¹.

c. Pressure-jump amplitudes and storm system intensity

The work of Bleeker and Andre (1950) indicates a relationship between pressure-jump amplitude and the intensity of the associated weather system. Bleeker and Andre found a linear relationship between amount of rainfall and the maximum pressure amplitude. A relationship of this type is to be expected on theoretical grounds because the pressure measured depends directly upon the height of the column of air cooled by evaporation as well as the magnitude of the density difference induced. These data suggest that statistically a trigger point can be chosen on the basis of some threshold of storm intensity. The higher the pressure level chosen, the fewer the false triggers due to other sources with the larger storms detected preferentially. However, Bleeker and Andre (1950) found no clear relationship between storm intensity and maximum pressure amplitude until they removed from the analysis multicell data and data from thunderstorm cells that did not pass over a significant segment of their array.

3. Design considerations

The original pressure-jump detectors used internal volumes of 55 gal and cost approximately $200 at 1955 prices. They required a thermally stable environment for proper operation. But it is possible to decrease the size and cost while increasing reliability by using techniques developed for the detection of infrasound in the atmosphere. In addition, one can use commercial pressure switches, now available at reasonable cost, for the basic pressure sensor. Pressure switches manufactured in quantity for home appliances (e.g., clothes dryers) use a diaphragm that makes electrical contact when pressures above some desired level occur. These switches make convenient sensors. On the other hand absolute pressure sensors require another level of processing to distinguish pressure jumps from other changes and at this time seem to represent a more expensive and complex alternative.

a. High-pass filter configuration

A pressure switch operated in a high-pass acoustic filter configuration (Fig. 1) responds to sudden changes in pressure while suppressing response to long-period, large-amplitude disturbances. Such filters usually consist of a reference volume to which we connect one

side (in our case the negative pressure side) of a differential pressure sensor. A capillary leak from this reference volume to the atmosphere permits long-period pressure changes to leak through so that they appear on both sides of the pressure sensor simultaneously, thus suppressing long-period response. The capillary leak is an acoustic resistor, the value of which can be computed from the Hagen-Poiseuille relation

$$R = \frac{8\mu l}{\pi a^4},$$

where μ is the viscosity of air, l the length of the capillary, a the radius and R the flow resistance.

The reference volume is analogous to an electrical capacitor and, under the assumption that the pressure changes occur isothermally, the capacitor size can be computed from

$$C = \frac{V}{P_0},$$

where V is the internal volume, P_0 the static pressure and C the acoustic capacitance.

Thus, the combination of a pressure switch and a high-pass filter offers a simple solution to this detection problem. The particular time constant chosen must be short enough to suppress long-period pressure changes but long enough to insure reliable detection of the pressure jumps of interest.

In practice, complex equivalent circuits can occur, especially if the equivalent capacitance of the sensor is significant with respect to the reference volume C or if we cannot ignore the resistance of the tubing connecting the system together. For the simplest case considered here, the time constant τ of the system high-pass filter is the product RC. The acoustic resistor can take the form of a standard hypodermic needle and the capacitor constructed from any convenient volume that is structurally rigid and thermally insulated.

b. Structural rigidity

The requirement for structural rigidity becomes clear if we consider that a volume change of 0.01% in a closed volume will produce a pressure change of about 0.1 mb at standard conditions. If a volume of 250 cm³ is used this corresponds to a 0.025 cm³ volume change.

c. Temperature response

Another consideration is thermal response. If the temperature changes by 1°C in a closed volume of air the pressure will change more than 3 mb at standard conditions. Such thermally induced pressure changes appear superimposed on variations due to atmospheric pressure changes and, unless reduced, will dominate them.

One method of obtaining thermal stability is to bury the sensor while routing the sampling port to the surface. Geiger (1973) reviews data showing the diurnal variation of temperature as a function of depth. In sandy soil the daily temperature fluctuations at a depth of $\sim$40 cm are smaller by about one order of magnitude relative to those at the surface. Thus even relatively shallow burial can suppress the influences of local temperature changes.

Two techniques help greatly in reducing thermal effects. Using layered insulation for both an outer enclosure and around the backing volume itself increases the thermal time constants. Packing the volume with steel wool suppresses convection pressure noise and helps suppress short-period, thermally induced pressure changes because of the increased heat capacity.

We have built a low-cost pressure-jump detector following these design principles. It consists of a 250 cm³ volume, filled with stainless steel wool, with a standard hypodermic needle used as the flow resistor. These components are placed within foam insulation in a fiberglass box suitable for wall mounting. Use of reasonably priced commercial pressure switches keeps the cost of the assembly below $50 including lightning protectors, batteries and an electronic oscillator for sending data over phone lines.

d. Building installations

We have installed this type of pressure-jump detector inside buildings which has required attention to the building-atmosphere time constant and internal sources of pressure noise as well as the influence of the building on the streamlines of the flow and hence on the local pressure field.

One must insure that the building time constant is short enough that atmospheric pressure changes couple into the structure. Even a small leak is sufficient to insure this for most structures. For a tube 10 cm in length and 1 cm in radius the flow resistance is about 0.05 Ω. If a leak of such a size exists in a structure 10 m $\times$ 10 m $\times$ 3 m, the structure acts as a low-pass filter with a time constant of 15 s. Because of existing heating and ventilating ducts, most structures will have time constants much shorter than this estimate and thus permit accurate recording of atmospheric pressure jumps.

A further consideration applying to installation of such sensors in buildings is that modern air conditioners can develop significant pressure differences between the building and the outside atmosphere. Opening or closing of doors and windows of airconditioned buildings can introduce step functions of pressure in excess of 1 mb superimposed on the atmospheric pressure field. Venting the pressure sensor input directly to the atmosphere through a short tube is a simple solution to this problem.

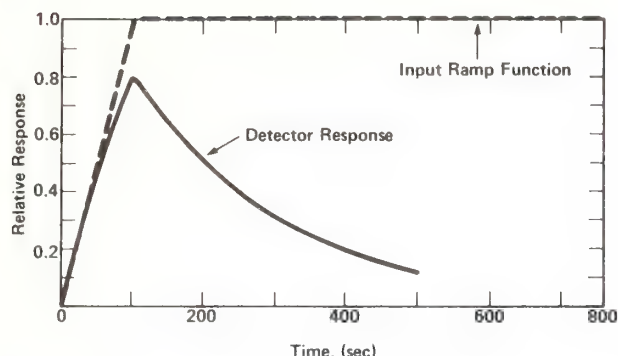Local turbulent flow fields can produce pressures that

FIG. 2. Response of detector to ramp function
with 100 s rise time.

are not representative of the atmospheric pressure field over some larger area. Small openings distributed over the surface of a building can provide some spatial integration of the pressure and give a more representative measurement. Underground burial also tends to help in this regard by placing the sensor below the atmospheric boundary layer, thus reducing wind-induced noise. In some extreme cases, a local-pressure-noise-reducing device, similar to that described by Daniels (1959) and Bedard (1977), could provide spatial averaging and added noise reduction.

e. Exposed installations

In practice, above-ground outdoor mounting of sensors might be desirable as in a low-lying area subject to flooding. Or mounting sensors on existing telephone poles could be expedient in rural areas with few buildings. In such cases a detector incorporating an increased thermal time constant is required.

Whereas the detector described above for use in thermally stable environments has a thermal time constant of about 45 min, a detector incorporating a larger (1000 cm^3) stainless steel thermos bottle and thicker insulation provides a thermal time constant of about 3 h. This model detector is mounted in a ventilated, white outside case to provide protection for the sensor from direct solar radiation.

f. Slowly varying pressure fields

An additional consideration is the influence of longer term pressure changes on detector response. For example a pressure rise or fall of 1 mb h^{-1} occurring for a time period of more than about 10 min will result in a limiting offset in the detector threshold of 0.042 mb for the choices of component values indicated later. By limiting offset is meant the maximum, constant pressure difference appearing across a differential pressure sensor equipped with a high-pass filter, resulting from the application of a constant rate of change of pressure. The offset will not exceed this limiting value though the change continues at a constant rate for many hours

(as is typical with atmospheric low or high pressure systems). As a result of such a pressure rise (fall) the threshold is decreased (increased) for a pressure jump of 1 mb by about 4%. Also, such changes, though they do cause variations of the threshold of array detectors, influence all of the array elements proportionally since the scale of low and high pressure areas is usually measured in hundreds of kilometers, whereas the array dimensions for pressure jump detectors now in use are less than 20 km in their longest dimension. Thus, the effect is small and will result in increases or decreases in the detection time for all the sensors of such arrays. The detection of events or velocity computations should not be changed except for pressure jumps just at the threshold of detection.

4. Pressure-jump detector component values

A goal is the choice of the shortest possible high-pass filter time constant that permits reliable detection of pressure jumps. This is because short time constants for a high-pass filter reduce response to unwanted long-period pressure fluctuations. Since typical atmospheric pressure jumps are more like ramp functions than step functions, one method of evaluating detector components is to numerically pass ramp functions with various rise times through a high-pass filter and evaluate the resultant response. The sequence of Figs. 2–4 illustrates the response of a high-pass filter with an RC of approximately 180 s to rise times of 100, 300 and 600 s. These figures show the relative response of both input wave forms and the filter output, normalized to the input peak value, plotted as a function of time. Note that for a rise time of 600 s (10 min) the pressure across the detector reduces to about one-third of the peak input value. The way to use these curves is to pick the minimum absolute peak pressure-jump detection threshold and the longest rise time of interest and determine if the detector would trigger. For example a threshold pressure of 2 mb with a rise time of 600 s would cause about 600 μb peak pressure across a sensor. If the sensor trigger point were set to 500 μb, the sensor would remain above the trigger level for over 300 s.
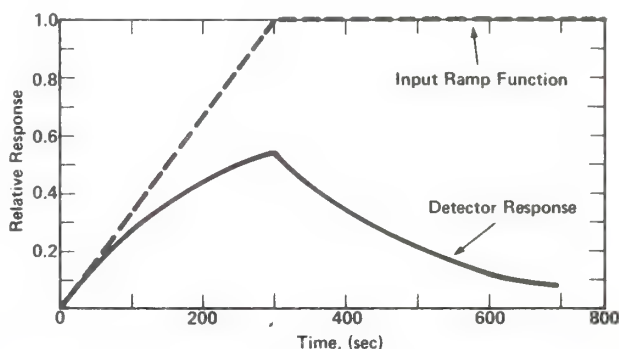

FIG. 3. As in Fig. 2 except for 300 s rise time.

Because of the variability in rise time that actually occurs with atmospheric pressure jumps, the trigger point occurs at different times for different rise times. This means that the time constants for arrays of these detectors must be matched. This disadvantage is balanced by the advantages of simple processing and low cost offered by such a detector. On the basis of past pressure-jump statistics the choice of an RC of 180 s and a trigger point of 0.5 mb seems reasonable. However, both the RC and the trigger point settings are adjustable and the optimum settings could be different for different weather systems or different regions.

Fig. 5 shows a plot of the maximum fractional pressure appearing across the detector switch as a function of the rise time of the pressure jump. It also shows the ranges of settings for the trigger level and the limits of the RC time constants for an initial manufacturing run. For the distribution of flow resistances used the time constant is between 165 and 196 s. (Note that one can tighten the tolerances considerably.) A chief problem associated with the mismatch of detectors occurs when the sensor is exposed to only a marginal amount of pressure to trigger. In such instances, whether or not a detector triggers at all is a function of the particular RC and trigger level. Another problem is that marginally triggered sensors may show variations in the initial trigger times. This results in errors in azimuth and velocity determinations that use the sequence of arrival information for an array of sensors. However, an event with a pressure amplitude of 1 mb and a rise time of 5 min will produce negligible azimuth and velocity errors for most applications, assuming an array spacing of about 1 km. We minimize error by matching sensor characteristics where close array spacings require the determination of arrival times to within 10 s. At a typical gust-front travel speed of 10 m s^{-1}, the transit time across a 1 km array is 100 s.

5. Calibration techniques

We apply several techniques to the task of evaluating and calibrating sensitive pressure switches and measuring the time constants of assembled pressure-jump
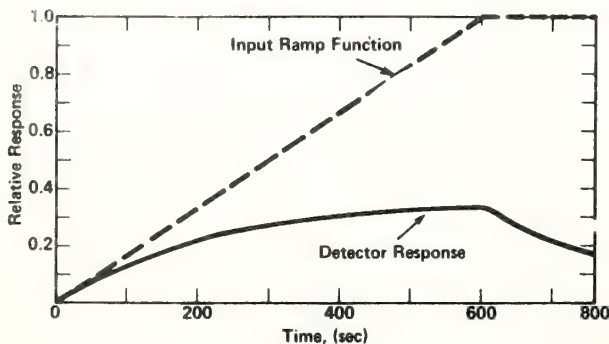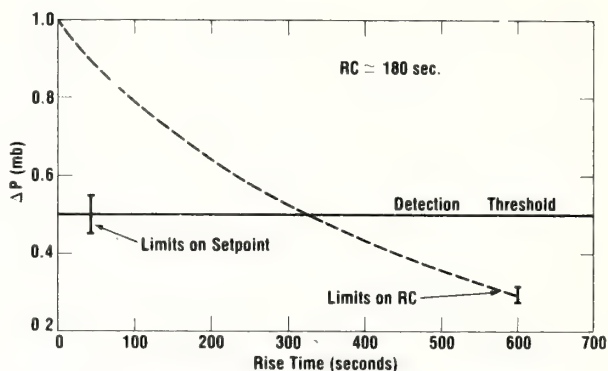

Fig. 5. Maximum pressure appearing across sensor for a 1 mb ramp function as a function of rise time.

detectors. Any method of calibration consists in a method of generation as well as a means of specification. To calibrate the trigger point of sensitive pressure switches, a water manometer primary standard can be used that measures pressure differences <0.001 inch of water; however, we also need to maintain and control very small pressures. To do this we match thermal time constants on both sides of the manometer and provide sufficient heat capacity and insulation to insure that changes occur slowly.

Matched lengths of tubing and insulated buffer volumes provide the matched time constants and stability. A variable volume element with a fine adjust capability permits us to adjust the differential pressure across the switch. When the calibration involves extremely small pressure changes (in the range of 0.1 to 25 μb), we use an alternate system, similar to that described by Bedard (1973).

We must also measure and check the calibration and time constants of the computed detectors. One means of doing this is to apply a known step function of pressure to the detector and measure the detector trigger time. Ideally, the output of a pressure-jump generator will not be influenced by the presence of the instrument being calibrated. A small fan with a variable rotation rate used in conjunction with a sensitive gage generates and specifies the desired pressures; simple switching arrangements permit the application of step functions. Note that the diaphragms of some types of pressure switches change their rest position (and hence calibration) significantly with different orientations relative to the gravitational force. Hence it is important to make calibrations for the orientation that will exist in actual use or insure that orientation effects are negligible.

6. Design details

Fig. 1 shows a schematic view of a pressure jump detector and Figs. 6 and 7 show details of our designs. We have used two types of pressure switches, one manufactured by Micro Pneumatic Logic and the other

Fig. 4. As in Fig. 2 except for 600 s rise time.
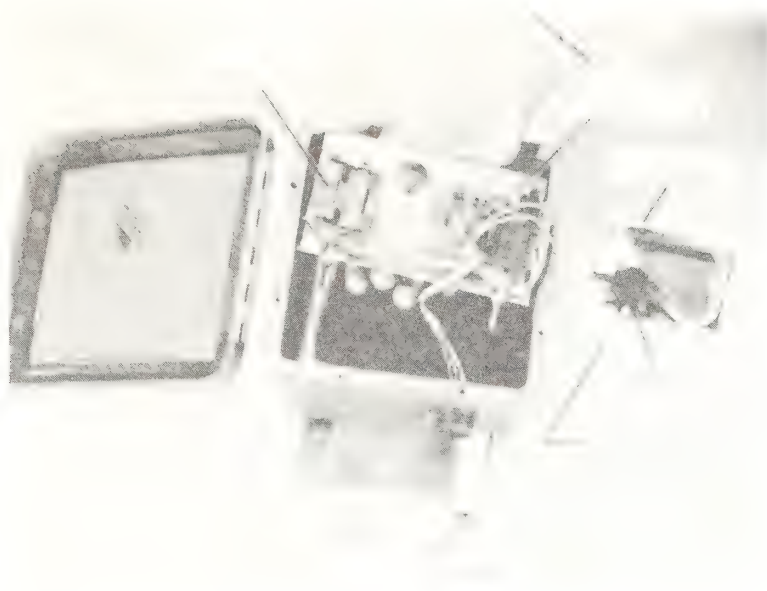
FIG. 6. Pressure-jump detector design for use in thermally stable environments.

by Fairchild Industrial Products. These or equivalent pressure switches will provide an electrical contact closure when the differential pressure across the switch exceeds some pre-set value. The 250 cm³ volume is made from standard PVC tubing and filled with medium-grade stainless steel wool. For a flow resistor we use a 2 inch long, 28 gauge hypodermic needle mounted in a length of rigid tubing for mechanical protection. The computed flow resistance is 725 000 Ω, which provides a time constant of 180 s at standard conditions.

Flow resistors built by manufacturers of fluidic components will work in this application. We have used flow resistors manufactured by Corning Fluidic Products. Using these or equivalent commercial products can simplify production greatly.

Fig. 8 shows the results of applying pressure step functions to the detector. The observed trigger duration agreed closely with that predicted from system component values. In practice we provide a battery across the switch contacts. Closure, resulting from a pressure jump, causes the battery voltage to appear across an
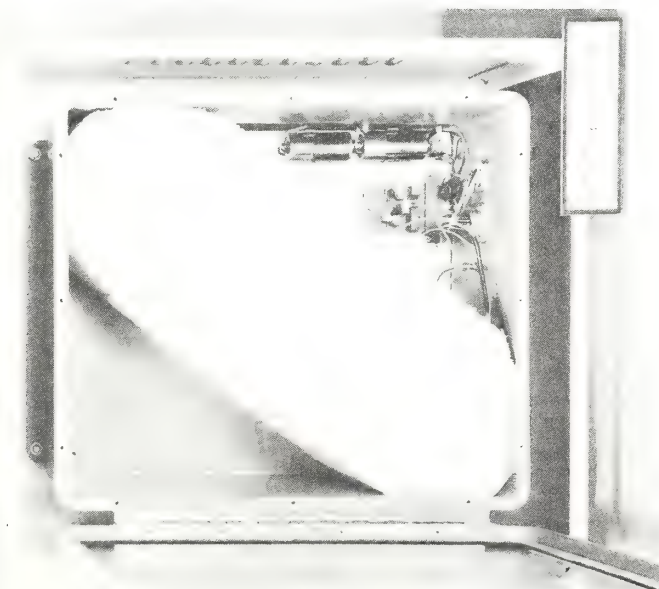
FIG. 7. Pressure-jump detector design for outdoor mounting.

oscillator, which sends a tone over a data line. This is only one of a number of possible methods of transferring data back from a remote location. A number of detectors with different tone frequencies can be multiplexed on a single dedicated data line. We are evaluating the potential of large arrays of these detectors for storm warning, particularly for gust-front systems and their associated wind shears which are hazardous to aircraft. Fig. 9 shows an example of a recording of a pressure jump (center trace) and three triggers from pressure-jump detectors located in a triangular array about 0.6 km on a side. The center trace of the curvilinear chart record is from a microbarograph used with an electronic high-pass filter (RC = 2200 s) to reduce very long-period pressure changes. The upper three traces are event markers corresponding to pressure jump detectors, with the lowest trace from a detector colocated with the microbarograph. The reference microbarograph used (Ball Engineering model EX 350b) or an equivalent sensor permits evaluation of the pressure-jump detector response to known atmospheric pressure changes.

7. Concluding remarks

We have described two alternate pressure-jump detector designs for use either within buildings or exposed locations. Comparisons between numerical results from pressure-jump simulations and laboratory calibrations indicate that the sensors operate as expected. A review of pressure-jump statistics and preliminary results from field tests also helped to guide our choice of detector components. Our tentative conclusion is that a pressure switch with a high-pass filter with about a 3 min time constant can reliably detect sudden pressure increases. The final choice of components and the evaluation of the sensor for thunderstorm gust-front detection will depend upon the accumulation of operating experience under well-defined meteorological conditions.

Concepts change from impractical to practical as a supporting technology progresses. We suggest that arrays of pressure-jump detectors may now be a practical tool for the meteorologist. Current field tests at Chicago's O'Hare Airport, at Dulles Airport, and in
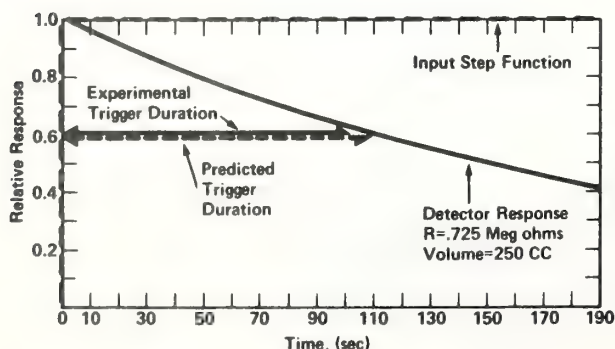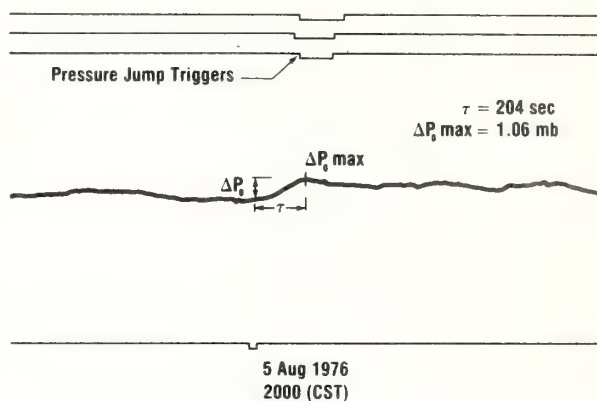
FIG. 9. Example of a pressure jump and associated pressure-jump detector responses recorded by an array operated during a National Severe Storms Laboratory gust front experiment.

conjunction with National Severe Storms Laboratory experiments in Oklahoma are evaluating their usefulness for the detection of thunderstorm gust fronts.

REFERENCES

Bedard, A. J. Jr., 1966: Some observations of travelling atmospheric pressure disturbances. NBS Rep. 9364, 63 p.
——, 1973: The design of a temperature independent dc flow resistor. *Fluid. Quart.*, **5**, No. 2, 31–50.
——, 1977: The dc pressure summator: Theoretical operation, experimental tests and possible practical uses. *Fluid. Quart.*, **9**, No. 1, 26–51.
——, and D. W. Beran, 1977: Detection of gust fronts using surface sensors. NOAA Tech. Memo. ERL WPL-20, 15 pp.
Bleeker, W., and M. J. Andre, 1950: Convective phenomena in the atmosphere. *J. Meteor.*, **7**, 195–209.
Bowman, H. S., and A. J. Bedard Jr., 1971: Observations of infrasound and subsonic disturbances related to severe weather. *Geophys. J. Roy. Astron. Soc.*, **26**, 215–242.
Charba, J., 1974: Application of gravity current model to analysis of squall-line gust front. *Mon. Wea. Rev.*, **102**, 140–156.
Daniels, F. B., 1959: Noise reducing line microphone for frequencies below 1 cps. *J. Acoust. Soc. Amer.*, **31**, 529–531.
Donn, W., R. Rommer, F. Press and M. Ewing, 1954: Atmospheric oscillations and related synoptic patterns. *Bull. Amer. Meteor. Soc.*, **35**, 301–309.
Fujita, T., 1959: Precipitation and cold air production in mesoscale thunderstorm systems. *J. Meteor.*, **16**, 454–466.
Geiger, R., 1973: *The Climate near the Ground.* Harvard University Press, 611 pp.
Goff, R. C., 1975: Thunderstorm-outflow kinematics and dynamics. NOAA Tech. Memo. ERL NSSL-75, 63 pp.
Tepper, M., 1950: A proposed mechanism of squall lines: The pressure jump line. *J. Meteor.*, **7**, 21–29.
Williams, D. T., 1948: A surface micro-study of squall-line thunderstorms. *Mon. Wea. Rev.*, **76**, 239–246.
——, 1953: Pressure wave observations in the central midwest, 1952. *Mon. Wea. Rev.*, **81**, 278–289.

FIG. 8. Experimental and predicted response of pressure-jump detector to applied stepfunction.

A RESEARCH LASER WEATHER IDENTIFICATION INSTRUMENT

K. B. Earnshaw and Brian Keebaugh

We describe an experimental laser weather identification instrument designed to test the feasibility of making automatic indentification of precipitation and other obscurations to visibility. The nature of the optical signals and electronic processing of these signals to make weather identification are discussed in detail. We have given instructions for preparing the instrument prior to taking data, as well as a complete set of electronic circuit diagrams needed for instrument maintenance.

PERFORMANCE TEST RESULTS FOR XONICS ACOUSTIC DOPPLER SOUNDER

Duane A. Haugen

In March and April 1976, a field program was conducted to evaluate the performance of a commercially-available acoustic Doppler sounder for measuring wind speeds. Wind speed profiles were measured over a height of 150 m with five in situ sensors. Several configurations of the sounder were tested, one of which proved to be suitable for acceptable wind speed measurements over a wind speed range of 1 to 10 m/sec.

A SECOND-GENERATION PASSIVE OPTICAL CROSSWIND MONITOR

G. R. Ochs, E. J. Goldenstein, and R. F. Quintana

The instruction book describes a compact battery-powered optical instru-
ment of improved design that measures crosswinds by observing the scintilla-
tion of naturally illuminated scenes. Operating instructions, adjustment
procedures, and circuit diagrams are included.

A SATURATION-RESISTANT OPTICAL SYSTEM FOR MEASURING AVERAGE WIND

G. R. Ochs, G. F. Miller, and E. J. Goldenstein

A optical system for measuring average crosswind in the presence of strong integrated refractive-index turbulence is described. Circuit diagrams and adjustment instructions for the instrument are included.

AN OPTICAL DEVICE FOR MEASURING REFRACTIVE-INDEX FLUCTUATION
IN THE ATMOSPHERE

G. R. Ochs, R. F. Quintana, and G. F. Miller

An instrument is described that measures the average value of the re-fractive-index structure constant (C_n^2) over optical paths from 80 to 800 meters. Corrections for the inner scale of turbulence and difficulties due to the saturation of scintillation, both present in previous optical tech-niques, are avoided by using an extended incoherent light source.

INFRARED PASSIVE WIND SENSING - A FEASIBILITY STUDY

G. R. Ochs and Ting-i Wang

We analyze the feasibility of measuring crosswinds by observing the scintillation of the natural background radiation in the wavelength region from 8 to 12 microns. Methods of signal analysis and experiment results for visual wavelengths are discussed. A signal-to-noise analysis and experimental results indicate that an infrared system is marginally possible, with S/N ratios approximately two orders of magnitude below that of a visual system.

A STELLAR SCINTILLOMETER FOR MEASUREMENT
OF REFRACTIVE-TURBULENCE PROFILES

G. R. Ochs, Ting-i Wang, and F. Merrem

An optical system for measuring refractive-turbulence profiles in the atmosphere is described. The instrument measures the profile along the light path to a star by analyzing the scintillation of the star by the atmosphere. The circuit diagram, computer program, and operating instructions for the instrument are included.

835

STELLAR SCINTILLOMETER MODEL II FOR MEASUREMENT
OF REFRACTIVE-TURBULENCE PROFILES

G. R. Ochs, Ting-i Wang, and F. Merrem

An optical system for measuring refractive-turbulence profiles in the atmosphere is described. The instrument measures the profile along the light path to a star by analyzing the scintillation of the star by the atmosphere, and is an improved version of an earlier system. The circuit diagram, computer program, and operating instructions for the instrument are included.

AN OPTICAL SYSTEM FOR PROFILING WIND
AND REFRACTIVE-INDEX FLUCTUATIONS

G. R. Ochs, Ting-i Wang, and E. J. Goldenstein

An instrument is described that measures the crosswind and the refractive-index structure parameter (C_n^2) at six locations along an optical path. Operator instructions, calibration procedures, and circuit diagrams are included.

MICROCOMPUTER-CONTROLLED ACOUSTIC ECHO SOUNDER

Edward J. Owens

This thesis is the result of research into new concepts of remote sensing of the atmosphere and includes a literature survey of the theory and practical application of atmospheric sounding using acoustic methods. The "state of the art" has been advanced in that a new type of system was designed, fabricated, and tested using modern digital methods. The major advances of replacing the typically troublesome facsimile recorder with a dot-matrix line printer using special characters called "tonels" and the development of a new and novel method of digital Doppler signal processing using a real covariance technique, is presented in detail.

The echosonde is capable of monitoring and displaying in real time the temperature fluctuations, turbulent velocity inhomogeneities, and vertical wind profile of the planetary boundary layer to a height of 680 meters and includes a microcomputer, a high-speed line printer, and various author-designed and -contributed digital and analog circuits.

User control of various system parameters and a wide choice of display possibilities make this a versatile and desirable atmospheric research tool.

FREQUENCY SPECTRUM ANALYZER FOR DOPPLER LIDAR

M. J. Post, R. E. Cupp, and R. L. Schwiesow

    This report describes an electronic apparatus that analyzes Doppler
returns from an infrared lidar system. By processing each spectral frequency
channel with a 100 percent duty cycle rather than with a swept filter ana-
lyzer, considerably better S/N is obtained.

A FREQUENCY DISCRIMINATOR VS. FFT DOPPLER EXTRACTION

R. Jeffrey Keeler

The Quantech 2415M frequency discriminator is compared to a Discrete Fourier Transform based mean frequency estimator for a doppler shifted acoustic echosonde application. Limited dynamic range and poor frequency tracking for SNR < 6 db make the Quantech a poor acoustic doppler shift estimator. An experiment with Haswell 1974 acoustic echosonde data demonstrates the superiority of the FFT technique.

Acoustic Doppler extraction by adaptive linear-prediction filtering

R. Jeffrey Keeler

Wave Propagation Laboratory, NOAA Environmental Research Laboratories, Boulder, Colorado 80302

Lloyd J. Griffiths

Department of Electrical Engineering, University of Colorado, Boulder, Colorado 80302

Acoustic echo sounders can be used to measure wind profiles in the lower atmosphere by estimating the Doppler shift from the range-gated received echoes. Instantaneous frequency estimates are estimated from the coefficients of an an adaptive linear- prediction filter (ALPF). These coefficients are updated at each sample time and provide a current estimate of the spectrum of the scattered acoustic echoes. The adaptive algorithm is derived in the context of a whitening filter and its convergence is shown to be rapid enough to track the vertical profile of wind in the lower atmosphere. An ALPF-derived profile is shown superior to an FFT-derived profile in both computational speed and estimator accuracy.

PACS numbers: 43.60.Cg, 43.28.Bj, 43.28.Py

INTRODUCTION

Remote sensing of the lower atmosphere using acoustic waves has been demonstrated to provide useful information to scientists who are investigating those properties of the atmosphere which may be characterized by temperature or velocity fluctuations. A propagating acoustic wave interacts strongly with these fluctuations to produce a scattered wave which can be detected by simple receiving equipment. Typically, a 100 msec long, 2-kHz pulse transmitted once every 8 sec provides quantitative measurements of the atmospheric structure,[1] wind profiles,[2] and temperature-inhomogeneity profiles[3] in the lower few hundred meters of the atmosphere. When the intensity of the backscattered echoes is plotted as a function of height and time on a facsimile recorder, the thermal structure of the atmosphere is clearly displayed as shown in Fig. 1.

Remote wind profiling by bistatic acoustic echo sounding can also provide accurate real-time wind profiles up to 600 m even in the noisy environment of a major airport.[4] The basis for wind profiling is estimating the mean Doppler shift of the returned echoes which have been contaminated with environmental acoustic noise. Because of turbulence within the scattering region, the echo is not a pure sinusoid but rather a continuum of sinusoids whose mean frequency changes because of the wind-induced gross motion of the scatterers. Thus the signal may be modeled as a nonstationary narrow-band random process, or equivalently as the output of a time-variant narrow-band filter that has white-noise input. The input noise can be modeled as a white Gaussian random process over the bandwidth of interest. Conventionally, one desires to reduce the effects of the noise and then to estimate the spectrum of the time-varying signal.

The Doppler shift of the echo is estimated by calculating the frequency shift from the transmitted frequency. This is usually done by computing the first moment (mean) of the filtered spectrum or by searching for the peak of the filtered spectrum or by some hardware device that performs a similar function, such as a frequency discriminator. A previous report[5] describes some deficiencies of one of the better analog frequency-discriminator devices. Workers in the area of spectrum estimation generally agree that digital computation of spectra potentially yields more information than most if not all analog devices, which normally generate only one parameter of the total spectrum, such as its mean. Hundreds of papers have been published describing various methods and modifications of spectrum estimation using Fourier-transform techniques, especially since the advent of the FFT. These conventional methods yield excellent spectrum estimates when a long stationary sequence of samples is available to achieve the required spectral resolution or when little spectral resolution is desired.

A. Conventional spectrum analysis

Conventional spectrum analysis may be divided into two broad classes: (1) spectra derived from the autocorrelation of the data, and (2) spectra derived from the data itself. Let $x(k)$ represent samples of a wide-sense stationary process, that is the mean and autocorrelation functions are not dependent on the observation interval. The autocorrelation function at lag l is given by

$$r_x(l) = E\{x(k)x(k+l)\}, \quad l = 0, \pm 1, \pm 2, \ldots, \tag{1}$$

where $E\{\ \}$ denotes expected value. The power spectrum for the sequence $\{x(k)\}$ can be shown to be

$$S_x(\omega) = \sum_{l=-\infty}^{+\infty} r_x(l)\, e^{-j\omega l}, \quad 0 \le \omega \le \pi. \tag{2}$$

Generally one has only a finite time series available, say $\{x(k)\}$, $k = 0, \ldots, N-1$. The first class of spectrum estimators requires that the autocorrelation sequence be estimated from the N samples by some technique. A biased autocorrelation estimate which generates a reasonable spectrum is

$$\hat{r}_x(l) = \frac{1}{N} \sum_{k=0}^{N-l-1} x(k)x(k+l), \quad l = 0, 1, \ldots, L \tag{3}$$

where L is usually less than $N/10$ to achieve a good accuracy in calculation of the autocorrelation values. By symmetry we require $\hat{r}_x(-l) = \hat{r}_x(l)$. The spectrum estimate $S_x(\omega)$ is then obtained by
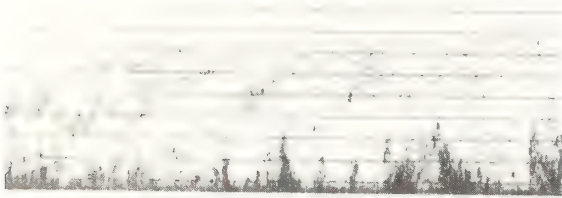
FIG. 1. Facsimile record showing thermal structure of lower atmosphere.

$$\hat{S}_x(\omega) \sum_{l=-L}^{+L} \hat{r}_x(l) W(l) e^{-j\omega l} , \qquad (4)$$

where $W(l)$ is a window function.[6,7] The ultimate resolution of a spectrum computed by this method is limited by the finite window length or equivalently the maximum autocorrelation lag. For the resolution desired in acoustic Doppler extraction, very long data sequences are necessary for computing the $\hat{r}_x(l)$ values. Translated to spatial distances for acoustic waves, this length corresponds to several tens of meters, over which the statistics of the Doppler spectrum, in particular the mean, are not stationary.

The alternative conventional spectrum estimate, known as the periodogram approach, is computed directly from the discrete Fourier transform of the windowed data as

$$\hat{X}(\omega) = \sum_{k=0}^{N-1} x(k) W(k) e^{-j\omega k}, \quad 0 \le \omega \le \pi \qquad (5)$$

and

$$\hat{S}_x(\omega) = |\hat{X}(\omega)|^2 .$$

In general the variance of each spectrum at any given frequency is larger when the power spectrum is a windowed periodogram than when the power spectrum is calculated from the autocorrelation values.[7,8] Therefore, some sort of averaging is necessary for accurate power-spectrum estimates. For acoustic Doppler applications this is easily done by (1) choosing a suitable range gate over which the Doppler spectrum may be assumed stationary, (2) calculating a periodogram for several successive pulses, and (3) averaging these consecutive periodograms to get a more accurate power-spectrum estimate at that range gate. If the averaging is done over a long enough period of time, Doppler spectrum contributions from short-term vertical motions of the atmosphere will be removed and the resulting averaged spectrum will include only Doppler information due to the mean horizontal wind.

A common disadvantage to both these conventional methods is the time and expense required to compute the spectrum estimates. A digital computer is absolutely required for a real-time application. The computation is time consuming for a pure software realization in a standard minicomputer even at acoustic rates. A hardware FFT peripheral unit, if not a limited use special purpose FFT computer, is desirable for real-time wind profiling with reasonably small range gates; say 30 m (~ 200 msec).

B. Maximum entropy spectrum analysis

Burg[9] suggested a method for improving the resolution of spectrum estimates based on linear-prediction filtering. This method is useful in the acoustic Doppler application because few autocorrelation lags are required to estimate the spectrum of a signal imbedded in noise. Consequently, only a short data sequence is necessary for computing these few autocorrelation values and greater spatial resolution is achievable. Burg named his method maximum entropy spectral analysis (MESA) and this method is widely used in geophysical data processing.[9-13] The MESA algorithm has been shown to be identical with the all-pole linear-prediction spectrum, or equivalently, to the autocorrelation method of linear prediction discussed in many recent publications on speech analysis[14-17] or also equivalently, to autoregressive filtering in the statistical literature.[18-21] Makhoul[22] gives an excellent tutorial presentation of all facets of linear prediction and Kailath[23] relates linear-prediction filtering to generalized linear least-squares theory in his survey article. Because of its actual method of realization, the technique is termed the "linear-prediction spectrum" throughout this paper.

C. Adaptive linear-prediction spectrum analysis

Riley and Burg[24] have further suggested that a linear-prediction filter could be modeled as a lattice structure involving reflection coefficients. This structure can be made time variable by updating the reflection coefficients at each sample time using a finite-time power-averaging algorithm. These reflection coefficients are then used to calculate the equivalent linear-prediction filter coefficients which define a linear-prediction spectrum estimate.

This paper summarizes the important features of an alternative implementation of an adaptive linear-prediction filter[25] in which the linear-prediction coefficients are updated using the data samples directly, rather than power averages of these samples. A least-mean-square gradient adaption algorithm is employed to adapt the filter coefficients. These continuously updated coefficients are then used to compute a simplified linear-prediction spectrum for the input sequence. The simple modification of the standard linear-prediction spectrum consists of removing the gain calculation and has the effect of producing a spectral estimate that is unaffected by changes in the input-signal strength and depends solely on the spectral width of the input-signal spectrum. Thus the resulting adaptive linear-prediction spectrum can not only track changes in the mean frequency of the received spectrum (and hence measure a wind component for the associated height) but can also track changes in the width of the Doppler spectrum (and hence measure the turbulence associated with a given height).

It will be shown that an assembly-language software implementation of the total adaptive linear-prediction Doppler estimator requires less storage and operates at about the same speed as a medium-speed hardware FFT unit used in conjunction with a conventional win-
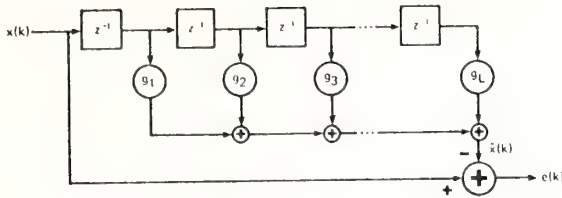
FIG. 2. Basic linear-prediction filter.

dowed periodogram-spectrum estimator. Additionally, the filtering algorithm itself and the coefficient update algorithm, which are the most time-consuming elements of the spectrum estimation algorithm, are very simple and can probably be implemented on a small microcomputer as a peripheral processing unit to a host minicomputer.

I. SPECTRAL ANALYSIS USING ADAPTIVE LINEAR-PREDICTION FILTERING

A. Classical linear prediction

The basic form of the classical linear-prediction filter G is shown in Fig. 2 where z^{-1} denotes a one sample time delay. The one-step prediction of the input sequence $x(k)$ is formed as a linear combination of L previous input values. Thus

$$\hat{x}(k) = \sum_{l=1}^{L} g_l x(k-l) , \qquad (7)$$

where g_l is the lth coefficient of the prediction filter. An error sequence is formed from the actual $x(k)$ by

$$\epsilon(k) = x(k) - \hat{x}(k) . \qquad (8)$$

The filter coefficients G^* which produce the minimum mean-square error (mmse), are well known and may be expressed in matrix form as

$$\underline{G}^* = \overleftrightarrow{R}_{xx}^{-1} \underline{P}_x , \qquad (9a)$$

where

$$\underline{G}^{*T} = [g_1^*, g_2^*, \ldots, g_L^*] , \qquad (9b)$$

$$\underline{P}_x^T = [r_x(1), r_x(2), \ldots, r_x(L)] , \qquad (9c)$$

$$\overleftrightarrow{R}_{xx} = \begin{bmatrix} r_x(0) & r_x(1) & \ldots & r_x(L-1) \\ r_x(1) & & & \\ \vdots & & & \vdots \\ r_x(L-1) & & \ldots & r_x(0) \end{bmatrix} , \qquad (9d)$$

and T denotes transpose.

The linear-prediction spectrum $M_x(\omega)$ can be expressed in terms of the optimum prediction filter coefficients[26] as

$$M_x(\omega) = r_x(0) - \sum_{l=1}^{L} g_l^* r_x(l) \bigg/ \bigg| 1 - \sum_{l=1}^{L} g_l^* e^{-j\omega l} \bigg|^2 . \qquad (10)$$

When the filter coefficients have their optimum value $\underline{G}^*$ the numerator of $M_x(\omega)$ is easily shown to be the mmse output power. Thus

$$M_x(\omega) = E\{\epsilon^2(k)\}_{min} \bigg/ \bigg| 1 - \sum_{l=1}^{L} g_l^* e^{-j\omega l} \bigg|^2 . \qquad (11)$$

An intuitive explanation of the structure of $M_x(\omega)$ can be given if one notes a result in the design of digital deconvolution filters. It is well known[27] that the finite impulse-response mmse whitening filter has a transfer function given by

$$H'(\omega) = 1 - \sum_{l=1}^{L} g_l^* e^{-j\omega l} \bigg/ E\{\epsilon^2(k)\}_{min}^{1/2} . \qquad (12)$$

Therefore, the linear-prediction spectrum estimate (11) is identical to the inverse of the magnitude-squared transfer function of the optimal whitening filter (12),

$$M_x(\omega) = \frac{1}{|H'(\omega)|^2} \qquad (13)$$

Equation (13) may be explained qualitatively by recalling the function of a whitening filter; to produce a white sequence from a colored input sequence. By utilizing z transform notation that is

$$H(z) = \sum_{k=0}^{\infty} h_k z^{-k} ,$$

the input sequence to the whitening filter $x(k)$ may be generated from a white sequence $w(k)$ modified by a coloring filter $S(z)$ as shown in Fig. 3. The whitening filter $H(z)$ attempts to remove the coloration of the input sequence $x(k)$ due to the poles and zeros of $S(z)$.

Alternatively, the filter $H(z)$ removes all predictable (or correlated) terms from $x(k)$ and the result is an optimally white sequence. The linear-prediction filter shown in Fig. 2 has no poles, only zeros, in its transfer function. The error sequence will be perfectly white only if $x(k)$ is generated by filtering a white-noise sequence with an all-pole filter containing P poles and the number of taps in the predictive filter L is equal to or greater than P, i.e., $L \geq P$[18]. In effect the linear-prediction filter must contain sufficient zeros to cancel the P poles of $S(z)$ used to color the original white sequence.

Since the zeros of $H(z)$ cancel the poles of $S(z)$, an equivalent way of calculating the linear-prediction power-spectrum estimate (13) is to evaluate $1/|H(z)|^2$ around the unit circle in the z plane.[28] In the denominator of (11), if $e^{-j\omega l}$ is replaced by z^{-l}, then the polynomial $H(z)$ has a leading coefficient of 1 and following coefficients equal to the negative of the prediction filter coefficients. Fast computational methods of evaluating polynomials in the complex z plane exist; consequently evaluating $M_x(\omega)$ is a straightforward operation. An alternate and slower method of evaluating $H(z)$ at discrete frequencies is to append zeroes to the whitening-filter impulse response and compute its FFT.

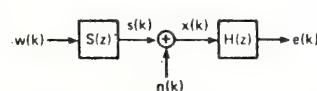It has been observed previously that the use of linear-

FIG. 3. Generation of input sequence and whitening filter.

prediction spectrum estimates (or equivalently, maximum entropy spectral estimates) leads to spiked spectrum estimates.[11,12] These spikes may be qualitatively explained in terms of whitening filters. If the input sequence contains a very narrow-band spectrum centered at ω_0, or equivalently the coloring filter has a pole very close to the unit circle, then the whitening filter places a zero at that frequency, also very close to the unit circle. The squared magnitude of the inverse transfer function (13) results in a large peak at ω_0, whose peak and width are solely determined by the zero's position relative to the unit circle. Since the zero placement is independent of the filter length, extremely sharp spectral peaks are possible even for short filters. More detailed analyses of linear-prediction spectrum estimation may be found in the literature.[22]

A modified linear-prediction spectrum estimate $Q_x(\omega)$ is used in this paper

$$Q_x(\omega) = \frac{1}{|H(z)|^2} = \frac{1}{|1 - \sum_{l=1}^{L} g_l^* e^{-j\omega l}|^2} . \tag{14}$$

The only difference between (14) and (11) is the removal of the $E\{\epsilon^2(k)\}$ gain factor. As a result, the integral of $Q_x(\omega)$ is not equal to the total input power; however, three distinct advantages arise from this change. Since the signals of the interest in acoustic Doppler-spectrum estimation are usually narrow-band spectra, they are quite predictable. It can be shown[25] that a perfectly predictable signal gives rise to a 0/0 indeterminacy in (11). Specifically, $E\{\epsilon^2(k)\} = 0$. If we replace $E\{\epsilon^2(k)\}$ by 1 as in (14), then the resulting 1/0 indeterminacy is computationally tractable as a limit. Secondly, it can be easily shown that $Q_x(\omega)$ is not affected by amplitude scale changes in the input spectra, which may be advantageous in some applications. Thirdly, the peak values of $Q_x(\omega)$ are related directly to the width of the spectra. Therefore, the amount of turbulence associated with the spectra can be related directly to the peak value of $Q_x(\omega)$ which is an immediate by-product of the estimation algorithm.

The modified linear-prediction spectrum $Q_x(\omega)$ in (14) depends directly on the optimal filter coefficients G^* defined by (9). Numerical solution of these equations requires knowledge of the autocorrelation values which in practice are unknown *a priori* and must be estimated from the data. Since acoustic Doppler signals have time-varying spectra, the autocorrelation estimates must be updated periodically to ensure that the linear-prediction filter remains accurate. In most applications, the data sequence is long compared with the maximum lag L, and the number of computations required to compute the autocorrelation estimates for use in (9) is several times larger than the number of computations required to solve the normal equation itself by a fast inversion algorithm.[28,29]

B. Adaptive linear-prediction filtering

In this section we present an alternative method of obtaining the prediction filter coefficients for the filter structure shown in Fig. 2. This method is a time-domain iterative technique which avoids the two-step procedure of first computing the autocorrelation values and and then solving the normal equations. The LMS algorithm was first derived by Widrow and Hoff.[30] Briefly, the algorithm may be described as follows: Denote the prediction filter coefficients at time k by

$$G^T(k) = [g_1(k), \; g_2(k), \; \ldots, \; g_L(k)] . \tag{15}$$

Then the prediction filter output at time k is

$$\begin{aligned}
\hat{x}(k) &= \sum_{l=1}^{L} g_l(k) x(k-l) \\
&= G^T(k) \underline{X}(k-1) \\
&= \underline{X}^T(k-1) G(k) ,
\end{aligned} \tag{16}$$

where

$$\underline{X}^T(k-1) = [x(k-1), \; x(k-2), \; \ldots, \; x(k-L)] \tag{17}$$

is the vector of data samples upon which the prediction is based. For a fixed coefficient vector G in (9), the mean-squared error is

$$\begin{aligned}
E\{\epsilon^2(k)\} &= E\{[x(k) - \hat{x}(k)]^2\} \\
&= E\{[x(k) - \underline{X}^T(k-1) G]^2\} \\
&= r_x(0) - 2\underline{P}_x^T G + G^T \overleftrightarrow{R}_{xx} G .
\end{aligned} \tag{18}$$

This equation is a quadratic function of G and since the matrix of second derivatives of (18) is positive definite for all G, a unique minimum exists, which is satisfied by G^* (9). Therefore a gradient-descent algorithm may be used to determine G^*. A common procedure is the method of steepest descent in which the coefficient vector is iterated in the direction of the negative gradient of the error surface (18). The negative gradient of (18) is

$$-\frac{\partial E\{\epsilon^2(k)\}}{\partial G} = 2[\underline{P}_x - \overleftrightarrow{R}_{xx} G] . \tag{19}$$

Therefore an algorithm which changes G in the direction of the negative gradient is

$$G(k+1) = G(k) + \mu[\underline{P}_x - \overleftrightarrow{R}_{xx} G(k)] , \tag{20}$$

where μ is scalar proportionality constant that controls the step size and convergence time.

The LMS algorithm is derived from (20) by replacing the average quantities $\underline{P}_x$ and $\overleftrightarrow{R}_{xx}$ with appropriate instantaneous values. Since

$$\underline{P}_x = E\{x(k) \underline{X}(k-1)\} \tag{21}$$

and

$$\overleftrightarrow{R}_{xx} = E\{\underline{X}(k-1) \underline{X}^T(k-1)\} , \tag{22}$$

the instantaneous values are the arguments of the expectations. Therefore the noisy LMS algorithm is given by

$$\begin{aligned}
G(k+1) &= G(k) + \mu[x(k) \underline{X}(k-1) - \underline{X}(k-1) \underline{X}^T(k-1) G(k)] \\
&= G(k) + \mu[x(k) - \hat{x}(k)] \underline{X}(k-1) \\
&= G(k) + \mu \epsilon(k) \underline{X}(k-1) .
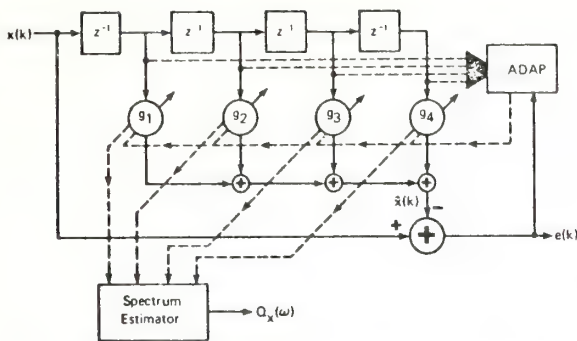\end{aligned} \tag{23}$$

An implementation is shown in Fig. 4.

FIG. 4. Basic adaptive linear-prediction spectrum estimator.

In order to use this algorithm, three parameters must be specified: the filter length L, the initial coefficient vector $G(0)$, and the proportionality constant μ. As previously stated, the filter length L must be large enough to generate sufficient zeros to cover the poles of a filter that generated the "all-pole" input sequence. Since acoustic Doppler data sequences can be modeled as a unimodal narrow-band signal spectrum embedded in wider-band noise spectra, an all-pole data model is a valid assumption. Experiments have shown that $L=4$ or 6 is a good compromise in filter length (computation time) versus minimum mean-squared error.

In the acoustic echo-sounder application, the time constant of adaption is rapid compared to the length of the data record. Thus only the initial portion of the output is affected by the choise of the initial coefficient vector $G(0)$. Experience has shown that slightly better results are obtainable if the data sequence is filtered in reverse order rather than time-sequential order. That is, adaption proceeds from a high range to a short range, starting in the low SNR region of an acoustic return sequence and progressing into larger SNR regions of the data sequences. For this reverse-filtering operation $G(0)=0$ usually suffices.

The third parameter of choice is the proportionality constant μ. A convergence analysis[25] shows that convergence is assured if

$$\mu = \alpha/Lr_x(0), \quad 0 < \alpha < 2 . \tag{24}$$

Since $r_x(0)$ is the power in the input-data sequence (the received echos), it is a function of time for the acoustic Doppler case. Thus a time-varying estimate of $r_x(0)$ must be maintained throughout the data sequence. If this is done, then experience again shows that $0.02 < \alpha < 0.2$ provides excellent results although assuredly this is dependent on the particular data studied. The processor performance seems relatively insensitive to changes in α by a factor of two within this range. A large α effects a rapid convergence and a large steady-state mean-squared error results. On the other hand, a small α effects very slow convergence but a small steady-state mean-squared error.

The time constant of the adaptive filter is a complicated parameter to evaluate since it depends in general on the choice of $G(0)$ and the eigenvalues of the auto-

correlation matrix. In application though, a reasonable estimate for the adaptive time constant is[25]

$$\tau_a \cong L/\alpha . \tag{25}$$

As an example let $\alpha = 0.1$ and $L = 4$; then $\tau_a = 40$, the number of samples of k that reduces the error term in the average coefficient vector to e^{-1} of its original value. For a monostatic acoustic echo sounder whose receiver is sampled at a rate of 1 kHz, this corresponds to a spatial propagation distance of only 7 m. Thus the average adaptive-filter time constant appears to be short enough to track expected variations in the Doppler spectrum.

The fact that the linear-prediction spectrum estimate can be made at any instant, merely by using the present value of G in (14) is important. Since the adaptive processor tracks the input-data statistics, specifically its instantaneous frequency, it can be shown that the coefficients of the filter represent an exponentially weighted average of the statistics of the previous input samples if the samples are uncorrelated.[31] Spectrum estimates can be made for any number of range gates within the maximum range of the sounder. The choice is based on the expected rate of change of the input spectrum and on the speed of the processor. For a normal application most of the processor time associated with the linear-prediction spectrum estimator is spent in the filtering and coefficient update procedure. Less than a quarter of the time is spent computing the spectral estimates by a computationally efficient polynomial evaluation routine which is based on a second-order system of state variable equations.[32]

C. Computational efficiency

As further evidence that the adaptive filter is computationally efficient in spectrum estimating, Table I shows the time required to extract a Doppler shift from a spectrum estimate using both conventional FFT methods and the adaptive-linear prediction filter (ALPF). The FFT estimate is derived from a weighted-mean-frequency estimate of the spectrum over the bandwidth of interest and the ALPF estimate utilizes the frequency corresponding to the peak of the smooth spectrum estimate. The reference computer is a NOVA 820 with hardware multiply/divide. Overhead calculations are considered in these timing estimates. As shown above, the adaptive-filter method is about seven times faster than the standard FFT calculation and of the same order of speed as a commercially available medium-speed hardware FFT unit. A side-by-side comparison of these two methods is being carried out in a field

TABLE I. Algorithm timing comparison.

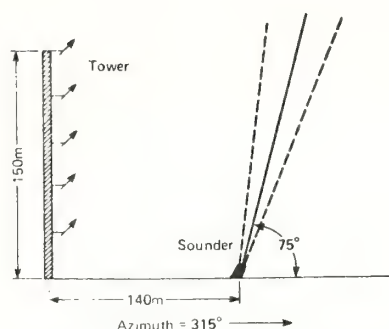| Method	Time (msec)
Assembly language FFT	370
Assembly language ALPF	52
Hardware MFFT unit	94

FIG. 5. Haswell 1974 acoustic sounder/tower configuration.

trial of an acoustic wind-profiling system in Boulder, Colorado.

II. APPLICATION TO ACOUSTIC DOPPLER ESTIMATION

A. Doppler profile example

The data used for the evaluation of the adaptive linear-prediction spectrum estimator were taken in March 1974 at Haswell, Colorado. A 150-m instrumented meteorological tower provided reference data for an acoustic sounder operating 140 m away at an azimuth of 315°. The monostatic sounder was tilted at an elevation angle of 75° away from the tower. Figure 5 shows a side view of the site configuration. Although the 75° elevation angle of the sounder is not optimal for horizontal wind sensing, it is nevertheless useable. The pulse-repetition period was 2 sec, creating an unambiguous range of 340 m, and the pulse duration was 50 msec at a center frequency of 2500 Hz.

A 100-Hz-bandwidth filtered version of the received echoes was heterodyned down to 250 Hz and digitized at a 1-kHz sampling rate using an effective 12-bit A-D converter. The time period analyzed was from 0825– 0835 on 24 March 1974. As shown in Fig. 1 a nocturnal inversion was breaking up with echoes to 240 m and some thermal plumes to 100 m were in the process of

FIG. 7. Doppler profile—raw data.

forming. A 4-m sec⁻¹ wind was blowing from the SE, creating Doppler shifts of about −15 Hz. The data analysis consisted of dividing the 2-sec pulse (340 m) into 100-msec (17 m) range gates and estimating the mean Doppler shift by use of the FFT/spectrum mean and the ALPF/spectrum peak algorithms, thereby generating a pair of Doppler profiles.

The behavior of the adaptive linear prediction filter can be demonstrated by considering this particular case. Figure 6 shows the behavior of the adaptive coefficients as the filter progresses through 2 seconds of data in the reverse direction, i.e., from right to left in the figure, from top to bottom in space. The initial coefficient vector $\underline{G}^T(0)$ is $[0, -1.389, 0, -0.482]$, corresponding to a pair of zeros at $\pm j0.83$ and a pair at 0.

The zeros of $H(z)$ may be calculated by finding the roots of $H(z)$, which is equivalent to finding the poles in $Q_x(z)$ in (14) and thus representing the spectrum of the input data. The two zeros nearest the unit circle are those most effective in whitening the signal and therefore estimating the signal spectrum, while those nearer the origin in the z plane attempt to whiten the narrowband noise, which is present in all real applica-

FIG. 6. Adaptive filter coefficients.
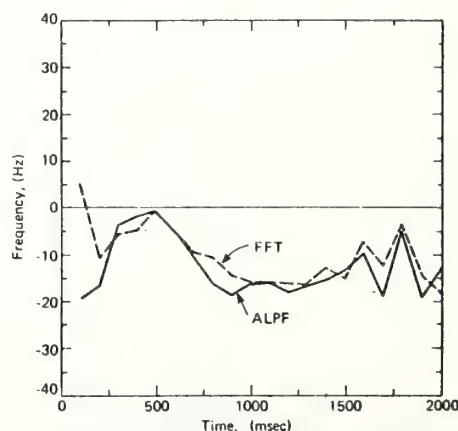
FIG. 8. Doppler profile—10 record averaged.

J. Acoust. Soc. Am., Vol. 61, No. 5, May 1977

846
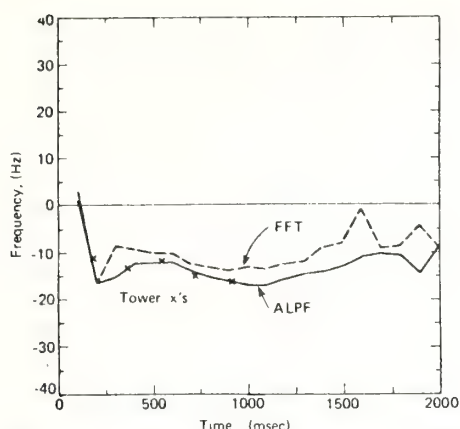
FIG. 9. Doppler profile—2 min averaged.

tions. Actually the zeros of $H(z)$ are placed to produce the whitest sequence in a mean-square sense with no consideration given to independently canceling the signal and noise poles. At the desired times, or ranges, the peak of $Q_x(\omega)$ can be calculated and a Doppler shift, or wind component, estimated.

If the prediction filter has more than two coefficients, then a multimodal spectrum estimate is possible. For small SNR's the zeros of the ALPF arrange themselves to whiten the input noise sequence, and small random variations will cause different zeros to be closest to the unit circle for different data sequences. Thus the peak of the spectrum will change rapidly throughout the low SNR data sequence. However since the noise is generally wide band, $Q_x(\omega)$ will be relatively small, that is, the spectrum estimate will be low and broad as opposed to the large spikey spectrum estimate obtained from a high SNR sequence. This, of course, is a direct result of the modification of the standard linear-prediction spectrum estimate as explained previously. In practice, the peak value of $Q_x(\omega)$ can be compared with a threshold below which the estimate is declared to be invalid. This threshold test was not done for the Doppler profile in this paper.

Figure 7 shows a raw (or immediate) Doppler profile. The solid line is the adaptive linear-prediction estimate and the dashed line is the FFT estimate. The correlation at all ranges is excellent except at $t \leq 100$ msec where the received data sequence was cut off because of antenna reverberation. Recall that the data is filtered from right to left in these diagrams. Figure 8 shows the average of all previous profiles using a 10-sec time constant. The profiles are much smoother and again well correlated. This short time constant seems ideal for measuring vertical atmospheric motions of thermal plume dimensions.

Figure 9 shows an averaged profile with a 2-min time constant. The x's represent tower data, i.e., the theoretical frequency shifts at anemometer heights that would be measured if the average wind, as measured by the tower, were present at those range gates.

The excellent agreement of the adaptive linear-prediction spectrum with the reference tower data may be attributed to the fast response time of the adaptive filter and to the smoothed spectrum of each single data sequence. The FFT generates a very spikey spectrum estimate based on a single data sequence. Therefore several individual spectra must be averaged to define a smooth spectrum from which a Doppler shift can be estimated by peak picking rather than from a spectrum mean calculation. The Doppler estimate obtained from a spectrum mean calculation around some center frequency tends to be biased slightly towards zero inversely proportional to its SNR. This evidence indicates that the adaptive linear-prediction spectrum estimator is an unbiased estimator of the mean Doppler shift.

B. Correlation analysis

The FFT and ALPF profiles were also averaged over both a 10- and a 2-min interval. The 10-sec average removes most medium-scale fluctuations and provides a good estimate of the short-term total wind component. The 2-min average smooths all vertical components of the total wind vector and leaves only the horizontal wind component, which can be directly compared with a similar average of tower data. Correlation statistics on the data were run and the profiles were plotted for a qualitative comparison.

Table II shows some pulse-to-pulse correlation coefficients for the unsmoothed Doppler profiles. That is, the correlation coefficient was computed for two sequences of Doppler-shift estimates. The two sequences each contained 20 elements and were derived from consecutive received echo sequences. For ten pairs of pulses sampled 1 min apart during the 10-min analysis period an average of 30%–40% correlation was observed. This seems reasonable since one would expect a fair correlation between wind measurements separated by only two seconds, regardless of whether the FFT method or the linear-prediction filter method was used.

In the following tables the regression coefficient is listed in addition to the correlation coefficient. The regression coefficient is the slope of the best least-squares fit line through the scatter diagram, which con-

TABLE II. Pulse/pulse correlations.

Pulse	FFT	ALPF
30	0.616	0.622
60	0.281	−0.193
90	0.595	0.561
120	0.459	0.158
150	0.394	0.399
180	0.299	0.149
210	0.680	0.632
240	0.122	0.565
270	0.419	0.393
300	0.124	−0.161
Average	0.399	0.312

J. Acoust. Soc. Am., Vol. 61, No. 5, May 1977

847

TABLE III. Correlation/regression coefficients between ALPF and FFT Doppler profiles all data (20 points).

Pulse	Raw	Averaged (2 min)
30	0.860/0.572	0.691/0.583
60	0.109/0.062	0.710/0.616
90	0.662/0.458	0.662/0.497
120	0.463/0.297	0.674/0.589
150	0.235/0.104	0.730/0.675
180	0.798/0.734	0.768/0.806
210	0.620/0.667	0.792/0.889
240	0.731/0.300	0.753/0.744
270	0.823/0.670	0.683/0.661
300	0.396/0.172	0.585/0.511
Average	0.570/0.409	0.705/0.657

sists of 20 points for all gates, and the lower 14 points for the high SNR cases. A characteristic of the regression line is that if the data have a low correlation, say 25%, then the least-squares line actually underestimates the slope of what appears to be a better fit. If isolated points in the scatter diagram exist, the regression coefficient may be grossly in error.

Table III shows the correlation and regression coefficients for all 20 points in a scatter diagram of ALPF-derived Doppler estimates versus FFT-derived Doppler estimates. The middle column tabulates nonaveraged Doppler-profile data and the right column lists 2-min averaged data. Note that the averaged profiles exhibit significantly higher correlations and regression coefficients. The relatively good 57% correlation for raw Doppler profiles and the very good 70% correlation for the averaged Doppler profiles lend credence to the near equivalence of the two estimators. Since the regression coefficient is less than one, for both cases, the adaptive-filter estimator generates somewhat larger values of Doppler shift than the FFT. This result may occur because the peak of the linear-prediction spectrum is used as opposed to the mean of the FFT spectrum, which would be biased toward zero Doppler shift from the additive noise spectrum.

Table IV shows the same calculation based on only 14 high SNR points of the Doppler profiles. The resulting correlations are about 6% and 22% larger than those in Table III for the raw- and averaged-data profiles, respectively. The high SNR, averaged profile correlation of 92% is remarkably high and the regression coefficient of 0.83 indicates excellent agreement between the two estimators, although again the adaptive linear-prediction estimates are slightly larger. The extreme variability of the raw-data correlations (over an order of magnitude) can be explained by recalling that the time constant of the adaptive linear-prediction estimator is short enough that two or three independent spectra may be estimated within the same data sequence that produces only one averaged spectrum by the FFT method. For a given 100-point sequence representing 17 m in space, the ALPF spectrum estimate is made after the 60th point. For performance of an FFT, 28 zeros are appended to the 100 data points. Thus the FFT-derived spectrum represents an average spectrum
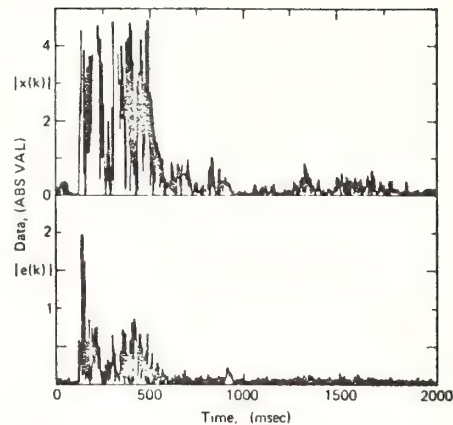
FIG. 10. Envelope of adaptive filter input and error time series.

over a perhaps nonstationary data sequence. In contrast the correlations of the 2-min averaged profiles are relatively constant over the 10-min period.

C. Specular target detection

Since the output of the $H(z)$ filter is the error signal between the predicted $x(k)$ and the actual $x(k)$; i.e., $\epsilon(k) = x(k) - \hat{x}(k)$, any unexpected event appearing in the input sequence (such as a specular reflection) will cause an abnormally large $\epsilon(k)$. The processor will eventually learn of its existence and converge to a proper configuration so that the effect of the unexpected event is removed and the error sequence is once again white, in a mmse sense at least. This abrupt increase in the error sequence may be used as a detector of specular reflections, although the amount of increase depends directly on the input-signal strength. This is in contrast to the spectrum estimate which is unaffected by the input-signal strength. This change in the error sequence is not evident when a distributed scatterer such as an elevated inversion layer is filtered. Apparently the adaptive processor is fast enough to adapt to changes in the input sequence caused by distributed scattering whereas it is not fast enough for changes caused by specular scattering. Figure 10 shows an

TABLE IV. Correlation/regression coefficients between ALPF and FFT Doppler profiles high SNR data (14 points).

Pulse	Raw	Average (2 min)
30	0.840/0.614	0.853/0.534
60	0.068/0.068	0.942/0.743
90	0.740/0.786	0.920/0.752
120	0.390/0.289	0.904/0.786
150	0.600/0.340	0.934/0.867
180	0.832/0.792	0.947/0.990
210	0.794/0.844	0.936/0.934
240	0.815/0.634	0.929/0.880
270	0.862/0.745	0.927/0.876
300	0.334/0.154	0.913/0.903
Average	0.629/0.526	0.921/0.827

J. Acoust. Soc. Am., Vol. 61, No. 5, May 1977

848

example of the envelope of an input and error time series. The low-level echoes correspond to a disintegrating nocturnal inversion with weak echoes from above the inversion. The lower trace shows the error voltage increasing sharply as the inversion is passed through and slightly as the waves are entered. At about 900 msec a specular reflection occurs and the error voltage increases unambiguously. Thus a possibly valuable by-product is available at no cost from the adaptive linear-prediction spectrum estimator.

III. SUMMARY

This paper has reviewed the design of an adaptive processor that estimates the digital instantaneous frequency of a time-varying input sequence, specifically samples of a bandpass-filtered and Doppler-shifted acoustic echo. So long as the variation of the frequency of the received sequence is slower than the convergence time of the adaptive linear-prediction spectrum estimator, then the processor accurately tracks changes in the Doppler shift. No time consuming calculations are involved, such as computing autocorrelation estimates and inverting matrices. Only simple but repetitive additions and multiplications are constantly performed on the input sequence. At an appropriate time (range) a spectrum estimate is quickly computed. Because of the very simple but repetitious prediction filtering and coefficient update task, these calculations lend themselves to implementation on a peripheral microprocessor, thereby freeing the main-frame minicomputer for more complex tasks.

The adaptive processor has been implemented on a CDC 6600 and was used to analyze a short portion of Haswell 1974 acoustic-sounder data. The processor is presently being used to extract Doppler information and generate wind profiles for the GATE acoustic-sounder data which were collected on board the OCEANOGRAPHER in the summer of 1974. In the fall of 1975 a side-by-side comparison of the adaptive processor with a hardware FFT unit was performed in a real-time environment. These tests were performed near a local meteorological tower for a period of several weeks. Based on the preliminary calculations and results presented in this paper and the GATE data analysis, the adaptive processor is expected to outperform even the hardware FFT unit.

An extension of this research would be to investigate the linear-prediction method of spectral estimation and the adaptive coefficient-adjustment algorithm and to determine whether or not acoustic echoes impose any advantageous or disadvantageous constraints on the algorithms. Peculiarities of atmospheric acoustic echo sounding such as phase-coherence distances, amplitude scintillations, and the like may prevent the unconstrained LMS algorithm from attaining its full capability as a spectrum estimator. A constrained algorithm would perhaps be more useful.

[1]C. G. Little, "Acoustic Methods for the Remote Probing of the Lower Atmosphere," Proc. IEEE, 571–578 (1969).

[2]D. W. Beran, F. F. Hall, B. C. Willmarth, R. J. Keeler, and D. E. Hunter, "Operational Test Results of Acoustic Doppler Wind Shear Detector," in Proc. 6th Conf. Aerosp. Acronaut. Met. (AMS, El Paso, TX, 1974).

[3]W. D. Neff, "Quantitative Evaluation of Acoustic Echoes from the Planetary Boundary Layer," U.S. Dept. Commer. Tech. Rep. NOAA TRERL 322-WPL 38 (US GPO, Washington, DC, 1975).

[4]D. W. Beran, "Remote Sensing Wind and Wind Shear System," Dept. Transp. Inter. Rep. FAA-RD-74-3 (1974).

[5]R. J. Keeler, "Frequency Discriminator vs FFT Derived Doppler Extraction Techniques," NOAA Tech. Memo. ERL WPL-17, Boulder, CO (1976).

[6]C. Bingham, M. D. Godfrey, and J. W. Tukey, "Modern Techniques of Power Spectrum Estimation," IEEE Trans. Audio ElectroAcoustic. AU-15, 56 (1967).

[7]R. B. Blackman and J. W. Tukey, The Measurement of Power Spectra (Dover, New York, 1958).

[8]G. M. Jenkins and D. G. Watts, Spectral Analysis and its Application (Holden–Day, San Francisco, 1968).

[9]J. P. Burg, "Maximum Entropy Spectral Analysis," 37th Annual Meeting of Society of Exploration Geophysicists, Oklahoma City, OK, 1967 (unpublished).

[10]J. A. Edward and M. M. Fitelson, "Notes on Maximum Entropy Processing," IEEE Trans. Inf. Theory IT-17, 232 (corresp.) (1973).

[11]R. T. Lacoss, "Data Adaptive Spectral Analysis Methods," Geophysics 36, 661 (1971).

[12]T. Ulrych, "Maximum Entropy Power Spectrum of Truncated Sinusoids," J. Geophys. Res. 77, 1396 (1971).

[13]E. R. Kanasewich, Time Sequence Analysis in Geophysics (Edmonton, University of Alberta, Alberta, Canada, 1973).

[14]J. Makhoul and J. Wolf, "Linear Prediction and Spectral Analysis of Speech," Bolt Beranek and Newman, Cambridge, MA BBN Report 2304 (AD 749-006) (1972).

[15]F. Itakura, "Minimum Prediction Residual Principle Applied to Speech Recognition," IEEE Trans. Acoust. Speech Signal Process. ASSP-23, 67 (1975).

[16]J. D. Markel, "Digital Inverse Filtering–A New Tool for Format Trajectory Estimation," IEEE Trans. Audio Electroacoust. ASSP-20, 129 (1972).

[17]B. S. Atal and S. L. Hanauer, "Speech Analysis and Synthesis by Linear Prediction of the Speech Wave," J. Acoust. Soc. Am. 50, 637 (1971).

[18]A. Van den Bos, "Alternative Interpretation of Maximum Entropy Spectral Analysis," IEEE Trans. Inf. Theory IT-17, 493 (corresp.) (1971).

[19]T. J. Ulrych and T. N. Bishop, "Maximum Entropy Spectral Analysis and Autoregressive Decomposition," Rev. Geophys. Space Phys. 13, 183 (1975).

[20]M. Kaveh, High Resolution Velocity Estimation in the Presence of Extended Clutter, Ph.D. dissertation (Purdue University, 1974) (unpublished).

[21]T. W. Anderson, Statistical Analysis of Time Series (Wiley, New York, 1958).

[22]J. Makhoul, "Linear Prediction - A Tutorial," IEEE Proc. 63, 561 (1975).

[23]T. Kailath, "A View of Three Decades of Linear Filtering Theory," IEEE Trans. Inf. Theory IT-20, 146 (1974).

[24]D. C. Riley and J. P. Burg, "Time and Space Adaptive Deconvolution Filters," 42nd Annual Meeting of Society of Exploration Geophysicists, Anaheim, CA, 1972 (unpublished).

[25]L. J. Griffiths, "Rapid Measurement of Digital Instantaneous Frequency," IEEE Trans. Acoust. Speech Signal Process. ASSP-23, 207 (1975).

[26]E. A. Robinson, Statistical Communication and Detection (Hafner, New York, 1967).

[27]K. L. Peacock and S. Treital, "Predictive Deconvolution: Theory and Practice," Geophysics 34, 155 (1969).

[28]L. R. Rabiner and G. Gold, Theory and Application of Digi-

J. Acoust. Soc. Am., Vol. 61, No. 5, May 1977

849

tal Signal Processing (Prentice Hall, Englewood Cliffs, NJ, 1975).

[29] N. Levinson, "The Wiener *RMS* Error Criterion in Filter Design and Prediction," J. Math. Phys. (Cambridge, Mass.) 25, 261 (1947).

[30] B. Widrow and M. E. Hoff, "Adaptive Switching Circuits," IRE 1960 WESCON Conv. Rec., Pt. 4, 96 (1960).

[31] L. J. Griffiths and P. E. Mantey, "Iterative Least-Squares Algorithms for Signal Extraction," *Proc. Second Hawaii International Conference of System Sciences* (Western Periodicals, N. Hollywood, CA, 1969), p. 767.

[32] G. Goertzel, "Fourier Analysis," *Mathematical Methods for Digital Computers* (Wiley, New York 1967), Vol. 1, Chap. 5, pp. 258–262.

J. Acoust. Soc. Am., Vol. 61, No. 5, May 1977

850

version is covered completely by Burg [6], and is also presented briefly by Haykin and Kesler [12]. Although there is recent interest in multichannel maximum entropy methods (see Ioannidis [13]), and successful results have been obtained, all multidimensional calculations begin with estimates of the autocovariances.

The main purpose of the present paper is to generalize the Burg reflection-coefficient estimation process to multichannel complex time series, and to show that the virtues of the single-channel Burg process carry over to the multichannel complex generalization. In particular, it will be shown that least-squares estimation of complex matrix reflection coefficients using inverse-power weighting provides a sequence of positive-definite power matrices, with a resulting positive-definite autocovariance matrix. The main theoretical results that apply to the single-channel Burg process will be shown to have their multichannel counterparts. Preliminary numerical results, some of which are presented in Section IV, indicate that superior spectral resolution can be expected from the new method, which we shall call the "multichannel Burg process."

II. Forward and Backward Filters and the Multichannel Levinson Algorithm

Let

$$y(t) = \begin{bmatrix} y_1(t) \\ y_2(t) \\ \cdot \\ \cdot \\ \cdot \\ y_p(t) \end{bmatrix}, \qquad t = \{n\Delta t\}_{n=-\infty}^{\infty}$$

be a complex zero-mean, wide-sense stationary p-channel time series. We can consider the *N-element forward filter* (or *forward filter of length N*) in the form

$$y(t) + \sum_{k=1}^{N} F_{kN}^* y(t - k\Delta t) = e_N(t). \qquad (2.1)$$

This is called a *forward* filter because $y(t)$ is predicted *ahead*, in terms of previous values $y(t - k\Delta t)$. Similarly, we consider the N-element *backward* filter[1]

$$y(t) + \sum_{k=1}^{N} B_{kN}^* y(t + k\Delta t) = b_N(t). \qquad (2.2)$$

In (2.1) and (2.2), the forward and backward filter coefficients, F_{kN} and B_{kN}, respectively, are complex $p \times p$ matrices. The asterisk * denotes the (Hermitian) conjugate transpose. We are concerned with *optimum* forward or backward filters (2.1) or (2.2), for which the expected mean-square value of $e_N(t)$ or $b_N(t)$ is a minimum. For (2.1) this involves determining $F_{1N}, F_{2N}, \cdots, F_{NN}$ such that

$$E[e_N^*(t)e_N(t)] = \text{minimum} \qquad (2.3)$$

where $E[\quad]$ is the expected value. Inserting the expression (2.1) for $e_N(t)$ into (2.3) and minimizing with respect to the coefficient matrices F_{kN}^* gives the system

$$RF_N = V. \qquad (2.4)$$

In (2.4) F_N (single subscript) is defined by $F_N^* = [I, F_{1N}^*, \cdots, F_{NN}^*]$ (commas indicate matrix partitions), I is the $p \times p$ identity, $V^* = [P_N, 0, \cdots, 0]$, $P_N^* = P_N$, $R = (R_{ij})$ where $R_{ij} = R_{j-i}$, $i, j = 1, 2, \cdots, (N+1)$, and the $p \times p$ block submatrices R_k are defined by

$$R_k = E[y(t)y^*(t - k\Delta t)], \qquad k = 0, 1, \cdots, N \qquad (2.5)$$

so that

$$R_{-k} = R_k^*. \qquad (2.6)$$

Multichannel Complex Maximum Entropy (Autoregressive) Spectral Analysis

OTTO NEALL STRAND

Abstract—The Burg reflection-coefficient method for maximum entropy (autoregressive) spectral estimation is generalized to apply to multichannel complex signals. It is shown that all resulting power matrices are positive definite. Preliminary numerical results obtained for a monochromatic signal with noise indicate that the determinants of the power matrices are rapidly reduced as the number of filter coefficients is increased, and that superior spectral resolution can be expected.

I. Introduction

Maximum entropy spectral estimation techniques have been successfully applied recently in many contexts. Extensive bibliographies citing such applications are given in recent papers by Makhoul [17] and Ulrych and Bishop [22]. The Burg reflection-coefficient method is receiving increased usage because it avoids major difficulties inherent in methods which begin with estimates of the autocovariances, and often provides superior spectral resolution. Good general references describing the single-channel Burg process are Ulrych and Bishop [22], cited above, Chen and Stegen [7], and Kanasewich [15]. The single-channel complex

851

The unknowns in (2.4) are F_N and the *forward power matrix* P_N. For an optimum forward filter [i.e, for F_N satisfying (2.4)] we have

$$P_N = E[e_N(t)e_N^*(t)]. \qquad (2.7)$$

Because F_N satisfies (2.4) it follows that

$$P_N = F_N^* R F_N. \qquad (2.8)$$

System (2.4) is identical to the system cited by Wiggins and Robinson [23] for real multichannel time series, except that matrix transposes have been replaced by Hermitian conjugates. Because of (2.6), the optimum backward filter satisfies

$$R'B_N = V' \qquad (2.9)$$

where $R' = (R_{i-j})$, $B_N^* = \{I, B_{1N}^*, \cdots, B_{NN}^*\}$ and $(V')^* = [P_N', 0, \cdots, 0]$. In this notation the primes indicate a reversal of time, F_N stands for "forward" and B_N stands for "backward." The *backward power matrix* P_N' for the resulting optimum backward filter is

$$P_N' = E[b_N(t)b_N^*(t)] \qquad (2.10)$$

and because of (2.9),

$$P_N' = B_N^* R' B_N. \qquad (2.11)$$

It is easily shown by block multiplication that

$$R' = URU^* \qquad (2.12)$$

where U is the block permutation matrix

$$U = U^* = \begin{bmatrix} 0 & & I \\ & \diagup & \\ I & & 0 \end{bmatrix}. \qquad (2.13)$$

Exact matrices R_k would, of course, determine F_N, B_N, P_N, and P_N' completely. However, since these exact matrices are not obtainable from a finite sample of a realization of $y(t)$, we must resort to approximations. In the remainder of this paper P_N and P_N' denote the result of substituting whatever approximations are being used into (2.8) and (2.11). Thus, a set of R_k may or may not give rise to a positive definite set $P_0, P_1, \cdots, P_N$ or $P_0', P_1', \cdots, P_N'$ as determined by recursive solution of (2.4) or (2.9). (If $A = A^*$, $A > 0$ denotes positive definiteness and $A \geq 0$ denotes positive semi definiteness.) By (2.12) and (2.13), $R' > 0$ if and only if (iff) $R > 0$. It can be shown [6] that $R > 0$ iff all $P_k > 0$, $k = 0, 1, \cdots, N$. Therefore all $P_k > 0$ iff all $P_k' > 0$. Since this paper is concerned with recursive solutions, we shall assume throughout that $P_k > 0$, $k = 0, 1, \cdots, (N-1)$. Then if R is not > 0, neither is P_N or P_N', and according to (2.7) and (2.10) systems (2.4) and (2.9) cannot define optimum filters. We assume for the moment that our approximation does give $P_N > 0$ (and $P_N' > 0$). It is known [13], [14], [6], that the maximum entropy (autoregressive) power spectral density, $S(f)$, a $p \times p$ matrix, can then be calculated from the forward filter F_N by

$$S(f) = \Delta t [F^{-1}(1/z)]^* P_N [F^{-1}(1/z)] \qquad (2.14)$$

where $F(z) = I + F_{1N}z + \cdots + F_{NN}z^N$, z is the complex scalar defined by $z = \exp[-2\pi i f \Delta t]$ and f is the frequency. The maximum entropy spectrum can also be computed from the backward filter B_N by

$$S(f) = \Delta t [B^{-1}(z)]^* P_N' [B^{-1}(z)] \qquad (2.15)$$

where $B(z) = I + B_{1N}z + \cdots + B_{NN}z^N$. Equation (2.15) can be obtained heuristically from (2.14) by replacing z by $1/z$, P_N by P_N', and F_N by B_N. It can be shown [6] that if $P_N > 0$, then all matrices $F(1/z)$ and $B(z)$ are nonsingular.

If $\{y_i\}_{i=1}^{N_d}$ is a sample of N_d consecutive vectors of a realization of $y(t)$, one may take

$$R_k = \frac{1}{N_d - k} \sum_{i=1}^{N_d - k} y_{k+i} y_i^*, \qquad k = 0, 1, \cdots, N \qquad (2.16)$$

as an unbiased estimator of R_k, where $N \ll N_d$. Unfortunately the resulting R matrix may fail to be positive definite, with disasterous consequences. Replacing the denominator in (2.16) by N_d gives biased estimators of R_k for which $R > 0$. The method in which such estimators are used in (2.4) will be called the *R-process* (it is sometimes called *Yule–Walker estimation* [22].) In this method, the spectral resolution may suffer, and the bias becomes more severe when the record is short, precisely the situation where maximum entropy spectral analysis has the most to offer [7], [21]. The *R-process* has been used with apparent success, however, by Ioannidis [13], among others.

Burg [6] has derived the following results concerning the recursive solution of (2.4) and (2.9). The forward and backward filters may be postulated in the form

$$F_N = \begin{bmatrix} F_{N-1} \\ 0 \end{bmatrix} + \begin{bmatrix} 0 \\ B_{N-1}' \end{bmatrix} C_N \quad \text{and} \quad B_N = \begin{bmatrix} F_{N-1} \\ 0 \end{bmatrix} C_N' + \begin{bmatrix} 0 \\ B_{N-1}' \end{bmatrix} \quad (2.17)$$

where $B_{N-1}' = [B_{N-1,N-1}^*, \cdots, B_{1N}^*, I]^*$ is the block reverse of B_{N-1}, and the $p \times p$ matrices C_N and C_N' are called *forward* and *backward reflection coefficients*, respectively. Then

$$\Delta_N + P_{N-1}' C_N = 0 \qquad (2.18)$$

$$P_{N-1} + \Delta_N' C_N = P_N \qquad (2.19)$$

$$\Delta_N' + P_{N-1} C_N' = 0 \qquad (2.20)$$

$$P_{N-1} + \Delta_N C_N' = P_N' \qquad (2.21)$$

where

$$\Delta_N = R_{-N} + \sum_{k=1}^{N-1} R_{-N+k} F_{k,N-1} \qquad (2.22)$$

$$\Delta_N' = R_N + \sum_{k=1}^{N-1} R_{N-k} B_{k,N-1}. \qquad (2.23)$$

According to (2.17), $C_N = F_{NN}$ and $C_N' = B_{NN}$. It is further shown by Burg [6] that

$$\Delta_N^* = \Delta_N' \qquad (2.24)$$

and that

$$\det R = \prod_{k=0}^{N} \det P_k' \qquad (2.25)$$

where $\det(\ )$ denotes the determinant. Finally [6], he indicates the relations

$$P_N = P_{N-1} - C_N^* P_{N-1}' C_N \qquad (2.26)$$

$$P_N' = P_{N-1}' - (C_N')^* P_{N-1} C_N', \qquad (2.27)$$

which are easily derived from (2.18)–(2.24). By the form of (2.26) [9], corresponding eigenvalues of $P_1, P_2, \cdots$, form nonincreasing sequences, as does the sequence of determinants. This is the multichannel analog to the fact that the P_k form a nonincreasing sequence in the single-channel case. The use of the equations derived above for the recursive solution of (2.4) and (2.9) is called the *modern Levinson algorithm* [6], [16].

In the remainder of this section we extend Burg's results as required to present the new algorithm. By (2.18) and (2.20), together with (2.24), C_N and C_N' satisfy the "generalized conjugate" relationship

$$C_N = (P_{N-1}')^{-1}(C_N')^* P_{N-1} \quad \text{and} \quad C_N' = (P_{N-1})^{-1} C_N^* P_{N-1}'. \quad (2.28)$$

The second equation of (2.28) follows from the first; both are written to display the symmetry. It follows from (2.12) and (2.13) that $\det R' = \det R$ and from (2.25) (with both direct and reversed time) that

$$\prod_{k=0}^{N} \det P_k' = \prod_{k=0}^{N} \det P_k.$$

Since $\det P_0 = \det P_0' = \det R_0$,

$$\det P_k' = \det P_k, \qquad k = 0, 1, \cdots; \tag{2.29}$$

If $p = 1$, then $\det P_{N-1} = P_{N-1} = P_{N-1}'$ and (2.28) reduces to $C_N' = C_N^*$, that is, "generalized conjugation" reduces to ordinary conjugation.

If one has a set $C_1, C_2, \cdots, C_N$ for which all $P_k > 0$, then the set $R_0, C_1, \cdots, C_N$ determines the set $R_0, R_1, \cdots, R_N$, as can be seen by recursively applying the formula

$$R_N = - \sum_{k=0}^{N-1} F_{k+1,N}^* R_{N-k-1} \tag{2.30}$$

obtained by taking the Hermitian conjugate of the last equation of (2.4). (One may also obtain R_N by applying the fast Fourier transform [8] to the maximum entropy spectrum.) We therefore reverse the point of view and instead of trying to solve (2.4) using approximations to the R_k, we derive a method of determining the C_N *directly from the data* so that P_N and P_N' are always positive definite and are rapidly reduced in magnitude as N is increased. The new method, presented in Section III, is a direct generalization of Burg's single-channel method [6].

III. The Multichannel Burg Process

Let $\{y_l\}_{l=1}^{N_d}$ be a sample of N_d consecutive observations of a realization of $y(t)$. We consider a set of $M = N_d - N$ consecutive $N + 1$-tuples of data and array each $N + 1$-tuple as a long vector y_m^N defined by

$$(y_m^N)^* = [y_{m+N}^*, y_{m+N-1}^*, \cdots, y_m^*], \qquad \begin{matrix} m = 1, 2, \cdots, N_d - N = M \\ N = 0, 1, \cdots, N_d - 1. \end{matrix} \tag{3.1}$$

For example,

$$y_m^0 = y_m, \ m = 1, 2, \cdots, N_d; \ y_m^1 = \begin{bmatrix} y_{m+1} \\ y_m \end{bmatrix} \Big\} 2p, \ m = 1, 2, \cdots, N_d - 1, \ \text{etc.}$$

According to (2.17), the outputs u_m and v_m of the forward and backward filters as applied to the mth $N + 1$-tuple are, respectively,

$$u_m = \left\{ [F_{N-1}^*, 0] + C_N^* [0, (B_{N-1}')^*] \right\} y_m^N \tag{3.2}$$

and

$$v_m = \left\{ (C_N')^* [F_{N-1}^*, 0] + [0, (B_{N-1}')^*] \right\} y_m^N. \tag{3.3}$$

We define the forward and backward residual p-tuples e_m^N and b_m^N as

$$e_m^N = [F_{N-1}^*, 0] y_m^N \quad \text{and} \quad b_m^N = [0, (B_{N-1}')^*] y_m^N. \tag{3.4}$$

Then (3.2) and (3.3) take the form

$$u_m = e_m^N + C_N^* b_m^N \tag{3.5}$$

and

$$v_m = (C_N')^* e_m^N + b_m^N. \tag{3.6}$$

However, substituting the generalized conjugation (2.28) into (3.6) gives

$$v_m = P_{N-1}' C_N P_{N-1}^{-1} e_m^N + b_m^N. \tag{3.7}$$

We seek to minimize the weighted power over the M $N + 1$-tuples by requiring that $SS(C_N) = $ minimum, where

$$SS(C_N) = \frac{1}{2} \sum_{m=1}^{M} W_m [u_m^* Q_1 u_m + v_m^* Q_2 v_m] \tag{3.8}$$

and $Q_i = Q_i^* > 0$, $i = 1, 2$ are weighting matrices. The W_m are positive scalar weights (usually all taken as $1/M$ in practice). In (3.8), u_m and v_m are given by (3.5) and (3.7), respectively. We continue to assume $P_{N-1} > 0$ and $P_{N-1}' > 0$ and ultimately seek to determine C_N. Expression (3.8) may be simplified by employing matrix trace operations as suggested by $x^* y = \operatorname{tr} x^* y = \operatorname{tr} y x^*$, $\operatorname{tr} AB = \operatorname{tr} BA$, and $\operatorname{tr} A^* = \overline{\operatorname{tr} A}$ for vectors x and y

and matrices A and B. We also define the $p \times p$ matrices B, G and E by

$$E = \sum_{m=1}^{M} W_m e_m^N (e_m^N)^*$$

$$G = \sum_{m=1}^{M} W_m b_m^N (e_m^N)^* \tag{3.9}$$

$$B = \sum_{m=1}^{M} W_m b_m^N (b_m^N)^*.$$

When convenient, we also use inner-product notation, i.e., $(u, v) = \overline{u^* v}$ and $\|v\|^2 = (v, v)$. It is easy to show that E and B are nonsingular unless the set of linear combinations of residuals e_m^N or b_m^N fails to span p-space. For E, note that if $(Ev, v) = 0$, $\|v\|^2 \neq 0$, then

$$\sum_{m=1}^{M} W_m v^* e_m^N (e_m^N)^* v = \sum_{m=1}^{M} W_m |(e_m^N, v)|^2 = 0.$$

Since all W_m are positive, it follows that v is orthogonal to all forward residuals e_m^N. Since this situation is so rare in the consideration of actual data, we shall assume it does not occur for any N under consideration. (The most extreme case, of course, is that all forward residuals are zero.) A similar argument for B allows us to assume throughout that E and B are nonsingular.

Let X and Y be any complex $p \times p$ matrices whatsoever. After some algebra one obtains

$$SS(Y) - SS(X) = \tfrac{1}{2}\operatorname{tr}(T_1^* B T_1) + \tfrac{1}{2}\operatorname{tr}(T_2^* Q_2 T_2) + \operatorname{Re}\operatorname{tr}(Y^* - X^*)L(X) \tag{3.10}$$

where

$$T_1 = (Y - X)Q_1^{1/2}, \qquad T_2 = P_{N-1}'(Y - X)(P_{N-1}^{-1} E P_{N-1}^{-1})^{1/2}$$

and

$$L(X) = BXQ_1 + GQ_1 + (P_{N-1}' Q_2 P_{N-1}')X(P_{N-1}^{-1} E P_{N-1}^{-1}) + P_{N-1}' Q_2 G P_{N-1}^{-1}.$$

The matrix $Q_1^{1/2} > 0$ is the Hermitian symmetric positive semidefinite square root of Q_1 and $(P_{N-1}^{-1} E P_{N-1}^{-1})^{1/2} > 0$ is the analogous square root of $P_{N-1}^{-1} E P_{N-1}^{-1}$ [4]. It follows from (3.10) that $L(X) = 0$ is a necessary and sufficient condition for X to minimize $SS(X)$. For sufficiency, if $L(X) = 0$, then, since the first two terms of (3.10) are nonnegative, we have $SS(Y) > SS(X)$ for any complex $p \times p$ matrix Y whatsoever. Conversely, suppose $L(X) \neq 0$. In particular, we may choose $Y = -\epsilon L(X) + X$, where ϵ is real and positive. Substituting this matrix Y into (3.10) gives

$$SS(Y) - SS(X) = \epsilon^2 \left\{ \operatorname{tr}[Q_1^{1/2} L^*(X)] B [L(X) Q_1^{1/2}] \right.$$

$$+ \operatorname{tr}\left[(P_{N-1}^{-1} E P_{N-1}^{-1})^{1/2} L^*(X) P_{N-1}' \right]$$

$$\left. \cdot Q_2 \left[P_{N-1}' L(X)(P_{N-1}^{-1} E P_{N-1}^{-1})^{1/2} \right] \right\} - \epsilon \operatorname{tr} L^*(X) L(X).$$

Since the first part of this expression is nonnegative, and $\operatorname{tr} L^*(X) L(X) > 0$, $SS(Y) - SS(X)$ now has the form $SS(Y) - SS(X) = \epsilon^2 q_1 - \epsilon q_2$, where $q_1 > 0$ and $q_2 > 0$. If $q_1 = 0$, then for any $\epsilon > 0$, $SS(Y) < SS(X)$. Also, if $q_1 > 0$, then for $0 < \epsilon < q_2 / q_1$, we have $SS(Y) < SS(X)$. Thus, if $L(X) \neq 0$, $SS(X)$ cannot be a minimum. Therefore the desired minimization occurs by means of C_N iff

$$BC_N Q_1 + GQ_1 + (P_{N-1}' Q_2 P_{N-1}')C_N (P_{N-1}^{-1} E P_{N-1}^{-1})$$

$$+ P_{N-1}' Q_2 G P_{N-1}^{-1} = 0. \tag{3.11}$$

This normal equation (3.11) is the multichannel equation for C_N that corresponds to the single-channel Burg process when arbitrary weights Q_1 and Q_2 are applied. We show that (3.11) has a unique solution if Q_1 and Q_2 are nonsingular. Clearly, we can reduce (3.11) (with $X = C_N$) to

the form

$$A_1 X + X A_2 = C \qquad (3.12)$$

where

$$A_1 = (P'_{N-1} Q_2 P'_{N-1})^{-1} B \qquad (3.13)$$

$$A_2 = (P_{N-1}^{-1} E P_{N-1}^{-1}) Q_1^{-1} \qquad (3.14)$$

$$C = -(P'_{N-1} Q_2 P'_{N-1})^{-1} G - (P'_{N-1} Q_2 P'_{N-1})^{-1} P'_{N-1} Q_2 G P_{N-1}^{-1} Q_1^{-1}. \qquad (3.15)$$

The relevant theory of equations such as (3.12) is given briefly by Bellman ([5, pp. 175–76 and 231]). Since C_N is a $p \times p$ matrix, the solution requires solution of a $p^2 \times p^2$ system of equations; however, the computational labor is not excessive, since (3.12) must be solved only once for each update, so that the number of required solutions is $0(N)$ for filters of length $1, 2, \cdots, N$. It turns out that if the unknown matrix elements x_{ij} are put in the order $x_{11} x_{12} \cdots x_{1p}, x_{21} \cdots x_{2p}, \cdots, x_{p1}, \cdots, x_{pp}$ as a column vector, and the elements c_{ij} are correspondingly arranged as $c_{11} \cdots c_{1p}, c_{21} \cdots c_{2p}, \cdots, c_{p1}, \cdots, c_{pp}$, then the coefficient matrix becomes

$$A_1 \otimes I + I \otimes A_2^T \qquad (3.16)$$

where $\otimes$ denotes the Kronecker (or tensor) product and T denotes ordinary transposition. In the numerical work reported in Section IV, the resulting equation was programmed, and excellent solution accuracy was observed. The coefficient matrix (3.16) is nonsingular provided that if λ_i, $i = 1, \cdots, p$ are the eigenvalues of A_1 and μ_j, $j = 1, \cdots, p$ are the eigenvalues of A_2, then $\lambda_i + \mu_j \neq 0$ (i.e., $\lambda_i + \mu_j$ is nonzero for every choice of i and j) ([5, p. 231]). We show that this condition is satisfied for (3.12) and, in fact that both the λ_i and μ_j are all positive. For this, suppose $A_2 v = \mu v$, that is,

$$P_{N-1}^{-1} E P_{N-1}^{-1} Q_1^{-1} v = \mu v$$

or

$$Q_1^{-1} v = \mu (P_{N-1}^{-1} E P_{N-1}^{-1})^{-1} v. \qquad (3.17)$$

Take the inner product of (3.17) with v to obtain

$$(Q_1^{-1} v, v) = \mu ((P_{N-1}^{-1} E P_{N-1}^{-1})^{-1} v, v). \qquad (3.18)$$

Since both sides of (3.18) are positive, it follows that $\mu > 0$. A similar argument shows that any eigenvalue of $A_1 = (P'_{N-1} Q_2 P'_{N-1})^{-1} B$ is also positive.

For Q_1 and Q_2 not necessarily nonsingular, (3.8) can be written in the form

$$2SS(C_N) = \mathrm{tr}\, C_N^* [B C_N Q_1 + G Q_1$$
$$+ (P'_{N-1} Q_2 P'_{N-1}) C_N (P_{N-1}^{-1} E P_{N-1}^{-1}) + P'_{N-1} Q_2 G P_{N-1}^{-1}]$$
$$+ \mathrm{tr}\, C_N [Q_1 G^* + P_{N-1}^{-1} G^* Q_2 P'_{N-1}] + \mathrm{tr}\, E Q_1 + \mathrm{tr}\, B Q_2 \qquad (3.19)$$

and if $\hat{C}_N$ is a solution of (3.11), then

$$2SS(\hat{C}_N) = \mathrm{tr}(E - \hat{C}_N^* B \hat{C}_N) Q_1$$
$$+ \mathrm{tr}\left[B - P'_{N-1} \hat{C}_N (P_{N-1}^{-1} E P_{N-1}^{-1}) \hat{C}_N^* P'_{N-1} \right] Q_2. \qquad (3.20)$$

The key to the multichannel Burg process is a proper assignment of the weight matrices Q_1 and Q_2. Early efforts involved assigning these matrices to reduce (3.11) to a simple form for which the solution did not involve Kronecker products. Such an assignment was

$$Q_1 = P_{N-1}^{-1} E P_{N-1}^{-1} \text{ and } Q_2 = (P'_{N-1})^{-1} B (P'_{N-1})^{-1} \qquad (3.21)$$

However, it was soon found by numerical experiment that (3.21) did not necessarily give $P_N > 0$, so that (3.21) was abandoned. It was then found

that the assignment

$$Q_1 = P_{N-1}^{-1} \text{ and } Q_2 = (P'_{N-1})^{-1} \qquad (3.22)$$

has the required properties and furthermore, reduces to the Burg process for a single channel, $p = 1$. According to (2.29), if $p = 1$, then $P'_k = P_k$ for all k and it is readily verified that (3.8) gives the same minimization as that presented by Burg [6], for which the solution is, by (3.11),

$$C_N = -2G/(E + B). \qquad (3.23)$$

For our multichannel case, the equation to be solved reduces to

$$B C_N + P'_{N-1} C_N P_{N-1}^{-1} E = -2G. \qquad (3.24)$$

It will be proved that the assignment (3.22) of Q_1 and Q_2 will always give rise to a positive definite matrix P_N, and preliminary numerical results presented in Section IV indicate that the power matrices are reduced considerably faster by this process than occurs with the R-method. There is another reason why (3.22) should be efficient. According to (2.7) and (2.10), if the residuals are approaching white noise with P_N remaining approximately unchanged as N increases, then the weighting given by (3.22) approximates that applied in the Gauss–Markov theorem [10]. In any case, weighting (3.22) may be justified by its apparent success.

We now prove that if $Q_1 = P_{N-1}^{-1}$ and $Q_2 = (P'_{N-1})^{-1}$, then the matrix P_N (and consequently P'_N) is always positive definite. The proof is slightly indirect and proceeds by first showing that a closely related matrix is positive definite, and then relating this to the theory of stable matrices to obtain the final result. By (3.24)

$$P'_N C_N = -(2G + B C_N) E^{-1} P_{N-1}, \qquad (3.25)$$

and substituting (3.25) into (2.26) gives

$$P_N = [E + C_N^* B C_N + 2 C_N^* G] E^{-1} P_{N-1}. \qquad (3.26)$$

Since $P_N = P_N^*$, one may also write

$$P_N = P_{N-1} E^{-1} [E + C_N^* B C_N + 2 G^* C_N]. \qquad (3.27)$$

Let H be defined by

$$2H = (E P_{N-1}^{-1}) P_N + P_N (P_{N-1}^{-1} E). \qquad (3.28)$$

Clearly, $H = H^*$; we prove that $H > 0$. By (3.28), (3.26), and (3.27),

$$H = E + C_N^* B C_N + C_N^* G + G^* C_N. \qquad (3.29)$$

Let v be any complex p-tuple for which $\|v\| = 1$. Then

$$(Hv, v) = v^* [E + C_N^* B C_N + C_N^* G + G^* C_N] v$$
$$= \mathrm{tr}[E + C_N^* B C_N + C_N^* G + G^* C_N](vv^*). \qquad (3.30)$$

By (3.19), $(Hv, v) = 2SS(C_N)$ as evaluated for $Q_1 = vv^*$ and $Q_2 = 0$. Consequently, $(Hv, v) > 0$ and $H > 0$. However, by (3.8), (Hv, v) cannot be zero unless v is orthogonal to all forward residuals, a case that has been ruled out. Consequently, H is strictly positive definite. By (3.28), P_N satisfies the matrix equation

$$(-E P_{N-1}^{-1}) X + X (-P_{N-1}^{-1} E) = -2H. \qquad (3.31)$$

By an argument similar to that given in connection with (3.18), it follows that all eigenvalues of $-E P_{N-1}^{-1}$ and $-P_{N-1}^{-1} E$ are negative, and that (3.31) has a unique solution. According to a known theorem ([11, pp. 270-278 and prob. 3, p. 278]) if A is a stable complex matrix, then if Q is any complex Hermitian symmetric positive definite matrix, the equation
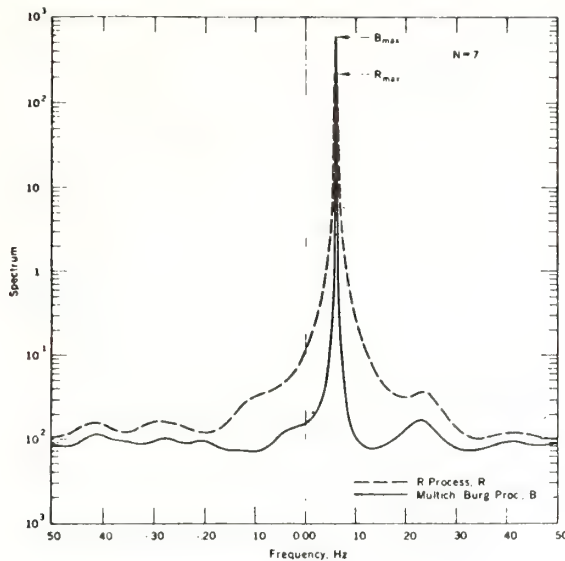
Fig. 1. 1-1 spectra, $S_{11}(f)$.
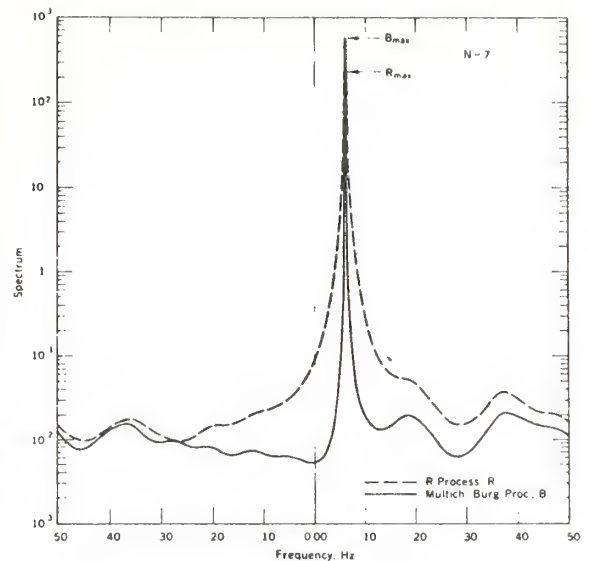
Fig. 2. 2-2 spectra, $S_{22}(f)$.

$$AX + XA^* = -Q \qquad (3.32)$$

has a positive definite Hermitian symmetric solution X. Here a *stable* matrix is defined as one for which all eigenvalues have negative real parts. Clearly, $A = -EP_{N-1}^{-1}$ is a stable matrix. Consequently, (3.31) has a positive definite solution X, and since the solution is unique, $X = P_N$ and P_N is positive definite. It was shown in Section II that this also implies that P_N' is positive definite.

In solving for C_N and C_N', one normally solves (3.24) for C_N and obtains C_N' from the "generalized conjugation" (2.28). However, one could equally well solve the dual equation [obtained by applying (2.28) to (3.24)]

$$EC_N' + P_{N-1}C_N'(P_{N-1}')^{-1}B = -2G^*. \qquad (3.33)$$

This equation can also be obtained from (3.24) by reversing the data in time. The definitions (3.4) and (3.1), together with (2.17), imply that

$$e_m^N = e_{m+1}^{N-1} + C_{N-1}^* b_{m+1}^{N-1} \quad \text{and} \quad b_m^N = b_m^{N-1} + (C_{N-1}')^* e_m^{N-1},$$

$$m = 1, 2, \cdots, N_d - N = M, N > 1. \quad (3.34)$$

We briefly review the computing procedure for the multichannel Burg process. First we compute $P_0 = P_0' = (\sum_{m=1}^{N_d} y_m y_m^*)/N_d$. Then we let $e_m^1 = y_{m+1}$ and $b_m^1 = y_m$, $m = 1, 2, \cdots, N_d - 1$, and compute E, B, and G (for 2-tuples) by (3.9). Then we solve (3.24) for C_1 and compute C_1' by (2.28). The power matrices P_1 and P_1' are then computed by (2.26) and (2.27), and the filter coefficients are updated by (2.17). The new forward and backward residuals e_m^2 and b_m^2 (for 3-tuples) are computed by (3.34), and the process continues. Spectra are computed, when desired, by (2.14). The methods described in this paper have been programmed in Fortran [19], and a few numerical results are presented in Section IV.

IV. NUMERICAL COMPARISONS

The simulations presented here give some indication of the behavior of the new method. We present the results as applied to the following data:

$$N_d = 128, \quad \Delta t = 1\,\text{s}, \quad p = 2$$

$$y_t = \begin{bmatrix} y_{1t} \\ y_{2t} \end{bmatrix}, \qquad t = 1, 2, \cdots, 128$$

$$\text{Re}\, y_{1t} = \cos\left(\frac{2\pi t}{16}\right) + 0.25(\text{Ranf} - 0.5)$$

$$\text{Im}\, y_{1t} = \sin\left(\frac{2\pi t}{16}\right) + 0.25(\text{Ranf} - 0.5) \qquad (4.1)$$

$$\text{Re}\, y_{2t} = \cos\left(\frac{2\pi t}{16} + 1\,\text{rad}\right) + 0.25(\text{Ranf} - 0.5)$$

$$\text{Im}\, y_{2t} = \sin\left(\frac{2\pi t}{16} + 1\,\text{rad}\right) + 0.25(\text{Ranf} - 0.5).$$

The quantity Ranf represents a pseudo-random number uniformly distributed between 0 and 1. The simulation was programmed so that the R-process (Section II) and the multichannel Burg process operated on precisely the same data. The simulation (4.1) was used mainly for check out, and the results presented here must be regarded as preliminary. Both the new method and the R-process can be expected to handle much lower signal-to-noise ratios than that of (4.1). If we denote the spectrum by

$$S(f) = \begin{bmatrix} S_{11}(f) & S_{12}(f) \\ S_{21}(f) & S_{22}(f) \end{bmatrix}, \qquad (4.2)$$

where f is the frequency in Hz, then the squared coherence is given by

$$\text{coh}^2(f) = \frac{|S_{12}(f)|^2}{S_{11}(f) S_{22}(f)}. \qquad (4.3)$$

A rough indication of the expected performance of either process is given by Akaike's FPE criterion [1], [2], given by

$$\text{FPE}(N) = \det P_N \left(\frac{N_d + 1 + pN}{N_d - 1 - pN}\right)^p. \qquad (4.4)$$

Other criteria exist [3], [18], but (4.4) should suffice for a crude comparison of the two methods. According to (4.4), a filter estimation process is performing well if $\det P_N$ is rapidly reduced as the filter length is increased through the first few values of N.

In the numerical check out of the programs, the exact equality of the two versions of the maximum entropy spectrum [(2.14) and (2.15)] was observed, as was the exact equality of $\det P_N$ and $\det P_N'$. The eigenvalues of P_N and P_N' were computed, and although not identical, they usually
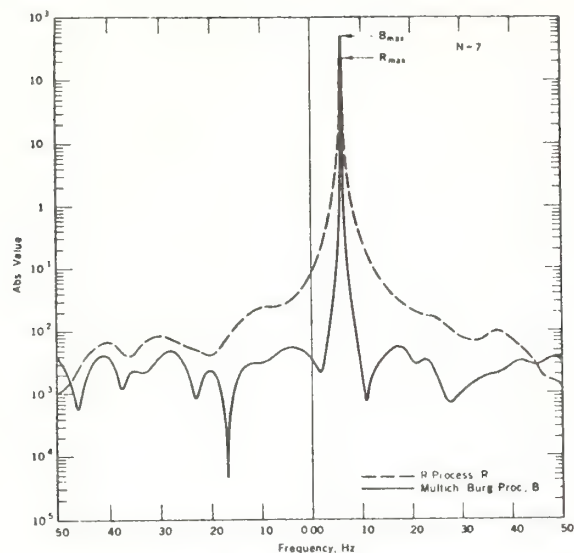
Fig. 3.   Absolute value of 1-2 spectra, $|S_{12}(f)|$.
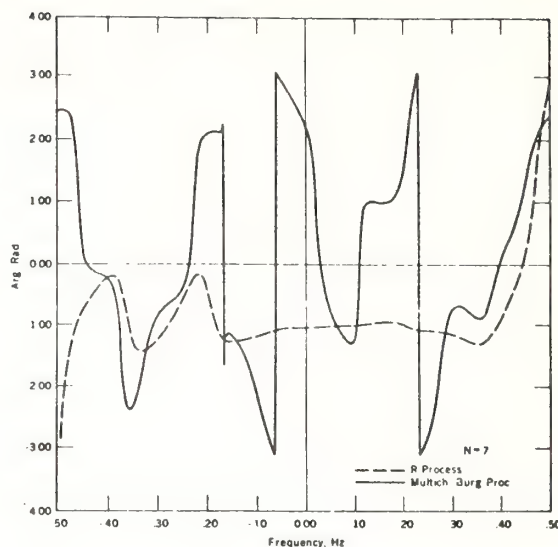
Fig. 4.   Phase of 1-2, spectra, $\arg S_{12}(f)$.
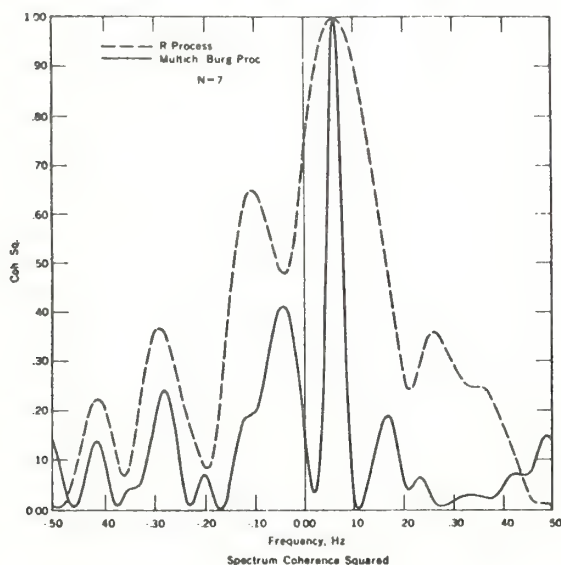
Fig. 5.   1-2 spectrum coherence squared, $|S_{12}(f)|^2 / S_{11}(f) S_{22}(f)$.
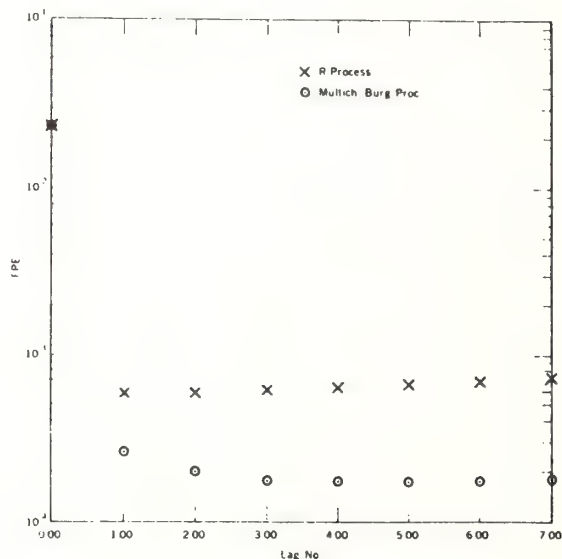
Fig. 6.   Determinants of P_N.

agree to at least 2–3 significant figures. Of course, these eigenvalues adjust themselves in such a way that $\det P_N = \det P_N'$. The case $p = 1$ was computed, and exact agreement was obtained with a separately-programmed Burg single-channel solution.

In the absence of random noise, the signal given by (4.1) would give $S_{11}(f) = S_{22}(f) = \text{const} \times \delta(f - 0.0625)$. The quality of the approximation obtained is indicated in Figs. 1 and 2. (The maxima shown are only approximate because of the discrete spacing of the FFT frequencies.) Note the superior resolution of the multichannel Burg process, as indicated by narrower "stems" at $f = 0.0625$. The corresponding results for $S_{12}(f)$ are shown (in amplitude and phase) in Figs. 3 and 4. The phases of the two methods differ markedly, but both appear to equal -1 radian at $f = 0.0625$ Hz. In Fig. 5, the corresponding squared coherences are compared. As it is intuitively reasonable that frequencies at which the data are random should give zero coherence, it appears that the multi-

channel Burg process gives a more reasonable squared coherence. Fig. 6 gives a comparison of $\det P_N$ for the two methods. Since the determinant of P_N is approximately a factor of four smaller for the multichannel Burg process with $N = 7$, it appears to be performing better than the R-process. Finally, the corresponding values of Akaike's FPE criterion are presented in Fig. 7. It is indicated that little difference in the performance of the multichannel Burg process would be expected for $N = 3, 4, \cdots, 7$. Results for $N = 3, 4, 5, 6$ were also obtained, and were quite similar to those presented here for $N = 7$. The multichannel Burg process also has been applied to data analogous to (4.1) with $p = 3$, with similar results. New Fortran computer programs have been written to implement the algorithm of this paper as well as the older R-process. These programs are available and are described in detail in a forthcoming report [19]. Various available single-channel programs are described in another report [20].
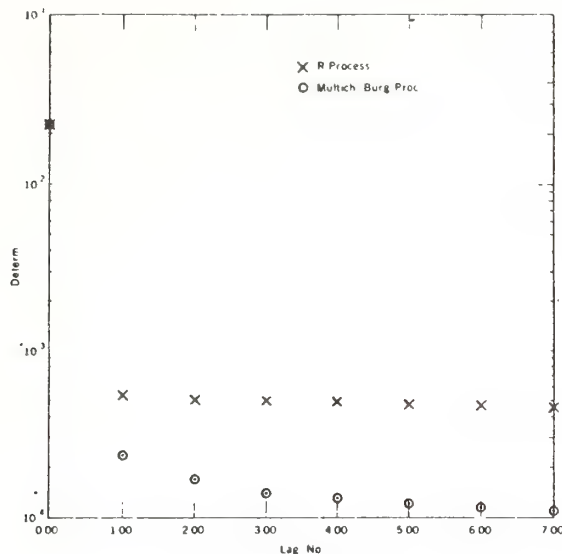
Fig. 7. Akaike's FPE criterion.

V. Conclusions

A multichannel complex generalization of the Burg reflection-coefficient process has been derived. It has been proven that all resulting power matrices are positive definite. Preliminary numerical results indicate a rapid reduction of $\det P_N$ and $\det P_N'$ as N is increased, as well as superior resolution.

Acknowledgment

The author gratefully acknowledges the contribution of J. P. Burg, who graciously provided a copy of his 1975 Stanford dissertation in which the essential foundation for the work of the present paper was laid. The author also acknowledges valuable conversations with J. M. Young, R. B. Chadwick, and W. B. Sweezy, all of the Wave Propagation Laboratory, and the contribution of J. A. Leise of CIRES, who read the manuscript and made valuable suggestions.

References

[1]   H. Akaike, "Fitting autoregressive models for prediction," *Ann. Inst. Statist. Math.*, vol. 21, pp. 243–247, 1969.
[2]   ——, "Autoregressive model fitting for control," *Ann. Inst. Statist. Math.*, vol. 23, pp. 163–180, 1971.
[3]   ——, "A new look at statistical model identification," *IEEE Trans. Automat. Contr.*, vol. AC-19, pp. 716–723, 1974.
[4]   A. Albert, *Regression and the Moore-Penrose Pseudoinverse*. New York: Academic, 1972.
[5]   R. Bellman, *Introduction to Matrix Analysis*. New York: McGraw-Hill, 1960.
[6]   J. P. Burg, "Maximum entropy spectral analysis," Ph.D. dissertation, Dep. Geophys., Stanford Univ., Stanford, CA, May, 1975.
[7]   W. Y. Chen and G. R. Stegen, "Experiments with maximum entropy power spectra of sinusoids," *J. Geophys. Res.*, vol. 79, pp. 3019–3022, 1974.
[8]   J. W. Cooley and J. W. Tukey, "An algorithm for the machine calculation of complex Fourier series," *Math. Comput.*, vol. 19, pp. 297–301, 1965.
[9]   R. Courant and D. Hilbert, *Methods of Mathematical Physics*, vol. 1. New York: Interscience, 1953.
[10] R. Deutsch, *Estimation Theory*. Englewood Cliffs, NJ: Prentice-Hall, 1965.
[11] J. N. Franklin, *Matrix Theory*. Englewood Cliffs, NJ: Prentice-Hall, 1968.
[12] S. Haykin and S. Kesler, "The complex form of the maximum entropy method for spectral estimation," *Proc. IEEE*, vol. 64, pp. 822–823, 1976.
[13] G. A. Ioannidis, "Application of multivariate autoregressive spectrum estimation to ULF waves," *Radio Sci.*, vol. 10, no. 12, pp. 1043–1054, 1975.
[14] R. H. Jones, "Identification and autoregressive spectrum estimation," *IEEE Trans. Automat. Contr.*, vol. AC-19, pp. 894–897, Dec. 1974.
[15] E. R. Kanasewich, *Time Sequence Analysis in Geophysics*. Edmonton, Canada: Univ. of Alberta Press, 1973.
[16] N. Levinson, "The Wiener rms (root mean square) error criterion in filter design and prediction," *J. Math. Phys.*, vol. 25, no. 4, pp. 261–278, 1947; also in N. Wiener, *Extrapolation, Interpolation, and Smoothing of Stationary Time Series*. Cambridge, MA: MIT Press, 1949.
[17] J. Makhoul, "Linear prediction: A tutorial review," *Proc. IEEE*, vol. 63, no. 4, pp. 561–579, 1975.
[18] E. Parzen, "Some recent advances in time series modeling," *IEEE Trans. Automat. Contr.*, vol. AC-19, pp. 723–730, 1974.
[19] O. N. Strand, "Computer programs for maximum entropy spectral analysis of real and complex multichannel time series," U. S. Dep. Commerce, Environmental Res. Lab., Boulder, CO, NOAA Tech. Rep.
[20] O. N. Strand, J. M. Young, and R. B. Chadwick, "Computer programs for maximum entropy spectral analysis of real and complex single-channel time series," U. S. Dep. Commerce, Environmental Res. Lab., Boulder, CO, NOAA Tech. Rep.
[21] T. J. Ulrych, "Maximum entropy power spectrum of truncated sinusoids," *J. Geophys. Res.*, vol. 77, no. 8, pp. 1396–1400, 1972.
[22] T. J. Ulrych and T. N. Bishop, "Maximum entropy spectral analysis and autoregressive decomposition," *Rev. Geophys. Space Phys.*, vol. 13, no. 1, pp. 183–200, 1975.
[23] R. A. Wiggins and E. A. Robinson, "Recursive solution to the multichannel filtering problem," *J. Geophys. Res.*, vol. 70, no. 8, pp. 1885–1891, 1965.

MULTICHANNEL COMPLEX MAXIMUM ENTROPY SPECTRAL ANALYSIS

Otto Neall Strand

NOAA/ERL/Wave Propagation Laboratory
Boulder, Colorado 80302

ABSTRACT

The Burg reflection-coefficient method for maximum entropy spectral estimation is generalized to apply to multichannel complex signals. The virtues of the single-channel Burg process, particularly superior resolution and a guarantee that all power matrices are positive definite, carry over to the generalization. Results of some numerical computations are presented in graphical form.

1. INTRODUCTION

The single-channel Burg reflection-coefficient method (Burg, 1968, 1975) for obtaining maximum entropy spectral estimates has been widely applied and has met with considerable success. Extensive bibliographies citing such applications are presented by Makhoul (1975) and Ulrych and Bishop (1975). The single-channel complex Burg process is described by Haykin and Kesler (1976), as well as by Burg (1975). In the present paper we present a generalization of Burg's technique to multichannel complex time series. In his recent dissertation Burg (1975) develops the modern multichannel Levinson algorithm for solving the Yule-Walker equations for the filter coefficients and states that no simple extension of the Burg technique to the multichannel case is possible. The purpose of this paper is to present just such an extension. This extension, which involves the least-squares determination of the reflection coefficients (defined in section 2) with inverse-power weighting, is a direct generalization of the single-channel Burg process, and has the same virtues; namely, superior resolution and a guarantee that all resulting power matrices are positive definite. Mathematical proofs and further details that are omitted here may be found in a forthcoming paper (Strand, 1977a). Available computer programs implementing the new method, as well as programs for the earlier Yule-Walker methods, are described in a separate report (Strand, 1977b). Another report (Strand, et al., 1977) describes analogous single-channel computer programs that are available.

2. THEORY

Many of the results presented in this section are adaptations of results obtained by Burg (1975). We consider the complex p-channel vector time series

$$y(t) = \begin{bmatrix} y_1(t) \\ y_2(t) \\ \cdot \\ \cdot \\ \cdot \\ y_p(t) \end{bmatrix} , \quad t = \{n\Delta t\}_{n=-\infty}^{\infty} \qquad (2.1)$$

where we assume that $y(t)$ is wide-sense stationary with zero mean. The <u>forward filter of length N</u> has the form

$$y(t) + \sum_{k=1}^{N} F_{kN}^* \, y(t-k\Delta t) = e_N(t) . \qquad (2.2)$$

The p vector $e_N(t)$ is called the <u>output</u> of the filter. The constant complex p x p matrices F_{kN} are called the <u>forward filter coefficients</u>, and the star * denotes the (Hermitian) conjugate transpose. Similarly, the <u>backward filter of length N</u> has the form

$$y(t) + \sum_{k=1}^{N} B_{kN}^* \, y(t + k\Delta t) = b_N(t) . \qquad (2.3)$$

We are concerned with <u>optimum</u> forward or backward filters (2.2) or (2.3), which result from imposing the condition that the expected mean-square value of $e_N(t)$ or $b_N(t)$ should be a minimum. For (2.2) this involves determining F_{1N}, F_{2N}, ..., F_{NN} such that

$$E\{[e_N(t)]^* \, [e_N(t)]\} = \text{minimum.} \qquad (2.4)$$

Inserting the expression (2.2) for $e_N(t)$ into (2.4) and minimizing with respect to the coefficients F_{kN}^* gives the system

$$RF_N \equiv \begin{bmatrix} R_0 R_1 & \cdots & R_N \\ R_{-1} R_0 & \cdots & R_{N-1} \\ \cdots & & \cdots \\ R_{-N} R_{-N+1} & \cdots & R_0 \end{bmatrix} \begin{bmatrix} I \\ F_{1N} \\ \cdot \\ \cdot \\ \cdot \\ F_{NN} \end{bmatrix} = \begin{bmatrix} P_N \\ 0 \\ \cdot \\ \cdot \\ \cdot \\ 0 \end{bmatrix} \qquad (2.5)$$

where I is the p x p identity matrix and the p x p block submatrices R_k are defined by

$$R_k = E[y(t)y^*(t-k\Delta t)], \quad k = 0,1, \ldots N \qquad (2.6)$$

so that

$$R_{-k} = R_k^* . \qquad (2.7)$$

As indicated, the coefficient matrix in (2.5) will be called the R-matrix or simply R. The vector of block matrices, F_N (single subscript), is defined by $F_N^* = [I|F_{1N}^*| \ldots F_{NN}^*]$. The forward power matrix for the resulting optimum filter (i.e., for F_N satisfying (2.5)) is

$$P_N = E\{e_N(t)e_N^*(t)\} . \qquad (2.8)$$

Because F_N satisfies (2.5), it follows that

$$P_N = F_N^* R F_N . \qquad (2.9)$$

System (2.5) is identical to the transposed form of the system resulting from the multichannel equations cited by Wiggins and Robinson (1965) for real time series, except that matrix transposes are replaced by Hermitian conjugates. Because of (2.7), the optimum backward filter satisfies

$$R'B_N \equiv \begin{bmatrix} R_0 R_{-1} & \cdots & R_{-N} \\ R_1 R_0 & \cdots & R_{-N+1} \\ \cdots & & \cdots \\ R_N R_{N-1} & \cdots & R_0 \end{bmatrix} \begin{bmatrix} I \\ B_{1N} \\ \cdot \\ \cdot \\ \cdot \\ B_{NN} \end{bmatrix} = \begin{bmatrix} P_N' \\ 0 \\ \cdot \\ \cdot \\ \cdot \\ 0 \end{bmatrix} \qquad (2.10)$$

where R' is the coefficient matrix in (2.10) and $B_N^* = [I|B_{1N}^*| \ldots B_{NN}^*]$. The primes indicate a reversal of time, F_N stands for "forward" and B_N stands for "backward". The backward power matrix P_N' for the resulting optimum filter is

$$P_N' = E\{b_N(t)b_N^*(t)\} \qquad (2.11)$$

and it follows from (2.10) that

$$P_N' = B_N^* R' B_N. \qquad (2.12)$$

The p x p matrix coefficients F_{NN} and B_{NN} will be called forward and backward reflection coefficients, respectively. They have special significance in that the optimum filter of length N can be computed from them if one has already determined the optimum filters of length N-1. Accordingly, we define

$$C_N = F_{NN} \text{ and } C_N' = B_{NN}. \qquad (2.13)$$

It can be shown that

$$P_N = P_{N-1} - C_N^* P_{N-1}' C_N \qquad (2.14)$$

and

$$P_N' = P_{N-1}' - (C_N')^* P_{N-1} C_N' . \qquad (2.15)$$

If one has determined the optimum filters of length N, then the maximum entropy power spectral density (a p x p matrix) can be computed in terms of the forward filter by the formula (Jones, 1974, Ioannidis, 1975)

$$S(f) = \Delta t[F^{-1}(1/z)]^* P_N[F^{-1}(1/z)] \qquad (2.16)$$

where $F(z) = I + F_{1N}z + \ldots + F_{NN}z^N$ and z is the complex scalar defined by $z = \exp[-2\pi i f\Delta t]$, and in terms of the backward filter by

$$S(f) = \Delta t[B^{-1}(z)]^* P_N'[B^{-1}(z)] \qquad (2.17)$$

where $B(z) = I + B_{1N}z + \ldots + B_{NN}z^N$. The calculation of $F(1/z)$ and $B(z)$ is done economically by fast Fourier transform.

The filter coefficient matrices F_{kN} and B_{kN} are obtained recursively from $F_{j,N-1}$ and $B_{j,N-1}$ by the Levinson algorithm:

$$F_{NN} = C_N; \quad F_{kN} = F_{k,N-1} + B_{N-k,N-1} C_N \qquad (2.18)$$

and

$$B_{NN} = C_N'; \quad B_{kN} = B_{k,N-1} + F_{N-k,N-1} C_N', k=1,2,\ldots(N-1). \qquad (2.19)$$

The following new result is crucial to the process to be developed in section 3. It has been shown (Strand, 1977a) that

$$C_N = (P_{N-1}')^{-1}(C_N')^* P_{N-1} \text{ and } C_N' = P_{N-1}^{-1} C_N^* P_{N-1}'. \qquad (2.20)$$

These relationships will be called "generalized conjugation". It is also known (Strand, 1977a) that $\det P_N = \det P_N'$ for all N, where $\det ( )$ denotes the determinant. Consequently, if p = 1, then $P_N' = P_N$ and we obtain $C_N = (C_N')^*$ so that generalized conjugation becomes ordinary conjugation.

If one had the exact values of the R_k, he could proceed recursively using the formulas listed above to obtain the maximum entropy spectrum. However, since these are not obtainable from a finite sample of a realization of y(t), we must resort to approximations. In what follows P_N and P_N' denote the results of substituting whatever approximations are being used into (2.9) and (2.12). Two basic approaches have been used for single-channel estimation and can be used for multichannel time series: approximation of the R_k or approximation of the C_k. In the first case,

if $\{y_\ell\}_{\ell=1}^{N_d}$ is a sample of N_d consecutive vectors of a realization of $y(t)$, one may take

$$\hat{R}_k = \frac{1}{N_d-k} \sum_{\ell=1}^{N_d-k} y_{k+\ell} y_\ell^*, \quad k=0,1,\ldots,N \tag{2.21}$$

as an unbiased estimator of R_k, where $N \ll N_d$. Unfortunately the resulting R-matrix often fails to be positive definite, with disasterous consequences. It can be shown that R is positive definite if and only if $P_0, P_1, \ldots, P_N$ are all positive definite; also P_k' is positive definite if and only if P_k is positive definite. Thus by (2.8) and (2.11), any choice of estimates of R_k for which R is not positive definite will result in disasterous consequences akin to obtaining negative variance. Replacing the denominator in (2.21) by N_d gives biased estimators of R_k for which the R-matrix is positive definite. The method in which such estimators are used will be called the R-process. (It is sometimes called Yule-Walker estimation). However, the resulting spectral resolution suffers, and the bias becomes more severe when the record is short, precisely the situation where maximum entropy spectral analysis has the most to offer. Because of these inherent difficulties Burg (1968, 1975) devised a single-channel method in which the autocovariance approach is bypassed and instead the reflection coefficients and resulting F_{kN} and $B_{kN}(=F_{kN}^*$ if p=1) are estimated directly from the data $\{y_\ell\}$ in a manner that gives both superior resolution and positive powers, P_N and P_N'. In the next section we generalize this method, known as the Burg reflection-coefficient method, to apply to a multichannel complex time series. This new generalization will be called the multichannel Burg process.

3. THE MULTICHANNEL BURG PROCESS

In this section we are concerned with a sample $(y_1, y_2, \ldots y_{N_d})$ consisting of N_d consecutive vector observations of a relization of a p-channel time series $y(t)$. The treatment is analogous to that of Burg (1975, pp. 51-54) or Kanasewich (1973, pp. 258-262). We may consider a set of $M=N_d-N$ consecutive N+1-tuples of data vectors and array each N+1-tuple as a long vector y_m^N as defined by

$$(y_m^N)^* = [y_{m+N}^* | y_{m+N-1}^* | \ldots y_m^*], \quad \begin{array}{l} m=1,2,\ldots,N_d-N=M \\ N=0,1,\ldots,N_d-1 \end{array}. \tag{3.1}$$

For example,

$$y_m^0 = y_m, \quad m = 1,2,\ldots,N_d; \quad y_m^1 = \left[\begin{array}{c} y_{m+1} \\ y_m \end{array}\right]\Big\}2p,$$

$m = 1,2,\ldots,(N_{d-1})$, etc. According to the Levinson algorithm, the outputs u_m and v_m of the forward and backward filters as applied to the mth N+1-tuple are, respectively

$$u_m = \{[F_{N-1}^*|0] + C_N^*[0|B_{N-1}^*]\}y_m^N \tag{3.2}$$

and

$$v_m = \{(C_N')^*[F_{N-1}^*|0] + [0|B_{N-1}^*]\}y_m^N. \tag{3.3}$$

We may define the forward and backward residual p-tuples e_m^N and b_m^N by

$$e_m^N = [F_{N-1}^*|0]y_m^N \text{ and } b_m^N = [0|B_{N-1}^*]y_m^N. \tag{3.4}$$

Then (3.2) and (3.3) become

$$u_m = e_m^N + C_N^* b_m^N \text{ and } v_m = (C_N')^* e_m^N + b_m^N. \tag{3.5}$$

However, according to the generalized conjugation (2.20), $(C_N')^* = P_{N-1}'C_N P_{N-1}^{-1}$. Substituting this result into (3.5) gives

$$v_m = P_{N-1}'C_N P_{N-1}^{-1} e_m^N + b_m^N \tag{3.6}$$

as the residual output of the backward filter. We choose C_N to minimize a weighted sum of squares of the forward and backward residual outputs of the filter of length N in the form $SS(C_N) = $ minimum, where

$$SS(C_N) = \frac{1}{2} \sum_{m=1}^M W_m[u_m^* Q_1 u_m + v_m^* Q_2 v_m]. \tag{3.7}$$

In (3.7), u_m is given by (3.5) and v_m is given by (3.6). The p x p weight matrices Q_1 and Q_2 are assumed Hermitian symmetric and positive semi-definite. The positive scalar weights W_m are usually all taken as $W_m = 1/M$. It has been proved (Strand, 1977a) that (3.7) has a unique solution for C_N if the matrices Q_1 and Q_2 are nonsingular. General normal equations have been derived for which the solutions have been programmed (Strand, 1977a, 1977b). However, the most useful choice appears to be

$$Q_1 = P_{N-1}^{-1} \text{ and } Q_2 = (P_{N-1}')^{-1}. \tag{3.8}$$

The reasonable assumption is made that for every N under consideration the matrix whose columns are the residual vectors has rank p. We define the p x p matrices E, G and B by

$$E = \sum_{m=1}^{M} W_m e_m^N (e_m^N)^* ; \quad G = \sum_{m=1}^{M} W_m b_m^N (e_m^N)^*$$

$$B = \sum_{m=1}^{M} W_m b_m^N (b_m^N)^* . \tag{3.9}$$

Then the equation giving the p x p matrix C_N that minimizes (3.7) under assumption (3.8) is

$$BC_N + P_{N-1}' C_N P_{N-1}^{-1} E = -2G. \tag{3.10}$$

If p = 1, then $P_k' = P_k$ for all k and (3.10) reduces to $C_N = -2G/(E+B)$ to give the same solution as that presented by Burg. In general, however, (3.10) has the form AX + XB = C, a p^2 x p^2 system of equations for which the relevant theory is given briefly by Bellman (1960, pp. 176-176 and 231). The computational effort is not excessive, as this equation must be solved only once for each update. It has been proved (Strand, 1977a) that the C_N given by the unique solution of (3.10) always gives rise to positive definite power matrices P_N and P_N' as given by, (2.14) and (2.15). After obtaining C_N, we obtain C_N by the "generalized conjugation" (2.20), and the filter coefficients by the Levinson algorithm (2.18) and (2.19), from which the spectrum is computed by (2.16) or (2.17). If desired, the R_k can also be obtained (Strand, 1977a). Superior resolution of the new method is indicated by the results in section 4.

4. NUMERICAL COMPARISONS

Computer programs to implement both the R-process (Yule-Walker) and the new multichannel Burg method have been written, checked out, and applied to various data. The simulation presented here is typical and gives some indication of the behavior of the new method. We present the results as applied to the following data

$$N_d = 128; \quad \Delta t = 1 \text{ sec}; \quad p = 2; \quad y_t = \begin{bmatrix} y_{1t} \\ y_{2t} \end{bmatrix};$$

$$t = 1, 2, \ldots, 128$$

$$\text{Re } y_{1t} = \cos(\frac{2\pi t}{16}) + .25(\text{Ranf}-.5);$$

$$\text{Im } y_{1t} = \sin(\frac{2\pi t}{16}) + .25(\text{Ranf}-.5) \tag{4.1}$$

$$\text{Re } y_{2t} = \cos(\frac{2\pi t}{16} + 1 \text{ rad.}) + .25(\text{Ranf}-.5);$$

$$\text{Im } y_{2t} = \sin(\frac{2\pi t}{16} + 1 \text{ rad.}) + .25(\text{Ranf}-.5).$$

The quantity Ranf represents a pseudo-random number uniformly distributed between 0 and 1.

The simulation was programmed so that the R-process and the multichannel Burg process operated on precisely the same data. If we denote the spectrum by

$$S(f) = \begin{bmatrix} S_{11}(f) & S_{12}(f) \\ \\ S_{21}(f) & S_{22}(f) \end{bmatrix}, \tag{4.2}$$

where f is the frequency in Hz, (that is, the diagonal elements are auto-spectra and S_{12} is the cospectrum) then the squared coherence is given by

$$\text{Coh}^2(f) = \frac{|S_{12}(f)|^2}{S_{11}(f)S_{22}(f)} . \tag{4.3}$$

A rough indication of the performance of either process is given by Akaike's FPE criterion (Akaike, 1969, 1971), given by

$$\text{FPE}(N) = \det P_N \left(\frac{N_d + 1 + pN}{N_d - 1 - pN} \right)^p . \tag{4.4}$$

Note that according to (4.4) a filter process is performing well if det P_N is rapidly reduced as the filter length is increased through the first few values of N.

In the numerical check out of the programs, the exact equality of the two versions of the maximum entropy spectrum ((2.16) and 2.17)) was observed, as was the exact equality of det P_N and det P_N'. The eigenvalues of P_N and P_N' were computed, and although not identical, they usually agree to at least 2-3 significant figures. Of course, these eigenvalues adjust themselves in such a way that det P_N = det P_N'. The case p = 1 was computed, and exact agreement was obtained with a separately-programmed Burg single-channel solution.

In this paper we present only $S_{11}(f)$, $\text{Coh}^2(f)$ and FPE(N). The remaining results, which are consistent with these, are presented elsewhere (Strand, 1977a). In the absence of random noise, the signal given by (4.1) would give $S_{11}(f)=S_{22}(f)=\text{const} \times \delta(f-.0625)$. The quality of the approximations obtained is indicated in figure 1. (The maxima shown are only approximate because of the nonzero spacing of FFT frequencies.) Note the superior resolution of the multichannel Burg process. In figure 2 we compare squared coherences. As it is intuitively reasonable that frequencies at which the data are random should give zero coherence, it appears that the multichannel Burg process gives an improved squared coherence. In figure 3 we present the corresponding values of Akaike's FPE criterion for the two methods. The new method gives a substantially smaller set of values, indicating better

performance. It is also apparent that little difference in the performance of the multichannel Burg process would be expected for N=3,4,...7. Results for N=3,4,5,6 were also obtained, and were quite similar to those presented here for N=7.
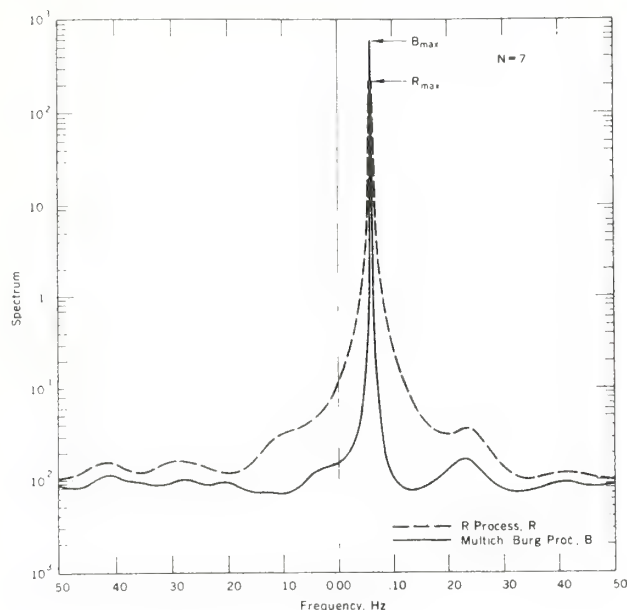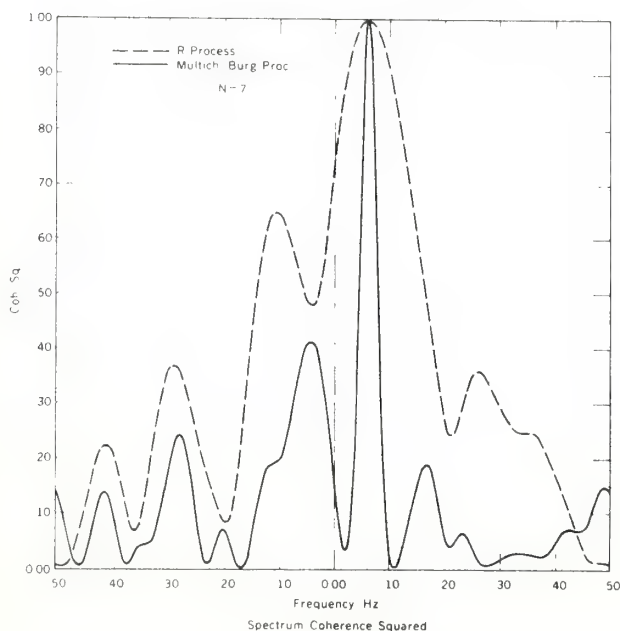

Figure 1. 1-1 Spectra, $S_{11}(f)$
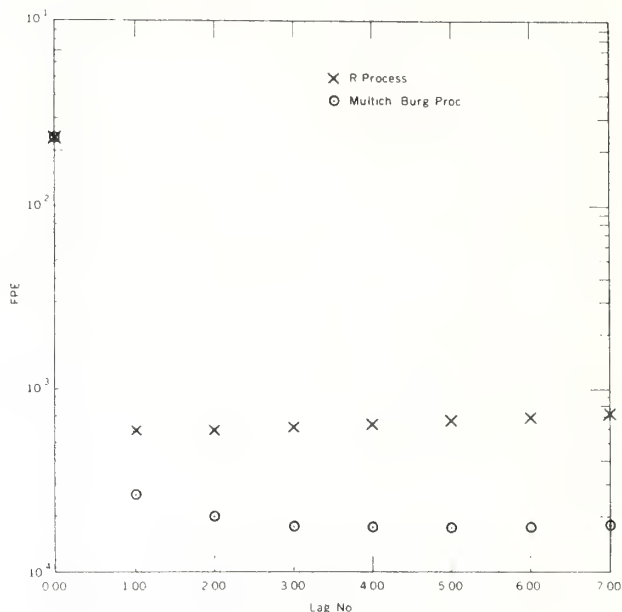

Figure 2. 1-2 Spectrum Coherence Squared

Figure 3. Akaike's FPE Criterion

References

Akaike, H. (1969), Fitting autoregressive models for prediction, Ann. Inst. Statist. Math, 21, 243-247.

Akaike, H. (1971), Autoregressive model fitting for control, Ann. Inst. Statist. Math, 23, 163-180.

Bellman, R. (1960), Introduction to Matrix Analysis, McGraw-Hill, New York.

Burg, J. P. (1968), A new analysis technique for time series data, paper presented at the Advanced Study Institute on Signal Processing, NATO, Enschede, Netherlands, 1968.

Burg, J. P. (1975), Maximum entropy spectral analysis, Ph.D. dissertation, Dept. of Geophysics, Stanford University.

Haykin, S. and S. Kesler (1976), The complex form of the maximum entropy method for spectral estimation, Proc. IEEE, 64, 822-823.

Ioannidis, G. A. (1975), Application of multivariate autoregressive spectrum estimation to ULF waves, Radio Science, 10, no. 12, 1043-1054.

Jones, R. H. (1974), Identification and autoregressive spectrum estimation, IEEE Trans. Automatic Control, AC-19, no. 6, 894-897.

Kanasewich, E. R. (1973), Time Sequence Analysis in Geophysics, Univ. of Alberta Press, Edmonton, Canada.

Makhoul, J. (1975), Linear prediction: a tutorial
    review, Proc. IEEE, 63, no. 4, 561-579.

Strand, O. N. (1977a), Multichannel complex
    maximum entropy spectral analysis, submitted
    to IEEE Trans. Automatic Control.

Strand, O. N. (1977b), Computer programs for
    maximum entropy spectral analysis of real
    and complex multichannel time series, in
    preparation as a technical report, NOAA,
    Wave Propagation Laboratory, Boulder,
    Colorado 80302.

Strand, O. N., J. M. Young and R. B. Chadwick
    (1977), Computer programs for maximum entropy
    spectral analysis of real and complex single-
    channel time series, in preparation as a
    technical report, NOAA, Wave Propagation
    Laboratory, Boulder, Colorado 80302.

Ulrych, T. J. and T. N. Bishop (1975), Maximum
    entropy spectral analysis and autoregressive
    decomposition, Reviews of Geophys. and Space
    Phys., 13, no. 1, 183-200.

Wiggins, R. A. and E. A. Robinson (1965), Recursive
    solution to the multichannel filtering
    problem, J. Geophys. Research, 70, no. 8,
    1885-1891.

COMPUTER PROGRAMS FOR MAXIMUM ENTROPY SPECTRAL ANALYSIS

OF REAL AND COMPLEX MULTICHANNEL TIME SERIES

(WITH MICROFILM PLOTS)

Otto Neall Strand

This report describes various FORTRAN computer programs for maximum entrophy spectral analysis of a complex or real vector time series. The descriptions include sufficient detail to permit the programs to be implemented correctly. All programs have been carefully checked out, and are available from the author on request.

COMPUTER PROGRAMS FOR MAXIMUM ENTROPHY SPECTRAL ANALYSIS
OF REAL AND COMPLEX SINGLE-CHANNEL TIME SERIES
(WITH MICROFILM PLOTS)

Otto Neall Strand, Jessie M. Young, and Russell B. Chadwick

We describe various FORTRAN computer programs for maximum entropy spectral analysis of a single real or complex time series. The descriptions are in sufficient detail to permit the methods to be correctly implemented. All programs have been carefully checked out, and are available from the authors on request.

Taylor's Hypothesis and High-Frequency Turbulence Spectra

J. C. Wyngaard

*Cooperative Institute for Research in Environmental Sciences, University of Colorado/NOAA, Boulder, Colo. 80309
and Wave Propagation Laboratory, NOAA, Boulder, Colo. 80302*

S. F. Clifford

Wave Propagation Laboratory, NOAA, Boulder, Colo. 80302

ABSTRACT

Lumley's model for interpreting frequency spectra of streamwise velocity in high-turbulence level flows assumes 1) that the convection velocity fluctuations and the convected finestructure are statistically independent, and 2) that the characteristic function of convection velocity fluctuations can be represented by the first two terms of its series expansion. The first assumption is consistent with numerous experimental results, and we test the second with an alternative assumption: that the convection velocity fluctuations are Gaussian. The two models are found to agree well up to moderately high fluctuation levels, thus giving support for Lumley's model in atmospheric boundary layer applications. We generalize his model to spectra of lateral velocity and a scalar, and calculate how various large-wavenumber spectral properties are disturbed by convection velocity fluctuations. The inertial subrange spectra are found to be affected relatively little, but serious spectral distortion is found at larger wavenumbers.

1. Introduction

Although the power spectral densities, or spectra, of turbulence theory are the spatial (wavenumber) variety, the experimentalist measures temporal (frequency) spectra. Taylor's (1938) hypothesis, which views turbulence as "frozen" in a field moving with mean streamwise speed U, is traditionally expressed in the form $\kappa_1 = \omega/U$ to relate the streamwise wavenumber κ_1 to angular frequency ω.

Experiments (see, e.g., Fisher and Davies, 1964) show that this application of Taylor's hypothesis may fail if different wavenumber components are convected at different velocities, or if temporal fluctuations, in a framework moving at the mean velocity, are important. Such fluctuations can be caused either by time variations in the pattern (non-frozen turbulence) or by fluctuations in the convection velocity.

Lumley (1965) has shown that when several criteria are satisfied, only the fluctuating convection velocity effect remains at high frequencies (inertial range and beyond). He constructed a model for the effect of a fluctuating convection velocity on the one-dimensional streamwise velocity spectrum.

A key assumption in Lumley's model is that the characteristic function of the convection velocity fluctuations can be represented by the first two terms in its series expansion. One would expect this approximation to fail for large fluctuation levels and for

large wavenumbers. In this paper we explore an alternative approximation: that the convection velocity fluctuations are Gaussian. This allows the characteristic function to be handled exactly, and provides a framework for judging the fluctuation level and wavenumber limits on Lumley's expansion.

We find that at the fluctuation levels typically found in the atmospheric boundary layer, and within the normally accessible wavenumber range, Lumley's expansion gives results very close to those of the Gaussian model. Consequently, we extend Lumley's model, which is easier to use, to spectra of lateral velocity and scalars. We find that convection velocity fluctuations can seriously distort spectral levels and shapes, introduce apparent anisotropy into measurements, and significantly affect the measured values of spectral constants.

2. The model

Following Lumley (1965), we take

$$u_i(\mathbf{x},t) = \int \exp[i\boldsymbol{\kappa}\cdot(\mathbf{x}-\mathbf{U}t)]dZ_i(\boldsymbol{\kappa}) \qquad (1)$$

$$\langle dZ_i(\boldsymbol{\kappa})dZ_j^*(\boldsymbol{\kappa}')\rangle = \begin{cases} 0, & \boldsymbol{\kappa} \neq \boldsymbol{\kappa}' \\ \phi_{ij}(\boldsymbol{\kappa})d\boldsymbol{\kappa}, & \boldsymbol{\kappa}' = \boldsymbol{\kappa} \end{cases} \qquad (2)$$

$$U_i = \bar{U}\delta_{1i} + v_i. \qquad (3)$$

The angle brackets denote ensemble averages and u_i is the turbulent velocity field that we assume is measured by the experimentalist as a time series at spatial point $\mathbf{x}$. The model of Eq. (1) says this turbulent field is swept past point $\mathbf{x}$ as a frozen pattern moving at velocity U_i. We take $\bar{U}$, the mean value of U_i, to be in the streamwise (x_1) direction and its fluctuations v_i to be three-dimensional.

We will extend Lumley's analysis to a scalar θ, writing analogously

$$\theta(\mathbf{x},t) = \int \exp[i\mathbf{\kappa}\cdot(\mathbf{x}-\mathbf{U}t)]d\Theta(\mathbf{\kappa})$$

$$\langle d\Theta(\mathbf{\kappa})d\Theta^*(\mathbf{\kappa}')\rangle = \begin{cases} 0, & \mathbf{\kappa}'\neq\mathbf{\kappa} \qquad (4) \\ S(\mathbf{\kappa})d\mathbf{\kappa}, & \mathbf{\kappa}'=\mathbf{\kappa}. \qquad (5) \end{cases}$$

The model development for θ parallels that for u_i. We will not show it in complete detail here.

Clearly the u_i and v_i fields are not distinct. However, we will be considering large Reynolds number turbulence, which has a wide range of scales (wavenumbers). We will be interested in how spectral measurements at large wavenumbers are affected by convection velocity fluctuations that lie in the low-wavenumber (energy containing) range. Thus we designate these large wavenumber (inertial range and beyond) components by u_i, and the low-wavenumber ones by v_i.

This scale separation is the basis for a key assumption in the model: that v_i and u_i, and v_i and θ, are statistically independent. This has some experimental and theoretical support (Tennekes and Lumley, 1972).

With this independence assumption, and Eqs. (1)–(3), we have

$$\langle u_\alpha(\mathbf{x},t)u_\alpha(\mathbf{x},t+\tau)\rangle = R_{\alpha\alpha}(\tau)$$

$$= \int \exp[i\kappa_1\bar{U}\tau]\langle\exp(i\mathbf{\kappa}\cdot\mathbf{v}\tau)\rangle\phi_{\alpha\alpha}(\mathbf{\kappa})d\mathbf{\kappa}. \quad (6)$$

The quantity $R_{\alpha\alpha}(\tau)$ (no sum on Greek indices) is the measured time correlation function. Its Fourier transform is the frequency spectrum $W(\omega)$, i.e.,

$$R_{\alpha\alpha}(\tau) = \int_{-\infty}^{\infty} \exp(i\omega\tau)W_{\alpha\alpha}(\omega)d\omega, \quad (7)$$

$$W_{\alpha\alpha}(\omega) = (1/2\pi)\int_{-\infty}^{\infty} \exp(-i\omega\tau)R_{\alpha\alpha}(\tau)d\tau. \quad (8)$$

Thus by transforming Eq. (6) we have

$$W_{\alpha\alpha}(\omega) = (1/2\pi)\int_{-\infty}^{\infty} \exp(-i\omega\tau)$$

$$\times\left[\int \exp(i\kappa_1\bar{U}\tau)\langle\exp(i\mathbf{\kappa}\cdot\mathbf{v}\tau)\rangle\phi_{\alpha\alpha}(\mathbf{\kappa})d\mathbf{\kappa}\right]d\tau. \quad (9)$$

In order to facilitate the interpretation of Eq. (9), we first consider the case where the convection velocity fluctuations v_i are negligible. Then

$$\langle\exp(i\mathbf{\kappa}\cdot\mathbf{v}\tau)\rangle\approx 1 \quad (10)$$

and

$$W_{\alpha\alpha}(\omega) = (1/2\pi)\int \exp(-i\omega\tau)$$

$$\times\left[\int \exp(i\kappa_1\bar{U}\tau)\phi_{\alpha\alpha}(\mathbf{\kappa})d\mathbf{\kappa}\right]d\tau$$

$$= (1/2\pi)\int \phi_{\alpha\alpha}(\mathbf{\kappa})$$

$$\times\left\{\int \exp[-i\tau(\omega-\kappa_1\bar{U})]d\tau\right\}d\mathbf{\kappa}$$

$$= \int \phi_{\alpha\alpha}(\mathbf{\kappa})\delta(\omega-\kappa_1\bar{U})d\mathbf{\kappa}$$

$$= \frac{1}{\bar{U}}F_{\alpha\alpha}\left(\frac{\omega}{\bar{U}}\right), \quad (11)$$

where $F_{\alpha\alpha}$ is the one-dimensional spectrum and

$$F_{\alpha\alpha}(\kappa_1) = \int_{-\infty}^{\infty}\int \phi_{\alpha\alpha}(\mathbf{\kappa})d\kappa_2 d\kappa_3. \quad (12)$$

Thus it is usual to infer the one-dimensional spectrum from the measured frequency spectrum,

$$F_{\alpha\alpha}(\kappa_1) = \bar{U}W_{\alpha\alpha}(\kappa_1\bar{U}), \quad (13)$$

which is Taylor's hypothesis.

In the general case, however, the model [Eq. (9)] indicates that convection velocity fluctuations cause spectral aliasing. To examine this more closely we will use two approaches to the solution of Eq. (9). In one we will assume that v_i is a Gaussian random variable, and in the other (Lumley's) we will approximate the characteristic function of v_i by the first two terms in its series expansion. Because the latter approach is much simpler to use, we will attempt to assess its range of applicability by comparing results from the two methods. To simplify this comparison we will take v_i to be isotropic, so that

$$\langle v_i v_j\rangle = \langle v^2\rangle\delta_{ij}, \quad (14)$$

but later we will allow v_i to be anisotropic.

a. Gaussian convection velocity

If v_i is a Gaussian random variable, it can be shown that (Tatarskii, 1971)

$$\langle\exp(i\mathbf{\kappa}\cdot\mathbf{v}\tau)\rangle = \exp(-\tau^2\langle(\mathbf{\kappa}\cdot\mathbf{v})^2\rangle/2). \quad (15)$$

Let us denote by a superscript m the one-dimensional spectrum obtained from the measured frequency spectrum by Taylor's hypothesis [Eq. (13)]. Then the Gaussian model gives, from (15) and (11),

$$F_{\alpha\alpha}^m(\kappa_1) = (\bar{U}/2\pi)\int_{-\infty}^{\infty}\exp(-i\omega\tau)\left\{\int\exp(i\kappa_1\bar{U}\tau)\right.$$

$$\left.\times\exp[-\tau^2\langle(\kappa\cdot v)^2\rangle/2]\phi_{\alpha\alpha}(\kappa)d\kappa\right\}d\tau$$

$$= (\bar{U}/2\pi)\int\phi_{\alpha\alpha}(\kappa)\int\exp[-i(\omega-\kappa_1\bar{U})\tau$$

$$-\tau^2\langle(\kappa\cdot v)^2\rangle/2]d\tau d\kappa$$

$$= \bar{U}\int\phi_{\alpha\alpha}(\kappa')\{(2\pi)^{-\frac{1}{2}}(\kappa')^{-1}\langle v^2\rangle^{-\frac{1}{2}}$$

$$\times\exp[-\bar{U}^2(\kappa_1-\kappa_1')^2/(2\kappa'^2\langle v^2\rangle)]\}d\kappa'. \quad (16)$$

Note that as $\langle v^2\rangle\to 0$,

$$\frac{\exp[-\bar{U}^2(\kappa_1-\kappa_1')^2/(2\kappa'^2\langle v^2\rangle)]}{\sqrt{2\pi}\kappa'\langle v^2\rangle^{\frac{1}{2}}}\to\delta(\kappa_1'\bar{U}-\kappa_1\bar{U})$$

$$=\frac{1}{\bar{U}}\delta(\kappa_1'-\kappa_1), \quad (17)$$

so that

$$F_{\alpha\alpha}^m(\kappa_1) = \int_{-\infty}^{\infty}\phi_{\alpha\alpha}(\kappa)d\kappa_2 d\kappa_3 = F_{\alpha\alpha}(\kappa_1). \quad (18)$$

Eq. (16) shows the nature of the spectral aliasing that occurs for finite $\langle v^2\rangle$. Regions in κ' space near the $\kappa_1'=\kappa_1$ plane contribute to the measured one-dimensional spectrum at κ_1. With an assumed form for $\phi_{\alpha\alpha}$, we can calculate the measured spectrum by carrying out the integration in Eq. (16), as shown later.

b. Lumley's two-term expansion

Lumley (1965) approximated the characteristic function of v_i by the first two terms in its series expansion:

$$\langle\exp(i\kappa\cdot v)\rangle\approx 1-\tfrac{1}{2}\langle(\kappa\cdot v)^2\rangle. \quad (19)$$

Thus Eq. (6) becomes, for isotropic v_i,

$$R_{\alpha\alpha}(\tau) = \int\exp(i\kappa_1\bar{U}\tau)F_{\alpha\alpha}d\kappa_1$$

$$-\frac{1}{2}\frac{\langle v^2\rangle}{\bar{U}^2}\int\exp(i\kappa_1\bar{U}\tau)\tau^2\bar{U}^2$$

$$\times\int\int\kappa^2\phi_{\alpha\alpha}d\kappa_2 d\kappa_3 d\kappa_1. \quad (20)$$

This can be written as

$$R_{\alpha\alpha}(\tau) = \int\exp(i\kappa_1\bar{U}\tau)\left[F_{\alpha\alpha}(\kappa_1)\right.$$

$$\left.+\frac{1}{2}\frac{\langle v^2\rangle}{\bar{U}^2}Z_{\alpha\alpha}''(\kappa_1)\right]d\kappa_1, \quad (21)$$

where

$$Z_{\alpha\alpha}(\kappa_1) = \int\int_{-\infty}^{\infty}\kappa^2\phi_{\alpha\alpha}d\kappa_2 d\kappa_3. \quad (22)$$

Fourier-transforming Eq. (21) then gives

$$F_{\alpha\alpha}^m(\kappa_1) = F_{\alpha\alpha}(\kappa_1)+\frac{\langle v^2\rangle}{2\bar{U}^2}Z_{\alpha\alpha}''(\kappa_1). \quad (23)$$

The results of Lumley's approach are expressed in Eqs. (22) and (23), while the Gaussian model gives Eq. (16). Because Lumley's approach is easier to use, in the next section we will attempt to learn its range of applicability by comparing results from the two methods.

3. Model solution comparisons

We continue to assume that v_i is isotropic, and also that the turbulence spectrum in the wavenumber range of interest is isotropic. Then (Batchelor, 1953)

$$\phi_{ij}(\kappa) = \frac{E(\kappa)}{4\pi\kappa^4}(\kappa^2\delta_{ij}-\kappa_i\kappa_j), \quad (24)$$

where E is the three-dimensional spectrum. For a scalar, isotropy implies $S(\kappa)=S(\kappa)$.

In using the two-term expansion results [Eqs. (22) and (23)] with isotropic wavenumber spectral forms, it is convenient also to have the expressions

$$F_{11} = \int\int_{-\infty}^{\infty}\phi_{11}d\kappa_2 d\kappa_3 = \frac{1}{2}\int_{\kappa_1}^{\infty}\frac{E}{\kappa}\left(1-\frac{\kappa_1^2}{\kappa^2}\right)d\kappa, \quad (25)$$

$$F_{22} = \int\int_{-\infty}^{\infty}\phi_{22}d\kappa_2 d\kappa_3 = \frac{1}{4}\int_{\kappa_1}^{\infty}\frac{E}{\kappa}\left(1+\frac{\kappa_1^2}{\kappa^2}\right)d\kappa, \quad (26)$$

$$F = \int\int S d\kappa_2 d\kappa_3 = 2\pi\int_{\kappa_1}^{\infty}\kappa^2\frac{S}{\kappa}d\kappa. \quad (27)$$

Lumley showed that the two-term expansion technique gives, from Eqs. (22) and (23),

$$F_{11}^m = F_{11}+\frac{1}{2}\frac{\langle v^2\rangle}{\bar{U}^2}[\kappa_1^2 F_{11}''-2F_{11}]. \quad (28)$$

Extending his model to F_{22} and F gives

$$F_{22}^m = F_{22} + \frac{1}{2}\frac{\langle v^2 \rangle}{\bar{U}^2}[2F_{22}+\kappa_1^2 F_{22}'' - 2\kappa_1 F_{22}' - 2E], \quad (29)$$

$$F^m = F + \frac{1}{2}\frac{\langle v^2 \rangle}{\bar{U}^2}[\kappa_1^2 F'' + 2\kappa_1 F']. \quad (30)$$

Here a prime denotes differentiation with respect to κ_1.

The corresponding results for the Gaussian model can be found from Eq. (16). We will now compare the predictions for various spectral properties found from the two approaches.

a. Inertial range behavior

In the inertial range, where according to Kolmogorov theory E, $\kappa^2 S$ (and therefore F_{11}, F_{22} and F) behave as $\kappa^{-5/3}$, the two-term expansion results of Eqs. (28)–(30) are simple:

$$F_{11}^m = F_{11}\left[1 + \frac{11}{9}\langle v^2 \rangle \Big/ \bar{U}^2\right], \quad (31)$$

$$F_{22}^m = F_{22}\left[1 + \frac{11}{36}\langle v^2 \rangle \Big/ \bar{U}^2\right], \quad (32)$$

$$F^m = F\left[1 + \frac{5}{9}\langle v^2 \rangle \Big/ \bar{U}^2\right]. \quad (33)$$

Note that these are independent of wavenumber; thus the model predicts that we will measure the inertial range power law correctly but overestimate the spectral levels.

The corresponding Gaussian model results were found by numerically integrating Eq. (16). The results for $\langle v^2 \rangle / \bar{U}^2 < 0.1$ follow well Eqs. (31)–(33) with coefficients agreeing within a few percent.

Beyond the inertial range the models predict that both spectral levels and shapes will be distorted by convection velocity fluctuations. Here the model solutions are more difficult. To survey the situation we will consider spectral moments, which can be evaluated exactly in each model.

b. Derivative variances

The "measured" value of $\langle (u_{1,1})^2 \rangle$ (we denote differentiation by a comma) from the u_1 time series is

$$\langle (u_{1,1})^2 \rangle^m = \frac{1}{\bar{U}^2}\langle (u_{1,t})^2 \rangle = \int_{-\infty}^{\infty} \kappa_1^2 F_{11}^m d\kappa_1, \quad (34)$$

whereas the true value is

$$\langle (u_{1,1})^2 \rangle = \int_{-\infty}^{\infty} \kappa_1^2 F_{11} d\kappa_1. \quad (35)$$

Therefore, by multiplying Eqs. (28)–(30) by κ_1^2 and integrating, we find for the two-term expansion

$$\langle (u_{1,1})^2 \rangle^m = \langle (u_{1,1})^2 \rangle[1 + 5\langle v^2 \rangle / \bar{U}^2], \quad (36)$$

$$\langle (u_{2,1})^2 \rangle^m = \langle (u_{2,1})^2 \rangle[1 + 2.5\langle v^2 \rangle / \bar{U}^2], \quad (37)$$

$$\langle (\theta_{,1})^2 \rangle^m = \langle (\theta_{,1})^2 \rangle[1 + 3\langle v^2 \rangle / \bar{U}^2]. \quad (38)$$

The Gaussian results are likewise obtained by multiplying Eq. (16) by κ_1^2 and integrating. For example,

$$\langle (u_{1,1})^2 \rangle^m = \frac{\bar{U}}{(2\pi\langle v^2 \rangle)^{\frac{1}{2}}} \int \frac{\phi_{11} d\kappa'}{\kappa'} \int$$

$$\times \exp[-\bar{U}^2(\kappa_1 - \kappa_1')^2/(2\kappa'^2\langle v^2 \rangle)]\kappa_1^2 d\kappa_1$$

$$= \int \phi_{11}(\kappa')d\kappa'\left[\kappa'^2\frac{\langle v^2 \rangle}{\bar{U}^2} + \kappa_1'^2\right]$$

$$= \langle (u_{1,1})^2 \rangle + \frac{\langle v^2 \rangle}{\bar{U}^2}[\langle (u_{1,1})^2 \rangle + \langle (u_{1,2})^2 \rangle$$

$$+ \langle (u_{1,3})^2 \rangle]. \quad (39)$$

For the assumed locally isotropic structure,

$$\langle (u_{1,1})^2 \rangle = \tfrac{1}{2}\langle (u_{1,2})^2 \rangle = \tfrac{1}{2}\langle (u_{1,3})^2 \rangle \quad (40)$$

so the result is

$$\langle (u_{1,1})^2 \rangle^m = \langle (u_{1,1})^2 \rangle\left[1 + 5\frac{\langle v^2 \rangle}{\bar{U}^2}\right], \quad (41)$$

in agreement with the two-term model Eq. (36). The results for lateral velocity and temperature also agree.

c. Second derivative variances

The second derivative variance weights even larger wavenumber regions of the spectrum. For example,

$$\langle (u_{1,11})^2 \rangle = \int_{-\infty}^{\infty} \kappa_1^4 F_{11}(\kappa_1) d\kappa_1. \quad (42)$$

Multiplying Eqs. (28)–(30) by κ_1^4 and integrating gives for the two-term expansion

$$\langle (u_{1,11})^2 \rangle^m = \langle (u_{1,11})^2 \rangle\left[1 + 14\frac{\langle v^2 \rangle}{\bar{U}^2}\right], \quad (43)$$

$$\langle (u_{2,11})^2 \rangle^m = \langle (u_{2,11})^2 \rangle\left[1 + \frac{28}{3}\frac{\langle v^2 \rangle}{\bar{U}^2}\right], \quad (44)$$

$$\langle (\theta_{,11})^2 \rangle^m = \langle (\theta_{,11})^2 \rangle\left[1 + 10\frac{\langle v^2 \rangle}{\bar{U}^2}\right]. \quad (45)$$

The Gaussian model gives

$$\langle (u_{1,11})^2 \rangle^m = \langle (u_{1,11})^2 \rangle \left[1 + 14 \frac{\langle v^2 \rangle}{\bar{U}^2} + 35 \frac{\langle v^2 \rangle^2}{\bar{U}^4} \right], \quad (46)$$

$$\langle (u_{2,11})^2 \rangle^m = \langle (u_{2,11})^2 \rangle \left[1 + \frac{28}{3} \frac{\langle i^2 \rangle}{\bar{U}^2} + \frac{35}{3} \frac{\langle v^2 \rangle^2}{\bar{U}^4} \right], \quad (47)$$

$$\langle (\theta_{,11})^2 \rangle^m = \langle (\theta_{,11})^2 \rangle \left[1 + 10 \frac{\langle v^2 \rangle}{\bar{U}^2} + 15 \frac{\langle v^2 \rangle^2}{\bar{U}^4} \right]. \quad (48)$$

Here the two methods give different results, in contrast to the situation for first derivative variances. For the second derivative variances of u_1, u_2 and θ, the agreement at $\langle v^2 \rangle / \bar{U}^2 = 0.1$ is within 15, 6 and 8%, respectively. Turbulence levels in the atmospheric boundary layer do not normally exceed this value unless we approach free convection.

In practice, noise resolution problems are usually serious at large wavenumbers, and seldom can spectra be resolved at κ_1 values larger than those dominating the second derivative variance. Thus our model comparison suggests that at resolvable wavenumbers, Lumley's two-term model is a useful and adequate representation of the effect of convection velocity fluctuations on measured boundary layer spectra. In the next section we will generalize the results for this model to the more realistic case of an anisotropic fluctuating convection velocity.

4. Anisotropic fluctuating convection velocity

We now consider only Lumley's two-term expansion model but let v_i be anisotropic. In this case we have

$$F_{\alpha\alpha}^m = F_{\alpha\alpha} + \frac{\langle v_1^2 \rangle}{2\bar{U}^2} P_{\alpha\alpha}'', \quad (49)$$

where

$$P_{\alpha\alpha} = \int\!\!\!\int\!\!\!\int_{-\infty}^{\infty} \left[\kappa_1^2 + \kappa_2^2 \frac{\langle v_2^2 \rangle}{\langle v_1^2 \rangle} + \kappa_3^2 \frac{\langle v_3^2 \rangle}{\langle v_1^2 \rangle} \right] \phi_{\alpha\alpha} d\kappa_2 d\kappa_3. \quad (50)$$

Analogous expressions hold for the scalar case.

Again assuming the isotropic forms for the wavenumber spectra, we find

$$P_{11}'' = \kappa_1^2 F_{11}'' - 2F_{11} - 2(\kappa_1 F_{11}' + F_{11}) \left\{ \frac{\langle v_2^2 \rangle}{\langle v_1^2 \rangle} + \frac{\langle v_3^2 \rangle}{\langle v_1^2 \rangle} - 2 \right\}, \quad (51)$$

which reproduces Lumley's result. For lateral spectra we find

$$P_{22}'' = \kappa_1^2 F_{22}'' + \kappa_1 F_{22}' \left[4 - 5 \frac{\langle v_2^2 \rangle}{\langle v_1^2 \rangle} - \frac{\langle v_3^2 \rangle}{\langle v_1^2 \rangle} \right]$$

$$+ F_{22} \left[2 + \frac{\langle v_2^2 \rangle}{\langle v_1^2 \rangle} - \frac{\langle v_3^2 \rangle}{\langle v_1^2 \rangle} \right] - 2 \frac{\langle v_2^2 \rangle}{\langle v_1^2 \rangle} E, \quad (52)$$

and for the scalar spectrum we find

$$P'' = F \left[2 - \frac{\langle v_2^2 \rangle}{\langle v_1^2 \rangle} - \frac{\langle v_3^2 \rangle}{\langle v_1^2 \rangle} \right] + \kappa_1 F' \left[4 - \frac{\langle v_2^2 \rangle}{\langle v_1^2 \rangle} - \frac{\langle v_3^2 \rangle}{\langle v_1^2 \rangle} \right] + \kappa_1^2 F''. \quad (53)$$

Eqs. (49)–(53) can now be used to evaluate the effects of fluctuating convection velocity on inertial range spectra and derivative variances.

a. Inertial range behavior

In a inertial subrange, we have

$$F_{11}^m = F_{11} \left(1 - \frac{1}{9} \frac{\langle v_1^2 \rangle}{\bar{U}^2} + \frac{2}{3} \frac{\langle v_2^2 \rangle}{\bar{U}^2} + \frac{2}{3} \frac{\langle v_3^2 \rangle}{\bar{U}^2} \right), \quad (54)$$

$$F_{22}^m = F_{22} \left(1 - \frac{1}{9} \frac{\langle v_1^2 \rangle}{\bar{U}^2} + \frac{1}{12} \frac{\langle v_2^2 \rangle}{\bar{U}^2} + \frac{1}{3} \frac{\langle v_3^2 \rangle}{\bar{U}^2} \right), \quad (55)$$

$$F^m = F \left(1 - \frac{1}{9} \frac{\langle v_1^2 \rangle}{\bar{U}^2} + \frac{1}{3} \frac{\langle v_2^2 \rangle}{\bar{U}^2} + \frac{1}{3} \frac{\langle v_3^2 \rangle}{\bar{U}^2} \right). \quad (56)$$

b. First derivative variances

Here we have

$$\langle (u_{1,1})^2 \rangle^m = \langle (u_{1,1})^2 \rangle \left[1 + \frac{\langle v_1^2 \rangle}{\bar{U}^2} + 2 \frac{\langle v_2^2 \rangle}{\bar{U}^2} + 2 \frac{\langle v_3^2 \rangle}{\bar{U}^2} \right], \quad (57)$$

$$\langle (u_{2,1})^2 \rangle^m = \langle (u_{2,1})^2 \rangle \left[1 + \frac{\langle v_1^2 \rangle}{\bar{U}^2} + \frac{1}{2} \frac{\langle v_2^2 \rangle}{\bar{U}^2} + \frac{\langle v_3^2 \rangle}{\bar{U}^2} \right], \quad (58)$$

$$\langle (\theta_{,1})^2 \rangle^m = \langle (\theta_{,1})^2 \rangle \left[1 + \frac{\langle v_1^2 \rangle}{\bar{U}^2} + \frac{\langle v_2^2 \rangle}{\bar{U}^2} + \frac{\langle v_3^2 \rangle}{\bar{U}^2} \right]. \quad (59)$$

These can be tested against results found in an entirely different way. The equations for total fluctuating velocity $u' = u_i + v_i$ and θ are (Lumley and Panofsky, 1964):

$$u_{i,t}' = -\bar{U}_{i,j} u_j' - u_{i,j}' \bar{U}_j - u_{i,j}' u_j' + \langle u_{i,j}' u_j' \rangle - P_{,i} + \nu u_{i,jj}', \quad (60)$$

$$\theta_{,t} = -\theta_{,j} \bar{U}_j - \bar{\Theta}_{,j} u_j' - \theta_{,j} u_j' + \langle \theta_{,j} u_j' \rangle + D\theta_{,jj}, \quad (61)$$

where repeated indices are summed and the notation is standard. Squaring and averaging gives equations for the time derivative variances. Heskestad (1965) showed that assuming statistical independence of large and small wavenumber structure, large Reynolds number turbulence and local isotropy give for $i=1$ in Eq. (60):

$$\frac{1}{\bar{U}^2} \langle (u_{1,t})^2 \rangle = \langle (u_{1,1})^2 \rangle \left[1 + \frac{\langle v_1^2 \rangle}{\bar{U}^2} + 2 \frac{\langle v_2^2 \rangle}{\bar{U}^2} + 2 \frac{\langle v_3^2 \rangle}{\bar{U}^2} \right], \quad (62)$$

which reproduces the result of Eq. (57), as pointed out earlier by Wyngaard and Pao (1972). Heskestad's

approach gives for $i=2$ and for a scalar θ:

$$\frac{1}{\bar{U}^2}\langle(u_{2,t})^2\rangle = \langle(u_{2,1})^2\rangle\left[1+\frac{\langle v_1{}^2\rangle}{\bar{U}^2}+\frac{1}{2}\frac{\langle v_3{}^2\rangle}{\bar{U}^2}+\frac{\langle v_3{}^2\rangle}{\bar{U}^2}\right], \quad (63)$$

$$\frac{1}{\bar{U}^2}\langle(\theta_{,t})^2\rangle = \langle(\theta_{,1})^2\rangle\left[1+\frac{\langle v_1{}^2\rangle}{\bar{U}^2}+\frac{\langle v_2{}^2\rangle}{\bar{U}^2}+\frac{\langle v_3{}^2\rangle}{\bar{U}^2}\right], \quad (64)$$

which agree with Eqs. (58) and (59), respectively.

c. Second derivative variances

The expressions here become

$$\langle(u_{1,11})^2\rangle^m = \langle(u_{1,11})^2\rangle\left[1+6\frac{\langle v_1{}^2\rangle}{\bar{U}^2}+4\frac{\langle v_2{}^2\rangle}{\bar{U}^2}+4\frac{\langle v_3{}^2\rangle}{\bar{U}^2}\right], \quad (65)$$

$$\langle(u_{2,11})^2\rangle^m = \langle(u_{2,11})^2\rangle\left[1-\frac{17}{3}\frac{\langle v_1{}^2\rangle}{\bar{U}^2}+13\frac{\langle v_2{}^2\rangle}{\bar{U}^2}+2\frac{\langle v_3{}^2\rangle}{\bar{U}^2}\right], (66)$$

$$\langle(\theta_{,11})^2\rangle^m = \langle(\theta_{,11})^2\rangle\left[1+6\frac{\langle v_1{}^2\rangle}{\bar{U}^2}+2\frac{\langle v_2{}^2\rangle}{\bar{U}^2}+2\frac{\langle v_3{}^2\rangle}{\bar{U}^2}\right]. \quad (67)$$

d. The stress cospectrum

We now consider a flow such as the atmospheric surface layer where the only nonzero off-diagonal element of $\langle v_i v_j\rangle$ is $\langle v_1 v_3\rangle$. Then a straightforward calculation from Eqs. (49) and (50) gives

$$F_{13}^m = \frac{-\langle v_1 v_3\rangle}{\bar{U}^2}\frac{\kappa_1{}^2}{2}F_{11}''. \quad (68)$$

In an inertial range of F_{11} we have

$$F_{13}^m = -\frac{20}{9}\frac{\langle v_1 v_3\rangle}{\bar{U}^2}F_{11}. \quad (69)$$

Note that this predicts a sign reversal in the measured stress cospectrum at large wavenumbers. In the energy-containing range F_{13}^m has the sign of $\langle v_1 v_3\rangle$, but according to the model the convection velocity fluctuations will alias enough spectral content into the measured cospectrum to force it to change sign at large κ_1.

5. Application to atmospheric boundary layer flow

The ratios of the standard deviations of the wind component fluctuations to the mean wind in the atmospheric boundary layer depend on a number of parameters, including the surface roughness, the boundary layer depth and the stability. Therefore, rather than attempting a general description of the behavior of these ratios, we will simply consider four illustrative cases.

The first three concern the surface layer. Here we will use data at 5.7 m from the 1968 Kansas experi-

TABLE 1. 1968 Kansas wind data at 5.7 m.

Case	Stability	$\dfrac{\langle v_1{}^2\rangle}{\bar{U}^2}$	$\dfrac{\langle v_2{}^2\rangle}{\bar{U}^2}$	$\dfrac{\langle v_3{}^2\rangle}{\bar{U}^2}$
1	very unstable $(L\approx-13\text{ m})$	0.048	0.084	0.012
2	moderately unstable $(L\approx-50\text{ m})$	0.040	0.036	0.0081
3	moderately stable $(L\approx 50\text{ m})$	0.026	0.0144	0.0081

ments (Haugen *et al.*, 1971). Table 1 summarizes these cases, which represent very unstable, moderately unstable and moderately stable conditions.

Case 4 represents conditions typical of the mid regions of the convective boundary layer over land. Here there is ample evidence, both from observations and model calculations, that the wind fluctuations scale with w_*, the convective velocity scale defined by

$$w_* = [(g/T)Q_0 Z_i]^{\frac{1}{3}}, \quad (70)$$

where Z_i is the convective layer depth and Q_0 the surface temperature flux. We will take typical mid-summer, overland convective conditions with $Z_i = 2.0$ km, $Q_0 = 0.25$ m s^{-1} °C, so that $w_* \approx 2.5$ m s^{-1}. Observations (Willis and Deardorff, 1974; Panofsky *et al.*, 1977; Kaimal *et al.*, 1976) indicate typical mid-layer values are

$$\langle v_1{}^2\rangle \sim \langle v_2{}^2\rangle \sim 0.3 w_*{}^2, \quad (71)$$

$$\langle v_3{}^2\rangle \sim 0.4 w_*{}^2. \quad (72)$$

Taking $\bar{U}=5$ m s^{-1} gives for case 4

$$\frac{\langle v_1{}^2\rangle}{\bar{U}^2} \sim \frac{\langle v_2{}^2\rangle}{\bar{U}^2} \approx 0.075, \quad (73)$$

$$\frac{\langle v_3{}^2\rangle}{\bar{U}^2} \sim 0.10. \quad (74)$$

We emphasize that these four cases are only typical; they do not cover all possibilities. Clearly the limiting case of free convection, where $\langle v^2\rangle/\bar{U}^2 \to \infty$, is not included.

In Table 2 we show the predicted influence on three types of spectral properties inferred from frequency spectra through the ordinary application of Taylor's hypothesis.

The first is the ratio of measured and true inertial range one-dimensional spectral levels, found from Eqs. (54)–(56). This is important in applications such as inferring dissipation rate ϵ and the temperature structure parameter $C_T{}^2$ directly, since (Wyngaard *et al.*, 1971)

$$F_{11} = \alpha_1 \epsilon^{2/3}\kappa_1{}^{-5/3}, \qquad F_{22} = \tfrac{4}{3}\alpha_1 \epsilon^{2/3}\kappa_1{}^{-5/3}, \quad (75)$$

$$F = 0.125 C_T{}^2 \kappa_1{}^{-5/3}, \quad (76)$$

TABLE 2. Influence of fluctuating convection velocity on spectral properties

Property	Flow Case			
	1	2	3	4
F_{11}^m/F_{11} (inertial range)	1.06	1.03	1.01	1.11
F_{22}^m/F_{22}	1.01	1.00	1.00	1.03
F^m/F	1.03	1.01	1.01	1.05
$\langle(u_{1,1})^2\rangle^m/\langle(u_{1,1})^2\rangle$	1.24	1.13	1.06	1.43
$\langle(u_{2,1})^2\rangle^m/\langle(u_{2,1})^2\rangle$	1.10	1.07	1.04	1.21
$\langle(\theta_{,1})^2\rangle^m/\langle(\theta_{,1})^2\rangle$	1.14	1.08	1.05	1.25
$\langle(u_{1,11})^2\rangle^m/\langle(u_{1,11})^2\rangle$	1.68	1.42	1.24	2.15
$\langle(u_{2,11})^2\rangle^m/\langle(u_{2,11})^2\rangle$	1.84	1.26	1.06	1.75
$\langle(\theta_{,11})^2\rangle^m/\langle(\theta_{,11})^2\rangle$	1.48	1.33	1.20	1.80

where α_1 is the one-dimensional Kolmogorov constant.

The second property is the ratio of measured and true streamwise derivative variances, found from Eqs. (57)–(59). These are useful in "direct" measurements of ϵ and the scalar variance destruction rate χ, since under local isotropy

$$\epsilon = 15\nu\langle(u_{1,1})^2\rangle = 7.5\nu\langle(u_{2,1})^2\rangle, \qquad (77)$$

$$\chi = 6D\langle(\theta_{,1})^2\rangle, \qquad (78)$$

where ν and D are the momentum and thermal diffusivities.

The third property is the ratio of measured and true fourth spectral moments calculated from Eqs. (65)–(67). These are of interest because of theoretical ideas (see Batchelor, 1953) that the spectral shape in the dissipative range should be the same in all turbulent flows of sufficiently large Reynolds number.

Table 2 shows that these spectral properties are all overestimated because of convection velocity fluctuations. Note that the spectral error increases with wavenumber κ. This is because at any (large) κ the measured spectrum is contaminated chiefly by aliased energy from faster moving, lower κ eddies, and as κ increases, the increasingly rapid spectral falloff increases the aliasing error.

Table 2 shows also that the convection velocity fluctuations can introduce apparent local anisotropy into measurements. For example, the quantity $\langle(u_{2,1})^2\rangle/\langle(u_{1,1})^2\rangle$, which is 2.0 under local isotropy, is predicted to vary from 1.69 to 1.96 for the four cases. The ratio F_{22}/F_{11} in the inertial subrange, which is $\frac{4}{3}$ under local isotropy, ranges from 1.24 to 1.32. The second derivative variances can be related to the production rates of vorticity variance (Batchelor, 1953) and scalar gradient variance (Wyngaard, 1971) and thus under local isotropy can be related to derivative skewness (Wyngaard and Tennekes, 1970). Table 2 shows that checks of these relationships will be seriously affected by the induced errors in the second derivative variances.

6. Conclusions

Although these are only model calculations, it seems clear that serious errors in high-frequency spectral properties can be induced by a fluctuating convection velocity. We have shown that under typical conditions in the atmospheric boundary layer, fixed-point (tower-based) measurements will show apparent local anisotropy in velocity and temperature derivative statistics.

In aircraft measurements we avoid this problem by effectively raising the mean speed $\bar{U}$ so that the relative fluctuation level $\langle v^2\rangle/\bar{U}^2$ becomes negligible. The trade-off, of course, is that the finestructure is shifted to higher, and perhaps unmeasurable, frequencies.

There is increasing interest in atmospheric flows as a source of high Reynolds number turbulence for basic research, but our calculations indicate that errors induced by convection velocity fluctuations can obscure the phenomena being studied. Lumley's result [Eqs. (49) and (51)] and our extensions [Eqs. (52) and (53)] allow the experimentalist to correct his spectral results for these effects. There remains a continuing need for theoretical work on the effects on other properties, such as probability densities and moments and on measurement techniques that minimize the problem.

REFERENCES

Batchelor, G. K., 1953: *The Theory of Homogeneous Turbulence.* Cambridge University Press, 197 pp.

Fisher, M. J., and P. O. A. L. Davies, 1964: Correlation measurements in a non-frozen pattern of turbulence. *J. Fluid Mech.,* **18,** 97–116.

Haugen, D. A., J. C. Kaimal, and E. F. Bradley, 1971: An experimental study of Reynolds stress and heat flux in the atmospheric surface layer. *Quart. J. Roy. Meteor. Soc.,* **97,** 168–180.

Heskestad, G., 1965: A generalized Taylor hypothesis with application for high Reynolds number turbulent shear flows. *J. Appl. Mech.,* **87,** 735–739.

Kaimal, J. C., J. C. Wyngaard, D. A. Haugen, O. R. Coté, Y. Izumi, S. J. Caughey and C. J. Readings, 1976: Turbulence structure in the convective boundary layer. *J. Atmos. Sci.,* **33,** 2152–2169.

Lumley, J. L., 1965: Interpretation of time spectra measured in high-intensity shear flows. *Phys. Fluids,* **8,** 1056–1062.

——, and H. A. Panofsky, 1964: *The Structure of Atmospheric Turbulence.* Interscience, 239 pp.

Panofsky, H. A., H. Tennekes, D. Lenschow and J. C. Wyngaard, 1977: Wind fluctuations in the surface layer under convective conditions. Submitted to *Bound.-Layer Meteor.*

Tatarskii, V. I., 1971: The effects of the turbulent atmosphere on wave propagation. [NTIS Ref. No. TT68-50464.]

Taylor, G. I., 1938: The spectrum of turbulence. *Proc. Roy. Soc. London,* **A132,** 476–490.

Tennekes, H., and J. L. Lumley, 1972: *A First Course in Turbulence*. M.I.T. Press, 300 pp.

Willis, G. E., and J. W. Deardorff, 1974: A laboratory model of the unstable planetary boundary layer. *J. Atmos. Sci.*, **31**, 1297–1307.

Wyngaard, J. C., 1971: The effect of velocity sensitivity on temperature derivative statistics in isotropic turbulence. *J. Fluid Mech.*, **48**, 763–769.

——, and H. Tennekes, 1970: Measurements of the small-scale structure of turbulence at moderate Reynolds numbers. *Phys. Fluids*, **13**, 1962–1969.

——, and Y. H. Pao, 1972: Some measurements of the fine structure of large Reynolds number turbulence. *Statistical Models and Turbulence*, Vol. 12, *Lecture Notes in Physics*, Springer-Verlag, 384–401.

——, Y. Izumi and S. A. Collins Jr., 1971: Behavior of the refractive-index-structure-parameter near the ground. *J. Opt. Soc. Amer.*, **61**, 1646–1650.

Author Index

·

Einaudi, F.	79,84,85,86
Evans, M.W.	75,106,126
Fankhauser, J.C.	92
Fitzjarrald, D.E.	57
Farnk. H.W.	46,93,94
Friehe, C.A.	69
Frisch, A.S.	47,48,49,70,103
Fritz, R.B.	97
Fau, D.	85,86
Gaynor, J.E.	58,59,60
George T.M.	75,80,81,83
Goldenstein, E.J.	131,132,137
Gossard, E.E.	50,70,87,99,100
Greene, G.E.	94,95
Griffiths, L.J.	141
Guiraud, F.O.	24,32,33
Hall, F.F., Jr.	59,60,61,62,64,65,66,67,98,112
Hardesty, R.M.	113
Haugen, D.A.	36,71,108,130
Hennington, L.	26
Hill, R.J.	5,102
Hogg, D.C.	125
Hooke, W.H.	82,107,109
Huffaker, F.M.	6,114
Hulstrom, R.L.	11
Izumi, Y.	71
Jones, R.M.	27,73,83
Kaimal, J.C.	36,68,71,115
Keebaugh, B.	129
Keeler, R.J.	140,141
Kohn, N.M.	47,52,53

Post, M.J.	15,41,43,44,120,139
Pratte, F.	16
Pries, T.H.	119
Pueschel, R.F.	11
Quintana, R.F.	131,133
Ramm, H.E.	67
Ray, P.S.	25
Readings, C.J.	71
Rodriguez, R.	119
Rufenach, C.L.	28
Sand, W.R.	92
Schwiesow, R.L.	42,43,44,120,139
Sinclair, P.C.	43
Sirmans, D.	26
Snider, J.B.	21
Strand, O.N.	142,143,144,145
Strauch, R.G.	22,23,25,26,29,30,45,47,49,50, 92,110,111,113
Taylor, W.L.	96
Tennekes, H.	72
Wahr, A.B.	60
Walters, D.L.	119
Wang, T.	12,13,14,17,18,35,39,121,134, 135,136,137
Weber, B.L.	74,88,106
Westwater, E.R.	16,24,31,32,33
Wyngaard, J.C.	69,71,72,73,101,146
Young, J.M.	48
Zieske, P.	39
Zrnic', D.	26